

Sr, No.	Name of Author	Title of Paper	Page No.
1	Kailash Nemade and Sandeep Waghuley	Sodium Superoxide-Polypyrrole Composite for Photovoltaic Applications	1
2	Nitin P. Garad, Pallavi D. Hambarde and Ashok C. Kumbharkhane	High-Frequency Dielectric Study and Unveiling molecular Dynamics of Diol's Using TDR	6
3	S Habibuddin, R N. Kambale, A V Pansare, S Krishnakumar, Yugandhara S W, T S Hibare and Vaishali Bambole	Li doped nickel ferrite/PAni nanocomposite as an ecofriendly electrode material for energy storage device	12
4	C. R. Chaudhari and G. K. Reddy	Analytical approach of Communication between RFID technology and PC	19
5	A. G. Kshirsagar, G. D. Agrahari and D. S. Dhote	PLC-Based Induction Motor Operations	24
6	Aniket D. Bokhare, Haribhau M. Dhage , Milind P. Lokhande and Ashok C. Kumbharkhane	A comparison of the dielectric relaxation behaviour of 2-nitrotoluene-Dimethyl sulfoxide and toluene-Dimethyl sulfoxide mixtures using Time Domain Reflectometry	34
7	Nikita S. Korde and Sandeep A. Waghuley	Giant Magnetoresistance of Graphene Doped Iron and Nickel Thin Films	41
8	Deepika S. Yawale	Bioelectronic nose using bare graphene and carbon nanotube as a human olfactory receptor- a brief review	51
9	Y S Waghode, Bhagyashri B, S Habibuddin, T S Hibare, Aarav Mehta, R. R. Kalesh, R.N. Kamble and V A Bambole	Monitoring The Size Of CdSe Quantum Dots For Dye Sensitized Solar Cell With Temperature Gradient	57
10	V. A. Rana, K. C. Vaghela, H. P. Vankar and K.N. Shah	Complex Permittivity and Complex Impedance Analysis of Binary Mixtures of Ethylene Glycol Monophenyl Ether and Methanol	70
11	K. J. Agheda, N. A. Chaudhary, N. Garad, A. C. Kumbharkhane, B. S. Chakraborty and A. N. Prajapati	Molecular interaction through dielectric relaxation study of methanol-bromopropane mixtures as a function of composition	82
12	N. A. Chaudhary, K. N. Shah, S. P. Patel and A. N. Prajapati	Investigation of Some Physicochemical Properties of Binary Liquid Mixtures (n-Octanol +N, N Dimethylformamide) at Different Temperatures	93
13	Chitralekha Anil Kolhe and Shilpa G. Vidhale	Powering the Future: A Comprehensive Review of Polymer Solar Cells	103
14	S.A.Waghuley and S.M.Butte	Structural Properties of Polyindole for energy storage application	120
15	P. A. Saudagar, D. R. Bijwe and R. B. Pedhekar	Arduino Based Smart Controller for Greenhouse using Integrated Fuzzy Logic for Temperature Control	125
16	P.R. Konmare, S.H. Saknure and A.C. Kumbharkhane	Dielectric Relaxation and Hydrogen Bonding Studies Of 1,2,6-Hexanetriol From 10MHz- 50GHz	129
17	P. S. Awandkar , A. V. Tiwari, A. P. Deshmukh, S. P. Tiwari and S. P. Yawale	Synthesis and characterization of polyaniline & exploring it for CO ₂ gas sensing	134
18	Pravin Rathod, Vishnudas Bhosle and Ashok Ubale	Synthesis, Characterization, Photocatalytic, Antibacterial and Antifungal Study of ZnO Nanoparticles	139
19	P. U. Sah , A. P. Bangar and S. A. Waghuley	Exploring potential of CdS for Efficient Solar Cell incorporated with SiO ₂	148
20	S. A. Athawale , V. B. Bhise and R. M. Belekar	An investigation on the hardness of L- hydroxyproline-doped potassium aluminium sulphate dodecahydrate single crystal.	153
21	S. Bisan, S. Atre and Satish Sharma	Design of a Real-Time Hand to Text Sign Language Recognition System	158
22	Shilpa S.Patange and Ashok C. Kumbharkhane	Dielectric Relaxation studies of binary mixture of D-arabitol + Water using a Time Domain Reflectometry Technique	166
23	Vaishnavi V. Pandhe, Suraj V. Tayade and S. A.	Synthesis and Characterization of Graphene Decorated CuO	171

	Waghuley	Nanocomposite for Multifunctional application.	
24	Krishna Kumar and Bijaya Kumar Sahoo	Exploring Heat Rectification Behaviour of InGaN/GaN Interface: Towards Efficient Thermal Management in Optoelectronic Devices	176
25	V.S. Pabboj, H.N. Lakhamawad, G.T. Jinklor, D.N. Rander, K.S. Kanse, Y.S. Joshi and V.A. Rana	Dielectric and electrical characterization of ethyl cellosolve and ethanol binary mixtures in frequency range 20 Hz to 2 MHz	185
26	Arsala Zamir Khan, Zamir S. Khan, Leena G. Gahane, A. C. Kumbharkhane and M. P. Lokhande4	Dielectric relaxation and thermodynamic study of Amino Acid using time domain reflectometry technique	191
27	Shailesh P. Tiwari, A.P. Deshmukh, A.V. Tiwari, P.S. Awandkar, M.S.Dixit and S.P. Yawale	Synthesis and Characterization of Polyaniline Composite Incorporated with TiO ₂ Nanoparticles for Enhancement of Antibacterial Activity	196
28	A.P. Deshmukh, S. P. Tiwari, A.V. Tiwari, P.S. Awandkar, M.S.Dixit, D.P. Deshmukh, and S. P. Yawale	Structural Investigation of PEDOT-PSS Conducting Polymer Treated with Solvent	208
29	J.S.Tated, C.M.Jadhao, D.S.Dhote, and S.D.Gawande	Real-Time Soil Fertility Detection Using Colorimetric Technology: A Precision Farming Approach In Vidarbha Region of Maharashtra	216
30	Gitanjali F. Jadhav, Rushikesh R. Suryawanshi, Suhas S. Mohite, Pratik P. Raut and Rajaram S. Mane	Electrochemical Studies: Biomass-Derived Nitrogen-Doped Graphene Oxide	222
31	U. B. Tagade, N. S. Meshram and S. A. Singade	Study of AgCl ₃ , ZnCl ₂ and KCL Added Glycine Single Crystals by Slow Evaporation Method	234
32	Shantanu Raulkar and N R Pawar	Synthesis of Alpha Alumina (α - Al ₂ O ₃) nanoparticles by solution combustion method	241
33	Rupali Thete, Satish Sharma and Vishal R. Panse	Comparative Study of primary and secondary alcohols in a common solvent Nitrobenzene using Ultrasonic Pulse-echo technique	246
34	Rajesh R. Karhe, C.M Jadhao and S.S. Mhaske	Recurrent Neural Network-Based Classification of Scanned ECG Records for Cardiac Arrhythmia Detection	253
35	S. K. Ganvir and G. K. Reddy	Design of MATLAB GUI for COVID detection and tagging the results using Neuro Solution Software	260
36	Manisha S. Raut, and S. A. Waghuley	Efficient Synthesis and Detailed Analysis of Graphene Quantum Dots (GQDs) via Electrochemical Exfoliation	269
37	A. K. Patel, V. S. Patel, U. D. Raval, N. A. Chaudhary, K. N. Shah, and A. N. Prajapati	Frequency and Concentration Dependent Dielectric and Electrical Properties of N, N-Dimethylacetamide and n-Nonanol.	274
38	Radhika A. Gandhare, Aachal R. Kadu and Jitendra T. Ingle	Combustion Synthesis and Photoluminescence Study of Li ₂ ZnTi ₃ O ₈ :Mn ⁴⁺ Phosphor for Photo-catalytic Activity in Plants.	284
39	Ashish Choudhary and Sandeep Waghuley	CO ₂ and LPG Gas sensing study of chemically synthesized PPy based sensor.	290

40	Chitransh Malvia, M. D. Mehare and S. J Dhoble	Synthesis and luminescence study of Eu^{3+} activated KLaF_4 phosphor for W-LED application	294
41	Farhan Kaleem Ahmed, K. H. Adhau, U. A. Palikundwar, S. Acharya, M. Gaidhane and D. Taikar	Synthesis and Characterization of iron (Fe) Doped Tungsten Oxide (WO_3) as an Electrolyte Material	302
42	A.B. Nawale, G. Sutrale, H. Chaitwar and S. R. Jigajeni	Structural and Optical Properties Study of ZnO Thin Films Prepared by Spin Coating Method	312
43	Ankit R. Palewar, Yash D. Narad and Sanjay J. Dhoble	Spectroscopic investigation of photoluminescence properties of $\text{K}_2\text{CaMg}(\text{PO}_4)_2:\text{Eu}^{3+}$ phosphor for solid state lighting applications.	318
44	A. B. Nawale, H. Chaitwar, G. Sutrale and S. R. Jigajeni	Performance of TiO_2 based Dye Sensitized Solar Cell for Chlorophyll Based Natural Dyes	328
45	J. Joshi, S. Athawale, S. P. Tiwari and A. P. Deshmukh,	Synthesis of CuO Nanoparticles by Using Butea Monosperma by Green Approach.	338
46	K. D. Jagtap, R.V.Barde, K. R. Nemade, P.R. Malasane and S. A. Waghuley,	Electrochemical Study of 5% doped TiO_2 graphene nanocomposites electrode for Supercapacitor application	343
47	K. Sonkusare, D. R. Taikar and S. J. Dhoble,	Synthesis, luminescence characterization and energy transfer in rare earth doped apatite-type $\text{Ca}_9\text{La}(\text{PO}_4)_5(\text{SiO}_4)\text{Cl}_2$ phosphors.	348
48	M. R. Baccha, A. P. Deshmukh, S. P. Tiwari, M.S. Dixit and S.P. Yawale	Synthesis of pure PANI, PEDOT: PSS and their copolymer as a counter electrode for the application of photovoltaic cell using betanin as natural dye sensitizer.	361
49	Priyanka P Gole and Sandeep A. Waghuley.	Review On Rare Earth-Conducting Polymer Nanocomposites For Spintronics Application	370
50	S. S. Pakade, A.H. Kale, A.D. Bokhare, M.P. Lokhande and A.C. Kumbharkhane	Study Of Dielectric Relaxation in a water mixture of Adonitoland D-Arabitol using Time Domain Reflectometry Technique	378
51	S. V. Tiwari, V. N. Bombatkar, R. V. Barde and P.R. Malasane	Optical conductivity Study of Polyaniline/Cerium Oxide composites by using Ultraviolet Visible Spectroscopy	383
52	Shaikh Naved Shaikh Quasim, A. B. Nawale and S. R. Jigajeni	Synthesis Of Zinc Oxide (ZnO) Nanoparticles By Co-precipitation Method & It's Characterization	388
53	S. K. Khan, A. D. Bokhare Z. S. Khan, N .P. Garad, M. P. Lokhande and A. C. Kumbharkhane	Dielectric relaxation studies of binary mixture of Pyridine and iso-propanol by Time Domain Reflectometry	394
54	V. S. Patel, A. K. Patel, U. D. Raval, N. A. Chaudhary, K. N. Shah and A. N. Prajapati	Dielectric spectroscopic study of Chlorobenzene With n-Butanol at different temperature	401
55	Shrikant H. Nimkar, P. A. Fartode and S. B. Kondawar	Fabrication of Polyaniline / TiO_2 Nanocomposites Thin Film for CO_2 Gas Sensor	414

56	S. V. Warudkar, A.P. Deshmukh, P. S. Awandkar, S. P. Tiwari and S. P. Yawale	Synthesis and Sensing Characteristics of PEDOT:PSS/RGO composite as a Carbon Dioxide Gas Sensor	422
57	Suraj V. Tayade, A. P. Bangar and S. A. Waghuley	Evaluating Polyaniline-CuO Composite for Next- Generation Electromagnetic Interference Shielding"	432
58	S. S. Kosalge, S. D.Charape,S. Bharambe and P. G Bhatia	Study of gas sensing properties of nanostructured nickel ferrite thick film sensors in NH ₃ , H ₂ S, CO ₂ , and PLG environments	441
59	Deepak S. Dhote and Swapnil K. Shelke	Advanced System For The Measurement Of Blood Hemoglobin Non-invasively:an Investigative Approach	447
60	Syed Samiuddin and. M.E. Shelke	Synthesis, Characterization and Conductometric Study of Schiff's Bases and Their Metal Complexes: A Review	454
61	U.D. Raval, V.S. Patel, A.K. Patel, N.A. Chaudhary, K.J. Agheda, M.K. Prajapati, K. N. Shah and A. N. Prajapati	Physicochemical, Electrochemical and DFT Characterization of n – Butanol and Benzonitrile Binary Mixture	463
62	V. N. Bombatkar, S. V. Tiwari, R. V. Barde and O.P. Gunjkar	Synthesis, characterization and AC conductivity study of Polyindole/Stannic oxide nanocomposites	474
63	Ruby Khan, Akhila Nair and Vaishali Raikwar	Effect of Capping on Luminescence of Cadmium Sulfide/PVP Nanocomposite	480
64	Vaishnavi D. Nagmote, Suraj V. Tayade and, S. A. Waghuley	Exploring Polyaniline for Effective Electromagnetic Interference Shielding Applications	488
65	N. D. Kherde, A. O. Chauhan, P. A. Nagpure and S. K. Omanwar	Efficient Synthesis and Photoluminescence Properties of K ₂ Sr ₄ (BO ₃) ₃ Phosphors Doped with Gd ³⁺ , Bi ³⁺ , and Pb ²⁺ for Phototherapy Applications	493
66	Rupesh N. Patil and Jitendra T. Ingle	Combustion Synthesis and Photoluminescence Study of Ba ₃ Y ₂ (BO ₃) ₄ :Eu ³⁺ Phosphor for White LED.	500
67	S. G. Ibrahim and P. M. Gulalkari	Nickel ferrite Nanolayer thin film: A Review Study	506
68	P. S. Dikondwar	Supercapacitors: Opportunities and Challenges.	517
69	N. Thejo Kalyani, Ritesh Raikundliya, Droupadi Gingule and S.J. Dhoble	Synthesis and characterization of bis(8-hydroxyquinoline) (Strontium) organo- metallic fluorescent phosphor for solid state lighting	522
70	Shubham Kadam and Vivek Kapse	Hydrogen Sulfide Gas Sensing by Chemically Synthesized Cerium Oxide Nanoparticles	534
71	N R Thakare, V M Lokhande, S. A. Patil and V R Chinchamatpure	Stabilization of plastic phase of Lithium Sulphate using different electrolytes.	540
72	S. S. Bangade, V. M. Raut, P. D.Khadse and A. B. Ghanbahadur	Characterization of Iron and Zinc Nanoparticles Synthesized from Spirulina Extract: A Comprehensive Analysis Using UV, FTIR, SEM, TEM, DLS, and XRD Techniques	545

73	D. V. Diwedi, V. V. Mishra and S. J. Sharma	Smart Doctor Assistant System using Lab VIEW.	552
74	R. P. Ikhar, K. M. Mude, B. M. Mude, S. M. Yenorkar, R. R. Mistry, G. T. Lamdhade, A.O. Chauhan, R. B. Butley, C. C. Jadhao and K. B. Raulkar	NH ₃ Gas Sensing Applications of PPy Doped SnO ₂ Sensor to Study Sensitivity	559
75	R.N.Zade, B.M.Mude, K.M.Mude, S.M.Yenorkar, K.B.Raulkar, R.R.Mistry, S.M.Warbhe, S.K.Mude, A.N.Patange G.T.Lamdhade and P.S.Bodkhe	Coupling Reactions of Active Methylene Group for synthesis of 3(P-Methylphenyl)1-Phenylprop-2-en-1-one [Chalcone] using nanocomposite of Ceria embedded on zeolite	565
76	P. D. Shirbhate, S.D. Charpe, P. J. Jadhao and V. S. Kalyamwar	Synthesis and Characterization of Stannic Oxide Nanoparticles by the Sol–Gel Method	570
77	Dhananjay. P. Deshmukh, Ashitosh P. Deshmukh, Sushil D. Charpe	Electrical behavior (ac And dc Conduction) of Polythiophene composite thin films doped with Iodine.	574
78	P. D. Shirbhate, D. P. Deshmukh, S. P. Yawale and S. V. Pakade	Synthesis and Impedance Spectroscopy of PTh-PEO Polymer composite doped with LiClO ₄	584
79	A. R. Bhojane, D. R. Bijwe, A. V. Rajgure, S. P. Yawale, P. A. Saudagar and N. R. Pawar	Synthesis and Characterization of Lanthanum Oxide (La ₂ O ₃ NPs) Nanoparticles	590
80	Ankit Chavhan , N. R. Pawar , D. R. Bijwe and D. S. Chavhan	Synthesis and thermoacoustic study of Boehmite nanoparticles in Acetone	596
81	D. S. Chavhan, D. R. Bijwe, N. R. Pawar and A. D. Chavhan	Synthesis and Thermoacoustic Study of Boron Nitride Nanoparticles in Acetone	604
82	S N Jadhav and RNPathare (Dhokne)	Dielectric Characteristics of Nanoparticles Doped Polyvinyl Alcohol	612
83	Ms. D.P. Rathod, Dr. R.V. Barde, Dr. K. R.Nemade and Dr. S. A. Waghuley	Optical Study of Graphene/TiO ₂ nanocomposite by Ultraviolet–Visible Spectroscopy	618
84	P.D.Hambarde, N.P.Garad and A.C.Kumbharkhane	Dielectric Relaxation Study of tert-Butyl Acetate Using Time Domain Reflectometry Technique (TDR)	627
85	Daiwashala G. Dongre and Ashok.C. Kumbharkhane	Structural and dynamics behavior of nitriles through dielectric properties using a time domain reflectometry (TDR)	632
86	S.H. Saknure, P.R. Konmare and A.C.Kumbharkhane	Dielectric Relaxation study of Hydroxypropyl methyl cellulose – water mixture using Time Domain Reflectometry (TDR)	640
87	K. Y. Rokde and S. S. Shende	Design and Development of an Embedded System via Sending a Real Time Data of ECG Signal to the Cloud Server for Cardiologist Doctor	646
88	P.A.Fartode, S.P.Yawale and S.H.Nimkar	Transport And Electrical Properties Of Peo: Pvp: Nacl Based Polymer Electrolyte For Solid State Batteryapplication	656

89	A. R. Karule, S. P. Yawale and S. S. Yawale	D. C. Conductivity of polypyrrole-polyethylene oxide-SnO ₂ films synthesized by chemical oxidative polymerization method	667
90	P.P. Raut, G.T. Lamdhade, S. D. Charpe, P.D.Shirbhate, D. P. Deshmukh and V.U. Rahangdale	PVC-PMMA Electrolyte System Tailoring with Different Dopants: A Comprehensive Study	675
91	Parimal T Patwe, Neha A. Kumbharkhane and Gajanan R Mahajan	Comparative Analysis of Phantoms Used for Stereotactic Radiosurgery Patient-Specific Quality Assurance	684
92	Dr. Vinod M. Sherekar and Mr. Nilesh S. Padole	Synthesis, Characterization And Biological Evaluation Of 4-(4-Bromo-1-Hydroxy Naphthalen-2-Yl)-6-(3,4-Dimethoxy Phenyl)-5,6-Dihydropyrimidine-2(1h)-One	693
93	S. A. Athawale, B.A. Lone, S. E. Bhandarkar S. Athawale and M. A. Wani	Synthesis and Computational Approach of Cyclic Imines of Substituted 1, 3, 4-Thiadiazole with Special Reference to Theirs Antioxidant Activity	699
94	S. S. Birajdar, S. D. Sont, M. R. Bodke and D. B. Suryawanshi	A comparative experimental and theoretical approach to study structural and molecular aspects in binary solutions	708
95	B.M.Mude, K.M.Mude, R.N.Zade, S.M.Yenorkar, K.B.Raulkar, R.R.Mistry, S.M.Warbhe, S.K.Mude and S.P.Yawale	Enhancement in efficacy of gas sensor by doping metal oxide with conducting polymer	715
96	Dr. Niteen S. Mohod	Advancement In Biomedical Sensor Technologies And Future	719
97	Mr. M. C. Naidu and Dr. D. S. Dhote	Wearable Artificial Intelligence Biosensors and Bioelectronic Devices: A Comprehensive Review	722
98	A.B.More and G.T.Lamdhade	Exploring the Influence of Salicylic Acid Doping on the AC Conductivity and Dielectric Constant in PVC-PMMA Thin Films	732
99	Sarang S. Dhote, Priyadarshani Deshmukh and Sandip Dautpure	Comparative Study of Bismuth Silicate and Aminoplast Polymer as Adsorbents in Thin-layer Chromatography for Heavy Metal Identification using Computational Chromatography	738
100	R.K. Parate, K.M. Dhole and S.J. Sharma	Node MCU based Continuous Monitoring of Health Parameters using Android Device	744
101	Sidharaddi R. S., Yadav M. P., Mane A. A. and Sawant V. S.	Physicochemical and Air Purifying Characteristics of Electroplated Cu Films: Influence of Depositing Time	749
102	S. D. Gawande , D. S. Dhote and Dr. J. S. Tated	Detection of Disease on Citrus Plants Using Image Processing Technique	760
103	Sayli Guru, U. P. Manik and Amol Nande	Optical and Luminescence properties of Ca ₉ Al(PO ₄) ₇ :Eu ³⁺ inorganic phosphor	767
104	Naresh N. Sarkar and Shraddha M. Butte	The impact of sintering temperature on the magnetic and structural properties of spinel ferrite synthesized via sol-gel auto-combustion technique.	776

105	Dr. Gajanan S. Wajire	Versatile low voltage power supply using manually driven DC motor	785
106	D.R. Solanke and Y.B.Gandole	On the Implementation of Linear Position Control using Fuzzy Logic Approach	790
107	N. S. Wadatkar and S. A. Waghuley	Structural and optical characterization of polythiophene/polyindole/ferric chloride blended polymers for optoelectronic applications	802
108	Miss. Shraddha L. Bhagat and Dr. Shilpa Pande	Enhancing Supercapacitor Performance with Polyaniline-Metal Oxide Nanocomposites: Current Trends and Future Directions	810
109	Ashish Choudhary and Sandeep Waghuley	CO ₂ and LPG Gas sensing study of chemically synthesized PPy based sensor	828
110	R. B. Mankar and V. D. Kapse	Gas sensing potential of nanocrystalline SmFeO ₃ : A Review	832
111	Humera Khan and Pramod Kumar Malviya	Spectroscopic studies of transition metal complexes	840
112	P.N.Deshmukh, S.S.Dhote and S.V.Dautpure	Green route: Nanoparticles Synthesis, Characterization, a Sustainable Future	845
113	D. R. Taikar and S. J. Dhoble	Effect of Li ⁺ -ion on enhancement of photoluminescence in Sm ³⁺ doped CaSnO ₃ phosphor	855
114	C. T. Londhe	Study of potential energy curves of diatomic zirconium oxide molecule	861
115	V. U. Rahangdale and S. D. Charpe	Effect of Al ₂ O ₃ addition on the properties of Lead Titanate Glass-ceramics	867
116	Nita Shinde, Anil G. Beldar, Ashvini Pusdekar and N.S.Ugemuge	A Comprehensive Review on Nano Crystalline CdS, Ag ₂ S and CdS-Ag ₂ S Thin Films Synthesized by Chemical Bath Deposition & Modified Chemical Bath Deposition Method	870
117	Mr. S.S Mhaske and Dr. C.M. Jadhao	GUI based Heart Disease prediction model using Random Forest Algorithm	880
118	Kajal Sirtawar and Kishor Raulkar	Spectroscopic Studies of Polymethyl Methacrylate (PMMA) and Ethyl Cellulose (EC) Polyblend doped with Oxalic Acid	886
119	Krishna Sharma, Satishkumar A. Athawale , Rustam Ali and Utpal Deka	Investigation of Lower Hybrid Wave Instability in a Collisional Magnetized Gallium Arsenide (GaAs) Semiconducting Quantum Plasma System	896
120	N. B. Thakare, V. S. Kalyamwar, M. R. Belkhedkar and G. T. Lamdhade	Synthesis of SnO ₂ Nanoparticles by Solution Combustion Method	904

121	Raushan Shah R. Shah, P. R. Yawale , A. C. Dongapure and P. P. Choudhari*	Green Synthesis of Papaya (Carica papaya) Leaf Extract by using of Copper Oxide.	909
122	R.R.Mistry, B.M.Mude, K.M.Mude, K.B.Raulkar, S.M.Yenorkar, R.P.Ikhar, R.N.Zade and G.T.Lamdhade	Impact of Laser irradiation on seed germination, seed vigour and electric conductivity in Groundnut seeds	912
123	S.M.Yenorkar, B.M.Mude, K.M.Mude, K.B.Raulkar, R.R.Mistry, B.R.P.Ikhar, R.N.Zade and G.T.Lamdhade	Enhanced Ammonia Sensing Performance of NiO-WO ₃ Metal Oxide Composite Gas Sensors	918
124	S. R. Jaiswal, R. G. Korpe and P. A. Nagpure	Highly efficient green light-emitting K ₂ Sr(Gd, Y)(PO ₄) ₂ : Tb ³⁺ phosphor for Mercury Free Fluorescent Lighting and PDPs	925
125	S. Dubey, P.K. Sharma, A. Mishra, S.K. Joshi, A. Mansuri, S. Vyas	EXAFS studies of some Cu (II) complexes using Synchrotron Radiation Source	936
126	Dr.Shraddha Bansod-Pande and Dr.Seema Ubale	Effect of Sugarcane bagasse ash on the phase transformation and optical properties of Zinc-Borate glass	942
127	P.R. Kandalkar, Y.A. Gadhikar and S.A. Waghuley	ZnO Nanoparticles For Antibacterial Activity Against Clinically Extracted Gram-Positive And Gram-Negative Bacteria	948
128	Surabhi Jaju Rathi	Nanotechnology : A Revolution in The Era of Renewable Energy	953
129	Pritesh J.Jadhao, Kamlesh R Banarse, S.P. Yawale and S.S. Yawale	Electrical And Thermal Properties of Polyaniline –Cadmium Sulphide Nanocomposite with Photovoltaic Application	957
130	S. G. Ibrahim and D. S. Dhote	A Review Study on Indium Tin Oxide Thin Films: Synthesis and Characterizations	970
131	Aniket R.Deshmukh, Nilesh R.Thakare, Sanjay K Devade and Gaurav S.Chaudhari	A Literature Review of TiO ₂ -GO Composites in Solar Cells: Advances and Future Prospects	976
132	M. T. Mundhe, G. K. Biradar, G. B. Todkar and R. A. Kunale	Magnetic and electrical properties of nanosized M-type strontium hexaferrite prepared by sol-gel	981
133	S. Krishnakumar, Amol V. Pansare, Xavier Gama, Guruling. B. Todkar, G.K. Brajdar and Renuka. A. Kunale	Novel binary polymeric nanocomposite for high performance supercapacitor	988
134	Vijay R. Chinchamatpure and Nilesh R. Thakare	Thermoluminescence Properties of Fluorophosphate Materials Li ₉ Mg ₃ [PO ₄] ₄ F ₃ , Li ₂ Mg[PO ₄]F.	994
135	Sandip M. Parkhi, Shaukat A. Shah, Shruti Dhale, Ashvini Pusdekar, N. S. Ugemuge , S. V. Moharil	Combustion Synthesis and Luminescence in LiAl ₅ O ₈ :Ln ³⁺ (Ln ³⁺ = Ce, Gd) Phosphor for UV Applications	999
136	S. P. Pawar and P. M. Ardhapurkar	Experimental Investigation and Optimization of Wire Electric Discharge Machining Parameters for Shape Memory Alloy	1011

137	Dr. S. A. Patil and Dr. N. R. Thakare	A review of various Spectroscopic Techniques for cancer diagnosis	1020
138	Pankaj G. Waghmare, Vaibhav Y. Borokar, Ashwini S. Ghate, Manish G. Patil and Ashok M. Mahajan	Multilayer Deposition of TiO ₂ : A Versatile Approach for Battery and Biomedical Applications	1024
139	Atish Kohale and Sarika A. Khapre	Structure and properties of processible conductive polyaniline-polyethylene oxide composite	1033
140	P. R. Yawale , N. R. Thakare , P. P. Chaudhary, P. S. Parimal, D. S. Wartti and A. D. Ghatol	Water quality Assessment of Wagholi Lake, Dist. Amravati(MH)	1041
141	Bhupesh Nemmaniwar and Shyam Mokle	Rheological Study of 2,3-Dichloroaniline and 2-Ethoxyethanol at different Temperatures	1045
142	P.L. Harale, M.E. Shelke, D.T. Tayade and A.R. Kurhe	Anticancer Activity of Novel Thiocarbamide Derivatives by MTT Colorimetric Assay	1054
143	Anant S. Wadatkar	Study of variation of AC Electrical Conductivity of 4:1 PS PMMA Polyblend thin films doped with Oxalic Acid in different weight proportions	1059
144	Radhika G Deshmukh, Amruta Gaikwad and Sanjay J Dhobale	The Spectroscopic study compound Na ₂ BaCa(PO ₄) ₃ :Eu ³⁺ red-emitting phosphor for WLED application	1063

¹ Kailash Nemade
² Sandeep Waghuley

Sodium Superoxide-Polypyrrole Composite for Photovoltaic Applications



Abstract: - This study successfully investigated the photovoltaic (PV) properties of polypyrrole (PPy), sodium superoxide (NaO_2), and a sodium superoxide-polypyrrole (NaO_2 -PPy) composite. A simple and cost-effective ex-situ approach was used to prepare the composite. The NaO_2 -PPy composite-based PV cell exhibited a fill factor of 0.24 and a power conversion efficiency of 11.17%. This work demonstrates a straightforward and economical method for preparing NaO_2 -PPy composites for PV applications.

Keywords: composite materials; sodium superoxide; polypyrrole

¹ *Corresponding author: Kailash Nemade, Department of Physics, Indira Mahavidyalaya, Kalamb 445 401, India.

² Sandeep Waghuley, Department of Physics, Sant Gadge Baba Amravati University, Amravati 444 602, India
Copyright © JES 2024 on-line : journal.esrgroups.org

I. INTRODUCTION

To achieve the target of restricting global warming to 1.5 °C, a rapid reduction in carbon dioxide emissions due to heavy industrialization is essential. Therefore, energy production through green approaches plays a crucial role. In this quest, photovoltaic (PV) cells are leading the renewable energy field due to their excellent feature of clean energy production. On the other hand, efficient energy management is equally important, as energy storage remains challenging. Fortunately, supercapacitors offer a more straightforward solution for energy management.

Currently, conducting polymers such as polyaniline, polypyrrole, and polythiophene have garnered significant interest for energy production and storage applications due to their excellent physical properties. Among these, polypyrrole (PPy) stands out as a potent candidate for PV cell and supercapacitor applications due to its extraordinary characteristics, including electrical conductivity, optoelectrical properties, interesting redox properties, and stability against atmospheric changes.

Considering the above discussion, we planned to explore the photovoltaic properties of a novel sodium superoxide-loaded polypyrrole (NaO₂-PPy) composite. The fill factor and power conversion efficiency were measured from the current-voltage characteristics of PV cells. The main accomplishment of the present work is the positive synergistic effect between PPy and NaO₂, resulting in a noteworthy power conversion efficiency.

II. EXPERIMENTATION

For the preparation of NaO₂-PPy composite, analytical grade chemicals were used without further purification. Stable NaO₂ nanoparticles were prepared by following recipe reported by Nemade et al [4]. Whereas, PPy was directly procured from Sigma Aldrich. Ex-situ approach was adopted for the preparation of NaO₂-PPy composite. In this process, firstly 5 g PPy was added in 100 ml of acetone and kept under probe-sonication for 1 h. Then the 0.5 g of NaO₂ nanoparticles were added in the suspension of PPy and again kept for probe-sonication for 1 h. Finally, the suspension was filtered and blackish precipitated was kept for in oven for drying at 60 °C for 8 h. The structural, optical and morphological properties of composite investigated using X-ray diffraction (XRD, Rigaku Miniflex), ultraviolet-visible (UV-VIS, Agilent Cary 60 UV-VIS spectrophotometer) and field emission scanning electron microscopy (FESEM, ZEISS SIGMA SEM), respectively.

The <ITO/NaO₂-PPy/Al> type configuration was adopted for the fabrication of PV cells. Similarly, DN350 (indoline dye) was used for preparation of dye sensitized solar cells. Before fabrication process, ITO glass plates (Resistivity-28 Ω/cm²; Thickness-125 nm and Dimension-25mm × 25mm) were cleaned using mild detergent and DI water. On ITO layer, NaO₂-PPy composite as active layer was deposited using spin-coating film deposition technique at 1000 rpm. The aluminum foil as back contact of size 5 mm × 5 mm was fixed on active layer and kept cell for drying at 80 °C for 1h. By adopting same processes, PV cell based on PPy and NaO₂ were also fabricated.

Current-voltage (IV) characteristics of PV cells were recorded under the incandescent light source. All PV cell parameters such as open circuit voltage (V_{OC}), short circuit current (I_{SC}), fill factor (FF), and power conversion efficiency (η) were calculated from IV characteristics [5]. The data used in present paper is average of five sets of data, which does shows considerable deviation.

III. RESULTS AND DISCUSSION

Figure 1(a) shows the XRD patterns of sodium superoxide (NaO₂) and NaO₂-PPy composite. The XRD pattern of NaO₂ comprises characteristic peaks at 30.99°, 45.12°, 56.80° and 58.91° associated with planes (200), (220), (311) and (222), respectively [6]. XRD pattern of NaO₂-PPy composite indicates the successful incorporation of NaO₂ nanoparticles through its characteristic peaks. XRD pattern of composite comprises with broad hump peak at 27.09° and sharp peak indicates semi-crystalline nature of composite. Figure 1(b) shows the UV-Vis spectra of NaO₂-PPy composite, exhibiting the absorption tail around 534 nm results in band gap 2.32 eV of NaO₂-PPy composite. Figure 1(c) depicts the SEM image of NaO₂-PPy composite, showing the agglomerated nature of composite. SEM image also shows rough morphology of nanocomposite, which attributed to condensation of surface oxides on the flakes of PPy.

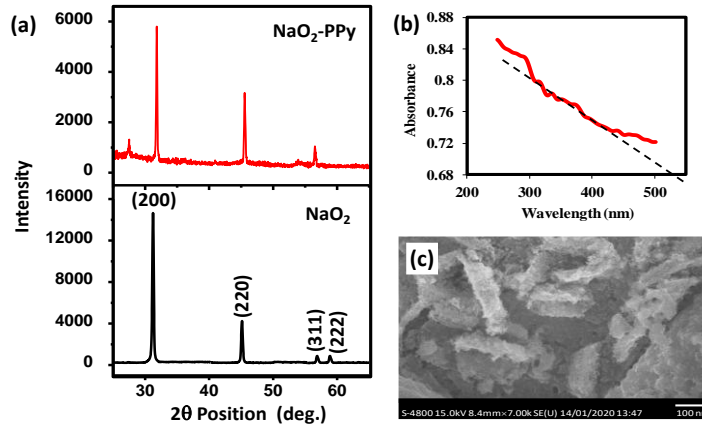


Figure 1. (a) XRD pattern of NaO₂ and NaO₂-PPy composite. (b) UV-Vis of NaO₂-PPy composite and (c) SEM image of NaO₂-PPy composite.

Figure 2(a-c) depicts the photovoltaic performance of the PPy, NaO₂ and NaO₂-PPy based PV cells, respectively. Figure 2(a-c) and displayed values of FF and power conversion efficiency of composite significantly more than the pure PPy and NaO₂. Figure 2(c) shows the promoted power conversion efficiency of PV cell after the incorporation of NaO₂ nanoparticles. It reveals that positive synergetic effect existed between PPy and NaO₂. The noteworthy efficiency of NaO₂-PPy based PV cells attributed to the interfacial behavior and morphology of an active layer. Improvement in efficiency also attributed to the charge separation process and good transport efficiency due to the chemical nature of superoxides, which reduces insulating characteristics of hybrid materials [7].

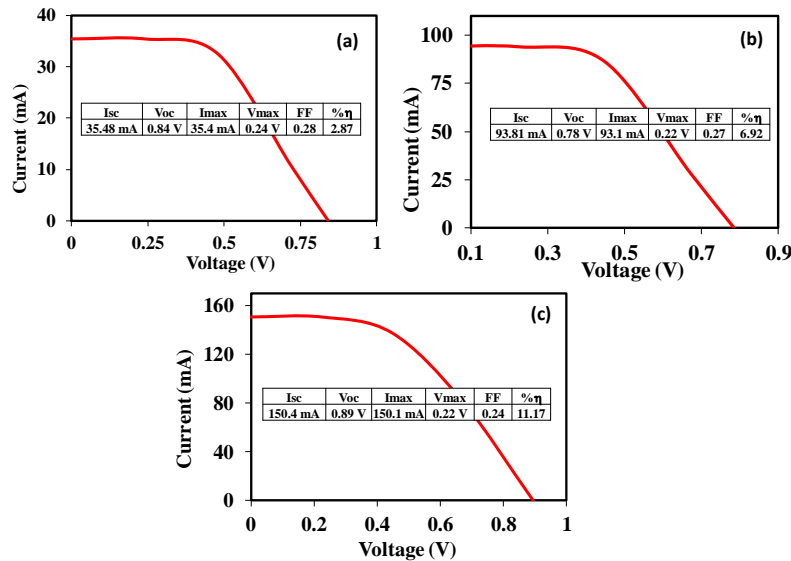


Figure 2. Photovoltaic response of (a) PPy, (b) NaO₂ nanoparticles and (c) NaO₂-PPy composite.

The enhanced power conversion efficiency (PCE) in the NaO₂-PPy composite compared to the individual components, PPy and NaO₂ nanoparticles, can be attributed to:

Sodium superoxide (NaO₂) nanoparticles possess unique electronic properties that facilitate efficient charge separation. When integrated into the PPy matrix, these nanoparticles can act as electron acceptors, effectively separating the photo-generated electron-hole pairs. Polypyrrole (PPy) is known for its good electrical conductivity and stability. It acts as an excellent hole transport material. The integration of NaO₂ nanoparticles into the PPy matrix ensures a continuous pathway for holes, reducing recombination losses and enhancing charge transport.

The composite structure of NaO₂-PPy enhances the light absorption across a broader spectrum. PPy has strong absorption in the visible region, while NaO₂ nanoparticles can contribute to absorbing different wavelengths. This broadens the range of absorbed light, leading to more efficient generation of charge carriers.

The interface between NaO₂ nanoparticles and the PPy matrix is crucial. The close contact between these materials ensures efficient transfer of electrons from the NaO₂ to the PPy, and holes from the PPy to the NaO₂. This efficient interface reduces the likelihood of charge recombination and enhances the overall efficiency.

The combination of NaO₂ and PPy creates a synergistic effect where the properties of each material complement and enhance the other's performance. The oxidative stability of PPy protects NaO₂ nanoparticles from degradation, while NaO₂ enhances the electrical properties of PPy.

The incorporation of NaO₂ nanoparticles into the PPy matrix can lead to a more favorable morphology for photovoltaic applications. A well-dispersed nanoparticle distribution within the polymer matrix can create a more extensive interfacial area for charge separation and transport.

Table 1 provides a comparison of the photovoltaic properties of various PPy-based composites with the results from the present work. The fill factor (FF) and power conversion efficiency (% η) are used to evaluate the performance of these materials. The results indicate that despite the lower fill factor, the NaO₂-PPy composite exhibits a significantly higher power conversion efficiency compared to other PPy-based systems. This highlights the effectiveness of the NaO₂-PPy composite in enhancing photovoltaic performance.

Table 1. Comparison of present work with previously reported literature on photovoltaic properties of PPy-based composites.

Photovoltaic Properties			
Material System	FF	% η	Ref.
PPy	0.71	9.48	[8]
PPy based DSSC	0.43	4.72	[9]
PPy/ZnO	0.51	0.02	[10]
NaO ₂ -PPy	0.24	11.17	This Work

IV. CONCLUSIONS

This research successfully demonstrated the photovoltaic properties of a novel sodium superoxide-polypyrrole (NaO₂-PPy) composite, highlighting its potential in renewable energy applications. A simple and cost-effective ex-situ approach was adopted to prepare the NaO₂-PPy composite. This method proved to be efficient in integrating sodium superoxide nanoparticles into the polypyrrole matrix. The NaO₂-PPy composite-based photovoltaic cell exhibited a fill factor of 0.24 and a power conversion efficiency of 11.17%. This represents a significant improvement over previously reported PPy-based photovoltaic systems. The composite structure showed a positive synergistic effect between NaO₂ and PPy, leading to enhanced charge separation and transport. This synergy was key to achieving the notable power conversion efficiency. This study provides a promising outlook on the use of NaO₂-PPy composites in photovoltaic technology, emphasizing the importance of continued research in this area to develop efficient and sustainable energy solutions.

ACKNOWLEDGMENT

Authors are very much thankful to Principal, Indira College, Kalamb Dist. Yavatmal for providing necessary facilities.

REFERENCES

- [1] W.-J. Kwak, Rosy, D. Sharon, C. Xia, H. Kim, L. R. Johnson, P. G. Bruce, L. F. Nazar, Y.-K. Sun, A. A. Frimer, M. Noked, S. A. Freunberger, and D. Aurbach, "Lithium-Oxygen Batteries and Related Systems: Potential, Status, and Future," *Chem. Rev.*, vol. 120, no. 14, pp. 6626-6683, Mar. 2020.
- [2] P. V. Radu, A. Szelag, and M. Steczek, "On-Board Energy Storage Devices with Supercapacitors for Metro Trains-Case Study Analysis of Application Effectiveness," *Energies*, vol. 12, no. 7, p. 1291, Apr. 2019.
- [3] S. Naeem, W. Younas, A. Awan, N. Ahmad, M. J. Iqbal, T. Razzaq, M. Azam, S. Naseem, and S. Riaz, "Electrochemical performance and large positive-negative magnetodielectric coupling in iron chromite spinels," *Arabian Journal of Chemistry*, vol. 15, no. 6, p. 103800, Jun. 2022.
- [4] K. Nemade and S. Waghuley, "Novel synthesis approach for stable sodium superoxide (NaO₂) nanoparticles for LPG sensing application," *International Nano Letters*, vol. 7, pp. 233-236, May 2017.
- [5] K. Nemade, P. Dudhe, and P. Tekade, "Enhancement of photovoltaic performance of polyaniline/graphene composite-based dye-sensitized solar cells by adding TiO₂ nanoparticles," *Solid State Sciences*, vol. 83, pp. 99-106, Sep. 2018.
- [6] C. Xia, R. Black, R. Fernandes, B. Adams, and L. F. Nazar, "The critical role of phase-transfer catalysis in aprotic sodium oxygen batteries," *Nat Chem.*, vol. 7, no. 6, pp. 496-501, Jun. 2015.

- [7] B.P. Nguyen, T. Kim, and C. R. Park, "Nanocomposite-Based Bulk Heterojunction Hybrid Solar Cells," *Journal of Nanomaterials*, vol. 2014, Article ID 243041, Jan. 2014.
- [8] X. Zhang, B. Zhang, X. Ouyang, L. Chen, & H. Wu, "Polymer Solar Cells Employing Water-Soluble Polypyrrole Nanoparticles as Dopants of PEDOT with Enhanced Efficiency and Stability," *J. Phys. Chem. C*, vol. 121, no. 34, pp. 18378-18384, Aug. 14, 2017.
- [9] K. Keothongkham, S. Pimanpang, W. Maiaugree, S. Saekow, W. Jarernboon, & V. Amornkitbamrung, "Electrochemically Deposited Polypyrrole for Dye-Sensitized Solar Cell Counter Electrodes," *International Journal of Photoenergy*, vol. 2012, Article ID 671326, Jan. 2012.
- [10] F.M.A. Almutaser, S. Majumder, P.K. Baviskar, J. V. Sali, & B. R. Sankapal, "Synthesis and characterization of polypyrrole and its application for solar cell," *Applied Physics A*, vol. 123, article number 555, Jul. 2017.

*Nitin P. Garad,
¹Pallavi D. Hambarde,
¹Ashok C. Kumbharkhane

High-Frequency Dielectric Study and Unveiling molecular Dynamics of Diol's Using TDR



Abstract: - This study investigates the molecular dynamics of various diols using high-frequency dielectric spectroscopy with Time-Domain Reflectometry (TDR). TDR offers a unique advantage in probing dielectric properties at high frequencies, providing insights into the relaxation behavior of diol molecules. The analysis focuses on extracting key dielectric parameters such as dielectric constant, relaxation time and Kirkwood correlation factor which offer valuable information about the polarity, orientation, and hydrogen bonding interactions within the diol structure. This approach sheds light on the dynamics of diol molecules at the molecular level, contributing to a deeper understanding of their material properties.

Keywords: Diol, dielectric spectroscopy, molecular dynamics, Kirkwood correlation factor, TDR,

I. INTRODUCTION

Dielectric spectroscopy is a powerful technique for investigating the interaction of electromagnetic waves with polar molecules. By analyzing the dielectric response of a material, researchers can glean valuable information about its molecular dynamics, including dipole moment, relaxation processes, and molecular interactions [1-3]. Traditional dielectric spectroscopy methods often operate at low frequencies, limiting the ability to probe fast molecular motions [4-5]. This study utilizes Time-Domain Reflectometry (TDR) as a high-frequency dielectric spectroscopy technique to unveil the molecular dynamics of diols. TDR offers several advantages, including its ability to measure the dielectric response over a broad frequency range, making it ideal for studying the fast dynamics of polar molecules [6-8].

Diols, also known as dihydric alcohols, are a class of organic molecules containing two hydroxyl groups (-OH) bonded to a hydrocarbon chain. These hydroxyl groups endow diols with unique properties, including polarity and the ability to form hydrogen bonds. Understanding the molecular dynamics of diols is crucial in various fields, including material science, physical chemistry, and development of diol-based materials. Many researchers have been done the investigation on the dielectric relaxation behavior of diols in presence of polar and non polar solvent to understand the molecular interaction between them [9-13]. In the present investigation the diols under consideration are 1, 2 & 1, 3-Propanediol, 1, 3 & 1, 4-Butanediol, 2, 4 & 1, 5-Pentanediol.

In this work, we employ TDR to characterize the dielectric constant and relaxation time of diol samples. To understand the effect of number of carbon atom and position of hydroxyl

group on the dielectric properties of liquids. By analyzing the high-frequency dielectric response, we aim to gain deeper insights into the rotational dynamics and intermolecular interactions within these molecules. The findings from this study will contribute to a more comprehensive understanding of diol behavior and inform the development of novel diol-based materials with tailored properties.

II. MATERIALS AND MEASUREMENT

All the samples are purchased commercially, as mentioned below in table 1 with their purity:

Table1. The names of the diols under study, their production company names and purity:

Chemicals	Supplier	Purity
1,3-Propanediol	Merck Specialities Pvt. Ltd.	$\geq 98\%$
1,2-Propanediol	Thermo-fisher Scientific Pvt. Ltd.	99%
1,4-Butanediol	S.D. Fine-chem. Ltd.	99%
1,3-Butanediol	Himedia Laboratories Pvt. Ltd.	99%
1,5-Pentanediol	Merck Specialities Pvt. Ltd.	$>97\%$
2,4-Pentanediol	Merck Specialities Pvt. Ltd.	99%

The measurement of dielectric complex permittivity spectra of all these samples were done in the 10 MHz to 30 GHz frequency range using TDR. The Tektronix DSA8300 sampling main frame oscilloscope with TDR module 80E10B has been used. The experimental set-up and calibration of the instrument has been done as mentioned [12-13].

III. RESULT & DISCUSSION

The complex dielectric permittivity spectra of all diols are shown fig.1 in the frequency range of 10 MHz to 30 GHz at 25⁰C. Which represent the variation in dielectric permittivity (ϵ') and dielectric loss (ϵ'') with respect to applied frequency. From fig.1 it is seen that the ϵ' decreases with increase in frequency this is due to at lower frequencies, molecules can align with the electric field, causing a greater ϵ' . Conversely, at higher frequencies, there's less time for molecular reorientation, resulting in reduced polarization and a lower ϵ' this phenomenon is known as dielectric dispersion [12]. From fig.1 it can also be seen that the ϵ' decreases as the carbon chain length increases this is due to decrease in polarizability with carbon chain length and increase in the close packing of electron cloud which can hinder the movement of the electron clouds in response to the electric field. The ϵ' is also depends on the position of

functional groups in the chain [12]. The shift in dielectric loss (ϵ'') peak was observed towards lower frequency as we move propanediol to pentanediol which indicate increase in dielectric increase in dielectric relaxation time.

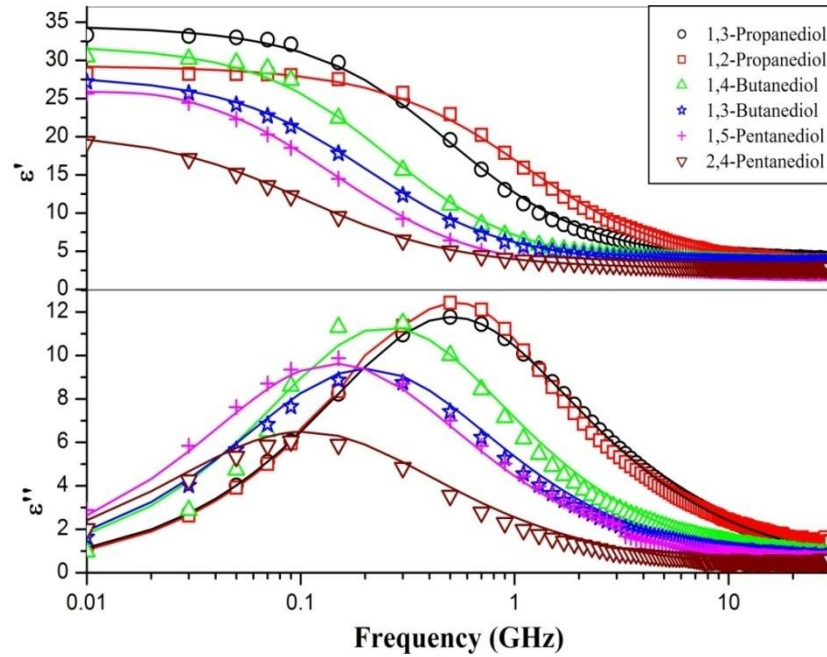


Fig.1. The complex dielectric permittivity spectra of diols at 25⁰C

The experimentally obtained complex dielectric was fitted to Cole-Davidson’s model to obtain the dielectric relaxation parameter [9]:

$$\epsilon^*(\omega) = \epsilon_\infty + \frac{(\epsilon_0 - \epsilon_\infty)}{[1 + (i\omega\tau)]^\beta} \quad (1)$$

Where ϵ_0 is the static dielectric constant, ϵ_∞ is the dielectric permittivity at high frequency, τ is the relaxation time in picoseconds and β is the distribution parameter which describes the broadness of dielectric loss peak. The obtained dielectric relaxation parameters for all diols are reported in table 2 agree very well with those reported in the literature [9, 13-15]. From table 2 it is observed that the static dielectric constant is depends on position of functional group and no. of carbon atoms present in it. In propanediol 1,3-propanediol having high dielectric constant than that of 1,2-propanediol this is due to 1,3-propanediol has two hydroxyl (OH) groups separated by carbon atoms, allowing it to form hydrogen bonds with neighboring molecules. However, 1,2-propanediol has its OH groups adjacent to each other on the same carbon atom, which hinders effective hydrogen bond formation between neighboring molecules. Similar effect we can observe for butane and pentanediols. From table 2 the relaxation time in diol increases with increase in carbon chain length this is due to increase in viscosity, which can indirectly affect relaxation time. Higher viscosity signifies a stronger resistance to flow, and this can also hinder the molecule's ability to rotate in response to the electric field.

The Kirkwood correlation factor ('g'), is a valuable parameter in understanding the orientational order and interactions within a polar liquid. It provides information about how effectively the permanent electric dipoles in the molecules are aligned with each other. The Kirkwood correlation factor can be calculated using the formula [9]:

$$\frac{(\epsilon_0 - \epsilon_\infty)(2\epsilon_0 + \epsilon_\infty)}{\epsilon_0(\epsilon_\infty + 2)^2} = g\mu^2 \frac{4\pi N\rho}{9kTM} \quad (2)$$

where M = molecular weight, ρ = density, μ = dipole moment for the corresponding liquids, N= Avogadro's number, k = Boltzmann constant, and T = temperature. The obtained values of 'g' are reported in table 2. From table 2 it can be observed that the values of g increasing with increase in number of carbon atom this may be due to the longer carbon chains can introduce flexibility, allowing the hydroxyl groups to explore a larger space and potentially interact with more neighboring diol molecules through hydrogen bonding. This increased intermolecular interaction could lead to a higher g value compared to shorter chain diols. In shorter chain diols, intramolecular hydrogen bonding within the molecule itself might be more favorable. However, with a longer chain, the increased distance between the hydroxyls might make intramolecular bonding less favorable. This can then shift the balance towards intermolecular hydrogen bonding with neighboring diols, potentially increasing g.

Table 2. Dielectric relaxation parameters for diols at 25^oC temperature.

Name of Compound	Static Dielectric Constant (ϵ_0)	Relaxation time (τ) in ps	Kirkwood correlation factor
1,3-Propanediol	34.65(09)	315.12(20)	2.35
1,2-Propanediol	29.35(07)	298.28(14)	2.44
1,4-Butanediol	32.60(90)	616.70(52)	2.55
1,3-Butanediol	28.21(11)	778.40(94)	2.40
1,5-Pentanediol	25.97(14)	1099.05(11)	2.54
2,4-Pentanediol	20.87(05)	1524.01(07)	3.13

Note: Bracketed term represent the error in last significant digit. Eg: 34.65±09.

IV. CONCLUSIONS

This study employed Time-Domain Reflectometry (TDR) to elucidate the relationship between molecular structure and dielectric relaxation in diols. Our results demonstrate that increasing the carbon chain length of diols leads to a decrease in the dielectric constant and an increase in the relaxation time. This observation can be attributed to the enhanced flexibility of longer chains, allowing for weaker intermolecular interactions and hindering the alignment of polar hydroxyl groups with the applied electric field. Additionally, the position of the hydroxyl group on the carbon chain appears to influence the dielectric constant and relaxation times, potentially due to variations in steric effects and hydrogen bonding capabilities. These findings contribute to a deeper understanding of the interplay between molecular dynamics and dielectric properties in diols. The increasing Kirkwood correlation factor (g) with a longer carbon chain length in diols attributed to two possible mechanisms: enhanced intermolecular interactions and a shift in hydrogen bonding preferences.

ACKNOWLEDGMENT

The authors would like to thank the DST (Grant number: SB/S2/LOP-032/2013) for their financial support, which made this research possible. We would like to thank the School of Physical Sciences, SRTM University Nanded, for providing the infrastructure and research environment necessary to conduct this study.

REFERENCES

- [1] Mounica P., Sahana R., Ramya K., Garad N. P., Kumbharkhane A. C., & Arivazhagan G. "Self and hetero-association in Benzaldehyde/Quinoline– Formamide solutions: Time Domain Reflectometry studies". *J. Mol. Liq.* (2024) 124744.
- [2] Bokhare A. D., Garad N. P., Lokhande M. P., & Kumbharkhane A. C. "Dielectric relaxation and hydrogen bonding interactions study of aqueous D-sorbitol using time domain reflectometry". *Phys. & Chem. Liq.*, 62(1), (2024) 1-8.
- [3] Khan Z. S., Khan A., Garad N., Kumbharkhane A. C., & Lokhande M. P. "Dielectric relaxation and thermodynamic study of aqueous Glycine using time domain reflectometry technique". *Ferroelectrics*, 616(1), (2023) 80-96.
- [4] Saknure S. H., Garad N. P., Gubre A. G., Joshi Y. S., & Kumbharkhane A. C. "Dielectric relaxation studies of cellulose-water mixtures using time and frequency domain technique". *Ind. J. Pure & App. Phys.*, (2023) 27-32.
- [5] Saknure S. H., Garad N. P., Gubre A. G., Joshi Y. S., & Kumbharkhane A. C. "Molecular interactions studies of methyl cellulose-water solutions using dielectric spectroscopy". *Phys. & Chem. of Liq.*, 61(4), (2023) 229-239.
- [6] Dongre D. G., Garad N. P., & Kumbharkhane A. C. "Dielectric Study of Nitriles Using Time-Domain Reflectometry". *Braz. J. of Phys.*, 54(3), (2024) 1-9.
- [7] Dhage H. M., Bokhare A. D., Garad N. P., Lokhande M. P., & Kumbharkhane A. C. "Dielectric relaxation studies of 1-nitropropane-dimethyl sulfoxide mixtures using a Time Domain Reflectometry". *Phys. & Chem. of Liq.*, (2024)1-10.
- [8] Dongre D. G., Deshmukh A. R., Garad N. P., Gubre A. G., Saknure S. H., & Kumbharkhane A. C. "Dielectric and hydrogen bonding studies of butyronitrile with 1, 4-dioxane using a time-domain reflectometry". *Can. J. of Phy.* (2024)
- [9] Garad N.P. and Kumbharkhane A.C., "Structural and dielectric relaxation studies of 1, 4, and 1, 3-butanediol–1, 4-dioxane mixtures using TDR technique". *Ferroelectrics*, 616(1), (2023) pp.70-79.
- [10] Garad N.P., Saknure S.H., Dongre D.G. and Kumbharkhane A.C., "Dielectric behaviour of 1, 3-butanediol-1, 4-dioxane mixtures". *App. Invo. Res.*(2023).
- [11] Hanna F.F., Gestblom B. and Soliman A., "Dielectric relaxation study of alcohol/diol (s) mixtures". *J.mol. liq.*, 95(1), (2002) pp.27-40.
- [12] Garad N.P., Saknure S.H., Gubre A.G. and Kumbharkhane A.C., "Study of dielectric relaxation and hydrogen bonding interaction of 1, 4-Butanediol-1, 4-Dioxane mixture using TDR technique". *Ind. J. Pure & App. Phys.*, (2023)
- [13] GARAD N.P., SAKNURE S., DONGRE D. and Kumbharkhane A.C., "High frequency dielectric study on the hydrogen bonding interaction on 1, 5-pentanediol+ 1, 4-dioxane binary mixtures". *Can. J. of Chem.*, (2024)
- [14] Mashalkar G.V., Chalikwar P.A. and Kumbharkhane A.C., Temperature-dependent dielectric relaxation study of polyhydric alcohols (propane-1, 3 and 1, 2-diol) using a TDR technique". *Phys. & Chem. of Liq.*, 53(3), (2015) pp.307-317.
- [15] Davidson D.W., "Dielectric relaxation in liquids: II. Isomeric pentanediols". *Can. J. of Chem.*, 39(11), (1961) pp.2139-2154.

¹S Habibuddin,
¹R.N.Kambale,
¹Yugandhara S W,
¹T S Hibare,
¹Vaishali Bambole*
²A V Pansare
³S Krishnakumar

**Li doped nickel ferrite/PAni nanocomposite
as an eco-friendly electrode material for
energy storage device**



Abstract: - Recently transition metal oxides as capacitive electrodes are finding place in supercapacitor. However, low specific energy and poor electrical conductivity are main drawbacks for energy storage applications. We report, Lithium doped nickel ferrite nanoparticles (LNF) and LNF/polyaniline (LNF/PAni) in the form of a nanocomposite as a better substitute to be the electrode for supercapacitor. These nanocomposites were prepared by sol gel auto-combustion and in-situ polymerization method and characterized by XRD. The XRD pattern revealed the single phase of highly crystalline LNF nanoparticles and crystalline- amorphous nature of nanocomposite. The surface morphology is studied by FEG-SEM which shows cubic structure of LNF nanoparticles and formation of core-shell of nanocomposite. Capacitance was measured by electrochemical measurements to examine the impact of introducing PAni in ferrite nanoparticles. The specific capacitance value increased due to high conductivity of PAni.

Keywords: ferrite nanoparticles, polyaniline, nanocomposites, electrochemical, specific capacitance.

¹ *Corresponding author: Department of Physics, University of Mumbai, Vidyanagari Campus, Kalina, Santacruz (E) Mumbai 400098, India.

² Author 2 Affiliation Lab Composites Group, Mechanical Systems Engineering, Empa - Swiss Federal Laboratories for Materials Science and Technology, Überlandstrasse 129, 8600 Dübendorf, Switzerland.

³ Department of Physics, Kittel Science College, Dharwad, Karnataka -580001 India.

I. INTRODUCTION

Some of the most significant global concerns of the twenty-first century include the ever-increasing need for energy, issues with portability, and the fast-dwindling hydrocarbon fuel sources. The scientific community has been prompted by all of these problems to develop economical, environmentally responsible, and efficient alternative energy conversion and storage methods. Supercapacitors have demonstrated their capacity to store energy efficiently, providing a range of benefits including high power densities, large specific capacitance, rapid charging and discharging times, extended cycle life, and clean electrochemical energy storage. One popular option for an environmentally friendly energy storage device is the supercapacitor [1-5].

Supercapacitors are unusual energy sources that operate on the basis of electrochemical energy conversion in all other respects. Supercapacitors are available in a variety of shapes and sizes and are transparent, tiny, thin, lightweight, and flexible. For portable electronics like laptops, cell phones, MP3 players, medical equipment, video cameras, and robotic vacuum cleaners, they serve as substitute power sources [6-7].

Supercapacitors have received a lot of interest because of their high-power density, long-term cycle capabilities, and high specific capacitance (SC). Three groups of materials are commonly explored for application in supercapacitors: (i) conducting polymers, (ii) metal oxides, and (iii) activated carbons [8-11].

Metal oxides have been used as supercapacitor electrode materials for many years. MFe_2O_4 ($M = Fe, Co, Ni, Mn, Cu, Zn$) ferrites, however, have drawn a lot of attention for researchers. Their good conductivity, redox chemistry, ease of synthesis, abundance, eco-friendliness, and 3D diffusion pathways make them valuable but pure metal oxides does not give satisfying electrochemical performance. So, the plan of synthesizing hybrids of MFe_2O_4 has evolved. Out of various conducting polymers, Polyaniline is chosen over all of them due to its significantly large electrical conductivity, fairly large pseudocapacitance, quick doping/dedoping kinetic during charging-discharging and moderate cost. Polyaniline and MFe_2O_4 based binary system may exhibit better electrochemical activities [12-13].

The nickel ferrite demonstrates an inverse spinel structure with Ni^{2+} ions at octahedral sites while Fe^{3+} ions are found at the tetrahedral and octahedral sites. Therefore, Li^+ ions occupy Ni^{2+} sites because of Li (0.59 \AA) ionic radius is very similar to Ni (0.55 \AA). For the existing study, Lithium-doped nickel ferrite nanoparticles and polyaniline nanocomposite are synthesized for better electrochemical performance.

II. EXPERIMENTAL

A. The synthesis of $Ni_{0.5}Li_{0.5}Fe_2O_4$ ferrite nanoparticles

$Ni_{0.5}Li_{0.5}Fe_2O_4$ ferrite (LNF) powder was prepared using a sol-gel auto-combustion technique. The detailed procedure is as follows. Stoichiometric amounts of $Ni(NO_3)_2 \cdot 6H_2O$, $Li(NO_3)_2 \cdot 6H_2O$, and $Fe(NO_3)_3 \cdot 9H_2O$ were each dissolved in deionized water, followed by the addition of a specific quantity of lemon juice to the metal nitrate solution. These cationic solutions were then combined and stirred continuously for one hour to ensure homogeneity. Ammonium hydroxide was gradually added dropwise to adjust the pH to approximately 7.0. Subsequently, the mixed solution was heated to $90^\circ C$ with constant stirring to form a dried gel, which underwent self-propagating combustion until all the gels were fully burnt, resulting in loose precursors. Finally, $Ni_{0.5}Li_{0.5}Fe_2O_4$ crystalline powder was obtained by calcining the loose precursors at $600^\circ C$ for 4 hours [14].

B. Preparation of $Ni_{0.5}Li_{0.5}Fe_2O_4/PAni$ nanocomposite

Lithium doped nickel ferrite nanoparticles/polyaniline (LNF/PAni) nanocomposite was synthesized using an in situ polymerization method. Initially, a specified amount of LNF ferrite nanoparticles was dispersed in 70 ml of 1 M HCl solution and stirred for 90 minutes to achieve a uniform dispersion. Subsequently, 2 ml of aniline (AN) monomer was added to the ferrite solution, followed by stirring for an additional two hours. A solution of 4.98 g of ammonium peroxydisulfate (ASP) in 40 ml of 1 M HCl was then prepared. This ASP solution was gradually added to the ferrite mixture under continuous stirring for two hours [15]. The resulting green solution was left to polymerize for 12 hours at temperatures ranging from $0^\circ C$ to $5^\circ C$. The mixture was

then filtered, thoroughly washed with 1 M HCl and double-distilled water, and finally dried in a vacuum oven at 80°C for 48 hours.

III. RESULT AND DISCUSSION

3.1 Structure and Morphology

Fig. 1 shows the X-Ray diffraction pattern of LNF ferrite nanoparticles and LNF/PAni nanocomposite. PAni shows the amorphous nature in a partially crystalline state having two diffraction peak $2\theta = 20.68^\circ$ and 25.6° in nanocomposite XRD pattern [16-17]. The LNF ferrite nanoparticles and composites showed the polycrystalline nature. From Fig.1, we can see that between LNF ferrite nanoparticles and LNF/PAni composite, there is no significant difference in crystalline nature, except the intensity. The average crystallite size (D) of LNF ferrite nanoparticles has been calculated from XRD data using Scherer's equation.

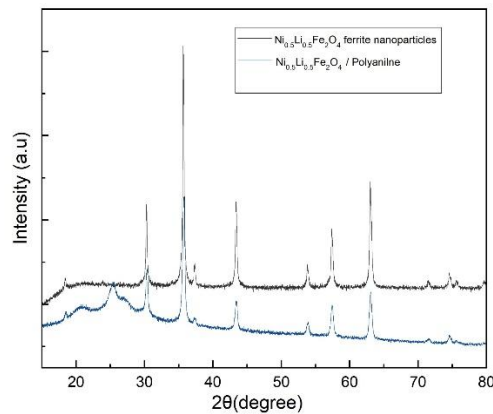


Fig. 1 XRD patterns of LNF ferrite nanoparticles and LNF/ PAni nanocomposite.

The FE-SEM images of LNF ferrite nanoparticles and the LNF/PAni nanocomposite are presented in Fig. 2 (a) and (b). In Fig.2 (a), the Lithium-doped Nickel ferrite nanoparticles exhibit a cubic structure. Fig. 2 (b) illustrates the polyaniline coating on LNF ferrite nanoparticles, where the nanoparticles are uniformly dispersed within the polymer matrix.

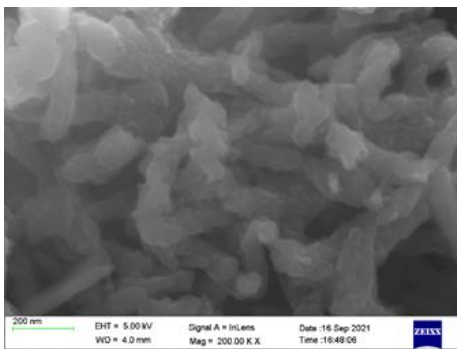
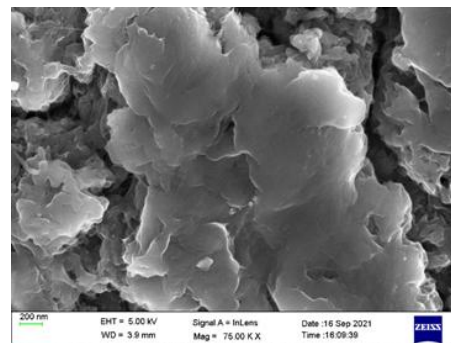


Fig. 2 (a) FE-SEM image of LNF nanoparticles



(b) FE-SEM image of LNF/PAni nanocomposite

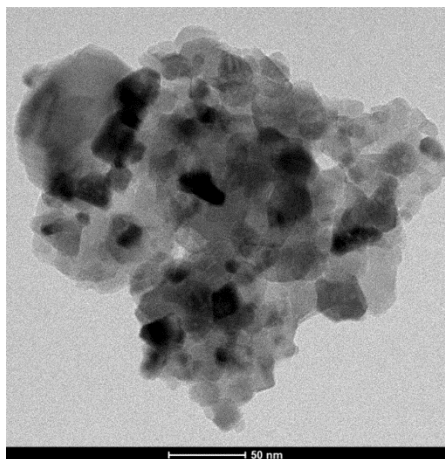


Fig. 3 (a) TEM image LNF nanoparticles

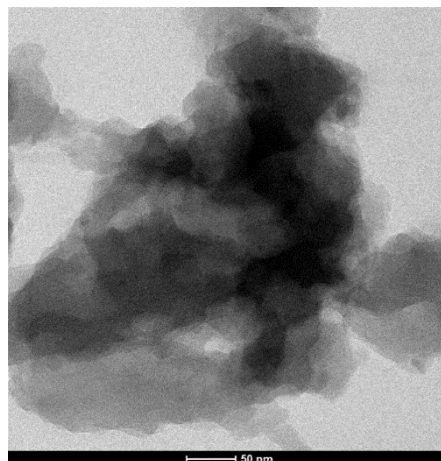


Fig. 3 (a) b) TEM image LNF/PAni Nanocomposite

The average particle size of LNF ferrite nanoparticles was determined using FEG-TEM images, yielding average particle size of 30 nm as calculated with ImageJ software. In Fig. 3 (b), the dark regions represent LNF ferrite nanoparticles, while the lighter areas correspond to amorphous polyaniline. The core of the nanocomposite consists of LNF ferrite nanoparticles enveloped by a polyaniline shell. The images clearly demonstrate that the synthesized ferrite nanoparticles are crystalline with a cubic structure and are uniformly distributed throughout the polymer matrix [18].

1. Electrochemical characterization

The electrochemical performance of the synthesized LNF and LNF/PAni electrodes was investigated at room temperature using a 2 M KOH electrolyte solution through cyclic voltammetry (CV). The CV plots of the prepared ferrite nanoparticles and nanocomposite electrodes in a three-electrode configuration at various scan rates (5 mV/s, 10 mV/s, 20 mV/s, 60 mV/s, 80 mV/s, and 100 mV/s) are presented in Fig. 4 (a) and (b). In Fig. 4 (a), pronounced oxidation/reduction peaks are observed for the LNF nanoparticles, indicating their pseudocapacitive properties related to electrochemical reactions at the electrode-electrolyte interface. The CV curves of the nanocomposites in Fig. 4 (b) show peaks attributable to the faradaic processes of both LNF and PAni components. The specific capacitance and surface area of the LNF/PAni nanocomposite are enhanced due to the improved conductivity of the composite. The inclusion of LNF in the PAni matrix results in a continuous conductive network that facilitates ion transport and redox reactions [19-23].

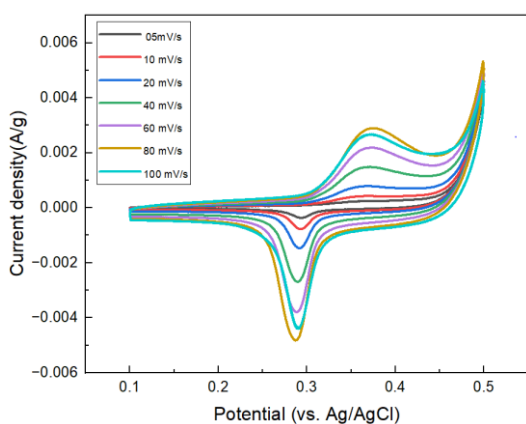


Fig. 4 C V curves of (a) NLF ferrite nanoparticles at different scan rates and potential.

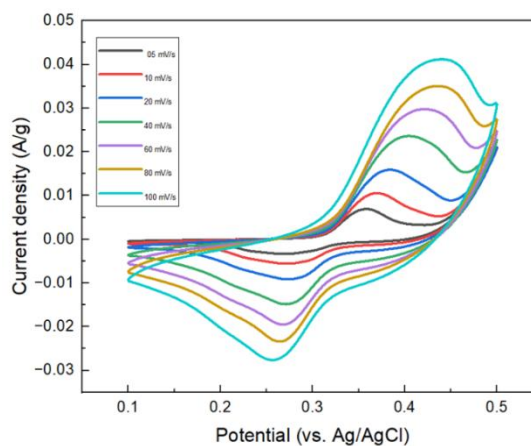


Fig. 4 C V curves of NLF/PAni nanocomposite at different scan rates and potential.

Additionally, LNF ferrite improves the electro-chemical performance of the LNF/PAni supercapacitor electrode by minimizing charge transfer resistances and enhancing the interfacial contact between LNF/PAni and electrolyte. The specific capacitance and energy density were computed using following equations,

Specific capacitance(F/g)

$$C_s = \frac{\int Idv}{v \times m \times \Delta V} \dots\dots\dots (1)$$

where, I- Integral area - Scan rate (mVs⁻¹),

m- Mass of the composites (milligram) and

ΔV- window potential (volt).

Energy density, E (Wh/kg)

$$E = \frac{0.5 \times C_s \times \Delta V^2 \times 1000}{3600} \dots\dots\dots (2)$$

The maximum specific capacitance values calculated for LNF nanoparticles and LNF/PAni nanocomposite are 51 Fg⁻¹ and 289.74 Fg⁻¹, respectively, at a scan rate of 5 mV/s. The energy density values for LNF nanoparticles and LNF/PAni nanocomposite are 0.637 Wh/kg and 14.487 Wh/kg, respectively.

IV. CONCLUSION

Lithium-doped nickel ferrite nanoparticles and Li-doped nickel ferrite/polyaniline nanocomposites were successfully synthesized using the sol-gel auto-combustion and in-situ polymerization methods. X-ray diffraction patterns confirmed the spinel cubic structure of the LNFF ferrite and the amorphous nature of polyaniline. The average particle size of the synthesized ferrite nanoparticles, determined from XRD, FE-SEM, and FE-TEM images, was approximately 30 nm. The maximum specific capacitance values for the NMF ferrite nanoparticles and LNF/PAni nanocomposite were calculated to be 17.28 Fg⁻¹ and 246 Fg⁻¹, respectively, at a scan rate of 5 mV/s. The LNF/PAni nanocomposite and LNF ferrite nanoparticles have energy densities of 5.48 Wh/kg and 0.38 Wh/kg, respectively. These findings imply that the materials that were produced are good choices for the anode electrodes of supercapacitors.

REFERENCES

- [1] Hsin-Yen Sun, Lu-Yin Lin, Ying-Yu Huang, Wei-Lun Hong, Nickel precursor-free synthesis of nickel cobalt-based ternary metal oxides for asymmetric supercapacitors, *Electrochimica Acta*, 281, (2018) 692-699.
- [2] X. Wang, Y. Fang, B. Shi, F. Huang, F. Rong, R. Que, Three-dimensional NiCo₂O₄@ NiCo₂O₄ core-shell nanocones arrays for high-performance supercapacitors, *Chem. Eng. J.* 344 (2018) 311–319.
- [3] Edmund Samuel, Ali Aldalbahi, Mohamed El-Newehy, Hany El-Hamshary, Sam S. Yoon, Nickel ferrite beehive-like nanosheets for binder-free and high-energy-storage supercapacitor electrodes, *Journal of Alloys and Compounds*, 852, (2021) 156929.
- [4] Laleh Saleh Ghadimi, Nasser Arsalani, Iraj Ahadzadeh, Abdollah Hajalilou, Ebrahim Abouzari-Lotf, Effect of synthesis route on the electrochemical performance of CoMnFeO₄ nanoparticles as a novel supercapacitor electrode material, *Applied Surface Science*, 494, (2019) 440-451.
- [5] S.M. Pawar, B.S. Pawar, P.T. Babar, A.T.A. Ahmed, H.S. Chavan, Y. Jo, S. Cho, J. Kim, B. Hou, A.I. Inamdar, Nanoporous CuCo₂O₄ nanosheets as a highly efficient bifunctional electrode for supercapacitors and water oxidation catalysis, *Appl. Surf. Sci.* 470 (2019) 360–367.

- [6] Q. Li, R. Hu, J. Qi, Y. Sui, Y. He, Q. Meng, F. Wei, Y. Ren, Y. Zhao, Facile synthesis of mesoporous CuCo_2O_4 nanorods@ MnO_2 with core-shell structure grown on RGO for high-performance supercapacitor, *Mater. Lett.* 249 (2019) 151–154.
- [7] K. Wang, X. Dong, C. Zhao, X. Qian, Y. Xu, Facile synthesis of $\text{Cu}_2\text{O}/\text{CuO}/\text{RGO}$ nanocomposite and its superior cyclability in supercapacitor, *Electrochim. Acta* 152 (2015) 433–442.
- [8] A.K. Rai, T.V. Thi, J. Gim, J. Kim, Combustion synthesis of $\text{MgFe}_2\text{O}_4/\text{graphene}$ nanocomposite as a high-performance negative electrode for lithium ion batteries, *Mater. Charact.* 95 (2014) 259–265.
- [9] Vidyadevi A. Jundale, Dilip A. Patil, Ganesh Y. Chorage, Abhijit A. Yadav, Mesoporous cobalt ferrite thin film for supercapacitor applications, *Materials Today: Proceedings*, 43, (2021) 2711-2715.
- [10] J. Yan, Y. Huang, C. Chen, X. Liu, H. Liu, The 3D CoNi alloy particles embedded Ndoped porous carbon foam for high-performance microwave absorber, *Carbon* 152 (2019) 545–555.
- [11] G. Wang, Q. Tang, H. Bao, X. Li, G. Wang, Synthesis of hierarchical sulfonated graphene/ MnO_2 /polyaniline ternary composite and its improved electrochemical performance, *J. Power Sources* 241 (2013) 231–238.
- [12] F. Miao, C. Shao, X. Li, K. Wang, N. Lu, Y. Liu, Electrospun carbon nanofibers/carbon nanotubes/polyaniline ternary composites with enhanced electrochemical performance for flexible solid-state supercapacitors, *ACS Sustain. Chem. Eng.* 4 (2016) 1689–1696.
- [13] Shaoyun Chen, Huan Cheng, Du Tian, Qi Li, Min Zhong, Jian Chen, Chenglong Hu, and Hongbing Ji, Controllable Synthesis, Core-Shell Nanostructures, and Supercapacitor Performance of Highly Uniform Polypyrrole/Polyaniline Nanospheres, *ACS Applied Energy Materials* (2021) 4, 3701-3711
- [14] Ravindra N. Kambale, Krishnakumar M. Sagar, Sunil M. Patange, Sagar E. Shirsath, K. G. Suresh, and Vaishali A. Bambole, Excellent Microwave Absorbing Properties of Nd^{3+} -Doped Ni–Zn Ferrite/PANI Nanocomposite for Ku Band, *Phys. Status Solidi (a)* applications and materials science, Wiley-VCH GmbH (2022), 2100505-1-2100505- 14. H index 113.
- [15] Ravindra N Kambale, Sunil M Patange, RA Pawar, Sagar E Shirsath, KG Suresh, Vaishali A Bambole, Magnetically recoverable $\text{CoFe}_{1.9}\text{Gd}_{0.1}\text{O}_4$ ferrite/polyaniline nanocomposite synthesized via green approach for radar band absorption, *Ceramics International* 47, 20 (2021) 28240-28251.
- [16] Shubhangi B. Bandgar, Madagonda M. Vadiyar, Yong-Chien Ling, Jia-Yaw Chang, Sung-Hwan Han, Anil V. Ghule, and Sanjay S. Kolekar, Metal Precursor Dependent Synthesis of NiFe_2O_4 Thin Films for High-Performance Flexible Symmetric Supercapacitor, *ACS Applied Energy Materials* (2018) 1, 638-648
- [17] Ravindra N. Kambale, Akhilesh Kumar Patel, K. G. Suresh, Sandeep Kumar, Vaishali Bambole, Green synthesis of rare-earth doped spinel ferrite and ferrite/PANI nanocomposite to microwave absorption in radar frequency range, *International Journal of Advance and Innovative Research.* 6, 1 (2019) 1-7.
- [18] Ravindra N. Kambale, Akhilesh Kumar Patel, Sandeep Kumar, K G Suresh, Vaishali Bambole, Green Synthesis, characterization and Microwave absorbing properties of Ni-Cu ferrite nanoparticles, *Research Journey International Multidisciplinary E-Research Journal*, V 168 (B) (2019) 69-72.
- [19] Amin Goljanian Tabrizi, Nasser Aرسالani, Zhwan Naghshbandi, Laleh Saleh Ghadimi, Abdolkhaled Mohammadi, Growth of polyaniline on $\text{rGO-Co}_3\text{S}_4$ nanocomposite for high-performance supercapacitor energy storage, *International Journal of Hydrogen Energy*, 43, Issue 27, (2018) 12200-12210.
- [20] Min Fu, Wei Chen, Xixi Zhu, Qingyun Liu, One-step preparation of one dimensional nickel ferrites/graphene composites for supercapacitor electrode with excellent cycling stability, *Journal of Power Sources*, 396, (2018) 41-48.
- [21] Tapas Das, Bhawna Verma, Synthesis of polymer composite based on polyaniline-acetylene black-copper ferrite for supercapacitor electrodes, *Polymer*, Volume 168, (2019) 61-69.
- [22] K. Hareesh, Sachin R. Rondiya, Nelson Y. Dzade, S.D. Dhole, Jim Williams, Samarin Sergey, Polymer-wrapped reduced graphene oxide/nickel cobalt ferrite nanocomposites as tertiary hybrid supercapacitors: insights from experiment and simulation, *Journal of Science: Advanced Materials and Devices*, 6, (2021) 291-301.

- [23] Anjali Gupta, Silki Sardana, Jasvir Dalal, Sushma Lather, Anup S. Maan, Rahul Tripathi, Rajesh Punia, Kuldeep Singh, and Anil Ohlan, Nanostructured Polyaniline/Graphene/Fe₂O₃ Composites Hydrogel as a High-Performance Flexible Supercapacitor Electrode Material, *ACS Applied Energy Materials* (2020) 3, 6434-6446.

© 2024. This work is published under
[https://creativecommons.org/licenses/by/4.0/legalcode\(the“License”\)](https://creativecommons.org/licenses/by/4.0/legalcode(the“License”)).
Notwithstanding the ProQuest Terms and Conditions, you may use this
content in accordance with the terms of the License.

¹Mr. C. R.
Chaudhari

²Dr. G. K. Reddy

**Analytical approach of
Communication between RFID
technology and PC**



Abstract: - The Internet is undergoing significant change and evolution. The Internet now facilitates human-to-human contact. The future need for the internet The Internet of Things (IoT) is noble machine-to-machine contact, improving system efficiency and quality. The Internet of Things is fast becoming a key component of wireless communication, with applications including home automation, healthcare, and industrial process management. The number of IoT devices is likely to grow dramatically in the decades to come. This paper describes the generic design of the Internet of Things which communicates between radio frequency identification technique (RFID) and IoT. It gives a larger idea of the personal computer employed for communication of IoT and Wireless Transceiver medium. development of intelligent systems. There are a lot radio IOT technologies These devices facilitate intelligent interaction between things. This technology can be used for a wide range of IoT applications. IoT applications are present in numerous aspects of our daily lives. Furthermore, important issues in the IOT industry are explored.

Keywords: Radio Frequency Identification (RFID), Near Field, M2M, V2V, Arduino, Internet of Things, MIMO, Visual Studio

¹ Mr. C. R. Chaudhari, Research Scholar, Department of Electronics, Mahatma Fule Arts, Commerce & Sitaramji Science Mahavidyalaya, Warud

² Dr. G. K. Reddy, Associate Professor, Department of Electronics, Mahatma Fule Arts, Commerce & Sitaramji Science Mahavidyalaya, Warud

I. INTRODUCTION

We have recently increased our emphasis on IoT due to the requirement for widespread connection in enhanced wireless communication. Mobile devices, Radio Frequency Identification (RFID), sensors, and Near Field Communication (NFC) have all seen significant progress in the past decade. These things interact to exchange information. IoT turns conventional tools into smart devices by integrating them with new technologies such as multiple access strategies, sensor networks, embedded devices, protocols, and computer software. IoT enables these devices to communicate with one another and with servers without requiring human involvement. Initially, radio frequency was considered crucial for IoT. However, today, numerous technologies, such as NFC, Machine to Machine Communication and Vehicular to Vehicular Communication have been developed to create smart IoT systems. IoT significantly impacts smart cities and industrial, medical, and commercial areas, making life easier and more comfortable as more devices connect to the internet through IoT applications. Planning an RFID network is crucial for establishing a large RFID system. The K-coverage-based deployment of RFID readers is essential for ensuring efficient transmission. The Plant Growth Simulation Algorithm is used to guarantee k-coverage for RFID readers.

The RFID scheme for channel identification instead of the Received Signal Strength Indication (RSSI) scheme. The RFID scheme is employed for identification purposes, whereas the RSSI scheme, which is based on the signal strength of a node, is often used in wireless communication networks for channel selection. RSSI represents the signal strength of the received radio frequency signal and is frequently used in wireless protocols to select channels. A clustering RFID system is typically focused on large-scale RFID networks. When a large number of nodes are involved in the network, existing tracking algorithms may not guarantee network efficiency. IoT connectivity techniques are classified based on coverage area: short-range techniques include Bluetooth, ZigBee, Wi-Fi, and Optical Wireless Communication (OWC), while long-range techniques cover wider areas, mainly outdoors, for specific applications such as unmanned aerial vehicles and environmental monitoring. This article primarily focuses on the general IoT architecture, various conventional and emerging network interface technologies, and addresses key challenges in designing innovative IoT applications

II. LITERATURE REVIEW

This paper advocates for using low-power wide area (LPWA) technologies as the backbone for Internet of Things (IoT) applications due to their wide coverage, long battery life, and low data rates. It reviews current trends, services, and challenges in LPWA technology, discusses industrial implementation models, and emphasizes the need for integrating different LPWA technologies. It also analyzes market opportunities, reviews recent research efforts to improve LPWA networks, and categorizes these efforts to aid researchers. Lastly, it identifies challenges and suggests future research directions. Bluetooth Low Energy (BLE) has grown significantly, but its original star topology design limits network coverage and lacks end-to-end path diversity. Competing technologies with mesh networks address these issues. To enable BLE mesh networks, academia, industry, and standards organizations have been developing solutions. However, there is no comprehensive overview in the literature. This paper offers a detailed survey of BLE mesh networking, starting with a taxonomy of solutions, then reviewing various approaches that leverage existing BLE functionality. It identifies key aspects of these solutions, discusses their advantages and disadvantages, and highlights open issues in the field. This letter explores the potential of blockchain in wireless IoT ecosystems, focusing on its ability to establish trust and consensus without central authority. It investigates the security performance of wireless blockchain networks using the RAFT consensus mechanism under malicious jamming conditions. By modelling blockchain transactions as a wireless network with uplink and downlink transmissions and assuming follower nodes' positions as a Poisson Point Process (PPP) with a designated leader, the study derives and validates the probability of

successful transactions through extensive simulations. The findings provide analytical guidance for the practical deployment of wireless blockchain networks. This letter investigates the potential of blockchain for wireless IoT ecosystems, focusing on trust and consensus without central authority. It examines the security of RAFT-based wireless blockchain networks under malicious jamming by modelling transactions as a wireless network with Poisson Point Process (PPP) positioned follower nodes and a designated leader. The study derives and validates the probability of successful transactions through simulations, providing guidance for deploying wireless blockchain networks. This review paper discusses Non-Orthogonal Multiple Access (NOMA) as a promising technique for enhancing bandwidth efficiency in future wireless cellular systems compared to conventional methods like orthogonal multiple access. NOMA offers better spectral efficiency and supports larger connectivity, especially in fading environments. Recently proposed by the Third Generation Partnership Project (3GPP) for 4G (LTE-A), NOMA aims to address the needs of 5G, advanced multimedia applications, and the Internet of Things by supporting massive heterogeneous data traffic. It provides a detailed overview of various NOMA techniques and the latest advancements in NOMA principles, including the power domain and its variants.

III. SENSING AND CONTROL TECHNIQUES

In any application, sensors and controller play a crucial role in establishing connections between network technologies and physical objects.

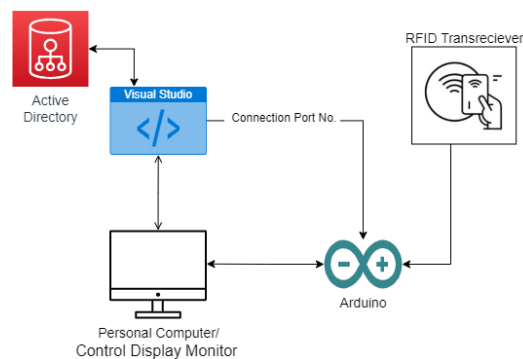


Figure 1 Block Diagram of Connectivity between Sensor and Actuator

- *Sensor – RFID -*

RFID is a vital sensing technology that uses radio waves for transmission and object identification. Its main components include a tag, a reader, and middleware. The reader transmits radio frequency signals through its antenna, and the tag gains energy from these waves to communicate with the system. Wireless Sensor Networks (WSNs) are employed in industrial environments, integrating embedded computing, sensors, and information processing techniques. WSNs collaboratively monitor, sense, and collect real-time information about various objects within the system. They offer flexibility, self-organization, lower costs, and intelligent processing capabilities.

- *Controller – Display , Database and Actuators -*

In critical applications such as gate controlling and water dividing, information control is paramount. Information and communication technology, combined with control techniques, is used in many internet applications.

1. *Network Interconnection Technologies -*

There are various wireless devices in future applications necessitating the development of advanced technologies to support massive connectivity. This section discusses existing wireless communication technologies that support extensive connectivity. These technologies are categorized based on coverage range into short-range and long-range IoT technologies. The dominant short-range technologies include Wi-Fi, Bluetooth, ZigBee, and Optical Wireless

Communication (OWC) technologies. This paper primarily focuses on short-range IoT technology and its applications. These technologies are designed to support wireless connectivity among devices within a small coverage area and are commonly used for indoor applications such as buildings, industries, or technical plants to meet connectivity requirements. The goal is to identify a specific IoT technology that can be integrated with NOMA to control particular applications. In this paper the Port of the Device is used as the mediator between the Arduino and the monitoring & controlling unit. The Port No. gets exchanged from Arduino to the Visual Studio server and the operation of the connectivity gets done without the interruption of any WIFI or internet within a network.

IV. THE KEY BENEFITS OF THIS COMMUNICATION SETUP INCLUDE:

- A. Real-Time Data Transfer : Immediate feedback from sensors and actuators connected to the Arduino can be processed and visualized in Visual Studio, facilitating dynamic interaction and control.
- B. Enhanced Debugging : Debugging Arduino code is simplified by utilizing Visual Studio's powerful debugging tools, enabling developers to diagnose issues more effectively.
- C. User Interface Development : Visual Studio's comprehensive design capabilities allow for the creation of sophisticated graphical user interfaces (GUIs) to control and monitor Arduino projects, making the systems more user-friendly and accessible.
- D. Data Logging and Analysis : Collected data from Arduino sensors can be logged and analysed within Visual Studio, supporting complex data processing and decision-making tasks.

By following the steps user can effectively bridge the gap between Arduino hardware and Visual Studio software, unlocking a wide range of possibilities for innovative project development. As technology continues to evolve, this method will remain a valuable tool for creating integrated systems in the field of Internet of Things (IoT) that leverage the strengths of both platforms.

V. CONCLUSION :

In the given research paper the communication between Arduino and Visual Studio through port connections offers a robust and efficient method for integrating Sensors and actuator together. By leveraging serial communication, user can create powerful and interactive systems that combine the physical capabilities of Arduino or any microcontroller with the extensive features of Visual Studio.

Throughout this exploration, we have demonstrated how to establish a serial connection between Arduino and Visual Studio, enabling seamless data exchange. This connection allows for real-time monitoring and control of Arduino-based projects directly from a Visual Studio application, enhancing both development and debugging processes.

V. REFERENCE :

- [1] Q. M. Qadir, T. A. Rashid, N. K. Al-Salihi, B. Ismael, A. A. Kist, and Z. Zhang, "Low power wide area networks: A survey of enabling technologies, applications and interoperability needs," *IEEE Access*, vol. 6, pp. 77454–77473, 2018
- [2] S. Darroudi and C. Gomez, "Bluetooth low energy mesh networks: A survey," *Sensors*, vol. 17, no. 7, p. 1467, 2017
- [3] H. Xu, L. Zhang, Y. Liu and B. Cao , "RAFT based wireless blockchain networks in the presence of malicious jamming" *IEEE Wireless Commun. Lett.*9, 2020, 817–821.

- [4] A.Imran, A. Zoha, L. Zhang, A. Qammer, “Grand Challenges in IoT and Sensor Networks”, *Frontiers in Communications and Networks*, vol1, December 2020.
- [5] Kokane, G. Nijhawan, S. Vashist, ‘Evaluation of Non-Orthogonal Techniques for Advance Wireless System’ in ‘*International Journal of Recent Technology and Engineering (IJRTE)*’, ISSN: 2277-3878 (Online), Volume-8 Issue-2, July 2019. Page No.: 1849-1854.

¹Mr. A. G. Kshirsagar²Dr. G. D. Agrahari³Dr. D. S. Dhote

PLC-Based Induction Motor Operations



Abstract: - Automation is the field in which controlling a particular task or process is done with the help of electronic and electrical devices without human assistance or with less human aid and replaced by manual control operations. As far as the various industrial applications are concerned, the different operations or processes with induction motors have one of the important tasks for the smooth conduction of the process. The paper includes detailed information regarding PLC-based control and power wiring connections to the motor to run in star delta connections, connections to operate the motor in forward and reverse directions, interlocking of motors, sequential operations of motors, operation based on conditions, further, it includes the designing of ladder logic programming to run the motor as per requirement of above operations.

Keywords: PLC, Hardware components- relay, Contactors, Push buttons, etc., Ladder diagram, System design process.

I. INTRODUCTION

A PLC is a computer-based controller used to control the processes or operations of the designed system of a particular application. The simplest operation to complex operation is to be controlled with the help of PLC. The PLC-based operations provide monitoring and controlling of the process as per conditions so that hazardous conditions occurring in a plant can be avoided to make a safe environment for processes and machinery used. The various advantages of induction motors make them suitable for industrial automation. It is used to drive fans, compressors, pumps, conveyors, elevators, cranes, etc. as per application need. Gas industries, oil industries, manufacturing plants, home appliances, power distribution, and refining plants are some examples where the controlling operations of induction motors are needed.

As per the process or operation conditions, one has to design ladder logic to control various functions. The paper covers some of the controlling functions of induction motors that are generally used. The understanding of PLC-based control and power wiring to run the motors as per the conditions and designing of the ladder logic program is an attempt at paper writing.

II. PLC BASED AUTOMATION

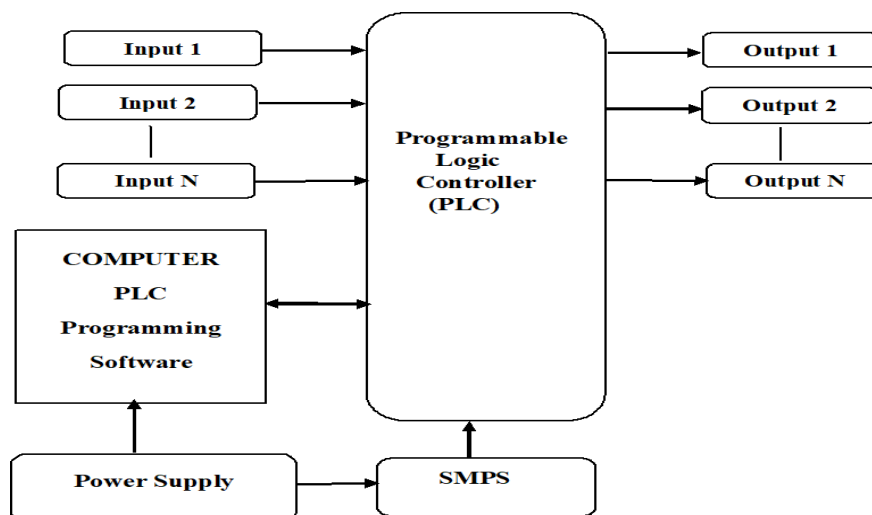


Fig 1: General Block Diagram

¹ *Department of Electronics, Shri Brijlal Biyani Science College, Amravati

² Department of Electronics, Shri Brijlal Biyani Science College, Amravati

³ Department of Electronics, Shri Brijlal Biyani Science College, Amravati

SYSTEM BLOCKS

Inputs – A mechanical device or sensors used to give a signal to a PLC to control a designed electrical circuit. There are two types of inputs i.e. analog and digital.

Programmable Logic Controller – A PLC is a computer-based controller that the industry uses to control the devices or processes according to the program of a particular operation or process. A PLC has three basic units i.e. power supply, processor, and input and output.

Outputs – There are two types of outputs i.e. analog and digital. To ON and OFF the devices or processes, the digital outputs are used. In the case of analog output, the continuous signal from PLC is fed to the field devices.

Computer and Programming Software – Programming software is required to program a PLC as per applications or the process requirement. The selection of particular programming software depends on the PLC selection.

Power Supply – The power supply Provides a 230 V AC voltage to the computer and SMPS.

SMPS – The SMPS provides a 24 V DC voltage to the PLC.

III. SYSTEM DESIGN PROCESS

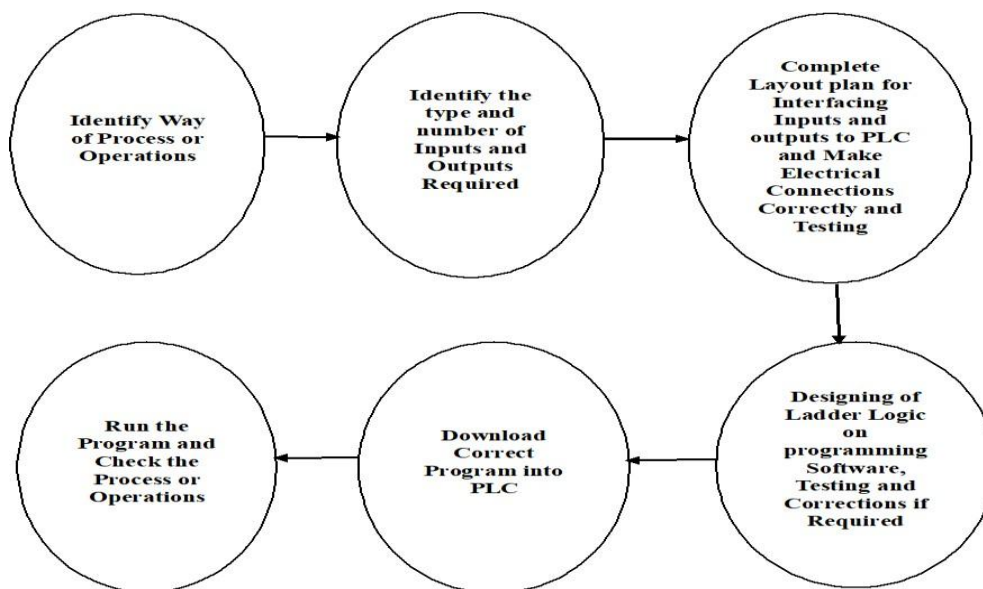


Fig 2: Blocks of System Design

IV. EXPERIMENTAL WORK

As per the need of various industrial applications, the operations or processes with induction motors have one of the important tasks to run the process smoothly. To run the motor as per the condition of the process or operations, the proper control and power wiring of the total system and correct ladder logic programming have equal importance.

- (1) The various operations included in the experimental part are as follows.
 - PLC-based control and power wiring to run the motor in star delta connections.
 - Electrical connections to operate the motor in forward and reverse direction.
 - Interlocking Operations of motors.
 - Sequential operations of motors,
 - Operation based on conditions.
- (2) Ladder logic design to run the process or operations.
- (3) Testing of ladder logic of designed process on the simulator. Make changes if required.
- (4) Verify the project
- (5) Download the correct program into PLC
- (6) Run the program

A. General Block Diagram

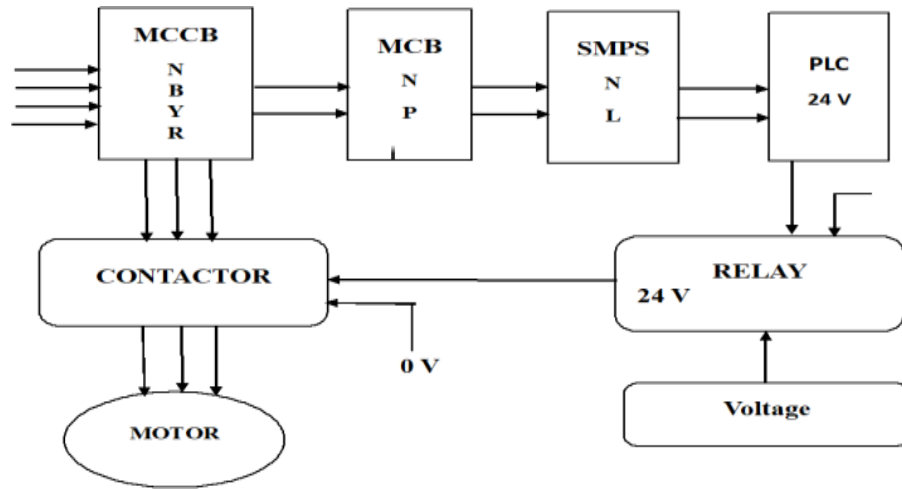


Fig 3: General Block Diagram – Wiring Connections

B. Star Delta Operation

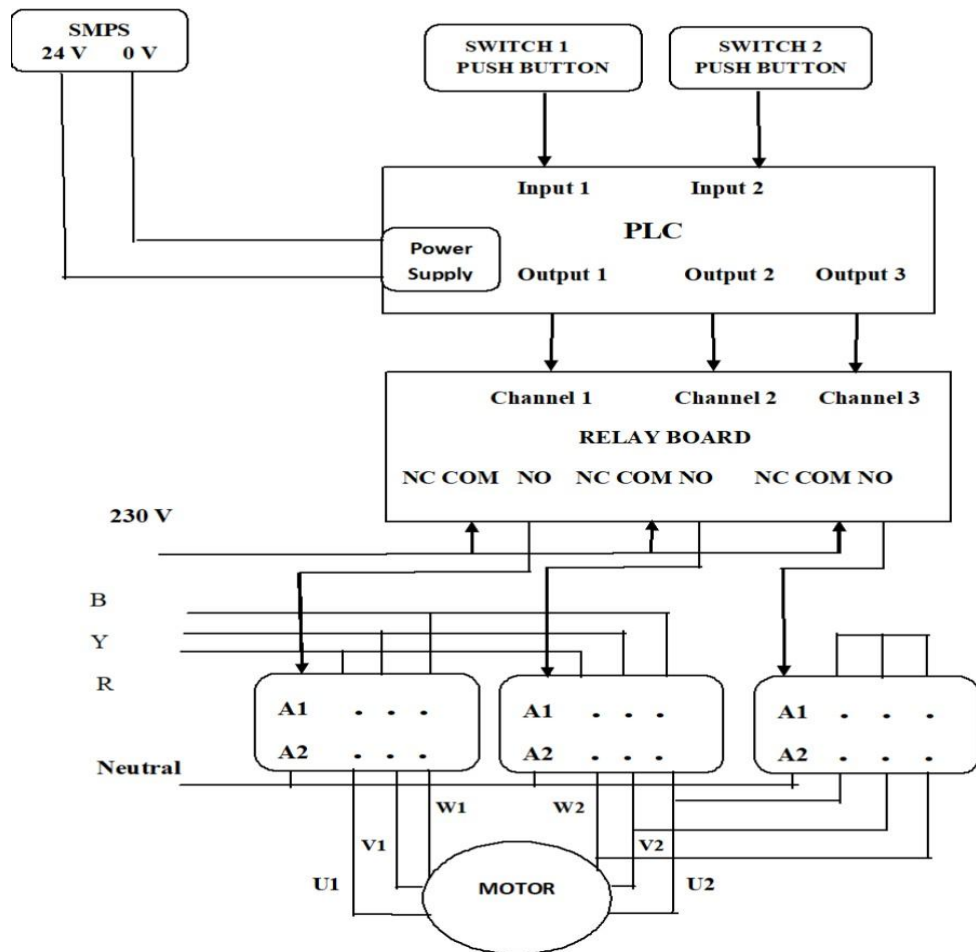
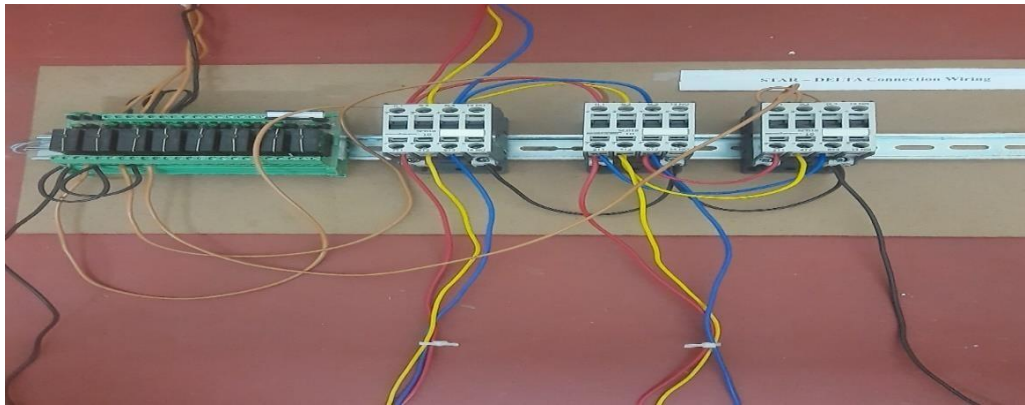
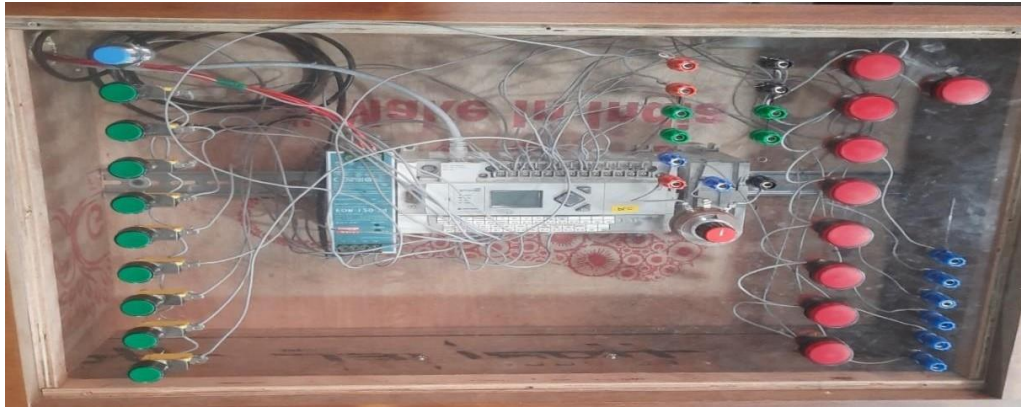
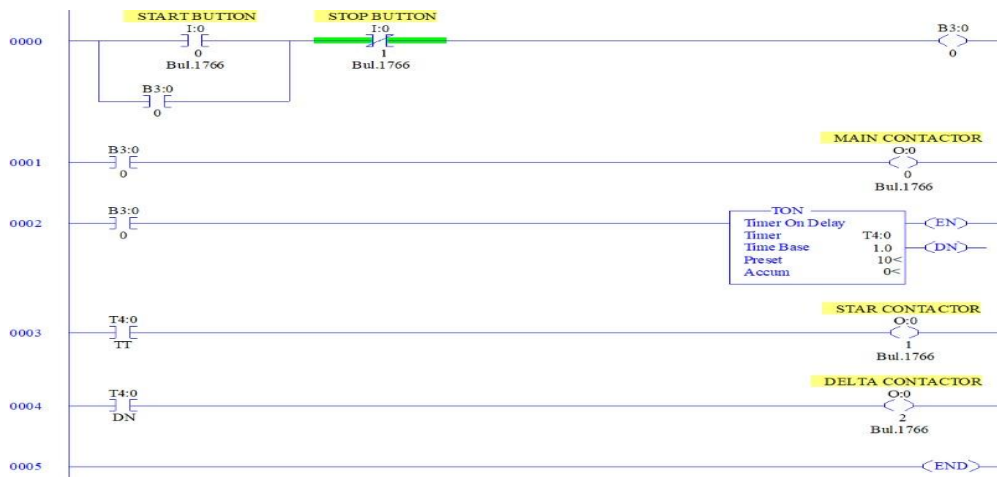
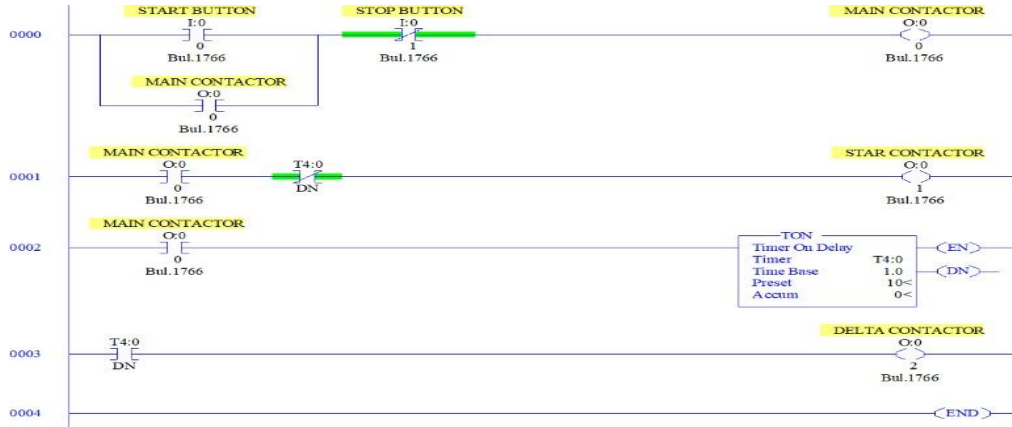
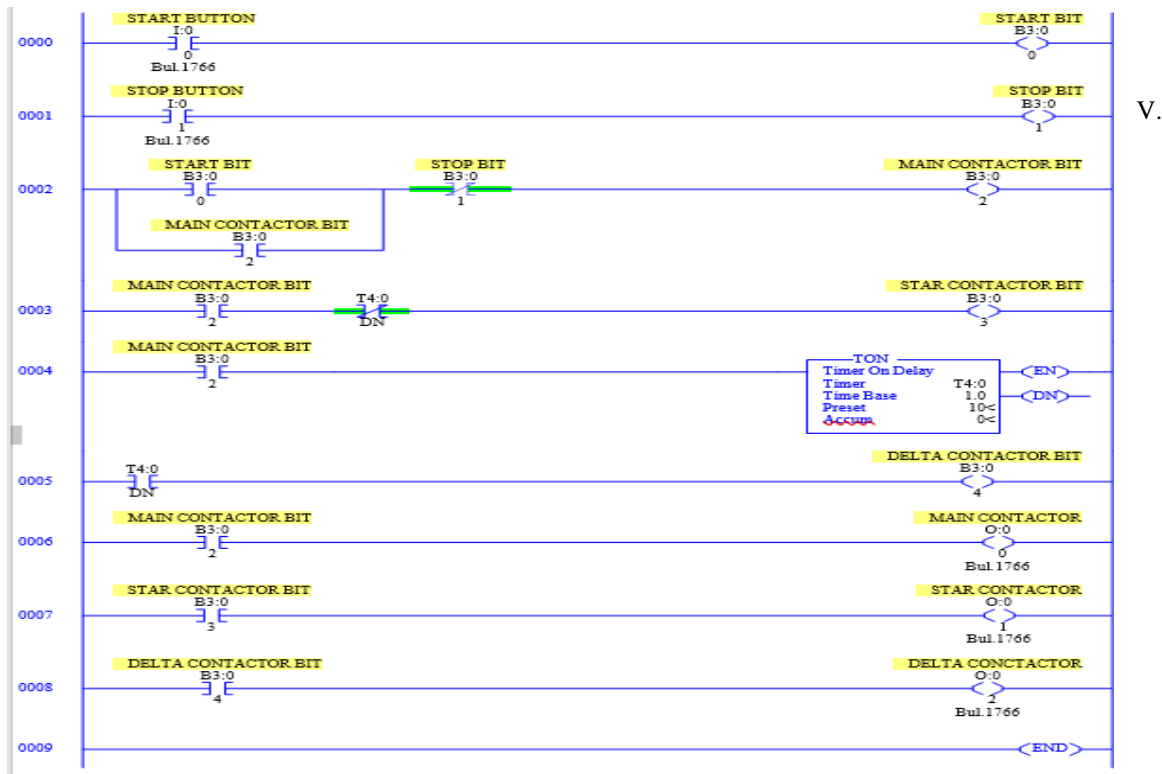


Fig 4: Star Delta Connections – Power and Control Wiring



VI. LADDER PROGRAM





(C) Direction Control Operation

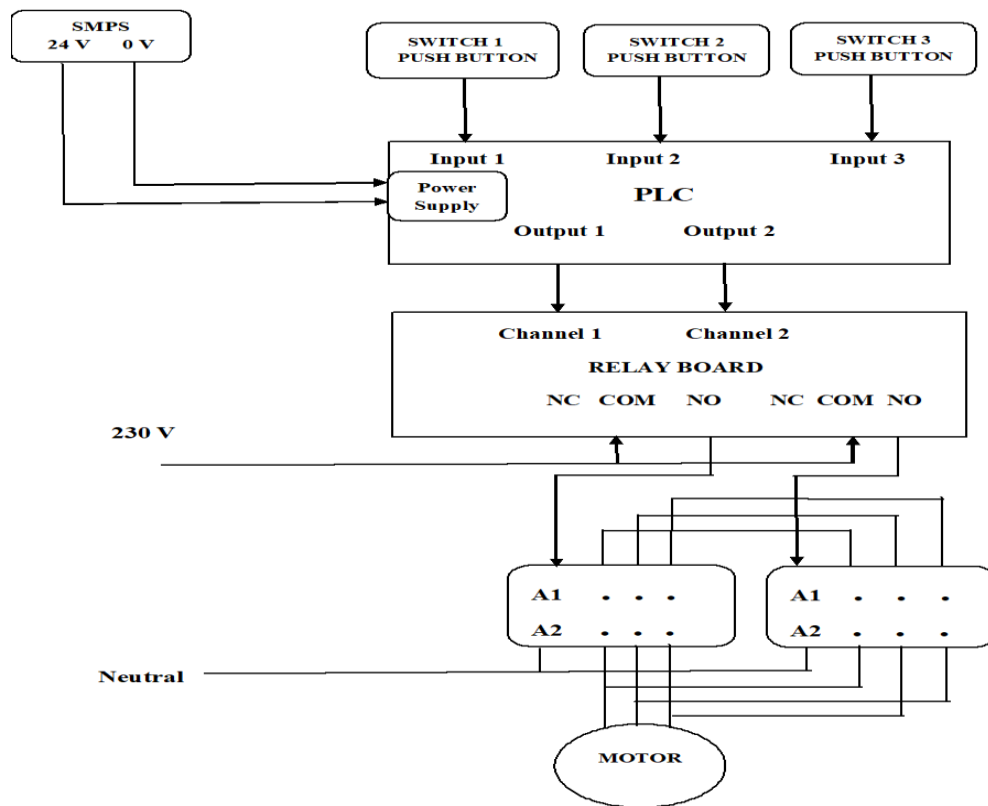
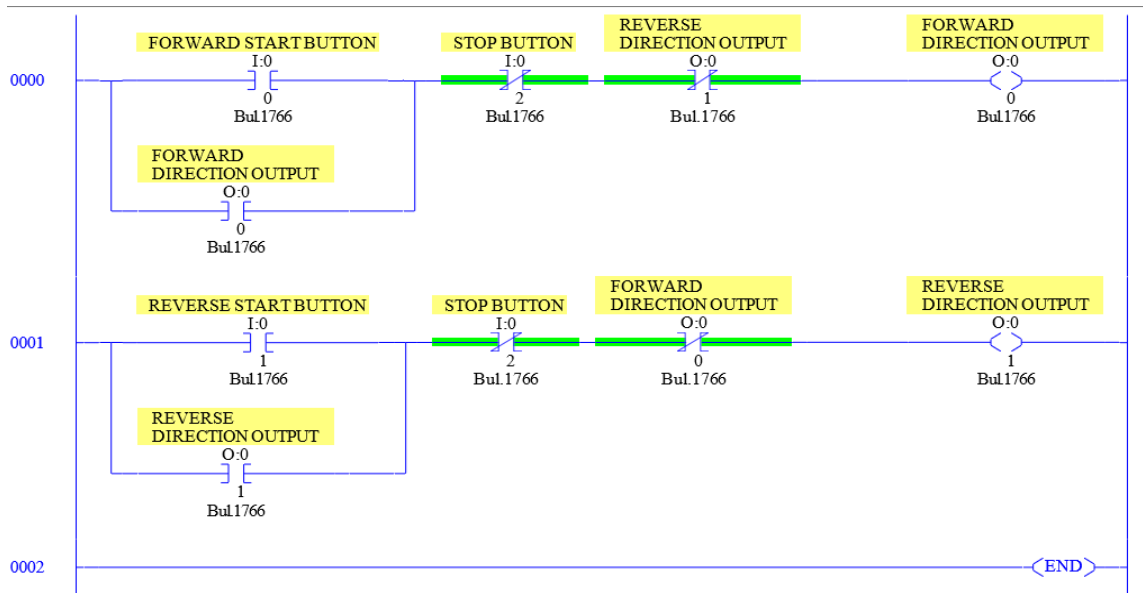
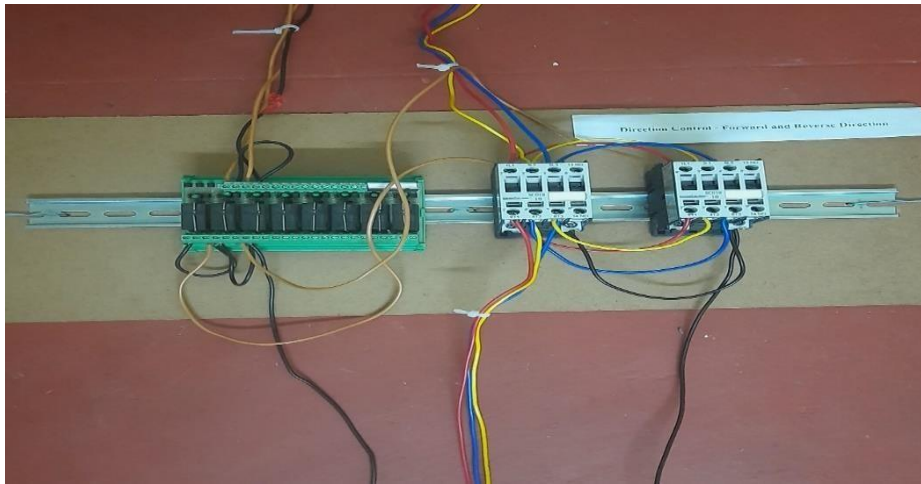
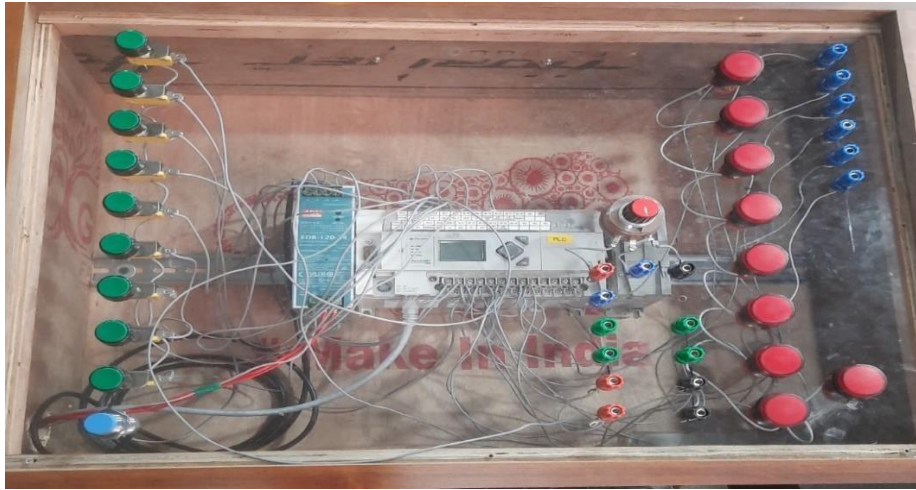
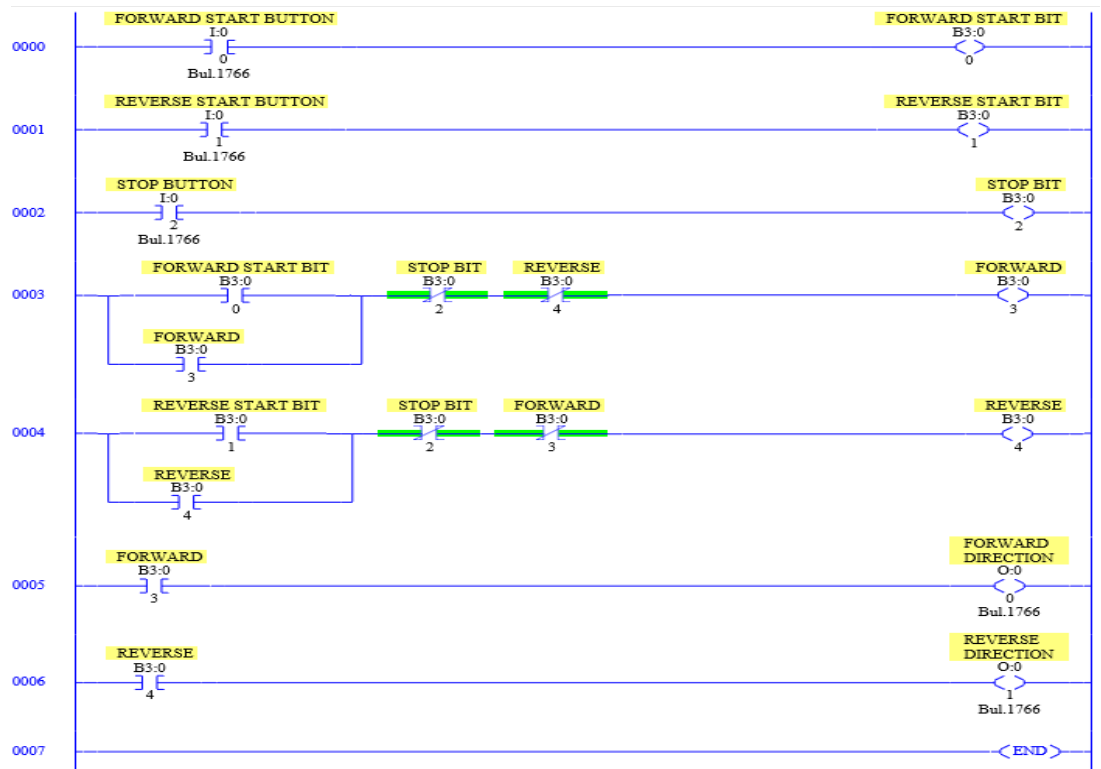


Fig 5: Forward and Reverse Direction Control





(D) Single Phase Operation

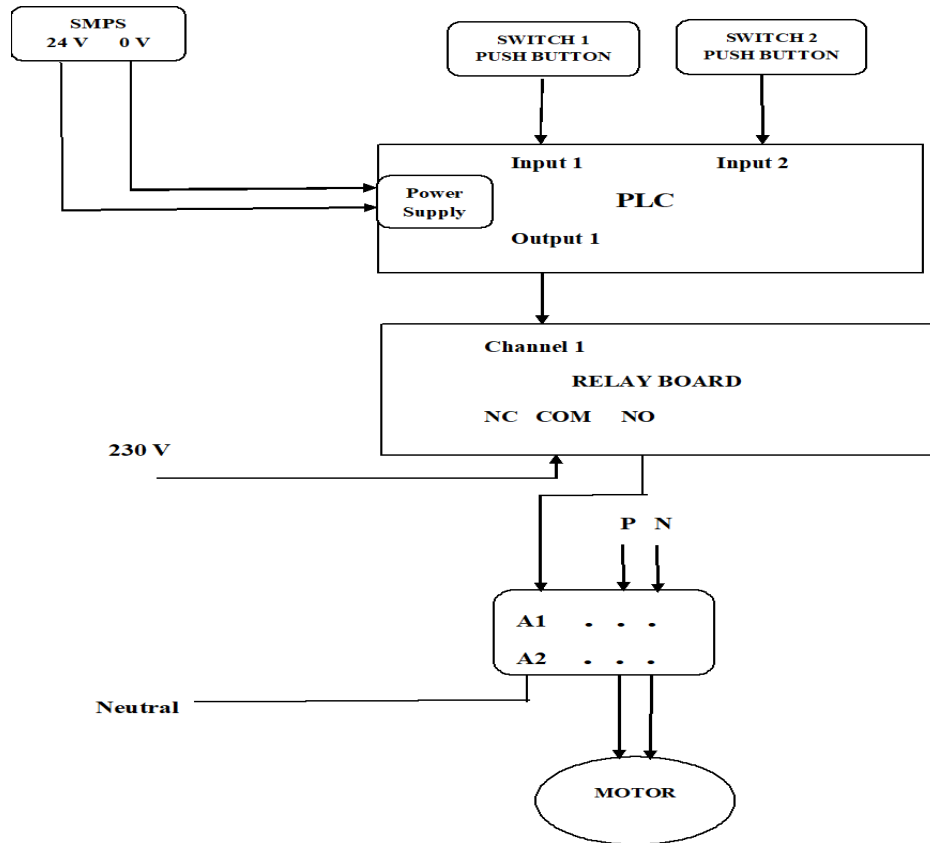
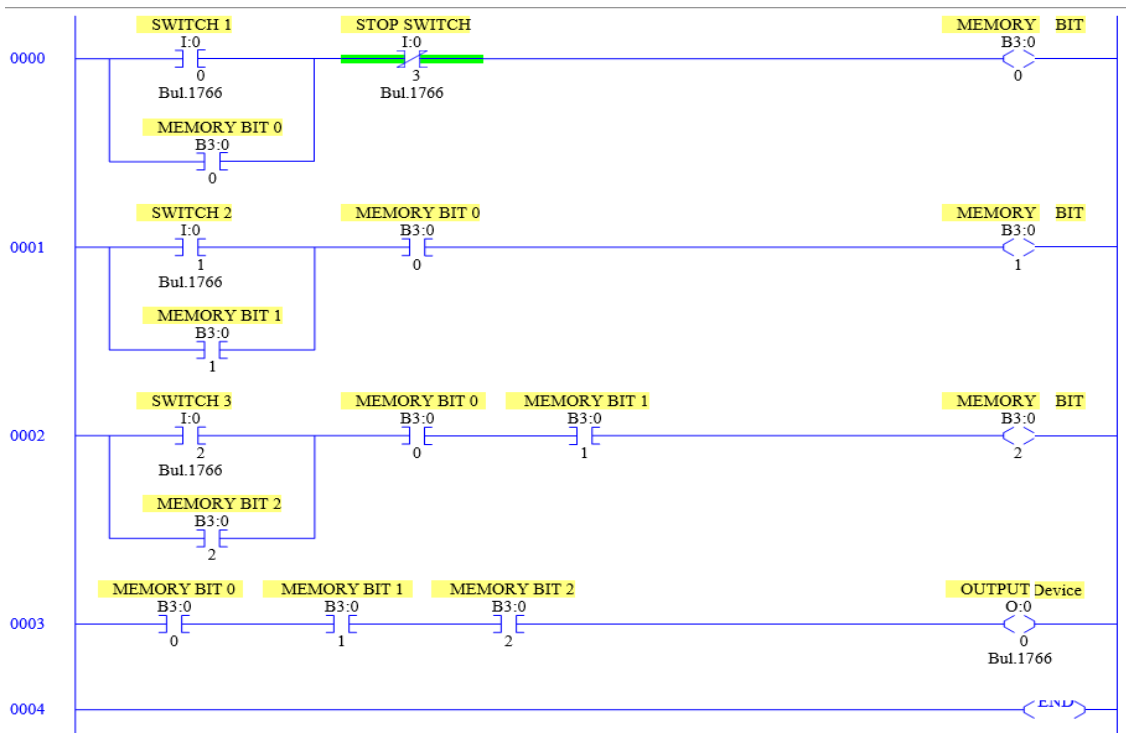
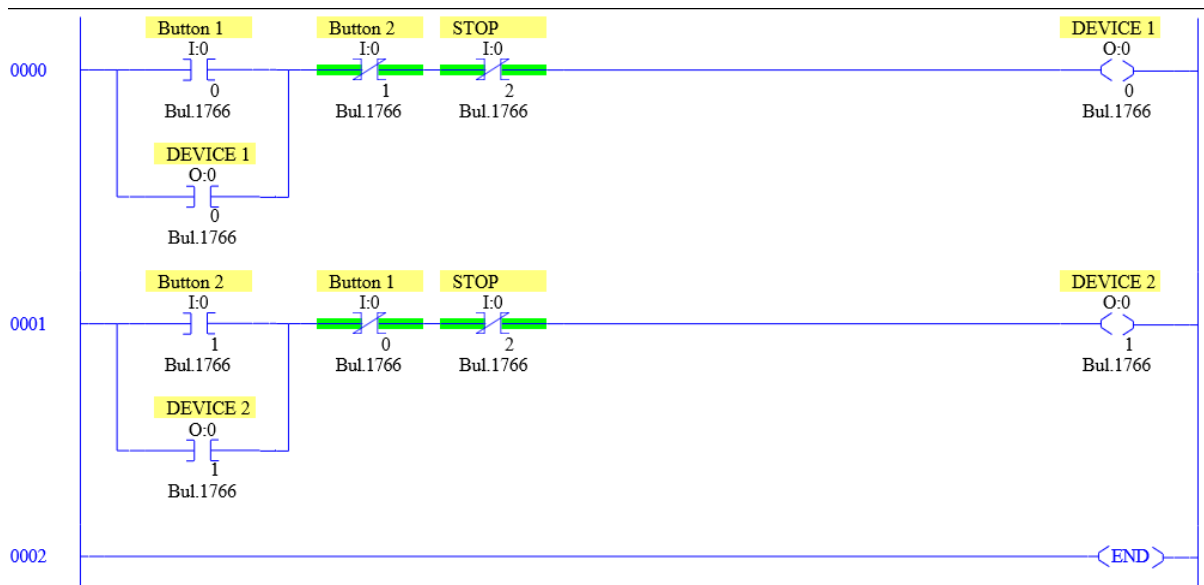


Fig 6: Single Phase – Connection Wiring

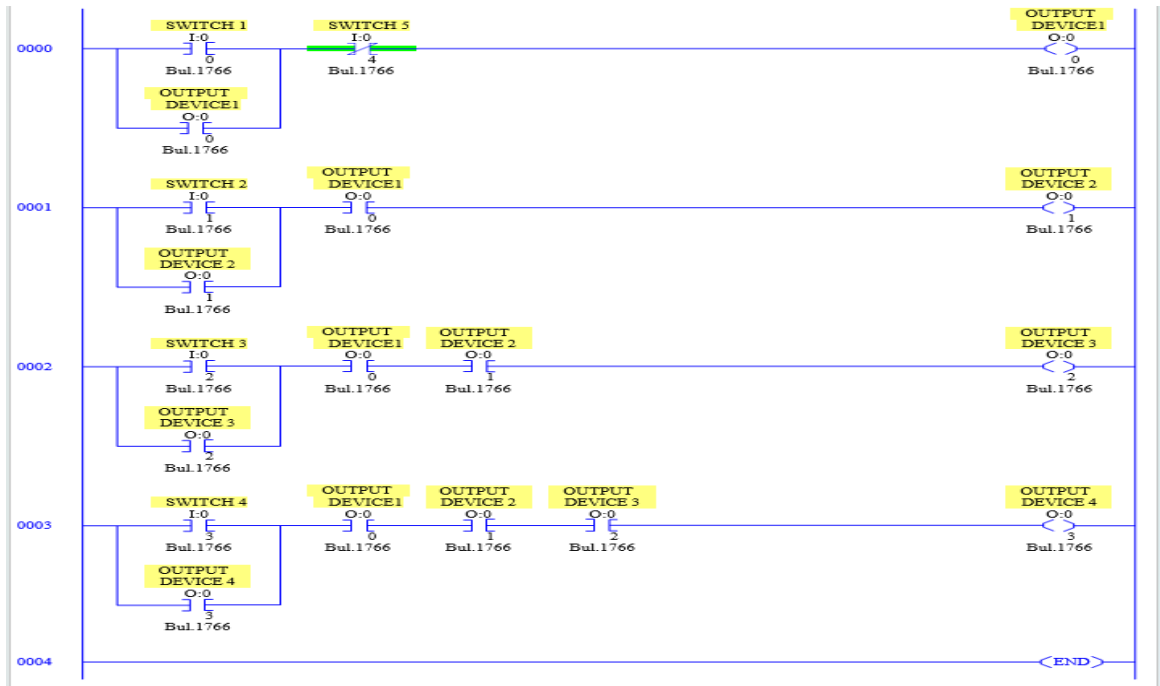
(E) Switches Priority Based Operation



(F) Interlocking Operations



(G) Sequential Start Operation

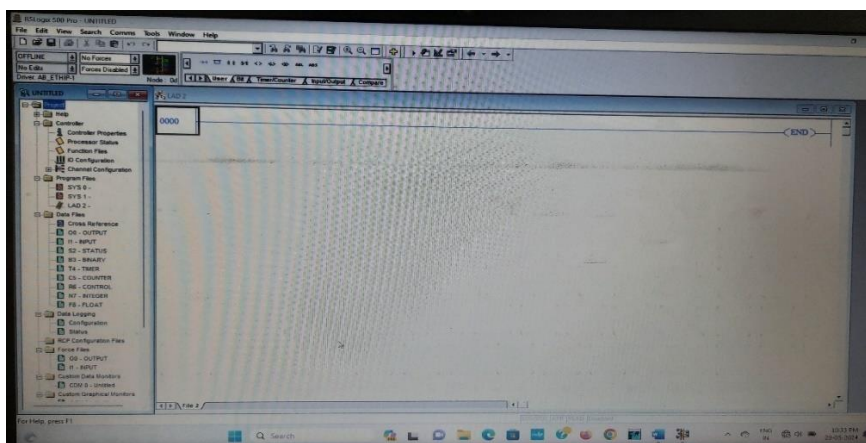


(H) Allen Bradley - MicroLogix 1400 PLC Panel

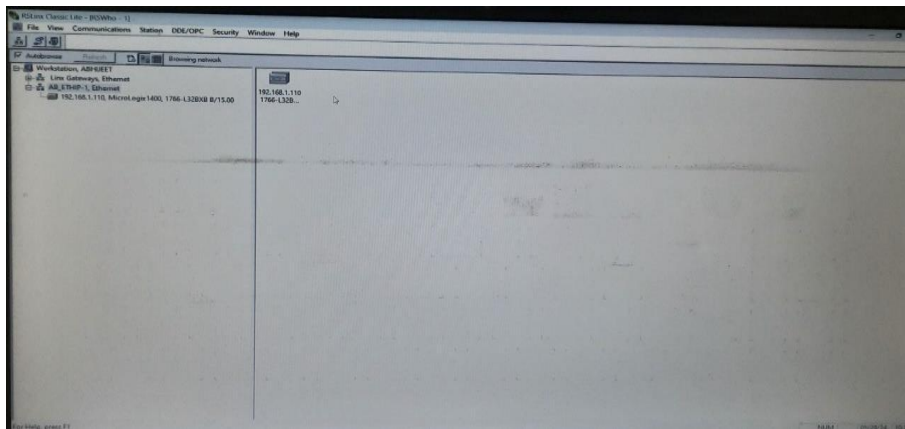


(I) Programming and Communication Software

RSLogix 500



RSLinx Classic



V. OUTCOME

- Low-cost controlling of induction motors for various operations using PLC is possible.
- By changing ladder logic programming controlling various processes or operations is possible.
- Provide automatic control over the process.
- A consistency in processing and safety is possible.
- The smooth handling of complex processes is also possible.

VI. CONCLUSION

The circuits for various PLC-based induction motor operations are successfully constructed and run by making a respective ladder logic program using RSLogix 500 and RSLinx Classic programming and communication software.

Controlling output devices based on a program for a particular process or operation is done successfully and makes an errorless operation. The designed work can monitor and control the process.

VII. REFERENCES

- [1] A. D. Vieira, E. A. P. Santos, M. H. de Queiroz, A. B. leal, A. D. de Paula Neto and J. E. R. Cury, "A Method for PLC Implementation of Supervisory Control of Discrete Event Systems", Published by IEEE Transaction on Control Systems Technology.
- [2] S. C. Ramesh, Dr. G. Kalivarathan, "A Reasonable Approach for Manufacturing System Based On Supervisory Control Using Discrete Event System" Published by IJECET, Volume 4, Issue 1. January – February (2013), PP. 92-98.
- [3] Andre B. Leal, Diogo L.L. da Cruz and Marcelo da S. Hounsell, "PLC Based Implementation of Local Modular Supervisory Control for Manufacturing System" www.intechopen.com
- [4] Belen C. Diego, Vidal M. Rodilla, Carlos F. Carames, Anibel C. Moran, Raul A. Santos "Applying a Software Framework for Supervisory Control of a PLC – based Flexible Manufacturing Systems" Published Online: 27 October 2009, Springer – Verlag London Limited 2009, Int J adv Manuf Technol (2010).
- [5] X. D. Koutsoukos, P. J. Antsaklis, J. A. Stiver and M. D. Lemmon, "Supervisory Control of Hybrid Systems", Proceedings of the IEEE, VOL. 88, NO. 7, July 2000.
- [6] Maria G. Ioannides, "Design and Implementation of PLC – Based Monitoring Control System for Induction Motor" IEEE Transactions on Energy Conversion, VOL. 19, NO. 3, September 2004.
- [7] Manisankar Dhabal, Durgesh Lingampalle, O P Ullas, " A Guide to Design a PLC and SCADA based Industrial Automation System", September 2021, IJIRT, Volume 8 Issue 4, ISSN : 2349-6002.

¹Aniket D. Bokhare,²Haribhau M. Dhage¹Milind P. Lokhande²A.C.Kumbharkhane

A comparison of the dielectric relaxation behaviour of 2-nitrotoluene-Dimethyl sulfoxide and toluene-Dimethyl sulfoxide mixtures using Time Domain Reflectometry



Abstract: - This study investigated the dielectric properties of 2-nitrotoluene (2NT)-dimethyl sulfoxide (DMSO) and toluene-DMSO mixtures across the entire concentration range using Time Domain Reflectometry (TDR) in the frequency range of 10 MHz to 50 GHz. The Debye model was employed to analyze the complex permittivity spectra and extract key parameters. The results revealed that 2NT-DMSO mixtures possess a higher static dielectric constant compared to toluene-DMSO mixtures, particularly at lower DMSO concentrations. This signifies a more prominent contribution of polar 2NT molecules to the overall polarity of the mixture as the concentration of the other polar component (DMSO) decreases. Additionally, 2NT-DMSO mixtures exhibited higher relaxation times compared to their toluene counterparts. This is likely attributed to the steric hindrance caused by the bulkier nitro group in 2NT, impeding its molecular reorientation, and potentially stronger interactions with DMSO molecules. These findings provide valuable insights into the interplay between molecular structure and dielectric behaviour in these binary mixtures

Keywords: Toluene, 2-nitrotoluene Complex permittivity, Relaxation time, Time domain reflectometry (TDR)

I INTRODUCTION

Understanding the dielectric properties of materials is crucial in various technological applications, including capacitors, sensors, and microwave devices. Dielectric properties are influenced by the interaction between an electric field and a material's constituent molecules [1]. In this study, we focus on binary mixtures of polar solvents: 2-nitrotoluene (2NT) and toluene with dimethyl sulfoxide (DMSO). The nitro

¹*Corresponding author: Author 1 Govt. Vidarbha Institute of Science and Humanities, Amravati-444604, MS, India

²Author 2 School of Physical Sciences, Swami Ramanand Teerth Marathwada University, Nanded-431606, MS, India

*Corresponding author: aniketbokhare13696@gmail.com

Copyright©JES2024on-line:journal.esrgroups.org

group (NO_2) in 2NT introduces a significant dipole moment, making it a more polar molecule compared to toluene. DMSO is another polar solvent with a high dielectric constant.

2NT has a benzene ring substituted with a nitro group ($-\text{NO}_2$) at the 2-position as shown in Fig. 1. The aromatic ring contributes to its overall polarity, but the presence of the methyl group ($-\text{CH}_3$) adds steric hindrance. Fig.2 shows structure of toluene. Toluene possesses a simpler structure with a methyl group ($-\text{CH}_3$) attached to a benzene ring. While the benzene ring in both molecules contributes to some overall polarity due to delocalization of electrons (movement of electrons throughout the ring), the key difference lies in the functional groups attached. DMSO was chosen as the solvent because of its high polarity and ability to dissolve a wide range of compounds [2-3].

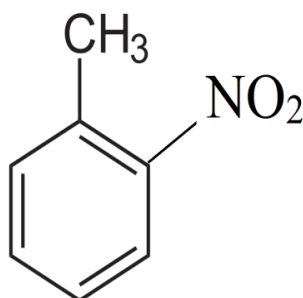


Fig. 1. Structure of 2-Nitrotoluene

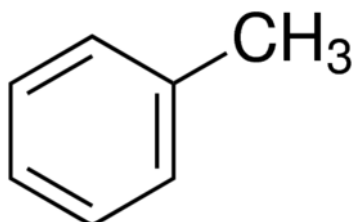


Fig. 2. Structure of toluene

We hypothesize that due to the stronger polarity of 2NT compared to toluene, the 2NT-DMSO mixtures will exhibit a higher overall dielectric constant (ϵ_0), especially at lower DMSO concentrations. Additionally, the bulkier structure of the nitro group in 2NT might lead to slower molecular reorientation, resulting in higher relaxation times for 2NT-DMSO mixtures compared to toluene-DMSO mixtures. This research aims to verify these hypotheses and provide a comprehensive understanding of the interplay between molecular structure and dielectric behaviour in these binary mixtures. We employ TDR as a reliable technique to measure the complex permittivity spectra of the mixtures in a wide frequency range (10 MHz to 50 GHz). By analyzing the complex permittivity spectra, we can gain valuable insights into the molecular dynamics and relaxation behaviour within these mixtures [4].

II EXPERIMENTAL METHOD

A. MATERIALS

2NT and toluene were purchased commercially from Loba Chemie Pvt. Ltd., Mumbai, with 99.00% purity. DMSO was obtained from S. D. Fine-Chem Ltd. The binary mixture of Toluene-DMSO and 2NT-DMSO was prepared at varying concentrations by volume fraction.

B. Measurements

The CPS were obtained using the TDR technique [5]. The Tektronix digital serial analyzer model no. DSA8300 sampling mainframe oscilloscope along with the dual channel sampling module 80E10B has been used for time domain reflectometer. The experimental setup and instrument calibration are carried out in accordance with the references [6, 7].

III RESULTS AND DISCUSSION

Fig. 3 and Fig. 4 display the frequency-dependent CPS for Toluene-DMSO and 2NT-DMSO at various concentrations respectively. The CPS obtained with TDR are fitted to the Havriliak - Negami expression using the non-linear least squares fit method [8-9].

$$\varepsilon^*(\omega) = \varepsilon_{\infty} + \frac{\varepsilon_0 - \varepsilon_{\infty}}{[1 + (j\omega\tau)^{1-\alpha}]^{\beta}} \quad (1)$$

Where ε_0 , τ , ε_{∞} , α and β are the fitting parameters. ω is the angular frequency. The Debye ($\alpha = 0$, $\beta = 1$) [10], Cole-Cole ($0 \leq \alpha \leq 1$ and $\beta = 1$) [11] and Davidson – Cole ($\alpha = 0$ and $0 \leq \beta \leq 1$) [12] relaxation models are the limiting cases of Havriliak - Negami expression.

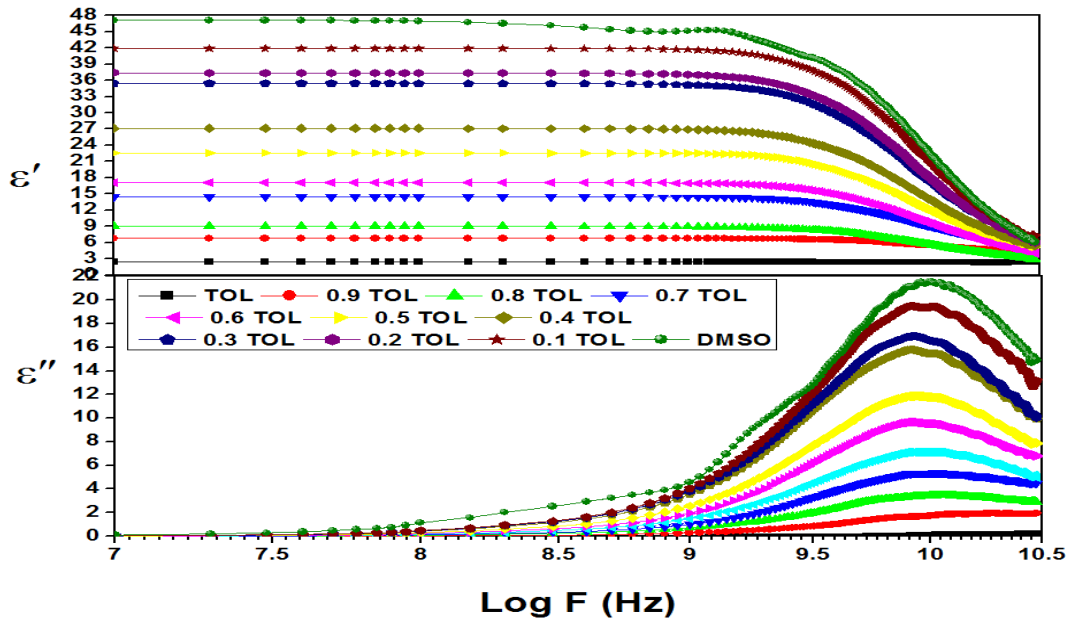


Fig. 3 Frequency dependent complex permittivity spectra for toluene +DMSO mixture at 25 °C.

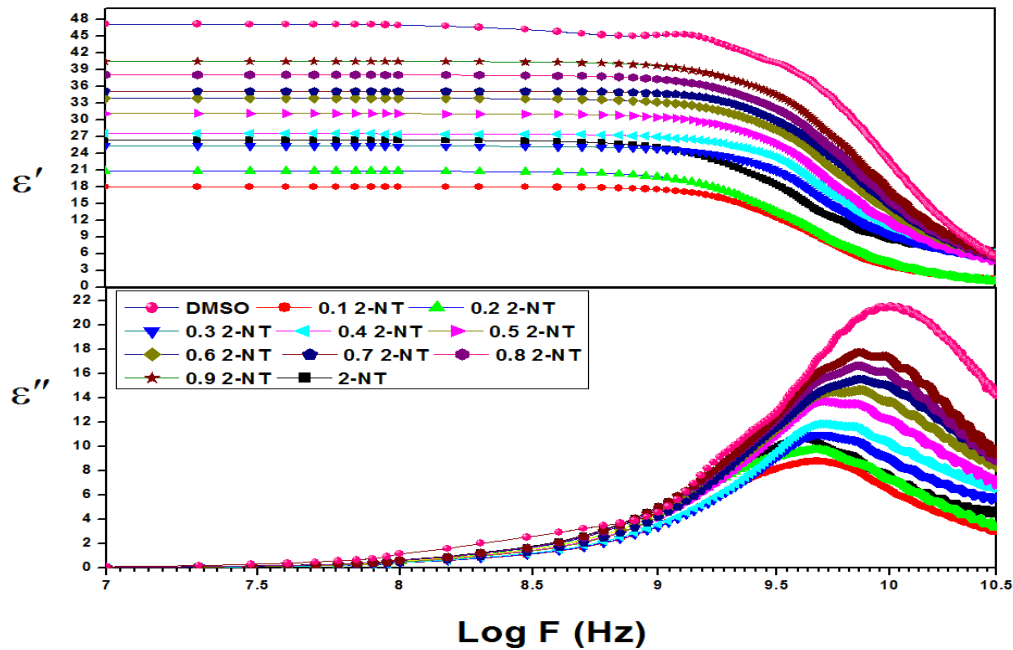


Fig. 4. Frequency dependent complex permittivity spectra for 2NT-DMSO mixtures at 25 ° C

The study compares ϵ_0 for 2NT-DMSO and Toluene-DMSO mixtures at 25°C for different volume fraction of DMSO at 25 °C as represented in Fig. 5. 2NT is a polar molecule due to the presence of the nitro group (NO_2). This group creates an uneven distribution of charge within the molecule, making it more susceptible to orienting itself in an electric field compared to Toluene (which has a methyl group instead of NO_2). As the concentration of DMSO (also polar) decreases in the 2NT-DMSO mixture, the influence of the polar 2NT molecules becomes more significant, leading to a higher overall dielectric constant compared to the Toluene-DMSO mixtures.

Comparison of relaxation time (τ in ps) for 2NT-DMSO and Toluene-DMSO mixtures for different volume fraction of DMSO at 25 °C is represented in Fig. 6. The value of τ of 2NT-DMSO mixtures found to be greater than Toluene-DMSO mixtures over different concentration ranges. The nitro group in 2NT makes it bulkier and hinders its movement compared to Toluene. Additionally, there might be stronger interactions between the polar 2NT and DMSO molecules, further slowing down the reorientation process. This translates to a higher relaxation time for 2NT-DMSO mixtures compared to Toluene-DMSO. This observation aligns with our initial hypothesis.

An intriguing trend emerges when analyzing the relaxation time (τ) as a function of DMSO concentration (Fig. 6). For 2NT-DMSO mixtures, τ exhibits a decreasing trend with increasing DMSO content. This suggests that the 2NT molecules reorient faster as the concentration of DMSO increases. This

behaviour can potentially be attributed to a dilution effect. As the concentration of DMSO rises, the relative number of 2NT molecules in the mixture diminishes. This reduces the overall influence of the bulky nitro group on the average reorientation time within the mixture, leading to faster overall molecular movement. Conversely, the relaxation time (τ) for toluene-DMSO mixtures exhibits an increasing trend with increasing DMSO concentration. This implies that the toluene molecules reorient slower at higher DMSO concentrations. This can be explained by the viscosity effect. DMSO is a relatively viscous liquid. As its concentration increases in the mixture, the overall viscosity of the system rises. This hinders the movement of both toluene and DMSO molecules, leading to a slower reorientation process and a higher relaxation time observed for toluene-DMSO mixtures.

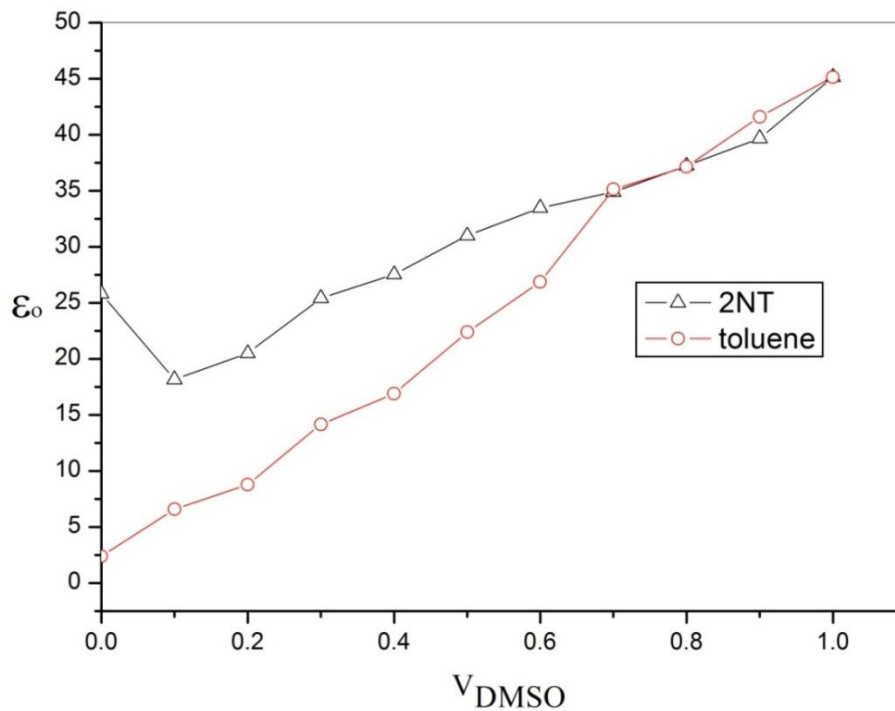


Fig. 5. Comparison of dielectric constant for 2NT-DMSO and Toluene-DMSO mixtures for different volume fraction of DMSO at 25 ° C

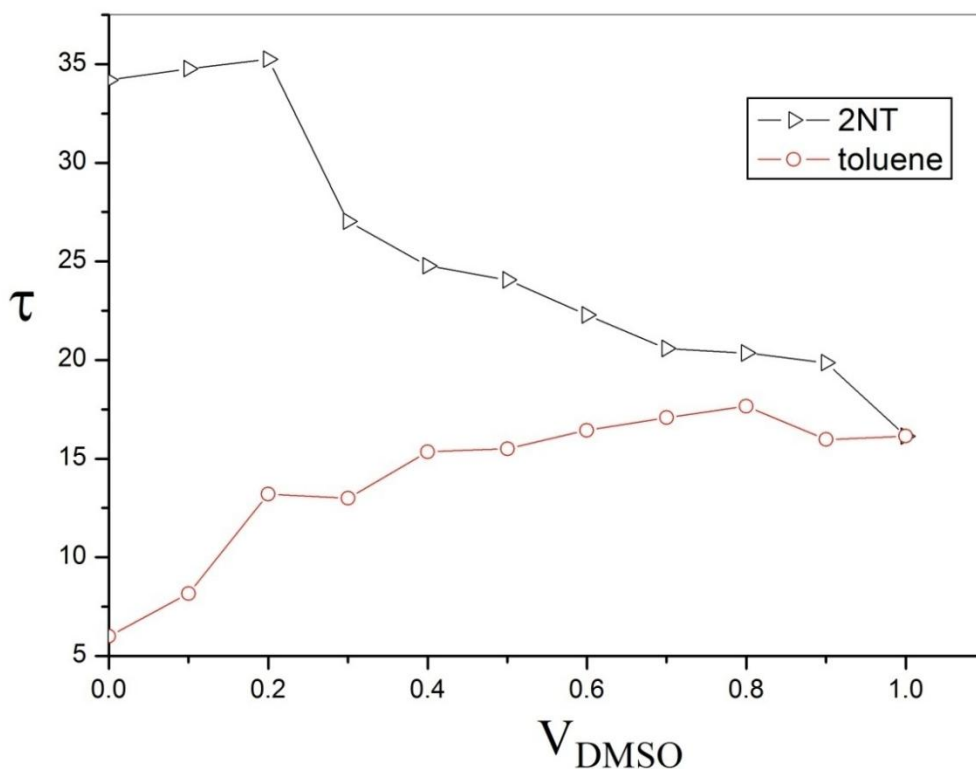


Fig. 6. Comparison of Relaxation time for 2NT-DMSO and Toluene-DMSO mixtures for different volume fraction of DMSO at 25 ° C

IV CONCLUSIONS

The interplay between the strong dipole moment of 2NT and the varying concentration of DMSO determines overall dielectric constant of the mixture. At low DMSO concentrations, the dominance of polar 2NT molecules leads to a higher dielectric constant compared to toluene-DMSO mixtures. The combined effect of steric hindrance from the nitro group and potential interactions with DMSO molecules leads to a slower reorientation process in 2NT-DMSO mixtures, manifested as a higher relaxation time compared to toluene-DMSO mixtures

Acknowledgement

Author Aniket D. Bokhare expresses gratitude to the Director of the Government Vidarbha Institute of Science and Humanities, Amravati. The School of Physical Sciences at SRT Marathwada University in Nanded (MS) is also acknowledged by the author for providing the laboratory equipment. Author acknowledges the fellowship received from the Chhatrapati Shahu Maharaja Research, Training, and Human Development Institute (SARTHI), Pune (CMSRF-2021). It is acknowledged that the DST, New Delhi, India, provided financial assistance for this project (Project number: DST PROJECT- SB/S2/LOP-032/2013).

REFERENCES

- [1] Stuerger, D., “Microwave-material interactions and dielectric properties, key ingredients for mastery of chemical microwave processes”. *Microwaves in organic synthesis*, pp.1-61,2006.
- [2] Dhage, H.M., Deshmukh, A.R., Birajdar, S.S. and Kumbharkhane, A.C., “Temperature dependent dielectric relaxation studies of 2-nitrotoluene-dimethyl sulfoxide mixture using time domain reflectometry”, 2022.
- [3] Dhage, H.M., Bokhare, A.D., Garad, N.P., Lokhande, M.P. and Kumbharkhane, A.C., . “Dielectric relaxation studies of 1-nitropropane-dimethyl sulfoxide mixtures using a Time Domain Reflectometry”. *Physics and Chemistry of Liquids*, pp.1-10.,2024
- [4] Bokhare, A.D., Garad, N.P., Lokhande, M.P. and Kumbharkhane, A.C.,. “Dielectric relaxation and hydrogen bonding interactions study of aqueous D-sorbitol using time domain reflectometry”. *Physics and Chemistry of Liquids*, 62(1), pp.1-8. 2024.
- [5] Cole, R.H., Berberian, J.G., Mashimo, S., Chryssikos, G., Burns, A. and Tombari, E.. ”Time domain reflection methods for dielectric measurements to 10 GHz”. *Journal of applied physics*, 66(2), pp.793-802,1989.
- [6] Kadam, S.S., Kanse, K.S., Joshi, Y.S., Rander, D.N. and Kumbharkhane, A.C., “Dielectric relaxation studies of 1, 3 and 1, 4-butanediol–water mixtures using time domain technique”. *Indian Journal of Physics*, 92, pp.1367-1372. 2018.
- [7] Mehrotra, S.C., Kumbharkhane, A. and Chaudhari, A.,. *Binary polar liquids: structural and dynamic characterization using spectroscopic methods*. Elsevier. 2017.
- [8] Havriliak, S. and Negami, S., “A complex plane analysis of α -dispersions in some polymer systems”. In *Journal of Polymer Science Part C: Polymer Symposia* (Vol. 14, No. 1, pp. 99-117). New York: Wiley Subscription Services, Inc., A Wiley Company., 1966.
- [9] Kaatze, U., “Microwave dielectric properties of liquids”. *Radiation Physics and Chemistry*, 45(4), pp.549-566, 1995.
- [10] Debye, P., 1929. Polar molecules, the chemical catalog company. *Inc., New York*, 89.
- [11] Cole, K.S. and Cole, R.H.,. “Dispersion and absorption in dielectrics I. Alternating current characteristics”. *The Journal of chemical physics*, 9(4), pp.341-351. ,1941.
- [12] Davidson, D.W. and Cole, R.H.,. “Dielectric relaxation in glycerine”. *The Journal of Chemical Physics*, 18(10), pp.1417-1417., 1950.

¹*Nikita S. Korde¹Sandeep A.
Waghuley

Regular paper

Giant Magnetoresistance of Graphene Doped Iron and Nickel Thin Films



Abstract: - A two-dimensional (2D) layered material becomes an ultimate candidate for spintronics devices because of its atomically thin and flat nature. In this work, graphene was synthesized by modified electrochemical exfoliation method while transition metal oxides were prepared by simple chemical co-precipitation method. The XRD and SEM study confirmed the structure of prepared nanocomposites. The particle size was found to be increased due to doping. The giant magnetoresistance (GMR) of Graphene doped iron and nickel thin films deposited on glass substrate using screen printing technique was measured by using two-probe method at room temperature. The GMR values for graphene doped iron and nickel thin films were found to be 3.97% and 3.38%.

Keywords: Graphene Nanocomposites, Transition Metal Oxides, Ferromagnetic Materials, Giant Magnetoresistance.

¹*Corresponding author: Nikita S. Korde, Research Scholar, Department of Physics, Sant Gadge Baba Amravati University, Amravati, Maharashtra, India, E-mail:- nikitakorde3@gmail.com

¹Faculty of Physics, Department of Physics, Sant Gadge Baba Amravati University, Amravati, Maharashtra, India
Copyright©JES2024on-line:journal.esrgroups.org

1 Introduction

According to Moore's law, exploiting new degrees of freedom has turned out to be an essential research direction to promote further development of electronic devices. The goal of spintronics is to make use of the spin degree of freedom of electrons to realize novel information storage and logic devices. A spintronics device has the superiority of faster speed, ultra-low heat dissipation, and non-volatility, making it an ideal candidate for future electronics [1]. Spintronics take advantage of spin degree of freedom together with the charge of an electron, providing more flexibility and control. Flipping the spin state of an electron with an external magnetic field needs greatly low power and exceptionally little time in comparison with the movement of electron over the circuit which comes about in high-speed and low-power spintronics devices as compared to conventional electronic devices [2]. The beginning of spintronics goes back to the primary understanding of the electrical conduction in transition metals by Mott in 1936, who characterized the conduction of electrons in ferromagnetic (F) substances as a combination of two individual current channels, one channel along with electrons with spins parallel to the magnetization axis of F and the other with electron spins oriented in opposite direction [3].

Magnetoresistance (MR), which is the change in a material's electrical resistance in response to an applied magnetic field, is of interest both from fundamental and technological point of view. A large value of MR in weak magnetic fields at room temperature is of special attention in producing magnetic sensors, magnetic memory and hard drives [4, 5]. The first magnetoresistive effect was observed by William Thomson, better called as Lord Kelvin, in 1856, but he was not able to lower the electrical resistance of anything by more than 5% [6]. The giant magnetoresistive (GMR) effect was found in 1988 in multilayered structures of ferromagnetic and non-ferromagnetic thin films by Grunberg, Binasch et al [7] as well as Fert, Baibich et al [8]. In principle, a typical GMR structure consists of a couple of ferromagnetic thin film layers separated by a non-magnetic conducting layer. The change in the resistance of this multilayer arises once the externally applied magnetic field aligns the magnetic moments of the successive magnetic layers [9]. In the presence of a magnetic field the spin-dependent electron scattering among the structure reduces and the electrical resistance decreases [10, 11]. GMR sensors are ideal for low cost applications since they are simply energized by applying a steady current and the yield voltage is a measure of the magnetic field [12].

Two-dimensional (2D) layered materials have an atomically thin and flat nature which makes it an ultimate candidate for spintronics devices [13]. Graphene has been broadly applied in different areas such as electronic circuitry components, energy production, and field-effect transistors because of its great electrical, optical and mechanical properties [14-19]. In expansion to the remarkable intrinsic electronic and mechanical properties of pure graphene, the structure and properties can too be modified and controlled by molecule adsorptions and atom-dopants [20]. On the other side, transition-metal

adsorbed on nanoscale carbon surface these days has been of great interest, which gives rise to interesting new phenomena. Many 3d-orbital adatoms carry a magnetic moment and binding to graphene presents a chemical route to localized magnetic moments [21–23]. Moreover, many studies suggest that introducing impurities into graphene can transform the electronic structure of graphene [17]. Shinji Yuasa et al [24] reported a giant MR ratio up to 180% at room temperature in single-crystal Fe/MgO/Fe MTJs. Xiong et al [25] studied the injection, transport and detection of spin-polarized carriers using an organic semiconductor as the spacer layer in a spin-valve structure, which results in low-temperature giant magneto-resistance effects upto 40 percent. Ali et al [4] reported the observation of an extremely large positive magnetoresistance at low temperatures in the non-magnetic layered transition-metal dichalcogenide WTe_2 : 452,700 percent at 4.5 kelvins in a magnetic field of 14.7 teslas, and 13 million per cent at 0.53 kelvins in a magnetic field of 60 teslas. Schmaus et al [26] demonstrated giant magnetoresistance across a single, non-magnetic hydrogen phthalocyanine molecule contacted by the ferromagnetic tip of a scanning tunnelling microscope. They measured the magnetoresistance to be 60% and the conductance to be $0.26G_0$. Theoretical analysis identified spin-dependent hybridization of molecular and electrode orbitals as the cause of the large magnetoresistance. Guan et al [27] examined the geometry and the magnetic and electronic properties of transitional-metal (TM) adsorption on graphene with line defect (LD). For different TMs such as Fe, Co, Mn, Ni, and V, the complex systems showed different magnetic and electronic properties.

In this work, we prepared graphene/transition metal oxide nanocomposites (Graphene doped Iron and Nickel) by a simple chemical co-precipitation method. The prepared samples were investigated by XRD and FTIR. Particle size of the materials was measured using Malvern's zetasizer ZS-90 and also Giant magnetoresistance was calculated by two-probe method.

2 Methodology

2.1 Materials and Methods

Analytical grade Ferric Chloride Hexahydrate ($\text{FeCl}_3 \cdot 6\text{H}_2\text{O}$), Acetone, Nickel Chloride Hexahydrate ($\text{NiCl}_2 \cdot 6\text{H}_2\text{O}$) and Sodium Hydroxide (NaOH) were used in the preparation of Graphene/Metal oxide composites.

2.2 Sample preparation

2.2.1 Preparation of Graphene and Metal oxides

Graphene was synthesized via electrochemical exfoliation method with a graphite rod, whereas Metal oxides were prepared by using simple co-precipitation method. By vigorous stirring, sodium hydroxide (NaOH) solution was added drop by drop to an aqueous solution of ferric chloride. The stirring operation

was continued until the brown precipitation of ferric oxide was obtained. This was filtered and rinsed in distilled water before being heated in a muffle furnace at 100°C and ground into a fine powder. Subsequently, the material was calcined at 450°C for 2 hours. Similarly, the light green colored nickel is obtained, which on calcinations, turns into black oxide.

2.2.2 Synthesis of Graphene/Metal oxide composite

The ex-situ approach was adopted to synthesize the Graphene/metal oxide composites in equal proportion (1:1 ratio). The composites were all synthesized using acetone as a solvent and then calcined at 100°C for an hour.

2.2.3 Preparation of Thin films using Screen printing technique

For the preparation of thin films of Graphene/Metal oxide composites, screen printing technique is used. In this method, the paste of graphene/metal oxide composite mixed with binder made from butyl glycol and terpinol is printed onto a glass plate with the help of a blade. The glass plates are then dried to fix the layer of thin film.

3 Result and discussions

3.1 X-Ray Diffraction Analysis

Characterization is necessary to establish understanding and controlled synthesis of nanostructure materials and their applications. XRD analysis was done by the X-ray diffraction of the samples using Rigaku Miniflex 600. X-ray Diffraction pattern were recorded from 10 degrees to 80 degrees using Cu-K α using an accelerating voltage of 40 KV. Data was collected at a rate of 10 degree/min.

The XRD pattern of pure graphene is shown in figure 1(a). The pure graphene shows (002) diffraction peak at $2\theta = 26.41^\circ$, corresponding to a d-spacing of 0.34 nm, which is almost the same as that of graphite.

The XRD pattern of Graphene doped Iron and Nickel is shown in figure 1(b). Graphene doped Fe shows the diffraction peak at $2\theta = 52.86^\circ$ (110), 75.1° (200) and 25.56° (002). The existence of small peaks of Graphene doped Ni at 2θ values 37.44° , 34.1° & 25.66° corresponding to Ni crystal planes of (111) (200) & (002) respectively matches with JCPDS 04-850[28].

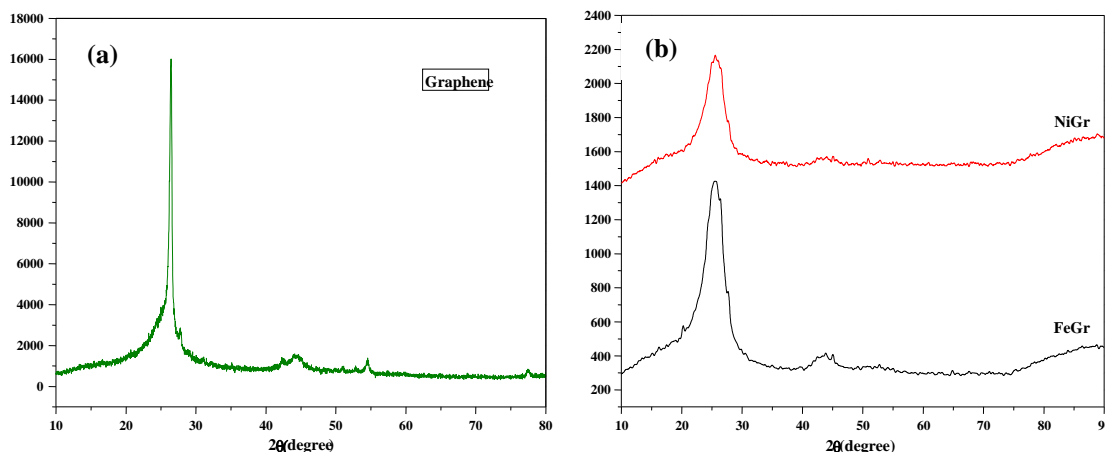


Figure 1: XRD analysis of (a) Pure Graphene and (b) Graphene doped Iron and Nickel.

3.2 SEM Analysis

Figure 2(a) & 2(b) depicts the SEM images of Graphene doped Nickel Oxide and Graphene doped Iron Oxide, respectively. Both SEM images show that the metal oxide nanoparticles nicely distributed over the surface of graphene sheets.

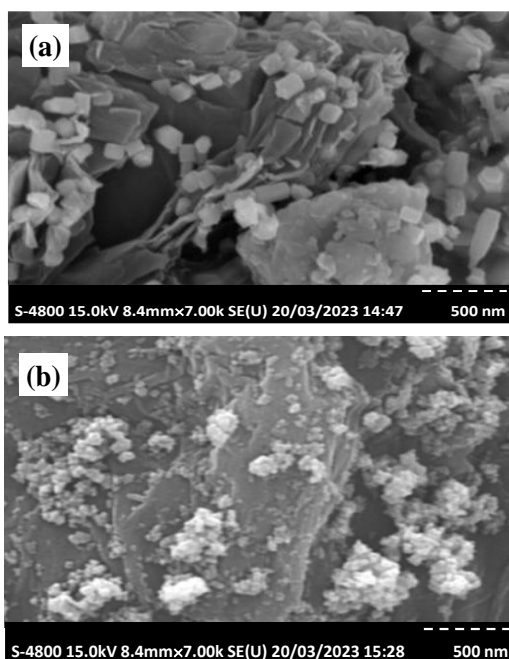


Figure 2: SEM images of (a) Graphene doped Nickel Oxide and (b) Graphene doped Iron Oxide.

3.3 Fourier Transform Infrared Spectra Analysis:

The FTIR spectra of the Graphene nanocomposite samples are shown in figure 3. The graphene oxide spectra show some peaks which relates to O-C bond in the range 968 to 1365 cm^{-1} , O=C shows existence through peaks in the range 1788 to 1803 cm^{-1} (carbonyl group), C=C bond at 1585 cm^{-1} and O-H bond at 3138 cm^{-1} (hydroxyl group). These fingerprints indicate that graphene was successfully

synthesized. Complete metal oxide bonding ($< 500 \text{ cm}^{-1}$) was not found due to limitations of the instrument. Only the peak of Fe, Ni - O is appearing in the range 430 to 476 cm^{-1} [29-33].

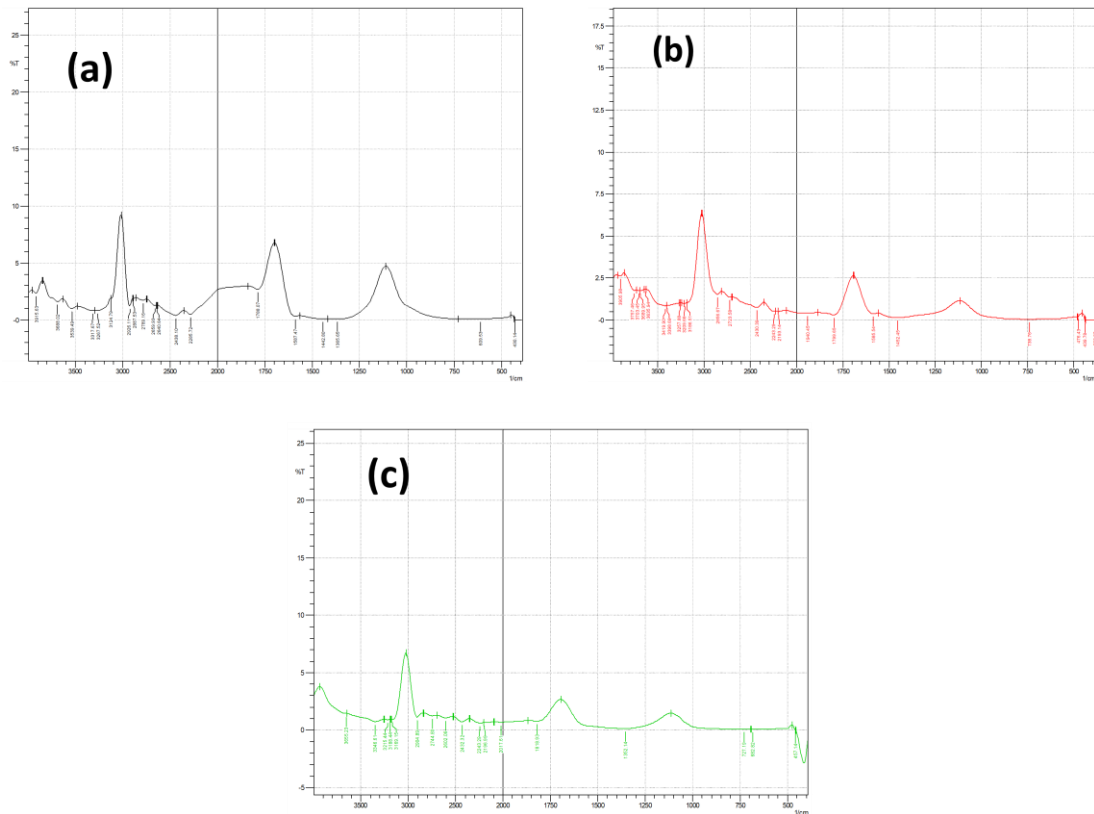


Figure 3: FTIR Spectrum of (a) Pure Graphene oxide, (b) Graphene doped Nickel Oxide, (c) Graphene doped Iron oxide.

3.4 Particle Size Analysis:

The particle sizes of graphene nanocomposites are determined by using Malvern's zetasizer ZS-90. The particle size of pure graphene is found to be 3 nm whereas the particle sizes of graphene doped iron and nickel are found to be 300 nm and 200 nm respectively as in figure 4. Thus due to the doping of ferromagnetic materials in graphene, the particle size of sample is increased.

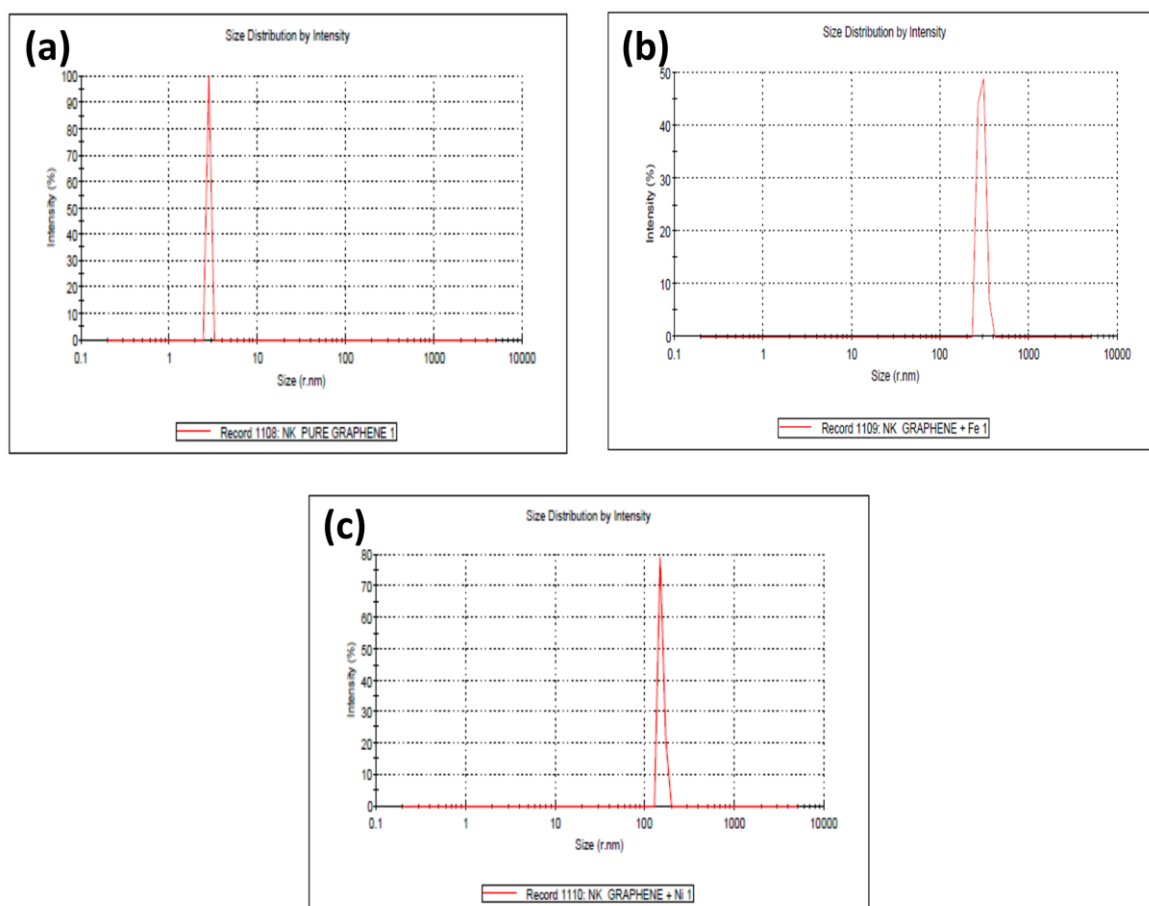


Figure 4: Particle size distribution (a) Graphene, (b) Graphene doped Fe, (c) Graphene doped Ni.

3.5 Determination of Giant Magnetoresistance:

The giant magnetoresistance of graphene doped ferromagnetic materials are calculated using two probe method. The GMR for graphene doped iron is found to be maximum than graphene doped nickel and cobalt as shown in the table 1. Thus graphene doped iron is more useful for spintronic devices as compared to others. The valencies of iron and nickel are four and two. The outer shell of the iron is having the four electrons in the same direction as compared to the nickel which is the maximum one. After applying the magnetic field to the outer electrons, they align in the same direction and give the maximum change in electrical resistance. Due to this, the iron is having the maximum magnetoresistance.

Table 1: GMR and average GMR values

Material	GMR=$\Delta\rho/\rho_0$	Average GMR
Graphene + Fe	<ol style="list-style-type: none"> 1. 5.33% 2. 4.49% 3. 3.34% 4. 2.71% 	3.97%
Graphene + Ni	<ol style="list-style-type: none"> 1. 5.35% 2. 3.43% 3. 2.62% 4. 2.12% 	3.38%

4 Conclusions

This study evaluated the structural and magnetic properties of graphene doped metal oxide nanocomposites. In this work, the graphene is doped with the ferromagnetic materials such as iron and nickel and their giant magnetoresistance is measured. The simple chemical co-precipitation method is used for the doping of the ferromagnetic materials in graphene. The XRD shows that due to doping of the ferromagnetic materials in graphene, the crystalline size is increased. The thin films of the doped samples are prepared by screen printing method. FTIR spectrum confirms the metal oxide bonding. The particle size of pure graphene, graphene doped iron, and nickel is found to be 3nm, 300nm and 200nm respectively. The Giant Magnetoresistance (GMR) of the prepared thin films calculated using two-probe method is found to be 3.97% (for Fe) and 3.38% (for Ni). These findings conclude that graphene doped with iron can be useful for spintronics device fabrication due to high GMR ratio than graphene doped nickel.

5 Acknowledgement

The authors would like to thank Department of Physics, Sant Gadge Baba Amravati University, Amravati for their support.

6 References

1. Y. Liu, C. Zeng, J. Zhong, J. Ding, Z. M. Wang, Z. Liu, Spintronics in Two-Dimensional Materials, *Nano-Micro Lett*, 12 (93), 1-26, 2020.
2. M. Gani, K. A. Shah, S. A. Parah, P. Misra, Room temperature high Giant Magnetoresistance graphene based spin valve and its application for realization of logic gates, *Phys. Lett. A.*, 384 (7), 126171, 2019.
3. M. Gurram, Spin transport in graphene-hexagonal boron nitride Van der Waals heterostructures[Groningem]: University of Groningen, 2018.

4. M. N. Ali, J. Xiong, S. Flynn, J. Tao, Q. D. Gibson, L. M. Schoop, T. Liang, N. Haldolaarachchige, M. Hirschberger, N. P. Ong, R. J. Cava, Large, non-saturating magnetoresistance in WTe₂, *Nature*, 514, 205-208, 2014.
5. V. N. Matveev, V. I. Levashov, O. V. Kononenko, V. T. Volkov, Large positive magnetoresistance of graphene at room temperature in magnetic fields up to 0.5 T, *Scr. Mater.*, 147(1), 37–39, 2018.
6. J. F. Brouckaert, R. Marsili, G. Rossi, R. Tomassini, Development and experimental characterization of a new non contact sensor for blade tip timing, *AIP Conf. Proc.*, 1457(1), 61-68, 2012.
7. G. Binash, P. Grunberg, F. Saurenbach, W. Zinn, Enhanced magnetoresistance in layered magnetic structures with antiferromagnetic interlayer exchange, *Phys. Rev. B.*, 39, 4828-4830, 1989.
8. M. N. Baibich, J. M. Broto, A. Fert, F. N. Van Dau, F. Petroff, Giant Magnetoresistance of (001) Fe/(001) Cr Magnetic Superlattices, *Phys. Rev. Lett.*, 61, 2472-2475, 1988.
9. V. K. Varadan, L. Chen, J. Xie, Nanomedicine: Design and Applications of Magnetic Nanomaterials, Nanosensors and Nanosystems, *John Wiley & Sons, Ltd.: West Sussex, UK*, 1-43, 2008.
10. L. Xu, H. Yu, M. S. Akhras, S. J. Han, S. Osterfeld, R. L. White, N. Pourmand, S. X. Wang, Giant magnetoresistive biochip for DNA detection and HPV genotyping, *Biosens. Bioelectron.*, 24(1), 99-103, 2008.
11. C. Gooneratne, C. Liang, I. Giouroudi, J. Kosel, An integrated micro-chip for rapid detection of magnetic particles, *J. Appl. Phys.*, 111(7), 07B327, 1-4, 2012.
12. Ce. Yang, Yang-Long. Hou, Song Gao, Nanomagnetism: Principles, nanostructures, and biomedical applications, *Chin. Phys. B*, 23(5), 057505, 1-9, 2014.
13. M. F. Khan, S. Rehman, M. A. Rehman, M. A. Basit, D. K. Kim, F. Ahmed, H. M. Waseem Khalil, I. Imtisal Akhtar, S. C. Jun, Modulation of Magnetoresistance Polarity in BLG/SL-MoSe₂ Heterostacks, *Nanoscale Res. Lett.*, 15(136), 1-8, 2020.
14. K. S. Novoselov, A. K. Geim, S.V. Morozov, D. Jiang, Y. Zhang, S.V. Dubonos, I. V. Grigorieva, A. A. Firsov, Electric field effect in atomically thin carbon films, *Science.*, 306(5696), 666-669, 2004.
15. S. Stankovich, D.A. Dikin, G. H. B. Dommett, K. M. Kohlhaas, E. J. Zimney, E. A. Stach, R. D. Piner, S. T. Nguyen, R. S. Ruoff, Graphene-based composite materials, *Nature*, 442, 282-286, 2006.
16. J. Ryou, S. Hong, First-principles study of carbon atoms adsorbed on MgO(100) related to graphene growth, *Curr. Appl. Phys.*, 13(2), 327-330, 2013.
17. Q. Zhou, Z. Fu, Y. Tang, H. Zhang, C. Wang, First-principle study of the transition-metal adatoms on B-doped vacancy-defected graphene, *Physica E.*, 60, 133-138, 2014.
18. M. Sun, Y. Peng, Study on structural, electronic and magnetic properties of Sn atom adsorbed on defective graphene by first-principle calculations, *Appl. Surf. Sci.*, 307, 158-164, 2014.
19. J. Zhou, Q. Wang, Q. Sun, X. S. Chen, Y. Kawazoe, P. Jena, Ferromagnetism in semi hydrogenated graphene sheet, *Nano Lett.*, 9(11), 3867-3870, 2009.
20. X. B. Yuan, Y. L. Tian, X. W. Zhao, W. W. Yue, G. C. Hu, J. F. Ren, Spin polarization properties of benzene/graphene with transition metals as dopants: First principles calculations, *Appl. Surf. Sci.*, 439, 1158–1162, 2018.
21. Y. Yagi, T. M. Briere, M. H. F. Sluiter, V. Kumar, A. A. Farajian, Y. A. Kawazoe, Stable geometries and magnetic properties of single-walled carbon nanotubes doped with 3d transition metals: first-principles study, *Phys. Rev. B.*, 69(7), 2004.

22. K. T. Chan, J. B. Neaton, M. L. Cohen, First-principles study of metal adatom adsorption on graphene, *Phys. Rev. B.*, 77(23), 235430, 2008.
23. Y. Mao, J. Yuan, J. Zhong, Density functional calculation of transition metal adatom adsorption on graphene, *J. Phys.: Condens. Matter.*, 20(11), 115209, 2008.
24. S. Yuasa, T. Nagahama, A. Fukushima, Y. SuZuki, K. Ando, Giant room- temperature magnetoresistance in single-crystal Fe/MgO/Fe magnetic tunnel junctions, *Nat. mater.*, 3, 868-871, 2004.
25. Z. H. Xiong, Di. Wu, Z. Vally Vardeny, S. Jing, Giant magnetoresistance in organic spin valves, *Nature.*, 427, 821-824, 2004.
26. S. Schmaus, A. Bagrets, Y. Nahas, T. K. Yamada, A. Bork, M. Bowen, E. Beaurepaire, F. Evers, W. Wulfhekel, Giant magnetoresistance through a single molecule, *Nat. Nanotechnol.*, 6, 185-189, 2011.
27. Z. Guan, S. Ni, S. Hu, First-Principles Study of 3d Transition-Metal-Atom Adsorption onto Graphene Embedded with the Extended Line Defect, *ACS Omega.*, 5(11), 5900-5910, 2020.
28. M. M. [Almutairi](#), E. E. [Ebraheim](#), M. S. [Mahmoud](#), M. S. [Atrees](#), M. E. M. [Ali](#), Y. M. [Khawassek](#), [Nanocomposite of TiO2 @ Ni- or Co-doped Graphene Oxide for Efficient Photocatalytic Water Splitting](#), *Egypt. J. Chem.*, 62(9), 1649-1658, 2019.
29. U. Narkiewicz, N. Guskos, W. Arabczyk, J. Typek, T. Bodziony, W. Konicki, G. Gazsiorek, I. Kucharewicz, E. A. Anagnostakis, XRD, TEM and magnetic resonance studies of iron carbide nanoparticle agglomerates in a carbon matrix. *Carbon.*, 42(5-6), 1127–1132, 2004.
30. N. Dharmaraj, P. Prabu, S. Nagarajan, C. H. Kim, J. H. Park, H. Y. Kim, Synthesis of nickel oxide nanoparticles using nickel acetate and polyvinyl acetate precursor, *Mater. Sci. Eng., B.*, 128(1-3), 111–114, 2006.
31. J. Zhang, C. Q. Lan, Nickel and Cobalt nanoparticles produced by laser ablation of solids in organic solution, *Mater. Lett.*, 62(10-11), 1521-1524, 2008.
32. H. Qiu, F. Qiu, X. Han, J. Li, J. Yang, Microwave-irradiated preparation of reduced graphene oxide-Ni nanostructures and their enhanced performance for catalytic reduction of 4-nitrophenol, *Appl. Surf. Sci.*, 407, 509-517, 2017.
33. K. Bhowmik, A. Mukherjee, M. K. Mishra, G. De, Stable Ni Nanoparticle–Reduced Graphene Oxide Composites for the Reduction of Highly Toxic Aqueous Cr(VI) at Room Temperature, *Langmuir.*, 30(11), 3209-3216, 2014.

¹ Deepika S. Yawale

Bioelectronic nose using bare graphene and carbon nanotube as a human olfactory receptor- a brief review



Abstract: - With the development of smart biosensing technology, the applications of biosensors are evident in every field. However, the operation of a single sensor is not sufficient many a times for variety of obstacles which may cater to high power consumption, high temperature, low sensitivity and less accuracy due to the effects of environmental changes. In the quest of battling such situations E-nose comes into picture which is nothing but a combination of gas sensor arrays (GSAs). The E-nose is created to impersonate the human nose with the better version and greater accuracy. This paper reviews the real-time detection sensor of amyl butyrate (AB) using olfactory receptor 2AG1 and G-protein coupled receptor (GPCR) rendered inactive on a bare graphene. The graphene resistor sensor is made out of drop-casting method and using 1,5-diaminonaphthalene (DAN). The sensor binded with the target and other similar structure targets clarifies how the sensor is efficient with selectivity. The field effect transistor (FET) like structure of p-type Si-wafer on which SWCNTs surface functionalize with 1,5 diaminonaphthalene using glutaraldehyde can be a good biosensor or receptor. The paper further lists the applications and future scope of this E-nose and concludes with the results and discussion and a brief conclusion.

Keywords: olfactory receptor, biosensor, E-nose, SWCNT, graphene

¹*Corresponding author: Dept of Physics & Electronics, Government Vidarbha Institute of Science and Humanities (Autonomous), Amravati-444604 (Maharashtra) India deepikayawale21@gmail.com

I. INTRODUCTION

The gas sensing Technology has gained huge popularity as sensors help in detecting and differentiating several chemical compounds and have a wide range of applications which include detecting diseases, hazard detection in our surrounding and freshness of edible materials [1].

These sensors usually give output in electrical form. They are cost effective and also profitable for industry manufacturers. Selection of specific gas sensor plays a crucial role another critical parameter includes its response time, stability, sensitivity, repeatability and longevity [15]. They offer different functions but the operation of single sensor is not sufficient many a times for variety of challenges which mainly include High power consumption, very high operating temperature, extremely low sensitivity ,not able to detect small gas, wrong selection due to the hindrance of other gases, drop in accuracy due to external factors namely humidity, temperature variations, etc.

In order to combat such lacking nature of the sensor technology has given rise to gas sensor array (GSA) which operates as a combination of multiple gas sensors with several and variety of operating potential.

The electronic nose, better known under the name E-nose [22] is a combination of such gas sensor arrays (GSAs). With the help of machine learning it blooms the result. The E-nose is designed to simulate human olfactory system [23] and its biological receptors. The E-nose basically combines gas sensor arrays (GSAs) with some machine learning to produce improved and better results. In E-nose, the selection of target gas and prediction of concentration is acquired through machine learning algorithms. The presented review highlights the detection of amyl butyrate (AB) using human olfactory receptor. Amyl butyrate is an odour-active volatile organic compound that has been identified as one of the main flavour constituents in banana fruit, apricot and Apples. It is widely used as food flavouring agent in chewing gums, candies and baked edibles. Human olfactory receptor used is G- protein coupled receptor (GPCRs) which has seven trans-membrane domains [2]. The G-protein coupled receptors (GPCRs) are largest and usually diverse group of membrane receptors present in eukaryotes [21]. These cell surface receptors act like an inbox for messages in the form of light energy, peptides, lipids, sugars and proteins such messages inform the cells about presence or absence of life sustaining light or nutrients in their environment, or they convey information sent by other cells. GPCRs play a vital role in an incredible line of functions in the human body and increased understanding of these receptors has largely affected modern medicine. Researchers have found that around 0.3% of the market drugs are tangled with GPCRs. A G-protein coupled receptor (GPCR) is incapacitated onto a grapheme resistor. Conceptually, the bioelectronic nose are much similar to human olfactory system [3].

II. ELECTRONIC OLFACTORY SYSTEM

1. E-nose

A Mammalian olfactory system and the electronic nose system have different stages of process building but it mainly deals with the sequence given in figure 1.

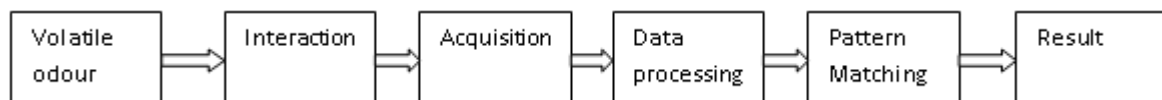


Fig 1: Different stages of electronic nose system

In Mammalian olfactory system, the volatile odour is first taken into the body then the olfactory receptors get activated. Next the olfactory bulb passes it to the brain cortex and the final stage has neuronal processing further it is stored in memory. However, in E-nose the first stage consists of the sensor array which collects the raw data and then processed signals are transmitted. In the final stage there is a data bank which further helps in pattern recognition and retrieval.[25]

2. E-nose working

Using a sensor array (an electronic chip) and onboard pattern recognition algorithms, the lightweight, portable device works by exposing an array of plastic composite sensors to the chemical components in a vapour. When the sensors come in contact with the vapour, the polymer expands like a sponge, changing the resistance of the composites. The presence of a pre-trained substance is done by quick and accurate diagnosis and determined by measuring the change in resistance of the sensor. The E-nose includes three major parts namely, sample delivery system, detection system and computing system. A breath analyzer is the best-known electronic nose as drivers breath into the device a chemical sensor measures the amount of alcohol in their breath. This chemical reaction is then converted into an electronic signal, allowing the police officer to read off the result as alcohol is easy to detect, because the chemical reaction specific and the concentration of the measured gas is fairly high.

A brief comparison between human nose and E-nose is reported in table 1[4-5].

Table 1: Brief comparison between human nose and E-nose

Human nose	v/s	E-nose
<ul style="list-style-type: none"> • 10^8 receptor cells • 10^3 types • Responds in a few seconds 		<ul style="list-style-type: none"> • 5-32 sensors • 5-32 types • Responds in tens of seconds to a few minutes
<ul style="list-style-type: none"> • Sensitivity in ppb/ppt • Massive neural processing in the brain • Receptors regenerated every few weeks (~30 days) 		<ul style="list-style-type: none"> • Sensitivity in ppm/ppb • Pattern recognition, AI, artificial neural nets • Sensors replaced on a maintenance schedule (depends on application)

C. Biosensor (Analogous e-receptors)

Biosensors are tools for the analysis of sample materials and perform function by converting the biological signal to electrical response. They occur in various types namely Immunosensors, DNA, enzyme-based, piezoelectric etc.[24]

Elements and Working

1) Samples: The first stage of a biosensor is sample which can contain food, water, soil, vegetation, cell, blood, urine, saliva, etc. as per needed.

2) Transducers: This stage is mainly divided into two substages i.e. i) Bioreceptor and ii) Electrical Interface. The bioreceptor may have nuclei acids, antibodies, cells or enzymes which are then combined with an electrical interface which can have Electrodes, array of nano wires, nanoparticles or FET devices. The Electrical interface stage converts the biological signal into an electrical one.

3) Electronic system: The third and last stage is the electronic system which is subdivided into three sections namely 1) Signal amplification 2) Signal Processing 3) Displaying the signal. In the transducer stage the biological signal is converted into electrical and then passed on to signal amplification. An amplifier is attached to get a filtered and amplified signal which is then passed on to the signal processing stage. In this stage, the amplified signal is processed and required observations and readings are noted down so as to pass it on to the last stage to display the variations on the screen (Fig 2).

D. Applications of Biosensor

1) Biosensor in packaging

For the safety of foods and to determine its freshness the packaging includes

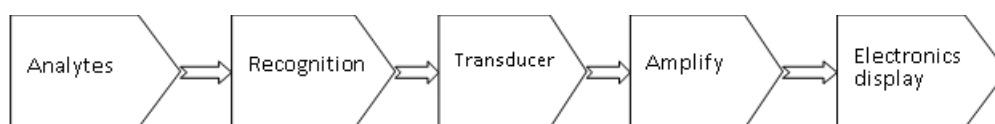


Fig 2: Block diagram of Electronic system

2) Biosensor in Cancer Research [18-19]

The nanoparticles of metal used in the making of biosensor have a large tendency for cancer cells.

3) Biosensor in safety of foods

The screening through biosensor depends mostly for the determination of contaminants in food like pesticides and to check the nutritional content in it.

III. WORKING MODELS OF E-NOSE SYSTEM

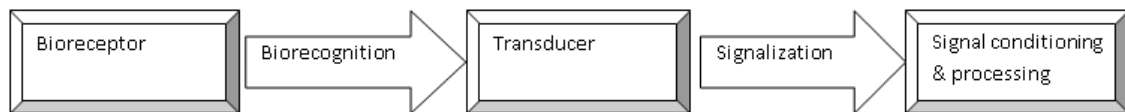
1. Model:1

The Authors [2] stated that Graphene was fabricated using chemical vapour deposition (CVD) using single layer graphene. The mechanical exfoliation has the highest electron mobility in the single layer graphene. 1,5-diaminonaphthalene (DAN) was deposited on the bare grapheme. After this deposition, glutaraldehyde was added to it then an olfactory receptor 2AG1 was immobilized in it.

B. Model: 2

The Authors [6-7] stated that a p-silicon wafer was embedded with a 1000 Å thick oxide layer. Using photolithography photoresist (PR) layer pattern was concealed with Polyethylene Glycol (PEG) toluene (PEG-toluene). The PEG has a silanol group due to which it got self-fabricated on the SiO₂ wafer. The PR was taken off using lift-off method. The wafer was then submerged in solution of swCNTs (0.1 mg/ml in 1,2-dichlorobenzene). The deposited swCNTs adsorbed 1,5-diaminonaphthalene. It was then activated using glutaraldehyde and followed by hOR2AG1.

Real-time current, voltage and resistance measurements were carried out using graphene sensor chip and obtained FE [12-13]. Measurements were taken in ambient conditions (at 20°C, normal atmospheric pressure). Current in response to a constant voltage of 40 mV was applied across the E-nose. Real-time measurement of resistance was carried out. In graphene by drop casting method and in SiO₂ wafer first with the blank measurement i.e. no solution followed by pentyl valerate, butyl butyrate and propyl butyrate and eventually with our target odorant i.e. amyl butyrate with increasing concentrations. The depiction can be arranged in the following series of events



IV. CURRENT APPLICATIONS AND FUTURE APPLICATIONS

- 1) E-nose is used by R&D labs and various production departments for several purposes which consists of
 - a) Monitoring the quality of meat
 - b) Labs in which quality control is needed
 - c) Vendor selection
 - d) Detection of contamination or adulteration
 - e) Observing storage conditions
 - f) Maintaining batch to batch consistency
- 2) Environmental monitoring can be done on a large scale using E-nose
- 3) Identification of volatile organic compounds in air, water and soil samples
- 4) In future, E-nose can be used as a drug detection method at airports. Similar to which detection of odorless [20] smells for bomb odours.
 - 5) Sensing of dangerous and harmful bacteria, such as MRSA (Methicillin resistant staphylococcus aureus)
 - 6) Detection of lung cancer or other medical diseases
 - 7) In addition to it, E-nose is used in automobile, analytical chemistry, packaging, drug and other two significant uses are in analysis of food grains and wines.
- i) They are used for categorizing and quality checking of wines [11]. Sensory and chemical properties of wine, especially colour, aroma and taste are important aspects of their quality
- ii) The aroma of grains is the primary criteria of fitness for consumption in many countries.

V. RESULT AND DISCUSSION

It is reported by authors [6-8] that the surface topography that was possessed by bare graphene before and after the drop-casting of DAN was characterized using atomic force microscopy (AFM). AFM showed clear changes in surface topology and surface roughness. The roughness of bare graphene was found to be 0.534 nm which escalated to 2.315 nm after DAN drop-casting.

Real-time resistance measurement was carried out with drop-casting and washing with 45 minutes drying period. There was substantial increment in resistance after DAN drop-cast. After that another noticeable increase in resistance was observed after addition of glutaraldehyde [16-17] then it was washed and allowed to dry. Addition of ORA2G1 receptor produced small changes in resistance. The final resistance was found to be higher than the bare graphene [9-11].

The functionalized sensor both graphene and FET [14] showed great tendency towards amyl butyrate (AB). However, OR2AG1 showed no response with aliphatic, alcohols, ketones, esters, butyl butyrate and propyl butyrate it addition of AB caused sharp decrease in resistance. Two structurally similar odorants i.e. butyrate and propyl butyrate were tested for its selectivity with which it showed no major changes. The response signals showed dramatically larger signal change for AB. These results indicate that implemented graphene biosensor offered greater selectivity towards amyl butyrate and the field effect transistor (FET) [26] like structure of p-type SiO₂ wafer on which swCNTs surface is functionalized with 1,5 diaminomaphthalene using glutaraldehyde can be a good biosensor receptor. By reviewing both the methods in which one carries drop cast method and the other has photolithography I feel that drop cast method is easy to adopt and cost effective in laboratory basis whereas the SiO₂ masking method in which Photolithography is done is more technical and complex but can be used to create such micro form of wafers which will be resembled like ICs on a large scale.

V. CONCLUSION

The biosensor was obtained using DAN drop-cast and immobilization of OR2AG1 protein. The sensor specifically detected the target odour i.e. Amyl butyrate (AB) recommending great capability for bioelectronic nose using combination of olfactory receptors. The operating method is simple, quick and cost effective for making selective sensing devices. The field effect transistor (FET) like structure of p-type SiO₂ wafer on which swCNTs surface is functionalized with 1,5 diaminomaphthalene using glutaraldehyde can be a good biosensor receptor on large scale and miniature forms.

VI. REFERENCES

- [1] L. Mahmood, M. Ghommem , Z.Bahroun, “Smart Gas Sensors: Materials, Technologies, Practical Applications, and Use of Machine Learning – A Review,” *Journal of Applied and Computational Mechanics*, 3rd ed., vol. 9, pp. 775-803, 2023
- [2] D. Goodwin, F. Walters, M. Munem Ali , E. Ahmadi and O. Guy, “Graphene Bioelectronic Nose for the Detection of Odorants with Human Olfactory Receptor 2AG1,” *Chemosensors*, vol. 9, pp. 174, 2021
- [3] S. Zozulya, F. Echeverri, T. Nguyen, “The human olfactory receptor repertoire,” *Genome Biol.*,vol.2, pp. 1-12, 2001
- [4] H. Venthur, J. Zhou, “. Odorant Receptors and Odorant-Binding Proteins as Insect Pest Control Targets: A Comparative Analysis,” *Front. Physiol.*,vol. 9, pp.1163, 2018
- [5] C. Sarafoleanu, C. Mella, M. Georgescu, C. Perederco, “The importance of the olfactory sense in the human behavior and evolution,” *J. Med. Life*, vol. 2, pp. 196-198, 2009
- [6] S. Lee, H. Jun Jin, H. Seok Song, S. Hong and T. Hyun Park, “ Bioelectronic nose with high sensitivity and selectivity using chemically functionalized carbon nanotube combined with human olfactory receptor,”*Journal of Biotechnology*, Elsevier, vol. 157, pp. 467-472, 2011
- [7] S. Firestein, “How the olfactory system makes sense of scents,” *Nat. Cell Biol.* , vol. 413, pp. 211-218, 2001
- [8] G. Archunan, “Odorant Binding Proteins: A key player in the sense of smell,” *Bioinformation*, vol. 14, pp. 36-37, 2018
- [9] S. Qiu, J. Wang, “The Prediction of Food Additives in the Fruit Juice Based on Electronic Nose with Chemometrics,” *Food Chemistry*,vol. 230, pp. 208-214, 2017
- [10] S. Srivastav, G. Mishra, H.N.Mishra, “Fuzzy Controller Based E-Nose Classification of Sitophilus Oryzae Infestation in Stored Rice Grain,” *food chemistry*,vol. 283,pp. 604-610, 2019
- [11] M. Rodríguez-Méndez, “Electronic Noses and Tongues in Wine Industry,” *Frontiers in Bioengineering and Biotechnology*, vol. 4, pp. 81, 2016
- [12] E.D Sitsanidis, J. Schirmer, A. Lampinen, K.K. Mentel, V.M. Hiltunen, V.Ruokolainen, A. Johansson, P. Myllyperkiö,M. Nissinen, M. Pettersson, “Tuning protein adsorption on graphene surfaces via laser-induced oxidation,” *Nanoscale Adv*, vol. 3, pp. 2065–2074, 2021
- [13] F. Walters, M.M. Ali,G. Burwell, S. Rozhko, Z. Tehrani, E.D. Ahmadi, J.E. Evans, H. Y. Abbasi, R. Bigham, J.J Mitchell, “A Facile Method for the Non-Covalent Amine Functionalization of Carbon-Based Surfaces for Use in Biosensor Development,” *Nanomaterials*, vol. 10, pp. 1808, 2020
- [14] S.R. Ahn, J.H. An, S.H. Lee, H.S. Song,J. Jang,T.H. Park, “Peptide hormone sensors using human hormone receptor-carrying nanovesicles and graphene FETs,” *Sci. Rep.*, vol. 10, pp. 388, 2020

- [15] S. Yu, Z. Wang, L. Gao, B. Zhang, L. Wang, J. Kong, L. Li, "A Highly Selective and Sensitive Peptide-Based Fluorescent Ratio Sensor for Ag⁺," *J. Fluoresc.*, vol. 31, pp. 237–246, 2021
- [16] T. Wasilewski, B. Szulczyński, M. Wojciechowski, W. Kamysz, J. Gębicki, "Determination of long-chain aldehydes using a novel quartz crystal microbalance sensor based on a biomimetic peptide," *Microchem. J.*, vol. 154, pp. 104509, 2020
- [17] T. Wasilewski, B. Szulczyński, M. Wojciechowski, W. Kamysz, J. Gębicki, "A Highly Selective Biosensor Based on Peptide Directly Derived from the HarmOBP7 Aldehyde Binding Site," *Sensors*, vol. 19, pp. 4284, 2019
- [18] H.J. Lim, T. Saha, B.T. Tey, W.S. Tan, O.C. Wei, "Quartz crystal microbalance-based biosensors as rapid diagnostic devices for infectious diseases," *Biosens. Bioelectron.*, vol. 168, pp. 112513, 2020
- [19] R. Ravina, A. Dalal, H. Mohan, M. Prasad, C. Pundir, "Detection methods for influenza A H1N1 virus with special reference to biosensors: A review," vol. 40, pp. BSR20193852, 2020
- [20] Y. Lu, Y. Yao, S. Li, Q. Zhang, Q. Liu, "Olfactory biosensor based on odorant-binding proteins of *Bactrocera dorsalis* with electrochemical impedance sensing for pest management," *Sens. Rev.*, vol. 37, pp. 396–403, 2017
- [21] C. Kotłowski, M. Larisika, P.M. Guerin, C. Kleber, T. Kröber, R. Mastrogiacomo, C. Nowak, P. Pelosi, S. Schütz, A. Schwaighofer, "Fine discrimination of volatile compounds by graphene-immobilized odorant-binding proteins," vol. 256, pp. 564–572, 2018
- [22] H.J. Jin, S.H. Lee, T.H. Kim, J. Park, H.S. Song, T.H. Park, S. Hong, "Nanovesicle-based bioelectronic nose platform mimicking human olfactory signal transduction," *Biosens. Bioelectron.*, vol. 35, pp. 335–341, 2012
- [23] Y. Hou, N. Jaffrezic-Renault, C. Martelet, A. Zhang, J. Minic-Vidic, T. Gorojankina, M.A. Persuy, E. Pajot-Augy, R. Salesse, V. Akimov, "A novel detection strategy for odorant molecules based on controlled bioengineering of rat olfactory receptor I7," vol. 22, pp. 1550–1555, 2007
- [24] T.A. Hopf, S. Morinaga, S. Ihara, K. Touhara, D.S. Marks, R. Benton, "Amino acid coevolution reveals three-dimensional structure and functional domains of insect odorant receptors," *Nat. Commun.*, vol. 6, pp. 1–7, 2015
- [25] S. Robin, S. Tacher, M. Rimbault, A. Vaysse, S. Dréano, C. André, C. Hitte, F. Galibert, "Genetic diversity of canine olfactory receptors," *BMC Genom.*, vol. 10, pp. 21, 2009
- [26] H. Yoon, S.H. Lee, O.S. Kwon, H.S. Song, E.H. Oh, T.H. Park, J. Jang, "Polypyrrole Nanotubes Conjugated with Human Olfactory Receptors: High-Performance Transducers for FET-Type Bioelectronic Noses," *Angew. Chem.*, vol. 121, pp. 2793–2796, 2009

© 2024. This work is published under <https://creativecommons.org/licenses/by/4.0/legalcode>(the "License"). Notwithstanding the ProQuest Terms and Conditions, you may use this content in accordance with the terms of the License.

¹Y S Waghode,
¹S Habibuddin,
¹Bhagyashri B,
¹T S Hibare,
²Aarav Mehta,
³R R Kalesh ,
¹R N Kamble,
¹V A Bambole

Monitoring The Size Of Cdse Quantum Dots For Dye-Sensitized Solar Cell With Temperature Gradient



Abstract: - Novel reaction parameters for synthesizing CdSe Quantum Dots (QD's) of particle size of unit dimensions measured in nanometer is claimed herewith. The investigation systematically explored various sets of reaction conditions, in particular, the impact of reaction temperature, on the structural, morphological, optical, and other atomic scale properties of the CdSe QD's. Particle Size, as small as, 1 nm and with stability at ambient temperature could be easily obtained with β ME as the capping agent. Characterization of, thus synthesized, CdSe QD's were done using XRD, UV-Visible spectroscopy, SEM, FTIR, HRTEM, EDX, and SAED techniques. The XRD results revealed that the size of the particles is between 2.4nm to 9nm and is in the cubic phase. SEM images clearly shows that the particle size increases with the increasing temperature. Further, HRTEM confirms the average particle size to be 3.6nm and smallest particle size as 1 nm. Also observed is intermixing of both, wurtzite and zinc blende structures. The EDX study confirms the percentage of Cd and Se to be 76.03 % and 23.96 % respectively. All the characterization techniques carried out, coherently lead to the conclusion of formation QD's of CdSe. The size of which could be controlled by varying the temperature. The CdSe QD's nanoparticles remained stable in ambient conditions over longer period of time.

Keywords: Quantum Dots (QD's), Capping agents, Colloidal Method, Wurtzite Structure, Dye-Sensitized Solar Cell.

¹Department of Physics, University of Mumbai, Vidyanagari Campus, Kalina, Santacruz (E), Mumbai 400 098, India.

²Hill Spring International School, Mumbai 400 034, India.

³Department of Physics, Institute of Science, 15, Madam Cama Road, Mantralaya, Fort, Mumbai 400 032, India.

Corresponding author Email: vaishali.bambole@physics.mu.ac.in

Copyright © JES 2024 on-line : journal.esrgroups.org

I. INTRODUCTION

Nanostructure material is 10^{-5} times smaller than a human hair's diameter; it is one billionth of a meter. On basis of dimensions, Nanomaterials are categorized as zero-dimensional, one dimensional, two-dimensional and three dimensional which are represented by 0D (Quantum dots), 1D (Nanorod), 2D (Nanosheet) and 3D (Nanoflowers) respectively [1]. The motion of electrons from conduction band and holes or excitons from valence band (bound pairs of conduction band electrons and valence band holes) are confined in all the three directions of a structure for quantum dots[2-4]. Since they were first identified in the 1980's, Semiconductor nanocrystals are also referred as Quantum Dots (QD's)[5-20]. A type of semiconductor nanocrystal known as Colloidal Quantum Dots has particle size smaller than the exciton Bohr radius of 5.4 nm for CdSe and their properties are dissimilar to those of bulk object due to few nanometers[21-26]. semiconductors QD's of II-VI group metal chalcogenides, especially ZnS, CdSe, and CdTe were extensively investigated due to their quantum confinement properties[27]. The quantum confinement effect occurs when the size of a particle is comparable to the electron's de Broglie wavelength. The Hot Injection method is a general procedure for synthesizing high-quality crystalline II-VI semiconductor material, where in initially Cadmium precursor $(\text{CH}_3)_2\text{Cd}$ or CdO is dissolved in coordination ligands such as Trioctylphosphine oxide, Hexylphosphine acid, or Tetradecylphosphonic acids. Next, the selenium precursor (Se dissolve in TOP) is quickly injected into the Hot coordination reaction mixture, initiating the nucleation process. Subsequent growth is carried out at a relatively lower temperature. This Process was first reported by Murray et al. [28], and later on, Peg et al. and Talpin et al. have developed the Hot Injection Procedure [29-36]. The synthesizing of CdSe QD's has been tried by numerous researchers using different techniques or by utilizing Cd and Se precursors. Lately, several methods have been tried to generate CdSe QD's: liquid paraffin with a combination[37], one-pot hydrothermal synthesis[38], microwave and electron beam irradiation[39,40], colloidal reaction temperature technique[41], and aqueous solution[42-45]. In contrast to these methods, the synthesis process that employ an aqueous solution have good water solubility and are easy, environmentally friendly, and highly reproducible.

When stimulated by UV light, QD's with diameters of 5-6nm emit longer wavelengths, while smaller ones with sizes between 2-3nm emit shorter wavelengths and larger bandgap. Because the electrons in quantum dots are restricted to specific energy levels that are determined by the size of the particle (the smaller the particle, the greater the bandgap) [46-47]. Hence, shorter wavelength means higher photon energy, which is required for Photovoltaic conversions. In this paper we are reporting to have synthesized CdSe QD's by the wet chemical method (colloidal method) in which water is used as a solvent, and the reaction happens at ambient temperature. The synthesis procedure is economic gives us very small quantum dot particles. Xray & SEM studies revealed interesting structural and morphological changes depending on temperature variation. highly pure form of CdSe QD's were obtained due to unique experimental setup. At temperature of 400C experiment of 5 hours small QD's of size 3.5nm were obtained. with the size of QD falling in the range of 3.5nm to 4nm and Bandgap of 2.60eV is obtained. So, we can claim that these quantum dots have the potential application in Photovoltaic and Dye-Sensitized solar cell.

II. MATERIALS AND METHODS:

1. Materials:

Cadmium Acetate Dihydrate $[\text{Cd}(\text{CH}_3\text{COO})_2]$ (reagent grade, 98%, Aldrich), Selenium Metal Powder (Se) (100 mesh, 99.99% trace metals basis, Aldrich), 2-Mercaptoethanol ($\text{HOCH}_2\text{CH}_2\text{SH}$) (99%, SRL) also known as β ME, Sodium Sulphite (Na_2SO_3) (Sodium Sulfite, $\geq 98\%$, Aldrich). All of the materials were employed without further purification because they were of analytical grade. Water as solvent had been twice distilled was used to produce each solution.

2. Synthesis of CdSe quantum dots:

Solution A as stock solution of Sodium Selenosulphite (Na_2SeSO_3) in two neck flasks was prepared by mixing of 0.6040 gm of Na_2SO_3 and 0.0948 gm of Se metal powder in 50ml of double distilled water (DDW). This solution was then heated at 90°C for an hour. The second solution B was prepared by adding 0.46 gm of $[\text{Cd}(\text{CH}_3\text{COO})_2]$ in 50ml of DDW at 40°C for a period of 10 minutes. Solution A is then added to Solution B till the colourless solution B changes from Milky to dark lemon colour. Then 0.4ml of 2-Mercaptoethanol (β ME) is added drop by drop till end of the experiment. A set of four experiment done at temperature 40°C, 55°C, 70°C, and 85°C for material T40°C, T55°C, T70°C and T85°C Respectively. Fig (1) showing pictorial graph of

experiment. The Prepared Quantum dots were washed by Double Distilled Water for 3-4 times and keep it in Oven to dry the samples and convert it into the Powder.

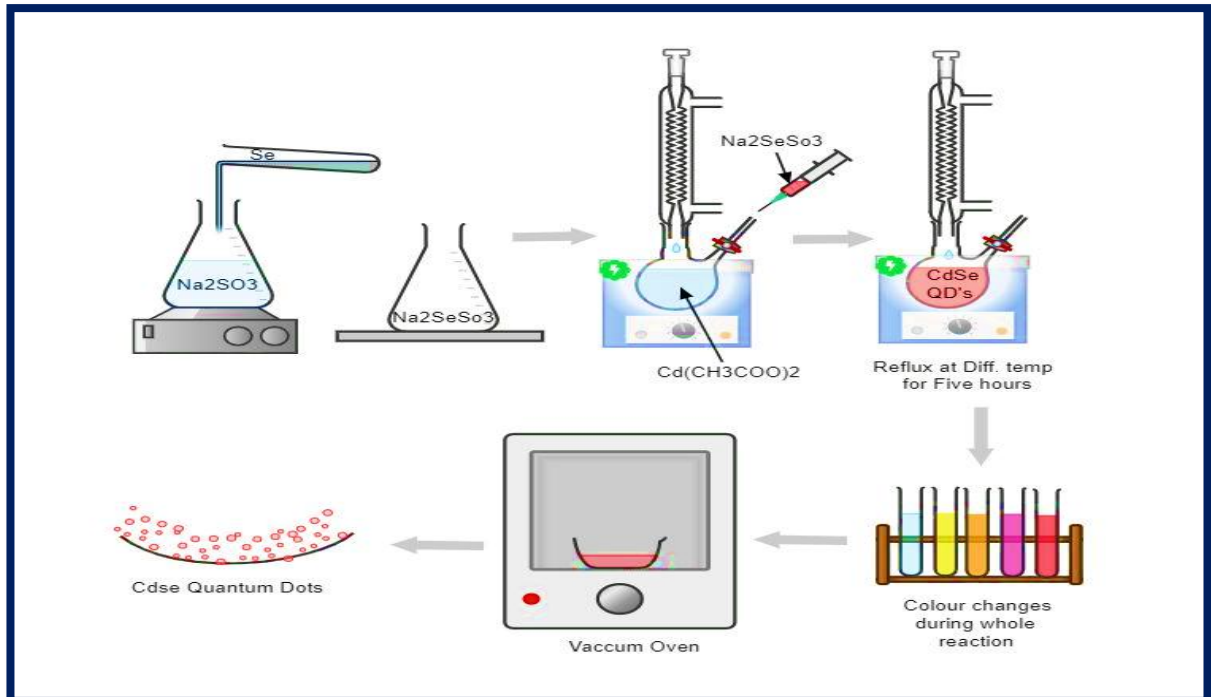


Fig. (1) Schematic illustration of the CdSe Colloidal Synthesis Process

III. RESULTS AND DISCUSSIONS:

1. Characterization and Evaluation:

An XPERT-PROMPD X-ray diffractometer with Cu-K α radiation ($\lambda = 1.5405 \text{ \AA}$) in the range of (100 to 800) was applied for the identification of materials, crystal composition and Phase identification. JEOL-IT300 for scanning electron microscopy (SEM). For Absorbance study, the UV-Visible Spectrometer (Perkin-Elmer, Lambda 750) was used. Using a Perkin-Elmer 1710, the Fourier Transform Infrared (FTIR) spectra was acquired at a resolution of 2cm⁻¹ across the 500-4000 cm⁻¹ range. Using Thermo Scientific- Talos F200X G2, a High-resolution transmission electron microscopy (HRTEM) was used for atomic-scale imaging of a sample of crystalline structure. Energy-dispersive X-ray spectroscopy (EDS) was carried out to identify the chemical compositions and Selected Area Electron Diffraction (SAED) was used to determine the significant level of crystallinity in the porous material.

2. XRD Characterization:

The structure, composition and crystallite size analysis of the prepared CdSe QD's was performed using an XPERT-PROMD X-ray diffractometer (XRD) instrument recorded between the 2θ angles 20° to 60° . The diffraction graph in the XRD shown in Figure(2). The standard [ICDD No. 19-191][48,49] and [JCPDS No. 19-191][50-60] have been three clear wide peaks could be identified at $2\theta = 26.08^\circ, 42.29^\circ, 46.28^\circ$ and 50.55° which corresponds to the lattice planes (111), (220) and (311). The formation of CdSe nanocrystalline structure is confirmed by peak broadening.

To calculate the crystallites size from Debye-Scherrer's formula,

$$D = \frac{K\lambda}{\beta \cos\theta} \quad (1)$$

Where,

D = crystallites size (nm)

K = 0.9 (Scherrer's constant)

$\lambda = 0.15406\text{nm}$ (wavelength of the x-ray sources)

$\beta = \text{FWHM}$ (radians)

$\theta = \text{Peak Position}$ (radians)

To using the same, the estimate crystallite size was found out to be of CdSe QD's is 0.2 nm to 0.6 nm. Fig.(2) is the X-ray diffraction pattern of temperature of 40°C,55°C,70°C, and 85°C synthesized materials.

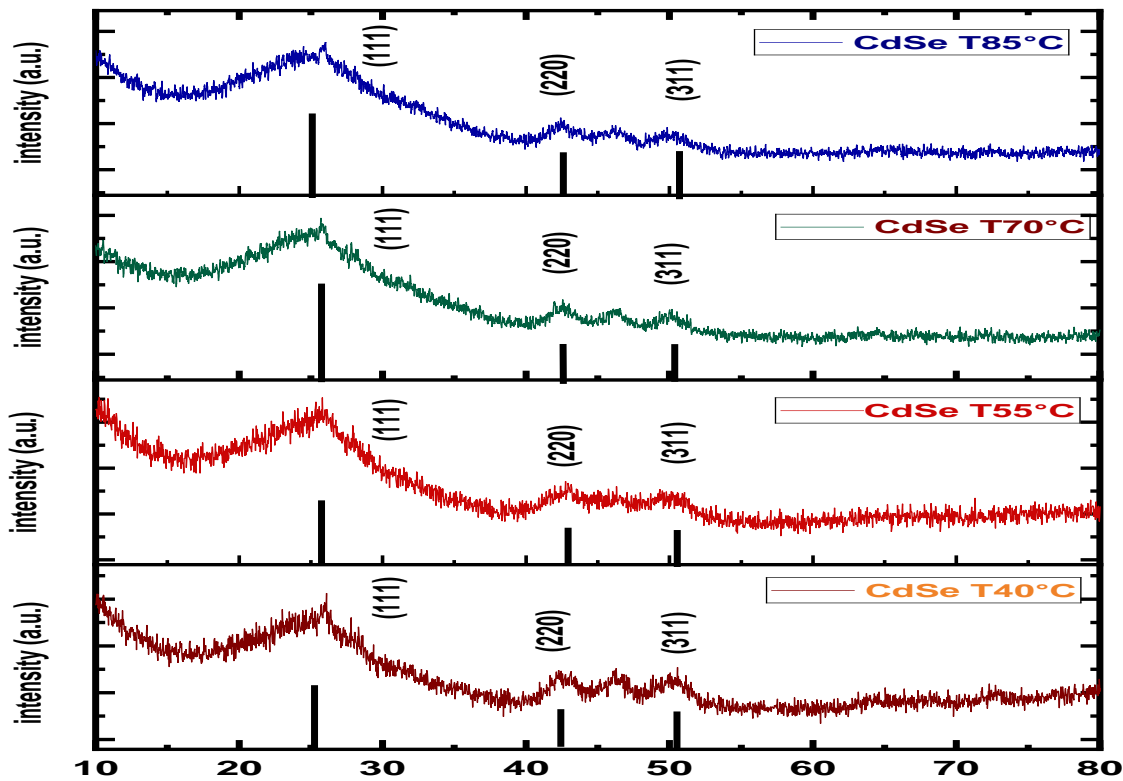


Fig (2): XRD pattern of CdSe QD's prepared at 40°C, 55°C, 70°C and 85°C

3. SEM Characterization:

Fig. (3) is the surface morphology of the CdSe Quantum dots for the temperature series of 40°C,55°C,70°C and 85°C of samples T40°C,T55°C,T70°C and T85°C are represented the SEM images of temperature series at 1000 magnification are represented in fig. a,b,c,and d and at 3000 magnification in fig. e,f,g,and h for sample T40°C,T55°C,T70°C and T85°C respectively. The particle size is being increases with increasing temperature. Also, Fig.3 is shows image of the uneven orientation of grains in the SEM image seems rough and agglomerated. It is preferable to trap charge carriers inside the gadget because of its rough construction, but doing so also reduces the device's responsiveness and mobility [61].

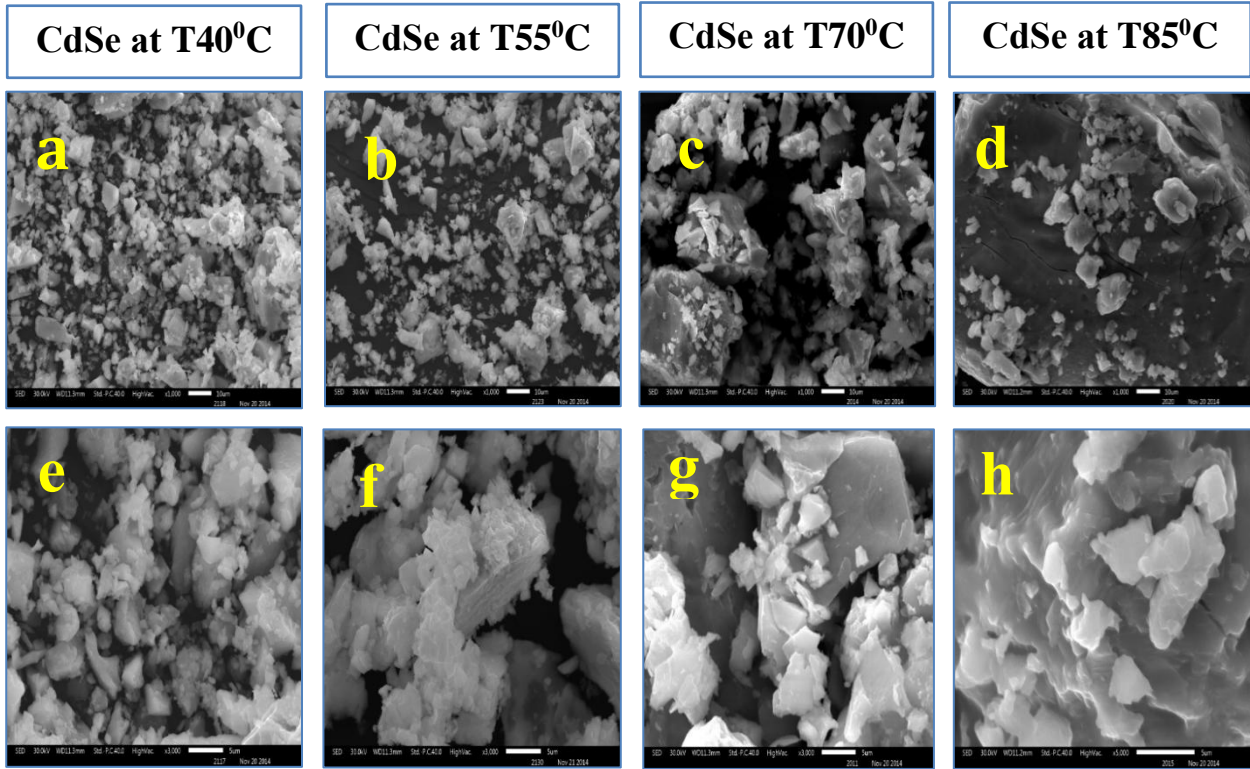


Fig. 3 (a-d) Temperature series of magnification rate 1000 and Fig. 3 (e-h) magnification rate 3000 for 40°C, 55°C, 70°C and 85°C of Samples T40°C, T55°C, T70°C and T85°C respectively

4. UV-Visible Spectroscopy:

Before being transferred into a quartz cuvette for analysis, a tiny portion of the powdered samples of T40°C, T55°C, T70°C and T85°C were sonicated in double distilled water to ensure appropriate dispersion. The UV-Vis absorption spectra confirms the red shift in colour implying increase in particle size [62-64]. The absorption spectra in Figure 3 shows how the particle size increases with temperature. Distinct peaks are observed at 595nm, 619nm, 599nm and 544nm with 40°C, 55°C, 70°C and 85°C respectively in all prepared CdSe QD's [65].

Bandgap determination:

Tauc's relation [2, 62, 66] was used to determine the optical transition energy from the absorption spectra.

$$(\alpha h\nu) = B (h\nu - E_g)^r \tag{2}$$

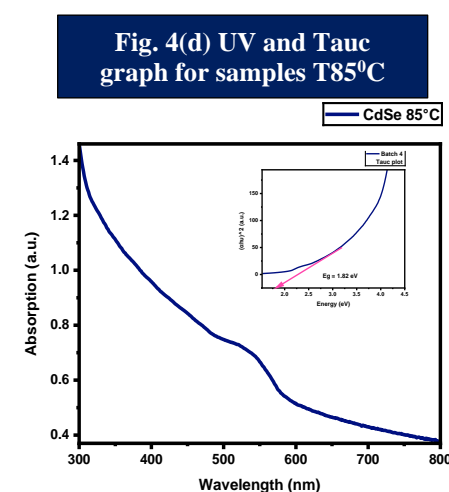
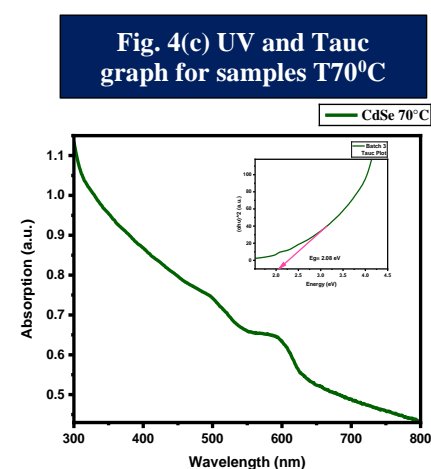
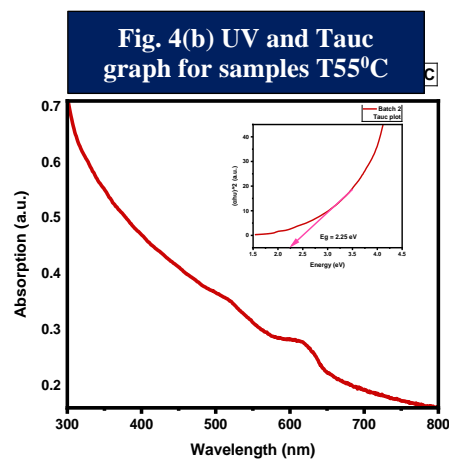
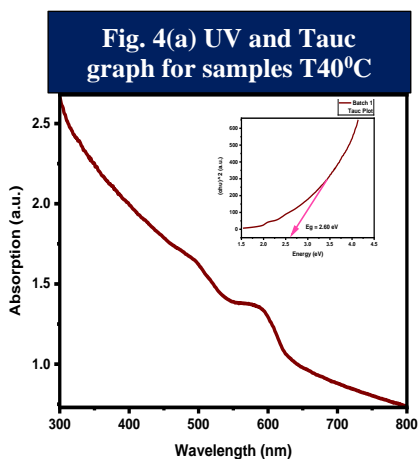
Where $h\nu$ is the photon energy, E_g is the optical bandgap, B is a constant, and r is an index that relies on the type of electronic transition that results in optical absorption. The values of r for allowed direct, allowed indirect, forbidden direct and forbidden indirect transitions are $1/2$, 2 , $3/2$, and 3 , respectively. [21]

CdSe known to have direct bandgap structure, For direct transitions, Eq. (1) becomes,

$$(\alpha h\nu) = B (h\nu - E_g)^{1/2} \tag{3}$$

The variation between $(\alpha h\nu)^2$ and $h\nu$ of the prepared CdSe QD's is shown in the inset spectra in each graph in Figure 3. The straight lines of the plots across a broad spectrum of photonic energy points to a direct transition. The bandgap for the samples prepared at 40°C, 55°C, 70°C and 85°C was determined to be 2.60 eV, 2.25 eV, 2.08 eV, and 1.89 eV, respectively, which exceeds the value of CdSe bandgap ($E_{gap} = 1.74$ eV) (1,21,67). The optical transition energy was obtained by extrapolating the linear region to the energy axis where $(\alpha h\nu)^2 = 0$.

Fig.4(a), 4(b), 4(c) and 4(d) shows UV and Tauc graph of samples 40°C, 55°C, 70°C and 85°C respectively.



5. FTIR Characterization:

The CdSe nonstructural material's organic species are identified and characterized by FTIR Spectroscopy. Figure 5 exhibits the FTIR analysis of CdSe QD's given below:

Sample No.	Wavenumber as per Analysis (Cm-1)	Analysis
T40°C	735	Cd - Se band stretching [72]
	992	CH2 rocking [4]
	1281	CH2 wagging [4]
	2607	symmetric stretching vibration of C – CH2 from the methylene chain [72]
	3762	weak band [72]
T55°C	742	Cd - Se band stretching [72]
	992	CH2 rocking [4]
	1289	CH2 wagging [54]
	1390	CH2 wagging [73]
	3279	O-H stretching of vibration peak [54]
T70°C	3435	the OH vibrations of hydroxyl group [74]
	742	Cd - Se band stretching [72]
	1000	C-O stretching [73]
	1421	CH2 bending [73]
	3279	OH group [73]
T85°C	2849	Symmetric stretching in CH2 vibrations of alkyl chain [73]
	633	C-S stretching [73]
	742	Cd - Se band stretching [72]
	992	CH2 rocking [4]
	1281	CH2 wagging [4]
T85°C	2888	Symmetric stretching in CH2 vibrations of alkyl chain [73]

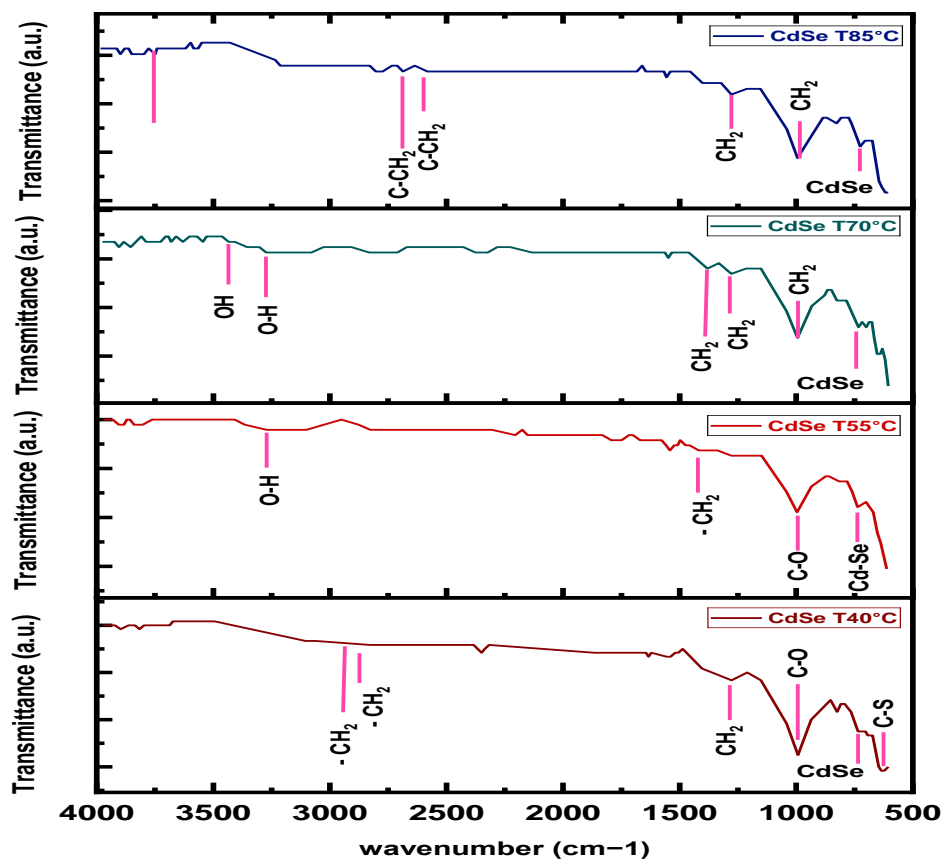


Fig. 5 FTIR Spectrum of the CdSe QD's

6. HR-TEM Characterization:

In Fig. 6(a) shows a HRTEM image of Samples T40°C, in which several CdSe QD's are clearly visible and seen crystalline in nature. Their average diameter is measured to be 3.65 nm. When compared to the size estimated from the XRD study, it was discovered that the quantum dots observed by HRTEM were slightly larger. The main reason of this result is due to the fact the X-ray only measures the nanocrystalline core size [68].

Fig. 6(b) shows a histogram of the measured QD's size distribution, Most of the QD's have diameters of between 3.5nm to 4 nm. Empirical functions provided by Lu et al. which correlated size with excitonic peak position indicate that their sizes and optical properties are consistent with one other (23,69,70,78,79). HRTEM of two QD's and their Fourier transformations are shown in Fig. 6(c) and (d).

The typical zig-zag pattern of the Wurtzite crystal structure appears by the Fourier transform in Fig. 6(c), and the QD's in Fig. 6(d) exhibit a Zinc blende crystal structure. The presence of CdSe QD's Quantum Yield (QY) increases as compared to the Wurtzite structure, Xia et al. hypothesized [69,71] that the Zinc blende structure in these particles leads to improved optoelectronic capabilities. The QD's revealed continuous lattice fringes of Wurtzite structured CdSe with an interplanar lattice spacing of 0.385 nm, according to HRTEM analysis in Fig. 6(e), the fringes are clearly shown in the same diagram at lower side. Intensity Profile obtained from the atomic column distance with lines in (e), with help of graph in Fig. 6(f) we have calculated the Interplanar Spacing in Fig. 6(e).

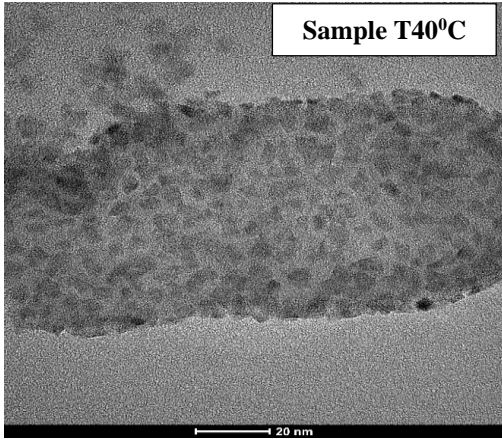


Fig. 6(a) HRTEM of CdSe QD's

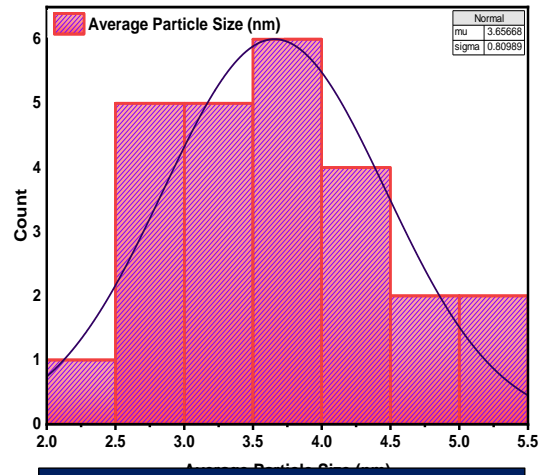


Fig. 6 (b) Histogram of CdSe QD's

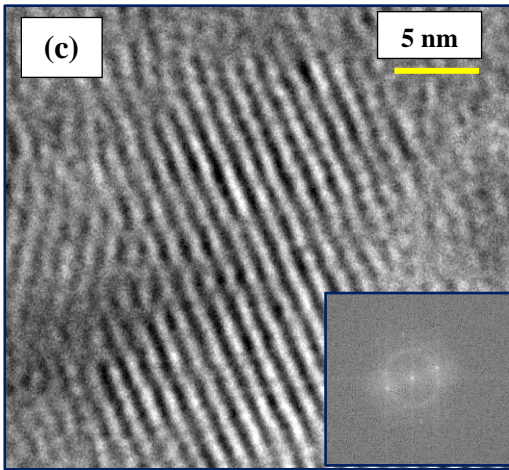


Fig. 6 (c) CdSe QD's with Wurtzite Structure

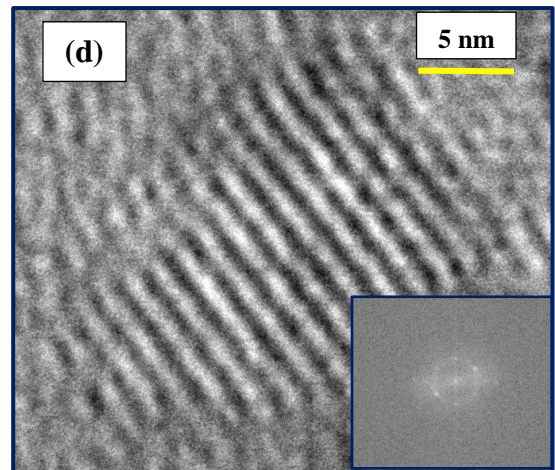


Fig. 6 (d) CdSe QD's with Zinc Blende Structure

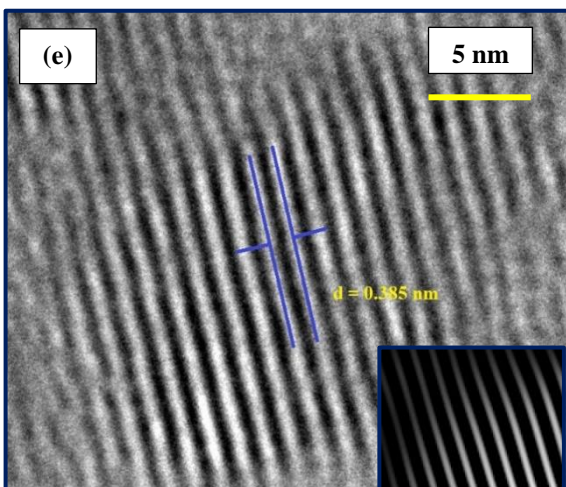


Fig. 6 (e) Interplanar Spacing of CdSe QD's

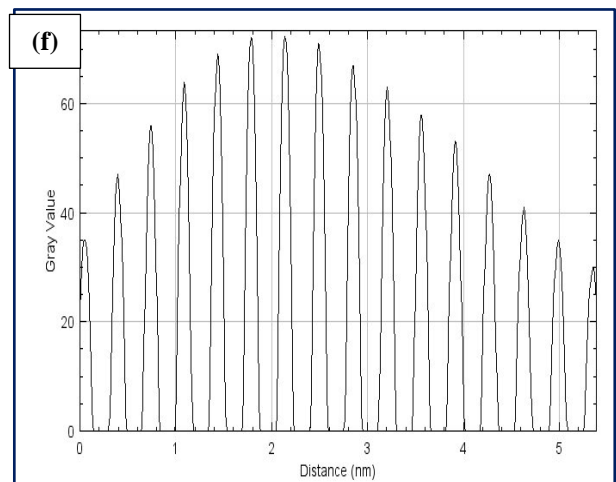
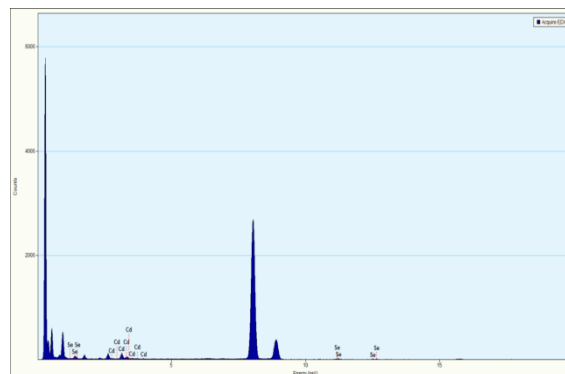


Fig. 6 (f) Intensity Profiles obtained from the atomic columns marked with lines in (e) with Interplanar Spacing

7. EDX Characterization:

In order to confirm the formation of CdSe QD's EDX analysis was performed. During the EDX measurement different areas were focused and the corresponding peaks are shown in Fig. 7. Both Cd and Se can be seen in the synthesized QD's in the EDX Spectrum. In Spectrum, the atomic quantity of Cd and Se were 76.03 and 23.96 respectively.

Details of the EDX Spectra of the CdSe QD's values measured as atomic and weight % are listed in Table 7 (i):



Element	Cadmium (Cd)L		Selenium (Se)K	
	Weight(%)	Atomic (%)	Weight (%)	Atomic (%)
CdSe QD's	81.87	76.03	18.12	23.96

Fig.7(i) EDX Spectra of CdSe QD's

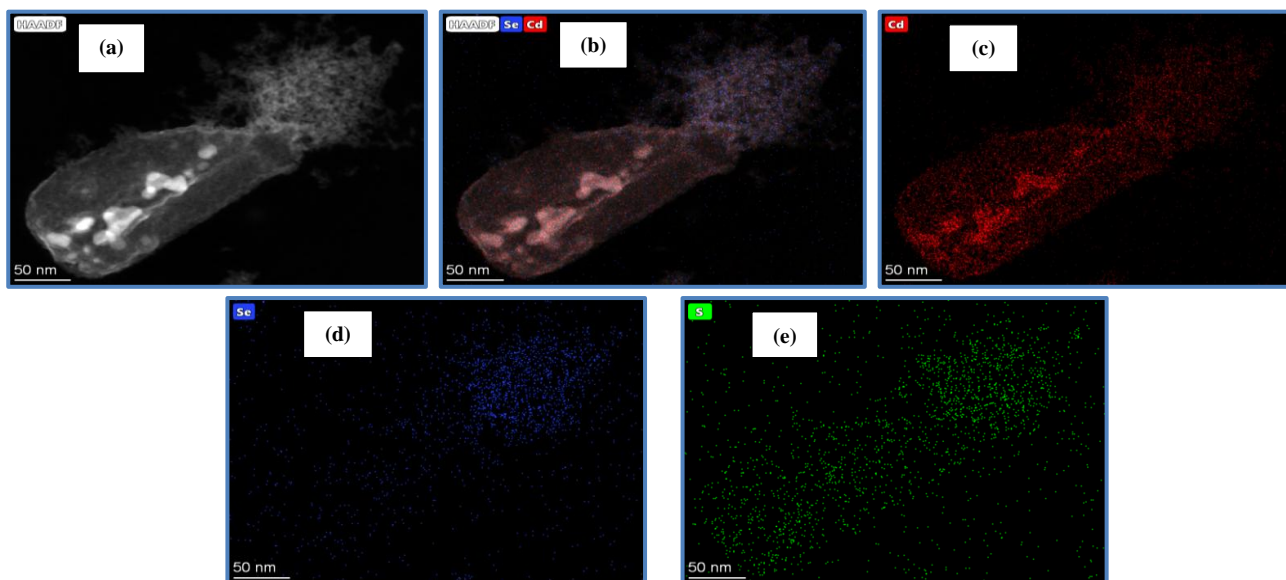


Fig. 7 Element distribution maps of CdSe QD's. (a-b) HAADF-STEM image, (c-e) positions of Cd, Se, and S atoms respectively.

Energy dispersion X-ray (EDX) Spectroscopy was used to generate element distribution maps in order to investigate the locations of Cd, Se, and S in CdSe QD's (Figure 7). Using Scanning transmission electron microscopy (STEM), a high angle annular dark field (HAADF) [23,78,79,80, 81] image of the sample CdSe QD's is displayed in Figure 7(a). The distribution of the Cd and Se elements in the same picture is shown in Figure 7(b). The positions of the atoms of Cd, Se, and S are shown in Figure 7(c-e). The intensity of the K (Se) or L (Cd) line in the EDX spectrum determines the colour brightness of a single selected pixel [23]. Element Cd distributed more in the lower half side as compared to the upper part of the structure in Fig. 7(c), Element Se distributed more in top right part of the structure in Fig.7 (d) and Element S is evenly distributed throughout the entire structure in Fig.7 (e).

8. SAED Characterization:

The SAED of the T400C sample is displayed in Figure 8(a); The Sample's good crystallinity is indicated by the presence of distinct diffraction rings. The lattice planes that emerged had smaller interplanar spacing (d) than the bulk and were indexed with cubic planes (111), (220), (311), (422), (511) and (531). These lattice planes are Polycrystalline clear diffraction rings structure associated with the CdSe QD's is cubic. [4,54, 68, 75, 76]. That XRD data by confirming that the Samples main phase has a Modified cubic structure. The polycrystalline clear diffraction rings structure of the produced CdSe nanoparticles' SAED pattern correlates to the lattice planes (111), (220), and (311), respectively, and is associated with cubic CdSe nanoparticles.

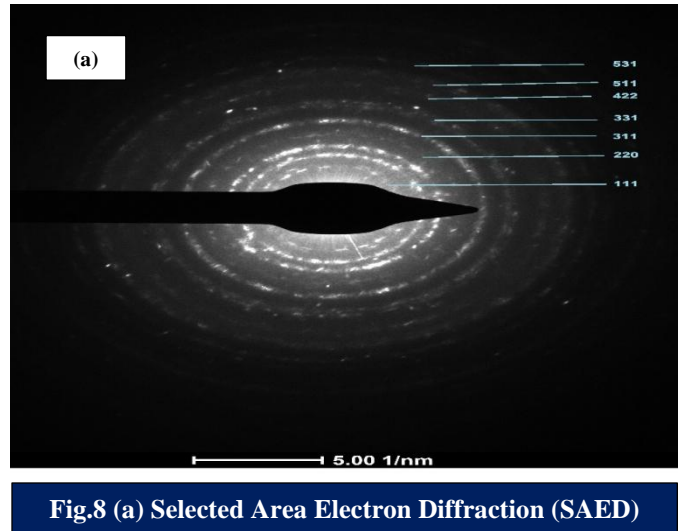


Fig.8 (a) Selected Area Electron Diffraction (SAED)

IV. CONCLUSION

Using the wet chemical method, CdSe QD's are synthesized. XRD results reveal 0.2nm to 0.6nm particle size, at temperature 40°C showing cubic phase with zinc blend structure of CdSe QD's. SEM morphology shows that the particle size increase with increasing temperature and the band gap decreases from 2.60 eV to 1.89 eV for temperature 40°C, 55°C, 70°C and 85°C respectively. Among all-material that we studied, the average particle size 3.65nm and the smallest particle size is 1nm as well as the Wurtzite crystal structure and Zinc blende crystal structure appears by the Fourier Transform of material of temperature 40°C. The surface area increases as the particle size decreases [82]. These CdSe QD's did not agglomerate even after 550 days without using any Stabilizing agent. With these results, we conclude that with temperature set at 400C is promising material for the Dye Sensitized Solar Cell application.

The typical zig-zag pattern of the Wurtzite crystal structure of CdSe QD's can be also confirmed by Fast Fourier Transform (FFT) which is a generalized through ImageJ plug in for the calculation of Fourier transform. In Fig. 6(c), and the QD's in Fig. 6(d) exhibit a zinc blende crystal structure.

V. ACKNOWLEDGEMENT

The authors extend their sincere gratitude to Government of Maharashtra's ISMAIL YUSUF COLLEGE of Arts, Science & Commerce, Mumbai, India for helping in FTIR, and Indian Institute of Technology Dhanbad, Jharkhand, India for helping with fine results of HRTEM.

VI. REFERENCES

- [1] Ameta, S.C., 2022. Nanomaterials: An Introduction. In The Science of Nanomaterials (pp. 1-18). Apple Academic Press.
- [2] Karan Surana, Pramod K Singh, Hee-Woo Rhee, B. Bhattacharya, "Synthesis, characterization and application of CdSe quantum dots", Journal of Industrial and Engineering Chemistry, Volume 20, Issue 6, Pages 4188-4193, 25 November 2014.
- [3] Karan Surana , Ibrahim T. Salisu , R.M. Mehra , Bhaskar Bhattacharya, "A simple synthesis route of low temperature CdSe-CdS core-shell quantum dots and its application in solar cell", Optical Materials, Volume 82, Pages 135-140, August 2018.
- [4] Mahesh Verma, D. Patidar, K. B. Sharma, and N. S. Saxena, "Synthesis, Characterization and Optical Properties of CdSe and ZnSe Quantum Dots", Journal of Nanoelectronics and Optoelectronics Vol. 10, 1-7, 2015.
- [5] Ekimov, A.I. and Onushchenko, A.A., 1982. Quantum size effect in the optical-spectra of semiconductor micro-crystals. Sov. Phys. Semicond, 16(7), pp.775-778.

- [6] Brus, L.E., 1984. Electron-electron and electron - hole interactions in small semiconductor crystallites: The size dependence of the lowest excited electronic state. *The Journal of chemical physics*, 80(9), pp.4403-4409.
- [7] Zhang, M., Bishop, B.P., Thompson, N.L., Hildahl, K., Dang, B., Mironchuk, O., Chen, N., Aoki, R., Holmberg, V.C. and Nance, E., 2019. Quantum dot cellular uptake and toxicity in the developing brain: Implications for use as imaging probes. *Nanoscale advances*, 1(9), pp.3424-3442.
- [8] Tang, X., Ackerman, M.M., Chen, M. and Guyot-Sionnest, P., 2019. Dual-band infrared imaging using stacked colloidal quantum dot photodiodes. *Nature photonics*, 13(4), pp.277-282.
- [9] Moon, H., Lee, C., Lee, W., Kim, J. and Chae, H., 2019. Stability of quantum dots, quantum dot films, and quantum dot light - emitting diodes for display applications. *Advanced Materials*, 31(34), p.1804294.
- [10] Chen, K.; Zhong, Q.; Chen, W.; Sang, B.; Wang, Y.; Yang, T.; Liu, Y.; Zhang, Y.; Zhang, H. Short-Chain Ligand-Passivated Stable α -CsPbI₃ Quantum Dot for All-Inorganic Perovskite Solar Cells. *Adv. Funct. Mater.* 2019, 29, 1900991.
- [11] Yan, D.; Shi, T.; Zang, Z.; Zhou, T.; Liu, Z.; Zhang, Z.; Du, J.; Leng, Y.; Tang, X. Ultrastable CsPbBr₃ Perovskite Quantum Dot and Their Enhanced Amplified Spontaneous Emission by Surface Ligand Modification. *Small* 2019, 15, 1901173.
- [12] Song, J.; Wang, O.; Shen, H.; Lin, Q.; Li, Z.; Wang, L.; Zhang, X.; Song, L. Over 30% External Quantum Efficiency Light-Emitting Diodes by Engineering Quantum Dot-Assisted Energy Level Match for Hole Transport. *Layer Adv. Funct. Mater.* 2019, 29, 1808377.
- [13] Ma, F.; Zhang, Q.; Zhang, C. Catalytic Self-Assembly of Quantum-Dot-Based MicroRNA Nanosensor Directed by Toehold-Mediated Strand Displacement Cascade. *Nano Lett.* 2019, 19, 6370–6376.
- [14] Shi, L.; Meng, L.; Jiang, F.; Ge, Y.; Li, F.; Wu, X.-G.; Zhong, H. In Situ Inkjet Printing Strategy for Fabricating Perovskite Quantum Dot Patterns. *Adv. Funct. Mater.* 2019, 29, 1903648.
- [15] Zhang, H.; Hu, N.; Zeng, Z.; Lin, Q.; Zhang, F.; Tang, A.; Jia, Y.; Li, L.S.; Shen, H.; Teng, F.; et al. High-Efficiency Green InP Quantum Dot-Based Electroluminescent Device Comprising Thick-Shell Quantum Dots. *Adv. Optical Mater.* 2019, 7, 1801602.
- [16] Yuan, J.; Bi, C.; Wang, S.; Guo, R.; Shen, T.; Zhang, L.; Tian, J. Spray-Coated Colloidal Perovskite Quantum Dot Films for Highly Efficient Solar Cells. *Adv. Funct. Mater.* 2019, 29, 1906615.
- [17] Chebroly, V.T.; Kim, H.-J. Recent progress in quantum dot sensitized solar cells: An inclusive review of photoanode, sensitizer, electrolyte, and the counter electrode. *J. Mater. Chem. C* 2019, 7, 4911–4933.
- [18] Li, X.; Lin, Q.; Song, J.; Shen, H.; Zhang, H.; Li, L.S.; Li, X.; Du, Z. Quantum-Dot Light-Emitting Diodes for Outdoor Displays with High Stability at High Brightness. *Adv. Opt. Mater.* 2020, 8, 1901145.
- [19] Sun, Y.; Su, Q.; Zhang, H.; Wang, F.; Zhang, S.; Chen, S. Investigation on Thermally Induced Efficiency Roll-Off: Toward Efficient and Ultrabright Quantum-Dot Light-Emitting Diodes. *ACS Nano* 2019, 13, 11433–11442.
- [20] Ouellette, O.; Lesage-Landry, A.; Scheffel, B.; Hoogland, S.; de Pelayo García Arquer, F.; Sargent, E.H. Spatial Collection in Colloidal Quantum Dot Solar Cells. *Adv. Funct. Mater.* 2020, 30, 1908200.
- [21] Waleed E. Mahmoud, Amal M. Al-Amri, S.J. Yaghmour, “Low temperature synthesis of CdSe capped 2-mercaptoethanol quantum dots”, *Optical Materials*, Volume 34, Issue 7, Pages 1082-1086, May 2012.
- [22] Yukun Gao and PG Yin, “Synthesis of cubic CdSe nanocrystals and their spectral properties”, *Nanomaterials and Nanotechnology Volume 7: 1–6 The Author(s) 2017*.
- [23] Kotin, P.A., Bubenov, S.S., Mordvinova, N.E. and Dorofeev, S.G., 2017. AgCl-doped CdSe quantum dots with near-IR photoluminescence. *Beilstein Journal of Nanotechnology*, 8(1), pp.1156-1166.
- [24] Alivisatos, A.P., 1996. Semiconductor clusters, nanocrystals, and quantum dots. *science*, 271(5251), pp.933-937.
- [25] Hoy, J., Morrison, P.J., Steinberg, L.K., Buhro, W.E. and Loomis, R.A., 2013. Excitation energy dependence of the photoluminescence quantum yields of core and core/shell quantum dots. *The Journal of Physical Chemistry Letters*, 4(12), pp.2053-2060.
- [26] Luther, J.M. and Pietryga, J.M., 2013. Stoichiometry control in quantum dots: a viable analog to impurity doping of bulk materials. *ACS nano*, 7(3), pp.1845-1849.
- [27] Ramalingam, G., Ragupathi, C., Kaviyarasu, K., Letsholathebe, D., Mohamed, S.B., Magdalane, C.M., Mola, G.T., Isaev, A.B. and Maaza, M., 2019. Up-scalable synthesis of size-controlled white-green emitting behavior of core/shell (CdSe/ZnS) quantum dots for LED applications. *Journal of nanoscience and nanotechnology*, 19(7), pp.4026-4032.
- [28] Cingrapu, S., Yang, Z., Sorensen, C.M. and Klabunde, K.J., 2012. Synthesis of CdSe/ZnS and CdTe/ZnS quantum dots: refined digestive ripening. *Journal of Nanomaterials*, 2012, pp.7-7.
- [29] D. Battaglia, J. J. Li, Y. Wang, and X. Peng, “Colloidal twodimensional systems: CdSe quantum shells and wells,” *Angewandte Chemie—International Edition*, vol. 42, no. 41, pp. 5035–5039, 2003.
- [30] X. Peng, L. Manna, W. Yang et al., “Shape control of CdSe nanocrystals,” *Nature*, vol. 404, no. 6773, pp. 59–61, 2000.
- [31] Z. A. Peng and X. Peng, “Formation of high-quality CdTe, CdSe, and CdS nanocrystals using CdO as precursor,” *Journal of the American Chemical Society*, vol. 123, no. 1, pp. 183–184, 2001.

- [32] L. Qu, Z. A. Peng, and X. Peng, "Alternative routes toward high quality CdSe nanocrystals," *Nano Letters*, vol. 1, no. 6, pp. 333–337, 2001.
- [33] D. V. Talapin, A. L. Rogach, A. Kornowski, M. Haase, and H. Weller, "Highly luminescent monodisperse CdSe and CdSe/ZnS nanocrystals synthesized in a hexadecylamine-trioctylphosphine oxide-trioctylphosphine mixture," *Nano Letters*, vol. 1, no. 4, pp. 207–211, 2001.
- [34] H. Yang, N. Fan, W. Luan, and S. T. Tu, "Synthesis of monodisperse nanocrystals via microreaction: open-to-air synthesis with oleylamine as a coligand," *Nanoscale Research Letters*, vol. 4, no. 4, pp. 344–352, 2009.
- [35] W. W. Yu and X. Peng, "Formation of high-quality CdS and other II–VI semiconductor nanocrystals in noncoordinating solvents: tunable reactivity of monomers," *Angewandte Chemie—International Edition*, vol. 41, no. 13, pp. 2368–2371, 2002.
- [36] Cingarapu, S., Yang, Z., Sorensen, C.M. and Klabunde, K.J., 2012. Synthesis of CdSe/ZnS and CdTe/ZnS quantum dots: refined digestive ripening. *Journal of Nanomaterials*, 2012, pp.7-7.
- [37] Liu J., Gu S., Pan K., ET AL.: 'Synthesis and photoluminescence properties of high-quality CdSe quantum dot in liquid paraffin', *Micro Nano Lett.*, 2011, 6, (11), pp. 964–966
- [38] Song X., Liu X., Yan Y., ET AL.: 'One-pot hydrothermal synthesis of thioglycolic acid-capped CdSe quantum dots-sensitized mesoscopic TiO₂ photoanodes for sensitized solar cells', *Sol. Energy Mater. Sol. Cells*, 2018, 176, pp. 418–426
- [39] Zhang T., Jin J., Yang C., ET AL.: 'Microwave synthesis CdSe quantum dot clusters via ribonuclease a protein', *Micro Nano Lett.*, 2012, 7, (12), pp. 1289–1291
- [40] Singh A., Tripathi V.S., Neogy S., ET AL.: 'Facile and green synthesis of 1-thioglycerol capped CdSe quantum dots in aqueous solution', *Mater. Chem. Phys.*, 2018, 214, pp. 320–329
- [41] Bhand G.R., Lakhe M.G., Rohom A.B., ET AL.: 'Synthesis and characterization of controlled size CdSe quantum dots by colloidal method', *J. Nanosci. Nanotechnol.*, 2018, 18, (4), pp. 2695–2701
- [42] Singh A., Guleria A., Kunwar A., ET AL.: 'Saccharide capped CdSe quantum dots grown via electron beam irradiation', *Mater. Chem. Phys.*, 2017, 199, pp. 609–615
- [43] Wang Y., Yang K., Pan H., ET AL.: 'Synthesis of high-quality CdSe quantum dots in aqueous solution', *Micro Nano Lett.*, 2012, 7, (9), pp. 889–891
- [44] Lan Y., Yang K., Wang Y., ET AL.: 'Aqueous synthesis of highly luminescent CdSe quantum dots with narrow spectra using hydrazine hydrate reduction selenium', *Micro Nano Lett.*, 2014, 9, (3), pp. 202–205
- [45] Akter, M., Khan, M.N.I., Mamur, H. and Bhuiyan, M.R.A., 2020. Synthesis and characterisation of CdSe QDs by using a chemical solution route. *Micro & Nano Letters*, 15(5), pp.287-290.
- [46] Brus, L.E. Electron-Electron and electron-hole interactions in small semiconductor crystallites: The size dependence of the lowest excited electronic state. *J. Chem. Phys.* 1984, 80, 4403–4409.
- [47] Sanmartín-Matalobos, J., Bermejo-Barrera, P., Aboal-Somoza, M., Fondo, M., García-Deibe, A.M., Corredoira-Vázquez, J. and Alves-Iglesias, Y., 2022. Semiconductor Quantum Dots as Target Analytes: Properties, Surface Chemistry and Detection. *Nanomaterials*, 12(14), p.2501.
- [48] Avinash Singh, Amit Kunwar, and M. C. Rath, "L-Cysteine Capped CdSe Quantum Dots Synthesized by Photochemical Route", *Journal of Nanoscience and Nanotechnology* Vol. 17, 1–8, 2017
- [49] Zainab H. Omran, Odai N. Salman* and A. K. Ali, "Preparation CdSe Quantum Dots using laser ablation technique for Dye-Sensitized Solar Cell", *International Journal of Nanoelectronics & Materials*. Vol. 14 Issue 1, p61-69. 9p, Jan2021.
- [50] Waleed E. Mahmoud, Amal M. Al-Amri, S.J. Yaghmour, "Low temperature synthesis of CdSe capped 2-mercaptoethanol quantum dots", *Optical Materials*, Volume 34, Issue 7, Pages 1082-1086, May 2012.
- [51] Mahesh Verma, D. Patidar, K. B. Sharma, and N. S. Saxena, "Synthesis, Characterization and Optical Properties of CdSe and ZnSe Quantum Dots", *Journal of Nanoelectronics and Optoelectronics* Vol. 10, 1–7, 2015.
- [52] Kale, R.B. and Lokhande, C.D., 2004. Band gap shift, structural characterization and phase transformation of CdSe thin films from nanocrystalline cubic to nanorod hexagonal on air annealing. *Semiconductor science and technology*, 20(1), p.1.
- [53] Kale, R.B. and Lu, S.Y., 2015. Air annealing induced transformation of cubic CdSe microspheres into hexagonal nanorods and micro-pyramids. *Journal of Alloys and Compounds*, 640, pp.504-510.
- [54] Jamble, S.N., Ghoderao, K.P. and Kale, R.B., 2017. Hydrothermal assisted growth of CdSe nanoparticles and study on its dielectric properties. *Materials Research Express*, 4(11), p.115029.
- [55] Raut, V.S., Lokhande, C.D. and Killedar, V.V., 2017. Studies on effect of pH on structural, optical and morphological properties of chemisynthesized CdSe grains. *International Journal of Engineering*, 10(1), p.2017.
- [56] Hodlur, R.M. and Rabinal, M.K., 2014. A new selenium precursor for the aqueous synthesis of luminescent CdSe quantum dots. *Chemical Engineering Journal*, 244, pp.82-88.
- [57] Kim, J., Choi, S., Noh, J., Yoon, S., Lee, S., Noh, T., Frank, A.J. and Hong, K., 2009. Synthesis of CdSe–TiO₂ nanocomposites and their applications to TiO₂ sensitized solar cells. *Langmuir*, 25(9), pp.5348-5351.

- [58] Akter, M., Khan, M.N.I., Mamur, H. and Bhuiyan, M.R.A., 2020. Synthesis and characterisation of CdSe QDs by using a chemical solution route. *Micro & Nano Letters*, 15(5), pp.287-290.
- [59] Kumar Gupta D., Verma M., Patidar D., ET AL.: 'Synthesis, characterization and optical properties of CdSe and ZnSe quantum dots', *Nanosci. Nanotechnol.–Asia*, 2017, 7, (1), pp. 73–79
- [60] Masteri-Farahani M., Mollatayefeh N.: 'Chiral colloidal CdSe quantum dots functionalized with cysteine molecules: new optical nanosensor for selective detection and measurement of morphine', *Colloids Surf. A, Physicochem. Eng. Aspects*, 2019, 569, pp. 78–84
- [61] Wang, Q. and Seo, D.K., 2006. Synthesis of deep-red-emitting CdSe quantum dots and general non-inverse-square behavior of quantum confinement in CdSe quantum dots. *Chemistry of Materials*, 18(24), pp.5764-5767.
- [62] Waleed E. Mahmoud, Amal M. Al-Amri, S.J. Yaghmour, "Low temperature synthesis of CdSe capped 2-mercaptoethanol quantum dots", *Optical Materials*, Volume 34, Issue 7, Pages 1082-1086, May 2012.
- [63] Waleed E. Mahmoud, A.A. Al-Ghamdi, F. El-Tantawy, S. Al-Heniti, *J. Alloys Compd.* 485 (2009) 59.
- [64] Waleed E. Mahmoud, *J. Cryst. Growth* 312 (2010) 3075.
- [65] Karan Surana, R.M. Mehra, B. Bhattacharya, "Quantum Dot Solar Cells with size tuned CdSe QDs exhibiting 1.51V", *Materials Today: Proceedings* 5, Volume 5, Issue 3, Part 1, Pages 9108-9113, 2018.
- [66] J. Tauc, *Amorphous and Liquid Semiconductors*, Plenum Press, New York, NY, 281 1974. 282.
- [67] Waleed E. Mahmoud, H.M. El-Mallah, *J. Phys. D: Appl. Phys.* 42 (2009) 035502.
- [68] Wageh, S., Al-Ghamdi, A., Jilani, A. and Iqbal, J., 2018. Facile Synthesis of Ternary Alloy of CdSe_{1-x}S_x Quantum Dots with Tunable Absorption and Emission of Visible Light. *Nanomaterials*, 8(12), p.979.
- [69] Fernández-Delgado, N., Herrera, M., Tavabi, A.H., Luysberg, M., Dunin-Borkowski, R.E., Rodríguez-Cantó, P.J., Abargues, R., Martínez-Pastor, J.P. and Molina, S.I., 2018. Structural and chemical characterization of CdSe-ZnS core-shell quantum dots. *Applied Surface Science*, 457, pp.93-97.
- [70] W.W. Yu, L. Qu, W. Guo, X. Peng, Experimental determination of the extinction coefficient of CdTe, CdSe, and CdS nanocrystals, *Chem. Mater.* 15 (2003) 2854–2860.
- [71] X. Xia, Z. Liu, G. Du, Y. Li, M. Ma, Wurtzite and zinc-blende CdSe based core/shell semiconductor nanocrystals: Structure, morphology and photoluminescence, *J.Lumin.* 130 (2010) 1285–1291.
- [72] P Sanjay , K Deepa, J Madhavan and S Senthil, "Synthesis and Spectroscopic Characterization of Cdse Nanoparticles for Photovoltaic Applications", *IOP Conf. Series: Materials Science and Engineering* 360,012010,(2018).
- [73] G. Ramalingam, K. Venkata Saravanan, T. Kayal Vizhi, M. Rajkumar and Kathirvelu Baskar, "Synthesis of water-soluble and bio-tagable CdSe@ZnS quantum dots", *RSC Adv.*, 8, 8516, 2018.
- [74] S. Reghuram, A. Arivarasan , R. Kalpana * and R. Jayavel, "CdSe and CdSe/ZnS quantum dots for the detection of C-reactive protein", *Journal of Experimental Nanoscience* ,Volume 10, Issue 10, 2015
- [75] Kale, R.B. and Lokhande, C.D., 2005. Systematic study on structural phase behavior of CdSe thin films. *The Journal of Physical Chemistry B*, 109(43), pp.20288-20294.
- [76] Nor Aliya Hamizi* , Mohd Rafie Johan, "Enhanced Ripening Behaviour of Cadmium Selenide Quantum Dots (CdSe QDs)", *Int. J. Electrochem. Sci.*, 7 8473 – 8480, (2012).
- [77] E.A. Larios-Rodríguez, F.F. Castellón-Barraza, R. Herrera-Urbina, U. Santiago, A. Posada-Amarillas, Synthesis of aucorepdshell nanoparticles by a green chemistry method and characterization by HAADF-STEM imaging, *J. Clust. Sci.* 28 (2017) 2075–2086
- [78] D.S. He, Z.Y. Li, J. Yuan, Kinematic HAADF-STEM image simulation of small nanoparticles, *Micron* 74 (2015) 47–53
- [79] N. Fernandez-Delgado, M. Herrera, J. Pizarro, P. Galindo, S.I. Molina, HAADF-STEM for the analysis of core-shell Quantum Dots, *J. Mater. Sci.* (2018).
- [80] Held, J.T., Hunter, K.I., Dahod, N., Greenberg, B., Reifsnnyder Hickey, D., Tisdale, W.A., Kortshagen, U. and Mkhoyan, K.A., 2018. Obtaining Structural Parameters from STEM–EDX Maps of Core/Shell Nanocrystals for Optoelectronics. *ACS Applied Nano Materials*, 1(2), pp.989-996.
- [81] Weigert, F., Müller, A., Häusler, I., Geißler, D., Skroblin, D., Krumrey, M., Unger, W., Radnik, J. and Resch-Genger, U., 2020. Combining HR-TEM and XPS to elucidate the core–shell structure of ultrabright CdSe/CdS semiconductor quantum dots. *Scientific reports*, 10(1), p.20712.
- [82] Alshora, D.H., Ibrahim, M.A. and Alanazi, F.K., 2016. Nanotechnology from particle size reduction to enhancing aqueous solubility. In *Surface chemistry of nanobiomaterials* (pp. 163-191). William Andrew Publishing.

¹V. A. Rana,
²K. C. Vaghela
³H. P. Vankar
⁴K.N. Shah

**Complex permittivity and Complex
 Impedance Analysis of Binary
 Mixtures of Ethylene Glycol
 Monophenyl Ether and Methanol**



Abstract: - Within the frequency range of 20Hz to 2MHz at 299.15 K, the relative complex permittivity (ϵ^*), electric modulus (M^*), alternating current (AC) electric conductivity, and complex impedance (Z^*) spectra of EGMPE, MeOH, and their binary mixtures are investigated. The HN model has been used to fit the complex permittivity data, and the Nyquist plot have been used to analyse the complex impedance data. The different formalisms such as complex electric modulus and complex impedance have been used to determine the geometric relaxation time (τ_g), ionic conductivity relaxation time (τ_σ), and electrode polarisation relaxation time (τ_{EP}). All these parameters are used to discuss in detail various processes responsible for electric/dielectric properties of binary mixture of EGMPE and MeOH.

Keywords: Dielectric spectrum, Electric modulus, Complex impedance

^{1,2}Department of Physics, School of sciences, Gujarat University, Ahmedabad-380009, Gujarat, India.

³Department of Physics, Government Science College, Vankal-394430, Gujarat, India.

⁴Department of Computer Science and Engineering, United world of Computational Intelligence, Karnavati University, Gandhinagar-382422, Gujarat, India.

¹ Corresponding author: K.C. Vaghela
 Email-addresses:² kishanvaghela389@gmail.com

Copyright © JES 2024 on-line: journal.esrgroups.org

I. INTRODUCTION

The technique of dielectric spectroscopy is broadly utilized to explain the molecular dynamics of organic polar liquids in both: their pure and mixed states. This method requires evaluating the complex permittivity of samples over a wide frequency range, either at a particular temperature or over a broad range of temperatures. A number of dielectric investigations on polar-polar and polar-non-polar liquid mixtures have been conducted to learn about molecular interactions and relaxation processes in the mixed states[1][2][3][4][5][6]. These studies helped to gain information on the dynamics of H-bonds[2][3][4][6]. One can use complex permittivity data to calculate electric modulus, electrical conductivity and complex impedance, which can give additional information about structural configurations, electrochemical properties and behavior of conducting species of binary mixtures. In past, very few researchers have studied the polar solvent dynamics with relevance to the evaluation of their structural behavior of EGMPE-MeOH mixtures [7] . In past, Chaube et al. [6] studied dielectric relaxation of a binary mixture of ethylene glycol mono phenyl ether and methanol by time domain reflectometry. They examined dielectric characterization in the microwave frequency range (10 MHz to 25 GHz) at four different temperatures. They obtained different dielectric parameters such as static permittivity, permittivity at optical frequency and relaxation time using CNLS fit method. Through this study they obtained valuable information about the orientation of dipole, hydrogen bonds, and molecular interaction. In present investigation, dielectric properties of EGMPE, MeOH and their binary mixtures of varying concentration in frequency range 20 Hz to 2MHz at 299.15 K have been studied. In the present study, we are examining the complex permittivity and complex impedance spectra in the lower frequency region. The HN model has been used to fit the complex permittivity data, and the Nyquist plot have been used to analyses the complex impedance data. This study differs from the previous study in their methodological approaches, frequency ranges and also outcomes based on different studied parameters.

EGMPE, commonly used as preservative and antioxidants, surface active agent, is a six-carbon aromatic ring with a phenyl group attached to one carbon atom of the ethylene glycol backbone. On the other hand, the methanol, sometimes known as wood alcohol, is one of the first organic chemicals to find widespread usage in the laboratories and industry[8][9]. Results reported in the present investigations will be helpful to understand the structural changes taking place among the industrially important compounds: EGMPE and MeOH, in their mixed state of varying composition.

II EXPERIMENTAL

1. Material

MeOH of HPLC grade with a minimum assay (GC) of 99.7% purity was given by Ranbaxy, while SRL Pvt. Ltd. provided EGMPE with a minimum assay (GC) of 99% purity. EGMPE and methanol were mixed to obtain binary mixtures at 21 various volume fraction concentrations. The mole fraction of EGMPE in MeOH was derived from the volume fraction [2], using relation

$$X_a = \frac{\rho_a \times V_a / M_a}{\rho_a \times V_a / M_a + \rho_b \times V_b / M_b} \quad (1)$$

Where, a = EGMPE, b = MeOH, M = Molecular weight, V = Volume, ρ = Density t° .

2. Measurement

Utilizing the capacitance measuring process the value of the complex relative dielectric function (ϵ^*) of EGMPE, MeOH, and their mixtures were determined over frequency span of 20 Hz to 2 MHz. Using an Agilent E4980A precision LCR meter, the parallel capacitance and parallel resistance of the measurements of Agilent

16452A four terminal liquid dielectric test setups without and with samples were obtained[10]. While calculating the values of the complex relative dielectric function, the correction coefficient for the test fixture was also taken into account to eliminate the influence of erroneous capacitance. Using a constant temperature water bath (Model Industrial Corporation, India manufacture) with an accuracy of +0.1 K, the temperature of the solutions was kept at the required constant level. All measurements were made at a fixed temperature of 299.15 K. Determination of various parameters such as complex function(ϵ^*), complex electric modulus(M^*),and complex impedance (Z^*) were evaluated using relations reported in reference[11][12][7].

III. RESULT AND DISCUSSION

Fig.1 illustrates the frequency and concentration dependence of the real part of the relative complex dielectric function (ϵ') of the binary mixture of EGMPE+ MeOH. The energy held in the material as a result of various polarizations is represented by the real component (ϵ') of the complex dielectric function ($\epsilon^*(\omega)$)[13]. Within the 20 Hz to 2 MHz frequency range, the spectra are split into two distinct parts. The ϵ' values in the low frequency region rise linearly as the frequency lowers by several orders of magnitude. On a log-log scale, the slope is negative and higher than unity. The presence of ionic impurities in the binary mixtures of polar liquids under study, result in the electrode polarization near to the surface of the measuring electrode/cell. This electrode polarization effect is manifested as enormously large values of ϵ' in the lower frequency range region, i.e. below 1 kHz. The electrode polarization effect is caused by the accumulation of ions and free charges at the interface between the dielectric material and electrode[14]. In the high frequency region beyond a few tens of kHz, ϵ' is frequency independent, giving the static dielectric constant. We have taken the ϵ' value at a frequency of 2 MHz as static dielectric constant[15]. The imaginary part (ϵ'') represents the energy loss as a result of dipole motion or movement of ionic species when there is an electric field present[13].

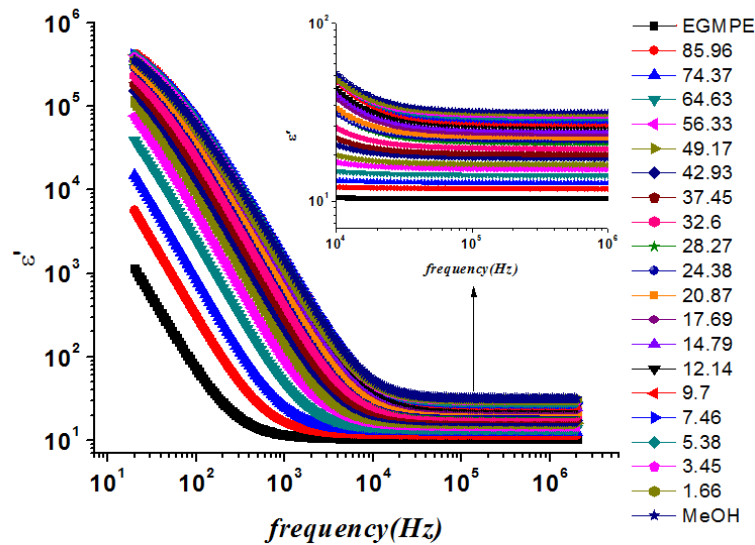


Fig.1 Frequency dependence of real part of relative complex dielectric function (ϵ') for binary mixtures of EGMPE and MeOH.

Fig. 2 displays the imaginary component of complex permittivity (ϵ'') versus frequency graph. The straight line in Fig. 2 with a negative slope, which results from decrement of (ϵ'') with frequency. shows that the material under investigation satisfies Ohm's law[16]. Ion jumps and conduction loss of migratory ions are the two causes of the significantly large value of (ϵ'') in the low frequency region.

The Havriliak-Negami (HN) model is frequently used expression to define the frequency dependence complex permittivity data for binary system of liquids and also explain motion extended to several molecular segment[17].

We fitted complex permittivity data to a single HN relaxation[17][18] model which is given by

$$\epsilon^* = \epsilon_\infty + \frac{\Delta\epsilon_{EP}}{[1+(j\omega\tau_{EP})^\alpha]^\beta} \tag{7}$$

$\Delta\epsilon_{EP} = \epsilon_\infty - \epsilon_0$; ϵ_∞ = High frequency limiting value of ϵ'

ϵ_0 = static permittivity at lower frequency

τ_{EP} = Electrode polarization relaxation time

α, β = asymmetry and broadness parameter of dielectric loss peak

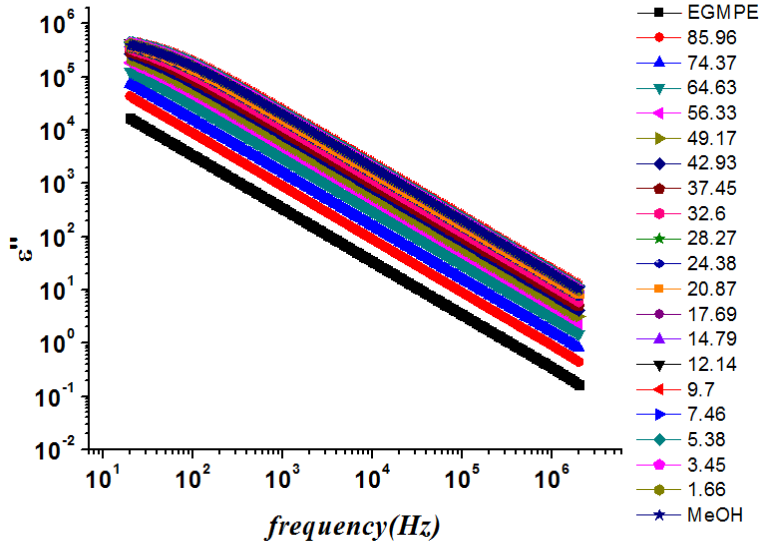


Fig.2 Frequency dependence of imaginary part of relative complex dielectric function (ϵ'') for binary mixtures of EGMPE and MeOH at 299.15K.

Table 1 Fitting parameters ϵ_0 , $\Delta\epsilon_{EP}$, τ_{EP} , α and β at 299.15 K temperature.

Concentration of EGMPE	ϵ_0	$\Delta\epsilon_{EP} \times 10^5$	τ_{EP} (ms)	α	β
1.0000	10.36	3.55	169	0.91	1.09
0.8597	11.71	4.51	82	0.90	1.09
0.7437	12.60	5.47	54	0.87	1.14
0.6463	13.91	6.07	33	0.86	1.15
0.5633	15.04	6.67	23	0.85	1.16
0.4917	16.01	7.42	19	0.83	1.19
0.4293	17.38	8.10	16	0.82	1.21
0.3745	18.29	8.63	14	0.81	1.23
0.3260	19.64	9.23	12	0.80	1.24
0.2827	21.06	9.14	9.1	0.78	1.26
0.2438	21.91	9.74	9.8	0.78	1.26
0.2087	22.88	10.02	9.4	0.78	1.27
0.1769	23.84	10.59	8.6	0.77	1.29
0.1479	24.74	10.99	8.3	0.76	1.30
0.1214	26.09	11.25	8.3	0.76	1.30
0.0970	27.09	11.26	7.6	0.76	1.31
0.0746	28.21	10.40	6.9	0.76	1.31
0.0538	29.26	11.49	7.9	0.75	1.32
0.0345	30.18	11.44	8.4	0.75	1.33
0.0166	30.89	11.42	9.0	0.74	1.35
0	31.74	11.42	8.4	0.71	1.39

Experimental and fitted plots of ϵ^* to the H-N model for EGMPE, MeOH and their binary mixtures are shown in Fig.3. From the figure, it can be seen that our data provides excellent fitting to the H-N model.

Fitting parameters $\Delta\epsilon_{EP}$, ϵ_o , τ_{EP} , α and β for all concentrations are tabulated in Table 1. The shape of dispersion is determined by the empirical parameters α and β , which usually displays Debye behavior at the low frequency end and an asymptotic long tail at the high frequency end. The objective function of CNLS fitting simultaneously includes the real and imaginary components of the complex permittivity to give a comprehensive fit. In Fig. 3, the plots of ϵ^* versus frequency demonstrate that EGMPE exhibits more significant electrode polarization (EP) compared to MeOH, which shows less significant EP.

The spectrum of frequency-dependent loss tangents ($\tan\delta$) for EGMPE, MeOH, and their binary mixtures are shown in Fig. 4. The relaxation frequency f_{EP} , at which bulk material properties and EP phenomena diverge is represented by the peak value of the $\tan\delta$ spectrum[19]. The relaxation time τ_{EP} (obtain from $\tan\delta$ spectra) was calculated using $\tau_{EP} = (2\pi f_{EP})^{-1}$ [20]. While f_{EP} is the frequency corresponding to the peak value of $\tan\delta$. The peak shifts to the lower frequency side when the EGMPE concentration in the mixture increases. The relaxation time of MeOH is 8.4 ms, and that of EGMPE is 169 ms.

Fig. 5(a) and 5(b) illustrate the graph of the complex modulus (M^*) for real and imaginary component versus frequency. The value of M' approaches zero for all concentration in the low frequency zone; this behavior is caused by an absence of a force that controls the movement of charge carriers when a low frequency electric field is present[21]. For above 10 kHz frequency range, the value of M' increases and approaches to constant level for all concentration range. In Fig.5(b), peak in M'' against frequency plot is seen in all the concentration solutions in the stated frequency range. The peak shifts to a higher frequency side as the MeOH in the mixtures becomes more concentrated. However, there is only a little shift of the M'' peak values to the lower frequency side in MeOH-rich regions. The M'' peak values diminishes from 0.0480 for pure EGMPE to 0.0157 for pure MeOH as the concentration of MeOH increases.

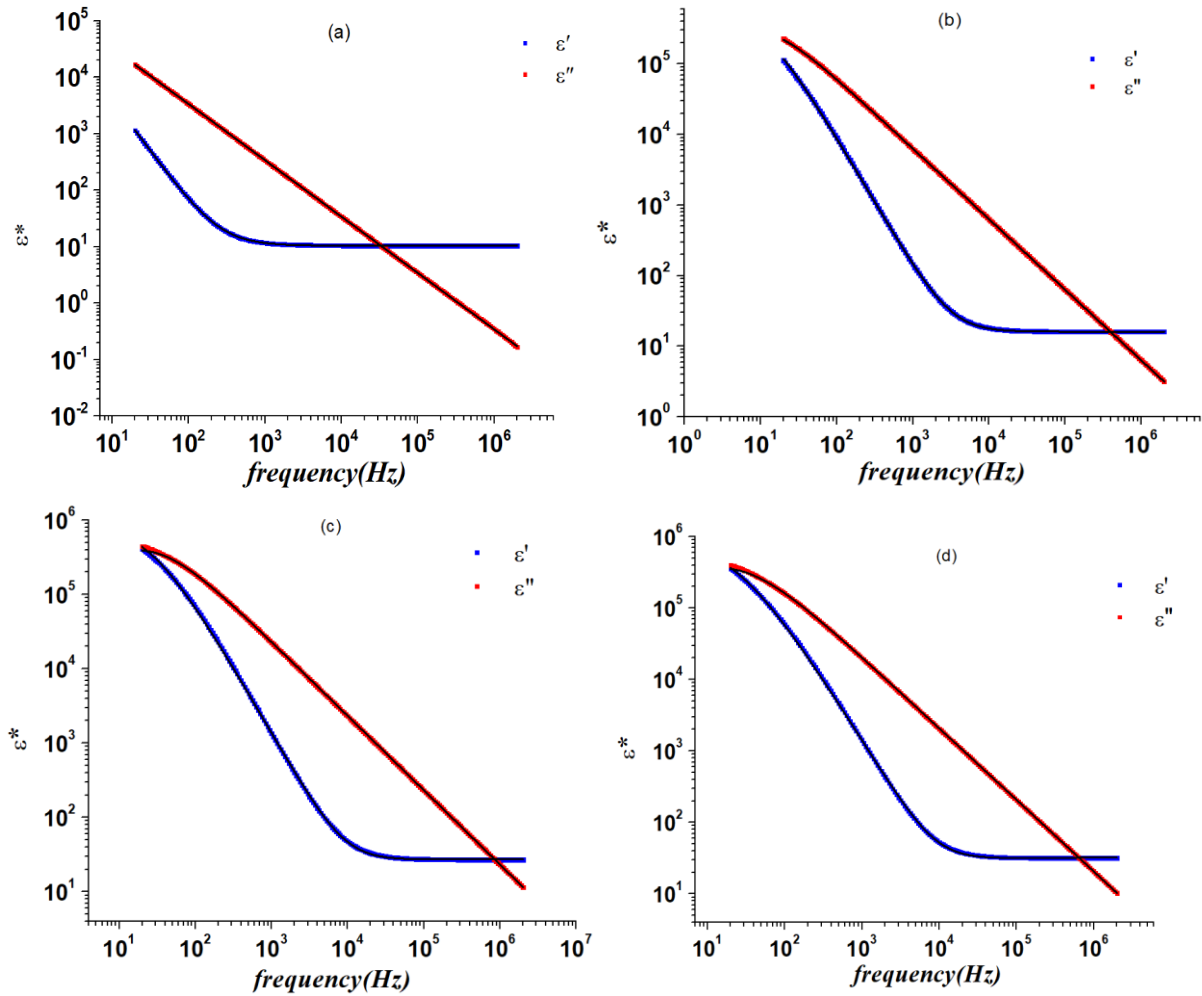


Fig.3 Complex dielectric function (ϵ^*) fitted to HN model by CNLS fitting for a) EGMPE b) mixture of EGMPE 49.17% + MeOH (50.83%) c) mixture of EGMPE (9.70%) + MeOH (90.30%) d) MeOH. Solid line represented fitted data.

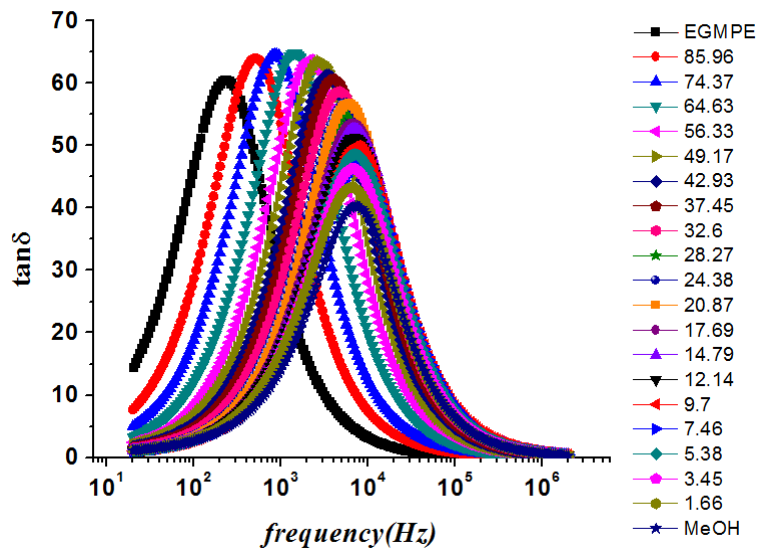


Fig.4 Frequency dependence of the loss tangents ($\tan\delta$) for binary mixtures of EGMPE and MeOH at 299.15K.

For EGMPE, peak value of M'' is much larger than the peak values of the other samples, because of its low static dielectric constant. The properties of the modulus spectrum indicate the presence of a hopping electrical conduction mechanism in binary mixtures[22]. The M'' spectra of those mixtures contain a peak in the indicated

frequency range, and the frequency associated with these peaks is related to the relaxation time of ionic conductivity τ_σ by the formula $\tau_\sigma = (2\pi f_\sigma)^{-1}$ [19] where the relaxation might be influenced by both short-range molecule mobility and charge carrier transfer. In Fig.6, the behavior of τ_σ with the volume fraction of EGMPE in the binary mixture of EGMPE and MeOH is depicted. As the concentration of EGMPE in MeOH rises, the relaxation time for ionic conductivity (τ_σ) increases. This may be due to the higher value of molecular size, density and viscosity of EGMPE in comparison with MeOH[5].

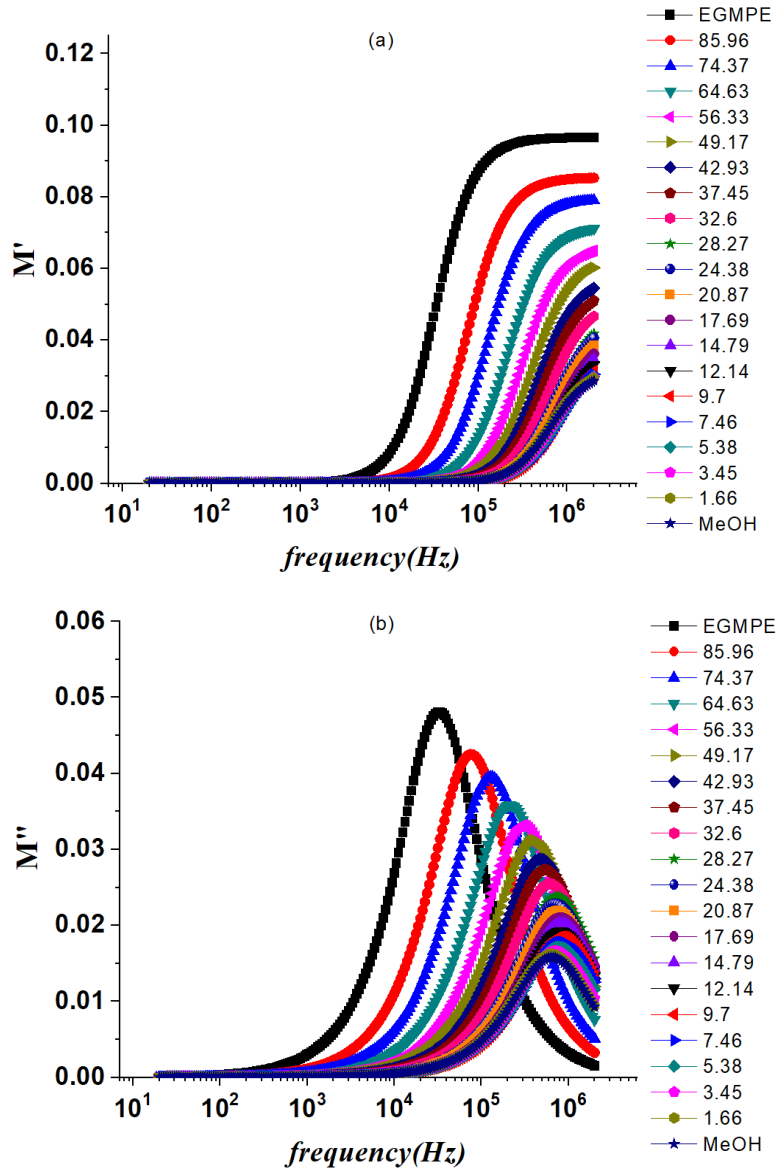


Fig.6 Frequency and concentration dependent (a) real part of the electric modulus (M') (b) imaginary part of the electric modulus (M'') for binary mixtures of EGMPE and MeOH.

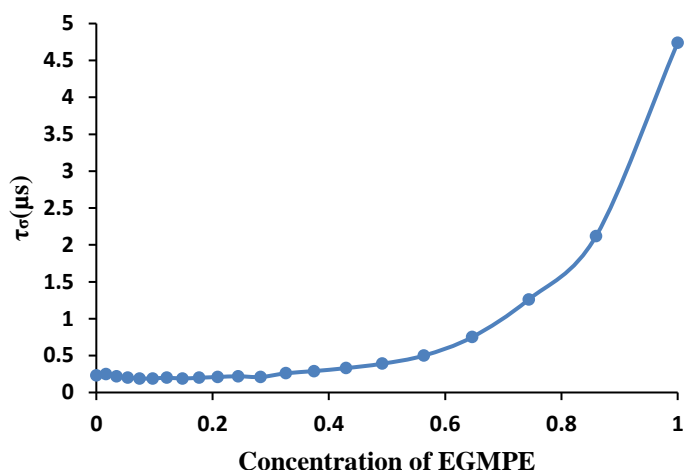


Fig.7 Ionic conductivity relaxation time (τ_σ) against concentration of EGMPE in MeOH at 299.15K temperature.

Fig. 7 shows the complex impedance in the plane plot for the binary mixture of EGMPE and MeOH. The impedance spectra show Debye-type semicircle in high frequency region followed by a tail in the low frequency region. The value of bulk resistance (R_b) is equal to the semi-circle's intercept with the real axis (Z'). The bulk resistance (R_b) separate semicircle in two regions higher frequency arc region represents the bulk material property and lower frequency arc represents the polarization of the electrode surface.

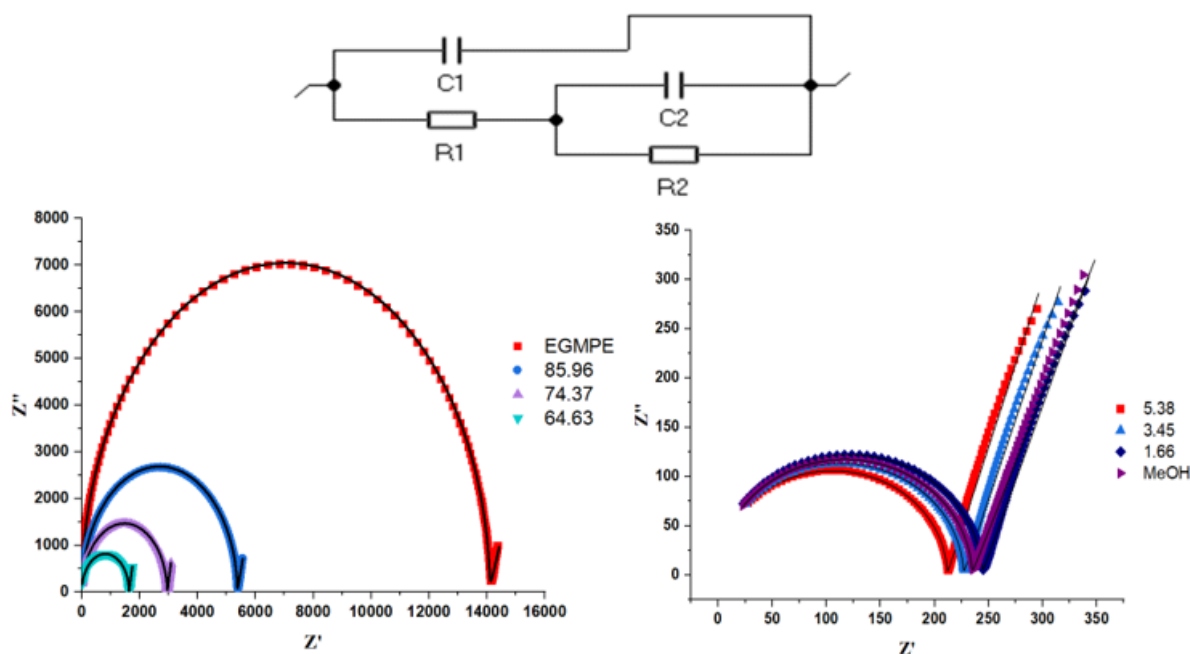


Fig.13 Plots of Z'' versus Z' with varying concentration for binary mixtures of EGMPE and MeOH. Solid line represents fitted curves to four terminal equivalent RC circuit.

A more significant tool for analyzing the impedance spectra of examined materials is electrochemical impedance spectroscopy (EIS). Experimental data points of impedance spectra for studied materials were fitted to the various equivalent circuit models with help of EC-Lab software. For pure EGMPE, MeOH, and their binary mixtures. It was found that the four-element equivalent illustrated in Fig.13 provide the best fit to the experimental data. From the fitted values of capacitor C_1 and resistor R_1 geometric time ($\tau_g = R_1 C_1$) was evaluated[23]. In Table 2 values of fitting parameters $R_1, C_1, R_2,$ & C_2 for all concentrations are presented.

It can be seen that at all concentrations, the ionic conduction relaxation time (determined from complex modulus spectra) and geometric time values (in Table 2) are nearly same. This suggests that R_1 and C_1 represent the bulk resistance and capacitance of samples, respectively, while τ_σ exhibits ionic conductivity relaxation.

The value of capacitance C_1 increases with a decreased concentration of EGMPE in MeOH, while the value of bulk resistance R_1 is reduced. For the materials under research, additional R_2 and C_2 indicate the reaction resistance and diffuse double layer capacitance of the polarization region near the electrode, respectively

Table 2 *Four equivalent RC circuit fitted parameters along with the geometric time constant (τ_g) and ionic conductivity relaxation time (τ_σ).*

Concentration of EGMPE(X_a)	R1 (Ω)	C1 (nF)	R2(Ω)	C2 (μ F)	τ_g (μ s)	τ_σ (μ s)
1.000	14117	0.3438	2931	6.93	4.85	4.74
0.8597	5385	0.3883	2549	9.76	2.09	2.12
0.7437	2958	0.4192	2523	11.48	1.23	1.26
0.6463	1641	0.4583	2285	13.24	0.75	0.75
0.5633	1044	0.4951	1935	14.64	0.51	0.50
0.4917	766.1	0.5263	1640	15.93	0.40	0.39
0.4293	593.9	0.5665	1418	16.98	0.33	0.33
0.3745	491.6	0.6015	1268	18.07	0.29	0.29
0.3260	406.1	0.6429	1141	19.06	0.26	0.26
0.2827	311.0	0.6909	1089	19.22	0.21	0.21
0.2438	314.8	0.7150	1028	20.11	0.22	0.22
0.2087	288.4	0.7444	978.9	21.05	0.21	0.21
0.1769	256.9	0.7693	910.8	21.23	0.19	0.20
0.1479	240.6	0.8012	860	21.93	0.19	0.19
0.1214	235.1	0.8471	847	22.18	0.19	0.20
0.0970	212.0	0.8828	816.5	22.62	0.18	0.19
0.0746	210.1	0.9246	884.4	21.44	0.19	0.19
0.0538	214.7	0.9624	799.9	22.95	0.20	0.20
0.0345	230.1	0.9917	801.7	22.26	0.22	0.22
0.0166	247.7	1.013	794.3	21.17	0.25	0.25
0	239.0	1.09	787.7	19.55	0.26	0.23

To determine the mobile ion concentration, ion mobility, ion diffusivity and Debye length, Klein et al. [24] developed a model. The Klein model was used to derive all the parameters for EGMPE, MeOH, and their binary mixture. Using the equation, the Debye length at the electrode surface was calculated.

$$\lambda_d = \frac{g}{2M} \tag{8}$$

where λ_d = Debye length at surface of electrode g = electrode gap and $M = \frac{\tau_{EP}}{\tau_\sigma}$

The value of Debye length for pure EGMPE is 3.60×10^{-9} m; for pure MeOH, it is 4.58×10^{-9} m. For all the other concentrations, it lies in between the pure values. Values are tabulated in Table 3. Ion mobility of the mixture is calculated using the equation:

$$\mu = \frac{qg^2}{4kTM\tau_{EP}} \tag{9}$$

where q is an electron charge, k is Boltzmann constant and T is absolute temperature.

Table 3 Calculated values for the binary mixtures of EGMPE and MeOH at 299.15 K for Debye length (λ_D), ion mobility (μ), mobile concentration (P_o), and ion diffusivity (D).

X(MeOH)	λ_D (nm)	μ^2 (m ² /Vs)	P_o (m ⁻³)	D (m ² /s)
0	4.21	1.48E-10	8.01E+23	3.73E-12
0.1403	3.88	2.81E-10	1.1E+24	7.09E-12
0.2562	3.50	3.85E-10	1.45E+24	9.72E-12
0.3537	3.41	6.13E-10	1.66E+24	1.55E-11
0.4367	3.26	8.42E-10	1.91E+24	2.13E-11
0.5083	3.08	9.62E-10	2.27E+24	2.43E-11
0.5706	3.09	1.15E-09	2.48E+24	2.9E-11
0.6254	3.11	1.32E-09	2.59E+24	3.33E-11
0.6740	3.25	1.61E-09	2.58E+24	4.06E-11
0.7173	3.46	2.26E-09	2.39E+24	5.71E-11
0.7561	3.37	2.04E-09	2.63E+24	5.15E-11
0.7912	3.35	2.12E-09	2.77E+24	5.35E-11
0.8230	3.49	2.41E-09	2.76E+24	6.08E-11
0.8520	3.43	2.46E-09	2.88E+24	6.21E-11
0.8786	3.61	2.59E-09	2.8E+24	6.53E-11
0.902933	3.75	2.93E-09	2.72E+24	7.4E-11
0.92539	4.13	3.55E-09	2.26E+24	8.98E-11
0.946152	3.80	2.85E-09	2.74E+24	7.21E-11
0.965406	3.93	2.78E-09	2.64E+24	7.02E-11
0.983309	4.17	2.75E-09	2.48E+24	6.94E-11
1	4.11	2.9E-09	2.45E+24	7.33E-11

Values of an ion diffusivity (D) and the mobile ion concentration (P_o) are determined using the following relation:

$$P_o = \frac{\sigma_{ac}}{q\mu} \quad \text{and} \quad D = \frac{\mu kT}{q} \tag{10}$$

Values of Ion mobility, ion diffusivity, and mobile ion concentration are stated in Table 3. Ion mobility and ion diffusivity increase as the concentration of MeOH increases. While the value of mobile ion concentration

decreases with an increase concentration of MeOH in EGMPE. Debye length increases with decreased concentration of EGMPE in MeOH.

Conclusion

This study analyses the complex permittivity and complex impedance formalism of EGMPE concentrations in MeOH at 293.15 K within frequencies ranging from 20 Hz to 2 MHz. In the low frequency domain, the complex dielectric function of these binary mixtures is influenced by electrode polarization and ionic conduction. The peak of the loss tangent shifts to the lower frequency side with an increase in the EGMPE concentration in the mixture. Experimentally established complex permittivity values for EGMPE + MeOH mixtures is fitted into the HN model. The value of M' approaches zero for all concentrations in the low-frequency zone; this behavior is caused by the absence of a force that controls the movement of charge carriers when a low-frequency electric field is present. The peak value of M'' shifts to a higher frequency side as the MeOH in the mixtures becomes more concentrated. The ionic conductivity relaxation time τ_σ increases with the concentration of EGMPE. The modulus spectra for all concentrations show Debye-type semicircles. The high-frequency arc representing the bulk effect and the low-frequency arc representing the electrode surface effect are easily distinguished in the Z'' vs Z' graphs for EGMPE and higher concentrations of EGMPE. When the concentration of MeOH in the mixture increases, it is seen that the size of the semi-circular arc (low-frequency arc) decreases. For every concentration, complex impedance values are fitted to an analogous four-element RC circuit. The loss tangent $\tan\delta$ and M'' demonstrate just one of either EDL or ionic relaxation processes. It is established that the polar liquids EGMPE and MeOH contain natural impurities. From the phenomenon of electrode polarization, the mobility and concentration of the natural impurities in pure EGMPE, MeOH, and their mixes are ascertained. An estimate was made of the thickness of the ion accumulated at the interface between the electrode and the dielectric medium, which was made up of the polar liquids EGMPE, MeOH, and their mixtures.

Acknowledgments

Authors are very much thankful to Department of Sciences and Technology (DST), New Delhi for providing financial support through the DST-FIST (Level-I) project (SR/FST/PSI-001/2006). Financial assistance provided by UGC, New Delhi through DRS-SAP program grant [No. F. 530/10/DRS/2010(SAP\I)] is also gratefully acknowledged. Authors are also thankful to Prof. V. A. Rana, Head, Department of Physics, School of Sciences, Gujarat University, Ahmedabad for his constant encouragement.

REFERENCES

- [1] H. A. Chaube, V. A. Rana, P. Hudge, and A. C. Kumbharkhane, "Dielectric relaxation studies of binary mixture of diethylene glycol mono phenyl ether and methanol by Time Domain Reflectometry," *J. Mol. Liq.*, vol. 211, pp. 346–352, 2015.
- [2] V. A. Rana and H. A. Chaube, "Static permittivity, density, viscosity and refractive index of binary mixtures of anisole with 1-butanol and 1-heptanol at different temperatures," *J. Mol. Liq.*, vol. 173, pp. 71–76, 2012.
- [3] R. J. Sengwa, S. Choudhary, and A. Bald, "Dielectric Dispersion and Electric Relaxation Processes Induced by Ionic Conduction in Formamide, 2-Aminoethanol and Their Binary Mixtures," *J. Solution Chem.*, vol. 42, no. 10, pp. 1960–1975, 2013, doi: 10.1007/s10953-013-0087-6.
- [4] V. A. Rana, N. S. Shah, K. N. Shah, and H. P. Vankar, "Dielectric spectroscopy and molecular dynamic simulation study of binary mixtures of benzaldehyde and methanol at 303.15 K," *J. Mol. Liq.*, vol. 369, p. 120829, 2023.
- [5] V. A. Rana, K. N. Shah, H. P. Vankar, and C. M. Trivedi, "Dielectric spectroscopic study of the binary mixtures of amino silicone oil and methyl ethyl ketone in the frequency range of 100 Hz to 2 MHz at 298.15 K temperature," *J. Mol. Liq.*, vol. 271, pp. 686–695, 2018.
- [6] H. A. Chaube, V. A. Rana, P. Hudge, and A. C. Kumbharkhane, "Dielectric relaxation studies of binary mixture of ethylene glycol mono phenyl ether and methanol by Time Domain Reflectometry," *J. Mol. Liq.*, vol. 193, pp. 29–36, 2014.
- [7] R. J. Sengwa and S. Sankhla, "Solvent effects on the dielectric dispersion of poly (vinyl pyrrolidone)-poly (ethylene

- glycol) blends,” *Colloid Polym. Sci.*, vol. 285, no. 11, pp. 1237–1246, 2007.
- [8] C. Carr and J. A. Riddick, “Physical properties of methanol-water system,” *Ind. Eng. Chem.*, vol. 43, no. 3, pp. 692–696, 1951.
- [9] F. Studt *et al.*, “The mechanism of CO and CO₂ hydrogenation to methanol over Cu-based catalysts,” *ChemCatChem*, vol. 7, no. 7, pp. 1105–1111, 2015.
- [10] D. T. Fixture, “Operation and Service Manual.” Agilent, 2000.
- [11] S. Manual, “Keysight 16452A Liquid Test Fixture.”
- [12] A. Kyritsis, P. Pissis, and J. Grammatikakis, “Dielectric relaxation spectroscopy in poly (hydroxyethyl acrylates)/water hydrogels,” *J. Polym. Sci. Part B Polym. Phys.*, vol. 33, no. 12, pp. 1737–1750, 1995.
- [13] K. F. A. El-Rahman, A. A. A. Darwish, S. I. Qashou, and T. A. Hanafy, “AC conductivity and dielectric relaxation behavior of Sb₂S₃ bulk material,” *J. Electron. Mater.*, vol. 45, no. 7, pp. 3460–3465, 2016.
- [14] A. Karmakar and A. Ghosh, “Dielectric permittivity and electric modulus of polyethylene oxide (PEO)–LiClO₄ composite electrolytes,” *Curr. Appl. Phys.*, vol. 12, no. 2, pp. 539–543, 2012.
- [15] J. Swiergiel and J. Jadzyn, “Electric relaxational effects induced by ionic conductivity in dielectric materials,” *Ind. Eng. Chem. Res.*, vol. 50, no. 21, pp. 11935–11941, 2011.
- [16] S. Choudhary and R. J. Sengwa, “Ionic conduction in binary mixtures of dipolar liquids,” *J. Mol. Liq.*, vol. 175, pp. 33–37, 2012.
- [17] T. A. Ezquerra, J. Majszczyk, F. J. Baltà-Calleja, E. López-Cabarcos, K. H. Gardner, and B. S. Hsiao, “Molecular dynamics of the α relaxation during crystallization of a glassy polymer: A real-time dielectric spectroscopy study,” *Phys. Rev. B*, vol. 50, no. 9, p. 6023, 1994.
- [18] S. Havriliak and S. Negami, “A complex plane analysis of α -dispersions in some polymer systems,” in *Journal of Polymer Science Part C: Polymer Symposia*, 1966, vol. 14, no. 1, pp. 99–117.
- [19] S. Zhang, S. Dou, R. H. Colby, and J. Runt, “Glass transition and ionic conduction in plasticized and doped ionomers,” *J. Non. Cryst. Solids*, vol. 351, no. 33–36, pp. 2825–2830, 2005.
- [20] R. J. Sengwa and S. Sankhla, “Dielectric dispersion study of coexisting phases of aqueous polymeric solution: Poly (vinyl alcohol)+ poly (vinyl pyrrolidone) two-phase systems,” *Polymer (Guildf.)*, vol. 48, no. 9, pp. 2737–2744, 2007.
- [21] M. H. Lakhdar, T. Larbi, B. Ouni, and M. Amlouk, “AC conductivity, dielectric relaxation and modulus behavior of Sb₂S₂O new kermesite alloy for optoelectronic applications,” *Mater. Sci. Semicond. Process.*, vol. 40, pp. 596–601, 2015.
- [22] A. K. Behera, N. K. Mohanty, S. K. Satpathy, B. Behera, and P. Nayak, “Investigation of complex impedance and modulus properties of Nd doped 0.5 BiFeO₃-0.5 PbTiO₃ multiferroic composites,” *Cent. Eur. J. Phys.*, vol. 12, no. 12, pp. 851–861, 2014.
- [23] B. A. Yezer, A. S. Khair, P. J. Sides, and D. C. Prieve, “Use of electrochemical impedance spectroscopy to determine double-layer capacitance in doped nonpolar liquids,” *J. Colloid Interface Sci.*, vol. 449, pp. 2–12, 2015.
- [24] R. J. Klein, S. Zhang, S. Dou, B. H. Jones, R. H. Colby, and J. Runt, “Modeling electrode polarization in dielectric spectroscopy: Ion mobility and mobile ion concentration of single-ion polymer electrolytes,” *J. Chem. Phys.*, vol. 124, no. 14, p. 144903, 2006.

¹ K. J. Agheda² N. A. Chaudhary³ N. Garad⁴ A. C. Kumbharkhane⁵ B. S. Chakraborty^{6*} A. N. Prajapati

**Molecular interaction through
dielectric relaxation study of
methanol-bromopropane
mixtures as a function of
composition**



Abstract: - For different mole fractions, investigations of the dielectric properties of binary mixtures of Methanol (MeOH) and Bromopropane (BRP) have been obtained as a function of frequency ranging from 10 MHz to 30 GHz using Time domain refractometry (TDR) at 283.15 K temperature. Complex permittivity data fitted Havriliak-Negami dielectric model to extract dispersion parameters using complex non-linear least square fitting (CNLS) program. Various dielectric parameters namely; static dielectric constant (ϵ_0), relaxation time (τ), effective Kirkwood correlation factor (g^{eff}), corrective Kirkwood correlation factor (g^{f}), Bruggeman factor (f_B) are determined and variation of these parameters are discussed in light of molecular interaction of between molecular constituents. Excess static dielectric constant (ϵ_0)^E, excess inverse relaxation time ($1/\tau$)^E are evaluated. Furthermore, several theoretical mixing models for static dielectric constant are validated and tested.

Keywords: Dielectric relaxation, Molecular Interaction, Excess properties, Time Domain Reflectometry

*Corresponding author: Department of Physics, Sardar Patel University, V. V. Nagar-388120, Gujarat, India

^{1,2,5} Department of Applied Physics, The M. S. University of Baroda, Vadodara-390001, Gujarat, India

^{3,4} School of Physical Sciences, Swami Ramanand Teerth Marathwada University Nanded, Maharashtra, India

⁶ Department of Physics, Sardar Patel University, V. V. Nagar-388120, Gujarat, India

I. INTRODUCTION

Recently, there has been considerable interest in researching the physicochemical characteristics and their corresponding excess properties. Understanding the physical condition and composition range is crucial for comprehending the mixing features, since these properties are directly impacted by them. Moreover, there is a significant need to investigate the connections between molecular structure and the qualities of mixtures [1-3]. Dielectric, and refractometric, measurements have been proven to be excellent methods for analysing the functional and structural properties of the mixtures [4]. Many researchers have extensively studied the dielectric relaxation in polar-polar binary mixtures, including the whole range of concentrations and temperatures [5, 6]. The objective of these investigations is to comprehend the molecular composition and assess both ideal and non-ideal mixture characteristics. 1-Bromopropane used as solvent for cleaning electronic parts, implanted prostheses, optical devices, and other supplies. Methanol finds applications such as automotive antifreeze, chemical synthesis, solvents, and fuel cells. The incalculable applications of these hydroxyl-based solvents make it necessary to investigate their mixing behaviour in order to enhance the solvents' characteristics in the many application domains [7]. In current study, we examined the dielectric characteristics of a combination containing MeOH and BRP at all concentrations at a temperature of 283.15 K. The frequency range of 10 MHz –30 GHz was used to acquire the complex permittivity spectra of the binary mixtures, using the TDR approach. The dielectric characteristics, including the static dielectric permittivity (ϵ_0) and relaxation time (τ), are assessed and analysed. In addition, we utilised a diverse set of theoretical mixing models for dielectric constant to suit our experimental findings. The Root mean square deviation (RMSD) estimations have also been implemented for their validation.

II. EXPERIMENTAL METHODS

Table 1 Experimental and reported values of the static dielectric constant (ϵ_0), refractive index (n) and relaxation time (τ) for the pure liquids.

	Static permittivity		Refractive index		Relaxation time	
	Expt.	Lit.	Expt.	Lit.	Expt.	Lit.
MeOH	38.95	38.59 ⁹	1.3326	1.3328 ¹¹	60.04	60.00 ^{13b}
1- BRP	11.14	11.81 ¹⁰	1.4402	1.4319 ^{12a}	7.00	13.50 ¹⁰

^aAt 298.15 K temperature, ^bAt 288.15 K temperature

MeOH (GC grade) and BRP (Synthesis Grade) were procured from LOBA Chemie, India. The solutions were made at eleven various volume percentages of BRP, ranging from 0% to 100% in increments of 10%. Utilising the following formula, the volume fraction has been altered into a mole fraction [3]. The complex permittivity ($\epsilon^*(f)$) of binary mixtures were measured in frequency span 10 MHz to 30 GHz using TDR setup [8]. Refractive index of liquid samples were measured using Abbe refractometer at sodium D-line. The measurement of the refractive index was found to have a maximum error of $\pm 0.015\%$. All measurement were carried out at constant temperature 283.15 K. It is seen that the

III. RESULT AND DISCUSSION

Complex permittivity spectra obtained from the time domain reflectometry (TDR) were fitted to Havriliak-Negami dielectric model using LEVMW software to obtain dielectric strength ($\Delta\epsilon = \epsilon_0 - \epsilon_\infty$) and dipolar relaxation time (τ) for the binary mixtures of MeOH + BRP [7]. It has been observed from figure 1(a) that the dielectric constant (ϵ') of complex spectra is independent of frequency up to 0.3 GHz, this plateau region yields to the static dielectric constant values of the binary mixtures of MeOH + BRP. As the concentration of BRP increases in MeOH + BRP mixture, ϵ' value decreases due to the diminution of polarizability of mixing molecules of binary mixtures under the influence of applied electric field. On the other hand, the ϵ'' peaks (figure 1(b)) moved to the higher frequency side, suggesting mixing molecules swing rapidly under the influence of an applied electric field, resulting in a decline in the relaxation time of binary mixtures.

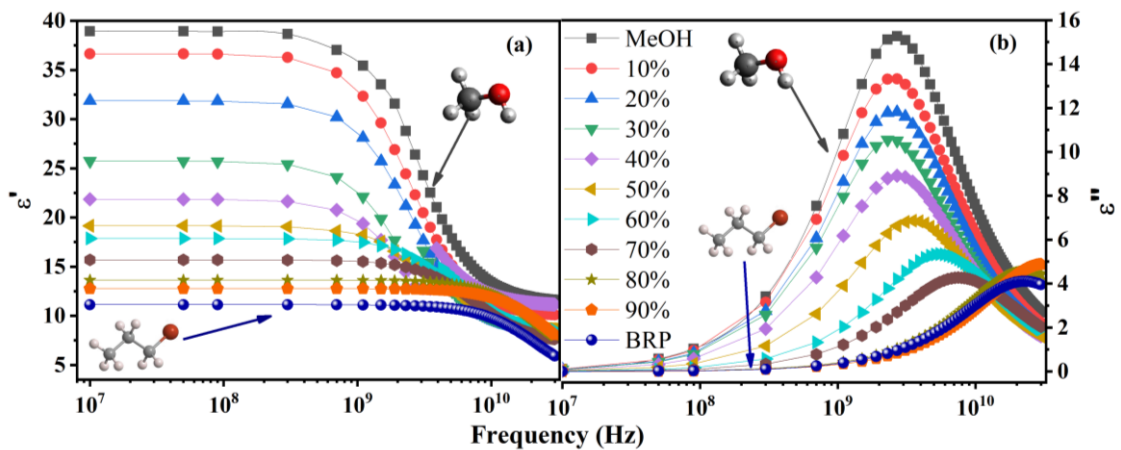


Figure 1. Display the dielectric constant (ϵ') and dielectric loss (ϵ'') part of complex permittivity spectra of MeOH + BRP binary mixtures at 283.15 K.

Table 1 makes it evident that the calculated values of the relaxation time (τ), refractive index (n), and static dielectric constant (ϵ_0) agree quite well with the values found in literature. Methanol has a greater relaxation time than 1-bromopropane. This is so because the structures of methanol include hydroxyl groups and intramolecular clusters joined by (O–H ---O) type of connection. Moreover, the system absorbs more energy as a result of the self-associated clusters; hence, molecules rest slowly, which lengthens the relaxation time. Its inflexible and non-associative character is suggested by the reduced relaxation time value of BRP. Refractive index (n), relaxation time (τ), and static dielectric constant (ϵ_0) values in an ideal mixture of polar liquids vary nonrectilinear as hetero molecules interact. Refractive index, relaxation duration, and static dielectric constant are shown in Figure 2 against the mole fraction of BRP. It is clear from figure 2 that the observed values (ϵ_0) and (τ) are decreases in a nonrectilinear manner as the concentration of BRP increases while the refractive index (n) values show opposite trend as the concentration of BRP increases in the mixture. The nonlinearity in (ϵ_0), (τ) and (n) indicate heteromolecular interaction between the MeOH molecules and BRP molecules in binary mixtures.

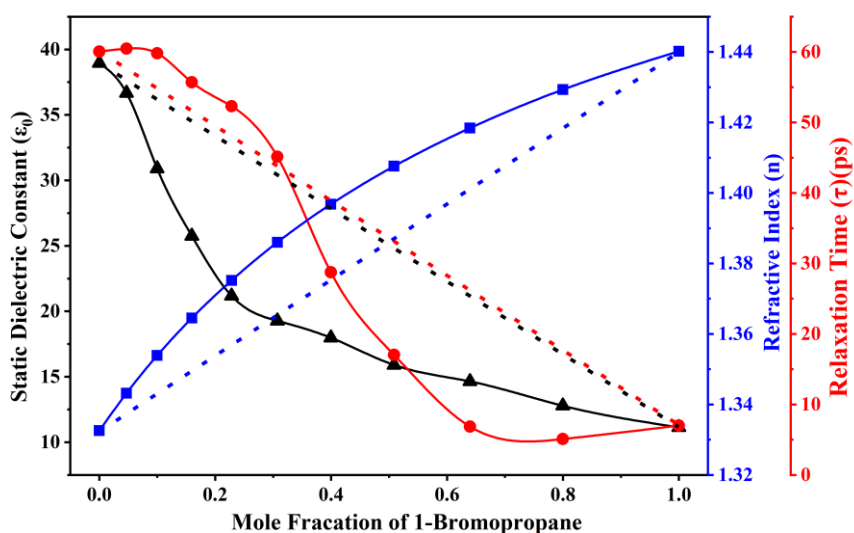


Figure 2 Variation of Static dielectric constant (ϵ_0), refractive index (n) and relaxation time (τ) against mole fraction of BRP. [Dotted lines indicate ideal behavior of mixture.]

There is a notable difference between the (ϵ_0) and (τ) values of MeOH and BRP. When BRP molecules added to MeOH molecules, the formation of MeOH-BRP clusters can lead to the occurrence of three distinct types of cooperative domains (CDs) in the combinations. These CDs may be categorised as follows: CD_{BRP} contains exclusively BRP molecules,

CD_{MeOH} contains exclusively MeOH molecules, and $CD_{MeOH-BRP}$ contains both MeOH and BRP molecules. The nonlinear trend in the evaluated values of τ in mixtures of MeOH and BRP give direct evidence of the interactions between the interacting molecules. In addition, the formation of uniform CDs by intermolecular hydrogen bonding enhances the obstacle to the overall rotational movements of the systems. The observed changes in τ values as the concentration fraction of BRP increases in the MeOH + BRP mixture provide evidence for the ongoing process of breaking and forming hydrogen bonds in the heterogeneous mixture [6].

The excess parameters related to (ϵ_0) , (τ) and (n) provide valuable information regarding interaction between the (MeOH + BRP) binary liquid mixtures shown in figure 3. The excess parameters are well-defined as [8].

$$(\epsilon_0)^E = (\epsilon_0)_M - (\epsilon_{0I}X_I + \epsilon_{0II}X_{II}) \quad (1)$$

$$(n)^E = (n)_M - (n_I X_I + n_{II} X_{II}) \quad (2)$$

$$(1/\tau)^E = (1/\tau)_M - [(1/\tau)_I X_I + (1/\tau)_{II} X_{II}] \quad (3)$$

Where subscript M suggests mixture of MeOH/BRP. Subscripts I and II suggest BRP and MeOH, respectively. Mehrotra et al. state that the interactions between molecules might cause changes in structure, leading to fluctuations in the dielectric permittivity value based on concentration. $(\epsilon_0)^E$ show a negative value at all MeOH-BRP concentrations, indicating significant intermolecular interaction because of hyper conjugation in these mixtures, which reduces the total number of dipoles [8]. It has been observed that $(1/\tau)^E$ show a negative deviation in the mole fractions $0 \leq X_I \leq 0.50$ and beyond $X_I > 0.50$ show positive deviation. This suggests that in mole fraction range $(0 \leq X_I \leq 0.50)$ the molecular complexion swings slowly under the influence of external field, Beyond $X_I > 0.50$ the molecular complexion swings quickly [12]. The $(n)^E$ show positive deviation over the entire range of concentration indicate dispersive attractive interaction between molecular species in the mixture constituents.

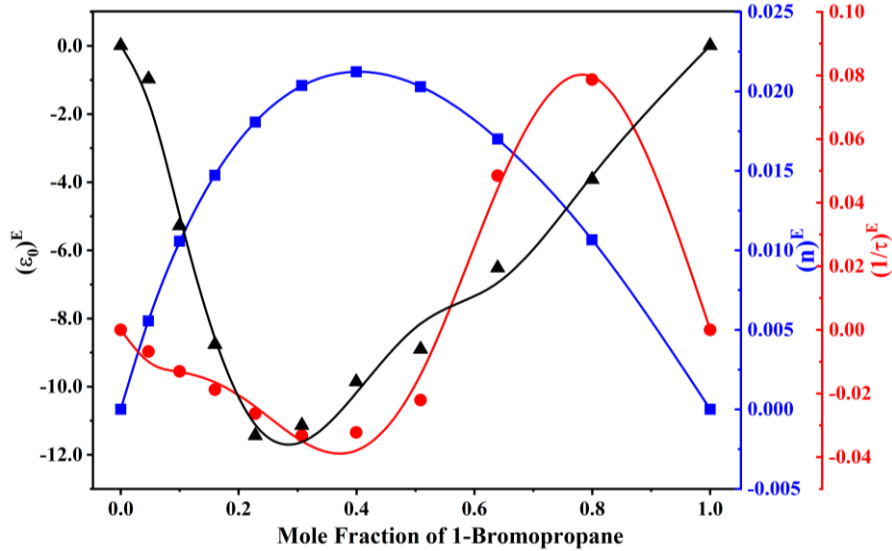


Figure 3 Variation of $(\epsilon_0)^E$, $(1/\tau)^E$ and $(n)^E$ against mole fraction of Bromopropane.

In binary mixtures, when different molecular species interact, there will be formation/breaking of inter/intra molecular bonds results in dielectric relaxation. To gain more information about such mechanism, knowledge of correlation of electric dipoles in binary mixture of polar liquids is essential. The Kirkwood correlation factor g [12]

$$g = \frac{9KTM}{4\pi\rho N\mu^2} \times \frac{(\epsilon_{0m} - \epsilon_{\infty m})(2\epsilon_{0m} - \epsilon_{\infty m})}{\epsilon_{0m}(\epsilon_{\infty m} + 2)^2} \tag{5}$$

In the given system, where μ denotes the dipole moment, ρ represents density, ϵ_0 the free space permittivity, ϵ_{∞} is dielectric permittivity at high frequency, K depicts the Boltzmann constant, M suggests the molecular weight, and N signifies the Avogadro's number. The equation has been adapted to analyse the alignment of electric dipoles in binary mixtures, as described by Kumbharkhane et al. [14]

$$\frac{4\pi N}{9KT} \left[\frac{\mu_I^2 \rho_I V_I}{M_I} + \frac{\mu_{II}^2 \rho_{II} (1 - V_I)}{M_{II}} \right] \times g^{eff} = \frac{(\epsilon_{0m} - \epsilon_{\infty m})(2\epsilon_{0m} - \epsilon_{\infty m})}{\epsilon_{0m}(\epsilon_{\infty m} + 2)^2} \tag{6}$$

g^{eff} represents the effective Kirkwood correlation factor for a binary mixture. It differs between g_I and g_{II} . 'I' represent for MeOH and 'II' for BRP. The value of g^{eff} for pure liquid MeOH is larger than one, indicating a significant presence of coordinated chainlike formations. While, g^{eff} values for BRP is close to unity suggesting the absence of dipole correlation.

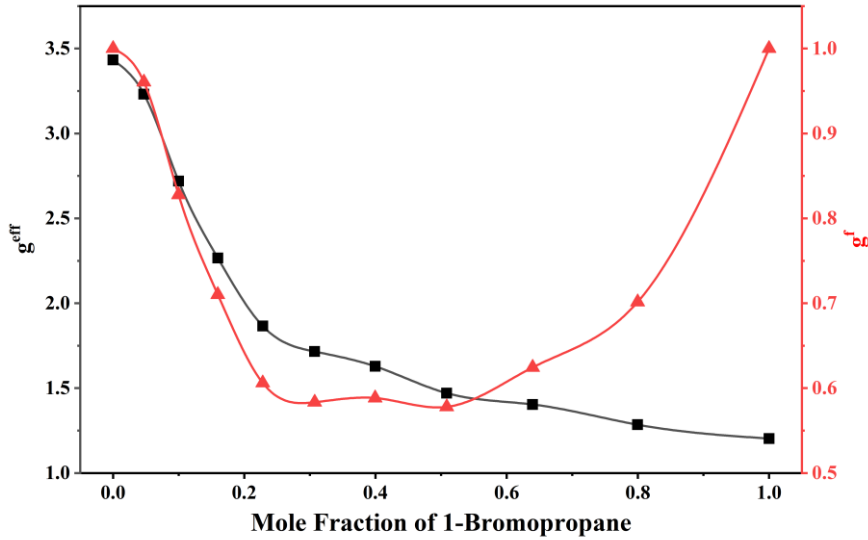


Figure 4 Variation of Effective Kirkwood correlation factor and corrective Kirkwood correlation factor versus mole fraction of 1-Bromopropane.

The corrective Kirkwood correlation factor g^f provides information on the heterogeneous interactions among the components of the mixture.

$$\frac{4\pi N}{9KT} \left[\frac{\mu_I^2 \rho_I g_I V_I}{M_I} + \frac{\mu_{II}^2 \rho_{II} g_{II} (1-V_I)}{M_{II}} \right] \times g^f = \frac{(\epsilon_{0m} - \epsilon_{\infty m})(2\epsilon_{0m} - \epsilon_{\infty m})}{\epsilon_{0m}(\epsilon_{\infty m} + 2)^2} \quad (7)$$

It is believed that g_I and g_{II} are influenced by a quantity g^f in the combination. As the concentration of BRP increases in the mixture, the g^{eff} value decrease nonlinearly. This trend indicates a reorientation of the molecules in the surrounding media of the MeOH + BRP polar liquids, result in a preference for aligning the dipoles in a parallel manner [7]. The variation of g^f against mole fraction of BRP is shown in Figure 4. g^f should equal one in an ideal non-interacting combination. Divergent interaction between the mixture's constituents is shown by the deviation from this value. In the lack of any interaction between the constituent molecules, Chaube et al. [8] found that the value of g^f will stay close to unity. if $g^f < 1$, Dipoles of both molecules will align in a way that produces effective dipoles less than the average value of the pure liquids. The Bruggemann equation (f_B) for the binary liquid solution [12] is expressed by the following equation:

$$f_B = \left(\frac{\epsilon_{0m} - \epsilon_{0II}}{\epsilon_{0I} - \epsilon_{0II}} \right) \left(\frac{\epsilon_{0I}}{\epsilon_{0m}} \right)^{1/3} = (1 - V_{II}) \quad (8)$$

The modified Bruggemann equation is derived to account for the nonlinear change of the Bruggemann equation (f_B) with respect to V_{II} which as follow,

$$f_B = 1 - (s - (1 - s)V_{II}) V_{II} \tag{9}$$

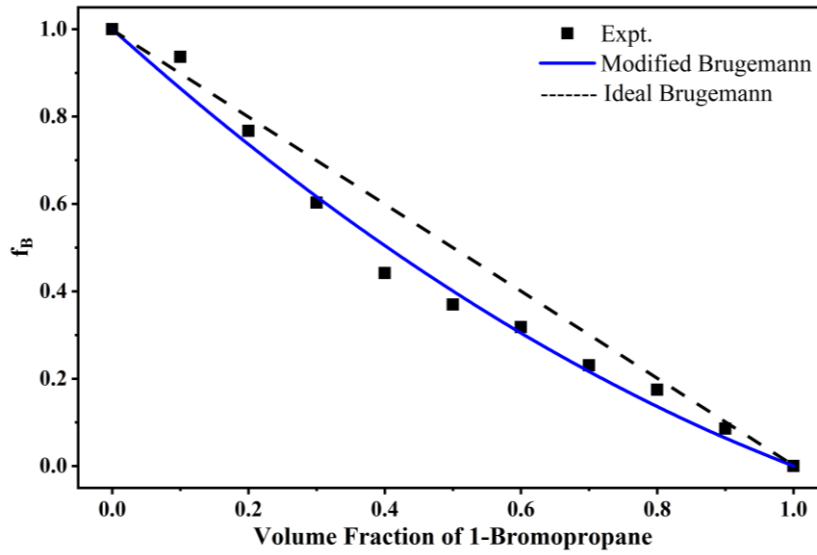


Figure 5 Plot of Bruggeman factor (f_B) against volume fraction of 1-Bromopropane.

As an interaction parameter, "s" in the following equation is evaluated using the least square fit approach which gives the information about the change in effective volume of the component of the binary mixtures [8]. The 's' values found to be greater than one indicates that the effective volumes of MeOH molecules get increases as concentration of BRP molecules increases in the mixtures (Figure 5).

The adjustable parameters (a, b, c, d, e) of excess static dielectric and excess inverse relaxation time are shown in Table 2 according to least square fitting. In the same table is also included the correlation coefficient (σ).

Table 2. Parameters of R–K equation for the mathematical illustration of deviation in excess quantities for MeOH + BRP.

Excess Properties	a	b	c	d	e	σ
$(\epsilon_0)^E$	-33.129	30.136	-84.509	10.5062	149.54	0.9952
$(1/\tau)^E$	-0.0684	0.6800	1.1243	-0.4422	-1.1739	0.9944
$(n)^E$	0.0816	-0.0313	0.0091	-0.0028	0.0071	0.9999

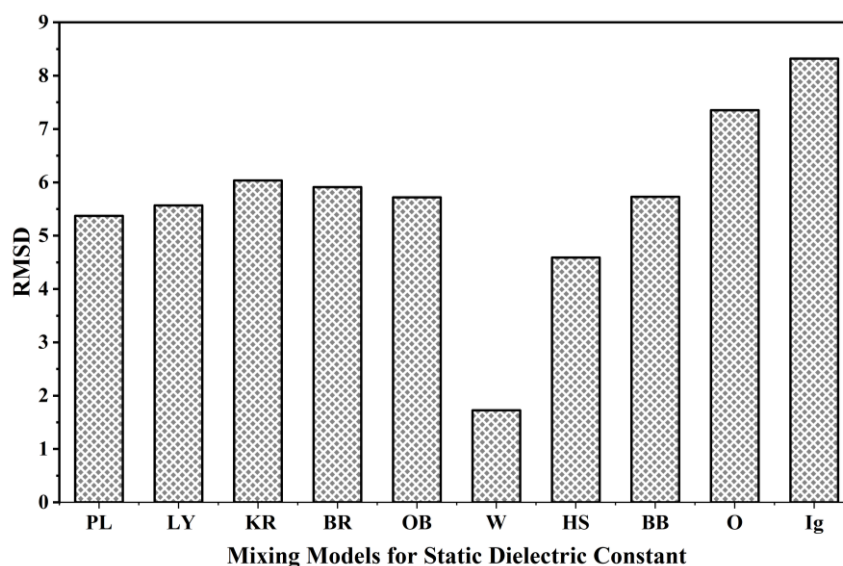


Figure 6 Plot of values of RMSD against various Mixing models

Theoretical Models

There are several molecular interactions since the components of the binary combinations are associated with distinct chemical classes. In this study, we tested ten mixing models such as Peon-Iglesias (PL), Looyenga (LY), Kraszewski (KR), Brown (BR), Iglesias (Ig), Wiener (W), Hasin-Shtrikman (HS), Bottcher & Bordewijk (BB), Oster (O), Onsager-Bottcher (OB) for experimental dielectric permittivity data of MeOH/BRP binary compositions shown in figure 6. The RMSD figures demonstrate that the dielectric permittivity values for all the combinations being studied are accurately anticipated. The Wiener (W) mixing model provides the most accurate prediction, whereas the Iglesias (Ig) mixing model does not accurately agree with experimental data on static dielectric permittivity.

IV. CONCLUSIONS

The complex permittivity spectra (ϵ^*) for the binary mixtures of (MeOH + BRP) were assessed at a constant temperature 283.15 K using a Time domain reflectometry (TDR) in the frequency span 10 MHz \rightarrow 30 GHz. The complex permittivity spectra fitted to Harviliak - Negami model using CNLS fitting program to obtain dielectric dispersion and relaxation parameters. There is a systematic non rectilinear variation observed in (ϵ_0), (τ) and (n) values as the concentration of mixture constituent changes which indicate heteromolecular interaction between the constituent of mixtures species. The excess parameters ($(\epsilon_0)^E$, $(1/\tau)^E$), Kirkwood parameters (g^{eff} and g^f) and Bruggeman parameters (f_B) are determined. Among the all fitted mixing models Wiener shows best fitted model using RMSD for dielectric permittivity.

V. ACKNOWLEDGMENTS

The School of Physical Sciences at S.R.T.M.U. Nanded, Maharashtra, desires recognition for providing the TDR facilities obtained under the DST project (DST PROJECT SB/S2/LOP-032/2013). The authors express their gratitude to the Head of the Applied Physics department in the Faculty of Technology and Engineering, The Maharaja Sayajirao University of Baroda, Vadodara.

VI. REFERENCES

- [1] V. A. Durov and I. Yu. Shilov, "Supramolecular structure and physicochemical properties of the mixture tetrachloromethane-methanol," *Journal of Molecular Liquids*, vol. 92, no. 3. Elsevier BV, pp. 165–184, Jul. 2001.
- [2] N. P. Garad, S. H. Saknure, D. G. Dongre, and A. C. Kumbharkhane, "High frequency dielectric study on the hydrogen bonding interaction on 1,5-pentanediol + 1,4-dioxane binary mixtures," *Canadian Journal of Chemistry*, vol. 102, no. 6. Canadian Science Publishing, pp. 391–396, Jun. 2024.
- [3] A. N. Prajapati, "Study of heterogeneous interaction through dielectric properties of binary mixtures of fluorobenzene with methanol," *Indian Journal of Pure & Applied Physics*, vol. 49, no. 7, pp. 478-484, Jul. 2011.
- [4] A. G. Gilani and A. Mirkhalili, "Dielectric, Volumetric, Refractometric, and Excess Properties of (Cycloalkanone + Pentanol Isomers) Systems at T = 298.15 K," *Journal of Chemical & Engineering Data*, vol. 66, no. 10. American Chemical Society (ACS), pp. 3934–3950, Oct. 2021.
- [5] V. A. Rana, H. P. Vankar, and H. A. Chaube, "Static Permittivity and Refractive Index of Binary Mixtures of 3-Bromoanisole and 1-Propanol at Different Temperatures," *Journal of Chemical & Engineering Data*, vol. 60, no. 11. American Chemical Society (ACS), pp. 3113–3119, Oct. 2015.
- [6] V. L. Jadhavpatil, P. B. Undre, and S. N. Helambe, "Dielectric relaxation in water-dimethylaminoethanol mixtures as a function of composition and temperature," *Integrated Ferroelectrics*, vol. 185, no. 1. Informa UK Limited, pp. 1–10, Nov. 2017.
- [7] P. Sivagurunathan, K. Dharmalingam, K. Ramachandran, B. Prabhakar Undre, P. W. Khirade, and S. C. Mehrotra, "Dielectric relaxation study of mixtures of alkyl methacrylates and 1-alcohols using time-domain reflectometry," *Philosophical Magazine Letters*, vol. 86, no. 5. Informa UK Limited, pp. 291–300, May 2006.

- [8] H. A. Chaube, V. A. Rana, P. Hudge, and A. C. Kumbharkhane, "Dielectric relaxation studies of binary mixture of ethylene glycol mono phenyl ether and methanol by Time Domain Reflectometry," *Journal of Molecular Liquids*, vol. 193. Elsevier BV, pp. 29–36, May 2014.
- [9] S. Mrad, C. Lafuente, M. Hichri, and I. Khattech, "Density, Speed of Sound, Refractive Index, and Viscosity of the Binary Mixtures of N,N-dimethylacetamide with Methanol and Ethanol," *Journal of Chemical & Engineering Data*, vol. 61, no. 9. American Chemical Society (ACS), pp. 2946–2953, Jul. 2016.
- [10] Shinde Ravindra V, Kumbharkhane A C, "Temperature dependent dielectric relaxation studies of halopropane from 10 Mhz to 50 Ghz using a time domain reflectometry (TDR)", *Applied Innovative Research*, vol. 2, no. 2. , pp. 1-4, Jun. 2020.
- [11] J. Wisniak, A. Apelblat, J. Zabicky, and I. Feingold, "Isobaric Vapor-Liquid Equilibria in the Binary Systems of 1-Bromopropane with Cyclohexane, Heptane, and 1-Butanol," *Journal of Chemical & Engineering Data*, vol. 40, no. 1. American Chemical Society (ACS), pp. 120–123, Jan. 1995.
- [12] V. V. Navarkhele and M. K. Bhanarkar, "Microwave dielectric response of binary mixture of N,N-dimethylformamide with propylene glycol using TDR method," *Molecular Physics*, vol. 107, no. 17. Informa UK Limited, pp. 1823–1830, Sep. 2009.
- [13] R. M. Shirke, A. Chaudhari, N. M. More, and P. B. Patil, "Temperature dependent dielectric relaxation study of ethyl acetate — Alcohol mixtures using time domain technique," *Journal of Molecular Liquids*, vol. 94, no. 1. Elsevier BV, pp. 27–36, Oct. 2001.
- [14] A. C. Kumbharkhane, S. M. Puranik, and S. C. Mehrotra, "Dielectric relaxation studies of aqueous N,N-dimethylformamide using a picosecond time domain technique," *Journal of Solution Chemistry*, vol. 22, no. 3. Springer Science and Business Media LLC, pp. 219–229, Mar. 1993.

¹N. A. Chaudhary²K. N. Shah³S. P. Patel⁴*A. N. Prajapati

**Investigation of Some
Physicochemical Properties of
Binary Liquid Mixtures (n-
Octanol + N, N-
Dimethylformamide) at
Different Temperatures**



Abstract: - Ultrasonic studies are widely used to analyze organic molecules, offering unique insights and finding applications across various fields. They enable the evaluation of physico-chemical properties of mixtures and enhance the interpretation of molecular interactions with greater reliability. Due to the extensive variety of molecular interactions between the polar liquids of N-N-dimethylformamide and n-Octanol, measurements of ultrasonic velocity (U_v), densities (ρ), and viscosity (η) have been carried out for these systems at different temperatures (293.15→313.15 K) and over the complete composition range (0.0→1.0). From the experimental data the physicochemical parameters such as molar volume (V_m), adiabatic compressibility (β), intermolecular free length (L_f), surface tension (σ) and relaxation time (τ) were calculated, which are more useful to predict and confirm the molecular interaction in the binary liquid mixtures. Excess measured acoustic parameters have been estimated and fitted into the R.- K. polynomial. The variations in the sign and magnitude of these parameters from the values expected for ideal mixing reveal the nature of intermolecular interactions in the liquid mixture. Further experimental data of these mixtures were also used to test the validity of various mixing rules/theories for ultrasonic velocity.

Keywords: Binary Mixture, Excess Properties, Mixing Models, Molecular Interaction, Ultrasonic Velocity

*Corresponding author: Department of Physics, Sardar Patel University, V. V. Nagar-388120, Gujarat, India.

^{1,3}Department of Applied Physics, The M. S. University of Baroda, Vadodara-390001, Gujarat, India.

²Department of Computer Engineering, Unitedworld School of Computational Intelligence, Karnavati University, Gandhinagar, Gujarat, India.

⁴Department of Physics, Sardar Patel University, V. V. Nagar-388120, Gujarat, India.

*Corresponding author email: anp3872@gmail.com

Copyright © JES 2024 on-line : journal.esrgroups.org

I. INTRODUCTION

Extensive studies on molecular interactions in liquid systems have been conducted using various physical methods such as the Raman technique, Infrared Radiation (IR) technique, NMR technique, Ultraviolet, and ultrasonic methods [1-2]. Understanding the intermolecular interactions between the molecules in a mixture requires doing studies on liquid mixtures using ultrasonic techniques. Ultrasonic sound vibrations can be used to investigate the properties of both liquid and solid materials. These studies have significant applications in a variety of industrial and scientific processes [3-4]. Liquid-liquid mixtures and solutions have found wide application in medical, pharmaceutical, chemical, and related industries [1-5]. The ultrasonic study of liquids and liquid mixtures has become increasingly important in recent years for understanding molecular interactions in both pure liquids and binary liquid mixtures. This ultrasonic measurement is a part of our study, which aims to investigate the molecular interactions between the components of binary mixtures of N, N-Dimethylformamide (DMF) and n-octanol systematically. The excess thermodynamic functions are sensitive not only to intermolecular forces but also to the size of the molecules [2]. The non-rectilinear behavior of ultrasonic velocity, compressibility, and other thermodynamic parameters in liquid mixtures also indicates the strength of interactions between molecules. Different acoustical parameters such as adiabatic compressibility, free length, molar volume, along with different excess parameters, are useful to obtain further insights into the nature and strength of molecular interactions. Ultrasonic methods have secured a permanent place in science, with new applications continually being found for solving both theoretical and practical problems [6-8].

Alcohol has been found in various applications and commercial uses in medical and other fields [9]. Recently, the longer-chain alcohol, n-octanol, has been recognized as a biofuel candidate derived from biomass-derived platform chemicals [10]. Notably, 1-octanol holds significance and is employed in synthesizing 1-octene, a key co-monomer in polyethylene production and petrochemical processes [11]. Amides are highly polar and have a strong ability to dissolve substances, making them crucial solvents in industries and biological processes. N, N-Dimethylformamide (DMF) is an important member of the amides solvent group and is used in the production of acrylic fibers and plastics [12]. It consists of two hydrophobic -CH₃ groups and one highly polar C=O group. DMF can easily form C-H...O and C=O...H type hydrogen bonds with other molecules, such as alcohols, enhancing its solvent capabilities [13].

In the present work, we are presenting the physicochemical properties of binary mixtures of n-octanol, and N, N-Dimethylformamide (DMF). The experimentally measured parameters include ultrasonic velocity (u), density (ρ), and viscosity (η). Additionally, we evaluated

several derived parameters, namely adiabatic compressibility (β), intermolecular free length (L_f), molar volume (V_m), surface tension (σ), and relaxation time (τ). These measurements were taken at temperatures ranging from 293.15 K to 323.15 K, in intervals of 10 K. This study aims to investigate the effect of concentration and different temperature variations on the different physico-chemical parameters of the n-Octanol and DMF binary mixture along with the molecular interactions between the mixtures.

II. EXPERIMENTAL DETAILS

n-Octanol (Synthesis Grade) and N, N-Dimethylformamide (DMF) (AR grade) were procured from Loba Chemi Pvt Ltd, India, and used without further purification. Binary mixtures of n-Octanol and DMF were prepared at eleven different volume-based concentrations. These concentrations were subsequently converted into the mole fraction of DMF using a referenced Equation [14].

The ultrasonic velocity (U_v) of the binary mixtures was measured using a digital ultrasonic interferometer (Model F-05, Mittal Enterprises, New Delhi, India) with an accuracy of ± 2 m/s. The densities (ρ) of the binary mixtures were determined using a specific gravity bottle with an accuracy of ± 0.1 . The viscosity (η) of the pure liquids and their binary mixtures was measured using an Ostwald viscometer with an accuracy of ± 0.1 . The binary liquid mixtures were kept at a constant temperature using a digital temperature bath, and all measurements were conducted at various fixed temperatures.

Acoustic Evaluated Parameters

Various acoustical parameters were derived from the measured values of ultrasonic velocity and density [8].

$$V_m = \frac{x_1 m_1}{\rho_1} + \frac{x_2 m_2}{\rho_2}$$

(1)

Where X and M are the mole fraction and molecular weight, respectively. The suffix 1, 2 and m represent liquid 1, liquid 2 and mixture, respectively.

$$\beta = \frac{1}{U^2 \rho}$$

(2)

$$L_f = k \cdot \beta^{\left(\frac{1}{2}\right)}$$

(3)

where K is called the Jacobson constant and is given by $K = (93.875 + 0.375 T) \times 10^{-8}$, where T is the temperature in Kelvin.

$$\sigma = 6.4 \times 10^{-10} U^{\frac{3}{2}} \rho$$

(4)

$$\tau = \frac{4}{3} \eta \beta$$

(5)

III. RESULTS AND DISCUSSION

Figure 1 (A) illustrates the variation of ultrasonic velocity (U_v) across the entire concentration range (mole fraction of DMF) in N, N-dimethylformamide (DMF) and n-Octanol mixtures at various temperatures (293.15 K \rightarrow 313.15 K). At all measured temperatures and concentrations, the plot is divided into two linear segments with different slopes, intersecting at a mole fraction of $X = 0.5768$, indicating a deviation from ideal mixing behavior, similar to the DMF/methanol system [8]. Additionally, the ultrasonic velocity (U_v) increases with the mole fraction of DMF and decreases with temperature. This linear increase in U_v with concentration suggests significant interactions between unlike molecules through hydrogen bonding (OH–O), causing displacement of electrons and nuclei [15]. Figure 1 (B) depicts the variation of density as a function of the mole fraction of DMF at different temperatures. The density increases nonlinearly with the concentration of DMF at all measured temperatures, indicating that the mixture becomes more compact with the addition of DMF. This suggests the presence of attractive interactions between the components, causing a nonlinear increase in density [16]. The rate of increase in density is higher in the lower and mid concentration range ($0 \leq X \leq 0.5768$) compared to the higher concentration range ($X > 0.5768$). For instance, at 293.15 K, the density of n-Octanol and DMF is 0.8254 g.cm^{-3} and 0.9470 g.cm^{-3} , respectively, which decreases to 0.8113 g.cm^{-3} and 0.9382 g.cm^{-3} at 313.15 K. This decrease in density with increasing temperature is observed in all n-Octanol and DMF mixtures, attributed to an increased intermolecular gaps at higher temperatures. Figure 1 (C) shows the variation in viscosity with varying DMF composition in the mixture at different temperatures. The viscosity increases nonlinearly with the mole fraction of DMF at all temperatures, consistent with reports by Yue et al. [17] and Fort and Moore [18], which observed nonlinear variation or higher viscosity values in polar liquid mixtures. This nonlinear increase in viscosity indicates specific interactions between mixture constituents, such as hydrogen bond formation and charge transfer complexes, leading to higher viscosity in the mixtures compared to pure components [19]. The experiment that measured U_v , η , ρ , value use determined acoustic parameters, namely surface tension (σ) and relaxation time (τ) for different concentrations and temperatures are presented in Table 1.

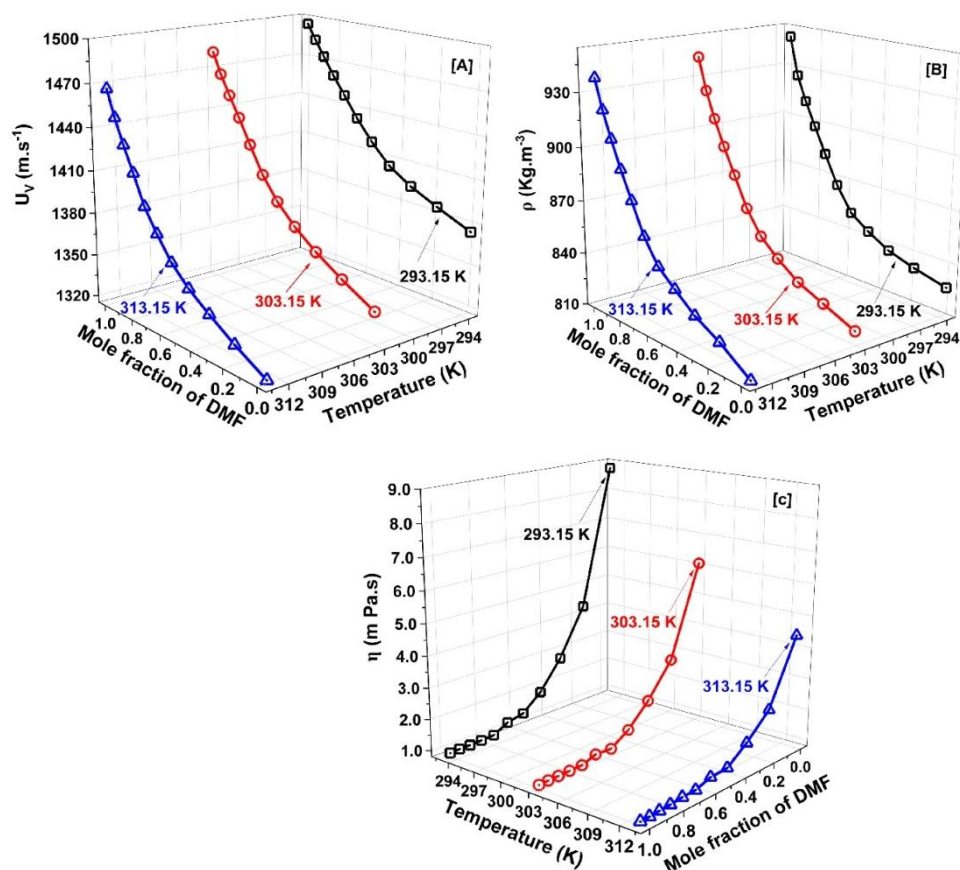


Figure 1. Experimental [A] ultrasonic velocity (UV), [B] density (ρ) and [C] viscosity (η) of mixtures as fraction of mole fraction of DMF (0.0→1.0) at various temperature.

Table 1. Evaluated parameters of surface tension (σ) and relaxation time (τ) for mole fraction of DMF (0.0→1.0) at various temperatures.

X	293.15 K		303.15 K		313.15 K	
	σ (N/m)	τ (10^{-12} S)	σ (N/m)	τ (10^{-12} S)	σ (N/m)	τ (10^{-12} S)
0.0000	26.5838	7.5196	25.3587	5.5463	24.5512	4.1794
0.1851	27.0257	3.6118	25.9652	2.8253	25.2558	2.1976
0.3382	27.4569	2.2740	26.5059	1.8389	25.8237	1.4976
0.4670	28.0028	1.4752	27.1401	1.2078	26.4214	1.0335
0.5768	28.6882	1.0340	27.8358	0.8690	27.0461	0.9846
0.6715	29.6214	0.9113	28.7453	0.8626	27.9333	0.8178
0.7541	30.6642	0.6966	29.8884	0.7082	28.9569	0.7786
0.8267	31.6084	0.6586	30.9328	0.6759	30.0871	0.7170
0.8910	32.5141	0.6318	31.8936	0.6469	31.1347	0.6748
0.9484	33.4138	0.6114	32.8700	0.6244	32.1849	0.6360
1.0000	34.6041	0.5806	34.0170	0.5923	33.3643	0.6050

The variation in surface tension indicates the attractive interactions between the two solutions. Table 1 shows that the surface tension of the mixture increases with the mole fraction of DMF. According to Karla Granados [20], strong interactions in the liquid mixture lead to an increase in the surface tension (σ) value. This suggests that the interactions in the mixture are strong, resulting in higher σ values as the mole fraction increases. Additionally, the observed decrease in surface tension with increasing temperature supports the fundamental concept of surface tension, where the formation of an interface involves the migration of species from a high surface tension liquid state to a low surface tension vapor state. Furthermore, observed in relaxation time (τ) value decreases with increase in concentration with temperature increasing τ value decreases. The relaxation time is contingent upon the viscosity of the liquid. The τ usually on the order of 10^{-12} seconds, results from the structural relaxation process. This suggests a cooperative rearrangement of molecules.

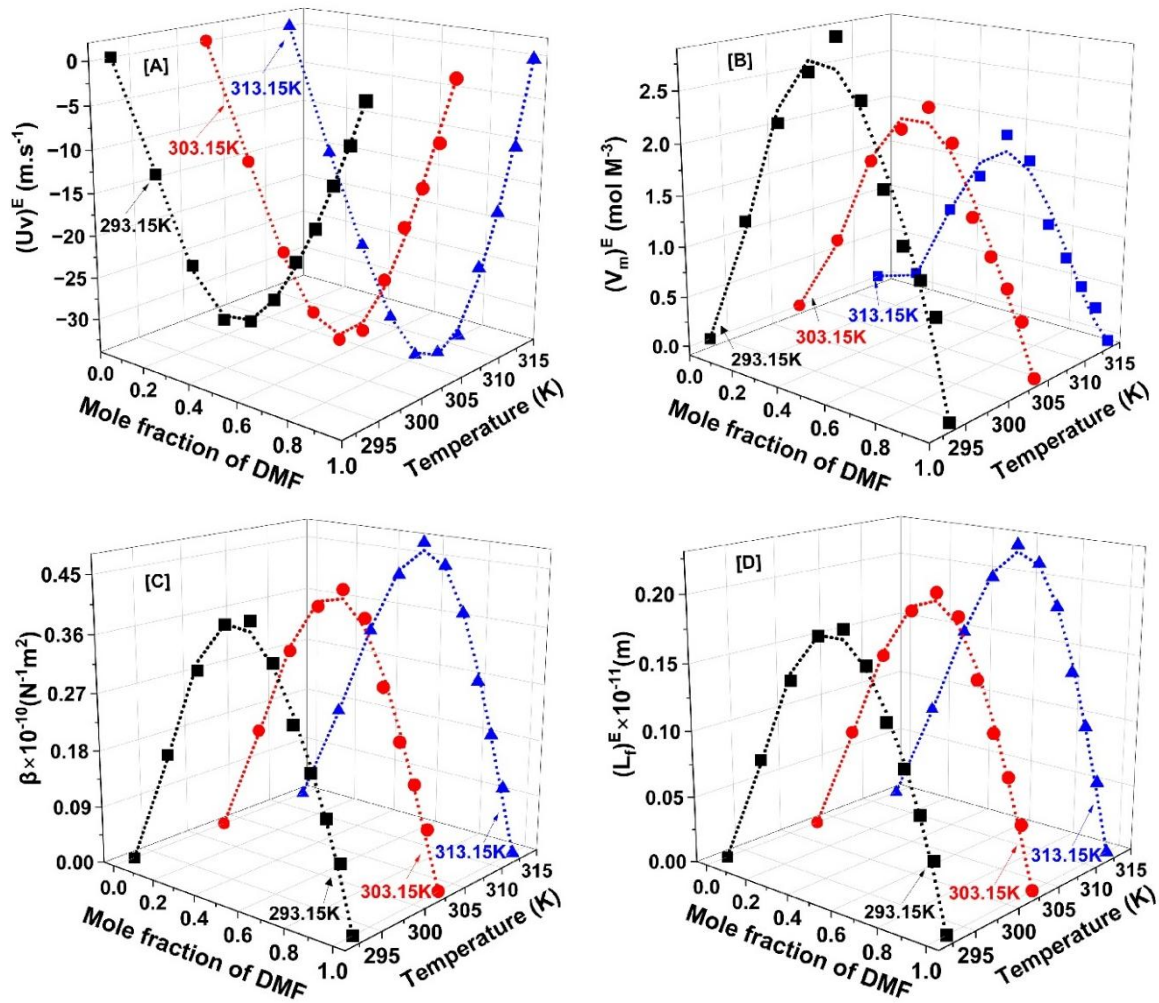


Figure 2. Variation of excess function (a) $(U)^E$, (b) $(V_m)^E$, (c) $(\beta)^E$ and (d) $(L_f)^E$ vs mole fraction of DMF in binary mixtures at different temperatures.

The excess values $(U)^E$, $(V_m)^E$, $(\beta)^E$, and $(L_f)^E$ are fitted to the R. K. polynomial equation using the least squares method. Table 2 lists the coefficients a_0 , a_1 , a_2 , and a_3 along with their standard deviation δ . In Figure 1 (A), the variation of $(Uv)^E$ across different mole fractions of DMF at three distinct temperatures is shown. Across the composition range, the excess velocity tends to become more negative as the interaction strength between the component molecules increases. Additionally, the decrease in negative deviation and the shift of the velocity maximum point towards higher 'X' values with increasing temperature suggest the presence of strong hydrogen bonding. This bonding reaches its peak at the minima, indicating a significant influence on the mixture's behavior. Figure 2 (B) presents the variation of excess molar volume $(V_m)^E$ with respect to the mole fraction of DMF across the entire composition range (0.0→1.0) at different temperatures. The strength of intermolecular interactions in liquid mixtures can be elucidated through the sign and magnitude of the $(V_m)^E$ values. Positive values of $(V_m)^E$ suggest a loose packing of molecules in the binary mixture compared to the pure components. In this figure, the $(V_m)^E$ values increase for the liquid mixtures as the interactions between unlike molecules weaken, particularly with the increase in the alkanol chain length. Figure 2(C) shows that positive adiabatic compressibility $(\beta)^E$ values indicate the presence of dispersive forces, suggesting weak interactions and structure-breaking tendencies between hetero-molecules in the mixtures. This leads to loosely packed molecular arrangements, reflecting positive deviations in $(\beta)^E$ in binary liquid systems. $(\beta)^E$ shows a higher deviation at around 0.578 mole fraction of DMF in n-Octanol, indicating significant attractive and repulsive forces between the components of the binary mixture. In Figure 2 (D), the excess free length $(L_f)^E$ in the DMF-n-Octanol mixture at various temperatures is depicted. At lower DMF mole fractions (around $X = 0.578$), $(L_f)^E$ rises, indicating strong interactions between different molecules. The shift to positive $(L_f)^E$ values suggests increased detachment between components, resulting in higher compressibility and volume.

Table 2. Values of coefficients (a_0, a_1, a_2, a_3) of R. K. polynomials with standard deviation (δ) at different temperatures.

	a_1	a_2	a_3	a_4	δ
<u>T = 293.15 K</u>					
$(U_v)^E$	-106.3373	-4.0390	45.7044	-23.7668	0.9994
$(V_m)^E$	11.7507	0.6303	-4.994	5.2441	0.9864
$(\beta)^E$	1.6226	0.1012	-0.6083	0.5407	0.9972
$(L_f)^E$	0.7434	0.0908	-0.231	0.2354	0.9974
<u>T = 303.15 K</u>					
$(U_v)^E$	-125.5903	-41.9581	40.3272	21.7376	0.9976
$(V_m)^E$	8.9209	1.3215	-5.6743	2.3600	0.9916
$(\beta)^E$	1.6472	0.397	-0.6756	-0.0467	0.9967
$(L_f)^E$	0.7703	0.225	-0.2559	-0.0204	0.9971
<u>T = 313.15 K</u>					
$(U_v)^E$	-146.4458	-85.2688	4.7219	40.5627	0.9990
$(V_m)^E$	6.4728	4.3948	-7.8021	-1.2111	0.9863
$(\beta)^E$	1.7618	-0.9076	-0.5702	-0.5187	0.9986
$(L_f)^E$	0.8287	0.4489	-0.1975	-0.2181	0.9988

IV. CONCLUSIONS

In the study of the n-Octanol+DMF binary system, the concentration-dependent behaviors of ultrasonic velocity (U_v), density (ρ), and viscosity (η) were examined across different temperatures. The non-linear changes observed in parameters like β , L_f , σ , and τ shed light on the intricate molecular interactions underlying complex formation via hydrogen bonding between solute molecules. Additionally, the contrasting positive and negative shifts in excess values concerning concentration and temperature for these acoustic parameters provided further evidence of interactions between unlike molecules.

V. ACKNOWLEDGMENT

Mr. Navin Chaudhary expresses gratitude to the SHODH Scheme (Ref. no. 2021017228) of the Government of Gujarat for financial support.

VI. REFERENCE

1. A. Ali, A. K Nain, and S. Hyder, "Study of molecular interaction in binary liquid mixtures through ultrasonic speed measurement." *Journal of Pure and Applied Ultrasonics*, 23, 73-79, 2001.
2. S. Anuradha, S. Prema and K. R. Rajagopal, "Ultrasonic studies on molecular interactions in binary mixtures of acetonitrile with carbonyl molecules", *Journal of Pure and Applied Ultrasonics*, 27, 49-54, 2005.
3. S. Thirumaran, J. Jayakumar, "Ultrasonic study of n-alkanols in toluene with nitrobenzene", *Indian Journal of Pure & Applied Physics*, 47, 265–272, 2009.
4. A. N. Prajapati, Acoustic and refractometric study of binary mixtures of 1-Propanol + Benzonitrile at 313 K, *Indian Journal of Pure & Applied Physics*, 55, 297-303, 2017.
5. S. T. Murugan and D. Priya, "Acoustical and excess thermodynamic studies of ternary liquid mixtures of some primary alkanols in mixed binary solvent at varying temperatures", *Indian Journal of Pure and Applied Physics*, 51, 413-420, 2013.
6. M. Gupta, J. P. Shukla, "Indian Ultrasonic investigation of molecular association in binary mixtures-Dioxan plus formic acid, salicylic acid and benzoic acid", *Indian Journal of Pure and Applied Physics*, 34, 769-772, 1966.
7. A. N. Kannappan, R. Palani, "Studies on molecular interaction in ternary liquid mixtures by ultrasonic velocity measurements", *Indian Journal of Physics*, 70, 59-65, 1996.
8. A. M. E. Raj, L. B. Resmi, V. B. Jothy, M. Jayachandran, C. Sanjeeviraja, "Ultrasonic study on binary mixture containing dimethylformamide and methanol over the entire miscibility range ($0 < x < 1$) at temperatures 303–323 K", *Fluid Phase Equilibria*, 281, 78–86, 2009.
9. S. P. Patel, A. N. Prajapati, H. P. Vankar and V. A. Rana, "Dielectric Dispersion Response of Binary Mixtures of n-Butanol and Valeronitrile", *Advance Material Research*, 1169, 73-77, 2022.
10. L. Cai, Y. Uygun, C. Togbe, H. Pitsch, H. Olivier, P. Dagaut, S. M. Sarathy, "An experimental and modeling study of n-octanol combustion", *Proceedings of the Combustion Institute*, 35, 419-427, 2015.
11. J. Julis and W. Leitner, "Synthesis of 1-Octanol and 1,1-Dioctyl Ether from Biomass-Derived Platform Chemicals", *Angewandte Chemie International Edition*, 51, 1-6, 2012.

12. L. Yang, K. Huang, X. Yang, Dielectric Properties of N, N-Dimethylformamide Aqueous Solutions in External Electromagnetic Fields by Molecular Dynamics Simulation. *Journal of Physical Chemistry A*, 114, 1185-1190, 2009.
13. R. J. Sengwa, V. Khatri, S. Sankhla, "Structure and hydrogen bonding in binary mixtures of N, N-dimethylformamide with some dipolar aprotic and protic solvents by dielectric characterization", *Indian Journal of Chemistry*, 48A, 512-519, 2009.
14. A. N. Prajapati, S. P. Patel, V. A. Rana, "Study of short range and long range molecular interactions in binary liquid mixtures of N, N-dimethylformamide (DMF) and 1-propanol", *Journal of Molecular Liquids*, 354, 118832, 2022.
15. M. Rastogi, A. Awasthi, M. Gupta, J. P. Shukla, "Molecular association of aliphatic ketones and phenol in a nonpolar solvent-ultrasonic and IR study", *Journal of Molecular Liquids*, 107, 185-204, 2003.
16. M. Chandra Sekhar, T. Madhu Mohan, T. Vijaya Krishna, A. Venkatesulu, K. Siva Kumar, "Density, refractive Index, speed of sound and computational studies of intermolecular interactions in binary mixtures of 2-Chloroaniline with butanols (1-butanol, 2-butanol) at T= (303.15–318.15) K", *Journal of Solution Chemistry*, 44, 237–263, 2015.
17. X. Yue, L. Zhao, L. Ma, H. Shi, T. Yang, J. Zhang, "Density, dynamic viscosity, excess property and intermolecular interplay studies for 1, 4-butanediol+ dimethyl sulfoxide binary mixture", *Journal of Molecular Liquids*, 263, 40–48, 2018.
18. R. J. Fort, W. R. Moore, "Viscosities of binary liquid mixtures", *Trans. Faraday Soc.* 62 1112–1119, 1966.
19. D. Rahul, T.S. Krishna, M. Gowrisankar, D. Ramachandran, "Molecular interactions and theoretical estimation of ultrasonic speeds using scaled particle theory in binary mixtures of 3-chloroaniline and 1-alkanols (C6–C10) at different temperatures", *Journal of Molecular Liquids*, 212 618–628, 2015.
20. K. Granados, J. G. Fredrique, "Refractive Index, Surface Tension, and Density of Aqueous Mixtures of Carboxylic Acids at 298.15 K". *Journal of Chemical Engineering Data*, 51, 1356-1360, 2006.

¹Chitralekha Anil
Kolhe

²Shilpa G. Vidhale

**"Powering the Future: A Comprehensive
Review of Polymer Solar Cells"**



Abstract: - Polymer solar cells (PSC) offer advantages like flexibility and lightweight but suffer from low efficiencies, due to issues like limited charge carrier mobility and rapid combination. The blending of two different polymers can improve the morphology of the active layer in Organic Photovoltaic (OPV) devices, promoting better mixing and distribution of components. This can lead to enhanced charge transport and reduced recombination, ultimately improving device performance. Metallic nanoparticles accelerate the charge transport by generating the conductive pathways and reducing the distance between the free charges need to travel in the active layer of polymer solar cells which decreases the losses due to recombination and increase current density. Their unique properties make them ideal for innovative applications and integration into everyday life, paving the way for a more sustainable and energy-efficient future.

Keywords: polymer solar cells, excitons, nanoparticles, active layer, etc.

^{1*} Research scholar at Department of Physics, Adarsha Science, Jairamdas Bhagchand Arts and Birla Commerce *Mahavidyalaya, Dhamangaon Rly.*, Dist. Amravati, Maharashtra. Sant Gadge Baba Amravati University Amaravati.

² Assistance professor at Department of Physics, Adarsha Science, Jairamdas Bhagchand Arts and Birla Commerce *Mahavidyalaya, Dhamangaon Rly.*, Dist. Amravati, Maharashtra, Sant Gadge Baba Amravati University Amaravati.

I. INTRODUCTION

Polymer solar cells are the great too used instead of traditional photovoltaic devices for great sustainable future. conjugate polymers are the best alternatives to the traditional photovoltaic devices. It promising the clean and renewable energy generation which ends our dependence on fossil fuels and mitigating environmental impact. The conjugate polymer has strong light absorption and compatibility with cost effective and production techniques on large scales.[1] from the past few years, the organic solar cells have been developing in the various part of the world, due to the rapid increase in power conversion efficiencies it is a point of attraction for scientific and economic interest around the world wide. The finding of new materials and improved materials engineering and simple device structures are the reasons behind this field growth. Today, solar power conversion efficiencies in excess of 3% have been accomplished with several device concepts. Though efficiencies of these thin-film organic devices have not yet reached those of their inorganic counterparts ($\approx 10\text{--}20\%$); the perspective of cheap production (employing, e.g., roll-to-roll processes) drives the development of organic photovoltaic devices further in a dynamic way. There are two techniques for the production of photovoltaic, wet solution processing or dry thermal evaporation of the organic constituents. In the development of light-emitting diodes (similar technologies) the organic solar cells are attracted the profit of the market recently. We review here the current status of the field of organic solar cells and discuss different production technologies as well as study the important parameters to improve their performance.[2] The two key factors such as efficient exciton dissociation and effective charge extraction are responsible for attending high photosensitivity in organic photovoltaic (OPV) devices, these processes are improved by charge transport fundamental properties of the donor-acceptor (DA) blends. To improve exciton dissociation the close contact between donor and acceptor materials has to be ensure by using the methods like as blending, codeposition, laminating and chemical linking. These techniques are the reasons behind the increase charge-trap densities and lead to reduced carrier mobilities in blend, but crystalline order and high purity is challenging task in this research. To answer these challenges, researchers focus on controlling the film morphology of the blends, by rearranging the acceptor and donor molecules within the blend. Researchers aim to improve charge transport properties while maintaining efficient exciton dissociation and charge extraction properties while maintaining efficient exciton dissociation and charge extraction. This research is pivotal for increasing the efficiency of these sustainable energy devices and advancing OPV technology.[3]

Excitons.[4] Are the states in the polymer solar cells or polymer light-emitting diodes (PLEDs) if they are excited electrically or optically. These excitons are able to move within the polymer material, this migration, known as exciton diffusion, is driven by excitation energy transfer to lower-energy sites. The distance travelled by the excitons during its lifetime is called as exciton diffusion length which is the key factors to

quantify this process.[5] Exciton diffusion plays important role the in polymer optoelectronic devices.[6] In PLEDs, quenching at the metallic cathode done by the exciton diffusion.[7] In polymer photovoltaic devices, the optimal morphology of the active layer depends on the ability of excitation to reach the polymer interface for dissociation.[8] Determining the exciton diffusion length is key point for understanding these processes. The spectral dependence of the photocurrent can be varied to estimate the exciton diffusion length. This variation provides valuable insights into the behavior and performance of these devices.[9]

II. BASIC WORKING OF POLYMER SOLAR CELLS

When light incident on the active layer of the solar cell, electrons get excites in the polymer materials which create electron-hole pairs called as excitons and the process is called excitation. This electron-hole diffuse through the active layer, which is typically a blend of a conjugated polymer, electron donor and electron acceptor.[10][11][12][13] At the interface between donor and acceptor, due to the energy difference between two materials excitons are separated into free electrons and holes.[14][15][16][17][18] The free electrons and holes move through their respective materials towards the electrodes. The electrons attracted towards the cathode meanwhile the holes attracted towards the anode.[19][20] This electron moves from cathode to the anode through external circuit generate an electric current, used in power electronic devices.[21] A blocking layer is often used between the active layer and the electrodes to prevent recombination of electrons and holes.[22]

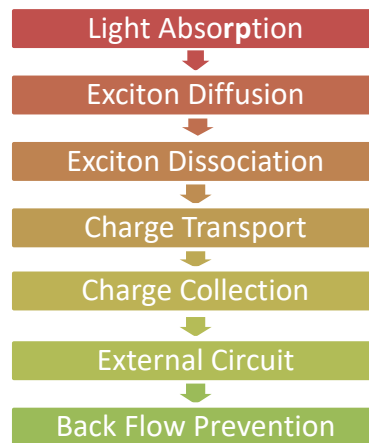


Figure 2: working of the polymer solar cells

III. HETEROJUNCTION PHOTOVOLTAIC:

The internal quantum efficiency has been controlled by the direct deposition of the metal cathode onto the active organic layers in the bilayer organic photovoltaic (OPV) devices. The layer can be inserted between the active layers and the metal cathode to address the issue must have the following properties.[23]

- It acts as a barrier to exciton transport, confining excitons to the active organic layers to prevent them from recombining at the cathode/organic interface.

- It can be efficiently transporting electrons from the acceptor layer to the metal cathode without significantly increasing the total cell series resistance.
- The material is able to withstand damage during cathode deposition.
- It will be transparent to the incident radiation to allow light to reach the active organic layers.

Also, the layer must be thick to absorb the maximum light incident on the photoactive layer and separate the metal cathode which improve the performance of the OPV devices.[24] If all layers of the OPV should be smaller than the exciton diffusion length (LD) then almost all photogenerated excitons reach to the donor-acceptor (DA) interface and efficiently dissociate into free electrons and holes.[25] The maximum numbers of excitons generated in the active layer are properly converted into charge carriers which maximize the efficiency of the devices by optimizing the thickness of the active layer.[26]

IV. INFLUENCE OF THE NANOPARTICLE'S INCORPORATIONS:

Polymer solar cells (PSCs) have potential of low-cost, highly portable, and deployable solar energy solutions, enabled by their flexibility and light weight.[27] when compared with inorganic solar cells, polymer solar cells (PSCs) have problems such as insufficient light absorption due to thin active layer for maintaining the short exciton diffusion length and low carrier mobilities.[28][29][30] To improve the power conversion efficiency (PCE) of polymer solar cells (PSCs) the metallic nanoparticles such as Au(gold) and Ag(silver) incorporated into the polymer layer by solution processing either in buffer layer or the active layer of the PSCs.[31][32][33]

Luyao Lu et al, are incorporated Ag NPs into PEDOT:PSS (Poly(3,4-ethylenedioxythiophene) (polystyrene sulfonate) layer results during the open-circuit, voltage (Voc) remained the same whereas in short-circuit, current density (Jsc) increased from 15.0 to 16.4 mA/cm², FF increased from 67.1 to 68.8%. As a result, Power Conversion Efficiency enhanced from 7.25 to 8.01%. Incorporating Au NPs into PEDOT layer shows similar improvement. Voc remained unchanged, Jsc improved from 15.0 to 16.7 mA/cm² and FF enhanced to 68.8%, leading to a PCE of 8.16%. Both Ag and Au NPs exhibit around 10% enhancement of PCE due to the notable enhanced Jsc and improved FF. [34]

Aruna P Wanninayake et al, investigated that Copper oxide (CuO) has band gap energy of 1.5 eV, which is close to the ideal 1.4 eV for optimal solar spectral absorption in solar cells, due to which incorporation of CuO nanoparticles in the active layer are the one for enhancing the performance of the polymer solar cells. When different weight percentage of CuO NPs incorporated in P3HT/PC70BM (Poly(3-hexylthiophene)) solar cells, the increase in the photo absorption in the active layer, due to which 24% increase in the power conversion efficiency compared to the reference cell. The short-circuit current increased from 5.234 mA cm⁻² to 6.484 mA cm⁻² in cells with 0.6 mg of CuO nanoparticles and FF improved from 61.15% to 68.0%.[35]

Marco Notarianni et al, explored the different methods to incorporate metallic nanoparticles into organic solar cells, also the methods to produce the metallic nanoparticles. To enhanced the power conversion efficiency the geometry, size, concentration, and placement of the nanoparticles has to be controlled. By adjusting the thickness of the deposited gold and the annealing temperature the size of the nanoparticles was controlled and the distance between the particles increase which prevent undesired reflection effects. This factor (distance between the particles and size of metallic nanoparticles) enhanced the power efficiency in organic solar cells.[36]

Feng-Xian Xie et al, achieved the 22% efficiency improvement in polymer solar cells (PSCs) by incorporating Au nanoparticles (NPs) into all polymer layers. When Au NPs incorporated in the poly-(3,4-ethylenedioxythiophene)(styrenesulfonate), it enhanced the hole collection in the active layer which increase optical absorption and balance charge transport. The study indicated that the absorption enhancement in the active layer is due to plasmon resonances with strong near-field distributions.[37]

Jyh-Lih Wu et al, investigated the plasmonic effects on polymer photovoltaic devices (OPVs). They form a blend of poly(3-hexylthiophene) (P3HT) and [6,6]-phenyl-C61-butyric acid methyl ester (PCBM). The localized surface plasmon resonance (LSPR) triggered by incorporating gold nanoparticles (Au NPs) into the anodic buffer layer which enhances the device performance. Steady-state photoluminescence (PL) measurements showed increased fluorescence intensity, indicating higher light absorption in P3HT due to LSPR which reduced the lifetime of photogenerated excitons and reducing exciton recombination. Due to this photocurrents and fill factors improved significantly. The power conversion efficiency increased from 3.57% to 4.24% due to the local enhancement of the electromagnetic field around the Au NPs.[38]

Dixon D. S. Fung et al, achieved a 13% improvement in power conversion efficiency (PCE) for polymer solar cells (PSCs) by incorporating PEG-capped Au nanoparticles (NPs) into the PEDOT layer, with enhancements primarily in short-circuit current density (J_{sc}) and fill factor (FF). The optimal Au NP concentration was 0.32 wt%. Although Au NPs showed minimal impact on absorption enhancement due to lateral distribution of near-field plasmonic resonance, they reduced the resistance of the PEDOT layer and increased interfacial roughness, improving hole collection and J_{sc} and FF. This study highlights the importance of considering both optical and electrical properties for enhancing PSC performance.[39]

Zhe Li et al, compared the transient photocurrent and photovoltage behaviour of P3HT/CdSe nanoparticle devices to study the impact of nanoparticle shape. For the P3HT/CdSe nano-dots system, significant charge trapping was observed, indicated by an initial photocurrent peak and a long tail after turn-off. This trapping limited charge collection. In contrast, the P3HT/CdSe nano-tetrapods system exhibited reduced charge trapping, with no initial photocurrent peak, less back injection of charge carriers, and longer charge carrier

lifetimes. These results show that nanoparticle shape significantly affects charge transport, with tetrapod improving electron transport and overall device performance. Reducing charge trapping by engineering the nanocrystal phase is crucial for enhancing hybrid solar cell efficiency.[40]

Hyosung Choi et al, achieved high-performance polymer solar cells using multipositional silica-coated silver nanoparticles to leverage the plasmonic effect. The strategic placement of these nanoparticles enhances light absorption and scattering through improved electric field distribution. Our device, incorporating nanoparticles between the hole transport layer and the active layer, achieved a power conversion efficiency of 8.92% with an external quantum efficiency of 81.5%. These efficiencies are the highest reported to date for plasmonic polymer solar cells using metal nanoparticles.[41]

Xuanhua Li et al, introduces a novel approach using a combination of Ag nanomaterials, including nanoparticles and nano prisms, synthesized via a simple wet chemical method, to enhance the power conversion efficiency (PCE) of organic solar cells (OSCs). Theoretical and experimental studies reveal that the PCE enhancement is due to the simultaneous excitation of plasmonic low- and high-order resonance modes, with the Ag nano prisms' high-order resonances contributing significantly to absorption enhancement. Incorporating these mixed nanomaterials into the active layer improves wide-band absorption, increasing short-circuit photocurrent density (Jsc) by 17.91% and PCE by 19.44% compared to pre-optimized control OSCs.[42]

V. CONSTRUCTION OF POLYMER SOLAR CELLS WITH NANOPARTICLES:

polymer solar cells (PSCs) with nanoparticles includes few important steps, which enhance the overall performance of the solar cells such as materials preparation, fabrication, optimization and characteristics.

1. Materials preparation

- Active Layer Materials: choose the polymer as a donor material (e.g., P3HT - Poly(3-hexylthiophene)) and as an acceptor material (e.g., PCBM - [6,6]-Phenyl C61-butyric acid methyl ester).[43]
- Nanoparticles: select the proper metallic nanoparticles (e.g., Au or Ag) with appropriate shapes and sizes. [44]

2. Fabrication steps

1) Substrate Preparation:

- Cleaning: Clean the substrate (e.g., indium tin oxide (ITO) coated glass) thoroughly using solvents like acetone, isopropanol, and deionized water, followed by drying. [45][46]

- Surface Treatment: Apply a UV-ozone treatment to improve surface wettability and adhesion.[47]

2) Hole Transport Layer (HTL):

A thin coating of poly(3,4-ethylenedioxythiophene) (styrene sulfonate) (PEDOT) is applied onto the substrate through spin coating. This particular layer plays a role in collecting and transporting holes. After the deposition, anneal the layer to eliminate any leftover solvents which will further enhance the quality of the film.[48]

3) Nanoparticle Incorporation:

- Synthesize metallic nanoparticles using methods such as chemical reduction, laser ablation etc.[49]
- Nanoparticles are then dispersed in a suitable solvent or directly mixed into the polymer blend solution.[50]
- Blend the nanoparticles directly into the polymer mix (materials with both donor and acceptor properties) to produce the active layer.
- On the other hand, nanoparticles may be applied independently either as an interface layer between PEDOT and the active layer or by putting them directly on top of each other in the active layer. [51]

4) Active Layer Deposition:

- The nanoparticle-polymer blend solution should be spin coated onto the HTL. It is important that the active layer be both thick and uniform as this greatly affects the performance of the device. [52]
- The active layer should then be annealed; this process will help in improving the crystallinity while enhancing phase separation between donor and acceptor materials.[53]

5) Electron Transport Layer (ETL):

- An ETL needs to be deposited (for example Zinc Oxide (ZnO) or a low-work-function metal like calcium) which will help in electron collection.[54]

6) Top Electrode:

- Thermal evaporate a top electrode (e.g., aluminum) under vacuum to deposit last layer, which acts as the cathode and finalizes the device structure.[55]

7) Encapsulation:

- Use an encapsulating material to protect your device from moisture and oxygen that would otherwise corrode its performance over time. Choose transparency when selecting this

material; encapsulation keeps off those harmful environmental factors for longevity of performance. [56]

3. Optimizing and characterizations
 - 1) Optimization:
 - Adjust the concentration, size, shape, and distribution of nanoparticles to maximize light absorption and charge transport while minimizing recombination losses.
 - Optimize the thickness of each layer for maximum efficiency.[57]
 - 2) Characterization:
 - Use techniques like UV-Vis spectroscopy, photoluminescence, and electron microscopy to analyse the optical and structural properties of the layers.[58]
 - Measure the photovoltaic parameters such as power conversion efficiency (PCE), short-circuit current density (J_{sc}), open-circuit voltage (V_{oc}), and fill factor (FF).[59]
 - 3) Electrical Testing:
 - Conduct current-voltage (J-V) measurements under simulated sunlight to assess the overall performance of the solar cells.
 - Evaluate the stability and durability of the PSCs over time.[60]

By carefully controlling the incorporation of nanoparticles and optimizing each step in the fabrication process, high-performance polymer solar cells can be constructed, offering improved efficiency and stability.

VI. ADVANTAGE OF INCORPORATING NANOPARTICLES IN POLAR SOLAR CELLS:

When the different metallic nanoparticles incorporating in polymer solar cells (PSCs) it enhances their performance and efficiency. Following are some advantages of the incorporating nanoparticles in polar solar cells

- The light absorption and trapping in the active layer of polymer solar cells is increase by incorporating the nanoparticles within the active layer, leading to generate the excitons in the active layer. (electron-hole pairs).[61]
- Localized surface plasmon resonance (LSPR), are induced by using the metallic nanoparticles like gold nanoparticles or silver nanoparticles, which enhances the local electromagnetic field and increase the light absorption in the active layer.[62]
- Metallic nanoparticles accelerate the charge transport by generating the conductive pathways and reducing the distance between the free charges need to travel in the active layer of polymer solar cells which decreases the losses due to recombination and increase current density.[63]
- Nanoparticles can increase the light absorption and charge transport due to which the power conversion efficiency increase in the polymer solar cells for real world application.[64]

- The stability and durability of the polymer solar cells improved by incorporating the nanoparticles which prevent the active layer degradation.[65]
- The optical properties of the polymer solar cells by controlling the size, shape, and material of nanoparticles which allowing better alignment with the absorption spectrum in the active layer.[66]
- The UV and near-infrared ray can be absorbed by the nanoparticles which enhanced the light harvesting capabilities of PSCs. [67]
- Nanoparticle incorporation make the active layer thinner which forms the lighter and more flexible solar cells.[68]

Therefore, it is concluded that the incorporating nanoparticles in PSCs can significantly improve their optical and electrical properties of the polymer solar cells

VII. FUTURE OF POLYMER SOLAR CELLS:

1. Efficiency Improvements

- Development of new donor and acceptor materials with higher absorption coefficients and better charge transport properties.[69]
- Continued improvement of non-fullerene acceptors, which have shown promise in achieving higher efficiencies.[70]
- Increasing efficiency by stacking multiple layers with complementary absorption spectra to capture a broader range of the solar spectrum.[71]

2. Stability and Longevity

- Enhanced encapsulation methods to protect PSCs from environmental degradation (moisture, oxygen, UV light).
- Development of more stable polymer materials and device architectures that can withstand prolonged exposure to sunlight and other environmental factors.[72]

3. Scalability and Manufacturing

- Advancements in scalable manufacturing techniques, such as roll-to-roll printing, to produce PSCs at a lower cost and higher volume.
- Improvement in printing technologies (inkjet, screen printing) for large-scale production and integration into flexible substrates. [73]

4. Integration with Other Technologies

- Combining PSCs with other types of solar cells (e.g., perovskite solar cells) to create hybrid devices that leverage the strengths of both technologies.[74]

5. Flexible and Wearable Electronics
 - Continued development of flexible and lightweight PSCs suitable for wearable electronics and portable power sources.[75]
6. Environmental and Economic Impact
 - Use of environmentally friendly and sustainable materials to reduce the ecological footprint of PSC production.[76]

VIII. WHY, POLYMER SOLAR CELLS:

There are several reasons why polymer solar cells (PSCs) are increasingly being sought as alternatives to silicon-based solar cells. Some of the reasons behind preference for polymer solar cells include the fact that PSCs are made from flexible materials, which allows them to be bent and rolled, making them applicable in a wide range of areas such as portable solar chargers, wearable electronics and even they can be integrated with building materials. In other words, PSCs are light making them suitable for portable devices and also, they can be used in aerospace or transport. In addition, low-cost materials like roll-to-roll printing can be used during fabrication of these types of PSCs thereby reducing overall costs significantly when compared with traditional silicon photovoltaic cells.[77] This is because manufacturing technologies for this kind of a cell could be easily scaled-up hence there is very less difficulty in meeting the increasing demand for renewable energy sources. The flexibility and lightweight Ness make PSCs useful in various innovative applications including textiles integration, packaging inclusion and transparent windows incorporation. Moreover, PSCs also offer an ability to design semi-transparent or coloured designs capable of harmonizing with architectural aesthetics without affecting their appearance.[78]

IX. APPLICATION OF POLYMER SOLAR CELLS:

Polymer solar cells (PSCs) have a range of applications due to their flexibility, lightweight nature, and potential for low-cost production. Here are some key applications:

1. **The small devices such tablet, smart phones and** wearable technology are able to use the PSCs, providing a lightweight and flexible energy source.
2. PSCs can be embedded in building materials like windows, facades and roofs, and used as a renewable energy source without compromising on the aesthetic and functional aspects of the building materials.
3. PSCs are flexible and can be integrated in textiles (clothes, backpacks and other wearable items), allowing for wearable electronics and for the charging of mobile electronic devices on the go.
4. PSCs can be applied in agriculture, e.g. in green houses. The semi-transparency of PSCs allows crops to grow beneath the panels while delivering electricity.

5. PSCs offer a lightweight, easy to carry, high energy density power source for remote and off-grid areas, including environmental sensors, communication tools and emergency lights.
6. PSCs can be part of general products like solar powered chargers, lamps and toys, encouraging the everyday use of renewable energy.
7. PSCs can drive IoT devices allowing for the massive deployment of sensors and smart objects in indoor, outdoor, and wearable environments, without the need for battery replacement.[79]

These applications highlight the versatility and potential of polymer solar cells in contributing to sustainable energy solutions across various sectors.

X. CONCLUSION:

The promising and versatile technology in the renewable energy is promising by the Polymer solar cells (PSCs) which provides many features over traditional silicon-based solar cells. It comes with different potential such as their flexibility, lightweight nature, and low-cost production which is best factors for various devices from portable electronics and wearable technology.

Also, the metallic nanoparticles such as gold nanoparticles or silver nanoparticles significantly enhance their performance. Nanoparticles can increase the light absorption and charge transport due to which the power conversion efficiency increase in the polymer solar cells for real world application Aesthetically appealing with environmental benefits PSC can be incorporated into different materials that are less toxic and have lower energy requirements for production.

In conclusion, polymer solar cells, particularly when enhanced with nanoparticles, offer a compelling combination of efficiency, flexibility, and sustainability. Their unique properties make them ideal for innovative applications and integration into everyday life, paving the way for a more sustainable and energy-efficient future. Continued research and development in this field will likely lead to further improvements in performance and broaden the scope of their applications

ACKNOWLEDGMENT

First and foremost, I would like to express my sincere gratitude to my advisor Shilpa G. Vidhale, for their continuous support, patience, and immense knowledge. Their guidance helped me in all the time of research and writing of this paper.

REFERENCES

1. Martin Helgesen, Roar Søndergaard and Frederik C. Krebs. (2009). Advanced materials and processes for polymer solar cell devices. *Journal of Materials Chemistry*, 20, 36-60.
2. Harald Hoppe and Niyazi Serdar Sariciftci. (2004). Organic solar cells: An overview. *Materials Research Society*, 19(7), 1924-1945.

3. Peter Peumans, Aharon Yakimov and Stephen R. Forrest. (2002). Small molecular weight organic thin-film photodetectors and solar cells. *JOURNAL OF APPLIED PHYSICS*, 93(7), 3693-3695.
4. Shawn R. Scully; Michael D. McGehee. (2006). Effects of optical interference and energy transfer on exciton diffusion length measurements in organic semiconductors. *J. Appl. Phys.*, 100(3).
5. J. J. M. Halls, K. Pichler, R. H. Friend, S. C. Moratti and A. B. Holmes. (1996). Exciton diffusion and dissociation in a poly(p-phenylenevinylene)/C60. *Appl. Phys. Lett.*, 68(22), 3120-3122.
6. Peter K. H. Ho, D. Stephen Thomas, Richard H. Friend, Nir Tessler*. (1999). All-Polymer Optoelectronic Devices. *American Association for the Advancement of Science*, 285, 233-236.
7. D. E. Markova and P. W. M. Blom. (2005). Exciton quenching in poly(phenylene vinylene) polymer light-emitting diodes. *APPLIED PHYSICS LETTERS*, 87.
8. Ahmed G. S. Al-Azzawi, Shujahadeen B. Aziz, Elham M. A. Dannoun, Ahmed Iraqi, Muaffaq M. Nofal, Ary R. Murad and Ahang M. Hussein. (2023). A Mini Review on the Development of Conjugated Polymers: Steps towards the Commercialization of Organic Solar Cells. *Polymers*, 15(164).
9. Oleksandr V. Mikhnenko, Hamed Azimi, Markus Scharber, Mauro Morana, Paul W. M. Blom, Maria Antonietta Loi. (2012). Exciton diffusion length in narrow bandgap polymers. *Energy Environ. Sci.*, 5, 6960–6965.
10. M. Stoessel; G. Wittmann; J. Staudigel; F. Steuber; J. Blässing; W. Roth; H. Klausmann; W. Rogler; J. Simmerer; A. Winnacker; M. Inbasekaran; E. P. Woo. ((2000)). Cathode-induced luminescence quenching in polyfluorenes. *J. Appl. Phys.*, 87(9), 4467–4475.
11. A. Haugeneder, M. Neges, C. Kallinger, W. Spirkel, U. Lemmer, J. Feldmann, U. Scherf, E. Harth, A. Gügel, and K. Müllen. (1999). Exciton diffusion and dissociation in conjugated polymer/fullerene blends and heterostructures. *Phys. Rev.*, 59(23), 15346.
12. Leif A. A. Pettersson; Lucimara S. Roman; Olle Inganäs. (1999). Modeling photocurrent action spectra of photovoltaic devices based on organic thin films. *J. Appl. Phys.*, 86(1), 487–496.
13. Tom J Savenije, John M Warman, Albert Goossens. (1998). Visible light sensitisation of titanium dioxide using a phenylene vinylene polymer. 287(1-2), 148-153.
14. Sariciftci, N. S. (1998). *Primary Photoexcitations In Conjugated Polymers: Molecular Exciton Versus Semiconductor Band Model*. World Scientific, 1998.
15. M. Chandross, S. Mazumdar, S. Jeglinski, X. Wei, Z. V. Vardeny, E. W. Kwock, and T. M. Miller. (1994). Excitons in poly(para-phenylenevinylene). *Phys. Rev.*, 50(19).
16. I. H. Campbell, T. W. Hagler, D. L. Smith, and J. P. Ferraris. (1996). Direct Measurement of Conjugated Polymer Electronic Excitation Energies Using Metal/Polymer/Metal Structures. *Phys. Rev. Lett.*, 76(11).
17. Martin Pope and Charles E. Swenberg. (1999). *Electronic Processes in Organic Crystals and Polymers (Monographs on the Physics and Chemistry of Materials)*. oxford university press.

18. Knupfer, M. ((2003)). Exciton binding energies in organic semiconductors. *Applied Physics A*, 77, 623–626.
19. Harald Hoppe and Niyazi Serdar Sariciftci. (2006). Morphology of polymer/fullerene bulk heterojunction solar cells. *Journal of materials chemistry*, 16(1), 45-61.
20. H Hoppe , T Glatzel, M Niggemann, A Hinsch, M Ch Lux-Steiner, N S Sariciftci. (2005). Kelvin probe force microscopy study on conjugated polymer/fullerene bulk heterojunction organic solar cells. *Nano Lett*, 5(2), 269-274.
21. Petritsch, K. (2000). *Organic Solar Cell*.
22. Thilo Glatzel, Harald Hoppe, Niyazi S. Sariciftci , Martha Ch. Lux-Steiner. (2005). Kelvin Probe Force Microscopy Study of Conjugated Polymer/Fullerene Organic Solar Cells. *Japanese Journal of Applied Physics*, 44(7B), 5370-5373.
23. Akira Tada, Yanfang Geng, Qingshuo Wei, Kazuhito Hashimoto, Keisuke Tajima. (2011). Tailoring organic heterojunction interfaces in bilayer polymer photovoltaic devices. *NATURE MATERIALS*, 10.
24. Seamus E. Burns, Dr. Nicola Pfeffer, Dr. Johannes Grüner, Dr. Marcus Remmers, Dr. Thomas Javoreck, Prof. Dieter Neher, Prof. Richard H. Friend. (2004). Measurements of optical electric field intensities in microcavities using thin emissive polymer films†. *Advanced materials*, 9(5), 395-398.
25. Thomas Stubinger and Wolfgang Brutting. (2001, OCTOBER 1). Exciton diffusion and optical interference in organic donor–acceptor photovoltaic cells. *JOURNAL OF APPLIED PHYSICS*, 90.
26. P. Peumans, V. Bulovic, and S. R. Forrest,. (2000, June). Efficient, high-bandwidth organic multilayer photodetectors. *Applied Physics Letters*, 76(26), 3855.
27. Gilles Dennler, Markus C. Scharber, Christoph J. Brabec. (2009). Polymer-Fullerene Bulk-Heterojunction Solar Cells. *Advanced Materials*, 21(13), 1323-1338.
28. Prof. Dieter Wöhrle, Dr. Dieter Meissner. (1991). *Organic Solar Cells*†. *Advance Materials*, 3(3), 129-138.
29. Vishal Shrotriya; Elbert Hsing-En Wu; Gang Li; Yan Yao; Yang Yang. (2006). Efficient light harvesting in multiple-device stacked structure for polymer solar cells. *Appl. Phys. Lett.*, 88(6).
30. P. W. M. Blom, V. D. Mihailechi, L. J. A. Koster, D. E. Markov. (2007). Device Physics of Polymer:Fullerene Bulk Heterojunction Solar Cells†. *Advanced Materials*, 19(12), 1551-1566.
31. Fang-Chung Chen; Jyh-Lih Wu; Chia-Ling Lee; Yi Hong; Chun-Hong Kuo; Michael H. Huang. (2009). Plasmonic-enhanced polymer photovoltaic devices incorporating solution-processable metal nanoparticles. *Appl. Phys. Lett.*, 95(1).
32. J.L. Wu, F.C. Chen, Y.S. Hsiao, F.C. Chien, P. Chen, C.H. Kuo, M. H. (2011). Surface Plasmonic Effects of Metallic Nanoparticles on the Performance of Polymer Bulk Heterojunction Solar Cells. *ACS Nano* 2011, 5, 2, 959–967, 5(2), 959–967.

33. Kyungkon Kim; David L. Carroll. (2005). Roles of Au and Ag nanoparticles in efficiency enhancement of poly(3-octylthiophene)/C60 bulk heterojunction photovoltaic devices. *Appl. Phys. Lett.*, 87(20).
34. Luyao Lu, Zhiqiang Luo, Tao Xu, and Luping Yu*. (2013). Cooperative Plasmonic Effect of Ag and Au Nanoparticles on Enhancing Performance of Polymer Solar Cells. | *Nano Lett.*, 59–64.
35. Aruna P Wanninayake, Subhashini Gunashekar, Shengyi Li, Benjamin C Church and Nidal Abu-Zahra. ((2015)). Performance enhancement of polymer solar cells using copper oxide nanoparticles. *Semicond. Sci. Technol.*
36. Marco Notarianni, Kristy Vernon, Alison Chou, Muhsen Aljada, Jinzhang Liu, Nunzio Motta. (2013). Plasmonic effect of gold nanoparticles in organic solar cells. *Solar Energy*, 23-37.
37. Feng-Xian Xie, Wallace C. H. Choy, a) Charlie C. D. Wang, Wei E. I. Sha, and Dixon D. S. Fung. (2011). Improving the efficiency of polymer solar cells by incorporating gold nanoparticles into all polymer layers. *Appl. Phys. Lett.*, 99(15).
38. Jyh-Lih Wu, † Fang-Chung Chen, Yu-Sheng Hsiao, Fan-Ching Chien, Peilin Chen, Chun-Hong Kuo, Michael H. Huang, and Chain-Shu Hsu. (2011). Surface Plasmonic Effects of Metallic Nanoparticles on the Performance of Polymer Bulk Heterojunction Solar Cells. *ACS Nano.*, 5(2), 959–967.
39. Dixon D. S. Fung, Linfang Qiao, Wallace C. H. Choy, Chuandao Wang, Wei E. I. Sha, Fengxian Xie and Sailing He. (2011). Optical and electrical properties of efficiency enhanced polymer solar cells with Au nanoparticles in a PEDOT–PSS layer †. *Journal of Materials Chemistry*, 1–9.
40. Zhe Li, Weiyuan Wang, a Neil C. Greenham and Christopher R. McNeil. (2014.). Influence of nanoparticle shape on charge transport and recombination in polymer/nanocrystal solar cells †. *Phys. Chem. Chem. Phys.*, 25684--25693.
41. Hyosung Choi, † Jung-Pil Lee, † Seo-Jin Ko, † Jae-Woo Jung, ‡ Hyungmin Park, † Seungmin Yoo, † Okji Park,. (2013). Multipositional Silica-Coated Silver Nanoparticles for High Performance Polymer Solar Cells. *Nano Lett.*, 2204–2208.
42. Xuanhua Li, Wallace Chik Ho Choy, * Haifei Lu, Wei E. I. Sha, and Aaron Ho Pui Ho. (2013). Efficiency Enhancement of Organic Solar Cells by Using Shape-Dependent Broadband Plasmonic Absorption in Metallic Nanoparticles. *Adv. Funct. Mater.*, 2728–2735.
43. Burak Kadem a, R.K. Fakher Alfahed b, Ahmed S. Al-Asadi c, Hussain A. Badran . (2020). PMorphological, structural, optical, and photovoltaic cell of copolymer P3HT: ICBA and P3HT:PCBM. *optik*, 164153.
44. Muheeb Ahmad Alkhalayfeh, Azlan Abdul Aziz, Mohd Zamir Pakhuruddin. (2021.). An overview of enhanced polymer solar cells with embedded plasmonic nanoparticles. *Renewable and Sustainable Energy Reviews*, 110726.
45. Susan E. Habas, Heather A. S. Platt, Maikel F. A. M. van Hest, and David S. Ginley*. (2010). Low-Cost Inorganic Solar Cells: From Ink To Printed Device. *chem. Rev.*, 6571–6594.

46. Bobins Augustine , Kari Remes , Gabriela S. Lorite , Jobin Varghese , Tapio Fabritius . (2019). Recycling perovskite solar cells through inexpensive quality recovery and reuse of patterned indium tin oxide and substrates from expired devices by single solvent treatment. *Solar Energy Materials and Solar Cells*, 74-82.
47. JA Poulis, A Kwakernaak. (2024). *UV/Ozone Surface Treatment of Polymers to Enhance Their Adhesion*. scrivener publishing LLC.
48. Bernhard Ecker , Jairo Cesar Nolasco , Josep Pallarés , Lluís Francesc Marsal , Jörg Posdorfer , Jürgen Parisi , and Elizabeth von Hauff. (2011). Degradation Effects Related to the Hole Transport Layer in Organic Solar Cells. *Adv. Funct. Mater.*, 2705–2711.
49. Jun Natsuki, Toshiaki Natsuki, Yoshio Hashimoto. (2015). A Review of Silver Nanoparticles: Synthesis Methods, Properties and Applications . *International Journal of Materials Science and Applications*, 325-332.
50. Johannes Pecher and Stefan Mecking*. (2010,). *Nanoparticles of Conjugated Polymers*. *Chem. Rev.*, 6260–6279.
51. J. Chandrasekaran , D. Nithyaprakash , K.B. Ajjan , S. Maruthamuthu , D. Manoharan , S. Kumar . (2011). Hybrid solar cell based on blending of organic and inorganic materials—An overview. *Renewable and Sustainable Energy Reviews*, 1228-1238.
52. Je-Heon Oh, Jin-Woo Park. (2021). Designing a solution-processable electron transport layer for transparent organic light-emitting diode. *Organic Electronics*, 106252.
53. Chaohua Cui, Yongfang Li. (2021). Morphology optimization of photoactive layers in organic solar cells. *Aggregate*.
54. Sandro Lattante. (2014). *Electron and Hole Transport Layers: Their Use in Inverted Bulk Heterojunction Polymer Solar Cells*. *electronics*.
55. Abhay Gusain, Aparna Thankappan & Sabu Thomas. (2020). Roll-to-roll printing of polymer and perovskite solar cells: compatible materials and processes. *journal of material science*, 13490–13542.
56. Ulf Blieske *, Gunther Stollwerck †. (2013). Chapter Four - Glass and Other Encapsulation Materials. *Semiconductors and Semimetals*, 199-258.
57. Sonali Dass Mohammad Jobayer Hossain Siu-Fung Leung , Anya Lenox , Yeonwoong Jung , Kristopher Davis , Jr-Hau He , Tania Roy. (2019). A leaf-inspired photon management scheme using optically tuned bilayer nanoparticles for ultra-thin and highly efficient photovoltaic devices. *Nano Energy*, 47-56.
58. Razieh Teimouri, Sajad Mehrvarz, Ali Ebrahimi, Mohammadreza Kolahdouz, Mahdi Darab. (2022). Performance of planar perovskite solar cells based on formamidinium cations: Simulation and fabrication. *International Journal of Energy Research*.

59. Zhicai He, Chengmei Zhong, Xun Huang, Wai-Yeung Wong, Hongbin Wu, Liwei Chen, Shijian Su, Yong Cao. (2011). Simultaneous Enhancement of Open-Circuit Voltage, Short-Circuit Current Density, and Fill Factor in Polymer Solar Cells. *Advanced Materials*, 4636-4643.
60. Yanbo Li, Jason K. Cooper, Wenjun Liu, Carolin M. Sutter-Fella, Matin Amani, Jeffrey W. Beeman, Ali Javey, Joel W. Ager, Yi Liu, Francesca M. Toma & Ian D. Sharp. (2016). Defective TiO₂ with high photoconductive gain for efficient and stable planar heterojunction perovskite solar cells. *Nature Communications* .
61. Leila Shabani, Ahmad Mohammadi & Tahmineh Jalali. (2021). High-efficiency polymer solar cells achieved by doping plasmonic metallic nanoparticles into dual charge selecting interfacial layers to enhance light trapping. *plasmonics*, 491–504.
62. O. O. Havryliuk, A. A. Evtukh, O. V. Pylypova, O. Yu. Semchuk, I. I. Ivanov & V. F. Zabolotnyi . (2020). Plasmonic enhancement of light to improve the parameters of solar cells. *Applied Nanoscience*, 4759–4766.
63. A. Pivrikas, N. S. Sariciftci, G. Juška, R. Österbacka. (2007). A review of charge transport and recombination in polymer/fullerene organic solar cells. *Progress in Photovoltaics*, 677-696.
64. Melad M. Olaimat, Leila Yousefi, and Omar M. Ramahi. (2021). Using plasmonics and nanoparticles to enhance the efficiency of solar cells: review of latest technologies. *Journal of the Optical Society of America B*, 638-651.
65. Lei Qian, Jihua Yang, Renjia Zhou, Aiwei Tang, Ying Zheng, Teng-Kuan Tseng, Debasis Bera, Jiangeng Xue and Paul. H. Holloway. (2011). Hybrid polymer-CdSe solar cells with a ZnO nanoparticlebuffer layer for improved efficiency and lifetime. *Journal of Materials Chemistry*, 3814-3817.
66. Holger Borchert. (2010). Elementary processes and limiting factors in hybrid polymer/nanoparticle solar cells†. *Energy & Environmental Science*, 1682-1694.
67. Jinyan Li, Yiming Bai, Bo Yang, Jin Zhang, Xiaohan Chen, Tasawar Hayat, Ahmed Alsaedi, Yun Yang, ORCID logo Jianhui Hou ORCID logo and Zhan' Tan ORCID logo. (2019). Multifunctional bipyramid-Au@ZnO core–shell nanoparticles as a cathode buffer layer for efficient non-fullerene inverted polymer solar cells with improved near-infrared photoresponse†. *Journal of Materials Chemistry A*, 2667-2676.
68. Sankara Rao Gollu , Ramakant Sharma , G. Srinivas , Souvik Kundu , Dipti Gupta. (2015). • Nanoparticle incorporation make the active layer thinner which forms the lighter and more flexible solar cells . *Organic Electronics*, 43-50.
69. Yongfang Li. (2012). Molecular Design of Photovoltaic Materials for Polymer Solar Cells: Toward Suitable Electronic Energy Levels and Broad Absorption. *cc. Chem. Res.*, 723–733.

70. Ardalan Armin, Wei Li, Oskar J. Sandberg, Zuo Xiao, Liming Ding, Jenny Nelson, Dieter Neher, Koen Vandewal, Safa Shoaee, Tao Wang, Harald Ade, Thomas Heumüller, Christoph Brabec, Paul Meredith. (2021). A History and Perspective of Non-Fullerene Electron Acceptors for Organic Solar Cells. *Advanced Energy Materials*.
71. Huiting Fu, Prof. Zhaohui Wang, Prof. Yanming Sun. (2018). Polymer Donors for High-Performance Non-Fullerene Organic Solar Cells. *Energy Storage and Conversion*, 4442-4453.
72. Agnès Rivaton, Aurélien Tournebize, Julien Gaume, Pierre-Olivier Bussière, Jean-Luc Gardette, Sandrine Therias. (2013). Photostability of organic materials used in polymer solar cells. *Polymer International*, 1335-1345.
73. Marwa Sayed. (2020). Efficiency of inkjet printing in fabrication Organic Solar cells. *ResearchGate*, 241-252.
74. Silvia Collavini, , Andrea Cabrera-Espinoza, and Juan Luis Delgado*. (2021). Organic Polymers as Additives in Perovskite Solar Cells. *Macromolecules*, 5451–5463.
75. Juanyong Wan , Ruopeng Zhang , Yaowen Li, Yongfang Li. (2024). Applications of organic solar cells in wearable electronics. *Wearable Electronics*, 26-40.
76. Seungjin Lee, Dahyun Jeong, Changkyun Kim, Changyeon Lee, Hyunbum Kang, Han Young Woo*, and Bumjoon J. Kim*. (2020). Eco-Friendly Polymer Solar Cells: Advances in Green-Solvent Processing and Material Design. *ACS Nano*, 14493–14527.
77. Kenjiro Fukuda, Kilho Yu, Takao Someya. (2020). The Future of Flexible Organic Solar Cells. *Advanced Energy Materials*.
78. Yongxi Lia, Xia Guo, Zhengxing Peng, Boning Que, , Hongping Yanf, Harald Ade, Maojie Zhang, and Stephen R. Forrest. (2020). Color-neutral, semitransparent organic photovoltaics for power window applications. 21147–21154.
79. M.R. Geiker, M.M. Andersen. (2009). 11 - Nanotechnologies for sustainable construction. *Sustainability of Construction Materials*, 254-283.

¹ S.A.Waghuley² S.M.Butte

Structural Properties of Polyindole for energy storage application



Abstract: - The present research work specifies the novel formation of the Polyindole (PIn) by the chemical oxidative polymerization of the indole monomer. The highly focus of this article is on the structural analysis of the polyindole. The XRD confirms the Formation of semicrystalline nature of the PIn. The FTIR confirms the formations of PIn and the bonding are observed in the spectrum are exactly matched. The Raman shows the C-H bending , C-N stretching and the C=C molecular ring formation the sample. The SEM shows the porous nature of the material and so it is highly preferable for the energy storage application such as fuel cell, Photovoltaics, supercapacitor, pseudo capacitor, batteries etc..

Keywords: Polyindole(PIn), Chemical oxidative polymerization, Structural properties

I. INTRODUCTION

Polyindole, a polymer made from indole monomers, has become an area of great interest in material science and engineering. This interest is due to its unique combination of electronic, optical, and mechanical properties, which makes it suitable for a wide range of applications, including conductive materials, sensors, electrochemical devices, and biocompatible materials. Compared to other conductive polymers such as polyaniline and polypyrrole, polyindole offers remarkable stability and conductivity, making it a highly promising material for various advanced technological applications.[1]

The process of synthesizing polyindole (PIn) typically involves oxidative polymerization of indole monomers, which can be achieved through either chemical or electrochemical methods. The method chosen for polymerization significantly affects the properties of the resulting polymer, such as molecular weight, conductivity, and structural integrity. Chemical polymerization usually involves oxidizing agents like ammonium persulfate, while electrochemical polymerization is conducted in an electrochemical cell.[2] Each method has its own set of advantages and limitations, and optimizing these processes is essential to customize the properties of polyindole for specific uses.[3]

Polyindole's electrical properties make it highly suitable for use in organic electronics, including the creation of transistors, light-emitting diodes, and photovoltaic cells. Its high conductivity and stability under ambient conditions are particularly advantageous for these applications. Additionally, polyindole's ability to form composites with other materials broadens its range of applications. For instance, polyindole-carbon nanotube composites have been found to have enhanced mechanical strength and electrical conductivity, making them ideal for flexible electronic devices and sensors.[4][5]

In the field of sensing applications, polyindole shows considerable promise due to its responsiveness to environmental changes. [6]Gas sensors, in particular, benefit from the high surface area and conductive properties of polyindole, which improve the detection of various gases. Furthermore, the electrochemical activity of polyindole allows for the development of highly sensitive and selective biosensors, capable of accurately detecting biological molecules.

Polyindole also holds significant potential in energy storage and conversion applications. Its electrochemical properties make it a suitable material for use in supercapacitors and batteries, where it can serve as an efficient electrode

¹ Author 1 Department of Physics, Sant Gadge Baba Amravati University Amravati 444602, Maharashtra, India

² *Corresponding author: Author 2 Department of Physics, Shri Shivaji Science College Amravati 444603, Maharashtra, India

Copyright © JES 2024 on-line : journal.esrgroups.org

material.[7] Polyindole-based electrodes have demonstrated high specific capacitance, long cycle life, and excellent energy density, making them competitive with traditional electrode materials.[8]

Another noteworthy attribute of polyindole is its biocompatibility, which paves the way for its use in biomedical applications. Polyindole can interface with biological tissues without causing adverse reactions, making it suitable for drug delivery systems, tissue engineering, and biosensing devices. Ongoing research aims to explore the full potential of polyindole in these areas, seeking to develop new therapeutic and diagnostic tools.[8][9]

In conclusion, polyindole is a multifaceted polymer with a broad range of applications. Its synthesis methods, unique properties, and potential uses in various fields make it an exciting subject for further research. As research and development efforts continue, the capabilities of polyindole are expected to be further uncovered, leading to innovative applications in both technology and medicine.[10]

II. EXPERIMENTAL

1. Materials

Indole Monomer (SD fine) Ferric Chloride (FeCl_3) (98% purity, SD fine), Hydrogen peroxide (H_2O_2) (30% purity, Merck specialities PVT Ltd.) are used as precursors. The de-ionised water was used in the experiment.

2. Method

A monomer indole (oxidant) anhydrous iron chloride FeCl_3 , hydrogen peroxide (H_2O_2) used as a catalyst these all chemicals are used for analytic grade and product from SD fine chemical India. The monomer was used for synthesis of PIn without further purification through the chemical oxidative technique using a FeCl_3 as an oxidant. The polymeric materials were prepared the monomer and oxidant FeCl_3 is used in Stoichiometric ratio were dissolved in deionized water the H_2O_2 (0.1M) was added into the reaction mixture for the enhanced the rate of reaction and conjointly yield. Then the reaction mixture was allowed for constant stirring for 12 hour to complete polymerisation reaction with magnetic stirrer at 30°C . Then the precipitate was washed with copious amount of triply distilled water until the washing were clear. Then the sample kept overnight for filtration process. Infrared lamp (IR) is used for drying at 15 to 16 hours[11].

III. CHARACTERIZATIONS

The structural characterization of the samples performed by using Bruker D8 advance with $\text{Cu K}\alpha$ radiation ($\lambda = 1.5406 \text{ \AA}$) is used to identify structure and phase purity of samples at room temperature. The pattern recorded with step height of 0.02 with scan rate 6.00. The d-spacing (D) corresponding to the highest intense crystalline peak was determined by the Debye–Scherrer (powder) method using Bragg's relation.

$$2d \sin\theta = n\lambda \quad (1)$$

where n is an integer, λ is the wavelength of the X-ray, θ is the angle between the incident and reflected rays. The crystallite size (D) of the highest intense crystalline peak was determined from the Scherrer relation.[12][13]

$$D = K\lambda / \beta \cos\theta \quad (2)$$

Where, K is the shape factor for the average crystallite (0.91 \AA), β is the full width at half maxima of the crystalline peak in radians. The inter-chain separation length (R) corresponding to the highest intense crystalline peak was determined from the relation given by Klug and Alexander.

$$R = 5\lambda / (8 \sin\theta) \quad (3)$$

The FTIR spectra of the pure PIn were recorded using Shimadzu Infinity IR -1 370 spectrometer at room temperature over a range of $400\text{--}4000 \text{ cm}^{-1}$ with resolution of 2 cm^{-1} .

The FE-SEM images were obtained from Zeiss make Model SIGMA IV.

The RAMAN Spectra were recorded on Horiba make Xplora Plus (France).

IV. RESULT AND DISCUSSIONS.

This section shows the structural properties of the Polyindole. In this section the X-Ray diffraction shows the structural confirmation. The FE-SEM shows the surface morphology. The RAMAN and FTIR shows the bond formation.

1. X-Ray Diffraction Analysis :

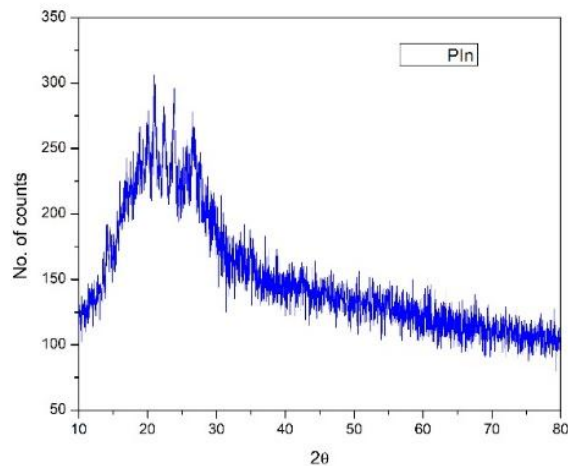


Fig. 1. X-Ray Diffraction of PIn

The XRD pattern of Polyindole shown is the figure 1. The broad peak with the intense peaks observed at 21.04, 23.08, 26.62 confirms the formation of Polyindole nanoparticles. the broadness of the above peaks shows the amorphous and the semi-crystalline nature of the polyindole. With the help of this broad peak we find out the FWHM and using equation number 1,2 and 3 we determine crystalline size 2.266 nm and Chain separation length of 2.4198 Å

2. FE-SEM Analysis

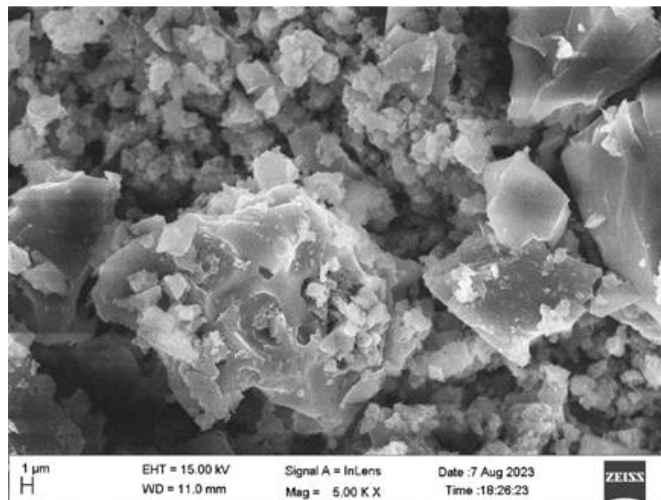


Fig. 2 FE-SEM image of Polyindole

The above fig 2 Shows the shows the formation of surface of PIn polymer. The synthesized polyindole reveals that the formation of irregularly shaped particles. The polymer clusters are observed. The particles are agglomerated in some region also the particles are porous in nature. The porous structure is most favorable for the energy storage. The layers are also seen in the structure. The porous nature of the PIn makes the material suitable for various application like energy storage, batteries, supercapacitors, solar cells, fuel cells etc.

3. RAMAN Spectroscopy

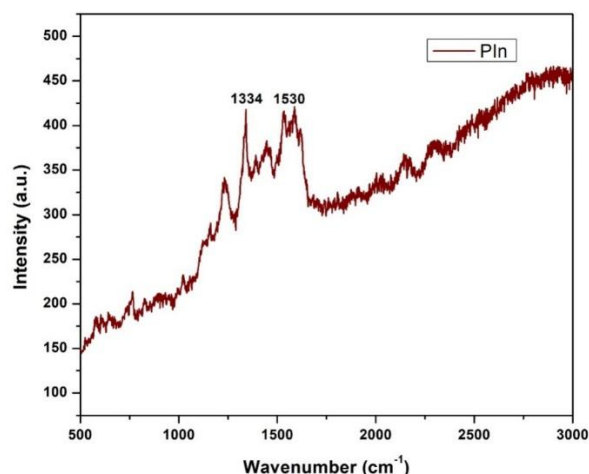


Fig 3 RAMAN spectroscopy of PIn

The above Fig. 3 shows the RAMAN spectra of PIn. The raman spectra shows the molecular structure and its properties. The peak observed at around 1023 cm^{-1} corresponds to C-H bending vibration in the polyindole ring. The lower intense peak shows the polyindole is polymerized properly and has a higher degree of polymerization. The next peak observed at the 1334 cm^{-1} it reveals the bond between C-N stretching in the indole ring. The intensity of the peak tells about the incorporation of nitrogen and the chemical information about the environment of polymer chain. The peak observed at 1530 cm^{-1} and 1594 cm^{-1} attributes to C=C stretching vibrations of the aromatic ring in the Polyindole. Also it tells about the electronic structure of the PIn and conjugate backbone C=C stretching presence.[14]

4. FTIR Spectroscopy

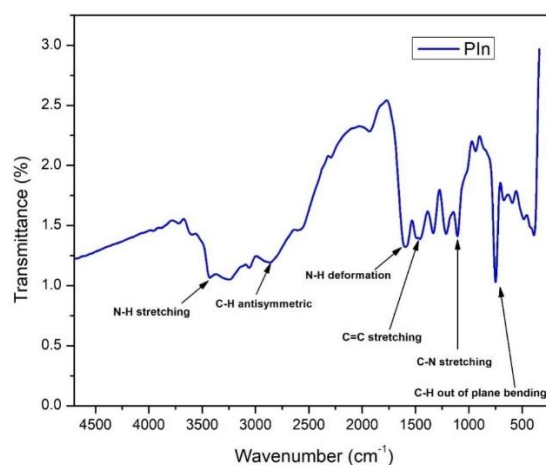


Fig 4. FTIR Spectra of PIn

The fig. 4 shows the FTIR spectrum of Polyindole ranging from $100\text{-}5000\text{ cm}^{-1}$. The N-H stretching is observed in the range of 3428.28 cm^{-1} . The C-H antisymmetric bond is formed at 2853 cm^{-1} . The N-H deformation and C=C stretching are found at 1604 cm^{-1} and 1473 cm^{-1} . The C-N stretching is formed at 1098 cm^{-1} . The C-H out of plane bending is at 753 cm^{-1} . The FTIR confirms the formation of Polyindole and the bonding are observed in the spectrum are exactly matched. [15]

V. CONCLUSIONS :

The above research article gives the idea about the synthesis method of the polyindole nanoparticle through the chemical oxidative polymerization method. The XRD gives the confirmation of the formation of the semi crystalline PIn. The SEM gives the porous nature of the PIn. the FTIR and RAMAN spectroscopy gives the confirmation of the bond structure and the

presence of the C=C molecular ring, N-H Stretching. The porous nature of the PIn makes the material suitable for various application like energy storage, batteries, supercapacitors, solar cells, fuel cells etc.

VI. ACKNOWLEDGEMENT

Authors are very much thankful to the Head, Department of Physics, Sant Gadge Baba Amravati University, Amravati, India, for providing necessary facilities.

VII. COMPLIANCE WITH ETHICAL STANDARDS

Conflict of Interest: The authors declare that they have no conflict of interest

- [1] E. A. Mollamehmetoğlu and M. Alanyahoğlu, "A Flexible Reduced Graphene Oxide-based Paper for Supercapattery Design: Effect of Polyindole Thin Films and Zinc Oxide Nanoparticles," *ChemistrySelect*, vol. 9, no. 21, p. e202400838, Jun. 2024, doi: 10.1002/slct.202400838.
- [2] C. Zhijiang, S. Xingjuan, and F. Yanan, "Electrochemical properties of electrospun polyindole nanofibers as a polymer electrode for lithium ion secondary battery," *J. Power Sources*, vol. 227, pp. 53–59, 2013.
- [3] S. Li *et al.*, "Facile preparation of poly (indole/thiophene) for energy storage and sensor applications," *Electrochimica Acta*, vol. 358, p. 136919, 2020.
- [4] M. Majumder, R. B. Choudhary, S. P. Koiry, A. K. Thakur, and U. Kumar, "Gravimetric and volumetric capacitive performance of polyindole/carbon black/MoS₂ hybrid electrode material for supercapacitor applications," *Electrochimica Acta*, vol. 248, pp. 98–111, 2017.
- [5] M. Majumder, R. B. Choudhary, and A. K. Thakur, "Hemispherical nitrogen-doped carbon spheres integrated with polyindole as high performance electrode material for supercapacitor applications," *Carbon*, vol. 142, pp. 650–661, 2019.
- [6] R. Wang *et al.*, "Highly efficient electrochemical energy storage of fluorinated nano-polyindoles with different morphology," *Electrochimica Acta*, vol. 349, p. 136410, 2020.
- [7] Q. Guo, J. Li, B. Zhang, G. Nie, and D. Wang, "High-Performance Asymmetric Electrochromic-Supercapacitor Device Based on Poly(indole-6-carboxylic acid)/TiO₂ Nanocomposites," *ACS Appl. Mater. Interfaces*, vol. 11, no. 6, pp. 6491–6501, Feb. 2019, doi: 10.1021/acsami.8b19505.
- [8] S. Taherkhani, F. Ghamari, J. Arjomandi, A. Nasri, and H. Shi, "Interwoven of γ -MnO₂ and V₂O₅ nanostructures with polyindole grafted reduced graphene oxide nano-platform for high-efficient supercapacitors: A collaborated insight of experimental and surface morphological studies," *Fuel*, vol. 353, p. 129167, 2023.
- [9] A. R. Athira, B. B. Raj, and T. S. Xavier, "Microwave-induced polyindole on cobalt MOF-electrodes for high-performance supercapacitors," *J. Electrochem. Soc.*, vol. 168, no. 12, p. 120524, 2021.
- [10] M. M. Y. Zaghloul, S. Ebrahim, M. Anas, M. Soliman, and J. El Nady, "Synthesis and characterization of nanocomposites of polyaniline and polyindole with multiwalled carbon nanotubes for high performance supercapacitor electrodes," *Electrochimica Acta*, vol. 475, p. 143631, 2024.
- [11] S. A. Hashemi *et al.*, "Synergic effect of laser-assisted graphene with silver nanowire reinforced polyindole/polypyrrole toward superior energy density," *Carbon*, vol. 188, pp. 276–288, 2022.
- [12] N. N. Sarkar, K. G. Rewatkar, V. M. Nanoti, P. S. Hedao, and M. N. Giriya, "Cation distribution of Zn_{0.5}Me_{0.5}Fe₂O₄ (Me= Co, Ni And Cu) on the basis of rietveld refinement and magnetization measurement," *Mater. Sci. Res. India*, vol. 14, no. 2, pp. 169–175, 2017.
- [13] N. N. Sarkar, K. G. Rewatkar, N. S. Meshram, and V. M. Nanoti, "Structural and magnetic studies of (Ni_{0.5}M_{0.5}Fe₂O₄) where M= Zn, Cu," *Ferroelectrics*, vol. 519, no. 1, pp. 209–212, 2017.
- [14] R. B. Choudhary, S. Ansari, and B. Purty, "Robust electrochemical performance of polypyrrole (PPy) and polyindole (PIn) based hybrid electrode materials for supercapacitor application: A review," *J. Energy Storage*, vol. 29, p. 101302, 2020.
- [15] R. P. Raj, P. Ragupathy, and S. Mohan, "Remarkable capacitive behavior of a Co₃O₄-polyindole composite as electrode material for supercapacitor applications," *J. Mater. Chem. A*, vol. 3, no. 48, pp. 24338–24348, 2015

¹P. A. Saudagar*

²D. R. Bijwe

³R. B. Pedhekar

Arduino Based Smart Controller for Greenhouse using Integrated Fuzzy Logic for Temperature Control



Abstract: - This paper proposes a design of smart controller for green house using Integrated Fuzzy Logic for temperature Control. The proposed system is designed using Arduino Mega so as to have the flexibility in the design and to reduce the hardware. Also, maximum facilities like Analog to Digital Converter, PWM, I/O lines, etc. are available on-chip. An Integrated fuzzy logic controller is designed using the concepts of Fuzzy Logic and PID control. Fuzzy rules were used for the control action to be taken by the controller to maintain the temperature at the set point value.

Keywords: Smart Controller, Fuzzy Logic, IFLC, Fuzzy Inference, AI in Agriculture.

¹*Corresponding author: Department of Electronics, Bajaj College of Science, Wardha (MS) India. email: saudagar.pa@gmail.com

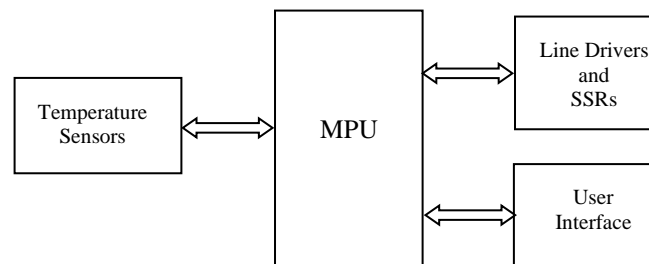
²Department of Physics, G. S. Tompe Arts, Commerce and Science College, Chandur Bazar, Dist. Amravati (MS) India.
email: drbijwe28@gmail.com

³Department of Physics, M. J. Fule Commerce, Science & V. Raut Arts College, Bhatkuli, Dist. Amravati (MS) India.
email: rajeshpedhekar@gmail.com

I. INTRODUCTION

The greenhouse is a structure covered with a material that is transparent to the visible part of the electromagnetic spectrum, which is used to grow plants. Greenhouse performance is best when the temperature is neither too hot nor too cold. It is necessary to maintain a suitable temperature at the growth stage of several plants. The controlled environment of the greenhouse makes it possible to increase the quality and quantity of crops per unit area in the shortest possible time [1]. There are a number of conventional methods for controlling temperature, but they are less effective because they are based either on proportional methods or on on-off control. Fuzzy logic has been widely used in industrial controls and domestic electrical appliances [2]. A key technique in fuzzy control is the automatic learning of fuzzy rules. In this work, a controller has been designed to control the temperature of a plant. The temperature is continuously monitored and compared with the setpoint. An integrated fuzzy logic approach [3][4] has been used to decide the output.

II. SYSTEM BLOCK DIAGRAM



III. HARDWARE AND SOFTWARE

1. Hardware

The system was designed using an Arduino Mega 2560 board which, after initialization, reads the sensors, displays the indoor and outdoor temperature values on the LCD of the user interface and acts according to the algorithm. The temperature sensors used to measure the inside and outside temperature of the greenhouse were National Semiconductor's LM 35 ICs. The analog outputs of these sensors were connected to the analog inputs available on the board. They were then converted to their digital equivalent using an on-chip 10-bit A/D converter. The current temperature values are displayed on a 20x4 LCD module. This LCD module has four rows of twenty characters each. The PWM pins available on the Arduino board were used to control the heating and cooling systems. These PWM output pins are connected to the solid-state relays (SSR) via line driver IC ULN2808. The cooling and heating systems have been connected to these SSRs in order to maintain the desired temperature [5].

2. Software

The software modules have been designed to control the system, so that the system can be upgraded module by module. After a power-on reset, the initialization module loads the variables and other necessary registers to their default values set by the programmer, initializes the timers and starts them. The user interface module makes it easy for the user to set the internal temperature and displays the settings and temperature values on the LCD screen. The sensor module reads the indoor and outdoor temperatures one after the other, converts them into a digital format and stores them in the system's memory. All user settings are stored in EEPROM so that they can be restored in the event of a power failure.

IV. INTEGRATED FUZZY LOGIC CONTROLLER (IFLC)

In this work, an integrated fuzzy logic controller (IFLC) [5][6][7] was used to maintain the greenhouse temperature at the user-set value. Integrated Fuzzy Logic Controller is an integration of Fuzzy Logic Controller and PID controller. The block diagram of the IFLC is shown in Fig. 4.1.

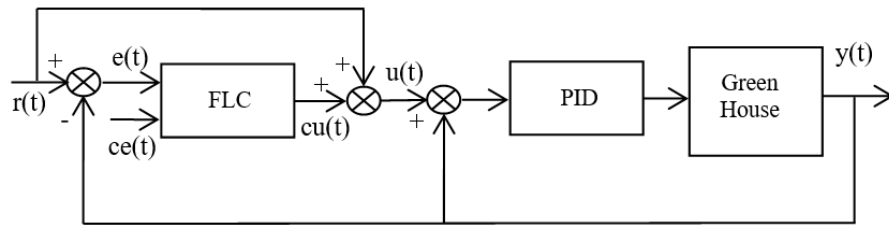


Fig. 4.1 Block diagram of IFLC

An FLC was designed and given two input variables, e and ce . The e is the error value of the temperature, calculated as-

$$e = \text{temperature set point} - \text{current value of temperature}$$

and change in error ce is computed as-

$$ce = \text{current } e - \text{previous } e$$

The values of ce and e are of a crisp nature and it is necessary to convert them into fuzzy values. The triangular membership function was used to fuzzify error e within the universe of discourse with eleven linguistic values NVVL (Negative Very Very Large), NVL (Negative Very Large), NL (Negative Large), NM (Negative Medium), NS (Negative Small), Z (Zero), PS (Positive Small), PM (Positive Medium), PL (Positive Large), PVL (Positive Very Large) and PVVL (Positive Very Very Large). The universe of discourse for e was $(-40, +40)$ °C.

Similarly, triangular membership function was used to convert change in error ce into non-crisp values with three linguistic values NEG (Negative), Z (Zero) and POS (Positive).

The important part of the fuzzy control system has been designed based on the expert knowledge, experience and previous work in this area. The decision-making stage consists of fuzzy rules that are used to decide what action needs to be taken. The rule base consists of 33 rules as shown in Table 4.1.

Table 4.1 Fuzzy Logic rule base

$\begin{matrix} ca \\ ce \\ e \end{matrix}$	NVVL	NVL	NL	NM	NS	Z	PS	PM	PL	PVL	PVVL
NEG	VH	VH	H	LH	M	VL	M	LH	H	VH	VH
Z	VH	VH	VH	H	LH	VL	LH	H	VH	VH	VH
POS	VL	VL	VL	VL	VL	VL	VL	VL	VL	VL	VL

Control actions are taken using If-Then rules. For example, IF e is NS and ce is POS, then the control action is VL. This process is called inferencing. The inference process relates the fuzzy state variables e and ce to the control action ca . The triangular membership function was used to fuzzify the control actions with the linguistic values VL (very low), L (low), M (middle), LH (slightly high), H (high) and VH (very high).

The error value was used to select either the cooling or heating system. If the error is positive, the heating system is selected, otherwise the cooling system is selected and the control action apply to the selected system.

For decision making, the fuzzy rule-based Mamdani inference [2][3] is used. These outputs are fuzzy values as shown in figure 4.2 that are defuzzified into crisp values. To defuzzify, the fuzzy values obtained from the decision stage were converted into non-fuzzy or crisp values as shown in figure 4.3[8] using the Center of Gravity (COG) method, also known as Center of Area or Centroid. This method proved to work efficiently and accurately [4].

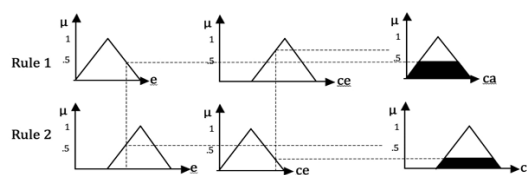


Fig. 4.2 Fuzzy Inference

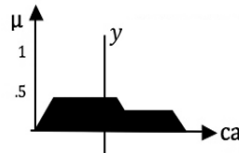


Fig. 4.3 Crisp output y

The crisp value (y) obtained from the defuzzification stage for the values of e and ce were scaled and stored in the internal memory as a look-up table, and the values of e and ce were used to access these crisp values from the look-up table. The value retrieved from the look-up table was added to the setpoint and treated as the new PID controller setpoint as shown in the system block diagram. The current temperature value was subtracted from the new setpoint and the difference was used as the error value for the PID controller. The PID controller generates the new control action v_n , which is implemented by means of the velocity equation [6][7]-

$$v_n = v_{n-1} + k_p(e_n - e_{n-1}) + k_i(e_n)T + k_d/T(e_n - 2e_{n-1} + e_{n-2})$$

where,

- v_n : Control action by PID controller
- v_{n-1} : previous control action
- e_n : current error value of PID controller
- e_{n-1} : previous error value of PID controller
- e_{n-2} : previous to previous error value to PID controller
- k_p : proportional gain
- k_i : integral gain
- k_d : differential gain
- T : cycle time

After power-on, the error values and v_n were initialized to zero. The value calculated by the above equation was scaled within limits and used to generate PWM output. In order to maintain the temperature of the system according to the setpoint, this procedure was repeated.

V. CONCLUSION

The performance of the system as a whole has been tested. The interface worked well, allowing various parameters to be set as required. As soon as the set point has been set, the software acts accordingly and generates the PWM outputs in the IFLC that are necessary to maintain the set temperature in the system. Current temperature values and setpoints are continuously displayed on the screen. The use of the Arduino board demonstrated the stable performance of the system

REFERENCES

- [1] A. Sriraman and R. V. Mayorga, "A Fuzzy Inference System Approach for Greenhouse Climate Control", Environmental Informatics Achieves, Vol. 2, pp699-710, 2004.
- [1] John Yen, Reza Langari, "Fuzzy Logic Intelligence, Control and Information" Pearson Education, 2003.
- [2] Timothy J. Ross, "Fuzzy Logic With Engineering Applications" Wiley-India, 2005.
- [3] Scott S. Lancaster and Mark J. Wierman, Empirical Study on Defuzzification, IEEE, pp121-126, (2003).
- [4] Ming-Yuan Shieh and Tznu-Hseng S. Li, "Integrated Fuzzy Logic Controller Design", IEEE, pp279-284, 1993.
- [5] S. S. Patil and P. Bhaskar, "Design and Real Time Implementation of Integrated Fuzzy Logic Controller for a High Speed PMDC Motor", International Journal of Electronic Engineering Research, Vol.1 No.1, pp13-25, (2009).
- [6] S. S. Patil, P. Bhaskar and L. Shrimanth Sudheer, Design and Implementation of An Integrated Fuzzy Logic Controller for a Multi-Input Multi-Output System, Defence Science Journal, Vol. 61, No. 3, pp219-227, May 2011.
- [7] Saudagar, P. A., Fuzzy and Integrated Fuzzy Logic Controller for Greenhouse Climate Control (Unpublished doctoral thesis), Sant Gadge Baba Amravati University, Amravati, India, 2013.

¹* P.R. Konmare,
²S.H. Saknure
²A.C.Kumbharkhane

Dielectric Relaxation and Hydrogen Bonding Studies Of 1,2,6-Hexanetriol



Abstract: - This study investigates the dielectric relaxation properties of binary mixtures containing 1,2,6-Hexanetriol and dimethyl sulfoxide (DMSO) in the frequency range of 10 MHz to 30 GHz using Time Domain Reflectometry (TDR). The research unveils a connection between the static dielectric constant (ϵ_0) and relaxation time (τ) of the mixtures with the prevalence of hydrogen bonding. The observed initial rise in ϵ_0 at lower concentrations followed by a decrease at higher 1,2,6-hexanetriol content suggests a saturation of available hydrogen bonding sites. The increasing trend in τ with concentration signifies a growing hindrance to dipole rotation as the number of 1,2,6-Hexanetriol molecules increases. These findings elucidate the interplay between hydrogen bonding and molecular dynamics at high frequencies in 1,2,6-Hexanetriol-DMSO mixtures.

Keywords: Dielectric Relaxation, Hydrogen Bonding, DMSO, 1,2,6Hexanetriol Mixtures, Time Domain Reflectometry (TDR).

1. INTRODUCTION

Polyhydric alcohols, like 1,2,6-hexanetriol, have a higher glass transition temperature (T_g) compared to other liquids of similar size. Triol has a linear backbone with OH groups attached to each carbon, and the dynamics of these OH groups are crucial to the material's properties. The number of OH groups likely plays a significant role, as they are dielectrically active [2,3]. Several studies have explored the dielectric properties of triols for this reason [2-4]. 1,2,6-Hexanetriol specifically has three hydroxyl groups (OH) bonded to a six-carbon chain. This colorless, odorless, and viscous liquid is immiscible with non-polar solvents but readily mixes with water and polar organic solvents. Due to its versatility, 1,2,6-hexanetriol finds applications in various fields. Notably, it serves as a solvent for dielectric studies, particularly for compounds that struggle to dissolve in non-polar liquids [5]. This makes it a valuable tool in pharmaceutical and cosmetic research.

¹*Corresponding author: Author prkonmare96@gmail.com ¹ School of Physical Sciences, Swami Ramanand Teerth Marathwada University, Nanded-431606, MS, India

² Author School of Physical Sciences, Swami Ramanand Teerth Marathwada University, Nanded-431606, MS, India

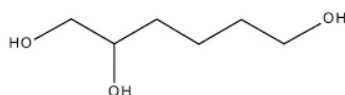


Fig.1 Structure of 1,2,6-hexanetriol

This research focused on how 1,2,6-hexanetriol behaves in its pure form and when mixed with DMSO (dimethyl sulfoxide). To achieve this, the study employed Time Domain Reflectometry (TDR) to analyze the dielectric relaxation of 1,2,6-hexanetriol in DMSO at a constant temperature of 25°C. The investigation covered a frequency range of 10 MHz to 30 GHz. By applying a least square fit method to the measured complex permittivity spectra, able to extract key parameters like the static dielectric constant, the high-frequency dielectric constant, the relaxation time, and the relaxation distribution parameter.

2. EXPERIMENTAL METHOD

The 1,2,6-hexanetriol was acquired commercially from S. D. Fine Chemical Limited in India and utilized without additional purification. The solutions were carefully prepared using various volume fractions of benzylamine in 1,2,6-hexanetriol.

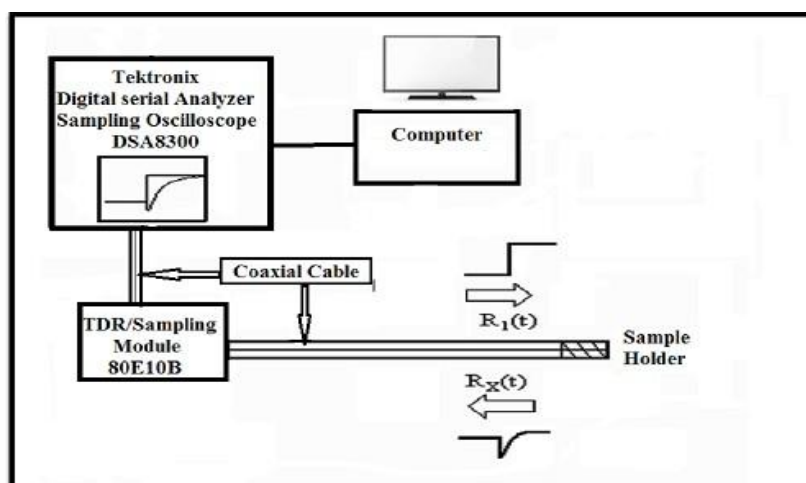


Fig.2. Block diagram of Time Domain Reflectometry

dielectric spectra were obtained using a time domain reflectometry (TDR) technique. As shown in Figure 2, the measurement was performed using the Tektronix model no. DSA8300 Digital Serial Analyzer sampling mainframe and the sampling module 80E10B. A fast-rising voltage pulse of 12 ps was fed through a 50 Ω coaxial line system. The sampling oscilloscope measures changes in the step pulse after reflection from the end of the line. Reflected pulses without sample $R_1(t)$ and with sample $R_x(t)$ were

recorded in a 5-ns time window and digitized at 2000 points. The pulses were Fourier transformed, and data was analyzed earlier to determine the complex permittivity spectra using the non-linear least squares fit method.[6-10]

3. RESULTS AND DISCUSSION

The complex permittivity spectra of 1,2,6-Hexanetriol-DMSO mixture were measured using the Time Domain Reflectometry (TDR) technique in the frequency range of 10MHz to 30 GHz at 25°C. It can be seen that the value of permittivity (ϵ') decreases and dielectric loss (ϵ'') shifts towards lower frequency as the concentration of 1,2,6-Hexanetriol in DMSO, that is, the loss peak shifted to words lower frequency side, including greater relaxation time as shown in Fig.2

The complex permittivity spectra are fitted to the Havriliak - Negami expression using the non-linear least squares fit method . [11]

$$\epsilon^*(\omega) = \epsilon_{\infty} + \frac{\epsilon_0 - \epsilon_{\infty}}{[1 + (j\omega\tau)^{1-\alpha}]^{\beta}}$$

where ϵ_0 - static dielectric constant, τ - relaxation time, ϵ_{∞} - dielectric constant at high frequency , ω is the angular frequency, α and β -distribution parameters. In this study the aqueous solutions of 1,2,6-Hexanetriol shows Cole–Davidson type dispersion.[12]

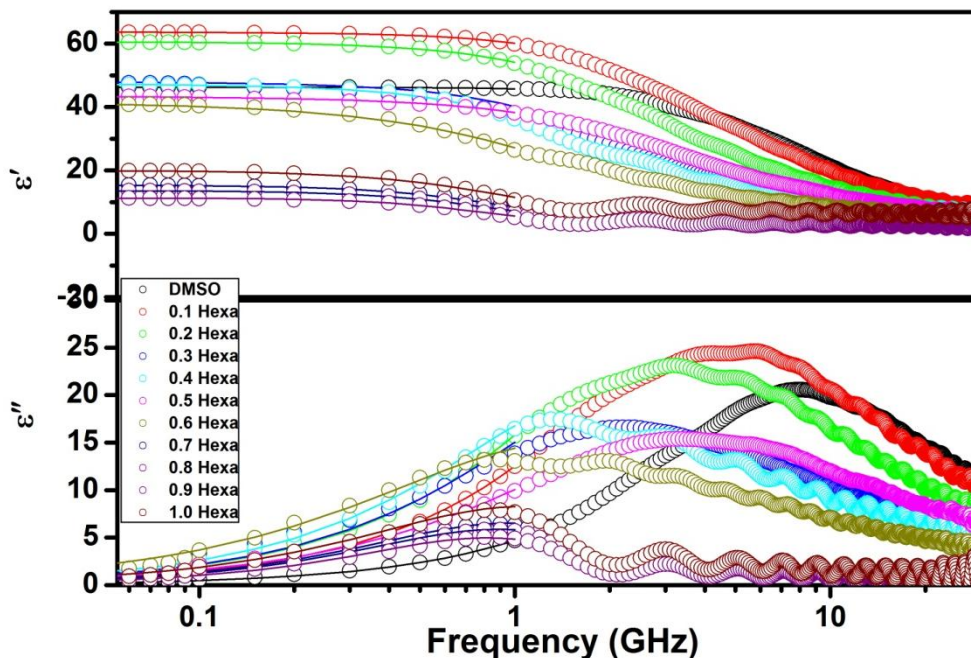


Fig. 3 The complex permittivity spectra for 1,2,6-Hexanetriol + DMSO Mixture

The dielectric parameters of various concentrations of 1,2,6-Hexanetriol in DMSO are shown in Table no 1. It has been found that values of dielectric constant decrease with the increase in quantity of 1,2,6-Hexanetriol in DMSO. The relaxation time τ (Ps) increases with increasing of 1,2,6-Hexanetriol in DMSO.

This indicates that the presence of 1,2,6-Hexanetriol in DMSO affects the polarization and dielectric relaxation behavior of the system. The decrease in dielectric constant suggests a decrease in the ability of the medium to store electrical energy, while the increase in relaxation time indicates a slower response to an applied electric field.

TABLE 1. Dielectric parameters for 1,2,6-Hexanetriol-DMSO mixture at 25°C

Volume fraction of 1,2,6-Hexanetriol	ϵ_0	τ (ps)
0	46.29	17.03
0.1	63.71	32.55
0.2	60.66	46..17
0.3	47.99	61.66
0.4	47.29	81.84
0.5	43.60	44.08
0.6	41.56	103.88
0.7	15.35	164.23
0.8	13.55	178.03
0.9	11.22	194.87
1.0	20.04	150.09

4. CONCLUSION

The results revealed a correlation between the static dielectric constant (ϵ_0), relaxation time (τ), and the prevalence of hydrogen bonding within the mixtures. At lower concentrations of 1,2,6-hexanetriol, there was an initial rise in ϵ_0 followed by a decrease at higher concentrations, indicating saturation of available hydrogen bonding sites. Additionally, the observed increase in τ with concentration suggests a hindrance to dipole rotation as the number of 1,2,6-hexanetriol molecules increases.

ACKNOWLEDGEMENT

The financial support from the Department of Science and Technology, New Delhi is greatly acknowledged (Project No DST PROJECT-SB/S2/LOP-032/2013). I would also like to express my special thanks of gratitude to the School Of Physical Sciences Swami Ramanand Teerth Marathwada University, Nanded.

REFERENCES

- [1] N. Masahiro and N. Ryusuke, Dynamics and structure of hydrogen-bonding glass formers: Comparison between hexanetriol and sugar alcohols based on dielectric relaxation, *J. Phys. Rev.* 81, 041501 (2010).
- [2] P. Lunkenheimer, A. Pimenor, B. Schiener, R. Bohmer and A. Loidal, High-frequency dielectric spectroscopy on glycerol, *Eur. Phys. Lett.* 33, 611 (1996).
- [3] V. I. Zhuravlev, N. V. Lifanova and T. M. Usacheva, Structure of some liquid alcohols, diols and triols: an analysis of dielectric data, *J. Mol. Liq.* 120, 107 (2005).
- [4] M. B. Swami, V. P. Pawar, P. G. Hudge and A. C. Kumbharkhane, Dielectric relaxation study of amines in 2,3-butanediol mixture using picosecond time domain reflectometry technique, *J. Mol. Liq.* 190, 178 (2014).
- [5] N. V. Lifanova, T. M. Usacheva, V. I. Zhuravlev and V. K. Matveev, Dielectric properties of 2,5-hexanediol, *Rus. J. Phys. Chem.* 77, 477 (2003).
- [6] Dhage, Haribhau M., et al. "Dielectric relaxation studies of 1-nitropropane-dimethyl sulfoxide mixtures using a Time Domain Reflectometry." *Physics and Chemistry of Liquids* (2024): 1-10
- [7] Saknure, Shankar H., and Ashok C. Kumbharkhane. "Dielectric and Hydration Study of Aqueous Cellulose Derivative Solutions." *Journal of Macromolecular Science, Part B* (2024): 1-7.
- [8] Garad, Nitin P., et al. "Study of Dielectric Relaxation and Hydrogen Bonding Interaction of 1, 4-Butanediol-1, 4-Dioxane Mixture using TDR Technique." (2023).
- [9] Joshi, Y. S., and A. C. Kumbharkhane. "Study of dielectric relaxation and hydrogen bonding in water+ 2-butoxyethanol mixtures using TDR technique." *Fluid Phase Equilibria* 317 (2012): 96-101.
- [10] Deshmukh, Avadhut R., and Ashok C. Kumbharkhane. "Dielectric relaxation studies of aqueous primary amines using a time domain reflectometry." *Indian Journal of Physics* 96.11 (2022): 3105-3115.
- [11] S. Havriliak, S. Negami, *J. Polym. Sci. C* 14 (1966) 99–117.
- [12] Davidson, Donald W., and Robert H. Cole. "Dielectric relaxation in glycerol, propylene glycol, and n-propanol." *The Journal of Chemical Physics* 19.12 (1951): 1484-1490.

¹ P. S. AWANDKAR² A. V. TIWARI³ A. P. DESHMUKH⁴ S. P. TIWARI⁵ S. P. YAWALE

Synthesis and characterization of polyaniline & exploring it for CO₂ gas sensing



Abstract: - Polyaniline was synthesized through chemical oxidative polymerization at room temperature. The polyaniline sample was analysed by XRD, FTIR and impedance spectroscopy. Through the XRD and FTIR analysis it was confirmed the synthesis of the polyaniline. The sensor fabricated from polyaniline was exposed to the CO₂ gas at ambient temperature. The sensor was tested by voltage variation and impedance spectroscopy to determine the sensitivity of the polyaniline at room temperature which was found to be the 0.35 and 0.33. The polyaniline sensor shows capacitance like nature after exposure in air and gas. The response and recovery time of the sensor was found to 144 and 43 s.

Keywords: Polyaniline, CO₂, sensitivity, sensor, Impedance spectroscopy.

I. INTRODUCTION

CO₂ gas detection has been a area of interest in the area of the gas sensor due to increase in the pollution with the increase in the advancement in industrialization and pollution. The major research is to develop a gas sensor that should be thermally stable, low in cost, have fast response and recovery time and have better sensitivity and selectivity. Polyaniline is used as a sensor film due to its properties such as electrical conductivity, thermally stable, and synthesis cost. Various researchers have fabricated the sensor based on polyaniline to detect various gases. The sulfonated polyaniline in combination with polyvinyl alcohol has been used to fabricate a sensor to detect CO₂ gas at room temperature [1]. This sensor has shown increased in sensitivity toward the CO₂ gas at room temperature than the pure sample. Polyaniline with graphene has used as sensor for CO₂ gas sensing [2]. Polyaniline is used to detect NH₃ gas by forming it composite with TiO₂ fibers. The sensor was found to be highly sensitive than the pure polyaniline sensor [3]. Polyaniline has been also tested for gas sensing with a carbon nanotube to sense NH₃ at room temperature [4]. Polyaniline copper ferrite composite based sensor has been fabricated for sensing NH₃ gas at room temperature [5]. Polyaniline graphene has been used as the NH₃ gas sensor [6].

II. MATERIAL USED

Aniline and HCL were obtained through S D fine, FeCl₃, distilled water.

III. SYNTHESIS

Synthesis of polyaniline

The 5ml of aniline was added to the 1M of HCL and was stirred for 1hr at room temperature. 12.5 g of fecl₃ is added to 50 ml of distilled water [7]. Then this solution of fecl₃ was added drop by drop in solution of aniline and stirred for 1 hr. The polymerization was initiated at normal temperature. The solution was kept for 24 hr so that the fine polyaniline powder was produced. The solution is filtered and dried at room temperature to obtain polyaniline.

^{1*} Corresponding author **P.S.AWANDKAR** (pranavawandkar@gmail.com) ¹ *Material Research Laboratory, Department Of Physics Government Vidarbha Institute of Science and Humanities VMV Road, Amravati Maharashtra -444 604, India.*

²**A.V.TIWARI** (tiwariaditya992@gmail.com), ³**A.P. DESHMUKH** (deshmukh41@gmail.com), ⁴**S. P. TIWARI** (tiwarishaillesh26@gmail.com), ⁵**S.P. YAWALE** (spyawale@rediffmail.com)
Material Research Laboratory, Department Of Physics Government Vidarbha Institute of Science and Humanities VMV Road, Amravati Maharashtra -444 604, India.

IV. CHARACTERIZATION

XRD analysis

Polyaniline sample was characterized through XRD analysis. The range of measurement was from $2\theta = 10^\circ$ to 80° . The peak observed at $2\theta = 15.13, 20.89$ and 25.51 shown in fig. 1. Similar peaks have been observed by other researcher which indicates the formation of the polyaniline as this is the characteristic peak of the polyaniline [8].

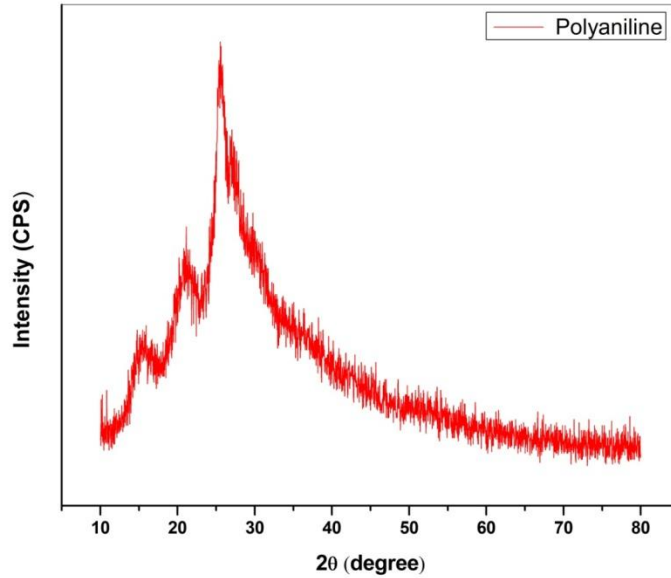


Figure 1. XRD of polyaniline

FTIR analysis

Polyaniline sample was characterize through FTIR spectroscopy shown in fig. 2. The peak obtained of the sample were nearly same as the peaks observed by the other researcher [9]. The peak at 1237.6 cm^{-1} corresponds to the C-N protonated group. Peak at 1400.8 cm^{-1} are related to C=C stretching mode of benzoid ring.

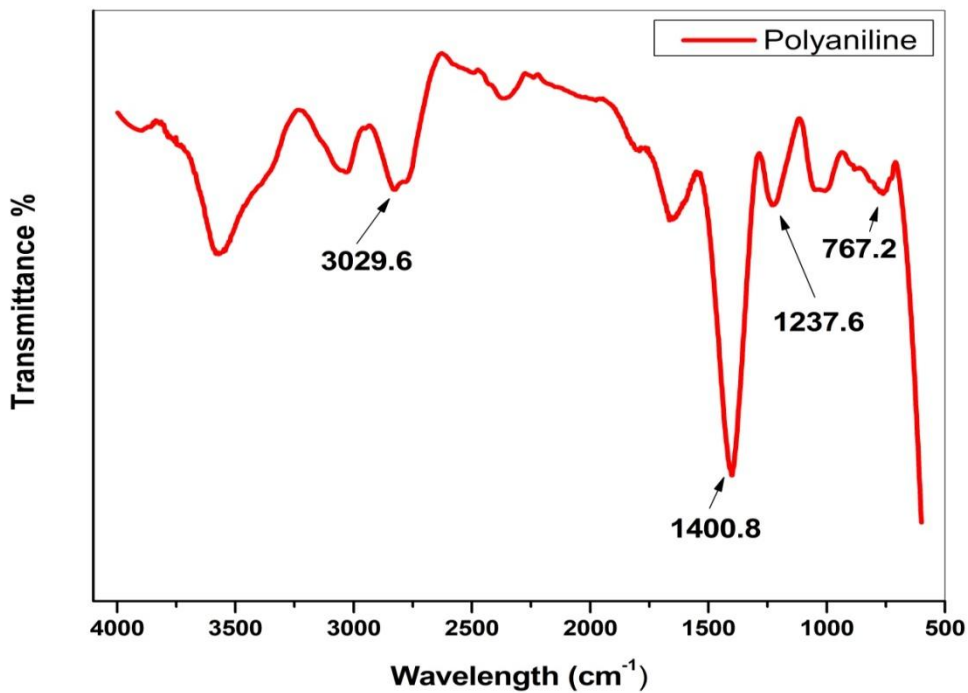


Figure 2. FTIR of polyaniline.

Impedance spectroscopy

The polyaniline sensor film was exposed to the CO₂ gas for 150 ppm for the frequency of 1Hz to 5MHz at 1V. Here the Z' signifies the real impedance of the sensor film. The intercept on the Z' at the lower frequency range indicates the resistance at the grain boundaries (R_{gb}) and at the higher frequency range indicates resistance at the grain (R_g). From the figure of Z' VS Z'' shown in fig. 3 we can observe that here the R_{gb} increase for the polyaniline sensor film after the exposure of the gas at room temperature. However the variation in the R_g is small as compared to the R_{gb} which indicates that the polyaniline is highly sensitive toward the CO₂ gas at room temperature. Here the relaxation peak as observed by the graph of the log frequency Vs Z'' shows that it increases in height after the exposure of the sensor in the CO₂ gas. The polyaniline sensor shows the phase angle greater than - 45° which indicates its capacitive nature [10]. Table 1 shows the resistance at grain boundary and resistance at grain in air and gaseous environment.

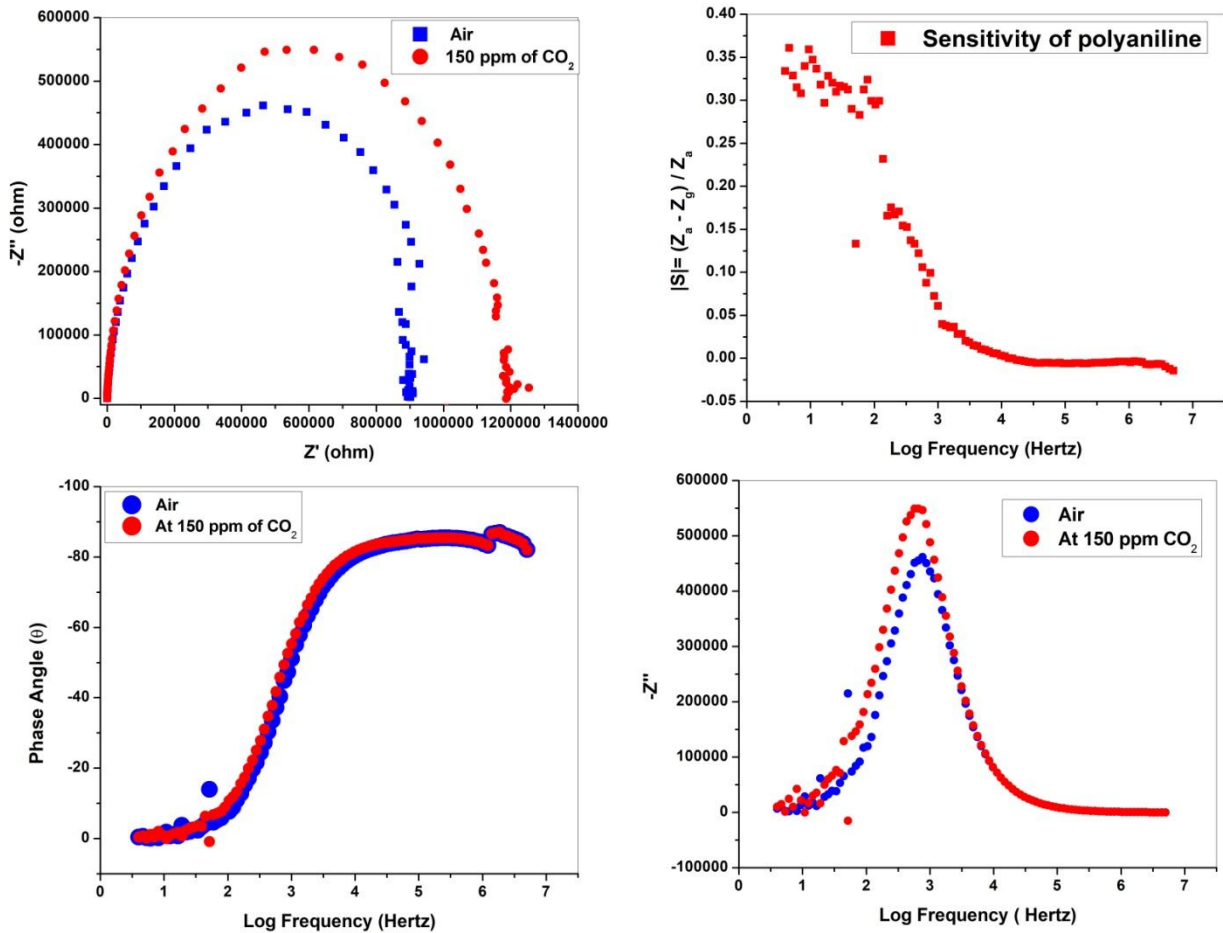


Figure 3. Impedance spectra of polyaniline in air and after exposure to the gas.

Table 1. The resistance at grain boundary (R_{gb}) and resistance at grain (R_g) in air and gaseous environment.

R _g (air)	122.1117
R _{gb}	895833.2
R _g (gas)	120.3664
R _{gb}	1195155

The sensor sensitivity was determined from the formula

$$|S| = \frac{Z_a - Z_g}{Z_a} \quad (1)$$

Where Z_a and Z_g are impedance in air and gas. The sensitivity from impedance spectroscopy was found to be 0.33.

V. GAS SENSING

Here the polyaniline sensor was introduced to the CO₂ gas at 150 ppm at room temperature to determine its sensitivity toward the gas. The response and recovery time of the sensor were found to be 144 & 43 s. The sensitivity of the sensor was calculated by the formula

$$|S| = \frac{R_a - R_g}{R_a} \quad (2)$$

Where R_a and R_g are resistance observed in air and gas. The sensitivity of the polyaniline by voltage variation method was found to be 0.35. Through impedance spectroscopy and change in voltage method it can be seen that the sensitivity of the polyaniline gas sensor was found to be nearly the same. Fig. 4 shows the sensing response of the polyaniline sensor.

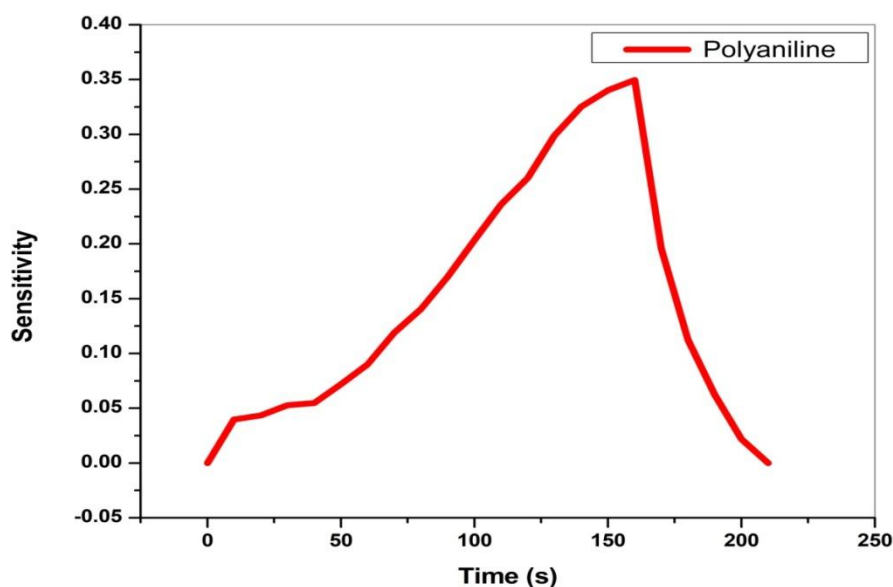


Figure 4. Sensor response of the polyaniline sensor.

VI. CONCLUSION

The polyaniline was synthesized by the chemical oxidative polymerization method at the room temperature. The gas sensor was exposed to the CO₂ gas at 150 ppm at room temperature. The polyaniline film was tested through the impedance spectroscopy and voltage variation method to determine its sensitivity. The sensitivity determined by both methods was found to be nearly the same. The phase angle of the polyaniline determined by the impedance in air and gas indicates its capacitive nature.

VII. REFERENCES

1. Tin C.D. Doan, Rajesh Ramaneti, Jacob Baggerman, J. Franc van der Bent, Antonius T.M. Marcelis, Hien D. Tong, Cees J.M. van Rijn, Carbon dioxide sensing with sulfonated polyaniline, *Sensors and Actuators B: Chemical*, Volume 168, 2012, Pages 123-130, ISSN 0925-4005, <https://doi.org/10.1016/j.snb.2012.03.065>.
2. Abdali, Hanan & Heli, Bentolhoda & Ajj, Abdallah. (2019). Stable and sensitive amino-functionalized graphene/polyaniline nanofiber composites for room-temperature carbon dioxide sensing. *RSC advances*. 9. 41240-41247. 10.1039/c9ra06223h.
3. Ultrasensitive NH₃ Gas Sensor from Polyaniline Nanograin Enchased TiO₂ Fibers, Jian Gong, Yinhua Li, Zeshan Hu, Zhengzhi Zhou, and Yulin Deng, *The Journal of Physical Chemistry C* 2010 114 (21), 9970-9974, DOI: 10.1021/jp100685r
4. Lina Xue, Wen Wang, Yunlong Guo, Guangqing Liu, Pengbo Wan, Flexible polyaniline/carbon nanotube nanocomposite film-based electronic gas sensors, *Sensors and Actuators B: Chemical*, Volume 244, 2017, Pages 47-53, ISSN 0925-4005, <https://doi.org/10.1016/j.snb.2016.12.064>.
5. Xingwei Wang, Likun Gong, Dongzhi Zhang, Xiaoxi Fan, Yingbo Jin, Liang Guo, Room temperature ammonia gas sensor based on polyaniline/copper ferrite binary nanocomposites, *Sensors and Actuators B: Chemical*, Volume 322, 2020, 128615, ISSN 0925-4005, <https://doi.org/10.1016/j.snb.2020.128615>.

6. Zuquan Wu, Xiangdong Chen, Shibu Zhu, Zuowan Zhou, Yao Yao, Wei Quan, Bin Liu, Enhanced sensitivity of ammonia sensor using graphene/polyaniline nanocomposite, *Sensors and Actuators B: Chemical*, Volume 178, 2013, Pages 485-493, ISSN 0925-4005, <https://doi.org/10.1016/j.snb.2013.01.014>.
7. Yasuda, A., Shimidzu, T. Chemical Oxidative Polymerization of Aniline with Ferric Chloride. *Polym J* 25, 329–338 (1993). <https://doi.org/10.1295/polymj.25.329>.
8. Wang, Z., Han, JJ., Zhang, N. *et al.* Synthesis of polyaniline/graphene composite and its application in zinc-rechargeable batteries. *J Solid State Electrochem* 23, 3373–3382 (2019). <https://doi.org/10.1007/s10008-019-04435-x>
9. Jiang, L., Cui, Z. One-step synthesis of oriented polyaniline nanorods through electrochemical deposition. *Polym. Bull.* **56**, 529–537 (2006). <https://doi.org/10.1007/s00289-005-0494-y>
10. Laschuk, Nadia & Easton, E. & Zenkina, Olena. (2021). Reducing the resistance for the use of electrochemical impedance spectroscopy analysis in materials chemistry. *RSC Advances*. 11. 27925-27936. 10.1039/D1RA03785D.

*¹P. P. Rathod²V.K. Bhosle³ A.U. Ubale

Synthesis, Characterization, Photocatalytic, Antibacterial And Antifungal Study of ZnO Nanoparticles



Abstract: - This study presents a comprehensive investigation into the synthesis, characterization, photocatalytic, antibacterial and antifungal study of zinc oxide (ZnO) nanoparticles. The nanoparticles were synthesized using a chemical precipitation and cost-effective method, followed by detailed characterization utilizing various analytical techniques such as X-ray diffraction (XRD), Scanning electron microscopy (SEM), Fourier Transform Infrared Spectroscopy (FTIR), and UV-Vis spectroscopy. The structural, morphological, and optical properties of the synthesized nanoparticles were thoroughly examined. The crystallite size was determined using the Debye Scherrer formula within the range of 29 nm and an optical band gap of 3.0 eV determined by Tauc plot. Moreover, the photocatalytic activity of the ZnO nanoparticles was evaluated through the degradation of Methylene blue dye under UV irradiation. The results demonstrate the efficient photocatalytic performance of the synthesized nanoparticles, indicating their potential applications in wastewater treatment and environmental remediation. Additionally, the antibacterial and antifungal activities of ZnO nanoparticles were assessed against pathogenic microorganisms and fungus, elucidating its significant bactericidal effects. Overall, this study provides valuable insights into the multifunctional properties of ZnO nanoparticles, highlighting its promising prospects in diverse fields such as environmental remediation and biomedical applications.

Keywords: XRD, SEM, FTIR, UV-Visible, ZnO, Photocatalysis, Antibacterial, Antifungal, Nanoparticles

I. INTRODUCTION

In recent years, the exploration of nanocatalysts has significantly expanded the realm of possibilities in various scientific fields, particularly in environmental remediation and medicine. The nanocatalysts have unique optical and electrical properties which opened up lots of doors for optoelectronic applications such as Solar cells [1], Hybrid solar cells [2], Sensors [3], LED [4], Lasers [5], etc. Among these nanocatalysts, zinc oxide (ZnO) nanocatalysts have emerged as a promising candidate due to their exceptional dual action potential of photocatalytic and antibacterial properties [6]. ZnO nanoparticles possess unique characteristics that make them highly efficient photocatalyst. Their wide band gap of 3.37 eV [7] with exciton binding energy of 60 meV at room temperature [8], the large specific surface area of up to $98 \text{ m}^2 \text{ g}^{-1}$ [9], high pore volume of up to $0.6 \text{ m}^3 \text{ g}^{-1}$ [10], low toxicity [11], and excellent electron-transport [12] these properties make it a promising material for chemical absorbents [13], polymer additives [14] and visible light driven photocatalytic activity [15]. The emergence of antibiotic-resistant bacteria has become a global health concern, prompting the search for alternative antimicrobial agents. ZnO nanoparticles exhibit remarkable antibacterial activity against a broad spectrum of pathogenic bacteria [16], including both Gram-positive and Gram-negative strains [17]. Their efficacy arises from a combination of factors, including their unique physicochemical properties, such as high surface area-to-volume ratio, surface reactivity [18], and ability to generate reactive oxygen species (ROS) under light or ambient conditions [19]. Varying morphologies at the nanoscale are widely used for antibacterial activity for various bacterial species. ZnO nanomaterials have a high refractive index and high binding energy so they can be used in many products such as medicine, cosmetics, rubber, solar cells, and foods [20-21]. ZnO nanomaterials can be synthesized by various chemical and physical techniques. The chemical method is easy in which the morphology of nanoparticles can be controlled by optimizing various reaction conditions such as pH, concentration of precursors, temperature, and reaction time. Moreover, the method is low cost and

^{*1,2} Author: Dept of Physics, Government Vidarbha Institute of Science and Humanities, Amravati

³ Author : Dept of Physics, Govt. Institute of Forensic Science, Chhatrapati Sambhaji Nagar
Email: rathodpp11yc@gmail.com

effective than the physical method [22-24]. There are various chemical methods for synthesizing nanomaterials such as sol-gel, hydrothermal, flame spray pyrolysis, and precipitation [25–28]. In the present work, we have synthesized the ZnO nanomaterials through the chemical precipitation method and investigated their structural, optical, morphological properties, and studied their photocatalytic, antibacterial and antifungal activities. The structural, optical, and morphological properties were studied by using XRD, UV absorbance, FTIR, and SEM characterization techniques respectively.

II. MATERIALS AND METHODS

Materials and chemicals such as Zinc acetate (99.99%) and Ethanol all analytical grades purchased from SDFine LTD. For the synthesis of ZnO nanoparticles, 16 gm of zinc acetate was dissolved in 100 mL of ethanol under continuous stirring for 1 h at 1000 rpm and kept without stirring for 16 h. On the next day, the solution was washed 2-3 times with ethanol, and the resulting residue was heated at 400°C in a muffle furnace for 1 h to obtain ZnO nanoparticles. The study of phase purity of ZnO nanopowder was performed by X-ray diffractometer (Model: Mini flex-II, Rigaku, Japan) with Cu K α radiation ($\lambda = 1.5406$ Å) operating at 40 kV and 30 mA. Surface morphology was studied using a Scanning Electron Microscope (SEM, Model: JEOL JSM-6360, Japan). Fourier transmission infrared (FTIR) spectra of the samples (as pellets in KBr) were recorded using FT-IR Spectrometer (Shimadzu, Japan) in the range of 4000-400 cm⁻¹. The optical absorption spectra were measured in the range of 300-800 nm by using a UV-visible spectrometer (UV-1800 Spectrophotometer, Shimadzu, Japan). The photocatalytic activities of all the samples were evaluated by exposing the aqueous MB dye solutions with or without catalysts. To investigate the photocatalytic performance of the samples, the photocatalyst test was done. First, 10 mg of the synthesized ZnO was immersed into the 50 mL of MB solution with an initial concentration of 2mg per liter under the visible light irradiation produced by a 150 W lamp (OSRAM, Germany). A 420 nm cut-off filter located at 30 cm above the solution. Then, the MB suspension containing the photocatalyst was magnetically stirred in the dark for 60 min at room temperature to calculate the equilibrium for absorption and desorption between the dye molecules and photocatalyst. After a certain time interval, 2 mL of the solution was extracted to determine the concentration of MB by UV-Vis Unico 2100 spectrophotometer at the maximum peak of the MB spectrum (664 nm). Antimicrobial activity of the prepared samples was tested in both gram-negative and gram-positive bacteria namely Escherichia coli and Staphylococcus aureus by disc diffusion method. The 24 h bacterial cultures were swabbed in Muller Hinton agar plates.

III. RESULTS

1. Structural Analysis

The XRD pattern of prepared ZnO nanoparticles was taken. All the XRD peaks were indexed by the hexagonal wurtzite phase of ZnO (JCPDS Card No. 01-089-0510) as shown in figure 1. The XRD pattern indicates the formation of the hexagonal wurtzite phase of ZnO. The peak broadening in the XRD pattern indicates that small nanoparticles are present in the samples. The sharp diffraction peaks indicate the good crystallinity of the prepared nanoparticles. In our study we obtained all peak at angle (2θ) 31.55°, 34.18°, 36.02°, 47.37°, 56.38°, 62.62°, 66.22°, 67.68°, 68.85° and 76.85° which corresponds to the reflection from (100), (002), (101), (102), (110), (103), (200), (112), (201), and (202) crystal planes of the hexagonal wurtzite zinc oxide structure. The absence of additional peaks in the XRD pattern confirms that the purity of ZnO nanoparticles. The crystallite size of the ordered ZnO nanoparticles has been estimated from the full width at half maximum (FWHM) and the Debye-Scherrer formula as given below

$$D = \frac{K\lambda}{\beta_{hkl}\cos\theta} \quad (1)$$

Where β_{hkl} is the integral half width, K is a constant equal to 0.90, λ is the wave length of the incident X-ray ($\lambda = 0.1540$ nm), D is the crystallite size, and θ is the Bragg angle. The crystallite size obtained for synthesized ZnO nanoparticles given in table 1. For hexagonal structure, the plane spacing d is related to the lattice constant a, c and the Miller indices by the following relation

$$\frac{1}{d_{hkl}^2} = \frac{4}{3} \left(\frac{h^2 + hk + k^2}{a^2} \right) + \frac{l^2}{c^2} \quad (2)$$

With the first-order approximation, $n = 1$

$$\sin^2 \theta = \frac{\lambda^2}{4a^2} \left[\frac{4}{3} (h^2 + hk + k^2) + \left(\frac{a}{c} \right)^2 l^2 \right] \quad (3)$$

The lattice constant “a” for (100) plane is calculated by

$$a = \frac{\lambda}{\sqrt{3} \sin \theta} \quad (4)$$

And lattice constant “c” for (002) plane is calculated by

$$c = \frac{\lambda}{\sin \theta} \quad (5)$$

The lattice constants ($a = b = 3.2644 \text{ \AA}$ and $c = 5.6541 \text{ \AA}$, $c/a = 1.7320$) and diffraction peaks corresponding to the planes (100), (002), (101), (102), (110), (103) obtained from X-ray diffraction data. The interplanar spacing (d_{hkl}) calculated from XRD is compared with JCPDS data card and corresponding (hkl) planes. The dislocation density (d), which represents the amounts of defects in the sample is defined as the length of dislocation lines per unit volume of the crystal and is calculated using the equation

$$\delta = \frac{1}{D^2} \quad (6)$$

Where D is the crystallite size and the obtained dislocation density is mentioned in table 1. The Zn-O bond length can be determined using the relation and the calculated value is 2.0417 \AA for (100) plane.

$$L = \sqrt{\left(\frac{a^2}{3} + \left(\frac{1}{2} - u \right)^2 c^2 \right)} \quad (7)$$

Where u is the positional parameter in the wurtzite structure and is a measure of the amount by which each atom is displaced with respect to the next along the ‘c’ axis. ‘u’ is given by the relation

$$u = \frac{a^2}{3c^2} + 0.25 \quad (8)$$

Positional parameter value for ZnO nanoparticles is 0.3611.

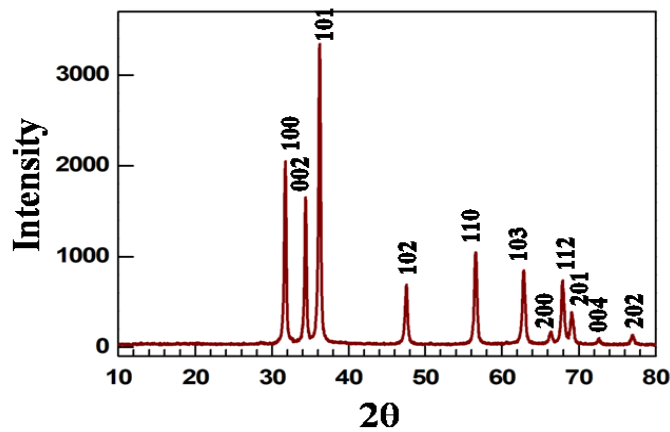


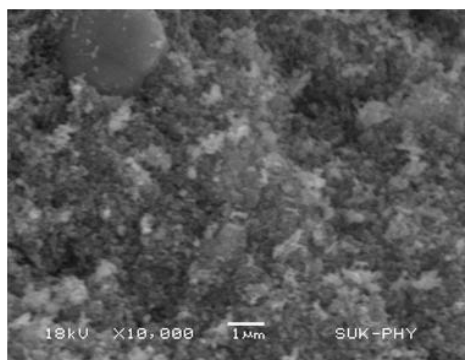
Fig 1:XRD pattern of ZnO nanoparticles

Table 1: Different 2 θ angle and their corresponding FWHM, Crystallite size and lattice parameters

Peak 2 θ	D (nm)	Strain (ϵ) = $\beta/4$ $\tan \theta$	Dislocation density δ (nm ⁻²)	FWHM β	Lattice parameters						
					a=b (Å)	c (Å)	c/a	V (Å) ³	U	APF (gcm ⁻³)	L (Å)
31.623	29.91	0.0042	0.00112	0.276	3.2644	5.6541	1.732	52.18	0.3611	0.697	2.04
34.293	29.48	0.0039	0.00115	0.282	3.0170	5.2256					
36.108	28.81	0.0038	0.00121	0.29	2.8700	4.9710					
47.403	27.98	0.0030	0.00128	0.31	2.2127	3.8326					
56.434	30.77	0.0023	0.00106	0.293	1.8812	3.2583					
62.728	25.42	0.0026	0.00155	0.366	1.7089	2.9599					
66.32	27.11	0.0023	0.00136	0.35	1.6261	2.8165					
67.822	27.27	0.0022	0.00135	0.351	1.5942	2.7614					
68.996	29.84	0.0020	0.00112	0.323	1.5704	2.7200					
72.42	24.61	0.0023	0.00165	0.4	1.5056	2.6078					
76.755	24.12	0.0023	0.00172	0.42	1.4326	2.4814					

2. Morphological analysis

The SEM image of the sample is shown in figure 2. In the higher resolution SEM images, the uniform and compact structure is observed.

**Fig 2:SEM image of ZnO nanoparticles**

3. Optical analysis

The UV-visible spectrum of the sample is shown in figure 3. The sample absorbs the radiations in the UV range up to 370.03 nm which is shown in figure 3 and almost all the visible spectrum radiations are transmitted by the ZnO nanoparticles. The band gap energy (E_g) can be calculated using a Tauc plot, which involves plotting $(\alpha h\nu)^2$ versus photon energy ($h\nu$), where α is the absorption coefficient. The linear portion of the plot is extrapolated to intersect the energy axis, giving the band gap value of 3.0 eV. The plotted Tauc plot is shown in figure 4. Chemical bonding in a material can be evaluated by using FTIR technique. The absorption and transmission peaks in the FTIR spectrum depend on crystalline structure, chemical composition, and also on the morphology of a material. The FTIR curve for ZnO nanoparticles is shown in figure 5. A series of absorption peaks from 1000 to 4000 cm^{-1} can be found, corresponding to the carboxylate and hydroxyl impurities in materials. To be

more specific, a broad band at 3427.51 cm^{-1} is assigned to the O-H stretching mode of the hydroxyl group. Peaks between 2830 and 3000 cm^{-1} are due to the C-H stretching vibration of alkane groups. The peaks observed at 1537.27 and 1386.82 cm^{-1} are due to the asymmetrical and symmetrical stretching of the zinc carboxylate, respectively. As the size of the nanoparticles increases, the content of the carboxylate (COO^-) and hydroxyl ($-\text{OH}$) groups in the samples decreased. The carboxylate probably comes from reactive carbon-containing plasma species during synthesis and the hydroxyl results from the hygroscopic nature of ZnO.

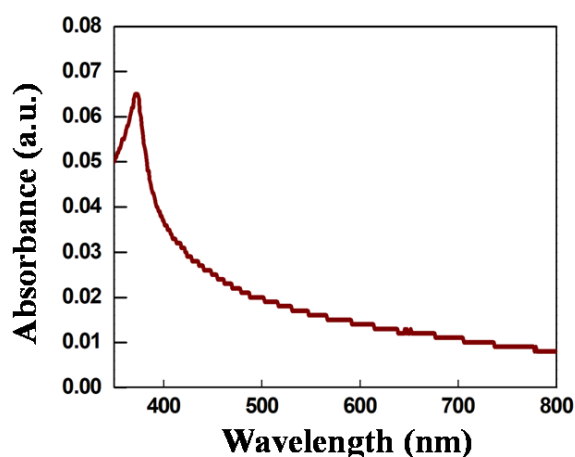


Fig 3:UV-Vis absorbance spectrum of ZnO nanoparticles

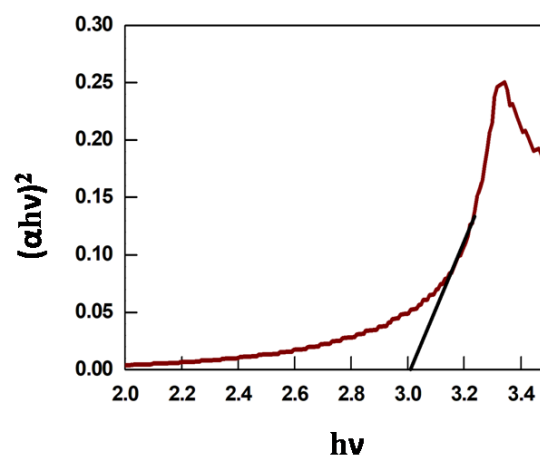


Fig 4: Tauc plot of ZnO nanoparticles

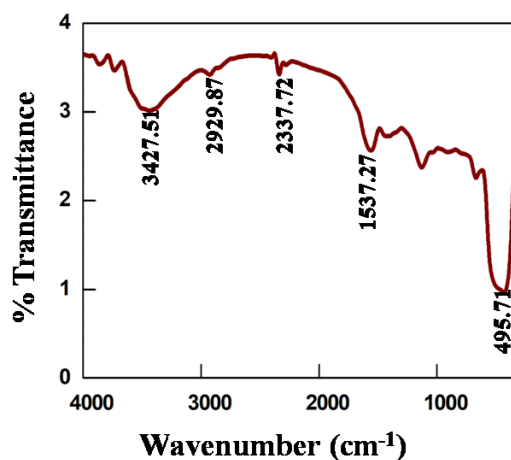


Fig 5:FTIR spectrum of ZnO nanoparticles

4. Photocatalytic Degradation of Methylene Blue

The photocatalytic activity of the ZnO nanoparticles was evaluated by exposing the aqueous MB dye solutions with or without catalysts. Methylene blue dye was chosen as it is a commonly used organic pollutant for water. The MB is a phenothiazine dye, with a monomer-dimer equilibrium, that can be observed by absorption maxima at 664 nm and 614 nm , respectively [29–31]. First, 10 mg of the synthesized ZnO was immersed into the 50 mL of MB solution with an initial concentration of 2 mgL^{-1} under the visible light irradiation produced by 150 W lamp (OSRAM, Germany) with a 420 nm cut-off filter located at 30 cm above the solution. Then, the MB suspension containing the photocatalyst was magnetically stirred in the dark for 60 min at room temperature to calculate the equilibrium for absorption and desorption between the dye molecules and photocatalyst. After a

certain time interval, 2 mL of the solution was extracted to determine the concentration of MB by UV–Vis Unico 2100 spectrophotometer at the maximum peak of the MB spectrum (664 nm). The obtained results confirm the degradation of MB dye as depicted in figure 6. The result shows good degradation efficiency for the synthesized ZnO nanoparticles. The percentage degradation is calculated using the formula [32]

$$\text{Degradation rate}(\%) = ((C_0 - C)/C_0) \times 100 \quad (9)$$

Where C_0 is the concentration of MB dye at equilibrium and C is the concentrations of non-degraded dye after different irradiation time intervals. In the photocatalytic mechanism the first stage of photoreaction, the ZnO NPs are illuminated by a light source having photon energy greater or equal to the band gap ($E_{\text{photon}} \geq E_{\text{Bandgap}}$) [33]. This adsorption of photons energy causes formation of electron-hole pairs ($e^- + h^+$). In the second step, photons generated electron hole pair ($e^- + h^+$) move toward the surface of the ZnO nanoparticles, due to their small size [34] In the next step, electrons (e^-) are introverted from the conduction band by oxygen (O_2) molecules and form an anion radical ($\bullet O_2^-$). The holes present in the valence band serve as trap for adsorbed water (H_2O_{ads}) or hydroxyl ions (OH_{ads}^-) and produces hydroxyl radicals ($\bullet OH$)[35]. The radicals generated in the process attack the organic dye molecules, finally leading to their degradation and formation of harmless products like CO_2 , H_2O , SO_2^{4-} , NO_3^- , and NH_4^+ [36].

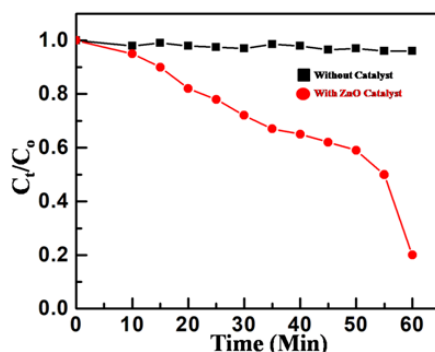


Fig 6:Photocatalytic degradation of Methylene blue

5. Antibacterial and Antifungal test

The antibacterial activities of synthesized ZnO-NPs were tested against human pathogens like Gram-negative strains *E. coli* and gram-positive strains *S. aureus* concerning Ofloxacin. The antibacterial activity is listed in Table II. From the results, it was observed that the synthesized ZnO-NPs showed preferred antibacterial activity against Gram-negative strains *E. coli* and gram-positive strains *S. aureus*. The obtained diameter of the inhibition zone for gram-positive *S. aureus* and for gram-negative *E. coli* are 11 mm and 12 mm for the synthesized ZnO particles respectively. The antifungal activity of the ZnO-NPs was investigated against *C. albicans* using the disc-diffusion susceptibility method. The obtained diameter of the inhibition zone is 12 mm and for standard reference diameter of the inhibition zone is 14 mm. ZnO nanoparticles are good candidates for the antifungal against *C. albicans*.

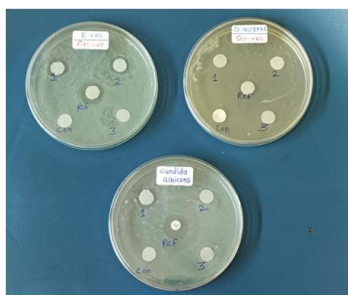


Fig 7:Antibacterial and Antifungal activity of ZnO nanoparticles (Sample 1)

Table 2:Antibacterial and Antifungal activity of ZnO nanoparticles

S. No	Compound Name	Antibacterial Sensitivity Test against Bacteria and Fungus, After 24 hrs at 37° C temp and Fungus at room temp (Zone of inhibition in mm)		
		Gram + ve bacteria	Gram - ve bacteria	Fungus
		Staphylococcus aureus	Escherichia coli	Candida Albicans
1.	ZnO	11 mm	12 mm	12 mm
2.	Standard Ofloxacin (2 mcg) for bacteria	12 mm	12 mm	---
3.	Standard Fluconazole (25mcg) for fungus	--	--	14 mm

IV. DISCUSSION

In this study, we investigated the photocatalytic, antibacterial, and antifungal activities of ZnO nanoparticles. The results demonstrated significant photocatalytic degradation of methylene blue, potent antibacterial effects against *E. coli* and *S. aureus*, and effective antifungal activity against *Candida albicans*. The photocatalytic activity of ZnO nanoparticles can be attributed to their high surface area due to nanoparticles size and the generation of reactive oxygen species under UV light. The antibacterial effects are likely due to both ROS production and the release of Zn^{2+} ions, which disrupt bacterial cell membranes. The antifungal activity study shows ZnO nanoparticles' efficacy against *Candida albicans* through cell wall disruption. These findings contribute to the growing evidence of ZnO nanoparticles' multifunctional properties. Compared to other nanomaterials, ZnO's relatively low cost and ease of synthesis make it a promising candidate for widespread environmental and biomedical applications. The demonstrated photocatalytic efficiency suggests that ZnO nanoparticles could be utilized in wastewater treatment to degrade organic pollutants. The potent antibacterial and antifungal activities indicate potential applications in medical device coatings and agricultural fungicides, providing a dual benefit of protecting human health and enhancing crop yields. One limitation of this study is the potential for aggregation of ZnO nanoparticles, which can reduce surface area and activity. Additionally, the study was conducted under controlled laboratory conditions, which may not fully replicate real-world environments. Further research is needed to explore the long-term stability and safety of ZnO nanoparticles in practical applications.

V. CONCLUSION

In the present study, zinc oxide nanoparticles were synthesized using the chemical precipitation method. The nanoparticles were characterized using UV-visible spectroscopy which showed a band gap of 3.0 eV. The crystal structure of ZnO nanoparticles was studied using X-ray Diffraction and the peak position of XRD confirmed the wurtzite hexagonal structure of zinc oxide nanoparticles. The FTIR was also carried out to characterize the zinc oxide nanoparticles. The morphology of the nanoparticles was studied using SEM. The antibacterial study was carried out against *E.coli* and *Staphylococcus aureus*, and the zone of inhibition was measured. The maximum zone of inhibition was in *E. coli*. The antifungal study was carried out against *Candida albicans*. The photocatalytic study was carried out against methyl blue. The maximum percentage of dye degradation was obtained after 60 minutes. Our research suggests that ZnO NPs formed by this method have potential application in wide areas of study ranging from wastewater treatment to antimicrobials.

ACKNOWLEDGMENT

All authors thank the Department of Physics and Electronics, GVISH, Amravati for providing XRD and FTIR facilities. All authors thank the Department of Physics, Shivaji University Kolhapur for providing an SEM facility.

REFERENCES

1. S. Siva Kumar, P. Venkateswarlu, V. RangaRao and G. NageswaraRao, Synthesis, characterization and optical properties of zinc oxide nanoparticles, *Int. Nano Lett.* 3 (2013) 3-30.
2. A.K. Singh, Synthesis, characterization, electrical and sensing properties of ZnO nanoparticles, *Adv.Powder Technol.* 6 (2010) 609-613.
3. M. Kahouli, A. Barhoumi, A. Bouzid, A. Al-Hajry, S. Guermazi, Structural and optical properties of ZnO nanoparticles prepared by direct precipitation method, *SuperlatticesMicrostruct.* 85 (2015) 7-23.
4. A. Dakhlaoui, M. Jendoubi, L. S. Smiri, A. Kanaev, N. Jouini, Synthesis, characterization and optical properties of ZnO nanoparticles with controlled size and morphology, *J. Cryst. Growth* 311 (2009) 3989-3996.
5. F.S.F. Morgenstern, D. Kabra, S. Massip, T.J.K. Brenner, P.E. Lyons, J. N. Coleman, R.H. Friend, Ag-nanowire films coated with ZnO nanoparticles as a transparent electrode for solar cells, *Appl. Phys. Lett.* 99 (2011) 183307.
6. Kumar, Nishant, Akhshay Singh Bhadwal, MayankGarg, Reema Sharma, Suman Singh, and Boris Mizaikoff. "Photocatalytic and antibacterial biomimetic ZnO nanoparticles." *Analytical methods* 9, no. 33 (2017): 4776-4782.
7. G.Wisz, I. Virt, P. Sagan, P. Potera, R.Yavorskyi, Structural, Optical and Electrical Properties of Zinc Oxide Layers Produced by Pulsed Laser Deposition Method, *Nanoscale Res. Lett.* 12 (2017) 253.
8. Klingshirn, C., 2007. ZnO: material, physics and applications. *ChemPhysChem*, 8(6), pp.782-803.
9. S. Kaluza, M. K. Schröter, R. N. d'Alnoncourt, T. Reinecke, M. Muhler, High Surface Area ZnO Nanoparticles via a Novel Continuous Precipitation Route, *Adv. Funct. Mater.* 18 (2008) 3670-3677.
10. D. An, Y. Li, X. Lian, Y. Zou, G. Deng, Synthesis of porous ZnO structure for gas sensor and photocatalytic applications, *Colloids Surf. A Physicochem. Eng. Asp.* 447 (2014) 81-87.
11. S. Pasupuleti, S. Alapati, S. Ganapathy, G. Anumolu, N.R. Pully, B.M. Prakhya, Toxicity of zinc oxide nanoparticles through oral route, *Toxicol. Ind. Health* 28 (2012) 675-686.
12. Liu, Chunhui, Chengyi Xiao, and Weiwei Li. "Zinc oxide nanoparticles as electron transporting interlayer in organic solar cells." *Journal of Materials Chemistry C* 9, no. 40 (2021): 14093-14114.
13. J.O. Primo, C. Bittencourt, S. Acosta, A. Sierra-Castillo, J.F. Colomer, S. Jaeger, V.C. Teixeira, F.J. Anaisi, Synthesis of Zinc Oxide Nanoparticles by Ecofriendly Routes: Adsorbent for Copper Removal from Wastewater, *Front. Chem.* 8 (2020) 571790.
14. T. V. D. Berg, M. Ulbricht, Polymer Nanocomposite Ultrafiltration Membranes: The Influence of Polymeric Additive, Dispersion Quality and Particle Modification on the Integration of Zinc Oxide Nanoparticles into PolyvinylideneDifluoride Membranes, *Membr.J.* 10 (2020) 197.
15. S. Akir, A. Barras, Y. Coffinier, M. Bououdina, R. Boukherroub, A. D. Omrani, Eco-friendly synthesis of ZnO nanoparticles with different morphologies and their visible light photocatalytic performance for the degradation of Rhodamine B, *Ceram. Int.* 42 (2016) 10259-10265.
16. Shinde, Sandip S. "Antimicrobial activity of ZnO nanoparticles against pathogenic bacteria and fungi." *Sci Med Central* 3 (2015): 1033.
17. Emami-Karvani, Zarrindokht, and PegahChehrazi. "Antibacterial activity of ZnO nanoparticle on gram-positive and gram-negative bacteria." *Afr J Microbiol Res* 5, no. 12 (2011): 1368-1373.
18. Anders, C.B., Eixenberger, J.E., Franco, N.A., Hermann, R.J., Rainey, K.D., Chess, J.J., Punnoose, A. and Wingett, D.G., 2018. ZnO nanoparticle preparation route influences surface reactivity, dissolution and cytotoxicity. *Environmental Science: Nano*, 5(2), pp.572-588.
19. Ma, H., Wallis, L.K., Diamond, S., Li, S., Canas-Carrell, J. and Parra, A., 2014. Impact of solar UV radiation on toxicity of ZnO nanoparticles through photocatalytic reactive oxygen species (ROS) generation and photo-induced dissolution. *Environmental pollution*, 193, pp.165-172.

20. A.M. Alsaad, Q.M. Al-Bataineh, A.A. Ahmad, Z. Albataineh, A. Telfah, Optical band gap and refractive index dispersion parameters of boron-doped ZnO thin films: A novel derived mathematical model from the experimental transmission spectra, *Optik*, 211 (2020) 164641.
21. C. Klingshirn, ZnO: Material, Physics and Applications, *ChemPhysChem*. 8 (2007) 782-803.
22. A. Rayerfrancis, P.B. Bhargav, N. Ahmed, B. Chandra, S. Dhara, Effect of pH on the morphology of ZnO nanostructures and its influence on structural and optical properties, *Physica B Condens.* 457 (2015) 96-102.
23. M.A. MoghriMoazzen, S.M. Borghei, F. Taleshi, Change in the morphology of ZnO nanoparticles upon changing the reactant concentration, *Appl. Nanosci.* 3(2013) 295-302.
24. C. Pholnak, C. Sirisathitkul, S. Suwanboon, D.J. Harding, Effects of precursor concentration and reaction time on sonochemically synthesized ZnO nanoparticles, *Mater. Res.* 17 (2013) 405-411.
25. Y.T. Chung, M.M. Ba-Abbad, A.W. Mohammad, N.H.H. Hairom, A. Benamor, Synthesis of Minimal-Size ZnO Nanoparticles through Sol-gel Method: Taguchi Design Optimisation, *Mater. Des.* 87 (2015) 780-787.
26. M. M. ElFaham, A. M. Mostafa, E. A. Mwafy, The effect of reaction temperature on structural, optical and electrical properties of tunable ZnO nanoparticles synthesized by hydrothermal method, *J. Phy. Chem. Sol.* 154 (2021) 110089.
27. R. Wallace, A.P. Brown, R. Brydson, K. Wegner, S.J. Milne, Synthesis of ZnO nanoparticles by flame spray pyrolysis and characterisation protocol, *J. Mater. Sci.* 48 (2013) 6393-6403.
28. S. Rajan, A. Venugopal, H. Kozhikkalathil, S. Valappil, M. Kale, M. Mann, P. Ahuja, S. Munjal, Synthesis of ZnO nanoparticles by precipitation method: Characterizations and applications in decipherment of latent fingerprints, *Mater. Today Proc.* (2023).
29. Asjadi, F.; Yaghoobi, M. Characterization and dye removal capacity of green hydrothermal synthesized zno nanoparticles. *Ceram. Int.* 2022, 48, 27027-27038.
30. 58. Oksuz, A.E.; Yurddaskal, M.; Kartal, U.; Dikici, T.; Erol, M. Zno nanostructures for photocatalytic degradation of methylene blue: Effect of different anodization parameters. *J. Korean Ceram. Soc.* 2022, 59, 859-868.
31. Dhatwalia, J.; Kumari, A.; Chauhan, A.; Mansi, K.; Thakur, S.; Saini, R.V.; Guleria, I.; Lal, S.; Kumar, A.; Batoo, K.M.; et al. Rubusellipticus sm. Fruit extract mediated zinc oxide nanoparticles: A green approach for dye degradation and biomedical applications. *Materials* 2022, 15, 3470.
32. Akir, S., Barras, A., Coffinier, Y., Bououdina, M., Boukherroub, R. and Omrani, A.D., 2016. Eco-friendly synthesis of ZnO nanoparticles with different morphologies and their visible light photocatalytic performance for the degradation of Rhodamine B. *Ceramics International*, 42(8), pp.10259-10265.
33. R. M. Tripathi, A. S. Bhadwal, R. K. Gupta, P. Singh, A. Shrivastav and B. R. Shrivastav, *Journal of Photochemistry and Photobiology B: Biology*, 2014, 141, 288-295.
34. X. Li, C. Hu, X. Wang and Y. Xi, *Applied Surface Science*, 2012, 258, 4370-4376.
35. A. Nezamzadeh-Ejhih and S. Khorsandi, *Journal of Industrial and Engineering Chemistry*, 2014, 20, 937-946.
36. D. Kale and P. Thakur, *Journal of Porous Materials*, 2015, 22, 797-806.

^{1*} Priya U. Sah
² Akshay P. Bangar
³ S. A. Waghuley

Regular paper
Exploring potential of CdS for
Efficient Solar Cell incorporated with
SiO₂



Abstract: - This study explores the potential of cadmium sulfide (CdS) for efficient solar cells enhanced by silicon dioxide (SiO₂). CdS nanoparticles were synthesized via chemical precipitation, and SiO₂ nanoparticles through solid-state diffusion using silicic acid. Characterization with UV-Visible spectroscopy and X-ray diffraction (XRD) showed polycrystalline films with hexagonal and cubic structures, preferentially oriented at (111), and nanoparticles averaging 6.8 nm. UV-Vis absorption spectra (300-800 nm) revealed crucial optical characteristics for the effectiveness of solar cells. Incorporating SiO₂ into CdS solar cells improved photovoltaic performance by enhancing light absorption and reducing electron-hole recombination, demonstrating the potential for high-performance, cost-effective solar cells.

Keywords: Cadmium sulfide, Silicon, Solar cell, XRD.

*Corresponding author: Priya U. Sah, ^{1,2,3} Department of Physics, Sant Gadge Baba Amravati University, Amravati, India ,444 602. Email : priyasah652001@gmail.com

INTRODUCTION

The constant rise in the development of technology, global warming, and enhanced living standards globally is a precursor in the search for fresh, safe, and reliable energy resources. For support the sustainable growth of human society and environmental protection according to fixed fossil fuel energy sources are insufficient [1]. Everyday sun sends out great amount of energy in the form of radiations and heat called solar energy. Solar energy is available at no cost which is a limitless source of energy [2]. The major benefit of solar energy over other conventional power generators is that the sunlight can be directly harvested into solar energy with the use of small and tiny photovoltaic (PV) solar cells [3].

The PV effect, first observed in 1839 by Alexandre -Edmond Becquerel, led to the invention of the modern silicon solar cell in 1946 by Russel Ohl [4]. Unlike noisy power pumping devices, small solar cells operate silently, making them less disruptive. Traditional solar photovoltaic batteries, while more expensive and bulky, are suitable for small-scale or household use, not large solar plants [5]. Early photovoltaic cells transformed sunlight into electrical power using thin silicon wafers. Modern technology relies on creating electron-hole pairs in semiconductor layers (p-type and n-type materials). When a photon hits the junction, it ejects an electron, generating electrical power [5]. Materials for photovoltaic cells include silicon (single crystal, multi-crystalline, amorphous), cadmium-telluride, copper-indium-gallium-selenide, and copper-indium-gallium-sulfide [6].

CDS

CdS (Cadmium Sulphide) particles are type II–VI semiconductor materials with a 2.42 eV band gap, displaying excellent physical and chemical properties, especially in their nano-crystalline form with varying band gaps. These properties are attributed to their crystallite size, which differs from bulk particles. CdS serves as a significant semiconductor photocatalyzer. [7]. However, there has been limited research dedicated to understanding the impact of manipulating the concentration of Cd²⁺ ionic species, which could significantly influence the properties of CdS. In our study, we employed a simple and cost-effective synthetic technique for preparing CdS NCs through chemical precipitation, focusing on the effect of molar concentrations of the cadmium source, CdSO₄. Our various characterizations revealed a strong dependence on the concentration of CdSO₄ used [8].

SiO₂

In solar cells, the key requirements include enhancement of photon absorption and generating charge carriers. Thus, therefore, nanomaterials (such as nanorods, nanoparticles, ultrathin film and gratings) have been demanded due to their significant properties which can boost the conversion efficiency of the solar cells [9]. SiO₂ nanoparticles, known for their excellent electrical and optical properties, are utilized as anti-reflection coating materials in solar cells. Additionally, SiO₂ finds applications in the fabrication of sensors, piezoelectric devices, fuel cells, antireflection coatings, and catalysts [10].

MATERIALS AND EXPERIMENTAL

The current study, aqueous solutions of sodium sulphide (Na₂S) (of 99.99% purity) cadmium sulphate (CdSO₄) (of 99.0% purity) were selected as main precursors for the preparation of CdS nanoparticle. CdS NCs was prepared at room temperature from 0.1 M aqueous solution of Na₂S CdSO₄ 0.1. Each solution dissolved separately in 25 ml of de-ionized and stirred for 10 min. After completely dissolving Na₂S solution was blended with slowly dropping to CdSO₄ solution for 30 min below stirring. No buffer modification has been added. Throughout this process, wet yellow precipitate was collected. The final product was dried in an oven for 48 hours at 80 °C.

Chemical reactions that take place is given by the equation 1

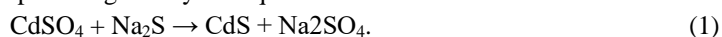


Figure 1 shows the photograph of CdS NPs after the drying process

As obtained Cds nanoparticules were used to prepare composite with SiO₂ using Solid state diffusion method. For this, silicic acid was utilized as source of SiO₂. The heating of silicic acid above 200⁰C, result in oxidation of silicic acid. And we prepared a sample of CdS loaded SiO₂ rich composite shown in fig 2.



Figure 1 CdS nanoparticle

Figure 2 SiO₂ nanoparticle

RESULTS AND DISCUSSIONS

XRD STUDY

The physical-chemical analysis of prepared samples was done through various analytical tools. The structural study of samples was completed using X-ray diffraction (XRD). Hexagonal and cubic crystal phases are seen in CdS. When CdS is deposited, its polycrystalline hexagonal and cubic forms take on random orientations and show multiple prominent diffraction peaks. It is therefore established that samples of excellent purity were created. The X-ray diffraction patterns of CdS NCs at 0.5 M concentration are displayed in Figure 1's blue color spectrum. Differentiating between cubic (1 1 1) and HCP (200), cubic (2 2 0) and HCP (1 1 0), is a challenging task. Additional CdSO₄ concentrations caused the XRD to show new hexagonal structure peaks. This event was expected to represent a phase shift in the application of higher CdSO₄ concentrations. It was thought that the hexagonal phase had replaced the combinations of the cubic and hexagonal phases.

The index was created using the various peaks in the diffraction gran, and matching values for the surfaces spacing "d" were computed and compared to the typical values of the JCPDS data. The most notable finding from the data is the observation of increased crystallinity in response to a precursor's concentration levels shifting. The strongest peak is used in the Debye-Scherrer equation to estimate the average crystallite sizes of various cadmium salt concentrations.

$$D = 0.94\lambda / B \cos \theta$$

Wavelength, and B is the full width at half maximum (FWHM) of the diffraction peak, respectively. The d-spacing for all samples can be estimated from the position of the main peak at 26.6° and by the Bragg condition

$$n\lambda = 2d \sin \theta$$

Where, d is the distance between the planes parallel to the incident beam's axis, θ is the diffraction angle, λ is the incident X-ray's wavelength, and n is the order of diffraction. Crystallite sizes computed using d-spacing. All of the deposited films were polycrystalline with a preferred orientation and a hexagonal and cubic structure, according to XRD (111). The estimated size of the nanoparticles is 6.8 nm, based on the surface morphologies micrographs and X-ray diffraction peaks.

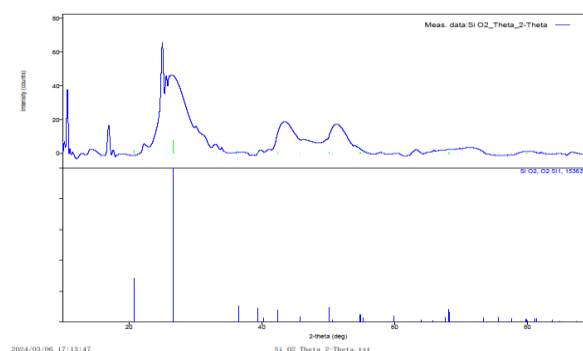


Figure 3 : XRD of CdS nanoparticles.

Figure 2 show the XRD pattern of CdS incorporated SiO₂ nanocomposites. XRD pattern clearly show the presence of characteristics peaks of CdS with correct diffraction peak position and marginal intensity. The signatures peaks of CdS exactly match with JCPDS card No: 06-0464. The broad hump with some shoulder peak appears between 25- 35 indicates the presence of SiO₂ in composites. It reveals that CdS/SiO₂ nanocomposites is crystalline in nature.

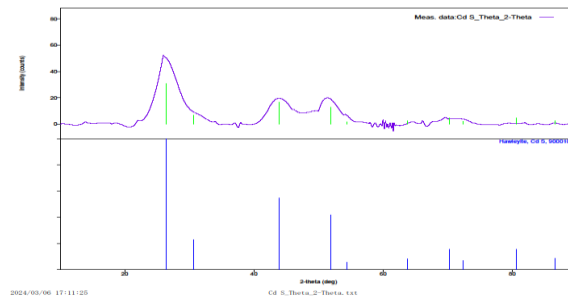


Figure 4 : XRD of CDS/SiO₂ nanoparticles.

UV-VIS SPECTROSCOPY STUDY

To evaluate the efficiency of the solar cells the optical properties play a significant role. Fig. 3 shows the UV–Vis absorption spectra of CdS nanoparticules between the wavelength of 300-800 nm. Fig.3. Impact on the optical characteristics of CdS nanoparticules. As a consequence of increased concentration, it was found that there is a slight change in absorption.

Basically, a sharper absorber edge shows fewer defects and impurities in the film. In fact, when CdS begins absorbing light, CdS nanoparticules presented interference patterns through a sudden decrease of transmission nearby the band edge, resulting from the excellent crystallinity of nanoparticles. The linear part of the curves to the interception of the horizontal axis, the optical band gaps of all samples were achieved to be between 2.36 and 2.4 eV which is ideal for buffer materials.

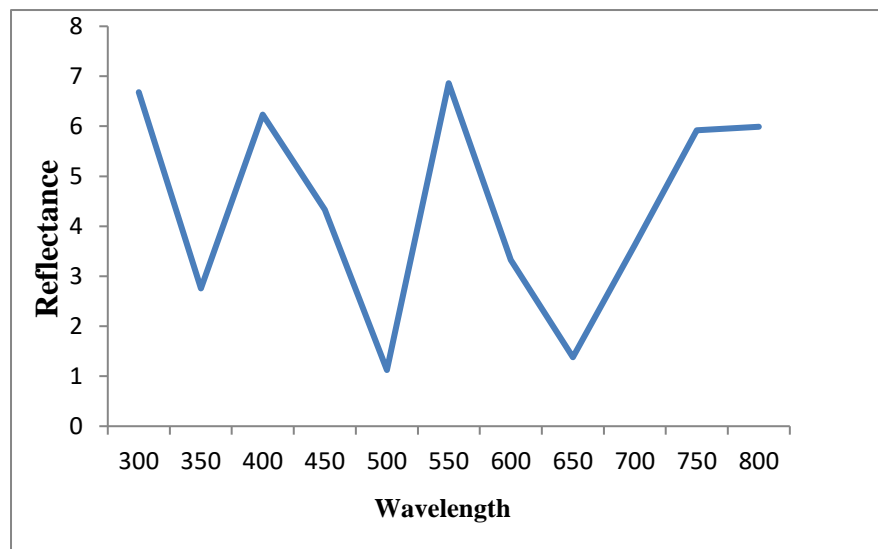


Figure 5: UV-visible spectra of CdS nanoparticles.

CONCLUSIONS

In summary, the incorporation of silicon dioxide (SiO₂) into cadmium sulfide (CdS) significantly enhances solar cell efficiency. XRD analysis showed that all the deposited films were polycrystalline with hexagonal and cubic structures, exhibiting preferential orientation (111). From the X-ray diffraction the nanoparticle size was estimated to be around 6.8 nm. The broad hump with a shoulder peak indicates the presence of SiO₂ in the composites, revealing that the CdS/SiO₂ nanocomposites are crystalline in nature. The UV-Vis absorption spectra of CdS nanoparticles, recorded between wavelengths of 300-800 nm, showed a slight change in absorption, with a sharper absorption edge indicating fewer defects and impurities in the film. These findings indicate that SiO₂ integration can effectively advance CdS-based solar cell technology, offering a promising route for developing high-performance, cost-effective solar energy solutions.

REFERENCES

- [1] Moskowitz, P. D., & Fthenakis, V. M. (1990). Toxic materials released from photovoltaic modules during fires: health risks. *Solar cells*, 29(1), 63-71.
- [2] Chu, Y., & Meisen, P. (2011). Review and comparison of different solar energy technologies. *Global Energy Network Institute (GENI), San Diego, CA*, 1, 1-52.
- [3] Choubey, P. C., Oudhia, A., & Dewangan, R. (2012). A review: Solar cell current scenario and future trends. *Recent Research in Science and Technology*, 4(8).
- [4] Yadav, A., Kumar, P., & Rpsgoi, M. (2015). Enhancement in efficiency of PV cell through P&O algorithm. *International Journal for Technological Research in Engineering*, 2(11), 2642-2646.
- [5] [5]Sharma, S., Jain, K. K., & Sharma, A. (2015). Solar cells: in research and applications—a review. *Materials Sciences and Applications*, 6(12), 1145.
- [6] Srinivas, B., Balaji, S., Nagendra Babu, M., & Reddy, Y. S. (2015). Review on present and advance materials for solar cells. *International Journal of Engineering Research-Online*, 3(2015), 178-182.
- [7] Ashok, C. H., Rao, K. V., Chakra, C. S., & Rajendar, V. (2014). Structural properties of CdS nanoparticles for Solar cell applications. *Int. J. Pure Appl. Sci. Technol*, 23(1), 8-12.
- [8] Najma. A. S, Munna. F. T, Impact of cadmium salt concentration on CdS nanoparticles synthesized by chemical precipitation method, Vol.17, No. 11, November 2020, https://chalcogen.ro/537_NajmAS.
- [9] Dubey, R. S., & Ganesan, V. (2017). Reflectance modulation using SiO₂/TiO₂ multilayer structures prepared by sol-gel spin coating process for optical applications. *Superlattices and Microstructures*, 111, 1099-1103.
- [10] H.Gleiter, Nanostructured materials : state of the art and perspectives, *Journal of Nanostructured Materials* 6,pp.3-14,2001.

¹S. A. Athawale
²V. B. Bhise
^{*3}R. M. Belekar

An investigation on the hardness of L-hydroxyproline-doped potassium aluminium sulphate dodecahydrate single crystal.



Abstract: A single crystal of L-hydroxyproline-doped potassium aluminium sulphate dodecahydrate (LHPKASD) single crystal is obtained by using the slow evaporation solution technique (SEST). Good quality and transparent single crystals were obtained, having dimensions $8 \times 8 \times 6 \text{ mm}^3$ within 37 days. Vickers microhardness test was used to examine the mechanical properties of a solution-grown LHPKASD single crystal with a load range of 10 to 60 g. The calculated Meyer's index number "n" is 1.83, categorizing the LHPKASD single crystal as a soft material. Additionally, indentation patterns, mechanical parameters and hardness contour were also determined.

Keywords: Slow Evaporation Solution Technique (SEST), Vickers Microhardness (VM), Indentation (I), Meyer's Index Number (MIN).

I. INTRODUCTION

Potassium aluminium sulphate (potassium alum) or (potash alum) is the double sulphate salt of potassium and aluminium having molecular formula $\text{KAl}(\text{SO}_4)_2$ [1]. Alum possesses a cubic crystal system and has a monoclinic crystal structure. On the basis of atomic arrangement, these structures are divided into three types: α , β and γ [2,3] reported that potassium aluminium sulphate dodecahydrate crystal. Kishimura et al. [4] found a phase transition from a crystalline to an amorphous phase of $\text{KAl}(\text{SO}_4)_2 \cdot 12\text{H}_2\text{O}$. Potash alum has been used in many applications, such as food additives, antiperspirants, cleansing products, and skin care products. Furthermore, it has been used in Raman laser converters [5] and has potential applications in optical limiting and switching [6,7]. Recently, research found that potash alum has shown some medical applications. Antibacterial effect and antibiotics to killing microorganisms studied by Ali [8], and it has excellent antimicrobial inhibitory effects on microorganisms, especially commixed with antibiotics. Uzkul and Alkan [9] dyed the silk fabric by using green walnut shell extract, which has an antimicrobial effect, and they used potash alum as a mordant. Wang and Lu [10] used potash alum to fabricate oral ulcer powder, and they studied it by temperature-dependent X-ray diffraction technique. In this paper, we focus on investigating the mechanical properties of a semi-organic L-hydroxyproline potassium aluminium sulphate single crystal was grown using the slow evaporation technique (SEST). We specifically study the relationship between the hardness number (Hv), applied load, diagonal length, and Meyer's index number of the LHPKASD single crystal.

II. METHOD AND MATERIALS

L-hydroxyproline and potassium aluminium phosphate (AR-Grade) S-D fine chemicals were used as starting materials, which were dissolved in doubled distilled water then L-hydroxyproline was added into the mother solution and kept on a magnetic stirrer for 8 hours until it became the homogeneous solution. Afterwards, the homogeneous solution was filtered using high-quality Whatman filter paper and transferred to a clean, dry borosilicate glass beaker. It was then allowed to slowly evaporate in a constant-temperature water bath for crystallization. To control the growth rate of the LHPKASD solution, kept at a constant temperature, the water bath was covered with a silver foil sheet containing a minimum number of holes. After recrystallizing several times, good-quality seed crystals were harvested after 37 days from the mother solution.

^{*}Corresponding author: Department of Physics, Government Institute of Science, Nagpur 440 001, Maharashtra, India.
 Author 1 Department of Physics and Electronics, Government Vidarbha Institute of Science and Humanities, Amravati 444 604, Maharashtra, India.
 Author 2 Department of Physics, L. P. G. Arts and Science Mahavidyalaya, Shirpur (Jain), Washim, 444 504, Maharashtra, India
 Copyright © JES 2024 on-line: journal.esrgroups.org

VI.

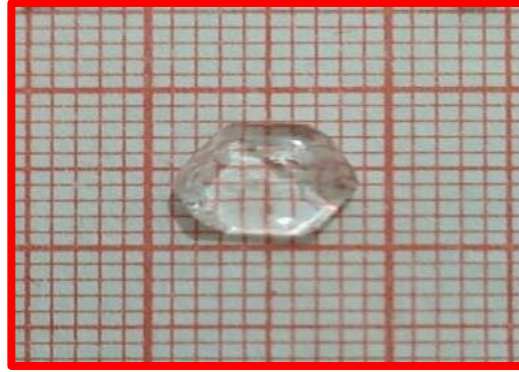


Fig.1-L-hydroxyproline potassium aluminium sulphate (LHPKASD) single crystal

III. RESULT AND DISCUSSION

A. Vicker's microhardness number.

Vickers microhardness is an important factor to consider when choosing the crystal processing steps (cutting, grinding, and polishing) in the device fabrication process. Microhardness is a universal method for determining binding strength and also serves as a metric for bulk strength. To prevent surface flaws, the LHPKASD crystal was carefully polished. For the mechanical study, we used Mututuoya - HM 210B with AVPAK-20V2.0 software Part No. 11AAC666) at room temperature in which the indenter has a pyramidal with a square base shape with semi-apex angle θ equal to 680 at different places on the surfaces of crystal which shows indentation patterns. To prevent any mutual interaction between the indentations, the space between any two indentations was made three times larger than the diagonal length. The Vicker's microhardness value was evaluated by following the formula [11].

$$Hv = \frac{1.8544}{d^2} P \text{ (kg/mm}^2\text{)}$$

Where Hv is the Vickers hardness number (kg/mm²), P applied load in gm and d² is the diagonal length, and 1.8544 is the constant of a geometrical factor for the diamond factor for the diamond pyramid. When the diagonal length (d) is measured in micrometres, the applied load (P) in grams can be used. The graph plotted for load (P) versus hardness number (Hv) is shown in Fig. 3(a). A plot of the microhardness as a function of the applied load clearly indicates that the hardness of the LHPKASD crystal increases with an increase in load up to 40 g and has a maximum hardness number at 40 g of load.



Fig. 2 (a) without applied load indentation image.

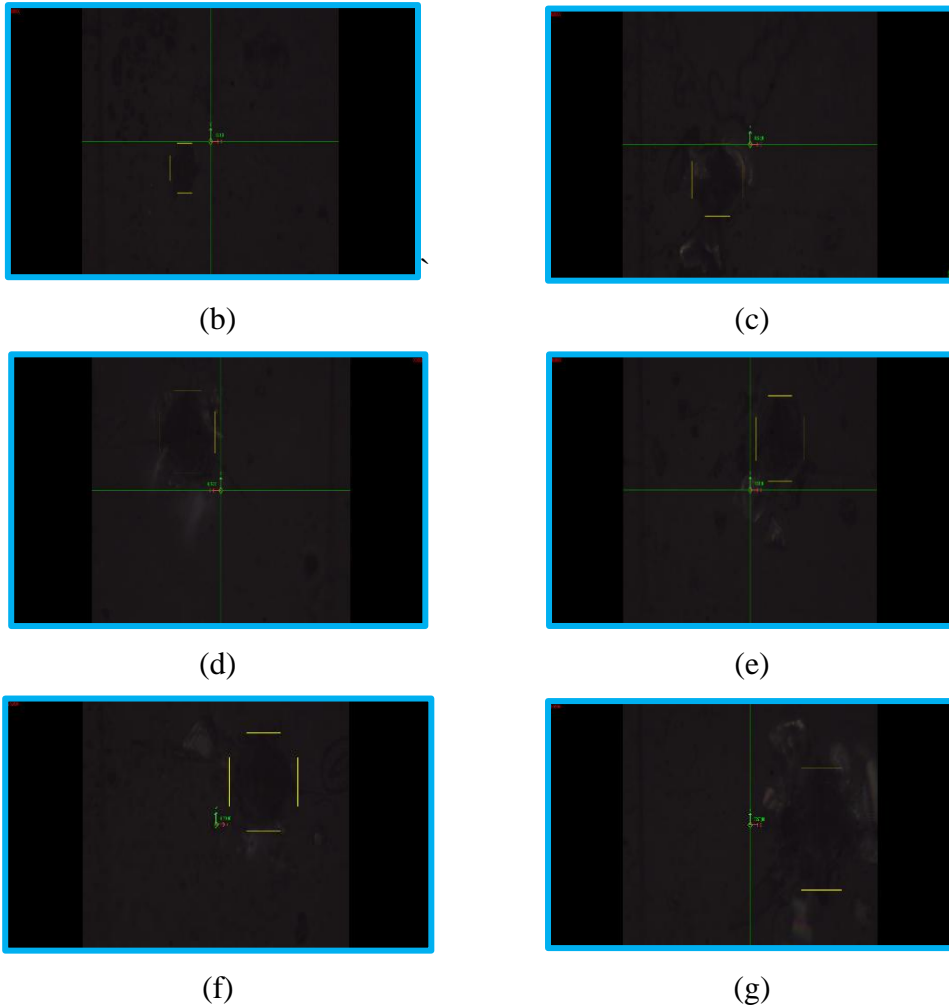


Fig. 2 (b),(c),(d),(e),(f) and (g) an applied load of 10g, 20g, 30g, 40g, 50g, 60g, indentation image pattern respectively of LHPKASD single crystal.

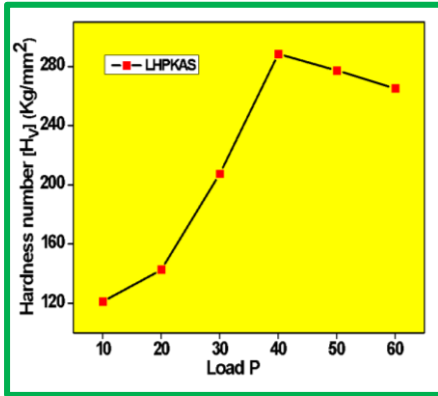


Fig. 3 (a): Load P (gm) versus Hv

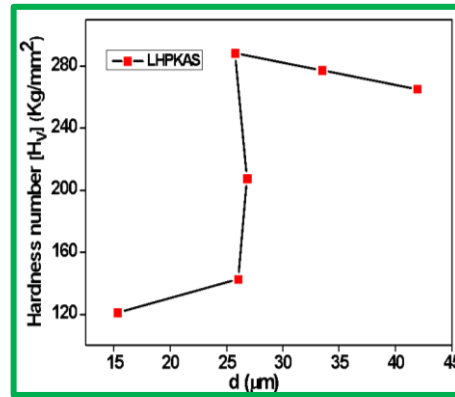


Fig. 3 (b): diagonal length d (μm) versus Hv

1. B. Mayer Index (n)

The simplest method to describe the Indentation size effect phenomenon is Meyer's Law [12]

$$P = A d^n$$

In this case, where A is the standard hardness, which is determined by the intercept, d diagonal length and n is Mayer's index, also known as the work hardening coefficient, which is determined from the slope of the plot of log P and log d, which, gives a straight line, as shown in Figure 3 (c). The work hardening coefficient (n) in the current study is n = 1.83 for LHPKASD crystals.

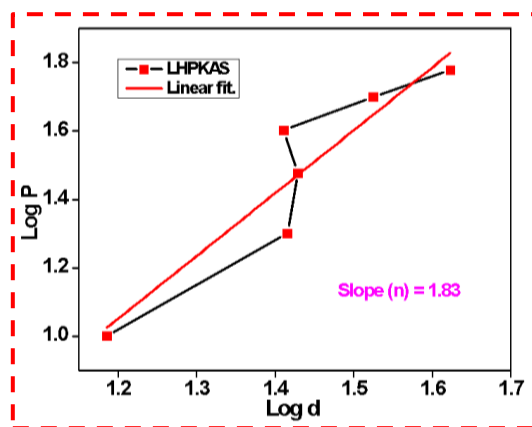


Fig. 3 (c) log d versus log P

IV. CONCLUSION

In this present work, a good-quality and transparent LHPKASD single crystal was successfully grown by the slow evaporation solution techniques (SEST). Vickers microhardness number, or hardness coefficient number, is calculated as 1.83, revealing that the given materials belong to the soft materials category. Vickers's microhardness number increases while increasing the load value, this is known as the reverse indentation size effect (RISE). LHPKASD crystal sustains the load up to 40 g and then decreases due to the crack up to 50 to 60 g, so the Hv value decreases, which depicts the grown crystal that has been used for device fabrication, such as detectors and sensors.

VII. V CONFLICTS OF INTEREST

The authors declare that they have no conflict of interest.

VI. DECLARATION OF COMPETING INTEREST

The authors report no declarations of interest.

ACKNOWLEDGMENT

The authors, S. A. Athawale is thankful to BARTI, Pune, Maharashtra, India [Fellowship/ BANRF-2020/21- 22/850 & 16/02/2022] for providing the senior research fellowship. The authors are thankful to Centre for Functional Materials VIT, Vellore, Tamil Nadu, India for providing microhardness measurement facility.

REFERENCES

- [1] Abdulwahab, A M, Yusra Abdullah, Ahmed Al-magdash, Abdo Meftah, Dyab A Al-eryani, and A A Qaid. 2019. "Growth, Structure, Thermal, Electrical and Optical Properties of Potassium Aluminum Sulphate Dodecahydrate (Potash Alum) Single Crystal." Chinese Journal of Physics 60 (February): 510–21. <https://doi.org/10.1016/j.cjph.2019.05.034>.
- [2] Lipson, H, and C A Beevers. 1935. "The Crystal Structure of the Alums," 664–80. <https://doi.org/10.1098/rspa.1935.0040>.
- [3] Bosetti, Luca, and Marco Mazzotti. 2020. "Study of Secondary Nucleation by Attrition of Potassium Alum Crystals Suspended in Different Solvents." <https://doi.org/10.1021/acs.cgd.9b01700>.
- [4] Access, Open. 2014. "Dehydration of Potassium Alum Induced by Shock Loading Dehydration of Potassium Alum Induced by Shock." <https://doi.org/10.1088/1742-6596/500/18/182020>.
- [5] Hauss S, A A Kaminskii, and E Hauss., 2004. "α-Alums: K, Rb, Tl and NH₄ Al (SO₄)₂ · 12H₂O – a New Family of χ (3) -Active Crystalline Materials for Raman Laser Converters with Large Frequency Shifts" 211 (4): 205–11. <https://doi.org/10.1002/lapl.200310050>.
- [6] V. Natarajan, T. Sivanesan, S. Pandi, Indian J. Sci. Technol., 2010 3 (8): 656–658
- [7] Miah, M Idrish, Uzzal Acharjee, and Lubna Naheed. 2014. "Optik Optical Limiting and Its Mechanism

in Potash Alum.” *Optik - International Journal for Light and Electron Optics* 125 (22): 6727–29.
<https://doi.org/10.1016/j.ijleo.2014.08.068>.

- [8] Ali, Zahra Muhsin. 2018. “Synergistic Antibacterial Interaction Antibiotics on Some Microorganisms between an Alum And,” no. x: 47–51.
- [9] Uzkul, Hülya, and Rezan Alkan. 2018. “Kocaeli Journal of Science and Engineering (KOJOSE) Antimicrobial Properties of Silk Fabrics Dyed with Green Walnut Shell (*Juglans Regia L.*)” 1(2): 28–32.
- [10] Wang, Yang, and Dayong Lu. 2018. “New Materials and Intelligent Manufacturing (NMIM) STUDY ON ORAL ULCER POWDER USING TEMPERATURE-DEPENDENT X-RAY” 1: 104–6.
- [11] Deepthy, A, and H L Bhat. 2001. “Growth and Characterization of Ferroelectric Glycine Phosphite Single Crystals” 226: 287–93.
- [12] Vizhi, R Ezhil, R Ashok Kumar, D Rajan Babu, and K Sathiyarayanan. 2011. “Synthesis, Crystal Growth, structural, Dielectric and Ferroelectric Properties of N-Acetyl Glycine Phosphite (AGPI) Single Crystals,” 291–300. <https://doi.org/10.1080/00150193.2011.531194>.

¹ Sankalp Bisan

² S. K. Atre

³ Satish Sharma

Design of a Real-Time Hand to Text Sign Language Recognition System



Abstract: - Sign language is a very powerful and effective tool for communication among the dumb and deaf. It plays a significant role in ensuring accessibility and inclusion for the individuals with hearing impairment. The proposed work attempts to bridge the communication gap between verbal and non-verbal communicators. In the present work, Indian Sign Language (ISL) is considered for conversion into text form since sign languages are region specific. The designed system uses flex sensors, an inertial measurement unit (IMU) and microcontroller unit as the main processing unit that provides voltage values according to the hand and finger movements. Data as measured using the wearable glove has been analyzed using the Long Short Term Memory (LSTM) algorithm for training the ML model. The in-house system accepts ISL signs as a real time input via flex sensor and IMU those are classified into the appropriate gestures. The classified gesture is then converted into an appropriate label as output in the corresponding legible text format. It is observed that in-house designed system is very simple and reliable for conversion of Indian sign gestures into legible text format.

Keywords: Indian Sign Language (ISL), Flex Sensor, Inertial Measurement Unit (IMU), Machine Learning (ML), Long Short Term Memory (LSTM).

¹ *Department of Electronics and Computer Science, RTMNU Campus, Nagpur – 440 033, Maharashtra, India.
Email: sankalpbisan07@gmail.com

² Department of Electronics and Computer Science, RTMNU Campus, Nagpur – 440 033, Maharashtra, India.
Email: atreshivk@gmail.com

³ Department of Electronics and Computer Science, RTMNU Campus, Nagpur – 440 033, Maharashtra, India.
Email: sharmasat@gmail.com

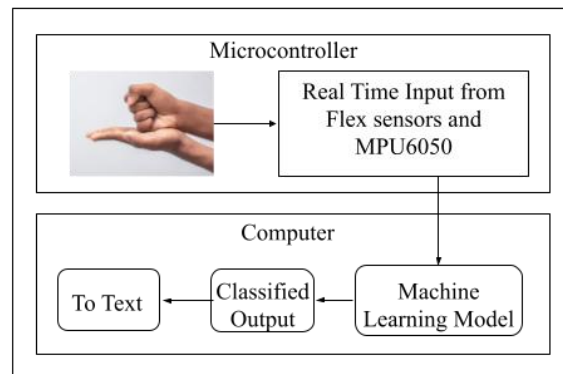
I. INTRODUCTION

Communication is not only limited to the exchanging or sharing of information verbally, but also the information can be exchanged through human emotions, facial expressions, body language and signs performed by hands. Although, verbal communication is far more crucial than other means of communication. But there are people who cannot comprehend verbal communication because they are unable to listen and to speak. Such people are called as Deaf-Mute people and thus they use sign languages which are region specific as their only mode of communication. But the verbally communicating people do not understand sign languages unless they have learnt it. This results in a communication gap between the verbal communicators and Deaf-Mute people. To bridge this gap, a system has been developed which takes the signs performed by the user via hand in real time and aims to convert it into text. This will significantly help the Deaf-Mute people to form relationships, collaborate, grab opportunities and to express their own opinions and feelings to the entire world.

Several researchers have worked in this direction to design an effective communication system. The basic sign gestures like numbers and alphabets can be obtained by using Arduino Nano and comparing its values with predefined values and converting the text into speech format via smartphone via text to speech engine within it [1]. The classification can also be done using some machine learning algorithm like support vector machine to attain high accuracy [2]. Another way of identifying the sign gestures is by using the state estimation method proposed in [3] which aims to track the motion of the hand in 3D space using Raspberry Pi, flex sensor and IMU. The system records the data of hand motion and compares it to a predetermined database. The hand and fingers movement can be determined by the EMG sensor which uses electrical signals generated from the muscles for determining the movements. The classification of these EMG based data along with IMU is done based on LSTM. However, the individual based model outperforms the general model, because the gestures performed vary from person to person [4].

In the present work, a wearable glove with the flex sensors and IMU mounted on it are used along with the STM32F103C8T6 MCU for the processing the data which is solely responsible for taking input from the sensors and then processing of the ML model for sign gesture classification is done on computer.

II. METHODS



A. SYSTEM DESCRIPTION

Fig.1: Block Diagram of the System

Fig.1 shows the block diagram of the system designed in the laboratory. Sign gesture performed by hand using a wearable glove fused with flex sensors and IMU is taken as an input. The Flex sensors account for the bending of fingers whereas MPU6050, the IMU, accounts for the angular momentum of the hand. Flex sensors are used to measure the resistance across the strip. The bending resistances may vary from 45 to 125 Kohms. MPU6050 is a 6-axes motion tracking device, in which 3-axes acts as accelerometer and rest 3-axes act as gyroscope. Thus, it gives a total of 6 values as measured output which defines the shift in angular momentum of the hand from one instance to the another. The input data collected by these sensors is fed to the microcontroller (STM32F103C8T6) for further processing. It performs computations on the measured voltage values received from the sensors and returns its values to the computer in a specified way.



Fig.2: Wearable Glove

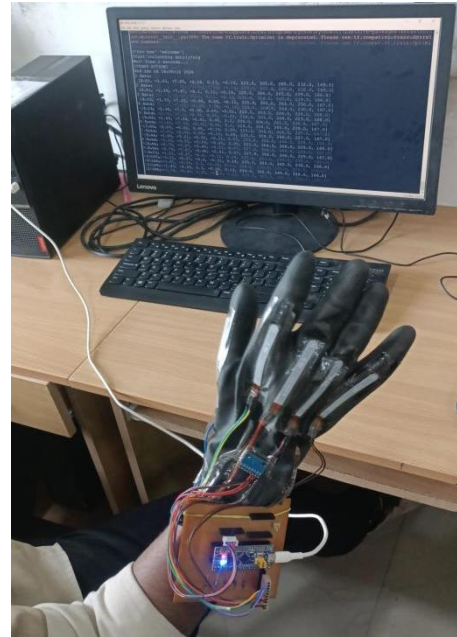


Fig.3: Complete Setup of the System

All the electronic components have been mounted onto a PCB so as to make the system portable and light. The sensors are connected to the PCB board via connectors provided by the supplier. Flex sensors are attached to each finger of the rubber glove for recording the bending movement of five fingers and MPU6050 is attached alongside it for capturing hand movements. Fig. 2 shows the wearable glove whereas Fig. 3 shows a screen shot of the complete system for conversion of ISL signs into legible text.

B. SOFTWARE

The design and development of the present system is divided into hardware and software. Flex sensor is procured from the <https://quartzcomponents.com> site. Most of the electronic components are soldered on the PCB for its convenience and compactness. For software development and, data acquisition and analysis, Arduino IDE and Python language are used. The software part includes collecting data, preprocessing it, training the preprocessed data and deploying the model on STM32F103C8T6. Data is collected and stored into csv file format. In the present work, as the preliminary testing, the dataset consists of two categories of data i.e. for two signs 'welcome' and 'bye-bye'. Data is collected by a single subject and with 30 samples for each sign. Thus, making it a total of 60 csv files. Each csv file contains 50 rows as time points and 11 columns as sensor values. The labeling is done in annotated form, the file name is the label itself [5]. This data is preprocessed and converted into numpy format for more efficient machine learning model training. The model is trained based on the LSTM algorithm with 30 epochs that achieved almost 100% accuracy with the validation data.

III. RESULTS

The collected dataset for two sign gestures is showing variations when their values are plotted into a graph. Although there are slight variations in between them still these signs are differentiable. In time series data, the instance of a particular time point plays a significant role. The values at the initial time point and at the end point depict a significant difference, however it is tough to describe these time points on a graph, which could give a path or pattern of how exactly data is moving/behaving.

The graphical representation of the dataset results in better understanding of the data. To represent all the 30 samples of data into a single graph is challenging and complex at the same time and when the 30 samples were plotted on a graph, the data points were cluttered into each other and were a bit complex to interpret. Therefore, to reduce its complexity, the average of the same cell of all samples has been calculated and the average values for each cell is stored into another csv file. This was calculated for each cell of the data, like, the value in the position [5,5] has been averaged with the values of all csv files on the same position. This similar calculation was completed for each position. This resulted in a new csv file of dimension 50x11. The graph for this csv file represents the data in a concise way. It represents a similar pattern to the pattern formed after plotting all data in a graph.

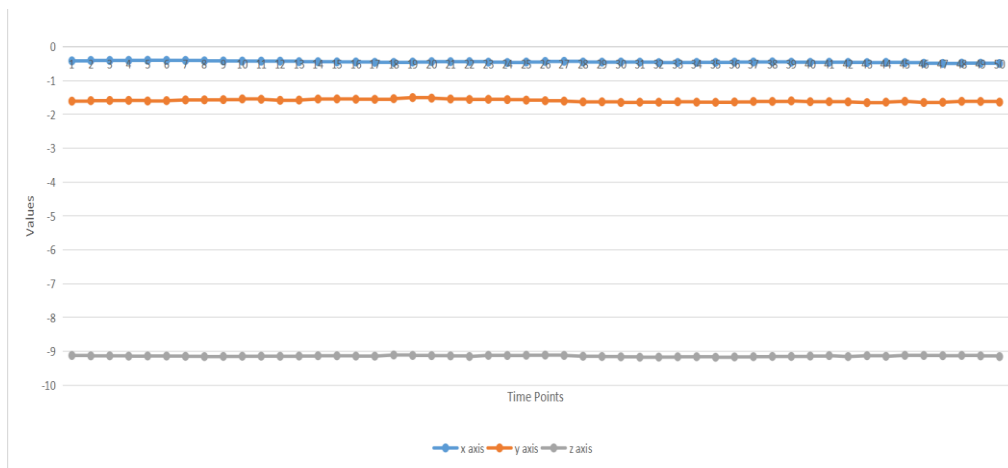


Fig.4: Variation of Accelerometer Sensors' Output with Time for "WELCOME"

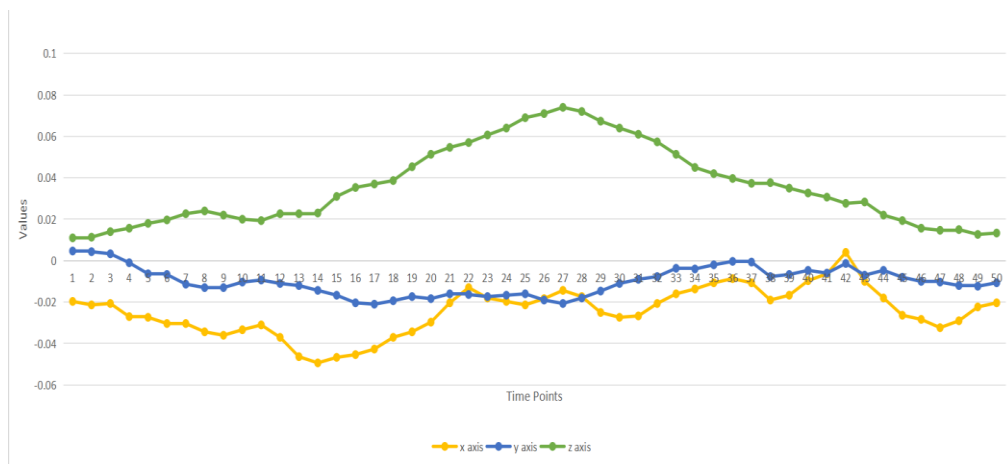


Fig.5: Variation of the Gyroscope Sensors' Output with Time for "WELCOME"

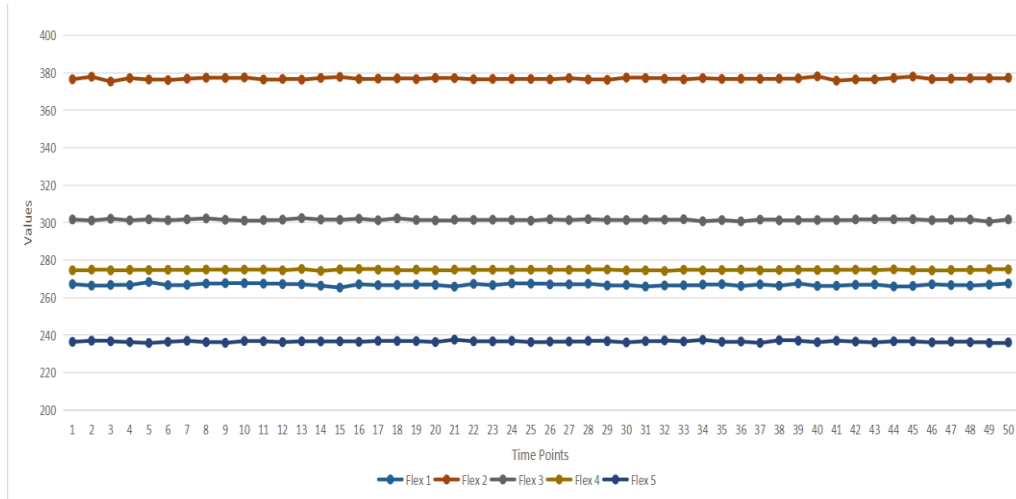


Fig.6: Variation of Flex Sensors' Output with Time for "WELCOME"

Fig. 4 and Fig. 5 represent the pattern of the x, y and z axes of the accelerometer and gyroscope, respectively for the "WELCOME" gesture. The accelerometer shows gradual fluctuations in the output signal values along each axis. This shows that the data collected for "WELCOME" gesture at each x, y, z axis is almost similar for all the samples. Thus, it can be significantly distinguished from other gesture signs. Whereas, the output signals at the gyroscope shows noticeable fluctuations. These fluctuations are within an extremely small range which represents the values collected for this sign does not include the angular movement of the hand as "WELCOME" gesture is typically a horizontal movement of hand from a distance from the chest towards chest with palm of hand facing the sky. Also, this sign does not involve any flex (finger) movements, therefore the values of all the flex sensors remain constant in the graph as shown in Fig. 6.

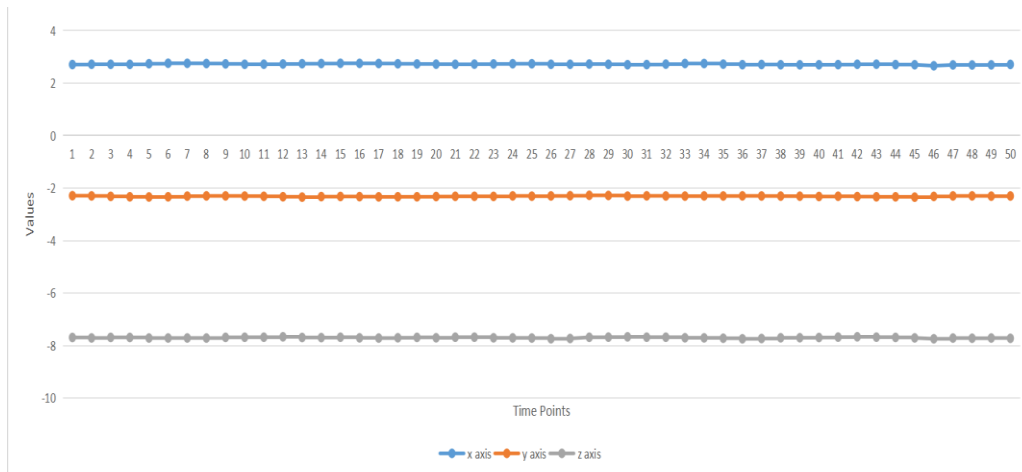


Fig.7: Variation of Accelerometer Sensors' Output with Time for "BYE-BYE"

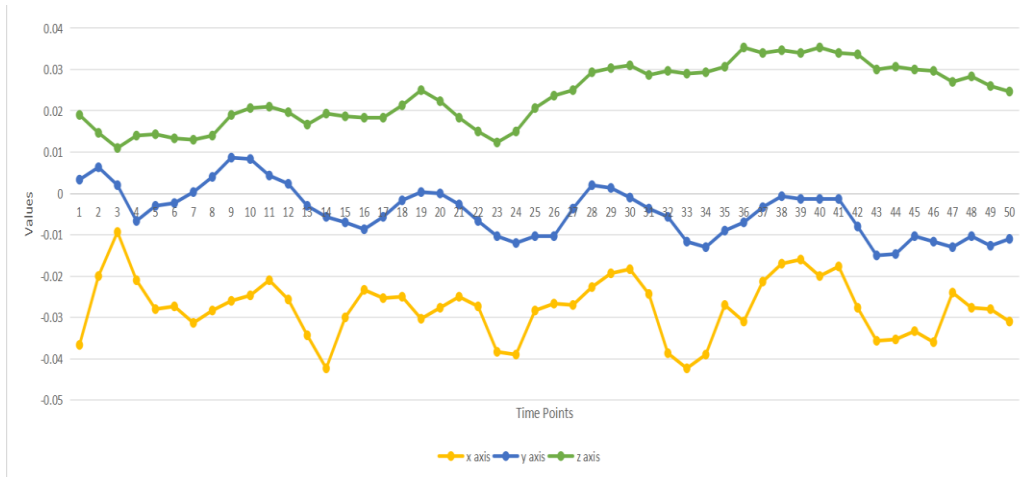


Fig.8: Variation of Gyroscope Sensors' Output with Time for "BYE-BYE"

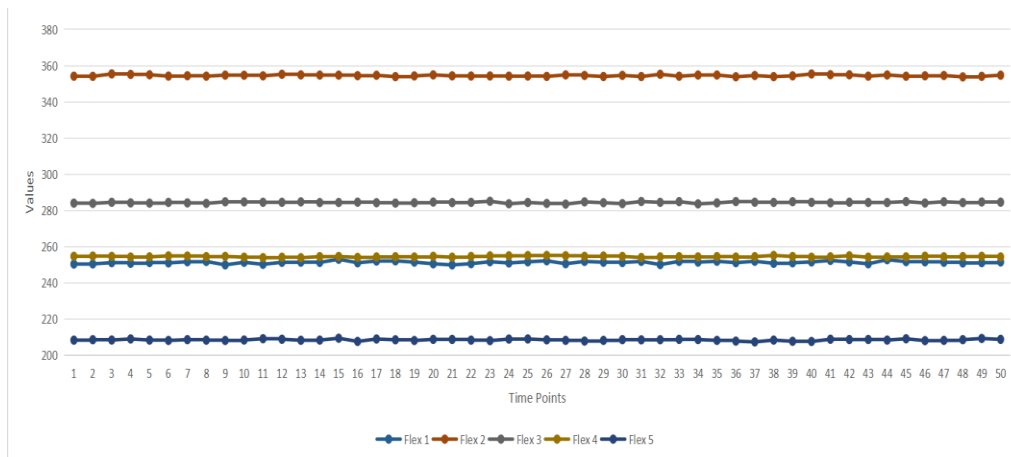


Fig.9: Variation of Flex Sensors' Output with Time for 'Bye-Bye'

The figures 7, 8 and 9 show variation of the output signals at the accelerometer, gyroscope and flex sensors, respectively for the sign "BYE-BYE". The accelerometer output signal values are not varying much as expected and almost follow the straight line with different values as compared to the "WELCOME" gesture. The gyroscope output signal values are slightly in a higher range than that of "WELCOME" gesture values and it has formed a pattern, which depicts that the repeated action has occurred which sounds convincing because the "BYE-BYE" gesture is just similar to what everyone performs to signal indicating departure. This action includes the movement of the hand and its action is just like waving a hand. Therefore, "BYE-BYE" sign gesture is also distinguishable with other gestures as per the data collected.

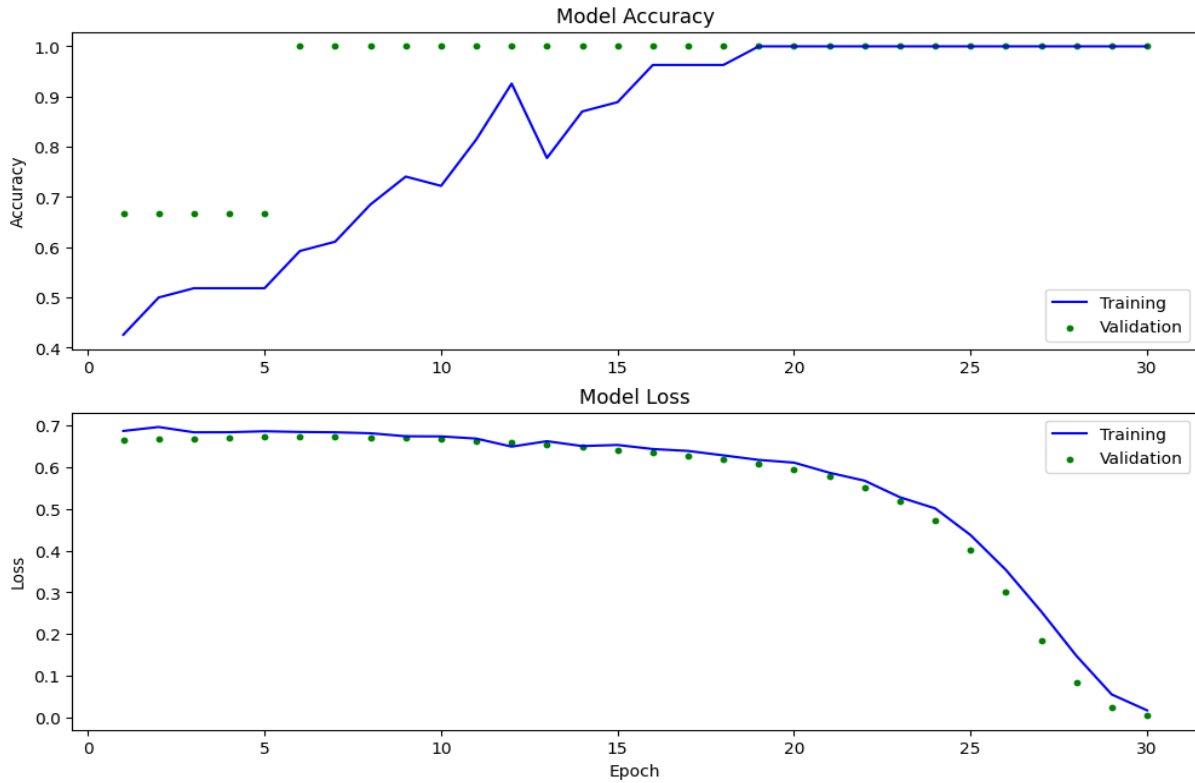


Fig.10: Loss and Accuracy Graph of ML model.

Fig. 10 shows that the model achieved a profound accuracy of 100% after 10-12 epochs. The model has only been trained with 60 samples of data collected from a single person. The ML model is trained based on the LSTM algorithm with 30 numbers of epochs.

IV. CONCLUSION

The work presented formulates the sign gestures and converts the two hand gesture signs, “WELCOME” and “BYE-BYE” into text format. The present work is able to distinguish between the “WELCOME” and “BYE-BYE” sign gestures in real time with the machine learning model running on the computer itself. Although, the classification of the gestures is more promising when the model is tested with the person’s gesture whose data has been collected for training ML model. More data can be collected from various users in order to get more promising results which will certainly add the flexibility trait to the present work.

REFERENCES

- [1] Y. Jhunjhunwala, P. Shah, P. Patil, and J. Waykule, "Sign Language to Speech Conversion using Arduino", *Int. J. Recent Innov. Engg. Res.*, vol. 2, pp. 37-44, 2017
- [2] M. M. Chandra, S. Rajkumar, and L. S. Kumar, "Sign Languages to Speech Conversion Prototype using the SVM Classifier", *TENCON 2019 - 2019 IEEE Region 10 Conference*, pp. 1803-1807, Kochi, India, 2019
- [3] K. A. Bhaskaran, A. G. Nair, K. D. Ram, K. Ananthanarayanan, and H. R. Nandi Vardhan, "Smart gloves for hand gesture recognition: Sign language to Speech Conversion system", *International Conference on Robotics and Automation for Humanitarian Applications (RAHA)*, pp. 1-6, Amritapuri, India, 2016
- [4] S. Shin, Y. Baek, J. Lee, Y. Eun, and S. H. Son, "Korean Sign Language Recognition using EMG and IMU Sensors based on Group-dependent NN Models", *IEEE Symposium Series on Computational Intelligence(SSCI)*, pp. 1-7, Honolulu, USA, 2017
- [5] E. Abraham, A. Nayak, and A. Iqbal, "Real-Time Translation of Indian Sign Language using LSTM," *2019 Global Conference for Advancement in Technology (GCAT). IEEE*, Oct. 2019
- [6] S. Y. Heera, M. K. Murthy, V. S. Sravanti, and S. Salvi, "Talking hands - An Indian Sign Language to Speech Translating Gloves", *International Conference on Innovative Mechanisms for Industry Applications (ICIMIA)*, pp. 746-751, Bengaluru, India, 2017
- [7] K. Suri and R. Gupta, "Convolutional Neural Network Array for Sign Language Recognition using Wearable IMUs", *6th International Conference on Signal Processing and Integrated Networks (SPIN)*, pp. 483-488, Noida, India, 2020

¹*Shilpa S
Patange
²Ashok C
Kumbharkhane

Dielectric Relaxation studies of binary mixture of D-arabitol + Water using a Time Domain Reflectometry Technique



Abstract: The complex dielectric permittivity measurements of binary mixture of D-arabitol + water have been carried out in the frequency range 10 MHz to 30 GHz using a Time Domain Reflectometry technique at 25°C. The measurements have been carried out for different mole fractions of Arabitol in Water. The Cole – Davidson relaxation model is appropriate to describe the complex permittivity spectra of this binary mixture. The static dielectric constant (ϵ_0) and relaxation time (τ in ps) are calculated from the complex permittivity spectra using the non linear Least Square Fit method.

Keywords: Time Domain Reflectometry, Dielectric permittivity , Relaxation time

I. INTRODUCTION

Polyhydric Alcohols or Polyols are the sugar alcohols with the general formula ($C_nH_{n+2}OH_n$) in carbohydrate classification. Polyols are a broad class of compounds that are categorized based on the number of carbon atoms in the molecules backbone and are named based on the number of OH groups, e.g., n=2 for diol, n=3 for triol, n=4 for tetritol, n=5 for pentitol and so on [1]. These sugar alcohols are frequently employed in place of sucrose in commercial meals, typically in conjunction with strong artificial sweetener to counteract their poor sweetness. D-arabitol is a sugar alcohol also referred to as arabinitol (polyol). It can be generated through the reduction of arabinose or lyxose. It has the molecular formula $C_5H_{12}OH_5$. figure 1 shows the structure of D-arabitol [1,2].

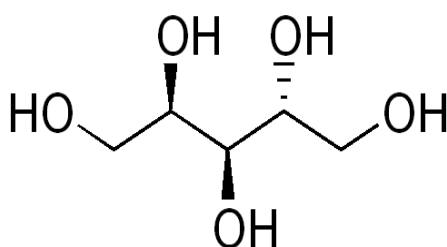


Fig 1: structure of D- arabitol

Dielectric relaxation spectroscopy has proven to be a useful method for determining the dynamics and structural characteristics of liquids that are mostly hydrogen bond based. In our previous paper, we have conducted the dielectric relaxation studies of aqueous xylitol solution using TDR technique[3]. L. Carpentier et al. have conducted the dielectric studies of the mobility in pentitols in the broad frequency range $10^{-2} \leq \nu \leq 10^6$ Hz [4]. There were not many investigations done on the arabitol.

In this work, the impact of intermolecular interactions is shown in water and D-arabitol at different concentrations and at 25°C temperature. Variations in the dielectric characteristics have been investigated in the frequency range 10 MHz to 30 GHz .using the Least Square Fit method, the dielectric constant (ϵ_0) and relaxation time (τ) have been calculated and discussed.

II. Experimental

A Materials

D-arabitol was obtained commercially from Alfa Aesar Ltd and used without further purification . The water used in the preparation of binary mixture was distilled water. The solutions were made with varying mole fractions of D-arabitol in water while keeping the water weight constant.

B. Measurement :

The TDR technique was used to obtain the dielectric spectra[5]. For The Time Domain Reflectometre, The dual channel sampling module 80E10B and the Tektronics model number DSA8200 sampling mainframe were utilized. Figure 2 shows the block diagram of TDR. A 12 ps incident pulse and 15 ps rising time pulse are provided by the sampling module. These pulses are reflected pulse without sample $R_1(t)$ and with sample $R_x(t)$ were recorded in a time window of 5 ns and digitised in 2000 points and are shown in figure. To provide the pulse , coaxial cable with an inner diametre of 0.28 mm and an outside diametre of 1.19 mm , and an impedance of 50 ohms was used. The addition $[q(t)=R_1(t)+R_x(t)]$ and subtraction $[p(t) = R_1(t) - R_x(t)]$ of these pulses are done in the oscilloscope memory . these subtracted and added pulses are delivered to computer for further analysis. The non linear Least Square Fit method was used to get the complex permittivity spectra in the frequency range 10 MHz to 30 GHz by completing the Fourier transformation of these pulses and data analysis beforehand. The temperature of the test sample has been maintained using a calibrated temperature controller system with an accuracy of $\pm 0.1^\circ\text{C}$.

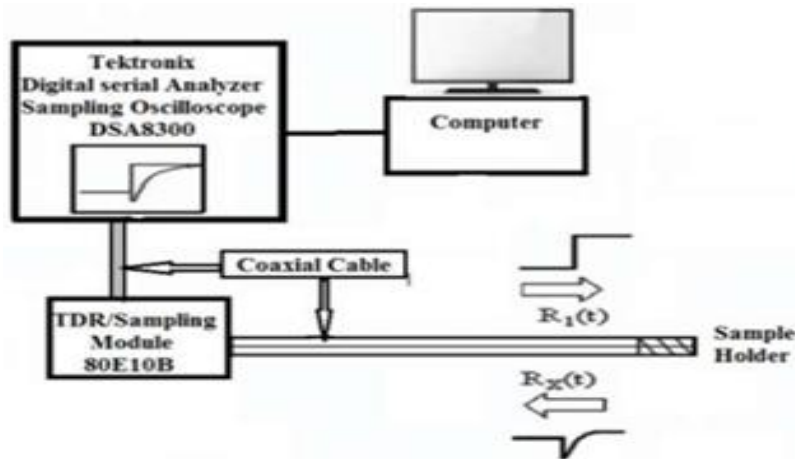


Fig2. Block diagram of Time Domain Reflectometre (TDR)

III Results and Discussion

A. Complex Permittivity Spectra

The relative complex permittivity offer's an important insights into the common dielectric relaxation and absorption processes throughout a broad frequency range. A materials complex permittivity spectrum can be used to infer properties such as dielectric loss, polarity, conductivity, dipolar relaxations and atomic / electronic resonances [6].

Figure 3 shows the frequency dependent complex permittivity spectra for D-arabitol – Water at various concentrations using the Time Domain Reflectometry Technique (TDR) at 25°C . The dielectric permittivity falls as D-arabitol concentration in water increases and as frequency increases, indicating dielectric dispersion. Additionally the graph indicates that when the amount of D-arabitol in the water increases, certain frequencies exhibit peaks in the dielectric loss that are moved towards lower frequencies.

The non linear Least Square Fit approach is used to fit the complex permittivity spectra obtained with TDR to the Havriliak – Negami formula

$$\varepsilon^*(\omega) = \varepsilon_\infty + \frac{\varepsilon_0 - \varepsilon_\infty}{[1 + (j\omega\tau)^{1-\alpha}]^\beta}$$

Where ε_0 is the static dielectric constant which represents the equilibrium behaviour, ε_∞ is the permittivity at high frequency which represents the instantaneous behaviour, τ is the relaxation time, α and β are the shape parameters describing the symmetric and asymmetric distribution of relaxation time respectively. ω is the angular frequency [7].

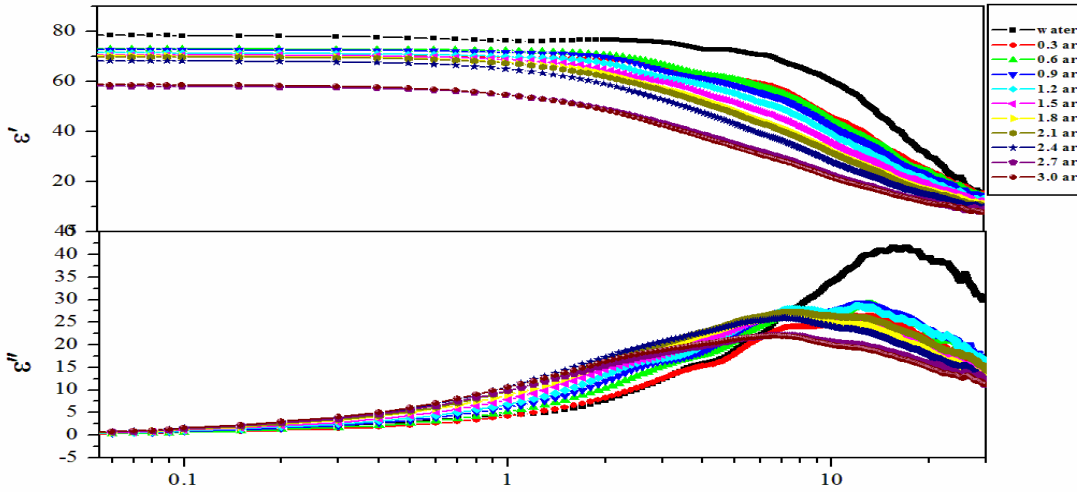


Fig 3.Frequency Dependent Dielectric Complex Permittivity Spectra of D-arabitol – Water mixture for various concentrations at 25

B. Static Dielectric constant (ϵ_0)

Fig 4 shows that the dielectric constant (ϵ_0) of D-arabitol aqueous solution decreases as the amount of D-arabitol in water increases. This may be due to the significant impact of hydrocarbon chain branching on the correlation of permanent electric dipole moment orientation [8] and the decrease in this dipole moment magnitude as the mole fraction of D-arabitol in water increases [9].

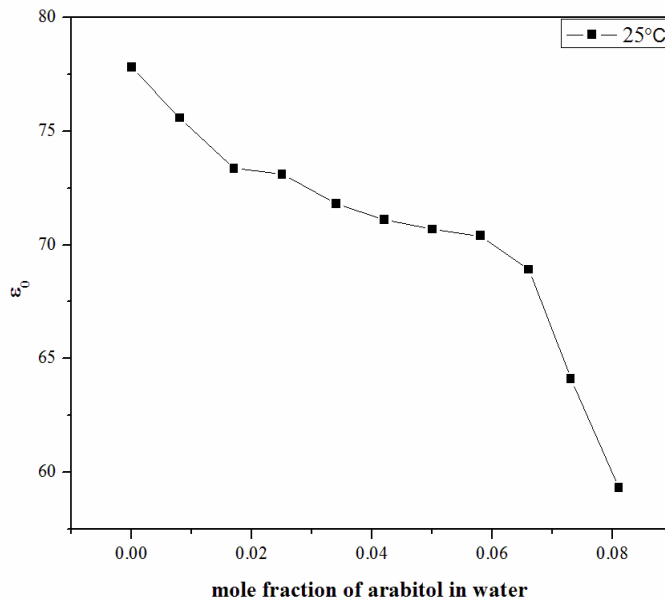


Fig 4. Variation of Static dielectric constant (ϵ_0) with mole fraction of D-arabitol in water

C. Relaxation time (τ)

As shown in fig 5, the dielectric relaxation time value grows linearly with increasing mole fraction of D-arabitol in water. The reason behind the gradual rise in relaxation time could be that the effective dipole moment rotates more slowly in the field produced by the intermolecular interaction [9]. Additionally, It is noted that the complex permittivity spectrum is descending from the Debye to Cole – Davidson type as the concentration of D-arabitol in water increases [10].

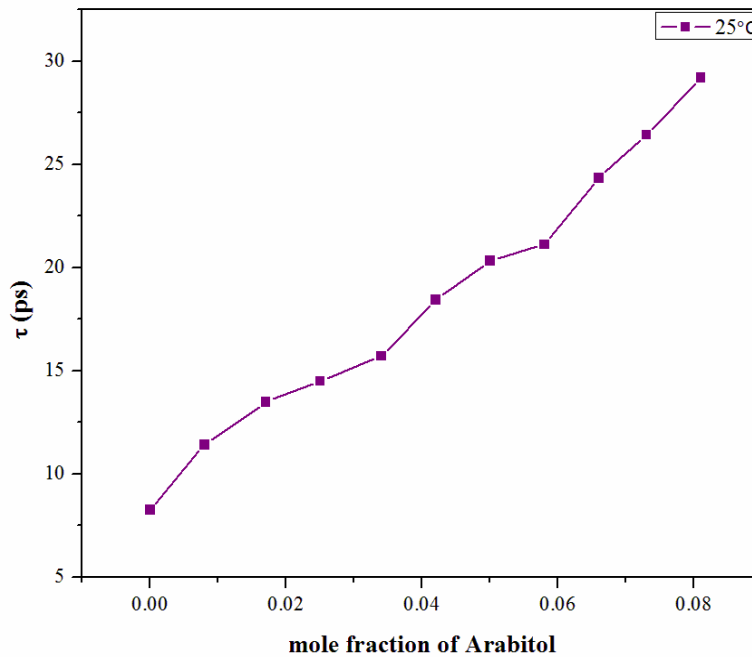


Fig 5.variation of relaxation time with mole fraction of D-arabitol in water at 25°C

IV Conclusion

This study used TDR to investigate how arabitol concentration affects the electrical properties of D-arabitol-water mixtures. The findings show that increasing D-arabitol concentration weakens the mixtures dielectric response, likely due to D-arabitol disrupting water molecule alignment. Additionally, τ indicating response speed to electric field, increases with more arabitol.

V. Acknowledgement

The author S S Patange expresses gratitude to the School of Physical Sciences, SRTM University, Nanded, Maharashtra and DST, New Delhi (project no. DST PROJECT – SB LOP – 032/2013) for providing financial support and allowing the use of their instrument facilities.

REFERENCES :

- [1] Carpentier, L., Paluch, M., & Pawlus, S. (2011). Dielectric studies of the mobility in pentitols. *The Journal of Physical Chemistry B*, 115(5), 1062-1066.
- [2] Awuchi, C. G., & Echeta, K. C. (2019). Current developments in sugar alcohols: Chemistry, nutrition, and health concerns of sorbitol, xylitol, glycerol, arabitol, inositol, maltitol, and lactitol. *Int J Adv Acad Res*, 5(11), 1-33.
- [3] <https://ijsrst.com/paper/11965.pdf>
- [4] Carpentier, L., Paluch, M., & Pawlus, S. (2011). Dielectric studies of the mobility in pentitols. *The Journal of Physical Chemistry B*, 115(5), 1062-1066.
- [5] Cole, R. H., Berberian, J. G., Mashimo, S., Chryssikos, G., Burns, A., & Tombari, E. (1989). Time domain reflection methods for dielectric measurements to 10 GHz. *Journal of applied physics*, 66(2), 793-802.
- [6] Bennett, E. L., Song, C., Huang, Y., & Xiao, J. (2019). Measured relative complex permittivities for multiple series of ionic liquids. *Journal of Molecular Liquids*, 294, 111571.
- [7] Volkov, A. S., Kuposov, G. D., & Perfiliev, R. O. (2018). On the physical meaning of disperse parameters of frequency dependence of dielectric permittivity in the Havriliak–Negami model. *Optics and Spectroscopy*, 125, 379-382.
- [8] Wang, F., Pottel, R., & Kaatze, U. (1997). Dielectric properties of alkanediol/water mixtures. *The Journal of Physical Chemistry B*, 101(6), 922-929.
- [9] Haggis, G. H., Hasted, J. B., & Buchanan, T. J. (1952). The dielectric properties of water in solutions. *The Journal of Chemical Physics*, 20(9), 1452-1465.
- [10] Begum, S., Vardhan, A., Chaudhary, A., & Subramanian, R. (2016). Disruption of the self-molecular association of pentanol in binary mixtures with alkylbenzoates: a dielectric relaxation spectroscopy study. *RSC advances*, 6(2), 1260-1267.
- [11] Davidson, D. W., & Cole, R. H. (1951). Dielectric relaxation in glycerol, propylene glycol, and n-propanol. *The Journal of Chemical Physics*, 19(12), 1484-1490.

Vaishnavi V. Pandhe¹,
Suraj V.Tayade²,
S. A. Waghuley³.

Regular paper
Synthesis and Characterization
of Graphene Decorated CuO
Nanocomposite for
Multifunctional application.



Abstract: - This work discusses the synthesis of graphene-based CuO nanocomposite using various methods, including the co-precipitation method and electrochemical exfoliation method. The electrochemical exfoliation method is identified as the most efficient for creating graphene nanocomposite, while the co-precipitation method is preferred for synthesizing CuO nanoparticles. These CuO nanoparticles are then decorated with graphene nanocomposite through a solution mixing method known as the ex-situ approach. The crystallographic structure, phases, and quantitative analysis of the materials were studied using X-ray Diffraction (XRD), while the chemical composition, molecular structure, and interactions within the sample were analysed using Fourier Transform Infrared (FTIR) spectroscopy. Graphene-based nanocomposite exhibit exceptional mechanical, electrical, thermal, and optical properties, making them suitable for numerous applications such as supercapacitors, biomedical uses, EMI shielding, solar cells, and gas sensors.

Keywords: CuO; Graphene; Nanocomposite; Advanced applications.

INTRODUCTION

Nanotechnology is the field of application-based research in Nanoscience. It has expanded to include environmental remediation applications. The micrometer is approximately 1 to 100 nanometres, which is 10^9 meters in length (2D). There are many types of nanosciences, such as nanotubes, nanoparticles, graphene, quantum dot, nano-medicine, nanocomposites and manufacturing composite materials. A nanoparticle is a particle that is 1 to 100 micrometers in size and consists of a macromolecule material containing the active ingredient. They are found in nature and can also be created by human activities. Due to their small size, nanoparticles have unique material properties and can be used in a variety of applications, such as medicine, engineering catalysis, environmental remediation, and manufacturing nanoparticles. Nanocomposites has The electrical, thermal, mechanical, magnetic, chemical, radioactive, and watt ability properties of nanocomposites vary if the nanomaterial converts from bulk to nanoscales.

Graphene: Graphene is an allotropes of carbon, is the thin, almost see through sheet that is only one atom thick. it is incredibly lightweight but also incredibly strong , with a strength 100 times that of steel additionally, it has the unique property of being able to conduct electricity. of carbon consisting of a single layer of atoms arranged in a two dimensional honeycomb lattice nanostructures. Its has become a valuable and useful nanomaterial due to its exceptionally high tensile strength this nanomaterial has made it desirable and practical. Transparency, electrical conductivity, and the world's thinnest two-dimensional substance Graphene is a single sheet of pure carbon arranged in a flat hexagon pattern. It has use in electronics, transportation, and medicine, among other fields. the high quality graphene also provide bto be sparingly easy to isolate, Andre Geim Konstantin at the University of Manchester won the Nobel Prize in physics in 2010”for groundbreaking experiments regarding the Two-dimensional material graphene. The elements of other allotropes , including graphite , charcoal, carbon nanotubes and fullerene.

Synthesis of graphene by electrochemical exfoliation method:

Few layer graphene synthesized from graphite flakes using electrochemical exfoliation method, in this copper rod act as a cathode electrode, and then the graphite rod and copper rod were inserted with the 5cm separation. Now H_2SO_4 (99.99%) in diluted distilled water and form the ionic solution and give the dc (10 volt) at room temperature.(303k), then the few layer graphene collected through cellulose nitrate filter paper, then washed the precipitate with distilled water , then obtained Sample dried at 100^0c for 2hr.

Synthesis of CuO nanoparticle:

CuO nanoparticles were made using the co-precipitation approach, which involved dissolving one mole of $CuSO_4$ in 100 milliliters of distilled water. and then placing the necessary solution in a magnetic stirrer and stirring it for two hours. Copper sulphate and sodium hydroxide were utilized in this process. The reaction continued for two hours after the NaOH was simultaneously dissolved in 50 milliliters of distilled water and introduced drop wise to the $CuSO_4$ solution that was already on the magnetic stirrer while being continuously stirred. After that, rinse the precipitation with distilled water. The precipitate now dries overnight at 800 degrees Celsius.

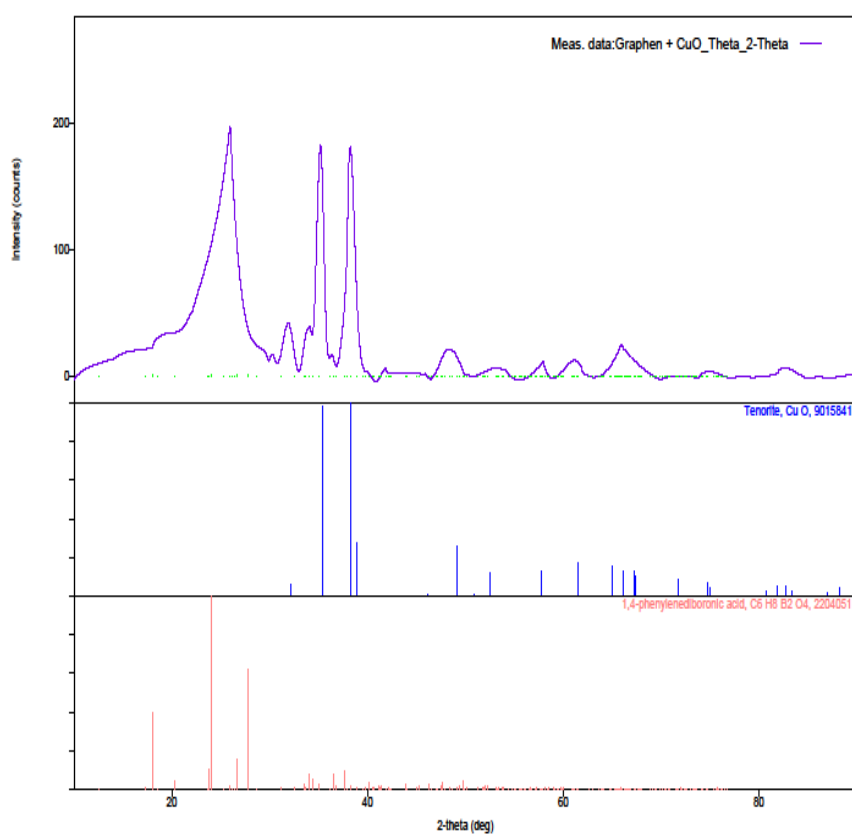
Synthesis method of CuO nanoparticle decorated by graphene:

The CuO nanoparticle was doped with graphene using the solution mixing method of the Ex-situ approach. In this method, 0.5 moles of graphene and 0.5 moles of CuO were mixed in 10 ml of acetone, and the mixture was stirred for 20 minutes on a magnetic stirrer. The remaining precipitate was then obtained in a petry dish after the acetone evaporated

Results and discussions:**X-Ray Diffraction (XRD) of CuO decorated by graphene-nanocomposite:**

In the provided figure, the XRD pattern of the CuO nanoparticle coated with graphene revealed diffraction peaks absorbed at 26.50 values. Using the Debye Scherer formula, the average crystallite size (D) of the graphene-based CuO nanoparticle was determined as follows: $D_{h,k,l} = 0.9\lambda / (\beta_{h,k,l} \cos\theta)$, where β is the line's full width at maximum (FWHM) and $\lambda = 1.50429 \text{ \AA}$, the wavelength. With the hexagonal symmetry, the Scherer constant is 0.98. $D = k\lambda / \beta \cos\theta$ is the formula; using this formula, the value of 2θ is found to be 25.58 and provided for the 1,1,-1 h, k, and l value.

where θ is the diffraction angle. Based on this, we computed the crystallite size, which came out to be 41.7374 nm. This illustrates the prepared sample; all of the peak spectra are ascribed to CuO, which exhibits monoclinic symmetry; the graphene peak, located at position 25.



2024/04/02 16:24:12

Graphen + CuO_Theta_2-Theta.txt

FT-IR of graphene based CuO nanocomposites:

From the above graph, which kind of functional group present in given compound of CuO nanoparticle. And give an idea about the functional group present at particular peak on the graph broad peak noticed at the 2759.84cm^{-1} attributed to O-H stretching of moisture content. The FTIR spectrum of CuO nano powder was shown in fig. The CuO nanoparticle exhibited vibration modes at 432cm^{-1} , 511cm^{-1} and 611cm^{-1} were Assigned for Cu-O stretching vibrations, rocking vibrational modes of water molecule at 886cm^{-1} . the band at 1125cm^{-1} indicated triply degenerative ν_3 mode of SO_4^{2-} ion and the absorption bands at 1630cm^{-1} were bending and stretching mode of vibration of water molecule. In FT-IR spectroscopy of CuO nanoparticle decorated by graphene, in the graph, it give an idea about the functional group contained in the given doped sample, and this is determined by the different peak value at particular peak on the graph.

Peak(cm^{-1})	Peak assignments
3784.47, 3673.87, 3460.69, 3319.21, 329.62	N-H stretch
3017.50, 2978.59,	C-H stretch
2766.72	O-H stretch
2484.00, 2394.41, 2161.32, 2121.59	C=O stretch
2065.67, 2014.14, 1909.89, 1686.81,	N-H stretch

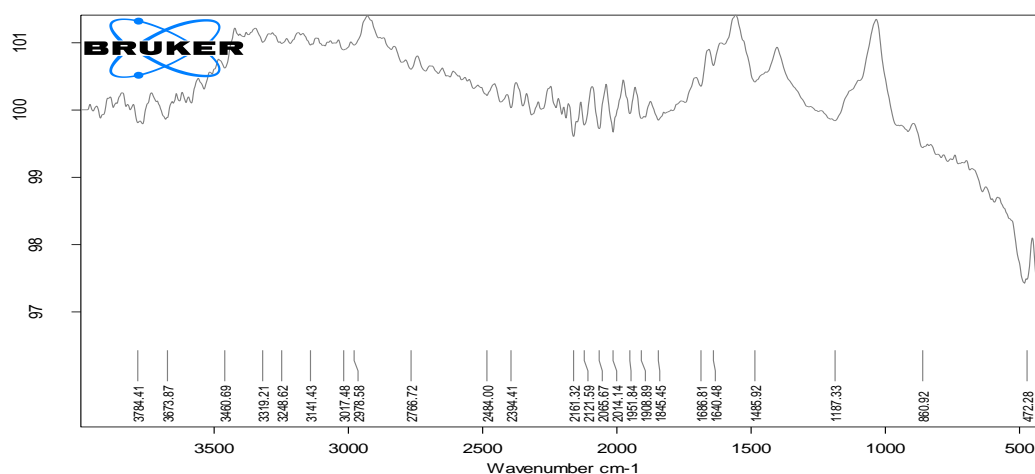


Fig: FT-IR for graphene based cuo nanocomposites

Conclusions:

There are several ways to create graphene-based Nanocomposites, including Hummer's method, Sol- gel method, electrochemical, and hydrothermal methods; however, the co-precipitation method is the most effective way to create nanoparticles, and the most effective method was the electrochemical Exfoliation method to fabricate graphene. In the various Research into graphene potential uses as a semiconductor has expanded globally because to its robust, flexible, lightweight, high resistance, thinness, and conductivity. Furthermore, a study of multiple applications focusing on future aspects was carried out. These comprised the most advantageous uses in highly promising domains like solar cells, super capacitors, EMI shielding, and sensors. as in the NO₂ gas detection use of graphene oxide.CuO and graphene nanocomposites offer a synergistic combination of properties mechanical strength, chemical stability , conductivity that enhance their utility and performance in advanced applications.

References:

- [1] Pan, S., & Liu, X. (2012). ZnS–Graphene nanocomposite: Synthesis, characterization and optical properties. *Journal of Solid State Chemistry*, 191, 51-56
- [2] Ojha, G. P., Pant, B., Park, S. J., Park, M., & Kim, H. Y. (2017). Synthesis and characterization of reduced graphene oxide decorated with CeO₂-doped MnO₂ nanorods for supercapacitor applications. *Journal of colloid and interface science*, 494, 338-344.
- [3] Saranya, et al(2016). Graphene-zinc oxide (G-ZnO) nanocomposite for electrochemical supercapacitor applications. *Journal of Science: Advanced Materials and Devices*, 1(4), 454-460.
- [4] Mandhare, et al (2020). Preparation and thermal conductivity investigation of reduced graphene oxide-ZnO nanocomposite-based nanofluid synthesised by ultrasound-assisted method. *Materials Research Innovations*
- [5] Gayathri, S. *et al* Synthesis of ZnO decorated graphene nanocomposite for enhanced photo catalytic (2015). *Structural ceramic nanocomposites:properties.* 2014 *,Journal of Applied Physics*, 115(17)
- [6] Pena *et al.* have been prepared by the Go onto functionalized Fe₃O₄-NP₅ surface by the carbodimide method.(2021) (Graphene-based nanocomposites in analytical extraction processes. *TrAC Trends in Analytical Chemistry*, 142, 1163030
- [7] Kumar, N *et al.* (2015). Facile synthesis of zno–reduced graphene oxide nanocomposites for NO₂ gas sensing applications. *European journal of inorganic chemistry*, 2015(11), 1912-1923.
- [8] Alamelu, K *et al* (2018). Biphasic TiO₂ nanoparticles decorated graphene nanosheets for visible light driven photocatalytic degradation of organic dyes. *Applied Surface Science*, 430, 145-154

¹ Krishna Kumar
² Bijaya Kumar
Sahoo

**Exploring Heat Rectification
Behaviour of InGaN/GaN Interface:
Towards Efficient Thermal
Management in Optoelectronic
Devices**



Abstract: - This study provides intention on InGaN/GaN interface which shows sign of heat rectification due to asymmetric thermal transport behaviour across the interface. Reviewed built-in-polarization (BIP) effect on thermal parameters of InGaN alloys and theoretically estimated phonon transmission coefficient (Γ) for InGaN/GaN interfaces for various Indium composition which provides possible way to tailored thermal boundary resistance (TBR) and thermal conductivity (k) of the material which play key role in movement of heat energy from an interface of materials. Small value Γ observed for the direction of GaN to InGaN layer as compared to opposite direction and magnitude of this asymmetric nature can change using Indium composition. In addition, the BIP effect reduced thermal conduction in both directions. This special property of interface shows off the sign of thermal rectifier and strength of rectification strongly depends on amount of Indium with their polarization effect. Insights from this study can inform the development of next-generation thermal management solutions capable of addressing the increasing thermal challenges in high-power and high-brightness InGaN/GaN-based devices.

Keywords: Heat rectification, InGaN/GaN heterostructure, Built-in-polarization (BIP) effect, Internal heat, phonon transmission, Thermal boundary resistance (TBR)

¹ *Corresponding author: kkumar.phy@nitrr.ac.in Department of Physics, National Institute of Technology Raipur -492010 (C.G) India

² Department of Physics, National Institute of Technology Raipur -492010 (C.G) India

Copyright © JES 2024 on-line : journal.esrgroups.org

I. INTRODUCTION

InGaN/GaN heterostructures have garnered significant attention for their remarkable electronic and optoelectronic applications. It is used in fabrication of active region in LEDs, laser, sensors, and many other electronic components. However, performance of such devices is limited in the high-power application due to unwanted heat dissipation. Therefore, heat management is a critical aspect of modern electronics and optoelectronic devices and presently researchers are going to find a unique model which removes or minimizes this limit. Therefore, a heat rectifier nature is highlighted as a suitable model to develop heat management in such devices.

$\text{In}_x\text{Ga}_{1-x}\text{N}$ material is suitable for electron confinement because of the band gap lower than the GaN which enhances possibility of recombination to emit light in optoelectronic devices. Higher order of recombination rates signs of better internal quantum efficiency in LEDs. However, there are some non-radiative recombination and internal heat generation which reduces quantum efficiency under high current operating known as efficiency droop. This droop phenomenon strongly depends on thermal parameters and polarization mechanism of material. Any semiconductors are grown by different grown technique usually contains single crystalline structure. If two different semiconductors joined with different lattice parameters produces severe strain at the interface [1]. This strain developed an opposite field often known as built-in-polarization electric field (BIP) which has potential to change various ideal parameters of the material. The amount of heat flow decides by the thermal conductivity (k) of material. Typically, an optoelectronic device requires a high thermal conductive material to minimize self-heating, on the other hand a thermoelectric device requires low thermal conductive material to absorb and good response for heat energy [2]. In the case of heterostructure and superlattices (SLs), thermal boundary resistance (TBR) at the interface reduces k which resists heat transfer during perpendicular from one layer to another [3]. Various recent study concentrated on management of TBR by phonon transmission model which is based on variable parameter introduces as phonon transmission coefficient (Γ) which depends on specific heat (C_p), phonon velocity (v), and Debye temperature (θ_D) of the material [4].

The role of these thermal parameters on heat management are highlighted in previous study explained for III-V nitride semiconductors [4]. However, deviation due to polarization effect on each thermal parameter remains unexplored for InGaN/GaN interfaces. This study explored those parameters which have key role to control unwanted heat generation and observed an important feature of InGaN/GaN heterostructure as a thermal rectifier nature which is proposed for a heat management. A thermal rectifier is a device that allows heat to flow preferentially in one direction while resisting in opposite direction. This property is typically achieved through an asymmetric structure or material properties that create directional heat flow and it may be utilized in reduction of unwanted heat dissipation electronic and thermal isolation within the devices. Theoretical framework for thermal rectifier is proposed, and its functioning parameter like phonon transport, BIP effect, heat capacity is analyzed those function of TBR which controls transmission of phonons. Various observations characterized in result section which correlate with thermal rectifier. In the conclusion part, the main observation and its basic applications and advantages are briefly discussed.

II. THEORETICAL FRAMEWORK

1. Built-in-Polarization effect in InGaN/GaN

Asymmetry of wurtzite structure with large ionicity of InGaN and GaN contains highly polar molecules which creates internal electric field due to spontaneous polarization (P^{sp}) and lattice parameter of InGaN alloy (epitaxial layer) is different as compared to GaN (sapphire substrate) layer which developed strong strain which causes piezoelectric polarization (P^{pz}) at the interface. Therefore, built-in-polarization can be estimates by including of both tow polarization components as introduces as $P = P^{sp} + P^{pz}$. Piezoelectric polarization can be estimated by Eq. (1) including strain component and piezoelectric constants investigated in previous studied [5].

$$P^{pz} = \varepsilon_1 e_{31} + \varepsilon_2 e_{32} + \varepsilon_3 e_{33} \quad (1)$$

Here, P^{pz} is piezoelectric charge density (in C/cm^2), e_{kl} ($k=1,2,3$ & $l=1, 2, \dots, 6$) stands for piezoelectric constant and ε_l represent for strain components in various axis. Simple layout of InGaN/GaN heterostructure mentioned in Fig. (1) which act as a two-dimensional electron gas (2DEG) model. Deformation of a material under any strain is described by elastic constants of the material. Therefore 2D (two-dimensional) polarization surface charge density can be estimated by following Eq. (2) extracted from the literature [6]. Where, a is lattice

constant for epitaxial layer, a_0 is lattice constant for sapphire(substrate) layer and C_{13} , C_{33} are elastic constant. These all-essential parameters for $In_xGa_{1-x}N$ material system is mentioned in Table. 1

$$P = P^{sp} + \frac{2(a-a_0)}{a} [e_{31} - e_{33} \left(\frac{C_{13}}{C_{33}}\right)] \quad (2)$$

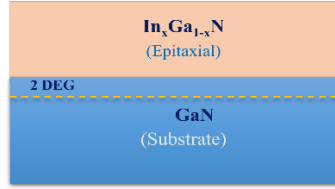


Figure 1: InGaN/GaN heterostructure

Table 1: Parameters for InN, GaN and its alloys [7]

Parameters	InN	GaN	$In_xGa_{1-x}N$
$P^{sp} (C/m^2)$	-0.042	-0.034	$-0.034 + 0.029x - 0.037x^2$
$e_{15} (C/m^2)$	-0.57	-0.30	$-0.57x - 0.30(1-x)$
$e_{31} (C/m^2)$	-0.56	-0.55	$-0.56x - 0.55(1-x)$
$e_{33} (C/m^2)$	1.09	1.12	$1.09x + 1.12(1-x)$
$a (\text{Å})$	3.54	3.19	$3.54x + 3.19(1-x)$
ϵ	15.3	9.5	$15.3x + 9.5(1-x)$
$\rho (Kg/m^3)$	6810	6150	$6810x + 6150(1-x)$
$C_{44} (GPa)$	48	105	$48x + 105(1-x) - 16x(1-x)$
$C_{33} (GPa)$	224	398	$224x + 398(1-x) - 38x(1-x)$

2. Polarization Effect on Phonon Transportation

Phonons are responsible for transporting heat energy in crystalline materials. Phonons are quantized lattice vibrations and velocity of phonons (v) describes by direction magnitude of phonon wave vector. It is introduced by combination of longitudinal velocity (v_L) and transverse velocity (v_T) along X, Y and Z direction. The magnitude of velocity along X and Y directions are same therefore total group velocity of phonons expressed as.

$$v = [(2 v_T^{-1} + v_L^{-1}) / 3]^{-1} \quad (3)$$

In acoustic phonons, their transverse and longitudinal velocity relates elastic constant of the material as $v_T = \sqrt{(c_{44}/\rho)}$ and $v_L = \sqrt{(c_{33}/\rho)}$. Combined phonon velocity (v) and effect of BIP on it (v_p), for an $In_xGa_{1-x}N$ alloy studied in previous study [2, 5] and extracted a short method for different Indium compositions (x), mentioned in Eq. (4) for without BIP, and Eq. (5) with BIP:

$$v = 3234x + (1-x) 4931 - 258x(1-x) \text{ (m/s)} \quad (4)$$

$$v_p = 3572x + (1-x) 5277 - 328x(1-x) \text{ (m/s)} \quad (5)$$

The lattice vibration also depends on operating temperature. Temperature that responsible highest mode of lattice vibration known as Debye temperature denoted by $\theta_D = hw_D/k_B$. Here, h is the Plank's constant, k_B is Boltzmann's constant and w_D is Debye frequency. Debye frequency $w_D = v(3N/4\pi V)^{1/3}$, Where V stand for volume, and N is the number of atoms in unit cell. The value of Debye temperature for $In_xGa_{1-x}N$ alloy estimated in previous study [7]. Its value for without polarization effect (θ_D), and with polarization effect (θ_{Dp}) can be estimates using Eq. (6), and Eq. (7) respectively.

$$\theta_D = 660x + (1-x) 600 - 54x(1-x) \quad (6)$$

$$\theta_{Dp} = 729x + (1-x) 645 - 69x(1-x) \quad (7)$$

3. Heat Capacity

The amount of heat required to change one unit of temperature within unit mass is known as heat capacity (specific heat). To determine lattice specific heat for wurtzite-nitride structure, Debye's, and Einstein's models for specific heat are utilized in experimental study [8], as constant pressure specific heat C_p (in J/mol K) can be calculates using Eq. (8).

$$C_p(T) = C_D(T) + C_E(T) = 3 N_A k_B 3 \left(\frac{T}{\theta_D}\right)^3 f\left(\frac{T}{\theta_D}\right) + 3 N_A k_B^3 \frac{\frac{\theta_D}{T}}{(e^{\frac{\theta_D}{T}} - 1)^2} \quad (8)$$

Where, $C_D(T)$, $C_E(T)$ represents Debye's, Einstein's specific heat, and θ_E, θ_D are represents corresponding temperatures and N_A, k_B are stands for Avogadro number, Boltzmann constant and addition integrating function referred as Eq. (9).

$$f\left(\frac{\theta_D}{T}\right) = \int_0^{\theta_D/T} \frac{x^4 e^x}{(e^x - 1)^2} dx \quad (9)$$

From literature study [9], the Einstein temperature (θ_E) and (θ_D) are related as $\theta_D = \sqrt{3/5} \theta_E \approx 0.77 \theta_E$. Overview on specific heat indicates, it has key role in heat conduction phenomenon, and its functioning parameters deviated due to polarization effect. In the literature, its value for binary nitride compound was reported by a research group with good accuracy [10, 1]. However, specific heat for $In_xGa_{1-x}N$ alloy and effect of polarization effect on it, remains unexplored.

4. Mechanism of Heat Rectification

1) Thermal Boundary Resistance

Framework of heat rectifier nature of an InGaN/GaN interface begins with properties of heat flow in the material which is governed by the phonon propagation model. These two materials are separated by the Thermal Boundary Resistance (TBR) which decides the amount of heat flow (see Fig). Its analysis is subjected to interface engineering [17]. Magnitude of a TBR may be different depending on changing the direction of measurement at the same interface. It means as per the Fig. (2), TBR from material 2 to material 1 is different as compared material 1 to material 2. This special behavior of interface may be utilized to control heat carrier movement from the interface and these properties indicated uses of interface as a thermal rectification to heat management.

Typically, TBR acts as electrical resistance in case the carrier is electron. However, we assumed heat carrier is phonons and phonons movement from the interface restricted by TBR. It can be estimates for material i to material j , using Eq. (11) [2, 4]

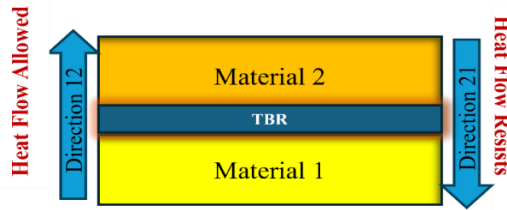


Figure 2: Schematic representation of heat rectifier

$$R_{ij} = \frac{4\pi^2 \hbar^3 v_i^2}{k_B^4 \Gamma_{ij} T_i^3} \left[\int_0^{\frac{\theta_D}{T_i}} \frac{x^4 e^x}{(e^x - 1)^2} dx \right]^{-1} \quad (10)$$

Where, v_i stand for velocity of phonon in layer i , \hbar is modified plank constant, k_B is Boltzmann constant and transmission coefficient of phonon from material i to j is represented by Γ_{ij} . Functioning parameters of TBR show significant change while we considered polarization effect and therefore, we need to explore phonon transmission coefficient which has inversely related with TBR.

2) Interface Nature of Heteostructure

Phonon transmission through the interface of materials is a critical aspect of thermal transport, especially in heterogeneous systems like superlattices, thin films, and nanocomposites. When phonons encounter an interface between two different materials, they can be either transmitted across the interface or reflected. The likelihood of these events depends on the nature of interface. Fig. (3).

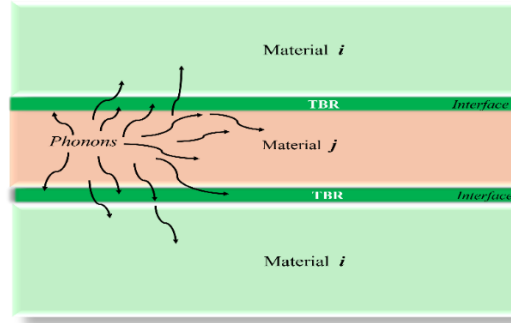


Figure 3: Phonons propagation in superlattice

The probability of accounting of phonon transmits beyond to the interface measured by transmission coefficient from one layer to another. When phonons smoothly transmitted beyond to the interface, it's called Acoustic mismatch model (AM). It provides maximum possibilities of transmission which is based on modification of their path and frequencies and wave properties are conserved [12]. However, 100% transmission of phonons through interface practically not possible therefore one another model has come known as Diffuse mismatch (DM) model which based on rough interface between the layers. This interface model leads to thermalization of interface, and it has independent to phonon path and wave property [17]. Transmission coefficient in AM based model (τ_{ij}^S) from layer (i) to layer (j) can be estimated using Eq. (12) [13].

$$\tau_{ij}^S = \frac{4Z_i Z_j}{(Z_i + Z_j)^2}; \quad (11)$$

where $Z_i = v_i \rho_i$ is known as acoustic impedance with v_i, v_j and ρ_i, ρ_j are the phonon velocity and material density in material i and j respectively. Similarly, in the DM based model (τ_{ij}^D) it can be estimated with the help of Eq. (13). Including C_i, C_j are representing specific for the layer i and j respectively.

$$\tau_{ij}^D = \frac{C_j v_j}{(C_i v_i + C_j v_j)}; \quad (12)$$

Theoretical and experimental analysis claim that we can't make interface with perfect AM nor purely DM based interface [2, 15]. Therefore, transmission coefficient can be estimates by coupling both models and one specular probability parameter (p) introduced. If $p=1$, then it indicates 100% transmission of phonons are possible. However, practically it can't obtain therefore, resulting transmission coefficient Γ_{ij} be estimates using Eq. (14). Similarly, in both directions, average transmission coefficient can be obtained using Eq. (15).

$$\Gamma_{ij} = p\tau_{ij}^S + (1-p)\tau_{ij}^D \quad (13)$$

$$\Gamma = \frac{\Gamma_{ij} + \Gamma_{ji}}{2} \quad (14)$$

From this phenomenon, it is highlighted that DM model of interface responsible for heat generation and is totally dependent on phonons velocity and specific heat of both material which provides possible way to control heat flow through the interface.

III. OBSERVATION AND RESULTS WITH DISCUSSION

1. Specific Heat with of polarization effect

The first attempt to determine the specific heat of GaN wurtzite structure at constant pressure reported [18] as function of temperature (T) estimates using $C(T) = 38.1 + 8.96 \times 10^{-1} T$ (J /mol. K) and obtained room temperature specific heat $C_p = 40.78$ (J /mol. K). Similarly for InN, reported $C(T) = 9.1 + 2.9 \times 10^{-1} T$ (cal. /mol. K) which shows at room temperature $C_p = 41.67$ (J/ mol. K) [15]. Using 400 mg of InN specific heat measured through experimentally from 140K to 300 K room temperature which showed C_p of InN at 300 K to be 39.80 J /mol.K (≈ 308 J/kg K) [19]. Another experimental work reported for specific heat of materials like GaN and InN can vary slightly depending on temperature and crystal structure. Specific heat capacity of GaN at room temperature (around 25° C) is approximately 320 J/kg. K [21]. The specific heat capacity of InN can vary more widely due to its dependence on crystal structure and impurities. However, a rough estimate on room temperature is around 270 J/kg.K [22].

These all investigations deeply explored specific heat only for binary nitride compounds. However, the effect of polarization on it, still unexplored for binary nitrides as well as $In_x Ga_{1-x} N / GaN$ interfaces. Therefore, first

we have studied the influence of polarization effect on specific heat, found that it does not directly affect the phonon because it has no charge quantity. However, phonon propagation totally depends on crystal structure which significant changes under the polarization electric field (PEF) due to BIP. Therefore, its velocity and other transport parameters change under the influence with PEF. Such modification of transport parameters such as phonon velocity (v_p), Debye temperature (θ_{DP}) which has already discussed in previous study [2, 7].

Here, we have theoretically estimated specific heat (C_p) for GaN and InN using Eq. (8, 9) including with and without PEF at room temperature in Table. 2 with good agreement with reported experimental value. Similarly in the Fig. (4a, 4b) shows change of specific heat with various temperature with and without considering influence of PEF.

Table 2: Observation of specific heat for nitride semiconductor (at 300 K)

Sample	Specific Heat J/kg. K (without BIP)	Specific Heat J/kg. K (with BIP)	Decreases % (Due to BIP)	From literature (J/kg. K)
GaN	421	401	4.75	320 [21] without BIP
InN	256	236	7.81	270[22] without BIP

From Table. 2 showed that our observed value of specific heat for GaN is 421 J/kg K (35.25 J /mol.K) which reduces approximately 4.75 % when we considered BIP. Polarization enhanced phonon group velocity as well as Debye temperature [7]. We investigated reasons behind this reduction assumed enhancement of phonon mean free path (MFP) including polarization field which increases phonon group velocity (v_p) and phonon vibration frequency (ω_p), these factors internally contribute to enhancement of temperature and need less amount of heat to change one unit of temperature which is already discussed in reference [7]. Based on literature [2, 5], we estimated specific heat for InGaN alloy which reduced when increases Indium composition showed in Fig. (5b). Similarly, in characterized for various temperatures with indium compositions $x = 0.2, 0.4$ considering with and without BIP. It is observed that specific heat strongly increased with temperature up to $T \approx 600$ K, after this limit characterization showed stable for higher temperature.

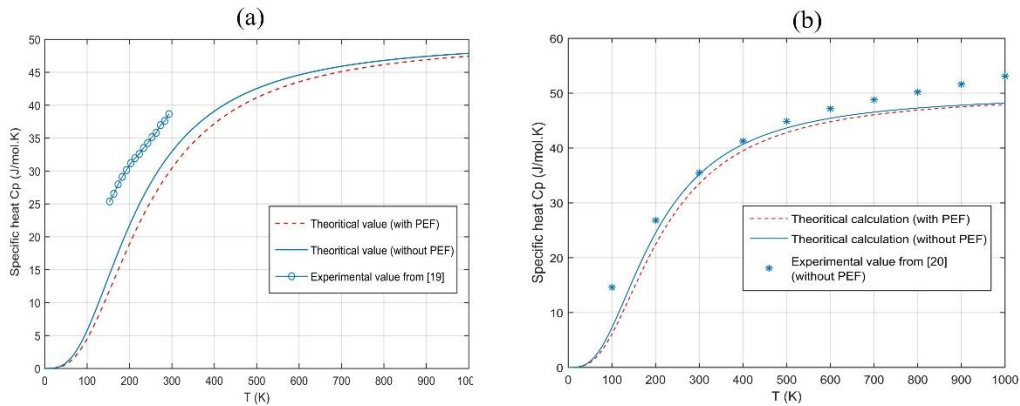


Figure 4: (a) Specific heat of InN, and (b) Specific heat of GaN under various temperatures including and excluding with polarization.

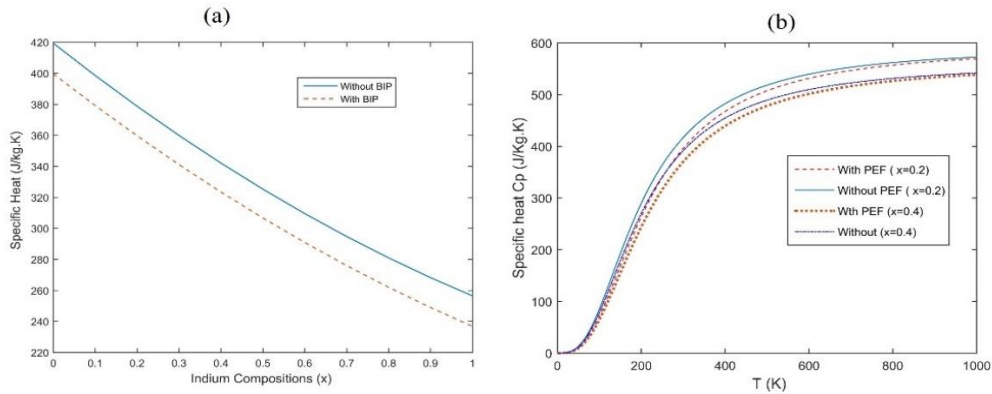


Figure 5: (a) Specific heat of $In_xGa_{1-x}N$ alloy for various Indium compositions x ; (b) Specific heat for $x=0.2, 0.4$ including with and without BIP effect under the various temperatures.

Based on the above observation we have developed the second order's polynomial equations to direct estimate specific heat (in J/kg. K) for a given Indium composition (x) mention in Eq. (16) and Eq. (17).

$$C \text{ (without BIP)} = 50.58 x^2 - 213.5 x + 419.4 \quad (15)$$

$$C_p \text{ (with BIP)} = 46.02 x^2 - 208.8 x + 399.6 \quad (16)$$

2. Interface nature of InGaN/GaN

Acoustic mode transmission (τ_{ij}^S) is totally based on phonon group velocity which significant change under the consider of polarization electric field (PEF) which we have already discussed. However, diffusion-based model (τ_{ij}^D) is depending specific heat of destination layer which significant changes observed due to Indium composition in InGaN alloy and polarization effect. In this order we theoretically estimated the transmission behavior of phonons in $In_xGa_{1-x}N/GaN$ interfaces.

1) *Specular (acoustic) mismatch*: Specular interface provides a suitable way to conduct heat carrier through an interface without any disturbance [24]. We have analyzed specular transmissivity for an $In_xGa_{1-x}N/GaN$ interface using Eq. (12) for various Indium compositions and observation illustrated in Fig. (6a)

Magnitude of specular transmissivity independent to the direction of heat flow, i.e. from $In_xGa_{1-x}N$ to GaN transmissivity equal to from GaN to $In_xGa_{1-x}N$. However, polarization effect enhanced transmissivity due enhancement of group velocity of phonons. Therefore, higher Indium composition significantly reduces magnitude of transmissivity which indicates transmission of phonons can be controlled using Indium content in $In_xGa_{1-x}N$ alloy. We have estimated mathematical tools to directly reach AM based transmissivity for given Indium compositions (x) mentioned in Eq. (18) for without BIP and Eq. (19) for with BIP.

$$\tau_{ij}^S = \tau_{ji}^S = -0.02714x^2 + 0.002245x + 0.9999 \quad (17)$$

$$\tau_{ijp}^S = \tau_{jip}^S = -0.02084x^2 + 0.0002087x + 1 \quad (18)$$

2) *Diffusive mismatch*: Heat generates when the nature of interface rough contact which basically depends on the specific heat of material 2 and group velocity of phonons. So that, in this way transmission coefficient slightly different in the both direction and we have characterized DM based transmissivity mentioned in Fig. 6(b)

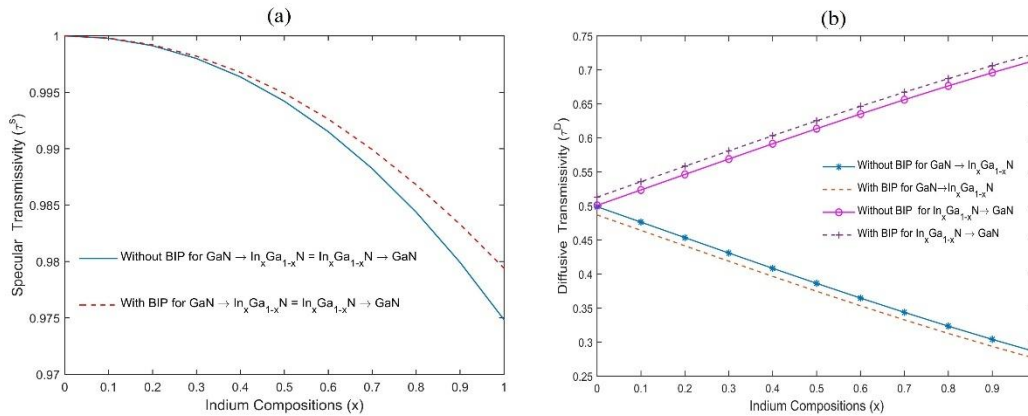


Figure 6:(a) Specular transmissivity, and (b) Diffusive transmissivity for $In_xGa_{1-x}N/GaN$ interface for various Indium compositions

Based on our observation, we have developed equations to direct estimate for given Indium composition (x) mentioned in Eq. (20, 22) as without BIP and Eq. (21, 23) with considering BIP. We observed that magnitude of transmissivity high from $In_xGa_{1-x}N$ to GaN transmissivity as compared GaN to $In_xGa_{1-x}N$, and the magnitude of changes increased when we increased Indium amount. In addition, significant changes were observed due to BIP in both directions.

$$\tau_{ij}^D = 0.02365x^2 - 0.2387x + 0.4998 \quad (19)$$

$$\tau_{ijp}^D = 0.0262x^2 - 0.239x + 0.4877 \quad (20)$$

$$\tau_{ji}^D = -0.02365x^2 + 0.2387x + 0.5002 \quad (21)$$

$$\tau_{jip}^D = 0.0262x^2 + 0.239x + 0.5123 \quad (22)$$

3. Heat Rectification Behaviour of InGaN/GaN interface

The interface quality between InGaN and GaN plays a critical role. AM based interface leads lower TBR while DM based interface lead higher TBR value. However, resultant nature of interface can tuned between these two mismatch models. Various research group [17, 25] have chosen possibilities of AM mismatch model (specular) parameter $p = 0.5$ (i.e. half specular and half diffusive). Based on this assumption we have estimated

transmission coefficient in this way characterized in Fig. (7a) which shows that measurement of transmission coefficients are different in both direction which indicates amount of heat carrier will be different in both direction. This special feature of InGaN/GaN interface showed off as behavior of heat rectification. From Eq. (11), it seen that TBR (from material i to material j) proportionally depended on v_i^2 while invers proportionally with the Γ_{ij} . So that a factor as $\frac{v_i^2}{\Gamma_{ij}}$ gives predicted value of TBR for given $In_xGa_{1-x}N/GaN$ and higher value of this factor for a direction indicates lower heat transmission in that direction. We observed higher heat transmission in the direction of $In_xGa_{1-x}N$ to GaN as compared to opposite direction. The strength of such transmission increased with increasing amount of Indium composition. In addition, BIP effect reduced magnitude of heat transmission in both directions mention in Fig. (7b). This asymmetry $In_xGa_{1-x}N/GaN$ interface highlighted as sign of heat rectification.

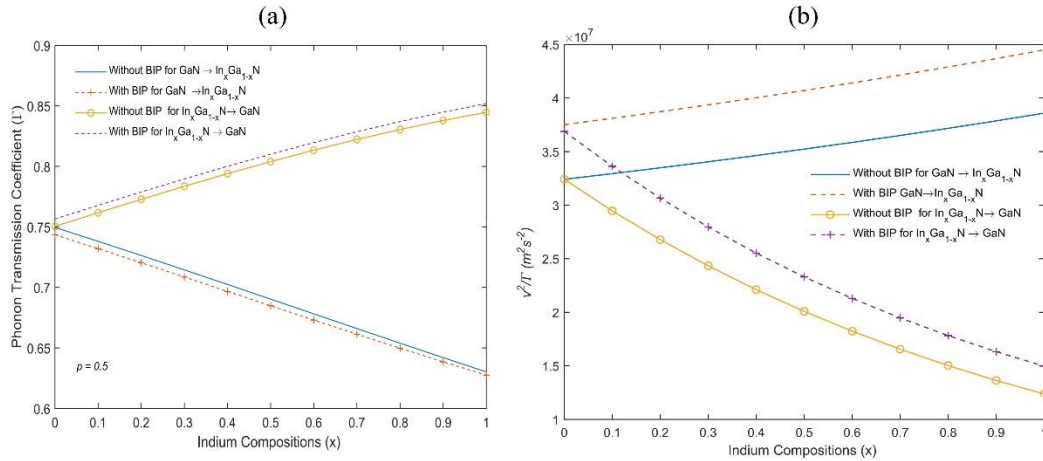


Figure 7: (a) Transmission coefficient for $In_xGa_{1-x}N/GaN$ interface, and (b) Thermal rectifier sign as factor ($\frac{v_i^2}{\Gamma_{ij}}$) for various Indium compositions

IV. CONCLUSIONS

In this study, interfacial thermal properties of InGaN/GaN heterostructure and superlattices (SLs) are theoretically investigated. Significant changes observed due to BIP effect in thermal parameters which provides possible way to modify thermal properties of materials. This BIP effect reduces specific heat and we observed 4.75% and 7.81% reduction on room temperature specific heat for GaN and InN wurtzite. Specific heat of $In_xGa_{1-x}N$ alloy reduces as increasing of Indium composition (x). However, enhancement on phonons group velocity observed due to BIP in previous studies. Changing of these two parameters modified phonon transmission coefficient (Γ) in both directions. Numerical value Γ observed higher for $In_xGa_{1-x}N/GaN$ than $GaN/In_xGa_{1-x}N$ inverse direction and amount of this changing increased by BIP effect. The magnitude of this asymmetrical nature of heterostructure enhanced for higher Indium compositions. This unique properties of heterostructure may be utilized in thermal rectifier and we observed amount of thermal rectification approx. We have characterized its sign of rectification with observations 11% and 25% for $x = 0.1$ and 0.2 respectively. These special properties can be implemented in active region of LEDs, laser to heat management and isolated thermal behavior where required. By taking more attention on this field, performance of devices can be improved.

REFERENCES

- [1] Terry M. Tritt.: Thermal Conductivity Theory, Properties, and Applications. Kluwer Academic / Plenum Publishers, New York. P-153 (2004)
- [2] Sahu S. S., Sahoo B. K.: Reduction of in-plane and cross-plane thermal conductivities by polarization electric field induced in $In_xGa_{1-x}N/GaN$ superlattice. Journal of Alloys and Compounds 898, 162927 (2022)
- [3] Mei S., Knezevic I.: Thermal conductivity of III-V semiconductor superlattices. J. Appl. Phys. 118, 175101(2015).
- [4] Alvarez F.X., Alvarez-Quintana J., Jou D., Viejo J. R.: Analytical expression for thermal conductivity of superlattices. Journal of Applied Physics 107, 084303(2010)

- [5] Gedam V., Sahoo B. K.: Built-in-polarization and thermal conductivity of $\text{In}_x\text{Ga}_{1-x}\text{N}/\text{GaN}$ heterostructures. *Physica E* 93, 63-69(2017).
- [6] Bernardini F., Fiorentini V., and Vanderbilt D.: Spontaneous polarization and piezoelectric constants of III-V nitrides: *Physics Review B*, volume 56, pp. R10024– R10027(1997).
- [7] Sahu S.S., Sahoo B. K.: Reduction of thermal conductivity due to interfacial polarization mechanism of $\text{GaN}/\text{In}_x\text{Ga}_{1-x}\text{N}$ superlattice. *Physica E* 134, 114849(2021).
- [8] Danilchenko B.A., Paszkiewicz T., Wolski S., Jezowski A., Plackowski T.: Heat capacity and phonon mean free path of wurtzite GaN. *Applied Physics Letters* 89, 061901(2006).
- [9] Grimvall G.: *Thermophysical properties of material*. ELSEVIER, The Royal Institute of Technology, Stockholm, Sweden (1999)
- [10] Davydov V. Y., Kitaev Y. E., Goncharuk I. N., Smirnov A. N., Graul J., Semchinova O., Uffmann D., Smirnov M. B., Mirgorodsky A. P., and Evarestov R. A.: Phonon dispersion and Raman scattering in hexagonal GaN and AlN, *Physics Review B* 58, 12899 (1998).
- [11] Yan W. S., Zhang R., Xie Z. L., Xiu X. Q., Zheng Y. D., Liu Z. G., Xu S., and He Z. H.: The contributions of the acoustic modes and optical modes to the primary pyroelectric coefficient of GaN. *Applied Physics Letters* 94, 242111 (2009).
- [12] Alvarez F. X., Alvarez-Quintana J., Jou D., and Rodriguez Viejo J.: Analytical expression for thermal conductivity of superlattices. *Journal of Applied Physics* 107, 084303(2010)
- [13] Mei S., Knezevic I.: Thermal conductivity of III-V semiconductor superlattices. *Journal of Applied Physics* 118, 175101(2015).
- [14] Wang Y. , Vallabhaneni A., Hu J. , Qiu B., Chen Y. P., and Ruan X.: Phonon Lateral Confinement Enables Thermal Rectification in Asymmetric Single-Material Nanostructures, *Nano Letters* 14, 2, 592–596(2014).
- [15] Dehaghani M. Z., Molaei F., Spitas C., Mashhadzadeh A. H.: Thermal rectification in nozzle-like graphene/boron nitride nanoribbons: A molecular dynamics simulation. *Computational Materials Science* 207, 111320(2022).
- [16] Yousefi F., Khoeni F., Rajabpour A.: Thermal conductivity and thermal rectification of nanoporous graphene: A molecular dynamics simulation, *International Journal of Heat and Mass Transfer* 146, 118884(2020).
- [17] Sahu S. S., Sahoo B. K.: Thermal boundary resistance enhancement through interfacial polarization electric field induced in $\text{GaN}/\text{In}_x\text{Ga}_{1-x}\text{N}$ superlattice. *Superlattices and Microstructures* 159, 107035(2021).
- [18] Barin I., Knacke O. and Kubaschewski O.: *Thermochemical Properties of Inorganic Substances*, Springer, Berlin (1977).
- [19] Krukowskia S. et al.: THERMAL PROPERTIES OF INDIUM NITRIDE: *J. Phys. Chem Solids* Vol 59, No. 3, pp. X39-295(1998).
- [20] Lee S., Kwon S. Y., and Ham H. J.: Specific Heat Capacity of Gallium Nitride. *Japanese Journal of Applied Physics* 50, 11RG02 (2011)
- [21] Kiv A. E., Zaitsev A. V., and Starikov V. V.: Specific heat capacity of bulk GaN crystal. *Journal of Applied Physics*, vol. 99, no. 6, 063527(2006).
- [22] Sridhara S. G., Gerberich H. R., and Hopkins R. H.: Thermal properties of bulk and thin film InN and In-rich InGaN. *Journal of Applied Physics*, vol. 96, no. 11, pp. 6523-6529 (2004).
- [23] Slack, G.A., Tanzili, R.A., Pohl, R.O. and Vandersande, J.W., *J. Phys. Chem. Solids*, 1987, 48, 64.
- [24] Chen G.: Size and Interface Effects on Thermal Conductivity of Superlattices and Periodic Thin-Film Structures. *Journal of Heat Transfer*, Vol. 119, 220-229 (1997).

¹V. S. Pabboj
¹H. N. Lakhamawad
¹G. T. Jinklor
¹D. N. Rander
¹K. S. Kanse
¹Y. S. Joshi*
²V. A. Rana
³A. C. Kumbharkhane

**Dielectric and electrical
 characterization of ethyl
 cellosolve and ethanol binary
 mixtures in frequency range 20
 Hz to 2 MHz**



Abstract: - The measurement of complex permittivity $\epsilon^*(\omega)$ and loss tangent ($\tan \delta$) spectra for binary mixtures of ethyl cellosolve also known as ethylene glycol mono ethyl ether (EGMEE) and ethanol (EtOH) at various concentrations has been done using a precision LCR meter. The study has been carried out using frequency domain technique in frequency range 20 Hz to 2 MHz at room temperature 27°C . The dielectric parameters like static dielectric permittivity (ϵ_s) recorded at 2 MHz, the electrical parameters like complex electric modulus $M^*(\omega)$ and complex electrical conductivity $\sigma^*(\omega)$ have been computed. All these complex parameters are utilized to discuss various dielectric and electrical properties. The non-linear nature in ϵ_s values of binary mixtures indicates the existence of heteromolecular interactions. The minima in the value of excess static dielectric permittivity (ϵ_s^E) is observed at $X_E = 0.502$ indicating strong hydrogen bond interaction. The real part of $\sigma^*(\omega)$ is used to confirm the presence of ionic traces in the mixture.

Keywords: Ethyl cellosolve, LCR, Hydrogen bonding, Static dielectric permittivity, Dielectric parameters.

¹ Department of Physics and Electronics, Lal Bahadur Shastri Mahavidyalaya, Dharmabad 431809 (India)

² Department of Physics, Electronics and Space Science, Gujarat University, Ahmedabad 380009 (India)

³ School of Physical Sciences, S. R. T. M. University, Nanded 431606 (India)

First Author E-mail: pabbojvishal@gmail.com

Corresponding Author E-mail: yjosh@rediffmail.com

Copyright © JES 2024 on-line: journal.esrgroups.org

I. INTRODUCTION

The present study investigates the dielectric and electrical properties of the ethylene glycol mono ethyl ether and ethanol binary solutions. The ethyl cellosolve is an organic molecule containing etheric ($-\text{O}-$) and hydroxyl ($-\text{OH}$) functional groups in a single structure. The $-\text{OH}$ group at one of its terminals makes it polar. Understanding the physical and chemical properties of the polar liquid materials helps to improve their applicability in the various fields like industries, pharmaceuticals, electronics etc. The EGMEE is widely used for biological, pharmaceutical, industrial and condensed matter physics applications [1]. The literature reveals that the binary mixtures of EGMEE with various solvents have already been studied using time domain dielectric spectroscopic method. Y.S. Joshi et al. [1] has used time domain reflectometric technique to examine the dielectric relaxation behaviour of aqueous binary solutions of ethyl cellosolve. The hydrogen bonding interaction between the ethyl cellosolve and ethyl methyl ketone has been discussed by K.L. Pattebahadur et al. [2] using dielectric and conformational studies. P.W. Khirade et al. [3] have computed the static dielectric constant and relaxation time for the binary mixtures of dimethyl sulfoxide with ethyl cellosolve along with other solvents. The dielectric dispersion study for binary liquid mixtures provides valuable information about molecular interactions through hydrogen bonding in aqueous or alcoholic binary liquid mixture [4]. Despite the extensive use of this compound, there is a noticeable absence in the literature regarding the study of dielectric and electric properties of EGMEE and ethanol binary mixtures in the 20 Hz to 2 MHz frequency range.

II. EXPERIMENTAL

1. Materials

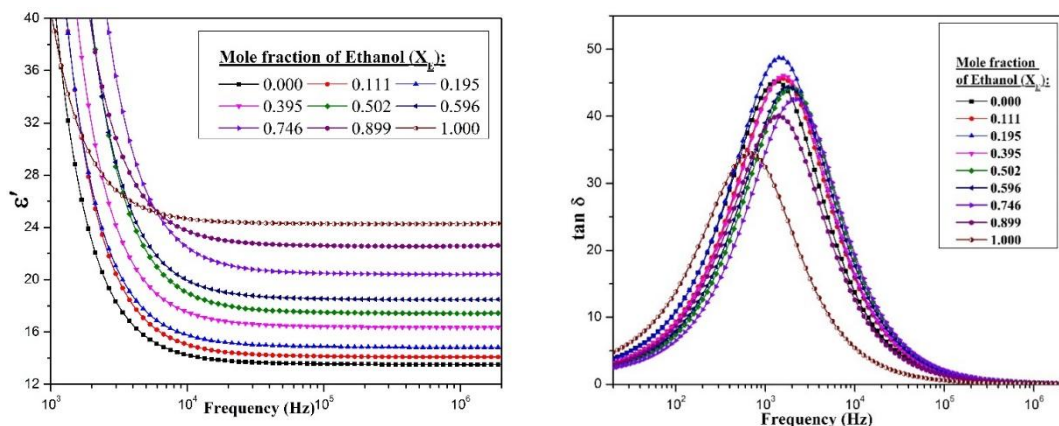
The ethyl cellosolve also known as 2-ethoxy ethanol or ethylene glycol mono ethyl ether (EGMEE) was purchased from TCI, Japan with purity 99.0% and ethanol from Merck, Germany with a purity of 99.9%. These materials are utilized without any further purification. The binary mixtures were prepared with different mole fractions of ethanol in EGMEE.

2. Measurements

The dielectric measurements of all the prepared binary solutions have been done using Agilent (E4980A) precision LCR meter along with liquid dielectric test fixture (16452A). The observations have been recorded at room temperature of 27 °C. The “Capacitive measurement technique” has been used to evaluate the permittivity values [4]. The short circuit compensation and the correction coefficient for dielectric cell have been examined to reduce the impact of stray capacitance effect on frequency dependant complex dielectric permittivity values [5].

III. RESULTS AND DISCUSSION

The frequency domain dielectric spectroscopy has been applied for the pure and binary mixtures of EGMEE and ethanol to extract the dielectric properties of corresponding liquid samples within the frequency range of 20 Hz to 2 MHz. The Fig. 1 (a) and (b) shows the frequency dependent real part of dielectric spectra (ϵ') and loss tangent ($\tan \delta$) respectively. A sharp rise in the ϵ' value at lower frequency (Fig. 1(a)) is due to the existence of ionic impurities in the sample which is a characteristic of polar liquids [6]. The movement of these ionic impurities within the dielectric material causes electrode polarization (EP) and electric double layer (EDL) forms near the electrode surfaces causing the net rise in total capacitance. In this way the low-frequency dielectric spectroscopy can be used to discover the presence of ions and free charges in polar liquids even in their purest form [7]. The relaxation peaks in loss tangent spectra (Fig. 1(b)) gives the EP relaxation times for corresponding liquid sample.



(a) (b)
Fig. 1: (a) Dielectric permittivity (ϵ') spectra (b) spectra of loss tangent ($\tan \delta$) EGMEE – Ethanol binary mixtures at 27 °C.

In the present case, the ϵ' values are observed to become frequency independent within the frequency range of 10 kHz - 40 kHz. Hence the static dielectric permittivity (ϵ_s) values are recorded at 2 MHz and presented in Table 1 as well as plotted in Fig. 2 as a function of molar concentration of ethanol in EGMEE. The non-linearity observed in ϵ_s values is due to the presence of hydrogen bonding interactions among the associating molecules [8].

The Fig. 3 presents a plot of excess static dielectric permittivity (ϵ_s^E) vs. mole fraction of ethanol (X_E). The ϵ_s^E values are calculated by using a linear equation as discussed in our earlier research paper [6]. The values of ϵ_s^E are negative in entire range of concentrations indicating decrease in effective number of dipoles in the solution confirming the presence of strong H-bond interactions among the associating molecules in the mixture [9]. For the present system, the negative peak of ϵ_s^E curve is observed at $X_E = 0.502$ indicating strongest hydrogen bonding strength.

At 25 °C, the literature values for static dielectric permittivity of neat EGMEE are 14.45 [1] and 13.97 [2]. In the present research work, the ϵ_s value for neat EGMEE is obtained to be 13.51. This is in good agreement with the fact that, values of ϵ_s decrease with the increase in temperature [1,2,4,6]. For the aqueous solution of EGMEE, minima in ϵ_s^E value was reported at stoichiometric ratio of 1:2.3 (EGMEE:water) [1], but for its alcoholic solution, the minima in ϵ_s^E value is at near about equimolar concentration i. e. at stoichiometric ratio of 1:1 (EGMEE: ethanol).

Table 1: Static dielectric permittivity (ϵ_s), dc electrical conductivity (σ_{dc}) and ionic conduction relaxation time (τ_{ion}) for EGMEE – ethanol binary mixtures measured at 27 °C.

X_E	ϵ_s	σ_{dc} (S/m)	τ_{ion} (s)	X_E	ϵ_s	σ_{dc} (S/m)	τ_{ion} (s)
0.000	13.51	1.06×10^{-4}	1.12×10^{-6}	0.596	18.48	1.88×10^{-4}	8.42×10^{-7}
0.111	14.08	1.29×10^{-4}	9.45×10^{-7}	0.746	20.43	2.38×10^{-4}	7.51×10^{-7}
0.195	14.82	1.36×10^{-4}	8.92×10^{-7}	0.899	22.61	1.61×10^{-4}	1.19×10^{-7}
0.395	16.36	1.55×10^{-4}	8.92×10^{-7}	1.000	24.30	7.01×10^{-5}	2.82×10^{-6}
0.502	17.43	1.89×10^{-4}	7.95×10^{-7}				

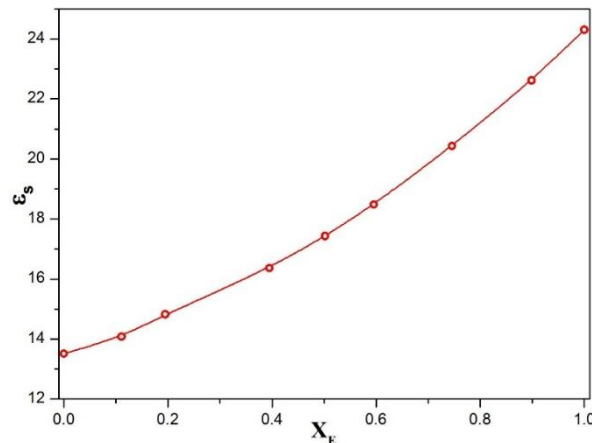


Fig. 2: Static dielectric permittivity (ϵ_s) vs. mole fraction of ethanol (X_E)

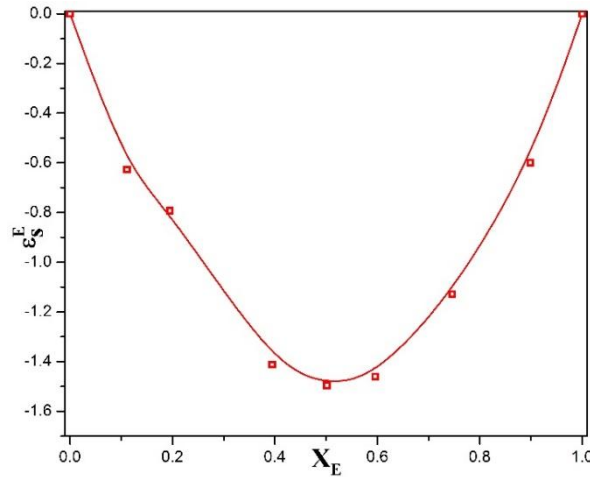


Fig. 3: Excess static dielectric permittivity (ϵ_s^E) vs. mole fraction of ethanol (X_E)

The conductivity characteristics of materials can be related to the mobility of charge carriers or the reaction of materials to an externally applied electric field [10]. The complex electric conductivity (σ^*) values, which can be utilized to describe the ionic traces in neat as well as the binary mixtures of EGMEE and ethanol, have been evaluated using the relation [11]

$$\sigma^*(\omega) = \sigma' + j\sigma'' = \omega\epsilon_0\epsilon'' + j\omega\epsilon_0\epsilon' \quad (1)$$

Where, σ' and σ'' are the real and imaginary parts of ac conductivity of the samples respectively and ϵ_0 is the dielectric permittivity of free space ($\epsilon_0 = 8.854 \times 10^{-12} \text{ F m}^{-1}$). The Fig. 4 shows the plot of real part of ac conductivity (σ_{ac}) for EGMEE – ethanol binary mixtures. The σ_{ac} values are very small at lower frequencies as the ionic impurities are accumulated at electrode surfaces participating in EP phenomena [12]. At the frequencies near about 10 KHz, the conductivity values start to rise. It is an effect of rise in number of mobile charges. Further these mobile charges cause decrease in EP effect. Eventually σ_{ac} becomes frequency independent creating plateau region. When these plateau regions are extended to σ' axis, their intercepts give dc values of electric conductivities (σ_{dc}). The σ_{dc} values for EGMEE - ethanol binary solutions measured at 27 °C are reported in Table 1. The dc conductivities of binary solutions are observed to be greater than the σ_{dc} values of neat EGMEE and ethanol.

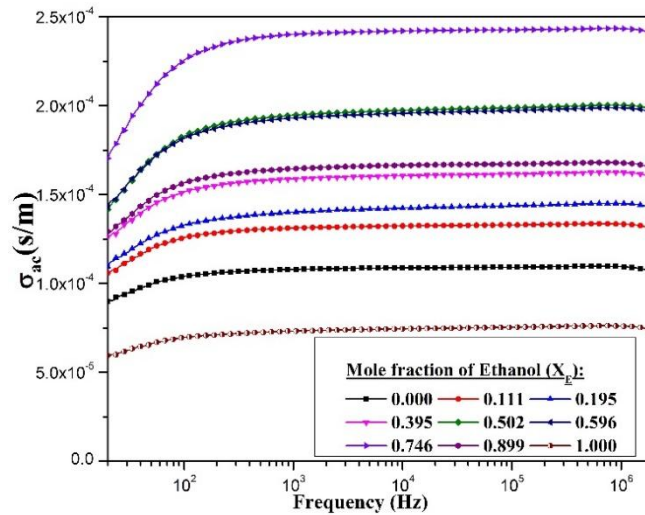


Fig. 4: Complex ac conductivity vs. frequency

The huge permittivity induced due to charge accumulation at the electrode surface can obscure the bulk relaxation process of the material. Due to this the dielectric behaviour of material will get difficult to be examined [13]. In such cases, the complex electric modulus (M^*) can be used as a significantly powerful tool to explore the relaxation process due to ionic conductivity taking place in the polar liquids. The M^* values are evaluated from the following equation [13]

$$M^*(\omega) = M' + jM'' = \frac{\epsilon'}{\epsilon'^2 + \epsilon''^2} + j \frac{\epsilon''}{\epsilon'^2 + \epsilon''^2} \quad (2)$$

The frequency dependent real part (M') and imaginary parts (M'') of complex electric modulus for EGMEE – ethanol binary mixtures are presented in fig. 5 (a) & (b) respectively.

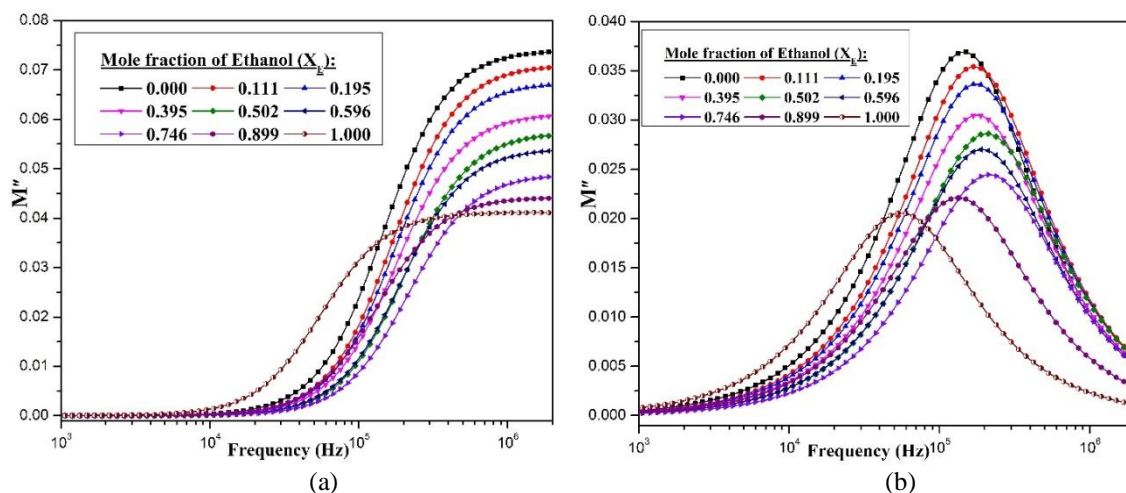


Fig. 5: (a) Real part (M') and (b) imaginary part (M'') of complex electric modulus vs. frequency

The M' values are very low and show negligible increase in the frequency region less than 10 KHz. Then these values observed to be increasing linearly with increase in frequency and approaches a constant value in MHz region. In M'' spectra, the relaxation peaks for different mole fractions of ethanol in EGMEE are observed in the order of rise in M' values. These peaks are associated with the ionic conductivity relaxation time (τ_{ion}) [14]. The concentration dependent τ_{ion} values for EGMEE – ethanol binary mixtures are reported in Table 1.

IV. CONCLUSIONS

The dielectric and electrical properties for neat ethyl cellosolve, neat ethanol and their binary mixtures have been studied using frequency domain dielectric spectroscopy with the help of LCR meter in the frequency range 20 Hz to 2 MHz. From the study, the following conclusions are made:

1. The electrode polarization effect has been observed at lower frequencies which is a result of charge accumulation at the electrode surface producing EDL.
2. The existence of heteromolecular hydrogen bonding has been predicted from the non-linear nature of static dielectric permittivity.
3. The strongest hydrogen bonding interaction strength is observed at equimolar concentration.
4. The polar liquids studied in this research work exhibits small but finite values of electrical conductivities due to presence of free charges in the sample.
5. The ionic conductivity relaxation process has been explained by using complex electric modulus.


The present study can be utilized further for developing/improving the use of ethyl cellosolve in electrical, industrial or pharmaceutical applications.

ACKNOWLEDGMENT

The financial support from the SERB, Department of Science and Technology, New Delhi is gratefully acknowledged (project No. SR/FTP/PS-203/2012 and Project no. DST Project-SB/S2/LOP-032/2013). For the financial support, the author V. S. Pabjoj thanks to Mahajyoti fellowship (award No. MAHAJYOTI/Nag./Fellowship/2021-22/1042(370)).

REFERENCES

- [1] Y. S. Joshi, P. G. Hudge, A. C. Kumbharkhane, "Dielectric relaxation study of aqueous 2-ethoxyethanol using time domain reflectometry technique", *Indian J. Phys.*, vol. 85, No. 11, 2011, pp. 1603-1614, doi: 10.1007/s12648-011-0176-6.
- [2] K. L. Pattebahadur, S. D. Deshmukh, A. G. Mohod, P. B. Undre, S. S. Patil, P. W. Khirade, "Dielectric and conformational studies of hydrogen bonded 2-ethoxyethanol and ethyl methyl ketone system", *AIP Conf. Proc.* 1953, 2018, pp. 050038, doi: 10.1063/1.5032693.
- [3] P. W. Khirade, A. Chaudhari, J. B. Shinde, S. N. Helambe, S. C. Mehrotra, "Static Dielectric Constant and Relaxation Time Measurements on Binary Mixtures of Dimethyl Sulfoxide with Ethanol, 2-Ethoxyethanol, and Propan-1-ol at 293, 303, 313, and 323 K", *J. Chem. Eng. Data*, vol. 44, 1999, pp. 879-881, doi: 10.1021/je980118j.
- [4] Y. S. Joshi, K. S. Kanse, D. N. Rander, A. C. Kumbharkhane, "Dielectric relaxation and molecular interaction study of aqueous amides", *IJPAP*, Vol. 54, 2016, pp. 621-628.
- [5] R. J. Sengwa, S. Choudhary, S. Sankhla, "Low frequency dielectric relaxation processes and ionic conductivity of montmorillonite clay nanoparticles colloidal suspension in poly (vinyl pyrrolidone) – ethylene glycol blends", *Express Polym. Lett.*, 2008, pp. 800-809.
- [6] V. S. Paboj, H. N. Lakhmawad, G. T. Jinklor, D. N. Rander, K. S. Kanse, Y. S. Joshi, A. C. Kumbharkhane, "H-bonding interaction study for binary mixtures of methyl cellosolve and ethanol: a dielectric, FTIR spectroscopic and volumetric approach", *Phys. Scr.*, Vol. 99, No. 5, 2024, pp. 055401, doi: 10.1088/1402-4896/ad37de.
- [7] S. Choudhary, P. Dhatarwal, R. J. Sengwa, "Characterization of conductivity relaxation processes induced by charge dynamics and hydrogen-bond molecular interactions in binary mixtures of propylene carbonate with acetonitrile", *J. Mol. Liq.*, Vol. 231, 2017, pp. 491-498.
- [8] D. N. Rander, Y. S. Joshi, K. S. Kanse, A. C. Kumbharkhane, "Dielectric relaxation and thermodynamic study of polyhydric sugar alcohols in DMSO using TDR technique", *Thermochim. Acta*, vol. 652, 2017, pp. 97-102, doi: 10.1016/j.tca.2017.03.018.
- [9] A. Mahendraprabu, A. C. Kumbharkhane, Y. S. Joshi, S. S. Shaikh, P. P. Kannan, N. K. Karthick, G. Arivazhagan, "Spectroscopic and time domain reflectometry studies on acetonitrile - Ethylene glycol binary solutions", *J. Mol. Struct.*, Vol. 1136, 2017, pp. 303-308, doi: 10.1016/j.molstruc.2017.02.017.
- [10] S. Ramesh, A. K. Arof, "Ionic conductivity studies of plasticized poly (vinyl chloride) polymer electrolytes", *Mater. Sci. Eng. B.*, Vol. 85, 2001, pp. 11-15.
- [11] V. A. Rana, K. N. Shah, H. P. Vankar, C. M. Trivedi, "Dielectric spectroscopic study of the binary mixtures of amino silicone oil and methyl ethyl ketone in the frequency range of 100 Hz to 2 MHz at 298.15 K temperature", *J. Mol. Liq.*, Vol. 271, 2018, pp. 686-695.
- [12] V. A. Rana, D. K. Barot, H. P. Vankar, "AC/DC conductivity and dielectric relaxation behavior of aqueous solutions of 1-butyl-3-methylimidazolium chloride." *IJPAP*, Vol. 57, 2019, pp. 453-460.
- [13] F. Tian, Y. Ohki, "Electric modulus powerful tool for analyzing dielectric behavior", *IEEE T. Dielect. El. In.*, Vol. 21, No. 3, 2014, pp. 929-931, doi: 10.1109/TDEI.2014.6832233.
- [14] Y. S. Joshi, B. A. Rathod, K. S. Kanse, A. C. Kumbharkhane, "Molecular interaction study of some ethylene glycol ethers in 1,4 dioxane through dielectric and volumetric properties", *J. Mol. Liq.*, Vol. 198, 2014, pp. 347-353, doi: 10.1016/j.molliq.2014.07.036.

<p>Arsala Zamir Khan¹ Zamir S. Khan^{2*}, Leena G. Gahane² A. C. Kumbharkhane³, M. P. Lokhande⁴</p>	<p>Dielectric relaxation and thermodynamic study of Amino Acid using time domain reflectometry technique</p>	
<p>ABSTRACT</p> <p>Using the Time Domain Reflectometry technique in the frequency range of 10 MHz to 50 GHz, the complex permittivity spectra of amino Acids (AA's) with water combinations have been determined for one mole fraction and in the 10-25^o C temperature range. The Cole-Davidson model was used to fit the intricate permittivity spectra for AA's and water.</p> <p>The non-linear least square fit method has been used to compute the static dielectric constant (ϵ_0), relaxation time (τ) and thermodynamic parameters (activation enthalpy and activation entropy). An automated density and sound velocity metre, the Anton Paar DSA 5000 M and viscosity with Lovis 2000 M/ME, was used to measure the density, sound velocity, and viscosity of aqueous solutions. FT-IR spectra are used to identify the conformation assessments of hydrogen bonding development between complicated mixtures.</p> <p>Keywords: Amino acids, complex permittivity, static dielectric constant (ϵ_0), relaxation time (τ); FT-IR</p>		

I. INTRODUCTION

The dielectric relaxation time of the solution obtained from this spectroscopy is very helpful in engineering and biomedical applications[1-6]. In the amino acid, the carbonyl oxygen atom is most secure. The water molecules form an –OH band with the carbonyl oxygen group (–COOH) rather than the (–NH₂) amino group. A water molecule donates a proton to the carbonyl oxygen atom as well as accepts a proton from the hydroxyl group to form a complex structure. Three water molecules in the chain which bridges the carboxylic acid and the amino groups [7]. Dielectric relaxation studies are paying a lot of attention on biological compounds, especially amino acids, for the reason of their hydrogen bonding network and zwitterionic nature. Amino acids, which compose the majority of proteins, are also essential for several chemical reactions, the body's synthesis and transfer of energy, and muscular contraction. These amino acids' dielectric relaxation properties have multiple commercial and healthcare applications in addition to basic ones.

In this paper, we present the complex dielectric permittivity study of Amino Acid – water mixtures from 10MHz to 50 GHz using TDR technique for different temperatures. The dielectric relaxation behaviour of these mixtures is explained by the Cole–Davidson model. The changes in dielectric and relaxation parameters are associated with frequency; temperature and concentration have been calculated by non-linear least square fit method. Measurements of density, speed of sound and viscosity of aqueous solutions were carried out using an automated density and sound velocity meter, Anton Paar DSA 5000 M and viscosity with Lovis 2000 M/ME. The conformation analyses of formation of hydrogen bonding between complex mixtures are identified using FT-IR spectra.

II. EXPERIMENTAL METHOD

Material and sample preparation

Binary mixtures were prepared using HPLC grade water obtained from Fisher scientific India Pvt. Ltd. Valine and Tyrosine was obtained from sigma Aldrich, having a purity of 99.9% and used without further Purification. The Amino Acid - Water solution was prepared very carefully to obtain homogenous medium. One molar fraction solutions were prepared for AAs - Water. The mixtures were prepared by weighing appropriate amounts of the constituents of in a suitable flask. In order to avoid the uptake of moisture from the air, solution should be kept in tightly packed flask. The solutions were prepared carefully and maintained at room temperature for about 10 to 15 min before conduct of experiment.

2*Corresponding author: zamirsk75@gmail.com

1 Department of Physics, YeshwantraoChavan College of Engineering, Nagpur, Maharashtra, India - 441110

*2Department of Physics, Anjuman College of Engineering and Technology, Sadar, Nagpur, Maharashtra, India -440001

3School of Physical Sciences, Swami RamanandTeerthMarathwada University, Nanded, Maharashtra, India-431606

4Department of Physics & Electronics, Government VidarbhaInstitute of Science & Humanities (Autonomous), Amravati, India-444604

III. RESULTS AND DISCUSSION

1. **Density, speed of sound and viscosity measurement:**

Measurement of density, speed of sound and viscosity of aqueous solutions were carried out using an automated density and sound velocity meter, Anton Paar DSA 5000 M and viscosity with Lovis 2000 M/ME [8]. It consists of two miniaturized inline cells to simultaneously measure the density, sound velocity and viscosity of liquid samples. All the measurements were done at ambient atmospheric pressure of 101.3 kPa.

The formation of strong H-bonding between Amino Acid- water, density and viscosity decreases as temperature increases, whereas speed of sound increases as temperature increases due to this formation of more cluster or coagulation takes place and group molecular rotation increases the time period of rotation. The formation of strong hydrogen bonding and different structural arrangements causes increase in the viscosity and relaxation time of a molecule. The density, speed of sound and viscosity for Amino acid - water mixture are reported in Table.1



	Density	Speed of sound	Viscosity
Pressure range		0 – 0.3 MPa	
Temperature range		273 -343K	
Measurement range	0 –3000 kg/m ³	1000–2000 m/s	0.3–10000 mPa.s
Measurement time		1 – 4 min	
Total sample volume		≈ 3 cm ³	
Repeatability	0.001 kg/m ³	0.1 m/s	
Uncertainty	0.005 kg/m ³	0.5 m/s	

Fig.1: Anton Paar DSA 5000 Mand viscosity with Lovis 2000 M/ME

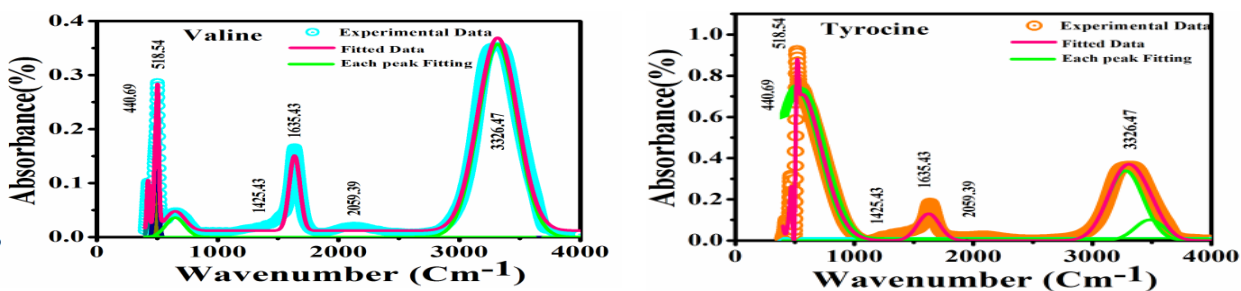
One Molar conc. of Amino Acid	Temperature (Kelvin)	Density (g/cm ³)	Speed of sound (m/s)	Viscosity (mPa.s)
Tyrosine	298	0.997953	1495.25	0.8981
	303	0.996550	1507.87	0.8020
Valine	298	1.006319	1526.49	1.0234
	303	1.004818	1537.58	0.9115

Table 1: The density, speed of sound and viscosity for Amino acid -Water mixtures

2. **FTIR studies:**

To evaluate the chemical composition of Amino acid -Water mixture in aqueous solution, FTIR spectroscopy has been carried out, which is an extremely useful tool for examination of molecular structure of chemical compounds. All chemical compounds have their own typical IR spectrum. The FTIR spectrum of Amino acid –Watermixture in aqueous solution in 1M concentrations were recorded by Perkin-Elmer FTIR spectrophotometer in the range of 4000 cm⁻¹ to 400 cm⁻¹ at room temperature. One mole conc. of Amino acid mixed with KBr and spectra were recorded in the entire frequency region. The precession of the equipment on measurement is approximately 1.0 cm⁻¹. On increasing the concentration of the solution to maximum, we observed 0.21 molar au/vibrating group. These values are matches with Cabaniss et al [9-10].

There are two main reasons for this broadening (i) the weakening of hydrogen-bonding network and (ii) formation of water clusters with solute molecules. The band 3326.47 cm-1 is –OH stretch of pure water, at the same time the water molecule that has not been strong bonded to the carboxyl group but bonded. The band 2059.39 cm-1 shows a slight hump with broaden region, which indicates the aqueous Amino Acids than the pure water. The assignments of mixture validate the bonding of Amino Acids –water.



a) Fitted FT-IR spectrum of Valine

b) Fitted FT-IR spectrum of Tyrosine

Fig.2: Fitted FT-IR spectrum of one mole solution of Amino Acids –water

3. Thermodynamic parameters

Thermal parameters enthalpy (ΔH) and entropy (ΔS) were calculated by using Eyring's equation (11) from the obtained relaxation time

$$\tau = (h/ kT) \exp^{(\Delta H/RT)} \exp^{(-\Delta S/R)}$$

here, ΔH is the enthalpy of activation in KJ/mol, ΔS is the entropy of activation in J/mol, τ is the relaxation time in picoseconds (ps), T is the temperature in degree Kelvin, h is the plank's constant, R is the gas constant and k is the Boltzmann's constant. The activation energy (ΔS and ΔH) are obtained by leastsquare fit method and are reported in Table 2.

One Mole conc. of AA's	Enthalpy of Activation DH (kJ mole ⁻¹)	Entropy of Activation DS (J mole ⁻¹ K ⁻¹)
Tyrosine	9.04(5)	0.22(3)
Valine	6.69(2)	0.217(4)
Water	9.03 (1)	0.226 (5)

Table 2: Thermodynamic parameters for Amino Acid -Water mixtures

The value of active energy of one molar solution of Tryptophan and Tyrosine is more compare to water, leading to the conclusion that Tyrosine requires more energy for rotation than hydrogen bonds in pure water.

The value of active energy of one molar solution of Valine is less compare to water, leading to the conclusion that Valine requires less energy for rotation than hydrogen bonds in pure water.

4. Dielectric Measurement:

The dielectric permittivity (ϵ'), dielectric loss (ϵ''), static dielectric constant (ϵ_0) and relaxation time (τ) were measured using time domain reflectometry (TDR) in the frequency range from 10 MHz to 50 GHz. Frequency and temperature dependent Complex Permittivity Spectra (CPS) for pure and binary mixtures was determined using Tektronix digital serial analyzer (DSA 8300) with sampling mainframe oscilloscope having dual channel sampling module 80E10B has been used. A sampling module provides 12ps incident and 15ps reflected rise time pulses generated by tunnel diode was fed through a coaxial line system having 50 Ω impedance. The inner and outer diameters of used coaxial cable were 0.28mm and 1.19mm respectively. Sampling oscilloscope recorder the changes in step pulse after reflection from the end of line. The reflected pulse without sample $R_1(t)$ and with sample $R_x(t)$ were recorded in the time window of 5ns and digitized in 2000 points. The Fourier transform of the pulse and data analysis was performed to establish complex permittivity spectra $\epsilon^*(\omega)$ using non linear least square fit method [12-13].

Complex permittivity spectra obtained by the time domain reflectometry technique (TDR) in the frequency range from 10 MHz to 50 GHz at 10- 25 °C for binary mixtures of Amino acid in water at one mole concentrations. From figure 3 it is observed that the dielectric permittivity goes on decreasing as the frequency increases this indicates the dielectric dispersion. The dielectric losses are shifted towards higher frequency and exhibit the Debye type dispersion. The values of different dielectric parameters for aqueous Amino Acid -water solutions obtained by the Havriliak-Negami equation [14] are represented in Table 3.

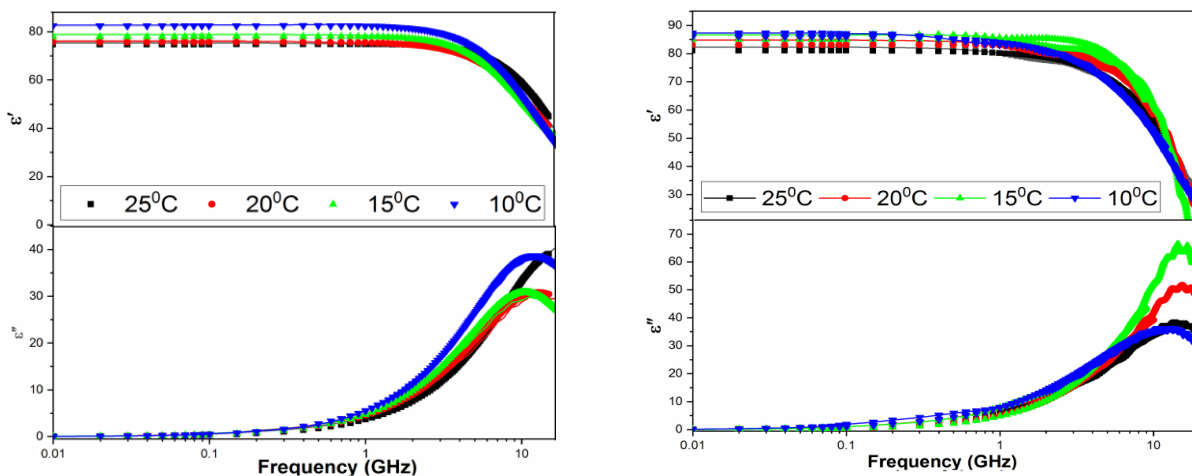


Fig. 3: Frequency dependent dielectric permittivity and dielectric loss of Tyrosine-water and Valine-water mixtures at 10-25°

Molar conc. (X_L)	25°C		20°C		15°C		10°C	
	(ϵ_0)	τ (ps)	(ϵ_0)	τ (ps)	(ϵ_0)	τ (ps)	(ϵ_0)	τ (ps)
Valine	81.17	10.11	83.06	10.84	84.94	11.88	86.14	12.36
Tyrosine	74.75	9.07	75.61	12.52	77.80	15.27	82.43	16.33
Water	77.78	9.14	78.65	9.50	81.98	10.38	85.95	11.64

Table 3: Dielectric relaxation parameters for an aqueous solution of Amino Acid -Water mixtures at 10-25 °C

5. Static dielectric constant (ϵ_0)

The static dielectric constant of liquids is depends on many factors such as nature of intermolecular forces, dipole-dipole correlation, number of carbon atoms present in molecule, temperature etc. **Figure 4** shows the temperature dependent static dielectric constant of Valine and Tyrosine (Amino Acids).Static dielectric constant, ϵ_s increases as the temperature decreases which may be due decrease in molar volume and increases in dipole – dipole interaction. At higher temperatures there are more thermal fluctuations and dis-orderness in dipoles.

6. Relaxation time (τ)

The temperature dependent study of Amino Acids-Water mixture shows that there is decrease in relaxation time with increase in temperature as shown in **Figure 5** The temperature dependent relaxation time values of Amino Acids-Water mixture have been established in the order of Tyrosine>Valine. Decrease in relaxation time with increase in temperature may be due to faster reorientation of molecules and rate of loss of energy increases due to large number of collisions. This effect may be due to decrease of hindrance and subsequently increase in molecular reorientation of Amino Acids-Water molecules with increase in temperature. Supplementary cause for decrease in relaxation time may be an increase in the effective length of the dipole with increase in temperature.

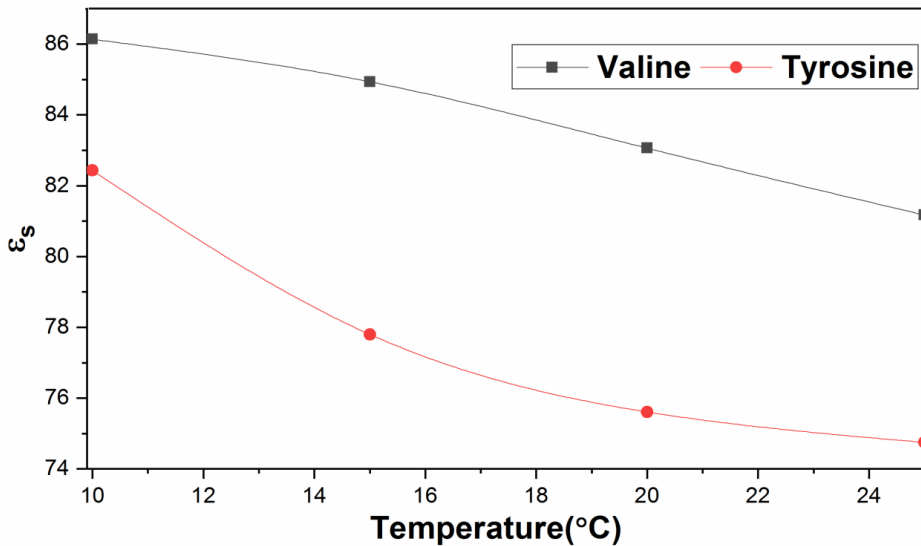


Figure 4: Temp. Vs. Static Dielectric constant of Amino Acids -Water

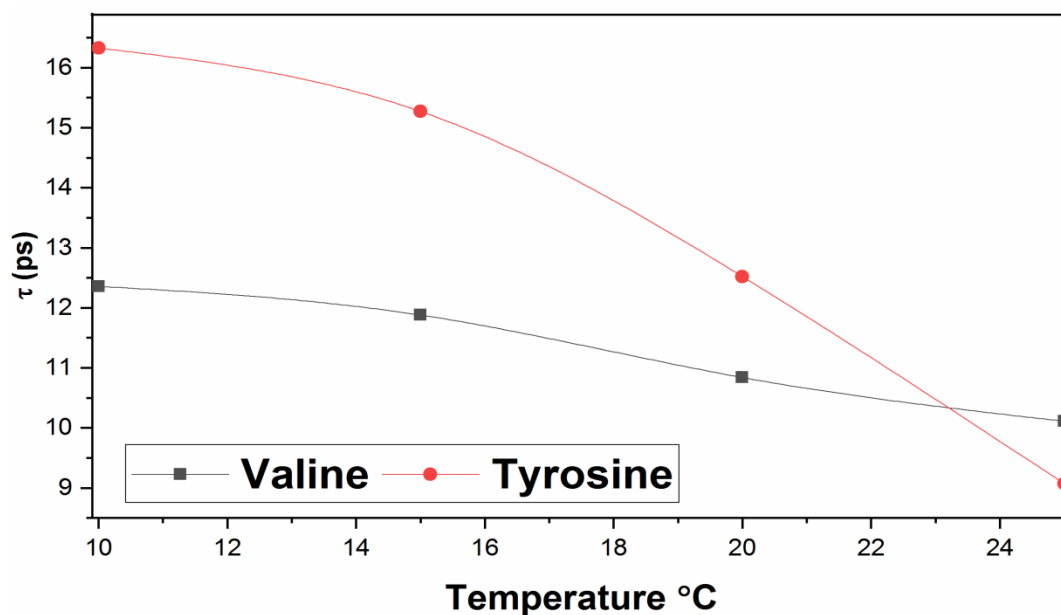


Figure 7.5 Relaxation time (τ) Vs. temperature for Amino Acids-Water

V. CONCLUSION

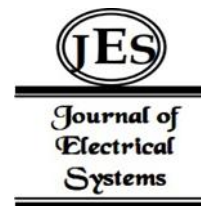
In this paper, we present the complex dielectric permittivity study of Amino Acid – water mixtures from 10MHz to 50 GHz using TDR technique for different temperatures. One mole of valine exhibits a dielectric constant which is higher than one mole of tyrosine at 25°C. The changes in dielectric and relaxation parameters are associated with frequency; temperature and concentration have been calculated by non-linear least square fit method. Measurements of density, speed of sound and viscosity of aqueous solutions were carried out using an automated density and sound velocity meter, Anton Paar DSA 5000 M and viscosity with Lovis 2000 M/ME. The conformation analyses of formation of hydrogen bonding between complex mixtures are identified using FT-IR spectra.

VI. REFERENCES

- [01] Madhuriama V, Murthy VRK & Shobhanadri J: *Ind. J. Pure Appl. Phys.* 36 (1998) 85
- [02] Madhuriama V, Murthy VRK & Shobhanadri J: *Ind. J. Pure Appl. Phys.* 36 (1998) 144
- [03] Sengwa RJ, Madhuri & Abhilasha: *J. Mol. Liq.* 123(2006)92
- [04] Sato T, Chiba A & Nozaki R: *J. Mol. Liq.* 96-7(2002)327
- [05] Sato T, Chiba A & Nozaki: *J. Chem. Phy.* 112(2000)2924
- [06] Hudge PG, Gond DS, Gacche RN, Lokhande MP & Kumbharkhane AC: *Ind. J. Phy.* 87-6(2013)543
- [07] Junyan Sun, ZhuoXu, XiaoJieLiu, *Chem. Phys.* 528 (2020) 110528
- [08] T.J. Fortin et al. *J. Chem. Thermodynamics* 57 (2013) 276–285
- [09] Cabaniss S E & Mcrey I F, *SpectrochimActa A*, 51 (1995)2385.
- [10] Cabaniss S E, Leeinheer J A & Mcrey I F, *SpectrochimActa A*, 54 (1998) 449.
- [11] S. Glasstone, K.J. Laidler, H. Eyring. *The Theory of Rate Processes* McGraw Hill, New York (1941)
- [12] R.H. Cole, J.G. Berberian, S. Mashimo, G. Chryssikos, A. Burns, & E. Tombari, *J. Appl. Phys.* 66 (1989) 793.
- [13] AC Kumbharkhane, A Puranik, SC Mehrotra, *J. Chem. Soc. Faraday Trans.* 87 (1991)1569
- [14] Anand K D J S, et al. Dielectric properties and analysis of H-bonded interaction study in complex systems of binary and ternary mixtures of polyvinyl alcohol with water and DMSO, *Flu. Pha. Equi.* 382 (2014) 300

^{1*} S. P. Tiwari
² A. P. Deshmukh
² A. V. Tiwari
² P. S. Awandkar
² M. S. Dixit
² S. P. Yawale

Synthesis and Characterization of Polyaniline Composite Incorporated with TiO₂ Nanoparticles for Enhancement of Antibacterial Activity



Abstract - In this study we synthesized pristine Polyaniline (PANI), and PANI-TiO₂ nanocomposites by chemical oxidative polymerization method. The nanocomposites were prepared with various amount of TiO₂ by wt. % method to observe its effect on microbial activity. The obtained samples were characterized by using X-Ray diffraction method and the XRD study validates the well-organized arrangement of TiO₂ nanoparticles (NPs) inserted into the polymer matrix. The crystallite size in a nanocomposite was found to be in the range of 10-50 nm. The structural and the functional group confirmation of the nanocomposites were characterized by FTIR and UV-Visible analysis. FT-IR spectra and UV study revealed the interaction of TiO₂ NPs with PANI matrix. All the prepared nanocomposites were tested for antibacterial activity. PANI-TiO₂ nanocomposite showed higher antibacterial activity than that of pure PANI and TiO₂ nanoparticles. The highest inhibition zone was obtained for 5 wt. % of TiO₂ per aniline monomer. Hence PANI-TiO₂ nanocomposite is a remarkable material for biological activity and can be used as future biosensor. Thus, it can be exploited as antibacterial agent in ointments, paints and food packaging materials.

Keywords:

Conducting polymer, polyaniline, Titanium dioxide, Nanocomposites, Antibacterial properties.

I. Introduction

The organic intrinsic conducting polymers (ICPs) have gained a much interest in a field of research due to its versatile and unique physical, chemical, structural and electrical properties such as better electrical conductivity, special doping mechanism, low ionization potential, low energy optical transitions and high electron affinity due to their π - electron backbone arrangement [1]. They have attracted the researchers as a novel material for potential applications such as biosensors, gas sensors, actuators, super capacitors, electronic devices, solar cells, and electrochemistry etc. Among these conducting polymers polyaniline (PANI), has received considerable attention and proposed as a most promising material because of its excellent electrical, electrochemical, mechanical and optical properties, ease of synthesis, low cost of monomer, lightweight, high thermal and environmental stability

^{1*}Corresponding author: Government Vidarbha Institute of Science and Humanities, Amravati 444604, India.
Email id- tshailesh737@gmail.com

² Government Vidarbha Institute of Science and Humanities, Amravati 444604, India

[2,3]. The efficient polymerization of aniline can be obtained in an acidic medium only in which aniline acts as a cation [4, 5]. PANI is categorized in various forms which differ in chemical and physical properties as: Leucoemeraldine is a fully reduced form and is yellow, Protoemeraldine is brown, Emeraldine is green, nigraniline is blue and Pernigraniline is violet [6-8]. Metal nanoparticles and oxides of metal are widely used for the synthesis of nanocomposites. They show many excellent properties such as large surface to volume ratio, good electrical properties, strong adsorption ability, small particle size, and high surface reaction activity. [9-11]. Several metal oxides have been widely used for the investigation of antibacterial, antifungal and biological activity such as ZnO, MnO₂, TiO₂, WO₃, ZrO₂, CuO and so many [12,13]. Titanium dioxide (TiO₂) has received a special attention of researchers due to its good stability, nontoxicity, excellent physical and chemical properties due to 'd' electrons, crystalline structure, as well as wide range of applications such as paints, plastic, paper industries, fabrics and bio-electrochemistry [14-15]. Thus, the TiO₂ was selected as the Nano filler with PANI matrix to enhance the microbial activity. In this article, we report a simple method for the synthesis of conducting PANI-TiO₂ nanocomposites, which could be easily applied industrially. The structural, morphological and functional group study were done by XRD, FTIR, and UV-visible. Another objective of this study was to incorporate the TiO₂ nanoparticles into the PANI matrix using *in-situ* polymerization method for enhancement of antibacterial activity.

II. EXPERIMENTAL

A. *Materials and methods*

All the reagents and chemicals used in this study were analytical grade. Aniline (99.5% monomer) and the oxidant ammonium peroxydisulfate [APS, (NH₄)₂S₂O₈] were purchased from SD Fine. HCL (35% Loba chemicals), TiO₂ Nanoparticles, acetic acid (Aldrich), were used to synthesize the material without any further purification. Whatmann grade one filter papers were used for filtering the product. Distilled water is used for all synthesis as well as washing the product.

B. *Synthesis of PANI and its Nanocomposites*

The chemical oxidative polymerization method was adopted for polymerization of aniline to polyaniline. An appropriate amount of aniline (3.64 ml) and 1M HCL was mixed together in a beaker containing distilled water such that its volume becomes 50ml and stirred for 15 minutes. Keep the solution for 30 min. as it is. Dissolve ammonium peroxydisulfate (APS) in 50 ml of distilled water to form a 0.0025M solution and kept as it is for 30 minutes at room temperature. This APS solution was added drop wise to monomer solution till polymerization took place and the reaction mixture was stirred for 4 hours constantly at room temperature. A dark green precipitate is formed which is kept for 24 hours. The polymer obtained was filtered, washed several times with distilled water, ethanol and acetone to remove the impurities [2, 12]. The obtained precipitate was dried in oven at 60° C for 24 hours. Now, to synthesize PANI/TiO₂ nanocomposites, various amount of prepared anatase TiO₂ were added in the above solution and sonicated for 30 min. for homogeneous dispersion. The amount of TiO₂ nanoparticles added were calculated to be 5, 15, and

25 weight per cent (wt. %) per weight of aniline monomer. Repeat the same procedure as above mentioned and the dark green fine powder of PANI/TiO₂ nanocomposite was obtained and named as PT5%, PT15%, and PT25% respectively.

C. Antibacterial activity of prepared nanocomposites

The antibacterial activities of pristine PANI, anatase TiO₂ and PANI-TiO₂ nanocomposites were determined by agar well diffusion method. We have used two strains of bacteria such as gram-positive bacteria *Staphylococcus aureus* (S. aureus) and gram-negative bacteria *Escherichia coli* (E. coli). The commonly used antibiotics (OFLOXACIN) were taken as a reference. The bacteria and the antibacterial reagents were cultured and incubated individually on Muller-Hinton Agar Plates at 37° C for 24 hr. After the incubation period, the zone of inhibition was recorded and measured.

III. Result and Discussion

A. X-ray Diffraction Analysis

Fig.1 shows the XRD spectra of pristine PANI, TiO₂ NPs, and PANI-TiO₂ nanocomposite. For the pure PANI, the XRD spectra showed broad amorphous diffraction peak at $2\theta = 25.22^\circ$ and low intensity at $2\theta = 15.17^\circ$ and 20.39° indicates the disordered structure of long chain polymer matrix. The presence of strong diffraction peaks at 2θ values 25.4° , 37.8° , 48.19° , 54.0° , and 62.8° corresponds to the crystal planes of (101), (004), (200), (105) and (204). This shows the formation of anatase TiO₂ nanoparticles (JCPDS card No. 21-1272) [16]. The XRD spectrum of PANI-TiO₂ composite was analogous to the pure TiO₂. In case of PANI-TiO₂ composite the amorphous peak of PANI at $2\theta=25.22^\circ$ is found to be slightly shifted to a higher diffracting angle at $2\theta= 25.3^\circ$, this shifting of peaks occurred due to strong interaction between availability of empty orbitals of transition metal with the polar segments of PANI. This indicates the successful incorporation of TiO₂ on polymer matrix [17]. The mean crystallite sizes of nanocomposite were calculated using Scherrer formula: $D = K\lambda / B\cos\theta$, where D is the crystal size, K is the Scherrer constant (0.891), λ is the X-ray wavelength (0.154056 nm), B is the half-height width of the diffraction peak, and θ is the diffraction angle. The particle size of anatase TiO₂ was found 48.42 nm and that of PANI- TiO₂ nanocomposite were found to be 9.46nm, 38.97nm, 42.67nm, 27.29nm, 37.44nm and 36.53nm for 5%, 10%, 15%, 20%, 25% and 30% respectively. As no impurity peaks were observed the prepared samples are considered to be pure.

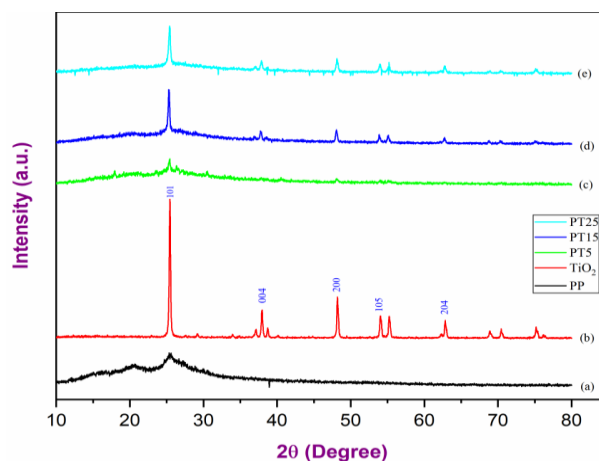


Fig.1. XRD pattern of Pure PANI, TiO₂ NPs and PANI with different content of TiO₂ nanoparticles.

B. FTIR Spectroscopy

The fig.2 shows the comparative study of FTIR spectra of pristine PANI, TiO₂ NPs, and PANI/TiO₂ nanocomposites with different amount of loaded TiO₂ nanoparticles. FTIR spectroscopy confirms the interaction between conducting PANI with TiO₂. The strong absorption band of PANI at 1525 cm⁻¹ was assigned to the C=C stretching of quinoid group. Also, the peak at 1467 cm⁻¹ was the vibration absorption peak of C=C in a benzene type ring. The spectrum shows the bands at 2862 cm⁻¹ which are attributed to C-H stretching of PANI. The peak at 3444.87 and 3128.54 cm⁻¹ corresponds to the stretching vibration absorption peak of N-H and the weak peak at the 1647 cm⁻¹ represents deformation vibration absorption peak of N-H bond. The peak at 1170 cm⁻¹ was the vibration absorption peak of ⁻H⁺N=C related to a quinone type ring. Along with that one more peak was observed at 1327 cm⁻¹, which represents stretching absorption peak of C-N bonding. The stretching and out of plane bending vibrations of C-H benzenoid ring were observed at 825 and 671 cm⁻¹ [18]. The position of these peaks matched with the characteristic peak ranges of an amine group, the range of stretching vibration absorption peak of N-H is 3500-3100 cm⁻¹. 1350-1000 cm⁻¹ and 1640-1560 cm⁻¹ was the range of stretching vibration absorption and the deformation vibration peaks of C-N respectively. These results indicated that polymerization of aniline molecule took place during the reaction [19]. Due to addition of TiO₂ nanoparticles in the polymer matrix the electron densities of PANI chain were affected and it led to the shifting of some peaks to lower frequencies like [2862 to 2864 cm⁻¹ for C-H, 3444 to 3448 and 3128 to 3130 cm⁻¹ for N-H, 825, 671 to 839,678 resp. for C-H etc.] Also, the main absorption peak 1525 and 1467 cm⁻¹ were shifted to lower wavenumbers, this is because of strong PANI quinoid and benzene ring [18].

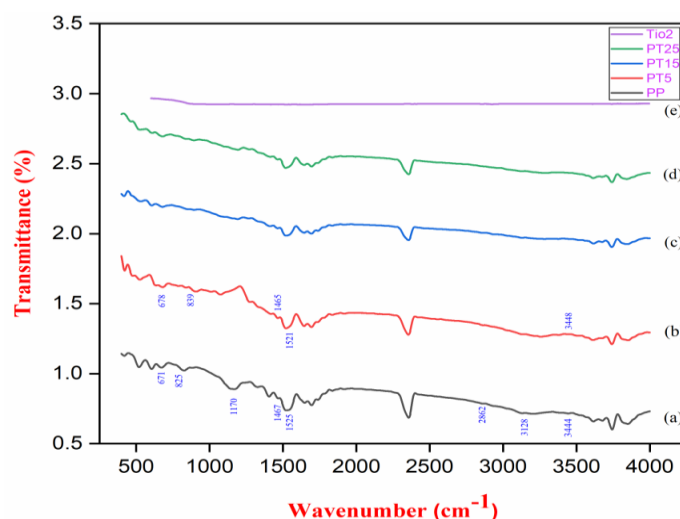


Fig. 2. FTIR spectra of Pristine PANI, TiO₂ NPs, and PANI- TiO₂ Nanocomposites.

C. UV Visible analysis

UV-Visible absorption spectra of pristine PANI, PANI with various weight percentages of TiO₂ nanoparticles was shown in fig.3. The absorption spectra of PANI indicated the maximum absorption at 213 nm and 244 nm respectively. These bands were corresponding to the $n - \pi^*$ transition. The weak reflection peak at wavelength 305 nm is assigned to the $\pi-\pi^*$ transition. Moreover, the band at 305 nm represents the quinoid structure presents in PANI matrix [20]. The characteristic peak observed in PANI at 900 nm is ascribed to the π - polaron transition [21]. The filling of TiO₂ nanoparticle affected the relative intensity of pure PANI matrix. From the UV-Vis. Spectrum of Nano composites it was confirmed that the intensity of the absorption peaks of all Nano composites was higher than that of pure polymer. More specifically, the absorbance of the peak 244 nm has shifted to the higher wavelength at 277 nm for 5 wt% of composites. The intensity and absorption bands of the prepared composites were found to be increased with increase in concentration of TiO₂. These noticeable changes reveal that there is strong intermolecular interaction between the added TiO₂ NPs with aniline molecules. In addition to this, the optical band gap of the PANI-TiO₂ Nano composite has been determined using Tauc's plot equation; $(\alpha h\nu)^n = B(h\nu - E_g)$, where $h\nu$ is the energy of incident photon and $n = 2$ for direct and $1/2$ for indirect allowed transitions [22-23]. Fig.4. represents the direct optical energy band gap of different content of TiO₂ nanoparticles incorporated with polyaniline. The tangent drawn to the linear portion of curve gives the energy band gap values of the synthesized composites. It is observed that the energy band gap values were decreasing as we increase the quantity of TiO₂ NPs due to semiconducting nature of TiO₂.

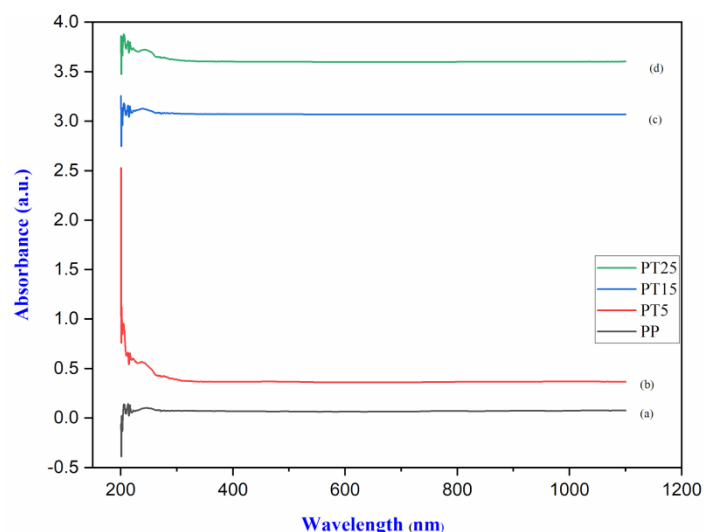


Fig.3. UV-Visible spectra of prepared samples: (a) Pure PANI, (b) PT5, (c) PT15 and (d) PT25.

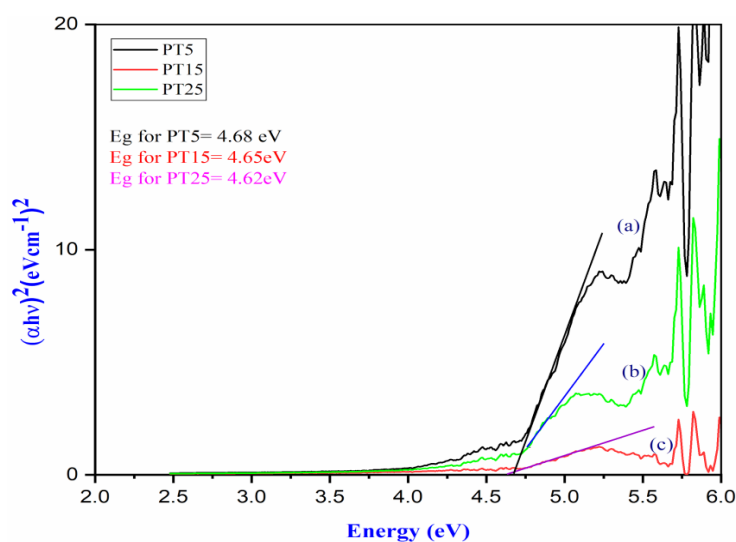


Fig.4. Variation in direct energy band gap of PANI-TiO₂ Nanocomposites.

D. Antibacterial Activity

The PANI, TiO₂ NPs, and PANI- TiO₂ nanocomposite were studied against human pathogenic microorganisms like gram positive (*S. aureus*) and gram negative (*E. Coli*) bacteria using disc diffusion method as shown in fig. (6). These pathogens were commonly found on the surface of contaminated wound and waste water. The bacterial strains were prepared, inoculated in nutrient broth and incubated for 24 hours before using bacterial assay. Sterile Muller-Hinton agar plates were prepared. Ofloxacin was used as standard reference and dimethyl sulfoxide (DMSO) were used as positive control. The plates were incubated at 37° C for 24 hrs. The values of inhibition zone diameter of pure PANI, TiO₂ NPs, and PANI- TiO₂ nanocomposite were recorded and tabulated as shown in table no.1. [29].

Table No. 1: The inhibition zone diameter values in (mm) scale of Pure TiO₂, Pristine PANI and PANI-TiO₂ Nano composite with different weight % of TiO₂ (5%,15%,25%) respectively tested against gram positive (*S. Aureus*) and gram negative (*E. Coli*) bacterial pathogens.

Sr. No.	Samples	Inhibition zone diameter in mm	
		<i>S. Aureus</i> (Gram positive)	<i>E. Coli</i> (Gram negative)
1.	Ofloxacin (Ref.)	22 mm	22 mm
2.	TiO ₂	16	8
3.	PP	10	8
4.	PT5	20	22
5.	PT15	18	0
6.	PT25	10	10

The result indicates that synthesized TiO₂ nanoparticles have shown the excellent antibacterial effects against the bacterial strains. The bactericidal activity of TiO₂ NPs is more effective than that of pristine PANI which shows somewhat poor antimicrobial activity against the both bacterial strains. This may be due to the non-crystalline nature of PANI. The study reveals that the antibacterial activity enhanced after addition of TiO₂ nanoparticles and is found maximum for 5 wt. % of added TiO₂. The synergistic effects occurred when the TiO₂ nanoparticles were incorporated into the PANI matrix. The result clearly demonstrates that PANI-TiO₂ nanocomposite has excellent antibacterial activity against both pathogenic bacteria. Sample PT5 has shown the highest bactericidal activity amongst all the samples which is almost equal to that of the standard Ofloxacin. Also, the sample PT5 showed the maximum zone of inhibition for *E. Coli* as compared to the *S. Aureus*. These results may be observed because of the variation in the structure of bacterial cell wall, where the gram-positive bacteria have a thicker cell wall of peptidoglycan than that of gram negative which in turn restricts the tunneling of TiO₂ nanoparticles. Moreover, as we increase the loading of TiO₂ NPs the bactericidal property decreases. The nanocomposite PT15 showed a clear zone of 18 mm and 0 mm for the both microorganisms *S. Aureus* and *E. Coli* respectively. It is because of the fact that the antibacterial activity also depends on the morphology of the particles [30]. The reason behind the excellent biocidal activity of PANI-TiO₂ nanocomposite is the lower particle size of freshly prepared samples. These nanoparticles can easily penetrate the bacterial cell wall through small pores present on the surface of cell which may leads to the perturbation in metabolic process and hence cell death [31-32]. The crystallite size of the particles calculated from the XRD data of PT5, PT15 and PT25 nanocomposite were found to be 9.46 nm, 42.67 nm and 37.44 nm respectively. The enhancement in antibacterial activity is because of added TiO₂ NPs. Since the TiO₂ has ability to trigger the free hydroxyl [HO[•]] radicles when dispersed in the solution. As these hydroxyl radicles are highly toxic and readily reactive in the

oxidation of organic substances. These $[HO^\cdot]$ radicals inhibit the microbial growth by targeting the DNA and enzyme in the nucleus of cell [24-25]. Also, the reactive oxygen species (ROS) like H_2O_2 , OH and O_2^\cdot are responsible to rupture the cell membrane and make it porous which may lead to bacterial destruction [26-28]. The variation in inhibition zone diameter vs. different nanocomposites is graphically represented in figure 5.

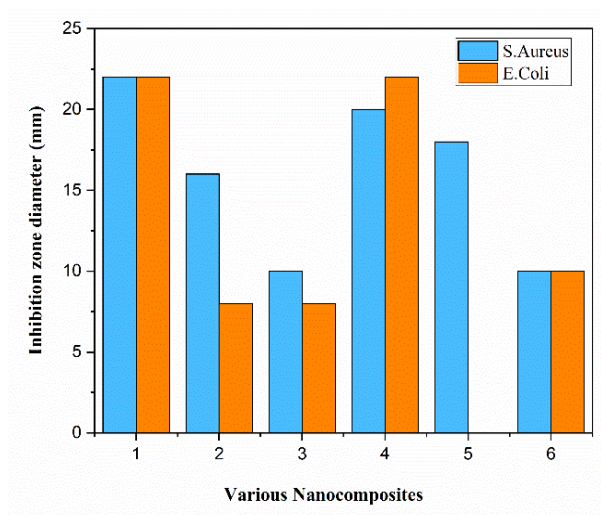


Fig.5. Bar Chart of Inhibition zone diameter vs. synthesized samples, where 1, 2, 3,4,5,6 correspond to Ofloxacin, TiO_2 , Pure PANI, PT5%, PT15%, and PT25% respectively against pathogenic bacteria.

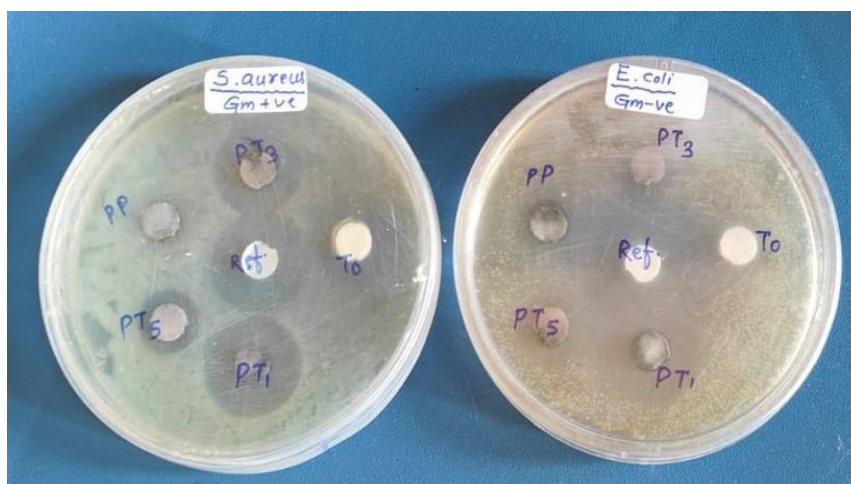


Fig.6. Antibacterial activity of Pure PANI, TiO_2 NPs, and various PANI/ TiO_2 Nano composites PT1 (5%), PT3 (15%) and PT5 (25%) tested against gram positive (*S. aureus*) and gram negative (*E. coli*) bacterial strains.

IV. Conclusion

The above discussion can be summarized as, synthesis of PANI- TiO_2 nanocomposites were done by in-situ chemical oxidative polymerization reaction. The TiO_2 nanoparticles were successfully incorporated within the PANI matrix with various amounts of TiO_2 using APS as oxidant. The applied method was simple, low cost and so easy that a very less chemical required unlike other

methods. The presence of TiO₂ NPs and strong chemical interaction between PANI-TiO₂ nanocomposite was confirmed by FTIR analysis. The synthesis of broad long chain polymers with some degree of crystallinity were confirmed by the XRD data. XRD study reveals that the crystalline TiO₂ NPs are well incorporated into the PANI surface. The particle size was obtained using Scherer equation and is in the range of 10 - 50 nm. The UV-Vis. Spectra confirms the strong intermolecular interaction of each individual particle with polymer. The optical band gap energy for different nanocomposite has been calculated using Tauc's Plot. The band gap energy was found to be decreased with loading of TiO₂ NPs. In addition to this the proposed research was further studied to the antibacterial study. The results confirmed that novel PANI-TiO₂ nanocomposites have shown the great resistance to the bacterial growth. The sample PT1 (PANI with 5% TiO₂) showed the best bactericidal activity against both pathogenic strains. With increase in the amount of TiO₂ the inhibition zone decreases. This may be due to the small particle size and agglomeration of polymer on the surface of TiO₂ nanoparticles. Thus, we conclude that loaded TiO₂ nanoparticles enhanced the antibacterial activity and these biomaterials can further used for the packaging of food product, paint industries, textile, pharmaceutical and medicine.

Acknowledgment

The proposed work was carried out at the Dept. of Physics and Electronics, Government Vidarbha Institute of Science and Humanities, Amravati (Autonomous). Author wish to thanks both Dr. S.P.Yawale H.O.D. Physics and Electronics, the Director, Govt.V.I.S.H. Amravati (Autonomous). This research did not receive any specific grant from funding agencies in the public, commercial, or not-for-profit sectors.

References

- 1) Özerol, E. A., Bozdoğan, A. Ç., Şenkal, B. F., & Okutan, M. (2016). The effect on the impedance characteristics of the metal oxides (Al₂O₃ and ZnO) doping into polyaniline Materials Science in Semiconductor Processing, 56, 357-361.
- 2) Cheng, Y. J., Yang, S. H., & Hsu, C. S. (2009). Synthesis of conjugated polymers for organic solar cell applications. Chemical reviews, 109(11), 5868-5923.
- 3) Oh, M., Park, S. J., Jung, Y., & Kim, S. (2012). Electrochemical properties of polyaniline composite electrodes prepared by in-situ polymerization in titanium dioxide dispersed aqueous solution. Synthetic metals, 162(7-8), 695-701.
- 4) Stejskal, J., Hajná, M., Kašpárková, V., Humpolíček, P., Zhigunov, A., & Trchová, M.(2014). Purification of a conducting polymer, polyaniline, for biomedical applications. Synthetic Metals, 195, 286-293.
- 5) Manjunatha, B., Shetty, A. N., Kaveri, S., Mety, S. S., Anjaneya, K. C., Reddy, R., & Kalyane, S. (2020). Chemical Mediated Synthesis of Polyaniline/Tungstenoxide (PANI/WO₃) Nanocomposites and Their Antibacterial Activity Against Clinical Pathogenic Bacteria. BioNanoScience, 10, 73-80.

- 6) Molapo, K. M., Ndagili, P. M., Ajayi, R. F., Mbambisa, G., Mailu, S. M., Njomo, N., ... & Iwuoha, P. B. I. (2012). Electronics of conjugated polymers (I): polyaniline. *International Journal of Electrochemical Science*, 7(12), 11859-11875.
- 7) Chiang, C. K., Druy, M. A., Gau, S. C., Heeger, A. J., Louis, E. J., MacDiarmid, A. G., ... & Shirakawa, H. (1978). Synthesis of highly conducting films of derivatives of polyacetylene, (CH)_x. *Journal of the American Chemical Society*, 100(3), 1013-1015.
- 8) Jotiram, K. P., Prasad, R. G. S. V., Jakka, V. S., Aparna, R. S. L., & Phani, A. R. (2012). Antibacterial Activity of Nanostructured Polyaniline Combined With Mupirocin. *Nano Biomedicine & Engineering*, 4(3).
- 9) Palaniappan, S., & John, A. (2008). Polyaniline materials by emulsion polymerization pathway. *Progress in polymer science*, 33(7), 732-758.
- 10) Jain, R., Jadon, N., & Pawaiya, A. (2017). Polypyrrole based next generation electrochemical sensors and biosensors: A review. *TrAC Trends in Analytical Chemistry*, 97, 363-373.
- 11) Zhao, P., Li, N., & Astruc, D. (2013). State of the art in gold nanoparticle synthesis. *Coordination Chemistry Reviews*, 257(3-4), 638-665.
- 12) Babazadeh, M., Zalloi, F., & Olad, A. (2015). Fabrication of conductive polyaniline nanocomposites based on silica nanoparticles via in-situ chemical oxidative polymerization technique. *Synthesis and Reactivity in Inorganic, Metal-Organic, and Nano-Metal Chemistry*, 45(1), 86-91.
- 13) Revathi, T., & Thambidurai, S. (2018). Immobilization of ZnO on Chitosan-Neem seed composite for enhanced thermal and antibacterial activity. *Advanced Powder Technology*, 29(6), 1445-1454.
- 14) Ramesan, M. T., & Sampreeth, T. (2018). In situ synthesis of polyaniline/Sm-doped TiO₂ nanocomposites: evaluation of structural, morphological, conductivity studies and gas sensing applications. *Journal of Materials Science: Materials in Electronics*, 29, 4301-4311.
- 15) Ramesan, M. T., Santhi, V., Bahuleyan, B. K., & Al-Maghrabi, M. A. (2018). Structural characterization, material properties and sensor application study of in situ polymerized polypyrrole/silver doped titanium dioxide nanocomposites. *Materials Chemistry and Physics*, 211, 343-354.
- 16) Venkatasubbu, G. D., Baskar, R., Anusuya, T., Seshan, C. A., & Chelliah, R. (2016). Toxicity mechanism of titanium dioxide and zinc oxide nanoparticles against food pathogens. *Colloids and Surfaces B: Biointerfaces*, 148, 600-606.
- 17) Cogal, S., Ali, A. K., Erten-Ela, S., Celik Cogal, G., Kulicek, J., Micusik, M., ... & Oksuz, A. U. (2018). Plasma-based preparation of polyaniline/graphene and polypyrrole/graphene composites for dye-sensitized solar cells as counter electrodes. *Journal of Macromolecular Science, Part A*, 55(4), 317-323.

- 18) Hosseini, M. G., & Sefidi, P. Y. (2017). Electrochemical impedance spectroscopy evaluation on the protective properties of epoxy/DBSAdoped polyaniline-TiO₂ nanocomposite coated mild steel under cathodic polarization. *Surface and Coatings Technology*, 331, 66-76.
- 19) Tang, W., Li, L., & Zeng, X. (2015). A glucose biosensor based on the synergistic action of nanometer-sized TiO₂ and polyaniline. *Talanta*, 131, 417-423.
- 20) Sampreeth, T., Al-Maghrabi, M. A., Bahuleyan, B. K., & Ramesan, M. T. (2018). Synthesis, characterization, thermal properties, conductivity and sensor application study of polyaniline/cerium-doped titanium dioxide nanocomposites. *Journal of Materials Science*, 53(1), 591-603.
- 21) Xia, H., & Wang, Q. (2003). Preparation of conductive polyaniline/nanosilica particle composites through ultrasonic irradiation. *Journal of Applied Polymer Science*, 87(11), 1811-1817.
- 22) Morsi, M. A., Rajeh, A., & Al-Muntaser, A. A. (2019). Reinforcement of the optical, thermal and electrical properties of PEO based on MWCNTs/Au hybrid fillers: nanodielectric materials for organoelectronic devices. *Composites Part B: Engineering*, 173, 106957.
- 23) Morsi, M. A., Rajeh, A., & Menazea, A. A. (2019). Nanosecond laser-irradiation assisted the improvement of structural, optical and thermal properties of polyvinyl pyrrolidone/carboxymethyl cellulose blend filled with gold nanoparticles. *Journal of Materials Science: Materials in Electronics*, 30, 2693-2705.
- 24) Abutalib, M. M., & Rajeh, A. (2020). Preparation and characterization of polyaniline/sodium alginate-doped TiO₂ nanoparticles with promising mechanical and electrical properties and antimicrobial activity for food packaging applications. *Journal of Materials Science: Materials in Electronics*, 31, 9430-9442.
- 25) Özyıldız, F., Güden, M., Uzel, A., Karaboz, I., Akil, O., & Bulut, H. (2010). Antimicrobial activity of TiO₂-coated orthodontic ceramic brackets against *Streptococcus mutans* and *Candida albicans*. *Biotechnology and Bioprocess Engineering*, 15, 680-685.
- 26) Yamamoto, O. (2001). Influence of particle size on the antibacterial activity of zinc oxide. *International Journal of Inorganic Materials*, 3(7), 643-646.
- 27) Kumar, R., Umar, A., Kumar, G., & Nalwa, H. S. (2017). Antimicrobial properties of ZnO nanomaterials: A review. *Ceramics International*, 43(5), 3940-3961.
- 28) Lakshmi Prasanna, V., & Vijayaraghavan, R. (2015). Insight into the mechanism of antibacterial activity of ZnO: surface defects mediated reactive oxygen species even in the dark. *Langmuir*, 31(33), 9155-9162.
- 29) Ramakrishnan, S., & Rajakarthishan, S. (2020). Antimicrobial study on gamma-irradiated polyaniline–aluminum oxide (PANI–Al₂O₃) nanoparticles. *International Nano Letters*, 10, 97-110.

- 30) Kanmani, P., & Rhim, J. W. (2014). Properties and characterization of bionanocomposite films prepared with various biopolymers and ZnO nanoparticles. *Carbohydrate polymers*, 106, 190-199.
- 31) Costa, C. O. N. T. E., Conte, A., Buonocore, G. G., & Del Nobile, M. A. (2011). Antimicrobial silver-montmorillonite nanoparticles to prolong the shelf life of fresh fruit salad. *International Journal of Food Microbiology*, 148(3), 164-167.
- 32) Zhang, L., Jiang, Y., Ding, Y., Daskalakis, N., Jeuken, L., Povey, M., ... & York, D. W. (2010). Mechanistic investigation into antibacterial behavior of suspensions of ZnO nanoparticles against *E. coli*. *Journal of Nanoparticle Research*, 12, 1625-1636.

¹*A. P. Deshmukh¹S. P. Tiwari²A. V. Tiwari¹P.S.Awandkar³M. S. Dixit⁴D. P. Deshmukh¹S. P. Yawale

Structural Investigation of PEDOT-PSS Conducting Polymer Treated with Solvent



Abstract: - In this study, the PEDOT-PSS (Poly 3, 4-ethylenedioxythiophene-Polysodium 4-styrenesulfonate) has been synthesized with the help of chemical oxidative method. The structure of composites were studied with the help of Fourier transform infrared (FTIR) spectroscopy over the wavelength range of 600-4000 cm^{-1} and it shows the various group position of the molecules. The X-Ray diffraction (XRD) technique reveals the amorphous nature of the samples. The characterization of Ultraviolet Visible (UV- visible) spectra and is used to study the direct and indirect transition and optical band gap. The surface morphology has been studied with the help of Scanning Electron Microscopy (SEM). The behavior of electrical conductivity at different temperature of PEDOT -PSS in the ratio of EDOT: PSS (1:1, 1:2, 1:3, 3:1 and 5:1) has been taken on the conducting paper by treated with Methanol, Ethanol and DMSO (Dimethyl Sulphoxide). The 1:1 ratio material sample was more conductive as compare to other ratio. For the 3:1 ratio the conductivity found to be less than other ratio.

Keywords: PEDOT-PSS, APS, SEM, XRD, UV- Visible, Electrical Conductivity

I. INTRODUCTION

With the objective to construct organic electrochemical and optoelectronic devices, conducting polymers, including doped conducting polymers and intrinsic semiconducting conjugated polymers, are considered essential. Researchers have recently turned their attention to studying a novel kind of thiophene group called PEDOT (Poly 3,4-ethylenedioxythiophene) polymers. Because of its straightforward synthesis method and special qualities—such as mechanical flexibility, adjustable electrical conductivity, environmental stability, low cost, and solution processability—the P-type of PEDOT is an essential material [1-2]. The PEDOT-PSS (Polysodium 4-styrenesulfonate) polymer exhibits a high electrical conductivity, with hydrophobic PEDOT molecules coated in hydrophilic PSS molecules. As a result of the selective removal of PSS, the hydrophilic ethylene glycol solvent gets increasingly ineffective [3]. H.Ziyanget. al, suggests that by enhancing PEDOT-PSS, conductivity has a significant role in improving short circuit current and fill factor [4]. PEDOT exhibits superior qualities compared to other π -conjugated polymers because of its exceptional stability, electro-optical, transparency, and conductivity, while being employed in just a handful of uses [5]. Due to PSS's polyelectrolyte nature and PEDOT's solubility in water, PEDOT and PSS form a conjugated polymer. While PEDOT imparts a positive charge, PSS carries a negative charge [6]. Pristin PEDOT-PSS is utilized as a transparent electrode because of its poor conductivity. The effectiveness of electrical conductivity using organic solvent is dependent on a change in the PEDOT backbone structure; as a result, the electrical characteristics of the final nanomaterials can be adjusted by modulating the conductivity of PEDOT-PSS using dopant, although the exact mechanism is still unresolved [7]. PEDOT's conductivity exhibits an excess of insulating limit, which has an impact on its application in low resistance [8]. The composition ratio has a significant impact on PEDOT-PSS electrical conductivity, and it exhibits ideal conditions for the Hopping charge carrier [9]. By reorienting the polymer chain, PEDOT-PSS treated with solvent enhances the quality of conductivity and mobility charge carrier. This occurs because the addition of nanoparticles improves the overall electrochemical performance by reducing the coulomb contact that causes a screening effect in the PEDOT-PSS molecule [10,11,12].

¹*Corresponding author: A. P. Deshmukh

Department of Physics, Government Vidarbha Institute of Science and Humanities, Amravati-444604.

²Department of Physics, ShriMathura Das Mohota College of Science, Nagpur -440009, Maharashtra.

³JagadambaMahavidyalaya, Achalpur, Amravati-444806.

⁴Lt. R. Bharti Arts, Comm. And Smt. S. R. Bharti Sci. College, Arni, Dist.- Yavatmal.

Copyright@JES2024on-line:journal.esrgroups.org

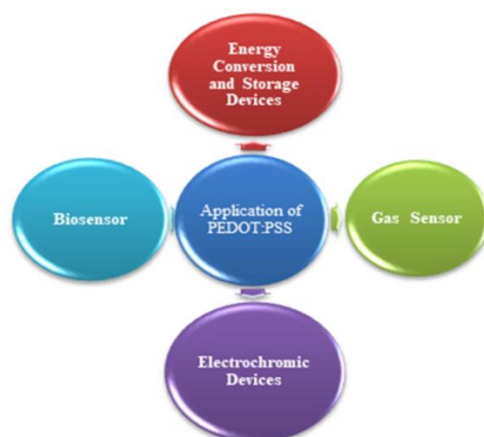


Fig 1. Applications of PEDOT-PSS to different fields.

PEDOT-PSS has a broad application area due its high electrical conductivity, good stability in air, high mechanical flexibility and high transparency shown in fig.1.

In the present research work, the synthesis of PEDOT-PSS (Poly 3,4-ethylenedioxythiophene-Polysodium-4-styrenesulfonate) has been done with the help of insitu chemical oxidative method using Ammonium Persulphate (APS) and Ferric Chloride Anhydrous (FeCl_3). The characterization of sample is carried out by XRD (X-Ray diffraction), Fourier transform infrared spectroscopy (FTIR) , Ultraviolet-Visible Spectroscopy (UV- Visible) and Scanning Electron Microscopy (SEM). The electrical conductivity and activation energy of PEDOT-PSS sample with different solvent has been examined.

II. EXPERIMENTAL SECTION

1. Materials and Reagents

Poly(sodium-4-styrenesulfonate) (PSS) ($M_w = 75,000$ g/mol) is procured from Sigma Aldrich and EDOT (3,4-ethylenedioxythiophene) monomer acquired from TCI (Tokyo Chemical Industries), Ferric Chloride Anhydrous (FeCl_3) from Hi Media ,DMSO, Ammonium Persulphate (APS) from Fisher Scientific, Ethylene Glycol and Ammonium Persulphate (APS) from Fisher Scientific.

2. Preparation of PEDOT-PSS

The 50 ml solution of PSS is prepared in the ratio 1:1 (EDOT-PSS) in distilled water. This solution is ultrasonicated for 45 minutes to get homogenous mixture of PSS solution. After sonication EDOT monomer is added into PSS solution and well mixed with the help of magnetic stirrer. Add APS at 1:2 mass ratio (EDOT : APS) directly in the above mixture and dissolve then add drop by drop FeCl_3 solution which is prepared at 1:0.6 mass ratio (EDOT : FeCl_3)[13]. The Polymerization reaction started as the drop of FeCl_3 mixed in the above mixture then color changes into blue and vigorously stirred it up to 2 h at room temperature during polymerization reaction. Keep this solution for 16 hours as it is. The obtained product was filtered with the help of filter paper and washed several times with distilled water. The obtained product is dried at 60° on the filter paper in oven for 24 h. Finally we get bluish black product and crushed it in the Agate Mortar Pestle to obtain fine powder. The same procedure is repeated for 1:2, 1:3, 5:1, 3:1 mass ratio (EDOT : PSS) without changing the ratio for APS and FeCl_3 with respect to EDOT monomer that will remain as it is for the polymerization reaction. The nomenclature of the samples PSS 5:1, 3:1, 1:1, 1:2 and 1:3 ratio were denoted as A0, A, B, C, D and E.

3. Fabrication of conducting Polymer

The synthesized conducting polymer PEDOT-PSS was fabricated on Whatmann filter paper by using chemical bath deposition (CBD) method to investigate the electrical conductivity at various temperatures. Firstly the conducting sample was added in 10 ml of Ethylene Glycol with a constant stirring about 2 h and was ultrasonicated for the next 1 h. A small piece of Whatmann filter paper has been added in the above mixture and was left undisturbed over 4 h. The sample was dried in the oven. Again this sample was added in the beaker of EG. Repeatedly the procedure was followed to obtain the layer by layer deposition of the sample on the Whatmann filterpaper.

4. Characterization

The XRD data is obtained from Rigaku MiniFlex 600 X-ray spectrophotometer which is operated at maximum voltage 40 kV and 15 mA Current. The FTIR analysis is carried out from Alpha Brooker Instrument spectrometer. The direct indirect transition and optical band gap was studied with the help UV-Visible

spectrometer. The surface morphology has been studied with the help of SEM and the compositions of elements were confirmed by Energy Dispersive X-Ray Spectroscopy (EDX). The electrical conductivity of the PEDOT-PSS was measured with the help of two probe methods and showed the conductivity at different temperature.

III. RESULTS AND DISCUSSION

1. X-Ray Diffraction (XRD)

The investigation of XRD pattern of synthesized samples was recorded in the 2θ ranges from 10° - 80° . All the spectra of PEDOT-PSS ratio and pure PSS are shown in fig 2. The pure PSS showed peak at $2\theta = 31.8^\circ$ which is observed due to the presence of Na in PSS. A broad peak in samples A, B, C, D, E were observed ranging from 20.15° to 28° confirmed the successful formation of insitu polymerization of EDOT: PSS monomer [14]. The increase in the concentration of PSS did not influence any crystallinity in this composite. Consequently, PEDOT-PSS sample with varying ratio were indicate the complete amorphous in nature.

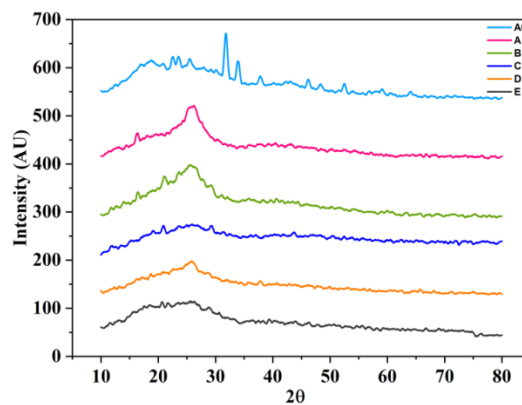


Fig 2. XRD of sample A0, A, B, C, D and E

2. FTIR Analysis

Fig 3 shows the FTIR spectra of PEDOT-PSS with varying ratio of all samples in 4000 - 600 cm^{-1} wavenumber range. From the FTIR spectra it is observed that O-H stretching is present which confirms from the peak at 3691 cm^{-1} for C sample and it is seen varies for the other samples of increasing concentration of PSS too [15]. The C-H bonding is confirmed by the distinctive absorption spectra, which have a peak at 2877 cm^{-1} [16, 17]. Additionally, the strong bond and significant vibration polarity of the carbonyl are investigated at 1709 cm^{-1} through C=O [18]. The weak vibrations caused by C=C stretching are responsible for the peak that was recorded at 1568 cm^{-1} . The presence of PEDOT-PSS is confirmed by the band at frequency of 1135 cm^{-1} , which corresponds to stretching modes for the aromatic sulfonate ester group and (C-O-C) stretching in the ethylenedioxy groups of the PEDOT units. The weak stretching vibration of the C-O bond is associated with the band at frequency 1065 cm^{-1} .

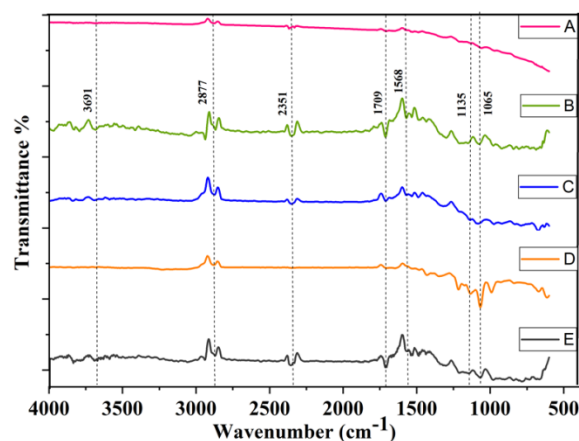


Fig 3. FTIR of all the samples.

3. Scanning Electron Microscopy (SEM)

Fig. 4a, b, c shows the surface morphology of PEDOT-PSS samples A, C and D and studied with the help of SEM. The SEM image of samples A, C and D of EDOT: PSS ratio (5:1, 1:1 and 1:2) shows the agglomeration of particles. The Fig. 4 (a) the compact cluster of discrete particles just like a broccoli vegetable. The smooth structure morphology indicates the poor electrical conductivity because it is not good for transfer of electron in the polymer chain. The SEM images of sample C and D reveals rough surfaces as a result of this both the samples is good electrical conductivity. From the surface morphology it observed that as the rough surface increase the electrical conductivity also increase due the addition of PSS leads to the formation of microparticle. The charge transfer mechanism plays an important role in the system. The Energy Dispersive X-Ray Spectroscopy (EDX) reveals that the chemical composition of elements in the polymer sample A, C and D is as shown in fig. 5. From the study of EDX shows that it contains composition of Carbon, Nitrogen, Sulphur and Oxygen element. In case of preparation of sample A the carbon atom contributes more but in case of sample C oxygen atom is less and large amount of oxygen is present in the sample D. The interconnection in the elements leads to change in the conductivity of PEDOT-PSS.

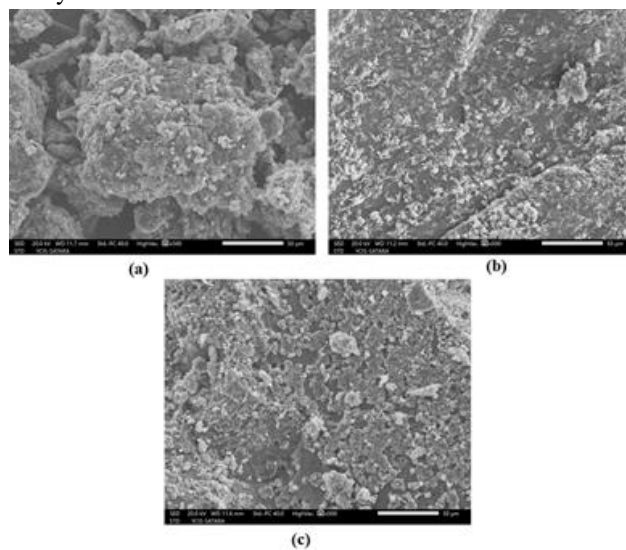


Fig 4 SEM images for (a) A, (b) C, (c) D samples of PEDOT: PSS.

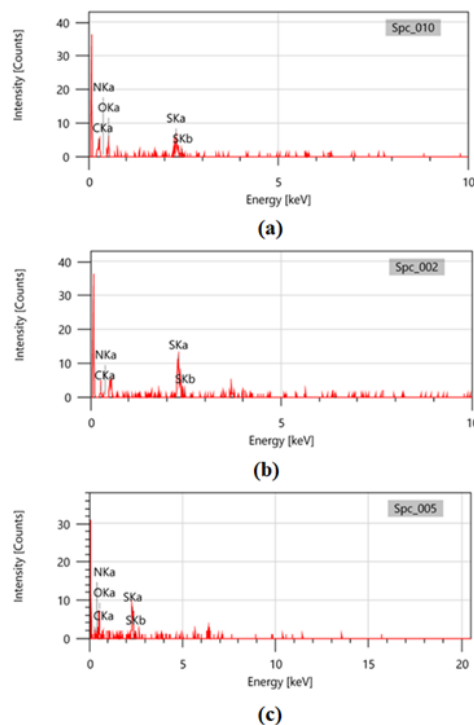


Fig 5 EDAX study for (a) A, (b) C, (c) D samples of PEDOT: PSS.

4. UV-Visible Spectra

The UV- Visible spectra is use to study the direct and indirect transition and to find at the optical energy band gap over a wavelength range 200 to 800 nm. The fig 6 reveals the UV-Visible spectra of synthesized PEDOT-PSS by changing the ratio of EDOT to PSS. A broad absorption peak was observed in between 200 to 420 nm near the UV region which slightly changes but very similar to the previously reported composite PEDOT-PSS sample as shown in Fig 6 (a) [21]. The peak were observed as a result of the bonding to antibonding in the range of 200 to 300 nm occurred due to the p-p* transition A, B, D and E [22] but in case of C two peaks were present. Both the peaks occurred due to the presence of aromatic ring in PSS but the peak present at 350 nm shows the bonding to nonbonding, p-n transition [23]. From the spectra it clearly indicates that lower concentration of PSS shows the higher absorption spectrum. The optical energy band gap is determined by Tauc's plot and its relation is given by equation no.(1):

$$\alpha \cdot h \cdot v = A (h \cdot v - E_g)^n \dots\dots\dots (1)$$

The Table 1. shows the direct transition of optical energy band gap for varying concentration of PSS. The Optical Energy band gap of Conducting samples of PEDOT-PSS is shown in the fig 6 (b).It illustrates that the optical energy band gap of sample A found to be more 2.41eV than sample E, therefore the nature of the sample found to be in semiconducting due to optical energy band gap lie between conductor and insulator.

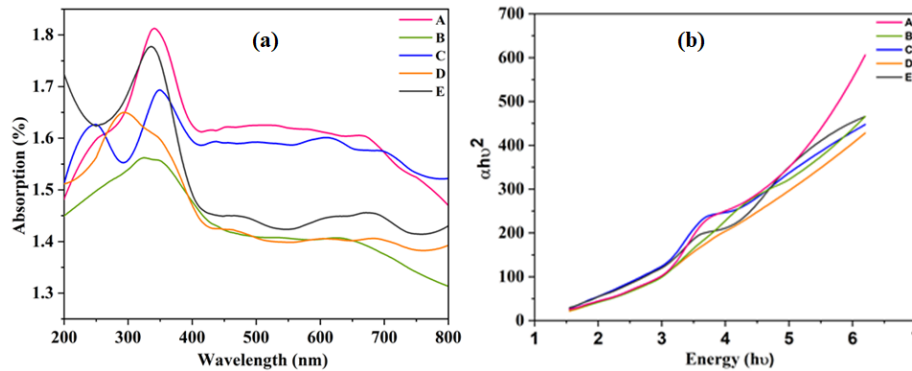


Fig 6. (a) A plot of UV-vis absorption spectra and (b) The Optical Energy band gap of all Conducting samples of PEDOT-PSS.

Table 1. Optical energy band gap for varying concentration of PEDOT: PSS.

Sr.No.	Concentration of EDOT:PSS	Optical Energy Band Gap (eV)
1.	A	2.41
2.	B	2.05
3.	C	2.14
4.	D	1.85
5.	E	1.81

5. DC Electrical Conductivity Analysis

The DC electrical conductivity was studied with the help of two probe method. Fig 7 illustrates the variation of DC electrical conductivity of synthesized PEDOT-PSS material with a varying concentration of PSS. The DC Electrical Conductivity of the conducting samples was determined by using Arrhenius equation (2),

$$\sigma = \sigma_0 \exp (-\Delta E / K T) \dots\dots\dots (2)$$

The Arrhenius plot, which indicates the temperature dependence of the DC electrical conductivity for solvents such as methanol, ethanol, and DMSO treated with varying concentrations of EDOT, was applied to PSS samples A (5:1), B (3:1), C (1:1), D (1:2), and E (1:3). The DC electrical conductivity was then investigated in the temperature range of 303-358K. The DC electrical conductivity rises in accordance with temperature. This is revealed by fig 7 (a). As in case of pure sample E found to be more conducting and sample A is the least. The ultimate reason is the change in the concentration of PSS. According to Fig 7(b), Sample C has the highest electrical conductivity in the DMSO instance, while Sample A has the lowest conductivity compared to the other samples. Similarly Fig. 7(c) and 7(d), these figures show that Sample E and Sample C were more conductive than

the other samples. Additionally, in all cases, sample A had the lowest DC electrical conductivity. The addition of methanol, ethanol, DMSO indicates that the change in the morphology of thin film due to the hopping of charge carriers. The variations of different solvents with the concentration verses conductivity is shown in the fig 8. Pure and ethanol have highest conductivity in sample E while DMSO and methanol has highest conductivity to sample C. The fig 9 represents the change in conductivity with various concentrations of PSS. It is observed that a 1:2 ratio greatly impacts electrical conductivity for pure samples. We also got the same results for ethanol and methanol. Large electrical conductivity was seen in sample C (1:1), much as in the case of DMSO. As a result, conductivity changed barely in terms of temperature, indicating that conductivity did not vary as temperature rose. The concentration of PSS and the changes in behavior produced by solvents actively participating in the activation energy and charge carriers that were able to move into the conducting site of the polymer matrix are other factors that affect conductivity. Table 2 displays the activation energy of different solvents for each of the samples A, B, C, D, and E.

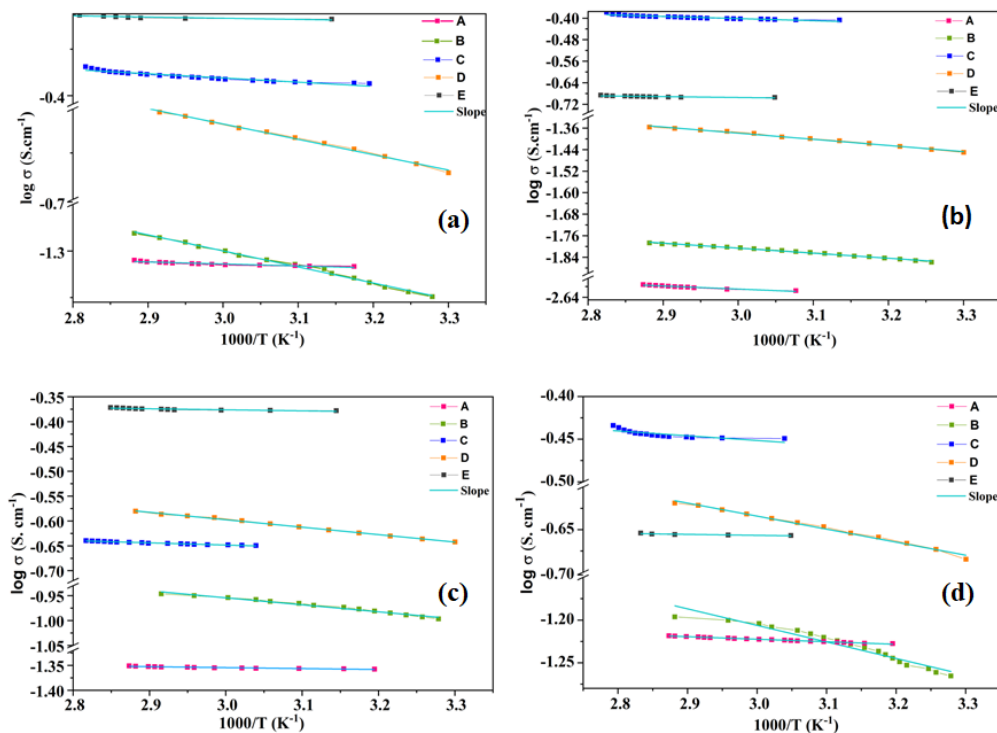


Fig 7. DC Electrical Conductivity as a function of temperature for (a) Pure, (b) DMSO, (c) Ethanol and (d) Methanol for all the samples.

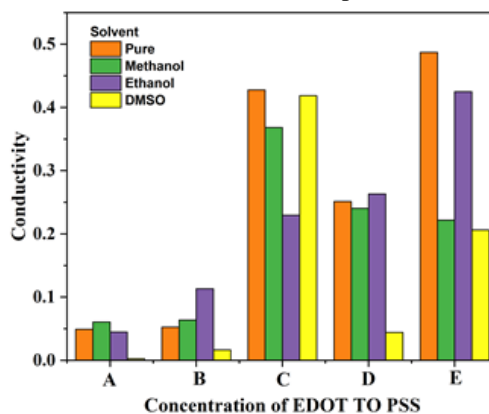


Fig 8. The plot of concentration of EDOT to PSS versus conductivity

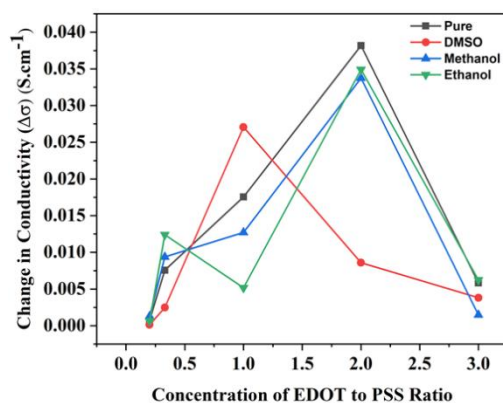


Fig 9. The plot of concentration of EDOT to PSS verses change in conductivity.

Table 2. Activation energy of various solvents for all samples of PEDOT:PSS.

Concentration of EDOT to PSS	ΔE Pure ($\times 10^{-3}$ eV)	ΔE Methanol ($\times 10^{-3}$ eV)	ΔE Ethanol ($\times 10^{-3}$ eV)	ΔE DMSO ($\times 10^{-3}$ eV)
A	1.840591	2.564419	1.627751	9.846646
B	14.847953	16.697161	12.154279	16.106035
C	3.889714	4.799669	3.814746	6.92893
D	14.199954	13.14351	12.897064	19.726898
E	1.108146	0.978891	1.789751	0.978891

IV. CONCLUSION

The samples of PEDOT-PSS polymer were prepared with the help Chemical Oxidative method by varying concentration of PSS in the ratio of 5:1, 3:1, 1:1, 1:2 and 1:3 EDOT to PSS. This synthesized sample was treated with solvents Methanol, Ethanol and DMSO. The structural investigation of sample was characterized by XRD, FTIR, SEM and UV-Visible spectra. From the XRD it is conclude that sample PEDOT-PSS possess the amorphous nature. The FTIR indicates the various positions of the molecules and the frequency of band at 1135 cm^{-1} confirm the bonding of PSS with PEDOT. Also the vibrational polar and strong bond of carbonyl is $\text{C}=\text{O}$ represent by the presence of peak at 1709 cm^{-1} . Surface Morphology of sample A, C and D has been studied with the help of SEM. The image shows the agglomeration of the particle in polymeric matrix and from EDX it confirms that the element C, N, S and O are present. The UV-Visible spectra determine the optical energy band gap. The smallest concentration of PSS shows the highest energy band gap among all. The activation energy of the PEDOT-PSS sample were find to be in the range of 10-3 eV. The 1:2 ratio reveals the largest change in conductivity with concentration of PSS. In the similar fashion all the parameters of various ratios of PEDOT-PSS samples treated with solvents were studied.

ACKNOWLEDGMENT

The authors would like to thanks Prof. S. P. Yawale Head, Department of Physics and Electronics, Government Vidarbha Institute of Science and Humanities, Amravati for their guidance and support during this study. Authors also acknowledge Director, Government Vidarbha Institute of Science and Humanities, Amravati for providing necessary facilities to complete this study.

REFERENCES

- [1] Groenendaal, L., Jonas, F., Freitag, D., Pielartzik, H. and Reynolds, J.R., 2000. Poly (3, 4-ethylenedioxythiophene) and its derivatives: past, present, and future. *Adv. Mater.*, pp.12-481.
- [2] Wang, Y., 2009, March. Research progress on a novel conductive polymer—poly (3, 4-ethylenedioxythiophene)(PEDOT). In *Journal of Physics: Conference Series* (Vol. 152, No. 1, p. 012023). IOP Publishing.
- [3] Kim, G.H., Shao, L., Zhang, K. and Pipe, K.P., 2013. Engineered doping of organic semiconductors for enhanced thermoelectric efficiency. *Nature materials*, 12(8), pp.719-723.
- [4] Hu, Z., Zhang, J., Hao, Z. and Zhao, Y., 2011. Influence of doped PEDOT: PSS on the performance of polymer solar cells. *Solar Energy Materials and Solar Cells*, 95(10), pp.2763-2767.
- [5] Groenendaal, L., Jonas, F., Freitag, D., Pielartzik, H. and Reynolds, J.R., 2000. Poly (3, 4 - ethylenedioxythiophene) and its derivatives: past, present, and future. *Advanced materials*, 12(7), pp.481-494.

- [6] Ko, I.H., Kim, S.J., Lim, J., Yu, S.H., Ahn, J., Lee, J.K. and Sung, Y.E., 2016. Effect of PEDOT: PSS coating on manganese oxide nanowires for lithium ion battery anodes. *Electrochimica Acta*, 187, pp.340-347.
- [7] Zhou, J. and Lubineau, G., 2013. Improving electrical conductivity in polycarbonate nanocomposites using highly conductive PEDOT/PSS coated MWCNTs. *ACS applied materials & interfaces*, 5(13), pp.6189-6200.
- [8] Kim, Y.H., Sachse, C., Machala, M.L., May, C., Müller - Meskamp, L. and Leo, K., 2011. Highly conductive PEDOT: PSS electrode with optimized solvent and thermal post - treatment for ITO - free organic solar cells. *Advanced Functional Materials*, 21(6), pp.1076-1081.
- [9] Horii, T., Hikawa, H., Katsunuma, M. and Okuzaki, H., 2018. Synthesis of highly conductive PEDOT: PSS and correlation with hierarchical structure. *Polymer*, 140, pp.33-38.
- [10] Pumera, M., 2011. Graphene in biosensing. *Materials today*, 14(7-8), pp.308-315.
- [11] Ouyang, J., 2013. Solution-processed PEDOT: PSS films with conductivities as indium tin oxide through a treatment with mild and weak organic acids. *ACS applied materials & interfaces*, 5(24), pp.13082-13088.
- [12] Ouyang, J., Xu, Q., Chu, C.W., Yang, Y., Li, G. and Shinar, J., 2004. On the mechanism of conductivity enhancement in poly (3, 4-ethylenedioxythiophene): poly (styrene sulfonate) film through solvent treatment. *Polymer*, 45(25), pp.8443-8450.
- [13] Feng, X., Wang, X., Wang, M., Zhou, S., Dang, C., Zhang, C., Chen, Y. and Qi, H., 2021. Novel PEDOT dispersion by in-situ polymerization based on sulfated nanocellulose. *Chemical Engineering Journal*, 418, p.129533.
- [14] Ram, J., Singh, R.G., Singh, F., Kumar, V., Chauhan, V., Gupta, R., Kumar, U., Yadav, B.C. and Kumar, R., 2019. Development of WO 3-PEDOT: PSS hybrid nanocomposites based devices for liquefied petroleum gas (LPG) sensor. *Journal of Materials Science: Materials in Electronics*, 30, pp.13593-13603.
- [15] A. Pasha, A. Roy, M. Murugendrappa, O. Al-Hartomy and S.Khasim, Conductivity and dielectric properties of PEDOT-PSS doped DMSO nano composites thin films, *J Mater Sci: Mater Electron*, 2016.
- [16] J. Lee, S. Lee, F. Kim, H. Choi and J. Kim, Simultaneous enhancement of the efficiency and stability of organic solar cells using PEDOT: PSS grafted with a PEGME buffer layer, *Org. Electron*. 26, 191, 2015.
- [17] D. Mengistie, P. Wang and C.Chu, Effect of molecular weight of additives on the conductivity of PEDOT: PSS and efficiency for ITO-free organic solar cells, *J. Mater. Chem. A1*, 9907, 2013.
- [18] M. Tadesse, C. Loghin, Y. Chen, L. Wang, D. Catalin and V. Nierstrasz, Effect of liquid immersion of PEDOT:PSS-coated polyester fabric on surface resistance and wettability, *Smart Mater. Struct.* 26, 065016, 2017.
- [19] J. Lee, W. Choi, Surface Modification of Sulfur Cathodes with PEDOT:PSS Conducting Polymer in Lithium-Sulfur Batteries, *J. Electrochem. Soc.* 162, A935, 2015.
- [20] J. Ram, R. Singh, F. Singh, V. Kumar, V. Chauhan, R. Gupta, U. Kumar, B. Yadav, R. Kumar, Development of WO₃ - PEDOT: PSS hybrid nanocomposites based devices for liquefied petroleum gas (LPG) sensor, *Journal of Materials Science: Materials in Electronics*, 2019.
- [21] Bhowal, A.C., Talukdar, H. and Kundu, S., 2019. Preparation, characterization and electrical behaviors of PEDOT: PSS-Au/Ag nanocomposite thin films: An ecofriendly approach. *Polymer Bulletin*, 76, pp.5233-5251.
- [22] Alemu, D., Wei, H.Y., Ho, K.C. and Chu, C.W., 2012. Highly conductive PEDOT: PSS electrode by simple film treatment with methanol for ITO-free polymer solar cells. *Energy & environmental science*, 5(11), pp.9662-9671.
- [23] Kim, H., Pique, A., Horwitz, J.S., Mattoussi, H., Murata, H., Kafafi, Z.H. and Chrisey, D.B., 1999. Indium tin oxide thin films for organic light-emitting devices. *Applied physics letters*, 74(23), pp.3444-3446.

Article in a conference proceedings:

© 2024. This work is published under

[https://creativecommons.org/licenses/by/4.0/legalcode\(the“License”\)](https://creativecommons.org/licenses/by/4.0/legalcode(the“License”)).

Notwithstanding the ProQuest Terms and Conditions, you may use this content in accordance with the terms of the License.

¹Dr.J.S.Tated
²Dr.C.M.Jadhao
³Dr.D.S.Dhote
⁴Dr.S.D.Gawande

Real-Time Soil Fertility Detection Using Colorimetric Technology: A Precision Farming Approach In Vidarbha Region of Maharashtra



Abstract: - Agriculture is a wide economic sector and plays a vital role within the overall economic development of the nation. Over fertilization is a serious issue that affects farmers around the world. Unplanned use of fertilizers leads to inferior quality of crops and various environmental problems like water pollution, soil contamination, bio-magnification and poor food quality. Technological advancements in the sector of agriculture can ascertain to enhance the ability and quality of assured farming activities. Bad quality crop production is often because of either unnecessary use of fertilizer or insufficient addition of fertilizer. Now a day it is most important to maintain the proper ratio of nutrients for better growth and yield of the crop through organic and inorganic fertilizers. The aim of our developed system is to detect the N (nitrogen), P (phosphorus) and K (potassium) contents of soil in situ and based on the result; farmers will use the necessary fertilizers as per need. In this system we used optical technique is used for soil micronutrients detection.

Keywords: Color Sensor, Soil Fertility, NPK nutrients, Arduino, I2C OLED Display, Microcontroller, Cloud, IoT.

I. INTRODUCTION

Agriculture is the backbone of Indian economy. In India, around 70% of the population earns its earnings from agriculture[1]. Soil physical and chemical conditions play a very important role in the crop production cycle. Moreover, farmers can also add organic or inorganic nutrients to the soil in precise ratios. Therefore, soil fertility detection plays a vital role in plant growth and improved yield[2]. Continuing to cultivate without properly measuring soil nutrients can lead to decreased soil fertility and yields. Identification of soil nutrients is essential for proper plant growth and effective fertilization[3]. In the current scenario, technological developments are having a valuable impact on the agricultural sector. The use of new technologies has brought about major changes from traditional to modern farming. One modern farming method that increases productivity is precision farming. Use sensors, controls, and software systems to obtain real-time information to improve crop cultivation[4]. The general soil testing is take place in laboratories which are maximum available at district level also it take a considerable time to generates the results. Hence this process is time consuming and costly too[5]. Moreover the overall soil fertility changes with change in weather conditions. Thus a system required which will detect the soil nutrients in real time.

The system is based on colorimetric analysis technology. A color sensor is used as a soil nutrient sensor. Different reagents are added to the aqueous solution of the soil to be tested, which changes color depending on the concentration of micronutrients present. The light emitted from the color sensor hits the solution and the reflected light is received by the color sensor detectors, which converts the (R, G, B) values into electrical signals. Further use of threshold values previously stored in the microcontroller's database helps in detecting the micronutrient levels present in the soil sample.

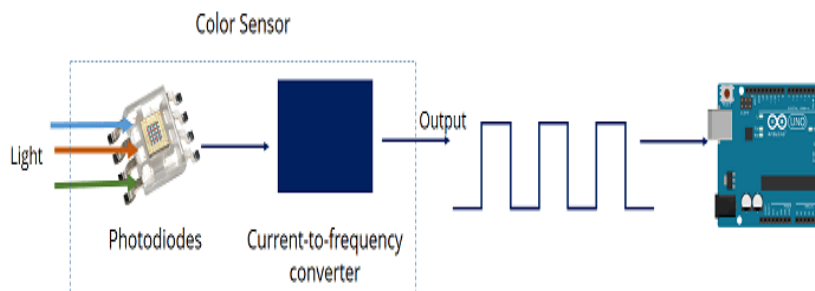





Figure 1 Concept of Colorimetric Technology

¹ Research Scholar, Post Graduate Department of Electronics, Brijlal Biyani Science College, Amravati, Dist. Amravati, M.S., India

*Corresponding author e-mail: jayesh.tated@gmail.com

Copyright © JES 2024 on-line : journal.esrgroups.org

Table 2 Importance of Nitrogen, Phosphorous and Potassium Detection

Macronutrients	Adequate	Inadequate	Results
Nitrogen	Promotes the growth of leaves and vegetation.	Tree doesn't get average height. Leaves become yellow.	
Phosphorous	Promotes root and shoot growth.	Growth of plant stops.	
Potassium	Promotes flowering, fruiting and general hardiness.	Leaves become reddish yellow on the edges while inner part of the leaves remain green.	

II. LITERATURE SURVEY

In 2015, Dhanapriya.M et al. proposed a system to test the levels of micronutrients and macronutrients in soil using portable kits. The collected data was transmitted to the target via GPRS and the ground location was identified using GPS. Simulations were performed using PROTEUS software and the results were analyzed[6]. Muhammad E.H. Chowdhury et al. developed a high-density optical sensor based on photometric nutrient detection in soil using high-precision photodiodes and light-emitting diodes in 2016. The quality of the sensor was experimentally investigated and the results were compared with those obtained with a conventional spectrophotometer and color card[3]. In 2016, D. Rupa et al. had shown a new approach to soil testing using an embedded system. The researchers developed a testing device that can analyse soil by detecting nitrogen, potassium, phosphorus, and pH levels. They measured the concentration of soil nutrients N and K using nitrate and phosphorus ISEs. They explain how to use enough fertilizer to meet the needs of your plants while taking advantage of nutrients already present in the soil[7]. The study, "Using electrical conductivity of in situ soil solutions to assess mineral nitrogen in commercial orchards: preliminary results," was published by Elena Baldi and her research group in 2020. The aim of this study is to investigate the effectiveness of soil electrical conductivity (EC) testing as a rapid method to assess inorganic nitrogen (N) in orchards and to define accurate nitrogen inputs that can help farmers avoid fertilizer waste[8]. Gagandeep Singh Kukreja and his research group published a paper on IoT for enhancing agriculture and soil nutrient storage. The research focused on essential components for plant development such as nitrogen, phosphorus, and potassium, and how to effectively control these nutrients. The proposed system uses RGB color sensors, humidity sensors, and pH sensors, all connected to a NodeMCU[9]. Agni Biswas et al. published an article in 2015 describing how they can provide farmers with tools to increase information and make their farms more productive. In it, the authors monitor soil moisture, pH, humidity, and temperature, then turn valves on or off on pipes based on input from these factors[10]. Rapid technological advances and swift legislative action not only helped India avert a food disaster but also ensured a steady increase in food production.

III. MATERIAL AND METHODOLOGY

Accurate measurement and analysis are crucial for any application. Many of these applications require low-power, low-cost portable devices. The aim is to determine various soil parameters by developing modern embedded systems that are low-power, low-cost and portable[2]. The most important consideration is to recognize the soil macronutrients, which are the main nutrients in soil for plant growth. Therefore, the nutrients nitrogen, phosphorus and potassium need to be measured for further analysis. Thus the required equipment description is as follows.

1. Arduino Nano V3

The Arduino NANO V3 is the smallest open source embedded development board from Arduino, based on the Atmega328 SMD package microcontroller. It is a surface mount breadboard friendly board with an integrated mini USB port[11]. It has 30 DIP style male I/O connectors, small in size and less expensive. The development board has everything for system development i.e. Reset, oscillator

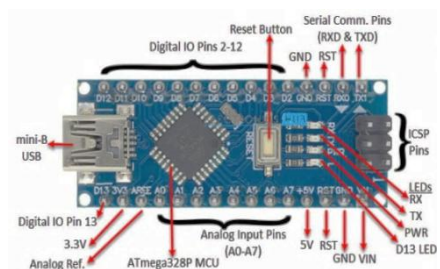


Figure 2 Arduino Nano Board Layout 217

circuit, USB to UART circuit, I2C, analog and digital I/O pins, ICSP programming headers etc.[12].

2. *TCS3200 Color Sensor*

The TCS3200 is a programmable color light-to-frequency converter with silicon photodiodes and a current-to-frequency converter on a single CMOS IC. The output is a square wave with a 50% duty cycle and frequency directly proportional to the light intensity. In the TCS3200, the light-to-frequency converter reads an 8 x 8 array of photodiodes. 16 photodiodes have blue filters, 16 photodiodes have green filters, 16 photodiodes have red filters, and 16 photodiodes have no filters. The photodiodes are 110 μm x 110 μm in size and are spaced 134 μm apart[13].



Figure 3 Schematic of TCS3200 sensor

3. *ESP8266 Wi-Fi Module*

The ESP8266 is a low-cost Wi-Fi microchip with integrated TCP/IP networking software and microcontroller capabilities. Each ESP8266 module is pre-programmed with AT commands. The ESP8266 represents a highly integrated Wi-Fi SoC solution that enables low power consumption, small size, and reliable performance for the Internet of Things, and can also be used as a Wi-Fi adapter for any microcontroller design via SPI/SDIO or UART interfaces[14].



Figure 4 Schematic of ESP8266

4. *1.3' I2C OLED Display*

This 1.3' I2C OLED display is a 128x64 monochrome dot-matrix display module with I2C interface. It is ideal when you need a super small display. Compared to LCD, OLED screens are significantly more competitive and have many advantages such as high brightness, self-illumination, high contrast ratio, slim outline, wide viewing angle, wide temperature range and low power consumption. It is compatible with 3.3V, 5V microcontrollers such as Arduino[15].

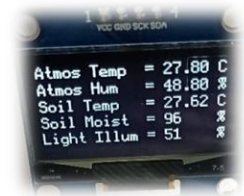


Figure 5 Schematic of 1.3' OLED Display

IV. MODELING AND ANALYSIS

To solve the above problems, we have developed a soil fertility detection system based on colorimetric technology.

1. *System Block Diagram*

In this system, the color sensor works by shining white light on a sample of soil water solution i.e. aqueous solution (The aqueous solution is made with the help of soil testing kit with standard procedure) and measuring the intensity of the reflected light using the 8x8 photodiode chip available in the TCS3200 sensor. The results obtained from the sensor is analyzed by microcontroller and displayed on the OLED display. At the same time, it is stored in a cloud server called ThingSpeak.com using an ESP8266 Wi-Fi module, and is displayed as a graph on the cloud server according to the deviation of the sensor values. Using the ThingView mobile app, users can view these results anytime and anywhere for further analysis.

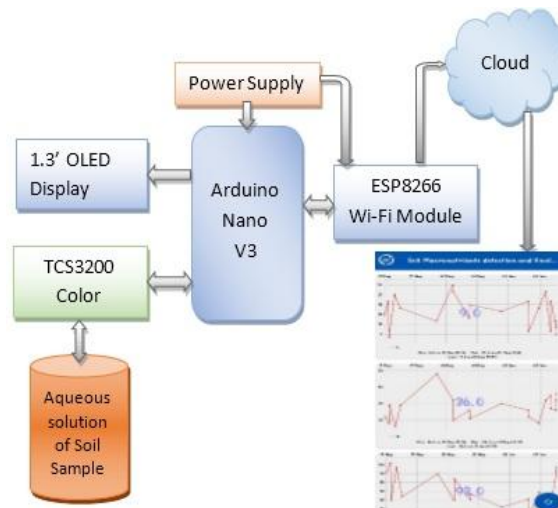


Figure 6 System Block Diagram

2. System Circuit design and Working Flowchart



Figure 7 Making of Aqueous Solution

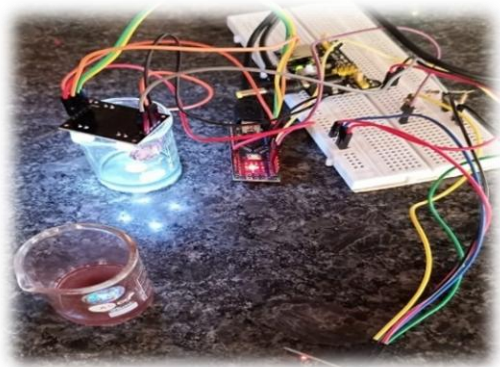


Figure 8 Schematic of System Design

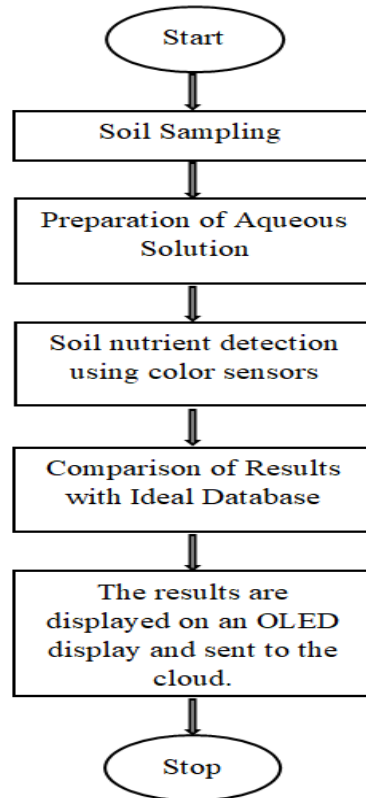
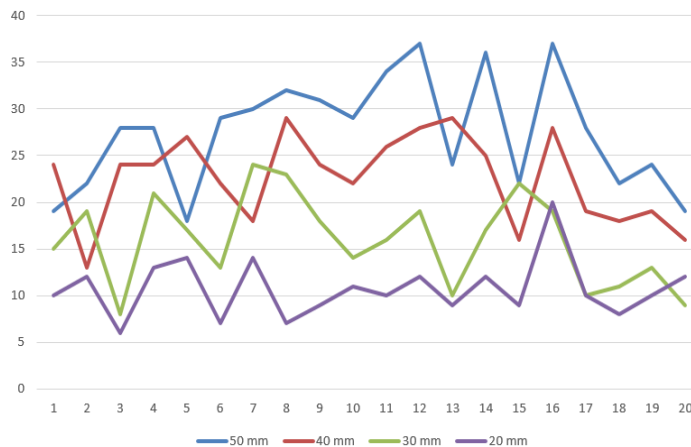


Figure 9 Working Flowchart of System

V. RESULT AND DISCUSSION

This embedded system is designed to detect different soil parameters such as nitrogen, phosphorus, and potassium. An Arduino Nano V3 microcontroller was programmed for this. The received data is sent to the computer through a serial communication cable. The data received from Arduino is processed using the open source software "Arduino IDE" that supports C and C++ languages and the results are displayed on the OLED display. At the same time, the received data was sent to the cloud using an Esp8266 Wi-Fi module. The results obtained with the developed embedded system are discussed below.

In this system, we first took 20 samples at different locations of Vidarbha region and set the optimal distance by varying the length between the sample and the sensor: 50mm, 40mm, 30mm, and 20mm. Then we selected the distance where the incidence and reflection angles were most accurate, i.e 30mm/3cm.

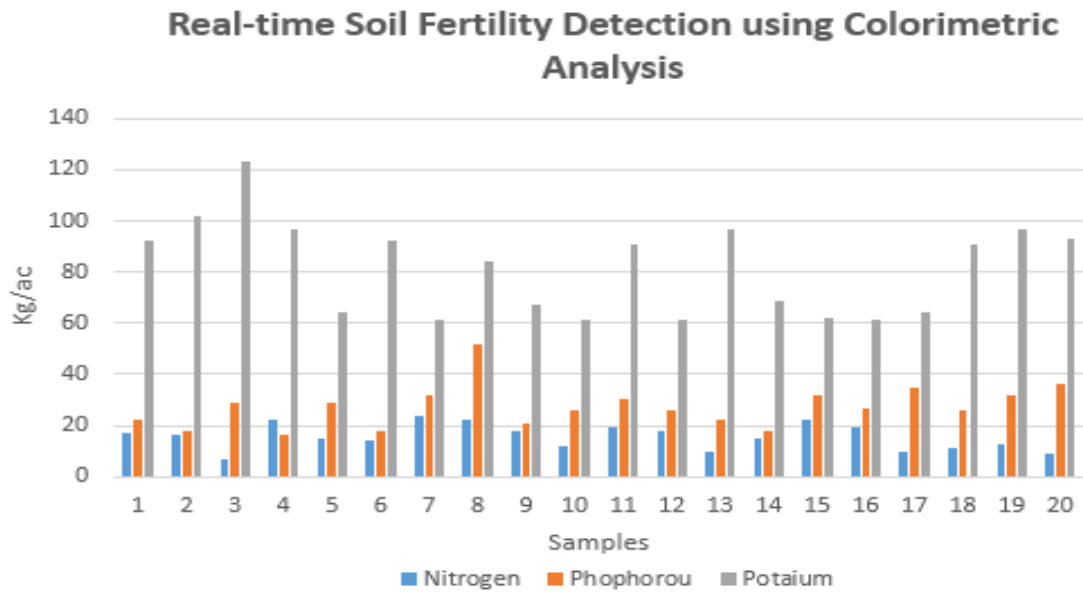


Graph 1 Different distance N values

Table 2 Color Intensity Threshold Levels for Nitrogen, Potassium and Phosphorous

Nutrients	V Low	Low	Medium	High	V High
Nitrogen	0 - 9	10 - 20	20 - 30	30 - 40	> 40
Phosphorus	0 - 15	15 - 25	25 - 35	35 - 45	> 45
Potassium	0 - 30	30 - 60	60 - 90	90- 120	> 120

After all customization measures, we have found the following sample results:

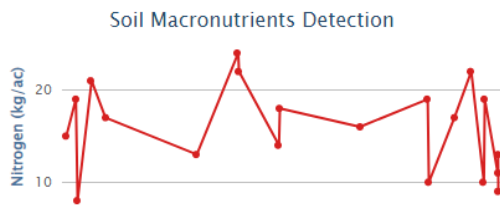


Graph 2 Result Analysis of the system

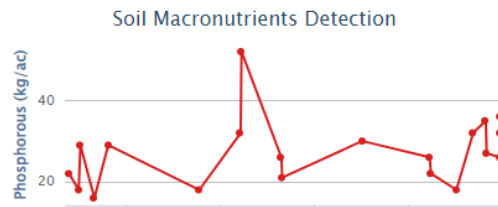
The above bar graph shows the different samples tested from different locations and found that the NPK values are varying from one location to another also the results are varying with atmospheric condition. The threshold values for soil N, P and K content are also given in Table 2, which shows the range of colour intensity values for N, P and K in the form of low, medium and high.

1. Cloud data Loading and Visualization:

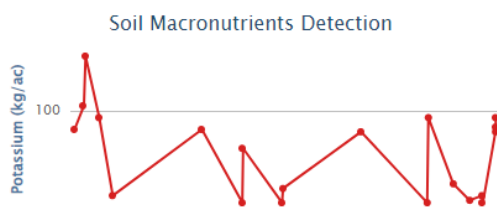
As the result is detected by Sensor and received at microcontroller all data is transferred to cloud for further analysis and future reference. The Graph 3, 4, 5 are the cloud data store images.



Graph 3 Nitrogen content available in different samples



Graph 4 Phosphorous content available in different samples



Graph 5 Potassium content available in different samples

VI. CONCLUSION AND FUTURE SCOPE

The study concludes that the TCS3200 color sensor with Arduino Nano has been effectively designed and tested to measure nutrients N, P, and K in soil. This finding may improve other farmers' problems in determining and measuring the amount of nutrients in soil at a lower cost than traditional methods. It may also help reduce the amount of fertilizers unnecessarily added to soil.

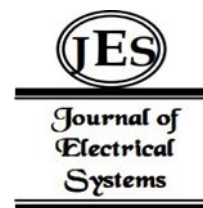
Future learning efforts will expand this method further and introduce an Android application that will display all the data about a farmer's field, including macronutrient values and levels, fertilizer recommendations, atmospheric conditions, and crop price close to market.

REFERENCES

- [1] M. Chetan Dwarkani, R. Ganesh Ram, S. Jagannathan, and R. Priyatharshini, "Smart farming system using sensors for agricultural task automation," *Proc. - 2015 IEEE Int. Conf. Technol. Innov. ICT Agric. Rural Dev. TIAR 2015*, no. Tiar, pp. 49–53, 2015, doi: 10.1109/TIAR.2015.7358530.
- [2] A. T. Madhumathi R and Shruthi R, "Soil NPK and Moisture analysis using Wireless Sensor Networks," *11th Int. Conf. Comput. Commun. Netw. Technol. ICCCNT* ., 2020.
- [3] M. E. H. Chowdhury, M. B. Hossain, T. Adhikary, M. M. Toufikur Rahman, and M. A. Razzaque, "Remote analysis of soil macronutrients using optical sensor for precision agriculture," *Int. J. Appl. Sci. Eng.*, vol. 14, no. 2, pp. 87–99, 2016.
- [4] R. Madhumathi, T. Arumuganathan, and R. Shruthi, "Soil Nutrient Detection and Recommendation Using IoT and Fuzzy Logic," *Comput. Syst. Sci. Eng.*, vol. 43, no. 2, pp. 455–469, 2022, doi: 10.32604/esse.2022.023792.
- [5] Department of Agriculture & Cooperation Ministry of Agriculture Government of India, "Soil Testing in India," 2011. [Online]. Available: https://agriculture.uk.gov.in/files/Soil_Testing_Method_by_Govt_of_India.pdf.
- [6] M. Dhanapriya and R. Maheswari, "Estimation of micro and macro nutrients in the soil of remote areas," *J. Chem. Pharm. Sci.*, vol. 2015-July, no. 10, pp. 67–73, 2015.
- [7] D. R. G. Rupa, B. Arunmohan Raj, K. Gowtham, R. Raashmi, "A Novel Approach for Soil Testing using Embedded System," *Int. J. Innov. Res. Electr. Electron. Instrum. Control Eng.*, vol. 4, no. 7, pp. 2321–2004, 2016, doi: 10.17148/IJREEICE.
- [8] E. Baldi, M. Quartieri, E. Muzzi, M. Noferini, and M. Toselli, "Use of in situ soil solution electric conductivity to evaluate mineral n in commercial orchards: Preliminary results," *Horticulturae*, vol. 6, no. 3, pp. 1–11, 2020, doi: 10.3390/horticulturae6030039.
- [9] G. S. Kukreja, V. Bagyaveereswaran, S. Menon, and G. Agrawal, "IoT to inculcate Smart Farming and Soil Nutrient Retention," *Proc. 2021 IEEE Int. Conf. Innov. Comput. Intell. Commun. Smart Electr. Syst. ICSES 2021*, 2021, doi: 10.1109/ICSES52305.2021.9633822.
- [10] A. Biswas and S. Prakash, "Farming technology for India agriculture based sensorics and indicative systems," *Proc. - 2015 IEEE Int. Conf. Technol. Innov. ICT Agric. Rural Dev. TIAR 2015*, no. Tiar, pp. 72–78, 2015, doi: 10.1109/TIAR.2015.7358534.
- [11] N. Datasheet, "Arduino Nano (V3.0) user manual," *Gravitech*, pp. 1–4, 2009, [Online]. Available: <http://creativecommons.org/licenses/by-sa/2.5/>.
- [12] TheEngineeringProjects.com, "Arduino Nano V3," 2018. <https://www.theengineeringprojects.com/wp-content/uploads/2018/06/introduction-to-arduino-nano-13-1.png>.
- [13] TAOS TCS3200, "TCS3200, TCS3210 Programmable Color Light-To-Frequency Converter," *The Lumenology*, no. 972, pp. 1–14, 2009.
- [14] E. Systems, "ESP8266EX Datasheet," *Espr. Syst.*, p. 31, 2020, [Online]. Available: https://www.espressif.com/sites/default/files/documentation/0a-esp8266ex_datasheet_en.pdf.
- [15] "1.3' I2C OLED Display," [Online]. Available: https://www.electroniccomp.com/1.3-inch-i2c-iic-128x64-oled-display-module-4-pin-white?gad_source=1&gclid=EAIaIQobChMI_o_U6LG3hgMVOoJmAh2hYjZOEaQYASABEgJURvD_BwE.

¹Gitanjali F. Jadhav*²Rushikesh R.
Suryawanshi³Suhas S. Mohite⁴Pratik P. Raut⁵Rajaram S. Mane

Electrochemical Studies: Biomass-Derived Nitrogen-Doped Graphene Oxide



Abstract: - Heteroatom doping is an effective method for customizing the optical, electrical and magnetic properties of carbon-based energy storage materials. In the present work, biomass-derived nitrogen-doped graphene oxide (NGO) is synthesized using a simple cost-effective, low-temperature auto-combustion process having more than 10.01 at.% nitrogen (N) doping content. The presence of nitrogen in GO has been corroborated by the electron dispersion X-ray analysis. The effect of nitrogen doping on electrochemical properties are studied using cyclic-voltammetry (CV) and electrochemical impedance spectroscopy (EIS) measurements. Three-electrode-based half-cell analysis performed within 0 to -1.0 V operating potential window vs. Ag/AgCl has approved 6.531 F g^{-1} specific capacitance for NGO nanobud-like electrode at 0.4 Ag^{-1} current density with about 92.13% stability, which is superior to pristine GO electrode material, suggesting the importance of nitrogen doping for improving electrochemical properties. This could pave the way for forming nitrogen-doped biomass-based electrode materials for high-performance electrochemical devices.

Keywords: Graphene oxide; Structural analysis; Biomass-Derived; Surface morphology; Nitrogen doping; Supercapacitor.

I. INTRODUCTION

The scarcity of fossil fuel resources, growing current energy demands, and global warming have created a pressing need for sustainable energy sources [1, 2]. Currently, e-mobile items (aircraft and automobiles) require a significant amount of energy; consequently, building a sustainable transportation system is critical. These e-mobile devices necessitate significant energy and power densities. Batteries have a high energy density but limited power density [3]. Furthermore, batteries increase the weight/volume of mobile devices, which contradicts the goal of reducing energy use. As a result, there is a demand for energy-storage devices with high energy and power density that can also serve as a structural component of e-mobiles [4]. It is becoming increasingly necessary to develop new technologies for clean, inexpensive, and reliable power [5, 6]. Electrochemical supercapacitors (ESs) are revolutionary electrochemical energy storage devices, bridge the current gap between batteries and regular capacitors by capturing energy and

¹ * Centre for Nanomaterials & Energy Devices, School of Physical Sciences, Swami Ramanand Teerth Marathwada University, Nanded-431606, M.S., India.

² Centre for Nanomaterials & Energy Devices, School of Physical Sciences, Swami Ramanand Teerth Marathwada University, Nanded-431606, M.S., India

³ Bharati Vidyapeeth's (deemed to be University) Yashwantrao Mohite College of Arts, Science and Commerce, Erandwane, Pune-411038, India

⁴ Centre for Nanomaterials & Energy Devices, School of Physical Sciences, Swami Ramanand Teerth Marathwada University, Nanded-431606, M.S., India

⁵ Centre for Nanomaterials & Energy Devices, School of Physical Sciences, Swami Ramanand Teerth Marathwada University, Nanded-431606, M.S., India

Copyright © JES 2024 on-line : journal.esrgroups.org

providing high power in a short period of time [7]. They are also known to store energy in the electrical double-layer capacitors region *via* ion adsorption. Furthermore, because of their quick reversible faradaic reactions, pseudocapacitors are sometimes considered as supercapacitors [8]. One of the new materials of solution is two-dimensional carbon sheets i.e. graphene where a single layer of sp^2 -hybridized carbon atoms is tightly packed through a honeycomb-like structure. Due to unique properties such as high Young's modulus, fracture strength, thermal conductivity, charge carrier mobility, and specific surface area, it has been the focus of significant global research. Unfortunately, graphene's poor solubility in both polar and nonpolar fluids has severely hampered its preparation and applications. However, due to the abundance of oxygen functional groups on its basal plane and edges, graphene oxide (GO) is hydrophilic in nature. Although GO has the same lamellar structure as graphene, due to functional groups, such as good dispersion stability in aqueous and other organic solvents, it has potentially more promising properties [9]. The low electronic conductivity and weak microbial adherence of GO are preventing an efficient transfer of charge [10]. Reducing GO can partially restore the ideal graphene structure, which is advantageous for boosting its conductivity. However, because of van der Waals interactions, the decreased GO frequently experiences irreversible agglomeration and re-stacking, which can produce a negative impact on its electrochemical performances by decreasing specific surface area [11]. Additionally, the presence of hydrophilic oxygenated surface area and hydrophobic pristine graphene in GO boosts its surface heterogeneity and improves its capacity to bind with various pollutants *via* hydrophobic interactions, van der Waals interactions, electrostatic interactions, π -stacking, and H-bonding [12]. In most cases, conductive polymers like polypyrrole and polyaniline and metallic oxides [13] like TiO_2 and SnO_2 [14] were coupled with GO. Hence, doping or functionalization was added at the carbon basal planes and the edge sites to get over this restriction, which creates new opportunities for practical applications [15].

The perfect sp^2 hybridization of the carbon atoms is typically disrupted by substitutional doping of graphene with various atoms (such as B, N, S, F, and Si), which locally can promote significant changes in its electrical characteristics. Since nitrogen has five valence electrons available to make powerful valence bonds with carbon atoms and a similar atomic size to other prospective dopants, it has garnered a lot of attention [16]. As a result, it can be easily incorporated into the carbon lattice to enhance the graphene's binding capabilities and electron-donor properties. N-doping could also improve the carbon nanomaterials' capacity for efficient extracellular electron transfer, which is advantageous for biosensing [17] and bioelectricity generation applications [18]. For example, electrocatalysts for Oxidation Reduction Reaction (ORR) [19], enormous promise in high-frequency semiconductor devices [20], and improved catalysis for energy conversion and storage [21] are just a few of the exciting features that N-doping promises. Both, one-step and two-step N-doping strategies have been used to accomplish N doping in graphene. The one-step N-doping strategy frequently includes Chemical Vapor Deposition (CVD), flame treatment, and solvothermal method while, the two-step N-doping strategy primarily consists of thermal annealing, pyrolysis, N_2H_4 treatment, wet chemical synthesis, microwave treatment, supercritical reaction, hydrothermal method, microwave-assisted hydrothermal method, and lyophilization-assisted heat treatment [22]. However, the majority of these methods have

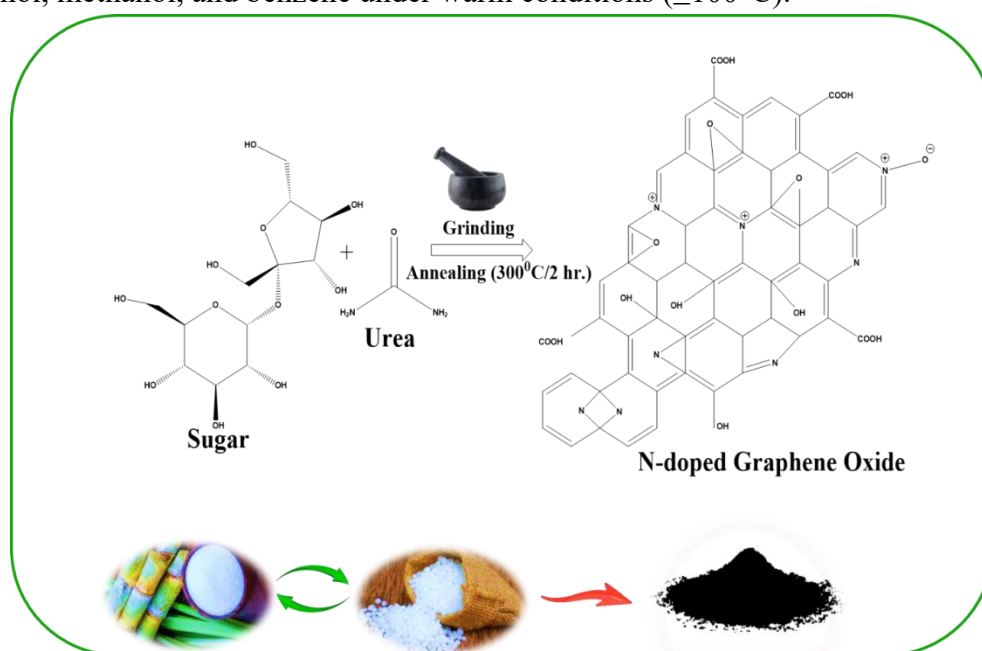
restrictions that prevent them from being used for mass manufacturing, including low yield, significant energy use, and severe environments. The CVD approach, for example, is expensive and requires high temperatures (800–1100°C), while other synthesis processes are difficult and time-consuming, requiring either a certain environment or poisonous precursors [23]. By these circumstances, the development of a low-cost, effective, economical, and ecologically acceptable process for nitrogen doping of graphene materials under benign conditions is very desirable. Graphene-based SC technology can be greener and substantially safer than traditional battery technology because it operates without bursting or overheating.

Hence, as part of our ongoing research on the synthesis of the GO and doped-GO for various applications, here we prepared GO and nitrogen-doped graphene oxide (NGO) by carbonizing tabletop sugar [24] and carbonizing urea with tabletop sugar, respectively. Both GO and NGO were used for physical characterization initially and then envisaged for electrochemical measurements in a 6 M KOH electrolyte solution. The aim of this article was to see the effect of N-doping on electrochemical energy storage performance of biomass-derived GO.

II. EXPERIMENTAL SECTION

A. Preparation of GO and NGO

The pure GO and NGO electrode materials were prepared by carbonization process. Periodic heating of dry table sugar with and without organic urea can be a common technique for creating NGO and GO, respectively. Scheme 1 provides an illustration of the scientific details. Dry table sugar and dry table sugar combined with 50 wt.% organic urea were grounded into powders using a mortar pestle which were then transferred to transparent laboratory petri-dishes. These organic, affordable and environmentally benign powdered samples were carbonized for two hours at 300°C in a closed furnace. The treated dark powders were crushed and used without being further annealed. In both instances, the product yield was between 50-57% of the synthesis material used. The resulting black powder was found to be somewhat soluble in dimethyl sulfoxide, but insoluble in water, ethanol, methanol, and benzene under warm conditions ($\leq 100^\circ\text{C}$).



Scheme 1. Schematic showing synthesis of NGO using table top sugar and urea.

B. Electrode preparation

A slice of Ni-Foam (1.0 cm × 1.5 cm) was sonicated for 30 min in a 1% HCl solution with deionized water to remove contaminants before being rinsed with deionized water for 10 minutes and air dried at room-temperature for 24 h. Both GO and NGO electrodes were prepared by coating 1 mg active material powder mixed with polyvinyl alcohol (PVA) binder equally on the surface of Ni-foam which was dried at 175 °C for 6 h to form the cathode electrodes.

C. Physical and electrochemical characterizations

Field emission scanning electron microscopy (FE-SEM) Hitachi, S-4800 operated at 15 kV accelerating voltage and equipped with energy dispersive X-ray spectroscopy (EDX) was used for surface morphology analysis. X-ray photoelectron spectroscopy (XPS) (Omicron ESCA) to analyze the valence states of the surface chemical elements and their associated molecular species. Raman spectroscopy (Horiba Scientific France, Xplora Plus system at a Laser wavelength of 532 nm & 785 nm) was considered to confirm the change in the band position of GO after N-doping and X-ray diffraction (XRD) (XRD, D8-Discovery Bruker, Cu K, 40 kV, 40 mA) was used to know structural change if there any.

Cyclic-voltammetry (CV), galvanostatic charge-discharge (GCD), and electrochemical impedance spectroscopy (EIS) measurements were used in a three-electrode system utilizing the IVIUM electrochemical workstation for electrochemical analysis. The working, reference, and counter electrodes were respectively GO or NGO coated Ni-foam, Ag/AgCl, a platinum. The CV measurement was performed at scan rates ranging from 5 to 100 mV/s between 0 and -1.0 V potential range in a 6 M KOH aqueous electrolyte. The EIS was operated using an alternating current perturbation with an amplitude of 0.3V and a frequency range of 1 Hz to 45 kHz. The specific capacitance (C_{sp}) of both electrodes was calculated with the help of CV and GCD plots using the following (1);

$$C_{sp} = \frac{I \cdot \Delta t}{m \cdot \Delta V} \quad \dots(1)$$

Where, I is the current density, Δt is the discharge duration, ΔV is the potential difference, and m is the mass of the active material [13].

III. RESULTS AND DISCUSSION

A. Surface morphology confirmation

The successor urea was used to modify the surface of GO by doping N. The FE-SEM pictures adduce the surface morphology difference between GO and NGO scanned at different magnifications as shown in Fig. 1(a), indicating that the presence of urea affects the surface morphology/contents of NGO. A comprehensive look at the FE-SEM pictures of the NGO electrode, as shown in Fig. 1b, suggests the growth of cabbage-like floral nano-buds. The height of a single nano-bud is remarkable due to their close proximity. The presence of large open gaps between these nano-buds has been proven, allowing for the easy and rapid movement of charge/electrolyte ions within electrode material for minimum diffusion resistance. Fig. 1 (c) and (d) support the calculation of weight percentages of elements present on pristine GO and NGO electrode surfaces, respectively.

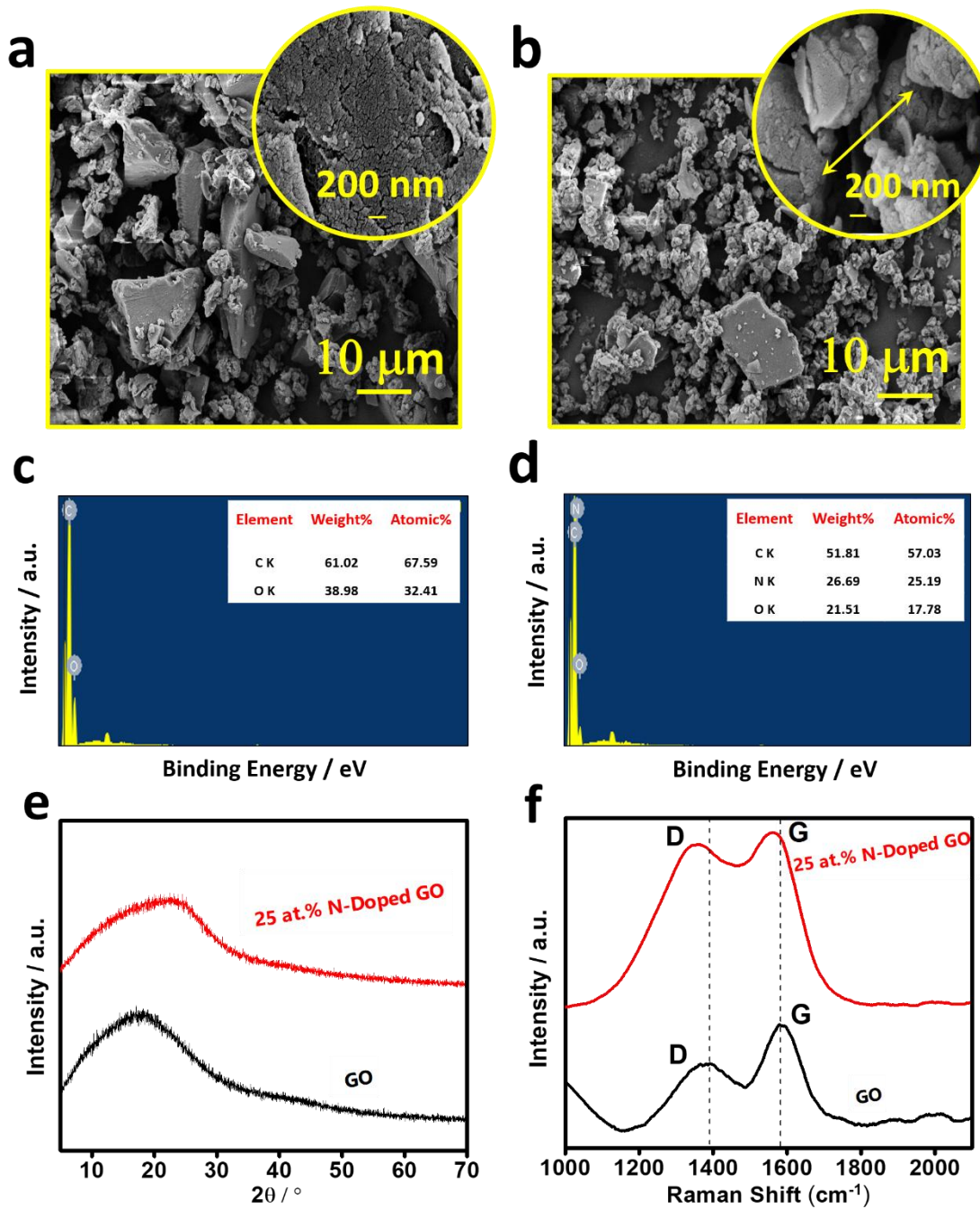


Fig. 1. (a, b) FE-SEM of GO, and NGO powders scanned at different magnifications and. (c, d) EDAX mapping showing the weight percentages of C, O and N elements. (e, f) XRD and Raman shift spectra of GO and NGO powders.

Raman spectroscopy was used to estimate the degree of defects in the graphene structures. Because of the predominance of pyrrolic-N and pyridinic-N configurations determined by XPS, the NGO G-band, when compared to the GO G-band, has been shifted to a lower frequency by up to 28 cm⁻¹ for NGO. The density of defects is connected with the D band. The average peak intensity of the D band relative to the G band (I_D/I_G) was used to determine the defect level. The peak intensity ratios (I_D/I_G) between the D and G bands represent the density and dispersion of the defects that were used to estimate the defect density. Equation (2) was used to calculate the distance between defects (L_D);

$$L_D = (4300 * (I_D/I_G)^{-1} / E_L^4)^{1/2} \quad \dots (2)$$

Where, E_L is the laser energy (2.41 eV, $\lambda = 514.5$ nm). Because of the introduction of defects during N doping, NGO has the greatest I_D/I_G value with the smallest L_D than GO [18]. The Raman spectrum of the NGO has confirmed two prominent peaks at roughly 1341 cm^{-1} (D band) and 1558 cm^{-1} (G band), respectively (Fig. 1f). The D-band (disorder-induced) correlates to the aromatic rings' breathing mode, whereas the G-band (in-plane vibration) corresponds to the tangential vibration of the C sp^2 atoms [25]. Raman mapping of NGO I_D/I_G is higher than that of GO, most likely due to the insertion of defects during N doping, which is consistent with earlier results. The I_D/I_G values increased after N doping. Nonetheless, the I_D/I_G ratios for GO and NGO were 0.6996 and 0.9424, respectively. The higher I_D/I_G value of NGO suggests a more disordered structure than GO, which could be attributable to the high nitrogen doping level due to urea as an "internal" doping source [26].

B. Analysis of the XRD and XPS spectra

Fig. 1e depicts the XRD patterns of the GO and NGO. It is worth noting that GO had a significant height at $2\theta = 17.8^\circ$. However, the peak changed from $2\theta = 17.8^\circ$ in GO to $2\theta = 22.4^\circ$ in NGO, suggesting the successful doping of the N in GO [24]. The patterns also show that the peak intensity at $2\theta = 22.4^\circ$ in NGO decreased and broadened. The broadening of the NGO peak could be related to differences in interlayer spacing caused by the presence of functional groups such as hydroxyl and epoxide on the surface of GO, which were eliminated after air annealing, resulting in the narrow peak [27, 28].

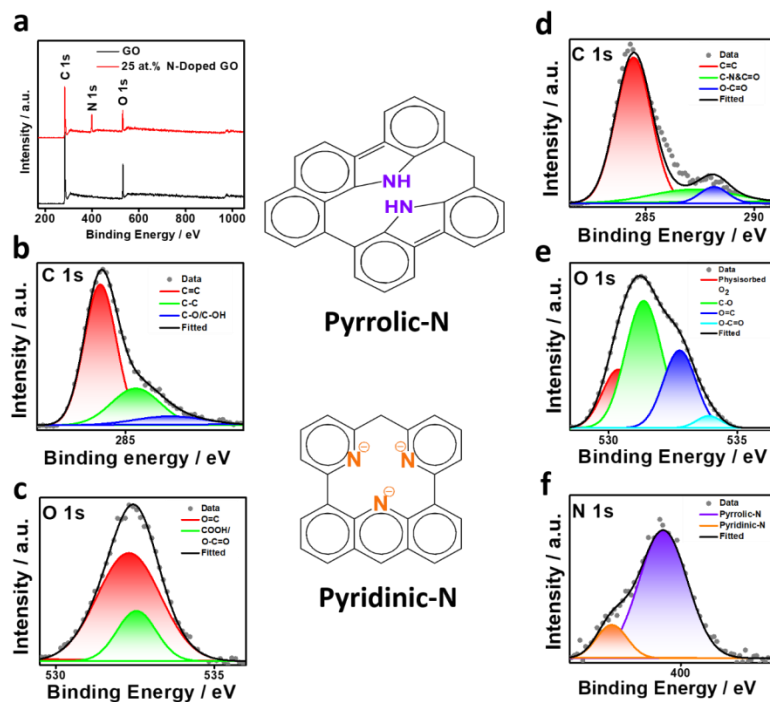


Fig. 2. The proposed structures of pyridinic-N and pyrrolic-N along with; (a) full range XPS survey spectrum, (b-f) high-resolution deconvoluted of GO (b: C1s scan; c: O1s scan) and NGO (d: C1s scan; e: O1s scan; f: N1s scan) spectra.

The XPS spectra of GO, and NGO were collected to examine the surface elemental proportions and chemical states. Elements like C, N, and O elements were observed on NGO surface. The XPS survey spectra, as shown in Fig. 2a, confirmed no single N in the GO. In Fig. 2b, the C 1s spectrum of the GO electrode exhibits three prominent peaks at 284.23, 285.76, and 286.15 eV for the C=C (sp^2), C-C (sp^3), and C-OH/epoxy, respectively. The

high-resolution O1s XPS from GO in Fig. 2c has revealed additional peaks at 532.25, 532.48 ascribed to C=O and COOH/O-C=O, respectively. A significant doping level (graphitic-N = 25.19%) was evidenced that may contribute high catalytic efficiency [26]. Fig. 2(d-f) presents the high-resolution deconvoluted spectra of NGO. In Fig. 2e, O1s spectrum three peaks with binding energies of 532.73, 531.11, and 533.84 eV corresponding to C=O, C-O, and O=C-O adsorption were fitted [29]. Furthermore, as illustrated in Fig. 2d, the C1s spectrum was divided into three peaks spanning 284 to 288 eV. The three binding energies at 284.26, 287.83, and 288.4 eV for C=C, C=O, and O-C=O bonds, respectively, were noticed [30]. The peak for C=O at 287.8 eV could be superimposed by C-N at roughly 287.5 0.5 eV [29, 31]. The asymmetric N1s peak (Fig. 2f.) was split into two components, indicating that nitrogen atoms were doped in two distinct locations on the graphene skeleton. At 398.32 eV, the pyridinic-N (bonded with two sp^2 hybridized carbon atoms in a hexagonal ring) contributes one p-electron to the π -conjugated system in the graphene structure, while the pyrrolic-N (bonded with two sp^2 hybridized carbon atoms in a pentagonal ring) contributes two p-electrons in the π -conjugated system). Fig. 2 also depicts the placement of N atoms on the graphene skeleton. N-doping has been found to disturb the sp^2 hybridized carbon arrangement of GO, weakening the chemical inertness of the carbon for better catalytic activity. In short, graphitic N, in particular, has the potential to induce electron transfer from neighboring carbon atoms to N, hence improving catalytic efficiency [32].

IV. ELECTROCHEMICAL STUDIES

A. Half-cell electrochemical measurements

The electrochemical energy storage properties of GO and NGO were measured in a three-electrode system with a 6 M KOH electrolyte solution within a potential window ranging from 0 to 1 V vs. an Ag/AgCl reference electrode. Fig. 3a depicts the CV curves of the GO attempted at 5-100 mV/s scan rates, indicating the participation of pseudocapacitive behavior due to the presence of oxygen functional groups connected to the surface of GO [24].

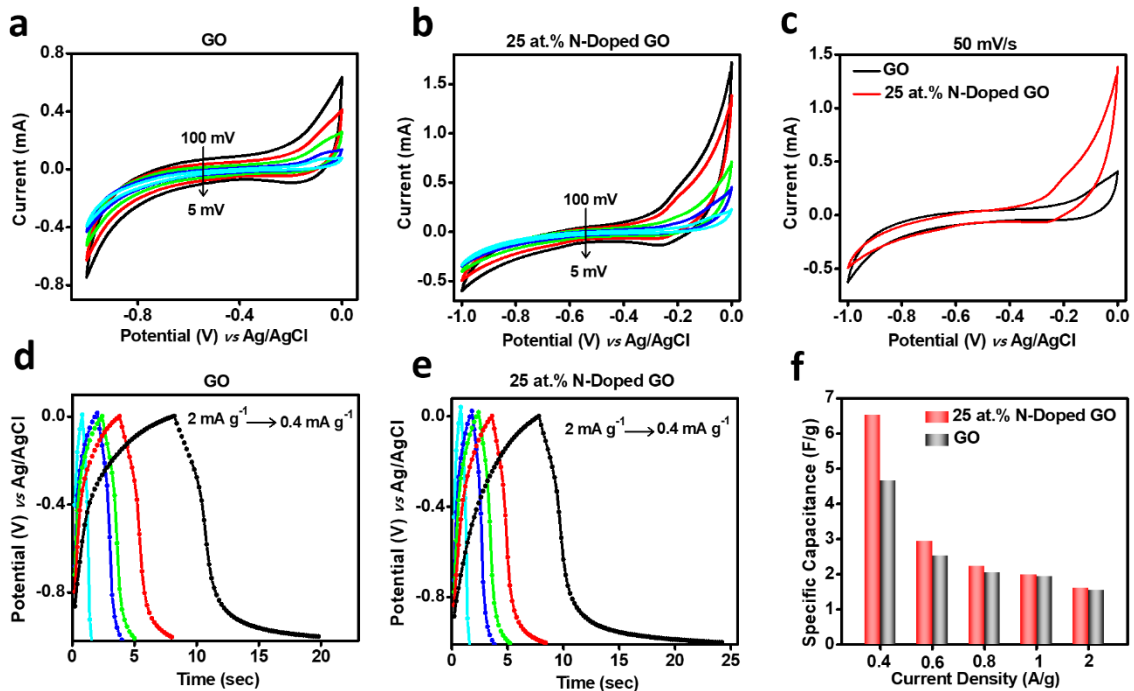


Fig. 3. Electrochemical measurements of; a-b) CV, and d-e) GCD of the GO and NGO electrodes. c) CV @ 50 mV/s scan rate and f) comparative SC vs. current density revelation of the GO and NGO electrodes.

The CV curves of the NGO measured at different scan rates ranging from 5 to 100 mV/s are shown in Fig. 3b. Furthermore, when the scan rate increases, the obtained current increases, and a significant change in redox peaks is observed at 100 mV/s, indicating a fairly good rate of response. At 0.8 A/g, the C_{sp} values of the GO and NGO were 2.0552 F/g and 2.2371 F/g, respectively, indicating that the C_{sp} of the NGO electrode is greater than that of GO, highlighting the contribution of the redox pseudocapacitance from doping. These C_{sp} values were 6.531, 2.637, 2.237, 1.939, and 1.613 F/g for current densities of 0.4, 0.6, 0.8, 1 and 2 A/g, respectively. The SC computed from the mass of the NGO loaded on the Ni-foam electrode was 6.531 F/g, resulting in a capacitance retention of 92.13%. Fig. 3c depicts the CV plots of both the GO and NGO electrode materials at 50 mV/s, illustrating a large area under the curve and hence an impressive capacitive nature of NGO electrode over GO. NGO's better capacitance performance could be attributed to its high pyridinic-N and pyrrolic-N contents, as well as different surface morphology, which could provide excellent electrical conductivity and pseudocapacitance with good electrolyte penetration [23].

The GCD curves of the NGO electrode were measured in a potential window of 0 to -1.0 V at 0.4, 0.6, 0.8, 1 and 2 A/g current densities where a disturbed saw-tooth pattern is observed, and the discharge time of the NGO was longer than that of GO at both high and low current densities. Both electrodes' GCD curves were almost symmetric, indicating that the as-obtained GO and NGO were availing good electrochemical capacitive properties. The C_{sp} values of the GO and NGO electrodes were derived from the discharging curves at different current densities (Fig. 3(d-e)). We clearly see that the C_{sp} decreases with an increase in current density for both electrodes. The C_{sp} values calculated by using eq. 1, in accordance with current density, are also plotted in Fig. 3f. As previously stated, due to a poor combustion synthesis impact, the as-obtained C_{sp} for the NGO was slightly lower. Based on the XPS fitting data, it is clear that after increasing the temperature over 180 °C an increase

in the proportion of pyrrolic N takes place. N-doped GO commonly results in four binding configurations inside the carbon lattice: graphitic N (sp^2), pyridinic N (sp^2), oxidized N (sp^2), and pyrrolic N (sp^3). The reduced sp^2 species in oxidized, graphitic, and pyridinic conformations might have permitted increased electron transference due to negative doping. As a result, positive charge delocalization could result in greater bacterial affinity *via* electrostatic contact. The absence of graphitic N (sp^2) and oxidized N (sp^2) configurations can be attributed to a low-temperature annealing [27]. The increased SC of the NGO compared to the GO could be attributed to the creation of additional defect sites as a result of N-doping doping in the GO. The *in-situ* produced defects could allow for a more efficient active site and a faster charge transfer mechanism, resulting in improved electrochemical performance.

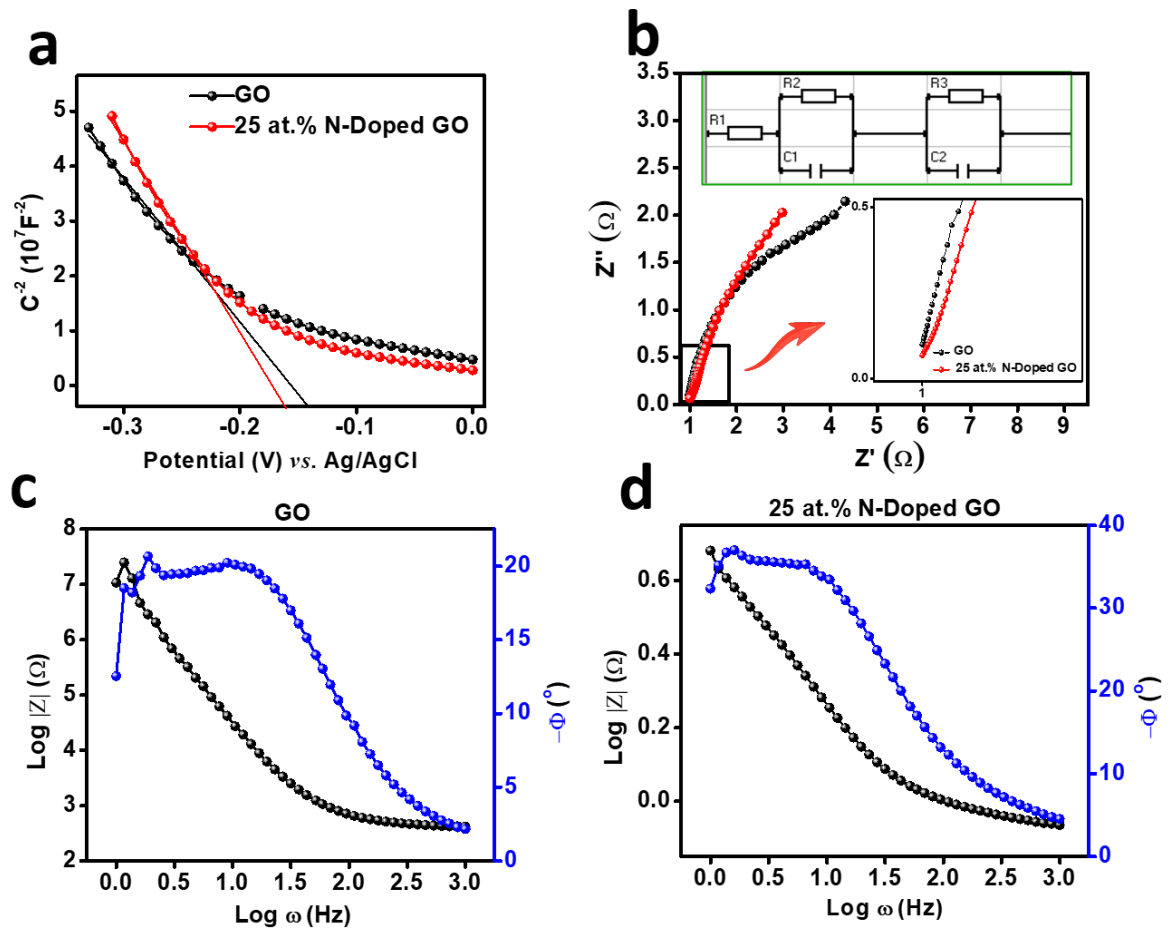


Fig. 4. a) The Mott-Schottky, and b) Nyquist (along with simple circuit model that explains current flow across a metal oxide contact), and c-d) Bode plots of the GO and NGO electrodes.

Fig. 4(a) depicts the Mott-Schottky plots where n -type behavior for both the GO and NGO electrodes was noted. The plot collects the values of forbidden energies i.e., $E_{FB}^{GO} = -0.1428$, $E_{FB}^{NGO} = -0.1621$ from their respective slopes. The Nyquist plots of the NGO and GO electrode materials are shown in Fig. 4(b), along with; (a) an equivalent resistor-capacitor circuit and (b) the behavior of these two electrodes at higher frequency as an inset,

where both have the approximate same real axis intercept (i.e., $R_s = 1.0 \Omega$). Non-Faradaic current is correlated with an interfacial capacitance (C_{int}), whereas Faradaic current is correlated with a charge transfer resistance (R_{ct}). A series resistance (R_s) is depicted to indicate the resistance caused by the wires, contacts, and solutions that complete the circuit.

Fig. 4c and d, shows the Bode magnitude and phase angle plots the GO and NGO electrodes with respect to frequencies. For both of the electrodes, as the frequency increases, the impedance decreases; which can be attributed to the capacitive behavior of the electrodes. A similar observation was found for the phase angle, confirming that the capacitive behavior is dominant at higher frequencies [19]. Cycling life is a key consideration in supercapacitor applications. Thus, we investigated the cycling life tests of the NGO as measured by the GCD curve over 1000 cycles (Fig. 5) where NGO demonstrated good capacitance retention, and displayed acceptable cyclic life, approving moderate chemical stability and considerable mechanical robustness over GO for its use in portable devices.

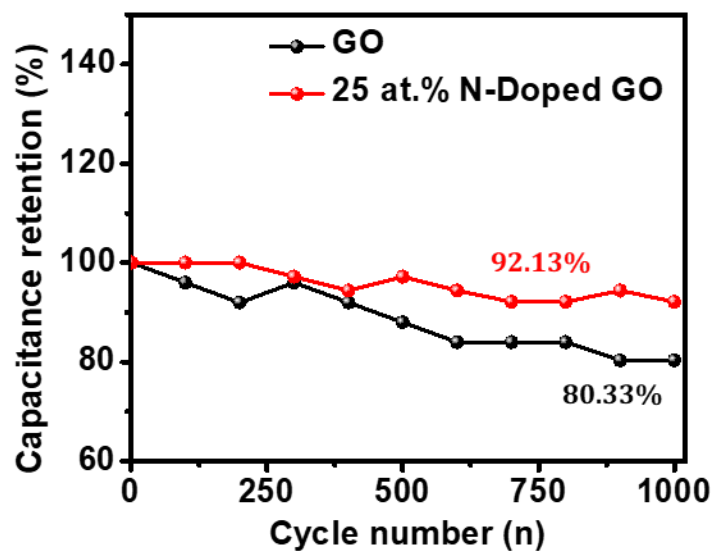


Fig. 5. Cycling stability of the GO and NGO electrodes.

Introduction

V. CONCLUSION

The nitrogen-doped graphene oxide (NGO) has successfully been produced utilizing a cheap, easy, and safe auto-combustion process using tabletop market quality sugar. Both GO and NGO are characterized and examined for their physical and electrochemical energy storage properties. The XRD patterns revealed that the GO has been effectively synthesized and doped with nitrogen. Raman spectrum measurement has demonstrated that NGO induces a shift in the D and G bands as a result of structural distortion caused by the differing bond lengths of C-C and C-N. The presence of two forms of N is confirmed by deconvoluted XPS spectra of N1s: pyridinic-N (N in 6-membered ring) and pyrrolic-N (N in 5-membered ring). Furthermore, surface analysis shows that the NGO has formed characteristic floral buds on the surface. Finally, heavily nitrogenated graphene oxide appears to be a suitable material for supercapacitor applications as confirmed here, NGO electrode reveals a reasonable specific capacitance of 6.531 F g^{-1} and a superior cycling life of 1000 cycles with just 7.9%

performance loss, suggesting its usability as biomass-derived electrode materials in energy storage devices.

ACKNOWLEDGMENT

This work was supported by “SARTHI award number CSMNRF-2021/2021-22/896.”

REFERENCES

- [1] Vattikuti, S.P., Devarayapalli, K.C., Sekhar, M.C., Nallabala, N.K.R., Dang, N.N. and Shim, J., 2021. Electrochemical performance of coin cell-type symmetric supercapacitor electrode consisting of three-dimensional molybdenum disulfide microflowers. *Materials Letters*, 285, p.129203.
- [2] Devarayapalli, K.C., Lee, K., Do, H.B., Dang, N.N., Yoo, K., Shim, J. and Vattikuti, S.P., 2021. Mesoporous g-C₃N₄ nanosheets interconnected with V₂O₅ nanobelts as electrode for coin-cell-type-asymmetric supercapacitor device. *Materials Today Energy*, 21, p.100699.
- [3] Deka, B.K., Hazarika, A., Kim, J., Kim, N., Jeong, H.E., Park, Y.B. and Park, H.W., 2019. Bimetallic copper cobalt selenide nanowire-anchored woven carbon fiber-based structural supercapacitors. *Chemical Engineering Journal*, 355, pp.551-559.
- [4] Qian, H., Kucernak, A.R., Greenhalgh, E.S., Bismarck, A. and Shaffer, M.S., 2013. Multifunctional structural supercapacitor composites based on carbon aerogel modified high performance carbon fiber fabric. *ACS applied materials & interfaces*, 5(13), pp.6113-6122.
- [5] Bauen, A., 2006. Future energy sources and systems—Acting on climate change and energy security. *Journal of Power Sources*, 157(2), pp.893-901.
- [6] Aemro, Y.B., Moura, P. and de Almeida, A.T., 2021. Experimental evaluation of electric clean cooking options for rural areas of developing countries. *Sustainable Energy Technologies and Assessments*, 43, p.100954.
- [7] Pandolfo, A.G. and Hollenkamp, A.F., 2006. Carbon properties and their role in supercapacitors. *Journal of power sources*, 157(1), pp.11-27.
- [8] Xu, J., Gu, X., Cao, J., Wang, W. and Chen, Z., 2012. Nickel oxide/expanded graphite nanocomposite electrodes for supercapacitor application. *Journal of Solid State Electrochemistry*, 16, pp.2667-2674.
- [9] Chen, D., Feng, H. and Li, J., 2012. Graphene oxide: preparation, functionalization, and electrochemical applications. *Chemical reviews*, 112(11), pp.6027-6053. [10]
- [10] Yao, Y., Chen, X., Zhu, J., Zeng, B., Wu, Z. and Li, X., 2012. The effect of ambient humidity on the electrical properties of graphene oxide films. *Nanoscale research letters*, 7, pp.1-7.
- [11] Chua, C.K. and Pumera, M., 2014. Chemical reduction of graphene oxide: a synthetic chemistry viewpoint. *Chemical Society Reviews*, 43(1), pp.291-312.
- [12] Duan, F., Yang, Y., Li, Y., Cao, H., Wang, Y. and Zhang, Y., 2014. Heterogeneous Fenton-like degradation of 4-chlorophenol using iron/ordered mesoporous carbon catalyst. *Journal of Environmental Sciences*, 26(5), pp.1171-1179.
- [13] Ghule, B.G., Shinde, N.M., Nakate, Y.T., Jang, J.H. and Mane, R.S., 2022. Bismuth oxide-doped graphene-oxide nanocomposite electrode for energy storage application. *Colloids and Surfaces A: Physicochemical and Engineering Aspects*, 651, p.129690.
- [14] Kaur, P., Park, Y., Sillanpää, M. and Imteaz, M.A., 2021. Synthesis of a novel SnO₂/graphene-like carbon/TiO₂ electrodes for the degradation of recalcitrant emergent pharmaceutical pollutants in a photo-electrocatalytic system. *Journal of Cleaner Production*, 313, p.127915.
- [15] Zhang, J., Wang, G., Liao, Z., Zhang, P., Wang, F., Zhuang, X., Zschech, E. and Feng, X., 2017. Iridium nanoparticles anchored on 3D graphite foam as a bifunctional electrocatalyst for excellent overall water splitting in acidic solution. *Nano Energy*, 40, pp.27-33.
- [16] Li, P., Li, X., Huang, J., Qu, W., Pan, X., Chen, Q., Klemeš, J.J., Wang, B., Wang, J. and Tao, H., 2022. Nitrogen-doped graphene oxide with enhanced bioelectricity generation from microbial fuel cells for marine sewage treatment. *Journal of Cleaner Production*, 376, p.134071.
- [17] Dumont, J.H., Martinez, U., Artyushkova, K., Purdy, G.M., Dattelbaum, A.M., Zelenay, P., Mohite, A., Atanassov, P. and Gupta, G., 2019. Nitrogen-doped graphene oxide electrocatalysts for the oxygen reduction reaction. *ACS Applied Nano Materials*, 2(3), pp.1675-1682.
- [18] Kim, J., Mat Teridi, M.A., Mohd Yusoff, A.R.B. and Jang, J., 2016. Stable and null current hysteresis perovskite solar cells based nitrogen doped graphene oxide nanoribbons hole transport layer. *Scientific Reports*, 6(1), p.27773.
- [19] Buldu-Akturk, M., Toufani, M., Tufani, A. and Erdem, E., 2022. ZnO and reduced graphene oxide electrodes for all-in-one supercapacitor devices. *Nanoscale*, 14(8), pp.3269-3278.
- [20] Xu, H., Ma, L. and Jin, Z., 2018. Nitrogen-doped graphene: Synthesis, characterizations and energy applications. *Journal of energy chemistry*, 27(1), pp.146-160.
- [21] Ray, S., 2015. Applications of graphene and graphene-oxide based nanomaterials. William Andrew.
- [22] Amari, A., Elboughdiri, N., Ghernaout, D., Lajimi, R.H., Alshahrani, A.M., Tahoona, M.A. and Rebah, F.B., 2021. Multifunctional crosslinked chitosan/nitrogen-doped graphene quantum dot for wastewater treatment. *Ain Shams Engineering Journal*, 12(4), pp.4007-4014.

- [23] Faisal, S.N., Haque, E., Noorbehesht, N., Zhang, W., Harris, A.T., Church, T.L. and Minett, A.I., 2017. Pyridinic and graphitic nitrogen-rich graphene for high-performance supercapacitors and metal-free bifunctional electrocatalysts for ORR and OER. *RSC advances*, 7(29), pp.17950-17958.
- [24] Ghule, B.G., Shaikh, S., Ekar, S.U., Nakate, U.T., Gunturu, K.C., Shinde, N.M., Naushad, M., Kim, K.H., O'Dwyer, C. and Mane, R.S., 2017. Natural carbonized sugar as a low-temperature ammonia sensor material: experimental, theoretical, and computational studies. *ACS applied materials & interfaces*, 9(49), pp.43051-43060.
- [25] Wilson, N.R., Pandey, P.A., Beanland, R., Rourke, J.P., Lupo, U., Rowlands, G. and Römer, R.A., 2010. On the structure and topography of free-standing chemically modified graphene. *New Journal of Physics*, 12(12), p.125010.
- [26] Hirani, R.A.K., Asif, A.H., Rafique, N., Wu, H., Shi, L., Zhang, S., Duan, X., Wang, S., Saunders, M. and Sun, H., 2022. Three-dimensional nitrogen-doped graphene oxide beads for catalytic degradation of aqueous pollutants. *Chemical Engineering Journal*, 446, p.137042
- [27] Lei, Z., Lu, L. and Zhao, X.S., 2012. The electrocapacitive properties of graphene oxide reduced by urea. *Energy & Environmental Science*, 5(4), pp.6391-6399.
- [28] Indrawirawan, S., Sun, H., Duan, X. and Wang, S., 2015. Low temperature combustion synthesis of nitrogen-doped graphene for metal-free catalytic oxidation. *Journal of Materials Chemistry A*, 3(7), pp.3432-3440.
- [29] Wang, Y., Shao, Y., Matson, D.W., Li, J. and Lin, Y., 2010. Nitrogen-doped graphene and its application in electrochemical biosensing. *ACS nano*, 4(4), pp.1790-179.
- [30] Qu, Y., Wang, J., Ma, Q., Shen, W., Pei, X., You, S., Yin, Q. and Li, X., 2018. A novel environmental fate of graphene oxide: Biodegradation by a bacterium *Labrys* sp. WJW to support growth. *Water research*, 143, pp.260-269.
- [31] Malitesta, C., Losito, I., Sabbatini, L. and Zambonin, P.G., 1995. New findings on polypyrrole chemical structure by XPS coupled to chemical derivatization labelling. *Journal of Electron Spectroscopy and Related Phenomena*, 76, pp.629-634.
- [32] Tao, H., Yan, C., Robertson, A.W., Gao, Y., Ding, J., Zhang, Y., Ma, T. and Sun, Z., 2017. N-Doping of graphene oxide at low temperature for the oxygen reduction reaction. *Chemical Communications*, 53(5), pp.873-876.

U. B.Tagade^{a/}
N.S.Meshram^b,
.B.A.Singade^c

**Study of AgCl₃,ZnCl₂ and KCl Added
Glycine Single Crystals by Slow
Evaporation Method**



Abstract: - AgCl₃,ZnCl₂ and KCl added glycine single crystals have been grown in 1M% proportion by slow solvent evaporation method .The powder XRD study confirms that the grown crystals doped with KCl and ZnCl₂ have gamma glycine crystal structure and it crystallizes into a hexagonal structure with a non-centro symmetric space group of P3₁and glycine crystal doped with aluminium chloride belongs to monoclinic system The FTIR spectrum was recorded to identify the expected functional groups. Optical absorbance spectrum recorded in the wavelength range of UV-VIS revealed that this crystal has good optical transparency in the range 250-1100nm.

Keywords: UV-VIS(Ultraviolet-Visible Spectroscopy),XRD(X-ray Diffraction),FTIR(Fourier Transform Infrared Spectroscopy).

¹ ^aS. Chandra Mahila Mahavidyalaya Amgaon441902, Maharashtra, India.

^bGondwana University Gadchiroli 442605, Maharashtra, India .

^cBhawabhuti College Amgaon 441902, Maharashtra, India.

Correspondence:-uttara25vaidya@gmail.com

1. Introduction

NLO crystals were used in optoelectronics, laser crystals, light modulation and optical storage etc. due to their second harmonic generation efficiencies and transparent in the visible and ultraviolet ranges. Amino acids crystals were famous organic materials shows NLO properties due to the fact that they have chiral symmetry and crystallize in non-centro symmetric space group[1]. Glycine ($\text{NH}_2\text{-CH}_2\text{-COOH}$) is a simplest amino acids and it exist in three forms of α , β and γ when reacts with inorganic salts. Some of the glycine compound exhibit ferroelectric and NLO properties[2]. The growth of gamma glycine single crystals have been grown using additive such as potassium chloride with various concentration like 4g,12g,18g in 100ml of water [3] by slow evaporation method. Single crystals of gamma glycine were grown from aqueous solution of glycine and zinc chloride in 1:0.5 molar ratio[4]. Some other gamma glycine crystals already reported doping with inorganic compound such as potassium fluoride[5], zinc sulphate, magnesium sulphate[6], lithium bromide, lithium acetate, sodium chloride[7]. Jyotsna R Pandey (2011) has reported that new organic GOA (glycine oxalic acid) crystals of appreciable sizes were grown from solution method in 2-3 weeks time. XRD studies revealed orthorhombic crystal structure. The cell parameters were dependent on the concentration of oxalic acid in the crystals. The UV visible studies showed wide transparency window between 188 nm to 700 nm suggesting the use of grown materials for non linear optical applications. Glycine Magnesium Chloride (GMC) single crystal was grown by Suresh Sahadevan et al. (2017) in slow evaporation technique was of good quality. From the single crystal XRD data obtained, it was proved that the crystals belong to hexagonal crystal system. The higher values of dielectric constant occurs at higher temperature. Narayan Bhat and Dharm (2002) were grown gamma glycine single crystals have been grown using additive such as with sodium nitrate various concentration. T. Balkrishnan, K. Ramamurthi (2008) were studied that grown gamma glycine single crystals doped with zinc chloride in the 1:1 ratio by temp reduction method. M. Esthaku Peter, P. Ramasamy (2010) were grown gamma glycine single crystals of triglycine zinc chloride in 2:1 molar ratio by slow solvent evaporation technique. In the present work, gamma glycine crystal have been grown by slow evaporation method by doping KCl , ZnCl_2 with molar 1M%. Also doping of AgCl_3 with molar 1M% for the growth of gamma glycine single crystal for the first time. The various characterization studies have been carried out and the results are discussed.

2. Materials and Method

2.1 Materials used

Glycine ($\text{C}_2\text{H}_5\text{NO}_2$ -amino acetic acid). AR(99.5%), M.Wt: 75.07g/mol, potassium chloride (KCl) M.Wt: 74.555g/mol, zinc chloride (ZnCl_2) M.Wt: 136.286g/mol, aluminium chloride (AlCl_3) M.Wt: 133.33g/mol and distilled water were used for the crystal growth

2.2 Slow evaporation crystal growth method.

It is the low temperature solution growth technique. In this technique crystals can be grown from solution, if the solution is supersaturated i.e. It contains more solute than it can be equilibrium with the solid. The driving force that is the super saturation is carried out by solvent evaporation. This method is used to grow bulk crystal which possess high solubility and variation in solubility with temperature.

The saturated aqueous solution of sample was prepared and stirrer continuously using magnetic stirrer. The solution is filtered two or three times. Then the solution is a transfer into a clean vessel. The vessel is placed in a constant temperature bath which are controlled by microprocessor. The growth of samples by this method may take weeks or months to grow crystal. The non-toxic solvent like water is taken mainly to evaporation into the atmosphere. The Crystal growth condition

take temperature stabilization to about $\pm 0.005^{\circ}\text{C}$. The deficiency of temperature control system have more effect on crystal growth rate. The size of Crystal produced is small in this technique [8]. Experimental setup as shown in Fig.1.



Fig.1 Experimental setup(both a&b)

Gamma glycine was synthesized by mixing saturated glycine solution with doping of dopants with 1M% of KCL, 1M% of ZnCl_2 and 1M% of AlCl_3 in the different vessel and distilled water taken as solvent. The solution was stirred well for about 2 hour at room temperature and saturated solution was filtered with what man filter paper in clean vessel. The vessel where covered with perforated polythene sheet and kept in the constant temperature bath 35°C the solution was allowed for slow evaporation and grown crystal obtained within 35 days as shown in Fig.2.

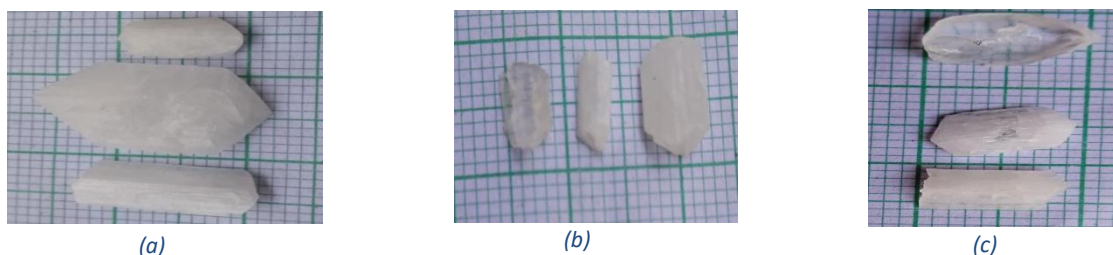


Fig.2: (a) ZnCl_2 doped glycine (b) KCl doped glycine (c) AlCl_3 doped glycine

3. Results and discussion

3.1 X-ray diffraction analysis

The diffraction pattern of a sample get into peak position and intensities. The position of the lines are shows spacing between planes in the lattice and the intensities depends on the atoms position on particulars sites. In the present work Powder x-ray diffraction analysis of the grown γ -glycine and α -glycine has been carried out using Lynx Eye X-ray diffractometer with $\text{K}\alpha$ radiation ($\lambda = 1.54060$) at room temp 25°C for structural analysis of the crystal.

Finely crushed powder of the grown crystal was used for the analysis. The Powder sample was stand over the range $10 - 80^{\circ}$. The intensity of the diffracted beam was recorded as the function of 2θ and the peaks were indexed which are agree with the literature report [9][8]. The observed values are in good agreement with data in JCPDS Card NO:06-0230 for gamma glycine and JCPDS CARD NO:32-1702 for alpha glycine.

Glycine crystal doped with aluminium chloride belongs to monoclinic system and gamma glycine doped with zinc chloride and potassium chloride belongs to hexagonal crystal system as given in Table1.

Table 1

Crystal parameter	Gamma glycine doped with zncl_2	Gamma glycine doped with kcl	Gamma glycine doped with alcl_3
Polymorph structure	γ	γ	α
structure	hexagonal	hexagonal	monoclinic
Lattice parameter	$a=7.0454\text{\AA}$ $b=7.0454\text{\AA}$ $c=5.4901\text{\AA}$ $\alpha=90^\circ$ $\beta=90^\circ$ $\gamma=120^\circ$	$a=7.0409\text{\AA}$ $b=7.0409\text{\AA}$ $c=5.49881\text{\AA}$ $\alpha=90^\circ$ $\beta=90^\circ$ $\gamma=120^\circ$	$a=5.3405\text{\AA}$ $b=11.801\text{\AA}$ $c=5.1281\text{\AA}$ $\beta=111.72^\circ$

The index XRD pattern for the grown crystal are shown in Fig.3. Appearance of sharp and strong peaks confirms the good crystallinity of the grown sample. The characteristics peak at $2\Theta = 25.278$ for kcl doped glycine and prominent planes are (110), (101), (210), (102). The characteristics peak at $2\Theta = 25.261$ for zncl_2 doped glycine and prominent planes are (110), (101), (210), (102), (200). The characteristics peak at $2\Theta = 29.666$ for alcl_3 doped glycine and prominent planes are (040), (021), (-110), (044).

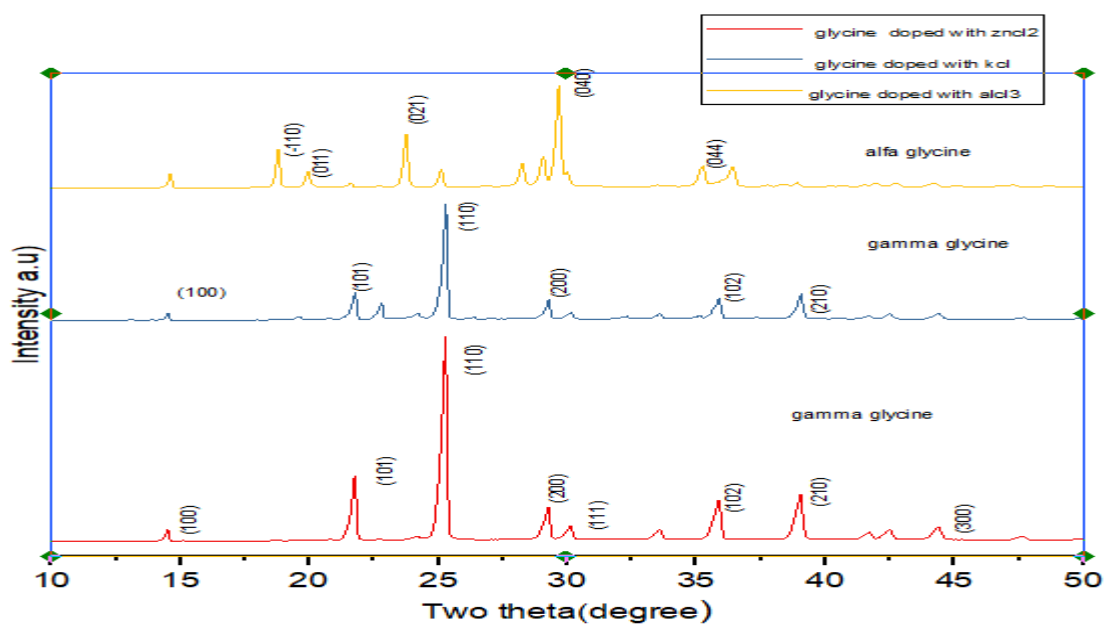


Fig.3 Powder XRD pattern of glycine single crystal

3.2 FTIR studies

The recorded FTIR spectra of powdered doped glycine is shown in Fig.4. The observed functional groups of grown α and γ glycine single crystal are well agree with reported result [9],[3],[5],[6]. From the report of α -glycine doped AlCl_3 , it is observed that the functional group 503,607,697 cm^{-1} are corresponding to the carboxylic groups, while 1504 cm^{-1} corresponding to the NH_3^+ group.

In the FTIR spectra of γ -glycine doped ZnCl_2 , the functional group 503,607,695 cm^{-1} are corresponding to the carboxylic groups, while 1497 cm^{-1} corresponding to the NH_3^+ group. The observed at 1043 cm^{-1} and 889 cm^{-1} are corresponding to C-C-N Asymmetric stretching vibration C-C-N symmetric stretching vibration in the FTIR spectra of γ -glycine doped KCl. The observed frequencies and their assignment of the glycine single crystal are shown in table 2.

Table 2 . FTIR Analysis

Alcl3 doped glycine (α - glycine)cm ⁻¹	Zncl2 doped glycine (γ - glycine) cm ⁻¹	Kcl doped glycine (γ - glycine) cm ⁻¹	Band assignment
3169	3106	3105	NH ₃ ⁺ asymmetric stretching vibration
2612	2603	2601	NH ₃ ⁺ stretching vibration
2123	2169	2169	Combinational bond
1611	1595	1575	asymmetric CO ₂ stretching vibration
1504	1497	1495	NH ₃ ⁺
1411	1391	1390	COO ⁻ Symmetric stretching vibration
1332	1334	1334	CH ₂ twisting
1111	1126	1127	NH ₃ ⁺ Rocking
1033	1042	1043	CCN Asymmetric stretching vibration
910	929	929	CH ₂ Rocking
891	889	889	CCN symmetric stretching vibration
697	685	686	COO ⁻ Bending
607	607	603	COO ⁻ wagging
503	503	502	COO ⁻ rocking

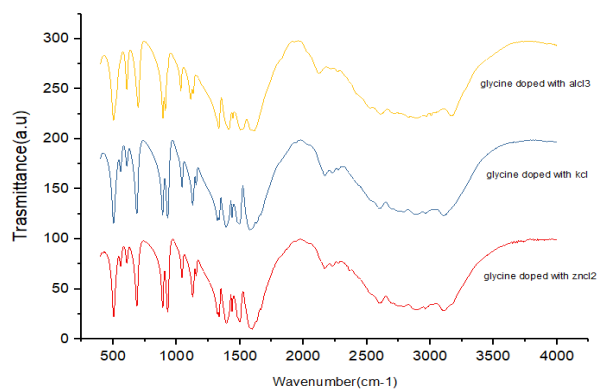


Fig. 4. FTIR Analysis of glycine single crystal

3.3 UV-Visible spectrum Analysis

The recorded UV-Vis NIR transmission spectrum of grown crystal as shown Fig.5 . The spectral where recorded in the range of 200-1100 nm. From spectrum it is notice that, crystal has lower cut off wavelength at 300 nm and there is no significant absorption observed in the entire region of the spectrum .The crystal is transparent in the entire visible region. It suggest that crystal is suitable for frequency doubling process.

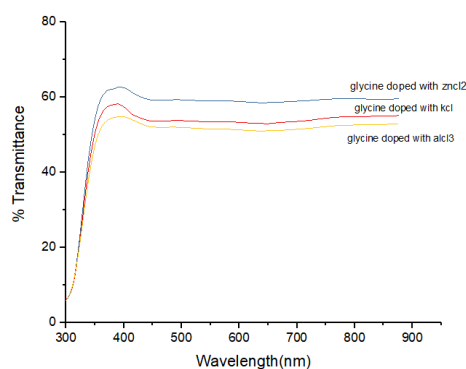


Fig. 5. UV spectra of glycine single crystal

4. Conclusion

We have grown gamma glycine single crystal with doping of zncl_2 , kcl and alcl_3 with 1M% concentration by slow evaporation method. From Powder XRD analysis, aluminium chloride doped glycine crystallize in monoclinic system and Kcl , Zncl_2 crystallize in hexagonal system .The appearance of sharp and strong peak confirm the good crystallinity of the grown crystal.

FTIR analysis confirm the presence of various functional group. From UV analysis, it is notice that, The lower cutoff frequency at 300nm and transmitters range 300-900nm. The absence of absorption of light in the visible region is the important property of amino acids.

REFERENCES

- [1] M. M. Anne, S. Perumal, and K.M.Prabu “Growth, structural & optical studies on pure L-Histidine doped single crystals of copper sulphate”, *Int.J.Res.Eng. Technol*, Vol.4 no.7, PP.2319-7308, 2015.
- [2] M.Senthil Pandian, P.Ramasamy “ Growth and characterization of solution-grown tetra glycine barium chloride (TGBC) single crystals”, *J.Cryst Growth* ,310, 2563-68. (2008).
- [3] C.Sekar, R.Parimaladevi “Effect of KCl addition on crystal growth and spectral properties of glycine single crystals”, *Spectrochimica Acta aprt A* 74(2009)1160-1167.
- [4] S.G.Pushpalatha Gracelin, C.Krishnan, P.Selvarajan, “Studies of gamma glycine crystals grown in the aqueous solution of zinc chloride”, *Internat.Journal* Vol.2, p.no.229-237, 2017.
- [5] G. R. Dillip, P.Raghavaiah, K.Mallikarjuna, C.MadhukarReddy, G.Bhagavannarayana, V.Ramesh kumar, B.Devaprasad Raju, “Crystal growth and characterization of -glycine grown from potassium fluoride for photonic applications”, *Spectrochimica Acta aprt A* 79, 1123-1127, 2011.
- [6] V.Vijayalakshmi, P.Dhanaeskan, “Growth and characterization study of γ -glycine crystal grown using different mole concentrations of zinc sulphate as structure-directing agents”, *J. Cryst.growth* ,498, 372-376(2018).
- [7] P.V.Dhanraj, N.P.Rajesh, “ Growth and characterization of nonlinear optical -glycine single crystal from lithium acetate as solvent” *mater.chem.phys.*115(2009)413-417.
- [08] J.C.Brice, P.Rudolph, *crystal growth*. blackie and son(1986)
- [09] S.Anbu Chudar Azhagan, S.Ganesan, “Structural, mechanical, optical and second harmonic generation (SHG) studies of gamma glycine single crystal”, *International Journal of Physical Sciences* Vol. 8(1), pp. 6-11, 9 January, 2013.

¹Shantanu Raulkar
²N R Pawar

**Synthesis of Alpha Alumina
(α -Al₂O₃) nanoparticles by
solution combustion method.**



Abstract: - In this study, Aluminium Nitrate Nonahydrate Al(NO₃)₃.9H₂O and Urea NH₂CONH₂ were used as raw materials to synthesize Alpha Alumina (α - Al₂O₃) nanoparticles by solution combustion method. The synthetic process and properties of nano-powder (α - Al₂O₃) was studied by X-ray diffraction, Scanning Electron Microscopy and Transmission Electron Microscopy. The product was sphere-shaped particle with good dispersity.

Keywords - (α - Al₂O₃) , Solution Combustion method., XRD , SEM , TEM

INTRODUCTION

Metal oxide nanoparticles have found many uses in engineering, medicine and materials.[1-8] Alumina (Al_2O_3) has been used in different applications because of its various importance and beneficial properties. The chemical compound of alumina composed of aluminum and oxygen and most widely used ceramic materials among others ceramic material such as aluminum nitride, zirconia, silicon carbide, etc. Various applications that used alumina are as a biomedical implants, catalyst support and absorbents, fire retardants, polymer matrix composite, insulator and in clinical field, electronic fields, etc. [9]. Nowadays, metal oxide nanoparticles have found many uses in engineering, medicine and materials. Al_2O_3 nanoparticles are used for a wide range of adsorbent and catalyst applications including the adsorption of catalysts in polyethylene production, in hydrogen peroxide production, as a selective adsorbent for many chemicals including arsenic, fluoride, in sulfur removal from gas streams. The oxides of aluminium materials are widely used in ceramics, refractories and abrasives due to their hardness, chemical inertness, high melting point, non-volatility and resistance to oxidation and corrosion.[10]

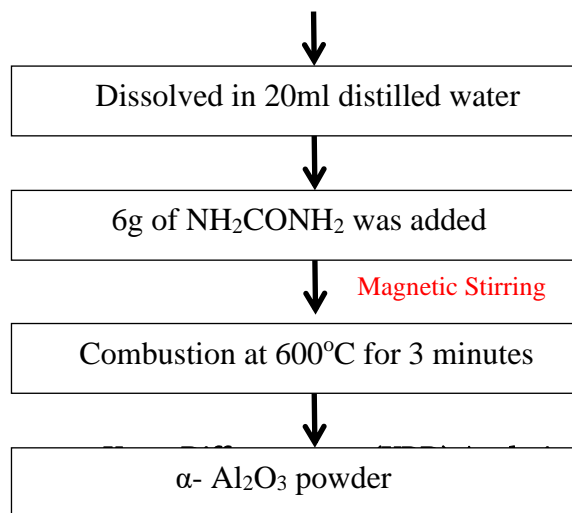
Alumina can be synthesized into different phases including alpha, beta, gamma, and delta. All of these phases can be attained at different temperature during synthesizing of alumina. Each phase has its own features which are different for application used. However, among these phases the alpha alumina is most stable structure and popular among researchers due to its superior properties such as high hardness, high stability, high insulation and transparency.[11]

EXPERIMENTAL DETAILS / ANALYSIS

Every chemical used was of analytical grade.

A certain amount of Aluminium Nitrate (98%) Non Hydrate [$\text{Al}(\text{NO}_3)_3 \cdot 9\text{H}_2\text{O}$] was dissolved in 20ml distilled water. Then about 6 g (6.00399g) of urea [NH_2CONH_2] was added and the solution was stirred using a magnetic stirrer for one hour. Then the solution was combusted at 600°C for 3 minutes in preheated furnace. A solid in foam form was obtained. The solid was then crushed to obtain a fine powder.

$\text{Al}(\text{NO}_3)_3 \cdot 9\text{H}_2\text{O}$ was taken as precursor



X-ray Diffractometry (XRD) Analysis

Fig 1 shows XRD pattern of synthesized nano-powder after combustion. The peaks were observed at 25.656° , 35.236° , 37.857° , 43.436° , 52.613° , 57.5644° , 66.592° and 68.276° . The crystalline size calculated according to debye scherrer formula was found out to be 28.22365039 nm.

It can be seen that the XRD data is agreeable with the standard diffraction chart of α - Al_2O_3 in JCPDS 00-001-1296, indicating the α - Al_2O_3 phase has good crystalline structure but some impurities were observed.

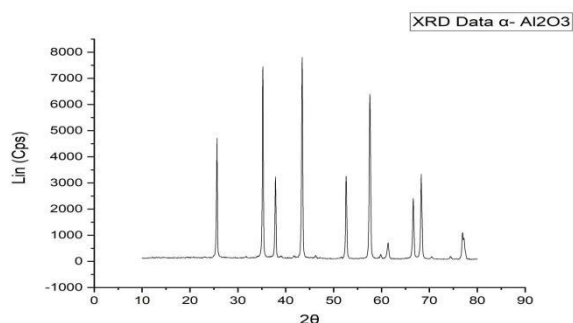


Fig 1 - XRD pattern of synthesized α - Al_2O_3 nano-powder after combustion.

SEM and TEM Analysis

SEM study is carried out to observe the overall surface morphology and crystallite sizes of the prepared nanomaterials. From the SEM images are observed under 10 micrometer resolutions which shows the foam like surface morphology as shown in figure In the depicted images of Al_2O_3 nanomaterials, it can be clearly seen that the crystallite sizes may vary from a $10\ \mu\text{m}$ to few microns range if we magnify further. The crystallites look like having a sharp surface edge as well as crystalline grains and the particles foam-like morphology can be formed from highly agglomerated crystallites. Also, it is confirmed that the crystallite sizes are nearly equal for all sample.

TEM analysis was carried out to confirm the actual size of the particles, their growth pattern and the distribution of the crystallites. Figure 3 shows the as synthesized TEM image of sphere-like shaped of α - Al_2O_3 nanoparticles. The alumina nanoparticles were formed with size in the range of 20-35 nm

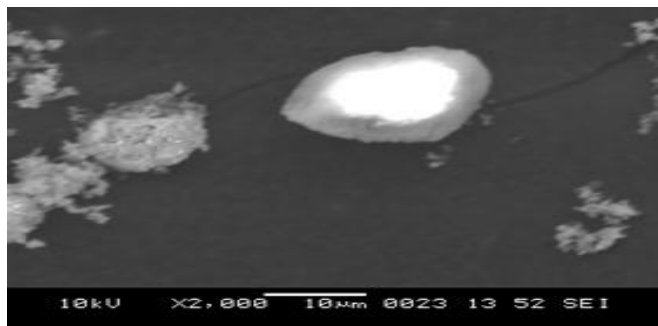


Fig 2 - SEM images of the as-prepared α - Al_2O_3 nanoparticles.

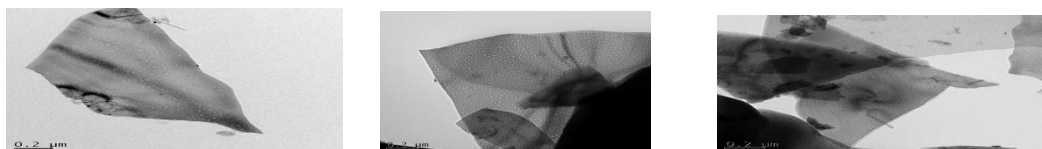


Fig 3 - TEM images of the as-prepared α - Al_2O_3 nanoparticles.

Conclusion- It was concluded that urea served not only as a fuel for the process running but also as a “catalyst” for the formation of alpha alumina from alumina nitrate. The use of Urea as a accelerating fuel to form chelants leads to formation of fine α - Al_2O_3 nanoparticles. The powder was nanocrystalline in nature with average crystallite size of about 28 nm as confirmed by XRD

References -

[1] Farahmandjou M. Magnetocrystalline properties of Iron Platinum (L10-FePt) nanoparticles through phase transition. *Iran Journal of Physical Research*, 2016, 16: 1-5.

<https://doi.org/10.18869/acadpub.ijpr.16.1.1>

[2] Farahmandjou M and Ramazani M. Fabrication and Characterization of Rutile TiO_2 Nanocrystals by Water Soluble Precursor. *Physical Chemistry Research*, 2015, 3: 293-298.

<https://doi.org/10.22036/pcr.2015.10641>

[3] Farahmandjou M, Honarbakhsha S and Behrouziniab S. PVP-Assisted Synthesis of Cobalt Ferrite (CoFe_2O_4) Nanorods. *Physical Chemistry Research*, 2016, 4: 655-662.

[4] Akhtari F, Zorriasatein S, Farahmandjou M, et al. Structural, optical, thermoelectrical, and magnetic study of $\text{Zn}_{1-x}\text{Co}_x\text{O}$ ($0 \leq x \leq 0.10$) nanocrystals. *International Journal of Applied*

Ceramic Technology, 2018, 15: 723-733.

<https://doi.org/10.1111/ijac.12848>

[5]Khoshnevisan B, Marami MB and Farahmandjou M. Fe³⁺-Doped Anatase TiO₂ Study Prepared by New Sol-Gel Precursors. Chinese Physics Letters, 2018, 35: 027501-027505.

<https://doi.org/10.1088/0256-307X/35/2/027501>

[6]Jafari A, Khademi S and Farahmandjou M. Nano-crystalline Ce-doped TiO₂ Powders: Sol-gel Synthesis and Optoelectronic Properties. Materials Research Express, 2018, 5: 095008.

[7]Jurablu S, Farahmandjou M and Firoozabadi TP. Sol-gel synthesis of zinc oxide (ZnO) nanoparticles: study of structural and optical properties. J Sci Islamic Republic of Iran, 2015, 26: 281-285.

[8]Dastpak M, Farahmandjou M and Firoozabadi TP. Synthesis and Preparation of Magnetic Fe-Doped CeO₂ Nanoparticles Prepared by Simple Sol-Gel Method. Journal of Superconductivity and Novel Magnetism, 2016, 29(11): 2925-2929.

<https://doi.org/10.1007/s10948-016-3639-3>

[9] Siti Nur Syakirah Mohamad et al 2019 IOP Conf. Ser.: Mater. Sci. Eng. 701012034

[10]Majid Farahmandjou1Nazafarin Golabiyani Synthesis and characterisation of Al₂O₃ nanoparticles as catalyst prepared by polymer co-precipitation method .

[11]V. Piriawong, V. Thongpool, P. Asanithi, and P. Limsuwan, J Nanomater. 2012 (2012).

Comparative Study of primary and secondary alcohols in a common solvent Nitrobenzene using Ultrasonic Pulse-echo technique

Abstract: - This work focuses on studying the Liquid mixtures to identify their nature and behavior. Variations are studied on the basis of different physical parameters using ultrasonic characterization techniques. This work depicts the study of the binary mixture of ethanol and iso-propanol in a common solvent where the nitrobenzene for the temperature range is 1°C-10°C. The temperature stabilizer -Julabo F32 is noted with an accuracy of $\pm 0.1^\circ\text{C}$. Ultrasonic attenuation and velocity are studied in both the mixtures. Both the alcohols have been witnessed to have the similar nature of the curves with a sharp change in the values of critical molar concentrations and critical temperatures.

Keywords: Ultrasonic pulse echo technique, ultrasonic velocity of propagation, ultrasonic absorption, critical mixture

I. INTRODUCTION

The Liquids or liquid mixtures are of a meticulous importance as dynamic processes occur near their critical points. Further, they possess a sharp phase transition near their critical temperature. Propagation of ultrasonic wave through the liquid or liquid mixture introduces thermal agitations in it. This perturbs the system and a relaxation phenomenon is encountered. Further, Absorption in liquids is result of the combined effects of viscosity and conduction of heat. Absorption due to structural relaxation shows significant velocity dispersion over the relaxation region. The measurement of thermodynamic parameters is possible using ultrasonic relaxation for which stoichiometric nature of perturbed equilibrium is to be studied. This study is generally executed using systematic variations in chemical composition. Many researchers have studied different alcohols and their mixtures in different solvents [1-11]. Perturbation in the chemical combination of the mixtures provides variations in the values of ultrasonic attenuation.

In the given study, nitrobenzene is a common solvent for ethanol and iso-propanol. Both alcohols have varied molecular combinations where Ethanol is a primary alcohol and iso-propanol is the secondary.

¹ *Corresponding author: 1Department of Physics, G H Raisoni College of Engineering, Nagpur-440016, India

²Department of Electronics and Computer Science, Rashtrasant Tukadoji Maharaj Nagpur University, Nagpur-440 033, India

³ Late B. S. Arts Prof N. G. Science and A. G. Commerce College, Sakharkherda Dist -Buldhana-443201, India

Copyright © JES 2024 on-line: journal.esrgroups.org

The measurements are done using pulse echo technique with Transducer of 10 MHz frequency. The temperature stabilization is done with the usage of Julabo Thermostat with an accuracy of ± 0.10 C. The variations of attenuation and velocity show that the critical temperature and concentration values are different for both the alcohols which prove to be the basis for comparison.

II. EXPERIMENTAL

A. Materials

Ethanol and isopropyl alcohol and nitrobenzene used are of AR grade. The mixtures are prepared without further filtration or distillation of the sample.

The cell is specially designed to measure ultrasonic velocity and attenuation in liquid mixtures with utmost accuracy. It has a variable path length which can be changed as we move the transducer probe up and down. It is made up of stainless steel with grooves to avoid internal reflections, corrosion, and non-reactivity with the sample under study. Sample holder is a two layered cylinder where the outer cylinder is used to circulate water from the thermostat to maintain temperature stability and the inner cylinder is used to hold a sample.

Pulse echo is one of the best techniques to study the liquid samples. This has several benefits, which includes its feature to send a short train of sound waves through the medium to the receiver where a acoustic energy passes through the medium of liquid mixture for only a short time avoiding local heating of the sample. In the present work, in-house designed pulse echo set-up is used with 10MHz frequency [12]. Kalman Filter is used in this system which helps the system to extract signals from the noise.

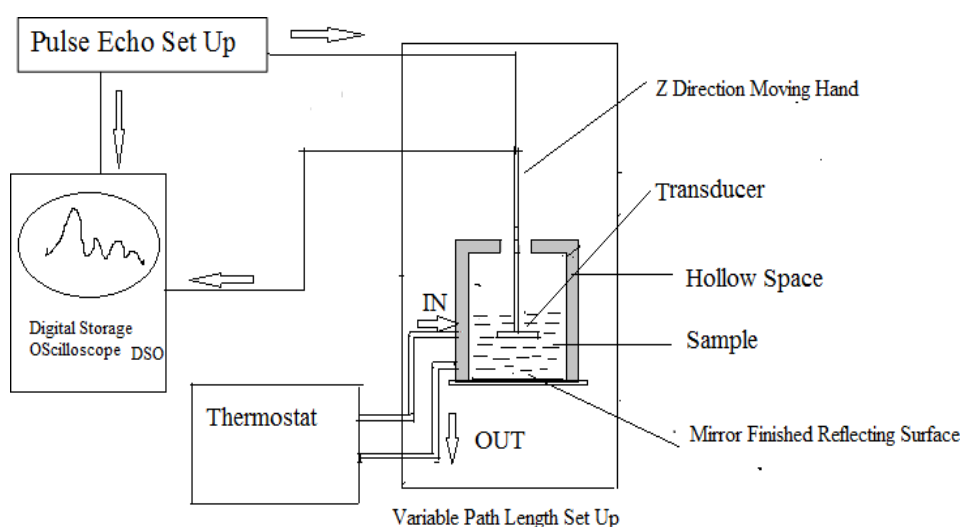


Figure 1. Schematic diagram for experimental set-up

B. Method

This method starts with the process of the cell being rinsed with the sample three times. The sample is then carefully poured in a cell or a sample holder to avoid the formation of any air bubble. This step is followed by switching on the thermostat and the sample is left for uniform circulation of water through the sample holder. The temperature of the sample is initially raised to the desired value, and then readings are noted down in a decreasing fashion to minimize the hysteresis. Figure 1 represents experimental set-up. Ultrasonic velocity and attenuation are calculated by noting the time of flight and amplitudes of respective echoes. The measurement for time of flight using echo pattern is as shown in figure 2 and measurement for attenuation is as shown in figure 3.

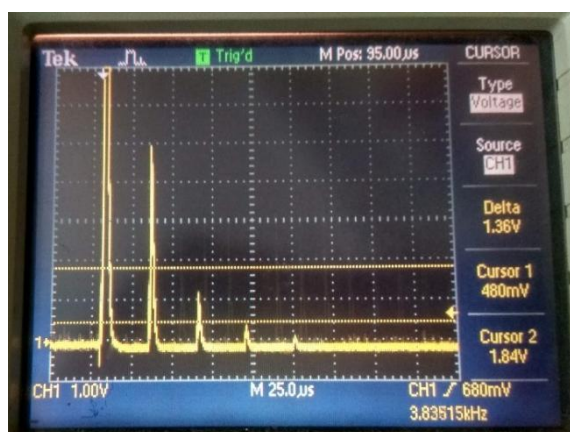
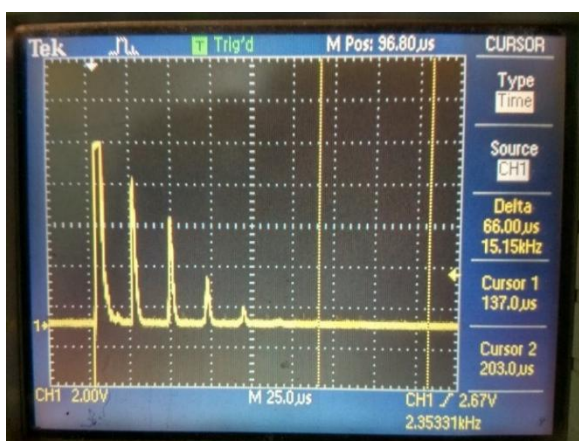


Figure 2. Echo Pattern on a digital oscilloscope to measure
Figure 3. Echo Pattern on a digital oscilloscope to measure amplitude time of flight

C. RESULTS AND DISCUSSION

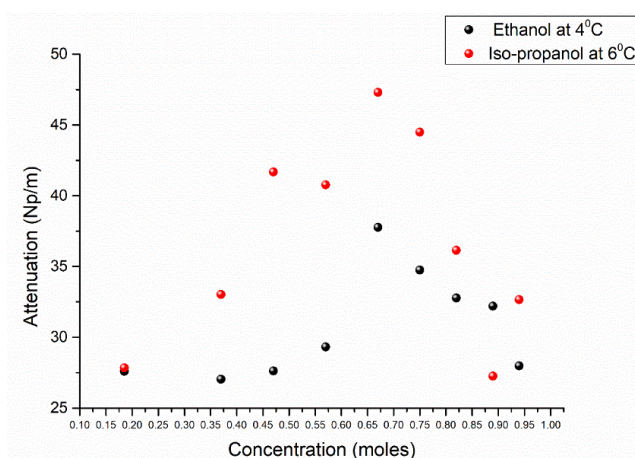


Figure 4. Variation of attenuation with respect to concentration for mixtures ethanol and iso-propyl alcohol in nitrobenzene

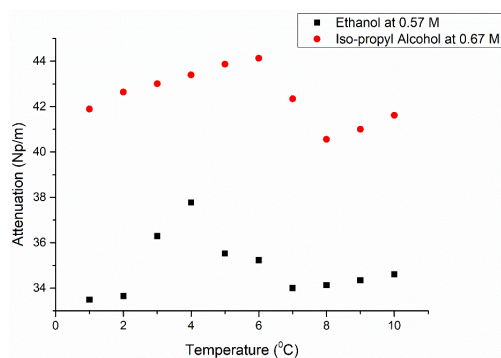


Figure 5. Variation of attenuation with respect to temperature for mixtures of ethanol and iso-propyl alcohol in nitrobenzene

Ultrasonic attenuation measurement is a tool for studying variations in molecular structure in a sample. Temperature is a major factor in the structural relaxation that occurs in many samples. Romanov proposed a concentration fluctuation model that explains the effect of concentration on the physical properties of mixtures. Researchers [13-18] have studied the variation of attenuation for temperature and concentration. Figure 4 represents the changes in attenuation for the variations in its concentration. As we continue to add ethanol or isopropyl alcohol to the nitrobenzene, the attenuation initially increases, reaches a maximum, and gradually decreases. This is a mixture of associated and non-associated liquids, where hydrogen bonding is a factor in the attenuation of ultrasound [19-20]. Dispersion of ultrasonic waves is observed due to relaxation phenomenon. The graph shows that the attenuation is on the higher side for isopropyl alcohol with respect to concentration. Ethanol, being a primary alcohol, has a lower charge, showing attenuation at lower temperatures and lower concentrations. On the other hand, iso-propyl alcohol is a secondary alcohol and tightly bonds atoms with the OH functional group on the second carbon atom. Thus, structural relaxation is dominant in the isopropyl blend. The interaction between the open-ended O-H group in ethanol with nitrobenzene is a dipole-dipole interaction, while the interaction with iso-propyl alcohol having an O-H bond on the second carbon atom induces a dipole-dipole interaction. Ethanol, being a primary alcohol, has an attenuation peak at a lower temperature compared to the attenuation experienced by isopropyl alcohol as shown in figure 5. Temperature changes show that smaller packing fractions and functional group relaxation at free carbon, led to a decrease in temperature [21-22].

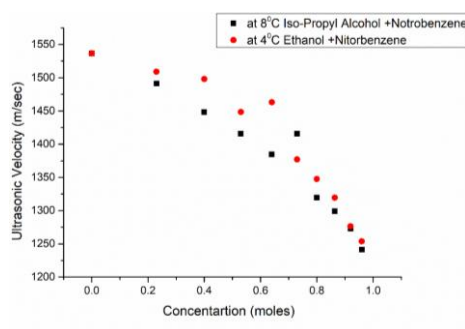


Figure 6. Variation of velocity with respect to concentration for mixtures of ethanol and iso-propyl alcohol in nitrobenzene

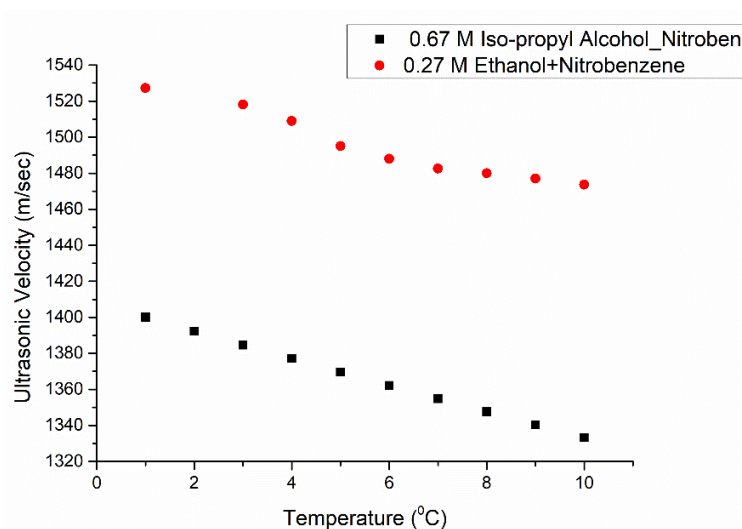


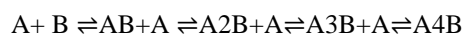
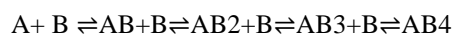
Figure 7. Variation of velocity with respect to temperature for mixtures of ethanol and iso-propyl alcohol in nitrobenzene

Ultrasonic velocity measurement is used to study the effect of intermolecular forces in a mixture. Ethanol is with the functional group at first carbon. Isopropyl alcohol has it on the second carbon atom in the chain that alters the reactivity of the material. The influence of temperature and concentration on the speed of ultrasound is monitored. The ultrasonic speed of nitrobenzene is highest in its pure form. The velocity of the mixture lowers with rising concentrations of the individual alcohols as shown in Figure 6. The polar nature of the alcohols and the hydroxyl group exhibiting a self-associative nature are responsible for such variations. Isopropyl alcohol has a lower density [9]. Dipole-induced interactions can be witnessed on mixing of associated and non-associated liquids. The changes in temperature are observed in Figure 7. A decrease in ultrasound velocity is observed as the increase in temperature weakens the molecular forces. A strong dipole-dipole interaction between hydrogen, oxygen, or nitrogen is generally called a hydrogen bond. Due to larger partial positive charge on the hydrogen atom and the large partial negative charge on the oxygen or nitrogen atom, there is a large difference in electronegativity. In the primary alcohol, electronegative oxygen atom will exhibit a dipole-dipole interaction, while when the secondary alcohol molecules interact with the nitrobenzene, it exhibits an induced dipole force. As the temperature increases, these forces weaken [15].

D. CONCLUSION

A comparative study is done for primary and secondary alcohol using ethanol as primary and isopropyl alcohol as secondary alcohol. Following are the conclusions after studying the samples. The first factor to focus on is the position of the OH group present in ethanol and isopropyl alcohol. This factor affects the chemical reaction taking place between the solute and the solvent. With increasing concentration of alcohols in nitrobenzene the interaction between the OH functional group and nitrogen in nitrobenzene

is due to the large variance in the electro negativity of hydrogen and nitrogen. Complexes are formed in both mixtures as follows [23].



This complete discussion is in the light of Fixman's approach of concentration fluctuation [24-25]. The dependency of absorption on temperature and concentration influences the behaviour of mixtures. Different critical temperatures and concentration values provide a good comparison between the two alcohols.

E. DECLARATIONS

Ethical Approval

This is to declare that the authors have not conducted any experiments on any humans or animals. Also, the presented work is the part of my doctoral research.

Competing interests

One of the authors is grateful to Dr. Satish Sharma Head of the Department of Electronics and Computer Science, Rashtrasant Tukadoji Maharaj Nagpur University, Nagpur, for providing the necessary facilities to carry out the work.

Authors' contributions

One of the authors, Rupali Thete, confirms sole responsibility for the following: studying the sample, selecting the system, data collection, analysis and interpretation of results. Both authors Rupali Thete and Satish Sharma, reviewed the results and agreed fully on the final version of the manuscript.

Funding

This is to declare that no specific grant is received for this research from any funding agency.

Availability of data and materials

Supporting data for the findings of this study are available and can be produced on request from the corresponding author, Rupali Thete.

F. REFERENCES

- [1] T. Homowski, "Ultrasonic Absorption Coefficient and Propagation Velocity in Critical Benzonitrile- Isooctane Mixture, *Acta Phys.Pol.*", 82(6), 1992, pp. 961-966.
- [2] J. Blitz, *Fundamentals of Ultrasonics*, (Butterworth Publishers, London, 1963)
- [3] K. F. Herzfeld and T.A. Litovitz, *Absorption and Dispersion of Ultrasonic Waves*, (Academic Press, New York and London, Pubs., 1959)
- [4] C. Shanmug Priya, C. Nithya, C. Velraj and A. N. Kanappan, "Molecular interaction studies in liquid mixture using Ultrasonic technique," *Int. Jr Adv. Sci. & Tech.* 18, 2010, pp 59-73.
- [5] M. Sri Laxmi, "Theoretical Evaluation of Ultrasonic Velocities in Binary Liquid Mixtures containing Cyclohexane," *Int. J. Pharm. & Chem. Sci.* 1(4), 2012, pp. 1856-1862.
- [6] V. C. Agrawal and A. K. Gupta, "Acoustic attenuation and velocity measurements in a methanol and cyclohexane," *J. Phy D. Phys.* 8, 1975, pp. 2232-2236.
- [7] Issam R. Abdelraziq, S. S. Yun and F. B. Stumpf, "Critical behavior of the ultrasonic attenuation and velocity & shear viscosity for the binary mixture of nitrobenzene-n-hexane," *J. Acoost. Soc. Am.* 88(4), 1990, pp. 1836-1831
- [8] S.S. J Shrinivas, B. Tulasi Koteswari Bai, K Baburao, K Narendra and M. Sarath Babu, "Studies of densities, viscosities and ultrasonic speeds of binary mixtures containing isopropyl alcohol and ketones at different temperatures," *Int. Letters. of Chem., Phy. and Astronomy*, 15, 2013, pp. 151-158.
- [9] S. Elangovan, "Ultrasonic studies on Intermolecular Interaction in Binary Mixtures of N-Methyl with 1-Butanol at 308 K," *Int. J. of Chem. Tech Research* 8(1), 2015, pp. 223-227.
- [10] D. Sette, "Measurements of Ultrasonic Absorption in Various Mixtures of Nitrobenzene," *J. Acoust. Soc. Am.* 23(3), 1951, pp. 359-363.
- [11] P. S. Nikam, "Density and Viscosity of Mixtures of Nitrobenzene with Methanol, Ethanol, Propan-1-ol, Propan-2-ol, Butan-1-ol, 2-Methylpropan-1-ol, and 2-Methylpropan-2-ol at 298.15 and 303.15 K," *J. Chem. Eng. Data*, 40, 1995, pp. 931-934.
- [12] S. U. Dubey, "Real Time Implementation of Kalman Filter to improve accuracy on the measurement of time of flight in an ultrasonic pulse-echo setup," *Rev. Sci. Instrum.* 90, 025105, 2019, pp. 1-6 <https://doi.org/10.1063/1.5048966>
- [13] C. J. Burton, "A Study of Ultrasonic Velocity and Absorption in Liquids," *J. Acoust. Soc. Am.* 20(2), 1948, pp. 781-782.
- [14] Govindrajan S., Kannappan V., Naresh M. D., Muthukrishnan M., Arumugam V., Rajaram A, and Lokandam B. J. *Pure Appl. Ultrason.* 33, 2011, pp. 33-38
- [15] B. Jacobson, "Intermolecular free lengths in the liquid state; Adiabatic and Isothermal compressibility," *Acta. Chim. Scand.* 6, 1952, pp. 1485-1497.
- [16] M. J. Blandamer, *Introduction to Chemical Ultrasonics*, Academic Press, London and New York, 1973
- [17] V. P. Romanov and V. A. Solov'ev, "Concentration fluctuation and their influence on sound absorption, Consultants Bureau," New York, 2, 1971, pp. 1-11.
- [18] A. Ali and A. K. Nain, "Study of molecular interactions in non-aqueous binary liquid mixtures through ultrasonic measurements," *J. Pure & Appl. Ult.* 22, 2000, pp. 10-15.
- [19] Dukhin A.S. and Goetz P. J. 2010 *Characterization of Liquids, Nano- and Micro-particulates and Porous Bodies using Ultrasound Studies in Interface Science*, Elsevier Publication
- [20] S. Rajagopalan, "Ultrasonic Absorption in Mixture of Dioxane and Benzene," *J. Phy. Soc. Japan*, 27(4), 1969, pp. 1020-1021.
- [21] Rupali Thete, Satish Sharma and S. Rajagopalan, "Ultrasonic Propagation in Critical Mixture of Nitrobenzene and Ethanol", *AIP Conference Proceedings* 2220, 140052, 2020, pp. 1-5. <https://doi.org/10.1063/5.0001142>
- [22] Rupali Thete, Satish Sharma and S. Rajagopalan, "Study of Positional isomerism in N-propyl and Isopropyl alcohol using ultrasonic technique", *Journal of Physics: Conference Series* 1913, 012009, 2021, pp. 1-7. DOI 10.1088/1742-6596/1913/1/012009
- [23] S. Rajagopalan and G. S. Verma, "On coexistence of chemical relaxation in mixtures of dioxane and glycerol", *Il Nuovo Cimento B* (1965-1970) 67, pages13-28 (1970)
- [24] M. Fixman, "Absorption and Dispersion of Sound in Critical Mixtures," *J. Chem. Phys.* 36(8), 1961-1964 (1961)
- [25] M. Fixman, "Ultrasonic Attenuation in the Critical Region," *J. Chem. Phys.* 33(5), 1363-1370 (1961)

¹Dr. Rajesh R. Karhe

²Dr. C.M Jadhao

³Mr. S.S. Mhaske

Recurrent Neural Network-Based Classification of Scanned ECG Records for Cardiac Arrhythmia Detection



Abstract: - The Electrocardiogram (ECG) is a valuable tool for diagnosing cardiac arrhythmias without invasive procedures. This study utilizes an arrhythmia detection system to analyze scanned ECG paper images, distinguishing between normal and arrhythmic patterns. Artificial Neural Networks (ANN) serve as the backbone of this system, with various models trained separately using different hidden layers and training algorithms (trainrp, trainbr, trainscg, trainlm). Performance metrics such as accuracy, execution time, and several performance functions like MSE, SSE, SAE, and MAE are compared to identify the most effective ANN models. Results indicate that the Recurrent Neural Network (RNN) achieves the highest accuracy of 85.71% in detecting arrhythmias from scanned ECG data. Additionally, the comparison between training algorithms highlights trainrp as the most efficient one for this arrhythmia detection system.

Keywords: Feedforward Neural Networks, Patternnet Neural Networks, cascade forward Neural Network, Recurrent Neural Network.

¹ Professor, Department of Electronics & Telecommunication, Mauli College of Engineering and technology, Shegaon, India

² Professor and Principal, Department of Electronics & Telecommunication, Mauli College of Engineering and technology, Shegaon, India

³ Assistant Professor, Department of Electronics & Telecommunication, Mauli College of Engineering and technology, Shegaon, India
Copyright © JES 2024 on-line: journal.esrgroups.or

I. INTRODUCTION

The Electrocardiogram (ECG) signal reflects the heart's electrical activity and offers crucial insights into heart-related diseases. This research aims to analyze and detect arrhythmias using Neural Network classifiers. The process involves digitizing ECG images, detecting QRS complexes in the signal, extracting features from these complexes, and finally, classifying them using Neural Networks.

Artificial Neural Networks (ANN) have become popular for arrhythmia detection, with the back propagation neural network (BPNN) being a favored model trained using a back propagation algorithm. Different ANN models mimic the behavior of neurons in the human brain, making them suitable for arrhythmia detection. Researchers have employed various ANN models with different performance metrics, highlighting the need to identify the most effective model for arrhythmia detection.

This work aims to develop an arrhythmia detection system utilizing different ANN models, including feedforward neural networks, cascade neural networks, pattern net neural networks, and recurrent neural networks. The paper is structured into sections: background, details about Artificial Neural Networks, detection and classification of arrhythmias from scanned ECG paper records images, results and decision, and conclusion.

II. BACKGROUND

Several recent studies in the field of arrhythmia detection and analysis are summarized here. Dallali et al. [2] conducted an analytical investigation of ECG signals to identify uncommon heart rhythms, employing time-frequency filters to reduce noise. Kutlu et al. [3] proposed a system for arrhythmia detection based on morphological features and utilized a wrapper feature selection algorithm. Fatin A Flhaj et al. [4] analyzed five types of beat classes of arrhythmia using principal component analysis of DWT coefficients, achieving high accuracy with SVM and neural network methods.

Manu Thomos et al. [5] introduced a computer-aided diagnosis system for cardiac diseases utilizing DTCWT technique and a multi-layer backpropagation neural network for classification. Hongqiang Li et al. [6] implemented feature extraction and classification of ECG signals using GA-BPNN and WPD. Andrew Y. Ng et al. [7] proposed a convolutional neural network algorithm for detecting various arrhythmias from ECG signals.

Latha Parthiban et al. [8] suggested a Coactive NeuroFuzzy Inference System for arrhythmia prediction, combining genetic algorithm, neural networks, and fuzzy logic. Maedeh Kiani Sarkalehm et al. [9] utilized DWT transform for feature extraction and MLP for classification. Mohd. Khalid Awang et al. [10] developed a Heart Disease Management Information System integrated with a neural network simulator. Ali Sadr et al. [11] compared Multi-layer Perceptron and Radial Basis Function for ECG signal classification.

Mehmet Engin et al. [12] proposed a fuzzy-hybrid neural network for ECG signal classification. Yuksel Ozbay et al. [13] used Artificial Neural Networks to classify ten different arrhythmias, achieving 96% accuracy with backpropagation. V. S. Chauhan et al. [14] introduced a modified slope of the ECG signal as a new feature for feature extraction and classification.

III. ARTIFICIAL NEURAL NETWORK

Artificial Neural Networks (ANNs) are data processing mathematical models composed of units known as nodes or neurons, organized into layers. These layers include an input layer, one or more hidden layers, and an output layer. The neurons in these layers are interconnected through weights and biases. The input layer receives the initial data, and each subsequent layer is connected to the one before it. The output layer generates the final result of the ANN. Training an ANN can be accomplished using the Back Propagation algorithm, which involves the following equations.

$$U_k(t) = \sum_{j=1}^n w_{jk}(t) * x_j(t) + b_k(t) \quad (1)$$

$$Y_k(t) = \varphi(U_k(t)) \quad (2)$$

Where:

- $w_{jk}(t)$: Weight assigned by neuron k to input j at time t
- $x_j(t)$: Input value of j at time-step t

- $b_k(t)$: The bias of k-neuron at time t
- ϕ : Nonlinear activation function
- $y_k(t)$: Output from neuron k at time t

The target output T_k is compared with the output Y_k using the error function given by Equation 3:

$$\delta_k = (T_k - y_k) y_k (1 - y_k) \quad (3)$$

For neurons in the hidden layer, the error is given by Equation 4:

$$\delta_k = y_k (1 - y_k) \sum (\delta_k * w_k) \quad (4)$$

Where:

- δ_k : Error term of the output layer
- w_k : The weight between the output and hidden layers

The error from the output layer is fed back to the input layer for updating the weights of each connection as follows:

$$w_{jk}(t+1) = w_{jk}(t) + \eta \delta_k y_k + \alpha (w_{jk}(t) - w_{jk}(t-1)) \quad (5)$$

Where:

- η : Learning rate
- α : Momentum variable

Cascade-forward networks are similar to feed-forward networks, but they include connections from the input and every previous layer to subsequent layers. Layer recurrent neural networks are also similar to feed-forward networks, except that each layer has a recurrent connection with an associated tap delay.

PatternNet is a feed-forward network used for pattern recognition problems and can be trained to classify inputs according to target classes.

The difference between the desired output and the actual output is given by the mean square error (MSE), a performance function that needs to be minimized during ANN training.

In this research paper, four ANN training algorithms were used to train four models separately to identify the best one for arrhythmia recognition:

- Bayesian Regularization algorithm (TRAINBR)
- Levenberg-Marquardt algorithm (TRAINLM)
- Resilient Back Propagation (TRAINRP)
- Scaled Conjugate Gradient Back Propagation (TRAINSCLG)

IV. DETECTION AND CLASSIFICATION OF ARRHYTHMIAS FROM SCANNED ECG IMAGES

The proposed algorithms were tested on 32 images from a normal patient and 32 images from patients with arrhythmias. These ECG images were pre-processed and digitized using Dijkstra's shortest path algorithm, as illustrated in Figure 4. Harris Corner features were utilized for the detection and classification of arrhythmias from the digitized ECG signals using a Neural Network.

In this study, different ANN models were used separately for arrhythmia detection. Each of these models was constructed individually, consisting of input layers, various hidden layers, and output layers. The ECG paper recordings needed to be scanned. Figure 2 shows an example of a scanned ECG paper recording.

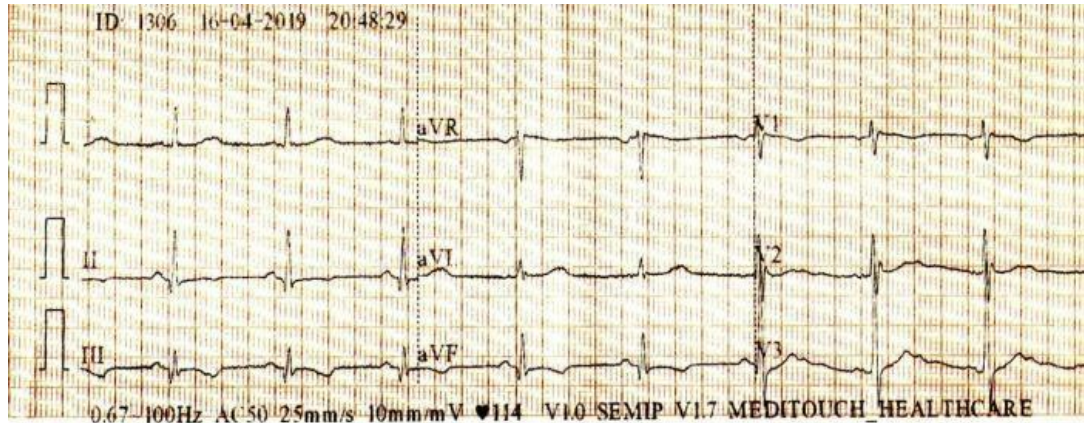


Fig 2: Scanned ECG Document

The first step is carried out to select and crop one of the 12-lead ECG signals as shown in the figure 3 for cropping III lead

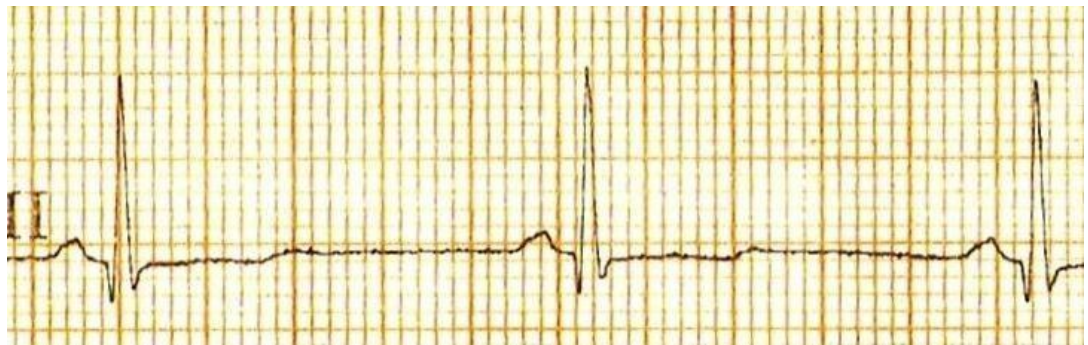


Fig 3: Cropped ECG Image.

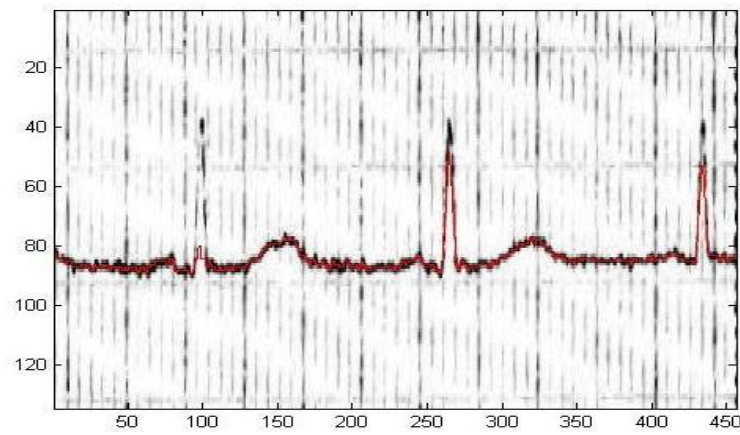


Fig 4: ECG curve plot on the original ECG image.

V. RESULTS AND DISCUSSIONS

MATLAB was utilized to develop the simulation programs for four models: feedforward, cascade-forward, Patternnet, and layrecnet. The performance of these ANN models for arrhythmia detection was evaluated based on accuracy and execution time. The evaluation considered varying the number of hidden layers (5, 10, 15, 20, 25) and different neural network architectures for each number of hidden layers, as shown in Table I. The training function considered here is ‘trainlm’ and performance function for neural network is ‘MSE’.

Table I Performance of Neural Network for various numbers of hidden layers

Accuracy					
Number of Hidden Layers	5	10	15	20	25
FeedForward Neural Network	73.4375	78.125	51.5625	87.5	87.5
Patternnet	87.5	87.5	87.5	73.4375	87.5
CascadedForwardNet	81.25	87.5	75	65.625	75
LayrecNet	85.7143	85.7143	85.7143	85.7143	85.7143
Execution Time					
Number of Hidden Layers	5	10	15	20	25
Feedforward Neural Network	2.0562	3.4534	25.2505	48.0734	92.9652
Patternnet	3.7723	8.2157	31.4473	38.4494	70.9846
CascadedForwardNet	2.946	8.5766	43.6273	59.3516	99.4319
LayrecNet	4.3282	1.831	1.9357	2.8307	3.9387

Table II Performance of ‘LayrecNet’ Neural Networks for Different Training Functions

Accuracy					
Number of Hidden Layers	5	10	15	20	25
Trainlm	87.5	50	87.5	87.5	87.5
Trainbr	87.5	87.5	87.5	87.5	87.5
Trainscg	87.5	84.375	87.5	84.375	87.5
Trainrp	87.5	85.9375	87.5	85.9375	87.5
Execution Time					
Number of Hidden Layers	5	10	15	20	25
Trainlm	133.5743	37.5393	16.7896	63.897	212.8488
Trainbr	1.55E+03	1.61E+03	1.66E+03	1.74E+03	5.41E+03
Trainscg	89.7128	9.837	15.0933	3.4528	3.1374
Trainrp	4.3282	1.831	1.9357	2.8307	3.9387

The table II shows that for LayrecNet the accuracy of all training functions is best. The execution time of ‘trainrp’ is less (average2.97). Hence considering the execution time and accuracy together, it’s been concluded that the ‘trainrp’ is the best for arrhythmias detection.As concluded from the above results, LayrecNet networks with ‘trainrp’ function performs better for arrhythmia detection from actual time scanned ECG image data. Here we have compared the performance of LayrecNet neural networks using different neural network performance functions including ‘MSE’, ‘SSE’, ‘SAE’, and ‘MAE’.

Table III depicts the performance of LayrecNet neural networks with ‘trairp’ function for types of arrhythmias detection.

Table III Performance of LayrecNet Neural Networksfor different Performance Functions

Accuracy					
Error Function	5	10	15	20	25
MSE	85.7143	85.7143	85.7143	85.7143	85.7143
SSE	50	50	87.5	87.5	75
SAE	87.5	89.0625	92.1875	87.5	81.25
MAE	85.9375	50	87.5	87.5	87.5
Execution Time					
Error Function	5	10	15	20	25
MSE	4.3282	1.831	1.9357	2.8307	3.9387
SSE	14.9897	10.6785	34.9405	71.7529	127.2963
SAE	44.8688	16.0932	14.253	19.0926	38.1863
MAE	28.1004	10.2087	13.1454	11.0549	34.6919

The overall accuracy and execution time of 'MSE' is best for arrhythmias detection with LayreCNet neural networks.

VI. CONCLUSIONS

In this study, neural network classification was employed to classify scanned ECG images. Various neural network models were assessed based on accuracy, execution time, and different performance metrics, including MSE, SSE, SAE, and MAE. For the scanned ECG images, a layered neural network using the 'trainrp' training function and 'MSE' as the performance metric proved to be the most effective. Future work will focus on investigating additional types of arrhythmias and reducing the time and storage requirements for the ECG image database.

VII. REFERENCES

- 1) WHO. Cardiovascular diseases (CVDs) [Internet]. [Cited 2015 Dec 25]; Available from: <http://www.who.int/mediacentre/factsheets/fs317/en>
- 2) A. Dallali, "Integration of HRV, WT and Neural Networks for ECG Arrhythmias Classification", in ARPN Journal of Engineering and Applied Sciences, vol. 6, no. 5, May 2011.
- 3) Yakup Kutlu n, Damla Kuntalp A multi-stage automatic arrhythmia recognition and classification system Computers in Biology and Medicine41 (2011) 37–45.
- 4) Fatin A. Elhaj Arrhythmia recognition and classification usingcombined linear and nonlinear features of ECGsignalsFatin com puter method s and programsin biomedicine.
- 5) Manu Thomas, Manab Kr Das*, Samit Ari Automatic ECG arrhythmia classification using dual tree complexwavelet based features International Journal of Electronics and Communications (AEÜ).
- 6) Hongqiang Li1, Danyang Yuan1, Xiangdong Ma1, Dianyin Cui1 & Lu Cao Genetic algorithm for the optimization of features and neural networks in ECG signals classification.
- 7) Pranv Rajpurkar, Awni Y. Hannun, Masoumeh, Codie Bourn, Andrew Y. Ng, Cardiologist-Level Arrhythmia Detection with Convolutional Neural Networks, IEEE Transactions on Biomedical Engineering, Vol. 55, No. 1,Pp. 108-118, July 2017.
- 8) Latha Parthiban, R. Subramanian, Intelligent Heart Disease Prediction System using CANFIS and Genetic Algorithm, International Journal of Biological and Medical Sciences 3:3 2008

- 9) MAEdeh Kiani Sarkalehm, Asadollah Shahbahrami, Classification of ECG Arrhythmias using Discrete Wavelet Transform and Neural Networks, International Journal of Computer Science, Engineering and Applications (IJCSEA) Vol.2, No.1, February 2012
- 10) Mohd Khalid Awang and Fadzilah Siraj. Utilization of an Artificial Neural Network in the Prediction of Heart Disease, International Journal of Bio-Science and BioTechnology Vol. 5, No. 4, August, 2013
- 11) Ali Sadr, Najmeh Mohsenifar, Raziye Sadat Okhovat. Comparison of MLP and RBF neural networks for Prediction of ECG Signals,
- 12) Mehmet Engin. ECG beat classification using neurofuzzy network, Elsevier, Pattern Recognition Letters 25, 1715–1722, 2004
- 13) Yüksel Özbay and Bekir Karlik. A Recognition of ECG Arrhythmias Using Artificial Neural Networks, Proceedings – 23rd Annual Conference – IEEE/EMBS Oct.25-28, 2001, Istanbul, Turkey.
- 14) V. Chouhan, "Delineation of QRS-complex, P and T-wave in 12-lead ECG", in International Journal of Computer Science and Network Security, vol. 8, no. 4, April 2008.
- 15) I. Romero and L. Serrano., "ECG frequency domain features extraction: a new characteristic for arrhythmias classification", in Engineering in Medicine and Biology Society, 2001. Proceedings of the 23rd Annual International Conference of the IEEE., 2001.
- 16) Sean Franklin, Joseph Wallcave. Cardiac Condition Detection using Artificial Neural Networks, Senior Project Electrical Engineering Department, California Polytechnic State University, San Luis Obispo, June 2013.
- 17) Yildirim, Ö., Pławiak, P., Tan, R.-S., & Acharya, U. R. Arrhythmia detection using deep convolutional neural network with long duration ECG signals. Computers in Biology and Medicine – 2018.
- 18) Argyro Kampouraki, George Manis, and Christophoros Nikou, Member, IEEE, Heartbeat Time Series Classification with Support Vector Machines, IEEE Transactions on Information Technology in Biomedicine, Vol. 13, No. 4, July 2009

¹Mr.Siddharth K.
Ganvir

²Dr.G.K.Reddy

Design of MATLAB GUI for COVID detection & tagging the results using Neuro Solution Software



Abstract: - Traditional diagnostic methods faces limitations in discerning between different viral strains promptly. This research focuses on advancing the state-of-the-art in COVID-19 variant detection by harnessing the power of X-ray imaging and deep learning, implemented using MATLAB as the development environment. The utilization of neural networks, a subset of deep learning models, offers a promising avenue for automating the identification of Omicron and Delta variants based on radiological patterns captured in CT scan images. This Research paper focuses on designing a MATLAB GUI for COVID detection & tagging the results using Neuro Solution Software.

Keywords: COVID, X-Ray Images, CT Scan Images, MATLAB, Neuro Solution Software.

I. INTRODUCTION

Radiographs such as X-rays and computed tomography (CT) scans are cost-effective and widely available at public health facilities, hospital emergency rooms (ERs), and even at rural clinics, they could be used for rapid detection of possible COVID-19-induced lung infections. Therefore, toward automating the COVID-19 detection, we propose a viable and efficient deep learning-based chest radiograph framework to analyse COVID-19 cases with accuracy. A unique dataset is prepared from available sources containing the chest view of CT scan & X-ray data for COVID-19 cases. Our Designed framework leverages a data augmentation of radiograph images algorithm for the COVID-19 data, by adaptively employing the MATLAB and NeuroSolution on COVID-19 infected chest images to generate a train a robust model.

¹*Corresponding author : Research Scholar, Dept. of Electronics, Mahatma Fule, Arts, Commerce & Sitaramji Choudhari Science Mahavidyalaya, Warud, INDIA., siddharthgnvr@gmail.com

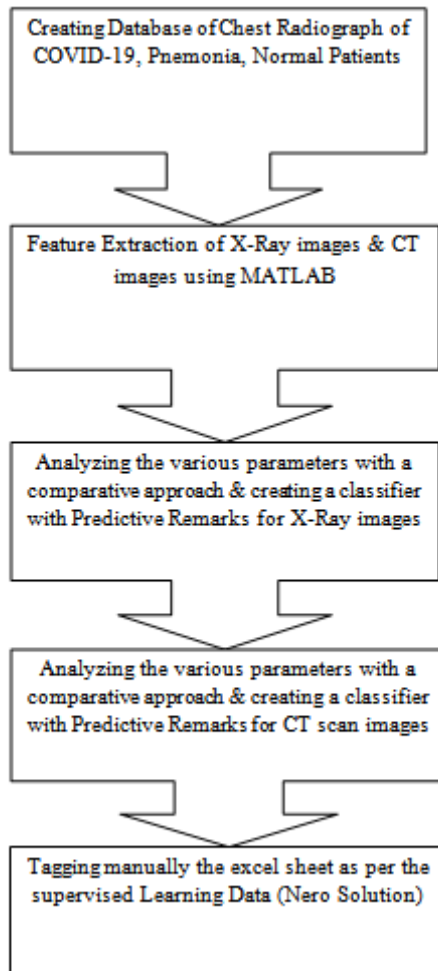
²Associate Professor, Dept. of Electronics, Mahatma Fule, Arts, Commerce & Sitaramji Choudhari Science Mahavidyalaya, Warud, INDIA., reddygiridhar4@gmail.com

II. RELATED LITERATURE REVIEWED

Sr.No.	Name of Researcher	Topic	Year	Method
1	S. Karanam, R. Li, F. Yang, W. Hu, T. Chen, and Z. Wu,	“Towards contactless patient positioning,” <i>IEEE Transactions on Medical Imaging</i> , vol. 39, no. 8, pp. 2701–2710, Aug. 2020.	2020	Image processing
2	M. Hosseiny, S. Kooraki, A. Gholamrezanezhad, S. Reddy, and L. Myers	Radiology perspective of coronavirus disease 2019 (COVID-19): Lessons from severe acute respiratory syndrome and middle east respiratory syndrome,” <i>American Journal of Roentgenology</i> , vol. 214, no. 5, pp. 1078– 1082, May	2020	Image processing
3	W. Wang	“Detection of SARS-CoV-2 in different types of clinical specimens,” <i>Journal of the American Medical Association (JAMA)</i> , vol. 323, no. 18, pp. 1843–1844, May 2020, doi:10.1001/jama.2020.3786.	2020	Image processing
4	G. D. Rubin	“The role of chest imaging in patient management during the COVID-19 pandemic: A multinational consensus statement from the Fleischner society,” <i>Radiology</i> , vol. 296, no. 1, pp. 172–180, Jul. 2020, pMID: 32255413, doi: 10.1148/radiol.2020201365.	2020	Image processing
5	M. Hosseiny, S. Kooraki, A. Gholamrezanezhad, S. Reddy, and L. Myers,	“Radiology perspective of coronavirus disease 2019 (COVID-19): Lessons from severe acute respiratory syndrome and middle east respiratory syndrome,” <i>American Journal of Roentgenology</i> , vol. 214, no. 5, pp. 1078– 1082, May	2020	Image processing
6	T. Ai	Correlation of chest CT and RT-PCR testing for coronavirus disease 2019 (COVID-19) in China: A report of 1014 cases,” <i>Radiology</i> , vol. 296, no. 2, pp. E32–E40, Aug. 2020, pMID: 32101510, doi: 10.1148/radiol.2020200642.	2020	Image processing
7	A. Dangis	“Accuracy and reproducibility of low-dose submillisievert chest CT for the diagnosis of COVID-19,” <i>Radiology: Cardiothoracic Imaging</i> , to be published, doi: 10.1148/ryct.2020200196.	2020	Image processing
8	A. Jacobi, M. Chung, A. Bernheim, and C. Eber,	“Portable chest X-ray in coronavirus disease-19 (COVID-19): A pictorial review,” <i>Clinical Imaging</i> , vol. 64, pp. 35–42, Aug. 2020, doi: 10.1016/j.clinimag.2020.04.001.	2020	Image processing
9	M. Mossa-Basha, C. C. Meltzer, D. C. Kim, M. J. Tuite, K. P. Kolli, and B. S. Tan	“Radiology department preparedness for COVID-19: radiology scientific expert review panel,” <i>Radiology</i> , vol. 296, no. 2, pp. E106–E112, Aug. 2020, pMID:	2020	Image processing

		32175814, doi: 10.1148/radiol.2020200988.		
10	R. Vaishya, M. Javaid, I. H. Khan, and A. Haleem,	“Artificial Intelligence (AI) applications for COVID-19 pandemic,” <i>Diabetes & Metabolic Syndrome: Clinical Research & Reviews</i> , vol. 14, no. 4, pp. 337–339, Jul.-Aug. 2020, doi: 10.1016/j.dsx.2020.04.012.	2020	Image processing
11	J. Zhang, Y. Xie, Y. Li, C. Shen, and Y. Xia,	“COVID-19 screening on chest X-ray images using deep learning based anomaly detection,” <i>arXiv preprint arXiv:2003.12338</i> , Mar. 2020.	2020	Image processing
12	A. Abbas, M. M. Abdelsamea, and M. M. Gaber	, “Classification of COVID-19 in chest X-ray images using DeTraC deep convolutional neural network,” <i>arXiv preprint arXiv:2003.13815</i> , May 2020.	2020	Image processing

III. RESEARCH METHODOLOGY



IV. TOOLS USED

A. MATLAB

MATLAB is a software package for mathematical calculations

MATLAB is a programming language developed by MathWorks. Image processing in MATLAB provides technique to convert an image into digital format and perform operations on it to get an enhanced image or extract some useful information from it. Changes that take place in images are usually performed automatically and rely on carefully designed algorithm. Image processing is a multidisciplinary field, with contributions from different branches of science including mathematics, physics, optical and electrical engineering. Moreover, it overlaps with other areas such as pattern recognition, machine learning, artificial intelligence and human vision research.

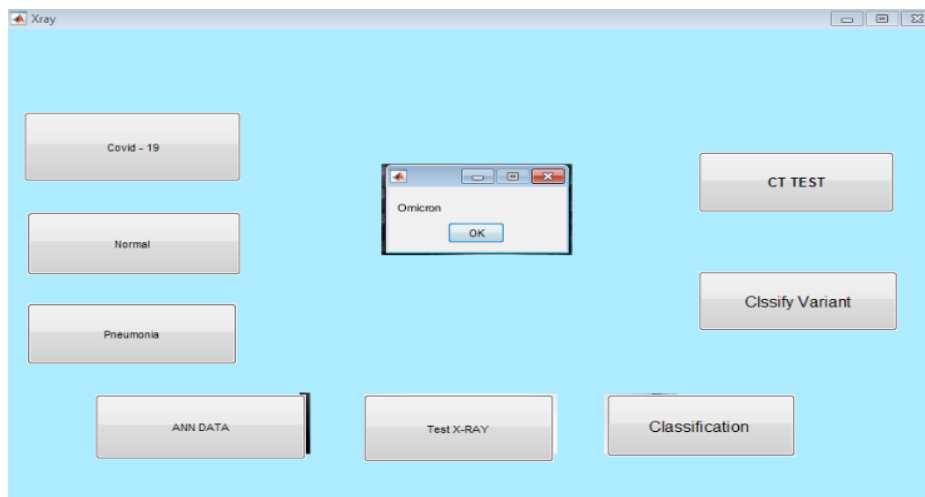
B. NeuroSolutions (Neural Network Software)

NeuroSolutions is an easy-to-use neural network software package for Windows. It combines a modular, icon-based network design interface with an implementation of advanced artificial intelligence and learning algorithms using intuitive wizards or an easy-to-use Excel interface. Perform sales forecasting, sports predictions, medical classification, and much more with NeuroSolutions. NeuroSolutions helps to Analyze and preprocess data from SQL Server, Excel, or text files into relevant information to create highly accurate predictive neural network models. NeuroSolutions is capable to Automatically mine your data for hidden relationships on small or large data sets using advanced neural networks and artificial intelligence. It has the Harness the massive processing power of graphics cards and distributed processing on a single machine or thousands & also Quickly deploy your neural network solutions for Windows or All Platforms applications.

V. SIMULATING RESULTS

A. MATLAB GUI for Medical Image Classification: Functionality Overview

The MATLAB Graphical User Interface (GUI) designed to classify medical images into categories such as COVID-19, normal (healthy), and pneumonia. The GUI incorporates eight buttons, each dedicated to a specific function: selecting COVID-19 images, selecting normal images, selecting pneumonia images, training an Artificial Neural Network (ANN), testing X-ray images, classifying images, testing CT images, and classifying COVID-19 variants. The GUI serves as a user-friendly platform to streamline the process of medical image analysis and classification.



Button 1: Selection of COVID-19 Images

The first button in the GUI is designated for the selection of COVID-19 images. When this button is pressed, it opens a file selection dialog that allows the user to choose multiple images from their file system. These images are stored in a global variable for subsequent use in training the ANN. The selection process involves using the `uigetfile` function with the 'MultiSelect' option enabled, which facilitates the selection of multiple image files at once. This functionality is critical for gathering the necessary dataset to train the classification model.

Button 2: Selection of Normal Images

The second button functions similarly to the first but is used for selecting images of normal (healthy) lungs. Upon pressing this button, a file selection dialog appears, enabling the user to select multiple normal images. These images are also stored in a global

variable. This step ensures that the dataset includes a balanced representation of normal images, which is essential for accurate model training and evaluation.

Button 3: Selection of Pneumonia Images

The third button is dedicated to selecting pneumonia images. This button, like the previous two, triggers a file selection dialog for choosing multiple images indicative of pneumonia. These images are stored in a global variable, completing the dataset needed for training the ANN. Having a comprehensive and diverse dataset is crucial for the model to learn distinguishing features across different classes effectively.

Button 4: ANN Training

The fourth button is for training the Artificial Neural Network (ANN). Before initiating the training process, the GUI checks whether images have been selected for all three categories: COVID-19, normal, and pneumonia. If any category is missing, an error dialog prompts the user to complete the selection. Once the image datasets are confirmed, the training process begins. This involves loading and preprocessing the images, such as resizing and normalization, followed by feeding them into the ANN for training. The training function includes defining the network architecture, configuring training parameters, and iterating through the dataset to optimize the network weights. Upon completion, the trained model is stored in a global variable for future classification tasks.

Button 5: X-ray Image Test

The fifth button allows users to test individual X-ray images. When this button is pressed, a file selection dialog opens for the user to select a single X-ray image. The selected image undergoes preprocessing steps, such as resizing and normalization, to ensure it matches the input format expected by the ANN. The preprocessed image is then fed into the trained ANN, which outputs a classification result indicating whether the image is classified as COVID-19, normal, or pneumonia. The result is displayed to the user, providing immediate feedback on the classification.

Button 6: Classify Images

The sixth button is used for classifying images using the trained ANN. This button can be used after the ANN has been trained. It allows the user to classify a batch of images or a single image selected from their file system. The selected images are preprocessed similarly to the training data before being passed through the ANN for classification. The classification results are then displayed, showing the predicted category for each image. This functionality is essential for validating the ANN's performance on new, unseen data and for practical diagnostic purposes.

Button 7: CT Image Test

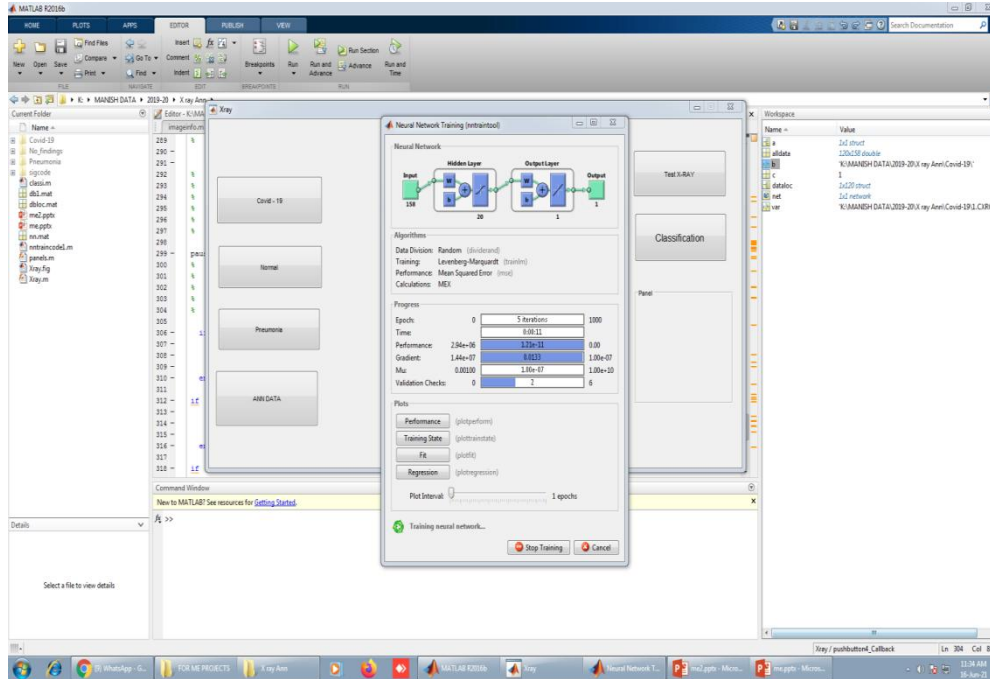
The seventh button is designated for testing CT images. Similar to the X-ray image test, this button opens a file selection dialog for the user to choose a CT image. The selected CT image undergoes the same preprocessing steps as X-ray images to ensure compatibility with the ANN input requirements. The preprocessed image is then classified by the ANN, and the result is displayed. This functionality extends the application of the GUI to different types of medical imaging modalities, enhancing its versatility.

Button 8: Classify COVID-19 Variant

The eighth and final button in the GUI is for classifying COVID-19 variants. This functionality is particularly relevant in the context of identifying different strains of the COVID-19 virus from medical images. When this button is pressed, the user selects an image suspected of containing a COVID-19 variant. The image is preprocessed and then analyzed by the ANN, which has been trained to differentiate between various COVID-19 strains. The classification result, indicating the specific variant, is displayed to the user. This advanced functionality aids in the detailed analysis and tracking of COVID-19 mutations.

MATLAB GUI, though simple with a single button for selecting a folder containing COVID-19 images, plays a crucial role in streamlining the workflow for medical image analysis. By enabling users to efficiently select and load a bulk set of images, it sets the stage for subsequent image processing tasks. This functionality is particularly valuable in medical research and diagnostics, where handling large datasets is common. The clear and intuitive design of the GUI ensures that users can quickly and accurately select the necessary image data, thereby enhancing the efficiency and effectiveness of their analytical workflows.

B. MATLAB GUI for ANN Training with Normal, COVID-19, and Pneumonia Images: Functionality Overview



MATLAB GUI, with its interface, provides a robust and user-friendly platform for selecting and processing image datasets needed for training an ANN. By enabling users to select images of normal lungs, COVID-19 affected lungs, and pneumonia-affected lungs separately, the GUI ensures that each dataset is accurately compiled and ready for neural network training. The integrated preprocessing and training functions further streamline the workflow, making it accessible for users to develop and train models efficiently. This GUI thus serves as an essential tool in medical image analysis and the development of diagnostic models using machine learning techniques

C. CLASSIFICATION PROCESS

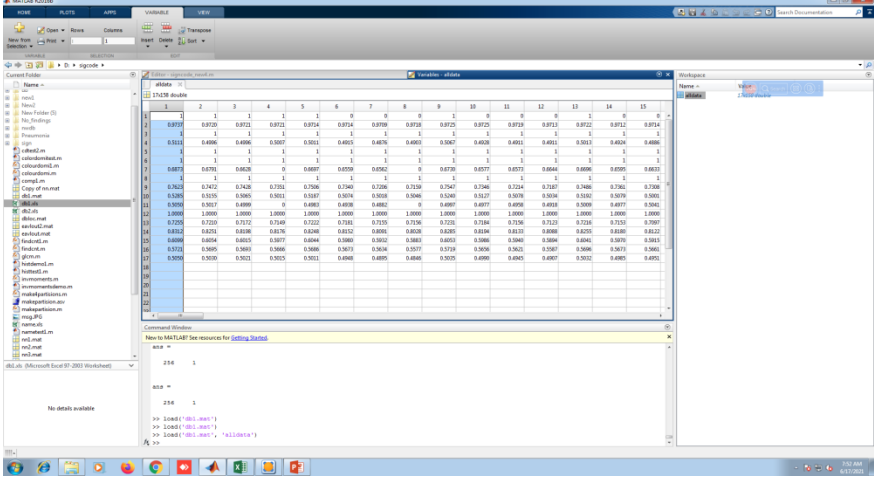
The classification process involves several steps:

1. **Loading Selected Images:** The images from the selected paths are loaded into MATLAB using the `imread` function. Each image is read and stored in an appropriate data structure for further processing.
2. **Preprocessing Images:** The loaded images are preprocessed to ensure they are in the correct format for classification. Common preprocessing steps include resizing the images to a standard size and normalizing pixel values.
3. **Classifying Images:** The preprocessed images are then passed through a pre-trained neural network model for classification. The model outputs the predicted class for each image, which could be categories such as normal, COVID-19, or pneumonia.

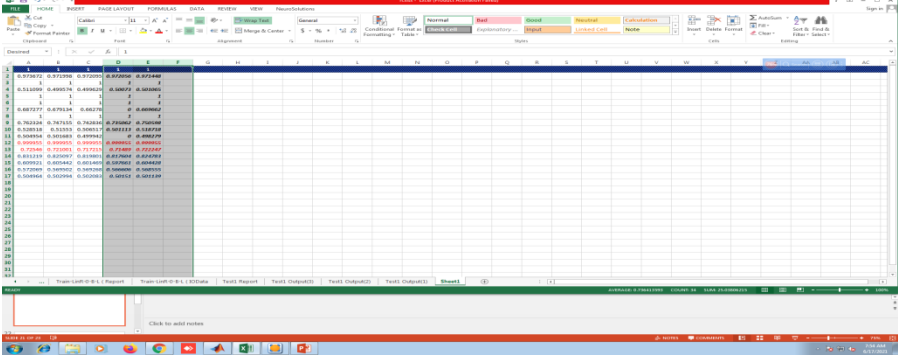
D. NeuroSolutions Results

NeuroSolutions provides an easy-to-use and intuitive user interface for Microsoft Excel. It simplifies and enhances the process of getting data into and out of a NeuroSolutions neural network. It also benefits both novice and advanced neural network developers by offering an easy-to-use, yet extremely powerful and exclusive features. The Excel interface is accessible by clicking on the "Launch Excel with NeuroSolutions" button from the launcher OR by launching Excel directly. This quick tutorial will provide you with high level details of tagging your data, building a neural network, training it and finally testing the performance. For in-depth information on NeuroSolutions features in Excel please refer to the NeuroSolutions for Excel Help Documentation. Excel provides the perfect interface for presenting data for neural networks. It can work with any column-formatted data such as comma-separated files (.csv), tab-delimited files (.txt) and of course Excel files (.xls and .xlsx).

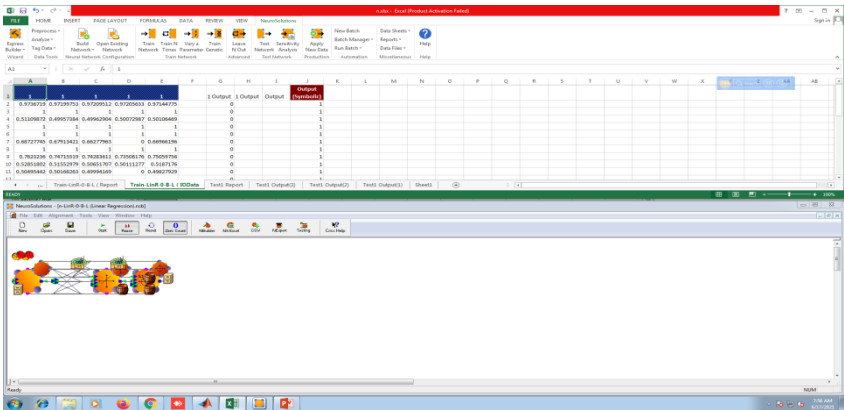
Segmentation of Image



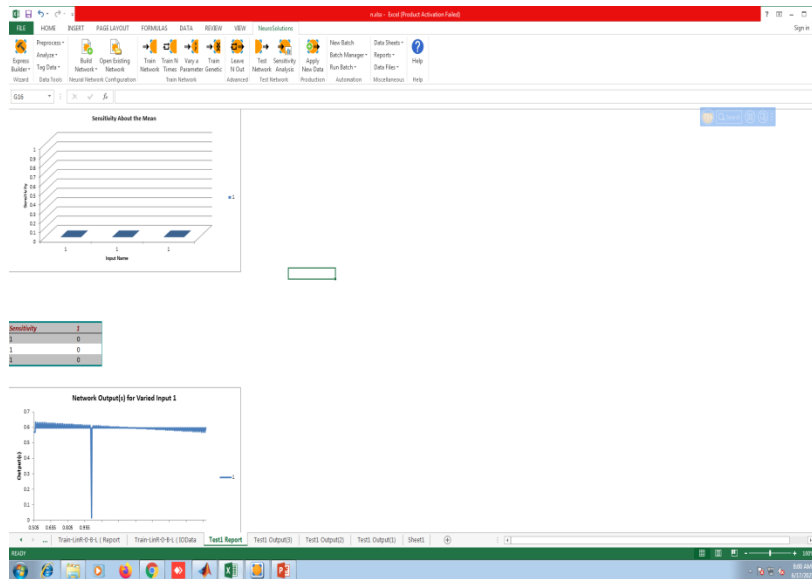
Data export to Excel



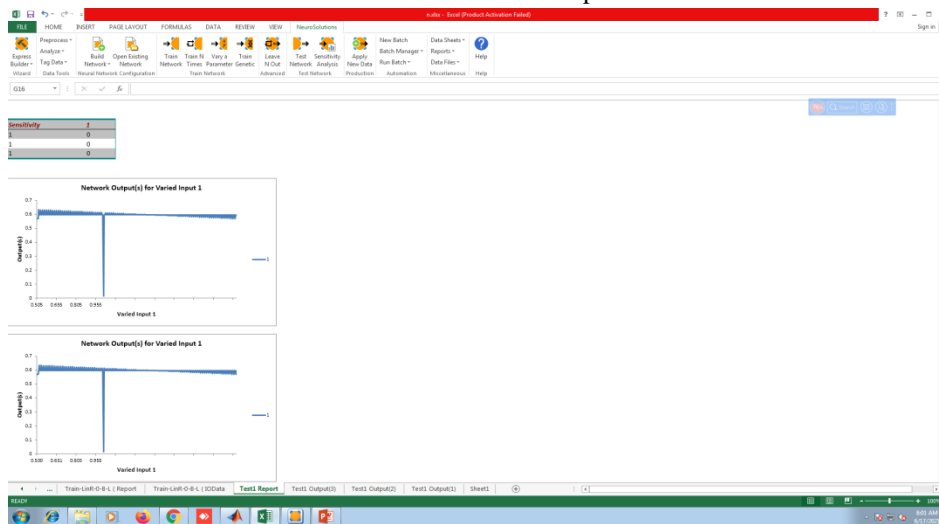
Neurosolutions Process



Neurosolutions Test Report



Neurosolutions Test Report



VI. CONCLUSION

The Designed framework leverages a data augmentation of radiograph images algorithm for the COVID-19 data, by adaptively employing the MATLAB and NeuroSolution on COVID-19 infected chest images to generate a train a robust model. The training data consisting of actual and synthetic chest images are fed into our customized neural network model, which achieves COVID-19 detection with good accuracy. Furthermore, through this it is possible to efficiently automate COVID-19 Variant detection from CT scan images to provide a fast and reliable evidence of COVID-19 infection in the lung that can complement existing COVID-19 diagnostics modalities.

REFERENCES

[1] “WHO coronavirus disease (COVID-19) dashboard.” World Health Organization (WHO). <https://covid19.who.int/> (accessed Jul. 15, 2020).

[2] W. Wang et al., “Detection of SARS-CoV-2 in different types of clinical specimens,” *Journal of the American Medical Association (JAMA)*, vol.323, no. 18, pp. 1843–1844, May 2020, doi:10.1001/jama.2020.3786.

[3] G. D. Rubin et al., “The role of chest imaging in patient management during the COVID-19 pandemic: A multinational consensus statement from the Fleischner society,” *Radiology*, vol. 296, no. 1, pp. 172–180, Jul.2020, PMID: 32255413, doi: 10.1148/radiol.2020201365.

[4] M. Hosseiny, S. Kooraki, A. Gholamrezanezhad, S. Reddy, and L. Myers, “Radiology perspective of coronavirus disease 2019 (COVID-19): Lessons from severe acute respiratory syndrome and middle east respiratory syndrome,” *American Journal of Roentgenology*, vol. 214, no. 5, pp. 1078–1082, May 2020, doi: 10.2214/AJR.20.22969.

[5] “ACR recommendations for the use of chest radiography and computed tomography (CT) for suspected COVID-19 infection.” American College of Radiology (ACR). <https://www.acr.org/Advocacy-and-Economics/ACR-Position-Statements/Recommendations-for-Chest-Radiographyand-CT-for-Suspected-COVID19-Infection> (accessed Jul. 15, 2020).

¹*Manisha S.Raut²*S. A. Waghuley

Regular paper
**Efficient Synthesis and Detailed
 Analysis of Graphene Quantum
 Dots (GQDs) via Electrochemical
 Exfoliation**

**Abstract: -**

Graphene quantum dots (GQDs), have been attracting a lot of attention recently because of their unique electrical, optical, and chemical properties, which make them highly attractive for a variety of uses in biomedicine, optoelectronics, sensing, and catalysis. Here, we provide an extensive examination of the synthesis of GQD by electrochemical exfoliation method and characterization with particular emphasis on the precise control of their dimensions, structure, and properties. XRD shown Broaden sharp peak at 26.26° , which shows crystalline nature of GQD. UV shown great peak of absorption at 236 nm, and FTIR shown absorption peaks of GQD are 3588, 3775, 2341, 1593, and 1245 cm^{-1} . The produced GQDs exhibited great high quantum yield, and minimal cytotoxicity, which made them attractive options for a range of uses.

Keywords: Graphene Quantum Dots (GQD), Graphite flaks, Exfoliation etc.

I. Introduction

Graphene quantum dots (GQDs), a novel and interesting zero-dimensional substance of the carbon family, have been the subject of a great deal of interest in recent years because of their remarkable and desired optical, chemical, physical, electrical, and biological properties. These special, size-dependent qualities serve to illustrate the many uses in the optoelectronic and medicinal fields. They are a reflection of the combined structural features of very small graphene sheets, which include edge effects and quantum confinement. Due to this, applications of GQDs have also increased in the areas of biomedical (bio-sensing, bio-imaging, drug delivery, anti-bacterial activity, and photo-thermal/dynamic therapy) and optoelectronic (light-emitting diodes and solar cells).[1]

New opportunities in the field of nanotechnology because GQD have several additional advantages over graphene, such as a tunable bandgap, excellent aqueous solubility, good biocompatibility, high fluorescence quantum yield, and the presence of several active functional groups. GQDs have unique electrical and structural characteristics. Their small size allows them to have special optical characteristics and the ability to release electrons selectively. GQDs thus appear very promising for use in biological applications. The material's unique properties make them very attractive alternatives for use in the biomedical industry. Because of their special physical and chemical characteristics, such as their small size, chemical inertness, excellent photoluminescence stability, minimal cytotoxicity, and strong biocompatibility, GQDs stand out as exceptional and universal fluorophores.[2]

GQDs are zero-dimensional fluorescent nanomaterials based on carbon that have an internal graphene lattice. Their solubility is superior to that of carbon nanotubes. Their typical size is less than 20 nm, while their maximum size of 60 nm has been recorded. Their small size allows them to easily pass through biological membranes. Lower pH levels and high electrolyte concentrations cause the GQD solution to become very stable. Many of the biological uses of

¹* Manisha S. Raut, Department of physics SGBAU Amravati university,444602, Maharashtra, India.
rautmanisha488@gmail.com

²* S. A. Waghuley, Department of physics SGBAU Amravati university 444602, Maharashtra, India.
sandeepwaghuley@sgbau.ac.in

graphene quantum dots (GQDs), such as biosensing and bioimaging, become feasible by their fluorescence, which is one of its well-studied luminescence features. They have a greater quantum yield. GQDs have a huge surface area, great crystallinity, and outstanding GQDS are disc-shaped, single-layered carbon nanoparticles with SP² hybridization carbon.[3]

The shape of most synthesized GQDs is circular or elliptical, although triangular, quadrate and hexagonal GQDs have been synthesized as well.[4] In this paper, The synthesized GQD were characterized using various techniques to determine their structural and optical properties. we report the synthesis of GQD by using electrochemical exfoliation of graphite. The materials are analyzed by XRD, ultraviolet- visible (UV- VIS) and Fourier Transform Infrared Spectroscopy (FT-IR).

II. Experimental

Materials

Sulphuric acid (H₂SO₄) AR grade from Alpha chemika, distilled water was used for making ionic solution, Graphite flaks, copper wire or rod, cellulose nitrate filter paper and Acetone these all materials was used for synthesized of GQD.

Synthesis of GQD

Graphene quantum dots were synthesized by the electrochemical exfoliation of graphite. Firstly, graphene was synthesized from graphite flake. Graphite flaks were used as an anode and source of graphene. The copper electrode was used as a cathode. The graphite flake and silver electrode were inserted into the ionic solution of sulphuric acid (H₂SO₄) with a separation of 5 cm. AR-grade chemicals was used in this investigation for the preparation of an ionic solution. The ionic solution was prepared by taking 4.8 g of sulphuric acid (H₂SO₄) diluted in 100 ml.[5]

The exfoliation process was carried out by a DC bias arrangement (10 V). Exfoliated graphene was collected through cellulose nitrate filter paper and washed with double distilled water then again with acetone. After filtration of material, ultra sonication was carried out for 18 h by ultrasonic homogenizer probe sonicator, then material calcinations at 100°C for 2 h and got fine materials. Relative to other processes, electrochemical exfoliation is easier to perform since it only requires one step and takes a some hours, whereas many other procedures required longer times for preparation and the finished material to stabilize. [2]

Result and Discussion

Material Characterization

X-ray Diffraction (XRD) gives information of atomic and molecular structure of a crystal sample. When incident X-rays are directed upon a sample, they diffract into a variety of distinct directions. The crystalline structure of the sample can be determined by measuring the angles and intensities of the diffracted beam.[6]

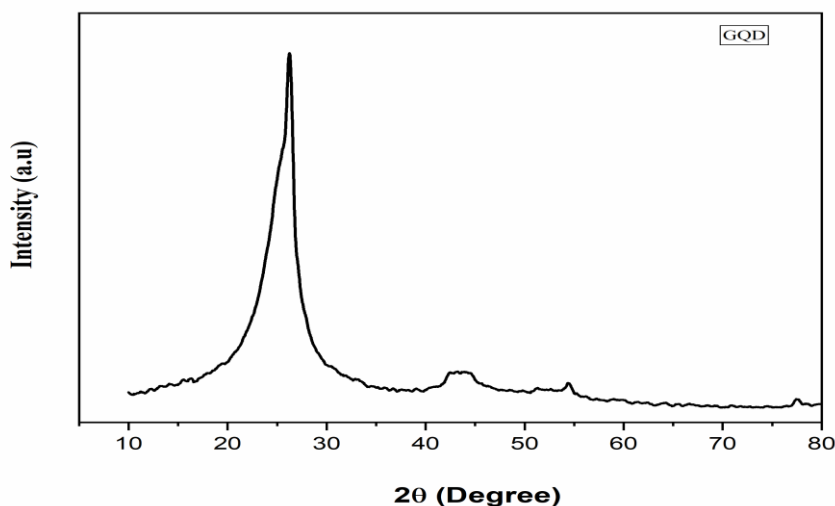


Fig 1: XRD pattern of GQD

Figure 1 shows the XRD pattern of GQD. The XRD pattern shown in Figure 1 indicates the formation of graphene quantum dots. There are two peaks (002) and (100), which are the main peaks of graphene quantum dots. GQD exhibits sharp peaks at $2\theta = 26.26^\circ$ and 43.93° , which is due to its crystalline nature. $2\theta = 26.26^\circ$ indicates a highly organized structure. Using the Debye-Scherrer equation, it was found to be 10.6 nm.

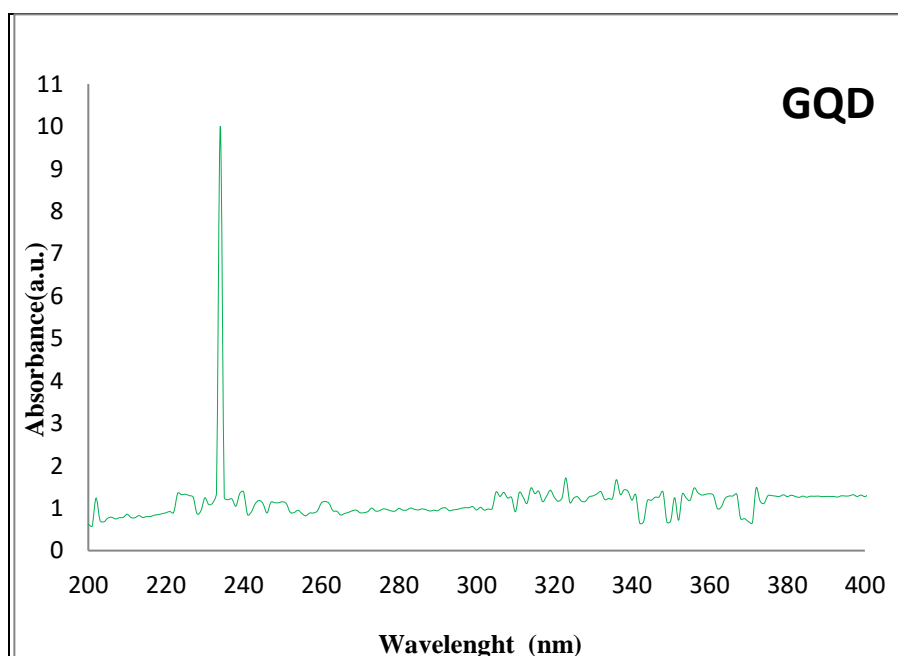
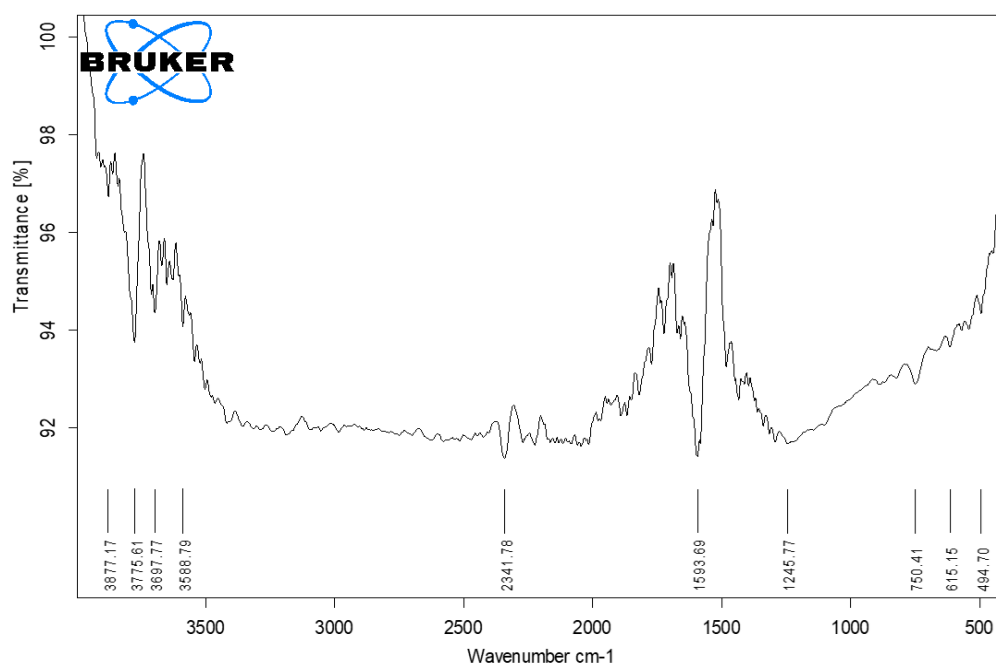


Fig 2: UV pattern of GQD

The UV-visible spectra of the GQD are shown in figure 2. The strong peak obtained at 236 nm indicates the presence of GQD. The energy gap between the electronic energy levels of small molecules is high. Therefore, the excitation of a molecule from a lower electronic energy level to a

high level needs a high-energy photon of a shorter wavelength. A peak is always obtained between 230 and 250 nm relative to the π - π^* transitions of the C=C aromatic bond and, therefore, to the sp² hybridization domains. Associated with the n- π transitions of C=O bonds, due to the presence of oxygen groups on the surface of GQD, can also be observed in the region of 280–300 nm. These longer wavelengths can be diminished through the chemical reduction of GQD, which removes the oxygen functionalities [7].



A

Fig 3: FT-IR pattern of GQD

Fourier Transform Infrared Spectroscopy (FT-IR) spectra of the GQD are shown in figure 3. FTIR spectra demonstrated the reduction of the C-O-C and C-OH functional groups in GQD. The absorption peaks of GQD are 3588, 3775, 2341, 1593, and 1245 cm⁻¹. The absorption peak of GQD within 3588–3000 cm⁻¹ can be assigned to O-H stretching vibration. It was found that the absorption peaks of carbonyl stretching and carboxylate symmetry vibrating at 1750 cm⁻¹ and 1593 cm⁻¹ had no apparent decrease, whereas the absorption band of the C-O group at 1245 cm⁻¹ almost disappeared in the FT-IR spectra of GQD.[8]

Conclusion

The synthesis of graphene quantum dots (GQDs) using the electrochemical exfoliation method and their consequent characterization were extensively investigated in this study. Particular attention was given to the precise control of the size, structure, and characteristics of the GQDs. The crystalline characteristics of the GQDs were shown by an enlarged, sharp peak at 26.26° observed in the X-ray diffraction (XRD) examination. Their optical activity was confirmed by an apparent absorption peak observed at 236 nm using UV-Vis spectroscopy. A peak is always obtained between 230 and 250 nm relative to the π - π^* transitions of the C=C aromatic bond and, therefore, to the sp² hybridization domains. Absorption peaks have been observed at 3588, 3775, 2341, 1593, and 1245 cm⁻¹ by Fourier-transform infrared (FTIR) spectroscopy. These peaks are indicative of different functional groups that are present on the surface of GQD, which that demonstrated the reduction of the C-O-C and C-OH functional groups in GQD. The synthesized GQDs are interesting alternatives for many kinds of applications due to their high quantum yield and low cytotoxicity. These characteristics highlight the adaptability of GQDs produced by electrochemical exfoliation and bring up promising

opportunities for future study and application. Future research will concentrate on studying GQD inclusion into functional devices and developing synthesis techniques to increase yield and flexibility.

Acknowledgment

The author M. S. Raut express our deepest gratitude to Department of physics SGBAU university Amravati for providing the facilities and resources necessary to conduct this research. Special thanks to Dr. S. A. Waghuley for their invaluable guidance support and allowing the use of their instrument facilities throughout this project throughout this work. We are also grateful to our colleagues for their insightful discussion.

References

- [1] S. Kadian, S. K. Sethi, and G. Manik, "Recent advancements in synthesis and property control of graphene quantum dots for biomedical and optoelectronic applications," *Materials Chemistry Frontiers*, vol. 5, no. 2. Royal Society of Chemistry, pp. 627–658, Jan. 21, 2021. doi: 10.1039/d0qm00550a.
- [2] M. Handayani *et al.*, "Development of graphene and graphene quantum dots toward biomedical engineering applications: A review," *Nanotechnology Reviews*, vol. 12, no. 1. Walter de Gruyter GmbH, 2023. doi: 10.1515/ntrev-2023-0168.
- [3] T. K. Henna and K. Pramod, "Graphene quantum dots redefine nanobiomedicine," *Materials Science and Engineering C*, vol. 110. Elsevier Ltd, May 01, 2020. doi: 10.1016/j.msec.2020.110651.
- [4] W. Han, Z. Wu, Y. Li, and Y. Wang, "Graphene family nanomaterials (GFNs)—promising materials for antimicrobial coating and film: A review," *Chemical Engineering Journal*, vol. 358. Elsevier B.V., pp. 1022–1037, Feb. 15, 2019. doi: 10.1016/j.cej.2018.10.106.
- [5] C. Y. Su, A. Y. Lu, Y. Xu, F. R. Chen, A. N. Khlobystov, and L. J. Li, "High-quality thin graphene films from fast electrochemical exfoliation," *ACS Nano*, vol. 5, no. 3, pp. 2332–2339, Mar. 2011, doi: 10.1021/nn200025p.
- [6] W. Ka and K. M. Phil, "SYNTHESIS OF NITROGEN-DOPED GRAPHENE QUANTUM DOTS AND ITS ANTIBACTERIAL PROPERTY," 2018.
- [7] M. H. M. Facure, R. Schneider, L. A. Mercante, and D. S. Correa, "A review on graphene quantum dots and their nanocomposites: From laboratory synthesis towards agricultural and environmental applications," *Environmental Science: Nano*, vol. 7, no. 12. Royal Society of Chemistry, pp. 3710–3734, Dec. 01, 2020. doi: 10.1039/d0en00787k.
- [8] S. Chen, Y. Quan, Y. L. Yu, and J. H. Wang, "Graphene Quantum Dot/Silver Nanoparticle Hybrids with Oxidase Activities for Antibacterial Application," *ACS Biomater Sci Eng*, vol. 3, no. 3, pp. 313–321, Mar. 2017, doi: 10.1021/acsbiomaterials.6b00644.

¹ A. K. Patel
² V. S. Patel
³ U. D. Raval
⁴ N. A. Chaudhary
⁵ K. N. Shah
^{6*} A. N. Prajapati

Frequency and Concentration Dependent Dielectric and Electrical Properties of N, N- Dimethylacetamide and n-Nonanol



Abstract: - A precision LCR meter using a liquid dielectric cell was utilized to measure the complex dielectric function ($\epsilon^*(\omega)=\epsilon'-j\epsilon''$) of binary mixtures consisting of n-Nonanol and N, N-Dimethylacetamide (DMA) within the frequency spectrum ranging from 100 Hz to 2 MHz at a constant temperature of 303.15 K. Different dielectric and electrical parameters such complex electric modulus $M^*(\omega)$, complex electrical conductivity $\sigma^*(\omega)$, and complex impedance $Z^*(\omega)$ were calculated from complex relative dielectric function $\epsilon^*(\omega)$. Further, complex permittivity data was used to fit the Coelho model. This model provides insights into the electrode polarization relaxation time, which is associated with the relaxation processes of the electric double layer. Various relaxation times, such as electrode polarization (τ_{EP}) and ionic conduction relaxation time (τ_{σ}), were determined. It was observed that the real part of the dielectric permittivity corresponds to the static dielectric permittivity of these mixtures within the frequency range of 500 kHz to 2 MHz. This behavior shows the significant effect of absorbed charge impurities on the dielectric polarization of these dipolar liquids at low frequencies. Different parameters such as Debye Length (λ_D), Ion Mobility (μ), Mobile Ion Concentration (P_0), and Ion diffusivity (D) were determined. This study is useful for gaining knowledge about the effect of the concentration on different dielectric and electrical properties of the mixtures.

Keywords: Coelho Model, Electrode Polarization Relaxation Time, n-Nonanol, N, N Dimethylacetamide, Precision LCR meter.

*Corresponding author: Department of Physics, Sardar Patel University, V. V. Nagar-388120, Gujarat, India

^{1,2,3,6}Department of Physics, Sardar Patel University, V. V. Nagar-388120, Gujarat, India

⁴Department of Applied Physics, The M. S. University of Baroda, Vadodara-390001, Gujarat, India

⁵Department of Computer Engineering, United world School of Computational Intelligence, Karnavati University, Gandhinagar-382422, Gujarat, India

I. INTRODUCTION

Dielectric spectroscopy is often used as the techniques for interpreting the molecular interaction in binary liquid systems [1]. It is used to investigate the molecular dynamics of liquids, capturing the rapid variations in both intermolecular and intramolecular structures as they evolve [1]. Investigation of the dielectric properties of binary mixtures of polar liquids has garnered growing attention in scientific communities [2]. Low-frequency dielectric dispersion studies offer intricate understandings of the charge dynamics and electrical conduction mechanisms within liquids [3]. These insights are directly correlated with the molecular structure and polarization strength of the liquids, providing valuable information about their behavior [3]. The exploration of the molecular structures and dynamics of amides, particularly regarding their hydrogen bonding, remains a focal point of scientific investigation. Amides serve as valuable models for understanding hydrogen-bonded peptide linkages and find utility as electrolyte solvents. Additionally, the pronounced self-association via strong hydrogen bonding in alcohols has established them as common solvents since the early days of solution chemistry [4-6]. Therefore, there is a deep interest in investigating the static permittivity of amides when mixed with alcohols, aiming to elucidate their molecular conformations and potential applications across various scientific and technological domains [7-14]. Studying the dielectric characteristics of binary mixtures containing both associative and non-associative polar liquids offers valuable insights into the molecular interactions occurring within the solution [14-16]. Among the associative liquids, Alcohols hold significant industrial and scientific relevance as organic compounds, with their physical and chemical properties predominantly dictated by the presence of the hydroxyl group [17]. Alcohol, being a versatile organic liquid, finds wide application in chemical industries as a solvent for oils and resins, as well as serving as an antifreeze agent for explosives [18]. Among the non-associative liquids, Amides have high polarity, potent solvating capabilities, and a wide liquid range making them indispensable solvents with substantial industrial and technological significance. The amide linkage ($-\text{CO}-\text{NH}-$) serves as a crucial functional group across various disciplines, including chemistry, biochemistry, pharmaceuticals, and material science [9,19]. N, N-dimethylacetamide (DMA) is a clear liquid that readily mixes with water and a wide range of organic solvents, such as alcohols, ethers, and ketones, in any proportion. DMA's high solubility in water and excellent solvent efficiency, especially for high molecular weight polymers and resins, contribute to its extensive use in synthetic Fibers and polyurethane [20].

In the present investigation, an attempt is made to determine the dielectric and electrical properties of the binary mixtures of n-Nonanol + DMA at 303.15 K temperature with the help of an Agilent precision LCR meter in the frequency range 100 Hz to 2 MHz. Different parameters such as electrode polarization relaxation time, ionic conduction relaxation time, DC conductivity, and static dielectric constant are calculated from different formalisms. This study is useful for studying different polarization mechanisms involved in liquid mixtures. This work contributes to the understanding of how n-Nonanol-DMA binary liquid mixtures are affected by concentrations and frequency.

II. EXPERIMENTAL DETAILS

n-Nonanol and N, N-Dimethylacetamide (DMA) of AR Grade were procured in their analytical grades from SISCO Chem P Ltd., India, and utilized without undergoing any purification processes. Eleven different binary mixture samples with differing mole fractions (X_A) of DMA in n-Nonanol were prepared.

An Agilent E-4980 precision LCR meter with a cylindrical capacitor fixture as a sample holder was used to measure the resistor and capacitance with and without samples in the frequency range of 100 Hz to 2 MHz. The cylindrical capacitance fixture was designed in our laboratory, featuring an outer cylinder, inner cylinder, connectors, and Teflon spacers. The detailed calibration process is described cited literatures [21,22]. The temperature of the solutions being tested was precisely controlled using a constant temperature water bath, with a precision of ± 0.1 K, to maintain consistency and accuracy throughout the experimental process.

III. RESULTS AND DISCUSSION

Figure 1 (a) and (b) display the real (ϵ') and imaginary (ϵ'') parts of the complex dielectric permittivity, $\epsilon^*(\omega)$ spectra, for n-Nonanol + DMA binary mixtures across different mole fractions of DMA at 303.15 K temperature.

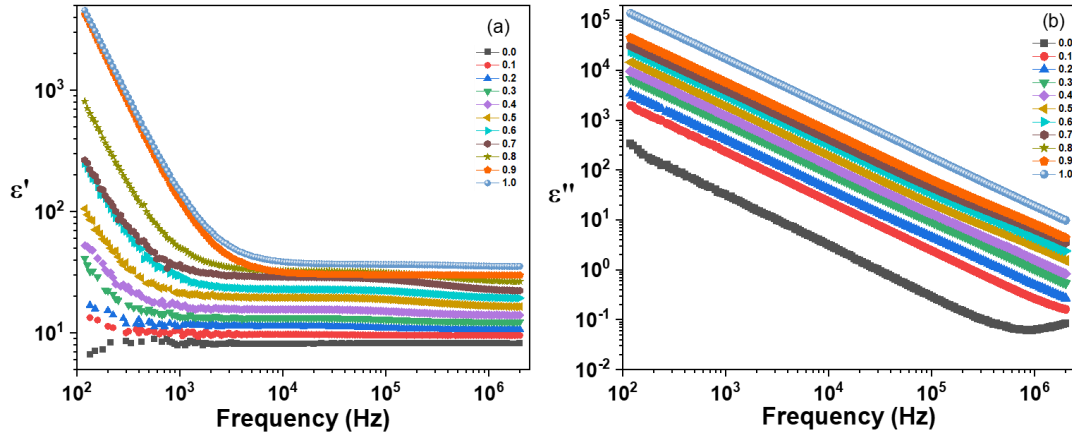


Fig.1 (a) variation of dielectric constant against frequency (b) variation of dielectric loss against frequency

In Figure 1(a), the spectra are divided into two different regions: a higher-frequency region and a lower-frequency region. Within the higher frequency region, which extends beyond 5 kHz, the real part of the permittivity spectrum demonstrates a frequency-independent behavior, converging towards a stable value over time. On the other hand, the real part of the permittivity spectrum shows a significant augmentation in the lower frequency range, below 5 kHz, which is connected with an increase in the DMA (Dimethylacetamide) volume fraction. This finding highlights various behaviors at different frequency ranges and implies a dependence on the system's frequency. The real part of the dielectric permittivity, particularly noticeable at lower frequencies, is predominantly attributed to electrode polarization (EP). This phenomenon arises from the establishment of electric double layer (EDL) capacitances, wherein ions and free charges accumulate at the interface between the dielectric material and the electrode surfaces, especially in a planar geometry setup. This accumulation, particularly of ions drifting over longer distances, significantly impacts the observed dielectric behavior of the system, leading to the pronounced elevation in ϵ' values at low frequencies [23-25]. In polar dipolar liquids, the strength of the electrode polarization (EP) effect weakens with increasing frequency. This weakening is a result of the reduced long-range mobility of free charges within the liquid dielectric material, which is caused by the rapid reversal of the applied AC electric field as the frequency rises. At a specific frequency where the EP effect vanishes entirely, the real part (ϵ') of the dielectric permittivity for the liquid dipolar materials approaches to its static permittivity value (ϵ_0). As the frequency increases, the real part (ϵ') of the dielectric permittivity decreases linearly until it reaches a steady state at specific frequencies. For pure n-Nonanol and DMA, these steady-state values occur at approximately 300 Hz and 5 kHz, respectively. This suggests a transition to a state where the electrical properties of the material are no longer influenced by the polarization effect induced by the applied electric field [26-29]. The observed phenomenon provides clear evidence for the existence of thermally activated ionic impurities within the polar solvent DMA (dimethylacetamide).

The spectra of ϵ'' (Fig. 1(b)) for DMA, n-Nonanol, and their binary mixtures exhibit a linear decrease with increasing frequency, considered by a slope of approximately -1.00 (± 0.02) when plotted on a log-log scale. This consistent behavior confirms the presence of an Ohmic-type ionic conduction mechanism within these dipolar liquid materials. Such behavior is observed across various dipolar liquids and their binary mixtures [26,27,29,30,31]. Initially, at a frequency of 20 Hz, the ϵ'' values of DMA and n-Nonanol mixtures are nearly in the order of magnitude six, showing a linear decrease as the frequency increases up to 1 MHz. It appears that these values approach the minimum value at the higher frequency side.

The complex permittivity data obtained from experiments are affected by the electrode polarization (EP) effect, mainly in the lower frequency range ($< 10^4$ Hz) within the investigated mixtures [32]. To analyze this data, we applied the Coelho model by keeping the values of α & β to one, which is given by

$$\epsilon^*(\omega) = \epsilon_0 + \frac{\Delta\epsilon_{EP}}{[1+(i\omega\tau_{EP})^\alpha]^\beta} \quad (1)$$

Where, $\Delta\epsilon_{EP} = \epsilon_{0(EP)} - \epsilon_0$

$\epsilon_{0(EP)}$ = Low-frequency dielectric constant in the presence of EP

ϵ_0 = Static permittivity and

τ_{EP} = Electrode polarization relaxation time.

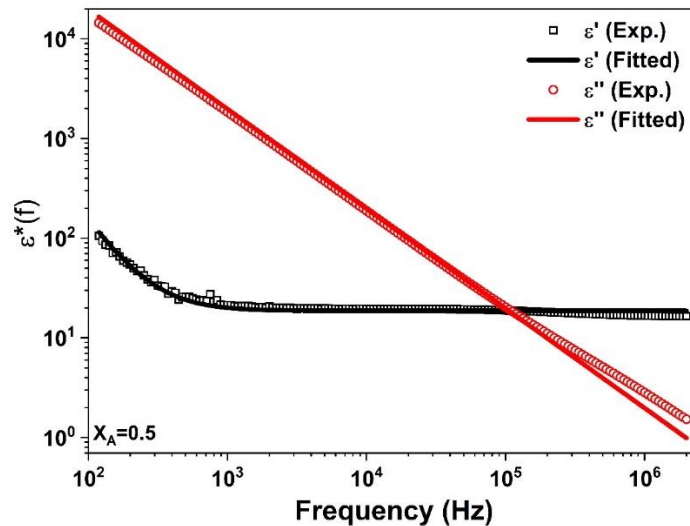


Fig. 2 Experimental and fitted data of complex permittivity spectra using the CNLS method for the concentration range for the mole fraction $X_A=0.5$.

Complex Nonlinear Least Square (CNLS) fitting procedure, as outlined in the reference [33] was used to fit experimental data to Eq. (1). The fitting parameters that were taken in this process were τ_{EP} , ϵ_0 , and $\Delta\epsilon_{EP}$. Fig. 2 represents the graph of experimental and fitted data points of $\epsilon^*(\omega)$ to the Coelho model (equation (1)) for $X_A = 0.5$. The Coelho model gives the best fitting for all the concentration ranges. The different fitted parameters for all the concentration ranges are tabulated in Table 1. It can be seen from Table 1 that as the concentration of DMA increases in the mixtures the value of the static dielectric constant increases. The electronic double-layer relaxation time decreases as the concentration of DMA increases in the mixtures.

Table 3: Fitted parameters ϵ_0 , $\Delta\epsilon_{EP}$ and τ_{EP} using CNLS fitting procedure.

X_A	ϵ_0	$\Delta\epsilon$	τ_{EP}
0.0	8.170	9.0526E+08	-
0.1	9.590	6.3514E+05	432.85
0.2	11.144	7.5318E+06	279.60
0.3	12.630	1.4290E+06	265.97
0.4	14.514	1.8378E+06	238.51
0.5	18.687	2.8662E+06	230.66
0.6	22.001	2.9220E+06	141.71
0.7	28.215	3.7734E+06	160.51
0.8	28.253	2.5501E+06	67.795
0.9	30.791	4.2809E+06	38.103
1.0	37.367	3.7688E+06	33.883

An actual approach for investigating the features of ionic conductivity relaxation processes while minimizing the effect of Electric Double Layers (EDLs) dynamics in ion-conductive materials is to apply the change of dielectric spectra into electric modulus. The spectra of electric modulus explain to avoid the space charge effect observed in dielectric spectra [34]. The complex electric modulus $M^*(\omega)$ is expressed as the inverse of the complex permittivity ($\epsilon^*(\omega)$), written as $M^*(\omega) = 1/\epsilon^*(\omega)$. It is given by the relation: [1]

$$M^*(\omega) = M' + jM'' = \frac{\epsilon'}{\epsilon'{}^2 + \epsilon''{}^2} + j \frac{\epsilon''}{\epsilon'{}^2 + \epsilon''{}^2} \tag{2}$$

Where ϵ' and ϵ'' show the real and imaginary parts of permittivity.

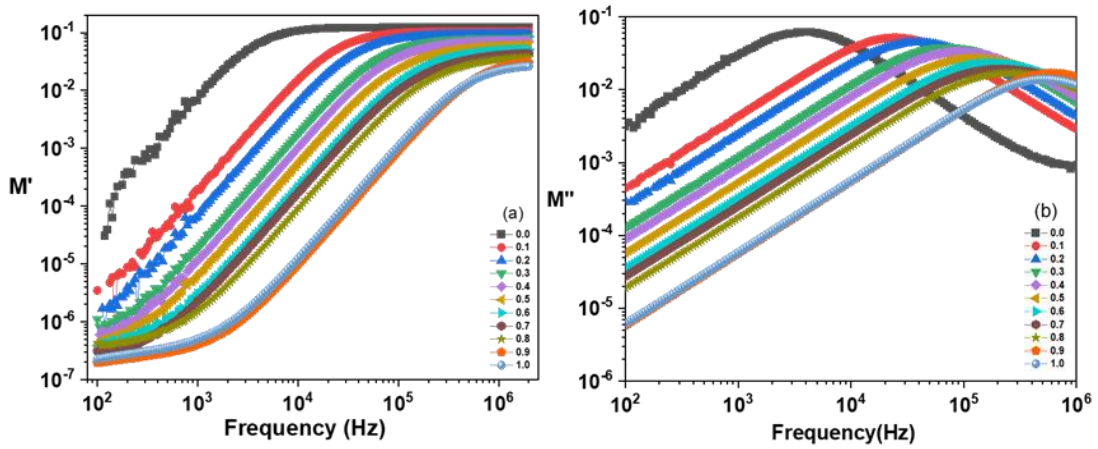


Fig.3 (a) variation of real part of electric modulus against frequency (b) variation of imaginary part of modulus against frequency

Fig. 3(a) and 3(b) depicts the plots of real and imaginary parts of modulus spectra. These binary mixtures show behavior consistent with the Debye function, a characteristic common by other dipolar liquids and ionic electrolytes [26,35]. It can be seen from the Fig. 3 (a) that values of the M' spectra increase exponentially up to 104 Hz for n-Nonanol and higher concentrations of n-Nonanol. While beyond the frequency range 104 Hz, for the same concentration, it remains constant. It is observed that for the pure DMA and higher concentration of DMA, the spectra of M' increase exponentially up to MHz frequency range and then remain slightly constant. The defeat of high capacitance phenomena within the modulus formalism leads to relatively low values of M' over the frequency range dominated by EP, with only a slight increase. From Fig. 3(a) it is clear that M' experiences a significant increase with frequency, finally stabilizing at the endpoint. The M'' spectra (Fig. 3(b), when represented on a logarithmic scale, show a linear increase across the low and intermediate-frequency regions, with concentration dependent peaks observed in the high-frequency range. These peaks match to the conductivity relaxation process, reflecting observations made earlier in several dielectric liquids [26,27]. In Fig. 3(b), as the concentration of DMA increases, the peak is observed in the higher frequency region, while a decrease in DMA concentration leads to a shift of the peak towards lower frequencies. The frequency f_{σ} associated with the peak value of M'' is directly associated to the relaxation time τ_{σ} for ionic conductivity, expressed as $\tau_{\sigma}=1/2\pi f$ [1]. It can be seen from Table 2 that the values of ionic conductivity relaxation time for pure n-Nonanol is 39.904 μ S. As we are adding a small amount of DMA into the n-Nonanol, the ionic conductivity relaxation time decreases from 39.904 to 6.324 μ S. Ionic conductivity relaxation time further decreases as the concentration of DMA increases in n-Nonanol and it approaches to 0.299 μ S for pure DMA.

Table 4 Ionic conductivity relaxation time ($\tau\sigma$), and experimentally and theoretically determined DC conductivity values (σ_{dc}) for various concentrations of DMA at 303.15 K.

X_A	Ionic conductivity relaxation time $\tau\sigma$ (μS)	σ_{dc} ($\mu\text{S/m}$) (From Fig. 4 (a))	σ_{dc} ($\mu\text{S/m}$) (From Eq. (4))
0.0	39.904	1.63E-06	1.81E-06
0.1	6.324	1.36E-05	1.34E-05
0.2	4.227	2.60E-05	2.33E-05
0.3	2.244	5.32E-05	4.98E-05
0.4	1.782	7.79E-05	7.21E-05
0.5	1.337	1.22E-04	1.24E-04
0.6	0.893	2.04E-04	2.18E-04
0.7	0.752	2.70E-04	3.32E-04
0.8	0.632	3.75E-04	3.96E-04
0.9	0.252	1.00E-03	1.08E-03
1.0	0.299	1.01E-03	1.11E-03

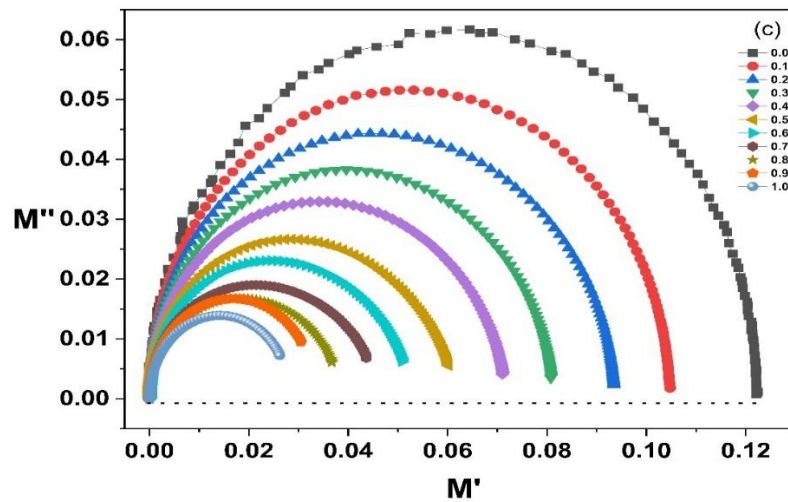


Fig.3 (c) Spectra of M'' versus M' for the binary mixtures of DMA-n-N-Nonanol

Figure 3(c) depicts the spectra of M'' versus M' plots for binary mixtures of DMA and n-Nonanol at 303.15 K temperature, indicating conformity to the Debye function, similar to other dipolar liquids and ionic electrolytes [26,36]. In the electric modulus plane plots, the absence of spikes at low frequencies assists as confirmation that the $M^*(\omega)$ spectra are not inclined by the EP effect [34]. The size of the Debye semicircle for DMA in the electric modulus is relatively small. A decrease in DMA concentration within the mixtures leads to a regular increase in the semicircle size, ascribed to higher relaxation frequencies $\epsilon^*(f)$ values of the concentrations.

The real part (σ') and imaginary part (σ'') of the complex electric conductivity ($\sigma^*(\omega)$) of the liquid mixtures were determined using the provided equation [25].

$$\sigma^*(\omega) = \sigma' + j\sigma'' = j\omega\epsilon_0\epsilon''(\omega) = \omega\epsilon_0\epsilon'' + j\omega\epsilon_0\epsilon' \tag{3}$$

In this equation, ϵ_0 is the value of the permittivity for the free space.

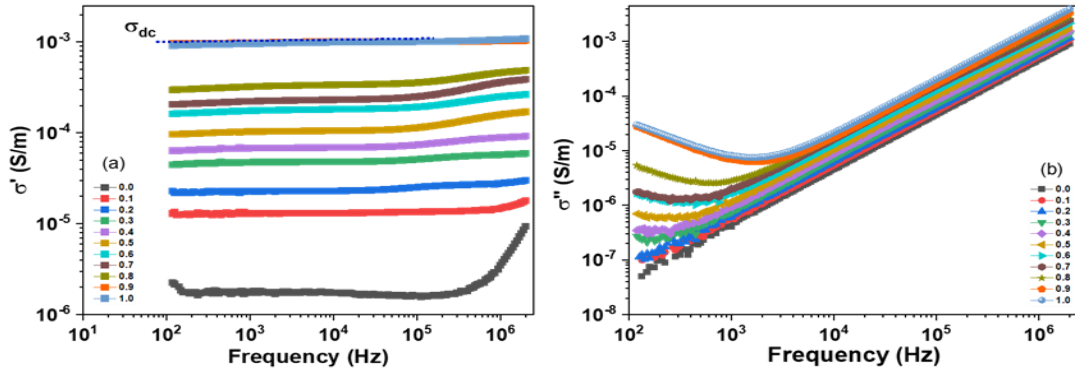


Fig.4 (a) variation of real part of electric conductivity against frequency (b) variation of imaginary part of conductivity against frequency

Observations from Figure 4(a) indicate that the values of σ' initially slightly increase irregularly across the experimental frequency range, then suggesting frequency independence. The duration of this steady-state frequency range depends upon the composition of DMA+ n-Nonanol mixtures. The σ' values remain constant, suggesting the direct current (DC) electrical conductivity (σ_{dc}) of these binary mixtures. In the spectral plot of Fig. 4 (a), the solid line at σ' indicates the direct current (DC) conductivity, denoted as " σ_{dc} ". Table 2 provides the dc conductivity values for the (DMA + -n-Nonanol) mixtures at 303.15 K temperature. The direct current (DC) conductivity (σ_{dc}) values for (DMA + -n-Nonanol) binary mixtures are observed to be within the range of a few $\mu\text{S/m}$. It is observed from Table 2 that values of dc conductivity are $1.63 \mu\text{S/m}$. As the small amount of DMA increases in the n-Nonanol, the value of dc conductivity increases to $13.6 \mu\text{S/m}$. It increases as the concentration of DMA increases in the mixtures of n-Nonanol. Value of the dc conductivity is also calculated using the below relation:

$$\sigma_{dc} = \frac{\epsilon_0 \epsilon_v}{\tau_\sigma} \tag{4}$$

Where, ϵ_v is the permittivity of the vacuum, τ_σ = Ionic conductivity relaxation time and ϵ_0 is the permittivity of the free space.

It can be seen from Table 2 that values of dc conductivity determined from the σ' spectra are in good agreement with values determined from the above relation. It is in good agreement for all the concentrations of the binary mixtures as well as for n-Nonanol and DMA.

The σ'' spectra of the DMA + n-Nonanol liquid mixtures at 303.15 K are shown in Fig. 4(b). σ'' spectra can also be used to understand EDL dynamics in dipolar liquids [37]. It shows the minimum peak for DMA and higher concentration of DMA in the lower frequency region up to 10 kHz and beyond the same it increases linearly up to 2 MHz frequency region. The minimum peak is shifting towards the lower frequency side as the concentration of the mixtures decreases in DMA. For pure n-Nonanol and higher concentrations of n-Nonanol, it increases linearly through the all-frequency range. Moreover, they prove a linear rise with increasing frequency, indicating the predominant effect of direct current (DC) ionic conduction within this frequency range. However, a deviation from linearity in the initial slight frequency gap (100 Hz to around 10 kHz) suggests the significant contribution of the electrode polarization (EP) effect in the mixtures of DMA + n-Nonanol [19,30].

Figure 5 (a) and (b) represent the impedance spectra, showcasing both the resistive part (Z') and the capacitive reactance part (Z'') of the DMA + n-Nonanol binary mixtures at 303.15 K temperature.

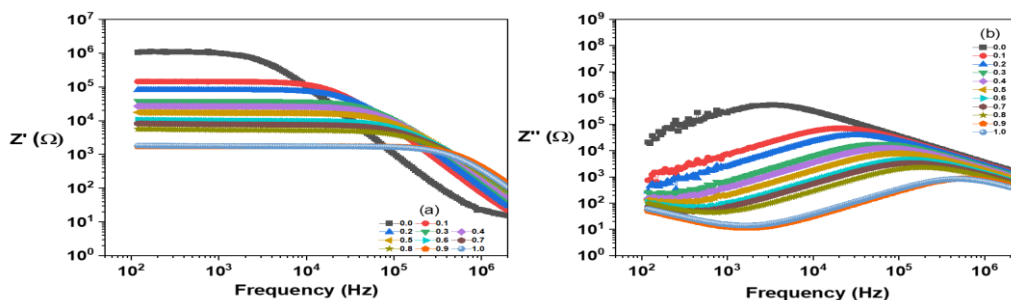


Fig.5 (a) variation of real part of electric impedance against frequency (b) variation of imaginary part of impedance against frequency

Notably, the Z' values display near-constant behavior up to 10^4 Hz, beyond 10^4 Hz it decreases non-linearly. Furthermore, it is observed that the Z' values for pure n-Nonanol are particularly higher in comparison to those of pure DMA. It can be seen from Fig. 5 (b) that a maxima peak is observed for pure n-Nonanol in the MHz frequency range. While for the higher concentration of n-Nonanol, $Z''(\omega)$ spectra increase linearly as the frequency increases. For pure DMA and also for the higher concentration of DMA, it shows minima and maxima both peak. The minima peak is shifting towards the higher frequency side as the concentration of DMA increases and vice versa the maxima peak shifts towards the lower frequency side. Minima and maxima peaks in the pure DMA and higher concentrations of DMA exhibit both the EDL and ionic conductivity relaxation process in the given frequency range.

Table 5 Values of the Debye length (λ_D), ion mobility (μ), mobile ion concentration (P_0), and ion diffusivity (D) for the mixtures of n-Nonanol and DMA at 303.15 K.

X_A	λ_D (nm)	μ (m^2/vs^{-1})	P_0 (m^{-3})	D (m^2/s)
0.1	24.11	3.51E-12	2.32E+25	9.18E-14
0.2	2.50	5.64E-14	2.53E+27	1.47E-15
0.3	13.92	3.30E-12	9.04E+25	8.63E-14
0.4	12.33	3.26E-12	1.31E+26	8.52E-14
0.5	9.56	2.62E-12	2.50E+26	6.83E-14
0.6	10.40	4.63E-12	2.44E+26	1.21E-13
0.7	7.73	3.04E-12	4.73E+26	7.94E-14
0.8	15.39	1.43E-11	1.46E+26	3.74E-13
0.9	10.90	1.80E-11	3.47E+26	4.72E-13
1.0	14.57	2.71E-11	2.27E+26	7.09E-13

The determination of Debye Length (λ_D), ion mobility (μ), mobile ion concentration (P_0), and ion diffusivity (D) within the concentration range ($0.0 \leq X_A \leq 1.0$) was performed by applying the model equation proposed by Klein et. al. [38] in their paper. Table 3 shows the values of Debye Length (λ_D), ion mobility (μ), mobile ion concentration (P_0), and ion diffusivity (D) for all the concentration ranges. The thickness of the ion layer formed at the electrode surface was determined using the provided equation.

$$\lambda_D = \frac{g}{2 \frac{\tau_{EP}}{\tau_\sigma}} \tag{5}$$

Where τ_{EP} is the electrode polarization relaxation time, τ_σ is the ionic conductivity relaxation time, g is the gap between two electrodes.

λ_D denotes to the thickness of the ion layer collected at the electrode surface. The value of λ_D for DMA is 14.57 nm. The value of λ_D shows anomalous behavior with changes in the concentrations in the mixtures.

Ion mobility is determined over the use of the following equation:

$$\mu = \frac{g^2}{4kTM\tau_{EP}} \tag{6}$$

where $M = \frac{\tau_{EP}}{\tau_\sigma}$, q is charge of electron, k is Boltzmann constant, and T is temperature.

The mobile ion concentration (P_0) and ion diffusivity (D) are derived from the ion mobility calculations,

$$P_0 = \frac{\sigma_{dc}}{q\mu} \tag{7}$$

$$D = \frac{\mu RT}{F} \tag{8}$$

Where, F is Faraday's constant and R is ideal gas constant.

As the concentration of DMA increases, there is an increase observed in ion diffusivity. Table 3 displays the variations in ion concentration across all concentrations ($0.0 \leq X_A \leq 1.0$). The ion mobility displays an increasing trend with the rising concentration of DMA in the mixture, reaching its maximum value at the highest concentration. This specifies that at this concentration, specific molecular structures are formed that allow ions to

diffuse more easily over the medium. As the concentration of DMA increases, the ion concentration and Debye length displays a nonlinear behavior.

IV. CONCLUSIONS

This study investigates the dielectric and electrical properties of n-Nonanol, N, N-Dimethylacetamide (DMA), and their binary mixtures as a function of concentration within the frequency range of 100 Hz to 2 MHz at a temperature of 303.15 K. Electrode polarization phenomena has happened under the effect of an AC electric field in the lower frequency region. The value of the dielectric loss is higher in the lower frequency region due to ionic conduction losses. The Coelho model is used to fit the complex permittivity data of the mixtures and provides the best fitting for all the binary mixtures. The value of the static dielectric constant increases as the concentration of the DMA increases in the mixtures. The values of electrode polarization relaxation time and ionic conduction relaxation time decrease as the concentration of DMA increases in the mixtures. Determined values of dc conductivity from the real part of conductivity spectra is in good agreement with the values derived theoretically. The thickness of ion accumulation is useful to understand the interface between the electrode and the dielectric medium, comprising polar liquids like n-Nonanol, DMA, and their mixtures.

V. ACKNOWLEDGMENT

We are thankful to Head, Department of Physics, Sardar Patel University, Vallabh Vidyanagar, for their continuous encouragement.

VI. REFERENCE

1. H. P. Vankar, V. A. Rana, "Electrode polarization and ionic conduction relaxation in mixtures of 3-bromoanisole and 1-propanol in the frequency range of 20 Hz to 2 MHz at different temperatures", *Journal of molecular liquids*, 254, 216-225, 2018.
2. N. S. Shah, H. P. Vankar and V. A. Rana, "Study of Complex Permittivity Spectra of Binary Mixtures of 2-chloroaniline and Methanol in Frequency Range 10 KHz to 2 MHz at Different Temperatures", *American institute of physics*, 1837, 040036, 2017.
3. R. J. Sengwa, S. Choudhary and P. Dhatarwal, "Dielectric and electrical behavior over the static permittivity frequency regime, the refractive indices and viscosities of PC-PEG binary mixtures", *Journal of Molecular Liquids*, 252, 339-350, 2018.
4. J. Barthel, R. Buchner, B. Wurm, "The dynamics of liquid formamide, N-Methylformamide, N, N- Dimethyl formamide and NN- Dimethylacetamide. A Dielectric relaxation studies", *Journal of Molecular Liquids*, 98-99, 51-69, 2002.
5. Y. Lei, H. Li, H. Pan, and S. Han, "Structures and Hydrogen Bonding Analysis of N, N-Dimethylformamide and N, N-Dimethylformamide-Water Mixtures by Molecular Dynamics Simulations", *Journal of physical chemistry*, 107, 1574-1583, 2003.
6. M. D. Elola, B. M. Ladanyi, "Computational study of structural and dynamical properties of formamide water mixtures", *Journal of chemical physics*, 125, 184506, 2006.
7. B. Wurm, M. Munsterer, J. Richardi, R. Buchner, J. Barthel, "Ion association and solvation of perchlorate salts in N, N-dimethylformamide and N, N-dimethylacetamide: A dielectric relaxation study", *Journal of molecular liquids*, 119, 97-106, 2005.
8. B. Wurm, C. Baar, R. Buchner, J. Barthel, "Dielectric relaxation spectroscopy of ion-solvent interactions in formamide and N-methylformamide", *Journal of molecular liquids*, 127,14-20, 2006.
9. A. Greenberg, C. M. Breneman, J. F. Liebman, "The Amide Linkage: Structural Significance in Chemistry, Biochemistry and Materials Science", Wiley, New York, 2002.
10. N. E. Hill, W. E. Vaughan, A. H. Price, M. Davies, "Dielectric Properties and Molecular Behavior", Van Nostrand Reinhold Co., London, 1969.
11. R. J. Sengwa, V. Khatri, S. Sankhla, "Static Dielectric Constants and Kirkwood Correlation Factor of the Binary Mixtures of N-Methylformamide with Formamide, N, N-Dimethylformamide and N, N-Dimethylacetamide", *Journal of solution chemistry*, 38, 763-769, 2009.
12. R. J. Sengwa, S. Sankhla, V. Khatri, "Dielectric constant and molecular association in binary mixtures of N, N-dimethylethanolamine with alcohols and amides", *Fluid Phase Equilibria*, 285, 50-53, 2009.
13. R. J. Sengwa, S. Sankhla, V. Khatri, S. Choudhary, "Static permittivity and molecular interactions in binary mixtures of ethanolamine with alcohols and amides", *Fluid Phase Equilibria*, 293, 137-140, 2010.
14. R. J. Sengwa, V. Khatri, "Study of static permittivity and hydrogen bonded structures in amide-alcohol mixed solvents", *Thermochimica Acta*, 506, 47-51, 2010.
15. R. J. Sengwa, V. Khatri, S. Sankhla, "Structure and hydrogen bonding in binary mixtures of N, N-dimethylformamide with some dipolar aprotic and protic solvents by dielectric characterization", *Indian Journal of Chemistry*, 48/A, 512-519, 2009.

16. A. N. Prajapati, V. A. Rana, A. D. Vyas and D. H. Gadani, "A study of molecular interaction in binary mixtures of 1-Propanol with N, N-Dimethylformamide at different temperatures", *Advanced Materials Research*, 665, 317-325, 2013.
17. M. S. Manjunath, P. Sivagurunathan, and J. Sannappa, "Studies of Hydrogen Bonding Between N, N-Dimethylacetamide and Primary Alcohols, *Journal of Chemistry*", 6, 143-146, 2009.
18. G. Ravi, P. B. Undre, K. Ramachandran, K. Samuvel, "Dielectric relaxation study of amides with alcohol mixtures by time domain reflectometry", *South African Journal of Chemical Engineering*, 24, 71-81, 2017.
19. J. Barthel, H. Gores, "A cutting edge in modern electrochemical technology. In: Mamantov, G., Popov, A.J. (eds.) *Chemistry of Nonaqueous Solutions-Current Progress*", *Journal of Solution chemistry*, VCH, New York, 1994.
20. A. Ali, A. K. Nain, "Interactions in binary N, N-dimethylacetamide + ethanol and ternary lithium nitrate + N, N dimethylacetamide + ethanol mixtures", *Physics and Chemistry of Liquids*, 37, 161-174, 1999.
21. K. N. Shah, V. A. Rana, C. M. Trivedi, H. P. Vankar, "Dielectric properties of binary mixtures of methyl iso butyl ketone and amino silicone oil", in: *AIP Conference Proceeding*, AIP Publishing, 1837, 040026, 2017.
22. D. H. Gadani, A. D. Vyas, V. A. Rana, S. P. Bhatnagar, A. N. Prajapati, "Dielectric Spectroscopy of Dry and Wet Soils in Frequency region from 20 Hz to 20 GHz", in: *Solid State Phenomena*, Trans Tech Publication, 209, 23-26, 2014.
23. N. Shinyashiki, R. J. Sengwa, S. Tsubotani, H. Nakamura, S. Sudo, S. Yagihara, "Broadband Dielectric Study of Dynamics of Poly (vinyl pyrrolidone) – Ethylene Glycol Oligomer Blends", *Journal of physical chemistry*, 110, 4953-4957, 2006.
24. N. Gondaliya, D. K. Kanchan, P. Sharma, M. S. Jayswal, M. Pant, "Conductivity and dielectric behavior of AgCF3SO3 doped PEO polymer films", *Integrated Ferroelectric*, 119, 1-12, 2010.
25. R. J. Sengwa, S. Sankhla, S. Choudhary, "Dielectric relaxation processes and ionic conduction behavior in poly (ethylene oxide)-montmorillonite clay nanocomposite aqueous colloidal suspensions", *Colloid and Polymer Science*, 287, 1013-1024, 2009.
26. R. J. Sengwa, S. Choudhary, A. Bald, "Dielectric dispersion and electric relaxation processes induced by ionic conduction in formamide, 2-aminoethanol and their binary mixtures", *Journal of Solution chemistry*, 42, 1960-1975, 2013.
27. R. J. Sengwa, S. Choudhary, P. Dhatwarwal, "Effect of ionic contaminants on dielectric dispersion and relaxation processes over static permittivity frequency region in neat liquid poly (ethylene glycol)", *Journal of Molecular Liquid*, 220, 1042-1048, 2016.
28. R. J. Sengwa, S. Sankhla, "Characterization of ionic conduction and electrode polarization relaxation processes in ethylene glycol oligomers", *Polymers Bulletin*, 60, 689-700, 2008.
29. R. J. Sengwa, S. Sankhla, "Characterization of solvent effect on low-frequency dielectric dispersion and relaxation behavior of ethylene glycol oligomers", *Journal of Molecular Liquid*, 141, 73-93, 2008.
30. J. Jadzyn, J. Swiergiel, "On intermolecular dipolar coupling in two strongly polar liquids: dimethyl sulfoxide and acetonitrile", *Journal of Physical Chemistry*, 115, 6623-6628, 2011.
31. J. Swiergiel, J. Jadzyn, "Conductivity dynamics and static dielectric permittivity of highly conducting molecular liquids studied with impedance spectroscopy Formamides", *Journal of Physical Chemistry*, 113, 14225-14228, 2009.
32. J. Barthel, K. Bachhuber, R. Buchner, J. B. Gill, M. Kleebauer, "Dielectric spectra of some common solvents in the Microwave region. Dipolar aprotic solvents and amides", *chemical physics letters*, 167, 62, 1990.
33. J. R. Macdonald, "LEVM/LEV MW Manual-CNLS (Complex Nonlinear Least Squares) Immittance, Inversion, and Simulation Fitting Programs for WINDOWS and MS-DOS", abgerufen am 20.09. 2013.
34. S. Choudhary, P. Dhatwarwal, R. J. Sengwa, "Characterization of conductivity relaxation processes induced by charge dynamics and hydrogen-bond molecular interactions in binary mixtures of propylene carbonate with acetonitrile", *Journal of Molecular Liquids*, 231, 491, 2017.
35. R. J. Klein, S. Zhang, S. Dou, B.H. Jones, R.H. Colby, J. Runt, "Modeling electrode polarization in dielectric spectroscopy: Ion mobility and mobile ion concentration of single-ion polymer electrolytes", *Journal of Chemical Physics*, 124, 144903, 2006.
36. J. Jadzyn, J. Swiergiel, "Electric relaxational effects induced by displacement current in dielectric materials", *Industrial and Engineering chemistry research*, 51, 807-813, 2012.
37. V. A. Rana, K. N. Shah, H. P. Vankar, C. M. Trivedi, "Dielectric Spectroscopic Study of the Binary Mixtures of Amino Silicone Oil and Methyl Ethyl Ketone in the Frequency Range of 100 Hz to 2 MHz at 298.15 K Temperature", *Journal of molecular liquids*, 271, 686-695, 2018.
38. R. J. Klein, S. Zhang, S. Dou, B. H. Jones, R. H. Colby, Modeling electrode polarization in dielectric spectroscopy: Ion mobility and mobile ion concentration of single-ion polymer electrolytes", *Journal of chemical physics*, 124, 144903 2006.

© 2024. This work is published under

<https://creativecommons.org/licenses/by/4.0/legalcode>(the "License")
). Notwithstanding the ProQuest Terms and Conditions, you may use this content in accordance with the terms of the License.

¹Radhika A.
Gandhare
²Aachal R. Kadu
^{3*}Jitendra T. Ingle

**Combustion Synthesis and Photoluminescence
Study of $\text{Li}_2\text{ZnTi}_3\text{O}_8:\text{Mn}^{4+}$ Phosphor for Photo-
catalytic Activity in Plants.**



Abstract: - In view of multifunctional applications of optical materials, an ultraviolet activated $\text{Li}_2\text{ZnTi}_3\text{O}_8:\text{Mn}^{4+}$ red emitting phosphor is synthesized by simple route of solution combustion technique, the synthesis was based up on the exothermic reaction between the fuel (Urea) and oxidizer (Nitrate), the heat release in reaction was utilized for auto combustion of ingredients, the phase formation and crystal structure of prepared borates material was determined by powder XRD technique. The sample belongs to spinel cubic crystal structure and there are abundant $[\text{TiO}_6]^{8-}$ octahedron sites can be occupied by Mn^{4+} . The $\text{Li}_2\text{ZnTi}_3\text{O}_8:\text{Mn}^{4+}$ shows the red emission in the region of 600-800 nm with a maximum at ~647 nm under 330 nm excitation, which can promote the plant growth. The optimal Mn^{4+} doping concentration is ~0.3 mol%, which is higher than that of other hosts. Furthermore, the characteristics of thermal quenching are also studied. All data suggest that $\text{Li}_2\text{ZnTi}_3\text{O}_8:\text{Mn}^{4+}$ phosphor can be a potential application in plant-cultivation and enhance photocatalytic activity.

Keywords: Combustion synthesis, photoluminescence, phosphors, photo catalytic activity.

I. INTRODUCTION

In present scenario of environmental pollution, human being faced with food, energy, resources which are all closely related to plant production. Light is pioneer source in plant growth and development [1-5]. As we all known, chlorophyll and carotenoids are the main contributions to plant photosynthesis. Their absorption bands are located in the blue light region of 400–520 nm and the red-light region of 610–720 nm, respectively [6-8]. In photosynthesis, blue light is conducive to protein synthesis, has a greater impact on plant growth and bud formation, can inhibit plant elongation and make plants short and strong. While red light is conducive to the synthesis of sugar and carbohydrate, accelerating the development of plant stem nodes. Phytochrome in plants has two forms: PR and PFR, which mainly absorb about 660 nm red light and 730 nm far red light, respectively [9]. Therefore, in order to solve the food problems faced by human beings, it is necessary to supply light to promote plant growth and improve crop yield and quality.

Therefore, In search of an efficient phosphor which emit deep red light in 610 nm -720 nm by using the Mn^{4+} ion as color centre, we undertake $\text{Li}_2\text{ZnTi}_3\text{O}_8$ as host material. Mn^{4+} , because of its excellent luminous properties and low cost, is used to instead of Eu^{2+} or Ce^{3+} . In addition, Mn^{4+} can absorb light from 250 to 550 nm, and can emit the red light of 600–750 nm. Mn^{4+} exhibits a wide excitation band that is the result of $^4\text{A}_{2g} \rightarrow ^2\text{T}_{2g}$, $^4\text{A}_{2g} \rightarrow ^4\text{T}_{1g}$, and $^4\text{A}_{2g} \rightarrow ^4\text{T}_{2g}$ transitions, and the $^2\text{E} \rightarrow ^4\text{A}_{2g}$ transition leads to its red emission band [10]. In structural context, Mn^{4+} ion can shows stable octahedral or

*Corresponding author: Government Vidarbha Institute Of Science and Humanities, Amravati 444604,India.

Emailid: inglejt2013@gmail.com

¹ Government Vidarbha Institute Of Science and Humanities, Amravati 444604,India

distorted octahedral coordinated site .we first time report combustion synthesis and photoluminescence properties under UV excitation, results are in favors to use for plant growth.

II. EXPERIMENTAL

Combustion synthesis of $\text{Li}_2\text{ZnTi}_{3-x}\text{O}_8:x\text{Mn}^{4+}$

$\text{Li}_2\text{ZnTi}_{3-x}\text{O}_8:x\text{Mn}^{4+}$ powders with various Mn^{4+} -doped concentrations are prepared by modified route of solution combustion technique. $\text{Zn}(\text{NO}_3)_2$ (LOBA CHEMIE, 98%), TiO_2 (Addendum, 98%), LiNO_3 (Star Chem Fine Chemicals 98%), and MnO_2 (LOBA CHEMIE) are chosen as the starting materials. The preparation process is as follows. Firstly, stoichiometric amounts of starting ingredients were calculated as per the balance inorganic reaction indicated in table no.1 and weighted precisely. Secondly, all starting ingredients like MnO_2 , TiO_2 were converted into $\text{Mn}(\text{NO}_3)_2$ and $\text{Ti}(\text{NO}_3)_4$ by mixing MnO_2 and TiO_2 into few ml of dil. HNO_3 , then these starting ingredients were weighed on High Precision Balance (WENSAR ISO 0001 CERTIFIED), then weighed quantities of each metal nitrate and urea were mixed together by adding little D.D. water and place on heating menthol for about 30 minute to obtained homogenous, clear and thick solution, it then transferred in to a preheated muffle furnace maintained at 550°C .

The mixture boils, froths, ignites and undergoes dehydration and then decomposition with liberation of NH_3 and NO_2 gases. The heat generated in reaction between fuel (urea) and oxidiser (ammonium nitrate) used for the auto-combustion of precursors. The process being highly exothermic, continues to liberates gases swell, the mixture glows into large voluminous foamy substrate, the entire process complete within 5 minutes.

The prepared material is then taken out of the furnace and the foamy product is crushed into a fine power and heated at 800°C for about 1 hour, some of phosphors reported by this technique [11-15].

Table 1. The molar ratios of ingredients used in the synthesis and corresponding balanced chemical reactions.

S.N.	Phosphors.	Balanced chemical reaction with molar ratios of ingredients.
1.	$\text{Li}_2\text{Zn}(3-x)\text{TiO}_8:x\text{Mn}^{4+}$ ($x=0.1, 0.3, 0.5$)	$2\text{Li}(\text{NO}_3)_3 + \text{Zn}(\text{NO}_3)_2 + (3-x)\text{Ti}(\text{NO}_3)_4 + 9\text{CO}(\text{NH}_2)_2 + 4.5 \text{NH}_4\text{NO}_3 + x\text{Mn}(\text{NO}_3)_2 \xrightarrow{550\text{ }^\circ\text{C}} \text{Li}_2\text{ZnTi}_3\text{O}_8:x\text{Mn}^{4+} + \text{Gaseous Products } (\text{H}_2\text{O}\uparrow, \text{NH}_3\uparrow \text{ and } \text{NO}_x\uparrow)$

III. CHARACTERIZATION

Phase formation and structural properties of all samples are measured using powder X-ray diffraction analysis (XRD), which performed on Rigaku Miniflex \times 600 X-ray Diffractometer using $\text{Cu K}\alpha$ radiation with 0.15405 \AA wavelengths. The XRD data were obtained at the scanning angle ranging from 10° to 80° with the step of 0.2° per sec at room temperature. Rietveld refinement analysis and the structural model of the sample are put into effect by the general structure analysis system (GSAS) software. The photoluminescence spectra (excitation and emission) were recorded on Hitachi F-7000 fluorescence spectrophotometer.

IV. STRUCTURE ANALYSIS AND PHASE PURITY.

The XRD patterns of various Mn^{4+} concentrations doped $\text{Li}_2\text{ZnTi}_3\text{O}_8$ phosphor are shown in Fig. 1. It can be clearly observed that with the increase of the doping concentration of Mn^{4+} , except for the change of intensity, all the diffraction

peaks data of $\text{Li}_2\text{ZnTi}_3\text{O}_8:x \text{Mn}^{4+}$ ($0.01 \leq x \leq 0.4$) samples are in conformity with standard card JCPDS No. 86-1512 in shape and position, and no other impurity phase is observed. These data express that the samples of $\text{Li}_2\text{ZnTi}_3\text{O}_8:x \text{Mn}^{4+}$ are single phase and that Mn^{4+} ion is successfully entered into host $\text{Li}_2\text{ZnTi}_3\text{O}_8$ lattices but do not cause clearly the change of crystal structure. There are no additional diffraction peaks can be observed, all the diffraction peaks are in accordance with Bragg position, which indicates that the sample is pure phase [16-17]. The parameters of crystal structure $\text{Li}_2\text{ZnTi}_3\text{O}_8:x \text{Mn}^{4+}$ samples are obtained. $\text{Li}_2\text{ZnTi}_3\text{O}_8$ belongs to spinel cubic crystal system, P4332 (212) space group, and the crystal cell factors are $a = b = c = 8.3710 \text{ \AA}$ and the crystal cell volume was $V = 586.59 \text{ \AA}^3$, respectively. Fig. 2 illustrated unit cell of the crystal structure of the sample and coordination environments of TiO_6 octahedrons. In the $\text{Li}_2\text{ZnTi}_3\text{O}_8$ host lattice, there are two types coordination sites of lithium ions. One is the Li and Zn ions which are bonding with four oxygen atoms, and the other is the independent Li ions bonding with six oxygen atoms occupy the octahedrons in the crystal lattice. Moreover, the Ti ions are coordinated by six O atoms and they form an octahedron [18-19]. The $\text{Li}_2\text{ZnTi}_3\text{O}_8$ host lattice has a great deal with TiO_6 octahedral and LiO_6 octahedral.

In general, the Mn^{4+} ion can occupy octahedral or distorted octahedral site with 6-fold coordination where it can exist stably in general. Structural results confirms Ti^{4+} and Li^+ are 12.4% and 41.1%, which can further confirm that when Mn^{4+} ions entered the host lattice, it prefers to occupy the Ti^{4+} sites.

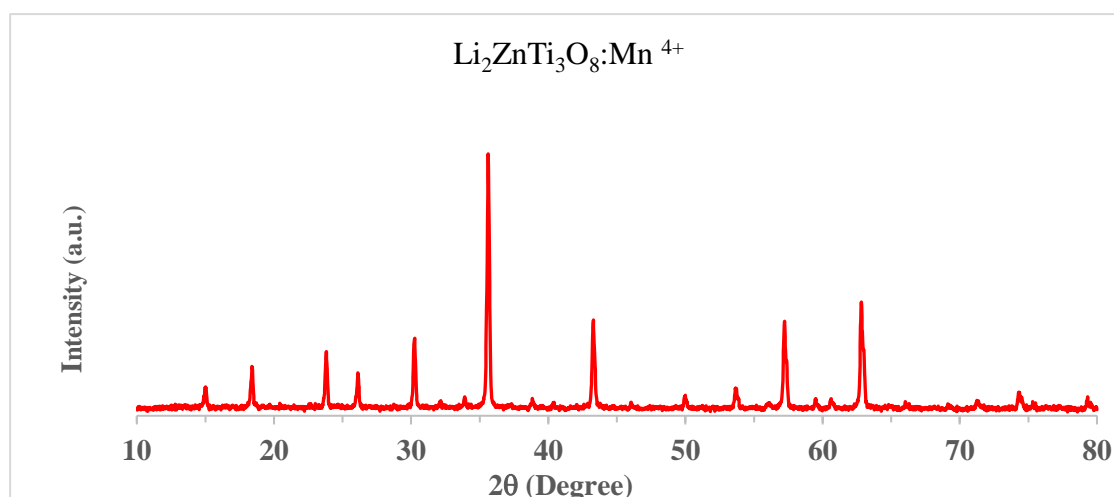


Fig. 1 Observed XRD pattern for $\text{Li}_2\text{ZnTi}_{2.7}\text{Mn}_{0.3}\text{O}_8$

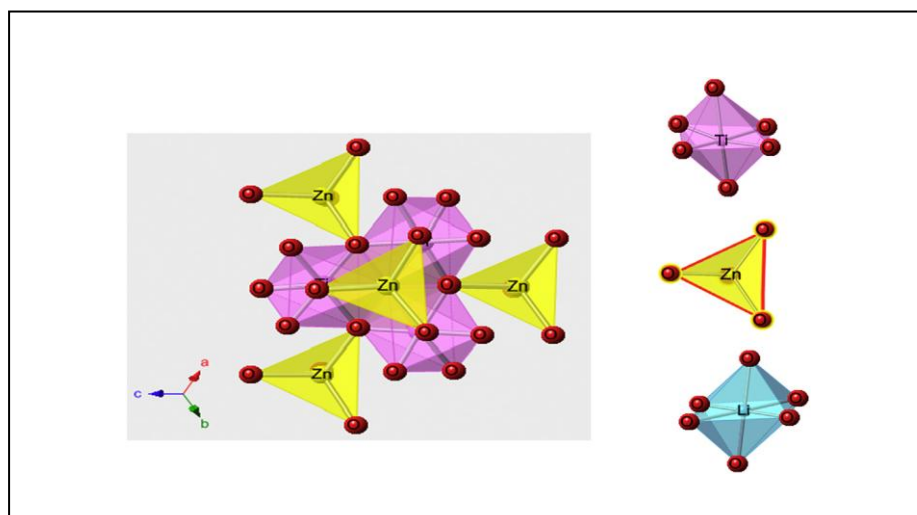


Fig. 2 Unit cell representation of the crystal structure of $\text{Li}_2\text{ZnTi}_3\text{O}_8:\text{Mn}^{4+}$

(a) TiO₆ and (b) LiO₂ octahedron (Li/Zn)O₄ Tetrahedron

V. PHOTOLUMINESCENCE PROPERTIES

Fig. 3 presented the PLE spectrum and PL spectrum of Li₂ZnTi₃O₈:0.3Mn⁴⁺ red phosphor, it can be used to investigate the luminescent properties of the phosphors. The excitation spectrum of Li₂ZnTi₃O₈:0.3Mn⁴⁺ monitored at 681 nm contains broad emission regions from 325 to 350 nm. The, PLE spectrum between 325 and 355 nm. There are three peaks centering at 335 nm. A strong excitation peak appears at approximately 330 nm, which is almost in line with earlier report [20-22].

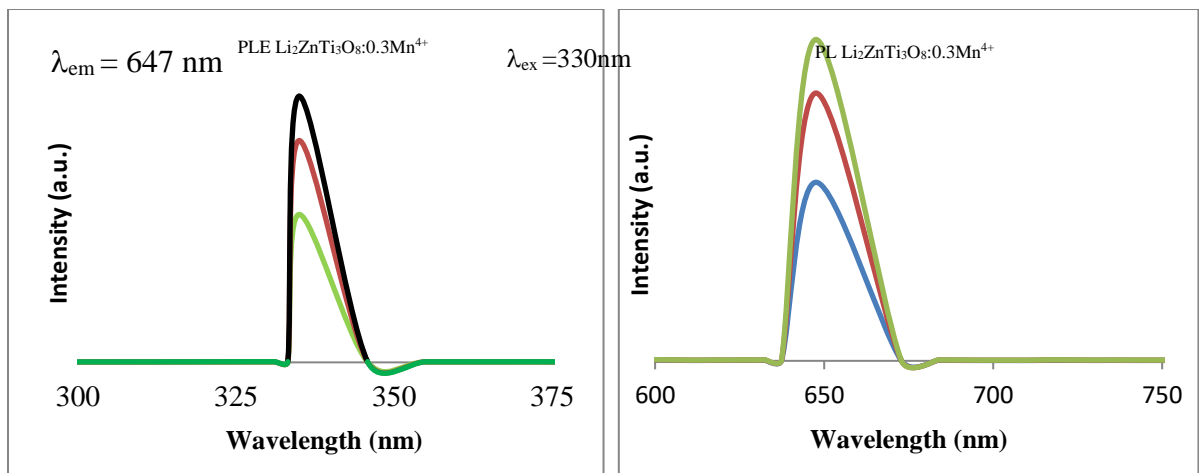


Fig. 3 PLE (Excitation) left and PL(Emission) right spectra of Li₂ZnTi₃O₈:0.3Mn⁴⁺ Phosphor

Under 330 nm excitation, Li₂ZnTi₃O₈:Mn⁴⁺ samples exhibit a strong deep red emission with a sharp emission peaks at 647 nm, corresponding to the different level transition modes of spin-forbidden ²E_g → ⁴A_{2g} transition and can be absorbed by the plant needed to promote plant growth. It can be universally known Mn⁴⁺ is a special transition metal ion and its 3d-3d transition band can be excited by near-ultraviolet light. The 3d electron level splits into three degenerate states T_{2g} and the double degenerate state E_g in the octahedron field, and special spin parity and forbidden transition ²E_g → ⁴A_{2g} can emit red light, which is consistent with our experimental results.

VI. CONCLUSION

In this Paper, a new type of Mn⁴⁺-activated red phosphor is prepared by solution combustion method firing at 550°C for 5 min. The phase structure and characteristics of luminescence have been studied in detail. Crystal structure of Li₂ZnTi₃O₈ was analyzed by XRD characterization and structural refinement. Ti⁴⁺ located in the octahedron center is very suitable for substitution by Mn⁴⁺ ions. The excitation spectrum of samples is ranged from 300 to 375 nm that can match well with the ultraviolet chip. Under 330 nm excitation, the Li₂ZnTi₃O₈: Mn⁴⁺ phosphors exhibit emission peak centering at 647 nm, ascribed to the ²E_g → ⁴A_{2g} transitions of 3d³ electrons. The red light emitted by the sample can promote the plant growth and found suitable application as plant-cultivation light-emitting phosphors.

ACKNOWLEDGMENT

The authors would like to thank Head, Department of Physics and Electronics, Government Vidarbha Institute of Science and Humanities, Amravati for their guidance and support during this study. Authors also acknowledge Director, Government Vidarbha Institute of Science and Humanities, Amravati for providing necessary facilities to complete this study.

REFERENCES

- [1] Z. Zhou, M. Xia, Y. Zhong, S.J. Gai, S.X. Huang, Y. Tian, X.Y. Lu, N. Zhou, Dy³⁺-Mn⁴⁺-co-doped Ca₁₄Ga_{10-m}Al_mZn₆O₃₅ far-red emitting phosphors with high brightness and improved luminescence and energy transfer properties for plant growth LED lights, *J. Mater. Chem. C* 5 (2017) 8201–8210.
- [2] Z. Zhou, Y. Zhong, M. Xia, N. Zhou, B.F. Lei, J. Wang, F.F. Wu, Tunable dual emission of Ca₃Al₄ZnO₁₀:Bi³⁺, Mn⁴⁺ via energy transfer for indoor plant growth lighting, *J. Mater. Chem. C* 6 (2018) 8914–8922.
- [3] J.Y. Chen, C.F. Guo, Z. Yang, T. Li, J. Zhao, Li₂SrSiO₄:Ce³⁺, Pr³⁺ phosphor with blue, red, and near-infrared emissions used for plant growth LED, *J. Am. Ceram. Soc.* 99 (2016) 218–225.
- [4] J.M. Xiang, J.Y. Chen, N.M. Zhang, H.B. Yao, C.F. Guo, Far red and near infrared double-wavelength emitting phosphor Gd₂ZnTiO₆:Mn⁴⁺, Yb³⁺ for plant cultivation LEDs, *Dyes Pigments* 154 (2018) 257–262.
- [5] M. Xia, X.B. Wu, Y. Zhong, Z. Zhou, W.-Y. Wong, A novel Na₃La(PO₄)₂/LaPO₄:Eu bluered dual-emitting phosphor with high thermal stability for plant growth lighting, *J. Mater. Chem. C* 7 (2019) 2385–2393.
- [6] X. Yang, Y. Zhang, X.J. Zhang, J. Chen, H.S. Huang, D.S. Wang, X.R. Chai, G.N. Xie, M.S. Molokeev, H.R. Zhang, Facile synthesis of the desired red phosphor Li₂Ca₂Mg₂Si₂N₆: Eu²⁺ for high CRI white LEDs and plant growth LED device, *J. Am. Ceram. Soc.* 103 (2020) 1773–1781.
- [7] R. Hernández, C. Kubota, Physiological responses of cucumber seedlings under different blue and red photon flux ratios using LEDs, *Environ. Exp. Bot.* 121 (2016) 66–74.
- [8] Z. Zhou, J. Zheng, R. Shi, N. Zhang, J. Chen, R. Zhang, H. Suo, E.M. Goldys, C.F. Guo, Ab initio site occupancy and far-red emission of Mn⁴⁺ in cubic-phase La(MgTi)_{1/2}O₃ for plant cultivation, *ACS Appl. Mater. Interfaces* 9 (2017) 6177–6185.
- [9] G. Tamulaitis, P. Duchovskis, Z. Bliznikas, K. Breive, R. Ulinskaite, A. Brazaityte, A. Novičkovas, A. Žukauskas, High-power light-emitting diode based facility for plant cultivation, *J. Phys. D: Appl. Phys.* 38 (2005) 3182.
- [10] R.P. Cao, T. Chen, Y.C. Ren, T. Chen, H. Ao, W.S. Li, G.T. Zheng, Synthesis and photoluminescence properties of Ca₂LaTaO₆:Mn⁴⁺ phosphor for plant growth LEDs, *J. Alloys Compd.* 780 (2019) 749–755.
- [11] Ingle JT, Gawande AB, Sonekar RP, Omanwar SK, Wang Y, Zhao L, Combustion synthesis and optical properties of Oxy-borate phosphors YCa₄O(BO₃)₃: RE³⁺ (RE = Eu³⁺, Tb³⁺) Under UV, VUV excitation *J. Alloys and Compounds* 2014; 585:633–636.
- [12] Ingle JT, Sonekar RP, Omanwar SK, Wang Y, Zhao L. Combustion Synthesis and Photoluminescence Study of Novel Red Phosphor (Y_{1-x-y}, Gd_x)BaB₉O₁₆:yEu³⁺ for Display and Lighting *J. Alloys and Compounds* 2014; 608 : 235–240.
- [13] Ingle JT, Sonekar RP, Omanwar SK, Wang Y, Zhao L. Combustion Synthesis and VUV Photoluminescence Studies of Borate Host Phosphors YBO₃:Re³⁺ (Re=Eu³⁺, Tb³⁺) For PDPs Applications *Combust. Sci. Technol.* 2013; 186:83–89.

- [14] Ingle JT, Sonekar RP, Omanwar SK, Wang Y, Zhao L. Solution combustion synthesis and optimization of phosphors for plasma display panels. *Optical materials*, 2014;36:1299–4.
- [15] Ingle JT, Sonekar RP, Omanwar SK, Wang Y, Zhao L. Combustion Synthesis and Luminescent Properties of Metal Yttrium Borates $M_3Y_2(BO_3)_4:Eu^{3+}$ (M=Ba, Sr) For PDPs applications. *Solid State Sciences* 2014;33:19-24.
- [16] X.Y. Huang, H. Guo, Finding a novel highly efficient Mn^{4+} -activated $Ca_3La_2W_2O_{12}$ far-red emitting phosphor with excellent responsiveness to phytochrome PFR: towards indoor plant cultivation application, *Dyes Pigments* 152 (2018) 36–42.
- [17] H.Y. Yan, Z.T. Wei, M.G. Zhang, Q. Wei, Exploration of stable stoichiometries, ground-state structures, and mechanical properties of the W–Si system, *Ceram. Int.* 46 (2020) 17034–17043.
- [18] Q. Sun, S.Y. Wang, B. Li, H. Guo, X.Y. Huang, Synthesis and photoluminescence properties of deep red-emitting $CaGdAlO_4:Mn^{4+}$ phosphors for plant growth LEDs, *J. Lumin.* 203 (2018) 371–375.
- [19] R.P. Cao, Z.H. Shi, G.J. Quan, T. Chen, S.L. Guo, Z.F. Hu, P. Liu, Preparation and luminescence properties of $Li_2MgZrO_4:Mn^{4+}$ red phosphor for plant growth, *J. Lumin.* 188 (2017) 577–581.
- [20] R.D. Shannon, Revised effective ionic radii and systematic studies of interatomic distances in halides and chalcogenides, *Acta Cryst.* 32 (1976) 751–767.
- [21] E. Song, J. Wang, J. Shi, T. Deng, S. Ye, M. Peng, J. Wang, L. Wondraczek, Q. Zhang, Highly efficient and thermally stable $K_3AlF_6:Mn^{4+}$ as a red phosphor for ultrahigh performance warm white light-emitting diodes, *ACS Appl. Mater. Interfaces* 9 (2017) 8805–8812.
- [22] Y.J. Zhu, Z.X. Qiu, B.Y. Ai, Y.T. Lin, W.L. Zhou, J.L. Zhang, L.P. Yu, Q.H. Mi, S.X. Lian, Significant improved quantum yields of $CaAl_{12}O_{19}:Mn^{4+}$ red phosphor by co-doping Bi^{3+} and B^{3+} ions and dual applications for plant cultivations, *J. Lumin.* 201 (2018) 314–320.

© 2024. This work is published under <https://creativecommons.org/licenses/by/4.0/legalcode>(the“License”).
Notwithstanding the ProQuest Terms and Conditions, you may use this content in accordance with the terms of the License.

¹Ashish Choudhary
²Sandeep Waghuley

CO₂ and LPG Gas sensing study of chemically synthesized PPy based sensor



Abstract: - The polypyrrole (PPy) was prepared by chemical oxidative polymerization route. X-ray diffraction (XRD), scanning electron microscopy (SEM) and ultraviolet-visible spectroscopy were used to evaluate the as-synthesized PPy sample. The SEM results showed that PPy sample shows accumulated nature with cotton-like structure. PPy sensor was fabricated using screen printing method. The sensing response of PPy based resistive gas sensor was observed for both liquid petroleum gas (LPG) and carbon dioxide (CO₂) gas. The PPy sensor was more selective towards carbon dioxide (CO₂) gas.

Keywords: Polypyrrole, Gas sensing, Oxidative polymerization

INTRODUCTION

Conducting polymers, such as polypyrrole (PPy) have been used as room temperature operated gas sensors. The PPy has many better characteristics like high sensitivities, ease of synthesis, environmental stability, high conductivity and short response and recovery time at room temperature. It has various applications in sensors, batteries, optical and nanoelectronic devices etc. [1-2]. Carbon dioxide has the greatest potential of all these gases to accelerate global warming. The two main causes of CO₂ emissions into the atmosphere are the industrial revolution and the burning of fossil fuels. LPG is a fuel that can be utilized for a variety of purposes but mishandling LPG can lead to flames, explosions, and most importantly deaths.

A room-temperature, flexible, polymer-based chemiresistive CO₂ gas sensor was fabricated by Zahra Shahrbabaki et al. [3] Waghuley et al prepared SnO₂/PPy Screen-Printed Multilayer CO₂ Gas Sensor for detection of CO₂ gas at room temp for different concentration. This sensor exhibits improved stability with ~ 2 min response time and ~ 10 min recovery time [4]. Bulakhe et al. reported on a room temperature operating LPG sensor based on a PPy-TiO₂ heterojunction [5]. A titanium dioxide (TiO₂)-reduced graphene oxide (r-GO) composite LPG sensor was prepared by Navin Chaurasiya et al. to detect LPG gas at ambient temperature [6].

Polypyrrole has been successively synthesized using simple chemical oxidative polymerization route. UV-VIS spectroscopy and scanning electronic microscopy (SEM) were used to characterize the PPy. Polypyrrole film was produced using the screen printing technique on a glass substrate that served as a PPy-based resistive gas sensor. The PPy sensor was then used to study CO₂ and LPG gases at room temperature (303K).

EXPERIMENTAL

In this work PPy sample prepared by chemical oxidative polymerization route using monomer pyrrole and ammonium persulphate in a 50:50 wt% ratio. Screen printing was the method used to deposit the PPy film. The two-probe method was used to calculate the value of the resistance change in the presence of gas. The sensing response of CO₂ and LPG gas was studied at room temperature (303K) by varying their concentrations. The powdered PPy was investigated with SEM, and XRD and U-V spectroscopy.

RESULT AND DISCUSSION

XRD ANALYSIS

The XRD patterns of as-synthesized PPy samples made with a 50:50 weight percent stoichiometry are displayed in Figure 1. Using a step height of 0.02 degrees, the XRD scanning was done in the 2θ range, which spans from 10 to 70°. The pattern displays nearly erratic forms with a few pointed peaks, which indicate that PPy has a semicrystalline structure. The wide hump peak in the region of 15–25° also analyzes the semicrystalline nature [7]. Oriented amorphous polymers have a different X-ray diffraction

¹ * Department of Physics, Shri Shivaji Arts, Commerce and Science College, Akot 444101, India.

² Department of Physics, Sant Gadge Baba Amravati University, Amravati 444 602, India
 Corresponding author e-mail: ashishchou78@gmail.com (A.R.Choudhary)

pattern than unoriented polymers. The Sharp peaks in the XRD pattern, exhibits high degree of crystallinity and unoriented polymerization.

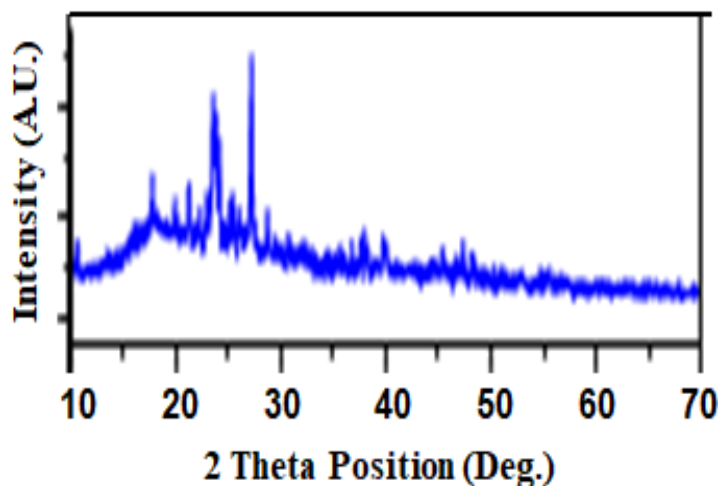


Figure 1: XRD pattern of as-synthesized PPy sample

The average chain separation values play key role in altering physical properties of materials and it has a great impact on electrical properties of polymeric materials also. In present case, we were detecting presence of gas by resistive method so its estimation is must.

Table 1: Average chain separation values and average particle size of as-synthesized sample

Sample name	Composition (wt %)	Peak position of amorphous halo (2θ)	Average chain separation (Å)	Average Particle size (nm)
S1	50:50	16.92°	1.027	15.93

SEM

The surface morphology of as-synthesized PPy sample was investigated using SEM micrograph as shown in figure 2. An extended open interconnected network is formed when the surfaces of the collected samples are randomly connected to one another. The synthesized sample show accumulated nature with cotton like structure. This asymmetrical structure is appropriate for gas sensing application.

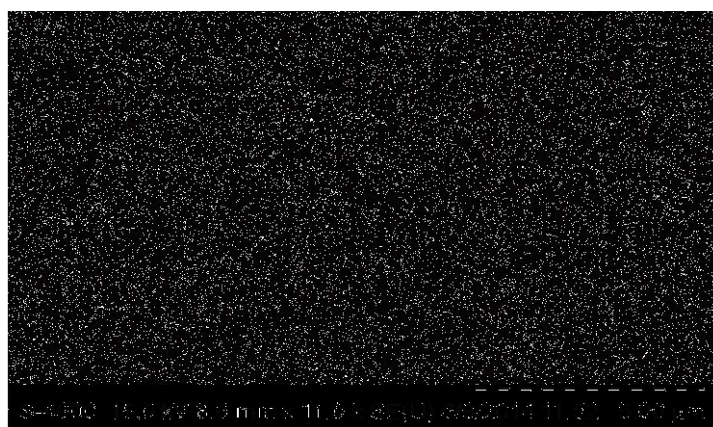


Figure 2: SEM micrographs of as-synthesized PPy sample

UV- VIS SPECTROSCOPY

Plot of the optical band gap for PPy sample is shown in figure 3. Polymerization is an inconsistent process therefore there is no correlation between the concentration of oxidant or monomer and the optical band gap values. This happens is due to monomers are joined in random numbers to a polymeric chain. Thus there is no obvious correlation between the concentration of the oxidant or monomer and the physical properties of organic materials.

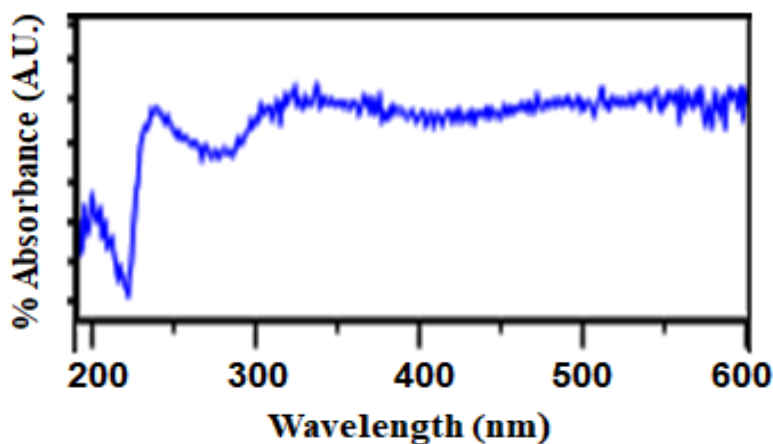


Figure 3: UV-VIS Spectra of as-synthesized PPy sample

GAS SENSING RESPONSE

Figure 4 shows the selectivity response of as-fabricated sensors. Selectivity is the ability of a material to detect a specific gas. Fabricated sensors have optimum response towards CO₂ gas than LPG for dose of 500 ppm at room temperature. The sensing response of sensors to CO₂ gas is better than that of LPG at 500 ppm dose at room temperature. When the sensing response is measured, it is found that resistance of film increases in the presence of CO₂ gas whereas, resistance decreases in the presence of LPG. It indicates that the materials being studied for gas sensing are n-type, or electron-rich. When exposed to CO₂ gas, the as-synthesized PPy sensing materials exhibit a high sensing response.

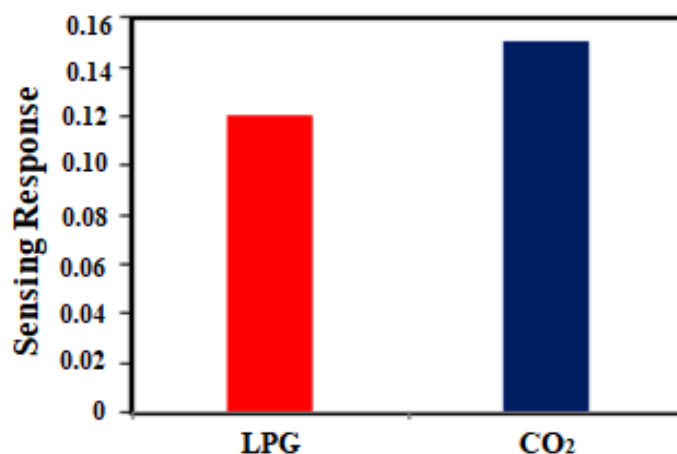


Figure 4: Selectivity responses of PPy sample towards the 500 ppm LPG and CO₂ gas concentration at RT

Figure 5 demonstrates sensing behavior PPy-based sensors towards CO₂ gas in terms of sensing. Up to 1000 ppm, the sensor response was found to be almost linear. The resistance of sensing film rise in the presence of CO₂ gas (oxidizing gas),

indicating the n-type behavior of sensing materials. The prepared sample exhibits a better sensing response due to the high degree of polymerization.

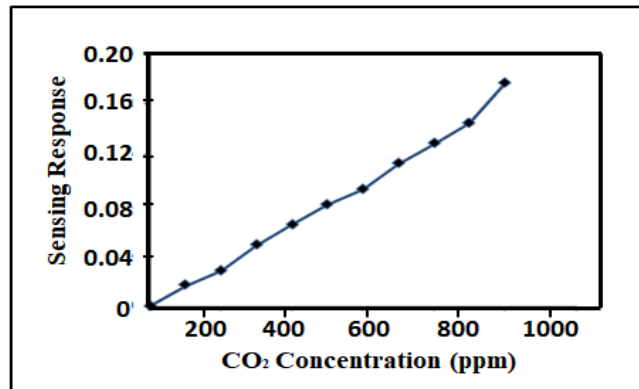


Figure 5: Gas sensing response of PPy sample towards the CO₂ gas at RT

CONCLUSIONS

In present work, we effectively synthesized PPy sample utilizing ammonium persulphate as an oxidant and pyrrole in a 50:50 wt% ratio, employing a chemical oxidative polymerization technique. The UV spectroscopic study describes the chemical composition of the as-prepared sample, which prominently demonstrates formation of PPy. The XRD pattern shows essentially erratic forms with a few sharp peaks, indicating a semicrystalline structure of PPy. Using XRD data, average polymer chain separation of as-synthesized PPy was determined which is found to be 1.027 Å, with an average particle size of 15.93 nm. The SEM micrograph shows accumulated nature with cotton like appearance. This asymmetrical structure is appropriate for gas sensing application. The sensor linear response curve is highly dependent on CO₂ gas concentration.

REFERENCES

- [1] Grgur B.N., Ristic V., Gvozdenovic M.M, Maksimovic M.D., Jugovic B.Z., J. Power Sources 180 (2008) 635.
- [2] D. Li, J.X. Huang, R.B. Kaner, Acc. Chem. Res. 42 (2009) 135
- [3] Shahrabaki Z., Farajikhah S, Mohammad B. Ghasemian, Oveissi F., Rath R.J, Yun J., Dehghani F, Adv. Mat. Tech. vol 8 (2023) 02-11.
- [4] Waghuley S. A., Yenorkar S. M., Yawale S. S., Yawale S. P Sen. & Trans. Jour, vol.79, (2007) 1180-1185.
- [5] Bulakhe R. N., Patil S. V., Deshmukh P. R., Shinde N. M., Lokhande C. D., Sens. Act. B 181 (2013) 417– 423.
- [6] Chaurasiya N, Singh A , Kumar K., Yadav B.C., Yadawa P.K., Singh S.K., Dey K.K., Sens. & Diagnostics 2 (2023) 1215-1227.
- [7] Choudhary A. R., Waghuley S. A., Optoelectronics and Adv. Mater. 12 (2018) 117-124.

•

¹ Chitransh D. Malvi^{*1,2} M.D. Mehare¹ S.J.Dhoble

Synthesis and luminescence study of Eu³⁺ activated KLaF₄ phosphor for W-LED application



Abstract: The present study reported the synthesis of Eu³⁺ activated KLaF₄ fluoride-based phosphor via conventional high-temperature solid-state reaction method. The identification of the crystalline structure of the prepared phosphor was characterized by XRD analysis, confirming the formation of cubic crystal structure with space group Fm-3m. The emission (PL), and excitation (PLE) spectra were investigated by photoluminescence spectroscopy, exhibiting that excitation peaks are centered at 260 nm, 395 nm, 466 nm, and 534nm attributes to O²⁻ → Eu³⁺ transition charge transfer band, ⁷F₀ → ⁵L₆, ⁷F₀ → ⁵D₂, and ⁷F₀ → ⁵D₁ transitions of Eu³⁺ ions, respectively. Optimum luminescent intensity was observed at 0.7mol% doping concentration of Eu³⁺ ions, which further studied at different excitation wavelengths, under the excitation of 466nm emission intensity observed at 612nm in the red region of the spectrum with CIE coordinates located at (0.6620, 0.3488) and color purity 97.66%. The obtained outcomes suggested that, the reported phosphor may be a promising candidate as blue exciting red-emitting phosphor for w-LEDs.

Keywords: Phosphor; LED; solid state diffusion; CIE co-ordinates; photoluminescence

¹ Department of Physics, RTM Nagpur University, Nagpur 440033, India

² *Corresponding Author: Department of Applied Physics, Priyadarshini College of Engineering, Nagpur 440019, India
Copyright © JES 2024 on-line: journal.esrgroups.org

I. INTRODUCTION

In the recent era, great research interest has been inclined toward the development of rare earth (RE³⁺) doped nanocrystalline phosphor materials owing to their numerous advantages in display and illumination. White light emitting diodes (w-LEDs) gain prime attention due to their exceptional optical performance, long operational lifetime, high luminous efficiency, remarkable chemical and thermal stability, and environmental friendliness which are expected to replace the conventional source of light worldwide in the near future [1–5]. Among the various reported inorganic phosphors, fluoride-based host phosphor gains more attention owing to their high refractive index with low photon energy resulting in a longer lifetime of their excited state along with optimum luminescence yields [6–8]. The various RE³⁺ activated fluoride based phosphors are extensively studied includes β -YF₃:Tm³⁺/Yb³⁺ [9], GdF₃:Eu³⁺ [10], KLaF₄:Tb³⁺[6], KLaF₄:Eu³⁺[11], KLaF₄:Ce³⁺[12], NaYF₄:Eu/Sr [13], NaYF₄:Yb,Er[14] exhibits special characteristics of host matrix which could strongly influence the emissive nature of RE³⁺ ions. The various parameters such as site occupancy, relative energy of the 4f emitting level of RE³⁺ ions along guest-host interaction greatly impact the emission mechanism of RE³⁺ ions in the host matrix. The Eu³⁺ ions as activator exhibits intense emission in the red region (~612nm) which is widely used in most commercial red-emitting phosphors. The crystal structure of the host matrix and local site symmetry substitution of activator in the host are the prominent factors responsible for intra-4f-shell down-conversion transitions (⁵D₀→⁷F_J, J=1,2,3,4) of Eu³⁺ ions in the host [15,16]. In the present work, we report the synthesis of KLaF₄:xEu³⁺ phosphor first time via solid state reaction method. The formation of crystal structure will be confirmed from XRD analysis, along with luminescent properties of as-synthesized phosphor materials were studied at different excitation wavelengths. The obtained outcome revealed that the reported phosphor is best suitable as blue exciting red-emitting phosphor for w-LEDs.

II. EXPERIMENTAL

A. Materials and Preparation

The Phosphor KLaF₄:xEu³⁺ (x=0.1, 0.2, 0.5, 0.7 & 1 mol %) has been synthesized by conventional high-temperature solid state reaction method. The starting materials such as Lanthanum Oxide [La₂O₃ (99.90%), Potassium Carbonate [K₂CO₃ (99.90%)], Ammonium Fluoride [NH₄F (99.90%)], and Europium Oxide [Eu₂O₃(99.90%)] are all analytical grade were employed as reactants. All the reactant materials were weighted according to stoichiometric ratio and mixed homogeneously in an agate mortar and pestle for 1hr. The fine powder of the samples was transfer into ceramic crucible calcinate at 400 °C for 2h inside a muffle furnace. The obtained powder was grounded and reheated again at 800°C for 24h. After having cooled down to room temperature in the furnace, the samples were grounded into powder for further characterization.

B. Characterization

X-ray diffraction (XRD) characterization of as-synthesized phosphor was carried out using a Bruker Advance D8 diffractometer with Cu-K α radiation (X-ray tube operated at 40KV and 40mA) scanning in 2 θ pattern was noted in the range of 20-70° with step size 0.021 and 0.5s per step. The photoluminescence excitation (PLE) and emission (PL) spectra were recorded at room temperature using a SHIMADZU spectrofluorophotometer RF-5301 PC equipped with 150W xenon flash lamp and spectral width of 1.5nm. The Commission Internationale de l'éclairage (CIE) chromaticity coordinates were analyzed using an Osram Sylvania Color calculator with high accuracy.

III. RESULTS AND DISCUSSION

1. XRD analysis

The Phase composition, purity, and crystalline structure of as-synthesized phosphor material was studied using XRD analysis. The X-ray diffraction pattern of the prepared phosphor material shown in Figure 1, exhibits excellent crystalline structure.

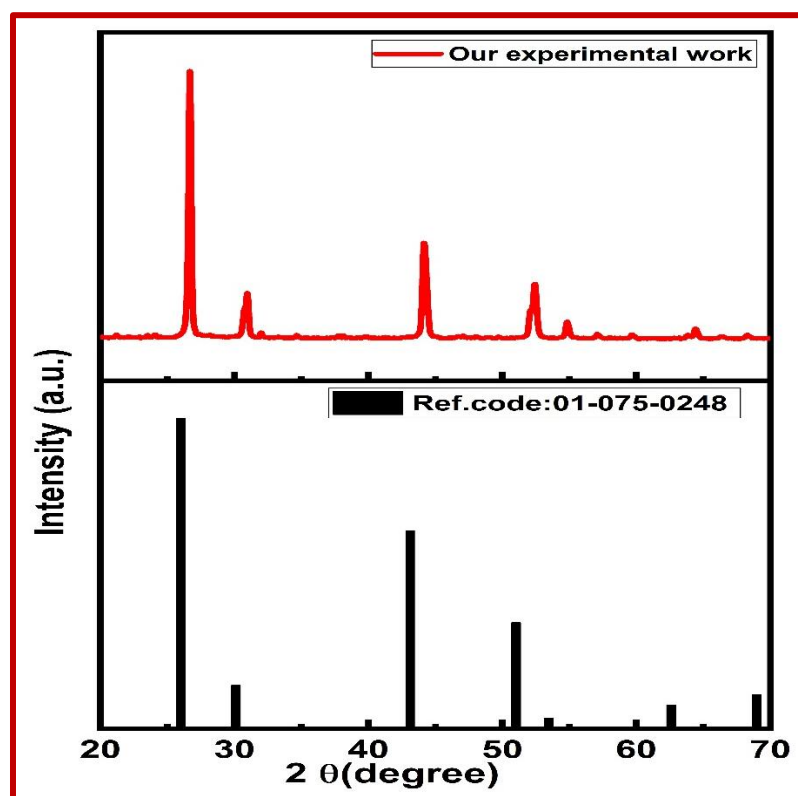


Fig 1: XRD pattern of KLaF₄ phosphor.

All the diffraction peaks are well indexed with standard Reference Code 01-075-0248, confirming the formation of single-phase material. The crystal structure of as-synthesized KLaF₄ phosphor is shown in Figure 2. This revealed a cubic crystal structure with space group Fm-3m (225) [6]. The crystallographic data and lattice parameter of the KLaF₄ phosphor are shown in Table 1.

Table1. Crystallographic data and lattice parameter of KLaF₄ phosphor

Crystal parameter	KLaF ₄ phosphor from crystallographic information file (CIF) no.
Crystal structure	Cubic
Space group	Fm-3m
Volume (V)	208.633394Å ³
Lattice parameter	a= 5.93100 Å b=5.93100 Å c=5.93100 Å α=90° β = 90° γ = 90°

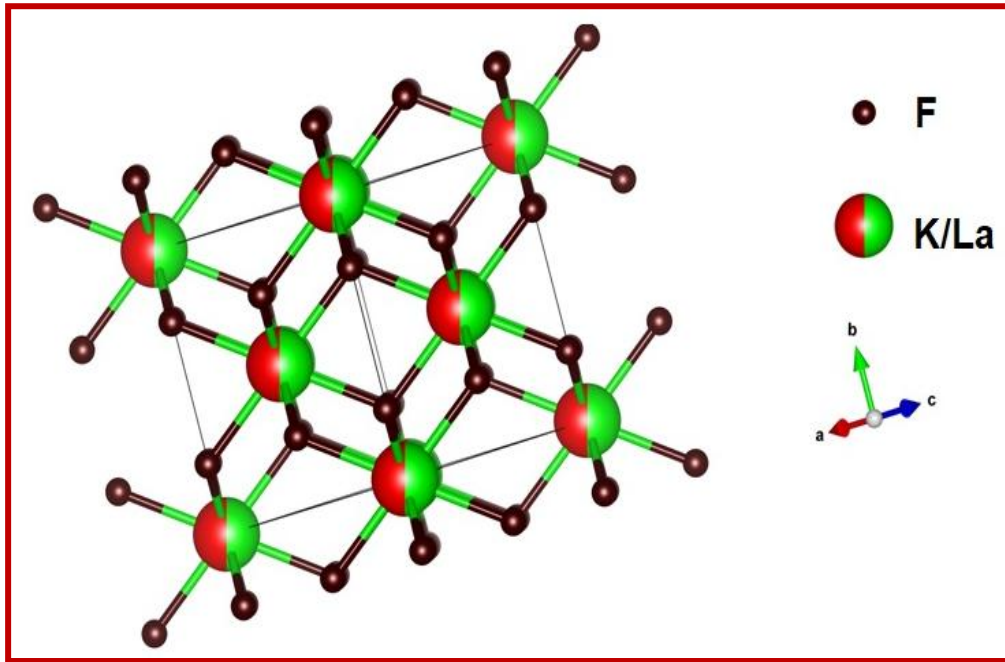


Fig 2: Crystal structure diagram of KLaF_4 phosphor.

2. Photoluminescence Characterization

The PL excitation spectrum of $\text{KLaF}_4:0.7\text{Eu}^{3+}$ phosphor monitor at 612nm attributed to $^5\text{D}_0 \rightarrow ^7\text{F}_2$ transition of Eu^{3+} ions is depicted in Figure 3. The PLE spectrum comprises a broad excitation band from 220 to 310nm. From the figure, it is clear that the broad excitation band centered at 260nm corresponds to the $\text{O}^{2-} \rightarrow \text{Eu}^{3+}$ charge transfer band (CTB) owing to electron transfer from filled 2p orbital of O^{2-} ions to the empty state of 4f orbital of Eu^{3+} ions [17,18]. In addition, several excitation peaks are observed assigned to intra-configurational 4f-4f forbidden transition of Eu^{3+} ions centered at 395nm, 466nm, 534nm attributed to $^7\text{F}_0 \rightarrow ^5\text{L}_6$, $^7\text{F}_0 \rightarrow ^5\text{D}_2$, and $^7\text{F}_0 \rightarrow ^5\text{D}_1$ transition of Eu^{3+} ions in the host [19–21]. Among all the excitation peaks the strongest excitation peak is centered in the blue region at 466nm. The PL emission spectrum for $\text{KLaF}_4:0.7\text{Eu}^{3+}$ phosphor at the different excitation wavelengths of 395nm, 466nm, and 534nm located in the wavelength range of 550nm to 650nm is shown in Figure 4. The sharp emission peaks for all excitation wavelengths are observed at 579nm, 592nm, 612nm, and 622nm corresponding to $^5\text{D}_0 \rightarrow ^7\text{F}_0$, $^5\text{D}_0 \rightarrow ^7\text{F}_1$, $^5\text{D}_0 \rightarrow ^7\text{F}_2$, and $^5\text{D}_0 \rightarrow ^7\text{F}_3$ transition of Eu^{3+} ions in the host [22]. From the emission spectrum, it is clear that, emission intensity at 612nm ($^5\text{D}_0 \rightarrow ^7\text{F}_2$) assigned to an electric dipole (ED) transition was much higher in comparison with emission wavelength of 592nm ($^5\text{D}_0 \rightarrow ^7\text{F}_1$) which is attributed to the magnetic dipole of Eu^{3+} ions in the host. When the Eu^{3+} ion is located at the crystallographic site followed by inversion symmetry, the magnetic dipole transition $^5\text{D}_0 \rightarrow ^7\text{F}_1$ transition is dominant, moreover if it site without inversion symmetry the electric dipole $^5\text{D}_0 \rightarrow ^7\text{F}_2$ transition will be dominant [23,24]. The obtained outcomes revealed that the local symmetry of Eu^{3+} ions sites belong to the non-centrosymmetric in the host lattice.

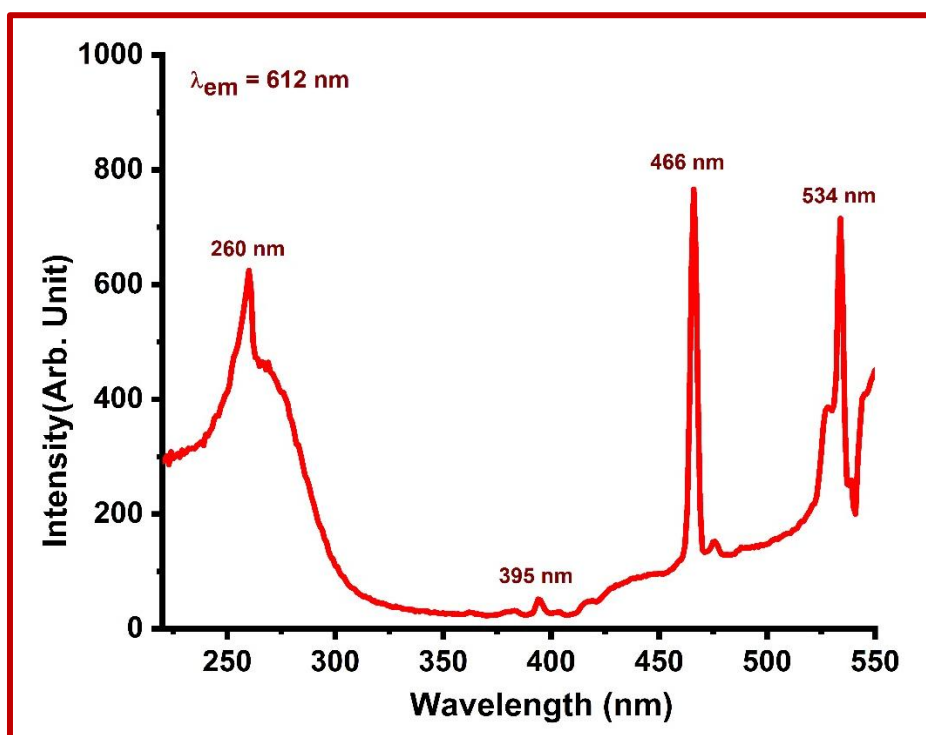


Fig 3: PL excitation spectra of KLaF₄: Eu³⁺ phosphor under 612 nm emission wavelength.

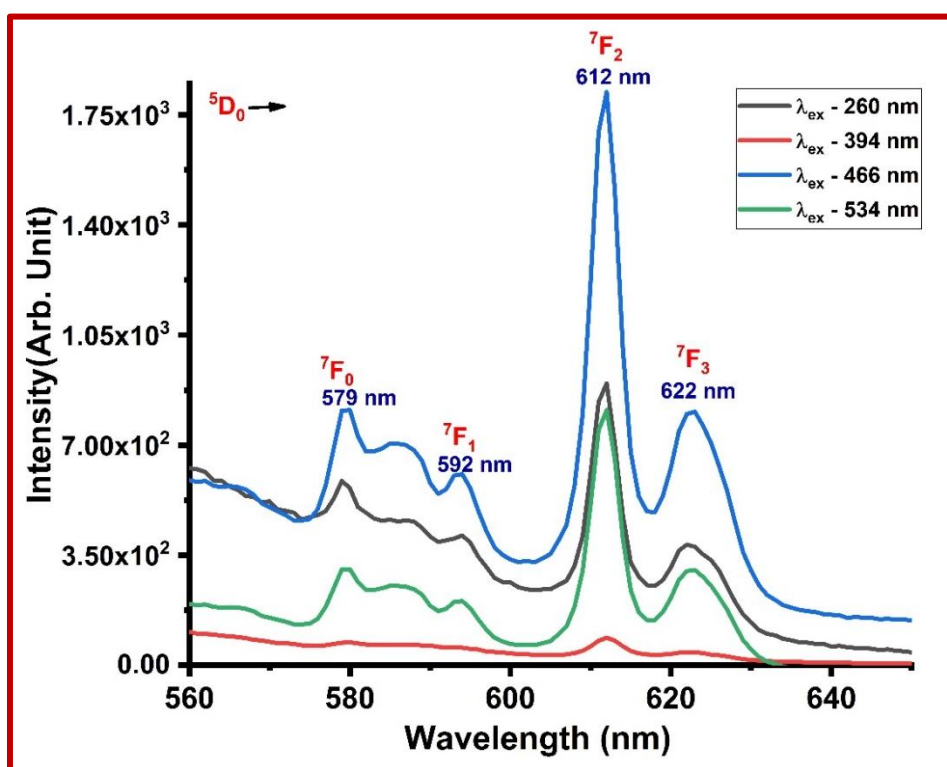


Fig 4: Emission spectra of KLaF₄:0.7mol% Eu³⁺ phosphor with different excitation wavelengths.

3. CIE Chromaticity

To optimize the credential of synthesized phosphor for w-LED application, the PL spectra were analyzed using Commission de l'Eclairage chromaticity (CIE) coordinates, which is most important parameter to confirm luminous quality of the phosphor. The CIE chromaticity diagram of KLaF₄:0.7Eu³⁺ phosphor under the excitation wavelength of 236nm, 394nm, 466nm, and 534nm is depicted in figure 5. The obtained values of CIE coordinates along with color purity and color correlated temperature (CCT) at the different excitation

wavelengths for 0.7mol% Eu^{3+} doped KLaF_4 phosphor is demonstrated in Table 2. The color purity of the phosphor is evaluated by the formula given below [3–5,25].

$$\text{color purity} = \frac{\sqrt{(x-x_i)^2+(y-y_i)^2}}{\sqrt{(x_d-x_i)^2+(y_d-y_i)^2}} \times 100\% \quad (1)$$

where, (x, y) and (x_i, y_i) are denoted for the color coordinate of the prepared phosphor and luminescent point of the standard CIE (1931) source respectively. (x_d, y_d) represent the chromaticity coordinate of the dominant wavelength of a light source.

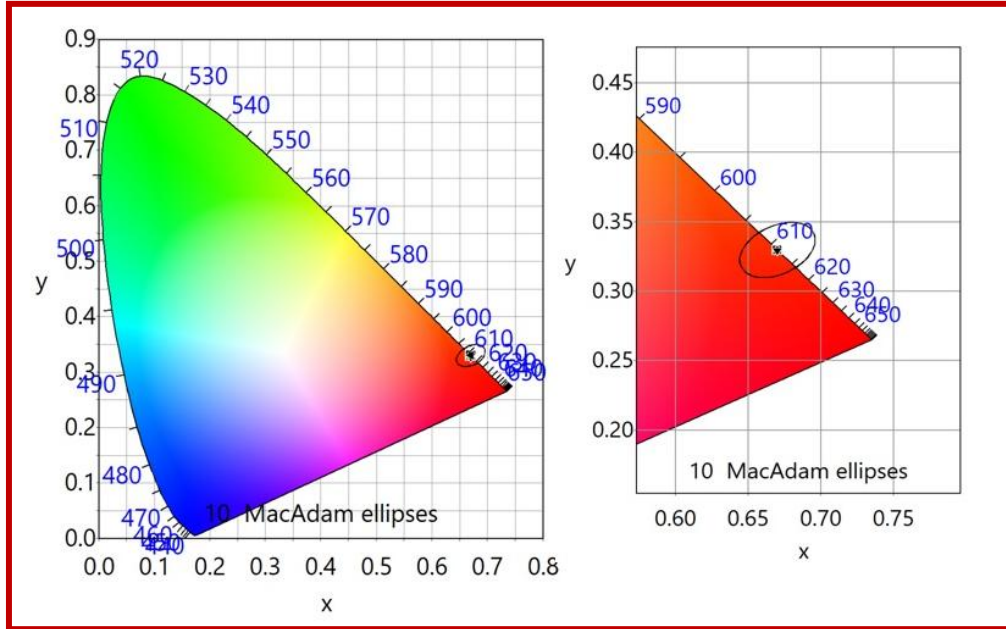


Fig 5: CIE chromaticity diagram of $\text{KLaF}_4:0.7\text{molEu}^{3+}$ doped phosphor

The quality of the white light can be examined using correlated color temperature (CCT) value, which can be evaluated using Mc Camy empirical formula [26].

$$\text{CCT} = -499n^3 + 3525n^2 - 6823.3n + 5520.33 \quad (2)$$

where, $n = \frac{x-x_e}{y-y_e}$, and $(x_e, y_e) = (0.332, 0.186)$ term as chromaticity epicentre. Normally, CCT values of the studied phosphor were found to vary from 1871-6125K. Generally, a CCT value of more than 5000K revealed the cold white light used for commercial lighting purposes. The CCT value of standard daylight at noon (D65, 6500K) is suitable for cold near white light emission [27]. The obtained value of CCT is depicted in Table 2.

Table 2: CIE Chromaticity coordinates, color purity and CCT

S.No.	Excitation Wavelength (nm)	x	y	Color purity (%)	CCT (K)
A.	266	0.6542	0.3454	95.357	2422
B.	395	0.6506	0.3461	94.31	2363
C.	466	0.6620	0.3488	97.66	2433
D.	534	0.6619	0.3378	97.60	2731

IV. CONCLUSION

In summary, Eu^{3+} activated KLaF_4 phosphor has been successfully synthesized by a high-temperature solid-state reaction method. The crystal structure has been characterized by XRD analysis. All diffraction peaks are in good agreement with standard reference code 01-075-0248 revealing the formation of a single-phase cubic structure with space group Fm-3m . The luminescent intensity of $\text{KLaF}_4: 0.7\text{mol}\%$ Eu^{3+} phosphor has been examined at

different excitation wavelengths and revealed sharp emission positions at 579nm, 592nm, 612nm, and 622nm corresponding to $^5D_0 \rightarrow ^7F_0$, $^5D_0 \rightarrow ^7F_1$, $^5D_0 \rightarrow ^7F_2$, and $^5D_0 \rightarrow ^7F_3$ transition of Eu^{3+} ions in the host. At the excitation of 466nm, emission intensity at 612nm ($^5D_0 \rightarrow ^7F_2$) is much higher than 592nm ($^5D_0 \rightarrow ^7F_1$), exhibits dominance of electric dipole (ED) transition. The CIE values are located at (0.6620, 0.3488) with color purity 97.66% confirm that the reported sample is a potential candidate as a blue exciting red-emitting phosphor for w-LEDs.

REFERENCES

- [1] R. P. de Oliveira, J. Benvenuti, and D. C. R. Espinosa, "A review of the current progress in recycling technologies for gallium and rare earth elements from light-emitting diodes," *Renew. Sustain. Energy Rev.*, vol. 145, no. January, p. 111090, 2021, doi: 10.1016/j.rser.2021.111090.
- [2] H. Lin *et al.*, "Stable and efficient hybrid Ag-In-S/ZnS@SiO₂-carbon quantum dots nanocomposites for white light-emitting diodes," *Chem. Eng. J.*, vol. 393, no. March, p. 124654, 2020, doi: 10.1016/j.cej.2020.124654.
- [3] M. D. Mehare, C. M. Mehare, H. C. Swart, and S. J. Dhoble, "Recent development in color tunable phosphors: A review," *Prog. Mater. Sci.*, vol. 133, no. August 2022, p. 101067, 2023, doi: 10.1016/j.pmatsci.2022.101067.
- [4] M. D. Mehare, "Synthesis and novel emission properties of Bi³⁺-doped Ca₂BO₃Cl phosphor for plant cultivation," no. November 2022, pp. 4–11, 2023, doi: 10.1002/bio.4418.
- [5] C. M. Mehare, N. S. Dhoble, C. Ghanty, and S. J. Dhoble, "Photoluminescence and thermoluminescence characteristics of CaAl₂Si₄O₁₂:Dy³⁺ new phosphor prepared by combustion synthesis," *J. Mol. Struct.*, vol. 1227, p. 129417, 2021, doi: 10.1016/j.molstruc.2020.129417.
- [6] S. Ahmad, S. Das, R. Nagarajan, and G. Vijaya Prakash, "Optical properties of Tb³⁺ doped KLaF₄ in cubic and hexagonal symmetries," *Opt. Mater. (Amst.)*, vol. 36, no. 2, pp. 396–401, 2013, doi: 10.1016/j.optmat.2013.09.031.
- [7] R. Kumar, M. Nyk, T. Y. Ohulchanskyy, C. A. Flask, and P. N. Prasad, "Combined optical and MR bloimaging using rare earth ion doped NaYF₄ nanocrystals," *Adv. Funct. Mater.*, vol. 19, no. 6, pp. 853–859, 2009, doi: 10.1002/adfm.200800765.
- [8] S. Sivakumar, F. C. J. M. Van Veggel, P. S. May, V. Uni, and P. O. Box, "Near-Infrared (NIR) to Red and Green Up-Conversion Emission from Silica Sol - Gel Thin Films Made with Energy Transfer (Hetero-LEET): A New Up-Conversion Process," *J. Am. Chem. Soc.*, no. c, pp. 620–625, 2007.
- [9] D. Chen, Y. Wang, Y. Yu, and P. Huang, "Intense ultraviolet upconversion luminescence from Tm³⁺/Yb³⁺:β-YF₃ nanocrystals embedded glass ceramic," *Appl. Phys. Lett.*, vol. 91, no. 5, pp. 30–33, 2007, doi: 10.1063/1.2767988.
- [10] X. Zhang, T. Hayakawa, M. Nogami, and Y. Ishikawa, "Variation in Eu³⁺ luminescence properties of GdF₃:Eu³⁺ nanophosphors depending on matrix GdF₃ polytype," *J. Alloys Compd.*, vol. 509, no. 5, pp. 2076–2080, 2011, doi: 10.1016/j.jallcom.2010.10.143.
- [11] S. Das, A. Amarnath Reddy, S. Ahmad, R. Nagarajan, and G. Vijaya Prakash, "Synthesis and optical characterization of strong red light emitting KLaF₄:Eu³⁺ nanophosphors," *Chem. Phys. Lett.*, vol. 508, no. 1–3, pp. 117–120, 2011, doi: 10.1016/j.cplett.2011.04.029.
- [12] Y. X. Han, Q. N. Li, H. Y. Shen, and Q. H. Yang, "Synthesis, Characterization and Optical Property of KLaF₄:Ce³⁺ Nano Particle," *Appl. Mech. Mater.*, vol. 778, no. 3, pp. 183–186, 2015, doi: 10.4028/www.scientific.net/amm.778.183.
- [13] G. Wang and Q. Peng, "Tunable photoluminescence of NaYF₄:Eu nanocrystals by Sr²⁺ codoping," *J. Solid State Chem.*, vol. 184, no. 1, pp. 59–63, 2011, doi: 10.1016/j.jssc.2010.10.030.
- [14] G. Yi, H. Lu, S. Zhao, Y. Ge, and W. Yang, "Synthesis, Characterization, and Biological Application of Size-Controlled Nanocrystalline NaYF₄:Yb,Er Phosphors," *Nano Lett.*, vol. 4, no. 11, pp. 2191–2196, 2004.
- [15] Y. Huang, L. Shi, E. S. Kim, and H. J. Seo, "Site-selective spectroscopy and crystallographic sites of Eu³⁺ ions doped in Gd₂BaZnO₅," *J. Appl. Phys.*, vol. 105, no. 1, pp. 5–10, 2009, doi: 10.1063/1.3056167.
- [16] Q. Ma, Y. Zhou, A. Zhang, M. Lu, G. Zhou, and C. Li, "Synthesis and optical properties of novel red phosphors YNbTiO₆:Eu³⁺ with highly enhanced brightness by Li⁺ doping," *Solid State Sci.*, vol. 11, no. 6, pp. 1124–1130, 2009, doi: 10.1016/j.solidstatesciences.2009.02.018.
- [17] G. Annadurai *et al.*, "Novel Eu³⁺-activated Ba₂Y₅B₅O₁₇ red-emitting phosphors for white LEDs: high color purity, high quantum efficiency and excellent thermal stability," *RSC Adv.*, vol. 8, no. 41, pp. 23323–23331, 2018, doi: 10.1039/c8ra03059f.
- [18] Y. Zhu *et al.*, "Chemical bond parameters, charge transfer band in Eu³⁺-activated La₂Mo₂O₉ phosphors based on complex chemical bond theory," *Ceram. Int.*, vol. 46, no. 11, pp. 18184–18192, 2020, doi: 10.1016/j.ceramint.2020.04.140.
- [19] H. Guo, X. Huang, and Y. Zeng, "Synthesis and photoluminescence properties of novel highly thermal-stable red-emitting Na₃Sc₂(PO₄)₃:Eu³⁺ phosphors for UV-excited white-light-emitting diodes," *J. Alloys Compd.*, vol. 741, pp. 300–306, 2018, doi: 10.1016/j.jallcom.2017.12.316.
- [20] R. Guo, S. Tang, B. Cheng, and D. Tan, "A new red emitting phosphor: La₂SrB₁₀O₁₉:Eu³⁺," *J. Lumin.*, vol. 138, pp. 170–173, 2013, doi: 10.1016/j.jlumin.2013.02.008.
- [21] H. Y. Chen, H. L. Lai, R. Y. Yang, and S. J. Chang, "Effect of different alkali carbonate on the microstructure and photoluminescent properties of YInGe₂O₇:Eu³⁺ phosphors," *J. Mater. Sci. Mater. Electron.*, vol. 27, no. 3, pp. 2963–2967, 2016, doi: 10.1007/s10854-015-4116-7.

- [22] W. B. Dai, M. Zhou, Z. Y. Xian, and L. K. Zeng, "Structure and photoluminescence characteristics of europium(iii) doped in $\text{CaAl}_2\text{Si}_2\text{O}_8$ phosphors," *RSC Adv.*, vol. 4, no. 49, pp. 25470–25478, 2014, doi: 10.1039/c4ra02213k.
- [23] X. Huang, B. Li, H. Guo, and D. Chen, "Molybdenum-doping-induced photoluminescence enhancement in Eu^{3+} -activated CaWO_4 red-emitting phosphors for white light-emitting diodes," *Dye. Pigment.*, vol. 143, pp. 86–94, 2017, doi: 10.1016/j.dyepig.2017.04.037.
- [24] Q. Zhang, X. Wang, X. Ding, and Y. Wang, "A Potential Red-Emitting Phosphor $\text{BaZrGe}_3\text{O}_9:\text{Eu}^{3+}$ for WLED and FED Applications: Synthesis, Structure, and Luminescence Properties," *Inorg. Chem.*, vol. 56, no. 12, pp. 6990–6998, 2017, doi: 10.1021/acs.inorgchem.7b00591.
- [25] P. N. Parale, A. R. Kadam, K. V Dabre, and S. J. Dhoble, "Design efficient energy transfer $\text{Dy}^{3+}, \text{Eu}^{3+}$ activated / co-activated $\text{NaMg}(\text{PO}_3)_3$ phosphor for WLEDs : Photochromaticity and structural analysis," *Inorg. Chem. Commun.*, vol. 154, no. June, p. 110974, 2023, doi: 10.1016/j.inoche.2023.110974.
- [26] P. Dewangan, D. P. Bisen, N. Brahme, and S. Sharma, "Structural characterization and luminescence properties of Dy^{3+} doped $\text{Ca}_3\text{MgSi}_2\text{O}_8$ phosphors," *J. Alloys Compd.*, vol. 777, pp. 423–433, 2019, doi: 10.1016/j.jallcom.2018.10.390.
- [27] S. Som *et al.*, "The energy transfer phenomena and colour tunability in $\text{Y}_2\text{O}_2\text{S}:\text{Eu}^{3+}/\text{Dy}^{3+}$ micro-fibers for white emission in solid state lighting applications," *Dalt. Trans.*, vol. 43, no. 26, pp. 9860–9871, 2014, doi: 10.1039/c4dt00349g.

¹Farhan Kaleem
Ahmed

^{2*}Kalpana H Adhau

³Smita Acharya

⁴Mahesh Gaidhane

⁵Deepak Taikar

^{6*}Umesh A
Palikundwar

Synthesis and Characterization of iron (Fe) Doped Tungsten Oxide (WO₃) as an Electrolyte Material



Abstract

The fuel cell generates electricity by taking the natural gases as fuel. One of great advantages of fuel cell is its efficiency. Electrolyte materials in solid oxide fuel cells (SOFCs) play as key role for deciding its operating temperature. Nowadays, researchers are trying to increase the ionic conductivity of electrolyte material at low temperature which is a challenging task. In this research paper, 2%Fe doped WO₃, is used as an electrolyte material for low-temperature SOFCs (LTSOFCs). X-ray diffraction pattern revealed monoclinic structure with the P21/n space group. Scanning electron microscopic study (SEM) shows the surface morphology with highly dense structure which results in better electrochemical performance than other electrolyte material. FTIR analysis revealed the chemical bonds present in the material. The electrochemical study at different temperature shows that Fe doped WO₃ exhibits significant potential as an electrolyte material for Low temperature SOFC.

Keywords: Solid oxide fuel cell, SEM, Electrochemical characterization, electrolyte

¹Author 1 Affiliation X-ray Research Laboratory, Department of Physics, Rashtrasant Tukadoji Maharaj Nagpur University, Nagpur 440033

^{2*}Author 2 Affiliation Department of Physics, Institute of Science, Nagpur 440002

³Author 3 Affiliation Advanced Materials Research Laboratory, Department of Physics, Rashtrasant Tukadoji Maharaj Nagpur University, Nagpur 440033

⁴Author 3 Affiliation Department of Physics, Shri Lemdeo Patil Mahavidyalaya, Mandhal, Nagpur 440001

⁵Author 3 Affiliation Department of Physics, Shri Lemdeo Patil Mahavidyalaya, Mandhal, Nagpur 440001

^{6*}Author 3 Affiliation X-ray Research Laboratory, Department of Physics, Rashtrasant Tukadoji Maharaj Nagpur University, Nagpur 440033

*Email id:

kalpana.nagle@gmail.com (Kalpana H. Adhau)

uapali@yahoo.com (Umesh A. Palikundwar)

Introduction

Solid oxide fuel cells (SOFCs) use natural gases as fuel and convert them into electricity via an electrochemical reaction, resulting in a high efficiency of around 60% [1]. SOFCs made up of a cathode electrolyte and an anode. The electrolyte plays a crucial role in determining the operating temperature of SOFCs. Moreover, many researchers have focused on developing high-ionic conductive electrolyte materials at low temperatures to reduce operating temperature [2]. Next-generation energy sources need to rely less on fossil fuel burning because to variable fuel costs and environmental concerns. SOFCs are projected to significantly impact the future of energy technology [3]. It is a well-known fact that the lower operating temperature, 450-650°C, can improve stability and minimize costs by reducing thermal and chemical stresses, expanding material options, reducing energy usage, and enabling faster start-up times for portable applications. SOFCs operating temperature can be reduced by lowering the electrolyte resistance. The resistance of electrolyte material will be reduced by replacing well-established yttrium-stabilized zirconium (YSZ) electrolyte with the materials having better ionic conductivity [4]. The low ionic conductivity of YSZ's makes it unsuitable for use as an electrolyte in SOFCs at temperatures below 800°C [5].

According to literature survey it has been observed that Fe-doped WO_3 increases the dielectric parameter due to polarization and in turn the ionic conductivity [6-8]. Therefore, in present work an attempt was done for the synthesis of the 2% doped WO_3 (abbreviated as FW02) as an electrolyte material at low temperature.

Experimental

FW02 was prepared using the aqueous nitrate sulfate solution method. Ferric nitrate (Himedia Hi-AR purity 99.000-102.00%), and tungsten oxide (WO_3) were used as initial ingredients. All initial ingredients were taken in stoichiometric amounts for the preparation of FW02. The sulfate solution of WO_3 and the nitrate solution of ferric nitrate were prepared. Later, both solutions were mixed and stirred for 10 minutes to form a homogeneous mixture. The final solution was then dried overnight in the furnace at 200 °C. The dried powder was crushed using a mortar and pestle, calcined at 500 °C for 5 hours to remove nitrate and sulfate contents. Then 2 to 3 drops of PVA (Polyvinyl Alcohol) were added as a binding agent to make the pellets. The final heat treatment of pellets was done at 950 °C for 12 hours. The samples were cooled in a furnace to room temperature. Here, tungsten oxide WO_3 (W0) with a Himedia purity of 98%, was used as the standard sample for comparison purpose.

X-ray powder diffraction (XRD) study was used to characterize the sample using a Rigaku table top X-ray diffractometer with a copper target ($\text{CuK}\alpha = 1.5405 \text{ \AA}$, filament current = 15mA, operating voltage = 40 kV). The step size was kept at 0.04 and the scanning speed was 5 degrees per minute. The microstructural investigation of sintered pellets was performed with the help of scanning electron microscopy (SEM) utilizing Model ZIESS EVO18 with accelerating voltage of 0.2 to 5 kV and filament current of 2.56 A. FT-

IR spectroscopy was performed to detect the different bonds in the samples under study using the JASCO 4700 FTIR model.

The electrochemical performance of the NW02 sample was determined using electrochemical impedance spectroscopy. NW02 pellets were coated with silver paste using xylene to achieve a homogenous paste. To ensure appropriate contact between the pellet and the electrode, the silver paste was first dried at room temperature before being baked for 5 hours in an oven at 150 °C. An impedance study was performed at 300-400°C using the Metro ohm Auto lab model 204. The optimum AC voltage was 25mV in a frequency range of 0.1Hz to 1MHz. The collected EIS data were finally analyzed using the Nova 2.1.1 software.

Results and Discussion

X-ray powder diffraction

Figure 1 shows the comparison of X-ray diffraction patterns of FW02 and pure tungsten oxide (W0) with standard COD file (No. 1010618). The XRD peaks of W0 and FW02 are indexed, showing a highly crystalline monoclinic phase of both pure and doped material. The 2 % Fe doped material attained monoclinic phase which is in good agreement with reported data[9, 10]. The main diffraction peaks of all samples under study are located at 2θ of 23.1, 23.6, 24.4, 33.3, 34.06, 34.18, 41.50, 41.86 and 49.94 and well indexed to (002), (020), (200), (022), (20 $\bar{2}$), (220), (220), (22 $\bar{2}$) and (400) planes, respectively corresponds to a typical monoclinic structure. A detailed examination of Figure 1 of FW02 shows the absence of secondary phases, demonstrating the effective replacement of the W⁶⁺ ions by the Fe³⁺ ions. Thus, it can be conclude that Fe goes entirely to the site of tungsten oxide. Figure 2 shows a magnified image of the X-ray powder diffraction patterns in the 2θ range, 22 to 26 degrees of W0 and FW02. A close look of Figure 2 shows that the diffraction peaks (002), (020), and (200) are shifted to higher angle after 2% doping of Fe. Strong evidence for the existence of WO₃ in the monoclinic phase is provided by this matching planes more intense triplet [11]. The shift in lattice parameter values confirms that Fe has been effectively doped into WO₃[8].

Rietveld refinement analysis is done using FullProf software. Rietveld refinement analysis of FW02 is given in Figure 3 which confirms the monoclinic phase with space group P2₁/n. The bottom curve displays the discrepancy between estimated and refined intensities to the crystallographic model and experimental measurements. The locations of the Bragg reflections are indicated by the vertical tick marks. The comparison of lattice parameters of W0 and FW02 are listed in Table 1, which shoes increase in lattice parameter, is good agreement of earlier reported lattice parameter by TengZhanga et al[9].

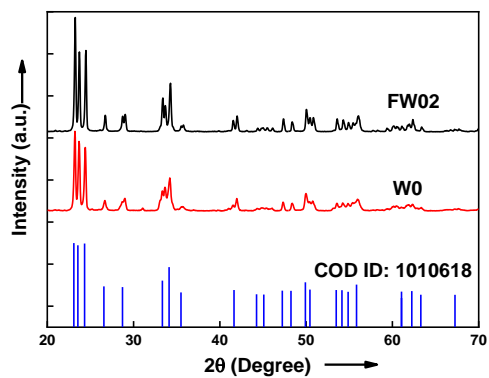


Fig.1 XRD patterns of W0 and FW02 with standard COD pattern.

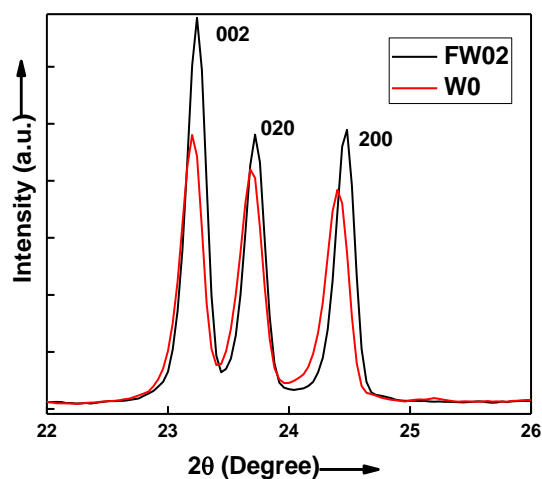


Fig.2 Enlarged views of X-ray powder diffraction patterns in 2θ range of 22 to 26 degree of W0 and FW02.

Fig.1 XRD patterns of W0 and FW02 with standard COD pattern.

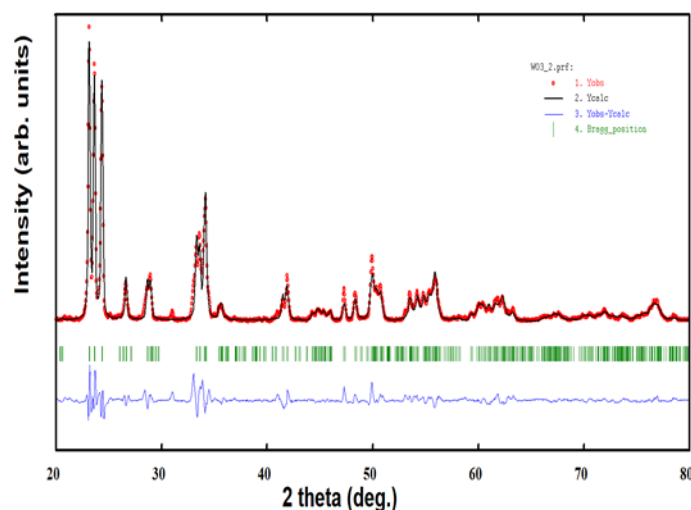


Fig.3Rietveld refinement of FW02.

Table1. Comparison of lattice parameters of standardW0 and FW02.

Samples	a (Å)	b (Å)	c (Å)	α	β	γ
W0	7.298391	7.531981	7.684532	90	89.287	90
FW02	7.310525	7.528165	7.686395	90	89.218	90

Scanning electron microscopy (SEM)

Figure 4 shows the scanning electron microphotographs of FW02. A cursory look at the Figure 3 clearly indicates that FW02 becomes more dense and homogenous after sintering. The statistically analysis of particle size distribution was determined using the ImageJ software. The particle size distribution map reveals particle sizes ranging from 0.5 to 3 microns, with an average size of 2 microns. Therefore, the average grain size of FW02 is 2 μm . So, it can be said that this densified material can be used as an electrolyte for SOFCs.

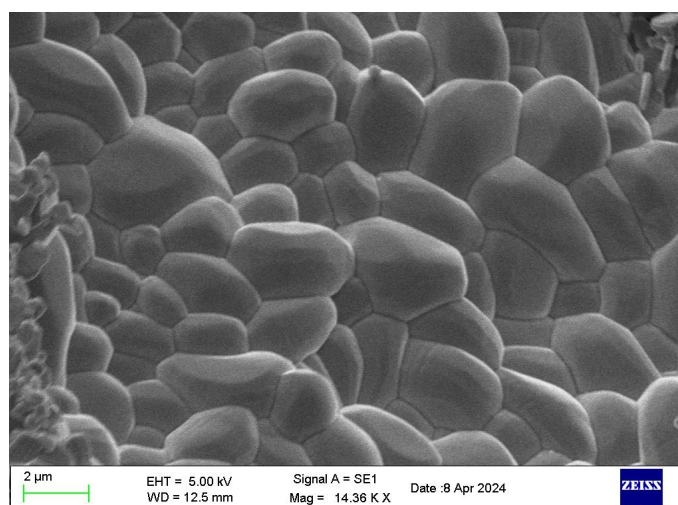


Fig.4SEM images of Sintered FW02.

Fourier Transform Infrared spectroscopy (FTIR)

Figure 5 shows the FTIR spectra of W0 and FW02 in the range of 500 to 4000 cm^{-1} . All spectra show comparable IR active bands. The wide bands of about 600 cm^{-1} are attributed to stretching vibrations of the O-W-O bond [13]. The band at 3660 cm^{-1} represents the hydrogen-bonded OH stretching vibrations of water molecules that are absorbed by KBr from moisture. The band at 1397 cm^{-1} is caused by stretching vibrations of the C-O bond, while the band at 1065 cm^{-1} is caused by C-O-C stretching of adsorbed CO_2 molecules from the atmosphere [14]. It is interesting to note here that the iron oxide bands are absent which indicates that the Fe^{3+} ions are successfully incorporated at WO_3 lattice site. This is also in good agreement with earlier reporting [8].

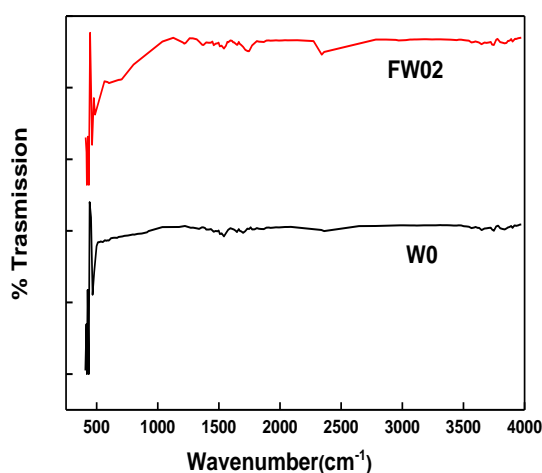


Fig. 5 FTIR spectra of W0 and FW02.

Electrochemical impedance spectroscopy (EIS)

EIS data in the low temperature range were collected and used to calculate their ionic conductivities and represented in Figure 6. The EIS of FW02 was carried out of temperatures range 300 to 400°C with intervals of 50°C. Ionic conductivity data is extracted from fitted data using equation 1.

$$\sigma = L / (R \times S) \quad \dots \dots \quad (1)$$

Where S is the area of pellet in cm^2 , R is the bulk resistance in ohm (Ω), and L is the thickness of pellet in cm [17].

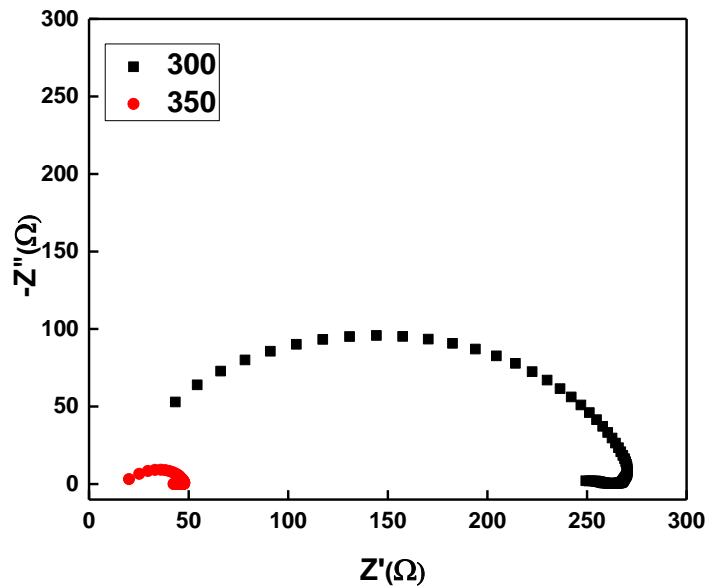


Fig.6 Impedance spectra of FW2 sample at different temperatures

Bulk resistance is represented by the high frequency side semicircle passing through the origin, whereas the grain boundary is represented by the arc in the middle frequency band. The low frequency range is characterized by complicated electrode behavior, including many arcs [15]. It is clear from Figure 6 that electrolyte's grain boundary arc's radius reduces with increase in temperature.

The semicircle has a minimum radius of FW02 pellet at temperature 400°C. Increased carrier ions and ionic mobility can cause a decrease in bulk resistance[16]. Impedance spectra of FW02 with equivalent circuit diagram at 300 °C is depicted in Figure 7. The polarisation and ohmic resistances (R_s and R_p) provide information about the charge transfer. Furthermore, the Ohmic resistance (R_s) corresponds to the intersection of the EIS curve at the high frequency on the real axis of resistance, which is usually provided by the ionic transport resistance in the electrolyte layer.

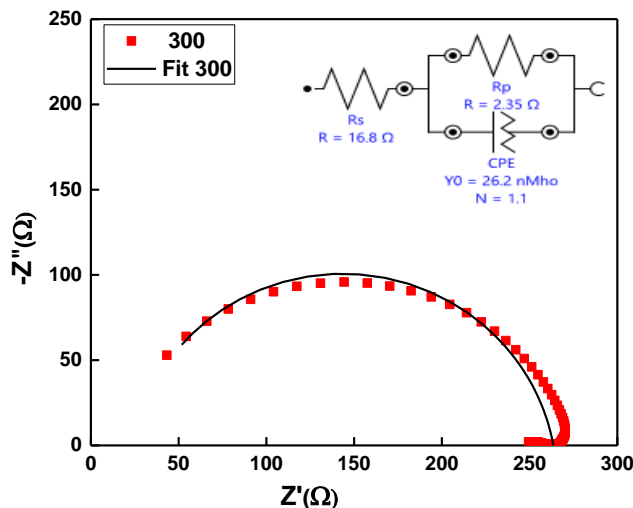


Fig.7 Impedance spectra with fitted line along with equivalent circuit diagram of FW02 at 300 °C.

The ionic conductivity of the FW02 listed in table 3 with respect to temperature. It is evident that conductivity increases with temperature. Due to the thermal vibrations of the ceramic lattice and the increasing ion vacancies, It can be seen that the conductivity increases with increasing temperature due to the increased ion vacancies and the thermal vibrations of the ceramic lattice. This indicates that doping of Fe in place of W increases the faster charge diffusion and mass transfer processes. Parameters obtained from fitting of experimental EIS spectra for FW02 are given in table 2. By observing the fitted data of FW02, it is shown that while the Rp value decreases with respect to temperature, which leads to increase in FW02 ionic conductivity.

Table2. Parameters obtained from fitting of experimental EIS spectra for FW02.

Samples	a (Å)	b (Å)	c (Å)	α	β	γ
W0	7.298391	7.531981	7.684532	90	89.287	90
FW02	7.310525	7.528165	7.686395	90	89.218	90

Table3. Ionic Conductivities of FW02 at different temperature.

Temp(°C)	Rs(Ω)	Rp(Ω)	CPE1(nMho)
300	23.5	240	12.7
350	15	31.2	155

Temp (°C)	σ (S/cm)
300	0.0096
350	0.01504

It is found that ionic conductivity increases after 2% Fe doping in WO₃. The ionic conductivity of value of FW02 is 0.01504 S/cm at 350 °C.

Conclusion

In present study, a new dopant iron (Fe) is used in tungsten oxide system as an electrolyte material. A monoclinic crystal structure is obtained for FW02. FTIR study indicate the presence of W-O bond in FW02 sample. The ionic conductivity is 0.01504 S/cm at 350°C. The value of ionic conductivity is more as compared to other system mentioned in the literature at 350°C. In nutshell, it can be said that FW02 can be considered as potential electrolyte material for low temperature SOFCs.

References

- [1] Wachsman, E. D., & Lee, K. T. (2011). Lowering the temperature of solid oxide fuel cells. *Science*, 334(6058), 935-939.
- [2] Lee, K. T., Yoon, H. S., & Wachsman, E. D. (2012). The evolution of low temperature solid oxide fuel cells. *Journal of Materials Research*, 27(16), 2063-2078.
- [3] Wachsman, E. D., & Singhal, S. C. (2009). Solid oxide fuel cell commercialization, research, and challenges. *The Electrochemical Society Interface*, 18(3), 38.
- [4] Jung, D. W., Duncan, K. L., & Wachsman, E. D. (2010). Effect of total dopant concentration and dopant ratio on conductivity of $(\text{DyO}_{1.5})_x (\text{WO}_3)_y (\text{BiO}_{1.5})_{1-x-y}$. *Acta Materialia*, 58(2), 355-363
- [5] Etsell, T. H., & Flengas, S. N. (1970). Electrical properties of solid oxide electrolytes. *Chemical Reviews*, 70(3), 339-376.
- [6] Jimenez-Angeles, F., Ehlen, A., & de la Cruz, M. O. (2023). Surface polarization enhances ionic transport and correlations in electrolyte solutions nanoconfined by conductors. *Faraday Discussions*, 246, 576-591
- [7] Dos Santos, A. P., Jimenez-Angeles, F., Ehlen, A., & Olvera de la Cruz, M. (2023). Modulation of ionic conduction using polarizable surfaces. *Physical Review Research*, 5(4), 043174.
- [8] Antony, A. J., Joel, C., Bennie, R. B., Kala, S. M. J., & Jemima, J. R. (2023). Enhancing the optical, temperature-dependent electrical and dielectric properties of WO_3 through Fe doping for optoelectronic applications. *Journal of Materials Science: Materials in Electronics*, 34(8), 761.
- [9] Zhang, T., Zhu, Z., Chen, H., Bai, Y., Xiao, S., Zheng, X., & Yang, S. (2015). Iron-doping-enhanced photoelectrochemical water splitting performance of nanostructure WO_3 : a combined experimental and theoretical study. *Nanoscale*, 7(7), 2933-2940.
- [10] Pitak, G., Srisodsai, S., & Termtanun, M. (2018). Effect of doping Fe/Cu/Ti on WO_3 on furfural degradation. In *MATEC Web of Conferences* (Vol. 192, p. 03048). EDP Sciences
- [11] Sivakumar, R., Raj, A. M. E., Subramanian, B., Jayachandran, M., Trivedi, D. C., & Sanjeeviraja, C. (2004). Preparation and characterization of spray deposited n-type WO_3 thin films for electrochromic devices. *Materials Research Bulletin*, 39(10), 1479-1489.
- [12] Yang, M., Lu, F., Zhou, T., Zhao, J., Ding, C., Fakhri, A., & Gupta, V. K. (2020). Biosynthesis of nano bimetallic Ag/Pt alloy from *Crocus sativus* L. extract: Biological efficacy and catalytic activity. *Journal of Photochemistry and Photobiology B:*

Biology, 212, 112025.

- [13] Aslam, I., Farooq, M. H., Iqbal, M. W., Boddula, R., Abid, M., Ashfaq, M., & Ghani, U. (2019). Synthesis of $\text{WO}_3 \cdot \text{H}_2\text{O}$ spherical particles for efficient photocatalytic properties under visible light source. *Materials Science for Energy Technologies*, 2(2), 187-193.
- [14] Jiang, W., Yang, K., Vachet, R. W., & Xing, B. (2010). Interaction between oxide nanoparticles and biomolecules of the bacterial cell envelope as examined by infrared spectroscopy. *Langmuir*, 26(23), 18071-18077.
- [15] Shirbhate, S., Nayyar, R. N., Ojha, P. K., Yadav, A. K., & Acharya, S. (2019). Exploration of atomic scale changes during oxygen vacancy dissociation mechanism in nanostructure co-doped ceria: as electrolytes for IT-SOFC. *Journal of The Electrochemical Society*, 166(8), F544.
- [16] Bredar, A. R., Chown, A. L., Burton, A. R., & Farnum, B. H. (2020). Electrochemical impedance spectroscopy of metal oxide electrodes for energy applications. *ACS Applied Energy Materials*, 3(1), 66-98
- [17] Zhu, F., Bao, H., Wu, X., Tao, Y., Qin, C., Su, Z., & Kang, Z. (2019). High-performance metal-organic framework-based single ion conducting solid-state electrolytes for low-temperature lithium metal batteries. *ACS applied materials & interfaces*, 11(46), 43206-43213.

Ashok B. Nawale1*,
Gayatri Sutrale1,
Harshali Chaitwar1,
Satyappa R. Jigajeni1

Structural and Optical Properties Study of ZnO Thin Films Prepared by Spin Coating Method



Abstract: - Here we report the preparation of ZnO thin films by spin coating method. The as prepared ZnO thin films were found to be polycrystalline in nature having hexagonal (wurtzite) structure as confirmed by X-ray diffraction. The ZnO crystallites are preferentially oriented along (002) planes parallel to the substrate surface for the films annealed for 2hrs of duration which are then becomes polycrystalline with increasing the duration time from 4hrs to 6 hrs. The films have high transparency which is observed to be decreased with increasing the number of cycles. The transparency of the films is also found to be dependent of the annealing temperature and annealing time. The absorption spectra analysis of the as prepared films shows the direct nature of band-to-band transitions. The band gap energy is found to be increases with increasing the number of deposition cycles. The band gap energy is also found to be dependent on the annealing temperature and duration of annealing temperature. Moreover, interestingly the tauc plot show the intermediate energy level for all the samples in between 2.88 eV to 2.91 eV, which is found to be influenced by the preparation conditions. The structural and optical properties were correlated with the preparation parameters of the ZnO thin films.

Keywords: Defects, Spin Coating, X-ray Diffraction, ZnO

I. INTRODUCTION

Among the various semiconductors zinc oxide is an inexpensive n-type semiconductor having wide band gap of 3.37 eV which is observed in two different structural forms namely hexagonal wurtzite and cubic zinc blende [1]. It is widely used in various applications such as ceramics, paints, pigments, lubricant, paste, ferrites, batteries, food industry and so on [2]. The various methods are used for the preparation of thin films of zinc oxide such as Sol-Gel [3], Chemical Bath Deposition [4], Spray Pyrolysis [5], SILAR [6], Laser Ablation [7], Chemical Vapor Deposition [8], Spin Coating [2]. Out of these the sol-gel spin coating method is more suitable due to their advantages such as easy to prepare, control of chemical compositions, ability to produce fine structures and control on film thickness and low cost. Various researchers have already been reported the relation between spin coating parameters with structural and optical properties of ZnO thin films.

Here we report the preparation of zinc oxide thin films by spin coating method. The effect of number of cycles and calcination temperature on structural and optical properties is reported.

II. EXPERIMENTAL

ZnO films were deposited on glass substrate using the spin-coating method (Model No.: HO-TH05) at room temperature and atmospheric pressure. Glass substrates were cleaned with distilled water, acetone and ethanol successively in an ultrasonic bath, and then dried under IR Lamp. The precursor solution for spin coating deposition was prepared by dissolving 1gm of zinc acetate in 10 ml ethanol. Then ammonia solution was added drop wise to form amino complex of zinc until the pH of solution was adjusted to ~10. This solution was then stirred for 15 min at room temperature to obtain a homogeneous solution. The obtained solution was deposited on the glass substrate by spin coating method at a spin rate of 1000 rpm for 30 sec. The deposited films were dried at a 55°C under IR lamp for 10 min. The films were prepared by repeating a 10, 15, 20 & 50 number of cycles of spin coating. For each deposition the film was dried under IR lamp for 10 minutes before the next cycle. Finally, the films which were prepared by repeating a 10, 15 and 20 number of cycles were annealed at 350, 400 and 450 degrees for 2hr, 4hr, 6hr respectively for complete oxidation. Whereas, the films which were prepared by repeating a 50 number of cycles was annealed at 450 degrees for 2hr, 4hr and 6hrs respectively.

III. RESULT AND DISCUSSION

Structural Analysis:

The crystal structure analysis of as prepared ZnO thin films is carried out by using X-ray diffraction method. Fig.3. shows X-ray diffraction patterns of ZnO thin films prepared for 10, 15 and 20 cycles and heat treated for 350 degrees, 400 degrees and 450 degrees respectively. It is clearly observed that all the samples show a very small peaks observed at around 2θ equal to 34.28, 31.36 and 31.14 degree corresponds to (100), (002) & (101) reflections respectively. Which are in agreement with those of the expected peaks of wurtzite structure of ZnO. These peaks are superposed to the diffuse scattering produced by the amorphous silica glass substrate. The observed diffraction peaks can be indexed to standard hexagonal wurtzite ZnO Structure.

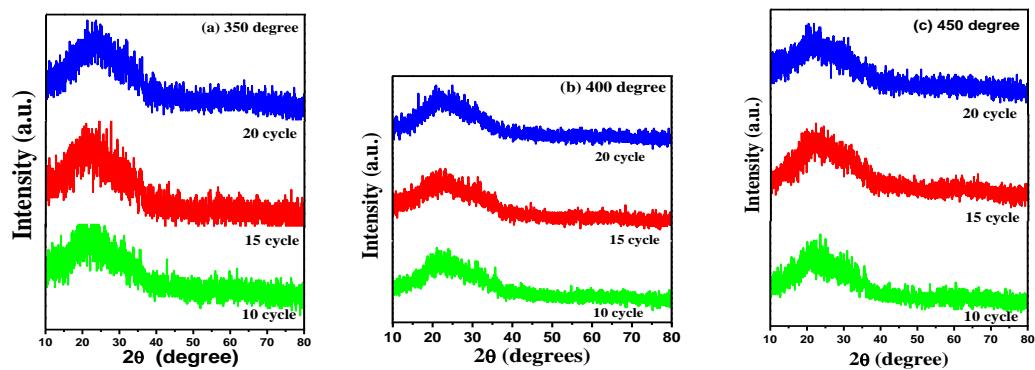


Fig.1.: X-ray diffraction patterns of ZnO thin films prepared for 10, 15 and 20 cycles and heat treated for a) 350 degree, (b) 400 degree and (c) 450 degree respectively.

To elaborate the impact of heating temperature and reaction media on growth of zinc oxide nanostructures the films are deposited for large number of cycles i.e. 50 cycles. Fig.2 (a) shows the normal XRD pattern of the films deposited for 50 cycles and heat treated at 2 hrs, 4hrs and 6 hrs respectively whereas the Fig.2. (b) shows the slow scan of the same films in between the 2θ values of 30 to 40 degree. It is observed that all the deposited and heat treated films show the broad peaks at around 2θ equal to 34.28, 31.36 and 31.14 degree corresponds to (100), (002) & (101) reflections respectively. Moreover, as we increase the heating temperature the peaks are observed to shift towards the lower 2θ values at the same time the peak intensity also decreases. The film heat treated at 2hrs show the (002) orientation which gradually decreases with increasing the heating time. Therefore, with increasing the heating period films get relaxed and transforms into the perfect Wurtzite structure of ZnO. The broad peaks observed in the XRD patterns are indicative of small particles.

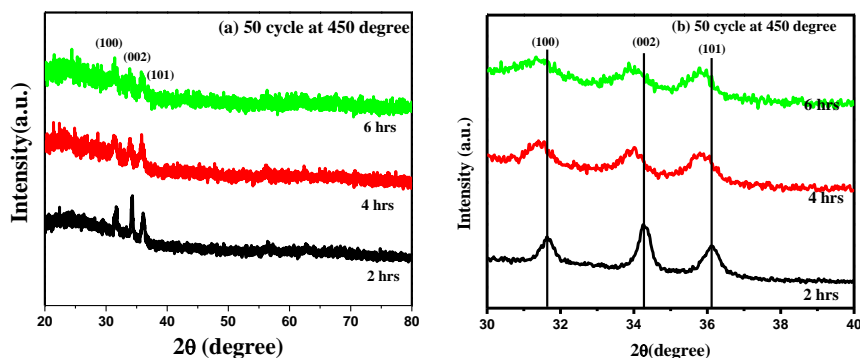


Fig. 2: (a) Normal X-ray diffraction pattern and (b) Slow scan of ZnO thin films prepared at 50 cycles and heat treated for 450 degrees for 2hrs, 4hrs and 6hrs respectively.

Furthermore, the increase of intensity, preferably the c-axis orientation along (002) plane was observed for the sample heated for 2 hours. It is worth to note that, the samples with a deposition of 50 cycles, as the heating time increases the intensity of (002) orientation decreases. This indicates that the crystallinity quality of ZnO film is cultivated with changing the heating time.

The crystallite size (D) of ZnO sample prepared at 50 cycles were calculated by using the well-known of Debye-Scherrer equation as follows:

$$D = 0.94 \lambda / B \cos \theta$$

Where, λ is the wavelength incident X-ray ($\lambda=1.5406\text{\AA}$) B is the full width at half maximum (FWHM), and θ is the diffraction angle at which the peak of a particular orientation occurs. The observed crystallite size for the samples calcined at 2hr, 4hr and 6hr was found to be around 25 nm, 14nm and 55 nm respectively.

Optical Properties Study:

UV-Visible Spectroscopy Study:

Fig.3. shows the absorbance spectra of the films prepared at 350, 400 and 450 degrees for 10, 15 and 20 cycles and heated at 2hr respectively. The inset of each graph shows the respective Tauc plot of $(\alpha h\nu)^2$ versus $h\nu$ which gives the band gap energy (E_g) for deposited material. The absorbance spectra of each sample shows the strong absorbance in the 300 nm to 400 nm of wavelength range. Moreover, each sample shows the small knee near the 360 nm of wavelength which indicates the presence of defect state. The band gap values calculated from the Tauc plots for ZnO thin films deposited for 10, 15 and 20 cycles via spin coating method and heat treated at 350, 400 and 450 degrees and are given in Table.1. The band gap value of ZnO thin films is found to be 3.98 eV, 3.95 eV, 3.97 eV and 3.88 eV for the deposition cycles of 10, 15, 20 and 50 and heat treated for 2 hrs. respectively. The observed increase in band gap value with increasing the number of deposition cycles is quite obvious due to the increase in film thickness with the number of deposition cycle.

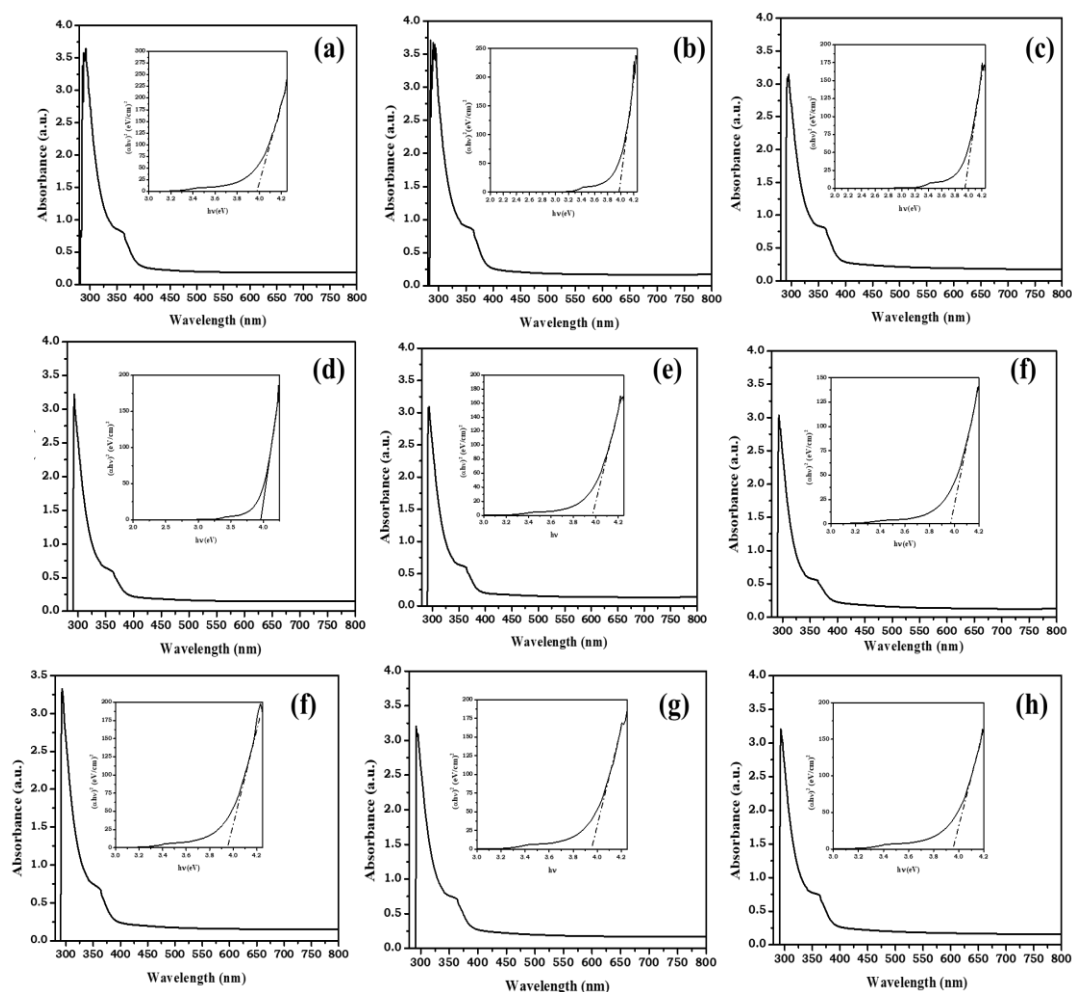


Fig.3.: The absorbance spectra of the films prepared at 350, 400 and 450 degrees for 10, 15 and 20 cycles and heated at 2hrs respectively.

Table.1.: Calculated band gap for thin films deposited for 10, 15, 20 and 50 cycles.

Heating Temperature (for 2hrs.)	BandGap values (eV)	BandGap values (eV)	BandGap values (eV)	BandGap values (eV)
	10 cycle	15 cycles	20 cycles	50 cycles
350	3.98	3.97	3.95	3.88eV(2 hrs)
400	3.98	3.97	3.95	3.86eV(4 hrs)
450	3.95	3.97	3.95	4.01eV(6 hrs)

Fig.4. shows the absorbance spectra of the samples prepared at 50 cycle and heated at 450 degree for 2hrs. 4 hrs. and 6 hrs respectively. The inset shows the tauc plots of the respective samples. The band gap value of ZnO thin films is found to be 3.88 eV, 3.86 eV and 4.01 eV for the samples heat treated at 2hrs. 4 hrs. and 6 hrs. respectively.

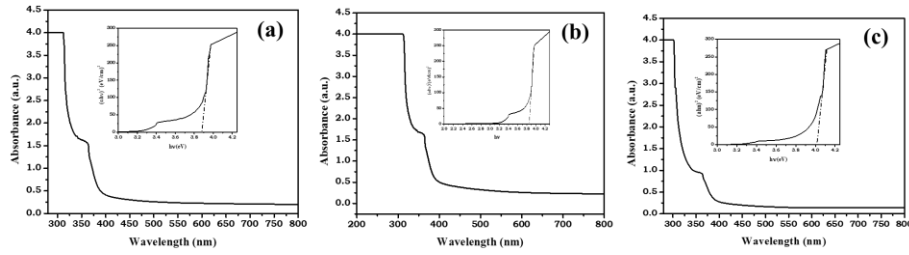


Fig.4.: The absorbance spectra of the samples prepared at 50 cycle and heated at 450 degrees for 2hrs. 4 hrs. and 6 hrs. respectively.

Fourier Transform Infrared Spectroscopy:

A typical FTIR spectrum of the ZnO in the frequency range from 500 to 4500 cm^{-1} is shown in Fig.5. It is observed that, the peaks appearing in the spectra are characteristics of the material structure. It is observed that the broad peak observed in the spectra at around 500 cm^{-1} of wavenumber corresponds to prominent symmetric stretching vibration of low frequency Zn-O band in ZnO lattice. All the samples show this band confirms the formation of ZnO structure and absence of any other peak in the spectra gives the purity of the sample.

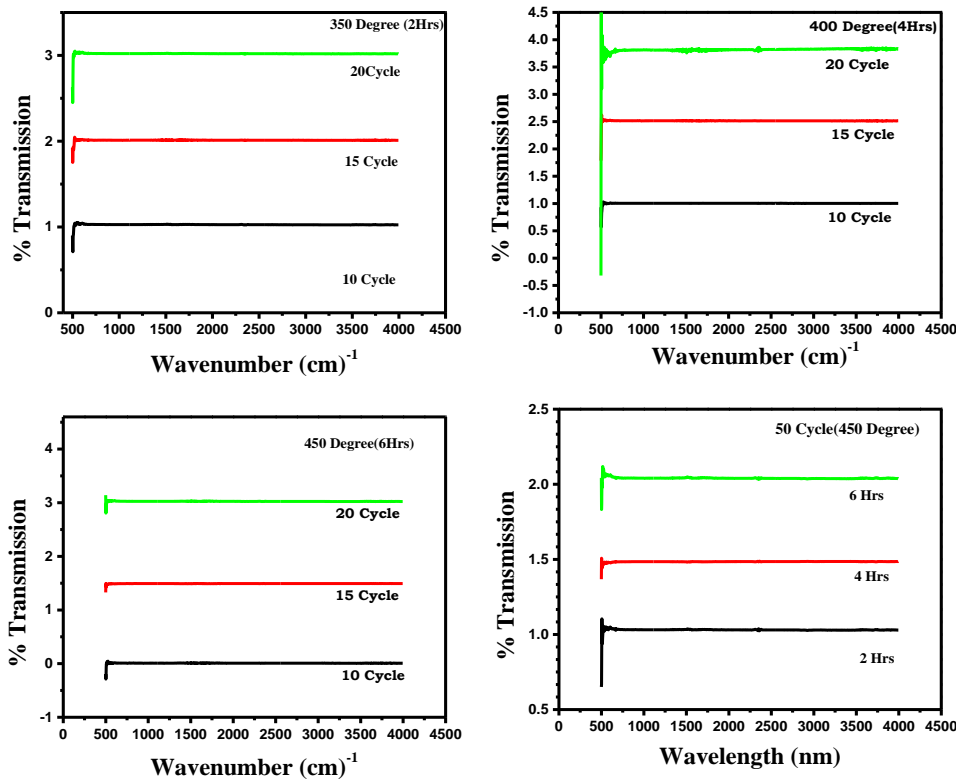


FIG. 5.: FTIR SPECTRA OF AS PREPARED ZnO THIN FILMS.

IV. CONCLUSION

In conclusion we have successfully prepared the ZnO thin films by spin coating method. An attempt has been made to prepare the ZnO thin films for different deposition cycles. The phase formations of all samples were confirmed by XRD study. The preferential growth of the film along c-axis oriented along (002) direction is observed for the sample heated at different temperature for 2hrs. As the heating period increases the sample becomes more polycrystalline having wurtzite structure. We have studied the effect of deposition cycles on the crystallinity and size of the crystallite. The crystallite size is observed to be increased with increasing the period of heating from 2hrs to 6hrs. The band gap calculation was done from tauc plots for all the as prepared samples. The value of band gap is found to be increased with increasing the deposition cycles as well as the heating temperature and duration of heating. FTIR analysis shows the presence of broad peak observed near 500 cm⁻¹ of wavenumber which corresponds to Zn-O stretching in ZnO lattice.

ACKNOWLEDGMENT

The authors would like to thanks Head, Department of Physics and Electronics, Government Vidarbha Institute of Science and Humanities, Amravati for their guidance and support during this study. Authors also acknowledges Director, Government Vidarbha Institute of Science and Humanities, Amravati for providing necessary facilities to complete this study.

REFERENCES

- [1] T. Srinivasulu, K. Saritha, K.T. Ramakrishna Reddy; Synthesis and characterization of Fe-doped ZnO thin films deposited by chemical spray pyrolysis; *Modern Electronic Materials* 3 (2017) 76–85.
- [2] M. Smirnov, C. Baban, G.I. Rusu; Structural and optical characteristics of spin-coated ZnO thin films; *Applied Surface Science* 256 (2010) 2405–2408.
- [3] Nanda Shakti, P.S. Gupta, Structural and optical properties of sol-gel prepared ZnO Thin film; *Appl. Phys. Res.* 2 (2010) 19–28.
- [4] S. K. Shaikh, S. I. Inamdar, V. V. Ganbavle and K. Y. Rajpure; Chemical bath deposited thin film based UV photoconductive detector; *J. alloys and compounds*; 664 (2016) 242-249.
- [5] F. Lmai, R. Moubah, A. El Amiri, Y. Abid, I. Soumahoro, N. Hassanain, S. Colis, G. Schmerber, A. Dinia, H. Lassri, Spin wave study and optical properties in Fe doped ZnO thin films prepared by spray pyrolysis technique, *Opt. Mater.* 57 (2016) 28–33.
- [6] G. Yergaliuly, B. Soltabayev, S. Kalybekkyzy, Z. Bakenov, A. Mentbayva; Effect of thickness and reaction media on properties of ZnO thin films by SILAR; *Scientific Reports* 12 (851) 2022.
- [7] X. M. Fan, J. S. Lian, Z. X. Guo and H. J. Lu; ZnO thin film formstion on Si (111) by laser ablation on Zn target in oxygen atmosphere; *J. Crystal Growth*, 279 (3-4) (2005) 447-453.
- [8] H. Deng, J. J. Russell, R. N. Lamb, B. Jiang, Y. Li, X. Y. Zhou; Microstrcture control of ZnO thin films prepared by single source chemical vapour deposition; *Thin Solid Films*; 458 (1-2) (2004) 43-46.

© 2024. This work is published under

[https://creativecommons.org/licenses/by/4.0/legalcode\(the“License”\)](https://creativecommons.org/licenses/by/4.0/legalcode(the“License”)).

¹Ankit R. Palewar²Yash D. Narad³Yatish R. Parauha⁴Sanjay J. Dhoble

**Spectroscopic investigation of
photoluminescence properties of
K₂CaMg(PO₄)₂:Eu³⁺ phosphor for
solid state lighting applications**



Abstract: - Phosphate based phosphors have been a major area of interest in solid state lighting devices. In the presented study, we report various concentrations of Europium (Eu³⁺) activated K₂CaMg(PO₄)₂ prepared via the standard solid-state diffusion synthesis method. The prepared phosphor is characterized using Photoluminescence (PL) spectroscopy. In the PL study, the PL excitation spectra exhibit excitation band at 395 nm wavelength along with a charge transfer band (CTB) centred at 258 nm. The PL emission spectra observed shows peaks at 594 nm (Orange Region) and 614 nm (Red Region) due to the 5D₀→7F₁ and 5D₀→7F₂ transitions of Eu³⁺ ions. The sample is also characterized using X-Ray Diffraction (XRD), Scanning Electron Microscopy (SEM), and Commission Internationale de l'Éclairage (CIE) techniques. The CIE diagram shows CIE coordinates in the orange-red region. According to obtained results, we suggest that the prepared phosphor have huge potential for future investigation in the field of solid state lighting (SSL) and display devices.

Keywords: Phosphor; Photoluminescence; Phosphate; Solid State Lighting (SSL)

¹ *Corresponding author: Department of Physics, RTM Nagpur University, Nagpur- 440033, India

² Department of Physics, RTM Nagpur University, Nagpur- 440033, India

³ Department of Physics, Shri Ramdeobaba College of Engineering and Management, Nagpur, 440013, India

⁴ Department of Physics, RTM Nagpur University, Nagpur- 440033, India

I. INTRODUCTION

Light emitting diodes (LEDs) have revolutionized the lighting industry with their energy efficiency, durability and versatility of applications [1–3]. One crucial component that contributes significantly to the performance of LEDs is phosphor. LEDs phosphors play a very vital role in converting blue light emitted by LEDs into various colours, thereby enhancing light quality and efficiency. The future of LEDs phosphors is promising, with ongoing research and development focusing on addressing current challenges and unlocking new opportunities. **Key areas of interest include:** Advanced Materials: Exploring novel phosphor materials with improved efficiency, stability, and spectral characteristics [4,5]. Smart Lighting: Integrating phosphors with smart lighting technologies for dynamic colour tuning and enhanced energy savings [6,7]. Health and Well-being: Developing LED phosphors that mimic natural sunlight spectra to promote circadian rhythm regulation and improve human well-being [8]. Environmental Sustainability: Emphasizing eco-friendly phosphor formulations and recycling strategies to reduce environmental impact [9]. LED phosphors play a critical role in the performance and versatility of LED lighting systems. Understanding their principles, types, applications, and ongoing advancements is essential for realizing the full potential of LEDs in various sectors, from everyday lighting to advanced display technologies and beyond. Some reports suggest that 22% of the electric power is consumed in the field of lighting [10]. Thus, how to reduce lighting energy consumption has become the research direction of many researchers. With the help of light-emitting diode (LED) light sources, energy consumption could be reduced by about 1000 TW [11].

Currently, the creation of W-LEDs has typically depended on combining a blue-emitting gallium nitride (GaN) light-emitting diode with yellow-emitting materials like cerium-doped yttrium aluminium garnet (YAG: Ce³⁺) [12,13]. However, due to a lack of red-light component, this type of WLED has some drawbacks, such low colour render index value (CRI) and high color correlated temperature (CCT), which restricts the areas in which WLEDs may be used (e.g., indoor illumination and screen display) [14,15]. While the human eye perceives the blend of blue and yellow light as white (cold white light), the CRI is typically low (<70). Especially, in certain lighting domains that demand excellent warm white illumination, such as photography, surgery, museums, cinematography, and art galleries, CRI rating needs to exceed 90 [16–18]. Currently, numerous research papers focus on advancing orange-red emitting phosphors and enhancing the luminescent characteristics of existing phosphors. Particularly, there has been detailed investigation into Eu³⁺ activated phosphors. The Eu³⁺ ion has an electronic configuration of [Xe]4f⁶, where the 4f orbitals are shielded from external influences by the closed outer shells of 5s² and 5p⁶. Importantly, the ground state energy level ⁷F₀ and the significant excited state energy level ⁵D₀ of Eu³⁺ are nondegenerate and unaffected by the crystal-field effect imposed by the host material. This key characteristic simplifies the interpretation of experimental absorption and luminescence spectra properties related to Eu³⁺. Numerous reports have demonstrated when Eu³⁺ ions occupy non-centrosymmetric sites, they emit vibrant red light corresponding to the ⁵D₀→⁷F₂ transitions [19–22].

It is well established that the optical properties of luminescent phosphors doped with rare earth ions are greatly influenced by the properties of the host matrix. Typically, it is widely recognized that the light-emitting characteristics of rare earth doped phosphors heavily rely on the host materials. Hence, choosing suitable host materials is a crucial endeavor in advancing rare earth activated phosphors for WLEDs. With various groups of materials emerging as good host materials for synthesis of phosphors, a great emphasis has certainly been on Phosphate materials. It is variably reported that, the formation of phosphate-based solid solution could improve the luminescence efficiency, so it is of great scientific significance to systematically study this influence mechanism [23,24]. Phosphate based phosphors doped with Eu³⁺ has been a field which has been extensively studied and reported [23–27]. Recently, Helode et al. investigated the optical spectroscopic studies and concentration quenching effects on Sr₉MgK(PO₄)₇: Eu³⁺ using the Dexter analysis [28]. Also, in 2021, Bin Yu et al. reported a novel mixed ion phosphate Cs₂Bi₂Sr(P₂O₇)(PO₄)₂ doped with Eu³⁺ synthesized using solid state reaction method and studied its optical characteristics and crystal structure [29]. Nandanwar et al. studied the photoluminescence properties and structural study of Sr₃La(PO₄)₃:Eu³⁺ phosphor prepared by wet chemical synthesis route [30]. Alongside, other researchers also studied various other phosphate type host materials doped with Eu³⁺, Ca₅(PO₄)₃F [31], NaMgPO₄ [32], K₄Ca(PO₄)₂ [33], Ca₉Y(PO₄)₇ [34], etc. are some of the examples of such recently prepared phosphors.

In this work, multiple concentrations of K₂CaMg(PO₄)₂:Eu³⁺ phosphor have been synthesized by conventional solid state diffusion synthesis method. In addition, PL properties of the proposed sample were

investigated. As per our best knowledge, $\text{K}_2\text{CaMg}(\text{PO}_4)_2:\text{Eu}^{3+}$ phosphor is first time reported by the authors and obtained result of proposed sample shows excellent PL properties for future studies of WLEDs and display devices.

II. EXPERIMENTAL

The presented paper reports various concentrations ($x = 0.5, 0.7, 1.0, 1.3$ and 1.5 mol%) of Eu^{3+} doped $\text{K}_2\text{CaMg}(\text{PO}_4)_2$ phosphor prepared by conventional solid state diffusion synthesis method. Potassium Carbonate (K_2CO_3), Calcium Carbonate (CaCO_3), Magnesium Carbonate (MgCO_3) and Ammonium Dihydrogen Phosphate ($\text{NH}_4\text{H}_2\text{PO}_4$) were used as starting material to prepare the host material which was subsequently doped with Europium Oxide (Eu_2O_3). All the precursors were weighed in stoichiometric ratio in the process. All the weighed materials were placed in agate mortar and pestle. For thirty minutes, every sample was constantly crushed to turn the combination into a homogenous fine powder. The resulting mixture was put in a muffle furnace after being transferred to ceramic crucibles. The muffle furnace was continuously operated at 800°C for 24 hours. After the period, sample was allowed to cool down to the room temperature and then further crushed using agate mortar pestle for 5 minutes per sample. Further characterizations were conducted using the powdered samples that were obtained.

The phosphor was characterized using a variety of techniques, including XRD, SEM, PL, and CIE. Glass samples were analyzed using the Rigaku Miniflex D 600 X-ray diffractometer with $\text{Cu K}\alpha$ radiation ($\lambda = 0.154059$ nm) at 40 kV and 15 mA to identify phases and crystalline structures. The diffraction pattern was detected between 10° and 80° at a scanning rate of $0.04^\circ/\text{sec}$. A scanning electron microscopy (SEM) analysis was carried out to analyse the morphology of the produced samples. The photoluminescence (PL) excitation and emission spectra of the glass sample were acquired with a SHIMADZU Spectrofluorophotometer RF-5301 PC. A 50 W Xenon lamp was used as an excitation source to measure the photoluminescence (PL) spectrum.

III. RESULTS AND DISCUSSION

1. X-Ray Powder Diffraction

Figure 1 depicts the XRD patterns of the proposed material, which were recorded in the 10° to 80° range. To the best of our knowledge, no research group has reported this material. This is first time prepared material using the solid-state diffusion approach. Furthermore, the standard data for the proposed host material were not available in the literature/JCPDS/ICDD/ICSD data, therefore the XRD pattern of the synthesized material was not compared. The major diffraction peaks are found in the 30° to 50° range. The XRD pattern exhibits sharp and narrow diffraction peaks, indicating the crystalline nature of the produced phosphor. As per the literature and ionic radii database, the ionic radii of Eu^{3+} is around 1.07 \AA and ionic radii of Ca^{2+} is around 1.12 \AA . Therefore, ionic radii of Ca^{2+} is greater than the ionic radii of Eu^{3+} . As per the ionic radii matching rule, it was expected that Eu^{3+} ions occupy the Ca^{2+} sites without significantly varying the structure of host lattice.

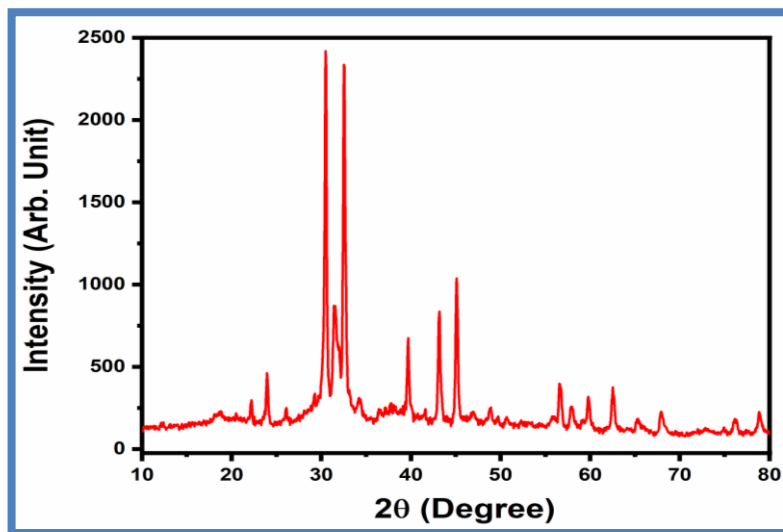


Figure 1: X-Ray Powder diffraction Spectra of $\text{K}_2\text{CaMg}(\text{PO}_4)_2: 0.5 \text{ mol}\% \text{Eu}^{3+}$.

2. Scanning Electron Microscopy (SEM)

Figure 2 shows the SEM images of the $0.5 \text{ mol}\% \text{Eu}^{3+}$ material. The SEM images were captured with magnification of $1 \mu\text{m}$ to $2 \mu\text{m}$. The size of particles varied in submicron range. The captured SEM images showed the high agglomeration and porous nature of the particles. This high agglomeration may be obtained due to the non-uniformities in heating and high temperature synthesis. The irregular shapes may also be arising due to the difference in the time period of crushing or the use of agate mortar and pestle. The porous nature of the particles as seen in the images is attributed to the of carbon dioxide and ammonia from the reaction mixture while heating.

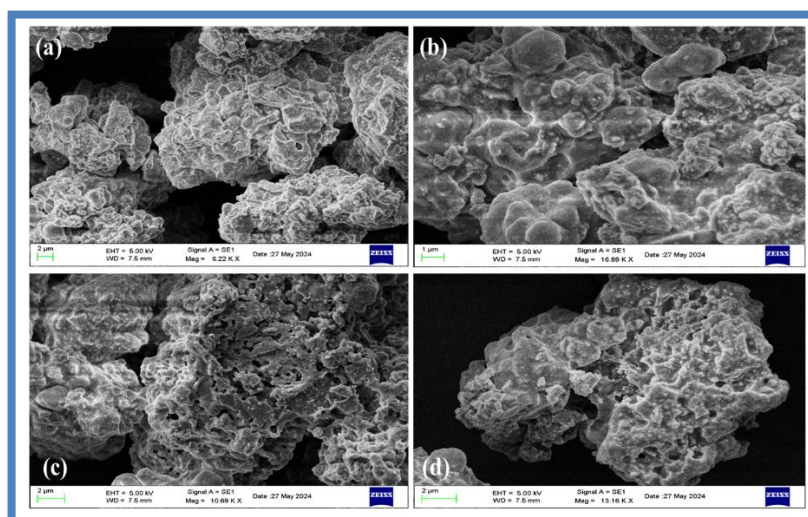


Figure 2: SEM images of $\text{K}_2\text{CaMg}(\text{PO}_4)_2:0.5 \text{ mol}\% \text{Eu}^{3+}$.

3. Photoluminescence Spectra

Figure 3 represents PL excitation spectra of $\text{K}_2\text{CaMg}(\text{PO}_4)_2$: 1 mol% Eu^{3+} phosphor, which is recorded in the range of 220-500 nm under 616 nm emission wavelength. The excitation spectrum depicts broad absorption band from 220-300 nm centred at 260 nm, this band also known as the Charge Transfer (CT) band. The CT band may be arising due to the charge transition from Oxygen 2p orbital (O^{2-}) to the vacant europium 4f orbital (Eu^{3+}) ions. In addition, multiple sharp absorption bands are observed at 320 nm, 363 nm, 383 nm and 395 nm, which may be arise due to ${}^7\text{F}_0 \rightarrow {}^5\text{H}_3$, ${}^7\text{F}_0 \rightarrow {}^5\text{D}_4$, ${}^7\text{F}_0 \rightarrow {}^5\text{L}_7$ and ${}^7\text{F}_0 \rightarrow {}^5\text{L}_6$ transitions of Eu^{3+} ions [35,36]. From the excitation spectrum, we clearly observed that 395 nm absorption band exhibits strong excitation intensity. As per the literature we found that near ultraviolet (NUV) absorption is suitable for WLEDs application. Here we observed that Eu^{3+} doped $\text{K}_2\text{CaMg}(\text{PO}_4)_2$ phosphor have absorption in the NUV region which suggests that our prepared sample may have potential for future studies in the field of WLEDs.

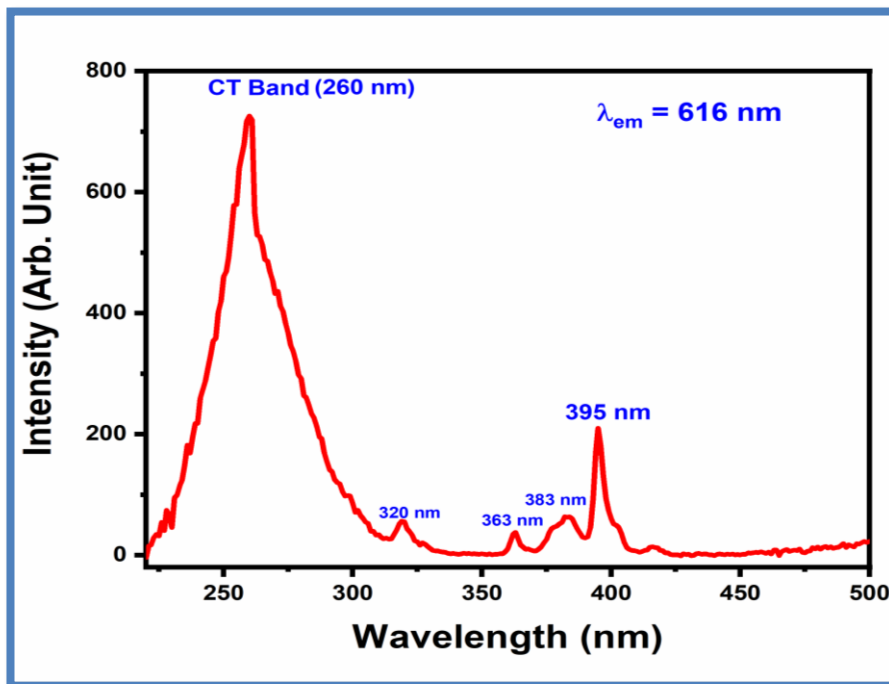


Figure 3: PL excitation spectrum graph of $\text{K}_2\text{CaMg}(\text{PO}_4)_2$: Eu^{3+} phosphor monitored at emission wavelength of 616 nm.

Figure 4 (a) and (b) represents PL emission spectra of the $\text{K}_2\text{CaMg}(\text{PO}_4)_2$: x mol% Eu^{3+} (x= 0.5, 0.7, 1.0, 1.3, 1.5 mol%) phosphor under 260 nm and 395 nm respectively. The emission spectrum is recorded in the range of 500-700 nm. The observed emission spectrum represents two strong emission bands around at 594 and 616 nm which may be observed due to the ${}^5\text{D}_0 \rightarrow {}^7\text{F}_1$ and ${}^5\text{D}_0 \rightarrow {}^7\text{F}_2$ transitions of Eu^{3+} ions [19]. Under 260 nm and 395 nm excitation, emission spectrum shows similar nature of the spectrum, only PL intensities are varied with variation of excitation wavelength, with emission peak at 616 nm being more intense as compared to the emission peak at 594 nm. As per the literature, it is known that the peak observed at 594 nm (${}^5\text{D}_0 \rightarrow {}^7\text{F}_1$) is due to magnetic dipole transitions which is not dependent on the coordination surrounding and are insensitive to site symmetry. Whereas the peak observed at 616 nm (${}^5\text{D}_0 \rightarrow {}^7\text{F}_2$) is due to the electric dipole transitions of Eu^{3+} ions from the chemical environment surrounding the dopant [37,38]. Furthermore, the orange-red emissions due to electric dipole transition shows higher intensity as compared to the magnetic dipole transitions.

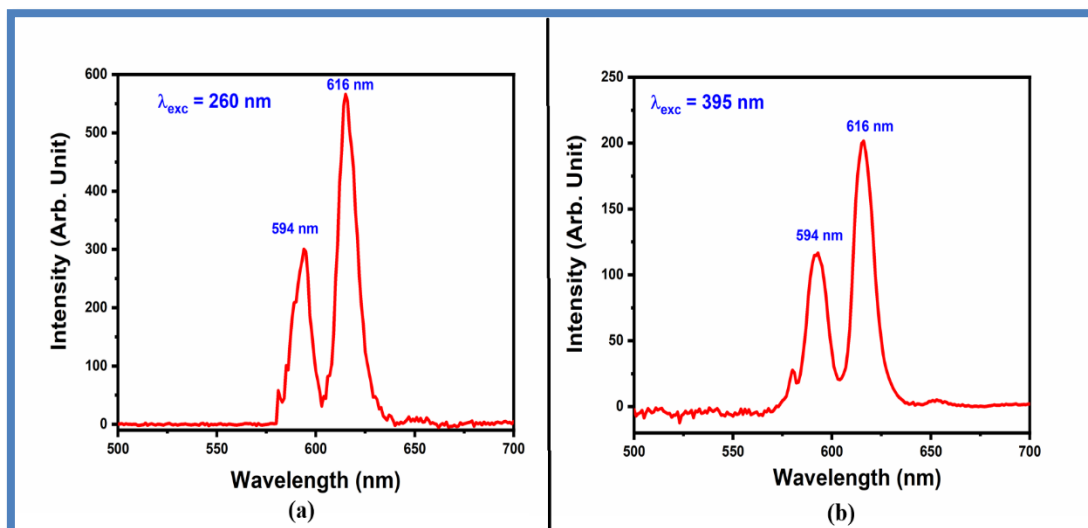


Figure 4 (a) : PL emission spectrum graph of K₂CaMg(PO₄)₂:Eu³⁺ phosphor monitored at excitation wavelength of 260 nm. **(b)** PL emission spectrum graph of K₂CaMg(PO₄)₂:Eu³⁺ phosphor monitored at excitation wavelength of 395nm.

4. Concentration Quenching

Concentration of dopant ions play a very important role in the PL spectra of a compound as it can significantly affect the luminescence properties of a material. Thus in order to find an optimal concentration of Eu³⁺ ions a series of K₂CaMg(PO₄)₂: x mol% Eu³⁺ (x= 0.5, 0.7, 1.0, 1.3, 1.5 mol%) has been synthesized. It is observed that, with variation in the concentration of Eu³⁺ ions there is no change in the position of peaks but it does have an effect on the emission intensity of the material. Figure 5 given below shows the trends observed by varying concentration of dopant ions in the case of K₂CaMg(PO₄)₂:Eu³⁺. The graph suggests an increase in the emission intensity with an increase in the concentration of Eu³⁺ ions till a maximum value of x= 1.0 mol% and then the emission intensity decreases with subsequent increase in Eu³⁺ concentration. This phenomenon is termed as concentration quenching [37,38].

Literature survey suggests the critical distance (R_c) is a very important factor as it suggests the type of energy transfer between the dopant and host. If R_c < 5Å, the energy is transferred due to exchange interaction, whereas when R_c > 5Å the energy is transferred via electric multipolar interaction. Blasse’s pointed out that critical distance is approximately equal to twice the radius of the sphere with the volume of unit cell and is expressed by the formula [37,38]:

$$R_c = 2 \left(\frac{3V}{4\pi X_c Z} \right)^{1/3} \dots \dots \dots (1)$$

where V is the volume of the unit cell, X_c is the critical concentration of Eu³⁺ ions, and Z is the number of available sites for the dopant in the unit cell. The type of the interaction can be further ascertained by the equation proposed by Dexter [19,26,39]:

$$\frac{I}{x} = K[1 + \beta(x)^{\theta/3}]^{-1} \dots \dots \dots (2)$$

This equation can be approximated as:

$$\text{Log} \frac{I}{x} = c - \frac{\theta}{3} \text{log}(x) \dots \dots \dots (3)$$

Where I is the PL emission intensity and x is the value of concentration of Eu³⁺ ions and K, β and c are constants in the same excitation conditions. According to Van Uitert, when the value of θ=6 then it presents the electric dipole-dipole (d-d) interaction, if the value of θ=8 then it presents the electric dipole- electric quadruple (d-q) interaction, and if the value of θ=8 then it presents the electric quadruple-electric quadruple (q-q) interactions [19,26,39]. Figure 6 (a,b) depicts the linear fitting graph of K₂CaMg(PO₄)₂: Eu³⁺ at excitation wavelengths 260 nm and 395 nm respectively. The graph is plotted as a function of Log(x) against Log(I/x) and is represented as a straight fitted line with negative slope value (-θ/3). According to linear fit for excitation value 260 nm the slope is (-θ/3) ≈ -1.63. Thus, the value of θ is calculated to be θ ≈ 4.89. As for figure 5(b) with excitation wavelength 395 nm, the slope was measured to be (θ/3) ≈ -1.93 which suggests the value of θ

to be about $\theta = 5.99$. As both the values of θ are closer to 6, this means the dipole- dipole (d-d) interaction leads to concentration quenching mechanism in case of $K_2CaMg(PO_4)_2: Eu^{3+}$ phosphor.

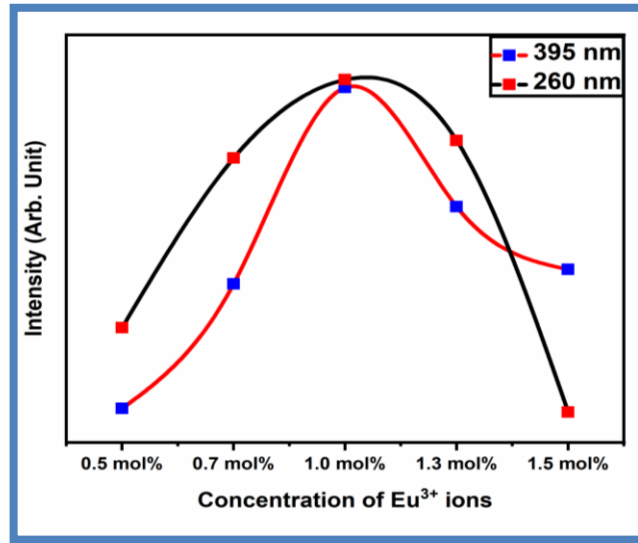


Figure 5: Concentration Quenching graph of $K_2CaMg(PO_4)_2:Eu^{3+}$.

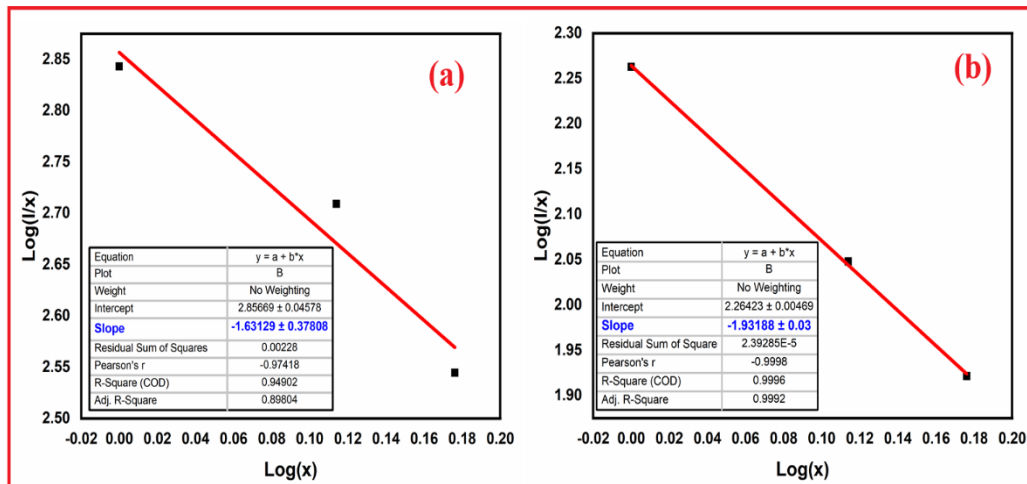


Figure 6: Linear fitting graph between $\text{Log}(x)$ and $\text{Log}(I/x)$ at excitation wavelength (a) 260 nm (b) 395 nm

5. CIE Chromaticity

Figure 7 represents the Commission Internationale de l'Éclairage (CIE) diagram for $K_2CaMg(PO_4)_2: 1 \text{ mol\% } Eu^{3+}$ phosphor observed under the excitation wavelengths of 260 and 395 nm, respectively. The diagram was plotted using OSRAM SYLVANIA Colour Calculator. The CIE coordinates are observed in the red region, which confirms strong red emission of the proposed material. Colour purity and CCT are also significant parameters for WLED applications. Equations 4 and 5 present a mathematical equation for colour purity and CCT computation. Using these equations and obtained CIE coordinates, we determine the values of colour purity and CCT as shown in Table 1 [40,41].

$$Color Purity = \frac{\sqrt{(x-x_i)^2+(y-y_i)^2}}{\sqrt{(x_d-x_i)^2-(y_d-y_i)^2}} \times 100\% \dots\dots\dots (4)$$

Where (x, y) are the CIE colour coordinates of the $K_2CaMg(PO_4)_2: 1 \text{ mol\% } Eu^{3+}$ sample, (x_i, y_i) are the white light coordinates, and (x_d, y_d) are the dominant wavelength coordinates. The colour purity of the suggested sample was calculated at 260 and 395 nm excitation wavelengths, and the computed colour purity values were more than 80%, indicating that the proposed phosphor is suitable for use in WLEDs as a red emitter.

$$CCT = -499 n^3 + 3525 n^2 - 6823.3 n + 5520.33 \dots\dots\dots (5)$$

Where,

$$n = \frac{x - x_e}{y - y_e}$$

Previous research has revealed that if the CCT value is larger than 4000 K, it produces cool light, and if it is less than 4000 K, it produces warm light [26]. The calculated value of CCT is around 1500 K, indicating that proposed sample is appropriate for warm WLEDs.

Table 1: CIE Chromaticity coordinates, Color purity and CCT values of $\text{K}_2\text{CaMg}(\text{PO}_4)_2$: 1 mol% Eu^{3+} phosphor under 260 nm and 395 nm excitation wavelengths

	x	y	x_d	y_d	Colour Purity	CCT
A(395 nm)	0.6038	0.3957	0.6775	0.3224	80.61%	1511 K
B(260 nm)	0.6188	0.3807	0.678	0.3281	83.94%	1524 K

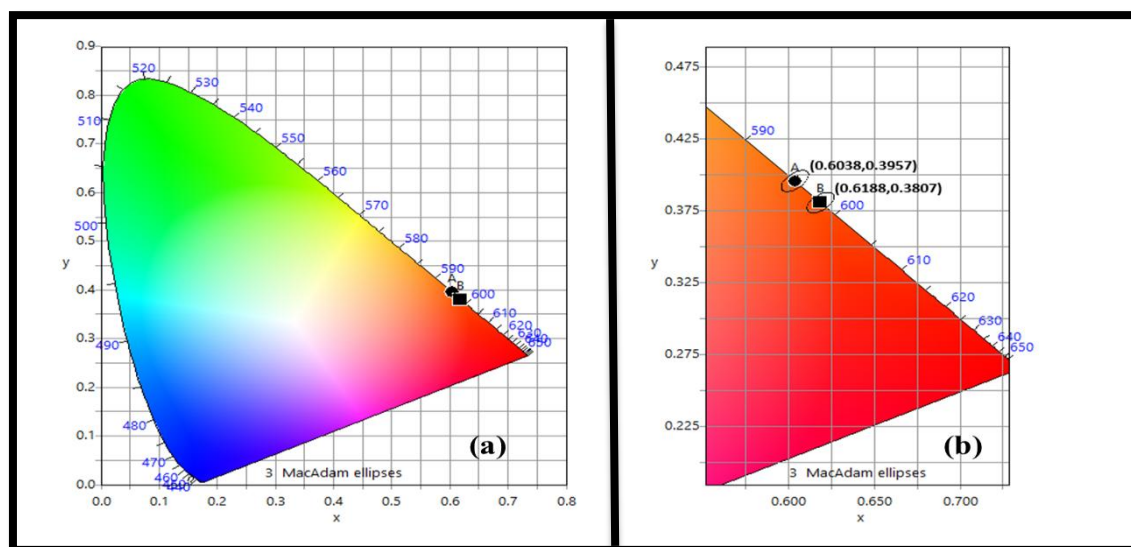


Figure 7: CIE diagram for $\text{K}_2\text{CaMg}(\text{PO}_4)_2$: 1 mol% Eu^{3+} phosphor

IV. CONCLUSION

In the present work, a series of Eu^{3+} doped $\text{K}_2\text{CaMg}(\text{PO}_4)_2$ was prepared by the conventional solid state diffusion method. The prepared phosphor was characterized using XRD, SEM, PL excitation, PL emission and CIE techniques. The XRD spectra of the prepared phosphor showed definite sharp peaks suggesting the crystalline nature of the phosphor. The SEM images suggested the porous nature of the phosphor due to emission of various gases during the synthesis of material. The PL emission spectra of the Eu^{3+} doped $\text{K}_2\text{CaMg}(\text{PO}_4)_2$ shows peaks at 594 nm due to the $^5\text{D}_0 \rightarrow ^7\text{F}_1$ and at 616 nm due to $^5\text{D}_0 \rightarrow ^7\text{F}_2$ transitions of Eu^{3+} ions. The concentration quenching graphs suggested the emission intensity to continuously increase upto 1 mol % Eu^{3+} ions and then decreasing, thus confirming 1.0 mol% to be an optimal doping concentration. Further the CIE diagram of the prepared phosphor indicated emission in intense red region of the spectra and the CIE coordinates were observed at (0.6038, 0.3957) for 395 nm excitation and at (0.6188, 0.3807) for the 260 nm excitation. The presented research thus indicates that the prepared phosphor has a great potential in red light emitting phosphors for eco-friendly white light generation.

REFERENCES

- [1] D. Nayak, R.B. Choudhary, A survey of the structure, fabrication, and characterization of advanced organic light emitting diodes, *Microelectron. Reliab.* 144 (2023) 1–7. <https://doi.org/10.1016/j.microrel.2023.114959>.
- [2] M. Loi, A. Villani, F. Paciolla, G. Mulè, C. Paciolla, Challenges and opportunities of light-emitting diode (Led) as key to modulate antioxidant compounds in plants. a review, *Antioxidants.* 10 (2021) 1–35.

- <https://doi.org/10.3390/antiox10010042>.
- [3] M. Zhao, Q. Zhang, Z. Xia, Narrow-band emitters in LED backlights for liquid-crystal displays, *Mater. Today*. 40 (2020) 246–265. <https://doi.org/10.1016/j.mattod.2020.04.032>.
 - [4] Q. Yao, P. Hu, P. Sun, M. Liu, R. Dong, K. Chao, Y. Liu, J. Jiang, H. Jiang, YAG:Ce³⁺ Transparent Ceramic Phosphors Brighten the Next-Generation Laser-Driven Lighting, *Adv. Mater.* 32 (2020) 1–7. <https://doi.org/10.1002/adma.201907888>.
 - [5] J. Qiao, S. Zhang, X. Zhou, W. Chen, R. Gautier, Z. Xia, Near-Infrared Light-Emitting Diodes utilizing a Europium-Activated Calcium Oxide Phosphor with External Quantum Efficiency of up to 54.7%, *Adv. Mater.* 34 (2022). <https://doi.org/10.1002/adma.202201887>.
 - [6] O. Ayan, B. Turkey, IoT-Based energy efficiency in smart homes by smart lighting solutions, 2020 21st Int. Symp. Electr. Appar. Technol. SIELA 2020 - Proc. (2020). <https://doi.org/10.1109/SIELA49118.2020.9167065>.
 - [7] S. Gorgulu, S. Kocabey, An energy saving potential analysis of lighting retrofit scenarios in outdoor lighting systems: A case study for a university campus, *J. Clean. Prod.* 260 (2020). <https://doi.org/10.1016/j.jclepro.2020.121060>.
 - [8] G.B. Nair, H.C. Swart, S.J. Dhoble, A review on the advancements in phosphor-converted light emitting diodes (pc-LEDs): Phosphor synthesis, device fabrication and characterization, *Prog. Mater. Sci.* 109 (2020) 1–8. <https://doi.org/10.1016/j.pmatsci.2019.100622>.
 - [9] Y. Qi, R. Liu, Z. Li, Y. Song, C. kui Wang, L. Cai, Microcavity forming electrode for efficient color-tunable semitransparent perovskite light-emitting diodes, *Opt. Laser Technol.* 169 (2024) 1–6. <https://doi.org/10.1016/j.optlastec.2023.110002>.
 - [10] R. Pode, Organic light emitting diode devices: An energy efficient solid state lighting for applications, *Renew. Sustain. Energy Rev.* 133 (2020) 1–8. <https://doi.org/10.1016/j.rser.2020.110043>.
 - [11] N.U. Islam, M. Usman, T. Jamil, Energy-savings using solid-state lighting: A case study of India, Pakistan, and Bangladesh, *Energy Policy*. 160 (2022) 1–8. <https://doi.org/10.1016/j.enpol.2021.112676>.
 - [12] C.M. Mehare, Y.R. Parauha, N.S. Dhoble, Chandan Ghanty, S.J. Dhoble, Synthesis of novel Eu²⁺ activated K₃Ca₂(SO₄)₃F down-conversion phosphor for near UV excited white light emitting diode, *J. Mol. Struct.* 2 (2020) 127957. <https://doi.org/10.1016/j.molstruc.2020.127957>.
 - [13] S. Wang, Z. Song, Q. Liu, Recent progress in Ce³⁺/Eu²⁺-activated LEDs and persistent phosphors: focusing on the local structure and the electronic structure, *J. Mater. Chem. C*. 11 (2022) 48–96. <https://doi.org/10.1039/d2tc02639b>.
 - [14] C. Gandate, Y.R. Parauha, S.G.M. Mushtaque, S.J. Dhoble, Current progress and comparative study of performance of the energy saving lighting devices: a review, *J. Phys. Conf. Ser.* 1913 (2021) 012018. <https://doi.org/10.1088/1742-6596/1913/1/012018>.
 - [15] Y.R. Parauha, R.S. Yadav, S.J. Dhoble, Enhanced photoluminescence via doping of phosphate, sulphate and vanadate ions in Eu³⁺ doped La₂(MoO₄)₃ downconversion phosphors for white LEDs, *Opt. Laser Technol.* 124 (2020). <https://doi.org/10.1016/j.optlastec.2019.105974>.
 - [16] B. Karadza, H. Van Avermaet, L. Mingabudinova, Z. Hens, Y. Meuret, Efficient, high-CRI white LEDs by combining traditional phosphors with cadmium-free InP/ZnSe red quantum dots, *Photonics Res.* 10 (2022) 155. <https://doi.org/10.1364/prj.428843>.
 - [17] D. Yan, S. Zhao, Y. Zhang, H. Wang, Z. Zang, Highly efficient emission and high-CRI warm white light-emitting diodes from ligand-modified CsPbBr₃ quantum dots, *Opto-Electronic Adv.* 5 (2022) 1–14. <https://doi.org/10.29026/oea.2022.200075>.
 - [18] D. Yan, Q. Mo, S. Zhao, W. Cai, Z. Zang, Room temperature synthesis of Sn²⁺-doped highly luminescent CsPbBr₃ quantum dots for high CRI white light-emitting diodes, *Nanoscale*. 13 (2021) 9740–9746. <https://doi.org/10.1039/d1nr01492g>.
 - [19] D.J. Dhiman, Y.R. Parauha, A.B. Chourasia, S.J. Dhoble, Synthesis and luminescence properties of Eu³⁺-activated Mg₃(PO₄)₂ phosphors and substitution of phosphate with molybdate, tungstate and sulphate, *Radiat. Eff. Defects Solids*. 3 (2024). <https://doi.org/10.1080/10420150.2024.2369121>.
 - [20] K. Singh, P. Pradhan, S. Priya, S. Mund, S. Vaidyanathan, *Dalton Transactions*, (2023) 3–7.
 - [21] G. Wu, J. Xue, X. Li, Q. Bi, M. Sheng, Z. Leng, A novel red-emitting Na₅W₃O₉F₅:Eu³⁺ phosphor with high color purity for blue-based WLEDs, *Ceram. Int.* 49 (2023) 10615–10624. <https://doi.org/10.1016/j.ceramint.2022.11.249>.
 - [22] J. Lakde, C.M. Mehare, K.K. Pandey, N.S. Dhoble, S.J. Dhoble, Recent development of Eu³⁺-doped phosphor for white LED application: A review, *J. Phys. Conf. Ser.* 1913 (2021). <https://doi.org/10.1088/1742-6596/1913/1/012029>.
 - [23] W. Liu, X. Wang, Q. Zhu, J.G. Li, Tb³⁺/Mn²⁺ singly/doubly doped Sr₃Ce(PO₄)₃ for multi-color luminescence, excellent thermal stability and high-performance optical thermometry, *J. Alloys Compd.* 829 (2020) 154563. <https://doi.org/10.1016/j.jallcom.2020.154563>.
 - [24] L. Reddy, T.J. Nkosi, P.L. Masiteng, A. Balakrishna, H.C. Swart, O.M. Ntwaeaborwa, Violet-blue-shift of emission and enhanced luminescent properties of Ca₃(PO₄)₂:Ce³⁺ phosphor induced by substitution of Gd³⁺ ions, *Curr. Appl. Phys.* 20 (2020) 696–702. <https://doi.org/10.1016/j.cap.2020.02.017>.
 - [25] V. Singh, Y.R. Parauha, S.J. Dhoble, V.K. Kummara, N. Ravi, Orange light emission from co-precipitation derived CaZr₄(PO₄)₆ doped with Sm³⁺ phosphor, *Optik (Stuttg.)* 242 (2021) 167229. <https://doi.org/10.1016/j.ijleo.2021.167229>.
 - [26] Y.R. Parauha, S.J. Dhoble, Structural and photoluminescence properties of Dy³⁺-activated NaCaPO₄ phosphor derived from solution combustion, *Luminescence*. 37 (2022) 141–152. <https://doi.org/10.1002/bio.4155>.
 - [27] S.K. Ramteke, A.N. Yerpude, S.J. Dhoble, N.S. Kokode, Luminescence characterization of KBaPO₄:RE (RE =

- Sm³⁺,Eu³⁺,Dy³⁺) phosphors, *Luminescence*. 35 (2020) 969–973. <https://doi.org/10.1002/bio.3792>.
- [28] S.J. Helode, S.D. Kadam, Abhijeet R, Structure, luminescence investigation in Dy³⁺, Eu³⁺ and Ce³⁺, Dy³⁺ co-activated Sr₉MgK(PO₄)₇ phosphors by energy transfer mechanism, *J. Solid State Chem.* 325 (2023) 124149.
- [29] S. Guo, P. Chen, L. Song, P. Guo, J. Gao, A new mixed-anion phosphate Cs₂Bi₂Sr(P₂O₇)(PO₄)₂: Synthesis, characterization, structure and its Eu³⁺-activated luminescence, *J. Solid State Chem.* 288 (2020) 1–7.
- [30] C.M. Nandanwar, N.S. Kokode, R.M. Yerojwar, A.N. Yerpude, R.S. Meshram, Wet chemical synthesis and photoluminescence study of Eu³⁺ activated orthophosphate-based phosphor for n-UV-based solid-state lighting, *J. Opt.* 53 (2024) 70–75. <https://doi.org/10.1007/s12596-023-01130-z>.
- [31] B. Lin, Y. Zhang, Z. Zhao, H. Zhao, J. Yu, Tunable red/ blue emitting of Ca₅(PO₄)₃F: Eu²⁺, Eu³⁺ and remote-excited color convertor for NUV-WLED, *Opt. Mater. (Amst)*. 137 (2023) 1–7. <https://doi.org/10.1016/j.optmat.2023.113609>.
- [32] A. Balakrishna, L. Reddy, O.M. Ntwaeaborwa, H.C. Swart, Remarkable influence of alkaline earth ions on the enhancement of fluorescence from Eu³⁺ ion doped in sodium ortho-phosphate phosphors, *J. Mol. Struct.* 1203 (2020) 1–7. <https://doi.org/10.1016/j.molstruc.2019.127375>.
- [33] S.G.M. Mushtaque, V.B. Pawade, S.J. Dhoble, Optical and thermal properties of rare earth-doped K₄Ca(PO₄)₂ phosphor, *Luminescence*. 38 (2023) 469–476. <https://doi.org/10.1002/bio.4470>.
- [34] H. Dahiya, M. Dalal, A. Singh, A. Siwach, M. Dahiya, S. Nain, V.B. Taxak, S.P. Khatkar, D. Kumar, Spectroscopic characteristics of Eu³⁺-activated Ca₉Y(PO₄)₇ nanophosphors in Judd–Ofelt framework, *Solid State Sci.* 108 (2020) 106341. <https://doi.org/10.1016/j.solidstatesciences.2020.106341>.
- [35] A. Siwach, D. Kumar, Structural and optical behavior of nano-scaled luminous green-emitting Ca₉Y(PO₄)₇:Tb³⁺ phosphor for competent lighting devices, *Chem. Phys. Lett.* 772 (2021) 2–10. <https://doi.org/10.1016/j.cplett.2021.138547>.
- [36] S. Guo, P. Chen, L. Song, P. Guo, J. Gao, A new mixed-anion phosphate Cs₂Bi₂Sr(P₂O₇)(PO₄)₂: Synthesis, characterization, structure and its Eu³⁺-activated luminescence, *J. Solid State Chem.* 288 (2020) 121411. <https://doi.org/10.1016/j.jssc.2020.121411>.
- [37] S.R. Bargat, Y.R. Parauha, G.C. Mishra, S.J. Dhoble, Combustion synthesis and spectroscopic investigation of CaNa₂(SO₄)₂:Eu³⁺ phosphor, *J. Mol. Struct.* 1221 (2020). <https://doi.org/10.1016/j.molstruc.2020.128838>.
- [38] Y.R. Parauha, S.J. Dhoble, Synthesis and luminescence characterization of Eu³⁺-doped Ca₇Mg₂(PO₄)₆ phosphor for eco-friendly white light-emitting diodes and thermoluminescence dosimetric applications, *Luminescence*. 36 (2021) 1837–1846. <https://doi.org/10.1002/bio.3900>.
- [39] J.R. Jose, A. M S, S.A. Oommen, C. Joseph, P.R. Biju, Tailoring high purity orange-red emission in Sm³⁺ activated SrTi(PO₄)₂ phosphor for lighting and display devices, *J. Mol. Struct.* 1312 (2024) 1–7. <https://doi.org/10.1016/j.molstruc.2024.138442>.
- [40] W. Ullah Khan, Z. Ye, M. Boubeche, T. Liu, Z. Guo, Y. Zhang, Robust thermal performance and color purity of samarium based deep red emitting phosphor for near-UV chip-based high-color-rendering, *J. Alloys Compd.* 888 (2021) 161538. <https://doi.org/10.1016/j.jallcom.2021.161538>.
- [41] N. Shaishta, W.U. Khan, S.K.B. Mane, A. Hayat, D.D. Zhou, J. Khan, N. Mehmood, H.K. Inamdar, G. Manjunatha, Red-emitting CaSc₂O₄:Eu³⁺ phosphor for NUV-based warm white LEDs: structural elucidation and Hirshfeld surface analysis, *Int. J. Energy Res.* 44 (2020) 8328–8339. <https://doi.org/10.1002/er.5376>.

Ashok B. Nawale^{1*},
Harshali Chaitwar¹,
Gayatri Sutrale¹,
Satyappa R.
Jigajeni¹

Performance of TiO₂ based Dye Sensitized Solar Cell for Chlorophyll Based Natural Dyes



¹Department of Physics, Government Vidarbha Institute of Science and Humanities (Autonomous) Amravati, MS, India

*E-mail: anwale11@gmail.com

Abstract:

Here we report the performance of TiO₂ based dye sensitized solar cell for chlorophyll based natural dyes. The TiO₂ films were deposited on a conductive glass substrate (FTO) by using doctor blade method which was used as a working electrode. Dyes, extracted from plant leaves of spinach, neem and mint were used as a natural dye. Their performance was compared with commercially available Rose Bengal dye. The as prepared TiO₂ electrode were found to be polycrystalline in nature having tetragonal structure with anatase phase as confirmed by X-ray diffraction. The band gap of the as prepared film was found to be 3.9 eV as confirmed by UV-vis analysis. Moreover, the dye absorption on the TiO₂ film was also confirmed by UV-visible spectroscopy. The absorption spectra analysis of the dye adsorbed films clearly shows the increase in absorbance in visible range. Finally, the performance of the as prepared dye sensitized films were studied by fabricating the cell. Among the different natural dyes spinach extracted in acetone shows the highest performance as compared with others.

Keywords: Natural Dyes, Doctor Blade Technique, Absorbance, TiO₂

INTRODUCTION:

Among all the renewable energy option solar energy stands out as the most viable choice to meet our energy demand as solar energy striking the earth is 1400 W/m². The abundance of this energy reaching earth can be fruitfully utilized in various ways namely solar fuel, photovoltaics, solar electricity and solar thermal solutions. Photovoltaic cells can be categorized by four main generations first, second, third and fourth generation. A dye sensitized solar cell, a third generation cell, is a low-cost solar cell belonging to the group of thin film solar cells [1]. It is based on a semiconductor formed between a photo-sensitized anode and an electrolyte a photo electrochemical system. The modern version of dye sensitized solar cell also known as the Gratzel cell.

In 1960s, it was discovered that electricity can be generated through illuminated organic dyes in electrochemical cells [2]. At the University of California at Berkeley, chlorophyll was extracted from spinach [3]. First chlorophyll-sensitized zinc oxide (ZnO) electrode was synthesized in 1972 [4].

For the first time, through electron injection of excited dye molecules into a wide band gap of semiconductor photons were converted into electricity.

A lot of research has been done on “ZnO” single crystals but the efficiency of these dye-sensitized solar cells was very poor, as the monolayer of dye molecules was able to absorb incident light only up to 1% [5].

Thus, the efficiency was improved by optimizing the porosity of the electrode made up of fine oxide powder [6]. So that the absorption of dye over electrode could be enhanced and as a result light harvesting efficiency could also be enhanced. As a result, Nano-porous titanium dioxide (TiO₂) electrodes with a roughness factor of Ca. 1000 were discovered, and in 1991, DSSCs with 7% efficiency were invented [7]. These cells also known as Gratzel cells, were originally co-invented in 1988 by Brian O'Regan and Michael Gratzel at UC Berkeley and were further developed by aforementioned scientists at Ecole Polytechnique federate de Lausann (EPFL) till 1991[8].

Here we report the fabrication and performance of dye sensitized solar cell by using the commercially available TiO₂ powder for the various dyes such as synthetic Rose Bengal and different natural dyes like spinach, neem and mint.

EXPERIMENTAL PROCEDURE:

Materials used: Commercially available TiO₂ Nano powder, ethyl cellulose, Triton-X-100, ethanol, Lithium Iodide, iodine, acetonitrile, Rose Bengal (dye), spinach leaves, neem tree leaves, mint leaves. Distilled water, acetone. FTO, glass slides.

Formation of Paste: A known amount (0.20 gm) of commercially available TiO₂ Nano powder was mixed in 2 ml ethanol using pestle and mortar and grinded for 5 minutes. Similarly, a known amount (0.12gm) of ethyl cellulose was mixed with 2 ml ethanol using pestle and mortar for 5 minutes. Then both the solutions were ultrasonicated for one hour to have a uniform dispersion of TiO₂ and dissolution of ethyl cellulose in ethanol using ultrasonic bath separately. After ultrasonication they were mixed together and grinded in pestle mortar for one and half hour to have a homogeneous solution. In this homogeneous solution, 3 drops of Triton X-100 were added as a surfactant and again grinded for 15 minutes. Ethanol was added as required during each step of grinding to maintain the viscosity of the paste. In this way the paste is ready for the use.

Extraction of Dyes: Dye is one of the important materials of DSSC. Its main function is to absorb the sun rays and transmit the photoelectron, to TiO₂. The most common dye used in DSSC is organic and natural dyes. The synthetic dyes possess higher optical absorption than natural dye in visible region. Thus, the photovoltaic performances of the DSSC utilizing synthetic dyes are relatively higher than that of the device using natural dye. A natural dye as a sensitizer in DSSC is designed according to the nature of photosynthesis principle. Natural dyes contain carboxyl, hydroxyl and so on which can easily react with the surface of TiO₂ nanoparticle. Moreover, the dyes containing higher percentage of chlorophyll content used

in the DSSC was shown the better performance. Natural dyes can be directly extracted from plants with no pollution, no tedious synthesis and separation and purification process is relatively simple. It could be achieved by a variety of natural dye sensitization to absorb sunlight of all band range.

In the present work two types of dyes were used for preparation of DSSC namely; commercially available Rose Bengal dye and naturally prepared dyes using plant leaves extract such as spinach, neem and mint.

Commercially available Rose Bengal dye: For the preparation of Rose Bengal dye two types solvents were used i.e., ethanol and acetonitrile. 0.001M Rose Bengal Dye were dispersed into 10ml of each solvent separately. Then the mixture was stirred for 15 min under dark condition and the dyes are ready to use.

Naturally prepared dyes using plant leaves extract: Natural dyes were prepared by using different plant leaves extract. Initially, plant leaves were properly cleaned and leaves were dried under natural condition. Spinach leaves were dried for a week, Neem leaves were dried for 4-5 days and the Mint leaves were dried for 2-3 days. Finally, the dried leaves were crushed in mortar and pestle till it becomes powder.

Different types of solvents were used for preparation dye. The spinach dye was prepared in acetone, acetonitrile and ethanol whereas; mint dye was prepared in only ethanol solvent. Here, known amount (1 gm) of both the dyes powder were dispersed into 20 ml of each solvent separately. Let them rest for 18 hours under dark condition and then filter them. Solvent is added if required and the dye is ready to use. For the preparation of Neem dye, two types of solvent were used namely ethanol and acetonitrile. Initially, 1 gm of Neem leaves powder were dispersed 20 ml of each solvent separately and the mixture is heated for 1 hour at 80°C. After heating the mixture is kept as it is for 18 hours and then it is get filtered with Whatman filter paper and the dye is ready to use.

Working electrode assembly: FTO (fluorine doped tin oxide) glass, which was used as a current collector was first cleaned in a distilled water for approximately 15 min, and then sequentially with acetone and ethanol for 15 min each using an ultrasonic bath. The edges of the FTO glass were covered with adhesive tape as a frame to control the film thickness and provide non-coated areas for electrical contact. The TiO₂ paste was coated on an FTO glass plate using the doctor-blade technique. After application, the TiO₂ films were air-dried for approximately 5 min to reduce the surface irregularities. The films were then heated to 450 °C in air for 1 hour to remove the organic loads and facilitate interconnection of the TiO₂ nanoparticles. Then the films were dipped into dyes for 24 hours. After dye adsorption, the film was cleaned with respective solvent to remove the excess dye and dried for 10 minutes. The size of the TiO₂ electrodes used was 0.36cm².

Preparation of Counter Electrode: The counter electrode in DSSCs collects electron in the external circuit and catalyzes the reduction of the redox electrolyte and hole transport in the solid electrolyte. Thus, it undoubtedly has an important impact on the photovoltaic performance, long-term stability, and cost of

DSSCs. FTO was cleaned as mention above. To make a counter electrode, a thin layer of carbon suit was developed on an FTO plate. A carbon black electrode was easily made by moving the substrate (conductive side of FTO) above the flame of a candle. The substrate becomes black after some time and then it was cooled. The size of the counter electrode used was 0.36 cm^2 .

Preparation of Electrolyte Solution: The electrolyte plays one of the most significant roles in the process of light-to-electricity conversion, since it works as an electron transfer mediator with the function of regenerating the dye sensitizer from the oxidized state. The iodide/triiodide (I-/I₃⁻) was used as the electrolyte solution. It is prepared by taking 0.1M Lithium Iodide and 0.05M Iodide in acetonitrile. The solution was then mixed thoroughly by using magnetic stirrer for 1 hour.

Fabrication of DSSC: The prepared working electrode and counter electrode are used to fabricate sandwiched type DSSC. The spacing between the two electrodes were formed by taping the working electrode twice by scotch tape. A drop of electrolyte solution as mentioned above was injected between the working electrode and counter electrode. Crocodile pins are used for contacts from the fabricated solar cell. After fabrication of solar cells, a tungsten lamp of constant light source ($200\text{mW}/\text{cm}^2$) is used to study the performance of DSSC. The performance of the DSSC is be evaluated in terms of short circuit current (JSC) open circuit voltage (VOC), fill-factor (FF) and power conversion efficiency (η).

RESULT AND DISCUSSION:

Structural Analysis:

The crystal structure analysis of as prepared TiO₂ working electrode and commercially available TiO₂ Nano powder which is used for the preparation of working electrode is carried out by using X-ray diffraction method. The X-ray diffraction machine model Rigaku Miniflex 600 is used to perform qualitative and quantitative analysis of polycrystalline materials. Fig.1. shows the XRD pattern of commercial available TiO₂ powder, as prepared TiO₂ film and FTO substrate. The XRD patterns of commercial TiO₂ powder, as prepared TiO₂ film consists of seven peaks raised at $2\theta = 25.62^\circ, 38.11^\circ, 48.30^\circ, 54.13^\circ, 55.38^\circ, 62.88^\circ, 75.19^\circ$ corresponding to (101), (004), (200), (105), (211), (204) and (215) planes of Anatase structure of TiO₂. Moreover, the TiO₂ film consists of some extra peaks which are corresponding to the FTO substrate as confirmed from XRD pattern of FTO substrate. There are no any other peaks observed in the sample confirms the purity of the film.

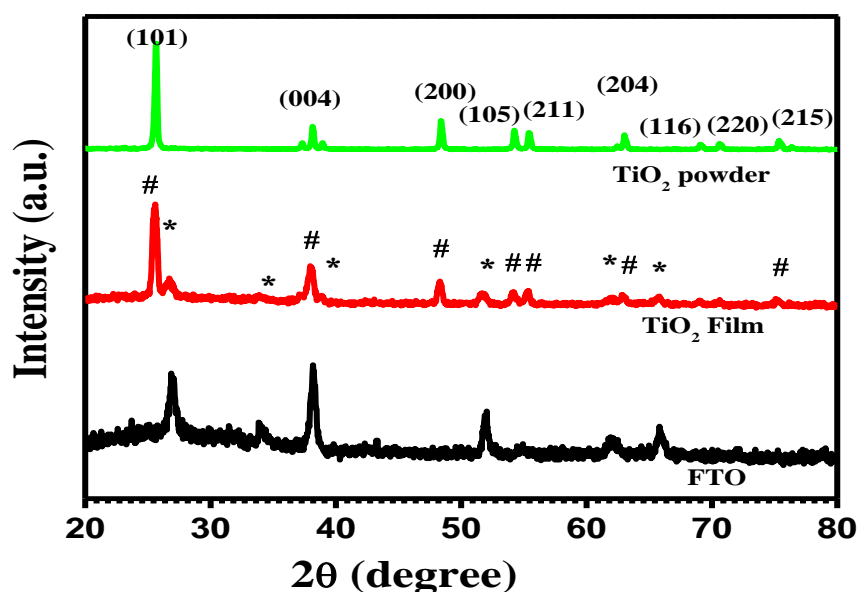


Fig. 1.: X-ray diffraction pattern of commercial TiO₂ powder, as prepared TiO₂ film and FTO substrate respectively.

The average crystallite size (t) of TiO₂ powder and film is estimated by using Debye-Scherrer formula given by:

$$t = \frac{0.94 \lambda}{\beta \cos \theta}$$

where λ is the wavelength of CuK α = 1.54 Å, β the full-width at half-maximum of diffraction peak measured in radian and θ is the Bragg's angle of the X-ray pattern at maximum intensity. The estimated crystallite size of TiO₂ powder was found to be around 40 nm whereas, for the TiO₂ film it is found to be 23 nm.

Optical Properties of TiO₂: The optical analysis of the as prepared working electrode is carried out by taking the absorbance spectra using UV-vis spectrometer model: UV-1800, SHIMADZU. The absorbance spectra of as prepared film, different dyes such as Rose Bengal and Spinach and TiO₂ films loaded with different dyes has been recorded and shown in Fig. 2. Care full observation of spectra shows that the dyes are successfully adsorbed on the TiO₂ film. The absorption data obtained from UV-vis spectrometer for TiO₂ film are used to calculate the bandgap energy. To calculate the band gap of TiO₂ film the Tauc plot has been plotted as shown in Fig 2. (b). the band gap of TiO₂ film was found to be 3.9 eV. However, the obtained bandgap is higher than the reported bandgap (3.2 eV) of bulk TiO₂. It is well reported that, with decrease in size of crystal, the value of band gap increases.

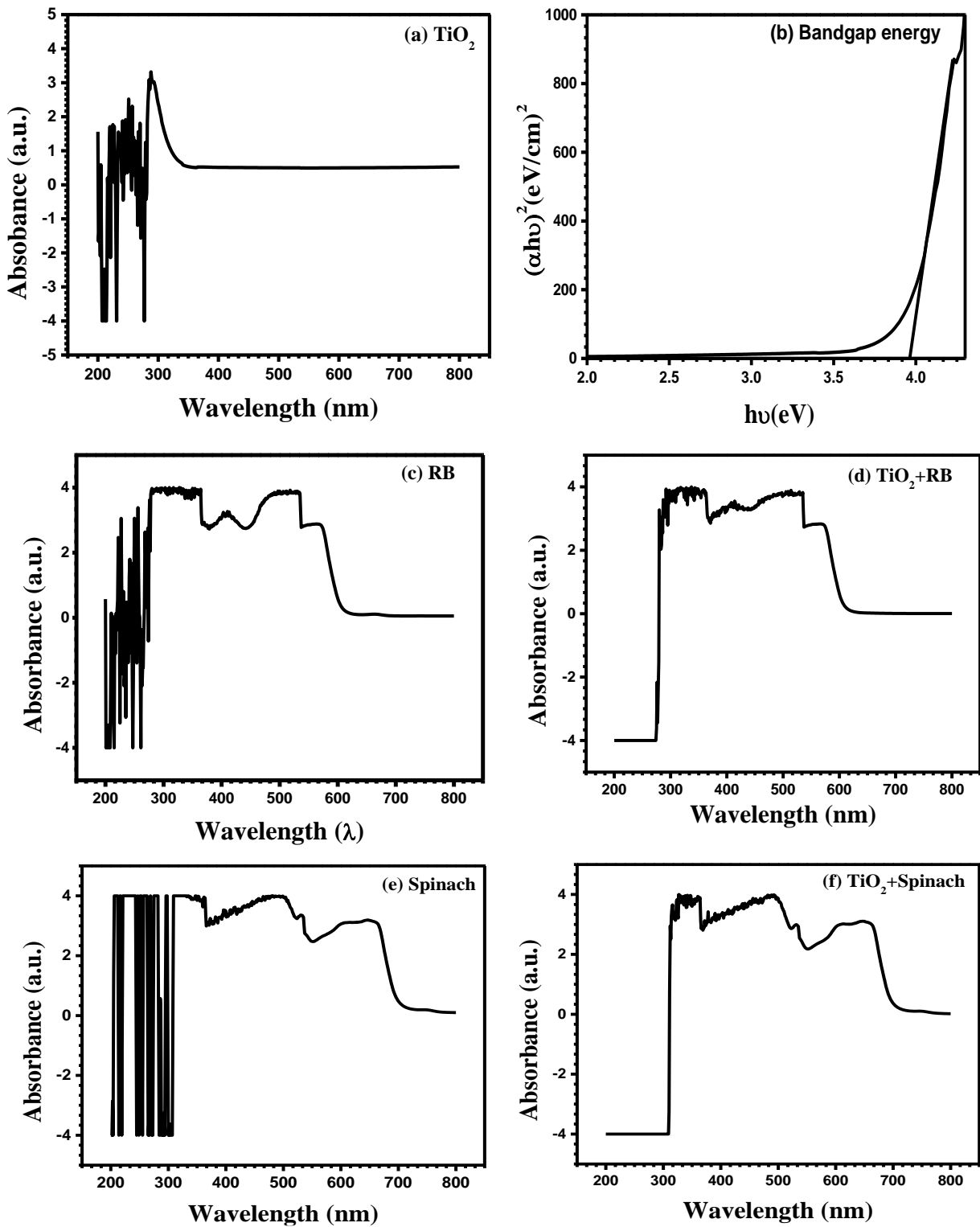


Fig. 2.: UV- visible absorbance spectra of a) TiO₂ film, c) Rose Bengal dye, d) TiO₂ film loaded with Rose Bengal dye, e) Spinach dye, f) TiO₂ loaded with spinach dye and b) Tauc plot of TiO₂ film.

I-V characteristics of DSSC: Different DSSCs were prepared using TiO₂ with different Dyes. To study the performance of these DSSCs, the I-V characteristics of these cells were recorded in the lab under tungsten lamp of 200W power. Fig. 3. Shows the I-V plots of as prepared different DSSCs. The resultant values of various parameters cells are summarized In Table 1. It is clearly found that the power conversion efficiency of commercially prepared Rose Bengal dye is greater than that of the naturally prepared dyes using plant leaves extract. Which is observed to be $\eta = 0.85125\%$. Similarly, the other factors like JSC, VOC, Vm and Jm has higher value for Rose Bengal dye than naturally prepared dyes.

Table 4.1.: Various parameters of as prepared different DSSCs obtained from I-V characteristics.

Sr. No.	Dye	Solvent	J_{max} ($\mu\text{A}/\text{cm}^2$)	V_{max} (V)	J_{sc} ($\mu\text{A}/\text{cm}^2$)	V_{oc} (V)	Fill Factor	Power Conversion Efficiency (%)
1	Rose Bengal	Ethanol	6.9356	0.00959	8.04151	0.01508	0.5484	0.85125
		Acetonitrile	0.016512	0.020021	0.03909	0.02907	0.29091	0.0004231
2	Spinach	Ethanol	0.019206	0.018074	0.044762	0.02798	0.27714	0.0004443
		Acetonitrile	0.035846	0.016966	0.105518	0.02590	0.2224	0.00077841
		Acetone	0.027757	0.070164	0.055072	0.10004	0.35348	0.0024929
3	Neem	Ethanol	0.00827	0.010033	0.021914	0.01802	0.210126	0.00010621
		Acetonitrile	0.01941	0.025044	0.066563	0.03412	0.214134	0.0006225
4	Mint	Ethanol	0.019121	0.023945	0.055297	0.03798	0.218013	0.00058608

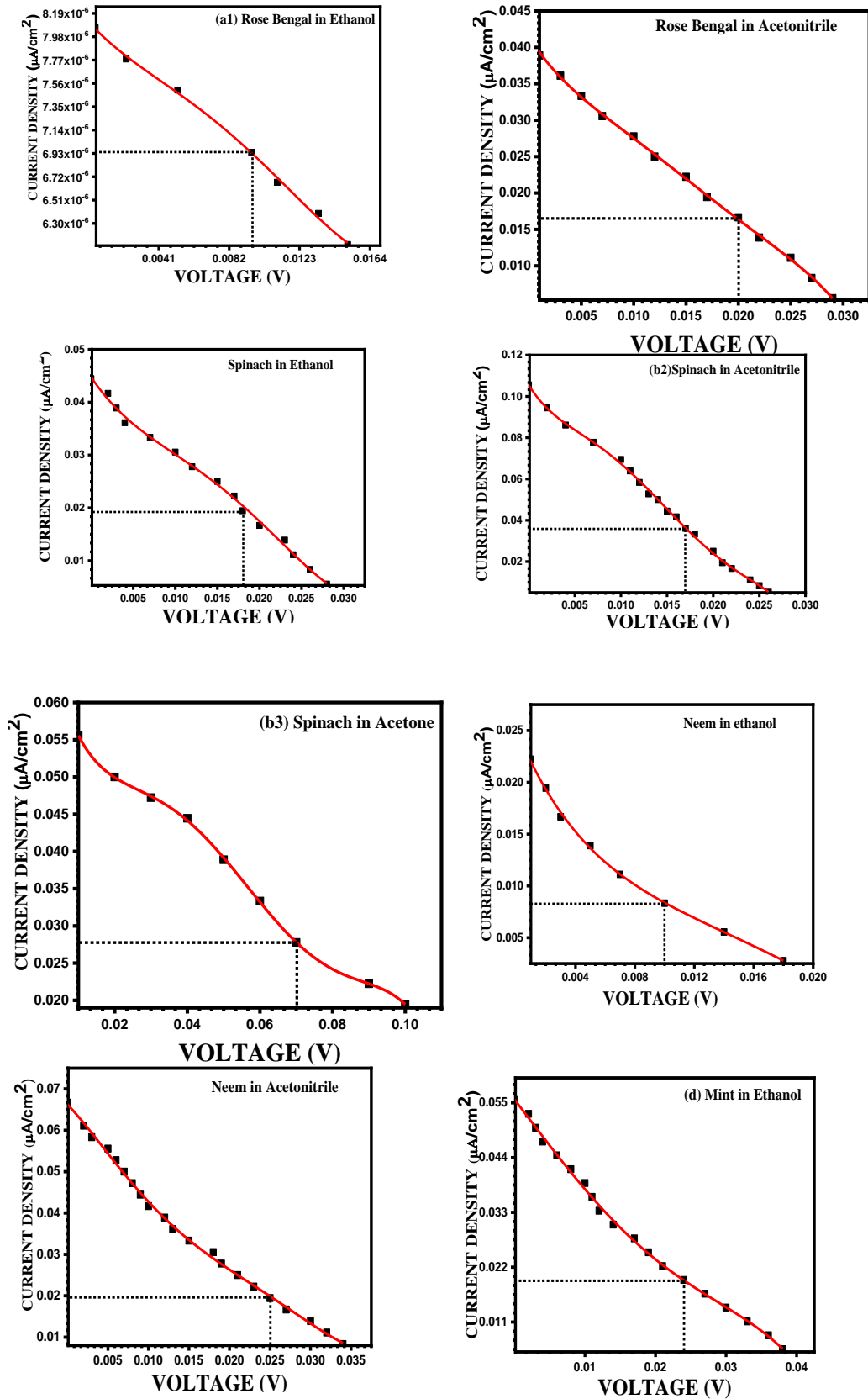


Fig. 3. I-V Characteristics of as prepared different DSSCs.

CONCLUSION:

In conclusion, an attempt has been made to fabricate the dye sensitized solar cell by using commercially available TiO₂ nano powder for the various dyes such as synthetic Rose Bengal, and different natural dyes like spinach, neem and mint. The working electrode was prepared by making the paste of commercially available TiO₂ nano powder on FTO substrate using doctor blade technique. The X-ray diffraction study of as prepared film shows the anatase phase of TiO₂. The band gap of the as prepared film was found to be 3.9 eV as confirmed by UV-vis analysis. Moreover, the dye absorption on the TiO₂ film was also confirmed by UV-visible spectroscopy. The extraction, preparation and photovoltaic performance of DSSCs based on commercially available Rose Bengal dye and naturally prepared dyes using plant leaves extract were optimized. Dye loaded film clearly shows the enhancement in absorbance in the visible region. Finally, the performance of the as prepared cell has been checked. It is observed that the film loaded with Rose Bengal dye gives the high efficiency 0.85125 percent as compared to the natural dyes. The other parameters of the cell were also calculated. Natural dyes can be easily and safely extracted by simple techniques. Among the natural dyes spinach extracted in acetone gave the highest performance as compared with other dyes. Therefore, it can be concluded that the natural dyes which are extracted from plants leaves may be used as the promising dye for dye sensitized solar cell.

References:

- [1] S.N. Karthick, K.V. Hemalatha, C. Justin Raj, A. Subramania, Hee-Je Kim; Preparation of TiO₂ paste using poly (vinylpyrrolidone) for dye sensitized solar cells; Nanoscience and Technology, Pondicherry University; 520(2); 7018-7021;2012.
- [2] Khushboo Sharma, Vinay Sharma and S.S. Sharma; Dye-Sensitized Solar Cells: Fundamentals and Current Status; Nanoscale Research Letter; 381(13); 1-46; 2018.
- [3] Ahmed M. Ammar, Hemdan S. H. Mohamed, Moataz M. K. Yousef, Ghada M. Abdel-Hafez, Ahmed S. Hassanien, and Ahmed S. G. Khalil; Dye-Sensitized Cells (DSSCs) Based on Extracted Natural Dyes; Nanomaterials; 1867271(3); 1-11; 2019.
- [4] Abhishek Attri; Dye-Sensitized Solar Cell Synthesis Using Green Extract: Natural Approach; Science and Research (IJSR); 2319(5); 71-89; 2018.
- [5] D. Sinha, D. De, D. Goswami and A. Ayaz; Fabrication of DSSC with Nanostructured ZnO Photo Anode and Natural Dye Sensitizer; Science Direct; 5(4); 2056-2063; 2018.

[6] Jose A. Castillo-Robles, Entique Rocha-Rangel, Jose A. Ramirez-de-Leon, Frida C. Caballero-Rico and Eddie N. Armendariz-Mireles; Advances on Dye-Sensitized Solar Cells (DSSCs) Nanostructured and Natural Colorants: A Review; Composites Science; 288(5); 1-25; 2021.

[7] Sofyan A. Taya, Taher M. El-Agez, Hatem S. El-Ghamri, and Monzir S. Abdel-Latif; Dye-Sensitized Solar Cell using fresh and dried natural dyes; Material Science and Applications; 2(2); 37-42; 2013.

[8] Monzir S. Abdel-Latif, Mahooud B. Aburban, Taher M. El-Agez and Sofyan A. Taya; Dye-Sensitized Solar Cells Using Dyes Extracted from Flowers, Leaves, Parks and Roots of Three Trees; Renewable Energy Research; 5(3); 293-310; 2015.

© 2024. This work is published under

<https://creativecommons.org/licenses/by/4.0/legalcode> (the “License”).

Notwithstanding the ProQuest Terms and Conditions, you may use this content in accordance with the terms of the License.

¹Janhavi Joshi
¹ShubhangiAthawale
² Shailesh Tiwari
²Ashitosh Deshmukh
³DeepaliGulwade

Synthesis of CuO Nanoparticles by Using *Butea Monosperma* by Green Approach



Abstract: - Green synthesis of nanoparticles aims in decreasing the use of toxic chemicals. Plants leaves contain reducing as well as the very good capping agents. Synthesis of CuO nanoparticles by green approach is extremely promising because of its environmentally friendly behavior and their versatile application. In this study we use *Butea monosperma* for synthesis of CuO nanoparticles under atmospheric condition. The synthesis of CuO nanoparticles were confirmed by spectral characterization using UV- visible spectrometry, FTIR and XRD studies.

Keywords: *Butea monosperma*, CuO nanoparticles, capping agents.

V. INTRODUCTION

The 'Nano' is referred to as Greek prefix meaning 'dwarf' or something very small and depicts one thousand millionth of a meter. Nanoparticles are the fundamental component of nanotechnology. Nanoparticles are the particulate matter with at least one dimension less than 100nm. They can be made up of carbon, metal, metal oxides or organic matter. There are vast applications of nanoparticles synthesized by eco-friendly way they are used in wastewater treatment for degradation of dyes, as antimicrobial agents for bio imaging, drug delivery system, biosensor, tissue engineering, multicolor optic coding, protein detection, cancer treatment therapy and in many other fields.

VI. MATERIALS AND METHODS

1. Fresh leaves of *Butea monosperma* were collected from Amravati, Maharashtra, India. The fresh leaves then wash thoroughly with tap water and then with deionized water. Out of that 5 gram of leaves were crushed in mortar and pestle by adding ethanol and then followed by filtration.
2. 5 gram of previously washed leaves were boiled from 200 to 50 ml in distilled water with stirring and then filtered with filter paper. The filtrate were stored in refrigerator for further use .

III . SYNTHESIS

1. Synthesis of CuO nanoparticles using NaOH

Copper sulphate (0.5m) solution was prepared in 50ml of distilled water. Then 10 ml of leaf extract prepared in ethanol were added drop wise with dropper. Heating and stirring process was done for 60 minutes at 80 degree

¹Corresponding author: Janhavi Joshi, Department of Chemistry Government Vidarbha institute of science and humanities Amravati (MS) INDIA

^{1,2,3}Department of Chemistry/Physics Government Vidarbha institute of science and humanities Amravati (MS) INDIA

Copyright©JES2024on-line:journal.esrgroups.org

Celsius on hot plate with magnetic stirrer. Then 0.5 molar of NaOH solution were added drop wise for 45 minutes at 80 degree Celsius. Then nanoparticles were allowed to settle for overnight. Sonicate the product for 30 minutes. Suspension was taken out by syringe and filtered with help of whatman filter paper. These particles were dried in hot air oven and then kept in muffle furnace to remove further moisture and impurities at temperature 360 degree Celsius for 1 hour.

2. Synthesis of CuO nanoparticles without using NaOH

On hot plate with magnetic stirrer 0.5 molar of copper sulphate solution was prepared in 50ml of distilled water. Then 10 ml of extract prepared in distilled water were added drop wise with dropper. This process was done for 60 minutes at 80 degree Celsius on hot plate with magnetic stirrer. Then the particles were allowed to settle down for overnight. On next day sonication was done for 30 minutes. Suspension was taken out by syringe and filtered with help of whatman filter paper. Then particles were dried in hot air oven and then kept in muffle furnace to remove further moisture and impurities at temperature 360 degree Celsius for 1 hour.

IV. CHARACTERIZATION

➤ UV- VISIBLE ANALYSIS

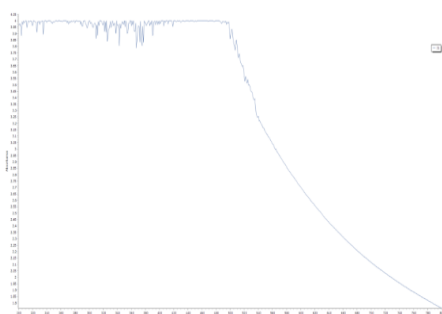


Fig.1

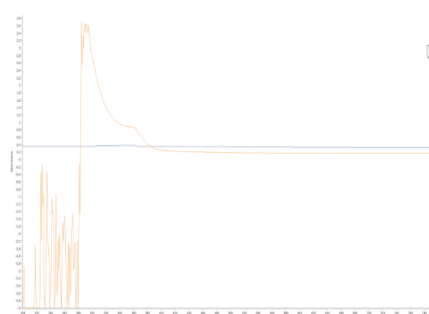


Fig.2

The UV-Visible absorbance spectra of CuO nanoparticles were recorded in range of 200-800nm using shimadzu 1800 spectrophotometer. In fig.1 [Extract in alcohol + NaOH] Solvent used for UV analysis was distilled water. The maximum absorbance found at 500nm. In fig.2 [Extract in H₂O without NaOH] Solvent used for UV analysis was distilled water. The maximum absorbance found at 280nm.

FT-IR Spectrum analysis

synthesized CuO nanoparticles was recorded by Bruker IR spectrophotometer.

Fig.3 [Extract in alcohol + NaOH] The IR spectrum of CuO nanoparticles shows the band between the ranges 550-780cm⁻¹. This indicates Cu-O stretching and formation of CuO nanoparticles. Fig.4 [Extract in H₂O without NaOH]. The IR spectrum of CuO nanoparticles shows the band between the ranges 550-780cm⁻¹. This indicates Cu-O stretching and formation of CuO nanoparticles. At 1000-2000cm⁻¹ shows band it means stretching in C-O and C-N bond due to presence of phytochemicals in plant extract.

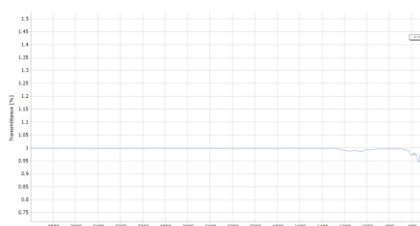


Fig. 3

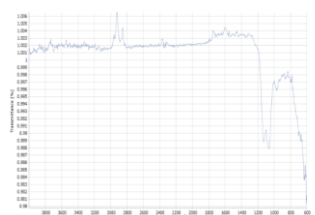


Fig. 4

➤ XRD Analysis

The spectrum of CuO nanoparticles was carried on Rigaku X-ray diffractometer.

Fig.5 [Extract in alcohol + NaOH]. The CuO nanoparticles synthesized with NaOH showed peak at angle $2\theta = 35.38, 38.81$ and 58.66 respectively with (111), (111), (202) intensity which corresponds to cubic lattice structure.

Fig.6 [Extract in H₂O without NaOH]. The CuO nanoparticles synthesized without NaOH showed peak at angle $2\theta = 35.67, 38.78$ and 58.34 respectively with (111), (202), (113) intensity which correspond to cubic lattice structure.

There is decrease in intensity if we compared Fig.5 and Fig.6

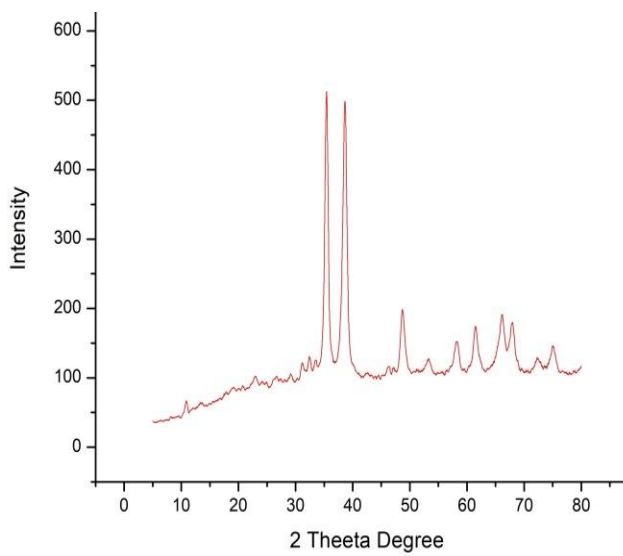


Fig. 5

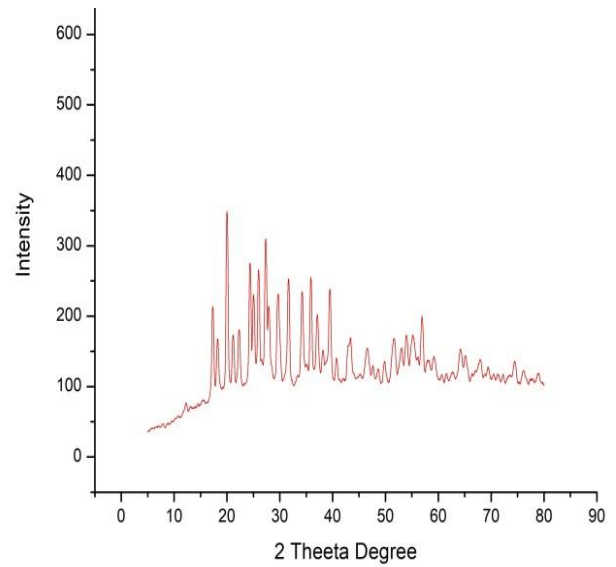


Fig. 6

V. BIOLOGICAL ACTIVITY

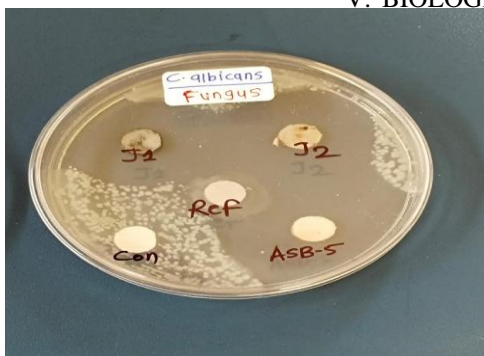


Fig. 7

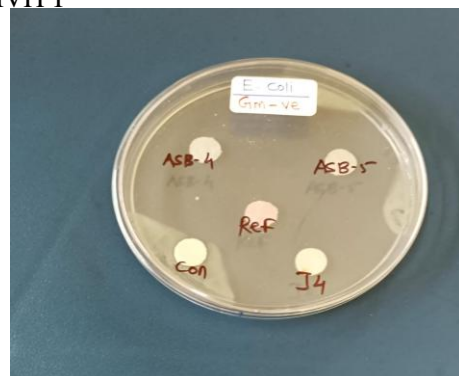


Fig. 8

Fig.6-CuO nanoparticles prepared from Extract in alcohol with NaOH (J1) are resistant to fungus *C.albicans*
 Fig.7-CuO nanoparticles prepared from Extract in H₂O without NaOH (J4) are resistant to gram negative

bacteria *E.coli*

CONCLUSION

The green synthesis of CuO nanoparticles was efficaciously performed using copper sulphate as precursor and *Butea monosperma* plant leaves extract as a powerful reducing agent. The applied technique is undemanding and easily biodegradable due to presence of phytochemicals and is carried out in short time.

The visible green color indicates the production of CuO nanoparticles. Further, demanding the reduction of Cu to CuO nanoparticles using UV-Visible spectroscopy. The ultraviolet spectroscopic absorption peak is at 500nm and 280nm. In the IR spectrum of CuO nanoparticles shows band between the ranges 550-780 cm^{-1} . The XRD pattern of synthesized CuO nanoparticles show intense peak at $2\theta = 35.38, 38.81$ and 58.66 which corresponds cubic lattice structure X-ray intensity vary when nanoparticles synthesized with NaOH and without NaOH.

ACKNOWLEDGMENT

The authors are grateful to the staff and laboratory of Department of Chemistry of Government Vidharbha Institute of Science and Humanities Amravati, Maharashtra, India, for providing all the facilities to carry out this study. The authors are also thankful to Department of physics Government Vidharbha Institute of Science and Humanities Amravati, Maharashtra, India for their assistance in instrumental analysis.

REFERENCES

- [1] R. Khani, B. Roostaei, G. Bagherzade and M. Moudi, Green synthesis of copper nanoparticles by fruit extract of *Ziziphus spina-christi* (L.) Willd.: Application for adsorption of triphenylmethane dye and antibacterial assay. *Journal of Molecular Liquids*, 255 (2018) 541-549.
- [2] S. Shende, A.P. Ingle, A. Gade and M. Rai, Green synthesis of copper nanoparticles by *Citrus medica* Linn. (Idilimbu) juice and its antimicrobial activity. *World Journal of Microbiology and Biotechnology*, 31 (2015) 865-873.
- [3] MW. Amer and A.M. Awwad, Green synthesis of copper nanoparticles by *Citrus limon* fruits extract, characterization and antibacterial activity. *Chem Int*, 7 (2021) 1-8.
- [4] J.K. Patra and K.-H. Baek, Green synthesis of silver chloride nanoparticles using *Prunus persica* L. outer peel extract and investigation of antibacterial, anticandidal, antioxidant potential. *Green Chemistry Letters and Reviews*, 9 (2016) 132-142.
- [5] A. Roy and N. Bharadvaja, Silver nanoparticles synthesis from a pharmaceutically important medicinal plant *Plumbago zeylanica*. *MOJ Bioequiv Availab*, 3 (2017) 00046.
- [6] P. Vanathi, P. Rajiv and S.Rajeshwari, *Bulletin of Materials Science* 39(5), 1165 (2016).
- [7] M.E.Elena, A.K. Aslan, I.S.Vitaly, Springer International Publishing Switzerland, 2016.
- [8] S.Yang, C.Wang, L.Chen, S. Chen, *Materials Chemistry and Physics* 120, 296 (2010).
- [9] M. B. Gawande, A. Goswami, F.-X. Felpin, T. Asefa, X. Huang, R. Silva, X. Zou, R. Zboril and R. S.Varma, Cu and Cu-based nanoparticles: synthesis and applications in catalysis, *Chem. Rev.*, 2016, 116, 3722-3811

[10] D. Vaidehi, V. Bhuvaneshwari, D. Bharathi, and B. P. Sheetal, "Antibacterial and photocatalytic activity of copper oxide nanoparticles synthesized using Solanum lycopersicum leaf extract," *Materials Research Express*, vol. 5, no. 8, Article ID 085403, 2018.

¹K.D. Jagtap,
²R.V. Barde,
³K.R. Nemade,
⁴P. R. Malasane,
⁵S. A. Waghuley,

Electrochemical Study of 5% doped TiO₂ graphene nanocomposites electrode for Supercapacitor application



Abstract: - Graphene, considered as the parent of all carbon materials, is a two-dimensional layered hexagonal lattice of sp² bonded carbon atoms. This work has been carried out to explore the electrochemistry graphene/titanium oxide nanocomposites. Herein the present article reports the synthesis of graphene-TiO₂ nanocomposites by ex-situ synthesis method. The synthesized nano-composites have been characterized by X-ray diffraction analysis (XRD). Electrochemical properties of the prepared nanocomposite electrodes and the supercapacitor have been studied using cyclic voltammetry (CV) in 3 M KOH as electrolyte. The 5% TiO₂ doped graphene nanocomposite electrode showed a specific capacitance of 167.5 F/g.

Keywords: Supercapacitors, Graphene, titanium oxide, nanocomposites, specific capacitance, cyclic voltammetry, X-ray diffraction and ex-situ synthesis.

I. INTRODUCTION

In the 21st century, the development of stored energy is a major concern for technology expansion. In particular, electronic devices such as mobile phones, laptops, and electric cars require energy supply from energy storage devices. However, most batteries have low power density, short life cycle time, and take a long time to charge memory to the device. [1] New technologies are therefore needed that can provide longer cycle times and more energy. It can be charged in a short time. Energy storage devices have great potential, and this field has attracted great interest among researchers to develop more efficient energy storage devices. One such device is the supercapacitor. [2]

Supercapacitors have much larger capacitance values than traditional capacitors. Supercapacitors have lower voltage limits that can even out the performance differences between rechargeable batteries and common electrolytic capacitors. [3] Issues associated with modern society's dependence on fossil fuels include rising fuel prices, pollution, global warming, and geopolitical concerns. Mitigating these problems is an increasingly important goal that can be achieved through the development of other energy sources and storage technologies. As a result, interest in high-performance, high-energy-density energy storage systems has recently increased. [4] Slow charge–discharge rate, short life cycles, and high weight of battery limit its applications in portable and wearable devices. At present-day, supercapacitors have been receiving a countless consideration, because of their significant features such as high energy density, great power density, light weight, fast charging–discharging rate and long life span.[5]

The performance of low-cost and eco-friendly energy conversion and storage components which are mostly requirements of electrical energy storage systems, such as batteries and electrochemical capacitors, depends on the physical and chemical properties of electrode materials.[6] Both EDL and pseudocapacitive behavior properties in supercapacitor electrodes can be achieved using advanced nanocomposites. At the same time, the performance of supercapacitors is also affected by the type of electrolyte. Therefore, the appropriate combination of electrode materials and electrolytes is important for the development of high-performance supercapacitors. [7] Various transition metal oxides (TMOs) such as TiO₂, RuO₂, MnO₂, V₂O₅, Fe₂O₃, Co₃O₄, etc. are used as electrode materials in the fabrication of supercapacitor devices. Most TMO-based supercapacitors operate via a pseudocapacitive charge storage mechanism. [8] To further

improve conductivity, TMO is often inserted/mixed into carbon-based nanostructures. Examples: graphene, carbon nanotubes (CNTs), activated carbon. As supercapacitor electrodes, his TMO carbon composites mentioned above are known to store charge through a combination of EDLC and pseudocapacitance mechanisms. Additionally, the TMO carbon composite electrode has a high specific surface area. In this study, graphene-TiO₂ nanocomposites were synthesized by ex situ synthesis method. In this method, TiO₂ nanoparticles are uniformly dispersed on the graphene layer. This method increases the specific surface area and power of the supercapacitor. [9]

*Corresponding author: Government Vidarbha Institute of Science and Humanities, Amravati 444604, India.
Email id: rajeshbarde1976@gmail.com

II MATERIALS AND METHODS

Synthesis of Graphene and Titanium oxide (TiO₂) nanoparticle

Graphene was synthesized by the electrochemical exfoliation method. We take and 480 ml double distilled water and 20 ml H₂SO₄ in beaker (96: 04 ratio of double distilled water and concentrated H₂SO₄). We use graphite electrode as anode (+ve terminal) and copper electrode as cathode (-ve terminal). Now We supply the dc voltage from the dc power source, (dimmer state via pair of diode 6A) in the range 9 - 12 v. We get precipitate after 24 Hours at the bottom of beaker. We filter this pot by using watmann filter paper and wash by double distilled water 3 times. To remove the moisture, we put this graphene powder in oven at 150°C for 2 Hours.

Titanium dioxide nanoparticles were synthesized by sol gel method. 12 ml TTIP (Titanium tetra Iso-prapoxide) was dissolved into 10 ml ethanol in 500 beaker and whole mixture was stirred for 30 minutes using magnetic stirrer for hydrolysis reaction, 3 ml of deionised water and 2 ml of hydrochloric acid were added to the solution dropwise. The mixed solution was then stirred constantly for 2 hours, to get homogenous solution. The PH value of solution was maintained in the acidity range of PH3. After 24 Hours, the gel was dried and then heated at 400°C dried in muffle furnaces.[10]

Preparation of Graphene-Zinc oxide (G-ZnO) Nanocomposite

Graphene doped with ZnO nanoparticles was synthesized by using an ethanolic solution of graphene and 5 wt.% concentration of ZnO using Ex-situ technique in wt.% stoichiometry.

III RESULT AND DISCUSSION

Fig. 1(a) represents the XRD of pure graphene which gives the intense peak at $2\theta = 26^\circ$ and $2\theta = 42.5^\circ$. Fig.(b) represents the XRD of TiO₂ nanoparticle. XRD pattern of TiO₂ shows characteristic diffraction peaks located at $2\theta = 25.3^\circ, 37.8^\circ, 48.0^\circ, 53.9^\circ, 55.0^\circ, 62.7^\circ, 68.7^\circ, 70.3^\circ,$ and 75.0° corresponding to the (101), (004), (200), (105), (211), (204), (116), (220) and (215) planes of tetragonal anatase TiO₂ (JCPDS card no. 21-1272), respectively.[11] Strong diffraction peaks at 25° and 48° indicating TiO₂ in the anatase phase. The peaks are sharp and well defined which reveal well crystalline nature of the nanoparticles. No characteristic peaks of other impurities were detected in the diffractogram. Furthermore, the XRD patterns of G-TiO₂ nanocomposite material are provided in figure 2. The presence of all diffraction peaks of pure graphene ($2\theta = 26^\circ$ and 42.5°) in Graphene-TiO₂ composite indicate that the addition of TiO₂ does not influence the preferable orientation of the graphene and other strong peaks at 25° and 48° confirm the presence of TiO₂.

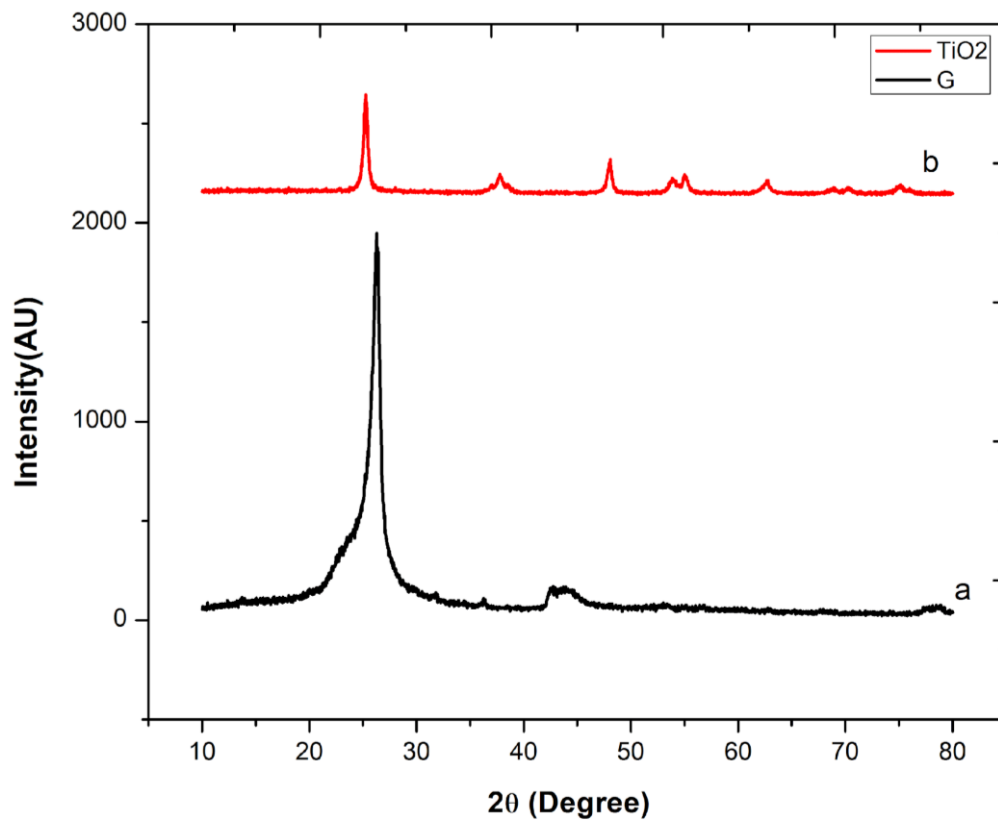


Fig. 1. a) XRD of pure graphene b) XRD of TiO_2 nanoparticle

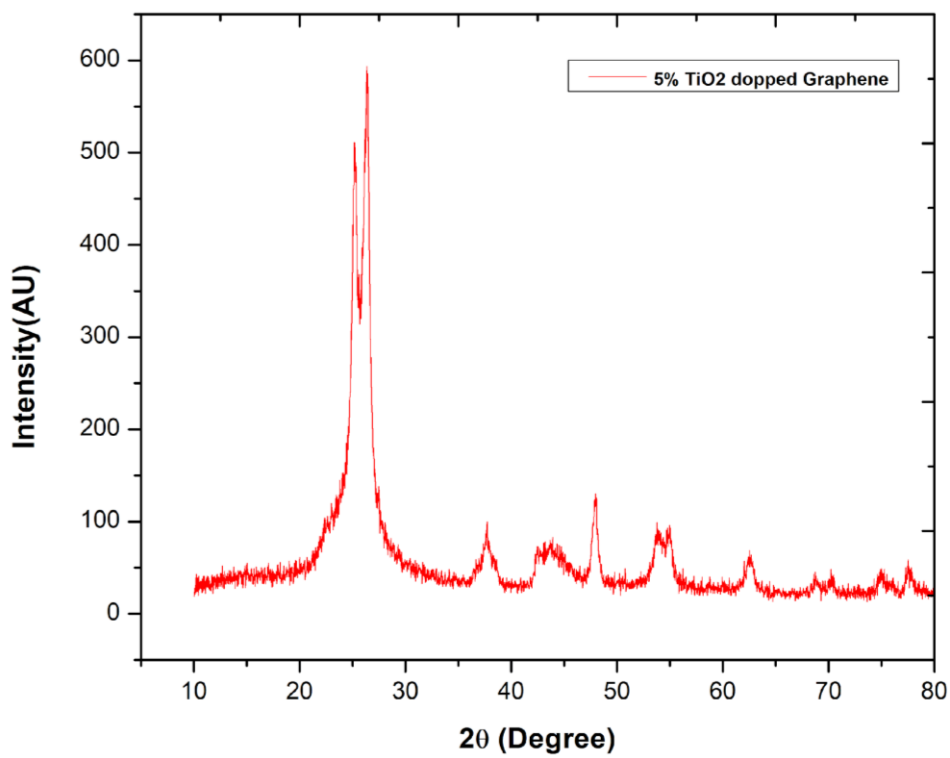


Fig. 2. XRD of 5 % TiO_2 doped Graphene

Supercapacitive study:

Electrochemical energy storage capacitance of 5 % TiO₂ doped graphene nanocomposite as electrode of electrochemical capacitor was evaluated from cyclic voltametric (CV) curves. Fig. 3 illustrates the cyclic voltammetry (CV) curves of graphene-TiO₂ nanocomposite recorded at a scan rate of scan rates 20 mv/s, 40 mv/s, 60 mv/s and 80 mv/s in 3 M KOH electrolyte solution, in potential range of 0 to 0.5 V, which shows quasi-rectangular graphs indicating a pseudo-capacitive behaviour. Specific capacitance has been estimated using the relation

$$C_p = \frac{A}{2mk\Delta V} \quad (1)$$

Where A is the area under the CV curve, m is the mass loaded, k is the scan rates and ΔV is the potential window.

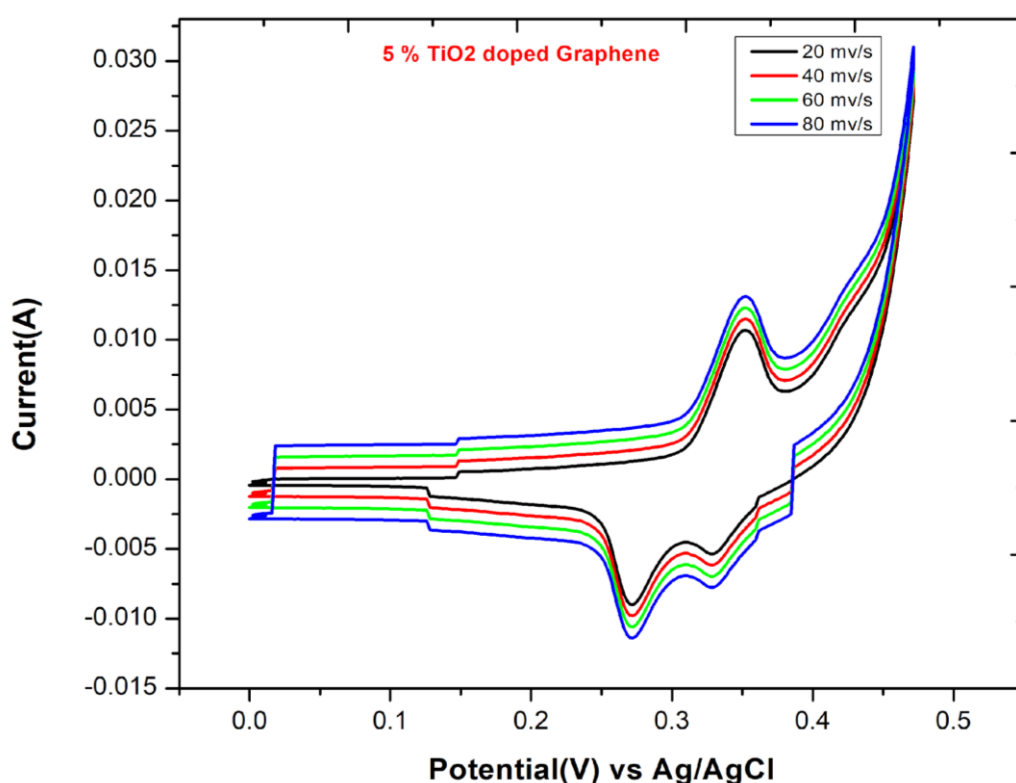


Fig. 3. CV Curve of 5 % TiO₂ doped graphene at scan rates 20 mv/s, 40 mv/s, 60 mv/s, 80 mv/s

According to Eq. (1), the calculated specific capacitance C_s values of the graphene-TiO₂ hybrid electrode are 167.5 F/g, 102.7 F/g, 81.2 F/g and 70.4 F/g at scan rate of 20 mv/s, 40 mv/s, 60 mv/s and 80 mv/s respectively.

IV SUMMARY

The 5% TiO₂ doped graphene hybrid nanostructure as an electrode material for supercapacitors was successfully synthesized using a ex-situ synthesis method. The structural and capacitive behaviours of the as-prepared materials were well investigated. XRD graph confirmed the structure of TiO₂ nanoparticles, pure graphene and TiO₂ doped graphene. Our results showed that the graphene-TiO₂ hybrid electrode exhibited a maximum specific capacitance of 167.5 F/g at a scan rate of 20 mV/s in 3 M KOH electrolyte solution. The improved specific capacitance of the graphene-TiO₂ hybrid

electrode was mainly attributed to the pseudocapacitance of the anatase phase of TiO₂ and was partially influenced by the intrinsic double-layer capacitance of the graphene sheets. [12]

References:

- [1] S.Sharma, A.K. Panwar, M.M. Tripathi,“Storage technologies for electric vehicles,” Journal of Traffic and Transportation Engineering (English Edition), Vol.7, Issue.3, pp.340-361, June 2020
- [2] A.D.Setyoputra, H. Ruffa, H. Sutanto, A. Subagio,“The Characterisation of MWCNT-rGO-TiO₂ Nanocomposite as Potential Electrode Material for Hybrid Supercapacitor,” Int. J. Electrochem. Sci, Vol.17,Issue.5, pp. 1-10, 2022
- [3] S.E. Umoru, “Capacity Imbalance and Diffusion Kinetic Between the Electrodes of Hybrid Supercapacitor: A Review”, International Journal of Scientific Research in Physics and Applied Sciences, Vol.12, Issue.1, pp.07-23, 2024
- [4] Ander González, Eider Goikolea, Jon Andoni Barrena , Roman Mysyk, “Review on supercapacitors: Technologies and materials,” Renewable and Sustainable Energy Reviews, Vol.58, Issue.5, pp.1189–1206, 2016
- [5] Santosh J. Uke, Vijay P. Akhare , Devidas R. Bambole , Anjali B. Bodade,Gajanan N. Chaudhari, “Recent Advancements in the Cobalt Oxides, Manganese Oxides, and Their Composite As an Electrode Material for Supercapacitor: A Review,” Frontiers in Materials, Vol.4, Issue.21, pp. 1-6, 2017
- [6] S.E. Umoru, “Hybrid Supercapacitor For Energy Storage Devices: A Review”, Journal of Physics and Chemistry of Materials Vol.10, Issue.4, pp.24-35, 2023
- [7] S. Sundriyal, V. Shrivastav, M. Sharma , S. Mishra, A. Deep, “Significantly enhanced performance of rGO/TiO₂ nanosheet composite electrodes based 1.8 V symmetrical supercapacitor with use of redox additive electrolyte,” Journal of Alloys and Compounds, Vol.790, Issue.35 pp.377-387,2019
- [8] S. Mandal, J. Hu, S.Q. Shi, “A comprehensive review of hybrid supercapacitor from transition metal and industrial crop based activated carbon for energy storage applications,” materialstodays COMMUNICATIONS Vol.790, Issue.3 pp.1-56,2023
- [9] P. Nagarajua , A. Alsalmeb , A. Alswielehb , R. Jayavela, “Facile in-situ microwave irradiation synthesis of TiO₂/graphene nanocomposite for high-performance supercapacitor applications,” Journal of Electroanalytical Chemistry, Vol. 808 Issue.1 pp. 90–100, 2018
- [10] M. M. Ahmad, S. Mushtaq, H. S. Al Qahtani, A. Sedky, M. W. Alam , “Investigation of TiO₂ Nanoparticles Synthesized by Sol-Gel Method for Effectual Photodegradation, Oxidation and Reduction Reaction,” crystals, Vol. 11 Issue.12 pp. 1-16, 2021
- [11] S.R. Damkale, S. S. Arbuji, G. G. Umarji, S. B. Rane and B. B. Kale, “Highly crystalline anatase TiO₂ nanocuboids as an efficient photocatalyst for hydrogen generation,” RSC Adv., Vol. 11 Issue.13 pp. 7587-7599, 2021
- [12] A. Ramadoss, S. J. Kim, “Improved activity of a graphene–TiO₂ hybrid electrode in an electrochemical supercapacitor,” Carbon, Vol. 63 Issue.1 pp. 434-445, 2013

¹ Kalpana Sonkusare

^{2,*} Deepak Taikar

¹ S. J. Dhoble

**Synthesis, luminescence
characterization and energy
transfer in rare earth doped
apatite-type
Ca₉La(PO₄)₅(SiO₄)Cl₂ phosphors**



Abstract: - Rare earth (RE) doped Ca₉La(PO₄)₅(SiO₄)Cl₂ phosphors were synthesized using the conventional solid state reaction method. The synthesized phosphors underwent various characterization techniques, including XRD, SEM, FTIR, and photoluminescence (PL). The XRD analysis confirmed the formation of a single-phase Ca₉La(PO₄)₅(SiO₄)Cl₂ compound in hexagonal form with space group P6₃/m. The SEM results indicated that the particles were agglomerated and non-uniform in nature, ranging from a few μm. The PL investigation revealed that Ca₉La(PO₄)₅(SiO₄)Cl₂:Eu²⁺ and Ca₉La(PO₄)₅(SiO₄)Cl₂:Sm³⁺ phosphors can be excited by near-UV (n-UV) LED chips, which emits light in blue (454 nm) and orange-red (602 nm) region, respectively. Additionally, the energy transfer between Ce³⁺ to Eu²⁺ and Ce³⁺ to Sm³⁺ was also examined, and the PL results indicate that Ca₉La(PO₄)₅(SiO₄)Cl₂:(Ce³⁺,Eu²⁺) and Ca₉La(PO₄)₅(SiO₄)Cl₂:(Ce³⁺,Sm³⁺) phosphors could be useful for n-UV excited LED, display devices and related applications.

Keywords: Ca₉La(PO₄)₅(SiO₄)Cl₂, Apatite, Rare earth, Energy transfer, LED.

I. INTRODUCTION

Compounds that possess the apatite-type structure have been the subject of extensive research, owing to their potential for use as luminescent materials [1-4]. These compounds are typically expressed as M₁₀(XO₄)₆Z₂, with M representing a metal cation that can be monovalent (Na⁺, Li⁺), divalent (Ca²⁺, Sr²⁺, Mg²⁺), or trivalent rare-earth ion (La³⁺, Y³⁺, etc); XO₄ representing a complex anionic group (SiO₄, PO₄, GeO₄, VO₄ etc.); and Z being an anion (F⁻, Cl⁻, O²⁻, S²⁻, etc.) [5]. Apatites crystallize in the hexagonal form with space group P6₃/m [6]. Furthermore, apatite materials have been shown to have superior physical and chemical stability, and a rigid crystal structure compared to sulfides and oxysulfides. Additionally, the structure is characterized by two cation sites, with the 4f site being symmetric at C₃ and the 6h site being symmetric at C_s [5,7]. It is well-suited to the luminescence of trivalent rare earth (RE) ions due to the feature of low symmetry [8].

Rare earth doped inorganic phosphors are becoming increasingly popular due to their versatility and usefulness in various applications. They have been utilized in luminescent devices, sensor technologies, optoelectronic devices, display devices, bio-molecule detection, and biochemical probes, to name a few. Their unique properties make them highly desirable for a range of different industries and research fields [9,10]. Rare earth activated phosphors are widely used in solid state lasers, color display devices, energy-saving fluorescent lamps, and other applications. Research activities related to the preparation and characterization of rare earth doped phosphors are being carried out throughout the world. There is a growing interest in developing cheap and efficient sources of white light for various purposes, such as displays, liquid crystal displays, field emission displays, backlight, and alternatives to general lighting (incandescent light bulb). The phosphors doped with RE ions are usually categorized into two groups. The first group includes ions like Eu²⁺ and Ce³⁺, which emit broad band light as a result of the 5d-4f transition. The second group consists of ions such as Eu³⁺, Sm³⁺, Tm³⁺, Tb³⁺, Gd³⁺, and Yb³⁺, which emit narrow band light due to the transition between the 4f levels [11].

L. Liang et al. [12] synthesized Eu²⁺ doped Ca₉La(PO₄)₅(SiO₄)Cl₂ phosphor via high temperature solid state reaction method and reported that the prepared phosphor can be useful as a blue-emitting phosphor for WLED application. H. Liu et al. [13] reported n-UV excitable white light emitting Dy³⁺ doped Ca₉La(PO₄)₅(SiO₄)Cl₂ phosphor synthesized by high temperature solid state reaction method. The luminescence property of Eu³⁺ doped Ca₉La(PO₄)₅(SiO₄)F₂ phosphor was successfully tailored by replacing F⁻ with Cl⁻ and (PO₄)³⁻ with

¹Department of Physics, R.T.M. Nagpur University, Nagpur-440033, India

²Department of Physics, Shri Lemdeo Patil Mahavidyalaya, Mandhal-441210, India

*Corresponding author: Deepak Taikar

(MoO₄)³⁻, (VO₄)³⁻, (WO₄)³⁻, and (SO₄)³⁻ [14]. Over the years, many apatite-type phosphors were developed and their luminescence property were investigated such as La₆Ba₄(SiO₄)₆F₂:Dy³⁺ [15], Sr_{10-x}(SiO₄)₃(SO₄)₃O:xEu²⁺ [16], Ca_{2+x}La_{8-x}(SiO₄)_{6-x}(PO₄)_xO₂:Eu³⁺ [17], Mn₂Gd₈(SiO₄)₆O₂ [18], Ca₉Mg(PO₄)₆F₂:Eu²⁺, Mn²⁺ [19], Ca₂Gd₈(SiO₄)₆O₂:Eu³⁺ [20], Na₆(SO₄)₂FCl:RE [21] Ca₄Y₆(SiO₄)₆O:Ce³⁺/Mn²⁺/Tb³⁺ [22]. In this article, we report the synthesis of Ca₉La(PO₄)₅(SiO₄)Cl₂ phosphor doped with different RE ions, and their PL study were investigated in detail.

II. MATERIALS PREPARATION AND ANALYSIS

A series of singly (Eu³⁺, Ce³⁺, Sm³⁺), doubly (Ce³⁺, Sm³⁺) and (Ce³⁺, Eu³⁺) doped Ca₉La(PO₄)₅(SiO₄)Cl₂ phosphors were synthesized by conventional solid state reaction method. According to the stoichiometric compositions (molar proportion) the starting reagents CaCO₃, La₂(CO₃)₃, (NH₄)₂HPO₄, SiO₂, NH₄HCl₂ (all A.R. grade) and RE activators Eu₂O₃, Ce₂O₃, Sm₂O₃ were weighed and thoroughly mixed by grinding together in a mortar pestle for 30 min. The mixture was finely ground and then carefully transferred to a ceramic crucible. The samples were then heat treated at 800°C for 24 hours in a controlled muffle furnace. After the samples were collected from the furnace at room temperature, they were ground into a fine powder for further analysis and characterization.

To obtain the X-ray diffraction (XRD) data, a Rigaku Miniflex 600 X-ray diffractometer was used with Cu-Kα radiation (λ= 1.5409 nm) over an angular range of 10° to 90° in 2θ. The particle size of prepared sample was investigated by using Scanning Electron Microscope (SEM) INSTRUMENT ZEISS EVO SEM 18. A Fourier transform infrared spectrum (FT-IR) was recorded on Bruker Alpha FT-IR Spectrometer to get the information about present vibrational bonds stretching in the synthesized material. The PL excitation and emission spectra of all prepared phosphors were recorded on SHIMADZU Spectrofluorophotometer RF-5301 PC with a Xenon flash lamp (150 W). The color chromaticity coordinates were obtained according to Commission International de l'Eclairage (CIE) using Radiant Imaging color calculator.

III. RESULTS AND DISCUSSIONS

1. XRD and Crystal Structure

The XRD pattern of the synthesized Ca₉La(PO₄)₅(SiO₄)Cl₂ phosphor is presented in Fig. 1, which exhibit sharp diffraction peaks. The obtained XRD patterns matched well with the standard data JCPDS file No. 73-1728, which indicating hexagonal structure with space group P6₃/m with cell parameters a = b = 9.67224 Å, c = 6.68289 Å, and the unit cell volume V = 541.438 Å³. Fig. 2 shows crystal structure of Ca₉La(PO₄)₅(SiO₄)Cl₂ compound. It consists of two inequivalent cation (Ca/La) sites namely 6h and 4f. The (Ca/La) atom situated at 6h site is bonded with five O²⁻ and two equivalent Cl⁻ atoms. The Ca-O bond length ranges from 2.30 to 2.50 Å, while both Ca-Cl bond lengths are of 2.97 Å. The (Ca/La) atom situated at 4f site is bonded with nine O²⁻ atoms with bond length ranges from 2.38 to 2.79 Å [23]. The (P/Si) is bonded in a tetrahedral geometry to four O²⁻ atoms, with bond length ranges from 1.53 to 1.55 Å.

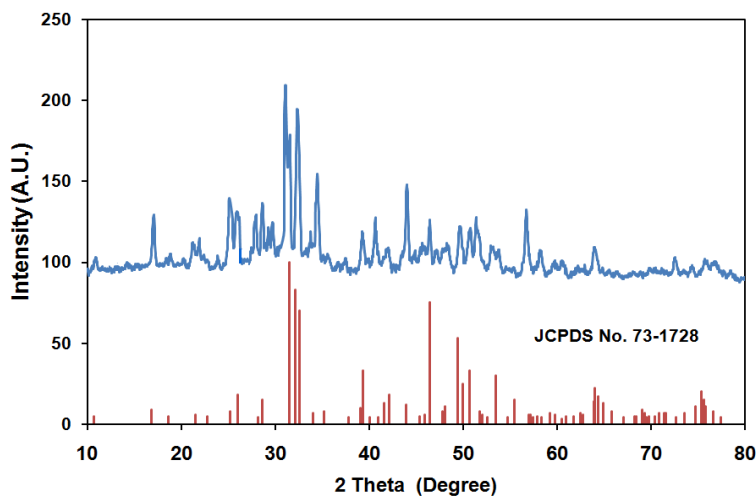


Fig.1. Powder XRD patterns of Ca₉La(PO₄)₅(SiO₄)Cl₂

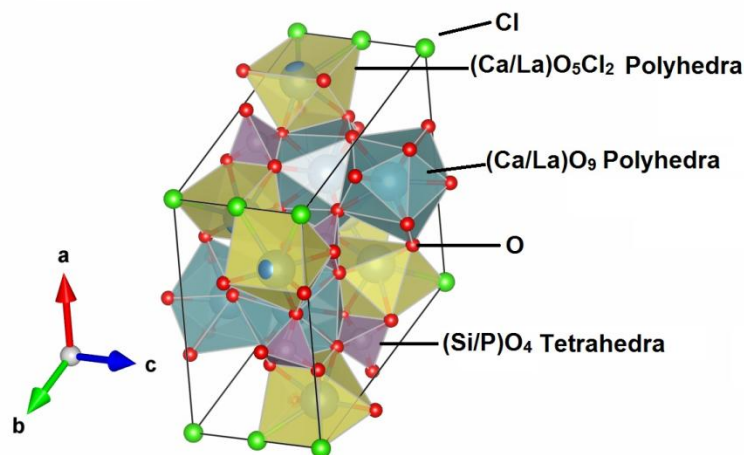


Fig.2. Crystal structure of $\text{Ca}_9\text{La}(\text{PO}_4)_5(\text{SiO}_4)\text{Cl}_2$ compound

2. SEM and FT-IR analysis

The surface morphology of synthesized material was studied by scanning electron microscopy (SEM) is presented in Fig. 3. The SEM images reveal that the particles were relatively agglomerated and non-uniform in nature due to the solid-state reaction method. The grain size distribution is broad and the average particle size ranges from 1 μm to 10 μm . The small particles are agglomerated forming bigger crystallites.

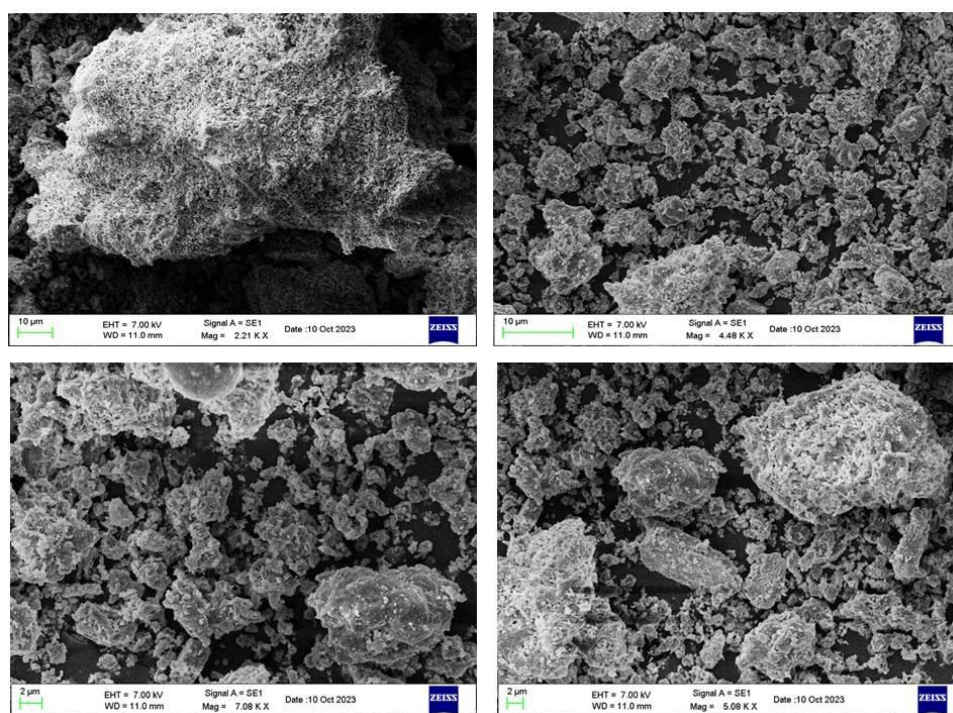


Fig.3. SEM images of $\text{Ca}_9\text{La}(\text{PO}_4)_5(\text{SiO}_4)\text{Cl}_2$

FT-IR spectroscopy is an analytical technique that is used to identify the functional groups present in a compound. The $\text{Ca}_9\text{La}(\text{PO}_4)_5(\text{SiO}_4)\text{Cl}_2$ sample with doping of 1 mol% Eu^{2+} ions was analyzed using this method, and result is presented in Fig. 4. The intense band situated at 557 and 607 cm^{-1} are attributed to the bending vibrations (ν_4) of O–P–O. The adsorption peak at 1024 cm^{-1} related to the P–O stretching vibration (ν_3) phosphate group (PO_4^{3-}) [24,25]. Some very weak peaks near 1600 cm^{-1} are due to O–H. These peaks are related to the presence of water molecules in the compound and moisture absorbed from the atmosphere.

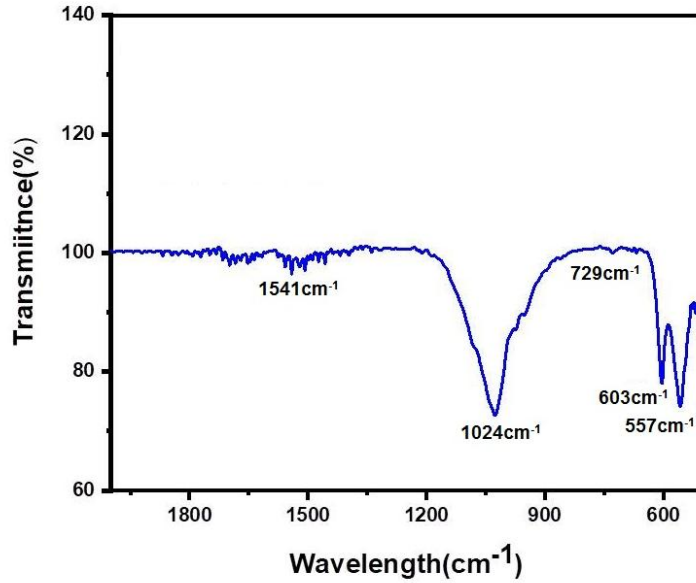


Fig.4. FT-IR spectrum of $\text{Ca}_9\text{La}(\text{PO}_4)_5(\text{SiO}_4)\text{Cl}_2$

3. PL of $\text{Ca}_9\text{La}(\text{PO}_4)_5(\text{SiO}_4)\text{Cl}_2:\text{Eu}^{2+}$

The PL excitation and emission spectra of Eu^{2+} doped $\text{Ca}_9\text{La}(\text{PO}_4)_5(\text{SiO}_4)\text{Cl}_2$ phosphor is presented in Fig. 5. The ground state electronic configuration of Eu^{2+} is $4f^7$. The excitation occurs from the transition between ground state $^8\text{S}_{7/2}$ of $4f^7$ configuration to the states belonging to $4f^65d^1$ configuration. It is important to note that the next $4f^7$ manifold ($^6\text{P}_j$) is situated at a higher energy level of approximately $28,000\text{ cm}^{-1}$, where as the lowest lying $4f^65d$ levels start near $34,000\text{ cm}^{-1}$ and are marked $^8\text{H}_j$ for the free ion. Usually, Eu^{2+} emits broad-band emission due to f-d transitions. The emission of Eu^{2+} originates from the lowest band of $4f^65d^1$ configuration to $^8\text{S}_{7/2}$ state of $4f^7$ configuration. The position of emission band varies from near-UV to the red region depending on the host lattice. This dependence is due to the crystal field splitting of the 5d levels. The impact of crystal field splitting on the $4f^65d$ levels is much greater than that on the $4f^7$ levels, mainly due to the larger spatial extent of the 5d orbitals. As a result, the $4f^65d$ levels often act as the metastable state or the lowest excited state in the presence of Eu^{2+} in a crystalline host [26]. It is important to note that the emission bands tend to shift towards longer wavelengths as the crystal field strength increases [27].

The PL emission spectra of $\text{Ca}_9\text{La}(\text{PO}_4)_5(\text{SiO}_4)\text{Cl}_2:\text{xEu}^{2+}$ ($\text{x}=0.5$ to 2 mol%) phosphor monitored at 352 nm excitation is presented in Fig. 5(b). It exhibit broad emission band ranging from 400 to 520 nm centered at 454 nm, assigned to the electric dipole allowed transition of Eu^{2+} ions from $4f^65d^1 \rightarrow 4f^7$ levels [28]. The PL excitation spectra (Fig. 5(a)) monitored at 454 nm emission exhibit broad excitation band centered at 352 nm, which is attributed to transition from $4f^7$ ($^8\text{S}_{7/2}$) $\rightarrow 4f^65d$ of Eu^{2+} ions, which could be effectively excited by UV LED chip. It is interesting to note that the concentration of Eu^{2+} in the $\text{Ca}_9\text{La}(\text{PO}_4)_5(\text{SiO}_4)\text{Cl}_2$ phosphors has a significant impact on the PL emission intensity. Specifically, as the concentration of Eu^{2+} increases from 0.5 mol% to 1.5 mol%, the PL emission intensity of the phosphor increases. However, beyond 1.5 mol%, the emission intensity falls due to concentration quenching. This phenomenon occurs when the excitation energy is lost via non-radiative decay processes. Importantly, there were no changes observed in the shape and peak position of the PL excitation and emission curve with varying Eu^{2+} concentration.

To determine the cause of concentration quenching, the critical distance (R_c) between the activator and the quenching site was calculated by the following expression [29,30]:

$$R_c = 2 \left(\frac{3V}{4\pi X_c N} \right)^{1/3} \dots \dots \dots (1)$$

Where, V = volume of the unit cell, X_c = optimum concentration of activator ions, and N = number of dopant sites available in the unit cell. In the present case, $V=541.438\text{ \AA}^3$, $X_c=1.5\%$, and $N=7$. From equation (1), it was found that the critical distance is 21.438 \AA , which is much greater than 5 \AA . This suggests that energy

transfer via exchange interaction is unlikely, and electric multipolar interaction is the dominant process that causes concentration quenching of Eu^{2+} ion in the prepared phosphors. Electric multipolar interaction includes dipole-dipole, dipole-quadrupole, and quadrupole-quadrupole interactions. According to Van Uiter's report, the emission intensity (I) per activator ion follows the equation [31].

$$\frac{I}{x} = K(1 + \beta(x)^{\theta/3})^{-1} \dots \dots \dots (2)$$

where I is emission intensity of phosphor, x is the concentration of activator, K and β are constants for a given host in the same excitation condition, and $\theta = 6, 8,$ and 10 corresponds to dipole-dipole, dipole-quadrupole, and quadrupole-quadrupole interactions, respectively. To get the value of θ , the relationship between $\log(I/x)$ and $\log(x)$ is plotted and is presented in fig. 6(a). The slope of fitting line which equal to $(-\theta/3)$ is determined to be -1.84 . Thus, the value of θ calculated to be 5.52 is close to 6 , revealing that the concentration quenching mechanism of Eu^{2+} doped $\text{Ca}_9\text{La}(\text{PO}_4)_5(\text{SiO}_4)\text{Cl}_2$ phosphors is dominated by the dipole-dipole interaction.

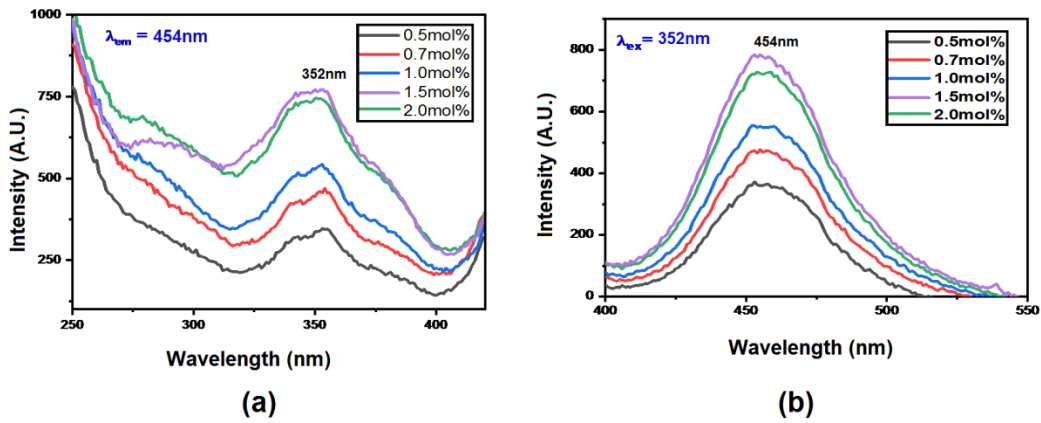


Fig.5. PL excitation emission spectra of $\text{Ca}_9\text{La}(\text{PO}_4)_5(\text{SiO}_4)\text{Cl}_2:\text{Eu}^{2+}$ phosphor (a) Eu^{2+} excitation for 454 nm emission, (b) Eu^{2+} emission for 352 nm excitation

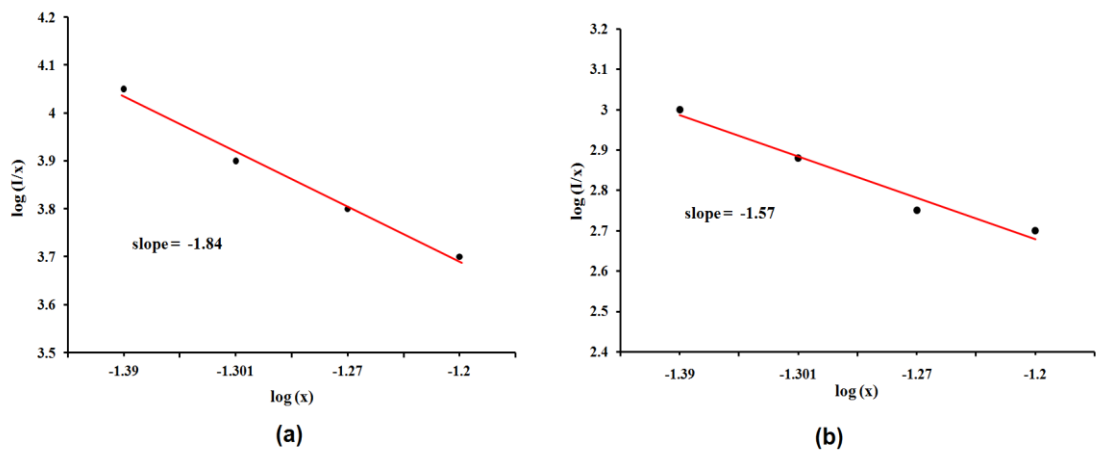


Fig.6. Curve of $\log(I/x)$ vs $\log(x)$: (a) $\text{Ca}_9\text{La}(\text{PO}_4)_5(\text{SiO}_4)\text{Cl}_2:\text{Eu}^{2+}$, (b) $\text{Ca}_9\text{La}(\text{PO}_4)_5(\text{SiO}_4)\text{Cl}_2:\text{Sm}^{3+}$

4. PL of $\text{Ca}_9\text{La}(\text{PO}_4)_5(\text{SiO}_4)\text{Cl}_2:\text{Sm}^{3+}$

Fig. 7 shows PL excitation and emission spectra of $\text{Ca}_9\text{La}(\text{PO}_4)_5(\text{SiO}_4)\text{Cl}_2$ phosphor activated with different doping concentration of Sm^{3+} . At 405 nm excitation, the phosphors exhibit characteristic emission lines at 563, 602, and 646 nm, as shown in Fig. 7(b). The emission peak centered at 563 nm

attributed to ${}^4G_{5/2} \rightarrow {}^6H_{5/2}$ transition of Sm^{3+} ion, which is originated due to purely magnetic dipole (MD) moment. The most intense emission peak at 602 nm attributed to the transition of Sm^{3+} ion from ${}^4G_{5/2} \rightarrow {}^6H_{7/2}$. The ${}^4G_{5/2} \rightarrow {}^6H_{7/2}$ transition is magnetic dipole allowed but electric dipole (ED) nature is more dominant with selection rule $\Delta J = \pm 1$, therefore it is allowed as both partially MD and partially ED. The least intense emission peak at 646 nm corresponds to ${}^4G_{5/2} \rightarrow {}^6H_{9/2}$ transition, which is originated due to purely ED moment with selection rule $\Delta J = \pm 2$ and is sensitive to the crystal field [32-34]. The ratio between the intensity of the ED and MD transitions indicates the symmetry of neighboring environment of the Sm^{3+} ions. If the intensity of ED transition is higher than MD, then it indicates asymmetry nature around the rare earth (RE) ions. It seems like the host matrix has a symmetric nature since the spectral intensity of the 646 nm emission peak is weaker than the other peaks in our current study [35]. At 602 nm emission, the phosphor exhibit excitation peaks at 345, 362, 376, 391, 405, and 418 nm attributed to the transitions of Sm^{3+} ions from ground state ${}^6H_{5/2} \rightarrow {}^4H_{9/2}$, ${}^4D_{3/2}$, ${}^4D_{1/2}$, ${}^4G_{11/2}$, ${}^4F_{7/2}$, and ${}^4M_{19/2}$ respectively [36-38]. The nature of excitation band in near-UV region suggests that the prepared phosphor can be effectively excited by UV LED chip. It is also observed from Fig. 7 that the position of emission and excitation band remains same with varying Sm^{3+} concentration. However, the emission intensity rises and show maximum intensity at 7 mol%, beyond that the emission intensity decreases due to concentration quenching effect. The critical distance for Sm^{3+} ions is 12.8 Å, which means that exchange interaction is not possible and electric multipolar interaction is the dominant process that causes concentration quenching of Sm^{3+} ion in the prepared phosphors. Additionally, the plot between $\log(I/x)$ and $\log(x)$ is plotted and is presented in fig. 6(b) shows a linear relation with a slope of about -1.57. Thus, the value of θ calculated to be 4.71 is close to 6, indicating that the concentration quenching mechanism of Sm^{3+} doped $Ca_9La(PO_4)_5(SiO_4)Cl_2$ phosphors is dominated by the dipole-dipole interaction.

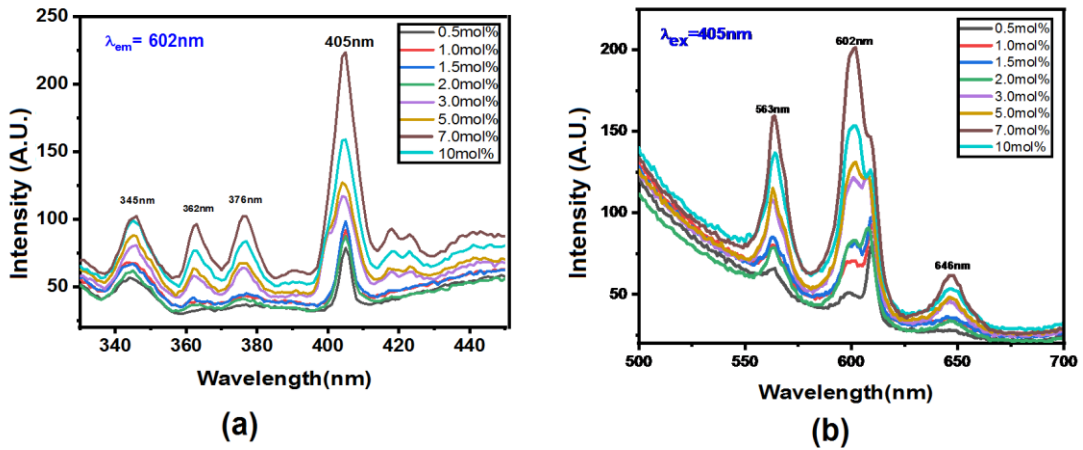


Fig.7. PL excitation emission spectra of $Ca_9La(PO_4)_5(SiO_4)Cl_2:Sm^{3+}$ phosphor
(a) Sm^{3+} excitation for 602 nm emission, (b) Sm^{3+} emission for 405 nm excitation

5. PL of $Ca_9La(PO_4)_5(SiO_4)Cl_2:Ce^{3+}$

The PL excitation and emission spectra of Ce^{3+} doped $Ca_9La(PO_4)_5(SiO_4)Cl_2$ phosphor is presented in Fig. 8. The Ce^{3+} is one of the lanthanide ion with an atomic number 58 and electronic configuration of $[Xe]4f^1$. The luminescence of Ce^{3+} ion comes from the transition between $4f^1$ ground state and $5d^1$ excited state. The 4f-shell is empty in the excited state and a single 5d-electron that interacts strongly with the crystal lattice. The interaction between the 5d-electron and the crystal lattice in the excited state seems to have a significant impact on the crystal field effects and phonon coupling [39]. It seems that the 2D_J excited state of $5d^1$ is particularly affected by this interaction, which can result in the splitting of the state into five Kramer's doublet by low symmetry [40]. On the other hand, the 2F_J ground state of $4f^1$ undergoes a split into two levels, namely ${}^2F_{5/2}$ and ${}^2F_{7/2}$, due to the spin orbit interaction. The separation of approximately 2000 cm^{-1} between these two levels [41]. The PL is usually intense because of parity allowed and spin-allowed 4f-5d transition. Due to strong crystal field interaction, the position of 5d band itself depends on the host and therefore the Stoke's shift and also the spectral positions of both the excitation and emission bands are host dependent [42]. Optical absorption in Ce^{3+} -doped crystals corresponds to the transitions from the ${}^2F_{5/2}$ ground state to the five $5d^1$ excited states. On the

other hand, the emission occurs as the transitions from the lowest $5d^1$ excited state to the $^2F_{5/2}$ and $^2F_{7/2}$ ground states. This is the reason for the double structure usually observed in the Ce^{3+} emission band.

In Fig. 8(b), we can see the PL emission spectrum of $Ca_9La(PO_4)_5(SiO_4)Cl_2:Ce^{3+}$ (10 mol%) when monitored at 311 nm excitation wavelength. The spectrum displays a broad band emission that ranges from 350 to 580 nm, with a peak at around 425 nm and a shoulder around 390 nm. These features are assigned to the Ce^{3+} ion transition between the $5d$ level to the ground state ($^2F_{5/2}$, $^2F_{7/2}$). The emission band can be separated into two Gaussian components (as indicated by the dotted lines in Fig. 8(b)) with maxima at 425 nm (23529 cm^{-1}) and 390 nm (25641 cm^{-1}). On an energy scale, the energy difference between these two components is about 2112 cm^{-1} , which agrees with the theoretical difference between the $^2F_{5/2}$ and $^2F_{7/2}$ levels (about 2000 cm^{-1}). When monitoring the excitation spectra at an emission wavelength of 425 nm, it can be observed that there is a significant band present around 311 nm. This band is associated with transitions from $4f^1 \rightarrow 5d^1$ configuration.

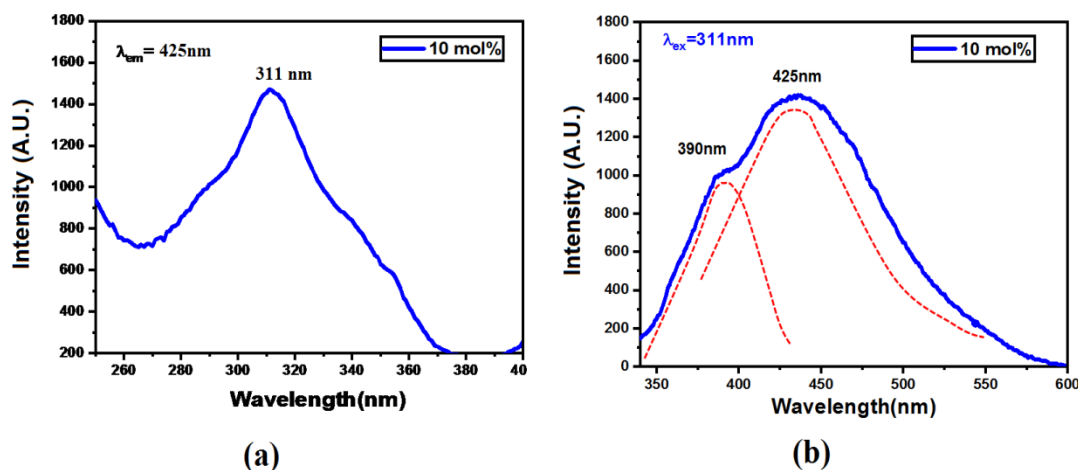


Fig.8. PL excitation emission spectra of $Ca_9La(PO_4)_5(SiO_4)Cl_2:Ce^{3+}$ phosphor (a) Ce^{3+} excitation for 425 nm emission, (b) Ce^{3+} emission for 311 nm excitation

6. PL of $Ca_9La(PO_4)_5(SiO_4)Cl_2:(Ce^{3+}, Eu^{2+})$

Due to the spectral overlap between the emission band of $Ca_9La(PO_4)_5(SiO_4)Cl_2:Ce^{3+}$ and excitation band of $Ca_9La(PO_4)_5(SiO_4)Cl_2:Eu^{2+}$, an energy transfer can be possible between Ce^{3+} to Eu^{2+} . The PL excitation spectra of $Ca_9La(PO_4)_5(SiO_4)Cl_2:(Ce^{3+}, Eu^{2+})$ phosphor monitored at 454 nm emission wavelength exhibit broad excitation band ranging from 250 to 400 nm is shown in Fig. 9(a). The excitation band centered at 311 nm with shoulders at 290 and 342 nm. At 311 nm excitation, the phosphor exhibit broad emission band that ranges from 350 to 550 nm, peaking at 454 nm and a shoulder at 390 nm as shown in Fig. 9(b). The 390 nm peak is assigned to Ce^{3+} emission, while intensity maxima occur at 454 nm is assigned to Eu^{2+} emission and both are confirmed from Fig. 5(b) and Fig. 8(b). The comparison of Ce^{3+} emission and Ce^{3+} to Eu^{2+} energy transfer emission is shown in Fig. 10. Fig. 13 shows Ce^{3+} to Eu^{2+} energy transfer mechanism. It seems that when Ce^{3+} ions absorb n-UV radiation, the energy is then transferred from the excited $5d$ level of Ce^{3+} ion to the excited $4f^65d^1$ state of Eu^{2+} ion. Afterward Eu^{2+} emission occur from excited $4f^65d^1 \rightarrow 4f^7$ levels of Eu^{2+} ion. It is observed that the emission intensity of Eu^{2+} increases when codoped with Ce^{3+} ion. A similar emission pattern is observed when phosphor is excited at 290 nm which is presented in Fig. 9(c). At 342 nm excitation the phosphor exhibit single broad band emission centered at 454 nm but does not any show shoulder in emission spectra shown in Fig. 9(d). It is also observed that, the PL emission intensity of $Ca_9La(PO_4)_5(SiO_4)Cl_2:(Ce^{3+}, Eu^{2+})$ phosphor increases as the Eu^{2+} doping concentration increases from 0.1 mol% to 0.7 mol%. Beyond 0.7 mol% the emission intensity falls because of concentration quenching phenomenon. Since the PL excitation curve of prepared phosphors matched with n-UV LED emission, it suggests that the prepared phosphors can be effectively excited by UV LED chip.

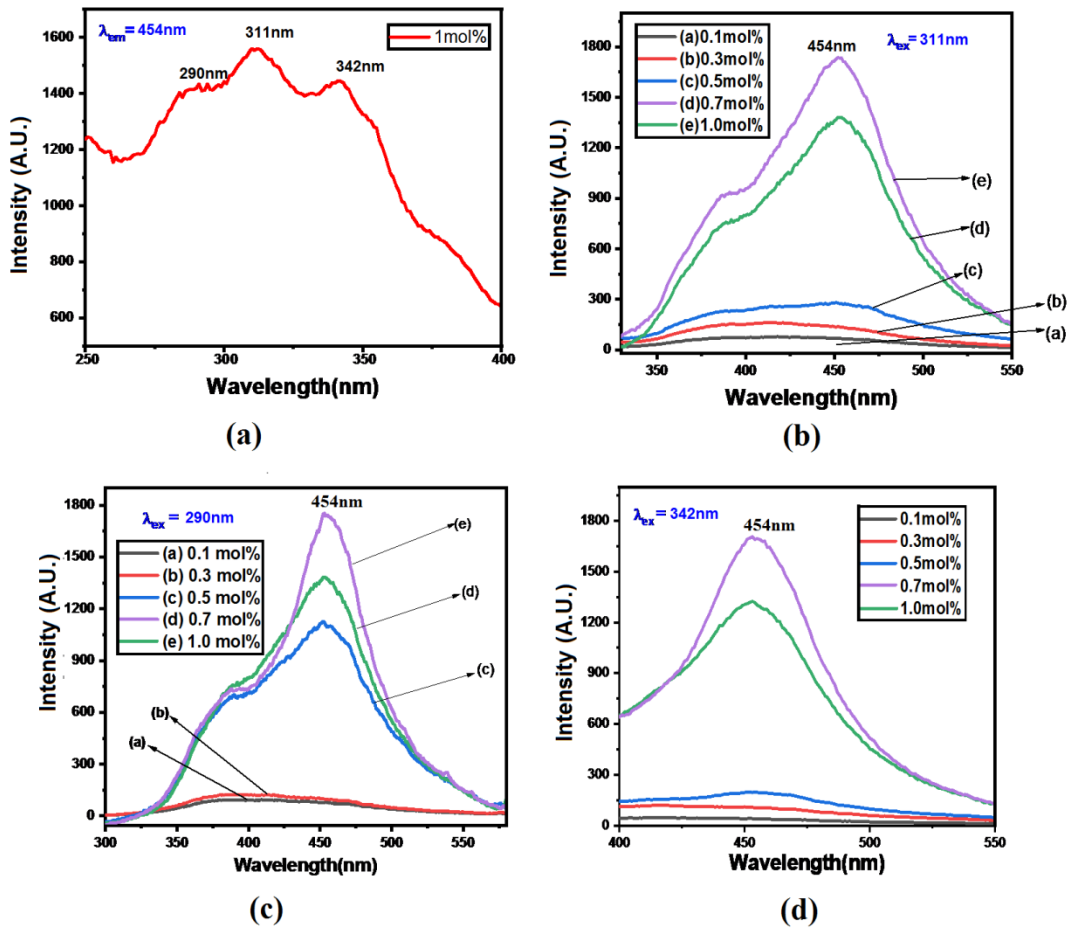


Fig.9. PL excitation emission spectra of $\text{Ca}_9\text{La}(\text{PO}_4)_5(\text{SiO}_4)\text{Cl}_2:(\text{Ce}^{3+}, \text{Eu}^{2+})$ phosphor
 (a) Excitation for 454 nm emission, (b) Emission for 311 nm excitation
 (c) Emission for 290 nm excitation, (d) Emission for 342 nm excitation

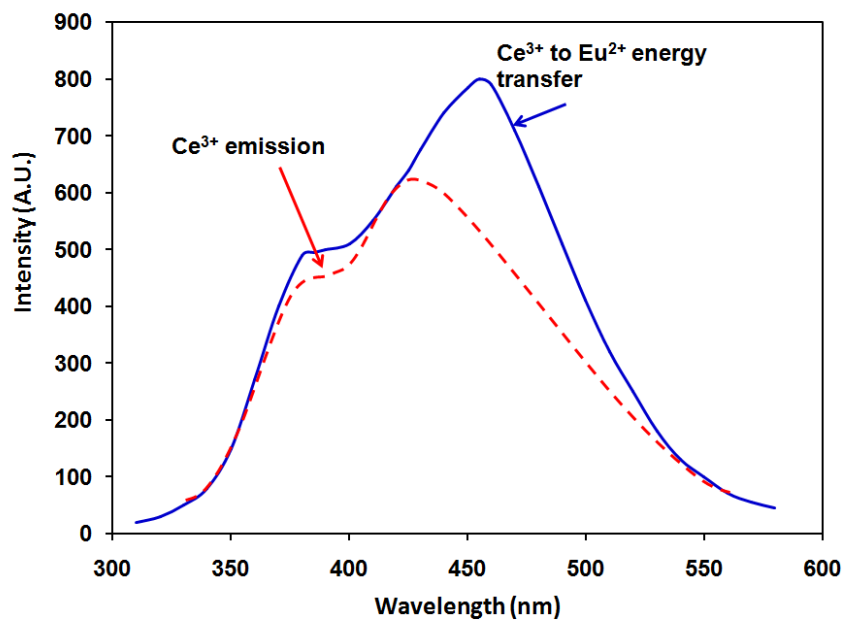


Fig.10. Comparison of Ce^{3+} emission and Ce^{3+} to Eu^{2+} energy transfer emission

7. PL of $\text{Ca}_9\text{La}(\text{PO}_4)_5(\text{SiO}_4)\text{Cl}_2:(\text{Ce}^{3+},\text{Sm}^{3+})$

The emission of $\text{Ca}_9\text{La}(\text{PO}_4)_5(\text{SiO}_4)\text{Cl}_2:\text{Ce}^{3+}$ phosphor and absorption of Sm^{3+} overlap in 350-450 nm region, suggesting that energy transfer may occur from Ce^{3+} to Sm^{3+} via 5d state of Ce^{3+} in $\text{Ca}_9\text{La}(\text{PO}_4)_5(\text{SiO}_4)\text{Cl}_2:(\text{Ce}^{3+},\text{Sm}^{3+})$ phosphor. In this phosphor, the concentration of Ce^{3+} was kept constant at 5 mol%, and the concentration of Sm^{3+} was varied, and the effect of variation of Sm^{3+} concentration on luminescence property was studied. The PL excitation and emission spectrum of $\text{Ca}_9\text{La}(\text{PO}_4)_5(\text{SiO}_4)\text{Cl}_2:(\text{Ce}^{3+},\text{Sm}^{3+})$ phosphor is presented in Fig. 11. The excitation spectra monitored at 602 nm emission exhibit excitation in n-UV and visible region attributed to the transition from ground state $^6\text{H}_{5/2}$ to various excited states of Sm^{3+} ions. At 405 nm, the phosphor emits broad band light (330-750 nm) due to Ce^{3+} ion's transition from 5d level to the ground state ($^2\text{F}_{5/2}, ^2\text{F}_{7/2}$), with peak at 425 nm and shoulder at 390 nm. Small emission peaks at 565 and 602 nm of similar intensity corresponding to $^4\text{G}_{5/2}$ to $^6\text{H}_{5/2}$ and $^6\text{H}_{7/2}$ transition of Sm^{3+} ion are also observed. The variation of Sm^{3+} emission intensity with respect to different Sm^{3+} concentration in prepared phosphors is presented in Fig. 12. Fig. 13 shows Ce^{3+} to Sm^{3+} energy transfer mechanism. Initially Ce^{3+} ions absorb N-UV radiation and then transfer the energy from the excited 5d¹ state of Ce^{3+} ion to the excited level of Sm^{3+} ions. This results in the emission of light due to $^4\text{G}_{5/2}$ to $^6\text{H}_{5/2}$ and $^6\text{H}_{7/2}$ transitions. The nature of excitation band in n-UV region suggests that the prepared phosphor can be effectively excited by UV LED chip.

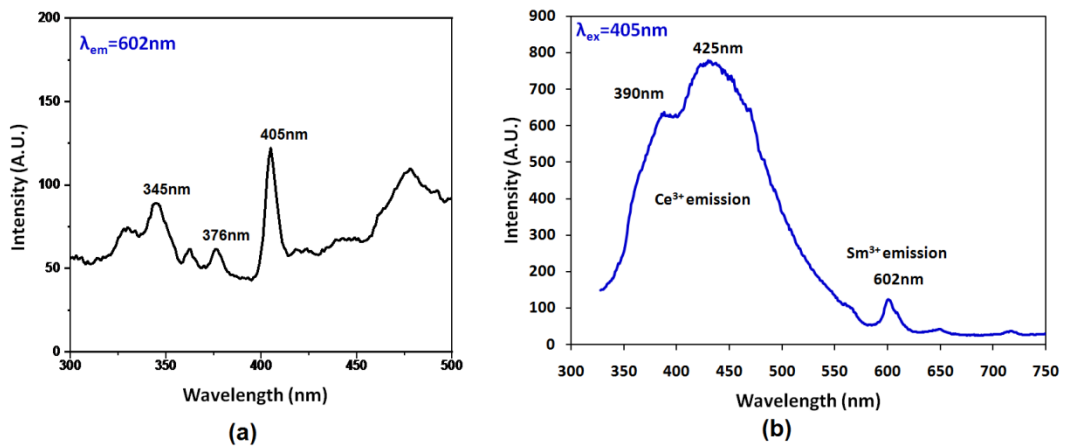


Fig.11. PL excitation emission spectra of $\text{Ca}_9\text{La}(\text{PO}_4)_5(\text{SiO}_4)\text{Cl}_2:(\text{Ce}^{3+},\text{Sm}^{3+})$ phosphor

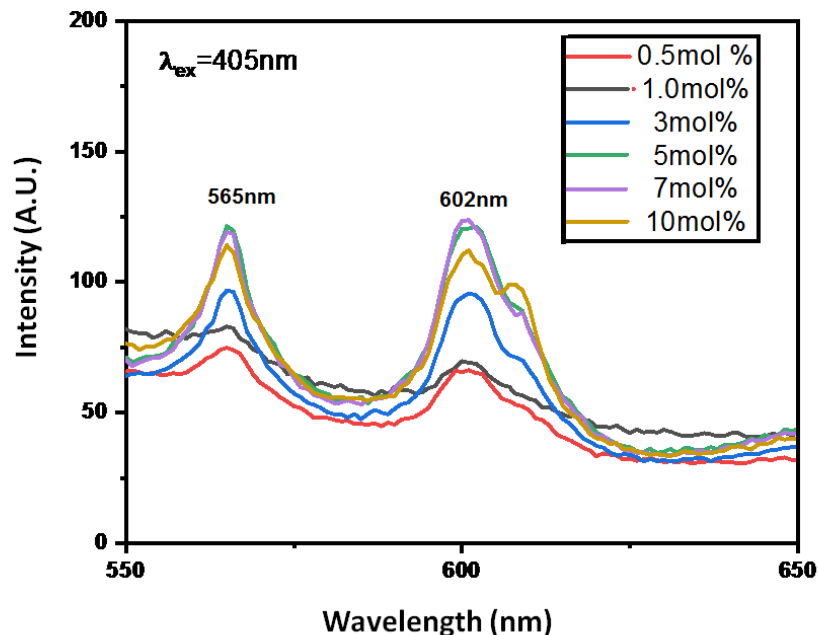


Fig.12. Variation of emission intensity as a function of Sm^{3+} concentration

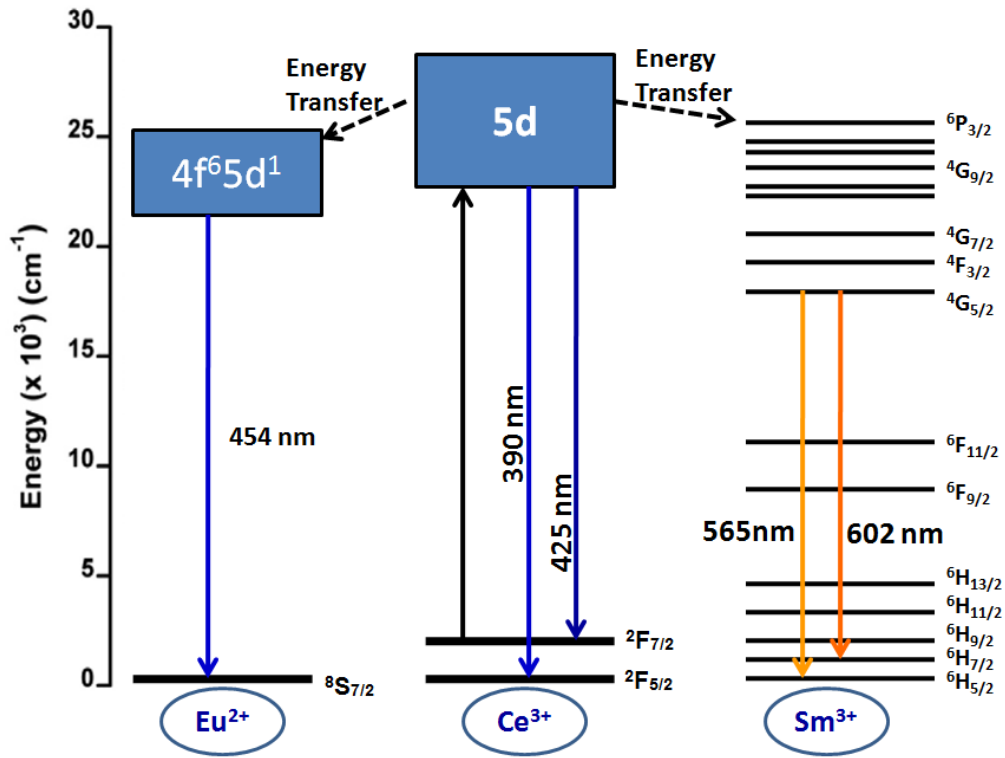


Fig.13. Energy transfer mechanism between Ce^{3+} to Eu^{2+} and Ce^{3+} to Sm^{3+}

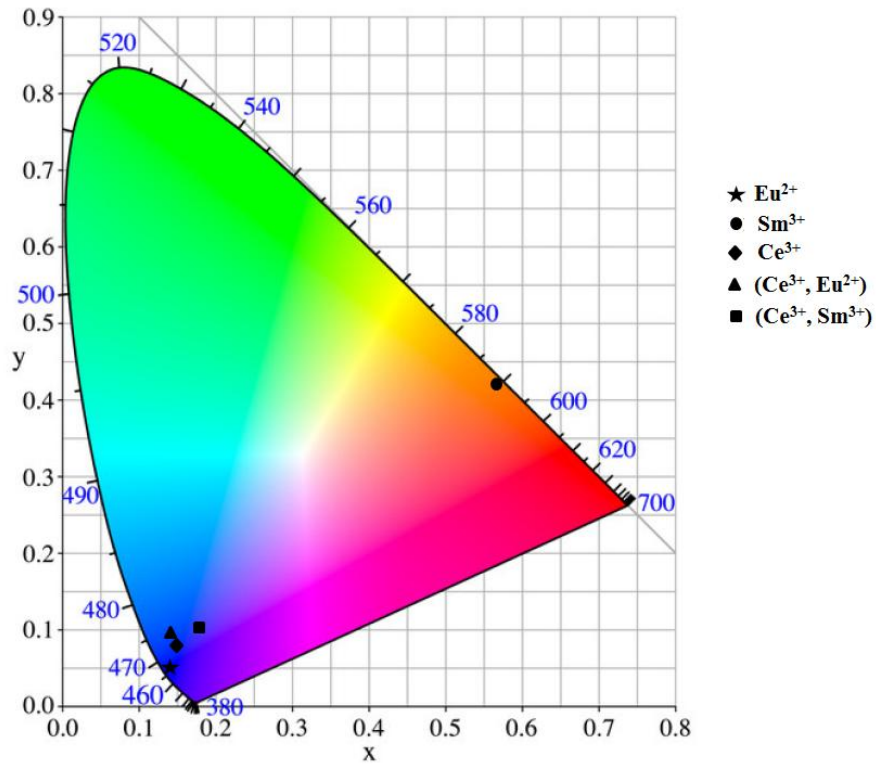


Fig.14. CIE chromaticity diagram

IV. COLOR CHROMATICITY

The color of the phosphor is very important in the field of luminescence and therefore the chromaticity diagram and CIE coordinates are calculated using PL data and interactive CIE software (CIE coordinate calculator). Fig. 14 shows CIE chromaticity diagram of synthesized phosphors. The color coordinates for prepared phosphors are summarized in table 1.

Table 1 Color coordinates for prepared phosphors

Compound	CIE-chromaticity co-ordinate (C_x, C_y)
$\text{Ca}_9\text{La}(\text{PO}_4)_5(\text{SiO}_4)\text{Cl}_2:\text{Eu}^{2+}$	(0.146, 0.0447)
$\text{Ca}_9\text{La}(\text{PO}_4)_5(\text{SiO}_4)\text{Cl}_2:\text{Sm}^{3+}$	(0.5681, 0.4231)
$\text{Ca}_9\text{La}(\text{PO}_4)_5(\text{SiO}_4)\text{Cl}_2:\text{Ce}^{3+}$	(0.1522, 0.0742)
$\text{Ca}_9\text{La}(\text{PO}_4)_5(\text{SiO}_4)\text{Cl}_2:(\text{Ce}^{3+}, \text{Eu}^{2+})$	(0.1481, 0.935)
$\text{Ca}_9\text{La}(\text{PO}_4)_5(\text{SiO}_4)\text{Cl}_2:(\text{Ce}^{3+}, \text{Sm}^{3+})$	(0.1859, 0.1051)

V. CONCLUSION

To summarize, a series of $\text{Ca}_9\text{La}(\text{PO}_4)_5(\text{SiO}_4)\text{Cl}_2$ phosphors doped with RE (Eu^{2+} , Sm^{3+} , Ce^{3+}) ions and co-doped with (Ce^{3+} , Eu^{2+}) and (Ce^{3+} , Sm^{3+}) were successfully synthesized via solid state reaction method. The XRD analysis of the resulting compound matches well with the standard JCPDS file. The blue light emission of the Eu^{2+} doped $\text{Ca}_9\text{La}(\text{PO}_4)_5(\text{SiO}_4)\text{Cl}_2$ phosphor at 454 nm assigned to the transition from $4f^65d^1$ to $4f^7$ level of Eu^{2+} ion, while the orange-red emission of the Sm^{3+} doped $\text{Ca}_9\text{La}(\text{PO}_4)_5(\text{SiO}_4)\text{Cl}_2$ phosphor at 602 nm is attributed to the transition from $^4G_{5/2}$ to $^6H_{7/2}$ level of Sm^{3+} ion. The Ce^{3+} doped $\text{Ca}_9\text{La}(\text{PO}_4)_5(\text{SiO}_4)\text{Cl}_2$ phosphor exhibit broad emission from 350 to 550 nm, assigned to transition of Ce^{3+} ion between 5d level and ($^2F_{5/2}$, $^2F_{7/2}$) levels. When Eu^{2+} and Sm^{3+} individually co-doped with Ce^{3+} in $\text{Ca}_9\text{La}(\text{PO}_4)_5(\text{SiO}_4)\text{Cl}_2$ host, efficient energy transfer was observed from Ce^{3+} to Eu^{2+} and partial energy transfer was observed from Ce^{3+} to Sm^{3+} . The excitation spectra of all prepared phosphors show good overlap with LED emission over n-UV region, making them attractive candidates for UV-LED converted phosphors, display devices and related applications.

REFERENCES

- [1] G. Blasse, The physics of new luminescent materials, Mater. Chem. Phys. 16 (1987) 201–236. [https://doi.org/10.1016/0254-0584\(87\)90100-3](https://doi.org/10.1016/0254-0584(87)90100-3).
- [2] T.J. Isaacs, A Study of Eu^{3+} Fluorescence in Some Silicate Oxyapatites, J. Electrochem. Soc. 120 (1973) 654. <https://doi.org/10.1149/1.2403526>.
- [3] J. Lin, Q. Su, Luminescence and energy transfer of rare-earth-metal ions in $\text{Mg}_2\text{Y}_8(\text{SiO}_4)_6\text{O}_2$, J. Mater. Chem. 5 (1995) 1151. <https://doi.org/10.1039/jm9950501151>.
- [4] S. Ferdov, R.A. Sá Ferreira, Z. Lin, Hydrothermal Synthesis, Structural Investigation, Photoluminescence Features, and Emission Quantum Yield of Eu and Eu–Gd Silicates with Apatite-Type Structure, Chem. Mater. 18 (2006) 5958–5964. <https://doi.org/10.1021/cm0617384>.
- [5] D. Kim, D. Park, N. Oh, J. Kim, E.D. Jeong, S.-J. Kim, S. Kim, J.-C. Park, Luminescent Properties of Rare Earth Fully Activated Apatites, $\text{LiRE}_9(\text{SiO}_4)_6\text{O}_2$ (RE = Ce, Eu, and Tb): Site Selective Crystal Field Effect, Inorg. Chem. 54 (2015) 1325–1336. <https://doi.org/10.1021/ic502113a>.
- [6] S. Slimi, P. Loiko, K. Bogdanov, A. Volokitina, R.M. Solé, M. Aguiló, F. Díaz, E. Ben Salem, X. Mateos, Structure and luminescent properties of Dy^{3+} activated $\text{NaLa}_9(\text{SiO}_4)_6\text{O}_2$ yellow-emitting phosphors for application in white LEDs, J. Alloys Compd. 896 (2022) 163109. <https://doi.org/10.1016/j.jallcom.2021.163109>.
- [7] H. Liu, Y. Luo, Z. Mao, L. Liao, Z. Xia, A novel single-composition trichromatic white-emitting $\text{Sr}_{3.5}\text{Y}_{6.5}\text{O}_2(\text{PO}_4)_{1.5}(\text{SiO}_4)_{4.5}:\text{Ce}^{3+}/\text{Tb}^{3+}/\text{Mn}^{2+}$ phosphor: synthesis, luminescent properties and applications for white LEDs, J. Mater. Chem. C. 2 (2014) 1619. <https://doi.org/10.1039/c3tc32003k>.
- [8] S. Wang, Y. Han, L. Shi, M. Jia, Y. Tong, B. Zhang, Z. Mu, X. Lu, Z. Zhang, A. Song, A novel single-phased $\text{Sr}_4\text{La}_6(\text{SiO}_4)_6\text{Cl}_2:\text{Dy}^{3+}$ phosphor for white-light-emitting diodes, Inorg. Chem. Commun. 117 (2020) 107948. <https://doi.org/10.1016/j.inoche.2020.107948>.
- [9] J. Du, O.Q. De Clercq, K. Korthout, D. Poelman, $\text{LaAlO}_3:\text{Mn}^{4+}$ as Near-Infrared Emitting Persistent Luminescence Phosphor for Medical Imaging: A Charge Compensation Study, Materials (Basel). 10 (2017) 1422. <https://doi.org/10.3390/ma10121422>.
- [10] J. Xu, D. Murata, Y. Katayama, J. Ueda, S. Tanabe, $\text{Cr}^{3+}/\text{Er}^{3+}$ co-doped LaAlO_3 perovskite phosphor: a near-infrared persistent luminescence probe covering the first and third biological windows, J. Mater. Chem. B. 5 (2017) 6385–6393. <https://doi.org/10.1039/C7TB01332A>.
- [11] E. Pavitra, G. Seeta Rama Raju, W. Park, J.S. Yu, Concentration and penetration depth dependent tunable emissions from Eu^{3+} co-doped $\text{SrY}_2\text{O}_4:\text{Dy}^{3+}$ nanocrystalline phosphor, New J. Chem. 38 (2014) 163–169.

- <https://doi.org/10.1039/C3NJ00987D>.
- [12] L. Liang, L. Mei, H. Liu, C. Wang, L. Liao, Intense broad-band absorption and blue-emitting $\text{Ca}_9\text{La}(\text{PO}_4)_5(\text{SiO}_4)\text{Cl}_2:\text{Eu}^{2+}$ phosphor under near-ultraviolet excitation, *J. Lumin.* 206 (2019) 154–157. <https://doi.org/10.1016/j.jlumin.2018.10.036>.
 - [13] H. Liu, L. Liao, Q. Guo, D. Yang, L. Mei, $\text{Ca}_9\text{La}(\text{PO}_4)_5(\text{SiO}_4)\text{Cl}_2:\text{Dy}^{3+}$: A white-emitting apatite-type phosphor pumped for n-UV w-LEDs, *J. Lumin.* 181 (2017) 407–410. <https://doi.org/10.1016/j.jlumin.2016.09.060>.
 - [14] C.M. Mehare, Y.R. Parauha, V. Chopra, S. Ray, N.S. Dhoble, C. Ghanty, S.J. Dhoble, Tailoring the luminescent properties of $\text{Ca}_9\text{La}(\text{PO}_4)_5(\text{SiO}_4)\text{F}_2:1 \text{ mol}\% \text{Eu}^{3+}$ phosphor via doping of chloride, molybdate, vanadate, sulfate, and tungstate ions, *J. Mater. Sci. Mater. Electron.* 31 (2020) 3426–3440. <https://doi.org/10.1007/s10854-020-02891-0>.
 - [15] J. Zhang, Q. Guo, L. Liao, Y. Wang, M. He, H. Ye, L. Mei, H. Liu, T. Zhou, B. Ma, Structure and luminescence properties of $\text{La}_6\text{Ba}_4(\text{SiO}_4)_6\text{F}_2:\text{Dy}^{3+}$ phosphor with apatite structure, *RSC Adv.* 8 (2018) 38883–38890. <https://doi.org/10.1039/C8RA08324J>.
 - [16] Q. Guo, B. Ma, L. Liao, M.S. Molokeev, L. Mei, H. Liu, Crystal structure and luminescence properties of novel $\text{Sr}_{10}(\text{SiO}_4)_3(\text{SO}_4)_3\text{O}:\text{xEu}^{2+}$ phosphor with apatite structure, *Ceram. Int.* 42 (2016) 11687–11691. <https://doi.org/10.1016/j.ceramint.2016.04.086>.
 - [17] R. El Ouenzerfi, G. Panczer, C. Goutaudier, M.T. Cohen-Adad, G. Boulon, M. Trabelsi-Ayedi, N. Kbir-Ariguib, Relationships between structural and luminescence properties in Eu^{3+} -doped oxyphosphate-silicate apatite $\text{Ca}_{2-x}\text{La}_{8-x}(\text{SiO}_4)_{6-x}(\text{PO}_4)_2\text{O}_2$, *Opt. Mater. (Amst)*. 16 (2001) 301–310. [https://doi.org/10.1016/S0925-3467\(00\)00090-2](https://doi.org/10.1016/S0925-3467(00)00090-2).
 - [18] H. Liu, L. Liao, Y. Zhang, T. Zhou, Q. Guo, L. Li, L. Mei, Structure refinement and luminescence properties of a novel apatite-type compound $\text{Mn}_2\text{Gd}_8(\text{SiO}_4)_6\text{O}_2$, *Dye. Pigment.* 140 (2017) 87–91. <https://doi.org/10.1016/j.dyepig.2017.01.033>.
 - [19] K. Li, D. Geng, M. Shang, Y. Zhang, H. Lian, J. Lin, Color-Tunable Luminescence and Energy Transfer Properties of $\text{Ca}_9\text{Mg}(\text{PO}_4)_6\text{F}_2:\text{Eu}^{2+}$, Mn^{2+} Phosphors for UV-LEDs, *J. Phys. Chem. C.* 118 (2014) 11026–11034. <https://doi.org/10.1021/jp501949m>.
 - [20] C. Peng, G. Li, Z. Hou, M. Shang, J. Lin, Electrospinning synthesis and luminescent properties of one-dimensional $\text{Ca}_2\text{Gd}_8(\text{SiO}_4)_6\text{O}_2:\text{Eu}^{3+}$ microfibers and microbelts, *Mater. Chem. Phys.* 136 (2012) 1008–1014. <https://doi.org/10.1016/j.matchemphys.2012.08.040>.
 - [21] P.S. Thakre, S.C. Gedam, S.J. Dhoble, R.G. Atram, Luminescence investigations on sulfate apatite $\text{Na}_6(\text{SO}_4)_2\text{FCl}:\text{RE}$ (RE=Dy, Ce or Eu) phosphors, *J. Lumin.* 131 (2011) 2683–2689. <https://doi.org/10.1016/j.jlumin.2011.06.050>.
 - [22] G. Li, Y. Zhang, D. Geng, M. Shang, C. Peng, Z. Cheng, J. Lin, Single-Composition Trichromatic White-Emitting $\text{Ca}_4\text{Y}_6(\text{SiO}_4)_6\text{O}:\text{Ce}^{3+}/\text{Mn}^{2+}/\text{Tb}^{3+}$ Phosphor: Luminescence and Energy Transfer, *ACS Appl. Mater. Interfaces.* 4 (2012) 296–305. <https://doi.org/10.1021/am201335d>.
 - [23] J. Cheng, J. Zhang, X. Bian, Z. Zhai, J. Shi, Photoluminescence properties, Judd-Ofelt analysis, and optical temperature sensing of Eu^{3+} -doped $\text{Ca}_3\text{La}_7(\text{SiO}_4)_5(\text{PO}_4)_2$ luminescent materials, *Spectrochim. Acta Part A Mol. Biomol. Spectrosc.* 230 (2020) 118057. <https://doi.org/10.1016/j.saa.2020.118057>.
 - [24] X. Shen, Q. Wang, Y. Liu, W. Xue, L. Ma, S. Feng, M. Wan, F. Wang, C. Mao, Manganese Phosphate Self-assembled Nanoparticle Surface and Its application for Superoxide Anion Detection, *Sci. Rep.* 6 (2016) 28989. <https://doi.org/10.1038/srep28989>.
 - [25] L.K. Bharat, J.S. Yu, $\text{Ba}_3(\text{PO}_4)_2$ hierarchical structures: synthesis, growth mechanism and luminescence properties, *CrystEngComm.* 17 (2015) 4647–4653. <https://doi.org/10.1039/C5CE00532A>.
 - [26] J.K. Lawson, S.A. Payne, *Phys. Rev. B.* 47 (1993) 14003–14010. <https://doi.org/10.1103/PhysRevB.47.14003>.
 - [27] G. Blasse, *Materials Science of the Luminescence of Inorganic Solids*, in: *Lumin. Inorg. Solids*, Springer US, Boston, MA, 1978: pp. 457–494. https://doi.org/10.1007/978-1-4684-3375-3_15.
 - [28] X. Fu, W. Lü, M. Jiao, H. You, Broadband Yellowish-Green Emitting $\text{Ba}_4\text{Gd}_3\text{Na}_3(\text{PO}_4)_6\text{F}_2:\text{Eu}^{2+}$ Phosphor: Structure Refinement, Energy Transfer, and Thermal Stability, *Inorg. Chem.* 55 (2016) 6107–6113. <https://doi.org/10.1021/acs.inorgchem.6b00648>.
 - [29] D.R. Taikar, S.J. Dhoble, White light emission via Pb^{2+} to Dy^{3+} energy transfer mechanism in CaTiO_3 phosphor, *Optik (Stuttg)*. 261 (2022) 169215. <https://doi.org/10.1016/j.ijleo.2022.169215>.
 - [30] G. Blasse, Energy transfer in oxidic phosphors, *Phys. Lett. A.* 28 (1968) 444–445. [https://doi.org/10.1016/0375-9601\(68\)90486-6](https://doi.org/10.1016/0375-9601(68)90486-6).
 - [31] L. Han, D. Xu, Q. Xu, Q. Di, J. Sun, Synthesis and luminescence properties of $\text{Sr}_3\text{GdNa}(\text{PO}_4)_3\text{F}:\text{Sm}^{3+}$ phosphor, *J. Mater. Sci.* 50 (2015) 2257–2262. <https://doi.org/10.1007/s10853-014-8788-9>.
 - [32] V. Naresh, S. Buddhudu, Analysis of energy transfer based emission spectra of (Sm^{3+} , Dy^{3+}): $\text{Li}_2\text{O}-\text{LiF}-\text{B}_2\text{O}_3-\text{CdO}$ glasses, *J. Lumin.* 147 (2014) 63–71. <https://doi.org/10.1016/j.jlumin.2013.10.035>.
 - [33] M.G. Ha, M.R. Byeon, T.E. Hong, J.S. Bae, Y. Kim, S. Park, H.-S. Yang, K.S. Hong, Sm^{3+} -doped CaTiO_3 phosphor: Synthesis, structure, and photoluminescent properties, *Ceram. Int.* 38 (2012) 1365–1370. <https://doi.org/10.1016/j.ceramint.2011.09.015>.
 - [34] D.R. Taikar, Synthesis and luminescence property of $\text{SrY}_2\text{O}_4:\text{M}$ (M = Eu^{3+} , Tb^{3+} , Sm^{3+} , Ce^{3+} , Bi^{3+}) phosphors, *J. Lumin.* 204 (2018) 24–29. <https://doi.org/10.1016/j.jlumin.2018.07.040>.
 - [35] S. Selvi, K. Marimuthu, G. Muralidharan, Structural and luminescence behavior of Sm^{3+} ions doped lead boro-telluro-phosphate glasses, *J. Lumin.* 159 (2015) 207–218. <https://doi.org/10.1016/j.jlumin.2014.11.025>.
 - [36] A.K. Vishwakarma, M. Jayasimhadri, Pure orange color emitting Sm^{3+} doped BaNb_2O_6 phosphor for solid - state lighting applications, *J. Lumin.* 176 (2016) 112–117. <https://doi.org/10.1016/j.jlumin.2016.03.025>.
 - [37] R. Yu, H. Mi Noh, B. Kee Moon, B. Chun Choi, J. Hyun Jeong, H. Sueb Lee, K. Jang, S. Soo Yi, Photoluminescence characteristics of Sm^{3+} doped $\text{Ba}_3\text{La}(\text{PO}_4)_3$ as new orange-red emitting phosphors, *J. Lumin.* 145 (2014) 717–722. <https://doi.org/10.1016/j.jlumin.2013.08.049>.
 - [38] L. Mei, H. Liu, L. Liao, Y. Zhang, R.V. Kumar, Structure and photoluminescence properties of red-emitting apatite-type phosphor $\text{NaY}_9(\text{SiO}_4)_6\text{O}_2:\text{Sm}^{3+}$ with excellent quantum efficiency and thermal stability for solid-state lighting, *Sci. Rep.* 7 (2017) 15171. <https://doi.org/10.1038/s41598-017-15595-z>.

- [39] L. Chen, X. Chen, F. Liu, H. Chen, H. Wang, E. Zhao, Y. Jiang, T.-S. Chan, C.-H. Wang, W. Zhang, Y. Wang, S. Chen, Charge deformation and orbital hybridization: intrinsic mechanisms on tunable chromaticity of $\text{Y}_3\text{Al}_5\text{O}_{12}:\text{Ce}^{3+}$ luminescence by doping Gd^{3+} for warm white LEDs, *Sci. Rep.* 5 (2015) 11514. <https://doi.org/10.1038/srep11514>.
- [40] M. Yamaga, T. Imai, H. Miyairi, N. Kodama, Substitutional disorder and optical spectroscopy of Ce^{3+} -doped CaNaYF_6 crystals, *J. Phys. Condens. Matter.* 13 (2001) 753–764. <https://doi.org/10.1088/0953-8984/13/4/321>.
- [41] M.G. Brik, N.M. Avram, Electron–vibrational interaction in the 5d states of Ce^{3+} ions in halosulphate phosphors, *Mater. Chem. Phys.* 128 (2011) 326–330. <https://doi.org/10.1016/j.matchemphys.2011.03.042>.
- [42] D.R. Taikar, S. Tamboli, S.J. Dhoble, Synthesis and photoluminescence properties of $\text{Li}_2\text{SO}_4:\text{RE}$ (RE = Eu^{3+} , Tb^{3+} , Gd^{3+} and Ce^{3+}) phosphors, *Optik (Stuttg).* 139 (2017) 111–122. <https://doi.org/10.1016/j.ijleo.2017.03.115>.

^{1*}Manasi R. Baccha

²A. P. Deshmukh

²S. P. Tiwari

²M. S. Dixit

²S. P. Yawale

Synthesis of pure PANI ,PEDOT:PSS and their copolymer as a counter electrode for the application of photovoltaic cell using betanin as natural dye sensitizer



Abstract: - This work presents the successful fabrication of natural dye sensitized solar cell (DSSC) using conducting polymers as counter electrode instead of expensive platinum .The CuO (copper oxide) nanoparticles were synthesized using co-precipitation method and these nanoparticles were used to synthesize TiO₂/CuO composites using ball milling method. Doctor blade method was adopted for the fabrication of TiO₂ and TiO₂/CuO working photo electrodes .The doping of CuO in TiO₂ revealed the enhancement in the stability of DSSC. The natural dye betanin was extracted from the beetroot, used as a dye-sensitizer for the fabrication of DSSC. In this study the variation of counter electrodes were carried out using conducting polyaniline (PANI), poly (3, 4-ethylenedioxythiophene) polystyrene sulfonate (PEDOT: PSS) and the copolymer of respective polymers. In-situ chemical oxidative polymerization method was utilized for the synthesis of pure PANI and PEDOT:PSS and the co-polymer of PANI/ PEDOT:PSS.

The structural study of synthesized material were done by using X-Ray diffraction (XRD) analysis. The functional group study of synthesized samples were done using Fourier Transform Infra-Red spectroscopy (FTIR) and UV-visible (UV-Vis) spectroscopy was carried out for the optical study .The VI-characteristics of DSSC were studied to investigate the parameters like open circuit voltage (V_{oc}), short circuit current (I_{sc}), fill factor (FF), voltage at maximum power (V_{mp}) and current at maximum power (I_{mp}). The efficiency of various solar cells so fabricated with the variation of counter electrode were also enlisted in this work. The efficiency of solar cell is found to be maximum for the pure PANI counter electrode as compared to other electrodes.

Keywords: Fluorine doped tin oxide (FTO), titanium dioxide (TiO₂), polyaniline (PANI), poly (3, 4-ethylenedioxythiophene) polystyrene sulfonate (PEDOT:PSS), PANI/PEDOT:PSS (PPP), dye sensitized solar cell (DSSC), copper oxide (CuO).

1. INTRODUCTION

In this era of new technology the demand for high energy supply is increasing day by day. So there is need to find the sustainable source of energy .The sun is abundant source of energy and solar energy is the most promising source of supply for this high energy demand. Dye sensitized solar cells (DSSC's) are most credible alternative to the P-N junction photovoltaic in both the technical and economic sense [1]. DSSC's are the third generation solar cell which are most efficient. The DSSC's are popular these days due to their remarkable properties such as low cost, non-toxic to environment ,good performance in the diverse light condition ,light weight, flexible ,semi-transparent ,bifacial and highly efficient [1].The four key parameters in the construction of DSSC are working electrode , sensitizer (dye) , redox mediator (electrolyte) and counter electrode .

The working electrodes are typically made from thin layer of semiconducting metal oxide such as titanium dioxide (TiO_2), zinc oxide (ZnO) on transparent conductive glass substrate such as FTO (Fluorine doped tin oxide) or ITO (Indium doped tin oxide). TiO_2 is the most promising material for the preparation of working electrode due to its higher energy band gap i.e. 3.2eV , non-toxic nature , less expensive and ease of availability [1-2]. However sensitizer (dye) is needed to broaden the absorption spectrum of metal oxide [4]. There is a formation of covalent bond between dye molecules and metal oxide layer .Organic dyes are less expensive and safer to use rather than expensive and toxic metal dyes[5]. These organic dyes can be easily extracted from flowers, leaves, roots of the plants by using some easy techniques [6]. Electrolytes have five main components that are redox couple, solvent, additive, ionic liquids and cations. Electrolyte can be made from KI and I_2 [9]. Typically counter electrodes for the efficient dye sensitized solar cell are made from expensive platinum .The cheaper and as efficient alternative is needed to be found out. The most promising alternative for the counter electrodes are the conducting polymers due to their remarkable properties such as high conductivity ,ease of synthesis , non -toxic and low cost . In this research work the variations of counter electrodes using various conducting polymers such as polyaniline (PANI), poly (3, 4-ethylenedioxythiophene) polystyrene sulfonate (PEDOT: PSS) and their copolymer were prepared and their photovoltaic study was carried out [3-13].

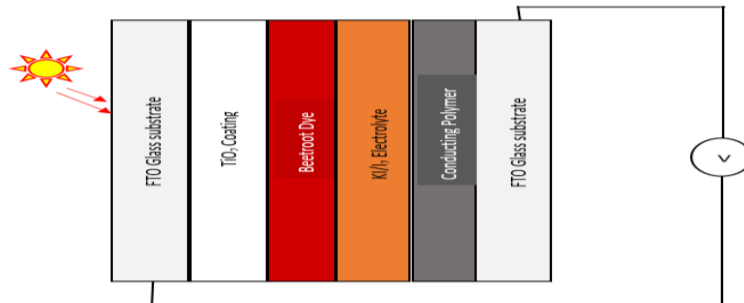


Fig 1:Shows the dye sensitized solar cell (DSSC) structure

2. EXPERIMENTAL TECHNIQUES

2.1.Preparation of working electrode

The semiconductor paste was prepared by blending 1g of commercial TiO_2 nano powder of anatase structure, 0.5g of ethyl cellulose, and 1.5ml of Butyl carbitol. The resulting suspension was stirred for 1hr and sonicated. Two edges of the FTO glass plate were secured with a layer of scotch tape to control the thickness of the film and to mask electric contact strips. Successively the TiO_2 paste was spread evenly on the substrate by sliding a glass rod along the tape spacer. The FTO glass spread TiO_2 nanoparticle were sintered at 100°C for about half an hour. After the sintering process was completed, the TiO_2 deposited electrode was cooled down from 100°C to 60°C at cooling rate of $3^\circ\text{C}/\text{min}$ to avoid cracking of glass. Then the TiO_2 electrodes was annihilated in blast furnace at 450°C for 1hr. Similar process was done for the $\text{TiO}_2/1\% \text{CuO}$ composite . The working electrodes then dipped in natural dye extracted from beetroot and henna leaves for 18 hr and then washed with ethanol to remove excess of unabsorbed dye from it's surface.

2.1.1. Preparation of $\text{TiO}_2/1\% \text{CuO}$ composite

The CuO was prepared by using co-precipitation method. In 0.2 M CuSO₄ , 0.4 M NaOH was added dropwise and solution was stirred for about 30 min at 80°C .Then the precipitate was filtered and heated at 400°C for 1 hr . Then 1% of CuO particles were doped with TiO₂ using *ex-situ* approach.

2.2. Preparation of conducting polymers

2.2.1. Synthesis of polyaniline (PANI)

PANI was chemically synthesized by oxidative polymerization. A monomer solution was prepared by adding 3.64 ml of aniline monomer into 3.32 mL of 1 M hydrochloric acid (HCl) along with 25 ml of distilled water. Next, 11.42 g of ammonium persulfate (APS) powder was mixed with 25 ml distilled water solution to form the initiator solution. Monomer and initiator solutions were then simultaneously dropped into a reactor glass, and the mixture was stirred for 30 min in ice bath (0-5°C) temperature. The flow rate of solution was controlled to get a homogeneous mixture. The solution will transform to a blackish-green color indicated the formation of PANI emeraldine salt (PANI-ES). The precipitate formed was settled for 16 hr and then filtered with whatman filter paper. The filtrate was then dried at 80°C for 3hr.

2.2.2. Synthesis of Poly(3,4ethylenedioxythiophene): polystyrene sulfonate (PEDOT:PSS)

Analytical reagent (AR) chemicals have been used for the synthesis. Conducting polymer PEDOT:PSS have been synthesized by chemical oxidative polymerization technique using oxidizing agent Ammonium Persulfate [(NH₄)₂S₂O₃] (APS) in aqueous medium. PSS was dissolved in 50 ml of distilled water at 1:2 mass ratio (EDOT:PSS) and stirred it well up to dissolve. Then the solution was sonicated for 45 min to get the homogeneous mixture of PSS solution. After the sonication EDOT monomer was added into PSS solution and stirred well using magnetic stirrer. Then oxidant APS was added at 1:2 mass ratio (EDOT:APS) directly in the above mixture with continued stirring. After this, the FeCl₃ solution which was prepared at 1:0.6 mass ratio (EDOT:FeCl₃) was added dropwise. The polymerization reaction started as the drop of FeCl₃ mixed in the above mixture. Physical appearance changes into blue and stirred it up to 2 hr at room temperature during polymerization reaction. After stirring, it was kept to settle for 16 hr. The obtained material was filtered with the help of filter paper and washed several times with distilled water. It was dried at 60 °C in oven for 24 hr. The bluish black material/polymer was obtained which was crushed in the Mortar pestle for fine powder.

2.2.3.Synthesis of copolymer of PANI/ PEDOT:PSS(PPP)

The copolymer was chemically synthesized by oxidative polymerization. A monomer solution was prepared by adding 2.662 g of PSS in 80ml distilled water and then sonicated for 30 min. In that solution 1 ml (1.33g) EDOT along with 2 ml aniline (2.0g) was added and stirred it. APS (6.66g) was directly added in mixture till it completely dissolved. 2 g of FeCl₃ was added in 20 ml distilled water then this solution was added dropwise to the above solution. The polymerization reaction started as the drop of FeCl₃ mixed in the above mixture.

2.3.Preparation of natural dye sensitizer

Beetroot extracts were prepared by crushing the 15g leaves and vegetables and adding them into 30 ml of ethanol and kept it as it for 1hr then it was filtered by using whatman filter paper. Extracts further purification was avoided to check whether an efficient sensitization could be achieved with negligible chemical methods. If properly stored, protected from direct sunlight and refrigerated at about 4°C, the acidic natural dye solutions (pH = 5.0) are usually stable, with a deactivation half-time of more than 12 months [5] .The formed dye was having pH 6.

2.4. Electrolyte preparation

To prepare liquid phase electrolyte 0.01M (0.126 g) I₂(Iodine) and 0.1M (0.8g) KI (Potassium iodide) was added into 10 ml of ethylene glycol and stirred for 30 minutes .Then this solution was stored in glass bottle and used as it is as electrolyte .

3. RESULT AND DISCUSSION

3.1. X-Ray Diffraction Analysis (XRD)

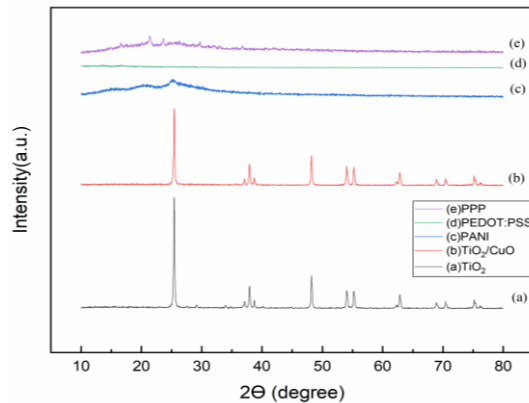


Fig 2. XRD pattern of TiO₂ ,TiO₂/CuO ,PANI ,PEDOT:PSS and PPP

Fig 2. Shows XRD pattern of TiO₂ ,TiO₂/CuO ,PANI ,PEDOT:PSS and PPP. For the pure PANI, the XRD spectra showed broad nebulous diffraction peak at $2\theta = 25.22^\circ$ and low intensity at $2\theta = 15.17^\circ$ and 20.39° indicates the disordered structure of long chain polymer matrix. For Pure PEDOT:PSS no sharp peaks were observed which indicates the amorphous nature of polymer. For the copolymer of PANI/PEDOT:PSS (PPP) , the XRD spectra showed broad nebulous diffraction peak at $2\theta = 21.42$ and 23.66° . Low intensity at $2\theta = 16.58^\circ$ and 29.39° indicates the disordered structure of long chain polymer matrix .The presence of highly intense diffraction peaks at 2θ values 25.4° , 37.8° , 48.19° , 54.0° and 62.8° corresponds to the crystallographic planes of (101), (004), (200), (105) and (204) . This shows the formation of anatase TiO₂ nanoparticles (JCPDS card No. 21–1272). For the TiO₂/ CuO composite only change in the intensity is observed and peak position remains the same[13-14] .

The mean crystallite size of nanocrystallites were calculated using Scherrer formula: $D = K\lambda / (B \cdot \cos\theta)$, where D is the crystalline particle size, K is the Scherrer constant (0.891), λ is the wavelength of X-ray (0.154056 nm), the half-height width of the diffraction peak is B, and θ is the angle of diffraction. The particle size of anatase TiO₂ was found to be 48.42 nm . The particle size of CuO was found to be 49.26 nm and for TiO₂/CuO composite was found to be 49.23 nm .

3.2. FTIR Spectroscopy analysis

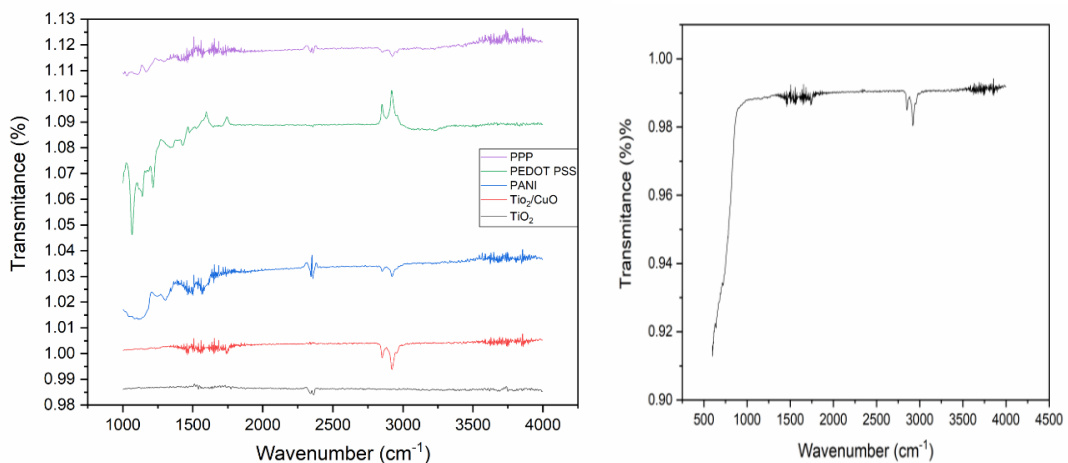


Fig 3. FTIR Spectra of TiO₂ ,TiO₂/CuO ,PANI ,PEDOT:PSS and PPP

Fig 3.1 : FTIR spectra of TiO₂/CuO

Fig 3. Shows the FTIR spectra of TiO₂ ,TiO₂/CuO ,PANI ,PEDOT:PSS and PPP . The FTIR spectrum of TiO₂ NPs clearly shows three groups. The first band is the broadest, and is observed around 2300 to 2400 cm⁻¹, corresponding to the stretching vibration of the hydroxyl group O-H of the TiO₂ NPs [7]. The next band is observed around 1630 cm⁻¹, corresponding to bending modes of water Ti-OH; the last is an important peak at

1383 cm^{-1} related to Ti-O modes.. The spectrum bands for CuO are observed at 601 cm^{-1} are characteristics of Cu-O bond formation along with TiO_2 for TiO_2/CuO [14].

The strong absorption band of PANI at 1525 cm^{-1} is assigned to the C=C stretching of quinoid group. Also, the vibration absorption peak of C=C in a benzene type ring is obtained at 1467 cm^{-1} . The spectra shows the bands at 2862 cm^{-1} which are attributed to C-H stretching of PANI. The peak at 3444.87 and 3128.54 cm^{-1} corresponds to the stretching vibration absorption peak of N-H and the weak peak at the 1647 cm^{-1} represents deformation vibration absorption peak of N-H bond. The position of these peaks matched with the characteristic peak ranges of an amine group- the range of stretching vibration absorption peak of N-H is 3500-3100 cm^{-1} . 1350-1000 cm^{-1} and 1640-1560 cm^{-1} is the range of stretching vibration absorption and the deformation vibration peaks of C-N respectively [3]. These findings showed that polymerization of aniline molecule took place throughout the reaction.

For the copolymer of PANI/PEDOT: PSS(PPP) the characteristics band of both PANI and PEDOT: PSS was observed simultaneously in FTIR spectra.

Table 1, Table 2 and Table 3 shows the FTIR analysis of TiO_2 , PANI and PEDOT:PSS [13,15].

Table 1. FTIR analysis of TiO_2

Sr. No	Wavenumber (cm^{-1})	Bonding/Stretching
1	2300 to 2400	hydroxyl group (O-H)
2	1630	bending modes of water Ti-OH
3	1383	Ti-O

Table 2. FTIR analysis of PANI

Sr. No	Wavenumber (cm^{-1})	Bonding /Stretching
1	1525	C=C of quinoid group
2	1467	C=C in a benzene type
3	2862	C-H
4	1170	$\text{H}^+\text{N}=\text{C}$
5	1327	C-N
6	3444, 3128	N-H
7	1647	Deformation of N-H

Table 3. FTIR analysis of PEDOT:PSS

Sr. No.	Wavenumber (cm^{-1})	Bonding /Stretching
1	1000	C-S stretching of the thiophene ring in PEDOT
2	1045-1145	S-O stretching SO_4^- from oxidant and S-phenyl in PSS
3	1095-1195	S=O stretching antisymmetric SO_4^- from oxidant
4	1094-1155	C-O stretching in PEDOT
5	1290-1370	C-C
6	1518-1640	C=C
7	2821-3070	C-H
8	3400	O-H stretching in PSS

3.3. UV-Visible Spectroscopy analysis

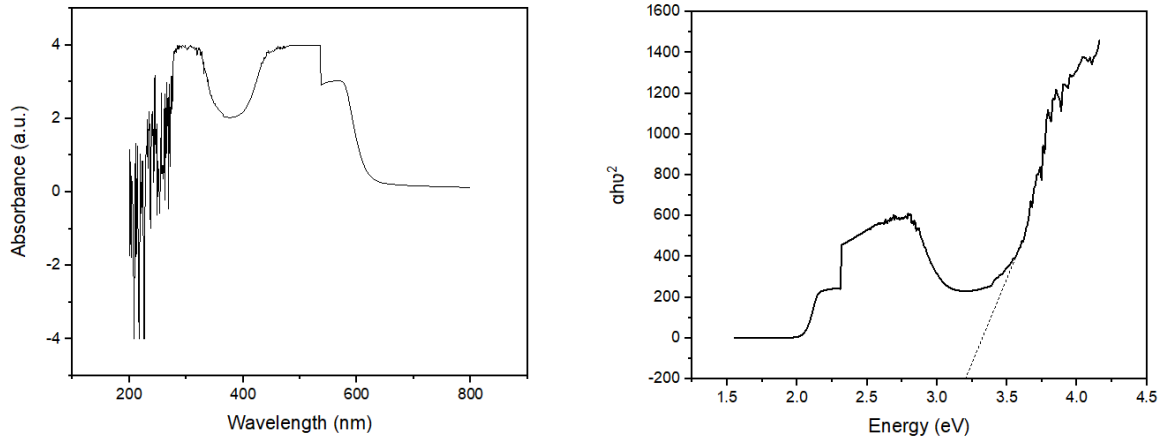


Fig 4. UV- Vi spectra of Beetroot dye

For the beetroot dye the maximum absorption was found to be in the range 450 to 550 nm of wavelength. The dip in the absorption curve was for 320 to 440 nm range. The band gap energy for the beetroot dye was found to be 3.2 eV(Fig 4 and 5) .

3.4. VI Characteristics

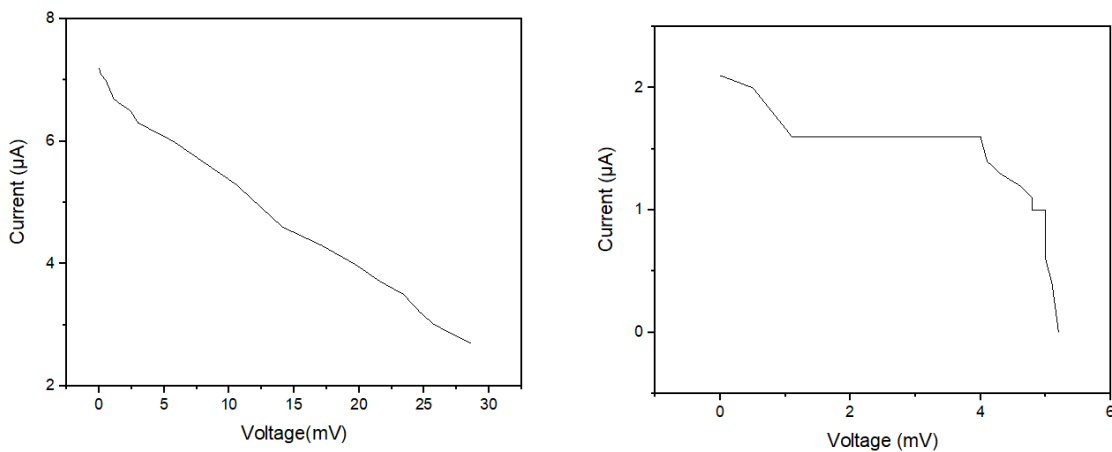


Fig 6. VI Characteristics of DSSC (TiO₂ + Beetroot+PANI)

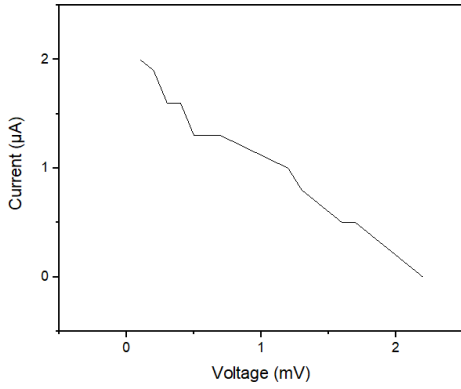


Fig 8. VI Characteristics of DSSC (TiO₂ + Beetroot+PEDOT:PSS)

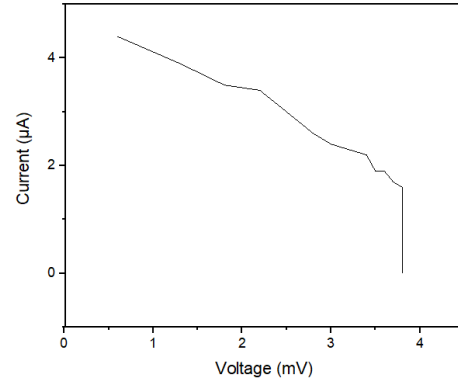


Fig 9. VI Characteristics of DSSC (TiO₂/1%CuO+ Beetroot+ PEDOT:PSS)

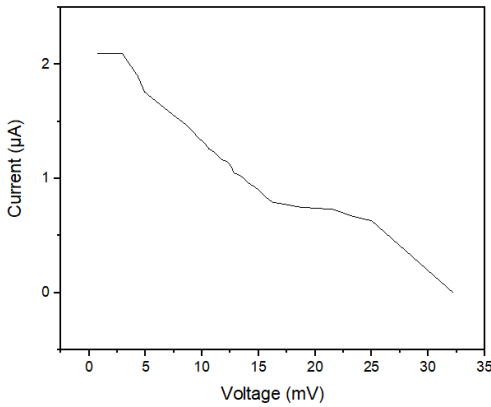


Fig 10. VI Characteristics of DSSC (TiO₂ + Beetroot+PPP)

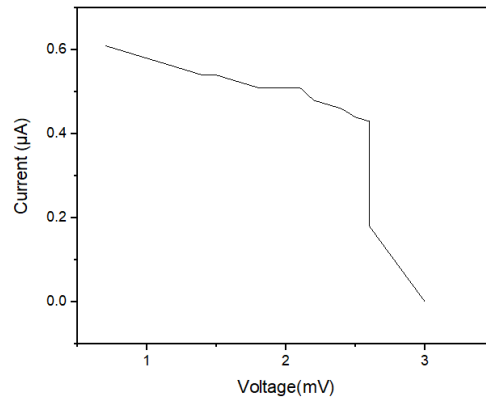


Fig 11. VI Characteristics of DSSC (TiO₂/1%CuO+ Beetroot+PPP)

Fig 6 to 11 shows the V-I characteristics of TiO₂ + Beetroot+PANI , TiO₂ /1%CuO+ Beetroot+PANI, TiO₂ + Beetroot+PEDOT:PSS , TiO₂/1%CuO+ Beetroot+ PEDOT:PSS , TiO₂ + Beetroot+PPP and TiO₂/1%CuO+ Beetroot+PPP DSSC respectively . For the TiO₂ + Beetroot+PANI the open circuit voltage is 42.8 mV which is found to be maximum amongst all prepared cells. Also short circuit current (I_{SC}) and efficiency is found to be maximum for this cell (Table 4). The table 4 depicts all values of the parameters for different prepared cells.

Table 4 . Open circuit voltage (V_{OC}) , short circuit current (I_{SC}), Voltage (V_{MP}) and current(I_{MP}) at maximum power , fill factor (FF) and efficiency of prepared DSSC .

Sr. No.	Working Electrode	Counter Electrode	Dye	V _{OC} (mV)	I _{SC} (µA)	V _{MP} (mV)	I _{MP} (µA)	FF	Efficiency (%)
1	TiO ₂	PANI	Beetroot	42.8	7.2	14.1	4.6	0.21	0.3
2	TiO ₂ /1% CuO	PANI	Beetroot	4.5	2.1	4	1.6	0.67	0.068
3	TiO ₂	PEDOT :PSS	Beetroot	2.2	2	1.2	1	0.27	0.005
4	TiO ₂ /1% CuO	PEDOT :PSS	Beetroot	3.8	4.4	3.4	2.2	0.45	0.03
5	TiO ₂	PPP	Beetroot	32.2	2.1	16.3	0.79	0.19	0.05
6	TiO ₂ /1% CuO	PPP	Beetroot	3	0.61	2.6	0.43	0.61	0.004

4. CONCLUSION

The work presents successful fabrication of natural dye sensitized solar cell (DSSC) using conducting polymers as counter electrode instead of expensive platinum. The DSSC made with pure PANI counter electrode and beetroot dye has maximum efficiency (0.3%) as compared to other electrodes. Doping of CuO in TiO₂ leads to enhancement in the stability of solar cell and fill factor of solar cell increases after addition of 1%CuO in TiO₂ which signifies power conversion efficiency of solar cell increase. Further optimizations in various parameters is needed for increase in the efficiency of solar cell.

5. AKNOWLEDGMENT

This proposed work was carried out at the Dept. of Physics and Electronics, Government Vidarbha Institute of Science and Humanities, Amravati (Autonomous). Author wish to thanks Dr. S.P.Yawale Head of Department Physics and Electronics for guiding this research work. The above research was not funded by any government or private agency.

6. REFERENCES

- [1] K. Sharma, V. Sharma S.S. Dye-Sensitized Solar Cells: Fundamentals and Current Status. *Nanoscale Res Lett* **13**, 381 (2018).
- [2] Michael Grätzel .Dye-sensitized solar cells (Review). *Journal of Photochemistry and Photobiology C: Photochemistry Reviews* 4, pp 145–153, 2003.
- [3] N.Patni, P.Sharma, K. Kumari and S.G. Pillai Synthesis of dye-sensitized solar cells using polyaniline and natural dye extracted from beetroot. *Research Journal of Recent Sciences* Vol.6, pp 35-39 (2017).
- [4] K .Soni ,A Sheikh , V Jain, N Lakshmi, Application of Natural Betalain Dye from Beetroot for Improved Efficiency in Dye Sensitized Solar Cell. *IOP Conf. Series: Materials Science and Engineering* vol.1187(2021).
- [5] C. Cari, Khairuddin, T. Y. Septiawan, P. M. Suciarmoko, D. Kurniawan, A. Supriyanto . The preparation of natural dye for dye-sensitized solar cell (DSSC). *AIP Conf. Proc.* 2014, 020106 (2018) .
- [6] Ahmed M. Ammar, Hemdan S. H. Mohamed, Moataz M. K. Yousef, Ghada M. Abdel-Hafez, Ahmed S. Hassanien, and Ahmed S. G. Khalil. Dye-Sensitized Solar Cells (DSSCs) Based on Extracted Natural Dyes. *Hindawi Journal of Nanomaterials* Vol 2019, Article ID 1867271 2019.
- [7] Soe Myat, Than Htay, San Nyein Khine, Kyaw San Oo, Tin Hla Yin, Tin Tin Mya, and Khin Phyu Phyu Tun .XRD and SEM Analysis, and Semiconductor Type Determination of TiO₂ for Dye-sensitized Solar Cell, *International Research Journal of Advanced Engineering and Science*, Volume 4, pp. 103-107, 2019.
- [8] Xiao Feng, Xijun Wang, Ming Wang, Shenghui Zhou, Chao Dang, Cunzhi Zhang, Yian Chen, Haisong Qi . Novel PEDOT dispersion by in-situ polymerization based on sulfated nanocellulose. *Chemical Engineering Journal* 2020.
- [9] MS Dixit, P.G. Khapekar, NS Dixit and SG Khaobragade . Study of dye sensitized solar cell using canna lily sensitizer nanocrystalline titanium dioxide photoanode. *International Journal of Science and Research Archive*, 2023, 08(02), 559–564 ,2023.
- [10] M. Khodadadi Yazdia , Gh. Hashemi Motlagha , S. Saeedi Garakani . Experimental and Theoretical Investigation of Ice Bath Polymerization for Polyaniline/Carbon nanotube Nanocomposites. *Proceedings of the 6th International Conference on Nanostructures (ICNS6)* pp 7-10, 2016.

- [11] Shahan Shah, N.N.S. Baharun, S.N.F. Yusuf, A.K. Arof. Efficiency Enhancement of Dye-Sensitized Solar Cells (DSSCs) using Copper Nanopowder (CuNW) in TiO₂ as Photoanode. Materials Science and Engineering 515 012002 IOP Publishing (2019).
- [12] A. Lanje , S. Sharma, R. Pode , R. Ningthoujam. Synthesis and optical characterization of copper oxide nanoparticles. Pelagia Research Library Advances in Applied Science Research, 1(2): 36-40(2010).
- [13] E. Nurazizah, A. Aprilia , R. Risdiana, L. Safriani, Different Roles between PEDOT:PSS as Counter Electrode and PEDOT:Carrageenan as Electrolyte in Dye-Sensitized Solar Cell Applications: A Systematic Literature Review,2023.
- [14] A. Asha Radhakrishnan, B. Baskaran Beena. Structural and Optical Absorption Analysis of CuO Nanoparticles Structural and Optical Absorption Analysis of CuO Nanoparticles. Indian Journal of Advances in Chemical Science 2 (2) pp158-161, 2014.
- [15] P. Sakunpongpitorn, K. Phasukom, N. Paradee, A. Sirivat. Facile synthesis of highly conductive PEDOT:PSS via surfactant templates, RSC Adv. 2019, 9, 6363, 2019.

© 2024. This work is published under
[https://creativecommons.org/licenses/by/4.0/legalcode\(the“License”\)](https://creativecommons.org/licenses/by/4.0/legalcode(the“License”)).
Notwithstanding the ProQuest Terms and Conditions, you may use this
content in accordance with the terms of the License.

¹Priyanka P Gole² Sandeep A.
Waghuley.

Regular paper
Review On Rare Earth-Conducting
Polymer Nanocomposites For
Spintronics Application

**Abstract: -**

Spintronics, a developing field at the intersection of electronics and magnetism, holds immense promise for revolutionizing information processing and storage technologies. Rare earth-conducting polymer nanocomposites have emerged as a novel class of materials with significant potential for advancing spintronic applications. This review provides a comprehensive overview of recent developments and applications in spintronics technology. It begins with an exploration of spin transport phenomena, elucidating concepts such as spin injection, spin polarization, and spin manipulation techniques. Subsequently, it delves into specific spintronics applications, including magnetic memory and storage solutions like spin-transfer torque MRAM and spin-orbit torque MRAM. Continued research efforts in this area are essential for realizing the full potential of rare earth-conducting polymer nanocomposites in practical spintronics applications.

Keywords: Spintronics, rare earth elements, conducting polymers, nanocomposites, applications.

¹*Priyanka P. Gole Department of Physics Sant Gadge Baba Amravati University, Amravati.444602

²*S. A. Waghuley, Department of Physics Sant Gadge Baba Amravati University, Amravati.444602
latapgole@gmail.com
sandeepwaghuley@sgbau.ac.in

I. INTRODUCTION

In the twenty-first century microelectronics devices face a number of difficulties, Researchers have been examining intrinsic properties of electrons called spin in an effort to focus on the present issues facing microelectronics devices,[1] such as power consumption and downscaling. New spin-related physics studied by gigantic magnetoresistance, tunneling magnetoresistance, and spin transfer torque have been investigate in the field of spin electronics, leading to spin based device application [2]. The detection and control of electron spin in solid-state physics is focus on electronics field known as spintronics [3]. These include the independent discoveries of massive magneto resistance made by Albert Fert in France and Peter Gruenberg in Germany in 1988[4, 5] have been observed spin polarized electron injection from ferromagnetic metal to a normal metal [6]. Nowadays in modern computer hard drives and other magnetic devices use a metal-based Spintronics [7,8].Ferromagnetic materials play a vital role in the spintronics application [9], leading to recent emphasis on the development of spintronics materials involving carbon materials, metal oxides, and conducting polymers [10]. In this review work on rare earth doped conducting polymer for spintronic application. Conducting polymer nanocomposites offer unique opportunities in spintronics due to their tunable electronic properties and compatibility with flexible and lightweight substrates. Here are some potential spintronics applications using conducting polymer nanocomposites [11].

II. CONDUCTING POLYMERS

Conducting polymers, with their 1D intrinsic property have been a focal point of both fundamental and applied research in fields like field-effect transistors, displays, and rechargeable batteries [12]. Polyaniline (PANI), Polypyrrole (PPy), Polythiophene (PTh) represent the extensively studied conducting polymers, in contrast to Polyindole, often referred to as PI/PIn/Pind, which has historically garnered less attention due to its lower polymerization efficiency. However, recent interest has surged owing to its remarkable environmental stability and electrical conductivity. Characterized by a distinctive benzene and pyrrole ring structure, coupled with properties such as good thermal stability, low degradation rate, and high storage capacity, to study helps us to under-stand the electric behavior of the samples whether capacitive or resistive type for which further studies can be conducted for sensor, anticorrosioncoating, and spintronic applications.[13]. The semiconducting and electrochemical behavior of rare earth based composites was investigated using four probe conductivity meter and cyclic voltammetry (CV) respectively. An overall view

of different the techniques show this material use in their various field of electronics and communication application is presented [14]. Pure phased rare earth doped ZnO nanoparticles for tetracycline degradation. They prepared sample were systematically characterized for structural, optical, and magnetic properties [15]. The influence of trivalent rare-earth dopants (Sm and La) on the structure-activity properties of CeO₂ was thoroughly studied for diesel soot oxidation [16]. Pure polyaniline (PANI) and Lanthanum oxide (La₂O₃) modified polyaniline were synthesized by using in-situ polymerization method. Dielectric constant of the samples increased as frequency increases and dielectric loss in the materials is also very minimal. The prepared samples may find applications in the electronics field industry [17]. The novel organic materials innovative devices and functionalized interfaces in organic spintronics are comprehensively introduced. First the fundamental concepts and parameters of organic spin devices are clarified. Subsequently the organic materials applied in organic spintronics are classified several types of spin-related devices in this field are introduced and discussed [18]. A carbon nanotube spin field-effect transistor device by the direct synthesis of single-walled carbon nanotubes (SWNTs) on substrates by alcohol catalytic chemical vapor deposition. They observed hysteretic magnetoresistance (MR) at low temperatures due to spin-dependent transport. In their devices[19]. Bimetallic Co–Ni-based spin FET device is fabricated, and its magnetoresistance behavior has been studied [20, 21]. Spin-injecting interfaces involving organic semiconductor (OSC) molecules and ferromagnetic metals are discussed. The inter-faces are classified in different categories depending on the type and strength of interface interaction and the relevant physics concerning energy level alignment and spin polarization of interface states are explained [22]. Organic spintronics is an emerging and potential platform for future electronics and display due to the intriguing properties of organic semiconductors. Studies have focused on three types of organic spintronic phenomena magnetic field effect, magnetoresistance effect, Spin valve [23]. In external spin injection and organic property-induced spin Polarization, according to the distinction between the sources of spin polarization [24]. The rare earth doped conducting polymer for spintronic applications is promising field of research. To synthesis of rare earth composite with conducting polymer some methods are used such as sol gel method, co-precipitation method, in-situ polymerization method, and combustion method, chemical oxidative polymerization method [25]. From the literature survey we can examine that to improve thermal and cyclic stability, capacity of energy storage in electronic device [26]. We conclude that the interaction between the stability, capacity of energy storage in electronic device. Conducting polymer nanocomposites offer unique opportunities in spintronics due to their tunable electronic properties and compatibility with flexible and lightweight substrates [27]. Here are some potential spintronics applications using conducting polymer nanocomposites:

- **Spin Injection Devices:** Conducting polymer nanocomposites can be used as spin injectors in spin valves and spin transistors. By incorporating magnetic materials into the nanocomposites, spin-

polarized currents can be injected into adjacent layers, enabling efficient spin transport and manipulation [28, 29, 30, 31].

- **Spin Filters:** Nanocomposites with controlled spin-dependent transport properties can act as spin filters, selectively allowing electrons with specific spin orientations to pass through while blocking others. This capability is crucial for spin-based logic and memory devices [32, 33].
- **Spintronic Memory Devices:** Conducting polymer nanocomposites can be employed in spintronic memory devices such as spin-transfer torque random access memory (STT-RAM) and magnetic random-access memory (MRAM). These devices utilize spin-polarized currents to write and read data, offering high-speed operation and non-volatility [34, 35].
- **Spintronic Sensors:** Nanocomposites can be used in spintronic sensors for detecting magnetic fields, spin currents, and spin polarization. Their flexibility and compatibility with diverse substrates make them suitable for wearable and flexible sensor application [36, 37].
- **Spintronic Logic and Computing:** Conducting polymer nanocomposites hold promise for developing spin-based logic and computing devices. Their tunable electronic properties and low-power operation make them attractive candidates for next-generation spintronic circuits and processors [38, 39,40].
- **Spintronic Energy Conversion:** Nanocomposites can be utilized in spintronic energy conversion devices such as spin Seebeck effect (SSE) generators and spin thermoelectric devices. These devices convert waste heat into useful electrical energy by utilizing the spin degree of freedom of electrons[41].
- **Spintronic Interconnects:** Conducting polymer nanocomposites can serve as efficient spin transport channels in spintronic interconnects, enabling low-loss transmission of spin information between different components in spin-based circuits and systems[41].

III. Rare Earth Elements

Rare earth elements (REEs) have garnered significant attention in spintronics research due to their unique electronic and magnetic properties, making them promising candidates for various spintronic applications[43]. This review explores the utilization of REEs in spintronics, focusing on their roles in enhancing spin transport, enabling novel device functionalities, and advancing spin-based technologies. Firstly, we discuss the fundamental properties of REEs that make them suitable for spintronics, including their high magnetic moments, long spin relaxation times, and robustness against oxidation. Next, we examine recent research efforts in incorporating REEs into spintronic devices, such as rare earth-based magnetic tunnel junctions (MTJs), spin valves, and spin field-effect transistors (SFETs). We highlight how REEs contribute to improving device performance, stability, and scalability, thereby expanding the potential applications of spintronics in data storage, sensing, computing, and communication [42].

IV. Application

- The largest technological application of GMR is in the data storage industry. IBM was first to place on the market hard disks based on GMR technology and these a day's all disk drives make use of this technology [44].
- Magnetoresistive materials and structures are used as sensors for magnetic recording, MRAM, motion Sensors or just simply to measure the strength of a magnetic field.[45,46]
- Other applications of GMR are as diverse as automotive sensors, solid-state compasses and non-volatile magnetic memories [47].
- Integrated spintronics biochips (neuroelectronic studies and biomedical imaging)[48].
- Spintronics devices are used in the field of mass-storage devices.

V. Conclusions

In this review observed that, the rare earth doped conducting polymer nanocomposites are best material for spintronics application a wide variety of new devices that combine logic, storage and sensor applications. Spintronics devices might lead to quantum computer and quantum communication based on electronics solid state devices, such as spin valve, spin FET Ultimately, significant advancements have been achieved in rare earth-conducting polymer spintronics concerning novel materials, apparatuses, and functionalized interfaces. But in order to gain industrial use, much more work needs to be done. Conducting material for spintronics is predicted to have a significant rise in the near future.

VI. REFERENCES

- [1] S. D. Sarma "Spintronics: A new class of device based on electron spin, rather than on charge, May yield the next generation of microelectronics" Vol. 89, No. 6 2001, pp. 516-523
<https://www.jstor.org/stable/27857562>.
- [2] Y.Tian, & S. Yan,. "Giant magnetoresistance: history, development and beyond". Science China Physics, Mechanics and Astronomy, 56(1),2012, 2–14.
- [3] S. Zegeye. "A Review Paper on Spintronics and Its Role to Improve Electronic Devices". American Journal of Quantum Chemistry and Molecular Spectroscopy. Vol. 3, No. 2, 2019, pp. 41-47. doi: 10.11648/j.ajqcms.20190302.13.
- [4] B.A.Gurney, "Giant magnetoresistance in magnetic recording". AAPPS Bull. 18, 2008,18–23.
- [5] H. Zabel, "Progress in spintronics. Superlattice. Microst". 46, 2009, 541– 553.
- [6] S. A.Wolf. "Spintronics, Proc". IEEE, Vol. 91, 2003pp. 5.

- [7] A. Rohit ,” International Journal of Advanced Computer Research”, (ISSN (print): 2249- 7277, Vol. 3, 2013 pp. 1.
- [8] M. RoukesL.” Caltech (August), Spin Electronics”, Univers, 2003 PP 4.
- [9] M. Ziese,and M.J.Thornton,” Spin Electronics (Lecture Notes in Physics series)”, Vol. 569.
- [10] L. Zhang, P. Wan “Polymer nanocomposite meshes for flexible electronic devices” Volume 107 2020, 101279,
- [11] S. Lanceros-Mendez, P. Martins “Tailoring polymer-based magnetoelectrics for Spintronics”volume 38,2024, 102216 <https://doi.org/10.1016/j.apmt.2024.102216>.
- [12] S.P. Koiry, V.Saxena, D.Sutar, S. Bhattacharya, D.K. Aswal,S.K. Gupta, & J. V. Yakhmi, “Interfacial synthesis of long polyindole fibers”. Journal of applied polymerscience, 103(1), 595-599.
- [13] M.G.Smitha, H.L.Sandeep Kumar and Shwetha Morphological, structural, electrical impedance, and equivalent circuit analysis of polypyrrole/barium substituted lanthanum manganite (La 0.7Ba 0.3MnO₃) perovskite nanocomposites,VOL. 28, NO. 3,241–255 <https://doi.org/10.1080/1023666X.2023.2201083>.
- [14] Rekha, A. Bisht, Ila Joshi, S. Sharma, S. Mehtab, N.K.Sand and M. Zaidi “Rare earth based conducting polymers”, International Journal of Chemical Studies 2019; 7(3): 1246-1250.
- [15] P.Dhiman, G. Rana, A. Kumar, Elmuez A. Dawi and G. Sharma” Rare Earth Doped ZnO Nanoparticles as Spintronics “and Photo Catalyst for Degradation of Pollutants,Molecules 2023, 28, 2838. <https://doi.org/10.3390/molecules28062838>
- [16] A. Rangaswamy, P. Sudarsanam , M.Benjaram Reddy “ Rare earth metal doped CeO₂-based catalytic materials for diesel soot oxidation at lower temperatures,” Volume 33, Issue 11, November 2015, Pages 1162-1169, [https://doi.org/10.1016/S1002- 0721\(14\)60541-X](https://doi.org/10.1016/S1002- 0721(14)60541-X)
- [17] L.N Gurunath “AnilkumarBidve Synthesis and Characterization of Lanthanum Oxide Doped Polyaniline (PANI/La₂O₃)” Journal of Survey in Fisheries Sciences10 (4S) 1023-1028 2023.
- [18] D. Li and G. Yu “Innovation of Materials, Devices”, and Functionalized Interfaces in Organic Spintronics, Adv. Funct. Mater. 2021, 2100550, <https://doi.org/10.1002/adfm.202100550>.
- [19] M. A. MohamedInami, N., Shikoh, E.Yamamoto, Y., Hori, H., & Fujiwara,” A fabrication of spintronics device by direct synthesis of single-walled carbon nanotubes from ferromagnetic electrodes”. Science and Technology of Advanced Materials. 9(2), 2008,025019.
- [20] T. Mohota and K. Nemade, “Integration of Bimetallic Co–Ni Thick Film-Based Devices for Spintronics”, a future issue of this journal. Content is final as presented, 10.1109/TED.2016.2596979.

- [21] M. D.Allendorf, R.Dong, X. Feng, S. Kaskel, D. Matoga, &V. Stavila, “Electronic Devices Using Open Framework Materials.ChemicalReviews”. (2020). doi:10.1021/acs.chemrev.0c00033.
- [22] Y. Zhan, M. Fahlman, “The Study of Organic Semiconductor/Ferromagnet Interfaces in Organic Spintronics” journal of polymer science part b: polymer physics 2012, 50, 1453–1462 DOI: 10.1002/polb.23157.
- [23] R. Geng, T. T.Daugherty, K. Do, H. M. Luong, T. D. Nguyen, “A review on organic spintronic materials and devices”. Magnetic field effect on organic light emitting diodes,2016.
- [24] K. Meng, L. Guo and X.Sun, “Strategies and applications of generating spin polarization in organic semiconductors” DOI: 10.1039/x0xx00000x.
- [25] P.chhattise, k. Handore , A. Horne, K. Mohite , A. Chaskar, S. Dallavalle and V.Chabukswar “Synthesis and characterization of Polyindole and its catalytic performance study as a heterogeneous catalyst “ Chem. Sci. Vol. 128, No. 3, (2016), pp. 467–475. DOI 10.1007/s12039-016-1040-1
- [26] J.D. MacKenzie, & C.Ho, “Perspectives on Energy Storage for Flexible Electronic Systems”. Proceedings of the IEEE, 103(4),(2015), 535–553. doi:10.1109/jproc.2015.2406340
- [27] R. carvalho, S. lanceros-mendez, P. martins “tailoring polymer-based magnetoelectric for spintronicsevaluating the converse effect” volume 38, (2024), 102216 <https://doi.org/10.1016/j.apmt.2024.102216>
- [28] P. Barla· V.Kumar Josh, S. Bhat “Spintronic devices: a promising alternative to CMOS devices” Journal of Computational Electronics (2021) 20:805–837 <https://doi.org/10.1007/s10825-020-01648-6>.
- [29] G Schmidt “Concepts for spin injection into semiconductors-a review” J. Phys. D: Appl. Phys.**38** (2005) R107–R122 doi:10.1088/0022-3727/38/7/R01.
- [30] S. M.Yakout” Spintronics: Future Technology for New Data Storage and Communication Devices” Journal of Superconductivity and Novel Magnetism (2020) 33:2557–2580 <https://doi.org/10.1007/s10948-020-05545>
- [31] M.Oestreich,J. Hübner,D. Hägele, P.J. Klar, W.Heimbrodt, W.W.Rühle,B. Lunn “Spin injection into semiconductors”. Applied Physics Letters, 74(9), (1999). 1251–1253. doi:10.1063/1.123515
- [32] M. G. Zeng,^{1,2} L. Shen,¹ Y. Q. Cai,¹ Z. D. Sha,¹ and Y. P. Feng Perfect spin-filter and spin-valve in carbon atomic chains. Applied Physics Letters, 96(4),(2010),042104. doi:10.1063/1.3299264 .
- [33] L.L. Manza, S.L.Stamer, A.J.Ham, S.G.Codreanu, & D.C.Liebler, “Sample preparation anddigestion for proteomic analyses using spin filters.” proteomics, 5(7), (2005), 1742–1745. doi:10.1002/pmic.200401063 .
- [34] W.PLin,S.J Liu., T. Gong, Q. Zhao & W. Huang, “Polymer-Based Resistive Memory material and Devices” .Advanced material,26(4),(2013),570-606 doi:10.1002/adma.201302637.

- [35] M. Ciorga, A. Einwanger, U. Wurstbauer, D. Schuh, W. Wegscheider and D. Weiss “Electrical spin injection and detection in lateral all-semiconductor devices”. *Physical Review B*,(2009),76(16) doi:10.1103/physrevb.79.165321.
- [36] X. Liu, K. H. Lam, K. Zhu , C. Zheng , X. Li1, Y. Du , Chunhua Liu , P. W. T. Pong, “Overview of Spintronic Sensors, Internet of Things, and Smart Living”2016.
- [37] M. A. Khan, J.Sun, B. Li, A. Przybysz and J. Kosel “ Magnetic sensors-A review and recent technologies Eng”. *Res. Express* 3 (2021) 022005.
<https://doi.org/10.1088/2631-8695/ac0838>
- [38] B. Dieny · R.C. Sousa “Spintronic Devices for Memory and Logic Applications”
 volume 19,2011,pages 107-127. <https://doi.org/10.1016/B978-0-444-53780-5.00002-8>
- [39] C. Pan, S.Chang; A. Naeemi “performance analyses and benchmarking for SPINTRONIC DEVICES AND INTERCONNECTS” 23-26, 2016
<HTTPS://DOI.ORG/10.1016/B978-0-444-53780-5.00002-8>
- [40] K.VANDAELE,S.J. WATZMAN,B. FLEBUS, A.PRAKASH, Y. ZHENG, S.R.BOONA & J.P. HEREMANS “THERMAL SPIN TRANSPORT AND ENERGY CONVERSION. MATERIALS TODAY PHYSICS” 1, 39–49.(2017)DOI:10.1016/J.MTPHYS.2017.05.00
- [41] Y.ZHANG,L. GUO,X.ZHU, & X.SUN, “THE APPLICATION OF ORGANIC SEMICONDUCTOR MATERIALS IN SPINTRONICS”. (2020) 8. DOI:10.3389/FCHEM.2020.589207.
- [42] S.GUPTA “EXOTIC RARE EARTH-BASED MATERIALS FOR EMERGING SPINTRONIC TECHNOLOGY”
 Volume 63,2023, Pages 99-140 <https://doi.org/10.1016/bs.hpre.2023.04.001>
- [43] W.Xia, Z. Pei, K.Leng, & X. Zhu,“Research Progress in Rare Earth-Doped Perovskite Manganite Oxide Nanostructures”.*Nanoscale Research Letters*, (2020)15(1). doi:10.1186/s11671-019-3243-0
- [44] [http://simple.wikipedia.Org/wiki/Giant magnetoresistance](http://simple.wikipedia.Org/wiki/Giant_magnetoresistance)
- [45]A. Hirohata, K.Yamada, Y.Nakatani, I.L Prejbeanu, B.Diény, P.Pirro, &B. Hillebrands, “ Review on spintronics: Principles and device applications”. *Journal of Magnetism and Magnetic Materials*, (2020). 509, 166711. doi:10.1016/j.jmmm.2020.16671.
- [46] A.Fert, & F.N. Van Dau, “Spintronics, from giant magnetoresistance to magnetic skyrmions and topological insulators”. *Comptes Rendus Physique*.(2019) doi:10.1016/j.crhy.2019.05.020.
- [47] M. Pinarbasi, A. D. Kent “Perspectives on spintronics technology development: Giant magnetoresistance to spin transfer torque magnetic random access memory”10, 02090 (2022)<https://doi.org/10.1063/5.0075945>.
- [48]P.PFreitas, V.C.Martins, F.A.Cardoso,E.Fernandes,T. Sobrino,J.Castillo,S.Cardoso, *SpintronicBiochips. Nanomagnetism: Applications and Perspectives*, 165–200. (2017). doi:10.1002/9783527698509.ch9

¹S. S. Pakade

¹A.H. Kale

²A.D. Bokhare

^{3*}M.P. Lokhande

⁴A.C.Kumbharkhane

Study Of Dielectric Relaxation in a water mixture of Adonitol and D-Arabitol using Time Domain Reflectometry Technique



Abstract: - Complex dielectric permittivity of two pentitol isomers, adonitol (C₅H₁₂O₅), D-arabitol(C₅H₁₂O₅) in water has been studied using time domain reflectometry technique in the frequency range of 10MHz to 30GHz. The measurements have been done at 250C temperature for different concentration. The dielectric relaxation behaviour of adonitol and water mixture has been fitted in Debye model while the D-arabitol and water mixture fitted in Cole-Davidson model. The dielectric parameters such as static dielectric constant and relaxation time have been calculated from complex permittivity spectra using the nonlinear least square fit method.

Keywords: Time domain reflectometry, Dielectric relaxation, Complex permittivity spectra.

*Corresponding author: Government Vidarbha Institute of Science and Humanities, Amravati 444604, India.
Email id:mplokhande123@gmail.com

¹ Government Vidarbha Institute of Science and Humanities, Amravati 444604, India

I. INTRODUCTION

The study of dynamical properties of organic solvents in binary mixtures with water, through their interaction with electromagnetic waves, provides valuable insights into molecular interactions and structures. Advanced spectroscopic techniques, particularly broadband dielectric spectroscopy, are instrumental in revealing these properties. Dielectric spectroscopy, using frequency and time domain methods, offers detailed information about frequency-dependent dielectric properties, essential for both fundamental research and practical applications. Time Domain Reflectometry (TDR), a key technique within time domain spectroscopy, enables precise measurement of complex dielectric permittivity over a wide frequency range in a single experiment. This versatile method is used in various applications, from assessing soil moisture content to detecting faults in electronic components. By studying dielectric dispersion and absorption spectra, significant molecular interactions, such as hydrogen bonding, can be elucidated, enhancing our understanding of the structural and dynamical behaviors of liquid mixtures.[1]

Adonitol and D-arabitol, five-carbon sugar alcohols (pentitol) or alditols are the polyhydroxylated molecules they are aliphatic, which has multiple vicinal hydroxy group[2]. The molecular formula of adonitol and D-arabitol is $C_5H_{12}O_5$, belong to the carbohydrate family. They naturally occur in certain microorganisms and some plants[3]. Adonitol, produced by the reduction of ribose, is found in nature in the plant *Adonis vernalis* and in some Gram-positive bacteria's cell walls as ribitol phosphate and teichoic acids. It is also a component of riboflavin and flavin mononucleotide (FMN), a nucleotide coenzyme used by various flavoproteins. Whereas, D-arabitol is primarily sourced from the reduction of arabinose, a pentose sugar found in plant cell walls, particularly in hemicellulose[4]. These sugar alcohols find diverse applications across various industries. In the food industry, they serve as low-calorie sweeteners and humectants, enhancing the texture and shelf life of product[5]. In pharmaceuticals, arabitol is explored as a non-toxic excipient in drug formulations. Their occurrence in microbial cell walls also makes them significant in biotechnological research. D-arabitol and adonitol's multifaceted properties underscore their importance in developing innovative products and processes.[6]

Water, as the biological basis of life, possesses unique properties primarily due to its structure and dynamics, dominated by hydrogen bond interactions. Similarly, D-arabitol and adonitol show a strong tendency to form hydrogen bonds[7]. Due to their multiple hydroxyl groups, D-arabitol and adonitol exhibit high solubility in aqueous media. Dielectric relaxation studies of their mixtures with water are crucial for understanding intermolecular interactions and hydrogen bonding, driven by dipole-dipole interactions. [8]

The primary objective of this research is to investigate the dielectric relaxation properties of D-arabitol water and adonitol-water systems using time domain reflectometry (TDR) in the frequency range of 10 MHz to 30 GHz. This study reports on the static dielectric constant, relaxation time, and excess dielectric permittivity for these mixtures, providing valuable insights into their structural and dynamic behavior.

II. EXPERIMENTAL

A. Material and sample preparation

D-arabitol and adonitol, each with a purity of 99%, were purchased from Alfa Aesar and utilized directly without any additional preparation. Double-distilled water was used to create the aqueous mixtures. Eleven different samples were prepared for each substance. The solutions were prepared at different mole fractions of water in adonitol and D-arabitol. The concentration series ranged from 0.3 M to 3 M, with one sample of pure water included as a control in both sets.

B. Measurements

The basic Time Domain Reflectometry (TDR) setup includes a broadband sampling oscilloscope, a TDR module, and a coaxial transmission line. For this experiment, a Tektronix DSA8200 sampling oscilloscope with a 30 GHz bandwidth and a TDR module 80E08 equipped with a step generator unit were used. A 250mV step pulse with an 18 ps rise time was sent through a 50 Ω coaxial line system. The sampling oscilloscope monitored the changes in the step pulse after it reflected from the sample. The reflected pulse without the sample, $R_1(t)$ and with the sample, $R_x(t)$, were recorded within a 5 ns time window and digitized into 2000 data points. The step pulses recorded with and without sample are $R_X(t)$ and $R_1(t)$ respectively and the addition $\{q(t) = [R_1(t) + R_x(t)]\}$ and subtraction $\{p(t) = [R_1(t) - R_x(t)]\}$ of these pulses are performed in the oscilloscope's memory. These added and subtracted pulses are then transferred to a PC for further analysis. Fourier transformations of the pulses

and subsequent data analysis were previously conducted to determine the complex permittivity spectra, $\epsilon^*(\omega)$, using the non-linear least squares fit method

III. RESULT AND DISCUSSION

1. Dielectric constant and relaxation time:

The dielectric relaxation for the solution of adonitol and water & D-arabitol and water system has been fitted in the Debye model(a) and the Cole- Davidson model(b) using nonlinear least square fit method respectively.

$$\epsilon^* = \epsilon_\infty + \frac{\epsilon - \epsilon_\infty}{(1 + j\omega\tau)} \quad \dots a$$

$$\epsilon^* = \epsilon_\infty + \frac{\epsilon - \epsilon_\infty}{(1 + j\omega\tau)^\beta} \quad \dots b$$

Where ϵ_0 is the static permittivity, ϵ_∞ is the permittivity at high frequency, τ is relaxation time α and β is the empirical parameter it gives how relaxation time distributed. Dielectric parameters like dielectric constant, relaxation time for (adonitol + water mixture) and (arabitol + water mixture) is shown below in table a and b. It is observed that the dielectric constant for both the sample are found to be decreasing with increase in concentration of Adonitol and Arabitol at room temperature 250C. This may be due to the lesser alignment of dipole or smaller value of dipole moment. The relaxation time is found to be increases continuously with increase in concentration of sample as shown below in fig.1. This due to the modified network of hydrogen bond by sample to increase the time, it shows linear relationship between the relaxation time and the viscosity of material [8].

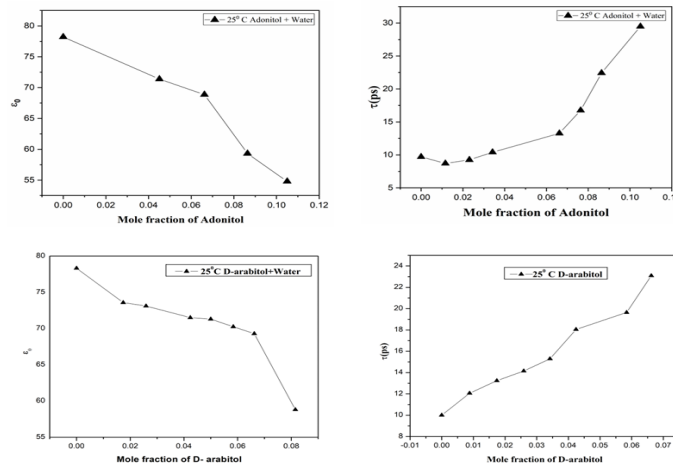


Fig .1

2. Complex permittivity spectra

The dielectric spectra is found out to be same for adonitol and D-arabitol [9]. The fig.2(a) and fig.2(b) shows the frequency dependent values of permittivity (ϵ') and dielectric loss (ϵ'') of adonitol-water and D-arabitol-water mixture at 250C. From the plot that values of dielectric permittivity (ϵ') and dielectric loss (ϵ'') shifted towards lower frequency side as the concentration increases the shifting of loss peaks towards lower frequency side with increase in concentration indicates increased relaxation time.[10]

Table a

Sr.no	Mole fraction of Adonitol ($X_{Adonitol}$)	ϵ_0	τ (ps)
1	0	78.21	9.71
2	0.0116	59.44	8.71
3	0.0231	57.56	9.25
4	0.0342	56.36	10.41
5	0.0451	71.38	12.44
6	0.0558	63.21	12.34
7	0.0662	68.87	13.27
8	0.0764	55.10	16.76
9	0.0864	59.31	22.42
10	0.0962	59.31	22.74
11	0.1050	54.79	29.48

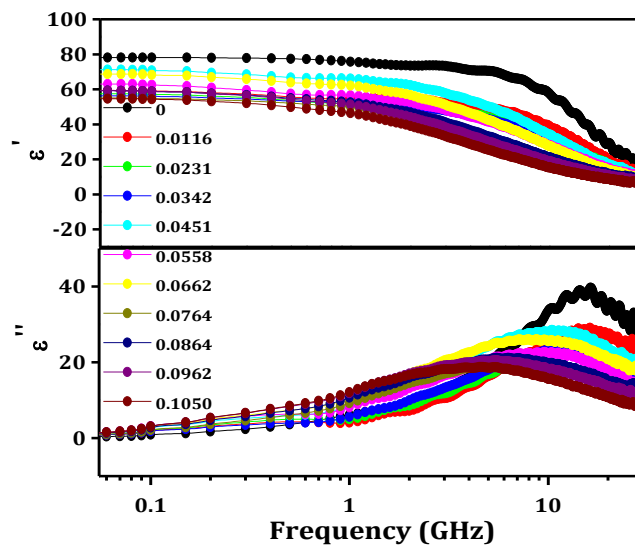


Fig.2(a) Complex permittivity spectra for mixture of Adonitol and water at 25°C.

Table b

Sr no.	Mole fraction of arabitol	ϵ_0	τ (ps)
1	0	78.32	10
2	0.00879	70.75	12.06
3	0.0174	73.58	13.24
4	0.0259	73.11	14.15
5	0.0342	71.52	15.29
6	0.0424	71.50	18.05
7	0.0500	71.30	20.06
8	0.0584	70.25	19.64
9	0.0662	69.29	23.09
10	0.0815	58.80	23.75
11	1	59.39	26.03

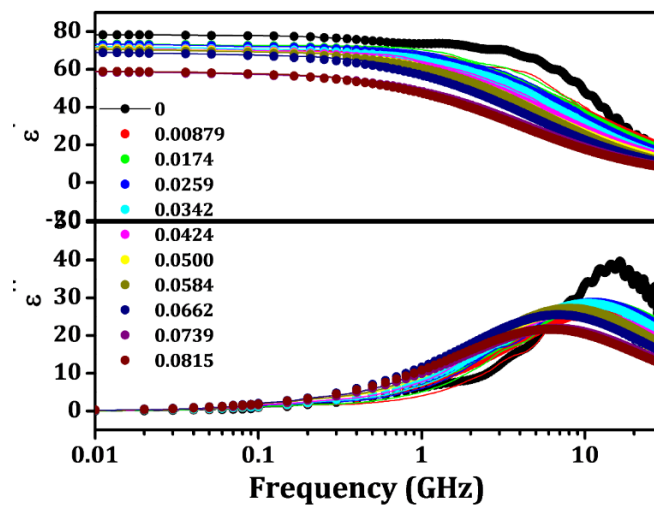


Fig.2(b) Complex permittivity spectra for mixture of D-arabitol and water at 25°C

IV. CONCLUSION

In this paper two out of seven sugar alcohol which are adonitol and D-arabitol have been studied by using time domain reflectometry at room temperature. Complex permittivity spectra of this polyols have been observed in the frequency range of 10MHz to 30GHz at 25°C temperature. The value of static dielectric constant and relaxation time for adonitol and D-arabitol in water were found out. One significant finding from the observed data is the decrease in the value of the static dielectric constant (ϵ_0) with increase in concentration of adonitol and D-arabitol in water. This suggests the formation of hydration sheaths around adonitol and D-arabitol molecules in the solution. Whereas relaxation time(Γ) was observed to increase in the presence of adonitol and D-arabitol in the water solution, which is due to the formation of structural arrangement around water molecules by polyol

molecules, inhibit their rotational motion. Our further approach is to comparatively study the dielectric parameter of different polyols with varying temperature.

ACKNOWLEDGMENT

The author would like to thank Head, Department of physics and electronics, Government Vidarbha Institute of science and humanities, Amravati for their guidance and support. Authors also thankful to Director, Government Vidarbha Institute of science and humanities, Amravati. Authors acknowledges Head, Swami Ramanand Teerth Marathwada University, Nanded for providing necessary facilities during this study.

REFERENCES

- [1] A.Deshmukh,R.Shinde,S.Ingole,A.Pathan,M.Lokhande,A.Sarode,A.Kumbharkhane,Dielectric relaxation and hydrogen bonding interaction of solvent using time domain reflectometry technique from 10MHz to 50GHz,Indian journal of pure and applied physics,vol 56,pp 346-352,2018.
- [2] I.Pena, M.Sanz, *E.Alonso, J.Alonso ,The multiple hydrogen bonding networks of the polyol ribitol,Chemistry- a European journal,vol 24(51), pp 13408-13412 , 2018
- [3] M. Grembecka, E. Techno, Sugar alcohols—their role in the modern world of sweeteners: a review, Vol 241,pp1–14,v2015.
- [4] Y. Ravikumar, S.Razack, L. Ponpandian, G. Zhang, J.Yun, J.Huang, D.Lee, X. Li, Y. Dou, X.Qi, Microbial hosts for production of D-arabitol: Current state-of-art and future prospects,trends in food science & technology, vol 120, pp 100-110 , 2022
- [5] B. Tong, Y. Yu, Z. Tan, C. Menga, L. Xiao, R. Liu, Thermodynamic investigation of several natural polyols (IV) Heat capacities and thermodynamic properties of adonitol, thermochimica Acta, vol 499, pp 117–122, 2010.
- [6] K. Mäkinen, Alcohol Sweeteners as Alternatives to Sugar with Special Consideration of Xylitol. Med Princ, vol,644,2011.
- [7] K.Makinen, Alcohol sweeteners as alternatives to sugar with special consideration of xylitol,med prime pact,2011.
- [8] P. Chalikwar, A. Pathan, A. Deshmukh, M. Lokhande, A. Kumbharkhane, Dielectric relaxation studies in water mixtures of dipropylene glycol using time domain reflectometry technique, 2018.
- [9] M. paluch, S. pawlus, Dielectric studies of the Mobility in pentitols, The journal of physical chemistry, vol 115, pp 1062-1066, 2011
- [10] S. Neware, P. Wahed, A. Kumbharkhane, A. Deshmukh, A. Haque, Y. Shaikh, Dielectric relaxation study of 1-pentanol–ethanol binary mixtures at 10 MHz–50GHz frequency range using TDR technique, physics and chemistry of liquid,2021

© 2024. This work is published under

[https://creativecommons.org/licenses/by/4.0/legalcode\(the“License”\)](https://creativecommons.org/licenses/by/4.0/legalcode(the“License”)).

Notwithstanding the ProQuest Terms and Conditions, you may use this content in accordance with the terms of the License.

¹S. V. Tiwari
²V. N. Bombatkar
^{3*}R. V. Barde
⁴P. R. Malasane

Regular paper
Optical conductivity Study of
Polyaniline/Cerium Oxide
composites by using Ultraviolet
Visible Spectroscopy



Abstract: - In this study, XRD, absorption, optical conductivity of PANI/CeO₂ composites were studied. The present work successfully demonstrated the preparation of Polyaniline (PANI) and PANI/CeO₂ nanocomposites prepared by in-situ chemical oxidative polymerization technique. XRD spectra shows broader peak at $2\theta=25.20$ indicating the amorphous nature of PANI. The mean crystallite size of CeO₂ nanocomposites was found to be 44.822 nm. The absorbance spectra and optical conductivity were obtained by UV-Vis spectroscopy at room temperature the absorption spectra shows an intense absorption dip in the wavelength region 240 nm to 276 nm and broad hump in the wavelength region 486 nm to 698 nm. The optical conductivity was also estimated it shows highest value for sample C1 (5%) whereas lowest value for sample C4 (20%).

Keywords: Polyaniline, cerium oxide, nanocomposites, optical conductivity, UV-Vis spectroscopy.

I. INTRODUCTION

Conducting polymers are conjugated polymers, which are organic molecules with an extended p-orbital structure that allows electrons to flow from one end of the polymer to the other [1]. Due to the excellent properties, of conducting polymers such as electrical property, optical and high mechanical properties, easy synthesis, effortless fabrication and high environmental stability over conventional inorganic materials they are extensively studied. [2]. Conducting polymers have the extra benefit of conductivity in the metallic or semiconducting regimes along with many of the benefits of plastics, such as flexibility and processing from solution, however, many applications are limited by the lack of straight-forward techniques to obtain inexpensive conductive polymer shapes/patterns [3].

Among all conducting polymers Polyaniline (PANI) is preferred due to its remarkable qualities, which include excellent electrical features, reasonable chemical and environmental stability, low cost, and a simple preparation process, it has potential applications in a variety of fields, including organic electronics, biomedical and anti-corrosion materials [4]. PANI is also well-known for being straightforward, stable in the environment, and dopable with protonic acids. By connecting the 1, 4-coupling of the aniline monomer components, PANI can be found [5].

Metal oxide is one of these nanostructures that attract the most attention due to its many uses, including electrical conductivity and transparency in the visible spectrum. These properties make them perfect for solar cells, fuel cells, supercapacitors, sensors, catalysis, and electrochromic windows [6]. Cerium is a lustrous, flexible, and malleable element. Iron-gray in hue, cerium metal exhibits a high degree of reactivity. It exists as cerium oxide when combined with oxygen atoms and is also referred to as a potent oxidizing agent. It can be found in compounds as either ceric (Ce⁴⁺, tetravalent state) or cerous (Ce³⁺, trivalent state) [7]. Anees et al studied the optical and electrical properties of electrochemically deposited PANI/cerium oxide film onto indium-tin-oxide (ITO) glass substrate by using UV-visible spectroscopy and I-V characteristic. The estimated band gap of the CeO₂ sample was 3.44 eV. The electrical properties of the PANI/CeO₂ hybrid nanocomposites film are mostly controlled by PANI doping, as demonstrated by optical and electrochemical characteristics [8]. Barde et al studied CeO₂ doped phospho-vanadate glass system. The values of direct band gap are greater than the corresponding values of indirect band gap. The samples exhibit a progressive rise in absorption around the 225 nm, which raises the refractive index and optical conductivity [9]. Anitha et al explains a novel synthesis for producing Polyaniline/CeO₂ nanocomposites with by in situ polymerization technique. The optical studies results for the PANI/CeO₂ nanocomposites shows the possible visible absorption peaks in the region of 273, 342, 634 and 872 (nm). Band gap energy of nanocomposites is discussed and calculated; it is 3.3 eV [10].

*Corresponding author: Government Vidarbha Institute of Science and Humanities, Amravati 444604, India.
 Email id: rajeshbarde1976@gmail.com

Inspiring from the above discussion, we planned to study the optical conductivity of PANI/CeO₂ nanocomposites. To the best of our knowledge, there is no information on the optical conductivity of PANI/CeO₂. The optical conductivity was estimated by using ultra violet (UV-Vis) spectroscopy.

II. EXPERIMENTAL

1. Synthesis of CeO₂ nanoparticles

A horn-type 20 KHz Sonic Sonifier was used to prepare the nanoparticle of CeO₂ through sonication. 5 gm of CeO₂ was dissolved in 100 ml double distilled water and stirred it for 20 min. This mixture was ultrasonicated for 30 min, light yellow precipitate was formed. This precipitate was washed by using double distilled water and then washed by ethanol, and then it dried out in an oven at 100°C for 3 h.

2. Synthesis of PANI/ CeO₂

The in-situ chemical oxidative method is preferred for the synthesis of polyaniline from aniline monomer. The typical preparation process is as follows 2.32 ml of aniline and 1.5 ml HCL were dissolved in 25 ml double distilled water to form uniform solution. The quantity of CeO₂ nanoparticles added were estimated as 5, 10, 15 and 20 weight percent (wt. %) per weight of aniline monomer solution. Now, the solution was stirred in the ice-bath (0-5°C) for 30 min. Dissolve 4 gm. of ferric chloride in the beaker containing 25 ml of double distilled water and this solution was added drop wise to above monomer solution till polymerization took place and the reaction mixture was stirred for 1-2 hours constantly at (0-5°C) temperature. A series of colour change occurred from blue to dark green and precipitate is formed which was kept for 24 hrs. For the polymerization, precipitate were filtered using Whatmann filter paper no 1 and washed with double distilled water and ethanol till filtrate becomes colourless. The obtained precipitate was dried for 24 h at 40°C. The dark green powder of PANI/CeO₂ nanocomposites were obtained. The nomenclature for Pure PANI, CeO₂, 5%, 10%, 15% and 20% PANI/CeO₂ were named as PP, C0, C1, C2, C3 and C4 respectively [11-12].

III. RESULT AND DISCUSSION

1. XRD Analysis

Fig. 1 shows X-ray diffraction patterns of the pure PANI, CeO₂ and PANI/CeO₂ composites. The XRD spectra of the pure PANI found to be broader indicating amorphous nature of PANI, the diffraction peak was observed at $2\theta=25.20$ and low intensity at $2\theta=14.880$ and 20.660 [13]. The peaks of CeO₂ is observed at 28.840 , 33.30 , 47.70 , 56.50 , 59.30 , 69.60 , 76.90 , and 79.400 . Corresponds to the crystallographic planes of (110), (200), (220), (311), (222), (400), (331) and (420) (JCPDS card no 34-0394). From the graph it is seen that the PANI/CeO₂ composites shows the similar peaks of CeO₂ indicating the crystal nature of CeO₂ nanoparticles in composites. Also, according to these study the inclusion of CeO₂ nanoparticles in amorphous PANI molecular chain. From XRD, it is also observed that as the concentration of CeO₂ increases peak intensity also increases, but the diffraction pattern of the composite does not change. It remains same as that of CeO₂. The mean crystallite sizes of nanocomposites were calculated using scherrer formula $D=K\lambda/(\beta \cos\theta)$ Where β is full width at half maximum, D is the crystalline particle size, K is the scherrer constant (0.891), λ is the wavelength of X-ray (0.154056 nm), θ is angle of diffraction. The particle size of CeO₂ nanocomposites was found to be 44.822 nm.

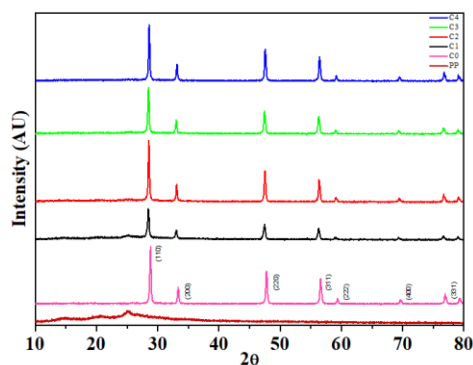


Fig. 1 XRD of Pure polyaniline, CeO₂, PANI/CeO₂ composites

2. Absorbance and Optical Conductivity

Fig. 2 represents the UV-VIS spectrum of the PANI/CeO₂ composites as a function of wavelength. The plot shows the intense absorption dip in the wavelength region 240 to 276 nm and a broad hump in the wavelength region of 486 nm to 698 nm. The absorption band in the region 200 nm to 400 nm are attributed to ligand to metal charge transfer and the band in the region 400 to 700 is due to the pair excitation processes. Sample C1 shows highest absorbance [14-15].

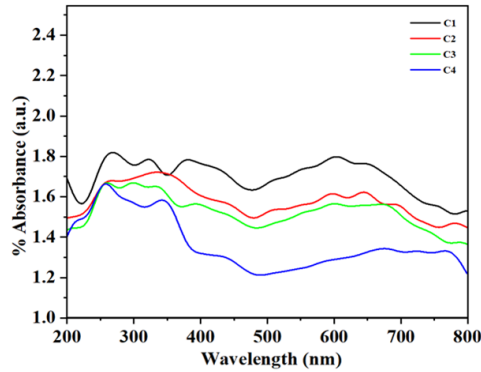


Fig.2 Absorption spectra of PANI/CeO₂ composites

Fig. 3(a) shows the variation of optical conductivity as a function of wavelength. The optical conductivity in terms of energy can be calculated as $\bar{\sigma} = (\alpha cn)/4\pi$ where α is the percent absorption c is speed of light and n is refractive index. The highest value of optical conductivity is associated with sample C1 whereas lowest with sample C4. From the plot it is observed that optical conductivity was tuned by concentration of CeO₂.

Fig. 3(b) shows the variation of optical conductivity with $h\nu$ (eV). Initially the optical conductivity increases with photon energy upto 2.04 eV. Beyond energy 2.04 eV optical conductivity decreases. It shows the linear increase in the region of energy 3 eV to 4 eV. Beyond 4 eV energy optical conductivity decreases. It shows higher optical conductivity for sample C1 and lower for sample C4 [16-17].

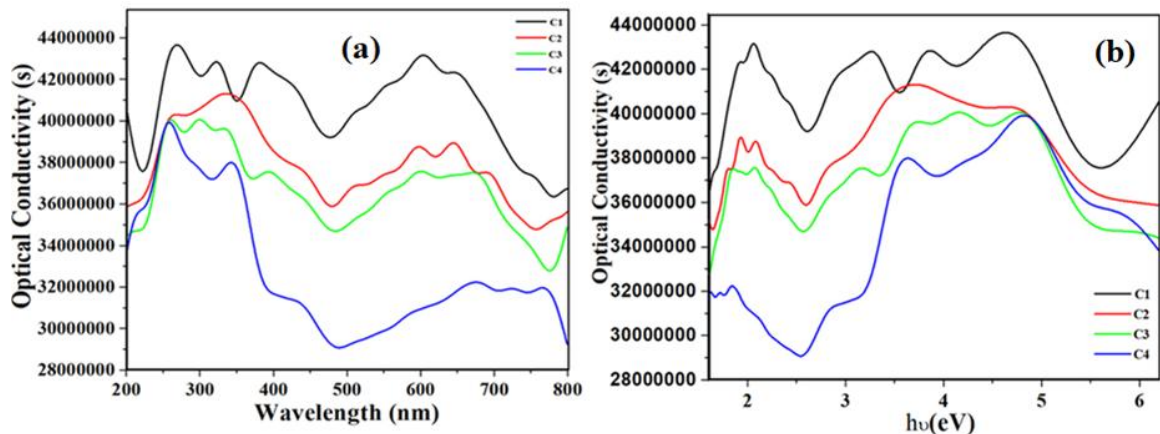


Fig.3 (a) Variation of optical conductivity as a function of wavelength and (b) Variation of optical conductivity as a function of photon energy.

IV. CONCLUSION

The present work successfully demonstrated the preparation of PANI/CeO₂ composites prepared by using in-situ technique. XRD spectra confirmed the amorphous nature of PANI. The mean crystallite size of CeO₂ nanocomposites was found to be 44.822 nm. The absorption spectra show an intense absorption dip in the wavelength region 240 to 276 nm and board hump in the wavelength region of 486 to 698 nm. The optical conductivity was also estimated it shows highest value for sample C1 whereas lowest value for sample C4.

ACKNOWLEDGMENT

The authors would like to thanks Head, Department of Physics and Electronics, Government Vidarbha Institute of Science and Humanities, Amravati for their guidance and support during this study. Authors also

acknowledges Director, Government Vidarbha Institute of Science and Humanities, Amravati for providing necessary facilities to complete this study.

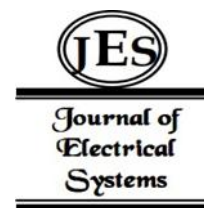
REFERENCES

- [1]. A. K. Mishra, Conducting Polymers: Concepts and applications, Journal of Atomic, Molecular, Condensate and Nano Physics, vol 5, pp 2349-6088, 2018.
- [2]. K. Namsheer, C. Sekhar Rout, Conducting polymers: a comprehensive review on recent advances in synthesis, properties and applications, The Royal Society of Chemistry, vol 11, pp 5659-5697, 2021.
- [3]. MacDiarmid, G Alan, Synthetic Metals: A Novel Role for Organic Polymers (Nobel Lecture). Angewandte Chemie International Edition, vol 40, pp 2581– 2590, 2001.
- [4]. M. Beygisangchin, A. Rashid, S Shafie, Sadrolhosseini A.R. Lim H.N. “Preparations, Properties, and Applications of Polyaniline and Polyaniline Thin Films—A Review Polymers”, Progress in polymer application, vol 13(12), 2003.
- [5]. Zh. Boeva, V. Sergeyev, polyaniline synthesis properties and applications Vysokomolekulyarnye Soedineniya, vol 56, pp 153-164, 2001.
- [6]. A. Henni and A. Karar, Properties and Applications of the Electrochemically Synthesized Metal Oxide Thin Films, chemically deposited nanocrystalline metal oxide thin films , pp 29-48, 2021.
- [7]. S. Khan, K. Akhtar, Introductory Chapter: Cerium Oxide - Applications and Attributes, 2018.
- [8]. A. Ansari, M. Khan, M. Khan, S. Alrokayan, M. Alhoshan, M. S. Alsalhi, Optical and electrical properties of electrochemically deposited polyaniline/CeO₂ hybrid nanocomposites film, journal of semiconductors, vol 32, 2011.
- [9]. R. Barde Influence of CeO₂ content on complex optical parameters of phosphovanadate glass system Spectrochimica Acta Part A: Molecular and Biomolecular Spectroscopy, vol 153, pp 160-164, 2016.
- [10]. R. Anitha, E. Kumar, S. Vella Durai, Structural, Optical, and Frequency Dependent Conductivity Properties of PANI/CeO₂ Nanocomposites by In Situ Polymerization Method, International Journal of Research in Advent Technology, vol 7, pp 2321-9637, 2019.
- [11]. Z. Zhanga, J. Denga, M. Wana, Highly crystalline and thin polyaniline nanofibers oxidized by ferric chloride, Materials Chemistry and Physics, vol 115, pp 275–279, 2009.
- [12]. E. Kumar, P. Selvarajan, D. Muthuraj, Preparation and characterization of polyaniline/cerium dioxide (CeO₂) nanocomposite via in situ polymerization, journal of Material Science vol 47, pp 7148–7156, 2012.
- [13]. I. Ashwini, J. Pattar, P. Anjaneyulu, D. Babu, R. Sreekanth, S.Manohara, M. Nagaraja , Synthesis and electrical properties of polyaniline–cerium oxide composites, synthetic metals, vol 270, pp 116588, 2020.
- [14]. K. Rahman, A. Kar, Structural and optical properties of ex-situ polymerized PANi-TiO₂ nanocomposites, Materials Today: Proceedings, vol 18, pp 1067–1071, 2019.
- [15]. R. Barde, K. Nemade, S. Waghuley, Complex optical study of V₂O₅–P₂O₅–B₂O₃–Dy₂O₃ glass systems, Journal of taibah university for science, vol 10, pp 340-344, 2016.
- [16]. R. Barde, K. Nemade, S. Waghuley Complex Optical Investigation of Sodium Superoxide Loaded Phosphovanadate Glass System in Ultra-Violet and Visible Region, trends in sciences, vol 19, 2016.
- [17]. R. Barde Influence of CeO₂ content on complex optical parameters of phosphovanadate glass system Spectrochimica Acta Part A: Molecular and Biomolecular Spectroscopy, vol 153, pp 160-164, 2016.

© 2024. This work is published under [https://creativecommons.org/licenses/by/4.0/legalcode\(the“License”\)](https://creativecommons.org/licenses/by/4.0/legalcode(the“License”)). Notwithstanding the ProQuest Terms and Conditions, you may use this content in accordance with the terms of the License.

¹Shaikh Naved
Shaikh Quasim
²Dr.A.B.Nawale
^{3*}Dr.S.R.Jigaeni

SYNTHESIS OF ZINC OXIDE (ZnO)
NANOPARTICLES BY CO-PRECIPIATION
METHOD & IT'S CHARECTERIZATION.



Abstract: ZnO nanoparticles are believed to be one of the most produced nanomaterials have a large surface area relative to their size and high catalytic activity. This present work aimed at the investigation of the structural, optical and chemical properties of synthesized ZnO nanoparticles by co-precipitation method. In this present work, we synthesized ZnO nanoparticles by co-precipitation method using zinc acetate [$Zn(CH_3COO)_2$] and sodium hydroxide [NaOH] as a precursors and further for purification ammonia solution was used. The synthesized ZnO sample was annealed at 400 °C for 4 hours. The characterization like X-ray diffraction (XRD), UV - visible spectroscopy and Fourier transmission infrared spectroscopy (FTIR) were done. The x-ray diffraction (XRD) study reveals that the prepared ZnO nanoparticles have wurtzite hexagonal structure and XRD patterns proved the presence of zinc oxide nanoparticles. Lattice parameter was derived from XRD data and particle size of the nanoparticles was also calculated by using Scherrer formula. The UV - visible spectroscopy was taken at room temperature. The UV-vis absorption spectrum shows an absorption band at 358 nm due to ZnO nanoparticles in addition the band-gap energy (3.107eV) of the nanoparticles were calculated using Tauc's equation. FTIR data was also used to analyze the various functional groups present in the synthesized nanoparticles.

Keywords: co-precipitation method , Nanoparticles, Zinc oxide, X-ray diffraction, UV – visible, FTIR .

INTRODUCTION

In recent years, metal oxide nanoparticles have been the subject of focused research due to their unique electronic, optical, mechanical, magnetic and chemical properties. Zinc oxide (ZnO) is the most promising compound in the II-VI semiconductor family[1]. The material ZnO is a wide direct band-gap semiconductor. That are significantly different from those of bulk counterpart. The nano zinc oxide has found wide ranging applications in various areas due to its unique and superior physical and chemical properties compared with bulk ZnO [2].The large specific surface area, high pore volume, nanostructured properties, low cost and low toxicity of nano ZnO make it a promising candidate, particularly in catalysts , photocatalysis, electrostatic dissipative coating, transparent UV protection films, and chemical sensors [3].Different synthesis technique could be used to prepare ZnO NPs. Also ZnO can be synthesized in different nanostructures and these nanostructures have unique optical properties. Actually different microstructure i.e. grain size, lattice constant, lattice strain and defects at grain boundaries strongly influence the optical properties of ZnO [4].Various methods such as thermal decomposition, chemical vapor deposition, sol gel, spray pyrolysis, and precipitation have been developed for the fabrication of nanosized ZnO particles with uniform morphology and size. In the present study simple and widely used co-precipitation technique has been used in this work for preparing ZnO NPs. The co-precipitation synthesis technique for preparation of nanostructures is based on bottom up approach [5]. In this process the product yield is low

*Corresponding author: Government Vidarbha Institute Of Science and Humainitie, Amravati 444604,India. Emailid: sjigajeni@gmail.com

¹ Government Vidarbha Institute Of Science and Humainitie, Amravati 444604,India

and the final product may contain some impurities or un-reacted raw materials. Therefore it is necessary to wash the final product several times by distilled water or by alcohol. However, this simple technique is very useful for synthesis of control nanostructure (i.e. size and shape) and for doping by other elements into semiconductor nano-crystals and the characterization of ZnO nanoparticles using X-ray diffraction, UV - visible spectroscopy and Fourier transmission infrared spectroscopy (FTIR)[6] .

EXPERIMENTAL

Synthesis of ZnO nanoparticles:

The present work describes synthesis of chemically synthesized ZnO nanoparticles prepared by co-precipitation method in our laboratory. For preparation of 5gm of ZnO nanoparticles the stoichiometric amounts of starting raw materials zinc acetate [$\text{Zn}(\text{CH}_3\text{COO})_2$] and sodium hydroxide [NaOH] of required amount & concentration was calculated and weighed with the help of weight balance[7].

Zinc acetate and sodium hydroxide were dissolved in 100 ml distilled water in two separate beakers with magnetic stirrer for proper solution. Then NaOH solution was added drop wise into the zinc acetate solution with constant stirring with temperature upto 70 C^0 until completely dissolution of solution[8].

The reaction was allowed to proceed for 3 hours after the complete addition of sodium hydroxide to form zinc hydroxide solution and precipitate. After the dissolving of solution was allowed to settle down and left the solution for 24 hours at room temperature overnight for final process [9]. Then the supernatant solution was separated carefully, and white precipitate was washed several times by distilled water & ethanol then solution was filtered with the help of 'whatman filter paper'. After getting white precipitate, dried it with the help of uv light lamp until its converted into white powder [10].

After the drying the resultant powder was collected then the calcination/annealing process was done at 400 C^0 with the help of 'Furnence' for 4 hours during this process $\text{Zn}(\text{OH})_2$ was completely converted into ZnO nanoparticles. [11]

CHARACTERIZATIONS

X-ray diffraction (XRD) is a powerful analytical technique used to analyze the crystal structure, phase composition, crystallinity, and lattice parameters of materials. XRD works by analyzing the diffraction pattern produced when X-rays interact with the crystal lattice of a material. In this work the X-ray diffraction analysis were carried out on Rigaku Miniflex 600 X-ray Diffractometer. The optical properties of the nanoparticles in solutions are studied using UV-Visible spectrophotometer in the wavelength range of 200–800 nm. Fourier transmission infrared spectroscopy (FTIR) technique also used to obtain an infrared spectrum or emission of ZnO. An FTIR spectrometer simultaneously collects high resolution spectral data over a wide range.

RESULTS AND DISCUSSION

The figure 1 shows the XRD pattern of prepared ZnO nanoparticles. The diffraction peaks at $2\theta^0 = 31.71^0, 34.37^0, 36.20^0, 47.51^0, 56.55^0, 62.84^0, 66.31^0, 69.02^0, 72.56^0, 76.95^0$ and corresponding (hkl) values are (100), (002), (101), (102), (110), (103), (112), (201), (004).

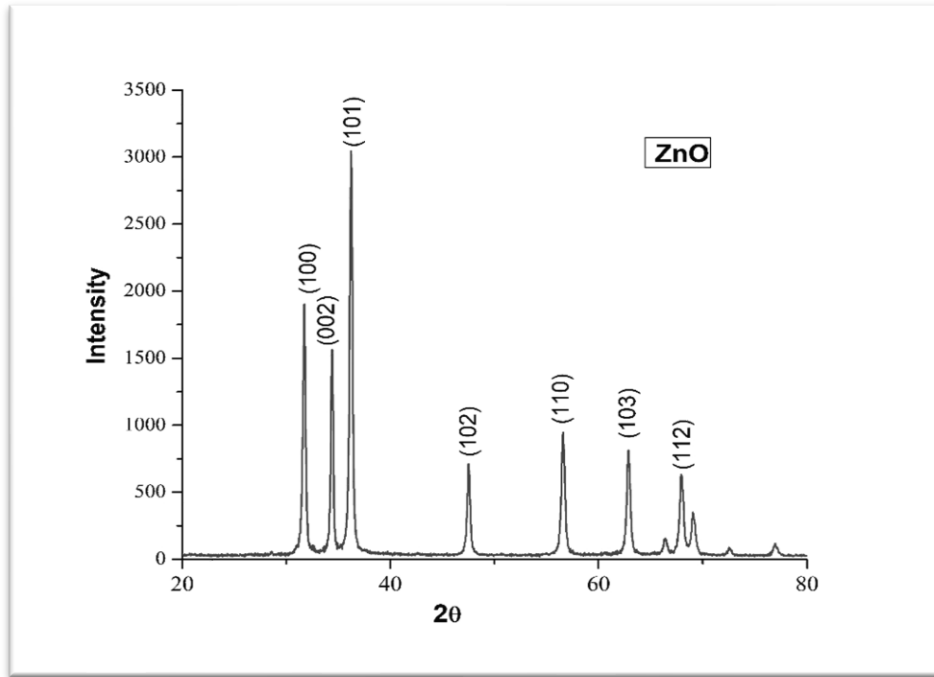


Figure 1.

The ZnO nanoparticles exhibit strong (101) diffraction peak. The XRD pattern shows polycrystalline nature of these prepared ZnO sample. The diffraction peak could be identified as hexagonal wurtzite structure of ZnO[7, 12,13]. The XRD pattern and calculated lattice parameters were compared with standard data (JCPDS PDF card No.230-0112).

The lattice parameters (a, c) of the prepared ZnO nanoparticles have been calculated by using following equation no 1 . The estimated value of lattice parameters are as follows $a = 3.247\text{\AA}$ & $c = 5.2129\text{\AA}$.The calculated c/a ratio of the lattice parameters was found as 1.606\AA [7, 14].

Lattice parameters	Standard values	Calculated values
a	3.2494\AA	3.247\AA
c	5.2054\AA	5.2129\AA
c/a	1.6019\AA	1.606\AA

The crystallite size (D) of the ZnO nanoparticles was calculated by ‘Scherrer equation’ which is given by equation no 2. The calculated crystallite size (D) of the ZnO nanoparticles was found $D = 33.917\text{ nm}$.

$$\frac{1}{d_{hkl}} = \left[\frac{4}{3} \left(\frac{h^2+hk+k^2}{a^2} \right) + \frac{l^2}{c^2} \right] \dots\dots\dots(1)$$

Where d_{hkl} represents the inter-planer spacing corresponding to the Miller indices (hkl).

$$D = \frac{k\lambda}{\beta \cos\theta} \dots\dots\dots(2)$$

Here D is average crystallite size, k is Scherrer const(0.9) . λ is wavelength of x-ray (1.5406\AA) and β is FWHM on $2\theta^\circ$ scale of the diffraction peaks.

Parameter	$\lambda(A)$	Peak position	FWHM	$D = \frac{\kappa\lambda}{\beta\cos\theta}$	D ...AVERAGE (nm)
K	$\lambda(A)$	2 Theta (O)_	Beta(O)		
0.9	0.15406	28.59	0.21	39.03869166	33.91717714
0.9	0.15406	31.712	0.283	29.18202758	
0.9	0.15406	32.59	0.09	91.96409578	
0.9	0.15406	34.378	0.233	35.68973904	
0.9	0.15406	36.204	0.286	29.22366282	
0.9	0.15406	47.517	0.278	31.2226446	
0.9	0.15406	50.69	0.29	30.31170385	
0.9	0.15406	56.554	0.329	27.41871653	
0.9	0.15406	62.849	0.315	29.55483368	
0.9	0.15406	66.31	0.33	28.75510323	
0.9	0.15406	67.909	0.317	30.2126717	
0.9	0.15406	69.02	0.344	28.02560408	
0.9	0.15406	72.567	0.38	25.93481763	
0.9	0.15406	76.951	0.34	29.84585984	
0.9	0.15406	81.36	0.37	28.31240725	
0.9	0.15406	89.569	0.4	27.98225491	

UV visible spectrum of prepared ZnO nanoparticle is shown in below figure no 2. It reveals that ZnO nanoparticles with absorption maxima at 358 nm. The ZnO nanoparticles exhibit silent exciton absorption features due to the relatively large binding energy.

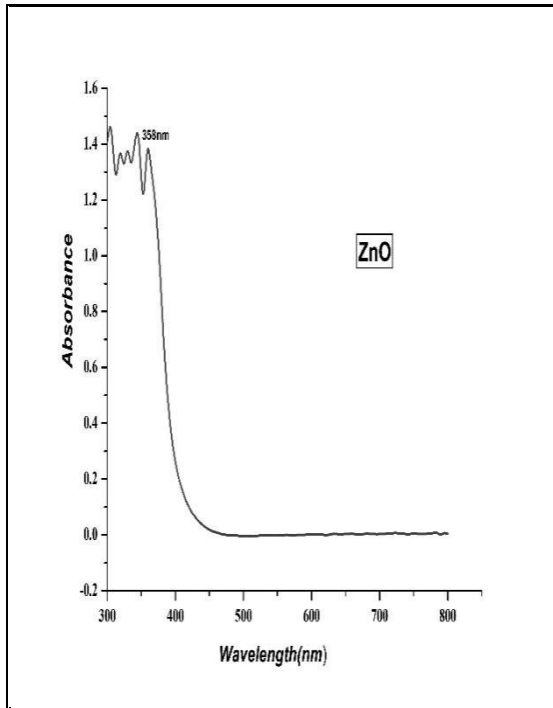


Fig -2:- UV spectra of ZnO

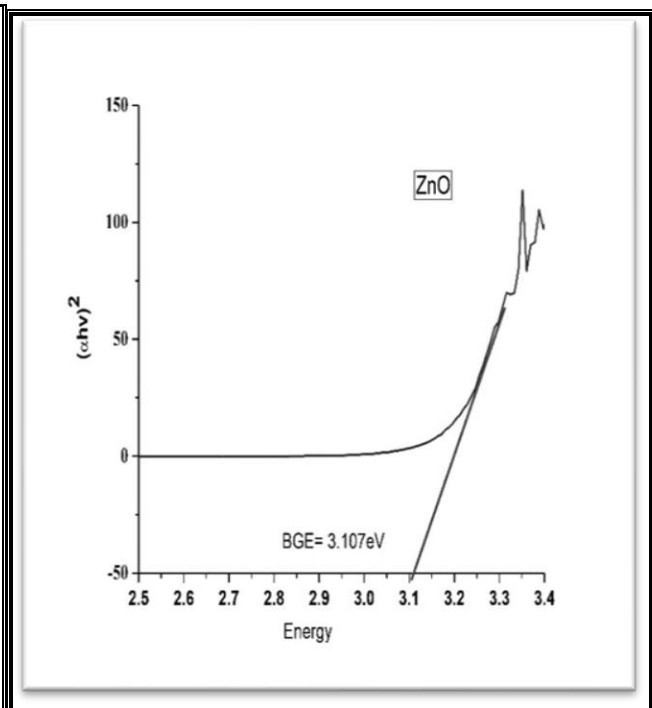


Fig-3 :- Binding energy of ZnO

The direct band gap energy of ZnO nanoparticles was found **3.107eV** by using the Tauc's equation. The Tauc plot uses the equation $(\alpha hv)^2 = A(hv - E_g)$ to plot the absorption coefficient (α) against the photon energy (hv) as shown in figure no. 3 [14].

FTIR spectroscopy could collect the infrared spectrum information of sample and provide the structural information to identify the molecules. The FTIR of ZnO shown in figure no. 4.

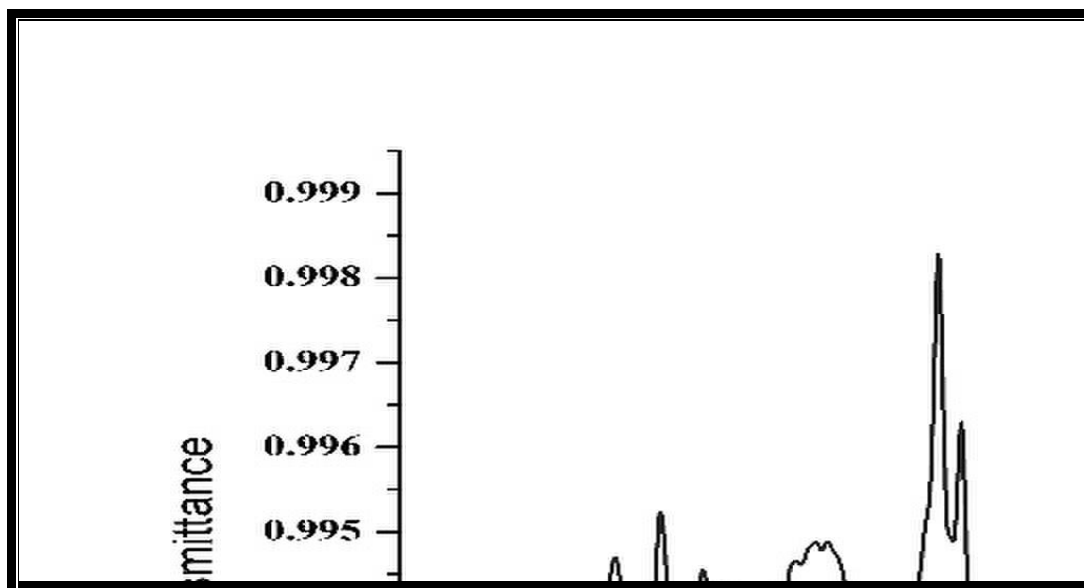


Figure- 4.

The peak indicates the characteristics functional group present in the synthesized ZnO nanoparticles, it is infrared that the ZnO have absorption peaks in the range of 3783cm^{-1} , 3687cm^{-1} , 2342cm^{-1} , 1563cm^{-1} , 1384cm^{-1} , 1074cm^{-1} , 863cm^{-1} . The peak at 1384cm^{-1} are described to primary alcohol in vibration of the OH bond of the alcohol[15]. The peak 3687cm^{-1} ascribed to stretching vibration of hydroxyl compounds. The following table shows peak and chemical bonds and their nature of vibration in ZnO[16].

Peak at wavenumber in cm^{-1}	Bond (stretching/bending)
863cm^{-1} .	C=C bending
1074cm^{-1}	C=C bending
1384cm^{-1}	O-H bending
1563cm^{-1}	N-H bending
3687cm^{-1}	O-H stretching

CONCLUSION

The present work describes the zinc oxide (ZnO) nanoparticles were prepared and synthesized by the 'co-precipitation method'. The XRD pattern and analysis revealed that the ZnO sample is crystalline and hexagonal wurtzite structure. The lattice parameters of prepared ZnO was found as $a = 3.247\text{\AA}$, $c = 5.2129\text{\AA}$ and c/a ratio = 1.606\AA . The crystallite size of ZnO prepared nanoparticles was determined by Debye-Scherrer's equation and it was found to be in nanometer range 33.19 nm . The results were compared with standard (JCPDS PDF card No. 230-0112) and the formation of ZnO nanoparticles was confirmed. The UV visible results shows the absorption maxima peak at 358 nm . And band gap energy of ZnO nanoparticles was found 3.107 eV by using the Tauc's equation. The FTIR result showed that the peak ascribed to stretching vibration of hydroxyl compounds and the OH bond is present in the prepared ZnO nanoparticles.

ACKNOWLEDGMENT

The authors would like to thank Head, Department of Physics and Electronics, Government Vidarbha Institute of Science and Humanities, Amravati for their guidance and support during this study. Authors also acknowledge Director, Government Vidarbha Institute of Science and Humanities, Amravati for providing necessary facilities to complete this study.

REFERENCES

- [1] Dutta S, Chattopadhyay S, Sarkar A, Chakrabarti M, Sanyal D, and D. Jana 2009 Progress in Materials Science, 54 89.
- [2] Pramanik S, Mondal S, Mandal A C, Mukherjee S, Das S, Ghosh T, Rajib Nath R, Manoranjan Ghosh M, Kuiri Probodh K 2020 Jr. Alloys and Compounds 849 156684.
- [3] Maciej Mazur; Electrochemistry Communications, 2004, 6, 400-403.
- [4] Sharma P K, Dutta R K, Choudhary R J and Pandey A C 2013 Cryst. Eng. Comm. 15 4438.
- [5] Tereshchenko A, Bechelany M, Viterc R, Khranovskyy V, Smyntyna V, Starodub N, Yakimova R 2016 Sensors and Actuators B 229 664.
- [6] Ghosh S, Khan G G, Das B, and Mandal K 2011 J. Appl. Phys. 109 123927.
- [7] Kharroubi B, Baghdad R, Abdiche A, Bousmaha M, Bousquet M, Zeinert A, Marssi M EI, K Zellama K and Hamzaoui S 2012 Phys. Scr. 86 015805.
- [8] Neogi S K, Ahmed Md A, Banerjee A and Bandyopadhyay S 2019 Appl. Sur. Sci. 481 443.
- [9] Zhao J, Yan X, Lei Y, Zhao Y, Huang Y and Zhang Y 2012 Advances in Materials Research.
- [10] Norton D P, Heo Y W, Ivill M P, Ip K, Pearton S J, Chisholm M F, and Steiner T 2004 Materials Today 34-40.
- [11] Tereshchenko A, Bechelany M, Viter R, Khranovskyy V, Smyntyna V, Starodub N, Yakimova R 2016 Sensors and Actuators B 229 664-677.
- [12] Koutu V, Shastri S, Malik M M 2016 Materials Science Poland, 34 819-827 [13] Elements of X-Ray Diffraction, By B. D. Cullity.
- [13] Elements of X-Ray Diffraction, By B. D. Cullity.
- [14] Efafi, B.; Ghamsari, M.S.; Aberoumand, M.A.; Ara, M.M.; Ghamsari, A.H.S.; Rad, H.H. Aluminum doped ZnO sol-gel derived nanocrystals: Raman spectroscopy and solid solubility characterization. *Phys. Status Solidi A* **2014**, *211*, 2426–2430.
- [15] Sundrarajan, M.; Ambika, S.; Bharathi, K. Plant-extract mediated synthesis of ZnO nanoparticles using *Pongamia pinnata* and their activity against pathogenic bacteria. *Adv. Powder Technol.* **2015**, *26*, 1294–1299.
- [16] Senthilkumar, N.; Nandhakumar, E.; Priya, P.; Soni, D.; Vimalan, M.; Potheher, I.V. Synthesis of ZnO nanoparticles using leaf extract of *Tectona grandis* (L.) and their anti-bacterial, anti-arthritis, anti-oxidant and in vitro cytotoxicity activities. *New J. Chem.* **2017**, *41*, 10347–10356.

© 2024. This work is published under <https://creativecommons.org/licenses/by/4.0/legalcode>(the“License”).
Notwithstanding the ProQuest Terms and Conditions, you may use this content in accordance with the terms of the License.

^{1*} Shakeel K. Khan,
²Aniket D. Bokhare,
³Zamir S. Khan,
²Milind P. Lokhande,
⁴Ashok C.
Kumbharkhane

Dielectric relaxation study of Isopropanol and pyridine mixtures using Time Domain Reflectometry



Abstract: - The dielectric relaxation behavior of isopropanol-pyridine mixtures was analyzed using Time Domain Reflectometry (TDR) across the frequency range of 10 MHz to 10 GHz, covering all concentrations. The obtained complex permittivity spectra were modeled using the Cole-Davidson relaxation model to account for the non-exponential distribution of relaxation times typical in polar mixtures. Additionally, the static dielectric constant and relaxation times were derived using a nonlinear least squares fitting method.

Keywords: Dielectric constant, Complex permittivity, Relaxation time, Time domain reflectometry (TDR)

^{1*}Department of Physics, B.S. Patel Arts Commerce and Science College, Pimpalgaon Kale, 443403, Maharashtra

²Govt. Vidarbha Institute of Science and Humanities, Amravati-444604, MS, India

³Department of Physics, Anjuman College of Engineering and Technology, Sadar, Nagpur

⁴School of Physical Sciences, Swami Ramanand Teerth Marathwada University, Nanded-431606, MS, India

*Corresponding author: shakeelkhan264@gmail.com

1. Introduction

The study of dielectric relaxation in mixtures of isopropanol and pyridine using Time Domain Reflectometry (TDR) offers significant insights into the molecular interactions and dynamics within the system. Dielectric relaxation, which refers to the delay in the dielectric constant of a material in response to a changing electric field, provides critical information about the molecular structure and behavior of liquids and their mixtures [1].

Isopropanol, a simple alcohol, and pyridine, a basic heterocyclic organic compound, both have unique dielectric properties. Isopropanol is known for its hydrogen bonding capabilities, while pyridine, due to its aromatic structure and nitrogen atom, can engage in specific interactions such as π -stacking and hydrogen bonding with suitable partners. The combination of these two compounds in a mixture presents a complex system where various molecular interactions can be probed using dielectric relaxation techniques.

Previous studies have demonstrated the efficacy of TDR in analyzing the dielectric properties of various liquid mixtures [2-4]. For instance, Bokhare et al. (2024) investigated the dielectric relaxation behavior of d-sorbitol and water mixtures, revealing critical insights into their molecular interactions and dynamics [4]. Similarly, the dielectric study of 1-nitropropane and Dimethyl sulfoxide mixtures by Dhage et al. (2024) highlighted the significance of intermolecular interactions and its impact on the dielectric properties of the system [3].

In this study, we aim to explore the dielectric relaxation behavior of isopropanol and pyridine mixtures using TDR. By analyzing the relaxation times and dielectric constants, we seek to understand the nature of interactions between isopropanol and pyridine molecules, and how these interactions influence the overall dielectric properties of the mixture in frequency range 10 MHz to 10 GHz. This research not only contributes to the fundamental understanding of molecular interactions in binary mixtures but also has potential implications for various applications in chemical and pharmaceutical industries where such mixtures are prevalent.

2. Experimental

2.1. Materials

Binary Mixtures of Isopropanol and pyridine of changed concentrations were prepared by volume fraction.

2.2. Measurements

TDR is a powerful method used to study the dielectric properties of materials over a wide frequency range. TDR measures the reflection of a short voltage pulse transmitted through a material, providing detailed information about the dielectric relaxation processes occurring within the system.

Meticulously prepared solutions were held at a constant temperature for 10-15 minutes before TDR measurements [3-5] using a conventional setup with a signal source, a 50 Ω coaxial transmission line, and a high-speed Tektronix DSA 8300 sampling oscilloscope equipped with a dual-channel 80E10B module. This module generated fast-rise time pulses (12 ps incident and 15 ps reflected) using a tunnel diode, launching

them into the coaxial line. The reflected pulse response, $R_1(t)$ for the empty line and $R_x(t)$ for the sample-filled line, was captured within a 5 ns window and digitized with 2000 points by the sampling oscilloscope. Fourier transform and non-linear least squares analysis were then applied to extract the complex permittivity spectra ($\epsilon^*(\omega)$) of pure solutions and binary mixtures for frequency dependence.

3. Results and Discussion

3.1 Complex permittivity spectra

The frequency-dependent complex permittivity spectra for isopropanol-pyridine mixtures, obtained using Time Domain Reflectometry (TDR) at 25 °C, show that dielectric permittivity decreases with increasing frequency. This is because at higher frequencies, polar molecules cannot reorient quickly enough with the changing electric field. Consequently, their alignment diminishes, leading to lower dielectric permittivity. The complex permittivity spectra obtained with TDR are fitted to the Havriliak - Negami expression using the non-linear least squares fit method [6-7].

$$\epsilon^*(\omega) = \epsilon_\infty + \frac{\epsilon_0 - \epsilon_\infty}{[1 + (j\omega\tau)^{1-\alpha}]^\beta} \tag{1}$$

where ϵ_0 is the static dielectric constant which represents the equilibrium behaviour, ϵ_∞ is the permittivity at high frequency which represents the instantaneous behaviour, τ is relaxation time, α and β are the shape parameters describing symmetric and asymmetric distribution of relaxation time, respectively, and ω is the angular frequency. The Debye ($\alpha = 0, \beta = 1$)[8], Cole-Cole ($0 \leq \alpha \leq 1$ and $\beta = 1$) [9] and Davidson – Cole ($\alpha = 0$ and $0 \leq \beta \leq 1$)[10] relaxation models are the limiting cases of H-N expression. The static dielectric constant (ϵ_0) and relaxation time (τ) for Isopropanol-pyridine mixtures at different temperatures are shown in table 1.

Table 1. Dielectric parameters: a) Dielectric constant (ϵ_0) b) relaxation time (τ) for Isopropanol + pyridine mixture.

Volume fraction of Pyridine	Static dielectric constant	Relaxation time(ps)
1	12.23	5.804
0.9	13.35	6.717
0.8	14.26	6.232
0.7	15.78	12.69
0.6	16.20	14.61
0.5	16.72	27.66
0.4	17.30	40.91
0.3	17.82	82.01
0.2	18.63	123.64
0.1	20.04	180.6
00	20.28	157.05

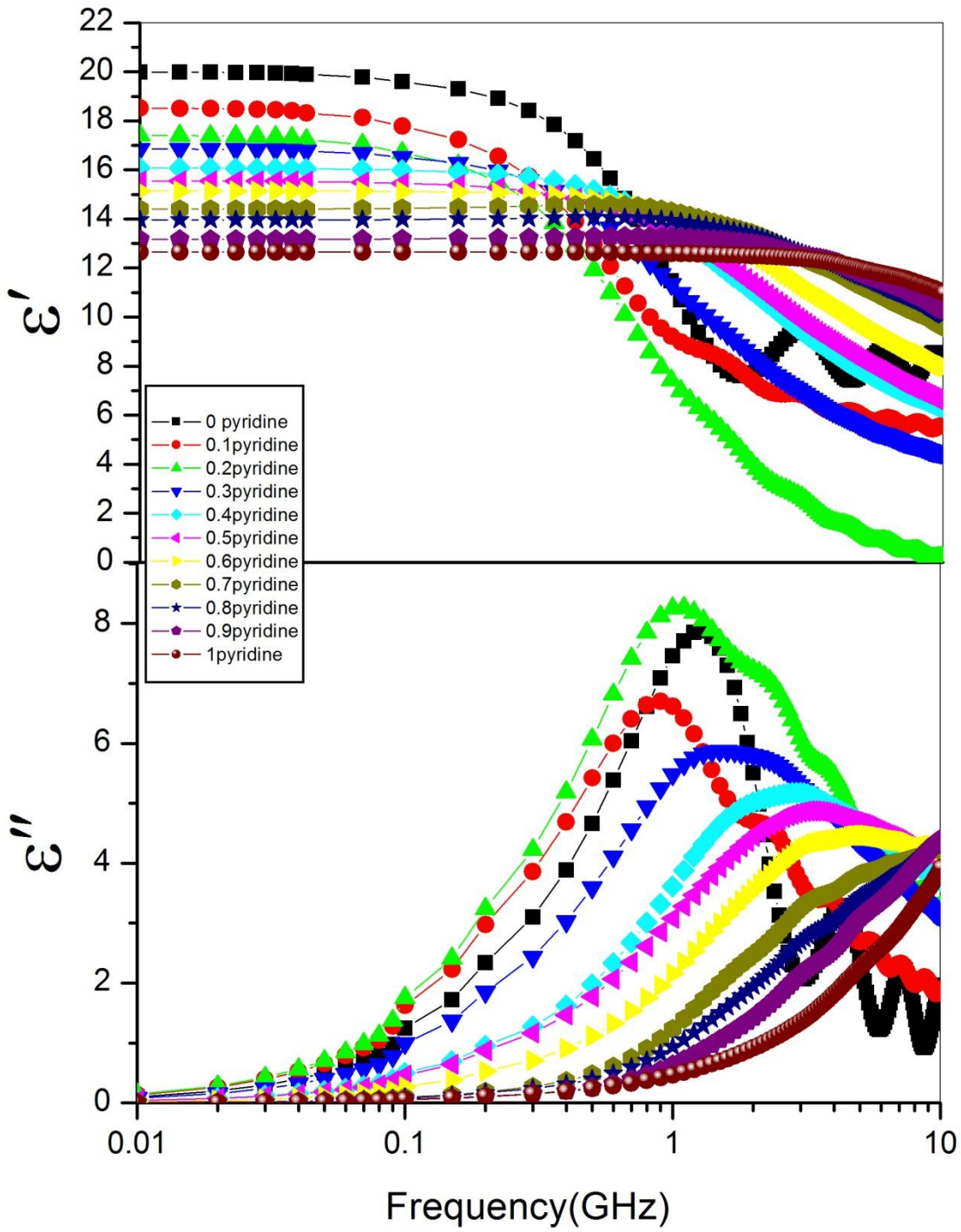


Figure 1 Complex permittivity spectra for Isopropanol + pyridine mixtures at 25°C.

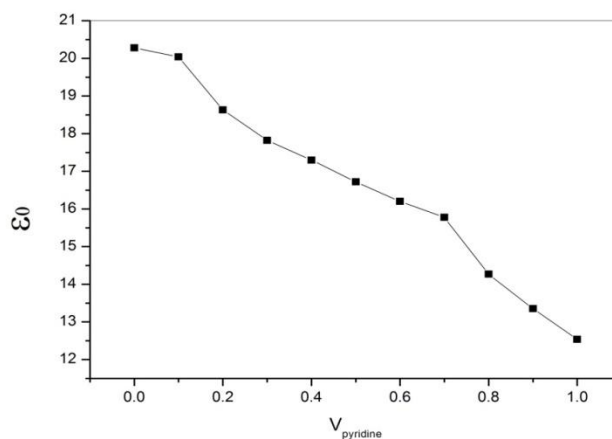


Figure 2: Static Dielectric constant versus Volume fraction of Pyridine for Isopropanol+ pyridine mixtures at 25°C

Figure 2 reveals that the static dielectric constant of the mixture decreases as the volume fraction of pyridine increases for Isopropanol+pyridine mixtures. The static dielectric constant of a mixture is influenced by the individual dielectric constants of the components and their ability to polarize in an electric field. Isopropanol has a higher dielectric constant due to its strong hydrogen bonding capability, which facilitates greater polarization. Pyridine, on the other hand, has a lower dielectric constant because it is less polarizable compared to isopropanol. As the volume fraction of pyridine increases, the overall polarizability of the mixture decreases, leading to a reduction in the static dielectric constant. This is because the pyridine molecules disrupt the hydrogen bonding network of isopropanol, thereby reducing the mixture's ability to align with the electric field and store electric energy.

Figure 3 reveals that the relaxation time of the mixture decreases as the volume fraction of pyridine increases for Isopropanol + pyridine mixtures. In isopropanol-pyridine mixtures, the addition of pyridine alters the molecular environment, affecting the ease with which molecules can reorient. Pyridine's molecular structure and interactions within the mixture likely result in a faster relaxation process compared to isopropanol alone. As the volume fraction of pyridine increases, the dominance of pyridine's molecular environment leads to a reduction in relaxation time.

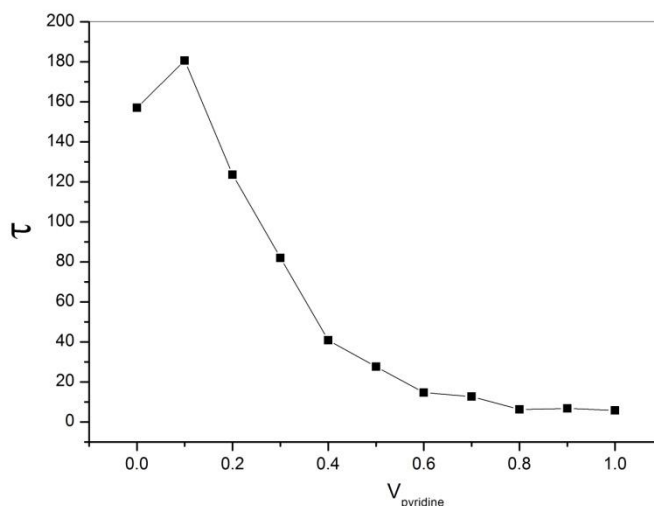


Figure 3: Relaxation time versus Volume fraction of Pyridine for Isopropanol+ pyridine mixtures at 25°C

4. Conclusion

The dielectric relaxation study of isopropanol-pyridine mixtures using Time Domain Reflectometry (TDR) reveals three key trends: a frequency-dependent decrease in dielectric permittivity, a reduction in static dielectric constant with increasing pyridine volume fraction, and a corresponding decrease in relaxation time. These findings illustrate the complex molecular interactions within the mixture, with the observed trends suggesting limitations in molecular reorientation, disruptions in hydrogen bonding networks induced by pyridine, and an accelerated relaxation process influenced by pyridine's molecular environment. Such insights are crucial for applications in chemical and pharmaceutical industries.

Acknowledgement

Author Shakeel K. Khan is thankful to Director of Government Vidarbha Institute Of Science and Humanities, Amravati and School of Physical Sciences, SRT Marathwada University, Nanded (MS) For availing the laboratory facility. It is acknowledged that the Department of Science and Technology (DST), New Delhi, India, provided financial assistance for this project (Project number: DST PROJECT-SB/S2/LOP-032/2013). . Additionally, the author AD Bokhare would like to extend gratitude to the Chhatrapati Shahu Maharaja Research, Training, and Human Development Institute (SARTHI), Pune, for a fellowship (CSMNRF-2021).

References

- [1] Feldman Y, Gusev YA, Vasilyeva MA. Dielectric relaxation phenomena in complex systems. Tutorial, Kazan Federal University, Institute of Physics. 2012.
- [2] Gubre AG, Kumbharkhane AC. Dielectric relaxation and hydrogen bonding studies of chlorobutane-dioxane mixtures using a time domain technique. *Journal of the Indian Chemical Society*. 2023 Jun 1;100(6):101016.
- [3] Dhage HM, Bokhare AD, Garad NP, Lokhande MP, Kumbharkhane AC. Dielectric relaxation studies of 1-nitropropane-dimethyl sulfoxide mixtures using a Time Domain Reflectometry. *Physics and Chemistry of Liquids*. 2024 Jan 21:1-0.
- [4] Bokhare AD, Garad NP, Lokhande MP, Kumbharkhane AC. Dielectric relaxation and hydrogen bonding interactions study of aqueous D-sorbitol using time domain reflectometry. *Physics and Chemistry of Liquids*. 2024 Jan 2;62(1):1-8.
- [5] Cole RH, Berberian JG, Mashimo S, Chryssikos G, Burns A, Tombari E. Time domain reflection methods for dielectric measurements to 10 GHz. *Journal of applied physics*. 1989 Jul 15;66(2):793-802.
- [6] Havriliak S, Negami S. *J. Polym. Sci., Part C: Polym. Symp. In J. Polym. Sci. Part C: Polym. Symp* 1966 (Vol. 14, p. 99).
- [7] Kaatze U. Microwave dielectric properties of liquids. *Radiation Physics and Chemistry*. 1995 Apr 1;45(4):549-66.
- [8] P. Debye, *Pressure Broadening and Debye's Relaxation Equation Polar molecules*. New York: chemical catalog;1929.
- [9] Cole KS, Cole RH. Dispersion and absorption in dielectrics I. Alternating current characteristics. *The Journal of chemical physics*. 1941 Apr;9(4):341-51.
- [10] Davidson DW, Cole RH. Dielectric relaxation in glycerine. *The Journal of Chemical Physics*. 1950 Oct;18(10):1417.

© 2024. This work is published under

[https://creativecommons.org/licenses/by/4.0/legalcode\(the“License”\)](https://creativecommons.org/licenses/by/4.0/legalcode(the“License”)).

Notwithstanding the ProQuest Terms and Conditions, you may use this content in accordance with the terms of the License.

¹ V. S. Patel
² A. K. Patel
³ U. D. Raval
⁴ N. A. Chaudhary
⁵ K. N. Shah
^{6*} A. N. Prajapati

Dielectric spectroscopic study of Chlorobenzene With n-Butanol at different temperature



Abstract: - The complex permittivity $\epsilon^*(f)$, complex electric modulus $M^*(f)$, complex electrical conductivity $\sigma^*(f)$ and complex impedance $Z^*(f)$ over the frequency range from 100 Hz to 2 MHz for the Chlorobenzene and n-Butanol mixtures spanning the entire mixing range (0.0→1.0) have been investigated at different temperature (303.15 K, 313.15 K and 323.15 K). The complex permittivity data were analyzed using dielectric relaxation models by applying the complex nonlinear least square fitting method (CNLS). The dielectric relaxation parameters were extracted from the best fitted model (Debye model). By examining the concentration dependence of these parameters, insights into the molecular interactions among the constituents of the mixtures were obtained. These analyses were utilized to determine various parameters, including the ionic conduction relaxation time (τ_σ), the DC conductivity (σ_{dc}) and activation energy (E_a). Modulus and conductivity spectra are utilized to gain insights into how variations in concentration of the components in the mixtures affect their electrical properties.

Keywords: chlorobenzene, n-Butanol, dielectric relaxation spectroscopy (DRS), Relaxation time.

1. INTRODUCTION

Confirming the structure of primary alcohols under varying environmental conditions presents an intriguing and multifaceted challenge that captivates researchers across various scientific domains, encompassing chemistry, physics, biology, electronics engineering [1,3]. Dielectric spectroscopic study is an important tool for material characterization and is used to understand inter/intra-molecular interactions as well as molecular structures of molecular system [4-10]. Frequency-dependent dielectric properties are highly beneficial for comprehending the fundamental characteristics of liquids, including their structural

*Corresponding author: Department of Physics, Sardar Patel University, V. V. Nagar-388120, Gujarat, India

^{1,2,3,6}Department of Physics, Sardar Patel University, V. V. Nagar-388120, Gujarat, India

⁴Department of Applied Physics, The M. S. University of Baroda, Vadodara-390001, Gujarat, India

⁵Department of Computer Engineering, Unitedworld School of Computational Intelligence, Karnavati University, Gandhinagar-382422, Gujarat, India

persistence and dynamics. These properties also play a crucial role in various practical applications, providing insights into molecular interactions and behavior under different conditions [10]. Alcohols are integral to many chemical reactions due to their capacity for self-association into diverse internal structures. Their versatility makes them widely utilized in industrial and scientific contexts, serving as reagents, solvents, and fuels [11-13]. n-Butanol (n-BuOH) finds extensive applications in pharmaceuticals, textiles and automobile industries. The simplest of the chlorobenzenes, consists of a benzene ring with a single chlorine atom substituted at one of its positions Chlorobenzene, which has a low dielectric constant, is a non-aqueous solvent widely used in chemical synthesis and various industrial applications.

In the present paper we report complex dielectric spectra $\epsilon^*(f)$, electric modulus spectra $M^*(f)$, electric conductivity spectra $\sigma^*(f)$ and impedance spectra $Z^*(f)$ for CB, n-BuOH and their binary mixtures in the frequency span 100 Hz to 2 MHz at different temperatures.

I. EXPERIMENTAL

Chlorobenzene (CB) and Butanol (n-BuOH) both the ACS grades were procured from Merck Life Science Pvt. Ltd. (India). They were used without further purification. Eleven samples of the binary mixtures of different mole fraction of CB in n-BuOH were prepared. A precision LCR meter (Agilent E-4980A) and a coaxial capacitor as the sample holder was used to measure the complex permittivity of the liquid samples. In our laboratory, we designed and fabricated a cylindrical capacitor. The capacitor features an outer cylinder, an inner cylinder, connectors, and Teflon components. The manufacturing process was executed by a local manufacturer. Before measurements calibration was performed for cylindrical liquid test fixture as described in literature [5]. The temperature of the binary liquid samples throughout measurement was controlled by constant temperature water bath with a precision of 0.1K.

Table 1. Comparison of the pure liquid static dielectric constant (ϵ_0) with literature values.

Compound Name	Temperature	Static dielectric constant (ϵ_0)	
		Exp.	Lit.
Chlorobenzene	303.15 K	5.41	5.61[17]
	313.15 K	5.25	5.51[18]
	323.15 K	4.93	5.33[18]
n-Butanol	303.15 K	16.33	16.91[15]
	313.15 K	15.57	15.66[35]
	323.15 K	14.36	14.54[35]

II. RESULTS AND DISCUSSION

The measured values of ϵ' and ϵ'' over the entire range of frequency (100 Hz to 2 MHz) for various mixture concentration (CB + n-BuOH) at different temperatures are shown in Fig. 1 (A), (B), (C). The permittivity spectra exhibit a division into two distinct regions: a higher-frequency region and a lower-frequency region.

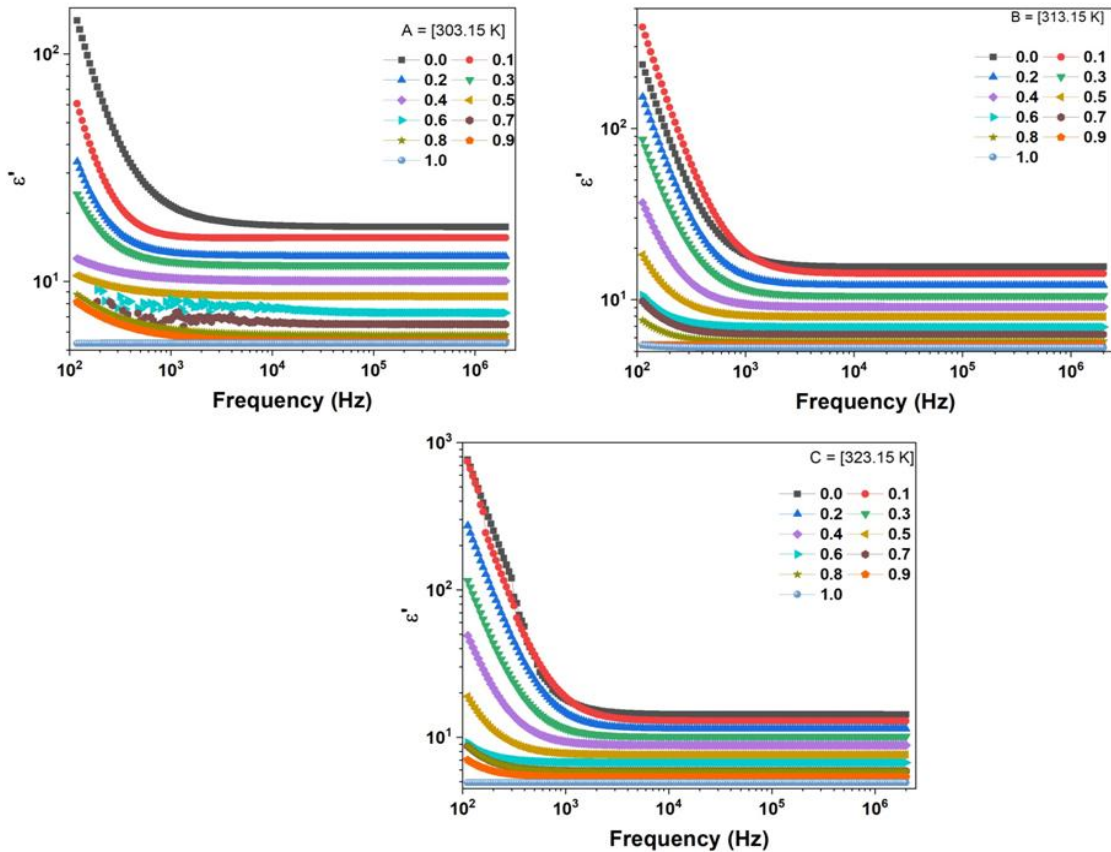


Fig. 1. Plots of the real part of permittivity (ϵ') versus frequency for binary mixtures of CB + n-BuOH at (A) 303.15K (B) 313.15 K and (C) 323.15 K temperatures.

In the higher frequency region, typically above 10^3 Hz, the real part of the permittivity spectra remains constant and independent of frequency. As the frequency increases within this range, the permittivity stabilizes or attenuates to a steady state. From Fig. 1(A) (B) (C), it can be seen that the real part of permittivity (ϵ') remains constant over the entire frequency range Chlorobenzene (CB) rich region. This constancy of ϵ' indicates the absence of ionic impurities in CB, as ionic impurities typically cause a frequency-dependent variation in the dielectric constant. For the high concentration of n-Butanol real part of permittivity (ϵ') is high in the low-frequency region and decreases rapidly with increasing frequency. The higher value of the real part of the permittivity (ϵ') in the lower frequency region indicates a dominant effect of electron polarization (EP). At a low frequency, it is observed that the real part of permittivity ϵ' values in the low-frequency region (electrode polarization dominant region) increase with the temperature rise. This suggests that the ion concentration in the

electrical double layers (EDLs) increases with temperature increases [2]. In high frequency rang ϵ' values are decrease with increase of temperature. Figure 2 (A),(B),(C) shows the imaginary part of permittivity spectra (ϵ'') for the different mole fractions of CB in n-BuOH. It can be seen from the figure that in the low frequency region for n-Butanol and higher concentration of Butanol, values of imaginary part of permittivity (ϵ'') exhibit strong dependence on the frequency. It is independent of frequency for higher concentration of CB and pure CB. The large value of ϵ'' for pure n-Butanol and high concentrations of n-Butanol confirms the presence of free ionic impurities in the n-BuOH. The high value of ϵ'' at lower frequencies is due to the dominance of ionic conduction loss. This indicates that at low frequencies, the ionic impurities significantly contribute to energy dissipation, resulting in a higher dielectric loss [4,13,14]. Fig. 2 (A),(B),(C) shows that increased frequency with Dielectric loss (ϵ'') of pure n-BuOH rapidly decrease at 10^3 Hz frequency. When the temperature of binary mixture was increases with ϵ'' increase at high frequency range. At low frequency rang ϵ'' decrease with increase temperature. Experimental complex dielectric data were fitted to Debye Model and specifically utilized the Havriliak–Negami (HN) [7,12] to obtain static dielectric constant (ϵ_0), electrode polarization relaxation time (τ_{EP}).

Transforming dielectric spectra into electric modulus is a useful way to investigate ionic conductivity relaxation processes [2]. The real part M' and imaginary part M'' of complex modulus $M^*(f)$ are evaluated from the following equation [13,14].

$$\epsilon^* = M' + jM'' = \frac{\epsilon'}{(\epsilon')^2 + (\epsilon'')^2} + j \frac{\epsilon''}{(\epsilon')^2 + (\epsilon'')^2} \quad (1)$$

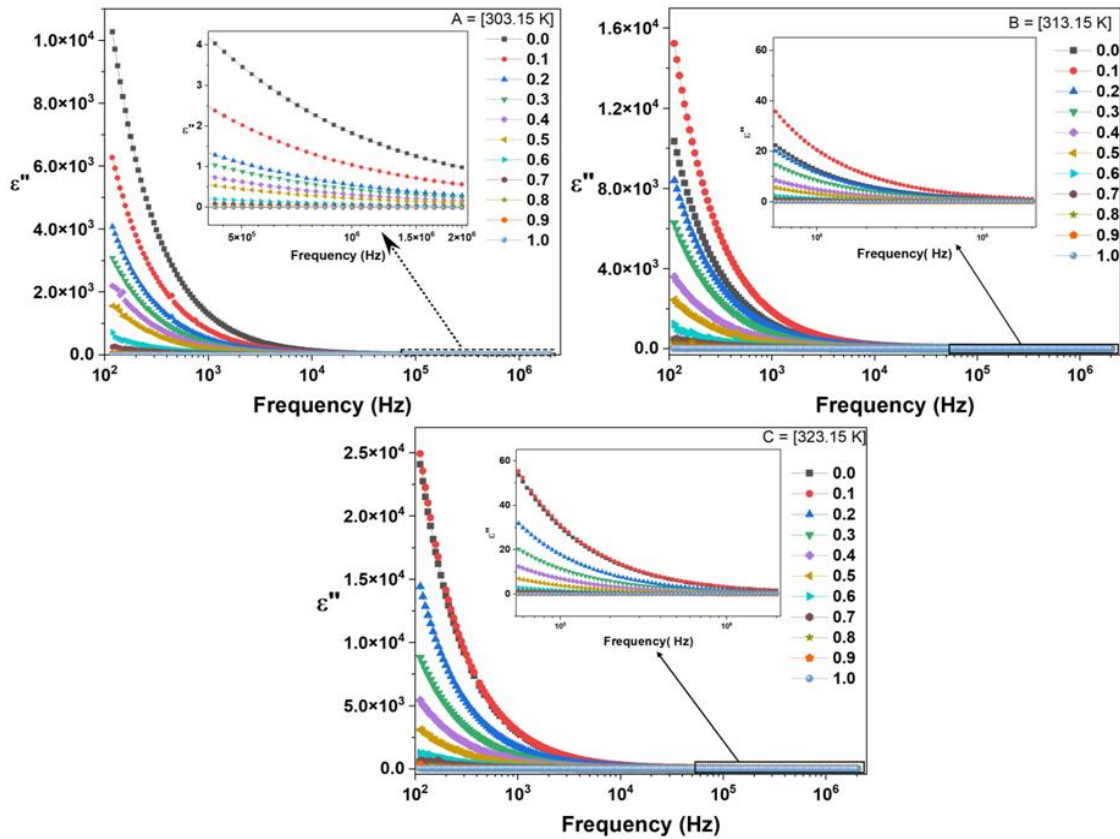


Fig. 2. Plots of (ϵ'') versus frequency for binary mixtures of CB + n-BuOH at (A) 303.15 K (B) 313.15 K and (C) 323.15 K temperatures.

Where ϵ' is the real part of permittivity, and ϵ'' is the imaginary part of permittivity. The plot of real part of modulus spectra M' for the binary mixture of CB + n-BuOH at different temperatures are shown in Fig. 3 (A), (B), (C). In the n-BuOH rich region, M' increases linearly in the frequency range up to 10^5 Hz, after which it reaches a constant value. As the concentration of CB increases, the constant region reaches up to kHz frequency range. Figure 3(A), (B), (C) shows that the temperature increase of pure n-BuOH decreases with the first concentration of CB, then increases with CB increase at 313.15 K and 323.15 K. In Fig. 4, the imaginary part M'' spectra, plotted on a logarithmic scale, exhibit a linear increase with frequency and reach the maximum point in the intermediate frequency range and then decrease in the higher frequency range. These peaks correspond to the ionic conductivity relaxation process in the mixtures, a phenomenon previously observed in several dielectric liquids [2,13,14]. It is clear from the modulus spectra that (Fig. 4) M'' , peak for pure n-BuOH observed at the high-frequency side, but as the concentration of CB increases, the peak shifts from the high-frequency side to the low-frequency side. The ionic conductivity relaxation time ($\tau_\sigma = 1/2\pi f_\sigma$) is determined using the frequency (f_σ) corresponding to the maximum value of M'' .

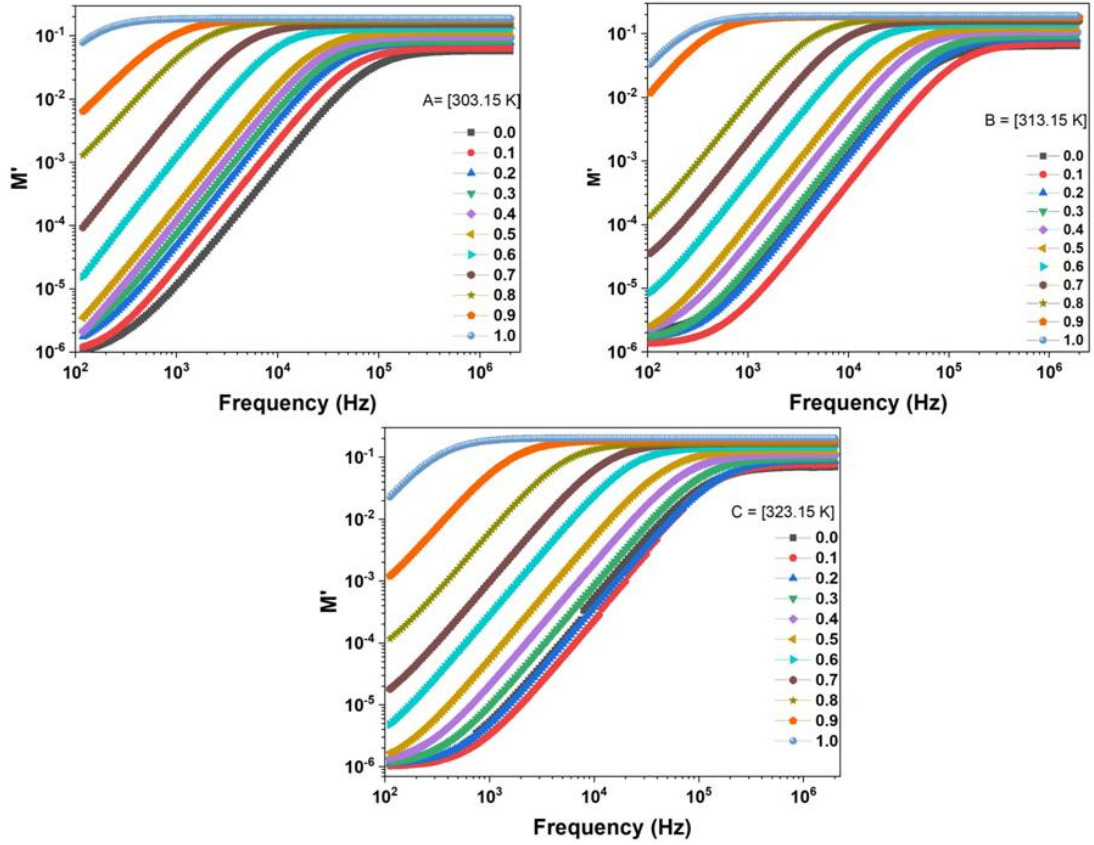


Fig.3. Plots of real part of modulus (M') versus frequency for binary mixtures of CB + n-BuOH at (A) 303.15K (B) 313.15 K and (C) 323.15 K temperatures.

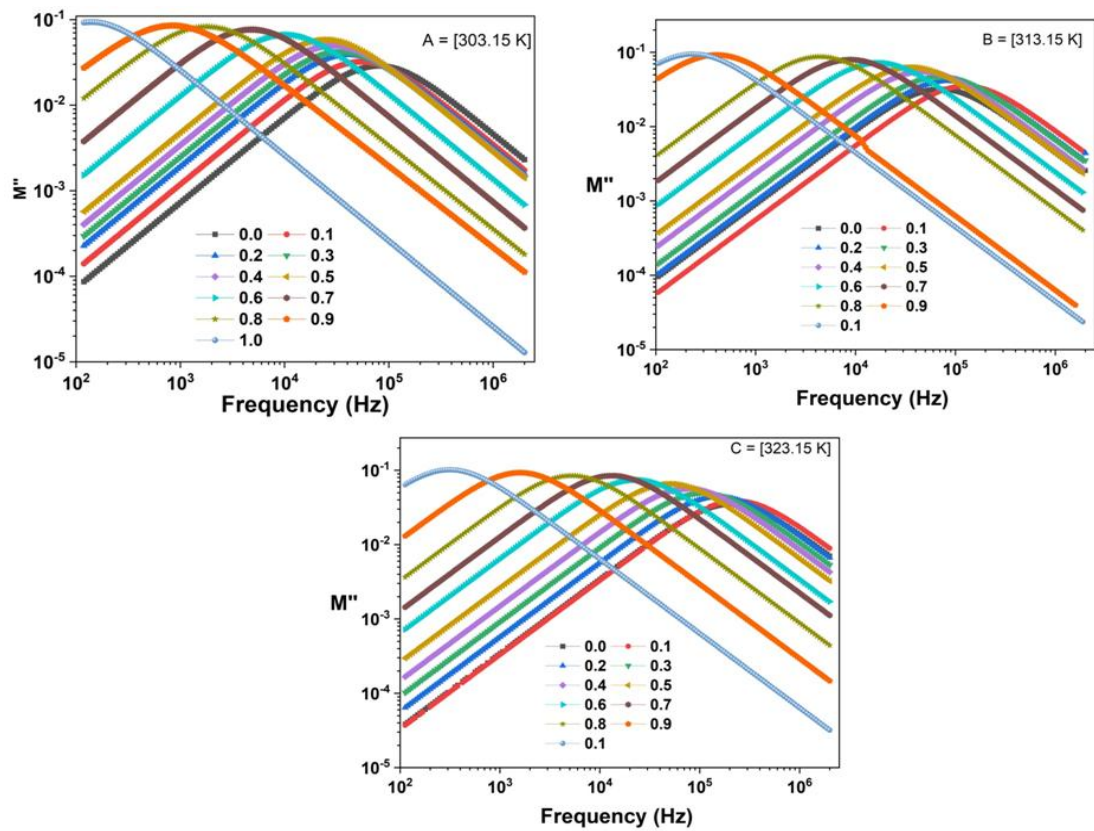


Fig.4. Plots of real part of modulus (M'') versus frequency for binary mixtures of CB + n-BuOH at (A) 303.15K (B) 313.15 K and (C) 323.15 K temperatures.

Determined values of ionic conductivity relaxation time for binary mixtures for all the temperature ranges are tabulated in Table 2. It can be observed from the Table 2 that the values of ionic conductivity relaxation time increase as the concentration of the CB increases in the mixture at particular 303.15 K temperature. However, at 313.15 K and 323.15 K, the ionic conductivity relaxation time exhibit anomalous behavior.

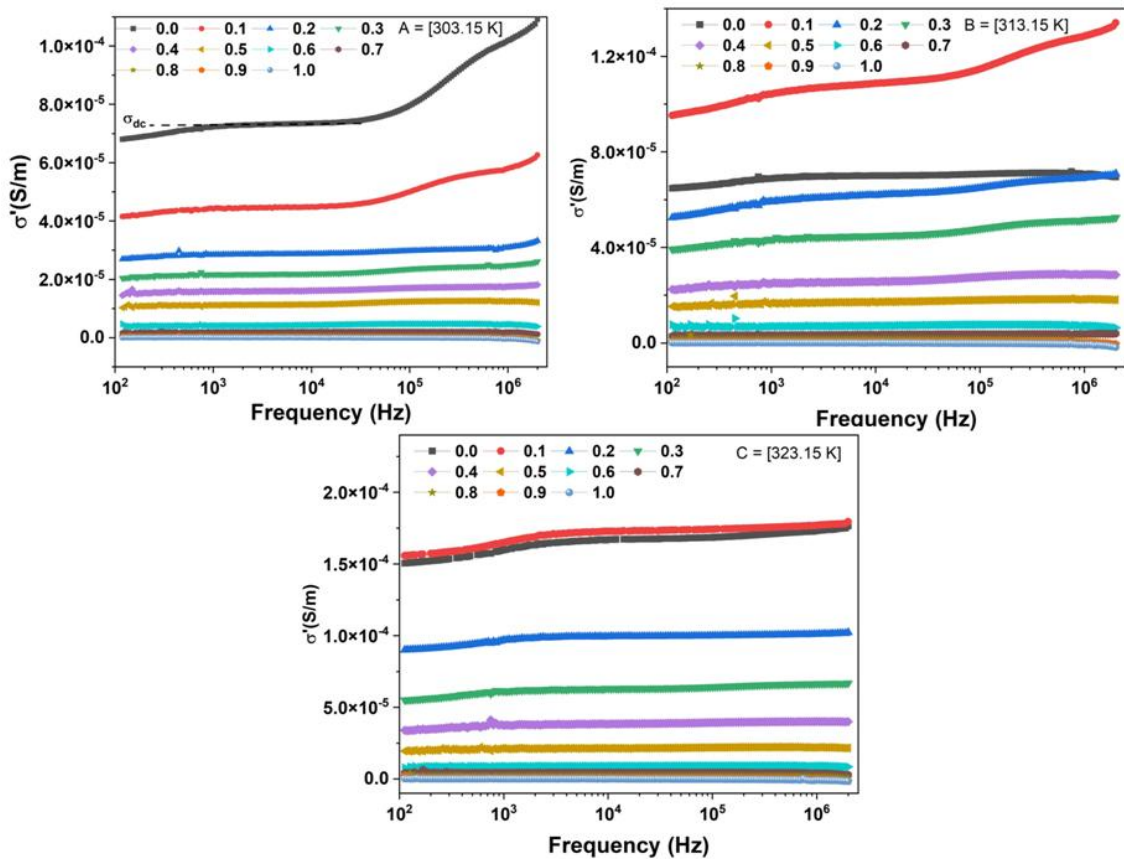


Fig.5. Plots of (σ') versus frequency for the binary mixture Chlorobenzene with n-Butanol at (A) 303.15K (B) 313.15 K and (C) 323.15 K temperatures.

The complex electrical conductivity of the binary liquid mixtures were obtained from the equation [13,14]:

$$\sigma^*(\omega) = \sigma' + j\sigma'' = \omega\epsilon_0\epsilon'' + j\omega\epsilon_0\epsilon' \tag{2}$$

The variation of σ' with against frequency for the binary mixtures (CB + n-BuOH) is shown for three different temperature are shown in Fig. 5 (A), (B), (C).

For the concentrations, 0.0 and 0.1 of CB, the real part of the conductivity (σ') increases with increasing frequency in the high-frequency region (above 10^5 Hz) and it becomes constant in the intermediate frequency range. For lower concentration of n-Butanol it shows the plateau region in all the frequency ranges. The σ_{dc} values are determined from this

frequency-independent area of the stability region of the σ' spectra. Similarly direct current electrical conductivity (σ_{dc}) computed from the relation $\sigma_{dc} = \epsilon_0 \cdot \epsilon_v / \tau_\sigma$. It has been observed that dc conductivity values are decreases with increasing concentration of chlorobenzene, as shown in Table (2). It decreases also with the increase in the temperature for all the concentration ranges. The low value of dc conductivity of pure CB indicates the absence of ionic impurities in CB making it an insulating liquid [14]. The graph of the imaginary part of complex conductivity spectra with frequency is shown in Fig. 6 (A), (B), (C). It can be seen from the figure, that a minima peak is observed in the pure n-BuOH and higher concentration of n-BuOH. While it remains linear in all the frequency regions and for the concentration ranges.

Table 2. Values of ionic conductivity relaxation time (τ_σ), and experimental and theoretical derived DC conductivity (DC) at different temperature

X_A	$\tau_\sigma(\mu s)$	$\sigma_{dc}(\mu s/m)$ fig.6 From fig	$\sigma_{dc}(\mu s/m)$ (Eq.5) From equation
T = 303.15 K			
0.0	2.00	7.35E-05	7.22E-05
0.1	2.82	4.49E-05	4.61E-05
0.2	3.77	2.88E-05	3.00E-05
0.3	4.48	2.19E-05	2.29E-05
0.4	5.64	1.61E-05	1.55E-05
0.5	6.70	1.14E-05	1.11E-05
0.6	15.00	4.36E-06	4.30E-06
0.7	33.56	1.99E-06	1.71E-06
0.8	70.96	6.12E-07	7.36E-07
0.9	178.24	2.18E-07	2.74E-07
1.0	1061.72	1.89E-08	4.52E-08
T = 313.15 K			
0.0	2.12	7.00E-05	6.90E-05
0.1	1.59	1.09E-04	7.77E-05
0.2	1.68	6.18E-05	6.32E-05
0.3	2.00	4.48E-05	4.61E-05
0.4	2.99	2.56E-05	2.66E-05
0.5	3.99	1.67E-05	1.76E-05

0.6	8.43	7.20E-06	7.23E-06
0.7	14.16	3.46E-06	3.89E-06
0.8	33.57	1.45E-06	1.51E-06
0.9	188.80	4.15E-07	2.58E-07
1.0	893.33	7.14E-08	5.21E-08
T = 323.15 K			
0.0	1.34	1.67E-04	9.48E-05
0.1	1.12	1.73E-04	1.02E-04
0.2	1.00	9.92E-05	1.01E-04
0.3	1.42	6.31E-05	6.29E-05
0.4	2.00	3.83E-05	3.90E-05
0.5	3.17	2.13E-05	2.12E-05
0.6	6.70	8.98E-06	8.88E-06
0.7	11.25	4.46E-06	4.63E-06
0.8	25.18	2.01E-06	1.99E-06
0.9	79.62	4.27E-07	6.01E-07
1.0	188.80	1.04E-07	2.37E-07

The complex impedance spectra of the binary liquid mixture of CB + n-Butanol are evaluated by the below Equation [6,14]:

$$Z^*(\omega) = Z' + Z'' = \frac{R_P}{1+(\omega C_P R_P)^2} - j \frac{\omega C_P R_P}{1+(\omega C_P R_P)^2} \quad (3)$$

Where, C_P and R_P are electric capacity and resistance of the sample. The real part of complex impedance (Z') spectra for all temperatures are shown in Fig. 7(A), (B), (C). Z' spectra remains constant up to 10^4 Hz for the lower concentration of chlorobenzene in n-Butanol, and then decreases rapidly in the high frequency range ($>10^4$ Hz). It decreases linearly for the higher concentration of CB and pure CB with increases frequency. Fig.8 (A), (B), (C) shows the plot of the imaginary part of the complex impedance spectra at different temperature. In this plot, for lower concentrations of chlorobenzene, Z'' exhibit a minima and maxima peak is observed.

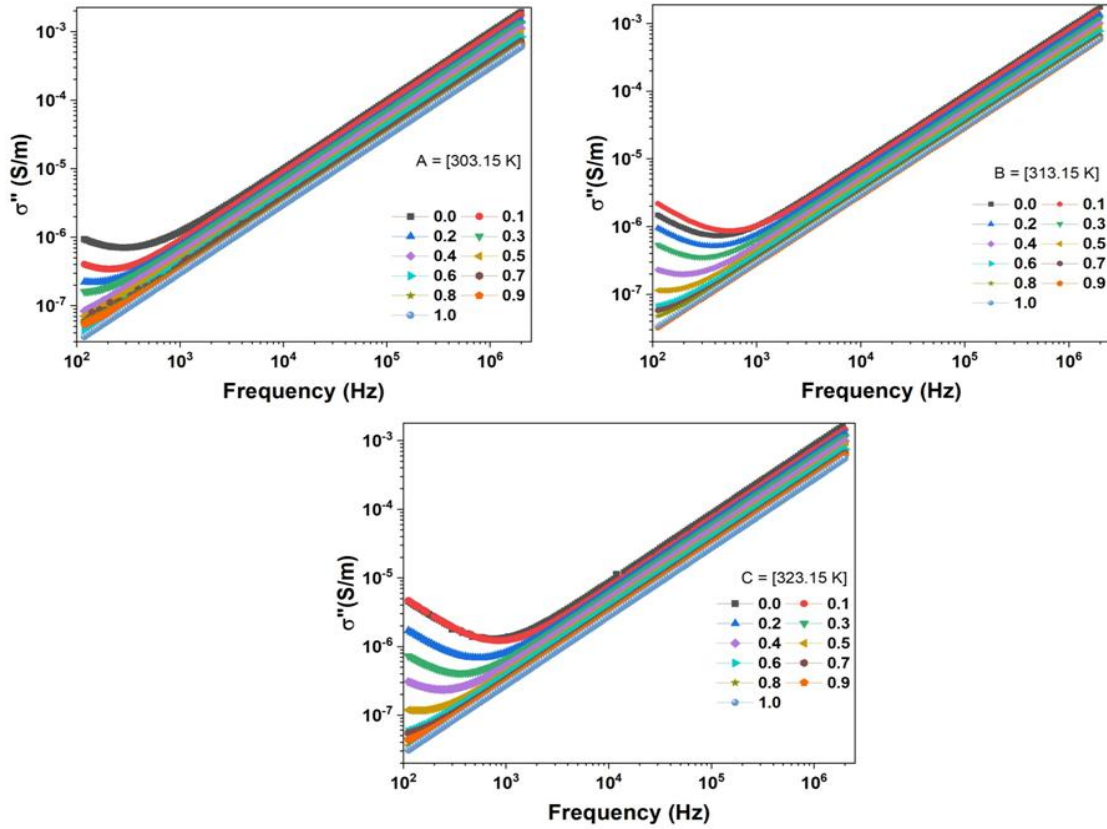


Fig.6. Plot of (σ'') versus frequency for CB + n-BuOH binary mixtures at (A) 303.15K (B) 313.15 K and (C) 323.15 K temperatures.

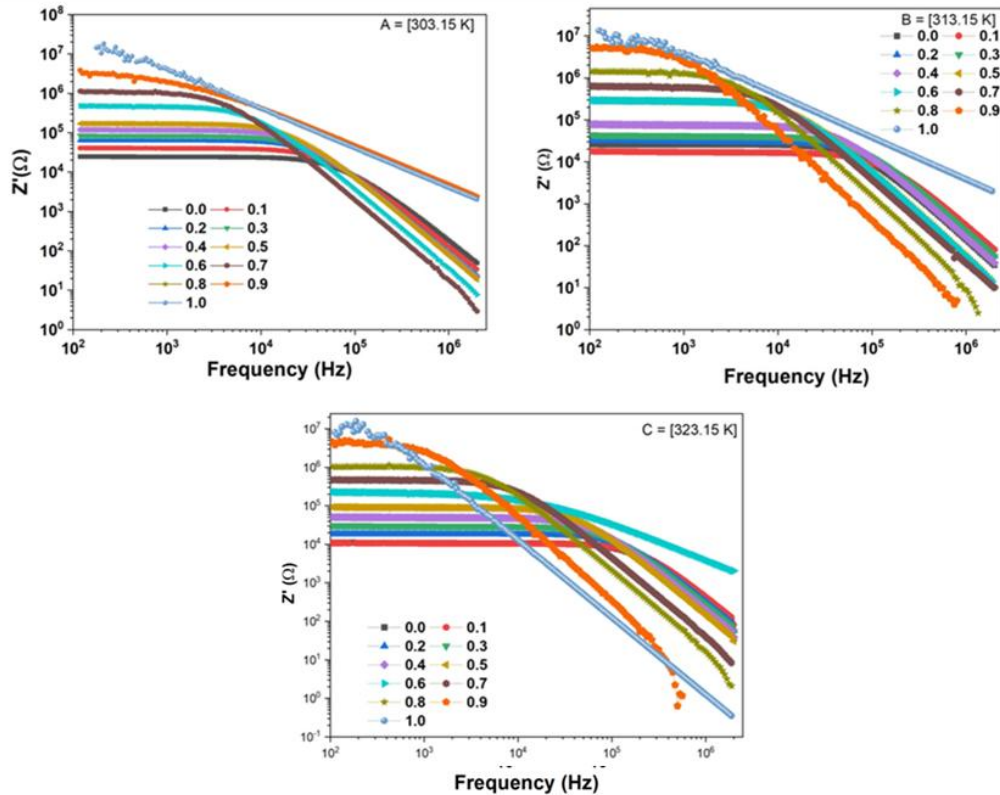


Fig. 7. Plot of Z' versus frequency for the binary mixture of CB and n-BuOH at (A) 303.15K (B) 313.15 K and (C) 323.15 K temperatures.

Concentrations of chlorobenzene in n-Butanol Z'' increases with frequency reach the maximum point than decreases with increases frequency range.

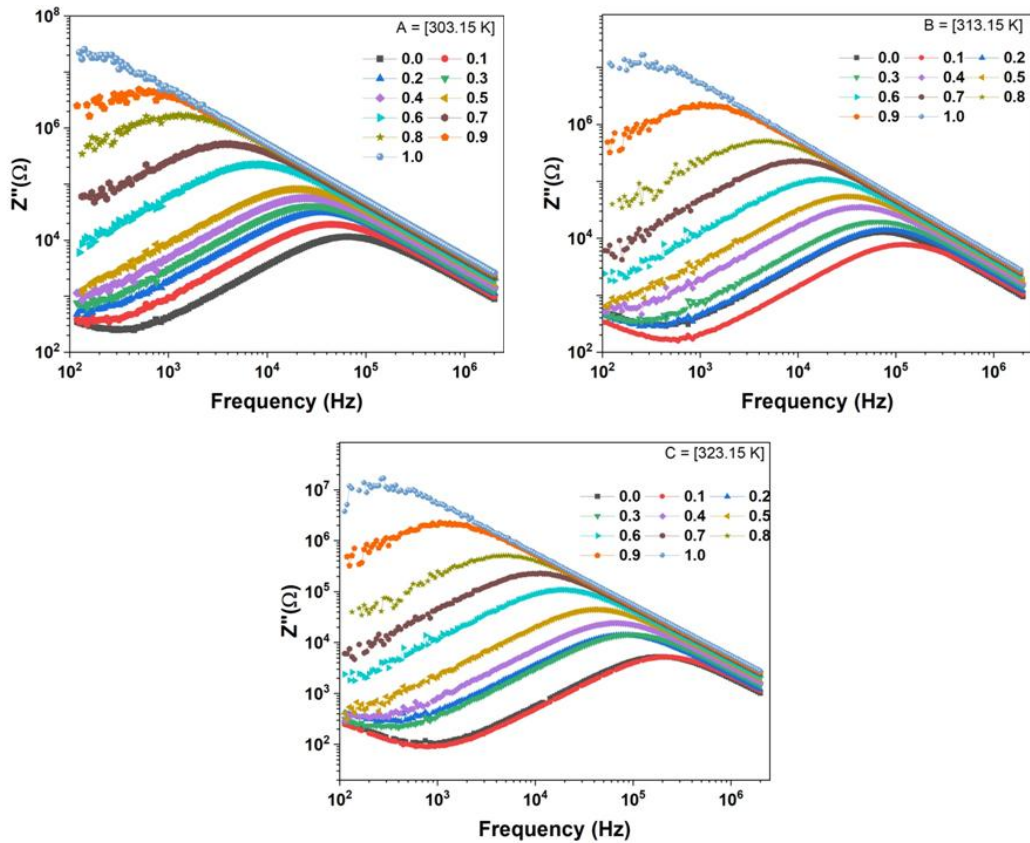


Fig. 8. Plot of Z'' versus frequency for the binary mixture of CB and n-BuOH at (A) 303.15K (B) 313.15 K and (C) 323.15 K temperatures.

III. CONCLUSIONS

This paper presents the complex dielectric and electrical spectra for pure Chlorobenzene and their mixtures (CB + n-BuOH) for the different temperature ranges (303.15 K, 313.15 K and 323.15 K). The complex permittivity parameter indicates that an EP phenomenon is more prominent at lower frequency. The dielectric loss value is high in the lower frequency region due to ionic conduction loss. At low frequencies, the ionic impurities significantly contribute to energy dissipation, resulting in a higher dielectric loss. The ionic relaxation time τ_σ is evaluated from the maximum value of M'' . As the concentration of chlorobenzene increases, the ionic relaxation time (τ_σ) increases at 303.15 K. However, at 313.15 K and 323.15 K, the ionic relaxation time (τ_σ) exhibit anomalous behavior. Direct current electrical conductivity σ_{dc} is evaluated from the constant region of the real part of σ' . It is observed that as the concentration of chlorobenzene increases, the value of σ_{dc} decreases.

IV. ACKNOWLEDGMENT

We are thankful to Head, Department of Physics, Sardar Patel University, Vallabh Vidyanagar, for their continuous encouragement.

V. REFERENCES

1. H. A. Chaube, V. A. Rana, "Dielectric and Electrical Properties of Binary Mixtures of Anisole and Some Primary alcohols in the Frequency Range 20 Hz to 2 MHz", *Advanced Materials Research*, 665, 194-201, 2013.
2. H. P. Vankar, V.A. Rana, "Electrode Polarization And Ionic Conduction Relaxation In Mixtures of 3-Bromoanisole and 1-Propanol in The Frequency Range Of 20 Hz to 2 MHz at Different Temperatures", *Journal Of Molecular Liquids*, 254, 216–225, 2018.
3. R.J. Sengwa, V. Khatri , S. Sankhla, "Structure and hydrogen bonding in binary mixtures of N, N—dimethylformamide with some dipolar aprotic and protic solvents by dielectric characterization", *Indian Journal of Chemistry*, 48, 512–519, 2009.
4. V. A. Rana, K. N. Shah, H. P. Vankar, C. M. Trivedi, "Dielectric spectroscopic study of the binary mixtures of amino silicone oil and methyl ethyl ketone in the frequency range of 100Hz to 2MHz at 298.15K temperature", *Journal of Molecular Liquids*, 271, 686-695, 2018.
5. K. N. Shah, V. A. Rana, C. M. Trivedi, H. P. Vankar, "Dielectric properties of binary mixtures of methyl iso butyl ketone and amino silicone oil", in: *AIP Conference Proceeding*, AIP Publishing, 1837, 040026, 2017.
6. S. Choudhary, P. Dhatarwal, and R. J. Sengwa, "Characterization of conductivity relaxation processes induced by charge dynamics and hydrogen-bond molecular interactions in binary mixtures of propylene carbonate with acetonitrile", *Journal of Molecular Liquids*, 231, 491–498, 2017.
7. A. R. Deshmukh, R. V. Shinde, S. A. Ingole, A. W. Pathan, M. P. Lokhande, A. V. Sarode, A. C. Kumbharkhane, "Dielectric relaxation and hydrogen bonding interaction of solvents using time domain reflectometry technique from 10 MHz to 50 GHz", *Indian Journal of Pure & Applied Physics*, 56, 346-352, 2018.
8. R. D. Bezman, E. F. Casass, and R. L. Kay, "The temperature dependence of the dielectric constants of alkanols", *Journal of Molecular Liquids*, 73-74, 397402, 1997.
9. A. N. Prajapati, "Dielectric Study of Binary Mixtures of 1-Butanol With N, N Dimethylformamide", *AIP Conference Proceedings*, 2220, 040030, 2020.
10. D. C. Majak , A. Bald, R. J. Sengwa, "Static permittivities of n-propanol mixtures with ethanol, isomers of propanol, and butanol at temperature (288.15–308.15) K", *Journal of Molecular Liquids*, 179, 72–77, 2013.

11. N. V. SASTRY and P. N. DAVE, “Dielectric behaviour of acrylic ester-organic solvent mixtures”, *Journal of Chemical Sciences*, 109, 211, 1997.
12. V. P. Pawar, S. C. Mehrotra, “Dielectric Relaxation Study of Liquids Having Chloro Group with Associated Liquids. I. Chlorobenzene with Methanol, Ethanol, and 1-Propanol”, *Journal of Solution Chemistry*, 31, 559–576, 2002.
13. R. J. Sengwa, S. Sankhla, S. Choudhary, “Dielectric relaxation processes and ionic conduction behaviour in poly (ethylene oxide)–montmorillonite clay nanocomposite aqueous colloidal suspensions”, *Colloid and Polymer Science*, 287, 1013–1024, 2009.
14. R. J. Sengwa, S. Choudhary, P. Dhatarwal, “Effect of ionic contaminants on dielectric dispersion and relaxation processes over static permittivity frequency region in neat liquid poly(ethylene glycol)”, *Journal of Molecular Liquids*, 220, 1042–1048, 2016.

© 2024. This work is published under

[https://creativecommons.org/licenses/by/4.0/legalcode\(the“License”\)](https://creativecommons.org/licenses/by/4.0/legalcode(the“License”)).

Notwithstanding the ProQuest Terms and Conditions, you may use this content in accordance with the terms of the License.

- 1) Shrikant H. Nimkar^{a*}
- 2) Poonam. A. Fartode^b
- 3) S. B. Kondawar^c

Fabrication of Polyaniline / TiO₂ Nanocomposites Thin Film for CO₂ Gas Sensor



Abstract: Polyaniline/Titanium dioxide (PANI/TiO₂) nanocomposites synthesized by solution route technique and the thin film of nanocomposite was deposited on glass substrate during polymerization. The PANI/TiO₂ nanocomposites have been analyzed by using XRD, SEM, and FTIR. PANI/TiO₂ thin film sensor synthesized by solution route technique and it was exposed to CO₂ gas at different temperature and studied cross selectivity. The gas sensing measurement reveals that, on exposing of CO₂ gas (1000ppm) at different temperature the resistance of thin film was increased and it shows highest response at 46⁰C which was very closed to room temperature. XRD graph reveals that TiO₂ nanoparticle was present in PANI chain structure and SEM image showed agglomerated structure of PANI/TiO₂ helps for adsorption process. Electronic structure modification of PANI chain due to the presence of TiO₂ was confirmed by FTIR.

Keywords: Conducting polymer, Polyaniline (PANI), Titanium dioxide (TiO₂), nanocomposites, thin film, and CO₂ gas sensor.

1. Introduction

High concentrations of CO₂ gas in confined areas can be potentially dangerous. However, the chemical inertness of carbon dioxide has caused many difficulties in developing CO₂ chemical sensors [1]. Conventional methods of detecting CO₂ include using infrared spectroscopy and gas chromatography. The commercial equipment's available based on the above techniques are bulky and expensive. Due to these reasons research on sensing materials has been focused to design a high performance and elevated efficiency gas sensing elements with suitable sensing materials which can sense high concentration of carbon dioxide (CO₂) gas in atmosphere [2].

Organic and inorganic materials are used as gas sensing materials. ZnO, TiO₂ and SnO₂ have been well studied for gases detection in inorganic category. For organic materials category, conducting polymers such as polyaniline, polypyrrole, and polythiophene have been widely investigated as effective materials for chemical sensors [3].

¹* Physics Research Laboratory, Shri Shivaji Arts, Commerce and Science College, Akot Dist: Akola, (MS) (India),

² Shri Shivaji Science College, Amravati (MS) (India)

³ Department of Physics, Rashtrasant Tukadoji Maharaj Nagpur university, Nagpur (India)

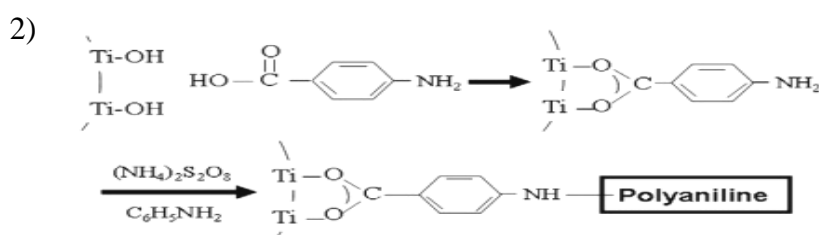
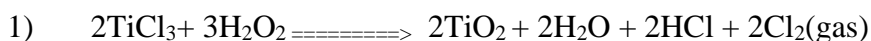
*Corresponding author. Tel: (+91) 8459616611; E-mail: shrikantnimkarsscakot@gmail.com

Among the conducting polymers polyaniline (PANI) is frequently used because of its ease of synthesis, environmental stability, intrinsic redox reaction, high electrical conductivity [4]. Mixing semiconductive metal oxide with PANI to form nanocomposites was found to be an effective way to improve the gas sensing properties of PANI. However, the problem with these conducting polymers is their low processing ability, poor mechanical strength, and chemical stability [5]. There is a tremendous approach for the enhancement of the mechanical strength and characteristics of sensors by combining the organic materials with inorganic counterparts to form composites. Among the inorganic materials, Titanium dioxide (TiO₂) was chosen due to its unique physical and chemical properties such as large energy gap, dielectric constant, and environmental-friendliness and easy to synthesis [6].

However, very few researchers have studied the composite PANI/TiO₂ for sensor application. In the present paper, we report fabrication of Polyaniline/TiO₂ nanocomposite thin film CO₂ gas sensors synthesized by solution route technique.

2. Experimental

Solution route technique is the effective method for synthesis of PANI/TiO₂ nanocomposites thin film [7]. In this technique aniline monomer was distilled under reduced pressure. Initially, 0.3 M of TiCl₃, was hydrolyzed, in 50 ml of double distilled water (DDW) with constant stirring and it's pH was maintained at ≤4, using 3-4 drops of concentrated HCl. 10 ml of Hydrogen peroxide (H₂O₂) was added in the above solution, which oxidizes titanium ions to tin oxide, the brown colored solution is obtained. Take 40 ml of solution from it and add 0.1 M of aniline, and keep it for constant stirring for 15 minutes and that reaction mixture kept on ice bath for 30 minutes. After that add (Drop by drop) ammonium persulphate (APS) ((NH₄)₂S₂O₈) solution in the above mixture and simultaneously inserted pre-cleaned glass substrates vertically. It was found that solution color change to dark green indicating the polymerization and formation of PANI/TiO₂ composites and the growth of film on the glass substrate. The precipitate produced in the reaction was removed by filtration, washed repeatedly with DDW and dried under vacuum for 24 hours. The composite powder was conductive emeraldine salt (ES) form of PANI/TiO₂ nanocomposite.



3. Results

3.1. XRD

The XRD pattern of PANI/ TiO₂ nanocomposites showed diffraction peaks along (1 1 0), (1 0 1), (1 1 1), (2 0 0), (2 1 0) centered at $2\theta = 23.68^\circ$, 26.28° , 30.62° , 32.92° , 38° and 41.04° respectively. On comparing the observed XRD peaks and corresponding planes with the standard (h k l) planes of the TiO₂ reported elsewhere [8-9]. A good matching was seen between the two sets, confirming that the nanocomposites consist of TiO₂ having tetragonal rutile phase [10]. The peaks related to the TiO₂ nanoparticles became sharper and more crystalline in composites. These peaks are slightly shifted from their respective standard positions, may be due to presence of PANI matrix. This confirmed that PANI/TiO₂ nanocomposites become more crystalline as the concentration of TiO₂ is increased and PANI deposited on the surface of TiO₂ particles has no effect on the crystallization behavior of TiO₂ particles in the nanocomposites [11-13].

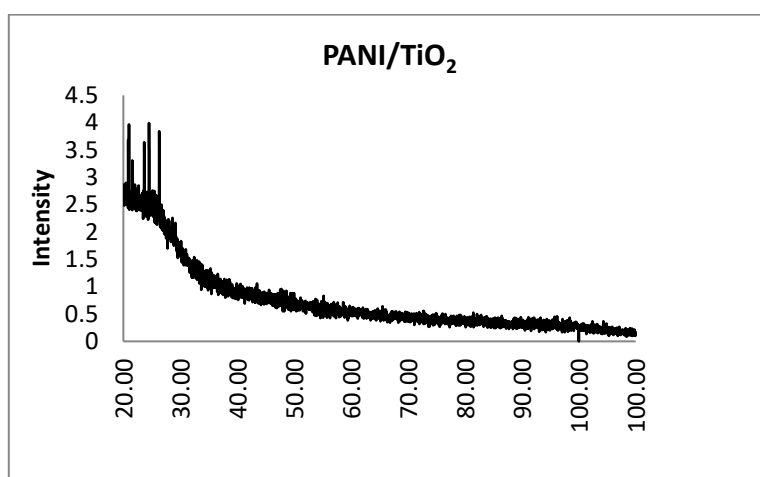


Fig.1 XRD pattern of PANI/ TiO₂ nanocomposites.

3.2. SEM

The surface morphology of PANI/TiO₂ nanocomposite is determined by scanning electron microscopy (SEM) as shown in Fig. 2a and Fig. 2b for two different magnification ranges. The SEM images of composites with diameters about 167 nm and 183 nm, respectively. The decrease in composite particle diameter might have been due to an increase in TiO₂ content, which caused a relative decrease in PANI content. The pure PANI exhibits a completely amorphous region [14]. The SEM images clearly reveals that surface of PANI/TiO₂ is not smooth and uneven lumps and holes are visible which are suitable for gas adsorption. It is found that the doping of TiO₂ strongly affected the morphology of the resulting PANI/TiO₂ composites. In case of PANI/TiO₂ composite, the SEM micrograph revealed that the composite particles are highly dispersed with agglomeration with an interlocking arrangement of granular particles (Fig. 2a) [15-17].

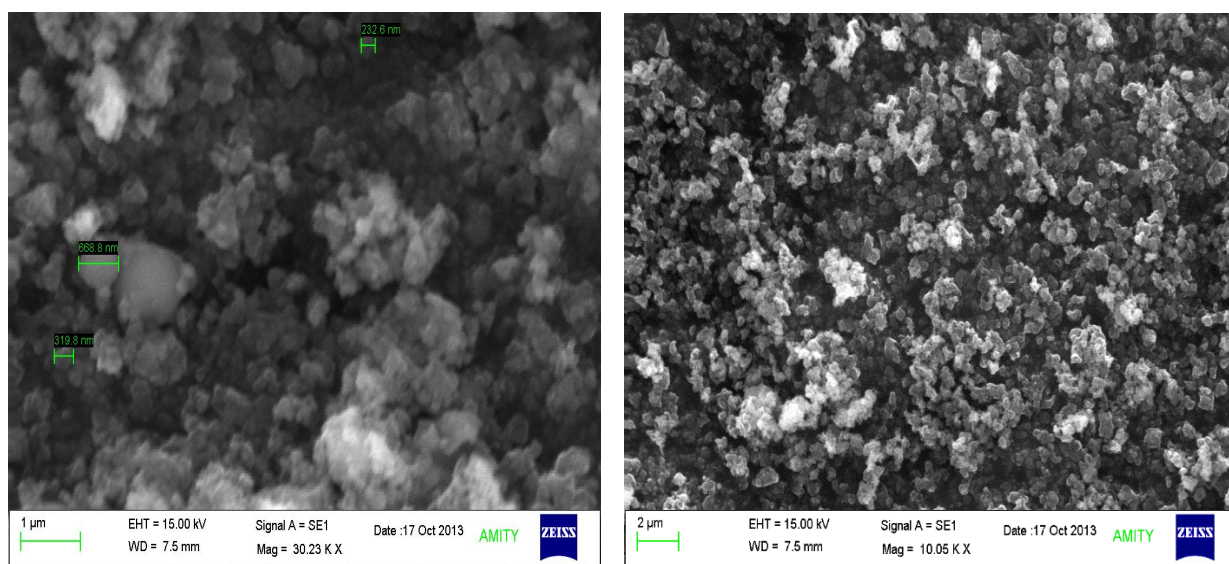
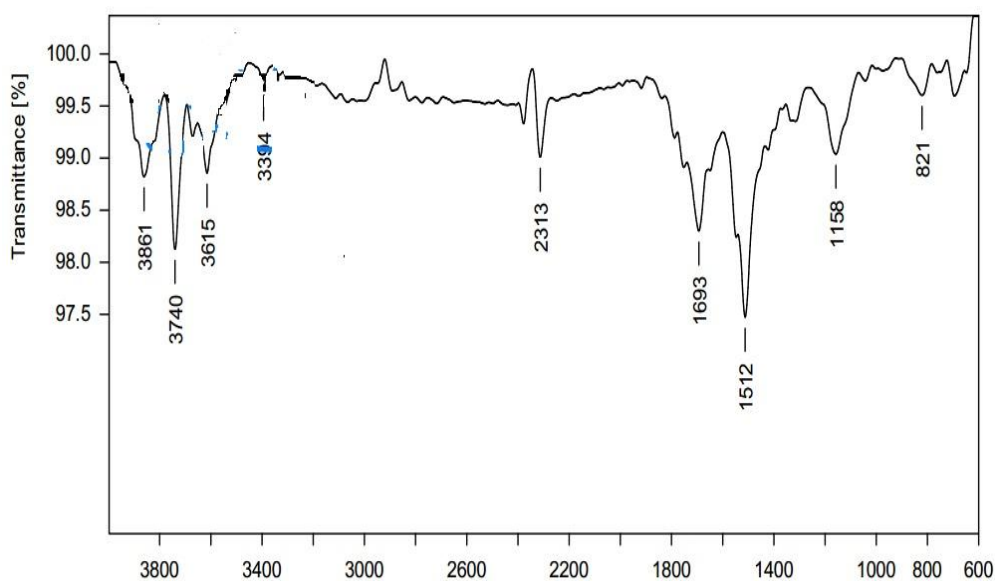


Fig.2a SEM

images of PANI/ TiO₂ nanocomposites. Fig.2b SEM images of PANI/ TiO₂ nanocomposites.

3.3. Fourier- Transform Infrared Spectroscopy (FTIR)

The FTIR spectra reveal the presence of Ti-O-Ti vibrational peak and characteristic vibrational peaks of PANI indicating the interaction of TiO₂ particles in PANI matrix. The peak at 3861-3394 cm⁻¹ is attributed to N-H stretching vibration [18]. The vibration band at 1158-1100 cm⁻¹ range is the characteristic band of PANI corresponding to charge delocalization proving the protonation which is shifted towards higher wavelength side due to the interaction of TiO₂ in PANI matrix [19-21]. It is also observed that the peaks at around 800-850 cm⁻¹ corresponds to the C-H bending out of the plane for 1, 4 substituted aromatic rings indicating the linear structure which is slightly deviated due to the presence of TiO₂ particles. There are strong peak at 761.23 and 686 cm⁻¹ which are due to the antisymmetric Ti-O-Ti mode in TiO₂ [22].

Fig. 3 FTIR spectra of PANI/TiO₂ nanocomposites

3.5. Gas Sensing Measurement

The gas sensing setup used to measure variation in resistance as shown in Fig.5.



Fig. 4 Gas sensing setup used in present work

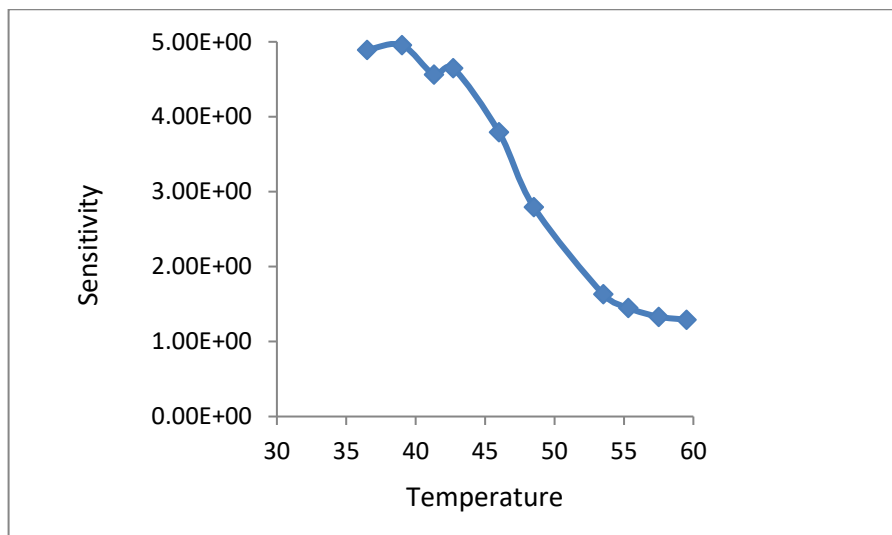


Fig. 5 Sensitivity Vs Temperature graph of PANI/TiO₂ nanocomposites

PANI/TiO₂ thin was exposed to CO₂ gas for 1000 ppm at different temperature resistance start increasing due to porous structure of PANi/TiO₂ films leads to the predominance of surface phenomena over bulk material phenomena, which may again be due to surface adsorption effect [23-26]. The sensitivity of PANI/TiO₂ nanocomposite for CO₂ with increasing temperature was found to be as shown in fig. 5. This graph shows that sensitivity of nanocomposite is higher at normal temperature and it goes on decreasing with increasing temperature The response/recovery time is an important parameter use for characterizing a sensor. Table 1 show the time and resistance change of PANI/TiO₂ composite for CO₂ gas for constant concentration of gas i.e. 1000 ppm. It is revealed that the response time was found to be 70 to 80 s, if CO₂ concentration increased from 1000 ppm and more response time may decreases as found. This may be

because of high surface area due to porous structure of exposed film which facilitates rapid diffusion of gas molecules into the film [27-28]. The response S_{gas} of the sensor is calculated from following equation.

$$\text{Sensitivity}(\text{gas}) = \frac{R_{\text{gas}} - R_{\text{air}}}{R_{\text{air}}}$$

where R_{air} is the sensor resistance in pure synthetic air and R_{gas} is the sensor resistance in the presence of the test gas. Response and recovery times are defined as the time necessary for the sensor to reach 90% of the final resistance value during gas exposure and at the end of gas exposure, respectively [29-30].

Sr. No.	Time (sec)	Resistance (ohm)
1	10	3.79E+03
2	20	3.82E+03
3	30	3.69E+03
4	40	3.56E+03
5	50	3.00E+03
6	60	2.36E+03
7	70	1.43E+03
8	80	1.36E+03
9	90	1.35E+03
10	100	1.41E+03

Table 1: Best sensing performance of the PANI/TiO₂ nanocomposite for CO₂ gas

4. Conclusions

The PANI/TiO₂ nanocomposite was successfully synthesized and deposition of thin film by using solution route technique. The composites have poorer crystallinity than TiO₂, because of amorphous structure of PANI and agglomeration interlocking arrangement of granular particles and high surface area have been observed in XRD and SEM images. The gas sensing measurements were carried out for different temperature, but at room temperature PANI/TiO₂ thin film sensor gives more sensitivity than higher temperature and also response time was 70 to 80 sec. which was considerable towards CO₂ gas.

References:

- [1] Chi-Ju Chiang, Kang-Ting Tsai, Yi-Huan Lee, Hung-Wei Lin, Yi-Lung Yang, Chien-Chung Shih, “In situ fabrication of conducting polymer composite film as a chemical resistive CO₂ gas sensor”, *Microelectronic Engineering*, 2013, 111, 409-415.
- [2] Mohammad Hafizuddin Haji Jumali, Izura Izzuddin, Norhashimah Ramli, Muhamad Mat Salleh, and Muhammad Yahaya, *Solid State Science and Technology*, 2009, 17, 126.
- [3] Kondawar S. B., S. P. Agrawal, S. H. Nimkar, H. J. Sharma, P. T. Patil, *Conductive polyaniline-tin oxide nanocomposites for ammonia sensor* *Adv. Mat. Lett.* 2012, 3(5), 393-398.
- [4] Pawar S. G., S. L. Patil, M. A. Chougule, B. T. Raut, S. A. Pawar and V. B. Patil, “Fabrication of Polyaniline/ TiO₂ Nanocomposite Ammonia Vapor Sensor”, *Sensors & Transducers*, 2011, 125(2), 107-114.
- [5] Duong Ngoc Huyen, Nguyen Trong Tung, Nguyen Duc Thien and Le Hai Thanh, “Effect of TiO₂ on the Gas Sensing Features of TiO₂/PANi Nanocomposites”, *Sensors* 2011, 11, 1924-1929.
- [6] Subodh Srivastava, Sumit Kumar, V.N. Singh, M. Singh, Y.K. Vijay, “Synthesis and characterization of TiO₂ doped polyaniline composites for hydrogen gas sensing, international journal of hydrogen energy”, 2011, 36, 6343-6349.
- [7] Deshpande N.G., Gudage Y. G., Sharma R. Vyas J.C.; Kim, J.B. Lee, Y.P. “Studies on tin oxide-intercalated polyaniline nanocomposite for ammonia gas sensing applications” *Sensors and Actuators B*, 2009, 138, 76-84.
- [8] Huiling Tai, Yadong Jiang, Guangzhong Xie and Junsheng Yu, “Preparation, Characterization and Comparative NH₃-sensing Characteristic Studies of PANI/inorganic Oxides Nanocomposite Thin Films”, *J. Mater. Sci. Technol.*, 2010, 26(7), 605-609.
- [9] Pi-Guey Su, Lin-Nan Huang, “Humidity sensors based on TiO₂ nanoparticles/polypyrrole composite thin films”, *Sensors and Actuators B*, 2007, 123, 501-507.
- [10] Parveen, Ameena; Koppalkar, Anilkumar; Roy, Aashis S, “ Liquefied Petroleum Gas Sensing of Polyaniline-Titanium Dioxide Nanocomposites”, [Sensor Letters](#), 2013, 11, 242-247.
- [11] Huiling Tai, Yadong Jiang, Guangzhong Xie, Junsheng Yu, Xuan Chen, “Fabrication and gas sensitivity of polyaniline–titanium dioxide nanocomposite thin film, *Sensors and Actuators B*, 2007, 125, 644-652.
- [12] S. Deivanayagi, V. Ponnuswamy, S. Ashokan, P. Jayamurugan, R. Mariappan, “Synthesis and characterization of TiO₂-doped Polyaniline nanocomposites by chemical oxidation method”, *Materials Science in Semiconductor Processing*, 2013, 16, 554-561.
- [13] Sitao Yang, Yoshie Ishikawa, Hiroshi Itoh, Qi Feng, “Fabrication and characterization of core/shell structured TiO₂/polyaniline nanocomposite”, *Journal of Colloid and Interface Science*, 2011, 356, 734-738.
- [14] Gupta Shipra Mital & Tripathi Manoj, “A review of TiO₂ nanoparticles”, *Chinese Science Bulletin*, 2011, 56 (16), 1639-1646.
- [15] Mohammad Reza Nabid, Maryam Golbabaee, Abdolmajid Bayandori Moghaddam, Rassoul Dinarvand, Roya Sedghi, “Polyaniline/TiO₂ Nanocomposite: Enzymatic Synthesis and Electrochemical Properties”, *Int. J. Electrochem. Sci.*, 2008, 3, 1117-1123.
- [16] Wang, H., Yang, Y., Li, X., Li, L., Wang, C., “Preparation and characterization of porous TiO₂/ZnO composite nanofibers via electrospinning”, *Chinese Chemical Letters*, 21, 2010, 1119–1123.

- [17] Nirmala, R., Kim, H., Yi, C., Barakat, N., Navamathavan, R., “Electrospun nickel doped titanium dioxide nanofibers as an effective photocatalyst for the hydrolytic dehydrogenation of ammonia borane”, *International journal of hydrogen energy*, 37, 2012, 10036-10045.
- [18] Mahanty, S., Roy, S., Sen, S., “Effect of Sn doping on the structural and optical properties of sol-gel TiO₂ thin films”, *Journal of Crystal Growth*, 261, (2004), 77–81.
- [19] Ma X, Wang M, Li G, Chen H, Bai R. Preparation of polyaniline-TiO₂ composite film with in situ polymerization approach and its gas sensitivity at room temperature. *Mater Chem Phys* 2006, 98, 241-247.
- [20] Cruz-Silva R, Romero-García J, Angulo-Sánchez JL, FloresLoyola E, Farías MH, Castillo’n FF, “Comparative study of polyaniline cast films prepared from enzymatically and chemically synthesized polyaniline”, *Polymer*, 2004, 45:47, 11-17.
- [21] Li X, Wang G, Lu D., “Surface properties of polyaniline/nanoTiO₂ composites”, *Appl Surf Sci* 2004, 229, 395-401.
- [22] S. Sen, P. Kanitkar, A. Sharma, K.P. Muthe, A. Rath, S.K. Deshpande, M. Kaur, R.C. Aiyer, S. K. Gupta, J.V. Yakhmi, “Growth of SnO₂/W₁₈O₄₉ nanowire hierarchical heterostructure and their application as chemical sensor”, *Sens. Actuators B*, 147, 2010, 453–460.
- [23] Jianbo Lu, Bijandra Kumar, Mickaël Castro, Jean-François Feller, “Vapour sensing with conductive polymer nanocomposites (CPC): Polycarbonate-carbon nanotubes transducers with hierarchical structure processed by spray layer by layer”, *Sensors and Actuators B* 2009, 185-192.
- [24] Xianping Chen, K.Y. Wong, Cadmus A. Yuan, Guoqi Zhang, Nanowire-based gas sensors, *Sensors and Actuators B*, 2013, 177, 178–195.
- [25] D.S. Dhawale, D.P. Dubal, V.S. Jamadade, R.R. Salunkhe, S.S. Joshi, C.D. Lokhande, Room temperature LPG sensor based on n-CdS/p-polyaniline heterojunction, *Sensors and Actuators B*, 2010, 145, 205–210.
- [26] S. Stegmeier, M. Fleischer, A. Tawil, P. Hauptmann, “Stepwise improvement of (hetero-) polysiloxane sensing layers for CO₂ detection operated at room temperature by modification of the polymeric network”, *Sensors and Actuators B*, 2010, 148, 450–458.
- [27] E. Brunet, T. Maiera, G.C. Mutinaria, S. Steinhauer, A. Köck, C. Gspan, W. Grogger, “Comparison of the gas sensing performance of SnO₂ thin film and SnO₂ nanowire sensors”, *Sensors and Actuators B*, 2012, 165, 110–118.
- [28] Suresh Mulmia, Azfar Hassan, Pedro Pereira-Almao, Venkataraman Thangadurai, “Detecting CO₂ at ppm level in synthetic air using mixed conducting double perovskite-type metal oxides”, *Sensors and Actuators B*, 2013, 178, 598–605.
- [29] L. I. Trakhtenberg, G. N. Gerasimov, V. F. Gromov & T. V. Belysheva, O. J. Ilegbusi, “Gas Semiconducting Sensors Based on Metal Oxide Nanocomposites”, *Journal of Materials Science Research*, 2012, 1.1(2), 56-68.
- [30] Bin Sun, Guangzhong Xie, Yadong Jiang, Xian Li, “Comparative CO₂-Sensing Characteristic Studies of PEI and PEI/Starch Thin Film Sensors”, *Energy Procedia*, 2011, 12, 726 – 732.

^{1*}Shubham V. Warudkar
²A.P. Deshmukh
³P.S. Awandkar
⁴S.P. Tiwari
⁵S. P. Yawale

*Synthesis and Sensing
 Characteristics of
 PEDOT:PSS/RGO composite
 as a Carbon Dioxide Gas Sensor*



Abstract: - The utilization of conducting polymer composites for gas sensing applications has gathered significant interest due to their unique properties, such as high surface area, tunable conductivity, and chemical stability. In this study, a composite material consisting of poly(3,4-ethylenedioxythiophene):poly(styrene sulfonate) (PEDOT:PSS) (1:2) and reduced graphene oxide (RGO) was synthesized and characterized for its potential application as CO₂ gas sensor. The PEDOT:PSS/RGO composites at 5, 10, 15 and 20 wt. % RGO in PEDOT:PSS were prepared via chemical oxidative *in-situ* polymerization technique using oxidizing agent Ammonium Persulphate (APS), followed by deposition onto a paper substrate. For electrical contacts, Copper electrodes were attached on adjacent sides of the sensor film. The structural and chemical properties of the composite were analyzed using techniques such as XRD and FTIR. Sensitivity of sensors was measured by a voltage drop method at room temperature (312 K) at 100 ppm CO₂ gas concentration. It is analysed that PEDOT:PSS+10% RGO composite shows effective (maximum) sensing toward CO₂ gas but has comparative longer response and recovery time. Whereas, PEDOT:PSS+20 % RGO composite has rapid response and recovery time but it is less efficient to sense the gas.

Keywords: Conducting polymer, PEDOT:PSS, Reduced graphene oxide, CO₂ gas sensing, Carbonaceous materials, Composite.

I. INTRODUCTION

Sensors made of conducting polymers have many particular characteristics such as a higher sensitivity to produce stronger signals, shorter response time, and room temperature operating ability. These gas sensors play a critical role in environmental monitoring, industrial safety, and indoor air quality control. Literature surveys have indicated that several metal oxides are promising material for various types of gas sensing, including CO₂. However, less attention has been paid to electrically conducting polymers such as polypyrrole, polythiophene, PEDOT:PSS, and polyaniline, etc. These polymers possess unique properties, including low density, versatile production methods, high anisotropy of electrical conduction, [1] and non-metallic temperature dependence of conductivity, which could be advantageous for CO₂ gas sensing. Poly(3,4-ethylenedioxythiophene):poly(styrenesulfonic acid) (PEDOT:PSS), one of the most important and successful conducting polymers. PEDOT has good thermal and chemical stability until 150 °C. Due to its high conductivity, good thermal stability, excellent environmental stability, and electrochemical stability, PEDOT is used in a wide range of applications such as light-emitting diodes, electrochromic devices (ECDs), sensors and batteries [2]. On the other hand, reduced graphene oxide, due to its unique two-dimensional carbon nanostructure, offers significant potential for various applications such as gas sensing, transparent conducting electrodes, ultracapacitors, and thin film transistors. As point of view of gas sensor, it provides a large surface area per unit volume, allowing every atom at the surface to potentially interact with gases. Additionally, its ease of functionalization with different materials enables the development of selective capture agents, enhancing its suitability for sensing specific target gases[3-5].

The present investigation mainly deals with the preparation of CO₂ gas sensor of PEDOT:PSS/ RGO composite. It was found that composite of conducting polymers shows more sensitivity to carbon dioxide gas. PEDOT:PSS polymer is chosen for the conducting layer because of its high stability in air, while RGO is selected for its high surface area-to-volume ratio[6,7]. Chemical and structural properties of PEDOT:PSS conducting polymer can be improved by its combination with Carbon nanomaterials[8]. Both PEDOT:PSS and RGO have hydrophilic properties, enabling uniform deposition onto sensor substrates as thin films, which is essential for sensor technology applications [9]. The CO₂ gas sensor based on the synthesized hybrid composite of SnO₂-RGO exhibited excellent response, good linearity, and low detection limit. The excellent gas interaction of the SnO₂-RGO hybrid composite could be attributed to its high conductivity[10]. In one of the research work it is

^{1*}Corresponding author: Government Vidarbha Institute of Science and Humanities, Amravati 444604, India.
 Email id: spyawale@rediffmail.com, shubhamwarudkar112@gmail.com

observed that as compared to the pure PEDOT:PSS, the Chemically modified graphene (CMG)/PEDOT:PSS hybrid system exhibited more promising sensing behavior on H₂ gas. The sensing behavior of the RGO/PEDOT:PSS composite sensor indicates that the sensing material is a n-type. Also, GO/PEDOT:PSS shows better H₂ gas sensing properties than RGO/PEDOT:PSS[11]. The earlier study reveals that the research work on PEDOT:PSS embedded with RGO is found to be scanty. Hence, the composites were prepared with an intention to exploit these materials as CO₂ gas sensor.

In the present study, pristine PEDOT:PSS, RGO and PEDOT:PSS/RGO composites were prepared using *in-situ* chemical oxidative polymerization method. Several amounts of reduced graphene oxide has been loaded to prepare a composite by weight percent method. The structural, morphological and functional group study were done by XRD and FTIR spectroscopic techniques. Sensitivity of sensors was measured by a voltage drop method at room temperature (312 K).

II. EXPERIMENTAL

A. Materials

Poly(Sodium4-styrenesulfonate) (PSS) (Mw=75000 g/mol, Aldrich) procured from Sigma Aldrich and EDOT (3,4-ethylenedioxythiophene) monomer acquired from TCI (Tokyo Chemical Industries), Ferric Chloride Anhydrous (FeCl₃), DMSO from Hi Media, Ammonium Persulphate (APS) from Fisher Scientific, Graphite powder from Loba Chemie.

B. Synthesis of conducting polymer PEDOT:PSS

Conducting polymer PEDOT:PSS have been synthesized by chemical oxidative polymerization technique using oxidizing agent Ammonium Persulphate [(NH₄)₂S₂O₈] (APS) in aqueous medium. For that PSS was dissolved in 50 ml of distilled water at 1:2 mass ratio (EDOT:PSS) and stirred it well to dissolve. Then the solution was ultrasonicated for 45 min to get the homogeneous mixture of PSS solution. After the sonication EDOT monomer was added into PSS solution and stirred well using magnetic stirrer. Then oxidant APS was added at 1:2 mass ratio (EDOT:APS) directly in the above mixture with continued stirring. After this, the FeCl₃ solution which was prepared at 1:0.6 mass ratio (EDOT:FeCl₃) was added dropwise. The polymerization reaction started as the drop of FeCl₃ mixed in the above mixture. Physical appearance changes into blue and stirred it up to 2 h at room temperature during polymerization reaction. After stirring, it was kept unagitated for 16 h. The obtained material was filtered with the help of filter paper and washed several times with distilled water. It was dried at 60 °C in oven for 24 h. The bluish black material / polymer was obtained which was crushed in the Mortar pestle to get fine powder [12].

C. Synthesis of Reduced Graphene Oxide (RGO)

The modified Hummer's method was used for producing Reduced Graphene Oxide (RGO) by oxidizing graphite powder using oxidant KMnO₄. Firstly Graphene Oxide (GO) was obtained which on reduction gives reduced graphene oxide.

Step 1: Synthesis of Graphene Oxide

2 g Graphite powder was dispersed into cold conc. 46 ml H₂SO₄ in a beaker which was kept in an ice bath and stirred using a magnetic stirrer. Slowly, 3 g of KMnO₄ was added while ensuring that the temperature of the solution do not rise above 10 °C. Then the reaction vessel was removed from ice bath, the temperature was brought to 35 °C and the reaction vessel was allowed to sit for 30 min to an h. Over this time, the solution thickened and turned a brownish gray in color. Next, 100 ml of deionized water was slowly and carefully added to the reaction vessel. At this time, temperature of the solution was rose to 100 °C. The solution was kept at this elevated temperature for 15 min, during which it became brown in color. After that, 300 ml deionized water with 3 % H₂O₂ was added to the reaction vessel/beaker. Finally the solid products was washed with 5 % HCl and deionized water 5 times to remove all the impurities. and, dried at 60 °C in an oven to obtain the Graphene Oxide Powder [13,14].

Step 2: Reduction of Graphene Oxide:-

Suspension of GO (1 mg/ml) was prepared by sonicating dried GO in distilled water. To it's 500 ml, 500 mg of ascorbic acid was added. The pH of the solution was adjusted to 10 by adding NH₃ solution. The mixture was stirred at 65 °C. The resulting solution was filtered using filter paper. Then it was washed with distilled water and dried at 50 °C in an oven [15].

D. Composite preparation of PEDOT:PSS and RGO (In-situ approach).

Composite was prepared by weight percent method. 4.26 g PSS was dissolved in 50 ml distilled water at 1:2 mass ratio (EDOT:PSS) and stirred it well to dissolve. 40 mg (5 %) RGO was added to the solution. (80 mg -10 %, 120 mg -15 %, 160 mg -20 %). Then the solution was ultrasonicated for 45 minutes to get the homogeneous mixture. After the sonication, 2.13 g (1.6 ml) EDOT monomer was added into solution and stirred well using magnetic stirrer for 2 to 3 h. Then oxidant APS (4.26 g) was added at 1:2 mass ratio (EDOT:APS) directly in the above mixture with continued stirring. After this, the FeCl₃ solution was prepared at 1:0.6 mass ratio (EDOT:FeCl₃) by adding 1.29 g of FeCl₃ in 20 ml distilled water, and was added dropwise. After stirring it was kept unagitated for 16 h. The obtained material was filtered with the help of filter paper and washed several times with distilled water. It was dried at 60 °C in oven for 24 h. The bluish black material /polymer was obtained which was crushed in the mortar pestle for fine powder. Thus four samples P1 –PEDOT:PSS + 5 % RGO, P2- PEDOT:PSS + 10 % RGO, P3- PEDOT:PSS + 15 % RGO and P4- PEDOT:PSS + 20 % RGO were obtained.

E. XRD & FTIR characterizations

The X-ray diffraction analysis was performed using a Rigaku Miniflex benchtop X-ray diffractometer, equipped with an advanced detector and Cu K α radiation, at department of physics and electronics, Government Vidarbha Institute of Science and Humanities, Amravati. The resulting diffractogram was recorded in terms of 2θ , having the range of 0° to 80°. Fourier Transform Infrared Spectroscopy (FTIR) was obtained to examine the various molecular stretches and bonds between the molecules and functional groups of the material. The spectra were recorded using a Bruker Alpha II FTIR with a diamond crystal ATR, covering the vibrational range of 400-4000 cm⁻¹.

F. Fabrication of sensor and Sensing technique

The sensor was fabricated by using screen printing technique. For that, whatman filter paper was cut into 2 cm \times 2 cm dimensions. The binder for screen-printing was prepared by thoroughly mixing 8 wt% butyl carbitol with 92 wt% ethyl cellulose in 1:2 ratio of ethyl cellulose to composite material. The paste formed was screen printed on the desired prepared paper substrate such that uniform coating is obtained. Then it was kept for 24 h to dry at room temperature and then heated at 80-90 °C for 2.5 h to remove the binder. Thus, four sensors were obtained by printing paper with P1,P2,P3 and P4. The electrical resistance of the film was measured by using a voltage drop method [16]. Copper electrodes were used. The gas chamber having dimensions 30 cm \times 30 cm \times 30 cm with an attached CO₂ gas flow meter was used for keeping the sensors for testing.

III. RESULTS AND DISCUSSION

A. XRD Analysis

XRD analysis, is used to identify the crystalline phases present in a material. It is seen from fig.1, the diffraction angle of pure PEDOT:PSS (1:2) polymer (PO sample) is at $2\theta = 26^\circ$ and the amorphous hump is found at $2\theta = 33^\circ$. This scattering, corresponds to the (0 2 0) crystalline plane of the orthorhombic unit cell of PEDOT crystals. The XRD spectrum signifies amorphous or semi-crystalline nature of PEDOT:PSS polymer due to the absence of sharp peaks[17]. XRD analysis of RGO typically reveals characteristic peak at around $2\theta = 25^\circ$. The presence and intensity of this peak confirm the restoration of sp² hybridized carbon atoms in the RGO structure after reduction from graphene oxide (GO). RGO can be considered to have both amorphous and crystalline characteristics. The relative proportions of these characteristics depend on factors such as the degree of reduction, synthesis method, and processing conditions[18].

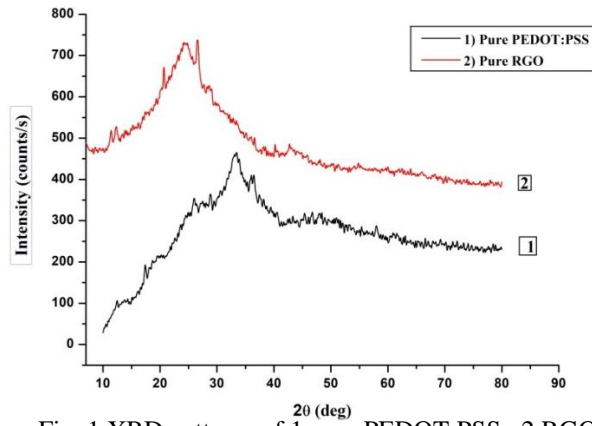


Fig. 1 XRD patterns of 1) pure PEDOT:PSS, 2) RGO

The peaks and amorphous hump observed for the PEDOT:PSS/RGO composites at different wt % of RGO are as shown in fig. 2. In XRD pattern of composites, the peaks at 29.32° (p4), 30.5° (p3), 31° (p2,p1) are due to presence of pure PEDOT:PSS in composite. Whereas, peaks at 26.28° (p4), 26.92° (p2), 26.36° (p3), 26.65° (p1) are due to presence of RGO. It is found that the peaks are shifted as compared to pure samples. This shifting proves the dispersion of RGO sheets within the PEDOT:PSS polymer structure. Also, it is observed that the intensity of diffraction peaks increases with increasing Reduced Graphene Oxide concentration. This means, the extent of crystallinity of the particular plane is proportional with the RGO amounts. The intensity of peaks of PEDOT:PSS is decreasing with increase in extent of RGO. This shows that reduced graphene oxide (RGO) is showing dominant nature in composite.

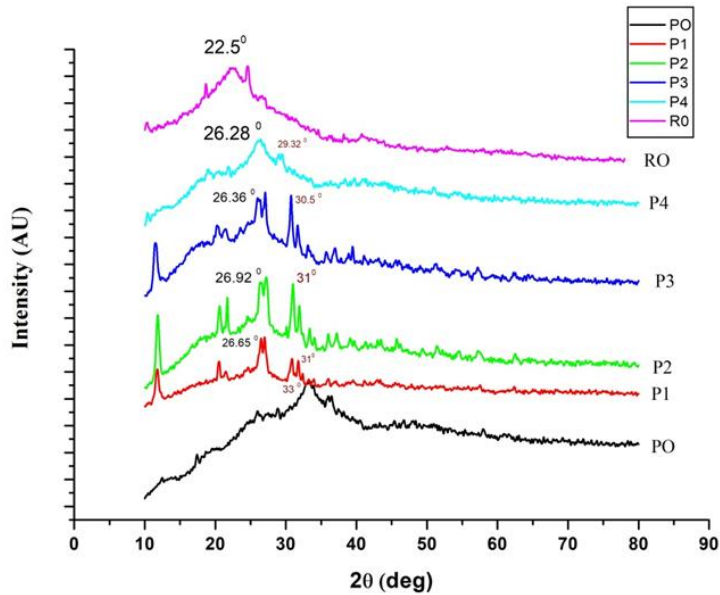


Fig.2 XRD patterns of pure PEDOT:PSS (P0), RGO (R0), and (PEDOT:PSS/RGO) at different wt % of RGO (5 %-P1, 10 %-P2, 15%-P3, 20 %-P4).

The average crystallite size of PEDOT:PSS/RGO composites was calculated by using Scherrer’s formula given by

$$D = \frac{K\lambda}{\beta \cos\theta} \tag{1}$$

Where λ is the wavelength of incident X-Ray radiation (nm), D is the crystallite size, K is the shape factor, which can be assigned a value of 0.94, θ is the diffraction angle at maximum peak intensity, and β is the full width at half maximum of diffraction angle in radians.

Table 1 :- Crystallite size of PEDOT:PSS/RGO (5-20 %) composite

Sr.No.	Composite Sample	Crystallite Size (nm)
--------	------------------	-----------------------

1.	PEDOT:PSS+ 5% RGO	6.93
2.	PEDOT:PSS+ 10% RGO	28.59
3.	PEDOT:PSS+ 15% RGO	14.50
4.	PEDOT:PSS+ 20% RGO	1.19

B. FTIR Analysis

In FTIR spectra, presence of functional groups and types of bonds between constituent atoms are observed. fig.3 shows FTIR spectra of PEDOT:PSS/RGO composites at different wt.% of RGO in PEDOT:PSS conducting polymer.

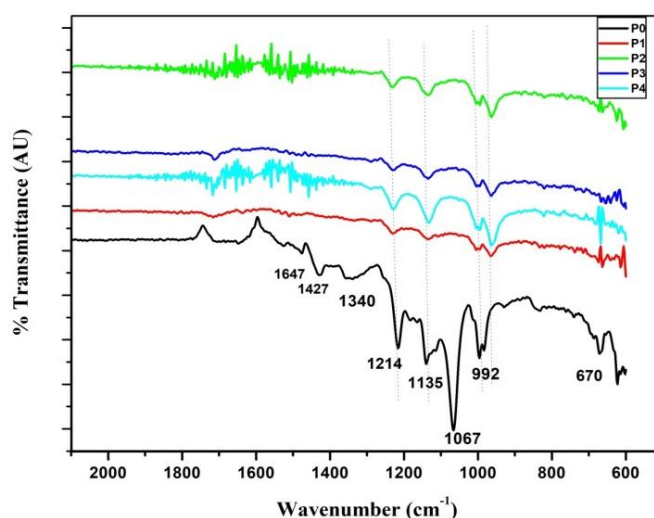


Fig. 3 FTIR spectrum of pure PEDOT:PSS (P0), and (PEDOT:PSS/RGO composite) at different wt % of RGO (5 %-P1, 10 %-P2, 15 %-P3, 20 %-P4).

In FTIR spectrum of Pure PEDOT:PSS, a peak at around 1228 cm^{-1} typically corresponds to the stretching vibration of the C-O bond (PEDOT), which shows the presence of the oxygen atoms and other oxygen-containing functional groups present in PEDOT:PSS. Peak at 1427 cm^{-1} corresponds to CH_2 bending. The strong peak at 1067 cm^{-1} is associated with the C-O stretching. Peak at 992 cm^{-1} corresponds to aromatic $=\text{C-H}$ bending which confirm presence of aromatic ring in PSS structure. The bending vibration of C-S bonds present in thiophene rings gives rise to the peak at approximately 670 cm^{-1} . The peak at 1136 cm^{-1} indicates the stretching vibration of the Carbon-Oxygen-Carbon (C-O-C) bond in the Ethylenedioxy (EDOT) units of the PEDOT polymer. This peak is characteristic of the PEDOT component in the composite. [18]

In FTIR spectrum of PEDOT:PSS/RGO (5%-20%) composite one extra peak is found along with peaks in pure PEDOT:PSS FTIR, which is observed at $1712\text{-}1716\text{ cm}^{-1}$. This peak typically corresponds to the stretching vibration of the C=O bond. It indicates the presence of carbonyl groups, which may originate from residual oxygen-containing functional groups (like aldehydes, carboxylic acid, ketones, alcohol, etc.) on the reduced graphene oxide (RGO) sheets. Slight shifts are observed compared to original peak which proves the dispersion of RGO sheets within the PEDOT:PSS polymer structure. As there is change in crystallite size, it also contribute to shifts in the FTIR peaks. [19]

Table 2: showing Peaks and chemical bonds and their nature of vibration in sample

Peak at wavenumber in cm^{-1}	Bond (stretching/bending)
1228 cm^{-1}	C-O, Stretching,
1427 cm^{-1}	CH_2 bending
992 cm^{-1}	Aromatic ($=\text{C-H}$) Bending
670 cm^{-1}	C-S, Bending

1136 cm ⁻¹	C-O-C, Stretching
1712-1716 cm ⁻¹	C=O, Stretching
1067 cm ⁻¹	C-O stretching

C. CO₂ Gas Sensing Analysis

The sensor response is defined as

$$S = \frac{R_g - R_a}{R_a} = \frac{\Delta R}{R_a} \tag{2}$$

Where, R_a is the resistance of sensor in air and R_g is the resistance in CO₂ gas, respectively. The resistance of all sensors are found to increase with increasing the CO₂ gas concentration [16, 20].

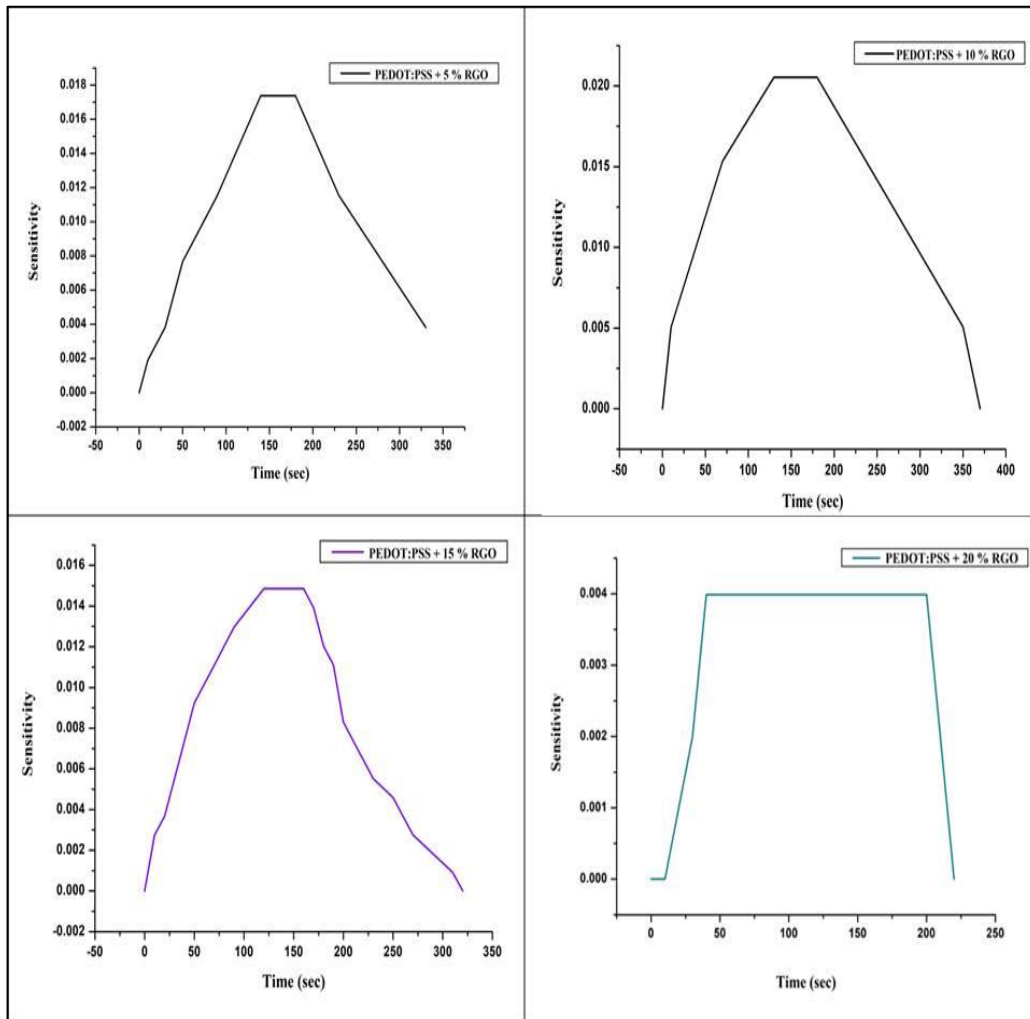


Fig.4:- Static response of sensors for CO₂ gas at 100 ppm . Plot of time vs sensitivity

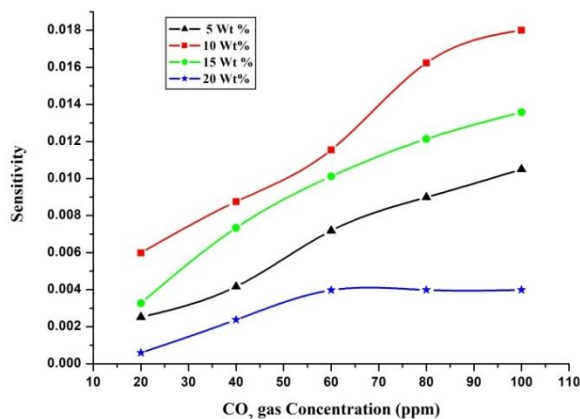


Fig.5 :- Plot showing CO₂ gas concentration (ppm) vs Sensitivity

The plot (fig.5) shows that PEDOT:PSS+10% RGO composite shows effective (max.) sensing toward CO₂ gas whereas PEDOT:PSS+20 % RGO composite is less efficient to sense the gas.

The response time and recovery time were defined as the times to reach 90 % of the final equilibrium value. The response time and recovery time are reported in the following table 3.

Table 3 :- The Response time and Recovery time of gas sensor at 100 ppm

Sr.No.	RGO wt % in Composite Sample	Response Time (s)	Recovery Time (s)
1.	5	126	135
2.	10	130	172
3.	15	120	144
4.	20	40	18

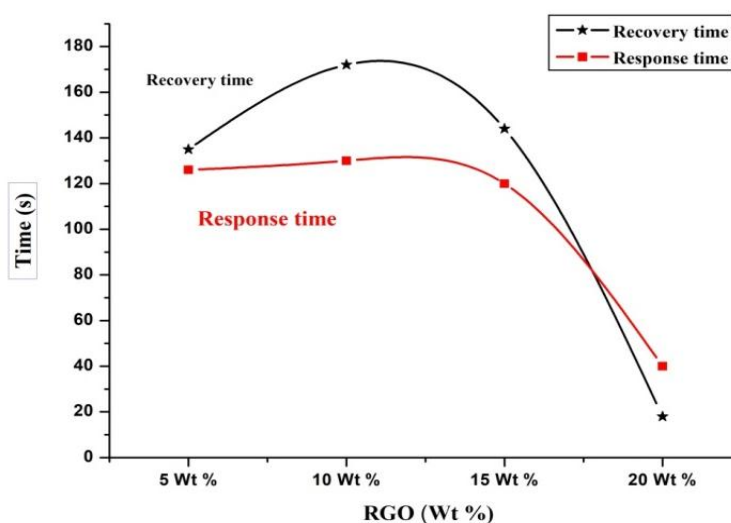


Fig. 6: Plot of Response time and recovery time against RGO (Wt. %) in composite

From the data and above corresponding plot (fig. 6) it can be inferred that, though PEDOT:PSS+20%RGO has less sensitivity toward CO₂ gas but it has rapid response and recovery time than other composites ; which is characteristic property of good gas sensor. Whereas , PEDOT:PSS+10% RGO composite sensor having highest sensitivity have a slow response and recovery time than others.

Table 4:- Gas Sensitivity at 100 ppm of gas sensors

Sr.No.	RGO wt % in Composite Sample	Sensitivity at 100 ppm	In %
1.	5	0.0174	1.74
2.	10	0.0205	2.05
3.	15	0.0148	1.48
4.	20	0.00406	0.41

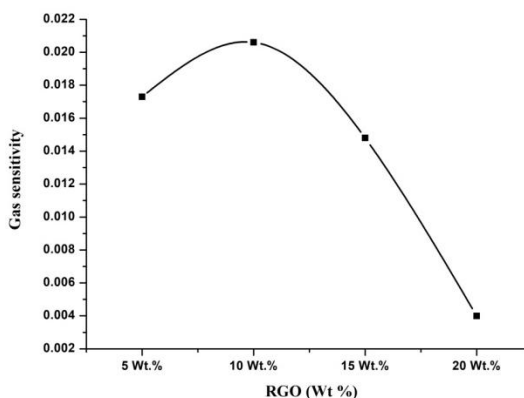


Fig.7:- Plot showing RGO (Wt.%) and sensitivity at 100 ppm

Fig. 7 shows that PEDOT:PSS+10% RGO composite has highest sensitivity than other composites. It can be also analyzed that the sensitivity of sensor is decreasing with increased proportion of RGO in composite. From fig. 8, it is found that composite having more crystallite size have higher sensitivity and that having less crystallite size has less sensitivity. Sensitivity is decreasing with decreased crystallite size. The reason is that it provides more surface area to volume ratio.

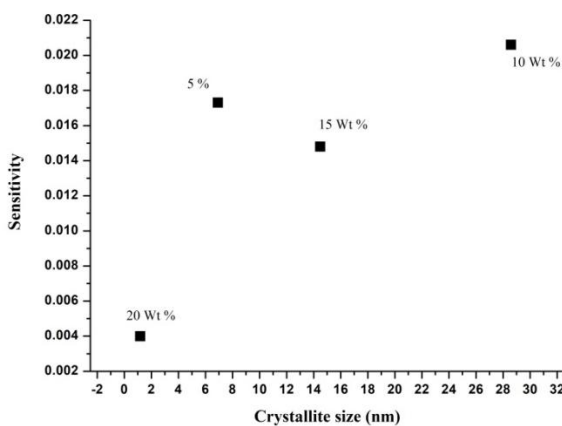


Fig.8 : Variation of sensitivity with Crystallite size in a sample

Thus , the response of PEDOT:PSS/RGO composites from 5% to 20 % (RGO) to CO₂ gas at 100 ppm was evaluated at room temperature (38 °C). It is observed that the sensitivity of PEDOT:PSS+10 %RGO composite is high having maximum response and recovery time. Whereas, PEDOT:PSS+20 %RGO have low sensitivity and quick response and recovery time than other sensors/composite. Also by comparing crystallite size and sensitivity it is found that , sensitivity is decreasing with decrease in crystallite size . The composite having less crystallite size also found to be giving quick response as well as recovery which is property of good gas sensor. Increased proportion of RGO in composite causing quick response and recovery but the sensitivity is found to be low as compared to composite having less RGO amount.

D. Gas Sensing Mechanism

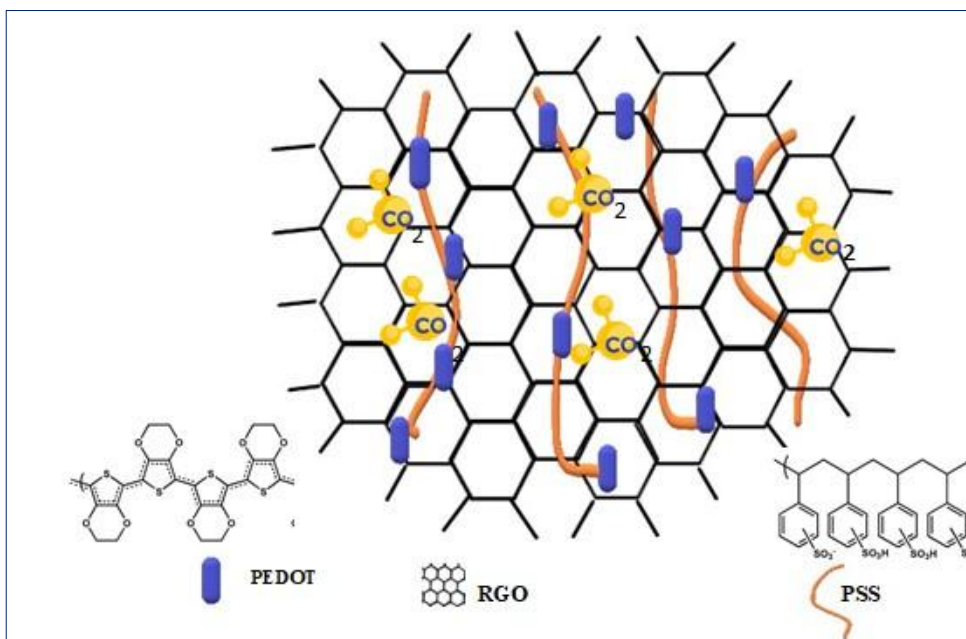


Fig. 9 Schematic illustration of the preparation of PEDOT:PSS/RGO composite and its interaction with CO₂ gas.

CO₂ molecules are adsorbed onto the surface of the composite material. The RGO component, with its large surface area and functional groups, plays a significant role in adsorbing CO₂ molecules. The interaction between CO₂ molecules and the composite material can be physical or chemical. The presence of oxygen-containing groups on RGO can enhance the chemical interaction with CO₂. When CO₂ molecules are adsorbed onto the surface of composite, they interact with the electron cloud of the conducting polymer and RGO. This interaction can lead to a change in the charge distribution within the composite. CO₂ is an electron acceptor and can withdraw electrons from the composite material. This results in a change in the electrical conductivity of the PEDOT:PSS/RGO composite.[21] The adsorption of CO₂ causes a reduction in the number of charge carriers (electrons) in the composite, leading to an increase in resistance or a decrease in conductivity. The degree of change in electrical conductivity is proportional to the concentration of CO₂ in the environment. Similar type of schematic (fig. 9) is reported by Miao Zhang [22].

IV. CONCLUSION

PEDOT:PSS and its composites with Reduced Graphene Oxide are synthesized and characterized to produce thin films by screen printing technique for CO₂ gas sensing application. The 'static response' method is used for gas sensing, taken at 100 ppm CO₂ gas concentration at room temperature (312 K). XRD and FTIR characterizations are used to identify the structure, nature, molecular bondings and presence of functional groups in pure PEDOT:PSS/RGO(5-20 wt.%). From XRD characterization it is concluded that PEDOT:PSS has amorphous or semi-crystalline nature. The crystallinity increases with increase in RGO concentration. In FTIR analysis, it is concluded that there are C-O bond, C=C bond, =C-H, C-O-C and C-S bond in pure PEDOT:PSS. From gas sensing analysis it is concluded that the PEDOT:PSS/RGO composite shows good response to CO₂ gas. PEDOT:PSS+10% RGO composite shows effective (max.) sensing toward CO₂ gas but has longer response and recovery time. Whereas PEDOT:PSS+20% RGO composite is less efficient to sense the gas but has quick response and recovery time. Also, the sensitivity of sensor is found to be decreasing with increased proportion of RGO in composite. If crystallite size and sensitivity of four composites are correlated, it is observed that composite having more crystallite size have higher sensitivity and that having less crystallite size have less sensitivity. Sensitivity is decreasing with decreased crystallite size.

Thus, the PEDOT:PSS/RGO composite holds good potential for applications in CO₂ gas sensing at room temperature.

ACKNOWLEDGMENT

The authors would like to thanks Head, Department of Physics and Electronics, Government Vidarbha Institute of Science and Humanities, Amravati for his guidance and support during this study. Authors also acknowledges Director, Government Vidarbha Institute of Science and Humanities, Amravati for providing necessary facilities to complete this study.

REFERENCES

- [1] E. Ruckenstein, J.S. Park, New method for the preparation of thick conducting polymer composites, *J. Appl. Poly. Sci*, vol 42, pp 925–934, 1991.
- [2] L. V. Kayser and D. J. Lipomi, *Stretchable Electronics, Stretchable Conductive Polymers and Composites based on PEDOT and PEDOT:PSS*, vol 10, 2019.
- [3] N. Sharma, V. Sharma, Y. Jain, M. Kumari, R. Gupta, S. K. Sharma, and K. Sachdev, *Macromolecular Symposia, Synthesis and Characterization of Graphene Oxide (GO) and Reduced Graphene Oxide (RGO) for Gas Sensing Application*, vol 376, 2017.
- [4] M. Czerniak-Reczulska, A. Niedzielska and A. Jędrzejczak, *Advances in materials science, Graphene as a material for solar cells applications*, vol.15, pp 46, 2015.
- [5] S. Pang , Y. Hernandez , X. Feng , and K. Müllen , *Advanced materials, Graphene as Transparent Electrode Material for Organic Electronics*, vol 23, pp 2779–2795, 2011.
- [6] Y. Seekaew, S. Lokavee, D. Phokharatkul, A. Wisitsoraat, T. Kerdcharoen & C. Wongchoosuk, *Low-cost and flexible printed graphene–PEDOT:PSS gas sensor for ammonia detection*, *Organic Electronics*, vol 15, pp 2971–2981, 2014.
- [7] S. M. Majhi , A. Mirzaei, H. W. Kim and S. S. Kim , *Reduced Graphene Oxide (RGO)-Loaded Metal-Oxide Nanofiber Gas Sensors: An Overview*, *Sensors*, vol 21, pp 1352, 2021.
- [8] M. Hakimi, A. Salehi, F.A. Boroumand, *Fabrication and characterization of an ammonia gas sensor based on PEDOT-PSS with N-doped graphene quantum dots dopant*, *IEEE Sens. J.* vol 16, pp 6149–6154, 2016.
- [9] P. W. Sayyad, S. S. Khan, N. N. Ingle, G. A. Bodkhe, T. Al-Gahouari, M. M. Mahadik, S. M. Shirsat & M. D. Shirsat, *Chemiresistive SO₂ sensor: graphene oxide (GO) anchored poly(3,4-ethylenedioxythiophene):poly(4styrenesulfonate) (PEDOT:PSS)*, *Applied Physics A*, 126:857, 2020.
- [10] Z. Y. Lee, H. F. B. Hawari ,G. W. B. Djaswadi and K. Kamarudin, *A Highly Sensitive Room Temperature CO₂ Gas Sensor Based on SnO₂- RGO Hybrid Composite*, *Materials* , vol 14, pp 522, 2021.
- [11] Y. Zheng , D. Lee, H. Young Koo and S. Maeng, *Carbon 8I, Chemically modified graphene/PEDOT:PSS nanocomposite films for hydrogen gas sensing*, pp 54 –62, 2015.
- [12] X. Feng, X. Wang, M. Wang, S. Zhou, C. Dang, C. Zhang, Y. Chen, & H. Qi, *Novel PEDOT dispersion by in-situ polymerization based on sulfated nanocellulose*, *Chemical Engineering Journal*, vol 418, 2021.
- [13] N. Yadav, B. Lochab, *A Comparative Study of Graphene Oxide: Hummers, Intermediate and Improved method*, *FlatChem*, 2019.
- [14] Ji Chen, B. Yao, Chun Li & G. Shi, *An improved Hummers method for eco-friendly synthesis of graphene oxide*, *ScienceDirect, carbon*, vol 64, pp 225 – 229, 2013.
- [15] K. Kanishka H. De Silva, H. Huang & M. Yoshimura, *Progress of reduction of graphene oxide by ascorbic acid*, *Applied Surface Science*, vol 447, pp 338–346, 2018.
- [16] S.A. Waghuley , S.M. Yenorkar, S.S. Yawale and S.P. Yawale, *Sensors and Actuators B chemical, Application of chemically synthesized conducting polymer-polypyrrole as a carbon dioxide gas sensor*, vol 128, pp 366–373, 2008.
- [17] Sura.K. Jebur , Auda J. Braihi and Ali S. Hassan, *Materials Today: Proceedings, Graphene effects on the structural, morphological and optical properties of PEDOT:PSS thin films*, vol 49, pp 2733–2740, 2022.
- [18] A. B. D. Nandiyanto, R. Oktiani and R. Ragadhita, *How to Read and Interpret FTIR Spectroscopy of Organic Material*, *Indonesian Journal of Science & Technology*, vol 4 (1), pp 97–118, 2019.
- [19] P. C. Mahakul, K. Sa, B. Das, B. V. R. S. Subramaniam, S. Saha , B. Moharana, J. Raiguru, S. Dash, J. Mukherjee, and P. Mahanandia, *Journal of Materials Science, Preparation and characterization of PEDOT:PSS/ reduced graphene oxide–carbon nanotubes hybrid composites for transparent electrode applications*, vol 52, pp 5696–5707, 2017.
- [20] P. Awandkar & S. P. Yawale, *Polymer-Plastics Technology and Materials, Sensing analysis of polyaniline – stannous chloride pentahydrate composite of CO₂ gas sensors*, vol 63, pp 605-612, 2024.
- [21] P. Shankar & J. B. B. Rayappan, *Gas sensing mechanism of metal oxides: The role of ambient atmosphere, type of semiconductor and gases - A review*, *Science Letters Journal*, vol 4: 126, 2015.
- [22] M. Zhang, W. Yuan, B. Yao, C. Li, and G. Shi, *Solution-Processed PEDOT:PSS-Graphene Composites as Electrocatalyst for Oxygen Reduction Reaction*, *ACS Appl. Mater. Interfaces*, 2024.

© 2024. This work is published under [https://creativecommons.org/licenses/by/4.0/legalcode\(the“License”\)](https://creativecommons.org/licenses/by/4.0/legalcode(the“License”)). Notwithstanding the ProQuest Terms and Conditions, you may use this content in accordance with the terms of the License.

Suraj V. Tayade^{1*},
A. P. Bangar²,
S. A. Waghuley³

Regular paper
**"Evaluating Polyaniline-CuO
Composite for Next-Generation
Electromagnetic Interference
Shielding"**



Abstract: - The rapid advancement of wireless technology has introduced a new form of pollution known as Electromagnetic Interference (EMI), which adversely affects electronic devices and poses potential risks to human health. Copper is traditionally employed for EMI shielding due to its superior electrical conductivity, malleability, and durability. Recently, polyaniline (PANI), an intrinsically conductive polymer, has gained attention for EMI shielding applications owing to its notable properties such as electrical conductivity, lightweight nature, corrosion resistance, and flexibility. This study focuses on the synthesis of polyaniline-based copper oxide (CuO) composites with varying CuO weight percentages, incremented by 5%. The structural, optical properties and interfacial interaction of these composites were characterized using X-ray diffraction (XRD), ultraviolet-visible (UV-Vis) spectroscopy and Fourier Transform Infrared (FTIR) spectroscopy. The findings suggest that PANI/CuO composites hold promise for effective Electromagnetic Interference EMI shielding applications.

Keywords: Polyaniline; Copper Oxide; Electromagnetic Interference Shielding.

Introduction:

In recent years, the rapid use of telecommunication and electronic devices such as cell phones, computers, radio, microwaves, radar system, laptops, and arrival of 5G era, wireless electromagnetic wave technology so on have produced the unique form of electronic pollution in the environment [3]. Increasing the market of Wi-Fi portable devices and the rapid expansion of information technology have congested the space of electromagnetic waves, due to which it causes the chaos in multiple communication channels. Packed electronic equipment having high integrated circuitry also emits the electromagnetic radiation which are very harmful which interfere with the operation of surrounding gadgets causing them to fail [6]. Electromagnetic interference is an electromagnetic pollution caused by electromagnetic noise originated either from natural source (lighting, solar flares, etc.) or man-made devices (electrical circuit, electronic devices ,etc.) over a frequency range (depends on the source) that affects or degrades the performance of another electronic device/electrical circuit and loss of stored data. These disturbances may be caused by electromagnetic coupling, electromagnetic induction or conduction[2]. Therefore, it is very necessary to explore effective methods and control for electromagnetic pollution. The best way is to create the shield termed as electromagnetic shielding. Which uses electromagnetic shielding materials to block electromagnetic wave, by means of physical phenomenon like reflection, absorption, multiple internal reflection, transmission in space, which has caused extensive research by many researchers [1].

Electromagnetic radiation: Electromagnetic radiation (EMR) consists of waves of the electromagnetic (EM) field, which propagate through space and carry momentum and electromagnetic radiant energy. It includes radio waves, microwaves, infrared, (visible) light, ultraviolet, X-rays, and gamma rays. All of these waves are the part of the electromagnetic spectrum which is discussed ahead. Basically Electromagnetic radiation consists of electromagnetic waves, which are synchronized oscillations of electric and magnetic fields. Depending on the frequency of oscillation, different wavelengths of electromagnetic spectrum are produced. Electromagnetic wave (EMW) is described in terms of wavelength (λ), frequency (ν) and speed (v). In vacuum (or free space), it propagates in a straight line with the speed of light i.e (c). In the material medium, its speed varies with the density of the medium. However, the frequency of electromagnetic wave (EMW) remains unchanged in the material medium.

EM Spectrum: The electromagnetic spectrum is the range of frequencies (the spectrum) of electromagnetic radiation and their respective wavelengths and photon energies. The electromagnetic spectrum covers electromagnetic waves with frequencies ranging from below one hertz to above 10^{25} hertz, corresponding to wavelengths from thousands of kilometres down to a fraction of the size of an atomic nucleus. This frequency range is divided into separate bands, and the electromagnetic waves within each frequency band are called by different names; beginning at the low frequency (long wavelength) end of the spectrum these are: radio waves, microwaves, infrared, visible light, ultraviolet, X-rays, and gamma rays at the high-frequency (short wavelength) end. The electromagnetic waves in each of these bands have different characteristics, such as how they are produced, how they interact with matter, and their practical applications.

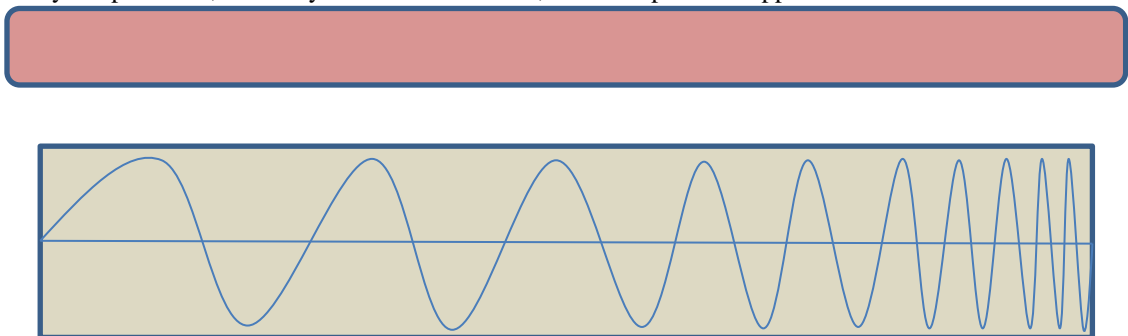


Figure (a): Graphical representation of the EM spectrum

In fig(a) shows that Extreme ultraviolet, soft X-rays, hard X-rays and gamma rays are classified as ionising radiation because their photons have enough energy to ionise atoms, causing chemical reactions. As per the study the Exposure to ionizing radiation can be a health hazard, causing radiation sickness, DNA damage and cancer. Radiation of visible light and longer wavelengths are classified as non ionizing radiation because they have insufficient energy to cause these effects. Different factors like exposure time to EMR, the frequency and the intensity of the EMR decide their negative impact on human health. For example, ionising radiation breaks the bond of biological cells instantly whereas long-term exposure of non-ionising radiation produces a heating effect on the human body due to the use of mobile phone for 15 minutes.

Electromagnetic interference: Electromagnetic interference is an electromagnetic pollution caused by electromagnetic noise originated either from natural source (lighting, solar flares, etc.) or man-made devices (electrical circuit, electronic devices, etc.) over a frequency range (depends on the source) that affects or degrades the performance of another electronic device/electrical circuit and loss of stored data. The disturbance may be caused by electromagnetic coupling, electromagnetic induction or conduction [2].

Electromagnetic coupling is when the electromagnetic field in one circuit induces charge or voltage in others. **Electromagnetic Induction:** it is a current produced because of voltage production (electromotive force) due to a changing magnetic field. This either happens when a conductor is placed in a moving magnetic field (when using an AC power source) or when a conductor is constantly moving in a stationary magnetic field. **Electromagnetic Conduction:** The process where a conductor placed in a changing magnetic field (AC) causes the generation of a voltage across the conductor. Therefore, there is an urgent need for high-efficiency Electromagnetic Interference (EMI) shielding materials to attenuate electromagnetic waves to protect the normal operation of electronic equipment and human health [16].

Electromagnetic interference Shielding: The phenomenon involving reflection and/or absorption of electromagnetic (EM) waves by a specifically designed material is called Electromagnetic interference (EMI) shielding [7]. An electromagnetic interference (EMI) shielding material is a material that attenuates radiated electromagnetic energy. EM radiation can be divided into two subclasses; one is near field and another one is far field regions. In near field, the EM signal can be predominately an electric or magnetic vector depending upon the nature of the incident radiation. In case of far field, plane waves exist in which the electric and magnetic vectors lie in an equal ratio and they are in phase and orthogonal to each other [14]. EMI shielding in electronic devices and equipment is the use of manufacturing techniques and material to protect signals from being disrupted by external electromagnetic signals as well as preventing generated signals from interfering with surrounding components. When em radiation falls on the material there are three physical phenomenon's can happen and those are as follows shown in fig(b)

Reflection, Absorption, Transmission and Multiple internal reflections. These Physical phenomenon's give us a shielding of em radiation.

These Physical phenomenon's shown in the fig(b) given.

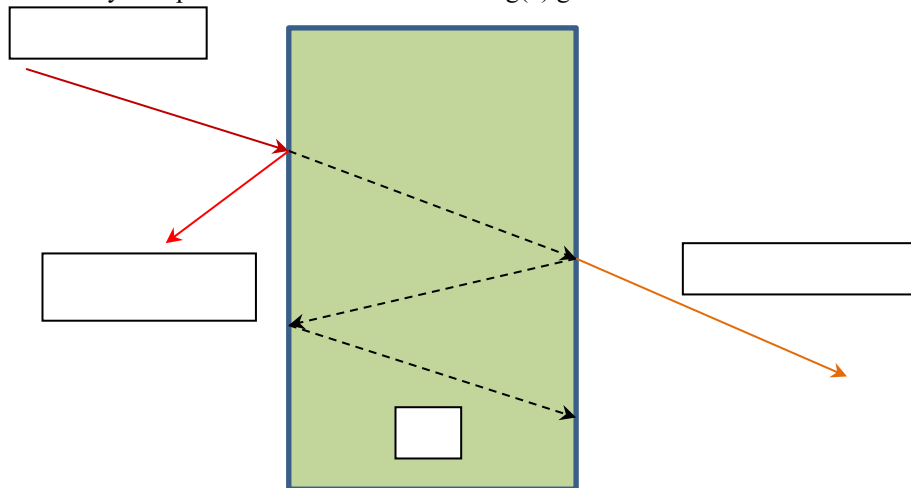


Fig (b) Schematic diagram of the mechanism of EMI shielding

The EM radiation blocking efficiency of a shield is measured in terms of a logarithmic quantity called shielding effectiveness that can be expressed as in (1): [14]

$$\text{Emi SE(dB)} = 10 \log_{10}(P_t/P_i) = 20 \log_{10}(E_t/E_i) = 20 \log_{10}(H_t/H_i) \quad (1)$$

EMI shielding efficiency presents the material ability to block waves in terms of percentage. For commercial application, EMI SE of 20 dB is required, which corresponds to 99% blockage of incident radiation. EMI shielding effectiveness [dB] is converted into EMI shielding efficiency [%] by (2) : [23]

$$\text{Shielding efficiency (\%)} = 100 - (1/10^{SE/10}) \times 100 \quad (2)$$

Nowadays, the Schelkunoff formula based on transmission line model is widely used to calculate the shielding effectiveness of uniform shielding materials.

The specific form of shielding effectiveness is given by eq (3):

$$\text{SE(dB)} = \text{SE}_A \text{ (dB)} + \text{SE}_R \text{ (dB)} + \text{SE}_M \text{ (dB)} \quad (3)$$

Where SE_A is a shielding effectiveness due to the absorption

SE_R is a shielding effectiveness due to reflection

SE_M is a shielding effectiveness due to multiple reflections

Shielding efficiency due to reflection is given by following (4)

$$\text{SE}_R \text{ (dB)} = 39.5 + 10 \log(\sigma/2\pi f\mu) \quad (4)$$

Where σ is a conductivity of material, μ is a permeability of material

Hence shielding effectiveness due to reflection can be enhanced by increasing a conductivity of material or by decreasing the permeability of material.

Shielding efficiency due to absorption expressed by (5)

$$\text{SE}_A \text{ (dB)} = 8.7d \sqrt{(\pi f \mu \sigma)} \quad (5)$$

Where d is thickness of material

Shielding efficiency due to multiple internal reflections is given by following equation

$$\text{SE}_M \text{ (dB)} = 20 \log(1 - e^{-2d/\delta}) \quad (6)$$

Where δ is the skin depth, defined as the thickness below the outer surface at which the incident field is attenuated to $1/e$ of its initial value, given by [18]

$$\delta = \sqrt{(\pi f \mu \sigma)} \quad (7)$$

Materials synthesis:

Synthesis of Polyaniline: Monomer Aniline of 10 ml was taken and dissolved in 150 ml HCl solution in a beaker. This solution is kept on the magnetic stirrer. Then another solution was made of 10 gm of ammonium persulfate which was dissolved in 50 ml Double distilled water and this solution is added to aniline solution drop wise. For the proper mixing of chemicals in the solution, ammonium persulfate is added in drop wise. After 5 hours of stirring process, diamond green solution was formed. The whole reaction system was kept still at temperature of 25°C to 30°C. Then the stirred solution was filtered, and the obtained product was washed by double distilled water. The resulting polyaniline was dried in a vacuum oven at 40°C, yielding Polyaniline powder.

Synthesis of CuO nanoparticle: CuO nanoparticles were made using the co-precipitation approach, which involved dissolving one mole of CuSO_4 in 100 milliliters of distilled water. and then placing the necessary solution in a magnetic stirrer and stirring it for two hours. Copper sulphate and sodium hydroxide were utilized in this process. The reaction continued for two hours after the NaOH was simultaneously dissolved in 50 milliliters of distilled water and introduced drop wise to the CuSO_4 solution that was already on the magnetic stirrer while being continuously stirred. After that, rinse the precipitation with distilled water. The precipitate now dries overnight at 800 degrees Celsius.

Synthesis of Polyaniline- CuO Nanocomposite : The composites between CuO and PANI was prepared by ex situ approach. The different composites were prepared by altering the wt% of CuO in PANI, with an interval 5 wt% as 5wt%(S1), 10wt%(S2), 15wt%(S3), 20wt%(S4) and 25wt%(S5). Both these chemicals were mixed in the presence of organic media that is acetone.

Results and discussion:

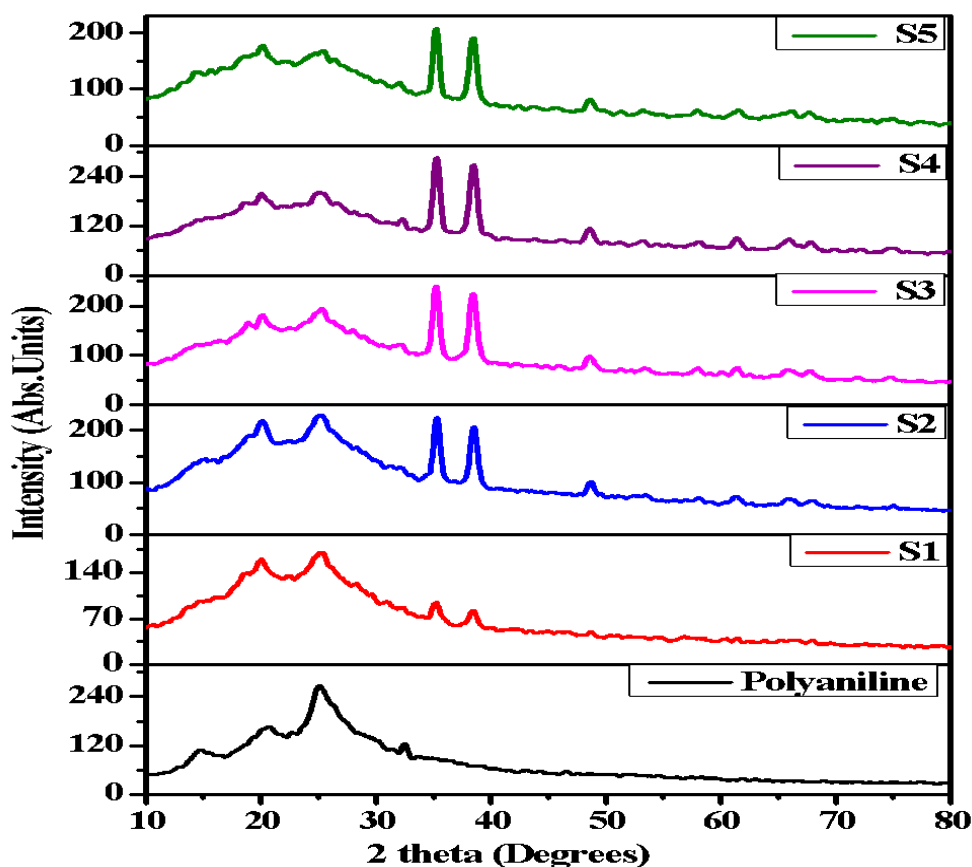


Fig.(c) XRD patterns of PANI, different samples of wt% of CuO loaded PANI matrix

The X-ray diffraction (XRD) patterns of the as-prepared composites were recorded using an X-ray diffractometer. Figure (c) illustrates the XRD patterns of pure polyaniline (PANI), various samples of copper oxide (CuO) incorporated into the PANI matrix. The characteristic peaks of CuO at 36° and 38° confirm its structural purity, with no impurity peaks detected. The XRD pattern of PANI displays its amorphous nature, represented by a broad hump in the 2θ range of 20° – 30° . Sharp peaks appear on the broad hump of PANI, indicating an improvement in the degree of crystallinity. This enhancement in crystallinity, which contributes to a rougher surface, is expressed in terms of the degree of crystallinity, quantifying the extent of material crystallinity. The main change observed in the XRD pattern of the CuO-loaded PANI matrix is the variation in peak width with different CuO concentrations. A detailed examination of the XRD patterns of all five composites shows that the successful incorporation of CuO into the PANI matrix.

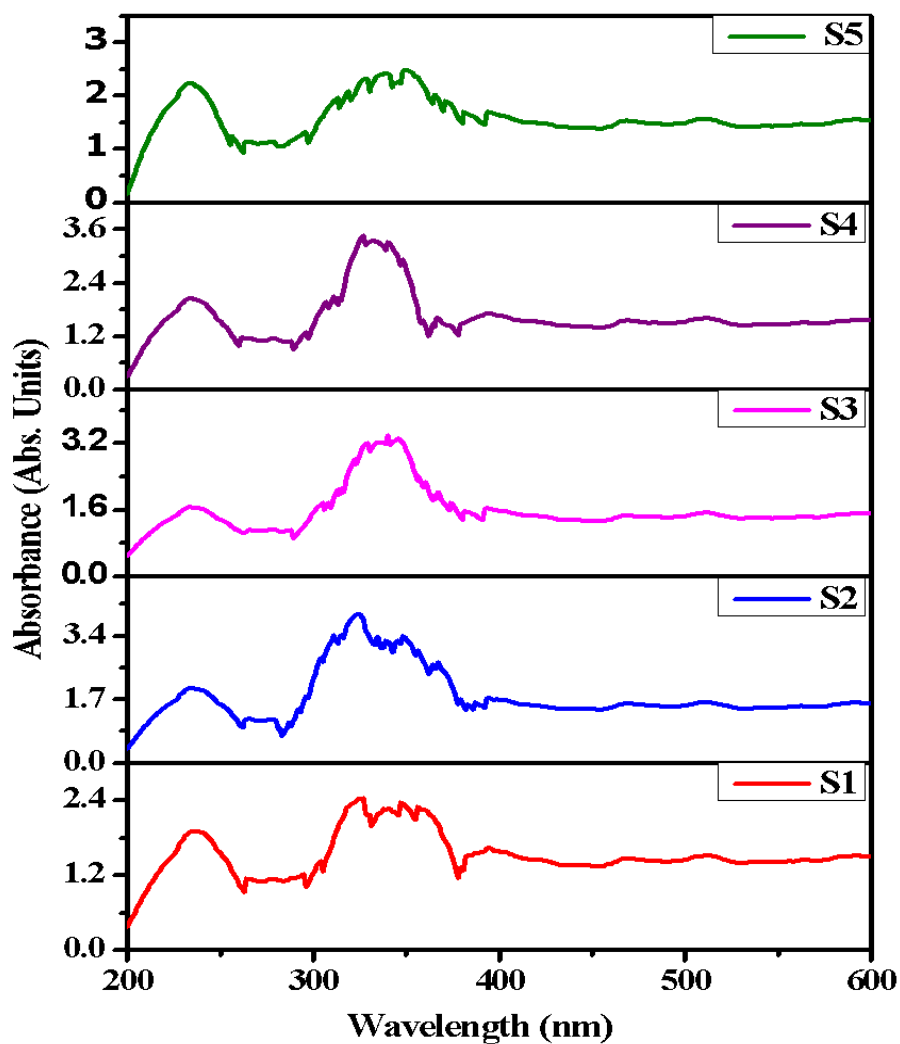


Fig.(d) UV–VIS spectrum of different wt% of CuO loaded PANI

Figure (d) shows that UV–VIS spectrum of different wt% of CuO from 5 to 25 wt% by interval of 5 wt% loaded PANi matrix recorded in the range 200–600 nm. It is observed that absorption coefficient magnitude nearly linear in the range 400–600 nm. The absorption curve of samples shows broad peaks in the range 200–225 nm, which attributed to p–p* transition in polymeric materials [25]. With the standard result it is confirms that peaks of PANi and CuO shifts minutely to lower energy [24]

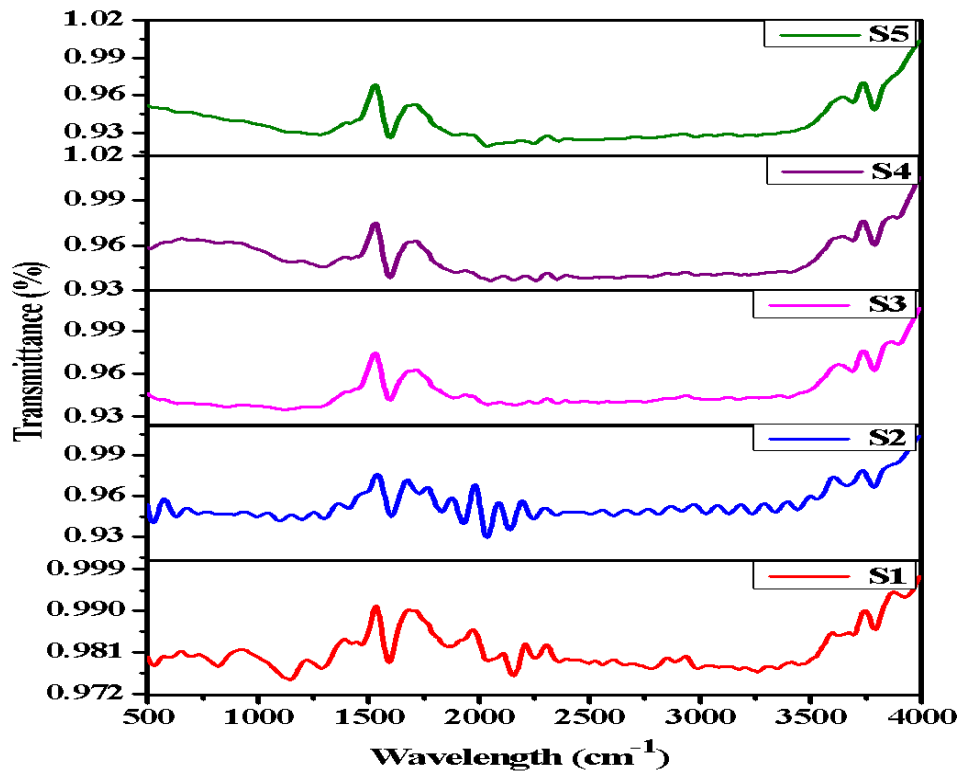


Fig.(e) FTIR spectrum of different wt% of CuO loaded PANI

In general, FTIR spectroscopy is a versatile analytical technique used to identify functional groups within molecules and confirm the purity of compounds while detecting impurities. The FTIR spectrum for PANI-CuO Composites reveals various peaks across the wave number region of 4000 to 400 cm^{-1} . Notable peaks observed in the nanocomposite include those at 541, 1293, 1593, 2028, 2980, 3588, 3695, and 3775 cm^{-1} . Additionally, the spectrum exhibits a broad absorbance peak at 3775 cm^{-1} , which is attributed to the O-H stretching mode, indicating the presence of hydroxyl groups. Moreover, distinct peaks are observed for C-H stretching at 2980 cm^{-1} , and C-O stretching at 1293 cm^{-1} and 1593 cm^{-1} , each displaying strong absorbance. These peaks provide further insight into the molecular composition and bonding within the PANI-CuO Composites.

Conclusions:

Metallic materials possess high conductivity due to the mobility of electrons, making them dominant in many applications. Conversely, polymers are valued for their lightweight, flexibility, and corrosion resistance. As a result, there's a growing demand for polymer-based EMI shielding composites with excellent shielding properties. The synthesis of PANi-CuO nanocomposites has been successful, with structural studies (XRD) indicating that CuO nanoparticles are uniformly dispersed within the PANi matrix. UV-Vis spectra demonstrate enhanced absorption efficiency in PANi-CuO composites, suggesting improved performance of the material. Furthermore, FTIR spectra reveal significant shifts in characteristic absorption peaks, indicating distinct interfacial interactions between CuO nanoparticles and the PANi matrix. These findings underscore the potential of PANi-CuO nanocomposites for EMI shielding applications, offering a combination of electrical conductivity from metals and mechanical properties from polymers.

References:

- [1]. Chen, Y., Li, J., Li, T., Zhang, L., & Meng, F. (2021). Recent advances in graphene-based films for electromagnetic interference shielding: Review and future prospects. *Carbon*, *180*, 163-184.
- [2]. Jiang, D., Murugadoss, V., Wang, Y., Lin, J., Ding, T., Wang, Z., ... & Guo, Z. (2019). Electromagnetic interference shielding polymers and nanocomposites-a review. *Polymer Reviews*, *59*(2), 280-337.
- [3]. Nazir, A. (2022). A review of polyvinylidene fluoride (PVDF), polyurethane (PU), and polyaniline (PANI) composites-based materials for electromagnetic interference shielding. *Journal of Thermoplastic Composite Materials*, *35*(10), 1790-1810.
- [4]. Cheng, J., Li, C., Xiong, Y., Zhang, H., Raza, H., Ullah, S., ... & Che, R. (2022). Recent advances in design strategies and multifunctionality of flexible electromagnetic interference shielding materials. *Nano-Micro Letters*, *14*(1), 80.
- [5]. Omana, L., Chandran, A., John, R. E., Wilson, R., George, K. C., Unnikrishnan, N. V., ... & Paul, I. (2022). Recent Advances in Polymer Nanocomposites for Electromagnetic Interference Shielding: A Review. *ACS omega*, *7*(30), 25921-25947.
- [6]. Kumar, P., Narayan Maiti, U., Sikdar, A., Kumar Das, T., Kumar, A., & Sudarsan, V. (2019). Recent advances in polymer and polymer composites for electromagnetic interference shielding: review and future prospects. *Polymer Reviews*, *59*(4), 687-738.
- [7]. Kumar, K. S., Rengaraj, R., Venkatakrishnan, G. R., & Chandramohan, A. (2021). Polymeric materials for electromagnetic shielding-A review. *Materials Today: Proceedings*, *47*, 4925-4928.
- [8]. Zhang, H. Y., Li, J. Y., Pan, Y., Liu, Y. F., Mahmood, N., & Jian, X. (2022). Flexible carbon fiber-based composites for electromagnetic interference shielding. *Rare Metals*, *41*(11), 3612-3629.
- [9]. Guo, H., Chen, Y., Li, Y., Zhou, W., Xu, W., Pang, L., ... & Jiang, S. (2021). Electrospun fibrous materials and their applications for electromagnetic interference shielding: A review. *Composites Part A: Applied Science and Manufacturing*, *143*, 106309.
- [10]. Shahapurkar, K., Gelaw, M., Tirth, V., Soudagar, M. E. M., Shahapurkar, P., Mujtaba, M. A., ... & Ahmed, G. M. S. (2022). Comprehensive review on polymer composites as electromagnetic interference shielding materials. *Polymers and Polymer Composites*, *30*, 09673911221102127.
- [11]. Wanasinghe, D., & Aslani, F. (2019). A review on recent advancement of electromagnetic interference shielding novel metallic materials and processes. *Composites Part B: Engineering*, *176*, 107207.
- [12]. Chung, D. D. L. (2020). Materials for electromagnetic interference shielding. *Materials Chemistry and Physics*, *255*, 123587.
- [13]. Dhakate, S. R., Subhedar, K. M., & Singh, B. P. (2015). Polymer nanocomposite foam filled with carbon nanomaterials as an efficient electromagnetic interference shielding material. *Rsc Advances*, *5*(54), 43036-43057.
- [14]. Ganguly, S., Bhawal, P., Ravindren, R., & Das, N. C. (2018). Polymer nanocomposites for electromagnetic interference shielding: a review. *Journal of Nanoscience and Nanotechnology*, *18*(11), 7641-7669.
- [15]. Safdar, F., Ashraf, M., Javid, A., & Iqbal, K. (2022). Polymeric textile-based electromagnetic interference shielding materials, their synthesis, mechanism and applications—A review. *Journal of Industrial Textiles*, *51*(5_suppl), 7293S-7358S.
- [16]. Liang, C., Gu, Z., Zhang, Y., Ma, Z., Qiu, H., & Gu, J. (2021). Structural design strategies of polymer matrix composites for electromagnetic interference shielding: a review. *Nano-Micro Letters*, *13*(1), 181.
- [17]. Liu, H., Wu, S., You, C., Tian, N., Li, Y., & Chopra, N. (2021). Recent progress in morphological engineering of carbon materials for electromagnetic interference shielding. *Carbon*, *172*, 569-596.
- [18]. Shukla, V. (2019). Review of electromagnetic interference shielding materials fabricated by iron ingredients. *Nanoscale Advances*, *1*(5), 1640-1671.
- [19]. Wang, X. Y., Liao, S. Y., Wan, Y. J., Zhu, P. L., Hu, Y. G., Zhao, T., ... & Wong, C. P. (2022). Electromagnetic interference shielding materials: recent progress, structure design, and future perspective. *Journal of Materials Chemistry C*, *10*(1), 44-72.
- [20]. Wu, N., Hu, Q., Wei, R., Mai, X., Naik, N., Pan, D., ... & Shi, Z. (2021). Review on the electromagnetic interference shielding properties of carbon based materials and their novel composites: Recent progress, challenges and prospects. *Carbon*, *176*, 88-105.
- [21]. Yao, Y., Jin, S., Zou, H., Li, L., Ma, X., Lv, G., ... & Shu, Q. (2021). Polymer-based lightweight materials for electromagnetic interference shielding: A review. *Journal of Materials Science*, *56*, 6549-6580.

- [22]. Zahid, M., Anum, R., Siddique, S., Shakir, H. F., & Rehan, Z. A. (2021). Polyaniline-based nanocomposites for electromagnetic interference shielding applications: A review. *Journal of Thermoplastic Composite Materials*, 08927057211022408.
- [23]. Li, H., Lu, X., Yuan, D., Sun, J., Erden, F., Wang, F., & He, C. (2017). Lightweight flexible carbon nanotube/polyaniline films with outstanding EMI shielding properties. *Journal of Materials Chemistry C*, 5(34), 8694-8698.
- [24] Jundale, D. M., Navale, S. T., Khuspe, G. D., Dalavi, D. S., Patil, P. S., & Patil, V. B. (2013). Polyaniline–CuO hybrid nanocomposites: synthesis, structural, morphological, optical and electrical transport studies. *Journal of Materials Science: Materials in Electronics*, 24, 3526-3535.
- [25] A. Kaushik, J. Kumar, M.K. Tiwari, R. Khan, B.D. Malhotra, V. Gupta, S.P. Singh, J. Nanosci. Nanotechnol. 8, 1757 (2008)
- [26] Katore, M. S., Nemade, K. R., Yawale, S. S., & Yawale, S. P. (2016). Photovoltaic application of architecture ITO/graphene oxide–polyaniline/aluminum. *Journal of Materials Science: Materials in Electronics*, 27, 9828-9835.

¹Swapnil S. Kosalge
²Sushil D. Charpe
³Sandhya Bharambe
¹Pushpinder G. Bhatia

Study of Gas Sensing Properties Of Nanostructured Nickel Ferrite Thick Film Sensors In NH₃, H₂S, CO₂, And LPG Environments



Abstract: - The nickel ferrite was prepared using the sol-gel auto combustion glycine method, and the sensor element was prepared using the screen printing method and investigated for NH₃, LPG, CO₂, and H₂S gases. The sensor is found to be more sensitive to NH₃ gas as compared to LPG, CO₂, and H₂S gases. The structural, surface morphological and elemental analyses were done using X-ray diffraction and scanning electron microscopy attached to EDAX, respectively. The synthesized nickel ferrite exhibits a crystalline size of ~ 68.65 nm, and an x-ray density of ~ 4986 Kg/m³. The response and recovery time of sensor for H₂S was found to be ~ 81 seconds and ~ 108 seconds respectively. The mechanism of gas sensing of nickel ferrite film has been explained on the basis of oxygen adaption kinetics.

Keywords: Nickel Ferrite, NH₃ Gas Sensor, Screen Printing Method, Sol-Gel Auto Combustion Method.

I. INTRODUCTION

Gas sensors are an essential tool in detecting and monitoring the presence of harmful gases in the environment and in industrial settings [1]. They are available in various types, including those based on organic and inorganic and polymer materials [2]. Among these, semiconductor metal oxide gas sensors are favoured for their cost-effectiveness and simplicity [3]. Recently, researchers have focused on fabricating gas sensors based on spinel ferrite. Spinel ferrites, known for their magnetic, semi-conducting, gas adsorption, and catalytic properties. The primary advantage of spinel ferrite over conventional sensor materials based on single metal oxides is its capacity to control conductivity through modifications to stoichiometry, annealing temperatures, or cation composition [4, 5]. The use of nanostructured materials has been shown to significantly enhance the gas sensing properties of semiconductor sensors, particularly for spinel-ferrite-type gas sensors. This has led to a growing interest in the synthesis of nanostructured ferrites for gas sensing applications [6]. In this context, various methods for synthesizing nanostructured ferrites have been reported in the literature, co-precipitation, sol gel, hydrothermal micro-emulsion reverse micelle, etc. among these and sol gel auto-combustion methods has great potential in the preparation of spinel ferrite nanomaterials. Sol gel auto-combustion method offers mixing of metal precursors at the molecular level, precise control over stoichiometry, enhanced reactivity, and produce fine particle size and high surface area [7].

Gases and volatile organic compounds (VOCs) were examined in various spinel ferrites. The co-precipitation method was used to prepare the CdFe₂O₅ nanoparticles, which showed good sensitivity to LPG, methanol, and ethanol [8-10]. The hydrothermal method used to prepare NiFe₂O₄ has demonstrated good sensitivity to LPG, toluene, and acetone [11-13]. Sol-gel-prepared ZnFe₂O₄ has demonstrated good sensitivity to NH₃ and LPG. [14]. Sol-gel-prepared CuFe₂O₄ has demonstrated good sensitivity to LPG [15], H₂S [16], co-precipitation MgFe₂O₄ has demonstrated good sensitivity to LPG [17], CO₂ [18], and the solvothermal method used to prepare COFe₂O₄ has demonstrated high sensitivity to n-butanol [19].

^{1*} Corresponding author: Swapnil S. Kosalge ,Guru Nanank College of Arts, Science and Commerce, GTB Nagar Mumbai-400037 , India

²Department of Physics, J.D. Patil Sangludkar Mahavidyalaya, Daryapur, Dist. - Amravati, 444803, India

³Department of Physics, S.I.E.S Graduate school of technology Nerul -400706, India

Copyright © JES 2024 on-line : journal.esrgroups.org

¹ *Corresponding author: Author 1 Affiliation

² Author 2 Affiliation

Copyright © JES 2024 on-line : journal.esrgroups.org

Among the various spinel ferrites, nickel ferrite stands out as one of the most versatile due to its catalytic activity, magnetic properties, low conductivity, and high electrochemical stability. Its catalytic efficiency in oxidation reactions stems from its high oxygen ion mobility at the film surface, making it particularly appealing for the development of gas sensors [20]

In the paper, we synthesize NiFe₂O₄ and analyzed its gas sensing properties for NH₃, H₂S, LPG, and CO₂ gases.

II. MATERIAL AND EXPERIMENTAL

The nickel-ferrite nanoparticles were synthesized by the sol-gel auto combustion method. The synthetic procedure to prepare nickel ferrite is depicted in Fig.1. The starting material is nickel nitrate hexahydrate [Ni (NO₃)₂ · 6H₂O], Ferric Nitrate [Fe (NO₃)₃ · 9H₂O] and glycine (NH₂CH₂COOH) and Ammonia (NH₃) were purchased from Merck. The starting materials of metal nitrates and glycine are taken in the molar ratio of 1:2. All metal nitrates and glycine were dissolved in a stoichiometric amount of de-ionized water and stirred continuously using a magnetic stirrer attached to a hot plate. During constant stirring, NH₃ solution was added drop-wise to reach pH 7. The mixed nitrate solution was heated at 60°C with constant stirring for 6 hours. Then the solution was kept in the hot air oven at a temperature of 120°C for 12 hours. During the process, the mixed nitrate solution gets transformed into gel, and the gel gets completely dried in 12 hours and then heated to 200°C to initiate a self-sustaining auto combustion reaction. The dried sample was ground using a mortar and pestle and then annealed in a muffle furnace at 600°C for 2 hours and cooled slowly to room temperature.

The sensing element is composed of a 1 cm x 0.5 cm thick film prepared using the screen-printing method. The binder for printing thick films was created by mixing organic solvents such as butyl cellulose, butyl carbitol acetate, and turpineol [21]. To make the thixotropic paste, stannic oxide, ethyl cellulose (a temporary binder), and the organic binder were combined, maintaining a 75:25 ratio of inorganic to organic components. The ratio of nickel-ferrite to ethyl cellulose was set at 95:05. These thixotropic pastes were then screen printed in desired patterns on glass substrates that had been cleaned with acetone. The freshly prepared films were fired at 500°C for 30 minutes to remove the organic binders. Silver paste was applied for electrical measurements. The film thickness ranged from 30 to 40 μm. The electrical resistance of the film was measured using the two-probe method, followed by gas sensing properties being assessed with a computer-monitored static gas sensing system.

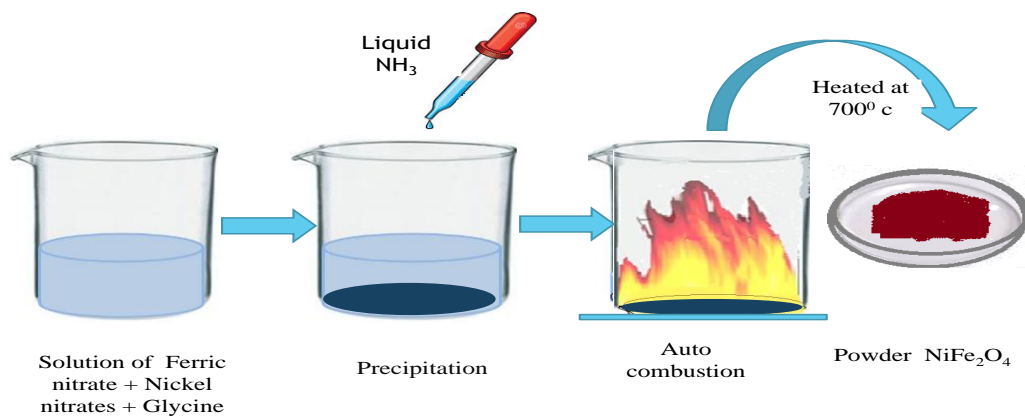


Figure 1: Synthesis Procedure of NiFe₂O₄

III. RESULTS AND DISCUSSION

Fig.2 shows the X-ray Diffractometer patterns of Nickel-Ferrite of sample. Spinel structure of annealed powders of the Nickel ferrite samples confirmed by the XRD patterns from JCPDS No. 22-1086 for NiFe₂O₄ has been presented in Fig.2 Eight obvious diffraction peaks corresponding to (220), (311), (222), (400), (422), (511), (440) and (533) planes shows the peak positions.

The average crystallite size is calculated from the most intense peak (311) using the Scherrer's formula [22]

$$D = k\lambda / \beta \cos\theta \dots\dots\dots (1)$$

D represents the average crystalline size, k is the Scherrer constant, λ is the X-ray wavelength and θ is the Bragg's angle in degrees unit, β is the angular bandwidth of half maximum intensity. The results are shown in Table 1. The lattice parameter value is found 8.3594Å.

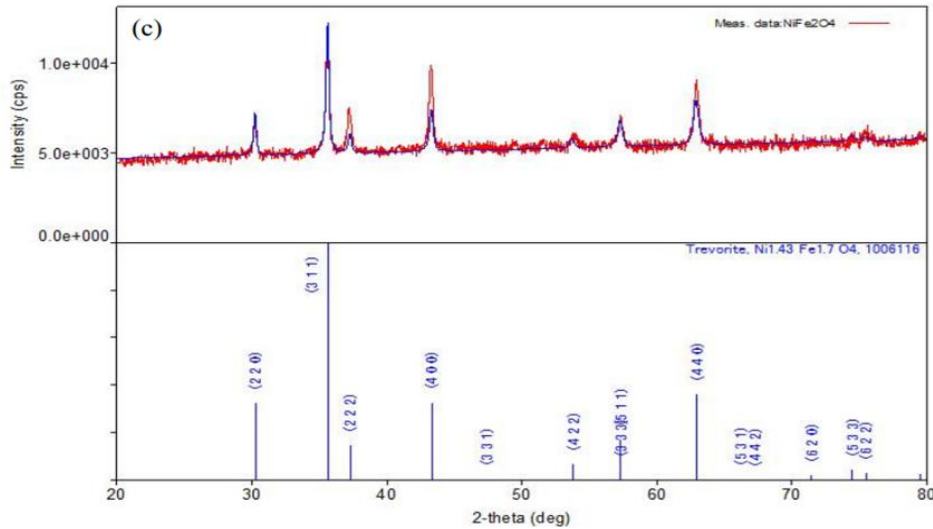


Figure 2: X-ray diffraction Patterns of NiFe₂O₄ Sample

The X-ray density (the theoretical density) ρ was calculated using the relation

$$\rho = \frac{8M}{N_A a^3} \dots\dots\dots (2)$$

where M is the molar mass of the ferrite, ‘a’ is the lattice parameter, and N_A is Avogadro's number [23]. From XRD patterns and Scherrer's formula, mean crystallite sizes of the samples is found to be around 68 nm and X-ray density is 4986 Kg/m³ by sol-gel auto combustion method.

The distances between the centers of adjacent ions (hoping length) in the tetrahedral A-sites (L_A) and octahedral B-sites (L_B) is given by the following relations [24].

$$L_A = \left(\frac{\sqrt{3}}{4}\right) a \dots\dots\dots (3)$$

$$L_B = \left(\frac{\sqrt{2}}{4}\right) a \dots\dots\dots (4)$$

Table 1. XRD Analysis of NiFe₂O₄ Sample

Sample	Inter-planar spacing (d) Å	Lattice parameter (a) Å	Crystallite size (D)Å	Density (ρ) Kg/m ³	L _A (Å)	L _B (Å)
NiFe ₂ O ₄	2.5204	8.3594	6.8659	5466	3.6197	2.9554

The SEM image (Fig.3) reveal grains with irregular shapes and varying sizes, along with noticeable agglomeration. Elemental analysis clearly shows that the mixing of Ni, Fe, and O atoms is homogeneous, as no impurity peaks are observed in the EDX spectrum, indicating the sample's purity. The compositional stoichiometry of the nickel ferrites observed in the EDX spectra (Fig.3) aligns well with the stoichiometric calculations.

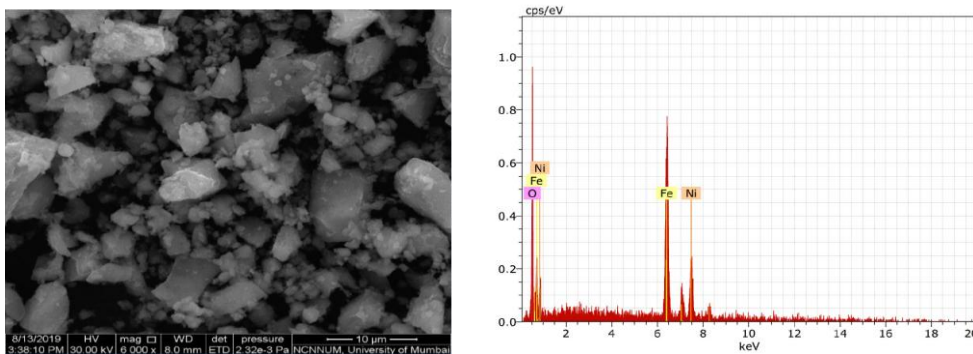


Figure 3: SEM and EDX image of NiFe₂O₄

To investigate the gas sensing properties of nickel ferrite for NH₃, LPG, CO₂, and H₂S, the film's resistance was initially stabilized for 30 minutes and recorded as R_a. After introducing the gas into the chamber, the

resistance was recorded as R_g . This procedure was repeated across a temperature range of 30 °C to 500 °C, and the sensitivity was calculated using the following formula:

$$\text{Sensitivity (NH}_3, \text{H}_2\text{S, LPG)} = R_a/R_g \dots\dots\dots (5)$$

$$\text{Sensitivity (CO}_2) = R_g/R_a \dots\dots\dots (6)$$

The sensitivity variation of NH₃, LPG, H₂S, and CO₂ at 500 ppm is illustrated in Fig. 4 NiFe₂O₄ shows the highest sensitivity to NH₃, moderate sensitivity to LPG and CO₂, and the lowest sensitivity to H₂S.

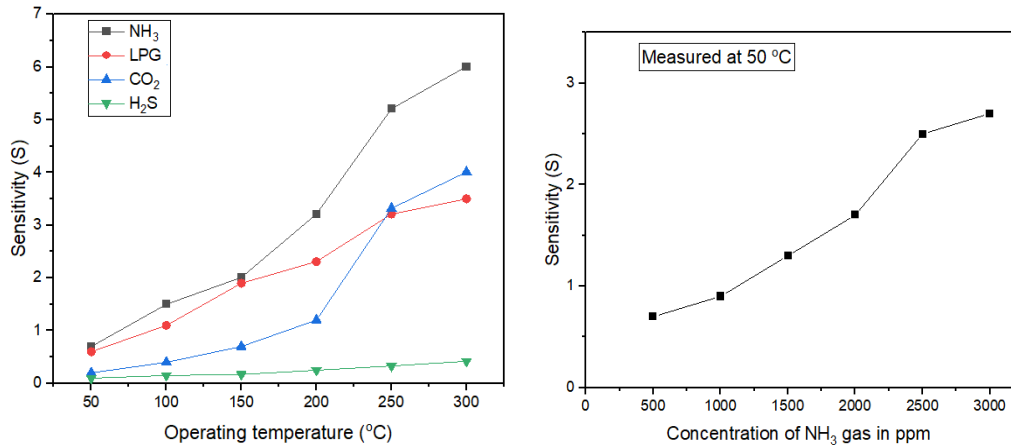


Figure 5: Variation in Sensitivity of NH₃ Gas Measure in ppm

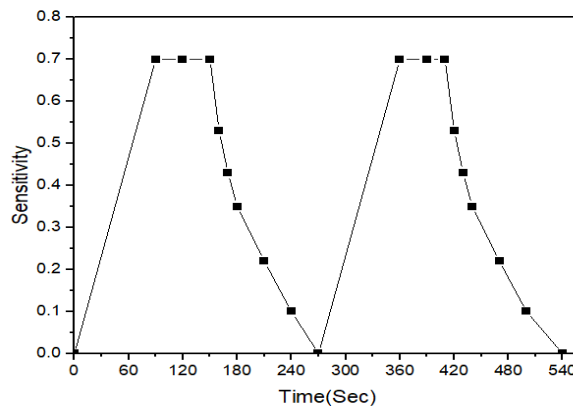


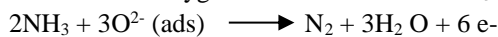
Figure 6: Recovery and Response Time for NH₃ Gas Sensor

Fig. 5 and Fig.6 shows the variation in sensitivity of NH₃ gas and the response as well as recovery time of NiFe₂O₄ film was ~ 81 seconds and ~ 108 seconds respectively. The sensitivity of NH₃ increases with an increase in NH₃ concentration and stagnates above 2500 ppm.

The response time of NiFe₂O₄ film is 90 seconds and Recovery time is found to 120 seconds .When NiFe₂O₄ film is heated above 100 °C, the surface is characterized by adsorption of oxygen ions (O⁻ or O²⁻). The kinetics of the adsorption of oxygen on the NiFe₂O₄ surface is given by the following reaction:



The adsorbed oxygen extracts electrons from the Ni or Fe crystal atoms and forms electron deficiency in the crystal, thereby increasing the resistance of the sensor element. When reducing gas NH₃ interacts with the sensor, surface adsorbed oxygen O²⁻ reacts with the NH₃ and releases electrons, and the resistance of the film decreases.



IV. CONCLUSIONS

The self-gel auto-combustion process was successfully used to prepare nickel ferrite in nano-crystalline form. The screen-printing technique was successfully used to prepare the sensor element. The crystalline size of nickel ferrite is found to be 68.659 nm. Nickel ferrite was more sensitive to NH₃ than it was to CO₂, H₂S, and LPG gases. The response and recovery times of the sensor element are found to be ~ 81 seconds and ~ 108 seconds, respectively. Thus, the nickel ferrite-based sensor element is robust, affordable, easy to produce, and capable of detecting NH₃ gas at ambient temperature.

REFERENCES

- [1] Khomarloo, N., Mohsenzadeh, E., Gidik, H., Bagherzadeh, R., & Latifi, M. (2024). Overall perspective of electrospun semiconductor metal oxides as high-performance gas sensor materials for NO_x detection. *RSC advances*, *14*(11), 7806-7824.
DOI: 10.1039/D3RA08119B
- [2] Pathania, A., Dhanda, N., Verma, R., Sun, A. C. A., Thakur, P., & Thakur, A. (2024). Metal Oxide Chemoresistive Gas Sensing Mechanism, Parameters, and Applications. *ECS Sensors Plus*, *3*(1), 013401.
DOI 10.1149/2754-2726/ad2152
- [3] Nikolic, M. V., Milovanovic, V., Vasiljevic, Z. Z., & Stamenkovic, Z. (2020). Semiconductor gas sensors: Materials, technology, design, and application. *Sensors*, *20*(22), 6694.
<https://doi.org/10.3390/s20226694>
- [4] Šutka, A., & Gross, K. A. (2016). Spinel ferrite oxide semiconductor gas sensors. *Sensors and actuators B: chemical*, *222*, 95-105.
<https://doi.org/10.1016/j.snb.2015.08.027>
- [5] Shedam, R. M., Kashid, P. P., Mathad, S. N., Deshmukh, R. B., Shedam, M. R., & Gadkari, A. B. (2022). Ferrites gas sensors: A Review. *Physics and Chemistry of Solid State*, *23*(3), 626-640.
<https://doi.org/10.15330/pcss.23.3.626-640>
- [6] Zhang, R., Qin, C., Bala, H., Wang, Y., & Cao, J. (2023). Recent Progress in Spinel Ferrite (MFe₂O₄) Chemiresistive Based Gas Sensors. *Nanomaterials*, *13*(15), 2188.
<https://doi.org/10.3390/nano13152188>
- [7] Sutka, A., & Mezinskis, G. (2012). Sol-gel auto-combustion synthesis of spinel-type ferrite nanomaterials. *Frontiers of Materials Science*, *6*, 128-141.
<https://doi.org/10.1007/s11706-012-0167-3>
- [8] Liu, X., Xu, Z., Liu, Y., & Shen, Y. (1998). A novel high performance ethanol gas sensor based on CdO Fe₂O₃ semiconducting materials. *Sensors and Actuators B: Chemical*, *52*(3), 270-273.
[https://doi.org/10.1016/S0925-4005\(98\)00278-0](https://doi.org/10.1016/S0925-4005(98)00278-0)
- [9] Xiangfeng, C. (2003). Sulfide-sensing characteristics of MFe₂O₄ (M= Zn, Cd, Mg and Cu) thick film prepared by co-precipitation method. *Sensors and Actuators B: Chemical*, *96*(3), 504-508.
[https://doi.org/10.1016/S0925-4005\(03\)00626-9](https://doi.org/10.1016/S0925-4005(03)00626-9)
- [10] Singh, S., Singh, A., Yadav, B. C., & Tandon, P. (2014). Synthesis, characterization, magnetic measurements and liquefied petroleum gas sensing properties of nanostructured cobalt ferrite and ferric oxide. *Materials Science in Semiconductor Processing*, *23*, 122-135.
<https://doi.org/10.1016/j.mssp.2014.02.048>
- [11] Xiangfeng, C., Dongli, J., & Chenmou, Z. (2007). The preparation and gas-sensing properties of NiFe₂O₄ nanocubes and nanorods. *Sensors and Actuators B: Chemical*, *123*(2), 793-797.
<https://doi.org/10.1016/j.snb.2006.10.020>
- [12] Zhang, Y., Jia, C., Wang, Q., Kong, Q., Chen, G., Guan, H., & Dong, C. (2019). Highly sensitive and selective toluene sensor of bimetallic Ni/Fe-MOFs derived porous NiFe₂O₄ nanorods. *Industrial & Engineering Chemistry Research*, *58*(22), 9450-9457.
<https://doi.org/10.1021/acs.iecr.9b01497>
- [13] Srivastava, R., Yadav, B. C., Singh, M., & Yadav, T. P. (2016). Synthesis, characterization of nickel ferrite and its uses as humidity and LPG sensors. *Journal of Inorganic and Organometallic Polymers and Materials*, *26*, 1404-1412.
<https://doi.org/10.1007/s10904-016-0425-4>
- [14] Raut, S. D., Awasarmol, V. V., Ghule, B. G., Shaikh, S. F., Gore, S. K., Sharma, R. P., & Mane, R. S. (2018). γ -irradiation induced zinc ferrites and their enhanced room-temperature ammonia gas sensing properties. *Materials Research Express*, *5*(3), 035702.
DOI 10.1088/2053-1591/aab3eb
- [15] Singh, S., Yadav, B. C., Prakash, R., & Bajaj, B. (2011). Synthesis of nanorods and mixed shaped copper ferrite and their applications as liquefied petroleum gas sensor. *Applied Surface Science*, *257*(24), 10763-10770.
<https://doi.org/10.1016/j.apsusc.2011.07.094>
- [16] Haija, M. A., Abu-Hani, A. F., Hamdan, N., Stephen, S., & Ayesh, A. I. (2017). Characterization of H₂S gas sensor based on CuFe₂O₄ nanoparticles. *Journal of Alloys and Compounds*, *690*, 461-468.
<https://doi.org/10.1016/j.jallcom.2016.08.174>
- [17] Hankare, P. P., Jadhav, S. D., Sankpal, U. B., Patil, R. P., Sasikala, R., & Mulla, I. S. (2009). Gas sensing properties of magnesium ferrite prepared by co-precipitation method. *Journal of Alloys and Compounds*, *488*(1), 270-272.
<https://doi.org/10.1016/j.jallcom.2009.08.103>
- [18] Sumangala, T. P., Pasquet, I., Presmanes, L., Thimont, Y., Bonningue, C., Venkataramani, N., & Barnabé, A. (2018). Effect of synthesis method and morphology on the enhanced CO₂ sensing properties of magnesium ferrite MgFe₂O₄. *Ceramics International*, *44*(15), 18578-18584.

- [19] Xu, Y., Sun, D., Hao, H., Gao, D., & Sun, Y. (2016). Non-stoichiometric Co (II), Ni (II), Zn (II)-ferrite nanospheres: size controllable synthesis, excellent gas-sensing and magnetic properties. *RSC advances*, 6(101), 98994-99002.
<https://doi.org/10.1039/C6RA21990J>
- [20] Bajorek, A., Berger, C., Dulski, M., Zubko, M., Lewińska, S., Prusik, K., & Randrianantoandro, N. (2022). Tuning physical properties of NiFe₂O₄ and NiFe₂O₄@ SiO₂ nanoferrites by thermal treatment. *Metallurgical and Materials Transactions A*, 53(4), 1208-1230.
- [21] Patil, Y., Pedhekar, R. B., Patil, S., Kosalge, S., & Raghuvanshi, F. C. (2021, March). Chemically synthesized ZnO and Cd-ZnO thick films as Ethanol sensor. In *IOP Conference Series: Materials Science and Engineering* (Vol. 1126, No. 1, p. 012046). IOP Publishing.
10.1088/1757-899X/1126/1/012046
- [22] Nejati, K., & Zabihi, R. (2012). Preparation and magnetic properties of nano size nickel ferrite particles using hydrothermal method. *Chemistry Central Journal*, 6, 1-6.
<https://doi.org/10.1186/1752-153X-6-23>
- [23] Sontu, U. B., Yelasani, V., & Musugu, V. R. R. (2015). Structural, electrical and magnetic characteristics of nickel substituted cobalt ferrite nano particles, synthesized by self combustion method. *Journal of Magnetism and Magnetic Materials*, 374, 376-380.
<https://doi.org/10.1016/j.jmmm.2014.08.072>
- [24] Mustafa, G., Islam, M. U., Zhang, W., Jamil, Y., Anwar, A. W., Hussain, M., & Ahmad, M. (2015). Investigation of structural and magnetic properties of Ce³⁺-substituted nanosized Co–Cr ferrites for a variety of applications. *Journal of alloys and compounds*, 618, 428-436.
<https://doi.org/10.1016/j.jallcom.2014.07.132>

© 2024. This work is published under

[https://creativecommons.org/licenses/by/4.0/legalcode\(the“License”\)](https://creativecommons.org/licenses/by/4.0/legalcode(the“License”)).

Notwithstanding the ProQuest Terms and Conditions, you may use this content in accordance with the terms of the License.

¹ Swapnil K. Shelke
² Deepak S. Dhote

ADVANCED SYSTEM FOR THE MEASUREMENT OF BLOOD HEMOGLOBIN NON- INVASIVELY: AN INVESTIGATIVE APPROACH



Abstract: - Numerous components make up blood, including hemoglobin, platelets, red blood cells, white blood cells, and plasma. The primary component of human blood is hemoglobin, which transports carbon dioxide from other areas of the body back to the lungs and oxygen from the lungs to other areas of the body. Hemoglobin measurements assist medical professionals in diagnosing a variety of illnesses based on a patient's health. These days, invasive techniques that include drawing blood from the patient and analyzing it are employed to measure the hemoglobin content. In addition to the discomfort associated with taking blood samples, another drawback of this approach is the time lag between collection and analysis of the blood, which prevents real-time patient monitoring in emergency scenarios. A non-invasive approach makes it possible to monitor patients continuously without pain and with a low risk of infection. It also makes it easier to monitor data in real time, enabling quick clinical responses to the recorded data. In this noninvasive technique, Near Infrared (NIR) Spectroscopy and Photoplethysmography (PPG) methods are used for the detection of hemoglobin level. Here sensor system different LEDs are used of different wavelength and photodiode are used. Proposed system provides expected results for the blood samples.

Keywords: blood, hemoglobin, non-invasive, LED, Photo diode.

I. INTRODUCTION

Blood consists of different parameters such as hemoglobin, white blood cell, red blood cell, platelets and plasma [17]. Hemoglobin is made up of four protein molecules, called globulin chains; each globulin chain contains an important central structure called the heme molecule [19]. Hemoglobin is a metal protein present in the red blood cells of blood plasma [18]. The primary component of human blood is hemoglobin, which transports carbon dioxide from other areas of the body back to the lungs and oxygen from the lungs to other areas of the body. Hemoglobin measurements assist medical professionals in diagnosing a variety of illnesses based on a patient's health. One of the most popular blood tests is the measurement of hemoglobin (Hb) concentration, which is typically done as part of a complete blood count (CBC). Anemia of different kinds, bleeding, erythropoietin deficiency (from kidney disease), lead poisoning, malnourishment, iron, folate, vitamin B12, and vitamin B6 nutritional deficiencies, over hydration, and red blood cell destruction related to transfusion reaction can all cause a lower than normal hemoglobin level. Increased red blood cells from too much erythropoietin, corpulmonale, pulmonary fibrosis, polycythemia vera, and congenital heart disease can all contribute to higher-than-normal hemoglobin levels. Decrease in Hb level due to different causes leads to symptoms of various types of anemia, wherein iron deficiency anemia (IDA) is the most prevalent among Asians (UNICEF 2004) [7]. A hemoglobin test reveals how much hemoglobin is to be found in the blood. With this information anemia (a low hemoglobin level) and polycythemia vera (a high hemoglobin level) can be a diagnosed and monitored [14].

Hemoglobin concentration is currently measured using invasive techniques that require drawing blood from the patient and analysis thereafter. In addition to the discomfort associated with taking blood samples, another drawback of this approach is the time lag between blood collection and analysis, which prevents real-time patient monitoring in emergency scenarios [2][3]. After drawn blood is exposed to chemical analysis, the amount of hemoglobin in milligrams per deciliter of blood is determined. An experienced paramedical staff member is needed to carry out this procedure: In order to draw blood, a technician in the lab: Along with a pathologist, to carry out the chemical analysis: Interpreting and confirming the findings are necessary [10] [18]. The complete blood count (CBC), which measures the amount of hemoglobin in the blood by examining the blood component

¹Assistant Professor, Department of Electronics, Adarsha Science, J. B. Arts and Birla Commerce Mahavidyalaya, Dhamangaon Rly, Amravati, India (M.S.)

E-mail:swapnilkshelke1@gmail.com

²Principal, Brijlal Biyani Science College, Amravati, India (M.S.)

E-mail:dr.deepak.dhote@gmail.com

Copyright © JES 2024 on-line : journal.esrgroups.org

in the tube, is one of the invasive procedures. One way to gauge hemoglobin levels is by the use of biosensors [20]. In rural areas, the Sahli method, the filter paper test, or the pallor test have been used to evaluate hemoglobin levels [9]. The copper sulfate method, the centrifuge method, and the Lovibond type comparator method are a few more techniques for determining the amount of hemoglobin in a person's blood. Hemocue method, cyanmethemoglobin method, and grey wedge photometer method. These procedures involve taking a patient's blood and evaluating their hemoglobin levels with various reagents and tools [9]. Hemoglobin is chemically changed in the hemoglobinocyanide process to create cyanmethemoglobin, which has a maximum absorption at a wavelength of 540 nm. The process of absorption yields the hemoglobin concentration [19].

A noninvasive approach makes it possible to continuously monitor patients without pain and with a low risk of infection. It also makes it easier to monitor data in real time, enabling quick clinical responses to the recorded data. Near infrared spectroscopy has been developed into a non-invasive technique for biomedical sensing and clinical diagnostics since it was discovered that near infrared light could permeate biological tissues to a significant depth [2][3][19][15][28]. Non-invasive medical diagnostic methods, such as magnetic resonance imaging (MRI), thermography, ultrasound, and X-rays, have significantly decreased patient risk and improved our understanding of how the body functions. Non-invasive procedures have the advantages of leaving no scars or incisions, a reduced chance of infection, bleeding, or needing blood transfusions, a quicker healing period, and a quicker return to regular work [11]. Many non-invasive methods, including imaging, spectro-photometry, opto-acoustic spectroscopy, transmission spectroscopy, and reflection spectroscopy, have been proposed in the literature for the estimate of blood parameter as a pathological advancement [23][24].

II. MATERIALS AND METODS

In this system, Near Infrared (NIR) spectroscopy and Photoplethysmography (PPG) method is used for the determination of hemoglobin level in the blood sample. System also consists of Light Emitting Diodes (LEDs), Optical detector, Signal conditioning unit, Microcontroller and display unit.

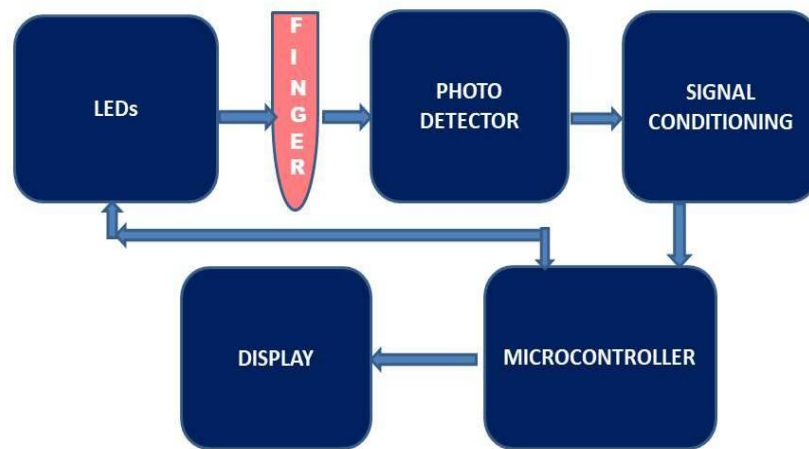


Figure (1): Block diagram of proposed system

The fundamental idea behind measuring hemoglobin is that blood plasma, oxygenated and, deoxygenated hemoglobin absorbs and transmits light differently in the red and near-infrared regions.

In this system idea is that hemoglobin in blood and tissue in the finger, respectively, causes absorption and dispersion. In the NIR spectroscopy optical sources such as LEDs are used of different wavelength as shown in the table 1.

Table (1): List of LEDs and its wavelengths

Sr. No.	LED	Wavelength (nm)
1.	APT2012LSYCK/J3-PRV	590
2.	AA3021LSYSK/J3-TR	590
3.	Cree-Xlamp ML-E LEDs	590
4.	APGO603SEC-E-TT	624

5.	VLD51535R-08	624
6.	APTR3216SRCPRV	640
7.	SML-LX15SRC-TR	660
8.	VSMY98145DS	810
9.	1541085A3060	850
10.	APT2012SF4C-P22	880
11.	VSMF3710	890
12.	APT2012F3C	940
13.	15414194BA210	940
14.	1541294A3060	940

Light is transmitted through the fingertip and detected by the Optical detector. Here we used optical detector such as PIN photodiode SFH2201, VEMD55A0C, TEFD4300, RDB-C152SM, OPT101 Monolithic Photodiode and Trans- impedance Amplifier are used. Here Photoplethysmography method is used for the detection of light intensity depending of the hemoglobin level. Output of the detector is given to the Signal conditioning system that makes all the necessary changes such as signal attenuation, signal amplification, signal filtering etc. Output of signal conditioning system is given to the Microcontroller unit which makes all the necessary processing and send to the display unit. Display unit will indicate the readings of hemoglobin.

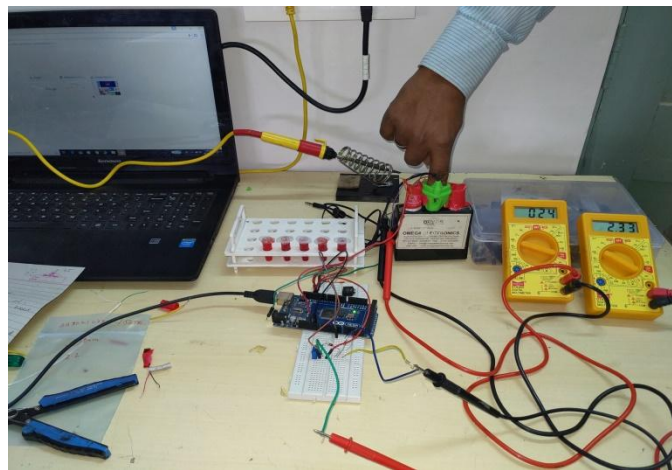


Figure (2): set up of proposed system

Here we have taken five different blood samples of the patients who suggested for the Complete Blood count.

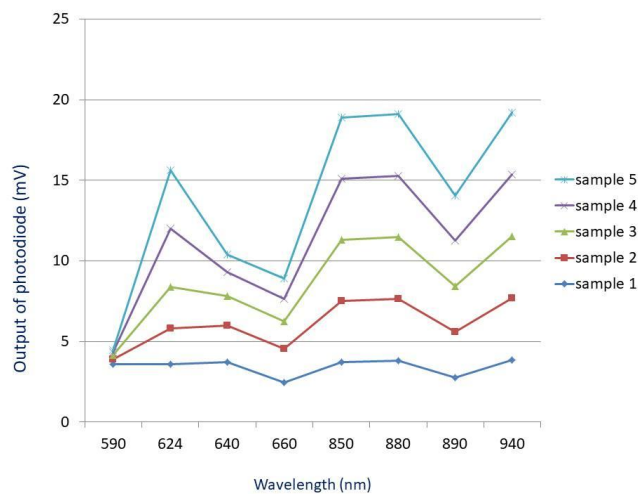


Figure (3): Graph between Wavelength and Photodiode output

Katsuyasu Saigo et al. (2004) investigated the Astrim device to measure hemoglobin levels by combining the analysis of optical pictures captured by a charge-coupled device camera situated on the other side of light sources with the principle of near-infrared spectroscopy. The suggested approach was predicated on the idea that

hemoglobin in blood and tissue in the finger, respectively, causes absorption and dispersion. Astrim detects images of blood vessels using light sources with wavelengths of 660, 805, and 880 nm. It then computes hemoglobin levels depending on the wavelengths that are absorbed [1]. Jens Kraitl et al. (2011, 2006) presented NIR spectroscopy and photoplethysmography for measurement of hemoglobin. They have created the laser-based photometric device PMD-I, which generates light at wavelengths of 670, 808, 905, 980, and 1300 nm through five laser diodes. They employed laser diodes with wavelengths of 670, 808, 905 and 980 since this is the therapeutic window region where hemoglobin derivatives dominate blood absorption and water absorption predominates at 1300 nm. Additionally, they created the LED-based photometric device PMD-II, which employs three LEDs with wavelengths ranging from 670 to 1300 nm [2] [3] [4]. Marlin Wayne Causey et al. (2011) presented optical spectroscopy method for the measurement of hemoglobin using Masimo Radical-7 SpHb station [5].

Aditya Bhat et al. (2015) investigated the use of rainbow R120L pulse co-oximeter with Masimo Radical 7 finger probe sensor for optical spectroscopy hemoglobin measurement [6]. K. Abo Alam et al. (2009) reported optical method in which Wang-Mendel method based fuzzy expert system is used to generate fuzzy rule base for measurement of hemoglobin [8]. The optical photoplethysmography method for hemoglobin measurement was presented by Nirupa J et al. (2014). A photodiode is used on one side of the fingertip while red and infrared LEDs with wavelengths of 624 nm and 850 nm, respectively, are used on the other [10]. A Mohamed Abbas et al. (2016) presented signal to image photo-plethysmo-graphic method. They used LED that transmits light in the near infrared region through fingertip or earlobe and a photodiode to detect the signals. The output of proposed system was obtained using regressive analysis and the hemoglobin content was displayed in the LabVIEW program [18].

Table (2): Displaying the authors' various techniques, sample size, correlation coefficient, and calibration technique.

Sr. no.	Author / Year	Technique / Method	Sample size	Correlation coefficient (r)	Calibration Method
1.	Katsuyasu Saigo (2004)	Near-infrared spectroscopy	97	0.626	Sysmex SE-9000
2.	Jens Kraitl (2011)	Near-infrared Spectroscopy and photoplethysmography	43	0.918	Hemocue TM device
3.	J. Kraitl (2006)	Multispectral near-infrared spectroscopy	19	Sq r =0.85	Hemocue TM device
4.	Marlin Wayne Causey (2011)	Optical Spectroscopy	60	0.78	Lab hemoglobin method
5.	Aditya Bhat (2015)	Optical Spectroscopy	150	0.94	Automated lab Analyzer Cyanmethemoglobin method
6.	Vaishal V. Agte (2009)	Nail color scale method	52 (2007) 175	Sq r = 0.77 0.75	Cyanmethemoglobin method
7.	K. Abo Alam (2009)	Optical method	122	0.977	Invasive reference method
8.	Kumar R.(2013)	Optical Method	100	-	Cyanmethemoglobin method
9.	Nirupa J. (2014)	Optical Photoplethysmography	69	-	Conventional chemical analysis
10.	Dr. Raid Saleem	Single wavelength	10	-	Look up table

	Al-Baradie (2013)	spectrophotometry			
11.	U. Timm (2011)	Optical Spectroscopy	48	-	Hemocue (R) tester
12.	Tristan Knutson (2013)	Optical Spectroscopy	127	-	Arterial blood gas analyzer
13.	Cedrick Zaouter (2012)	Optical Spectroscopy	9	-	Arterial blood gas analyzer
14.	Timm U. (2010)	Optical method	-	-	Blood Gas Analyzer
15.	Khunawat Luangrat (2013)	Optical Spectroscopy	8 / 5	-	-
13.	Mohamed Abbas (2016)	Photoplethysmography	10	-	-
16.	Rajashree Doshi (2013)	Optical pulse photometric method	58	-	-
17.	Setsuo Takatani (1988)	Optical Spectroscopy	-	-0.966 to -0.9988	-
18.	Dong-Sik Kim (2011)	Optical Spectroscopy	33	-	-
19.	Francesco Fabbri (2003)	Near-infrared spectroscopy	9	-	-
20.	Chetan Sharma (2012)(2013)	Photoplethysmography	-	-	-
21.	Philips J.P. (2011)	Optical and Capacitance	-	-	-
22.	O. Abdallah (2008)	Optical Spectroscopy & Photoplethysmography	-	-	-
23.	Eran Hadar	Occlusion Spectroscopy	63	Sd=0.86	LH-750 Beckman Coulter counter

III. RESULT AND DISCUSSION

Proposed system shows significance reading of different blood samples at different wavelengths. Output of the detector system shows appreciable reading according to the hemoglobin level of the blood sample. Samples observe at LEDs wavelength of 660 nm and 940 nm gives significant result for the further system. Output of the detector is minimum at 660 nm and maximum at 940 nm wavelength. Relation observed between Wavelength of the LED and Output of the photodiode shows good response curve.

IV. CONCLUSION

Proposed system uses Near Infrared (NIR) spectroscopy and Photoplethysmography (PPG) method for the measurement of hemoglobin. In the proposed work appreciable results are observed with the given system. For the non-invasive measurement of hemoglobin and other blood related parameters optical sources such as LEDs with 660 nm and 940 nm wavelength further may be used in the Biomedical instrumentation systems. NIR Since many of the methods covered here have shown to have excellent hemoglobin measurement sensitivity, specificity, and accuracy, a variety of non-invasive methods will be used in the future for different applications. For non-invasive hemoglobin measurement, a fingertip sensor is mostly used; however, earlobe sensors might be a better option for systems down the road because they use less power than fingertip sensors.

ACKNOWLEDGMENT

We thank all peoples who directly and indirectly help us during this work. We also thank all the volunteers who actively participate in this study.

REFERENCES

- [1] Katsuyasu Saigo, Shion Imoto, Mokoto Hashimoto, Hisashi Mito, Junko Moriya, Tadanobu Chinzei, Yoshitsugu Kubota, Shigehiro Numada, Toshiyuki Ozawa, Shunichi Kumagai, "Noninvasive monitoring of hemoglobin: The Effects of WBC Counts on Measurements," *American Journal of Clinical Pathology*, vol. 121, pp. 51-55, 2004.
- [2] Jens Kraitl, Ulrich Timm, Hartmut Ewald, Elfed Lewis, "Non-invasive sensor for an in vivo hemoglobin measurements," *IEEE Sensors conference*, pp. 276-279, 2011.
- [3] Jens Kraitl, Ulrich Timm, Hartmut Ewald, Elfed Lewis, "Non-invasive measurement of blood components: Sensor for an in vivo hemoglobin measurement," *IEEE fifth International conference on sensing technology*, pp. 253-257, 2011.
- [4] J. Kraitl, H. Ewald, H. Gehring, "Analysis of time series for non-invasive characterization of blood components and circulation patterns," *Nonlinear analysis Hybrid Systems 2*, pp. 441-455, 2006.
- [5] Marlin Wayne Causey, Seth Miller, Andrew Foster, Alec Beekley, David Zenger, Matthew Martin, "Validation of noninvasive hemoglobin measurements using the Masimo Radical-7 SpHb station," *The American Journal of Surgery*, pp. 592-598, 2011.
- [6] Aditya Bhat, Amit Upadhyay, Vijay Jaiswal, Deepak Chawla, Dharamveer Singh, Mithilesh Kumar, C.P. Yadav, "Validity of non-invasive point-of-care hemoglobin estimation in healthy and sick children-a method comparison study," *European Journal of Pediatrics*, pp. 171-179, 2015.
- [7] Vaishal V. Agte, Rucha Tillu, "Development of a nail color scale as a noninvasive tool for predicting hemoglobin in humans," *Journal of Public Health*, pp. 315-319, 2009.
- [8] K. Abo Alam, O. Abdallah, A. Bolz, "New Estimation Approach for total Hemoglobin Concentration Based on a Fuzzy Expert system," *IFMBE Proceedings 25/VII*, pp. 396-398, 2009.
- [9] Kumar R., Dr. Ranganathan H, "Noninvasive Sensor Technology for Total Hemoglobin Measurement in blood," *Journal of Industrial and Intelligent information*, vol. 1, No. 4, pp. 243-246, 2013.
- [10] Lourdes Albina Nirupa J., Jagadeesh Kumar V, "Non-invasive Measurement of Hemoglobin Content in Blood," *IEEE International symposium on Medical Measurements and Applications*, pp. . 2014.
- [11] Dr. Raid Saleem Al-Baradie, Mr. Anandh Sam, Chandra Bose, "Portable Smart Non-Invasive Hemoglobin Measurement System," *10th International Multi-conference on systems, Signals and devices (SSD)*, pp. 1-4, 2013.
- [12] U. Timm, S. Andruschenko, M. Hinz, S. Koball, G. Leen, E.Lewis, J. Kraitl, H. Ewald, "Optical Sensor System for Continuous Non-Invasive Hemodynamic Monitoring in Real-Time," *IEEE Sensors Application Symposium (SAS)*, pp. , 2011.
- [13] Tristan Knutson, David Della-Giustina, Eric Tomich, Brandon Wills, Emily Luerssen, Penny Reynolds, "Evaluation of a New Noninvasive Device in Determining Hemoglobin Levels in Emergency Department Patients," *West Journal Emergency Medicine*, pp. 283-286, 2013.
- [14] Timm U., Lewis E., Leen G., McGrath D., Kraitl J., Ewald H., "Non-invasive continuous online hemoglobin monitoring system," *IEEE Sensors Applications Symposium (SAS)*, pp. 131-134, 2010.
- [15] U. Timm, G. Leen, E. Lewis, D. McGrath, J. Kraitl, H. Ewald, "Non-Invasive Optical Real-time Measurement of Total Hemoglobin Content," *Proceedings Eurosensors XXIV*, pp. 488-491, 2010.
- [16] Khunawat Luangrat, Prapat Suriyaphol, Yodchanan Wongsawat, "Hemoglobin Prediction System from Pulse Signal," *Signal and information processing association Annual summit and conference (APSIPA)*, pp. , 2013.
- [17] Khunawat Luangrat, Yunyong Punsawad, Prapat Suriyaphol, Yodchanan, "On the Development of Using the Non-Invasive Blood Oxygen Level Sensor for Quantifying Hemoglobin Concentration," *World congress on Medical Physics and Biomedical Engineering, IFMBE Proceedings 39*, pp. 1428-1430, 2013.
- [18] A. Mohamed Abbas, S. Ashok, S. Prabhu Kumar, P. Balavenkateswarlu, "Haemoglobin Detection in Blood by Signal to Image Scanning using Photo-Plethysmo-Graphic-Technique (PPG)," *Indian Journal of Science and Technology*, vol. 9(1), pp. 1-4, 2016.
- [19] Rajashree Doshi, Anagha Panditrao, "Optical Sensor System for Hemoglobin Measurement," *International Journal of Computational Engineering Research*, Vol. 3, issue 7, pp. 41-45, 2013.
- [20] Setsuo Takatani, Hiroyuki Noda, Hisateru Takano, Tetsuzo Akutsu, "A Miniature Hybrid Reflection Type Optical Sensor for Measurement of Hemoglobin Content and Oxygen Saturation of Whole Blood," *IEEE transactions on Biomedical Engineering*, vol. 35, no. 3, pp. 187-198, 1988.
- [21] Dong-Sik Kim, Jae-Hoon Choi, Myung-Hyun Nam, Ji-Woon Yang, "LED and CMOS image sensor based hemoglobin concentration measurement technique," *Sensors and Actuators B: Chemical*, pp. 103-109, 2011.
- [22] Francesco Fabbri, Michael E. Henry, Perry F. Renshaw, Shalini Nadgir, Bruce L. Ehrenberg, Maria Angela Franceschini, Sergio Fantini, "Bilateral near-infrared monitoring of the cerebral concentration and oxygen-saturation of hemoglobin during right unilateral electro-convulsive therapy," *Brain Research* 992, pp. 193-204, 2003.
- [23] Chetan Sharma, Sachin Kumar, Anshul Bhargava, Shubhajit Roy Chowdhury, "Field Programmable Gate Array based embedded system for Non-invasive estimation of Hemoglobin in Blood using Photoplethysmography," *International Journal on Smart Sensing and Intelligent Systems*, vol. 6, no. 3, pp. 1267-1282, 2013.
- [24] Chetan Sharma, Komal Pandey, Shubhajit Roy Chowdhury, "A non invasive robust device for the detection of blood hemoglobin using photoplethysmography," *Research article, Biotechnology Bioinformatics Bioengineering*, pp. 573-579, 2012.
- [25] Philips J.P., Hickey M., Kyriacou P.A., "Electro-optical plethysmography for non-invasive estimation of hemoglobin concentration," *Annual international conference of IEEE on Engineering in Medicine and Biology Society EMBC*, pp. 4348-4351, 2011.

- [26] O. Abdallah, K.Abo Alam, A. Bolz, "Towards Noninvasive Monitoring of Total Hemoglobin Concentration and Fractional Oxygen Saturation Based on Earlobe Pulse Oximetry," IFMBE Proceedings 22, pp. 1738-1742, 2008.
- [27] Cedrick Zaouter, Gerald S. Zavorsky, "The measurement of carboxyhemoglobin and methemoglobin using a non-invasive pulse CO-oximeter," Respiratory Physiology and Neurobiology, pp. 88-92, 2012.
- [28] J. Kraithl, D. Klinger, D. Fricke, U. Timm, H. Ewald, "Non-invasive Measurement of Blood Components Sensors for an In-Vivo Haemoglobin Measurement," Advancement in Sensing Technology SSMI 1, pp. 237-262, 2013.
- [29] Eran Hadar, Oded Raban, Tal Bouganin, Kinneret Tenebaum-Gavish, Moshe Hod, "Precision and Accuracy of Non Invasive Hemoglobin Measurements during Pregnancy," Clinical publication, pp.2503-2506, 2012.
- [30] Swapnil Shelke, Deepak Dhote, "ENUMERATE BLOOD HEMOGLOBIN BY NON-INVASIVE TECHNIQUES: A REVIEW," GLOBAL JOURNAL OF ENGINEERING SCIENCE AND RESEARCHES, pp. 152-161, 2018.

^{1*}Syed Samiuddin¹M.E. Shelke¹

Synthesis, Characterization and Conductometric Study of Schiff's Bases and Their Metal Complexes: A Review

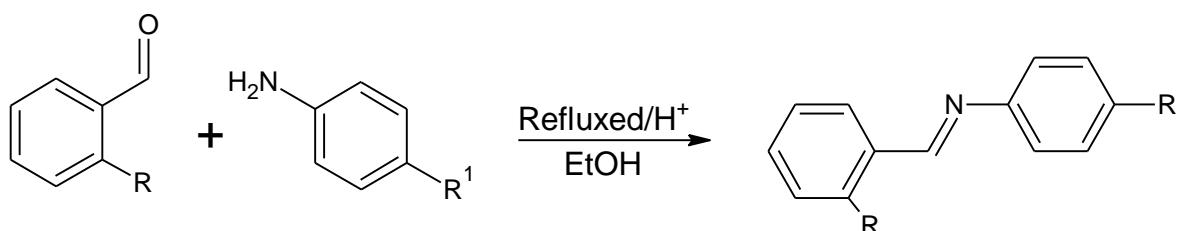


Abstract: - The Schiff's bases ligand and its metal complexes has been found extensive use in the field of interest. Schiff's bases and their metal complexes are best known for their antibacterial, antifungal, anti-tumour, anti-hypertensive, anti-depressants, anti-HIV, clinical, pharmaceuticals, herbicidal and anti-corrosive activities. Conductometric measurements of a solution containing electrolyte brought useful knowledge about solubility and permeability of drugs. Mixed solvents are very attractive and compulsive for study of ion association reaction by conductometry in behalf of addition of even pinch of organic components to water alter physical properties of solvent mixture. The conductometric techniques is based on measurements of electrical current in an electrolytic solution.

Keywords: Schiff's base, metal complex, spectral studies, conductivity

I. INTRODUCTION

The Schiff's bases having enamine linkage are usually derived by the condensation of Aldehydes or ketones with primary amines. (Scheme 1) such Schiff's bases and its metal complexes are found more effective in various biological activities such as anticancer, anti-tumor, anti-hypertensive, anti-depressants, antifungal, anti-viral and antioxidants over the years, a lot of research work carried out on synthesis of Schiff's bases.



(Scheme 1 : Enamine linkage formation reaction)

Conductometry techniques plays a significant role in pharmacodynamic. To study solubility product conductometric method is widely used because of its various advantages such as low cost, eco-friendly, less time consuming, proper, thermodynamics calculation with different parameters and most important easy to operate. Using conductometric method, researcher can calculate all the thermodynamics parameter for specific reactions and also investigate solubility of product.

^{1*,1} Department of Chemistry, Government Vidarbha Institute of Science and Humanities Amravati (MS) INDIA

II. LITERATURE REVIEW

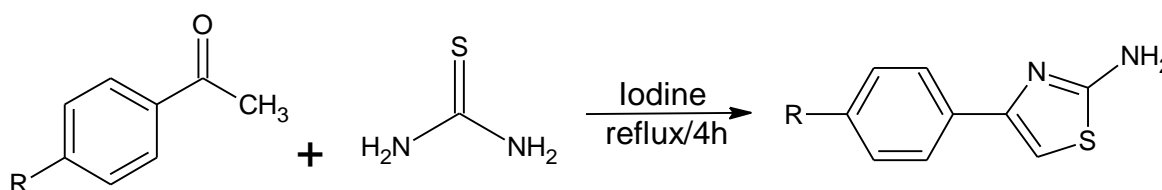
The available studies on synthesis of Schiff's base ligands and its metal complexes to study conductometric measurements are reviewed based on their applications in pharmacodynamic.

Munira Fatin Mannan ahad *et al* [1] (2012) carried out synthesis, characterization and physico-chemical data analysis of *O*-phenylenediamine Schiff's base ligand, elemental analysis like I.R, H^1 , C^{13} NMR, U.V-Visible, XRD were used to study molecular formula. The samples for electrical conductivity measurements were prepared from the Schiff's base metal complex and lithium Schiff's base in the form of pellets. These pellets were placed between two electrode and contact were tested to be ohmic.

Compounds	Conductivity value ($\Omega^{-1} \text{ cm}^{-1}$)
(API) ISA	7.2371×10^{-10}
$[(\text{API})\text{ISA}]_2\text{Co}$	4.4367×10^{-10}
Li-(API)ISA	3.0941×10^{-10}

fig. 1.1 – table showing conductivity values of complex compounds

S.R Kelode [2] (2023) has studied electrical conductivity of (Scheme 2) Vo(IV), Zr(IV) and $\text{UO}_2(\text{VI})$ metal complexes from thiazole Schiff's base. Elemental analysis like NMR, FT-IR, UV, XRD were done for the determination of structure and molecular formula. It was observed that the electrical conductivity of Metal complexes varies with their nature and temperature.



(Scheme 2 : Synthesis of 4-(substituted)-2 amino thiazole)

1. Electrical conductivity of the complexes lies in the range of 1.16×10^{-8} to $6.69 \times 10^{-7} \Omega^{-1} \text{ cm}^{-1}$ at temperature 373k.
2. The electrical conductivity of these complexes at 273K follows the order $\text{UO}_2 > \text{VO} > \text{Zr}$
3. The activation energy of electrical conduction of the complexes has been found to increase in the order $\text{Zr} < \text{VO} < \text{UO}_2$.

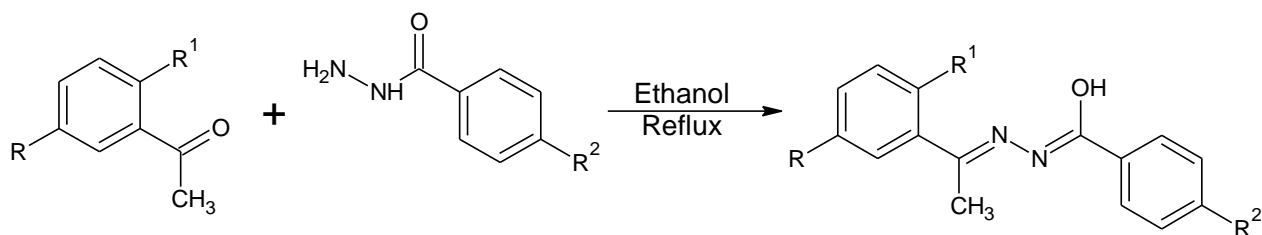
Atinafu Abayneh *et al* (3) had studied synthesis, characterization, conductivity and electrochemical studies of Schiff's base ligand and its copper complexes. The Schiff's base ligand was prepared by the condensation of 0.44715 gram of 4-aminoantpyrine with 0.057 ml glyoxal in absolute ethanolic solution. (Scheme 3) the resulting mixture was then reflux for 2 hours the yellow precipitate formed was filtered and recrystallized from ethanol to give yellow needles. Elemental analysis like NMR, FT-IR, UV, XRD were done for the determination of structure and molecular formula of Schiff's base and its coordination complexes.

Compound s	Molecular weight	Colour	Conductivity $\Omega\text{cm}^2 \text{ mol}^{-1}$
$[\text{CuL}_1]\text{Cl}_2$	562.5	Brown	240
$[\text{CuL}_1](\text{NO}_3)_2$	615.5	Dark Brown	235

Table 1.2. Elemental analysis and electrical conductance data

Amit R. Yaul *et al* [4] (2018) studied synthesis and electrical conductivity of some Schiff's base and their metal complexes. The hydrazone ligands H_2L_1 and H_2L_2 , and resulting product was filter washed several times with ethanol

diethyl ether and subsequently hydride over CaCl_2 in a desiccator. Elemental analysis like NMR, FT-IR, UV, XRD were done for the determination of structure and molecular formula. (Scheme 3)



(Scheme 3: Synthesis of Schiff's base)

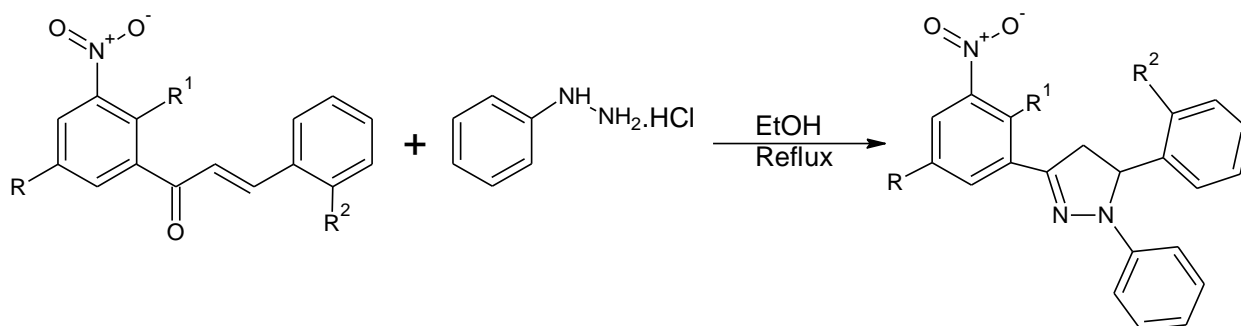
The electrical conductivity (dc) of the complex was studied in the temperature range 310-413 K. in all cases the conductivity increases with increasing temperature indicating that these complexes lie in the range of semiconductor.

i

Compounds	Colour	Electrical Conductivity σ ($\text{ohm}^{-1} \text{cm}^{-1}$)
$[\text{VOL1}(\text{H}_2\text{O})]$	Dark olive	2.40×10^{-8}
$[\text{Zr}(\text{OH})_2\text{L1}(\text{CH}_3\text{OH})_2]$	Cannery yellow	3.06×10^{-9}
$[(\text{Th}(\text{HL1})_2(\text{NO}_3)_2)]$	Cannery yellow	7.00×10^{-10}
$[(\text{UO}_2)\text{L1}(\text{CH}_3\text{OH})]$	Volcana	3.00×10^{-9}

Table 1.3 showing conductivity values of complexes

Shubhangi Y. Deshmukh *et al* [5] (2022) carried out work on synthesis, spectroscopic characterization electrical conductivity of heterocyclic Schiff's base metal complexes. The condensation reaction between Chalcone (E)-1-2-hydroxy-5-methyl-3-nitrophenyl)-3-(2-hydroxyphenyl) prop-2-en-1-one and hydrazine hydrochloride (Scheme 5) was carried out by the reflux for 2 hours. The crude product pores into the water and solid obtained washed by petroleum ether and dried in oven. (Scheme 4)



(Scheme 4 : Synthetic method of Schiff's base)

Structural characterization viz. NMR, FT-IR, XRD, UV, magnetic behaviour and FAB mass analysis were used to determine its molecular formula.

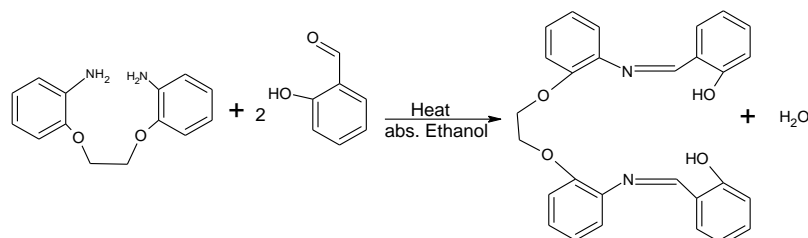
The conductivity values for 2-(5-(2-hydroxyphenyl)-1-phenyl-4,5-dihydro-1H-pyrazol-3-yl)-4-methyl-6-nitrophenol in DMF found to be very low i.e. 5.86 and 4.72 $\Omega^{-1} \text{ cm}^2 \text{ mol}^{-1}$.

Chao Meng *et al* [6] (2023) were synthesised poly Schiff's base from Para benzaldehyde and hydrazine according to the procedure reported elsewhere, briefly *p*-benzaldehyde (0.12mol) was dissolve in 180 ml. of absolute ethanol and then the solution was slowly dropped under the protection of N₂ to the solution of para phenylenediamine, sonicated for 15 minute, filtered and washed with distilled water and absolute ethanol. The intrinsic conductivity of all synthesised poly Schiff's bases in iron salt is summarised in the table.

Poly (Schiff's base)	Conductivity S/cm
L1	5.0×10^{-8}
L2	2.6×10^{-8}
C1	4.3×10^{-7}
C2	5.6×10^{-6}

Table 1.4 showing conductivity values of poly Schiff's base

Hamid Temel *et al* [7] (2003) carried out research work on the synthesis, characterization and conductance study of Cu (II), Ni(II), and Zn(II) complexes with Schiff's base derived from 1,2-bis-(*O*-amino phenoxy)ethane and salicylaldehyde according to them, the reaction steps for synthesis of H₂L are given in figure, the first step is synthesis of 1,2-bis-(*O*- nitrophenoxy)ethane from reaction of sodium ortho nitrophenolate and 1,2- dibromoethane. In the second step 1,2-bis-(*O*-nitrophenoxy)ethane and Pd/C as Catalyst in hydrazine hydrate were reacted to obtain 1,2-bis-(*O*-amino phenoxy)ethane in the third step *N-N'*-bis(Salicylidene)-1,2-bis-(*o*-aminophenoxy)ethane (H₂L) (Scheme 5)



(Scheme 5 : Synthesis of ligand (H₂L) N-N'-bis(Salicylidene)-1,2-bis-(*o*-aminophenoxy)ethane)

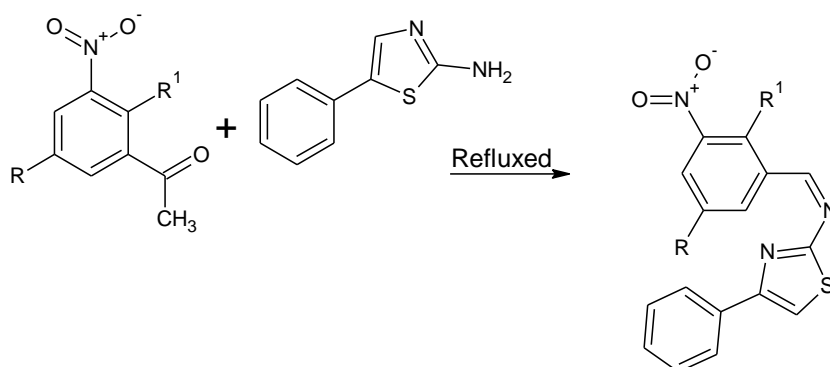
Y Z Ahmed *et al* [8] (1993) were carried out the synthesis of Schiff's base metal complexes and predicted it's conductometric measurement, when a solution of one mole of metal salt in absolute ethanol was added dropwise to a well stirred solution of Schiff's base N-(2-hydroxy)-benzylidene- β -alanine (L), a coloured compound precipitate immediately which was collected after evaporation of solvent the product obtained was purified by repeated washing with ethanol. During the course of study of electrical properties of organic compound measurements have been made on resistivity or conductivity as a function of temperature of a large number of samples.

V.D Patel *et al* [9] (2015) were synthesized enamine by the condensation of *p*-Dimethylaminobenzaldehyde (1.4919 gm. 0.1 mol.) solution in ethanol and *o*-phenylenediamine (1.0814 gm 0.1 mol.) Solution in hot water were taken in the round bottom flask, 50 ml absolute ethanol was added and reflux. Filtered and washed with distilled water

An Electrical conductivity of all crystals was measured at different temperature. A uniform thin layer of silver paste was applied on both the sides of the pallets of crystal providing electric contacts. average diameter and thickness of each pallet were measured and found 6 mm.

Abdel-Amir M. Fenjan *et al* [10] (2015) were reported preparation of Schiff's bases derived from 7-hydroxy-4-methyl Coumarin, according to them a mixture of compound (0.29 gm) from various aldehyde or ketone was dissolve in 15 ml of ethanol, a drop of glacial acetic acid was added then the mixture was refluxed for 6 hours. The solid product was filtered, dried and recrystallized with hot ethanol.

S.R Kelode [11] (2021) has reported electrical conductivity of Cr[III], Mn [III] and Fe[III] metal complexes of 2-Hydroxy-5-Methyl-3-Nitroacetophenone Thiazole Schiff's base 2-hydroxy-5-methyl-3-nitro acetophenone (HMNA) and 2-amino-4-phenyl thiazole was prepared by known methods. (Scheme 6)



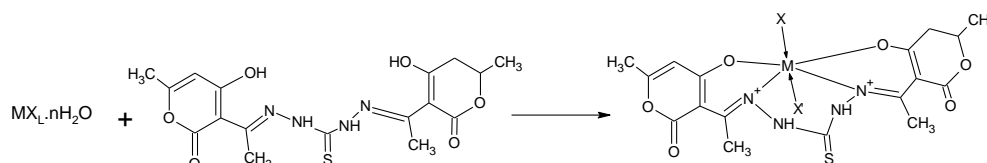
(Scheme 6 : Synthesis of enamine linkage)

The electrical conductivity resistivity of the different metal chelated can be measured either with ac. or dc methods. However, in this work the dc method was used for resistivity measurements, over a wide range of temperature. The electrical conductivity of metal complexes varies with their nature and temperature.

Metal		Cr(III)	Mn(III)	Fe(III)
HCAT	$\sigma \Omega^{-1}$	4.89 x	1.89 x	4.24 x
	cm^{-1}	10^{-8}	10^{-8}	10^{-7}
	Ea (eV)	0.0188	0.0124	0.1636

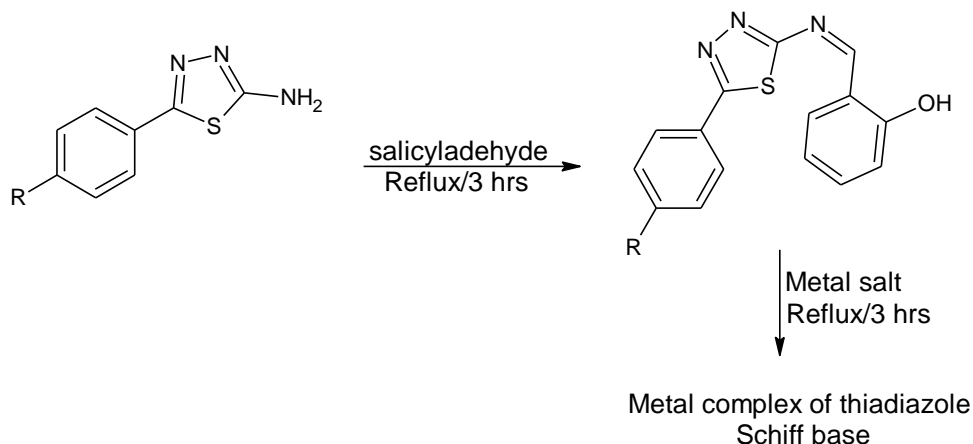
Table 1.5: Showing electrical conductivity of Cr, Mn and Fe (III) complexes.

N.J. Suryavanshi *et al* [12] (2013) carried out synthesis, characterization, thermal and electrical conductivity studies of Schiff's base metal complexes derived from 3-acetyl-6-methyl-pyran-2,4(3H)-dione (dihydroacetic acid) and thiocarbohydrazide. It was observed that the electrical conductivity of the complexes had positive temperature coefficient i.e. with an increase in temperature, conductivity increases exponentially.



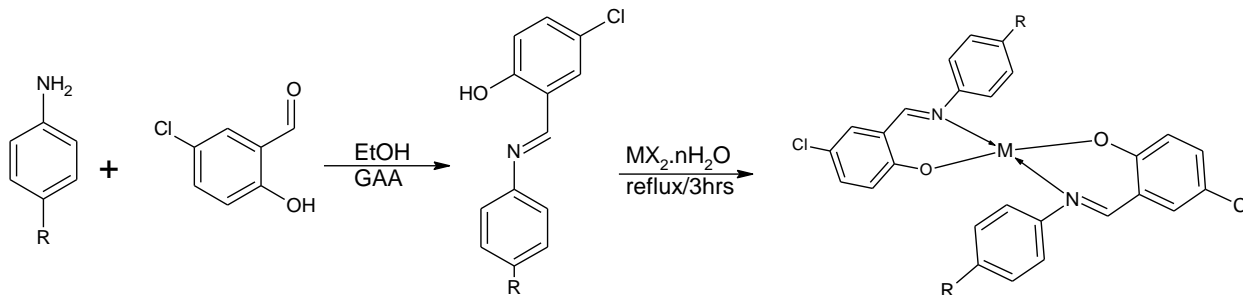
(Scheme 7 : Synthesis of Schiff's base and its metal complex)

Emad Yousif *et al* (13) 2013 were prepared Schiff's base from substituted thiadiazole react with salicylaldehyde formed inamine linkage further they prepared its metal complexes by mixing it in metallic salt. The complex was diamagnetic and conductivity measurement in DMF shows that the complex was conducting.



(Scheme 8. Synthesis of thiadiazole Schiff's base and its metal complex)

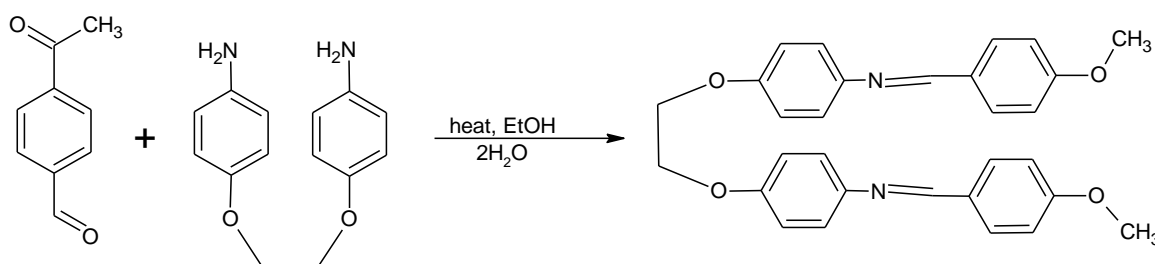
F.K Omenya *et al* (14) 2020 were carried out synthesis, characterization and electrical conductivity of Schiff's base, 4-Chloro-2-((E)-[4 Fluorophenyl]imino)methyl]phenol Metal (II) complexes. (Scheme 9). The conductivity values of synthesized compounds in DMSO were measured at room temperature. The conductivity value indicating that this complex compound was non electrolytic in nature.



(Scheme 9 : Synthesis of Schiff's base and metal complex)

Esmaceli *et al* (15) 2023 were predicted conductivity of new Schiff's base and its Zn(II) metallopolymer according to them the electrical conductivity of Zn(II) and it's complex (ZnL) increased by increasing the temperature in which the conductivity varied from 4.18×10^{-10} to $10^{-5-1} \text{ cm}^{-1} \cdot \text{L}$.

Umit Cakir *et al* (16) 2019 were reported the spectroscopic studies of transition metal complexes with a Schiff's base derived from 4-Methoxybenzaldehyde and 1,2-bis(*p*-Aminophenoxy)ethane. (Scheme 10) according to them Ni(II), Zn(II) and Cu(II) complexes are non-electrolytes shown by their conductivity measurements in DMF.



(Scheme 10. A reaction showing synthesis of Schiff's base)

Suman Malik *et al* (17) 2015 were carried out spectral characterization and thermal behaviour of Schiff's base metal complex derived from 2-aminobenzimidazole they were reported that Schiff's bases are the condensation reaction

product of aldehydes/ketones with primary amines. Further they reported its complex formation reaction. After completion of reaction product was characterized by spectral studies.

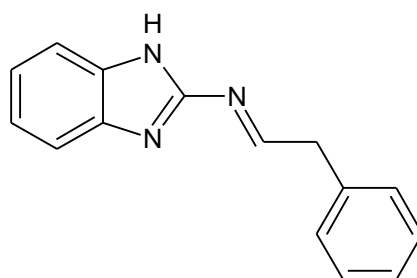
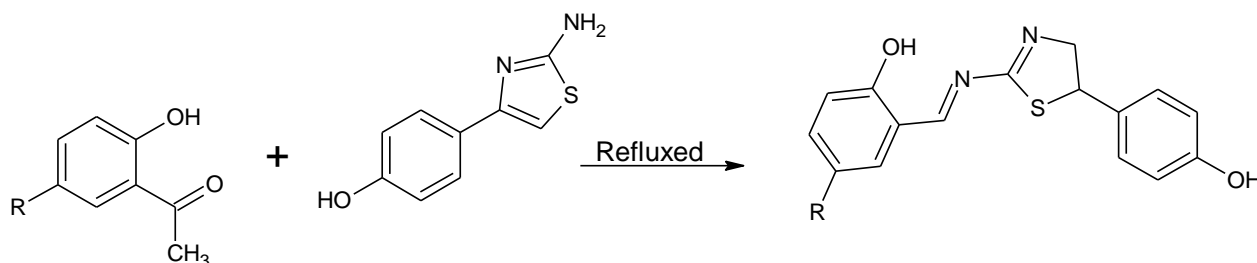


(Figure: Structure of synthesized Schiff's base)

Kelode S.R et al (18) 2020 were investigated the electrical conductivity of Co (II), Ni (II) and Cu (II) complexes derived from bidentate thiazole Schiff's base. In such reaction process 4-hydroxy acetophenone and thiourea was taken as a starting material. 4-(2-hydroxyphenyl)-2-amino thiazole was obtained as a product, it was further reacted with 2-hydroxy-5-chloro acetophenone to form HCAT. (Scheme 12)



(Scheme 12. reaction showing synthesis of Schiff's base compound)

III. CONCLUDING REMARK

The various studies have been carried out on the synthesis and characterization of Schiff's base metal complexes using different approach by researcher. The concluding remarks based on their studies will be follows.

- The study shows the variety of possible structure of metal complexes of Schiff's base ligands depends upon the aldehydes/ketones and amines used.
- The specific industrial, pharmaceutical applications of metal complexes based upon the orientation of Schiff's base metal complexes.
- This study can be extended with the use of different aldehydes, ketones and amines to evaluate conductometric measurements use in the field of pharmacodynamics.
- The synthesized Schiff's base and their metal complexes will be widely used in field of medicine.
- The synthesized Schiff's base metal complex may have great application in chemical analysis and also be helpful in agricultural purpose.
- Schiff's base metal complexes have found to be more effective in various biological applications, such as anticancer, anti-tumor and antibacterial.
- The Schiff's base formed can undergo reactions with number of metal ions for example Mn(II), Fe (II), (III), Co (II/III), Ni(II) and Cu(II) etc.
- The study shows that electrical conductivity is a temperature dependant property.
- This study shows that every complex compound has their own electrical conductivity value.
- This study also shows that normally organic compounds are non-conductor and if they have delocalised pi-electrons their conductivity can be increased by chemical treatment.

IV. ACKNOWLEDGEMENT

The authors are thankful to The Director and Head Department of Chemistry, Government Vidarbha Institute of Science and Humanities, Amravati for providing laboratory, internet and library facilities.

V. CONFLICT OF INTEREST:

The author has declare that they have no conflict of interest.

VI. ETHICAL APPROVAL

This has not been published elsewhere and is not currently under consideration for Publishing elsewhere.

VII. REFERENCES

- 1) Muneera Fatin Manan, Karimah Kasim, Mohd Abdul Fateh Abdul Mannan "Synthesis Characterization and conductivity studies of Schiff's base ligand derived from isatin and o-Phenylenediamine with its cobalt (II) metal complex and lithium -Schiff's base compound" The Malaysian Journal of Analytical Sciences, Vol. 16 pp. 318-324 2012
- 2) S. R. Kelode "Electrical conductivity and biological activities of Vo (iv), Zr (iv) and Uo2, (vi) complexes derived from thiazole Schiff's base European Chem. Bull Vol. 12 (8) pp.705-709 2023
- 3) Atinafu Abayneh, Tesfey Gebretsadik, Sisay Tadesse, Madhu Thomas "Synthesis, spectroscopic, structural characterization, conductivity and electrochemical studies of Schiff's base ligand and its copper complexes" Advances in Chemical Engineering and Sciences Vol. 8 pp. 241-254 2018
- 4) Amit R. Yaul, Vijaya V. Dhande, Gaurav B. Pethe, and Anand S. Anwar "Synthesis, Characterization, Biological and Electrical Conductivity Studies of Some Schiff's Base Metal Complexes" Bull. Chem. Soc. Ethiop. Vol 28(2) pp. 255-264 2014
- 5) Shubhangi Y. Deshmukh, Nilesh S. Padole, "Synthesis, Spectroscopic Characterization, Electrical Conductivity and Biological Studies of Heterocyclic Schiff's Base Metal Complexes" Journal of Emerging Technologies and Innovative Research Vol.9 (2) a794-a801 2022
- 6) Chao Meng, Zheng Gu, Jianfa Wang, Jinyong Sui, Shaokai Hu, Susu Zhang, Xiaoyi Zhang, Peiyao Zhang, Peiyao Li, Wengin Liu, Yifan Hu,"Synthesis and Characterization of aldamine condensed Schiff's bases and their iron salts" Vol. 68(2) pp.99-105 2023
- 7) Hamdi Temel, Umit Cakir, H. Ibrahim Ugras and Memet Sekersi "The Synthesis, Characterization, and Conductance Studies of New Cu(II), Ni(II) and Zn(II) Complexes with Schiff's Base Derived from 1,2-Bis-(o-aminophenoxy)Ethane and Salicylaldehyde"Vol.56 J. Coord. Chem. Vol. 56 (11), pp.943-951 2003
- 8) Y Z Ahmed, S R Selim, R S Frag & M EI Nawawy "Electrical properties and spectral studies of some Schiff's base complexes" Indian Journal of Chemistry, Vol. 33A, pp.20-25, 1994 January
- 9) V.D. Patel, K.R. Patel, K.P. Patel, M.N. Parmar, "Activation Energy of Electrical Conductivity of Some Binary Crystal" Vol.4 (3) pp.41-43 2015
- 10) Abdel-Amir M. Fenjan, Inas S. Mahdi, Selvana Adwar Yousif "Synthesis and Characterization of Some New Schiff's bases Derived from 7-hydroxy-4-methyl Coumarin"International Journal of Science and Research Vol.6(3) pp.1539-1545, 2017
- 11) S.R. Kelode "Electrical Conductivity of Cr(III), Mn(III) and Fe(III) Metal Complexes of 2-Hydroxy-5-Methyl-3-Nitroacetophenone Thiazole Schiff's Base" International Journal of Scientific Research in Science and Technology Vol.8(1) pp.402-405 2021,

- 12) N.J Suryavanshi, G.B. Pethe, S.G. Bhadange, A.S. Aswar "Synthesis, Characterization, thermal, electrical conductivity and biological studies of Schiff's base metal complexes" J. Indian Chem. Soc. Vol.90 pp.1327-1333, 2013
- 13) Emad Yousif, Ahmed Majeed, Khulood Al-Sammarrae, Nadia Salih, Jumat Salimon, Bashar Abdullah "Metal Complexes of Schiff's base: Preparation characterization and antimicrobial activity" Arabian Journal of Chemistry pp. 1-6 2013
- 14) F.K Ommenya, E.A Nyawade, D.M. Andala and J. Kinyua "Synthesis, Characterization and antibacterial activity of Schiff's base, 4-Chloro-2-[(E)-(4-Fluorophenyl)imino] methyl]phenol Metal(II) Complexes. Handwriting Journal of Chemistry Vol.2020, 2020
- 15) Esmaeili Alireza, Grivani Gholamhossein, "New Schiff's Base and Its Zn (II) Metallopolymer and Solid-State Conductivity" Iran. J. Chem. Eng. Vol.42 (7) pp. 2131-2140 2023
- 16) Umit Cakir, Hamdi Temel, Salih Ilhan and H. Ibrahim Ugras "Spectroscopic and Conductance Studies of New Transition Metal Complexes with a Schiff's Base Derived from 4-Methoxybenzaldehyde and 1,2-bis(p-Aminophenoxy)ethane Spectroscopy Letters Vol.36,(5)(6) pp.430-440 2003
- 17) Suman Malik, Archana Singh, Nayak Ahmed "Spectral characterization and thermal behaviour of Schiff's base metal complexes derived from 2-aminobenzimidazole" Advances in Applied Science Research, Vol.6 (8) pp.199-204, 2015
- 18) Kelode S.R and Jagnit P.R "Electrical Conductivity of Co (II), Ni (II) and Cu (II), Complexes derived from bidentate thiazole Schiff's base" Int. Research. J. of Science & Engineering, sp. Issue A7 pp.6-10 2020
- 19) Sadi A.H, Idris M.I and Bashir S.S "Synthesis, Characterization and Antimicrobial Studies of Ru (II) Complexes with Schiff's Base Co-Ligand Derived from 5,6-Diamino-1,10-Phenanthroline and Benzene-1,4-Dicarbaldehyde Bayero Journal of Pure and Applied Sciences, Vol.10(1) pp.468-476, 2017
- 20) Dr. S.E. Bhandarkar, P.P. Pathare, B.P Khobragade "A Comparative Study of Schiff's Base Metal Complexes Based on Its Biological Application: A Review, Journal of Emerging Technologies and Innovative Research (JETIR) Vol.9, (7), 2022
- 21) T. H. Al-Noor, N.S. Al-barki, A.A. Maihub, M.M. El-ajaily "Synthesis and Spectroscopic Characterization of Some Mixed Schiff's Base Complexes" International Journal of Science and Research (IJSR), Vol. 6 (3) pp. 2421-2426 2017
- 22) S. O. Mohod and D.T. Tayade "To Study the Thermodynamic Parameter of Substituted Thiocarbamidophenol in 70% Mixed Solvens at Constant Temperature by Conductometric Method" Vol.6 (3) pp.1712-1716 2017
- 23) Magda Ayad, Hisham Abdellatef, Mervat Hosny and Nagla Kabil "Conductometric Determination of Certain Pharmacological Drugs Using Silver and Bismuth" International Journal of Pharmaceuticals and Applied Sciences Vol.3(4) pp. 140-148, 2013
- 24) A.B.Dikkar, G.B. Pethe, and A.S. Anwar "Solute-Solvent Interactions in Solutions of 2-Hydroxy-5-Chloro-3-nitroacetophenone Isonicotinoylhydrazone in N,N-Dimethylformamide at 298-313 K According to Ultrasonic and Viscometric Data" Russian Journal of Physical Chemistry Vol.89 (12) pp.2197-2203, 2015
- 25) A.U. Mandakmare, M.L. Narwade, D.T. Tayade and A.B. Naik "Intermolecular Interactions in Dioxane-Water Solutions of Substituted Coumarin according to Ultrasonic Data, Russian Journal of Physical Chemistry Vol. 88, (13) pp.2334-2338 2014

¹U.D. Raval²V.S. Patel³A.K. Patel⁴N.A. Chaudhary⁵K.J. Agheda⁶M.K. Prajapati⁷K.N. Shah^{8*}A.N. Prajapati

**Physicochemical, Electrochemical
and DFT Characterization of
n-Butanol and Benzonitrile Binary
Mixtures**



Abstract: - Density (ρ) and Refractive index (n) of the binary mixtures of n-butanol and benzonitrile across the entire concentration range ($0.0 \rightarrow 1.0$) were measured experimentally for temperature ranges 303.15 K to 323.15 K in the interval of 10 K. Various parameters were such as reduced free volume (V_m/R_m), molecular radius (r), and internal pressure (P_{int}) evaluated from the experimentally measured data. Excess parameters such as excess refractive index (n^E), excess reduced free volume (V_m/R_m^E), excess molecular radius (r^E) and excess internal pressure (P_{int}^E) were also determined. These parameters were fitted to Redlich-Kister polynomial equations using the least-square fit method to obtain fitting parameters. Different mixing models for refractive index have been validated and tested. The confirmation of hydrogen bond formation in the binary mixture systems was validated through Fourier-transform infrared (FT-IR) spectra analysis. Density functional theory (DFT) method was used to determine the dipole moment and HOMO-LUMO analysis of both pure compounds. The study confirms the stability and reactivity of molecules. These studies were analyzed to elucidate the nature of hetero-interactions, specifically interactions between, unlike molecules, within the mixtures.

*Corresponding author: Department of Physics, Sardar Patel University, Vallabh Vidyanagar-388120, Gujarat, India

^{1,2,3,8} Department of Physics, Sardar Patel University, Vallabh Vidyanagar-388120, Gujarat, India

^{4,5} Department of Applied Physics, The M.S. University of Baroda, Vadodara-390001, Gujarat, India

⁶ Gujarat Industrial Research and Development Agency, Vadodara-390008, Gujarat, India

⁷ Department of Computer Engineering, Unitedworld School of Computational Intelligence, Karnavati University, Gandhinagar-382422, Gujarat, India

*Corresponding author email: anp3872@gmail.com

Copyright © JES 2024 on-line : journal.esrgroups.org

Keywords: Binary mixture, Refractive Index, Hetero-molecular interactions, Electrochemical properties, DFT, FT-IR Analysis, HOMO-LUMO Analysis.

I. INTRODUCTION

Understanding the refractive index property of mixed solvents at various temperatures is a crucial aspect in determining their structure and characterizing them. Mixed solvents are often employed as effective media in numerous chemical, industrial, and biological processes because they offer a broad spectrum of mixtures with tailored properties [1]. Hydrogen bonding is crucial in both fundamental sciences and industrial applications. Despite numerous experimental and theoretical studies aimed at elucidating hydrogen bonding, it continues to be a dynamic area of research [2]. Combined with other thermodynamic data, refractive index measurements are valuable for practical engineering calculations. Additionally, the refractive index is instrumental in assessing substance purity and calculating molecular electronic polarizability [3]. FTIR spectroscopy provides absorption spectra unique to the molecular structure of compounds. It is also utilized to confirm the presence of intermolecular interactions between different molecules in the solution [4,5].

On the basis of their industrial importance the liquids for binary mixture were chosen i.e., Benzonitrile (BN) having -CN functional group is a significant compound within the nitrile family. Nitriles are aprotic liquid is a highly polar amphiphile, is the most important solvent that has been known to have only proton acceptor site. Its derivatives are extensively utilized in industrial, pharmaceutical, and medicinal applications. Due to its broad utility and straightforward structure, benzonitrile has been the subject of numerous studies. Alcohols (n-Butanol) having -OH functional group are commonly used solvents due to their protic nature and ability to self-associate. n-Butanol found applications in pharmaceutical industry, in medications for animals, and in the production of perfumes and paint removers [4-8]. Furthermore, alcohols and nitriles play a significant role in a diverse range of industrial and consumer applications. Consequently, detailed knowledge of their physical properties is essential for practical purposes.

The present investigation, reports refractive index (n) and density (ρ) of n-butanol with benzonitrile binary mixtures over the entire concentration range at three different temperatures. Furthermore, computational and spectroscopic analyses are performed to gain insights into the intermolecular interactions present in these binary mixture systems.

II. EXPERIMENTAL AND COMPUTATIONAL METHODS

Benzonitrile with 99% for synthesis (GC) and n-Butanol with 99.5% AR grade (GC) was also supplied by LOBA Chemie (India). Both liquids were used without any further

purification. The solution of Benzonitrile with n-Butanol was prepared at 11 different concentrations by volume fraction. The refractive index values of pure and binary liquid mixtures were determined using an Abbe refractometer, with sodium D light at constant temperature. To maintain a constant temperature, a temperature controller system equipped with a water bath was employed, ensuring temperature stability with an uncertainty of ± 0.1 K. Refractive index measurement uncertainty is ± 0.0001 . The density of pure liquids and their binary mixtures was determined using an airtight 10 ml glass density bottle. The volume of the mixture was kept constant, and the mass was measured using a digital balance with an accuracy of 0.0001 g. FT-IR spectra for both pure substances and equimolar binary mixtures were obtained in the 4000–400 cm^{-1} range using an ALPHA (Bruker, Germany) FTIR spectrometer with a precision of 0.05 cm^{-1} . Computational details The geometry optimization procedure was performed utilizing the Density Functional Theory (DFT) method with B3LYP functional calculations and the 6-311G (d,p) basis set in ORCA 5.0.0 code [9,10]. The experimental values of ρ and n for pure liquids at different temperatures are compared with literature values in Table 1 found quite good agreement with reported literature values.

Table 1. Experimental densities (ρ), and refractive index (n) for pure liquids at various temperatures and comparison with literature data.

Compound	T (K)	ρ ($\text{g}\cdot\text{cm}^{-3}$)		n	
		Expt.	Lit.	Expt.	Lit.
Benzonitrile	303.15	0.9960	0.9963[11]	1.5235	1.5252[11]
	313.15	0.9909	0.9871[11]	1.5210	1.5209[11]
	323.15	0.9828	-----	1.5185	-----
n-Butanol	303.15	0.8012	0.8019[1]	1.3985	1.3950[1]
	313.15	0.7942	0.7946[1]	1.3895	1.3935[1]
	323.15	0.7887	-----	1.3860	-----

III. THEORY

From the density (ρ) and refractive index (n) experimentally measured values, using it below mentioned optical and volumetric parameters were evaluated:

$$\text{Reduced free volume } (V_m/R_m), \quad V_m/R_m = \left[\frac{n^2+2}{n^2-1} \right] \quad (1)$$

$$\text{Molecular radii } (r), \quad r = \left[\left\{ \left(\frac{3}{4\pi N} \right) \left(\frac{n^2-1}{n^2+2} \right) \right\} V_m \right]^{\frac{1}{3}} \quad (2)$$

Internal pressure (P_{int}),
$$P_{int} = \frac{2^{1/6}RT}{2^{1/6}V_m - 2rN^{1/3}V_m^{2/3}} \quad (3)$$

Where X_1 , X_2 , M_1 and M_2 represent the volume fraction and molecular weight of pure components. N , R and T denote Avogadro number, Gas constant and absolute temperature, respectively. The excess parameters $(n)^E$, $(V_m/R_m)^E$, $(r)^E$ and $(P_{int})^E$ were determined and fitted in Redlich-Kister Polynomial [12] and the fitting parameters are listed in Table 2.

IV. RESULT AND DISCUSSION

A close perusal of Figure 1(A-D) shows that the variation of n , ρ , r and P_{int} of binary mixture increase as the concentration BZ increases in the mixture.

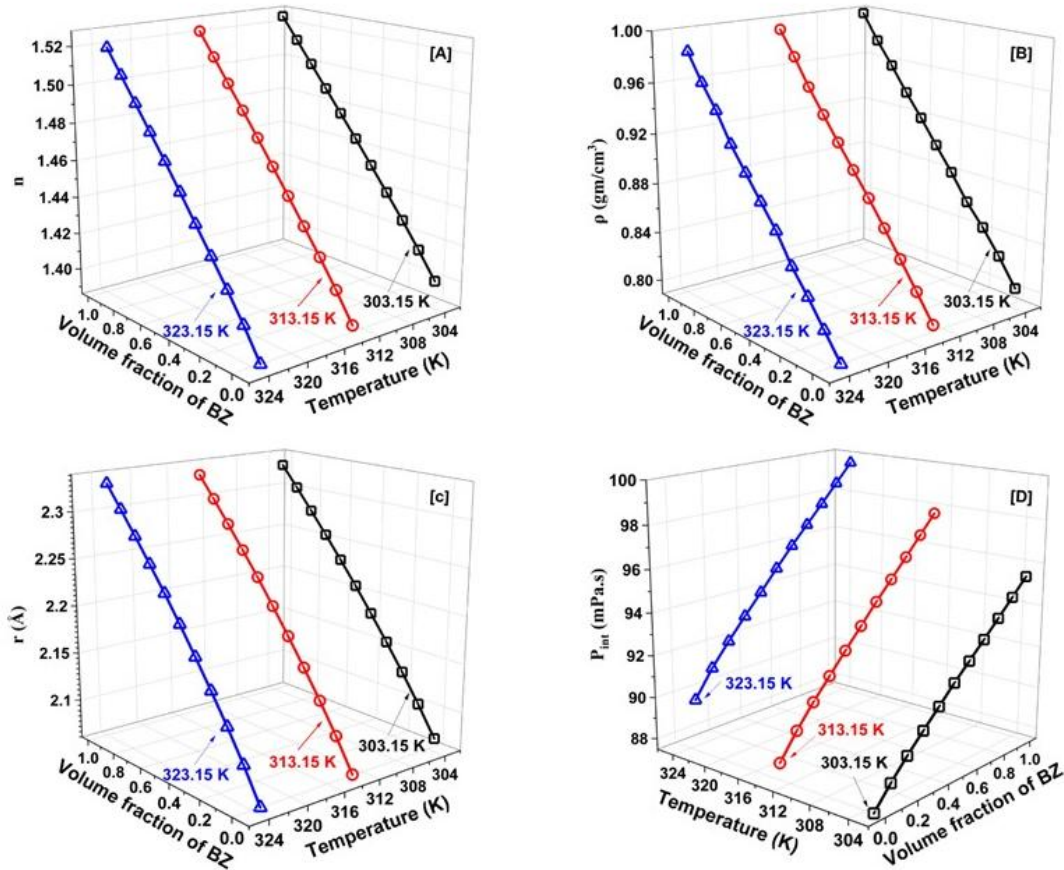


Figure 1(A-D). Variation of (n) , (ρ) , (r) and (P_{int}) against volume fraction of BZ in (n-BuOH+BZ) binary mixture at different temperature.

The excess functions provide insight into the degree to which liquid mixtures deviate from ideal behaviour, making these properties crucial for understanding intermolecular interactions and the molecular dynamics in hetero-molecular systems. In this study, we calculated the $(n)^E$, $(V_m/R_m)^E$, $(r)^E$ and $(P_{int})^E$ for binary mixtures. All these computed values were then fitted to the Redlich–Kister polynomial to model the non-ideal behaviour of the mixtures accurately.

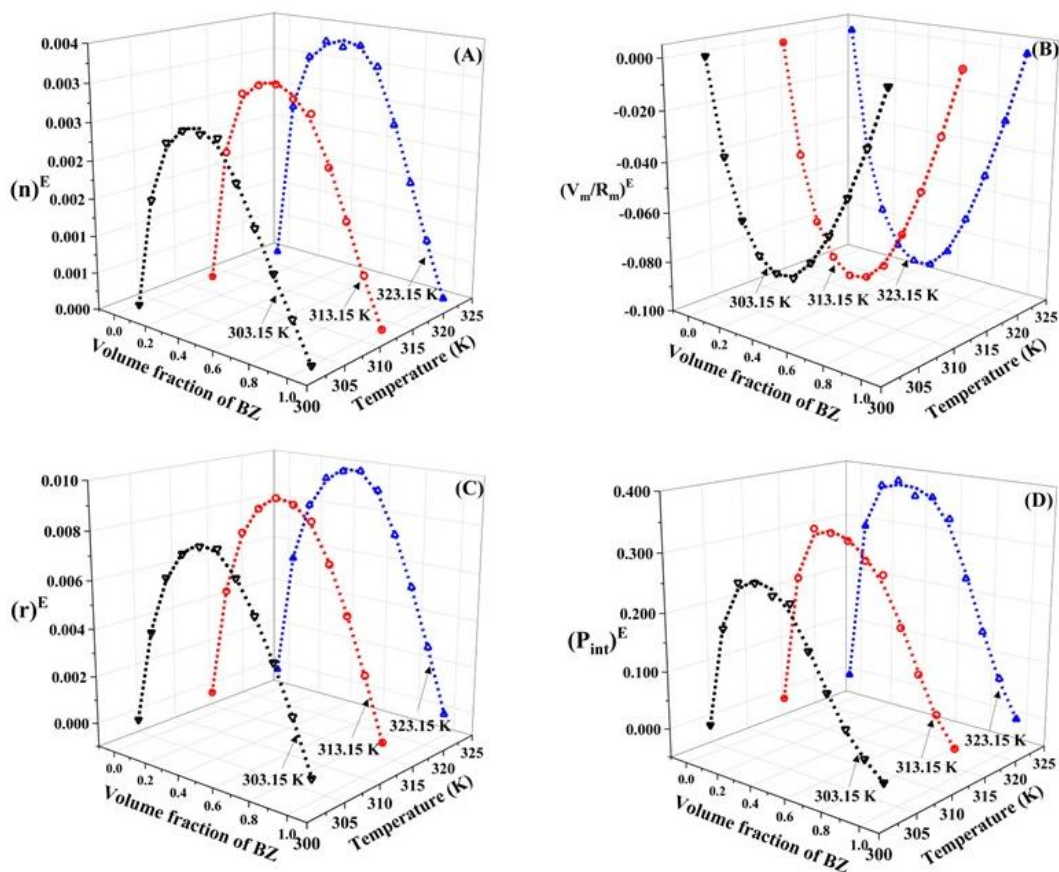


Figure 2(A-D). Plot of $(n)^E$, $(V_m/R_m)^E$, $(r)^E$ and $(P_{int})^E$ against volume fraction of BZ at different temperatures. (geometrical shapes show experimental data points and dotted line show R.K.fitted points).

Table 2. Values of coefficients (a_i) with correlation coefficient (δ) for the excess refractive index $(n)^E$, excess reduced free volume $(V_m/R_m)^E$, excess molecular radii $(r)^E$ and excess internal pressure $(P_{int})^E$ of n-Butanol + Benzonitrile mixture at different temperatures.

Parameters	Temperature (K)	a_1	a_2	a_3	a_4	a_5	δ
$(n)^E$	303.15	0.0096	-0.0055	-0.0006	-0.0025	0.0052	0.9987
	313.15	0.0111	-0.0040	0.0019	-0.0075	0.0037	0.9990
	323.15	0.0129	-0.0035	-0.0006	-0.0113	0.0102	0.9992
$\Delta(V_m/R_m)$	303.15	-0.3071	0.0876	-0.0154	0.0280	-0.0400	0.9999
	313.15	-0.3565	0.0904	-0.0356	0.0685	-0.0395	0.9999
	323.15	-0.3801	0.0918	-0.0168	0.1021	-0.0964	0.9999
$(r)^E$	303.15	0.0309	-0.010	0.0002	-0.0043	0.0070	0.9997
	313.15	0.0359	-0.0086	0.0039	-0.0112	0.0061	0.9997
	323.15	0.0388	-0.0082	-0.0009	-0.0171	0.0167	0.9998

$(P_{\text{int}})^E$	303.15	0.9183	-0.8297	-0.1035	-0.3664	0.7547	0.9977
	313.15	1.1489	-0.6202	0.2838	-1.1016	0.5283	0.9982
	323.15	1.4394	-0.5503	-0.1076	-1.6982	1.5089	0.9987

Figure 2(A-D) show positive deviation for $(n)^E$, $(r)^E$ and $(P_{\text{int}})^E$ are over the entire composition range (0.0 – 1.0) of BZ in binary mixtures with different magnitudes while $(V_m/R_m)^E$ shows negative deviation against volume fraction of BZ over the entire composition range (0.0 – 1.0). The positive deviation of $(n)^E$, $(r)^E$ and $(P_{\text{int}})^E$ on volume fraction basis can interpreted as the indication of intermolecular interaction between molecular species. Negative deviation $(V_m/R_m)^E$ suggests strong hetero molecular interaction. Further the positive deviation in $(P_{\text{int}})^E$ indicates that attractive forces are stronger than repulsive interactions within the mixture [6,7].

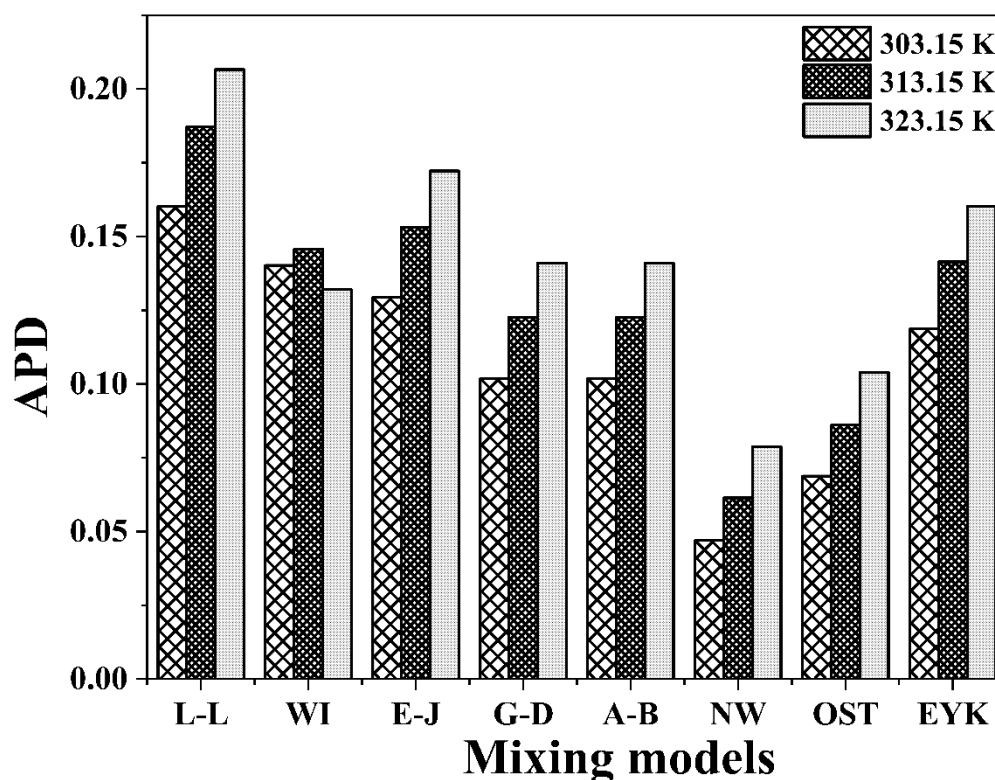


Fig. 3. Plot of APD versus Mixing models for theoretical comparison of refractive index values at different temperatures.

For many practical applications, predicting the nonideality of binary liquid mixtures using the physical parameters of the pure components is essential. The comparative analysis of refractive index (n) of liquid mixtures can be estimated by applying various mixing models available in the literature [6,7]. In the present study, eight mixing models were tested and validated. From the Figure 3 it is clear that among all mixing model, Newton (NW) show least

APD values at all studied temperatures which suggests that NW model fit refractive index data quite accurately among other mixing models for the studied system.

The FT-IR analysis demonstrates the presence of intermolecular hydrogen bonding within binary mixture of (n-BuOH + BZ). Figure 3(A-B) show FTIR spectra of pure compound and equimolar concentration of (n-BuOH + BZ). By comparing the FT-IR spectra of equimolar binary mixtures with those of the corresponding pure compounds, it is observed that magnitude of C-H stretching is suppressed in equimolar concentration (fig. 3(A)) while noticeable shift in broad O-H peak is observed (Fig 3(B)). The observed shifts are attributed to strong intermolecular interactions hydroxyl group in n-Butanol and the cyanide group in Benzonitrile [3,8].

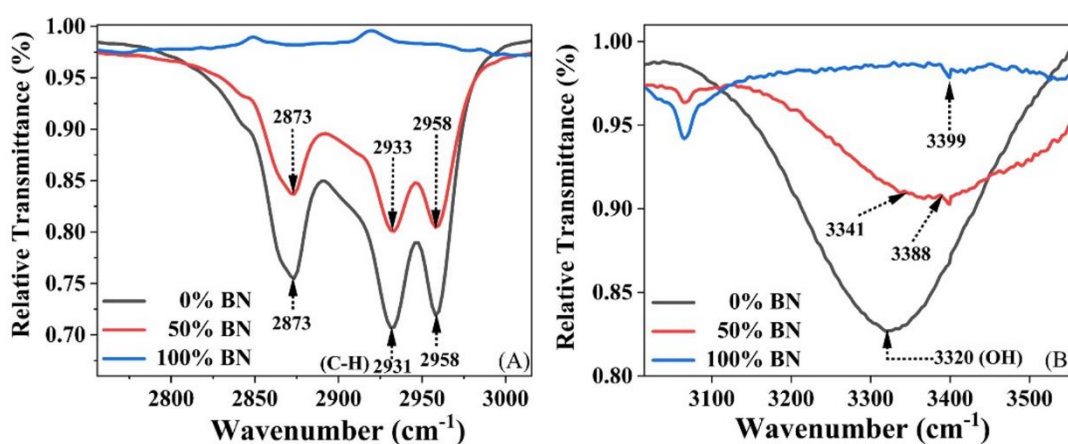


Fig. 4. FTIR spectra (A) C-H stretching and (B) O-H stretching vibration bond in Benzonitrile + n-Butanol.

The geometrical effect on component molecule intermolecular interaction was studied using DFT simulations. Avogadro software and ORCA 5.0 with a functional B3LYP and 6-311G (d,p) basic set optimized the structures of the pure and binary molecules (BZ, BZ + BU, BU) studied in a 1:1 ratio and exhibited them in Fig. 5 with dipole orientation [9,10]. Dipole moment values in the literature match theoretical values shown in Table 3.

Table 3. Dipole moments of the BZ, BU and equimolar binary mixture.

Compound Name	Dipole moment (Debye)	
	Theoretical Value	Literature Value
BZ	4.57	4.51 [13]
BZ + BT	3.36	----
BT	1.68	1.66 [10]

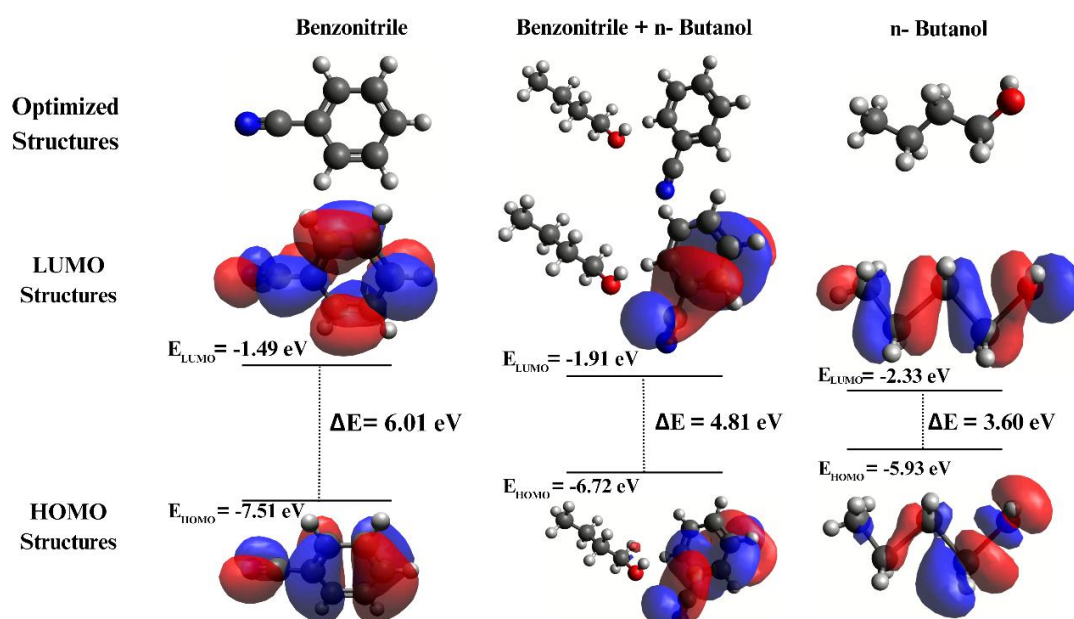


Fig. 5. Optimized and HOMO-LUMO structure of BZ, BZ + BU, and BU

The structures were optimized before HOMO-LUMO study. A molecule's electron-donating capacity is explained by its highest occupied molecular orbital (HOMO) and electron-absorbing ability by its lowest LUMO. Energy gap size, defined by the HOMO-LUMO energy differential, indicates molecular chemical stability. A bigger energy gap value suggests stability and low reactivity, whereas a lower number indicates molecular activity. We also learn about electrophilic and nucleophilic substitution in molecular electron density. The positive charge is concentrated in the red region, which contains many electrons, whereas the blue region has few. We estimated numerous parameters of BZ, BU, and their equimolar combination using HUMO-LUMO analysis. Properties such as HOMO and LUMO energies (E_H and E_L), electronegativity (χ), ionization potential (IP), energy gap (ΔE), electron affinity (EA), and chemical potential (μ) [10]. E_H and E_L values for all substances varied from -7.51 to -5.93 and -1.49 to -2.33 eV, respectively, according to Table 4. A 6.01 eV energy gap value

for BZ indicates the highest stability of all chemicals studied. BU has an energy gap ΔE of 3.60 eV. BZ molecules easily form hydrogen bonds with BU due to its greater polarity. The ionization potential of a molecule is closely correlated with the energy of its highest occupied molecular orbital (HOMO), which indicates its ability to donate electrons. Electron affinity is associated with both the energy level of the lowest unoccupied molecular orbital (LUMO) and the tendency to accept electrons. The chemical potential is a key factor in understanding the stability of a molecule and its tendency to undergo nonspontaneous disintegration. Electronegativity is a measure of the strength of the attraction between electrons.

Table 4. Various Electro-chemical parameters of the BZ, BU, and equimolar binary mixture.

Compounds Name	E_H	E_L	IP	EA	ΔE	χ	μ
				(eV)			
BZ	-7.51	-1.50	7.51	1.50	6.01	4.50	-4.50
BZ + BU	-6.72	-1.91	6.72	1.91	4.81	4.32	-4.32
BU	-5.93	-2.33	5.93	2.33	3.60	4.13	-4.13

V. CONCLUSIONS

Density (ρ) and refractive index (n) across the entire composition range (0.0 \rightarrow 1.0) of n-butanol and benzonitrile mixtures have been experimentally determined at 303.15, 313.15, and 323.15 K temperatures at atmospheric pressure. Different parameters namely, molar volume (V_m), molar refraction (R_m), reduced free volume (V_m/R_m), molecular radii (r), and internal pressure (P_{int}) as well as excess parameters (n)_E, (V_m/R_m)_E, (r)_E and (P_{int})_E have been computed and the results were fitted to the Redlich–Kister equation. The (n)_E, (r)_E, (PA)_E and (P_{int})_E values are positive over the entire composition range while the deviation in (V_m/R_m)_E is negative over the whole composition range suggest strong intermolecular interactions of n-butanol upon addition of benzonitrile, surpassing the hydrogen bond interactions between n-butanol and benzonitrile molecules. Additionally, the refractive index (n) of the binary mixtures were theoretically correlated using various mixing models based on pure component data. The best fit results are of Newton (NW) mixing model with minimum Average Percentage Deviation (APD). The FT-IR spectra indicate the formation of

intermolecular hydrogen bonds between the -CN group of benzonitrile and the -OH group of n-butanol ($C\equiv N\cdots H-O$). Additionally, computational studies using Density functional theory (DFT) were conducted to gain insight into the intermolecular interactions within the binary mixture systems being examined.

VI. ACKNOWLEDGMENTS

The authors are thankful to Head, Department of Physics, Sardar Patel University, Vallabh Vidyanagar for his constant encouragement and support.

VII. REFERENCES

- [1] M. Chandra Sekhar, T. Madhu Mohan, T. Vijaya Krishna, A. Venkatesulu, and K. Siva Kumar, "Density, Refractive Index, Speed of Sound and Computational Studies of Intermolecular Interactions in Binary Mixtures of 2-Chloroaniline with Butanols (1-Butanol, 2-Butanol) at $T = (303.15-318.15)$ K," *Journal of Solution Chemistry*, vol. 44, no. 2. Springer Science and Business Media LLC, pp. 237–263, Feb. 2015.
- [2] R. K. Shukla, P. Misra, S. Sharma, N. Tomar, and P. Jain, "Refractive index and molar refractivity of benzonitrile, chlorobenzene, benzyl chloride and benzyl alcohol with benzene at $T = 298.15, 303.15, 308.15$ and 313.15 K," *Journal of the Iranian Chemical Society*, vol. 9, no. 6. Springer Science and Business Media LLC, pp. 1033–1043, Aug. 21, 2012.
- [3] S. Deshmukh, A. Mohod, K. Pattebahadur, S. Patil, A. Kumbharkhane, and P. Khirade, "Influence of dielectric, Electro-Optic Kerr Effect and spectroscopic characterisation on polar–polar binary liquid mixture," *Physics and Chemistry of Liquids*, vol. 60, no. 1. Informa UK Limited, pp. 141–163, May 12, 2021.
- [4] L. Sakhtemanian and M. H. Ghatee, "Multi-structural feasibility in benzonitrile solvent through the multi hot-potential centers," *Journal of Molecular Liquids*, vol. 336. Elsevier BV, p. 116309, Aug. 2021. Doi: 10.1016/j.molliq.2021.116309.
- [5] A. N. Prajapati, V. A. Rana, and A. D. Vyas, "Study of molecular interaction between some primary alcohols and anilines using concentration dependent dielectric properties," *Indian Journal of Pure & Applied Physics*, vol. 51 pp. 104-111, Feb. 2013.
- [6] A. N. Prajapati, V. A. Rana, A. D. Vyas and D.H. Gadani, "Optical and volumetric study of molecular interactions in binary mixtures of 1-Propanol (1-PrOH) and Fluorobenzene (FB)," *Journal of International Academy of Physical Sciences*, vol. 16 pp. 387-398 Dec. 2012.

- [7] A. N. Prajapati, "Acoustic and refractometric study of binary mixtures of 1-Propanol + Benzonitrile at 313 K," *Indian Journal of Pure & Applied Physics*, vol. 55, no. 4, pp. 297-303, Apr. 2017.
- [8] F. A. Saif, P. B. Undre, S. A. Yaseen, S. S. Patil, and P. W. Khirade, "Conformational and dielectric relaxation studies on hydrogen bonded binary mixture of ethyl acetate in 1-butanol and 1-pentanol," *Ferroelectrics*, vol. 519, no. 1. Informa UK Limited, pp. 61–71, Oct. 26, 2017.
- [9] Sawant, Arun Balkesh, and Sunil G. Wagh, "Density, viscosity, DFT and FTIR study of tertiary butyl alcohol and ethanol with DMSO and DMF at room temperature," *Indian Journal of Pure & Applied Physics* vol. 56, no. 5, pp. 405-414, May 2018.
- [10] F. Akman, A. Demirpolat, A. S. Kazachenko, A. S. Kazachenko, N. Issaoui, and O. Al-Dossary, "Molecular Structure, Electronic Properties, Reactivity (ELF, LOL, and Fukui), and NCI-RDG Studies of the Binary Mixture of Water and Essential Oil of *Phlomis bruguieri*," *Molecules*, vol. 28, no. 6. MDPI AG, p. 2684, Mar. 16, 2023.
- [11] N. Chaudhary and A. Kumar Nain, "Physicochemical studies of intermolecular interactions in 1-butyl-3-methylimidazolium tetrafluoroborate + benzonitrile binary mixtures at temperatures from 293.15 to 318.15 K," *Physics and Chemistry of Liquids*, vol. 59, no. 3. Informa UK Limited, pp. 358–381, Jan. 22, 2020.
- [12] O. Redlich and A. T. Kister, "Algebraic Representation of Thermodynamic Properties and the Classification of Solutions," *Industrial & Engineering Chemistry*, vol. 40, no. 2. American Chemical Society (ACS), pp. 345–348, Feb. 1948.
- [13] K. Wohlfart, M. Schnell, J.-U. Grabow, and J. Küpper, "Precise dipole moment and quadrupole coupling constants of benzonitrile," *Journal of Molecular Spectroscopy*, vol. 247, no. 1. Elsevier BV, pp. 119–121, Jan. 2008.

© 2024. This work is published under

[https://creativecommons.org/licenses/by/4.0/legalcode\(the\"License\"\)](https://creativecommons.org/licenses/by/4.0/legalcode(the\).

Notwithstanding the ProQuest Terms and Conditions, you may use this content in accordance with the terms of the License.

¹V. N. Bombatkar²S. V. Tiwari³R. V. Barde*⁴O. P. Gunjkar

Regular Paper
Synthesis, Characterization and
AC Conductivity Study of
Polyindole/Stannic Oxide
Nanocomposites



Abstract: - The conducting polymer Polyindole (PI_n) is synthesized by chemical oxidative polymerization route and ex situ approach was used to produce PI_n/SnO₂ composites in weight % stoichiometry. AC electrical conductivity is analysed for PI_n/SnO₂ composites. The measurements are carried out by varying frequency ranges from 5kHz to 5 MHz XRD and FTIR characterization techniques confirms the crystalline structure and structural bonding of the composites. The highest concentration of SnO₂ shows the highest intensity peaks in XRD. AC conductivity increases with increase in frequency. The impedance plot also suggests to the increase in ac conductivity for the studied samples. The dielectric loss factor has higher value for lower concentration of Stannic oxide (SnO₂) sample.

Keywords: Polyindole, Stannic oxide, chemical oxidative polymerization, AC electrical conductivity.

I. INTRODUCTION

Numerous advancements have been made since conducting polymers were discovered in the late 1970s, and diverse uses may be found in the fields of science and engineering [1]. Conducting polymers, or CPs, can be easily and affordably produced on a large scale using chemical or electrochemical methods. CPs often has narrow, adjustable bandgaps. Particularly, CP's high conductivity and electroactive qualities enable them to catalyse redox reactions in fuel cells, dye-sensitized solar cells (DSSCs), biosensors, and other devices [2]. Additionally, CP nanomaterials are excellent candidates for use in optoelectronic and electronic sensing systems due to their large surface areas, biocompatibility, and ease of surface modification [3]. Because conducting polymers can inhibit the corrosion of a number of easily oxidizable materials, they have been employed as efficient coating against corrosion materials to protect metals. Examples of these polymers are polyaniline and polypyrrole. Polyindole is a suitable option for a number of applications, including organic electronics[4]. Compared to PANI and PPy, it has a slower rate of degradation, high redox activity, air stability, and good thermal stability[5]. It has several benefits in a range of electronics applications and other characteristics that set it apart from other conducting polymers [6]. The family of metal oxides have been useful in various fields at great extent. When oxides are combined, the materials overall electrical structure is altered. This includes changes to the surface and bulk properties [7]. SnO₂ is one of the most appealing and promising materials. Because SnO₂ nanoparticles have outstanding qualities like photosensitivity, environmental friendliness, and photostability, they are a good photocatalyst for the destruction of organic contaminants in aqueous solution. A growing interest in using SnO₂ anodes in lithium batteries has been observed recently. This is because of the oxides physical properties, such as transparency and semiconductivity, which make it a highly desirable oxide from a technological standpoint for gas sensors, white pigments for conducting coatings, transparent conducting coatings for solar cells, catalysts, and surge arrestors (varistors) [8,9].

As far as from the above discussion we have decided to study the AC electrical conductivity of PI_n/SnO₂ nanocomposites. To the greatest extend of our understanding there is not any data available in the study of AC electrical conductivity of PI_n/SnO₂.

¹*Corresponding author:

Government Vidarbha Institute of Science and Humanities, Amravati 444604, India.

Email id: rajeshbarde1976@gmail.com

¹ Government Vidarbha Institute of Science and Humanities, Amravati 444604, India

Copyright©JES2024on-line:journal.esrgroups.org

I. EXPERIMENTAL

1. Synthesis of SnO₂ nanoparticles

The nanoparticles of SnO₂ were prepared by sonication method. In this Athena Ultrasonic Homogenizer (Probe Sonicator) is used for sonication. Typically, 5 gm of SnO₂ was dissolved in 100 ml of double distilled water and was stir on magnetic stirrer about 20 min. Then this mixture was ultrasonicated for 30 min. a pale white colour precipitate was formed. This precipitate was filtered, washed in double distilled water and then wash by ethanol and dried out in an air oven at 100° C for 4 hours [10].

2. Synthesis of Polyindole

Polyindole was synthesis from the monomer indole by chemical oxidative route, where ferric chloride (FeCl₃) is used as an oxidizing agent. 1:1 M ratio is maintained of the indole monomer and ferric chloride. (1M) of the aqueous solution was taken in beaker and kept for 45 min at room temperature while being constantly stirred on a magnetic stirrer. A dropwise FeCl₃ is added to the indole solution and for the next 3 hours stirring is continued. After 8-10 hours the mixture is settled down and blackish green colour confirms the formation of polyindole. After filtering this mixture, the precipitate was washed several times with double-distilled water to get rid of the impurities. After four hours of drying at 60°C, the resulting PIn was crushed with a mortar and pestle [11-12].

3. Synthesis of PIn/SnO₂ nanocomposites

Ex-situ approach was used to produce the PIn/SnO₂ composites in weight% stoichiometry. The SnO₂ content was varied at intervals of 5 wt% to create the composites with respect to PIn. The range for preparing composites was set at 5 to 20 weight%. In this manner, samples were produced for additional characterization and AC electrical conductivity analysis at room temperature [13]. The samples were nomenclature as AP for pure PIn, A0 for SnO₂ and A1, A2, A3, A4 for PIn/5% SnO₂, PIn/10% SnO₂, PIn/15% SnO₂ and PIn/20% SnO₂.

II. RESULTS AND DISCUSSION

1. XRD Analysis

At room temperature, the XRD patterns of pure PIn, SnO₂ nanoparticles, and PIn/SnO₂ composites were recorded in 2θ ranges: 10°–80°. The diffractogram all samples are shown in Fig.1. Diffraction peaks of A0 coincide with the planes and are detected at (110), (101), (200), (111), (211), (220), (002), (310), (112), (301), (202) and (321) at 2θ diffraction angle 26.59°, 33.89°, 37.96°, 51.80°, 54.8°, 57.86°, 61.91°, 64.76°, 65.99°, 71.30° and 78.74° consecutively. These peaks are belonging to cassiterite crystal phase with tetragonal rutile structure [10]. SnO₂ mean crystallite size was determined to be 49.01 nm using the Debye-Scherrer formula $D = (k\lambda) / (\beta \cos\theta)$ where k is the Scherrer constant, λ is the X-ray wavelength, β is the full width half maximum, and θ is the Bragg's angle. As the concentration of SnO₂ increases in A0, A1, A3 and A4 the peak intensity also increases.

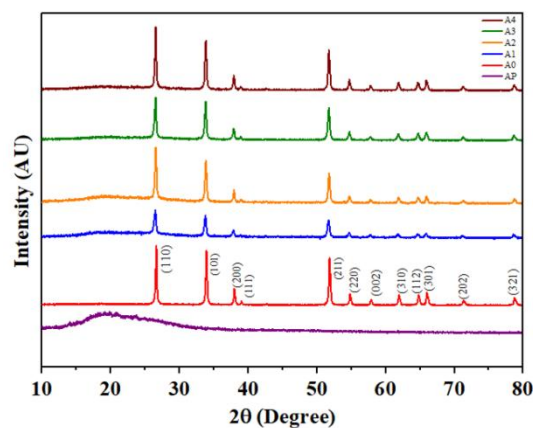


Fig 1 XRD analysis of AP, A0, A1, A2, A3 and A4.

2. FTIR Analysis

In the FTIR study of pure PIn (AP) the major peak is observed at 3404 cm⁻¹ which indicates the N-H stretching and the polymerization does not occur at nitrogen. The peak at 1601 cm⁻¹ provide us the details of C-C stretching of benzenoid ring indole. Also the C-N and C=N bond stretching is observed at peaks 1447 cm⁻¹ and 1331 cm⁻¹. The peak at 744 cm⁻¹ indicates out of plane deformation of benzene or we can say that C₂-H and C₃-H bonds are only present in case of indole. Besides the peaks at 1442, 1331, 1238 and 1092 cm⁻¹ are induced by different

stretching frequencies of aromatic ring. According to the FTIR spectra analysis the coupling in PIn occurred between the C2 and C3 monomer sites. But it is not possible to determine whether this structure is regular or random. The peak 2927 cm^{-1} are induced by the stretching vibrations of $-\text{CH}_2$ bond. [14, 15] The same peaks are observed for corresponding composites A1, A2, A3 and A4 respectively mentioned in fig 2.

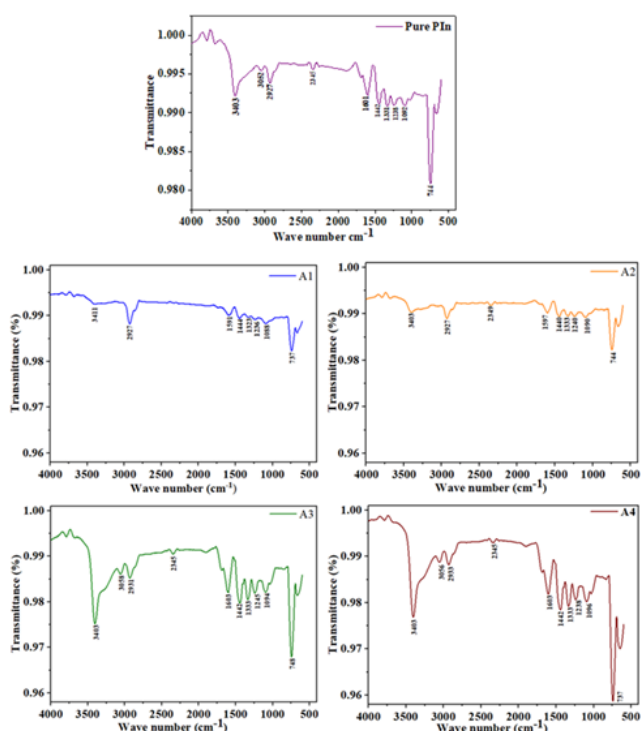


Fig 2 FTIR analysis of A0, A1, A2, A3 and A4.

3. AC Conductivity analysis

As the data is examined from the experiments in correlation with complex impedance and phase angle i.e. $|Z|$ and $|\theta|$ at higher frequency range. A graph is plotted between real and imaginary part (Z' and Z'') of impedance with increase in frequency as shown in fig 3 (a). Few conclusions are put forward the plot of Z' and Z'' tends to decrease linearly towards the origin implies that the conduction mechanism is active [16]. Polarization resistance acts as the charge transfer resistance at very low frequencies. In contrast, a high frequency will reduce the resistance [17].

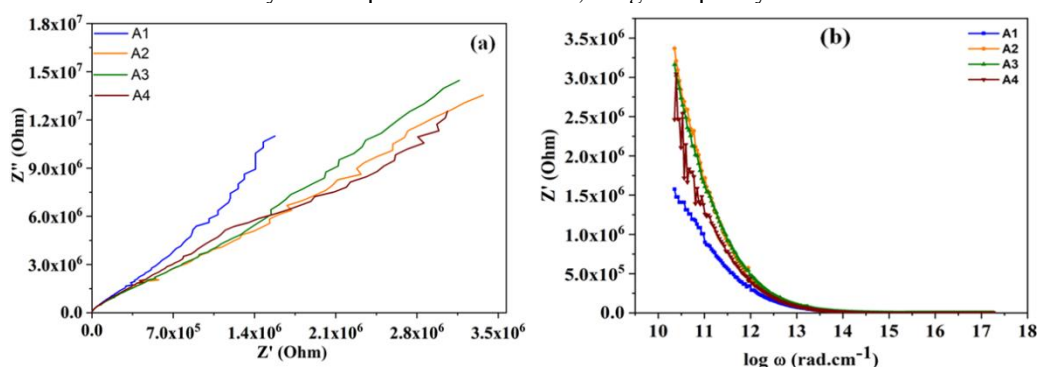


Fig 3.(a) Nyquist plot and (b) Plot of Z' as a function of frequency for all samples at room Temperature.

With an increase in frequency the value of real impedance tends to decrease suggesting to the increase in ac conductivity as shown in fig 3 (b). The values of Z' merge at higher frequency region for all the stoichiometric ratios. This behavior could be caused by the material's barrier potential decreasing and space charge releasing as the variation of composites rises [10].

Fig 4 (a) shows frequency- dependent conductivity plot of $\log(\sigma)$ versus $\log(\omega)$. The conductivity increases as frequency attains the higher values. Jonscher's universal law relation is employed to analyze the frequency dispersion characteristic throughout the high frequency region,

$$\sigma(\omega) = \sigma(0) + A\omega^n$$

Where, the sample's frequency-independent DC conductivity is denoted by $\sigma(0)$, the power law exponent, n , lies in the range $0 < n < 1$ [18, 19].

The conductivity data of all samples have been fitted to the above equation. The fitted curves are represented by the solid lines shows a fairly strong relation with the experimental values [20].

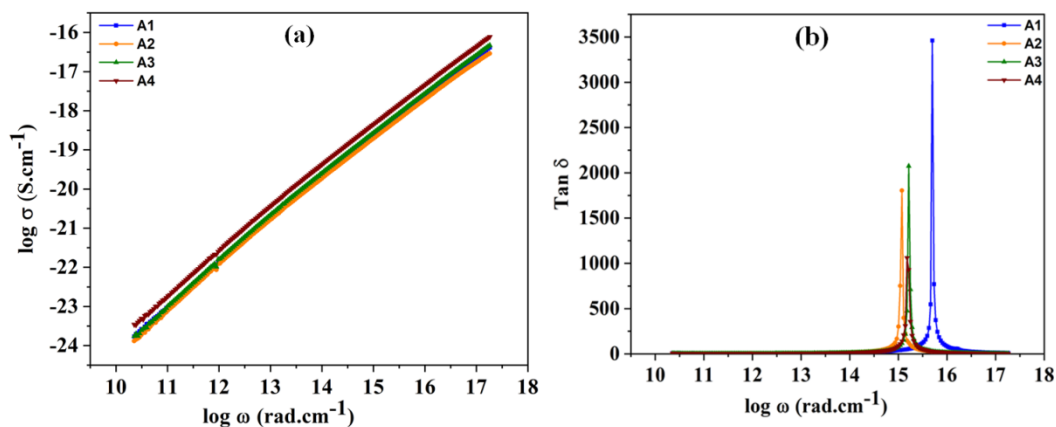


Fig 4 (a) Frequency dependent conductivity plot and (b) Plot of dielectric loss verses $\log(\omega)$ for all samples at room Temperature

At a given frequency, the phase difference caused by energy loss within the sample is reflected by the dielectric loss factor ($\tan \delta$). Fig 4 (b) displays the frequency dependence of $\tan \delta$ for all glass samples at various temperatures. Because the active component of the current increases quicker than the reactive component, $\tan \delta$ reaches a maximum at certain frequencies. $\tan \delta$ is observed to decrease with frequency at higher frequencies due to an increase in the reactive component despite the loss of an independent active component [21].

There could be two primary causes of the dielectric loss. The first section is the relaxation of Debye-type independently rotating dipoles that is thermally activated, where the only excitation source is thermal energy. The second portion arises at higher temperatures and is caused by an electrical scenario where there is an electron-phonon interaction. It rises with temperature [10,22].

An analogous method for evaluating a materials complex electrical response which minimizes or cancel the effect of electrode polarization. A plot between the real and imaginary part of electric modulus i.e., M' verses M'' is shown in fig 5 A semicircular arc in the midway of M' axis is observed which is because of some characteristic properties of the material. The impedance is hence shown as,

$$\frac{1}{Z_{CPE}} = Y_0(j\omega)^\beta$$

Where, Y_0 is admittance $|\frac{1}{|Z|}|$ and $0 < \beta < 1$ [23, 24].

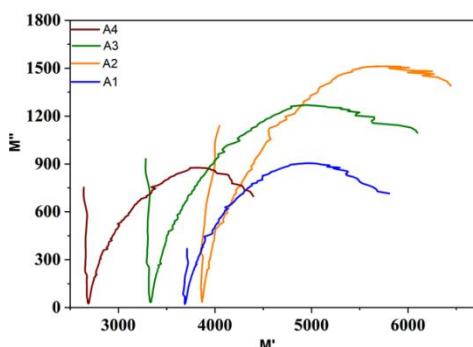


Fig 7. Nyquist plot of electrical modulus for all Samples at room Temperature.

III. CONCLUSION

In Summary, Polyindole was prepared by chemical oxidative method and FeCl_3 used as an oxidizing agent in the ratio 1:1 of PIn to FeCl_3 . The complex PIn- SnO_2 synthesized by Ex situ chemical method. The XRD shows the amorphous nature of pure polyindole and the composition of PIn- SnO_2 shows the crystallinity of material. The crystalline size of the material found to be 49.01 nm. The FTIR shows the major peak of N-H stretching at 3404 cm^{-1} and 1601 cm^{-1} indicate the C-C stretching of benzenoid ring indole. The AC conductivity of the given material rises with frequency behavior. The lowest concentration of SnO_2 indicates the large Dielectric loss factor. The impedance plot indicates the rise in AC conductivity behavior. From the above study it can be inference that all the parameters show the good surrounding for applicable to biological and optical studies.

ACKNOWLEDGMENT

The authors would like to thanks Head, Department of Physics and Electronics, Government Vidarbha Institute of Science and Humanities, Amravati for their guidance and support during this study. Authors also acknowledge Director, Government Vidarbha Institute of Science and Humanities, Amravati for providing necessary facilities to complete this study.

REFERENCES

- [1] B. Gupta, D. Chauhan and R. Prakash, Controlled morphology of conducting polymers: Formation of nanorods and microspheres of polyindole, *Materials Chemistry and Physics* vol.120,pp. 625–630, 2010.
- [2] Qingin Zhou and Gaoquan Shi, Conducting polymer-based catalysts, *Journal of the American chemical society*, pp. 2868-2876, 2016.
- [3] Chul Soon Park, Changsoo Lee and Oh Seok Kwon, Conducting polymer based Nano biosensors, *Polymers* 8,249, 2016.
- [4] S.Anandhi, M. Edward and V. Jaishankar, Synthesis, characterization and antimicrobial activity of polyindole/ ZrO_2 nanocomposites, *Materials today: proceedings*, 2020.
- [5] K.Phasukson, W. Prissanaroon-Ouajai, A.Srivat, Electrical conductivity response of methanol sensor based on conductive polyindole, *Sensors and Actuators B* 262,pp.1013-1023, 2018.
- [6] R. Barde, K. Nemade and S.Waghuley, Optimization of supercapacitive properties of polyindole by dispersion of MnO_2 nanoparticles, *Chemical physics impact*, vol 5, 100100, 2022.
- [7] S. Pusawale, Chemically Deposited Nanocrystalline Metal Oxide Thin Films,2, 2021.
- [8] C. Ararat Ibarquen, A. Mosquera, R. Parra, M. Castro, J. Rodriguez-Paez, Synthesis of SnO_2 nanoparticles through the controlled precipitation route, *Materials chemistry and physics* 101, pp.433-440, 2007.
- [9] S. Suthakaran, S. Dhanapadian, N. Krishnakumar and N. Ponpandian, Hydrothermal synthesis of SnO_2 nanoparticles and its photocatalytic degradation of methyl violet and electrochemical performance, *Materials research express*, 2019.
- [10] R. Barde, K. Nemade and S.Waghuley, AC conductivity and dielectric relaxation in $\text{V}_2\text{O}_5\text{-P}_2\text{O}_5\text{-B}_2\text{O}_3$ glasses, *Journal of Asian Ceramic Societies*, pp. 2187-0764, 2014.
- [11] P.Chhattise, K. Handore, and A.Horne, Synthesis and characterization of Polyindole and its catalytic performance study as a catalyst, *Journal of Chemical Sciences* 128 vol. 3, pp. 467-475, 2016.
- [12] S. Goel, N.Mazumder, and A.Gupta, Growth of One-Dimensional Polyindole Nanostructures, *Journal of Nanoscience and Nanotechnology*, Vol.
- [13] R.V. Barde, Preparation, characterization and CO_2 gas sensitivity of Polyaniline doped with Sodium Superoxide (NaO_2), *Materials Research Bulletin* 73,pp.70–76,2016.
- [14] S. An, T. Abdiryim, Y. Ding and I. Nurulla, A comparative study of the microemulsion and interfacial polymerization for polyindole, *Materials Letters* 62, pp.935–938, 2008.
- [15] P.Chhattise, K. Handore, and A.Horne, Synthesis and characterization of Polyindole and its catalytic performance study as a catalyst, *Journal of Chemical Sciences* 128 (3), pp. 467-475, 2016.
- [16] A. Bhide and K.Hariharan, Sodium ion transport in $\text{NaPO}_3\text{-Na}_2\text{SO}_4$ glasses, *Materials chemistry and physics* 105,pp.213-221,2007.
- [17] A. Elhamid, H. Shawkey, Ahmed A. Khalil and I. Azzouz, Graphene Functionalization towards Developing Superior Supercapacitors Performance, *Supercapacitors for next generation*, 2021.
- [18] C. Mariappan, G. Govindara, S. Rathan and G. Prakash, Preparation, characterization, ac conductivity and permittivity studies on vitreous $\text{M}_4\text{AlCdP}_3\text{O}_{12}$ (M=Li, Na, K) system, *Mat. Sci. Eng. B* 121, 2, 2005.
- [19] M H Makled, E Sheha, T. Shanap and M K El-Mansy, Electrical conduction and dielectric relaxation in p-type PVA/Cul polymer composite, *J. Adv.Res.* vol.4, pp.531-538, 2013.
- [20] R.V. Barde and S.A. Waghuley, Thermal and electrical properties of $60\text{V}_2\text{O}_5\text{-}5\text{P}_2\text{O}_5\text{-(}35\text{-x)B}_2\text{O}_3\text{-xCeO}_2$ ($1 \leq x \leq 5$) glasses, *Bull. Mater. Sci.*, Vol. 38, No. 2, pp. 557–563, 2015.
- [21] S. Chopra, S. Sharma, T.C. Goel and R.G. Mendiratta, *Solid State Commun.*, 127,4, pp. 299–304, 2003.
- [22] E. Shaishay, S. El-Desouki, I. Shaltout and A. Bahgat, *J. Mater. Sci. Technol.*, 22, pp. 701–707, 2006.
- [23] R.V. Barde and S.A. Waghuley, Study of AC electrical properties of $\text{V}_2\text{O}_5\text{-P}_2\text{O}_5\text{-B}_2\text{O}_3\text{-Dy}_2\text{O}_3$ glasses, *ceramic international*, vol.39, Issue 6, pp. 6303-6311, 2013.
- [24] R. Barde, K. Nemade and S.Waghuley, Impedance spectroscopy study of the AC conductivity of sodium superoxide nanoparticles doped vanadate based glasses, *material science for energy technologies*, vol. 4, , pp. 202-207, 2021.

Article in a conference proceedings:

© 2024. This work is published under
<https://creativecommons.org/licenses/by/4.0/legalcode>(the“License”
).

NotwithstandingtheProQuestTermsandConditions,youmayuse this
content in accordance with the terms of the License.

¹Ruby Khan²Akhila Nair³Vaishali Raikwar

Effect of Capping on Luminescence of Cadmium Sulfide/PVP Nanocomposite



Abstract: -Nanomaterials, with dimensions less than 100 nanometers, are the foundation of nanoscience and technology, with potential impacts in electronics, medicine, and other fields. Nanoparticles exhibit unique properties due to their small size, high surface to volume ratio, and quantum confinement. Cadmium sulfide (CdS) nanoparticles have sparked interest due to their unique optical and electronic properties, making them useful in optoelectronics, photovoltaics, and bioimaging. Their size-dependent tunability allows for customization to suit specific applications. The controlled chemical reaction of cadmium acetate is used to synthesize nanoscale CdS particles. CdS characterization is crucial for understanding and optimizing nanoparticle properties. Techniques like UV-Vis spectroscopy, X-ray diffraction (XRD), and transmission electron microscopy (TEM) are used to assess size, structure, and composition. These methods help tailor CdS nanoparticles for specific applications, such as bio medical applications and optoelectronics. XRD ensures reproducibility, while TEM images provide insights into nanoparticle shape and distribution.

Keywords: Cadmium sulfide, Nanotechnology, Capping agent, Nanocomposite, Photoluminescence property.

¹*Corresponding author: Vaishali Raikwar, Ramniranjan Jhunjhunwala College, Ghatkopar, Mumbai vaishaliraikwar@ricollege.edu.in

I. INTRODUCTION

Microscopic particles with at least one dimension smaller than or equal to 100 nanometers (nm) are known as nanoparticles. These materials are valuable in a variety of applications because they have distinct physical, chemical, and biological properties that set them apart from their bulk counterparts. Nanoparticles frequently exhibit properties that differ significantly from larger particles of the same substance. Because the average diameter of an atom is between 0.15 and 0.6 nm, a large portion of the nanoparticle's material is within a few atomic diameters of its surface. As a result, the surface layer's properties may take precedence over those of the bulk material. This effect is especially strong for nanoparticles dispersed in a medium of varying composition, as interactions between the two materials at their interface become significant [1]. Nanoparticles can be synthesized from desired material according to our needs. The properties of these synthesized nanoparticles are different from those of the parent material. This is because due to its small in size most of the materials are located on the surface, where their interaction with the surrounding environment is much more predominant than the bulk material. Moreover, they have high surface-to-volume ratio. These properties can drastically influence the behavior of the nanoparticles which is much more different from that of the parent or bulk material. This is the reason why they have different chemical and physical properties than bulk material. Another factor that makes these nanoparticles to be different is due to their property of quantum confinement. Due to their small size, in these nanoparticles, electrons are confined which is the basic requirement for quantum confinement which leads to changes in electronic properties such as energy level, optical properties, and many more. Due to this quantum confinement, quantum dots can be observed in nanoparticles [2, 3]. Larger quantum dots emit longer wavelengths corresponding to red, therefore their appearance is mostly red in color, while intermediate sizes emit yellow or orange wavelength hence appearing to be yellow or red and lastly smaller sizes emit green or blue wavelength giving the appearance green or blue. CdS nanoparticles are semiconductor nanocrystals that have sparked widespread interest due to their unique optical and electronic properties. These nanoparticles are known to absorb and emit visible light, making them useful in optoelectronics, photovoltaics, and bioimaging. The small size of CdS nanoparticles (typically 2-10 nm in diameter) causes quantum confinement effects, resulting in size-dependent optical and electronic properties. The ability to adjust the size of CdS nanoparticles to suit particular applications is a major benefit due to their size-dependent tunability [4, 5, 6].

Many methods are reported in literature to synthesize CdS nanoparticles. Synthesis and characterization of CdS nanoparticles was done by Preeti Sahare et al using simple, inexpensive aqueous precipitation method at room temperature [7]. The nanoparticles were characterized using XRD, SEM, FTIR and spectroscopic techniques. The calculated crystalline size was calculated using XRD and it was about 30 nm. Powder morphology and size of the nanoparticle were characterized by Scanning Electron Microscopy (SEM). Images obtained through SEM showed irregular particles agglomerated with many falling 30-50 nm size ranges. The infrared absorption spectra were analyzed using the FTIR spectrometer. The absorption peak in the range 3600-3100 cm^{-1} was attributed to the OH group of water, while that at 1635 cm^{-1} was assigned to CO_2 adsorbed on the surface of nanoparticles. The peak formed at 400-470 cm^{-1} indicates the formation of CdS nanoparticles. The UV-visible absorption of these nanoparticles showed a strong absorption at 345 nm. The preparation and characterization of CdS nanoparticles by chemical co-precipitation techniques with thiophenol as capping agent have been conducted by B. Srinivasa Rao et al. XRD studies revealed the calculated crystalline size was around 13 nm. PL, SEM, and TEM were also done [8]. H. L. Lee et al successfully synthesized the nanoparticle by heating cadmium chloride along with thiourea in ethanol. The reagents were of analytical purity and distilled water was used throughout the experiment. Solution A was prepared by dissolving cadmium chloride and thiourea into ethanol, while the solution was prepared by dissolving sodium hydroxide in ethanol. The mixture was held under reflux for 10 hours, forming a white precursor. The yellow precipitates were collected and dried in a vacuum oven. The XRD analysis showed a transformation from cubic to hexagonal crystalline phase. The UV-visible results indicated that the quantum confinement effect took place when compared to bulk CdS [9]. L. Dhatchinamurthy, et al used reagents cadmium acetate, thiourea, and Polyvinyl alcohol (PVA) to synthesize a CdS nanostructure thin film. The reagents were prepared using deionized water and stirred for 1 hour at 40°C. The PVA was then blended with CdS precursor materials and stirred for nearly around 8 hours. The solutions were coated on a glass substrate and dried at 50°C for 1 hour. The thin film's color changed from transparent to light yellow, indicating the formation of the CdS nanostructure [10].

Our work aims to synthesize CdS nanoparticles under two conditions: with and without PVP. Following synthesis, these nanoparticles were tested using various characterization techniques, including X-ray diffraction,

FTIR, UV-visible spectroscopy, Scanning Electron Microscopy, Transmission Electron Microscopy and Photoluminescence (PL) spectroscopy. The effect of capping was observed on the luminescence of CdS-PVP nanocomposite using fluorescence spectroscopy.

II. MATERIALS AND METHODS

The synthesis of cadmium sulfide (CdS) using cadmium acetate involves a controlled chemical reaction that leads to the formation of nanoscale CdS particles. According to stoichiometric calculations, weigh the required amount of cadmium acetate and dissolve it in 100 ml of distilled water. Stir the solution until complete dissolution. In a separate beaker, dissolve sodium sulphide in 25 ml of ethanol and prepare another solution. Pour the cadmium acetate solution into the reaction vessel equipped with a magnetic stirrer. While stirring, slowly add the Sodium sulphide solution to the cadmium acetate solution. Maintain a constant stirring rate to ensure homogeneity. Continue stirring the solution for a predetermined duration to allow the complete precipitation of CdS nanoparticles. After precipitation, separate the solid CdS nanoparticles by centrifugation. Discard the supernatant and wash the precipitate with deionized water and ethanol to remove impurities. They are further kept in a furnace at 200°C for about 2 hours. The synthesized CdS nanoparticles were characterized using techniques such as UV-Visible spectroscopy, X-ray diffraction (XRD), and transmission electron microscopy (TEM) to assess their size, composition, and crystal structure. This method is repeated again but this time capping reagent is PVP (Poly n-vinyl pyrrolidone) added before the formation of precipitation. Hence, two CdS samples are formed, one where CdS is formed by adding a capping agent and another without the capping agent. A capping agent, when added during the synthesis of nanoparticles like cadmium sulfide (CdS), plays a crucial role in controlling the size, shape, and stability of the nanoparticles. It forms a protective layer around the nanoparticles, preventing them from agglomerating and providing colloidal stability. This capping agent also influences the surface chemistry of the nanoparticles. The choice of capping material is essential as it directly impacts the function of nanoparticles and enhances the properties of nanoparticles and their performance in various practical applications.

Characterization of cadmium sulfide (CdS) is a critical step in understanding and optimizing the properties of the synthesized nanoparticles and to assess the size, structure, and composition of CdS nanoparticles. Techniques employed for characterization include UV-Vis spectroscopy, X-ray diffraction, and transmission electron microscopy (TEM). UV-Vis spectroscopy and Fluorescence spectroscopy is used to assess the optical properties of CdS nanoparticles, providing information on absorption and fluorescence spectra. XRD is employed to determine the crystal structure and phase purity of CdS, elucidating the material's composition and confirming its crystalline nature. TEM enables detailed imaging of the particle morphology and size distribution. The importance of characterization lies in tailoring CdS nanoparticles for specific applications. For instance, in optoelectronics, understanding the size-dependent bandgap of CdS through UV-Vis spectroscopy aids in designing materials with desired electronic properties. XRD ensures the reproducibility of the synthesized CdS, essential for applications wherein crystalline structure impacts performance. Characterization is indispensable for harnessing the unique properties of CdS in diverse fields, guiding the fine-tuning of synthesis parameters for optimal performance in applications ranging from sensors to photovoltaics.

III. RESULTS AND DISCUSSION

1. X-Ray Diffraction

The X-ray diffraction (XRD) pattern helps to identify the phases that are present in the synthesized sample by providing important details about the crystalline structure of materials. As shown in Figure 1 three distinct peaks at various angles are visible in the XRD pattern, suggesting the presence of a cubic zinc blend crystal phase. Broadened peaks are seen, which is a feature frequently connected to nanocrystalline materials. Because there are fewer lattice planes in nanocrystals than in bulk materials, this broadening occurs. Defects like twinning and dislocations also contribute to peak broadening by reflecting the crystal structure's micro straining. These flaws arise spontaneously during the course of the chemical reaction and are intrinsic to chemically synthesized nanocrystals. The XRD line's diffuse and broad character suggests that the CdS nanoparticles are very small in size. The phase is confirmed to be pure CdS by comparing the obtained "hkl" values with those found in the standard JCPDS file (10-0454). In particular, the XRD pattern shows clear peaks at 2θ scattering from the (111), (220), (311), and (335) planes. All things considered, the XRD analysis offers strong proof that the synthesized sample is composed of nanocrystalline CdS, with the observed peak characteristics pointing to a small particle size and a well-defined crystal phase. Figure 1(b) shows the X Ray

diffraction image of CdS capped with PVP. The peak position hasn't shifted confirming the fact that only coating of PVP has been formed and the crystal structure is the same as in pristine CdS sample.

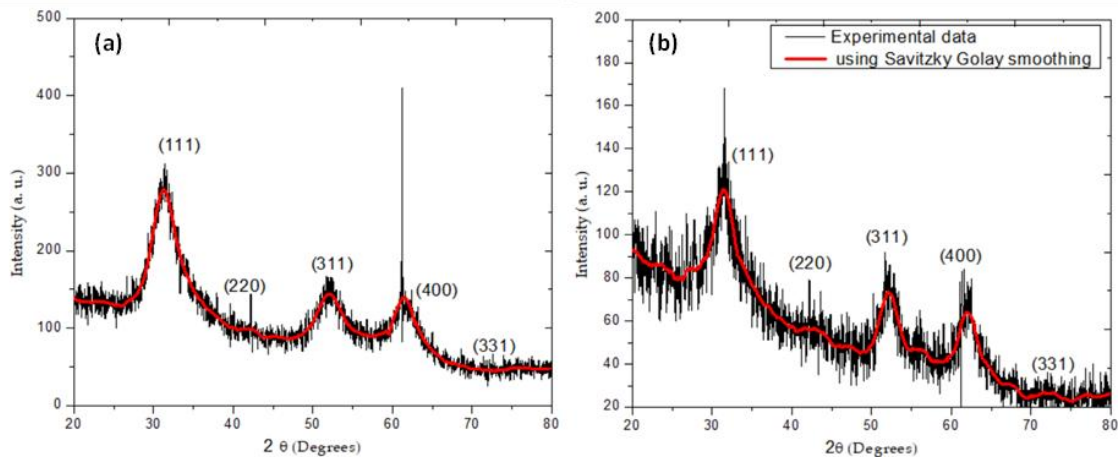


Figure 1: X-Ray diffraction pattern of CdS (a) without PVP and (b) capped with PVP [Smoothing by Savitzky-Golay smoothing function in origin software]

2. FTIR spectroscopy

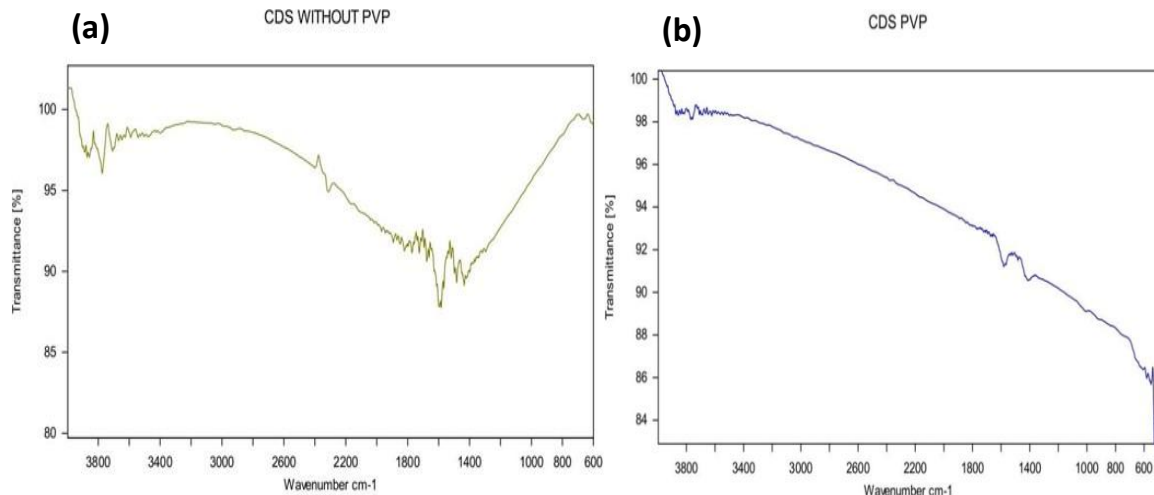


Figure 2: FTIR spectra of CdS (a) without PVP and (b) capped with PVP

The FTIR spectrum shows various bonds between the constituent atoms. Here, Absorption peaks in the range of 3700 cm^{-1} could be attributed to the group of water adsorbed by the sample. Small peaks near the 600 cm^{-1} range may be indicated as the formation of CdS as this region is assigned Metal Sulphur bond [Figure 2(a)]. On the other hand, the peak range between 1300 cm^{-1} and 1400 cm^{-1} corresponds to C-N stretching motion and C=O stretching motion of monomers for PVP respectively [Figure 2(b)]. A narrow absorption peak between 1500 cm^{-1} and 1700 cm^{-1} occurred due to C-H bonding due to the presence of PVP [11]. The relatively intense S-O stretching absorption bands in range 400 cm^{-1} to 600 cm^{-1} shows presence of Sulphur-oxygen compounds [12].

C. Scanning Electron Microscopy (SEM)

SEM is a helpful tool to be used for the characterization of materials because it exposes the sample to a high-energy electron beam that provides information about the material's topography, morphology, composition, chemistry, grain orientation, and other characteristics. Figure 2 is the SEM image of the synthesized CdS nanoparticles at a 5000 magnification. It shows the spherical CdS nanoparticles are arranged on the surface with rough morphology. It has been reported that the capping agent enhances the mono dispersive property. They show uniform crystal structure [13].

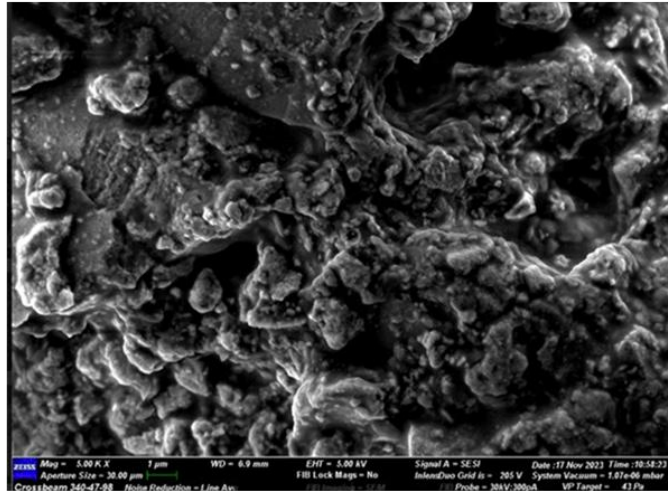


Figure 3: Scanning Electron Microscopy image of CdS capped with PVP

D. Transmission Electron Microscopy (TEM) Analysis

Figure 4 shows the HRTEM images of CdS nanoparticles without capping and with capping by PVP. The aggregated CdS nanoparticles form a bigger size cluster if not capped with PVP [Figure 4 (a)].

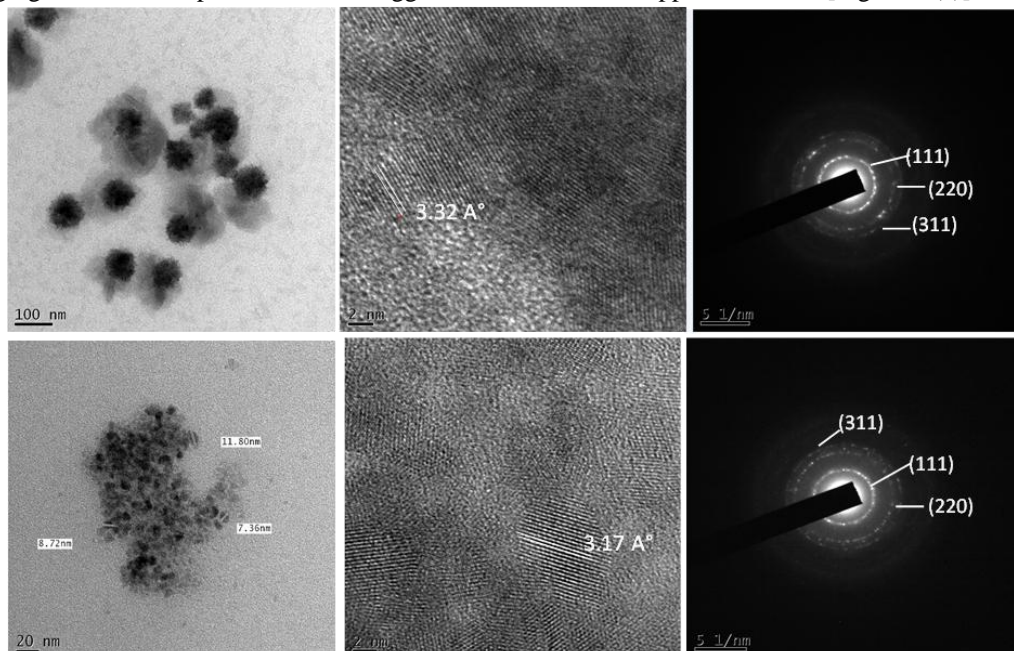


Figure 4: CdS sample without PVP (a) TEM image (b) HRTEM image (c) SAED pattern and CdS sample with PVP (d) TEM image (e) HRTEM image (f) SAED pattern

The Cluster of CdS nanoparticles are mostly spherical in nature with the size in the range of 50-60 nm. The SAED pattern shows the crystalline planes as revealed in XRD graphs [Figure 4 (b) and (c)]. When capped with PVP, the CdS nanoparticles could not form a cluster. They are uniformly distributed in the PVP matrix as shown in figure 4 (d). The layer of PVP decreases the growth rate of CdS nanoparticles and slows down the agglomeration by Oswald ripening and thereby narrowing down the size distribution. The average particles size is in the range of 7 nm – 12 nm. The corresponding SAED images for capped nanoparticles are shown in Figure 4 (e) and (f). The d-spacing of the plane (111) are observed to be fairly matching with that of the sample without PVP capping. This shows that the crystal structure is unaltered. The crystal planes are well matched with X Ray diffraction graph of capped CdS nanoparticles.

E. UV-Vis spectroscopy

The CdS semiconductor is II-VI direct band gap semiconductor having bandgap 2.42 eV for bulk material [14]. From the figure 5 (a), we can conclude that the maximum absorbance occurs at the wavelength 290 nm. It means that the electrons in the material are absorbing light strongly at that wavelength, undergoing electronic transitions that take them to higher energy levels. The absorbance at 290 nm in CdS is relatively weak, which is typical for ($n \rightarrow \pi$) transitions [15]. From the figure 5 (b), we can conclude that maximum absorbance range increases covering wavelengths from UV to visible region. The variation in absorbance wavelengths suggests that the interaction between the compound and PVP alters the electronic environment, potentially affecting the types of transitions occurring within the molecule. The shift from 290 nm to higher wavelength with the addition of PVP implies a change in the structural arrangement or electronic properties of the compound, highlighting the importance of considering the specific effects of PVP on the compound's UV-visible spectrum analysis. Here, CdS nanoparticles behave differently from expected since their maximum absorbance in UV-visible is usually observed at 400 nm. This may be due to specific experimental conditions, sample preparation, or other factors.

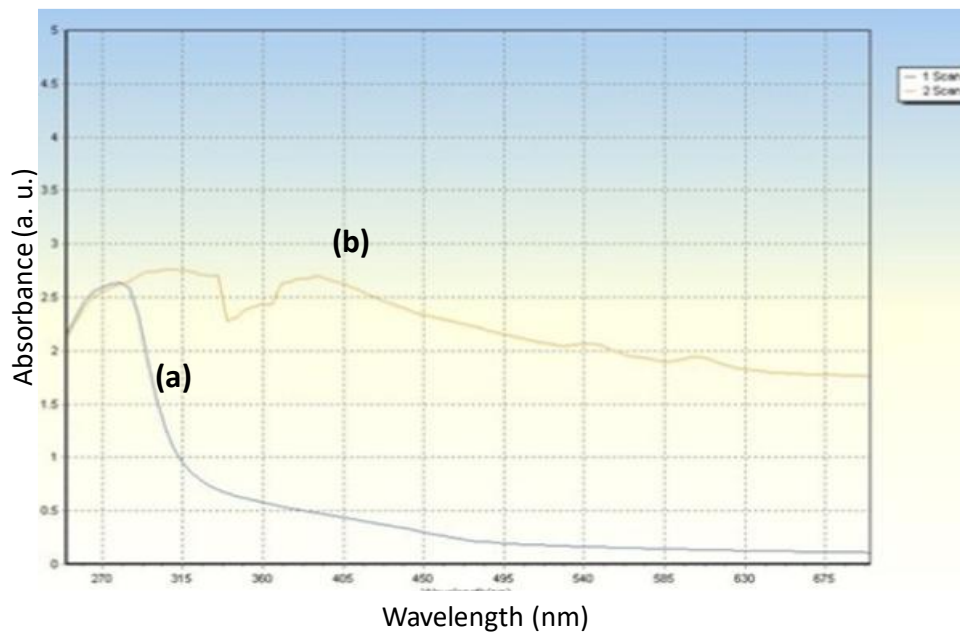


Figure 5: UV absorption spectra of (a) pristine CdS and (b) CdS capped with PVP

F. Photoluminescence properties

CdS nanoparticles are having good photostability and fluorescent property with broad excitation wavelength [16]. This excellent quality of CdS nanoparticles can be useful for many biomedical applications like bioimaging, drug delivery, and biosensors. The uncapped CdS nanoparticles emission spectrum is shown in Figure 6 (a). The sample shows varied emission intensity with change in excitation wavelengths such as 254 nm, 330 nm and 390 nm. The maximum intensity has been observed for 330 nm excitation wavelength. When the nanoparticles are capped by PVP, the intensity of CdS nanoparticles has been increased by many folds. The two major emission peaks at 415 nm and 450 nm retained their positions, but intensity has been increased by almost 70 times as shown in figure 6 (b). This enhancement in the luminescent property may be occurring due to surface modification of CdS nanoparticles by PVP molecules, thus minimizing surface defects and enhancing the electron hole recombination [17].

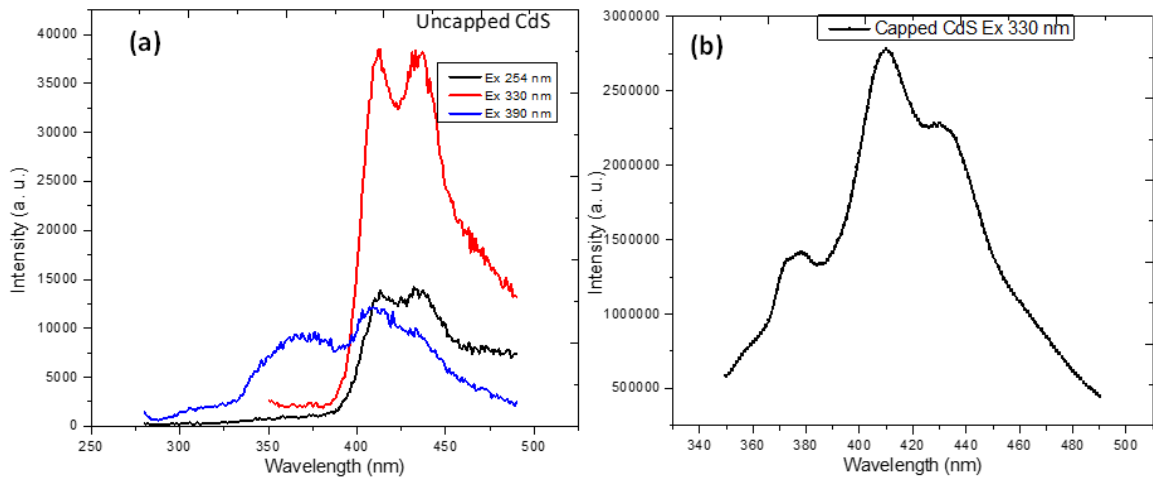


Figure 6: Photoluminescence property of CdS nanoparticles (a) without capping agent, (b) with capping agent PVP

IV. CONCLUSION

In summary, the CdS nanoparticles were prepared by facile controlled chemical precipitation technique. The PVP was used as a capping agent. The increase in PL intensity is observed after capping. The CdS nanoparticles vary in toxicity depending on their size and surface to volume ratio. They have high potential to act as antimicrobial agent or as anticancer agent. Also, the tunable PL intensity which is excitation wavelength dependent can be a crucial factor for bioimaging application. Thus, for biomedical applications CdS nanoparticles are potential candidates.

ACKNOWLEDGMENT

The authors are grateful to Ramniranjan Jhunjhunwala College, Mumbai for PG student's research support and SAIF, IIT, Bombay for HRTEM and fluorescence spectroscopy facility.

REFERENCES

- [1] Vollath, Dieter. *Nanomaterials: an introduction to synthesis, properties and applications*. John Wiley & Sons, 2013.
- [2] Hadi, Iman H., Khawla S. Khashan, and Doaa Sulaiman. "Cadmium sulphide (CdS) nanoparticles: Preparation and characterization." *Materials Today: Proceedings* 42 (2021): 3054-3056.
- [3] De La Cruz Terrazas, E. C., RC Ambrosio Lázaro, ML Mota Gonzalez, P. A. Luque, S. J. Castillo, and A. Carrillo-Castillo. "A simple method for the synthesis of CdS nanoparticles using a novel surfactant." *Chalcogenide Letters* 12, no. 4 (2015).
- [4] Aziz, Shujahadeen B., Mariwan A. Rasheed, Salah R. Saeed, and Omed Gh Abdullah. "Synthesis and characterization of CdS nanoparticles grown in a polymer solution using in-situ chemical reduction technique." *International Journal of Electrochemical Science* 12, no. 4 (2017): 3263-3274.
- [5] Zheng, Xinlong, Yuhao Liu, Yuqi Yang, Yiming Song, Peilin Deng, Jing Li, Weifeng Liu, Yijun Shen, and Xinlong Tian. "Recent advances in cadmium sulfide-based photocatalysts for photocatalytic hydrogen evolution." *Renewables* 1, no. 1 (2023): 39-56.
- [6] Harish, R., K. D. Nisha, S. Prabakaran, B. Sridevi, S. Harish, M. Navaneethan, S. Ponnusamy, Y. Hayakawa, C. Vinniee, and M. R. Ganesh. "Cytotoxicity assessment of chitosan coated CdS nanoparticles for bio-imaging applications." *Applied Surface Science* 499 (2020): 143817.
- [7] Preeti Sahare. "Synthesis and characterization of cds nanoparticles". *International Journal of Engineering Research & Technology (IJERT)*, 6(1), 2018.
- [8] B Srinivasa Rao, B Rajesh Kumar, V Rajagopal Reddy, T Subba Rao, and GJCL Chalapathi. "Preparation and characterization of cds nanoparticles by chemical co-precipitation technique". *Chalcogenide Lett*, 8(3):177-185, 2011
- [9] HL Lee, AM Issam, M Belmahi, MB Assouar, H Rinnert, and M Alnot. "Synthesis and character- izations of bare cds nanocrystals using chemical precipitation method for photoluminescence application". *Journal of Nanomaterials*, 2009:1-9, 2009.
- [10] L Dhatchinamurthy, P Thirumoorthy, L Arunraja, and S Karthikeyan. Synthesis and charac- terization of cadmium sulfide (cds) thin film for solar cell applications grown by dip coating method. *Materials Today: Proceedings*, 26:3595-3599, 2020.

- [11] Saravanan, L., S. Diwakar, R. Mohankumar, A. Pandurangan, and R. Jayavel. "Synthesis, structural and optical properties of PVP encapsulated CdS nanoparticles." *Nanomaterials and Nanotechnology* 1 (2011): 17.
- [12] Zawadzki, Mirosław, and Janina Okal. "Synthesis and structure characterization of Ru nanoparticles stabilized by PVP or γ -Al₂O₃." *Materials Research Bulletin* 43, no. 11 (2008): 3111-3121.
- [13] Guo, Lin, Shihe Yang, Chunlei Yang, Ping Yu, Jiannong Wang, Weikun Ge, and George KL Wong. "Highly monodisperse polymer-capped ZnO nanoparticles: Preparation and optical properties." *Applied physics letters* 76, no. 20 (2000): 2901-2903.
- [14] Biswas, Ankan, S. R. Meher, and Deepak K. Kaushik. "Electronic and band structure calculation of wurtzite CdS using GGA and GGA+ U functionals." In *Journal of Physics: Conference Series*, vol. 2267, no. 1, p. 012155. IOP Publishing, 2022.
- [15] Singh, V., Sharma, P. K., & Chauhan, P. Synthesis of CdS nanoparticles with enhanced optical properties. *Materials Characterization*, (2011) 62(1), 43-52.
- [16] Khaliq, Nilem, Muhammad Asim Rasheed, Maaz Khan, Muhammad Maqbool, Mashkoor Ahmad, Shafqat Karim, Amjad Nisar, Patrik Schmuki, Sung Oh Cho, and Ghafar Ali. "Voltage-switchable biosensor with gold nanoparticles on TiO₂ nanotubes decorated with CdS quantum dots for the detection of cholesterol and H₂O₂." *ACS Applied Materials & Interfaces* 13, no. 3 (2021): 3653-3668.
- [17] Liu, S. H., X. F. Qian, J. Yin, X. D. Ma, J. Y. Yuan, and Z. K. Zhu. "Preparation and characterization of polymer-capped CdS nanocrystals." *Journal of physics and chemistry of solids* 64, no. 3 (2003): 455-458.

Vaishnavi D.
Nagmote¹
Suraj V. Tayade²
S. A.Waghuley³

Regular paper
Exploring Polyaniline for Effective
Electromagnetic Interference Shielding
Applications



Abstract: - The study investigates Polyaniline (PANI) nanocomposite synthesized via chemical oxidative polymerization of aniline using ammonium peroxodisulfate as an oxidant. Characterization of the prepared PANI nanocomposite was conducted through UV-visible (UV-vis) absorption spectra, X-ray diffraction (XRD), and Fourier transform infrared spectroscopy (FTIR). XRD analysis revealed the amorphous nature of PANI. The formation of PANI was evidenced by its dark green coloration. In EMI shielding applications, the addition of metal nanocomposite enhanced the shielding effectiveness of PANI nanocomposite. Furthermore, PANI improved absorption efficiency of the material.

Keywords: Polyaniline; Nanocomposite; EMI shielding.

1.Introduction

1.1. Polyaniline (PANI) Polyaniline was invented by a German chemist, Carl Julius Fritzsche, in 1840. He first obtained colourless oil from indigo and called aniline due to the similarity of these two material in appearance and these oxidized this oil to Polyaniline. Since this invention of Polyaniline has attracted lots of attention of scientific community. Conducting polymers are a new class of polymers with electronic and ionic conductivity that were discovered in 1977 [1]. Polyaniline is considered one of the important members of this class of materials due to its low cost, low weight, environmental stability, corrosive resistance, and ease of conversion between base and salt by adding base (OH)⁻ or acid (H)⁺ [2]. Polyaniline has attracted attention due to its various structures [3]. Polyaniline has a rather unique polymeric structure which is mainly composed of sequentially alternating benzene rings and nitrogen atom. Polyaniline Nanocomposite can be regarded as a material consisting of PANI matrix and one or more components such as semiconductors metals nanoparticles, organic components inorganic compounds as well as biological and natural products in order to improved polymer backbone properties or extend its functionalities. The process of mixing materials with polymers is the result of polymeric composites.[4] The process of mixing material with Polyaniline results in polyaniline composites. [5] PANI has been used in many applications such as solar cells, batteries, supercapacitors, corrosion-resistant coatings, sensors and EMI shielding etc.[5] Polyaniline exhibits tremendous properties. It's physical properties depend on its three forms, which show different colours according to their chemical nature. The optical properties of polyaniline are used to study the oxidation level and protonation process of the polymer. Polyaniline shows noticeable differences in mechanical properties depending on the polymerisation method from which it was prepared. Polyaniline also has anticorrosive properties PANI films doped with boric acid show semiconducting properties. Due to its semiconducting properties, polyaniline is widely used in organic field transistors [5]. PANI exist in three different forms such as fully oxidised Pernigrtaniline (PAB), leucoemeraldine base (LEB) semi oxidised emeraldine base (EB) PANI [5] also have electrical conductivity only in the emeraldine form and other type do not show significant Polyaniline (PANI) continues to attract considerable attention because its electrical and optical properties can be changed by oxidation and protonation of the amine nitrogen atoms. PANI is known for its excellent thermal and environmental stability. [6]

1.2. Electromagnetic interference (EMI) Shielding Application: Electromagnetic interferences (EMI shielding) in which blocking of conducting or radiating electromagnetic radiation into shielding material. [7] EMI shielding in electronic device and equipment is the use of manufacturing techniques and materials to protect signal from being distorted by external electromagnet signals as well as preventing generated signals from interfering with surrounding. EMI shielding is the class of of an intelligent packaging. EMI an undesirable electromagnetic induction triggered by extensive use of alternating current or voltage that can produces corresponding induced signal in the nearby electronic circuit and make it reduced its performances. [7] It is necessary to reduced electromagnetic interference by decrease errors and noise in electronic systems. Due to EMI high density, corrosiveness, weak mechanical flexibility tedious and costly processing reduces the use of metals and metallic composites for EMI shielding nonmaterial's are trending mostly on polymeric matrix, carbon matrix, and ceramic matrix nanocomposite. Electrical and magnetic fields creates the improved EMI shielding effectiveness. Conducting Polyaniline composites are also

mainly used in EMI shielding purposes. EMI shielding is the material property that stops the transmission of EM waves.

Shielding by reflection (SER): The waves reflected due to the mismatch of incident electromagnetic waves with the shielding nanomaterials. The reflection occurs on the surface of the shielding material when incident on the EM waves. High electrical conductive materials containing free charge carriers which make them favorable reflection [7]

Shielding by absorption (SE_A): The rays in which microwave region comprise electric and magnetic field. The interaction due to these field ohmic losses occur as well as dipole of these shielding material electric and magnetic field of dipole are necessary shielding material of these of EM waves the absorption is primarily because of magnetic hysteresis losses and current generated in the shielding material that is ohmic losses. [7]

Shielding by multiple reflections (SE_{MR}): In the multiple reflections shielding efficiency and capability of the absorption associated with the shielding material. The electromagnetic (EM) radiation reflects at multiple borders within the shielding material when the shielding thickness is less compared to the skin effect. The nanomaterial having multiple boundaries in the structure are most important for multiple shielding.[7]

2.Experimental

Materials: Aniline monomer were used as the precursors and Ammonium per sulfate was used as oxidizing agent, Hydrochloric acid, Distilled Water etc.

Synthesis of Polyaniline: Polyaniline have been most widely synthesis chemical and electrochemical technique. Polyaniline can be synthesis by chemical oxidative polymerization method. The chemical oxidative polymerization process is of important for synthesis of Polyaniline on a large scale. In this work we used the oxidative polymerization method. The aniline monomer 10 ml was dissolved in 150 ml of HCL in a beaker. This solution was kept on the magnetic stirrer after that 10 gm of ammonium per sulfate was dissolved in 50 ml distilled water and this solution drop wise added by using burette in aniline solution. This reaction can take place 5 hours of stirring process dark green solution was formed the whole reaction was kept still at room temperature (25⁰) this stirrer solution was filtered and the obtained product was washed by using distilled water. The obtained product was dried in vacuumed oven at temperature of 40⁰ And then Polyaniline powder was obtained. [8]

3. Results and Discussion

3.1. X-Ray Diffraction: The XRD pattern of the synthesized Polyaniline (PANI) from (figure1) It can be observed that, three bands are ascribed to the periodic parallel and perpendicular features of the polymer chains of PANI. They are centered at $2\theta = 6.7^\circ$, 19.77° and 25.88° corresponding to (100), (11-1) and (400) crystallographic planes reflection of PANI respectively. The interlayer spacing (d) was evaluated according to Braggs law.

$$n\lambda = 2d\sin\theta \quad (1)$$

where n is an integer, λ is the XRD wavelength (0.154050 nm) and θ is the angle between the incident ray and the scattering planes. The XRD pattern show highest intensity peak at 25.88° which represent the characteristic peak in the PANI and it is consistent with reported data in literature . The 2θ value for the most prominent peak was used in calculating the interlinear spacing value (d) from Equation (1). 2.48509 Å⁰ or 0.248509 nm was obtained for synthesized PANI is shown that PANI is amorphous in nature.

3.2. UV- Visible Spectroscopy: The UV-visible spectra of the synthesized Polyaniline nanocomposite were measured using a UV-visible spectrophotometer in the wavelength range of 200-1000 nm as shown in (Figure 2.) The peaks at 339 nm is attributed to the π - π^* transition in benzenoid units of the polymer chains. The other band at 630 nm is associated with the π - π^* transition in quinonoid rings. [9] The absorption characteristic bands found at 599 nm. [10] It shows maximum absorption at 339 nm with respect to 659 nm. [11] These observation are consistent with literature report of PANI. Above 419 nm the absorption is gradually decreases and above 579 nm gradually increases up to 599 nm and above that also increases.

3.3. Fourier Transform Infrared Spectroscopy: FTIR spectra of PANI polymer displays the characteristic bands stretching deformation the spectra are collected using 4000 - 400 cm^{-1} . The FT-IR spectra good agreement with the previously reported results [10][11]. The FT-IR spectra of Polyaniline nanocomposite as shown in (Figure 3). The PANI polymer displayed the characteristic bands of secondary amine (N-H) at 3242.02 cm^{-1} , the C=C stretching deformation of the quinoid at 1582.52 cm^{-1} , benzenoid rings at 1501.92 cm^{-1} and the C-H stretching of the secondary aromatic amine at 1151.57 cm^{-1} , the C-H (out of plane) of stretching of the distributed benzene ring at 820.59 cm^{-1} . The PANI nanocomposite displayed almost identical characteristic bands at 3230 , 1568 , 1501 , 1289 , 824 cm^{-1} .

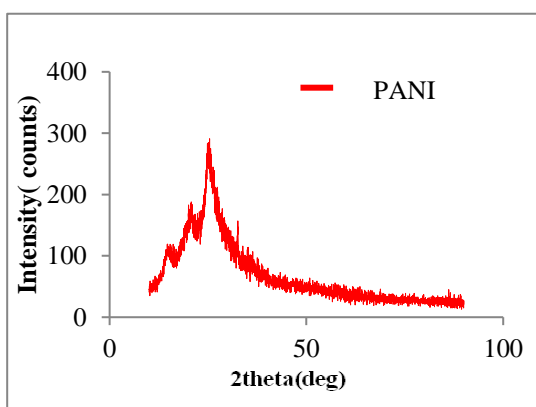


Figure 1. XRD pattern of PANI

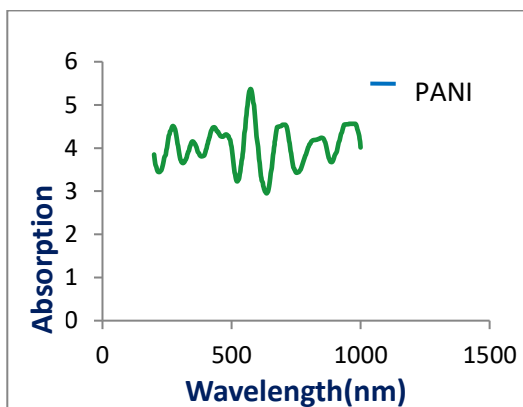
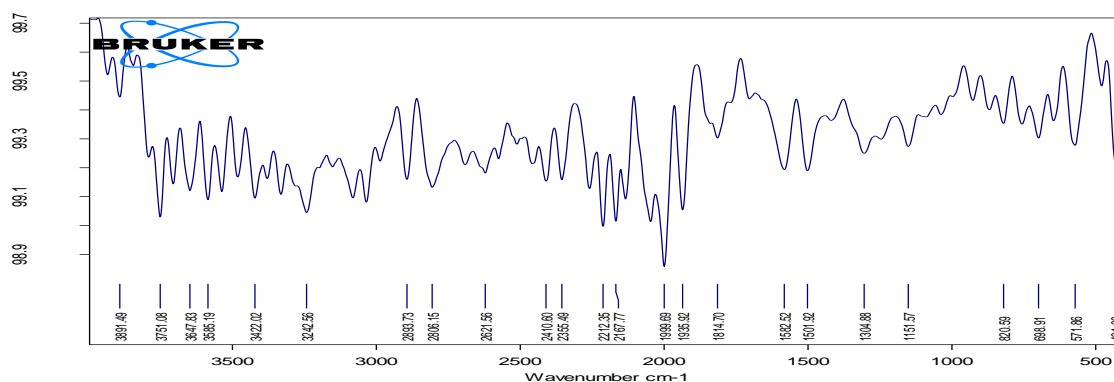


Figure 2 UV-Vis Absorption spectra of PANI



4. Conclusions

The polymerization of aniline monomer and conductive polyaniline nanocomposites were synthesized by chemical oxidative polymerization method. It has wider application, easy process and commercial production and molecular structure and it was confirmed by UV-visible spectroscopy X-ray diffraction and Fourier transform infrared spectroscopic techniques. The polyaniline nanocomposites were discussed as an application of electromagnetic interference shielding as absorption dominant in EMI shielding uv-visible spectra show highest absorption bands at 599 nm and 659 nm. PANI effective material for EMI shielding application.

References

- [1] Kyomuhimbo, H. D., & Feleni, U. (2023). Electroconductive Green Metal-polyaniline Nanocomposites: Synthesis and Application in Sensors. *Electroanalysis*, 35(2), e202100636.
- [2] Reddy, K. R., Lee, K. P., & Gopalan, A. I. (2008). Self-assembly approach for the synthesis of electromagnetic functionalized Fe₃O₄/polyaniline nanocomposites: effect of dopant on the properties. *Colloids and Surfaces A: Physicochemical and Engineering Aspects*, 320(1-3), 49-56.
- [3] Babel, V., & Hiran, B. L. (2021). A review on polyaniline composites: Synthesis, characterization, and applications. *Polymer Composites*, 42(7), 3142-3157.
- Baldissera, A. F., Souza, J. F., & Ferreira, C. A. (2013). Synthesis of polyaniline/clay conducting nanocomposites. *Synthetic metals*, 183, 69-72
- [4] Bavatharani, C., Muthusankar, E., Wabaidur, S. M., Alothman, Z. A., Alsheetan, K. M., mana AL-Anazy, M., & Ragupathy, D. (2021). Electrospinning technique for production of polyaniline nanocomposites/nanofibres for multi-functional applications: A review. *Synthetic Metals*, 271, 116609.
- [5] Majeed, A. H., Mohammed, L. A., Hammoodi, O. G., Sehgal, S., Alheety, M. A., Saxena, K. K., ... & Salmaan, N. U. (2022). A Review on polyaniline: Synthesis, properties, nanocomposites, and electrochemical applications. *International Journal of Polymer Science*, 2022.
- [6] Ali, M. A., Saion, E., Yahya, N., Kassim, A., Dahlan, K. M., & Hashim, S. (2007). Synthesis of conducting polyaniline nanocomposites by radiation doping. *Journal of Engineering Science and Technology*, 2(1), 111-118.
- [7] Zahid, M., Anum, R., Siddique, S., Shakir, H. F., & Rehan, Z. A. (2023). Polyaniline-based nanocomposites for electromagnetic interference shielding applications: A review. *Journal of Thermoplastic Composite Materials*, 36(4), 1717-1761.
- [8] Sivalingham, D., Elangovan, H., Subramanian, M., Kandasamy, S. K., & Govindasamy, M. (2013). Synthesis and characterization of PANI/ferric chloride composite for fabrication of electrodes in supercapacitor. *Advanced Materials Research*, 768, 334-337.:
- [9] Ayad, M., El-Hefnawy, G., & Zaghlol, S. (2013). Facile synthesis of polyaniline nanoparticles; its adsorption behavior. *Chemical engineering journal*, 217, 460-465.
- [10] Huang, Y. F., & Lin, C. W. (2012). Facile synthesis and morphology control of graphene oxide/polyaniline nanocomposites via in-situ polymerization process. *Polymer*, 53(13), 2574-2582.
- [11] Wankhede, Y. B., Kondawar, S. B., Thakare, S. R., & More, P. S. (2013). Synthesis and characterization of silver nanoparticles embedded in polyaniline nanocomposite. *Advanced Materials Letters*, 4(1), 89-93.

N. D. Kherde
A. O. Chauhan
P. A. Nagpure
S. K. Omanwar

Efficient Synthesis and Photoluminescence Properties of $\text{KSr}_4(\text{BO}_3)_3$ Phosphors Doped with Gd^{3+} , Bi^{3+} , and Pb^{2+} for Phototherapy Applications



Abstract: - In this paper we have reported the synthesis and the photoluminescence properties of the phosphor $\text{KSr}_4(\text{BO}_3)_3:\text{Gd}^{3+}$, Bi^{3+} , and Pb^{2+} phosphors. This phosphor material were first time prepared by a recrystallization method followed by the sintering at 900°C for 2 hours. The structural properties of the phosphor were studied by X-ray Diffraction Pattern which was studied using Rigaku miniflex II X-Ray Diffractometer. The excitation and emission spectra were measured by using fluorescence spectrophotometer at the room temperature. The structural and morphological characteristics i.e. particle size and shape of particle were studied by using scanning electron microscopy. Elemental analysis provides verification of the elements present and a qualitative chemical composition of the synthesized materials via energy dispersive X-ray analysis (EDX). This shows the application of the phosphor in various fields like photocopying, phototherapy.

Keywords: Photoluminescence, EDX, SEM, Phototherapy

¹ *N. D. Kherde , 1 Department of Physics, Shri Shivaji Science College, Amravati 444 603, (Affiliated to S.G.B.A. University, Amravati) Maharashtra, India.

² A. O. Chauhan, 2 Department of Physics, Vidya Bharati Mahavidyalaya Amravati 444 602, (Affiliated to S.G.B.A. University, Amravati) Maharashtra, India.

³ P. A. Nagpure, 3 Department of Physics, Shri Shivaji Science College, Amravati 444 603, (Affiliated to S.G.B.A. University, Amravati) Maharashtra, India.

⁴ S. K. Omanwar ,4 Department of Physics, S.G.B.A. University, Amravati 444 602, Maharashtra, India.
Copyright © JES 2024 on-line : journal.esrgroups.org

I. INTRODUCTION

The host and activators may have a significant impact on photoluminescence. It may cover the entire electromagnetic spectrum, from ultraviolet to infrared. Most often, inorganic substances like phosphate, borate, sulphates, and fluorides are utilized as hosts, and rare earths with desired distinctive emission and excitation spectra are used as activators. Host lattices do not appreciably impact the electronic transitions of rare earth ions. [1] Applications for UV emitting phosphors are numerous. In addition to being used to create phototherapy lamps, UV-emitting phosphors are also utilized in low-pressure lamps, photochemistry, X-ray imaging equipment, water filtration and other applications.[2]

Phototherapy has a long history of use in the treatment of skin conditions. The causes and signs of different skin illnesses vary, but phototherapy is a very effective treatment for them. Since phototherapy has the fewest negative effects of all the treatments, the demand for phototherapy lamps on the global market is rising daily. Additionally helpful for treating various skin diseases and skin renewal, phototherapy is a good treatment option. [3] The primary and most crucial factors for treating the specific condition with phototherapy are the wavelength of the light selected for the treatment and the duration of the exposure.

UV light is divided into UVC (100–280 nm), UVB (280–315 nm), and UVA (315–400 nm). Whereas UV light (100-400 nm) is appropriate for treating skin problems, phototherapy that uses UVA light with the medication psoralen is referred to as PUVA phototherapy, while UVB phototherapy uses UVB light. For luminous ions, borate materials make ideal host lattices. Numerous rare earth doped borate compounds have high optical damage thresholds and UV transparency, making them excellent hosts for UV emitting phosphors. Due of their well defined UV emission, Gd³⁺-activated phosphors have received a great deal of attention. The high efficiency of gadolinium borate phosphors, which range from orthoborates to pentaborates, has shown them to be potential candidates for use in optoelectronic devices. [4-8].

We have described the phosphor K₄(BO₃)₃ doped with different activator Gd³⁺, Bi³⁺, Pb²⁺ in this study. For the first time, these phosphors were created using the re-crystallization technique. The optical characteristics of these phosphors were explored. The borate group contains a variety of useful phosphors, such as LaB₅O₉:Ce³⁺ [9], LaMgB₅O₁₀:Ce³⁺ [10], Na₂La₂B₂O₇:Ce³⁺ [11], and LiSrBO₃:Gd³⁺.

II. EXPERIMENTAL

The phosphors K₄(BO₃)₃:Gd³⁺, Bi³⁺, Pb²⁺ were synthesized first time by a recrystallization method. This process has a few key advantages, such as a relatively low temperature route, improved controllability, and ease of solubility. [12-13] Stoichiometric quantities of the metal nitrates K(NO₃), Sr(NO₃)₂, boric acid, and gadolinium nitrate Gd(NO₃)₂, Bismuth nitrate Bi(NO₃)₃, Lead nitrate Pb(NO₃)₂ were used to make the phosphor. In a little volume of double-distilled water, the starting ingredients K(NO₃) and Sr(NO₃)₂ were first dissolved. A magnetic stirrer was used to stir constantly for a few minutes while the stock solution of activators was added in nitrate form. By vigorously stirring for a few minutes at 50 °C, boric acid was dispersed in double-distilled water. Next, a drop at a time of this solution was poured into the mixture. After that, the entire homogeneous solution was put on a hot plate set to 70°C to gradually evaporate any extra water. Finally, heat and crushing were applied to the dried precursor. A white crystalline powder of K₄(BO₃)₃:Gd³⁺, Bi³⁺, Pb²⁺ were obtained after crushing the dry precursor and heating it for two hours at 900°C. A spectrophotometer, powder XRD, scanning electron microscopy, and EDX were then used to characterize the resulting powder sample.

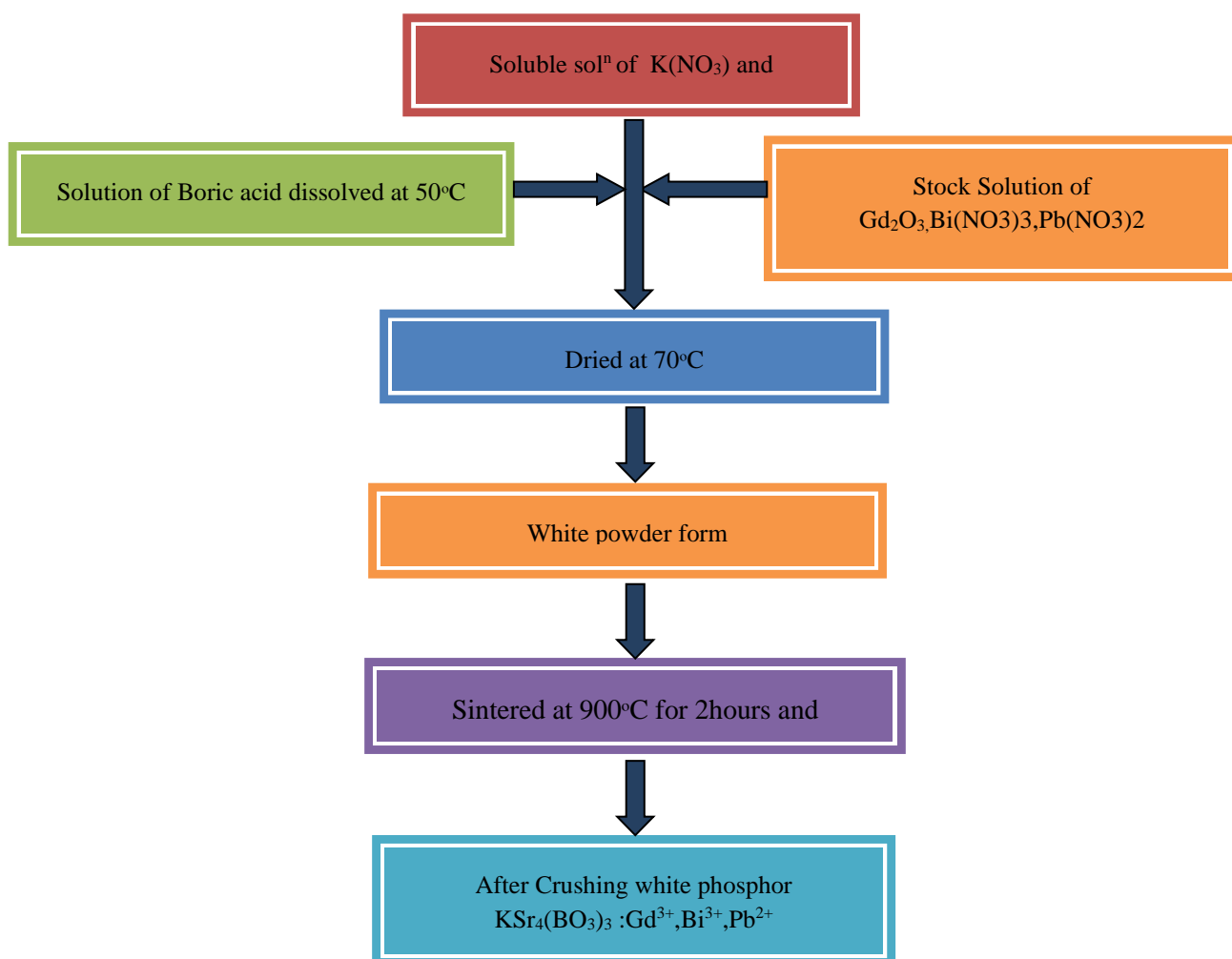


Figure1. -Flowchart of synthesis of phosphors by re crystallization method

III. RESULT AND DISCUSSION

The phosphor $\text{KSr}_4(\text{BO}_3)_3$ doped with different activator $\text{Gd}^{3+}, \text{Bi}^{3+}, \text{Pb}^{2+}$ were analysed using an X-ray Diffractometer with a scan speed of $5.000^\circ/\text{min}$ in the range of $10\text{-}80^\circ$, and the results of the XRD analysis verified the crystallinity and phase purity of the compound. At room temperature, a fluorescence spectrophotometer was used to measure the excitation and emission spectra. The photomultiplier tube (PMT) detector voltage, spectral resolution, scan speed, and the width of monochromatic slits (0.1 nm) were all held constant throughout the examination of the samples. Scanning electron microscopy was used to examine the structural and morphological properties, including particle size and shape.

1. XRD analysis-

The XRD pattern, examined using a Rigaku Miniflex II X-Ray Diffractometer, confirmed the phase purity and crystalline structure of the produced phosphor. The XRD patterns for $\text{KSr}_4(\text{BO}_3)_3$ are shown in Figure 2. Each diffraction peak corresponds to the pure phase of the prepared sample, matching well with the standard data for $\text{KSr}_4(\text{BO}_3)_3$. The strong and precise diffraction peaks indicate that the sample has been properly crystallized. The Rietveld refinement data for the $\text{KSr}_4(\text{BO}_3)_3$ phosphor revealed lattice parameters of $a = 11.0384 \text{ \AA}$, $b = 11.9897 \text{ \AA}$, and $c = 6.8845 \text{ \AA}$, belonging to the space group $\text{Ama}2$ (No. 40). The unit cell volume is 911.174 \AA^3 , with $Z = 4$, and the angles $\alpha = 90.00^\circ$, $\beta = 90.00^\circ$, and $\gamma = 90.00^\circ$. The refinement achieved goodness-of-fit coefficient values of $R_b = 11.03\%$ and $R_{wb} = 15.22\%$.

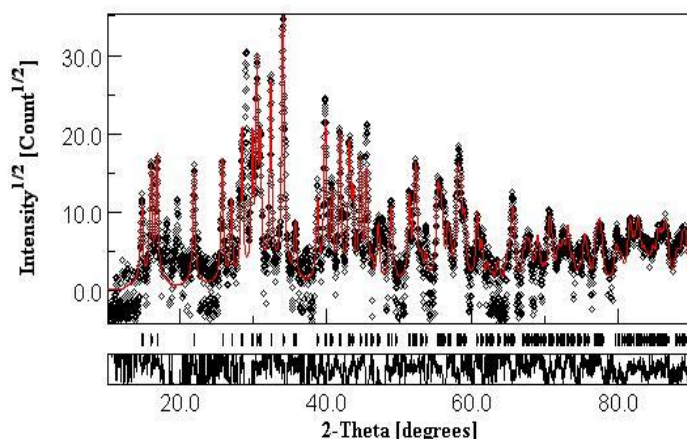


Figure2.- Reitveld analysis patterns for X-ray powder diffraction data of $\text{K Sr}_4(\text{BO}_3)_3$.

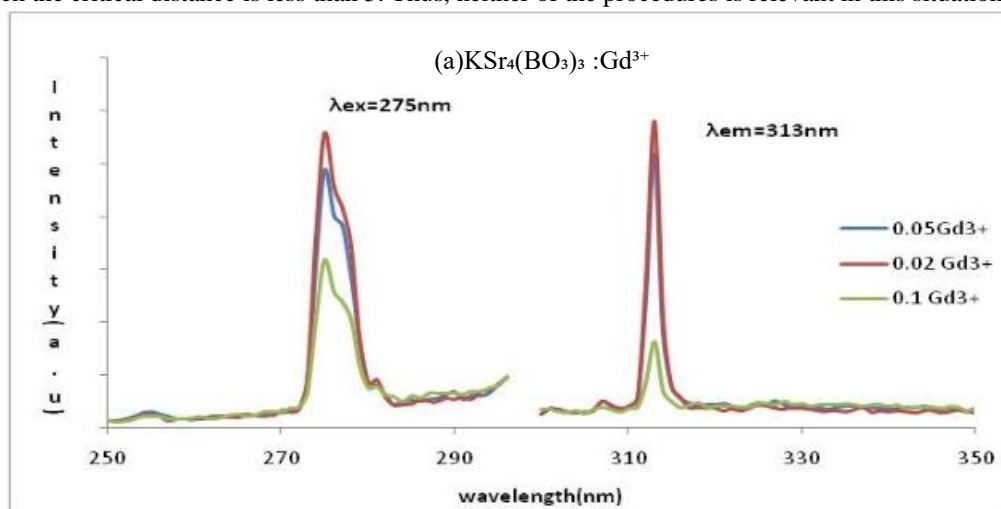
2. Photoluminescence Spectroscopy-

The accompanying figure 3 presents the excitation and emission spectra of $\text{K Sr}_4(\text{BO}_3)_3 : \text{Gd}^{3+}$, Bi^{3+} , Pb^{2+} , obtained using a Hitachi F-7000 fluorescence spectrophotometer at room temperature. The phosphor $\text{K Sr}_4(\text{BO}_3)_3 : \text{Gd}^{3+}$ shows an excitation peak at 275 nm and an emission peak at 313 nm when excited at this wavelength. This emission at 313 nm, under 275 nm excitation, corresponds to the ${}^6\text{P}_{7/2} \rightarrow {}^8\text{S}_{7/2}$ transition.

Figure 3 (a). illustrates how the PL intensity increases with the concentration of the dopant Gd^{3+} ions up to 2 mol%, after which it begins to decline due to concentration quenching. Concentration quenching primarily occurs due to photon reabsorption, multipole-multipole phonon interaction, and non-radiative energy transfer between dopant ions. The likelihood of energy transfer between activator ions is determined by the n th power of the distance between them. As the concentration of dopant ions increases, the distance between them decreases, leading to increased energy transfer. The critical distance for energy transfer (R_c) can be determined using the equation given below

$$R_c = 2 \left[\frac{3V}{4\pi X_c Z} \right]^{\frac{1}{3}}$$

R_c stands for the critical distance, V for the unit cell's volume, Z for the number of cations, and X_c for the critical concentration of the activator ion (Gd^{3+}). The critical distance is discovered to be 17.09 \AA for the phosphor $\text{K Sr}_4(\text{BO}_3)_3 : \text{Gd}^{3+}$ at $V=911.144 \text{ \AA}^3$, $X_c=0.02$, and $Z=4$. Nonradiative energy transfer is primarily caused by three processes: exchange interaction, radiative reabsorption, and multipole-multipole contact. When excitation and emission spectra match, there is radiation reabsorption; nevertheless, exchange interaction is considered when the critical distance is less than 5. Thus, neither of the procedures is relevant in this situation. [14]



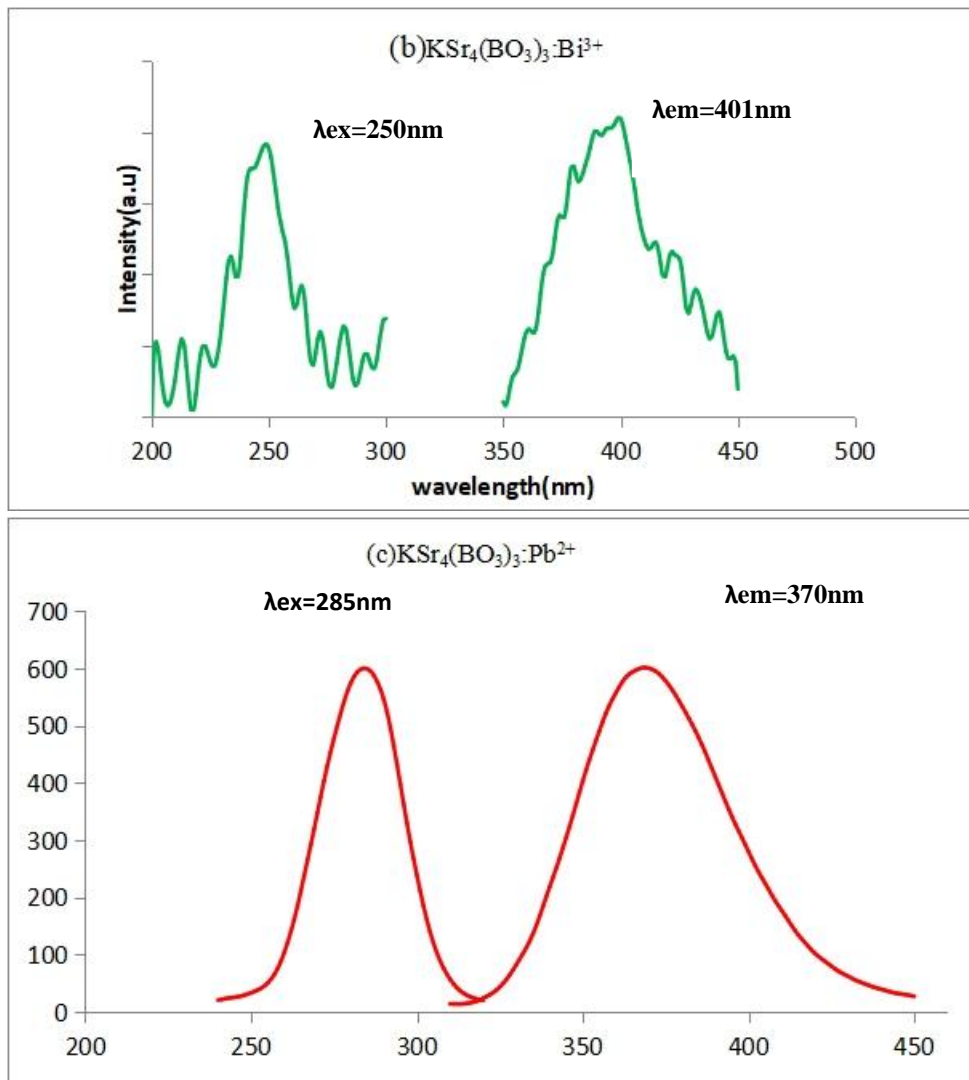


Figure3. - PL excitation and emission spectra of (a) $\text{K Sr}_4(\text{BO}_3)_3:\text{Gd}^{3+}$ (b) $\text{K Sr}_4(\text{BO}_3)_3:\text{Bi}^{3+}$ (c) $\text{K Sr}_4(\text{BO}_3)_3:\text{Pb}^{2+}$

In Figure 3(b), broad excitation bands are observed between 220 nm and 290 nm, with a peak at 251 nm, corresponding to the $^1\text{S}_0 \rightarrow ^3\text{P}_1$ transition of Bi^{3+} . When excited at 251 nm, an emission band appears at 401 nm, indicating the transition from the $^3\text{P}_1$ excited state to the $^1\text{S}_0$ ground state. The absence of splitting or multiple bands in the emission spectra suggests that Bi^{3+} ions are likely occupying the positions of Sr^{3+} ions in the lattice. According to extensive literature on the luminescence of Bi^{3+} in inorganic hosts, Bi^{3+} typically absorbs light in the 220–290 nm range and emits in the 350–450 nm range. Figure 3(c) shows the photoluminescence spectrum of Pb^{2+} doped in the $\text{K Sr}_4(\text{BO}_3)_3$ host material. The excitation band for the synthesized $\text{K Sr}_4(\text{BO}_3)_3:\text{Pb}^{2+}$ phosphor was observed at 285 nm, corresponding to the $^1\text{S}_0 \rightarrow ^3\text{P}_1$ transition, and the emission band was observed at 370 nm, corresponding to the transition from the $^3\text{P}_1$ excited state to the $^1\text{S}_0$ ground state. This spectrum is characterized by the $^1\text{S}_0 \rightarrow ^3\text{P}_1$ transition, originating from the $6s^2 \rightarrow 6p$ interconfigurational transition. Typically, at room temperature, emission is observed from the $^3\text{P}_1 \rightarrow ^1\text{S}_0$ transition, although at low temperatures, the highly forbidden $^3\text{P}_0 \rightarrow ^1\text{S}_0$ emission is also seen. There is not any splitting or multiple bands in the emission spectra observed, indicating that the Pb^{2+} ions are incorporated at only one site (Sr^{2+} ion site) in the crystal lattice. In many inorganic hosts, the emission band of the Pb^{2+} ion is in the UV region, but in some hosts, Pb^{2+} can emit in the visible region. This variability depends strongly on the site occupied by Pb^{2+} ions, the crystal structure of the host lattice, temperature and the electronegativity of the ligand.[15]

3. FE-SEM analysis-

By using the FE-SEM technique, as demonstrated in figure 4, the microstructural evaluation of the $\text{K Sr}_4(\text{BO}_3)_3$ phosphors was carried out. The synthesised phosphors crystalline shape showed microgranularity

with a particle size range of 1 to 100 nm. This is appropriate for the high-energy emissions and absorptions from the phosphor particles outer surface. The luminescence intensity, which is controllable, is always impacted by the particle size and surface shape. The SEM scans show both larger and smaller individual particles, indicating that the particle sizes and shapes are random. Recrystallization is a gentle chemical method that saves time and money. It can be seen in the figures below that certain little particles with irregular shapes are present on top of the larger particles.

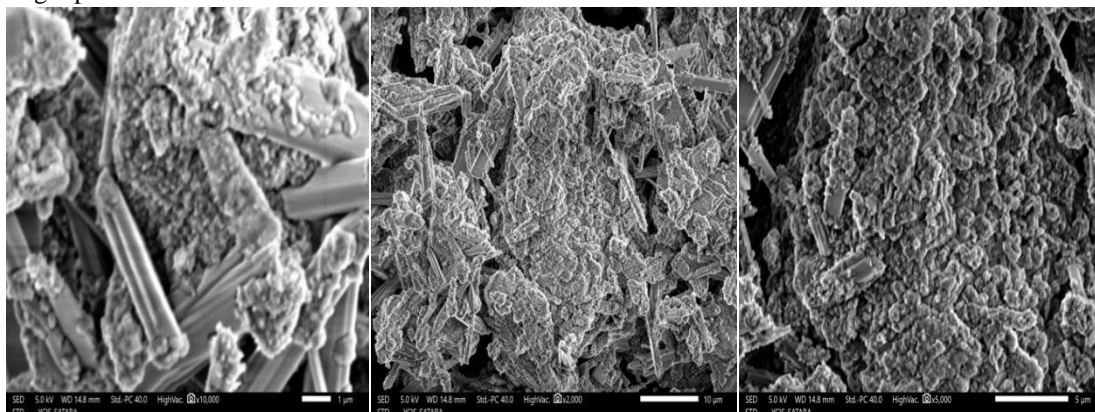
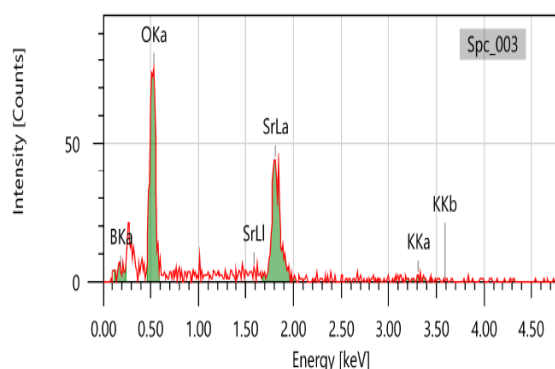


Figure 4.-SEM images of $\text{K}_2\text{Sr}_4(\text{BO}_3)_3$

4. Energy Dispersive X-ray Analysis-

Through energy dispersive X-ray analysis, elemental analysis verifies the components in the produced materials and determines their qualitative chemical makeup (EDX). $\text{K}_2\text{Sr}_4(\text{BO}_3)_3:\text{Gd}^{3+}$, Bi^{3+} , Pb^{2+} were formed by recrystallization method, and their formation was confirmed by EDX element analysis. The results shown in the next graphs figure 5 demonstrate how well the EDX data agree. However, it is quite challenging to use an EDX detector to find light elements like lithium and boron. However, the EDX graph's constant proportionality between the components demonstrates how the phosphors $\text{K}_2\text{Sr}_4(\text{BO}_3)_3$ were formed correctly.



Element	Line	Mass%	Atom%
B	K	nd	nd
O	K	18.92+0.91	54.16+2.60
K	K	5.32+3.69	6.24+4.33
Sr	L	75.76+5.47	39.60+2.86
Total		100.00	100.00

Figure 5. EDX analysis of $\text{K}_2\text{Sr}_4(\text{BO}_3)_3$

IV. CONCLUSION

Recrystallization was employed to effectively synthesize the inorganic borate host phosphors $\text{K}_2\text{Sr}_4(\text{BO}_3)_3$ doped with Gd^{3+} , Bi^{3+} , Pb^{2+} . This method is simple, rapid, low-temperature, and cost-effective. Photoluminescence (PL) studies indicate that this technique is particularly effective for synthesizing inorganic compounds with a borate host. When excited at 275 nm, $\text{K}_2\text{Sr}_4(\text{BO}_3)_3$ doped with Gd^{3+} emits strongly at 313 nm. For $\text{K}_2\text{Sr}_4(\text{BO}_3)_3$ doped with Bi^{3+} , an excitation at 251 nm results in an emission band at 401 nm, corresponding to the transition from the $^3\text{P}_1$ excited state to the $^1\text{S}_0$ ground state. For the synthesized $\text{K}_2\text{Sr}_4(\text{BO}_3)_3:\text{Pb}^{2+}$ phosphor, the excitation band was observed at 285 nm, corresponding to the $^1\text{S}_0 \rightarrow ^3\text{P}_1$ transition, with an emission band at 370 nm, corresponding to the transition from the $^3\text{P}_1$ excited state to the $^1\text{S}_0$ ground state. $\text{K}_2\text{Sr}_4(\text{BO}_3)_3$ phosphors doped with Gd^{3+} , Bi^{3+} , Pb^{2+} exhibit UV-B emission bands, making them highly suitable for phototherapy applications.

REFERENCES

- [1] Nimbalkar M, Yawalkar M, Mahajan N, Dhoble SJ, Potential of Luminescent Materials In Phototherapy, Photodiagnosis and Photodynamic Therapy 33 (2020) 102082-102099
- [2] R.S. Palaspar A.B. Gawande R.P. Sonekar S.K. Omanwar, $\text{Eu}^{3+} \rightarrow \text{Eu}^{2+}$ reduction in $\text{BaAl}_2\text{B}_2\text{O}_7$ phosphor in oxidizing environment, Optik - International Journal for Light and Electron Optics, 15 (2015) pp.1122-1134.
- [3] Energy transfer from Pr^{3+} to Gd^{3+} ions in $\text{BaB}_8\text{O}_{13}$ phosphor for phototherapy lamps Sumedha Tamboli, Govind B. Naira, S.J. Dhoble, D.K. Burghate, Physica B :Physics of Condensed Matter, 535(2018) pp.232-236.
- [4] P. S. Hemne, R. G. Kungthakar, S. J. Dhoble, S.V. Moharil, V. Singh, Phosphor for phototherapy: Review on psoriasis, The journal of biological and chemical luminescence, 32 (2017) 260–270.
- [5] E Runkle ,UV Radiation and Applications in Horticulture, (2018) pp.33-46
- [6] Ya Zhuo, J. Zhong , J. Brgoch , Controlling Eu^{2+} Substitution towards a Narrow-Band Green-Emitting Borate Phosphor $\text{NaBaB}_9\text{O}_{15}:\text{Eu}^{2+}$, ChemRxiv 1(2019) pp.773-795.
- [7] X. Liu, B. Lei ,Y. Liu, The Application of Phosphor in Agricultural field, Springer Science ,(2016)pp.234-258
- [8] N. Singh, Jung-Kul Lee, M. Mohapatra, R.M. Kadam, V. Singh, UV emitting Gd incorporated $\text{LiBaB}_9\text{O}_{15}$ phosphors: An ESR and photoluminescence investigation , journal of luminescence, 223 (2020) pp. 117239
- [9] X. Lei, Gen Li, M. Zeng , B. Zhou, Z. Yuan , Y. Hu, H. Gu, Y. Li, Wei Chen, Europium-doped $\text{NaBaB}_9\text{O}_{15}$ phosphors with controllable blue/red dual-band emissions through self-reduction for plant growth LEDs, Journal of luminescence, 237(2021), pp.118166
- [10] P. A. Nagpure, S. K. Omanwar, UV emitting borate phosphors for phototherapy lamps, Indian Journal of pure and Applied Physics. 53(2015) pp. 77-81
- [11] P. A. Nagpure, S. K. Omanwar, Red and blue emitting borate phosphor excited by near Ultraviolet Light, Journal of Optics, 46-2(2016) pp. 91-94
- [12] V. Singh, K. Swapna, S. Kaur, A.S. Rao and J.L. Rao, “Narrow-Band UVB-Emitting Gd-Doped SrY_2O_4 Phosphors”, Journal Of Electronics material, 49(2020) , pp. 5-13.
- [13] A.O. Chauhan, A.B. Gawande, S.K. Omanwar, ” Narrow band UVB emitting phosphor $\text{LaPO}_4:\text{Gd}^{3+}$ for phototherapy lamp “ Optik (2016) pp.334-367
- [14] S. Tamboli, B. Rajeswari and S. J. Dhoble, Investigation of UV-emitting Gd^{3+} -doped LiCaBO_3 phosphor ,The journal of biological and chemical luminescence (2016) Luminescence, 31(2016) pp. 551–556.
- [15] A. B. Gawande, 1 R. P. Sonekar, 2 and S. K. Omanwar, Synthesis and Photoluminescence Study of Bi^{3+} and Pb^{2+} Activated $\text{Ca}_3(\text{BO}_3)_2$, International Journal of Optics Volume 2014 pp223-454

© 2024. This work is published under [https://creativecommons.org/licenses/by/4.0/legalcode\(the“License”\)](https://creativecommons.org/licenses/by/4.0/legalcode(the\).

Notwithstanding the ProQuest Terms and Conditions, you may use this content in accordance with the terms of the License.

¹ Jitendra T. Ingle² Rupesh N. Patil

Combustion Synthesis and Photoluminescence Study of $\text{Ba}_3\text{Y}_2(\text{BO}_3)_4:\text{Eu}^{3+}$ Phosphor for White LED.



Abstract: - As a progressive research in optical materials, $\text{Ba}_3\text{Y}_2(\text{BO}_3)_4:\text{Eu}^{3+}$ red emitting phosphor is synthesized by simple route of solution combustion technique, the synthesis was based up on the exothermic reaction between the fuel (Urea) and oxidizer (Nitrate), the heat release in reaction was utilized for auto combustion of ingredients, the phase formation and crystal structure of prepared borates material was determined by powder XRD technique. The emission spectrum exhibited one strong red emission at 613 nm, corresponding to the electric dipole ${}^5\text{D}_0\text{-}{}^7\text{F}_2$ transition of Eu^{3+} , under 365 nm excitation. The emission spectrum at 613 nm indicated that the $\text{Ba}_3\text{Y}_2(\text{BO}_3)_4:\text{Eu}^{3+}$ phosphor was effectively excited by ultraviolet (UV) (254, 365 and 400 nm) and blue (470 nm) light. The optimal Eu^{3+} doping concentration is ~5 mol%, which is higher than that of other hosts. Furthermore, CIE coordinates are $x=0.64$ & $y=0.36$ the characteristics of thermal quenching are also studied. All data suggest that $\text{Ba}_3\text{Y}_2(\text{BO}_3)_4:\text{Eu}^{3+}$ phosphor found potential candidate in white light converted LEDs.

Keywords: Combustion synthesis, photoluminescence, phosphors, w-LEDs.

Introduction

The current development in cutting edge technology of lighting industry, fascinates more reliable and environment friendly light emissive devices. Nowadays, saving energy and reducing greenhouse gas emissions has become the consensus of people all over the world [1-6]. Usage of Lighting for daily is a large proportion of energy consumption, so replacing inefficient lighting technologies is greatly important in terms of sustainable development and environmental protection. White light emitting diodes (white LEDs) are more and more recognized and developed rapidly in the current solid-state lighting field [7-8], since they have many advantages over traditional incandescent lamps and fluorescent lamps, such as energy saving, high efficiency, long working life, easy control and environmental friendliness [9-12]. Energy-efficient white LED lighting technologies have already been widely applied to replace all inefficient old lighting systems. The most mature method for fabricating white LEDs involves the combination of InGaN-based blue LED chips and commercial $\text{Y}_3\text{Al}_5\text{O}_{12}:\text{Ce}^{3+}$ yellow phosphors [13-15], but the obtained white-light emission exhibits a low color rendering index ($\text{CRI} < 75$) and a high correlated color temperature ($\text{CCT} > 4500 \text{ K}$) due to inadequate red light component [33,34]. An alternative approach, which uses the near-ultraviolet (near-UV) LED chips to excite red/green/blue tri-color phosphors, has been proposed to fabricate white LEDs with high CRI and low CCT values [16-18]

¹ Department of Physics, Luminescence & Optical Material Research Laboratory, Govt. Vidarbha Institute of Science and Humanities, Amravati

² Department of Physics, Vidnyan Mahavidyalaya, Malkapur, Dist-Buldhana

Copyright © JES 2024 on-line : journal.esrgroups.org

Therefore, In search of efficient red phosphor, we undertake borate host $\text{Ba}_3\text{Y}_2(\text{BO}_3)_4$ which emit red light at 613 nm by using the Eu^{3+} ion as color center, which can efficiently excited by UV and blue light because of its excellent luminous properties and low cost.

Experimental

Combustion synthesis of $\text{Ba}_3\text{Y}_2(\text{BO}_3)_4:\text{Eu}^{3+}$

$\text{Ba}_3\text{Y}_2(\text{BO}_3)_4:\text{Eu}^{3+}$ powders samples with optimized concentration o Eu^{3+} are prepared by modified route of solution combustion technique. $\text{Ba}(\text{NO}_3)_2$ (LOBA CHEMIE, 98%), $\text{Y}_2(\text{NO}_3)_3$ (Star Chem Fine Chemicals 98%), and Eu_2O_3 (IRE Ltd.) are chosen as the starting materials. The preparation process is as follows. Firstly, stoichiometric amounts of starting ingredients were calculated as per the balance inorganic reaction indicated in table no.1 and weighted precisely. Secondly, all starting ingredients like $\text{Y}_2\text{O}_3, \text{Eu}_2\text{O}_3$ were converted into $\text{Y}(\text{NO}_3)_3$ and $\text{Eu}(\text{NO}_3)_3$ by mixing Y_2O_3 and Eu_2O_3 into few ml of dil. HNO_3 , then these starting ingredients were weighed on High Precision Balance (WENSAR ISO 0001 CERTIFIED), then weighed quantities of each metal nitrate and urea were mixed together by adding little D.D. water and place on heating mantle for about 30 minute to obtain homogeneous, clear and thick solution, it then transferred in to a preheated muffle furnace maintained at 550°C .

The mixture boils, froths, ignites and undergoes dehydration and then decomposition with liberation of NH_3 and NO_2 gasses. The heat generated in reaction between fuel (urea) and oxidiser (ammonium nitrate) used for the auto-combustion of precursors. The process being highly exothermic, continues to liberate gases swell, the mixture glows into large voluminous foamy substrate, the entire process complete within 5 minutes.

The prepared material is then taken out of the furnace and the foamy product is crushed into a fine powder and heated at 800°C for about 1 hour, some of the phosphors reported by this technique [19-23].

Table 1. The molar ratios of ingredients used in the synthesis and corresponding balanced chemical reactions.

S.N.	Phosphors.	Balanced chemical reaction with molar ratios of ingredients.
1.	$\text{Ba}_3\text{Y}_{(2-x)}(\text{BO}_3)_4:$ $x\text{Eu}^{3+}$ ($x= 5 \text{ mol}\%$)	$\text{Ba}(\text{NO}_3)_2 + (2-x)\text{Y}(\text{NO}_3)_3 + 4\text{H}_3\text{BO}_3 + 3 \text{NH}_4\text{NO}_3 + 11 \text{CO}(\text{NH}_2)_2 +$ $x\text{Eu}(\text{NO}_3)_3 \xrightarrow[550^\circ\text{C}]{\text{heat}} \text{Ba}_3\text{Y}_2(\text{BO}_3)_4:\text{Eu}^{3+} + \text{Gaseous Products } (\text{H}_2\text{O}\uparrow,$ $\text{NH}_3\uparrow \text{ and } \text{NO}_x\uparrow)$

Characterizations

Phase formation and structural properties of all samples are measured using powder X-ray diffraction analysis (XRD), which performed on Rigaku Miniflex $\times 600$ X-ray Diffractometer using $\text{Cu K}\alpha$ radiation with 0.15405 \AA wavelengths. The XRD data were obtained at the scanning angle ranging from 10° to 80° with the step of 0.2° per sec at room temperature. Rietveld refinement analysis and the structural model of

the sample are put into effect by the general structure analysis system (GSAS) software. The photoluminescence spectra (excitation and emission) were recorded on Hitachi F-7000 fluorescence spectrophotometer.

Structure analysis and phase purity

The crystal structure of $\text{Ba}_3\text{Y}_2(\text{BO}_3)_4$ is of an orthorhombic phase with $pc21n$ space group, and the lattice parameter is $a=0.7686$ nm, $b=1.6498$ nm, and $c=0.89559$ nm (JCPDS No. 48- 0307). The XRD pattern of $\text{Ba}_3\text{Y}_2(\text{BO}_3)_4:\text{Eu}^{3+}$ with 15 mol% Eu^{3+} is present. Most peaks are indexed to the $\text{Ba}_3\text{Y}_2(\text{BO}_3)_4$ phase, which agrees well with JCPDS No, 48-0307. It indicates that the doping of Eu^{3+} ions does not form new phases in the synthesis process.

The structure of $\text{Ba}_3\text{Y}_2(\text{BO}_3)_4$ is formed with isolated BO_3 triangles, barium-oxygen polyhedra, and yttrium-oxygen polyhedra. The trivalent yttrium ions occupy two different crystallographic sites (Y1 and Y2), and every Y^{3+} has an eight-fold coordination to form YO_8 polyhedra. The bond valence of Y1 is stronger than that of Y2, therefore, Eu^{3+} prefers to occupy the Y2 site. Y_2O_8 polyhedral columns are built by sharing edges along the c -axis. The distance between Y1 and Y2 is equal to the value of the c -constant, and the environment around Y^{3+} is not centrosymmetric. The structure of $\text{Ba}_3\text{Y}_2(\text{BO}_3)_4$ indicates that the long distance between the rare-earth ions results in a higher doping concentration, and the imperfect symmetry of Eu^{3+} leads to the pure red emission.

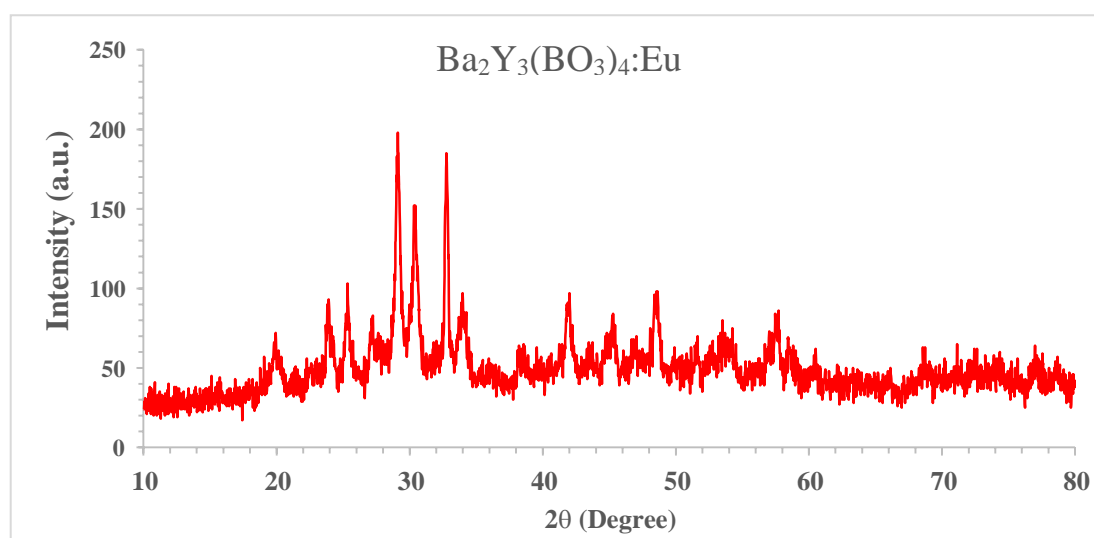


Fig. 1 XRD pattern of $\text{Ba}_3\text{Y}_2(\text{NO}_3)_4:\text{Eu}^{3+}$

Photoluminescence properties

Fig.2 shows the emission spectrum of $\text{Ba}_3\text{Y}_2(\text{NO}_3)_4:\text{Eu}^{3+}$ phosphor under 254 nm excitation with 15mol % Eu^{3+} . Several narrow bands are observed between 580 and 700 nm. The main peak at 613 nm is assigned to the electric dipole transition of ${}^5\text{D}_0\text{-}{}^7\text{F}_2$, of Eu^{3+} , which is because Eu^{3+} occupies the noncentrosymmetric position in the crystal structure of $\text{Ba}_3\text{Y}_2(\text{NO}_3)_4$. Other peaks corresponds to the

transitions of ${}^5D_0-{}^7F_j$ ($j=1, 2, 3$), such as, the peaks at 599, 632 and 654 nm, assigned to ${}^5D_0-{}^7F_1$, ${}^5D_0-{}^7F_2$ and ${}^5D_0-{}^7F_3$ transitions of Eu^{3+} respectively.

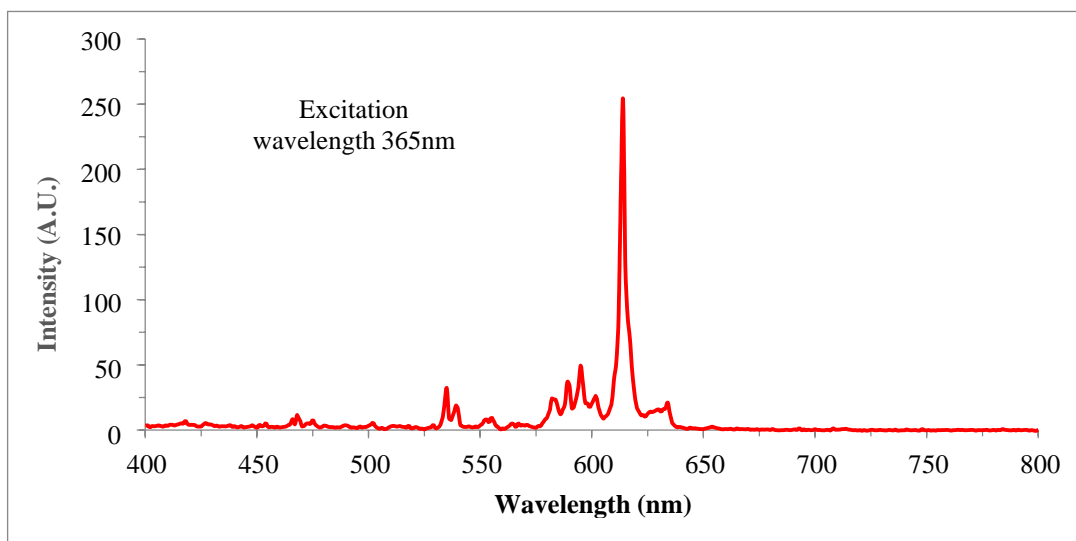


Fig.2 Emission spectrum of $\text{Ba}_3\text{Y}_2(\text{NO}_3)_4:\text{Eu}^{3+}$ at 365 nm.

Fig. 3 shows the broadband at 254 nm is assigned to the charge transition band of $\text{O}^{2-}-\text{Eu}^{3+}$. The bands between 200 and 375 nm are observed, which means that the $\text{Ba}_3\text{Y}_2(\text{NO}_3)_4:\text{Eu}^{3+}$ phosphor exhibits a satisfactory red performance under UV-vis excitation. One band centred at 390 nm is observed in the excitation spectrum, which means that the phosphor has sufficient absorption at the emission wavelength of the blue diode. It is suitable for a red light source, which is combined with InGaN based yellow phosphor materials.

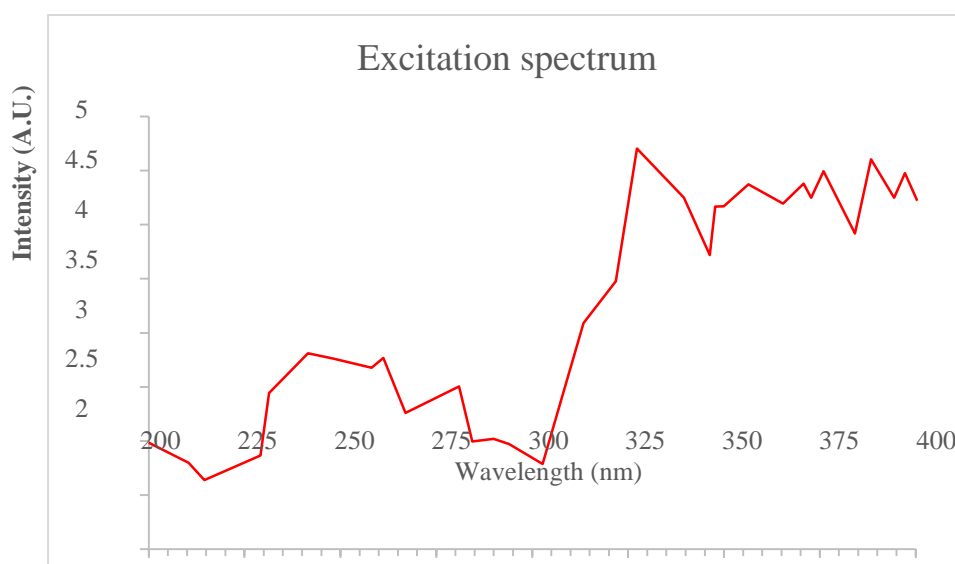


Fig. 3 Excitation spectrum of $\text{Ba}_3\text{Y}_2(\text{NO}_3)_4:\text{Eu}^{3+}$ at emission 613 nm.

The excitation and emission spectra, it is noted that $\text{Ba}_3\text{Y}_2(\text{NO}_3)_4:\text{Eu}^{3+}$ is a promising red phosphor for white LED. The effect of Eu^{3+} concentration on the emission intensity of ${}^5\text{D}_0-{}^7\text{F}_2$ (613 nm) transition. The Eu^{3+} concentration varies from 5 mol % to 25mol %. The emission intensities increase with increasing Eu^{3+} concentration, and reach the maximum at $x=15\text{mol}$ %. However the emission intensity of the $\text{Ba}_3\text{Y}_2(\text{NO}_3)_4:\text{Eu}^{3+}$ phosphor is higher under the 365 nm excitation than under the 254 nm excitation at the same Eu^{3+} doped concentration.

Conclusion

The $\text{Ba}_3\text{Y}_2(\text{NO}_3)_4:\text{Eu}^{3+}$ red phosphor was synthesized and the luminescent characteristics were investigated. The phosphor was effectively excited by UV and blue light, and the intense pure emission, on account of the ${}^5\text{D}_0-{}^7\text{F}_2$ transition of Eu^{3+} , was observed in $\text{Ba}_3\text{Y}_2(\text{NO}_3)_4:\text{Eu}^{3+}$ under 254 nm excitation. The CIE chromaticity (x,y) of $\text{Ba}_3\text{Y}_2(\text{NO}_3)_4:\text{Eu}^{3+}$ was $x=0.641$, $y=0.359$. The results indicated that $\text{Ba}_3\text{Y}_2(\text{NO}_3)_4:\text{Eu}^{3+}$ was a promising red emission phosphor converting for white LED.

References

- [1] L. Sun *et al.* Luminescence investigation of $\text{Eu}^{2+}/\text{Ce}^{3+}/\text{Mn}^{2+}$ doped $\text{Y}_2\text{Mg}_2\text{Al}_2\text{Si}_2\text{O}_{12}$ phosphors J. Lumin. (2022)
- [2] S.K. Baghel *et al.* Luminescence properties of a novel cyan-blue light emitting Ce^{3+} doped $\text{SrZrSi}_2\text{O}_7$ phosphor Opt. Mater. (2022)
- [3] X. Zhang *et al.* Photoluminescence properties of Eu^{2+} doped Ba_2ZnS_3 phosphor for white light emitting diodes Mater. Lett.(2007)
- [4] V.S. Hingwe *et al.* Eu^{3+} doped N-UV emitting LiSrPO_4 phosphor for W-LED application Optik (2017)
- [5] J. Chan *et al.* Cation substitution induced highly symmetric crystal structure in cyan-green-emitting $\text{Ca}_2\text{La}_{1-x}\text{Lu}_x\text{Hf}_2\text{Al}_3\text{O}_{12}:\text{Ce}^{3+}$ solid-solution phosphors with enhanced photoluminescence emission and thermal stability: toward full-visible-spectrum white LEDs Mater. Today Phys. (2023)
- [6] Z. Zhang *et al.* Using an excellent near-UV-excited cyan-emitting phosphor for enhancing the color rendering index of warm-white LEDs by filling the cyan gap Mater. Today Chem. (2021)
- [7] F. Liu *et al.* Garnet-based red emitting phosphors $\text{Li}_6\text{MLa}_2\text{Nb}_2\text{O}_{12}:\text{Eu}^{3+}$ (M = Ca, Sr, Ba): photoluminescence improvement by changing crystal lattice Ceram. Int.(2014)
- [8] J.Y. Park *et al.* Deep red-emitting $\text{Ca}_{14}\text{Al}_{10}\text{Zn}_6\text{O}_{35}:\text{Mn}^{4+}$ phosphors for WLED applications J. Alloys Compd.(2017).
- [9] X. Huang *et al.* Preparation, crystal structure, and photoluminescence properties of high-brightness red-emitting $\text{Ca}_2\text{LuNbO}_6:\text{Eu}^{3+}$ double-perovskite phosphors for high-CRI warm-white LEDs J. Lumin. (2020)
- [10] F. Gu *et al.* Combustion synthesis and photoluminescence of $\text{MgO}:\text{Eu}^{3+}$ nanocrystals with Li^+ addition J. Cryst. Growth (2006)
- [11] R. Yu *et al.* Synthesis and luminescence properties of a novel red-emitting phosphor $\text{Ba}_3\text{La}(\text{PO}_4)_3:\text{Eu}^{3+}$ for solid-state lighting J. Alloys Compd.(2013)
- [12] J.Y. Park *et al.* Versatile fluorescent $\text{CaGdAlO}_4:\text{Eu}^{3+}$ red phosphor for latent fingerprints detection J. Alloys Compd. (2020)
- [13] Z.-w. Zhang *et al.* Synthesis and characterizations of novel $\text{Ba}_2\text{La}_8(\text{SiO}_4)_6\text{O}_2:\text{Eu}^{3+}$ oxyapatite phosphors Dyes Pigm. (2017)
- [14] Y. Hua *et al.* Synthesis and photoluminescence $\text{Sr}_2\text{LaTaO}_6:\text{Mn}^{4+}$ phosphors with ultrahigh color purity for good CRI warm-WLED devices Optik (2021)
- [15] K. Ding *et al.* A potential red-emitting phosphor $\text{Ca}_2\text{YTaO}_6:\text{Eu}^{3+}$: luminescence properties, thermal stability and applications for white LEDs J. Rare Earth. (2021)
- [16] H. Guo *et al.* Synthesis and photoluminescence properties of novel highly thermal-stable red-emitting $\text{Na}_3\text{Sc}_2(\text{PO}_4)_3:\text{Eu}^{3+}$ phosphors for UV-excited white-light-emitting diodes J. Alloys Compd. (2018)
- [17] C. Ji *et al.* High thermal stability and colour saturation red-emitting $\text{Ba}_2\text{AGe}_2\text{O}_7:\text{Eu}^{3+}$ (A = Mg, Zn) phosphors for WLEDs J. Lumin. (2019)

- [18] S. Long *et al.* High quantum efficiency red-emission tungstate based phosphor $\text{Sr}(\text{La}_{1-x}\text{Eu}_x)_2\text{Mg}_2\text{W}_2\text{O}_{12}$ for WLEDs application *Ceram. Int.*(2013)
- [19] Ingle JT, Gawande AB, Sonekar RP, Omanwar SK, Wang Y, Zhao L, Combustion synthesis and optical properties of Oxy-borate phosphors $\text{YCa}_4\text{O}(\text{BO}_3)_3: \text{RE}^{3+}$ (RE = Eu^{3+} , Tb^{3+}) Under UV, VUV excitation *J. Alloys and Compounds* 2014; 585:633–636.
- [20] Ingle JT, Sonekar RP, Omanwar SK, Wang Y, Zhao L. Combustion Synthesis and Photoluminescence Study of Novel Red Phosphor $(\text{Y}_{1-x-y}, \text{Gd}_x)\text{BaB}_9\text{O}_{16}: y\text{Eu}^{3+}$ for Display and Lighting *J. Alloys and Compounds* 2014; 608 : 235–240.
- [21] Ingle JT, Sonekar RP, Omanwar SK, Wang Y, Zhao L. Combustion Synthesis and VUV Photoluminescence Studies of Borate Host Phosphors $\text{YBO}_3: \text{Re}^{3+}$ (Re= Eu^{3+} , Tb^{3+}) For PDPs Applications *Combust. Sci. Technol.*2013; 186:83–89.
- [22] Ingle JT, Sonekar RP, Omanwar SK, Wang Y, Zhao L. Solution combustion synthesis and optimization of phosphors for plasma display panels. *Optical materials*, 2014;36:1299–4.
- [23] Ingle JT, Sonekar RP, Omanwar SK, Wang Y, Zhao L. Combustion Synthesis and Luminescent Properties of Metal Yttrium Borates $\text{M}_3\text{Y}_2(\text{BO}_3)_4: \text{Eu}^{3+}$ (M=Ba, Sr) For PDPs applications. *Solid State Sciences* 2014;33:19-24.

¹ S. G. Ibrahim

² P. M. Gulalkari

Nickel ferrite Nanolayer thin film: A Review Study



Abstract: - Nickel ferrite is a pretty fascinating material in the research community because of their broad range of applications in many areas like magnetic recording, gas sensor, supercapacitor microwave devices, transformers, transducers and inductors and even in biomedical fields as magnetic nanoparticles. It is a type of soft magnetic materials composed of nickel and iron atoms arranged in a specific structure that have fabulous electrical, magnetic, optical properties. Resistivity, magnetoresistivity, engineered band gap, frequency-dependent behavior, high saturation magnetization, less coercivity, and permeability is the interesting properties of nickel ferrites. This review aims to explore simple, cost-effective and ecofriendly synthesis routes, unique properties and assorted applications of nickel ferrite.

Keywords: Nickel ferrite, Electrical property, magnetic property, chemical bath deposition method (CBD)

¹ *Corresponding author 1: Department of Physics, Prof. Ram Meghe College of Engineering & Management, Badnera-444701, Maharashtra, India

² Author 2 Student of, Prof. Ram Meghe College of Engineering & Management, Badnera-444701, Maharashtra, India

Copyright © JES 2024 on-line: journal.esrgroups.org

1. INTRODUCTION

Ferrite are the remolded structure of iron without carbon and these are a combination of two or more sets of different transition metals. On the bases of magnetic material there are of two types that is soft ferrite and hard ferrite. On the other hand, on the bases of structure it classified in spinel, garnet, ortho, and hexagonal ferrite. Spinel ferrite material is the type of magnetic material that belong to the spinel group of material. They are classified as normal, inverse, and mixed ferrite. The structure of this material is unique known as spinel structure. Their chemical formula is AFe_2O_4 where A can be a divalent metal cation such as Cu, Cd, Ni, Zn, Mg etc. all types of ferrites have their own properties among them is nickel ferrite ($NiFe_2O_4$) is one of the promising ferrite materials for many applications in various field because it shows the superior electrical, magnetic and optical properties. Because of low coercivity, low hysteresis losses, moderate saturation magnetization it belongs to soft ferrite. By doping of other material, size of particles, different synthesis methods, cationic distribution are affected the properties of material. Number of synthesis methods are suitable for prepare the nickel ferrite i.e., sol-gel method [1-3], co-precipitation method [4-6], spray pyrolysis method [7,8], successive ionic layer adoption and reaction method [9], chemical bath deposition method [10,11], spin coating method [12], pulsed laser deposition [13]. What this material will used for which application it depends on its properties. Nickel ferrite mostly used as a adsorbents and catalysts in many industrial applications. Due to dielectric constant, dielectric loss and heating coefficient of the nanoparticles they are used in Microwave applications [14]. nickel ferrite applicable gas sensor can detect hydrogen, ethanol [15] ammonia [16], petroleum gas [17] carbon monoxide, and more gases. It is applicable in memory device application. bismuth [18], cerium [19] doped nickel ferrite is good composite for memory device application, high capacity, excellent cycling stability make this material capable for energy storage [7-9,11,20-26] ascribed to magnetic properties of nickel ferrite. Nickel ferrite nanoparticles are useful for various biomedical applications including antifogging [27], detergent free self-cleaning, drug delivery systems, magnetic hyperthermia treatment for cancer [28], and magnetic resonance imaging (MRI) contrast agents.

2. WHY CHOOSE NICKEL FERRITES?

Nickel ferrite is a fascinating material that has attracted significant research interest for several reasons. One of the key reasons is its unique magnetic properties. Nickel ferrite is a type of ferrite material which adduce exhibits high magnetic permeability and low electrical conductivity, making it ideal for various applications in electronics and telecommunications as well as it shows their applicability in potential applications i.e. microwave devices, sensors, magnetic recording media, and catalysts. Its magnetic properties make it useful in data storage technologies like hard drives, magnetic tapes and even biomedical applications such as targeted drug delivery and hyperthermia treatment for cancer. Moreover, nickel ferrite is relatively inexpensive and easy to synthesize, which succeed it a cost-effective material for various industrial applications. Understanding the synthesis methods, structure-property relationships, and potential uses of nickel ferrite can lead to advancements in materials science, nanotechnology, and other fields. Overall, the unique magnetic properties, diverse applications, cost-effectiveness, and ease of synthesis make nickel ferrite an exciting research topic for researcher looking to explore new materials with promising properties and applications.

3. METHODS OF SYNTHESIS TO PREPARE NIKEL FERRITES

Various synthesis techniques are available to synthesis Nickel ferrite nanolayer thin film. The most common method of synthesis nickel ferrite is chemical bath deposition method (CBD), successive ionic layer adsorption and reaction (SILAR) method, Spray pyrolysis method, co-precipitation method, Spin coating technique, sol-gel method. The application base structural, electrical and magnetic properties of thin films depend on preparation method. Therefore, it is important to choose the method carefully.

3.1 CHEMICAL BATH DEPOSITION METHOD (CBD):

Chemical bath deposition method [10,11,21,22,29-31] is a handy and traditional method to synthesize nanomaterials. Normally It is need to inorganic salt (nitrate, chloride, sulphate, etc.) Dissolve the salts separately in distilled water [10] or ethanol [11] to make individual stock solutions. mix them together in the desired ratios to achieve the desired composition for the nickel ferrite thin film. Add a complexing agent to stabilize the metal ions in the solution, add a complexing agent such as ammonia or citric acid [32]. The complexing agent helps to prevent the precipitation of metal hydroxides. sodium hydroxide or sulfuric acid is use as an adjuster to adjust the pH of the solution at desired level. The pH value is crucial for controlling the deposition process. Thoroughly clean the substrate doubled distilled water [32] Ensure that it is free from any contaminants or impurities that could affect the quality of the coating Immerse the cleaned substrate into the chemical bath, ensuring that it is fully submerged and in contact with the solution. Control the deposition parameters such as Control the temperature, immersion time, and stirring rate according to the specific requirements of the deposition process [21]. These parameters can influence the thickness, morphology, and quality of the nickel ferrite thin film. After the desired deposition time, remove the substrate from the bath and rinse it thoroughly with distilled water to remove any residual chemicals. Then, carefully dry the substrate using a gentle stream of nitrogen or by air-drying. S.M. Chavan et.al. prepared the nickel zinc ferrite thin film using chemical bath deposition method successfully by varying concentration of nickel (II) chloride, zinc (II) chloride [10]. Xiaoyan Yan et al. successfully synthesis nickel sulfide nanoflake arrays are and investigate their electrical properties for supercapacitor [11]. Yedluri Anil Kumar et al.

prepared $\text{NiCo}_2\text{O}_4 @ \text{NiCo}_2\text{O}_4$ composite as an electrode material [21]. Anil Kumar Yedluri et al. synthesis binary metal oxides NiCo_2O_4 nanostructure by chemical bath deposition method it shows and good electrical properties for lightweight, flexible supercapacitor [22]. Fenglin Zhao et al. successfully synthesis hierarchical nickel cobalt oxides (NiCo_xO_y) and flaky nickel cobalt sulfides (NiCo_xS_y) with chemical composition 1.164 g $\text{Ni}(\text{NO}_3)_2 \cdot 6\text{H}_2\text{O}$, 2.328 g $\text{Co}(\text{NO}_3)_2 \cdot 6\text{H}_2\text{O}$ and 2.414 g by using chemical bath deposition method and investigate their electrical properties for application of supercapacitor [30]. Kanaka Durga Ikkurthi et al. prepared $\text{NiS}@\text{ZnS}$ nanostructure with varying chemical composition by using chemical bath deposition method on nickel foam substrate and demonstrated their applicability as electrode material for supercapacitor [31].

3.2 SUCCESSIVE IONIC LAYER ADSORPTION AND DEPOSITION METHOD (SILAR):

SILAR method is simple cost-effective technique. using this technique deposited thin film or coating the nanoparticle onto solid substrate. For deposition Nickel ferrite nano particle on suitable substrate prepare a precursor solution of nickel and iron (nitrate, chloride, sulphate, etc.) dissolve in distilled water. Use the stabilizer solution to control the nucleation and growth of the nanoparticles such as polyvinyl alcohol (PVA) or polyethylene glycol (PEG). Combine the nickel and iron precursor solutions in the desired molar ratio to achieve the desired composition for the nickel ferrite nanoparticles. Use a pH adjuster, such as sodium hydroxide or ammonia [9], to adjust the pH of the precursor solution to the desired level. The pH value is crucial for controlling the nanoparticle formation and stability. Gradually add the stabilizer solution to the precursor solution while stirring continuously. The stabilizer helps to prevent agglomeration and control the size and dispersion of the nanoparticles. After adding the stabilizer, it is important to sonicate the solution for a few minutes to ensure proper mixing and dispersion of the nanoparticles. Then take clean glass substrate and immerse it into the prepared solution and withdraw the substrate slowly to allow the nanoparticles to deposit onto its surface. Repeat this process multiple times to achieve the desired thickness and coverage and allow it to air-dry at room temperature anneal at specific temperature as per requirement.

3.3 SPRAY PYROLYSIS METHOD:

spray pyrolysis technique [7,8,15,33] is simple and cost-effective technique use to deposited nanostructure thin film. In this technique dissolve suitable nickel and iron salts in a solvent like water or ethanol. The concentration of the salts may vary as per required properties. For deposition, droplets of solution sprayed on heating substrate such as glass [8,12], stainless-steel silicon wafer. As the precursor droplets come into contact with the heated substrate, the solvent evaporates, leaving behind a thin film of the precursor material. The heat also initiates the decomposition and reaction of the precursors, leading to the formation of nickel ferrite nanoparticles. After the spray deposition, the film can be subjected to annealing at a high temperature. Annealing helps in the crystallization and growth of the nickel ferrite nanoparticles, improving their properties. S. S. Kumbhar et al. prepared the thin film using spray pyrolysis technique by varying the concentration. they are using the nickel nitrate, zinc acetate precursor. [8]. Rao et al. successfully prepare $\text{Cu}:\text{NiFe}_2\text{O}_4$ by using spray pyrolysis deposition technique by varying concentration and sintering temperature. [15]. R. Chavan, et al. synthesis $\text{NiFe}_{2-x}\text{Al}_x\text{O}_4$ nanostructure film by using spray pyrolysis technique. They are using the nickel nitrate hexahydrate, aluminum nitrate nonahydrate as an analytical reagent grade chemicals [33]. There are several advantages of spray pyrolysis technique such as easy of scalability, uniform particle size distribution, and versatility in synthesis a wide range of nanoparticle including metal oxide, semiconductor, magnetic material.

3.4 CO-PRECIPIATION METHOD:

Co-precipitation is an easy, inexpensive and low temperature synthesis method. This method often yields nanoparticles with high purity. By carefully controlling the reaction conditions, such as pH and temperature, as a result nanoparticles with a high degree of chemical homogeneity form. It controls of particle size and composition by adjusting the concentration of the precursor salts and the reaction parameters. Normally in this method inorganic Nickel and iron salts (nitrate, chloride, sulphate, etc.) are used. To adjust the pH of the precursor solutions, Sodium hydroxide (NaOH) or ammonia (NH_3) can be used as pH adjusters. During the co-precipitation method, the nickel and iron precursor solutions are mixed together while maintaining a controlled pH. This causes the precipitation of nickel and iron hydroxides, which eventually form nickel ferrite when subjected to further processing steps like drying and annealing. S. Sagadevan et al. synthesis NiFe_2O_4 prepare by Co-precipitation method with annealing temperature 80°C and nanoparticles of size 28 nm obtain by this method. Seema Joshi et.al. synthesis NiFe_2O_4 nanoparticles with the help of as starting materials sodium hydroxide, Nickel and ferric nitrate using co-precipitation method and investigated temperature dependent properties. Temperature varying between the $250\text{--}550^\circ\text{C}$. the size of particle obtains in range of 8nm –20 nm [4]. T. Vigneswari et al. using co-precipitation method calcium doped nickel ferrite ($\text{Ni}_{1-x}\text{Ca}_x\text{Fe}_2\text{O}_4$) nanoparticle was obtain in range 22-34 nm and display their applicability in memory device application [5]. S.M. Patange et al. synthesis $\text{NiAl}_x\text{Fe}_{2-x}\text{O}_4$ nanoparticle using co-precipitation by varying the concentration of chemical composition [6]. Ali A. Ati et al. synthesis $\text{Ni}_{(1-x)}\text{Co}_x\text{Fe}_{2-x}\text{Al}_x\text{O}_4$ with different composition using co-precipitation method. The nanocrystal size in between range 15-19 nm to get the appropriated signal-to-noise ratio appropriate in application of high-density recording media [34].

3.4 SOL-GEL METHOD:

Spin coating technique is a valuable technique for producing high-quality materials with tailored properties, offering control, versatility, and homogeneity in the synthesis of thin films, coatings, and other nanostructured materials. In solid particles of ions, molecular suspension or colloidal suspension is called sol and when the solvent in sol evaporated, the particles forsaken start to assemble into a continues network that's class gel. Sol-gel solution prepared by dissolving nickel and iron precursor. Nag S et al. reported zinc acetate, nickel nitrate, ferric nitrate and erbium nitrate as a starting precursor and heated on 110°C for 60 min for prepare the nanoparticle [1]. Most commonly ammonium solution is use to controlled the pH of the solution. Prepare sol-gel solution may apply using techniques like spin coating, dip coating, spray coating. Sonia et.al. synthesis Gadolinium doped nickel ferrite using Nickel and ferrite nitrate hexahydrate precursor [2]. P.S.J. Bharadwaj et al using sol-gel route, NCFO-AC composite synthesis with different mole ratio and invested their electrical properties for supercapacitor application [3]. H. Arabi et al. investigated the structural as well as magnetic properties of NiCoMn ferrite on calcination temperatures using sol-gel technique. This technique is very simple and cost-effective also.

COMPARISON OF SYNTHESIS METHODS

Recently since some years researchers are taking great interested in nickel ferrite material and their synthesis methods. The synthesis method and other parameters influences its properties of material. Therefore, choosing the appropriate method of synthesis is important. Several synthesis methods have been used in many reviews of literature, including Chemical bath deposition method, Successive ionic layer adsorption and deposition method, Spray pyrolysis method, co-precipitation method, Spin coating technique, sol-gel method. Overall, from review chemical bath deposition method is most suitable method for synthesis of nickel ferrite as compared to other methods. Chemical bath deposition method is more consistent and precise for film deposition because it provides the better control over the film thickness and uniformity due to control chemical reaction that take place in the solution bath. This method can be used for wide range of material and substrate. Also, this method is comparatively cost-effective choice for thin film deposition because it does not require expensive equipment or high temperature. As well as chemical bath deposition method is relatively simple and does not involve complex procedures, making it easier to implement and control compared to other techniques.

4 CHARACTERIZATION OF NICKEL FERRITES:

Nickel ferrites characterized by using various instruments and extensively study the relation between particle size, area and surface, composition, and shape of ferrites to find their structural, electrical, magnetic and optical properties. These are as follows:

4.1. X RAY DIFFRACTION STUDY:

XRD is the predominant technique used to analyses the crystal structure of material. It also providing the valuable information about its composition and phase identification. To understand the properties and behavior of different materials at the atomic level. This technique, which relies on penetrating radiation interacting with a crystal's ordered scattering centers to produce interference effects, is extensively utilized in various fields to investigate the crystal's internal structure. X-rays have the essential penetrating power and show interference effects. Many researchers have studied the consequence of calcination temperature on the structure of the crystal and found that if increasing calcination temperature crystallite size, intensity of XRD peaks, agglomeration of particles is also increase and decrease the impurity. Sanchayita Nag et al. investigated the XRD patterns of samples which exhibited the important pattern of NZE0, NZE25, NZE35 and NZE50. Without giving addition heating treatment it shows the cubic spinel structure [1]. A.R. Chavan et al. reported that $\text{NiFe}_{2-x}\text{Al}_x\text{O}_4$ exhibits single phase cubic spinel structure and observe the systematic variation in values of peak intensity [10]. Xiaoyan Yan et al. reported polycrystalline spinel cubic structure of nickel zinc ferrite thin films. The nature of thin film is uniform and smooth. nickel content is affected the intensity of diffracted plane. It is increase and shifted slightly [11]. G. Dixit et al. observes to increase the crystallite size and lattice parameter with annealing temperature up to 800 °C and above 1000°C. it was decreases [13]. Manohar K et al. synthesis $\text{Ni}_x\text{Mn}_{1-x}\text{Fe}_2\text{O}_4$ thin films by spray pyrolysis method. Using Scherrer formula calculated the average grain size 33.38 nm [20]. Yedluri, A. K. et al. successfully prepared $\text{NiCo}_2\text{O}_4@ \text{NiCo}_2\text{O}_4$ nanocomposite, XRD show the crystal structure. During observation show the strong diffraction peak at 44.5° and 52° [21]. Anil Kumar Yedluri et al. prepare nickel cobaltite nanostructure thin film by CBD method and identified interconnected honeycomb nanostructure [22]. D. Y. Kim et al. fabricated NiCo_2S_4 by chemical bath deposition method and investigate the strong peak at 43.93° and 44.77° and at 74.90° high intense peak was show. [29] Pawar D. K. et al. calculated crystallite size 29.80 nm using Scherrer's formula. And observe their cubic spinel crystal structures [32]. P.B. Belavi et al. observe that by increase Cd^{2+} content in the ferrite systems then X-ray density and porosity is also increase [35]. A.A. Kadam et al. synthesis dysprosium doped $\text{Ni}_{0.8}\text{Co}_{0.2}\text{Fe}_{2-x}\text{Dy}_x\text{O}_4$ ferrite show the spinel structure. if dysprosium content is increase then peak of intensity is decrease [36]. K. Kamala Bharathi et al. reported lattice parameter which vary from 8.335 to 8.348 Å. And observe the rhombohedral distortion in $\text{NiFe}_{1.925}\text{-Sm}_{0.075}\text{O}_4$ and $\text{NiFe}_{1.925}\text{-Sm}_{0.075}\text{O}_4$ from splitting of the (440) peak [37]

4.2 FOURIER TRANSFORM INFRARED STUDY:

FTIR allow to analyze the chemical composition and molecular structure of material, identify functional groups present in a compound, determine the presence of specific bonds, and provide information about the molecular vibrations within a sample. P.B. Belavi et al. observe nickel–copper ferrites spectra using FTIR and recorded their range from 400 to 800 cm^{-1} and two observation band in rang of 600 cm^{-1} improve to vibrations of tetrahedral and octahedral complexes respectively [35]. D.K. Pawar et al. noticed in their study that the FTIR spectra displayed prominent absorption peaks at approximately 600 cm^{-1} , which are characteristic of the cubic spinel crystal structure. The absorption bands observed at 573, 1020, and 163 cm^{-1} were linked to the stretching vibrations of the tetrahedral group, indicating the formation of lepidocrocite in the annealed $\text{Ni}_{0.8}\text{Zn}_{0.2}\text{Fe}_2\text{O}_4$ thin films. [32]. Suresh Sagadevan et al. Recorded NiFe_2O_4 nanoparticles spectra with the help of Bruker IFS 66W Spectrometer. They observe frequency range of 4000-5000 cm^{-1} and also observe, generally IR bands of solids are responsible for to the vibration of ions in the crystal lattice. tetrahedral and octahedral modes of nickel ferrite showing this bands at 552 cm^{-1} and 464 cm^{-1} [38]. A.A. Al-Ghamdi et al. used mechanochemical technique to fabricate $\text{Ni}_{1-x}\text{Cu}_x\text{Fe}_2\text{O}_4$ nano ferrites and recorded strong absorption peak in the range of 552.8 to 596.1 cm^{-1} . This peak is constituted to the dilating of metal-oxygen bonds in tetrahedral sites. As well as cantered peak is assigned to the vibration of metal oxygen (M-O) bonds in octahedral sites [39]. M. Maria Lumina Soni et al. analyze gadolinium doped nickel ferrite by FTIR and recorded the Infra-Red spectra of ferrites which show the two major (ν_1) wave in range of 600-550 cm^{-1} by the dilating vibrations of the metal-oxygen bonds existing in the tetrahedral sub-lattice (A) sites. Because of relative changes in bond length (Fe–O) at tetrahedral (A) sites and octahedral (B) sites create the difference in their value [2]. Swapnil A. Jadhav et al. successfully synthesis NiFe_2O_4 nanoparticles and recorded higher frequency band ν_1 in between the range of 600 cm^{-1} to 500 cm^{-1} [40]. T. Vigneswari et al. recorded cubic spinel structure with single phase of nanoparticles and found that due to increasing the Ca 2p substitution, are increase the crystallite size and lattice constant also [5].

4.3 MORPHOLOGY STUDY:

The study of morphology of nickel ferrite material is important for elucidate the properties of material. The surface morphology of material and size of the particle is depended on use of preparation technique and sintering temperature. For complete studying the morphology of nickel ferrite many characterization techniques are use such as scanning electron microscopy (SEM), atomic force microscopy (AFM), transition electron microscope (TEM). FESEM provide the high-resolution image than SEM. Because its superior imaging capability. Ali A. A et al. reported FESEM study in which agglomerated particles are found due to the interactions of magnetic nanoparticles having grain size is 20nm [41]. Xiaoyan Yan et al. reported that FESEM showed uniform nanoflakes with a shape 10nm [11] Kumbhar S. S et al. reported that prepared thin film is smooth and uniform in nature and having spinel cubic structure [7]. Manohar K. et al. reported SEM study in which crystal shape found like rice. But increasing concentration of nickel the grain length was decreased and we have got desired spherical structure at $x = 0.8$ [8]. Rao P. et al. studied with the help of SEM in which comparing the pure nickel ferrite and copper doped nickel ferrite with different concentration and recorded micrographs show remarkable change in the microstructure and porosity. pure nickel ferrite having a petal like structure but copper doping nickel ferrite having a grain like structure because of increase in number of voids [15]. Peishuang Miao et al. fabricate 3D NF/G by one-step hydrothermal approach, The thickness of graphene nanosheets NF having thickness 10nm which is recorded by SEM and it is propose for large surface area. as well as XPS used to analyze the chemical structure of NF/G. [20] T. Chtouki et al. recorded surface morphologies of Ni doped CdS thin film with different nickel content. the shape and size of crystal is spherical and hexagonal with an average of 35 nm. it observes that morphology of this film totally depends on doping concentration of nickel. AFM clear that the incorporation of the doping is affected film roughness [12]. R.B. Waghmode et al. by using SEM recorded the hierarchical nanostructures of NiCo_2O_4 which is capable to provide a more active surface area for effective intercalation of electrolyte ions. TEM show the disoriented nanorods of nickel ferrite. lattice fringe structure recorded by HRTEM [23]. Souvik Ghosh et al. recorded the study of HR-TEM which shows rough needle-like structure of NCG. FFT calculate the higher magnification lattice fringes of NCG composite SEAD pattern with HR-TEM image was found some bright spots and rings which suggest the polycrystallinity or poor crystallinity of NCG composite [24].

4.4 MAGNETIZATION STUDY:

To study the magnetic properties like saturation magnetization, remenant magnetization and coercivity used the vibrating sample magnetometer (VSM), magnetization hysteresis ($M - H$) loops and electron spin resonance (ESR) hysteresis loop measurements. G. Dixit et al. recorded high resistivity and phase and stoichiometry of a film affected by annealing temperature. This parameter controlled the structural and magnetic properties of the film [13]. Bharathi et al successfully demonstrated little amount Fe with Sm and Ho doped in Nickel ferrite and enhancing the dielectric constant, magnetocapacitance, and electrical resistivity [37]. P.B. Belavi et al. using double sintering ceramic technique to prepare Polycrystalline ferrites with composition $\text{Ni}_{0.95-x}\text{Cd}_x\text{Cu}_{0.05}\text{Fe}_2\text{O}$ and recorded Saturation magnetization, magnetic moment and Y–K angles are increase with cadmium content [35]. A.A. Kadam et al. complex impedance analysis at room temperature exhibited semicircles accredited to the high resistance values at lower frequencies. if Dy doping concentration is increase then

increase the x-ray density in range from 5.34 to 5.59 g/cc and porosity also increase from 28.23 to 31.22% [36]. Sanchayita Nag et al. recorded magnetization, coercivity, and remnant magnetization value i.e. $M_g=24$, $M_r = 4.40$ and $H_c=127.46$. according Mössbauer spectra at room temperature all the samples undergo superparamagnetic relaxation cause finite size effect along with some anomalous magnetic interactions for NZE25 and NZE35 [1]. P.S.J. Bharadwaj et al. synthesized NCF0-AC composite and recorded magnetic properties. they observe when the size of crystal is increase then the magnetization saturation is also increasing no matter the crystal structure and shape of the particles [3]. Samaila Bawa Waje et al. prepare $\text{Co}_{0.2}\text{Ni}_{0.3}\text{Zn}_{0.5}\text{Fe}_2\text{O}_4$ composite and observe $M_s = 0.61$ emu/g and $H_c = 5.92$ Oe [42]. Swapnil A. Jadhav et al. prepared NiFe_2O_4 nanoparticles successfully by using sol-gel method. And recorded superparamagnetic nature, that is, the value of saturation magnetization is 46.20 emu/gm, coercivity value is 383.2 Oe, and rest magnetization values are 25.27 emu/gm respectively. Against degradation of dye this nanoparticle showing the good photocatalytic activity and reusability [40]. T. Prabhakaran et al. recorded saturation magnetization of 42.5 emu/g and coercivity of 112. if the nickel ferrite is increase then saturation of PVDF/ NiFe_2O_4 composites is also increased. PNF20 compositions indicated higher value of saturation magnetization of 1.05 emu/g [43]. Ali A. At et al. synthesis $\text{Ni}_{1-x}\text{Co}_x\text{Fe}_{2x}\text{Al}_x\text{O}_4$ with varying concentration using co-precipitation method. The size of nanocrystal in between 15 and 19 nm. and they observe if the dopant concentration is increased then improved the magnetic properties which is useful for the application in microwave and memory devices [34].

4.5 ELECTROCHEMICAL STUDY:

Electrochemical properties can measure using cyclic voltammetry (CV), galvanostatic charge–discharge (GCD) and electrochemical impedance spectroscopy [21] which perform electrochemical workstation. through this study we investigate how material interact with electricity and chemical reaction.it can help to understand the properties like conductivity, reactivity, and stability. study of electrochemical properties plays very crucial role in various fields like energy storage technology (battery and supercapacitor), corrosion prevention, and sensor development. Xiaoyan Yan et al. observe nickel ferrite nanoflake arrays thin film is preferable than pure nickel oxide because it exhibited outstanding retention of specific capacitance up to 593 F g^{-1} after 3000 cycles.as well as recorded good energy density of about 14.1 Wh kg^{-1} at 40 Ag^{-1} and show their applicability in supercapacitor [11]. S. S. Kumbhar et al. they use spray pyrolysis method for synthesis $\text{Ni}_x\text{Zn}_{1-x}\text{Fe}_2\text{O}$ with different concentration and recorded by increasing temperature, resistivity (ρ) of thin films decreases due to samples showing semiconducting nature [7]. Manohar K. Zate et al. is exploring the nickel manganese ferrite as an electrical material and recorded maximum specific capacitance up to 47.27 Fg^{-1} along with energy density of this material is 19.5 Wh kg [8]. Peishuang Miao et al. 3D NF/G synthesis by using ne-step hydrothermal approach and observe that due to its precise hierarchical porous structure it provides the large surface are for fast redox reaction and increase the capacity of charge storage [20]. Apparao R. Chavan et al. prepare the aluminum doped nickel ferrite and observe that if the aluminum doping is increase then band gap is decrease but increase the resistivity up to $278 \times 10^6 \Omega\text{-cm}$ to $4.612 \times 10^7 \Omega\text{-cm}$. because of increasing resistivity dielectric loses is decrease it show their applicability in energy storage devices and transformer core [33]. Souvik Ghosh et al. synthesis $\text{NiCo}_2\text{Se}_4/\text{RGO}$ composite material and recorded highest specific capacitance 1776 Fg^{-1} at 2 Ag^{-1} it shows the maximum energy density of 66.2 W h Kg^{-1} and power densities 1500 W kg^{-1} the specific capacitance after 5000 GCD cycles is near ~93.5% [24] Kaliaraj et al. successfully deposited thin film of Ni-ZnS on stainless steel substate using RF magnetron co-sputtering method and observe that, Ni doped ZnS remarkable change the surface morphology and also increase the porosity of the material for enhanced electrochemical performance [25]. Muhammad Faisal Iqbal et at. conform that, GO–NSNP thin film suitable for pseudocapacitor supercapacitor application because of their excellent electrical conductivity, specific capacitance and specific energy value i.e., 1745.50 Fg^{-1} and 87.30 Wh Kg^{-1} at 5 mAcm^2 [26]. Based on the cyclic voltammogram, it is evident that the composite NCF0-AC exhibits superior capacitive behavior when compared to the plain carbon substrate SDAC800. It achieves a current density of 2 A/g and maintains 98.34% capacity after 10,000 cycles. [3].

5. APPLICATIONS OF NICKEL FERRITES:

Today era is the era of electronics. In every field we get to see electronic equipment. It is essential part of our life that's why researcher have a great interest to find the new materials and enhance the properties of existing material for electronics interest. Nickel ferrite is the most promising material. we can see the usefulness of nickel ferrite in many fields because of their outstanding electronics, magnetic and optical properties. Because of their outstanding properties it used in many applications like Microwave devices [13,14,44,45], Gas sensors [15,48-51], Memory devices [6,19,47], Energy storage applications [3,7,8,11,20-26], Memory devices [6,19], Biomedical applications [27,28,52-54].

5.1. MICROWAVE DEVICES:

Nickel ferrite is commonly used in microwave devices owing to its high electrical resistivity, low electrical conductivity, low dielectric losses and excellent magnetic properties. Its ability to maintain stable magnetic characteristics at high frequencies makes it ideal for applications in microwave components. G. Dixit et al. observe different annealing temperature affected the behavior of magnetic property, phase and stoichiometry of the film. Due to increasing the annealing temperature defect concentration decreases that the result coercivities also decreases. That's why it can be used for microwave application [13].

Kiran Naz et al. synthesis the $\text{Ni}_x\text{Cu}_{1-x}\text{Fe}_2\text{O}_4$ nanoparticles that react to electromagnetic radiation. Therefore, these nanoparticles can be effectively utilized in microwave devices. [14]. V.K. Sankaranarayanan et al. developed single phase nickel nitrate at low temperature using self-ignition reaction from citrate precursor. And it shows their high frequency applications [44]. John jaco et al. observes the three different grain sizes and two sintered samples and investigated dielectric properties. And all parameters are size dependent [45]. Overall, nickel ferrite is very good candidate for microwave devices.

5.2. GAS SENSORS:

Because of high sensitivity to various gases stability and relatively low cost compare to other material make the nickel ferrite good candidate for gas sensor devices. Rao et al. synthesis $\text{Cu: NiFe}_2\text{O}_4$ by spray pyrolysis deposition technique at different temperature and found that copper doped nickel ferrite responds well to ethanol gas [15]. Seema Joshi et al. pure cobalt good response to the carbon monoxide and ethanol gases but lacks selectivity. so, when in that adding the Ni^{2+} ions into cobalt ferrite enhancing the sensing properties [48]. S. Kotresh et al. has developed the polyaniline–nickel ferrite composite successfully to sense liquefied petroleum gas (LPG) at room temperature [49]. Rajesh Kashyap et. al. investigated at temperature 250°C observe ammonium gas as well as Nickel ferrite provide the excellence repeatability and stability to gas sensor [50]. A. Sutka et al. found that substituting nickel ions with zinc ions in nickel ferrite is completely unfavorable for gas sensing purposes because in Ni-Zn ferrite, quantity of zinc in composition is increase then sensing response is decreases [51]. this review indicates that, nickel ferrite-based gas sensor can detect hydrogen, ammonia, carbon monoxide, and more gases.

5.3. MEMORY DEVICES:

Due to magnetic properties of nickel ferrite, it is applicable for memory device application. M. Banerjee et al, developed the bismuth doping nickel ferrite nanoparticle and observe that doping of bismuth is increase than decrease the ferroelectric polarization. as well as increase the resistivity and decrease the dielectric loss that's why it is promising material at room temperature for memory devices application [47]. Aize Hao et al. developed cerium doped nickel ferrite thin film on various types of substrate and observe that doping of cerium in nickel ferrite improve the electrical properties for resistance switching memory devices [19]. S.M. Patange et al. synthesis $\text{Ni}_{(1-x)}\text{Co}_x\text{Fe}_{2-x}\text{Al}_x\text{O}_4$ by co-precipitation technique in temperature 600°C and investigate there magnetic properties for application of memory device[6]. Overall nickel ferrite has the superior properties that make them suitable for use in magnetic memory devices. the unique magnetic characteristics of nickel ferrite, such as high magnetic anisotropy and stability, make it a promising material for storing and retrieving data in memory devices.

5.4. ENERGY STORAGE APPLICATIONS:

Nickel ferrites have been coming up as electrode materials in the last few decades because they have a high capacity, great cycling stability, and are cost-effective. Electrodes based on nickel ferrite have been found to show good electrochemical behavior, like having a high specific capacity and a long life. We can make nickel ferrite properties better by controlling the size, shape, and composition of nickel ferrite nanoparticles. Transition metal-doped nickel ferrites are used in many energy storage devices because of their good electrical properties like high electrical conductivity, which is important for efficient charging and discharging rates, providing a high surface area for electrochemical reactions, and ensuring good stability. Muhammad Faisal Iqbal et al. synthesize GO–NSNP and found the specific capacitance 1745.50 Fg^{-1} . it can show their applicability in both symmetric and asymmetric supercapacitor [26]. P.S.J. Bharadwaj et al. successfully prepared NCFO-AC by sol-gel method it provides the specific capacitance of 1790.9 F/g and show the high stability its capacitance retention is 98.34% after 10,000 cycles [3]. S. S. Kumbhar et al. Nickel-zinc ferrite thin film deposited by spray pyrolysis technique with annealing temperature at 600°C for 2 hrs. and studied the AC conductivity to understand the conduction mechanism [7]. Manohar K. Zate et al. prepared Nickel-manganese ferrite with different concentration and exhibited the maximum specific capacitance that is 47.2 Fg^{-1} [8]. Xiaoyan Yan et al. prepare NiS nanoflake arrays by using chemical bath deposition method. The electrode material indicates a maximum specific capacitance of 718 Fg^{-1} Its outstanding electrochemical stability is shown by the electrode material maintaining a high capacitance over 3000 continuous charge-discharge cycles. [11]. Peishuang Miao et al. synthesis the three-dimensional graphene nickel ferrite by one-step hydrothermal method. due to three-dimensional graphene obtain the large specific surface area and short ion channel lengths [20]. Yedluri Anil Kumar et al. fabricate the $\text{NiCo}_2\text{O}_4@/\text{NiCo}_2\text{O}_4$ nanoplates and investigated the electrochemical properties. Its properties are much better than NiCo_2O_4 electrode. Their specific capacitance is 800 F g^{-1} [21]. Yedluri A. et al. prepared the nickel cobalt ferrite nanoparticle by CBD method obtaining outstanding specific capacitance and remarkable stability with 94.2% for 5000 cycles [23]. Souvik Ghosh et al. reported that $\text{NiCo}_2\text{Se}_4/\text{RGO}$ are synthesized by two-step hydrothermal technique. and these nanoparticles are suitable for supercapacitor application [24]. Gobi Saravanan Kaliaraj et al. fabricated Ni–ZnS thin film with the help of RF magnetron co-sputtering method. It reported excellent cycling stability after 3500 cycles and show their applicability for hybrid supercapacitors as an electrode material [25].

5.5. BIOMEDICAL APPLICATIONS:

Nickel ferrite nanoparticles are useful for various biomedical uses including drug delivery systems, magnetic hyperthermia treatment for cancer, and magnetic resonance imaging (MRI) contrast agents. H. J. Kardile et al. prepared nickel ferrite thin film and investigate surface wettability properties by using contact angle method. This film shows their applicability in antifogging, detergent free self-cleaning, anti-fouling, water-oil separation etc. [27]. Shazia Bano et al. fabricated NiFe_2O_4 with different three biopolymers. It shows the good biocompatibility and higher T_2 relaxivity, due to nontoxicity, hydrophilicity, and cancer-specific capability it can us for cancer treatment [28]. Marwa H. Sabbar et al use co-precipitation approach to synthesis $\text{Co}_{1-x}\text{Ni}_x\text{Fe}_2\text{O}_4$ ferrites nanoparticles. Which show good antibacterial potential, especially against gram-positive strain bacteria [52]. Maxwell Fazeli et al. developed the miniaturized implantable ferrite antenna. Due to dip-coated ferrite film decreases the resonant frequency and improve the bandwidth as well as non-toxic nature that why it shows their applicability in RF biomedical applications [53]. Noppakun Sanpo et al. investigated that microstructure; crystal structure and antibacterial property of the cobalt ferrite nanoparticles are affected due to substitution of transition metals in cobalt ferrite. They are showing antibacterial properties against the bacteria's [54].

CONCLUSION

The synthesis of nickel ferrite nanoparticle has increase in past few years. This is because nickel ferrites have impressive qualities compared to other soft ferrites, like high electrical resistivity, magnetic permeability, and Curie temperature. Researchers are keen on making these ferrites, and they find the chemical bath deposition method ideal for creating thin films because it's straightforward, affordable, and eco-friendly. This paper has discussed the various applications of Nickel ferrites, including biomedical, microwave device, memory device and energy storage applications. Additional study in this area may result in the production of new materials with enhanced properties and novel applications, which could have a significant impact on various industries.

REFERENCES

- [1] Nag S., Roychowdhury A., Das D., Da S., Mukherjee S. (2018). Structural and magnetic properties of erbium (Er^{3+}) doped nickel zinc ferrite prepared by sol-gel auto-combustion method. *Journal of Magnetism and Magnetic Materials*, 466, 172–179. doi: 10.1016/j.jmmm.2018.06.084
- [2] Sonia M. M. L., Anand S., Vinose V. M., Janifer M. A., Paulin S., Manikandan A. (2018). Effect of lattice strain on structure, morphology and magneto-dielectric properties of spinel $\text{NiGd}_x\text{Fe}_{2-x}\text{O}_4$ ferrite nano-crystallites synthesized by sol-gel route. *Journal of Magnetism and Magnetic Materials*, 466, 238–251. doi: 10.1016/j.jmmm.2018.07.017
- [3] Bharadwaj P. S. J., Gannavarapu K. P., Kollipara V. S., Dandamudi R. B. (2021). Study of magneto-supercapacitance properties of nickel cobalt ferrite-activated carbon composite. *Journal of Energy Storage*, 36, 102-444. doi: 10.1016/j.est.2021.102444
- [4] Joshi S., Kumar M., Chhoker S., Srivastava G., Jewariya M., Singh V. N. (2014). Structural, magnetic, dielectric and optical properties of nickel ferrite nanoparticles synthesized by co-precipitation method. *Journal of Molecular Structure*, 1076, 55–62. <https://doi.org/10.1016/j.molstruc.2014.07.048>
- [5] Vigneswari T., Raji P. (2017). Structural and magnetic properties of calcium doped nickel ferrite nanoparticles by co-precipitation method. *Journal of Molecular Structure*, 1127, 515–521. doi: 10.1016/j.molstruc.2016.07.116
- [6] Patange S. M., Shirsath S. E., Jadhav S. P., Hogade V. S., Kambl S. R., Jadhav K. M. (2013). Elastic properties of nanocrystalline aluminum substituted nickel ferrites prepared by co-precipitation method. *Journal of Molecular Structure*, 1038, 40–44. doi: 10.1016/j.molstruc.2012.12.05
- [7] Kumbhar S. S., Mahadik M. A., Mohite V. S., Rajpure K. Y., Bhosale C. H. (2014). Synthesis and Characterization of Spray Deposited Nickel-Zinc Ferrite Thin Films. *Energy Procedia*, 54, 599–605. doi: 10.1016/j.egypro.2014.07.301
- [8] Zate M. K., Shaikh S. M. F., Jadhav V. V., Tehare K. K., Kolekar S. S., Mane R. S., Hui, K. N. (2015). Synthesis and electrochemical supercapacitive performance of nickel–manganese ferrite composite films. *Journal of Analytical and Applied Pyrolysis*, 116, 177–182. doi: 10.1016/j.jaap.2015.09.012
- [9] Gund G. S., Lokhande C. D., & Park H. S. (2018). Controlled synthesis of hierarchical nanoflake structure of NiO thin film for supercapacitor application. *Journal of Alloys and Compounds*, 741, 549–556. doi: 10.1016/j.jallcom.2018.01.166
- [10] Chavan S. M., Babrekar M. K., More S. S., Jadhav K. M. (2010). Structural and optical properties of nanocrystalline Ni–Zn ferrite thin films. *Journal of Alloys and Compounds*, 507(1), 21–25. doi: 10.1016/j.jallcom.2010.07.171

- [11] Yan X., Tong X., Ma L., Tian Y., Cai Y., Gong C., Liang, L. (2014). Synthesis of porous NiS nanoflake arrays by ion exchange reaction from NiO and their high-performance supercapacitor properties. *Materials Letters*, 124, 133–136. <https://doi.org/10.1016/j.matlet.2014.03.067>
- [12] Chtouki T., El Kouari Y., Kulyk B., Louardi A., Rmili A., Erguig H., Sahraoui B. (2017). Spin-coated nickel doped cadmium sulfide thin films for third harmonic generation applications. *Journal of Alloys and Compounds*, 696, 1292–1297. doi: 10.1016/j.jallcom.2016.12.089
- [13] Dixit G., Singh J. P., Srivastava R. C., Agrawal H. M., Choudhary R. J., Gupta A. (2010). Annealing effect on the structural and magnetic properties of nickel ferrite thin films. *Surface and Interface Analysis*, 42(3), 151–156. doi:10.1002/sia.3195
- [14] Junaid K. N., Khan K., Khalid M., Akhtar M.S., Gilani Z. A., H.M. Noorul Huda Khan Asghar, Gaber A. M. Mersal, Mohamed M. Ibrahim, A. Muhammad, M.G.B. Ashiq (2022) Structural, dielectric, impedance and electric modulus analysis of Ni substituted copper spinel ferrites nanoparticles for microwave device applications. *Materials Chemistry and Physics*, 285, 126091 <https://doi.org/10.1016/j.matchemphys.2022.126091>
- [15] Rao P., Godbole R. V., Bhagwat S. (2016). Copper doped nickel ferrite nano-crystalline thin films: A potential gas sensor towards reducing gases. *Materials Chemistry and Physics*, 171, 260–266. doi: 10.1016/j.matchemphys.2016.01
- [16] Kashyap R., Kumar R., Devi S., Kumar M., Tyagi S., Kumar D. (2019). Ammonia Gas Sensing Performance of Nickel Ferrite Nanoparticles. *Materials Research Express*, 6, 1-22. doi:10.1088/2053-1591/ab55b5
- [17] Kotresh S., Ravikiran Y. T., Vijayakumari S. C., Thomas S. (2016). Interfacial p-n heterojunction of polyaniline-nickel ferrite nanocomposite as room temperature liquefied petroleum gas sensor. *Composite Interfaces*, 24(6), 549–561. doi:10.1080/09276440.2017.1241523
- [18] Wu L., Dong C., Wang X., Li J., Li M. (2019). Annealing effect on the bipolar resistive switching memory of Ni-Zn ferrite films. *Journal of Alloys and Compounds*, 779, 794–799. doi: 10.1016/j.jallcom.2018.11.345
- [19] Hao A., He S., Qin N., Chen R., Bao D. (2017). Ce-doping induced enhancement of resistive switching performance of Pt / NiFe₂O₄ / Pt memory devices. *Ceramics International*, 43, S481–S487. doi: 10.1016/j.ceramint.2017.05.21
- [20] Miao P., He J., Sang Z., Zhang F., Guo J., Su D. Ji H. (2018). Hydrothermal growth of 3D graphene on nickel foam as a substrate of nickel-cobalt-sulfur for high-performance supercapacitors. *Journal of Alloys and Compounds*, 732, 613–623. doi: 10.1016/j.jallcom.2017.10.243
- [21] Yedluri A. K., Kim H.-J. (2018). Preparation and electrochemical performances of NiCo₂O₄@NiCo₂O₄ composite of nanoplates for high performances supercapacitor applications. *New Journal of Chemistry*, 42, 19971-19978. doi:10.1039/c8nj05401k
- [22] Yedluri A. K., Kim H. J. (2019). Enhanced electrochemical performance of nanoplate nickel cobaltite (NiCo₂O₄) supercapacitor applications. *RSC Advances*, 9(2), 1115–1122. doi:10.1039/c8ra09081e
- [23] Waghmode R. B., Maile N. C., Lee D. S., Torane A. P. (2020). Chemical bath synthesis of NiCo₂O₄ nanoflowers with nanorods like thin film for flexible supercapacitor application-effect of urea concentration on structural conversion. *Electrochimica Acta*, 350, 136-413. doi: 10.1016/j.electacta.2020.136413
- [24] Ghosh S., Samanta P., Murmu N. C., Kuila T. (2020). Investigation of electrochemical charge storage in nickel-cobalt-selenide/reduced graphene oxide composite electrode and its hybrid supercapacitor device. *Journal of Alloys and Compounds*, 835,155-432. doi: 10.1016/j.jallcom.2020.155432
- [25] Kaliraj G. S., Ramadoss A. (2020). Nickel-zinc sulfide nanocomposite thin film as an efficient cathode material for high-performance hybrid supercapacitors. *Materials Science in Semiconductor Processing*, 105, 104-709. doi: 10.1016/j.mssp.2019.104709
- [26] Iqbal M. F., Yousef A. K. M., Hassan A., Hussain S., Ashiq M. N., Mahmood Ul-Hassan Razaq A. (2021). Significantly improved electrochemical characteristics of nickel sulfide nanoplates using graphene oxide thin film for supercapacitor applications. *Journal of Energy Storage*, 33, 102091. doi: 10.1016/j.est.2020.102091
- [27] Kardile H. J., Pandit A. A., Jadhav K. M. (2021). hydrophilic nature of nickel ferrite thin film deposited by spray pyrolysis technique. *A Double-Blind Peer Reviewed & Refereed Journal* 17, 617-620.
- [28] Bano S., Zafar T., Akhtar S., Buzdar S. A., Waraich M. M., Afzal M. (2016) Biopolymers coated superparamagnetic Nickel ferrites: Enhanced biocompatibility and MR imaging probe for breast cancer. *Journal of Magnetism and Magnetic Materials*, S0304-8853(16), 130760-0. <http://dx.doi.org/10.1016/j.jmmm.2016.05.063>
- [29] Kim D.Y., Ghodake G. S., Maile N. C., Kadam A. A., Sung Lee D., Fulari V. J., Shinde S. K. (2017). Chemical synthesis of hierarchical NiCo₂S₄ nanosheets like nanostructure on flexible foil for a high-performance supercapacitor. *Scientific Reports*, 7(1), 1-10. doi:10.1038/s41598-017-10218z

- [30] Zhao F., Huang W., Zhou D. (2018). Chemical bath deposition synthesis of nickel cobalt oxides/sulfides for high-performance supercapacitors electrode materials. *Journal of Alloys and Compounds*, 755, 15–23. doi: 10.1016/j.jallcom.2018.04.304
- [31] Ikkurthi K. D., Srinivasa Rao S., Ahn J. W., Sunesh C. D., Kim, H. J. (2018). Cabbage leaves like nanostructure of NiS@ZnS composite on Ni foam with excellent electrochemical performance for supercapacitors. *Dalton Transactions*. 48, 578-586. doi:10.1039/c8dt04139c
- [32] Pawar D. K., Pawar S. M., Patil P. S., Kolekar S. S. (2011). Synthesis of nanocrystalline nickel–zinc ferrite ($\text{Ni}_{0.8}\text{Zn}_{0.2}\text{Fe}_2\text{O}_4$) thin films by chemical bath deposition method. *Journal of Alloys and Compounds*, 509(8), 3587–3591. doi: 10.1016/j.jallcom.2010.12.079
- [33] Chavan A. R., Birajdar S. D., Chilwar R. R., Jadhav K. M. (2018). Structural, morphological, optical, magnetic and electrical properties of Al^{3+} substituted nickel ferrite thin films. *Journal of Alloys and Compounds*, 735, 2287–2297. doi: 10.1016/j.jallcom.2017.11.326
- [34] Ati A. A., Othaman Z., Samavati A., Doust F. Y. (2014). Structural and magnetic properties of Co–Al substituted Ni ferrites synthesized by co-precipitation method. *Journal of Molecular Structure*, 1058, 136–141. doi: 10.1016/j.molstruc.2013.10.04
- [35] Belavi P. B., Chavan G. N., Naik L. R., Somashekar R., Kotnala R. K. (2012). Structural, electrical and magnetic properties of cadmium substituted nickel–copper ferrites. *Materials Chemistry and Physics*, 132(1), 138–144. doi: 10.1016/j.matchemphys.2011.11.009
- [36] Kadam A. A., Shinde S. S., Yadav S. P., Patil P. S., Rajpure K. Y. (2013). Structural, morphological, electrical and magnetic properties of Dy doped Ni–Co substitutional spinel ferrite. *Journal of Magnetism and Magnetic Materials*, 329, 59–64. doi: 10.1016/j.jmmm.2012.10.008.6
- [37] Bharathi K. K., Markandeyulu G., Ramana C. V. (2010). Structural, Magnetic, Electrical, and Magnetoelectric Properties of Sm- and Ho Substituted Nickel Ferrites. *The Journal of Physical Chemistry C*, 115(2), 554–560. doi:10.1021/jp1060864
- [38] Sagadevan S., Chowdhury Z. Z., Rafique R. F. (2018). Preparation and Characterization of Nickel ferrite Nanoparticles via Co-precipitation Method. *Materials Research*, 21(2), 1-5. doi:10.1590/1980-5373-mr-20160533
- [39] Al-Ghamdi A. A., Al-Hazmi F. S., Memesh L. S., Shokr F. S., Bronstein L. M. (2017). Evolution of the structure, magnetic and optical properties of $\text{Ni}_{1-x}\text{Cu}_x\text{Fe}_2\text{O}_4$ spinel ferrites prepared by soft mechanochemical method. *Journal of Alloys and Compounds*, 712, 82–89. doi: 10.1016/j.jallcom.2017.04.052
- [40] Jadhav S. A., Khedkar M. V., Somvansh S. B., Jadhav K. M. (2021). Magnetically retrievable nanoscale nickel ferrites: An active photocatalyst for toxic dye removal applications. *Ceramics International*, 47(20), 28623–28633. doi: 10.1016/j.ceramint.2021.07.021
- [41] Ati A. A., Othaman Z., Samavati A., Doust F. Y. (2014). Structural and magnetic properties of Co–Al substituted Ni ferrites synthesized by co-precipitation method. *Journal of Molecular Structure*, 1058, 136–141. doi: 10.1016/j.molstruc.2013.10.04
- [42] Bawa Waje S., Hashim M., Ismail I. (2011). Effects of sintering temperature on grain growth and the complex permeability of $\text{Co}_{0.2}\text{Ni}_{0.3}\text{Zn}_{0.5}\text{Fe}_2\text{O}_4$ material prepared using mechanically alloyed nanoparticles. *Journal of Magnetism and Magnetic Materials*, 323(11), 1433–1439. doi: 10.1016/j.jmmm.2010.12.032
- [43] Prabhakaran T., Hemalatha, J. (2016). Magnetoelectric investigations on poly(vinylidene fluoride)/ NiFe_2O_4 flexible films fabricated through a solution casting method. *RSC Advances*, 6(90), 86880–86888. doi:10.1039/c6ra18032a
- [44] Sankaranarayanan V. K., Sreekumar C. (2003). Precursor synthesis and microwave processing of nickel ferrite nanoparticles. *Current Applied Physics*, 3(2-3), 205–208. doi:10.1016/s1567-1739(02)00202-x
- [45] Jacob J., Khadar M. A., Lonappan A., Mathew K. T. (2008). Microwave dielectric properties of nanostructured nickel ferrite. *Bulletin of Materials Science*, 31(6), 847–851. doi:10.1007/s12034-008-0135-9
- [46] Agarwala R. C. (2005) Electroless Ni–P–ferrite composite coatings for microwave applications. 65 (5), 959–96. <https://www.ias.ac.in/article/fulltext/pram/065/05/0959-0965>
- [47] Banerjee M., Mukherjee A., Chakrabarty S., Basu S. Pal M. (2019). Bismuth-Doped Nickel Ferrite Nanoparticles for Room Temperature Memory Devices. *ACS Applied*, 2, 7795-7802 DOI:10.1021/acsanm.9b01828
- [48] Joshi S., Kamble V. B., Kumar M., Umarji A. M., Srivastava G. (2016). Nickel substitution induced effects on gas sensing properties of cobalt ferrite nanoparticles. *Journal of Alloys and Compounds*, 654, 460–466. <https://doi.org/10.1016/j.jallcom.2015.09.119>
- [49] Kotresh S., Ravikiran Y. T., Vijayakumari S. C., Thomas S. (2016). Interfacial p-n heterojunction of polyaniline-nickel ferrite nanocomposite as room temperature liquefied petroleum gas sensor. *Composite Interfaces*, 24(6), 549– 561. doi:10.1080/09276440.2017.1241523
- [50] Kashyap R., Kumar R., Devi S., Kumar M., Tyagi S., Kumar D. (2019). Ammonia Gas Sensing Performance of Nickel Ferrite Nanoparticles. *Materials Research Express*, 6, 1-22. doi:10.1088/2053-1591/ab55b5

- [51] Sutk A., Mezinskis G., Lusi A., Stingaciu M. (2012). Gas sensing properties of Zn-doped p-type nickel ferrite. *Sensors and Actuators B: Chemical*, 171-172, 354–360. doi: 10.1016/j.snb.2012.04.059
- [52] Sabbar M.H., Mubarak1 T. H., Ahmad S.N. (2022). Synthesis and characterizations of Nano magnetic particles (Co-NiFe₂O₄) ferrite by co-precipitation and biomedical application. *International Journal of Nanoelectronics and Materials*, 18, 2222-8373 <https://dx.doi.org/10.24237/djps.1804.600C>
- [53] Fazeli M., Hong Y. K., Lee W., Park J. (2016). Implantable ferrite antenna for biomedical applications. *Microwave and Optical Technology Letters*, 58(11), 2745–2749. doi:10.1002/mop.30148
- [54] Sanpo N., Berndt C. C., Wen C., Wang J. (2013). Transition metal-substituted cobalt ferrite nanoparticles for biomedical applications. *Acta Biomaterialia*, 9(3), 5830–5837. doi: 10.1016/j.actbio.2012.10.037

¹Priyanka Dikondwar

Supercapacitors: Opportunities and Challenges



Abstract: - In the realm of energy storage devices, for the upcoming generations, supercapacitors and ultracapacitors are considered as most potential options. Supercapacitors have become the most popular and significant energy conversion and storage system in current renewable and sustainable nanotechnology. Supercapacitors are one of the advanced breakthroughs in energy applications due to their large energy capacity and supply with relatively short time and longer lifetime. These devices have earned their significance in frequent applications, viz., to power hybrid electric/electric vehicles and other power and electronic systems that require electrical energy for their operation. Supercapacitors are considered multipurpose devices, used to transfer electrical energy in a short time in a long shelf life. Therefore, supercapacitors are always in larger market demands, hence they need long-term progress for advancement and their commercialization. Meanwhile, there are some potential technical challenges regarding supercapacitors including, establishing electrical parameter models, consistency testing, and establishing industrial standards. This article pinpoints the challenges and future opportunities of supercapacitors. The current perspective also provides deeper insight into corresponding guidance and directions for the development of supercapacitors.

Keywords: supercapacitor, challenges and opportunities, energy storage

I. INTRODUCTION

Energy harvesting from renewable energy sources has been the prime goal of the research community in recent times of energy scarcity. Researchers involved in this area are engaged in devise methods to store electrical energy. Supercapacitors are one of the most efficient energy storage devices as they possess high specific capacity, high power density, long cycle life, economic efficiency, environmental friendliness, high safety, and fast charge/discharge rates. Hence, Supercapacitors form a bridge between conventional capacitors and secondary ion batteries [1–7]. Supercapacitors are low cost, easy maintenance, and no pollution to the environment.

The nanostructured materials have better chemical kinetics, chemical activity, shorter ionic diffusion path lengths, high surface area, and a surplus of active sites for electrochemical reactions. It became one of the hotspots of interdisciplinary research [8, 9] as it involves materials, energy, chemistry, electronic devices, and other disciplines. As a new type of energy storage device with excellent performance, great application values, and market potential, it can be excavated in many fields such as industrial control, power, transportation, intelligent instruments, consumer electronic products, national defence, communications, medical equipment like defibrillators, pulsed lasers, new energy vehicles, and so on [5,9–13].

Supercapacitors are being researched extensively in smart electronics applications like flexible, biodegradable, transparent, wearable, flexible, on-chip, and portable energy storage. In comparison with capacitors, supercapacitors use materials with a high specific surface area as electrodes [14, 15] in supercapacitors, higher vicinity and thinner dielectrics bring about extra precise capacitance and power density. In comparison with traditional capacitors that have a capacitance of micro or mili farad, the capacitance of a supercapacitor unit can reach thousands of Farads [16]. The supercapacitor faces enormous challenges even though it has unlimited potential and opportunities [17-21].

II. DEVELOPMENT OF SUPERCAPACITORS:

A supercapacitor was developed in the 1970s and 1980s and is an electrochemical device to stores energy by polarized electrolytes. It is unlike the traditional chemical power supply. It is a kind of device with performance between traditional capacitors and batteries [22].

Supercapacitors are classified into two groups based on their charge storage mechanism i.e., Electrostatic double layer capacitor (EDLC) includes electrostatically ion adsorption/ desorption at the interface of electrode and electrolyte, in a pseudocapacitor, a reversible faradaic redox reaction takes place between electrolyte ion and

¹*Corresponding author: Department of Physics, Amolakchand Mahavidyalaya, Yavatmal-445001.
Copyright © JES 2024 on-line : journal.esrgroups.org

electroactive material. And the combination of both is hybrid supercapacitor, in which an electrical double layer capacitance and faradaic or battery capacitance both reactions take place [23–26]. Research and commercialization on supercapacitors began out early in Japan, Russia, Switzerland, South Korea, the United States, France, and different European and American countries. Helmholtz discovered the properties of double-layer capacitance and proposed the concept of double-layer, but it is only in recent decades that double-layer was used for energy storage in early 1879 [22]. In 1957, according to Bcker, smaller capacitors could be used as energy storage devices, which had a specific energy close to that of batteries. A patent for making double-layer capacitors from carbon materials with high specific surface area was proposed by Standard Oil Company Sohio in 1968. After that, the patent era changed into transferred to NEC, and in 1979, they commenced to supply supercapacitors for beginning structures of electrical vehicles. Simultaneously, Panasonic studied supercapacitors with activated carbon as the electrode material and organic solution as the electrolyte. Later, supercapacitors have begun to be industrialized on a large scale, and various kinds of supercapacitors have been introduced. Supercapacitor's industrialization began in the 1980's-Generation-1980 NEC/Tokin and 1987 Panasonic and Mitsubishi Products. In the 1990s, Econd and ELIT mixed released the electrochemical capacitors for high-energy start-up energy applications. Currently, companies such as Panasonic, NEC, EPCOS, Maxwell, and NESS are very active in the research of supercapacitors.

Supercapacitors have shown many unique advantages over the past few years.

III. CHALLENGES FOR SUPERCAPACITORS:

Supercapacitors play a vital role in energy storage due to their distinctive properties since they possess high specific capacity, high power density, long cycle life, economic efficiency, environmental friendliness, high safety, and fast charge/discharge rates. Because of the excellent characteristics of supercapacitors, they are widely used in transportation, industry, military, consumer electronics, and other fields. Though, these devices have some shortcomings. Some of the challenges faced by the supercapacitors are as follows.

1. *Industrial standard*

Supercapacitors possess short development time and a fast speed. Enterprises involved in the supercapacitor industry have different levels. The healthful improvement of supercapacitors can't be separated from enterprise and marketplace supervision, which pursuits to formulate sensible enterprise standards, country wide standards, or even worldwide standards. A set of technical standard systems includes the classification model naming method, the electrical performance test method, safety technical requirements, general specification, electrode material specification, electrolyte specification, charger specification series, production technical requirements, transportation requirements, recovery, and destruction requirements should be established for supercapacitors. For example, general requirements and storage and management requirements of supercapacitor monomers and modules in the disposal of scrap, including the dismantling of scrap monomer and supercapacitor modules and handle recycling, plate processing, the processing of the diaphragm and other aspects, electrolyte capacitor shell processing, aims to guide and standardize the supercapacitor industry achieve the goal of low cost, green recycling disposal. Hence it is an essential means to promote the healthy development of the industry.

2. *Technical problems of supercapacitors*

It is observed that the energy densities of supercapacitors are not very high, there is still a certain gap between supercapacitors ($<20 \text{ Wh kg}^{-1}$) and batteries ($30\text{--}200 \text{ Wh kg}^{-1}$) in terms of energy densities and how to improve the energy density is still the research focus and difficulty in the field of supercapacitors [5, 27, 28]. An effective way to improve the storage capacity of supercapacitors is to improve the manufacturing process and technology, but in the long run, it is essential and difficult to find new electrolyte and electrode active materials with higher corresponding electrochemical performance. Because of the low energy density of the supercapacitor, a bulkier device is produced and is not compact. By increasing the effective surface area of electrode materials in double-layer capacitors or increasing the operation voltage window or both, the energy densities of supercapacitors increase. It is observed that research is going on to develop novel materials with high surface area and using suitable organic electrolytes that can endure a larger voltage window. If these expanses are properly addressed energy densities of supercapacitors can become equivalent to batteries.

3. *Establishment of electrical parameter model*

The supercapacitor model can be equivalent to the ideal model in some areas but in military applications, especially in power supply applications of satellites and spacecraft, some non-ideal parameters may bring potential risks, which cannot be unheeded. Resonance caused by ordinary signal, filter, and energy storage capacitors has a mature solution since it has limited energy. Supercapacitors have the capability of

instantaneous throughput and huge energy because of their high energy. Consequently, it is very vital to have a reliable design to study the impact on load nature, load fluctuation or external environment, and accidental disturbance on the system stability [29].

4. *Consistency detection*

The rated voltage of a supercapacitor is very low i.e. less than 2.7 V, which requires a lot of series connections for practical applications. Since the need for high current charging and discharging in applications, and overcharging has a serious impact on the life of capacitors, it is very significant whether the voltages on individual capacitors in series are consistent or not.

IV. FUTURE OPPORTUNITIES OF SUPERCAPACITORS:

Technical aspect

1. *Intelligentization and transparency*

Due to the speedy development of intelligent electronic devices, people are in urgent need of intelligent and controllable multifunctional electrochemical energy storage devices. The intelligence of electronic devices permits manufacturers and users to program them to perform different functions for different requirements in real life. The development of new materials and design of new structures combined with supercomputer simulation and artificial intelligence, an expectation to develop customizable devices to create user-friendly and personalized future interactions between wearable and bio-integrated electronics [30].

2. *Hybridization*

The problem of low energy density of supercapacitors can be solved by constructing hybrid battery-supercapacitors. Hybrid battery supercapacitor systems contain one electrode that stores charge by a battery-type Faradaic process while the other stores charge based on a capacitive mechanism. Devices such as lithium/sodium/potassium/magnesium ion hybrid battery-supercapacitors inherit the high power ($\sim 0.1\text{--}30\text{ kW kg}^{-1}$) of supercapacitors and the high energy density ($\sim 5\text{--}200\text{ Wh kg}^{-1}$) of secondary batteries. These gadgets have the benefits of strong long-cycle overall performance and occasional cost [5, 9, 31].

3. *Flexible device*

With fast development in portable electronic products and the concept of wearable electronics, flexible energy storage devices have become popular with researchers. It is of great inference to develop energy storage devices that are flexible and small but endowed with high electrochemical properties [32–34]. The traditional supercapacitors, due to the unbending nature of the electrode, are greatly limited to the shape of the device, and in the preparation of the electrode, the metal collector, and the bonding agent, which also reduces the electrochemical performance of the supercapacitor [35]. Thus a flexible supercapacitor matched with a portable electronic product will be the development direction of the next generation of flexible storage devices.

V. APPLICATION ASPECT

1. *Requirement of the society*

The application aspects of supercapacitors are of major importance since to meet social needs and promote industrial development. Due to the rapid development of the electronic industry, the demand for high-capacity portable power supply has become more and more decisive. People all over the globe are paying more and more attention to energy consumption and environmental protection and they are eager for more and more clean energy to be used. Hence mankind is actively seeking solutions. Development of the electronics industry leads to an urgent need to provide high-capacity, portable backup power for all kinds of electronic devices, which drives the development of supercapacitors. These social demands encourage the rapid development of the supercapacitor industry to a certain extent, and the market prospect is very broad.

2. *Improvement of the cost performance*

The most significant criterion to be considered for any industry to endure is to improve product performance and reduce production costs. To improve the technology of the supercapacitor itself, in addition to improving the manufacturing process and technology, to find stable and effective electrode and electrolyte materials to Performance, and on the identical time to lessen the fee is likewise the studies attention on this field. Full Power Technologies is an American firm that developed low-cost ultracapacitors. From the manner of value discount analysis, one has to find new low-cost raw materials like natural mineral resources.

VI. CONCLUSION

Supercapacitor is an excellent energy storage device. It possesses high specific capacity, high power density, long cycle life, economic efficiency, environmental friendliness, high safety, and fast charge/discharge rates. However, there are various challenges faced by the supercapacitors like industrial standard, technical problems of

supercapacitors, establishment of electrical parameter model and consistency detection. This paper also covers the opportunities of supercapacitors in terms of technical and application aspects.

REFERENCES

- [1] J. M. Tarascon, M. Armand, "Issues and challenges facing rechargeable lithium batteries". *Nature*, 414, 359–367, 2001. <https://doi.org/10.1038/35104644>.
- [2] V. Etacheri, R. Marom, R. Elazari, G. Salitra, and D. Aurbach, "Challenges in the development of advanced Li-ion batteries: a review". *Energy Environ. Sci.* 4(9), 3243–3262, 2011.
- [3] A. Manthiram, "Materials Challenges and Opportunities of Lithium Ion Batteries". *J. Phys. Chem. Lett.* 2(3), 176–184, 2011.
- [4] A. Vlad, N. Singh, J. Rolland, S. Melinte, P. M. Ajayan, J. F. Gohy, "Hybrid supercapacitor-battery materials for fast electrochemical charge storage". *Sci Rep.* 7; 4:4315, 2014. doi: 10.1038/srep04315.
- [5] D. Tie, S. Huang, J. Wang, Y. Zhao, J. Ma, J. Zhang, Y. Zhao, Hybrid energy storage devices: Advanced electrode materials and matching principles. *Energy Storage Mater.* 21, 22–40, 2019.
- [6] W. Miao, Y. Zhao, X. Zhang, R. Qi, S. Shi, Z. Li, Q. Wang, and Y. Zhao, *Electrochim. Acta* 272, 184–191 (2018).
- [7] M. Wang, F. Jin, X. Zhang, J. Wan, S. Huang, X. Zhang, S. M. Orcid, Y. Zhao, and Y. Zhao, "Multihierarchical Structure of Hybridized Phosphates Anchored on Reduced Graphene Oxide for High Power Hybrid Energy Storage Devices". *ACS Sustain. Chem. Eng.* 5(7), 5679–5685, 2017.
- [8] F. Yao, D. T. Pham, Y. H. Lee, "Carbon-Based Materials for Lithium-Ion Batteries, Electrochemical Capacitors, and Their Hybrid Devices". *ChemSusChem* 8(14), 2284–2311, 2015.
- [9] W. Zuo, R. Li, C. Zhou, Y. Li, J. Xia, J. Liu, "Battery-Supercapacitor Hybrid Devices: Recent Progress and Future Prospects". *Adv Sci (Weinh)*. 21; 4(7):1600539, 2017. doi: 10.1002/adv.201600539.
- [10] Y. Wang, Y. Song, and Y. Xia, "Electrochemical capacitors: mechanism, materials, systems, characterization and applications". *Chem. Soc. Rev.* 45(21), 5925–5950, 2016.
- [11] F. Díaz-González, A. Sumper, O. Gomis-Bellmunt, R. Villafáfila-Robles, *Renewable Sustainable Energy Rev.* 16(4), 2154–2171, 2012.
- [12] Y. Zou, X. Hu, H. Ma, S. E. Li, "Combined State of Charge and State of Health estimation over lithium-ion battery cell cycle lifespan for electric vehicles". *J. Power Sources* 273, 793–803, 2015.
- [13] L. Zhang, Z. Hu, Z. Wang, F. Sun, D. G. Dorrell, "A review of supercapacitor modeling, estimation, and applications: A control/management perspective". *Renewable Sustainable Energy Rev.* 81, 1868–1878, 2018.
- [14] C. J. Chen, Y. Zhang, Y. J. Li, J. Q. Dai, J. W. Song, Y. G. Yao, Y. H. Gong, I. Kierzewski, J. Xie, L. B. Hu. "All-wood, low tortuosity, aqueous, biodegradable supercapacitors with ultra-high capacitance". *Energy Environ. Sci.* 2017, 10, 538–545, 2017.
- [15] Y. J. Heo, J. h. Lee, S. H. Kim, S. J. Mun, S. Y. Lee, S. J. Park, "Paper-Derived Millimeter-Thick Yarn Supercapacitors Enabling High Volumetric Energy Density". *ACS Appl. Mater Interfaces*, 114, 42671–42682, 2022.
- [16] N. Kumar, S. B. Kim, S. Y. Lee, S. J. Park, "Recent Advanced Supercapacitor: A Review of Storage Mechanisms, Electrode Materials, Modification, and Perspectives". *Nanomaterials*. 12(20):3708, 2022. DOI. <https://doi.org/10.3390/nano12203708>.
- [17] C. Zhong, Y. Deng, W. Hu, J. Qiao, L. Zhang, J. Zhang, "A review of electrolyte materials and compositions for electrochemical supercapacitors". *Chem. Soc. Rev.* 44(21), 7484–7539, 2015.
- [18] A. González, E. Goikolea, J. A. Barrena, "Mysyk R. Review on supercapacitors: Technologies and materials". *Renewable Sustainable Energy Rev.* 58, 1189–1206, 2016.
- [19] Z. S. Iro, C. Subramani, "Dash S. A Brief Review on Electrode Materials for Supercapacitor". *Int. J. Electrochem. Sci.* 11(12), 10628–10643, 2016.
- [20] A. Borenstein, O. Hanna, R. Attias, S. Luski, T. Brousse, D. Aurbach, Carbon-based composite materials for supercapacitor electrodes: a review. *J. Mater. Chem. A* 5(25), 12653–12672, 2017.
- [21] M. Vangari, T. Pryor, L. Jiang, "Supercapacitors: Review of Materials and Fabrication Methods". *J. Energy Eng.* 139 (2), 72–79, 2012.
- [22] V. A. Boicea, "Energy storage technologies: The past and the present". *Proc. IEEE* 102(11), 1777–1794, 2014.
- [23] Z. Ma, Z. Zhang, Y. Qu, F. Lai, Q. Li, X. Wu, Q. Wu, H. Li, H. Wang, H. Huang, "Microporous Mesoporous Mater. 281, 50–56, 2019.
- [24] S. Yu, X. Zhu, G. Lou, Y. Wu, K. Xu, Y. Zhang, L. Zhang, E. Zhu, H. Chen, and Z. Shen, *Mater. Design.* 149, 184–193 (2018).
- [25] H. Zhuo, Y. Hu, Z. Chen, and L. Zhong, "Cellulose carbon aerogel/PPy composites for high-performance supercapacitor", *Carbohydr. Polym.* 215, 322–329, 2019.
- [26] H. Tang, J. Wang, H. Yin, H. Zhao, D. Wang, and Z. Tang, "Growth of polypyrrole ultrathin films on MoS₂ monolayers as high-performance supercapacitor electrodes". *Adv. Mater.* 27(6), 1117–1123, 2015.
- [27] Y. Zhao, W. Ran, J. He, Y. Song, C. Zhang, D. B. Xiong, F. Gao, J. Wu, Y. Xia, "Oxygen-Rich Hierarchical Porous Carbon Derived from Artemia Cyst Shells with Superior Electrochemical Performance". *ACS Appl. Mater. Interfaces* 7(2), 1132–1139, 2015.
- [28] Y. Zhao, Z. Zhang, Y. Ren, W. Ran, X. Chen, J. Wu, and F. Gao, *J. Power Sources* 286, 1–9 (2015)
- [29] S. Buller, E. Karden, D. Kok, D. D. Doncker, Modeling the Dynamic Behavior of Supercapacitors using Impedance Spectroscopy. *IEEE Industry Applications Conference, 36th IAS Annual Meeting (IEEE, 2001)*, 2001.
- [30] Z. Lv, W. Li, L. Yang, X. J. Loh, and X. Chen, Custom-Made Electrochemical Energy Storage Devices. *ACS Energy Lett.* 4(2), 606–614, 2019.
- [31] Z. Chen, D.-B. Xiong, X. Zhang, H. Ma, M. Xia, and Y. Zhao, *Nanoscale* 8(12), 6636–6645, 2016.
- [32] Q. Xu, C. Wei, L. Fan, W. Rao, W. Xu, H. Liang, and J. Xu, *Appl. Surf. Sci.* 460, 84–91, 2018.
- [33] Y. He, W. Chen, X. Li, Z. Zhang, J. Fu, C. Zhao, and E. Xie, Freestanding three-dimensional graphene/MnO₂ composite networks as ultralight and flexible supercapacitor electrodes. *ACS Nano* 7(1), 174–182, 2012.

- [34] Y. Shi, L. Pan, B. Liu, Y. Wang, Y. Cui, Z. Bao, and G. Yu, Nanostructured conductive polypyrrole hydrogels as high-performance, flexible supercapacitor electrodes. *J. Mater. Chem. A* 2(17), 6086–6091, 2014.
- [35] K. H. Choi, S. J. Cho, S. J. Chun, J. T. Yoo, C. K. Lee, W. Kim, Q. Wu, S. B. Park, D. H. Choi and S. H. Lee, “Heterolayered, one-dimensional nanobuilding block mat batteries”. *Nano Lett.* 14(10), 5677–5686, 2014.

© 2024. This work is published under
<https://creativecommons.org/licenses/by/4.0/legalcode> (the“License”).
Notwithstanding the ProQuest Terms and Conditions, you may use this
content in accordance with the terms of the License.

¹N. Thejo Kalyani^{2,3,*}Ritesh Raikundliya²Droupadi Gingule²S.J. Dhoble

**Synthesis and characterization
of
bis(8-hydroxyquinoline)
(Strontium) organo- metallic
fluorescent phosphor for solid
state lighting**



Abstract: - The synthesis of bis(8-hydroxyquinoline) (Strontium) – Srq₂ (where Sr = Strontium, q = 8-hydroxy-quinoline) at various pH (4 – 9: insteps of 0.5) were carried out at room temperature. Structural, morphological, thermal, optical and photometric investigations were carried out to evaluate the aptness of the synthesized complex for solid state lighting applications. The crystalline character of the complex was implied by the strong and sharp diffraction peaks registered in the XRD pattern. The outcome of FTIR verifies the formation and structure of the Srq₂. Surface morphology of the pigment reveals sheet like morphology with crystalline size estimated to be in the range of 20 μm. TGA curve infers that the complex has higher stability upto 395°C. Excitation spectra of Srq₂ phosphor show broad peak ranging from 250 nm to 400 nm, centred in between 340-350 nm, depending on the pH of the precipitate. Emission spectra shows broad peak that ranges from 400 nm to 550 nm, centred at 455-465 nm in accordance with pH. The emission falls in visible spectrum that peaks in greenish-blue region. Photoluminescence and photometric analysis indicate the sensitivity of pH towards emission intensity of organic phosphor. This infers that pH of the precipitate play a vital role in tuning the emission wavelength, which in this case, registered in blue/greenish blue region(456 to 462 nm) of the visible spectrum. Such phosphors have wide applications in solid state lighting through Organic Light Emitting Diodes(OLEDs) and flat panel displays.

Keywords: Quinoline complex, Srq₂, fluorescent phosphor, energy efficient, environmentally friendly, solid-state lighting, OLEDs

¹ Department of Applied Physics, Laxminarayan Innovation Technological University, Nagpur-440033, India

² Department of Physics, RTM Nagpur University, Nagpur-440033, India

³ Department of Physics, Shri. Lemdeo Patil Mahavidhyalaya, Mandhal, Kuhl, Nagpur – 441210, India

*Corresponding author: Ritesh Raikundliya , E-mail : raikundliyaritesh19@gmail.com

Copyright © JES 2024 on-line : journal.esrgroups.org

I. INTRODUCTION

Since a few decades, lighting technology has advanced beyond its limitations, and because it greatly enhances the quality and productivity of human existence, it now has the potential to replace the current lighting power consumption for domestic illumination. Although our primate predecessors used fire 2–6 million years ago, it is still regarded as a prime example of a human invention[1,2]. The so-called developed technologies still have a way to go before offering solid state lighting (SSL) that is both energy-saving and environmentally compatible. Millions of people still use climate-hazardous fuel-based lighting worldwide. As a result, there is a growing focus on employing technology to improve lighting practises with the intention of using green lighting called Solid state lighting (SSL), which has the potential to have a higher power efficiency than conventional lighting sources. Organic light emitting devices (OLEDs) have recently received a great deal of interest from producers, product designers, and end users due to its favorable technology for the developing display and lighting markets[3-5].

8-hydroxyquinoline organo-metallic complexes have gained consideration owing to their gorgeous applications for OLEDs [6] and glow in dark cotton fabric, coated by luminescent phosphor[7]. However, these complexes can also be used as pigment in the formulation of luminous paints. Centre of attention has been mainly on quinoline based metallic complexes particularly on Alq_3 , Znq_2 and Mgq_2 [Al: Aluminium, Zn: Zinc, Mg: Magnesium and q is 8-hydroxyquinoline] [8-11] as emissive layer electron transport layer in OLEDs. Almost negligible work has been carried out on Mq_n complexes: 8-hydroxyquinoline amalgamated with rare earth, some group II and group III elements that includes Pbq_2 , Tbq_3 , Srq_2 , Caq_2 , Cdq_2 , Euq_3 , Rhq_3 , Irq_3 , Biq_3 [Pb: Lead, Tb: Terbium, Sr: Strontium, Ca: Calcium, Cd: Cadmium, Eu: Europium, Ir: Iridium, Bi: Bismuth], to name a few. As widely reported in the literature, the nature of an attached metal ion influences the emission, colour, efficiency, stability, and evaporability of metal quinoline derivatives. These organometallic complexes are widely used as fluorescent phosphor in opto-electronic devices due to their good luminescence properties, contrast level with high intensity. Particularly, the metal quinolate (Mq_2), possess good anticorrosive property with higher stability as coating material [12]. Hence, the present study propose the synthesis of quinoline organometallic complex with strontium as metal ligand by simple cost-effective precipitation method, formulation of fluorescent paint and its evaluation.

II. EXPERIMENTAL

1. Materials

8-Hydroxyquinoline (8-HQ) (C_9H_7NO , M.wt. - 145.16 g/mol), acetic acid (CH_3COOH , M.wt - 60.052), strontium nitrate ($Sr(NO_3)_2$, M.wt - 211.63 g/mol), ammonia (NH_3OH , M.wt - 35.04g/mol) and Potassium hydroxide (KOH, M.wt - 56.10 g/mol) of Loba with AR grade were used as precursors. The recorded literature [13-14] states that by varying the pH from 4 to 9, blue light emitting Srq_2 organo-metallic complexes were synthesized by low cost precipitation method

at room temperature. We exclusively used analytical (AR) grade reagents and solvents during the synthesis of Srq_2 complex. All reactions were carried out with afresh distilled solvents, in an inert and anhydrous atmosphere.

2. Synthesis

According to a method described in the literature, Srq_2 has been made using a low-cost acid-base co-precipitation method at room temperature [14]. Fig. 1 and 2 reflects the synthesis scheme and the structure of the synthesised complex, respectively.

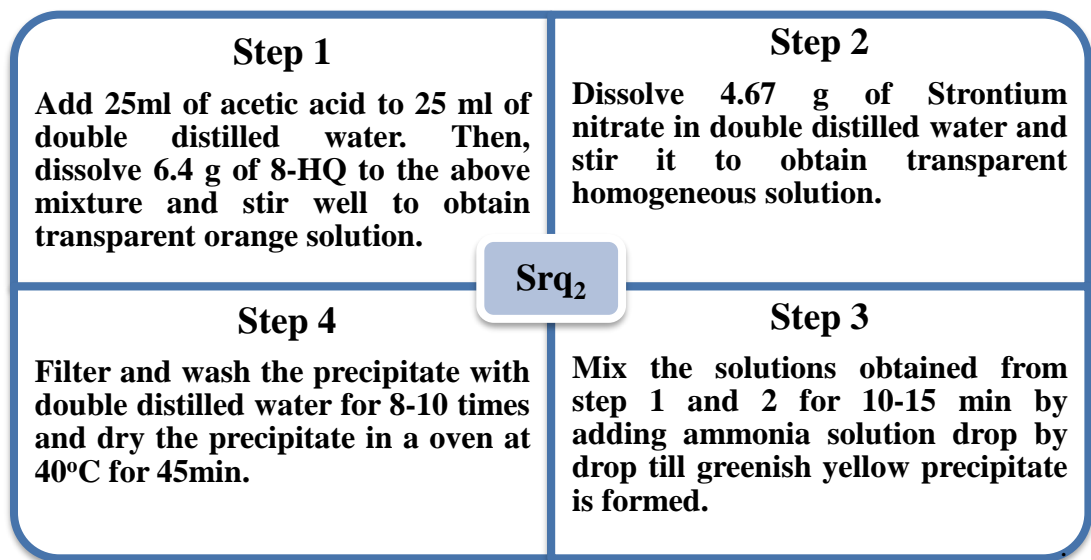


Fig.1: Synthesis scheme of Srq_2 organo-metallic complex

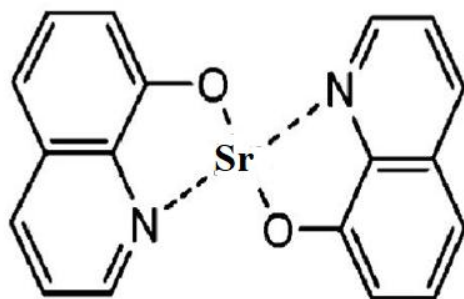


Fig.2: Chemical structure of Srq_2

III. CHARACTERIZATION

Suitability of the synthesized Srq_2 tunable light emitting phosphor which has potential application as emissive layer for an OLED, display devices that proffer SSL was assessed by various

characterization techniques. Crystal structure was confirmed through X-ray diffraction technique using Rigaku's Miniflex 600 (Cu-K α radiation). The bonding and chemical structure was analyzed through FTIR spectroscopy using Bruker Alpha FTIR Spectrometer (ATR Mode). The Photoluminescence spectra were recorded using the PL spectrometer Shimadzu RF5301PC to assess the emission wavelength and its intensity. 1931CIE colour calculator program radiant imaging was used to assess CIE coordinates of Srq₂. Shimadzu DTG-60 simultaneous DTATG apparatus is used for TGA –DTA analysis of the complex.

1. X-ray Diffraction (XRD) Analysis

X-ray Diffraction patterns of Srq₂ complex (pH 8.0, 8.5, 9.0) are shown in Fig.3. XRD profiles are in good agreement with ICDD PDF File No. 00-039-1857 of 8-hydroxyquinoline belong to orthorhombic crystal system. The sharp diffraction peaks of Srq₂ reveal good crystalline nature of synthesized complex. The XRD pattern has 5 noticeable major peaks at 14.15°, 23.354°, 23.504°, 25.622° and 28.046° for (400), (460), (111), (311) and (151) h k l planes respectively. The 100% relative intensity of synthesized Srq₂ organo-complex was observed to be 1901 a.u. at different pH with the value of 2 θ of 14.480° [15].

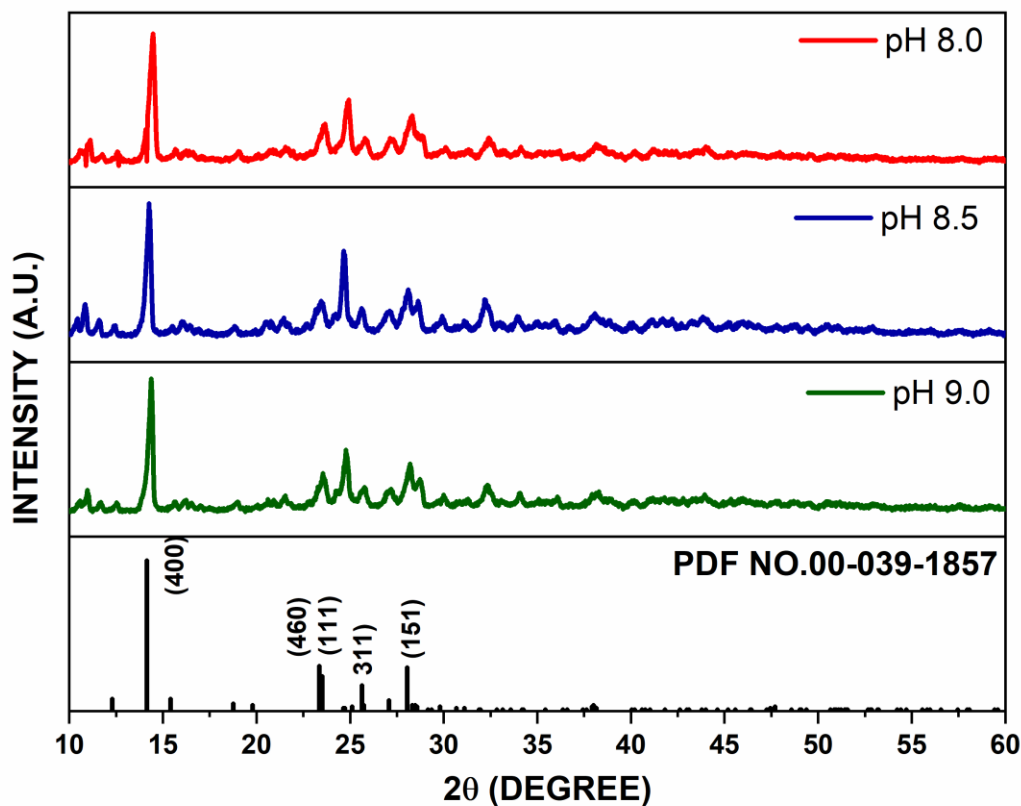


Fig. 3: X-ray diffraction pattern of Srq₂ complex

2. Fourier transform infrared spectroscopy (FTIR) analysis

Before you begin to format your paper, first write and save the content as a separate text file. Keep your text and graphic files separate until after the text has been formatted and styled. Do not use hard tabs, and limit use of hard returns to only one return at the end of a paragraph. Do not add any kind of pagination anywhere in the paper. Do not number text heads-the template will do that for you. Structure formation and the absorption peaks of the synthesized complexes in infrared region were explored by FTIR technique at different pH ranging from 8 to 9[20]. As shown in Fig. 4, the relationship between wave number (cm^{-1}) and transmittance (%) is plotted along the X and Y axes, respectively, and was recorded spanning the range of 4000 to 500 cm^{-1} .

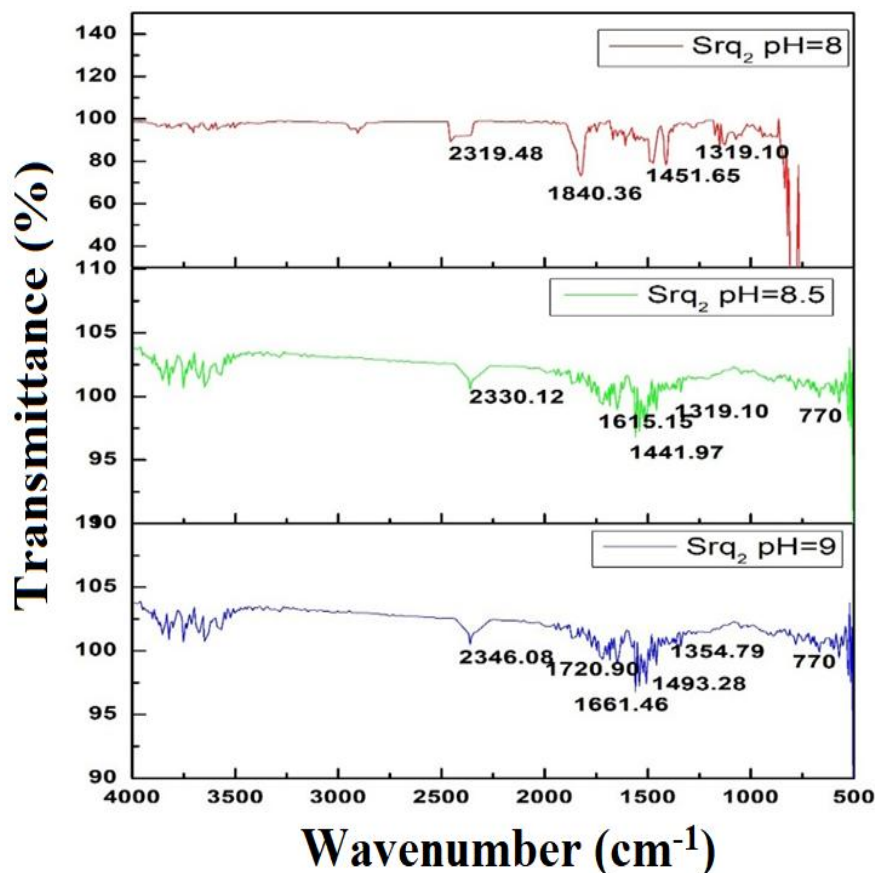


Fig. 4: FTIR spectra of Srq₂ complex

Srq₂ shows prominent peaks in its FT-IR spectra. The nature of these spectra was found to be same even at different pH values. Metal stretching vibrations were found at 2330.12 with C=O=O bonding of carbon dioxide, 1707.06 with C=O stretching of conjugated aldehyde, at 1615.15 with C=C bonding of alpha- Beta unsaturated ketone, at 1441.97 with O-H bending of carboxylic acid, 1451.65 with C-H bonding of alkane group, at 1319.19 with O-H bonding of phenol group, at 770.28 with C-H bonding of 1, 2, 3-trisubstituted group[21]. The result thus validates the Srq₂ complex's structural integrity.

3. SEM Analysis

Fig.5. shows the SEM images of the synthesized Srq_2 organo-complex, observed at different magnifications at scale of about $20\ \mu\text{m}$. The surface of Srq_2 complex portrays the formation of agglomerated particles with sheet like morphology [22]. Crystal size was found to be $27.535\ \mu\text{m}$.

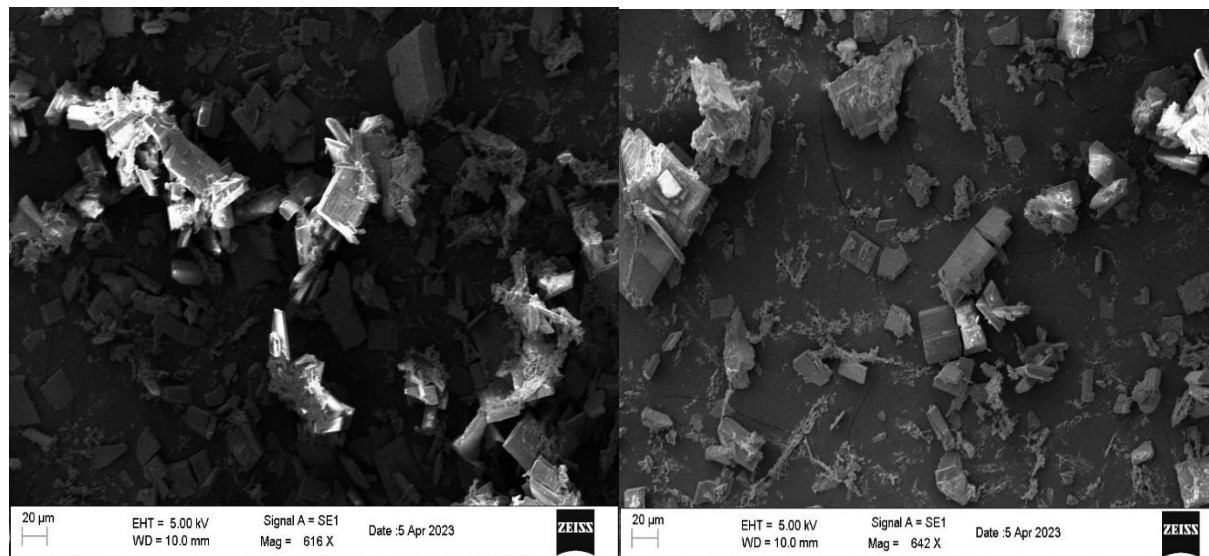


Fig.5: Morphology of Srq_2 organo-complex at the range of $20\ \mu\text{m}$.

4. Thermogravimetric and Differential Thermal Analysis

Thermogravimetric analysis (TGA) is a technique that assesses how a substance changes in weight in a controlled environment as a function of temperature or time. It also explains how temperature and time affect the relation between weight and heat changes. Thermal analysis provides details on how material properties change with temperature. The thermo-gravimetric analysis of Srq_2 complexes were carried out in the range of $0-550^\circ\text{C}$. As shown in Fig. 6, there is continuous loss in weight from 60 to 500°C in slow manner. But rapid decrease in weight starts from 80°C which is due to loss of water. The degradation temperature of Srq_2 is nearly 395°C .

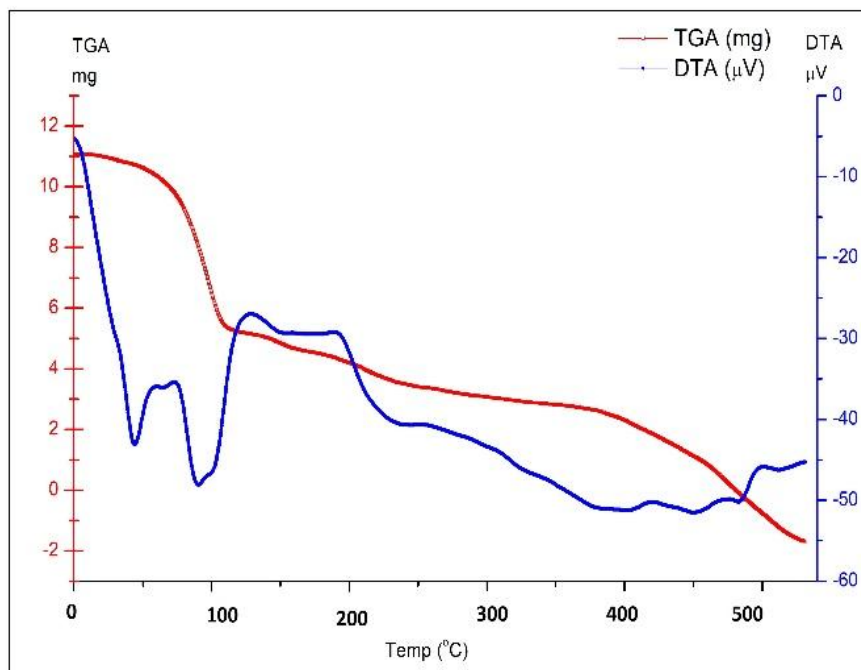


Fig.6: TGA/DTA Graph of Srq₂ Complex

The complex exhibits a nearly 8% to 9% weight loss up to 200°C, represented by the curved position in the graph. Chemical processes that occur during heating, the release of adsorbed species, and (iii) the breakdown process may be the cause of this mass loss [23,24]. DTA curve of Srq₂ complex exhibits endothermic and exothermic peaks. The endothermic peak, around 100°C and 175°C, is caused by the deformation of water and the evaporation of any moisture that may still be present on the surface of the synthesized complex. The decomposition of leftover organic material is indicated by an exothermic peak with a Centre temperature of around 210°C. Performance of OLEDs is ultimately determined by the thermal stability and melting point of the synthesized complex, which prevent morphological change, distortion, and material degradation during operation of the electroluminescent devices.

5. Photoluminescence Spectra

Photoluminescence (PL) property of the synthesized Srq₂ complex at different pH was carried out on Spectro fluorophotometer. PL spectra portrays different excitation wavelengths peaked at a wavelength of 456 nm as shown in Fig.7(a). When stimulated at 349 nm, bright emission wavelengths at 462 nm, 461 nm, 460 nm, and 456 nm were seen, as illustrated in Fig.7(b). It is evident that when pH increased from 4 to 5, a red shift of 1 nm was observed and a blue shift of 5 nm was witnessed in the pH range between 5.5 and 7.6. On the other hand, 8 to 9 pH range, red shift of 6 nm was attained. This suggests that the pH of the precipitate is crucial in adjusting the wavelength. It's interesting to note that intensity was found to be greatest at and near neutral pH [16].

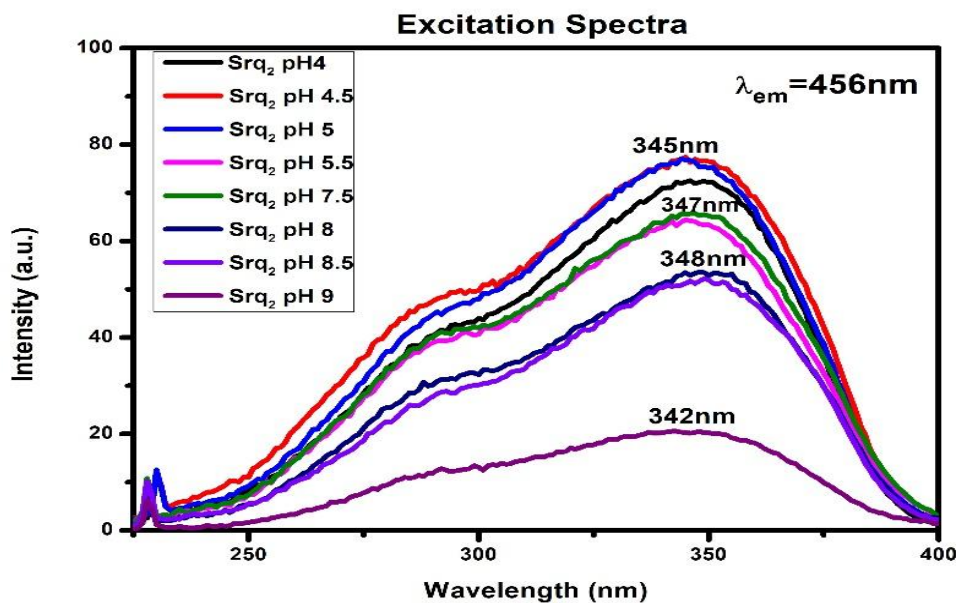


Fig. 7. (a) PL Excitation Spectra of Srq₂ Organometallic-complex at emission wavelength 456nm.

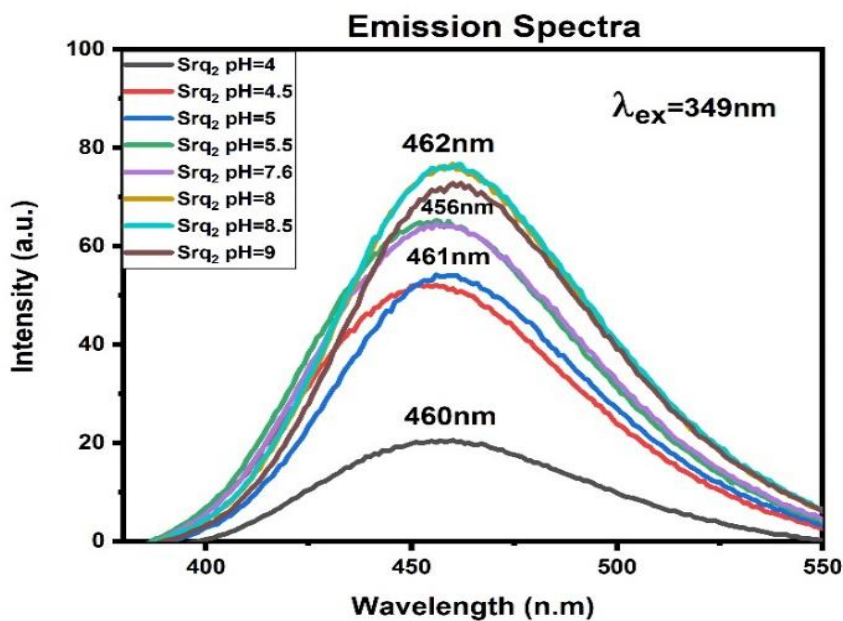


Fig.7(b) PL Emission Spectra of Srq₂ organo-complex at excitation wavelength 349 nm

This may be due to the fact that Sr²⁺ is planarly coordinated to the quinoline ligand and hence the electronic states responsible for fluorescence are very specific to the state of ionization of the molecule, and thus the energy transfer(ET) from the ligand to the metal ion is more effective [17]. Also, change in pH leads to molecular bonding or dissociation of H⁺ ion that changes the electronic wavefunction and hence intensity.

6. Photometric Analysis

CIE colour coordinates of Srq₂ organo-metallic complex [18] were evaluated from PL emission spectra. With chromaticity coordinates of (0.1379, 0.1314), (0.1379,0.1336), and (0.1371,0.1371) for pH values of 8, 8.5, and 9, respectively, the synthesized organo-complex Srq₂ exhibited greenish-blue emission with varying shades as depicted in Fig.8.

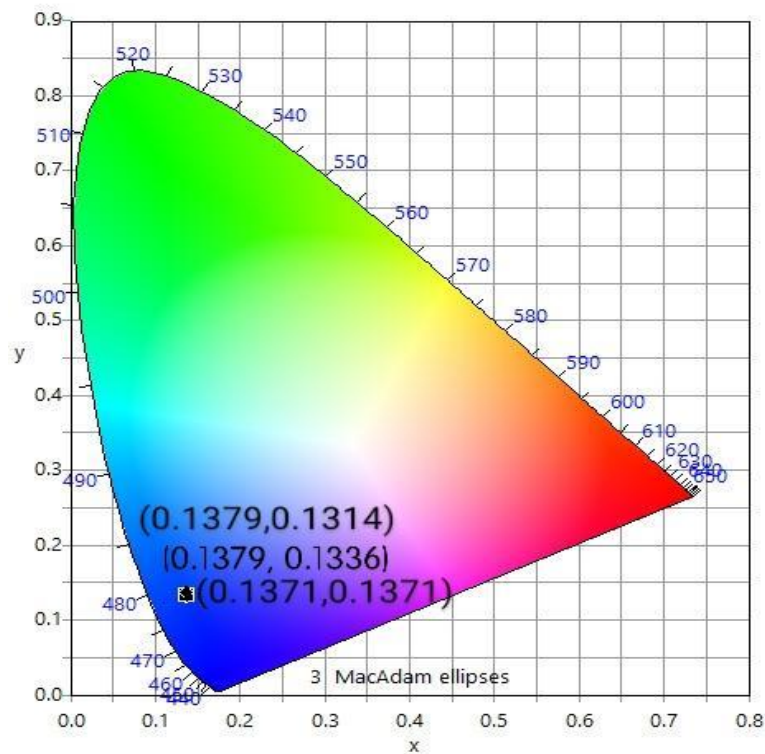








Fig. 8: CIE chromaticity diagram of Srq₂ at various pH

Table 1: Comparison of optical and Photometric properties of Srq₂

Srq ₂ Complex	pH	Under Normal Light	Under UV Light	λ_{em} (nm)	λ_{exc} (nm)	CIE Co-ordinates (x,y)	CCT (K)
	8.0			462	349	(0.1379,0.1314)	7030
	8.5			462	349	(0.1379,0.1336)	7327
	9.0			462	349	(0.1371,0.1371)	7723

IV. CONCLUSION

The present investigation reports the synthesis and characterization of Srq₂ (Strontium 8-hydroxyquinoline) organo-complex at different pH ranging from 4 to 9. XRD analysis confirms that the synthesized organo-metallic complex is crystalline in nature. FTIR analysis confirmed that the synthesized organo-complex have some vibrational stretching, bending and bonding of Srq₂(Strontium 8-hydroxyquinoline) organo-complex, which confirmed the functional group of organo-complex. SEM image reveals agglomerated fine particles that are in micrometer range. TGA curve infers the thermal stability of Srq₂ up to 150°C. According to DTA, the endothermic peak that lie between temperatures of less than 100 °C and around 175 °C corresponds to the deformation of water and the evaporation of any moisture that may still be present on the surface of the synthesised complex. An exothermic peak with at roughly 210°C shows the decomposition of leftover organic material. When stimulated at 349 nm, bright emission wavelengths at 462 nm, 461 nm, 460 nm, and 456 nm were demonstrated. CIE colour coordinates of Srq₂ organo-metallic complex were found to be (0.1379, 0.1314), (0.1379,0.1336), and (0.1371,0.1371) for pH values of 8, 8.5, and 9, respectively, thus revealing that the synthesized Organo-complex Srq₂ exhibited blue light emission with lighter to darker shade. These results prove that the synthesized srq₂ organo-complex have the ability to harvest blue component solid state lightning, which is likely utilized for energy-efficient lighting applications.

REFERENCES

1. Geffroy, Bernard, Philippe Le Roy, and Christophe Prat. "Organic light-emitting diode (OLED) technology: materials, devices and display technologies." *Polymer international* 55.6 (2006): 572-582.
2. Vij, D. R., ed. *Luminescence of solids*. Springer Science & Business Media, 2012.
3. Shiang, Joseph J. and Anil R. Duggal "Organic Electroluminescence", *Luminescence: From Theory to Applications* (2007).
4. Podes Ramchandra. "Organic light emitting diode devices: An energy efficient solid state lighting for applications." *Renewable and Sustainable Energy Reviews* 133 (2020): 110043.
5. Zhu, Dandan, and Colin J. Humphreys. "Solid-state lighting based on light emitting diode technology." *Optics in our time* (2016): 87-118.
6. Rajhans, Vyankatesh, N. Thejo Kalyani, Ritesh Raikundliya, and S. J. Dhoble. "Wavelength tuning from Cadmium based 8-HQ luminous paints formulated with contrasting resins." *Optik* 272 (2023): 170211.
7. Feezell, Daniel, and Shuji Nakamura. "Invention, development, and status of the blue light-emitting diode, the enabler of solid-state lighting." *Comptes Rendus Physique* 19, no. 3 (2018) 113-133.
8. Minakshi Ghate H. K. Dahule N. Thejo Kalyani S. J. Dhoble; Synthesis and characterization of high quantum yield and oscillator strength 6-chloro-2-(4-cynophenyl)-4-phenylquinoline (Cl-CN-DPQ) organic phosphor for solid-state lighting, *Luminescence –The journal of biological and chemical luminescence* (2017)1–8.
9. S.Y. Mullemwar, G.D. Zade, N. Thejo Kalyani, S.J. Dhoble; Blue light emitting P-Hydroxy DPQ phosphor for OLEDs, *Optik* 127 (2016) 10546–10553.
10. S. A. Bhagat, S. V. Borghate, N. Thejo Kalyani and S. J. Dhoble, Novel Na⁺ doped Alq₃ hybrid materials for organic light-emitting diode (OLED) devices and flat panel displays, *Luminescence* (30)(2015)251–256.
11. Ahmad, Ahmad A., et al. "Photoluminescence, Optical, and Electrical Properties of Bis (8-Hydroxyquinoline) Zinc and Tris-(8-Hydroxyquinoline) Aluminum Organometallics and Their Films." *Journal of Electronic Materials* (2023): 1-9.
12. Yang, Zhengqing, et al. "A multifunctional Sr (HQ) 2 filler-reinforced coating for self-healing and physical barrier properties on aluminum alloy." *Progress in Organic Coatings* 180 (2023): 107567.
13. Varghe, Prajakta P., N. Thejo Kalyani, P. G. Shende, and S. J. Dhoble. "Synthesis and characterization of energy-efficient Mq₂ (M= Zn, Cd, Ca, and Sr) organometallic complexes for OLED display applications." In *Energy Materials*, pp. 505-521. Elsevier, 2021.
14. Shahedi, Zahra, Mohammad Reza Jafari, and Abdol Ali Zolanvari. "Synthesis of ZnQ 2, CaQ 2, and CdQ 2 for application in OLED: optical, thermal, and electrical characterizations." *Journal of Materials Science: Materials in Electronics* 28 (2017): 7313-7319.
15. N. Thejo Kalyani, Prajakta P.Varghe, P.G.Shende, S.J. Dhoble, Mq₂(M= Zn, Cd, Ca and Sr) organometallic functional complexes for luminous paints; Concept, Mechanism and Theoretical Approach of Functional Materials and Their Applications; Elsevier (2022) Ch 15, pp. 477- 492; ISBN:978-0-323-85788-8.
16. Pratik Shinde, Shekhar Pandharipande, N. Thejokalyani, S.J. Dhoble; Exploration of photophysical properties of green light emitting bis(8-hydroxyquinoline) zinc (Znq₂) metal chelate under various environments; *Optik* 162 (2018) 151–160
17. Chitnis, Dipti, N. Thejo Kalyani, and S. J. Dhoble. "Structural and optical investigation of novel europium hybrid organic complex for OLEDs and solid state lighting." *Journal of Materials Physics and Chemistry* 5, no. 1 (2017): 1-10.

18. Ramos, M. Luísa, Licinia LG Justino, Andreia IN Salvador, Andreia RE de Sousa, Paulo E. Abreu, Sofia M. Fonseca, and Hugh D. Burrows. "NMR, DFT and luminescence studies of the complexation of Al (III) with 8-hydroxyquinoline-5-sulfonate." *Dalton Transactions* 41, no. 40 (2012): 12478-12489.
19. Huang, Shan, Guangming Pang, Xiangkui Li, Jianping Li, and Hongcheng Pan. "Nanowires of metal (Cd, Cu) halide complexes with 8-hydroxyquinoline for photoelectrochemical and electrochemiluminescence sensing." *Journal of Nanoparticle Research* 19 (2017): 1-9.
20. Xu, Yuna, Xueming Zhong, Yanrong Li, Junchen Liu, Shiting Wu, and Hongze Zeng. "Synthesis and characterization of bis-(8-hydroxyquinoline) strontium (SrQ2) in water medium." *Journal of the Society for Information Display* 28, 9 (2020): 721-730.
21. Wang, Ruifang, Yali Cao, Dianzeng Jia, Lang Liu, and Fang Li. "New approach to synthesize 8-hydroxyquinoline-based complexes with Zn²⁺ and their luminescent properties." *Optical Materials* 36, no. 2 (2013): 232-237.
22. Rafiqi, Ferooze Ahmad, and Kowsar Majid. "Synthesis, characterization, photophysical, thermal and electrical properties of composite of polyaniline with zinc bis (8-hydroxyquinolate): a potent composite for electronic and optoelectronic use." *RSC advances* 6, no. 26 (2016): 22016-22025..
23. Ghamsarizade, R., Sh Najafi, A. A. Sarabi, Sh Roshan, and H. Eivaz Mohammadloo. "Synthesis of pH sensitive microcapsules containing ZAPP, SAPP, and 8-HQ, and evaluation of their anti-corrosion performance, and mechanical enhancement of epoxy coating." *Progress in Organic Coatings* 174 (2023): 107290.
24. Erdem, Bilge, Adnan Özcan, and A. Safa Özcan. "Adsorption and solid phase extraction of 8-hydroxyquinoline from aqueous solutions by using natural bentonite." *Applied Surface Science* 256, no. 17 (2010): 5422-5427.
25. Liu, Tong, Lingwei Ma, Xin Wang, Jinke Wang, Hongchang Qian, Dawei Zhang, and Xiaogang Li. "Self-healing corrosion protective coatings based on micro/nanocarriers: A review." *Corrosion Communications* 1 (2021): 18-25.
26. Ding, ChenDi, JianHua Xu, Ling Tong, GuangCai Gong, Wei Jiang, and Jiajun Fu. "Design and fabrication of a novel stimulus-feedback anticorrosion coating featured by rapid self-healing functionality for the protection of magnesium alloy." *ACS Applied Materials & Interfaces* 9, no. 24 (2017): 21034-21047.

¹ Shubham Kadam

² Vivek Kapse

Hydrogen Sulfide Gas Sensing by Chemically Synthesized Cerium Oxide Nanoparticles



Abstract: - In this study, a highly sensitive and efficient sensor for detecting Hydrogen sulfide (H₂S) has been developed using Cerium Oxide (CeO₂) nanoparticles synthesized via the co-precipitation method. The structural and morphological characteristics of the CeO₂ nanoparticles were meticulously analysed using X-ray diffraction (XRD) and Scanning Electron Microscopy (SEM). The results indicate that the CeO₂-based sensor demonstrates remarkable sensing performance, characterized by high sensitivity, excellent stability, and rapid response and recovery times. These findings underscore the potential of CeO₂ nanoparticles as an efficient material for resistive gas sensors, advancing the field of gas detection technology.

Keywords: Cerium Oxide, Hydrogen sulfide, Gas Sensing

¹ *Corresponding author: Shubham Kadam; Department of Physics, Prof. Ram Meghe College of Engineering and Management Amravati- 444701, Maharashtra, India. (shubhamkadam@gmail.com)

² Vivek Kapse; Department of Physics, Arts, Science and Commerce College, Chikhaldara- 444807, Maharashtra, India.

Copyright © JES 2024 on-line : journal.esrgroups.org

I. INTRODUCTION

Cerium oxide (CeO_2) has emerged as a critical material in the field of gas sensing due to its unique chemical and physical properties. Its high oxygen storage capacity and excellent redox behavior make CeO_2 an ideal candidate for detecting various gases, particularly those with significant environmental and industrial relevance. The material's ability to operate effectively at room temperature and its sensitivity to changes in the surrounding atmosphere enable the development of highly responsive and selective sensors. CeO_2 nanostructured forms, such as nanoparticles, nanorods, and hollow spheres, further enhance its surface area and catalytic activity, leading to improved gas sensing performance. The versatility and effectiveness of CeO_2 in gas sensing applications underscore its importance in advancing sensor technology, providing crucial solutions for environmental monitoring, industrial safety, and public health.

The development of gas sensors based on Cerium Oxide (CeO_2) nanoparticles has garnered significant interest due to their potential for high sensitivity and selectivity.

Various studies have explored the synthesis, characterization, and gas sensing performance of CeO_2 -based sensors. Oosthuizen et al. (2020) synthesized CeO_2 nanoparticles using a chemical precipitation method with varying ethanol concentrations to evaluate their gas sensing characteristics towards H_2S and NO_2 . The study found that CeO_2 nanoparticles with different ethanol concentrations exhibited different gas responses depending on their crystallite sizes and defect concentrations. CeO_2 nanoparticles showed a higher response to H_2S at room temperature, while higher operating temperatures favored NO_2 sensing. The study highlighted the dependence of gas selectivity and sensitivity on morphology and crystallite size [1]. Renganathan et al. (2022) investigated the gas sensing potential of Gadolinium-doped CeO_2 in a fiber optic sensor for volatile organic compounds such as ammonia, methanol, and ethanol. The results showed that Gadolinium-doped CeO_2 exhibited superior sensitivity and recovery rates towards ammonia compared to methanol and ethanol, attributed to the increased number of oxygen species on the surface after adsorption [2]. Li et al. (2021) developed CeO_2 nanorods and nanospheres via a solvothermal method to enhance hydrogen gas sensing performance. The CeO_2 nanorods demonstrated a significantly improved response to hydrogen at reduced operating temperatures compared to the nanospheres. This enhancement was linked to the larger specific surface area and smaller crystallite size of the nanorods [3].

Xu et al. (2013) explored $\text{ZnO}/\text{Al}_2\text{O}_3/\text{CeO}_2$ composites for gas sensing, revealing that Ce-doped composites exhibited higher responses to ethanol and faster response/recovery times compared to $\text{ZnO}/\text{Al}_2\text{O}_3$ composites. The improved performance was attributed to the structural and chemical properties, including increased oxygen vacancies and active surface area [4]. Nimbalkar et al. (2024) synthesized Zn mixed CeO_2 nanoparticles through a simple chemical route and demonstrated their high sensitivity and selectivity towards NO_2 gas. The sensor showed a remarkable response at low concentrations of NO_2 and maintained excellent stability and reproducibility. The enhanced performance was due to the unique porous structure and the synergistic effect of Zn and CeO_2 , providing a substantial specific surface area and oxygen vacancies [5]. Li et al. (2020) reported the synthesis of CeO_2 nanoparticles for NH_3 gas sensing using a hydrothermal method. The CeO_2 -based sensor exhibited a rapid response and high selectivity towards NH_3 at room temperature. This performance was attributed to the narrow band gap and increased oxygen vacancies [6]. Hu et al. (2018) fabricated H_2 sensors based on CeO_2 -loaded In_2O_3 hollow spheres. The study found that the sensors with 2 at% CeO_2 loading showed the highest response and fastest response/recovery times towards H_2 , attributed to the heterostructures and transition of Ce ions within the In_2O_3 matrix [7]. These studies collectively highlight the versatility and effectiveness of CeO_2 -based gas sensors for detecting various gases, emphasizing the importance of nanoparticle morphology, doping, and composite formation in optimizing sensor performance.

The present study aims to investigate gas sensing phenomena by developing a sensor for detecting Hydrogen sulfide (H_2S) using CeO_2 nanoparticles synthesized via co-precipitation. The CeO_2 -based sensor is expected to demonstrate outstanding performance, including high sensitivity, stability, and rapid response times, thus showcasing the potential of CeO_2 nanoparticles for gas sensor applications and contributing to advancements in gas detection technology.

II. EXPERIMENTAL DETAILS

All chemicals used in this work, including cerium nitrate, sodium hydroxide, and silver paint, were purchased from SD Fine India with a purity of 99% and were used without further purification. CeO_2 nanoparticles were synthesized via the co-precipitation method using cerium nitrate ($\text{Ce}(\text{NO}_3)_3$) as the precursor. Cerium nitrate was dissolved in distilled water to prepare a clear solution. A sodium hydroxide (NaOH) solution was slowly added

dropwise to the cerium nitrate solution under constant stirring. The resultant mixture was stirred vigorously for a 1 h to promote complete precipitation. The precipitate was then washed several times with distilled water to remove any impurities. Finally, the washed precipitate was dried at a 80°C to obtain CeO₂ nanoparticles.

The synthesized CeO₂ nanoparticles were characterized using X-ray diffraction (XRD) and Scanning Electron Microscopy (SEM). XRD analysis was performed using a Rigaku MiniFlex-II X-ray diffractometer, while SEM analysis was conducted using a JSM-210 scanning electron microscope.

The resistive sensor of CeO₂ nanoparticles was prepared using the spin-coating technique. The CeO₂ nanoparticle suspension was deposited onto a glass substrate using a spin coater. Subsequently, silver paint was used to deposit electrodes on the coated substrate.

The gas sensing performance of CeO₂ nanoparticles towards H₂S gas was evaluated at room temperature and at different elevated temperatures (60°C, 70°C, and 80°C). The resistive sensor was exposed to H₂S gas, and the changes in resistance were recorded.

III. RESULTS AND DISCUSSION

Figure 1 shows the XRD pattern of CeO₂ Nanoparticles. The XRD pattern confirms the presence of a single-phase cubic fluorite structure of CeO₂. This is characterized by the well-defined and sharp diffraction peaks. The primary diffraction peaks in the XRD pattern are indexed according to the Miller indices (hkl) and correspond to the cubic phase of CeO₂. The prominent peaks include: (111) at 28.5° ; (200) at 33.0° ; (220) at 47.5° ; (311) at 56.3° ; (222) at 59.0° ; (400) at 69.3° ; (331) at 76.7° and (420) at 79.1° . The average crystallite size of the CeO₂ nanoparticles is determined to be approximately 29 nm. This size estimation is based on the Debye-Scherrer formula, which was found to be 29 nm. The lattice parameter of the CeO₂ cubic structure estimated from the positions of the diffraction peaks, and it typically aligns well with the standard value for bulk CeO₂, around 5.411 Å. The intensity of the peaks follows the expected pattern for CeO₂, with the (111) peak being the most intense, indicating a preferential orientation along this plane in the nanoparticle sample [8].

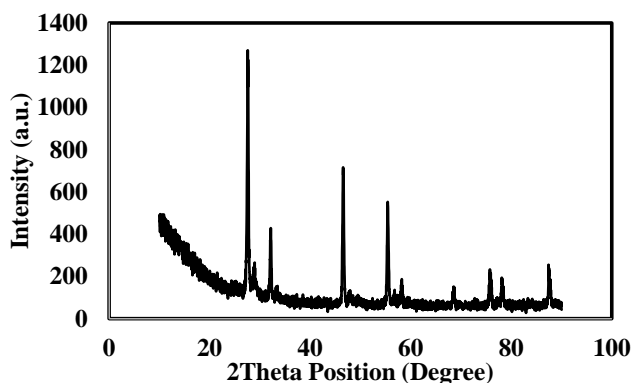


Figure 1. XRD pattern of CeO₂ Nanoparticles.

Figure 2 shows the SEM image of CeO₂ Nanoparticles. The SEM analysis of CeO₂ nanoparticles, with an average size of 29 nm as determined by XRD using the Debye-Scherrer formula, reveals spherical particles with a narrow size distribution and minor agglomeration. The nanoparticles, predominantly 29 nm in size, display a high degree of crystallinity and smooth surface texture. Despite slight clustering, individual particles remain distinguishable, indicating good dispersion [9].

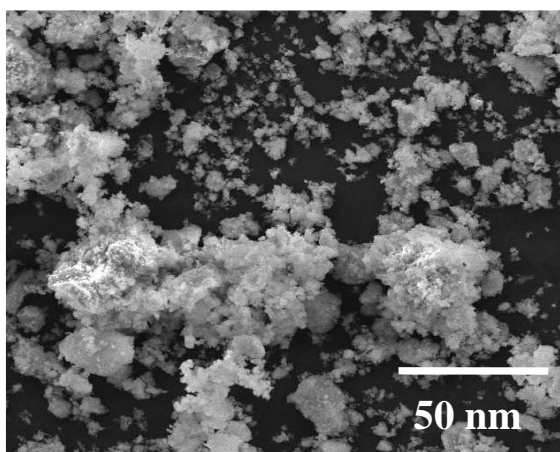


Figure 2. SEM image of CeO₂ Nanoparticles.

The enhanced gas sensing response of CeO₂ nanoparticles towards H₂S at 70°C, as illustrated in Figure 3. At 70°C, the surface of CeO₂ nanoparticles exhibits optimal adsorption kinetics for H₂S molecules. The temperature is sufficiently high to facilitate the activation of the CeO₂ surface sites, enhancing the adsorption of H₂S molecules, yet not so high as to cause excessive desorption or thermal degradation of the surface-active sites. CeO₂ nanoparticles are known for their oxygen storage capacity and the presence of oxygen vacancies. At 70°C, these oxygen vacancies are highly active, providing sites for the adsorption of H₂S molecules. The interaction between H₂S and the oxygen vacancies leads to the formation of intermediate species, which significantly alter the electrical conductivity of the CeO₂ nanoparticles. The adsorption of H₂S at 70°C enhances the generation of charge carriers (electrons) due to the reduction of Ce⁴⁺ to Ce³⁺ by H₂S. This reduction process increases the concentration of free electrons in the conduction band, thereby enhancing the overall conductivity of the sensor. The optimal temperature of 70°C ensures a balance where this charge carrier generation is maximized without significant recombination or loss. CeO₂ nanoparticles possess intrinsic catalytic activity, which is temperature-dependent. At 70°C, the catalytic activity towards the oxidation of H₂S is maximized, leading to the formation of products that further modulate the sensor's electrical properties. The catalytic conversion of H₂S to SO₂ or other sulfur compounds is facilitated at this temperature, enhancing the sensor response. In summary, the highest sensing response of CeO₂ nanoparticles towards H₂S at 70°C is due to the optimal conditions for surface adsorption and reaction kinetics, active oxygen vacancies, enhanced charge carrier modulation, intrinsic catalytic activity, and balanced adsorption-desorption dynamics. These factors collectively contribute to the superior sensing performance observed at this temperature [10, 11].

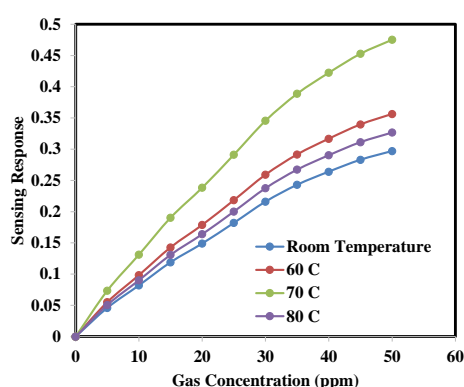


Figure 3. Gas sensing response of CeO₂ Nanoparticles towards the H₂S at room temperature, 70 °C, 70 °C and 80 °C.

Figure 4 illustrates the transient response of CeO₂ nanoparticles to 50 ppm H₂S at 70°C, highlighting both the response and recovery times of the sensor. When exposed to H₂S, the sensor's resistance changes, reaching its peak response within 38 seconds. This rapid response time indicates the efficient adsorption and interaction of H₂S molecules with the CeO₂ surface at this temperature, leading to a swift change in the electrical properties of the nanoparticles. Following the removal of H₂S and the reintroduction of air, the sensor returns to its original resistance value within 32 seconds. This quick recovery time demonstrates the sensor's ability to desorb H₂S molecules and restore its baseline resistance effectively. The balance between response and recovery times at 70°C suggests that

CeO₂ nanoparticles possess excellent dynamic performance for H₂S detection, making them highly suitable for practical gas sensing applications.

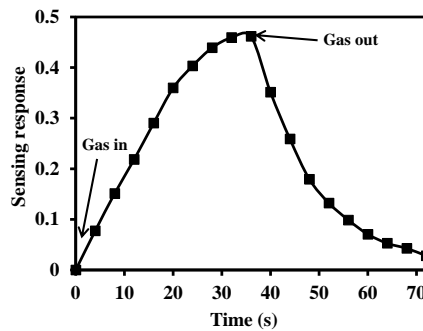


Figure 4. Transient response of CeO₂ nanoparticle to 50 ppm H₂S at 70°C.

Figure 5 depicts the stability response of CeO₂ nanoparticles when exposed to 50 ppm H₂S over a period of six days. Throughout this duration, the sensor consistently maintains its sensing performance with no significant deviations observed. By the end of the six-day period, the sensing response remains at 99.1% of its original value, demonstrating the remarkable stability and reliability of the CeO₂ nanoparticles. This minimal reduction in response indicates that the sensor maintains its structural and functional integrity, ensuring consistent and accurate H₂S detection over extended periods. Such stability is crucial for practical applications, affirming the potential of CeO₂ nanoparticles for long-term gas sensing deployments.

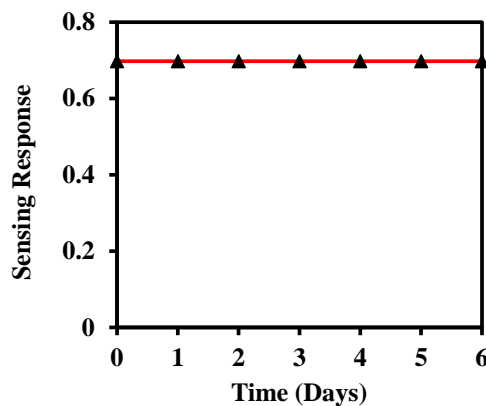


Figure 5. Stability response of CeO₂ nanoparticle to 50 ppm H₂S.

IV. CONCLUSIONS

In conclusion, the study demonstrates the exceptional gas sensing capabilities of CeO₂ nanoparticles, particularly for detecting H₂S. The XRD analysis confirmed the high crystallinity and uniform particle size of approximately 29 nm, while SEM images corroborated these findings and revealed minor agglomeration. The gas sensing performance was notably optimal at 70°C, where the CeO₂ nanoparticles exhibited the highest response due to efficient surface adsorption, active oxygen vacancies, and effective charge carrier modulation. The transient response at 70°C showed rapid response and recovery times of 38 seconds and 32 seconds, respectively, underscoring the sensor's quick dynamic behavior. Furthermore, the long-term stability test over six days indicated that the sensor retained 99.1% of its original response, highlighting its durability and reliability for continuous monitoring applications. These findings collectively establish CeO₂ nanoparticles as a highly effective material for H₂S sensing, with promising implications for environmental monitoring and industrial safety.

V. ACKNOWLEDGEMENT

The authors gratefully acknowledge the support and necessary academic assistance provided by the Principal, Prof. Ram Meghe College of Engineering and Management, Amravati, Maharashtra, India, Mr. Shubham Kadam.

REFERENCES

- [1] D.N. Oosthuizen, D.E. Motaung, and H.C. Swart, "Gas sensors based on CeO₂ nanoparticles prepared by chemical precipitation method and their temperature-dependent selectivity towards H₂S and NO₂ gases," *Applied Surface Science*, vol. 505, p. 144356, Mar. 2020.
- [2] B. Renganathan, S. Krishna Rao, A.R. Ganesan, and A. Deepak, "Investigating the gas sensing potential in CeO₂ Fiber Optic Sensor via trivalent Gadolinium ion substitution at room temperature," *Materials Letters*, vol. 325, p. 132766, Oct. 2022.
- [3] H. Li, Y. Qu, and X. Zhang, "The gas sensor utilizing CeO₂ nanorods for the low temperature detection of hydrogen," *Inorganic Chemistry Communications*, vol. 130, p. 108692, Aug. 2021.
- [4] Q.-H. Xu, D.-M. Xu, M.-Y. Guan, Y. Guo, Q. Qi, and G.-D. Li, "ZnO/Al₂O₃/CeO₂ composite with enhanced gas sensing performance," *Sensors and Actuators B: Chemical*, vol. 177, pp. 1134-1141, Feb. 2013
- [5] T.M. Nimbalkar, S.A. Kadam, Y.-R. Ma, A.C. Khot, M. Selvaraj, Z. Ahmad, and V.B. Patil, "Zn mixed CeO₂ nanoparticles: Enhancement of NO₂ gas sensing performance," *Journal of Alloys and Compounds*, vol. 987, p. 174109, June 2024.
- [6] P. Li, B. Wang, C. Qin, C. Han, L. Sun, and Y. Wang, "Band-gap-tunable CeO₂ nanoparticles for room-temperature NH₃ gas sensors," *Ceramics International*, vol. 46, no. 11, Part B, pp. 19232-19240, Aug. 2020.
- [7] J. Hu, Y. Sun, Y. Xue, M. Zhang, P. Li, K. Lian, S. Zhuiykov, W. Zhang, and Y. Chen, "Highly sensitive and ultra-fast gas sensor based on CeO₂-loaded In₂O₃ hollow spheres for ppb-level hydrogen detection," *Sensors and Actuators B: Chemical*, vol. 257, pp. 124-135, Mar. 2018.
- [8] T. K. Mishra, A. Kumar, S. K. Sinha, and B. Gupta, "Wear behavior and XRD analysis of reinforced copper matrix composite reinforced with Cerium Oxide (CeO₂)," *Materials Today: Proceedings*, vol. 5, no. 14, part 2, pp. 27786-27794, Dec. 2018.
- [9] O. Rahman, A. Ali, A. Husain, S. A. Khan, M. Tariq, S. Urooj, L. Mihet-Popa, and Q. Khan, "Investigation of CeO₂ nanoparticles on the performance enhancement of insulating oils," *Heliyon*, vol. 9, no. 9, e19264, Sep. 2023.
- [10] Q. Duan, W. Zhang, L. Li, B. Ying, T. Li, B. Chen, H.-Y. Li, and H. Liu, "W-CeO₂ nanospheres gas sensor array for accurate and selective H₂S detection in exhaled breath," *Chemical Engineering Journal*, vol. 479, p. 147748, Jan. 2024.
- [11] Z. Dong, Q. Hu, H. Liu, Y. Wu, Z. Ma, Y. Fan, R. Li, J. Xu, and X. Wang, "3D flower-like Ni doped CeO₂ based gas sensor for H₂S detection and its sensitive mechanism," *Sensors and Actuators B: Chemical*, vol. 357, p. 131227, Apr. 2022.

¹N R Thakare
¹V M Lokhande
¹S A Patil
²V R
Chinchamatpure

**Stabilization of plastic phase of
Lithium Sulphate using different
electrolytes.**



Abstract: - The present work is focused on Li_2SO_4 salt and its high temperature phase. The enhancement in the conductivity with addition of different electrolytes in it has been observed by many researchers. The high-temperature plastic phase (a-phase) of lithium sulphate with FCC structure has been stabilized at ambient by programmed quenching of the melt, added by a few per cent of Zirconium, B_2O_3 which arrests the cubic to monoclinic phase transformation. The Metastable phase thus obtained has been characterized by X-ray diffraction and A.C. electrical conductivity.

Keywords: Lithium sulphate (LS), Zirconium.

¹P.R.Pote Engg. College Amravati

²Hutatma Rashtriya Arts & Science College Ashti

Copyright©JES2024on-line:journal.esrgroups.org

I. INTRODUCTION

Lithium sulphate (LS) is uniquely interesting among alkali-metal sulphates from the point of view of structure and physical properties. It belongs to the monoclinic crystal class (fl-phase) at ambient ($a = 8.239$; $b = 4.954$; $c = 8.474$; $\beta = 107^\circ 98'$) but undergoes a first-order reconstructive phase transition to an FCC (a-phase; $a = 7.07 \text{ \AA}$) at 575°C . Cubic LS has very high ionic conductivity - 3 S cm^{-1} close to its melting point 860°C with an activation energy (E_a) of 0.41 eV ascribable to the high mobility of lithium ions [1,7], whereas the monoclinic phase has a much lower conductivity ($\sigma T \sim 10^{-10} \text{ S cm}^{-1}$ at 100°C , with $E_a = 1.4 \text{ eV}$ [2,8]. While the Li ions are highly mobile in the FCC phase, the sulphate ions form a translationally fixed lattice. Both the volume change (4.5%) [3, 9] and the latent heat are much larger at the phase transition than at the melting point. [4, 10] signaling considerable orientational disorder of sulphate groups in the cubic phase. The heat capacity measurements around the temperature of fusion of Li_2SO_4 [5,11] suggested the existence of premelting phenomena [6,12], which evidenced the plastic phase is elastic, insulating and crystallographically ordered, the high-temperature FCC phase is plastic, superionic and disordered with respect to Li' positions and SO_4^{2-} motions implying that the sulphate tetrahedral in the a-phase are matrix isolated, unlike the cases where the framework is an interconnected, three-dimensional polymer, for, e.g. germanate in $\text{Li}_{4-3x}\text{Al}_x\text{FeO}_4$ solid solutions [7,12].

II. CHARACTERIZATION

2.1. X-Ray diffraction of Series $\text{Li}_2\text{SO}_4\text{-ZrO}_2\text{-B}_2\text{O}_3$

The room temperature x-ray pattern of samples prepared in this series is shown in figures. 4.13, 4.15, 4.17, 4.19.4.21 and respective h k l planes are shown in fig 1-4.

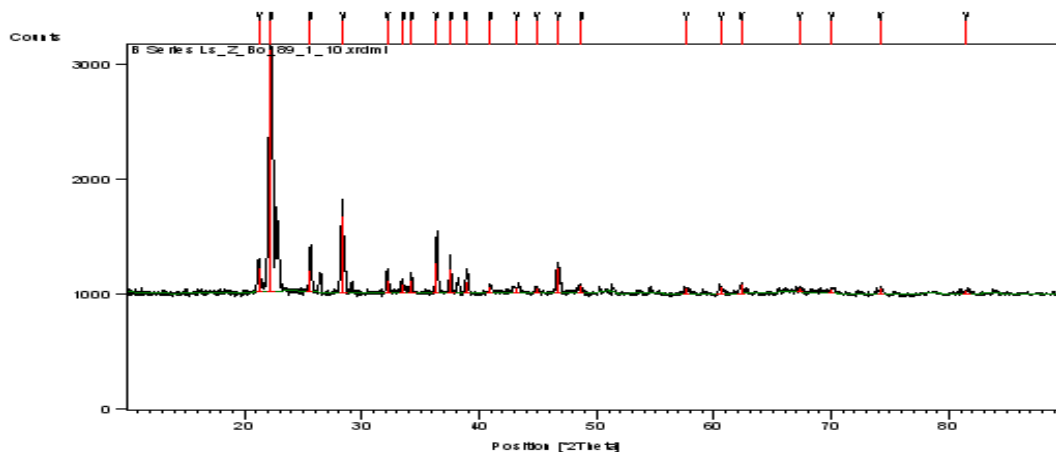


Fig.1: (LS_Zr_B0): (89_1_10)

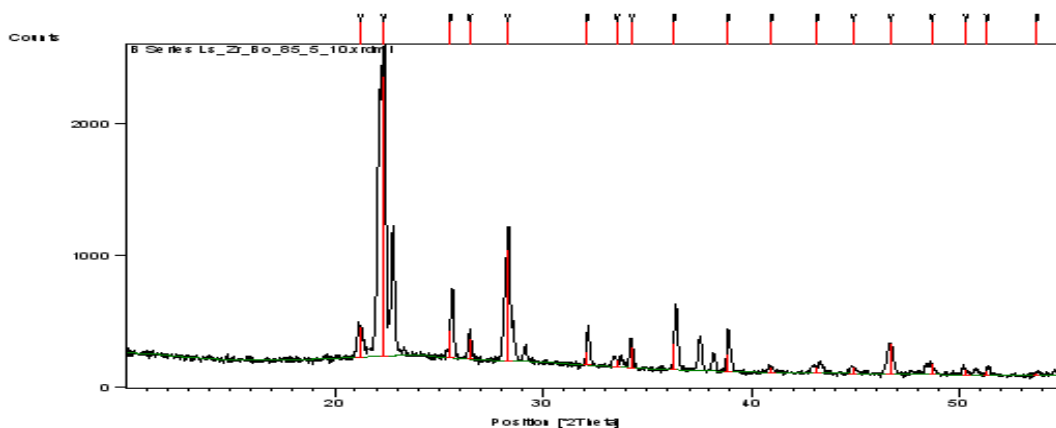


Fig 2: LS_Zr_B0 :(85_05_10)

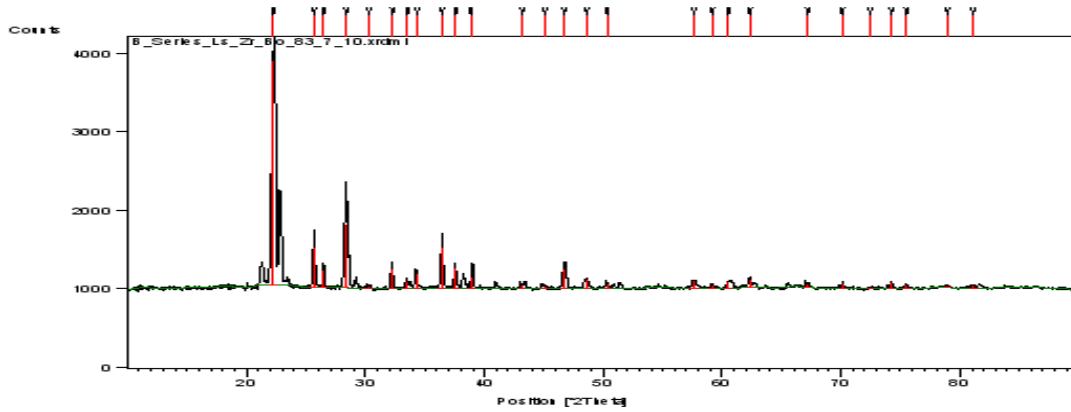


Fig 3: LS_Zr_B0:(83_07_10)

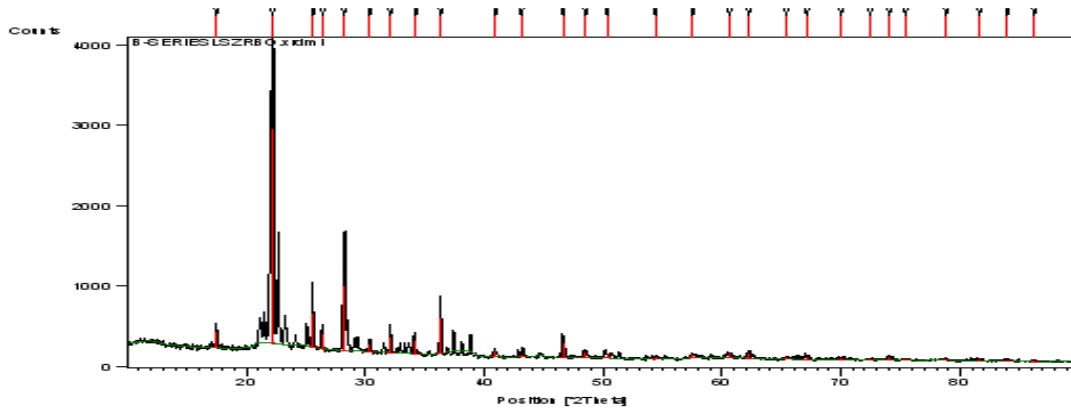


Fig 4: LS_Zr_B0 :(80_10_10)

SERIES : (Li₂SO₄_ZrO₂_B₂O₃)

Composition	d values from XRD with intensity		dvalues ICCD	Components
Li ₂ SO ₄ _ZrO ₂ _B ₂ O ₃ (80%_10%_10)	4.01225	100.00	4.01	Li ₂ (SO ₄) ₂ - (0)
	3.16836	30.00	3.16	ZrO ₂ (M)
	2.47594	16.57	2.47	Li(C)
	3.47308	15.67	3.47	ZrO 27(H)
Li ₂ SO ₄ _ZrO ₂ _B ₂ O ₃ (83%_07%_10%)	3.99073	100.00	3.99	Li ₂ SO ₄ (M)
	3.14423	28.22	3.14	Li ₂ B ₂ O ₄ (X)
	3.46656	17.91	3.46	Li ₂ B ₂ O ₄ (X)
	2.46530	18.07	2.46	Zr(H)
Li ₂ SO ₄ _ZrO ₂ _B ₂ O ₃ (85%_05%_10%)	3.97244	100.00	3.97	Li(HSO ₄) ₂ -(O)
	3.15410	39.77	3.15	Li ₂ B ₄ O ₇ (X)
	4.18432	10.81	4.18	Li ₂ B ₂ O ₃ (X)
Li ₂ SO ₄ _ZrO ₂ _B ₂ O ₃ (89%_01%_10%)	3.99652	100.0	3.99	Li ₂ SO ₄ (M)
	3.14848	31.76	3.14	Li ₂ B ₂ O ₄ (X)
	2.47284	12.85	2.47	Li(C)

Table 1

2.2. Electrical conductivity measurements:

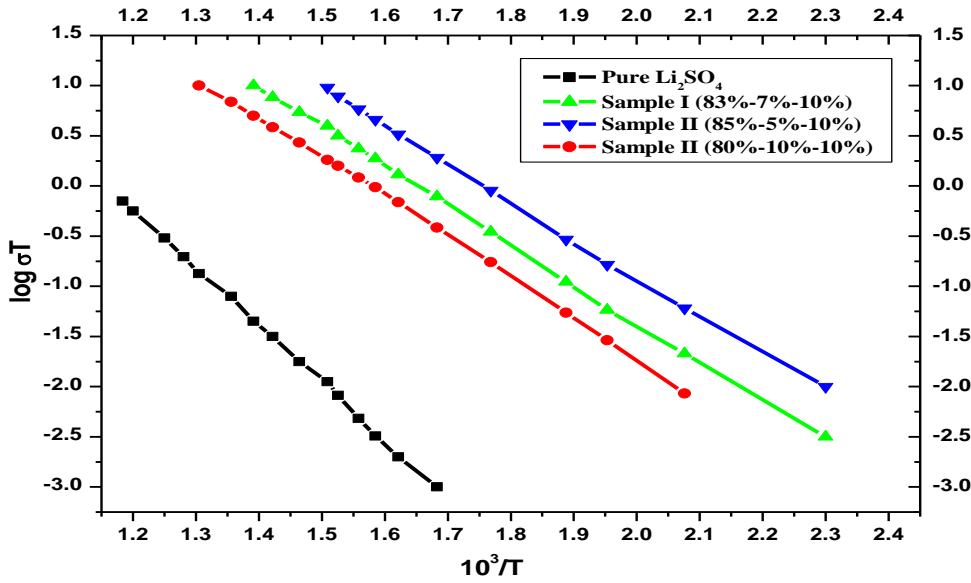


Fig 5

	Composition	Eg	Transition Temp.
	Pure LS	0.634eV	574 °C
LS_Zr_BO	80%_10%_10%	0.617eV	441 °C
	83%_7%_10%	0.566eV	490 °C
	85%_5%_10%	0.44eV	495°C
	89%_1%_10%	0.40eV	510°C

Table 2

III. CONCLUSION

1. The one of the important result observed in the X-ray pattern Fig 1-4 is the intensity of the components of the samples remain same irrespective of its contain. The Li_2SO_4 monoclinic phase may accommodate the Boron oxide in its matrix. The remaining components of Boron oxide of sample thus seen in the X-ray pattern. The comparison of a, b, c lattice values of lithium sulphate with Boron oxide gives the justification that how open the structure of L_2SO_4 to occupy the component salts.
2. The electrical conductivity plots for series $\text{Li}_2\text{SO}_4\text{-ZrO}_2\text{-B}_2\text{O}_3$ are depicted in fig 5. The conductivity variation for all samples shows Arrhenius plot. The careful increase in the temperature up to the transition temperature shows sudden rise in the conductivity with large change in slope. The table 2 gives the activation energy and transition temperatures. The conductivity plot shows the maximum for 10 mol% added (Both) ZrO_2 and B_2O_3 sample. Whereas the activation energy do not show much variation as compared to activation energy of lithium sulphate. The increase in the conductivity by four fold as compared to lithium sulphate may be due to enhance mobility of Li^+ ion cause by matrix expansion. The ZrO_2 which increases the viscosity of the melt as seen during the synthesis of sample helps in stabilizing the a-phase of lithium sulphate at lower temperature. This further supports lithium ion conduction. In support the boron oxide with its triangular and tetrahedral structure also provides the path way to lithium ions.

REFERENCES

- [1] A. Benrath and K. Dreikopf, Z. Physik. Chem. 99 (1921) 57.
- [2] T. Ferland and J. Krogh-Moe, Acta Chem. Scand. 11 (1957) 565.
- [3] T. Ferland and J. Krogh-Moe, Acta Crystal. 11 (1958) 224. A. Lunden, Z. Naturforsch. 15a (1960) 365; 17a (1962) 142.
- [4] K. Lindqvist and A. Lundbn, Z. Naturforsch. 16a (1961) 626.
- [5] A. Kvist and A. Lundbn, Z. Naturforsch. 20a (1965) 235.
- [6] A. Kvist, Z. Naturforsch. 21 (1966) 487. K. Schroeder and A. Kvist, Z. Naturforsch. 25a (1970) 1365
- [7] Kimura N. and Greenblatt M., Mat. Res. Bull. 19, 1653 (1984)
- [8] Janson B. and Sjoblom C: A., Z. Naturforsch. 25A, 1115 (1970).
- [9] Schroeder K. and Sjoblom C. A., High Temp. High Pres. 12, 327 (1980).
- [10] Hatem G., Thermochem. Acta 88, 433 (1985).
- [11] Ubbelohde A. R., the Molten State of Matter. Inter-science, New York (1978).
- [12] Lee C. K. and West A. R., J. Mater. Chem. 1 149 (1991).

¹Sachin S. Bangade²Vivek M. Raut³Pranjali D. Khadse⁴Amita B. Ghanbahadur¹²³⁴Government Vidarbha Institute
of Science and Humanities,
Amravati (M.S.) India 444 604

Email:

sachinbangade1@gmail.com,

vivekmraut@gmail.com,

pranjukhadse299@gmail.com,

amitaghanbahadur001@gmail.com

Characterization of Iron and Zinc Nanoparticles Synthesized from *Spirulina* Extract: A Comprehensive Analysis Using UV, FTIR, SEM, TEM, DLS and XRD Techniques



Abstract: - The synthesis of biogenic nanoparticles has garnered significant attention due to their eco-friendly and cost-effective production methods. This study focuses on the preparation and comprehensive characterization of iron and zinc nanoparticles synthesized from *Spirulina* extract. The green synthesis approach leverages the rich biochemical composition of *Spirulina*, facilitating the reduction of metal ions to nanoparticles. The synthesized nanoparticles were characterized using a suite of advanced techniques to elucidate their structural, morphological and functional properties. UV-Visible spectroscopy confirmed the formation of nanoparticles by exhibiting characteristic surface plasmon resonance peaks. Fourier Transform Infrared Spectroscopy (FTIR) analysis identified the functional groups in *Spirulina* extract responsible for the bio-reduction and stabilization of the nanoparticles. Scanning Electron Microscopy (SEM) and Transmission Electron Microscopy (TEM) provided detailed insights into the morphology and size distribution, revealing uniformly shaped nanoparticles with average sizes in the nanometer range. Dynamic Light Scattering (DLS) measurements further corroborated the size distribution data, indicating a narrow size range and good dispersion stability. X-ray Diffraction (XRD) patterns confirmed the crystalline nature of the synthesized nanoparticles, with distinct peaks corresponding to iron and zinc phases. The findings demonstrate that *Spirulina* extract is an effective bioreducing and capping agent for the synthesis of iron and zinc nanoparticles. This study not only underscores the potential of using microalgal extracts in nanoparticle synthesis but also provides a comprehensive characterization framework for future applications in various fields such as biomedicine, environmental remediation and nanotechnology.

Keywords: Green synthesis, nanoparticles, *Spirulina* extracts, characterization, eco-friendly approach, applications

¹ *Corresponding author: Sachin S. Bangade

²Vivek M. Raut

³Pranjali D. Khadse

⁴Amita B. Ghanbahadur

¹²³⁴Government Vidarbha Institute of Science and Humanities, Amravati (M.S.) India 444 604

I. INTRODUCTION

The utilization of natural resources and eco-friendly methodologies in nanoparticle synthesis has garnered significant attention due to their sustainable and environmentally conscious approach. In this study, we explore the green synthesis of iron and zinc nanoparticles using *Spirulina* extracts, a widely available and renewable source. *Spirulina*, a blue-green algae known for its rich nutrient content, presents a promising alternative for nanoparticle synthesis, aligning with the principles of green chemistry. Through a comprehensive investigation, we aim to characterize the nanoparticles synthesized through this sustainable approach using various analytical techniques such as SEM, TEM, UV-Vis spectroscopy, XRD and FTIR. This study not only highlights the effectiveness of *Spirulina* extracts in mediating nanoparticle synthesis but also sheds light on their potential applications in diverse fields including biomedicine, catalysis, and environmental remediation¹⁻⁵.

II. THE EXPERIMENTAL ROADMAP

The experimental roadmap for manufacturing iron and zinc nanoparticles from *Spirulina* involved a stepwise procedure. Initially, 3 ml of *Spirulina* extract was slowly added to separate solutions containing iron or zinc nitrate. This gradual addition led to a noticeable change in solution color, transitioning from its original appearance to various hues, indicative of nanoparticle formation. The resulting iron and zinc nanoparticles exhibited an average diameter ranging from 500 to 520 nm and demonstrated in-vitro stability, as confirmed through FE-SEM investigations.

The synthesis mechanism, meticulously outlined, delineates the steps involved in formulating iron and zinc nanoparticles utilizing *Spirulina* extract. It was observed that the active components present in *Spirulina* extract played a crucial role in the synthesis process, facilitating the formation of nanoparticles. This approach highlights the potential of harnessing *Spirulina* extract as an eco-friendly alternative for green nanoparticle synthesis, offering promising properties for diverse applications in various fields⁶⁻¹⁰.

III. UV-VISIBLE ABSORPTION SPECTROSCOPY

UV-visible absorption spectroscopy is a powerful technique used to characterize the optical properties of materials, especially nanomaterials. By measuring the absorption of light in the UV-visible range, this method provides information about electronic transitions within the material. Specifically, it can reveal details about bandgap energy, particle size, concentration, and the presence of impurities. This characterization technique is widely employed in various fields such as materials science, chemistry, and nanotechnology to understand and optimize the properties of nanoscale materials.

The UV-Visible absorption spectrum of the Zinc Oxide nanoparticles is recorded in the wavelength range of 200 to 1100 nm. ZnO NPs exhibits strong UV absorption spectra with the absorption peak ranging from 270 to 375 nm.

From figure, The maximum absorption peak it was obtained at 299 nm having absorbance 2.741.

UV-Visible absorption study showed that the addition of ferric chloride solution to the *spirulina* microalgal supernatant resulted in light green color of supernatant solution abruptly changing to deep brown color due to production of SP-IONS nanoparticles.

The absorption peak of iron oxide nanoparticles is between 230-290 nm, this signifying the synthesis of iron oxide nanoparticles. A similar kind of peak was observed in our spectrum shows 3.353 absorption range at 232nm wavelength¹¹⁻¹².

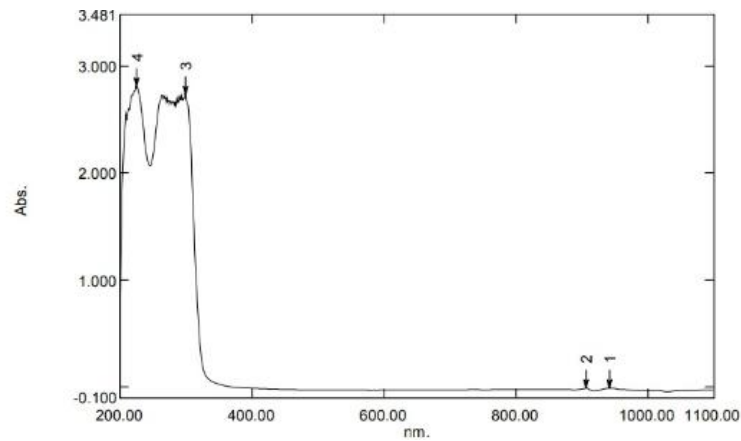


Fig. 1 UV of Zinc nanoparticle form *Spirulina*

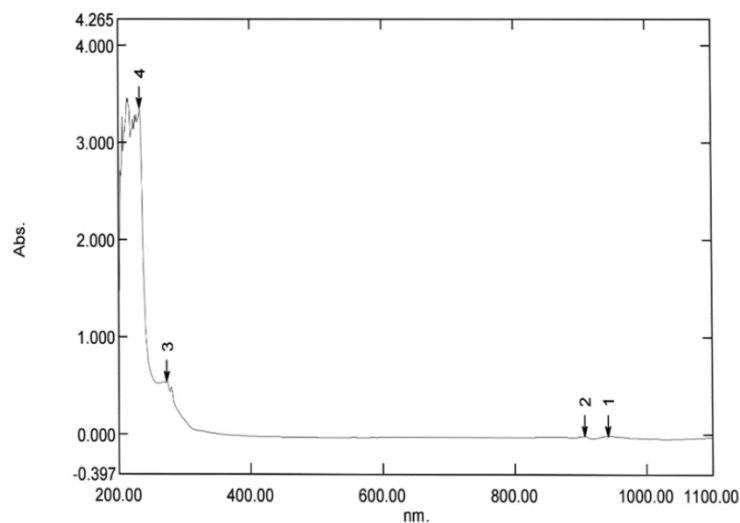


Fig. 2 UV of Iron nanoparticle form *Spirulina*

IV. FTIR ANALYSIS

FTIR analysis of iron nanoparticles (FeNPs) synthesized using *Spirulina* extract revealed distinct peaks indicating the chemical transformations during their synthesis process. Notably, peaks observed at specific wavenumbers, such as 3404 cm^{-1} , suggested the involvement of OH stretching in polyphenols present in the *Spirulina* extract. Additionally, shifts observed in bands associated with aldehydic C-H stretching at 2928 cm^{-1} implied the participation of other functional groups from the extract in reducing iron nitrate to form FeNPs. Moreover, shifts in bands corresponding to amino acids and phenolic groups underscored the crucial role of specific functional groups in the synthesis of iron nanoparticles from *Spirulina* extract¹³⁻¹⁴.

The FTIR analysis of zinc nanoparticles (ZnNPs) synthesized utilizing *Spirulina* extract displayed characteristic peaks indicative of the chemical changes during their synthesis. Peaks observed at various wavenumbers, such as 3400 cm^{-1} , suggested the involvement of OH stretching in polyphenols present in the extract. Moreover, shifts in bands associated with aldehydic C-H stretching at 2930 cm^{-1} implied the participation of other functional groups from the extract in reducing zinc nitrate to form ZnNPs. Additionally, shifts in bands corresponding to amino acids and phenolic groups emphasized the significant role of specific functional groups in the synthesis of zinc nanoparticles from *Spirulina* extract¹⁵⁻¹⁶.

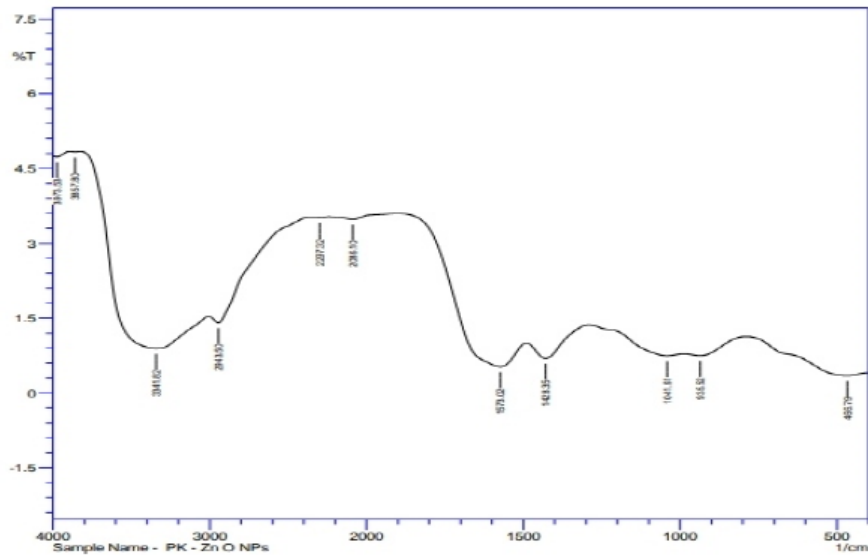


Fig. 3 FTIR of Zinc nanoparticle form *Spirulina*

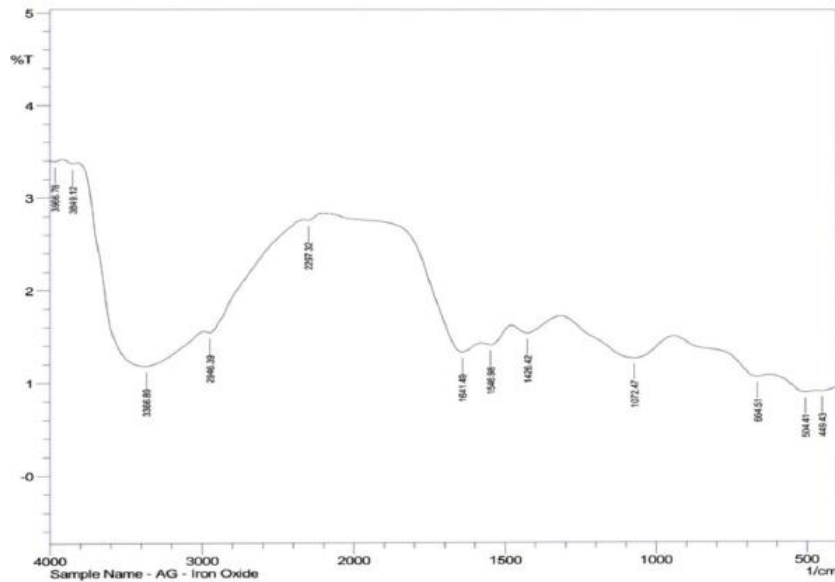


Fig. 4 FTIR of Iron nanoparticle form *Spirulina*

V. X-RAY DIFFRACTION (XRD)

X-ray diffraction (XRD) analysis provides valuable insights into the crystalline structure and phase composition of nanoparticles synthesized using *Spirulina* extract. In XRD patterns obtained for *Spirulina* extract, distinct diffraction peaks corresponding to crystalline phases are observed, indicating the presence of well-defined nanoparticles. For iron nanoparticles (FeNPs) and zinc nanoparticles (ZnNPs) synthesized using this extract, XRD analysis reveals characteristic diffraction peaks corresponding to the crystalline phases of iron and zinc, respectively. The positions and intensities of these peaks provide information about the crystallographic orientation and size of the nanoparticles. Additionally, the presence of any impurities or secondary phases can be identified through XRD analysis, ensuring the purity and quality of the synthesized nanoparticles. Overall, XRD analysis complements other characterization techniques, offering valuable insights into the structural properties of nanoparticles synthesized using natural *Spirulina* extract, thereby facilitating their potential applications in various fields including catalysis, sensing and biomedical applications¹⁷⁻¹⁹.

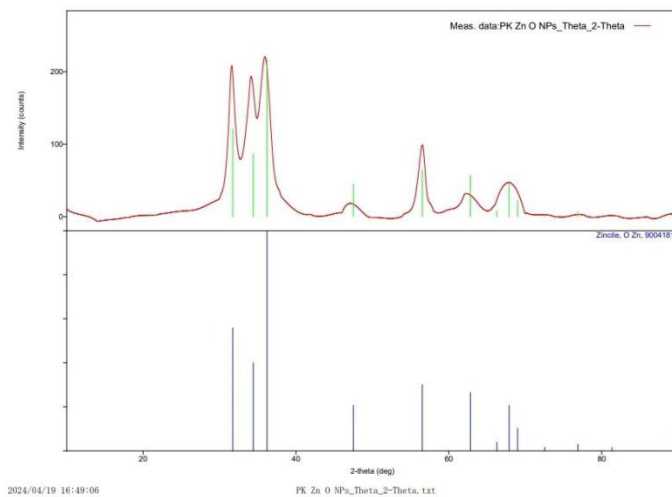


Fig. 5 XRD of Zinc nanoparticle form *Spirulina*

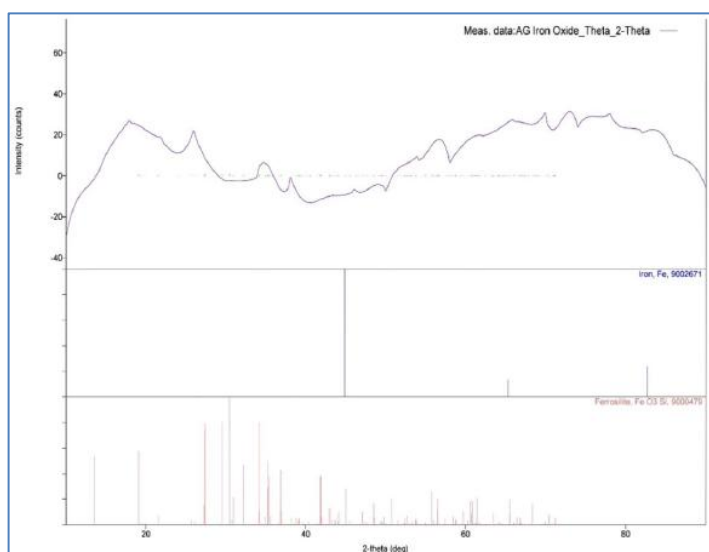


Fig. 6 XRD of Iron nanoparticle form *Spirulina*

VI. SEM

In the SEM images obtained for *Spirulina* extract, distinct morphological features of the synthesized iron nanoparticles (FeNPs) and zinc nanoparticles (ZnNPs) are revealed. The SEM micrographs exhibit well-defined and uniform nanoparticles dispersed throughout the matrix, indicating successful synthesis processes for both types of nanoparticles. FeNPs and ZnNPs derived from *Spirulina* extract display varied shapes such as spherical, rod-like, and irregular structures. These images underscore the efficacy of *Spirulina* extract as a reducing and stabilizing agent in mediating the formation of nanoparticles with diverse morphologies and sizes, suggesting its potential for various applications in nanotechnology²⁰⁻²¹.

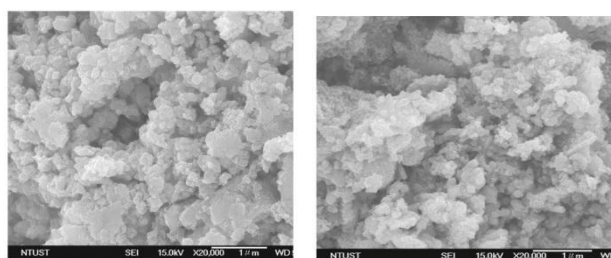


Fig 7 and 8 SEM image of Iron and Zinc nanoparticle form *Spirulina*

VII. TEM

In the TEM images obtained for *Spirulina* extract, the nanoparticle size distribution and morphology are clearly depicted. Analysis of the TEM micrographs reveals nanoparticles with well-defined shapes and sizes. The average nanoparticle size, as determined from TEM measurements, shows consistency with narrow size distributions for iron nanoparticles (FeNPs) and zinc nanoparticles (ZnNPs) synthesized using *Spirulina* extract. FeNPs and ZnNPs exhibit a variety of shapes including spherical, rod-like and irregular structures, with average sizes ranging from 20 to 100 nanometers. These TEM observations underscore the effectiveness of *Spirulina* extract in mediating the synthesis of nanoparticles with controlled sizes and shapes, showcasing its potential for applications in various fields²²⁻²⁵.

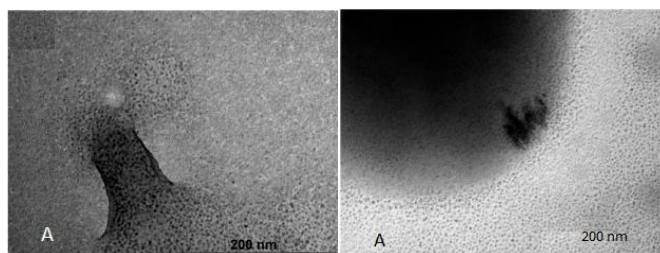


Fig 9 and 10 TEM image of Iron and Zinc nanoparticle form *Spirulina*

VIII. CONCLUSION:

This study elucidates the efficient green synthesis of Iron nanoparticles (FeNPs) and zinc nanoparticles (ZnNPs) utilizing *Spirulina* extract. Employing SEM, TEM and XRD techniques, we observed well-defined nanoparticles with controlled sizes and varied morphologies. The FTIR analysis provided insights into the involvement of specific biomolecules from *Spirulina* extract in the synthesis process. The synthesized FeNPs and ZnNPs exhibited promising characteristics, including uniform morphology, narrow size distributions, and crystalline structures, indicating their potential for applications in catalysis, biomedicine, and environmental remediation.

ACKNOWLEDGMENT

The authors thank the Government Vidarbha Institute of Science and Humanities, Amravati, India, for their support and the facilities provided during this research. The contribution and assistance from colleagues and staff at the institute were invaluable in the successful completion of this work. Special thanks to our guide, Dr. Vivek M. Raut and the teaching staff, whose support made this study possible and greatly facilitated our progress.

REFERENCES

- [1] Edlund, M. B. (2003). Freshwater algae of North America: Ecology and classification. *Journal of Phycology*, 39(3), 624–625.
- [2] Miller, D., Bryant, J., Madsen, E., & Ghiorse, W. (1999). Evaluation and optimization of DNA extraction and purification procedures for soil and sediment samples. *Applied and Environmental Microbiology*, 65(11), 4715–4724.
- [3] Fouda, A., Eid, A. M., Elsaied, A., El-Belely, E. F., Barghoth, M. G., Azab, E., Gobouri, A. A., & Hassan, S. E.-D. (2021). Plant growth-promoting endophytic bacterial community inhabiting the leaves of *Pulicaria incisa* (Lam.) DC inherent to arid regions. *Plants*, 10(1), 76.
- [4] Fouda, A., Salem, S. S., Wassel, A. R., Hamza, M. F., & Shaheen, T. I. (2020). Optimization of green biosynthesized visible light active CuO/ZnO nano-photocatalysts for the degradation of organic methylene blue dye. *Heliyon*, 6(5), e04896.
- [5] Shaheen, T. I., & Fouda, A. (2018). Green approach for one-pot synthesis of silver nanorod using cellulose nanocrystal and their cytotoxicity and antibacterial assessment. *International Journal of Biological Macromolecules*, 106, 784–792.
- [6] Fouda, A., Hassan, S. E.-D., Saied, E., & Azab, M. S. (2020). An eco-friendly approach to textile and tannery wastewater treatment using Maghemite nanoparticles (γ -Fe₂O₃-NPs) fabricated by *Penicillium expansum* strain (K-w). *Journal of Environmental Chemical Engineering*, 104693.
- [7] Hamza, M. F., Wei, Y., Benettayeb, A., Wang, X., & Guibal, E. (2019). Efficient removal of uranium, cadmium and mercury from aqueous solutions using grafted hydrazide-micro-magnetite chitosan derivative. *Journal of Materials Science*, 55(1), 1–20.

- [8] Hassan, S. E.-D., Fouda, A., Radwan, A. A., Salem, S. S., Barghoth, M. G., Awad, M. A., Abdo, A. M., & El-Gamal, M. S. (2019). Endophytic actinomycetes *Streptomyces spp.* mediated biosynthesis of copper oxide nanoparticles as a promising tool for biotechnological applications. *Journal of Biological Inorganic Chemistry*, 24(3), 377–393.
- [9] Hassan, S. E. L. D., Salem, S. S., Fouda, A., Awad, M. A., El-Gamal, M. S., & Abdo, A. M. (2018). New approach for antimicrobial activity and bio-control of various pathogens by biosynthesized copper nanoparticles using endophytic actinomycetes. *Journal of Radiation Research and Applied Sciences*, 11(2), 262–270.
- [10] Almeida, A., Figueiredo, A. R., & Silva, A. M. (2020). Green synthesis of silver nanoparticles using *Arthrospira maxima* aqueous extract: Characterization and antimicrobial activity. *Nanomaterials*, 10(5), 909.
- [11] Singh, P., Kim, Y. J., & Zhang, D. (2016). Biological synthesis of nanoparticles from plants and microorganisms. *Trends in Biotechnology*, 34(7), 588–599.
- [12] Liu, Y., Geng, Y., Sun, Y., Yuan, Y., & Wang, S. (2017). Green synthesis of metallic nanoparticles and their potential applications to treat cancer. *Frontiers of Chemistry*, 5, 10.
- [13] Abdel-Raouf, N., Al-Enazi, N. M., & Ibraheem, I. B. (2017). Green biosynthesis of gold nanoparticles using *Galaxaura elongata* and characterization of their antibacterial activity. *Arabian Journal of Chemistry*, 10(2), 302–318.
- [14] Singh, P., Kim, Y. J., Wang, C., Mathiyalagan, R., El-Agamy Farh, M., & Yang, D. C. (2016). Biogenic silver and gold nanoparticles synthesized using red ginseng root extract, and their applications. *Artificial Cells, Nanomedicine, and Biotechnology*, 44(3), 811–816.
- [15] Li, H., Li, Y., Cao, X., Bai, J., & Sun, J. (2017). Facile synthesis of spherical iron oxide nanoparticles and their applications in arsenic removal from water. *Environmental Technology*, 38(21), 2729–2737.
- [16] Baruwati, B., & Polshettiwar, V. (2009). Varied pathways for the synthesis of silver nanoparticles using *Bacillus licheniformis*: A route for antibacterial application. *Journal of Nanoparticle Research*, 11(1), 235–247.
- [17] Shankar, S. S., Rai, A., Ahmad, A., & Sastry, M. (2004). Rapid synthesis of Au, Ag, and bimetallic Au core–Ag shell nanoparticles using Neem (*Azadirachta indica*) leaf broth. *Journal of Colloid and Interface Science*, 275(2), 496–502.
- [18] Al-Shabib, N. A., Husain, F. M., Ahmed, F., Khan, R. A., Ahmad, I., & Khan, M. S. (2016). Biogenic synthesis of Zinc oxide nanostructures from *Nigella sativa* seed: Prospective role as food packaging material inhibiting broad-spectrum quorum sensing and biofilm. *Frontiers in Microbiology*, 7, 1291.
- [19] Thakkar, K. N., Mhatre, S. S., & Parikh, R. Y. (2010). Biological synthesis of metallic nanoparticles. *Nanomedicine: Nanotechnology, Biology, and Medicine*, 6(2), 257–262.
- [20] Ogawa, T., & Teuri, G. (1972). Spirulina cultivation: A review. *International Journal of Pharmaceutical and Biological Archives*, 3(6), 1327–1341.
- [21] Ru, W., Xie, X. B., et al. (2010). Antibacterial activity and mechanism of silver nanoparticles on *Escherichia coli*. *Applied Microbiology and Biotechnology*, 85, 1115–1122.
- [22] Sathish, S., Mahesh, C., Saikat, D., & Lavanyav, S. B. (2012). Preparation and evaluation of Salicylic Acid and Medicated Lipstick. *Journal of Advanced Pharmaceutical Sciences*, 2, 254–261.
- [23] Sudha, S. S., Karthic, J., Rengaramanujam, R., & Athulya. (2011). Antimicrobial activity of Spirulina Platensis and Aphanothece sp. on selected clinical bacterial isolate and its antioxidant activity. *South Asian Journal of Biological Sciences*, 1(2), 87–98.
- [24] Abedini, M., Shariatmadari, F., Karimi Torshizi, M. A., & Ahmadi, H. (2018). Effects of zinc oxide nanoparticles on the egg quality, immune response, zinc retention, and blood parameters of laying hens in the late phase of production. *Journal of Animal Physiology and Animal Nutrition*, 102, 736–745.
- [25] Food and Drug Administration (FDA). (2015). Select Committee on GRAS Substances (SCOGS) Opinion: Tannic acid (hydrolyzable gallotannins). In *GRAS Substances (SCOGS) Database*. Rockville, MD, USA.

¹Diwakar V. Diwedi

²Vipul V. Mishra

³Satish J. Sharma

Smart Doctor Assistant System using LabVIEW



Abstract: The medical examination and treatment of patients, particularly in rural areas is suffering due to a lack of medical infrastructure, facilities of biomedical instruments and a low doctor -to-patient ratio. The presented work aims at developing a suitable doctor assistant system for detecting real time health parameters such as height, weight, body mass index, temperature, blood pressure, ECG, SpO2 and heart rate of a patient, required by the doctor prior to the diagnosis. This monitoring system assists the doctor in carrying out medical tests in a synchronised manner thereby providing quick results and generating a pre-diagnostic report. A variety of sensors including temperature, pressure, oxygen level, ECG, heart rate, height and weight have been incorporated in the system to generate an excel report. The sensors are integrated using LabVIEW through microcontroller to provide a GUI based environment and monitoring parameters are displayed on the LabVIEW front panel. An early diagnosis report of every patient consisting of name, age, height, weight, temperature, blood pressure, SpO2, ECG and heart rate will be generated and stored for future use. This system can assist doctors to directly jump to the main diagnosis with the pre diagnostic report readily available.

Keywords: Health parameters, height, weight, body mass index temperature, blood pressure, ECG, SpO2, heart rate, microcontroller, LabVIEW, GUI.

¹ * Corresponding author: Department of Electronics and Computer Science, RTM Nagpur University, Nagpur-440033 (MS)

^{2,3}Department of Electronics and Computer Science, RTM Nagpur University, Nagpur-440033 (MS)

Copyright © JES 2024 on-line : journal.esrgroups.org

I. INTRODUCTION

Lack of appropriate medical facilities has been a serious issue in a growing country like India, particularly in villages or remote areas. Inadequate medical care and diagnosis is mostly due to the low doctor-to-patient ratio in rural areas. There is a need to improve the efficacy of patient treatment. Hence, there is need to develop the doctor assistant system in a more efficient manner. The major disadvantage of the existing patient's health parameter measuring facility is the necessity for the doctor or a medical person to be physically present in the neighborhood of the patient at all times and requirement of multiple devices to measure various health parameters which is an expensive affair for both doctors as well as patients. As a result, it is vital to build a system embedded with all the necessary sensors and required circuitry to measure all the primary health parameters of the patients prior to the doctor consultation [1,7].

Because of the developments in bioinstrumentation and telecommunication technology, it is now possible to construct a standalone doctor assistant system which is capable of acquiring, recording, displaying, and transmitting physiological information from the human body to any place. Doctors can use the suggested doctor assistant system to measure height, weight, temperature and monitor key biosignals such as ECG, respiration, heart rate, and body blood pressure of the OPD patients. The clinical output of the recorded patient's data is then transferred to an excel sheet and can be uploaded to the cloud server, where the clinician may view it from anywhere. As per the initial health parameters of the patients recorded by using the doctor assistant system, the doctor can also make necessary recommendations and provide required prescriptions. In many ways, this doctor assistant system collects physiological indicators such as ECG, SpO₂, heart rate, temperature and blood pressure, pre-processes them, and displays them in a graphical user interface developed using LabView [2,4].

In the developed system the LabVIEW's versatility has been used to capture, process, and display vital health data of the patients in real-time. The doctor assistant system is a state-of-the-art approach to healthcare technology. It satisfies the requirement for thorough and ongoing monitoring, empowering medical professionals to act quickly and with appropriate knowledge. LabVIEW makes data sharing and interoperability easier in this age of linked healthcare ecosystems, enabling smooth integration with Electronic Health Record (EHR) systems. As a result, a more comprehensive approach to patient care is supported by ensuring that the health information of the patient is not only tracked in real-time but also integrated into the larger healthcare data landscape [3].

II. EXPERIMENTAL

In this presented work, multiple sensors have been used to sense various body parameters such as height sensor, weight sensor, pulse and heart rate sensor, ECG sensor and blood pressure sensor, a microcontroller to process the data and generate the output as per the algorithm, a buzzer to generate alert signals and LabView software for designing a graphical user interface (GUI) to visualize the sensors data in readable form and control the system easily [9].

1. Hardware Architecture

As shown in fig. 1, one end of all the necessary fundamental sensors are connected to the patient's body to read the various body parameters and another end is connected to the microcontroller with the necessary signal conditioning circuits. The sensors will sense patients' height, weight, temperature, SpO₂, heart rate, ECG and blood pressure and feed these data to microcontroller the microcontroller will process the data as per the written program and transfer the data to the GUI developed using LabVIEW for the graphical representation of the sensors data.

It was made sure that every sensor was calibrated separately in advance to ensure that the project could be completed without any systematic errors. Then, the separate configuration of the sensors were combined so that the complete system works seamlessly accomplish the primary objective of the present work.

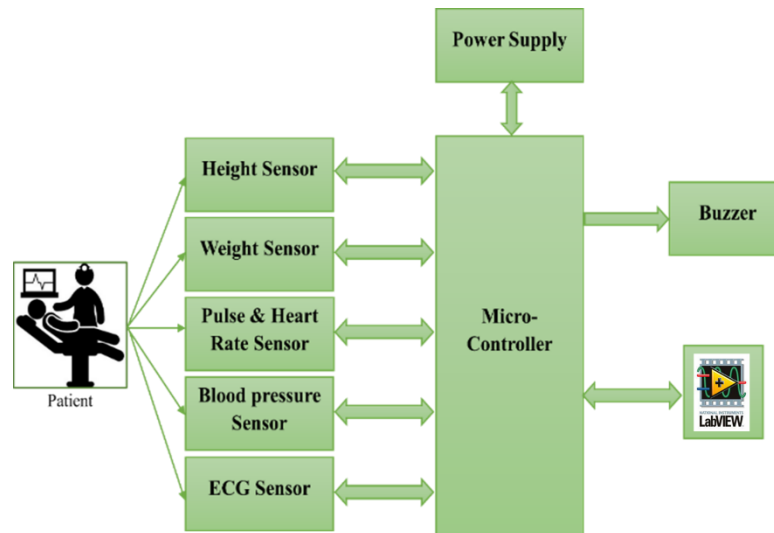


Fig. 1: Block Diagram of the system

1) Sensor Integration:

a. Height and Weight Sensor:

- Measure height and weight of the patient.
- Evaluates body composition and BMI.

$$BMI = \frac{\text{Weight(kg)}}{\text{Height (m}^2\text{)}}$$

- Gives baseline physical measurements for evaluating health.

b. SpO2 and Heart Rate Sensor:

- Helps to read patients' SpO2 and pulse rate.
- Keeps an eye on heart rate to assess cardiovascular health.
- Finds anomalies and irregularities in the pulse.

c. ECG Sensor:

- Records and examines cardiac electrical activity.
- Helps to detect irregularities and cardiac rhythms.

d. Blood Pressure Sensor:

- Assesses both the diastolic and systolic blood pressure.
- Vital for tracking cardiovascular health.

e. Buzzer:

- Integrated to provide prompt notifications in the event of a critical health event.
- Increases the system's capacity to react quickly in emergency situations.

2. Software Architecture:

Software integration is one of the most crucial components of a doctor assistant system, thereby working as the brain of the system. The software architecture of the doctor assistant system consists of the use of the Micro-Controller IDE, LabVIEW and MS-Excel as shown in fig. 2. The Arduino IDE, an open-source programme that makes it simple to upload code to a development board and extracts the sensors data has been used. The LabVIEW (Laboratory Virtual Instrument Engineering Workbench), is an interactive programming environment where graphical notation can be used to create programs is used to design the system GUI.

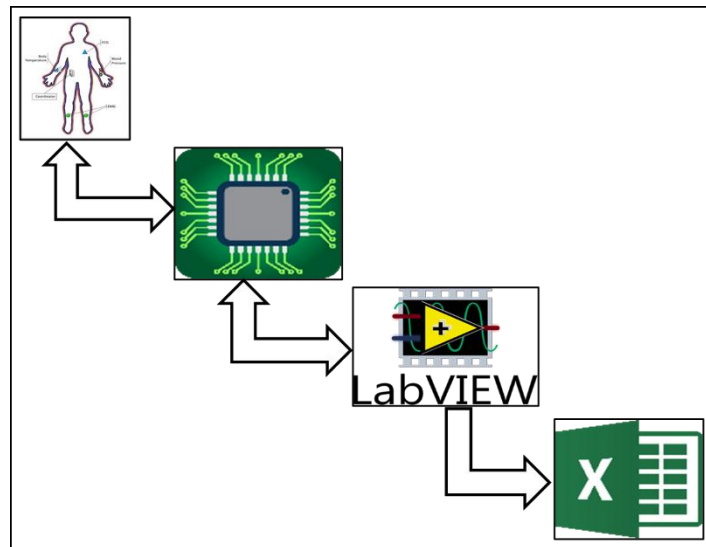


Fig. 2 Software architecture of the system

1) *LabVIEW-Based GUI is Developed for:*

a. Data Visualization:

- Real-time data from the integrated sensors is presented in an easily understandable format on the GUI.
- Provides graphical representation of anomalies and trends.

b. User Communication:

- Allows medical professionals to communicate with the system via a user-friendly interface.
- Enables system settings and alert thresholds to be customised.

Once the patient's necessary data is collected and displayed over GUI, the data can be saved to an MS- Excel sheet generated to save patients record and the saved data can be forwarded to the doctors for further treatment and diagnosis.

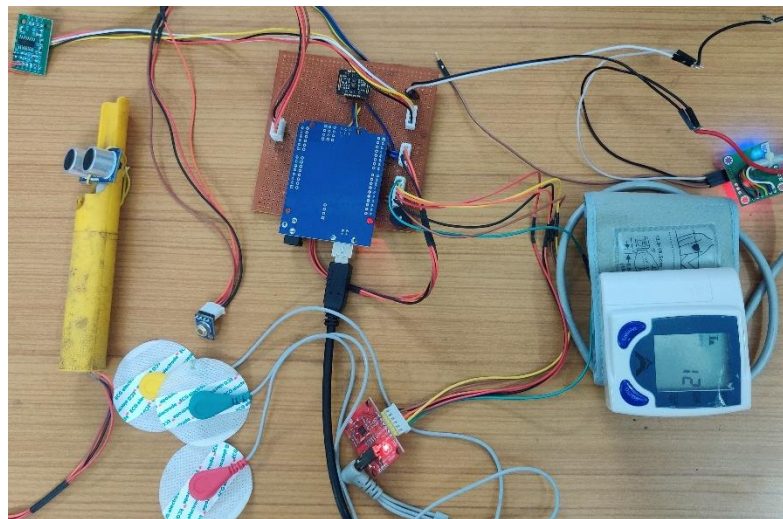


Fig. 3. Experimental setup of the system

Fig. 3 shows the experimental setup of the doctor assistant system in which all the required sensors are connected with the microcontroller and the microcontroller is connected with the computer to see the real time data acquire by the sensors.

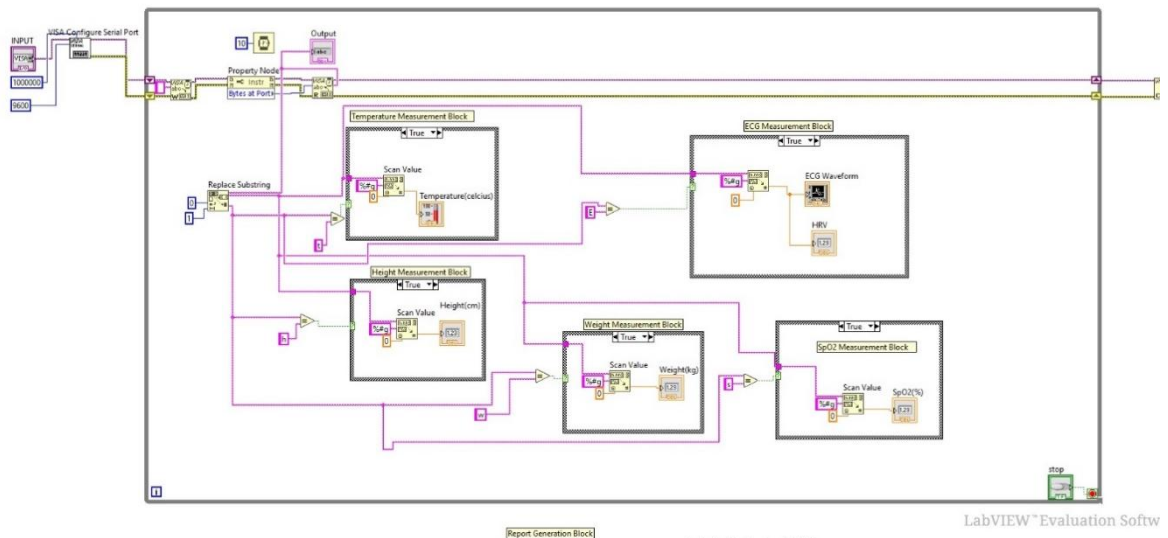


Fig. 4. Block diagram of the system in LabView

Fig. 4 shows the LabVIEW block diagram of the presented system. The LabVIEW block diagram of a doctor assistant system uses various LabVIEW elements to represent the functionality of the system visually. The main elements of such a block diagram are:

A) Data Acquisition:

LabVIEW is frequently utilised to interface with sensors and processing unit for obtaining patients' health data. Components for data acquisition, such as nodes or functions to read signals from devices measuring parameters like height, weight, temperature, blood pressure, heart rate, etc., would be represented in the block diagram.

B) Signal Processing:

Once the data is acquired, it may go through signal processing for filtering, noise reduction, or other preprocessing procedures. To improve the quality of the acquired data, LabVIEW offers a variety of signal processing tools and functions that can be integrated into the block diagram.

C) Data Analysis:

One can carry out variety of data analysis tasks with LabVIEW. Sections for analysing the health parameters, such as calculating trends, spotting patterns, or looking for abnormal values, would probably be included in the block diagram. This could involve custom algorithms, statistical analysis, or mathematical functions.

D) User interface (UI):

LabVIEW allows to design an user-friendly interfaces. Fig. 5 shows the graphical user interface (GUI) of the doctor assistant system designed using elements found in the block diagram. The physicians and other healthcare workers can use it to acquire patients' data. This includes graphs, charts, and indicators showing patient data in real time.

E) Communication:

Number of communication protocols are supported by LabVIEW. Here, in the presented system serial communication is used to communicate between the microcontroller and LabVIEW.

F) Alarm and Notification System:

Alarms and alerts based on preset thresholds can be configured with LabVIEW. Components for real-time data monitoring and alerts or notifications in the event that any health parameter surpasses a threshold could be included in the block diagram.

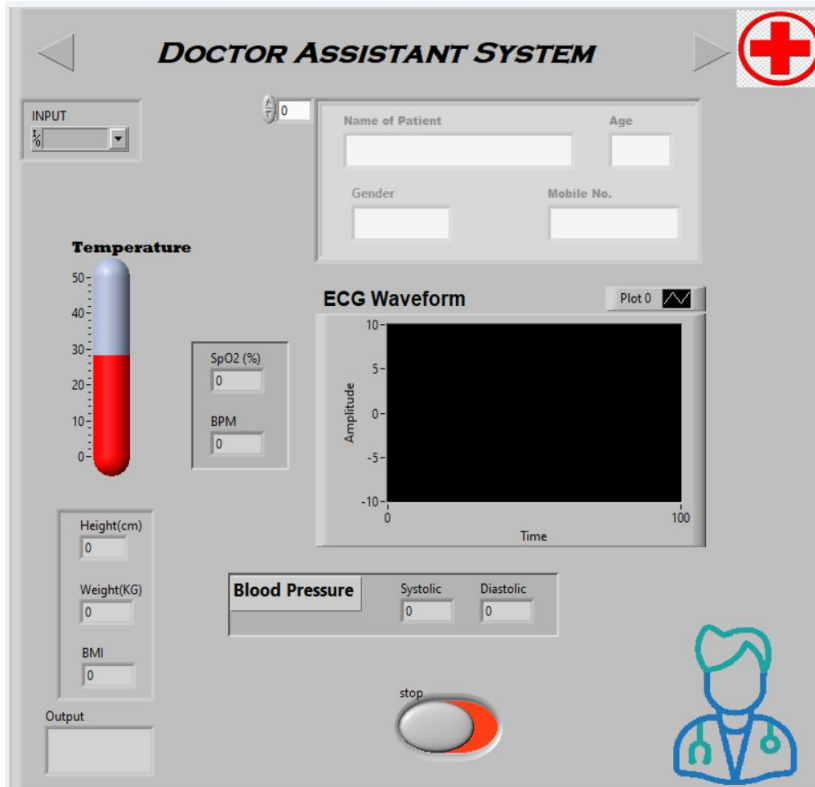


Fig. 5. Designed GUI of the system

III. RESULTS

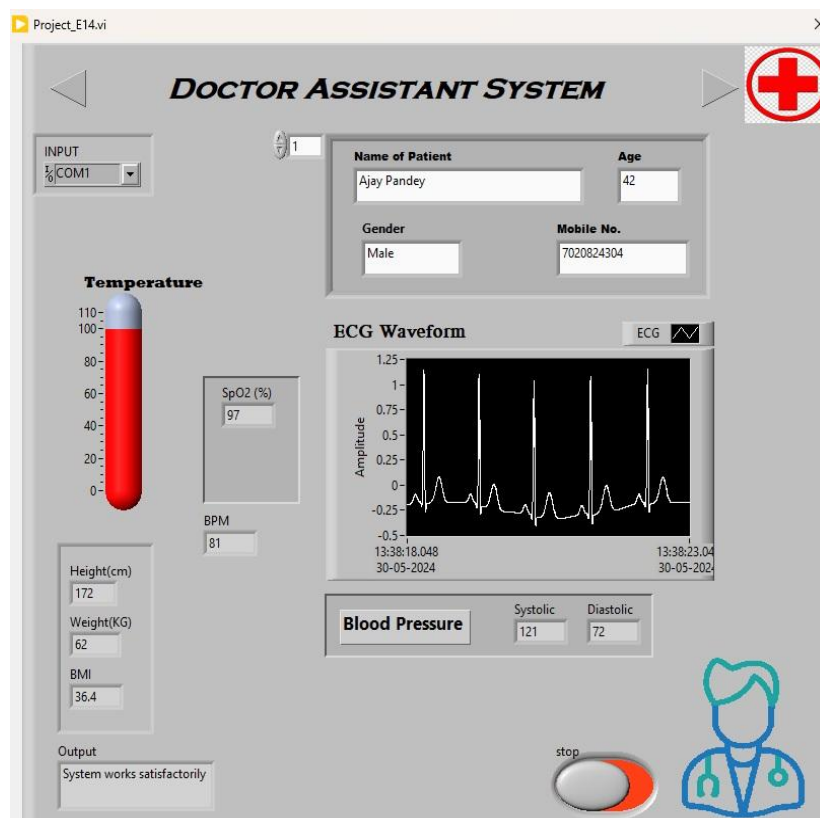


Fig. 6. GUI of the system in run mode with sensors data

The experimental findings demonstrate the effective integration of LabVIEW-based GUI for data validation with physiological sensors. With real-time monitoring and prompt alerts in emergency scenarios, the doctor assistant system shows promise as an all-inclusive tool for medical practitioners.

IV. CONCLUSION

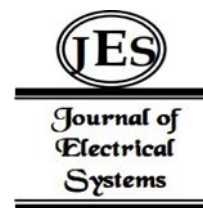
This experimental work, which combines physiological sensors with a LabVIEW-based GUI, represents a major step forward in the development of a doctor assistant system. The integrated system has the potential to improve patient care and strengthen healthcare professionals' ability to make prompt, well-informed decisions, especially when combined with the alert buzzer. Its practical applicability in clinical settings will increase with additional improvements and validations.

REFERENCES

- [1] Md. R. Ruman, A. Barua and W. Rahman, "IoT Based Emergency Health Monitoring System", *int. con. Indu. 4.0 tech.* pp. 169-162, Feb 2020.
- [2] A. Kaur and A. Jasuja, "Health Monitoring Based on IoT using RASPBERRY PI" *Int. Con. Comp. Comm. and Auto.*, pp. 1335-1340, May 2017,
- [3] Nikam P. Sujatha K., "LabVIEW based real time data monitoring and control system", *Int. J. Sci., Engg & Tech. Res.*, pp. 4064, December 2015
- [4] Kumar, R., & Rajasekaran, M. P, "An IoT based patient monitoring system using raspberry Pi", *IEEE Int. Conf. Comp. Techn. Intell. Data Engin.*, pp. 1-4, January 2016.
- [5] Kulkarni, C., Karhade, H., Gupta, S., Bhende, P. and Bhandare, S., "Health companion device using IoT and wearable computing." *IEEE int. Conf. Inter. Things Appl.*, pp. 152-156, January 2016.
- [6] R. K. Parate and S. J. Sharma, "Design of a Client Server based Body Signal Monitoring System", *Int. J. Engg. Res. & Appl.*, pp. 46-49, December 2020.
- [7] M. Hamim, S. Paul, S. I. Hoque, M. N. Rahman and I. Baqee, "IoT Based Remote Health Monitoring System for Patients and Elderly People," *Int. Conf. Robot., Elect. Sig. Pro. Tech.*, pp. 533-538, Feb 2019.
- [8] R. Harini and B. Rama Murthy, "Development of a Wireless Blood Pressure Monitoring System by using Smartphone", *Int. J. Adv. Res. in Electro. & Commu. Engg.*, 6(12), 1383-1386, (2017)
- [9] <https://www.ni.com/docs/en-US/category/labview-docs>

¹R. P. Ikhar,
²K. M. Mude,
³B. M. Mude,
⁴S. M. Yenorkar,
⁵R. R. Mistry,
⁶G. T. Lamdhade,
⁶A.O. Chauhan
⁶R. B. Butley
⁶C. C. Jadhao
⁶K. B. Raulkar

NH₃ Gas Sensing Applications of PPy Doped SnO₂ Sensor to Study Sensitivity



Abstract: - In the present work, SnO₂ and PPy were prepared using standard chemicals under conditions and SnO₂ is doped by polypyrrole (PPy) in the proper stoichiometry. By changing doping percentage of PPy, four sensors S₁, S₂, S₃ and S₄ are prepared. Au electrodes and Platinum wires were used. Each sensor was calcinated at about 500°C for 1h in ambient environment. To improve stability and repeatability, fabricated sensors were kept in N₂ environment for 2.5 h at about 180°C and then in air for about 1.5 h. XRD technique was used for the phase characterization study of the prepared materials and SEM (scanning electron microscopy) was used for porosity measurement. The resistances of the prepared sensors were measured with the help of voltage drop method and then sensitivity was determined. Sensitivity of sensor was checked at different concentration of ammonia.

PPy doped SnO₂ composite; S3 sensor (15%PPy+ 85%SnO₂) showed enhanced sensitivity among the prepared sensors due to high porosity and high ionization absorption at the surface of sensor. PPy acted as assistant catalyst to increase conductivity. Sensitivity (R_g/R_a) was found to be maximum, 18.23 at 62 ppm of NH₃ gas concentration at an operating temperature of 30°C. Also stability of the sensor was checked and found to be most stable.

Keywords: PPy, SnO₂ sensor, chemical precipitation method, sensitivity, stability, NH₃ gas, Screen Printing Technique

I INTRODUCTION

SnO₂ is a popular material for fabrication of gas sensors as it is best for reducing gasses detection. SnO₂ is a n-type semiconductor and its concentration of electron is established by concentration of stoichiometric defects such as oxygen vacancy like other metal oxide. Due to low cost, low weight, more porosity, simple design and high response, stannic oxide is generally used as best material. Many researchers stated that the sensitivity of SnO₂ can be enhanced by doping PPy [1-2].

Now a day, the atmosphere is being uncomfortable for breathing due to the many dangerous gasses present in the atmosphere. Therefore, it is vital to detect such dangerous and harmful gases in order to prevent human life, control air pollution, and protect nature from being damaged. Many people are facing problems with toxic, combustible and volatile gases in the atmosphere including domestic, laboratorial, and industrial places. Ammonia, one such hazardous and toxic gas and hence its detection is very important part. NH₃ is used in many places and in many applications, such as for cooling purposes in the industries and medical diagnoses and research. As hydrogen produced by the decomposition exerts high reduction effect on SnO₂, ammonia is a strong reducing gas [3-4]. Thus in the present work, it was decided to fabricate and use the sensors produced by using PPy doped in SnO₂ to sense ammonia gas. These prepared sensors had shown better response and stability during NH₃ gas detection.

II. EXPERIMENTAL

2.1 Synthesis of SnO₂ Nanoparticles:

GR grade chemicals of Sd-fine, India had been used for the study having purity 99.99%. SnO₂ had been prepared by taking 2g (0.1 M) of stannous chloride dehydrate (SnCl₂.2H₂O) which was dissolved in 100 ml H₂O. With magnetic stirring, after complete dissolution, 4 ml ammonia solution was added to this aqueous solution. Solution was stirred for about 30 minutes to get white gel precipitate [5-6].

Precipitate was left to settle for 9 to 10 h. The thick precipitate was then filtered and cleaned with distilled water 3-4 times by using de-ionized water. The washed and cleaned precipitate was combined with 0.27g carbon black powder (charcoal activated). The mixer was kept in vacuum oven at 85°C for about 1 day to obtain the mixer in powder form. The dried sample then grinded to obtain fine powder. This fine product of nanopowder of SnO₂ was calcinated at 700°C upto 7 h in the auto-controlled muffle furnace (Gayatri Scientific, Mumbai, India.) to eliminate the impurities from product completely.

2.2 Synthesis of Polypyrrole (PPy):

The Py monomer, anhydrous iron (III) chloride (FeCl₃) and methanol were used for synthesis of PPy [19]. The solution of 7 ml methanol and 1.892 g FeCl₃ was first prepared in round bottom flask. Then 8.4 ml Py monomer was added to (FeCl₃+methanol) solution with constant stirring in dark. The amount of Py monomer added to the solution (1/2.33 times of FeCl₃) was in such a way to get maximum yield. The resulting black precipitates were filtered and washed with copious amount of distilled water until the washings are clear. PPy so obtained was dried by keeping in oven at 600°C for 3 h [7].

2.3 Preparation of Sensors:

PPy is doped with SnO₂ with different percentage. A paste is produced by using binder (butyl carbitol and ethyl cellulose). On clean glass plate with Al₂O₃ base, paste is screened out with the help of screen printing technique. Electrodes are formed on the side edge of the sensors for electrical connections.

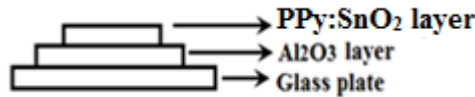


Fig. 1.Preparation of sensors

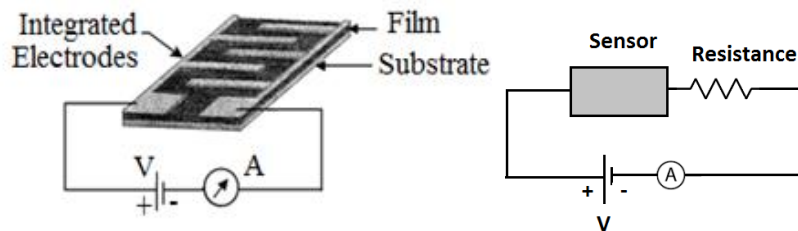


Fig. 2.Voltage drop method

For an hour, the prepared films were dried at 80-100°C in calibrated oven. Due to this, all the organic materials (in the form of binders) and organic impurities were evaporated [8-9]. The surface resistance measurements were done by forming electrodes of silver paint on adjacent sides of the films. For drying the silver paint, the films were further heated at about 80°C for half an hour. The prepared sensors are listed below in table 1.

Table 1:

Sr. No.	Composites	Sample codes
1.	5% PPy + 95% SnO ₂	S1
2.	10% PPy + 90% SnO ₂	S2
3.	15% PPy + 85% SnO ₂	S3
4.	20% PPy + 80% SnO ₂	S4

2.4 Sensitivity measurement:

Sensitivity [10-11] is defined as the ratio of resistance of the sensor due to presence of gas to the resistance in air environment and is given by

$$S = \frac{\text{Resistance in presence of gas}}{\text{Original resistance in air}} = \frac{R_{\text{gas}}}{R_{\text{air}}}$$

Where,

R_{gas} = Resistance of the sensor in presence of NH₃ gas environment and

R_{air} = Resistance of the sensor in presence of air.

III. RESULTS AND DISCUSSIONS

3.1 XRD Characteristics Study:

Fig.3 shows the X-ray powder diffraction (XRD) pattern of PPy doped SnO₂ materials.

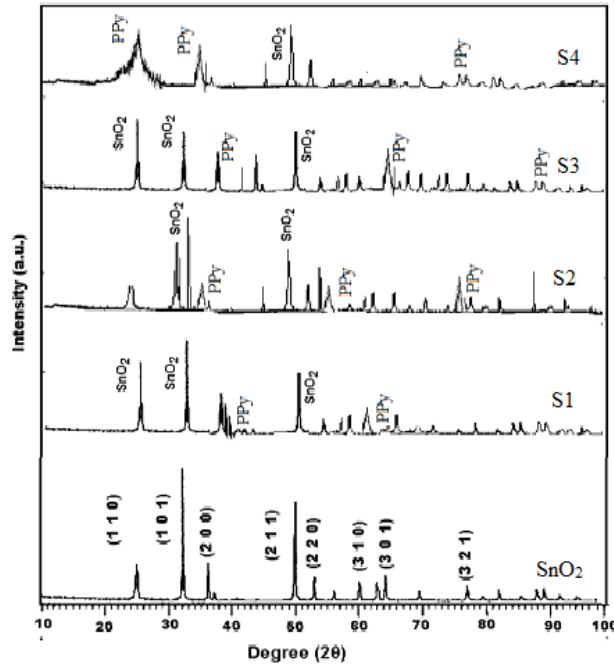
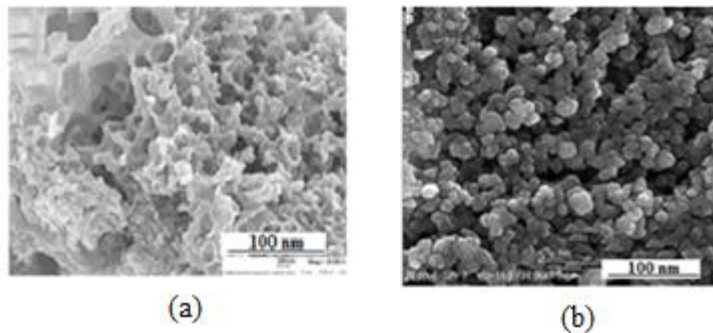


Fig.3.XRD of S₁, S₂, S₃ and S₄ sensors

As shown in XRD, even after calcinations at 600°C for 1.5 h, phase was not changed and no new phase was seen.

X-Ray diffraction pattern of PPy exhibited that, it was amorphous in nature. The broad peak occurred at 24° and it is characteristics of amorphous nature of polypyrrole. The broad peak occurs due to the scattering of X-rays from polymer chains at the interplaner spacing. The maximum intensity position of amorphous also depends on monomer to oxidant ratio. The X-ray diffraction patterns of composites of PPy, SnO₂ and pure SnO₂, calcinated at 200°C. Main peak, in case of pure SnO₂, is observed at 26.6° and this peak corresponds to the plane (1 1 0) of SnO₂ in tetragonal structure (JCPDS Card No.3-1114) with 100% intensity and the average crystalline size by using Scherer's formula was found to be 92.24 nm [12-13]. All the peaks are for the composites materials for molar weight percentage of various samples that are perfectly matched.

3.2 SEM (Scanning Electron Microscope) Study:



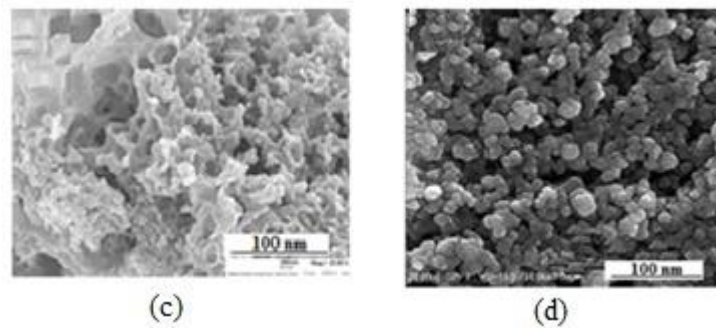


Fig.4.SEM of S₁, S₂, S₃ and S₄ sensors

From the SEM pictures, Fig. 4, it is observed that in every inch of the region, number of pores was different and an average number of pores was taken for comparative study. From every photo, porosity was calculated for one inch region. From figures, it is found that number of porosity of 15%PPy+ 85%SnO₂ (S₃ sensor) composition is more among the prepared and pure samples. Due to high porosity [14-15], gas absorptive nature increases. This leads to the more NH₃ gas absorption and hence resistance of the S₃ sensor is more and also sensitivity is found to be enhanced. Some of the pores are cylindrical and some are spherical, some are elongated and some pores have elliptical shapes. All these pores formed cavity which helped in the absorption of the gas.

3.3 Sensitivity Measurement:

Variation of sensitivity of sensors with concentration of Ammonia gas is shown in the following Fig. 5.

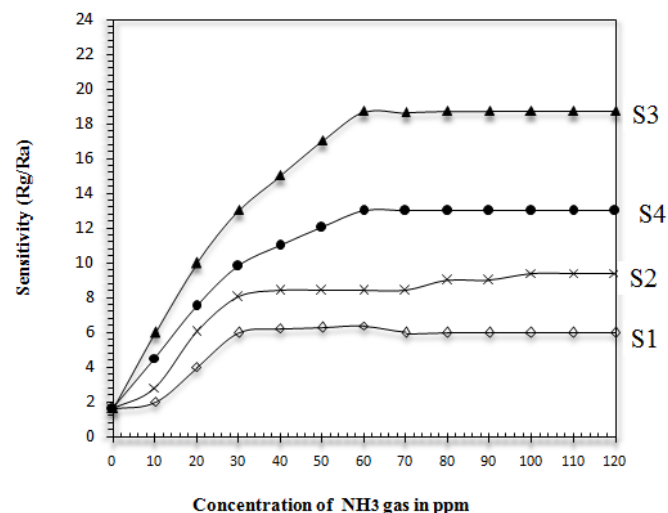


Fig.5.Variation of sensitivity with NH₃ gas concentration

As shown in Fig. 5, sensitivity of S₁, S₂ and S₄ sensors is low as compared to that of S₃ sensor. It was found that sensitivity of all the sensors increases linearly upto 60 ppm concentration of ammonia gas and then remains nearly constant. Maximum sensitivity (R_g/R_a) was recorded 18.23 at 62 ppm of NH₃ gas for S₃ sensor (15%PPy+ 85%SnO₂).

The semiconductor gas sensor is based on the change of conductivity of the semiconductor material due to its interaction with gas. Electron transfer occurs between the semiconductor and the adsorbates when molecules of the gas are adsorbed on the surface of semiconductor. The adsorbates accept electrons from the semiconductor when the electron's affinity of the adsorbates larger than the work functions of the n-type semiconductor [16-17]. This transfer of electrons and absorption of electrons continue until Fermi-level of the gas-adsorbed semiconductor surface becomes equal to that of the bulk. Due to this, accumulation of charges occurs near the semiconductor surface and causes the induction of potential barrier. This enhances the resistance of the material thereby increases sensitivity. Free electrons generating from oxygen vacancies causes electrical conductivity.

3.4 Stability Measurement:

Variation of sensitivity of prepared sensors with time is shown in the following Fig. 6.

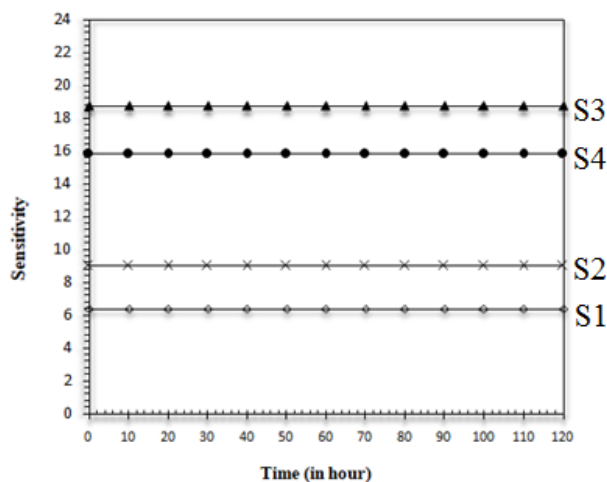


Fig.6.Variation of sensitivity with time (in hour)

The sensitivity variation [18] with time was checked for 120 hrs, and it was found that sensitivity was not changing with time i.e. sensors showed more stability.

III. CONCLUSION

PPy doped SnO₂ composite; S3 sensor (15%PPy+ 85%SnO₂) showed enhanced sensitivity among the prepared sensors due to high porosity and high ionization absorption at the surface of sensor. PPy acted as assistant catalyst to increase conductivity. Sensitivity was found to be maximum, 18.23 at 62 ppm of NH₃ gas concentration at an operating temperature of 30°C. Also stability of the sensor was checked and found to be most stable.

IV. ACKNOWLEDGEMENT

The author would like to acknowledge Department of Physics, Vidya Bharati Mahavidyalaya, Amravati (India) for providing Research center to carry on this work.

REFERENCES

- [1] Ly A., Luo Y., Cavailles G., Olivier M.G., Debliquy M. and Lahem D., (2020). Ammonia Sensor Based on Vapor Phase Polymerized Polypyrrole, *Chemosensors*, 8, 30.
- [2] Tai H., Wang S., Duan Z. and Jiang Y., (2020). Evolution of breath analysis based on humidity and gas sensors: Potential and challenges, *Sens. Actuators B Chem.*, 318, 128104.
- [3] Wang C., Lei S., Li X., Guo S., Cui P., Wei, X., Liu W. and Liu H., (2018), A Reduced GO-Graphene Hybrid Gas Sensor for Ultra-Low Concentration Ammonia Detection, *Sensors (Basel)*, 18(9), 3147.
- [4] Guntner A.T., Righettoni M. and Pratsinis S.E. (2016). Selective sensing of NH₃ by Si-doped -MoO₃ for breath analysis, *Sens. Actuators B Chem.*, 223, 266–273.
- [5] Chitte H. K., Bhat N.V. and Vasant E., (2011), Synthesis of Polypyrrole Using Ferric Chloride (FeCl₃) as Oxidant Together with Some Dopants for Use in Gas Sensors, *Journal of Sensor Technology*, 1, 47-56.
- [6] Devi R.S., Venkatesh R. and Sivaraj R., (2014), Synthesis of Titanium Dioxide Nanoparticles by Sol-Gel Technique, *IJIRSET*, 10, 15206-211.
- [7] Dighore N., Dhonde S., Gaikwad S. and Rajbhoj A., (2016), Synthesis of conducting polymer Polypyrrole-MoO₃ nanocomposites, *Mor. J. Chem.*, 4, 797-804.
- [8] Chartuprayoon N., Hangarter C.M., Rheem Y., Jung H. and Myung N.V. (2010), Wafer-scale fabrication of single PPy nanoribbon-based ammonia sensor, *J. Phys. Chem.*, 114, 11103–11108.

- [9] Hernandez S.C., Chaudhuri D., Chen W. and Myung N.V., (2007). Maskless electrodeposited contact for conducting polymer nanowires, *Appl. Phys. Lett.* 92, 073104.
- [10] Sachan, A., Castro, M., Choudhary V. and Feller J.F., (2018). Influence of Water Molecules on the Detection of Volatile Organic Compounds (VOC) Cancer Biomarkers by Nanocomposite Quantum Resistive Vapor Sensors vQRS, *Chemosensors*, 6, 64.
- [11] Hamouma O., Kaur N., Oukil D., Mahajan A. and Chehimi, M. M., (2019), Paper strips coated with polypyrrole-wrapped carbon nanotube composites for chemi-resistive gas sensing, *Synth. Met.*, 258, 116223.
- [12] Nakhleh, M.K., Amal H., Jeries R., Broza Y.Y., Aboud M., Gharra A., Ivgi H., Khatib S., Badarneh S. and Har-Shai, L., (2017). Diagnosis and Classification of 17 Diseases from 1404 Subjects via Pattern Analysis of Exhaled Molecules, *ACS Nano*, 11, 112–125.
- [13] Shang Y., Wang X., Xu E., Tong C. and Wu J. (2015), Porous Silicon Structures as Optical Gas Sensors, *Anal Chim Acta*, 15(8), 19968–19991.
- [14] Wang Y., Jia W., Strout T., Schempf A., Zhang H., Li B., Cui J. and Lei Y., (2009), Preparation, Characterization and Sensitive Gas Sensing of Conductive Core-sheath TiO₂-PEDOT Nanocables, *Sensors (Basel)*, 9(9), 6752–6763.
- [15] Hua B. and Gaoquan S., (2007). Gas Sensors Based on Conducting Polymers, *Sensors*, 7, 267-307.
- [16] Shanga Y., Wanga X., Xu E., Tong C. and Wu J., (2011). Optical ammonia gas sensor based on a porous silicon rugate filter coated with polymer-supported dye, *Analytica Chimica Acta*, 685, 58-64
- [17] Yang J, Lim H and Han S., (1999). Influence of binder on the sensing and electrical characteristics of WO₃-based gas sensors, *Sen. Actu. B*, 60(1), 71–77
- [18] Romppainen P and Lantto V., (1998). The effect of microstructure on the height of potential energy barriers in porous tin dioxide gas sensors, *J. Appl. Phys.*, 63(10):5159–5165.

^{1*}R.N.Zade
²B.M.Mude
³K.M.Mude
⁴S.M.Yenorkar
⁵K.B.Raulkar
⁶R.R.Mistry
⁷S.M.Warbhe
⁸S.K.Mude
¹⁰A.N.Patange
⁵G.T.Lambdhade
⁹P.S.Bodkhe

Coupling Reactions of Active Methylene Group for synthesis of 3(P-Methylphenyl)1-Phenylprop-2-en-1-one [Chalcone] using nanocomposite of Ceria embedded on zeolite



Abstract: - Chalcones are prominent secondary metabolites and precursors of flavonoids and isoflavonoids in plants. The 'enone' moiety is present in many biologically active molecules and it is considered to be primarily responsible for eliciting the biological response in such molecule. Chalcones in general are reported to exhibit various pharmacological activities such as anticancer, antimalarial, anti-inflammatory, immunomodulatory, antibacterial, immunosuppressive, antiprotozoan, trypanocidal, and leishmanicidal properties. Though there are many methods for preparation of chalcone, there is need to explore its synthesis using a simple, cheaper yet efficient method based on heterocatalytic embedded system. Here we have prepared chalcone using ceria embedded zeolite using cheaply available base compounds and allowed to undergo Michael addition at ambient temperature using very less amount of solvent and extraneous material. This provides a new route to prepare chalcone vide simple, cheaper, minimum solvent yet efficient synthesis at ambient temperature. This confirms the stability, nontoxicity and cost effectivity of ceria-zeolite nanocomposite for preparation of chalcone.

Keywords:Chalcone, active methylene group, ceria, zeolite, nanocomposite

^{1*}Dept. of Chemistry, Siddharth College, Fort, Mumbai-400001 (M.S.) India

²Dept. of Physics, Ramnarain Ruia College, Matunga(E)-400019 (M.S.) India

³Dept. of Physics, Bhavan's College, Andheri(W)-400058 (M.S.) India

⁴Dept. of Physics, Shri Shivaji College, Parbhani-431 401 (M.S.) India

⁵Dept. of Physics, Vidyabharti Mahavidyalaya, Amravati-444602 (M.S.) India

⁶Dept. of Physics, Deogiri College, Chhat. Sambhajinagar-431005 (M.S.) India

⁷ Dept. of Mathematics, Vidyabharti Mahavidyalaya, Amravati-444602 (M.S.) India

⁸ Dept. of AI & DS, Thakur College of Engineering and Technology, Kandiwali(E), Mumbai-400101 (M.S.) India

⁹Dept. of Chemistry, Vidyabharti Mahavidyalaya, Amravati-444602 (M.S.) India

¹⁰Dept. of Chemistry, Bhavan's College, Andheri(W)-400058 (M.S.) India

e-mail Corresponding Author : rzade07@yahoo.co.in

Copyright©JES2024on-line:journal.esrgroups.org

I. INTRODUCTION

Synthetic organic chemistry has its own charm in simulation of natural products synthesis and creating new fantastic molecules. Both the ways it is providing platform for other fields like agriculture, pharmaceutical, petroleum etc. It has gained pace after the use of catalysts enormously. Though organic synthesis has its place in classical and applied research, it is constantly encountered with certain problems of separation of materials other than desirable products, huge organic volatile solvent usage, protection and deprotection of functional groups, low absolute yield etc. These limitations are amplified enormously in synthesis of fine and specialty chemicals [1,2]. So, there is a growing need for more environmentally acceptable processes in the chemical industry. This trend towards what has become known as 'Green Chemistry'. After considerable literature survey we find Ceria embedded zeolite very useful in various organic transformation involving reaction between active methylene group for formation of chalcone.

Limitations of classical organic synthesis have been overcome by green chemistry approach especially in terms of reducing waste by replacing stoichiometric reagents with recyclable solid acid and bases, preferably in catalytic amounts[1]. Bio catalysis has many attractive features in the context of green chemistry such as mild reaction conditions (physiological pH and temperature), an environmentally compatible catalyst (an enzyme) and solvent (often water) combined with high activities and chemo-, regio- and stereoselectivities in multifunctional molecules[1,2,10]. Solid acids, such as zeolites, acidic clays and related materials, have many advantages in this respect They are often truly catalytic and can easily be separated from liquid reaction mixtures, obviating the need for hydrolytic work-up, and recycled. Zeolite-catalysed Friedel-Crafts acylation by Rhône-Poulenc (now Rhodia) may be considered as a benchmark in this area [1,6,9].

II. MATERIALS AND METHODS

Synthesis of Chalcone Derivative

1,3-Diaryl-2-propen-1-ones, commonly known as chalcones are prominent secondary metabolites and precursors of flavonoids and isoflavonoids in plants. Structurally in such compounds two phenyl rings are flanked by 2-propenone moiety and this arrangement makes them 'privileged structure' The 'enone' moiety is present in many biologically active molecules and it is considered to be primarily responsible for eliciting the biological response in such molecule.

Chalcones in general are reported to exhibit various pharmacological activities such as anticancer, antimalarial, antiinflammatory, immunomodulatory, antibacterial, immunosuppressive, antiprotozan, trypanocidal, and leishmanicidal properties. Licochalcone-A, a natural product, isolated from the licorice root, is known to have a wide variety of anticancer effects. They have recently been reported as antiproliferative and antitumor agents and interest in this class of molecules in identifying potent anticancer agents is renewed. These molecules with enone moiety inhibit several enzymes which render them the therapeutic potential. The ease of preparation, the potential of oral administration, and safety also support the feasibility of chalcone based compounds to be used as chemotherapeutic agents. Tremendous amount of work is reported on the synthesis, bio-evaluations, and mechanism of action of these compounds including their interference in microtubule formation and many cellular signaling pathways.

A number of chalcones with hydrophobic moieties and hydrophilic substituents attached to the aromatic rings such as adamantanyl and steroidal substituents were prepared and showed potent anticancer activity against different cancer cell lines. Chalcone undergo Buchwald- Hartwig Coupling /Michael Addition reaction with primary amine and with aldehyde to give 4-Quinolones. It is highly biologically active molecule [5].It can undergo Multicomponent Stereoselective Synthesis of 3-Amino-2(1*H*)-pyridinones Using CeCl₃·7H₂O/NaI, primary amine and oxazolone. Heterocycles incorporating a 2(1*H*)-pyridinone framework constitute an extensively studied class of compounds owing to their diverse biological activities ranging from anti-HIV, antibacterial and antifungal to free radical scavenger [3,4].A Ce(III)-catalyzed expeditious multicomponent stereoselective synthesis of 3-mercapto-2(1*H*)-pyridinones [12] is achieved using chalcone, primary amine and oxathiolanone. One of the drug namely Cyclopropralamine (Loprox) is approved by the FDA as a broad spectrum antifungal drug and is presently in clinical use for the treatment of various skin diseases. Polysubstituted 2(1*H*)-pyridinones are of special interest due to their anxiolytic activity with improved side effect profiles. In addition, dihydro and tetrahydro derivatives of 2(1*H*)-pyridinone have been applied as scaffolds for the construction of constrained amino acids [5].Synthesis of benzylaminocoumarin derivative was catalyzed by surfactant Triton X-100 using water as solvent [7].

The basic structure of chalcone [8] include following nucleus. R & R₁ can be –OH, CH₃, C₂H₅Cl, NH₂, and many complicated groups.

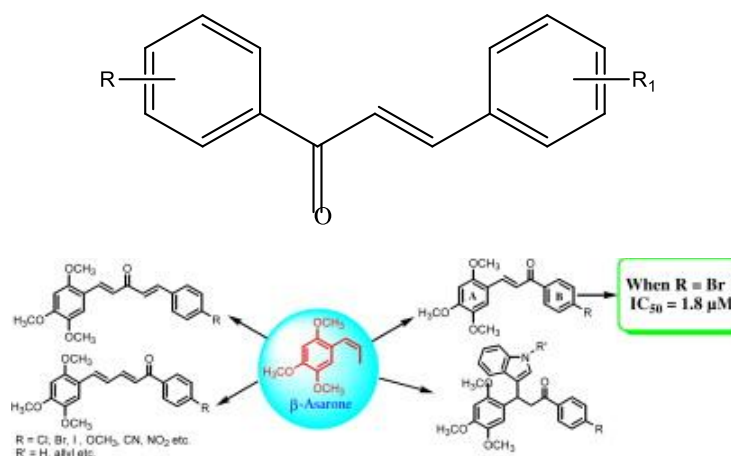


Figure.1. Basic structure of chalcone

Active Methylenes:

These are compounds in which methylene group (CH₂) is attached to electron withdrawing group such as CN, COOEt, NO₂ as shown in the following compounds.

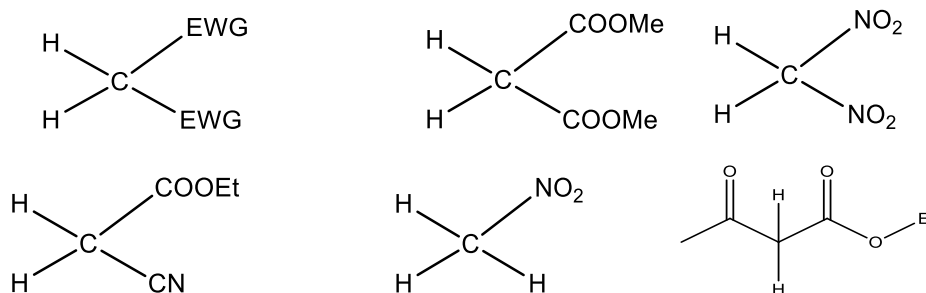


Figure2. Active Methylenes

These compounds are having acidic methylene hydrogens. These can be abstracted by base, forming a carbanion. These carbanions are stabilized due to resonance by EWG group. These also form enolate ion. These enolates are able to give nucleophilic addition over carbon double bond.

Synthesis of Ceria:

Cerium is a rare earth element belonging to the lanthanide series. Even if is a rare earth element, the earth crust is relatively rich in this element, being the most abundant from the lanthanides. After europium, cerium has the highest reactivity among the rare earth metals, passing easily into oxidized stage at room temperature. While most of the rare earths exist in trivalent state, cerium also occurs in 4+ state and may alternate between the two in a redox reaction. cerium oxide nanoparticles prolong cellular longevity by scavenging free radicals generated during their lifetime. The distinct structure of ceria nanoparticles, regarding the valence, support cell longevity as benefit of its antioxidant properties. Antioxidant behaviour is strongly influenced by the co-existence of both Ce³⁺ and Ce⁴⁺ oxidation states in CeO₂ nanoparticles.

The synthesis of CeO₂nps was achieved by precipitation method by using an aqueous cerium nitrate solution (0.2 M) as the cerium precursor and excess of ammonia solution (0.2 M) as precipitating reagent. The reaction was carried out at room temperature under continuous magnetic stirring. A stream of O₂ was bubbled into the reactor to oxidize Ce³⁺ to Ce⁴⁺. Firstly, a white precipitate came out in the solution. Subsequently, the colour of precipitate turned into purple, and gradually became light yellow. The post-precipitation stage consisted of a 24 hrs. aging, separation by filtering and drying. The sample was washed with ethanol for three times.

III. RESULT AND DISCUSSION

Structural Analysis

FT-IR spectra

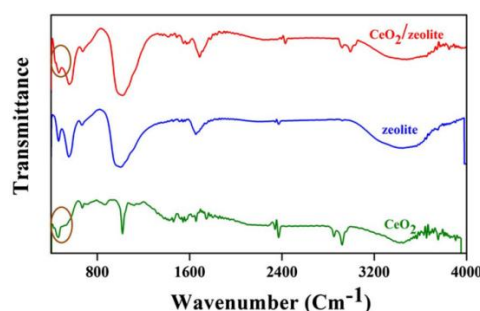


Figure 3. FT-IR Spectra of CeO₂, zeolite and CeO₂/zeolite

FT-IR spectra in the 400–4000 cm⁻¹ range were shown in Fig. 3 for CeO₂, zeolite, and CeO₂/zeolite nanocomposite. O-H stretching and bending vibrations of adsorbed water are responsible for the broad peak located at 3437 and 1646 cm⁻¹, respectively. The peak at 1013 cm⁻¹ in the zeolite spectrum is indicative of the Si–O–Si stretching vibration. The weak peaks correspond to Si–O–Si bending vibration and are located between 460 and 800 cm⁻¹. The signal at 426 cm⁻¹ in the FT-IR spectra of CeO₂ is indicative of the Ce–O bond. Because of the interaction between CeO₂ and zeolite, the Si–O–Si peaks are located at 1013 and 1032 cm⁻¹, respectively, and are associated with zeolite and CeO₂/zeolite nanocomposite.

XRD

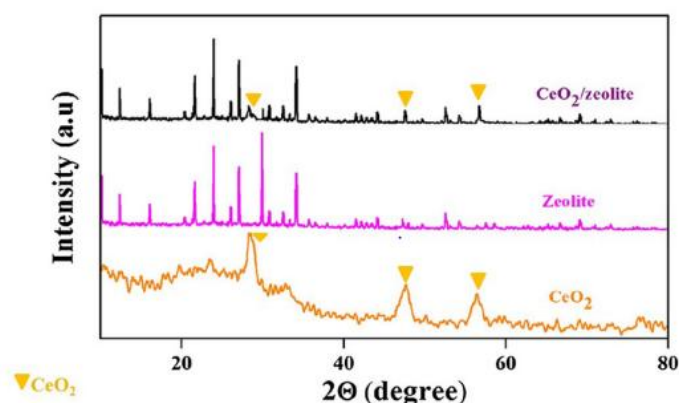


Figure 4. XRD pattern of pure CeO₂, Zeolite and CeO₂ embedded on Zeolite

Figure 4 displayed the XRD patterns of the zeolite, CeO₂, and CeO₂/zeolite. Zeolite's XRD pattern and JCPDS card No. 37-0072 agree well. The characteristic peak of CeO₂ is typically found at $2\theta = 28.56$ (111), 47.4(220), and 56.58 (311) (JCPDS card No. 89-8436). The CeO₂/zeolite XRD pattern showed the presence of both CeO₂ and zeolite peaks, indicating the entry of CeO₂ nanoparticles into the zeolite framework. Scherrer's formula was used to determine the average crystallite size.

$$D = 0.9\lambda / \beta \cos\theta$$

where D is the average diameter, θ is the Bragg angle in degrees, λ is the breadth line of the diffraction peaks in radians, and is the X-ray wavelength. For CeO₂/zeolite, the average CeO₂ size is determined to be 10.53 nm.

Zeolites are effective materials for segregation, adsorption, and catalytic activity. This immense focus is due to their extraordinary properties, which include a characteristic fluorite-type structure, a stable framework, and the versatile ability of cerium's tetravalent (Ce⁴⁺) and trivalent (Ce³⁺) valence states to undergo reduction and oxidation processes. Rare earth oxides like ceria have a wide range of applications, including electrocatalysis, solar and fuel cells, and photocatalysis. Although, CeO₂ is abundant with oxygen vacancies the drawback of limited surface area, lower visible-light harvesting capability, and high recombination of electron-hole pair has limited its independent application. Various strategies have been employed such as doping with metals and non-metals, support material, and fabricating over support materials. However, to the best of our knowledge, the application of zeolite and CeO₂ photocatalyst composite for the removal of endocrine disrupting compound like caffeine is unexplored. In this study, we developed a CeO₂ decorated zeolite nanocomposite

To prepare various pharmaceutical intermediates such as chalcones derivatives of various active methylene groups, cleaved epoxide, indole derivative, benzothiazepine, using various coupling reactions, C-C, C-N, C-O, C-X bond formation methodologies. All these reactions will be carried out in minimum solvent Ceria embedded zeolite as efficient catalyst. Along with core reaction, effect of temperature, solvent, concentration of catalyst, synergistic effect of various factors also is studied.

IV. CONCLUSION

Though classical organic synthetic methods are rampant for synthesis of chalcone derivatives of active methylene groups, we felt the need to develop green protocol using an efficient catalyst. So, we attempted to develop ceria embedded zeolite as a green catalyst for preparation of chalcone derivative which are biologically active intermediates. It also helps in expediting the steps in preparation of drugs which are potentially anticancer, antimalarial, anti-inflammatory, immunomodulatory, antibacterial, immunosuppressive, antiprotozoan.

REFERENCES

- [1] *Green Chemistry and Catalysis*. I. Arends, R. Sheldon, U. Hanefeld Copyright © 2007 WILEY-VCH Verlag GmbH & Co. KGaA, Weinheim ISBN: 978-3-527-30715-9
- [2] James H. Clark, Catalysis for green chemistry*, *Pure Appl. Chem.*, Vol. 73, No. pp. 103–111, 2001. © 2001 IUPAC
- [3] Organocatalytic cascade reactions as a new tool in total synthesis ,Christoph Grondal^{1*}, matthieu Jeanty² and dieter enders^{2*} Nature Chemistry Review article 19 Feb. 2010.
- [4] Synthetic Communications: An International Journal for Rapid Communication of Synthetic Organic Chemistry, A Straightforward Method for the Synthesis of Alkylidene and Arylidene Malonates Through Proline- Catalyzed Knoevenagel Condensation Giuliana Cardillo a , Serena Fabbioni a , Luca Gentilucci a , Massimo Gianotti a & Alessandra Tolomelli ao
- [5] Buchwald–Hartwig Coupling/Michael Addition Reactions: One-Pot Synthesis of 1,2-Disubstituted 4-Quinolones from Chalcones and Primary Amines ,Xiang-Dong Fei,[a] Zhou Zhou,[a] Wen Li,[a] Yong-Ming Zhu,*[a] and Jing-Kang Shen*[b] European Journal of Organic Chemistry. DOI: 10.1002/ejoc.201200172
- [6] Efficient and Eco-friendly Syntheses of 1,5-Benzothiazepines and 1,5-Benzodiazepines Catalyzed by [Hmim][NO₃] under Mild Conditions .Hossein Loghmani-Khouzani,a* Panteha Tamjidi,a Iraj Mohammadpoor-Baltork,a Marzieh Yaeghoobi,b Noorsaadah Abd. Rahman,b Ahmad Reza Khosropour,a Majid Moghadam,a Shahram Tangestaninejad,a Valiollah Mirkhani,a Mohammad Hossein Habibi,a Ayana Kashima,c and Takayoshi Suzukic DOI 10.1002/jhet.1827, published online in Wiley online library.
- [7] A mild ring opening fluorination of epoxide with ionic liquid 1-ethyl-3-methylimidazolium oligo hydrogen fluoride (EMIMF)(HF)2.3 Hideaki Yoshino, Kenichi Nomura, Seiji Matsubara,* Koichiro Oshima, Kazuhiko Matsumoto, Rika Hagiwarab, Yasuhiko Itob , Journal of Fluorine Chemistry 125 (2004) 1127–1129
- [8] Synthesis of polysubstituted pyridines via reactions of chalcones and malononitrile in alcohols using Amberlite IRA-400 (OH) , Kiumars Bahrami a, Mohammad M. Khodaei a, Fardin Naali a, Behrooz H. Yousefi b, Tetrahedron Letters 54 (2013)
- [9] Amberlyst-15 as a new and reusable catalyst for regioselective ring-opening reactions of epoxides to β-alkoxy alcohols. Yu-Heng Liu, Qiu-Shuang Liu, Zhan-Hui Zhang, Journal of Molecular Catalysis A: Chemical 296 (2008) 42–46
- [10] Regio- and Stereoselective Ring Opening of 2,3-Diaryl Oxiranes by LiBr/Amberlyst 15: A New Stereocontrolled Access to 1,2-Diaryl-2-bromo Alcohols . Arlette Solladie'-Cavallo,† Paolo Lupattelli,* ,‡ and Carlo Bonini‡ JOC article Received November 3, 2004
- [11] Opening an Aladdin's cave: the Suzuki coupling in a room-temperature ionic liquid Nicholas E. Leadbeater^a *Chem. Commun.*, 2014,**50**, 1515-1518.
- [12] A recyclable and base-free method for the synthesis of 3-iodothiophenes by the iodoheterocyclisation of 1-mercapto-3-alkyn-2-ols in ionic liquids Raffaella Mancuso,*^a Christian S. Pomelli,^b Cinzia Chiappe,^b Richard C. Larock^c and Bartolo Gabriele*^a *Org. Biomol. Chem.*, 2014,**12**, 651-659
- [13] Brønsted acid ionic liquid catalyzed facile synthesis of 3-vinylindoles through direct C3 alkenylation of indoles with simple ketones Amir Taheri,^a Changhui Liu,^a Bingbing Lai,^a Cheng Cheng,^a Xiaojuan Pan^a and Yanlong Gu*^{ab} *Green Chem.*, 2014,**16**, 3715-3719
- [14] Recent trends on application of Ionic Liquids in organic synthesis. P.CSERJESL . K. BELAFI-BAKO , N.NEMOSTOTHY , L. GUBICZA, HUNGARIAN JOURNAL OF INDUSTRIAL CHEMISTRY vol.36 (1-2)pp 27-34 (2008).

¹ P. D. Shirbhate

⁴Corresponding author: Department of Physics,

S.D. Charpe

2Department of Physics, J. D. Patil Sangludkar

P. J. Jadhao

³Department of Physics, Gondwana University, Gadchiroli 442605 India.

⁴V. S. Kalyamwar

4 Department of Physics, Bharatiya Mahavidyalaya, Amravati, 444405 India.

*Corresponding author: Dr. P. D. Shirbhate

Synthesis and Characterization of Stannic

Oxide Nanoparticles by the Sol–Gel Method ^{nal 4452}

Mahavidyalaya Daryapur Dist.-Amravati 444803, India.



**Journal of
Electrical
Systems**

Abstract: - In this work, the nanoparticles of stannic oxide (SnO₂) were synthesized using the sol-gel method, using stannic chloride dehydration (SnCl₂·2H₂O) as the precursor, ammonia solution (NH₃) as a solvent, and distilled water as a medium. Comprehensive structural studies have been conducted using X-ray diffraction (XRD). The SnO₂ NPs exhibit a typical tetragonal structure, as shown by the XRD spectra. The average crystalline size of SnO₂ NPs was determined to be around 23.18 nm using the Debye-Scherrer formula. XRD analysis shows that the synthesized sample is free of impurities.

Keywords: SnO₂ Nanoparticles; Sol-gel method, XRD.

I. INTRODUCTION

Nanotechnology stands at the forefront of modern materials science, offering unprecedented opportunities to engineer materials with tailored properties at the nanoscale [1-5]. Among the myriad of nanomaterials, stannic oxide (SnO₂) nanoparticles have emerged as a promising candidate owing to their diverse applications spanning catalysis [6], gas sensing [7], energy storage [8], and optoelectronics [9-10]. The precise control over their size, morphology, and surface properties is crucial for optimizing their performance in various applications.

The sol-gel method [11] represents a versatile and cost-effective approach for the synthesis of nanoparticles, enabling precise control over particle size, uniformity, and crystallinity. Leveraging this method for the synthesis of stannic oxide nanoparticles presents an avenue for achieving tailored properties to meet specific application demands.

This paper presents a comprehensive investigation into the synthesis and characterization of stannic oxide nanoparticles via the sol-gel method [12-13]. By meticulously controlling the synthesis parameters such as precursor concentration, solvent composition, and reaction conditions, we aim to elucidate the influence of these factors on the morphology, crystallinity, and physicochemical properties of the resulting nanoparticles.

II. EXPERIMENTAL

2.1 Materials

All the chemicals used in the experiment were of analytic reagent (AR) grade. Stannous chloride dehydrates (SnCl₂·2H₂O), distilled water, ammonia solution (NH₃) was available pure form.

2.2 Synthesis of SnO₂ NPs by sol gel method

SnO₂ NPs was synthesized by using sol-gel method. By dissolving 2 g (0.1 M) of stannous chloride dehydrate in 100 ml of distilled water, SnO₂ nanopowders were obtained. Ammonia solution was added to the previous solution dropwise while stirring after it had completely dissolved. The resultant gels were filtered and dried for 24 hours at 80°C to eliminate water molecules. Finally, tin oxide nanopowders are produced after two hours at 550°C.

III. RESULTS AND DISCUSSION

3.1. X-Ray Diffraction (XRD)

The crystallinity of the powdered sample of as-prepared SnO₂ NPs was examined using the X-ray diffraction technique. The SnO₂ NPs' XRD pattern is shown in Fig. 1. Cu K α ($\lambda=1.542\text{\AA}$) patterns were obtained between 5° and 99° using an accelerating voltage of 40 KV. The counting rate used to gather the data was 0.0170°/min. The K α doublets have good resolution. XRD data can be used for estimating the crystalline size using Debye Scherrer's formula [14]

$$D = \frac{0.9\lambda}{\beta \cos\theta}$$

where, D is the crystallite size of the particles, shape factor is 'K'. ' λ ' is the incident X-ray wavelength (1.54056 Å, CuK α), θ is the diffraction angle and β is the full width half maximum. Further, JCPDS card number 01-077-0447

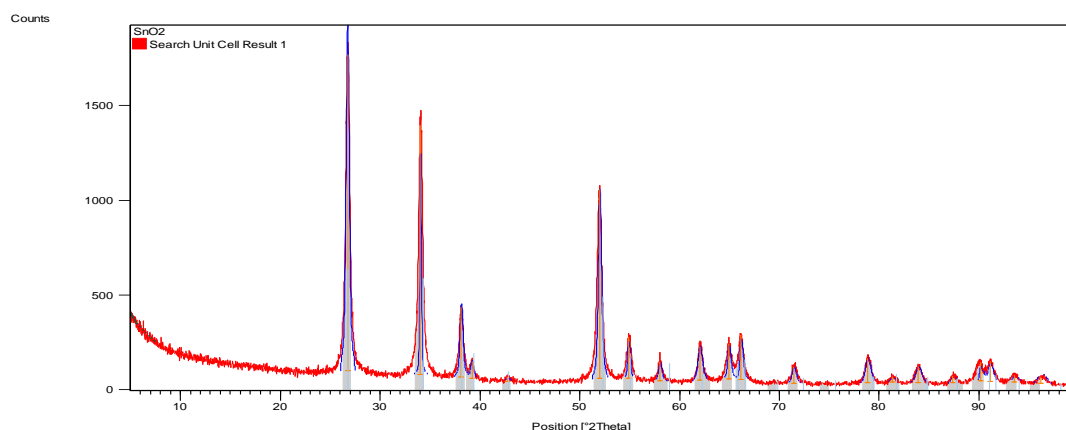


Figure 1: X-Ray Diffraction pattern of SnO₂ NPs synthesized by sol-gel method.

As illustrated in Fig. 1, the produced SnO₂ sample's XRD pattern showed greater intensity peaks at 2θ - 26.7399, 34.0409, 38.1412, 39.1911, 51.9902, and 54.8983. Sharp peaks in the SnO₂ XRD pattern indicate that the material is highly crystalline in nature. A distinct broadening of the XRD peaks suggests that the material that has been manufactured contains particles in the nanoscale range. Using the Debye-Scherrer formula, the crystalline size was determined to be 23.18 nm for the highest peak (26.7399°). The higher peak intensities of an XRD pattern are due to the better crystallinity [15]. The corresponding X-ray diffraction peak for planes confirm the formation of a typical tetragonal structure of SnO₂ (DB card number = = 01-077-0447). Further, Using PDXL software which provided with RigakuMinflex 600 model, it is confirmed that synthesized powder contains Sn and O elements only without any impurity. Table 1 shows the 2θ values and FWHM of as-synthesized SnO₂ NPs.

Table 1: 2θ values and FWHM of as-synthesized SnO₂ NPs.

Pos. [$^{\circ}2\theta$.]	Height [cts]	FWHM [$^{\circ}2\theta$.]	d-spacing [Å]	Rel. Int. [%]
26.7399	1669.65	0.3680	3.33396	100.00
34.0409	1318.93	0.1338	2.63376	78.99
38.1412	369.55	0.3346	2.35953	22.13
39.1911	89.93	0.3346	2.29871	5.39
42.7872	23.38	0.4015	2.11347	1.40
51.9902	999.45	0.3346	1.75895	59.86
54.8983	222.48	0.2342	1.67245	13.32

58.0259	101.08	0.3346	1.58954	6.05
62.0197	176.44	0.4684	1.49643	10.57
64.9482	188.88	0.3346	1.43585	11.31
66.1715	236.28	0.3011	1.41225	14.15
71.4220	90.01	0.4015	1.32078	5.39
78.8175	129.52	0.5353	1.21436	7.76
81.2984	31.74	0.4015	1.18346	1.90
83.8797	85.79	0.6022	1.15349	5.14
87.3687	36.99	0.4684	1.11619	2.22
90.1785	100.67	0.2676	1.08858	6.03
91.0976	104.26	0.4684	1.07997	6.24
93.5561	38.07	0.5353	1.05795	2.28
96.2056	35.08	0.9792	1.03487	2.10

IV. CONCLUSIONS

Using the sol-gel method, pure SnO₂ NPs were successfully synthesized. As synthesized, SnO₂ NPs have a tetragonal crystal structure with an average particle size of 23.18 nm, as confirmed using XRD. The sharp peaks in XRD at particular intensities denote the good crystallinity of sol-gel-synthesized SnO₂ NPs.

Conflict of interest

There are no conflicts to declare including any financial interest.

References

- [1] Dai, L. (Ed.). (2006). Carbon nanotechnology: recent developments in chemistry, physics, materials science and device applications.
- [2] Logothetidis, S. (2011). Nanotechnology: Principles and applications. In *Nanostructured materials and their applications* (pp. 1-22). Berlin, Heidelberg: Springer Berlin Heidelberg. https://doi.org/10.1007/978-3-642-22227-6_1
- [3] Nasrollahzadeh, M., Sajadi, S. M., Sajjadi, M., & Issaabadi, Z. (2019). An introduction to nanotechnology. In *Interface science and technology* (Vol. 28, pp. 1-27). Elsevier. <https://doi.org/10.1016/B978-0-12-813586-0.00001-8>
- [4] Kumar, R., Kumar, M., & Luthra, G. (2023). Fundamental approaches and applications of nanotechnology: A mini review. *Materials Today: Proceedings*. <https://doi.org/10.1016/j.matpr.2022.12.172>
- [5] Sahu, M. K., Yadav, R., & Tiwari, S. P. (2023). Recent advances in nanotechnology. *International Journal of Nanomaterials, Nanotechnology and Nanomedicine*, 9(1), 015-023. <https://doi.org/10.17352/2455-3492.000053>
- [6] Mai, L. (Ed.). (2023). *Nanowire Energy Storage Devices: Synthesis, Characterization and Applications*. John Wiley & Sons.
- [7] Izydorczyk, W., & Izydorczyk, J. (2021). Structure, Surface morphology, chemical composition, and sensing properties of SnO₂ thin films in an oxidizing atmosphere. *Sensors*, 21(17), 5741. <https://doi.org/10.3390/s21175741>
- [8] Jahnke, T., Raafat, L., Hotz, D., Knöllner, A., Diem, A. M., Bill, J., & Burghard, Z. (2020). Highly porous free-standing rGO/SnO₂ Pseudocapacitive cathodes for high-rate and long-cycling Al-ion batteries. *Nanomaterials*, 10(10), 2024. <https://doi.org/10.3390/nano10102024>
- [9] Jang, B., Kang, H., Lee, W. Y., Bae, J. H., Kang, I. M., Kim, K., ... & Jang, J. (2020). Enhancement mode flexible SnO₂ thin film transistors via a UV/Ozone-assisted sol-gel approach. *IEEE Access*, 8, 123013-123018. [10.1109/ACCESS.2020.3007372](https://doi.org/10.1109/ACCESS.2020.3007372)

- [10] Agrawal, R. M., Charpe, S. D., Raghuwanshi, F. C., & Lamdhade, G. T. (2015). Synthesis and characterization of magnesium oxide nanoparticles with 1: 1 molar ratio via liquid-phase method. *International Journal of Application or Innovation in Engineering & Management*, 4(2), 141-145.
- [11] Charpe, S. D., & Raghuwanshi, F. C. (2015). Synthesis, structural and gas sensing properties of pure Zinc Oxide nano thick film. *Journal of Electron Devices*, 21, 1854-1861. <https://doi.org/10.5281/zenodo.10774434>
- [12] Onkar, S. G., Raghuwanshi, F. C., Kalyamwar, V. S., & Charpe, S. D. Synthesis and characterization of SnO₂-ZnO composites nano particles. <https://doi.org/10.5281/zenodo.10774443>
- [13] Aziz, M., Abbas, S. S., & Baharom, W. R. W. (2013). Size-controlled synthesis of SnO₂ nanoparticles by sol-gel method. *Materials Letters*, 91, 31-34. <https://doi.org/10.1016/j.matlet.2012.09.079>
- [14] Bokuniaeva, A. O., & Vorokh, A. S. (2019, December). Estimation of particle size using the Debye equation and the Scherrer formula for polyphasic TiO₂ powder. In *journal of physics: Conference series* (Vol. 1410, No. 1, p. 012057). IOP Publishing. 10.1088/1742-6596/1410/1/012057
- [15] Ahvenainen, P., Kontro, I., & Svedström, K. (2016). Comparison of sample crystallinity determination methods by X-ray diffraction for challenging cellulose I materials. *Cellulose*, 23(2), 1073-1086. <https://doi.org/10.1007/s10570-016-0881-6>
- thin films in an oxidizing atmosphere. *Sensors*, 21(17), 5741. <https://doi.org/10.3390/s21175741>
- [8] Jahnke, T., Raafat, L., Hotz, D., Knöller, A., Diem, A. M., Bill, J., & Burghard, Z. (2020). Highly porous free-standing rGO/SnO₂ Pseudocapacitive cathodes for high-rate and long-cycling Al-ion batteries. *Nanomaterials*, 10(10), 2024. <https://doi.org/10.3390/nano10102024>
- [9] Jang, B., Kang, H., Lee, W. Y., Bae, J. H., Kang, I. M., Kim, K., ... & Jang, J. (2020). Enhancement mode flexible SnO₂ thin film transistors via a UV/Ozone-assisted sol-gel approach. *IEEE Access*, 8, 123013-123018. [10.1109/ACCESS.2020.3007372](https://doi.org/10.1109/ACCESS.2020.3007372)
- [10] Agrawal, R. M., Charpe, S. D., Raghuwanshi, F. C., & Lamdhade, G. T. (2015). Synthesis and characterization of magnesium oxide nanoparticles with 1: 1 molar ratio via liquid-phase method. *International Journal of Application or Innovation in Engineering & Management*, 4(2), 141-145.
- [11] Charpe, S. D., & Raghuwanshi, F. C. (2015). Synthesis, structural and gas sensing properties of pure Zinc Oxide nano thick film. *Journal of Electron Devices*, 21, 1854-1861. <https://doi.org/10.5281/zenodo.10774434>
- [12] Onkar, S. G., Raghuwanshi, F. C., Kalyamwar, V. S., & Charpe, S. D. Synthesis and characterization of SnO₂-ZnO composites nano particles. <https://doi.org/10.5281/zenodo.10774443>
- [13] Aziz, M., Abbas, S. S., & Baharom, W. R. W. (2013). Size-controlled synthesis of SnO₂ nanoparticles by sol-gel method. *Materials Letters*, 91, 31-34. <https://doi.org/10.1016/j.matlet.2012.09.079>
- [14] Bokuniaeva, A. O., & Vorokh, A. S. (2019, December). Estimation of particle size using the Debye equation and the Scherrer formula for polyphasic TiO₂ powder. In *journal of physics: Conference series* (Vol. 1410, No. 1, p. 012057). IOP Publishing. 10.1088/1742-6596/1410/1/012057
- [15] Ahvenainen, P., Kontro, I., & Svedström, K. (2016). Comparison of sample crystallinity determination methods by X-ray diffraction for challenging cellulose I materials. *Cellulose*, 23(2), 1073-1086. <https://doi.org/10.1007/s10570-016-0881-6>

¹Dhananjay. P.
Deshmukh

²Ashitosh P.
Deshmukh

³Sushil D. Charpe

Electrical behavior (ac And dc Conduction) of Polythiophene composite thin films doped with Iodine.



Abstract: - Thin solid films of PTh-PVAc doped with Iodine (Pure, 5.5, 10.4, 14.9, 18.9 and 22.5 wt %) were synthesized by chemical oxidative polymerization method in order to study the electrical properties such as dc and ac conductivity at various temperature ranges. Amorphous nature of the sample was confirmed by the XRD technique of sample. Temperature dependent conductivity (313-363K) of PTh-PVAc films doped with Iodine follows Arrhenius nature which depicts dc parameters such as activation energy, pre-exponential factors etc. The impedance spectra of films (323-343K over frequencies from 0.1-200 KHz) found to consist of only one arc suggest various parameters such as relaxation time, bulk resistance, bulk capacitance, dielectric activation energy etc.

Keywords: Poly(vinyl acetate) (PVAc), Polythiophene (PTh), Iodine, dc,ac

I. INTRODUCTION

Due to electron hopping transport, PTh is arose as a better conducting polymer and a leading field of investigation amongst conducting polymers. A number of applications have been proposed for PThs, such as field effect transistors, electroluminescent devices, solar cells, photochemical resists, nonlinear optic devices, batteries, diodes and chemical sensors [1]. A high performance is seen in various electronic devices and memory devices of PTh conductive polymers, due to recent developments of materials having improved process ability and ambient stability relative to the earlier systems. Due to high conductivity and fascinating structural properties, PTh has been involved in a wide range of applications.

These conjugating polymers thin films have been studied by many workers, because of special electrical properties, considerable thermal stability and oxidation resistance that are favorable in applications such as optoelectronic, biosensors, electro chromic displays and chemical sensors [2-3]. Roncali [4] surveyed the electrochemical synthesis and the electronic properties of substituted PThs in 1997. The overall review on chemical synthesis of PThs and applications as chemical sensors, organic memory devices, photo conductivity, etc., is given by many researchers [5,6]. Temperature-dependent conductivity, in the case of ion conducting solid electrolytes, is more completely explained by Vogel-Tamman-Fulcher (VTF) [7-9] rather than other models. Ryu et al. [10] predicted that PTh powder prepared by electrochemical method, shows better results than that prepared by the fast oxidation method. Yildiz et al. [11] synthesized poly (ethylene oxide)-copolymer-polythiophene (PEO-co-PTh) by electrochemical copolymerization and from characterization, they predicted the exploitation of electrochromic devices. Barde et al [12] observed the variation in ionic conductivity in polypyrrole (PPy)-poly (vinyl acetate) (PVAc) films synthesized by oxidative polymerization. An investigation in electrical, structural properties and impedance spectroscopy in PTh-PVAc composite films doped with Iodine was carried out by Bobade et al and Deshmukh et al [13-14].

The present paper focuses on comparison in electrical properties of Polythiophene composite thin films doped with Iodine.

II. EXPERIMENTAL PROCEDURE

A) STRUCTURE

For structure determination, X-ray diffractometer PANalytical PW: 3040/60, Netherland was used. All the PTh PVAc samples doped with iodine were characterized at Vishveshwaraia National Institute of Technology (VNIT), Nagpur.

¹*Corresponding author: Asst. Prof., Late R. Bharti Arts, Commerce And Smt. S. R. Bharti Science College, Arni, Dist. Yavatmal

²Research Scholar, GVISH, Amravati

³Asst. Prof, J.D. Patil Sangludkar Mahavidyalaya, Daryapur

Copyright©JES2024on-line:journal.esrgroups.org

B) DC CONDUCTIVITY MEASUREMENT

The dc conductivity of the samples was measured by the two probe method [12, 13], in a temperature range of 313 – 363 K. A dc regulated power supply and a picoammeter with a resolution of 1 pA was used for the measurement of resistance of the sample. Samples being tested were sandwiched between two conducting copper electrodes of the sample holder and then placed in a muffle furnace. The heating rate of the sample was $1^{\circ}\text{C min}^{-1}$.

C) AC CONDUCTIVITY MEASUREMENT

ac conductivity of the samples was recorded on LCR meter (Wayne Kerr, UK) having range of frequencies from 0.1-200 KHz at temperature in the range 323-343K with heating rate $1^{\circ}\text{C min}^{-1}$. A constant voltage is applied to the sample and corresponding impedance and phase angle was measured at constant temperature for all frequency range. Sample holder and furnace used is same as that of dc conductivity measurement.

III. RESULTS AND DISCUSSION

A) STRUCTURE

The XRD spectra of the PTh-PVAc composite films with different wt % of Iodine are shown in the figure 1.

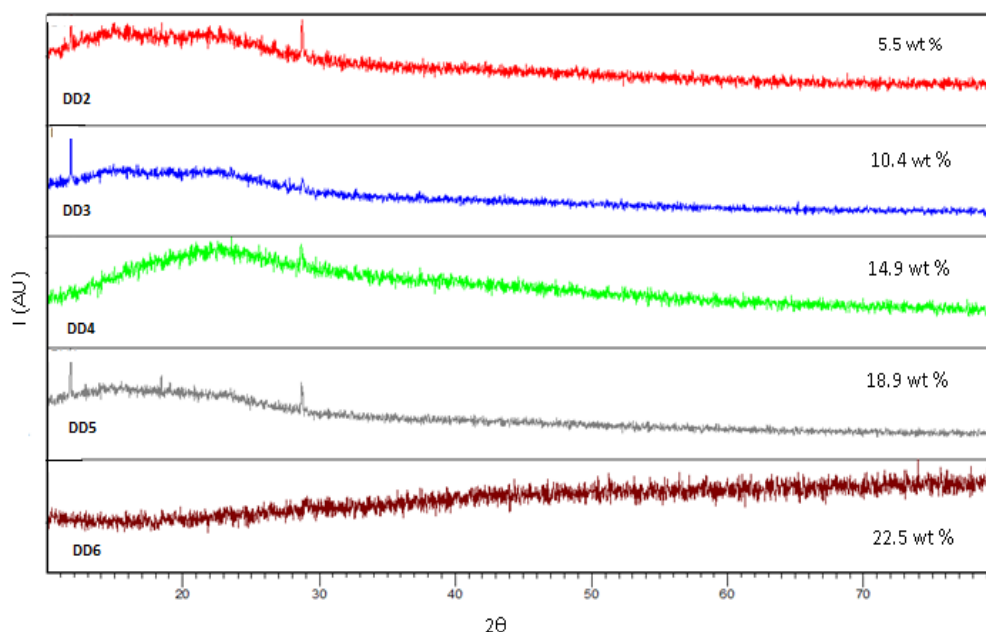


Fig 1 XRD Spectra of PTh-PVAc films doped with Iodine

Absence of peak in the intensity versus 2θ curve represents complete amorphous state of the sample [6]. Indication of peak or peaks in the curve suggests the formation of phase or phases in the composite during polymerization process.

All the spectra for different PThs having wt % of Iodine reveal a hump in low 2θ region. It is due to short range order and indicating that these PTh-PVAc composite films doped with Iodine are amorphous. Increase in concentration of dopant Iodine does not induce any crystallinity in these composite films. This also explains the homogeneous nature of the samples. The sharp peaks observed may be due to presence of Iodine in the sample. Since the samples of PTh-PVAc films doped with Iodine were indicating total amorphous nature this characterization is limited for these films only.

B) DC CONDUCTIVITY OF PTH-PVAC FILMS DOPED WITH IODINE

The dc conductivity of samples of iodine wt % 5.5 – 22.5 was measured at a temperature range of 313 – 363 K, by measuring the resistance of the samples; it was observed that the conductivity depends upon composition as well as temperature. The variation of DC conductivity vs. concentration of iodine wt % for composite films at

330 K is shown in Figure1. Initially, the conductivity increased, reached $9.78 \times 10^{-10} \text{ S cm}^{-1}$ for 10.4 wt % of iodine and then rapidly decreased with iodine concentration.

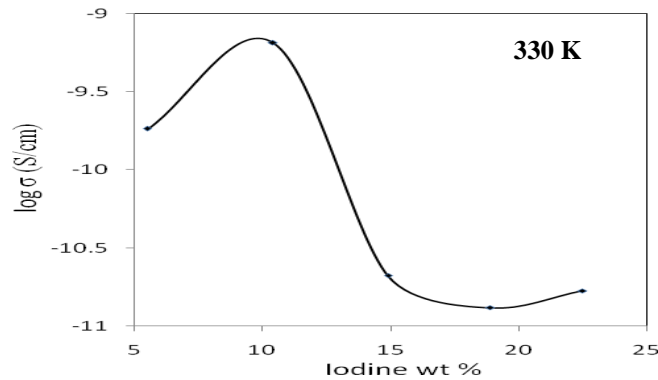


Fig.2: Variation of Conductivity with Iodine wt % at 330 K

Many researchers [11, 14-16] reported a similar conductivity isotherm. In the case of PTh composites [16-20], percolation behavior was reported even for a low concentration of PTh. The temperature dependence of conductivity for different iodine wt % is shown in Figure 2. From this plot it is observed that the conductivity increased with increase in temperature, due to an increase in mobility of the ions. Ionic conductivity for 10.4 wt % of iodine showed maximum conductivity, which can be attributed to the fact that ionic motion is improved by polymer segmental motion for the particular concentration. Also the formation of PTh-PVAc^{-I} has much contribution to the ionic conductivity.

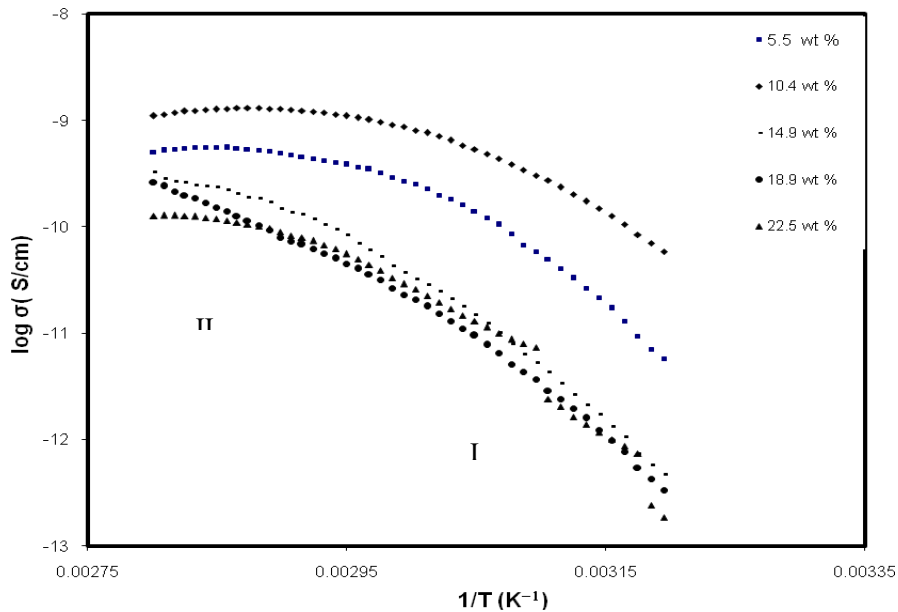


Fig. 3: Variation of logσ with 1/T for different wt. % of Iodine

From the fig.3 it is observed that initially the rate of increase of conductivity is fast and after certain temperature the rise is slow. Thus it leads to two activation region (I and II as shown in fig.3) giving two different activation energies. The samples synthesized by concentration of Iodine (5.5, 10.4, 14.9 and 22.5 wt %), show the curvature type behavior below a certain temperature T_c , called knee temperature, and above which the curves are nearly linear in nature. The non-linearity in Arrhenius plot for samples synthesized at 5.5, 10.4, 14.9 and 22.5 wt % of Iodine indicates the ionic transport facilitates by the segmental motion of polymer chains. Thus Vogel-Tamman-Fulcher (VTF) [9-11] equation may more effectively represent the results. And the sample with 18.9 wt % of Iodine indicates straight line nature to which VTF equation could not be applied.

$$\sigma = \frac{A}{T^{1/2}} \exp\left[-\frac{B}{k(T - T_0)}\right] \dots\dots\dots(1)$$

where T is the absolute temperature; 'A', 'B' and T₀ are the fitting constants and 'k' is Boltzmann constant. 'A' is the pre-exponential factor, which is related to the number of charge carriers. 'B' is the pseudo activation energy related to activation energy of the ion transport. It is related to critical volume for displacement in free volume model [9] and to the energy barrier for rotational motion of polymer segment in configuration entropy model [21]. T₀ is the critical (ideal glass transition) temperature, usually it is 30-50 K below 'T_g'. It is the temperature at which configuration entropy or free volume disappears.

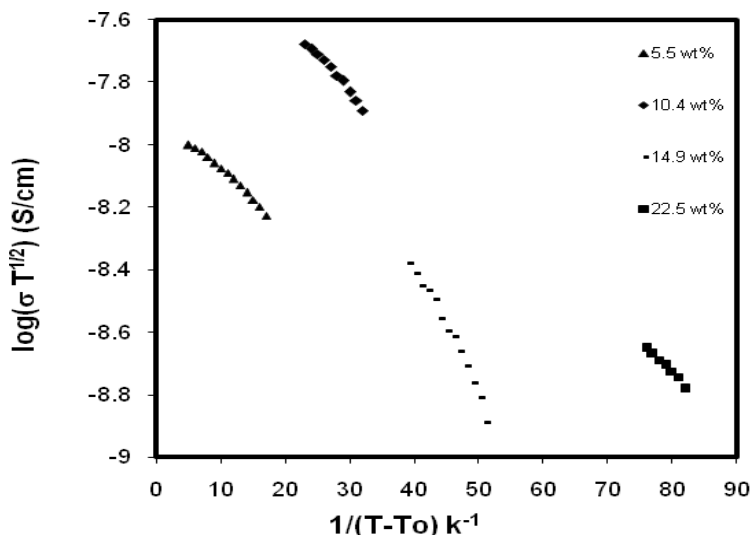


Fig. 4 VTF plots for PTh-PVAc films for different wt % of

The exploration of equation 1) gives the VTF fit parameters (fig.4) which are summarized in Table 1. It is evident that the activation energy value 'B', for the sample prepared with 5.5 wt % of Iodine is minimum. The values of T₀ increases with rise in concentration of Iodine. Such dependence of T₀, with respect to concentration of salt, has been reported in polymer electrolytes [22]. In high temperature region (fig.3) the curves no longer fits the VTF equation. The cross over from VTF to Arrhenius is clearly visible in the high temperature region. This type of cross over in conductivity behavior generally observed in polymer electrolyte systems [9-11].

Arrhenius equation is,

$$\sigma = \sigma_0 \exp\left[-\frac{E_a}{kT}\right] \quad \dots \dots \dots (2)$$

Where E_a is the Activation energy and σ₀ is the pre-exponential factor.

Table 1: VTF equation fitting parameters for the PTh-PVAc films for different Iodine wt %

Concentration of Iodine (wt%)	Ionic Transference number (tion)	Energy E _a (eV)	Temperature T _c (K)	Pre-exponential factor A (SK ^{1/2} cm ⁻¹)	Pseudo activation energy B(eV)	Ideal glass transition temperature T _o (K)
5.5	0.96	0.149	388	2.3319 x10 ⁻⁷	0.00009	327
10.4	0.94	0.188	385	1.6538 x10 ⁻⁷	0.00019	330
14.9	0.95	0.420	362	1.0124 x10 ⁻⁸	0.00058	332
22.5	0.87	0.150	380	1.7047 x10 ⁻⁸	0.00010	341

B) AC CONDUCTIVITY OF PTh-PVAc FILMS DOPED WITH IODINE

ac conductivity of the pure PTh-PVAc sample and doped with different Iodine wt % was measured at various temperatures 323-343K by applying a wide range of frequencies from 0.1-200 KHz. Fig.5-8 shows Nyquist plots of the samples Pure, 5.5 wt%,10.4 wt% and 14.9 wt% samples and it is observed that the resistance of all the samples is found to be decreasing with the rise in temperature.

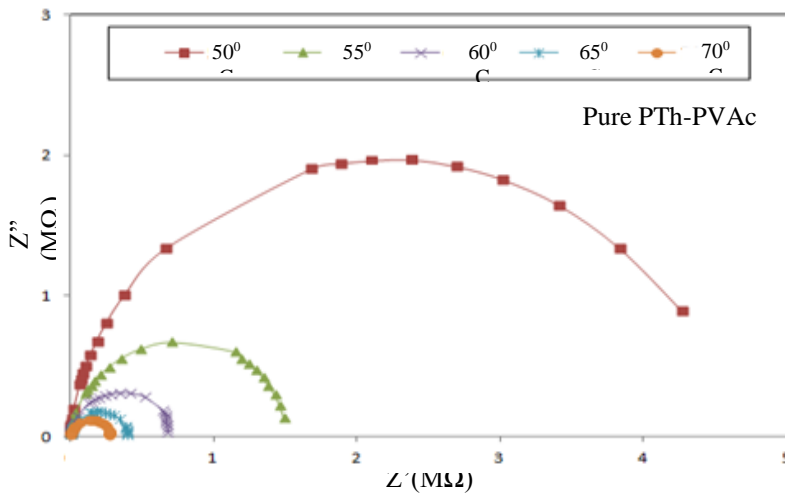


Fig. 5

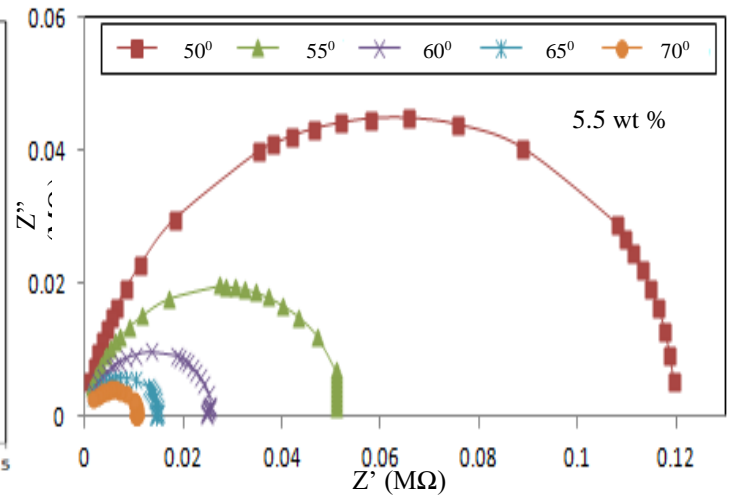


Fig. 6

All the curves show the same trends in the temperature range 323-343 K. Many researchers [23-26] reported a similar conductivity isotherm. The impedance spectrum of PTh-PVAc pure film and doped with Iodine is found to consist of only one arc (fig. 5-8) which may be taken to mean that the conduction processes have identical time constants [27].

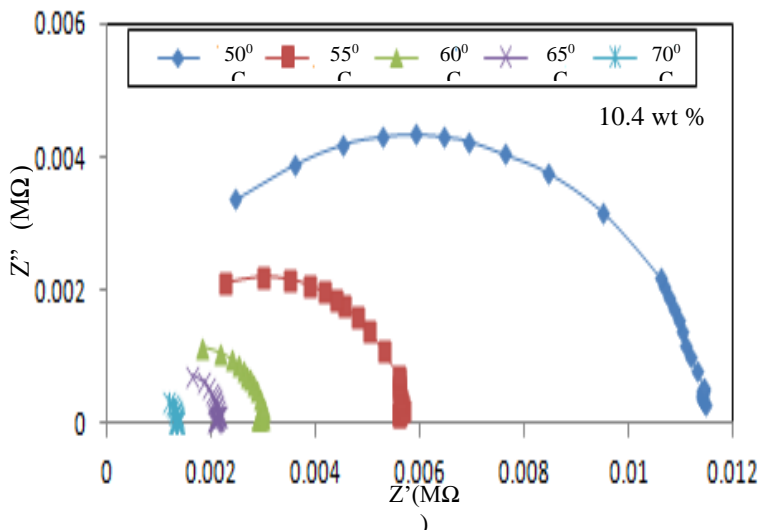


Fig. 7

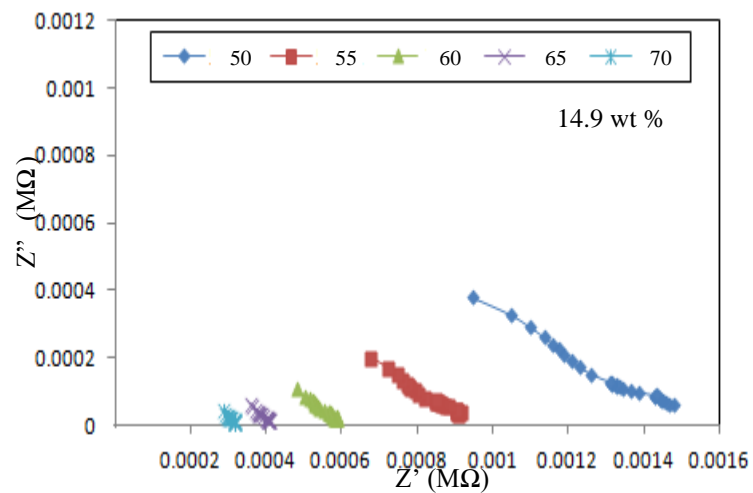


Fig. 8

All the curves show the same trends in the temperature range 323-343 K. Many researchers [23-26] reported a similar conductivity isotherm. The impedance spectrum of PTh-PVAc pure film and doped with Iodine is found to consist of only one arc (fig. 5-8) which may be taken to mean that the conduction processes have identical time constants [27].

Also it may be argued that as the temperature increases the arc of semicircle reduces, indicating the increase in conductivity. The basic features of the spectra seem to be qualitatively similar to those obtained by Johnson et al. [28] for polythiophene films and Komura et al. [24] for polypyrrole polystyrenesulfonate composite films in a similar configuration. The arcs are found to be highly depressed for the all films for different temperatures which indicate the distribution of relaxation times [29]. From the semicircle, the values of bulk resistance are calculated and noted in table 3.2.1. The variation of real axis Z' with $\log f$ for the samples is shown in fig 9-12.

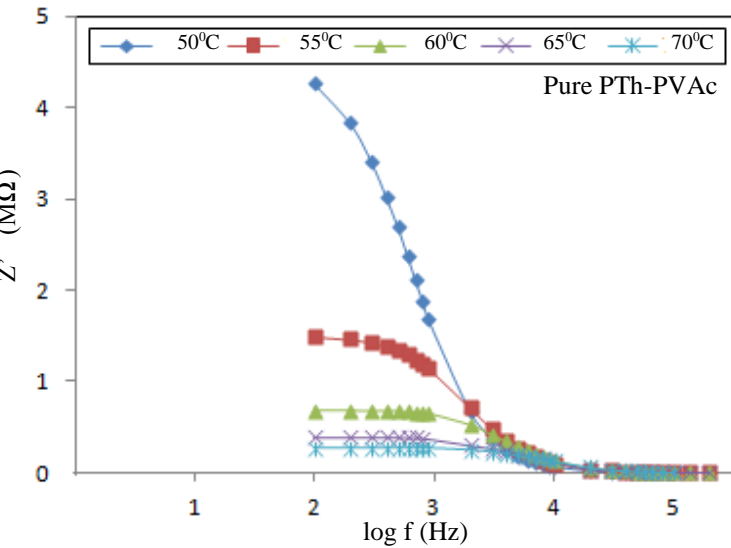


Fig. 9

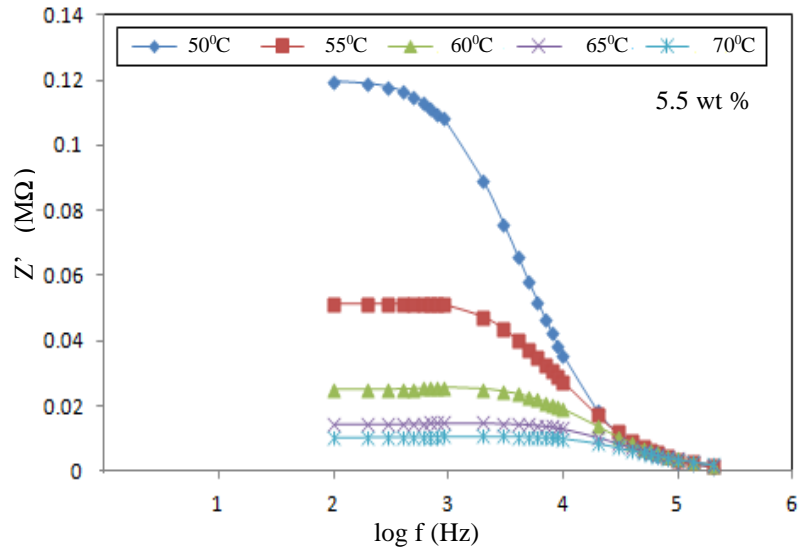


Fig. 10

From the fig.9-12, it is observed that the pure PTh-PVAc sample shows the wide variation of resistance with respect to real axis at all frequencies. As the frequency increases the resistance of the sample is found to be decreasing in a continuous manner and then it became constant. Also as the concentration of the dopant Iodine is increasing, the sample exhibits much lesser resistance for higher frequencies. The values of resistance are decreasing with rise in frequency and temperature. The magnitude decreases on increasing temperature in the low- frequency range which merges in the high-frequency region irrespective of temperature. This nature may be due to the release of space charge [30].

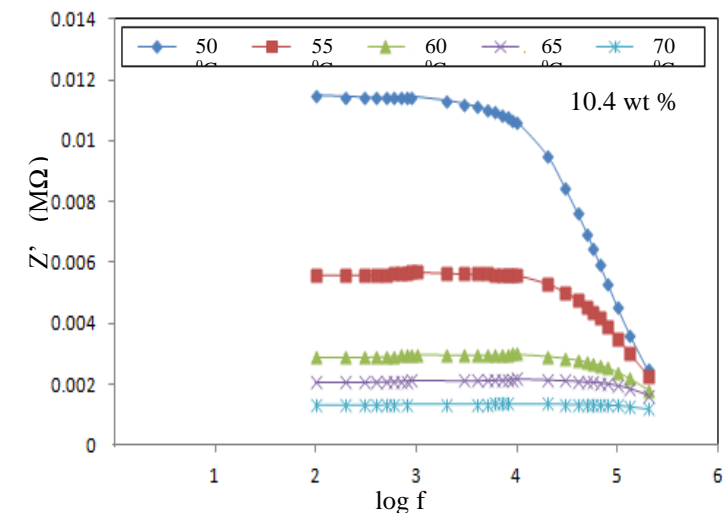


Fig. 11

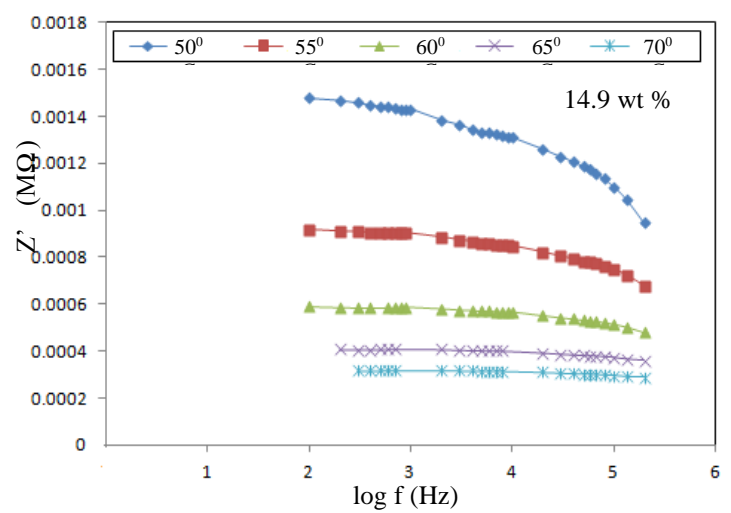


Fig. 12

The reduction in barrier properties of the materials with rise in temperature may be a responsible factor for enhancement of ac conductivity of the materials at higher frequencies [31-32]. Further, in the low frequency region, there is a decrease in magnitude with rise in temperature showing negative temperature coefficient of resistance (NTCR) behavior [33]. This behavior is changed drastically in the high frequency region showing complete merge of plot above a certain fixed frequency.

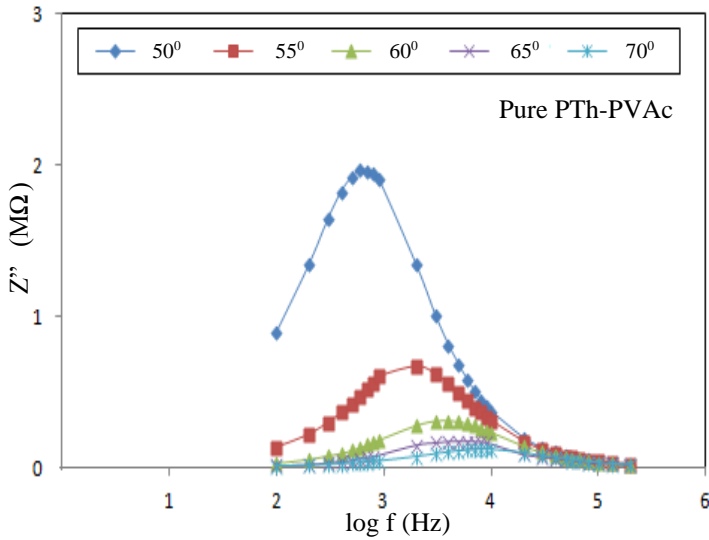


Fig. 13

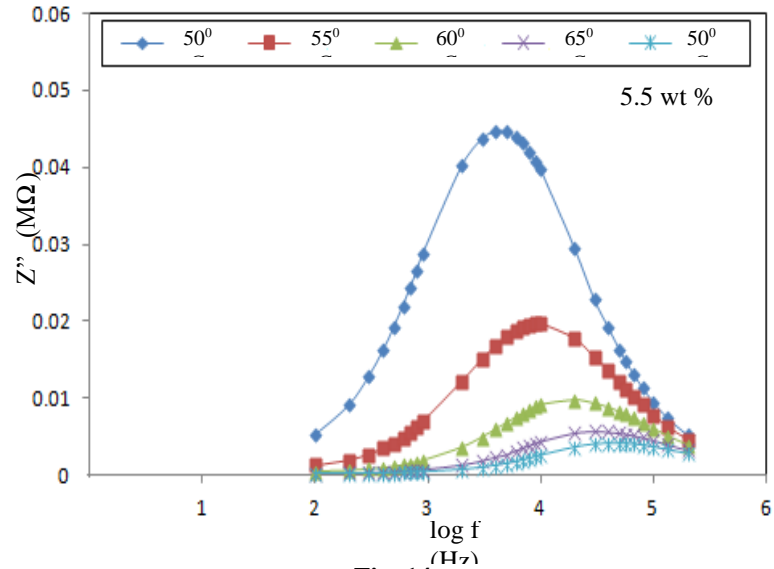


Fig. 14

The variation of log f versus Z'' in fig. 13-16 shows asymmetric peaks at different temperatures. Each peak is associated with a maximum frequency called as relaxation frequency (f_r). As the temperature increases the relaxation frequency is found to be shifting towards higher frequency side and it finally merges in the high frequency region which is an indication of the accumulation of space charge in materials.

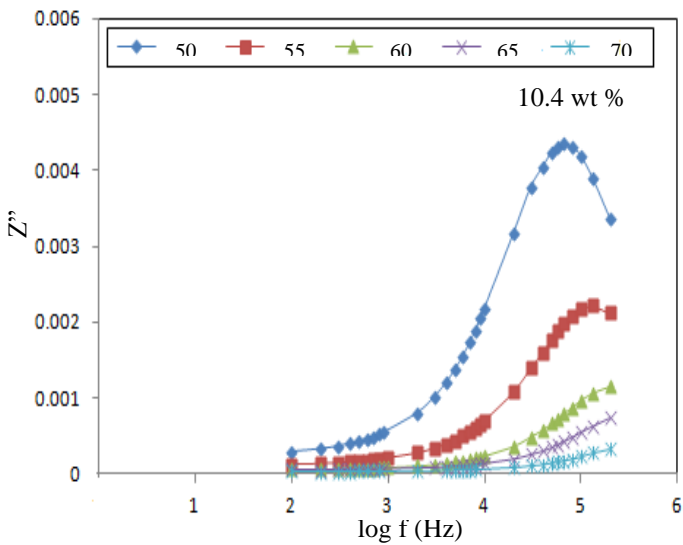


Fig. 15

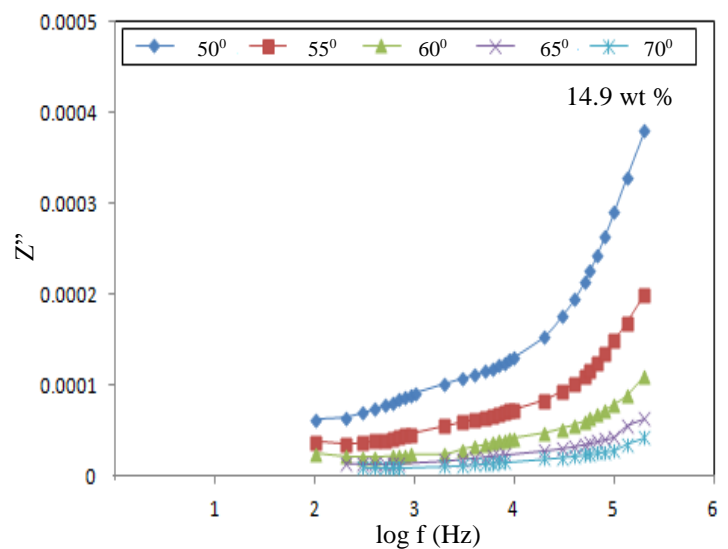


Fig. 16

The relaxation frequency (f_r) follows the Arrhenius behavior as,

$$f_r = f_0 \exp\left(\frac{-\Delta E}{kT}\right)$$

Or

(3.2.1)

$$\tau = \tau_0 \exp\left(\frac{-\Delta E}{kT}\right)$$

This equation is explored to find out the dielectric relaxation activation energy (ΔE) and relaxation time (τ). The calculated values of relaxation frequencies are plotted against the $1/T$ as shown in fig 17-19.

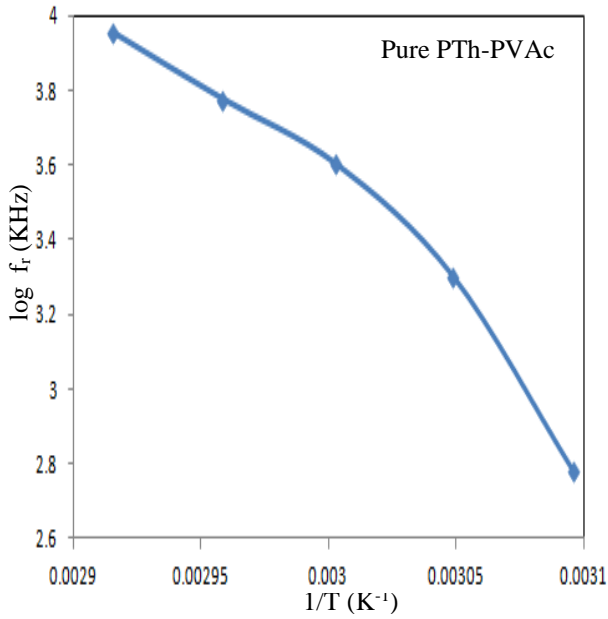


Fig. 17

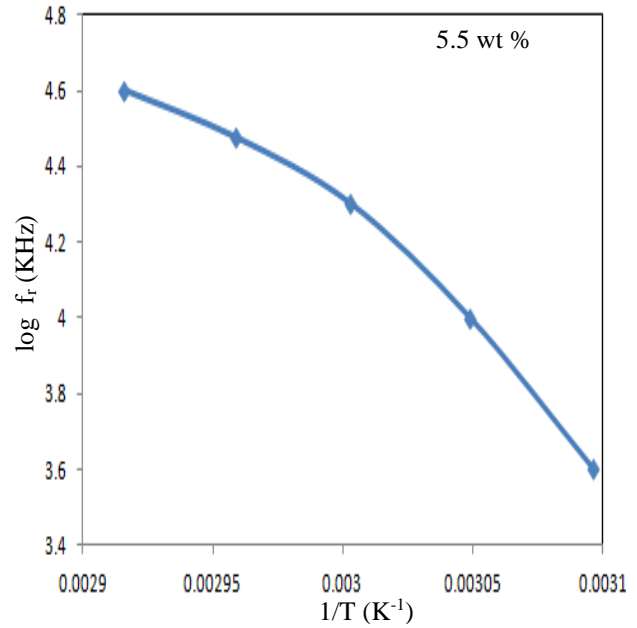


Fig. 18

The variation of log fr versus $1/T$ for the sample pure, 5.5 wt% and 10.4 wt% shows a straight line nature [34-36]. From this straight lines dielectric relaxation activation energy (ΔE) and relaxation time (τ) is noted in table 2.

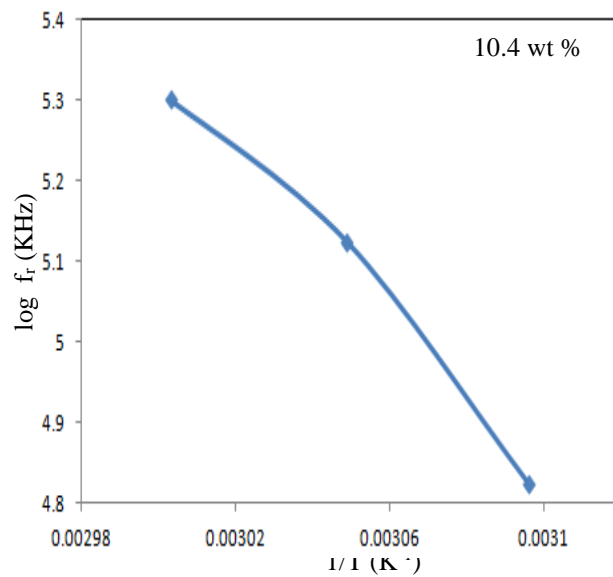


Fig. 19

Table 2 Dielectric relaxation activation energy and Relaxation time of PTh-PVAc film doped with Iodine

Sr.No.	Iodine wt %	ΔE (eV)	τ (μ s)
1	Pure PTh-PVAc	0.542	79.43
2	5.5	0.475	15.85
3	10.4	0.443	3.72
4	14.9	-	-

From the table 2 it is observed that, dielectric relaxation activation energy and relaxation time is maximum for Pure PTh-PVAc sample and minimum for 10.4 wt % of Iodine.

The values of bulk resistance (R_b) from fig. 5-8 and bulk capacitance (C_b) for peak frequencies from fig.9-12 are noted in table 3. From the table 3 it is observed that the bulk resistance of the sample decreases with the increase in temperature. The bulk capacitance is found to be maximum for the sample with 5.5 wt % Iodine.

Table 3 Bulk resistance and Bulk capacitance of PTh-PVAc film doped with Iodine at different temperature

Iodine wt %	323 K		328 K		333 K		338 K		343 K	
	$R_b(K\Omega)$	$C_b(pF)$	$R_b(K\Omega)$	$C_b(pF)$	$R_b(K\Omega)$	$C_b(pF)$	$R_b(K\Omega)$	$C_b(pF)$	$R_b(K\Omega)$	$C_b(pF)$
Pure PTh-PVAc	4850	54.72	1550	51.36	690	57.69	400	66.68	275	64.26
5.5	120	331.74	51	312.22	25.1	317.20	15.1	351.51	10.2	390.28
10.4	11.8	202.31	5.6	213.27	3.1	256.83	2.2	-	1.4	-
14.9	1.6	-	0.99	-	0.61	-	0.42	-	0.33	-

IV. CONCLUSION

Amorphous nature of the sample was confirmed by the XRD technique of sample. Temperature dependant conductivity for the samples 5.5, 10.4, 14.9 and 22.5 wt % of Iodine dopant follows the VTF equation [7-9] except 18.9 wt % sample. The cross over from VTF to Arrhenius observed in present system may be due to some sort of transition in energetic of local ion motion and reduction in effective ion density on undergoing order-disorder transition at temperature T_c . Thus T_c can be linked to order-disorder temperature. Below T_c the curves follows VTF equation. When the ionic conduction follows the VTF equation, a linear relation between $\log(\sigma T^{1/2})$ and $1/(T - T_0)$ is expected as shown in fig.3.1.3. The impedance spectra of PTh-PVAc films doped with Iodine consist of only one arc which may be taken to mean that the conduction processes have identical time constants. The variation of real axis Z' with $\log f$ shows negative temperature coefficient of resistance (NTCR). The variation of imaginary axis Z'' versus $\log f$ shows asymmetric peaks at different temperatures that lead to Debye type of relaxation. On the basis of impedance spectra various parameters such as relaxation time, bulk resistance, bulk capacitance, dielectric activation energy etc. are calculated. Dielectric relaxation activation energy and relaxation time is maximum for Pure PTh-PVAc sample and minimum for 10.4 wt % of Iodine. The bulk capacitance is found to be maximum for the sample with 5.5 wt % Iodine.

REFERENCES

- [1] Heuer HW, Wehrmann R, Kirchmeyer S. Adv. Funct. Mater. 2002, 12, 89 – 94.
- [2] E. M. Genes, A. Boyle, M. Lapkowski and C. Tsintavis, Synth Met., 36 (1990) 139.
- [3] P. Novak, K. Muller, K. Santhanam and O. Haas, Chem Rev., 97 (1997) 207.
- [4] Roncali J. Chem. Rev. 1997, 97, 173 – 205.

- [5] McCullough RD. *Adv. Mater.* 1998, 10, 93 – 116.
- [6] Reddinger JL, Reynolds JR. *Adv. Polym. Sci.* 1999, 145,57 – 122.
- [7] Fulcher GS. *J. Am. Chem. Soc.* 1925, 8, 339.
- [8] Vogel H. *Phys. Z.* 1922, 22, 645.
- [9] G. Tamman, W. Hesse, *Z. Anorg. Allg. Chem.* 156 (1926)245.
- [10] Ryu KS, Lee Y, Han KS, Kim MG. *Mater. Chem. Phys.* 2004,84, 380 – 384.
- [11] Yildiz HB, Kiralp S, Toppare L, Yagci Y, Ito K. *Mater. Chem. Phys.* 2006, 100, 124 – 127.
- [12] Barde WS, Pakade SV, Yawale SP. *J. Non Cryst. Solids* 2007,353, 1460 – 1465.
- [13] Bobade RS, Pakade (Yawale) SV, Yawale SP. *J. Non Cryst. Solids* 2009, 355, 2410 – 2414.
- [14] Deshmukh Dhananjay P, Yawale Sangita S, Yawale Shrikrishna P, *Journal of Polym Eng* 32 (2012): 103–110.
- [15] Wong HP, Dave BC, Levioux F, Harreld J, Dunn B, Nazer LF. *J. Matter Chem.* 1998, 8, 1019 – 1027.
- [16] Yin W, Lin H, Yin B, Yan T, Gu T. *Eur. Polym. J.* 1998, 34,779.
- [17] Yin W, Yan T, Gan LM, Lin H, Gan LH. *Eur. Polym. J.* 1998, 34,1763.
- [18] Aguilar-Hernandez J. *J. Phys. D: Apply. Phys.* 2001, 34,1700 – 1711.
- [19] Ruckenstein E, Yang S. *Polymer* 1993, 34, 4655.
- [20] Mandal TK, Mandal BM. *Synth. Metals* 1996, 80, 83.
- [21] M.H. Cohen, D. Turnbull, *J. Chem. Phys.* 31(1964).
- [22] M. Chakraborty, D.C. Mukherjee and B.M. Mandal, *Synth. Metals*, 98 (1999)193.
- [23] Abdel Salam Hamdy, *Int. J. Electrochem. Sci.*, pp.171-180, 1(2006).
- [24] T. Komura, S. Goisihara, T. Yamaguti, K. Takahashi, *J. Electroanal. Chem.*, pp.121, 456 (1998).
- [25] J. Ross Macdonald, *Annals of Biomedical Engineering*, pp.289-305, 20 (1992).
- [26] R Padma Suvama, *Bull. Mater. Sci.*, pp.647-651, 25(7), (2002).
- [27] J. Hwang, *Solid State Ionics*, pp.93-104, 98(1997).
- [28] B.W. Johnson, D.C. Read, *J. Electroanal. Chem.*, pp.103, 364 (1994).
- [29] J. Ross Macdonald, *J. Electroanal. Chem*, pp.25-50,223 (1987).
- [30] Macedo P.B; Moynihan C.T.; Bose R.; *Phys. Chem.*, pp.171,13(1972).
- [31] Provenzano V.; Boesch L.P.; *J. Am. Ceram. Soc.*, pp.492, 55(1972).
- [32] Jain H.; Hsieh C.H.; *J. Non-Cryst. Solids*, pp.1408, 172(1994).
- [33] S.K. Rout, Ali Hussian, *J. Allo. and Comp.*, pp.706-711,477 (2009).
- [34] S.K. Rout, Ali Hussian, *J. Allo. and Comp.*, pp.706-711,477 (2009).
- [35] P S Sahoo, A Panigrahi, *Bull. Mater. Sci.*, pp. 129–134,33(2), (2010).
- [36] R. Tripathi, A. Kumar, 'Pramana' *J. Phys.*, pp. 969-978,72(6),(2009).

© 2024. This work is published under

[https://creativecommons.org/licenses/by/4.0/legalcode\(the“License”\)](https://creativecommons.org/licenses/by/4.0/legalcode(the“License”)).

NotwithstandingtheProQuestTermsandConditions,youmayusethis content
in accordance with the terms of the License.

¹ P. D. Shirbhate
² D. P. Deshmukh
³ S. P. Yawale
⁴ S. V. Pakade

Synthesis and Impedance Spectroscopy of PTh-PEO Polymer composite doped with LiClO₄



Abstract: In this present work Polythiophene-Polyethylene oxide (PTh-PEO) polymer composite were synthesized by *in situ* chemical oxidative polymerization method. The structural and electrical properties of PTh-PEO polymer composite films were investigated by several experimental techniques including Fourier transform infrared (FTIR) spectroscopy, scanning electron microscopy (SEM) and impedance spectroscopy. The FTIR results confirmed the incorporation of LiClO₄ into PTh-PEO matrix. The SEM showed a uniform distribution of LiClO₄ and The impedance spectroscopy of PTh-PEO composite doped with LiClO₄ was measured at various temperatures over a wide range of frequencies from 0.1-200 KHz. The impedance spectrum of PTh-PEO polymer composite consist of only one arc which shows that the conduction processes have identical time constants. The Cole–Cole plots show that well-defined semicircles. The single semicircular plot for a given temperature suggests that the device can be considered as a parallel combination of bulk resistor (R_b)–bulk capacitor (C_b) network. The impedance plots suggest Debye type behaviour and single relaxation mechanism.

Keywords: Polythiophene- Polyethylene oxide (PTh,- PEO), Lithium Perchlorate (LiClO₄), Polymer Composite

I. INTRODUCTION

Now a days Polythiophene based materials have emerged as one of the most promising materials due to the easiness of its synthesis, its environmental stability and the possibility to modify it with different chemical groups [1-2]. And good thermal and electrical stability that exhibit some unique advantages of PTh for the development of various applications including organic field effect transistor, solar cells, sensors, electrochromic devices, and light emitting diodes [3-4]. Polythiophene composite have received a great deal of attention due to its flexibility, ease of doping, and good thermal and electrical stability that exhibit some unique advantages of PTh for the development of various applications [5-6] Although Polyethylene oxide (PEO) based polymer electrolyte has attracted great attention for high energy density and high power lithium-ion batteries because of its ease formation of complex with lithium salt, flexibility, stable mechanical properties, comparatively high mobility of charge carriers, etc. Among the polymeric materials reported, polyethylene oxide (PEO) based polymer electrolytes are the most commonly studied. The purpose of this investigation is to synthesize a composite material with good environmental and thermal stability and higher conductivity so that it would be useful for human being in developing and sustaining life.

In the present work PTh-PEO Polymer composite films doped with Lithium Perchlorate (LiClO₄) were synthesized by *in situ* chemical oxidative method. Their characterization is done through following various techniques, with an intension to exploit PTh Polymer composites for various applications.

¹ Corresponding author: 1Department of Physics, Gopikabai Sitaram Gawande Mahavidyalaya, Umarched, Dist. Yavatmal 445206, India.

²Department of Physics, Late R. Arts, Comm. And Smt. S.R. B. Science College Arni- 445103 (India)

³Department of Physics, Government Vidarbha Institute of Science and Humanities, Amravati-444604, (India)

⁴Director, Government Pre- IAS Training Centre, Amravati-444604, (India)

*Corresponding author: Dr. P. D. Shirbhate

Email: shirbhate@gsgcollege.edu.in

Copyright©JES2024on-line:journal.esrgroups.org

II. EXPERIMENTAL METHODS

2.1 Chemicals used :

Thiophene (Th) Polyethylene oxide (PEO, Mw 100,000) were obtained from Acros organic, New Jersey, USA. Lithium Perchlorate (LiClO_4), was purchased from LobaChem Mumbai. Methanol and Anhydrous FeCl_3 were acquired from S.d. fine, Mumbai. All the chemicals were used as received.

2.2 Synthesis of PTh-PEO polymer Composite doped with LiClO_4 :

PTh-PEO composite doped with LiClO_4 was synthesized at room temperature (303 K) by *in situ* chemical oxidative polymerization method [7]. Anhydrous FeCl_3 was used as a oxidizing agent. A solution of PEO was first prepared in methanol by stirring for 6 hours and kept over a night. Appropriate amount of Anhydrous FeCl_3 and LiClO_4 were added and stirred for 15 minutes. When monomer thiophene was added drop by drop to the solution a dark brown homogeneous solution was obtained. The solution was then poured on a polypropylene dishes (Petri dishes), to prepare the composite films. The thiophene polymerization progresses because the evaporation of the solvent increases the oxidation potential of cast solution. After evaporation of the solvent, the composite films were formed.

III. RESULTS AND DISCUSSION

3.1 Fourier transforms infrared (FTIR) spectroscopy:

An infrared spectrum of PTh-PEO polymer composite films doped with 4 wt. % of Lithium Perchlorate (LiClO_4) is shown in figure 1. The spectral studies of the synthesized polymer composite films show number of absorption peaks. The major peaks at 1076.28 cm^{-1} and 1643.35 cm^{-1} are due to the presence of C-S and C=C bonds in polythiophene respectively. The strong intensity of the 827.46 cm^{-1} band which is characteristic of 2,5-disubstituted Thiophene rings indicates that the coupling of thiophene ring occurs preferentially at 2,5 positions which shift to 846.68 , 846.30 and 904.61 cm^{-1} due to addition of Lithium salt. The absorption band at the region of $650\text{-}600 \text{ cm}^{-1}$ shows the ion-ion interactions in PEO $-\text{Li}^+$ ions. This band has been assigned to the stretching of ClO_4^- ions, and is conveniently used to identify the degree of ion pairing. The shoulder peak near 636 cm^{-1} is apparent in lithium salt containing PEO composite. Two medium peaks at 1473 and 1450 cm^{-1} are assigned to stretching vibrational modes of the thiophene ring [8].

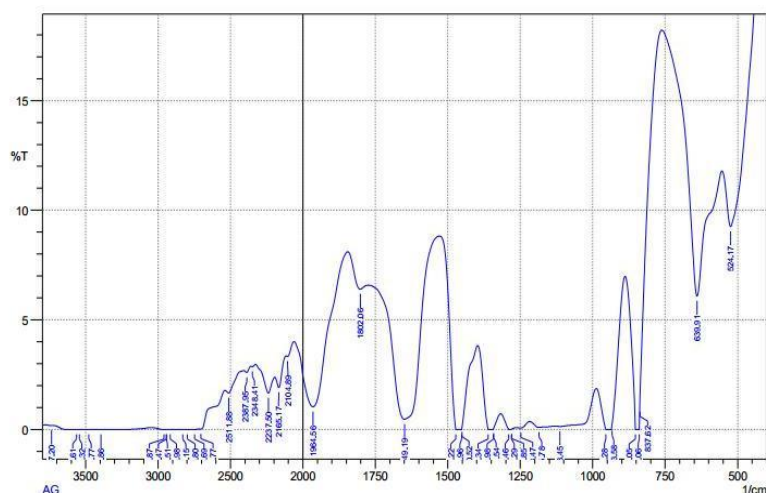


Figure 1. FTIR Spectra of PTh-PEO polymer Composite doped with LiClO_4

3.2 Scanning electron microscopy (SEM)

Figure 2 shows the morphology of PTh-PEO composite doped with LiClO_4 . The surface morphology changes severely from rough to smooth. PTh-PEO composite doped with LiClO_4 shows further drastic

improvement of surface morphology as appears in Fig.2 in which cluster of particles and voids are observed. The average size of the particles is 0.5µm to 100 nm, as shown in Fig 2 From the PTh-PEO composites image, the clusters of particles resulting from the aggregation of the composite particles can be seen. However, several aggregated phases and separate phase domains can be detected.

The smooth morphology is closely related to the reduction of PEO crystallinity in presence of the salt. The reduction of PEO crystallinity arises from random distribution and dissociation of salt which may introduce the topological disorder in the composite. The reduction of crystallinity will produced more amorphous phase in the system. The amorphous phase makes the electrolyte more flexible and results in increase of the segmental motion of the polymer.

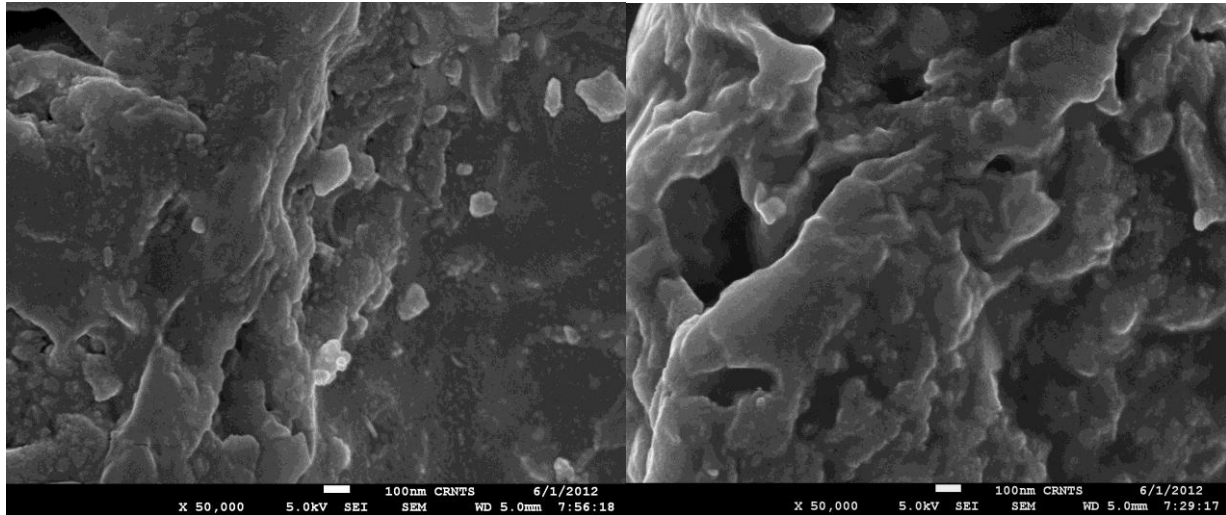


Figure 2 SEM Micrographs of PTh-PEO polymer Composite doped with LiClO₄

3.3 Impedance spectroscopy

Figure 3 shows the Nyquist plots (Cole-Cole plots i.e. $Z''=Z \sin\theta$ versus $Z'=Z \cos\theta$ which is also called as Nyquist plots) of the optimized samples for different temperatures. The incomplete semicircle shown in figure 3 for all temperatures, are caused by the unavailable higher range of frequencies. It can be noted from impedances spectrum that the value of bulk resistance shifts to higher frequency region of the spectrum as the temperature increases.

The entire impedances spectrum shows the same trends in the temperature range 303-328K. Many researchers [9] reported a similar conductivity isotherm. The impedance spectrum of PTh-PEO composite doped with LiClO₄ is found to be consist of only one arc as shown in fig. which may be taken to mean that the conduction processes have identical time constants [10]. Also it may be argued that as the temperature increases the arc of semicircle reduces, indicating the increase in conductivity.

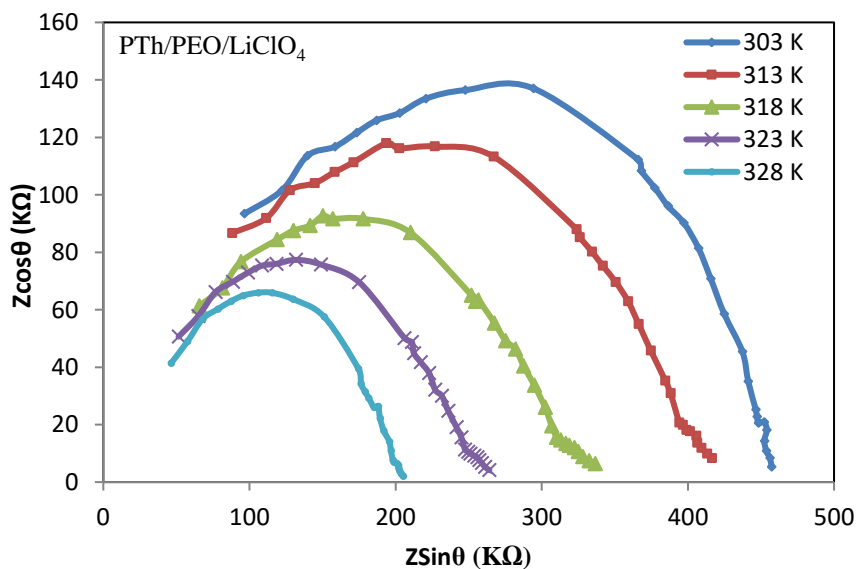


Figure 3: Cole-Cole plots for PTh-PEO polymer composite doped with LiClO₄

The basic features of the spectra seem to be qualitatively similar to those obtained for polythiophenefilms[11] The arcs are found to be highly depressed for the all films for different temperatures which indicate the distribution of relaxation times [12].

The Bulk resistance (R_b) and bulk capacitance (C_b) can be calculated from the impedance plots. It is well known from the theory of complex impedance plane analysis that the value of R_b is obtained from the real axis intercept. The capacitance value is obtained from the frequency values corresponding to the maximum of the semicircle in the Impedance plot, using the relation $\omega R_b C_b = 1$ [13]. It is observed that the bulk resistance of the sample decreases with the increase in temperature. The Cole–Cole plot (Fig.3) shows that well-defined semicircles. The single semicircular plot for a given temperature suggests that the device can be considered as a parallel combination of bulk resistor (R_b)–bulk capacitor (C_b) network. The impedance plots suggest Debye type behavior and single relaxation mechanism.

The variation of $\log f$ versus $Z\cos\theta$ at different temperature is as shown in figure 4. From the figure it is observed that the PTh-PEO sample shows the wide variation of resistance with all frequencies. The resistance of the sample is found to be decreased with increase in frequency.

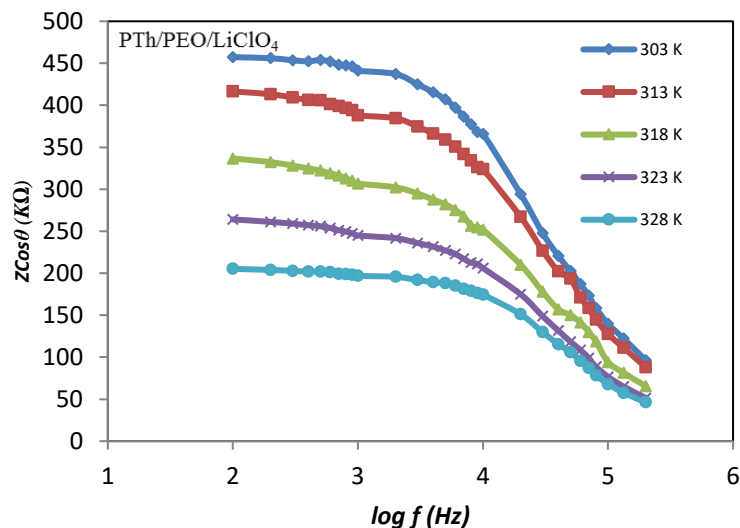


Fig.4 :Variation of real axis $Z\cos\theta$ with $\log f$ of PTh-PEO Composite doped with of LiClO_4

The magnitude decreases on increasing temperature in the low frequency range which merges in the high-frequency region irrespective of temperature. This nature may be due to the release of space charge [14]. The reduction in barrier properties of the materials with rise in temperature may be a responsible factor for enhancement of AC conductivity of the materials at higher frequencies [15]. Further, in the low frequency region, there is a decrease in magnitude with rise in temperature showing negative temperature coefficient of resistance (NTCR) behavior [16]. This behavior is changed drastically in the highfrequency region showing complete merger of plot above a certain fixed frequency.

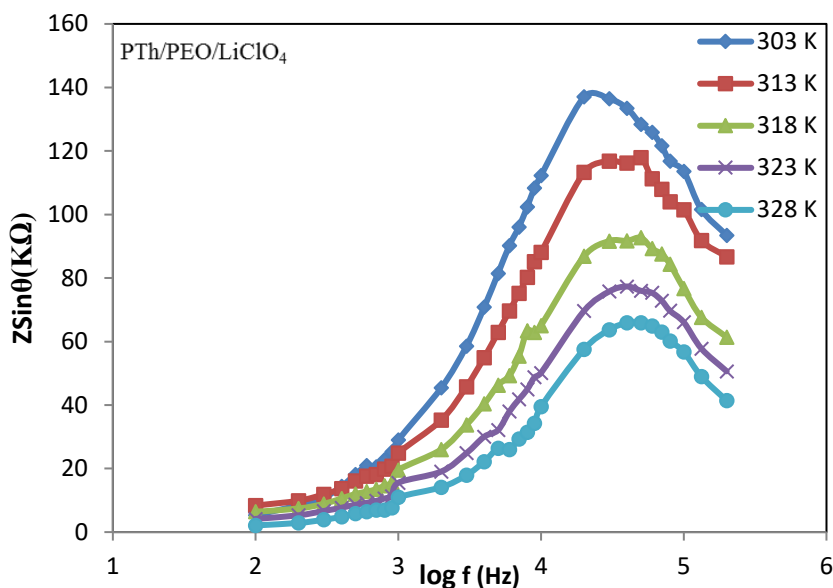


Fig.5: Variation of $Z\sin\theta$ with $\log f$ of PTh-PEO Composite doped with of LiClO_4

The variation of $\log f$ versus $Z\sin\theta$ in figure 5 shows asymmetric peaks at different temperatures. Each peak is associated with a maximum frequency called as relaxation frequency (f_r). As the temperature increases the relaxation frequency is found to be shifting towards higher frequency side and it finally merges in the high frequency region which is an indication of the accumulation of space charge in materials [17, 18].

IV. CONCLUSIONS

Polythiophene-Polyethylene oxide (PTh-PEO) polymer composite doped with of LiClO_4 were prepared successfully by *in situ* chemical oxidative polymerization of thiophene. FTIR spectra confirm the successful polymerization of thiophene and formation of PTh-PEO composite. SEM micrograph shows the semi crystalline morphology with the addition of LiClO_4 improves the surface morphology of composite. The impedance spectrum of PTh-PEO composite doped with LiClO_4 consist of only one arc which shows that the conduction processes have identical time constants. The Cole-Cole plots show that well-defined semicircles were obtained. The single semicircular plot for a given temperature suggests that the device can be considered as a parallel combination of bulk resistor (R_b)-bulk capacitor (C_b) network. The impedance plots suggest Debye type behaviour and single relaxation mechanism. The variation of real axis $Z'(Z\cos\theta)$ with $\log f$ shows negative temperature coefficient of resistance (NTCR).

V. REFERENCES

- [15] Roncali, J. (1992). Conjugated poly (thiophenes): synthesis, functionalization, and applications. *Chemical reviews*, 92(4), 711-738..
- [16] Nicolas, M., Guittard, F., & G ribaldi, S. (2006). Synthesis of stable super water-and oil-repellent polythiophene films. *Angewandte Chemie*, 118(14), 2309-2312.
- [17] Tsumura, A., Koezuka, H., & Ando, T. (1988). Polythiophene field-effect transistor: Its characteristics and operation mechanism. *Synthetic metals*, 25(1), 11-23.
- [18] Karim, M. R., Yeum, J. H., Lee, M. S., & Lim, K. T. (2008). Synthesis of conducting polythiophene composites with multi-walled carbon nanotube by the γ -radiolysis polymerization method. *Materials Chemistry and Physics*, 112(3), 779-782.
- [19] Deshmukh, D. P., Shirbhate, P. D., Yawale, S. S., & Yawale, S. P. (2012). Application of Vogel-Tamman-Fulcher (VTF) model to polythiophene composite thin films.
- [20] Park, D. H., Kim, B. H., Jang, M. K., Bae, K. Y., Lee, S. J., & Joo, J. (2005). Synthesis and characterization of polythiophene and poly (3-methylthiophene) nanotubes and nanowires. *Synthetic metals*, 153(1-3), 341-344.
- [21] Shirbhate, P. D., Pakade, S. V., & Yawale, S. P. (2016). Preparation and characterization of polythiophene polymer composite. *Transactions of the Indian Institute of Metals*, 69, 669-672.

- [22] Chu, P. P., Reddy, M. J., & Tsai, J. (2004). Structural and transport characteristics of polyethylene oxide/phenolic resin blend solid polymer electrolytes. *Journal of Polymer Science Part B: Polymer Physics*, 42(21), 3866-3875.
- [23] Suvama, R. P., Rao, K. R., & Subbarangiah, K. (2002). A simple technique for ac conductivity measurements. *Bulletin of Materials Science*, 25, 647-651.
- [24] Hwang, J. H., Kirkpatrick, K. S., Mason, T. O., & Garboczi, E. J. (1997). Experimental limitations in impedance spectroscopy:: Part IV. Electrode contact effects. *Solid State Ionics*, 98(1-2), 93-104..
- [25] Johnson, B. W., Read, D. C., Christensen, P., Hamnett, A., & Armstrong, R. D. (1994). Impedance characteristics of conducting polythiophene films. *Journal of Electroanalytical Chemistry*, 364(1-2), 103-109.
- [26] Kulkarni, A. R., & Maiti, H. S. (1984). Electrode effects in lithium conducting oxyfluorophosphate glasses. *Solid state ionics*, 14(4), 309-317.
- [27] Macedo, P. B., Moynihan, C. T., & Bose, R. (1972). The long time aspects of this correlation function, which are obtainable by bridge techniques at temperatures approaching the glass transition. *Phys. Chem. Glasses*, 13, 171.
- [28] Provenzano, V., Boesch, L. P., Volterra, V., Moynihan, C. T., & Macedo, P. B. (1972). Electrical relaxation in Na₂O·3SiO₂ glass. *Journal of the American Ceramic Society*, 55(10), 492-496.
- [29] Jain, H., & Hsieh, C. H. (1994). 'Window'effect in the analysis of frequency dependence of ionic conductivity. *Journal of non-crystalline solids*, 172, 1408-1412.
- [30] Rout, S. K., Hussian, A., Lee, J. S., Kim, I. W., & Woo, S. I. (2009). Impedance spectroscopy and morphology of SrBi₄Ti₄O₁₅ ceramics prepared by soft chemical method. *Journal of Alloys and Compounds*, 477(1-2), 706-711.
- [31] Sahoo, P. S., Panigrahi, A., Patri, S. K., & Choudhary, R. N. P. (2010). Impedance spectroscopy of Ba₃Sr₂DyTi₃V₇O₃₀ ceramic. *Bulletin of Materials Science*, 33, 129-134.
- [32] Tripathi, R., Kumar, A., & Sinha, T. P. (2009). Dielectric properties of CdS nanoparticles synthesized by soft chemical route. *Pramana*, 72, 969-978.
- [33]

¹ A. R. Bhojane
² D. R. Bijwe
³ A. V. Rajgure
⁴ S. P. Yawale
⁵ P. A. Saudagar
⁶ N. R. Pawar

Synthesis and Characterization of Lanthanum Oxide (La₂O₃NPs) Nanoparticles



Abstract: The utilization of lanthanum oxide nanoparticles (La₂O₃ NPs) in industrial and biotechnological applications, dielectric devices, optical devices, and sensors makes them an efficient rare earth metal oxide. In this study, we describe the sol-gel production of La₂O₃ NPs in their hexagonal phase using ammonia. X-ray diffraction investigations (XRD) and Fourier transform infrared spectroscopy (FTIR spectroscopy) were used to examine the produced La₂O₃ NPs Also the La₂O₃ doped with Polythiophene (PTH). The average La₂O₃ crystallite nanoparticle size as well as the La₂O₃ doped with Polythiophene (PTH) size was determined using the Scherrer formula from powered X-ray diffraction, and it was found to be around 29.1 nm and 24 nm. FTIR spectroscopy was then utilized to examine the chemical structure of the produced material.

Keywords: FTIR, spectroscopy, X-ray diffraction, nanoparticles, lanthanum oxide, Polythiophene, PTH.

I. INTRODUCTION

These days, thanks to advancements in integrated circuit and micro and nano electronic component research. The low-cost, high-performance electronic device creation with low power consumption is the main focus of research [1-3]. Because they are widely employed in electrical devices, optical devices, sensors, adsorbents, gate indicators, and superconductors, lanthanum oxide (La₂O₃) nanoparticles are an effective rare earth metal oxide [4–8]. Due to their varying sizes, the two-step procedure used to easily synthesize the transition metal oxides La₂O₃ and La₂C₂O₅ as nanoparticles exhibits distinct characteristics. There are several easy and environmentally benign methods for creating lanthanum oxide nanoparticles [9-10]. Lanthanum oxide nanoparticles have several uses in industry and biology. The approach for synthesizing (La₂O₃) nanoparticles from plant extract is successful or not [11-14]. The green production of mesoporous metal oxides via stoichiometric metal nitration has been established. Pluronic surfactants and their influence on surface area during synthesis operations. Lanthanum oxide and cupric oxide have recently been employed for water treatment, potentially as photocatalysts and adsorptive materials for pollution disposal [15-17, 21]. Lanthanum oxide's unusual physical properties have recently garnered interest. This oxide's solid forms are durable, thermally resilient, have good mechanical qualities, and are light emitting. The catalytic performance of La₂O₃ was observed that the initial transesterification rate catalyzed by the synthesized La₂O₃ catalyst was three times greater than its commercial equivalent, which is connected to strength and high crystallinity [18-19]. Thanks to its electrical arrangement, lanthanum proved to be the most beneficial atom in these series. Additionally, metal hydroxide and oxide have several uses in electrical components [20–22], pharmaceuticals for the environmentally friendly manufacture of La₂O₃ [22–23], biological events utilizing lasers [23–24], antibacterial action against *Staphylococcus aureus* [24–25], water defluoridation [25–26], and microwave fields [26–28]. Humidity sensing response is demonstrated by lanthanum doped tin oxide [27]. The photocatalytic activity is shown by the lanthanum nanoparticles [28]. SEM research is used to examine the surface properties of La₂O₃ [29]. Because of the necessary nanoparticle sizes and shapes, nanotechnology offers a wide range of lovely applications (NPs)[30].

In this study, we describe the synthesis and characterisation of La₂O₃ NPs using the sol-gel technique, employing lanthanum nitrate as the precursor material and ammonia as a reducing agent. At 500 °C, the material is calcined. La₂O₃ NPs were examined using XRD and FTIR properties.

^{1,2,3}Dept. of Physics, G. S. Tompe Arts, Commerce and Science College, Chadur Bazar- 444704 India

⁴Dept. of Physics & Electronics, Government Vidarbha Institute of Science and Humanity, Amravati-444604 India

⁵Dept. of Electronics, Bajaj College of Science, Wardha -442001, India

⁶Dept. of Physics, Arts, Commerce and Science College, mategao – 445303, India

Corresponding Author : d_bijwe@rediffmail.com

II. EXPERIMENTAL DETAIL

1. Chemical used

Lanthanum (III) Nitrate hexahydrate ($\text{La}(\text{NO}_3)_3 \cdot 6\text{H}_2\text{O}$), Ammonia (NH_4OH), ethanol, and double-distilled water were used to synthesize La_2O_3 nanoparticles. All used AR-grade chemical.

2. Synthesis of La_2O_3 nanoparticles

0.1 M of lanthanum nitrate was dissolved in 100 ml of double distilled water and stirred vigorously to get the transparent solution at 60 °C. To maintain the pH of solution, the liquid ammonia is added drop wise to get pH of reaction at 10. After that the solution was kept separately without any disturbances to get precipitated. Then precipitate was collected and washed with water or ethanol to remove impurity. The washed product was dried in hot air oven overnight at 80 °C. The collected dry powder was grounded by mortar and pestle then calcinated in a muffle furnace at 500 °C for 3 hr to get ultra fine nanoparticles.

3. Characterization

The structural properties of prepared lanthanum oxide nanoparticles have been analyzed by XRD with use of $\text{K}\alpha$ radiation source ($\lambda = 1.5059 \text{ \AA}$) operated at 40 kV and 15 mA. The functional groups present on prepared La_2O_3 nanoparticles were studied by FTIR spectrometer, which indicated the hexagonal structure of material synthesis.

III. RESULT AND DISCUSSION

1. Structural Property

La_2O_3 NPs sample were studied by XRD measurement for their crystalline size, crystallinity and phase composition. The XRD pattern of sample is shown in figure 1. XRD pattern of the prepared La_2O_3 NPs sample were recorded at room temperature. The different peaks are observed at 19.07°, 27.09°, 31.38° and 44.98° correspond respectively to crystal planes (2 1 1), (2 2 2), (1 0 0) and (1 1 0) which confirm the hexagonal structure of La_2O_3 calcinated at 500° C for 3 Hr. the value of cell parameter were $a=11.3920$, $b=11.3920$ and $c=11.3920$ (PDF Card No.1531467). Also XRD pattern of the prepared polythiophene La_2O_3 NPs sample were recorded at room temperature. The different peaks are observed at 23.96°, 32.64°, 44.52° and 59.25° correspond respectively to crystal planes (1 0 1), (1 1 1), (2 0 0) and (2 1 1) which confirm the hexagonal structure of PTH doped La_2O_3 calcinated at 80° C for 3 Hr. the value of cell parameter were $a=4.0670$, $b=4.0670$ and $c=9.0630$ (PDF Card No.1509432) as shown in figure 2. The Debye –Scherrer formula (Eq.1) [1-10] was used to analyse the average crystalline size (D) of the synthesised La_2O_3 .

$$D = \frac{K\lambda}{\beta \cos\theta} \quad (1)$$

Where θ is diffraction angle, K is constant (=0.9), λ is the wavelength (0.15059 nm) and β is the full width at half maximum.

The crystalline size of La_2O_3 NPs found to be 29.1 nm and The crystalline size of PTH doped La_2O_3 NPs found to be 24 nm. It should be noted that sample has wider and lower intense peak. The hexagonal phase La_2O_3 was more useful in gas sensor, supercapacitor and catalysis application [3].

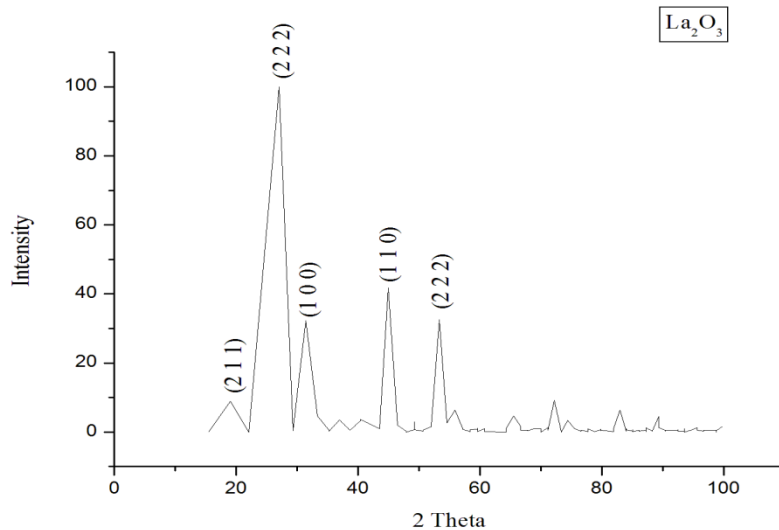


Figure 7 XRD Technique for La_2O_3 nanoparticles

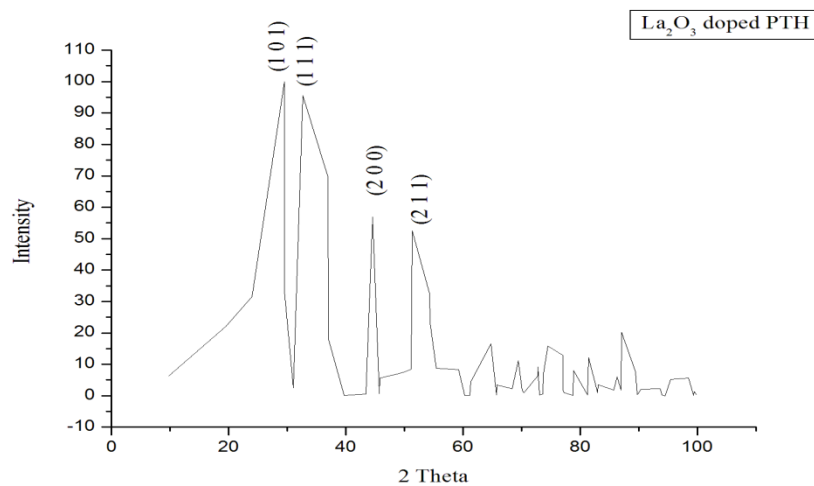


Figure 8 XRD Technique for PTH Doped La_2O_3

2. FTIR Property

FTIR spectra, in the wave number range from 4000 to 400cm^{-1} for synthesized La_2O_3 NPs sample as shown in figure 3. The broad absorption peak at 3556.89cm^{-1} for sample can be assigned to the O-H stretching vibrations of water molecule due to presence of moisture in sample [1,10] the small peak observed at 2500cm^{-1} indicates CH₂ stretching vibration [10,23,27]. A small sharp absorption peak observed at 422 , 501 , 601 , and 852cm^{-1} were assigned the stretching vibration of La-O bond in La_2O_3 [4,5,29]. FTIR spectra, in the wave number range from 4000 to 400cm^{-1} for synthesized PTH doped La_2O_3 NPs sample as shown in figure 4. The broad absorption peak at 3379.43cm^{-1} for sample can be assigned to the O-H stretching vibrations of water molecule due to presence of moisture in sample. The small peak observed at 2495.99cm^{-1} indicates CH₂ stretching vibration. A small sharp absorption peak observed at 447.50 , 488.98 , 661.61 , and 844.86cm^{-1} were assigned the stretching vibration of La-O bond in La_2O_3 .

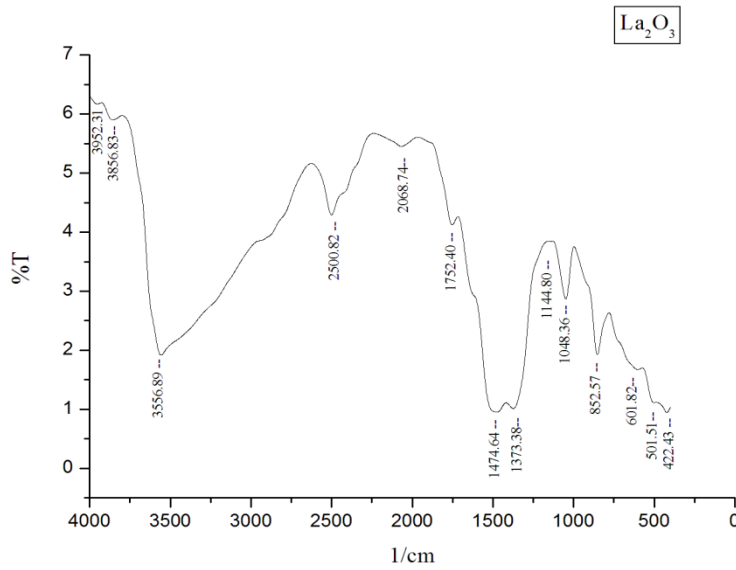


Figure 9 FTIR Technique for La_2O_3

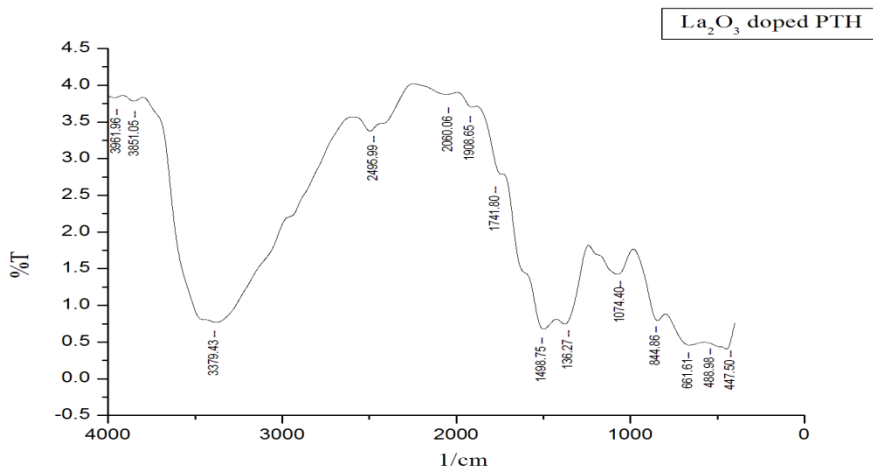


Figure 10 FTIR Technique for PTH doped La_2O_3

3. Conclusion

La_2O_3 nanoparticles were successfully synthesized by sol-gel method and calcinated at 500°C for 3Hr. physical properties of the sample was analyzed by XRD and FTIR spectroscopy technique. The XRD Result reveal the hexagonal phase with high intensity peak (2 2 2) of the sample and average crystalline size approximately 29nm. FTIR spectra confirm the La_2O_3 phase presence in the sample. From that it is conclude that the synthesized La_2O_3 nanoparticles may be used for gas sensing and dielectric application. PTH doped La_2O_3 nanoparticles were successfully synthesized by sol-gel method and calcinated at 80°C for 3Hr. physical properties of the sample was analyzed by XRD and FTIR spectroscopy technique. The XRD Result reveal the hexagonal phase with high intensity peak (1 0 1) of the sample and average crystalline size approximately 24nm. FTIR spectra confirm the PTH Doped La_2O_3 phase presence in the sample. From that it is conclude that the synthesized PTH Doped La_2O_3 nanoparticles may be used for gas sensing and dielectric application.

ACKNOWLEDGMENT

The author acknowledges gratitude to Dr. R. S. Ramteke, principal of G.S.Tompe college, Chandur Bazar for providing facilities to conduct research work. And thankful to Shri Shivaji Science college, Amravati to helping for used of XRD and FTIR Technique.

REFERENCES

- [1] P. N. Bhautik, Dr. R.P. Ugwekara , K. Singh, “Review on synthesis of Lanthanum oxide (La₂O₃) and characterization techniques” *Gradiva Review Journal*, volume 7 ISSUE 12 2021, ISSN NO : 0363-8057(260-273)
- [2] M. Rosynek, D. Magnuson, “Preparation and Characterization of Catalytic Lanthanum Oxide” *Journal of Catalysis* 46,402-413 (1977)
- [3] S. Karthikeyan, K. Dhanakodi, K. Shanmugasundaram, S Surendhiran, “Synthesis and characterization of lanthanum oxide nanoparticles: A study on the effect of surfactants,” *Materials Today*, in press.
- [4] L. P. Lingamduninne, J. Reddy Koduru, Y. Young Chang, S.Hong Kong, J. K. Yang, “Facial synthesis , characterization, and adsorption insights of lanthanum oxide nanorods” *Metals* 2020, 10, 1001;doi:10.3390/met10081001.
- [5] S.I. Boldish, W. B. White, “ Vibrational spectra of crystal with the A- type rare earth oxide structure.La₂O₃ and Nd₂O₃.” *Spectrochim. Acta Part A* 1979, 35, 1235
- [6] J. Gouteron, D. Michel, A. M. Lejus, J. Zarembowitch, “ Raman spectra of lanthanide sesquioxide single crystals: Correlation between A and B type structures.” *Journal Of Solid State Chemistry* 38, 288-296 (1981)
- [7] S. W. kang, S. W. Rhee, “deposition of La₂O₃films by direct liquid injection mettallorganic chemical vapour deposition.” *J. Electrochem. Sos.* 2002,149,345.
- [8] A. M. De Asha, J. T. S.Critchley, R. M. Nix, “Molecular adsorption characteristics of lanthanum oxide surfaces: The interaction of water with oxide overlayer grown on Cu.” *Surface Science*, 405, 1998, 201.
- [9] Hamideh Saravani , Malihe Khajehali, “Synthesis and Characterization of Lanthanum Oxide and Lanthanum Oxid Carbonate Nanoparticles from Thermalizes of [La(acacen)(NO₃) (H₂ O) Complex” *Orient. J. Chem.*, Vol. 31(4), 2351-2357 (2015).
- [10] W. M. Khalaf, Md. H. Al-Mashhadani, “synthesis and characterization of lanthnum oxide La₂O₃net-like nanoparticles by new combustion method.” *Biointerface research in applied chemistry*, Valume 12, Issue 3, 2022, 3066-3075.
- [11] R. F. Madani, I. Sofianty, A.G.P. Sari, R. Maryanti, A. B. D. Nandiyanto, “Synthesis method and green synthesis of lanthanum nanoparticles: A review.” *Arabian J. chemical and Enviromental Research*, Vol 08 Issue 2, 2021, 287-314.
- [12] S. Shubhashish, S. J. Karasik, I. Perera, S. March, L. F. Posada, Ali Mansour, S. L. Suib, “Stoichiometric Metal Nitration Based Novel Green Synthesis of Mesoporous Metal Oxides and Their Enhanced Heterogeneity” <https://www.elsevier.com/open-access/userlicense/1.0/>
- [13] M. N. Almarri , M. M. Khalaf, M. Gouda , F. El-Taib Heakal , A Elmushyakh , M. F. Abou Taleb, H. M. Abd El-Lateef, “Chemical, surface, and thermal studies of mixed oxides cupric oxide (CuO), lanthanum oxide (La₂O₃), and graphene oxide for dye degradation from aqueous solution” <https://doi.org/10.1016/j.jmrt.2023.01.152>.
- [14] Sk M. Rahaman, M.,Chakraborty, S. Kundu, S. Dhivar, D Kumar, S. M. Ibrahim , M. Chakravarty , B. Saha, “Controlled synthesis of samarium trifluoride nanoparticles in a water-in-oil microemulsion: Effects of water-to-surfactant ratio on particles and phosphate removal” *Journal of Hazardous Materials Advances* 11 (2023) 100348.
- [15] M. Mylarappa, C. Selvam, H. K. Sanjeevappa , S. G. Prasanna Kumar , G . Krishnamurthy , N .Kalasad Muttanagoud, “Reduced graphene oxide loaded La₂O₃ nanocomposite for dye degradation and antioxidant studies”, *Results in Surfaces and Interfaces* 14 (2024) 100202.
- [16] D. Rattanaphra , P. Soodjit , A. Thanapimmetha, M. Saisriyoot , P. Srinophakun, “Synthesis, characterization and catalytic activity studies of lanthanum oxide from Thai monazite ore for biodiesel production” */Renewable Energy* 131 (2019) 1128-1137.
- [17] A. Kumar, A. Bisht, A. Singh, S Kumar “Synthesis and biological applications of lanthanum-based nanoparticles: A review” *Biochem. Cell. Arch.* Vol. 24, No. 1, pp. 575-586, 2024.
- [18] A. A. Ansari, M. A. Siddiquib, A. Khan , N. Ahmad , A. A. Al-Khedhairy, “Synthesis, optical properties and toxic potentiality of photoluminescent lanthanum oxide nanospheres” *Colloids and Surfaces A* 607 (2020) 125511
- [19] B.Balusamy, Y.G. Kandhasamy, A Senthamizhan , G. Chandrasekaran, M. Siva Subramanian, K. Tirukalikundram S, “Characterization and bacterial toxicity of lanthanum oxide bulk and nanoparticles.” *Journal Of Rare Earths*, Vol. 30, No. 12, Dec. 2012, P. 1298
- [20] Amit Bansiwala, D. Thakrea, N. Labhshetwar, S. Meshram, S. Rayalu, “Fluoride removal using lanthanum incorporated chitosan beads.” *Colloids and Surfaces B: Biointerfaces* 74 (2009) 216–224
- [21] K.Chena, S. Guo, Y. Zeng , W. Huang , J.Penga, L. Zhang , S.Yin, “Facile preparation and characterization of lanthanum oxide powders by the calcination of lanthanum carbonate hydrate in microwave field” *Ceramics International*, in press.
- [22] U. Choudhari, S.Jagtap, “Lanthanum doped tin oxide: Synthesis, characterization and application” *Materials Today*, in press.

- [23] M.Ghiasi, A. Malekzadeh, "Synthesis, characterization and photocatalytic properties of lanthanum oxy-carbonate, lanthanum oxide and lanthanum hydroxide nanoparticles" *Superlattices and Microstructures* 77 (2015) 295-304.
- [24] G. A. M. Hussein, B. C. Gates, "Characterization of porous lanthanum oxide catalysts Microscopic and spectroscopic studies" *J. Chem. SOC., Faraday Trans.*, 1996,92(13), 2425-2430
- [25] S. L. Wagh, U. J. Tupe, A. V. Patil, "Review on: synthesis approaches and applications of lanthanum oxide nanoparticles" *JETIR* January 2019, Volume 6, Issue 1.
- [26] Sneha Jagtap, M. Yenkie, S. Das, S. Rayalu, "Synthesis and characterization of lanthanum impregnated chitosan flakes for fluoride removal in water" / *Desalination* 273 (2011) 267–275, <http://dx.doi.org/10.1016/j.desal.2010.12.032>
- [27] G. Maheshwaran a , R. Selva Muneeswari, A. Nivedhitha Bharathi, M. Krishna Kumar, S. Sudhahar, "Eco-friendly synthesis of lanthanum oxide nanoparticles by Eucalyptus globulus leaf extracts for effective biomedical applications" *Materials Letters* 283 (2021) 128799.
- [28] N.Ramjeyanthi, M.Alagar, D.Muthuraman, "Synthesis, Structural and Optical Characterization of Uncalcined Lanthanum Oxide Nanoparticles by Co-Precipitation Method" *International Journal of Interdisciplinary Research and Innovations* Vol. 6, Issue 3, pp: (389-395), Month: July - September 2018,
- [29] X. Wang , M. Wang , Hua Song, B. Ding, "A simple sol–gel technique for preparing lanthanum oxide nanopowders" *Materials Letters* 60 (2006) 2261–2265
- [30] M. Moothedan, K.B. Sherly, "Synthesis, characterization and sorption studies of nano lanthanum oxide" *Journal of Water Process Engineering* 9 (2016) 29–37

¹ Ankit Chavhan² N. R. Pawar³ D. R. Bijwe⁴ D. S. Chavhan

Synthesis and thermoacoustic study of Boehmite nanoparticles in Acetone

Abstract:

Boehmite nanoparticles has been synthesized via sol-gel method. The size, morphologies and bonding states of synthesized boehmite nanoparticles were investigated by X-ray diffraction (XRD) and scanning electron microscopy (SEM). The thermoacoustic properties of boehmite nanoparticles in acetone were studied with purpose of applications in various fields. X-ray diffraction (XRD) results indicated the major phases of boehmite. Scanning electron microscopy (SEM) images shows that boehmite particles mainly composed of crystalline nanoparticles. Average particle size of SiC nanoparticle has been estimated by using Debye-Scherrer formula, it was found to be 50 nm. The thermoacoustic properties of nanomaterials related to the surface of nanoparticles and nanoparticle surfactant interactions, these properties of boehmite nanosuspension were studied by non-destructive technique.

Keywords: Boehmite nanoparticles; Sol-gel technique; Nanosuspension, XRD

I. INTRODUCTION

In nanoparticle synthesis it is very important to control not only the particle size but also the particle shape and morphology as well. In the present investigation, the synthesis of boehmite Nanoparticles via sol-gel method and their thermodynamic studies in acetone-based solvent were discussed. Sol-gel technique is an easy, simple, cost effective and convenient route for preparing nanoparticles [1-3]. Boehmite nanoparticles have seen a flurry of research in recent years as nanotech researchers, engineers, and manufacturers discover its myriad applications across various fields of interest. As with many nanoparticles, it must be handled with care to avoid issues of toxicity. In this paper, Boehmite nanosuspension were prepared by two step method and their thermoacoustic properties were studied by non-destructive technique.

Synthesis of Boehmite Nanoparticles:

6.49 g of NaOH dissolved in, 50 ml of distilled water and 20 g of $\text{Al}(\text{NO}_3)_3 \cdot 9\text{H}_2\text{O}$ dissolved in 30 ml distilled water were prepared. $\text{Al}(\text{NO}_3)_3 \cdot 9\text{H}_2\text{O}$ is the source of aluminum. Sodium hydroxide solution is added to aluminium solution at the rate 2.94 ml/min Vigorous stirring up to 17 min [4-5]. Milky mixture was subjected with ultrasonic bath for 3h at room temperature. Mixture filtered and washed with distilled water. The precipitate was kept in 220-degree temp for 10 h. The sample so obtained was grinded to get it in powdered form.

XRD Pattern of Boehmite Nanoparticles:

Figure 1 shows the XRD pattern of AlOOH nanoparticles. The XRD measurement carried out by using "PAN analytical" X-ray diffractometer keeping the parameter constant at start position [$^{\circ}2\theta$.]: 10.0154 End Position [$^{\circ}2\theta$.]: 89.9834, Step Size [$^{\circ}2\theta$.]: 0.0170, Scan Step Time [s]: 5.7150, Scan Type: Continuous, Measurement Temperature [$^{\circ}\text{C}$]: 25.00 Anode Material: Cu, K-Alpha1 [\AA]: 1.54060. It is seen that the materials are well crystalline in nature and well agreed with standard JCPDS file number 021-1307. The estimate size of AlOOH nanoparticles using Debye Scherrer formula is found about 50 nm.

Corresponding Author: pawarsir1@gmail.com

¹ Department of Physics, Matoshri Nanibai Gharphalkar Science College, Babhulgaon - 445 101, India.

² Department of Physics, Arts, Commerce and Science College, Maregaon - 445 303, India

³ Department of Physics, G. S. Tompe Arts, Commerce and Science College, Chandur Bazar - 444 704, India

⁴ Department of Physics, Amolakchand Mahavidyalaya, Yavatmal - 445 001, India

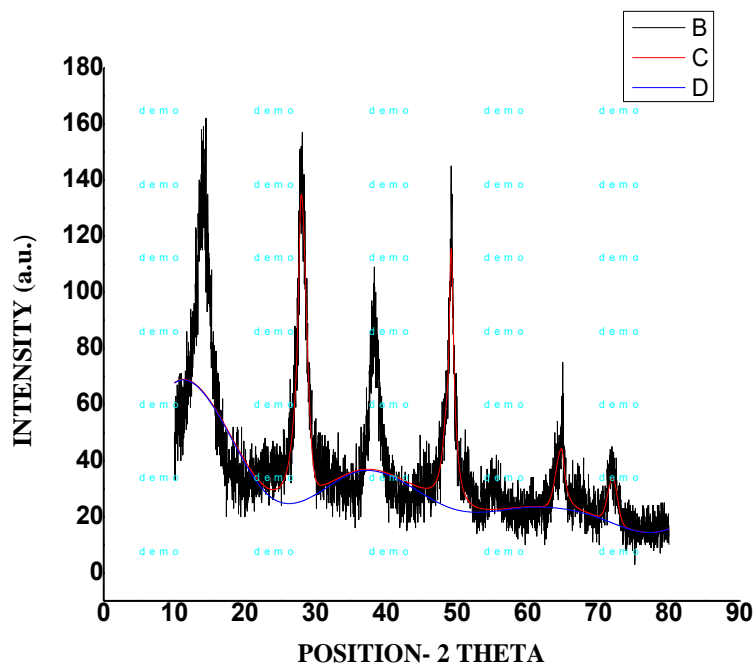


Fig. 1 X- ray diffraction pattern of Boehmite nanoparticles

SEM images of Boehmite nanoparticles:

SEM study is carried out to observe the overall surface morphology and crystallite sizes of the prepared nanomaterials. This material has been synthesis by sol-gel method. From the SEM images are observed under 10 micrometer resolutions which shows the foam like surface morphology as n shown in figure 2. In the depicted images of Boehmite (AlOOH) nanomaterials, it can be clearly seen that the micrograph crystallite sizes may vary from a 10 μm to few microns range if we magnify further. The crystallites look like having a sharp surface edge as well as crystalline grains and the particles foam-like morphology can be formed from highly agglomerated crystallites. Also, it is confirmed that the crystallite sizes are nearly equal for all sample.

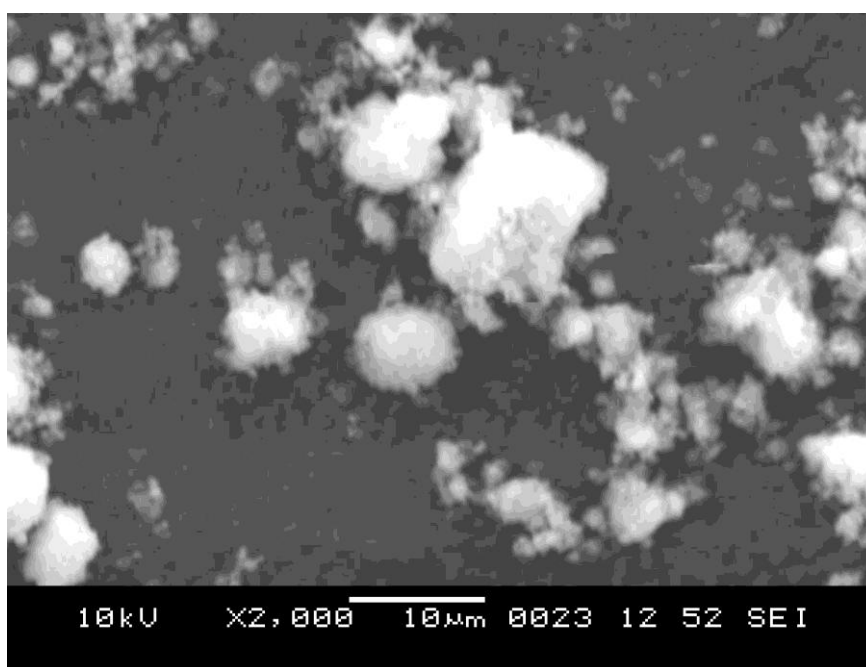


Fig 2. SEM image of Boehmite Nanoparticles

RESULTS AND DISCUSSION

The experimentally measured values of ultrasonic velocity, density and viscosity are used to derive thermoacoustic parameters such as viscosity, adiabatic compressibility, Acoustic impedance, free length, free Volume, internal Pressure, isothermal compressibility, isothermal bulk modulus, molar compressibility, molar sound velocity, molar volume, Poisson ratio, relaxation time, Van der Wall's Constant, volume expansivity, effective mass and thermal conductivity. These parameters are represented are given in tables 1 (A) and 1 (B). In boehmite acetone based nanosuspension there might be nanoparticle fluid interaction favors in increase in ultrasonic velocity [6]. Rise in ultrasonic velocity may concluded as the strong interaction between nanoparticles of boehmite and microsize molecules of acetone hence there is agglomeration of boehmite nanoparticles due to polar nature of acetone base fluid. Therefore sound will travel faster through the more compact structure by means of longitudinal waves [7-13].

Ultrasonic velocity gets increases with increasing the molar concentration of the boehmite nanoparticles in acetone this shows that the physical parameters of the sample changes by increasing the molar concentration. Nanoparticles suspensions do not settle which provides a long self- life which imparts ultrasonic velocity to them. For boehmite nanoparticle the velocity of the nanosuspension is higher than acetone and also by increasing the molar concentration of the boehmite nanoparticle the velocity gets high values at 0.8. This represents strong aggregation of boehmite nano suspension in acetone -based fluid at these molar concentrations. The cause behind this increase of ultrasonic velocity with increase in molar concentration (x) is due to strong interaction between nanosized particle and micro sized fluid molecule and also due to increase in density of nanosuspension with increase of molar concentration. Ultrasonic velocity can be interpreted as the nanosized boehmite particles have more surfaces to volume ratio and which can absorb more acetone molecules on its surface, which enhances the ultrasonic velocity. The decrease of ultrasonic velocity with increase in concentration is due weakening of interaction between boehmite nano sized particles and micro sized fluid molecules of methanol.

Densities of the nanosuspension were calculated by measuring the weight of the nanofluid using 25 ml of specific gravity bottle and also by using the standard value of density of water. Nanosuspension has more density than acetone. Increase in density indicates the close packing between the boehmite nanoparticles in acetone-based fluids.

When boehmite nanoparticles suspended in acetone fluid, motion of particle becomes more rapid, lighter the particles, faster the motion and denser the particles slower the motion. Also suspended nanoparticles do not settle and they have long self-life. Hence, they can be easily suspended despite high solid density. The densities of boehmite nanoparticles in acetone based nanosuspension shows that the density steeply increases with increase in concentration. This increase in density decreases the volume indicating association of SiC nanoparticles in nanosuspension. It may be increase due to structural reorganization.

The viscosity slightly increases with increase in molar concentration of boehmite nanoparticles in acetone base nanosuspension. As the motion of nanoparticles becomes more rapid when the temperature of the medium was raised which lowers the viscosity of the medium as the size of the particles was reduced. Hence viscosity of nanosuspension decreases with increase in temperature.

The viscosity of boehmite nanoparticle strongly depends on structure of boehmite nanoparticles and consequently interactions between the boehmite nanoparticles and molecules of the fluid. Thus, the viscosity depends on interactions between components of nanosuspension as well as on the size and shape of the boehmite nanoparticles. Measurements of viscosity of nanosuspension yield some reliable information in the study of nano cluster. The viscosity gives the strength of interaction between the interacting boehmite nanoparticles and molecules of acetone. The interactions between boehmite nanoparticles and molecules of acetone increase the viscosity of nanosuspension.

The adiabatic compressibility (β_a) decreases with increase in molar concentration indicating strong interaction between boehmite nanoparticles and molecules of acetone showing aggregation of nanoparticles. The surface area of the material is increased by the reduction in particle size. Due to this higher percentage of the boehmite Nanoparticles can interact with surrounding fluids. It may due to decrease in interspacing of boehmite nanoparticles in nanosuspension with increase in molar concentration. It is a measure of association or dissociation or repulsion. It also determines the orientation of the nanoparticles in nanosuspension. Kiyohara

and Benson [14] suggest that adiabatic compressibility is the result of several opposing effects like strong interactions between nanoparticles and molecules of the fluids also interstitial accommodation leads to a more compact structure and decreases adiabatic compressibility. The magnitudes of the various contributions depend mainly on the relative size of the boehmite nanoparticles. Isothermal compressibility (β_i) and adiabatic compressibility (β_a) exhibits similar trend and both decreases with increase in molar concentration of boehmite nanoparticles in nanosuspension.

The relaxation time slightly decreases with increase in molar concentration of boehmite nanoparticles indicating less stability of nanoparticles in boehmite nanosuspension. For the nanoparticles in nanosuspension, the gravitational pull is not stronger than the random thermal motion of the particles hence nanoparticles do not settle which provides long self life at these molar concentrations which increases the relaxation time. Stability of boehmite nanoparticles in nanosuspension is totally depends on its surface energy. Less surface energy more stable will be the boehmite nanoparticles. The relaxation is caused by the energy transfer between translational and vibrational degrees of freedom and all these degrees take part in the process observed [15].

Free length is the distance between the surfaces of the neighboring boehmite nanoparticles. The free length slightly decreases with increase in molar concentration and then increases. The free length (L_f) of a nanosuspension is a measure of attraction between boehmite nanoparticles and molecules of the acetone in nanosuspension. Decrease in free length is a result of increase in surface to volume ratio of boehmite nanoparticles with acetone molecules, association through interactions between nanoparticles and molecules of the constituents of the nanosuspension.

The internal pressure (π_i) and free volume (V_f) versus molar concentration of boehmite nanoparticles in nanosuspension represented that the internal pressure as well as free volume in nanosuspension is a measure of attraction between their constituents. In this nanosuspension, free volume decreases and internal pressure increases. Further, the increase in free volume and decrease in internal pressure with rise in concentration clearly show the increasing magnitude of interactions [16]. Such behavior of internal pressure and free volume generally indicates the association through interactions between boehmite nanoparticles and molecules of acetone.

Acoustic impedance is found reciprocal to that of adiabatic compressibility [17-20]. It is in good agreement with the theoretical requirements. As the size of the material decreases, the percentage of surface atoms increases, hence large amount of substance comes in contact with surrounding materials. This results in increase in acoustic impedance. The increase in acoustic impedance (Z) with molar concentration can be explained on the basis of the interactions between components of the nanosuspension, which decreases the distance of their components.

The molar volume (V_m) of boehmite nanoparticles depends on the structural arrangement and interactions between the components of the nanosuspension medium. The structural arrangement may be decided by the interaction forces in the nanosuspension medium. It decreases with increase in molar concentration because the molecular weight is directly proportional to the molar volume. The molar volume is found to have similar type of trend as that of molar compressibility [21-30]. The change in Vander Waal's constant (b) would be due to a change in geometry of the boehmite nanoparticles.

The sound velocity (R) increases due to increase in surface to volume ratio. It shows similar trends as that of ultrasonic velocity as it depends on it. The molar compressibility (W) decreases with increase in molar concentration of boehmite nanoparticles in acetone based nanosuspension due to aggration of boehmite nanoparticles in the medium. As it is function of adiabatic compressibility, its variation is similar as that of adiabatic compressibility. The isothermal Bulk modulus (B_i) increases with increase in molar concentration, it exhibits similar trends as that of ultrasonic velocity and inverse trend as that of isothermal compressibility. The volume expansivity decreases with increase in molar concentration due to aggration of boehmite nanoparticles in nanosuspension. As it depends on internal pressure and isothermal compressibility it shows their resultant effects.

The effective thermal conductivity of nanosuspension increases with temperature. It has substantially higher values at 08. The thermal conductivity enhancements are highly dependent on specific surface area of nanoparticle, with an optimal surface area for the highest thermal conductivity. There is strong relationship between Brownian motion and temperature of nanoparticles. Furthermore, the effect of temperature on thermal

conductivity is not very well understood and documented. It is reported that it shows the similar behavior as that of ultrasonic velocity.

Table 1(A) Experimental values of thermoacoustic Parameters at 5 MHz

X	U (m/s)	ρ (Kg/m ³)	η^*10^{-3} (NS/m ²)	βa^*10^{-10} (m ² /N)	βi^*10^{-10} (ms ² /kg)	τ^*10^{-10} (s)	$L_r^*10^{-11}$ (m)	$\pi_i^*10^6$ (N/m ²)	$V_f^*10^{-7}$ (m ³ /mol)
293 K									
0.1	1385	750.37	0.5193	6.95	8.34	4.81	5.17	4.4419	2.19
0.2	1369	766.22	0.5239	6.96	8.36	4.86	5.18	4.5331	2.13
0.3	1383	778.39	0.5184	6.72	8.06	4.64	5.09	4.5165	2.21
0.4	1386	792.14	0.5182	6.57	7.89	4.54	5.03	4.5465	2.23
0.5	1389	806.07	0.5256	6.43	7.72	4.51	4.98	4.6099	2.21
0.6	1380	821.48	0.5342	6.39	7.67	4.55	4.96	4.7040	2.14
0.7	1379	834.09	0.5493	6.31	7.57	4.62	4.92	4.8024	2.06
0.8	1412	858.68	0.5485	5.84	7.01	4.27	4.74	4.8172	2.15
0.9	1350	871.14	0.6117	6.29	7.56	5.14	4.92	5.2333	1.71
298 K									
0.1	1394	743.38	0.4992	6.92	8.31	4.61	5.17	4.3140	2.34
0.2	1378	759.21	0.5067	6.94	8.33	4.69	5.18	4.4164	2.26
0.3	1392	771.25	0.5013	6.69	8.02	4.47	5.09	4.3999	2.35
0.4	1395	785.23	0.5021	6.54	7.85	4.38	5.03	4.4348	2.36
0.5	1398	799.34	0.5083	6.41	7.68	4.34	4.98	4.4936	2.34
0.6	1389	814.36	0.5172	6.36	7.63	4.39	4.96	4.5869	2.27
0.7	1388	827.29	0.5323	6.27	7.52	4.45	4.92	4.6865	2.18
0.8	1421	851.72	0.5314	5.81	6.97	4.12	4.74	4.7009	2.27
0.9	1359	864.69	0.5946	6.26	7.51	4.96	4.92	5.1171	1.81
303 K									
0.1	1402	738.36	0.4808	6.89	8.27	4.42	5.21	4.3460	2.50
0.2	1386	752.33	0.4896	6.92	8.31	4.52	5.22	4.4493	2.40
0.3	1400	764.44	0.4843	6.67	8.01	4.31	5.12	4.4332	2.49
0.4	1403	778.24	0.4839	6.53	7.84	4.21	5.07	4.4628	2.52
0.5	1406	792.19	0.4911	6.39	7.67	4.18	5.02	4.5274	2.48
0.6	1397	807.33	0.5003	6.35	7.62	4.24	5.01	4.6251	2.40
0.7	1396	820.25	0.5154	6.26	7.51	4.31	4.96	4.7282	2.31
0.8	1429	844.32	0.5144	5.81	6.96	3.98	4.78	4.7419	2.41
0.9	1367	857.82	0.5776	6.24	7.49	4.81	4.96	5.1727	1.90
308 K									
0.1	1409	733.46	0.4627	6.87	8.24	4.24	5.25	4.3039	2.65
0.2	1393	745.39	0.4726	6.91	8.29	4.35	5.26	4.4050	2.54
0.3	1407	757.37	0.4674	6.67	8.01	4.16	5.17	4.3887	2.63
0.4	1410	771.26	0.4669	6.52	7.82	4.06	5.11	4.4183	2.66
0.5	1413	785.13	0.4745	6.38	7.66	4.04	5.06	4.4856	2.61
0.6	1404	800.43	0.4835	6.34	7.61	4.09	5.04	4.5840	2.53
0.7	1403	813.24	0.4986	6.25	7.51	4.16	5.01	4.6886	2.42
0.8	1436	837.29	0.4975	5.79	6.95	3.84	4.82	4.7024	2.53
0.9	1374	850.76	0.5607	6.23	7.48	4.66	5.01	5.1391	1.99
313 K									
0.1	1415	727.45	0.4427	6.87	8.24	4.05	5.29	4.2457	2.87
0.2	1399	738.47	0.4557	6.92	8.31	4.21	5.31	4.3591	2.71
0.3	1414	750.35	0.4506	6.67	8.01	4.01	5.22	4.3412	2.82
0.4	1416	764.28	0.4501	6.53	7.83	3.92	5.16	4.3726	2.84
0.5	1420	778.23	0.4572	6.37	7.65	3.88	5.11	4.4373	2.80
0.6	1410	793.53	0.4668	6.34	7.61	3.95	5.09	4.5412	2.70

0.7	1409	806.18	0.4789	6.25	7.51	3.99	5.05	4.6326	2.61
0.8	1442	830.84	0.4807	5.78	6.95	3.71	4.86	4.6635	2.70
0.9	1380	843.71	0.5439	6.22	7.47	4.51	5.04	5.1041	2.11

Table-1 (B) Experimental values of thermoacoustic Parameters at 5 MHz

X	Z*10 ⁶ (kg/m ² s)	Vm*10 ⁻² (m ³ /mol)	b*10 ⁻⁵ (m ³ /mol)	R*10 ⁻⁴ (m ³ /mol) (m/s) ^{1/3}	W*10 ⁻⁴ (m ^{19/7} /S ¹)	Bi*10 ⁹ (N/m ²)	α*10 ⁻⁵ (1/K)	T*10 ⁻³ (W/mK)	Meff (mol)
293 K									
0.1	1.0392	7.7656	1.9946	590.89	1.54	1.09	1.39	3.22	58.271
0.2	1.0489	7.6299	1.9945	580.64	1.51	1.08	1.44	3.05	58.462
0.3	1.0765	7.5352	1.9946	584.14	1.50	1.09	1.41	2.98	58.653
0.4	1.0979	7.4285	1.9946	582.63	1.48	1.10	1.40	2.89	58.844
0.5	1.1196	7.3238	1.9946	581.14	1.47	1.12	1.41	2.81	59.035
0.6	1.1336	7.2097	1.9946	574.36	1.45	1.12	1.44	2.71	59.226
0.7	1.1502	7.1236	1.9946	571.65	1.43	1.13	1.45	2.62	59.417
0.8	1.2124	6.9418	1.9947	580.30	1.41	1.19	1.38	2.63	59.608
0.9	1.1760	6.8645	1.9945	552.76	1.38	1.11	1.60	2.45	59.799
298 K									
0.1	1.0362	7.8387	1.9945	596.59	1.55	1.09	1.33	3.24	58.271
0.2	1.0461	7.7004	1.9945	586.25	1.53	1.09	1.36	3.07	58.462
0.3	1.0735	7.6049	1.9946	589.75	1.52	1.10	1.34	2.99	58.653
0.4	1.0953	7.4939	1.9946	588.13	1.50	1.12	1.33	2.90	58.844
0.5	1.1174	7.3855	1.9946	586.54	1.48	1.13	1.34	2.82	59.035
0.6	1.1311	7.2727	1.9946	579.78	1.46	1.13	1.36	2.72	59.226
0.7	1.1482	7.1821	1.9946	576.95	1.44	1.14	1.38	2.63	59.417
0.8	1.2102	6.9985	1.9947	585.59	1.42	1.20	1.31	2.64	59.608
0.9	1.1751	6.9157	1.9945	557.82	1.39	1.13	1.52	2.46	59.799
303 K									
0.1	1.0351	7.8919	1.9945	601.37	1.57	1.11	1.30	3.25	58.271
0.2	1.0427	7.7708	1.9945	591.45	1.54	1.10	1.34	3.08	58.462
0.3	1.0702	7.6727	1.9945	594.90	1.53	1.11	1.32	3.00	58.653
0.4	1.0918	7.5612	1.9946	593.27	1.51	1.12	1.31	2.92	58.844
0.5	1.1138	7.4521	1.9946	591.66	1.49	1.14	1.31	2.84	59.035
0.6	1.1278	7.7336	1.9946	584.81	1.47	1.14	1.34	2.74	59.226
0.7	1.1450	7.2438	1.9946	581.93	1.46	1.15	1.36	2.64	59.417
0.8	1.2065	7.0599	1.9947	590.60	1.44	1.21	1.29	2.66	59.608
0.9	1.1726	6.9710	1.9945	562.60	1.40	1.14	1.50	2.47	59.799
308 K									
0.1	1.0334	7.9447	1.9945	605.71	1.58	1.11	1.28	3.25	58.271
0.2	1.0383	7.8431	1.9945	596.27	1.56	1.10	1.32	3.08	58.462
0.3	1.0656	7.7443	1.9945	599.72	1.54	1.12	1.30	3.00	58.653
0.4	1.0874	7.6296	1.9945	598.02	1.53	1.13	1.29	2.92	58.844
0.5	1.1093	7.5191	1.9946	596.39	1.51	1.14	1.30	2.84	59.035
0.6	1.1238	7.3993	1.9945	589.42	1.49	1.14	1.32	2.74	59.226
0.7	1.1409	7.3062	1.9945	586.52	1.47	1.16	1.34	2.64	59.417
0.8	1.2023	7.1192	1.9947	595.15	1.45	1.22	1.27	2.66	59.608
0.9	1.1689	7.0289	1.9945	567.04	1.41	1.14	1.49	2.47	59.799
313 K									
0.1	1.0293	8.0103	1.9945	609.96	1.59	1.12	1.21	3.26	58.271
0.2	1.0331	7.9166	1.9944	600.70	1.57	1.11	1.26	3.09	58.462
0.3	1.0609	7.8168	1.9945	604.58	1.56	1.12	1.23	3.01	58.653
0.4	1.0822	7.6993	1.9945	602.39	1.54	1.14	1.23	2.92	58.844
0.5	1.1050	7.5858	1.9946	601.11	1.52	1.15	1.23	2.84	59.035
0.6	1.1188	7.4636	1.9945	593.65	1.50	1.15	1.26	2.74	59.226

0.7	1.1359	7.3702	1.9945	590.75	1.48	1.16	1.27	2.65	59.417
0.8	1.1980	7.1744	1.9947	599.18	1.46	1.23	1.22	2.66	59.608
0.9	1.1643	7.0876	1.9944	571.10	1.43	1.15	1.42	2.48	59.799

REFERENCES

- [1] Kumar D.H., Patel H.E., Kumar V.R.R., Sundararajan T., Pradeep T. and Das S.K., Model for heat conduction of nanofluids, *Physical Review Letters*, 94(14) (2004) 1-3.
- [2] Rajagopalan S., Sharma S.J. and Nanotkar V.Y., Ultrasonic Characterization of Silver Nanoparticles, *Journal of Metastable and Nanocrystalline Materials*, 23(2005) 271-274.
- [3] Peng C., Zhang J., Xiong Z., Zhao B. and Liu P., "Fabrication of porous hollow α -Al₂O₃ nanofibers by facile electro spinning and its application for water remediation", *Microporous and Mesoporous Materials*, 215 (2015) 133-142, (2002) 1896-1899. doi:10.1557/JMR.2002.0281.
- [4] Iglesias M.; Orge B.; Pineiro M.M.; de Cominges B.E.; Marino G.; Tojo J.: Thermodynamic Properties of the Ternary Mixture Acetone + Methanol + Ethanol at 298.15 K. *J.Chem.Eng.Data* 43 (1998) 776-780
- [5] Tourino A.; Casas L.M.; Marino G.; Iglesias M.; Orge B.; Tojo J.: Liquid phase behaviour and thermodynamics of acetone + methanol + n-alkane (C₉-C₁₂) mixtures. *Fluid Phase Equilib.* 206 (2003) 61-85
- [6] W. Guo, H. Xiao, W. Xie, J. Hu, Q. Li, P. Gao. A new design for preparation of high performance recrystallized silicon carbide. *Ceramics International*. 2012. 38: 2475-2481.
- [7] A. G. Murugkar and A. P. Maharolkar, Investigation on some thermo physical properties of methanol and nitrobenzene binary mixtures, *RJCABP*, Vol.1, pp-39-43, (2014)
- [8] Atoyán V.A.; Mamedov I.A.: Acoustic and Viscosity Properties of Liquid Ketones at Constant Volumes as a Function of Molecular Weight. *Zh. Fiz. Khim.* 54 (1980) 856-860
- [9] Babak S.F.; Udovenko V.V.: The Viscosity of Systems Containing Nicotine Vingson Solomon Jeevaraj, Ultrasonic Studies on Zink Oxide Nanofluids, *Journal of Nanofluids* 1 (2012) 97-100
- [10] R. Kiruba, M. Gopalkrishnan, T. Mahalingam, and A. Kingson Solomon Jeevaraj, Ultrasonic Studies on Zink Oxide Nanofluids, *Journal of Nanofluids* 1 (2012) 97-100
- [11] A. G. Murugkar and A. P. Maharolkar, I nvestigation on some thermo physical properties of methanol and nitrobenzene binary mixtures, *RJCABP*, Vol.1, pp-39-43, (2014)
- [12] Rao N P & Ronald E Verrall, *Can J Chem*, 65, (1987)
- [13] Thirumaran S & Deepesh George, *Arpan J of Engineering Appl. Sci*, 4, 4, (2009)
- [14] Rao N P & Ronald E Verrall, *Can J Chem*, 65, (1987)
- [15] Thirumaran S & Deepesh George, *Arpan J of Engineering Appl. Sci*, 4, 4, (2009)
- [16] Kiyohara O & Benson G C, *J Chem. Thermodyn*, 11, (1979) 861.
- [17] Bogumil B J Linde&Lezhnev N B, *J of Molecular Structure*, 754, (2005) 111.
- [18] Dhana Lakshmi & Sekhar S, *Ind J Pure Appl. Ultrasons*, 21, 3, (1999) 97
- [19] Chimankar O P, Sangeeta Jajodia, ShriwasRanjeeta & V A Tabhane, *Arch Appl Sci Res*, 3, 3, (2011) 252.
- [20] Tabhane V A & Patki B A, *Acustica*, 52, (1982).
- [21] J. Madhumitha, N. Santhi, G. Alamelumangai, M. Emayavaramban *International Letters of Chemistry, Physics and Astronomy*4 (2012) 82-95.
- [22] D.Ubagaramary, P.Neeraja *International Refereed Journal of Engineering and Science (IRJES) ISSN Volume 1, Issue 4(2012) 54-77.*
- [23] Riyazuddeen & Sadaf Afrin, *J Chem Eng*, 55, (2010) 2643.
- [24] N. R. Pawar and O. P. Chimankar, *J Pure & Appl.Ultrasonic*, 37(2015) 1-4.
- [25] P.D. Bageshwar, O.P. Chimankar and N.R. Pawar, *J Pure & Appl Ultrasonic*, 38(2016) 40- 42.
- [26] G.M. Jamankar, M.S. Deshapandeand N.R. Pawar, *J Pure & Appl Ultrasonic*, 38(2016) 10 – 13.
- [27] N.R. Pawar, O.P. Chimankar, S.J. Dhobleand R.D. Chavhan *Journal of Acoustical Society of India*, 43(3), (2016), 1-6.
- [28] K.Vaidyanathan, A.Venkateswaran & R.Ramaswamy, *Agricultural Chemistry*, Priya Publications, Karur 2000.

- [29] S.Chauhan, Kuldeep Kumar, and B.S. Patial., Indian Journal of Pure and Applied Physics, Vol 51 p.p 531-541 August 2013.
- [30] K.Ramanathan, S.Ravichandran, Journal of Pure and Applied Ultrasonics, 26,p.p 12-17 ,2004.

¹D. S. Chavhan

²D. R. Bijwe

³N. R. Pawar

⁴A. D. Chavhan

Synthesis and Thermoacoustic Study of Boron Nitride Nanoparticles in Acetone

Abstract: - Boron nitride nanoparticles (BN) were synthesized via high chemical route method and its characterization has been carried out by X ray diffraction (XRD), SEM, etc. Acetone based BN Nanosuspension were synthesized by two step method. Average particle size of BN nanoparticle has been estimated by using Debye-Scherrer formula. It was found to be 70 nm. Thermoacoustic properties of nanomaterials related to the surface of nanoparticles and nanoparticle surfactant interactions, these properties of BN nanosuspension was studied by non-destructive technique.

Keywords: BN, XRD, Debye-Scherrer formula, Nanosuspension, Thermoacoustic properties.

Corresponding Author: dbijwe@rediffmail.com

¹Department of Physics, Amolakchand Mahavidyalaya, Yavatmal - 445 001, India.

²Department of Physics, G.S.Tompe Arts, Commerce and Science College, Chandurbazar – 444704, India.

³Department of Physics, Arts, Commerce and Science College, Maregaon - 445 303, India.

⁴ Department of Physics, Matoshri Nanibai Gharphalkar Science College, Babhulgaon - 445 101, India.

I. INTRODUCTION

Nanoparticle of metals, metal oxide and semiconductor exhibited significantly distinct physical, chemical, optical, magnetic and biological properties from their matter because of their high surface to volume ratio. When a small number of nanoparticles dispersed in host fluids, can provide dramatic improvements in the thermal properties of the fluids. More recently there has been an increasing interest in the thermoacoustic properties of nanosuspensions in base fluids. Characterization of nanoparticle is important to understand and to control nanoparticle synthesis for various applications [1-3].

Boron nitride nanoparticles possess high thermal conductivity, and are a good conductor of heat. They are also a good electrical insulator, and have high-temperature lubricity features. Boron nitride nanoparticles are graded as an irritant and could possibly causes serious eye irritation, and allergy or asthma symptoms or breathing difficulties if inhaled. Boron nitride nanoparticles should be sealed in vacuum and stored in cool and dry room so as to avoid damp reunion as it would affect its dispersion performance and other usage effects.

Synthesis of Boron nitride Nanoparticles:

Boron Nitride is synthesized by using 6.18g boric acid (H_3BO_3 , Merck) dissolved in 200 ml distilled water. The solution is kept at $100^{\circ}C$. The 6.30g melamine $C_3H_6N_6$ Merck is now added to the solution. The material prepared is placed up to 48 hours in room temperature. $B_4N_3O_2H$ is obtained after filtering and drying the solution. This is the precursor of BN. Then it is heated at $500^{\circ}C$ temperature for three hours without any gas flow. After that, material heated under nitrogen gas flow. Nitrogen gas flow is allowed for one hour with $800^{\circ}C$. The sample so obtained was grinded to get it in powdered form [4-6].

XRD Pattern of Boron nitride Nanoparticles:

Many techniques are used to identify the various properties of nanomaterials. Some of the most important techniques are discussed below. X-ray diffraction [7-9] is a versatile, non-destructive technique that reveals details information about the chemical composition and crystallographic structure of natural and manufactured materials. In a crystalline solid, the constituent particles are arranged in regular periodic manner. An interaction of a particular crystalline solid with X-ray helps in investigation of its actual structure. Crystal is found to act as diffraction grating for X-ray and this indicates that the constituent particles in the crystal are arranged in planes at close distance in repeating patterns. The 2θ a value corresponding to peak in the X- ray diffraction is an important tool to understand the properties of characterizes materials. In nanomaterials number of atoms is very small. Nanoparticles cannot be considered as an infinite arrangement at of atoms. In case of amorphous nanoparticles broad diffraction peaks are expected to occur similar to amorphous bulk solid materials. However, in case of nanoparticles atoms do not have ordered lattices, some changes in diffraction are to be expected as compared to single crystal. Nanoparticles do not have grain boundaries. It has been found that diffraction peaks in nanocrystalline particles are broadened compared to a single or polycrystalline solid of same materials. From WRD pattern, Debye Scherrer gives an equation to determine nanoparticles size as,

$$D = \frac{0.9\lambda}{\beta \cos\theta} \quad \dots \dots \dots (3.1)$$

In above equation β is the broadening caused by nanoparticles size, θ is the Bragg's angle and λ is the wavelength of X-ray beam.

Figure 1 shows the XRD pattern of Boron nitride (BN) nanoparticles. The XRD measurement carried out by using "PAN analytical" X-ray diffractometer keeping the parameter constant at start position [$^{\circ}2\theta$.]: 10.0154 End Position [$^{\circ}2\theta$.]: 89.9834, Step Size [$^{\circ}2\theta$.]: 0.0170, Scan Step Time [s]: 5.7150, Scan Type: Continuous, Measurement Temperature [$^{\circ}C$.]: 25.00 Anode Material: Cu, K-Alpha1 [\AA .]: 1.54060. It is seen that the materials are well crystalline in nature and well agreed with standard JCPDS file number 034-0421. The estimate size of BN nanoparticles using Debye Scherrer formula is found about 70 nm.

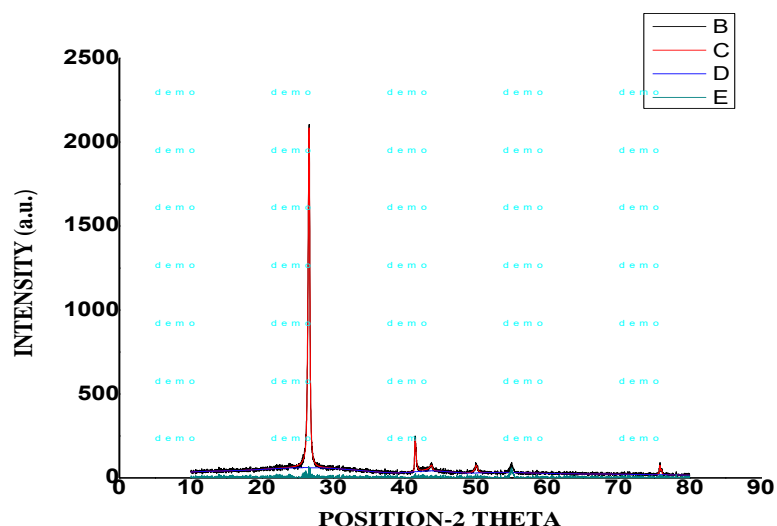


Fig. 1 X- ray diffraction pattern of Boron nitride nanoparticles

SEM image of BN Nanoparticle:

SEM study is carried out to observe the overall surface morphology and crystallite sizes of the prepared nanomaterials. This material has been synthesis by sol-gel method. From the SEM images are observed under 10 micrometer resolutions which shows the foam like surface morphology as n shown in figure 2. In the depicted images of BN nanomaterials, it can be clearly seen that the micrograph crystallite sizes may vary from a 10 μm to few microns range if we magnify further. The crystallites look like having a sharp surface edge as well as crystalline grains and the particles foam-like morphology can be formed from highly agglomerated crystallites. Also, it is confirmed that the crystallite sizes are nearly equal for all sample.

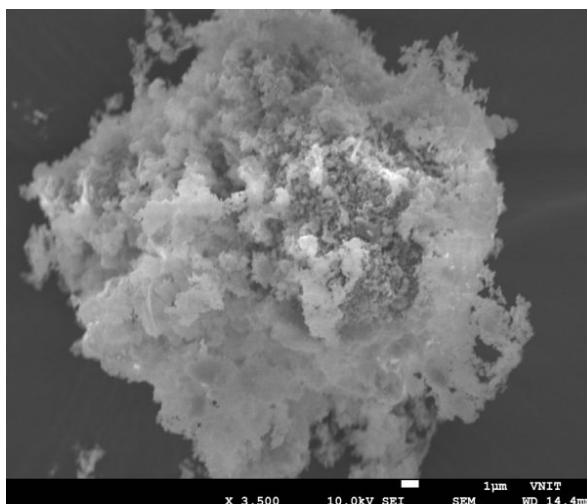


Fig 2. SEM image of BN Nanoparticles

RESULTS AND DISCUSSION

The experimentally measured values of ultrasonic velocity, density and viscosity are used to derive thermoacoustical parameters such as viscosity, adiabatic compressibility, Acoustic impedance, free length, free Volume, internal Pressure, isothermal compressibility, isothermal bulk modulus, molar compressibility, molar sound velocity, molar volume, Poisson ratio, relaxation time, Van der Wall's Constant, volume expansivity, effective mass and thermal conductivity. These parameters are represented are given in tables 1 (A) and 1 (B). In BN acetone based nanosuspension there might be nanoparticle fluid interaction favors in increase in ultrasonic velocity [10]. Rise in ultrasonic velocity may concluded as the strong interaction between nanoparticles of Boron Nitride (BN) and microsize molecules of methanol hence there is agglomeration of BN nanoparticles due to polar nature of acetone base fluid. Therefore sound will travel faster through the more compact structure by means of longitudinal waves [11-13].

Ultrasonic velocity gets increases with increasing the molar concentration of the BN nanoparticles in acetone this shows that the physical parameters of the sample changes by increasing the molar concentration. Nanoparticles suspensions do not settle which provides a long self- life which imparts ultrasonic velocity to them. For BN nanoparticle the velocity of the nanosuspension is higher than acetone and also by increasing the molar concentration of the BN nanoparticle the velocity gets higher value at 0.6. This represents strong aggregation of BN nano suspension in acetone-based fluid at this molar concentration. The cause behind this increase of ultrasonic velocity with increase in molar concentration (x) is due to strong interaction between nanosized particle and micro sized fluid molecule and also due to increase in density of nanosuspension with increase of molar concentration. Ultrasonic velocity can be interpreted as the nanosized BN particles have more surfaces to volume ratio and which can absorb more methanol molecules on its surface, which enhances the ultrasonic velocity. The decrease of ultrasonic velocity with increase in concentration is due weakening of interaction between BN nano sized particles and micro sized fluid molecules of acetone. Nonlinear variation of ultrasonic velocity may due to the Brownian motion of BN nanoparticles. Brownian motion is the erratic and constant motion of suspended nanoparticles in fluid. Motion of the particle becomes more rapid with increase in temperature of the medium which enhances ultrasonic velocity of the nanosuspension. Aggregation of BN nanoparticles in nanosuspension may occurs due to the interstitial accommodation of BN nanoparticles in nanosuspension or due to lack of perfect symmetry and decrease in available space between the components of the nanosuspension.

Densities of the nanosuspension were calculated by measuring the weight of the nanosuspension using 25 ml of specific gravity bottle and also by using the standard value of density of water. Nanosuspension BN has more density than acetone. Increase in density indicates the close packing between the BN nanoparticles in acetone -based fluids. Nonlinear variation of density may be due to Brownian motion of BN nanoparticles in acetone.

When BN nanoparticles suspended in acetone fluid, motion of particle becomes more rapid, lighter the particles, faster the motion and denser the particles slower the motion. Also suspended nanoparticles do not settle and they have long self-life. Hence, they can be easily suspended despite high solid density.

The densities of BN nanoparticles in acetone based nanosuspension shows that the density steeply increases with increase in concentration. This increase in density decreases the volume indicating association of BN nanoparticles in nanosuspension. It may be increase due to structural reorganization.

The viscosity slightly increases with increase in molar concentration of BN nanoparticles in acetone base nanosuspension. As the motion of nanoparticles becomes more rapid when the temperature of the medium was raised which lowers the viscosity of the medium as the size of the particles was reduced. Hence viscosity of nanosuspension decreases with increase in temperature.

The viscosity of BN nanoparticle strongly depends on structure of BN nanoparticles and consequently interactions between the BN nanoparticles and molecules of the fluid. Thus, the viscosity depends on interactions between components of nanosuspension as well as on the size and shape of the BN nanoparticles. Measurements of viscosity of nanosuspension yield some reliable information in the study of nano cluster. The viscosity gives the strength of interaction between the interacting BN nanoparticles and molecules of acetone. The interactions between BN nanoparticles and molecules of acetone increase the viscosity of nanosuspension.

The adiabatic compressibility (β_a) decreases with increase in molar concentration indicating strong interaction between BN nanoparticles and molecules of acetone showing aggregation of nanoparticles. The surface area of the material is increased by the reduction in particle size. Due to this higher percentage of the BN Nanoparticles can interact with surrounding fluids. It may due to decrease in interspacing of BN nanoparticles in nanosuspension with increase in molar concentration. It is a measure of association or dissociation or repulsion. It also determines the orientation of the nanoparticles in nanosuspension. Kiyohara and Benson [14] suggest that adiabatic compressibility is the result of several opposing effects like strong interactions between nanoparticles and molecules of the fluids also interstitial accommodation leads to a more compact structure and decreases adiabatic compressibility. The magnitudes of the various contributions depend mainly on the relative size of the BN nanoparticles. Isothermal compressibility (β_i) and adiabatic compressibility (β_a) exhibits similar trend and both decreases with increase in molar concentration of BN nanoparticles in nanosuspension.

The relaxation time slightly decreases with increase in molar concentration of BN nanoparticles indicating less stability of BN nanoparticles in nanosuspension. For the nanoparticles in nanosuspension, the gravitational

pull is not stronger than the random thermal motion of the particles hence nanoparticles do not settle which provides long self life at these molar concentrations which increases the relaxation time. Stability of BN nanoparticles in nanosuspension is totally depends on its surface energy. Less surface energy more stable will be the BN nanoparticles. The relaxation is caused by the energy transfer between translational and vibrational degrees of freedom and all these degrees take part in the process observed [15].

Free length is the distance between the surfaces of the neighboring BN nanoparticles. The free length slightly decreases with increase in molar concentration at 0.7. The free length (L_f) of a nanosuspension is a measure of attraction between BN nanoparticles and molecules of the acetone in nanosuspension. Decrease in free length is a result of increase in surface to volume ratio of BN nanoparticles with acetone molecules, association through interactions between nanoparticles and molecules of the constituents of the nanosuspension.

The internal pressure (π_i) and free volume (V_f) versus molar concentration of BN nanoparticles in nanosuspension represented that the internal pressure as well as free volume in nanosuspension is a measure of attraction between their constituents. In this nanosuspension, free volume decreases and internal pressure increases. Further, the increase in free volume and decrease in internal pressure with rise in concentration clearly show the increasing magnitude of interactions [16]. Such behavior of internal pressure and free volume generally indicates the association through interactions between BN nanoparticles and molecules of acetone.

Acoustic impedance is found reciprocal to that of adiabatic compressibility [17-20]. It is in good agreement with the theoretical requirements. In this case, acoustic impedance increases with increase in the molar concentration of BN nanoparticles in nanosuspension at 0.7. As the size of the material decreases, the percentage of surface atoms increases, hence large amount of substance comes in contact with surrounding materials. This results in increase in acoustic impedance. The increase in acoustic impedance (Z) with molar concentration can be explained on the basis of the interactions between components of the nanosuspension, which decreases the distance of their components.

The molar volume (V_m) of BN nanoparticles depends on the structural arrangement and interactions between the components of the nanosuspension medium. The structural arrangement may be decided by the interaction forces in the nanosuspension medium. It is decreases with increase in molar concentration because the molecular weight is directly proportional to the molar volume. The molar volume is found to have similar type of trend as that of molar compressibility [21-30]. The Vander Waal's constant increases with increase in molar concentration and decreases beyond 0.7. This is because of the association of the interacting molecules inside the fluid medium. The change in Vander Waal's constant (b) would be due to a change in geometry of the BN nanoparticles.

The sound velocity (R) increases at 0.7, it may due to increase in surface to volume ratio. It shows similar trends as that of ultrasonic velocity as it depends on it. The molar compressibility (W) decreases with increase in molar concentration of BN nanoparticles in acetone based nanosuspension due to aggration of BN nanoparticles in the medium. As it is function of adiabatic compressibility, its variation is similar as that of adiabatic compressibility. The isothermal Bulk modulus (B_i) increases with increase in molar concentration, it exhibits similar trends as that of ultrasonic velocity and inverse trend as that of isothermal compressibility. The volume expansivity decreases with increase in molar concentration due to aggration of BN nanoparticles in nanosuspension. As it is depends on internal pressure and isothermal compressibility it shows their resultant effects.

The effective thermal conductivity of nanosuspension increases with temperature. It has substantially higher value at molar concentration 0.7. The thermal conductivity enhancements are highly dependent on specific surface area of nanoparticle, with an optimal surface area for the highest thermal conductivity. There is strong relationship between Brownian motion and temperature of nanoparticles. Furthermore, the effect of temperature on thermal conductivity is not very well understood and documented. It is reported that it shows the similar behavior as that of ultrasonic velocity.

Table-1(A) Experimental values of thermoacoustic Parameters at 5 MHz

X	U (m/s)	ρ (Kg/m ³)	$\eta \cdot 10^{-3}$ (NS/m ²)	$\beta a \cdot 10^{-9}$ (m ² /N)	$\beta i \cdot 10^{-10}$ (ms ² /kg)	$\tau \cdot 10^{-10}$ (s)	$L_f \cdot 10^{-11}$ (m)	$\pi_i \cdot 10^6$ (N/m ²)	$V_f \cdot 10^{-8}$ (m ³ /mol)
293 K									
0.1	1190	748.71	0.4988	9.43	1.13	6.27	5.99	6.27	1.69
0.2	1225	751.91	0.5099	8.86	1.06	6.02	5.80	6.02	1.55

0.3	1310	761.87	0.6001	7.65	9.18	6.12	5.39	6.12	1.22
0.4	1418	770.09	0.5998	6.46	7.75	5.17	4.96	5.17	1.23
0.5	1550	777.82	0.6052	5.35	6.42	4.32	4.51	4.32	1.24
0.6	1710	785.51	0.6106	4.35	5.22	3.54	4.07	3.54	1.25
0.7	1710	790.73	0.6194	4.32	5.18	3.57	4.05	3.57	1.06
0.8	1530	798.56	0.6532	5.35	6.42	4.66	4.51	4.66	7.15
0.9	1470	803.15	0.6584	5.76	6.91	5.06	4.68	5.06	5.63
298 K									
0.1	1199	745.17	0.4815	9.33	1.1196	5.99	6.01	5.99	1.8
0.2	1234	748.46	0.4926	8.77	1.0524	5.76	5.82	5.76	1.65
0.3	1319	758.12	0.5827	7.58	9.096	5.89	5.42	5.89	1.28
0.4	1427	767.02	0.5822	6.40	7.68	4.97	4.98	4.97	1.3
0.5	1559	774.87	0.5877	5.31	6.372	4.16	4.53	4.16	1.3
0.6	1719	782.51	0.5931	4.32	5.184	3.42	4.09	3.42	1.31
0.7	1719	787.27	0.6018	4.30	5.16	3.45	4.08	3.45	1.12
0.8	1539	795.71	0.6356	5.31	6.372	4.50	4.53	4.50	7.51
0.9	1479	800.12	0.6408	5.94	7.128	5.08	4.79	5.08	5.91
303 K									
0.1	1138.4	742.89	0.4643	9.24	1.11	5.72	6.03	5.72	1.9178
0.2	1207	745.5	0.4754	8.70	1.04	5.51	5.85	5.51	1.7588
0.3	1242	755.17	0.5655	7.52	9.02	5.67	5.44	5.67	1.3543
0.4	1327	763.88	0.5651	6.36	7.63	4.79	5.01	4.79	1.3693
0.5	1435	772.01	0.5704	5.28	6.34	4.02	4.56	4.02	1.3723
0.6	1567	779.69	0.5757	4.30	5.16	3.30	4.11	3.30	1.3812
0.7	1727	784.47	0.5844	4.27	5.12	3.33	4.10	3.33	1.1777
0.8	1727	792.16	0.6181	5.27	6.32	4.34	4.55	4.34	7.8952
0.9	1547	797.56	0.6233	5.80	6.96	4.82	4.78	4.82	6.2141
308 K									
0.1	1214	739.21	0.4472	9.18	1.1	5.47	6.06	5.47	2.05
0.2	1249	742.83	0.4582	8.63	1.04	5.27	5.88	5.27	1.87
0.3	1334	752.22	0.5484	7.47	8.96	5.46	5.47	5.46	1.43
0.4	1442	760.17	0.5479	6.33	7.6	4.62	5.04	4.62	1.44
0.5	1574	768.75	0.5532	5.25	6.3	3.87	4.59	3.87	1.45
0.6	1734	776.48	0.5585	4.28	5.14	3.19	4.14	3.19	1.45
0.7	1734	781.07	0.5671	4.26	5.11	3.22	4.13	3.22	1.24
0.8	1554	789.63	0.6008	5.24	6.29	4.20	4.58	4.20	8.29
0.9	1494	794.24	0.6063	5.64	6.77	4.56	4.75	4.56	6.52
313 K									
0.1	1220	736.39	0.4302	9.12	1.09	4.04	6.10	5.23	2.1852
0.2	1255	739.77	0.4413	8.58	1.03	5.23	5.92	5.05	1.9975
0.3	1340	749.19	0.5313	7.43	8.92	5.05	5.51	5.26	1.5091
0.4	1448	757.7	0.5308	6.29	7.55	5.26	5.07	4.45	1.5247
0.5	1580	765.56	0.5361	5.23	6.28	4.45	4.62	3.74	1.5248
0.6	1740	773.64	0.5414	4.27	5.12	3.74	4.17	3.08	1.5317
0.7	1740	778.13	0.5513	4.24	5.09	3.08	4.16	3.12	1.2999
0.8	1560	786.99	0.5837	5.22	6.26	3.12	4.62	4.06	8.7121
0.9	1500	791.19	0.5892	5.62	6.74	4.06	4.79	4.42	6.8501

Table-1(B) Experimental values of thermoacoustic Parameters at 5 MHz

X	Z*10 ⁶ (kg/m ² s)	Vm*10 ⁻² (m ³ /mol)	b*10 ⁻⁵ (m ³ /mol)	R*10 ⁻⁴ (m ³ /mol) (m/s) ^{1/3}	W*10 ⁻⁴ (m ^{19/7} /S ¹)	Bi*10 ⁹ (N/m ²)	α*10 ⁻⁵ (1/K)	T*10 ⁻³ (W/mK)	Meff (mol)
293 K									
0.1	8.9096	7.3131	1.9935	497.63	1.42	0.885	1.94	2.04	54.754
0.2	9.2108	6.8396	1.9935	500.97	1.34	0.943	1.96	2.16	51.428

0.3	9.9805	6.3137	1.9937	521.63	1.27	1.09	1.94	2.44	48.102
0.4	10.9198	5.8146	1.9939	549.35	1.19	1.29	1.73	2.79	44.778
0.5	12.0562	5.3291	1.9942	583.28	1.13	1.56	1.51	3.23	41.450
0.6	13.4322	4.8534	1.9946	623.75	1.06	1.92	1.31	3.80	38.124
0.7	13.5214	4.4009	1.9943	603.73	0.958	1.93	1.46	4.05	34.799
0.8	12.2179	3.9411	1.9933	520.67	0.832	1.56	2.22	3.90	31.472
0.9	11.8063	3.5045	1.9926	481.05	0.732	1.45	2.80	4.05	28.146
298 K									
0.1	8.9345	7.3479	1.9935	502.19	1.43	0.893	1.93	2.04	54.754
0.2	9.2359	6.8712	1.9935	505.42	1.35	0.950	1.95	2.17	51.428
0.3	9.9996	6.3449	1.9937	526.08	1.27	1.10	1.99	2.45	48.102
0.4	10.9453	5.8379	1.9939	553.57	1.20	1.30	1.84	2.80	44.778
0.5	12.0802	5.3493	1.9942	587.41	1.13	1.57	1.66	3.24	41.450
0.6	13.4513	4.8721	1.9945	627.83	1.06	1.93	1.49	3.81	38.124
0.7	13.5331	4.4202	1.9943	607.79	9.63	1.94	1.65	4.06	34.799
0.8	12.2459	3.9552	1.9933	524.35	8.36	1.57	2.36	3.92	31.472
0.9	11.8337	3.5177	1.9926	484.61	7.32	1.40	2.83	4.07	28.146
303 K									
0.1	8.9666	7.3704	1.9935	506.06	1.44	0.901	1.89	2.05	54.754
0.2	9.2591	6.8985	1.9934	509.37	1.36	0.962	1.91	2.18	51.428
0.3	10.0211	6.3697	1.9937	529.96	1.28	1.11	1.95	2.46	48.102
0.4	10.9616	5.8619	1.9939	557.43	1.21	1.31	1.81	2.81	44.778
0.5	12.0974	5.3691	1.9942	591.15	1.14	1.58	1.64	3.25	41.450
0.6	13.4655	4.8896	1.9945	631.51	1.06	1.94	1.47	3.81	38.124
0.7	13.5478	4.4361	1.9943	611.34	9.67	1.95	1.63	4.07	34.799
0.8	12.2547	3.9729	1.9933	527.86	8.41	1.58	2.33	3.92	31.472
0.9	11.8597	3.5291	1.9926	487.74	7.36	1.44	2.72	4.08	28.146
308 K									
0.1	8.9740	7.4071	1.9934	509.84	1.45	0.909	1.88	2.05	54.754
0.2	9.2779	6.9233	1.9934	512.86	1.37	0.962	1.91	2.19	51.428
0.3	10.0346	6.3947	1.9936	533.45	1.29	1.12	1.95	2.46	48.102
0.4	10.9616	5.8905	1.9939	561.06	1.21	1.32	1.82	2.81	44.778
0.5	12.1001	5.3919	1.9942	594.63	1.14	1.59	1.64	3.26	41.450
0.6	13.4641	4.9098	1.9945	634.94	1.07	1.95	1.48	3.82	38.124
0.7	13.5437	4.4553	1.9942	614.71	9.72	1.96	1.64	4.07	34.799
0.8	12.2708	3.9857	1.9932	530.82	8.44	1.59	2.35	3.93	31.472
0.9	11.8659	3.5438	1.9926	490.72	7.43	1.48	2.63	4.09	28.146
313 K									
0.1	8.9839	7.4355	1.9934	513.01	1.45	0.917	1.81	2.06	54.754
0.2	9.2841	6.9519	1.9934	516.03	1.37	0.971	1.85	2.19	51.428
0.3	10.0391	6.4205	1.9936	536.57	1.29	1.12	1.90	2.47	48.102
0.4	10.9715	5.9097	1.9939	564.01	1.22	1.32	1.76	2.82	44.778
0.5	12.0958	5.4143	1.9942	597.72	1.15	1.59	1.60	3.26	41.450
0.6	13.4613	4.9279	1.9945	637.92	1.07	1.95	1.43	3.82	38.124
0.7	13.5394	4.4721	1.9942	617.61	9.76	1.96	1.59	4.08	34.799
0.8	12.2770	3.9991	1.9932	533.46	8.47	1.60	2.27	3.94	31.472
0.9	11.8678	3.5574	1.9925	493.32	7.46	1.48	2.53	4.10	28.146

REFERENCES

- [31] S. K. Thakur and S. Chauhan, A Study of acoustical behavior of drug colimax in aqueous mixture of methanol at 250C, *Advances in Applied Science Research*, 2 (2) pp. 208-217, (2011)
- [32] T. M. Aminabhavi, M. I. Arulaguppi S. B. Harogoppad, R. H. Balundgi, Densities, viscosities, refractive indices, and speeds of sound for methyl acetoacetate + aliphatic alcohols (C1C8) , *J. Chem. Eng. Data* 38 (1), pp.31-39, (1993)
- [33] U. B. Kadam, A. P. Hiray, A. B. Sawant, M. Hasan, Densities, viscosities, and ultrasonic velocity studies of binary mixtures of trichloromethane with methanol, ethanol, propan-1-ol, and butan-1-ol at T= (298.15 and 308.15) K, *J. Chem. Thermodyn.* 38, pp.1675-1683, (2006)
- [34] Iglesias M.; Orge B.; Pineiro M.M.; de Cominges B.E.; Marino G.; Tojo J.: Thermodynamic Properties of the Ternary Mixture Acetone + Methanol + Ethanol at 298.15 K. *J.Chem.Eng.Data* 43 (1998) 776-780
- [35] Tourino A.; Casas L.M.; Marino G.; Iglesias M.; Orge B.; Tojo J.: Liquid phase behaviour and thermodynamics of acetone + methanol + n-alkane (C9-C12) mixtures. *Fluid Phase Equilib.* 206 (2003) 61-85
- [36] R. Kiruba, M. Gopalkrishnan, T. Mahalingam, and A. K. Zh. *Obschch. Khim.* 20 (1950) 2124-2126
- [37] A. G. Murugkar and A. P. Maharolkar, Investigation on some thermo physical properties of methanol and nitrobenzene binary mixtures, *RJCABP*, Vol.1, pp-39-43, (2014)
- [38] Atoyan V.A.; Mamedov I.A.: Acoustic and Viscosity Properties of Liquid Ketones at Constant Volumes as a Function of Molecular Weight. *Zh. Fiz. Khim.* 54 (1980) 856-860
- [39] Babak S.F.; Udovenko V.V.: The Viscosity of Systems Containing Nicotine Vingson Solomon Jeevaraj, *Ultrasonic Studies on Zink Oxide Nanofluids*, *Journal of Nanofluids* 1 (2012) 97-100
- [40] R. Kiruba, M. Gopalkrishnan, T. Mahalingam, and A. Kingson Solomon Jeevaraj, *Ultrasonic Studies on Zink Oxide Nanofluids*, *Journal of Nanofluids* 1 (2012) 97-100
- [41] A. G. Murugkar and A. P. Maharolkar, Investigation on some thermo physical properties of methanol and nitrobenzene binary mixtures, *RJCABP*, Vol.1, pp-39-43, (2014)
- [42] Rao N P & Ronald E Verrall, *Can J Chem*, 65, (1987)
- [43] Thirumaran S & Deepesh George, *Arpan J of Engineering Appl. Sci*, 4, 4, (2009)
- [44] Rao N P & Ronald E Verrall, *Can J Chem*, 65, (1987)
- [45] Thirumaran S & Deepesh George, *Arpan J of Engineering Appl. Sci*, 4, 4, (2009)
- [46] Kiyohara O & Benson G C, *J Chem. Thermodyn*, 11, (1979) 861.
- [47] Bogumil B J Linde & Lezhnev N B, *J of Molecular Structure*, 754, (2005) 111.
- [48] Dhana Lakshmi & Sekhar S, *Ind J Pure Appl. Ultrasons*, 21, 3, (1999) 97
- [49] Chimankar O P, Sangeeta Jajodia, ShriwasRanjeeta & V A Tabhane, *Arch Appl Sci Res*, 3, 3, (2011) 252.
- [50] Tabhane V A & Patki B A, *Acustica*, 52, (1982).
- [51] J. Madhumitha, N. Santhi, G. Alamelumangai, M. Emayavaramban *International Letters of Chemistry, Physics and Astronomy* 4 (2012) 82-95.
- [52] D. Ubagaramary, P. Neeraja *International Refereed Journal of Engineering and Science (IRJES) ISSN* Volume 1, Issue 4 (2012) 54-77.
- [53] Riyazuddeen & Sadaf Afrin, *J Chem Eng*, 55, (2010) 2643.
- [54] N. R. Pawar and O. P. Chimankar, *J Pure & Appl. Ultrasonic*, 37 (2015) 1- 4.
- [55] P.D. Bageshwar, O.P. Chimankar and N.R. Pawar, *J Pure & Appl Ultrasonic*, 38 (2016) 40- 42.
- [56] G.M. Jamankar, M.S. Deshapande and N.R. Pawar, *J Pure & Appl Ultrasonic*, 38 (2016) 10 – 13.
- [57] N.R. Pawar, O.P. Chimankar, S.J. Dhoble and R.D. Chavhan *Journal of Acoustical Society of India*, 43 (3), (2016), 1-6.
- [58] K. Vaidyanathan, A. Venkateswaran & R. Ramaswamy, *Agricultural Chemistry*, Priya Publications, Karur 2000.
- [59] S. Chauhan, Kuldeep Kumar, and B.S. Patial., *Indian Journal of Pure and Applied Physics*, Vol 51 p.p 531-541 August 2013.
- [60] K. Ramanathan, S. Ravichandran, *Journal of Pure and Applied Ultrasonics*, 26, p.p 12-17, 2004.

¹S N Jadhav
²RNPathare (Dhokne)

Dielectric Characteristics of Nanoparticles Doped Polyvinyl Alcohol



Abstract: -A comparative study of structural characterization and dielectric properties of Polyvinyl alcohol, after insertion of Zinc oxide (ZnO) and Aluminum oxide (Al₂O₃) to form sample composite in the form of films at frequencies varying from 1Hz to 100 Hz and for several temperatures from 288k to 353k has been done. Structural characterization of PVA-Zn and PVA-Al done by x-ray diffraction (XRD), Fourier Transform Infrared Spectroscopy (FTIR) and Field emission Electron Microscopy (FESEM). It is confirmed that ZnO and Al₂O₃ was well incorporated in PVA matrix. Together composites of ZnO and Al₂O₃ with PVA tested by electrical properties like dielectric constant (ϵ') and dielectric loss (ϵ'') which shows the dispersed values at lower range of frequencies and seen to decreased at higher ranges at all temperatures, interprets the interfacial polarization. Imaginary part of electric modulus (M'') has been determined by studying the dielectric relaxation properties of both composites. The modulus graph shows that the peaks position transfer near higher frequencies with rise in temperatures. The time of dielectric relaxation is determined from peak frequencies of M'' plot; lessened with temperature rise.

Keywords: Dielectric Properties, XRD, FTIR, FESEM

I. INTRODUCTION

Polymer composite films have imperative applications in supercapacitors, sensors like gas sensors, batteries and many more as a result of their good thermal stability with better ionic conductivity. Now a days polymer incorporated with ceramic fillers improves electronic properties and thus opens for vast applications in fields like electronic packaging, angular acceleration accelerometers, integrated decoupling capacitors, etc. So, for the same probable technical applications, it is most imperative to study dielectric properties. It is significant to consider charge transfer mechanism in polymer composites for perspective of technological and fundamental mode. In highly doped polymers ions or charge carriers are localized, hence movement of the carriers happens by tunnelling or hopping mechanism among the localized states. One of the known charge transfer mechanisms is Variable Range Hopping (VRH), in which charge transfer happens in consecutive localized states by attaining phonon thermal energy [1-5]. Temperature dependent polymer is also called as polar polymer complex when inserted through metal salts in view to increase the ionic conductivity. The polymer composites can be easily process into films and also have electrochemical stability, hence received excessive attraction but cored downside is its low conductivity. It may improve the conductivity of polymer composites by incorporating the ceramic materials [6]. As Polyvinyl Alcohol (PVA) is compatible with each type of fillers so that it acknowledged a lot of industrial applications like food, cosmetics, packaging, pharmaceutical etc as well as it is biocompatible, non-toxic, hydrophilic and semicrystalline polymer and hence preferred for present work [7]. Present work emphasizes on the comparative structural and dielectric study of PVA with Al₂O₃ and ZnO to synthesize polymer composite by solvent casting technique for temperatures varies from 288 k to 353 k.

II. EXPERIMENTAL

The required polymer (PVA) of 86–89% degree of saponification, has molecular weight of 124000 mol⁻¹, analytical grade Zinc oxide (ZnO) of molecular weight 81.39 and Al₂O₃ of molecular weight 101.9 were together collected from SDFCL, Mumbai, India.

Films of pristine PVA, PVA-ZnO and PVA-Al₂O₃ composite were synthesised by simple and cost-effective solution casting method [8 -11]. As per method, first, 1g PVA powder is liquified in 30 ml highly double distilled water. The transparent solution was prepared by stirring the solution continuously at ambient temperature. Vacuum dried ZnO of 10 weight percentage, was placed into the congruent solution by simultaneous heating at 50°C for 1 h. The mixture after cooling transported on plane glass surface and left to evaporate at normal temperature and finally dehydrated at 40°C temperatures. Prepared layers of composite were then unwrapped from petri dishes which then kept separately in the vacuum chamber. Film thickness was measured by thickness profilometer, is found 114-120 μm . Similarly, PVA-Al₂O₃ composite is synthesized by the equal phenomenon and entitled as PVA-Zn, PVA-Al.

¹*Corresponding author: snjadhav@dbatu.ac.in, Dr B.A. T. U. Lonere, Raigad, Maharashtra

²SES Amravati's Science College, Nagpur, Maharashtra

Structural study of composites has been done by X-ray diffraction analysis, on Bruker D8 advance x-ray diffractometer, Germany of wavelength 1.5406 \AA , FTIR of SHIMADZU 8400 spectrophotometer, Japan over the range of $400\text{-}4000 \text{ cm}^{-1}$ and FESEM with EDAX of HITACHI S-4800. The dielectric properties were analysed on Novocontrol concept 80 with Alpha A high resolution Analyzer linked to a computer of frequency starts from 0.1 Hz to 1 MHz and for temperature in between 288K to 353K .

III. RESULT AND DISCUSSION

XRD spectra of PVA, PVA-Zn, PVA-Al sample composite are revealed in Fig 1. XRD peak of PVA is wide retorting to (101) plane at $2\theta = 19^\circ$ suggesting semi crystalline form of PVA [12-14]. In PVA-Zn film (JCPDS Card No. 36-1451 and 80-0075) the ZnO peaks had orientation from 100, 002, 101, 102, 110, 103, 110, 200, 112 and 201 planes for which the scattering angles are 31.6° , 34.4° , 36.16° , 47.52° , 56.48° , 61.56° , 62.88° , 66.24° , 67.84° , 68.96° respectively which designates that ZnO has the structure of hexagonal wurtzite [15-17]. The general PVA-Zn composite film XRD spectra reveals that Zinc Oxide kept its unique structure in composite film [18,12,17]. From XRD spectrum of PVA-Al composite film, it reveals that width of broad hump of PVA has been enlarged somewhat in size with lessened in height. Besides the intensity peak at 66.3° , no other peaks and features are detected in PVA-Al composite film, which shows the amorphous structure of composite. This is occurred due to smaller crystallites and very strong interface of Al with PVA. Size of Crystallites is calculated from Debye-Scherrer formula, is nearly equal 3.16 nm .

Fig. 2 shows FTIR spectra of PVA, PVA-Zn, PVA-Al composite films. Strong and broad hydrogen bond (O-H group) of alcohol in PVA is detected in between $3617\text{-}2738 \text{ cm}^{-1}$, which is then shifted to $3617\text{-}3451 \text{ cm}^{-1}$ in PVA-Zn composite and $3635\text{-}3452 \text{ cm}^{-1}$ in PVA-Al composite, occurs because of adsorption of water during creation of PVA-Zn composite films. Existence of hydrogen bond in PVA-Zn and PVA-Al composite confirmed by the occurrence of hydroxy group of PVA. For 2964 cm^{-1} and 2963 cm^{-1} medium stretching of C-H bond are seen in PVA-Al and PVA-Zn composite films. O-H bonding of acetyl group is occurred at 1131 cm^{-1} in PVA which then switched almost to 1139 cm^{-1} in PVA-Zn composite. Bending vibrations of O-H group is detected at 1270 cm^{-1} as a result of vibrations at gas phase, next it is shifted to 1288 cm^{-1} . The bending of C-H bond in $-\text{CH}_2$ group is at 1457 cm^{-1} and 620 cm^{-1} . The M-O bond of Zinc-oxide (Zn-O) is occurred at 578 cm^{-1} in PVA-Zn and of Al-O is formed at 765 cm^{-1} in PVA-Al composite film, which approves the presence of ZnO and Al_2O_3 content in composite film [19-23].

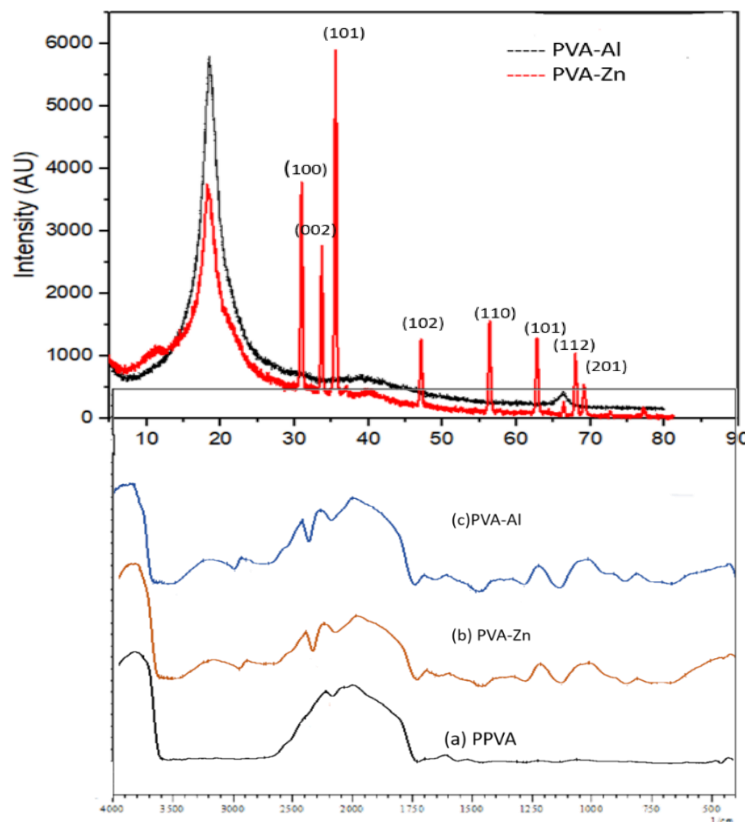


Figure 1. X Ray Diffraction of PVZn-10 and PVAI-10

Figure 2. FTIR of PVA, PVZn-10 and PVAI-10

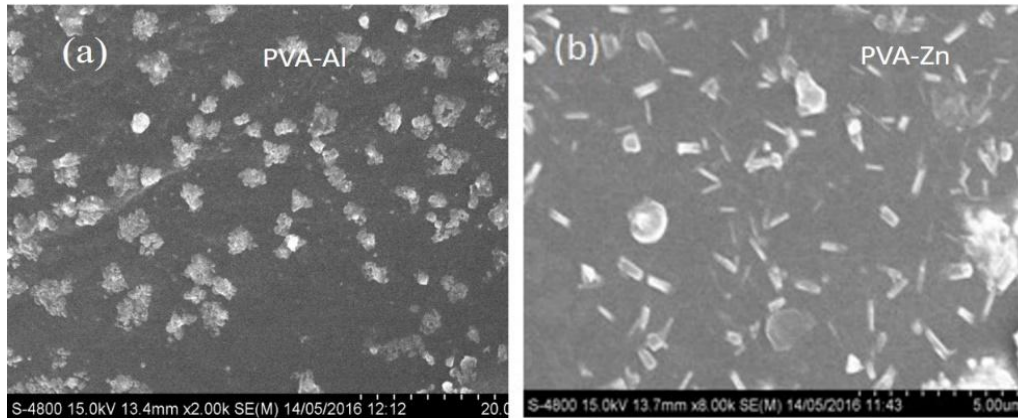


Figure 3. FESEM of a) PVZn-10 and b) PVAI-10

Figure 4: EDAX of PVZn-10 and PVAI-10

The FESEM image of PVA-Al and PVA-Zn is revealed in Fig. 3a and 3b. From Figure 3a, it is predicted that PVA when induced in ZnO, particles were dispersed arbitrarily on the surface and looks tube like constructions. The EDAX of PVA-Zn composite is depicted in Figure 4a shows presence of Zn and O element in composite film [24 -25]. Similarly, in PVA-Al micrograph the shape of Al_2O_3 particles becomes irregular and it spreads over the whole surface shows homogeneity of the film depicted in Figure 3b. The EDAX images of PVA-Al composite is shown in Figure 4b, specifies that energy of release of characteristics X-Ray spectrum for k-series of Al is 1.486keV and that of oxygen for k-series is 0.525 keV, directs the existence of Al and Oxygen in synthesized PVA-Al composite film [26-27].

The graph of (ϵ') of PVA, PVA-Al and PVA-Zn composite film with frequency from 100Hz to 1MHz is presented in Fig 4a. It is depicted that value of ϵ' for both composites fall with rising $\log f$ value and shows high values at low frequencies, because it gets enough relaxation time for the setback of ions with field arise as a result of interfacial polarization. It may arise due to electrode polarization in which charge carriers which are stored at electrodes easily follows with field reversal resulting in rised value of ϵ' . However, at higher frequencies, the charges not trails the field because of ionic and electronic polarization, which results in fall in ϵ' [28-30].

Besides PVA has minimum value of ϵ' which is formerly increased with doping of Al_2O_3 and ZnO into PVA due to oxide structure [23]. Fig. 4b shows the variance of ϵ' for temperatures varying from 288k to 353k. It is detected from graph that ϵ' grows with temperature for all composite films due to improvement in flexibility of polymer chain at high temperatures, thereby increases mobility of molecules. At low-temperature (288k), the polarization procedure slows down as of excess viscosity of polymer thus alignment of dipoles can't follow with the field setback results in lesser value of ϵ' . As temperature rises above 288k, the thick nature of polymer decreases, inscription of easier alternation of dipole with field thereby increase in ϵ' . Rise in density of charge carrier and mobility of molecules with temperature can be well explained by,

$$N = n_0 \exp\left(-\frac{U}{\epsilon' k_B T}\right) \text{-----1}$$

Where, N is charge carrier Density, K_B is Boltzmann constant and U is the dissociation energy. Debye relaxation model is used to describe dielectric relaxation in polymer having only one relaxation time can be given by,

$$\epsilon^* = \epsilon_\infty + \frac{\epsilon_s - \epsilon_\infty}{1 + i\omega\tau} \text{-----2}$$

ϵ' is given by,

$$\epsilon' = \epsilon_\infty + \frac{\epsilon_s - \epsilon_\infty}{1 + \omega^2\tau^2} \text{-----3}$$

Where, ϵ_∞ is the limiting value of the ϵ' at high frequencies, ϵ_s is the static ϵ' , $\omega = 2\pi f$ is the angular frequency and τ is the relaxation time. Polar and nonpolar polymers show diverse behaviour of ϵ' with temperature. In polar polymer ϵ' increases with temperature whereas remain independent of temperature in non-polar polymers [31].

Variation of dielectric loss with frequency and temperature for PVA, PVA-Al and PVA-Zn is depicted in Fig.5a and 5b. It is observed from Fig.5a that at down frequencies, dielectric loss (ϵ'') illustrates scattered nature, while at upper frequencies its value decreases and reaches to zero. As at lesser frequencies charges contributes to field alignment because of sufficient time span but at up frequencies, ϵ'' value decreases and thereby lessening in ϵ'' . Besides the rising of ϵ'' value with the temperature because of increased flexibility of charges with high thermal energy is described in Fig.5b. It trails the DC involvement which is temperature dependent, results in increment of both conductivity and the dielectric loss [32].

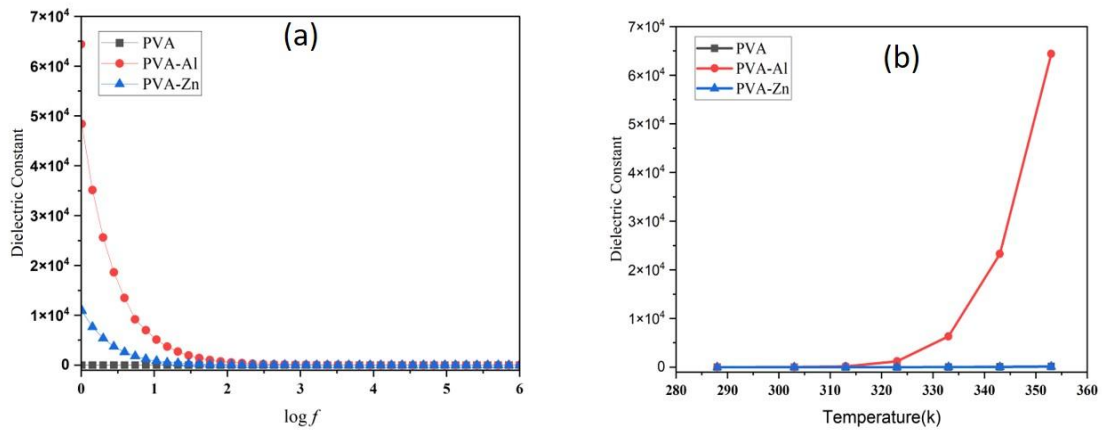


Figure 4. A plot of Dielectric constant of PVA, PVA-Al and PVA-Zn with (a) log f and (b) Temperature (k)

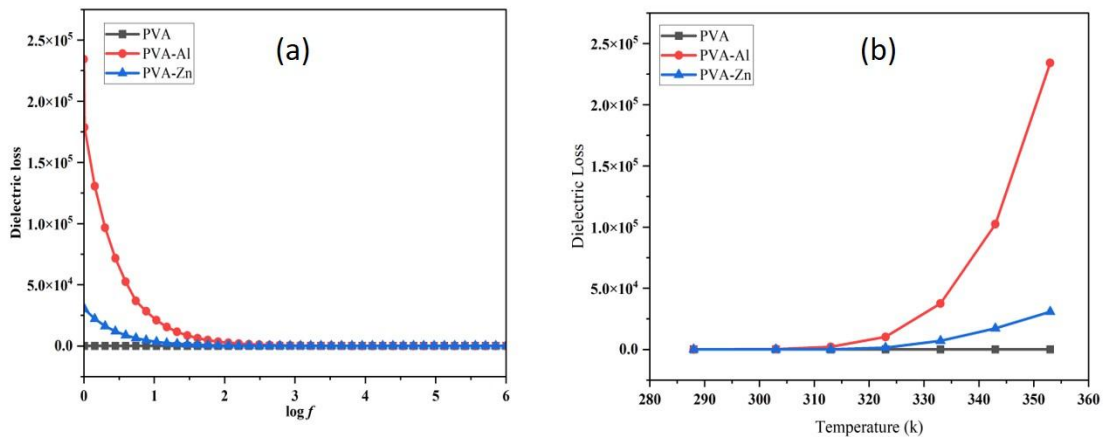


Figure 5. A plot of Dielectric loss (ϵ'') of PVA, PVA-Al and PVA-Zn with (a) log f and (b) Temperature k

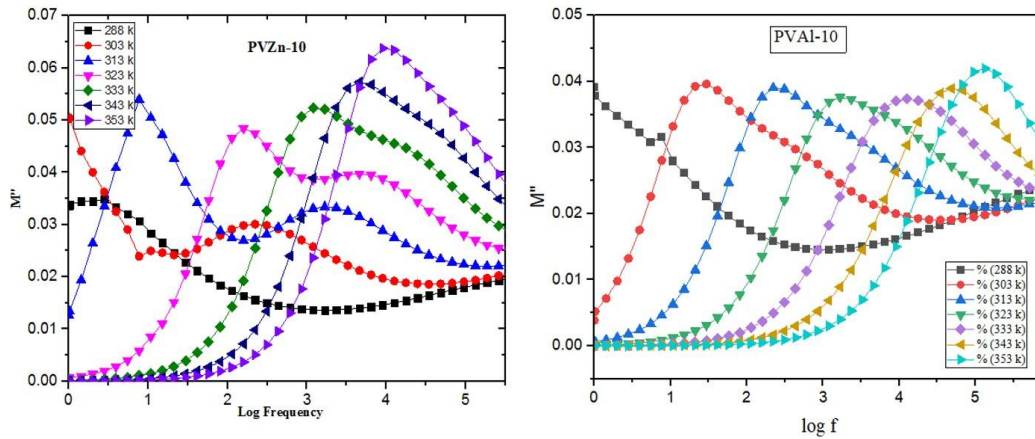


Figure 6 A plot of M'' of PVAI-10 and PVZn-10 with $\log f$ for different Temperature (k)

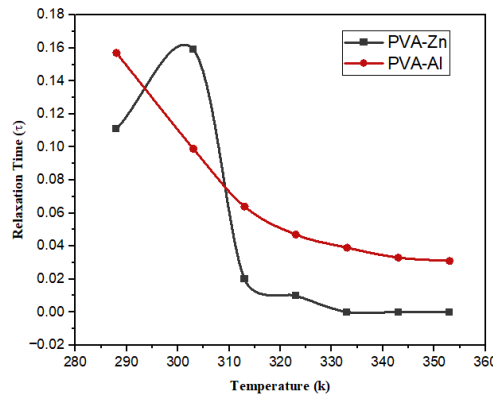


Figure 7 Variation of relaxation time with temperature of PVA-Zn and PVA-Al composite films

Dielectric relaxation can likewise be explored by studying electric modulus M'' of samples composite. M'' is stated in terms of ϵ'' ,

$$M = \frac{1}{\epsilon} \text{-----}4$$

$$M^* = M' + M'' \text{-----}5$$

Where M' is real part and M'' is the imaginary part of the electric modulus and it can likewise inscribed as,

$$M' = \frac{\epsilon'}{\epsilon'^2 + \epsilon''^2} \quad \text{and} \quad M'' = \frac{\epsilon''}{\epsilon'^2 + \epsilon''^2} \text{-----}6$$

A plot of electric modulus M'' for PVZn-10 and PVAI-10 composite verses frequency for temperature changes from 288k to 353k is shown in Figure (a) and (b) respectively. Both plots show the peaks at each temperature which suggests the dielectric relaxation process in which peaks are transferring towards higher frequencies with rise in temperatures. The shifting of peaks towards higher frequency sides depicts that ions are responsible for electric conduction. This is because at higher temperatures, carriers become thermally activated thereby decreasing the relaxation time. The relaxation time for PVZn-10 and PVAI-10 composites is calculated from the M'' Vs frequency plot is depicted in Figure, by using the relation,

$$\tau = \frac{1}{2\pi f_{max}} \text{-----}7$$

Where, f_{max} frequency of a peak for all temperatures.

Figure shows the relaxation time varies with rise in temperature from 288k to 353k. It clearly confirms that for both PVZn-10 and PVAI-10 composite relaxation time decreases sharply with increase in temperature which results in increasing conductivity of composites [33-34].

IV. CONCLUSIONS

PVA-ZnO and PVA-Al₂O₃ composite films were synthesized and characterized by structural and dielectric characterization that are dielectric constant ϵ' , dielectric loss ϵ'' and electric modulus M'' at temperatures starts from 288k to 353k. FESEM of both composites indicates well dispersion of dopant into PVA matrix. Values of ϵ' and ϵ'' for both dopant varies with temperature and frequency, might be due to viscosity of polymer. The electric modulus graph with frequency for both fillers show peaks for every temperature, was shifts with rising temperature to higher frequency range, depicts ions are the charge carriers. The time of dielectric relaxation, was calculated from electric modulus plot, decreased with temperature. This is happened due to charge carriers become thermally activated at upper temperatures. Improved dielectric properties of PVA-ZnO and PVA-Al₂O₃ composite are applicable in fields like thin film transistors for high k dielectric layer, capacitors, optoelectronics devices etc.

REFERENCES

- [1] Polu AR, Kumar R, Kumar KV (2012), *Adv Mater Lett* 3:406–409
- [2] Aziz SB, Abidin ZHZ (2015) *J Appl Polym Sci* 132(15):41774-1–41774-10
- [3] Aziz SB (2016) *Adv Mater Sci Eng* 2013. doi:[10.1155/2016/2527013](https://doi.org/10.1155/2016/2527013)
- [4] Salleh NS, Aziz SB, Aspanut Z, Kadir MFZ (2016) *Ionics* 22(11):2157–2167
- [5] Patil R, Roy AS, Anilkumar KR, Jadhav KM, Ekhelikar S (2012) *Compos Part B Eng* 43(8):3406–3411
- [6] Polu AR, Kumar R (2011) *Bull Mater Sci* 34(5):1063–1067
- [7] Nigrawal A, Chand N (2013) *Prog Nanotechnol Nanomater* 2(2):25–33
- [8] Sangawar VS, Moharil NA (2012) *Chem Sci Trans* 1(2):447–455
- [9] Rathod SG, Bhajantri RF, Ravindrachary V, Pujari PK, Sheela T (2014) *J Adv Dielectr* 4(04):1450033
- [10] More, S., Dhokne, R., & Moharil, S. (2018), *Polymer Bulletin*, 75, 909-923.
- [11] Guirguis OW, Moselhey MTH (2012) *Nat Sci* 4(1):57–67
- [12] Shuhaimi NEA, Teo LP, Woo HJ, Majid SR, Arof AK (2012) *Polym Bull* 69(7):807–826
- [13] Mansour AF, Mansour S F and Abdo MA 2015 *IOSR J. Appl. Phys.* 7 60–9
- [14] Hemalatha KS, Rukmani K, Suriyamurthy N and Nagabhushana B M 2014 *Mater. Res. Bull.* 51 438–46
- [15] Pal K, Banthia AK and Majumdar D K 2007 *Aaps Pharm Sci Tech* 8 E142–6
- [16] Bouropoulos N, Psarras G C, Moustakas N, Chrissanthopoulos A and Baskoutas S 2008 *Phys. Status Solidi a* 205 2033–7
- [17] Srikanth C, Sridhar BC, Prasad MV N and Mathad R D 2016 *J. Adv. Phys.* 5 105–9
- [18] Gong X, Tang CY, Pan L, Hao Z and Tsui CP 2014 *B* 60 144–9
- [19] Roy AS, Gupta S, Sindhu S, Parveen A and Ramamurthy PC 2013 *B* 47 314–9
- [20] Kumar N BR, Crasta V, Bhajantri RF and Praveen B M 2014 *J. Polym.*
- [21] Sugumaran S, Bellan CS and Nadimuthu M 2015 *Iran. Polym. J.* 24 63–74
- [22] Mallakpour S, Dinari M (2013), *J Rinf Plast Compos* 32(4):217-224 41AZ
- [23] Labidi N, SDjbaili A et al (2008) *J J Minor Mater Charact Eng* 7(02):147
- [24] Gurunathan k Amalnerkar Dp, Trivedi DC (2003) *Materials Letter* 57(9):1642-164
- [25] Vishwas M, Rao K N, Priya D N, Raichur A M, Chakradhar R P S and Venkateswarlu K 2014 *Proc. Mater. Sci.* 5 847–54
- [26] Prajapati G K and Gupta P N 2014 *50 MeV Ionics* 20 37–44
- [27] Amin GAM, Abd-El Salam MH (2014) *Mater Res Express* 1(2):025024
- [28] Aziz SB, Abidin ZHZ, Arof AK (2010) *Express Polym Lett* 5:300–310
- [29] Sheng J, Chen H, Li B and Chang L 2013 *Appl. Phys. A* 110 511–5
- [30] Jean-Mistral C, Sylvestre A, Basrou S and Chaillout J J 2010 *Smart Mater. Struct.* 19 075019
- [31] More, Shital, Ragini Dhokne, and Sanjiv Moharil. *Materials Research Express* 4.5 (2017): 055302.
- [32] Makled MH, Sheha E, Shanap TS, El-Mansy MK (2013) *J Adv Res* 4(6):531–538
- [33] Sinha S, Chatterjee S K, Ghosh J and Meikap A K 2015 *J. Mater. Sci.* 50 1632–45
- [34] Tsangaris G M, Psarras G C and Kouloumbi N 1998 *J. Mater. Sci.* 33 2027–37

¹Ms. D.P. Rathod²Dr. R.V. Barde³Dr. K. R.Nemade⁴Dr. S. A. Waghuley

Optical Study of Graphene/TiO₂ nanocomposite by Ultraviolet–Visible Spectroscopy



Abstract: - Outstanding photoelectrochemical characteristics of graphene (GR) include its huge specific surface area, distinct structure, chemical stability, high conductance, and quick electron transport. In this work, ex-situ method was used to create graphene/TiO₂ composites. A series of graphene/TiO₂ composite were created. Using the doctor blade process, the produced Graphene/TiO₂ composites were deposited on Indium Tin Oxide (ITO) glass substrates. XRD spectra determined that the characteristics peak intensity of graphene and TiO₂. The conformation of anatase phase in TiO₂ was done through X-ray diffraction analysis. Material's bonding information in given materials is studied by FTIR. optical parameters like absorbance, direct band gap, indirect band gap, refractive index, optical conductivity was analyzed using ultraviolet–visible spectroscopy.

Keywords: UV-Vis Spectroscopy; Optical Conductivity; Band Gap.

¹Shri Shivaji Science College, Amravati, India.

²Government Vidarbha Institute of Science and Humanities, Amravati, India.

³Indira Mahavidyalay, Kalamb, India.

⁴Sant Gadge Baba Amravati University, Amravati, India.

²Corresponding author: rajeshbarde1976@gmail.com

1. Introduction:

Metal oxide are compounds composed of a metal element and oxygen. They form when a metal reacts with oxygen, resulting in the creation of an oxide. In the 19th century, the synthesis of various metal oxides expanded, laying the foundation for modern materials science. Metal oxides have some specific uses in electronics and semiconductor, energy storage, magnetic storage device, construction and building materials. Metal oxides nanoparticles are the most used nanomaterials. In recent years most of metal oxide nanomaterials such as Ag₂O, FeO, MnO₂, CuO, ZnO, TiO₂, CaO, Al₂O₃ are used in various fields. Various semiconductors such as Fe₂O₃, TiO₂, ZnO, CdS, and ZnS, have been used electronic and optical components [1,2]. Among all these semiconductors, TiO₂ is the most commonly utilized because of its non-toxic nature, stability at different reaction conditions, high oxidizing power under irradiated by UV, low cost and being environmentally friendly [3-6]. TiO₂ may exist in three major polymorphs namely anatase, rutile and brookite. Anatase phase TiO₂ for offer better photocatalytic performance than rutile phase for photo-induced electron transfer properties of the thermodynamically metastable [7]. But anatase TiO₂ has a higher band gap (~3.2 eV) as compared to rutile (~3.0 eV) that causes large recombination of charge carriers [8]. To solve these problems modification of TiO₂ can be an effective way which is done in some research [9,10]. Due to their unique characteristics in environmental applications carbonaceous materials such as graphene and graphene oxide, are the most important ingredients for TiO₂ [11].

Among various carbonaceous materials, graphene showed some attractive properties such as excellent transmittance, high electron mobility (250,000 cm² /V/s), large specific surface area (2630 m² /g), good chemical stability and excellent electrical conductivity [12,13]. Graphene has a two-dimensional (2D) structure consisting of single-layer carbon atoms and is considered as the thinnest and toughest material. The interdisciplinary properties of graphene have various uses which is useful in various technologies [14-16]. In some literature observed that the energy bandgap of graphene is in the range of 0.11 eV to 1.62 eV [17]. Due to some special properties of graphene such as large bandgap and high charge carrier mobility, there are lots of applications of graphene in electronic and optoelectronic applications. Graphene has been doped with other materials to enlarge the bandgap [18].

There are various methods available for the synthesis of Graphene/TiO₂ nanocomposite such as spin coating method, simple coating approach [19]. In this paper Graphene/TiO₂ nanocomposite was prepared by ex-situ approach. In this research Structural, microstructural and optical properties of Graphene/TiO₂ nanocomposite was studied using XRD, FTIR, UV-VIS characterization technology and they are discussed here.

2. Experimental

2.1. Materials:

Graphite rod used for preparation of Graphene. Distilled water, Sulfuric acid, titanium tetrachloride, sodium hydroxide, acetone etc.

2.2 Preparation of Graphene:

Graphene will be synthesized from graphite rod using a modified electrochemical exfoliation method. Mixture of distilled water and sulfuric acid should be taken in 1:4 proportion in a beaker. After this put the graphite rod in the mixture and give continue AC supply to it with the help of dimmer. Exfoliation of graphite rod will have started. After few hours, the bottom of beaker will be covered with graphene powder. Now filter the graphene powder with the help of filter paper. After drying the graphene powder, heat it in a furnace at 70⁰ for one hour and finally you get graphene.

2.3 Preparation of TiO₂:

TiO₂ will be prepared by Co-precipitation method. The material used for the preparation of TiO₂ are titanium tetrachloride, sodium hydroxide, distilled water. For preparation of TiO₂ mixture of titanium tetrachloride and sodium hydroxide should be taken in 1:4 proportion. Provide normal stirring to the mixture with the help of magnetic stirrer until you get the precipitate. After filtering the precipitate, keep it for heating in furnace at 100⁰ C for two to three hours. In this way our final product is prepared.

2.4 Preparation of Graphene/TiO₂composites:

For preparation of composite, we use ex-situ approach and by using this method we prepare Graphene/TiO₂ composite series by adding various concentration of TiO₂ nanoparticles from 5 wt% to 25 wt% in graphene. Mix the mixture with the help of magnetic stirrer until acetone get evaporated. After this, if the mixture is wet, heat it in a furnace at 50-60⁰ C. The nomenclature for 5% Graphene/TiO₂ nanocomposites, 10% Graphene/TiO₂ nanocomposites, 15% Graphene/TiO₂ nanocomposites, 20% Graphene/TiO₂ nanocomposites and 25% Graphene/TiO₂ nanocomposites was named as S1, S2, S3, S4 and S5 respectively.

3 Results and Discussion

3.1 X-ray Diffraction Analysis:

Fig. 1 shows the XRD patterns of the TiO₂ samples synthesized by Co-precipitation method. The diffraction patterns of TiO₂ nanoparticles prepared by this method exhibit good crystalline peaks, and they correspond to the anatase phase of TiO₂. The TiO₂ sample shows nearly similar peak which has been observed by other researchers as well [20]. The diffraction peaks corresponding to the anatase phase of TiO₂. From the graph TiO₂ nanoparticles shows diffraction peaks located at the Bragg diffraction angles (2θ) of 25.43, 38.13 48.24, 54.20, 55.16, 62.89, 68.99, 70.59 and 75.27 which are indexed to (101), (004), (200), (105), (211), (204), (116), (220) and (215) lattice planes respectively [21]. Strong diffraction peaks at 25.43° and 48.24° indicating TiO₂ in anatase phase [22]. The peak of graphene exists in these XRD spectra shown in fig.2. The graphene peak is close to the peak of anatase TiO₂ nanoparticles which is at the diffraction angle of 25.84° which is nearer to diffraction angle studied in research paper [23]. The XRD pattern of Graphene/TiO₂ composite for various concentration of TiO₂ particle from 5 wt% to 25 wt% in graphene is shown in fig. 3

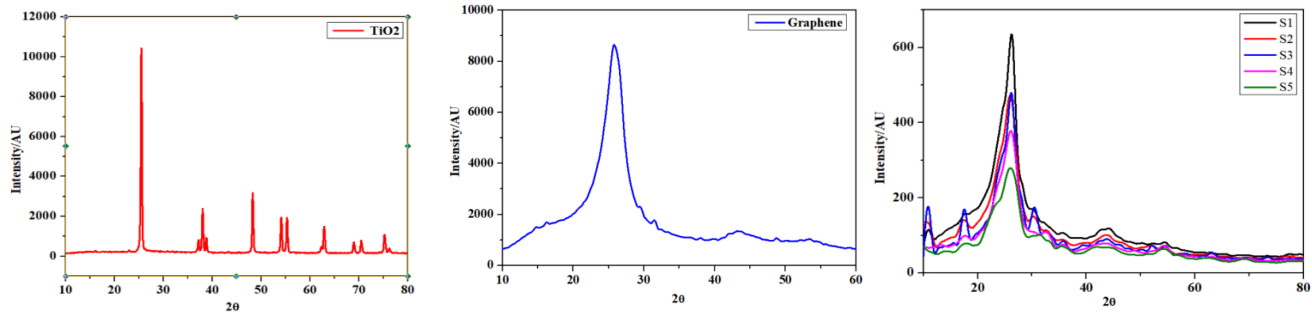
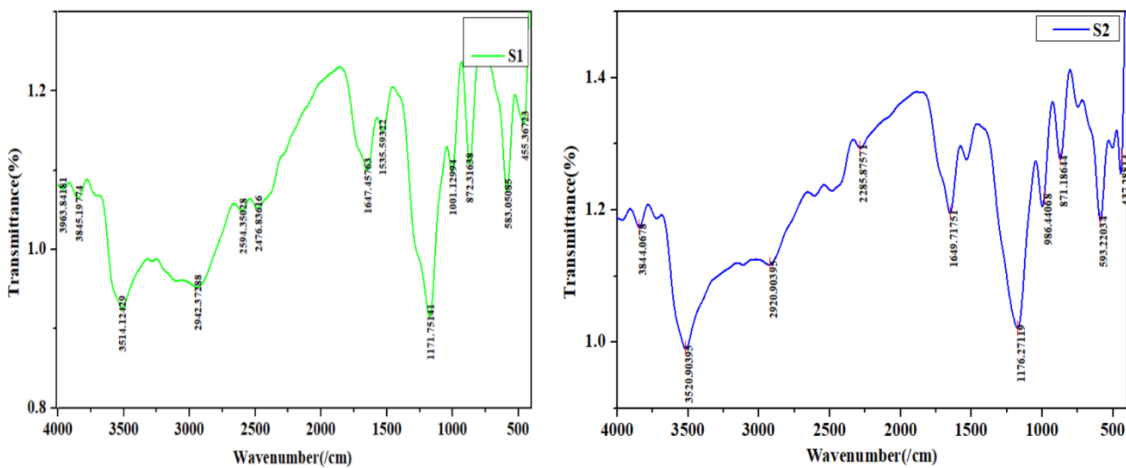


Fig. 1 Fig. 2 Fig. 3 XRD of Graphene/TiO₂ Composites

3.2 FTIR Analysis:

FTIR analysis is used to identify molecular compounds. We observe absorbance of infrared radiation by sample and resulting spectrum was used to identify the functional groups present in that sample. In this study on x-axis the wavenumber is plotted against transmittance within the range 4,000 to 400 cm⁻¹. FTIR measures the absorbance or transmittance of light through a sample as a function of wavelength and provides information regarding the identity of functional groups [24]. The spectrum shows highly reduced peaks in region ~3000 cm⁻¹ to ~3500 cm⁻¹ representing the reduction of OH group due to deoxygenation [25,26]. The band at 3514 cm⁻¹ and 1647 cm⁻¹ was attributed to strong O-H and C=C stretching mode. C-O strong stretching vibration band observed at 1171 cm⁻¹. The spectrum resulting from the analysis at TiO₂ solid microspheres showed one band at ~1000 cm⁻¹ characteristic of the Ti-O bonds observed in fig 4 [27].The spectrum shows a broad peak at 550-800 cm⁻¹ caused by the Ti-O-Ti band.



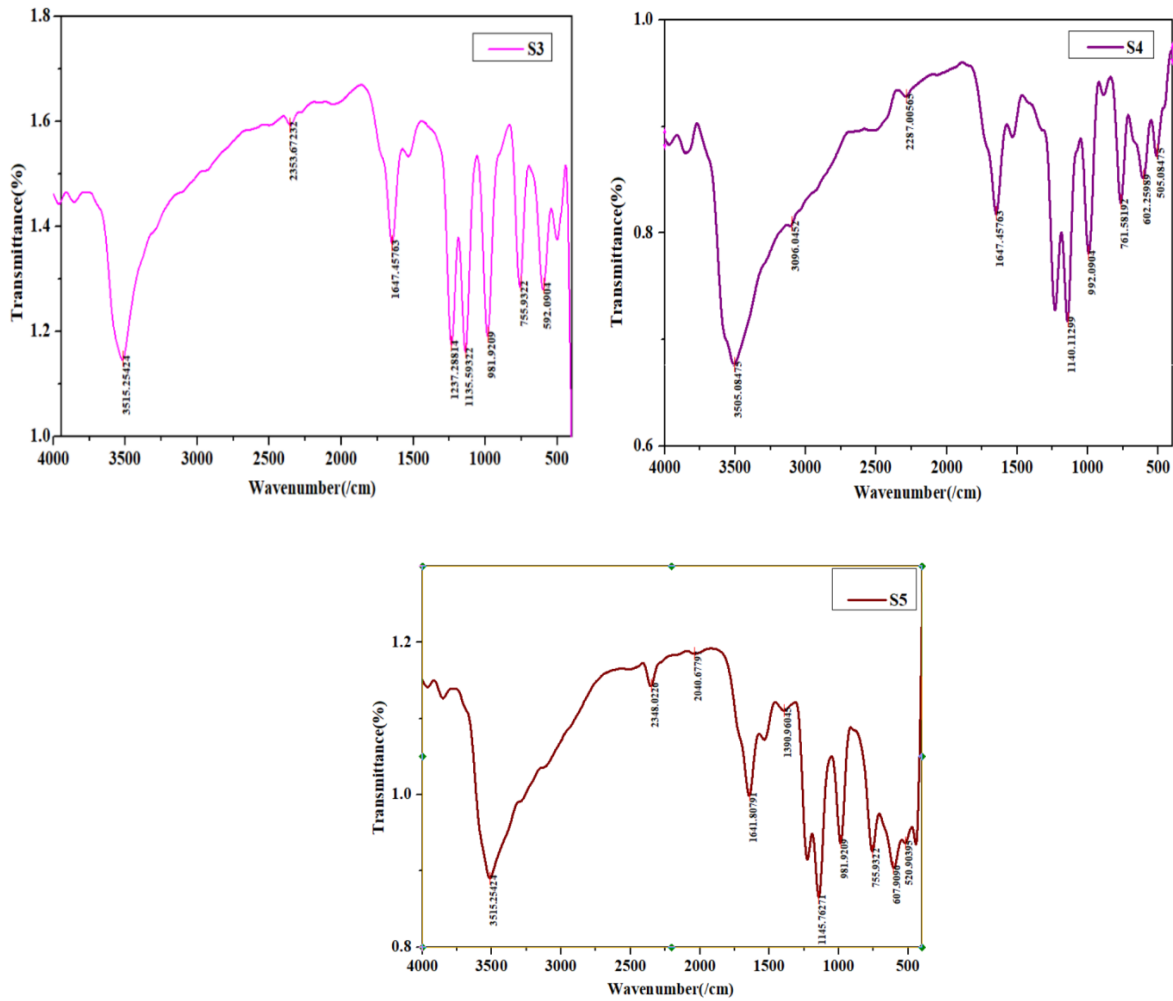


Fig. 4 FTIR spectra of Graphene/TiO₂ Composites

3.3 UV-VIS spectroscopy analysis:

UV-visible (UV-VIS) spectroscopy is an effective optical characterization technique to understand the optical properties of materials. Fig. 5 shows UV-VIS spectrum of the Graphene/TiO₂ composites as a function of wavelength against absorbance. The absorbance band appears at approximately in the range 200-400 nm.

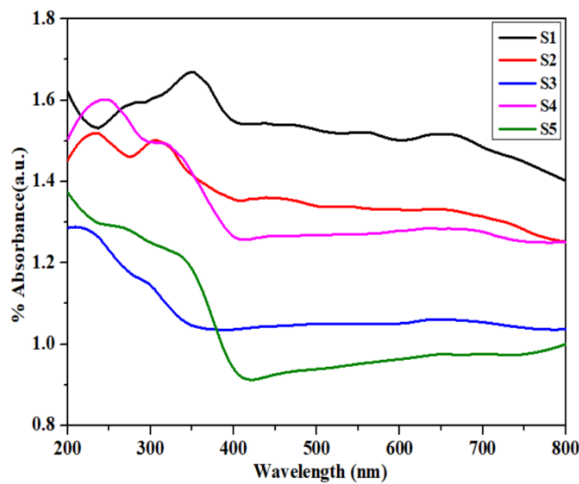


Fig. 5 Variation of absorbance as a function of wavelength

Fig. 6 shows Tauc plot for indirect band gap energy of different composition of Graphene/TiO₂ composites. The indirect band gap energy for sample S1, S2, S3, S4 and S5 are 2.34, 2.49, 2.73, 2.86 and 3.00 eV respectively. The indirect bandgap varies between 3.00 to 2.42 eV.

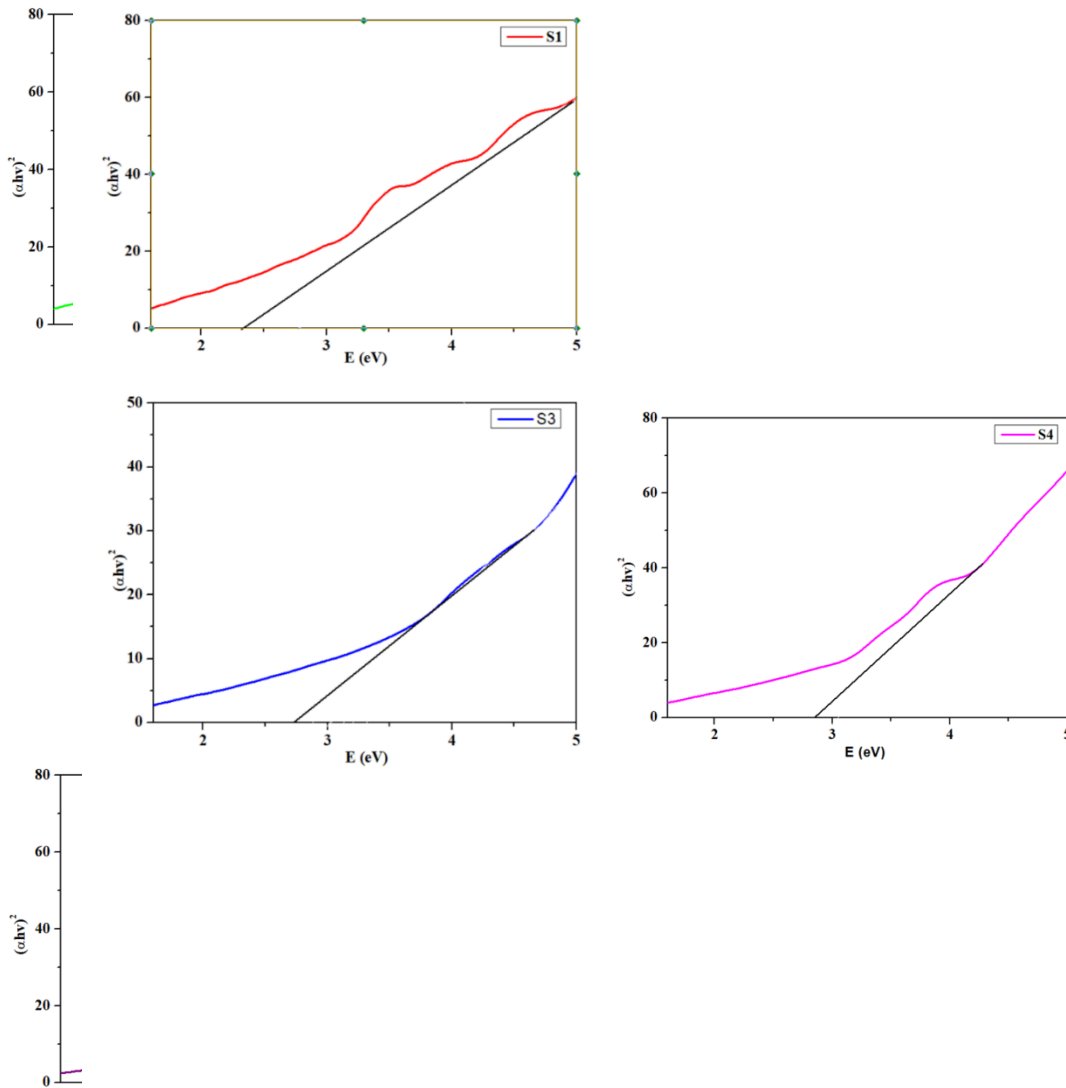
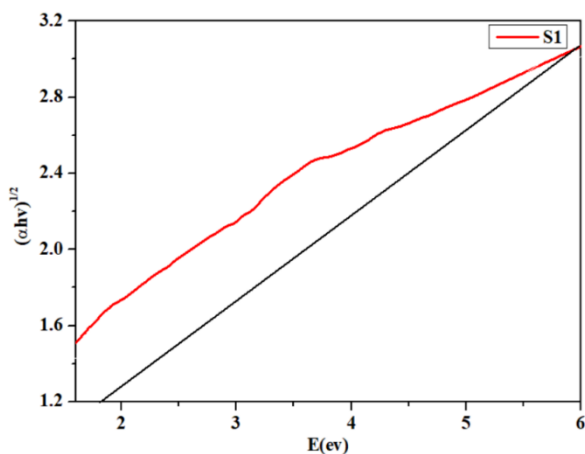


Fig. 6 shows Tauc plot of $(\alpha h\nu)^2$ versus photon energy for different composition of Graphene/TiO₂

Fig. 7 shows the Tauc plot for direct band gap energy of different composition of Graphene/TiO₂ composites. The direct band gap energy for sample S1, S2, S3, S4 and S5 are 1.81, 1.86, 2.25, 2.37 and 2.52eV respectively. It was observed that the bandgap obtained in Graphene/TiO₂ composites vary from 2.52 to 1.81 eV. Similar result observed in some research paper [18]. Sample S5 shows higher indirect as well as direct bandgap.



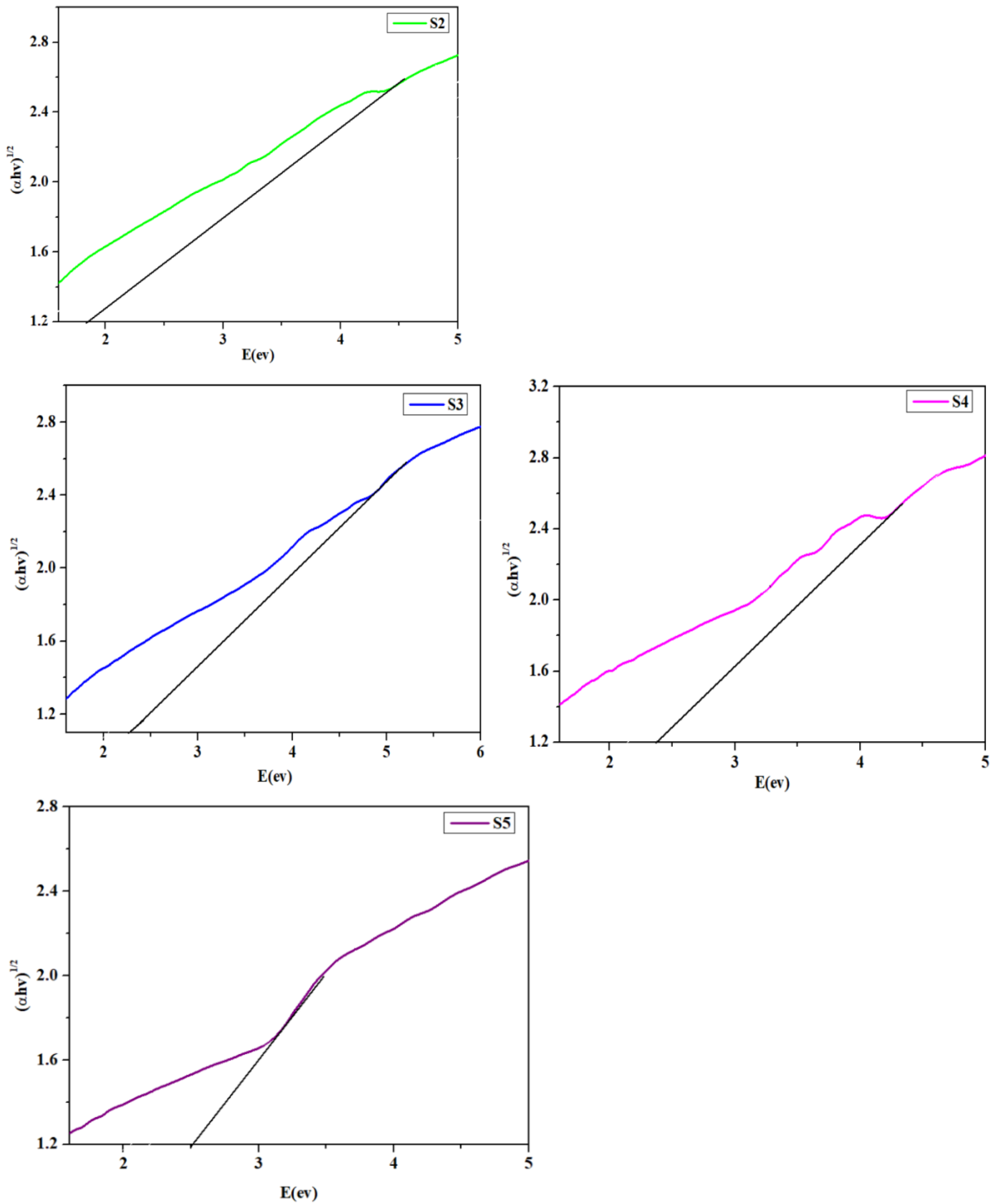


Fig. 7 Tauc plot of $(\alpha h\nu)^{1/2}$ versus photon energy for different composition of Graphene/TiO₂

Fig. 8 shows a graph of refractive index with wavelength. From fig we can say that low refractive index on shorter wavelength side was low whereas value of refractive index increases on longer wavelength side up to 358 nm. Beyond 358 nm refractive index decreases gradually. The highest value of refractive index is observed for S1 at 358 nm with change in the concentration of TiO₂ refractive index for S1, S2, S3, S4 and S5 samples decrease. [28,29].

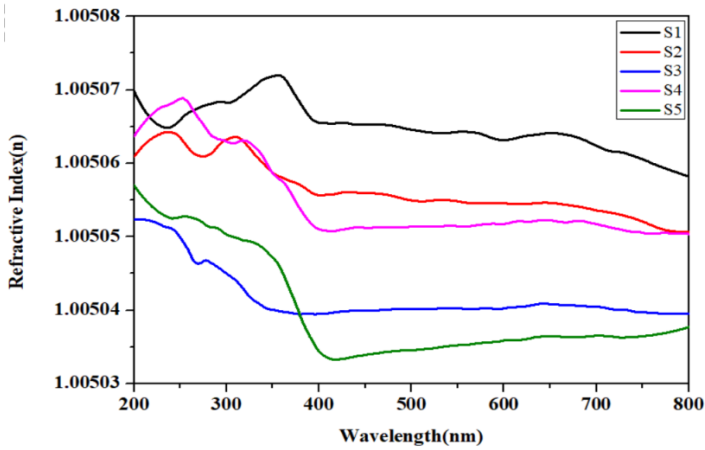


Fig. 8 variation of refractive index as a function of wavelength

Fig. 9 shows the variation of optical conductivity as a function of wavelength. The highest value of optical conductivity is associated with sample S1 whereas lowest with sample S5. From the Graph it is observed that optical conductivity was altered by changing the concentration of TiO₂.

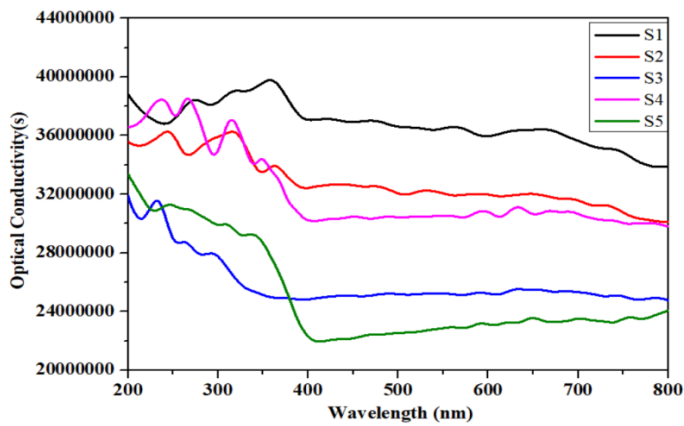


Fig. 9 variation of optical conductivity as a function of wavelength

Fig. 10 shows the variation of optical conductivity with $h\nu$ (eV). Initially the optical conductivity increases linearly in the region of energy 1.82 to 2.97 eV. Beyond energy 2.97 eV optical conductivity decreases up to 3.1 eV and then sudden increase up to 5.28 eV and again start decreasing. Graph shows higher optical conductivity for sample S1 and lower for sample S5. From graph it is observed that optical conductivity tuned by varying the concentration of Graphene/TiO₂ composites [30].

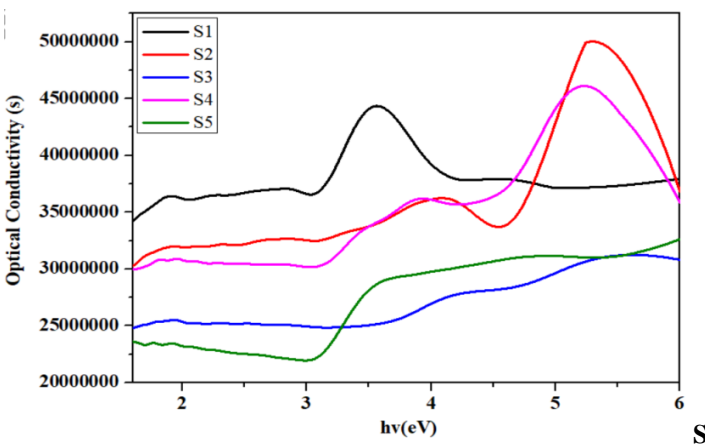


Fig. 10 variation of optical conductivity as a function of photon energy

4. Conclusion:

In present study Graphene and TiO₂ nanoparticles were synthesized successfully and from XRD it will clear that Graphene and anatase TiO₂ is formed. Graphene/TiO₂ nanocomposites with different weight present of TiO₂ were successfully synthesized by ex-situ approach. FTIR spectroscopy was used to verify the functional group present in the prepared sample. Graphene/TiO₂ nanocomposites were characterized to study their optical properties with the help of UV-VIS spectroscopy. Maximum absorbance of samples appears at approximately in the range 200-400 nm. The value of indirect and direct band gap was successfully estimated for the prepared sample. Initially refractive index is less and it increases on longer wavelength side up to 358 nm. After 358 nm refractive index gradually decreases. The optical conductivity for sample S1 was higher whereas lowest for sample S5.

References:

- [1] S. Anandan, Y. Ikuma, K. Niwa, "An Overview of Semi-Conductor Photocatalysis: Modification of TiO₂ Nanomaterials," *Solid State Phenom*, 162 (2010),pp.239–260.
- [2] M.R. Hoffmann, S.T. Martin, W. Choi, D.W. Bahnemann, "Environmental Applications of Semiconductor Photocatalysis," *Society*. 95 (1995),pp.69–96.
- [3] N. Arconada, A. Durán, S. Suárez, R. Portela, J.M. Coronado, B. Sánchez, Y. Castro, "Synthesis and photocatalytic properties of dense and porous TiO₂-anatase thin films prepared by sol-gel," *Appl. Catal. B Environ.* 86 (2009),pp.1–7.
- [4] S. Tek, E. Mutlugun, I.M. Soganci, N.K. Perkgoz, D. Yucel, G. Celiker, H. V Demir, "Comparative study of optically activated nanocomposites with photocatalytic TiO₂ and ZnO nanoparticles for massive environmental decontamination," *J. Nanophotonics*. 1 (2007).
- [5] T.K. Tseng, Y.S. Lin, Y.J. Chen, H. Chu, "A review of photocatalysts prepared by sol-gel method for VOCs removal," *Int. J. Mol. Sci.* 11 (2010),pp.2336–2361.
- [6] A. Hernández-Ramírez, I. Medina-Ramírez, Photocatalytic Semiconductors, in:A. Hernández-Ramírez, I. Medina-Ramírez (Eds.), *Photocatalytic Semicond.*, Springer International Publishing, Cham, 2015: 1– 289.
- [7] D. R. Eddy et al., "Heterophase Polymorph of TiO₂ (Anatase, Rutile, Brookite, TiO₂ (B)) for Efficient Photocatalyst: Fabrication and Activity," vol. 2, 2023.
- [8] S. Islam, S. Nagpure, D. Kim, S. Rankin, "Synthesis and catalytic applications of non-metal doped mesoporous Titania," *Inorganics*. 5 (2017) 15.
- [9] D. Zhao, G. Sheng, C. Chen, X. Wang, "Enhanced photocatalytic degradation of methylene blue under visible irradiation on graphene@TiO₂ dyade structure," *Appl. Catal. B Environ.*, 111–112 (2012),pp.303–308.
- [10] H. Park, Y. Park, W. Kim, W. Choi, "Surface modification of TiO₂ photocatalyst for environmental applications," *J. Photochem. Photobiol. C Photochem. Rev.* 15 (2013),pp.1–20.
- [11] R. Leary, A. Westwood, "Carbonaceous nanomaterials for the enhancement of TiO₂ photocatalysis," *Carbon N. Y.* 49 (2011),pp.741–772.
- [12] J.H. Byeon, Y.-W. Kim, *ACS Appl. Mater. Interfaces* 5 (2013) pp.3959–3966.
- [13] H. Wang, Y.H. Hu, *Energy Envi*"ron. Sci. 5 (2012) pp.8182–8188.
- [14] J. Shu, Z. Qiu, D. Tang, "Self-referenced smartphone imaging for visual screening of H₂S using Cu x O-polypyrrole conductive aerogel doped with graphene oxide framework," *Analyt. Chem.* 90 (16) (2018),pp.9691–9694.
- [15] T.A. Saleh, M.M. Nur, "Synthesis of polyacrylic-melamine grafted graphene as efficient inhibitor for shale stabilization in water-based drilling fluid," *Mater. Today Commun.* 35 (2023), 106264.
- [16] T.A. Saleh, "Protocols for synthesis of nanomaterials, polymers, and green materials as adsorbents for water treatment technologies," *Environ. Tech. Innov.* 24 (2021), 101821.
- [17] R. Nandee, M.A. Chowdhury, A. Shahid, N. Hossain, M. Rana, "Band gap Formation of 2D material in graphene: future prospect and challenges," *Results Eng.* (2022).
- [18] Nayem Hossain, Rajib Nandee, Mohammad Asaduzzaman Chowdhury, MD Arefin Kowser, Sagar Kumer Nondy, Md. Rasadujjaman, Assadullah Al Mostazi, Md. Baizid Molla, Sosmoy Barua, Md. Masud Rana, Md. Sherajul Islam, "Bandgap formation in graphene doped with BN, TiO₂, Al₂O₃ and ZnO by sintering process," *Results in Chemistry* 6(2023), 101229.
- [19] A. Timoumi, S. N. Alamri, H. Alamri "The Development of TiO₂ -Graphene oxide Nano composite thin films for solar cells," *Results in Physics* (2018), S2211-3797(17),32577-9.
- [20] Kaur H, Kumar S, Verma NK, Singh P, "Role of pH on the photocatalytic activity of TiO₂ tailored by W/T mole ratio," *J Mater Sci Mater Electron*, 2018,29:16120e35
- [21] Shen P-S, Tai Y-C, Chen P, Wu Y-C, "Clean and time-effective synthesis of anatase TiO₂ nanocrystalline by microwave assisted solvothermal method for dye-sensitized solar cells," *J Power Sources* 2014,247:444e51
- [22] N. Lakshmi, Kumavat Soni, Rakesh Jain, Aarti Rani Chandra and Arzoo Sheikh, "Study of Sulphur doped TiO₂ dye sensitized solar cell," *Materials Today* 29, (2020), 275–277.
- [23] M.Y.A. Rahman*, S.N. Sadikin, A.A. Umar, T.H.T. Aziz, "Improvement of dye-sensitized solar cell performance by utilizing graphene-coated TiO₂ films photoanode," *Superlattices and Microstructures* volume 128, (2019),pp.92-98.
- [24] Douglas H. Adamson, Zhihao Zhang, Hannes C. Schniepp, *carbon* 154(2019),pp.510-521.
- [25] F.T. Thema, M.J. Moloto, E.D. Dikio, N.N. Nyangiwe, L. Kotsedi, M. Maaza, M. Khenfouch, "Synthesis and characterization of graphene thin films by chemical reduction of exfoliated and intercalated graphite oxide," *Journal of Chemistry* 3, (2013), 150536.
- [26] T. Rattana, S. Chaiyakun, N. Witit-Anun, N. Nuntawong, P. Chindaudom, S. Oaew, C. Kedkeaw, P. Limsuwan, "Preparation and characterization of graphene oxide nanosheets," *Procedia Eng.* 32, (2012),pp.759–764

- [27] V.R.A. Ferreira, M.A. Azenha, C.M. Pereira, A.F. Silva, "Crystallization of hollow TiO₂ into anatase at mild conditions, for improved surface recognition in selective photocatalysis" *Applied Catalysis A, General* 648 (2022), 118912.
- [28] Rajesh Barde, Kailash Nemade and Sandeep Waghuley, "Complex Optical Investigation of Sodium Superoxide Loaded Phosphovanadate Glass System in Ultra-Violet and Visible Region," *TRENDS IN SCIENCES* 2022, 19(23), 2077.
- [29] R.V. Barde, K.R. Nemade, S.A. Waghuley, "Complex optical study of V₂O₅ -P₂O₅-B₂O₃-GO glass systems by ultraviolet-visible spectroscopy *Optical Materials*," Volume 40, (2015), pp.118-121.
- [30] R.V. Barde, "Influence of CeO₂ content on complex optical parameters of phospho vanadate glass system," *Spectrochimica Acta* 1386-1425(2015)30182-7.

¹P.D.Hambarde*²N.P.Garad²A.C.Kumbharkhane

Dielectric Relaxation Study of tert-Butyl Acetate Using Time Domain Reflectometry Technique (TDR)



Abstract: - Temperature dependent complex permittivity spectra of tert-butyl Acetate were measured in the frequency range from 10MHz to 30 GHz using the Time Domain Reflectometry Technique. The dielectric constant and dielectric relaxation time have been determined by the Least Squares Fit method.

Keywords: Time Domain Reflectometer, dielectric relaxation time, dielectric constant.

I. INTRODUCTION

The dielectric relaxation Spectroscopy (DRS) technique essentially reveals details about the dynamics of a material's response regarding the electric field, namely the rate at which its polarization might vary. Knowing this information is essential for comprehending a variety of material features, including charge transposition, material dynamics, dielectric properties, etc. Dielectric relaxation techniques are primarily used to measure the **relaxation time** of a material [1-2]. In high-frequency applications, relaxation time is especially important because it determines how quickly a material responds to rapidly changing electric fields [3]. It has applications in many fields like Dielectric Material Characterization, Charge Transport Studies, and Biological Systems.

tert-Butyl acetate [C₆H₁₂O₂] is a carboxylic ester that is manufactured by the esterification of acetic acid and isobutylene. It is a colorless flammable liquid that smells like blueberries or camphor. It is employed as a solvent in the manufacturing of industrial cleaners, lacquers, enamels, inks, adhesives and thinners [4]

Previous research has examined the dielectric relaxation behavior of esters such as methyl acetate (MA), ethyl acetate (EA), and butyl acetate (BA) with different alcohols to examine the molecular behavior of the O-H group with the oxygen atom of the ester molecule at different temperatures and concentrations. S.S. Birajdar et al. has investigated dielectric relaxation spectroscopy of esters using time domain spectroscopy [5]. To comprehend the intermolecular interaction in the mixture, R.M. Shirke et al. used the time domain technique to analyze the temperature dependent dielectric relaxation behavior of acetate-alcohol mixtures in the frequency range of 10 MHz to 20 GHz [6]. Dielectric characteristics of binary mixtures of esters with hydrocarbons at 303 K are investigated by M. Meenachi and P. Krishnamurthi [7]. S. Kumar et al. Studied dielectric relaxation of methyl acetate with 2- Alkoxyethanols using time domain reflectometry [8].

¹*Corresponding Author 1 hambardepallavi47@gmail.com²School of Physical Sciences, Swami Ramanand Teerth Marathwada University, Nanded

²Author 2 School of Physical Sciences, Swami Ramanand Teerth Marathwada University, Nanded

In the present paper, the frequency and temperature dependent dielectric relaxation investigation on tert – Butyl Acetate have been done using the TDR technique. This technique can offer high-resolution information about the dynamics of H-bonds [9]. Based on the obtained complex permittivity spectra, the static dielectric constant (ϵ_0), and dielectric relaxation time (τ) were determined using the Least Squares Fit method to investigate the molecular dynamics and intermolecular interaction.

II. MATERIALS AND MEASUREMENT

Tert-butyl acetate was commercially obtained from Spectrochem Pvt. Ltd. Mumbai, India with 99% purity and was used without further purification. The dielectric spectra of tert-butyl acetate have been recorded using time domain reflectometry (TDR). The TDR Tektronix Digital Serial Analyzer model no. DSA8300 sampling main frame oscilloscope along with TDR sampling module 80E10B was used. The detailed experimental set-up and calibration of the instrument were done as mentioned in [10]. The experimental set-up of TDR is shown in Fig. 1. The dielectric relaxation parameters were investigated in the frequency range of 10 MHz to 30 GHz.

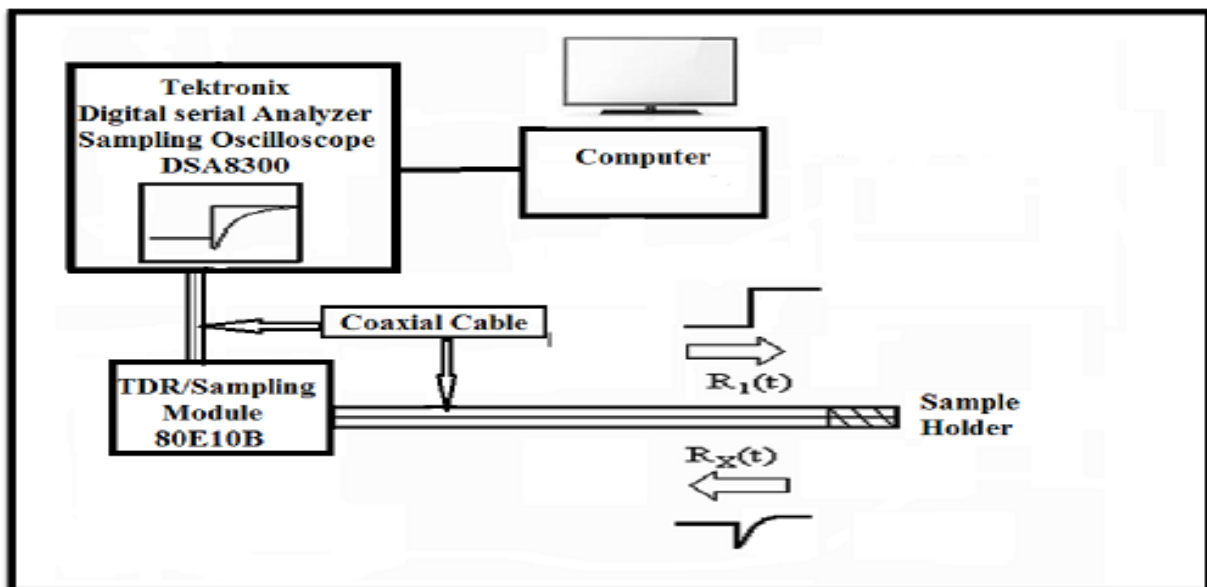


Fig.1.Experimental setup of TDR

III. RESULT AND DISCUSSION

A temperature and frequency dependent complex dielectric permittivity spectra (CPS) of tert-butylacetate is shown in Fig.2 in which ϵ' is static dielectric permittivity and ϵ'' is the dielectric loss.

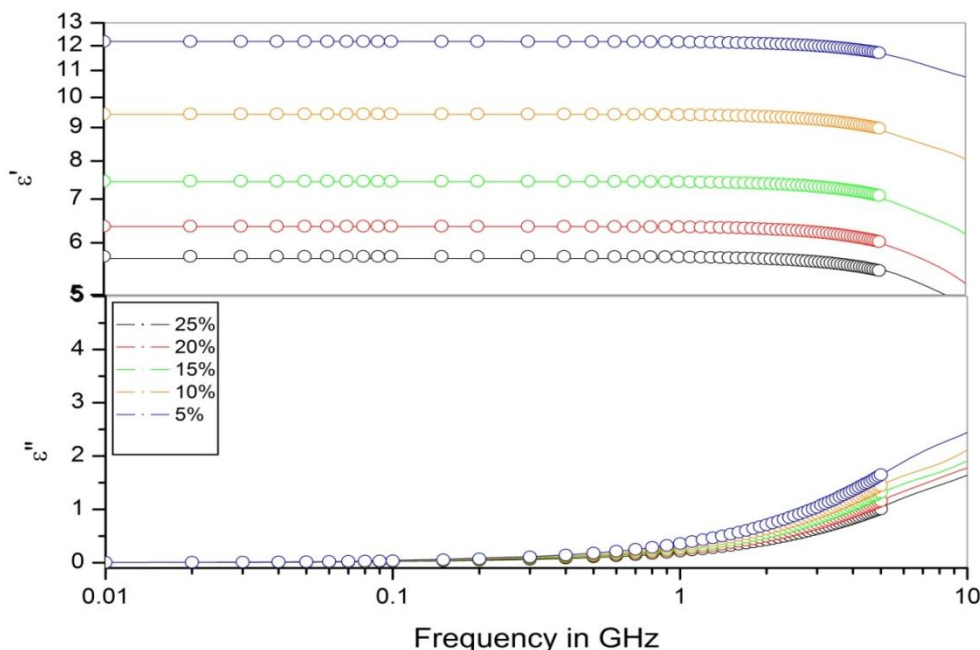


Fig 2. Temperature and frequency dependent complex permittivity spectra of tert-butylacetate

The experimentally obtained CPS is fitted to the Havriliak-Negami equation to obtain the dielectric parameters [11,12].

$$\epsilon^*(\omega) = \epsilon_\infty + \frac{\epsilon_0 - \epsilon_\infty}{[1 + (j\omega\tau)^{1-\alpha}]^\beta} \tag{1}$$

Where ϵ_0 is the static dielectric constant, τ is relaxation time, and α & β are the distribution parameters. The values of ϵ_0 and τ at various temperatures are reported in Table 1. The values are in good agreement with earlier work [13].

Table 1. Dielectric relaxation parameters of tert-Butyl Acetate at different temperatures.

Temperature in $^{\circ}\text{C}$	ϵ_0	τ
25 $^{\circ}\text{C}$	5.72(1)	7.88(1)
20 $^{\circ}\text{C}$	6.36(1)	8.98(1)
15 $^{\circ}\text{C}$	7.45(1)	9.21(1)
10 $^{\circ}\text{C}$	9.43(1)	13.61(1)
5 $^{\circ}\text{C}$	12.71(1)	13.01(1)

Numbers in the bracket denote uncertainties in the least significant digit obtained by the least squares fit method, e.g., 5.72(1) means 5.72 ± 0.01 .

Static dielectric constant (ϵ_0) and relaxation time (τ) of the molecule depend on molecule chain length, temperature, viscosity, Polarizability, etc. From Table 1, values of ϵ_0 and τ increase with a decrease in temperature indicating a reduction in the thermal motion of the molecule. Lower temperatures mean less thermal energy in the material, which translates to reduced random motion of the molecules or ions within the material. Relaxation time refers to the time it takes for the dipoles in a material to respond and realign with a changing electric field. Lower temperature translates to a "thicker" or more viscous environment for the dipoles, resulting in relaxation time increases. Also, Strong affectionate bonds between them account for the higher value of relaxation time [14-15].

IV. CONCLUSION

Frequency dependent complex permittivity spectra of tert-butyl Acetate were studied by using the TDR technique in the frequency range 10 MHz to 30 GHz at different temperatures which shows Cole-Cole type dispersion. The dielectric parameters such as static dielectric constant, and dielectric relaxation time are reported. As temperature decreases dielectric constant and the relaxation time increases due to viscous resistance.

ACKNOWLEDGMENT

We are thankful to the School of Physical Sciences at S. R. T. M. U. Nanded, Maharashtra, and DST, New Delhi (Project Number DST PROJECT SB/S2/LOP-032/2013) for financial support.

REFERENCES

- [1] Jonscher, A.K., 1999. Dielectric relaxation in solids. *Journal of Physics D: Applied Physics*, 32(14), p.R57.
- [2] Sylvester, M.M., Ganesh, T., Karunakaran, D.A., Hudge, P. and Kumbharkhane, A.C., 2014. Time domain dielectric relaxation studies of amphiphilics in solution state. *Journal of Molecular Liquids*, 194, pp.57-61.
- [3] Thostenson, E.T. and Chou, T.W., 1999. Microwave processing: fundamentals and applications. *Composites Part A: Applied Science and Manufacturing*, 30(9), pp.1055-1071.
- [4] https://en.wikipedia.org/wiki/Tert-Butyl_acetate
- [5] Birajdar, S.S., Deshmukh, A.R., Kumbharkhane, A.C. and Suryawanshi, D.B., 2023. Dielectric Relaxation Spectroscopy of Esters Using Time Domain Reflectometry. *Russian Journal of Physical Chemistry B*, 17(4), pp.990-995.

- [6] Chaudhari, A., Shirke, R.M., Nore, N.M., and Patil, P.B., 2002. Dielectric study of n-butyl acetate–alcohol mixtures by time-domain reflectometry. *Journal of solution chemistry*, 31(4), pp.305-315.
- [7] Meenachi, M. and Krishnamurthi, P., 2015. Dielectric characteristics of binary mixtures of esters with hydrocarbons at 303K. *Rasayan J Chem*, 8, pp.98-104.
- [8] Kumar, S., Guganathan, L., Malathi, M., Mohan, A. and Amalanathan, R., 2018. Dielectric relaxation studies of methyl acetate with 2-alkoxyethanols using time domain reflectometry technique. *Int. J. Sci. Res. Phys. Appl. Sci*, 6, pp.27-40.
- [9] Sinclair, W.E. and Pratt, D.W., 1996. Structure and vibrational dynamics of aniline and aniline–Ar from high-resolution electronic spectroscopy in the gas phase. *The Journal of Chemical Physics*, 105(18), pp.7942-7956.
- [10] Garad, N.P., Saknure, S.H., Gubre, A.G. and Kumbharkhane, A.C., 2023. Study of Dielectric Relaxation and Hydrogen Bonding Interaction of 1, 4-Butanediol-1, 4-Dioxane Mixture using TDR Technique. *Indian Journal of Pure & Applied Physics (IJPAP)*, 61(3), pp.158-164.
- [11] Kaatze U. Microwave dielectric properties of liquids. *Radiat Phys Chem*. 1995;45(4):549 566
- [12] Birajdar, S.S., Deshmukh, A.R., Kumbharkhane, A.C. and Suryawanshi, D.B., 2023. Study of cooperative dynamics and thermo-dielectric parameters of n-butyl acetate-xylene solutions using dielectric spectroscopy.
- [13] Lide DR: ‘CRC Handbook of Chemistry and Physics’, *Taylor and Francis* (2007) Boca Raton
- [14] Joshi YS, Kanse KS, Rander DN, et al. Dielectric relaxation and molecular interaction study of aqueous amides. *IJPAP*. 2016;54:621–628.
- [15] Birajdar, S.S., Suryawanshi, D.B., Deshmukh, A.R., Shinde, R.V., Ingole, S.A. and Kumbharkhane, A.C., 2021. Dielectric relaxation behavior of ethyl acetate-xylene mixtures using time domain reflectometry. *Physics and Chemistry of Liquids*, 59(4), pp.503-511.

¹ Daiwashala G.
Dongre*
²Ashok.C.
Kumbharkhane

**Structural and dynamics behavior of
nitriles through dielectric properties
using a time domain reflectometry
(TDR)**



Abstract: - Dielectric relaxation properties of Nitriles(NT) -1, 4-Dioxane(DX) binary mixtures have been measured at 25°C using Time Domain Reflectometry (TDR) in the frequency range of 10 MHz to 30 GHz. The complex permittivity spectra of Nitriles- 1, 4-Dioxane mixtures shows Debye type relaxation processes. The dielectric constant (ϵ_0) and relaxation times (τ in ps), in the mixture has been obtained using least square fir method. The molecular association is studied through excess dielectric properties, Kirkwood Correlation and Bruggeman, Factor..

Keywords: Complex Dielectric permittivity, Time Domain Reflectometry, Dielectric Relaxation Time, Luzar Model.

¹ * Daiwashala G. Dongre: daiwashala@gmail.com School of Physical Sciences ,S.R.T.M.U .Nanded

² Ashok.C. Kumbharkhane: School of Physical Sciences ,S.R.T.M.U. Nanded

Copyright © JES 2024 on-line : journal.esrgroups.org

I. INTRODUCTION

To understand molecular structure and dynamics with other polar or non-polar molecules, dielectric relaxation behavior in polar liquids is of great interest. Polar organic liquids nitriles have a significant dipole moment. Large dipole moments cause significant intermolecular interactions and molecule association. Nitriles are liquid at room temperature, non-hydrogen bonded, and has a strong dipole moment, and therefore dielectric researches were done on them. Acetonitrile(ACN), Acrylonitrile(ACRN), Propionitrile(PPN), and Butyronitrile(BTN) are aprotic nitriles(NT) and polar non-hydrogen bonded organic solvents with high dipole moments utilized in the chemical industry. The major by product of Acrylonitrile is Acetonitrile ACN is the simplest organic nitrile, while ACRN has vinyl group. ACN is a polar aprotic solvent for chemical synthesis and butadiene purification. Its high dielectric constant makes it popular in battery applications. ACRN is mostly a monomer for poly acrylonitrile, high flammability and toxicity. Producers of pesticides and fertilizers utilize propionitrile. Thus, pesticide and fertilizer demand is rising worldwide due to agricultural methods. It also makes high-voltage electrical double-layer capacitors [1]. Butyronitrile is mostly used to make amprolium for poultry and also used to make ethylamine [2]. However, 1,4-dioxane (DX) is a non-hydrogen bonded liquid with a small electric dipole moment and has been considered as a non-polar solvent. The dielectric permittivity varies as a function of frequency, temperature and concentration for the binary liquid mixtures [3-8]. Understanding the frequency-dependent dielectric properties of binary liquid mixtures is useful in both fundamental researches of liquid structure determination and dynamics, as well as practical applications. The frequency-dependent dielectric behavior of liquid mixtures also reveals information about molecular interactions and process mechanisms.

In this paper, we present a detailed study of the dielectric behavior of acetonitrile (ACN), acrylonitrile (ACRN), propionitrile (PPN), and butyronitrile (BTN) in 1, 4-dioxane (DX) using time-domain reflectometry (TDR) at 25⁰C in the frequency range 10 MHz to 30 GHz. The static dielectric constant and relaxation time were calculated from the measured dielectric spectra using the least squares fit method. Excess dielectric permittivity and the Kirkwood correlation factor are also calculated to investigate intermolecular interactions in different molecules.

II. MATERIALS AND EXPERIMENTAL METHOD

We purchased ACN, ACRN, PPN, BTN, and 1,4 DX from S.D. Fine Chem. Ltd. in 99% purity. The solutions were made in NT at different 1,4DX volume fractions. The TDR method was used to obtain the Complex permittivity spectra. The specific experimental setup and protocol have already been covered in previous discussions [9, 10].

III. RESULTS AND DISCUSSIONS:

A. Complex Permittivity Spectra:

The frequency-dependent complex permittivity spectra of nitrile are as shown in Figure 1. It is observed that with increasing frequency, dielectric permittivity (ϵ') decreases. At high frequencies, the response of permanent electric dipoles decreases, resulting in a decrease in (ϵ') [14]. An observation has been made that the value of the dielectric loss (ϵ'') is highly dependent on the frequency of the field that is being applied. These internal motions include the reorientation of electric dipoles, and the dielectric loss peak is evidence that these motions are occurring. The dielectric loss ϵ'' approaches maximum in the frequency range 25 GHz to 30 GHz for all nitriles. The general form of relaxation model can be explained by Havriliak-Negami equation [11, 12].

$$\epsilon^*(\omega) = \epsilon_{\infty} + \frac{\epsilon_0 - \epsilon_{\infty}}{[1 + (j\omega\tau)^{1-\alpha}]^{\beta}} \quad (1)$$

where, ϵ_0 , ϵ_{∞} , τ , α and β as fitting parameters. The equation (2) shows the Debye ($\alpha = 0$, $\beta = 1$), Cole-Cole ($\beta = 1$) and Davidson- Cole ($\alpha = 0$) relaxation models.

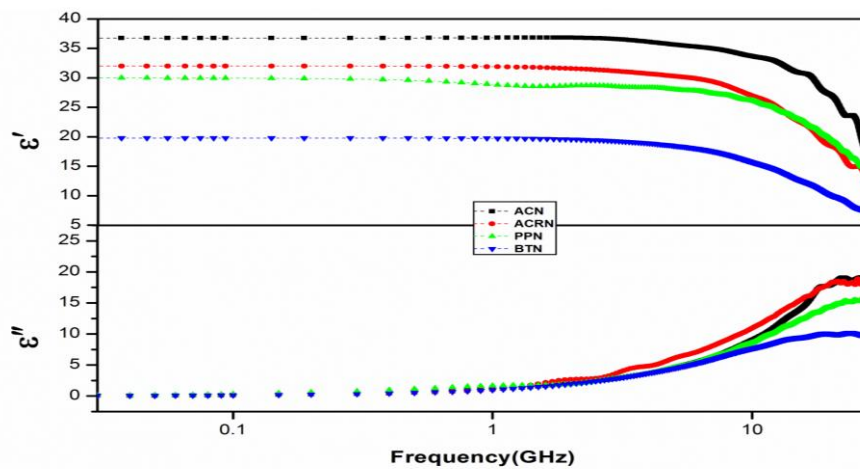


Figure 1: Complex Permittivity spectra for pure Nitriles at 25°C

B. Static Dielectric constant and Relaxation time

The static dielectric constant (ϵ_0) and relaxation time (τ) in picoseconds are calculated from equation (1). Table 1 shows nitrile-dioxane mixtures with 1,4 dioxane volume fraction at 25°C. Static dielectric constants depend on dipole moment, carbon atom number, intermolecular force, temperature, and chain length [13]. The molecular bond decreases with increasing carbon atom chain length, reducing the static dielectric constant of amines, alcohols, and ester compounds [14]. Experimental values of dielectric parameters (ϵ_0 and τ) for Nitriles and 1,4 Dioxane synchronize with previous reports [15,16]. Nitriles with higher Dioxane volume fractions have lower static dielectric constants. Maximum relaxation time in nitriles increases with Dioxane concentration. It means stronger molecule bonding increases molecular size at these concentrations.

Table 1 : Static dielectric constant and relaxation time of Nitrile -1,4 DX mixtures 25°C.

Syst	ACN+DX		ACRN+DX		PPN+DX		BTN+DX	
	ϵ_0	$\tau(\text{ps})$	ϵ_0	$\tau(\text{ps})$	ϵ_0	$\tau(\text{ps})$	ϵ_0	$\tau(\text{ps})$
0.0	36.43(2)	4.20(3)	33.34(1)	5.96(1)	29.15(5)	5.77(1)	23.67(1)	8.40(2)
0.1	32.58(1)	4.81(1)	29.24(1)	5.98(3)	25.71(4)	6.28(3)	19.53(2)	9.88(5)
0.2	30.75 (1)	4.91(1)	27.67(1)	6.28(2)	25.46(1)	6.29(3)	16.76(1)	10.01(7)
0.3	26.57(2)	5.57(2)	24.74(7)	6.77(2)	18.93(1)	6.87(1)	14.87(3)	10.28(1)
0.4	23.69(2)	7.30(1)	22.33(1)	7.20(1)	15.07(1)	8.08(2)	11.24(4)	11.76(3)
0.5	21.36(1)	7.43(1)	18.99(2)	8.02(3)	12.47(1)	8.76(1)	9.31(4)	13.24(3)
0.6	18.17(2)	8.19(1)	15.40(2)	8.28(1)	12.33(1)	7.58(2)	7.21(1)	16.49(9)
0.7	13.92(1)	9.76(4)	11.95(1)	9.27(1)	10.39(1)	6.66(3)	6.17(2)	13.32(4)
0.8	10.42(1)	10.42(4)	8.44(1)	10.17(2)	7.79(1)	6.38(4)	5.04(1)	12.41(3)
0.9	8.13(1)	12.47(1)	4.48(1)	13.08(1)	4.68(1)	5.16(1)	3.94(1)	11.33(7)
1.0	2.50(3)	3.95(1)	2.50(3)	3.95(1)	2.50(3)	3.95(1)	2.50(3)	3.95(1)

Digits in brackets show errors in the corresponding value. e.g.29.24(1) means 29.24 ± 0.01

C. Excess dielectric permittivity

Intermolecular bonds' contribution to mixture dielectric properties is also examined in terms of excess static dielectric permittivity. Excess dielectric permittivity is [12].

$$\epsilon_0^E = (\epsilon_0)_M - [(\epsilon_0)_1 X_1 + (\epsilon_0)_2 (1 - X_1)] \quad (2)$$

where the subscripts M, 1 and 2 represent mixtures of solvent (DX) and solute (ACN, ACRN, PPN, and BTN), respectively, and X1 represents the volume fraction of DX in solute (ACN,ACRN, PPN, and BTN). In a binary liquid mixture, the excess dielectric constant shows intermolecular interaction strength and physical form. The strength of unlike-molecule interactions is shown by excess permittivity values.

Fig. 3 plots excess permittivity versus DX volume fraction. The plot has a sharp maximum and is negative across the concentration range. These negative values for nitrile-dioxane mixtures indicate intermolecular bonding between dissimilar molecules, reducing the number of effective dipole moments contributing to excess permittivity.

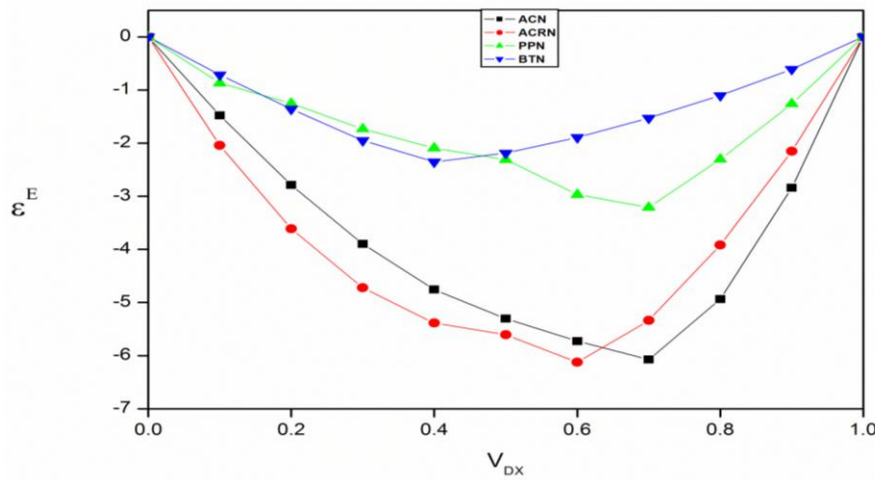


Fig. 3: Excess dielectric permittivity for nitriles with 1,4Dioxane at 25°C.

D. Kirkwood Correlation Factor:

The Kirkwood-Frohlich equation gives helpful information on the degree of orientation correlation between dipoles in pure liquid systems [17].

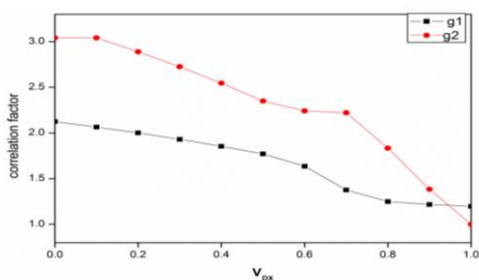
$$\frac{(\epsilon_0 - \epsilon_\infty)(2\epsilon_0 + \epsilon_\infty)}{\epsilon_0(\epsilon_\infty + 2)^2} = g\mu^2 \frac{4\pi N\rho}{9kTM} \quad (3)$$

where N is the Avogadro's number, ρ is the liquid density, ε₀ is the static dielectric constant, ε_∞ is the dielectric constant at high frequency, g is the Kirkwood correlation factor, and T is the Temperature. Kirkwood correlation factor from dielectric constant demonstrates molecular orientation correlation. Intermolecular bonding is measured by Kirkwood correlation factor “g” deviation from unity. Without assumptions, a static dielectric constant cannot determine average correlation factor g₁ and g₂. Luzar presented a hydrogen-bonded mixture model using mean field approximation [18]. Equation [18] calculates g₁ and g₂ correlations.

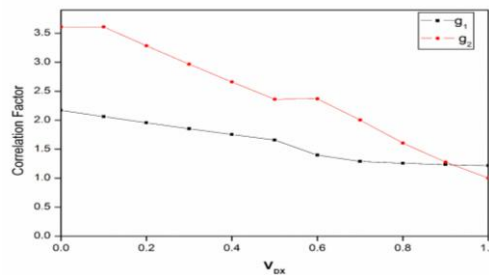
$$g_1 = 1 + Z_{11} \cos \varphi_{11} + Z_{12} \cos \varphi_{12} \left(\frac{\mu_2}{\mu_1} \right). \quad (4)$$

$$g_2 = 1 + Z_{21} \cos \varphi_{21} \left(\frac{\mu_1}{\mu_2} \right) \quad (5)$$

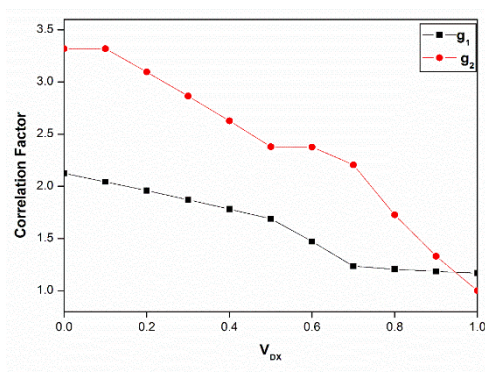
where , $Z_{11} = 2\langle n_{HB}^{11} \rangle$, $Z_{12} = 2\langle n_{HB}^{12} \rangle$ and $Z_{21} = 2\langle n_{HB}^{21} \rangle V_{DX} / (1 - V_{DX})$ represents the average particle number involved in the formation of hydrogen bonds with solute-solute, solute-solvent, and solvent-solute pairings, whereas φ₁₁, φ₁₂, and φ₂₁ represent the angles in nearby dipoles of the molecules. We explained the solute-solvent mixture's static dielectric permittivity with the model. Fig. 2 shows correlation factor g₁ and g₂ for (a) ACN-DX (b) ACRN-DX (c) PPN-DX and (d) BTN-DX vs V_{DX} at 25°C.



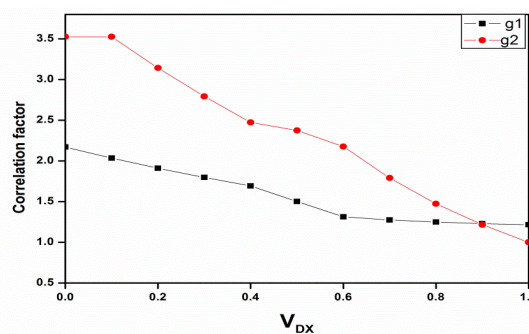
(a)



(b)



(c)



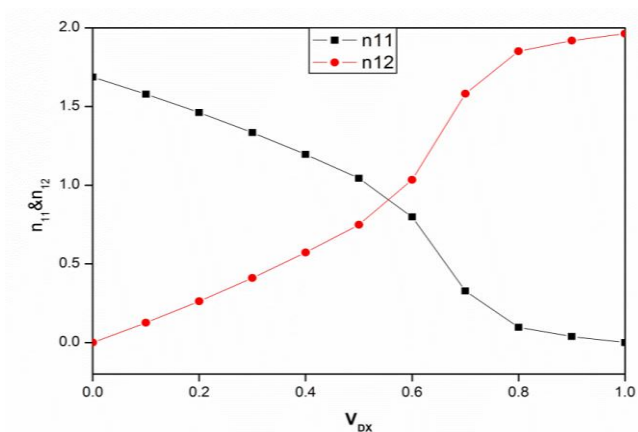
(d)

Fig. 2: Correlation factor vs V_{DX} for (a) ACN-DX (b) ACRN-DX (c) PPN-DX and (d) BTN-DX mixtures at $25^{\circ}C$.

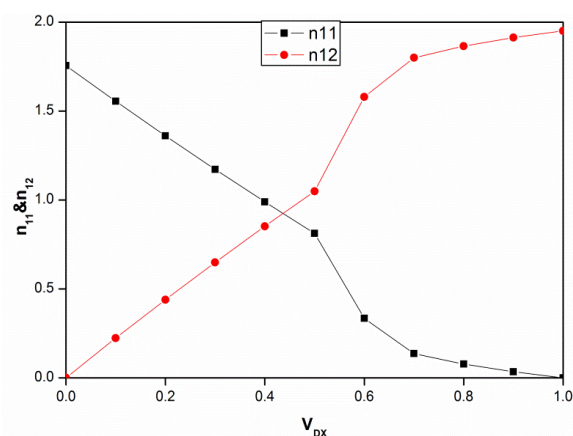
The following connection determines the average number of hydrogen bonds and solvent molecules for $1i$ pairs ($I = 1, 2$).

$$\langle n_{HB}^{1i} \rangle = \frac{n_{1i}}{n_1} \omega_{1i} \tag{6}$$

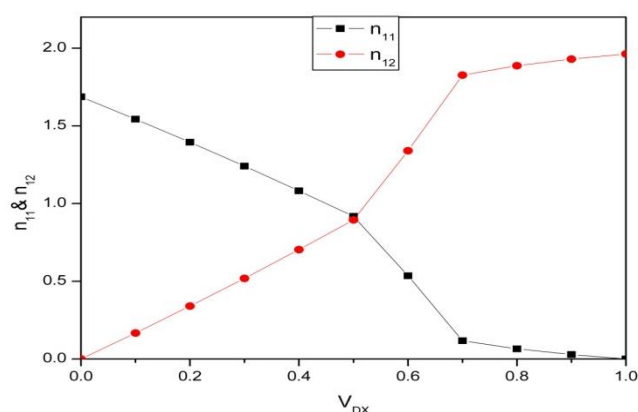
where $\omega_{1i} = \frac{1}{1 + \alpha^{1i} e^{-\beta E^{1i}}}$ is the solute-solvent bond probability, n_1 is DX number density. The energy levels for non-hydrogen-bonded pairs in solute solvent bonds are E_{11} and E_{12} , with $\beta = 1/kT$ and α^{1i} as the ratio of the two sub volumes of the phase space. The hydrogen bonding densities between solute-solvent, n_{12} , and solute-solute, n_{11} and calculate the formation of solute-solute and solute-solvent. Solute-solvent mixture values rely on solvent concentration. Fig. 3 shows the average hydrogen bonds compared to V_{DX} between pairings 11 and 12 for (a) ACN-DX, (b) ACRN-DX, (c) PPN-DX, and (d) BTN-DX mixes at $25^{\circ}C$.



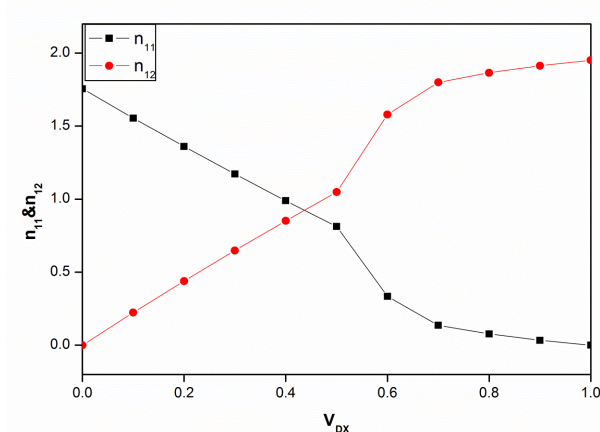
(a)



(b)



(c)



(d)

Fig. 3: Average number of hydrogen bonds in NT-NT (pair11) and NT-1,4-DX (pair 12) against V_{DX} .for(a) ACN-DX (b) ACRN-DX (c) PPN-DX and (d) BTN-DX mixtures at 25°C

It shows how the solute-solvent combinations' values of $\langle n^{11}HB \rangle$ and $\langle n^{12}HB \rangle$ are influenced by the solvent. Fig.3 shows the average number of hydrogen bonds between pairings 11 and 12, relative to V_{DX} . The values of $\langle n^{11}HB \rangle$ and $\langle n^{12}HB \rangle$ are determined by the density of hydrogen bonds between NT-NT and NT-DX molecules. From above figure it shows that as the values of $\langle n^{11}HB \rangle$ decreases with increasing V_{DX} and that of $\langle n^{12}HB \rangle$ has maxima at specific V_{DX} concentration. This result proves the formation of the Solute-Solvent and Solute-Solute hydrogen bonds in given system.

IV. CONCLUSION:

The complex dielectric spectra of Nitrile- 1, 4-Dioxane mixture have been studied using the time domain reflectometry technique in the frequency range of 10 MHz to 30 GHz. The complex permittivity spectra for all nitriles show systematic variation with frequency and concentration, as well as a Debye relaxation mechanism. The structure of nitriles and 1,4 dioxane molecules, based on Luzar's proposed hydrogen bonding model, is used to explain the concentration-dependent dielectric properties.

ACKNOWLEDGMENT

The financial support from the Department of Science and technology, New Delhi is gratefully acknowledge (Project no. DST project SB/S2/LOP-023/2013).

REFERENCES

- [1] <https://en.wikipedia.org/wiki/Propionitrile>
- [2] <https://en.wikipedia.org/wiki/Butyronitrile>
- [3] S.N. Helambe, M.P. Lokhande, A.C. Kumbharkhane, S.C. Mehrotra, S.C. Doraiswamy, *PRAMANA J. of Physics*, 44(1995)405-410.
- [4] R. Jellema, J. Bulthuis, G. van der Zwan, *Journal of Molecular Liquids*, 73,74(1997)179-193.
- [5] V.V. Ramana, A.B.V. Kiran Kumar, M. Ashok Kumar, M.K. Moodley, *Journal of Chemistry*, Article ID 687106(2013)1-4.
- [6] O. Mehmet, *Bull. Korean Chem. Soc.*, 35(2014)1469.
- [7] S.N. Helambe, A.S. Chaudhari, S.C. Mehrotra, *Journal of Molecular Liquids*, 84(2000)235-244.
- [8] S. N. Helambe, M.P. Lokhande, A.C. Kumbharkhane, S.C. Mehrotra, *PRAMANA J. of Physics*, 45(1995) 19-24.
- [9] Deshmukh, A. R., Shinde, R. V., Ingole, S. A., Pathan, A. W., Lokhande, M. P., Sarode, A. V., & Kumbharkhane, A. C. *Pure Appl. Phys.* 56 346 (2018)
- [10] S. H Saknure, N. P. Garad, A. G. Gubre, Y. S. Joshi & A. C. Kumbharkhane *Ind. J. Pure & App Phy.* 61, 27-32(2023).
- [11] U Kaatze, Microwave dielectric properties of liquids. *Radiation Physics and Chemistry*, 45(4), 549-566. (1995).
- [12] A.C. Kumbharkhane, S.M. Puranik, S.C. Mehrotra, *J Chem Soc Faraday Tran*, 87(1991)1569–1573.
- [13] A. R. Deshmukh, R. V. Shinde, S. A. Ingole, A. W. Pathan, M. P. Lokhande, A. V. Sarode, & A. C. Kumbharkhane, *Pure Appl. Phys.* 56 346 (2018)
- [14] S.C. Mehrotra, A.C Kumbharkhane and A.S.: 'Chaudhari *Binary Polar Liquids 1st edition*, Elsevier (2017).
- [15] D.G. Dongre, A.G. Gubre, N.P. Garad, S.H. Saknure & A.C. Kumbharkhane, *Physics and Chemistry of Liquids*, (2024)
- [16] S.N. Helambe, M.P. Lokhande, A.C. Kumbharkhane, S.C. Mehrotra, S.C. Doraiswamy, *PRAMANA J. of Physics*, 44(1995)405-410.
- [17] J.G. Kirkwood, *J Chem Phys*, 7(1939)911-919.
- [18] A. Luzar, *J Mol Liq*, 46(1990)221-238.

¹S.H. Saknure²P.R. Konmare²A.C.Kumbharkhane

**Dielectric Relaxation study of
Hydroxypropyl methyl cellulose – water
mixture using Time Domain Reflectometry
(TDR)**



Abstract: - The Complex permittivity spectra of Hydroxypropyl methyl cellulose (HPMC)15 cPs -Water mixture has been determined using the time domain reflectometry technique in the frequency range of 10 MHz to 30 GHz over the entire temperatures at 5°C - 20°C. The lowest temperature processes are analyzed in terms of dipole relaxation. The complex permittivity spectra for HPMC-water were fitted in the Debye model. The static dielectric constant (ϵ_0), relaxation time (τ) and thermodynamic parameters have been calculated by a non-linear least square fit method.

Keywords: Time domain reflectometry, complex permittivity spectra, static dielectric constant, relaxation time, thermodynamic parameters

1. INTRODUCTION

Polysaccharides, like cellulose, have garnered considerable research interest in recent years due to their unique properties and diverse applications in various industries. Understanding the relationship between a polysaccharide's chemical structure and conformation and its behavior in solution is crucial for optimizing its functionality. Numerous studies have explored polysaccharide-solvent interactions, highlighting their importance.

Cellulose, a key structural component of plant cell walls, is a complex carbohydrate built from β -D-glucose units linked by β (1 \rightarrow 4) glycosidic bonds to form cellobiose units. This unique structure imparts strength and resilience, making cellulose essential for plants and a valuable dietary fiber [2]. Hydroxypropyl methyl cellulose (HPMC), a water-soluble derivative of cellulose, finds applications in various sectors, including pharmaceuticals [1-3]. Understanding the interaction between HPMC and water is crucial for optimizing its performance in these applications.

Dielectric spectroscopy offers a powerful tool to investigate these interactions at the molecular level. Dielectric properties are sensitive to how molecules are arranged and interact with each other [4]. By studying the dielectric behavior of HPMC-water mixtures, we can gain valuable insights into the strength and nature of the interactions between HPMC and water molecules [5].

*Corresponding author: shankarsaknure@gmail.com ¹School of Physical Sciences, Swami Ramanand Teerth Marathwada University, Nanded, India-431606

² School of Physical Sciences, Swami Ramanand Teerth Marathwada University, Nanded, India-431606

Copyright © JES 2024 on-line: journal.esrgroups.org

This research presents a detailed investigation of the effect of water addition on HPMC. We focus on the complex permittivity spectra of a 15 cPs HPMC-water mixture across a temperature range of 5°C to 20°C and a frequency range of 10 MHz to 30 GHz. Time domain reflectometry (TDR) serves as the chosen technique for this analysis. Specifically, we analyze the data at the lowest temperature processes in terms of dipole relaxation. The Debye model is employed to fit the complex permittivity spectra of the HPMC-water mixture. Utilizing a non-linear least square fit method, we aim to extract key parameters such as the static dielectric constant (ϵ_0), relaxation time (τ), and relevant thermodynamic parameters. This study sheds light on the molecular interactions within the HPMC-water mixture at varying temperatures.

2. Experimental

2.1 Materials

The hydroxypropyl methyl cellulose 15 centipoise (cPs) (HPMC) was used from S. d. Fine-Chemical Limited, whereas water was used after deionization. Milimolar HPMC solution in water was prepared at various concentrations.

2.2 Measurement

The investigation of dielectric properties in the HPMC-water mixture employed Time Domain Reflectometry (TDR) for its ability to analyze a broad frequency range (10 MHz to 30 GHz). Measurements were conducted at a constant temperature of 25°C across various HPMC concentrations. A Tektronix Digital Signal Analyzer DSA8300 sampling mainframe oscilloscope with the dual-channel sampling module 80E10B facilitated the TDR measurements, ensuring accurate data acquisition [6-7].

3. Result and discussion

3.1 Complex permittivity spectra

Fitting complex permittivity spectra to the Havriliak-Negami equation using nonlinear least squares is a common technique in the study of dielectric materials [8].

$$\epsilon^*(\omega) = \epsilon_\infty + \frac{(\epsilon_0 - \epsilon_\infty)}{[1 + (i\omega\tau)^{1-\alpha}]^\beta} \quad (1)$$

Where:

- $\epsilon^*(\omega)$ is the complex permittivity at angular frequency ω .
- ϵ_∞ is the high-frequency permittivity (permittivity at infinite frequency).
- τ is the relaxation time.
- α and β are dimensionless parameters that characterize the shape of the relaxation spectrum.

Fig.1 shows the complex permittivity spectra ($\epsilon^* = \epsilon' - \epsilon''$) for an aqueous HPMC solution, where ϵ' is the dielectric permittivity and ϵ'' is the dielectric loss, as a function of frequency (GHz) at 20°C.

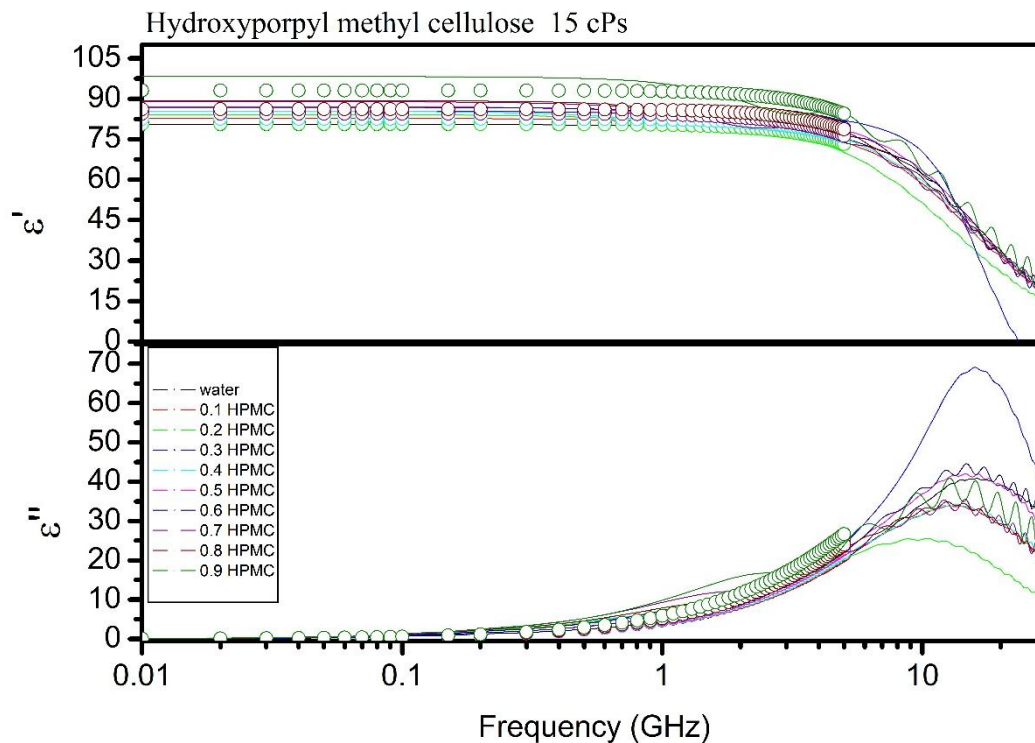


Fig.1 Complex permittivity spectra for HPMC 15 Cps-water mixture at 20°C using TDR

The observed decrease in permittivity (ϵ') with increasing frequency is attributed to the HPMC-water mixture's polar molecules struggling to reorient with the rapidly changing electric field at higher frequencies, resulting in a lower ability to store electrical energy. Furthermore, the shift in the dielectric loss peak towards lower frequencies with increasing concentration suggests a change in relaxation time (τ). Relaxation time represents the time required for molecules to realign with the field. At lower HPMC concentrations, water molecules have greater freedom, leading to a faster relaxation process (higher frequency peak). Conversely, as HPMC concentration increases, water molecules become restricted, resulting in a slower relaxation process (lower frequency peak).

3.2 Dielectric constant & Relaxation time

The Havriliak-Negami equation is a versatile tool for studying relaxation phenomena, including the material of HPMC in water. This equation is used to investigate the dielectric properties of HPMC in aqueous mixtures. Table 1. presents dielectric parameters, such as dielectric constant (ϵ_0) and relaxation time (τ), for various concentrations of HPMC at different temperatures. This data provides insights into how HPMC concentration and temperature affect the dielectric behavior of the solution.

Conc. of HPMC	5 ^o C		10 ^o C		15 ^o C		20 ^o C	
	ϵ_0	τ	ϵ_0	τ	ϵ_0	τ	ϵ_0	τ
00	92.27	13.80	89.4	13.04	85.09	11.36	80.67	10.42
0.1	105.40	12.27	96.41	10.89	85.64	9.94	81.41	9.43
0.2	103.45	13.51	93.19	11.78	85.49	10.75	84.65	10.26
0.3	108.27	12.85	97.96	11.07	95.87	9.99	85.81	9.35
0.4	104.30	12.68	94.55	10.90	81.86	10.02	82.60	9.51
0.5	105.73	12.77	96.23	10.92	84.72	10.10	85.74	9.57
0.6	106.62	13.20	95.46	11.63	84.23	10.70	84.90	10.08
0.7	105.99	12.92	93.31	11.52	81.70	10.78	84.53	10.63
0.8	107.39	13.07	96.54	11.31	84.85	10.45	86.18	9.95
0.9	105.83	13.21	98.46	11.45	86.66	10.51	88.10	10.03
1	116.82	15.50	109.02	12.96	94.15	11.34	93.12	10.28

Table 1. Dielectric relaxation parameters for an aqueous solution of HPMC 15 Cps-water at various temperature ranges (5^oC – 20^oC) and different concentrations.

We observe that as the concentration of HPMC increases, the dielectric constant increases as well. This suggests that the presence of HPMC enhances the material's ability to store electrical energy. Similar to the relaxation time at each concentration, the relaxation time tends to decrease as the temperature increases. This suggests that higher temperatures facilitate faster relaxation of the material.

Overall, the data suggests a complex interplay between HPMC concentration, temperature, and dielectric properties, highlighting the importance of understanding these factors in applications involving HPMC-water mixtures, such as in pharmaceuticals, food products, and industrial processes.

3.3 Thermodynamic properties

Eyring's rate equation was employed to determine the thermodynamic energy parameters for the HPMC-water mixture [9].

$$\tau = h/kT \exp(\Delta H/RT) \exp(-\Delta S/R) \quad (2)$$

This equation relates the relaxation time (τ) to temperature (T), activation enthalpy (ΔH), and activation entropy (ΔS). Table 2 presents the activation enthalpy (ΔH) and entropy (ΔS) values, which offer insights into the structural changes within the molecules. Positive ΔH values suggest an endothermic process across all HPMC-water mixture concentrations, while positive ΔS values indicate random orientation within the mixture. Fig.2 illustrates the Arrhenius behavior of the temperature-dependent dielectric relaxation time of the HPMC-water mixture.

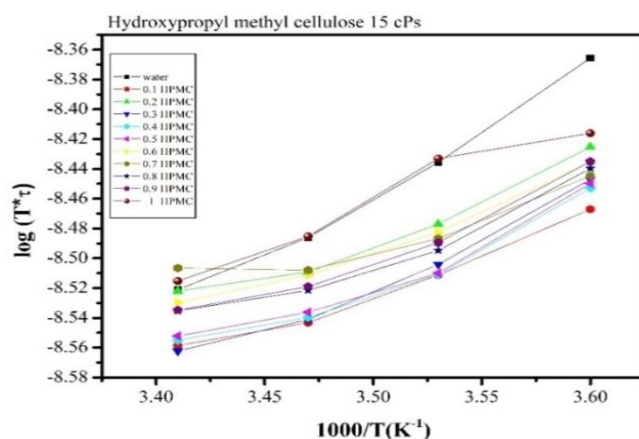


Fig. 2 shows the Arrhenius behavior of the temperature-dependent dielectric relaxation time of the HPMC-Water mixture.

Conc. of HPMC 15 cPs	ΔH	ΔS
00	9.74	0.2283
0.1	7.81	0.2225
0.2	9.16	0.2266
0.3	10.10	0.2305
0.4	7.37	0.2209
0.5	7.59	0.2216
0.6	7.47	0.2208
0.7	6.22	0.2164
0.8	7.64	0.2215
0.9	7.84	0.2222
1	12.86	0.2389

Table 2. Thermodynamic parameters for HPMC-water mixtures.

Conclusion

Time Domain Reflectometry (TDR) was used to analyze the complex permittivity spectra of HPMC-water mixtures, revealing information about the static dielectric constant and relaxation time for various HPMC concentrations. This technique provides insights into the interactions between HPMC and water molecules. Also, by using Eyring's rate equation to determine the activation energy for these relaxation processes.

The observed trends in dielectric constant, relaxation time, and thermodynamic parameters underscore the complexity of interactions within the mixture. Understanding these factors is crucial for various applications involving HPMC-water mixtures, ranging from pharmaceuticals to industrial processes.

Acknowledgment

The financial support from the Department of Science and Technology, New Delhi, is gratefully acknowledged (project no. DST PROJECT- SB/S2/LOP-032/2013). The author, Saknure S.H., would like to express his gratitude to the Chhatrapati Shahu Maharaja Research, Training, and Human Development Institute (SARTHI) for giving him the Chief Minister Special Research Fellowship - 2021. (CMSRF-2021).

References

- [1] Bowtell, R., Sharp, J.C., Peters, A., Mansfield, P., Rajabi-Siahboomi, A.R., Davies, M.C. and Melia, C.D., 1994. NMR microscopy of hydrating hydrophilic matrix pharmaceutical tablets. *Magnetic resonance imaging*, 12(2), pp.361-364.
- [2] Tritt-Goc, J. and Piślewski, N., 2002. Magnetic resonance imaging study of the swelling kinetics of hydroxypropylmethylcellulose (HPMC) in water. *Journal of Controlled Release*, 80(1-3), pp.79-86.
- [3] Fyfe, C.A. and Blazek, A.I., 1997. Investigation of hydrogel formation from hydroxypropylmethylcellulose (HPMC) by NMR spectroscopy and NMR imaging techniques. *Macromolecules*, 30(20), pp.6230-6237.
- [4] Kremer, F., 2002. Dielectric spectroscopy—yesterday, today and tomorrow. *Journal of Non-crystalline solids*, 305(1-3), pp.1-9.
- [5] Xiang, T.X. and Anderson, B.D., 2017. Molecular dynamics simulation of amorphous hydroxypropylmethylcellulose and its mixtures with felodipine and water. *Journal of pharmaceutical sciences*, 106(3), pp.803-816.
- [6] Saknure, S.H., Garad, N.P., Gubre, A.G., Joshi, Y.S. and Kumbharkhane, A.C. Dielectric Relaxation Studies of Cellulose-Water Mixtures Using Time and Frequency Domain Technique. *Indian J. Pure Appl. Phys.* 2023 61, pp.27-32.
- [7] Kumbharkhane, A.C., Puranik, S.M. and Mehrotra, S.C. Dielectric relaxation studies of aqueous N, N-dimethylformamide using a picosecond time domain technique. *J. Solution Chem.* 1993, 22, pp.219-229.
- [8] Havriliak, S. and Negami, S., *Journal of Polymer Science Part C: Polymer Symposia* (1966) (Vol. 14, No. 1). New York: Wiley Subscription Services, Inc., A Wiley Company.
- [9] Eyring, H., 1936. Viscosity, plasticity, and diffusion as examples of absolute reaction rates. *The Journal of chemical physics*, 4(4), pp.283-291.

^{1*} K. Y. Rokde² S. S. Shende

Design and Development of an Embedded System via Sending a Real Time Data of ECG Signal to the Cloud Server for Cardiologist Doctor

Abstract: - This research paper deals with the embedded system via sending a real time data of ECG signal to the cloud server for cardiologist doctor. In this research paper, we introduce a way to interact with Smartphone devices using ECG signals. The Electrocardiogram (ECG or EKG) is the electrical manifestation of the contractile activity of the Heart and is recorded non-invasively by placing electrodes on limbs and chest. It provided information about the rhythm and rate of Heart Beat and morphology. It is a diagnostic tool routinely used to assess the muscular and electrical functions of the Heart. The two applications are presented for android-based devices: SmartApp and Image view. SmartApp is used to select and run any application which is installed on the device while Image View is used to view and manipulate images. Nowadays, Smart mobile devices are widely used in daily life activities. Our proposed system suggests that the ECG signal will directly transfer to the cloud server and then it will transfer on the application which is used by user. The designed proposed system must be used to health care system. In rural areas poor people can't afford the heart attack diagnosis easily, so the idea is to related embedded device which can help poor people as well as for remote location when the patient is in critical condition and is admitted in intensive care unit (ICU) or is being operated upon in the operation theatre (OT). This monitoring is necessitated on account of the immediate response required for support of patients who are suffering from heart diseases to show their heart signal [ECG] report to the doctor may seat from the city via internet using cloud server technology. The doctor can monitor and study the real time waveforms of the patient in this Smartphone or a desktop.

Keywords: Cloud, ECG, smart phone, real time data etc.

I. INTRODUCTION

Physiological parameters were monitored since the earliest days of medicine. Vital signs or physiological parameters of human being consisted of a group of most important parameters that indicated the status of the body's life sustaining functions. These parameters were measured to help in assessing the general physical health of a person. It also gave clues to possible diseases and the progress towards stability and recovery. The normal ranges of vital signs varied with age, weight, gender and the overall health. In the realm of medical care, early information or warning scores emerged, consolidating individual vital sign values into a unified metric. This approach stemmed from the recognition that changes in vital signs or physiological parameters frequently heralded the onset of a medical crisis. Healthcare professionals undertook a range of assessments and interventions to thoroughly evaluate a patient's health status. Evaluating a patient's vital parameters typically constituted the initial assessment conducted by medical practitioners [1].

Medical Research proved that the most important parameters were those related to cardio and respiratory system. They described the state of health in the best possible manner. Mainly there were three primary physiological parameters, namely, Body Temperature, Blood Pressure, Heart Rate or Pulse, Respiratory Rate, ECG Signals. They were often noted as **BT**, **BP** and **HR**. However, depending on the clinical setting and the requirements, more physiological parameters, called the fourth and fifth physiological parameters, were included in monitoring. The below table 1.1 shows the basic idea of physiological parameters out of number of parameters we had taken only the one parameters i.e ECG signal measurement and then it is sent to cloud server for doctors' measurement [2].

^{1*} Assistant Professor, Department of Electronics, Dr. Ambedkar College, Nagpur, India.

krokde4@gmail.com

² Assistant Professor, Department of Electronics, Sharadchandra Pawar Mahavidyalaya, Lonand, India

Table 1. List of Physiological Parameters

Measured Parameter	Physiological Parameter Analysed	Nature of Measurement
Temperature	Body Temperature	Numeric Value
Blood Pressure	Systolic And Diastolic Blood Pressure	Time Function, Numeric Value
Pulse	Heart Work Rate	Mean Numeric Value
ECG	Variation of Electrical Vector of Heart	Time Function, Mean Numeric Value
SPO ₂	Blood Oxygen Saturation	Numeric, Percentile

1.1 ECG & Pulse

The Electrocardiogram (ECG or EKG) serves as the electrical representation of the heart's contractile activity and is captured through non-invasive means by positioning electrodes on the limbs and chest. This diagnostic tool furnishes insights into both the rhythm and rate of the heartbeat, as well as its morphology. Widely employed in clinical practice, the ECG plays a pivotal role in the routine evaluation of both the muscular and electrical aspects of cardiac function [3].

Previously, we delved into the intricacies of the heart's electrical activity. Central to the rhythmic contractile activity of the heart are coordinated electrical events orchestrated by a specialized conduction system, intrinsic and exclusive to the heart itself. The cardiac cycle, encompassing the entirety of these events, is meticulously analyzed utilizing the distinctive features of P waves, QRS complex, and T waves. Figure 3.6 illustrates a standard ECG, delineating the various waves and intervals that characterize this vital physiological process [4].

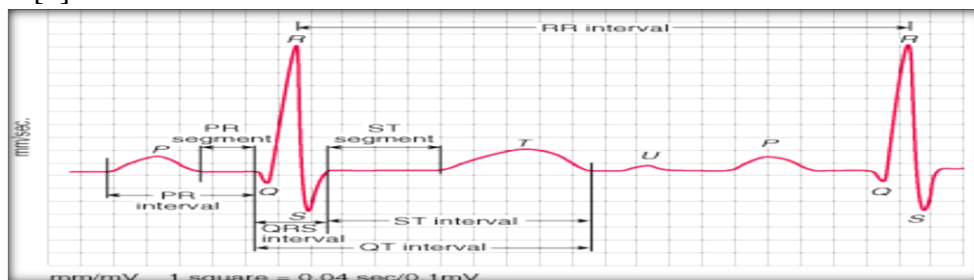


Figure 1. ECG with Different Waves

Table 2. Interpretation of each wave and interval in ECG

Wave / Interval	Interpretation / Event Occurred
P wave	Sequential activation/depolarisation of the Right and Left Atria
QRS Complex	Right and Left Ventricular depolarisation (normally the ventricles are activated simultaneously)
ST-T wave	Ventricular Re-polarisation
U wave	Represents After-depolarisations in the Ventricles
PR interval	Time interval from the onset of Arterial Depolarisation (P wave) to onset of Ventricular Depolarization (QRS complex)
QRS duration	Duration of Ventricular Muscle Depolarisation
QT interval	Duration of Ventricular Depolarisation and Re-polarisation
RR interval	Duration of the Ventricular Cardiac Cycle - an indicator of the Ventricular Rate
PP interval	Duration of the Arterial Cycle - an indicator of the Arterial rate

1.2 Measurement of ECG

The electrical activity of the heart is gauged through non-invasive means by situating electrodes at specific locations on the human body. The Electrocardiogram (ECG) captures these electrical impulses through

electrodes affixed to various points on the body. A total of twelve leads are generated using ten electrodes [5].

Table 3. Positions of these ten electrodes

Nature	Electrode	Position
Extremity Electrodes	LA	Left Arm
	RA	Right Arm
	RL	Right Leg (Neutral)
	LL	Left Leg
Chest Electrodes	V1	In the 4 th Intercostal Space, Right of Sternum
	V2	In the 4 th Intercostal Space, Left of Sternum
	V3	Between V2 and V4
	V4	In the 5 th Intercostal Space, in the mid-clavicular line
	V5	Between V4 and V6
	V6	In the mid-axillary line at the same height as V4

1.3 Pulse

The pulse is characterized as the palpable rhythmic expansion of an artery, resulting from the increased volume of blood propelled into the vessel by the heart's contraction and relaxation [29]. It is typically measured at locations where an artery can be compressed against a bone, such as the neck (Carotid Artery), inside of the elbow (Brachial Artery), wrist (Radial Artery), groin (Femoral Artery), behind the knee (Popliteal Artery), near the ankle joint (Posterior Tibial Artery), and foot (Dorsalis Pedis Artery). The count of arterial pulses per minute correlates with the heart rate [30], influenced by various factors including age, existing medical conditions like fever, medications, and fluid status. As a parameter characterizing heart rhythm, the pulse can be easily derived from an ECG. This involves measuring the distance between the largest peaks, typically the R peaks, and calculating the duration of the R-R interval. The pulse rate can then be determined using the formula:

$$\text{Pulse} = 60 / \text{R-R} [6].$$

A notable and precise technique for pulse measurement is the photoplethysmograph. This method defines the pulse based on arterial blood oxygenation, assessing light absorption by blood. Light emitted by sensors, typically infrared light with a wavelength around 940nm, interacts with arterial blood constituents, primarily hydroxyl groups, leading to changes in absorption. Light detectors measure alterations in scattering, indicating variations in blood flow volume and hence, the pulse rate. This principle underlies the functionality of heartbeat sensors [7].

II. METHODOLOGY

The block diagram of proposed system is shown below which consists various hardware and software connectivity. The following Wearable BCI system model to be constructed aims to provide a flexible system. The model is divided into two parts i.e. hardware and software part, where hardware part is used for collecting, processing and transmitting the ECG signal lie waveform data from patient and software part shows values of the ECG signal parameters and upload it to the medical or physicians server.

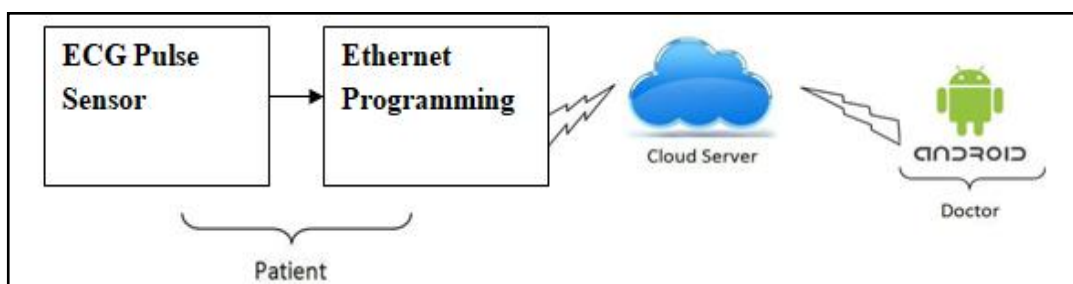


Figure 2. Block Diagram of System

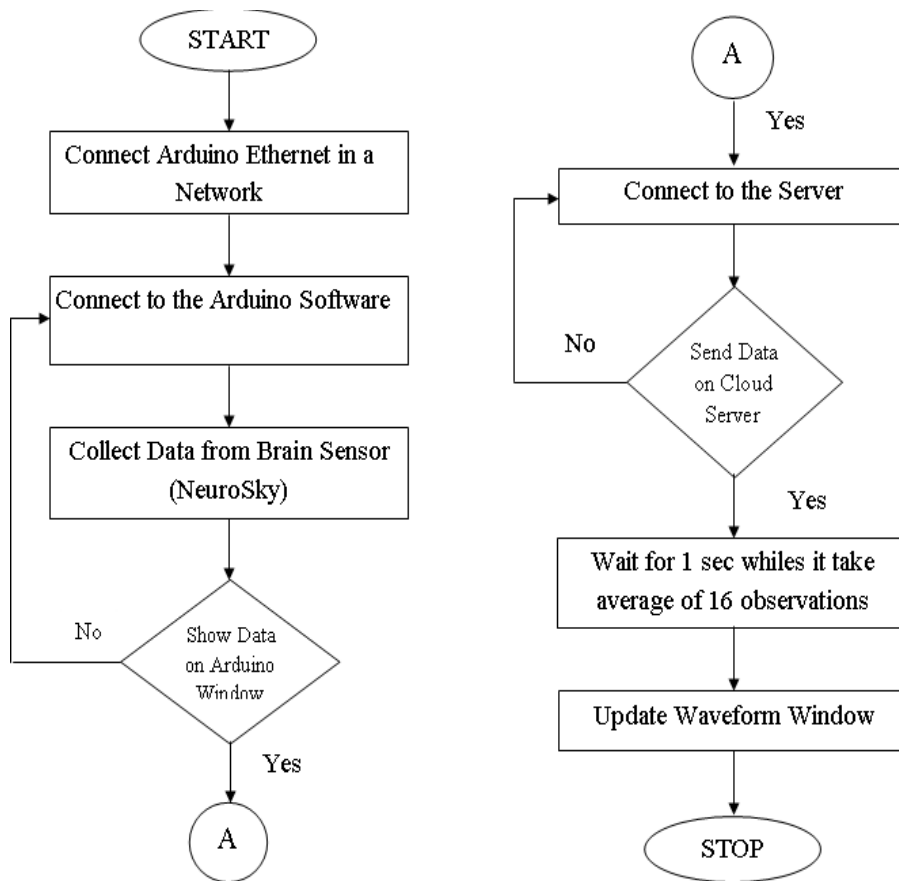


Figure 3. Flow Chart of Proposed System

The flow chart of how the ECG signal data is transmitted and received between the remote patient and the physician carried is shown below. The flow chart shows the communication of the patient with the physician and what are the steps of the communication.

The flow is designed above which shows how the whole system works. Figure shows the flow of the system from remote patient to the physician. As per the proposed method for sending the ECG signal waveform to the cloud server firstly we will connect Arduino Ethernet board in a network by assigning IP address and MAC address then we will collect the ECG sensor live waveforms from human ECG Signal on Arduino microcontroller with the help of Bluetooth and it will send these ECG signal waveform to the Ethernet module. After that with the help of Ethernet it will send to the cloud server and from the cloud server it will real time monitor on any android based application or a desktop [8].

III. EXPERIMENTAL WORK

The system consists of Arduino board and Arduino Ethernet shield. The circuit diagram is constructed as per the block diagram. Figure 4. Shows the circuit diagram of the system.

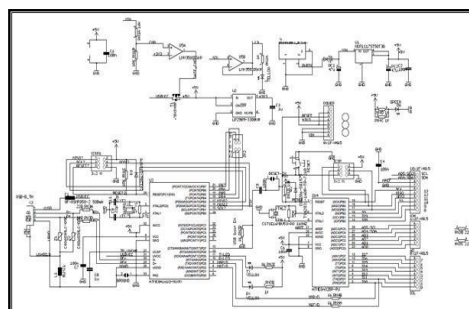


Figure 4. Circuit Diagram of Arduino interface with Arduino Ethernet

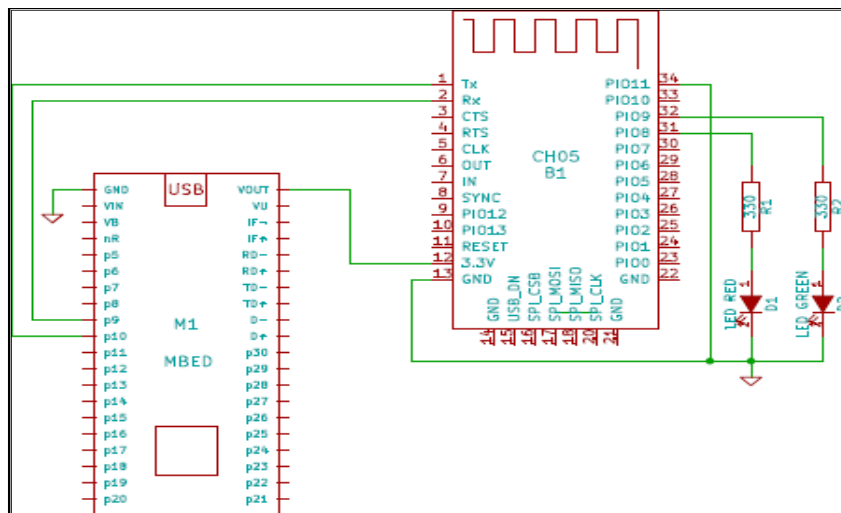


Figure 5. Circuit Diagram of Arduino Bluetooth Interfacing

In proposed system, ATmega328 microcontroller which was used to power mode, the work instruction set, peripherals and the immediate wake autonomous over time is an 8-bit microcontroller. However, some designs, such as the LilyPad run at 8 MHz and onboard voltage regulator due to specific form factor restrictions dispense with Arduino board, a 5 volt linear regulator and a 16 MHz crystal oscillator (or in some variants ceramic resonator) are included. Arduino microcontroller on a single chip flash memory for boot loader that simplifies uploading of programs with pre-programmed, other devices that typically need an external programmer is compared with. As the programmer by allowing the use of a simple computer uses an Arduino simpler. Arduino software stack, all boards using an RS-232 serial connection is programmed [9].

Serial Arduino boards Rs 232 and a level shifter circuit to convert the TTL level signals occurs. Current Arduino boards are programmed via USB, USB-to-serial adapter chips such as the FTDI FT232 is implemented using. HC-05 Bluetooth receiver connected to ATmega328. DTE (Data Terminal Equipment) and DCE (Data Communication Equipment) RS232 serial communication between the MAX232 IC and an asynchronous serial communication between the computers is acting as. Serial communication is not directly communicated with the computer not the first time that it sends signals via Bluetooth HC-05. eSense values microcontroller to read from the computer to send signals, RS232 is used. It is for reading and writing data. Microcontroller physical data from the sensors is processed by the brain and to the local PC via Bluetooth transmitter HC-05 will be notified. The hardware part of the research work, which is shown below as a sensor interface and a receiver circuit consisting of the brain is shown [10].

Tools used for Circuit

The hardware components that are required for implementing this research work.

4.1 Arduino Board:

The Atmel 8-bit AVR microcontroller boasts additional circuit components, accommodating either 16 or 32 with Arduino board programming capabilities. The flexibility extends to Arduino shield interchangeability, a pivotal feature enabled by its standard connectors, facilitating CPU connections to diverse modules. Notably, official Arduinos utilize megaAVR, particularly ATmega8, ATmega168, ATmega328, ATmega1280, and ATmega2560 series chips. While other processors have found utility in Arduino compatibles, utilizing an Arduino programmer streamlines tasks by enabling seamless compatibility with common computers



Figure 6. Arduino circuit board

For serial RS-232 communication with Arduino boards, a level shifter circuit is employed to convert signals between TTL and RS-232 levels. Presently, Arduino boards are programmed via USB utilizing FTDI FT232 USB-to-serial adapter chips. Some UNO board iterations offer flexibility by integrating FTDI chips within their headers, enabling reprogramming of the onboard AVR chip with alternative USB-to-Serial firmware via ICSP [11].

Arduino microcontroller boards offer versatile I/O pin capabilities for interfacing with external circuits. Models such as Decimal, Duemilanove, and Uno currently feature 14 digital I/O pins and six analog inputs, with the flexibility to repurpose six digital pins as needed. These boards sport a pin header layout of 0.10 inches (2.5 mm), facilitating easy connection via female headers. Additionally, various plug-in shields are commercially available to extend functionality.

The Arduino Nano and compatible bare bones boards feature male header pins on the underside, enabling direct insertion into solder less breadboards. Multiple variants of Arduino and compatible boards exist, offering similar functionalities and interchangeability. They are commonly employed in educational settings for constructing projects like buggies and small robots, often leveraging additional output drivers for enhanced functionality. While some variants maintain compatibility with standard shields, others may undergo form factor adjustments. This diversity extends to the use of different processors, providing users with options tailored to their specific needs. Figure 7. Illustrates a typical Arduino board configuration [12].

4.2 Arduino Ethernet Board:

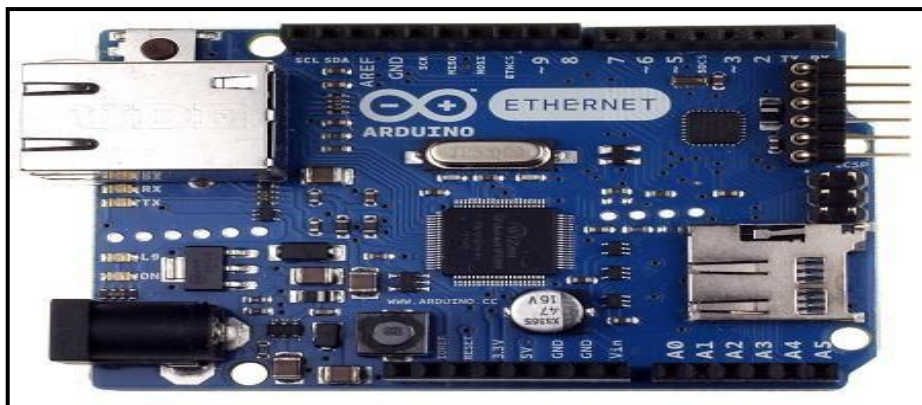


Figure 7. Arduino Ethernet Board

The Arduino Ethernet board is equipped with an ATmega328 microcontroller, boasting 14 digital input/output pins, along with 6 analog inputs and a 16 MHz crystal oscillator. Notably, it includes an RJ45 connection, a power jack, an ICSP header, and a reset button. It's essential to note that pins 10, 11, 12, and 13 are exclusively reserved for interfacing with the Ethernet module and should not be repurposed.

Despite offering 4 PWM outputs, the use of the Ethernet module reduces the available pins to 9. Additionally, users have the option to integrate Power over Ethernet modules into the board. What sets the Arduino Ethernet apart is its utilization of a wiznet Ethernet interface instead of an onboard USB-to-serial driver chip, akin to that found on the Ethernet shield.

Furthermore, it features an onboard micro-SD card reader, facilitating file storage for network operations, accessible through the SD Library. Pin 10 is dedicated to the wiznet interface's SS for the SD card, compatible with FTDI USB cables or Sparkfun and Adafruit FTDI-style basic USB pin 4. Moreover, it boasts a 6-pin serial programming header compatible with USB-to-serial adapters and serial Breakout boards, enabling automatic reset functionality for seamless uploading without manual intervention [13].

In operation, the Arduino Ethernet board can be powered via a USB-to-serial adapter.

Table 4. Specification of Arduino Ethernet board

Microcontroller	ATmega328
Operating Voltage	5V
Input Voltage Plug (limits)	6-20V
Input Voltage PoE (limits)	36-57V
Digital I/O Pins	14 (of which 4 provide PWM output)
Analog Input Pins	6
DC Current per I/O Pin	40 mA
DC Current for 3.3V Pin	50 mA
Flash Memory	32 KB of which 0.5 KB used by boot loader
SRAM	2 KB (ATmega328)
EEPROM	1 KB (ATmega328)
Clock Speed	16 MHz

4.3 Bluetooth (HC-05)

Bluetooth, a wireless technology standard utilized for exchanging data within a short distance, operates within the 2.4 GHz radio wave spectrum in the UHF band. This technology, known as Bluetooth Personal Area Network (PAN), typically covers a range of approximately 10 meters (30 feet). Arduino Bluetooth modules, characterized by their affordability, leverage this standard effectively. These modules often integrate an 8 MB flash chip for storage, and in some cases, can interface with external memory for more complex tasks. For further information on Bluetooth applications and related processes, visit wego.co.in.

4.4 Software Platform:

This section describes the Software platforms used for programming the microcontroller and the software platforms for the development of web page. The software is as follows.

A. Bootloader:

Arduino IDE controller and makes it special boot loader which microcontroller Arduino board and the power of integration is living inside a small piece of code. With boot loader erased when you try to program from the IDE, the controller will not understand anything. In simple terms, the boot loader Arduino IDE controller and acts as a translator between. Before you integrate with Arduino controller board (from a programmer) is to load the boot loader [14].

B. IDE (Integrated Development Environment):

Arduino IDE is installed in the computer. IDE is a compiler, serial version of the C ++ language, and monitoring Arduino C ++ programs, at least it looks like. The program, written, compiled and uploaded to the board's IDE. Language is very simple. An IDE controller with various options to choose from different versions of the Arduino board and also options where Arduino board is connected to the particular communications port is selected [15].

IV. RESULT ANALYSIS

Proposed system consists of both hardware and software implementation. Hardware part consists of ECG measurement, Arduino microcontroller board, Bluetooth HC-05 and RS232 for serial communication. Software part consists of simulation of ECG data coming on com port by using Arduino Software.



```

COM11
|
Connecting Arduino to network...
Arduino connected to network using DHCP
Connecting
HTTP/1.1 200 OK
Content-Type: text/html; charset=utf-8
Transfer-Encoding: chunked
Connection: close
Status: 200 OK
X-Frame-Options: ALLOWALL
Access-Control-Allow-Origin: *
Access-Control-Allow-Methods: GET, POST, PUT, OPTIONS, DELETE
Access-Control-Allow-Headers: origin, content-type, X-Request-Id
Access-Control-Max-Age: 1800
ETag: "ed3d2c21991e3bef5e069713af9fa6ca"
Cache-Control: max-age=0, private, must-revalidate
Set-Cookie: request_method=POST; path=/
X-Request-Id: 253069d7-650f-467c-aa68-9d7f67878542
X-Runtime: 0.014714
X-Powered-By: Phusion Passenger 4.0.57
Date: Wed, 09 Sep 2015 09:22:44 GMT
Server: nginx/1.9.3 + Phusion Passenger 4.0.57

```

Figure 8. Assigning the IP Address and MAC Address for Arduino Ethernet Board

Sample the Incoming Raw ECG Data:

The program is written to generate new sample objects that will add themselves as observers of the mindset DataStream (following the observer pattern), and fill up an array of raw ECG data until it reaches the set sample size. This size was set to 128 data points, so each sample takes 1280 milliseconds to complete (data is updated every 10ms). There are two simple reasons for this: FFT analysis needs a frame that is of a reasonable length, or else it will be difficult to do any accurate analysis and the FFT algorithm in the program needs an input array were the size of it is a power of two.

```
PoorQuality: 0 Attention: 30 Time since last packet: 994
PoorQuality: 26 Attention: 30 Time since last packet: 1000
PoorQuality: 0 Attention: 50 Time since last packet: 995
PoorQuality: 0 Attention: 64 Time since last packet: 997
PoorQuality: 0 Attention: 66 Time since last packet: 1000
PoorQuality: 0 Attention: 87 Time since last packet: 994
PoorQuality: 0 Attention: 78 Time since last packet: 1002
PoorQuality: 0 Attention: 70 Time since last packet: 994
PoorQuality: 0 Attention: 70 Time since last packet: 1001
PoorQuality: 0 Attention: 80 Time since last packet: 991
PoorQuality: 25 Attention: 80 Time since last packet: 997
PoorQuality: 0 Attention: 83 Time since last packet: 996
PoorQuality: 0 Attention: 90 Time since last packet: 1007
PoorQuality: 0 Attention: 100 Time since last packet: 985
```

Figure 9. Observed Attention Level from User

Expected ECG waveform From Cloud Server:

ECGs of different patients were recorded using the designed instrument. The output received was stored for further processing. The photographs of the analog output displayed using Oscilloscope for samples are given below



Figure 10. ECG Waveform on CRO

The stored ECG was filtered for removing the noise and other artefacts. The graphs shown below give the plot of unfiltered and filtered ECG.

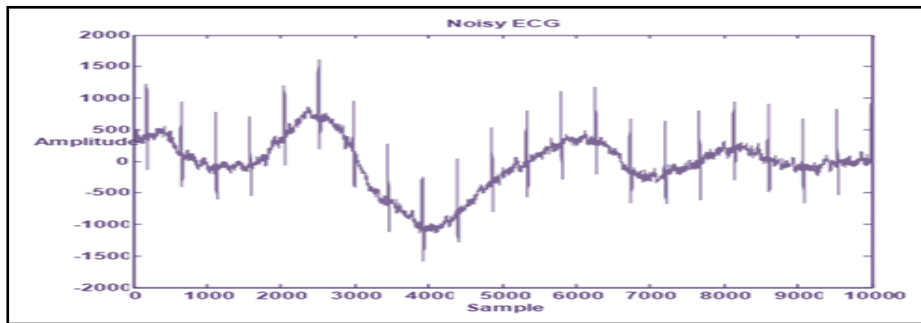


Figure11. Plot Showing Noisy ECG

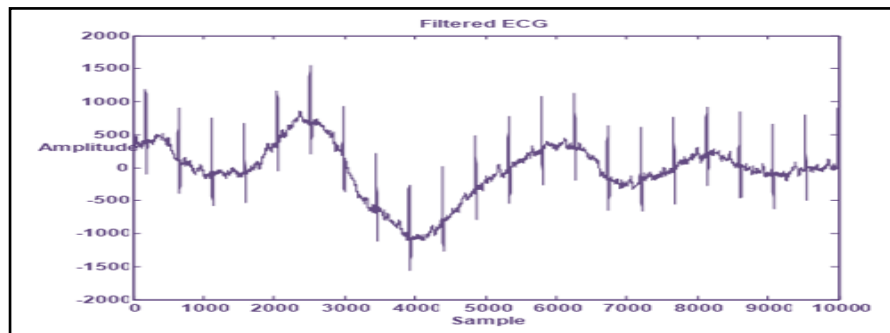


Figure 12. Plot Showing Filtered ECG

After filtering, the features of ECG were extracted. The peaks values were calculated. These values were compared against the medically standardized values to conclude whether the ECG was normal or not.

V. CONCLUSION

This work described results that show it is possible to build a Human ECG Interface system that allows users to monitor and controlling it with their heart signal waveform via cloud server. ECG signals waveforms from the user are sent to the computer via Bluetooth. The signal is then processed and the wave's band power is calculated using the Fourier transform. ECG worked as an effective diagnostic tool, routinely used to assess the muscular and electrical functions of the Heart. It provided information about the rhythm and rate of Heart Beat and morphology. A sequence of co-ordinated electrical events occurs in the Rhythmic Contractile Activity of the Heart, termed as the Cardiac Cycle. Each event in the cycle gave rise to a particular wave. Each wave had its own amplitude and duration. The procedure for measuring ECG (giving the position of electrodes) and different methods used for the recording, like Single-channel Recording, Three-channel Recording, Vector Cardiogram and Holter Recording, were also studied [16].

The results and the subsequent conclusions proved that the users preferred using the Patient Monitoring System i.e ECG measurement developed as it provided a single instrument and provided to the doctors through the cloud server. Also, they found it more effective and efficient for self-monitoring. The information collected was complete and decipherable by any layman. Initially, there were mixed feelings regarding the accuracy of the information collected through the system. This was mainly attributed to the lack of training conducted for the potential users of the system. Results showed that the reports generated by the system when used by properly trained persons were faster and more accurate [17].

REFERENCES

- [1] Malcolm Elliott, Alysia Coventry, Critical care: The Eight Vital Signs of Patient Monitoring, British Journal of Nursing, 2012, vol. 21, no.10, 621-625.
- [2] Tuba Yilmaz, Robert Foster, Yang Hao, Detecting Wireless Vital Signs with Wearable Wireless Sensors, Sensors (Basel), Dec 2010, vol.10, no. 12, 10837-862.

- [3] Leslie Cromwell, Fred J Weibell, Erich A Pfeiffer, Biomedical Instrumentation and Measurements, Second Edition, Eastern Economy Edition, 2005, 244-251.
- [4] Sund-Levander M, Forsberg C, Wahren LK, Normal, Oral, Rectal, Tympanic and Axillary Body Temperature in Adult Men and Women: A Systematic Literature Review, Scand J Caring Science, 2002, vol. 16, no. 2, 122–8.
- [5] Elert, Glenn, Temperature of a Healthy Human (Body Temperature), The Physics Factbook, 2005.
- [6] Harrison's Principles of Internal Medicine, ed. Dan L. Longo, T.R. Harrison, 2011, New York: McGraw-Hill, 142 -143.
- [7] Kelly G S, Body Temperature Variability II: Masking Influences of Body Temperature Variability and A Review of Body Temperature Variability in Disease, Altern Med Rev, March 2007, vol. 12, no. 1, 49–62.
- [8] A Dosinas, M Vaitkūnas, J Daunoras, Measurement of Human Physiological Parameters in the Systems of Active Clothing and Wearable Technologies, Electronics And Electrical Engineering (*Elektronika Ir Elektrotechnika*), 2006, vol 7, no. 71.
- [9] Lynne Mccullough, Sanjay Arora, Diagnosis and Treatment of Hypothermia, American Family Physician, Dec 2004, vol. 70, no. 12, 2325-2332.
- [10] James L Glazer, Management of Heatstroke and Heat Exhaustion, American Family Physician, Jun 2005, vol. 71, no. 11, 2133-2140.
- [11] Gasim I Gasim, Imad R Musa, Mohamed T Abdien, Ishag Adam, Accuracy of Tympanic Temperature Measurement Using an Infrared Tympanic Membrane Thermometer, Bio Med Central Research Notes 2013.
- [12] Blankertz, B., Dornhege, G., Krauledat, M., Müller, K.-R., Kunzmann, V., Losch, F., et al.(2006, June). The Berlin Brain-Computer Interface: EEGbased communication without subject training. *IEEE transactions on neural systems and rehabilitation engineering: a publication of the IEEE Engineering in Medicine and Biology Society*, 14(2), 147–52.
- [13] Fabiani, G. E., McFarland, D. J., Wolpaw, J. R., & Pfurtscheller, G. (2004, September). Conversion of EEG activity into cursor movement by a brain- computer interface (BCI). *IEEE transactions on neural systems and rehabilitation engineering: a publication of the IEEE Engineering in Medicine and Biology Society*, 12(3), 331–8.
- [14] Felzer, T., & Freisleben, B. (2003, December). Analyzing EEG signals using the probability estimating guarded neural classifier. *IEEE transactions on neural systems and rehabilitation engineering: a publication of the IEEE Engineering in Medicine and Biology Society*, 11(4), 361–71.
- [15] Blankertz, B., Dornhege, G., Krauledat, M., Müller, K.-R., Kunzmann, V., Losch, F., et al.(2006, June). The Berlin Brain-Computer Interface: EEGbased communication without subject training. *IEEE transactions on neural systems and rehabilitation engineering: a publication of the IEEE Engineering in Medicine and Biology Society*, 14(2), 147–52.
- [16] Fabiani, G. E., McFarland, D. J., Wolpaw, J. R., & Pfurtscheller, G. (2004, September). Conversion of EEG activity into cursor movement by a brain- computer interface (BCI). *IEEE transactions on neural systems and rehabilitation engineering: a publication of the IEEE Engineering in Medicine and Biology Society*, 12(3), 331–8.
- [17] Felzer, T., & Freisleben, B. (2003, December). Analyzing EEG signals using the probability estimating guarded neural classifier. *IEEE transactions on neural systems and rehabilitation engineering: a publication of the IEEE Engineering in Medicine and Biology Society*, 11(4), 361–71.

¹P.A.Fartode²S.P.Yawale³S.H.Nimkar

**TRANSPORT AND ELECTRICAL
PROPERTIES OF PEO: PVP: NaCl
BASED POLYMER
ELECTROLYTE FOR SOLID
STATE BATTERY APPLICATION**



Abstract: - Polymers PEO, PVP were taken separately at three different ratio with NaCl as (40:50:10), (35:50:15), (30:50:20), (25:50:25), (20:50:30) and (15:50:35) for preparation of polymer electrolyte by solution cast technique. Electrical conductivity is measured in the temperature range 313K to 343K.

Electrochemical cells have been fabricated with the configuration Na/(Electrolyte)/ I₂ + C, Na/(Electrolyte)/I₂ + C + Electrolyte power and their discharge characteristics were studied. Also other cell parameters were calculated such as OCV, SCC etc. The values of OCV and SCC for different cells found to be 0.253V, 0.652V and 24.7μA, 63.1 μA respectively. The other cell parameters were also measured for all this system at room temperature such as current density, energy density etc. by using 10kΩ load.

Keywords: Polymer electrolyte ,PEO,PVP and NaCl.

I. INTRODUCTION

The polymer electrolyte consists of an inorganic salt dissolved in a polymer host. Conductive polymer-salt complexes were first described in 1970's and it was quickly adopted by electrochemical community, who recognized the potential of a flexible, plastic, ion transporting medium for vital applications such as energy storage and electrochemical displays. In contrast to the cases of brittle glassy, polymer materials are suited for application together with intercalation materials, such as the anode and cathode in a rechargeable battery. Polymer electrolytes do not leak any harmful chemical hence they are safer than liquid electrolytes. Polymer electrolytes based on PEO complexed with NaClO₃, AgNO₃ and NaYF₄ etc. have been reported by many research workers [1]-[6]. Also the polymer electrolytes based on PVP complexed with NaClO₃ have been prepared by Kumar et al [7] and Sathiyamoorthi et al [8]. The polymer electrolytes based on PEO, PVP complexed with NaClO₃ were studied by Selladurai et al [9]. Keeping this view in mind, authors have prepared polymer electrolytes based on PEO, PVP complexed with NaCl. These polymer electrolytes were characterized by Impedance spectroscopy, Transference Number and DC Conductivity.

¹ * Assistant Professor, Department of Physics, Shri Shivaji Science College, Amravati. Maharashtra

² Head of Physics Department, Govt. Vidarbha Institute of Science and Humanities, Amravati-444604. Maharashtra

³ Assistant Professor, Department of Physics, Shri Shivaji Arts, Commerce and Science College, Akot. Maharashtra

II. EXPERIMENTAL

The chemicals used for preparation are Poly ethylene oxide (PEO) , Poly vinyl pyrrolidone (PVP) and Sodium chloride (NaCl).

Following components were prepared in laboratory by AR grade chemicals. PEO:PVP:NaCl (40:50:10), PEO:PVP:NaCl (35:50:15), PEO:PVP:NaCl (30:50:20), PEO:PVP:NaCl (25:50:25), PEO:PVP:NaCl (30:50:20), PEO:PVP:NaCl (35:50:15).

Each component dissolved in methanol with proper composition in wt% .The solution was stirred well for 24 Hr. for homogeneousness and poured onto the polypropylene dishes. The solution was slowly evaporated at room temperature. Thus, thin film of polymer electrolyte formed. The films were crushed to form a powder to obtain a pellet.

Thickness of all samples was measured by using digimatic micrometer (Mitutoyo Make, Japan) with least count 1 μ m. Thickness of the samples varies from 0.164 to 0.379 mm.

The ionic/electronic transference number (t_{ion}/t_e) was measured using dc polarization technique suggested by Wagner and Wagner 1957. The dc conductivity of the samples is measured by two-probe method, in which resistance of the sample, was measured. Sample under test was sandwiched between two electrodes of the sample holder. Impedance measurements were carried using the WAYNE KERR (UK), Digital LCR meter (Model 4230). The optimization of conductivity with NaCl concentration is done at 323K. The sample which has the highest conductivity as a polymer electrolyte was used for cell fabrication. Using that polymer electrolyte we fabricated two cells having configurations Na/Electrolyte/I₂+C and Na/Electrolyte/I₂+C+Electrolyte powder. The discharge characteristics of cell under constant load 10 k Ω are studied. Copper plates were used as a current collector on both side of the cell. The composite cathode material was prepared in the ratios (1:1, and 1:1:1 for Graphite + Iodine And Graphite + Iodine + Electrolyte Powder). The cell parameters such as open circuit voltage, short circuit current, current density, power density ,discharge time, discharge capacity etc. were measured.

III. Results and discussion

1 Impedance spectroscopy

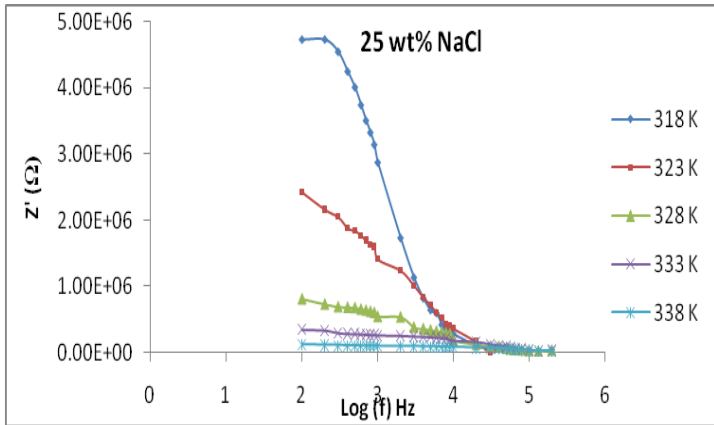


Figure 1 Z' versus frequency at different temperatures for PEO:PVP composite with NaCl 25 wt%

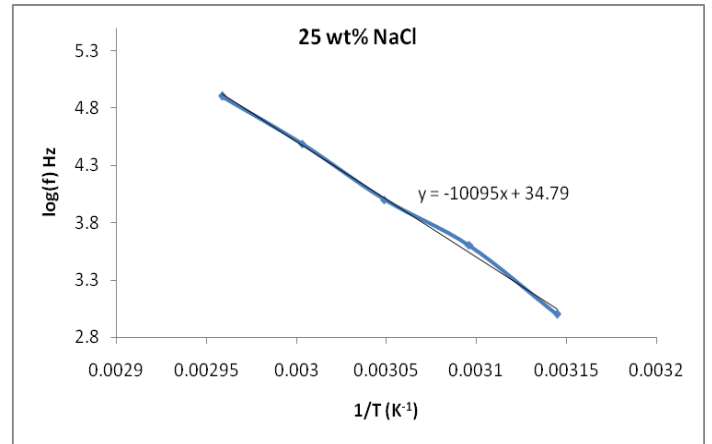


Figure 3 $\text{Log}(f)$ versus $1/T$ plot for PEO:PVP composite with NaCl 25 wt%

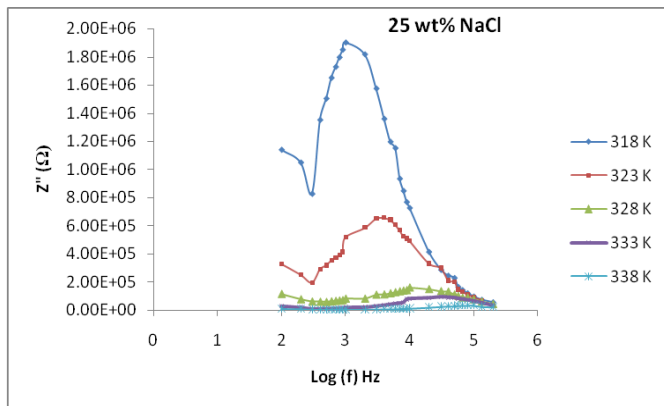


Figure 2 Z'' versus frequency at different temperatures for PEO:PVP composite with NaCl 25 wt%

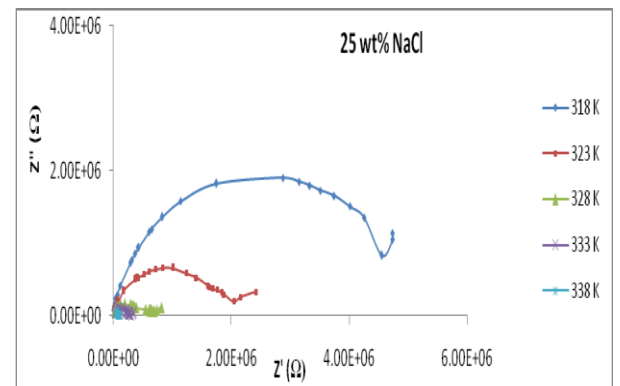


Figure 4 Nyquist diagram for PEO:PVP composite with 25 wt% NaCl at different temperatures

Frequency dependence of real part of impedance (Z') at different temperatures for PEO:PVP composite samples with 25 wt% NaCl is shown in figure 1. It is observed that the magnitude of Z' decreases with increase in both frequency as well as temperature. The Z' values of all temperatures merge above 10KHz. The curve also display single relaxation process and indicate an increase in an ac conductivity with temperature and frequency.

Figure 2 shows the variation of the imaginary part of impedance (Z'') with frequency at different temperatures for optimized PEO:PVP composite with 25 wt% NaCl, shows that the value of Z'' initially decreases then increases and again decreases with increase in frequency at lower temperature. It is also observed that the Z'' peaks are found to shift towards higher frequency side with the increase in temperature. All these curves are merge at the higher frequency.

The relaxation times (τ) were calculated from the frequency at which Z''_{max} is observed. The frequency for the maximum Z'' , called relaxation frequency (f_r). Relaxation frequency (f_r) shifts to higher values with increasing temperature indicating increase loss in the sample.

The variation of relaxation frequency with temperature for PEO:PVP composite samples with 25 wt% NaCl is shown in figure 3.

The relaxation frequency obeys the Arrhenius relation given by equation (1),

$$f_r = f_0 \exp(-E_a/kT) \quad (1)$$

Where, f_0 is the pre-exponential factor, k is the Boltzmann's constant, T is the absolute temperature and E_a is the activation energy.

Relaxation times at different temperature of PEO:PVP composite samples with 25 wt% NaCl is 0.162×10^{-34} s. Relaxation time for other samples can not be calculated due to absence of relaxation peaks in Z'' versus $\log f_r$ plot.

Impedance data taken over wide range of frequency (10^2 to 10^5 Hz) at different temperatures and obtained the Nyquist diagram. Nyquist diagrams for PEO:PVP composite samples with 25 wt% NaCl is shown in figure 4, it is observed that each curve ends with spike (residual tail) which is the characteristics of a blocking double layer capacitance. Sasikala et al [10] have been observed such type of result.

Again it is observed that with the increase in temperature slope of the line decreased and deviates towards real axis (Z') and at temperature above 328 K, semicircle could be traced, indicating increase in the conductivity of the sample. The semicircle diameter gives the electrical resistivity of the sample at the specified temperature and the maximum value corresponds to the relaxation frequency, $f_r = 1/2\pi RC$. Initially at low temperature, when the sample resistance is too high, a small portion of the impedance dispersion profile can be detected in the measured frequency range and thus making data analysis impossible. Since the impedance measurements performed for all the samples below the temperature 338 K did not present semicircle.

For higher temperature we get semicircle plots. It provides information about the nature of dielectric relaxation. As the Nyquist plots are single semicircle with the center located on Z' axis, relaxation process is pure monodispersive Debye process. For polymer dispersive relaxation, these argand plane plots are close to circular arcs with the end points on the axis of reals and the center below this axis. The complexed impedance in such situations is known as Cole-Cole formalism[11].

$$Z^*(\omega) = Z' + iZ'' = \frac{R}{\left(1 + i\omega/\omega_0\right)^{1-\alpha}} \quad (2)$$

Where, α represents the magnitude of the departure of the electrical response from an ideal condition and this can be determined from the location of the center of the Cole-Cole circles. When α goes to zero ($1 - \alpha \rightarrow 1$), equation (2) gives rise to the classical Debye's

formalism. Figures 4 shows full semicircle i.e. semicircle centered on the abscissa axis ($\alpha = 0$), suggest that the relaxation to be of Debye type.

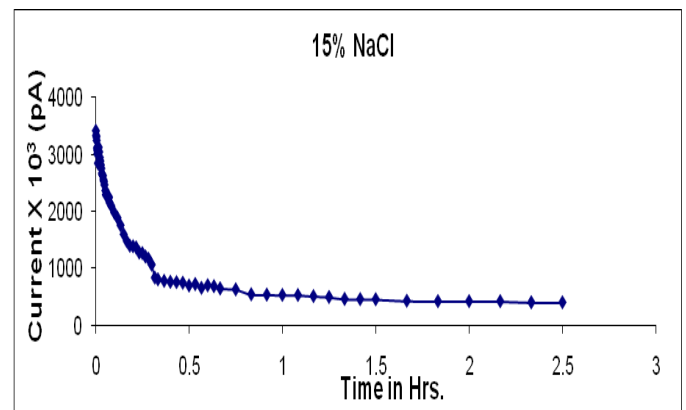
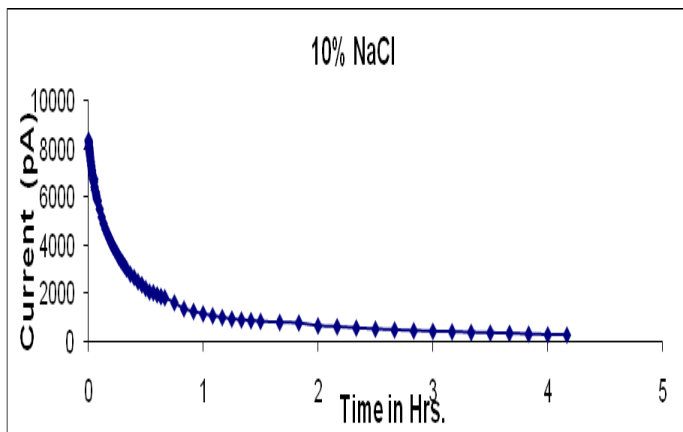
From these semicircles values of bulk resistance R_b and bulk capacitance C_b can be calculated for different temperatures. These values are reported table 1 .

Table 1: Values of bulk resistance R_b and bulk capacitance C_b of optimized NaCl sample at different temperatures

Sr. No.	Temperature (K)	Relaxation frequency (kHz)	Bulk resistance (R_b) (M Ω)	Bulk capacitance (C_b) (pF)	$2\Pi f_r R_b C_b$
1	318	1	4.55	34.98	1
2	323	4	2.04	19.50	1
3	328	10	0.73	21.80	1
4	333	30.77	0.29	17.84	1
5	338	80	0.12	16.58	1

From above table values of $2\Pi f_r R_b C_b$ are found to be equal to 1, which supports classical Debye formalism. The impedance plane plots for optimized NaCl are two well separated semicircles , represented by constructing two series RC elements. Corresponding values of R_b and C_b at different temperatures are given in the table 1.

2 Transference Number



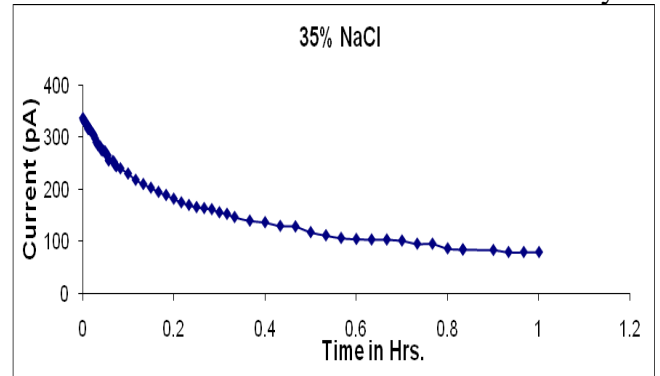
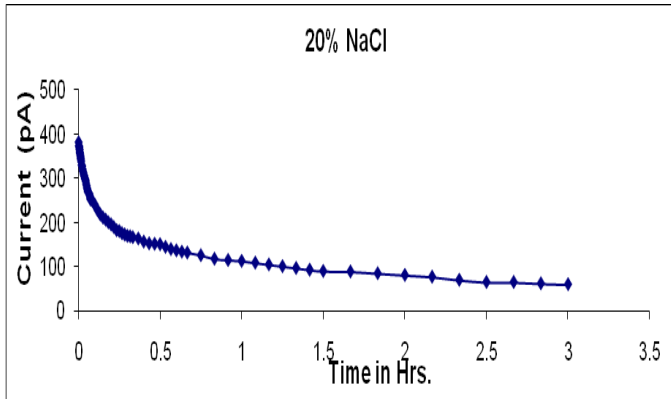


Fig. 5- Current versus time plot for different NaCl Concentration

10,15,20,25,30 and 35 wt%

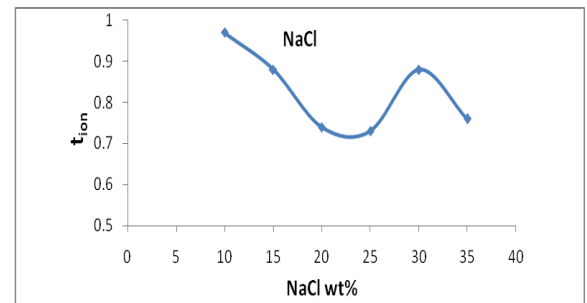
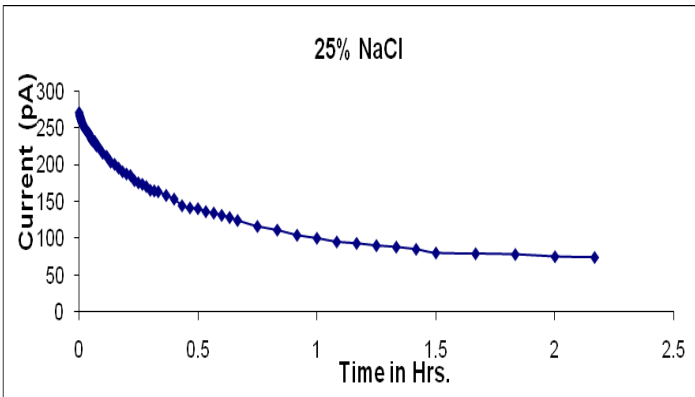
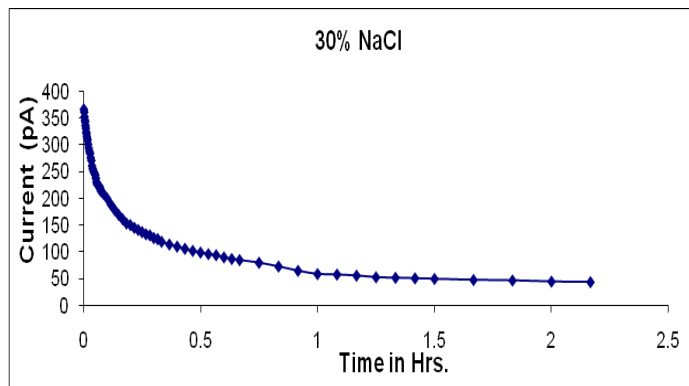


Figure 6- Variation of ionic transference number with NaCl wt%



The transference number gives quantitative information of the extent of ionic and electronic contribution to the total conductivity.

The ionic/electronic transference number can be defined as,

$$t_{ion} = \sigma_{ion} / \sigma_T = I_{ion} / I_T \tag{3}$$

$$t_e = \sigma_e / \sigma_T = I_e / I_T \tag{4}$$

Where, σ_{ion}/σ_e and I_{ion}/I_e are the conductivity and current contribution due to ions/ electrons respectively.

The ionic/electronic transference number was measured by using dc polarization technique [12], in which a PEO:PVP:NaCl polymer electrolytes are sandwiched between blocking (Graphite) and non-blocking (Silver) electrodes. A constant dc voltage (0.5V) is applied across the sample and the resultant current (pA) was recorded as a function of time.

The current versus time plot of the PEO:PVP:NaCl polymer electrolyte with different NaCl wt% is shown in fig. 5 The high current has been observed at initial time period and it starts decreasing with time and then the total current becomes nearly constant at some non zero value. All the samples show the same trend. The final residual current is mainly due to electrons/ holes. The ionic transference number is calculated separately for the polarization current versus time plots using equation (4). The values of transference numbers for different NaCl wt% are found to be in the range of 0.97 to 0.73.

The Variation of ionic transference number with NaCl wt% is shown in figure 6, we see that as concentration increases transference number decreases then increases and then again it will decreased. The values of transference number is greater than 0.5 so the conduction is due the movement of ions through the electrolyte [13].

3 DC Conductivity

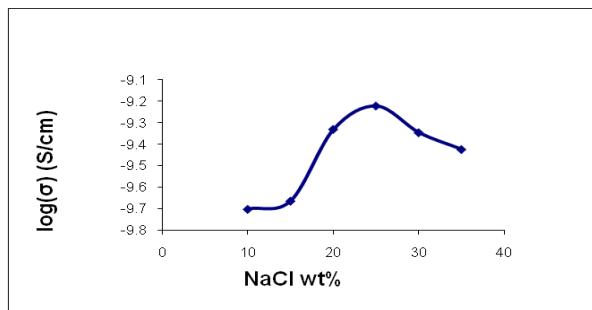


Figure 7- Variation of conductivity with NaCl wt% at 323 K

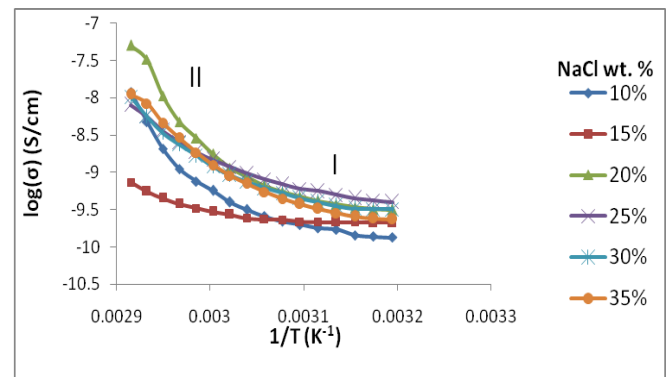


Figure 8 – Temperature dependence of conductivity for different NaCl wt %

DC conductivity of the samples of different NaCl wt% was measured in the temperature range 313 to 343K by measuring the resistance of the samples. It is observed that the value of resistance depends on temperature.

The variation of dc conductivity with wt% of NaCl, for NaCl doped PEO-PVP composite films at 323K is shown in figure 7, it is observed that as concentration increases conductivity also increases then it reaches to the maximum value and then decreases. For the 25 wt% the concentration of NaCl the conductivity shows maximum value .

The temperature dependence of conductivity for different NaCl wt % is shown in figure 8. The conductivity versus temperature curves of the samples shows increase in conductivity and plot follows the Arrhenius behavior throughout, but the nonlinear behavior of the curve suggests the two activation regions (I and II) with two different activation energies. Initially the rate of increase in conductivity is slow and after a certain temperature the rise is fast. The increase in conductivity may be due to the transition from the semi crystalline to amorphous phase. [14-17]. The values of activation energy varies from 0.03 to 0.84 eV .

The behaviour of $\log \sigma$ Vs $1/T$ suggests the polaron ionic hopping conduction; which may be due to Na^+ ions only. The PEO can acts like base material but the conductivity is entirely due to sodium ions.

4 Solid State Cell (Batteries)

From figure 7 it is observed that the sample which contains 25 wt % of NaCl has the highest conductivity. So, this sample is used as a (polymer) electrolyte for the preparation of cells with configuration Na/ PEO:PVP:NaCl/I₂+C, Na/PEO:PVP:NaCl/ I₂+C+ Electrolyte powder.

The calculated values of cell parameters are represented in table 2. The discharge characteristic of cells are studied under constant load 10k Ω . The discharge curve for all two cell configuration are represented in the figures 9 and 10 for Na/PEO:PVP:NaCl/I₂+C and Na/PEO:PVP:NaCl /I₂+C + Electrolyte powder respectively

Table 2– Values of cell parameters for PEO:PVP:NaCl based polymer electrolyte for different cell configuration

Cell parameter at 30°C for load of 10k Ω	Cell configuration	
	1	2
	Na/PEO:PVP:NaCl/ I ₂ +C	Na/PEO:PVP:NaCl/ I ₂ +C+ Electrolyte powder
Area of the cell (cm ²)	1.047	1.047
OCV (V)	0.652	0.253
SCC (μA)	63.1	24.7
Current Density ($\mu\text{A}/\text{cm}^2$)	60.27	23.59
Discharge time (h)	175	150
Discharge capacity ($\mu\text{A}/\text{h}$)	0.36	0.16
Power density (w/kg)	0.14	0.02
Energy density (wh/kg)	24.5	3

The discharge characteristic of cells are studied under a constant load of 10kΩ. The discharge curve for all two cell configuration are represented in figures 9 and 10 for Na/PEO:PVP:NaCl/I₂+C and Na/ PEO:PVP:NaCl /I₂+C + Electrolyte powder respectively.

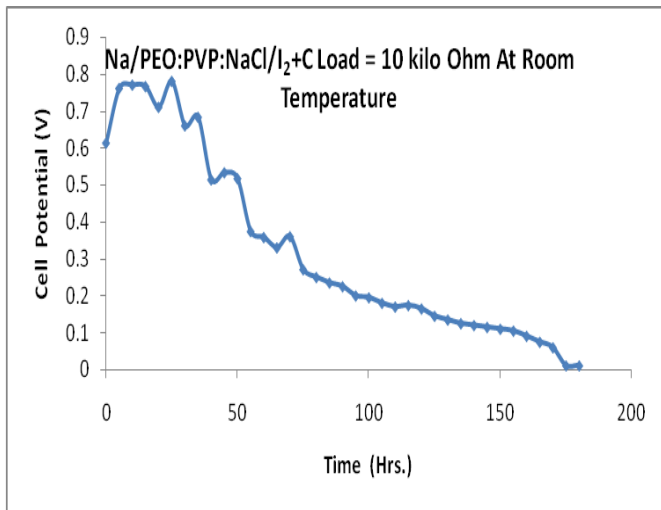


Figure 9- Discharge characteristic curve for cell configuration Na/ PEO:PVP:NaCl/I₂ + C

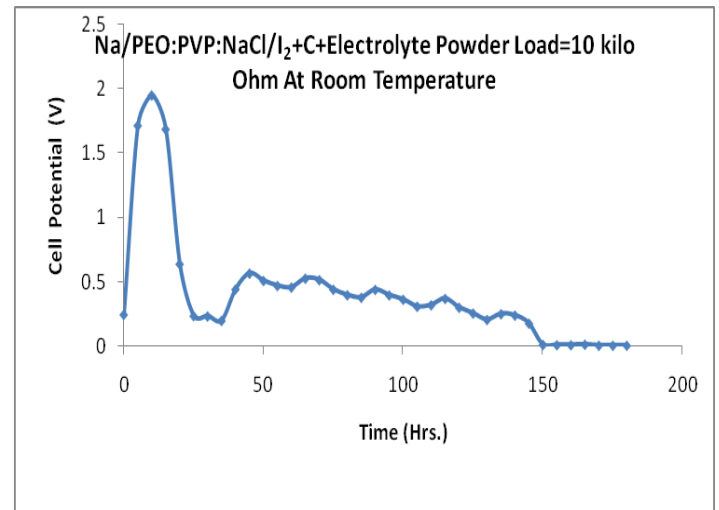


Figure 10- Discharge characteristic curve for cell configuration Na/ PEO:PVP:NaCl / I₂+ C + Electrolyte Powder

From figures 9 and 10 it is observed that initially we get maximum voltage(cell potential) and it decrease with time and it becomes zero after some time.

The discharge capacity of two cells was found to be 0.36 μA/h and 0.16 μA/h respectively.

In the cell configuration Na/Electrolyte/I₂+C open circuit voltage was found to be 0.652 V with a short circuit current 63.1 μA. This voltage increases upto 0.8V for 10kΩ load and then decreases and becomes zero after 175 Hr..

Similarly for second cell in which the counter electrode is I₂+C+Electrolyte powder (1:1:1) the open circuit voltage is found to be 0.253V, with short circuit current 24.7 μA. This voltage increases to 2 V then it decreases and then it completely discharges after 150 Hr..

It is observed that the OCV decreases with the addition of Electrolyte powder and the discharge time also decreases.

IV. Conclusion

From impedance spectroscopy result, it is observed that magnitude of Z' decreases with increase in both frequency as well as temperature. The Z' values of all temperatures merge above 10KHz. The curve also display single relaxation process and indicate an increase in an ac conductivity with temperature and frequency. It is observed that the peaks in the Z'' versus frequency are found shifted towards higher frequency side with the increase in temperature. All these curves are merge at the higher frequency. The relaxation times (τ) were calculated from the frequency at which Z''max is observed. The frequency for the maximum Z'', called relaxation frequency (fr). Relaxation frequency (fr) shifts to higher values with increasing temperature indicating the increase loss in the sample. Relaxation times at

different temperature of PEO:PVP composite samples with 25 wt% NaCl is 0.162×10^{-34} s. From Nyquist diagram, it is observed that with the increase in temperature slope of the line decreased and deviates towards real axis (Z') and at temperature above 328 K, semicircle could be traced, indicating increase in the conductivity of the sample. From these semicircles, values of bulk resistance R_b and bulk capacitance C_b can be calculated for different temperatures. The values of $2\pi f R_b C_b$ are found to be equal to 1, which supports classical Debye formalism.

Transference number for PEO:PVP:NaCl polymer electrolytes with different NaCl was found to be greater than 0.5, which suggest the presence of ionic conduction.

The conductivity versus temperature curves of the samples shows increase in conductivity and plot follows the Arrhenius behavior throughout, but with the two activation regions (I and II) with two different activation energies. Initially the rate of increase in conductivity is slow and after a certain temperature the rise is fast. The increase in conductivity may be due to the transition from the semi crystalline to amorphous phase. The variation of dc conductivity with wt% of NaCl doped PEO-PVP composite films at 323K shows the highest conductivity for sample with 25 wt% of NaCl.

The same sample i.e. 25wt% NaCl:PEO:PVP was used as electrolyte for two different cell configurations. Amongst these two cells, the cell Na/ PEO:PVP:NaCl/I₂+C generating higher potential than other. Also the short circuit current is found to be more for this cell. The other cell parameters such as current density, discharge time, discharge capacity, power density and energy density are found to be reasonable.

It is concluded that the cell configuration Na/ PEO:PVP:NaCl/I₂+C has better performance.

V. References

- [1] J. Shiva Kumar, A. R. Subrahmanyam, M. J. Reddy and U. V. Subba Rao, *J. Ionics*, 60 (2006) 3346-3349.
- [2] R. Chandrasekaran and S. Selladurai, *Solid State Ionics*, 50(2001) 89-94.
- [3] R. Chandrasekaran, I. R. Mangani, R. Vasanthi and S. Selladurai, *J. Solid State Ionics*, 1(2000) 88-93.
- [4] R. Chandrasekaran and S. Selladurai, *J. Solid State electrochemistry*, 5 (2000) 355-361
- [5] S. S. Rao, K. V. Satyanarayana Rao, Md. Shareefuddin, U. V. Subha Rao and S. Chandra, *Solid State Ionics*, 67 (1994) 331-334.
- [6] S. S. Rao, M. J. Reddy, K. N. Reddy and U. V. Subba Rao, *Solid State Ionics*, 74 (1994) 225-228.
- [7] K. N. Kumar, T. Sreekanth, M. J. Reddy and U. V. Subba Rao, *J. Power Sources*, 101 (2001) 130-133.
- [8] R. Sathiyamoorthi, R. Chandrasekaran, S. Selladurai and T. Vasudevan, *J. Ionics*, 9 (2003) 404-410.
- [9] S. Selladurai, R. Chandrasekaran, I. R. Mangani and R. Vasanthi, *Ion Conducting Material : Theory and Applications*, (2001) 213-219.
- [10] U. Sasikala, P. N. Kumar, V. V. R. N. Rao and A.K. Sharma, *IJESAT*, 2(2012) 722-730.
- [11] K. S. Cole and R.H.Cole, *J.Chem.Phys.*, 9(1941)341.
- [12] J. B. Wagner Jr. and C. J. Wagner, *J. Chem. Phys.*, 26(1957) 1595.
- [13] U. Sasikala, P. N. Kumar, P. C. Sekhar, V. V. R. N. Rao and A.K. Sharma, *ESTIJ*, 2(2012) 340-343.
- [14] M. J. Reddy, T. Shreekanth, M. Chandrashekar and U. V. Subba Rao, *J of Material Science*, 35(2000) 2841- 2845.
- [15] K. V. Kumar, G. S. Sundari, M. C. Sekhar and A.S.Rao, *IJCBS*, 1(2012)59-64.
- [16] B. L. Papke, M. A. Ratnar and D. F. J. Shriver, *J. of Electrochemical Society*, 129(1992)1434.
- [17] K. K. Maurya, N. N. Shrivastava, N. S. Hashmi and J. Chandra, *J. of Material Science* ,27(1992)6357.

¹Dr. A. R. Karule²Dr. S. P. Yawale³Dr. S. S. Yawale

**D. C. Conductivity of polypyrrole-
polyethylene oxide-SnO₂ films
synthesized by chemical oxidative
polymerization method**



Abstract: - Polypyrrole (PPy) - Polyethylene oxide (PEO) - Tin oxide (SnO₂) composite thin films were synthesized by chemical oxidative polymerization method with the solution of ferric chloride (FeCl₃) oxidant in methanol. The surface morphology of (PPy-PEO-SnO₂) polymer composite films was studied by scanning electron microscopy (SEM). Their dc conductivity as a function of temperature (308 to 338 K) was measured. The transference numbers for the PPy-PEO films, synthesized with different wt% of SnO₂, were determined by dc polarization technique. The values of transference number are found to be in the range of 0.67-0.94. This shows the ionic conduction. The dc electrical conductivity of the films, at 318K, first increases with wt% of SnO₂ and attains the maximum value ($\sigma = 2.14 \times 10^{-7}$ S/cm) at 5 wt% of SnO₂. However, further increase in wt% of SnO₂, decreases the conductivity of the films. The temperature dependence of conductivity shows cross over from Vogel-Tamman-Fulcher (VTF) to Arrhenius behaviour. The cross over from VTF to Arrhenius takes place at different temperatures for the films synthesized with different concentration of SnO₂.

Keywords: PPy-PEO-SnO₂ composites, SEM, Conductivity.

¹ *Dr. Ankita R. Karule, Lecturer in Physics, Government Polytechnic, Nagpur

² Prof. S. P. Yawale, Head, Dept of Physics and Electronics, GVISH, Amravati

Copyright © JES 2024 on-line : journal.esrgroups.org

I. INTRODUCTION

Conducting polymers, as their name suggests, are a group of conjugated polymers that exhibit excellent electrical conductivity. Conducting polymers belong to a novel class of materials that are being evaluated for application in charge storage devices (batteries, capacitors), electromagnetic screens, Sensors, membranes, Corrosion protective coatings [1]. Conducting polymers from five-member heterocyclic compounds are very interesting. Among conducting polymers, polypyrrole has been one of the most studied polymers because of its physical and electrical properties that have led to several applications such as solid state devices and sensors [2].

However, the typical polypyrrole, which is insoluble and infusible, exhibits poor processability and lacks essential mechanical properties. Efforts to overcome these drawbacks have led to numerous research on the synthesis of polypyrrole. Among them a significant strategy to approach both high electrical conductivity and desirable mechanical properties is through the use of bulky organic sulfonate dopants [3-9] or preparing composites of polypyrrole with other insulating polymers having desirable mechanical properties [10-12]. In other words, a combination of a conventional polymer with conductive polymer allows the creation of new polymeric materials with specific electrical properties. Apart from the knowledge of electrical and mechanical properties of composites, a thorough understanding of charge transport mechanism is important. Many articles have been published regarding the charge transport behavior of such composite films.

Many research workers have studied synthesis and charge transport in composites and blends, like PPy-poly vinyl chloride (PPy-PVC) [13], PPy-ferric oxide nanocomposites [14], poly methyl methacrylate-polyaniline (PMMA-PAn) [15], PPy-poly vinyl alcohol (PPy-PVA) [16], polystyrene-polyaniline (PS-PAn) [17], and nanocomposites of PPy and iron oxide [18], PPy-poly (alkyl methacrylates) [19]. Most of them explained the charge transport behavior as a charge carrier hopping (Mott's VRH) between localized states. On the other hand, in the case of ionically conducting solid polymer electrolytes, the temperature dependent behavior of conductivity is more completely explained by the VTF (Vogel-Tamman-Fulcher) equation [20-22].

Dhawan and Trivedi [23] deposited a thin conducting PPy film on an insulating surface by vapour phase technique. They observed that the electrical or mechanical properties of the polypyrrole film depended upon the method of synthesis and the synthesis conditions including strength of oxidizing or reducing agent, the doping concentration, the temperature of polymerization, and the polymerization time. Therefore, research on the preparation and characterization of polypyrrole is still a focus of investigation for research workers.

The present paper focuses on the synthesis of PPy-PEO-SnO₂ films by oxidative (chemical) polymerization and effect of the doping concentration on electrical conductivity of composite films to know the conduction mechanism and structural behavior.

II. EXPERIMENTAL

Anhydrous Ferric chloride (FeCl₃) (AR-grade), stannous chloride (SnCl₄), Ammonia from S. D. Fine Chem (India), pyrrole from Sisco (India) (AR-grade), PEO from Across Organic (USA) are obtained. All these chemicals were used as purchased.

A. Synthesis of nano SnO₂

0.1M of stannous chloride dehydrate (SnCl₄.2H₂O) is dissolved in 100 ml distilled water. After complete dissolution, about 4 ml ammonia solution is added. White gel precipitate is immediately formed. It is allowed to settle for 24 h. Then it is filtered and washed with water 2-3 times so that clear solution is obtained. The obtained mixture is dried for 24 h at 70°C. Dried powder is crushed and heated at 600°C for 4 h. Fig.1 shows TEM picture of pure SnO₂. Tin oxide particles are of spherical nature to form multiparticle aggregates, presumably because of weak antiparticle interactions. The grain size of SnO₂ is found to be from 10 to 20 nm.

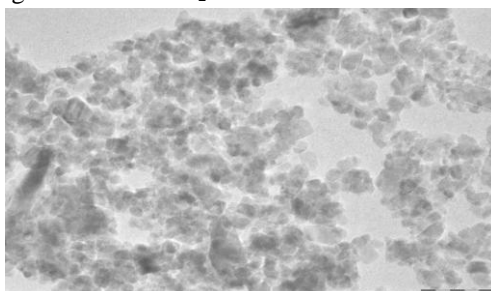


Fig. 1

B. Sample preparation

The PPy-PEO-SnO₂ composites were prepared by chemical oxidative polymerization by using FeCl₃ as oxidant in methanol solvent. Firstly, PEO dissolved in methanol. This solution was kept in test tube for 12 h. A suitable amount of oxidizing agent (0.2M) was added to the solution. PEO- FeCl₃ solution was homogenized by constant magnetic bar stirring. Further to study the effect of dopant SnO₂, Pyrrole (40 wt %), PEO (50 wt %) and FeCl₃ concentrations were kept constant and weight % of SnO₂ was changed. Films of different weight % of SnO₂ were synthesized viz. 4, 5, 6, 7 wt%. When monomer pyrrole was added dropwise to the homogeneous solution of PEO, FeCl₃ and SnO₂, under constant stirring for 3-4 h, a dark black homogeneous solution was obtained which was then poured on chemically cleaned polypropylene plane dish to prepare the films of composite. After evaporation of solvent the thin films were formed.

C. SEM characterization

Surface morphological study of composite films was done by using Field Emission Gun - Scanning Electron Microscope (JSM-7600 F) operating with an accelerating voltage of 0.1 to 30 KV at SAIF, IIT Bombay, Powai, Mumbai.

D. Transference number measurement

The transference number gives quantitative information of the extent of ionic and electronic contribution to the total conductivity. The ionic/electronic transference number can be defined as:

$$t_{ion} = \sigma_{ion} / \sigma_T = I_{ion} / I_T \quad (1)$$

$$t_e = \sigma_e / \sigma_T = I_e / I_T \quad (2)$$

Where, σ_{ion} / σ_e and I_{ion} / I_e are the conductivity and current contribution due to ions / electrons respectively.

The ionic / electronic transference number was measured by using dc polarization technique [24] in which a PPy-PEO-SnO₂ film is sandwiched between blocking (Graphite) and non-blocking (Silver) electrodes. A constant dc voltage (1V) is applied across the sample and the resultant current (pA) was recorded as a function of time.

E. DC conductivity measurement

The dc electrical conductivity of the samples was measured by two-probe method, in which resistance of the sample was measured. A dc regulated power supply and a pico ammeter with resolution of 1 pA is used for measurement. The composite film was sandwiched between two conducting electrodes and then placed in a muffle furnace. Temperature of the furnace was increased from room temperature 303 to 338 K.

III. RESULTS AND DISCUSSION

A. SEM analysis

The surface morphology of the composite films of 4, 5 and 6 wt % of SnO₂ was analyzed by SEM and the pictures are shown in figs. 2(a), 2(b) and 2(c) respectively. SEM images show the presence of round shaped crystals. These crystals are connected to each other. The average crystallite size is found to be of the order of 10 to 20 nm. Nanocrystallites of SnO₂ are seems to be deposited on the circular crystals of polypyrrole. Alongwith this hair cracks and rough morphology is seen. The smaller and bigger voids are also seen randomly.

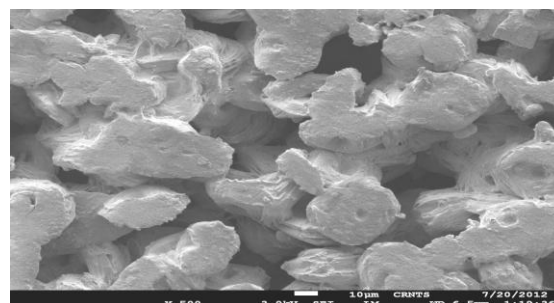


Fig. 2(a)

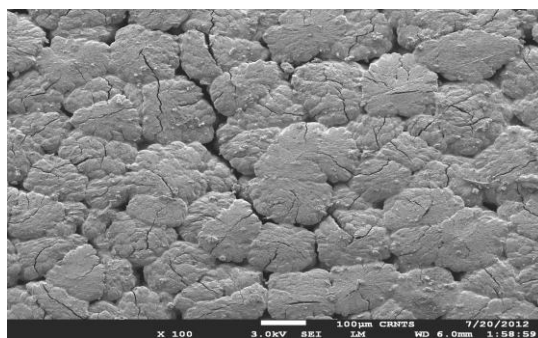


Fig. 2(b)

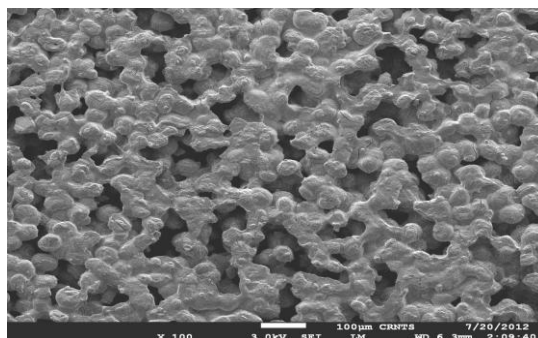


Fig. 2(c)

B. Ionic transference number

The current versus time plots of the SnO₂ doped PPy-PEO films with different wt % of SnO₂ are obtained which exhibit typical behaviour of ionic charge transport. The sample plots are shown in Figs. 3(a to c).

As seen from figs. the total current becomes nearly constant at some non-zero value after some time. The final residual current is mainly due to electrons/holes. The ionic and electronic transference numbers were calculated separately from the polarization current versus time plot using the Eqs. (1) and (2). The values of transference number are found to be in the range of 0.67-0.94. Thus values of transference number suggest that, ionic conduction becomes predominant at 5 wt% of SnO₂.

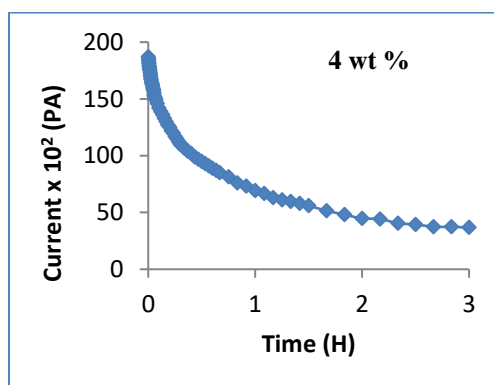


Fig.3(a)

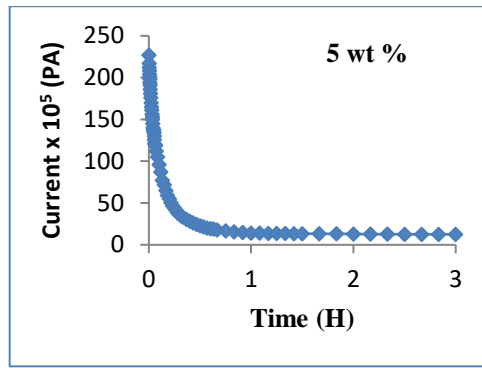


Fig.3(b)

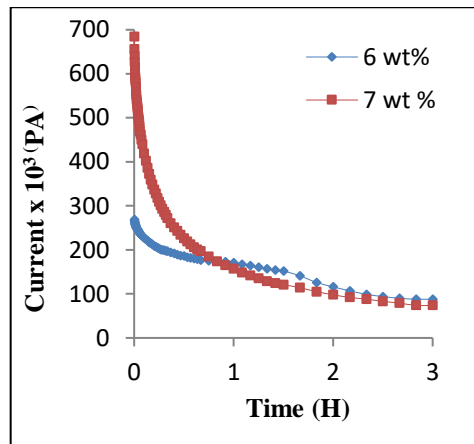


Fig.3(c)

C. DC conductivity

The variation of $\log \sigma_{dc}$ with wt % of SnO₂ for PPy-PEO-SnO₂ composite films at temperature 318 K is shown in Fig. 4.

Initially the conductivity increases reaches to 2.14×10^{-7} S/cm and then decreases with SnO₂ concentration. In case of PPy composites [25-29] percolation behavior was reported even for low concentration of PPy. The increase in conductivity of composite [26, 27] can be explained on the basis of formation of conducting PPy network due to well-dispersed polypyrrole in structure of composites. While decrease in conductivity has been attributed to the over oxidative reaction and formation of poor conducting PPy with low bulky density.

However, in case of PPy-thermoplastic polyurethane (PPy-TPU) composites [30] it has been reported that PPy in the composites facilitate the ionic transport. Yamaski *et al* [31] have also been reported that addition of polyaniline to polyethylene oxide/ LiClO₄ system increases the ionic conductivity.

The temperature dependence of conductivity for different wt % of SnO₂ is shown in fig. 5.

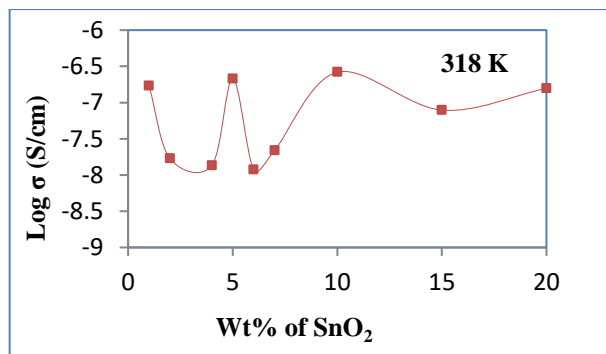


Fig.4: Variation of conductivity with wt % of SnO₂ at 318 K.

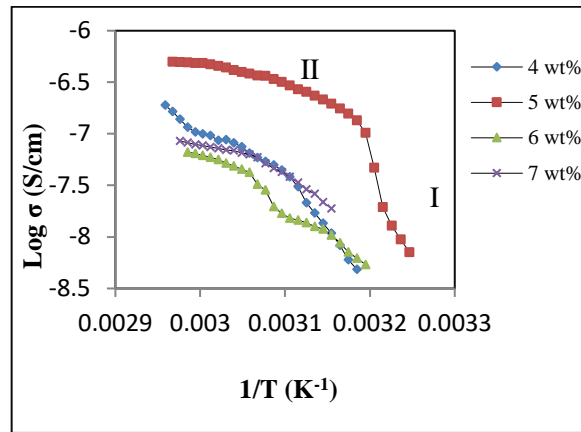


Fig. 5: Temperature dependence of conductivity for different wt % of SnO2

The conductivity versus temperature curves of the samples shows increase in conductivity. Initially the rate of increase of conductivity is slow and after a certain temperature the rise is fast. Thus it leads to two activation regions (I and II as shown in fig 5) giving two different activation energies. Above curves shows the curvature type behavior below a certain temperature T_c , called knee temperature, and above which the curves are nearly linear in nature. The non-linearity in Arrhenius plot indicates the ionic transport facilitates by the segmental motion of polymer chains. Thus Vogel-Tamman-Fulcher (VTF) [32-34] equation may more effectively represent the results.

$$\sigma = \frac{A}{T^{1/2}} \exp\left(\frac{-B}{k(T-T_0)}\right) \quad (3)$$

Where ' T ' is the absolute temperature; ' A ', ' B ' and ' T_0 ' are the fitting constants and ' k ' is Boltzmann constant. ' A ' is the pre-exponential factor, which is related to the number of charge carriers. ' B ' is the pseudo activation energy related to activation energy of the ion transport. It is related to critical volume for displacement in free volume model [35] and to the energy barrier for rotational motion of polymer segment in configuration entropy model [36]. ' T_0 ' is the critical (ideal glass transition) temperature. Usually it is 30-50 K below ' T_g '. It is the temperature at which configuration entropy or free volume disappears.

In high temperature region the curves no longer fits the VTF equation. The cross over from VTF to Arrhenius is clearly visible in the high temperature region. This type of cross over, in conductivity behavior, generally observed in polymer electrolyte systems [37-39]. The Arrhenius equation:

$$\sigma = \sigma_0 \exp\left(\frac{-E_a}{kT}\right) \quad (4)$$

fits the region above T_c , where ' E_a ' is the activation energy and ' σ_0 ' is the pre-exponential factor.

The VTF fits plot for SnO₂ doped PPy-PEO composite films are shown in fig. 6.

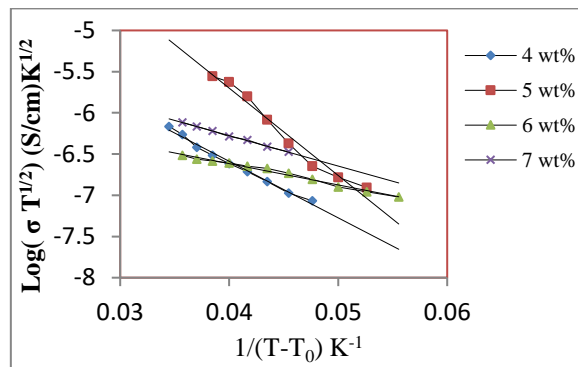


Fig.6: VTF plots for different wt % of SnO2

As seen from fig. 5 it is observed that VTF law is not valid for entire range of temperatures used for experiment. But above a certain temperature T_c , which is different for different samples, the rate of increase of conductivity with temperature slows down. As reported in block copolymer electrolytes based on poly (methyl methacrylate) and poly (oligo oxyethylene methacrylate) (PMMA-b-POEM) [40], the cross over from VTF to Arrhenius observed. In present study this may be due to some sort of transition in energetic of local ion motion and reduction in effective ion density on undergoing order-disorder transition at temperature T_c . Thus T_c can be linked to order-disorder temperature. Below T_c the curves fits the VTF equation. When the ionic conduction follows the VTF equation, a linear relation between $\ln(\sigma T^{1/2})$ and $1/(T-T_0)$ is expected. Such relationships are explored in fig. 6 for different wt % of SnO₂ composite samples. The correspondence between dependence of pseudoactivation energy 'B' with concentration of SnO₂ (Table 1) is observed. The minimum pseudoactivation energy 'B' (0.0022 eV) is observed for 6 wt % of SnO₂.

The VTF fit parameters are summarized in table 1.

It is evident that the activation energy value 'B' for the sample prepared with 6 wt % of SnO₂, is minimum. The value of value of T_0 increases with increase in concentration of SnO₂

IV. CONCLUSION

The PPy-PEO-SnO₂ composites were prepared by chemical polymerization of pyrrole by different concentration of SnO₂. The surface morphology of polymer composite films were characterized through scanning electron microscopy (SEM). The average crystallite size is found to be of the order of 10 to 20 nm. Due to addition of SnO₂ nanopowder in optimized PPy-PEO, large number of SnO₂ grains are seen deposited on crystals of polypyrrole which leading to high porosity and large effective surface area available for adsorption of gas species. The transference number measurement reveals that the charge transport in the PPy-PEO-SnO₂ films is predominantly due to ions. The temperature dependent conductivity behaviour of the PPy-PEO-SnO₂ composite shows a VTF to Arrhenius crossover. The correspondence between dependence of pseudoactivation energy 'B' with concentration of SnO₂ is observed. The minimum pseudoactivation energy 'B' (0.0022 eV) was observed for 6 wt % of SnO₂.

ACKNOWLEDGMENT

Authors are thankful to Director, Professor and Head of the Physics Department, from Government Vidarbha Institute of Science and Humanities, Amravati for providing laboratory facilities.

Table 1: Arrhenius and VTF equation fitting parameters for different SnO₂ wt%.

Sr No	SnO ₂ wt %	Activation Energy Ea (eV) (Region II)	Pre-exponential factor σ_0 (S/cm) (Region II)	Pseudo Activation energy B (eV) (Region I)	Pre-exponential factor σ_0 (S/cm) (Region I)	Knee temperature T_c (K)	Ideal glass transition temperature T_0 K
1	4	0.35	2.22×10^5	0.0059	1.43×10^{-4}	323	293
2	5	0.13	2.21×10^{-2}	0.0108	3.45×10^{-2}	319	289
3	6	0.24	0.98×10^1	0.0022	2.62×10^{-6}	325	295
4	7	0.14	3.19×10^{-3}	0.0031	1.58×10^{-5}	326	296

REFERENCES

- [1] Jude, O.I. and Kirill L. (2002) Electrochemical synthesis of polypyrrole / polyimide conducting composite using a polyamic acid precursor. *J. Euro. Polym*, **38**, 1547-1550.
- [2] Migahed, M.D., Fahmy, T., Ishra, M. and Barakat, A. (2004) Preparation, characterization, and electrical conductivity of polypyrrole composite films. *J. Polym*, **23**, 361-365.
- [3] Kiani, M.S. and Mitchell, G.R. (1992) Structure Property Relationship in Electrically Conducting Co-polymers Formed From Pyrrole and N-Methyl Pyrrole. *Synth Met*, **46**, 293-306.

- [4] Wernet, W., Monkenbusch, M. and Wegner, G. (1984) A New Series of Conducting Polymers with Layered structure :Polypyrrole n-alkylsulfates and n-alkylsulfonates. *Macromol Chem Rapid Commun* **5**, 157-164.
- [5] Cheung, K.M., Bloor, D. and Stevens, G.C. (1990) The influence of unusual counterions on the electrochemistry and physical properties of polypyrrole. *J. Mat.Sci* **25**, 3814-3837.
- [6] Buckley, L.J., Royland, D.K. and Wnek, G.E. (1987) Influence the Dopant Ion and Synthesis Variables of Mechanical Properties of Polypyrrole Film. *J Polym Sci Part B Polym Phys* **25**, 2179-2188.
- [7] Takeoka, S., Hara, T., Fukushima, K., Yamamoto, K. and Tsuchida, E. (1998) Antioxidative dopant for thermalresisting polypyrrole and its mechanism. *Bull Chem Soc Jpn* **71** (6), 1471-1476.
- [8] Bunting, R.K., Swarat, K. and Yan, D. (1997) Synthesis and characterization of a Conducting polymer: An electrochemical experiment for general chemistry. *J Chem Edu* **74** 4, 421.
- [9] Warren, L.F. and Anderson, D.P. (1987) Polypyrrole films from aqueous electrolytes: The effect of anions upon order. *J Electrochem Soc* **134** (1), 101.
- [10] Niwa, O. and Tamamura, T. (1984) Electrochemical polymerization of pyrrole on polymer-coated electrodes. *J Chem Soc Chem Commun* **470**, 817-818.
- [11] Otero, T.F. and Sansinena, J.M. (1996) Influence of synthesis conditions on polypyrrole-poly(styrenesulphonate) composite electroactivity. *J Electroanal Chem* **412**, 109-116.
- [12] Yan, F., Xue, G., Chen, J. and Lu, Y. (2001) Preparation of a conducting polymer / ferromagne composite film by anodic-oxidation method. *Snth Met* **123** (1), 17-20.
- [13] V. Mano, M.I. Felisberti, T. Malencio, Marco A. De. Paoli, *Polymer* **37** (1996) 5165.
- [14] R. Gangopadhyay, A. Das, *J. Appl. Phys.* **87** (2000) 2363.
- [15] M. Reghu, C.O. Yoon, C. Yang, D. Moses, A.J. Heeger, Y. Cao, *Macromolecules* **26** (1993) 7245.
- [16] V. Jousseume, M. Morsli, A. Bonnet, D. Tesson, S. Lefrant, *J. Polym. Sci. Polym. Chem. Ed.* **67** (1998) 1205.
- [17] E. Benseddik, A. Bonnet, S. Lefrant, *J. Polym. Sci. Polym. Chem. Ed.* **68** (1998) 709.
- [18] Komilla Suri, S. Annapoorni, R.P. Tandon, *Bull. Mater. Sci.* **24** (2001) 563.
- [19] Eli Ruckenstein, Shiyong Yang, *Polymer* **34** (1993) 4655.
- [20] H. Vogel, *Phys. Z.* **22** (1922) 645.
- [21] G.S. Fulcher, *J. Am. Chem. Soc.* **8** (1925) 339.
- [22] G. Tamman, W. Hesse, *Z. Anorg. Allg. Chem.* **156** (1926) 245.
- [23] S.K. Dhawan, D.C. Trivedi, *Bull. Mater. Sci.* **16** (1993) 371.
- [24] Wagner, J. B. Jr. and Wagner, C. J., (1957) *J. Chem. Phys.*, **26** 1595.
- [25] Eli Ruckenstein, Shiyong Yang, (1993) *Polymer* **34** 4655.
- [26] W. Yin, H. Liu, B. Yin, T. Yan, T. Gu, (1998) *Eur. Polym. J.* **34** 779.
- [27] W. Yin, T. Yan, L.M. Gan, C.H. Chew, H. Liu, L.H. Gan, (1998) *Eur. Polym. J.* **34** 1763.
- [28] T.K. Mandal, B.M. Mandal, (1996) *Synth. Metal* **80** 83.
- [29] M. Chakraborty, D.C. Mukherjee, B.M. Mandal, (1999) *Synth. Metal* **98** 193.
- [30] T.C. Wen, S.L. Hung, M. Digar, (2001) *Synth. Metal* **118** 11.
- [31] S. Yamasaki, T. Koga, H. Ohura, (1996) *J. Mater. Sci.* **15** 225.
- [32] H. Vogel, (1922) *Phys. Z.* **22** 645.
- [33] G.S. Fulcher, (1925) *J. Am. Chem. Soc.* **8** 339.
- [34] G. Tamman, W. Hesse, (1926) *Z. Anorg. Allg. Chem.* **156** 245.
- [35] M.H. Cohen, D. Turnbull, (1964) *J. Chem. Phys.* **31**.
- [36] G. Adam, J.H. Gibbs, (1964) *J. Chem. Phys.* **31**
- [37] T.H. Joykumar Sing, S.V. Bhat, (2003) *Bull. Mater. Sci.* **26** 707.
- [38] D. Bamford, A. Reiche, G. Dlubek, F. Alloin, J.Y. Sanchez, M.A. Alam, (2003) *J. Chem. Phys.* **118** 9420.
- [39] D. Bamford, A. Reiche, M.A. Alam, W. Meyer, P. Galvosas, F. Rittig, (2003) *J. Chem. Phys.* **115** 7260.
- [40] A.V. Ruzette, P.P. Soo, D.R. Sadoway, A.M. Mayes, (2001) *J. Electrochem. Soc.* **148** 537.

1*P.P. Raut,
 1G.T. Lamdhade,
 2S. D. Charpe, 3P.D.Shirbhate,
 4D. P. Deshmukh,
 5V.U. Rahangdale

PVC-PMMA Electrolyte System Tailoring with Different Dopants: A Comprehensive Study



Abstract: - Polyvinyl chloride (PVC) and polymethyl methacrylate (PMMA) are types of plastic materials widely used in various scientific and technological fields. In this study, we prepared thin films of PVC and PMMA by doping them with oxalic acid (OA) and cinnamic acid (CA) adopting the isothermal evaporation method. The thickness of the thin films was calculated using a digital micro-meter screw gauge. We characterized the thin films using analytical techniques including Fourier transform infrared (FT-IR) spectroscopy, scanning electron microscopy (SEM), and X-ray diffraction (XRD). FT-IR spectrum analysis confirmed the successful formation of homogeneous 1:1 (PVC: PMMA) thin films by observing characteristic peaks resulting from the addition of oxalic acid and cinnamic acid. XRD analysis revealed that all thin films had an amorphous nature. The scanning electron micrograph images of the samples supported the results obtained from FT-IR and XRD analyses.

Keywords: PVC-PMMA Electrolyte, (C₂H₂O₄), C₉H₈O₂, Analytical Techniques

I. INTRODUCTION

Polymers and their mixtures are a diverse class of materials that have wide applications in various industries [1–5]. The way these materials are synthesized has a major influence on their molecular structure and, consequently, their properties. Understanding these synthesis methods is crucial to adapting polymers to specific requirements. In addition, the electrical conductivity and dielectric properties of polymers are of the utmost importance, especially in areas such as electronics and energy storage. The ability to modify these properties through doping, the integration of nanomaterials, and the design of structures opens up opportunities for innovation.

Polymer electrolytes, a type of plastic material, have garnered significant attention due to their versatile uses in different scientific and technological sectors. The unique characteristics and versatile nature of polymer electrolytes make them a valuable material for numerous applications, driving ongoing research and technological advancements in this area. Hence, a polymer electrolyte, defined as a membrane made of salts dissolved polymer matrix which having in a high-molecular-weight, is known as a polymer electrolyte [6]. These ionic conduction-friendly, solid, solvent-free systems find extensive use in a range of electrochemical tools, such as lithium-ion batteries and solid-state and rechargeable batteries.

Fenton *et al.* originally introduced the notion of preparing polymer electrolytes in 1973 [7], but S. Rao *et al.* [8] realized and understood their technological relevance a few years later. The first polyelectrolyte to be suggested and investigated for solid polymer electrolyte (SPE) Li rechargeable batteries was poly (ethylene oxide) [9, 10]. The majority of solid polymer electrolytes (SPEs) are made either by dispersion in the solid state. Additionally, an effort is made to use covalent bonding or another chemical or physical technique to block the anion in the polymer medium [11].

^{1*} Corresponding author: P.P. Raut, Research Scholar, Department of Physics, Vidya Bharti Mahavidyalaya, Amravati, India

¹Department of Physics, Vidya Bharti Mahavidyalaya, Amravati, India

²Department of Physics, J.D. Patil Sangludkar Mahavidyalaya, Daryapur, Dist. - Amravati, 444803, India

³Department of Physics, Gopikabal Sitaram Gawande College, Umarched Dist. Yavatmal, 445206, India

⁴Department of Physics, Lt. R. B. Arts, Commerce and Smt. S. R. B. Sci. College, Arni, Dist- Yavatmal-445001, India

⁵Department of Physics, Jagat Arts, Commerce and I.H.P. Science College, Goregaon Dist. Gondia 441801, India

Polymer electrolytes comprise a wide range of substances that are specially designed to fulfill particular needs and uses in electrochemical devices. These electrolytes are generated by complexing low-lattice energy

salts with solvent polymers [12-13]. Chemical and physical methods are the two main types of polymer film production technology. The flexibility is provided by the electrolytes of solid polymers, which can be easily produced as soft films with a thickness of only a few microns. This allows continuous contact with solid electrodes throughout the operation, facilitating the creation and deployment of various electrochemical devices. The preparation of polymer films is the main topic of this research. Many techniques for producing high-quality polymer films have been described in literature and some really good reviews are available [14-16].

The characteristics, compositions, and ion transport methods of these materials differ, giving rise to several types of polymer electrolytes. Typical polymer electrolyte types include [17-18]. Poly(ethylene oxide), Poly(vinyl alcohol), Poly(methyl methacrylate), Poly(caprolactone), Poly(chitosan), Poly(vinyl pyrrolidone), Poly(vinyl chloride), Poly(vinylidene fluoride), and Poly(imide) are a few typical polymers utilized in these electrolytes. These polymers can all be customized for certain uses and have distinctive qualities.

Polymer electrolytes are fundamental components in many fields, including biomedical engineering, energy storage, electrochemical conversion, sensing, and actuation [19-22]. They are essential for tackling societal issues and promoting technological innovation in a variety of sectors due to their special set of properties.

Also, dopants play vital role in changing electrical parameters like electrical conductivities, which includes ac as well as dc, and dielectric constant. Values of these parameters will determine which applications the desired material will be used. In this study, the same polymer electrolyte system has two different types of dopants. If these dopants completely miscible in polymer electrolyte then it will definitely causes electrical parameters of casting thin films [23-25]. Only the idea of dopant miscibility in specific polymer electrolytes will be examined in this thorough investigation.

II. MATERIAL AND EXPERIMENTAL

All chemicals were of AR grade. Polyvinyl chloride (PVC) and Polymethyl methacrylates (PMMA) were supplied by SIGMA –ALDRICH, Co., USA having purity 99.99%. . While, oxalic acid and cinnamic acid by Merck specialties private limited, India and Tetrahydrofuran by E-Merck India Ltd., India is being used as a solvent for mixing process of two base materials PVC and PMMA. . In this work, the isothermal evaporation process was used to cast thin films [26-29].

A. Preparation of Thin Films

1) Preparation of a 1:1 (PVC-PMMA) Base Polyblend Thin Film

In this work, the isothermal evaporation technique has been used due to the rapid and easy mixing process. The two polymers, PVC and PMMA, have been taken with different weight ratios (i.e. 1:1) as required, and dissolved in the same solvent, tetrahydrofuran (THF). To create a homogeneous solution, the solution was let to stand for three to four days, allowing the polymers to fully dissolve. A glass plate (10 cm x 10 cm) was thoroughly cleaned with water and later with acetone as the substrate. In order to achieve a perfect level (and uniform thickness of the films), a pool of mercury was used in a plastic tray. After being placed onto the glass plate, the solution was given time to evenly spread across the substrate in all directions. The complete assembly was kept at ambient temperature in a dust-free environment. As a result, the solvent in the mixture was left to totally evaporate and turn into dried air. After removing the film from the glass substrate and splitting it into small, appropriate-sized pieces, the surface contaminants were eliminated by acetone rinsing. In this way, the films were prepared with the isothermal evaporation process.

2) Preparation of 1:1 (PVC-PMMA) Polyblend Thin Films Using Dopant Oxalic Acid (OA)

The two polymers PVC and PMMA were taken in weight ratio 1:1, and dopant oxalic acid was taken in doping percentage 5%. All three were dissolved separately in a 10 ml THF solution. After allowing them to completely dissolve, all three solutions were mixed together. A glass plate (10 cm x 10 cm) was cleaned with hot water and then used as a substrate with acetone. To achieve a perfect leveling and uniformity in the thickness of the film, a pool of mercury was used in the plastic box in which the glass plate was placed. After being placed onto the glass plate, the solution was given time to evenly spread across the substrate in all directions. The complete assembly was kept at ambient temperature in a dust-free environment. As a result, the solvent in the mixture was left to totally evaporate and turn into dried air. After removing the film from the glass substrate and splitting it into small, appropriate-sized pieces, the surface contaminants were eliminated by acetone rinsing. In this way, the films were prepared with the isothermal evaporation process.

3) Preparation of 1: 1 (PVC-PMMA) Polyblend Thin Films Using Dopant Cinnamic Acid (CA)

The 5 % of cinnamic acid (dopant) was taken and soluble in the mixture of PVC-PMMA solutions. After attainment homogenous solution, the above mentioned above (2) procedure was repeated to prepare the film using isothermal evaporation technique.

B. Measurements and Analytical Characterizations

The thickness of film is crucial for their structural and electrical properties. Various techniques can be used to measure film thickness. In this study, the thickness of all the samples was calculated using a Digital micrometer provided by Mitutoyo Corporation in Japan. This micrometer has a precision of 0.001 mm and a measurement range of 0 to 25 mm. It can be operated between 50°C and 400°C, with an instrumental error of +2 μm at 20°C. Additionally, it features a digital display with 6 digits and a minus sign for easy and clear readings.

Three samples were chosen for further investigation from a series based on optimization study results. Table 1 contains a list of optimized samples along with their weight percentage, sample codes, and thicknesses.

Table 1 Sample codes and thickness of 1:1 (PVC-PMMA) composite thin films doped with oxalic acid and cinnamic acid

Sr. No	Sample description	Sample code	Thickness
1	1:1 (PVC-PMMA)	S ₁	0.041 mm
2	1:1 (PVC-PMMA) OA 5%	S ₂	0.024 mm
3	1:1 (PVC-PMMA) CA 5%	S ₃	0.073 mm

The films' ultraviolet (UV) absorption spectra were obtained at ambient temperature. FT-IR measurements were conducted using the Bruker Model: Vertex 70, which has a wide wave number range (50 cm^{-1} to 15,000 cm^{-1}). This equipment allows recordings in both transmission and reflection geometries, with a high resolution scale of 0.5 cm^{-1} . The FT-IR spectra of all samples fall within the range of 500-4000 cm^{-1} .

XRD is analytical technique that provides valuable insights into the lattice structure of a material. It provides details on the phases, average grain size, crystallinity, and crystal flaws, among other structural characteristics. In this study, X-Ray Diffraction (XRD) of the samples was performed by the Bruker D8 Advance XRD system, obtained from the UGC-DAE Consortium for Scientific Research, Indore. Scanning electron microscopy was also carried out at the Department of Physics; RTM Nagpur University, by the Philips Model: XL-30. This analysis aimed to examine the surface structure, identify defects and how much miscibility of dopant presents in the samples.

III. RESULTS AND DISCUSSION

A. FT-IR Spectroscopic Analysis

In current study, FTIR Bruker Model: Vertex 70 was use in the transmittance mode from 500 cm^{-1} – 4000 cm^{-1} . To get the FTIR profiles, the final scan was recorded by averaging 100 scans at a resolution of 8.0. The measurements obtained a resolution of 4 cm^{-1} .

In our case, we have studied the FTIR of samples having 1:1 (PVC: PMMA), 1:1 (PVC: PMMA) OA 5%, 1:1 (PVC: PMMA) CA 5%. Fig. 1, 2 and 3 shows FTIR spectra of sample S₁, S₂ and S₃ respectively.

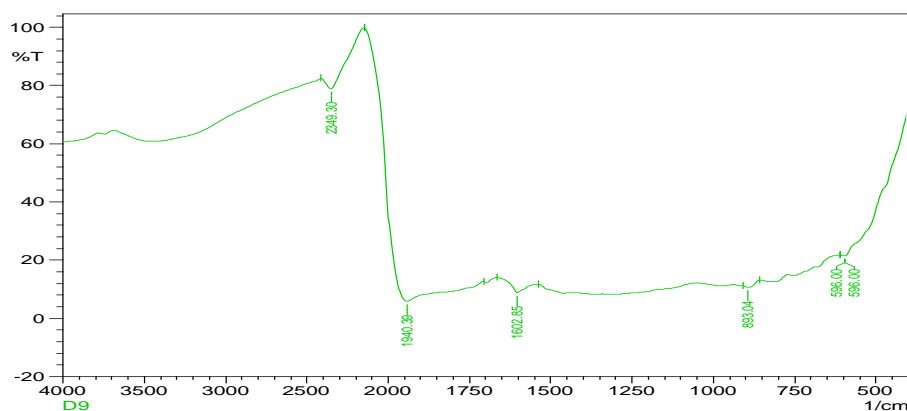


Figure 1 FT-IR of S₁ Sample

Fig. 1 shows 1:1 (PVC: PMMA) spectra. The PMMA carbonyl band has slightly shifted to a lower wave number, according to the spectra. The shift of peak is about 4-6 cm^{-1} within the domain of miscibility of the two polymers. The miscibility of 1:1 (PVC: PMMA) is due to a specific interaction of the hydrogen bonding type between Carbonyl (C = O) of PMMA and hydrogen (from CHCl) group of PVC [30].

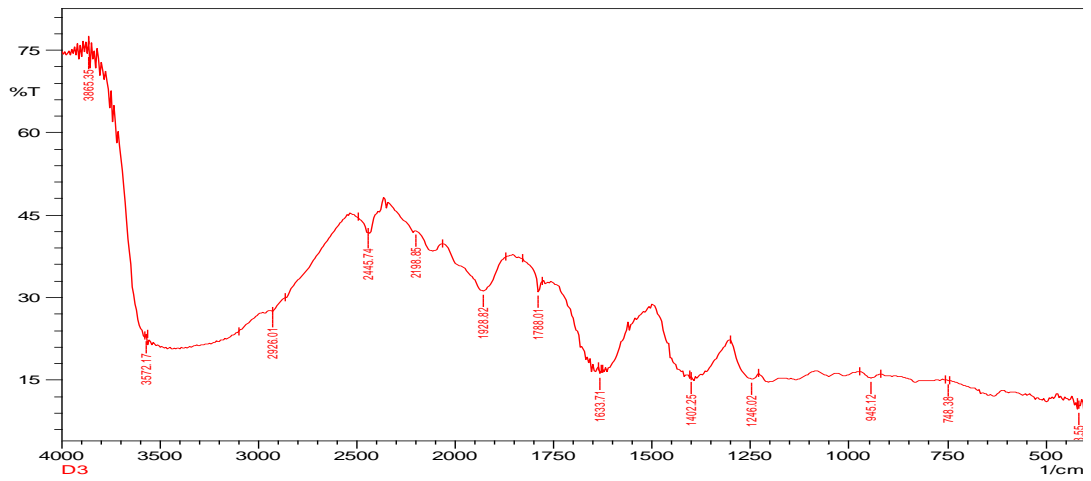


Figure 2 FT-IR of S₂ Sample

Fig. 2 shows 1:1 (PVC: PMMA) OA 5% spectra. The peak location for C = O stretching (i.e. 1732.08 cm⁻¹) in thin film shows minor shifting for the blend within the domain of miscibility.

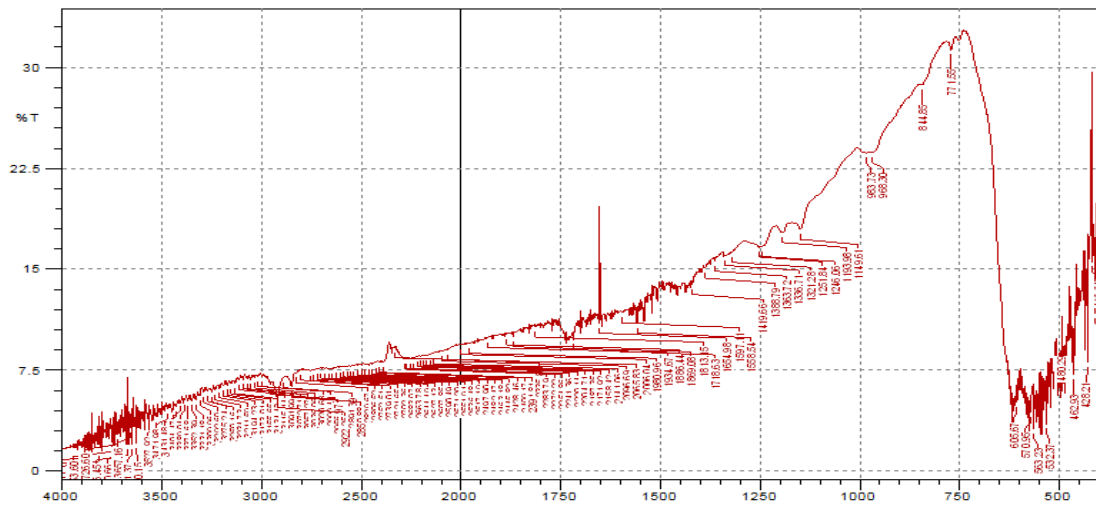


Figure 3 FT-IR of S₃ Sample

While Fig. 3 shows 1:1 (PVC: PMMA) CA 5% spectra. It shows large number peaks at different positions, so it may causes to shift for the blend within the domain of immiscibility [31.32].

B. XRD Analysis

XRD patterns of all samples were taken, and all the sample spectra show a similar nature. So for simplicity only three XRD spectra are shown here. XRD pattern of 1:1 (PVC: PMMA), 1:1 (PVC: PMMA) OA 5%, 1:1 (PVC: PMMA) CA 5% are shown in Fig. 4, 5 and 6 respectively.

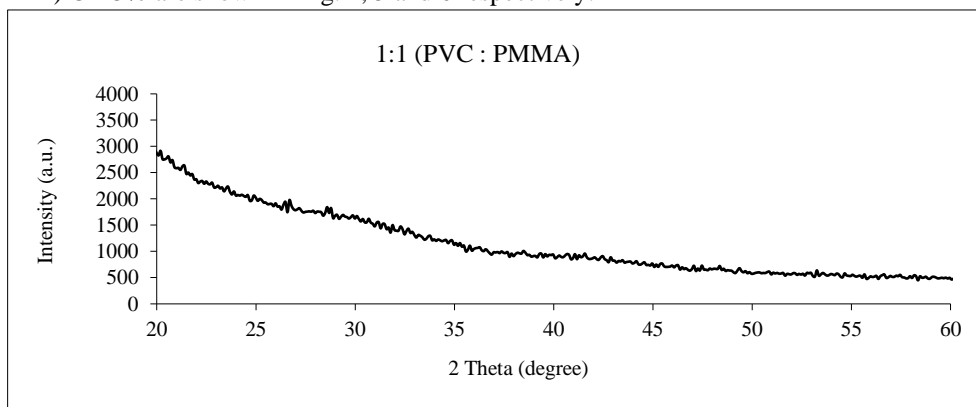
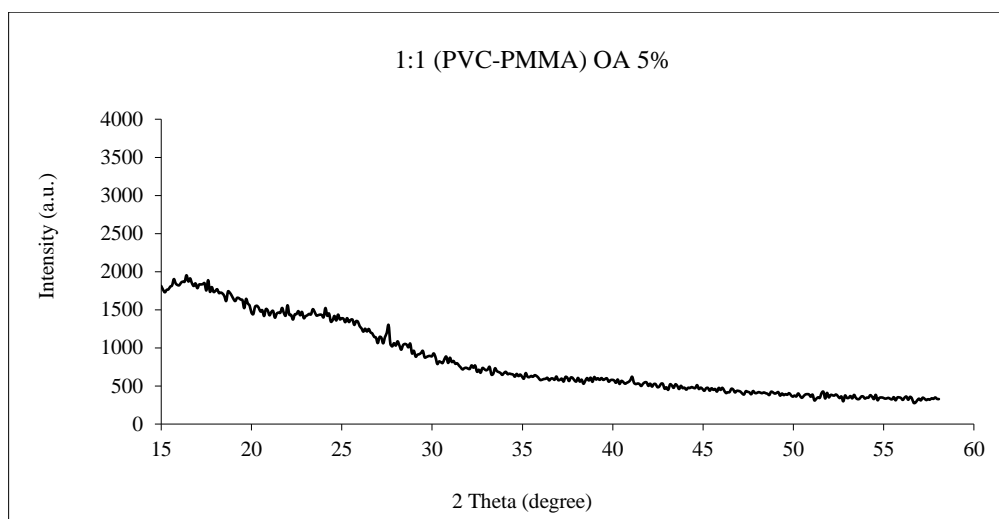
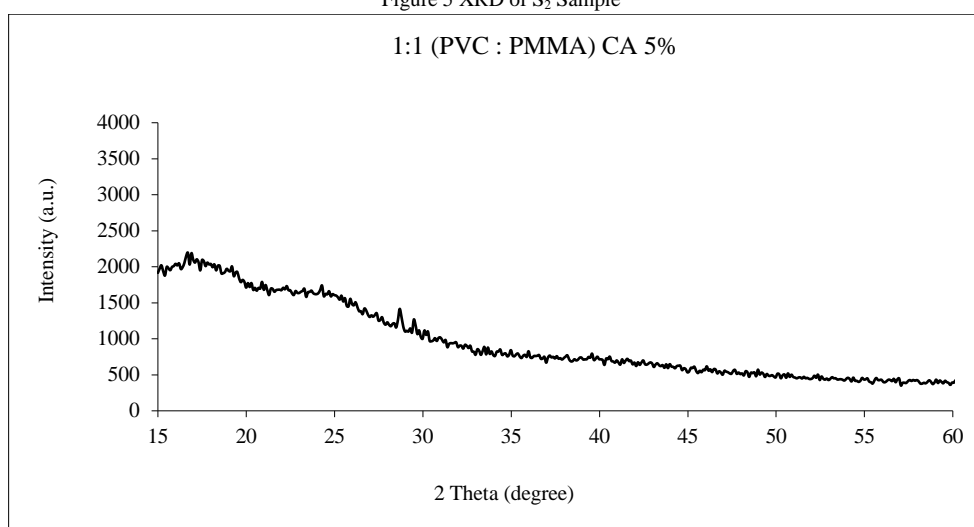


Figure 4 XRD of S₁ Sample

Figure 5 XRD of S₂ SampleFigure 6 XRD of S₃ Sample

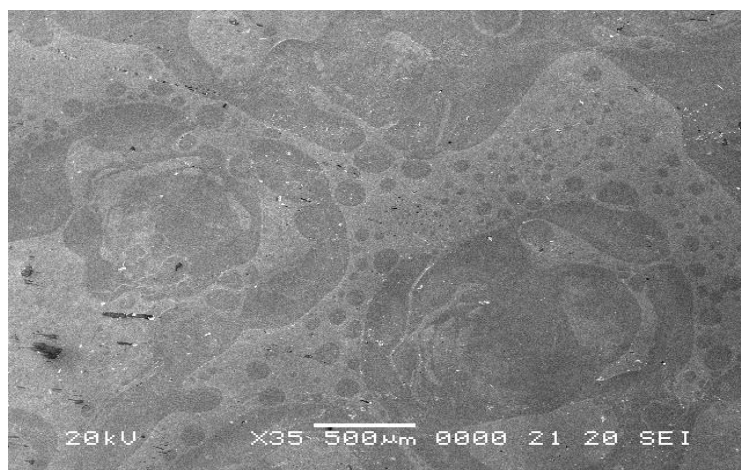
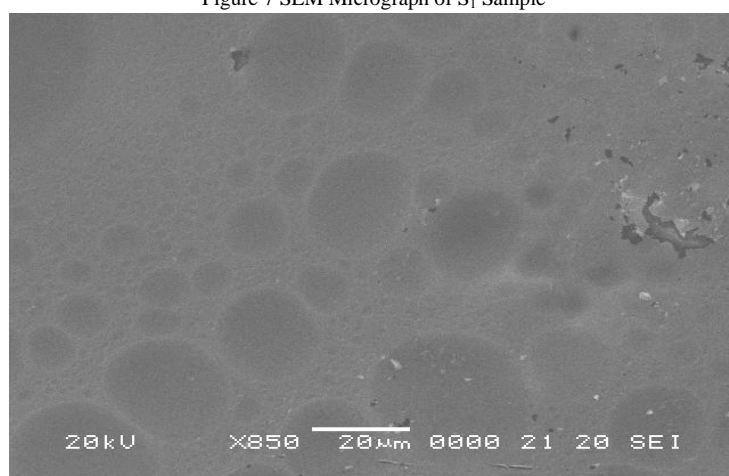
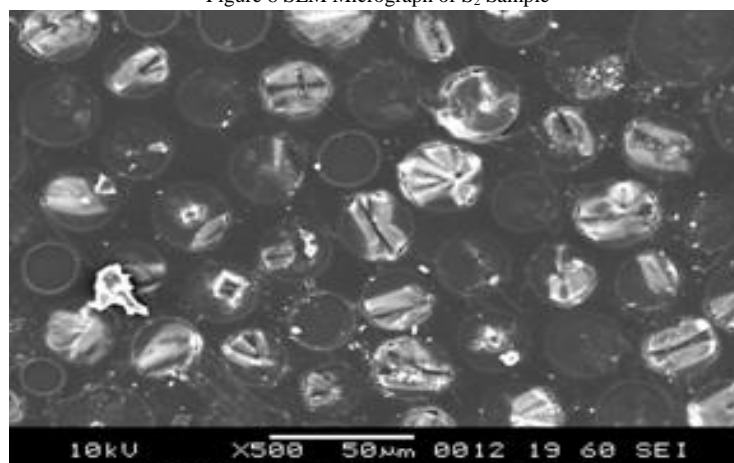
Generally, a polymer consists of both a crystalline region and an amorphous region. The conductivity parameter of the polymeric materials is characterized by their amorphous nature.

From Fig. 4, 5, and 6, it can be observed that the sample exhibit noisy spectra. A peak was observed around 25°, which is attributed to the amorphous nature [33, 34]. Therefore, the X-ray diffractograms of all the samples confirm the amorphous nature, showing large diffraction maxima that decrease at larger diffraction angles. The first main maximum shape indicates the order of the polymer chain packaging. The intensity and shape of the second maximum are related to the order effect within the main chain. The large humps observed in the XRD spectrum indicate the existence of very small crystallites. The absence of any prominent peak in the films demonstrates the mainly amorphous nature of the films. This is in agreement with many reports [35, 36].

C. Scanning Electron Microscopy

Scanning electron micrographs of blended materials were taken across composition for the 1: 1 (PVC: PMMA) blends are shown Fig. 7, 8 and 9. Micrographs show a heterogeneous structure of two base materials i.e. PVC and PMMA, but the size of the dispersed phase changes with composition.

As expected, the pore size maximums for the sample S₁ polymer blend. The tendency of PVC and PMMA to combine is revealed by the change in shape of particles from a spherical shape. As a result, PMMA coordinates with PVC and forms a complexation. In a literature survey, it was found that a higher pore size leads to less phase separation and forms a more homogeneous polymer electrolyte system [37, 38].

Figure 7 SEM Micrograph of S₁ SampleFigure 8 SEM Micrograph of S₂ SampleFigure 9 SEM Micrograph of S₃ Sample

Additionally, the morphology of the blends shows a phase-separated region, as shown in Fig. 7. Therefore, at the same concentration of PVC and PMMA, the phase split-up ultimately leads to the miscibility of the blend.

Fig. 8 and 9 clearly show that the 1:1 (PVC: PMMA) blend contains some impurities compared to Fig. 7. From a comparative study of Fig. 8 and 9, it is also observed that the dopant oxalic acid is more miscible as compared to cinnamic acid in 1:1 (PVC:PMMA) solution. Therefore, it can be concluded that the 1:1 (PVC: PMMA) blend with 5% oxalic acid forms a more homogeneous mixture, leading to the formation of a homogeneous thin film of PVC: PMMA with oxalic acid as a dopant. On the other hand, in the case of the 1:1 (PVC: PMMA) blend with 5% cinnamic acid, a homogeneous mixture was not formed, resulting in a thin film that was not homogeneous. This is because the thin film of the 1:1 (PVC: PMMA) blend with 5% cinnamic acid still shows some crystal particles of cinnamic acid, indicating that cinnamic acid was not completely miscible, i.e., immiscible with the 1:1 (PVC: PMMA) solution. This can also be explained by the fact that immiscible mixtures show several glass transition temperature areas, whereas miscible blends only show one [39].

IV. CONCLUSIONS

It was found that 1:1 (PVC: PMMA) CA 5% show maximum thickness among other samples. In short, in given study successfully casted the composites thin films of 1:1 (PVC: PMMA) with dopant oxalic acid (OA) and cinnamic acid (CA). The FT-IR spectrum study agrees us to conclude that successful formation of 1:1 (PVC: PMMA) homogenous thin films with OA and CA as dopant and characteristic peaks shows with addition of oxalic acid and cinnamic acid. XRD analysis shows amorphous nature all thin films. SEM micrographs of samples attribute FTIR and XRD's results. Also, the thin film of the 1:1 (PVC: PMMA) blend with 5% cinnamic acid still shows some crystal particles of cinnamic acid, indicating that cinnamic acid was not completely miscible, i.e., immiscible with the 1:1 (PVC: PMMA) solution. This can also be explained by the fact that immiscible mixes show several glass transition temperature areas, whereas miscible blends only show one [39]. As miscibility of dopant in polymer electrolyte system increase which cause to change in electrical parameters like electrical conductivities (AC and DC) and dielectric constant [40, 41].

REFERENCES

- [1] Chao, S., & Wrighton, M. S. (1987). Characterization of a solid-state polyaniline-based transistor: water vapor dependent characteristics of a device employing a poly vinyl alcohol/phosphoric acid solid-state electrolyte. *Journal of the American Chemical Society*, 109(22), 6627-6631.
<https://doi.org/10.1021/ja00256a011>
- [2] Gray, F. M. (1991). *Solid polymer electrolytes: fundamentals and technological applications*. Wiley-VCH, Weinheim.
- [3] Burley, S. K., Bhikadiya, C., Bi, C., Bittrich, S., Chen, L., Crichlow, G. V., & Zhuravleva, M. (2021). RCSB Protein Data Bank: powerful new tools for exploring 3D structures of biological macromolecules for basic and applied research and education in fundamental biology, biomedicine, biotechnology, bioengineering and energy sciences. *Nucleic acids research*, 49(D1), D437-D451.
<https://doi.org/10.1093/nar/gkaa1038>
- [4] Patel, A., Arik, M., & Sarkar, A. (2024). An Undergraduate Laboratory Module Integrating Organic Chemistry and Polymer Science. *Journal of chemical education*.
<https://doi.org/10.1021/acs.jchemed.3c01194>
- [5] Burford, R. (2019, January). Polymers: a historical perspective. In *Journal and Proceedings of the Royal Society of New South Wales* (Vol. 152, No. 473/474, pp. 242-250).
- [6] Ngai, K. S., Ramesh, S., Ramesh, K., & Juan, J. C. (2016). A review of polymer electrolytes: fundamental, approaches and applications. *Ionics*, 22, 1259-1279.
<https://doi.org/10.1007/s11581-016-1756-4>
- [7] Fenton, D. (1973). Complex of alkali metal ions with poly (ethylene oxide). *polymer*, 14, 589.
- [8] Rao, S. S., Rao, K. S., Shareefuddin, M., Rao, U. S., & Chandra, S. (1994). Ionic conductivity and battery characteristic studies on PEO⁺ AgNO₃ polymer electrolyte. *Solid state ionics*, 67(3-4), 331-334.
- [9] Xia, Y., Fujieda, T., Tatsumi, K., Prosini, P. P., & Sakai, T. (2001). Thermal and electrochemical stability of cathode materials in solid polymer electrolyte. *Journal of Power Sources*, 92(1-2), 234-243.
[https://doi.org/10.1016/S0378-7753\(00\)00533-4](https://doi.org/10.1016/S0378-7753(00)00533-4)
- [10] Meabe, L., Huynh, T. V., Lago, N., Sardon, H., Li, C., O'Dell, L. A., & Mecerreyes, D. (2018). Poly (ethylene oxide carbonates) solid polymer electrolytes for lithium batteries. *Electrochimica Acta*, 264, 367-375.
<https://doi.org/10.1016/j.electacta.2018.01.101>
- [11] Huang, S., Kong, X., Xiong, Y., Zhang, X., Chen, H., Jiang, W., & Ren, C. (2020). An overview of dynamic covalent bonds in polymer material and their applications. *European Polymer Journal*, 141, 110094.
<https://doi.org/10.1016/j.eurpolymj.2020.110094>
- [12] Armand, M. B., MacCallum, J. R., & Vincent, C. A. (1987). *Polymer electrolyte reviews*. by MacCallum JR and Vincent CA Elsevier, London.
- [13] Mikitaev, A. K., Ligidov, M. K., & Zaikov, G. E. (2006). *Polymers, polymer blends, polymer composites and filled polymers: Synthesis, properties and applications*. Nova Publishers.
- [14] Markovic, G., & Visakh, P. M. (2017). *Polymer blends: State of art. Recent Developments in Polymer Macro, Micro and Nano Blends*, 1-15.
<https://doi.org/10.1016/B978-0-08-100408-1.00001-7>
- [15] Utracki, L. A., & Wilkie, C. A. (Eds.). (2002). *Polymer blends handbook* (Vol. 1, p. 2). Dordrecht: Kluwer academic publishers.
- [16] Dalhat, M. A., & Al-Adham, K. (2023). Review on laboratory preparation processes of polymer modified asphalt binder. *Journal of Traffic and Transportation Engineering (English Edition)*.
<https://doi.org/10.1016/j.jtte.2023.01.002>
- [17] Chae, W., Kim, B., Ryoo, W. S., & Earmme, T. (2023). A brief review of gel polymer electrolytes using in situ polymerization for lithium-ion polymer batteries. *Polymers*, 15(4), 803.

- <https://doi.org/10.3390/polym15040803>
- [18] Hallinan Jr, D. T., & Balsara, N. P. (2013). Polymer electrolytes. *Annual review of materials research*, 43, 503-525.
<https://doi.org/10.1146/annurev-matsci-071312-121705>
- [19] Sequeira, C., & Santos, D. (Eds.). (2010). *Polymer electrolytes: fundamentals and applications*. Elsevier.
- [20] Smitha, B., Sridhar, S., & Khan, A. A. (2005). Solid polymer electrolyte membranes for fuel cell applications—a review. *Journal of membrane science*, 259(1-2), 10-26.
<https://doi.org/10.1016/j.memsci.2005.01.035>
- [21] Di Noto, V., Lavina, S., Giffin, G. A., Negro, E., & Scrosati, B. (2011). Polymer electrolytes: Present, past and future. *Electrochimica Acta*, 57, 4-13.
<https://doi.org/10.1146/annurev-matsci-071312-121705>
- [22] Li, S., Li, L., Yang, H., Zhao, Y., & Shan, Y. (2024). A review of composite polymer electrolytes for solid-state lithium-sulfur batteries: Synthesis methods, optimal design, and critical challenges. *Chemical Engineering Journal*, 149433.
<https://doi.org/10.1016/j.cej.2024.149433>
- [23] Bhadra, J., Madi, N. K., Al-Thani, N. J., & Al-Maadeed, M. A. (2014). Polyaniline/polyvinyl alcohol blends: Effect of sulfonic acid dopants on microstructural, optical, thermal and electrical properties. *Synthetic metals*, 191, 126-134.
<https://doi.org/10.1016/j.synthmet.2014.03.003>
- [24] Basha, S. S., Kumar, K. V., Sundari, G. S., & Rao, M. C. (2018). Structural and electrical properties of grapheme oxide-doped PVA/PVP blend nanocomposite polymer films. *Advances in materials Science and Engineering*, 2018, 1-11.
<https://doi.org/10.1155/2018/4372365>
- [25] Machado, J. M., Schlenoff, J. B., & Karasz, F. E. (1989). Morphology, doping, and electrical properties of poly (p-phenylenevinylene)/poly (ethylene oxide) blends. *Macromolecules*, 22(4), 1964-1973.
<https://doi.org/10.1021/ma00194a074>
- [26] Charpe, S. D., Agrawal, R. M., & Shirbhate, P. D. Dielectric Constant Properties of UV-irradiated Pure and Polyblends Polystyrene-Polyvinyl acetate Thin Films.
<https://doi.org/10.5281/zenodo.6406594>
- [27] Chang, C. C., Pai, C. L., Chen, W. C., & Jenekhe, S. A. (2005). Spin coating of conjugated polymers for electronic and optoelectronic applications. *Thin solid films*, 479(1-2), 254-260.
<https://doi.org/10.1016/j.tsf.2004.12.013>
- [28] Dhokne, R. J., Sangawar, V. S., Chikhalikar, P. S., Thool, V. S., Ubale, A. U., & Junghare, A. R. (2008). Structural characterization and electrical conductivity of naphthalene doped polyblend films of polystyrene (PS) and polymethyl methacrylate (PMMA). *Indian Journal of Physics*, 82, 1309-1318.
- [29] Raut, P. P., Lamdhade, G. T., Raghuvanshi, F. C., Raulkar, K. B., Shripathi, T., & Ganesan, V. (2019). Investigations of Polymer Blends: Variation of Conductivity and Dielectric Constant Versus Frequency.
- [30] Subban, R. H. Y., & Arof, A. K. (2004). Plasticiser interactions with polymer and salt in PVC–LiCF₃SO₃–DMF electrolytes. *European Polymer Journal*, 40(8), 1841-1847.
<https://doi.org/10.1016/j.eurpolymj.2004.03.026>
- [31] Sudharsan Reddy, K., Prabhakar, M. N., Kumara Babu, P., Venkatesulu, G., Rao, K., Sajan, U., & Subha, M. C. S. (2012). Miscibility studies of hydroxypropyl cellulose/poly (ethylene glycol) in dilute solutions and solid state. *International journal of carbohydrate chemistry*, 2012.
<https://doi.org/10.1155/2012/906389>
- [32] Cyriac, V., Sudhakar, Y. N., Mishra, K., Rojudi, Z. E., Murari, M. S., & Noor, I. M. (2024). Effect of dopant on ion-dynamics of sodium ion-based flexible polyblend electrolyte for electrochemical device application. *Materials Research Bulletin*, 169, 112498.
<https://doi.org/10.1016/j.materresbull.2023.112498>
- [33] Zakaria, N. A., Isa, M. I. N., Mohamed, N. S., & Subban, R. H. Y. (2012). Characterization of polyvinyl chloride/polyethyl methacrylate polymer blend for use as polymer host in polymer electrolytes. *Journal of Applied Polymer Science*, 126(S2), E419-E424.
<https://doi.org/10.1002/app.36940>
- [34] Deshmukh, S. H., Burghate, D. K., Akhare, V. P., Deogaonkar, V. S., Deshmukh, P. T., & Deshmukh, M. S. (2007). Electrical conductivity of polyaniline doped PVC-PMMA polymer blends. *Bulletin of Materials Science*, 30(1), 51-56.
<https://doi.org/10.1007/s12034-007-0009-6>
- [35] Sangawar, V. S., & MOHARIL, N. A. (2012). Study of electrical, thermal and optical behavior of polypyrrole filled PVC: PMMA thin film thermoelectrets. *Chemical Science Transactions*, 1(2), 447-455.
- [36] Heiba, Z. K., El-naggar, A. M., Kamal, A. M., Aldhafiri, A. M., & Mohamed, M. B. (2024). Influence of polyaniline on the structural, linear/nonlinear optical, and dielectric characteristics of poly (vinyl chloride/poly(ethyleneoxide) blends. *Journal of Macromolecular Science, Part B*, 63(5), 343-360.
<https://doi.org/10.1080/00222348.2023.2270269>
- [37] Abbasi, M. R., Abzan, M. S., Alavi, A., & Ahmadi, S. (2024). PVC/acrylic blends, IPNs, and gels. In *Poly (vinyl chloride)-Based Blends, IPNs, and Gels* (pp. 101-153). Elsevier.
<https://doi.org/10.1016/B978-0-323-99474-3.00006-9>

- [38] Flores-Guía, T. E., Caldera-Villalobos, M., Cabrera-Munguía, D. A., Cano-Salazar, L. F., & Claudio-Rizo, J. A. (2024). Poly (vinyl chloride)/vinyl plastic blends, interpenetrating polymeric networks, and gels. In *Poly (vinyl chloride)-Based Blends, IPNs, and Gels* (pp. 155-177). Elsevier.
<https://doi.org/10.1016/B978-0-323-99474-3.00001-X>
- [39] Velayutham, T. S. (2024). Miscibility and immiscibility in PVC-based blends, IPNs, and gels. In *Poly (vinyl chloride)-Based Blends, IPNs, and Gels* (pp. 377-400). Elsevier.
<https://doi.org/10.1016/B978-0-323-99474-3.00011-2>
- [40] Chang, Y., Huang, Y. H., Lin, P. S., Hong, S. H., Tung, S. H., & Liu, C. L. (2024). Enhanced electrical conductivity and mechanical properties of stretchable thermoelectric generators formed by doped semiconducting polymer/elastomer blends. *ACS Applied Materials & Interfaces*, 16(3), 3764-3777.
<https://doi.org/10.1021/acsami.3c15651>
- [41] Althobiti, R. A., Morsi, M. A., Alzahrani, E., & Al-Muntaser, A. A. (2024). Enhancing the performance of PVC/PMMA polymer blend through hybrid nanofiller of TiO₂ NPs/GNPs for capacitive energy storage applications. *Ceramics International*, 50(11), 19039-19047.
<https://doi.org/10.1016/j.ceramint.2024.03.001>

© 2024. This work is published under
<https://creativecommons.org/licenses/by/4.0/legalcode>(the“License”).
Notwithstanding the ProQuest Terms and Conditions, you may use this
content in accordance with the terms of the License.

¹Parimal T Patwe²Neha A.
Kumbharkhane³Gajanan R Mahajan

Comparative Analysis of Phantoms Used for Stereotactic Radiosurgery Patient-Specific Quality Assurance



Abstract: - The use of Stereotactic Radiosurgery (SRS) or fractionated SRS (f-SRS) to treat brainmet has increased significantly. As this treatment technique delivers a high amount of radiation dose to a stereotactically localized, small target volume, dose delivery verification before actual patient treatment is of paramount importance. The objective of this study was to evaluate the performance of the Gafchromic EBT-3, ArcCheck phantom, and the amorphous silicon-based aS1200 Electronic Portal Imaging Device (EPID) for pre-treatment quality assurance (PSQA) of SRS and f-SRS treatment plans. Thirty treatment plans were selected retrospectively in order to treat brainmet. The dose administered via SRS was 18 Gy in a single fraction, whereas it was 27 Gy in three fractions for FBRT. We used three separate devices to conduct the PSQA: Gafchromic EBT-3 radiotherapy film, ArcCHECK, and a S1200 EPID. For SRS and f-SRS PSQA, aS1200 EPID demonstrated the highest pass rates at less stringent gamma criteria (3%/3mm and 2%/2mm). However, at tighter criteria (5%/1mm and 1%/1mm), the EBT-3 film surpassed the aS1200 EPID in performance, suggesting greater sensitivity to detect small dose deviations and higher confidence in pinpointing discrepancies. ArcCHECK consistently displayed lower pass rates across all criteria compared to the other two devices for small targets. The present work highlight the selection of an appropriate phantom for performing SRS and f-SRS PSQA.

Keywords: Stereotactic Radiosurgery (SRS), Patient specific quality assurance (PSQA), Gafchromic film, ArcCheck phantom, Electronic Portal Imaging Device (EPID)

¹ Author 1: School of Physical Sciences, Swami Ramanand Tirth Marathwada University, Nanded, Maharashtra, India-431 606

² Author 2: Department of Physiology, B. J. Govt. Medical College, Pune, MH, India - 411001

³ *Corresponding author: Dept. of Physics, Shri Datta Arts, Commerce and Science College, Hadgaon, Nanded, MH, India-431 712
drgrmahajan@rediffmail.com

I. INTRODUCTION

Brain metastases (BM) account for 8.5–9.6% of all adult cancer cases and are the most common intracranial malignant neoplasms [1, 2]. Approximately half of these patients have a single BM, while roughly 70% have two or more metastases [3, 4]. At the time of presentation, BM can result in significant morbidity and mortality, including acute cognitive impairment [5, 6]. The primary treatment options are surgery and radiotherapy. Historically, whole brain radiotherapy (WBRT) has been the standard treatment for these individuals. Nonetheless, WBRT may not provide adequate control and is associated with serious side effects [7 – 12]. Recent research indicates that both stereotactic radiosurgery (SRS) and fractionated stereotactic radiosurgery (f-SRS) can achieve comparable survival rates for up to ten lesions without WBRT [13]. The hallmarks of SRS include pinpoint accuracy, extremely conformal radiation distributions, and high doses delivered in a single fraction. When fractionated up to five fractions, it becomes fSRS. Several studies have found that these approaches have fewer cognitive side effects than WBRT [7, 10, 14, 15]. As a result, SRS/fSRS is being used to treat BM.

A key aspect of the SRS workflow is the complete pre-treatment quality assurance (QA) of the generated treatment plan, also known as patient specific quality assurance (PSQA). Usually, the SRS/f-SRS technique is used to treat small targets, indicating that they are associated with small fields. Small-field dosimetry requires a detector with a high spatial resolution because of issues like volume-averaging effects and loss of lateral charge particle equilibrium. The availability of such a detector is of the utmost importance in accurately identifying the steep dose gradients that are linked to SRS and f-SRS techniques. This ensures that the desired dose distribution is administered correctly.

In routine, PSQA SRS plan validation was performed using film dosimetry or other high-resolution detectors. While film dosimetry offers advantages in spatial resolution and tissue equivalent, it can be a labor-intensive and time-consuming process. The advent of sophisticated QA devices, such as the ArcCheck phantom (Sun Nuclear Corporation, USA) and the amorphous silicon based aS1200 Electronic Portal Imaging Device (EPID) from Varian (A Siemens Healthineers Company), presents opportunities for carrying out PSQA before actual treatment. These devices and their associated analysis software have witnessed significant refinements in recent years. The objective of this study is to evaluate the performance of these commercial PSQA devices for pre-treatment verification of SRS and f-SRS treatment plans.

II. MATERIAL AND METHODS:

Thirty treatment plans (either f-SRS or SRS) were chosen retrospectively in order to treat brain mets. f-SRS was utilized when the target volume (TV) was in close proximity to vital structures such as the optic nerves, brainstem, or optic chiasm, or if it had multiple mets or was significantly larger in size. In the Eclipse treatment planning system (Version 13.6), treatment plans were generated with the aid of the volumetric modulated radiotherapy (VMAT) delivery technique. During the planning phase, 6MV FFF x-ray beam from the TrueBeam linac was utilized. The average volume of the target was 14.7 cc, ranging from 1.1 cc to 34 cc. Nine of the thirty plans were of SRS treatments, while twenty-one were of f-SRS. The dose administered via SRS was 18 Gy in a single fraction, whereas it was 27 Gy in three fractions for f-SRS. To conduct the PSQA, each plan was executed using three separate phantoms: aS1200 EPID, Gafchromic EBT-3 radiotherapy film, and ArcCHECK. Using Gamma criteria, the PSQA outcomes were compared. Gamma criteria is a metric utilized to evaluate the degree of agreement between the planned dose distribution from the TPS and the dose that is actually delivered to the patient using TrueBeam linac.

1. Detectors:

1) Gafchromic EBT-3 film:

Gafchromic films are designed to provide fast and highly accurate measurements for radiotherapy applications. When used with specifically designed Film QA software, Gafchromic film provides the most complete and accurate dosimetric measurement. A scan was performed on the slab phantom using a Discovery RT CT-Scanner with a slice thickness of 1.25mm. Using the slab phantom, the CT images were imported into Eclipse TPS (13.6), and the patient's plan was recalculated. As depicted in Fig. 1, the dose was delivered to each film using 6 MV x-rays at a depth of 10 cm, with a 100 cm distance between the source and the film, a field size of 10 cm x 10 cm, and a backscatter of 10 cm. For EBT-3 film to be utilized for PSQA, it must be calibrated to a known dose.

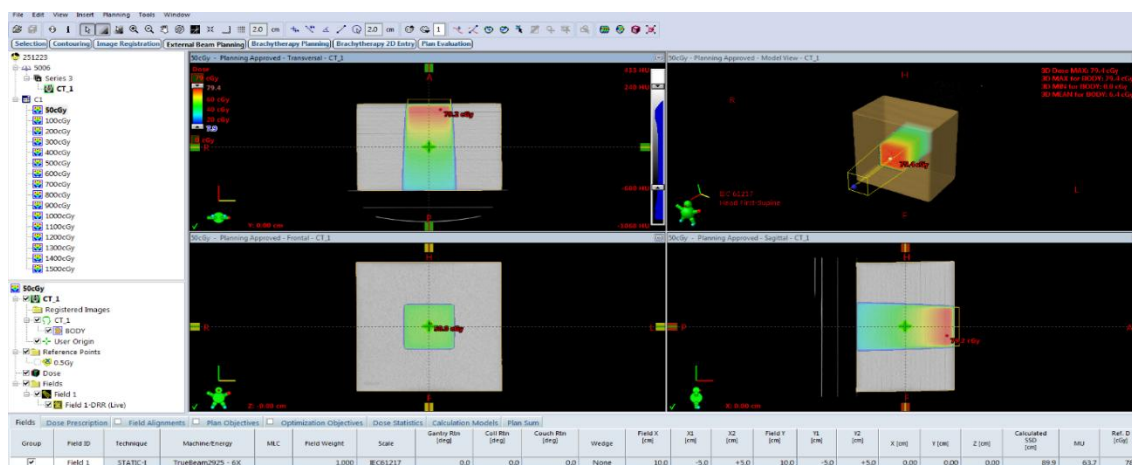


Figure 11 Slab phantom with EBT-3 film at a depth of 10 cm from the phantom surface.

The workflow commonly employed for film calibration is illustrated in Fig 2. Doses that were applied to the films varied between 50 cGy and 1500 cGy. Twenty-four hours later, an Epson 11000XL flatbed scanner manufactured by Seiko Epson Corporation in Suwa, Nagano, Japan, was utilized to scan the film. The digitization was executed at a resolution of 72 dpi, utilizing the triple channel technique, with no color corrections. Film dosimetry was utilized to generate the calibration curve via the SNC Patient QA software. Utilizing the identical slab phantom and film positioned in the coronal plane with respect to a 6 FFF X-ray beam from the TrueBeam linac, the PSQA plan was carried out. The SNC Patient QA software was utilized to import the film image and dose distribution from the Eclipse TPS in.tiff format onto the same plane as the film. Gamma analysis was employed to compare the delivered dose with the TPS calculated dose.

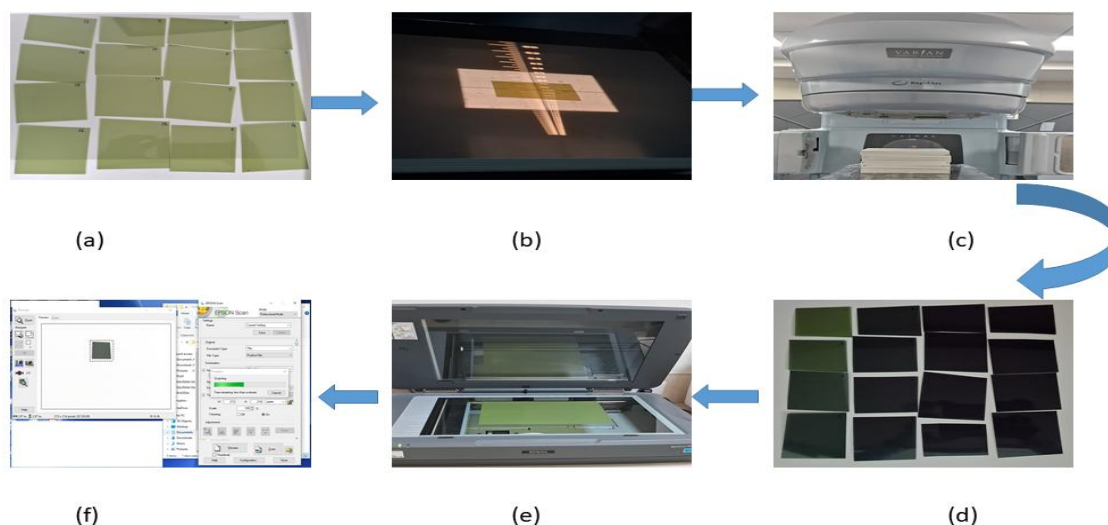


Figure 12 Film dosimetry workflow (a) EBT-3 film (b) EBT-3 film positioned on slab phantom at the isocenter of TrueBeam linac (c) EBT-3 film sandwiched between slab phantom (d) EBT-3 film exposed to various dose levels (e) The EBT-3 film is being scanned using the EPSON 11000XL scanner (f) EPSON 11000XL software.

2) *SNC ArcCHECK*

Fig. 3 depicts the implementation of virtual computed tomography (CT) images of the ArcCHECK within the Eclipse Treatment Planning System. We assigned the ArcCHECK a density of approximately 1.2 g/cc, whereas we assigned the rods a density of 1.4 g/cc. We recalculated PSQA plans using Eclipse TPS on this virtual ArcCHECK phantom and then transferred it to the SNC Patient software. The SNC Patient application imports a three-dimensional dose file and converts it into a two-dimensional format. This PSQA plan is considered a reference. Then the same plan was delivered using TrueBeam linac on the ArcCHECK phantom, and data was collected using the same SNC Patient software. We conducted gamma analysis to determine the degree of agreement between the measured and reference plans.

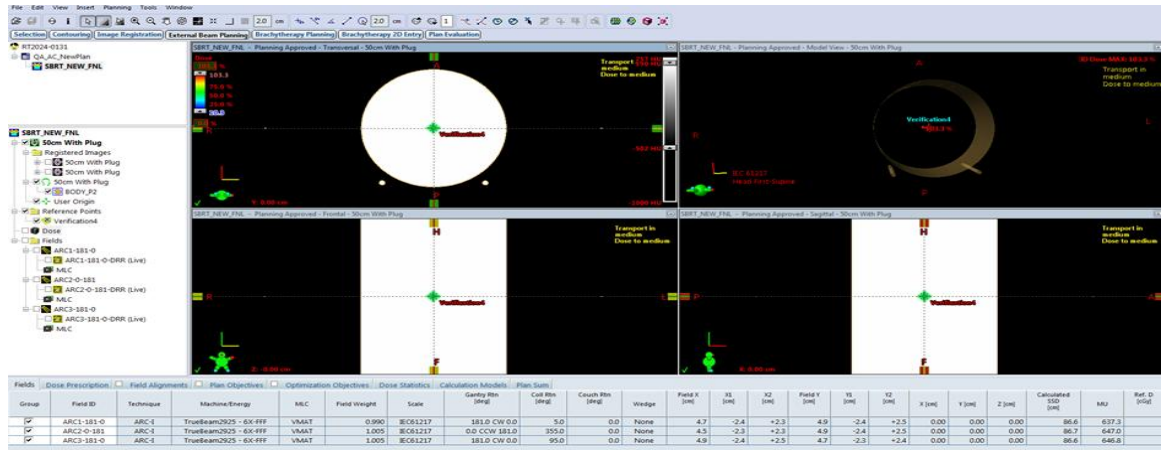


Figure 13 Virtual ArcCHECK phantom in Eclipse TPS

3) *aSi1200 EPID*

Varian’s aSi1200 EPID consists of a 43 cm × 43 cm array of amorphous-silicon (a-Si) photodiode flat panel detectors serving as the active layer. The design has a copper build-up layer that is 1 mm thick, a gadolinium oxysulfide (GOS)-based phosphor screen scintillation layer, an amorphous silicon photodiode readout layer, and a backscatter layer made of aluminum and lead plates that is 4 mm thick as shown in Fig 4. The pixel resolution is 1280 × 1280 pixels, with each pixel having an active area of approximately 0.113 mm². The EPID can handle FFF beams with a high dose rate and is capable of withstanding up to 7000 cGy/min without experiencing saturation effects [16, 17]. Couch rotation was set to zero, but all gantry and collimator rotation parameters were observed for each treatment plan. Portal dosimetry plans were generated and delivered utilizing 100 source-imager distances, as depicted in Fig 5.

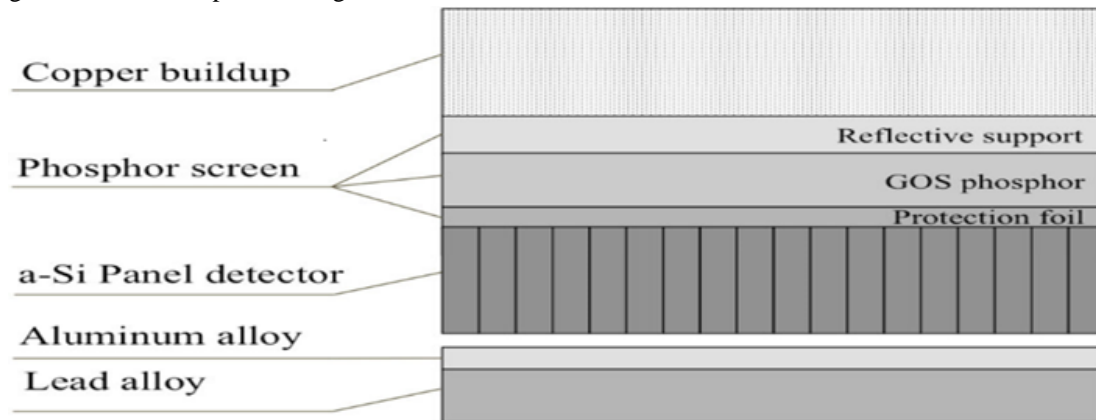


Figure 14 A cross-sectional view of the pertinent layers of the Varian aSi1200 Digital Megavolt Imager EPID



Figure 15 EPID in the planned position to carry out PSQA

The portal dosimetry images were evaluated in the Eclipse TPS using the Portal Dosimetry workspace. The analysis was performed with a pre-defined dose threshold of 10% and focused on the field plus a 2cm area of interest. Fig. 6 presents an EPID analysis of a 2.6 cc target using 3%/3mm gamma criteria.

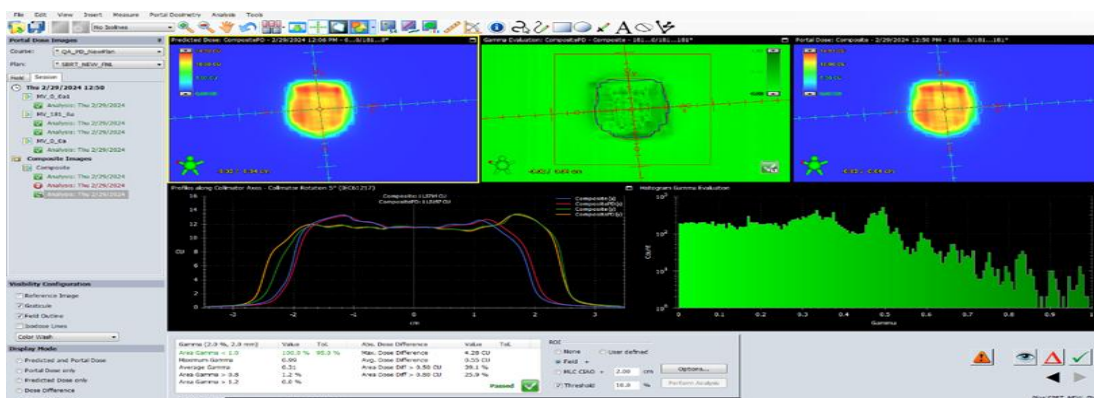


Figure 16 Portal dosimetry workspace in Eclipse TPS

III. RESULTS AND DISCUSSION:

Gamma analysis was used to test PSQA on three devices: EBT-3 Film, ArcCHECK, and aS1200 EPID. The criteria used were 3%/3mm, 2%/2mm, 5%/1mm, and 1%/1mm. Table 1 summarizes the average gamma pass rates for each device for SRS plans.

EBT-3 films average gamma analysis passing rates were found to be 96.43% ($\pm 1.8\%$), 93.08% ($\pm 1.96\%$), 91.67% ($\pm 2.31\%$), and 74.51% ($\pm 4.74\%$) for 3%/3mm, 2%/2mm, 5%/1mm, and 1%/1mm gamma criteria, respectively.

The ArcCHECK average gamma analysis passing rates were found to be 94.69% ($\pm 1.42\%$), 90.81% ($\pm 1.86\%$), 89.43% ($\pm 3.1\%$), and 68.63% ($\pm 3.8\%$) for 3%/3mm, 2%/2mm, 5%/1mm, and 1%/1mm gamma criteria, respectively.

The aS1200 EPID average gamma analysis passing rates were found to be 98.22% ($\pm 1.93\%$), 92.24% ($\pm 1.76\%$), 87.51% ($\pm 2.25\%$), and 72.36% ($\pm 5.71\%$) for 3%/3mm, 2%/2mm, 5%/1mm, and 1%/1mm gamma criteria, respectively.

Table 6 Average gamma pass rate for three PSQA devices for nine SRS plans

		Patient specific quality assurance devices	
Gamma Criteria	EBT-3 Film	Arc CHECK	aS 1200 EPID
3%/3mm	96.43% (± 1.8%)	94.69% (± 1.42%)	98.22% (± 1.93%)
2%/2mm	93.08% (± 1.96%)	90.81% (± 1.86%)	92.24% (± 1.76%)
5%/1mm	91.67% (± 2.31%)	89.43% (± 3.1%)	87.51% (± 2.25%)
1%/1mm	74.51% (± 4.74%)	68.63% (± 3.8%)	72.36% (± 5.71%)

The aS1200 EPID demonstrated the highest pass rates at less stringent gamma criteria (3%/3mm and 2%/2mm). However, at tighter criteria (5%/1mm and 1%/1mm), the EBT-3 film surpassed the aS1200 EPID in performance, suggesting greater sensitivity to detect small dose deviations and higher confidence in pinpointing discrepancies. ArcCHECK consistently displayed lower pass rates across all criteria compared to the other two devices.

The results of gamma analysis on three patient-specific QA devices (EBT-3 Film, ArcCHECK, and aS1200 EPID) in the context of f-SRS treatment plans can be seen in Table 2. Pass rates were determined across varying gamma criteria (3%/3mm, 2%/2mm, 5%/1mm, and 1%/1mm).

EBT-3 films average gamma analysis passing rates were found to be 98.79% (± 0.86%), 97.64% (± 1.49%), 95.38% (± 1.36%), and 94.51% (± 3.34%) for 3%/3mm, 2%/2mm, 5%/1mm, and 1%/1mm gamma criteria, respectively.

The ArcCHECK average gamma analysis passing rates were found to be 97.23% (± 1.63%), 96.63% (± 2.33%), 92.93% (± 2.84%), and 89.74% (± 5.68%) for 3%/3mm, 2%/2mm, 5%/1mm, and 1%/1mm gamma criteria, respectively.

The aS1200 EPID average gamma analysis passing rates were found to be 99.45% (± 1.12%), 97.88% (± 2.13%), 98.06% (± 1.46%), and 92.89% (± 3.76%) for 3%/3mm, 2%/2mm, 5%/1mm, and 1%/1mm gamma criteria, respectively.

Table 7 Average gamma result of 21 f-SRS plans

		Patient specific quality assurance devices	
Gamma Criteria	EBT-3 Film	Arc CHECK	aS 1200 EPID
3%/3mm	98.79% (± 0.86%)	97.23% (± 1.63%)	99.45% (± 1.12%)
2%/2mm	97.64% (± 1.49%)	96.63% (± 2.33%)	97.88% (± 2.13%)
5%/1mm	95.38% (± 1.36%)	92.93% (± 2.84%)	98.06% (± 1.46%)
1%/1mm	94.51% (± 3.34%)	89.74% (± 5.68%)	92.89% (± 3.76%)

IV. DISCUSSION

Choosing the appropriate phantom for pre-treatment verification of SRS and f-SRS plans is crucial to ensuring the safe and precise delivery of radiation doses. This study evaluated the performance of three commonly used PSQA devices (EBT-3 Film, ArcCHECK, and aS1200 EPID) by carrying out gamma analysis for SRS and f-SRS treatment plans.

Gafchromic EBT-3 films are widely regarded as the benchmark in dosimetry due to their numerous exceptional characteristics [18, 19]. Films possess a high spatial resolution, enabling the precise capture of dose distributions. This characteristic is crucial for SRS and f-SRS. In addition, EBT-3 films demonstrate exceptional similarity to human tissue and show minimal variation in response to different x-ray energies, accurately reflecting the actual doses received within the human body [16].

The data provided in both tables confirms the appropriateness of EBT-3 films for SRS and f-SRS PSQA. The high pass rates across all gamma criteria show that EBT-3 films are good at finding deviations from the intended dose distribution, even in the area of steep dose gradient. Although film dosimetry may require a significant amount of time and careful handling, its precision and accuracy are unmatched, especially in situations where the utmost confidence in dose verification is required.

In this study, EBT-3 failed to meet the 1%/1mm gamma criteria. One possible reason for this underperformance could be that film analysis methods are prone to systematic errors. Additionally, we used EBT 3 film, which has a maximum dose range of 15 Gy, to measure doses up to 18 Gy due to the lack of other high-dose range films. In order to fully utilize the spatial resolution capabilities of EBT-3 film, it is necessary to employ a precise technique that minimizes errors when studying dose distribution. Another potential explanation for this underperformance may be that film analysis methods might be susceptible to systematic errors. Lynch et al. studied how the optical density reading by flatbed scanners changes depending on the film's location and rotational rotation on the scanner [20]. The films showed up to 17% non-uniformity along the scanline and 7% perpendicular to the scanline when evenly irradiated and scanned at various points on the flatbed scanner. To make the most of the spatial resolution of EBT-3 film, a precise technique is needed to minimize errors in film dosimetry.

The diodes of the ArcCHECK are spaced at a distance of 10 millimeters from one another. The spacing between the diodes may cause only a single row of diodes to be within the field for very small targets, hence limiting the amount of collected data. Only a few rows of diodes receive direct radiation for small targets in the ArcCHECK device. Diodes positioned outside the primary beam also exhibit diminished sensitivity due to the limited radiation exposure in that region. Mhatre et al. examined the use of ArcCHECK for the purpose of ensuring the quality of a machine and concluded that it is suitable for advanced linac quality assurance [21]. ArcCHECK phantoms, which are specifically designed for conventional intensity-modulated radiotherapy (IMRT) and volumetrically modulated arc therapy (VMAT) patient-specific quality assurance (PSQA), have certain restrictions when used for SRS and f-SRS. Their intrinsic detector spacing of 10 mm is not adequate for accurately capturing complex dose distributions in SRS and f-SRS plans. Despite the implementation of the "merge" feature, which reduces spacing to 5 mm, there is still a risk of important dose information being lost between detectors. This could result in pass rates that are misleading. This constraint becomes much more evident in the case of multi-target PSQA, since the likelihood of neglecting inter-target dose information increases with larger target separations. Furthermore, the functionality of ArcCHECK phantoms is compromised for PSQA with couch kicks, which are commonly used in SRS treatments.

Utilizing EPID for portal dosimetry is a convenient method to quickly verify treatment plans before actual treatment. Originally, EPIDs were created to verify the patient's positioning just prior to commencing radiation therapy [22]. Shortly after its inception, it was discovered that the real-time portal images not only recorded visual data but also contained dose information, hence enhancing the efficiency of analysis compared to traditional films. As a result, it has been widely used to perform the quality assurance of linacs and verify the accuracy of dose delivery for modern treatments such as IMRT, VMAT, SRS, fSRS, and SBRT. Flat panel EPID systems with aSi technology are preferred because of their fast image capture, excellent spatial resolution, high sensitivity, compact size, and constant long-term performance. The aS1200 EPID is a helpful tool for PSQA [23]. EPID dosimetry also presents challenges for SRS and f-SRS QA. Since EPIDs are typically positioned perpendicular to the beam path in the absence of a couch, they fail to replicate the actual clinical setup with couch

angles. This incongruity can lead to discrepancies between measured and delivered doses, particularly in areas affected by couch movements.

According to our analysis, it is crucial that QA methods be customized to the unique features of SRS and f-SRS plans. In the present study, we outline important factors to consider when optimizing PSQA techniques.

EBT-3 films offer reliable dose information. On the other hand, the aS1200 EPID could be a good option when time is a constraint. ArcCHECK can be used when the target volume is larger. When choosing a device and determining gamma criterion thresholds, it is important to consider elements such as the fractionation scheme, target size, and complexity of dose delivery. For example, it may be necessary to use stricter gamma criteria for SRS plans that include delivering high doses in a single fraction to small targets. It may be necessary to reevaluate how strict the gamma criteria are, particularly for SRS plans where a high sensitivity to deviations can have a substantial influence on possible gamma pass rates. This analysis indicates that in specific situations involving SRS, using more stringent criteria could offer a more accurate evaluation of dose compliance.

V. LIMITATION OF THE STUDY

Each of the phantoms we used has its own pros and cons, which could have an impact on the gamma pass rate. Additionally, gamma analysis may not be optimal for regions characterized by an extremely sharp dose gradient. This study's limited sample size of 30 SRS/fSRS plans may affect the findings' generalizability.

VI. CONCLUSION:

Film dosimetry is still the best way to do PSQA for small targets because it has the best spatial resolution, but it is laborious to do and takes a long time. EPID-based PSQA is the best choice for high-throughput radiotherapy departments that need to be as efficient as possible. This is because it speeds up the PSQA process. For larger target volumes, ArcCHECK systems offer reliable gamma pass rates, so it can be used to perform SRS and f-SRS PSQA. A thorough examination of the departmental workflow and the necessary balance between accuracy and efficiency should guide the selection of an appropriate PSQA method.

REFERENCES

- [1] Barnholtz-Sloan J, Sloan A, Davis F, Vigneau F, Lai P, Sawaya R. Incidence Proportions of Brain Metastases in Patients Diagnosed (1973 to 2001) in the Metropolitan Detroit Cancer Surveillance System. *J Clin Oncol.* 2004 Jul; 22(14):2865-72.
- [2] Schouten L, Rutten J, Huvneers H, Twijnstra A. Incidence of brain metastases in a cohort of patients with carcinoma of the breast, colon, kidney, and lung and melanoma. *Cancer.* 2002; 94(10): 2698-2705.
- [3] Nussbaum E, Djalilian H, Cho K, Hall W. Brain metastases: Histology, multiplicity, surgery, and survival. *Cancer.* 1996; 78(8): 1781-88.
- [4] Delattre J, Krol G, Thaler H, Posner J. Distribution of Brain Metastases. *AMA Arch Neurol.* 1988; 45(7): 741-44.
- [5] Chang E, Wefel J, Hess K, Allen P, Lang F, Kornguth D, et al. Neurocognition in patients with brain metastases treated with radiosurgery or radiosurgery plus whole brain irradiation: a randomised controlled trial. *Lancet Oncol.* 2009; 10(11): 1037-44.
- [6] Koche M, Maarouf M, Bendel M, Voges J, Müller RP, Sturm V. Linac Radiosurgery Versus Whole Brain Radiotherapy for Brain Metastases. *Strahlenther Onkol.* 2004; 180(5): 263-67.
- [7] Pinkham M, Sanghera P, Wall G, Dawson B, Whitfield G. Neurocognitive Effects Following Cranial Irradiation for Brain Metastases. *Clin Oncol.* 2015; 27(11): 630-39.
- [8] Kocher M, Soffiatti R, Abacioglu U, Villà S, Fauchon F, Baumert B, et al. Adjuvant Whole-Brain Radiotherapy Versus Observation After Radiosurgery or Surgical Resection of One to Three Cerebral Metastases: Results of the EORTC 22952-26001 Study. *J Clin Oncol.* 2011; 29(2): 134-41.
- [9] Tsao M, Xu W, Wong R, Lloyd N, Laperriere N, Sahgal A, et al. Whole brain radiotherapy for the treatment of newly diagnosed multiple brain metastases. *Cochrane Database Syst Rev.* 2018; 1(1):CD003869.
- [10] Brown P, Ballman K, Cerhan J, Anderson S, Carrero X, Whitton A, et al. Postoperative stereotactic radiosurgery compared with whole brain radiotherapy for resected metastatic brain disease (NCCTG N107C/CEC-3): a multicentre, randomised, controlled, phase 3 trial. *Lancet Oncol.* 2017; 18(8): 1049-60.
- [11] Thomas E, Popple R, Wu X, Clark G, Markert J, Guthrie B, et al. Comparison of Plan Quality and Delivery Time Between Volumetric Arc Therapy (RapidArc) and Gamma Knife Radiosurgery for Multiple Cranial Metastases. *Neurosurgery.* 2014; 75(4): 409-18.

- [12] McDonald D, Schuler J, Takacs I, Peng J, Jenrette J, Vanek K. Comparison of radiation dose spillage from the Gamma Knife Perfexion with that from volumetric modulated arc radiosurgery during treatment of multiple brain metastases in a single fraction. *J Neurosurg*. 2014; 121(Suppl:51-9): 51-59.
- [13] Yamamoto M, Serizawa T, Shuto T, Akabane A, Higuchi Y, Kawagishi J, et al. Stereotactic radiosurgery for patients with multiple brain metastases (JLGK0901): a multi-institutional prospective observational study. *Lancet Oncol*. 2014; 15(4): 387-95.
- [14] Aoyama H, Shirato H, Tago M, Nakagawa K, Toyoda T, Hatano K, et al. Stereotactic Radiosurgery Plus Whole-Brain Radiation Therapy vs Stereotactic Radiosurgery Alone for Treatment of Brain Metastases. *JAMA*. 2006; 295(21): 2483-91.
- [15] Huss M, Barsoum P, Dodoo E, Sinclair G, TomaDasu I. Fractionated SRT using VMAT and Gamma Knife for brain metastases and gliomas — a planning study. *J Appl Clin Med Phys*. 2015; 16(6): 3-16.
- [16] Shi M, Myronakis M, Hu YH, Morf D, Rottmann J, Berbeco R. A Monte Carlo study of the impact of phosphor optical properties on EPID imaging performance. *Physics in Medicine & Biology*. 2018 Aug 20;63(16):165013.
- [17] James S, Al-Basheer A, Elder E, Huh C, Ackerman C, Barrett J, Hamilton R, Mostafaei F. Evaluation of commercial devices for patient specific QA of stereotactic radiotherapy plans. *Journal of Applied Clinical Medical Physics*. 2023 May 9:e14009.
- [18] Halvorsen PH, Cirino E, Das IJ, Garrett JA, Yang J, Yin FF, Fairbent LA. AAPM-RSS medical physics practice guideline 9. a. for SRS-SBRT. *Journal of applied clinical medical physics*. 2017 Sep;18(5):10-21.
- [19] Parwaie W, Refahi S, Ardekani MA, Farhood B. Different dosimeters/detectors used in small-field dosimetry: Pros and cons. *Journal of medical signals and sensors*. 2018 Jul;8(3):195.
- [20] Lynch BD, Kozelka J, Ranade MK, Li JG, Simon WE, Dempsey JF. Important considerations for radiochromic film dosimetry with flatbed CCD scanners and EBT film. *Medical physics*. 2006 Dec;33(12):4551-6.
- [21] Mhatre VR, Patwe PT. Evaluation of ArcCHECK SNC machine QA tool for modern linear accelerator. *Int. J. Cancer Ther. Oncol*. 2017;5.
- [22] Van Herk M, Meertens H. A matrix ionisation chamber imaging device for on-line patient setup verification during radiotherapy. *Radiotherapy and Oncology*. 1988 Jan 1;11(4):369-78.
- [23] Mhatre V, Pilakkal S, Chadha P, Talpatra K. Dosimetric comparison of a-Si 1200 and a-Si 1000 electronic portal imager for intensity modulated radiation therapy (IMRT). *J Nucl Med Radiat Ther*. 2018;9(2):1-6.

© 2024. This work is published under

[https://creativecommons.org/licenses/by/4.0/legalcode\(the“License”\)](https://creativecommons.org/licenses/by/4.0/legalcode(the“License”)).

Notwithstanding the ProQuest Terms and Conditions, you may use this content in accordance with the terms of the License.

¹Dr. Vinod M. Sherekar.

²Mr. Nilesh S. Padole

SYNTHESIS, CHARACTERIZATION AND BIOLOGICAL EVALUATION OF 4-(4-BROMO-1-HYDROXY NAPHTHALEN-2-YL)-6-(3,4-DIMETHOXY PHENYL)-5,6-DIHYDROPYRIMIDINE-2(1H)-ONE



Abstract: - 1-(4- Bromo -1-hydroxynaphthalen-2-yl)-ethan-1-one was prepared by refluxing 4- bromonaphthalen-1-ol with glacial acetic acid in presence of fused ZnCl₂. By condensing 1-(4- bromo -1-hydroxynaphthalen-2- yl)-ethan-1-ones with 3,4- dimethoxy benzaldehyde, to prepared by 1-(4- bromo -1- hydroxynaphthalen-2-yl)-3-(3,4-dimethoxy phenyl)-prop-2-en-1-one was synthesized. 1-(4- bromo -1- hydroxynaphthalen-2-yl)-3-(3,4-dimethoxy phenyl)-prop-2-en-1-one, urea and concentrated HCl in DMF were added and refluxed. Cool and pour in crushed ice. Treat it with cold NH₄OH solution to obtain titled compounds. The compounds thus synthesized have been characterized by physical and spectral data. All of these titled synthesized compounds have been screened for antimicrobial study and are found to possess excellent antimicrobial activities.

Keywords: Antimicrobial Activities, Cold NH₄OH Solution, Conc. HCl in DMF.

¹ *Corresponding author: Assistant Professor, Department of Chemistry, Vinaya Vidnyan Mahavidyalaya, Nandgaon Kh.

² Author 2 Affiliation: Assistant Professor, Department of Chemistry, Vinaya Vidnyan Mahavidyalaya, Nandgaon Kh.

Copyright © JES 2024 on-line: journal.esrgroups.org

INTRODUCTION

Dihydropyrimidin-2(1H)-one is designated hetero-cyclic compound with 2 Nitrogen atoms with pyrimidine ring in the six-member ring. Among the heterocycles, specially with Nitrogen containing heterocycles with pyrimidine ring nucleus is reckon as a the most useful framework for biological and pharmacological activities. This nucleus has wide applications in the physiological and industrial areas and proven to be most beneficial. They have been used extensively as important pharmacophore in the field of organic chemistry and drug designing. In this review, our focus will be on the 3,4-dihydropyrimidine (DHPM) ring. Basically, it is a selective review on dihydropyrimidinones. Literature of last two decades is incorporated in this review.

The pyrimidine is the most important heterocyclic moiety [1-2]. Dihydropyrimidinones (DHPMs) and their derivatives occupy a prominent place; these cores are of immense biological importance; play an important role as essential building blocks in the synthesis of DNA and RNA [3]. This review covers the recent synthesis and pharmacological advancement of dihydropyrimidinones/thiones moiety, along with covering the structure-activity relationship (SAR) of the most potent compounds, which may prove to become better, with more efficacy and safer agents [4]. In recent years, different varieties of building blocks have been accounted for the synthesis of Biginelli adducts and along these lines, the general proclamation about Biginelli reaction is, the reaction of aldehydes, 1,3-dicarbonyl compounds, and urea/thiourea to furnish 3,4-dihydropyridine-2(1H)-ones/thiones [5-7].

The synthesis of the dihydropyridine and their derivatives increasing tremendously significant because they generally show diverse medicinal properties [8-9]. Many reports exploring in Vivo and in Vitro dihydropyrimidin-2-one derivatives show variety of pharmacological activities such as active and safe tumor anti-initiating and multi-potent blocking agent [10], anxiolytic [11], antihypertensive agents [12], anticonvulsant [13], anticancer [14], analgesic activities [15], anti-bacterial [16], channel blockers [17], anti-HIV [18]. Their efforts are quite significant in literature hence considering the scope of dihydropyrimidine derivatives we have synthesized novel 4-(4-bromo-1-hydroxynaphthalen-2-yl)-6-(3,4-

dimethoxy phenyl)-5,6-dihydropyrimidine-2(1h)-one from 4- bromonaphthalen-1-ol and studied for their biological activities.

MATERIALS AND METHOD: -

Synthesis of 1-(4-Bromo-1-hydroxynaphthalen-2-yl)-ethan-1-one.

1-(4-Bromo-1-hydroxynaphthalen-2-yl) ethan-1-one was prepared by modified Nenchi method in which 4-bromo-naphthalen-1-ol was refluxed with glacial acetic acid in presence of fused $ZnCl_2$.

Synthesis of 1-(4-Bromo-1-hydroxynaphthalen-2-yl)-3-(3,4-dimethoxy phenyl)-prop-2-en-1-one.

1-(4-Bromo-1-hydroxynaphthalen-2-yl)-3-(3,4-dimethoxy phenyl)-prop-2-en-1-one was synthesized from 1-(4-Bromo-1-hydroxynaphthalen-2-yl) ethan-1-one by condensing it with 3,4-dimethoxy benzaldehyde were added in ethanol solvent and KOH mixture.

Synthesis of 4-(4-Bromo-1-hydroxy naphthalen-2-yl)-6-(3,4-dimethoxy phenyl)-5,6-dihydropyrimidine-2(1H)-one.

1. 4-(4-Bromo-1-hydroxy naphthalen-2-yl)-6-(3,4-dimethoxy phenyl)-5,6-dihydropyrimidine-2(1H)-one was prepared from 1-(4-Bromo-1-hydroxynaphthalen-2-yl)-3-(3,4-dimethoxy phenyl)-prop-2-en-1-one was reflux with urea and concentrated HCl in DMF. It was then treated with cold NH_4OH .

SCHEME: -

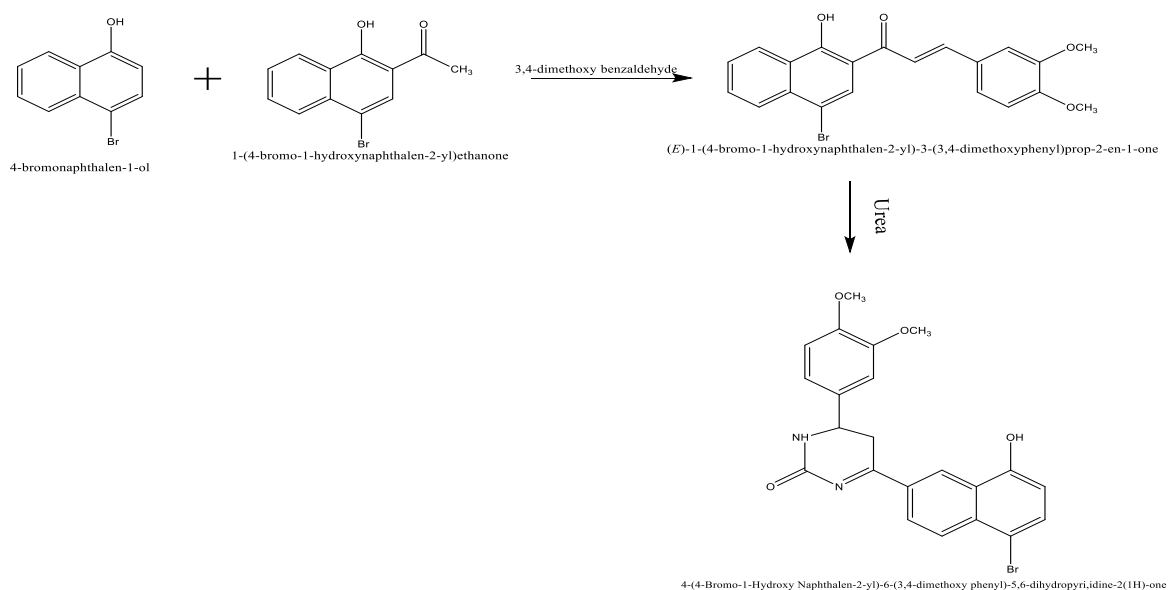


Table 1. PHYSICAL DATA OF SYNTHESIZED COMPOUNDS

Sr. no	Compound no	R1	R2	Molecular formula	Meltin g Point 0C	% Yield	% Nitrogen		R.F Value
							Found	Calculated	
1	1	-OCH3	-H	C21H17N2O3Br	258 ⁰ C	46%	6.63	6.64	0.58
2	2	-OCH3	-OCH3	C22H19N2O4Br	223 ⁰ C	47%	6.26	6.23	0.66
3	3	-H	-OH	C20H16N2OBr	229 ⁰ C	46%	6.91	6.81	0.56
4	4	-OH	-H	C17H16N2O2Br	258 ⁰ C	52%	5.86	5.84	0.57

SPECTRAL ANALYSIS: -

IR(vmax) (cm⁻¹): 1624 (C=O, str), 3342 (NH, str), 1568 (C=N),1172(C-O-C),757(monosubstituted Benzene

NMR (δ ppm): 1.3-1.9 (m, 2H, -CH₂ of pyrimidine), 10.33 (s, 1H, -OH),3.63 (s, 3H, -OCH₃),2.54 (s, 3H, CH₃,)

ANTIMICROBIAL STUDIES: -

All above synthesized 4-(4-Bromo-1-hydroxy naphthalen-2-yl)-6-(3,4-dimethoxy phenyl)-5,6-dihydropyrimidine-2(1H)-one has been studied for their antimicrobial activity against Escherichia coli, Proteus mirabilis, Staphylococcus aureus, Pseudomonas aeruginosa. The culture of each species was incubated at 370C and the zone of inhibition was measured after 24 hr. Results are tabulated in Table. Most of these compounds were found active

Sr. no	Compound Number	Antimicrobial Activity			
		E-coli	Proteus mirabilis	Staphylococcus aureus	Pseudomonas aeruginosa
1	1	17	18	16	10
2	2	16	10	18	14
3	3	18	12	14	17
4	4	15	14	12	13

Stron
gly

active, range 15-19 Weakly active, range 7-10 mm, moderately active, range 11-14mm, Inactive,

CONCLUSION: -

Thus, from above results it was observed that these heterocyclic compounds were found effective against *Escherichia coli*, *Proteus mirabilis*, *Staphylococcus aureus*, *Pseudomonas aeruginosa*. So those compounds can be easily be used for the treatment of diseases caused by test pathogens, only when they do not have toxic and other side effects.

REFERENCE: -

1. Kaur R, Chaudhary S, Kumar K, Gupta M.K, and Rawal R.K; Recent synthetic and medicinal perspectives of dihydropyrimidinones: A review; *Eur J Med Chem.* 2017; 26, 132: 108–134.
2. Naidu B.N et al; Synthesis and evaluation of C2-carbon-linked heterocyclic-5-hydroxy-6-oxo-dihydropyrimidine-4-carboxamides as HIV-1 integrase inhibitors. *Bioorg. Med. Chem. Lett.* 2015; 25, 717–720.
3. Francisco S.S et al; Synthesis of 3,4-Dihydropyrimidin(thio)one Containing Scaffold: Biginelli-like Reactions. *Pharmaceuticals.* 2022; 15(8): 948.
4. Khasimbi et al; Dihydropyrimidinones Scaffold as a Promising Nucleus for Synthetic Profile and Various Therapeutic Targets: A Review. *Curr. Org. Synth.* 2021; 18, 270-293.
5. Adole V A. Synthetic approaches for the synthesis of dihydropyrimidinones/ thiones (biginelli adducts): a concise review. *Wjpr.* 2020; 9(6): 1067-1091.
6. Ravichandran, S. and Karthikeyan, E. Microwave synthesis-a potential tool for green chemistry. *Int J Chem Tech Res.* 2011; 3(1): 466-470.
7. Sheldon, R.A. Green chemistry and resource efficiency: towards a green economy. *Green Chemistry.* 2016; 18(11): 3180-3183.
8. Lal J. Gupta S K. Thavaselvam C. Agarwal D D; Design, synthesis, synergistic antimicrobial activity and cytotoxicity of 4-aryl substituted 3,4-dihydropyrimidinones of curcumin. *Bioorg. Med. Chem. Lett.* 2012; 22. 2872–2876.
9. Ravi kumar K, Harika V L, Shaik A B. Synthesis, characterization and biological evaluation of 3,4-dihydropyrimidin-2(1H)-thione derivatives. *Arch.Appl. Sci. Res.* 2014; 6(6): 121-127.
10. Sherekar V M. Padole N S. Kakade K P. Synthesis, Characterization and Biological Evaluation of 4-(4-bromo-1-hydroxy naphthalen-2-yl)-6-(4-methoxy phenyl)-5,6-dihydropyrimidine-2(1h)-one). *Jetir.* 2022; 9(1): 15-19
11. Garg V. Jindal D. Singh R. Synthesis and Evaluation of antifungal activity of 4, 6- Diphenyl-3, 4- Dihydropyrimidine-2-(1h)-one derivatives. *tjpr.org.* 2020; 7(6): 8-12.
12. Malah-El-A. Mahmoud, Z. Salem, H.H. Abdou, A. Soliman, M. Hassan, R. Design, ecofriendly synthesis, anticancer and antimicrobial screening of innovative Biginelli dihydropyrimidines using β -aroylpyruvates as synthons. *Green Chem. Lett. rev.* 2020; 14(2): 220-232.

13. Maharramov A M. et al. Synthesis, investigation of the new derivatives of dihydropyrimidines and determination of their biological activity. *J. Mol. Struct.* 2017; 1141, 39-43.
14. Fandaklı S et al. MW Assisted Synthesis of New 4,6-diaryl-3,4-Dihydropyrimidines-2(1H)-thione Derivatives: Tyrosinase Inhibition, Antioxidant, and Molecular Docking Studies. *Cumhuriyet Sci. J.* 2023; 44(4):687-696.
15. Toraskar M P. Chaure R. Sonatakke S S. Novel Dihydropyrimidinones: Molecular Docking, Synthesis and Anti-Neoplastic Activity. *Asian J. Chem.* 2023; 35(7):1579-1584.
16. Shinde R R. Farooqui M. One-Pot and Solvent Free Synthesis of 3,4-Dihydropyrimidin-2(1 H)-Ones Using Recyclable Resin Purolite CT275DR as a Heterogeneous Catalyst via Three-Component Biginelli-Like Reactions. *Polycyclic aromatic compounds.* 2021; 42(2): 1-10.
17. Adhikari A et al. Synthesis, characterization and biological evaluation of dihydropyrimidine derivatives. *Saudi Pharm J.* 2012; 20(1): 75-79.
18. Sherekar V M, Padole N S. Synthesis, Characterization and Biological Evaluation of 4-(5- chloro-8-hydroxy naphthalen-2-yl)- 6-(4-methoxy phenyl)-5,6- dihydropyrimidine-2(1h)-one. *jetir.* 2022; 9(7): 104-110.

¹ S. A. Athawale
² B.A. Lone
³ S. E. Bhandarkar
³ S. Athawale
³ M. A. Wani

**Synthesis and Computational
Approach of Cyclic Imines of
Substituted 1, 3, 4-Thiadiazole with
Special Reference to Theirs
Antioxidant Activity**



Abstract: - 1,3,4-Thiadiazole moiety is a enormous curiosity to a large number of researchers due to their grand industrial and pharmaceutical significance and it is amazing that the synthetic publication extreme outweigh in numbers those concerning to all other fields. Substituted 1,3,4-thiadiazole moiety and derivatives considered as lead mixes for medicate union, and a few of them have exhibited higher antimicrobial movement in contrast with standard drugs. In present work a novel substituted 1, 3, 4-thiadiazole-2-amine and Schiff base were synthesized successfully by green approach. The newly synthesized compounds are further screening for their antioxidant activity. The difference between the profile activity between the Cl and NH₂ substituted 1,3,4-thiadiazole moiety intrinsically different antioxidant activity by DPPH method. Result of this study indicated that substituted 1, 3, 4-thiadiazole moiety and their derivatives are optimistic source of antioxidant activity. Hetero atom present in the compounds showing the enormous pharmacological activity.

Keywords: Synthesis, Computational and Biological Studies, H¹ NMR, IR, Antioxidant activity.

¹ *Corresponding author: S.A. Athawale, Department of Chemistry, Government Vidarbha Institute of Science and Humanities Amravati (MS) INDIA

^{2,3}, Department of Chemistry, Government Vidarbha Institute of Science and Humanities Amravati (MS) INDIA

³, Department of Physics, Government Vidarbha Institute of Science and Humanities Amravati (MS) INDIA

I. INTRODUCTION

Heterocyclic compounds are imperative in the metabolism of all living cells.¹ Heterocyclic chemical compound may be inorganic or organic compounds mostly contain at least one carbon. Although atoms that are neither carbon nor hydrogen are usually referred to in organic chemistry as heteroatom, this is habitually in contrast to the all-carbon backbone. But this does not prevent a compound such as borazine (which has no carbon atoms) from being labeled "heterocyclic". Thiadiazole² is a sub-family of azoles compounds. Structurally they are five-constituent heterocyclic compounds containing two nitrogen and sulfur atoms, and two double bonds. There are four probable structures exist depending on the virtual positions of the heteroatom these forms do not interconvert and hence are structural isomers. Schiff bases³ have a large number of synthetic uses in organic chemistry.

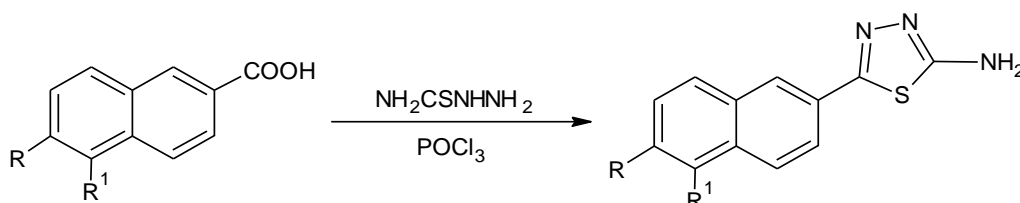
Acylation of Schiff bases by acid anhydrides, acid chlorides⁴ along with acyl cyanides is initiated by assault at the nitrogen atom and leads to net addition of the acylating agent. Schiff bases emerge to be a vital conciliator in a number of enzymatic reactions concerning interface of an enzyme with an amino or a carbonyl group of the substrate.

Free radicals of Reactive oxygen species resembling superoxide, singlet oxygen, hydroxyl radical and H₂O₂ encourage oxidation⁵ which damage the biological macromolecules and generate numerous health troubles such as malignancy, soreness, atherosclerosis⁶, antitubercular⁷ cardiovascular⁸ neurodegenerative⁹ diseases. The frontier molecular orbitals (HOMO and LUMO), HOMO-LUMO¹⁰ energy gap of newly synthesized compounds were calculated by using computing software.

II. EXPERIMENTAL

A novel synthesis of 5-(N-substitutednphthalen-2-yl)-1, 3, 4-thiadiazole-2-amine were synthesized by condensation of substituted aromatic acid with thiosemicarbazide in presence of POCl₃ by using 'green approach'. Progress of the reaction was monitored by TLC using appropriate solvent system. After cooling the reaction mixture was poured in ice-cold water with stirring till precipitation was complete to obtain titled product.

1) Reaction



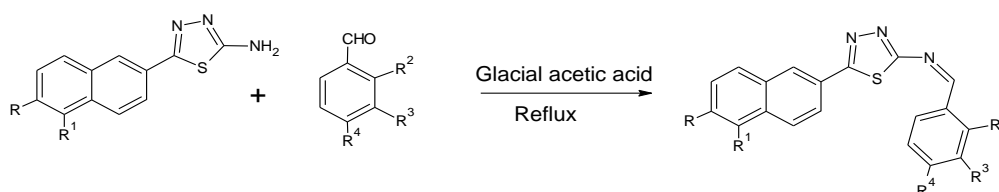
Where

R: -H, -NH₂, -Cl, -NO₂, -Br

R¹: -H, -Cl

2) Preparation of Schiff base

A mixture of 5-(6-substitutednaphthalene-2-yl)-1,3,4-thiadiazol-2-amine and aromatic aldehyde in glacial acetic acid was refluxed for two hours, cooled and poured in ice-cold water with stirring till precipitation was complete. The solid obtained was re-crystallized from ethanol.



R = -Cl, R₁ = -H. R₂ = -OH, -Cl, -H, R₃ = -NO₂, -H, R₄ = -Cl, -H

a) Characterization data

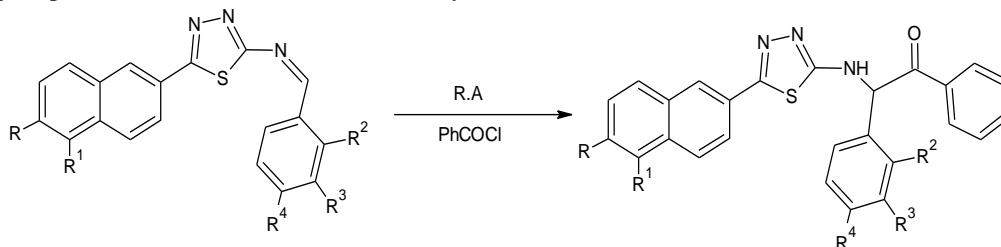
Compound **4b** was analyzed by IR and NMR spectra provided in supporting information.

IR: 1570.11 cm⁻¹ (-C=N), 883.23 cm⁻¹ (Para substitution)

^1H NMR: (DMSO d_6) δ (ppm) 8.32 (s, 1H), 7.35-7.98 (m, 10H)

3) Synthesis of benzoyl derivatives of Schiff base

A mixture of 5-(N-substitutednaphthalene 2-yl)-N-[(substituted) benzylidene]- 1,3,4-thiadiazole refluxed with benzoyl chloride in presence of sodium borohydride as a reducing agent for 3-4 hour, then poured into ice cold water. The precipitate was formed. Filtered it and recrystallized from ethanol.



$\mathbf{R} = -\text{Cl}$, $\mathbf{R}_1 = -\text{H}$, $\mathbf{R}_2 = -\text{OH}, -\text{Cl}, -\text{H}$, $\mathbf{R}_3 = -\text{NO}_2, -\text{H}$, $\mathbf{R}_4 = -\text{Cl}, -\text{H}$

a) Characterization data

Compound **4c** was analyzed by IR and NMR spectra provided in supporting information.

IR: 3250.25 cm^{-1} (N-H stretching), 1735.40 cm^{-1} (C=O stretching), 800.00 cm^{-1} (para substitution), 738.45 cm^{-1} (-Cl substitution)

^1H NMR: (DMSO d_6 in ppm): 4.36 (s 1H), 5.41(s 1H), 6.45-8.72 (m 10H)

III. RESULT AND DISCUSSION

3.1 Theoretical Calculations

The MM2 calculations and HOMO-LUMO¹⁰ energy levels of the newly synthesized compound by computational method using Chem. Draw for 3D optimization, ICD, I3D Pro 12.0.2 and Avogadro

Table 3.1.1

Sr. No.	Molecular formula	R	R ¹	R.F. value	M.P. ^{0c}	Yield %
1a	C ₁₂ H ₁₀ N ₄ S	-NH ₂	-H	0.5	161	61
2a	C ₁₂ H ₁₀ ClN ₃ S	-Cl	-H	0.5	128	57
3a	C ₁₂ H ₈ N ₄ O ₂ S	-NO ₂	-H	0.6	199	55
4a	C ₁₂ H ₈ BrN ₃ S	-Br	-H	0.45	210	61
5a	C ₁₂ H ₈ ClN ₃ OS	-H	-Cl	0.65	135	57

Table 3.1.2

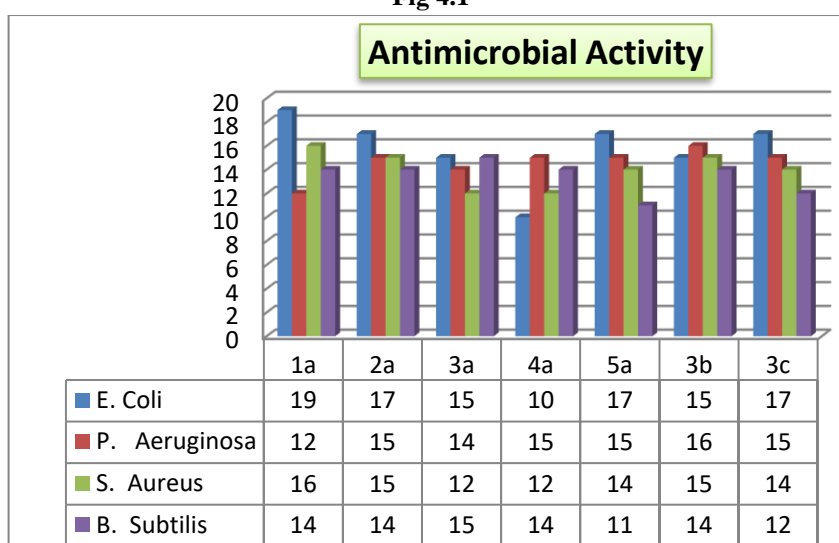
Sr. No.	Molecular formula	R	R ¹	R ²	R ³	R ⁴	M.P. ^{0c}	Yield %
1b	C ₂₁ H ₁₇ ClN ₄ S	-Cl	-H	-H	-H	-N(CH ₃) ₂	90	60
2b	C ₁₉ H ₁₂ ClN ₃ OS	-Cl	-H	-OH	-H	-H	219	58
3b	C ₁₉ H ₁₁ Cl ₂ N ₃ S	-Cl	-H	-H	-H	-Cl	110	61
4b	C ₁₉ H ₁₁ ClN ₄ O ₂ S	-Cl	-H	-H	-NO ₂	-H	160	59
5b	C ₂₁ H ₁₇ ClN ₄ S	-Cl	-H	-Cl	-H	-H	120	61

Table 3.1.3

Sr. No.	Molecular formula	R	R ¹	R ²	R ³	R ⁴	M.P. ^{0c}	Yield %
1c	C ₂₈ H ₂₃ ClN ₄ O ₃ S	-Cl	-H	-H	-H	-N(CH ₃) ₂	90	30
2c	C ₂₆ H ₁₈ ClN ₃ O ₂ S	-Cl	-H	-OH	-H	-H	180	55
3c	C ₂₆ H ₁₇ Cl ₂ N ₃ O ₃ S	-Cl	-H	-H	-H	-Cl	165	35
4c	C ₂₆ H ₁₇ ClN ₄ O ₃ S	-Cl	-H	-H	-NO ₂	-H	168	45
5c	C ₂₆ H ₁₇ Cl ₂ N ₃ O ₃ S	-Cl	-H	-Cl	-H	-H	128	42

4 Biological Assay

Antibacterial activity of newly synthesized compounds have high antimicrobial activity against *E. coli*, *S. Aureus* and *P. Seudomonas* and *B. Subtilus* studied by disk diffusion method using MH media. Antimicrobial activity of Schiff base of 5-(N-substitutednaphthalene-2-yl)-1, 3, 4-thiadiazole

Fig 4.1

5. Computational study

In this study we have perform the theoretical calculations viz. MM2, HOMO- LUMO energies and band gaps, bond of the newly synthesized molecules using ICD Pro 12.0, I3D Pro. 12.0 software of quantum mechanics.

5.1 Molecular mechanics

The mechanical molecular model considers atoms as spheres and bonds as springs. The mathematics of spring deformation can be used to describe the ability of bonds to stretch, bend, and twist.

Table 5.1.1

compo unds	S	B	S B	τ	Non 1,4-VDW	1,4-VDW	D/D	C/D and C/C	T E Kcal/mol
1a	0.919	5.174	0.003	-16.040	0.231	14.310	-3.128	-	1.558
2a	0.935	5.209	0.013	-13.920	0.363	15.402	-3.073	-	4.928
3a	1.049	6.091	0.023	-13.920	1.711	17.189	-2.994	-3.917	5.231
4a	0.945	5.250	0.023	-13.920	0.309	15.566	-3.077	-	5.100
5a	1.045	5.728	0.030	-12.860	1.215	15.656	-3.029	-	7.785
3b	1.407	7.700	0.055	-21.680	0.794	25.766	1.66	-	15.706
3c	2.131	7.547	0.132	-23.679	-2.216	31.819	-2.625	-	13.111

5.2 HOMO- LUMO

The energy difference between the HOMO and LUMO is termed the *HOMO–LUMO gap*. HOMO and LUMO HOMO- LUMO energy levels in molecule 1a-5a decreases when there are different substituent on naphthalene ring in thiadiazole moiety and its Schiff base i.e. in 2c and 3c molecule. Shown following table

Table 5.2.1

Compounds	HOMO (eV)	LUMO (eV)
1a	-6.128	-2.754
2a	-6.129	-3.071
3a	-6.908	-5.418
4a	-6.129	-3.120
5a	-6.130	-2.674
3b	-4.806	-3.111
3c	-6.042	-4.648

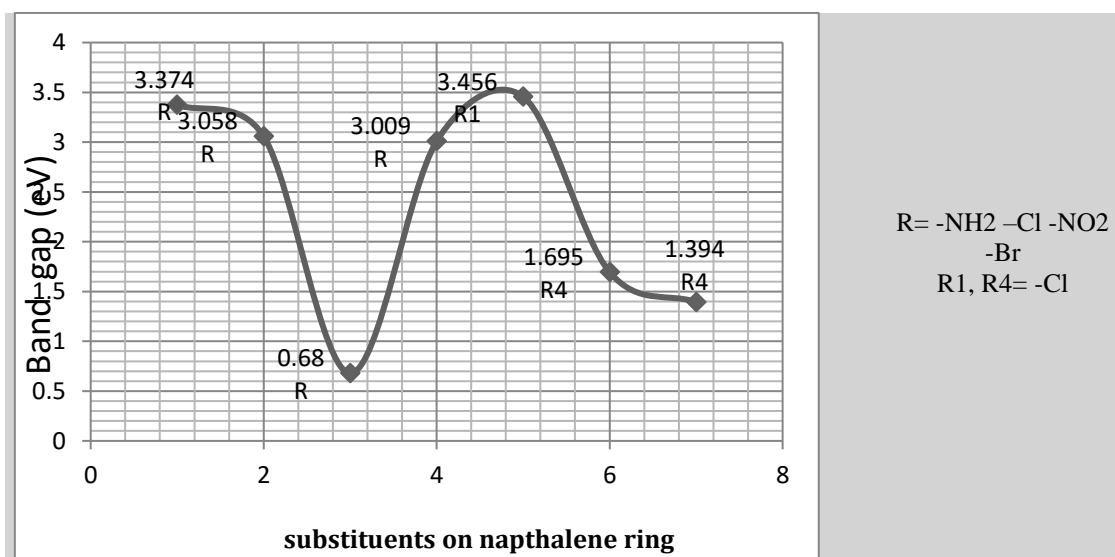


Fig 5.2.1

The graphical representation shows band gap in the molecules

5.3 Bond angle

When the substituent was changed on naphthalene ring the bond angle was also changed gradually. In amine (-NH₂) substitution on 6th position of naphthalene ring has lower bond angle rather than substitution of chlorine (-Cl) on 5th position of naphthalene ring. Shown in fig 6.3.1

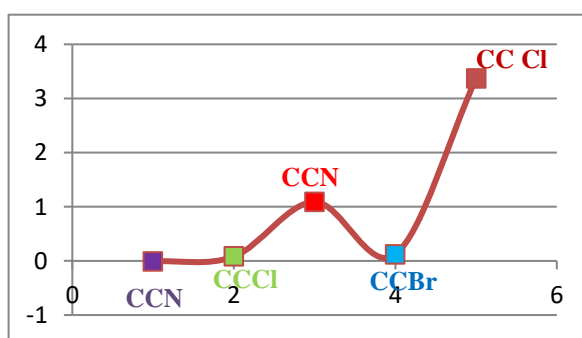


Fig 5.3.1

Fig 5.3.1

From the above representation it was seen that when the substituent was changed on naphthalene ring the bond angle was also changed gradually.

6 Antioxidant activities

6.1 Phenolic Contain

Total phenolic content was determined as described by Prior et al. [21]. Briefly, 500 μg of compound in 100 μL of methanol was mixed with 100 μL of 1 N Folin–Ciocalteu reagent. Following incubation for 5 min, 200 μL of 20% Na_2CO_3 was added. Absorbance at 730 nm was measured in plate reader after 10 min and the concentration of phenolic compounds was calculated using standard curve of gallic acid (500–5000 ng; $R^2=0.967$). The results were expressed as mg gallic acid equivalent (mg GAE) g^{-1} . Total phenolic content is obtained in molecule in 1a and 2a is 26.01 microgram GAE/mg and 8.1 microgram GAE/mg respectively.

6.2 Flavanoid

For flavanoid content, extract in 500 μL of distilled water was mixed with 30 μL of a 5% NaNO_2 solution and incubated for 5 min. 300 μL of 10% $\text{AlCl}_3 \cdot \text{H}_2\text{O}$ solution was added followed by 200 μL of 1 M NaOH and 200 μL of distilled water after 6 min. Absorbance was read at 510 nm and total flavanoids were calculated using quercetin as standard (10–100 μg ; $R^2=0.999$). The results were expressed as mg quercetin equivalent (mg GAE) g^{-1} .

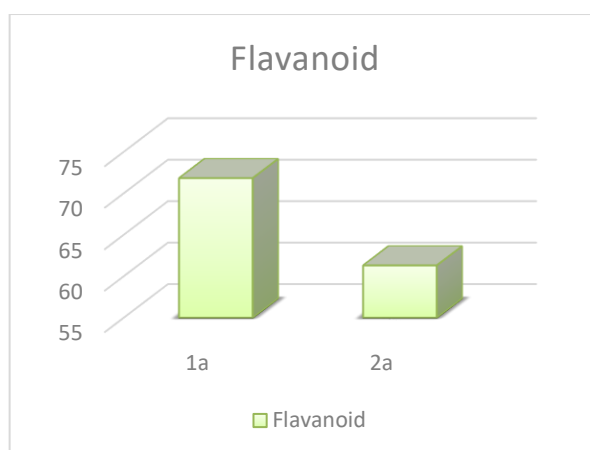


Fig. 6.2 Total flavanoid content is 54 microgram QER/mg and 57.33 microgram QER/mg in 1a and 2a respectively.

6.3 DPPH Assay

1,1-diphenyl-2-picrylhydrazyl (DPPH) radical scavenging assay, hydroxyl radical (OH^\cdot) scavenging activity, reducing power assay and chelation power of compound 1a and 2a was performed with a few modifications for plate reader analysis.

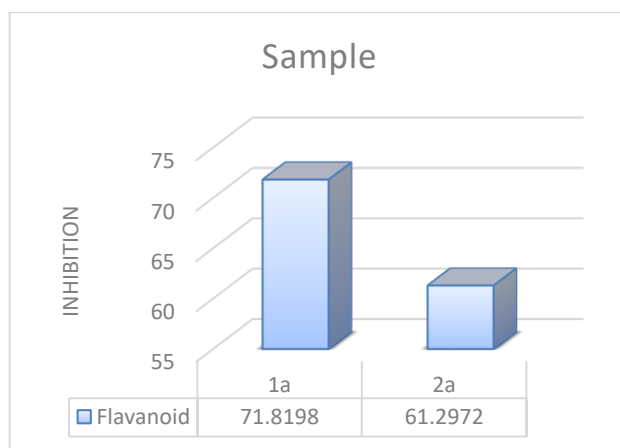
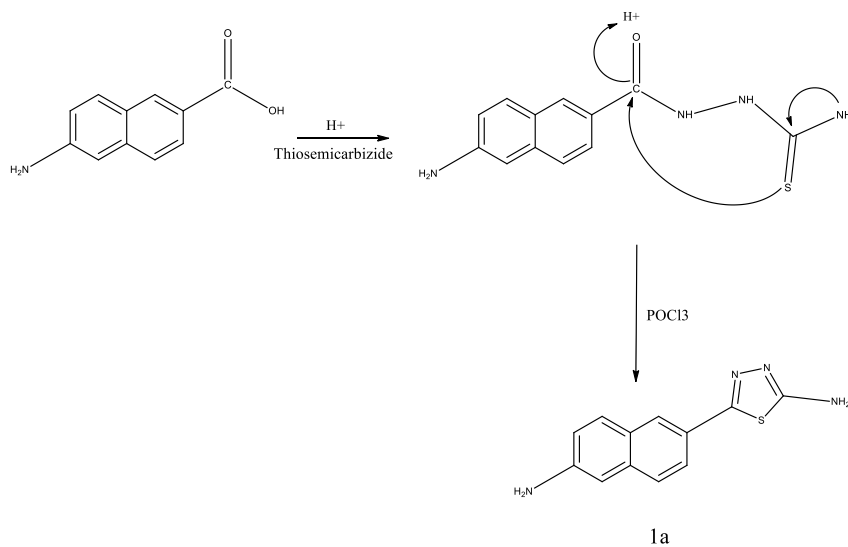


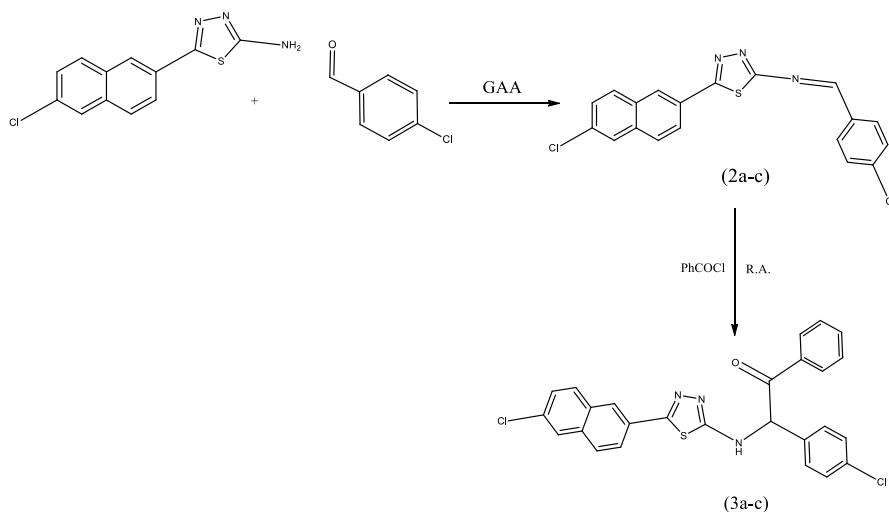
Fig 6.3.1 shows reducing power in 1a and 2a compounds

Reducing power of compounds **1a** and **2a** is obtained 71.81% and 61.29% respectively

IV. MECHANISM OF REACTION



-NH₂ in **1a** is replaced by -Cl, -NO₂, -Br in **2a**, **3a**, **4a** and **5a** respectively.



V. CONCLUSION

We have illustrated intriguing solvent free method to synthesized substituted naphthalene-1,3,4-thiadiazole moiety and their Schiff base was formed by single step reaction with moderate to good yield. The biological assay indicates high antimicrobial activity against *E. coli*, *P. Seudomonas*, *S. Aureus* and *B. Subtilis*. Computational data gives various strains, forces and energies HOMO- LUMO band gaps in the newly synthesized compounds. The parent molecule i.e. amino substituted and chloro substituted 1,3,4-thiadiazole moiety shows good antioxidant activity by DPPH assay.

VI. ACKNOWLEDGEMENT.

Author is thankful to IIM, Jammu for NMR analysis, S A appreciatively acknowledge Department of Physics G.V.I.S.H Amravati for IR analysis.

This research did not receive any specific grant from funding agencies in the public, commercial, or not-for-profit sectors.

VII. CONFLICT TO INTEREST

There is not conflict to interest.

VIII. REFERENCES

- [1] L. Mirta., Fascio, María Inés Errea , Norma Beatriz D'Accorso *European Journal of Medicinal Chemistry* 2014
- [2] K. Emma, D., J. Sperry *Org. Chem. Front.*, 2015
- [3] S. A. Athawale , B. A. Lone, S. E. Bhandarkar, *Indo American Journal of Pharmaceutical Sciences*, 05(01), S1-S4, 2018
- [4] S. A. Athawale, S. E. Bhandarkar *International Journal of Current Engineering and Scientific Research*, 6, 88, 2019
- [5] Katarina Jakovljević, a Milan D. Joksović, a Ivana Z. Matic, b , *Med. Chem. Commun.*, 2018, 3-33
- [6] L. Ziqiang, L. Yishuang., B. Xiaoguang, J. Deng, W. Juxian Wang, Z. Guoning, X. Chunling, M. Yaning, W. Yucheng *RSC Adv.*, 2015, 5, 97089
- [7] P. C. Fabienne, S. Xiangdong, V. Nigel, P. Mark, D. Thomas, S. Deborah, A. Heather, M. Halem, D. Michael, V. L. Barry., *Med. Chem. Commun.*, 2012, 3, 1117
- [8] N. Mihailović, V. Marković, Z. Ivana, S. Nemanja, S. Stanisavljevi Zivko, S. T. Jovanovi S, J. Ljubinka., *RSC Adv.*, 2017, 7, 8550
- [9] B. Zhou, Z. Hu, Y. Jiang, C. Zhong, Z. Sun, H. Sun, *Physical Chemistry Chemical Physics*, 20(30), 19759–19767. 2018 doi:10.1039/c8cp03135e

¹S. S. Birajdar
²S. D. Sont
³M. R. Bodke
⁴D. B. Suryawanshi

A comparative experimental and theoretical approach to study structural and molecular aspects in binary solutions



Abstract: - Heteromolecular interactions and hydrogen bonding between diverse entities at 8.845 GHz explains structural and molecular behavior. Frequency domain technique using X-band microwave bench with liquid dielectric cell is used to reveal the static dielectric properties of polar with non-polar binary solutions at 301 K. The effect of microwave frequency on binary mixtures of acetonitrile, chlorobenzene and Xylene is studied in terms of h-bonding association or disassociation between diverse molecules thereby obtaining and comparing static dielectric permittivity (ϵ') and effective Kirkwood correlation factor (g^{eff}) values with theoretically calculated static dielectric constant, g_1 and g_2 values using Luzar model. Values of polarizability, bonding energy and enthalpy were determined theoretically to authorize association or dissociation of hetero molecules.

Keywords: Static dielectric constant (ϵ'), Kirkwood correlation factor, Luzar model, hydrogen bonding, polarizability, bonding energy and frequency domain technique.

I. INTRODUCTION

Microwave spectroscopic techniques including time domain [1-4] and frequency domain has achieved finest results in the analysis of dielectric parameters to know physiochemical significance of the heteromolecules in the mixture. Frequency domain technique (FDT) [6-7] plays a remarkable role in perceptive of molecular assets and intermolecular exchanges through hydrogen bonding in binary liquids [8-9]. FDT is the most convenient method, provides exact static dielectric constant (ϵ') values of non-polar molecules in the microwave region. Exposure of microwaves to the binary liquid mixture causes variations in degree of solute-solvent and structural behavior such that it recognizes the heteromolecular interactions and intrinsic characteristics of dielectric properties. It is an interesting concept to distinguish effect of polarization in the mixture at different concentrations and to know how dipolar relaxations get affected for which a computational Luzar model is used for the mixtures [9].

Acetonitrile (ACN) is an organic colorless nitrile compound, polar, aprotic solvent, miscible in water and used in purification of butadiene [10]. Xylene is an aromatic compound, colorless, flammable liquid mostly used as a solvent [11-14]. Chlorobenzene (CBZ) is a non-associative liquid and is chlorine group molecule [15].

A comparative computational dielectric approach using Luzar model for the study of binary mixtures of CBZ, ACN and Xylene is revealed at 301 K employing FDT. In present context it is interesting to study the comparative effect of heteromolecular interactions among nitrile, C-H and chlorine group molecules in the system of binary mixtures. Kirkwood correlation factor reveals structuredness or orderedness of molecules in the mixture in its pure form and that of Luzar model reveals hydrogen bonding with concept of polarizability, enthalpy and associative energy required to bind hetero molecules and prediction of number of hydrogen bonds formed in the binary mixtures.

II. EXPERIMENTAL DETAILS - MATERIALS AND MEASUREMENTS

Source and purity of Acetonitrile, Chlorobenzene and Xylene components are tabulated in Table 1. Static dielectric parameters were measured at 8.845 GHz frequency by means of frequency domain technique using X-Band microwave bench. Analysis of data with procedure of frequency domain technique using X-Band microwave bench was systematically explicated formerly [5-8, 16-18]. The schematic diagram for setup of X-band microwave technique is shown in figure 1 [8].

¹S. S. Birajdar, Dept. of Physics and Electronics, Maharashtra Udayagiri Mahavidyalaya, Udgir, (MS)India-413517

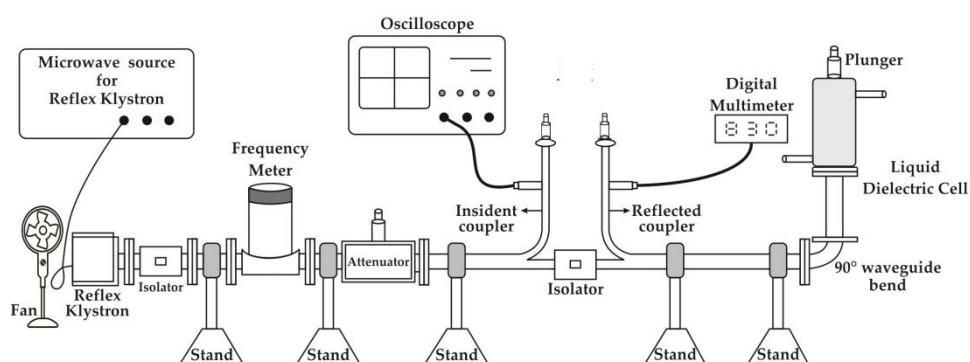
²S. D. Sont, Dept. of Chemistry, Maharashtra Udayagiri Mahavidyalaya, Udgir, (MS) India-431606

³M. R. Bodke, Dept. of Electronics, Modern College, Shivaji Nagar, Pune, (MS) India-411005

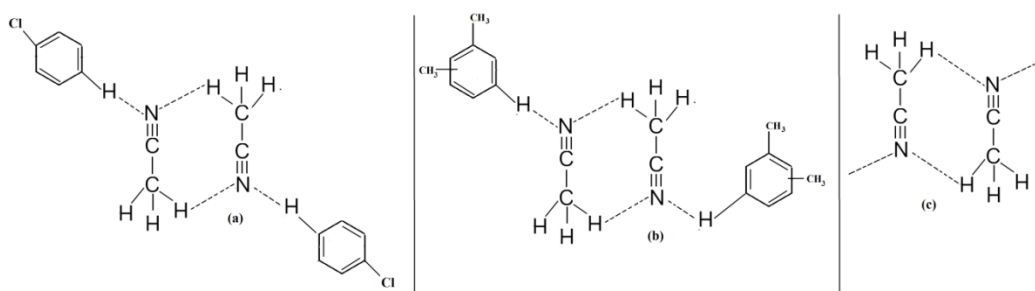
⁴*Corresponding author: D. B. Suryawanshi, Dept. of Physics and Electronics, Shri Havagiswami Mahavidyalaya, Udgir, (MS) India-413517.
 Email id: sdeelip123@gmail.com.

Table 1. Source and purity of liquids with literature values of polarity index and static dielectric constant.

Liquid	CAS Number	Supplier	Purity in Mass	Polarity Index [19-20]	Static dielectric constant [8, 16-18]
Acetonitrile	5-05-8	Sai Pharma. Pune	99.0%	5.8	33.549
Chlorobenzene	108-90-7	s d fiNE-Chem Limited, Bombay	99.0%	2.7	4.924
Xylene	1330-20-7	Himedia Laboratories, Pvt. Ltd. Mumbai	99.0%	2.5	2.642

**Fig. 1** Schematic diagram for experimental setup of X-band microwave technique.

An attempt is made to acknowledge hydrogen bonding interactions among complexes of different liquids and their mixtures, for which Luzar model [23] is used. Kirkwood-Froehlich theory is applied to separate g_1 and g_2 values from single ϵ' value, such that cross-related terms must be taken into concern. Average correlation factors g_1 and g_2 , average number of hydrogen bonds (n_{HB}^{11}) and (n_{HB}^{12}) per solute molecule for 1i pairs ($i = 1$ or 2) and static dielectric permittivity (ϵ') values have been calculated [23-24]. In present study, the probable bonding among hetero molecules is shown in figure 2.

**Fig. 2** Probable bonding between (a) ACN-CBZ, (b) ACN-Xylene and (c) ACN-ACN molecules.

III. RESULTS AND DISCUSSION

The variations of solute in solvent causes change in ϵ' value and is affected due to interactions [25-26] between hetero molecules which may create structural variations. As tabulated in table 1, dielectric constant values decrease with decrease in polarity index [21-22], in the order as ACN > CBZ > Xylene, thereby indicating effect of polarity index. Previous articles [8, 16-18] have been studied to reveal dielectric parameters of ACN, CBZ and Xylene binary solutions with an outcome of detailed dielectric parameters.

The dipole-dipole orientations are enlightened using Kirkwood correlation factor (g^{eff}) of distinct molecules in binary solution; is calculated from modified Kirkwood equation [27-28]. Kirkwood reveals concept of association and correlation among diverse molecules with structuredness [29-30] or orderedness of molecules or orientation of dipoles and is a measure of interruption in rotation of molecules. In present study, the effective Kirkwood correlation factor ' g^{eff} ' for Xylene is found to be 2.97, is greater than the values of ACN and CBZ, is

0.76, 0.60 at 301 K respectively, as tabulated in table 2. It seen that for all concentrations of all binary liquid mixtures (except xylene) the g^{eff} value is < 1 , is an indicative of unstructured nature [29-30], weak dipole-dipole interactions, parallel orientation of electric dipoles with [31-32] and insufficient interactions among them. In ACN+CBZ binary system, g^{eff} values rises with increases in V_{ACN} thereby confirming strong interaction in ACN rich region than that of CBZ region, is indication of deviation from unity [8, 30].

Table 2. Kirkwood correlation factor for different binary mixtures

V_{Solute}	g^{eff}		
	ACN+Xylene [18]	CBZ+Xylene	ACN+CBZ [8]
0	2.97	0.60	0.60
0.2	0.58	0.69	0.56
0.4	0.59	0.66	0.65
0.6	0.60	0.87	0.65
0.8	0.75	1.29	0.73
1.0	0.76	2.97	0.76

Hydrogen bonding effect between dipoles of heteromolecules is revealed using Luzar model. Variations in computationally obtained parameters were represented graphically in following figures. As stated in earlier paragraph of computational theoretical details, average correlation factors were determined from single value of ϵ' . As shown in figure 3, the values of correlation factor g_1 and g_2 increases with increasing solute and it is clear that the value of n_{HB}^{11} decreases and n_{HB}^{12} increases with increasing solute as shown in figure 4 (a), (b) and (c) respectively [31-33].

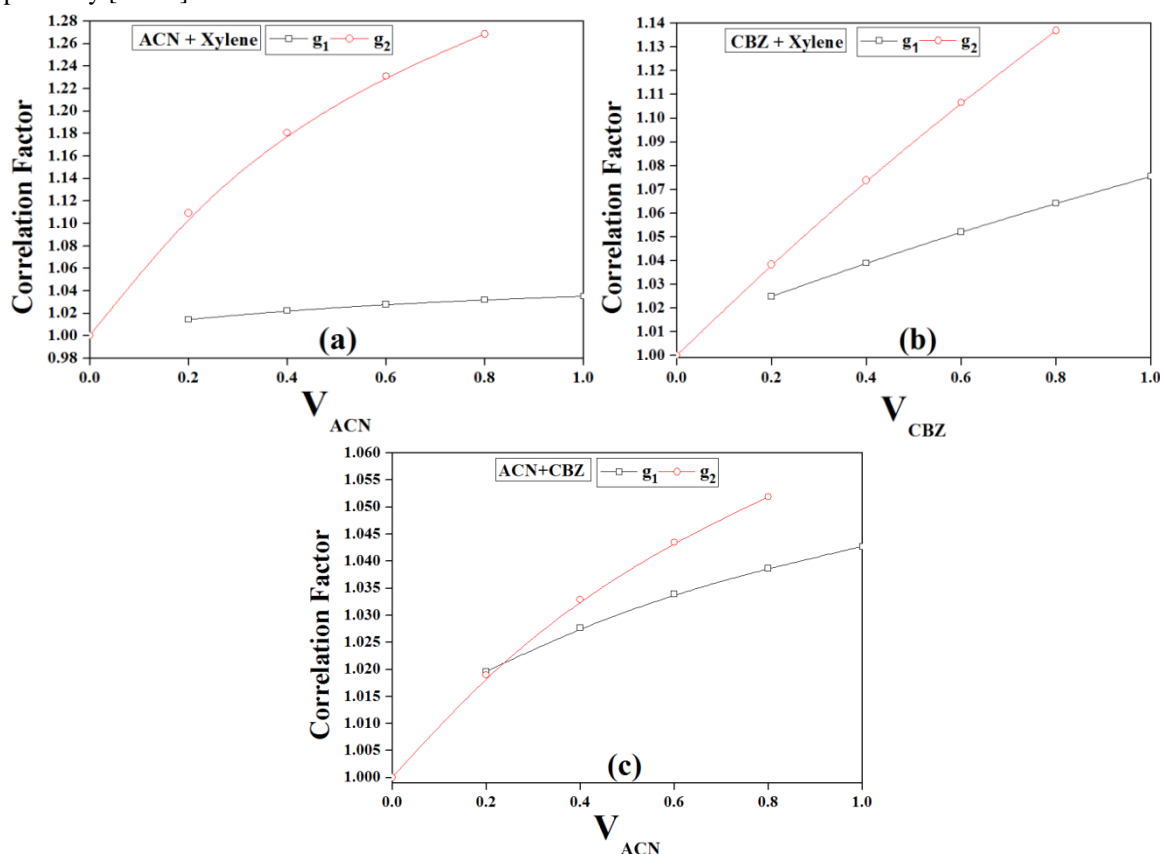


Fig. 3 Plots of correlation factor g_1 and g_2 at 301 K for (a) ACN+Xylene (b) CBZ+Xylene and (c) ACN+CBZ binary mixtures respectively.

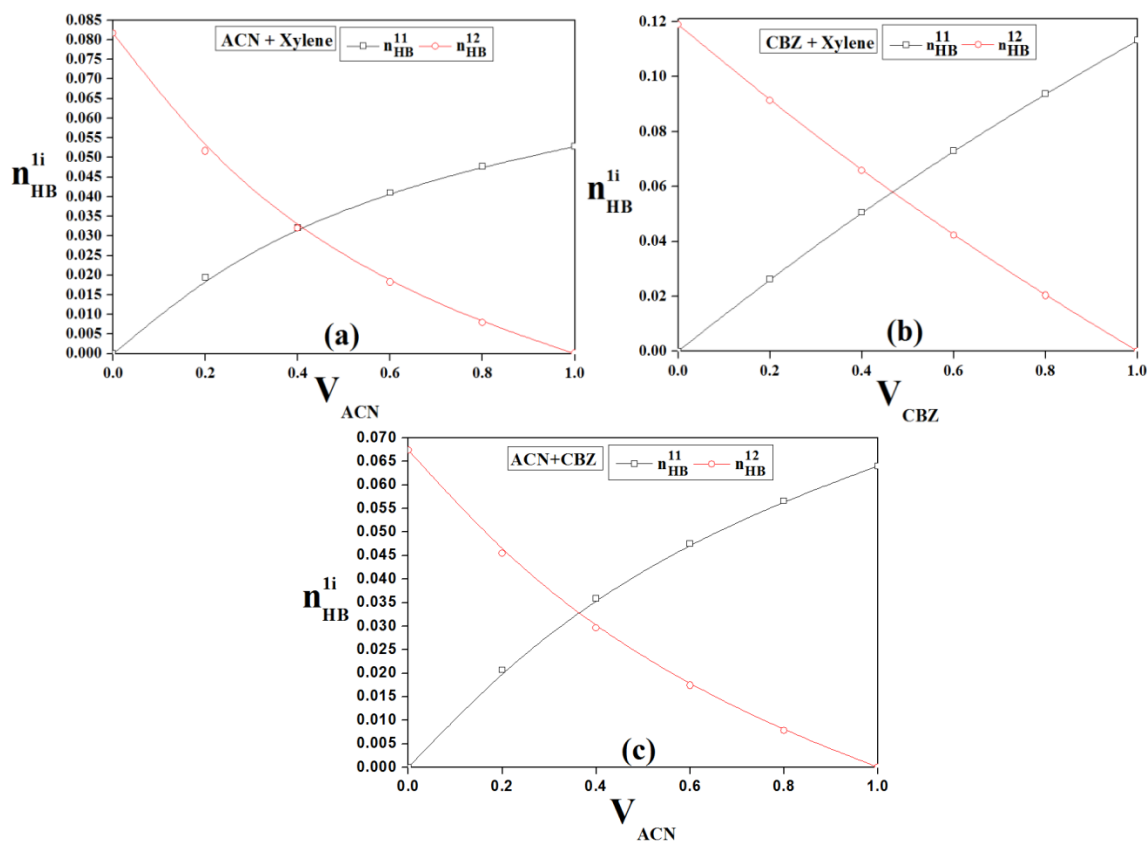


Fig. 4 Plot of average number of hydrogen bonds per unit volume at 301 K for (a) ACN+Xylene (b) CBZ+Xylene and (c) ACN+CBZ binary mixtures respectively.

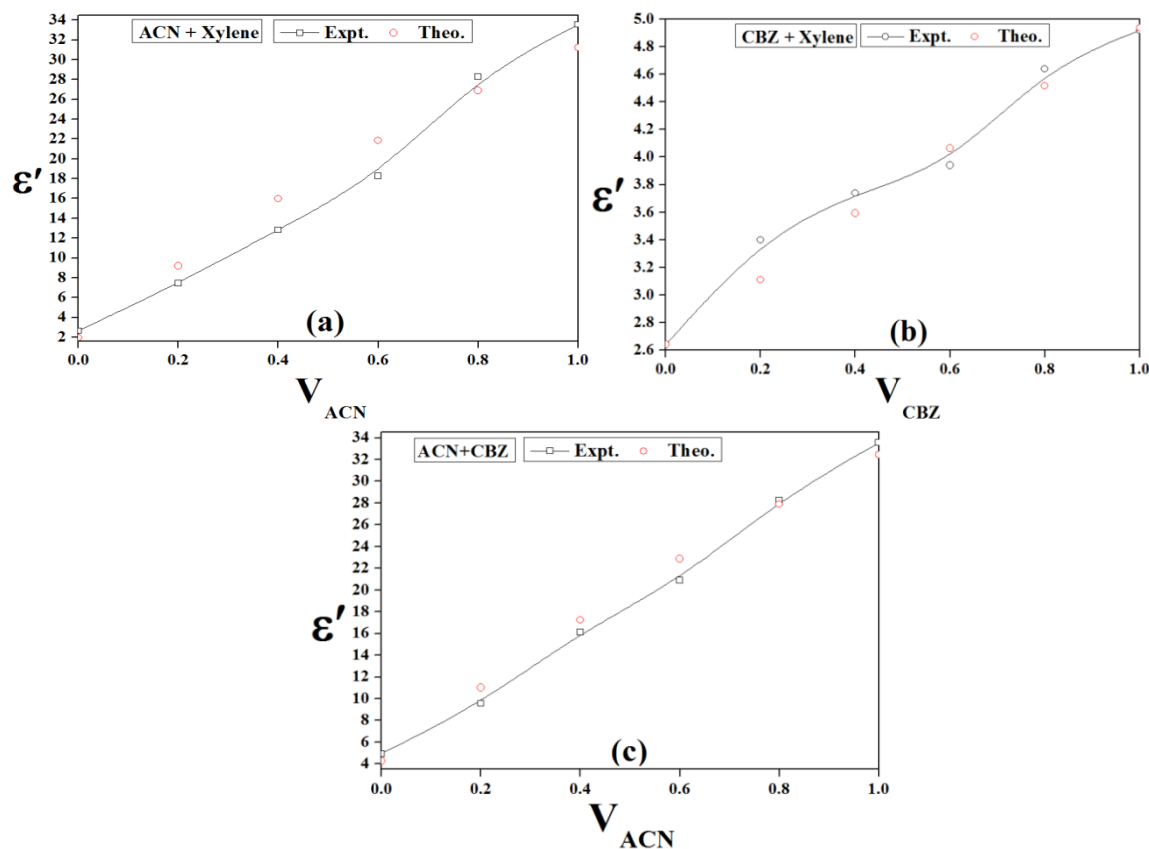


Fig. 5 Comparison of experimental and theoretical values of ϵ' at 301 K for (a) ACN+Xylene (b) CBZ+Xylene and (c) ACN+CBZ binary mixtures respectively.

From figure 4 it is clear that in these binary systems, CBZ+Xylene show maximum interactions such that the value of n_{HB}^{12} is 0.12 and that of in ACN+Xylene is 0.085 and in ACN+CBZ it is 0.070. In these binary systems, CBZ+Xylene show more associativeness rather than other two systems. The associativeness of the systems is in the order as, CBZ+Xylene>ACN+Xylene>ACN+CBZ respectively. Luzar model provides qualitative values of dielectric constant of ACN+Xylene, CBZ+Xylene and ACN+CBZ binary solutions as shown in figure 5. For all binary systems, predicted number of hydrogen bonds formed is two, such that probable values of molecular parameters with which ϵ' values are in good agreement with experimental values, as reported in Table 3.

Molecular parameters such as polarizability and bonding energy values differ in each system and these changes in the molecular parameters may be due to different physical parameters [34] such as structure, its nature, density, dipole moment and molecular weight of each molecule the liquid mixture system. In all binary systems, the value of polarizability increases with decrease in dipole moment and vice-versa as reported in the table 3. The polarizability of molecules in the mixture is in the order as, Xylene > CBZ > ACN. The value of bonding energy in each binary system is different such that the energy required in making and breaking of bonds is different. Comparatively in pure ACN-ACN and CBZ-CBZ molecules the bonding energy required is more in CBZ molecules than that of ACN molecules. In binary mixtures, value of bonding energy is in the order as, CBZ-Xylene > ACN-Xylene > ACN-CBZ.

Table 3. Molecular parameters utilized for computation of static dielectric constant (ϵ') for ACN+Xylene, CBZ+Xylene and ACN+CBZ binary solutions at 301 K.

Molecular Parameters							
ACN+Xylene			CBZ+Xylene			ACN+CBZ	
Effective Dipole Moment ^a of ACN		3.92	Effective Dipole Moment ^a of CBZ		1.5	Effective Dipole Moment ^a of ACN	3.92
Effective Dipole Moment ^a of Xylene		0.36	Effective Dipole Moment ^a of Xylene		0.36	Effective Dipole Moment ^a of CBZ	1.5
Polarizability ^b of ACN		1.1	Polarizability ^b of CBZ		9.2	Polarizability ^b of ACN	1.6
Polarizability ^b of Xylene		10.5	Polarizability ^b of Xylene		16.2	Polarizability ^b of CBZ	7.8
Bonding energy ^c of ACN-ACN		-0.5	Bonding energy ^c of CBZ- CBZ		-2.5	Bonding energy ^c of ACN-ACN	-1.0
Bonding energy ^c of ACN-Xylene		-1.0	Bonding energy ^c of CBZ-Xylene		-2.0	Bonding energy ^c of ACN-CBZ	-0.5
Enthalpy ^c of ACN-ACN		45	Enthalpy ^c of CBZ-CBZ		45	Enthalpy ^c of ACN-ACN	45
Enthalpy ^c of ACN-Xylene		35	Enthalpy ^c of CBZ-Xylene		35	Enthalpy ^c of ACN-CBZ	35
No. of Hydrogen Bonds		02	No. of Hydrogen Bonds		02	No. of Hydrogen Bonds	02

^aUnit: Debye; ^bUnit: A⁰³; ^cUnit: kJ/mol

IV. CONCLUSIONS

Static dielectric constant values of all binary systems were determined using frequency domain technique at 8.845 GHz. Dielectric constant values decrease with decrease in in polarity index, in the order as ACN>CBZ>Xylene. g^{eff} value is < 1 in all binary systems; indicate weak dipole-dipole and insufficient diverse molecular interactions, parallel orientation with unstructured nature for ACN & CBZ molecules in the mixture. Theoretically obtained values were compared with experimentally obtained dielectric parameter values using computational Luzar model, found to be good in agreement. Luzar model provides good qualitative information regarding static dielectric constant and Kirkwood correlation factors g_1 , g_2 and g^{eff} . Prediction of hydrogen bonds formed in all binary systems is two. Value of polarizability is in the order as Xylene > CBZ > ACN in the binary

systems. Bonding energy for all hetero molecules is in the order as, CBZ-Xylene > ACN-Xylene > ACN-CBZ. Thus from all binary systems studied, it is clear that the hetero molecules are less associative with each other in the system and among these three systems, CBZ+Xylene system shows more associativeness than other two systems.

ACKNOWLEDGMENT

Author S. S. Birajdar is thankful to Dept. of Chemistry for providing chemicals and also to Dept. of Physics & Electronics, Maharashtra Udayagiri Mahavidyalaya, Udgir for providing X-Band microwave setup and other facilities.

REFERENCES

- [1] A.C. Kumbharkhane, S.M. Puranik, S.C. Mehrotra, "Dielectric relaxation of tert-butyl alcohol-water mixtures using a time-domain technique", *J Chem Soc Faraday Trans*, no. 87 (1991): 1569-73. doi:10.1039/ft9918701569.
- [2] U. Kaatz, "Microwave dielectric properties of liquids", *Radiat Phys Chem*, no. 45 (1995): 549-66. doi: 10.1016/0969-806X(94)00070-Z.
- [3] S.S. Kadam, P.G. Hudge, D.B. Suryawanshi, A.C. Kumbharkhane, "Dielectric relaxation study of 2 and 3-chloroaniline and 2 and 3-methoxyaniline with 1, 4-dioxane mixtures using time domain technique", *Journal of Molecular Liquids*, no. 177 (2013): 426-431. doi.org/10.1016/j.molliq.2012.11.005.
- [4] S.S. Birajdar et al., Dielectric relaxation behaviour of ethyl acetate-xylene mixtures using time domain reflectometry, physics & chemistry of liquids 59 (4) (2021) 503-511, <https://doi.org/10.1080/00319104.2020.1743702>.
- [5] M.L. Sisodia, "Basic Microwave Techniques and Laboratory Manual", *Newagepublishers, India*, (2005).
- [6] T. Hengcharoena, K. Eaiprasertsaka and M. Fuangfoong, "Microwave Dielectric Measurement of Liquids by using Waveguide Plunger Technique", 2nd International Science, Social Science, Engineering and Energy Conference 2010: Engineering Science and Management, (2010) 270-274.
- [7] N. Thakur and D.R. Sharma, "Dielectric relaxation of acetonitrile in benzene solution from microwave absorption studies", *IJPAP*, no. 41 (2003): 806-809.
- [8] S.S. Birajdar, J.W. Gaikwad and D.B. Suryawanshi, "Microwave assisted co-operative dynamics and structural variations in chlorobenzene-acetonitrile solutions", *Bangladesh J. Sci. Ind. Res.* 57 no. 2 (2022) 85-90. doi.org/10.3329/bjsir.v57i2.60404.
- [9] Y.S. Joshi and A.C. Kumbharkhane, "Study of dielectric relaxation and hydrogen bonding in water +2 butoxyethanol mixture using TDR Technique", *Fluid Phase Equilibria*, no. 317 (2012): 96-101.
- [10] <https://en.wikipedia.org/wiki/Acetonitrile>.
- [11] <https://en.wikipedia.org/wiki/Xylene#Applications>.
- [12] R. Kandyala, S.P.C Raghavendra and S.T. Rajasekharan, Xylene: An overview of its health hazards and preventive measures, *Journal of Oral and Maxillofacial Pathology*, 14 (1) (2010) 1-5.
- [13] S.S. Birajdar, A.R. Deshmukh, A.C. Kumbharkhane and D.B. Suryawanshi, "Study of Thermodynamic and Dielectric Parameters of Xylene and Its Isomers Using Time Domain Dielectric Spectroscopy", *Polycyclic Aromatic Compounds*, (2022): 1-6. doi.org/10.1080/10406638.2022.2097273.
- [14] M. Meenachi and P. Krishnamurthi, "Dielectric Characteristics of Binary Mixtures of Esters with Hydrocarbons At 303 K", *Rasayan J. Chem*, no. 8 (2015): 98-104.
- [15] <https://en.wikipedia.org/wiki/Chlorobenzene>.
- [16] S. S. Birajdar, D.B. Suryawanshi, "Molecular & Structural Interaction Study of Chlorobenzene-Xylene Binary Mixture Using X-Band Dielectric Technique", *IJRSET* 6, no. 12 (2017): 22695-22698.
- [17] S.S. Birajdar, D.B. Suryawanshi, "Dielectric Properties of Chlorobenzene with Acetonitrile Using X-Band Microwave Dielectric Technique" *Research Journey*, no. 93, (2019): 51-54.
- [18] S.S. Birajdar, N.D. Vagshette, Shilpa S. Birajdar, D.B. Suryawanshi, A.R. Lathi, "Structural Characterization of Acetonitrile-Xylene Binary Mixtures At 301 K Using High Frequency X-Band Technique", *VIIRJ 12*, no. 1 (2021): 125-30.
- [19] <https://macro.lsu.edu/howto/solvents/polarity%20index.htm>.
- [20] <https://people.chem.umass.edu/xray/solvent.html>.
- [21] Z. Ahmad, Dielectric Materials - Polymer Dielectric Materials. October 3rd, 2012. DOI:10.5772/2781 and DOI: 10.5772/50638. ISBN : 978-953-51-6240-7.
- [22] R. M. Al Mohaimed et al., The Role of Solvent Environment on the Optical Behavior of Chemically Synthesized Silicon Nanoparticles. *Hindawi Journal of Spectroscopy*, (2018) 1-9. <https://doi.org/10.1155/2018/6870645>.
- [23] A. Luzar, "Dielectric behavior of DMSO-Water mixture a hydrogen bonding model", *Journal of Molecular Liquids*, no. 46 (1990): 221-238.
- [24] S. Sudo, N. Oshiki, N. Shinyashiki et al., "Dielectric properties of Ethyleneglycol-1,4-Dioxane mixtures using TDR method", *J Phy Chem A*. 111, no. 16 (2007) :2993-2998.
- [25] S.S. Birajdar, A.C. Kumbharkhane, S.N. Hallale, P.G. Hudge and D.B. Suryawanshi, "Thermodynamic and dielectric properties of Cyclohexanol-Xylene binary mixtures using dielectric spectroscopy", *Polycyclic Aromatic Compounds*, (2022): 1-9.
- [26] S.S. Birajdar et al., "Structural and molecular dynamics of methyl acetate-xylene solutions using dielectric relaxation spectroscopy", *Journal of the Indian Chemical Society* 99, no. 10 (2022): 1-4. doi.org/10.1016/j.jics.2022.100733.
- [27] J.G. Kirkwood, "The dielectric polarization of polar liquids", *Journal of Chemical Physics*, no. 7 (1939): 911.
- [28] H.M. Dhage et al., "Temperature dependent dielectric relaxation studies of 2-nitrotoluene-dimethyl sulfoxide mixture using time domain reflectometry", *Indian Journal of Chemistry*, no. 61 (2022): 1153-1158.
- [29] S.S. Birajdar et al. Study of structuredness and hydrogen bonding in binary solutions using microwave technique, *Indian Journal of Chemistry*, 63 (4) (2024) 383-389. doi: 10.56042/ijc.v63i4.6997.

- [30] Y. Marcus, The Structuredness of Solvents. *Journal of Solution Chemistry*, 21 (12) (1992) 1217–1230. <https://doi.org/10.1007/BF00667218>.
- [31] G. D. Rewar and D. Bhatnagar, “Dielectric relaxation in ternary mixtures of benzotrifluorides”, *Indian J. Pure Appl. Phys.*, no. 40 (2002): 430-435.
- [32] R. J. Sengwa, V. Khatri & S. Sankhla, Dielectric behavior and hydrogen bond molecular interaction study of formamide-dipolar solvents binary mixtures, *J Mol Liq*, 144 (2009) 89.
- [33] S.S. Birajdar, A.R. Deshmukh, D.B. Suryawanshi & A.C. Kumbharkhane, “Molecular interaction studies of isopropyl acetate-xylene mixture using dielectric relaxation approach”, *Indian Journal of Chemistry section A*, no. 60 (2021): 72-79. doi: 10.1080/10406638.2022.2032767.
- [34] D.R. Lide, Ed. “CRC handbook of chemistry and physics”, 87th ed. *Boca Raton (FL) Taylor and Francis* (2007).

© 2024. This work is published under

<https://creativecommons.org/licenses/by/4.0/legalcode>(the“License”).

Notwithstanding the ProQuest Terms and Conditions, you may use this content in accordance with the terms of the License.

¹B.M.Mude
²K.M.Mude
³R.N.Zade
⁴S.M.Yenorkar
⁵K.B.Raulkar
⁶R.R.Mistry
⁷S.M.Warbhe
⁸S.K.Mude
⁹S.P.Yawale

Enhancement in efficacy of gas sensor by doping metal oxide with conducting polymer



Abstract: - Recent uprising in gas sensor research shows substantial transfer to a enormous quantity of sensor devices for biomedical and environmental proficiency. These sensor devices have been made effective by suitable doping of metal oxides with conducting polymer PPy which can be formed by using solid electrolytes, insulators, metals, catalytic materials and classical semiconductors. A majority of polymers are unable to conduct electricity; their insulating properties are applied in the electronic industry. Such metal oxides gas sensors prepared by screen printing method. After validation of its properties viz. sensitivity, stability and characterization from FTIR and SEM etc. It has confirmed that enhancement in efficacy of gas sensor by doping metal oxide such as CuO, ZnO, SnO₂ with conducting polymer PPy.

Keywords: CuO, ZnO and SnO₂ gas sensors, Sensitivity and Stability

¹ * Dept. of Physics, Ramnarain Ruia College, Matunga(E)-400019 (M.S.) India

² Dept. of Physics ,Bhavan's College, Andheri(W)-400058(M.S.) India

³ Dept. of Chemistry, Siddharth College, Fort, Mumbai-400001(M.S.) India

⁴ Dept. of Physics, Shri Shivaji College, Parbhani-431 401 (M.S.) India

⁵ Dept. of Physics,Vidyabharti Mahavidyalaya, Amravati-444602(M.S.) India

⁶ Dept. of Physics, Deogiri College, Chhat. Sambhajinagar-431005 (M.S.) India

⁷ Dept. of Mathematics, Vidyabharti Mahavidyalaya, Amravati-444602(M.S.) India

⁸ Dept. of AI &DS, Thakur College of Engineering and Technology , Kandiwali(E),Mumbai-400101(M.S.) India

⁹ Dept. of Physics, Government Vidarbha Institute of Science & Humanities , Amravati-444604(M.S.) India

e-mail Corresponding Author : bhupeshmude@ruiacollege.edu

Copyright © JES 2024 on-line : journal.esrgroups.org

I. INTRODUCTION

The last century has seen increased industrial growth worldwide. A side effect of this development is an exponential increase in pollution of earth, air and water, especially in densely populated areas. While land pollution is locally restricted and great efforts have been made during the last decades to improve the quality of rivers and larger bodies of water, air pollution is not so easily reduced. Recently, there is a great interest in implementing sensing devices in order to improve environmental and safety control of gases. The most used gas sensor devices can be divided in three big groups depending on the technology applied in their development: solid state, spectroscopic and optic. While spectroscopic and optic systems are very expensive for domestic use and sometimes difficult to implement in reduced spaces as car engines, the so called solid state sensors present great advantages due to their fast sensing response, simple implementation and low prices [1-5]. These solid state gas sensors are based on the Change of the physical and /or chemical properties of their sensing materials when exposed to different gas atmospheres. Although the number of materials used to implement this kind of devices is huge, this work was centered in studying the semiconductor properties, in those material using SnO₂ and ZnO as sensing materials.

The main purpose of this paper is to study and develop CO₂ gas sensor with new materials for gas sensing elements starting from the knowledge in thick film production using screen-printing technique.

II. EXPERIMENTAL

2.1 Sensor preparation:

Ammonia solution (NH₃·H₂O): Used for pH adjustment. ZnO , SnO₂ and Al₂O₃ powders (AR grade) were calcinated at about 700 °C for 5-6 h and were crushed in mortal pestle to get fine powder of the samples. ZnO ,SnO₂ were characterized by SEM. The ink or paste of the sample was prepared by using screen-printing (thick film technique) technique. The binder for screen-printing was prepared by thoroughly mixing 8 wt% butyl carbitol with 92 wt% ethyl cellulose. On chemically cleaned glass plate, paste of Al₂O₃ was screen printed and it was kept for 24 hr to dry it at room temperature and then heated at 140°C for 2.5 h to remove the binder. The Al₂O₃ layer provides mechanical support as well as high thermal conductivity. Paste of ZnO and SnO₂ mixed in proper stiochometry was then screen printed on Al₂O₃ layer. Again plate was dried at room temperature for 24 h and binder was removed by heating it at 150°C for 2.5 h. Finally film is prepared by screen printing, whole plate was dried and again binder was removed as above. Fabrication of multilayer sensor is shown in following fig. (1)

Finally on the top surface of the sensor, interdigitate electrodes [6,9] were fabricated using conducting silver paste as shown in the Fig.1 (b)To measure the sensitivity, electrical resistance was measured with the help of voltage drop method, best one.

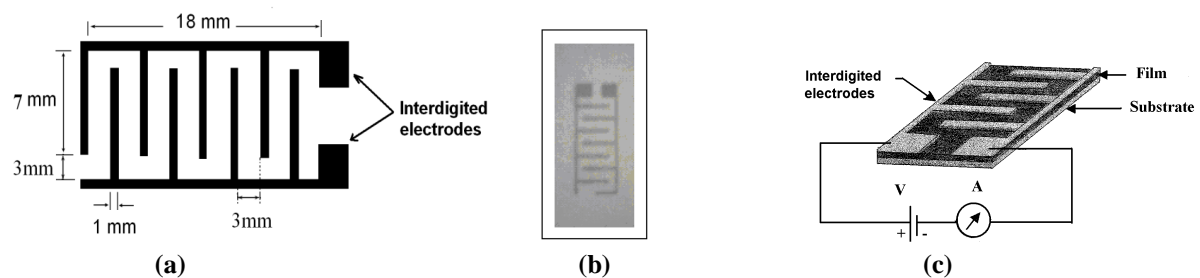


Fig. 1 (a) Fabrication of interdigitate Electrodes (b) Actual photograph of interdigitate electrodes (c) Circuit of resistance measurement using interdigitate electrodes.

III. RESULT AND DISSCUSSION

3.1 Scanning Electron Microscopy (SEM)

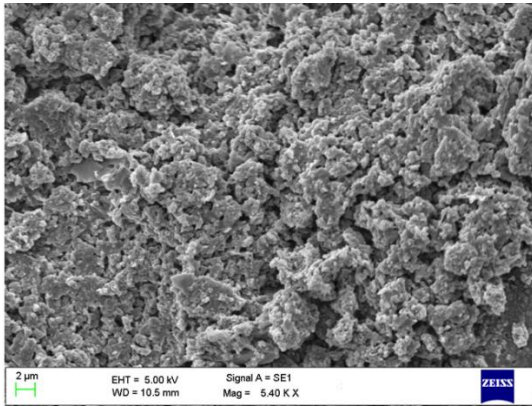


Fig 2 (a). SEM Pure ZnO

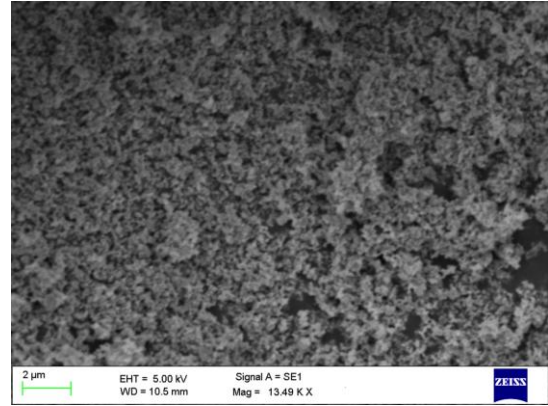


Fig.2 (b) SEM Pure SnO₂

Above SEM images shows some rods with fine voids over them which helps to enhance gas sensing properties. The surface morphologies of ZnO and SnO₂ materials were studied by SEM and the average diameter and number of pores per inch of ZnO and SnO₂ are as under.

Table .1 Average diameter of pore and number of pores per inch of pure samples and their compositions

Sr.No	Pure sample and their composition (mole %)	Average diameter of pore(nm)	No. of pores per inch (in x 2000 Magnification)
1	SnO ₂ doped with PPY	780	67
2	SnO ₂	740	61
3	ZnO	700	56

From the SEM pictures, it is observed that SnO₂ have maximum pores per inch (calculated for x 2,000 magnification for each composition) than ZnO. Thus SnO₂ have more surface area and exhibit more sensing nature.

3.2. Sensitivity of Sensor:

The sensitivity of the sensor is given by equation (2),

$$S = \left(\frac{R_{air} - R_{gas}}{R_{air}} \right) = \left(\frac{\Delta R}{R_{air}} \right) \tag{2}$$

Where, R_{air} and R_{gas} are the resistances of sensors in air and gas respectively. Maximum sensitivity was recorded for multilayer sensor at 70 ppm concentration of CO₂

Sr. No.	Sample	Codes
1	Pure SnO ₂	P1
2	Pure ZnO	P2
3	ZnO Doped with PPY	P3

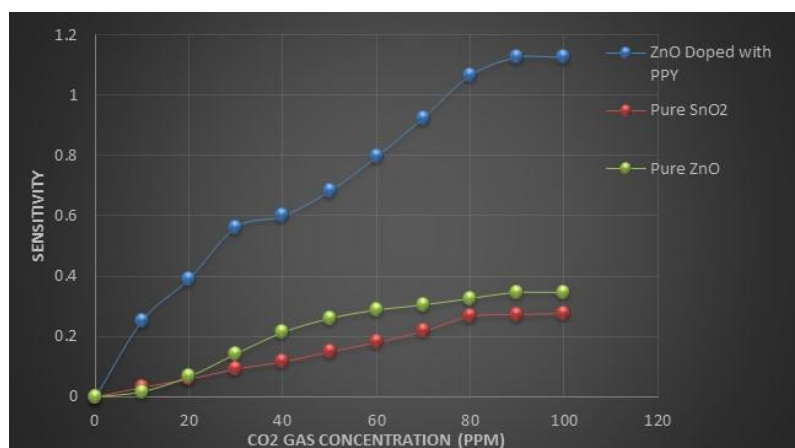


Figure 3: Variation of sensitivity with of CO₂ gas concentration for SnO₂, ZnO and ZnO doped PPY samples

It was observed that, in a typical case, the sensitivity increases gradually with temperature and becomes less gradual at higher temperature values. From linear dependency, it deviates to a maximum value and beyond this point the sensitivity falls rapidly, such behavior is being exhibited by almost all the metal oxide-based gas sensor

3.2. Stability of Sensor:

Rate of change of resistance of the sensor with respect to time defines the stability of the sensor. A sensor should be more stable for its better response. It is observed that resistance of SnO₂ sensor does not change drastically as that in case of ZnO samples.

IV. CONCLUSION

From SEM characterization it is concluded that the crystallite size of SnO₂ is smaller, more porous and hence has greater surface area and therefore shows greater response to CO₂ gas. Screen printing technique is the easiest for the preparation of sensor. SnO₂ sensor shows good stability than ZnO samples and dynamic response of SnO₂ is also fast. In present work we prepared a thick film of metal oxides SnO₂ and ZnO by using screen printing technique and analyzed by SEM.

REFERENCES

- [1] S.P.Yawale, S.S.Yawale, G.T.Lamdhade, *Sensors and Actuators A*, **135**, 388–393(2007). (5)
- [2] N. Pinna and M. Niederberger, *Angewandte Chemie International Edition*, **47**(29), 5292–5304 (2008).
- [3] Schultze, J.W.; Karabulut, H. Application potential of conducting polymers. *Electrochimica Acta*, **50**, 1739 (2005), *Journal of Chemical Devices*, Vol.10,2011, pp 433-437
- [4] S. A. waghuley, *Journal of electron devices*, vol.10,2011, pp 433-437
- [5] Asmus, T.; Wolf, G. K. Modification and structuring of conducting polymer films on insulating substrates by ion beam treatment. *Nucl. Instr. and Meth. in Phy. Res. B*. **166**, 732 (2000).
- [6] Mastragostino, M.; Arbizzani, C.; Soavi, F. Conducting polymers as electrode materials in super capacitors. *Solid State Ionics*, **148**, 493 (2002).
- [7] Dhawan, S.K.; Singh, N.; Rodrigues, D. Electromagnetic shielding behaviour of conducting polyaniline composites. *Science and Technology of Advanced Materials*, **4**, 105 (2003).
- [8] Koul, S.; Chandra, R.; Dhawan, S.K. Conducting polyaniline composite: a reusable sensor material for aqueous ammonia. *Sensors and Actuators B: Chemical*, **75**, 151(2001).
- [9] Jain, S.; Chakane, S.; Samui, A.B.; Krishnamurthy, V.N.; Bhoraskar, S.V. Humidity sensing with weak acid-doped polyaniline and its composites. *Sensors and Actuators B*: **96**, 124(2003).
- [10] Joon-Boo, Yu.; Hyung-Gi, B.; Myung-Suk, So.; Jeung-Soo, H. Analysis of diabetic patient's breath with conducting polymer sensor array. *Sensors and Actuators B*: **108**, 305 (2005)

¹Dr. Niteen S. Mohod

Advancement In Biomedical Sensor Technologies And Future



Abstract - Earlier, due to unavailability of the hi-tech biomedical equipments and the remote monitoring systems, advance diagnosis and its medication was an issue leading to higher death rate. With the advancement and upgradations in technologies, sophisticated biomedical sensors are available today and it has become easier not just to monitor but also to diagnose various diseases in advance, observing the varied physiological parameters and the changes taking place in them. Naturally, it leads to better life expectancy and health wise quality life. Through this paper, an attempt has been made to review the principles, types of sensors, and their applications. Also, the challenges in this field have been considered and the potential for future advancement is also discussed.

Keywords : Hi-tech biomedical equipments, Remote monitoring systems, Biomedical Sensor, Monitor, Diagnose, Physiological parameters, life expectancy, Health wise quality life.

¹* Asst. Prof. in Electronics, Shri Shivaji College of Arts, Commerce & Science, Dist: Akola, MS, India
Corresponding author e-mail : mohodniteen@gmail.com
Copyright©JES2024on-line:journal.esrgroups.org

I. INTRODUCTION

As every sensor functions, biomedical sensors detect physiological changes and transducer or convert them to measurable electrical signals. These sensors need to be very accurate in medical diagnostics, monitoring the patient's live and accordingly providing them the medication. During Covid-19 everyone has experienced this while measuring the body temperature and percentage oxygen in the blood maintaining social distance and more effectively while treating the patients.

II. PROMINENT ELEMENTS OF SENSOR

Broadly, every sensor system includes a Sensing element, Transducer, and Signal Processor as the basic blocks and is applicable to biomedical sensors too. Every block of sensor functions independently resulting in a signal that is sufficient to monitor, diagnose, and medicate the patient accordingly. The basic function of each block is as under;

1. **Sensing Element:** It senses/detects the physiological change occurring.
2. **Transducer:** It converts/transduces the detected biological signal / Physiological change into a measurable electrical signal.
3. **Signal Processor:** Processes the output of the Transducer (Electrical signal) for display or analysis purposes.

III. TYPES OF BIOMEDICAL SENSORS

Biomedical sensors are classified according to the parameters they measure or the technology they use;

- a) **Electrochemical Sensors / Analyzers:** Mainly measure biochemical reactions, commonly used in monitoring blood glucose, urea and dopamine [1].
- b) **Optical Sensor:** These sensor deals with the light. Used to detect changes in intensities of light on passing through blood in case of Pulsoximetry [2].
- c) **Acoustic Sensors:** Mainly detect changes in sound waves. Used in Ultrasound imaging [3].
- d) **Mechanical Sensors:** Deals with mechanical changes such as Pressure, Force, or Displacement mostly used in monitoring blood pressure [4].

IV. APPLICATIONS OF BIOMEDICAL SENSORS

- i. **Medical Diagnostics:** Biomedical sensors are mostly used in diagnostic devices for disease detection and in monitoring health conditions. Glucose sensors for diabetes management and biosensors for detecting biomarkers of diseases like cancer and cardiovascular conditions [5].
- ii. **Monitoring the Patient:** In emergencies, continuous monitoring of parameters like heart rate, blood pressure, and oxygen saturation is required. Under such circumstances wearable sensors are preferable enabling real-time monitoring and data collection [6].
- iii. **Wearable Health Devices:** Wearable sensors are integrated and embedded into fitness trackers and smart watches to monitor physical activity, sleep patterns, and other health metrics, promoting preventive healthcare and personalized medicine [7].
- iv. **Implantable Devices:** Implantable sensors are used for long-term monitoring of internal physiological conditions. Examples include cardiac pacemakers and glucose sensors implanted under the skin [8].

V. FUTURE TRENDS

a) Advances in Nanotechnology: Integrating nanomaterials like nanoparticles, nanowires, and nanotubes boost the sensitivity and specificity of biosensors. Nanotechnology allows miniaturization of biosensors making them portable and even more suitable for point-of-care applications [9].

b) Internet of Things (IoT): IoT-enabled biosensors help in transmitting real-time data to remote live monitoring systems and it has become the revolution in healthcare [10]

VI. CHALLENGES

Despite advancements, biosensors face challenges such as stability, reproducibility, and cost-effectiveness. Meeting these issues requires multidisciplinary efforts in materials science, biology, and engineering [11].

VII. CONCLUSION

Tremendous transformation in healthcare is becoming possible through biomedical sensors enabling precise monitoring and diagnostics. Advances in nanotechnology, AI, and IoT have added the feather enhancing the functionality and accessibility of these sensors. Overcoming current challenges will pave the way for innovative applications and improved healthcare outcomes.

REFERENCES

- [1] Heller, A., & Feldman, B. (2008). Electrochemical glucose sensors and their applications in diabetes management. *Chemical Reviews*, 108(7), 2482-2505.
- [2] Borisov, S. M., & Klimant, I. (2008). Optical sensors for continuous glucose monitoring. *Chemical Reviews*, 108(2), 423-461.
- [3] Szabo, T. L. (2004). *Diagnostic ultrasound imaging: Inside out*. Academic Press.
- [4] Chen, P. J., Rodger, D. C., Saati, S., Humayun, M. S., & Tai, Y. C. (2013). Microfabricated implantable Parylene-based wireless passive intraocular pressure sensors. *Journal of Microelectromechanical Systems*, 17(6), 1342-1351.
- [5] Wang, J. (2006). Electrochemical biosensors: Towards point-of-care applications. *Analyst*, 131(5), 657-662.
- [6] Heikenfeld, J., Jajack, A., Rogers, J., Gutruf, P., Tian, L., Pan, T., Li, R., Khine, M., Kim, J., & Wang, J. (2018). Wearable sensors: modalities, challenges, and prospects. *Lab on a Chip*, 18(2), 217-248.
- [7] Mishra, R. K., Barfidokht, A., & Karunakaran, C. (2017). Wearable chemical sensors: opportunities and challenges. *Electroanalysis*, 29(8), 1881-1892.
- [8] Merritt, C. R., Nagle, H. T., & Grant, E. (2009). Implantable medical devices. *Engineering in Medicine and Biology Magazine*, 18(3), 23-30
- [9] Wang, J. (2005). Nanomaterial-based electrochemical biosensors. *Analytical Chemistry*, 77(23), 7439-7452.
- [10] Park, S., Jayaraman, S., & Kim, J. (2017). Wearable biomedical devices: paradigms and challenges. *Smart Healthcare*, 1-23.
- [11] Turner, A. P. F. (2013). Biosensors: sense and sensitivity. *Science*, 290(5495), 1315-1317.

Mr. M. C. NAIDU¹,

Dr. D. S. Dhote²

1. Assistant Professor
Department of
Electronics Hislop
College, Nagpur, India

2. Professor and
Principal, Brijlal Biyani
Science College
Amravati, India.

Wearable Artificial Intelligence Biosensors and Bioelectronic Devices: A Comprehensive Review



Abstract

Wearable artificial intelligence (AI) biosensors and bioelectronic devices represent a burgeoning field at the intersection of advanced electronics, material science, and computational intelligence. These devices have the potential to revolutionize health monitoring, disease diagnosis, and personalized medicine by providing continuous, real-time data on various physiological parameters. This review paper aims to provide a comprehensive overview of the current state of wearable AI biosensors and bioelectronic devices, discussing their design, functionality, integration with AI, and applications in healthcare. The paper also addresses the challenges and future prospects of these technologies.

Keywords: Wearable Biomedical Devices, Biosensors, Bioelectronic devices, Polymers, Conductive Textiles, Nano particles , Nanomaterials, Nanowires, Nanoribbons, Artificial Intelligence, IoT, Remote Patient monitoring.

Introduction

The integration of wearable technology with AI has led to the development of sophisticated biosensors and bioelectronic devices capable of real-time health monitoring and disease management. These devices offer non-invasive, continuous monitoring of various physiological parameters, enabling timely intervention and personalized healthcare. The convergence of miniaturized electronics, advanced materials, and AI algorithms has opened new avenues for innovation in this field.

Design and Functionality of Wearable AI Biosensors

Materials and Fabrication Techniques

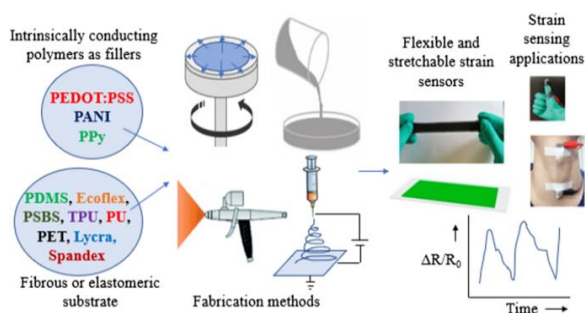
The materials used in wearable biosensors are crucial for their performance, comfort, and biocompatibility. Common materials include flexible polymers, conductive textiles, and advanced composites. Fabrication techniques such as inkjet printing, screen printing, and 3D printing have been employed to create flexible, stretchable, and wearable sensors. These materials and techniques enable the integration of sensors into everyday clothing and accessories, enhancing user comfort and compliance.

The choice of materials in wearable AI biosensors is critical to their performance, flexibility, biocompatibility, and overall user comfort. The materials must be capable of integrating advanced sensing functionalities while ensuring durability and wearability. This section delves into the key materials commonly employed in the construction of wearable AI biosensors, categorized based on their primary functions and properties.

Flexible Substrates

Polymers

Polymers are extensively used as substrates in wearable biosensors due to their flexibility, lightweight nature, and ease of fabrication. Common polymers include:



- **Polydimethylsiloxane (PDMS):** Known for its flexibility, biocompatibility, and ease of patterning. PDMS is often used in microfluidic devices and flexible electronics.

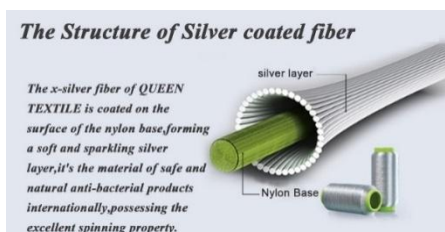
- **Polyimide (PI):** Offers excellent thermal stability and mechanical strength, making it suitable

for applications requiring robust performance.

- **Polyethylene terephthalate (PET):** Frequently used in flexible electronics due to its transparency, flexibility, and ease of processing.
- **Thermoplastic polyurethane (TPU):** Combines elasticity with durability, ideal for applications requiring stretchable and resilient materials.

Textiles

Conductive textiles integrate conductive materials into fabric, providing comfort and flexibility while maintaining electrical functionality. These include:



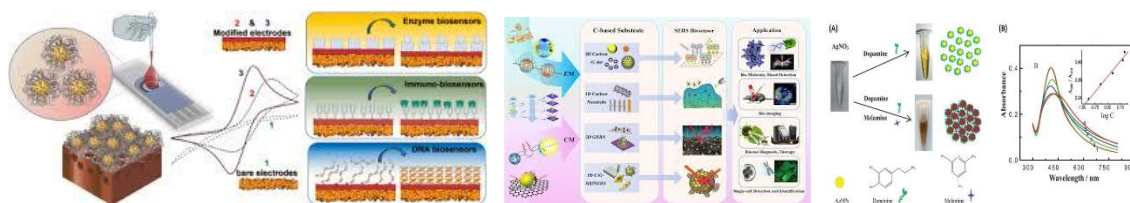
- **Silver-coated fibers:** Provide high conductivity and are used in fabrics for ECG and EMG monitoring.
- **Carbon-based textiles:** Utilize materials like carbon nanotubes or graphene, offering excellent conductivity and flexibility.

Conductive Materials

Metals

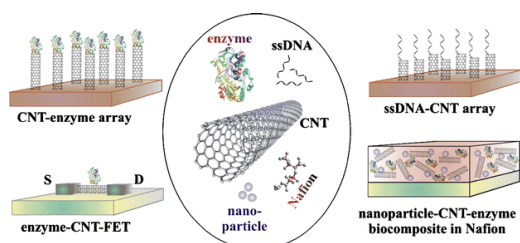
Metals are crucial for their high conductivity and are often used in interconnects and electrodes:

- **Gold (Au):** Highly conductive and biocompatible, though expensive.
- **Silver (Ag):** Offers excellent conductivity and is commonly used in wearable sensors for signal transmission.
- **Copper (Cu):** Known for its high conductivity and relatively lower cost, though less biocompatible than gold and silver.



Carbon-Based Materials

Carbon-based materials are popular due to their unique electrical properties and flexibility:



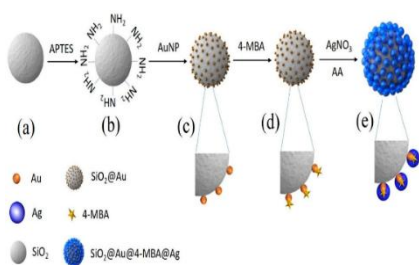
- **Graphene:** A single layer of carbon atoms with excellent electrical conductivity, flexibility, and mechanical strength.

- **Carbon Nanotubes (CNTs):** Cylindrical nanostructures with remarkable electrical, thermal, and mechanical properties.
- **Graphite:** Used in various forms, including composites, due to its good conductivity and cost-effectiveness.

Functional Nanomaterials

Nanoparticles

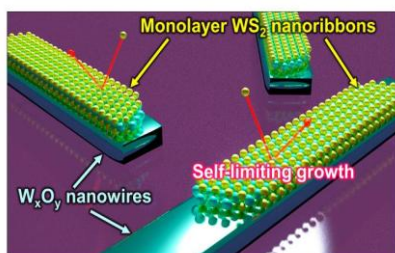
Nanoparticles enhance the sensing capabilities of wearable biosensors by providing high surface area and unique properties:



- **Gold nanoparticles (AuNPs):** Enhance electrochemical and optical sensing due to their excellent conductive properties and biocompatibility.
- **Silver nanoparticles (AgNPs):** Known for their antimicrobial properties and high conductivity, useful in biosensors and bioelectronics.
- **Silica nanoparticles:** Often used as carriers for biomolecules or drugs in targeted delivery systems.

Nanowires and Nanoribbons

These materials provide high sensitivity and flexibility for biosensors:



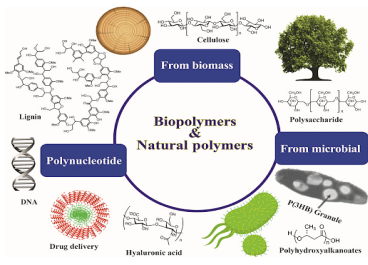
properties and chemical stability.

Biocompatible and Biodegradable Materials

Natural Polymers

- **Silicon nanowires (SiNWs):** Offer excellent electronic properties and high surface-to-volume ratio, enhancing sensitivity.
- **Metal oxide nanowires:** Materials like zinc oxide (ZnO) and tin oxide (SnO₂) are used for their unique electronic

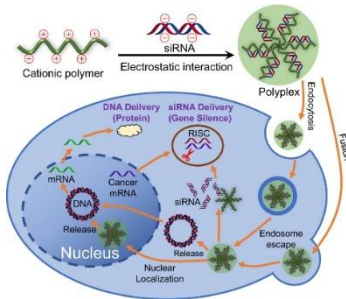
Natural polymers offer biocompatibility and biodegradability, making them suitable for temporary implants or disposable sensors:



- **Chitosan:** Derived from chitin, used for its biocompatibility, biodegradability, and ability to form films and fibers.
- **Alginate:** Extracted from seaweed, used for its gel-forming ability and biocompatibility.
- **Gelatin:** A protein-based polymer used for its biodegradability and film-forming properties.

Synthetic Biodegradable Polymers

These polymers degrade into non-toxic byproducts, suitable for transient sensors:

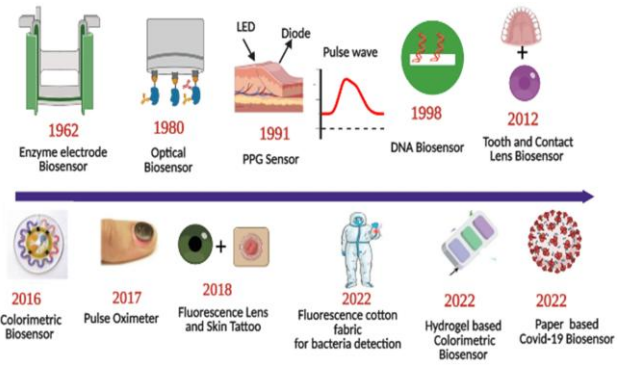
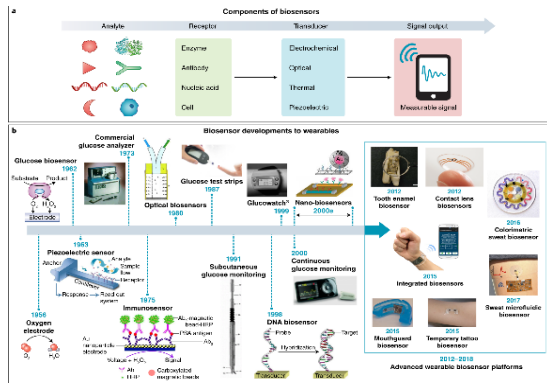


- **Poly(lactic acid) (PLA):** A biodegradable thermoplastic derived from renewable resources, commonly used in medical applications.
- **Poly(glycolic acid) (PGA):** Known for its high strength and biodegradability, used in sutures and implantable devices.
- **Polycaprolactone (PCL):** A biodegradable polyester with a low melting point, used in drug delivery systems and tissue engineering.

Sensing Mechanisms

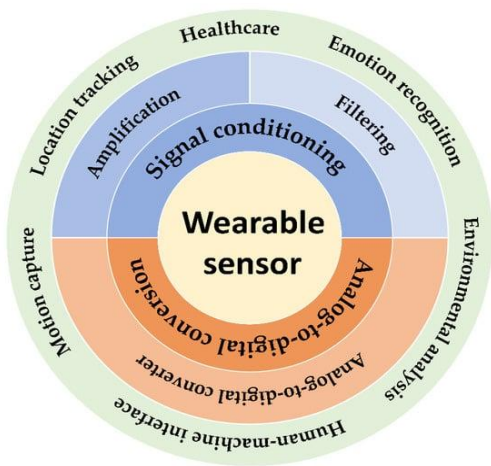
Wearable biosensors utilize various sensing mechanisms to detect physiological parameters:

- **Electrochemical sensors:** Measure biochemical markers such as glucose, lactate, and pH levels using enzymatic or non-enzymatic reactions.
- **Optical sensors:** Use light-based methods like photoplethysmography (PPG) and fluorescence to monitor parameters such as heart rate, oxygen saturation, and metabolic activity.
- **Mechanical sensors:** Detect physical parameters like strain, pressure, and motion, useful in monitoring activities like gait analysis and respiratory rate.



Data Acquisition and Processing

The integration of AI in wearable biosensors involves sophisticated data acquisition and processing techniques. These devices collect raw data from sensors and preprocess it to remove noise and artifacts. Machine learning algorithms are then applied to analyze the data, detect patterns, and provide actionable insights. Techniques such as deep learning, neural networks, and reinforcement learning have shown promise in improving the accuracy and reliability of these devices.



Applications in Healthcare

Chronic Disease Management

Wearable AI biosensors are particularly valuable in managing chronic diseases such as diabetes, cardiovascular diseases, and respiratory disorders. Continuous glucose monitors (CGMs) equipped with AI algorithms can predict glucose levels and suggest insulin doses for diabetic patients. Similarly, wearable ECG monitors can detect arrhythmias and predict potential cardiac events, enabling timely intervention.

Remote Patient Monitoring

Remote patient monitoring (RPM) has gained traction, especially in the context of the COVID-19 pandemic. Wearable biosensors enable healthcare providers to monitor patients' vital signs remotely, reducing the need for hospital visits and minimizing exposure risks. AI-driven analytics provide

healthcare professionals with real-time insights, facilitating early detection of health issues and personalized care.

Fitness and Wellness

The fitness and wellness industry has widely adopted wearable biosensors to monitor physical activity, sleep patterns, and overall health. Devices like smartwatches and fitness bands track metrics such as steps taken, calories burned, and sleep quality. AI algorithms personalize fitness recommendations and detect irregularities that may indicate health issues.

Rehabilitation and Physical Therapy

Wearable biosensors are increasingly used in rehabilitation and physical therapy to monitor patients' progress and ensure adherence to prescribed exercises. Motion sensors and AI algorithms analyze movement patterns, providing feedback to both patients and therapists. This technology enables tailored rehabilitation programs and enhances recovery outcomes.

Challenges and Future Prospects

Technical Challenges

- **Battery life and energy efficiency:** Ensuring long battery life while maintaining the device's functionality is a critical challenge.
- **Data security and privacy:** Protecting sensitive health data from breaches and ensuring user privacy is paramount.
- **Accuracy and reliability:** Enhancing the accuracy and reliability of biosensors to provide clinically relevant data is essential for widespread adoption.

Regulatory and Ethical Considerations

- **Regulatory approval:** Navigating the regulatory landscape to gain approval from bodies like the FDA and EMA is complex and time-consuming.
- **Ethical concerns:** Addressing ethical issues related to data ownership, consent, and the potential misuse of health data is crucial.

Future Directions

- **Integration with IoT:** Combining wearable biosensors with the Internet of Things (IoT) can enhance connectivity and data sharing, leading to more comprehensive health monitoring systems.
- **Advanced AI algorithms:** Developing more sophisticated AI algorithms to improve data analysis, prediction, and personalized recommendations.
- **New sensing technologies:** Exploring novel sensing technologies such as nanomaterials and biosynthetic sensors to expand the range of detectable biomarkers.

Conclusion

Wearable AI biosensors and bioelectronic devices are poised to transform healthcare by providing continuous, real-time monitoring of physiological parameters. Despite technical, regulatory, and ethical challenges, ongoing advancements in materials science, AI, and fabrication techniques hold promise for the future of this field. As these technologies continue to evolve, they have the potential to improve health outcomes, enhance patient care, and contribute to the development of personalized medicine.

References

1. Bandodkar, A. J., Jeerapan, I., & Wang, J. (2016). Wearable Chemical Sensors: Present Challenges and Future Prospects. *ACS Sensors*, 1(5), 464-482.
2. Heikenfeld, J., Jajack, A., Rogers, J., Gutruf, P., Tian, L., Pan, T., ... & Kim, J. (2018). Wearable sensors: modalities, challenges, and prospects. *Lab on a Chip*, 18(2), 217-248.
3. Ray, T. R., Choi, J., Bandodkar, A. J., Krishnan, S., Gutruf, P., Tian, L., ... & Rogers, J. A. (2019). Bio-integrated wearable systems: a comprehensive review. *Chemical Reviews*, 119(8), 5461-5533.
4. Pankratova, N., González-López, J. R., & Giannakopoulos, S. (2021). Wearable biosensors for monitoring mental health. *TrAC Trends in Analytical Chemistry*, 145, 116470.
5. Patel, S., Park, H., Bonato, P., Chan, L., & Rodgers, M. (2012). A review of wearable sensors and systems with application in rehabilitation. *Journal of NeuroEngineering and Rehabilitation*, 9(1), 21.
6. Jin X, Liu C, Xu T, Su L, Zhang X. Artificial intelligence biosensors: Challenges and prospects. *Biosensors and Bioelectronics*. 2020 Oct 1;165:112412.
7. Zhang Y, Hu Y, Jiang N, Yetisen AK. Wearable artificial intelligence biosensor networks. *Biosensors and Bioelectronics*. 2023 Jan 1;219:114825.

8. Qureshi R, Irfan M, Ali H, Khan A, Nittala AS, Ali S, Shah A, Gondal TM, Sadak F, Shah Z, Hadi MU. Artificial intelligence and biosensors in healthcare and its clinical relevance: A review. *IEEE Access*. 2023 Jun 13.
9. Zheng Y, Tang N, Omar R, Hu Z, Duong T, Wang J, Wu W, Haick H. Smart materials enabled with artificial intelligence for healthcare wearables. *Advanced Functional Materials*. 2021 Dec;31(51):2105482.
10. Goh GD, Lee JM, Goh GL, Huang X, Lee S, Yeong WY. Machine learning for bioelectronics on wearable and implantable devices: challenges and potential. *Tissue Engineering Part A*. 2023 Jan 1;29(1-2):20-46.
11. Jin X, Cai A, Xu T, Zhang X. Artificial intelligence biosensors for continuous glucose monitoring. *Interdisciplinary Materials*. 2023 Mar;2(2):290-307.
12. Smith AA, Li R, Tse ZT. Reshaping healthcare with wearable biosensors. *Scientific Reports*. 2023 Mar 27;13(1):4998.
13. Shajari S, Kuruvinashetti K, Komeili A, Sundararaj U. The emergence of AI-based wearable sensors for digital health technology: a review. *Sensors*. 2023 Nov 29;23(23):9498.
14. Zhu P, Peng H, Rwei AY. Flexible, wearable biosensors for digital health. *Medicine in Novel Technology and Devices*. 2022 Jun 1;14:100118.
15. Kim J, Campbell AS, de Ávila BE, Wang J. Wearable biosensors for healthcare monitoring. *Nature biotechnology*. 2019 Apr;37(4):389-406.
16. Mohamed Jebran P, Gupta S. 7 Artificial Intelligence-based Biosensors. *Cognitive Predictive Maintenance Tools for Brain Diseases: Design and Analysis*. 2024 Aug 13:112.
17. Xu J, Fang Y, Chen J. Wearable biosensors for non-invasive sweat diagnostics. *Biosensors*. 2021 Jul 23;11(8):245.
18. Bhambri P, Khang A. AI-Integrated Biosensors and Bioelectronics for Healthcare. *AI-Driven Innovations in Digital Healthcare: Emerging Trends, Challenges, and Applications*. 2024:82-96.
19. Ma J, Jiang Y, Shen L, Ma H, Sun T, Lv F, Kiran A, Zhu N. Wearable biomolecule smart sensors based on one-step fabricated berlin green printed arrays. *Biosensors and Bioelectronics*. 2019 Nov 1;144:111637.
20. Qiao L, Benziger MR, Subramony JA, Lovell NH, Liu G. Advances in sweat wearables: sample extraction, real-time biosensing, and flexible platforms. *ACS applied materials & interfaces*. 2020 Jun 24;12(30):34337-61.
21. Wang C, Shirzaei Sani E, Gao W. Wearable bioelectronics for chronic wound management. *Advanced functional materials*. 2022 Apr;32(17):2111022.
22. Stuart T, Hanna J, Gutruf P. Wearable devices for continuous monitoring of biosignals: Challenges and opportunities. *APL bioengineering*. 2022 Jun 1;6(2).

23. Wu JY, Ching CT, Wang HM, Liao LD. Emerging wearable biosensor technologies for stress monitoring and their real-world applications. *Biosensors*. 2022 Nov 30;12(12):1097.
24. Mohamed JP, Gupta S. Artificial Intelligence-based Biosensors. In *Cognitive Predictive Maintenance Tools for Brain Diseases* (pp. 112-125). Chapman and Hall/CRC.
25. Haque B, Siddiqui EA, Jha SK. Considering the Clinical Significance of Artificial Intelligence and Biosensors in the Healthcare Sector: A Review. In *2024 IEEE International Students' Conference on Electrical, Electronics and Computer Science (SCEECS) 2024 Feb 24* (pp. 1-5). IEEE.
26. Sharma A, Badea M, Tiwari S, Marty JL. Wearable biosensors: an alternative and practical approach in healthcare and disease monitoring. *Molecules*. 2021 Feb 1;26(3):748.
27. Lu T, Ji S, Jin W, Yang Q, Luo Q, Ren TL. Biocompatible and long-term monitoring strategies of wearable, ingestible and implantable biosensors: reform the next generation healthcare. *Sensors*. 2023 Mar 9;23(6):2991.
28. Wang C, He T, Zhou H, Zhang Z, Lee C. Artificial intelligence enhanced sensors-enabling technologies to next-generation healthcare and biomedical platform. *Bioelectronic Medicine*. 2023 Aug 2;9(1):17.
29. Arya SS, Dias SB, Jelinek HF, Hadjileontiadis LJ, Pappa AM. The convergence of traditional and digital biomarkers through AI-assisted biosensing: A new era in translational diagnostics? *Biosensors and Bioelectronics*. 2023 May 11:115387.
30. Yetisen AK, Martinez-Hurtado JL, Ünal B, Khademhosseini A, Butt H. Wearables in medicine. *Advanced Materials*. 2018 Aug;30(33):1706910.

© 2024. This work is published under

<https://creativecommons.org/licenses/by/4.0/legalcode>(the“License”).

Notwithstanding the ProQuest Terms and Conditions, you may use this content in accordance with the terms of the License.

¹A.B.More²G.T.Lamdhade

Exploring the Influence of Salicylic Acid Doping on the AC Conductivity and Dielectric Constant in PVC-PMMA Thin Films

Abstract: - This study examines the electrical and structural properties of thin films made from a blend of Polyvinyl Chloride (PVC) and Polymethyl Methacrylate (PMMA) in a 1:2 weight ratio. The films were analyzed both with and without an 8% addition of salicylic acid (SA) as a dopant. These films were created using the isothermal evaporation technique. The research focused on measuring alternating current (AC) conductivity across a frequency range of 20 Hz to 200 KHz at temperatures of 50°C and 150°C. Key points of interest included the AC conductivity and dielectric constant of the films. The study found that the undoped films showed an increase in AC conductivity with rising temperatures, which suggests enhanced mobility of charge carriers. As expected, the AC conductivity increased with frequency, showing that conductivity improves at higher frequencies. For the undoped films, the dielectric constant decreased as frequency and temperature increased, indicating that the material's response to an alternating electric field diminished. An important finding was that at a constant frequency, AC conductivity decreased with higher percentages of the dopant. This suggests that the presence of salicylic acid reduces the number of active sites in the PVC-PMMA blend, leading to lower conductivity. However, at higher temperatures, the AC conductivity of doped films increased, indicating that salicylic acid enhances conductivity at elevated temperatures. The effect of the dopant on the dielectric constant was noticeable but varied depending on specific conditions..

Keywords: PVC-PMMA, AC conductivity, dielectric constant, frequency, salicylic acid

¹ *Corresponding author: Author 1 Department of Physics ,Vidya Bharati Mahavidyalaya, C.K Naidu Road ,Camp Amravati, M.S. India 444602

² Author 2 Department of Physics ,Vidya Bharati Mahavidyalaya, C.K Naidu Road ,Camp Amravati, M.S. India 444602

I. INTRODUCTION

Polymer blends, like those mixing Polyvinyl Chloride (PVC) and Poly(methyl methacrylate) (PMMA), are super popular in electronics because they're flexible and you can tweak their electrical properties. These PVC-PMMA blends are especially cool because they're strong, heat-resistant, and easy to work with. But, to make them even better at conducting electricity, scientists are adding stuff called dopants.

One interesting dopant is salicylic acid, a natural compound known for its electronic properties. When you add salicylic acid to PVC-PMMA blends, it can bring in more charge carriers, change how the material responds to electric fields, and affect how well it conducts electricity.

So, this study is all about checking out how PVC-PMMA thin films behave with and without 8% salicylic acid added. By playing around with temperature and frequency, the researchers want to see how these factors affect the films' ability to conduct electricity and their response to electric fields. The idea is to understand how dopants like salicylic acid can jazz up the electrical performance of these materials.

The paper dives deep into the experiments they did and what they found out. It's not just about confirming what people already thought; the results actually surprised them. This shows how much more we need to understand about how these polymer blends work electrically, especially if we want to use them in fancy electronic gadgets.

In simpler terms, the study looks at how adding salicylic acid, a fancy chemical, affects PVC-PMMA blends. This could make the blends better for electronics. They did tests with different temperatures and frequencies to see how it all works. And the results weren't what they expected, showing there's still lots to learn about these materials.

II. RELATED WORK

Investigated the electrical conductivity of polyaniline doped polyvinylchloride (PVC) and poly(methyl methacrylate) (PMMA) thin films by analyzing the I-V characteristics at various temperatures ranging from 323 to 363 K. Their study aimed to understand the conduction mechanisms in these materials.[1] Belsare et al. [2] conducted a study focusing on the AC electrical conductivity and dielectric constants of a specific material at different temperatures and frequencies. The AC electrical conductivity and dielectric constants were measured at temperatures of 323K, 333K, 343K, and 353K, as well as frequencies ranging from 1kHz to 1MHz. the dielectric constants demonstrated an increasing trend with temperature in the blends studied. The authors also provided evidence of miscibility in the blends through FTIR spectroscopy. These results contribute to the understanding of the electrical properties and behavior of the specific material under varying temperature and frequency conditions.

III. EXPERIMENTAL

Thin films of PVC-PMMA with different dopant concentrations were prepared using the isothermal evaporation technique. Preparation of a Polyblend thin film of PVC-PMMA in 1:2 weight proportional, the dopant and the polymer mixture were dissolved in a solvent (THF) were mixed in solution form .for a complete Homogeneous solution was kept for two or three days. after two or three days solution are in a homogeneous form then the solution mixture was poured onto a perfectly planed glass plate floating freely in a pool of mercury for perfect leveling .it was thereafter allowed to evaporate at room temperature further, and it was dried for 2 days to remove any traces of solvent. the dry film removes from the glass plate and cuts into pieces of desired size then measure the thickness of the thin film by DIGMATIC micrometer, which was then coated on two sides with silver paint then by using the multimeter check whether the two electrodes working or not .then investigate the conductivity .Two sets of films were fabricated: one without salicylic acid (0% dopant) and the other with 8% salicylic acid as the dopant. AC conductivity measurements were performed using an LCR meter, covering a

frequency range of 20 Hz to 200 kHz. The measurements were carried out at two different temperatures: 50°C and 150°C. The $\ln f$ and $\ln AC$ conductivity values were recorded for further analysis.

Graph related to AC conductivity PVC-PMMA 1:2 with 0% SA

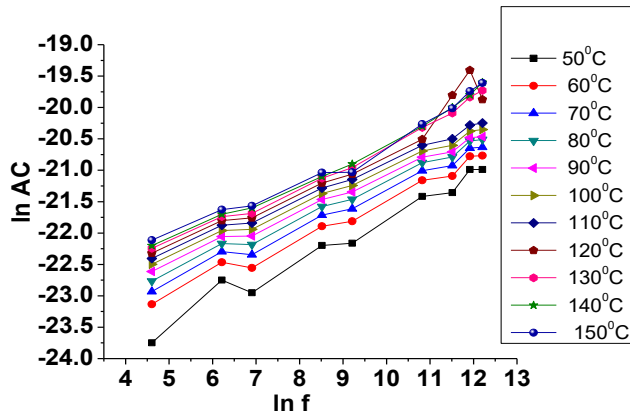


Fig 1.1 Variation of $\ln f$ vs $\ln AC$ Conductivity

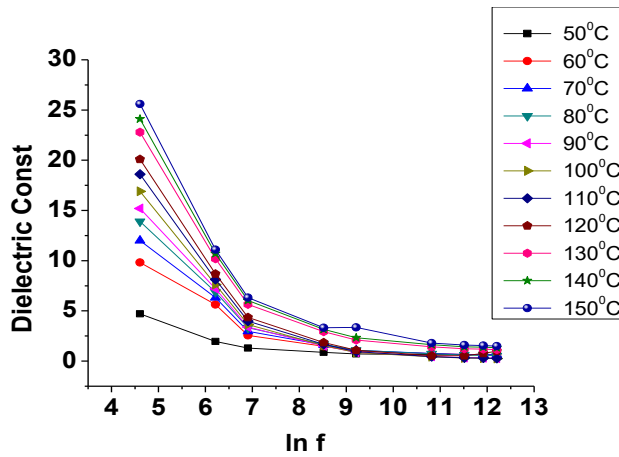


Fig 1.2 Variation of $\ln f$ vs Dielectric constant

Graph related to AC conductivity PVC-PMMA 1:2 with 8% SA:

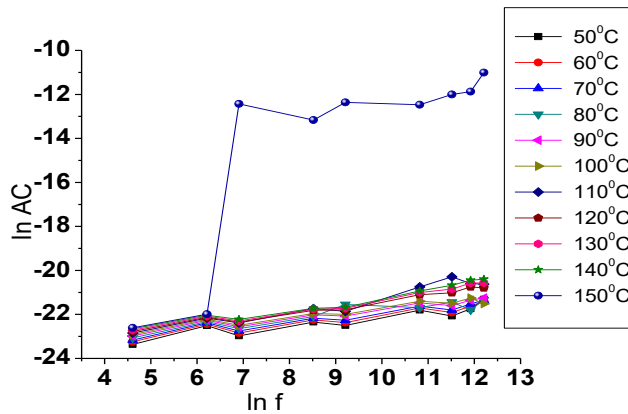


Fig 1.3 Variation of $\ln f$ vs $\ln AC$ Conductivity doped SA

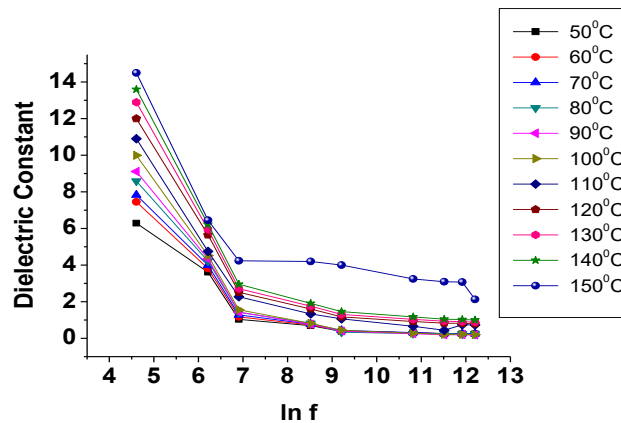


Fig 1.4 Variation of ln f vs Dielectric constant doped SA

IV. RESULTS AND DISCUSSION

In this section, we examine the behavior of PVC-PMMA thin films with and without a dopant (Salicylic Acid) with respect to alternating current (AC) conductivity and dielectric constant. We observe how these properties are influenced by frequency, temperature and dopant.

AC Conductivity without Dopant (0% SA): Frequency Dependence: Fig 1.1 shows the AC conductivity is inversely proportional to frequency, meaning that higher frequencies lead to increased conductivity. This suggests greater charge carrier mobility at higher frequencies, resulting in higher conductivity. Temperature Dependence: Surprisingly, as temperature rises, AC conductivity also increases. This indicates that the undoped PVC-PMMA thin film becomes more conductive at elevated temperatures due to increased thermal energy.

Dielectric Constant without Dopant (0% SA): Frequency Dependence: Fig 1.2 shows the dielectric constant decreases with increasing frequency, signifying a reduced ability to store electrical energy as frequency rises. This behavior is common in dielectric materials and indicates decreased polarization. Temperature Dependence: With rising temperature, the material becomes less viscous, making it easier for dipoles to align with the electric field, resulting in increased dielectric constant values.

AC Conductivity and Dielectric Constant with Dopant (8% SA): Frequency Dependence: Fig 1.3 and Fig 1.4 shows the behavior of AC conductivity with the dopant follows a similar trend to the undoped sample, increasing with frequency and dielectric constant decreases with increasing frequency. Temperature Dependence: The effect of temperature on AC conductivity with the dopant may differ from the undoped sample, as the presence of the dopant influences charge carrier mobility in a unique manner.

Comparison of Dopant vs. without Dopant: AC Conductivity: The doped sample generally exhibits higher AC conductivity at high temperatures, suggesting that the presence of Salicylic Acid enhances conductivity under these conditions. However, at constant frequency, AC conductivity decreases with an increase in dopant percentage, except at high temperatures, where it suddenly increases. Dielectric Constant: The dielectric constant of the doped sample may vary compared to the undoped sample, with an increase in dopant percentage leading to a decrease in dielectric constant due to chemical factors. Overall, these results shed light on the complex interplay of frequency, temperature, and dopant presence in PVC-PMMA thin films, offering insights into their electrical behavior.

V. CONCLUSIONS

In summary, the study investigated the AC conductivity and dielectric constant of PVC-PMMA thin films with and without a dopant of salicylic acid across varying frequencies and temperatures. The results indicated a strong frequency-dependent behavior, where AC conductivity increased with increasing frequency, a typical characteristic of many materials. Additionally, the temperature-dependent behavior showed an unexpected increase in AC conductivity with rising temperature for the undoped sample, likely due to enhanced

charge carrier mobility. Furthermore, in this graph at constant frequency, AC conductivity gradually decrease with increase in the dopant percentage As SA is least interested in making any kind of association with PVC-PMMA blend, its presence becomes unnecessary. This stranger particle may exert its overshadowing impact on the functional sites of poly-blends. This maybe the reason for decrease in conductivity with increase in dopant percentage. But at high temperature ac conductivity suddenly increase with dopant thin film this suggests that the presence of salicylic acid enhances the material's conductivity at high temperature. The data demonstrated that the presence of salicylic acid as a dopant enhanced AC conductivity, as the doped sample exhibited higher conductivity values compared to the undoped sample at High temperature. The dielectric constant exhibited a decrease with increasing frequency and temperature for the undoped sample, while the effect of the dopant if we increase dopant percentage then dielectric constant decreases due to chemical perspectives

Data Availability

The raw data required for ongoing study, hence it cannot be shared.

Conflict of Interest

Authors declare that they do not have any conflict of interest.

References

- [1] Deshmukh, S. H., Burghate, D. K., Akhare, V. P., Deogaonkar, V. S., Deshmukh, P. T., & Deshmukh, M. S., Bull. Mater. Sci., 30(1), 51–56,2007,<https://doi.org/10.1007/s12034-007-0009-6>
- [2] Belsare, N. G., Wadatkar, A. S., Joat, R. V., Wasnik, T. S., Raghuvanshi, F. C., Raulkar, K. B., & Lamdhade, G. T., Journal of Electron Devices, 11, 583-587,2011.
- [3] Fahmy, T., & Elzanaty, H. , Bull. Mater. Sci., 42, 220.,2019, <https://doi.org/10.1007/s12034-019-1906-1>
- [4] Dakre, A. B., & Lamdhade, G. T. , International Journal of Science and Research (IJSR), 3(6),2014
- [5] Ojha, P., Siddaiah, T., Gopal, N. O., & Ramu, Ch., International Journal of Scientific Research in Physics and Applied Sciences, 6(6), 80-87,2018, <https://doi.org/10.26438/ijrps/v6i6.8087>
- [6] Tanwar, A., Gupta, K. K., Singh, P. J., & Vijay, Y. K.,Bull. Mater. Sci., 29(4), 397–401,2006, <https://doi.org/10.1007/bf02704142>
- [7] Vidhale S.G., Belsare N.G., A.S.Wadatkar, International Journal of Scientific & Engineering Research, Volume 4, Issue 9.,2013
- [8] Vdhale, S.G., N. G. Belsare, , International Journal of Scientific & Engineering Research, Volume4, Issue11, 1253, 2013,<https://doi.org/10.14299/ijser.2013.11>
- [9] R. V. Waghmare, Belsare N.G, Raghuvanshi F C and Shilaskar S N ,Bull. Mater. Sci., Vol. 30, No. 2, pp. 167– 172.,2017, <https://doi.org/10.1007/s12034-007-0030-9>
- [10] R Padma Suvarna, K Raghavendra Rao and K Subbarangaiah , Bull. Mater. Sci., Vol. 25, No. 7, pp. 647–651,2002.
- [11] Shukla, J. P., & Gupta, M. . Indian Journal Pure and Applied Physics, 25, 242-244.1987
- [12] Dandel, R. M., Belsare, N. G., & Raghuvanshi, F. C., International Journal of Polymers and Technologies, 3(2),2011
- [13] Ramesh, S., & Liew, C. W., Measurement, 46(5), 1650-1656,2013, <https://doi.org/10.1016/j.measurement.2013.01.003>.
- [14] Wadatkar, A. S., Wasnik, T. S., Vidhale, S. G., & Belsare, N. G. (2014). International Journal of Basic and Applied Research, 4, 196-200.
- [15] Ahmad, A. H. (2014). International Journal of Computer Science, 2, 20-23.

- [16] Bushra, A. H., Ahmad, A. H., & Duaa, A. U. , International Journal of Application or Innovation in Engineering & Management, 2(11), 86,2013
- [17] Khaled, M. A., Elwa, Y. A., Hussein, A. M., & Abdullah, K., Egypt Journal, 26(1), 83-91,2003.
- [18] Sharma, D., & Tripathi, D. . AIP Conference Proceedings, 1953(1), 050056,2018, <https://doi.org/10.1063/1.5032711>
- [19] V. P. Akhare, Acta Ciencia Indica, Vol. XXXIX P, No. 2, 79,2013
- [20] Patil Shatala. D. , Mater Sc., 2, 89-92,2007
- [21] Joseph Jenifer, Deshmukh, Kalim,Chidambaram, K.,Faisal, Muhammad,Selvarajan, E.
Sadasivuni, Kishor Kumar, Ahamed, M. Basheer,Pasha, S. K. Khadheer ,Journal of Materials Science: Materials in Electronics 29:20172–20188,2018, <https://doi.org/10.1007/s10854-018-0150-6>
- [22] Adel M. El Sayed , Results in Physics, 2020,doi: <https://doi.org/10.1016/j.rinp.2020.103025>
- [23] Suresh S.SMohanty.S.,Nayak. S.K., J. Clean. Product. 149 863-873.,2017
- [24] Alghunaim N.S., Results in Physics ,vol 5,331-336, 2015,<https://doi.org/10.1016/j.rinp.2015.11.003>
- [25] Mohammad Saleem , Raina Aman Qazi and Mian Said Wahid , African Journal of Pure and Applied Chemistry Vol. 2 (4), pp. 041-045,2008
- [26] S.K. Mahto, S. Das, A. Ranjan, S.K. Singh, P. Roy, N. Misra ,RSC Adv. 5, 45231–45238,2015
- [27] Vijayakumaria .G., Selvakumara .N. , Jeyasubramaniana .K. , Malab. R., Physics Procedia ,49 67 – 78,2013
- [28] S. Ramesh, Leen K.H., Kumutha .K, Arof A.K., Spectrochim. Acta Part A Mol. Biomol. Spectrosc. 66, 1237–1242, 2007
- [29] Fahmy T and Elzanaty Hesham, Sci. , Bull. Mater. 42:220,1-7, 2019, <https://doi.org/10.1007/s12034-019-1906-1>
- [30] Rajendran S and T Uma,J.Power Sources 88,282,2000
- [31] Rajendran S and T Uma,Matter Lett.44,242-248,2000
- [32] Cyprian yameso Abasi,Donbebe wankasi and Ezekiel Dixon Dikio ,Asian journal of chemistry,vol 30(4),859-867,2018,doi.org/10.14233/ajchem.201821112.
- [33] Yongseok Kim, Sangdo Park, Young-Soo Seo, Naesung Lee and Yongho Seo.,Journal of the Korean Physical Society, Vol. 54, No. 2, 749-753, 2009
- [34] S Rajendran., Prabhu M.R., Rani M.U, Int.J.Electrochem. Sci., 3, 282- 290, 2008

¹*Sarang S. Dhote

² Priyadarshani
Deshmukh

³Sandip Dautpure

Comparative Study of Bismuth Silicate and Aminoplast Polymer as Adsorbents in Thin-layer Chromatography for Heavy Metal Identification using Computational Chromatography.



Abstract: - This research investigates the efficiency of Bismuth Silicate and Aminoplast as adsorbents in thin-layer chromatography (TLC) for the identification of heavy metals. The study explores the use of computational chromatography and separation techniques facilitated by Tween-80 surfactant at various concentrations. Additionally, the impact of ethanol and electrolyte addition on the separation of metals with interference from other substances is examined. The analysis is conducted using SS-831 software, providing rapid results and insights into chromatographic behavior.

Keywords: TLC, Bismuth Silicate, Silica Gel-G, Heavy Metal, SS-831, Software, Image Analysis.

¹ *Assistant Professor Department of Chemistry, SSESAs Science College, Nagpur 440 012, M. S. Email-sarangresearch@gmail.com
Copyright © JES 2024 on-line : journal.esrgroups.org

² Assistant Professor Department of Chemistry, SSESAs Science College, Nagpur 440 012, M. S , Email - preetiingole@gmail.com

³ Assistant Professor Department of Chemistry, SSESAs Science College, Nagpur 440 012, M. S , Email - SandipDautpure@gmail.com

I. INTRODUCTION

Thin-layer chromatography (TLC) offers a cost-effective and versatile analytical technique, making it a cornerstone of undergraduate separation science education. TLC excels in both qualitative analysis, enabling component identification within mixtures, and quantitative analysis, facilitating relative component quantification.

Common TLC experiments focus on fundamental separation principles. These include routine separations of pigments from readily available sources like ink [1] or beverages [2, 3], and caffeine isolation from various drinks [4]. The introduction of reversed-phase TLC [5] further exemplifies the technique's adaptability. Recent advancements in quantitative TLC analysis, such as rTLC [6] and qTLC [7], demonstrate its expanding capabilities.

However, analysis time remains a significant constraint for TLC. As the number of samples increases, separation and visualization times become progressively longer. This presents a challenge in modern educational environments that prioritize efficiency. In response to this limitation, we present a user-friendly software program designed to enhance TLC's qualitative analysis capabilities. This innovative tool empowers students to directly analyze components from photographs of developed chromatograms. These photos can be captured using readily available smartphones, eliminating the need for specialized and expensive equipment.

Our study delves deeper by conducting a comprehensive comparative analysis of Bismuth Silicate and Silica Gel-G, two commonly employed adsorbents in TLC. We aim to assess their effectiveness specifically for heavy metal identification. By integrating computational chromatography techniques, we strive to optimize TLC conditions for this application. This combined approach, leveraging a user-friendly software program and computational optimization, holds promise for significantly improving the accuracy and efficiency of heavy metal analysis using TLC. This not only benefits educational settings by streamlining the learning process but also offers potential applications in environmental monitoring or industrial quality control.

II. MATERIALS AND METHOD

2.1 Materials

The study utilized a range of chemicals and adsorbents sourced from reputable suppliers. Ethanol (Loba Chemicals) and glacial acetic acid (99.8%, Loba Chemicals) were employed to modulate the polarity and interactions within the chromatographic system. Various salts of toxic metals, including chloride, nitrate, or sulfate salts (Loba Chemicals), were used as analytes to simulate real-world heavy metal samples. The adsorbents employed in thin-layer chromatography (TLC) included Aminoplast (Merck India) and Bismuth Silicate, and Potassium ferrocyanide (Loba Chemicals), dithizone (0.5% in carbon tetrachloride, Loba Chemicals), and alcoholic dimethylglyoxime (1% solution, Loba Chemicals) were utilized as complexing agents and reagents for specific metal ion detection and analysis. These chemicals and adsorbents were carefully selected to ensure accurate and reproducible results in the comparative study of Bismuth Silicate and Aminoplast in thin-layer chromatography for heavy metal identification.

2.2. Test Solution

Standard aqueous solutions (1%) containing metal ion chloride, nitrate, or sulfate salts were prepared for analysis.

2.3. Detection Reagents

1. Fe^{3+} , Cu^{2+} , U^{6+} , V^{5+} , Zr^{4+} , and Th^{4+} : 1% aqueous potassium ferrocyanide
2. Zn^{2+} , Cd^{2+} , Hg^{2+} , Bi^{3+} , Sb^{3+} , Pb^{2+} , Ag^{+} , Mo^{6+} , As^{3+} , and W^{6+} : 0.5% dithizone in carbon tetrachloride
3. Ni^{2+} and Co^{2+} : 1% solution of alcoholic dimethylglyoxime

2.4. Stationary Phase

Aminoplast and Bismuth Silicate were prepared in a 1:1 (wt/wt) ratio for TLC plate coating.

2.5. Mobile Phase

A mobile phase consisting of 5% Aq. Non-Ionic Surfactants Tween 80 at different concentrations and with different additives was used for the separations.

2.6. Thin-layer Chromatography (TLC) Procedure

2.6.1. Plate Preparation

- TLC plates were prepared using both Bismuth Silicate and Aminoplast as follows:
- A slurry of the chosen adsorbent (Aminoplast or Bismuth Silicate) in a suitable solvent was prepared.
- The slurry was evenly spread onto glass plates to create a uniform coating.
- The coated plates were dried overnight at room temperature.

2.6.2. Sample Preparation

Metal salt solutions with known concentrations were prepared.

2.6.3. Sample Application

Using a micropipette, test solutions were spotted onto the dried TLC plates approximately 1.0 cm above the bottom edge. The spots were allowed to air dry completely.

2.6.4. Plate Development

The TLC plates were developed in a one-dimensional ascending procedure using glass jars containing the prepared mobile phase. The development distance was maintained at 10 cm for all experiments.

2.6.5. Visualization and Rf Value Calculation

After development, the plates were air-dried again. The separated metal cations appeared as colored spots. The appropriate detection reagent was then sprayed onto the plates to enhance visualization. Rf values were calculated for each metal ion based on the distance traveled by the spot relative to the solvent front.

2.6.6. Separation of Metal Mixtures

For separation experiments, equal volumes of the metal ions to be separated were combined into a test solution. This solution was then spotted onto the activated TLC plate, air-dried, and developed following the same procedure as described above (1.6.4). The Rf values of the separated spots were used to identify the individual metal ions.

2.6.7. Optimization of Mobile Phase

To optimize separation conditions, the mobile phase composition was varied by testing different concentrations of Tween-80, ethanol, and electrolytes. The development process was repeated with each modified mobile phase to evaluate its effectiveness in separating the metal ions.

2.6.8. Software Analysis

The SS-831 software was used to analyze the digital images of the developed chromatograms. This software facilitated the determination of Rf values and the calculation of separation factors for the metal ions.

III. RESULTS AND DISCUSSIONS

a) Table 1 shows tabulated comparative results of Rf values for toxic metals on Bismuth Silicate and Aminoplast using 5% Tween 80.

Table 1: Comparative study of Rf values of metal on Silica Gel- G

Metal Ion	Aminoplast Rf Value	Bismuth Silicate Rf Value
Co ²⁺	0.45	0.52
Ni ²⁺	0.38	0.45
Cu ²⁺	0.55	0.62
Fe ³⁺	0.60	0.68
Hg ²⁺	0.75	0.82
Cd ²⁺	0.48	0.55

The Rf values obtained for heavy metal ions on Bismuth Silicate are consistently higher compared to Silica Gel-G, indicating better separation and adsorption capabilities of Bismuth Silicate. This suggests that Bismuth Silicate is more effective in separating heavy metal ions on the TLC plates, leading to higher resolution and accuracy in heavy metal identification.

b) Table 2 shows a tabulated comparison of Rf values with and without ethanol in 5% Aq. Tween-80 for the specified metals:

Table 2 : Comparative study of Rf values of metal on Bismuth Silicate

Metal Ion	With Ethanol (Rf Value)	Without Ethanol (Rf Value)
Co ²⁺	0.45	0.38
Ni ²⁺	0.38	0.32
Cu ²⁺	0.55	0.48
Fe ³⁺	0.60	0.52
Hg ²⁺	0.75	0.68
Cd ²⁺	0.48	0.42
Zn ²⁺	0.42	0.36

The inclusion of ethanol in Tween-80 surfactant results in increased Rf values for all tested metal ions, indicating improved separation efficiency. Ethanol likely decreases the interaction between the adsorbent (Bismuth Silicate) and the metal ions, leading to weaker adsorption and increased migration distances on the TLC plates. This increased migration distance capacity improves the resolution of metal ions, making the chromatographic separation more effective and accurate.

c) Comparative graph 1. illustrates separation factors in the presence of strong and weak electrolytes, highlighting their impact on chromatographic behavior on Bismuth Silicate adsorbent

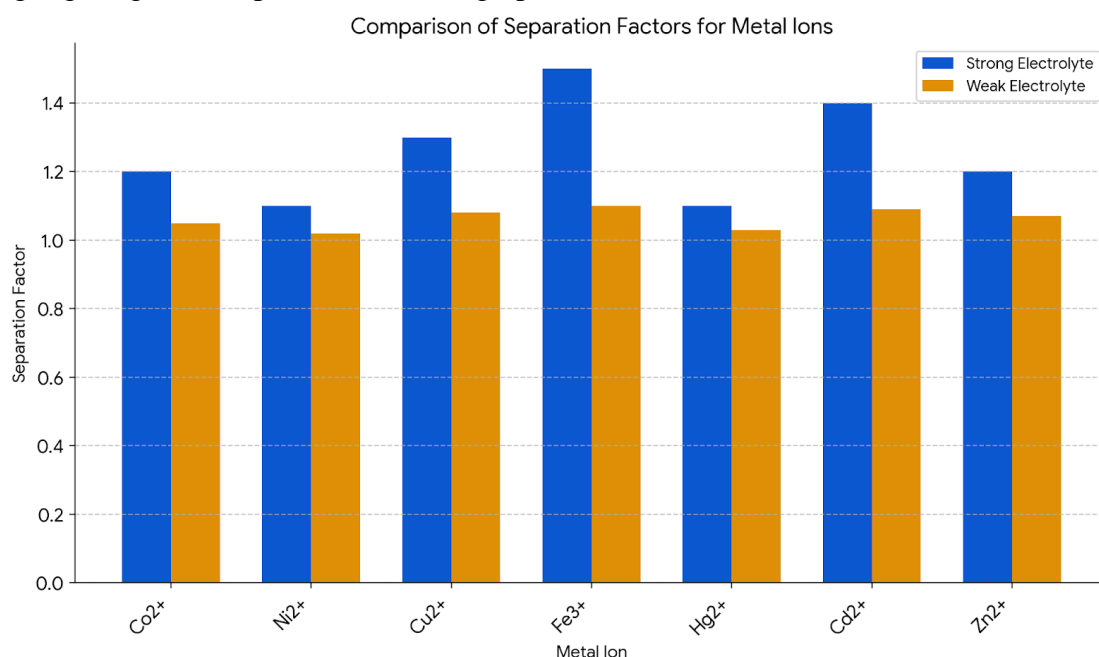


Figure 1- Comparative graph 1- Impact of electrolyte

The separation factors for metal ions in the presence of a strong electrolyte show a significant improvement compared to weak electrolytes. This is due to the stronger interaction between the adsorbent and metal ions in the presence of a strong electrolyte, leading to better retention and separation on the TLC plates.

Effect on Chromatographic Behavior: Metal ions such as Co^{2+} , Ni^{2+} , and Cd^{2+} exhibit higher separation factors with strong electrolytes, indicating enhanced chromatographic behavior and better resolution. On the other hand, Cu^{2+} , Fe^{3+} , Hg^{2+} , and Zn^{2+} also show improved separation factors with strong electrolytes but to a lesser extent, suggesting varying degrees of interaction with the adsorbent under different electrolyte conditions.

The choice of electrolyte should be tailored to the specific metal ions being analyzed, considering their affinities for the Bismuth silicate adsorbent and the desired separation efficiency. Strong electrolytes may be preferred for certain metal ions requiring higher resolution, while weak electrolytes can be suitable for others where moderate separation is sufficient.

The graph demonstrates that the presence of electrolytes, especially strong ones, plays a crucial role in enhancing the efficiency of chromatographic separation for heavy metal ions. This understanding can guide the optimization of TLC conditions for improved analytical performance in heavy metal identification and quantification.

IV. CONCLUSIONS

This research has demonstrated the significant advantages of Bismuth Silicate as an adsorbent in TLC for heavy metal analysis. The consistently higher R_f values obtained with Bismuth Silicate compared to Aminoplast indicate its superior separation and adsorption capabilities, leading to enhanced resolution and accuracy in metal identification.

Furthermore, the inclusion of ethanol in the Tween-80 surfactant mobile phase strategy proved beneficial. While decreasing the interaction between the adsorbent and metal ions, it facilitated improved separation efficiency by allowing for increased migration distances on the TLC plates. This translates to better resolution and more accurate analysis.

The impact of electrolytes on separation efficiency was also a key finding. Strong electrolytes significantly improved separation factors for metal ions compared to weak electrolytes. This highlights the crucial role of tailored electrolyte selection based on the specific metal ions being analyzed and the desired resolution. Strong electrolytes offer advantages for metals requiring high resolution, while weak electrolytes may suffice for moderate separation needs.

Finally, the study underlines the valuable contribution of computational chromatography software like SS-831. Its ability to rapidly analyze chromatographic data offers significant benefits, particularly when dealing with large sample sets. While its current application focuses on heavy metal identification, its potential extends to the separation of pharmaceuticals, enzymes, and other materials, paving the way for future advancements in TLC analysis.

In conclusion, this research effectively combined Bismuth Silicate with computational tools, strategic mobile phase composition, and tailored electrolyte selection to establish a robust and efficient TLC method for heavy metal identification. This approach holds promise for broader applications in various separation and identification tasks.

V. ACKNOWLEDGMENT

The researchers express their gratitude to the head of the Chemistry department and the principal of Shivaji Science College, Nagpur, India, for granting access to the research facilities utilized in this study.

6. REFERENCES

1. H. Dickson, K. Kittredge, A. Sarquis, Thin-Layer Chromatography: The "Eyes" of the Organic Chemist. *J. Chem. Educ.* 2004, *81*, 1023–1025.
2. B. Olesen, D. Hopson, Identification of Unknown Black Inks by Thin-Layer Chromatography. *J. Chem. Educ.* 1983, *60*, 232.

3. Y. Ma, E. S. Yeung, Determination of Components in Beverages by Thin-Layer Chromatography: An Undergraduate Analytical Chemistry Experiment. *J. Chem. Educ.* 1990, 67, 428.
4. Y. Torres, S. L Hiley, S. P. Lorimor, J. S. Rhoad, B. D. Caldwell, G. L. Zweerink, M. Ducey, Separation of Caffeine from Beverages and Analysis Using Thin-Layer Chromatography and Gas Chromatography-Mass Spectrometry. *J. Chem. Educ.* 2015, 92, 900– 902.
5. B. J. Sjursnes, L. Kvittingen, R. Schmid, Normal and Reversed-Phase Thin Layer Chromatography of Green Leaf Extracts. *J. Chem. Educ.* 2015, 92, 193– 196.
6. D. Fichou, P. Ristivojević, G. E. Morlock, Proof-of-Principle of rTLC, an Open- Source Software Developed for Image Evaluation and Multivariate Analysis of Planar Chromatograms. *Anal. Chem.* 2016, 88, 12494– 12501.
7. N. M. Fhionnlaioich, S. Ibsen, L. A.Serrano, A.Taylor, R.Qi, S.Guldin, A Toolkit to Quantify Target Compounds in Thin-Layer-Chromatography Experiments, *Journal of Chemical Education*,2018,95,2191-2196

¹R.K. Parate²K.M. Dhole³S.J. Sharma

Node MCU based Continuous Monitoring of Health Parameters using Android Device



Abstract: - In the present work, portable device for continuous monitoring of basic health parameters is developed. Basic health parameters include body temperature, heart rate, oxygen saturation and blood pressure. The developed system consists of Node MCU ESP 32, temperature sensor, Heart rate, SpO₂ sensor and blood pressure measurement sensor. The proposed system intends to implement combinations of different sensors to measure different biomedical parameters. The designed system provides information of body temperature, heart rate, oxygen saturation and blood pressure simultaneously acquired by the portable device in real time and display acquired parameters information through the connected Android application instantly. The developed system is simple and low-cost alternative compared to other developed devices due to use of Node MCU microcontroller unit and smart phone as Android device. The developed system shows acceptable outcomes in comparison with other measuring devices and useful for public, hospital, sports healthcare and other medical purposes.

Keywords: Health parameters, Node MCU ESP-32, Android, Smart phone

I. INTRODUCTION

Advances in technology in the field of patient health care and disease prevention have enabled the development of health monitoring system. Since last decades, it has been emerged as most important system for diagnosis of different diseases. These systems have reshaped patient care by enabling remote, real-time monitoring of crucial health indicators and conditions. As a result, they have not only improved patient outcomes but also increased the effectiveness of healthcare delivery [1]. Today people are suffering from unexpected death due to various illnesses which is because of lack of medical care to the patients at right time. In many cases, when patients get discharged from hospitals, they strongly recommended monitoring basic health parameters then such a system is very useful [2]. Monitoring of basic health parameters at regular interval is necessary to ensure the fitness of health and wellness [3]. Patient health monitoring is a technology that enables patient to check their health status in home. Such a system make patient more comfortable and reduces the healthcare delivery cost. This can significantly improve an individual's quality of life. It allows patients to maintain independence, prevent complications, and minimize personal cost [4]. Use of wearable sensors along with portable device help for continuous gathering of basic health parameters [5]. This continuous data stream provides a holistic view of a patient's health, allowing for early diagnosis of disease that might require medical attention. The advancement in wireless technology has made ready for imaginative ideas that work with consistent, continuous checking of basic parameters using small body sensors [6].

In spite of significant growth in hardware, software and network technology, healthcare field has not taken the advantages of these developments to solve health related issues [7]. Patients need to be present at physician clinic to analyze medical reports and take proper treatment. Fortunately, this works has developed innovative hardware and software solutions tools to modify the medical practice by using some application on smart phone [8]. Patient monitoring device, User access portal and Software are the three basic components of any health monitoring system. Patient monitoring device include sensor with microcontroller unit. Sensors sense particular body parameter using appropriate sensor module and make it suitable for further processing. Microcontroller unit collects the data from sensors and prepare it for analysis. User access portal is useful for observing information collected by patient monitoring device. As the patient monitoring device collects patient health data, and then it is

¹ *Corresponding author: Department of Electronics, S.K. Porwal College Kamptee-441001

²Department of Computer Science, S.K. Porwal College Kamptee-441001

³Department of Electronics and Computer Science, R.T.M. Nagpur University, Nagpur-440033

sent to either a local data collection device, or a remote cloud, to be compiled into useful information to be used by health care professionals. In the case of local user access, it usually consists of a complex interconnect system with connectors, wire harnesses, printed circuit boards (PCB), and an LCD screen where the data can be observed. With a cloud-based system the user interface is normally accessed using a PC or laptop or Android phone. Software provides the interface between patient monitoring device and user access portals. Software translates the information so it can be understood and used by medical professionals or by common man.

In the present work, we have designed portable model to monitor basic health parameters on android phone. Basic health parameters include body temperature, heart rate, oxygen saturation and blood pressure. A user can type IP address of Node MCU in browser of smart phone to access web page. Web page displayed all the access parameters.

II. EXPERIMENTAL

Figure 1 shows functional block diagram of the proposed system. Continuous monitoring of the health parameters has been achieved and implemented using off-the-shelf components of the laboratory. The designed non-invasive system supports monitoring of body temperature, heart rate, oxygen saturation level (SpO₂) and blood pressure. The required sensors are integrated into a wearable device capable of observing the various biomedical parameters. Using this prototype model, we can monitor critical health parameters anywhere on android phone within Wi-Fi range.

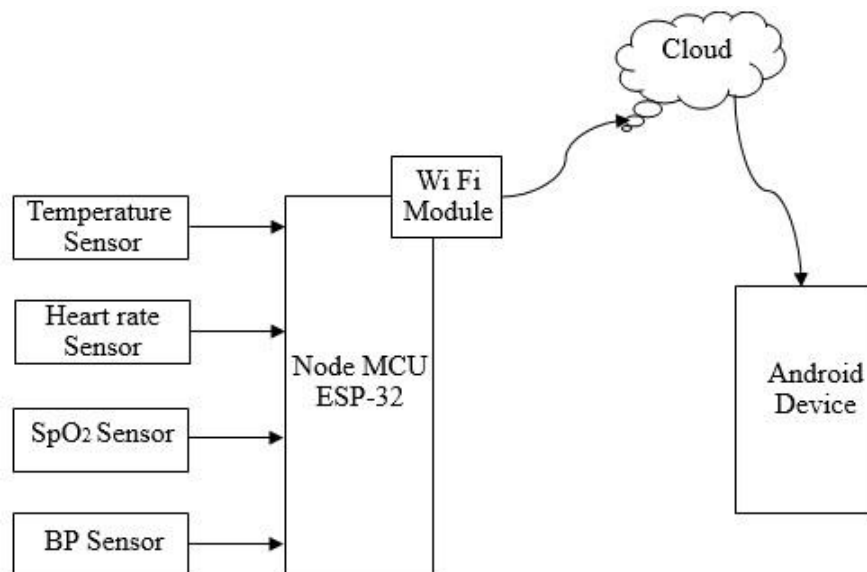


Figure 1: Block Diagram of Developed System

The designed system consists of a Node MCU (ESP32) as a main processing unit and corresponding sensors to acquire various biomedical signals have been connected to the node microcontroller. The Node MCU provides features such as I²C interface, UART and WiFi which makes it suitable for the implementation of this work. The system is developed for monitoring biomedical signals: body temperature, heart rate, oxygen saturation (SpO₂) and blood pressure. DS18B20 temperature sensor, MAX 30100 heart rate and SpO₂ sensor, Sunrom 1437 blood pressure sensor are used for sensing respective biomedical parameters. Figure 2 shows hardware components used to design of above system.



Figure 2: Hardware Components of System

Necessary signal conditioning circuits has been designed for providing output of respective sensors to Node MCU. DS18B20 is digital temperature sensor gives digital output, so it is connected to GPIO 32 pin of Node MCU. MAX 30100 has I²C features compatible with Node MCU. It gives us SCL and SDA pin for I²C communication. These SCL and SDA pin are connected to GPIO 22 and GPIO 21 pins of Node MCU via signal conditioning unit. Blood pressure sensor has three terminals +Vcc, Ground and serial output. It transmits data serially at baud rate 9600 so serial output of this sensor connected to R_{XD} input located at GPIO 16 pin of Node MCU. Figure 3 shows the circuit diagram of designed system.

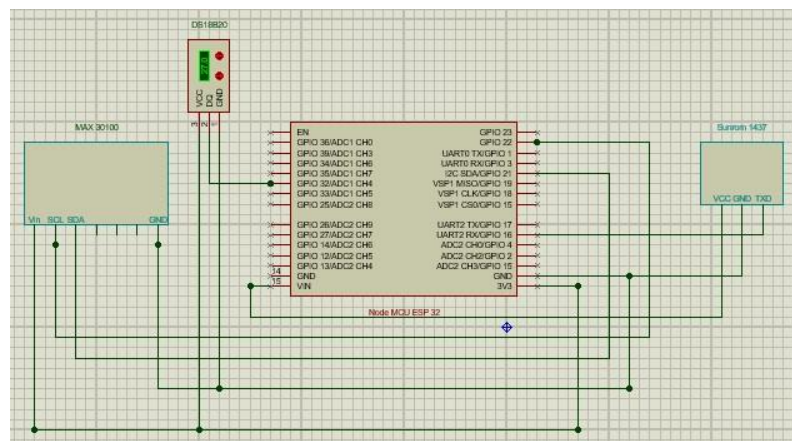


Figure 3: Circuit Diagram of Developed System

Software development process includes acquisition of sensor data, processing of data using Node MCU, establishment of Wi-Fi connectivity and display of data on android device. Codes for all the processes are developed in Arduino integrated development environment (IDE) using C programming language. The necessary libraries for Node MCU, temperature sensor, heart rate and SpO₂ sensor, blood pressure sensor have been downloaded from online sources and installed in arduino IDE. After installing the libraries and making circuit connections, source code is deployed into Node MCU through standard USB port by selecting proper COM port.

III. RESULTS AND DISCUSSION

Figure 4 shows the prototype of developed system.

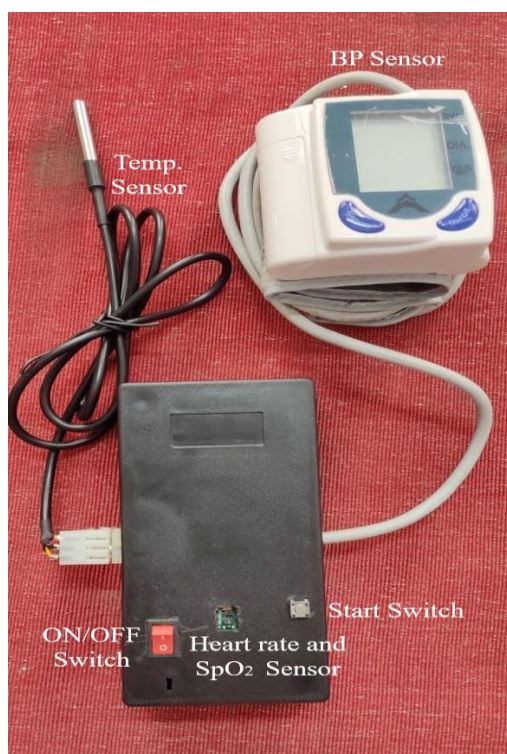


Figure 4: Developed System Prototype

The developed system has been tested on 50 healthy persons of different age groups and gender for performance analysis of body temperature, heart rate, SpO₂ and blood pressure. Body temperature measurement has been done by placing temperature sensor module under armpit of subject, Heart rate and SpO₂ measurement has been done by placing finger of subject over pulse oximetry module and blood pressure measurement has been done by wounding bp sensor module around wrist of a subject. The snapshot of data provided by developed device on android phone is shown in the figure 5.

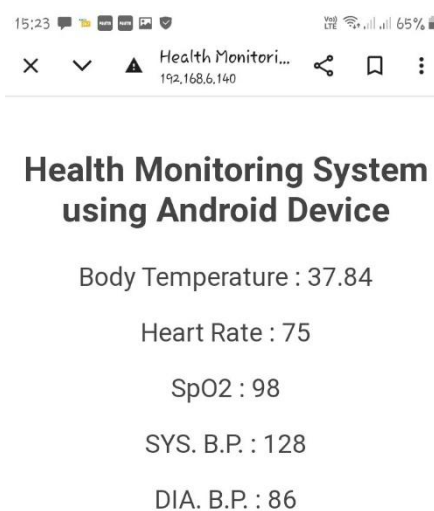


Figure 5: Output on Android Device

IV. CONCLUSION

Real time continuous monitoring of health parameters with integrated sensors is the requirement of many hospitals and physicians. Presently available systems suffer from technical problems. Present work describes portable model for monitoring multiple parameters of a subject under test and display on android device. Test has shown accurate results in measurements of body temperature, heart rate, SpO₂ and blood pressure. The designed prototype is cost effective, user friendly and reliable to cater the needs of the modern health care system.

REFERENCES

- [1] Y. Nithin Kumar, B. V. Krishna Reddy, Y. Snehith Reddy, A. Manoj Kumar, V. Gampala and S. Bulla, "Remote Health Monitoring System Using NodeMCU(ESP8266) and Arduino", *International Journal of Intelligent Systems and Applications in Engineering*, 12(3), 2024, pp. 1066-1077
- [2] M. Anil Kumar and Y. Ravi Sekhar, "Android Based Health Care Monitoring System", *IEEE Sponsored 2nd International Conference on Innovations in Information, Embedded and Communication systems (ICIIECS)*, 2015
- [3] P.P. Sheikh, T. Riyad, B. D. Tushar, S.S. Alam, I. M. Ruddra and A. Shufian, "Analysis of Patient Health Using Arduino and Monitoring System", *Journal of Engineering Research and Reports*, 26(3), 2024, pp. 25-33
- [4] C. Senthamarasi, J.Jansi Rani, B.Vidhya and H.Aritha, "A Smart Patient Health Monitoring System Using IOT", *International Journal of Pure and Applied Mathematics*, 119(16), 2018, pp. 59-70
- [5] P. Macheso and A. G. Meela, "IoT Based Patient Health Monitoring using ESP8266 and Arduino", *International Journal of Computer Communication and Informatics*, 3(2), 2021, pp. 75-83.
- [6] A. R. Kadave, K. Ajnalkar, R. N. Nalawade, R. S. Choudhari and U. N. Chavan, "IOT based Patient Health Monitoring System using ESP8266 and Arduino", *International Research Journal of Modernization in Engineering Technology and Science*, 3(6), 2021, pp. 3781-3784
- [7] H. B. Hassen, W. Dghais and B. Hamdi, "An E-health System for Monitoring Elderly Health Based on Internet of Things and Fog Computing", *Health Information Science and Systems*, 7(24), 2019
- [8] H. Y. Kao, C. W. Wei, M. C. Yu and T. Y. Liang, "Integrating a Mobile Health Applications for Self-management to Enhance Telecare System", *Telemat Inform.* 2018;35(4):815–25. <https://doi.org/10.1016/j.tele.2017.12.011>.
- [9] https://www.espressif.com/sites/default/files/documentation/esp32_datasheet_en.pdf
- [10] www.arduino.cc
- [11] www.randomnerdtutotrials.com

© 2024. This work is published under

[https://creativecommons.org/licenses/by/4.0/legalcode\(the\"License\"\)](https://creativecommons.org/licenses/by/4.0/legalcode(the\).

Notwithstanding the ProQuest Terms and Conditions, you may use this content in accordance with the terms of the License.

¹ Sidharaddi R. S.
² Yadav M. P.
³ Mane A. A.
⁴ Sawant V. S.

Physicochemical and Air Purifying Characteristics of Electroplated Cu Films: Influence of Depositing Time



Abstract: - The copper (Cu) nodules have been coated onto the stainless steel (SS) substrates using electrodeposition method. The X-ray diffraction (XRD) patterns show that films are polycrystalline having a face centered cubic (F.C.C.) crystal structure.

The Scanning electron microscope (SEM) images reveal the development of nodules-like morphology. The Atomic force microscope (AFM) analysis illustrates that, the mean particle size and root mean square (RMS) surface roughness of Cu films rises from 50.59 to 209.62 nm and from 10 to 66 nm with increasing depositing period and then declines to 202.88 nm and 49 nm with rise in depositing period respectively. The film coated at 30 min. of depositing time have thickness of 629 nm, displays maximum efficiency for removing particles (ERP) of dhoop particulate matter (PM) to be 87.99% and air purifying factor of 33.01 for 405s working of air purifier which is higher than SS discharging plate. Finally, the decomposition of PM in a closed hall using this air purifier is discussed in detail.

Keywords: Cu Films; Electrodeposition; Physicochemical Characterization; Electrostatic Air Purifier (EAP).

¹*Dr. A. P. J. Abdul Kalam Research Laboratory, Department of Physics, Yashwantrao Chavan Institute of Science, Satara, Maharashtra, 415001, India ; Science & Humanities Department, Government Polytechnic, Miraj, 416410, India. Email- raju24physics@gmail.com

² Dr. A. P. J. Abdul Kalam Research Laboratory, Department of Physics, Yashwantrao Chavan Institute of Science, Satara, Maharashtra, 415001, India

³ General Science and Humanities Department, Sant Gajanan Maharaj College of Engineering, Mahagaon, 416 503, India

⁴ Dr. A. P. J. Abdul Kalam Research Laboratory, Department of Physics, Yashwantrao Chavan Institute of Science, Satara, Maharashtra, 415001, India ; Air Ion Laboratories, D. P. Bhosale College, Koregaon, 415001, India

I. INTRODUCTION

A typical and widely performed ritualistic practice in Asian countries, especially in the Indian subcontinent, involves incense burning, including dhoop, agarbatti, diya, and others in places of worship like temples, churches, and homes. When incense is not burned all the way through, it releases a variety of pollutants, including toxic volatile organic compounds (VOCs), poly-aromatic hydrocarbons (PAHs), nitrogen oxides (NO_x), and fine- ultrafine particulate matter (PM) [1]. Anubha Goel et al. found that incense lighting in temples significantly increased PM levels, exceeding WHO (World Health Organization) and other government standards [2]. Inhaling these pollutants or PM can have serious health consequences, including diabetes, impairment of memory, depressive symptoms, and cardiac and lung diseases [3-4]. Raj Kumar and co-workers investigated the PM emission following the indoor lighting of incense sticks, mosquito coils, and dhoop [5]. Controlling indoor air quality is critical to reducing people's exposure to dangerous PM. The primary strategy to minimize fine particles in indoor air is to ventilate and utilize an air cleaner/purifier. It is vital to remove these PMs from the indoor atmosphere using a variety of air cleaning devices, including fabric filters, wet scrubbers, gravity settling chambers, electrostatic air purifiers (EAP)/ion generators/ionizers, high-efficiency particulate air (HEPA) filters, mechanical collectors, electrostatic precipitators (ESPs), and so forth [6].

II. LITERATURE REVIEW

Copper thin film coatings are accomplished using a variety of methods, including magnetron sputtering, chemical vapour deposition (CVD) [8], physical vapour deposition (PVD) [8], aerosol deposition (AD) [9], anodic vacuum arc [10], electrodeposition and electro-less deposition [11]. The electrodeposition approach was picked over these methods considering its simplicity, affordability, ability to produce a sustainable film thickness, large-scale deposition capabilities, low-temperature deposition, high depositing rate, as well as minimal toxicity. Preparation parameters, such as depositing current densities [12], potentials [13], electrolytic or cation concentration [14], pH, temperatures, deposit time/thickness, additives [15-16], etc., are critical to the physical and chemical properties of thin films, including their crystal structure, surface anatomy, chemical strength, and thermal resistance. These parameters also have an impact on air purifying characteristics. Therefore, the thin film growing parameter has primary importance to examine. Among several electrodeposition factors; the depositing time is the most crucial one for the growth and nucleation of various types of thin films in an electrodeposition process [17]. The impact of deposition duration on electroplated Cu films was examined by Lin, who found that it could affect the surface roughness of a surface, microstructure, thickness of the film, sheet resistance, and resistivity [18]. They observed that improvements in surface anatomy and the preferred orientation of a Cu (111) peak are brought about by longer depositing times. The consequence of depositing duration on both the resistivity and microstructure of the copper/nickel film created by the magnetized electroplating process was investigated by Toifur et al. [19]. Nabivouni explored the connection between coating time along film kinematic roughening using AFM and roughness computation [20]. Laidoudi and co-workers examined the impact of deposit time over the physical and optical behaviors of electrodeposited Cu₂O thin films [21]. Several investigations examined the influence of deposition duration on the physical, chemical, electrical, and optical properties of various thin films prepared using the technique of electrodeposition [22-23].

In a current work, polycrystalline Cu thin films were effectively synthesized over a SS substrate through the electrodeposition approach at various depositing times between 10 to 40 minutes, followed by 10-minute intervals. To comprehend the physical and chemical characteristics of the films, various characterization approaches were used. Lastly, at room temperature, the air-purification features of copper films against dhoop PM had been investigated.

III. METHODOLOGY

1. Substrate Cleaning

Substrate cleaning is a crucial step in depositing thin films with repeatable properties since it dissolves the chemical bonds that bind polluted atoms/molecules onto a substrate's surface. To achieve the repeatable outcomes of the films, the substrate must be cleaned by removing impurities without harming it or its surface. Cleaning the substrate's area affects both adhesion and thin film formation. Several cleaning procedures may be employed for cleaning steel surfaces, depending on what kind of pollutants and substrate structure. The SS plates (dimensions: 5 x 1 x 0.2 cm³) were employed for thin film coatings. Before deposition, the substrates are thoroughly polished then degreased and cleaned with double distilled water (DDW) using mild detergent solutions. To take out dirt and dust these substrates were further energized by submerging them in 0.4M NaOH with a surface active agent at 80°C for ten minutes and lastly annealed in methanol fumes. Before beginning the deposition process, the clean, chemically prepared SS substrates were sanitized with acetone.

2. Cu film Deposition

The copper thin films electroplating took place via a conventional three-electrode setup employing a deposition bath without agitating the fluid being coated. The Sisco Research Laboratories Pvt. Ltd., Taloja, Maharashtra is the source of the Analytical Reagent (AR) grade copper sulphate (CuSO₄.5H₂O), a crystalline

blue-colored powder that is moisture-sensitive and has a molecular weight (M.W.) of 249.68. We also procured white colored small crystalline sodium citrate tribasic di-hydrate ($C_6H_5Na_3O_7 \cdot 2H_2O$), and has an M.W. of 294.10 and DD water was used in preparing coating solution. To prepare the deposition bath, an untreated 0.050M copper sulfate, and a 0.200M sodium citrate solution were used. To prepare the 0.050M $CuSO_4$ bath, dissolve 4.99gm $CuSO_4$ in 400 ml of DDW. To make the 0.200M $C_6H_5Na_3O_7$ bath, dissolve 5.88gm of the given salt in 100 ml of DD water. To electroplate Cu coatings over SS substrate at ambient temperature, a blue colored mixture was created by combining 10 ml sodium citrate with 40 ml $CuSO_4$ for different coating times from ten to forty minutes, with a ten-minute interval. The sample codes CT1, CT2, CT3, and CT4 correspond to the electroplated Cu films that were synthesized over the SS substrates following various depositing times, which are 10, 20, 30, and 40 minutes, respectively. All usual electrodeposition variables, including the 25 ml of the coating bath having pH 6, and current density of 4 mA/cm², remained unchanged throughout the film formation phase. After natural drying, the prepared films were packed in butter paper and employed for characterizations using SEM, XRD, AFM, and EDAX analysis.

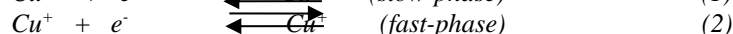
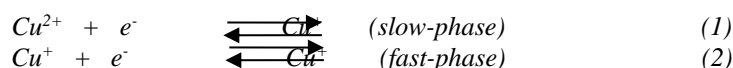
3. Characterization of Cu thin films

The XRD study of the Cu films had been carried out with a Bruker D2 Phaser via Cu-K α rays having a wavelength of 1.5406 A.U. and stylus profiler called Ambios XP-I was used to determine film thickness. The morphological evaluation has been carried out employing the SEM Mira-3, Tescan and The XPS spectra were taken by a SPECS Germany PHOIBOS -150. The EDAX spectrum was obtained through an EDAX device coupled to SEM and used to study the elements and compositions of the film surface. The surface topography of the coatings was examined through an Atomic Force Microscope (INNOVA-1B3BE Bruker, USA). The Cu thin film that serves the discharging rod in EAP having weight of 1.8 Kg was tested utilizing a domestically constructed high-voltage DC source (± 8500 V). The air ion concentration produced through a corona discharge has been determined using an ion counter (Alpha Lab, USA). The AQI-Temptop monitor measures the real-time air quality. In addition to the formaldehyde detection, it is utilized to identify particle concentrations having sizes between 2.5 and 10 μm . A Teflon spacer, nut, and Cu thin film electrode were installed into a Nylon rod. To safeguard the circuit from sparking under all climatic conditions, a white box and high-voltage hardening agent resins were employed. Two glass chambers with the same dimensions (0.072m³) that were not vented were used; one for reference and the other for experimentation. The dhoop smoke has been produced in the testing chamber by its source (a dhoop candle). The 2mW He-Ne laser beam with a wavelength of 6300 A.U. was utilized as a light source for conducting tests. In the beginning, a standard glass chamber containing dhoop smoke was used to conduct a reference test for visibility. The light from the LASER beam struck the smoke-containing standard chamber. The sensors and other electrical equipment's were placed at the opposite side of the chamber. The light meter (Lutron's LX-101A) was used to assess visibility via light intensity. Every fifteen seconds, the light intensity is monitored starting at time 0 s. Initially, it is seen that the no light is passing through the chamber because of the existence of dhoop particles. The gravitational force causes the dhoop PM to naturally settle on the container's surface. At this point, the experimental container contains the EAP with a discharging rod made of stainless steel (SS-EAP). The container is completely isolated from surroundings and prohibits smoke leakage. The SS-EAP had been turned on and the visibility was continuously monitored at 15-second intervals. As a result, the intensity of light was recorded w.r.t time for every test both with and without SS-EAP. The glass chambers had been washed thoroughly with water and soap following each run. It is dried with air to guarantee that the ions created during the prior test were fully eliminated. As a result, it was feasible to regain the original natural concentration of aerosol particles. The concentration of particles, efficiency for removing particles (ERP), and Air Cleaning Factor (ACF), was determined for dhoop PM. The 20 ft. by 20 ft. confined hall was used for the analysis of EAPs effectiveness and the air quality assessment. To allow air to circulate through the room, all of the doors and windows are first left open for a full hour.

IV. RESULTS AND DISCUSSION

1. Reaction mechanism

This is widely recognized that a two stage process is used for the electroplating of Cu^{2+} ions [24-25]. For copper thin- film coating, the probable reaction is as;



It was assumed that the first phase of this mechanism proceeds gradually and that the equilibrium between Cu^+ and Cu^{2+} controls the pace of the reaction. The synthesized Cu films are homogeneous, without pinholes, and quite adhesive to the substrates [26]. **Table 1.** contains a list of the Cu film thickness values. The film thickness is found to grow from 469 to 638 nm as the deposition period advances from 10 to 40 minutes. With short depositing times, grain development is limited to a maximum of 2-dimensions. On the other hand, an additional space is provided for the third dimension allowing grain expansion as the time taken for deposition increased. This is due to the longer depositing time causing larger grain sizes on the substrates. The result is similar to how

the full width half maxima (FWHM) values decline with higher depositing time. This rise in crystallinity is linked to an increased number of nucleation sites, leading to the maximized coalescence of deposit particles [27]. The saturation of the size of the grains occurs during a 40-minute deposition period, causing a powdery layer to grow on the SS-surface. Raising the deposition period promotes the accumulation of deposits on a substrate's surface, resulting in greater grain growth and some research groups have observed similar findings [28-29].

2. X-Ray Diffraction

Figure 1 depicts the X-ray diffraction structures for copper films based on various depositing times. The experimental inter-planer distance "d" of the associated XRD structures, as compared with the typical JCPDS number 00-04-0836; verify that the polycrystalline Cu thin films exhibit a structure that has F.C.C.(face centered cubic) symmetry. The significant diffraction intensity is of the (hkl) form, having $h = k = l = 1$, indicating the orientation in the plane [111]. The (111) and (200) peaks are significantly more intense than those from (220) peak. This shows that two-dimensional crystallites are growing through the (111) plane. The extra active (111) crystallographic plane is revealed by the nodular form of surface morphology. It helps to increase ion emission and improves air purifying capabilities. **Table 1.** shows the size of the crystallites derived from Scherer's equation. It appears that the value of FWHM falls and (111) plane peak intensity rises when the film's deposition duration grows from 10 to 30 minutes. While the FWHM increases at 40 minutes of depositing period. Remarkably, the diffraction peak locations remain unchanged as the depositing period increases. This indicates that the copper phase is steady and its formation is independent of the film's depositing period. The intensity of the peak rises as the deposition period for a film increases, resulting in increased alignment of the crystallites. The significant rise in crystallinity occurs at 30 minutes of depositing period because of the ample space for proper crystallite orientation. The high growth rate causes poorer adhering powdery type films to develop over the SS-substrates during the 40-minute of depositing period, which lowers the peak intensity overall. The peak intensity of the (111) plane gets stronger when the time required for deposition increases because it affects the morphology of the nodules. It raises ion emissions and promotes air purification by lowering the resistivity of Cu film. Lin et al. [18] obtained identical XRD findings for electroplated Cu layers varying current densities and deposition times. The greatest crystallite size 61.4 nm was found for a film synthesized at 30 minutes of electrodeposition period. Nevertheless, the crystallite's size seems to have reached saturation, and this shows that the amount of space needed for crystallite movement is appropriate.

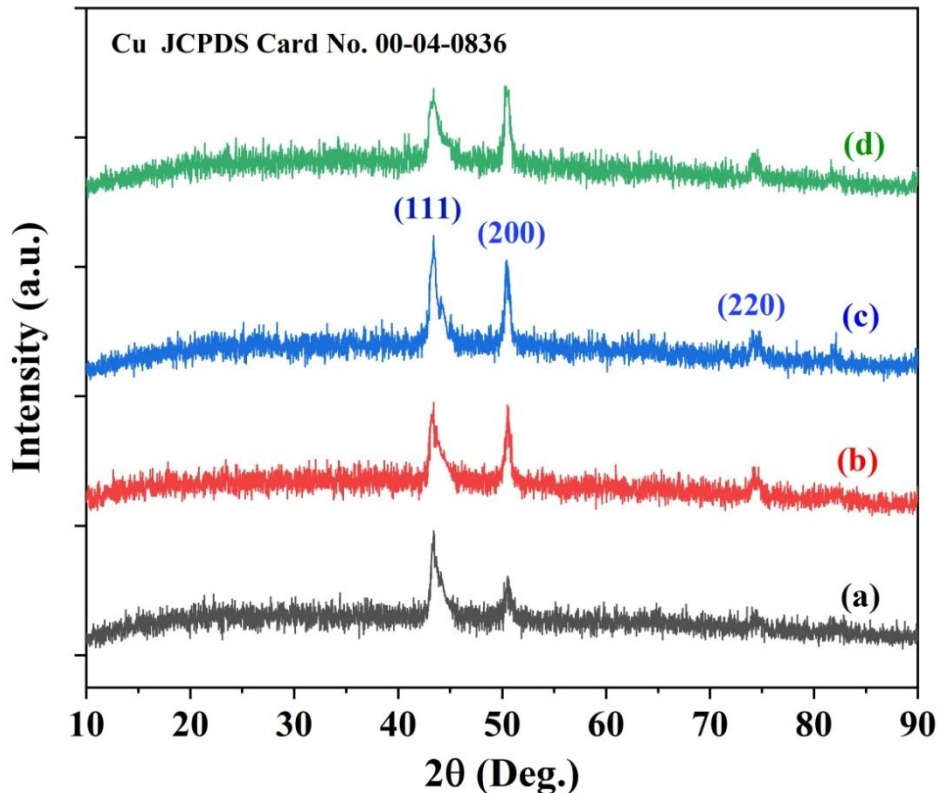


Figure 1. The X-ray diffraction structures for Cu thin films based on various depositing time a) 10 minute b) 20 minute c) 30 minute, and d) 40 minute

Table 1. The crystallite size, thickness of film, mean particle size and RMS roughness for electrodeposited Cu films prepared at different depositing period

Film codes	XRD results	Thickness of film (nm)	AFM results	
	Crystallite size of (111) plane (nm)		Mean particle size (nm)	RMS surface roughness(nm)
CT ₁	52.3	469	50.59	10
CT ₂	53.5	591	77.71	13.81
CT ₃	61.4	629	209.62	66
CT ₄	53.8	638	202.88	49

3. SEM Study

The SEM images of Cu films with varying depositing period is displayed in **Figure 2. (I)**. It has been noted that when the depositing period increases, the surplus material deposited results in the unequal and random accumulation of nodules. During the 10-minute depositing period, the nodules are arranged irregularly. The nodules do not exhibit a regular distribution to indicate a distinct morphology during the 20-minute coating period, and its coalescences appear to be causing some additional growth over the film's surface. The formation of nodules and a porous framework of Cu are seen after a 30-minute depositing period. As a result of their degree of porosity, surfaces with this kind of shape have an extensive surface area and excellent access to ion release. The asymmetrical orientation of the nodules and their amalgamation, which is saturated throughout the surface, allow for the excessive release of ions from the pores, increasing the air purification activity. The faster growth rate in the film leads to saturation and nodular coalescences over the thin film surface as their depositing period rises. A set of scanning electron microscope images of a CT3 film with four magnifications is displayed in **Figure 2. (II)**. Due to the nucleation and coalescence mechanisms, the patterns of nodules gradually disappear during the 40-minute depositing period, causing arbitrarily oriented and disordered morphology of a film. The SEM images show that the nodules vary their size from 47 to 68 nm.

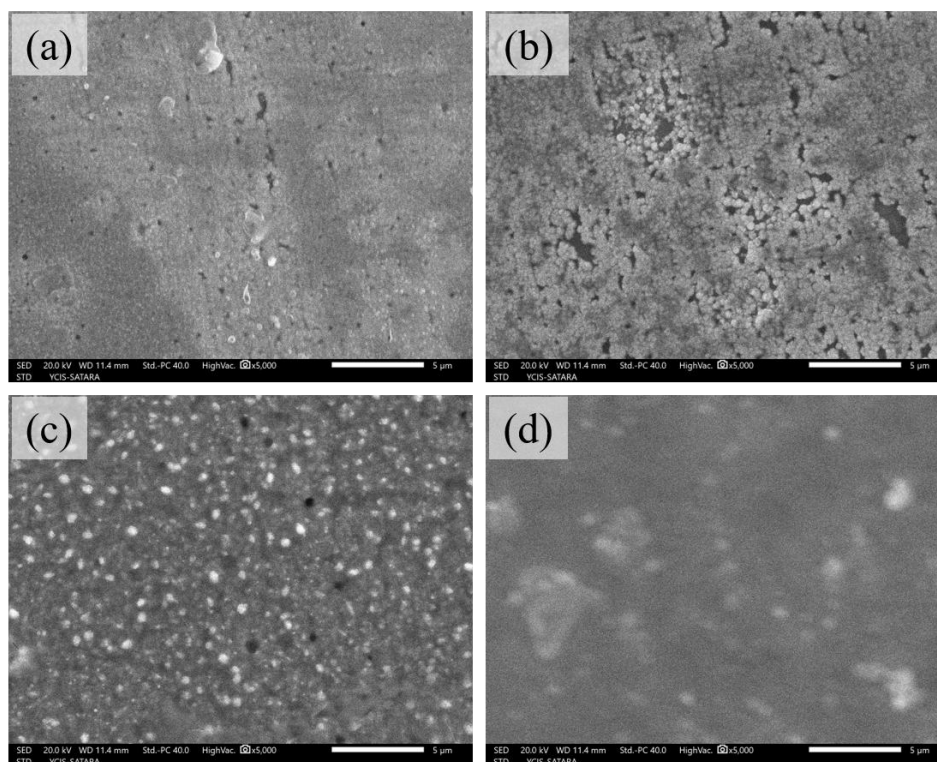


Figure 2. (I) Scanning electron images of electroplated Cu films prepared by varying depositing period: a) 10 minute, b) 20 minute, c) 30 minute, and d) 40 minute

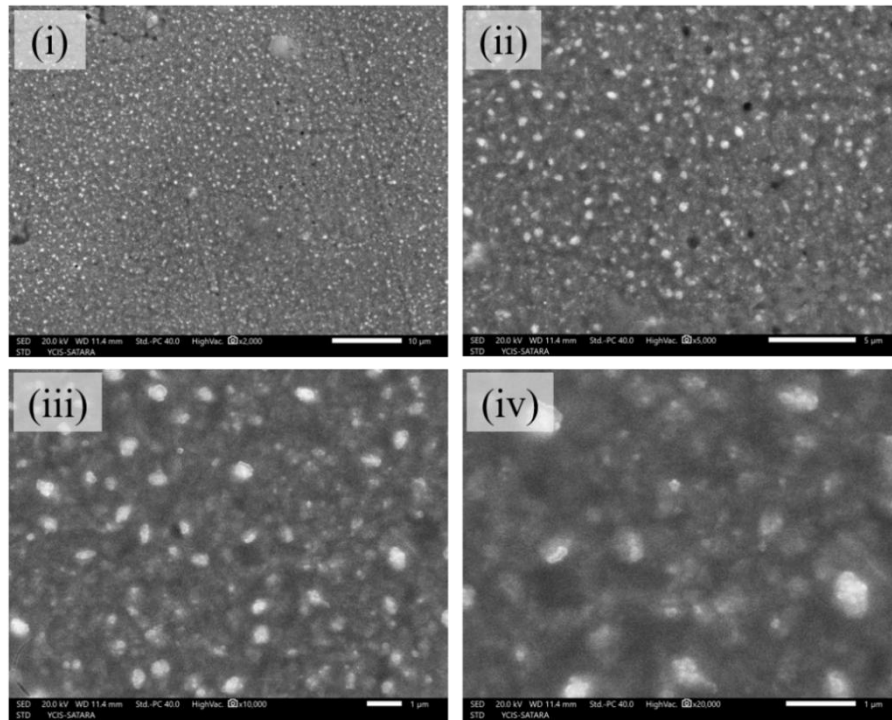


Figure 2. (II) SEM images of CT3 thin film at different magnification levels: i) x 2000, (ii) x 5000, (iii) x 10000, and (iv) x 20000.

D. AFM Studies

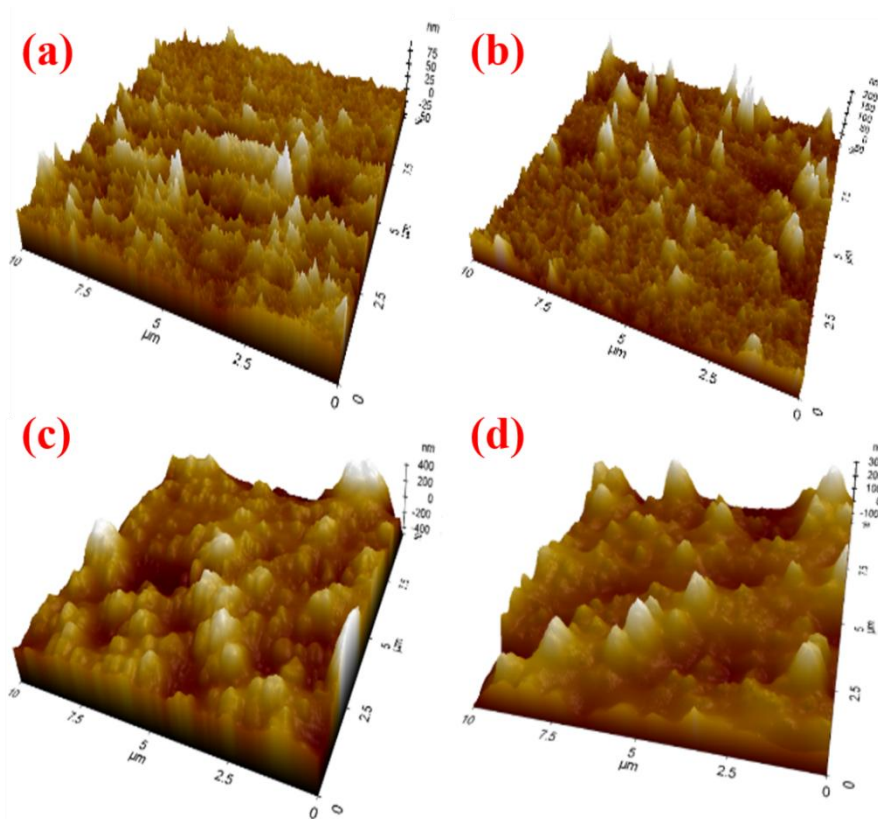


Figure 3. 3D AFM images of Cu thin films at varied depositing period a) 10 minutes, b) 20 minutes, c) 30 minutes, and d) 40 minutes.

AFM images in three dimensions (3-D) of Cu films that have various depositing period are shown in **Figure 3**, and **Table 1**, displays its average particle size and RMS roughness. It has been found that when the coating period goes up between 10 to 30 minutes, the RMS roughness for Cu films rises between 10 to 66 nm, while for the film formed at 40 minutes, it falls about 49 nm. Large valleys amid the particles are seen for the film created during 30 minutes of coating period indicating that the nodule coalescence process improved the resulting surface area and roughness, which is a favorable approach to release ions. Surface roughness decreases for film prepared at 40 minutes of depositing period, due to the irregular formation of nodules and hence a rate of ion emission also declines. Furthermore, the mean particle size rises between 50.59 to 209.62 nm when the coating period advances from 10 to 30 minutes, and subsequently falls to 202.88 nm for 40 minutes. Hanif and colleagues have also observed similar AFM outcomes [30]. The size of particles improves as small grains combine into larger grains over a thin film surface [31].

4. An Electrostatic Air Purifying Characteristics for Cu films

(i) Determining the concentration of smoke particulate matter

At an increments of 15 seconds, the light's intensity was measured. The light's visibility grows significantly over time since the negative ions produced by the EAP within the housing. We used easily produced dhoop smoke for our exploratory test. Beer Lambert's rule, as stated by equation (3) was used to calculate the PM concentrations for every fifteen seconds.

$$I = I_0 e^{-\alpha m} \quad (3)$$

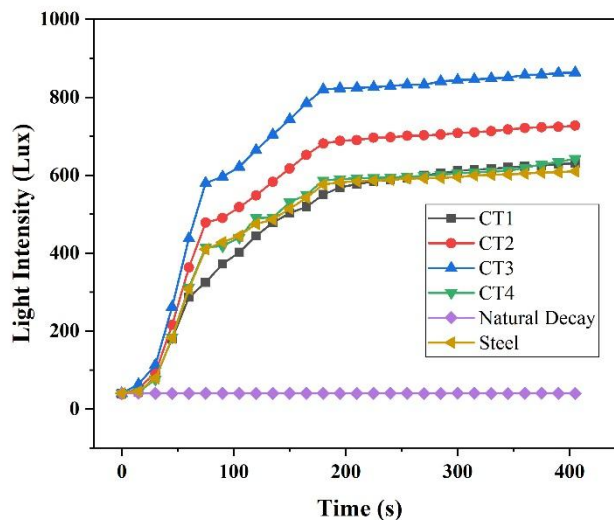
Where, I_0 is incident light intensity; I is observed light intensity; m is the number of particles and α is a scattering cross-section.

For smoke particles, $\alpha = 1.2 \times 10^{-11} / \text{cm}^2$ is considered [32].

Figure 4, displays the relation between light's intensity against time for smoke particulate matter. Both electroplated Cu films and SS substrates are employed as discharging rod for EAP in the present work. Numerous exploratory experiments were carried out for variable durations. For the studies with current set up, 8 minute time limit was found to be adequate. It has been observed that the dhoop particle matter degrades much slower naturally than when EAP is applied to produce an ionized atmosphere. Regarding dhoop particles, an examination was done comparing the transmission light intensity of Cu films and SS electrodes in EAP. It was discovered that Cu films have higher transmission light intensities for dhoop fumes than do SS rod in EAP. As the coating period rises from 10 to 30 minutes, the visibility of light improves and then falls for 40 minutes duration is listed in **Table 2**. This illustrates that a CT3 film requires 80 seconds to capture fifty per cent of the light that passes through container. As a result, CT3 film required less time than SS and other Cu films to increase visibility.

Figure 4. The light's intensity against time for smoke particulate matter

It is also seen that the natural disintegration of the smoke particles in the glass container remains nearly unchanged for 8 minutes. When using EAP, the amount of smoke particle matter drops exponentially with time. We discovered that CT3 film has



the fastest rate of smoke particle decomposition. It also minimal time to remove over 80 percent of the dhoop particulate matter compared to SS and other Cu film EAPs. The increased surface area and surface roughness of the CT3 film, which have been confirmed through SEM, AFM, and XRD, both contribute to the higher rate of generation of ions and are responsible for the noticed rise in particulate matter decay. Shiue et al. [33] and other researchers [34–35] reported similar curve types for different types of smoke particulate matter. However, the EAP with CT3 electrode exhibits a fast response time, which could be related to the nature of the discharging rod, the volume of the glass container, or the effectiveness of the EAP.

(ii) Efficiency for Removing Particles (ERP)

A natural decomposition of dhoop smoke particles served as a reference mark. The particle decay concentration was then determined using the EAP equipped with discharging rod made up of SS and of Cu thin films coated over a range of depositing period, between 10 to 40 minutes. The dhoop smoke decaying concentration were calculated when (1) EAP is turned off [$C_{Natural}(Pm, t)$] (2) EAP is turned on [$C_{EAP}(Pm, t)$]. The formula described in equation (4) was used to compute the ERP.

$$\text{Efficiency for removing particles} = \frac{C_{Natural}(Pm, t=0) - C_{EAP}(Pm, t)}{C_{Natural}(Pm, t=0)} \times 100 \% \quad (4)$$

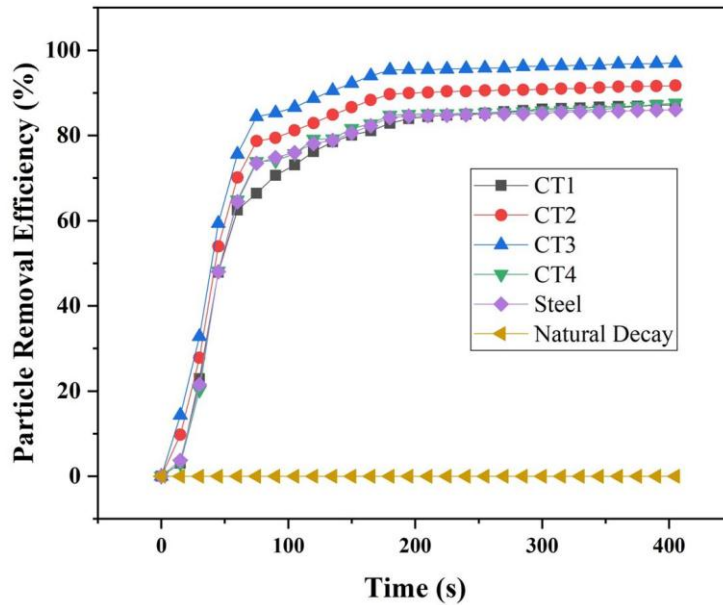


Figure 5. ERP versus time for dhoop particulate matter

Figure 5. depicts efficiency for eliminating dhoop particulate matter verses time utilizing Cu films and SS as discharging rod within EAP. It has been observed that the ERP for dhoop PM enhances in the atmosphere generated through electrostatic air purifier. An EAP with Cu coatings has a higher EPR than SS for dhoop particles. Table 2 indicates that for CT4 film synthesized at depositing period 40 minutes, the corresponding ERP decreases to 79.10 % and increases from 75.97 to 87.99 % as depositing period advances from 10 to 30 minutes. The powder coating that appears for CT4 films indicates a drop in ERP, which may be caused by very little ionic emissions. The highest value of ERP for CT3- EAP is owing to, the enhanced surface structure of Cu film and suggests that the rate of ion generation is larger for it which was further corroborated by AFM analysis. Grinshpun and co-workers had formerly published identical findings [36]. As a result, the time required for electrodeposition of the copper film is vital for particle removing process. The usage of EAPs, which produce ions that disintegrate the majority of smoke particulate concentration and purify the air.

(iii) Determination of Air Cleaning Factor (ACF) and Negative Ion Concentration

The ACF can be computed using the formula as;

$$ACF = \frac{C_{Natural}(Pm, t)}{C_{EAP}(Pm, t)} \quad (5)$$

The ACF has been calculated to measure the effectiveness of device for removing particulate matter by using the ions generated by it. Figure 6. (I) illustrates the way how the ACF value for EAPs made with SS and Cu films synthesized with different deposition periods varies over time. It is seen that the ACF is higher for Cu films relative SS. When the coating time of Cu is raised from 10 to 30 minutes, the ACF goes up from 7.48 to 30.80 while for 40 minutes of depositing time the ACF at 360 seconds reduces to 7.42. The highest value of ACF was observed to be 33.01 for CT3-EAP at 405 seconds, which is substantially greater than SS-EAP. A crucial factor in evaluating an air purifier's efficacy is the rate at which ions are created. We have selected a negatively polar ion generator because of its many advantages. It has been noticed that when CT3-EAP is employed, greater amounts of air ions are produced than when SS or other

discharging electrodes have been employed. Furthermore, **Figure 6. (II)** represents that, in contrast to the various kinds of EAPs, the CT3-EAP releases ions at reasonably consistent levels throughout time.

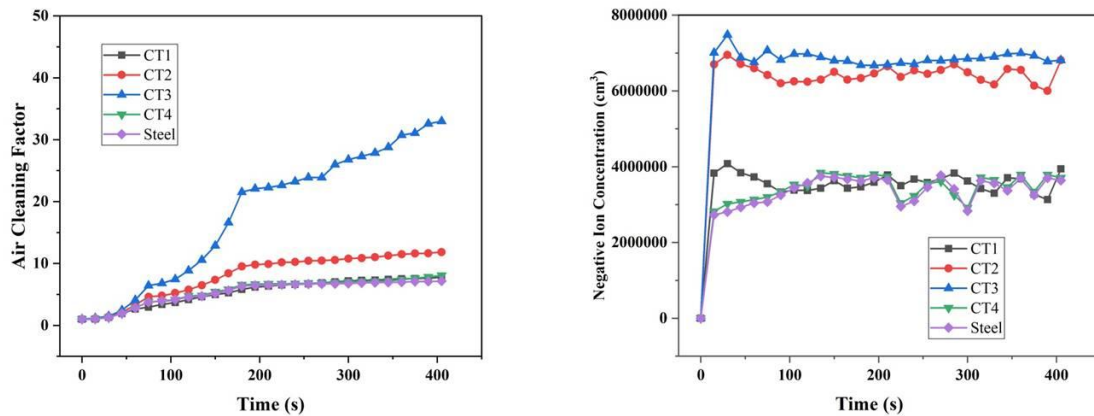


Figure 6. (I) Air-cleaning factor versus time **(II)** The negative ions concentration against time for dhoop particulate matter

Table 2. Reaction time for 80 % declining smoke particulate matter, duration for 50 % visibility, ERP after 120 s working of EAP and ACF at different time

Type of EAP	Reaction time for 80 % declining smoke particulate matter (s)	Duration for 50 % visibility (s)	ERP after 120 s EAP working (%)	ACF at different time (s)		
				120	240	360
CT ₁	150	135	75.97	4.21	6.68	7.48
CT ₂	105	90	82.61	5.69	10.19	11.51
CT ₃	75	80	87.99	8.90	23.31	30.80
CT ₄	120	120	79.10	4.09	6.70	7.42
SS	150	120	78.12	4.61	6.58	6.93

(iv) Studies on dhoop smoke particulate matter

Figure 7. (I) shows both particulate matter (PM_{2.5} and PM₁₀) declines substantially over duration equal to 150 s using CT₃-EAP. Unlike CT₃-EAP, the SS-EAP's creates less negative air ions, hence it disintegrates smoke particles less rapidly over time. During 120 s of CT₃-EAP execution, the hazardous PM levels in a non-ventilated room become normal, and the atmospheric condition improves. Similar studies on the amount of PM_{2.5} and PM₁₀ in houses were carried out by Nadali and colleagues using NAIs [37]. The drop in the no. of particles/liter as time goes on over a one-foot distance from the discharging rod is shown in **Figure 7. (II)** within a 4000 square-foot confined environment. The CT₃ film removes particulate concentrations rapidly than SS-EAP. As a result, it is feasible to enhance air quality inside the room by utilizing this kind of EAP.

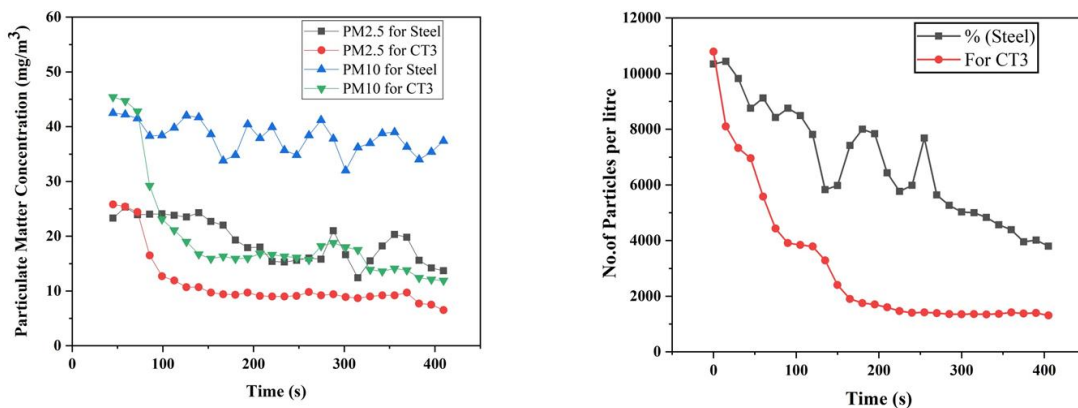


Figure 7. (I) the decay of PM_{2.5} and PM₁₀ particle matter concentrations over time **(II)** No. of particles/liter versus time inside a confined hall equipped EAP

V. CONCLUSIONS

The influence of depositing time over the physical, chemical and air purifying characteristics of copper films are being examined. The XRD investigation verifies the development of thin Cu films having a face-centered cubic structural symmetry. The SEM examination reveals that CT3 film prepared for 30 minutes depositing time results in a nodular morphology with minute pores. This structure is generated by the uneven orientation and aggregation of nodules with saturation across the surface. These nodules having size ranges from 47 to 68 nm. This form of surface provides a large surface area and aids in the extra emissions of ions via its pores, thereby improving air purifying activity. The AFM analysis demonstrates that increasing the deposition period from 10 to 30 minutes the mean particle size of Cu thin films rises from 50.59 to 209.62 nm, as does the RMS roughness of the surface, rising from 10 to 66 nm. With 40 minutes of deposition, mean particle size and RMS roughness fall to 202.88 nm and 49 nm, respectively.

The CT3 thin film, with a thickness of 629 nm, has a highest ERP in the range of 87.99% and an air cleaning factor of around 33.01 at 405 s of EAP operations for dhoop, which is significantly greater than the SS discharging plate. Additionally, it is shown that, in a closed, unventilated room, CT3's applied EAP causes the PM_{2.5} and PM₁₀ to decay from hazardous to acceptable levels at times of 120 and 60 seconds, respectively. The CT3 film has a greater amount of negative air ion production compared to SS and other Cu films made at varying depositing period. The physical and chemical features of Cu films show that as the time required for deposition grows, so do the surface morphology, crystal structure, its thickness, surface roughness creating a vibrant, vast surface available for ion emissions. Thus, a rise in the surface area for ion discharge by CT3-EAP due to an enhanced physical-chemical properties leads to a boost in the particle removal rate, negative ion production rate, air purification factor, and PM decay rate for dhoop PM, all of which contribute to a healthier indoor environment.

ACKNOWLEDGMENT

The Authors would like to acknowledge the SAIF and PIFC, Department of Physics, Shivaji University Kolhapur and YCIS, Satara for providing the research facilities and XRD, SEM and EDAX characterizations.

REFERENCES

- [1] Dubey, Stuti, Himanshi Rohra, and Ajay Taneja. "Assessing effectiveness of air purifiers (HEPA) for controlling indoor particulate pollution." *Heliyon* 7, no. 9 (2021)
- [2] Goel, Anubha, Roshan Wathore, Tirthankar Chakraborty, and Manish Agrawal. "Characteristics of exposure to particles due to incense burning inside temples in Kanpur, India." *Aerosol and Air Quality Research* 17, no. 2 (2017): 608-615.
- [3] Melody, Shannon M., Jane B. Ford, Karen Wills, Alison Venn, and Fay H. Johnston. "Maternal exposure to fine particulate matter from a large coal mine fire is associated with gestational diabetes mellitus: a prospective cohort study." *Environmental research* 183 (2020): 108956.
- [4] Petkus, Andrew J., Diana Younan, Keith Widaman, Margaret Gatz, JoAnn E. Manson, Xinhui Wang, Marc Serre et al. "Exposure to fine particulate matter and temporal dynamics of episodic memory and depressive symptoms in older women." *Environment international* 135 (2020): 105196.
- [5] Kumar R, Gupta N, Kumar D, Mavi AK, Singh K, Kumar M. Monitoring of indoor particulate matter during burning of mosquito coil, incense sticks and dhoop. *Indian J Allergy Asthma Immunol* 2014;28:68-73
- [6] Sung, Jin-Ho, Yeawan Lee, Bangwoo Han, Yong-Jin Kim, and Hak-Joon Kim. "Improvement of particle clean air delivery rate of an ion spray electrostatic air cleaner with zero-ozone based on diffusion charging." *Building and Environment* 186 (2020): 107335.
- [7] Giroire, Baptiste, M. Ali Ahmad, Guillaume Aubert, Lionel Teulé-Gay, Dominique Michau, James J. Watkins, Cyril Aymonier, and Angeline Poulon-Quintin. "A comparative study of copper thin films deposited using magnetron sputtering and supercritical fluid deposition techniques." *Thin Solid Films* 643 (2017): 53-59.
- [8] Quinet, Magali, Fabrice Lallemand, Laurence Ricq, J-Y. Hihn, P. Delobelle, Christelle Arnould, and Zineb Mekhalif. "Influence of organic additives on the initial stages of copper electrodeposition on polycrystalline platinum." *Electrochimica Acta* 54, no. 5 (2009): 1529-1536.
- [9] Lee, Dong-Won, Oh-Yun Kwon, Won-Ju Cho, Jun-Kwang Song, and Yong-Nam Kim. "Characteristics and mechanism of Cu films fabricated at room temperature by aerosol deposition." *Nanoscale research letters* 11, no. 1 (2016): 1-8.
- [10] Mukherjee, S. K., L. Joshi, and P. K. Barhai. "A comparative study of nanocrystalline Cu film deposited using anodic vacuum arc and dc magnetron sputtering." *Surface and Coatings Technology* 205, no. 19 (2011): 4582-4595.
- [11] Lu, W., V. S. Donepudi, J. Prakash, J. Liu, and K. Amine. "Electrochemical and thermal behavior of copper coated type MAG-20 natural graphite." *Electrochimica acta* 47, no. 10 (2002): 1601-1606.

- [12] Orhan, Gökhan, and Gökçe Hapçı. "Effect of electrolysis parameters on the morphologies of copper powder obtained in a rotating cylinder electrode cell." *Powder Technology* 201, no. 1 (2010): 57-63.
- [13] Ganesan, K. P., N. Anandhan, T. Marimuthu, R. Panneerselvam, and A. Amali Roselin. "Effect of deposition potential on synthesis, structural, morphological and photoconductivity response of Cu₂O thin films by electrodeposition technique." *Acta Metallurgica Sinica (English Letters)* 32, no. 9 (2019): 1065-1074.
- [14] Nikolic, Nebojsa D., Konstantin I. Popov, Ljubica J. Pavlovic, and Miomir G. Pavlovic. "Determination of critical conditions for the formation of electrodeposited copper structures suitable for electrodes in electrochemical devices." *Sensors* 7, no. 1 (2007): 1-15.
- [15] Sekar, R. "Synergistic effect of additives on electrodeposition of copper from cyanide-free electrolytes and its structural and morphological characteristics." *Transactions of Nonferrous Metals Society of China* 27, no. 7 (2017): 1665-1676.
- [16] Mohd Hanif, Asyikin Sasha, Siti Aisyah Azmal, Mohd Khairul bin Ahmad, and Fariza Mohamad. "Effect of Deposition Time on the Electrodeposited n-Cu₂O Thin Film." In *Applied Mechanics and Materials*, vol. 773, pp. 677-681. Trans Tech Publications Ltd, 2015.
- [17] Meng, Xiangdong, Yang Song, and Ting Shu. "Morphology control and optical characterization of three-dimensional ordered macroporous Cu films from template-assisted electrodeposition." *Journal of Porous Materials* 27, no. 4 (2020): 1069-1076.
- [18] Lin, Chien-Tai, and Kwang-Lung Lin. "Effects of current density and deposition time on electrical resistivity of electroplated Cu layers." *Journal of Materials Science: Materials in Electronics* 15, no. 11 (2004): 757-762.
- [19] TOIFUR, M. "The Effect Of Deposition Time On The Microstructure And Resistivity Of Cu/Ni Thin Film Prepared By Magnetized Electroplating."
- [20] Nabyouni, Gholamreza. "Effect of Deposition Time and Current Density on Kinetic Roughening of Electrodeposited Pt Thin Films." *ECS Transactions* 25, no. 24 (2010): 155.
- [21] Laidoudi, S., M. R. Khelladi, C. Dehchar, L. Lamiri, R. Yekhlef, S. Boudour, and R. Boufnik. "Effect of deposition time on the properties of Cu₂O thin film electrodeposited on ITO substrates." In *Iere Ecole d'hiver sur l'Analyse de cycle de vie Et L'Eco-conception*. 2018.
- [22] Tlemçani, Taoufik Slimani, Fouzia Cherkaoui El Moursli, Faiza Hajji, Zineb Edfouf, Mhamed Taibi, Hicham Labrim, Bouchra Belhorma et al. "Deposition time effect on the physical properties of Cu₂ZnSnS₄ (CZTS) thin films obtained by electrodeposition route onto Mo-coated glass substrates." *Energy Procedia* 84 (2015): 127-133.
- [23] Manjulavalli, T. E., and A. G. Kannan. "Effects of deposition time on structural, optical and electrical properties of chemically deposited Cu₂S thin films." *J. Chem. Tech. Res* 8, no. 11 (2015): 607-616.
- [24] Abd El Rehim, S. S., S. M. Sayyah, and M. M. El Deeb. "Electroplating of copper films on steel substrates from acidic gluconate baths." *Applied surface science* 165, no. 4 (2000): 249-254.
- [25] E. Mattsson, J. O'M. Bockris, *Trans. Faraday Soc.* 55 1959 Z. 1586.
- [26] Qiao, Feng, and Alan C. West. "The impact of cations on nucleus density during copper electrodeposition." *Electrochimica Acta* 150 (2014): 8-14.
- [27] Revathi, N., P. Prathap, and KT Ramakrishna Reddy. "Synthesis and physical behaviour of In₂S₃ films." *Applied Surface Science* 254, no. 16 (2008): 5291-5298.
- [28] Messaoudi, O., M. Gannouni, A. Souissi, H. Makhlof, A. Bardaoui, and R. Chtourou. "Structural, morphological and electrical characteristics of electrodeposited Cu₂O: effect of deposition time." *Applied Surface Science* 366 (2016): 383-388.
- [29] Cho, S. H., S. H. Kim, N-E. Lee, H. M. Kim, and Y. W. Nam. "Micro-scale metallization on flexible polyimide substrate by Cu electroplating using SU-8 photoresist mask." *Thin Solid Films* 475, no. 1-2 (2005): 68-71.
- [30] Mohd Hanif, Asyikin Sasha, Siti Aisyah Azmal, Mohd Khairul bin Ahmad, and Fariza Mohamad. "Effect of Deposition Time on the Electrodeposited n-Cu₂O Thin Film." In *Applied Mechanics and Materials*, vol. 773, pp. 677-681. Trans Tech Publications Ltd, 2015.
- [31] Y. F. Sun, S. B. Liu, F. L. Meng, J. Y. Liu, Z. Jin, L. T. Kong, J. H. Liu, "Metal oxide nanostructures and their gas sensing properties: A review," *Sensors* 12 (2012) 2610-2631.
- [32] *Solar Radiation* by N. Robinson, Elsevier Publishing Company, 1966, p-p 59.
- [33] Shiue, Angus, Shih-Cheng Hu, and Mao-Lin Tu. "Particles removal by negative ionic air purifier in cleanroom." *Aerosol and Air Quality Research* 11, no. 2 (2011): 179-186.
- [34] Sawant, V. S., G. S. Meena, and D. B. Jadhav. "Effect of negative air ions on fog and smoke." *Aerosol and Air Quality Research* 12, no. 5 (2012): 1007-1015
- [35] Wu, Chih Cheng, Grace WM Lee, Shinhao Yang, Kuo-Pin Yu, and Chia Ling Lou. "Influence of air humidity and the distance from the source on negative air ion concentration in indoor air." *Science of the total environment* 370, no. 1 (2006): 245-253.
- [36] Grinshpun, S. A., G. Mainelis, M. Trunov, A. Adhikari, T. Reponen, and K. Willeke. "Evaluation of ionic air purifiers for reducing aerosol exposure in confined indoor spaces." *Indoor air* 15, no. 4 (2005): 235-245.
- [37] P. Nadali, Azam, Hossein Arfaenia, Zahra Asadgol, and Mohammad Fahiminia. "Indoor and outdoor concentration of PM₁₀, PM_{2.5} and PM₁ in residential building and evaluation of negative air ions (NAIs) in indoor PM removal." *Environmental Pollutants and Bioavailability* 32, no. 1 (2020): 47-55.

© 2024. This work is published under

[https://creativecommons.org/licenses/by/4.0/legalcode\(the“License”\)](https://creativecommons.org/licenses/by/4.0/legalcode(the“License”)).

Notwithstanding the ProQuest Terms and Conditions, you may use this content in accordance with the terms of the License.

¹Dr.S. D. Gawande

²Dr. D. S. Dhote

³Dr. J. S. Tated

Detection of Disease on Citrus Plants Using Image Processing Technique



Abstract: India is rich in agricultural resources; more than 70% of the population is involved in agricultural activities and production. Farmers encounter great difficulties in detecting and controlling plant diseases. Detection and identification of plant leaf disease in early stage is very important to avoid farther economic loss as well as increase productivity. Visual inspection, spectral analysis, DNA – based analysis, IO T – based analysis and automated image analysis are some of the cutting - edge methods used for detection of plant diseases. This work focuses on Image processing technique that detects the plant disease in its early stage. The system has a set of algorithms that can identify the type of disease. Input image captured by the user undergoes various stages, such as image acquisition, pre-processing, segmentation, extraction features, and classification. Classification based on selecting appropriate features of images done by using SVM classifier. Android application that helps farmers for identifying plant diseases by uploading leaf images to the system. **Keywords:** Image Processing, Image Acquisition, Image Segmentation, Feature Extraction, Image Pre-processing, SVM classifier, Plant Diseases.

¹ Research Scholar, Post Graduate Department of Electronics, Brijlal Biyani Science College, Amravati, Dist. Amravati, M. S., India

*Corresponding author e-mail : sdgawande99@gmail.com

Copyright © JES 2024 on-line: journal.esrgroups.org

I. INTRODUCTION

The development of a nation's economy depends heavily on agricultural productivity, that is why disease diagnosis in plants has importance in the agriculture industry [9]. Manual inspection of plants is time-consuming and labor intensive and many times it may be ineffective [12]. Many technologies, such as remote sensing, geoinformatics, wireless sensor networks, and digital image processing, are now available to help the Indian farmers for smart agriculture. The most recent technical applications in this sector can assist Indian farmers in increasing agricultural efficiency and productivity. The image processing techniques based on mobile technology plays a significant role for disease detection and identification in which machine learning uses algorithms such as the K-means algorithm for detecting the features of plants which will be followed by the SVM process, the model is utilized for training and learning of captured images, which can successfully detect and identify plant disease. There are some challenges while image processing in disease detection. For example, the appearance of diseases varies significantly depending on disease stage. Also, diseases identification is difficult as it affects a small portion of the plant. The suggested approach is to identify plant diseases which is efficient substitute for prediction of disease in its early stage with in short time than deep learning strategies.

II. MOTIVATION

In citrus farming sector it is seen that, most of the plants regularly harmed by fungus, bacteria and viruses depending on immunity of plants. We found that most of the farmers do not know about the early symptoms of plant diseases affecting the leaf which might be an indication of hazardous disease found in plants. The affected tree has stunted growth and dies. Farmers encounter great difficulties in controlling plant diseases when it grows well. Thus, it is of great importance to diagnose plant diseases at early stages so that appropriate and timely action can be taken by the farmers to avoid further losses. There is no technology available in the market that can alert the farmer within low cost which can identify the disease in its early stage so as to avoid huge plant loss. Hence detecting the disease in its early stage in real-time on site is important. This research will be beneficial to the farmers, providing a knowledge of disease identification in early stage.

III. LITERATURE SURVEY

The automation of disease detection is a topic of major interest in the agriculture sector worldwide. Many studies are being done to find those diseases. To take preventive measures and protection researchers have done their study on various plants using different technique and technologies to detect various types of diseases. This study will carry out an idea and analyzing the identification of different types of diseases.

Wan Mohd Fadzil et al. [1], discussed a disease detection method for orchid plant leaves. The orchid plant leaflet images are received the usage of digital camera. The algorithm makes use of an aggregate of various strategies inclusive of border segmentation method, morphological processing and filtering technique used for categorizing input images into two disease class as black leaf spot and solar scorch. Vijay Jumb et al. [2], discussed a techniques of segmentation victimization Otsu's thresholding and K-means clustering. The first images area units regenerate to HSV color space and therefore the V part is used for multi-thresholding. The projected work compares this segmentation technique with different techniques like fuzzy C-means, region growing etc. These techniques area unit compared using two metrics i.e. peak signal to noise magnitude relation (PSNR) and mean sq. error (MSE).

Rong Zhou et al. [3], explained method for resilient and advance identify of leaflet patch in sugar beet. For capturing images, Nikon photographic camera was used that was mounted on a stand to stay constant distance. The author used white background whereas capturing images to avoid the additional complications in process. The method implements hybrid methods of guide matching and support vector machine. This technique usage color primarily forms options for segmentation, orientation code matching and support vector machine classifier for final malady classification.

Dheeb Al Bashish et al. [4], examined the strategy to detect the plant leaf disease exist on leaflet and cane. The presented system is together of K- Means segmentation method and neural network used for classification of segmented images. Classification demonstrated average precision of 93%.

Di Cui et al. [5], explains the image processing techniques for multispectral images to detecting rust on plant leaf and its growth amount of disease. The dataset contains the images collected from a greenhouse of research institute. The explained method uses the concept of evaluate centroid for each image for further processing.

J.S.Smith and A.Camargo [6], proposed a technique for recognizing the optical indications of plant leaf maladies by utilizing the image processing method. The accuracy of the algorithm is tested by matching the images, which were manually with those automatically segmented.

Murali Krishnan et al. [7], represent technique which discovers the contaminated plant leaf region with the use of K Means cluster and extracting the region of interest (ROI).

A. Camargo and J. S. Smith [8] used histogram equalization to spread the pixel intensities to get better quality images.

Omprakash Patel [9] studied several extended versions of histogram equalization. Their study found that Recursively Separated and Weighted Histogram Equalization gives lower mean error brightness and a higher peak to signal ratio.

S. B. Sayyad [10] used histogram equalization and compared Weiner filter and median filter. Padmavathi K. [11] the authors have compared RGB image and gray scale image to detect disease better. It was found that colored image gave good results than gray scale image.

Deepa. K. Jyothi.[12] used combination of median filter, Weiner filter and histogram equalization for image enhancement.

Zhou et al. [13] proposed K-Means clustering algorithm and faster R- CNN Fusion algorithm to detect rice diseases as well as to address several complications such as blurred image edge, noise, large background interference and low detection accuracy using 3010 images which captured by camera. And also faster 2D-Otsu algorithm was used to classify the rice disease images for getting output.

Sharma et al. [14] introduced the image preprocessing along with k- means clustering, segmentation and four classifiers such as logistic regression, SVM, KNN, and CNN to detect and classify leaf diseases automatically wherein logistic regression performs quite well due to classes but highest accuracy was provided by CNN.

Shafi et al. [15], it was suggested an incorporated method to create heterogeneous data from Normalized Difference Vegetation Index for achieving a rich and comprehensive knowledge of wheat's health using IoT sensors, machine learning such as SVM and NB and drone technology.

Sardogan et al. [16] presented a CNN model along with Learning Vector Quantization (LVQ) algorithm to identify and classify leaf diseases of 500 tomato leaf images from Plant Village dataset. Also, the different filters of convolutions were used to progress recognition level in classification method.

IV. METHODS

1. *Technique for Disease Ditection*

In process of disease detection, the Machine learning algorithms and Image processing digitally are two parts. In first part of disease detection as a Machine Learning algorithm we use SVM (support vector machine) to detect and analyze the feature of leaf and accuracy between training and testing data set. Before image processing sample goes through some steps like capturing of the images, image segmentation, feature extraction from images and last removal of noise.

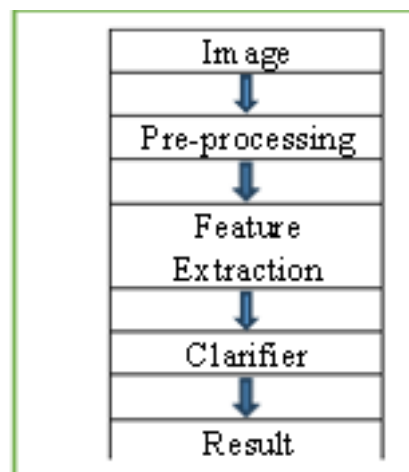


Fig. 1 Methodology

2. Working Include Following Steps

- Image Conversion

In image conversion we convert the RGB image to Grayscale image which is the most important factor, in this conversion some pixels given are converted to a single pixel which holds the information intensity and quantity of light. The image is black -white colors and grey shade sometimes, having lowest intensity contrast of black color and highest contrast intensity of white color.



Fig. 2 RGB to Gray Scale Conversion

- Edge Detection

Edge detection of leaf images is carried out by the detector that was developed by John F Canny for the detection of edges of images which is known as Canny Edge Detector used for edge detection.

- Thresholding

Thresholding converts image in to two parts foreground and background. It helps in conversion of gray scale image to binary form.

- Noise Reduction

In noise reduction the image is smoothen on the corners with decreasing contrast. There are many algorithm developed for this process. Output of this will give a smoothen images without noise in it. The noise in the plant leaf is in the form of shot noise, Gaussian noise, Pepper and salt.

Here we use Alex-Net Algorithm for the processing purpose of the image. It consists of five layers of convolutional and three layers fully connected. we can get the extracted features from the images multiple convolutional kernel [3]. In the single convolutional, multiple many numbers of kernels of equal size are seen.

classification is very important in plant disease detection system. In this process plant leaf images are categorized in accordance with identified diseases by providing a particular input image with one of the classes.

This process is useful in determining the disease causes, cures, and early diagnosis of disease. In this step we compile a dataset of plant leaf diseases, from which one by one image is processed for disease identification. While implementation of project, we need to connect the server and the mobile to same internet hotspot. After the establishment of connection with local host, we can take the images from data set. The captured images are send to the server side for further processing by using the Python web framework. Output is send back to the mobile with name of disease, causes, and remedies for disease. Classifier should distinguish the healthy and diseased life images. The SVM classification method is used for categorization of textural feature of input image and identifies the disease of plant.

3. Figures

RGB to Grayscale is the most important factor in which input image with some pixels and output is only a single pixel will be representing the quantity of light which will be holding only the information of the intensity of images. It is a black-white image only having these two colors and shade of grey sometimes. It will be having black color at the lowest intensity contrast [12] and white at a very highest intensity contrast.

- Scale Conversion from RGB to Gray

While processing any image segmentation process is very important tasks referred as surveillance purpose, image that can be used when we need and recognition of pattern.

The main motive or objective of the segmentation is to get better understanding of the image while identify the region around the images. It is mainly used to figure out the lines and boundaries in the image for better processing purpose. It will also help in see the curve in the images its intensity [14] and texture for good analyze purpose.

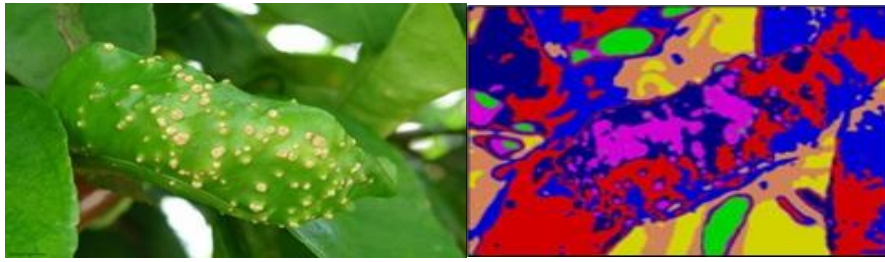


Fig 3. a. Original Image

Fig.3. b. Segmentation of Image

V. RESULT

The experimental work is carried out on the citrus species tree leaf. Different leaf having diseases shown over the surface of the leaf is selected for the image processing.

1. Insect Pest Diseases Citrus Leaf Miner

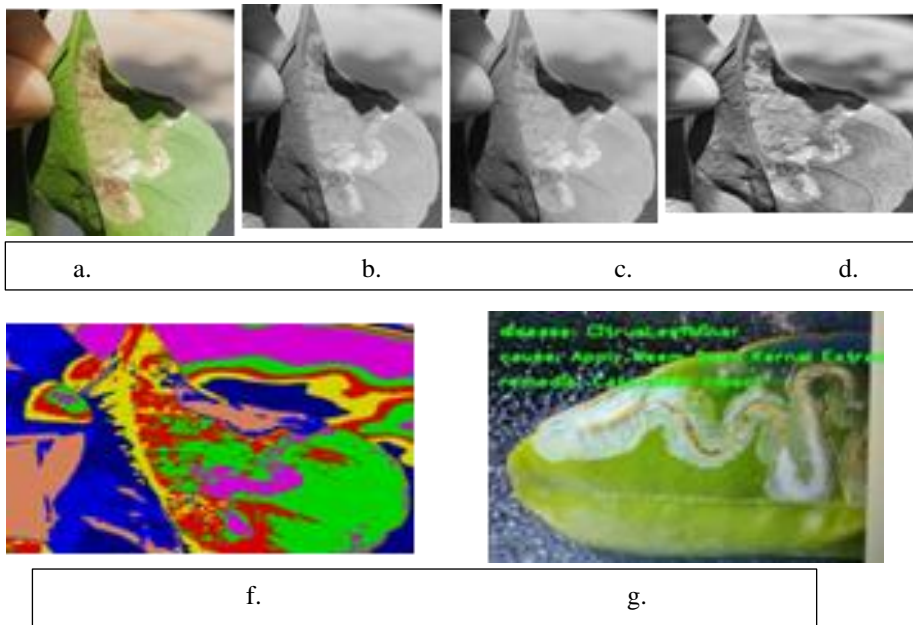
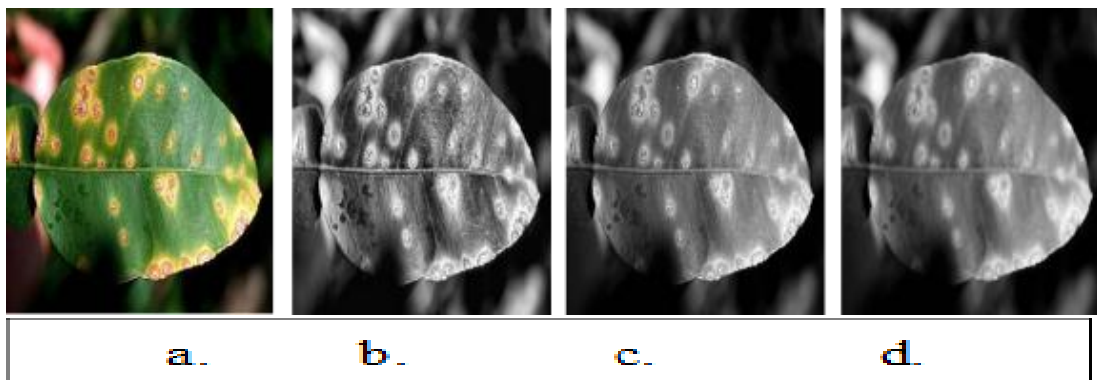


Fig.4 - a, b, c, d, e, f: - Citrus Leaf Miner original image, enhanced image, gray scale image, blur image, segmented image, final output with disease name, cause and remedy.

2. Bacterial Disease Citrus Canker



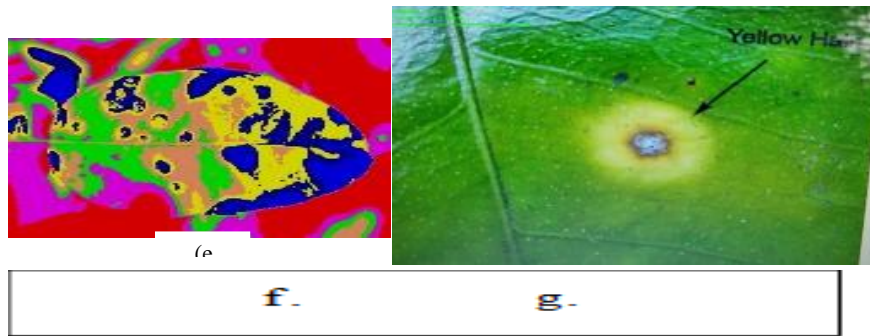


Fig..5. a, b, c, d, e, f: - Citrus Canker original image, enhanced image, gray scale image, blur image, segmented image, final output with disease name, cause and remedy

3. Healthy Image : Not Infected Leaf

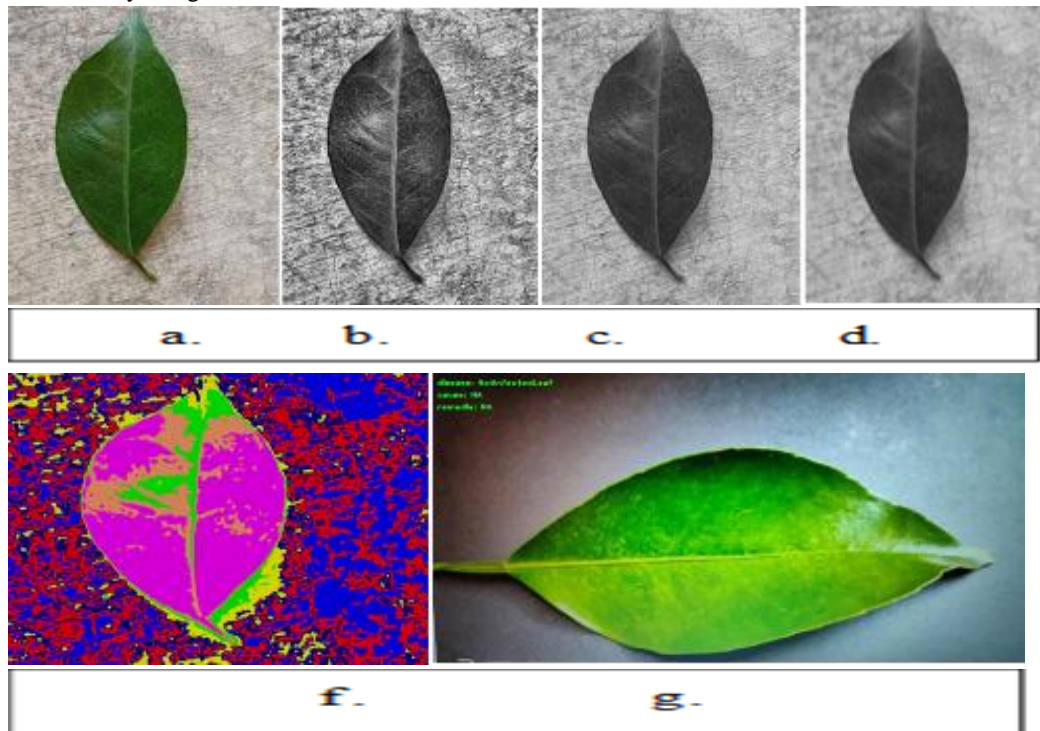


Fig. 6. Citrus not infected leaf original image, enhanced image, gray scale image, blur image, segmented image, final output with disease name, cause and remedy.

VI. CONCLUSION

The accurate detection of the plant disease is very important for the successful cultivation of crop and this can be done using image processing. The method reported in the thesis can be used to design a plant disease detector for farmers for the early detection of plant disease infection and getting appropriate cure for the diseases.

The research has been undertaken and motivated to help agriculture and horticulture fields. There are two modules in this project is the leaf name identification pertained to which plant and disease detection. Out of all available segmentation techniques, they are cost effective still there is chance to improve over the results.

The proposed method presented in this research is the integrated approach of K-means clustering which is beneficial for the proper segmentation of the leaf diseases. The analysis has been done to explore the techniques effective in the segmentation of the citrus plants leaves. The analysis is carried out on the available leaves images by performing various segmentation methods with the help of Python implementation. We have correctly analyzed citrus leaf disease through image processing using python.

REFERENCES

- [11] Wan Mohd Fadzil, Shah Rizam, Jailani R, Nooritawati M.T, "Orchid leaf disease detection using Border Segmentation technique," IEEE Conference on Systems, Process and Control (ICSPC), Vol.1, pp.168-179, December 2014.
- [12] Vijay Jumb, Mandar Sohani, Avinash Shrivastava, "Color Image Segmentation using K-means Clustering and Otsu's Adaptive Thresholding," International Journal of Innovative Technology and Exploring Engineering (IJITEE), Vol. 3, Issue 9, February 2014.
- [13] Rong Zhou, Shun'ichi Kaneko, Fumio Tanaka, Miyuki Kayamori, Motoshige Shimizu, "Early Detection and Continuous Quantization of Plant Disease Using Template Matching and Support Vector Machine Algorithms," IEEE International Symposium on Computing and Networking, 2013.Maxwell, 2013.
- [14] Al-Bashish, D.M.Braik and S. Bani-Ahmad, 2011, "Detection and classification of leaf diseases using K-means based segmentation and neural-networks based classification," Inform Technol, Vol.10, pp.267-275. 2011.
- [15] Di Cui, Qin Zhang, Minzan Li, Glen L. Hartman, Youfu Zhao, "Image processing methods for quantitatively detecting soybean rust from multispectral images",ELSEVIERScienceDirect,Vol.22,No.4, pp.186- 193, 2010.
- [16] A.Camargo, J.S.Smith, "An image-processing based algorithm to automatically identify plant disease visual symptoms," ELSEVIER, Vol. 17, No. 1, pp.9-21, 2009.on Electricity and Magnetism, 3rd ed., vol. 2. Oxford: Clarendon, 1892, pp.68–73.
- [17] Murali Krishnan, Dr.M.G.Sumithra, "A Novel Algorithm for Detecting Bacterial Leaf Scorch (BLS) of Shade Trees Using Image Processing",IEEE 11th Malaysia International Conference on Communications,November 2013.
- [18] Camargo A, Smith J S. "An image-processing based algorithm to automatically identify plant disease visual symptoms". Biosyst Eng 102:9-21, 2009.
- [19] Omprakash Patel, Yogendra P. S. Maravi and Sanjeev Sharma," A Comparative Study of Histogram Equalization Based Image Enhancement Techniques for Brightness Preservation and Contrast Enhancement", Signal & Image Processing: An International Journal (SIPIJ),4: 11-25, 2013.
- [20] Shaikh M A, Sayyad S B, "Color Image Enhancement Filtering Techniques for Agricultural Domain Using MATLAB",VIII International Symposium on Operational Remote Sensing Applications: Opportunities, Progress and Challenges; 9-2 December, Hyderabad,INDIA, 2014
- [21] Padmavathi K, Thangadurai K," Implementation of RGB and Grayscale Images in Plant Leaves Disease Detection – Comparative Study", Indian Journal of Science and Technology, 9(6):1–6, Feb 2016.
- [22] Deepa. K. Jyothi "A Robust and Efficient Pre Processing Techniques for Stereo Images" ICEECCOT, pp 89-92, 2017.
- [23] G. Zhou, W. Zhang, A. Chen, M. He, and X.Ma, "Rapid detection of rice disease based on FCM-KM and faster R-CNN fusion," IEEE Access, vol. 7, pp. 143190-143206, Sep. 2019.
- [24] P. Sharma ; P. Hans ; S. C. Gupta, "Classification Of Plant Leaf Diseases Using Machine Learning And Image Preprocessing Techniques," in Int. Conf. on Cloud Com., Data Sc. & Eng., Noida, INDIA, 2020
- [25] U. Shafi, R. Mumtaz, N. Iqbal, S. M. H. Zaidi, S. A. R. Zaidi, I. Hussain, Z. Mahmood, "A multi-modal approach for crop health mapping using low altitude remote sensing, Internet of Things (IoT) and machine learning," IEEE Access, vol. 8, pp. 112708-112724, Jun. 2020
- [26] M. Sardogan, A. Tuncer and Y. Ozen, "Plant Leaf Disease Detection and Classification based on CNN with LVQ Algorithm," in Int. Conf. on Comp. Sci. and Eng., Sarajevo, BOSNIA-HERZEGOVINA, 2018, pp. 382-385.

¹ Sayli Guru,
U. P. Manik
² Amol Nande

**Optical and
Luminescence
properties of
 $\text{Ca}_9\text{Al}(\text{PO}_4)_7:\text{Eu}^{3+}$
inorganic phosphor**



Abstract: A series of $\text{Ca}_9\text{Al}(\text{PO}_4)_7:\text{xEu}^{3+}$ samples was synthesized using energy efficient and ecofriendly co-precipitation method. These samples were synthesized by varying Eu^{3+} concentrations ($\text{x}=0.05\text{mol } \%, 0.15\text{mol } \%, 0.25\text{mol } \%, 0.5\text{mol } \%, 2\text{mol } \%, \text{ and } 7\text{mol } \%$). The formation of the $\text{Ca}_9\text{Al}(\text{PO}_4)_7$ and $\text{Ca}_9\text{Al}(\text{PO}_4)_7:\text{Eu}^{3+}$ compounds confirmed using X-ray diffraction (XRD) analysis. The results confirmed the formation of rhombohedral crystalline phase in both the compounds. Further, with increasing Eu^{3+} ion concentration the intensity of prominent peaks in the XRD patterns changed suggesting the doping had been taken placed in $\text{Ca}_9\text{Al}(\text{PO}_4)_7$ host matrix. The synthesized samples were subjected to SEM and EDS mapping analysis to confirm their morphological characteristics and elemental composition respectively. A comparison between $\text{Ca}_9\text{Al}(\text{PO}_4)_7$ and $\text{Ca}_9\text{Al}(\text{PO}_4)_7:\text{xEu}^{3+}$ EDS data suggested the Eu^{3+} ions successfully doped into the $\text{Ca}_9\text{Al}(\text{PO}_4)_7$ host matrix. UV- Vis spectral studies determined the band gap energy for the host which was found to be 4.2 eV respectively. The Photoluminescence (PL) spectra of the emission was examined at wavelength 395nm. The photoluminescence spectra clearly depicted that the prominent emission peak was observed at 613 nm corresponding to ${}^5\text{D}_0 \rightarrow {}^7\text{F}_2$ transitions. The highest luminescence emission intensity was obtained at 7mol % concentration of Eu^{3+} in the host matrix. The prominent red-orange emission observed for near UV-blue color wavelength excitation suggesting this phosphor can be used for red color light emitting devices.

Keywords: Co- precipitation synthesis, photoluminescence, X+-ray, Eu^{3+} , phosphate, UV.

¹ Author 1: S P College, Chandrapur, India

² *Corresponding author: G.N. College of Science, Ballarpur, India

I. INTRODUCTION

Luminescence have wide range of applications in displays, scientific research, lighting, medical diagnostics, entertainment and security. Their ability to emit light in response to various stimuli makes them valuable in many technological and biological contexts. Currently, there is significant enthusiasm for the application of phosphors for advancement of display and lighting technologies [1,2]. Despite extensive research on lighting devices, the field of luminescence continues to offer opportunities for further exploration, particular in areas such as color tuning, energy conversion, quantum yield enhancement, persistent luminescence and intensity variation [3,4]. These are quite few models of the diverse research topics within the area of luminescence, and ongoing studies continue to advance our understanding and unlock new applications for luminescent materials and phenomena. Both the host and activator (dopant) contribute equally to determine these luminescent properties [5]. Various types of host materials, including aluminates, sulphates, phosphates etc. exist among which phosphates are regarded as particularly promising host materials, as they are easy to prepare and good chemically stable [6]. Calcium based host like $\text{Ca}_9\text{Al}(\text{PO}_4)_7$ also known as Calcium Aluminium Orthophosphate have good thermal and chemical stability suggesting it can be act as a good luminescent host, making it valuable in phosphor applications for lighting , display technologies, catalysis, sensors and drug delivery systems[7].

The other requirement for luminescent material is dopant or activators. Rare earth elements plays a crucial role in the field of inorganic phosphors especially nanophosphors. Rare earth elements are incorporated into these nanophosphors to produce various colors and properties suitable for the discussed luminescence applications. The size and shape of nanophosphor particles can be controlled during synthesis to optimize their luminescence properties. Smaller particles mostly exhibit different emission characteristics compared to larger one due to quantum size effects. The specific rare earth element and its concentration in the nanophosphor, as well as the choice of host material and synthesis method, all impact the optical properties and suitability for particular application. Trivalent europium (Eu^{3+}) is mostly used dopant in the synthesis of nano- sized phosphors as a red color activator. When excited by blue or UV light, they emit red light, contributing to the full spectrum of colors in the display. Therefore, trivalent europium- doped nano-sized phosphors are valuable materials in the field of optoelectronics and are essential components in various technologies that rely on the emission of red light [8]. Phosphors containing rare-earth doped calcium aluminium phosphate are primarily made using a range of methods such as sol-gel, co- precipitation method, combustion and solid state reaction methods. In the synthesis of phosphates may require pre and post-heating treatments. It depends on the specific synthesis method and the desired properties of the phosphate material being produced. In this study, we employed the co- precipitation method for sample preparation due to its cost effectiveness, energy efficiency, and ability to yield finely crafted nanoscale products [9,14].

In this article, we synthesized a range of nanophosphors doped with Eu^{3+} in $\text{Ca}_9\text{Al}(\text{PO}_4)_7$ using co-precipitation method. Further, the synthesized sample were sent for various structural, micro-structural and optical characterizations. The structural and micro-structural analysis were performed using XRD and SEM analysis. However, the optical studies were carried out by performing UV-vis, FTIR and photoluminescence analysis.

II. SYNTHESIS OF $\text{Ca}_9\text{Al}(\text{PO}_4)_7$ AND $\text{Ca}_9\text{Al}(\text{PO}_4)_7 : x\text{Eu}^{3+}$ NANOPHOSPHORS

A range of nanophosphors with the composition $[\text{Ca}_9\text{Al}(\text{PO}_4)_7]:x\% \text{Eu}^{3+}$ (where $x= 0.05\%$, 0.15% , 0.25% , 0.5% , 2% and 7% molar concentrations) were prepared via the co-precipitation technique. The Synthesis involved the use of Calcium Nitrate $[\text{Ca}(\text{NO}_3)_2]$, Aluminium Nitrate $[\text{Al}(\text{NO}_3)_3]$, Di-ammonium hydrogen phosphate $[(\text{NH}_4)_2\text{H}(\text{PO}_4)_7]$ as precursors. The dopant precursor employed was Europium Oxide $[\text{Eu}_2\text{O}_3]$. Eu_2O_3 was transformed into its nitrate form by adding a small amount of nitric acid $[\text{HNO}_3]$ and subsequently heating it for a 1-2 minutes. Each reagents were of Analytical reagent grade and were used in accordance with their stoichiometric ratios.

The precursors $\text{Ca}(\text{NO}_3)_2$, $\text{Al}(\text{NO}_3)_3$, and $(\text{NH}_4)_2\text{H}(\text{PO}_4)_7$ was dissolved in distilled water in separate beaker and stirred magnetically for a duration of 15 to 20 minutes. Subsequently, Eu_2O_3 with HNO_3 , $\text{Ca}(\text{NO}_3)_2$, and $\text{Al}(\text{NO}_3)_3$ were combined to form a transparent mixture which stirred on magnetic stirrer for another 20 minutes. Following this, solution of $(\text{NH}_4)_2\text{H}(\text{PO}_4)_7$ was added into the mixture to induce the formation of a precipitate. Then they were left undisturbed for 24hours to allow the precipitation process for the completion. Following that, the precipitates underwent filtration and were thoroughly rinsed with double distilled water multiple times to remove the impurities present in the obtained precipitation. Next, the samples were kept in an oven at 80°C for a 24 hours. The resulting dried precipitates were collected, and crushed into a fine powder using a mortar and pestle for 1hr. The prepared samples were then annealed in muffle furnace at 700°C for 24 hr. Once the samples were cooled to room temperature, they were further ground in mortar and pestle for 1hr. The samples are now prepared for further characterization.

The XRD (X-ray diffraction) data was collected using Rigaku's Miniflex 600 benchtop X-ray diffractometer equipped with an advanced detector and Cu-K radiation, over a 2θ range spanning from 10° to 80° to identify its phase. The Scanning Electron Microscope (SEM) imaging was done through Carl Zeiss Model Supra 55. FTIR (Fourier Transform Infrared Spectroscopy) was carried out using the Bruker Alpha T FTIR spectrometer in the Attenuated Total Reflectance (ATR) mode. UV-Vis spectroscopy analysis was carried out to determine the band gap energy of the nanophosphor. The spectrum of optical absorption was determined with a UV-VIS-NIR spectrophotometer (Carry 100) in a range of 200-800nm. The Photoluminescence (PL) excitation – emission spectrum and lifetime were recorded using a fluorescence spectrophotometer (Horriba, Jobin Vyon – Fluorolog-3 model) with a xenon lamp of 450W.

III. RESULTS AND DISCUSSION

A. XRD analysis

The XRD (X-Ray diffraction) pattern of the Eu^{3+} doped $\text{Ca}_9\text{Al}(\text{PO}_4)_7$ samples annealed at 700°C , is displayed in Figure 1. The obtained patterns were compared with Joint Committee on Powder Diffraction Standards (JCPDS) card no : 49-1791 for $\text{Ca}_9\text{Al}(\text{PO}_4)_7$ compound. No additional phases were detected, resulting that obtained sample series are in single phase [10]. The position and intensities of observed peaks correspond well with the theoretical values further validating the phase purity and crystal structure of the synthesised compound. Its crystal structure is rhombohedral crystallised in trigonal R3C space group. The expected lattice parameters were $a = 10.4318 \text{ \AA}$, $b = 10.4318 \text{ \AA}$, $c = 37.3330 \text{ \AA}$ and predicted unit volume cell = $3518.37 * 10^6 \text{ pm}^3$ [11]. It is evident from the XRD data that as the doping concentration of Eu^{3+} increases its intensity is decreased. This suggested that small variation in the lattice parameters occur as Eu^{3+} concentration in the host matrix was increased with increasing doping concentration. The obtained XRD results in comparison with JCPDS data conclusively demonstrate that the obtained $\text{Ca}_9\text{Al}(\text{PO}_4)_7$ sample is of high purity and crystallinity, making it suitable for further applications and studies in various fields.

B. SEM analysis and EDS mapping

Major outcome of Scanning Electron Microscopy (SEM) analysis is shown in Figure 2 (a) - (d) of $\text{Ca}_9\text{Al}(\text{PO}_4)_7$ and (e)-(h) $\text{Ca}_9\text{Al}(\text{PO}_4)_7:7\%\text{Eu}^{3+}$. The SEM analysis of the synthesised $\text{Ca}_9\text{Al}(\text{PO}_4)_7:\text{Eu}^{3+}$ gives detailed insights of morphological characteristics of the $\text{Ca}_9\text{Al}(\text{PO}_4)_7$ and (e) -(h) $\text{Ca}_9\text{Al}(\text{PO}_4)_7:7\%\text{Eu}^{3+}$ nanophosphors. The SEM images shows that the particle possess a uniform and inhomogeneous distribution with not so well-defined shapes. Its microstructure shows typical agglomerated particles, which can exhibit a range of morphologies from spherical to irregular shapes. The average size of particle, obtained from SEM images falls within the range of 100nm to $1\mu\text{m}$ which indicates narrow size distribution.

1. EDS mapping

Figure 3 (a)-(d) shows presence of Oxygen (O), Phosphorus(P), Calcium(Ca) and Aluminium(Al) in $\text{Ca}_9\text{Al}(\text{PO}_4)_7$ host matrix. Further, Figure 3 (e) shows Energy Dispersive X-Ray Spectroscopy (EDS) analysis conducted in conjunction with Scanning Electron Microscopy (SEM) to determine the elemental composition and distribution within synthesised $\text{Ca}_9\text{Al}(\text{PO}_4)_7$ phosphor material. The EDS spectrum revealed the presence of calcium (Ca), aluminium (Al), phosphorous (P), oxygen (O), validating the formation of the $\text{Ca}_9\text{Al}(\text{PO}_4)_7$. The presence of Europium (Eu) was also detected in EDS spectrum, as shown in Figure 3 (f). The Eu peaks were less intense compared to host elements, reflecting the doping concentration is very low compared to the other host elements typically required to achieve the desired luminescent properties.

C. FT-IR analysis

Figure 4 displays FT-IR spectroscopy performed to evaluate the vibrational modes of chemical bonds in synthesised $\text{Ca}_9\text{Al}(\text{PO}_4)_7$ and $\text{Ca}_9\text{Al}(\text{PO}_4)_7:\text{Eu}^{3+}$ nanophosphor monitored in $500\text{-}4000\text{cm}^{-1}$. It displays a range of characteristic absorption bands and other functional groups within the sample. The most efficient peaks observed in FTIR spectrum includes $1140, 1536, 931, 934, 722 \text{ cm}^{-1}$. Ranging from $1000\text{-}1200\text{cm}^{-1}$ related to prominent peak at 1140cm^{-1} indicates PO_4 stretching vibrations of phosphate group. Peaks in the region ranging from $600\text{-}500\text{cm}^{-1}$ correspond to bending vibrations of phosphate tetrahedral structure of P-O. Peaks in the range of $700\text{-}800 \text{ cm}^{-1}$ are corresponding to Al-O stretching vibration modes [12]. Most efficient peaks in the range $800\text{-}1000 \text{ cm}^{-1}$ reported to be of Ca-O-Ca bonding in CaO phosphor [13]. Thus, FTIR results evaluate the phase purity and structural integrity of the material.

D. Diffuse reflectance spectrum

At room temperature, using a UV – Vis spectrometer, optical absorption spectrum of the $\text{Ca}_9\text{Al}(\text{PO}_4)_7$ compound was measured from 200 to 800 nm as shown in Figure 5. The UV-Vis absorption spectrum reveals

important information about electronic transitions and band gap energy of the material. The UV-vis absorption spectrum of $\text{Ca}_9\text{Al}(\text{PO}_4)_7$ exhibits distinct absorption bands at specific wavelengths, indicative of electronic transitions within the compound [14]. This absorption indicates the transition from valence band to the conduction band, providing insight into the bandgap energy. By analysing the absorption data and using Tauc plot method, the optical band gap energy of $\text{Ca}_9\text{Al}(\text{PO}_4)_7$ compound was calculated to be 4.2 eV. Equation used to calculate band gap energy is:

$$E_g = (ah\nu)^r$$

where,

$r = 1/2$ for direct allowed transition

$r = 3/2$ for direct forbidden transitions

$r = 3$ for indirect forbidden transitions.

E. Photoluminescence Studies

Figure 6 shows the Photoluminescence Emission (PLE) spectra of $\text{Ca}_9\text{Al}(\text{PO}_4)_7:\text{xEu}^{3+}$ nanophosphors. The PLE spectra of $\text{Ca}_9\text{Al}(\text{PO}_4)_7:\text{xEu}^{3+}$ nanophosphors were observed to investigate the luminescent properties of the material. Upon excitation at a 395nm wavelength, PL spectra exhibits distinct emission peaks indicating the material's strong luminescent behaviour [15]. The spectra reveal a prominent peak at 591 and 613nm were related to transitions $^5\text{D}_0 \rightarrow ^7\text{F}_1$ and $^5\text{D}_0 \rightarrow ^7\text{F}_2$ respectively. While the $^5\text{D}_0 \rightarrow ^7\text{F}_1$ transition is widely acknowledged to be primarily a magnetic dipole transition when Eu^{3+} ions are in elevated symmetry positions, the $^5\text{D}_0 \rightarrow ^7\text{F}_2$ transitions are significantly electric dipole transitions that occur only in instances where the Eu^{3+} ions are in positions lacking inversion symmetry. Emission intensities of the peaks grows with the increase in doping concentration from 0.015mol% to 7mol % suggesting the increasing in available luminescent centers with the doping concentrations. It is mostly assumed that as the concentration of Eu^{3+} ion doping increases, PL will also increase [16]. The PLE spectra of the synthesized nanophosphors demonstrate its potential for applications in optoelectronic devices, phosphors for lighting, and display technologies, owing to its strong and stable luminescent properties [17].

IV. CONCLUSION

The synthesis of $\text{Ca}_9\text{Al}(\text{PO}_4)_7:\text{Eu}^{3+}$ nanophosphors using co-precipitation method has been successfully employed with comprehensive characterization confirming the successful incorporation of Eu^{3+} ions into the $\text{Ca}_9\text{Al}(\text{PO}_4)_7$ host matrix. XRD patterns confirmed the successful formation of rhombohedral crystalline phase with high purity. The observed peaks matched well with the standard data, indicating that Eu^{3+} doping did not significantly disturb the host lattice structure. SEM images provided insights into the morphological features of the synthesised phosphors and confirmed the formation of nanophosphors. The homogeneous dispersion of Eu^{3+} ions within the matrix was evident, verifying the efficiency of co precipitation method for doping. FTIR spectra results the characteristic vibrational modes of the phosphate groups in $\text{Ca}_9\text{Al}(\text{PO}_4)_7$ structure and a comparison with the $\text{Ca}_9\text{Al}(\text{PO}_4)_7:7\%\text{Eu}^{3+}$ indicated the presence of Eu^{3+} ion in the nanophosphors. The presence of additional peaks corresponding to Eu-O bonds further confirmed the incorporation of Eu^{3+} ions into the lattice. The estimated band gap value of the host matrix and nanophosphors are 4.2 eV.

Photoluminescence (PL) spectra displayed the characteristic emission peaks of Eu^{3+} ions under 395nm excitation wavelength evaluating strong red emission. The intensity and position of these peaks were consistent with the expected electronic transitions ($^5\text{D}_0 \rightarrow ^7\text{F}_1$ and $^5\text{D}_0 \rightarrow ^7\text{F}_2$) of Eu^{3+} , confirming its appropriate incorporation and the sample's potential as a red – emitting phosphor for various applications, including in display and lighting technologies.

REFERENCES

- [1] Zhao, J., Dong, J., Ye, X., & Wang, L. (2021). A promising novel red-emitting Eu^{3+} -activated neodymium calcium phosphate phosphor with good thermal stability and excellent color purity for WLEDs. *Journal of Molecular Structure*, 1240. <https://doi.org/10.1016/j.molstruc.2021.130567>
- [2] Gupta, I., Singh, S., Bhagwan, S., & Singh, D. (2021). Rare earth (RE) doped phosphors and their emerging applications: A review. In *Ceramics International* (Vol. 47, Issue 14, pp. 19282–19303). Elsevier Ltd. <https://doi.org/10.1016/j.ceramint.2021.03.308>
- [3] Pawade, V. B., Swart, H. C., & Dhoble, S. J. (2015). Review of rare earth activated blue emission phosphors prepared by combustion synthesis. In *Renewable and Sustainable Energy Reviews* (Vol. 52, pp. 596–612). Elsevier Ltd. <https://doi.org/10.1016/j.rser.2015.07.170>
- [4] Khan, L. U., & Khan, Z. U. (2018). Rare earth luminescence: Electronic spectroscopy and applications. In *Handbook of Materials Characterization* (pp. 345–404). Springer International Publishing. https://doi.org/10.1007/978-3-319-92955-2_10

- [5] Jang, M. K., Kim, E. D., & Huh, Y. D. (2021). Photoluminescence properties of tunable emission (Sr_{1-x}Eu_x)₂Ga₂S₅ phosphors. *Optik*, 226. <https://doi.org/10.1016/j.ijleo.2020.165930>
- [6] Chand, S., Mehra, R., & Chopra, V. (2022). Recent advancements in calcium based phosphate materials for luminescence applications. *Journal of Luminescence*, 252, 119383. <https://doi.org/10.1016/J.JLUMIN.2022.119383>
- [7] El-Mesady, I. A., Alawsh, S. A., Hussein, A., El-Samman, H., & Othman, H. A. (n.d.). A Si activated Ca₉Al(PO₄)₇ Nanostructure: Synthesis and Thermoluminescence Characteristics. <https://ssrn.com/abstract=4122874>
- [8] Chaware, P., Nande, A., Dhoble, S. J., & Rewatkar, K. G. (2021). Structural, photoluminescence and Judd-Ofelt analysis of red-emitting Eu³⁺ doped strontium hexa-aluminate nanophosphors for lighting application. *Optical Materials*, 121. <https://doi.org/10.1016/j.optmat.2021.111542>
- [9] Mukhopadhyay, L., & Rai, V. K. (2018). UV excited downconversion luminescence properties of Eu³⁺: NaZnPO₄ phosphors. *AIP Conference Proceedings*, 1953. <https://doi.org/10.1063/1.5032752>
- [10] Pażik, R., Zawisza, K., Watras, A., Maleszka-Bagińska, K., Boutinaud, P., Mahiou, R., & Dereń, P. J. (2013). Thermal quenching mechanisms of the Eu³⁺ luminescence in Ca₉Al(PO₄)₇ obtained by citric route. *Materials Research Bulletin*, 48(2), 337–342. <https://doi.org/10.1016/j.materresbull.2012.10.034>
- [11] Lazoryak, B., X-ray Powder Diffraction Laboratory of Chemistry Technology, Moscow State Univ., Russia., ICDD Grant-in-Aid, (1998) Golubev, V., Lazoryak, B., *Izv. Akad. Nauk SSSR, Neorg. Mater.*, **27**, 376, (1991)
- [12] Goldberg, M. A., Protsenko, P. v., Smirnov, V. v., Antonova, O. S., Smirnov, S. v., Konovalov, A. A., Vorckachev, K. G., Kudryavtsev, E. A., Barinov, S. M., & Komlev, V. S. (2020). The enhancement of hydroxyapatite thermal stability by Al doping. *Journal of Materials Research and Technology*, 9(1), 76–88. <https://doi.org/10.1016/j.jmrt.2019.10.032>
- [13] Lee, J.-K., Bhat, A. A., Nande, A., Watanabe, S., Rao, T. K. G., & Singh, V. (2024). Optimized Mn⁴⁺ doped Sr₉Y₂W₄O₂₄ perovskite for enhanced far-red-emitting luminescent material. *Ceramics International*. <https://doi.org/10.1016/j.ceramint.2024.06.112>
- [14] Muthukumar, S., & Gopalakrishnan, R. (2012). Structural, FTIR and photoluminescence studies of Cu doped ZnO nanopowders by co-precipitation method. *Optical Materials*, 34(11), 1946–1953. <https://doi.org/10.1016/j.optmat.2012.06.004>
- [15] Kang, M., Liao, X., Kang, Y., Liu, J., Sun, R., Yin, G., Huang, Z., & Yao, Y. (2009). Preparation and properties of red phosphor CaO: Eu³⁺. *Journal of Materials Science*, 44(9), 2388–2392. <https://doi.org/10.1007/s10853-009-3298-x>
- [16] Yerojwar, R. M., Kokode, N. S., Nandanwar, C. M., & Zaveri Mahavidyalaya, M. (2023). Photoluminescence of Ca₉Al(PO₄)₇: Eu³⁺ phosphor Article in. *International Journal of Scientific Research in Science and Technology*. <https://doi.org/10.32628/IJSRST229346>
- [17] Wang, Q., Ci, Z., Zhu, G., Que, M., Xin, S., Wen, Y., & Wang, Y. (2012). Structure and Photoluminescence Properties of Ca₉Al(PO₄)₇: Ce³⁺, Mn²⁺ Phosphors. *ECS Journal of Solid State Science and Technology*, 1(3), R92–R97. <https://doi.org/10.1149/2.016203jss>

FIGURES

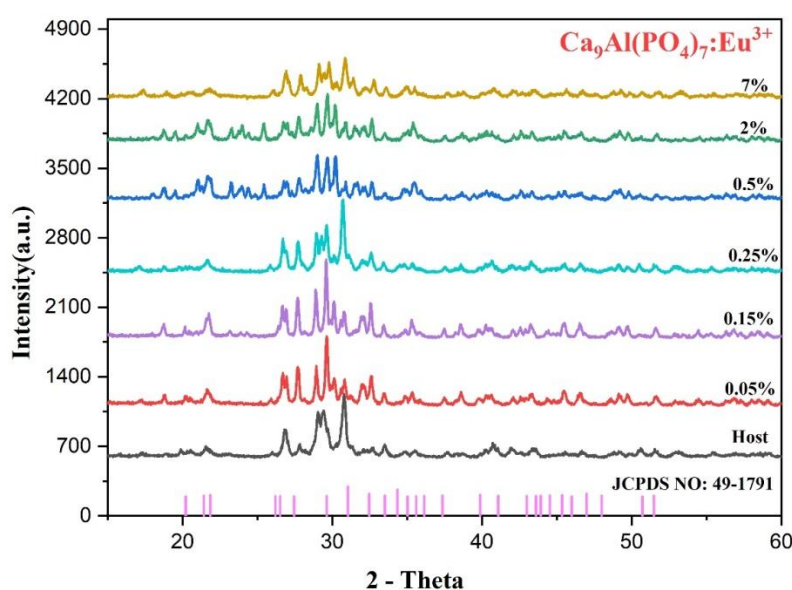


Fig 1. XRD patterns of Ca₉Al(PO₄)₇ and Ca₉Al(PO₄)₇:xEu³⁺ (x=0.05,0.15,0.25,0.5,2,7) with standard JCPDS card number 49-1791 .

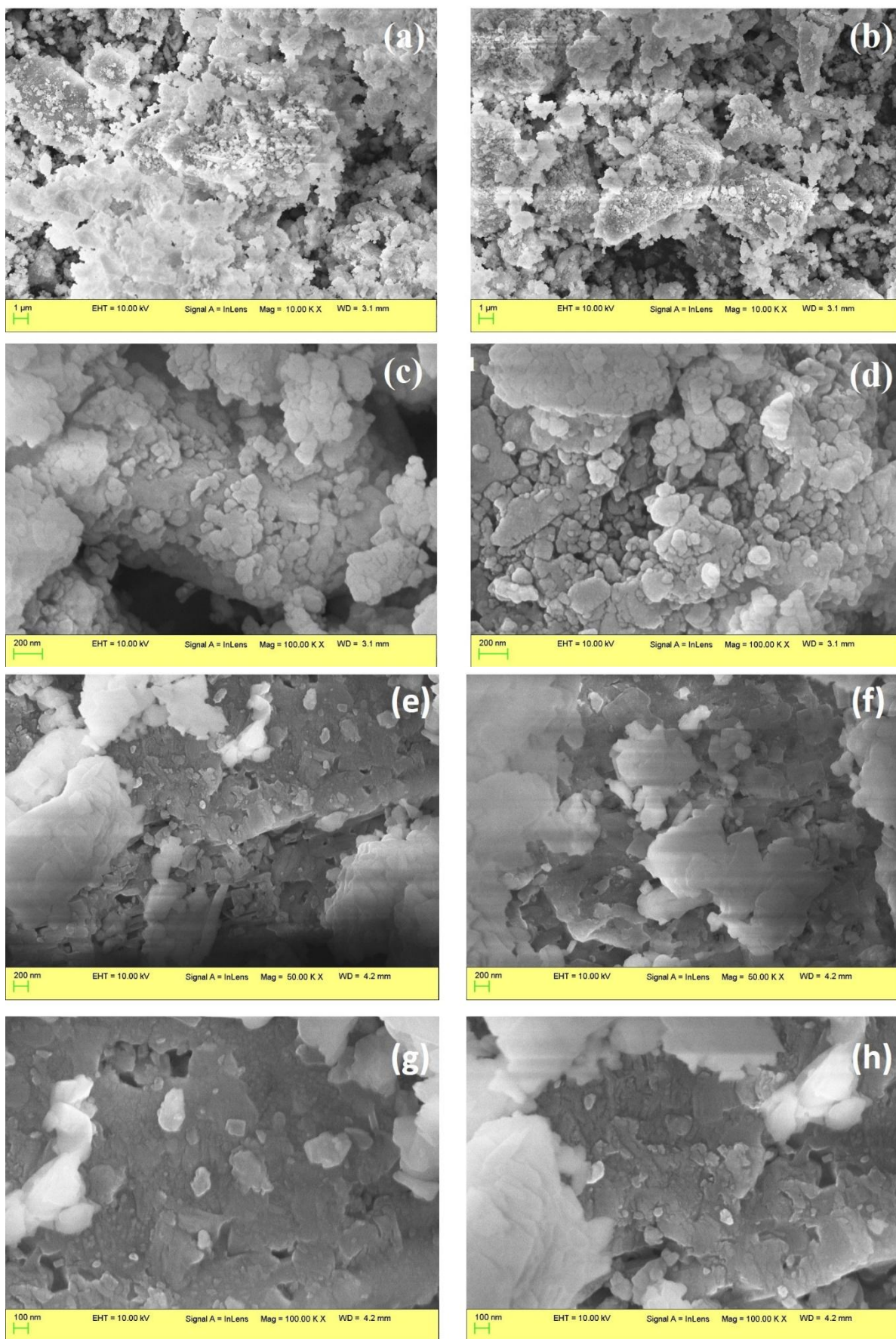
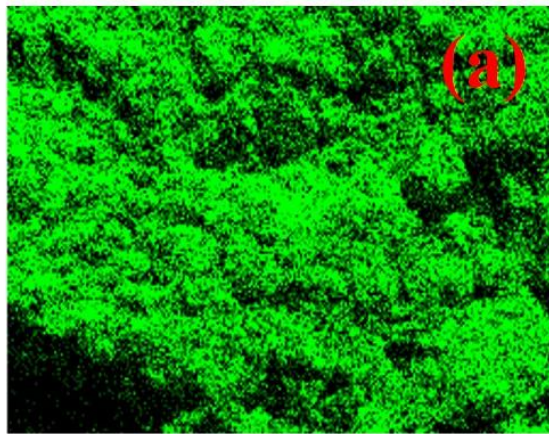
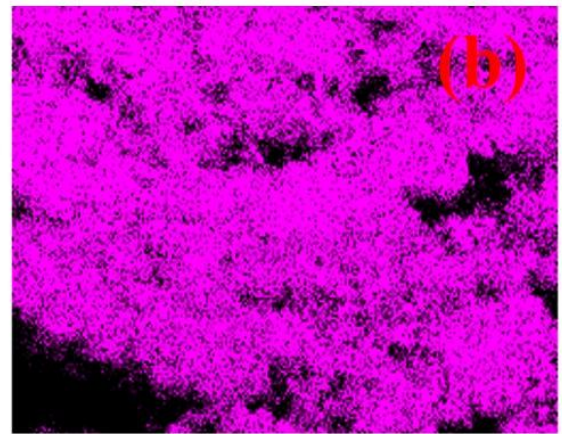


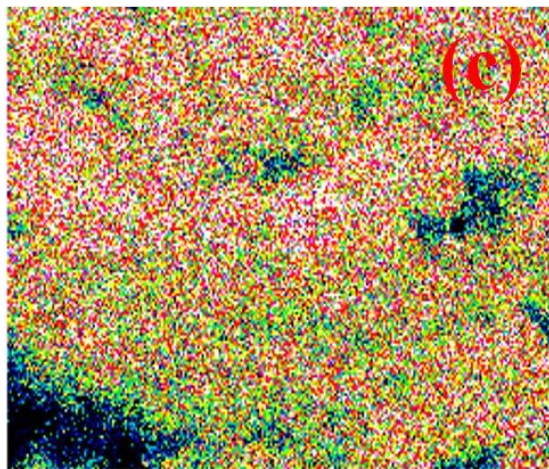
Fig 2. (a)-(d) SEM images of $\text{Ca}_9\text{Al}(\text{PO}_4)_7$ magnified at 100 K.X and 10 K.X and (e)-(h) shows SEM images of $\text{Ca}_9\text{Al}(\text{PO}_4)_7:7\%\text{Eu}^{3+}$ magnified at 100K.X and 50.00 K.X respectively



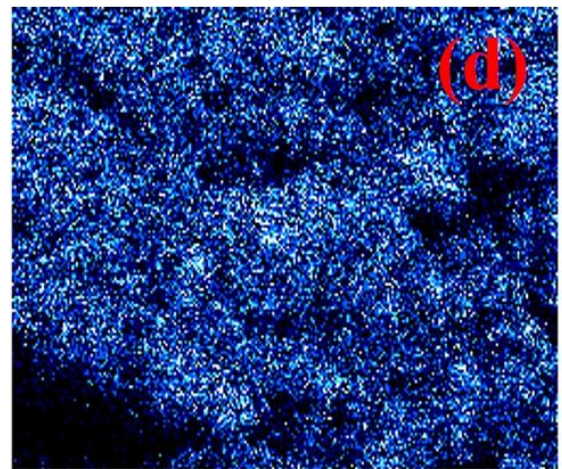
O Ka1



P Ka1



Ca Ka1



Al Ka1

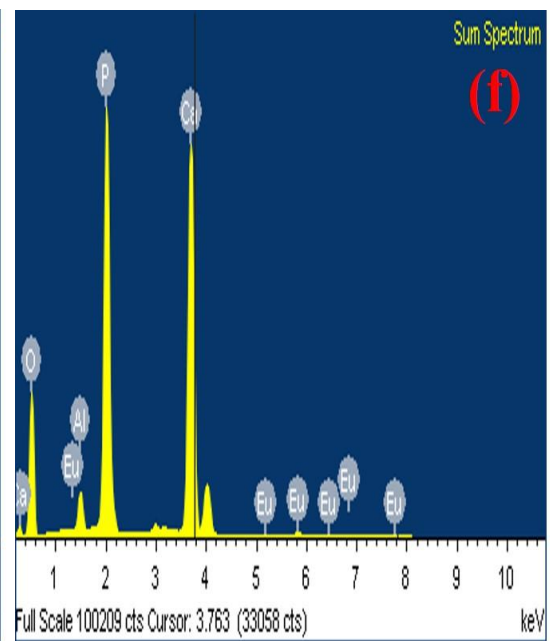
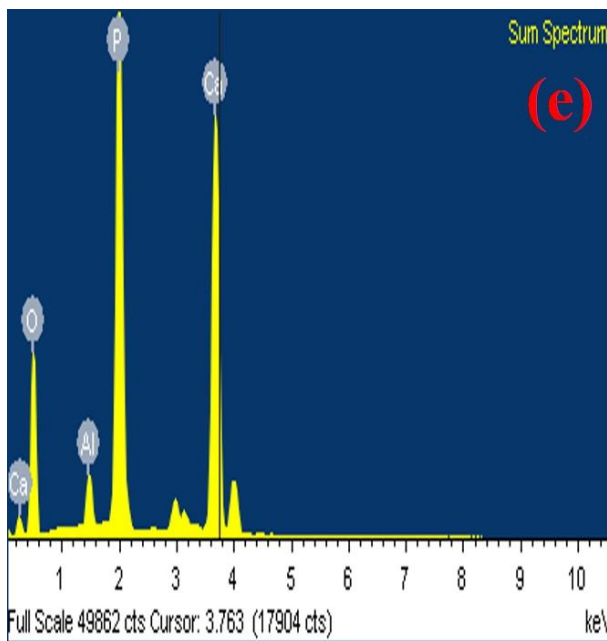


Fig 3. (a)-(e) EDS element mapping of pure $\text{Ca}_9\text{Al}(\text{PO}_4)_7$, and (f) EDS mapping of 7% of Eu^{3+} doped $\text{Ca}_9\text{Al}(\text{PO}_4)_7$.

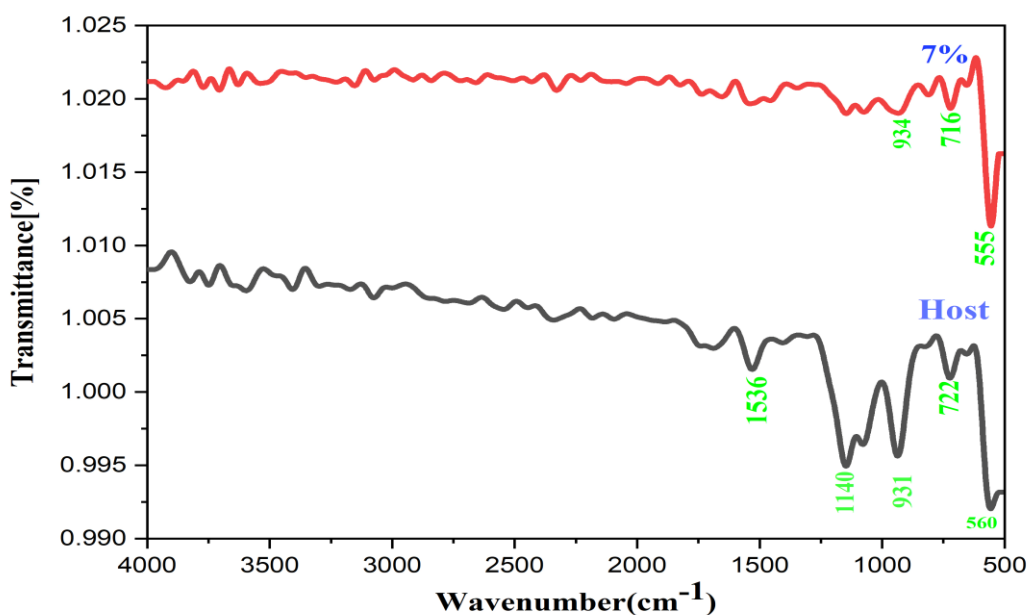


Fig 4. FTIR spectra of $\text{Ca}_9\text{Al}(\text{PO}_4)_7$ and $\text{Ca}_9\text{Al}(\text{PO}_4)_7 : 7\% \text{Eu}^{3+}$ nanophosphor

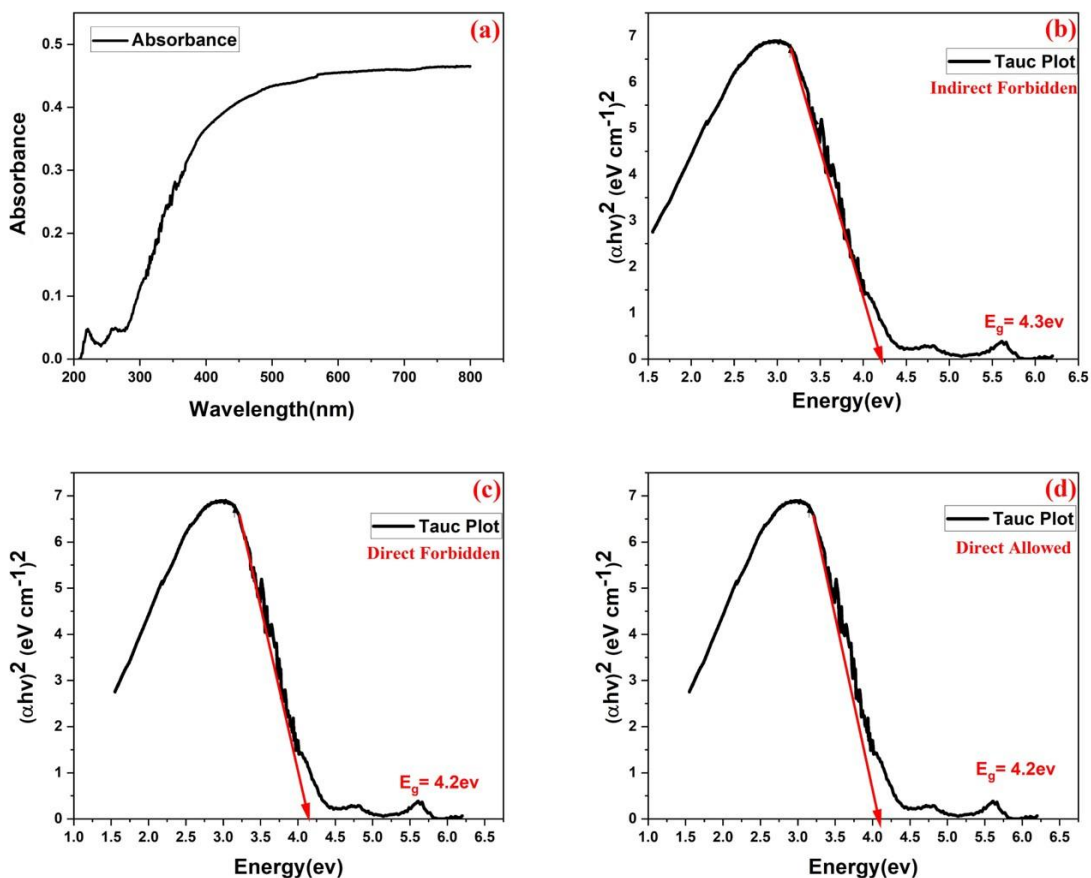


Fig 5. (a) UV Visible absorption spectra of $\text{Ca}_9\text{Al}(\text{PO}_4)_7$ compound and (b)-(d) Tauc plots for $\text{Ca}_9\text{Al}(\text{PO}_4)_7 : \text{Eu}^{3+}$ nanophosphors.

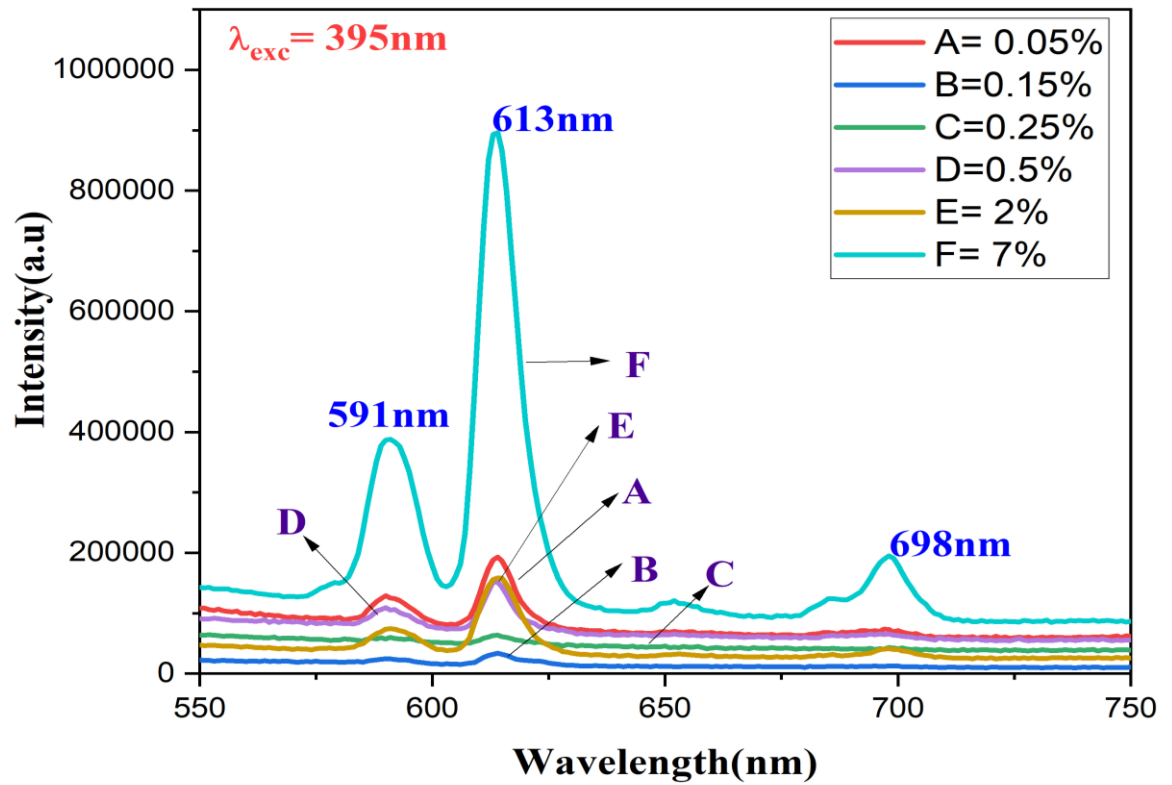


Fig 6. Emission spectra of $\text{Ca}_9\text{Al}(\text{PO}_4)_7:\text{xEu}^{3+}$ ($x = 0.05\%$, 0.15% , 0.25% , 0.5% , 2% and 7% molar concentrations) nanophosphor under 395 nm excited wavelength.

¹Naresh N. Sarkar²Shraddha M. Butte

The impact of sintering temperature on the magnetic and structural properties of spinel ferrite synthesized via sol-gel auto-combustion technique.



Abstract: - In this study, we aim to synthesize MgFe_2O_4 spinel ferrite through the Sol-Gel Auto-combustion method, employing various sintering temperatures. X-ray diffraction (XRD) analysis confirmed the material's single-phase crystalline structure, with lattice constants ranging from 8.246 to 8.514 Å. The crystalline size, estimated using the Debye-Scherrer formula, falls within the 100 nm scale. Scanning electron microscopy (SEM) characterization revealed the material's porous nature at lower sintering temperatures, with particle sizes ranging from 55 nm to 114 nm.

Keywords: Effect of sintering temperature, XRD, VSM, SEM

¹*Corresponding author: Naresh N. Sarkar,
Department of Physics, Mahatma Fule Arts, Commerce & Sitaramji Chaudhari Science
Mahavidyalaya Warud, Dist Amravati

² Shraddha M. Butte
Department of Physics, Shri Shivaji Science College Amravati

I. INTRODUCTION

Over the past few decades, magnetic materials, including ferrite, have seen extensive use across various industrial applications such as data storage devices, switching circuits, magnetic resonance imaging, and biomedical technologies, among others. Ferrite, with its broad spectrum of multidisciplinary applications, stands as a focal point for research endeavors. It is typically categorized into two groups: hard ferrite and soft ferrite, further classified into types like Hexagonal, Ortho, Garnet, and Spinel ferrite. Among these, Spinel ferrite falls under the soft ferrite category and serves as the focus of the current research module.

The fundamental formula for Spinel ferrite, denoted as MgFe_2O_4 , encompasses divalent cations represented by 'M' (e.g., Mg^{2+} , Zn^{2+} , Ni^{2+}) alongside trivalent cation Fe^{3+} . This research is centered on MgFe_2O_4 owing to its promising applications in various technological domains. Utilizing the sol-gel auto-combustion method, we synthesized MgFe_2O_4 nanomaterial and proceeded to examine its structural and magnetic properties across a range of sintering temperatures, spanning from 200°C to 1000°C over a 4-hour period.

Our objective was to optimize the material for specific applications by understanding how varying sintering temperatures affect its properties. Previous studies, such as those conducted by Bhondare et al., have investigated the impact of sintering temperature on Mn-ferrite, revealing fluctuations in both structural and magnetic attributes. Additionally, research by Patil et al. explored the gas response properties of magnesium ferrite to diverse gases.

In general, MgFe_2O_4 exhibits a mixed spinel ferrite composition expressed by the formula $(\text{Mg}_{1-x}\text{Fe}_x)_\text{T} [\text{Fe}_{2-x}\text{Mg}_x]_\text{O} \text{O}_4$, where 'T' and 'O' signify tetrahedral and octahedral sites respectively. The distribution of cations within these sites, determined using X-ray diffraction techniques, relies on factors like ionic radius, columbic interaction, and polarization order.[1, 2]

The structural and magnetic properties of the material directly correlate with the distribution of cations and the nature of doping. Considering the synthesis method and temperature effects, we embarked on a systematic investigation to ascertain the influence of sintering temperature on MgFe_2O_4 . [3, 4]

II. EXPERIMENTAL

For the Sol-Gel auto-combustion synthesis of MgFe_2O_4 nanoparticles, we utilized analytical grade raw materials including Magnesium nitrate $\text{Mg}(\text{NO}_3)_2 \cdot 6\text{H}_2\text{O}$, Ferric nitrate $\text{Fe}(\text{NO}_3)_3 \cdot 9\text{H}_2\text{O}$, and Urea $\text{NH}_2\text{-CO-NH}_2$. The stoichiometric ratio for producing 30 grams of MgFe_2O_4 involved 5.2543 grams of Magnesium nitrate, 16.5573 grams of Ferric nitrate, and

8.1965 grams of Urea. [5, 6] These reagents were dissolved in 100 ml of distilled water in a beaker, which was then heated on a hot plate at 80°C until gel formation occurred. Subsequently, the gel was subjected to microwave irradiation for 5 minutes at 800 M Watts, resulting in the formation of fluffy ash powder. This ash powder was then ground in a mortar and pestle for approximately 4 hours. The subsequent step involved sintering the sample in a furnace at 800°C. After sintering, the sample was crushed again in a mortar and pestle for 4 hours to obtain the final product, ready for further characterization.[7, 8]

III. RESULTS AND DISCUSSION

1. *Structural Analysis.*

The X-ray diffraction pattern of the synthesized sample, sintered at temperatures ranging from 200°C to 1000°C, is depicted in Figure 1. All observed diffraction peaks corresponding to planes (220), (311), (400), (422), (511), and (440) align with the standard pattern for MgFe_2O_4 as reported in JCPDS card No. 8-1935, confirming the formation of a single-phase cubic spinel structure with the space group $\text{Fd}\bar{3}\text{m}$. The crystallite sizes (D) of the sintered magnesium spinel ferrites were calculated using the Debye-Scherrer formula [$D = (0.94\lambda)/(\beta \cdot \cos \theta)$], employing the full width at half maximum (FWHM) of the most intense peak (311) in the XRD pattern. From the X-ray diffraction data, it is evident that the lattice constant increases from 8.246 Å to 8.514 Å with increasing sintering temperature from 200°C to 1000°C, respectively. Furthermore, Figure 1 illustrates that the intensity of diffraction peaks increases while peak width decreases with rising sintering temperature, confirming the enhancement of crystallinity. This indicates a transformation from a low degree of crystallization to a high degree of crystallization with increasing temperature.[9, 10] The lattice constant, crystalline size, and magnetization values are detailed in Table 1. Figure 2 illustrates the random shifting of the 2θ position of the most prominent peak (311) plane. From 200°C to 400°C, peaks shift to higher θ positions, and subsequently, from 400°C to 1000°C, they shift to lower θ positions. These lower and higher angle shifts in the 2θ position suggest non-uniform strain within the material. The compression and expansion of the material affect the d -value of the XRD data, which is inversely proportional to the 2θ value of the XRD results.[11, 12]

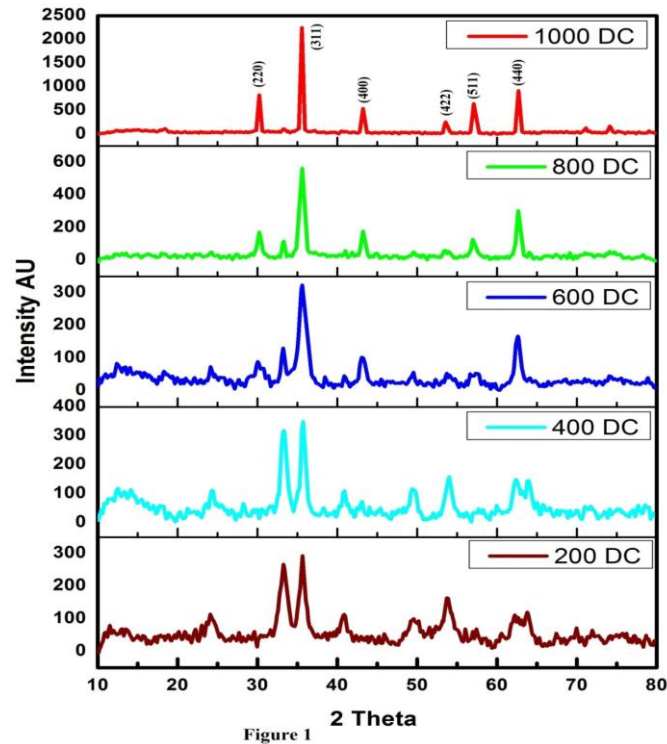


Figure 1 XRD Pattern of $MgFe_2O_4$

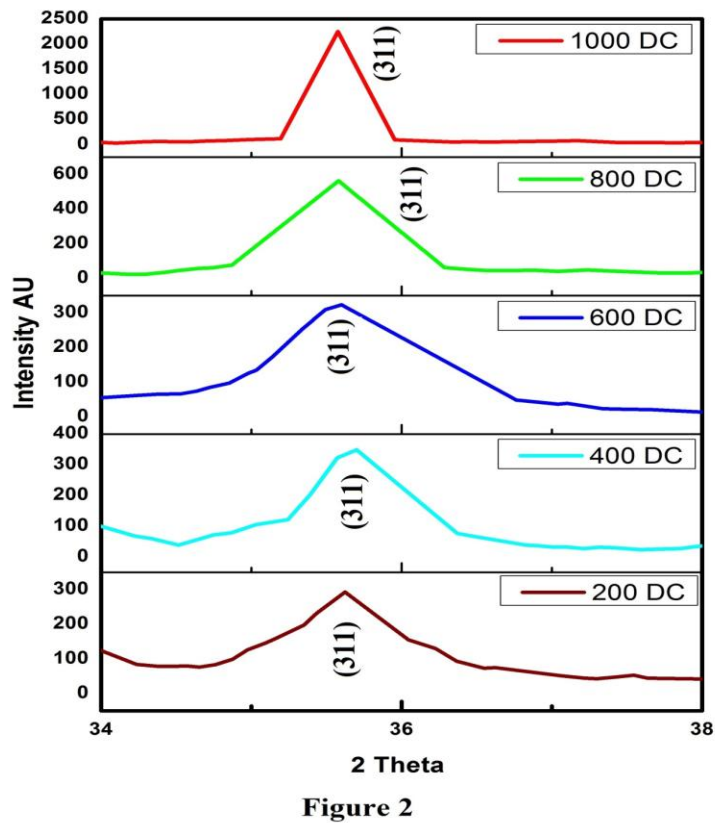


Figure 2 Stack XRD Pattern (311) Peak of $MgFe_2O_4$

Table 8 Lattice constant and Crystalline size

Sr. No	Sample name	Lattice constant a(Å)	Crystalline size D(nm)	Ms (emu/g)
1	200 DC	8.246	35	0.7580
2	400DC	8.253	49	0.3323
3	600DC	8.356	66	0.1676
4	800DC	8.421	84	0.01242
5	1000DC	8.514	98	0.01041

B. Morphological Analysis

Figure 3 presents SEM (scanning electron microscopy) images used to examine the microstructure morphology of the prepared sample. In Figure 3, SEM images labeled as 400°C, 600°C, 800°C, and 1000°C correspond to samples sintered at those respective temperatures. The particle size increases from the range of 50 nm to 100 nm as the sintering temperature rises. Additionally, it is evident from Figure 3 that at lower temperatures, the particles exhibit a higher degree of porosity compared to higher temperatures. At elevated temperatures, the removal of moisture from the material aids in the formation of molecular bonding during the sintering process. This results in higher crystallinity at higher temperatures, as observed in the X-ray diffraction study.[13,14, 15]

The SEM results demonstrate that increasing the sintering temperature significantly enhances the crystallization of the $MgFe_2O_4$ spinel structure. The SEM images clearly show that the morphology and size of the materials are notably influenced by the sintering temperature.

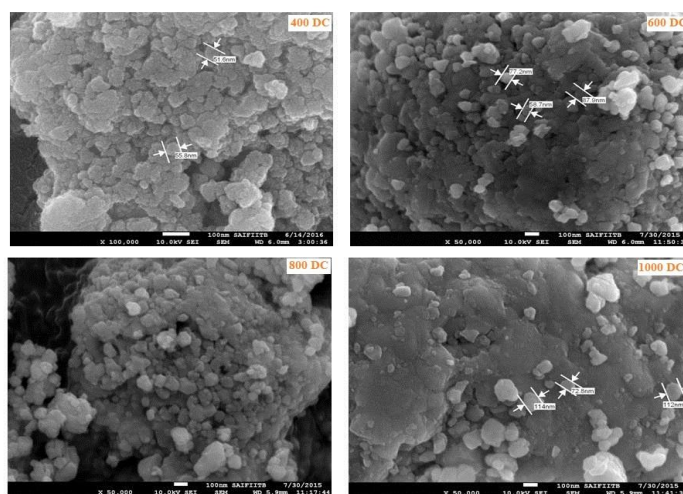


Figure 3

Figure 3: Surface Morphology of $MgFe_2O_4$

C. Magnetic Study

The Vibrating Sample Magnetometer (VSM) study, illustrated in Figure 4, presents the B-H curves for five samples sintered at temperatures of 200°C, 400°C, 600°C, 800°C, and 1000°C, respectively. The VSM results indicate that magnetization increases with sintering temperature. This is attributed to the higher degree of crystallinity and the optimal distribution of cations in the octahedral (A) and tetrahedral (B) sites of the $MgFe_2O_4$ structure at elevated temperatures. Enhanced magnetic interactions among the A-A, B-B, and A-B sites are observed due to this improved crystallinity. All five samples exhibit superparamagnetic behavior, evidenced by a squareness ratio of less than 0.5. The sample sintered at 200°C shows a larger B-H loop area, likely due to incomplete formation of the spinel structure at this lower temperature. This is corroborated by XRD characterization (Figure 1), which shows an additional peak at 2-theta position 32.1 in the 200°C sample, suggesting distortion in the material's lattice when subjected to an external magnetic field. SEM analysis reveals that the particles in the sample sintered at 400°C are denser compared to those in the 1000°C sample. When exposed to an external magnetic field, the particles in the 200°C sample are less free to align due to the dense neighboring particles, resulting in a larger B-H loop area compared to samples sintered at higher temperatures. [16, 17, 18]

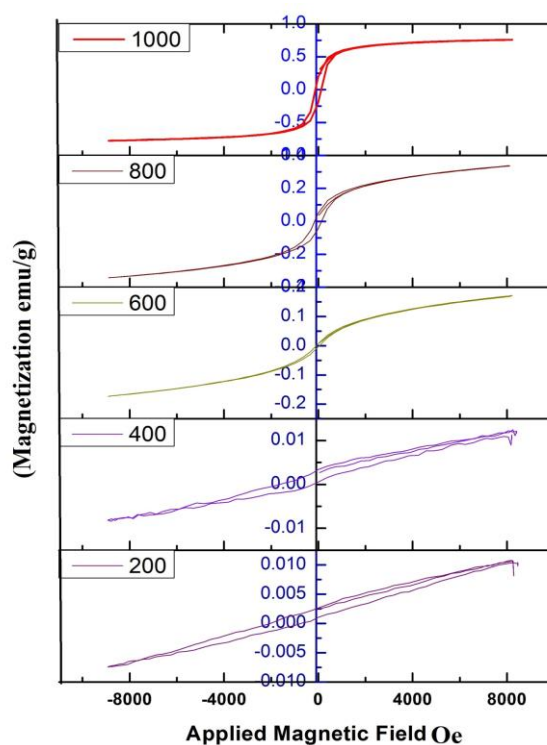


Figure 4

Figure 4 VSM graph of $MgFe_2O_4$

IV. CONCLUSION

Using the sol-gel auto-combustion method, we successfully synthesized single-phase MgFe₂O₄ spinel ferrite. X-ray diffraction analysis determined the lattice constant and crystalline size, both in the nanometer scale, confirming the material's nanoscale nature. We applied various sintering temperatures to the material and concluded that higher temperatures enhance crystallinity compared to lower temperatures. SEM images revealed greater porosity at lower sintering temperatures. The Vibrating Sample Magnetometer study indicated that the material is superparamagnetic, consistent with the XRD and SEM results.

REFERENCES

- [1] N. N. Sarkar, K. G. Rewatkar, V. M. Nanoti, P. S. Hedao, and M.N.Giriya, "Cation Distribution of Zn_{0.5}Me_{0.5}Fe₂O₄ (Me = Co, Ni And Cu) on the Basis of Rietveld Refinement and Magnetization Measurement," *Material Science Research India*, vol. 14, no. 2, pp. 169–175, Dec. 2017. Clerk Maxwell, A Treatise on Electricity and Magnetism, 3rd ed., vol. 2. Oxford: Clarendon, 1892, pp.68–73.
- [2] N. N. Sarkar, K. G. Rewatkar, N. S. Meshram, and V. M. Nanoti, "Structural and magnetic studies of (Ni_{0.5} M_{0.5} Fe₂O₄) where M = Zn, Cu," *Ferroelectrics*, vol. 519, no. 1, pp. 209–212, Oct. 2017, doi: 10.1080/00150193.2017.1361262. K. Elissa, "Title of paper if known," unpublished.
- [3] N. N. Sarkar, K. G. Rewatkar, V. M. Nanoti, and N. T. Tayade, "Structural, Magnetic-Electrical Behavior of Zr substituted Ni–Zn Spinel Ferrite," *Research Journal of Science and Technology*, vol. 10, no. 1, pp. 13–18, Mar. 2018, doi: 0.5958/2349-2988.2018.00003.7..
- [4] N. N. Sarkar, K. G. Rewatkar, V. M. Nanoti, P. S. Hedao, and M. N. Giriya, "Cation Distribution of Zn_{0.5}Me_{0.5}Fe₂O₄ (Me = Co, Ni and Cu) on the Basis of Rietveld Refinement and Magnetization Measurement," *Material Science Research India*, vol. 14, no. 2, pp. 169–175, Dec. 2017, doi: 10.13005/msri/140214.
- [5] B. P. Jacob, A. Kumar, R. P. Pant, S. Singh, and E. M. Mohammed, "Influence of preparation method on structural and magnetic properties of nickel ferrite nanoparticles," *Bulletin of Materials Science*, vol. 34, no. 7, pp. 1345–1350, 2011
- [6] H. M. El-Sayed and W. R. Agami, "Controlling of optical energy gap of Co-ferrite quantum dots in poly (methyl methacrylate) matrix," *Superlattices and Microstructures*, vol. 83, pp. 651–658, Jul. 2015, doi: 10.1016/j.spmi.2015.04.013 X. Zuo, B. Barbiellini, and C. Vittoria, "Calculation of exchange constants in manganese ferrite (MnFe₂O₄)," *Journal of Magnetism and Magnetic Materials*, vol. 272–276, pp. 306–311, May 2004, doi: 10.1016/j.jmmm.2003.12.466.

- [7] G. A. Sawatzky, F. VAN DER Woude, and A. H. Morrish, "Cation Distributions in Octahedral and Tetrahedral Sites of the Ferrimagnetic Spinel CoFe_2O_4 ," *Journal of Applied Physics*, vol. 39, no. 2, pp. 1204–1205, Feb. 1968, doi: 10.1063/1.1656224.
- [8] D. Stoppels, "Developments in soft magnetic power ferrites," *Journal of Magnetism and Magnetic Materials*, vol. 160, pp. 323–328, Jul. 1996, doi: 10.1016/0304-8853(96)00216-8.
- [9] J. Zhou, Z. Qiu, and P. Liu, "Electric and magnetic properties of $\text{Pb}(\text{Zr}_{0.52}\text{Ti}_{0.48})\text{O}_3\text{--CoFe}_2\text{O}_4$ particle composite thin film on the SrTiO_3 substrate," *Materials Research Bulletin*, vol. 43, no. 12, pp. 3514–3520, Dec. 2008, doi: 10.1016/j.materresbull.2008.01.019.
- [10] D. T. Margulies *et al.*, "Origin of the Anomalous Magnetic Behavior in Single Crystal Fe_3O_4 Films," *Phys. Rev. Lett.*, vol. 79, no. 25, pp. 5162–5165, Dec. 1997, doi: 10.1103/PhysRevLett.79.5162.
- [11] M. Sajjia, A. Baroutaji, and A. G. Olabi, "The Introduction of Cobalt Ferrite Nanoparticles as a Solution for Magnetostrictive Applications," in *Reference Module in Materials Science and Materials Engineering*, Elsevier, 2017. doi: 10.1016/B978-0-12-803581-8.09264-X.
- [12] A. Verma, T. C. Goel, R. G. Mendiratta, and M. I. Alam, "Dielectric properties of NiZn ferrites prepared by the citrate precursor method," *Materials Science and Engineering: B*, vol. 60, no. 2, pp. 156–162, Jun. 1999, doi: 10.1016/S0921-5107(99)00019-7.
- [13] I. H. Gul, W. Ahmed, and A. Maqsood, "Electrical and magnetic characterization of nanocrystalline Ni–Zn ferrite synthesis by co-precipitation route," *Journal of Magnetism and Magnetic Materials*, vol. 320, no. 3, pp. 270–275, Feb. 2008, doi: 10.1016/j.jmmm.2007.05.032.
- [14] F. Li, H. Wang, L. Wang, and J. Wang, "Magnetic properties of ZnFe_2O_4 nanoparticles produced by a low-temperature solid-state reaction method," *Journal of Magnetism and Magnetic Materials*, vol. 309, no. 2, pp. 295–299, Feb. 2007, doi: 10.1016/j.jmmm.2006.07.012.
- [15] Gh. R. Amiri, M. H. Yousefi, M. R. Abolhassani, S. Manouchehri, M. H. Keshavarz, and S. Fatahian, "Magnetic properties and microwave absorption in Ni–Zn and Mn–Zn ferrite nanoparticles synthesized by low-temperature solid-state reaction," *Journal of Magnetism and Magnetic Materials*, vol. 323, no. 6, pp. 730–734, Mar. 2011, doi: 10.1016/j.jmmm.2010.10.034.
- [16] W. Tang, Y. Su, Q. Li, S. Gao, and J. K. Shang, "Superparamagnetic magnesium ferrite nano-adsorbent for effective arsenic (III, V) removal and easy magnetic separation," *Water Research*, vol. 47, no. 11, pp. 3624–3634, Jul. 2013, doi: 10.1016/j.watres.2013.04.023.

- [17] M. Sedlář, V. Matějec, T. Grygar, and J. Kadlecová, “Sol–gel processing and magnetic properties of nickel zinc ferrite thick films,” *Ceramics International*, vol. 26, no. 5, pp. 507–512, Jun. 2000, doi: 10.1016/S0272-8842(99)00086-3.
- [18] H. M. Rietveld, “A profile refinement method for nuclear and magnetic structures,” *J Appl Cryst*, *J Appl Crystallogr*, vol. 2, no. 2, pp. 65–71, Jun. 1969, doi: 10.1107/S0021889869006558.

Dr. Gajanan S.
Wajire

Versatile low voltage power supply using manually driven DC motor



Abstract: This research paper explores the development and application of a low voltage power supply using a manually driven DC motor. The primary focus is on the design, implementation, and performance evaluation of such a system. The manually driven DC motor serves as a renewable and sustainable energy source, capable of generating low voltage electricity suitable for small-scale applications, such as charging batteries, powering small electronic devices, and emergency lighting. The study examines the mechanical and electrical components involved, the efficiency of energy conversion, and potential use cases. The results demonstrate the feasibility of this approach and highlight the advantages and limitations of manually driven power generation systems.

The law of conservation of energy states that, “The energy can neither be created nor be destroyed, rather it can be transform from one form to another form”. Using this principle, the whole scientific arena is taking much more efforts to explore the non-conventional and renewable energy sources for the advancement of the growing human being. The current research work in electricity generation from mechanical efforts is in initial stages, but has wide scope in future for the development of renewable and non-conventional energy resources. The undertaken research work describes the design aspect of such a non-conventional and renewable low power energy source in which manual efforts are used predominantly along with different electro-mechanical components. The designed low voltage power supply is state-of-the-art and provides multipurpose facilities in number of electrical applications.

Keywords: Versatile, manually driven, renewable, non-conventional, low voltage power supply, DC motor.

I. INTRODUCTION

In an era where sustainable energy solutions are increasingly critical, manually driven power generation systems offer a unique and practical alternative for low voltage and low power applications. A power supply is considered as an implanted circuit; which is able to converts unregulated AC into a constant DC supply. With the help of a rectifier, it converts AC supply into the DC supply. The type of stabilization used may be restricted to ensuring that the output remains within certain rated limits under various load and line conditions.

This paper elaborates and investigates a low voltage power supply system powered by a manually driven DC motor. The researcher has tried to make a versatile low voltage power supply which can be use in daily life. Most of the domestic electronic devices, that needs operating voltage up to 6 volts, can be operate effectively with the help of this versatile low power supply. Such systems can provide an immediate and reliable power source in the situations where conventional power sources are unavailable or impractical. Previous research has explored various methods of manually driven power generation, including pedal-powered generators, hand-crank generators, and flywheel energy storage systems. Studies have shown that manually driven systems can effectively convert mechanical energy into electrical energy with varying degrees of efficiency. These systems are particularly useful in remote areas, disaster recovery scenarios, and for educational purposes.

II. METHODOLOGY

The design of the manually driven low voltage power supply involves several key components as mentioned as follows:

1. **DC motor selection:** A small, efficient DC motor capable of generating electricity when rotated manually. A motor with low starting torque and high efficiency is selected. If the achievable shaft speed does not reach a sufficient back EMF, a suitable gear reduction can be added to increase the speed at motor shaft.
2. **Mechanical drive assembly:** A mechanism such as a crank, pedal or manually system to drive the motor. A hand-crank system can be considered to provide a consistent rotational force to the motor.
3. **Voltage regulation system:** A rectifier and voltage regulator are designed to convert and stabilize the generated voltage. A voltage regulator circuit is needed to ensure stable voltage output.
4. **Energy storage system:** Rechargeable batteries are integrated to store excess energy for later use. Batteries or capacitors can be used to store the generated electricity.
5. **Output Interface and connectors:** Connectors or adapters to use the generated power. The system is tested under various conditions to measure output voltage, current, and overall efficiency.
6. **Testing and Calibration:** Number of trial-and-error basis readings has been taken for proper testing and calibration of the system.

III. REAL-TIME SETUP OF THE POWER SUPPLY

The below mentioned figure shows the real-time setup and related diagram of the versatile manually driven low voltage power supply. The descriptions of each block are explained in the succeeding section.

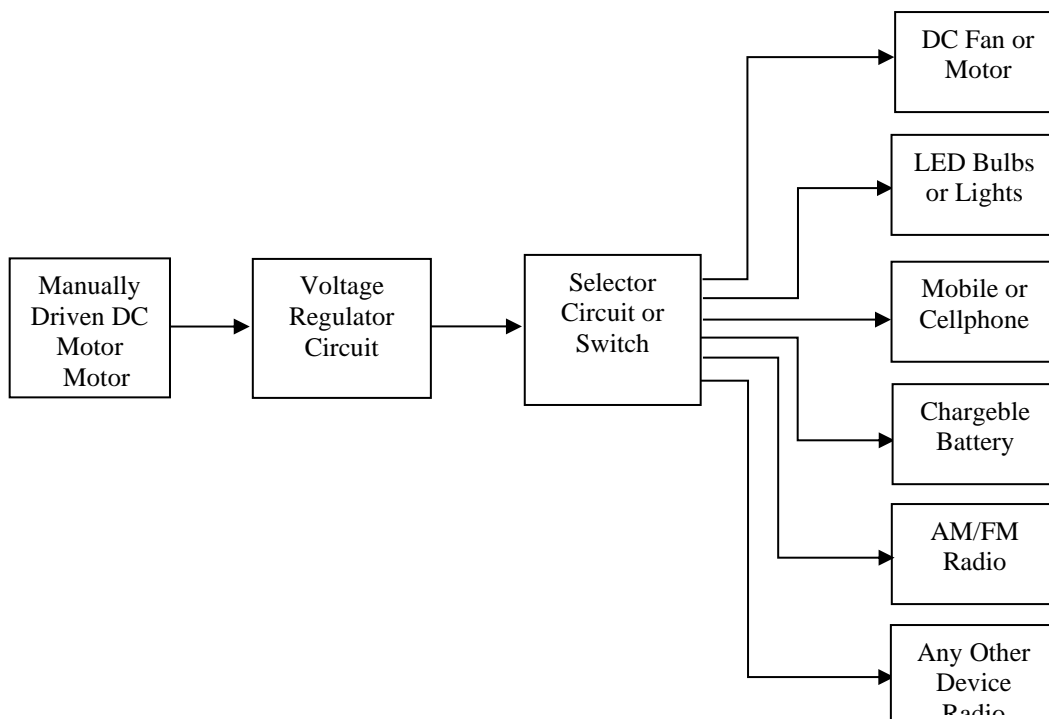


Figure: Realtime setup of the versatile low voltage power supply

A manually driven or hand cranked DC motor with suitable geared arrangements is used as generator to produce electricity across its output terminals. Such a DC motor can effectively function as a generator, converting mechanical energy into electrical energy. At this stage, multiple gear system was attached with the help of mechanical handle to apply mechanical energy.

A voltage regulator was designed to automatically maintain a constant voltage level. A voltage regulator may use a simple feed forward designs or may include negative feedback, if necessary. It may use an electro-mechanical mechanism, or electronic components. Depending upon the designs, these may be used to regulate one or more DC voltage levels.

Selection of the last stage utility has been prepared by using mechanical or electronic switch. For the sake of simplicity of the user, we have used here a mechanical ‘single pole multiple way’ switch with proper connections. Only one task will be selected and will be connected at any time of preferred position for the operation purpose. The generated as well as regulated dc voltage can be used to operate either of the device/gadget connected through the selector mechanism. For the sake of simplicity of the user as well as visitors, we have used here only limited utilities like DC fan or motor, LED bulbs or lights, mobile or cellphone set, chargeable battery, AM and/or FM radio set and any other low voltage operated electronic gadget. Many other number of available household devices can be connected as a load or a utility.

IV. SELECTION OF DC MOTOR

The selected DC motor can be served as a required generator in producing electricity by utilizing the Faraday’s principle of electromagnetic induction. Which states that ‘as a DC motor is rotated, it will generate the magnetic field’. Such a magnetic field will induce the current in nearby conductor or coil, known as the armature coil for current flow. This current can be collected and used as the generated electricity. To enhance the electricity generation, a pair of permanent magnets can be added to the motor's coil or core, which will act as an auxiliary power source. Here the most common types depend on on the forces produced by magnetic fields. Almost all types of DC motors have typical internal mechanisms, might be either electro-mechanical or electronic, to intermittently change the direction of current flow in the motor. Moreover, the motor used may be connected to secondary cell or the batteries, which can be charged by the rotating permanent magnets or by using the back-emf produce in the armature coil. By using such type of methods, a common type of DC motor can be excellently function as a generator, converting mechanical energy into an electrical energy. Multiple gear system was attached with the help of mechanical handle, to increase the number of rotations of the dc motor.

The manually driven DC motor system successfully generated a low voltage power supply. The key findings include as below:

- 1. Energy Conversion Efficiency:** The system achieved an efficiency of approximately 80-90% under optimal conditions.
- 2. Voltage Stability:** The voltage regulation circuit maintained a stable output within a range suitable for small electronic devices.
- 3. Usability:** The hand-crank or manually driven mechanism provided a practical and user-friendly interface for generating low power.
- 4. Applicability:** The system proved effective in charging small batteries, powering LED lights, DC fans and running small electronic devices like AM and FM radios.

V. AVAILABILITY AND APPLICATIONS

Various applications of such a low voltage power supply are mentioned as follows.

- 1) It can operate DC fans and motors of low voltage ratings.
- 2) LED bulbs and lighting loads can be easily operated.
- 3) Different types of mobile phones can be charge manually.
- 4) AM and/or FM radio sets can be operated as a real time loads.
- 5) Rechargeable batteries and small power banks can charge properly.
- 6) Can be use as regulated power supplies in various low power appliances.
- 7) Can be use as an emergency power supply in remote or rural areas.
- 8) Any other low power electronic gadgets can operate using this power supply.

Such a low voltage power supply can be used as a variable supply with slight modifications in the voltage regulator circuit.

VI. ADVANTAGES AND LIMITATIONS

a) Advantages are summarized as:

- **Renewable and sustainable:** Utilizes human mechanical energy, reducing reliance on traditional power sources.
- **Mechanical atomization:** Suggested circuitry can be attached to any mechanically automated driven system for continuous utilization of mechanical energy.
- **Portability:** Compact and lightweight design makes it easy to transport and use in various settings.
- **Emergency use:** Provides a reliable power source during power outages or in remote locations.

b) Limitations are summarized as:

- **Limited power output:** Suitable only for low voltage and low power applications.
- **Physical effort required:** Continuous manual, physical or automated effort is needed to generate power. In absence of any kind of efforts, electricity generation will stop.
- **Efficiency losses:** Energy conversion efficiency is relatively low compared to other power generation methods.

VII. CONCLUSION

The manually driven DC motor-based low voltage power supply is a viable solution for generating small amounts of electricity in an eco-friendly and sustainable manner. The undertaken research work describes the design aspect of one such non-conventional as well as renewable low power energy source in which manual or laborious efforts are used particularly along with different electro-mechanical components. The designed power supply is innovative and provides multipurpose utilities in number of applications. While it has limitations in power output and efficiency, its advantages make it a valuable tool for specific applications. Future work could focus on improving the efficiency of energy conversion and exploring hybrid systems that combine manual and other renewable energy sources.

VIII. REFERENCES

1. Bhattacharyya, S.C., & Palit, D. (2016). "Mini-grids for rural electrification of developing countries: Analysis and case studies from South Asia." Springer.
2. Gajanan S. Wajire (2018). "Multipurpose manual innovative power supply." *International Journal of Interdisciplinary Innovative Research and Development*, 2(2), ISSN: 2456-236X.
3. Okafor, E.C., & Uzodinma, U.E. (2008). "Renewable energy resources in Nigeria: The way forward." *Renewable and Sustainable Energy Reviews*, 12(1), 1-12.
4. Rehn, A., & Baek, C. (2012). "Design and Implementation of a Pedal Powered Generator for the Charge of Electrical Devices." *Energy Procedia*, 14, 212-216.
5. Gajanan S. Wajire (2022). "Effect of various cells on voltage generation from xerophytes." *Journal of Emerging Technologies and Innovative Research*, 9(3), ISSN: 2349-5162.
6. Vinoth Kumar, T., & Murugesan, R. (2016). "Design and fabrication of pedal powered battery charger." *International Journal of Applied Engineering Research*, 11(5), ISSN: 3163-3169
7. Gajanan S. Wajire & Yogendra B. Gandole (2015). "Obtaining the Potential Difference from Prickly Pear Plant." *International Journal of Informative and Futuristic Research*, 2(9), ISSN: 2347-1697.

¹ D.R.Solanke² Y.B.Gandole

On the Implementation of Linear Position Control using Fuzzy Logic Approach



Abstract: - This paper investigated a significant application of fuzzy set theory and fuzzy logic. The proposed work aimed to simulate Fuzzy Logic Controller (FLC) for linear position control. With this objective, an initiative is taken to design and simulate a Fuzzy Inference System (FIS) to control linear position in a computer-assisted environment. In this paper, the implementation of a Mamdani Fuzzy Inference System has been demonstrated with the application of controlling linear displacement. The design and simulation of conventional fuzzy logic controller (FLC) for a single input single output (SISO) system, is carried out. The system consists of a fuzzy logic controller that analyzes probable control situation based on the error distance and its error derivative. The controller determines the sufficient linear motion required to obtain the desired set-position while providing a smooth motion for the slider. The robustness of the proposed control scheme is verified by numerical simulation. The proposed scheme has better performance than the conventional method due to parameter variation and extraneous disturbance. To demonstrate its performance, the proposed control algorithm is applied to a real time position control system.

Keywords: Centroid, Defuzzification, Fuzzification, Mamdani Inference System

I. INTRODUCTION

Linear acceleration control is the main obligation of applications including machine tools and industrial machinery, in computer peripherals such as disk drives and printers, in space robotics, and in many other places where linear motion is required. It also used in the appliance requiring precise linear sliding movement and the wide range of linear motion products. The linear sliders provide advanced linear motion functionality in versatile linear motion solution. They are the component that ranges from ON/OFF devices with the simple linear controller to complex, user programmable modules that act as controllers within integrated multi-axis motion control systems. One of the major intricacies in realizing proposed Linear Position Control System (LPCS) is the controller design. Simple linear movement with simple velocity profile is relatively easy to design. The conventional position controller controls the position, not force while Fuzzy force controllers, regulate force without precise control of the movement trajectory. The hybrid position/force controllers, controlling position in one direction, have the advantage of simultaneously maintaining the desired movement path and force for the smooth movements. Several approaches were applied to model nonlinear system of LPCS. In present work, Fuzzy system modeling (model-based approach) has been used for our research purpose. Thus, the system had position control in one direction and speed-dependent force control in the opposite direction. One additional problem in designing the controller is the uncertainty about the subject and the nonlinear dynamics of the machine such as the Coulomb friction in the mechanism. In a classical design process, the control parameters are determined according to the system model. For a position control, the output load is also part of the dynamic system and the dynamic model of the subject is not as clear and invariable as the mechanical system. To solve this problem, fuzzy logic control is incorporated in the proposed LPCS. Fuzzy control is best known for tracking with nonlinear systems and systems that have uncertainty in its parameters. The uniqueness of a fuzzy modeling approach is its ability to utilize both qualitative and quantitative

¹ D. R. Solanke, Department of Applied Electronics, SGB Amravati University, Amravati, India (MS)

² Y.B.Gandole, Department of Electronics Adrasha Science JB Arts and Birla Commerce Mahavidyalaya Dhamangaon (Rly), Amravati, India (MS)

information. Qualitative information is human modeling expertise and knowledge, which are utilized in the form of fuzzy sets, fuzzy logic and fuzzy rules [1]. Many researchers have tried to maintain the stability by fine-tuning by enhancing the fuzzy rule set, through a stable linear proportional, integral, and derivative (PID) controller. Designing a controller for position control is more difficult because the external disturbance itself is subjected to another unresolved controller (the human control). Here we have designed a fuzzy logic controller using fuzzy logic toolbox in MATLAB (Version 7.0.0.499 R2010a 32 bit) software and simulate the designed model using the Simulink.

A major portion of research work on designing the hardware mechanism for automatic control system invariably revolves around the study of DC position control system. The present study has been designed with the objective in mind despite the constrained like friction, dead zone, nonlinearities due to driver saturation, motor current limitation and low speed of response associated with any mechanical system. The main purpose of the current study is to construct a linear position control system specialized for regulating a vehicle brake. The system, incorporating hybrid position/force control and fuzzy logic, shall be able to assist the subject in performing movements along the straight path inside the cylinder with specified loads. The specific goals of current work include design and simulation with control algorithm implementation and performance analysis of the proposed system. The schematic diagram in fig.1 shows various built-in subsystems which are now discussed in subsequent sections of this paper.

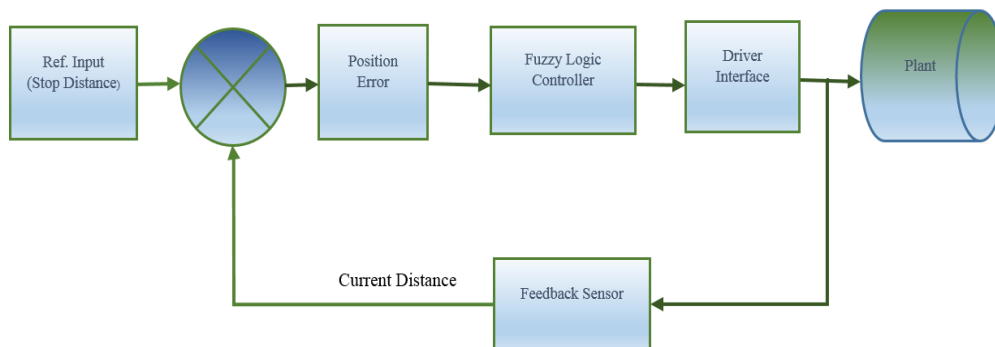


Fig. 1 Position control system

In [2] position control of a Brushless direct drive (BLDD) motor was proposed using a fuzzy logic controller (FLC), because of its simple structure and robust performance in a wide range of operating conditions. Although vehicle brake system is intrinsically nonlinear and its dynamics will be described by second order differential equations, it is often possible to obtain a linearized model of the system. If the system operates around target point and the error signals involved are small signals, a linear model that approximates the nonlinear system in the region of operation can be obtained. In [3] dynamics was derived using an integrated Fuzzy PID approach and the control was design by the equations linearized around steady-state value. Even though the controller is tested, but experimental results need to obtain to validate the simulation results and still not yet done. Thus, this paper presents investigations of performance comparison between conventional PID control and intelligent fuzzy logic control schemes for a position control experimentally. In this work, the LPCS was modeled to mimic the human mind to effectively employ modes of reasoning that are approximate rather than exact, to test controllers designed. Performances of both control strategy with respect to **Error distance** and **Error derivative** i.e. **Error rate** were examined if the error is being decreased with incremental error rate then motor speed should be

exponentially decreased. Comparative assessment of both control schemes to the LPCS system performance was analyzed and discussed.

II REVIEW OF LITERATURE

The control objective is to achieve the desired position and direction while maintaining the MTWIP (Mean Time to Work in Process) in a balanced state. The utilization of a Takagi-Sugeno model is employed to accomplish this. The results clearly indicate that the IT2 FLS performs better in the presence of modeling uncertainty and external disturbances.

Umesh Kumar Bansal [2] uses BLDD motor that has a PID controller to regulate its speed. The KP, KI, and KD gains of the PID controller are tuned based on fuzzy logic. The author noted that the specific characteristics of PID controllers and the adaptable characteristics of fuzzy controllers are both found in the fuzzy self-tuning PID controller. The simulation outcomes of the proposed work showed that the designed self-tuned PID controller achieved excellent dynamic characteristics of the BLDD motor. It revealed perfect speed tracking with minimal rise and settling time, minimal overshoot, minimal steady state error, and superior performance compared to a traditional PID controller.

Ivana Todic and her colleagues [3] conducted a study that specifically examined the regulation of Electro Mechanical Actuators (EMA) for aerospace purposes. The EMA is controlled utilizing a position regulator and a control mechanism that combines position and speed regulation. The author's research indicates that the operational limits of varying-speed motor drives are determined by the operational limits of single speed motors. This results in the system being underutilized and increases the risk of high power losses for the motor. The primary aim of his suggested research is to mitigate power losses, minimize heating, and reduce current consumption in the entire system.

Yongming Li and Shaocheng Tong [4] released a paper titled "Adaptive Fuzzy Control with Prescribed Performance for Block-Triangular-Structured Nonlinear Systems." This research utilizes fuzzy logic systems to ascertain the unidentified functions of nonlinear systems. A novel observer-based output-feedback control scheme is formulated using the adaptive fuzzy control theory and the back stepping design technique. The suggested control method effectively addresses the issue of excessive complexity in the back stepping design and eliminates the limiting assumption that unknown nonlinear functions must adhere to a global Lipschitz condition. The suggested strategy ensures that the tracking errors gradually approach a minimal residual set, while adhering to the specified performance limit. The simulation results of the chemical process control system are shown to further illustrate the efficacy of the proposed control technique.

In 2018, Bing Chen and his colleagues [5] conducted a study on the development of an observer and adaptive fuzzy control for nonlinear strict-feedback systems. The work proposed a robust fuzzy observer to estimate undetectable state variables of a system using the convex combination method. The proposed adaptive fuzzy output feedback controller ensures the convergence of the tracking error to a small region near the origin, while ensuring that all signals in the adaptive closed-loop system stay within specific constraints. We present the simulation's results to illustrate the efficacy of the proposed methodology.

The publication "Fuzzy Logic Controllers for specialty vehicles" was authored by Lishu Qin et.al [6] in 2017. Employing a fusion of phase plane analysis and the variable universe approach. Despite the small

amount of fuzzy rules in the rule base, it is possible to improve the accuracy of the fuzzy logic controller's performance. The application of Lyapunov stability theory ensures the stability of the closed-loop system. Implementing this design method can significantly alleviate the workload for fuzzy logic controller developers and reduce the time required for developing the fuzzy logic controller.

The paper titled "Task Space Control of an Autonomous Underwater Vehicle Manipulator System by Robust Single-Input Fuzzy Logic Control Scheme" was published by Pandurang S. Londhe et.al [7] in 2017. The numerical demonstration of the suggested control scheme's effectiveness is conducted on a planar undersea vehicle gripper system. The main goal of the proposed control strategy is to accurately follow the specified trajectory of the end-effector in the task space, even in the presence of external disturbances, ambiguities in the system, and internal sounds related to the AUVMS. Simulation outcomes have shown that the suggested control method enables the AUVMS to accurately follow the specified spatial trajectory and provide superior and reliable control performance.

The paper titled "Feedback Error Learning Control of Magnetic Satellites Using Type-2 Fuzzy Neural Networks with Elliptic Membership Functions" was published by Khanesar et.al [8] in 2014. The learning process is grounded on the feedback error learning approach, which enhances both the stability of the learning itself and the stability of the entire system. Additionally, this method allows for the inclusion of additional components in the control scheme to provide robustness. The simulation findings demonstrate that the suggested control algorithm outperforms traditional control techniques in terms of reduced steady state error and faster response to transients.

Haibo Du et.al [9] published a study on the development of a positioning-tracking device for a linear motion controller using vectorization technique. The primary aim of this work is to address the issue of position tracking control for a permanent magnet linear motor. This will be achieved by employing the discrete-time fast sliding mode control (SMC) method. An exhaustive analysis is presented to establish that the fast terminal sliding mode control law can provide superior precision compared to the conventional linear sliding mode control law. The suggested strategy is validated using computational simulations and empirical findings, which confirm its effectiveness and highlight the advantages of the discrete-time fast terminal sliding mode control (SMC) approach over previous methods.

The publication "A Modular Implementation Scheme for Non singleton Type-2 Fuzzy Logic Systems with Input Uncertainties" was authored by Zaheer et.al [10] in 2015. The recommended implementation method encompasses a comprehensive approach that includes both the fuzzyfiers and the membership functions. In order to assess the efficacy of the suggested approach, kind-2 fuzzy logic controllers are implemented for three distinct applications: controlling the altitude of an airplane, enabling obstacle avoiding for an autonomous vehicle, and facilitating wall following for a robot. The proposed system effectively handles all three uses. Furthermore, the performance outcomes in all three application configurations demonstrate that NS fuzzyfication can enhance the resilience of kind-2 fuzzy logic systems against significant uncertainties.

The paper titled "Adaptive Inverse Control of Cable-Driven Parallel System Based on Type-2 Fuzzy Logic Systems" was published by Tiechao Wang et.al [11] in 2015. The antecedents of the interval type-2 fuzzy nonlinear autoregressive model exogenous (NARX) forward models are constructed by establishing the monotonic property of the fuzzy NARX model. The antecedent parameters may then be derived based on

this property. In addition, the subsequent parameters of the advanced models are calculated offline using a constrained least squares approach. The experiment findings demonstrate that the suggested type-2 fuzzy control method successfully achieves the control objectives and exhibits excellent control performance.

Shaocheng Tong et.al [12] released an article on the design of adaptive fuzzy tracking control for single-input single-output uncertain non-strict feedback nonlinear systems. This work examines the topic of designing an adaptive fuzzy tracking control for the same system. The unified framework of adaptive back-stepping control design encompasses both adaptive fuzzy state feedback techniques and observer-based outcome feedback control design approaches. The robustness of the closed-loop systems is demonstrated by the utilization of Lyapunov value theory. The simulation examples are presented to validate the efficacy of the provided control strategies.

The publication "Observed-Based Adaptive Fuzzy Decentralized Tracking Control for Switched Uncertain Nonlinear Large-Scale Systems with Dead Zones" was authored by Shaocheng Tong et.al [13] in 2016. An adaptive fuzzy decentralized output-feedback tracking control strategy is created for the switched subsystem using the adaptive randomized back stepping implementation technique. The stability of the entire closed-loop system is demonstrated by the utilization of the Lyapunov function and the mean dwell-time approaches. The simulated example is presented to demonstrate the efficacy of the proposed control methodology.

Li Qiu and colleagues [14] have released a publication titled "Robust Cooperative Positioning Control of Composite Nested Linear Switched Reluctance Machines (LSRM)". The composite layered LSRMs across communication networks are represented as a Markov time-delay system to facilitate long distance movement and parallel close movement for industrial needs. The suggested robust collaborative positioning control system is tested through multiple experimental trials to confirm its effectiveness and practicality.

The publication "Position Control for Magnetic Rod less Cylinders with Strong Static Friction" by Hongjiu Yang et al. [15] was released in 2018. This work proposes a resilient controller based on an adaptive extended state observer (AESO). The suggested controller combines the benefits of a sliding-mode controller and a linear active disturbance rejection controller to achieve accurate and reliable control. The experimental results demonstrate a substantial enhancement in both reaction rate and position accuracy through the utilization of the strategy presented in this research.

Liang Sun and Zewei Zheng [16] published a paper titled "Disturbance Observer-Based Robust Layered Control for Spacecraft Proximity Makeovers." The papers present the design of a 6-DOF robust condition feedback saturated controller. This controller is capable of continuously monitoring relative position and synchronizing attitude. The stability of the closed-loop system that is used with this control method is rigorously established under mild presumptions. Furthermore, it is proven that both the relative position and with regard attitude converge to a small neighborhood around zero. The numerical simulation result provides evidence of the efficacy of the proposed strategy for designing controllers.

Li Qiu et.al [17] released a study on the design of a Networked H_∞ Controller for a Direct-Drive Linear Motion Control System. The network-induced random delay, which cannot be avoided, is represented by a Markov chain that has uncertain transition probabilities. This work presents a linear motion control system that utilizes a double-sided linear switched reluctance machine (DLSRM) in the experiments. The

experimental tests on the networked DLSRM system are conducted to validate the efficacy and feasibility of the proposed H_∞ control approach for industrial applications of networked control systems.

The 2015 paper by J. F. Pan et.al.[18] on high-precision dual-loop position control of an asymmetric bilateral linear hybrid switched reluctance motor, and the 2015 paper by Benoit Huard et.al.[19] on sensor-less force/position control of a single-acting actuator, both show better performance and faster rise time compared to single-loop control strategies.

Benoit Huard et.al [19] released a study titled "Linear Control of Switching Valve in Vehicle Hydraulic Control Unit (HCU) Based on Sensor less Solenoid Position Estimation." This study presents a novel approach to establish a real-time linear controller for the switching valve in the HCU. The approach involves integrating a new sliding-mode controller (SMC) with a nonlinear sliding-mode observer (SMO). The sensor less linear pressure controller's tracking capabilities was validated using simulations and experiments, which yielded findings that supported its performance across various conditions. This study offers a valuable approach to achieve real-time linear control of a high-frequency switching valve that is comparable to a high-performance proportional valve.

III. FUZZY LOGIC CONTROLLER

The cornerstone of fuzzy logic is rooted in the simulation of human views and perceptions to regulate any system. One approach to simplifying complicated systems is to accept a certain degree of imprecision, ambiguity, and uncertainty [10]. An experienced operator creates a versatile control mechanism utilizing often used phrases such as "suitable," "not very suitable," "high," "little high," "much high," "far," and "too much high" that are regularly seen in people's daily lives. Fuzzy logic control is built upon these logical linkages. Fuzzy sets are utilized to represent linguistic variables. Zadeh created Fuzzy Sets Theory in 1965 as a means to represent and manipulate imprecise knowledge [11, 12]. The relationship between fuzzy logic and fuzzy set theory is analogous to the relationship between Boolean logic and classical set theory. Fig.2 depicts a fundamental construction of a Fuzzy Logic Controller (FLC).

To enhance the performance of FLC, adjustments are made to the regulations and membership functions. The membership functions are modified by reducing the width of the membership functions in the vicinity of the ZE region, resulting in a higher level of control precision. Conversely, increasing the width of the area that is distance from the ZE zone results in a quicker response in terms of control. Furthermore, the performance can be enhanced by modifying the stringency of rules [4].

IV. EXPERIMENTAL MODEL DEVELOPMENT

The following assumptions are prepared while developing the model

- 1) Difference between Initial distance and stopping distance should not be zero.
- 2) The drive gears of the position control system do not slip.
- 3) The center of gravity of the position control system is at the center of the base.
- 4) All damping is viscous in nature, no Coulomb friction is included.
- 5) No backlash in the gears (DC motor) of the model.

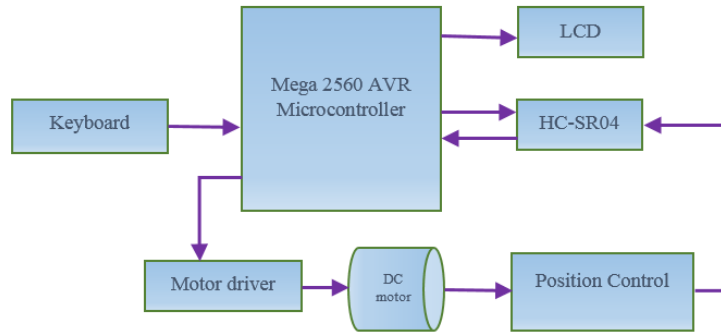


Fig. 2 The proposed system architecture

V. DESIGN OF FUZZY CONTROLLER

The structure of the control system with the proposed real time implementation of fuzzy controller is shown in Fig.2. The proposed fuzzy controller based on Mamdani’s fuzzy technique is implemented as a position controller.

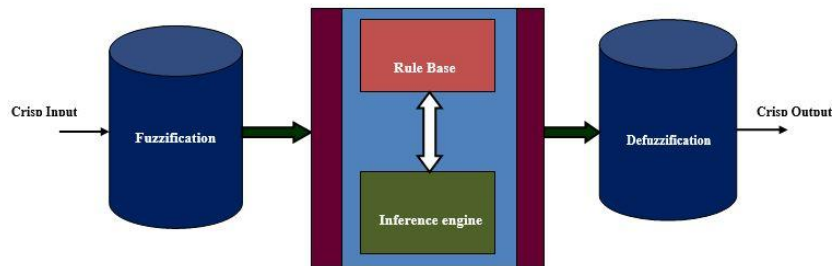


Fig. 3 Structure of fuzzy logic controller

The traditional Fuzzy Logic Controller usually works with input signals of the system error e and the derivative error ce in the error. The system error is defined as the difference between the reference point and the current output at the moment t :

$$e(t) = r(t) - y(t) \tag{1}$$

Hence the error derivative ce at the moment t will be:

$$ce(t) = e(t) - e(t - 1) \tag{2}$$

Proportional integral control technique is commonly using traditional control technique but the performance of the PID controller is mainly based on a suitable choice of the gains (Kp, Kd, Ki). Tuning of gains becomes the most difficult task. To overcome this problem a robust controller is needed. Fuzzy is one of these control technique which is robust about too many nonlinear procedures. The fuzzy controller uses a systematic method to control a nonlinear procedure based on human experience. This is defined as a heuristic method this can enhance the operation of closed loop system. The operation of the fuzzy controller is based on its capability to simulate several role implications at the same time, it results in the significantly comprehensive output. A well designed fuzzy controller can provide enhanced operation in

presence of variations in parameters, external perturbations, and load existence than conventional PID controllers. The design of fuzzy controller mainly consists of four building blocks: Fuzzyfication block, fuzzy knowledge-based (Membership Function and Fuzzy Rule Base) block, fuzzy Inference engine and Defuzzification block.

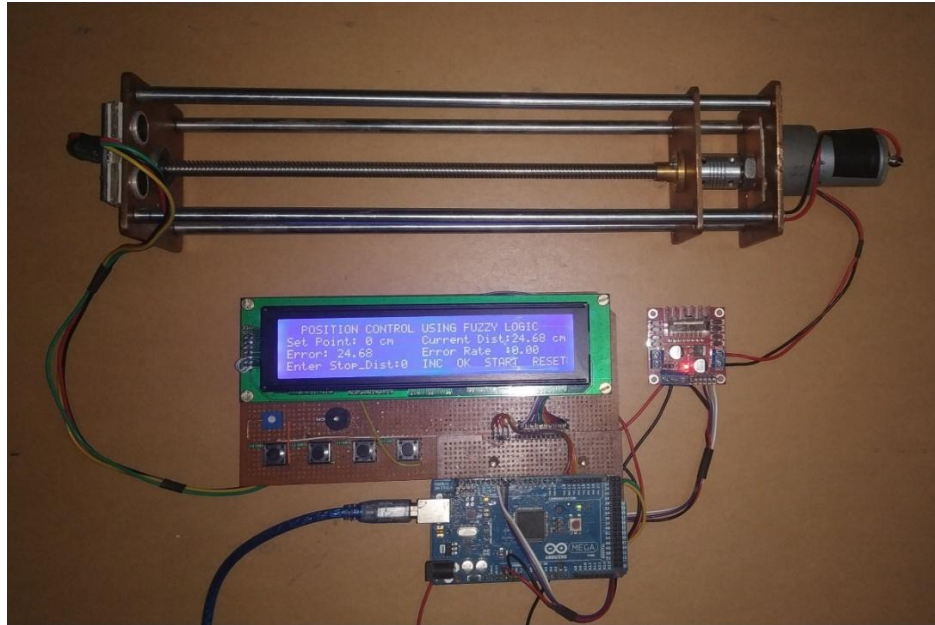


Fig 4: Experimental setup of model



Fig 5: LCD 40 x 4 Character Display

1. Fuzzyfication

The conversion of the crisp (classical) set to the fuzzy set is called the Fuzzification. Triangular fuzzifier is used among different fuzzifier such as Triangular, Trapezoidal, Singleton and Gaussian. By assigning some membership function to each and every input with the help of the fuzzifier is convert the input crisp value into the fuzzy set, [8, 9].

2. Membership Function

A graph of input crisp value and membership value which varies from 0 to 1 is called the membership function. It provides impreciseness to the fuzzy logic. The triangular membership function is used among the different membership functions such as trapezoidal, Gaussian, sigmoid, piecewise linear.

3. Fuzzy Rule Base

Fuzzy rule bases have garnered considerable interest in diverse disciplines because of their capacity to manage ambiguity and imprecise data. By integrating fuzzy logic into decision support block, proposed system will more accurately simulate how technical operator might tackle intricate situations with

significant levels of ambiguity. The fuzzy model offers a more predictable approach to input, membership functions, and inference rules, resulting in enhanced accuracy rates in mapping task between input crisp values to output crisp value. The rules established and applied in the fuzzy model take into account the most important factors and aid in defining the membership functions. Hence, the utilization of fuzzy rule bases enables the development of a complex framework that can be employed for our predefined events, such as the mapping the error and change in error to output duty cycle.

Table 9: The Fuzzy Rule Base

$\begin{matrix} & ce \\ e \end{matrix}$	NL	NM	NS	Z	PS	PM	PL
NL	NL	NL	NL	NM	NM	NS	Z
NM	NL	NM	NM	NS	NS	Z	PS
NS	NL	NM	NS	NS	Z	PS	PS
Z	NM	NS	NS	Z	PS	PS	PM
PS	NS	NS	Z	PS	PS	PM	PL
PM	NS	Z	PS	PM	PM	PL	PL
PL	Z	PM	PM	PM	PL	PL	PL

4. Inference Engine

Fuzzy inference engine consists of the knowledge base, in which the rules are framed. It can be broadly categorized into two types

- i. Mamdani method
- ii. Sugeno method

Sugeno method is generally based on mathematical analysis and calculations. But in Mamdani method linguistic logic used to make the rules which are very simple compared to the Sugeno method. Mamdani method is computationally efficient when compared to the Sugeno method. The fuzzy sets have been determined as NL(negative large), NM(negative medium), NS(negative small) and Z(zero), PS(Positive small), PM(positive medium), PL(positive large).

5. Defuzzification

Defuzzification is the last step of a fuzzy logic system, in which the fuzzy output of the inference engine gets converted into a precise value that can be received for further processing. This is achieved by identifying the most significant value or central point of the fuzzy output, which matches the level of membership in each fuzzy set. The interpretation of the outcomes of a fuzzy logic system and their use in implementation is a critical procedure. Converting the fuzzy output into a crisp value is an important step in the fuzzy logic system. This conversion allows for easy interpretation and utilization of the value in subsequent decision-making processes.

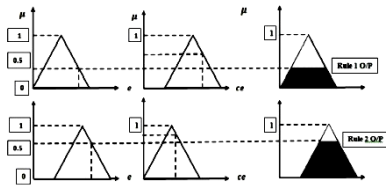


Fig 6. Understanding Defuzzification process

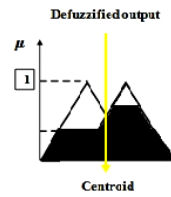


Fig. 7 Defuzzified Output

The Mamdani control strategy using PI and Fuzzy logic is implemented for linear position control using real time custom hardware and results are presented in this section. The performance of the Fuzzy logic controller is analyzed by using Steady State Error and error derivative analysis. The main objective of the Mamdani controller is to achieve target distance with minimum steady state error. The reference distance to the linear position controller is taken as 10 mm. The performance analysis using Fuzzy logic controller are shown in figure 21 to fig 24 .The resulting PWM with Total Period of 43 μ sec and frequency of 23.29 KHz of rectangular wave form is examined using dual channel storage type oscilloscope

Table 2: LCD Display Showing the Experimental results

T _{ON} (μ sec)	T _{OFF} (μ sec)	Duty Cycle	Error	Change in Error
10.75	32.25	25%	4.62	-1.14
20.64	22.36	48%	8.35	0.315
33.11	9.89	77%	14.7	0.929
41.71	1.29	97%	25	2.00

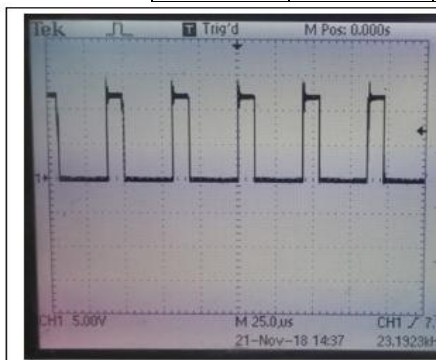


Fig 8: Resulting PWM for 25%

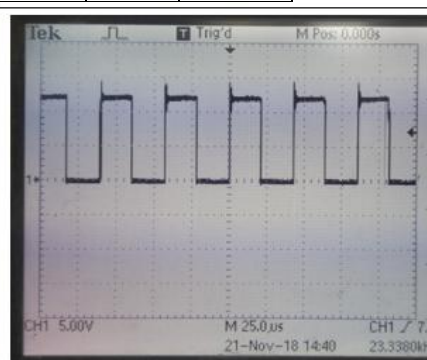


Fig 9: Resulting PWM for 48%

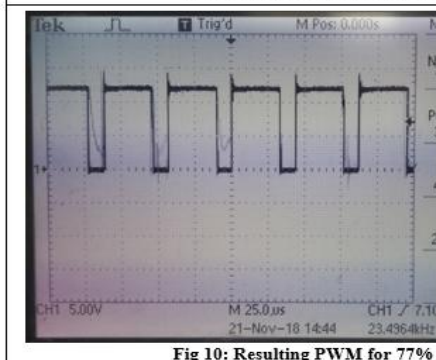


Fig 10: Resulting PWM for 77%

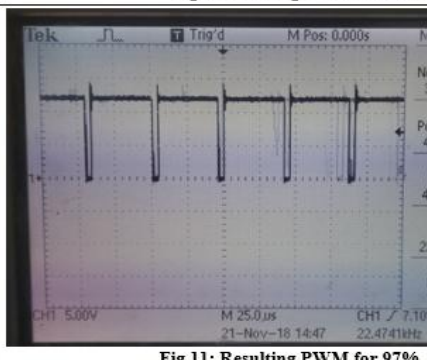


Fig 11: Resulting PWM for 97%

VII. CONCLUSION

This paper demonstrates the implementation and design of a fuzzy controller for linear position control of a mechanical plant. The structure of real-time implementation of the fuzzy controller has been introduced in this work. The Mamdani fuzzy technique is used to obtain the fuzzy controller. The fuzzy controller is developed as a two-term fuzzy controller using the system error and the derivatives of the error. This is evident from the obtained results, where the transient responses of the system output have shown an improvement after several rules with the implemented fuzzy controller. The experimental results realize a good transient behavior of the proposed system, it maintains a constant difference of target speed and output speed with a small system error and minimum error derivative. The system performance is satisfactorily verified with the validity and robustness of the proposed structure of the fuzzy controller.

REFERENCES

- 1] D. R. Solanke K. D. Chinchkhede, A. B. Manwar “ Design & Implementation of Fuzzy Inference System For Automatic Braking System ”, *proceeding of international conference on emerging trends in engineering and Technology*, sept 2017, pp no. 218-231.
- 2] Umesh Kumar Bansal and Rakesh Narvey, “Speed Control of DC Motor Using Fuzzy PID Controller” , *Advance in Electronic and Electric Engineering*, Volume 3, Number 9 (2013), pp. 1209-1220
- 3] Ivana Todic, Marko Milos and Mirko Pavisic, “Position and speed control of electromechanical actuator for aerospace applications”, *Technical Gazette*, Volume 20, Number 5(2013), pp 853-860
- 4] Yongming Li, Shaocheng Tong, “Adaptive Fuzzy Control With Prescribed Performance for Block-Triangular-Structured Nonlinear Systems”, *IEEE Transactions On Fuzzy Systems*, vol. 26, no. 3, pp. 1153-1163, June 2018.
- 5] Bing Chen, Xiaoping Liu, and Chong Lin, “Observer and Adaptive Fuzzy Control Design for Nonlinear Strict-Feedback Systems With Unknown Virtual Control Coefficients” *IEEE Transactions On Fuzzy Systems*, vol. 26, no. 3, pp. 1732-1743, June 2018.
- 6] Lishu Qin, Jianjun Hu, Hongxing Li, And Wang Chen, “Fuzzy Logic Controllers for Specialty Vehicles Using a Combination of Phase Plane Analysis and Variable Universe Approach”, *Special Section On Communication, Control And Computation Issues In Heterogeneous Vehicular Networks*, vol.5, pp. 1579-1588, March 2017.
- 7] Pandurang S. Londhe, M. Santhakumar, Balasaheb M. Patre, and Laxman M. Waghmare, “Task Space Control of an Autonomous Underwater Vehicle Manipulator System by Robust Single-Input Fuzzy Logic Control Scheme”, *IEEE Journal Of Oceanic Engineering*, vol. 42, no. 1, pp. 13-28 January 2017.
- 8] Mojtaba Ahmadi Khanesar, Erdal Kayacan, Mahmut Reyhanoglu, and Okyay Kaynak Khanesa M. A. et al., “Feedback Error Learning Control of Magnetic Satellites Using Type-2 Fuzzy Neural Networks With Elliptic Membership Functions”, *IEEE Transactions On Cybernetics*, vol. 45, no. 4, pp. 858-868 April 2015.
- 9] Haibo Du, Xiuping Chen, Guanghui Wen, Xinghuo Yu, and Jinhua, “Discrete-Time Fast Terminal Sliding Mode Control for Permanent Magnet Linear Motor”, *IEEE Transactions On Industrial Electronics*, vol. 65, no. 12, pp. 9916-9927, December 2018.
- 10] SheirAfgan Zaheer, Seung-Hwan Choi, Chang-Young Jung, and Jong-Hwan Kim, “A Modular Implementation Scheme for Non singleton Type-2 Fuzzy Logic Systems With Input Uncertainties”, *IEEE/ASME Transactions On Mechatronics*, vol. 20, no. 6, pp. 3182-3193, December 2015.
- 11] Tiechao Wang, Shaocheng Tong, Jianqiang Yi, and Hongyi Li, “Adaptive Inverse Control of Cable-Driven Parallel System Based on Type-2 Fuzzy Logic Systems”, *IEEE Transactions On Fuzzy Systems*, vol. 23, no. 5, pp 1803-1816, October 2015.
- 12] Shaocheng Tong, Yongming Li, and Shuai Sui, “Adaptive Fuzzy Tracking Control Design for SISO Uncertain Nonstrict Feedback Nonlinear Systems”, *IEEE Transactions On Fuzzy Systems*, vol. 24, no. 6, pp. 1441-1454 December 2016.
- 13] Shaocheng Tong, Lili Zhang, and Yongming Li, “Observed-Based Adaptive Fuzzy Decentralized Tracking Control for Switched Uncertain Nonlinear Large-Scale Systems With Dead Zones”, *IEEE Transactions On Systems, Man, And Cybernetics: Systems*, vol. 46, no. 1, pp. 37-47, January 2016.
- 14] Li Qiu, Yang Shi, Jianfei Pan, and Bo Zhang, “Robust Cooperative Positioning Control of Composite Nested Linear Switched Reluctance Machines With Network-Induced Time Delays”, *IEEE Transactions On Industrial Electronics*, vol. 65, no. 9, pp. 7447-7457, September 2018.
- 15] Hongjiu Yang, Jiahui Sun, Yuanqing Xia, and Ling Zhao, “Position Control for Magnetic Rodless Cylinders With Strong Static Friction”, *IEEE Transactions On Industrial Electronics*, vol. 65, no. 7, pp. 5806-5815, July 2018.
- 16] Liang Sun, and Zewei Zheng, “Disturbance Observer-Based Robust Saturated Control for Spacecraft Proximity

- Maneuvers”, *IEEE Transactions On Control Systems Technology*, vol. 26, no. 2, pp.684-692, March 2018.
- 17] Li Qiu, Yang Shi, Jianfei Pan, Member and Gang Xu, “ Networked H_∞ Controller Design for a Direct-Drive Linear Motion Control System”, *IEEE Transactions On Industrial Electronics*, vol. 63, no. 10, pp.6281-6291, October 2016.
 - 18] J. F. Pan, Yu Zou¹, Guangzhong Cao, Norbert C. Cheung, and Bo Zhang, “High-Precision Dual-Loop Position Control of an Asymmetric Bilateral Linear Hybrid Switched Reluctance Motor”, *IEEE Transactions On Magnetics*, vol. 51, no. 11, pp. 8600405, November 2015.
 - 19] Benoit Huard, Mathieu Grossard, Sandrine Moreau, and Thierry Poinot, “ Sensorless Force/Position Control of a Single-Acting Actuator Applied to Compliant Object Interaction”, *IEEE Transactions On Industrial Electronics*, vol. 62, no. 6, pp.3651-3661, June 2015.

¹ N. S. Wadtkar² S. A. Waghuley

Structural and optical characterization of polythiophene/polyindole/ferric chloride blended polymers for optoelectronic applications



Abstract: - The present work reports the complex optical properties of polythiophene/polyindole/ferric chloride (PTh/PIn/FeCl₃) blended polymers synthesized through novel one pot chemical oxidation copolymerization. The result of X-ray diffraction (XRD) analysis depicts the amorphous nature of these synthesized blended polymers. Field emission-scanning electron microscopy (FE-SEM) ensured the morphology of prepared samples. The complex optical parameters have been analyzed using ultraviolet-visible (UV-Vis) spectroscopy. The studied samples exhibited absorption around 240 - 300 nm. The optical band gap values were found to be 2.52 and 2.67 eV for 1:1:1 and 1:1:2 molar feed ratio of PTh/PIn/FeCl₃ blended polymers. The estimated optical energy band gap validated that the studied material has potential applications in optoelectronic devices.

Keywords: Chemical copolymerization, complex optical properties, optical conductivity.

I. INTRODUCTION

Recently, investigations are going on over the organic conjugated polymeric materials due to the demand of digital life style, energy storage system, hybrid vehicles and flexible portable electronic devices [1, 2]. These conjugated polymeric materials shows their wide applications in solid-state device technology likely photovoltaic, organic solar cells, sensors, light emitting diodes, field effect transistors, electrochemical lithium batteries etc. [3-9]. The conjugated conducting polymers and their copolymers exhibit sufficiently high optoelectronic properties, such materials are usually offered in low-cost electronic and optical devices [10]. For the active performance, most of the above said solid-state devices have been based on the conjugated conducting polymers such as polythiophene (PTh) and polyindole (PIn) due to their excellent electrical characteristics, thermal and environmental stability and solubility [11-13].

The characterizations of the prepared materials play a very crucial role in understanding the physico-chemical properties in order to design and implementation of such materials for their intended potential applications [14]. The optical characterization gives insight to different physical properties such as absorption, transmission, extinction coefficient, refractive index, electronic excitation energy, optical band gap, optical conductivity, etc. UV-Visible spectroscopy is one of the dominant tools in order to understand the complex optical properties of materials and numerous studies have been conducted earlier starting different methods of characterization [15, 16]. Using results of UV-Visible spectroscopy, by considering absorption, reflectance and other parameters, several models have been proposed to comprehend the properties of materials [17]. In light of this, we therefore describe the way to study the different complex optical properties of the prepared materials.

Gupta et al. [18] have been reported the successful performance of copolymerization of carbazole and indole through potentiostatic polymerization and the influence of the monomer concentrations ratio on copolymer formation have been investigated and found that the current density- voltage characteristic of the schottky diode is consequential in extracting the electronic parameters and the charge transport mechanism of the devices. Zhao et al. [19] have been successfully designed and synthesized three series of cis/trans isomers of benzimidazole-thiophene copolymers (PBDIT) with different length of n-alkyl chains and illuminated the relationship between the configurational isomerism and the optical and electrical properties. Wadtkar et al. [20] have been reported the successful chemical copolymerization of monomers, i.e. thiophene and indole in aqueous solution using FeCl₃ as an oxidant and studied the complex electrical behavior of as-synthesized copolymeric materials.

¹ *Corresponding author: Department of Physics, Government Polytechnic, Arvi 442201, India

² Department of Physics, Sant Gadge Baba Amravati University, Amravati 444602, India

Copyright © JES 2024 on-line : journal.esrgroups.org

There are some reports concerning the copolymerization of thiophene and indole [21], but no report on the chemically oxidative copolymerization of thiophene and indole is found in aqueous solution. In this article, we report on the novel one pot chemical synthesis of these oligomers in aqueous solution using FeCl_3 as an oxidant at room temperature. The as-synthesized PTh/PIn/ FeCl_3 blended polymers have been characterized through XRD, FE-SEM, and UV-Vis techniques.

II. EXPERIMENTAL

In experimental part of this research work, thiophene, indole monomers, anhydrous iron (III) chloride (FeCl_3), and other AR grade chemicals and reagents were purchased from commercial sources SD Fine, India and used without any further purification. The syntheses of blended polymers were done through in-situ chemical oxidative route. 0.1 M solution of thiophene and indole in deionized water has been mixed with variation of FeCl_3 as 1:1:1, 1:1:2. In this, FeCl_3 were used as an oxidant.

III. MATERIAL CHARACTERIZATIONS

The as-studied samples were characterized through XRD, FE-SEM and UV-Vis techniques to confirm the structural and optical properties. The XRD profile of powder samples were recorded on Rigaku miniflex-II X-ray diffraction using $\text{CuK}\alpha$ radiation ($\lambda = 1.54 \text{ \AA}$) in the 2θ range of $10\text{-}70^\circ$. The morphology of the samples was reported from FE-SEM (JEOL JSM-6360). The Characteristic UV-Vis analysis of as-synthesized samples was recorded on Perkin Elmer UV spectrophotometer in the range 200-800 nm.

IV. RESULTS AND DISCUSSION

XRD analysis

X-ray diffraction studies were carried out to examine the structure of studied samples. The patterns were recorded on Rigaku miniflex-II X-ray diffraction using $\text{CuK}\alpha$ radiation ($\lambda = 1.54 \text{ \AA}$) in the 2θ range of $10\text{-}70^\circ$. Fig. 1 depicts the XRD profile of PTh/PIn/ FeCl_3 blended polymers molar feed ratios as 1:1:1 and 1:1:2. The entire 2θ patterns do not shows any sharp peak, which is the characteristic of crystalline nature. Besides that patterns contains the broad humps between 20 and 30° , which pointed out the amorphous nature of synthesized samples of copolymer [20].

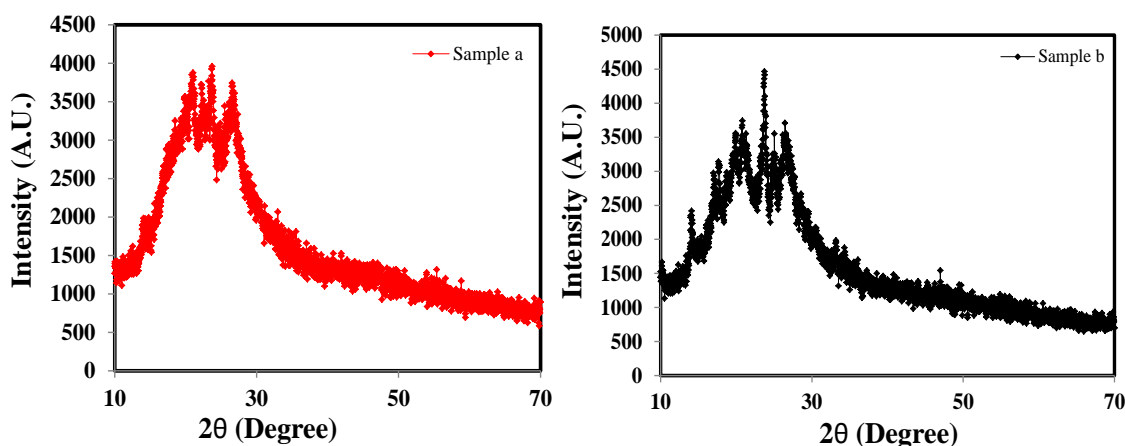


Fig. 1. XRD profile of PTh/PIn/ FeCl_3 blended polymers with molar feed ratios as (a) 1:1:1 and (b) 1:1:2.

FE-SEM Analysis

The physio-chemical properties are usually depends upon structure and morphology of materials. Conducting copolymers properties are correlated well with the morphology and structure. Thus, in order to analyze morphology of prepared samples, FE-SEM studies were carried out. Fig. 2 displays FE-SEM micrographs of PTh/PIn/ FeCl_3 blended polymers with molar feed ratios as 1:1:1 and 1:1:2. The micrographs of represents extremely rough, micro-globular porous structure and the surface particles are inhomogeneous in nature which attributes to random-ness in the structure of prepared samples [22].

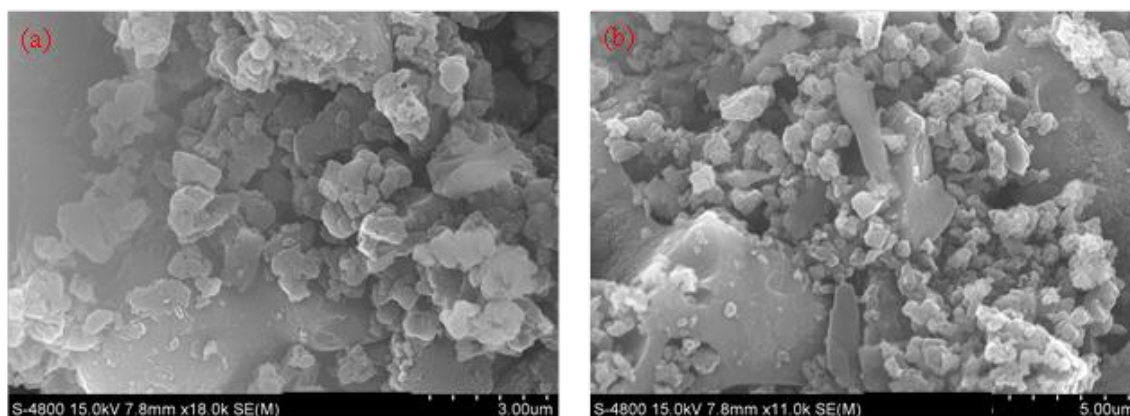


Fig. 2. FE-SEM micrograph of PTh/PIIn/FeCl₃ blended polymers with molar feed ratios as (a) 1:1:1 and (b) 1:1:2.

UV-Vis Analysis

Fig. 3 depicts the UV-Vis absorption spectra for PTh/PIIn/FeCl₃ blended polymers with molar feed ratios as 1:1:1 and 1:1:2 in the range 200 - 800 nm. The absorption spectra are one of the strongly used tools to examine the linear absorption properties of studied materials. The organic molecule of studied materials shows the electronic transitions usually occurs between bonding and non-bonding orbitals towards the non-occupied antibonding orbitals [23, 24]. The highly intense absorption peak of the synthesized samples was observed at 280 nm, frequently present in donor and acceptor in copolymer [25]. Peak ranging between 250-350 nm may ascribed due to the π - π^* electronic transitions of the conjugated polymer backbones [26].

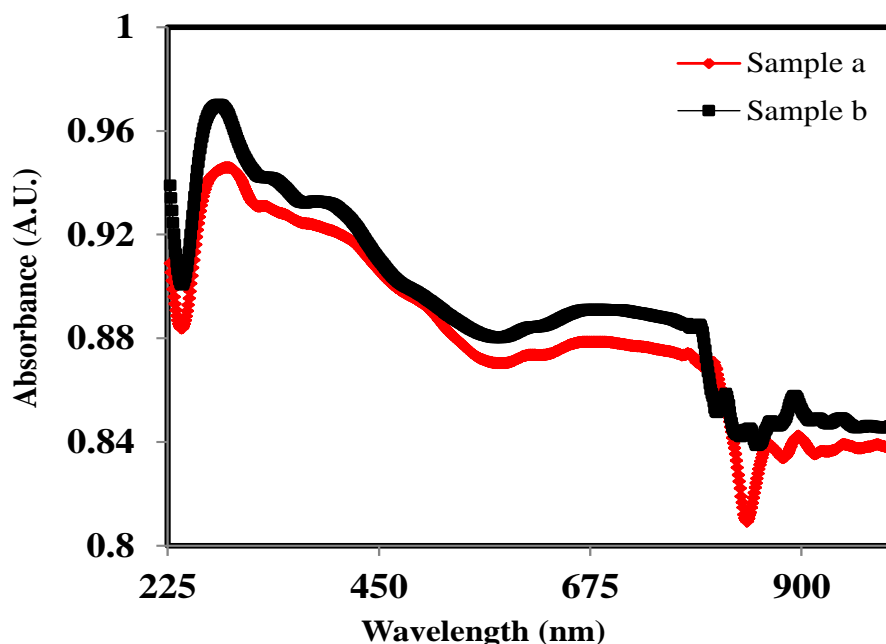


Fig. 3. UV-Vis spectra of PTh/PIIn/FeCl₃ blended polymers with molar feed ratios as (a) 1:1:1 and (b) 1:1:2.

Fig. 4 depicts the variation of extinction coefficient as a function of wavelength for PTh/PIIn/FeCl₃ blended polymers with molar feed ratios as 1:1:1 and 1:1:2. The plot clearly shows that extinction coefficient curve increases linearly with wavelength. The extinction coefficient represents the amount of trapping light [27]. Here, we conclude that wavelength beyond 240 nm trapped in the samples and there is a linear rise in the degree of trapping of light. Besides, the wavelength between 225 and 240 nm are not trapped in the samples. Since the variation of extinction coefficient between the wavelength range 225 and 240 nm is nearly constant. The highest value of extinction coefficient observed for the sample (b) having feed molar ratio as 1:1:2.

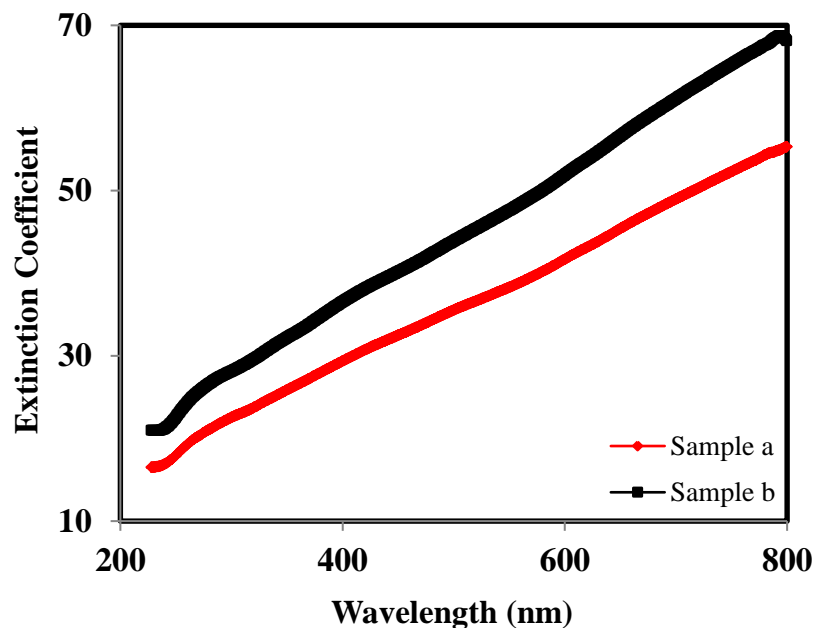


Fig. 4. Variation of extinction coefficient as a function of wavelength for PTh/PIn/FeCl₃ blended polymers.

Fig. 5 represents the variation of refractive index as a function of wavelength. The plot clearly shows that the samples offer low refractive index at smaller wavelength side, whereas the value of refractive index increases on higher wavelength side up to 560 nm. Beyond wavelength 560 nm, refractive index decreases gradually. The highest value of refractive index observed for the sample (a) having feed molar ratio as 1:1:1 at 560 nm.

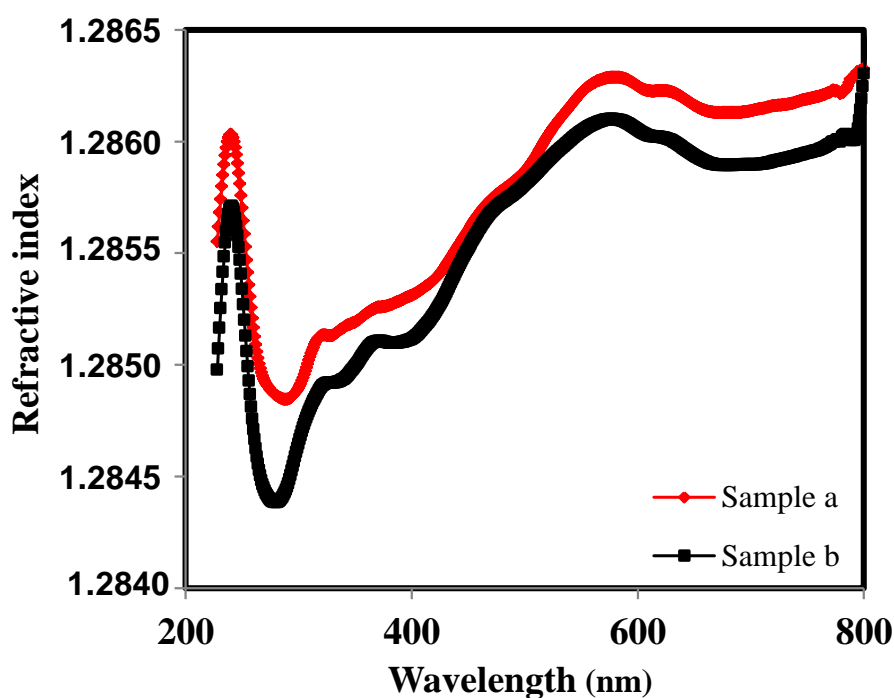


Fig. 5. Variation of refractive index as a function of wavelength for PTh/PIn/FeCl₃ blended polymers.

Fig. 6 shows the optical band gap curve for PTh/PIn/FeCl₃ blended polymers with molar feed ratios as 1:1:1 and 1:1:2. The relation between linear absorption coefficient (α) of material and incident photon energy ($h\nu$) is given by the well-known Tauc relation [28]:

$$\alpha h\nu = C (h\nu - E_g)^n \tag{1}$$

where, E_g is the optical band gap energy of material, C is a proportionality constant and n is 0.5 for direct allowed transition and equal 2 for indirect allowed transition, respectively. The optical band gap values for the

studied samples were found to be 2.52 and 2.67 eV for 1:1:1 and 1:1:2 molar feed ratios, respectively. The optical band gap energy values obviously conclude that, the prepared samples have potential application in optoelectronics devices [29-31].

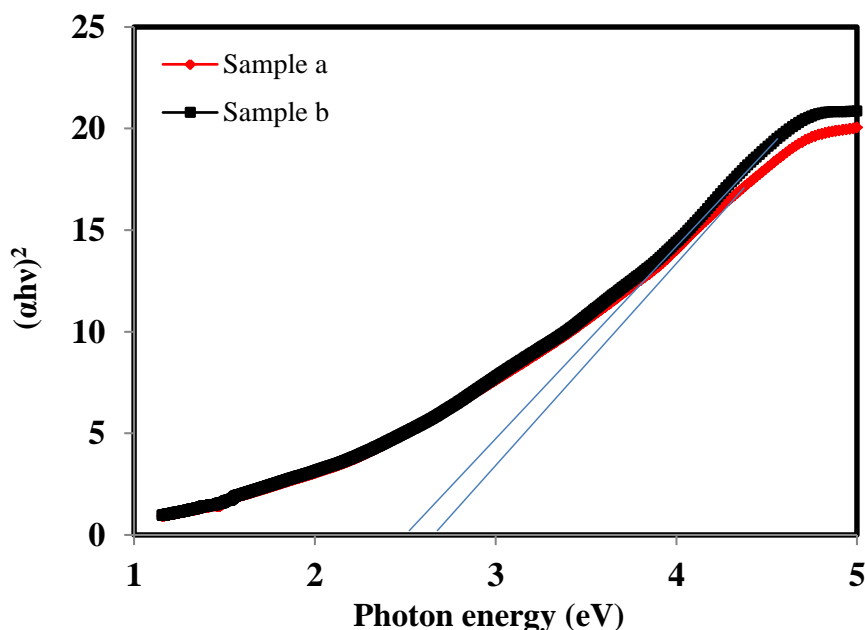


Fig. 6. Plot of $(\alpha hv)^2$ versus photon energy (hv) for PTh/PIn/FeCl₃ blended polymers.

The optical response of the materials is usually assessed in terms of the optical conductivity (σ) [30, 31]. Figure 7 shows the plot of the optical conductivity versus wavelength for samples PTh/PIn/FeCl₃ blended polymers with molar feed ratios as (a) 1:1:1 and (b) 1:1:2. The plot illustrates that, the optical conductivity directly depends upon the absorption coefficient and refractive index of the samples. Also, the optical conductivity found more at lower wavelength side which ascribed to the excitation of electrons towards that wavelength side [32]. The values of the optical conductivity for the samples of PTh/PIn/FeCl₃ blended polymers with molar feed ratios as (a) 1:1:1 and (b) 1:1:2 are estimated as 1.08×10^7 and 1.12×10^7 Scm⁻¹ at 280 nm respectively.

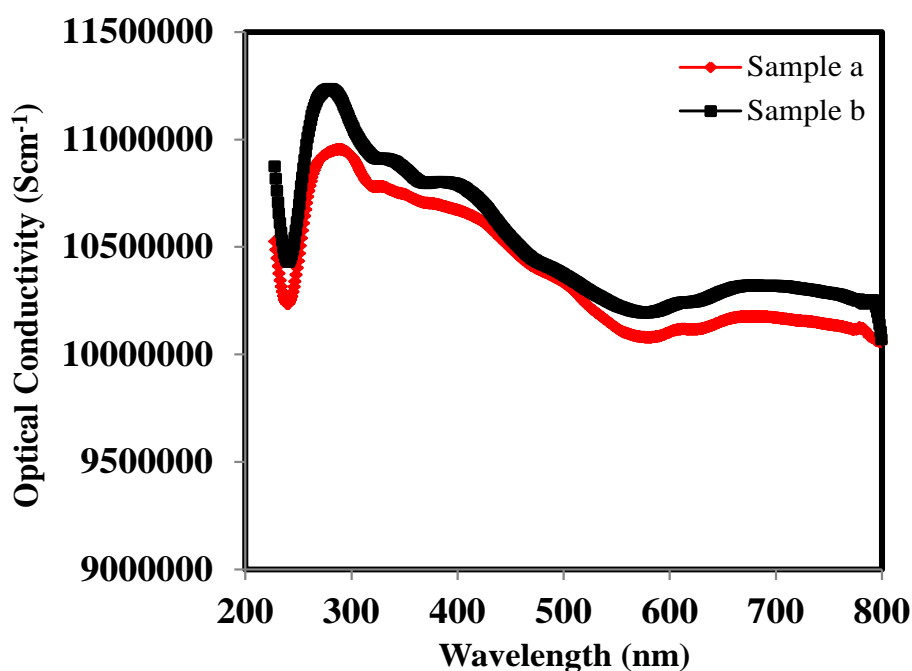


Fig. 7. Variation of optical conductivity for PTh/PIn/FeCl₃ blended polymers as a function of wavelength.

IV. CONCLUSIONS

In conclusion, we have studied the complex optical properties of PTh/PIn/FeCl₃ blended polymers. The absorption spectrum of synthesized samples were analyzed ranges over 200 - 800 nm for the determination of optical parameters. The optical band gap values for the studied were found to be 2.52 and 2.67 eV for 1:1:1 and 1:1:2 molar feed ratio of prepared blended materials, respectively. The optical conductivity shows their highest values around 280 nm for both samples. The critical analysis of results shows that all complex optical parameters vary with the concentration of oxidant. The estimated optical band gap energy has accepted value for photovoltaic activities and has potential for application in solar cells and optical devices.

Acknowledgements

The authors are very much thankful to Head, Department of Physics Sant Gadge Baba Amravati University, Amravati for providing the necessary facilities.

Funding

The study did not receive any external funding.

Conflict of interest

The authors declare that they have no conflict of interest.

Informed consent

Written informed consent was obtained from all individual participants included in the study.

Data and materials availability

All data associated with this study are present in the paper.

References

- [1] S. B. Aziz, "Modifying Poly(Vinyl Alcohol) (PVA) from Insulator to Small-Bandgap Polymer: A Novel Approach for Organic Solar Cells and Optoelectronic Devices," *J. Electron. Mater.*, vol. 45, pp 736–745, 2016.
- [2] B. Purty, R. B. Choudhary, M. Majhi, and R. Kerketta, "Augmented optical, dielectric and electrochemical performance for morphologically crushed nanorods decorated Fe:MnO₂/PIn nanocomposite," *Optik*, vol.158, pp 767–778, 2018.
- [3] L. Angiolini, V. Cocchi, M. Lanzi, E. Salatelli, D. Tonelli, and Y. Vlamidis, "Novel regioregular polythiophenes containing side-chain porphyrin groups for polymeric photovoltaic cells," *Mater. Chem. Phys.*, vol. 146(3), pp 464–471, 2014.
- [4] M. T. Dang, L. Hirsch, and G. Wantz, "P3HT:PCBM, Best Seller in Polymer Photovoltaic," *Research Adv. Mater.*, vol. 23, pp 3597–3602, 2011.
- [5] S. V. Kamat, V. Puri, and R. K. Puri, "Determination of the optical constants of a vacuum evaporated polythiophene thin film," *Physica Scripta*, vol. 84(4), pp 045801, 2011.
- [6] J. D. Myers, and J. Xue, "Organic Semiconductors and their Applications in Photovoltaic Devices," *Polym. Reviews*, vol. 52(1), pp 1–37, 2012.
- [7] R. Daik, and S. Maniam, "UV-Visible Absorption of Alkyl-Substituted Poly(thiophene) Solutions upon Exposure to Oxygen Gas," *Malays. J. Chem.*, vol. 9, pp 24–29, 2007.
- [8] M. Imperiyka, A. Ahmad, S. A. Hanifah, and F. Bella, "A UV-prepared linear polymer electrolyte membrane for dye-sensitized solar cells," *Phys. B Condens. Matt.*, vol. 450, pp 151–154, 2014.

- [9] K. Kesavan, C. M. Mathew, S. Rajendran, C. Subbu, and M. Ulaganathan, "Solid Polymer Blend Electrolyte Based on Poly (ethylene oxide) and Poly (vinyl pyrrolidone) for Lithium Secondary Batteries," *Braz. J. Phys.*, vol. 45(1), pp 19–27, 2015.
- [10] N. S. Wadtkar, and S. A. Waghuley, "A novel studies on electrical behaviour of chemically synthesized conducting polyindole," *Indian J. Phys.*, vol. 92(12), pp 1551–1559, 2018.
- [11] H. Mudila, P. Prasher, M. Kumar, A. Kumar, M. G. H. Zaidi, and A Kumar, "Critical analysis of polyindole and its composites in supercapacitor application," *Mater. Renew. Sustain. Energy*, vol. 8, pp 9–27, 2019.
- [12] N. S. Wadtkar, and S. A. Waghuley, "Studies on properties of as-synthesized conducting polythiophene through aqueous chemical route," *J. Mater. Sci: Mater. Electron.*, vol.27, pp 10573–10581, 2016.
- [13] P. Syed Abthagir, K. Dhanalakshmi, and R. Saraswathi, "Thermal studies on polyindole and polycarbazole," *Synth. Met.*, vol. 93(1), pp 1–7, 1998.
- [14] N. Dutta, D. Mohanta, I. Sulania, and A. Choudhury, "Studies of optical properties and SHI irradiation on PbS sensitized nanoporous TiO₂ network," *J. Optics*, vol. 38, pp 169–176, 2009.
- [15] N. S. Wadtkar, and S. A. Waghuley, "Optical Study of Chemically Synthesized Conducting Polythiophene Using UV–Vis Spectroscopy," *Macromol. Symp.*, vol. 362(1), pp 129–131, 2016
- [16] A. Murphy, "Band-gap determination from diffuse reflectance measurements of semiconductor films, and application to photoelectrochemical water-splitting," *Sol. Energy Mater. Sol. Cells*, vol. 91, pp 1326–1337, 2007.
- [17] T. G. Urs, G. K. Gowtham, M. B. Nandaprakash, D. Mahadevaiah, Y. Sangappa, and R. Somashekar, "Determination of force constant and refractive index of a semiconducting polymer composite using UV/visible spectroscopy: a new approach," *Indian J. Phys.*, vol. 91, pp 53–57, 2017.
- [18] B. Gupta, A. K. Singh, A. A. Melvin, and R. Prakash, "Influence of monomer concentration on polycarbazolepolyindole (PCz-PIn) copolymer properties: Application in Schottky diode," *Solid State Sci.*, vol. 35, pp 56–61, 2014.
- [19] Y. Zhao, X. Shen, S. He, X. Han, and Z. Ni, "Relationship between cis-trans isomerism and optical and electrical properties based on benzidimidazole-thiophene copolymer," *Synth. Met.*, vol. 245, pp 175–181, 2018.
- [20] N. S. Wadtkar, and S. A. Waghuley, "Electrical investigation on thiophene–indole conducting copolymers as-synthesized through in situ chemical copolymerization route," *Polym. Bull.*, vol. 77 pp 1–16, 2019.
- [21] A. S. Sarac, S. Ozkara, and E. Sezer, "Electropolymerization of indole and thiophene: conductivity-peak current relationship and in situ spectroelectrochemical investigation of soluble Co-oligomers," *Int. J. Polym. Anal. Chara.*, vol. 8, pp 395–409, 2003.
- [22] N. S. Wadtkar, and S. A. Waghuley, "Enhancement in the optical and carbon dioxide gas sensing properties of polythiophene by dispersion of manganese dioxide nanoparticles," *Sustain. Chem. Climate Action*, vol. 4, pp 100036, 2024.
- [23] N. S. Wadtkar, and S. A. Waghuley, "Complex optical and thermal studies on as-synthesized conducting polythiophene," *J. Elec. Mater.*, vol. 48(4), pp 2219–2225, 2019.
- [24] D. C. Hasija, J. Gopalakrishnan, A. V. Mishra, V. D. Ghase, and V. R. Patil, "Exploring copper as a catalyst for cost effective synthesis of polyfluorenes: an alternative to platinum and palladium," *SN Appl. Sci.*, vol. 2, pp 569–577, 2020.
- [25] N. S. Wadtkar, and S. A. Waghuley, "Further studies on complex optical performance of polythiophene-copolyindole conducting copolymers for optoelectronic applications," *Opt. Quant. Elec.*, vol. 54(9), pp 595–257, 2022.

- [26] M. A. Morsi, S. A. El-Khodary, and A. Rajeh, "Enhancement of the optical, thermal and electrical properties of PEO/PAM: Li polymer electrolyte films doped with Ag nanoparticles," *Phys. B Condens. Matt.*, vol. 539, pp 88–96, 2018.
- [27] K. R. Nemade, and S. A. Waghuley, "Role of defects concentration on optical and carbon dioxide gas sensing properties of Sb₂O₃/graphene composites," *Opt. Mater.*, vol. 36(3), pp 712–716, 2014.
- [28] A. Belhouni, P. Gredin, M. Mortier, and M. Diaf, "Structural, thermal and optical investigations of PbF₂:Eu³⁺ particles prepared by co-precipitation method," *Opt. Mater.*, vol. 83, pp 321–327, 2018.
- [29] N. S. Wadatkar, and S. A. Waghuley, "Complex optical studies on conducting polyindole as-synthesized through chemical route," *Egyp. J. Basic Appl. Sci.*, vol. 2, pp 19–24, 2015.
- [30] R. V. Barde, K. R. Nemade, and S. A. Waghuley, "Complex optical study of V₂O₅-P₂O₅-B₂O₃-GO glass systems by ultraviolet-visible spectroscopy," *Opt. Mater.*, vol. 40, pp 118–121, 2015.
- [31] N. S. Wadatkar, and S. A. Waghuley, "Exploring the electrical and complex optical properties of as-synthesized thiophene-indole conducting copolymers," *Heliyon*, vol. 5(4) pp e01534, 2019.
- [32] N. S. Wadatkar, and S. A. Waghuley, "Synthesis and Complex Optical Characterization of Polythiophene/Poly(vinyl acetate) Composite Thin Films for Optoelectronic Device Applications," *Ind. J. Pure & App. Phys.*, vol. 60(5), pp 430–436, 2022.

¹ Author Name: Miss.
Shraddha L. Bhagat

Dept. Of Physics RTMNU
Nagpur

²Authors Name :

Dr. Shilpa Pande

Dept. Of Applied Physics
L.I.T Nagpur

Regular paper

Paper Title: Enhancing Supercapacitor

Performance with Polyaniline-Metal Oxide

Nanocomposites: Current Trends and Future

Directions .



Review Paper

Abstract :-

Supercapacitors have gained significant attention in recent years due to their high power density, rapid charging/discharging capabilities, and long cycle life. Polyaniline (PANI) and metal oxides have been extensively explored as electrode materials for supercapacitors. The combination of PANI and metal oxides in the form of nanocomposites has shown enhanced electrochemical performance. This review focuses on the fabrication, characterization, and supercapacitor application of PANI-metal oxide nanocomposites, highlighting their potential for energy storage devices. And focuses on their Current Trends and Future Directions.

Keywords: PANI- Metal Oxide Nanocomposites, Supercapacitors, Electrochemical performance, Cyclic Stability, Hybrid Nanocomposites.

1. Introduction:-

Conductive polymers (CPs) have attracted great interest from academia and industry by offering the opportunity to combine the electrical properties of a semiconductor and metals with the traditional advantages of traditional polymers, such as polyaniline, polypyrrole, and polythiophene, together with their composites to improve the properties of conducting polymer materials. Conducting polymer possess conjugated bond system along the polymer backbone. They have been prepared through variety of techniques such as electrochemical oxidation/chemical oxidation of the conducting monomer. Polyaniline is one

of the most extensively studied and used conducting polymer in supercapacitor or battery electrode material. In this chapter, we explore conductive polymer-based composites for supercapacitors. For its applications in the field of energy storage, we critically review the application development and general design rules for energy storage devices, including supercapacitors, lithium and other ion batteries, and their limitations, current and future potential for moving forward energy storage technologies. We Hope that this review can facilitate to enhance the data regarding this conducting polymer and consequently lead to new areas of research.

¹ *Corresponding author: Author 1 Affiliation

² Author 2 Affiliation

Copyright © JES 2024 on-line : journal.esrgroups.org

Background :

Supercapacitors, also known as electrochemical capacitors or ultracapacitors, have gained significant attention in recent years due to their unique ability to generate high power density, quick charge-discharge cycles, and long cycle life. In contrast to traditional batteries, which store energy through chemical reactions, supercapacitors store energy by separating charges electrostatically. This basic difference enables supercapacitors to achieve substantially faster charge and discharge rates, making them ideal for applications needing brief bursts of energy, such as in electric vehicles, portable devices, and power backup systems .

1.1 Importance of Materials in Supercapacitors:

The electrode materials used in supercapacitors have a significant impact on their performance. Of the materials studied, conductive polymers and metal oxides have shown promise; metal oxides, such as titanium dioxide (TiO_2), ruthenium oxide (RuO_2), and manganese oxide (MnO_2), offer high specific capacitance, excellent electrochemical stability, and ease of synthesis. Conductive polymers, such as polyaniline (PANI), offer high capacitance, flexibility, and ease of synthesis.

Polyaniline (PANI)

According to its special qualities, including high conductivity, stability in the environment, and simplicity in synthesis and doping, polyaniline is one of the most researched conductive polymers. The primary factors influencing PANI's electrochemical behavior are its redox states, which are readily influenced by voltage and pH. Because of these qualities, PANI is a good option for supercapacitor electrodes. Unfortunately, PANI has limitations that restrict its practical applicability, such as poor cycle stability and mechanical degradation during long-term cycling.

Metal oxides

On the other hand, because of their many oxidation states, which promote quick and reversible redox reactions, metal oxides show exceptional capacitive behavior. For example, because of its low cost, environmental friendliness, and high theoretical capacitance, manganese oxide (MnO_4) is utilized extensively. Comparably, ruthenium oxide (RuO_2) is well-known for its remarkable capacitance and conductivity, but its exorbitant cost prevents it from being used widely. The stability and mild capacitance of titanium dioxide (TiO_2) are highly valued characteristics.

Polyaniline-Metal Oxide Nanocomposites:

Researchers have created polyaniline-metal oxide nanocomposites to get around the drawbacks of individual components. By combining the benefits of both parts, these composites provide materials with improved electrochemical performance. Improved specific capacitance, energy density, power density, and cycle stability are the results of the interaction between PANI and metal oxides. To improve electron transport, increase structural integrity, and provide more active sites for redox reactions, metal oxides can be included into the PANI matrix.[1-9]

1.2 Objective

The goal of this review is to present a thorough summary of the status of research on polyaniline-metal oxide nanocomposites for supercapacitors as it is right now. It will go through the several ways these nanocomposites are made, how they perform electrochemically, and how to characterize them. The assessment will also go over the difficulties encountered in this area and offer recommendations for future lines of inquiry to maximize these materials' usefulness.

1.3 Overview of supercapacitors:

Types of Supercapacitors

Supercapacitors, also known as ultracapacitors or electrochemical capacitors, are classified into three main types based on their charge storage mechanisms: electrochemical double-layer capacitors (EDLCs), pseudocapacitors, and hybrid capacitors.

Electrochemical Double-Layer Capacitors (EDLCs)

EDLCs store energy through the electrostatic separation of charges at the interface between the electrode and the electrolyte. They rely on the formation of an electric double layer to accumulate charge without any faradaic reactions (chemical reactions involving electron transfer). Materials with high surface area, such as activated carbon, carbon nanotubes, and graphene, are typically used as electrodes in EDLCs due to their ability to provide extensive surface area for charge accumulation .

Pseudocapacitors

Pseudocapacitors store energy through fast and reversible faradaic reactions occurring at the electrode surface. These reactions involve the transfer of charge between the electrode material and the electrolyte, leading to higher specific capacitance compared to EDLCs. Common electrode materials for pseudocapacitors include conductive polymers (e.g., polyaniline, polypyrrole) and transition metal oxides (e.g., manganese oxide, ruthenium oxide) .

Hybrid Capacitors

Hybrid capacitors combine the mechanisms of EDLCs and pseudocapacitors to leverage the advantages of both types. They typically use a combination of materials, such as a carbon-based material for the EDLC component and a metal oxide or conductive polymer for the pseudocapacitive component. This combination enhances the overall performance, offering improved energy density and power density .

Key Parameters of Supercapacitors

Several key parameters are used to evaluate the performance of supercapacitors, including specific capacitance, energy density, power density, and cycle stability.

Specific Capacitance

Specific capacitance (F/g) measures the amount of charge stored per unit mass of the electrode material. It is determined by cyclic voltammetry, galvanostatic charge-discharge, or electrochemical impedance spectroscopy. Higher specific capacitance indicates better energy storage capability .

Energy Density

Energy density (Wh/kg) represents the amount of energy stored per unit mass of the supercapacitor. It is influenced by the specific capacitance and the operating voltage window. Supercapacitors typically have lower energy density compared to batteries, but they offer higher power density .

Power Density

Power density (W/kg) indicates how quickly the stored energy can be delivered. Supercapacitors excel in delivering high power density due to their rapid charge-discharge capabilities. This makes them suitable for applications requiring quick bursts of energy .

Cycle Stability

Cycle stability refers to the ability of a supercapacitor to maintain its performance over repeated charge-discharge cycles. A high cycle life, often in the range of tens of thousands to millions of cycles, is a crucial advantage of supercapacitors over batteries. Materials used in the electrodes should exhibit minimal degradation over extended cycling .

1.4 Advantages and Applications of Supercapacitors

Supercapacitors offer several advantages over traditional batteries, including:

- ✧ **Rapid Charging and Discharging:** Due to their electrostatic storage mechanism, supercapacitors can be charged and discharged much faster than batteries.
- ✧ **Long Cycle Life:** They can endure hundreds of thousands to millions of charge-discharge cycles with minimal capacity loss.
- ✧ **High Power Density:** Supercapacitors can deliver high power outputs in short bursts, making them suitable for applications requiring quick energy release.
- ✧ **Wide Operating Temperature Range:** They perform reliably over a broad range of temperatures.
- ✧ These characteristics make supercapacitors ideal for various applications such as:
- ✧ **Energy Storage in Renewable Energy Systems:** To smooth out intermittent energy supply from sources like solar and wind.
- ✧ **Power Backup Systems:** For providing immediate power during outages and ensuring smooth power transitions.
- ✧ **Electric Vehicles (EVs):** To assist in regenerative braking and provide rapid acceleration.
- ✧ **Portable Electronics:** For quick charging devices such as cameras, laptops, and smartphones.
- ✧ **Industrial Applications:** Where high power bursts are needed, such as in cranes, forklifts, and other heavy machinery. [10-19]

2 Polyaniline in supercapacitor :

2.1 Introduction to polyaniline

Polyaniline (PANI) is one of the most intensively researched conducting polymers due to its unique qualities, including high conductivity, environmental stability, simplicity of manufacturing, and tunable electrochemical properties. PANI can exist in three oxidation states: leucoemeraldine (completely reduced), emeraldine (partially oxidized), and pernigraniline (totally oxidised). The emeraldine salt form is very conductive and is commonly utilized in electrochemical applications. PANI's redox characteristics and high capacitance make it a desirable material for supercapacitor electrodes.

2.2 Synthesis Methods

The synthesis of PANI typically involves chemical or electrochemical polymerization of aniline monomers. Common methods include:

Chemical Oxidative Polymerization: This method uses oxidizing agents such as ammonium persulfate to polymerize aniline in an acidic medium, resulting in a high yield of polyaniline with good conductivity .

Electrochemical Polymerization: This approach involves the deposition of PANI onto a conductive substrate through electrochemical oxidation of aniline in an acidic electrolyte. This method allows for better control over the thickness and morphology of the PANI film .

2.3 Electrochemical Performance

PANI-based supercapacitors operate on the principle of pseudocapacitance, where charge storage occurs through fast and reversible redox reactions. The electrochemical performance of PANI can be characterized by its specific capacitance, energy density, power density, and cycle stability.

Specific Capacitance: PANI exhibits high specific capacitance due to its redox-active nature. For instance, PANI electrodes can achieve specific capacitances ranging from 200 to 1000 F/g depending on the synthesis method and electrode configuration .

Energy Density and Power Density: PANI-based supercapacitors generally offer moderate energy density but high power density, which is suitable for applications requiring quick energy delivery. For example, PANI can deliver energy densities of 10-20 Wh/kg and power densities up to 10 kW/kg .

Cycle Stability: One of the main challenges with PANI is its cycle stability. The material tends to degrade over repeated charge-discharge cycles due to structural changes and mechanical stresses. However, strategies such as doping, composite formation, and using flexible substrates have been explored to enhance the durability of PANI electrodes .

2.4 Polyaniline-Metal Oxide Composites

To improve the performance and address the limitations of PANI, researchers have developed composites of PANI with various metal oxides. These composites leverage the high capacitance and conductivity of PANI with the stability and redox activity of metal oxides. Some notable examples include:

PANI-Manganese Oxide (MnO₂) Composites: MnO₂ is a popular choice for its high theoretical capacitance and environmental friendliness. PANI-MnO₂ composites exhibit synergistic effects, resulting in enhanced specific capacitance and better cycle stability compared to pure PANI .

PANI-Ruthenium Oxide (RuO₂) Composites: RuO₂ offers excellent capacitive properties, but it is expensive. Composites of PANI with RuO₂ can achieve very high specific capacitance and conductivity, though cost remains a challenge for large-scale applications .

PANI-Titanium Dioxide (TiO₂) Composites: TiO₂ is known for its stability and moderate capacitance. PANI-TiO₂ composites benefit from the good cycling stability of TiO₂ and the high capacitance of PANI, making them suitable for practical applications .

2.5 Applications and Future Prospects

PANI-based supercapacitors are being explored for various applications, including portable electronics, electric vehicles, and energy storage systems. The future of PANI in supercapacitors lies in overcoming challenges related to its mechanical stability and scalability. Continued research into nanostructuring, composite materials, and advanced fabrication techniques will be crucial in making PANI a viable option for commercial supercapacitors.[1,3,4,5,6,7,10,16,19]

3. Metal oxides in supercapacitor:

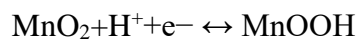
3.1 Introduction to Metal Oxides

Metal oxides are among the most promising materials for supercapacitor electrodes due to their excellent electrochemical properties, multiple oxidation states, high theoretical capacitance, and relatively low cost. They contribute to charge storage through faradaic reactions, which enable higher specific capacitance compared to carbon-based materials. Commonly studied metal oxides for supercapacitors include manganese oxide (MnO₂), ruthenium oxide (RuO₂), titanium dioxide (TiO₂), and nickel oxide (NiO) .

3.2 Types of Metal Oxides

Manganese Oxide (MnO₂)

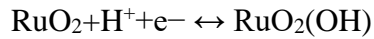
Manganese oxide is widely studied due to its high theoretical capacitance (~1370 F/g), natural abundance, low cost, and environmental friendliness. MnO₂ stores charge through the following redox reaction:



Despite these advantages, MnO₂ suffers from poor electrical conductivity and structural stability. Researchers have developed various strategies to address these issues, such as nanostructuring and combining MnO₂ with conductive materials like carbon nanotubes (CNTs) and graphene to enhance its electrochemical performance .

Ruthenium Oxide (RuO₂)

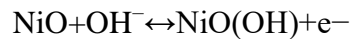
Ruthenium oxide is considered one of the best materials for supercapacitors due to its exceptional conductivity, high specific capacitance (up to 1700 F/g), and excellent cycle life. The charge storage mechanism involves the following redox reactions:



However, the high cost of RuO_2 limits its large-scale application. Efforts to reduce costs include synthesizing RuO_2 at the nanoscale to increase surface area and combining it with other, more affordable materials to maintain high performance while reducing the amount of RuO_2 used .

Nickel Oxide (NiO)

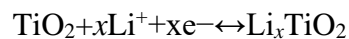
Nickel oxide is another promising candidate for supercapacitor applications due to its high specific capacitance, environmental friendliness, and abundance. NiO stores charge through the following redox reaction:



NiO, like other metal oxides, suffers from low conductivity. To address this, NiO is often combined with conductive substrates or nanostructured to enhance its electrochemical performance .

Titanium Dioxide (TiO₂)

Titanium dioxide is known for its excellent chemical stability, low cost, and safety. While TiO_2 has a lower specific capacitance compared to MnO_2 and RuO_2 , it provides good cycle stability and is often used in hybrid supercapacitors. Charge storage in TiO_2 occurs mainly through intercalation of ions:



TiO_2 's performance can be enhanced by nanostructuring and combining it with other active materials to improve conductivity and capacitance .

3.3 Synthesis Methods

Various synthesis methods are employed to produce metal oxide materials for supercapacitor electrodes, including:

Hydrothermal Synthesis: This method involves the use of a high-temperature and high-pressure aqueous solution to grow crystalline metal oxide nanostructures. It allows for precise control over the morphology and size of the particles.

Sol-Gel Method: In this process, metal alkoxides or metal salts are converted into a gel, which is then dried and calcined to form metal oxides. This method is useful for producing metal oxides with high purity and homogeneity .

Electrodeposition: This technique involves the electrochemical deposition of metal oxides onto a conductive substrate. It is advantageous for creating thin films with controlled thickness and uniformity .

Chemical Vapor Deposition (CVD): CVD is used to produce high-quality, thin metal oxide films by reacting gaseous precursors on a substrate. This method is suitable for creating well-adhered and uniform coatings .

3.4 Electrochemical Performance

The electrochemical performance of metal oxides in supercapacitors is evaluated based on several parameters, including specific capacitance, energy density, power density, and cycle stability.

Specific Capacitance: Metal oxides typically exhibit high specific capacitance due to their multiple oxidation states and the ability to undergo fast redox reactions. For example, MnO_2 can achieve specific capacitances ranging from 200 to 1370 F/g, depending on the synthesis method and electrode configuration .

Energy Density and Power Density: Metal oxides generally offer high energy density due to their pseudocapacitive behavior. However, their power density can be limited by their relatively low conductivity. Combining metal oxides with conductive materials like carbon nanotubes or graphene can enhance both energy and power densities .

Cycle Stability: The cycle stability of metal oxides is influenced by factors such as structural changes during cycling and dissolution of the active material. Strategies to improve cycle stability include nanostructuring, doping, and forming composites with other materials to provide mechanical support and prevent degradation .

3.5 Metal Oxide Composites

To enhance the performance of metal oxides in supercapacitors, researchers have developed various composites by combining metal oxides with other materials. These composites aim to synergize the advantages of each component, resulting in improved specific capacitance, conductivity, and cycle stability.

Metal Oxide-Carbon Composites: Combining metal oxides with carbon-based materials like graphene, carbon nanotubes, and activated carbon improves the overall conductivity and provides additional surface area for charge storage. For instance, MnO_2 -graphene composites exhibit enhanced specific capacitance and better rate capability compared to pure MnO_2 .

Metal Oxide-Polymer Composites: Conductive polymers such as polyaniline (PANI) and polypyrrole (PPy) are often combined with metal oxides to enhance electrochemical performance. These polymers provide high capacitance and flexibility, while the metal oxides contribute to stability and redox activity. For example, PANI- RuO_2 composites show high specific capacitance and excellent cycle stability .

Metal Oxide-Metal Oxide Composites: Combining different metal oxides can also yield superior performance by leveraging the unique properties of each oxide. For instance, NiO- MnO_2 composites benefit from the high capacitance of MnO_2 and the good cycle stability of NiO .

3.6 Applications and Future Prospects

Metal oxide-based supercapacitors are being explored for a wide range of applications, including energy storage systems, portable electronics, electric vehicles, and industrial equipment. The future of metal oxides in supercapacitors involves overcoming challenges related to conductivity, scalability, and cost. Advanced synthesis techniques, composite materials, and nanostructuring are key areas of focus to enhance the performance and practicality of metal oxide supercapacitors for commercial applications.[1,2,3,6,20,21]

4. Polyaniline metal-Oxide Nanocomposites for supercapacitor:

4.1 Introduction

Polyaniline (PANI)-metal oxide nanocomposites have emerged as promising materials for supercapacitor electrodes due to their synergistic properties. Combining PANI with metal oxides leverages the high capacitance and conductivity of PANI with the stability and redox activity of metal oxides, resulting in enhanced electrochemical performance.

4.2 Synthesis and Properties

Polyaniline can be combined with various metal oxides, such as manganese oxide (MnO_2), titanium dioxide (TiO_2), nickel oxide (NiO), and ruthenium oxide (RuO_2), to create nanocomposites with superior properties.

4.2.1. PANI-Manganese Oxide (MnO_2) Composites : MnO_2 is a widely used metal oxide in supercapacitors due to its high theoretical capacitance and environmental friendliness. PANI- MnO_2 composites exhibit enhanced specific capacitance and better cycle stability compared to pure PANI or MnO_2 . This improvement is attributed to the complementary redox activity and the conductive network formed by PANI, which facilitates efficient charge transfer and ion diffusion

Synthesis Example:Chemical Co-Precipitation: Aniline monomers and MnO_2 nanoparticles are mixed in an acidic medium, followed by the addition of an oxidizing agent to polymerize aniline and form the composite

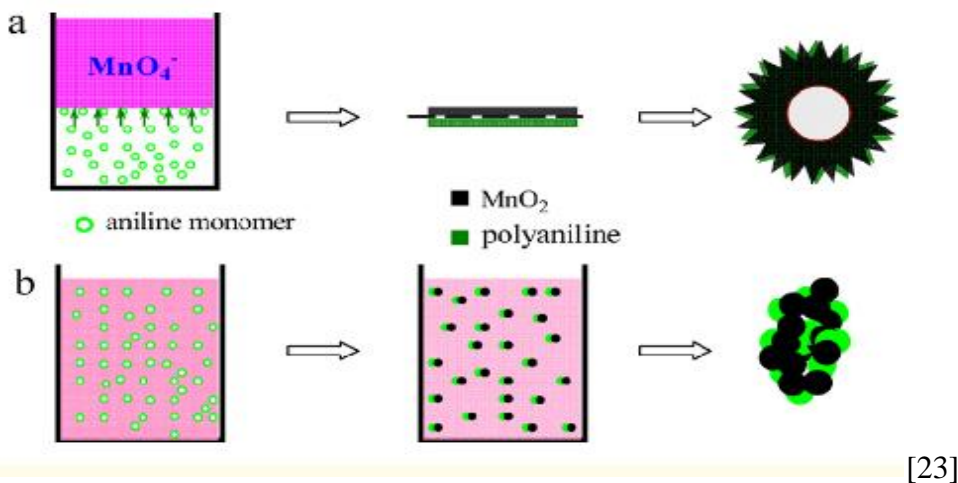


Figure1: Synthesis of PANI- MnO_2 Nanocomposites.

4.2.2 PANI-Titanium Dioxide (TiO_2) Composites : TiO_2 is known for its chemical stability and safety. PANI- TiO_2 composites benefit from the good cycling stability of TiO_2 and the high capacitance of PANI. These composites are particularly suitable for applications requiring long-term stability and durability .

Synthesis Example:

Sol-Gel Method: Titanium alkoxide is hydrolyzed to form TiO_2 nanoparticles, which are then mixed with aniline monomers. Polymerization of aniline in the presence of TiO_2 nanoparticles results in the formation of the composite .

4.2.3 PANI-Nickel Oxide (NiO) Composites: NiO is valued for its high specific capacitance and abundance. PANI-NiO composites combine the pseudocapacitive behavior of NiO with the conductive properties of PANI, resulting in high performance supercapacitor electrodes .

Synthesis Example:

In-Situ Polymerization: NiO nanoparticles are dispersed in an aniline solution, and polymerization is initiated by adding an oxidizing agent. This method ensures a uniform distribution of NiO within the PANI matrix .

4.2.4 PANI-Ruthenium Oxide (RuO₂) Composites: RuO₂ is one of the best performing metal oxides for supercapacitors due to its high specific capacitance and conductivity. However, its high cost limits its widespread use. PANI-RuO₂ composites can achieve very high specific capacitance and conductivity, making them suitable for high-performance applications .

Synthesis Example:

Electrochemical Deposition: RuO₂ is electrochemically deposited onto a conductive substrate, followed by the electrochemical polymerization of aniline to form the composite .

4.3 Characterization Techniques for Polyaniline-Metal Oxide Nanocomposites:

Characterizing polyaniline (PANI)-metal oxide nanocomposites is crucial to understanding their structure, morphology, and electrochemical performance. Here are some common characterization techniques used in the study of these nanocomposites:

4.3.1. Scanning Electron Microscopy (SEM)

SEM is used to observe the surface morphology and particle size of the nanocomposites.

It provides high-resolution images by scanning the surface with a focused beam of electrons. It helps in understanding the distribution and uniformity of metal oxide particles within the PANI matrix.[3]

4.3.2. Transmission Electron Microscopy (TEM)

TEM is used to analyze the internal structure and nanostructure of the composites. It offers detailed images of the internal composition and crystalline structure by transmitting electrons through an ultra-thin sample.[2]

4.3.3.X-ray Diffraction (XRD)

XRD is employed to identify the crystalline phases and crystallographic structures of the metal oxides and the nanocomposites.It provides information on the phase composition and crystallinity by measuring the diffraction patterns of X-rays interacting with the crystalline material.[9]

4.3.4. Fourier Transform Infrared Spectroscopy (FTIR)

FTIR is used to identify the functional groups and bonding interactions in the nanocomposites.

It measures the absorption of infrared light by the sample, providing information on the molecular vibrations and chemical bonds present.[1]

4.3.5. Thermogravimetric Analysis (TGA)

TGA evaluates the thermal stability and composition of the nanocomposites. TGA measures changes in the sample weight as a function of temperature, indicating the thermal decomposition and stability of the materials.[15]

4.3.6. Brunauer-Emmett-Teller (BET) Surface Area Analysis

BET analysis determines the surface area and porosity of the nanocomposites. It measures the amount of gas adsorbed onto the surface of the material, providing insights into its surface area and porosity, which are critical for supercapacitor performance.[2]

4.3.7. Cyclic Voltammetry (CV)

CV assesses the electrochemical behavior and capacitance of the nanocomposites. It measures the current response of the material to a cyclically varying voltage, providing insights into its redox behavior and electrochemical performance.[9]

4.3.8. Electrochemical Impedance Spectroscopy (EIS)

EIS evaluates the impedance and charge transfer resistance of the nanocomposites. It measures the impedance response of the material over a range of frequencies, providing information on the resistance, capacitance, and inductance of the system.[1]

These techniques provide comprehensive insights into the structural, morphological, thermal, and electrochemical properties of polyaniline-metal oxide nanocomposites, helping researchers optimize their performance for supercapacitor applications.

4.4 Electrochemical Performance:

PANI-metal oxide nanocomposites typically exhibit superior electrochemical performance compared to their individual components. Key performance metrics include:

Specific Capacitance:

The specific capacitance of PANI-metal oxide composites is significantly higher than that of pure PANI or metal oxides. For example, PANI-MnO₂ composites can achieve specific capacitances of 500-1000 F/g .

Energy and Power Density:

These composites offer higher energy and power densities due to the synergistic effects of PANI and metal oxides. For instance, PANI-RuO₂ composites can deliver energy densities of up to 50 Wh/kg and power densities exceeding 10 kW/kg .

Cycle Stability:

PANI-metal oxide composites generally show improved cycle stability compared to pure PANI, which tends to degrade over repeated cycling. The incorporation of metal oxides helps to stabilize the composite structure and maintain performance over many cycles .

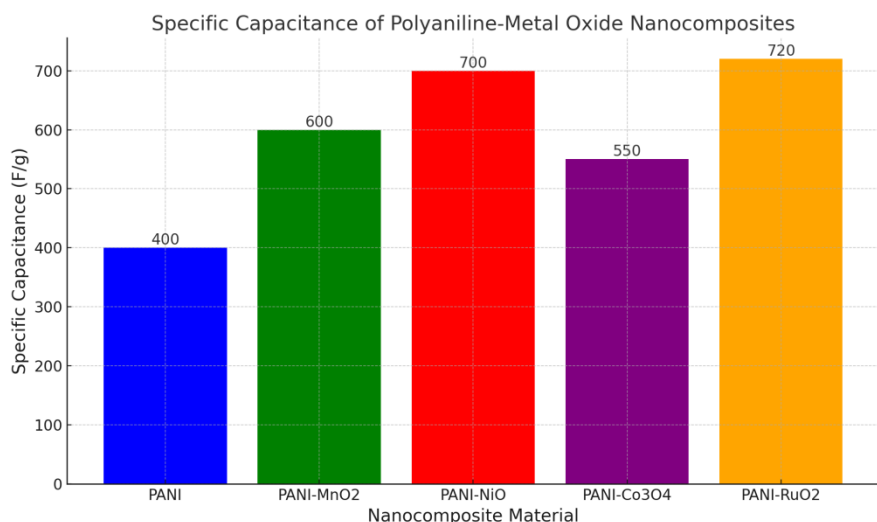


Figure2: Specific Capacitance of Polyaniline-Metal Oxide Nanocomposites. [1,2,3,9]

This graph compares the specific capacitance values of different nanocomposites, showcasing the superior performance of PANI-RuO₂ among the listed materials.

4.5 Applications and Future Prospects

PANI-metal oxide nanocomposites are being explored for various energy storage applications, including portable electronics, electric vehicles, and grid energy storage. The future of these materials lies in optimizing synthesis methods to enhance their electrochemical properties, scalability, and cost-effectiveness. Advanced techniques such as nanostructuring, doping, and hybridizing with other materials are expected to play crucial roles in the development of high-performance supercapacitor electrodes.[1,2,3,5,6,9]

5. Performance of Polyaniline-Metal Oxide Nanocomposites Compared to Other Materials:

Material	Specific Capacitance (f/g)	Energy Density (Wh/kg)	Power Density (kW/kg)	Cycle Stability (Retention after 1000 cycles)
PANI-MnO ₂ Nanocomposite	500-1000	20-30	5-10	>90%
PANI-TiO ₂ Nanocomposite	300-700	10-20	3-7	>85%
PANI-NiO Nanocomposite	600-800	15-25	6-8	>88%
PANI-RuO ₂ Nanocomposite	1000-1500	40-50	8-12	>95%
Pure Polyaniline	200-500	5-10	2-5	~80%

(PANI)				
Manganese Oxide (MnO ₂)	200-1370	5-20	2-10	70-90%
Nickel Oxide (NiO)	300-1000	10-30	3-6	80-90%
Ruthenium Oxide (RuO ₂)	1000-1700	40-50	8-15	>95%
Activated Carbon	100-300	5-10	3-7	~90%
Graphene	200-500	10-20	4-8	>90%

Table: Comparison of Electrochemical Performance of Various Supercapacitor Materials.[1,2,3,5,6,9]

5.1 Applications of Polyaniline-Metal Oxide Nanocomposites

Polyaniline-metal oxide nanocomposites have garnered significant interest for a range of applications due to their superior electrochemical properties, including high specific capacitance, excellent energy and power densities, and good cycle stability. Below are some of the key applications of these nanocomposites:

5.1.1. Energy Storage Systems

Supercapacitors:

- Portable Electronics: PANI-metal oxide nanocomposites are ideal for use in supercapacitors for portable electronic devices such as smartphones, laptops, and wearable technology. These devices require high power density and fast charging capabilities, which are efficiently provided by PANI-metal oxide supercapacitors .
- Electric Vehicles (EVs): The high energy density and rapid charge/discharge capabilities of PANI-metal oxide supercapacitors make them suitable for use in electric vehicles. They can be used in conjunction with batteries to provide additional power during acceleration and to capture energy during regenerative braking .
- Grid Energy Storage: PANI-metal oxide nanocomposites can be employed in grid energy storage systems to stabilize power grids and store energy from renewable sources like solar and wind. Their high cycle stability and ability to provide quick bursts of power are advantageous for maintaining grid reliability .

Battery-Supercapacitor Hybrids:

- High Energy Density Applications: PANI-metal oxide nanocomposites can be used in hybrid energy storage systems that combine the high energy density of batteries with the high power density of supercapacitors. This combination is useful for applications that require both high energy storage and rapid energy delivery .

5.1.2. Sensors and Actuators

Electrochemical Sensors:

- Environmental Monitoring: The high sensitivity and selectivity of PANI-metal oxide nanocomposites make them suitable for detecting environmental pollutants such as heavy metals and toxic gases. For example, PANI-TiO₂ composites have been used to detect trace amounts of lead and mercury in water .

- **Biomedical Sensors:** These nanocomposites can also be used in biosensors for detecting glucose, cholesterol, and other biomolecules. The excellent electrochemical properties of PANI-metal oxide nanocomposites enable the development of highly sensitive and accurate biosensors .

Actuators:

- **Artificial Muscles:** The combination of flexibility and conductivity in PANI-metal oxide nanocomposites makes them suitable for use in artificial muscles and soft robotics. These materials can undergo significant deformation in response to electrical stimuli, mimicking the behavior of natural muscles .

5.1.3. Electrocatalysis Fuel Cells:

- **Catalysts:** PANI-metal oxide nanocomposites can be used as catalysts in fuel cells due to their high surface area and excellent electrochemical properties. For instance, PANI-RuO₂ composites have been investigated for their catalytic activity in oxygen evolution reactions (OER) and hydrogen evolution reactions (HER) .

- **Electrolyzers:** These nanocomposites can also be employed in water electrolyzers to produce hydrogen fuel. Their high conductivity and catalytic activity enhance the efficiency of water splitting reactions .

5.1.4. Flexible and Wearable Electronics

Flexible Supercapacitors:

- **Wearable Devices:** PANI-metal oxide nanocomposites can be used to fabricate flexible supercapacitors for wearable electronics. These devices require materials that are both flexible and capable of storing significant amounts of energy. PANI-metal oxide composites meet these requirements and are being used to develop next-generation wearable technologies .

- **Smart Textiles:** Integrating PANI-metal oxide supercapacitors into textiles can lead to the development of smart clothing that can power electronic devices such as sensors and communication devices embedded in the fabric .

5.1. 5. Electromagnetic Interference (EMI) Shielding

EMI Shielding Materials:

- **Electronic Devices:** The excellent electrical conductivity of PANI-metal oxide nanocomposites makes them suitable for EMI shielding applications in electronic devices. These materials can prevent electromagnetic interference from affecting the performance of sensitive electronic components .

- **Communication Systems:** PANI-metal oxide composites can be used to protect communication systems from electromagnetic interference, ensuring reliable signal transmission.[1,2,3,5,6,9,20]

6.Challenges and Future Directions for Polyaniline-Metal Oxide Nanocomposites

6.1 Challenges:

6.1.1. Material Stability:

- **Degradation Over Time:** One major challenge is the long-term stability of polyaniline (PANI). PANI tends to degrade over repeated charge and discharge cycles, which reduces the performance of supercapacitors.

6.1. 2. Cost and Scalability:

- High Production Costs: Some metal oxides like ruthenium oxide (RuO_2) are expensive, making the large-scale production of these composites costly.

6.1. 3. Complex Synthesis Methods:

- Difficult Manufacturing Processes: Synthesizing PANI-metal oxide nanocomposites often involves complex and time-consuming processes, which can be a barrier to commercial production.

6.1.4. Electrochemical Performance:

- Optimization Needed: Achieving optimal electrochemical performance requires fine-tuning the composition and structure of the nanocomposites, which is a complex task.

6.2 Future Directions:

6.2.1. Improving Stability:

- Hybrid Materials: Combining PANI with other polymers or materials can enhance stability and prevent degradation..

6.2.2. Cost-Effective Materials:

- Alternative Metal Oxides: Research into more abundant and cheaper metal oxides like manganese oxide (MnO_2) or nickel oxide (NiO) could reduce costs.

6.2.3. Simplifying Synthesis:

- Innovative Methods: Developing simpler and more scalable synthesis methods can facilitate commercial production.

6.2.4. Enhancing Performance:

- Nanostructuring and Doping: Techniques like nanostructuring and doping with other elements can improve the electrochemical properties of the composites.

6.2.5. Exploring New Applications:

- Beyond Supercapacitors: PANI-metal oxide nanocomposites can be explored for other applications such as flexible electronics, sensors, and catalytic systems.

Conclusion:

Polyaniline (PANI)-metal oxide nanocomposites present a promising avenue for enhancing the performance of supercapacitors. These materials combine the high capacitance and conductivity of PANI with the stability and redox activity of metal oxides, resulting in composites with superior electrochemical properties. Despite the numerous advantages, several challenges such as material stability, production costs, complex synthesis methods, and the need for optimization remain.

To address these challenges, future research should focus on improving the stability of these composites through hybrid materials, exploring cost-effective and abundant metal oxides, and developing simpler synthesis methods. Additionally, advanced techniques like nanostructuring and doping can further enhance the electrochemical performance of PANI-metal oxide composites. Beyond supercapacitors, these

materials also hold potential for applications in flexible electronics, sensors, and catalytic systems, broadening their scope and impact.

Overall, PANI-metal oxide nanocomposites represent a versatile and effective solution for next-generation energy storage devices, with ongoing research likely to overcome current limitations and unlock new applications.

References:

1. Zhao, H., et al.(2020) Review on Polyaniline and its Composite Materials for Supercapacitor Applications: Synthesis, Characterization, and Performance Evaluation.
2. Wang, X., et al.(2019) Polyaniline-Metal Oxide Nanocomposites for Supercapacitors: A Review of Recent Advances.
3. Liu, J., et al.(2021)Advances in Polyaniline-Metal Oxide Composites for Energy Storage and Conversion Applications Journal of ACS Applied Materials & Interfaces.
4. Kim, Y., et al.(2018)Synergistic Effect of Polyaniline and Metal Oxides in Nanocomposites for Supercapacitors Journal of Nano Energy.
5. Simon, P., & Gogotsi, Y. (2008). Materials for electrochemical capacitors. *Nature Materials*, 7(11), 845-854.
6. Conway, B. E. (1999). *Electrochemical Supercapacitors: Scientific Fundamentals and Technological Applications*. Springer.
7. Wang, H., Casalongue, H. S., Liang, Y., & Dai, H. (2010). Mn₃O₄-graphene hybrid as a high-capacity anode material for lithium ion batteries. *Journal of the American Chemical Society*
8. Sharma, K., & Sudhakar, K. (2018). Green synthesis of polyaniline: a review of recent advancements. *Journal of Polymer Research*, 25(6), 144.
9. Subramanian, V., Zhu, H., & Wei, B. (2008). Nanostructured MnO₂: Hydrothermal synthesis and electrochemical properties as a supercapacitor electrode material. *Journal of Power Sources*
10. Frackowiak, E., & Beguin, F. (2001). Carbon materials for the electrochemical storage of energy in capacitors. *Carbon*
11. Wang, G., Zhang, L., & Zhang, J. (2012). A review of electrode materials for electrochemical supercapacitors. *Chemical Society Reviews*, 41(2)
12. Zhang, S., Pan, N. (2015). Supercapacitors Performance Evaluation. *Advanced Energy Materials*, 5(6), 1401401.
13. Chen, H., et al. (2018). Nanostructured materials for high-performance supercapacitors. *Journal of Materials Chemistry A*.
14. Zhu, Y., et al. (2011). Carbon-Based Supercapacitors Produced by Activation of Graphene.
15. Liu, C., et al. (2010). Advanced materials for energy storage. *Advanced Materials*, 22(8), E28-E62.

16. Yu, G., et al. (2013). Enhancement of supercapacitor performance by mixing CNT/graphene hybrid nanostructures. *Scientific Reports*, 3, 2470.
17. Miller, J. R., & Simon, P. (2008). Materials science—Electrochemical capacitors for energy management. *Science*, 321(5889), 651-652.
18. Wang, F., et al. (2012). Hybrid supercapacitors: A new era of energy storage. *Energy & Environmental Science*, 5(11), 8114-8121.
19. Zhu, J., et al. (2014). Recent progress in graphene-based hybrid supercapacitors. *Journal of Power Sources*.
20. Kang, Y. J., et al. (2011). All-solid-state flexible supercapacitors based on papers coated with carbon nanotube/MnO₂ nanocomposites. *Journal of Materials Chemistry*, 21(10), 3502-3507.
21. Hu, C. C., Chang, K. H., Lin, M. C., & Wu, Y. T. (2006). Design and tailoring of the nanotubular arrayed architecture of hydrous RuO₂ for next generation supercapacitors. *Nano Letters*, 6(12), 2690-2695.
22. Gautam, K.P., et al. (2022) Nickel Oxide-Incorporated Polyaniline Nanocomposites as an Efficient Electrode Material for Supercapacitor Application
23. Yang, D. (2012). Application of Nanocomposites for Supercapacitors: Characteristics and Properties. *Nanocomposites - New Trends and Developments*
24. Yang, Z., Ma, J., Bai, B., Qiu, A., Losic, D., Shi, D., & Chen, M. (2019). Free-standing PEDOT/polyaniline conductive polymer hydrogel for flexible solid-state supercapacitors. *Electrochimica Acta*, 322, 134769.
25. Wang, K., Wu, H., Meng, Y., & Wei, Z. (2014). Conducting polymer nanowire arrays for high performance supercapacitors. *Small*, 10(1), 14-31.
26. Shendkar, J. H., Zate, M., Tehare, K., Jadhav, V. V., Mane, R. S., Naushad, M., ... & Kim, K. H. (2016). Polyaniline-cobalt hydroxide hybrid nanostructures and their supercapacitor studies. *Materials Chemistry and Physics*, 180, 226-236.
27. Sharma, P., & Kumar, V. (2018). A brief review on supercapacitor. *Pramana Research Journal*, 8(3), 50-55.
28. Pande, S. A., Pandit, B., & Sankapal, B. R. (2017). Electrochemical approach of chemically synthesized HgS nanoparticles as supercapacitor electrode. *Materials Letters*, 209, 97-101.
29. Ghenaatian, H. R., Mousavi, M. F., & Rahmanifar, M. S. (2012). High performance hybrid supercapacitor based on two nanostructured conducting polymers: Self-doped polyaniline and polypyrrole nanofibers. *Electrochimica acta*, 78, 212-222.
30. Gangopadhyay, R., & De, A. (2000). Conducting polymer nanocomposites: a brief overview. *Chemistry of materials*, 12(3), 608-622.

31. Eftekhari, A., Li, L., & Yang, Y. (2017). Polyaniline supercapacitors. *Journal of Power Sources*, 347, 86-107.
32. Eftekhari, A., & Jafarkhani, P. (2014). Galvanodynamic synthesis of polyaniline: a flexible method for the deposition of electroactive materials. *Journal of Electroanalytical Chemistry*, 717, 110-118.
33. Das, T. K., & Prusty, S. (2012). Review on conducting polymers and their applications. *Polymer-plastics technology and engineering*, 51(14), 1487-1500.
34. Baker, C. O., Huang, X., Nelson, W., & Kaner, R. B. (2017). Polyaniline nanofibers: broadening applications for conducting polymers. *Chemical Society Reviews*, 46(5), 1510-1525.
35. Iro, Z. S., Subramani, C., & Dash, S. S. (2016). A brief review on electrode materials for supercapacitor. *Int. J. Electrochem. Sci*, 11(12), 10628-10643.
36. Giri, S., Das, C. K., & Kalra, S. S. (2012). Preparation and characterization of the cobalt doped polyaniline/MWCNT nanocomposites for supercapacitor application. *Journal of Materials Science Research*, 1(3), 10.
37. Gómez, H., Ram, M. K., Alvi, F., Villalba, P., Stefanakos, E. L., & Kumar, A. (2011). Graphene-conducting polymer nanocomposite as novel electrode for supercapacitors. *Journal of Power Sources*, 196(8), 4102-4108.
38. Jiang, H.; Ma, J.; Li, C. Mesoporous Carbon Incorporated Metal Oxide Nanomaterials as Supercapacitor Electrodes. *Adv. Mater.* 2012, 24, 4197–4202.
39. Wang, Y.; Xia, Y. Recent Progress in Supercapacitors: From Materials Design to System Construction. *Adv. Mater.* 2013, 25, 5336– 5342.
40. Wang, F.; Xiao, S.; Hou, Y.; Hu, C.; Liu, L.; Wu, Y. Electrode Materials for Aqueous Asymmetric Supercapacitors. *RSC Adv.* 2013, 3, 13059–13084.
41. Cericola, D.; Kötz, R. Hybridization of Rechargeable Batteries and Electrochemical Capacitors: Principles and Limits. *Electrochim. Acta* 2012, 72, 1–17.
42. Pell, W. G.; Conway, B. E. Peculiarities and Requirements of Asymmetric Capacitor Devices Based on Combination of Capacitor and Battery-Type Electrodes. *J. Power Sources* 2004, 136, 334–345.
43. Aravindan, V.; Gnanaraj, J.; Lee, Y.-S.; Madhavi, S. InsertionType Electrodes for Nonaqueous Li-Ion Capacitors. *Chem. Rev.* 2014, 114, 11619–11635.
44. Yadav, A. P., et al. "Nickel Oxide-Incorporated Polyaniline Nanocomposites as an Efficient Electrode Material for Supercapacitor Application." *Inorganics*, 2022.

¹Ashish Choudhary
²Sandeep Waghuley

CO₂ and LPG Gas sensing study of chemically synthesized PPy based sensor



Abstract: - The polypyrrole (PPy) was prepared by chemical oxidative polymerization route. X-ray diffraction (XRD), scanning electron microscopy (SEM) and ultraviolet-visible spectroscopy were used to evaluate the as-synthesized PPy sample. The SEM results showed that PPy sample was show accumulated nature with cotton like structure. PPy sensor was fabricated using screen printing method. The sensing response of PPy based resistive gas sensor was observed for both liquid petroleum gas (LPG) and carbon dioxide (CO₂) gas. The PPy sensor was more selective towards carbon dioxide (CO₂) gas.

Keywords: Polypyrrole, Gas sensing, Oxidative polymerization

INTRODUCTION

Conducting polymers, such as polypyrrole (PPy) have been used as room temperature operated gas sensors. The PPy have many better characteristics like high sensitivities, ease of synthesis, environmental stability, high conductivity and short response and recovery time at room temperature. It has various applications in sensors, batteries, optical and nanoelectronic devices etc.[1-2]. Carbon dioxide has greatest potential of all these gases to accelerate global warming. The two main causes of CO₂ emissions into the atmosphere are the industrial revolution and the burning of fossil fuels. LPG is a fuel that can be utilized for a variety of purposes but mishandling LPG can lead to flames, explosions, and most importantly deaths.

A room-temperature, flexible, polymer-based chemiresistive CO₂ gas sensor was fabricated by Zahra Shahrbabaki et al. [3] Waghuley et al prepared SnO₂/PPy Screen-Printed Multilayer CO₂ Gas Sensor for detection of CO₂ gas at room temp for different concentration. This sensor exhibit improved stability with ~ 2 min response time and ~ 10 min recovery time [4]. Bulakhe et al. reported on a room temperature operating LPG sensor based on a PPy-TiO₂ heterojunction [5]. A titanium dioxide (TiO₂)–reduced graphene oxide (r-GO) composite LPG sensor was prepared by Navin Chaurasiya et al. to detect LPG gas at ambient temperature [6].

Polypyrrole have been successively synthesized using simple chemical oxidative polymerization route. UV–VIS spectroscopy and scanning electronic microscopy (SEM) were used to characterize the PPy. Polypyrrole film was produced using the screen printing technique on a glass substrate that served as a PPy-based resistive gas sensor. The PPy sensor was then used to study CO₂ and LPG gasses at room temperature (303K).

EXPERIMENTAL

In this work PPy sample prepared by chemical oxidative polymerization route using monomer pyrrole and ammonium persulphate in a 50:50 wt% ratio. Screen printing was the method used to deposit the PPy film. The two-probe method was used to calculate the value of the resistance change in the presence of gas. The sensing response of CO₂ and LPG gas was studied at room temperature (303K) by varying their concentrations. The powdered PPy was investigating with SEM, and XRD and U-V spectroscopy.

RESULT AND DISCUSSION

XRD ANALYSIS

The XRD patterns of as-synthesized PPy samples made with a 50:50 weight percent stoichiometry are displayed in Figure 1. Using a step height of 0.02 degrees, the XRD scanning was done in the 2θ range, which spans from 10 to 70°. The pattern displays

¹ * Department of Physics, Shri Shivaji Arts, Commerce and Science College, Akot 444101, India.

² Department of Physics, Sant Gadge Baba Amravati University, Amravati 444 602, India
Corresponding author e-mail: ashishchou78@gmail.com (A.R.Choudhary)

nearly erratic forms with a few pointed peaks, which is indicate of PPy has semicrystalline structure. The wide hump peak in the region of 15–25°C also analyzes the semicrystalline nature [7]. Oriented amorphous polymers have a different X-ray diffraction pattern than unoriented polymers. The Sharp peaks in the XRD pattern, exhibits high degree of crystallinity and unoriented polymerization.

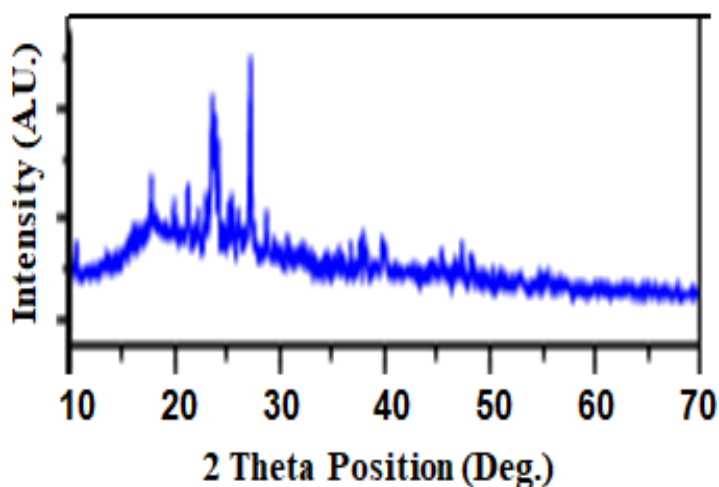


Figure 1: XRD pattern of as-synthesized PPy sample

The average chain separation values play key role in altering physical properties of materials and it has a great impact on electrical properties of polymeric materials also. In present case, we were detecting presence of gas by resistive method so its estimation is must.

Table 1: Average chain separation values and average particle size of as-synthesized sample

Sample name	Composition (wt %)	Peak position of amorphous halo (2θ)	Average chain separation (Å)	Average Particle size (nm)
S1	50:50	16.92°	1.027	15.93

SEM

The surface morphology of as-synthesized PPy sample was investigated using SEM micrograph as shown in figure 2. An extended open interconnected network is formed when the surfaces of the collected samples are randomly connected to one another. The synthesized sample show accumulated nature with cotton like structure. This asymmetrical structure is appropriate for gas sensing application.

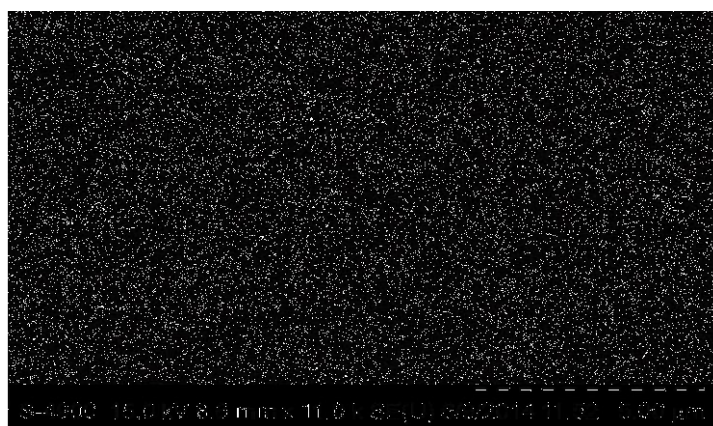
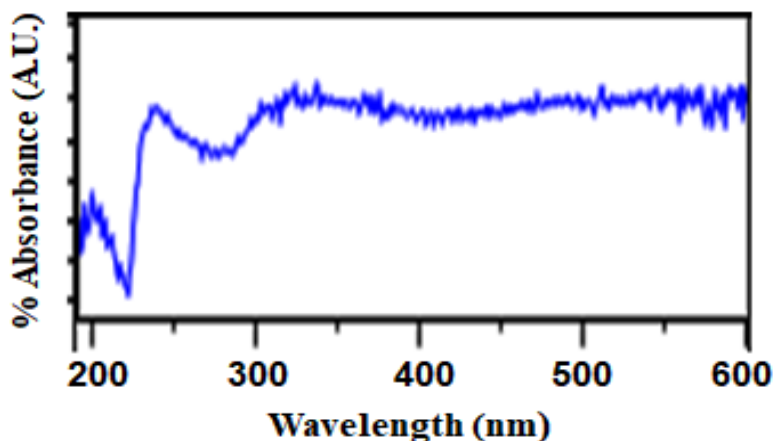


Figure 2: SEM micrographs of as-synthesized PPy sample

UV- VIS SPECTROSCOPY

Plot of the optical band gap for PPy sample is shown in figure 3. Polymerization is an inconsistent process therefore there is no correlation between the concentration of oxidant or monomer and the optical band gap values. This happens is due to monomers are joined in random numbers to a polymeric chain. Thus there is no obvious correlation between the concentration of the oxidant or monomer and the physical properties of organic materials.

**Figure 3:** UV-VIS Spectra of as-synthesized PPy sample

GAS SENSING RESPONSE

Figure 4 shows the selectivity response of as-fabricated sensors. Selectivity is the ability of a material to detect a specific gas. Fabricated sensors have optimum response towards CO₂ gas than LPG for dose of 500 ppm at room temperature. The sensing response of sensors to CO₂ gas is better than that of LPG at 500 ppm dose at room temperature. When the sensing response is measured, it is found that resistance of film increases in the presence of CO₂ gas whereas, resistance decreases in the presence of LPG. It indicates that the materials being studied for gas sensing are n-type, or electron-rich. When exposed to CO₂ gas, the as-synthesized PPy sensing materials exhibit a high sensing response.

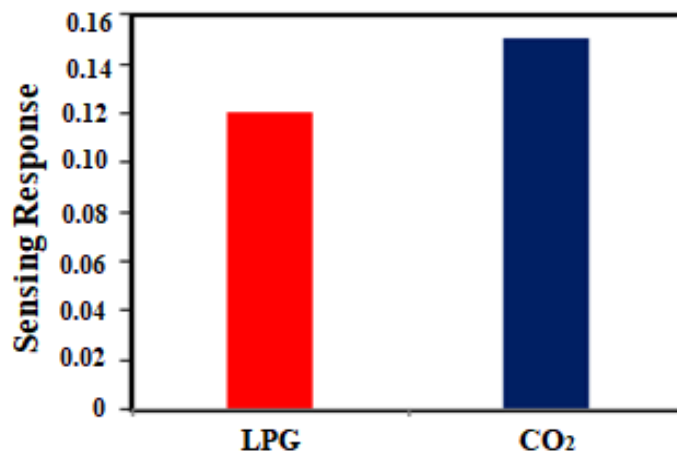
**Figure 4:** Selectivity responses of PPy sample towards the 500 ppm LPG and CO₂ gas concentration at RT

Figure 5 demonstrates sensing behavior PPy-based sensors towards CO₂ gas in terms of sensing. Up to 1000 ppm, the sensor response was found to be almost linear. The resistance of sensing film rise in the presence of CO₂ gas (oxidizing gas),

indicating the n-type behavior of sensing materials. The prepared sample exhibits a better sensing response due to the high degree of polymerization.

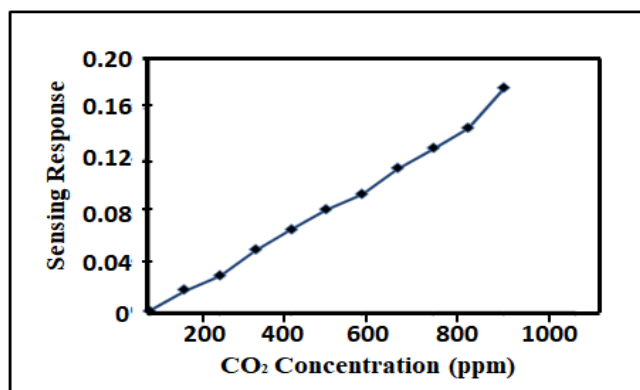


Figure 5: Gas sensing response of PPy sample towards the CO₂ gas at RT

CONCLUSIONS

In present work, we effectively synthesized PPy sample utilizing ammonium persulphate as an oxidant and pyrrole in a 50:50 wt% ratio, employing a chemical oxidative polymerization technique. The UV spectroscopic study describes the chemical composition of the as-prepared sample, which prominently demonstrates formation of PPy. The XRD pattern shows essentially erratic forms with a few sharp peaks, indicating a semicrystalline structure of PPy. Using XRD data, average polymer chain separation of as-synthesized PPy was determined which is found to be 1.027 Å, with an average particle size of 15.93 nm. The SEM micrograph shows accumulated nature with cotton like appearance. This asymmetrical structure is appropriate for gas sensing application. The sensor linear response curve is highly dependent on CO₂ gas concentration.

REFERENCES

- [1] Grgur B.N., Ristic V., Gvozdenovic M.M, Maksimovic M.D., Jugovic B.Z., J. Power Sources 180 (2008) 635.
- [2] D. Li, J.X. Huang, R.B. Kaner, Acc. Chem. Res. 42 (2009) 135
- [3] [Shahrbabaki Z.](#), [Farajikhah S.](#), [Mohammad B. Ghasemian.](#) [Oveissi F.](#), Rath R.J, [Yun J.](#), [Dehghani F.](#), Adv. Mat. Tech. vol 8 (2023) 02-11.
- [4] Waghuley S. A., Yenorkar S. M., Yawale S. S., Yawale S. P Sen. & Trans. Jour, vol.79, (2007) 1180-1185.
- [5] Bulakhe R. N., Patil S. V., Deshmukh P. R., Shinde N. M., Lokhande C. D., Sens. Act. B 181 (2013) 417– 423.
- [6] Chaurasiya N, Singh A , Kumar K., Yadav B.C., Yadawa P.K., Singh S.K., Dey K.K., Sens. & Diagnostics 2 (2023) 1215-1227.
- [7] Choudhary A. R., Waghuley S. A., Optoelectronics and Adv. Mater. 12 (2018) 117-124.

¹ R. B. Mankar² V. D. Kapse

Gas sensing potential of nanocrystalline SmFeO₃: A Review



Abstract: - Due to the ever increasing need for the development of highly sensitive and selective gas sensors, various semiconductor metal oxides have gained special attention. In this paper, different methods of synthesis of pure and modified SmFeO₃ along with advantages and disadvantages are reviewed in brief. Structural, electrical and gas sensing properties of SmFeO₃ are discussed together with its gas sensing principle. Being p-type semiconducting metal oxide, gas response of SmFeO₃ is attributed to the formation of electron-hole accumulation layer near the sensor surface and the change in concentration of holes in accumulation layer in presence of various gases. The physico-chemical properties of SmFeO₃ are associated with grain size and surface morphology. Effects of various dopants on morphology and gas sensing properties of SmFeO₃ are highlighted. Future scopes for improving the gas sensing performance of nanocrystalline SmFeO₃ are suggested.

Keywords: SmFeO₃, Nanocrystalline, Gas sensing, Sensitivity, Selectivity.

¹ *R. B. Mankar: Department of Physics, Smt. Radhabai Sarda Arts, Commerce and Science College, Anjangaon Surji 444705, Maharashtra State, India.

² Department of Physics, Arts, Science and Commerce College, Chikhaldara 444807, Maharashtra State, India.

Copyright © JES 2024 on-line : journal.esrgroups.org

I. INTRODUCTION

From past few decades, air pollution has been recognized globally as a serious issue. Various hazardous gases emitting continuously from the industrial exhausts have major impacts on air quality. Therefore, the need of detection of these gases in order to control air pollution has led the development of different gas sensors. In particular, semiconductor metal oxide (SMO) based gas sensors have always been attracted the researchers owing to their high sensitivity, selectivity, stability and reproducibility [1-2]. In fact, these gas sensing properties are related to the surface morphology and the physical and chemical properties of SMO. Till date, variety of SMOs including have been tested for their gas sensing potential. Meanwhile, SmFeO_3 has also gain a considerable attention due to its technological versatility. Potential of SmFeO_3 in the fabrication of chemoresistive gas sensors for the detection of oxidizing as well as reducing gases is highlighted by many researchers. In this paper, physico-chemical properties, different synthesis methods and the gas sensing properties of SmFeO_3 are reviewed.

II. CRYSTAL STRUCTURE AND PHYSICO-CHEMICAL PROPERTIES

SmFeO_3 belongs to the ABO_3 -type perovskite structure (A: rare earth, B: transition metal). It has orthorhombic crystal structure with the Pnma space group and mmm point group [3]. Sm^{3+} cations are present at the body centre and each Sm^{3+} cation is coordinated by 12 oxygen atoms. Fe^{3+} cations are present at each corner of unit cell and each Fe^{3+} cation is coordinated by 6 oxygen atoms to form the octahedron [4]. This FeO_6 octahedron is tilted towards the centre of the Sm^{3+} cation to maintain Sm^{3+} -O₂- bonding. The distorted structure of SmFeO_3 can be explained through Goldschmidt tolerance factor [3-4].

III. METHODS OF SYNTHESIS

Since methods of synthesis of nanomaterial strongly influence the microstructure, different synthesis techniques have been adopted by researchers for the synthesis of SmFeO_3 . M. C. Carotta et al synthesized ultrafine SmFeO_3 powder by thermal decomposition method [5]. S. M. Bukhari et al, reported that $\text{Sm}_{0.95}\text{Ce}_{0.05}\text{Fe}_{1-x}\text{Co}_x\text{O}_{3-\delta}$ ($x=0-0.10$) compounds prepared by thermal decomposition method were found to be stable even at 1350°C in air [6]. Z. Anajafi prepared $\text{SmFeO}_3/\text{ZnO}$ nanocomposite by thermal treatment method and obtained orthorhombic and wurzite phases for SmFeO_3 and ZnO respectively [7].

T. Han et al fabricated SmFeO_3 nanofibers by electro-spinning route [8]. As prepared SmFeO_3 nanofibers possessed the rough surface which increases contact area between target gases and material. Preparation of ultrafine SmFeO_3 nanofibers (diameter 220 nm) by electro-spinning method was also reported by Q. Hu et al [9].

M. Mori et al synthesized nano-sized SmFeO_3 particles by pyrolysis method at 600°C in ozone [10]. The obtained fine particles possessed high specific surface area with bimodal volume distribution which increased further with unimodal volume distribution by further classification of these fine particles.

Sol-gel method is one of the simple and cost-effective method used by many researchers for the synthesis of fine SmFeO_3 powder. Sol-gel method involves the preparation of separate metal nitrate solutions and citric acid solution and their mixing followed by drying, grinding and calcination. Owing to its various advantages, sol-gel method was adopted by many researchers for the synthesis of pure nanocrystalline SmFeO_3 [11-14]. S. Hernández et al, prepared $\text{Sm}_{1-x}\text{Ca}_x\text{FeO}_3$ ($0.1 \leq x \leq 0.5$) compounds by sol-gel based Pechini method at low temperatures and the resulting XRD data revealed a pure phase with perovskite structure for each composition [15]. Fig. 1 represents the procedure for preparation of SmFeO_3 by sol-gel method [14].

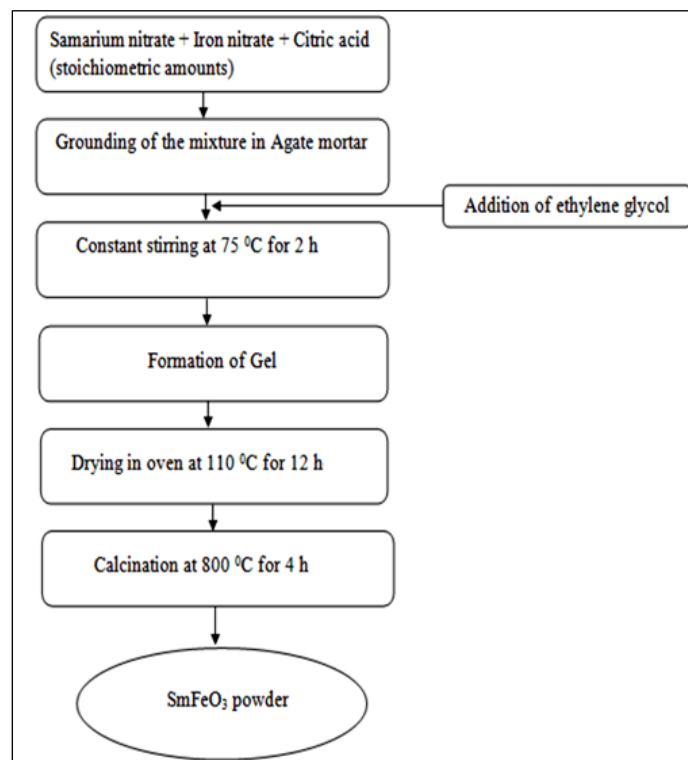


Fig. 1: Synthesis of SmFeO_3 by sol-gel method.

IV. GAS SENSING POTENTIAL

SmFeO_3 has been reported for the detection of various oxidizing gases such as O_3 and NO_2 . M. C. Carotta et al synthesized ultrafine SmFeO_3 powder by thermal decomposition method and reported that screen printed SmFeO_3 thick films were sensitive to the NO_2 gas

[5]. G. Martinelli et al also reported NO₂ gas sensing properties of SmFeO₃ thick films and observed the increased in sensitivity with increase in NO₂ concentration [16]. Considering microstructure affects sensitivity, H.T. Huang et al, fabricated porous hollow microspheres of SmFeO₃ with diameter of 2 μm and showed that SmFeO₃ microsphere exhibited higher sensitivity, selectivity and shorter response and recovery time towards NO₂ gas [17]. This enhanced sensing behavior was attributed to special morphology of the microsphere.

Y. Hosoya et al examined that SmFeO₃ based gas sensor was sensitive to ozone in sub-ppm levels at the temperatures above 240⁰C [18]. M. Mori et al also reported potential of SmFeO₃ for the detection of ozone in air [19].

In addition to oxidizing gases, SmFeO₃ has been also explored for the detection of various volatile organic compounds. H.T. Giang et al examined the response of SmFeO₃ towards methane (CH₄), propane (C₃H₈) and n-hexane (C₆H₁₄) gases and observed that SmFeO₃ exhibited the highest sensitivity to n-hexane [11]. The extreme sensitivity of SmFeO₃ to n-hexane was attributed to the oxygen adsorption that depends on the relative structural distortions of the SmFeO₃ lattices as well as the strength of carbon–hydrogen bonds in n-hexane compound. M. Mori also examined the effect of different VOCs with small concentrations (below 10 ppm) on the sensing properties of SmFeO₃ based gas sensor in temperature range 350⁰C to 500⁰C and concluded that the sensing behavior was characterized by power law [20]. SmFeO₃ nanofibers were fabricated by T Han et al by electrospinning route for detection of ethylene glycol [8]. The as-prepared SmFeO₃ nanofibers showed good response and selectivity to ethylene glycol (18.19 to 100 ppm and 2.18 to 5 ppm) at 240⁰C. The improved gas response was due to the rough surface of SmFeO₃ nanofiber which increases contact area between gases and material surface. In another work, T Han also investigated the effect of Ho doping on the sensitivity of SmFeO₃ nanofiber and concluded that Sm_{0.95}Ho_{0.05}FeO₃ based sensor exhibited improved response to ethylene glycol (26.12 to 100 ppm and 10.20 to 5 ppm) at 200⁰C [21].

The gas sensing performance of can also be improved by nanocomposite. Z. Anajafi et al reported the gas sensing properties of SmFeO₃/ZnO nanocomposite and demonstrated that, SmFeO₃/ZnO nanocomposite based sensor presented the high sensitivity towards low concentration of acetone and its enhanced performance was attributed to the formation of p-n heterojunction [7].

The available literature on gas sensing properties of SmFeO₃ for reducing gases revealed that the optimal operating temperature is very high. This high operating temperature has adverse effect on stability of sensor. Therefore, SmFeO₃ has rarely been explored for the detection of reducing gases like H₂, ethanol, CO etc. If attempt is made to achieve stability

by reducing sensor temperature, poor response will be the result. Hence, the practical and effective way to increase stability in reducing condition is the incorporation of dopants to SmFeO_3 . It has been proposed for ABO_3 -type perovskite oxides that, A-site cation generally affects stability and conductivity whereas B-site cation strongly influences the conductivity. S. M. Bukhari et al demonstrated that the partial substitution of Sm by Ce within the solubility limit prevents it from decomposing under reducing gas. Additionally, Co doping at Fe site to form $\text{Sm}_{0.95}\text{Ce}_{0.05}\text{Fe}_{1-x}\text{Co}_x\text{O}_{3-\delta}$ ($x=0-0.10$) had increased the electrical conductivities with cobalt concentration [6]. The higher conductivity in air was reported due to oxygen vacancies created as a result of cobalt doping and under reducing conditions (5% v/v H_2/N_2) stability is up to 800°C . Ma Zhao et al prepared $\text{SmFe}_{1-x}\text{Co}_x\text{O}_3$ ($x=0-1.0$) samples with a single-phase orthogonal perovskite structure and studied the effect of Co doping on microstructure, electrical and ethanol-sensing properties [13]. The results revealed that $\text{SmFe}_{0.7}\text{Co}_{0.3}\text{O}_3$ has the maximum response ($S = 80.78$) to 300 ppm ethanol at 215°C . Also, the decrease in lattice constant, unit cell volume and average grain size was reported with an increase in the CO concentration due to forming oxygen vacancies.

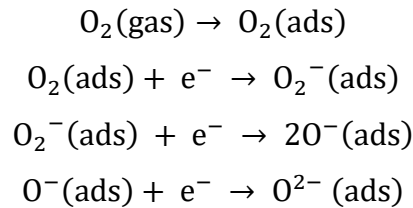
In another investigation, S. M. Bukhari et al prepared $\text{Sm}_{0.95}\text{Ce}_{0.05}\text{Fe}_{1-x}\text{Ni}_x\text{O}_3$ powders by a sol-gel citrate method and reported that materials with low Ni content ($x = 0-0.05$) show n-type conducting behavior while those of high Ni content ($x = 0.07-0.10$) show p-type conductivity [12]. The improved electrical conductivity for hydrogen detection is due to Ni doping. To study the effect of Ni dopants, Linfu Chen et al synthesized $\text{SmFe}_{1-x}\text{Ni}_x\text{O}_3$ nanocrystalline powder by a sol-gel citrate method [22]. Higher conductivities and lower optimal operating temperatures were obtained for $\text{SmFe}_{1-x}\text{Ni}_x\text{O}_3$ samples. The highest response was 57.8 for $\text{SmFe}_{0.95}\text{Ni}_{0.05}\text{O}_3$ based gas sensor at 260°C . It was also observed that sensitivity of $\text{SmFe}_{1-x}\text{Ni}_x\text{O}_3$ based sensor decreased for higher Ni concentrations.

The effect of Mg doping in SmFeO_3 was investigated by Xing Liu et al [23]. The highest response was reported to 300 ppm acetone gas for $\text{SmFe}_{0.9}\text{Mg}_{0.1}\text{O}_3$ based gas sensor at 260°C and its response increased with an increase in acetone gas concentration.

Instead of volume doping, as reported above, surface modification of SmFeO_3 by dipping method is also feasible. Our previous publications demonstrated the gas sensing potential of surface modified SmFeO_3 sensor. Co-modified SmFeO_3 sensor (dipping time 3 min) exhibited the highest response towards 50 ppm ammonia gas at 200°C [14]. Ce-modified SmFeO_3 sensor (dipping time 5 min) exhibited the excellent response towards 60 ppm ethanol gas at 100°C [24].

V. GAS SENSING MECHANISM

Being p-type semiconducting material, electron-holes are the majority charge carriers in SmFeO₃. In ambient air, oxygen species are adsorbed on the surface of SmFeO₃ sensor. These adsorbed oxygen species extract electrons from bulk SmFeO₃ due to their strong electron affinity. The adsorbed oxygen species are now converted to highly reactive atomic or molecular species O_2^- , $2O^-$ and O^{2-} depending on temperature. The conversion reactions are given below.



The extraction of electrons increases the concentration of holes and hole-accumulation layer is formed near the surface and sensor resistance decreases. When reducing gas is introduced, gas molecules interact with active species at the surface of sensor and the extracted electrons are returned back. Therefore accumulation layer gets elevated and sensor resistance increases. This change in resistance determines gas response. In case of oxidizing gas, more electrons are extracted and sensor resistance further decreases.

VI. CONCLUSION

SmFeO₃ is p-type semiconducting metal oxide which has orthorhombic crystal structure with the Pnma space group. Nanocrystalline SmFeO₃ can be synthesized by sol-gel method, thermal decomposition method, electrospinning method etc. It has potential to detect oxidizing and reducing gases. ABO₃-type perovskite structure of SmFeO₃ allows its modification for tailoring its properties in order to enhance gas sensing performance. Thus nanocrystalline SmFeO₃ is potential candidate in the fabrication of chemoresistive gas sensor for environmental monitoring.

REFERENCES

- [1] A Mirzaei, S.G. Leonardi and G. Neri, "Detection of hazardous volatile organic compounds (VOCs) by metal oxide nanostructures-based gas sensors: A review", *Ceramic International.*, vol. 42, Nov. 2016, pp. 15119–15141, doi: 10.1016/j.ceramint.2016.06.145.
- [2] Ali Mirzaei, H. R. Ansari, M. Shahbaz, Jin-Y. Kim, H. W. Kim and S. S. Kim, "Metal oxide semiconductor nanostructure gas sensors with different morphologies", *Chemosensors*, vol. 10, July 2022, pp. 289, Doi: 10.3390/chemosensors10070289.
- [3] S. Yuvaraj, S. Layek, S. Vidyavathy, S. Yuvaraj, D. Meyrick and R. Selvan, "Electrical and Magnetic properties of Spherical SmFeO₃ synthesized by aspartic acid assisted Combustion method," *Materials Research Bulletin*, vol. 72, Dec. 2015, pp. 77-82, Doi: 10.1016/j.materresbull.2015.07.013.

- [4] Ashwini Kumar, Jingdong Shen, Huihui Zhao, Qi. Zhengjian and Qi Li, "Crystallographic and magnetic properties of nanocrystalline perovskite structure SmFeO_3 orthoferrite," *Journal of crystal Growth*, vol. 490, May 2018, pp. 1-5, doi: 10.1016/j.jcrysgro.2018.03.001.
- [5] M.C. Carotta, G. Martinelli, Y. Sadaoka, P. Nunziante and E. Traversa, "Gas sensitive electrical properties of Perovskite-type SmFeO_3 thick films," *Sensors and Actuators B: Chemical*, vol. 48, May 1998, pp. 270-276, doi: 10.1016/S0925-4005(98)00011-2.
- [6] S. M. Bukhari and J. B. Giorgi, "Effect of cobalt substitution on thermal stability and electrical conductivity of $\text{Sm}_{0.95}\text{Ce}_{0.05}\text{FeO}_3$ in oxidizing and reducing conditions," *Solid State Ionics*, vol. 181, March 2010, pp. 392-401, doi: 10.1016/j.ssi.2010.01.017.
- [7] Z. Anajafi, M. Naseri and G. Neri, "Acetone sensing behavior of p- SmFeO_3 /n-ZnO nanocomposite synthesized by thermal treatment method," *Sensors and Actuators B: Chemical*, vol. 304, 2020, 127252 <https://doi.org/10.1016/j.snb.2019.127252>
- [8] T. Han, S.Y. Ma, X.L. Xu, X.H. Xu, S.T. Pei, Y. Tie, P.F. Cao, B.J. Wang and J.L. Zhang, "Rough SmFeO_3 nanofibers as an optimization ethylene glycol gas sensor prepared by electrospinning", *Materials Letters*, vol. 268 June 2020, pp. 127575, doi: 10.1016/j.matlet.2020.127575.
- [9] Q. Hu, B. Yue, D. Yang, Z. Zhang, Y. Wang, and J. Liu, "Electrochemical and magnetic properties of electrospun SmFeO_3 and SmCoO_3 nanofibers", *Journal of the American Ceramic Society*, vol. 105, Sept. 2021, pp. 1149-1158, doi: 10.1111/jace.18144.
- [10] M. Mori, A. Noguchi and Y. Itagaki, "VOC detection by p-type semiconducting sensors using nano-sized SmFeO_3 particles", *Sensors*, vol. 22, July 2022, pp. 5616, doi: 10.3390/s22155616.
- [11] H.T. Giang, H.T. Duy, P.Q. Ngan, G. H. Thai, D. T. Thu, and N. N. Toan, "Hydrocarbon gas sensing properties of nano-crystalline perovskite oxides LnFeO_3 ($\text{Ln}=\text{La}$, Nd and Sm)", *Sensors and Actuators B: Chemical*, vol. 158, Nov. 2011, pp. 246-251, doi: 10.1016/j.snb.2011.06.013.
- [12] S. M. Bukhari and J. B. Giorgi, "Ni doped $\text{Sm}_{0.95}\text{Ce}_{0.05}\text{FeO}_3$ perovskite based sensors for hydrogen detection", *Sensors and Actuators B: Chemical*, vol. 181, May 2013, pp. 153-158, doi: 10.1016/j.snb.2013.01.073.
- [13] M. Zhao, H. Peng, J. Hu, and Z. Han, "Effect of cobalt doping on the microstructure, electrical and ethanol-sensing properties of $\text{SmFe}_{1-x}\text{Co}_x\text{O}_3$ ", *Sensors and Actuators B: Chemical*, vol. 129, Feb. 2008, pp. 953-957, doi: 10.1016/j.snb.2007.10.012
- [14] R. B. Mankar, V. D. Kapse, and D. R. Patil, "Gas sensing properties of pure and Co-modified nanocrystalline SmFeO_3 thick film", *Asian Journal of Chemistry*, Vol. 35, 2023, pp. 1485-1490.
- [15] A.M. Huizar-Felix, T. Hernandez, S. de la Parra, J. Ibarra, and B. Kharisov, "Sol-gel based Pechini method synthesis and characterization of $\text{Sm}_{1-x}\text{Ca}_x\text{FeO}_3$ perovskite", *Powder Technology*, vol. 229, Oct. 2012, pp. 290-293, doi: /10.1016/j.powtec.2012.06.057.
- [16] G. Martinelli, M.C. Carotta, M. Ferroni, Y. Sadaoka, E. Traversa, "Screen-printed perovskite-type thick films as gas sensors for environmental monitoring", *Sensors and Actuators B: Chemical*, vol. 55, May 1999, pp. 99-110, doi: 10.1016/S0925-4005(99)00054-4.
- [17] H. T. Huang, W. L. Zhang, X. D. Zhang, and X. Guo, "NO₂ sensing properties of SmFeO_3 porous hollow microspheres", *Sensors and Actuators B: Chemical*, vol. 265, July 2018, pp. 443-451, doi: 10.1016/j.snb.2018.03.073.
- [18] Y. Hosoya, Y. Itagaki, H. Aono, and Y. Sadaoka, "Ozone detection in air using SmFeO_3 gas sensor", *Sensors and Actuators B: Chemical*, vol. 108, July 2005, pp. 198-201, doi: 10.1016/j.snb.2004.10.059.
- [19] M. Mori, J. Fujita, Y. Itagaki, and Y. Sadaoka, "Ozone detection in air using SmFeO_3 gas sensor for air quality classification", *Journal of Ceramic Society of Japan* vol. 119, 2011, pp. 926-928, doi: 10.2109/jcersj2.119.926.
- [20] M. Mori, Y. Itagaki, J. Iseda, Y. Sadaoka, T. Ueda, M. Nakatani, "Influence of VOC structures on sensing property of SmFeO_3 semiconductive gas sensor", *Sensors and Actuators B: Chemical*, vol. 202, Oct. 2014, pp. 873-877, doi: 10.1016/j.snb.2014.06.031.
- [21] T. Han, S. Ma, P. Yun, H. Sheng, X. Xu, P. Cao, S. Pei, and A. Alhadi, "Synthesis and characterization of Ho-doped SmFeO_3 nanofibers with enhanced glycol sensing properties", vol. 191, Sept. 2021, pp. 110378, doi: 10.1016/j.vacuum.2021.110378.

- [22] L. Chen, J. Hu, S. Fang, Z. Han, and Ma Zhao, "Ethanol-sensing properties of $\text{SmFe}_{1-x}\text{Ni}_x\text{O}_3$ perovskite oxides", *Sensors and Actuators B: Chemical*, vol. 139, 2009, pp. 407-410, doi: 10.1016/j.snb.2009.02.074.
- [23] X. Liu, J. Hu, B. Cheng, H. Qin, and M. Jiang, "Acetone gas sensing properties of $\text{SmFe}_{1-x}\text{Mg}_x\text{O}_3$ perovskite oxides", *Sensors and Actuators B: Chemical*, vol. 134, Sept 2008, pp. 483-487, doi :10.1016/j.snb.2008.05.024.
- [24] R. B. Mankar and V. D. Kapse, "Cerium modified nanocrystalline SmFeO_3 for ethanol sensing", *Oriental Journal of Chemistry*, vol. 40, 2024, pp. 362-368, doi: 10.13005/ojc/400206.

¹Humera Khan,
²Pramod Kumar
Malviya

Spectroscopic studies of transition metal complexes



Abstract: - The present study examines and evaluates the UV data of nano-crystalline transition metal complexes: Complex - **I** - Ni(0.8)Cu(0.2)Fe₂O₄ and Complex - **II** - (Ni(0.8)Co(0.2)Fe₂O₄). The bandgap value and band-edge structure play pivotal roles in the processes of excitation, movement, and the subsequent transition of photogenerated electrons. The band gap energy is determined through use of a Tauc plot method and analysis. The calculation of Tauc plot method has been done in Origin software under the head - First of all draw raw absorbance spectrum for the sample, then smoothed the data and taking the baseline procedure. Finally, calculated the energy ($h\nu$), absorbance coefficient (α), the factor $\alpha h\nu^{(1/\gamma)}$ and the curve of $\alpha h\nu^{(1/\gamma)}$ versus energy($h\nu$). From the comparison of our results, which is obtained by the direct method and indirect method, we found that the band gap energy not affected in both cases. From this calculation, we found that the band gap energy of studied complex I and II are $E_g = 1.425$ eV and $E_g = 3.201$ eV respectively.

Keywords: Nano-crystalline, transition metal, band gap.

¹*Corresponding author: Research Scholar, School of studies in Physics, Vikram University, Ujjain, M.P., India

² Author 2: Assistant Professor Physics Department, Govt. Madhav Science P.G. College, Ujjain, M.P., India

Copyright © JES 2024 on-line : journal.esrgroups.org

I. INTRODUCTION

Bandgap, which is also known as the forbidden bandwidth, refers to the energy difference between the bottom of the conduction band and the top of the valence band. With the increases in the bandgap value, solid materials are classified as metal conductors, semiconductors, and insulators. The bandgap value and band-edge structure play pivotal roles in the processes of excitation, movement, and the subsequent transition of photogenerated electrons. Based on these effects, bandgap engineering is proposed as a feasible method to control and modulate the macroscopic optical, electrical, and photoelectric properties of materials. According to the light energy, the absorption signal could be expanded from the Ultraviolet-visible (UV-Vis) region to the Infrared (IR) region. It should be noted that UV-Vis absorption spectroscopy has widespread applied in semiconductor investigations for the detection of band edge structure, bandgap value, and new band generation within the forbidden gap [1-3].

The present study examines and evaluates the UV data of nano-crystalline transition metal complex: Ni(0.8)Cu(0.2)Fe₂O₄ and Ni(0.8)Co(0.2)Fe₂O₄. The transition metals—copper, nickel, and ferric—make up the majority of these complexes. The word "nano" comes from the prefix "one billionth part." Particles smaller than 100 nanometres are referred to as nanoparticles. The stronger of one gram of nanoparticles is around ten times that of one gram of bulk material. Consequently, nanoparticles differ entirely from the original material in terms of their mechanical, electrical, physical, chemical, biological, electronic, etc. Properties of nano particles are completely different from the original material [4].

II. MATERIALS AND METHODS

Chemicals were used without additional purification after being purchased from well-known as renowned companies like E. Merck, Fluka, and Aldrich. For synthetic work, all solvents were utilised exactly as obtained, with an A.R. grade. Aldrich provided metal salt, whereas E. Merck provided Quinoline, Carbamide, Thiocarbamide, Melanic acid, and Dibenzoyl methane [5].

1. Synthesis of complexes

The chemical root method is used to synthesise nano-crystalline ferrites. To maintain the molar metal nitrate, a 1:3 ammonia solution is applied [6-10]. In this formula [M=Cu (II), Co, Ni], [X= 0.2, 0.4, 0.6, 0.8,], Chemical AR grad are used 99 % are nickel nitrate, ferric nitrate, copper nitrate, cobalt nitrate and citric acid are used for the synthesis.

2. UV visible spectroscopy

The Copper complex was characterized by namely UV-Visible Spectroscopy. The wavelength range of UV radiation is 200 nm- 400 nm. There are mainly two types of UV region. 1. 200 nm - 400 nm that is called near ultraviolet region. 2. Below 200 nm that is called far ultraviolet region. The wavelength of visible radiation is 400 nm- 800 nm. Wavelength in UV and visible region is expressed in nanometers or in angstroms. Absorption is expressed in terms of wave number (cm⁻¹). These data were analyzed by computer software Origin.

III. RESULTS AND DISCUSSION

Before you begin to format your paper, first write and save the content as a separate text file. Keep your text and graphic files separate until after the text has been formatted and styled. Do not use hard tabs, and limit use of hard returns to only one return at the end of a paragraph. Do not add any kind of pagination anywhere in the paper. Do not number text heads-the template will do that for you.

Finally, complete content and organizational editing before formatting. Please take note of the following items when proofreading spelling and grammar:

1. Band gap Measurement

Traditionally, the band gap energy is determined through use of a Tauc analysis, by which the band gap energy is related to the absorption coefficient through the following equation,

$$(\alpha \cdot hv)^{1/\gamma} = B(hv - E_g)$$

where h is the Planck constant, v is the photon's frequency, E_g is the band gap energy, and B is the slope of the linear portion of the Tauc plot and γ factor depends on the nature of the electron transition and is equal to 1/2 or 2 for the direct and indirect transition band gaps, respectively, α is the absorption coefficient. The Tauc plot is constructed by reporting the collected spectrum as αhv^(1/γ) vs. energy (eV). As absorbance is proportional to α through Beer's law, the collected absorbance can be used in place of the absorption coefficient to develop

the curve. The energy axis is determined by converting the analysed wavelength spectrum to energy through following equation

$$E = hv = hc/\lambda$$

where photon energy is represented by hv , the speed of light by c and E is the converted energy. By convention the calculated energy is converted from Jule to eV. From the curve a tangent line can be fit to the linear section of the data. The intersection of the tangent line with the X-axis denoted the estimated band gap energy of the material [11-13].

Using the methodology described earlier, Tauc Plots were constructed from the measurements for this samples. $[\text{Ni}(0.8)\text{Cu}(0.2)\text{Fe}_2\text{O}_4]$ has been studied and has a well-defined indirect band gap for the crystal structure analyzed here in. From the Tauc analysis, E_g was found to be 1.425 eV for studied complex.

In this section we present our result for calculating the band gap energy of nanomaterial based on Tauc Plot method. The calculating of Tauc Plot method in Origin software is given in Fig. 1 and Fig. 3 with respect to copper and cobalt complexes, which is raw data graph between wavelength and absorbance. First of all, we use the experimental data of absorbance spectrum for the samples. Now we smoothed the data and taking the baseline procedure and the results is given Fig. 2 and Fig. 4. We then calculated the energy ($h\nu$), absorbance coefficient (α), the factor $\alpha h\nu^{(1/\gamma)}$ and the curve of $\alpha h\nu^{(1/\gamma)}$ versus energy($h\nu$). The result is given in Fig. 3 and Fig. 6 with respect to Complex I and II. From this calculation, we found that the band gap energy of studied complexes, i.e., complex I and complex II are $E_g = 1.425$ eV and $E_g = 3.201$ eV respectively. From the comparison of our results, we found that the band gap energy of complex I is less than complex II. It means that when we replace the copper metal by cobalt metal whereas the other environment of complex remains same then the band gap energy increases. Hence, we can say that cobalt metal enhances the band gap energy and copper metal suppresses it.

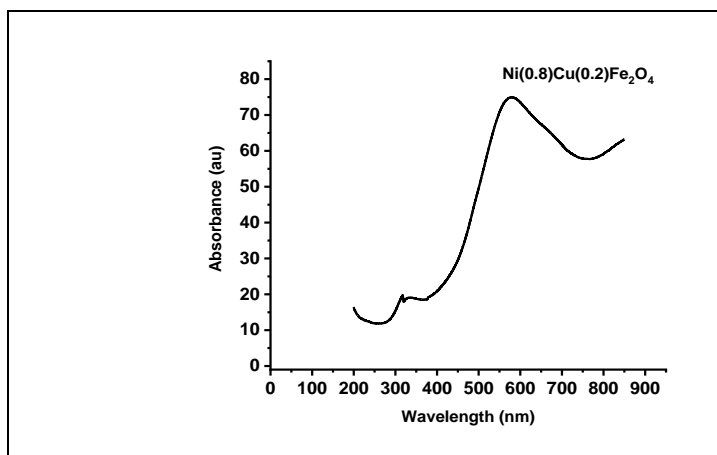


Fig. 1 - Raw data graph (absorption vs. wavelength)

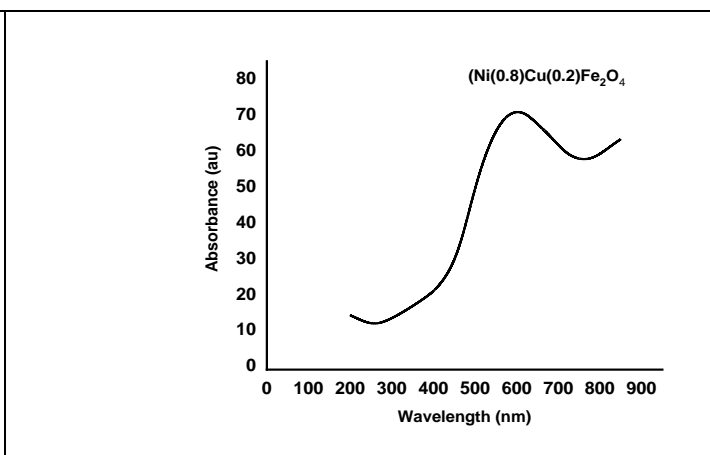


Fig. 2 – Smothed and baseline corrected graph (absorption vs. wavelength)

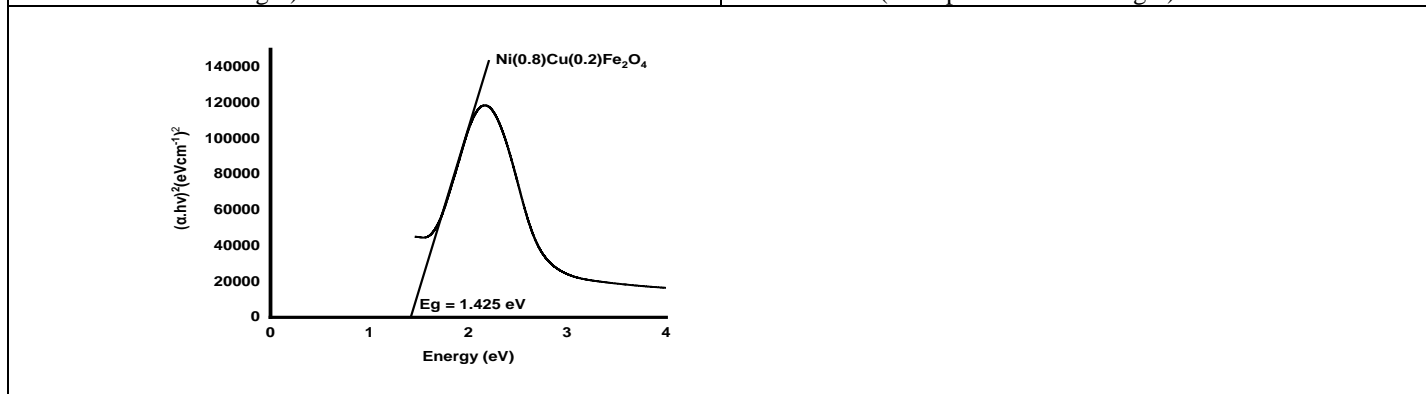


Fig. 3 – Indirect band gap (absorption factors vs. energy)

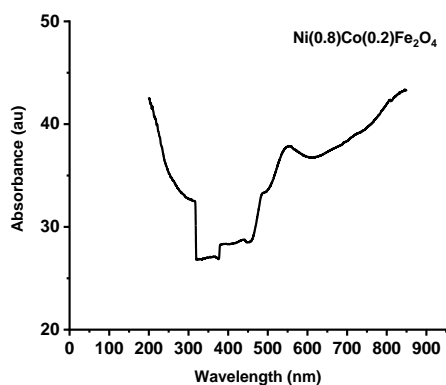


Fig. 4 - Raw data graph (absorption vs. wavelength)

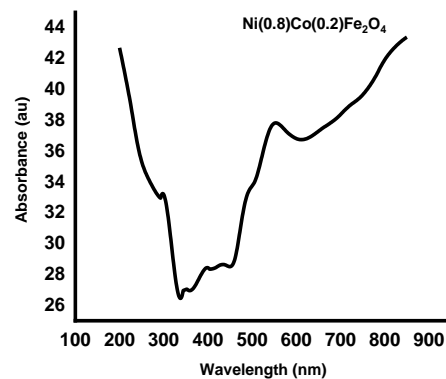


Fig. 5 – Smoothed and baseline corrected graph (absorption vs. wavelength)

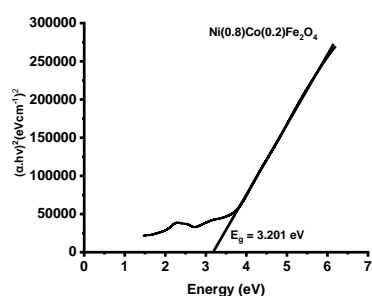


Fig. 6 – Indirect band gap (absorption factors vs. energy)

Table 1 – Band gap energy of transition metal copper and cobalt complexes

S. No.	Complex	Molecular formula	Band gap energy (eV)
1.	Complex I	[Ni(0.8)Cu(0.2)Fe ₂ O ₄]	1.425
2.	Complex II	[Ni(0.8)Co(0.2)Fe ₂ O ₄]	3.201

CONCLUSION

Using Origin Lab, we were able to derive the band gap energy based on the Tauc plot method under the three steps i.e., raw absorption graph, smoothed graph and baseline corrected graph. We then calculated the energy ($h\nu$), absorbance coefficient (α), the factor $\alpha h\nu^{(1/\gamma)}$ and the curve of $\alpha h\nu^{(1/\gamma)}$ versus energy($h\nu$). The band gap energy of studied complexes, i.e., complex I and complex II are $E_g = 1.425$ eV and $E_g = 3.201$ eV respectively. On comparing the results, we found that cobalt metal enhances the band gap energy and copper metal suppresses it.

REFERENCES

- [1] Tauc, J., Grigorovici, R., Vancu, A, Optical Properties and Electronic Structure of Amorphous Germanium, Phys. Status Solidi B, 1966, 15, 627– 637
- [2] Davis, E., Mott N., Conduction in non-crystalline systems V. Conductivity, optical absorption and photoconductivity in amorphous semiconductors., Philos. Mag. 1970, 22, 0903– 0922,
- [3] Mott, N. F., Davis, E. A., Electronic Processes in Non-Crystalline Materials; OUP Oxford, 2012.
- [4] Kubelka, P., Munk, F. A., Contribution to the Optics of Pigments. Z. Technol. Phys., 1931, 12, 593– 599
- [5] Omar Hamad Shehab, AL-Obaidil and Abdalhady R. H. Al-Hiti, American Chemical Science Journal, 2012, vol. 2(1), pp. 1-11.
- [6] Geete A., Shrivastava B. D. and Mishara A., Rasayan J. Chem., 2020, vol. 13 (3), pp. 1878-1884.

- [7] Iqbal J., Tirmizi S. A., Wattoo F.H., Imran M., Watto M.H.S., Sharfuddin S. and Latif S., 2006, Turkish, Journal of Biology, vol. 30(1).
- [8] Khalaji A.D., Nikookar M. and Das D., Journal of Thermal Analysis and Calorimetry, 2014, vol. 115(1), 409.
- [9] Chachaty C., Forchioni A. and Virlet J., Canadian Journal of Chemistry, 1975, vol. 53(5), 648.
- [10] Engelter C., Thornton D.A. and Ziman M.R., Journal of Molecular Structure, 1978, vol. 49(1), 7.
- [11] Makula, P., Pacia, M., Macyk, W, How to Correctly Determine the Band Gap Energy of Modified Semiconductor Photocatalysts Based on UV-Vis Spectra, J. Phys. Chem. Lett., 2018, 9, 6814–6817
- [12] Coulter, J. B., Birnie, D.P., Assessing Tauc Plot Slope Quantification: ZnO Thin Films as a Model System, Phys. Status Solidi B, 2018, 255, 1700393
- [13] López, R., Gómez, R., Band-Gap Energy Estimation from Diffuse Reflectance Measurements on Sol-Gel and Commercial TiO₂: A Comparative Study, J. Sol-Gel Sci. Technol., 2012, 61, 1-7

¹P.N.Deshmukh*²S.S.Dhote³S.V.DautpureGreen route: Nanoparticles Synthesis,
Characterization, a Sustainable Future

Abstract: - Nanotechnology nowadays is promising a sustainable future. Nanotechnology is eco-friendly and Sustainable due to its bioactive efficacy and resistance against various microbes its green route synthesis of different types of metal and metal oxide from leaf extracts, eggshells, moringa oleifera, fruit peels, and many more, proves itself a promising future of non-poisonous synthesis, and less harmful to the environment and mankind too. Nanotechnology is concerned with the method of synthesizing and manipulating particles of sizes between 1 and 100 nm. Nanoparticles (NPs) are often synthesized using a variety of processes, including laser ablation, chemical reduction, milling, sputtering, etc. Some traditional methods, including the chemical reduction method, which uses a variety of harmful chemicals to create NPs, because of their toxicity, present a variety of health issues and give rise to serious environmental problems, while other techniques are expensive and require a lot of energy. However, the biogenic synthesis technique used to produce NPs is ecologically friendly and free of chemical contaminants, making it ideal for medicinal applications where purity is a top requirement. Nature has devised various processes for the synthesis of nano and Micro-length scaled inorganic materials which have contributed to the development of the relatively new and largely unexplored area of research based on the biosynthesis of nanomaterials. In this article, more attention is given to ZnO nanoparticle synthesis as Zinc oxide is a chemical compound found naturally in the mineral called zincite and has attracted much attention in recent times due to its low cost and because it can be obtained by simple techniques. ZnO crystallizes in the typical wurtzite hexagonal structure where oxygen and zinc atoms are spatially arranged in a way that O atoms are arranged in a closed hexagonal structure, while the Zn atoms occupy the center of the distorted tetrahedron structure. Moreover, it is a semiconductor material of the II-VI group with a large energy gap around $E_g = 3.2$ eV, a large range of excitation energy, and controlled electrical conductivity, and when doped with transition metals exhibits the ferromagnetic phenomenon at room temperature, and because of that it has attracted much interest due to their potential applications in “spintronics”. The ZnO is insoluble in water

¹ *Corresponding author: SSESAs Science College, Nagpur.
preetiingole@gmail.com

and ethanol but is soluble in dilute mineral acids and is a fine powder, white or slightly yellow. In large quantities and high purity, it is recommended for use in the pharmaceutical, food, and cosmetic industries. Characterization is done with methods such as FTIR, UV-visible, DLS, SEM, TEM XRD, EDX, etc.

Keywords: ZnO Nanoparticles, Synthesis, Characterization. Anti-microbial Activity.

INTRODUCTION

A nanoparticle or ultrafine particle is usually defined as a particle of matter that is between 1 and 100 nanometres (nm) in diameter. The term is sometimes used for larger particles, up to 500 nm, or fibers and tubes that are less than 100 nm in only two directions. At the lowest range, metal particles smaller than 1 nm are usually called atom clusters instead. In general, the small size of nanoparticles leads to a lower concentration of point defects compared to their bulk counterparts, but they do support a variety of dislocations that can be visualized using high-resolution electron microscopes. However, nanoparticles exhibit different dislocation mechanics, which, together with their unique surface structures, results in mechanical properties that are different from the bulk material. Nanoparticles occur in a great variety of shapes, which have been given many informal names such as nanospheres, nanorods, nanochains, nanostars, nanoflowers, nano reefs, nanowhiskers, nanofibers, and nanoboxes. The shapes of nanoparticles may be determined by the intrinsic crystal habit of the material, or by the influence of the environment around their creation, such as the inhibition of crystal growth on certain faces by coating additives, the shape of emulsion droplets and micelles in the precursor preparation, or the shape of pores in a surrounding solid matrix. Some applications of nanoparticles may require specific shapes, as well as specific sizes or size ranges.

ZnO Nanoparticles

Zinc oxide is a chemical compound found naturally in the mineral called zincite and has attracted much attention in recent times due to its low cost and because it can be obtained by simple techniques. ZnO crystallizes in the typical wurtzite hexagonal structure where oxygen and zinc atoms are spatially arranged in a way that O atoms are arranged in a closed hexagonal structure, while the Zn atoms occupy the center of the distorted tetrahedron structure. Moreover, it is a semiconductor material of the II-VI group with a large energy gap around $E_g = 3.2$ eV, a large range of excitation energy, and controlled electrical conductivity, and when doped with transition metals exhibits the ferromagnetic phenomenon at room temperature, and because of that it has attracted much interest due to their potential applications in “spintronics”. The ZnO is insoluble in water and ethanol but is soluble in dilute mineral acids and is a fine powder, white or slightly yellow. In large quantities and high purity, it is recommended for use in the pharmaceutical, food, and cosmetic industries.

Zinc oxide is a transition metal and semi-metal that can react with both acids and bases providing water and salt. Because ZnO presents intermediate properties between acid and basic oxides it can behave as both acid and basic oxide. It is an intrinsic n-type semiconductor material that crystallizes in the hexagonal crystal system; it is relatively inexpensive, presents low toxicity, and is very effective in protecting against UV rays. ZnO is an excellent material for the manufacture of sunscreen because it absorbs ultraviolet (UV) rays and combat the potential problems associated with sun exposure. The search for nanostructured ceramic materials that result in high-performance materials has led to the development of several chemical methods on a laboratory scale. Among the various methods of chemical synthesis, there are the sol-gel method, spray pyrolysis, liquid combustion reaction, hydrothermal synthesis, spray drying, and the Pechini method, highlighting the combustion reaction method, which makes use of redox reactions between the decomposition products of nitrate and a fuel, such as urea.

Properties

Depending on end-use, ZnO may be considered as a bulk chemical or as a specialized semi-conductor. It has specific optical, electrical and thermal properties that are attractive for a range of very diverse applications. For example, its high refractive index (1.95–2.10) was useful in pigment applications, it can be an electrical conductor when suitably doped, and it is thermally stable to extremely high temperatures (at least ~1800 °C). The physical and chemical properties of ZnO powder ensure a large off-take as an additive in rubber. Alternatively, the high specific surface area of the ‘active’ grades permits them to be used in desulfurization processes in chemical plants. As a semiconductor, ZnO has applications in opto-electronics and in transparent conducting films. Awareness of its various properties is important, both for selection of this material for specific applications, and as input information for the producers of ZnO in its various forms.

1) Toxicology

Zinc oxide is generally categorized as a non-toxic material. Zinc oxide does not cause skin and eye irritation and there is no evidence of carcinogenicity, genotoxicity and reproduction toxicity in humans. However, the powder can be hazardous by inhalation or ingestion because it causes a condition known as zinc fever or zinc ague. The symptoms of this syndrome are chills, fever, cough, and tightness in the chest. Therefore appropriate safety precautions should be observed when preparing, packaging, transporting and handling ZnO. According to the recent EU hazard classifications, zinc oxide is classified as N; R50-53 (very toxic for the aquatic environment or ecotoxic). Therefore packages of ZnO in these jurisdictions must be labelled “UN3077-Class 9, Environmentally Hazardous Substance”. Soluble zinc compounds are considered ecotoxic for aquatic organisms despite them being necessary for humans, animals and plants in trace amounts. The human body, for example, contains around 2 g of Zn and a daily intake of 10–15 mg is required for metabolism. It has been shown that the ecotoxicity of ZnO to the model aquatic protozoan *Tetrahymena thermophila* is caused entirely by its solubilized fraction, i.e. [the Zn²⁺ ion]. Toxicities of bulk

ZnO, nano-ZnO, and soluble Zn²⁺ are similar once their different solubilities are taken into account, with 4-h effect concentration (EC50) values of about 4 or 5 mg bio-available Zn/L (5 ppm). These values are an order of magnitude lower than for soluble Cu²⁺] By comparison, the naturally occurring amount of Zn ions in seawater is three orders of magnitude smaller (5 ppb). Zinc oxide has a long history of use in sunscreen compositions to block UV radiation, with the nanoparticulate form having been introduced for this application in the late 1990s. There have been occasional concerns voiced about possible adverse effects on human health or the environment. However, the current evidence shows that ZnO particles or nanoparticles do not penetrate viable skin cells and remain on the outer layer of undamaged skin (the stratum corneum) with low systemic toxicity Toxicity to the aquatic environment would depend on whether any ZnO washed off sunbathers was solubilized in, for example, the seawater, and whether the local environmental concentration of Zn²⁺ could thereby exceed the roughly 5 ppm threshold mentioned earlier.

2) Crystal structures

There are three crystal structures of ZnO: hexagonal wurtzite, cubic zinc-blende structure, and a rarely-observed cubic rock-salt (NaCl-type). Under ambient conditions, the most thermodynamically stable structure is the wurtzite form. The zinc-blende structure is metastable and can be stabilized only by epitaxial growth on cubic substrates while the cubic rock-salt structure is usually only stable under extreme pressure (~2 GPa).

3) Surface properties

The surface properties of ZnO particles or thin films play a significant role in diverse fields, for example in sensing, catalysis, or optoelectronics. As a result, the topic has been extensively studied. Absorption of molecules onto the ZnO surface has been examined with some attention focused on the adsorbates for methanol synthesis from syn-gas (H₂, CO, CO₂). The wettability of ZnO surfaces has also been examined; flat ZnO substrates exhibit the maximum water contact angle of 109°. Super-hydrophobic ZnO has been prepared by surface treatment with fatty acids and reversibly switchable wettability between super-hydrophilicity and super-hydrophobicity has been observed by alternation of UV irradiation or oxygen plasma treatment. The hydrophobicity of ZnO additives is an important issue in polymer blending when seeking to obtain a homogeneous particle distribution or grafting of monomers onto the metal oxide. Since most polymers are hydrophobic and ZnO is hydrophilic, the surface of the surface of the particles may be modified for better compatibility with the polymer matrix.

Experimental Method

The zinc oxide nanostructure was synthesized by using the sol-gel method. In order to prepare a sol, 20 g of Zn acetate dihydrate is mixed into 150 ml of distilled water and stirred for about 20 minutes at 35⁰ c to produce a zinc acetate solution. Then 80 gm of NaOH powder is mixed into 80 ml of distilled water and stirred for around 20 min at 35⁰ c to form NaOH solution. After mixing both solutions, the titration reaction

by the addition of 100ml ethanol in a drop-wise manner accompanied by vigorous stirring for 90 minutes to obtain a gel-like product. Dry the gel at 80⁰ c overnight and calcify in an oven at 250⁰ c for 4hr and we get ZnO nanoparticle.

Synthesis of Zinc Oxide

Nanostructure Synthesizing Zinc Oxide nanostructure via sol-gel technique in this research includes the use of several materials such as Zinc Acetate Dihydrate ($\text{Zn}(\text{CH}_3\text{COO})_2 \cdot 2\text{H}_2\text{O}$) $\geq 99\%$ purity, Sodium hydroxide (NaOH) $\geq 98\%$ (Sigma Aldrich), Ethanol and distilled water. Zinc Acetate Dihydrate was used as a precursor and Ethanol was used as a reagent. Distilled water was used as a solvent medium.

Zinc Oxide Nanostructures

Based on the experimental work that has been done, there are a series of chemical reaction that takes place. The complete hydrolysis of zinc acetate with the aid of NaOH in an ethanolic solution should result in the formation of a ZnO colloid. The final product was obtained as a result of the equilibrium between the hydrolysis and condensation reaction. Due to the heating, Zinc Acetate within the solution undergoes hydrolysis forming acetate ions and zinc ions. The abundance of electrons in the oxygen atoms makes the hydroxyl groups (-OH) of alcohol molecules bond with the zinc ions⁵. The overall chemical reaction to form ZnO nano-powder when sodium hydroxide was used as a solvent is stated as follows in Eq. (1):



Zinc hydroxide acetate is an intermediate product of the hydrolysis reaction, formed in the presence of H₂O and OH ions. It can be easily transformed into ZnO at higher temperatures and with prolonged refluxing. Sodium acetate is water soluble and could therefore be removed from the end product. High purity ZnO nano-powder could therefore be obtained successfully by sol-gel technique⁶.

Synthesis of ZnO nanoparticles with different concentrations.

Sr.No	Amount of Zn acetate	Normality of NaOH
1	20g	0.1N
2	20g	0.2N
3	20g	0.3N

Characterization

Characterization of powders was determined by X-ray diffraction (XRD). The crystal structural analysis was analyzed by X-ray diffraction (XRD) with diffraction angles 2θ from ranging 10° to 90° and with Cu K α

radiation ($\lambda = 1.5406 \text{ \AA}$) as the radiation source. And antimicrobial activity. The synthesized calcium oxide nanoparticles were screened for antimicrobial activity.

Antimicrobial Activity:-Antibacterial analysis:

The bacterial culture for E. Coli was obtained from the department of Microbiology of Shri Shivaji Science College, Nagpur. The bacterial culture was incubated at 37°C for 24 hours by inoculation into nutrient agar. ZnO was stored dry at room temperature and Dissolved 20mg/ml in distilled water. The antibacterial activities of each compound were evaluated by the agar well-diffusion method. Mueller Hinton Agar Media was poured into the Petri dishes and allowed to solidify. After the spreading is complete allow the plate to dry for 5 minutes. Prepare an antibiotic solution of Zinc Oxide. Prepare wells of 10mm diameter with the help of a cork borer and add 20 μ L of each prepared antibiotic into wells. Incubate for 24 hours at 37°C. After incubation, the diameter of inhibition zones formed around each well was measured and expressed in millimeters (mm) to evaluate the antimicrobial activity.

Sr. no	NaOH	Bacteria
		E. Coil (Zone of inhibition)
1.	0.1N	11 mm
2.	0.2N	14 mm
3.	0.3N	8 mm

(Table-1)



Zone of Inhibition against E. Coil

X-ray diffraction pattern of ZnO

A series of XRD diffractograms of sample 1 as shown in Fig.1. Cu K radiation (1.5406 Å) was used to record the X-ray diffraction results. Data on intensity were gathered throughout a 2θ range between 20 and 80. Using the diffraction strength of the (101) peak, the Scherrer equation was used to estimate the average grain size of the samples. The synthesized materials were proven to be ZnO with wurtzite phase by x-ray diffraction examinations. All of the diffraction peaks corresponded with the reported JCPDS data¹⁵, and no distinctive peaks other than ZnO were seen. Using Scherrer equation¹⁶, the average grain size (D) of the particles was calculated from the XRD line broadening measurement.

$$D = 0.89\lambda / (\beta \cos\theta)$$

Where θ is the diffraction angle, β is the ZnO (101) line's full width at half-maximum (FWHM), and λ is the wavelength (Cu K). The diffraction peaks' distinct line broadening is a sign that the synthesized materials are in the nanoscale range. Depending on the growing conditions, it was discovered that the grain size ranged from 7 to 24 nm. Additionally, the predicted lattice parameters concurred with the reported values.

The reaction temperature greatly influences the particle morphology of as-prepared ZnO powders. Figure 1 shows that the XRD patterns of ZnO nanoparticles synthesized at various temperatures with 0.1N NaOH for 6 h. As the reaction temperature increases, FWHM decreases. Thus the size of ZnO nanoparticles increases as the temperature for

the hydrothermal synthesis increases. This is due to the change in growth rate between the different crystallographic planes.

Fig. 1. XRD patterns of ZnO nanoparticles synthesized from 0.1N NaOH at various temperatures for 6 h. Figure 2 and Figure 3 show the variation of FWHM and grain size of ZnO nanoparticles synthesized from 0.2 and 0.3 NaOH.

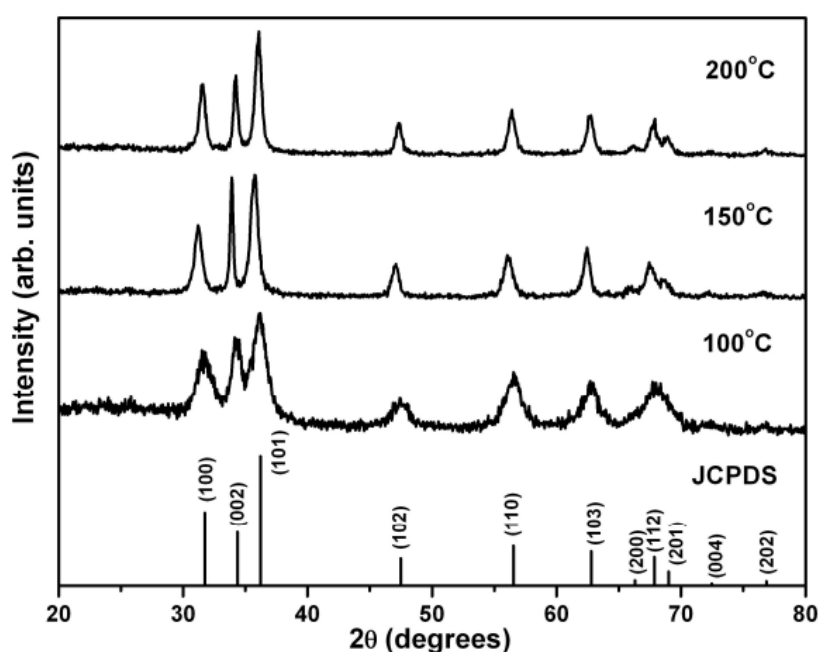


Fig.1 The XRD Diffractogram of sample 1

The reaction temperature greatly influences the particle morphology of as-prepared ZnO powders. Figure 1 shows that the XRD patterns of ZnO nanoparticles synthesized at various temperature with 0.1N NaOH for 6 h. As the reaction temperature increases, FWHM decreases. Thus the size of ZnO nanoparticles increases as the temperature for the hydrothermal synthesis increases. This is due to ZnO structures with different grain sizes can be obtained by controlling the concentration of the precursors. ZnO nanoparticles were synthesized by keeping the concentration of $\text{Zn}(\text{CH}_3\text{COO})_2 \cdot 2\text{H}_2\text{O}$ as 0.1 N in all reactions, the concentration of NaOH was varied from 0.2 N to 0.5 N at 200o C for 12 h. Figure.2 and Figure.3 shows the XRD pattern of ZnO nanoparticles synthesized by varying the concentration of precursors. All the peaks match well with the standard wurtzite structure and the FWHM of the (101) diffraction peak increases with the decreasing concentration of the NaOH.

These results reveal that the molar ratio of OH^- to Zn^{2+} is a dominant factor for the formation of the ZnO nanoparticles. The change of growth rate between the different crystallographic planes.

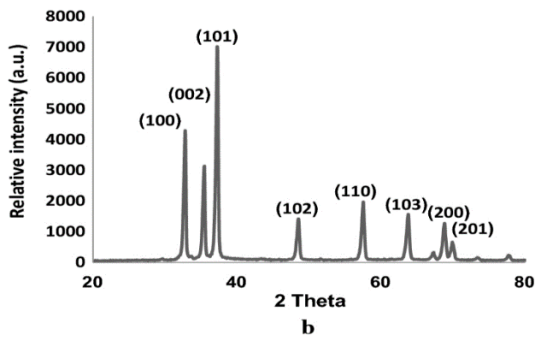


Fig.2 The XRD Diffractogram of sample 2

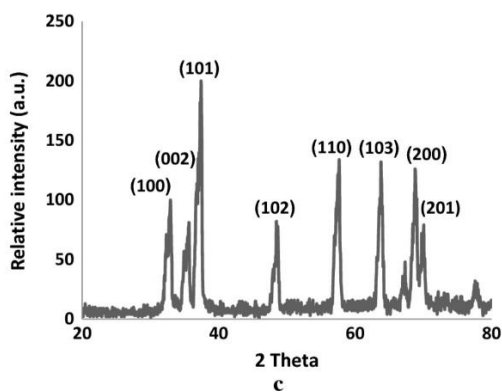


Fig.3 The XRD Diffractogram of sample 3

Antimicrobial activity result:-

The result of the antibacterial screening of the Zinc oxide nanoparticles at a concentration of 20 mg/ml against bacteria has been found. The inhibition zones were measured in mm and the results are shown in (Table). The result of antimicrobial screening indicates that ZnO shows significant activity against the Escherichia coil. When we increase concentration, the area of inhibited growth also increases.

Conclusion:-

The zinc oxide nanostructure was successfully synthesized by using the sol-gel method. The results showed that the ZnO rod-like structure was successfully synthesized by the sol-gel method in the nano-size range of about 84.98nm. The synthesized ZnO nano-powder obtained exhibits good crystallinity.

REFERENCES

1. Kargari, A., Tavakoli, A., & Sohrabi, M. (2007). A review of methods for synthesis of nanostructured metals with emphasis on iron compounds. *Chemical Papers*, 61(3), 151-170.
2. Research and market. (2013). *The Global Market for Metal Oxide Nanoparticles to 2020*. Retrieved from
3. Wahab, H.A & Salama, A.A et al. (2013). Optical, structural, and morphological studies of ZnO nano-rod thin film using sol-gel.3, 46-51.
4. Braga, D, Grepioni, F. *Acc. Chem. Res.* 27, 51, 1994
5. Klabunde, K. J, *Chemistry of Free Atoms and Particles*, Acad. Press, New York, 1980
6. Aitken, R. J, Creely, K. S, et al, *Nanoparticles: An occupational hygiene review*, Research Report 274, Institute of Occupational Medicine for the Health and Safety Executive, Edinburgh, 2004.
7. Nalwa, H.S, *Handbook of Nanostructured Materials and Nanotechnology*, Academic Press, New York, 1999
8. Chai, C. (2012). *The Global Market for Zinc Oxide Nanopowders 2012*. New Report on Global Zinc Oxide Nanopowder Market, 135-140.
9. Yung, K., Ming, H., Yen, C. & Chao, H., (2012). Synthesis of 1D,2D and 3D ZnO Polycrystalline Nanostructures Using Sol-Gel Method.*Journal of Nanotechnology*, 1-8
10. Bari, A. R., Shinde, M. D., Vinita. D. & Patil, L. A. (2009). Effect of Solvents on the Particle Morphology of Nanostructured ZnO. *Indian Journal of Pure & Applied Physics*, 47, 24-27.
11. Morkoç, H., &Özgür, Ü. (2009). Chapter 1 General Properties of ZnO. In *Zinc Oxide: Fundamentals, Materials and Device Technology*. Wiley-VCH.
12. Moezzi, A., McDonagh, A.M, & Cortie, M.B. (2012). Zinc oxide particles: Synthesis, properties and applications. *Chemical Engineering Journal*, 185–186, 1–22
13. "ISO/TS 80004-2: Nanotechnologies Vocabulary Part 2: Nano-objects" (<https://www.iso.org/obp/ui/#iso:std:iso:ts:80004:-2: ed-1:v1:en>). International Organization for Standardization. 2015. Retrieved 18 January 2018.
14. J.N Hasnidawani, Azlina, H. N., Norita, H., Bonnia, N. N., Ratim, S., & E. S. Ali, "Synthesis of ZnO Nanostructures Using Sol-gel method" *Procedia Chemistry*, 19, 211–216,(2016).
15. Surya P.G., " Synthesis and characterization of zinc oxide nanoparticles by sol-gel process", Master of Science in physics, National Institute of Technology Rourkela, Orissa, India, 1-36,(2012).
16. Vafaei, M. S.Ghamsari, "Preparation and characterization of ZnO nanoparticles by a novel sol-gel route," *Materials Letters*, 61(14-15), 3265–3268(2007).

^{1,*} D. R. Taikar² S. J. Dhoble

Effect of Li⁺-ion on enhancement of photoluminescence in Sm³⁺ doped CaSnO₃ phosphor



Abstract: - Photoluminescence (PL) study of Sm³⁺ doped CaSnO₃ phosphor and the effect of Li⁺-ion on PL property of CaSnO₃:Sm³⁺ were investigated. The phosphors were prepared by simple co-precipitation method using oxalic acid and annealed at 1100°C. The prepared phosphors were characterized using XRD, SEM and photoluminescence (PL) techniques. The result of x-ray powder diffraction (XRD) analysis confirmed the formation of single phase CaSnO₃. Photoluminescence measurements showed that the CaSnO₃:Sm³⁺ phosphor exhibited bright orange-red emission at about 610 nm attributed to ⁴G_{5/2} → ⁶H_{7/2} transition of Sm³⁺ ion under UV excitation. After introducing Li⁺ ion in CaSnO₃:Sm³⁺ phosphor, the luminescence efficiency enhanced due to the charge compensation. The PL study reveals that the prepared phosphors are useful in near UV excited LED, optoelectronic display devices and related applications.

Keywords: CaSnO₃, photoluminescence, Sm³⁺, co-precipitation.

I. INTRODUCTION

Host materials and active centers play a pivotal role in the process of luminescence [1,2]. Over the years, oxide phosphors are attracted more attention than the sulfide or halide phosphors due to their physical and chemical stability. SnO₄⁴⁻ anions are reported to be optically-inert, and could be a candidate for host materials. Alkaline earth stannates (MSnO₃, M = Ca, Sr, Ba), as a type of perovskite material, have garnered significant attention due to their potential applications in various fields such as display related application, thermally stable capacitors, photocatalysts, anode materials for lithium-ion batteries, and in many technical applications [3-6]. The luminescence properties of rare earth-doped alkaline earth stannates have been extensively documented, including examples such as CaSnO₃:Tb³⁺, MSnO₃:Eu³⁺ (M = Ca, Sr, and Ba), CaSnO₃:Sm³⁺, CaSnO₃:Er³⁺, Bi³⁺, CaSnO₃:(Eu³⁺, Pr³⁺, Tb³⁺), SrSnO₃:(Eu³⁺, Tb³⁺, Mg²⁺), Ca₂SnO₄:Eu³⁺, Sr₂SnO₄:(Eu³⁺, Eu³⁺, Ti⁴⁺) and Ba₂SnO₄:Eu³⁺ [7-19] phosphors. The Sm³⁺ ion is widely recognized as a crucial activator for a wide range of inorganic lattices, resulting in the emission of reddish-orange light due to its ⁴G_{5/2} → ⁶H_J (J = 5/2, 7/2, 9/2, 11/2) transitions [20].

This study delves into the synthesis and luminescence property of CaSnO₃:Sm³⁺ phosphor, with a specific focus on investigating the enhancements in its emission when co-doped with Li⁺ ions.

II. MATERIALS PREPARATION AND ANALYSIS

A series of Sm³⁺ doped CaSnO₃ phosphors and co-doped with Li⁺ ions were synthesized by co-precipitation method. For synthesis, initially stoichiometric amount of strontium chloride, stannic chloride and dopant (Samarium chloride) were dissolved separately in de-ionized water. Then the solutions were mixed. Ammonium carbonate (NH₄)₂CO₃ solution was then added slowly to the mixture. Precipitate thus obtained in carbonate form was separated by filtering, dried and thoroughly crushed to yield fine powder. The obtained white precipitate was decomposed by heating in air at 1100°C for 3 hour to yield Ca_(1-x)SnO₃:xSm³⁺ phosphors.

X-ray diffraction patterns were recorded on Philips PANalytical X'pert Pro diffractometer with Cu-K α radiation (λ = 1.5409 nm) over an angular range of 10° to 80° in 2 θ . Photoluminescence (PL) spectra in the spectral range 220-700 nm were recorded at room temperature on Hitachi F-4000 spectro-fluorimeter with a Xenon flash lamp (150 W) and spectral slit widths of 1.5 nm. The sample surface morphology was imaged

¹Department of Physics, Shri Lemdeo Patil Mahavidyalaya, Mandhal-441210, India

Email: deepak_taikar@yahoo.co.in

²Department of Physics, R.T.M. Nagpur University, Nagpur-440033, India

*Corresponding author: D. R. Taikar

using a S-3400, SEM (Hitachi, Japan). The color chromaticity coordinates were obtained according to Commission International de l'Eclairage (CIE) using Radiant Imaging color calculator.

III. RESULTS AND DISCUSSIONS

A XRD and Crystal Structure

The XRD pattern of the synthesized $\text{CaSnO}_3:\text{Sm}^{3+}$ (1mol%) phosphor is presented in Fig. 1, which exhibit sharp diffraction peaks. The obtained XRD patterns matched well with the standard data JCPDS file No. 77-1797, which indicating orthorhombic structure with space group Pbnm (62) with cell parameters $a = 5.52399 \text{ \AA}$, $b = 5.69628 \text{ \AA}$, $c = 7.90708 \text{ \AA}$, $\alpha = \beta = \gamma = 90^\circ$, and the unit cell volume $V = 248.8057 \text{ \AA}^3$.

Fig. 2 shows crystal structure of CaSnO_3 compound. CaSnO_3 is orthorhombic perovskite structured and crystallizes Pbnm space group. In this structure, Ca^{2+} atom has 4c site symmetry and is bonded to eight O^{2-} atoms to form CaO_8 polyhedron. The Ca–O bond distances ranging from 2.31-2.7 \AA . Sn^{4+} atom occupy 4b site in the lattice and is bonded to six O^{2-} atoms to form corner-sharing SnO_6 octahedra. The corner-sharing octahedral tilt angles range from 33-34°. The Sn–O bond length ranges from 2.049-2.054 \AA .

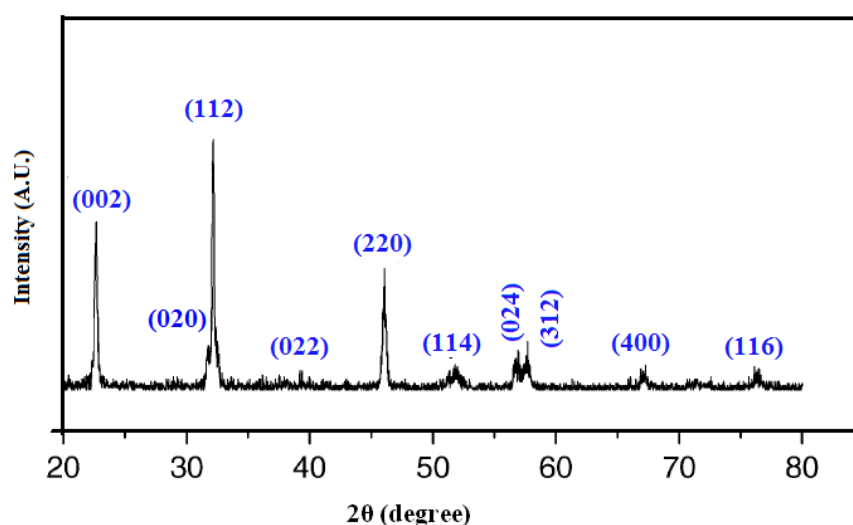


Fig.1. Powder XRD patterns of $\text{CaSnO}_3:\text{Sm}^{3+}$ (1mol%)

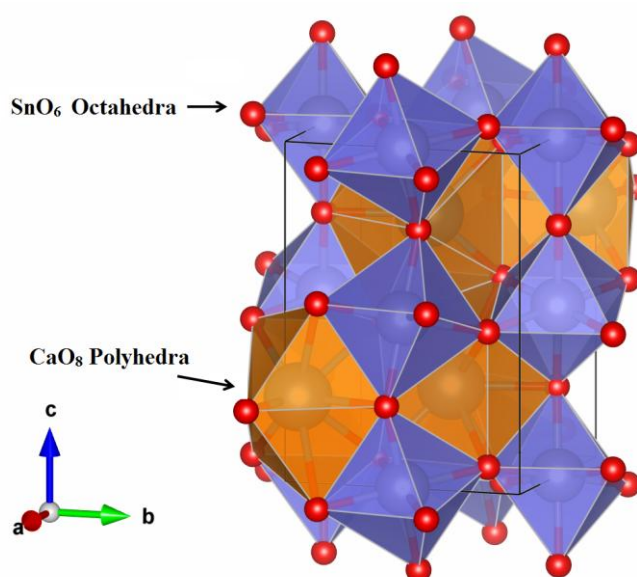


Fig.2. Crystal structure of CaSnO_3 compound

B SEM analysis

The surface morphology of synthesized material was studied by scanning electron microscopy (SEM) is presented in Fig. 3. The SEM images reveal that the particles were relatively agglomerated and non-uniform in nature. The grain size distribution is broad and the average particle size ranges from 1 μm to 10 μm . The small particles are agglomerated forming bigger crystallites.

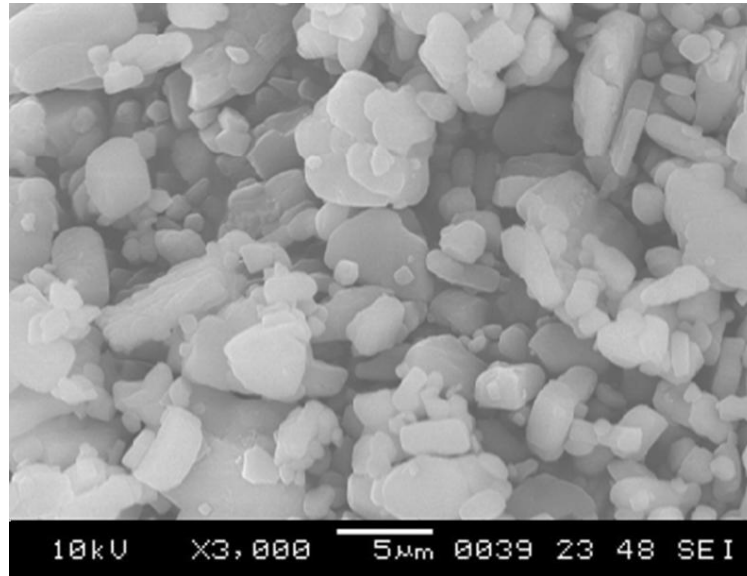


Fig.3. SEM images of $\text{CaSnO}_3:\text{Sm}^{3+}$

C Photoluminescence of $\text{CaSnO}_3:\text{Sm}^{3+}$ and $\text{CaSnO}_3:(\text{Sm}^{3+},\text{Li}^+)$

Fig. 4 shows results of PL excitation and emission spectra of CaSnO_3 doped with (1mol%) Sm^{3+} . At 409 nm excitation, the phosphor exhibits characteristic broad emission lines at 566, 574, 609, 616 and 660 nm. The 566 and 574 nm emission peaks can be attributed to ${}^4\text{G}_{5/2} \rightarrow {}^6\text{H}_{5/2}$ transition of Sm^{3+} ion, which is originated due to purely magnetic dipole (MD) moment. The most intense emission peaks at 609 and 616 nm attributed to the transition of Sm^{3+} ion from ${}^4\text{G}_{5/2} \rightarrow {}^6\text{H}_{7/2}$. The ${}^4\text{G}_{5/2} \rightarrow {}^6\text{H}_{7/2}$ transition is magnetic dipole allowed but electric dipole (ED) nature is more dominant with selection rule $\Delta J = \pm 1$, therefore it is allowed as both partially MD and partially ED. The least intense emission peak at 660 nm corresponds to ${}^4\text{G}_{5/2} \rightarrow {}^6\text{H}_{9/2}$ transition, which is originated due to purely ED transition with selection rule $\Delta J = \pm 2$ and is sensitive to the crystal field [21-23]. The emission intensity corresponds to ${}^4\text{G}_{5/2} \rightarrow {}^6\text{H}_{9/2}$ transition (660 nm) is weak when the Sm^{3+} ions are in the symmetric site and is strong when Sm^{3+} ions are in the asymmetric site. A PL spectrum indicates that 660 nm peak is weaker than other peaks i.e. most of the Sm^{3+} ions are in the symmetric site [24]. At 609 nm emission, the phosphor exhibit broad excitation band centered at 258 nm attributed to charge transfer band of $\text{Sm}^{3+}-\text{O}^{2-}$. The excitation spectra also shows series of sharp peaks at 348, 365, 380, 409, 422, 470 nm attributed to the transitions of Sm^{3+} ions from ground state ${}^6\text{H}_{5/2} \rightarrow {}^4\text{K}_{15/2}$, ${}^4\text{D}_{3/2}$, ${}^6\text{P}_{7/2}$, ${}^6\text{P}_{3/2}$, ${}^4\text{G}_{9/2}$, and ${}^4\text{I}_{13/2}$ respectively [25,26]. The nature of excitation band in near-UV region suggests that the prepared phosphor can be effectively excited by UV LED chip and can be useful for solid state lighting application. The effect of Sm^{3+} concentration on PL emission intensity is presented in Fig. 5. It is observed that the emission intensity rises as the concentration of Sm^{3+} increases from 0.3 mol% to 1.3 mol%. However, beyond 1.3 mol%, the emission intensity falls due to concentration quenching effect in which the excitation energy is lost via non-radiative decay process. No changes have been observed in the shape and peak position of PL excitation and emission curve with varying doping concentration.

It is anticipated that Sm^{3+} ions will take the place of Ca^{2+} ions in the CaSnO_3 host lattice. However, due to the difference in charge between Sm^{3+} and Ca^{2+} ions, maintaining charge balance in the lattice is challenging. As a result, Sm^{3+} ions are unable to be fully incorporated into the Ca^{2+} ion sites and form pairs by trapping an interstitial O^{2-} ion to maintain charge balance. In this study, Li^+ ions were selected as charge compensators due to their small ionic radius, which allows them to easily enter the lattice and conveniently provide charge compensation. Through the addition of Li^+ ions, it is possible for Sm^{3+} ions to fully occupy the Ca^{2+} ion sites in the lattice, leading to improved luminescence properties of the $\text{CaSnO}_3:\text{Sm}^{3+}$ phosphor. The impact of the

addition of Li^+ ion in the $\text{CaSnO}_3:\text{Sm}^{3+}$ (1.3 mol%) phosphor is depicted in fig 6. It is evident from the figure that the incorporation of Li^+ ion in $\text{CaSnO}_3:\text{Sm}^{3+}$ phosphor resulted in an increased intensity of the phosphor.

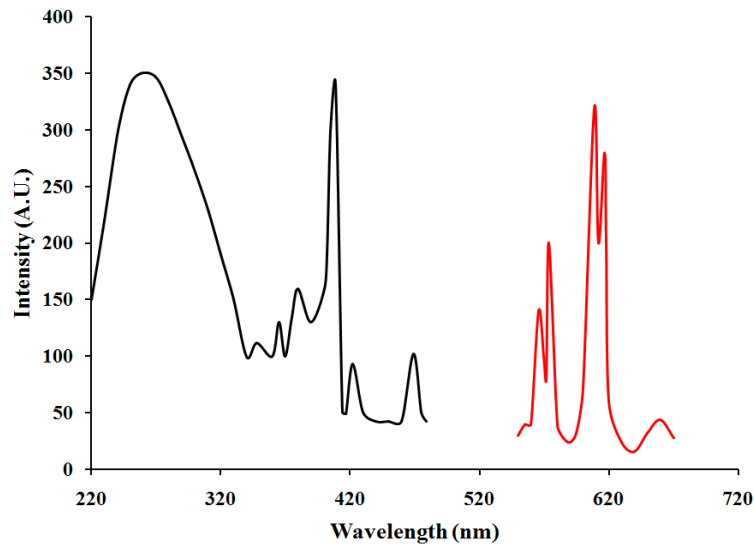


Fig. 4. PL excitation emission spectra of CaSnO_3 doped with (1 mol%) Sm^{3+} .

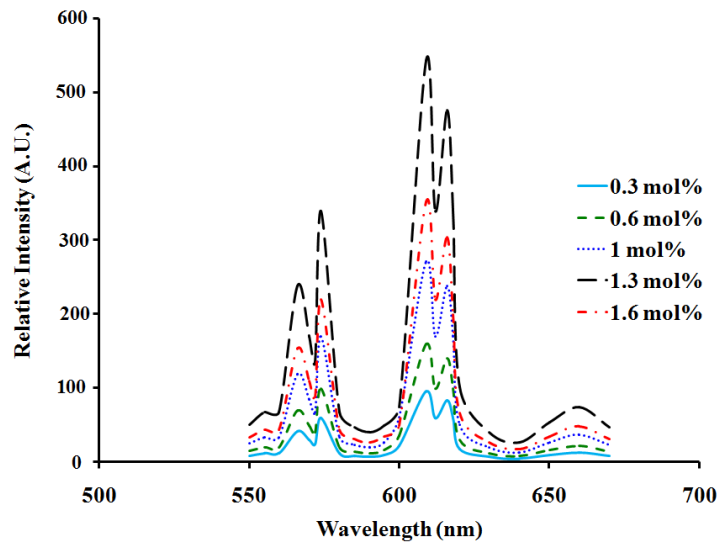


Fig. 5. Variation of emission intensity as a function of Sm^{3+} concentration

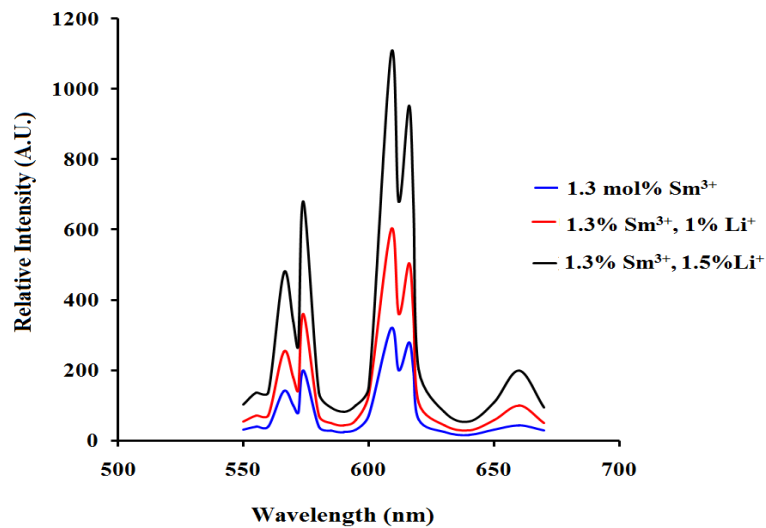


Fig. 6. Effect of addition of Li^+ in $\text{CaSnO}_3:\text{Sm}^{3+}$

D Color chromaticity

The color of the phosphor is very important in the field of luminescence and therefore the chromaticity diagram and CIE coordinates are calculated using PL data and interactive CIE software (CIE coordinate calculator). The CIE color coordinates for $\text{CaSnO}_3:\text{Sm}^{3+}$ phosphor was found to be (0.5902, 0.4091) as shown in Fig. 6.

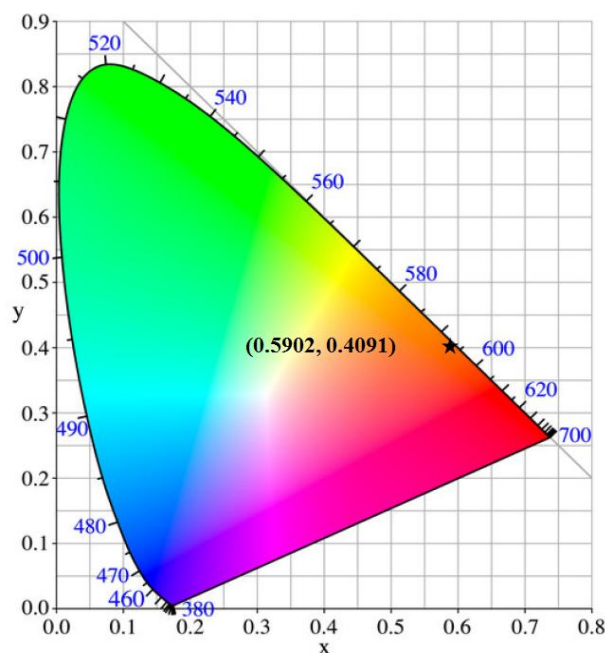


Fig. 6. CIE chromaticity diagram

IV. CONCLUSION

To summarize, a series of $\text{Ca}_{(1-x)}\text{SnO}_3:x\text{Sm}^{3+}$ ($x=0.3$ to 1.6 mol%) phosphors were successfully synthesized via co-precipitation method. The XRD analysis of the resulting compound matches well with the standard JCPDS file. $\text{CaSnO}_3:\text{Sm}^{3+}$ shows bright orange-red luminescence with a dominant emission peak at 609 nm attributed to ${}^4\text{G}_{5/2} \rightarrow {}^6\text{H}_{7/2}$ transition of Sm^{3+} ion under near UV excitation. After addition of Li^+ ion in $\text{CaSnO}_3:\text{Sm}^{3+}$ phosphor, the luminescence intensity enhanced significantly due to the charge compensation. Through the addition of Li^+ ions, it is possible for Sm^{3+} ions to fully occupy the Ca^{2+} ion sites in the lattice. The PL study reveals that the prepared phosphors can be useful in near UV excited LED, optoelectronic display devices and related applications.

REFERENCES

- [1] Z. Yu, Z. Xia, C. Su, R. Wang, Q. Liu, "Effect of Gd/La substitution on the phase structures and luminescence properties of $(\text{La,Gd})\text{Sr}_2\text{AlO}_5:\text{Ce}^{3+}$ solid solution phosphors," *J. Mater. Chem. C*, vol. 3, pp. 11629, 2015, <https://doi.org/10.1039/C5TC02325D>.
- [2] R. Cao, K. Chen, P. Liu, C. Cao, Y. Xu, H. Ao, P. Tang, "Tunable photoluminescence properties of $\text{Sr}_{1-y}\text{Ca}_y\text{MoO}_4:\text{Sm}^{3+}$ phosphors ($0 \leq y < 1$)," *Luminescence*, vol. 30, pp. 962, 2015, <https://doi.org/10.1002/bio.2845>.
- [3] A. Canimoglu, J. Garcia-Guinea, Y. Karabulut, M. Ayvacikli, A. Jorge, N. Can, "Catholuminescence properties of rare earth doped CaSnO_3 phosphor," *Appl. Radiat. Isotopes*, vol. 99, pp. 138, 2015, <https://doi.org/10.1016/j.apradiso.2015.02.026>.
- [4] S. Saha, S. Das, U. K. Ghorai, N. Mazumder, D. Ganguly, K. K. Chattopadhyay, "Controlling Nonradiative Transition Centers in Eu^{3+} Activated CaSnO_3 Nanophosphors through Na^+ Co-Doping: Realization of Ultrabright Red Emission along with Higher Thermal Stability," *J. Phys. Chem. C*, vol. 119, pp. 16824, 2015, <https://doi.org/10.1021/acs.jpcc.5b03500>.
- [5] X. Y. Chen, C. Ma, S. P. Bao, H. Y. Zhang, "Novel porous $\text{CaSnO}_3:\text{Eu}^{3+}$ and $\text{Ca}_2\text{SnO}_4:\text{Eu}^{3+}$ phosphors by co-precipitation synthesis and postannealing approach: A general route to alkaline-earth stannates," *J. Alloys Compd.*, vol. 497, pp. 354, 2010, <https://doi.org/10.1016/j.jallcom.2010.03.065>.
- [6] X. L. Pang, C. H. Jia, G. Q. Li, W. F. Zhang, "Bright white upconversion luminescence from $\text{Er}^{3+}-\text{Tm}^{3+}-\text{Yb}^{3+}$ doped CaSnO_3 powders," *Opt. Mater.*, vol. 34, pp. 234, 2011, <https://doi.org/10.1016/j.optmat.2011.08.019>.
- [7] B. Lei, B. Li, H. Zhang, W. Li, "Preparation and luminescence properties of $\text{CaSnO}_3:\text{Sm}^{3+}$ phosphor emitting in the reddish orange region," *Opt. Mater.*, vol. 29, pp. 1491, 2007, <https://doi.org/10.1016/j.optmat.2006.07.011>.
- [8] Z. Liang, J. Zhang, J. Sun, X. Li, L. Cheng, H. Zhong, S. Fu, Y. Tian, B. Chen, "Enhancement of green long lasting phosphorescence in $\text{CaSnO}_3:\text{Tb}^{3+}$ by addition of alkali ions," *Phys. B*, vol. 412, pp. 36, 2013, <https://doi.org/10.1016/j.physb.2012.12.013>.

- [9] Z. Fu, W. Li, S. Du, H. Yang, J. H. Jeong, "Hydrothermal Synthesis and Luminescent Properties of Uniform $\text{CaSnO}_3:\text{Eu}^{3+}$ Microcrystals with Controlled Morphology," *J. Electrochem. Soc.*, vol. 156, pp. J308, 2009, DOI 10.1149/1.3190536.
- [10] X. Pang, Y. Zhang, L. Ding, Z. Su, W. F. Zhang, "Upconversion Luminescence Properties of Er^{3+} - Bi^{3+} Codoped CaSnO_3 Nanocrystals with Perovskite Structure," *J. Nanosci. Nanotechnol.*, vol. 10, pp. 1860, <https://doi.org/10.1166/jnn.2010.2135>.
- [11] Z. Lu, L. Chen, Y. Tang, Y. Li, "Preparation and luminescence properties of Eu^{3+} -doped MSnO_3 ($M = \text{Ca}, \text{Sr}$ and Ba) perovskite materials," *J. Alloys Compd.*, vol. 387, pp. L1–L4, 2005, <https://doi.org/10.1016/j.jallcom.2004.06.036>.
- [12] Z. Liu, Y. Liu, "Synthesis and luminescent properties of a new green afterglow phosphor $\text{CaSnO}_3:\text{Tb}^{3+}$," *Mater. Chem. Phys.*, vol. 93, pp. 129–132, 2005, <https://doi.org/10.1016/j.matchemphys.2005.02.032>.
- [13] B. Lei, B. Li, H. Zhang, L. Zhang, Y. Cong, W. Li, "Synthesis and Luminescence Properties of Cube-Structured $\text{CaSnO}_3/\text{RE}^{3+}$ ($\text{RE} = \text{Pr}, \text{Tb}$) Long-Lasting Phosphors," *J. Electrochem. Soc.*, vol. 154 pp. H623–H630, 2007, DOI 10.1149/1.2734775.
- [14] K. Ueda, T. Yamashita, K. Nakayashiki, K. Goto, "Green, Orange, and Magenta Luminescence in Strontium Stannates with Perovskite-Related Structures," *Jpn. J. Appl. Phys.*, vol. 45, pp. 6981–6983, 2006, DOI 10.1143/JJAP.45.6981.
- [15] Y. C. Chen, Y. H. Chang, B.-S. Tsai, "Synthesis and the luminescent properties of europium-activated Ca_2SnO_4 phosphors," *Opt. Mater.*, vol. 27, pp. 1874–1878, 2005, <https://doi.org/10.1016/j.optmat.2004.12.006>.
- [16] H. M. Yang, J. X. Shi, M. L. Gong, "A novel red emitting phosphor $\text{Ca}_2\text{SnO}_4:\text{Eu}^{3+}$," *J. Sol. State. Chem.*, vol. 178, pp. 917–920, 2005, <https://doi.org/10.1016/j.jssc.2004.12.022>.
- [17] H. M. Yang, J. X. Shi, M. L. Gong, "A new luminescent material, $\text{Sr}_2\text{SnO}_4:\text{Eu}^{3+}$," *J. Alloys Compd.*, vol. 415, pp. 213–215, 2006, <https://doi.org/10.1016/j.jallcom.2005.04.221>.
- [18] Y. C. Chen, Y. H. Chang, B. S. Tsai, "Influence of processing conditions on synthesis and photoluminescence of Eu^{3+} -activated strontium stannate phosphors," *J. Alloys Compd.*, vol. 398, pp. 256–260, 2005, <https://doi.org/10.1016/j.jallcom.2005.02.019>.
- [19] H. Gao, Y. Wang, "Photoluminescence of Eu^{3+} activated Ba_2SnO_4 under ultraviolet–vacuum ultraviolet excitation," *J. Mater. Res.*, vol. 21, pp. 1857–1861, 2006, <https://doi.org/10.1557/jmr.2006.0230>.
- [20] B. Lei, Y. Liu, J. Liu, Z. Ye, C. Shi, "Pink light emitting long-lasting phosphorescence in Sm^{3+} -doped CdSiO_3 ," *J. Solid State Chem.*, vol. 177, pp. 1333, 2004, <https://doi.org/10.1016/j.jssc.2003.11.006>.
- [21] V. Naresh, S. Buddhudu, "Analysis of energy transfer based emission spectra of ($\text{Sm}^{3+}, \text{Dy}^{3+}$): $\text{Li}_2\text{O}-\text{LiF}-\text{B}_2\text{O}_3-\text{CdO}$ glasses," *J. Lumin.*, vol. 147, pp. 63–71, 2014, <https://doi.org/10.1016/j.jlumin.2013.10.035>.
- [22] M. G. Ha, M. R. Byeon, T. E. Hong, J. S. Bae, Y. Kim, S. Park, H.-S. Yang, K.S. Hong, " Sm^{3+} -doped CaTiO_3 phosphor: Synthesis, structure, and photoluminescent properties," *Ceram. Int.*, vol. 38, pp. 1365–1370, 2012, <https://doi.org/10.1016/j.ceramint.2011.09.015>.
- [23] D.R. Taikar, "Synthesis and luminescence property of $\text{SrY}_2\text{O}_4:\text{M}$ ($M = \text{Eu}^{3+}, \text{Tb}^{3+}, \text{Sm}^{3+}, \text{Ce}^{3+}, \text{Bi}^{3+}$) phosphors," *J. Lumin.*, vol. 204, pp.24–29, 2018, <https://doi.org/10.1016/j.jlumin.2018.07.040>.
- [24] S. Selvi, K. Marimuthu, G. Muralidharan, "Structural and luminescence behavior of Sm^{3+} ions doped lead boro-telluro-phosphate glasses," *J. Lumin.*, vol. 159, pp. 207–218, 2015, <https://doi.org/10.1016/j.jlumin.2014.11.025>.
- [25] W. T. Carnall, P. R. Fields and K. Rajnak, "Electronic Energy Levels in the Trivalent Lanthanide Aquo Ions. I. $\text{Pr}^{3+}, \text{Nd}^{3+}, \text{Pm}^{3+}, \text{Sm}^{3+}, \text{Dy}^{3+}, \text{Ho}^{3+}, \text{Er}^{3+}$, and Tm^{3+} ," *J. Chem. Phys.*, vol. 49, pp. 4424–4442, 1968, <https://doi.org/10.1063/1.1669893>.
- [26] E. Pavitra, G. Seeta Rama Raju, Yeong Hwan Ko and Jae Su Yu, "A novel strategy for controllable emissions from Eu^{3+} or Sm^{3+} ions co-doped $\text{SrY}_2\text{O}_4:\text{Tb}^{3+}$ phosphors," *Phys. Chem. Chem. Phys.*, vol. 14, pp. 11296–11307, 2012, <https://doi.org/10.1039/C2CP41722G>.

¹ C. T. Londhe**Regular paper****Study of potential energy curves of diatomic zirconium oxide molecule**

Abstract: - The spectrum of diatomic zirconium oxide was recently reported and the $B^1\Pi \rightarrow X^1\Sigma^1$ transition is analyzed by Jason J. Sorensen and Peter F. Bernath using a high resolution Fourier Transform Spectrometer. The zirconium oxide was produced using a carbon tube furnace that contained a few grams of ZrO_2 , charged 110 Torr helium and heated to 2390 K. The molecular constants derived in this analysis are used for the construction of RKR, Hulbert- Hirschfelder (H-H), and Generalized potential energy function. The percentage deviations from RKR curves are drawn at the same abscissa scale. The error curve shows that that both potential energy curve deviation is less than 2 % error with dissociation limit.

Keywords: *Potential energy curve, zirconium oxide, Hulbert- Hirschfelder Potential, Generalized potential energy function.*

¹ *Corresponding author: Department of Physics, Mahatma Gandhi Mahavidyalaya, Ahmedpur, Dist-Latur – 413515, India
Copyright © JES 2024 on-line : journal.esrgroups.org

I. INTRODUCTION

The potential energy function is a mathematical expression which represents the potential energy curve. The potential energy functions which play very important role in the determination of fundamental molecular constants that are related to the molecular structure [1]. In the calculations of Franck Condon factors, dissociation energies and thermodynamic quantities etc, the studies of potential energy curves are necessary [2]. The empirical potential energy functions like Morse [3], Rydberg [4] Varshni [5], Lippincott [6] and Hulbert-Hirschfelder [7] are usually applied and the potential energy curves are drawn. For all these calculations the Rydberg Klien Rees-Vanderslice RKR [8-12] curves are essential. Naturally to compute the turning points of various vibrational levels the accurate spectroscopic constants are required. The empirical potential functions also require these molecular constants.

Zirconium oxide molecule has astrophysical significance as it is observed in M and S type stars. The electronic band structure of zirconium oxide is complicated and possesses many strong bands which are characteristic of S type stars [1] as first reported by Merrill [13] and confirmed by Van Eck et al [14] in 2017. Zirconium oxide has been studied theoretically by Langhoff and Bauschlicher [15] in 1990 and reported spectroscopic constants. The review of zirconium oxide gives by Mc Kemmish et al [16]. In the present study the potential energy curves for the ground electronic states are constructed for the diatomic zirconium oxide molecule. The constants of ground state of Zirconium oxide are taken from Jason J. Sorensen and Peter F. Bernath [1] and reported in table 1.

Table 1: Molecular constants of the ground state of zirconium oxide molecule

μ	13.5790	B_e	0.4235669076442719
ω_e	976.40869	α_e	0.001918
$\omega_e x_e$	3.44152	D_e	63800
$\omega_e y_e$	0.00052	r_e	1.71199

Note: All constants are in cm^{-1} except r_e , which is in \AA and μ , is in amu

II. THE POTENTIAL ENERGY FUNCTIONS

The method of drawing potential energy curves based on the spectroscopic constant like ω_e , $\omega_e x_e$, B_e , α_e , r_e etc was developed by Rydberg, Klien and Rees [8-10,]. Further it was modified by Vanderslice [11, 12]. A brief account of RKR calculation is also given by Castano et al [17]. A programme for computing the turning point is developed by Le Roy [18].

1. *Generalized potential energy function:*

Surkus [19-29] has suggested a potential function which is known as GPEF. This function has the form

$$U_{GPEF}^{(r)} = g_0 w^2 \left(1 + \sum_{i=1}^N g_i - w_i \right) \text{---(1)}$$

$$\text{Where } w = w(R | P, n) = \left[\frac{r^p - r_e^p}{r^p - n r_e^p} \right] \text{---(2)}$$

Where $p \neq 0$, $n \neq -1$

And $s(p) = 1$ if $p > 0$, $s(p) = -1$ if $p < 0$

$W(R|-1,0)$ yields Dunham potential function

$W(R|1,0)$ yields SPF potential function

$W(R|P,0)$ yields Thakkar potential function

$W(R|1,1)$ yields Ogilvie-Tipping potential function

Thus all four potentials namely Dunham, Simon Parr Finlan (SPF), Thakkar and Ogilvie –Tipping are included in generalized potential energy function. The different parameters used in generalized potential energy function are calculated using turbo basic programme and shown in table 2.

2. *The Hulbert-Hirschfelder potential function:*

This function [7] is an extension of a Morse function and is defined as follows,

$$U_{H-H}(r) = D_e \{ [1 - \exp(-x)]^2 + cx^3(1 + bx) e^{-2x} \} \quad \dots\dots\dots (3)$$

Where $x = x_1(r - r_e)$; $x_1 = (\omega_e x_e / B_e)^{1/2} / r_e$

$$c = 1 + a_1 (D_e / a_0)^2; b = 2 - \{ [(7/12) - (D_e - (a_2 / a_0))] / c \}$$

$$a_0 = \omega_e^2 / 4 B_e; a_1 = -1 - \{ \omega_e x_e / (6B_e)^2 \} \text{ and}$$

$$a_2 = (5/4) a_1 - (2/3) (\omega_e x_e / B_e)$$

This function employs the spectroscopic constants like ω_e , $\omega_e x_e$, B_e and D_e etc. The potential energies U_{H-H} could be calculated by substituting the values of the constants and r values obtained from the RKR curves and the relevant parameters.

III. COMPUTATIONAL PROCEDURE

The data of turning points i.e. r_{\min} and r_{\max} values obtained from RKR curves of these molecules are substituted in equations 1 and 3 respectively for Generalized potential and Hulbert- Hirschfelder (H-H) potential energy function along with the corresponding parameters shown in Table 2.

Table 2 : Parameters of Generalized potential and Hulbert- Hirschfelder (H-H) potential energy function for the ground state of zirconium oxide molecule

Generalized potential energy function			
p	4.348	g₄	0.4352067
n	1	g₅	-0.3485827
g₀	117688.869	g₆	2.09569
g₁	-0.957269	g₇	-1.7358797
g₂	0.6875689	C_k	46572.55
g₃	-0.6346356	r_e(A⁰)	1.71199
Hulbert-Hirschfelder potential function			
a₀	562705.625	c	0.07728
a₁	2.74028	b=	0.27603
a₂	3.96971	X₁=	1.73471

The potential energies obtained plotted against r values yield a potential energy curve for that potential for that particular molecule. For comparison purposes all the potential energy curves of each molecule are drawn on same scale along with their respective RKR curve. The error curves i.e. the % deviation from RKR energies which are calculated by formula $[(U_{RKR} - U_{\text{potential}}) / D_e] \times 100$.

IV. RESULTS AND DISCUSSION

The RKR curves are plotted for the ground states of zirconium oxide molecule to the extent of 60 % of their dissociation energies. The potential energy curves drawn using Generalized potential energy functions are shown in Figure 1 and below these curves the % deviations from RKR curves are drawn as shown in Figure 2. The average deviation of RKR reported by Londhe et al.[30]. From the graph it is clear that both the potentials show good performance over a wider range. In case of the Hulbert- Hirschfelder potential energy curve almost overlap the RKR curves of the ground state of zirconium oxide molecule to high v values and show 1 % error to dissociation limit. On the other hand the Generalized potential energy function deviate from RKR with higher v values and show 2 % error to the dissociation limit.

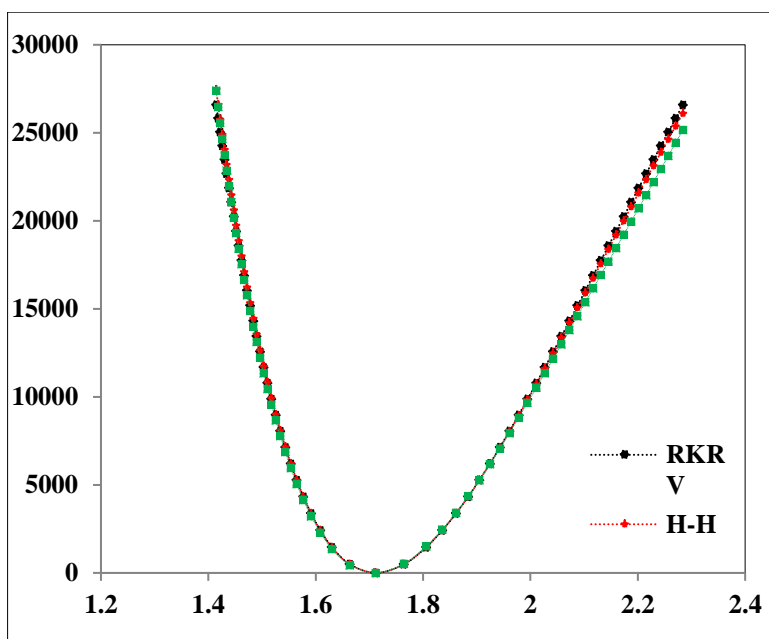


Figure 1: RKR, Generalized potential and Hulbert- Hirschfelder (H-H) potential energy curves for the ground state zirconium oxide molecule

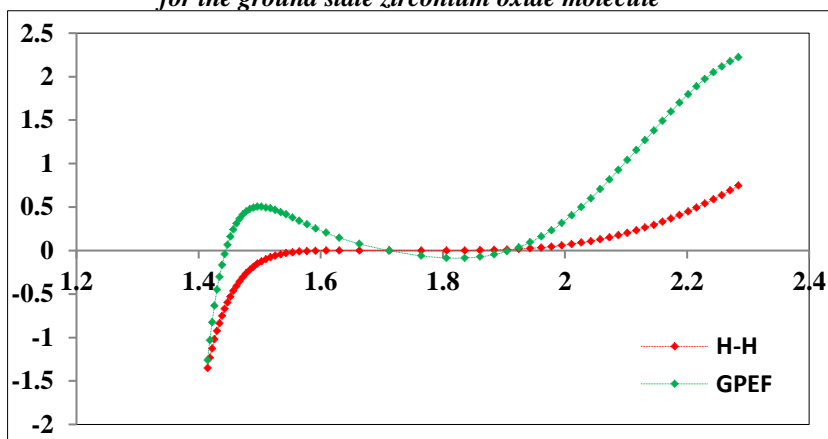


Figure 2: % Deviation of Generalized potential and Hulbert- Hirschfelder (H-H) potential energy curves for the ground state zirconium oxide molecule

V. CONCLUSION

The Generalized potential and the Hulbert-Hirschfelder potential energy function are almost overlap the RKR curves of the ground state of zirconium oxide molecule to high v values and show very little deviation from RKR potential.

ACKNOWLEDGMENT

I thank to Dr. S. H. Behere, Professor, Department of Physics, Dr. Babasaheb Ambedkar Marathwada University Aurangabad for their continuous encouragement during the course of this work.

REFERENCES

- [1] Jason J. Sorensen and Peter F. Bernath 2021 *ApJ* **923** 234
- [2] Hewa Y Abdullah, C. T. Londhe, *Iranian Journal of Science and Technology, Transactions A: Science* Vol. 43, Issue 3, pp.1361-1363 June 2019
- [3] P. M. Morse, *Phys Rev*, **34**, 57 (1929).
- [4] R. Rydberg, *Z Phys*, **73**, 376 (1931).

- [5] Y. P. Varshni, *Rev Mod Phys*, **29**, 664 (1937).
- [6] E. R. Lipponcott , *J Chem Phys*, **21**, 2070 (1953).
- [7] H. M. Hulbert and J. O. Hirschfelder, *J. Chem. Phys.*, **9**, 61, (1941) *ibid* 35, 1901 (1961)
- [8] R. Rydberg, *Z Phys.*, **80**,514 (1933)
- [9] O. Klein, *Z Phys.*, **76**,226 (1932)
- [10] A. L. G. Rees, *Proc. Phys. Soc.*, **59**,998 (1947)
- [11] J. T. Vanderslice, E. A. Meson, W. G. Maisch and E. R. Lippincott, *J. Chem. Phys.*, **33**,614 (1960)
- [12] J. T. Vanderslice, E. A. Meson, W. G. Maisch and E. R. Lippincott, *J. Mol. Spectrosc.*, **3**,17 (1959) and **5**, 83 (1960)
- [13] Merrill, P. W. 1922, *ApJ*, 56, 45
- [14] Van Eck, S., Neyskens, P., Jorissen, A., et al. 2017, *A&A*, 601, A10
- [15] Langhoff, S. R., & Bauschlicher, C. W. 1990, *ApJ*, 349, 369
- [16] McKemmish, L. K., Borsovszky, J., Goodhew, K. L., et al. 2018, *ApJ*, 867, 33
- [17] Castano J. de Juan and Martinez E., *J. Chem., Edu.*, 60 (1983) 291-294.
- [18] R. J. Le Roy, Uni. of waterloo, Chem., Phys. Research report (1992) CP-425.
- [19] A. A. Surkus, *Chem. Phys. Letters*, 180, 230 (1990).
- [20] A. A. Surkus, R J Rakauskaer and Bolotin A B, *Chem. Phys. Letters*, 105, 291(1984).
- [21] A. A. Surkus, *Chem. Phys. Letters*, 150, 416 (1991).
- [22] A. A. Surkus, *Chem. Phys. Letters*, 197, 530 (1992).
- [23] A. A. Surkus, *Lietuvos Fizikosrinkinys*, 32, 460 (1992).
- [24] A. A. Surkus, *Spectra chimica Acta*, 48A, 1501 (1992).
- [25] A. A. Surkus, *Spectra chimica Acta*, 50A, 2391 (1996).
- [26] A. A. Surkus, *Spectra chimica Acta, Part A* 52, 661 (1996).
- [27] A. A. Surkus, *Spectra chimica Acta,Part A* 52, 1925 (1996).
- [28] A. A. Surkus, *Chem. Phys. Letters*, 126, 356 (1997).
- [29] A. A. Surkus, *Chem. Phys. Letters*, 236, 279 (1997).
- [30] C. T. Londhe, N. H. Mhaske, S.H. Behere, *International Journal of Emerging Technologies in Computational and Applied Sciences*, 3(1), Dec.12-Feb., 2013, pp. 1-4.

¹*V. U. Rahangdale

²S. D. Charpe

Effect of Al₂O₃ addition on the properties of Lead Titanate Glass-ceramics



Abstract: - Glasses with different weight proportions of Al₂O₃ have been synthesized by melt-quench method. Prepared glasses were given two stage heat treatment to convert them into glass-ceramics. In these glass-ceramic samples it is observed that the density, room temperature dielectric constant and percentage of lead titanate phase increased with Al₂O₃ addition. These glass-ceramic samples have shown ferroelectric property and it has been observed that the value of remnant polarization increased with Al₂O₃ addition. The enhancement in the values of remnant polarization was due to increase in the volume fraction of PbTiO₃ phase as measured from XRD.

Keywords: Glass-ceramics, XRD, PbTiO₃, Dielectric constant, Ferroelectric properties.

¹ * Corresponding author: Jagat Arts, Commerce and I.H.P. Science College, Goregaon, Dist. Gondia. Maharashtra- 441801 India
Vijayrahangdale11@gmail.com

² Department of Physics, J. D. Patil Sangludkar Mahavidyalaya, Daryapur Dist. Amravati, Maharashtra-444803, India
Copyright © JES 2024 on-line : journal.esrgroups.org

I. INTRODUCTION

In 1950, Lead titanate was reported to be ferroelectric on the basis of its structural properties compared with BaTiO₃. The high transition temperature around 490 °C [1] exhibited by PbTiO₃ make this material useful for high temperature applications. Controlled crystallization of glasses led to a development of polycrystalline solids known as glass-ceramics [2]. These materials can be used as an insulator for high voltages, substrates for electronic circuits, dielectric and piezoelectric devices [2-3]. Lead titanate (PbTiO₃) is a typical ferroelectric material having perovskite structure with $T_c \sim 490$ °C. It is difficult to prepare the undoped lead titanate ceramic material due to large anisotropy. The glass-ceramic route, therefore, offers the possibility of fabricating lead titanate without cracking [4]. The lead titanate based glass-ceramic have been studied widely. However very few reports are available on the effect of Al₂O₃ addition on structural, dielectric and ferroelectric properties of lead titanate containing glass-ceramic.

In this work systematic addition of Al₂O₃ at the cost of B₂O₃ was done to enhance the dielectric and ferroelectric properties of these glass-ceramics.

II. EXPERIMENTAL

The glasses with composition 60PbO : 25TiO₂ : (15-X)B₂O₃ : XAl₂O₃ (with X= 0, 2.5, 5, 7.5 and 10 mol%) were prepared from highly pure chemicals. The mix dry powders with different weight proportions were transferred to 5 different 50 ml alumina crucibles, which then heated up to 1250-1300 °C. The melt was soaked for 1 h and homogenized by stirring it before quenching into the copper mould at room temperature. The resultant glass samples were annealed at 400 °C for three hours to remove the residual stresses. The glass transition temperature T_g and crystallization temperature T_c for the glass were determined from DTA. The glass samples were converted to glass-ceramics by following the two stage heat treatment. The glass samples were nucleated for 16 h and crystallized for 16 h, at 425 °C and 480 °C respectively. The density of these glass-ceramics was measured by Archimedes principle with toluene as an emersion liquid.

The XRD patterns of glass-ceramics were recorded with Xpert PANalytical diffractometer. In glass-ceramic samples it was desired to have maximum percentage of formation of perovskite PbTiO₃ phase. Therefore its (PbTiO₃) volume fraction was calculated from XRD. The room temperature dielectric constant of glass-ceramic samples was measured using high resolution dielectric alpha analyzer. The ferroelectric hysteresis measurements were performed using automatic PE loop tracer.

Times is specified, Times Roman or Times New Roman may be used.

If neither is available on your word processor, please use the font closest in appearance to Times. Avoid using bit-mapped fonts if possible. True-Type 1 or Open Type fonts are preferred. Please embed symbol fonts, as well, for math, etc.

III. RESULTS AND DISCUSSION

Density of the glass-ceramic samples has been observed to increase with Al₂O₃ addition. The maximum density 6.55 gm/cm³ was obtained for 10 mol % Al₂O₃ containing glass-ceramic sample. The increase in density with Al₂O₃ addition may be due to higher mass of Aluminum compared to that of Boron which increases the rigidity of glass-ceramic samples.

The XRD patterns of the glass-ceramic samples have been depicted in figure 1. XRD results shows that lead titanate is the major crystalline phase in the glass-ceramic samples. All the major peaks matched very well with the tetragonal lead titanate phase (JCPDS file no-78-0298). The volume fraction of lead titanate phase was calculated by comparing the integral intensities of amorphous, glass-ceramic and completely crystalline samples from X-ray diffraction patterns [5]. The volume fraction of PbTiO₃ phase is (shown in table 1) observed to increase with Al₂O₃ addition. The replacement of B₂O₃ by Al₂O₃ led to enhance the perovskite PbTiO₃ content in glass-ceramics as confirmed from XRD.

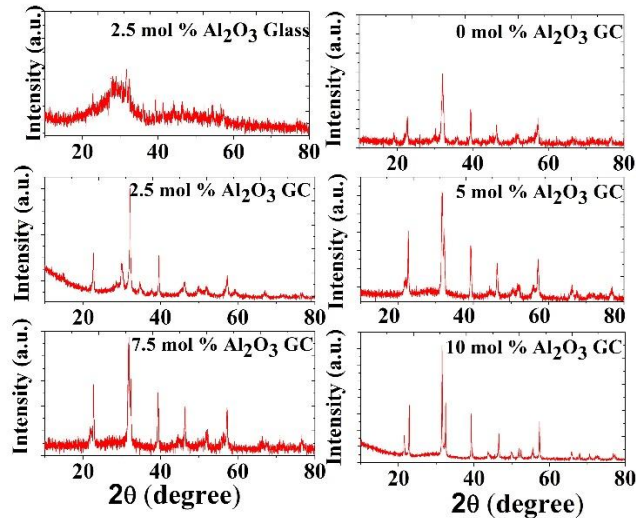


Fig 1. XRD Patterns for Glass-ceramic samples.

The room temperature dielectric constant of the glass-ceramic samples has been measured at 1 kHz which shows increasing trend with the Al_2O_3 addition (Table 1). The values of dielectric constant obtained in the present work are higher than those reported in the literature for PbTiO_3 containing glass-ceramics [6, 7]. The increase in dielectric constant may be correlated to the increased volume fraction of formation of tetragonal PbTiO_3 phase in glass-ceramic samples.

The ferroelectric hysteresis measurements were carried out at room temperature. The samples were poled at 5 kV for 30 minutes. The values of remnant polarization is given in table 1. From the table 1 it is observed that there is an increase in the values of remnant polarization with Al_2O_3 addition.

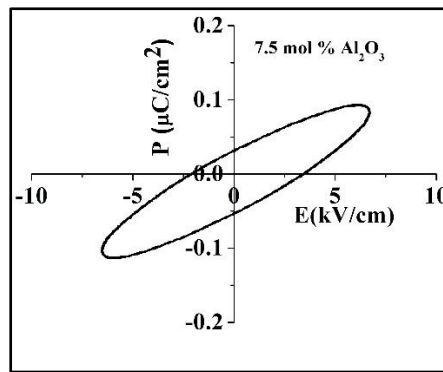


Fig 2. Representative PE Hysteresis Loop for 7.5 Al_2O_3 containing Glass-ceramic sample.

The observed increase in remnant polarization for glass-ceramic samples may be attributed to the formation of tetragonal lead titanate phase whose content was observed to increase with Al_2O_3 addition. Fig.2 shows the ferroelectric hysteresis loop for the 7.5 mol % Al_2O_3 containing glass-ceramic sample. The non-saturated loops were observed in all the samples which could be due to the presence of residual glass phase and the stress applied by the rigid glass matrix [8, 9]. The ceramic-glass interface plays an important role in causing the non-saturated hysteresis loops. This phenomenon is believed to be due to interfacial polarization [10, 11].

These are preliminary results, and further enhancement in P_r can be obtained by optimizing the processing parameters of the glass-ceramics.

TABLE 1. Values of Room Temperature Dielectric Constant, Volume Fraction of PbTiO₃, Remnant Polarization and Coercive Field for Glass-ceramic Samples.

Mol % Al ₂ O ₃	Dielectric Constant at 1 kHz	Volume Fraction of PbTiO ₃ (%)	P _r (μC/cm ²)
0	113	54.19	0.010
2.5	117	55.02	0.015
5	120	57.68	0.018
7.5	129	58.11	0.038
10	134	58.69	0.049

IV CONCLUSION

The density, dielectric constant and volume fraction lead titanate increases with Al₂O₃ addition. The presence of ferroelectricity in these glass-ceramic samples makes them useful for transducers applications for which further investigation is needed.

ACKNOWLEDGMENT

There is no specific funding to support this research.

REFERENCES

- [1] B. Jaffe, "Piezoelectric Ceramics", Academic Press, London, UK, 3rd edition, 1971.
- [2] P. Sooksaen, I. M. Reaney and D. C. Sinclair, *J. Electroceramics* **19**, 221-228 (2007).
- [3] G.J. Gardopee, R.E. Newnham, A. Halliyal, A.S. Bhalla, *Appl. Phys. Lett.* **36**, 817-818 (1980).
- [4] P. Sooksaen and I. M. Reaney, *J. Mater. Sci.* **43**, 1265-1269 (2008).
- [5] A. Ilinsky, V. Maslov, V. Nozenko, V. Brovko, *J. Mater. Sci.* **35**, 4495-4500 (2000).
- [6] J. Shyu, Y. Yang, *J. Mater. Sci.* **31**, 4859-4863 (1996).
- [7] J. Shankar and V. K. Deshpande, *Integrated Ferroelectrics*, **119**, 110-121, (2010).
- [8] J. Shyu, C. Chen, *Ceram. Int.* **29**, 447-453, (2003).
- [9] J. Seigwarth, *J. Appl. Phys.* **48**, 1- (1977).
- [10] E.P. Gorzkowski, M.J. Pan, B. Bender, C.C.M. Wu, *J. Electroceramics* **18**, 269-277 (2007).
- [11] M.J. Pan, J.E.P. Gorzkowski, B. Bender, C.C.M. Wu, Proceedings of 15th IEEE International Symposium on Ferroelectrics 25-28 (2006).

© 2024. This work is published under

[https://creativecommons.org/licenses/by/4.0/legalcode\(the\"License\"\)](https://creativecommons.org/licenses/by/4.0/legalcode(the\).

Notwithstanding the ProQuest Terms and Conditions, you may use this content in accordance with the terms of the License.

¹*Nita Shinde
²Anil G. Beldar
³Ashvini Pusdekar
³N.S.Ugemuge

**“A Comprehensive Review on
 Nano Crystalline CdS, Ag₂S and
 CdS-Ag₂S Thin Films Synthesized by
 Chemical Bath Deposition &
 Modified Chemical Bath Deposition
 Method”**



Abstract: Thin film solar cells offer several benefits over conventional first-generation technologies including lighter weight, flexibility, and a wider range of optoelectronic tunability.[1] This article provides an overview of the material properties of Nano crystalline cadmium sulphide (CdS), silver sulphide (Ag₂S) and CdS-Ag₂S thin films, the structural, microstructural, optical, and electrical characteristics of the thin films have been compared and reviewed for these nanocrystalline CdS and Ag₂S and CdS- Ag₂S. Nano crystalline cadmium sulphide (CdS), silver sulphide (Ag₂S) and CdS- Ag₂S thin films prepared from aqueous medium onto corning glass substrates and fluorine doped tin oxide (FTO) coated glass substrates using chemical bath deposition (CBD) and modified chemical bath deposition (M- CBD) methods has been discussed in detail in this paper [2]. This paper provides overview of characterization of the thin films deposited onto glass substrate. These thin-film solar cells' high absorption coefficient and appropriate band gap have also been shown to contribute to their comparatively good light management, according to analysis. Overall, this study offers background information on material properties and device performance and proposes primary research avenues to address the constraints.

Keywords: Nano crystalline Thin films,CBD& M-CBD techniques, structural, microstructural, optical, and electrical characteristics

¹*Corresponding author: ¹Department of Physics, L.A.D.& SMT. R.P. College for Women, Nagpur, 440007, India

²*Corresponding author: ² Department of Chemistry, P. S. G. V. P. Mandal's S. I. Patil Arts, G. B. Patel Science and S. T. K. V. Sangh Commerce College, Shahada, Nandurbar 425409, India

³ Department of Physics, Anand Niketan College, Anandwan, Warora, 442907, India

I. INTRODUCTION

In the science and technology thin films have become increasingly important due to their potential and technical importance. These thin films can be single or multi-component, compound, alloy, or multilayer coatings. To understand aspects of the subject these thin film materials are very important in modern technology, providing applicatory information. Thin film nanotechnology of films has modernized optics and electronics, manufacturing electronic components for high-speed digital, communications, computing, and automotive markets. Thin film nanotechnology used in various products, which includes delay lines, equalizers, filters, termination networks, précised resistors, inductors, and capacitors. For unconventional energy sources, researchers are exploring a thin-film solar energy conversion device which includes semiconductor-liquid (S-L) junction solar cells. These cells have built-in storage capacity, making them attractive over solid state solar cells, also prompts further research on their potential [3].

II. Cadmium Sulphide CdS Thin Films Research history

Wide band gap Group II-VI wide band materials produce thin films with appropriate blue and green crystal regions. It shows unique properties and performing amorphous polycrystalline materials, particularly at the nano range (20-80 nm). The II-IV group comprises cadmium sulfide, a yellow semiconductor with a 2.42 eV band gap that can exist in two crystal forms: cubic zinc blende and hexagonal wurtzite. CdS solar cells use its nano crystalline thin films, which belong to the cadmium chalcogenide family, as window material. [4-8]CdS, with its direct band gap, is highly valuable in solid state solar cells, optical coatings, light-emitting diodes, optoelectronic devices like gas sensors, transducers, photoconducting cells, photosensors, optical wave-guides, and non-linear integrated optical systems, [9-10] and is used to enhance dye-sensitized photoelectrochemical cells [11-12].

III. Silver Sulphide (Ag₂S) Thin Films Research History

Due to the potential applications in research and technology Silver sulfide (Ag₂S) Chalcogenide Substance, nanocrystalline semiconducting chalcogenide thin films have attracted attention [13]. Ag₂S observed in two primary allotropic modifications: cubic argentite (β -Ag₂S) and monoclinic acantite (α -Ag₂S). These thin, black solids are having applications in photoconductors, electrochemical storage cells. [14], and solar cells [15]. They are soluble in strong acids but destroyed in solvents. Its band gap ranges from 1-2 eV. Ag₂S thin films have been produced chemically by researchers in both acidic and alkaline solutions, making them an important resource for a variety of applications.

AgNO₃, thiourea, EDTA, and ammonia were used to create the Ag₂S thin films, which have been reported to have high absorbance, low reflectance, a fairly high refractive index, and a band gap of 1.8 eV by A. Ezenwa et al. [16]. These films can be applied to photovoltaic materials with evenly dispersed grains, antireflection coatings, and solar energy collecting. Ag₂S thin films were electrodeposited on an ITO substrate by Xing-Yu Guo et al. [17]; the best crystallization occurred at a deposition potential of -0.25 V. Ag₂S nanoparticles, with a mean particle diameter of 8.4 nm, were prepared by Rui Chem et al. [18] by the reaction of silver nanoparticles with sulphide gas.

Ximbo Wang et al. [19] produced hexagonal nano sulphide at room temperature by using AgNO₃ Sulphur in diethylamine both with and without PVP, which produces Ag₂S with crosswise lengths ranging from 100 to 120 nm. Sourich Banergy and associates [20] observed a decrease in resistivity with rising temperatures after depositing Ag₂S nanocrystals within a silica matrix. T. Ben Nasrallah et al. [21] conducted a physical investigation on Ag₂S thin films, revealing a solar efficiency of 0.11% synthesized by sequential thermal evaporation. Nahass et al. [22] deposited the thin films on glass and quartz substrates, enlightening a polycrystalline structure with a monoclinic structure of the thin films. As the thickness of the thin film increases dark electrical resistivity decreases.

IV. History of CDS-Ag₂S Thin Films Research

It has proven possible to create metal, metal sulfide, and ceramic Nano composites [23-25] with crystalline, amorphous, and polycrystalline materials that have special mechanical, chemical, magnetic, electrical, and optical properties. Silver and

cadmium sulphides are semiconducting materials that can be utilized in PEC for the conversion of solar energy. By employing these materials separately, all ECPV requirements might not be satisfied yet. In order to get around this multilayer and heterostructure films can adjust the band gap to match the solar spectrum. Hota et al. [26] synthesized CdS-Ag₂S composite nanoparticles, by using an AOT/n-heptane/water micro emulsion, which were observed to be well-defined and spherical in shape. Due to their importance in optoelectronic devices, wide band gap nanocrystalline materials have many uses nowadays. These materials' physico-chemical characteristics vary depending on the synthesis technique and substrate type. Large-area II-VI and I-VI compound nanocrystalline materials are economically attractive for producing a variety of devices. High absorption coefficient and an ideal band gap enable nanocrystalline CdS, Ag₂S, and CdS-Ag₂S thin films to handle the full solar spectrum.

V. Thin film deposition techniques

By using very thin layers of semiconductor materials thin film solar cells a type of solar panel that is made. Onto a substrate, like glass or plastic, using a thin film deposition technique these materials is applied. In the formation of solid-state microelectronic devices modern technology is heavily reliant on thin films, and the process of film deposition holds significant importance. There are numerous thin-film deposition techniques, but they are all atomistic in nature—that is, they grow films atom by atom. The methods employed for thin-film deposition can be divided into two groups based on the nature of the deposition process namely, physical and chemical as shown in fig.1.

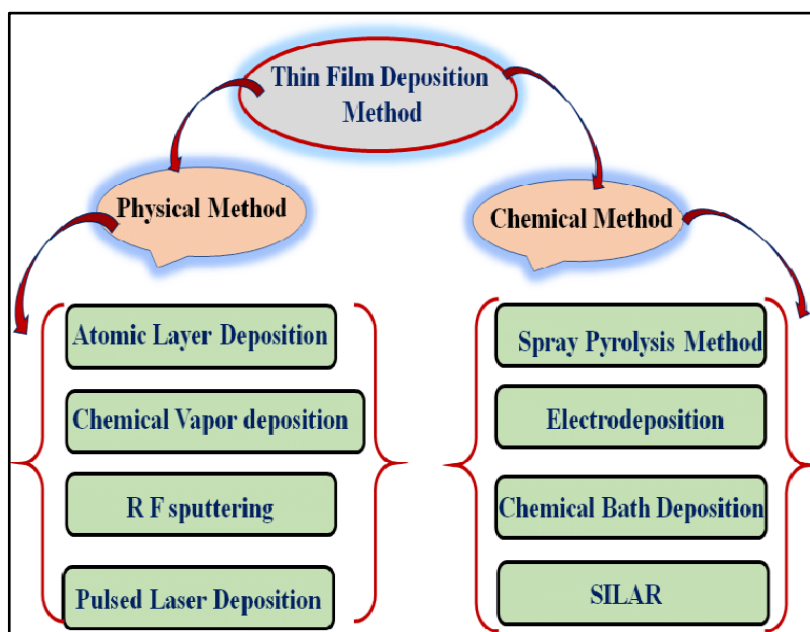


Fig. 1: Classification of deposition techniques [27]

V-a . Chemical Bath Deposition Method

Chemical Bath Deposition (CBD) method is a solution growth technique method which involves mixing of cationic and anionic solutions, which causes precipitation to form nuclei. This method is simple, inexpensive and for the large area deposition this method is very convenient. Precipitation is controlled using chemical equilibrium and metal complexing agents by the condensation of metal and oxide/sulfide/selenide/ ions over the substrate surface thin films are formed. Chalcogen ions and Complexation of metal ions are provided by reagents. So the stable concentration of metal cation for controlled homogenous precipitation on the solid substrate is possible. [28-29]

It does not require sophisticated instruments, like vacuum systems and other expensive equipments. It can be carried out in a glass beaker. A hot plate or a stirrer is the equipments needed. The starting chemicals are easily available and low cost. Using

CBD, a large number of substrates can be coated in a single run with a proper jig design. Electrical conductivity of the substrate is not a necessary requirement in chemical deposition unlike the electrodeposition [30]. Hence, any insoluble substrate to which the solution has free access will be a suitable for deposition. The low temperature deposition avoids oxidation and/or corrosion of metallic substrates. Chemical deposition results in pinholes free and uniform deposits as the solution from which these are deposited, always remains in touch with the substrates. It is possible to obtain Stoichiometric deposits easily since the basic building blocks are ions instead of atoms [31]. The film growth can take place, ion-by-ion condensation of the materials or by adsorption of colloidal particles from the solution on the substrate. There are no organo-metallic solvents and no toxic or pyrolytic gases are evolved. The initial parameters are easily controllable and improved grain structure, better orientation can be obtained [32]. Depending upon the deposition conditions such as, bath temperature, pH of solution, speed of rotation, concentration and reaction time period can be controlled to obtain uniform and adherent film deposition at low temperature [33]. This method can be used for the deposition of II-VI, I-VI, III-V, and IV-VI semiconducting thin films.

V-b. Modified Chemical Bath Deposition (M-CBD)

For the deposition of metal chalcogenide a relatively new and novel method firstly introduced; modified chemical bath deposition by Nicolau [34-35]. During last three decades, modified chemical bath deposition (M-CBD) commonly known as successive ionic layer adsorption and reaction (SILAR) method, has emerged as one of the solution methods to deposit a variety of compound materials in thin film form [36]. It is based on immersion of glass substrate into separately placed anionic and cationic precursors and rinsing between every immersion in double distilled water to avoid homogeneous precipitation technique, when substrate is immersed in cationic precursor, cations are adsorbed on the substrate surface. Rinsing the substrate in double distilled water can separate the unabsorbed or excess ions out and avoid homogeneous precipitation. When this substrate is immersed in anionic precursor solution, anions react with preadsorbed cation. The unreacted or powdery material can be removed by rinsing the substrate again in double distilled water. These steps are considered as one complete cycle. After repeating such appropriate number of cycles, multilayer film formation takes place. Thickness and Quality of the thin film depends mainly upon preparative parameters [37]. To obtain the good quality thin film the M-CBD method is inexpensive, simple and convenient. The initial requirements to obtain good quality thin films is the optimization of preparative parameters viz. concentration of the precursors, nature of complexing agent, pH of the precursor solutions [38-39].

VI Structural, Elemental, Microstructure, Optical, and Electrical properties of the Thin Films synthesized by the CBD method [40-41]

The optical absorption of thin films studied in the wavelength range 350 – 800 nm shows optical behavior in the visible range. The room temperature electrical resistivity of Nano crystalline thin film was $10^7 \Omega\text{-cm}$. from the electrical resistivity measurement, it was seen that the resistivity decreases with increase in temperature indicating semiconducting nature of the film. The structural, optical and electrical properties of thin film deposited by CBD and M-CBD method for CDS and Ag_2S are listed in Table 1. The thermoelectric studies showed n-type behavior of the thin films. It is now well known that thin film solar energy conversion devices have become important and are eco-friendly, non-conventional alternative sources of energy.

Table 1: The structural, optical and electrical properties of CdS and Ag₂S thin films deposited by CBD and M-CBD

Sr. No	Parameters	CdS thin film		Ag ₂ S thin film	
		CBD	M-CBD	CBD	M-CBD
1	Crystal structure	Cubic	Hexagonal	monoclinic (acanthite)	monoclinic (acanthite)
2	Grain size (nm)	40	38	25.61	21
3	Electrical resistivity (Ω-cm.)	6.463 x 10 ⁷	5.78 x 10 ⁶	4.8 x 10 ⁵	2.76 x 10 ⁶
4	Thickness (nm)	250	240	140	135
5	Band gap (eV)	2.46	2.20	1.76	2.09

VII. Electrochemical Photovoltaic (ECPV) Solar Cells

Solar cells at present provide the most important long duration power supply for our day to day life. Solar cells have been successfully employed in many fields of science and technology. The solar cell is a major alternative for obtaining energy from sun as it converts sunlight directly into electricity. It can provide nearly permanent power at low operating cost and is pollution free. It is now well known that thin film solar energy conversion devices have become important and are eco-friendly, non-conventional alternative sources of energy. There are several methods of converting solar energy in to electrical energy via photovoltaic, electrochemical photovoltaic, photochemical and photosynthetic using thin film. Thin film based electrochemical photovoltaic (ECPV) solar cells have wide applications due to their low fabrication cost, simple processing technique and ease of junction formation with the electrolyte. Photovoltaic conversion of solar energy is one of the most promising alternatives. The use of Photovoltaic for direct conversion of solar energy into electricity is the need at present. In such conversion, there is no direct contamination of environment. Solar cell utilizing semiconductor-liquid junction (S-L) is the simplest way suggested for solar energy conversion. The most attracting feature of an S-L junction solar cell over a solid state junction solar cell is that it has in-built storage capacity. Therefore S-L junction solar cells are being extensively studied. Solar cells of polycrystalline metal chalcogenide thin films of cadmium, zinc, silver and mixed cadmium are extensively studied in photovoltaic cells. Mixed metal chalcogenide are considered as semiconductor material due to manipulation of band gap to match solar energy spectrum.

The energy conversion by solid-liquid junction is now a subject of intensive research due to its several advantages over the solid-state counterpart. The electrochemical photovoltaic cell (ECPV) has the following advantages over conventional devices [43-47];

- 1) Easy and simple to construct.
- 2) Easy to form junction on immersion of semiconductor in the electrolyte solution.
- 3) A transparent epitaxial layer to reduce electron-hole recombination losses at the surface is not required.
- 4) Anti-reflecting coating for semiconductor is not required in ECPV cells.
- 5) It can be used for chemical storage.

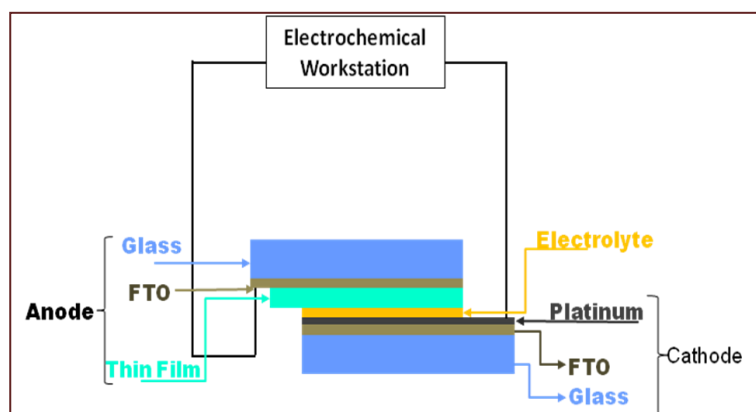


Fig.17: Construction of the ECPV cell

In ECPV solar cells, light energy may be converted into electrical and/or chemical energy, as shown in figure 2. In figure Red and Ox are reduced and oxidized species respectively, in the electrolyte and R represents the resistance in the external circuit or load. The performance and effectiveness of a solar cell device mainly depend upon its design and the properties of the photovoltaic materials included especially the light absorbers and their connections to the external circuit. The choice of the charge mediator involved may also be crucial.

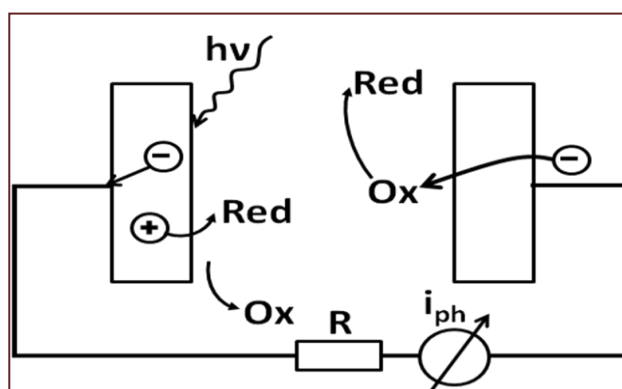


Fig. 18: The process of light-to-electrical energy conversion in electrochemical photovoltaic (ECPV) solar cell.

Light can be pictured as a stream of photons, energy packages of definite size or quantum's of electromagnetic wave energy, whose energy depends upon the frequency or color. Whenever light is absorbed by matter, photons transfer their energy and electrons are excited to higher energy states, usually followed by relaxation to their ground state. In a photovoltaic device, the relaxation may be avoided as the energy stored in the excited electrons is here quickly transferred to an external circuit, in order to do electrical work.

The development of thin films of compound of II-VI group has emerged as one of the alternative energy source due to their high absorption coefficient and matching band gap. Mixed metal chalcogenides are considered as important semiconductor material because of manipulability of band gap to match with solar distribution.

Many researchers have reported electrochemical photovoltaic properties of nanocrystalline as well as microcrystalline thin films of II-VI compounds [48-51]. Due to the small size of nanocrystallites, the mechanism of the space charge separation in these systems is very different from that in the conventional electrochemical photovoltaic cells using single or polycrystalline semiconductors, where the space charge layer controls the charge separation. In nanocrystalline film, it has been proposed that interfacial charge transfer kinetics controls the charge separation [52-55].

During the last few years, photoconversion processes at semiconductor-electrolyte and semiconductor-semiconductor have found new interest because of their solar and nonsolar applications. Cadmium sulphide and silver sulphide are promising semiconducting materials in the conversion of solar energy into electrical energy by means of photoelectrochemical and solid state conversion processes. However if each of them is considered separately it is impossible to fulfill all the desired requirement of semiconductor to be used because of the band gap of CdS (2.42eV) and Ag₂S (1.1eV) don't lie close to solar energy spectrum maximum. In this respect new solar energy materials need to be considered, which satisfy technical properties, such as maximum band gap match with solar spectrum, high mobility, life time of the charge carriers and low cost. It is found that by the formation of multilayer and heterostructure films by combination of two semiconductors, we will get better results in solar conversion. By the combination of CdS and Ag₂S it will tune the band gap between 2.42eV and 1.1eV so that it can match bang gap which is necessary towards solar energy conversion.

The ECPV cells have the following configuration:

FTO/CdS/polysulphide/Platinum,

FTO / Ag₂S / polysulphide / Platinum

FTO /n-CdS-Ag₂S/polysulphide /Platinum

Nanocrystalline CdS, Ag₂S and CdS₈₀Ag₂S₂₀ films deposited by CBD method showed n-type electrical conductivity. The performance parameters such as current density (J_{sc}), open circuit voltage (V_{oc}), series resistance R_s, shunt resistance R_{sh}, fill factor (FF) and efficiency (η) are analyzed from the I-V characteristics of these thin films under dark and illuminated conditions. In general the electrochemical photovoltaic cell (ECPV) properties of CdS, Ag₂S and CdS₈₀Ag₂S₂₀ thin films deposited by CBD are listed in Table 2. From Electrochemical photovoltaic (ECPV) studies, it is seen that the CdS, Ag₂S and CdS₈₀Ag₂S₂₀ photoelectrodes deposited by CBD method are photoactive.

Table 10: Electrochemical photovoltaic (ECPV) properties of CdS, Ag₂S and CdS₈₀Ag₂S₂₀ thin films

Sr.No.	Parameters	Thin films		
		CdS	Ag ₂ S	Cd ₈₀ Ag ₂ S ₂₀
1	Current density J _{sc} (mA/cm ²)	2.135	0.285	0.115
2	Open circuit voltage V _{oc} (V)	0.347	0.300	0.154
3	Series resistance R _s (Ω)	51.38	2181	52.28
4	Shunt resistance R _{sh} (Ω)	466.52	1855	855
5	Fill factor FF (%)	30	44.4	36
6	Efficiency □ (%)	0.222	0.038	0.0006
7	Type of conductivity	n	n	n

VIII. Results and Conclusions

The nanocrystalline CdS thin films deposited by CBD method were superior in adherence, uniformity than that of deposited by M-CBD method. There was no significant difference in other properties such as crystallite size, electrical resistivity etc.is observed. The nanocrystalline Ag₂S thin films deposited by CBD method were good quality and adherent to the substrate than that of deposited by M-CBD method. The crystallite size, and electrical resistivity obtained in the Ag₂S films deposited by M-CBD method were slightly less than the films deposited by CBD method. There is no significant change in the properties of CdS-Ag₂S films deposited by CBD method and that of CdS-Ag₂S films deposited by M- CBD method. The nanocrystalline CdS, Ag₂S and CdS₈₀Ag₂S₂₀ films deposited by CBD method show photoactivity in polysulphide electrolyte.

- **Characterization of nanocrystalline CdS thin films by chemical bath deposition (CBD) method [42].**

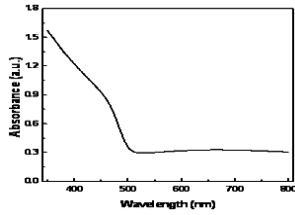


Fig. 4: Variation of absorbance of CdS with thin film with wavelength (λ)

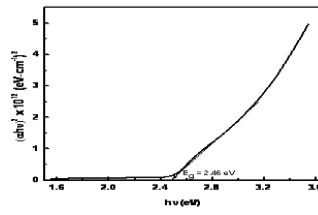


Fig. 5: Variation of $(\alpha h\nu)^2$ versus $h\nu$ of as-deposited CdS thin film

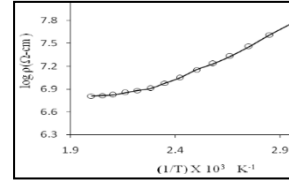


Fig. 6: Variation of electrical resistivity inverse of absolute temperature

- **Characterization of nanocrystalline CdS thin films by modified chemical bath deposition (M-CBD) method [41].**

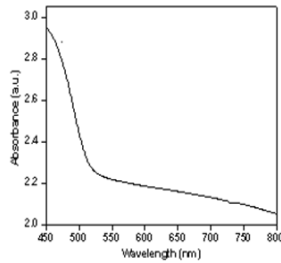


Fig. 7: The variation of optical absorption ' α ' with of wavelength ' λ '

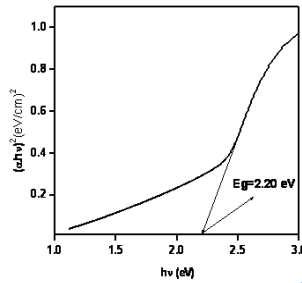


Fig. 8: Variation of $(\alpha h\nu)^2$ versus $h\nu$ as-deposited CdS thin film on glass substrate at room temperature.

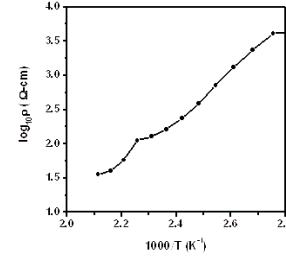


Fig. 9: The variation of logarithm($\log \rho$) with the inverse temperature ($1000/T$)

- **Characterization of nanocrystalline Ag₂S thin films by chemical bath deposition (CBD) method [41]**

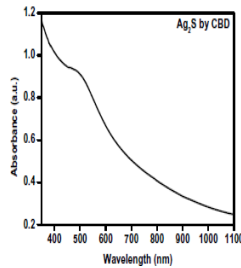


Fig. 10: Variation of ' α ' with of wavelength ' λ '

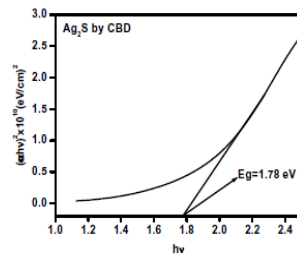


Fig. 11: Variation of $(\alpha h\nu)^2$ versus $h\nu$

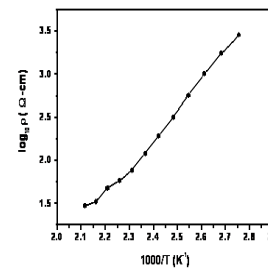


Fig. 12: The variation of $\log \rho$ with inverse of absolute temperature.

- **Characterization of nanocrystalline, Ag₂S modified chemical bath deposition (M-CBD)**

method [41].

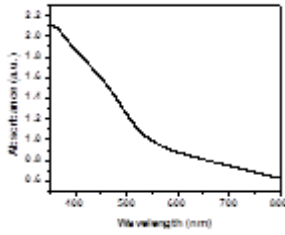


Fig. 13: Variation of (αt) against λ

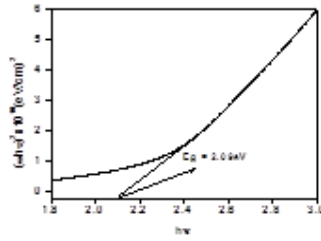


Fig. 14: Variation of $(\alpha hu)^2$ verses hu

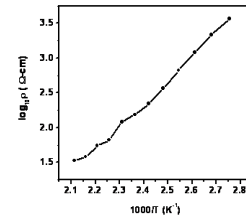


Fig.15: variation of logarithm of resistivity ($\log \rho$) with the inverse temperature ($1000/T$)

➤ Characterization of nanocrystalline CdS-Ag₂S thin films by chemical bath deposition (CBD) method [42]

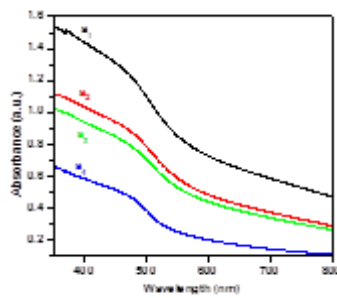


Fig. 16: Variation of (αt) against (λ) for CdS-Ag₂S thin films: (a) CdS₂₀Ag₂S₈₀, (b) CdS₄₀Ag₂S₆₀, (c) CdS₆₀Ag₂S₄₀ and (d) CdS₈₀Ag₂S₂₀.

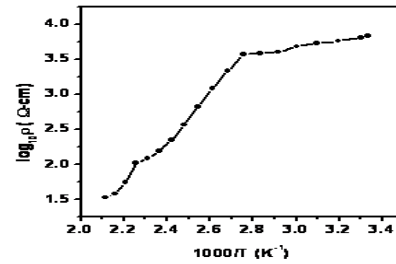


Fig.17: Variation of $\log \rho$ with $1000/T$ for CdS-Ag₂S thin films

➤ Characterization of nanocrystalline CdS-Ag₂S thin films by modified chemical bath deposition (M-CBD) method [41].

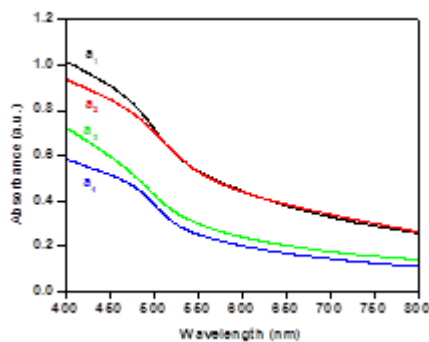


Fig. 18: Variation of (αt) against (λ) for CdS-Ag₂S thin films: (a) CdS₂₀Ag₂S₈₀, (b) CdS₄₀Ag₂S₆₀, (c) CdS₆₀Ag₂S₄₀ and (d) CdS₈₀Ag₂S₂₀.

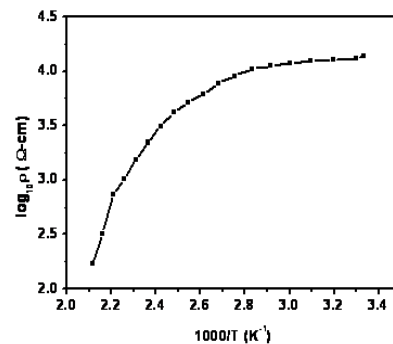


Fig. 19: The variation of logarithm of resistivity ($\log \rho$) with the inverse temperature ($1000/T$) CdS₈₀Ag₂S₂₀ thin film.

REFERENCES

- [1]Tobechi Okoroafor, Zacharie Jehl , Vivek Babu , “A comprehensive review on life cycle assessment of commercial and emerging thin-film solar cell systems”, *Renewable and Sustainable Energy Reviews* 186 (2023) 113652.
- [2] U. M. Jadhav, *Studies on chemical synthesis and characterization of nanocrystalline cds ags cds ags thin films*.Ph. D. Thesis, North Maharashtra Univ. Jalgaon, India (2013).
- [3] G. Nakato and H. Tsubomura, “Silicon photoelectrodes modified with ultrafine metal islands”, *Electrochem Acta*, 37 (1992) 897.
- [4]S. Kutzmutz, G. Lang, K. E. Heusler, “The electrodeposition of CdSe from alkaline electrolytes”, *Electrochem Acta*, 47 (2001) 955.
- [5] C. Shen, X. Zhang, H. Li, “Effect of pH on the electrochemical deposition of cadmium selenide nanocrystal films”, *Mater. Sci. Eng.*, B84 (2001) 265.
- [6] M. Soliman, A. B. Kashyout, M. Shabana, M. Elgamal, “Preparation and characterization of thin films of electrodeposited CdTe semiconductors”, *Semi. Renew. Energy*, 23 (2001) 471.
- [7] R. K. Sharma, G. Singh, A. C. Rastogi, “Pulsed electrodeposition of CdTe thin films: effect of pulse parameters over structure, stoichiometry and optical absorption” *Sol. Energy Mater. Sol. Cells*, 82 (2004) 201.
- [8] X. Mathew, G. W. Thompson, V. P. Singh, J. C. McClure, S. Velumani, Mathews, N. R., Sebastian, “Development of CdTe thin films on flexible substrates—a review” *P. J. Sol. Energy Mater. Sol. Cells*, 76 (2003) 293.
- [9] K. Senthil, D.Mangalaraj, S. K. Narayandass, Appl. “Structural and optical properties of CdS thin films” *Surf. Sci.*, 169/170, (2001) 476.
- [10]Y. Kanemitsu, T. Nagai and T. Kushida, “Free excitons in cubic CdS films” *Appl. Phys. Lett.*, 80 (2002)267.
- [11] H. Chen, W. Li, H. Liu, L. Zhu, “A suitable deposition method of CdS for high performance CdS-sensitized ZnO electrodes: sequential chemical bath deposition” *Solar Energy*, 84 (2010) 1201.
- [12] P. M. Bandaranayake, P. V. Jayaweera, K. Tennakone, “Dye-sensitization of magnesium-oxide-coated cadmium sulfide” *Sol. Energ. Mat. Sol. Cells*,76 (2003) 57.
- [13] A. Henglein, “Small-particle research: physicochemical properties of extremely small colloidal metal and semiconductor particles”, *chem. Rev.*, 89 (1989) 1861-1873.
- [14] H. M. Maghraoui, M. Dachraoui, S. Belgacem, K. D. Buhre, R. Kunst, P. Cowache, D. Lincot, “Structural, optical and transport properties of Ag₂S films deposited chemically from aqueous solution”, *Thin Solid Films*; 288 (1996) 217-223.
- [15] S. Tolansky, Academic press; New York, (1970).
- [16] I. A. Ezenwa, Okereka N.A., N. J Egwadnyenga, “*Int. J. of Sci and Tech*, 2(3)(2012).
- [17] Xing-Yu. Duo, Shu-Ying Cheng, Pei-Min Lu and Hai-Fang Zhao, “ *Mater. Sci. Forum* ,663-665 (2001) 910-913.
- [18] Rui Chen, Noel T Nuhfer, Laura Moussa, Hannah R Morris and Paul M Whitmore, “Silver sulfide nanoparticle assembly obtained by reacting an assembled silver nanoparticle template with hydrogen sulfide gas” *Nanotech.*, 19(2008) 455604.
- [19] Ximbo, Wang, Shuong, Zhicheng Zhang, “Synthesis of hexagonal nanosized silver sulfide at room temperature” *Materials Chem and Phy.*,107 (2008) 9-12.
- [20] Sourich Banergy, Santanu Bhattacharya and Dipankar Chakravorty, “Resistivity hysteresis of Ag₂S nanocomposites” *J. Phys. Chem*, (111) (2007), 13410-13413.
- [21]T. Ben Nasrallah, H Dlala, M amlouk, S belgacem, J. C. Barnede, “Some physical investigations on Ag₂S thin films prepared by sequential thermal evaporation” *Synthetic Metals*, (151) (2005) 225-230.

¹Mr. S.S Mhaske
²Dr. C.M. Jadhao

GUI based Heart Disease prediction model using Random Forest Algorithm



Abstract: - Cardiac disease is the primary cause of death globally. Diagnosis and accurate prediction of cardiac illness are difficult tasks. The mortality rate due to cardiac disease can be significantly decreased by routine monitoring and early detection of cardiac disease. The medical industry is seeing a considerable advancement in the application of machine learning techniques. Improved accuracy in predicting cardiac diseases has been obtained by interpreting the analyses done using this methodology. It has been demonstrated to explicitly attempt to uncover significant aspects of heart disease by giving ML. The classification algorithm Random Forest (RF) is used to train the model.

Keywords: Cardiac disease, Machine learning, Random Forest.

¹ Assistant Professor, Department of Electronics & Telecommunication, Mauli College of Engineering and technology, Shegaon, India

² Professor and Principal, Department of Electronics & Telecommunication, Mauli College of Engineering and technology, Shegaon, India

I. INTRODUCTION

An essential organ in the human body is the heart. It supplies blood to every bodily part. In the event that it malfunctions, the brain and several other organs will stop functioning, and the person will pass away in a matter of minutes. Any ailment that affects the heart might be collectively referred to as heart disease. Heart disease encompasses several disorders such as heart valve disease, cardiomyopathy, coronary heart disease, elevated blood pressure, cardiovascular disease, heart failure on one side, pulmonary failure, and more conditions. Heart disease risk factors can be acquired or inherited, and they can manifest at any age. Additionally, eating foods high in fat, like eggs or trans fats, smoking, overindulging in junk food, being overweight, abusing alcohol or soft drinks, living a sedentary lifestyle, diabetes, smoking, high blood pressure, and obesity are all contributing factors.

As per the article published by The Economic Times on September 29, 2023 [13], in India, cardiovascular diseases have turned into a silent epidemic of sorts and account for at least 27 percent of deaths.

II. LITERATURE REVIEW

The paper published by Sree et al., 2023 [1], presented a comprehensive analysis of risk prediction for heart disease using four machine learning algorithms. They had trained the model using four classification algorithms: Decision Tree (DT), K-Nearest Neighbors (K-NN), Random Forest (RF), and Support Vector Machine (SVM). They had measured four algorithms performance in a number of ways, including recall, accuracy, precision, and specificity. It has been demonstrated that SVM offers the best performance in this approach.

Jummelal, 2023 [2], presented a machine-learning method for identifying chronic heart failure using ECG recordings. The method, which includes filtering, segmenting, and feature extraction, outperforms a majority classifier by 15 percentage points and has an 87% recall rate among those with chronic heart failure.

The work presented by Alkurdi, 2023[3], used the Heart Disease UCI dataset to train machine learning models for heart disease diagnosis. Using preprocessing techniques like MEAN, normalization, SMOTE, and correlation, the data is pre-processed, and then this pre-processed data is forwarded to decision Tree, Random Forest, SVM, and k-NN classification algorithms. The methodology that has been suggested yields encouraging outcomes that distinctly underscore the importance and worth of preparing data. The obtained accuracy, precision, recall, F1 score, and ROC AUC scores all clearly demonstrate this.

Swain et al., 2023 [4], employed IoT to assess risk variables that are comparable to improperly managed cardiac conditions. They said that there has been a significant technological divide between researchers studying healthcare, patients, doctors, and machine learning architects. They have conducted an intense review of machine learning with the aim of taking advantage of new, cutting-edge technologies.

The research work presented by Swain et al., 2023[5], describes how an ML model can predict whether or not an individual would be at risk of CHD in the following ten years based on medical data and personal habits. They aim to determine the most accurate model for heart disease prediction using a variety of machine learning (ML) classification techniques, including random forests (RF), logistic regression (LR), artificial neural networks (ANNs), and decision trees (DT), where they have found out that RF has the best accuracy.

Zabeeulla et al., 2023[6], presented a machine learning algorithm to diagnose cardiac problems in which they achieved 98.8% accuracy. They have used a heart disease data set from Kaggle, which is open to all, and the dataset contained thirteen features. Finding out if the patient has a 10-year risk of developing coronary heart disease" (CHD) was the ultimate goal of their study.

To ascertain the effectiveness of various machine learning algorithms in categorization tasks, a thorough investigation is carried out by Hadiani, 2023 [7]. The experimentation dataset comes from a variety of patient populations, which increases the findings' generalizability. The study aims to determine the best machine learning approach for accurately predicting cardiac disease through thorough review and validation. Using Optuna's optimization technique, the author was able to increase the accuracy of heart disease forecasts.

Nayeem et al., 2022[8], used supervised machine learning algorithms to predict heart disease in patients. They had employed mean value and info-gain feature selection techniques to handle null values and remove unnecessary features. K-Nearest Neighbors, Naive Bayes, and Random Forest are used to calculate prediction accuracy, precision, recall, F1-score, and ROC. Out of all the models, Random Forest has the highest classification accuracy (95.63%), with the following values for precision, recall, F1-score, and ROC: 0.93, 0.92, 0.92, and 0.9.

The authors, Rindhe et al., 2021[9], performed the simulation on a dataset available in the UCI Machine Learning repository, which consists of 303 samples with fourteen input features and one output feature. They have used supervised machine learning algorithms like random forest and support vector machine as well as Artificial Neural Network. The web scraper responsible for gathering data for the model is programmed in Python. The accuracy achieved by them is 84.0%, 83.5%, and 80.0% for Support Vector Classifier, Neural Network, and Random Forest Classifier respectively.

Ruqiya, 2023[10], presented detailed review of the Cleveland Heart Disease Dataset using Machine Learning, and from the review, they suggested increasing the number of samples in the dataset for evaluation and implementing the deep learning approach after increasing the number of samples in the data set, as well as considering more features for classification.

The author, Handan Tanyildizi-Kökkülünk, 2023 [11], presented the work on Prediction of Heart Disease Using Machine Learning with Data Mining. Using multiple linear regressions (MLR), a machine learning technique, the categorization was achieved using the R Studio software. By employing the Akaike information criterion to identify characteristics that significantly contribute to the prediction, machine learning has been enhanced. The MLR model that was employed had an accuracy of 88%, a precision of 93%, a sensitivity of 86%, and a specificity of 91%.

Anusuya & Gomathi, 2021[12], presented a method that involved preprocessing, followed by feature selection, Eigen vector extraction, and classification. Moreover, multi-objective-based Ant Colony Optimization (MO-ACO) is used to choose the best features from the extracted features in order to increase the classification and clustering. The suggested approach was contrasted with the current methodology in terms of accuracy, recall, precision, NMI, and execution time, and came to the conclusion that the solution was more accurate for datasets of all sizes.

III. METHODOLOGY

The system flow for heart disease prediction is as shown in Figure 1. It involves steps like data preprocessing of the input data set, feature extraction, feature selection, splitting of data into test and train data sets, classification, and the output of the classifier, which is the prediction of heart abnormality.

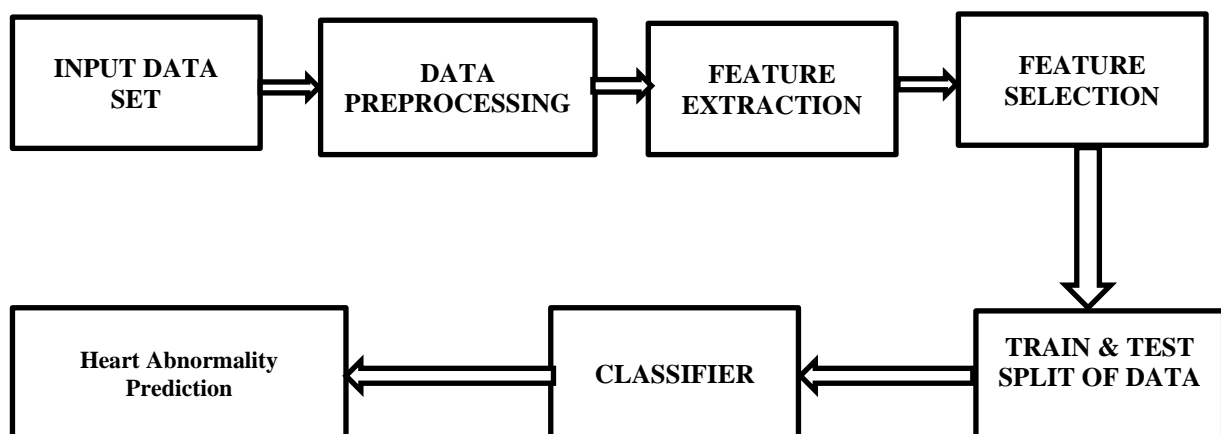


Fig 1: System flow for prediction of heart disease

The online data set from the github website [14] is used, which has 1025 data samples, and these data samples are used to train the random forest classifier. The various parameters like age, sex, CP, trestbps (the person's resting blood pressure), cholesterol, fbs (fasting blood sugar), restecg (resting electrocardiographic measurement), thalach (maximum heart rate), exang (exercise-induced angina), oldpeak, and slope are considered in the data set.

We have designed the GUI model using Python programming, in which the user has to provide various inputs like age, male or female. Chest pain type, blood pressure, cholesterol level, fasting blood sugar, resting ECG, max heart rate, exercise angina, ST depression, and slope of ST. Depending on the input provided by the user, the random forest classifier will give a prediction, either the possibility of heart disease or no heart disease.

IV. RESULTS

In order to assess the effectiveness of our created model, 21 inputs with varying parameter ranges were evaluated, and the outcomes were compared to the actual output. The model's output is displayed in Table No. 1 below.

Sr. No	Age	Sex	Cp	Trestbps	Chol	Fbs	Restecg	Thalach	Exang	Oldpeak	Slope	Target Output	Achieved Output
1	24	1	2	152	150	1	2	200	1	5	2	0	0
2	25	1	3	200	500	1	2	200	1	5	1	1	1
3	29	1	1	130	204	0	0	202	0	0	2	1	1
4	35	1	0	120	198	0	1	130	1	1.6	1	0	0
5	39	0	2	138	220	0	1	152	0	0	1	1	1
6	40	1	0	152	223	0	1	181	0	0	2	0	0
7	45	0	0	138	236	0	0	152	1	0.2	1	1	1
8	46	0	2	142	177	0	0	160	1	1.4	0	1	1
9	49	0	1	134	271	0	1	162	0	0	1	1	1
10	50	1	2	140	233	0	1	163	0	0.6	1	0	0
11	55	0	1	135	250	0	0	161	0	1.4	1	1	1
12	61	0	0	130	330	0	0	169	0	0	2	0	0
13	61	1	0	120	260	0	1	140	1	3.6	1	0	0
14	62	0	0	140	394	0	0	157	0	1.2	1	1	1
15	63	0	0	124	197	0	1	136	1	0	1	0	0
16	63	1	3	145	233	1	0	150	0	2.3	0	1	1
17	64	1	2	140	335	0	1	158	0	0	2	0	0
18	65	0	2	140	417	1	0	157	0	0.8	2	1	1
19	70	1	0	145	174	0	1	125	1	2.6	0	0	0
20	70	1	2	160	269	0	1	112	1	2.9	1	0	0
21	77	1	0	125	304	0	0	162	1	0	2	0	0

Figure 2 shows a screenshot of the predicted output as no heart disease for input sr. no. 1 from table no. 1, and Figure 3 shows the predicted output as the possibility of heart disease for input sr. no. 2 from table no. 1.

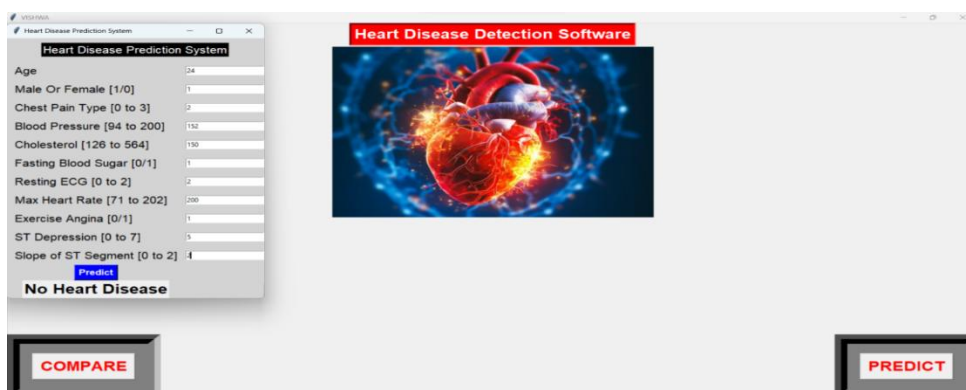


Fig 2: Screenshot showing the predicted output as no heart disease



Fig 3: Screenshot showing the predicted output as possibility of heart disease

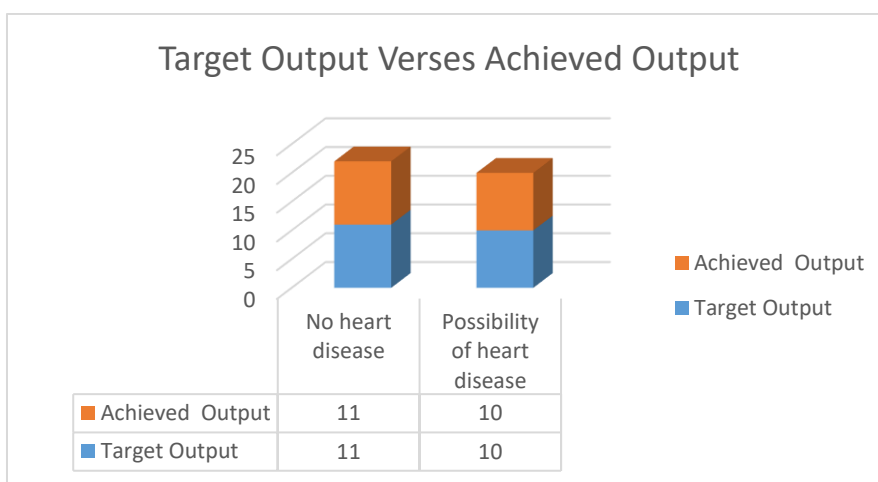


Fig 4: Graphical Representation of Target output to Achieved output.

A total of 21 inputs were tested on the model, out of which 11 were of no heart disease patience, and 10 were of the possibility of heart disease patience, and our model accurately identified the same, which is shown in figure 4.

V. CONCLUSION

One of the newest and most popular technologies is machine learning. The application of machine learning in the healthcare sector to forecast health issues in people is growing quickly and is essential to saving lives. The Using the Python programming language, we have created a GUI-based model for predicting heart illness based on a random forest method for this study, and the results show that we are getting 100% accuracy. The output response time of the GUI-based model is quite low, and it is very simple to comprehend and use.

VI. REFERENCES

1. Sree, P. K., Prasad, M., PBV, R. R., Ramana, C. V., Murty, P. T. S., Mallesh, A. S., & Raju, P. J. R. S. (2023, October 10). A Comprehensive Analysis on Risk Prediction of Heart Disease using Machine Learning Models. *International Journal on Recent and Innovation Trends in Computing and Communication*, 11(11s), 605–610. <https://doi.org/10.17762/ijritcc.v11i11s.8295>
2. Jummelal, K. (2023, May 29). *Chronic Heart Failure Diagnosis from Heart Sounds Using Machine Learning and Full-Stack Deep Learning*. <https://www.jclmm.com/index.php/journal/article/view/1065>

3. Alkurdi, A. A. H. (2023, January 1). *Enhancing Heart Disease Diagnosis Using Machine Learning Classifiers*. <https://doi.org/10.54216/fpa.130101>
4. Swain, S. K., Behera, N., Swain, A. K., Jayasingh, S. K., Patra, K. J., Pattanayak, B. K., Mohanty, M. N., Naik, K. D., & Rout, S. (2023, October 7). *Application of IoT Framework for Prediction of Heart Disease using Machine Learning*. *International Journal on Recent and Innovation Trends in Computing and Communication*. <https://doi.org/10.17762/ijritcc.v11i10s.7616>
5. Swain, S., Chakravarty, S., Paikaray, B., & Bhojar, H. (2023). Heart Disease Detection Using Machine Learning Techniques. *Lecture Notes in Electrical Engineering*, 273–284. https://doi.org/10.1007/978-981-19-9090-8_24
6. Zabeeulla, M., Sharma, C., & Anand, A. (2023, March 1). Early Detection of Heart Disease Using Machine Learning Approach. *CARDIOMETRY*, 26, 342–347. <https://doi.org/10.18137/cardiometry.2023.26.342347>
7. Hadiani, S. (2023, September 7). Optimization of The Machine Learning Approach using Optuna in Heart Disease Prediction. *Journal Medical Informatics Technology*, 59–64. <https://doi.org/10.37034/medinftech.v1i3.15>
8. Nayeem, M. J. N., Rana, S., & Islam, M. R. (2022, November 30). Prediction of Heart Disease Using Machine Learning Algorithms. *European Journal of Artificial Intelligence and Machine Learning*, 1(3), 22–26. <https://doi.org/10.24018/ejai.2022.1.3.13>
9. Rindhe, B. U., Ahire, N., Patil, R., Gagare, S., & Darade, M. (2021, May 12). Heart Disease Prediction Using Machine Learning. *International Journal of Advanced Research in Science, Communication and Technology*, 267–276. <https://doi.org/10.48175/ijarsct-1131>
10. Ruqiya. (2023, June 30). Review on Cleveland Heart Disease Dataset using Machine Learning. *Volume 21, Issue 1*, 21(1), 87–98. <https://doi.org/10.52584/qrij.2101.11>
11. H, T. K. (2023, January 5). Prediction of Heart Disease Using Machine Learning with Data Mining. *Physical Science & Biophysics Journal*, 7(1), 1–6. <https://doi.org/10.23880/psbj-16000228>
12. Anusuya, V., & Gomathi, V. (2021, March 25). An Efficient Technique for Disease Prediction by Using Enhanced Machine Learning Algorithms for Categorical Medical Dataset. *Information Technology and Control*, 50(1), 102–122. <https://doi.org/10.5755/j01.itc.50.1.25349>
13. Online, E. (2023, September 29). *World Heart Day: 27% of deaths in India are caused by cardiovascular diseases*. *The Economic Times*. <https://economictimes.indiatimes.com/magazines/panache/world-heart-day-27-per-cent-of-deaths-in-india-are-caused-by-cardiovascular-diseases/articleshow/104031929.cms>
14. D. (n.d.). *Datasets/DS/heart.csv at main · DataThinkers/Datasets*. GitHub. <https://github.com/DataThinkers/Datasets/blob/main/DS/heart.csv>

¹Kajal Sirtawar²Kishor Raulkar

**Spectroscopic Studies of Polymethyl
Methacrylate (PMMA) and Ethyl Cellulose
(EC) Polyblend doped with Oxalic Acid**



Abstract: Fourier transform infrared (FT-IR) and X Ray Diffraction (XRD) spectroscopy measurements for Polymethyl Methacrylate (PMMA) and Ethyl Cellulose (EC) polyblends (1:1 and 1:2) doped with different percentages (0%, 5% and 10%) of Oxalic Acid in tetrahydrofuran (THF) at room temperature were prepared using isothermal evaporation techniques. Polymers like Ethyl Cellulose (EC) and Poly Methyl Methacrylate (PMMA) being essentially insulating materials, the number of free charge carriers is very small and their mobility is very low. These measured spectra were then used to evaluate the optical energy gap in relation to blend composition. X-ray diffraction (XRD) was used to identify the molecular interaction arising in the mentioned polymer blend films. The peculiar deviation confirms the structural changes in the prepared samples.

Keywords: EC, PMMA, Oxalic Acid, Tetrahydrofuran, FT-IR, XRD

I. Introduction

Blending between two or more polymers can modify the structural and physical properties of polymers to specific requirements. So, the attention of material researchers has been attracted to polymers blend [1,2]. It involves physical mixing of biopolymers; leading to creation of a new material having some desirable properties that are superior to any one of the component polymers [3-5]. Polymer blending is an attractive route for producing new polymeric materials with tailored properties without having to synthesize totally new materials. Other advantages for polymer blending are versatility and simplicity [6]. There are many investigations on polymer blending. The most important of the cellulose ethers is ethyl cellulose (EC). Its electrical, mechanical and weathering properties are good in comparison with other cellulosic's, but not generally outstanding. Poly Methyl Methacrylate (PMMA) is a hard, rigid, transparent thermoplastic, which has good outdoor weatherability and is more impact resistant than glass. Poly Methyl Methacrylate

¹*Kajal Sirtawar Email. kajalsirtawar.ks@gmsil.com

²Kishor Raulkar Email. kbraulkar@gmail.com

^{1,2}Department of Physics, Vidya Bharti Mahavidyalaya, 444602, Amravati, India
Copyright©JES2024on-line:journal.esrgroups.org

(PMMA) is weakly polar [7]. The interest in organic and polymeric semiconductors has arisen, particularly because of their electro photo graphic and solar cell applications. The changes in the values of the optical energy gaps, dielectric constants, and the refractive index under different frequencies and blending ratio were related to the effects of structural changes in the amorphous domains, impurities, and space charge existing in the interfaces between the mixed phases [8-10].

In the past decades much effort has been devoted to investigating metal-polymer system, by the attachment of inorganic components and the performance of polymer matrix will be greatly enhanced with respect to electrical, mechanical, thermal and especially optical properties [11-13]. They have wide range of application in various sectors such as electronic devices, conductive composites, non-linear optical materials and so on [14]. Poly (methyl methacrylate) (PMMA) is one of the important transparent polymeric materials and it is used in various applications as dielectric in organic thin films, opto-elctronic devices, optical lenses in cameras, optical fibers and advanced electronic devices [15, 16]. Several researchers are focused on thermal and electrical properties of heterogeneous materials have gained momentum in recent years [17].

In the present work samples of different mass fractions (PMMA/EC) were prepared and their physical properties were studied by ordinary FT-IR and XRD with different glimpse. A new route for inquest the degree of miscibility was introduced depending on a spectroscopic quantitative measurement.

II. Experimental

A. Sample Preparation

In the present work, Isothermal Evaporation Technique has been used, as it is best suited to the laboratory. Polymers of Ethyl Cellulose (EC) and Poly Methyl Methacrylate (PMMA) were obtained from S.d. Fine Chem Ltd, Mumbai, India. The different quantities of given substances have been used for preparing film of thickness. The two polymers PMMA, EC were taken in pure form and in the ratio 1:1 were dissolved in the common solvent Tetrahydrofuran (THF).The solution was kept for 3-4 days to allow polymers to dissolve completely to yield uniform solution. A glass (15 cm X 15 cm) thoroughly cleaned with water and later with was used as a substrate. To achieve perfect levelling (and uniformity in thickness of the film), a pool of mercury was used in a plastic tray. The solution was poured on the glass plate and was allowed to spread uniformly in all directions on the substrate. The whole assembly was placed in a dust free chamber at room temperature. The solvent in the solution was thus allowed to evaporate completely and get air-dried. The film on the glass substrate was then removed and cut into small pieces of suitable sizes. In this way the films were prepared by isothermal evaporation technique. Further it was dried for 3 days to remove any traces of solvent. The dry film was removed from the plate and cut into pieces (samples) of desired size. The films of

other samples were prepared by the same method. The 0 %, 5 % and 10% of oxalic acid (doping) were taken and dissolved in the pure PMMA and EC and mixture of (1:1 and 1:2) PMMA/ EC solution.

B. Characterization

1. FT-IR analysis:

The FT-IR spectrum introduces information about the molecules present in the Specimen. The infrared (IR) spectra of the polymer were recorded on IRAffinity 1 model FTIR spectrophotometer in the region 400–4000 cm^{-1} .

2. X-Ray Diffraction:

In order to study the constitutional properties, the structure is resolved with a Rigaku Miniflex 600 model X-ray diffractometer used in this present work for identification and conformation of the compounds formed.

III. Results and Discussion

A. FT-IR Spectra:

FTIR spectra of PMMA and EC doped with different concentration of Oxalic Acid are depicted in Figure 1-6. From the figures it is apparent that the synthesized polymer blend contains characteristic transmittance vibration bands of polyblends PMMA/EC appear at range 1700 cm^{-1} (C=O) and 1400 cm^{-1} (C–O). The bands at 3000 and 2900 cm^{-1} correspond to the C–H stretching of the methyl group (CH_3) while the bands at 1300 and 1450 cm^{-1} are associated with C–H symmetric and asymmetric stretching modes, respectively. The 1200 cm^{-1} band is assigned to torsion of the methylene group (CH_2) and the 1100 cm^{-1} band corresponds to vibration of the ester group C–O, while C–C stretching bands are at 1000 and 800 cm^{-1} [18] The PMMA/EC with dopant 5%, 10% FTIR spectrum variation showed similar absorption peaks of functional groups, namely $-\text{CH}_3$, C=O ester, and C–O–C (ether). And other details of functional group are shown in table 1.

B. XRD

Figures 7-12 show the XRD pattern of the prepared pure PMMA/EC thin film and with dopant PMMA/EC films at Oxalic Acid concentration 5% and 10 wt%. From Figure 7 and 10 it seems clear that Pure PMMA/EC thin film possesses no crystalline structure therefore, we can say that amorphous structure. Some new peaks were observed in XRD patterns by doping with Oxalic Acid as shown in figures 8,9,11 and 12.

The 5% of oxalic acid in PMMA and EC polyblends in 1:1 and 1:2 proportions show microcrystalline nature but 10% of Oxalic Acid in PMMA and EC polyblends in 1:1 and 1:2 proportions show sharp peaks. And in 10% of 1:2 sample refraction provided by the three main peaks at $2\theta = 14.99, 24.33$ and 28.79° which are assigned to the lattice planes (1 0 1), (1 1 0) and (0 2 1). Oxalic Acid has crystalline nature and in present investigation by adding dopant the new peaks obtained this peak confirms the presence of Oxalic Acid and this behavior agrees with reference [19].

Acknowledgements

The authors wish to thanks for your valuable guidance. They are also extremely grateful to Dr. Pradnya S. yenkar, Principal, V. B. M. V. Amravati, for extending laboratory facilities to carry out the present work.

References

- [1] Elashmawi IS, Hakeem NA and Abdelrazek EM, "Spectroscopic and thermal studies of PS/PVAc blends", *Physica*, Vol 403, pp. 3547–52, 2008.
- [2] Sivakumar M, Subadevi R, Rajendran S, Wu HC and Wu NL, "Compositional effect of PVdF-PEMA blend gel polymer electrolytes for lithium polymer batteries", *Eur Polym J*, Vol. 43, pp. 4466–73, 2007.
- [3] Stephen AM, Kalyanasundaram S, Gopalan A, Muniyandi N, Renganathan NG and Saito Y, "Ionic conductivity and FT-IR studies on plasticized PVC/PMMA blend polymer electrolytes", *J. Power Sources*, Vol. 7, pp. 44–52, 2001.
- [4] Subban RHY and Arof AK, "Plasticizer interactions with polymer and salt PVC–LiCF₃SO₃–DMF electrolytes", *Eur Polym J*, Vol. 40, pp. 1841–7, 2004.
- [5] Sun Z, Wang W and Feng Z, "Criterion of polymer-polymer miscibility determined by viscometry", *Eur Polym J*, Vol. 28, pp. 1259–61, 1992.
- [6] Peesan M, Supaphol P, and Rujiravanit R, "Optical Study on Poly(methyl methacrylate)/Poly(vinyl acetate) Blends", *Journal of Applied Polymer Science*, vol. 105, pp. 1844, 2007.
- [7] Blythe AR, "Electrical properties of polymers" Cambridge: Cambridge University Press, Vol, 95 pp. 105, 1979.
- [8] Belsare NG, Wadatkar AS, Joat RV, Wasnik TS, Raghuwanshi FC, Raulkar KB and Lamdhade GT, "Polyvinyl chloride –Polymethylmethacrylate Micro-Composite polymers: Miscibility", *Journal of Electron Devices*, Vol. 11, pp. 583-587, 2011.
- [9] Kamira A and Naima BB, "Miscibility of PVC/PMMA blends by vicat softening temperature, viscometry, DSC and FTIR analysis", *Polymer Testing*, Vol. 25, pp. 1101-1108, 2006.

[10]Khan MS, Qazi RA and Wahid MS, “Miscibility studies of PVC/PMMA and PS/PMMA blends by dilute solution viscometry and FTIR”, African Journal of Pure and Applied Chemistry, Vol. 2(4), pp. 041-045, 2008.

[11] Singh H and Gupta NK,” Evolution of properties in ABS/PA6 blends compatibilized by fixed weight ratio SAGMA copolymer”, Journal of Polymer Research, Vol. 18, pp. 1365–1377, 2011.

[12] Qiao J, Fu J, Lin R, Ma J and Liu J, “ Alkaline solid polymer electrolyte membranes based on structurally modified PVA/PVP with improved alkali stability”, Polymer, Vol. 51, pp. 4850- 4859, 2010.

[13] Ramesan MT, Manojkumar TK, Alex R and Kuriakose B, “Investigations on the addition of styrene butadiene rubber in natural rubber and dichlorocarbene modified styrene butadiene rubber blends”, Journal of Material Science, Vol. 37, pp. 109-116, 2002.

[14] Ramesan MT, “Synthesis and characterization of magneto electric nanomaterial composed of Fe₃O₄ and polyindole”, Advances in Polymer Technology, Vol. 32, pp.928-934, 2013.

[15] Lampe IV, Schultze D and Zygalsky F, “Thermal degradation of poly (methacrylic acid) and Y–Ba–Cu poly methacrylate precursors for the preparation of high temperature superconductors”, Polymer Degradation and Stability, Vol. 73, pp. 87-92, 2001.

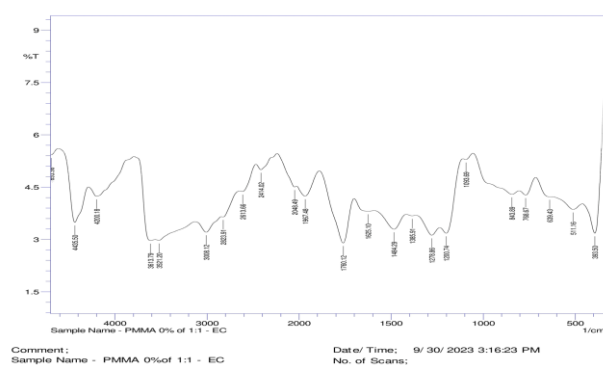
[16] Rusu M, Sofian N and Rusu D, “Mechanical and thermal properties of zinc powder filled high density polyethylene composites”, Polymer Testing, Vol. 20, pp. 409- 417, 2001.

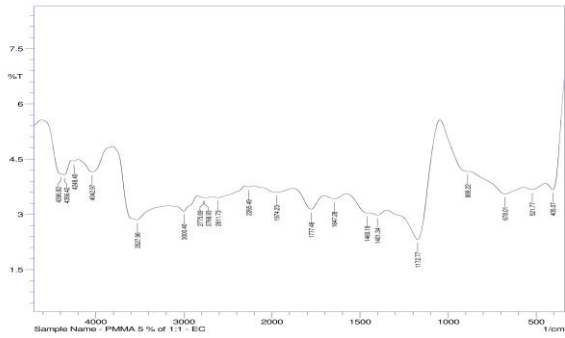
[17] Chae DW and Kim BC, “Characterization on polystyrene/zinc oxide nanocomposites prepared from solution mixing”, Polymers for Advanced Technologies, Vol. 16, pp. 846–850, 2005.

[18] Jayakrishnan P and Ramesan MT, “Synthesis, characterization and electrical properties of Fe₃O₄/poly (vinyl alcohol- co-acrylic acid) nanocomposites”, American Institute of Physics Conference Proceedings, Vol. 1620, pp. 165-172, 2014.

[19] Muthuselvi C, Arunkumar A and Rajaperumal G, “Growth and Characterization of Oxalic Acid Doped with Tryptophan Crystal for Antimicrobial Activity”, Der Chemica Sinica, Vol. 7(4), pp. 55-62, 2016.

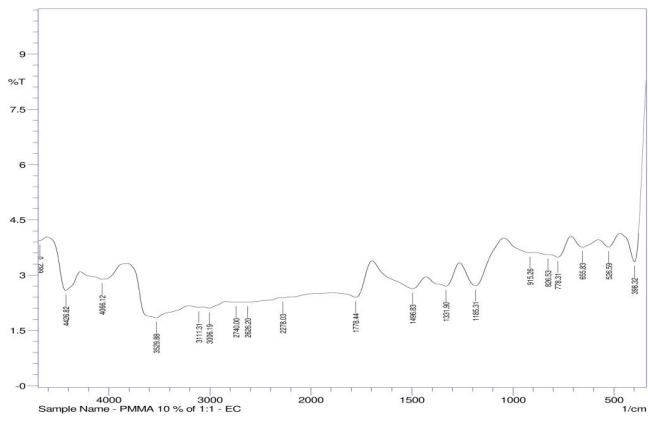
Figures and table:





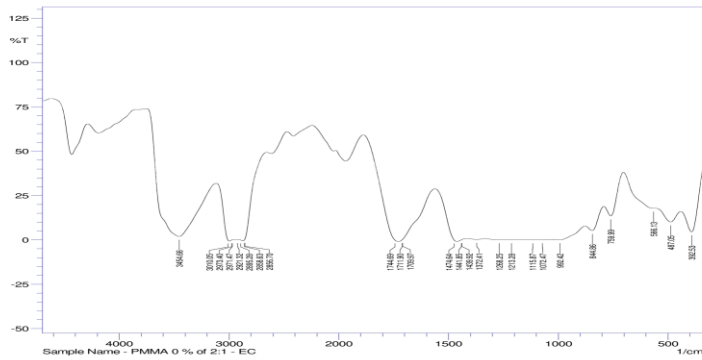
Comment:
Sample Name - PMMA 5 % of 1:1 - EC

Date/ Time: 9/ 30/ 2023 3:18:11 PM
No. of Scans:



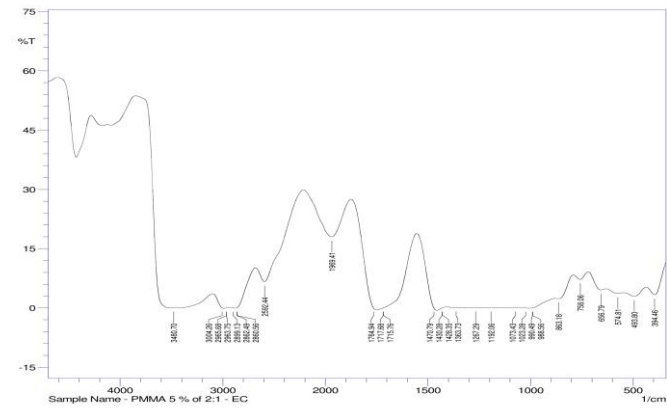
Comment:
Sample Name - PMMA 10 % of 1:1 - EC

Date/ Time: 9/ 30/ 2023 3:19:55 PM
No. of Scans:



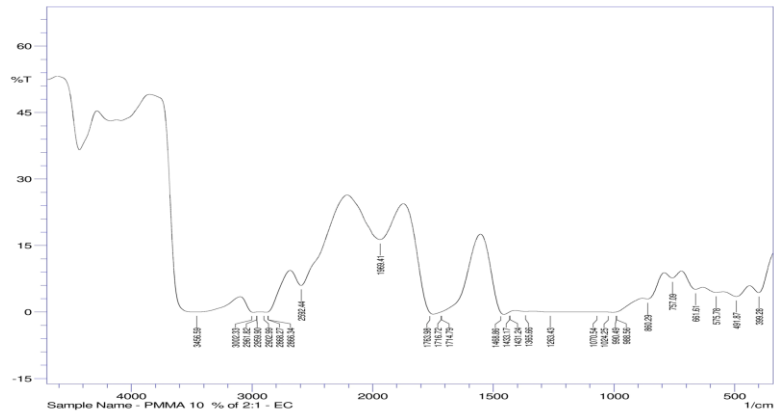
Comment:
Sample Name - PMMA 0 % of 2:1 - EC

Date/ Time: 9/ 30/ 2023 3:48:52 PM
No. of Scans:



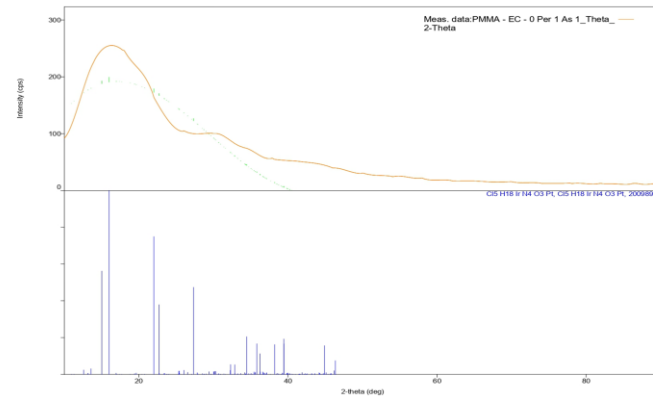
Comment:
Sample Name - PMMA 5 %of 2:1 - EC

Date/ Time: 9/ 30/ 2023 3:51:06 PM
No. of Scans:

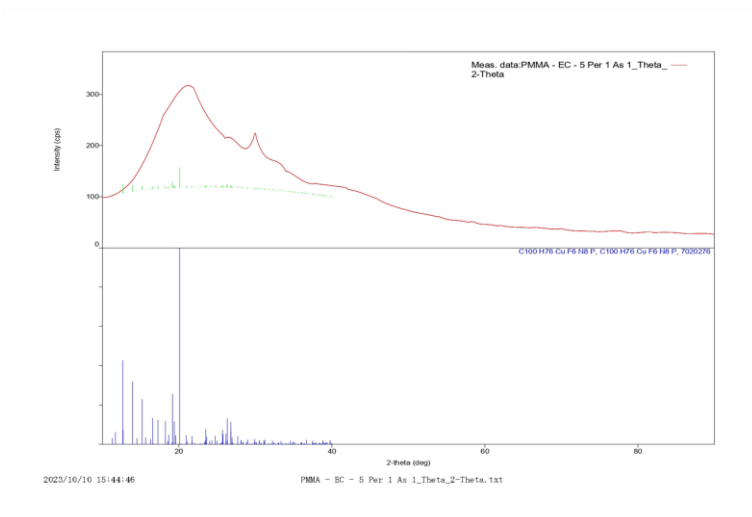


Comment:
Sample Name - PMMA 10 %of 2:1 - EC

Date/ Time: 9/ 30/ 2023 3:53:39 PM
No. of Scans:

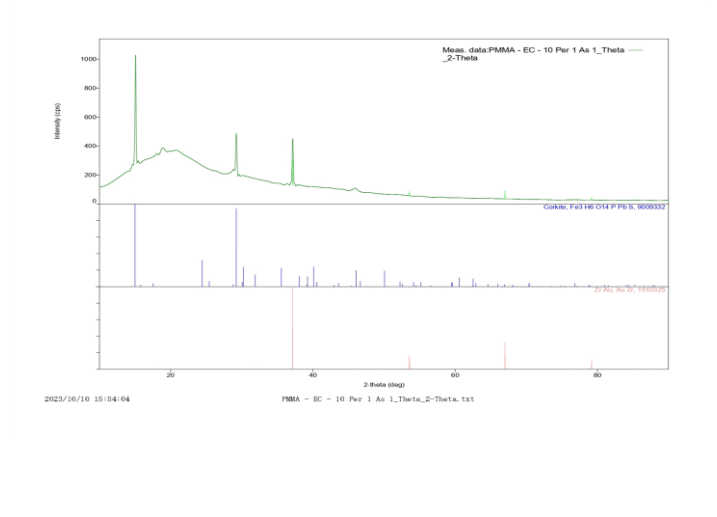


2023/10/10 13:43:09 PMMA - EC - 0 Per 1 As 1_Theta_2-Theta.txt



2023/10/10 15:44:46

PMMA - EC - 5 Per 1 As 1_Theta_2-Theta.txt



2023/10/10 15:54:04

PMMA - EC - 10 Per 1 As 1_Theta_2-Theta.txt

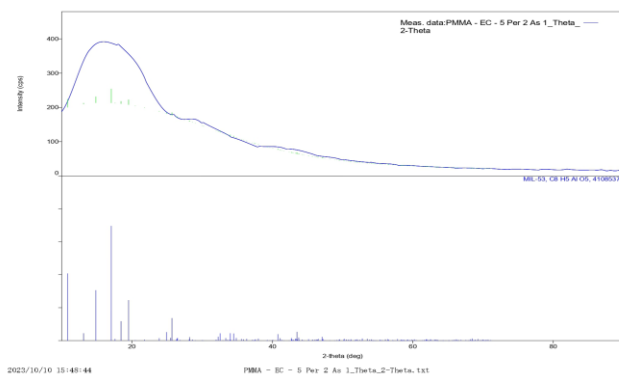


Fig.11. X- ray diffraction scans of 5% of PMMA/EC (1:2)

Vibrational modes	Peak No.	Wave Number (Cm ⁻¹)					
		PMMA/EC with Oxalic Acid					
		1:1			1:2		
Sample Code		0%	5%	10%	0%	5%	10%
-CH ₃ stretching	1	3008	3000	3006	3010	3004	3002
-CH ₃ stretching + -CH ₂ symmetric stretching	2	2961	2965	2973			
-CH ₂ antisymmetric Stretching	3	2823	2775	2740	2858	2862	2868
C=O stretching	4	1760	1777	1778	1744	1764	1763
C-H antisymmetric stretching	5	1484	1460	1496	1474	1470	1468
C-H deformation	6	1434	1401	1439	1430	1433	1433
C-H symmetric stretching	7	1385	1371	1372	1363	1365	1365
-CH ₂ twist	8	1200	1233	1213	1267	1237	1263
C-O-C stretching	9	1190	1172	1192	1192	1192	1190
C-O stretching	10			1115			
C-C stretching	11			992	988	990	990

Table1. Vibrational Modes observed in the PMMA/EC blends with dopant

^{1,2*} Krishna Sharma

³ Satishkumar A.
Athawale

⁴ Rustam Ali

^{2,5} Utpal Deka

Investigation of Lower Hybrid Wave Instability in a Collisional Magnetized Gallium Arsenide (GaAs) Semiconducting Quantum Plasma System



Abstract: - The study investigates the impact of electron-phonon and hole-phonon collisions on the lower hybrid waves (LHWs) instability induced by an external electron beam in a magnetized Gallium Arsenide (GaAs) semiconductor quantum plasma system. Utilizing the Quantum Hydrodynamic (QHD) model, we derive the dispersion relation by incorporating the collision term alongside various quantum corrections, such as quantum statistical pressure, exchange-correlation potential, and Bohmian force. Our analysis reveals that the inclusion of collision terms significantly influences the growth rate of LHWs instability. Additionally, the effects of propagation angle and beam streaming speed on the real part of frequency (phase speed) and growth rate of LHWs are thoroughly examined, showing that both parameters significantly affect the growth rate.

Keywords: Semiconductor plasma, QHD model, lower hybrid waves, collision, instability.

¹ *Corresponding author: Department of Physics, NBBGC, Tadong, Gangtok, Sikkim, 737102, India

² Department of Physics, Sikkim Manipal Institute of Technology, Sikkim Manipal University, Majitar, Sikkim, 737136, India

³ Department of Physics and Electronics, Government Vidarbha Institute of Science and Humanities, Amravati, Maharashtra, 444604, India

⁴ Department of Mathematics, Sikkim Manipal Institute of Technology, Sikkim Manipal University, Majitar, Sikkim, 737136, India

⁵ Department of Physics, Manipal Institute of Technology Bengaluru, Manipal Academy of Higher Education, Manipal, Karnataka, 576104, India

I. INTRODUCTION

The resonant interaction of Lower-hybrid waves (LHWs) with both ions and electrons, distinguish them from other electrostatic waves with lower-frequencies. The propagating frequencies of these waves lies between the ion and electron gyro frequencies. This distinctive feature allows LHWs to be effectively utilized for the heating and acceleration of plasma particles in both space and laboratory environments. Their ability to interact resonantly with a wide range of plasma constituents makes them particularly useful in various applications, including plasma heating, current drive-in fusion devices, and space plasma experiments [1-3]. Ion dynamics significantly influence the propagation of lower-hybrid waves (LHWs). At the lower-hybrid frequency, ions can move more freely across the magnetic field, whereas electrons are more affected by the magnetic field, resulting in distinct behaviors for the two types of particles. A diverse array of low-frequency electrostatic oscillations can be observed in semiconductor plasma [4], in the presence of a uniform magnetic field. Due to its high dielectric response function, the semiconductor is regarded as a plasma. Gaseous plasmas [5], composed of ions and electrons, exhibit electric fields that extend over significant distances. However, in semiconducting plasma system, plasma waves [6] arises due to interaction between electrons and holes, resulting in coherent motion that gives rise to acoustic modes.

Rasheed et. al. [3] investigated LHWs instability in semiconducting plasma. The study examines how various factors impact the phase speed and growth rates of LHWs, including the electron beam temperature, ratio of electron-to-hole number density, propagation angle, streaming speed, and cyclotron frequency. It's observed that higher streaming speed and electron number density intensify the instability. Similarly, decreasing the propagation angle alongside the magnetic field yields similar effects. However, the study did not take into account the impact of electron-phonon and hole-phonon collisions. Iqbal et. al. [7] investigated LHWs instability in a spin polarized degenerate plasma. The study reveals that beam streaming speed and electron spin polarization diminish both the k-domain and growth rate. Conversely, propagation angle and beam density amplify both parameters. Furthermore, the inclusion of the Bohm potential intensifies the growth of the instability. These observations suggest significant implications for instability and wave phenomena in spin-polarized plasmas. The ion-beam driven non-linear study of LHWs has been studied by Koshkarov et. al. [8]. They have examined the LHWs instability in both linear and nonlinear regimes through numerical simulations. Maslennikov et. al. [9] investigated the decay instability of LHWs. The study demonstrates that the decay instability is predominantly influenced by two factors: the propagation angle of the LHWs and external magnetic field, and the scattering angle of the wave. Depending on these angles, the instability is primarily controlled either by the plasma's nonlinear response to the propagating LHWs or by the oscillatory motion of electrons relative to ions.

Based on the literature review, it has become evident that lower hybrid waves (LHWs) have not been thoroughly investigated in semiconducting quantum plasma, particularly regarding the influence of electron-phonon and hole-phonon collisions. Therefore, this study aims to fill this gap by examining the instability of LHWs induced by an external electron beam while considering collision effects, along with various quantum phenomena such as the quantum statistical pressure, exchange-correlation potential, and Bohmian force. In this study, we propose to derive a normalized linear dispersion relation for LHWs in a collisional magnetized semiconducting quantum plasma system using the quantum hydrodynamic (QHD) model. This dispersion relation will be analyzed graphically to assess the impact of collision effects, propagation angle, and beam streaming speed on the growth rate of LHWs instability. Through this comprehensive investigation, we aim to provide a deeper understanding of the behavior of LHWs in semiconducting quantum plasma, shedding light on their potential applications and underlying physics.

II. MATHEMATICAL FORMULATION

In our investigation, we explore a semiconductor quantum plasma setup comprising both electrons and holes. We introduce an external magnetic field \mathbf{B}_0 along the \mathbf{z} -direction and an electron beam traveling parallel to \mathbf{B}_0 with a velocity v_0 . This beam of electrons, characterized by an equilibrium number density n_{b0} , serves as a source of free energy driving the instability. Throughout our analysis, subscripts e , b and h represent the electrons, beam electrons, and holes within the semiconductor plasma system, respectively. The effective masses of holes and electrons are denoted by m_h^* and m_e^* respectively. To derive the dispersion relation, we employ the quantum hydrodynamic (QHD) model, treating each plasma species as an independent fluid. The governing equations are given by [12];

$$\left(\frac{\partial}{\partial t} + \mathbf{v}_0 \cdot \nabla\right) \mathbf{v}_j = \frac{q_j}{m_j^*} \left(\mathbf{E} + \frac{1}{c} \mathbf{v}_j \times \mathbf{B}_0\right) - \frac{1}{n_{j0} m_j^*} \nabla P_j + \frac{\hbar^2}{4n_{j0} m_j^{*2}} \nabla(\nabla^2 n_{j1}) - \frac{\nabla(n_{j1}) V_{j,xc}}{n_{j0} m_j^*} - \xi \mathbf{v}_j \quad (1)$$

$$\frac{\partial n_{j1}}{\partial t} + \nabla \cdot (n_{j0} \mathbf{v}_j) = 0 \quad (2)$$

$$\nabla^2 \phi = -4\pi \sum_j q_j n_j \quad (3)$$

Here, $P_j = \frac{m_j^* v_{Fj}^2 n_{j0}^3}{3n_{j0}^2}$, $v_{Fj}^2 = \left[\frac{6 k_B T_{Fj}}{5} \frac{\pi^2}{m_j^*} \left(\frac{T_j}{T_{Fj}} \right)^2 \right]$ and $T_{Fj} = \frac{\hbar^2 (3\pi^2 n_{j0})^{2/3}}{2m_j^*}$ denotes the statistical pressure, Fermi speed and Fermi Temperature of j^{th} species respectively. Here, T_j and \mathbf{v}_j denotes the temperature and speed of j^{th} species. $V_{j,xc} = \frac{0.985}{3} \left(\frac{e^2}{\epsilon}\right) n_{j0}^{1/3} + \frac{0.985 \cdot 0.034}{3 a_{Bj}^*} \left(\frac{e^2}{\epsilon}\right) \frac{18.37 a_{Bj}^* n_{j0}^{1/3}}{1 + 18.37 a_{Bj}^* n_{j0}^{1/3}}$ denotes the exchange correlation potential. The third term on the right side of Equation (1) depicts the Bohmian force arising from the Bohm potential [11]. The final term in Equation (1) accounts for momentum transfer due to collisions. Here, ξ denotes the effective collision frequency encompassing both electron-phonon and hole-phonon collisions [12-14]. All the perturbed quantities responsible for the propagation of LHWs are proportional to $e^{-i(\omega t - k_x x - k_z z)}$ where k and ω and are the wave number vector and the angular frequency.

Solving (1), (2) and (3) gives the expression for velocity of the j^{th} species given by,

$$\mathbf{v}_j = \Phi \frac{q_j}{m_j^* (\omega^* + i\xi)} \left[\frac{(\omega^* + i\xi)^2}{(\omega^* + i\xi)^2 - \omega_{cj}^2} k_x \hat{i} + i \frac{\omega_{cj} \omega^*}{(\omega^* + i\xi)^2 - \omega_{cj}^2} k_y \hat{j} + k_z \hat{k} \right] \quad (4)$$

Where, $v_{tj}^2 = v_{Fj}^2 + \frac{\hbar^2}{4m_j^{*2}} k^2 + \frac{V_{j,xc}}{m_j^*}$ and $\Phi = \phi + \frac{m_j^*}{q_j} (v_{tj}^2 \frac{n_{j1}}{n_{j0}})$ gives the effective speed and the effective potential due to various quantum corrections and $\omega^* = (\omega - \mathbf{k} \cdot \mathbf{v}_0)$ is the doppler shifted frequency.

Now from (2), and using (4) we get the expression for perturbed particle density, given by;

$$n_{j1} = \phi \frac{q_j n_{j0}}{m_j^*} \frac{\left[\frac{k_x^2 (\omega^* + i\xi)}{\omega^* (\omega^* + i\xi)^2 - \omega_{cj}^2} + \frac{k_z^2}{\omega^* (\omega^* + i\xi)} \right]}{\left(1 - \frac{v_{tj}^2 (\omega^* + i\xi)}{\omega^* (\omega^* + i\xi)^2 - \omega_{cj}^2} k_x^2 - \frac{v_{tj}^2}{\omega^* (\omega^* + i\xi)} k_z^2 \right)} \quad (5)$$

The usual expression of n_{j1} of the dielectric medium is given by [15];

$$n_{j1} = -\chi_j \frac{k^2 \phi}{4\pi q_j} \quad (6)$$

where, χ_j is the dielectric susceptibility of j^{th} species. Now, comparing equation (5) and (6) gives,

$$-\chi_j \frac{k^2}{4\pi q_j} = \frac{q_j n_{j0}}{m_j^*} \frac{\left[\frac{k_x^2 (\omega^* + i\xi)}{\omega^* (\omega^* + i\xi)^2 - \omega_{cj}^2} + \frac{k_z^2}{\omega^* (\omega^* + i\xi)} \right]}{\left(1 - \frac{v_{tj}^2 (\omega^* + i\xi)}{\omega^* (\omega^* + i\xi)^2 - \omega_{cj}^2} k_x^2 - \frac{v_{tj}^2}{\omega^* (\omega^* + i\xi)} k_z^2 \right)}$$

Which gives,

$$\chi_j = -\frac{\omega_{pj}^2}{k^2} \frac{\left[\frac{k_x^2 (\omega^* + i\xi)}{\omega^* (\omega^* + i\xi)^2 - \omega_{cj}^2} + \frac{k_z^2}{\omega^* (\omega^* + i\xi)} \right]}{\left(1 - \frac{v_{tj}^2 (\omega^* + i\xi)}{\omega^* (\omega^* + i\xi)^2 - \omega_{cj}^2} k_x^2 - \frac{v_{tj}^2}{\omega^* (\omega^* + i\xi)} k_z^2 \right)} \quad (7)$$

Expressed through the dielectric susceptibilities, the dispersion relation $D(\omega, k)$ regulating Lower Hybrid Waves in a semiconductor quantum magneto plasma can be written as [3];

$$1 + \chi_b + \chi_e + \chi_h = 0 \quad (8)$$

With the assumption of the condition that the phase speed of LHWs is much smaller comparing to that of beam electrons i.e., the condition $\mathbf{k} \cdot \mathbf{v}_0 \gg \omega$ and $\omega_{pe}, \omega_{ce} \gg \omega$, we find the values of dielectric susceptibilities χ_b, χ_e and χ_h from equation (7) as,

$$\chi_b = -\frac{\omega_{pb}^2}{k^2} \frac{1}{(v_0^2 - v_b^2) - \frac{\xi^2}{k^2}} \quad (9)$$

$$\chi_e = \frac{\omega_{pe}^2}{k^2} \frac{k_x^2}{(\omega_{ce}^2 + v_{te}^2 k_x^2 + \xi^2)} \tag{10}$$

$$\chi_h = -\frac{\omega_{ph}^2}{k^2} \frac{k_x^2}{(\omega^2 - \omega_{ch}^2 - v_{th}^2 k_x^2 - \xi^2)} \tag{11}$$

Putting these values of χ_b, χ_e and χ_h in (8), we get the following dispersion relation for LHWs in a collisional magnetized semiconducting plasma system;

$$\omega^2 = \omega_{ch}^2 + v_{th}^2 k_x^2 + \xi^2 + \frac{(\omega_{ce}^2 + v_{te}^2 k_x^2 + \xi^2) \omega_{ph}^2 k_x^2}{k^2 (\omega_{ce}^2 + v_{te}^2 k_x^2 + \xi^2) - \omega_{pb}^2 (\omega_{ce}^2 + v_{te}^2 k_x^2 + \xi^2) \left((v_0^2 - v_b^2) - \frac{\xi^2}{k^2} \right)^{-1} + \omega_{pe}^2 k_x^2} \tag{12}$$

The presence of collision is evident in dispersion relation (12) through the collisional term ξ .

Normalizing (12) in the scale of ω_{ph}^2 gives;

$$\omega'^2 = \omega_{ch}^{\prime 2} + v_{th}^{\prime 2} k'^2 \cos^2 \theta + \xi'^2 + \frac{(\omega_{ce}^{\prime 2} + v_{te}^{\prime 2} k'^2 \cos^2 \theta + \xi'^2) k'^2 \cos^2 \theta}{k'^2 (\omega_{ce}^{\prime 2} + v_{te}^{\prime 2} k'^2 \cos^2 \theta + \xi'^2) - \omega_{pb}^{\prime 2} (\omega_{ce}^{\prime 2} + v_{te}^{\prime 2} k'^2 \cos^2 \theta + \xi'^2) \left((v_0^{\prime 2} - v_b^{\prime 2}) - \frac{\xi'^2}{k'^2} \right)^{-1} + \omega_{pe}^{\prime 2} v_{te}^{\prime 2} k'^2 \cos^2 \theta} \tag{13}$$

Where, we have considered $k_x = k \cos \theta$, $\omega'^2 = \frac{\omega^2}{\omega_{ph}^2}$, $\omega_{ch}^{\prime 2} = \frac{\omega_{ch}^2}{\omega_{ph}^2}$, $\omega_{ce}^{\prime 2} = \frac{\omega_{ce}^2}{\omega_{ph}^2}$, $v_0^{\prime 2} = \frac{v_0^2}{v_{Fh}^2}$, $v_b^{\prime 2} = \frac{m_h^* T_b}{m_e^* T_{Fe}}$, $\omega_{pe}^{\prime 2} = \frac{\omega_{pe}^2}{\omega_{ph}^2}$, $\omega_{pb}^{\prime 2} = \frac{\omega_{pb}^2}{\omega_{ph}^2}$, $k'^2 = \frac{v_{Fh} k^2}{\omega_{ph}^2}$, $v_{th}^{\prime 2} k'^2 = \frac{v_{th}^2 k^2}{\omega_{ph}^2}$, $v_{te}^{\prime 2} k'^2 = \frac{v_{te}^2 k^2}{\omega_{ph}^2}$, $v_{Fh}^2 = \frac{k_B \hbar^2 (3\pi^2 n_{ho})^{2/3}}{m_h^*}$ is the Fermi speed of hole at equilibrium.

III. RESULTS AND DISCUSSIONS

For the numerical and graphical analysis of the LHWs instability, we used $\omega' = \omega_r + i\gamma$ in equation (13), where ω_r denotes the real part of the frequency, indicating the phase speed, and γ represents the growth rate of the LHWs. Our investigation focused on a GaAs semiconductor plasma system with an external electron beam. The standard value of various parameters of GaAs semiconductor [3] is given by $n_{e0} = 4.7 \times 10^{16} \text{cm}^{-3}$, $\frac{m_e^*}{m_e} = 0.067$, $\frac{m_h^*}{m_e} = 0.5$ and dielectric constant $\epsilon = 12.8$. Figures 1-3 below provides a graphical representation of how the growth rate and phase speed vary with different parameters. In these figures, solid lines depict the growth rates (γ) while the dashed lines represent the real part of the frequency (ω_r).

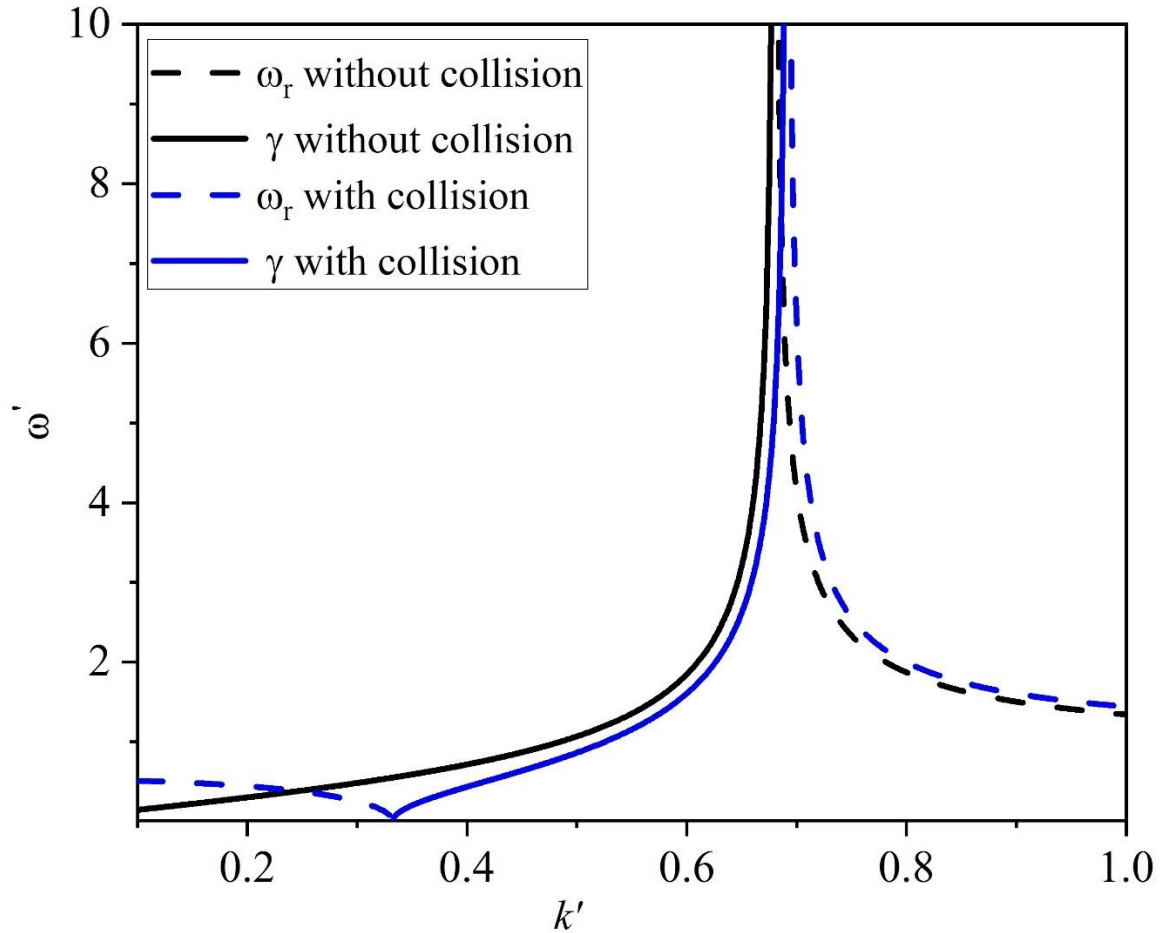


Figure 1: ω' versus k' curve to denote the effect of collision. For without collision $\xi' = 0$ and for with collision $\xi' = 0.5$. $\theta = 10^0$, $v'_0 = 5$, $v'_b = 3$ for all the curves.

Figure 1 illustrates the variation in the real part of frequency (ω_r) and growth rate (γ) with respect to the normalized wave number (k'). The figure demonstrates that the combined effects of electron-phonon and hole-phonon collisions significantly influence both the growth rate and the real part of the frequency.

When the collision term is not considered ($\xi' = 0$), the real part of the frequency is not observable at smaller values of k' . However, at larger values of k' , the real part of the frequency is present and decreases with increasing k' . Conversely, when the collision term is included ($\xi' = 0.5$), the real part of the frequency is observable at both smaller and larger values of k' , decreasing in both ranges as k' increases. Notably, at higher k' values, the real part of the frequency (ω_r) is higher in the collisional system compared to the non-collisional system. The figure also shows that the growth rate (γ) reduces with the inclusion of collisional effects. The trend of the growth rate's increase is similar in both the collisional and non-collisional systems, with a sharp increase beginning at ($k' = 0.6$). The reduction in the growth rate in the collisional system can be attributed to the redistribution of energy within the system, likely caused by the collisions.

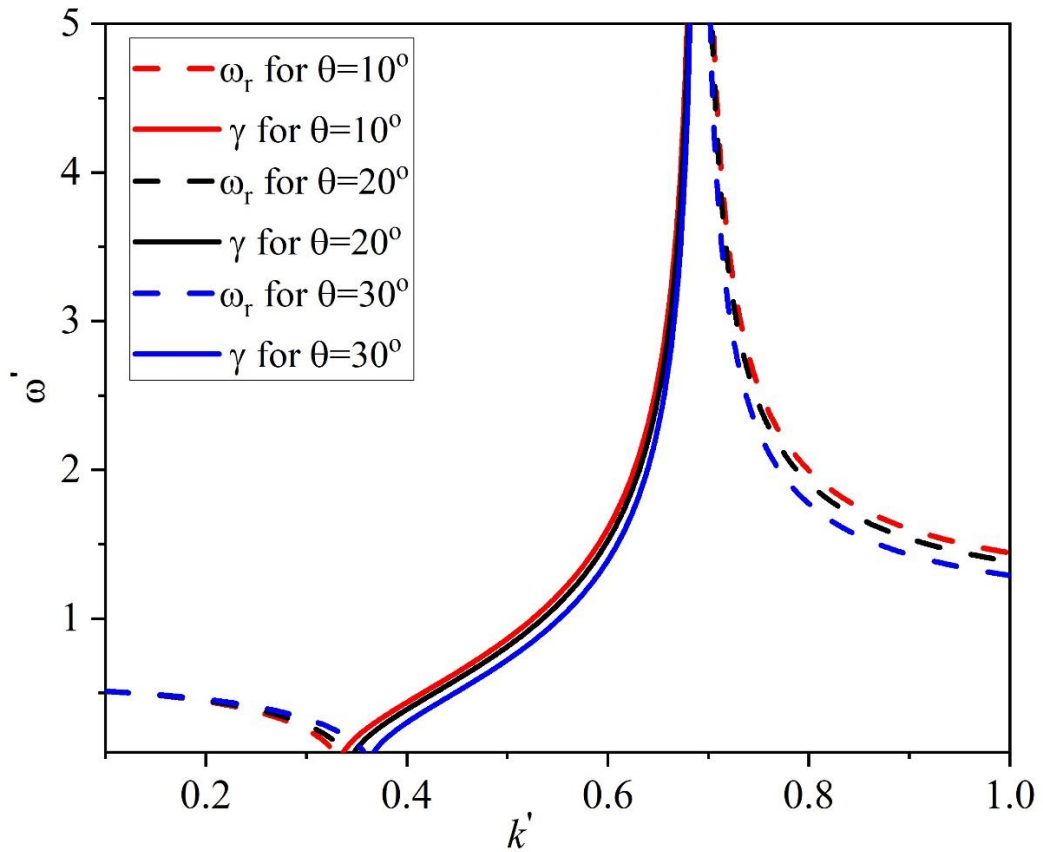


Figure 2: ω_r versus k' curve to denote the effect of propagation angle θ . $\xi' = 0.5, v'_0 = 5, v'_b = 3$ for all the curves.

Figure 2 depicts the variation in the real part of frequency (ω_r) and growth rate (γ) with respect to the normalized wave number (k') for three different propagation angles (θ). The data indicates that the real part of the frequency consistently decreases as the wave vector increases, across both the lower and higher ends of the wavelength range. In the higher wavelength range (corresponding to smaller k' values), ω_r increases with increasing θ . Conversely, in the shorter wavelength range, ω_r decreases with increasing θ . This behavior highlights the influence of the propagation angle on ω_r . Furthermore, the growth rate (γ) is observed to decrease with increasing θ . This trend suggests that larger propagation angles are more detrimental to lower hybrid wave (LHW) instabilities. The rapid redistribution of energy at lower angles likely enhances the conditions favorable for such instabilities to develop. Overall, the figure elucidates how propagation angle affects both the growth rates and the real part of the frequency, demonstrating that lower propagation angles facilitate a more rapid energy distribution, thereby promoting instability in the system.

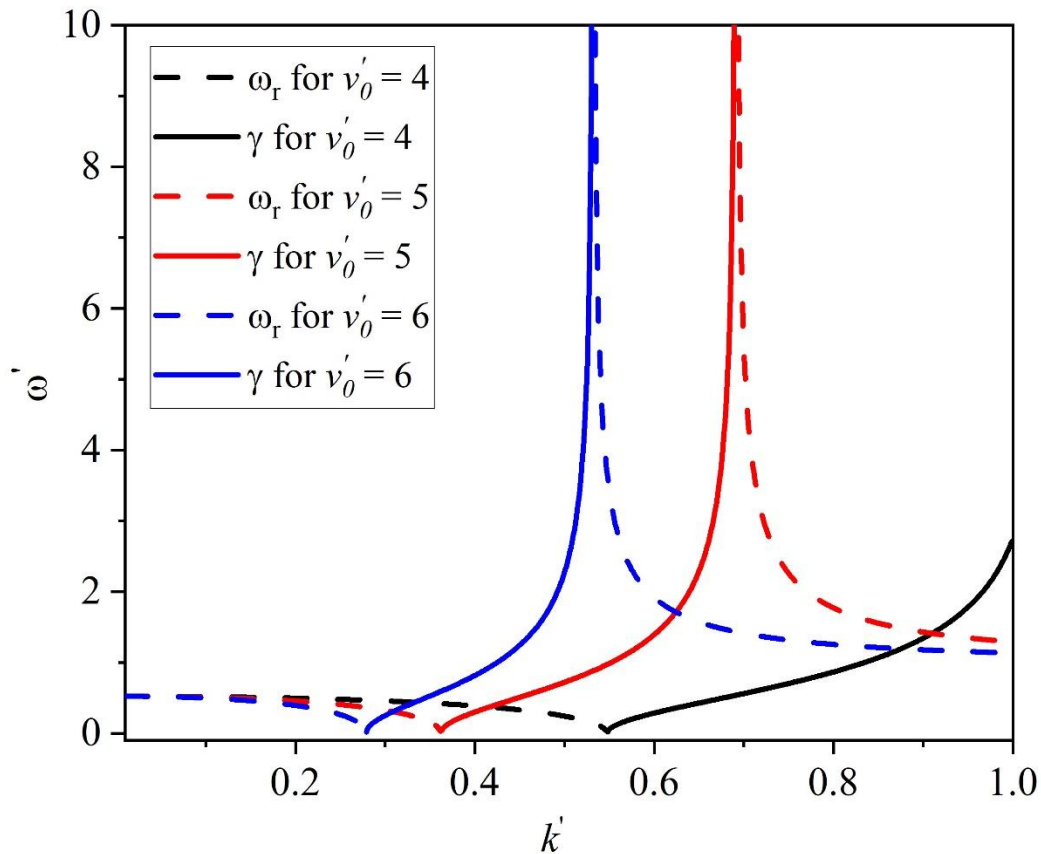


Figure 3: ω' versus k' curve to denote the effect of beam streaming speed v'_0 . $\xi' = 0.5, \theta = 30^\circ, v'_b = 3$ for all the curves.

Figure 3 illustrates the variation in the real part of frequency (ω_r) and growth rate (γ) with respect to the normalized wave number (k') for three different values of beam streaming speed (v'_0). The observed behaviour of ω_r is similar to that noted in previous analyses, where ω_r decreases with increasing k' across the spectrum. The growth rate (γ) increases with higher values of streaming speed. This indicates that higher streaming speeds introduce more energy into the system, thereby amplifying the instabilities. The figure also reveals that with increasing streaming speed, the resonance shifts towards the lower wavelength range.

IV. CONCLUSION

In this article, we have investigated the instability of Lower Hybrid Waves in a collisional magnetized GaAs semiconducting quantum plasma system. Using the Quantum Hydrodynamic (QHD) model, we derived a linear dispersion relation. Our findings suggests that the collisional term significantly affects the growth rate of the instability, specifically by decreasing its value. Additionally, consideration of the collisional term results in an increase in the real part of the frequency. We also investigate the effects of propagation angle and beam streaming speed on the system. Our results suggest that an increasing propagation angle reduces the growth rate, while a higher beam streaming speed increases the growth rates. These findings provide a deeper understanding of the dynamics within collisional magnetized GaAs semiconducting quantum plasma systems.

REFERENCES

- [1] Z. Iqbal, U. Khanum, and G. Murtaza, "Lower hybrid wave instability in a spin-polarized degenerate plasma," *Contributions to Plasma Physics*, vol. 59, no. 3, pp. 284-291, 2019.
- [2] V. D. Shapiro, V. I. Shevchenko, G. I. Solov'ev, V. P. Kalinin, R. Bingham, R. Z. Sagdeev, and J. J. Su, "Wave collapse at the lower-hybrid resonance," *Physics of Fluids B: Plasma Physics*, vol. 5, no. 9, pp. 3148-3162, 1993.
- [3] A. Rasheed, M. Jamil, F. Areeb, M. Siddique, and M. Salimullah, "Low frequency hybrid instability in quantum magneto semiconductor plasmas," *Journal of Physics D: Applied Physics*, vol. 49, no. 17, pp. 175109, 2016.
- [4] F. J. Zutavern, A. G. Baca, W. W. Chow, M. J. Hafich, H. P. Hjalmanson, G. M. Loubriel, et al., "Electron-hole plasmas in semiconductors," in *PPPS-2001 Pulsed Power Plasma Science 2001. 28th IEEE International Conference on Plasma Science and 13th IEEE International Pulsed Power Conference. Digest of Papers (Cat. No. 01CH37251)*, vol. 1, pp. 289-293, IEEE, June 2001.
- [5] T. Okuda, "The Fundamentals of Plasma," *Hyomen Kagaku*, vol. 5, no. 4, pp. 392-400, 1984.
- [6] D. M. Todorović, "Plasma, thermal, and elastic waves in semiconductors," *Review of Scientific Instruments*, vol. 74, no. 1, pp. 582-585, 2003.
- [7] Z. Iqbal, U. Khanum, and G. Murtaza, "Lower hybrid wave instability in a spin-polarized degenerate plasma," *Contributions to Plasma Physics*, vol. 59, no. 3, pp. 284-291, 2019.
- [8] O. Koshkarov, A. I. Smolyakov, A. Kapulkin, Y. Raitses, and I. Kaganovich, "Nonlinear structures of lower-hybrid waves driven by the ion beam," *Physics of Plasmas*, vol. 25, no. 6, 2018.
- [9] D. I. Maslennikov, V. S. Mikhailenko, and K. N. Stepanov, "Decay instability of a lower hybrid wave," *Plasma Physics Reports*, vol. 26, pp. 139-146, 2000.
- [10] M. R. Amin, "Modulation of electrostatic Langmuir waves in quantum electron-hole semiconductor plasmas," *Physica Scripta*, vol. 90, no. 1, p. 015601, 2014.
- [11] D. Bohm, "A Suggested Interpretation of the Quantum Theory in Terms of "Hidden" Variables. I.," *Physical Review*, vol. 85, no. 2, p. 166, 1952.
- [12] G. Manfredi, "How to model quantum plasmas," *Fields Inst. Commun.*, vol. 46, pp. 263-287, 2005.
- [13] I. Zeba, M. E. Yahia, P. K. Shukla, and W. M. Moslem, "Electron-hole two-stream instability in a quantum semiconductor plasma with exchange-correlation effects," *Physics Letters A*, vol. 376, no. 34, pp. 2309-2313, 2012.
- [14] A. R. Niknam, E. Rastbood, F. Bafandeh, and S. M. Khorashadizadeh, "Modulational instability of electromagnetic waves in a collisional quantum magnetoplasma," *Physics of Plasmas*, vol. 21, no. 4, 2014.
- [15] M. Jamil, A. Rasheed, C. Rozina, W. M. Moslem, and M. Salimullah, "Beam driven upper-hybrid-wave instability in quantized semiconductor plasmas," *Physics of Plasmas*, vol. 21, no. 2, 2014.

¹ N. B. Thakare
² V. S. Kalyamwar
¹ M. R. Belkhedkar
³ G. T. Lamdhade

Synthesis of SnO₂ Nanoparticles by Solution Combustion Method



Abstract: - The SnO₂ nanoparticles were synthesized by solution combustion method. It is also characterized for their structural and optical properties using various techniques including XRD, UV-Vis spectroscopy and FTIR. SnO₂ nanostructures have a tetragonal rutile structure, as determined by X-ray diffraction studies, with an average crystallite size of 11.47 nm. The bandgap was estimated as 3.72 eV from the UV-Visible spectra. The FTIR spectra provide evidence supporting the crystalline phase of SnO₂.

Keywords: SnO₂ nanoparticles, X-ray diffraction, UV-visible spectra, FTIR

¹Department of Physics, Shri Shivaji College of Arts Commerce and Science, Akola, (MS), India-444005

²Department of Physics, Vidhya Bharti Mahavidyalaya, Amravati, (MS), India- 444602

³Department of Physics, Bhartiya Mahavidyalaya, Amravati, (MS), India- 444602

Corresponding author: V. S. Kalyamwar

Email: vskalyamwar@gmail.com, nbtphy@gmail.com

I. INTRODUCTION

Transition-metal oxide nanoscale materials have sparked significant research interest due to their adaptive chemical, physical, and mechanical properties, which provide superior performance when compared to bulk materials [1,2]. The finite size, high surface-to-volume ratio, and possible appearance of quantum effects have a dramatic effect on nanomaterial properties [3]. Tin dioxide (SnO₂), an n-type semiconductor metal oxide, with a wide band gap ($E_g=3.65$ eV at 300 K) and a high excitation binding energy of 130 eV at ambient conditions [4,5]. With its remarkable physical and chemical characteristics, SnO₂ finds extensive utilization in various fields such as solar cells [6], gas sensors [7], transparent electrodes [8], transistors [9], batteries [10], and more. Several techniques have been used to prepare SnO₂ nanostructures, including sol-gel [11], hydrothermal [12], SILAR [13], precipitation [14], combustion-assisted sol-gel method [15], and microwave [16] among others.

Solution combustion method is a versatile, rapid, cost-effective, self-sustaining, energy efficient and scalable approach for the synthesizing of ultra-fine and uniform nanoscale materials [17,18]. This self-sustaining exothermal process involves the combustion of a uniform mixture of oxidizers (such as metal nitrates, metal sulfates, and carbonates) and fuels organic compounds like carboxylate and aliphatic amines (like urea, glycine, sucrose, and hydrazides) to produce a fine powder [17, 19]. In this study, we present the structural and optical properties of SnO₂ nanoparticles synthesized using a rapid and cost-effective solution combustion method.

II. EXPERIMENTAL:

2.1 Synthesis Of SnO₂ Nanoparticles

All the chemical reagents were analytical grade and used as purchased without further purification. Tin chloride pentahydrate (SnCl₄.5H₂O) and urea (CO(NH₂)₂) was purchases form Sigma Aldrich. Ammonia solution (35%) was obtained from S. D. Fine Chemicals, India. Urea was used as a fuel.

In a typical solution combustion method, 15 ml of 1M solution of SnCl₂.5H₂O were added to 150 ml of distilled water. The solution was stirred with a magnetic stirrer for 30 minutes at room temperature. Next, urea was added in the stoichiometric ratio under continuous stirring to the above solution and stirred for another hour to obtain a homogenous solution. The ammonia solution was used to adjust pH = 7, and the solution was stirred for 4 hours at 100 °C. Then, the resulting sol was further heated with magnetic stirring to remove the presence of water in the sol until a viscous gel was formed. The viscous gel was ignited by increasing the temperature up to 200 °C, and a brownish-gray powder of the sample was obtained. After cooling the powder to ambient temperature, it was delicately ground using an agate mortar and pestle. Finally, the powder was calcined at 500 °C for 5 hours to obtain tin oxide nanoparticles.

2.2 Characterization:

The crystal structure, purity, and phase identification of SnO₂ nanoparticles were examined using X-ray diffraction (XRD) using a Rigaku Miniplex-II instrument operating with Cu-K α radiation ($\lambda=1.5405$ Å) in the 20–80° (2 θ) range. A UV-visible spectrophotometer (Shimadzu Corporation, Kyoto, Japan) was used to characterize the optical properties of the product. The spectral range used was 200-800 nm. FT-IR spectra of dried samples were acquired with an Affinity-1S IR spectrometer (Shimadzu Corporation, Kyoto, Japan) over the 4000–500 wavenumber

III. RESULT AND DISCUSSION:

3.1 XRD Studies:

The presence of distinct peaks in the XRD pattern of the SnO₂ nanoparticles at $2\theta = 26.60, 33.83, 37.97, 51.79, 54.78, 57.81, 61.91, 65.99, 71.27, \text{ and } 78.74^\circ$ can be attributed to the (110), (101), (200), (211), (220), (002), (310), (301), (202), and (321) planes respectively [20]. All of the diffraction peaks can be indexed to the tetragonal rutile phase (P42/mmm) of SnO₂ (PDF Card No.: 1000062) [21]. The absence of any additional secondary phases of SnO₂ suggests that the synthesized product exhibits a high level of purity. The calculated mean lattice parameters, $a = b = 4.7357$ Å and $c = 3.1873$ Å, exhibit a strong agreement with the standard values [22]. The average crystallite size of nanoparticles (D, nm) was calculated from Debye-Scherrer's equation [23].

$$D = 0.9\lambda / \beta \cos\theta \quad \text{-----(1)}$$

where D is the size of a particle; λ is the wavelength of X-rays, which is equal to 0.154059 nm; β is a full width half maximum (FWHM) of the corresponding peak and θ is a diffracting angle. The average crystallite size of the SnO₂ nanoparticles synthesized in this method was obtained to be 11.47 nm. An overview of the structural parameters associated with the tetragonal SnO₂ lattice is listed in Table 1. These include unit

cell volume [24], lattice strain [25], dislocation density (δ), lattice distortion [26], number of unit cells per unit volume [27], specific surface area [28]. The quality of the synthesized SnO₂ nanoparticles appears to be fine, as δ is small and η is large compared to values reported in the literature [29].

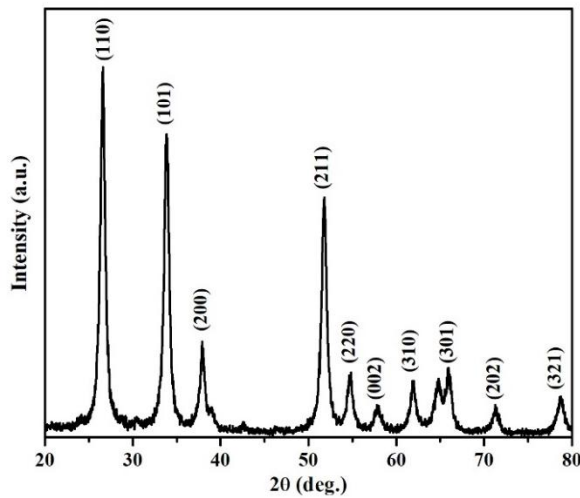


Fig.1: XRD pattern of SnO₂ nanoparticles

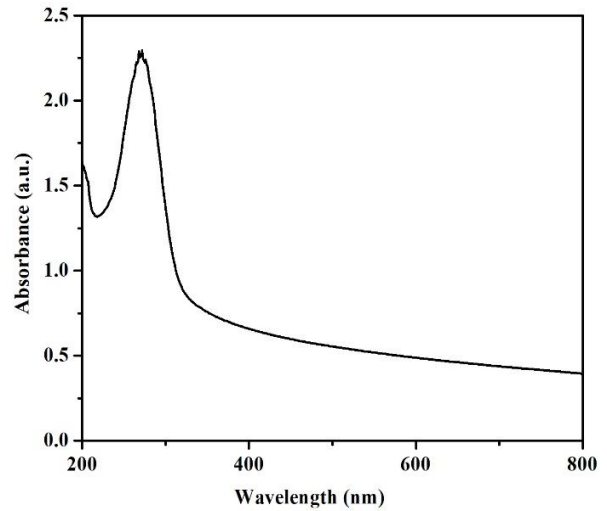


Fig. 2: UV-Vis. absorption spectrum of SnO₂ Nanoparticles

Table 1: Unit cell volume, strain, dislocation density, lattice distortion, number of unit cells per unit volume and specific surface area of SnO₂ nanoparticles.

Lattice Constant		Average Crystalline Size (nm)	Unit Cell Volume $V = a^2c$ (nm ³)	Lattice Strain $\epsilon = \beta / 4 \tan \theta$	Dislocation Density $\delta = 1/D^2$ lines/m ²	Lattice Distortion $U = a/c$	Unit Cells Per Unit Volume $n = \rho D^3 / 6V$	Specific Surface Area $S = 6/rD \cdot 10^3$ m ² / g
a=b (Å°)	c (Å°)							
4.7357	3.1873	11.47	71.48	2.156×10^{-3}	7.601×10^{16}	1.485	11.07×10^3	75.27

3.2 UV- Visible Study:

To examine the optical characteristics using UV-Vis. absorption spectroscopy, SnO₂ nanoparticles were dispersed in a solution containing 2-propanol and ethylene glycol in a 3:2 proportion. Fig. 4 shows the UV-Vis absorption spectra for tin oxide nanoparticles. The observed spectrum (Fig.2) exhibited a sharp absorption peak at 272 nm, at a shorter wavelength compared to bulk SnO₂ (344 nm) [30]. The band gap energy was estimated by analyzing the Tauc plot (Fig. 3) and was measured to be 3.74 eV.

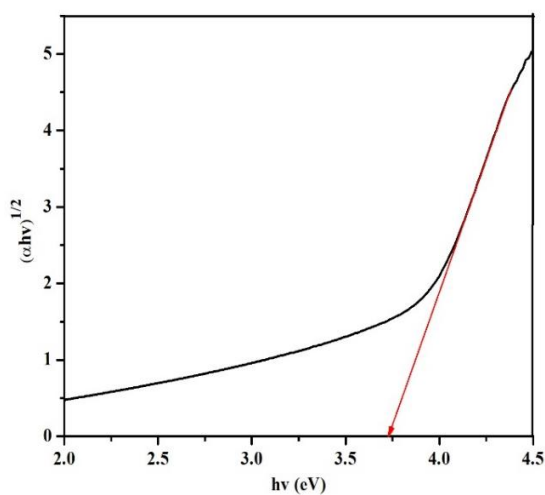


Fig. 2: Optical band gap of SnO₂ nanoparticles

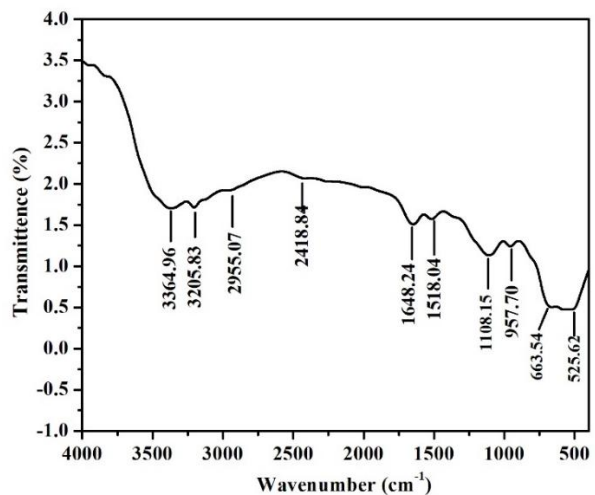


Fig.:4 FTIR Spectra of SnO₂ nanoparticles

3.3 Fourier transform infrared spectra (FTIR):

The FTIR spectrum of the dry SnO₂ nanoparticles sample is shown in Fig.4. The band noticed at 3364 and 3205 cm⁻¹ are due the O-H stretching O-H bending vibrations of water molecules reabsorbed from the ambient atmosphere by SnO₂ nanoparticles [29]. Bands at 1648 and 1518 cm⁻¹ were observed due bending vibration of H-O-H from water molecules entrapped inside the SnO₂ nanostructures [31]. The band area around 2955 and 2418 cm⁻¹ indicates the presence of C-H group [30]. The transmission in the region near 525 cm⁻¹ and 1108 cm⁻¹ is related to the vibration of Sn-O and Sn-OH bonds [32]. The O-Sn-O asymmetric stretching of SnO₂ appeared at 663 cm⁻¹ and ensured the existence of the SnO₂ crystalline phase [33].

IV. CONCLUSION:

SnO₂ nanoparticles were synthesized using straightforward solution combustion synthesis. The X-ray diffraction pattern confirms the formation of the tetragonal rutile system of SnO₂. The observed average size of the crystallites is 11.47 nm. UV-Vis. analysis showed an absorption peak at 272 nm, at a shorter wavelength compared to bulk SnO₂ (344 nm), confirming the blue shift. The band gap calculated using the Tauc relation is 3.74 eV, which is larger than that of bulk SnO₂. The asymmetric stretching vibrations of the O-Sn-O bond at 663 cm⁻¹ in the FTIR spectra ensure the formation of SnO₂. The Fourier transform infrared spectroscopy analysis indicated that water molecules were present on the nanoparticles as a result of reabsorption from the ambient atmosphere.

Acknowledgment

The author, N. B. Thakare, expresses gratitude to the Principal of Shri Shivaji College of Arts, Commerce, and Science, Akola, for his assistance and provision of research facilities.

References

- [1] Ibrahim Khan, Khalid Saeed, Idrees Khan, Nanoparticles: Properties, applications and toxicities, Arab. J. Chem., 12, 2019, 908-931, <https://doi.org/10.1016/j.arabjc.2017.05.011>.
- [2] Verma, G., Sheshkar, N., Pandey, C., Gupta A., Recent trends of silicon elastomer-based nanocomposites and their sensing applications, J. Polym. Res., 29, 195 (2022). <https://doi.org/10.1007/s10965-022-03044-z>.
- [3] Tawfik A. Saleh, Environ. Technol. Inno., Nanomaterials: Classification, properties, and environmental toxicities, 20, 2020, 101067, <https://doi.org/10.1016/j.eti.2020.101067>.
- [4] Chen, W., Ghosh, D. & Chen, S., Large-scale electrochemical synthesis of SnO₂ nanoparticles, J. Mater. Sci. 43, 2008, 5291–5299, <https://doi.org/10.1007/s10853-008-2792-x>.
- [5] M.A. Gondal, Q.A. Drmosh, T.A. Saleh, Preparation and characterization of SnO₂ nanoparticles using high power pulsed laser, Appl. Surf. Sci., 256, 2010, 7067-7070, <https://doi.org/10.1016/j.apsusc.2010.05.027>.
- [6] Haimang Yi, Dian Wang, Md Arafat Mahmud, Faiazul Haque, Mushfika Baishakhi Upama, Cheng Xu, Leiping Duan, and Ashraf Uddin Bilayer SnO₂ as Electron Transport Layer for Highly Efficient Perovskite Solar Cells, ACS Appl. Energy Mater., 1 (11), 2018, 6027-6039 <https://doi.org/10.1021/acsami.8b01076>.
- [7] Shukla, G. P., Pandey, C. K., Bajpai, M., Bhatnagar, M. C., & Dhar, R., Phase Transit., Ammonia gas sensor based on SnO₂ nanostructure with the enhanced sensing capability at low temperatures, 92(10), 2019, 939–947. <https://doi.org/10.1080/01411594.2019.1660878>.
- [8] R. Ramarajan, M. Kovendhan, K. Thangaraju, D. Paul Joseph, Indium-free large area Nb-doped SnO₂ thin film as an alternative transparent conducting electrode, Ceram. Int., 46, 2020, 12224-12231, <https://doi.org/10.1016/j.ceramint.2020.01.270>.
- [9] Priyadarshini D.M., Ramanjaneyulu Mannam, M.S. Ramachandra Rao, Nandita Das Gupta, Effect of annealing ambient on SnO₂ thin film transistors, Appl. Surf. Sci., 418, 2017, 414-417, <https://doi.org/10.1016/j.apsusc.2016.11.233>.
- [10] Jun Song Chen, Xiong Wen Lou, SnO₂-Based Nanomaterials: Synthesis and Application in Lithium-Ion Batteries, Small, 9 (11), 2013, <https://doi.org/10.1002/sml.201202601>.
- [11] Madzlan Aziz, Saad Saber Abbas, Wan Rosemaria Wan Baharom, Size-controlled synthesis of SnO₂ nanoparticles by sol-gel method, Mater. Lett., 91, 2013, 31-34, <https://doi.org/10.1016/j.matlet.2012.09.079>.
- [12] Nasrin Talebian, Farzaneh Jafarinezhad, Morphology-controlled synthesis of SnO₂ nanostructures using hydrothermal method and their photocatalytic applications, Ceram. Int., 39, 2013, 8311-8317, <https://doi.org/10.1016/j.ceramint.2013.03.101>.
- [13] M. Ali Yıldırım, Yunus Akaltun, Aytunç Ateş, Characteristics of SnO₂ thin films prepared by SILAR, Solid State Sci., 14, 2012, 1282-1288, <https://doi.org/10.1016/j.solidstatesciences.2012.07.012>.
- [14] K. Nejati, Cryst. Synthesis by precipitation method and investigation of SnO₂ nanoparticles, Res. Technol., 47,2012, <https://doi.org/10.1002/crat.201100633>.
- [15] Bongho Jang, Jaewon Jang, Jae Eun Jang, Hyuk-Jun Kwon, Combustion-assisted low-temperature solution process for high-performance SnO₂ thin-film transistors, Ceram. Int., 48, 14, 2022, 20591-20598, <https://doi.org/10.1016/j.ceramint.2022.04.026>.
- [16] Azam, A., Habib, S. S., Salah, N. A., & Ahmed, F. Microwave-assisted synthesis of SnO₂ nanorods for oxygen gas sensing at room temperature, Int. J. Nanomedicine, 8, 2013, 3875–3882. <https://doi.org/10.2147/IJN.S51206>.
- [17] Francesca Deganello, Avesh Kumar Tyagi, Solution combustion synthesis, energy and environment: Best parameters for better materials, Prog. Cryst. Growth Charact. Mater., 64, 2018, 23-61, <https://doi.org/10.1016/j.pcrysgrow.2018.03.001>.
- [18] Singanahally T. Aruna, Alexander S. Mukasyan, Combustion synthesis and nanomaterials, Curr. Opin. Solid State Mater. Sci., 12, 2008, 44-50, <https://doi.org/10.1016/j.cossms.2008.12.002>.
- [19] Emanuel Carlos, Prof. Rodrigo Martins, Prof. Elvira Fortunato, Prof. Rita Branquinho, Solution Combustion Synthesis: Towards a Sustainable Approach for Metal Oxides, Chem. Eur. J., 26, 2020, <https://doi.org/10.1002/chem.202000678>.

- [20] D. Dutta, S. Chandra, A.K. Swain, D. Bahadur, SnO₂ Quantum Dots-Reduced Graphene Oxide Composite for Enzyme-Free Ultrasensitive Electrochemical Detection of Urea, *Anal. Chem.*, 86, 2014, 5914-5921, <https://doi.org/10.1021/ac5007365>.
- [21] Y.-L. Wang, M. Guo, M. Zhang and X.-D. Wang, Hydrothermal preparation and photoelectrochemical performance of size-controlled SnO₂nanorod arrays, *Cryst. Eng. Comm*, 2010, 12, 4024-4027.
- [22] Qian Zhang, Peng Liu, Chunjie Miao, Zhiwen Chen, C. M. Lawrence Wub and Chan-Hung Shek, Formation of orthorhombic SnO₂ originated from lattice distortion by Mn-doped tetragonal SnO₂, *RSC Adv.*, 2015,5, 39285-39290, <https://doi.org/10.1039/C5RA04946F>.
- [23] Nirmal Prashanth M, Rajesh Paulraj, Ramasamy P, Vijayan N, One step synthesis of tin oxide nanomaterials and their sintering effect in dye degrdation, *Optik*, 135, 2017, 434-445, <https://doi.org/10.1016/j.ijleo.2017.01.068>.
- [24] Vijayaprasath, G., Murugan, R., Mahalingam, T. et al. Comparative study of structural and magnetic properties of transition metal (Co, Ni) doped ZnO nanoparticles. *J Mater Sci: Mater Electron* 26, 7205–7213 (2015). <https://doi.org/10.1007/s10854-015-3346-z>.
- [25] Khatter, J., Chauhan, R.P. Effect of temperature on properties of cadmium sulfide nanostructures synthesized by solvothermal method. *J Mater Sci: Mater Electron* 31, 2676–2685 (2020). <https://doi.org/10.1007/s10854-019-02807-7>.
- [26] A. Gaber, M.A. Abdel-Rahim, A.Y. Abdel-Latief, Mahmoud N. Abdel-Salam, Influence of Calcination Temperature on the Structure and Porosity of Nanocrystalline SnO₂ Synthesized by a Conventional Precipitation method, *Int. J. Electrochem. Sci.*, 9, 2014, 81-95, [https://doi.org/10.1016/S1452-3981\(23\)07699-X](https://doi.org/10.1016/S1452-3981(23)07699-X).
- [27] Rani, N., Jaggi, N. Effect of reaction temperature on the structural and electronic properties of stannic oxide nanostructures, *Bull Mater. Sci.* 43, 2020, 146, <https://doi.org/10.1007/s12034-020-02141-3>
- [28] Bikram Keshari Das, Tanushree Das, Kajal Parashar, Arun Thirumurugan & S. K. S. Parashar, Structural, bandgap tuning and electrical properties of Cu doped ZnO nanoparticles synthesized by mechanical alloying. *J Mater Sci: Mater Electron* 28, 2017, 15127–15134, <https://doi.org/10.1007/s10854-017-7388-2>.
- [29] Gauravkumar H. Patel, Sunil H. Chaki, Rohitkumar M. Kannaujiya, Zubin R. Parekh, Anilkumar B. Hirpara, Ankurkumar J. Khimani, M.P. Deshpande, Sol-gel synthesis and thermal characterization of SnO₂ nanoparticles, *Phys. B: Condens. Matter*, 613, 2021, 412987, <https://doi.org/10.1016/j.physb.2021.412987>.
- [30] Lin Tan, Lihong Wang and Yude Wang, Hydrothermal Synthesis of SnO₂ Nanostructures with Different Morphologies and Their Optical Properties, *J. Nanomater.*, <https://doi.org/10.1155/2011/529874>.
- [31] V. Senthilkumar, P. Vickraman, M. Jayachandran, C. Sanjeeviraja Synthesis and Characterization of SnO₂ Nanopowder Prepared by Precipitation Method, *J. Dispers. Sci. Technol.* 31, 2010, <https://doi.org/10.1080/01932690903223856>.
- [32] S. Roy, Amish G. Joshi, S. Chatterjee and Anup K. Ghosh, Local symmetry breaking in SnO₂ nanocrystals with cobalt doping and its effect on optical properties, *Nanoscale*, 2018,10, 10664-10682, <https://doi.org/10.1039/C7NR07427A>.
- [33] K. Karthik, V. Revathi & Tetiana Tatarchuk, Microwave-assisted green synthesis of SnO₂ nanoparticles and their optical and photocatalytic properties, *Mol. Cryst. Liq. Cryst.*, 67, 2018,17-23, <https://doi.org/10.1080/15421406.2018.1542080>

¹ Raushan Shah R. Shah

² P. R. Yawale

³ A. C. Dongapure

⁴ P. P. Choudhari*

Green Synthesis of Papaya (*Carica papaya*) Leaf Extract by using of Copper Oxide.



Abstract: - Green Synthesis is going on more use full and advance technique in resented year. It is nature preventive technique because less use of chemical and carry out in a simple manner. Development of green synthesis is eco-friendly and low cost method for bio synthesis of nano particle of 0.1 M Copper sulphate solution and papaya extract was made . 50 ml of papaya leaf extract and 150 ml Copper sulphate were taken. In Papaya extract we constant adding Copper sulphate solution with constant stirring at 50-60° C. It was observed that there was formation of nano particles of Copper. After the product was culled brown dark product gained. The bio synthesizes nano particle of copper sulphate are characterized by IR and XRD. At bond strength 3421.87 inert molecular H bond present in given sample. 3306.13 shows bond of NH it means amine group present in it. 2932.89 show saturated alkane present in this phytochemicals. 2155.54, 1655.00 shows conjugated nitriles and amide group present in given sample. 1337.69 bond strength shows nitro group present in it. 1154.45 shows alcohol phenol group present in copper nanoparticles. 664.51, 515.98 bond linkage in between given phytochemicals and nanoparticles.

Keywords: Green Synthesis, Nano Particle of Copper, Copper Sulphate, Papaya Leaf,

V. INTRODUCTION

Resent years green synthesis is become a more advance technique for synthesis of new compounds. Green synthesis use for the preparation of nano particle from various plants. Many physical and chemical methods are use for the synthesis of metal nano particles. Green synthesis of nano particle is clean, nontoxic and environmentally friendly procedures. Green synthesis of plant material provide an innovative research for the production of nano particles[1]. Plants provide better platform for the preparation for metal nano particles as they are free from the toxic chemicals as well as provide natural capping agents[2]. The extract of plants contains various organic compounds such as terpenoids which is surface active molecules that helps to stabilize the nano particles[3]. Copper nano particle is referred as effective bactericidal metal, it is non toxic to animal cell and there for consider to be safe for human being in the accept of food packaging and water treatment[4]. In literature survey the synthesis of copper nano particles from various methods such as vapour Deposition [5], electrochemical reduction[6], radiolysis[7], thermal decomposition[8], chemical reduction of metal salt[9], at room temperature synthesis using hydrazine hydrate and starch [10] In resented year green synthesis of Cu- nano particles was synthesis by using plant extract [11]

II Methods And material

Preparation leaf extract.

Papaya (*Carica*) leaves was used. Healthy leaves were collected and wash in running tap water and than by distilled water. The leaves were dried with absorbent paper. These papa leaves cut with a sterile knife. Take 50 gram of leaves and 100ml of distilled water in 250 ml beaker. This was boil at 60° C for 45 minutes. After completion of it was cool at room temperature and then filter with Whatmann filter paper the plant extract was collected in beaker.

Preparation of Copper Solution

Copper sulphate solution was prepare by adding 24.98 gm in 1000 ml distilled water, it is of 0.1 M solution of Copper Sulphate.

Preparation Cu- nano Partial

For the Synthesis of Cu-nano particle take 50 ml of papaya leaf extract in 250 ml beaker. Heat the solution about 60° C to 80° C and add gradually 0.1 M copper sulphate solution into the hot solution by continuous stirring. As result of colour of the solution changes gradually from greenish blue to green an heattiong was continue until dark green past was formed. The dark green past was cooled at room temperature. The collected powder was send to characterization using various analytical tools.

III Result And Discussion

The structural analysis of Cu-nano particle was analyze by XRD technique. Figure 1 represent the XRD pattern of green synthesis of Cu-NPs The specific diffraction peaks at 2- theta 14.30(2), 24.26(8), 30.07(4), 32.04(3), 37.19(13), 40.11(2), 42.508(19), 46.15(2), 49.34(3) and 67.177(19) The synthesized Cu-NP were well crystalline that was confirm by high intensity diffraction reflection peak. The crystal size was calculated $D=0.9\lambda / (B\cos\theta)$ [12]

¹Raushan Shah R. Shah :G. S. Tompe Arts, Commerce And Science College, Chandur Bazar , Amravati, Maharashtra,India ²P. R. Yawale, G. S. Tompe Arts, Commerce And Science College, Chandur Bazar, ³A. C. Dongapure Shankarlal Agrawal Science College, Salekasa, ⁴* P. P. Choudhari G. S. Tompe Arts, Commerce And Science College, Chandur Bazar , Amravati, Maharashtra,India Copyright©JES2024on-line:journal.esrgroups.org

Table 1 XRD Of Cu-Papaya Nano Particle

No.	2-theta (deg)	d (ang.)	Height (counts)	FWHM (deg)	Int.I (countsdeg)	Size (ang.)
254	14.30(2)	6.189(9)	87(9)	2.12(9)	347(8)	39.5(17)
255	24.26(8)	3.666(11)	45(7)	0.51(8)	30(4)	168(25)
256	30.07(4)	2.969(4)	21(5)	0.8(3)	35(5)	107(34)
257	32.04(3)	2.791(2)	91(10)	0.38(4)	50(3)	228(23)
258	37.19(13)	2.415(8)	21(5)	0.83(18)	30(4)	105(23)
259	40.11(2)	2.2460(13)	35(6)	0.45(7)	19(3)	198(31)
260	42.507(19)	2.1250(9)	18(4)	0.26(4)	5.8(7)	349(55)
261	46.15(2)	1.9655(9)	22(5)	0.34(14)	13.6(14)	267(114)
262	49.34(3)	1.8454(9)	15(4)	0.29(5)	7.2(7)	311(57)
263	67.177(19)	1.3924(4)	16(4)	0.20(5)	3.5(9)	486(121)

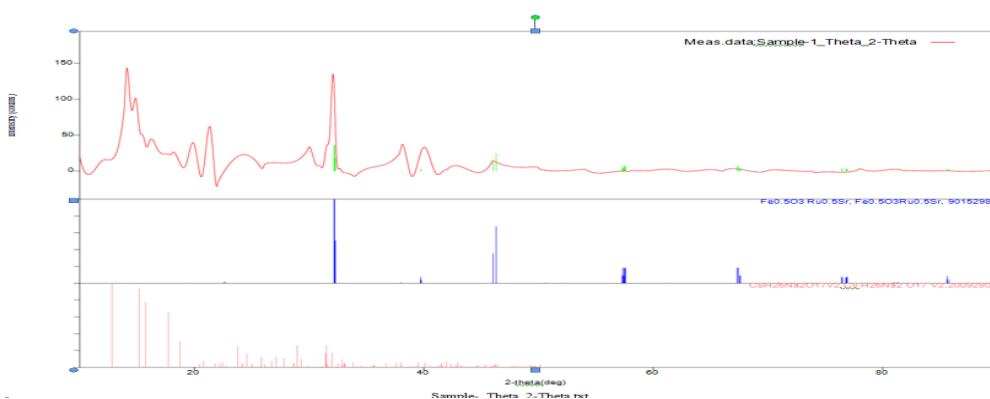


Figure No 1 XRD Of Cu-Papaya Nano Particle

FTIR spectroscopy analysis was carried out for the identification of functional groups involved in the formation of Cu-nano particles of papaya. Figure 2 shows the spectra of Papaya nano particles. The FTIR spectra of biosynthesized Cu-nano particles showed high-intensity sharp absorption peaks at 515 cm⁻¹, 1337 cm⁻¹, 664 cm⁻¹, showing the O-H bending functional group. Starching of C-O was identified by 1082 cm⁻¹. Absorption bands at 1545.05 cm⁻¹ and 1655 cm⁻¹ show the presence of a primary amide group. The presence of a primary amide group contributed from the protein content of the papaya, which provides the protein in the fruit peel. The absorption bands at 3306.13 cm⁻¹ and 3421.87 cm⁻¹ show O-H stretching. Other peaks at 2155 cm⁻¹, 2295.39 cm⁻¹, show the C-H stretching band.

Table 2 FTIR Of Cu-Papaya Nano Particle

No.	Peak	Intensity	Corr.Inte	Base(H)	Base(L)	Area	Corr.Are
1	515.98	0.6654	0.0537	621.11	406.03	464.874	3.9665
2	664.51	0.6821	0.0507	903.69	622.07	592.5568	2.9818
3	1082.11	0.6751	0.0788	1136.12	904.65	488.8063	4.4439
4	1154.45	0.7018	0.0094	1284.65	1137.09	315.2335	0.4135
5	1337.69	0.7297	0.0547	1486.22	1285.61	424.6372	3.7937
6	1545.05	0.7251	0.0518	1577.84	1487.18	192.0611	1.3568
7	1655	0.6034	0.3554	1990.62	1578.8	802.3108	22.5348
8	2155.54	1.8576	0.0174	2219.2	1991.59	393.5132	0.675
9	2295.39	1.8113	0.0193	2323.36	2220.16	179.1996	0.2236
10	2932.89	0.7016	0.3233	3019.69	2324.32	1329.560	18.4905
11	3306.13	0.6856	0.0698	3404.51	3020.66	810.6994	5.8283
12	3421.87	0.7013	0.0832	3807.65	3405.47	768.723	26.3214

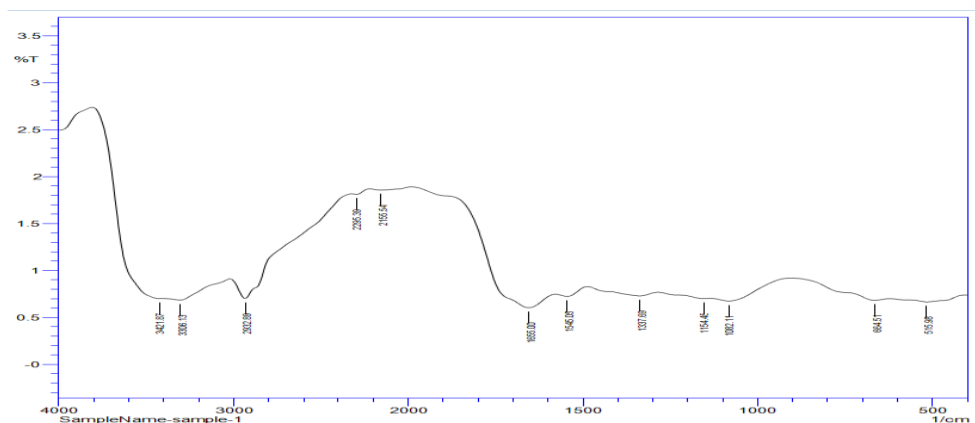


Figure No 2 FTIR Of Cu-Papaya Nano Particla

IV Conclusion

We Synthesis Cu Nano particle by using Papaya leaf and Copper Sulphate Solution. The characterization of this nano particle by XRD and FTIR technique. We observed that there were band observed 2- theta 14.30(2), 24.26(8), 30.07(4), 32.04(3), 37.19(13), 40.11(2), 42.508(19), 46.15(2), 49.34(3) and 67.177(19) shows the Cu-nano particle formation. The FTIR absorption band at 515 cm^{-1} , 1337 cm^{-1} , 664 cm^{-1} , shows the O-H bending, starching of C-O was identified by 1082 cm^{-1} , 2155 cm^{-1} , 2295.39 cm^{-1} , show the C-H streaching band. The band 3306.13 cm^{-1} and 3421.87 cm^{-1} show the O-H stretching, 1545.05 cm^{-1} and 1655 cm^{-1} show the presence of primary Amide group. The presence of primary Amide group contributed from the protein content of the papaya which provide the protein in the fruit peel. From this we can say that their presence of O-H, C-O, C-H and amide functional group.

ACKNOWLEDGMENT

I say thanks to Principal of G. S. Arts, Commerce and Science college and Chemistry department for providing me all facility for doing research work. I also thanks to my Guide Dr. Prafull P. Choudhari which give me very much support for work.

REFERENCES

1. I. Khan, K. Saeed and I. Khan, Arab. J. Chem. 12(7), P. P. 908–931, 2019.
2. 1) T. Imaoka, K. Yamamoto, Bull. Chem. Soc. Jpn. 92(5) P. P. 941–948, 2019.
2) A. Loureiro, N.G. Azoia, A.C. Gomes, A. CavacoPaulo, Curr. Pharm. Des. 22(10), P. P. 1371–1390, 2016.
3. E. Martis, R. Badve, M. Degwekar, Chronicles Young Sci. 3(1), P.P. 68–73, 2012.
4. A. Tadjarodi, R. Roshani, Curr. Chem. Lett. 3(4), P. P. 215–220, 2014.
5. C. Hyungsoo, P. Sung-Ho, “Seedless growth of free-standing copper nanowires by chemical vapor deposition”, J. Am. Chem. Soc. 126(20), P. P. 6248-6249, 2004.
6. L. Huang, H. Jiang, J. Zhang, Z. Zhang, P. Zhang, “Synthesis of copper nanoparticles containing diamond-like carbon films by electrochemical method”, Electro. Comm. 8(2), P. P. 262-266, 2006.
7. S.S. Joshi, S.F. Patil, V. Iyer, “Radiation induced synthesis and characterization of copper nanoparticles”, Nanostru. Mater. 10(7), P. P. 1135-1144, 1998.
8. N. Aruldas, C.P. Raj, A. Gedanken, “Synthesis, characterization, and properties of metallic copper nanoparticles”, Chem. Mater, 10(5), P. P. 1446-1452, 1998.
9. H. Hashemipour, M.E.Z. Rahimi, R. Pourakbari, P. Rahimi, “Investigation on synthesis and size control of 10 copper nanoparticle via electrochemical and chemical reduction method”, Int. J. Phys. Sci. 6(18), P. P. 4331-4336, 2011.
10. N.V. Surmawar, S.R. Thakare, N.T. Khaty, “One-Pot, single step green synthesis of copper nanoparticles: spr nanoparticles”, Inter. J. Green Nanotechnol. 3(4), P. P. 302-308, 2011
11. S. Gunalan, R. Sivaraj, R. Venkatesh, “Aloebarbadensis Miller mediated green synthesis of mono disperse copper oxide nanoparticles: optical properties”, Spectrochim. Acta. Mol. Biomol. Spectroscopy A Vol. 97, P. P. 1140-1144, 2012.
12. S. Flex, R. B. P. Chakkravarth, A. N. Grace, “Microwave assisted synthesis of copper oxide and its application in electrochemical sensing”, IOP Conf. Ser. Mater. Sci. Eng. 73, P. P. 12-15, 2015.

¹R.R.Mistry
²B.M.Mude
³K.M.Mude
⁴K.B.Raulkar
⁵S.M.Yenorkar
⁴R.P.Ikhar
⁶R.N.Zade
⁴G.T.Lamdhade

**Impact of Laser irradiation on
seed germination, seed vigour and
electric conductivity in
Groundnut seeds**



Abstract: - In this study, the groundnut seeds (*Arachis hypogaea* L.) were exposed to He-Ne laser. We had taken four varieties of groundnut seeds(TAG₂₄,SB₁₁&G₂), each varieties were divided into four groups. First group was the controlled group and received no radiation. Second, third and fourth group were irradiated 2, 4 and 6 minutes respectively by He-Ne laser with wavelength 632.8nm. from a distance of 45cm. Exposure with He-Ne laser gave significant results in increasing of germination percentages and vigour index but electrical conductivity has been decreased.

Keywords: Laser irradiation, germination rate, vigour index and electrical conductivity.

¹ * Dept. of Physics, Deogiri College, Chhat. Sambhajinagar-431005 (M.S.) India

² Dept. of Physics, Ramnarain Ruia College, Matunga(E)-400019 (M.S.) India

³ Dept. of Physics ,Bhavan's College, Andheri(W)-400058(M.S.) India

⁴ Dept. of Physics,Vidyabharti Mahavidyalaya, Amravati-444602(M.S.) India

⁵ Dept. of Physics, Shri Shivaji College, Parbhani-431 401 (M.S.) India

⁶ Dept. of Chemistry, Siddharth College, Fort, Mumbai-400001(M.S.) India

e-mail Corresponding Author : ranjeetphy18@gmail.com

Copyright © JES 2024 on-line : journal.esrgroups.org

I. INTRODUCTION

Light plays a major role in growing of plant. The effect of light during plant growth and germination process is undeniable. Laser can emit a high density of photons at small solid angle. The characteristics of the laser radiation, such as monochromatic, polarization, coherence and high density, can be used not only in all spheres of engineering but also in biology and plant growth [1-3]. The growing need for ecological agricultural products together with the increased demand of crop materials for food production as well as for other branches of industry imposes the necessity for searching new, safer decisions for raising the agricultural production [4-7]. Sustainable agriculture is a management system for renewable natural resource for food production income and livelihood for present and future generations [7-9]. Physical factors such as microwave and laser radiation are useful for plants enable to vegetable at higher energy level. It is based on the fact that physical methods increase the energy account by internal transformation of energy [10]. The germination of seed is dependent on both internal and external conditions. One of the most important external factors is light, which plays vital role in photosynthesis and non-photosynthesis processes involving action of light [11-15].

The previous studies showed that LED light and He-Ne laser presented a positive role in acceleration the plant growth, metabolism and increase their resistance to diseases, which suitable applications of laser irradiation improved germination capacity of plant seeds [4,16,17].

Laser irradiation is considered as a new branch in agriculture. This work aimed to study the effect of laser irradiation and exposure time on germination, vigour index and electric conductivity of groundnut seeds. Groundnut are the most important commercial crop playing a key role in economical and social affects of world continues to be acclaimed as king of oil seed.

II. MATERILAS AND METHOFDS

2.1. Seed materials:

Groundnut seeds (*Arachis hypogae* L.) used in this work were supplied by college of agricultural engineering and technology, Marathwada Krishi Vidyapeeth, Parbhani, India. The experiment were carried out at the department of physics , Shri Shivaji College, Parbhani.

2.2. Treatments:

Continuous laser irradiation at $\lambda = 632.8\text{nm}$ was obtain from He-Ne and intensity of beam is 5mW/mm^2 . The groundnut seeds of three verities (TAG₂₄, SB₁₁, G₂), each having 800 seeds were taken. Each varieties of seeds were divided into four groups. The first is the controlled (no irradiation) and rest of were irradiated to 2, 4, 6 minutes to He-Ne laser. The irradiation treatment of the seeds were performed in the dark room to avoid the influence of the Sun rays.

2.3. Germination test:

After the treatments, irradiated and controlled seeds were placed in water saturated towel paper. In each towel paper contained 200 seeds which were treated with time period of 0 min., 2min., 4min. and 6min. Sprayed the distilled water two times in a day to germination of groundnut seeds and count daily the number of seeds were germinated.

2.4. Seed Vigor Index:

Seed vigor index were calculated by determining the germination percentage and seedling length of the same seed lot. We were selected randomly 10 germinated seeds and measured seedling length.

The seed vigor index was calculated by using the formula

Vigor Index = germination % x Average seedling length (in mm)

2.5. Electrical conductivity test:

A seed sample of 10gm was sterilized with distilled water for 2-3 minutes. The clean sample was immersed in 100ml of water at $25 \pm 1^\circ\text{C}$ temperature for 10-12hr. After that the seeds were removed by a clean forcep. The steep water left was decanted and was termed as leachate. The conductivity meter was warmed about 30 minutes before testing by deeping in distilled water. First the conductance of distilled water was measured, then leachate was measured. The formula for calculate the electrical conductivity of seed extract was as follows.

E.C. = [Actual E.C. meter reading - E.C. of distilled water] x Cell constant factor.

Ammonia solution ($\text{NH}_3 \cdot \text{H}_2\text{O}$): Used for pH adjustment.

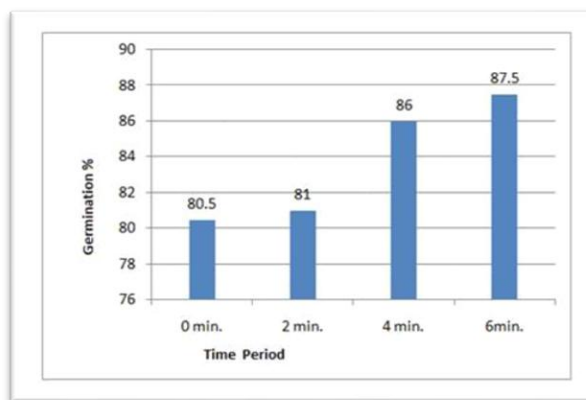
III. RESULT AND DISSCUSSION

3.1: GERMINATION PERCENTAGE

The results of germination test for all varieties based on irradiation time as shown in table.

Table (1) No. of seeds germinated per day for controlled and irradiated seeds of TAG24 variety

No. of Days	No. of seeds germinated per day			
	Controlled	Irradiation time period		
		2 min.	4 min.	6 min.
1	0	0	0	0
2	0	0	0	0
3	0	0	0	0
4	0	0	15	22
5	26	32	31	39
6	39	31	45	34
7	47	56	34	33
8	49	49	48	57
Total	161	162	172	175
%	80.5%	81%	86%	87.5%

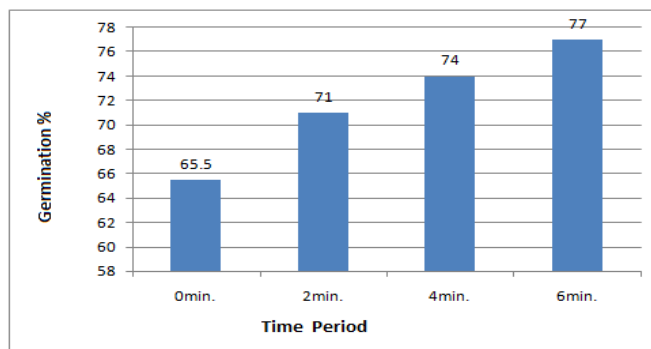


Graph 1) Germination % for TAG₂₄ Variety Vs irradiation time

From graph it was seen that as the time period of irradiation increases the germination percentage also increased from 80.5% for controlled seed to 87.5% for 6min. irradiated seed.

Table (2) No. of seeds germinated per day for controlled and irradiated seeds of SB₁₁ variety

No. of Days	No. of seeds germinated per day			
	Controlled	Irradiation time period		
		2 min.	4 min.	6 min.
1	0	0	0	0
2	0	0	0	0
3	0	0	0	0
4	0	0	12	14
5	19	28	25	26
6	24	25	24	34
7	40	42	41	38
8	48	47	46	42
Total	131	142	148	154
%	65.5%	71%	74%	77%

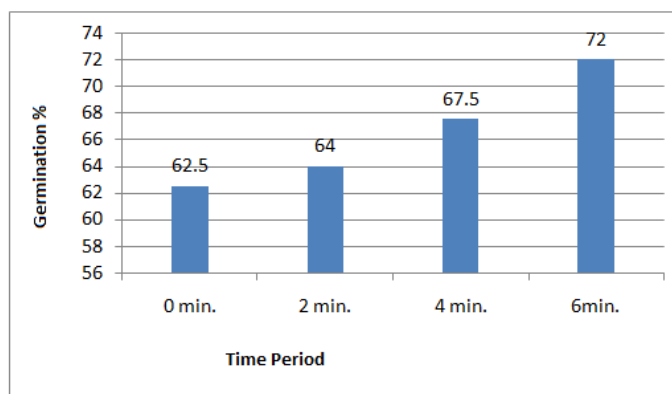


Graph 2) Germination % for SB₁₁ Variety Vs irradiation time

From graph it was seen that as the time period of irradiation increases the germination percentage also increased from 65.5% for controlled seed to 87.5% for 6min. irradiated seed.

Table (3) No. of seeds germinated per day for controlled and irradiated seeds of G₂ variety

No. of Days	No. of seeds germinated per day			
	Controlled	Irradiation time period		
		2 min.	4 min.	6 min.
1	0	0	0	0
2	0	0	0	0
3	0	0	0	0
4	0	9	12	15
5	21	26	32	24
6	26	33	31	30
7	36	34	28	35
8	42	36	32	40
Total	125	128	135	144
%	62.5%	64%	67.5%	72%



Graph 3) Germination % for G₂ Variety Vs irradiation time

From graph it was seen that germination % increases from 62.5% for controlled seed to 72% for 6min. irradiated seed. He-Ne laser irradiation enhanced the germination percentage of groundnut seed, after eight days germination % increases 7-11% of irradiated seed as compared to controlled seed. Germination rate of TAG₂₄ variety were more than SB₁₁ and G₂ varieties.

3.2. Vigour Index

The vigour test of the groundnut seed also shows the deflection in the vigour index of the controlled and irradiated seed. The seeds treated for more time period were more vigours than the controlled seed.

Table 4) Vigour index for TAG₂₄ Variety

Seed sample	Controlled (0min.)	2min.	4min.	6min.
Germination %	80.5	81	86	87.5
Seedling Length (mm)	75	80	82	85
Vigour Index	6037.5	6480	7052	7437.5

Table 5) Vigour index for SB₁₁ Variety

Seed sample	Controlled (0min.)	2min.	4min.	6min.
Germination %	65.5	70	74	77
Seedling Length (mm)	68	77	76	79
Vigour Index	4454	5467	5624	6083

Table 5) Vigour index for G₂ Variety

Seed sample	Controlled (0min.)	2min.	4min.	6min.
Germination %	62.5	62	67.5	72
Seedling Length (mm)	62	70	73	77
Vigour Index	3875	4340	4927.5	5544

The vigour index in all varieties i.e. TAG₂₄, SB₁₁ and G₂ increases with the irradiation time period. For TAG₂₄, the vigour index was increased from 6037.5 to 7437.5. For SB₁₁, the vigour index was increases from 4454 to 6083. For G₂, the vigour index was increases from 3875 to 5544. It was seen that as irradiation time increases Vigour index also increases.

3.3. Electrical Conductivity Test of Leachates.

The electric conductivity (E.C.) of the groundnut seed extract was measured by a digital electrical conductivity meter in $\mu\text{mhos/cm/gm}$.

Electrical conductivity of distilled water=3.8 ($\mu\text{mhos/cm/gm}$).

Cell constant factor=1.28

Table 7) . Electrical Conductivity of Leachates forTAG₂₄,SB₁₁ and G₂ varieties of groundnut seed.

Variety	Sample	Actual meter reading	Calculated E.C.
TAG ₂₄	0min.	6.0	2.816
	2min.	5.8	2.56
	4min.	5.2	1.792
	6min.	4.9	1.408
SB ₁₁	0min.	5.8	2.56
	2min.	5.5	2.176
	4min.	5.0	1.536
	6min.	4.8	1.28
G ₂	0min.	5.9	2.688
	2min.	5.4	2.408
	4min.	5.2	1.792
	6min.	4.7	1.152

Weakening of cell membrane is poor vigour seeds causes leakage of water soluble compounds like suger, amino acids electrolytes etc. when immersed in distilled water. It was seen that irradiation time increases , electrical conductivity goes on decreasing. It means that less water soluble compounds leakage for more time of irradiation.

IV. CONCLUSION

In the irradiation process the nucleus cell membrane of the DNA stands break and repairs the DNA stand. Because of reassembling of DNA stand the germination capacity and seed vigour index increases. Many researchers observed that irradiation of laser reduces seed born pathogen. Due to that significant increases in germination percentage and vigour index of all varieties of groundnut seed.

The time period of irradiation increases the electrical conductivity of irradiated seed was decreases. If the electrical conductivity is less the germination capacity of seed is more. The groundnut is one of the important oil seed. The area under groundnut is decreases day by day. To increase the groundnut production the irradiation treatment is used.

REFERENCES

- [1] A. Yasser, H. Osaman, Kareem M.K. El Tobgy and El Sayed A. El Sherbini, "Effect of Laser Radiation Treatment on Growth, Yield and chemical Constituents of Fennel and Coriander Plants", *Journal of Applied Sciences Research*, 5(3): 244-252, 2009.
- [2] St. Dinoev, M. Antonov, T. Stoyanov, Chr. Georgieva, "Spectral Impact of Low Power Radiation on Wheat and Maize Parameters", *Bulgarian Academy of Sciences, Sponsored by the Scientific National Fund-Ministry of Education and Science, Contract TS-816/98, Sofia*, 2004.
- [3] H. R. Behzadi, M. Qaryan, S. Shahil, "The Influence of LED Light on Basil seeds Before Sowing and its Effects on Growing and Germination", *International Journal of Plant research*, 2(4):108-110, 2012.
- [4] Yasemin Z. Rassam, Firdaws A. Al. Mashhadani, Amange F. Boya, "Laser Treatment may enhance growth and resistance to fungal infection of hard wheat seeds", *ISOR Journal of Agriculture and Veterinary Sciences*, volume 2, PP 47-51, Jan-Feb. 2013.
- [5] Soltani F., Kashi A., Arghavani M., "Effect of magnetic field on *Asparagus originalis* L Seed germination and seedling growth", *Seed Science and Technology*, 34(2), 2006, 349-353.
- [6] Vasilevski G. Perspectives of the Application of Biophysical Methods in Sustainable Agriculture. *BULG. J. PLANT PHYSIOL.*, 2003, 179-186.
- [7] aladjadjiyan A., The used of Physical Methods for Plant Growth Stimulation in Bulgaria *Journal of Central European Agriculture*, 8930, 2007, 369-380.
- [8] T. W. Li, W. Cai, X. I. Wang, "The effect of He-Ne laser treatment on seeds germination and growth of *atractylodes macrocephala*", *Chin. J. Appl. Laser* 16, 37-41, 1996.
- [9] Muszynski s., and Gladyszewska B., "Representation of He-Ne laser irradiation effect on radish seeds with selected germination indices", *International Agrophysics*, 22, 2008, 151-157.
- [10] Jiang X. L., "A preliminary experimental report on killing pests by laser. (Liangsh, zhuzang Hubifood school, wuhan, china 4, 1981), 33-36.
- [11] Dinoev St., Antonov M., Stoyanov T., Gerogieva Chr., "Spectral ipact of low power laser radiation on wheat and maize parameters", *Bulgarian Academy of Sciences*, 2004, 54.
- [12] Shinomura T., Phytochrome regulation of seed germination, *J. Plant Res.*, 110(1), 1997, 151-161.
- [13] Hartmann K. M. and Mollwo A., "The action spectra for maximum photosensitivity of germination", *Nature wissense hafteen*, 87, 200, 398-403.
- [14] Dukova E., "The activity of wheat grains and the effect of laser radiation", *Acta Phytotech.*, 49, 1993, 59-66.
- [15] Gladyszewska B., "Pre-sowing laser biostimulation of cereal grains", *Tech. Sci.*, 6, 2006, 33-38.
- [16] Wilczek M., Koper R., Cwintal M., Kornilowicz Kowalska T., "Germination Capacity And health status of hybrid alfalfa seeds afer laser treatment", *Int. Agrophys.*, 19, 2005, 257-261.
- [17] Y.P. Chen, L.Li, X.L. Wang, F.M. Li, "The effect of He-Ne laser and KT treatment on the seeds germination and growth of wheat", *Acta Laser Biol, Sinica*, 6, 412-416, 2002.

¹S.M.Yenorkar²B.M.Mude³K.M.Mude⁴K.B.Raulkar⁵R.R.Mistry⁴B.R.P.Ikhar⁶R.N.Zade⁴G.T.Lamdhade

Enhanced Ammonia Sensing Performance of NiO-WO₃ Metal Oxide Composite Gas Sensors



Abstract: - The detection and monitoring of ammonia gas have significant implications in various fields, including agriculture, environmental safety, and industrial processes. This abstract presents a comprehensive study of the utilization of NiO-WO₃ metal oxide composite gas sensors for the detection of ammonia. Nickel oxide (NiO) and tungsten trioxide (WO₃) are promising semiconducting materials known for their high sensitivity to reducing gases. The synergistic combination of these oxides in composite structures has garnered attention due to their enhanced sensing properties, such as improved selectivity, sensitivity, and response/recovery times. This study discusses the synthesis methods employed to fabricate NiO-WO₃ composites and highlights the influence of various parameters on the sensing performance, such as composition, morphology, and operating temperature. Moreover, the mechanisms underlying the gas-sensing behavior of NiO-WO₃ composites, including surface reactions and charge transfer processes, are elucidated. Furthermore, recent advances in nanostructuring and functionalization strategies to further enhance the gas-sensing performance of these composites are explored. Finally, the potential applications and future prospects of NiO-WO₃ composite gas sensors for ammonia detection are discussed, addressing challenges and opportunities for commercialization and widespread deployment in real-world sensing applications.

Keywords: NiO-WO₃ Composite ,Ammonia gas sensor , Sensitivity, Selectivity ,Response time and Recovery time.

¹ *Dept. of Physics, Shri Shivaji College, Parbhani-431 401 (M.S.) India

² Dept. of Physics, Ramnarain Ruia College, Matunga(E)-400019 (M.S.) India

³ Dept. of Physics ,Bhavan's College, Andheri(W)-400058(M.S.) India

⁴ Dept. of Physics,Vidyabharti Mahavidyalaya, Amravati-444602(M.S.) India

⁵ Dept. of Physics, Deogiri College, Chhat. Sambhajinagar-431005 (M.S.) India

⁶ Dept. of Chemistry, Siddharth College, Fort, Mumbai-400001(M.S.) India

e-mail Corresponding Author : smy20777@gmail.com

Copyright © JES 2024 on-line : journal.esrgroups.org

I. INTRODUCTION

The detection and monitoring of ammonia (NH_3) gas are of paramount importance in a wide range of applications spanning agriculture, environmental monitoring, and industrial processes[1- 4]. Ammonia, a colorless and pungent gas, is extensively used in fertilizers, refrigeration, and various chemical industries. However, its release into the atmosphere can pose serious health hazards to humans and animals, contribute to air pollution, and lead to environmental degradation. Therefore, the development of highly sensitive, selective, and reliable gas sensors for the detection of ammonia is crucial for mitigating its adverse effects and ensuring environmental safety.

Metal oxide semiconductor gas sensors[5-7] have emerged as promising candidates for detecting a variety of gases due to their high sensitivity, rapid response, and low cost. Among them, nickel oxide (NiO) and tungsten trioxide (WO_3) have garnered considerable attention owing to their semiconducting properties and affinity towards reducing gases such as NH_3 . Individually, NiO and WO_3 exhibit moderate sensitivity towards ammonia gas, but their composite structures have demonstrated enhanced gas-sensing performance attributed to synergistic effects.

The combination of NiO and WO_3 in composite gas sensors offers several advantages over single-component sensors, including improved sensitivity, selectivity, and stability. Moreover, the tunable properties of metal oxide composites enable the optimization of sensor performance for specific applications. Various synthesis methods, including sol-gel, hydrothermal, and co-precipitation techniques, have been employed to fabricate NiO- WO_3 composite gas sensors with tailored morphologies and compositions.

In this paper, we present a comprehensive review of the recent advancements in NiO- WO_3 metal oxide composite gas sensors for enhanced ammonia sensing performance[8-15]. We discuss the synthesis strategies, structural characterization techniques, sensing mechanisms, and factors influencing the gas-sensing properties of these composites. Furthermore, we highlight recent developments in nanostructuring and functionalization approaches aimed at further improving the sensitivity and selectivity of NiO- WO_3 composite gas sensors. Finally, we discuss potential applications and future directions in the field of metal oxide composite gas sensors for ammonia detection, emphasizing the importance of addressing challenges and optimizing sensor performance for real-world applications.

II. MATERIALS AND METHODS

2.1 Materials

The following chemicals were used in the synthesis of NiO- WO_3 composite nanomaterials:

Nickel nitrate hexahydrate ($\text{Ni}(\text{NO}_3)_2 \cdot 6\text{H}_2\text{O}$): Purchased from Sigma-Aldrich, used as the nickel precursor.

Ammonium tungstate ($(\text{NH}_4)_{10}[\text{H}_2\text{W}_{12}\text{O}_{42}] \cdot x\text{H}_2\text{O}$): Purchased from Sigma-Aldrich, used as the tungsten precursor.

Citric acid ($\text{C}_6\text{H}_8\text{O}_7$): Purchased from Merck, used as a complexing agent.

Ethanol ($\text{C}_2\text{H}_5\text{OH}$): Analytical grade, used as a solvent.

Deionized water (H_2O): Used in all aqueous solutions.

Ammonia solution ($\text{NH}_3 \cdot \text{H}_2\text{O}$): Used for pH adjustment.

2.2 Synthesis of NiO- WO_3 Composite Nanomaterials

The NiO- WO_3 composite nanomaterials were synthesized using a sol-gel method, followed by calcination.

2.2.1 Preparation of Precursors

Nickel Precursor Solution: Dissolve 0.01 mol of Nickel nitrate hexahydrate in 50 mL of deionized water under constant stirring to form a clear Ni^{2+} solution. Tungsten Precursor Solution: Dissolve 0.01 mol of Ammonium tungstate in 50 mL of ethanol under constant stirring to form a W^{6+} solution.

2.2.2 Mixing and Gel Formation

Gradually add the tungsten precursor solution to the nickel precursor solution under vigorous stirring. Add 0.02 mol of citric acid to the mixed solution to act as a complexing agent and stabilize the mixture. Slowly add ammonia solution dropwise to the mixture until the pH reaches 7-9, promoting the formation of hydroxides. Continue stirring the solution until a gel is formed. This process may take several hours, depending on the temperature and concentration.

2.2.3 Aging and Drying

Allow the gel to age for 24-48 hours at room temperature to enhance network formation. Dry the aged gel at 100-120°C in an oven for several hours to remove solvents and water, resulting in a xerogel.

2.2.4 Calcination

Calcine the dried gel at 500°C in an air atmosphere for 3 hours. This step decomposes the nitrates and converts the hydroxides to oxides, forming the NiO-WO₃ composite nanomaterial. Allow the calcined material to cool to room temperature naturally.

2.3 Characterization

The synthesized NiO-WO₃ composite nanomaterials were characterized using the following techniques:

2.3.1 X-ray Diffraction (XRD)

XRD analysis was performed using a Bruker D8 Advance diffractometer with Cu K α radiation ($\lambda = 1.5406 \text{ \AA}$). Scans were recorded in the 2θ range of 10-80° to determine the crystalline phases and estimate the crystallite size.

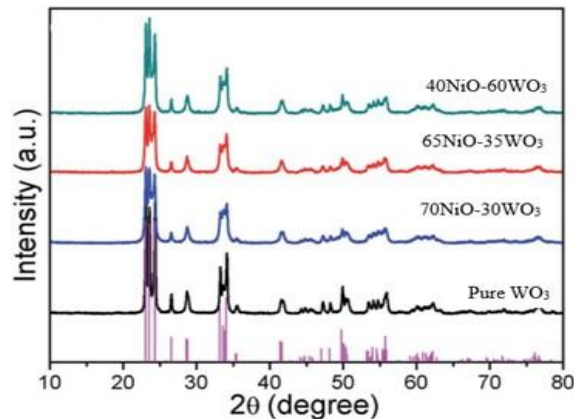


Fig. 1. XRD patterns of pure WO₃ and NiO-WO₃ composite sample

The phase composition and crystal structures of the synthesized pure WO₃ and NiO-WO₃ composite sample were analyzed using X-ray diffraction (XRD), as shown in Figure 1. The XRD patterns exhibit a series of strong diffraction peaks for all samples, which match well with the crystalline monoclinic WO₃ phase (JCPDS no. 43-1035)

The diffraction peaks for all NiO-WO₃ composite sample are broader compared to those of pure WO₃, suggesting smaller crystallite sizes in the composite material. The mean grain sizes were calculated using the Scherrer equation. The mean grain sizes for pure WO₃, 70NiO-30WO₃, 65NiO-35WO₃, and 40NiO-60WO₃ composite sample are 15.2 nm, 9.2 nm, 8.2 nm, and 10.3 nm, respectively. Clearly, the NiO-WO₃ composite sample have smaller grain sizes compared to pure WO₃. This reduction in grain size can be attributed to the NiO phase inhibiting the grain growth of WO₃ during heat treatment. Consequently, the 40 NiO-60WO₃ sample exhibit larger grain sizes than the 70NiO-30WO₃ and 65NiO-35WO₃, sample. Smaller mean grain sizes allow for more oxygen species to be adsorbed on the surface of the thick film.

2.3.2 Scanning Electron Microscopy (SEM)

SEM images were obtained using a JEOL JSM-7500F field emission scanning electron microscope. Samples were sputter-coated with a thin layer of gold to improve conductivity before imaging. The detailed morphology and microstructure of the pure NiO, WO₃, 65 NiO-35 WO₃ were investigated by SEM. Fig. 2 (a), (b) and (c) the morphology of the pure NiO shows sand like structure, WO₃ shows candy with smooth surface structures, 65NiO-35WO₃ appears to be small spherical structure and the average particle size is below 10 nm. 65NiO-35WO₃ composite material is more porous and therefore more sensitive to ammonia gas.

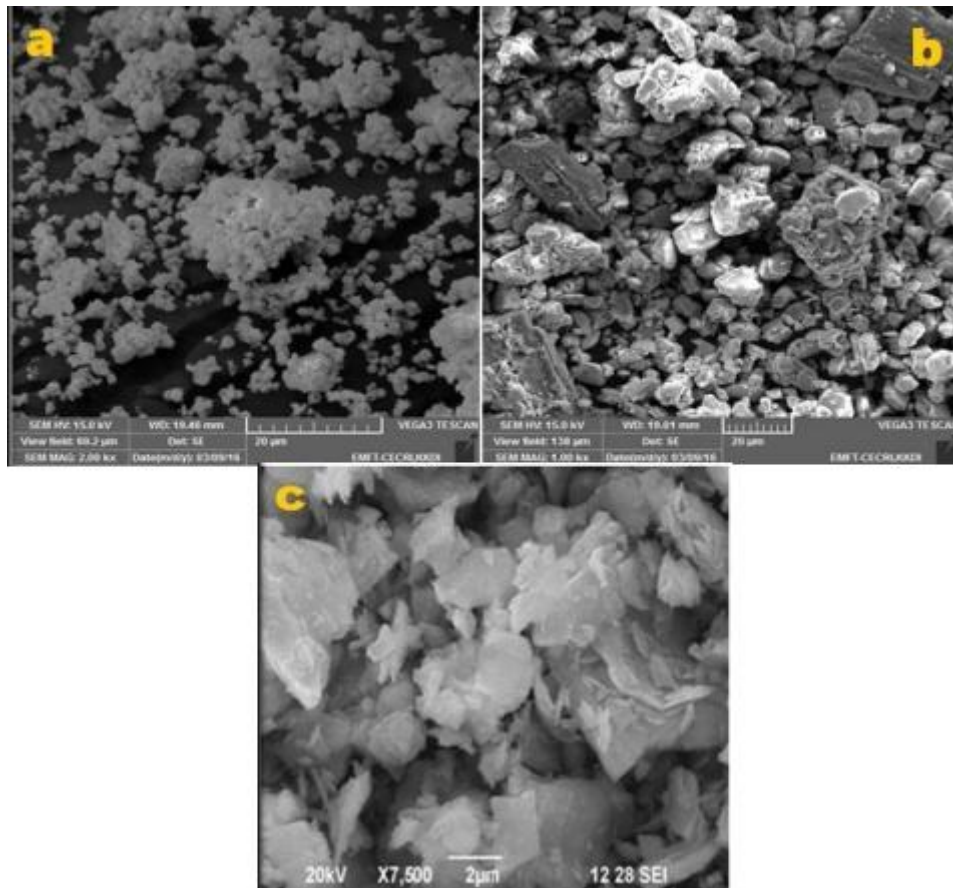


Figure 2: SEM image of (a) Pure NiO (b) Pure WO_3 and (c) 65NiO-35 WO_3 composite sample

2.4 Gas Sensing Measurements

The gas sensing performance of the NiO- WO_3 composite nanomaterials was evaluated using a custom-built gas sensing setup.

2.4.1 Sensor Fabrication

Thick films of semiconductor sensors were fabricated using standard screen printing method. So as to prepare these films, inorganic metal oxides was added to organic binder solution in the ratio of 70:30. Binder solution was prepared by using Butyl carbitol acetate (BCA) and ethyl cellulose (EC) in fixed ratio of 8:92. Metal oxides and binder solution were mixed meticulously for 30 minutes using mortar and pestle. This gave us stoichiometric slurry to make stable thick films over glass substrates.

Further small amount of BCA was mixed to above slurry drop wise to get gel like paste. This jelly paste is applied as thick film with dimension of 1 X 0.5 cm over clean and dry glass substrate. After the application of composite coat on glass, these films were dried in air for 20 minutes and subsequently under IR light for 30 minutes. Afterward these composite loaded glass plates were heated in muffle furnace at 100°C for approximately 2 hrs. After cooling these thick films were used for the study of its electrical properties using screen printed silver electrode for electrical contact with the circuit.

2.4.2 Gas Sensing Setup

Thick film sensors of metal oxide composites were examined for electrical characterization and gas detection. The gas detection execution was evaluated by a home-made gas sensor system as shown in fig 3.

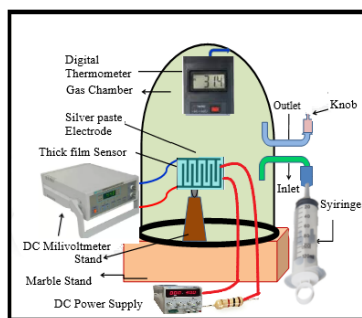


Fig.3.Gas sensor system

DC resistance of these composite sensor was measured, in the atmosphere of various temperatures with fair reliability. The temperature sensed by thermocouple was intentionally recorded by a digital thermometer. The gas is injected at ppm level inside the glass chamber by using a Syringe. The constant DC voltage was applied to the circuit. Sample resistance was measured in the ambient air and also in the presence of testing gas atmosphere at various temperatures. In this method, the resistance of $R = 1M\Omega$ was connected in series with the material and used DC Power supply (0-5V).(Fig 4).

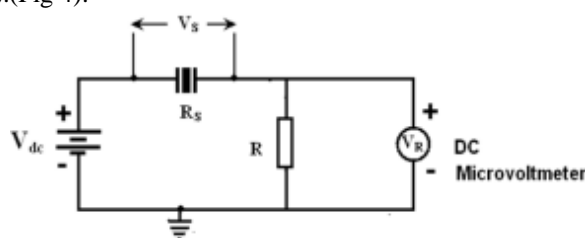


Fig. 4 Measurement of sample resistance

Sensitivity of gas sensor in terms of resistance of sensors can be given by an equation

$$Sensitivity(S) = \frac{R_{NH_3} - R_{Air}}{R_{Air}}$$

Where R_{NH_3} is the electrical resistance of thick film in presence of Ammonia gas (NH_3) and R_{Air} is electrical resistance of thick film in ambient air.

III. RESULT AND DISSCUSSION

1. Gas sensitivity

The variations of sensitivity of Pure NiO ,Pure WO_3 and 65NiO: 35 WO_3 compositions with concentration of ammonia gas at room temperature are shown in Fig.5.

From Fig. 5, it is observed that for Pure Oxide Samples like Pure NiO and Pure WO_3 sensitivity is less. It is observed from the cure sensitivity increases for composite samples and becomes maximum for 65NiO:35 WO_3 composition. From SEM picture, it is found that porosity of 65NiO:35 WO_3 composition is large as compared to other Pure NiO and Pure WO_3 , thus active surface area is more. Also the average crystallite size of 65NiO:35 WO_3 composition is small and it means large active surface area. That's why sensitivity of 65NiO:35 WO_3 composition is large as compared to other compositions and pure samples.

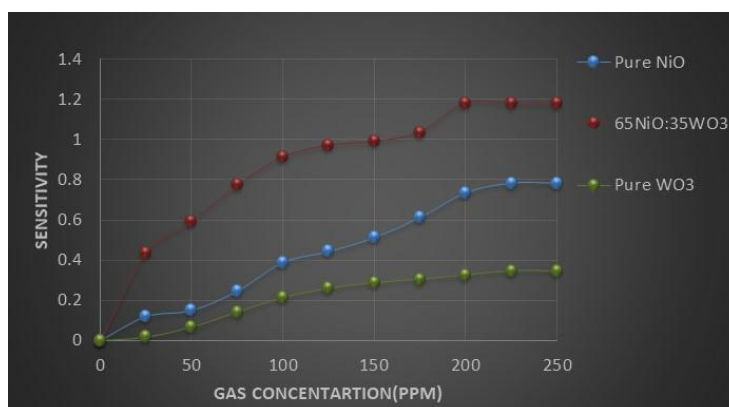


Fig. 5. Variation of sensitivity of Pure NiO,Pure WO_3 and 65NiO:35 WO_3 system with NH_3 gas concentration (ppm) at room temperature (303 K).

2. Stability of optimise sample

Sensor stability is expressed in terms of measurement of resistance with time. It is defined as the change in resistance of sensor with time [8,9]. The resistance values of optimize sensors, measured with time at room temperatures it gives stable response from fig 6.

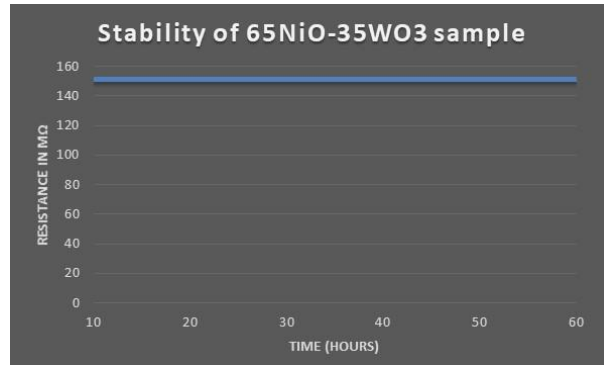
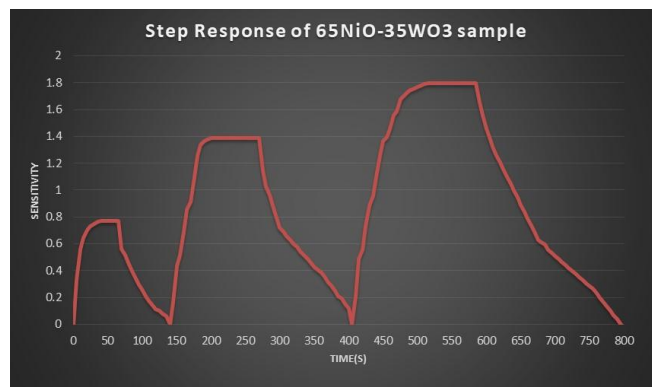


Fig. 6. Variation of resistance of sensors with time in air

3. Static response of optimise sample

Fig 7. Static response under static condition, it is observed that response is fast for 65NiO:35WO₃. It is also observed that recovery time for all sensors is very slow than the response time. The response and recovery time for all sensors for 50 ppm Ammonia gas concentration are calculated. Response time for optimize sensor i.e 65NiO:35WO₃ is 75 S and recovery time is 155S



IV. CONCLUSION

The gas-sensing properties of NiO:WO₃ films towards Ammonia Gas have been investigated and compared to those of single oxide WO₃ and NiO. The pure thick film of NiO and WO₃ sensors showed low response than the composite films to NH₃. In general, the best performances in terms of response, recovery, sensitivity and low detection limit were found in 65NiO:35WO₃ sensor. This sensor showed higher sensitivity than pure WO₃ and NiO.

REFERENCES

- [1] Insausti, M., Timmis, R., Kinnersley, R. and Rufino, M.C., 2020. Advances in sensing ammonia from agricultural sources. *Science of the total environment*, 706, p.135124.
- [2] Baruah, S. and Dutta, J., 2009. Nanotechnology applications in pollution sensing and degradation in agriculture: a review. *Environmental Chemistry Letters*, 7, pp.191-204.
- [3] Ghosh, A., Zhang, C., Shi, S.Q. and Zhang, H., 2019. High-temperature gas sensors for harsh environment applications: a review. *CLEAN-Soil, Air, Water*, 47(8), p.1800491.
- [4] Wilson, A.D., 2013. Diverse applications of electronic-nose technologies in agriculture and forestry. *Sensors*, 13(2), pp.2295-2348.

- [5] Nikolic, M.V., Milovanovic, V., Vasiljevic, Z.Z. and Stamenkovic, Z., 2020. Semiconductor gas sensors: Materials, technology, design, and application. *Sensors*, 20(22), p.6694.
- [6] Jaaniso, R. and Tan, O.K. eds., 2013. *Semiconductor gas sensors*. Elsevier.
- [7] Khomarloo, N., Mohsenzadeh, E., Gidik, H., Bagherzadeh, R. and Latifi, M., 2024. Overall perspective of electrospun semiconductor metal oxides as high-performance gas sensor materials for NO_x detection. *RSC advances*, 14(11), pp.7806-7824.
- [8] Li, X., Fu, L., Karimi-Maleh, H., Chen, F. and Zhao, S., 2024. Innovations in WO₃ gas sensors: Nanostructure engineering, functionalization, and future perspectives. *Heliyon*.
- [9] Maktoof, A.S., Mohammed, G.H. and Abbas, H.H., 2024. Effect of annealing process on structural and optical properties of Au-doped thin films (NiO: WO₃) fabricated by PLD technique. *Journal of Optics*, pp.1-12.
- [10] Saini, R.K., Rani, M., Shanker, U. and Sillanpää, M., 2024. Sunlight-mediated efficient remediation of organic pollutants from water by chitosan co-decorated nanocomposites of NiO loaded with WO₃: Green synthesis, kinetics, and photoactivity. *Inorganic Chemistry Communications*, 165, p.112450.
- [11] Nozar, S., Hosseini, S.M.P., Chaibakhsh, N. and Amini, M., 2024. Light-assisted catalytic ozonation for efficient degradation of ciprofloxacin using NiO/MoS₂ nanocomposite. *Journal of Photochemistry and Photobiology A: Chemistry*, 448, p.115343.
- [12] GV, A.R., Kumar, K.N., Sattar, S.A., Shetty, H.D., Prakash, N.G., Jafri, R.I., Devaraja, C., Manjunatha, B.C., Kaliprasad, C.S., Premkumar, R. and Ansar, S., 2023. Effect of post annealing on DC magnetron sputtered tungsten oxide (WO₃) thin films for smartwindow applications. *Physica B: Condensed Matter*, 664, p.414996.
- [13] Kwon, S., Lee, S., Kim, J., Park, C., Jung, H., Kim, H., Kim, C. and Kang, H., 2022. Effect of GNWs/NiO-WO₃/GNWs heterostructure for NO₂ gas sensing at room temperature. *Sensors*, 22(2), p.626.
- [14] Juang, F.R. and Wang, W.Y., 2021. Ethanol gas sensors with nanocomposite of nickel oxide and tungsten oxide. *IEEE Sensors Journal*, 21(18), pp.19740-19752.
- [15] Liu, F., Song, H., Wu, L., Zhao, J., Yao, X., Fu, K., Jin, Z., Liu, J., Wang, F. and Wang, Z., 2023. Excellent NO₂ gas sensor based on the oxygen inhibiting effect of Ni³⁺-doped WO₃. *Colloids and Surfaces A: Physicochemical and Engineering Aspects*, 666, p.131329.

¹S. R. Jaiswal*²R. G. Korpe²P. A. Nagpure¹Department of Physics, Shri
R. L. T. College of Science,
Akola. 444001 (INDIA)²Department of Physics, Shri
Shivaji Science College,
Amravati. 444602 (INDIA)*srjaiswal07@gmail.com**Highly efficient green light-
emitting K₂Sr(Gd, Y)(PO₄)₂: Tb³⁺
phosphor for Mercury Free
Fluorescent Lighting and PDPs**

Abstract: - The phosphors K₂Sr(Gd, Y)(PO₄)₂: Tb³⁺ were synthesized using the co-precipitation method. The vacuum ultraviolet (VUV) spectroscopical properties of these phosphors were studied. The outcomes illustrated that the efficient energy transfer (ET) from Gd³⁺ to Tb³⁺ happens in this system. The ET and visible quantum harvesting phenomenon was detected in a high Tb³⁺ concentration doped sample. The ET efficiency rises with growing Tb³⁺ doped concentrations, which is showed by the emission intensity of Gd³⁺ decreasing with increased the Tb³⁺ doping concentrations. In addition, it is found that by erratic the doping concentration of Tb³⁺, the emission color of K₂Sr(Gd, Y)(PO₄)₂: Tb³⁺ phosphors was transformed from blue to yellowish-green. The Phosphor K₂SrGd_{0.5}(PO₄)₂: 0.5Tb³⁺ illustrated the stoutest emission, which is about 75% of the profitable green-emitting phosphor Zn₂SiO₄: Mn²⁺ (ZSM) under the 172 nm excitation. This indicates that phosphor is a latent application for mercury-free fluorescent lighting (MFFL), Plasma display panels (PDPs), and Three-dimensional display.

Keywords: Quantum Cutting (QC), Vacuum Ultraviolet (VUV), Down-conversion, Mercury Free Fluorescent Lighting and PDPs

I. INTRODUCTION

The development of mercury-free fluorescent lightning such as Hg-free lamps, 3D displays, and plasma display panels (PDPs) has led to important research into the optical properties of luminescent materials under the VUV region (147 or 172 nm excitation wavelength).[1] In these devices, the materials absorbed VUV radiation and then were converted into visible light. [2] However, there have been many restrictions to achieving high quantum efficiency [absorbing one VUV photon and converting one visible photon], mostly because of intrinsic energy loss involved in the nonradiative relaxation processes present in most of the phosphors.[3] A visible quantum cutting (QC) is a phenomenon that a phosphor absorbs one VUV photon and emits two visible photons, and energy conversion efficiency can reach doubled i.e. 200% in theory, as a consequence, most of the effort has been taken to synthesize phosphor that could realize QC. [4,5] The strong visible emission can be realized in a suitable host lattice doped with Tb³⁺ ion under the VUV excitation due to spin-allowed 4f–5d transitions.[6] The process of QC has been established in some fluorides and oxides by using the combination Tb³⁺–Gd³⁺ ions pair such as K₂GdF₅: Tb³⁺, [7] BaGdF₅: Tb³⁺,

[8] $\text{GdPO}_4:\text{Tb}^{3+}$, $\text{Sr Gd (PO}_4)_3: \text{Tb}^{3+}$, [9] and $\text{GdBO}_3: \text{Tb}^{3+}$. [10] In these systems, the QC is understood via CRET by transitions lower $4f5d-^5D_3$ and $7F_6-^5D_4$ of Tb^{3+} ions. In the interim, the incidence of CRT between 5D_3 to 5D_4 and 7F_6 to 7F_0 , will result in tunable Tb^{3+} emissions from the blue to green regions, which is dependent on the doping concentration of Tb^{3+} and the host lattice. [11,12] It is generally considered that the $4f-4f$ absorption lines of Tb^{3+} overlapped well with the emission of the $\text{Gd}^{3+} \ ^6P_J - \ ^8S_{7/2}$ transition located at 273– 274 nm, so the incorporation of Gd^{3+} could improve the luminescence of Tb^{3+} by energy transfer (ET). [13,14] The crystal structure of $\text{KSrGd(PO}_4)_2$ has comparable with hexagonal LaPO_4 , excluding that the large eight-coordinated K^+ inhabits only half of the tunnel sites with the coordination polyhedron $[\text{KO}_8]$, and Gd^{3+} or Sr^{2+} ions statistically occupy the La^{3+} position. [15–17] Zhang et al [16] reported the VUV–UV spectroscopic properties in the system of $\text{KM Ln (PO}_4)_2$ ($\text{M} = \text{Ca, Sr; Ln} = \text{Y, La, Lu}$) doped with Ce^{3+} , Tb^{3+} , Tm^{3+} , Dy^{3+} , and Eu^{3+} . This work shows strong absorption of material below 200 nm wavelength. Motivated by this work, investigated the $\text{Gd}^{3+}-\text{Tb}^{3+}$ ET and examined the possibility of QC in $\text{KSr(Gd, Y)(PO}_4)_2: \text{Tb}^{3+}$.

II. EXPERIMENTAL

All the phosphors were successfully synthesized by the co-precipitation method. The preliminary chemicals Y_2O_3 (99.99%, AR), Gd_2O_3 (99.99%, A.R.), KNO_3 , SrNO_3 , and Tb_4O_7 (99.90%, AR) were mixed together in a china clay basin. A small quantity of double-distilled water (D.D.W.) was added and paste was formed. The HNO_3 was added drop by drop and the mixture was heated gradually at 60°C , till the paste dissolved completely. The solution was further heated to get the excess acid boiled off. A little quantity of D.D.W. was added again. Subsequent the solution was considered as $\text{K Sr (Y Gd) (NO}_3)_3: \text{Tb}$, to this soluble solution, the transparent solution of $(\text{NH}_4) \text{HPO}_4$ (A.R.) was added drop by drop to get precipitate. The precipitate was filtered and washed three to four times to remove extra impurities. The whole pest was then dried to obtain a dried powder. The dried precursor was finally crushed and heated at 1000°C up to 4 hr to get white crystalline powder of $\text{KSr(Gd, Y)(PO}_4)_2: \text{Tb}^{3+}$. The similar procedure has been constant for $\text{KSrGd(PO}_4)_2: \text{Tb}^{3+}$ phosphor. The comprehensive process intricate in the reaction was signified as a flow chart in Fig. 1.

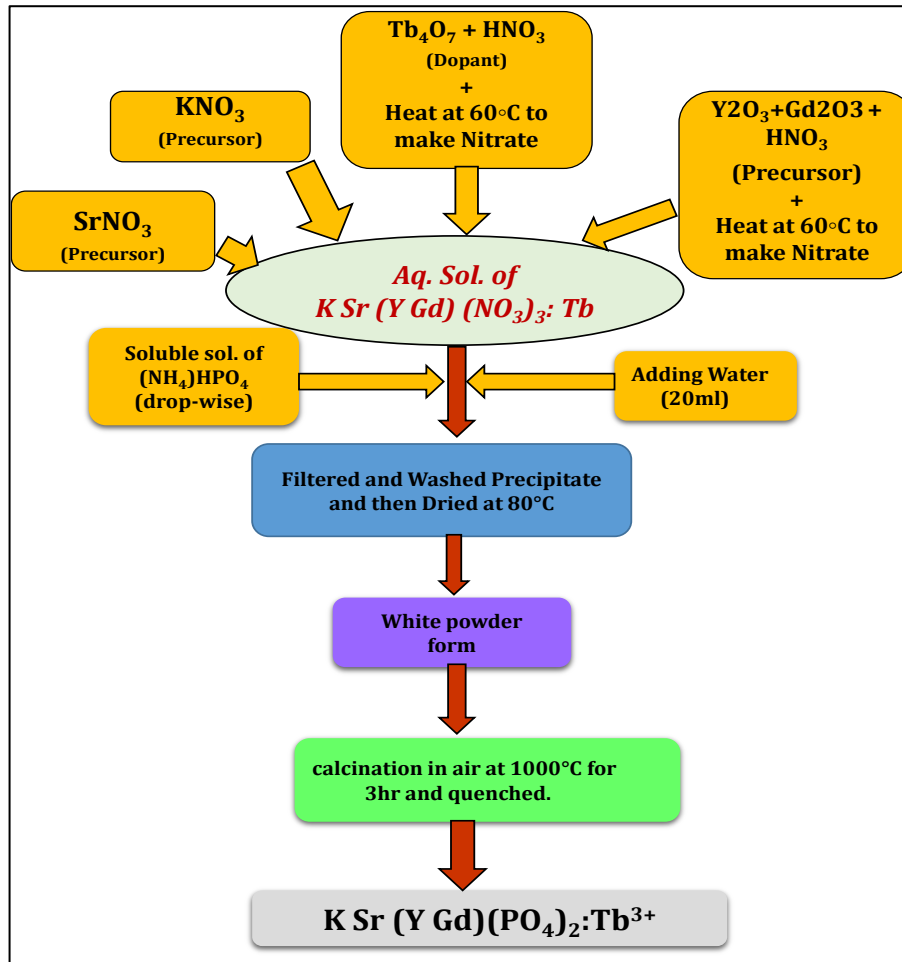


Fig. 1. Flow chart represented the complete synthesis process

The crystal structure of the phosphor powders was characterized by XRD analysis by using a Rigaku mini flex II X-ray diffractometer with a scan speed of $2.000^\circ/\text{min}$ and $\text{Cu K}\alpha$ ($\lambda = 0.15406 \text{ nm}$) radiation in the range of 10° to 80° . The PLE and PL spectra in the VUV region were measured at the 4B8-VUV spectroscopy experimental station on the beamline of the Beijing Synchrotron Radiation Facility (BSRF), P.R. China. All the measurements were performed at room temperature.

III. RESULTS AND DISCUSSION

A. Powder XRD Characterization

The figure 2 displays the XRD patterns of $\text{K Sr Gd}_{0.5}\text{Y}_{0.49}(\text{PO}_4)_2:0.01\text{Tb}^{3+}$ and $\text{K Sr Gd}_{0.5}(\text{PO}_4)_2:0.5\text{Tb}^{3+}$ samples and the reference data of JCPDS Card No. 34-0118 for pure $\text{K Sr Gd} (\text{PO}_4)_2$. It was testified that $\text{K Sr Gd} (\text{PO}_4)_2$ had a hexagonal crystal structure with the space group $P6_222$. [15,16]. Associated with standard data, all the samples show the peaks of pure hexagonal phase. In the XRD patterns, no second phase is detected, inadequate the successful doping of Y^{3+} and Tb^{3+} in $\text{K Sr Gd} (\text{PO}_4)_2$.

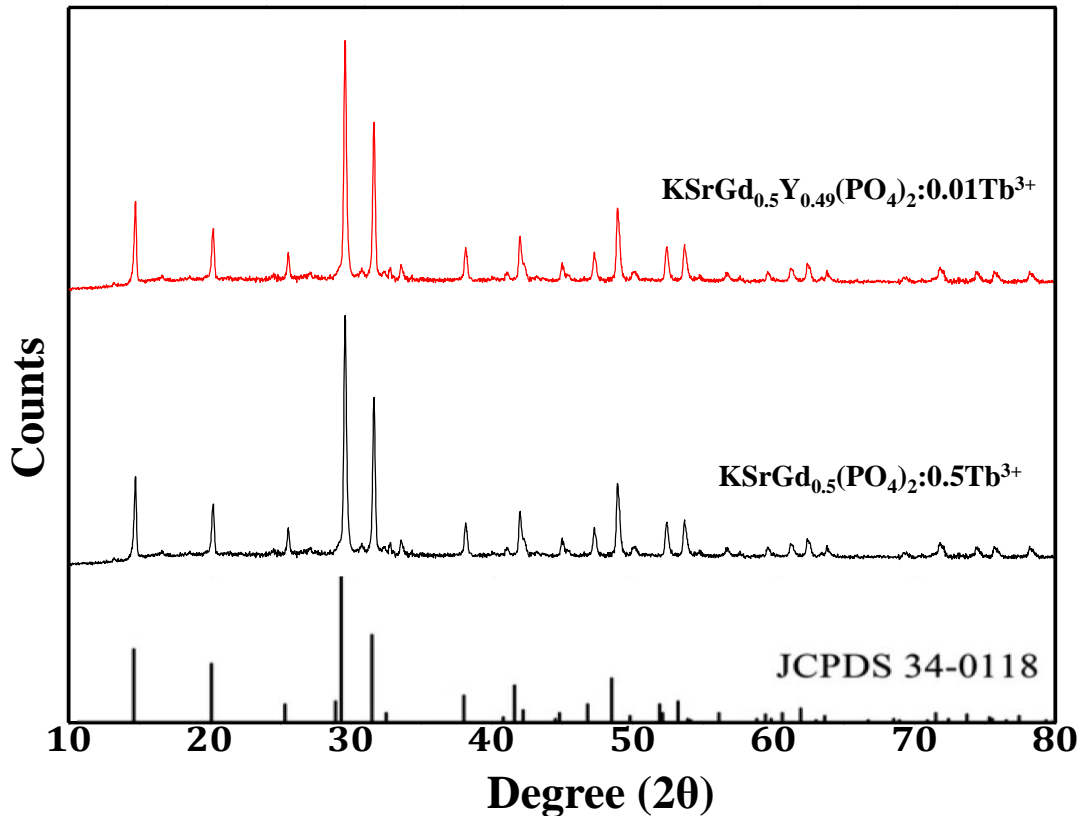


Fig. 2. XRD pattern of of $\text{K Sr Gd}_{0.5} \text{Y}_{0.49} (\text{PO}_4)_2 : 0.01 \text{Tb}^{3+}$ and $\text{K Sr Gd}_{0.5} (\text{PO}_4)_2 : 0.5 \text{Tb}^{3+}$ phosphors

B. Photoluminescence Properties and Tunable Emission

Figure 3 shows the VUV excitation spectra of $\text{K Sr Y}_{0.50} (\text{PO}_4)_2 : 50\% \text{Tb}^{3+}$, $\text{K Sr Gd}_{0.50} (\text{PO}_4)_2 : 50\% \text{Tb}^{3+}$, and $\text{K Sr (Gd}_{0.5}, \text{Y}_{0.49}) (\text{PO}_4)_2 : 1\% \text{Tb}^{3+}$.

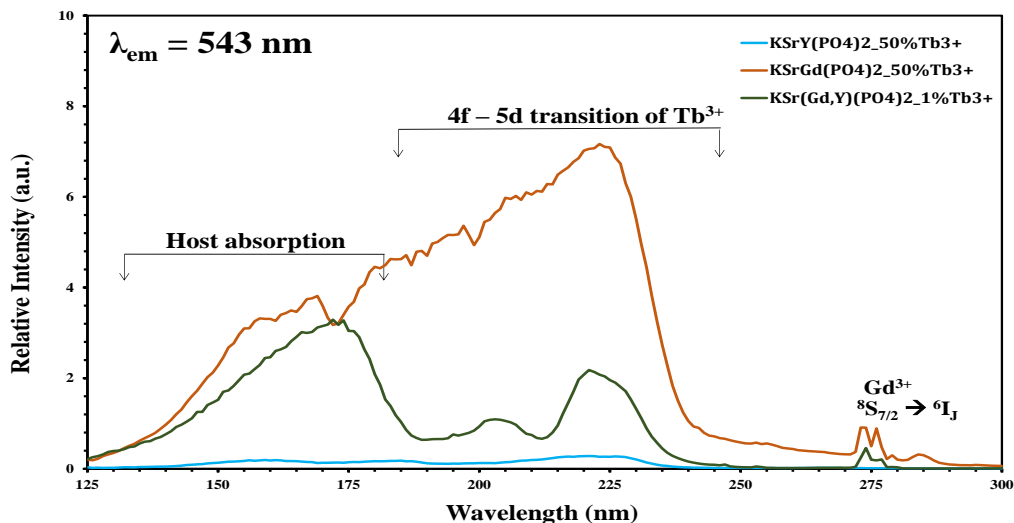


Fig. 3. VUV excitation spectra of $\text{K Sr Y}_{0.50} (\text{PO}_4)_2 : 50\% \text{Tb}^{3+}$, $\text{K Sr Gd}_{0.50} (\text{PO}_4)_2 : 50\% \text{Tb}^{3+}$, and $\text{K Sr (Gd}_{0.5}, \text{Y}_{0.49}) (\text{PO}_4)_2 : 1\% \text{Tb}^{3+}$ phosphors monitored at 543 nm.

These three excitation spectra show similar features but different intensities and are composed of several bands and broad bands. The first band in the range 125–180 nm is ascribed to the host absorption band, which is probably in connection with the transition from the valence band to the conduction band or

the absorption due to near excitation in the host. [16] The other two broad bands (maximized in 203 and 220 nm) in the range 180–250 nm is due to the split of the 5d excitation state of Tb^{3+} and assigned to the $4f^8-4f^75d^1$ spin allowed transitions of Tb^{3+} . When one electron of Tb^{3+} is promoted from the ground states $4f^8$ to the $4f^75d^1$ excited state, it can produce two kinds of $4f^8-4f^75d^1$ transitions: spin-allowed and spin-forbidden transitions. Some of the sharp and weak bands near 275 nm are attributed to the $^8S_{7/2} \rightarrow ^6I_J$ transition of Gd^{3+} . The presence of Gd^{3+} excitation line in the excitation spectrum of $\text{KSrGd}(\text{PO}_4)_2: \text{Tb}^{3+}$ measured by monitoring Tb^{3+} emission, indicating the occurrence of $\text{Gd}^{3+}-\text{Tb}^{3+}$ ET. [18]

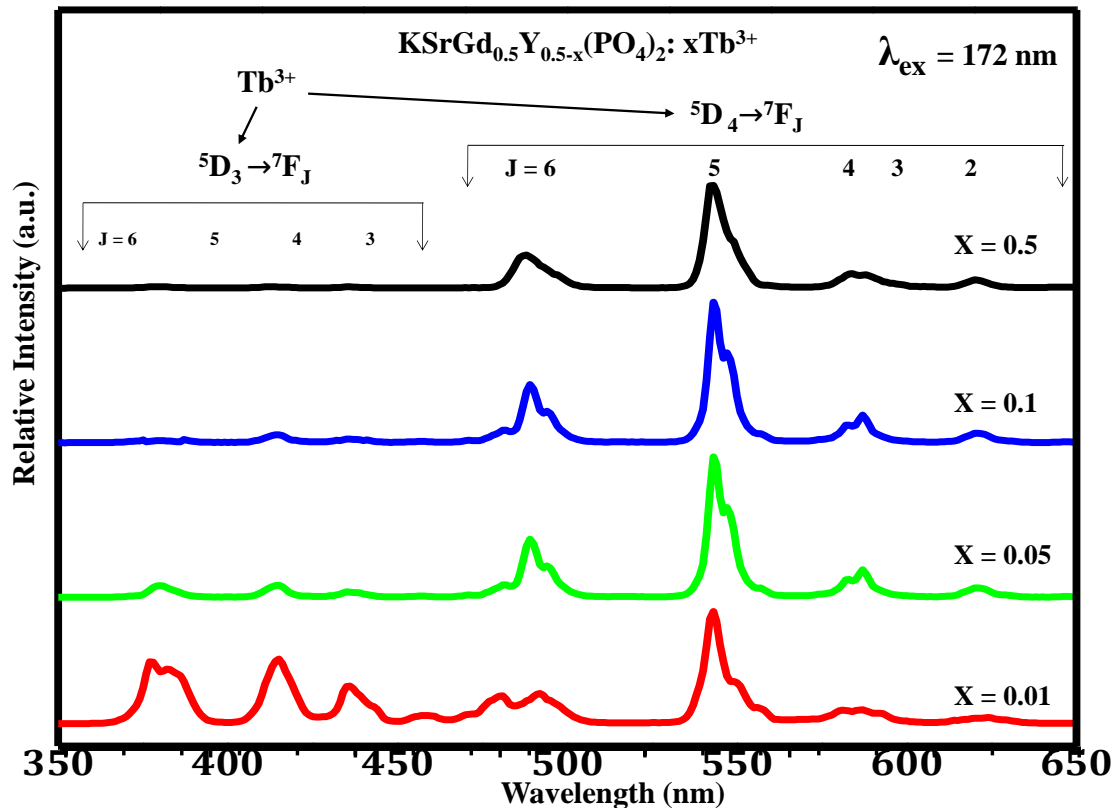


Fig. 4. PL emission spectrum of $\text{KSrGd}_{0.5}\text{Y}_{0.5-x}(\text{PO}_4)_2: x\text{Tb}^{3+}$ ($0.01 \leq x \leq 0.5$) phosphors monitored at 172 nm.

Figure 4 shows the emission spectra of samples $\text{KSrGd}_{0.5}\text{Y}_{0.5-x}(\text{PO}_4)_2: x\text{Tb}^{3+}$ ($0.01 \leq x \leq 0.5$) under 172 nm excitation. The emission spectra are a collection of emissions from $^5\text{D}_3$ and $^5\text{D}_4$ levels of Tb^{3+} . The emission from the $^5\text{D}_3$ excited level is mainly blue and the emission from the $^5\text{D}_4$ excited level is mainly green. With the increase of Tb^{3+} concentration, the distance of neighboring Tb^{3+} decreases, and the cross-relaxation process between $^5\text{D}_3$ to $^5\text{D}_4$, and $^7\text{F}_6$ to $^7\text{F}_0$ become more and more efficient, resulting in the quenching of $^5\text{D}_3$ emission. In this system, the emission intensity ratio of $^5\text{D}_3$ to $^5\text{D}_4$ decreases with increasing Tb^{3+} contents, which is attributed to the enhancement of the Tb^{3+} concentration-dependent cross-relaxation process between $^5\text{D}_3$ to $^5\text{D}_4$, and $^7\text{F}_6$ to $^7\text{F}_0$ correspondingly. [19] At about 1.0 mol% Tb^{3+} content, the intensity of $^5\text{D}_3$ emission is almost the same as that of $^5\text{D}_4$ emission. Then, the $^5\text{D}_4$ emission increases fast, and the $^5\text{D}_3$ emission decreases rapidly. Therefore, the color of samples $\text{KSrGd}_{0.5}\text{Y}_{0.5-x}(\text{PO}_4)_2: x\text{Tb}^{3+}$

($0.01 \leq x \leq 0.5$) is turned from blue to yellowish-green when Tb^{3+} doping concentration is varied from 0.01 to 0.5. Figure 5 (a) and (b) show the Spectral Power Distribution (SPD) and CIE chromaticity diagram, in which the CIE chromaticity coordinate position and luminescence photos of different samples are indicated.

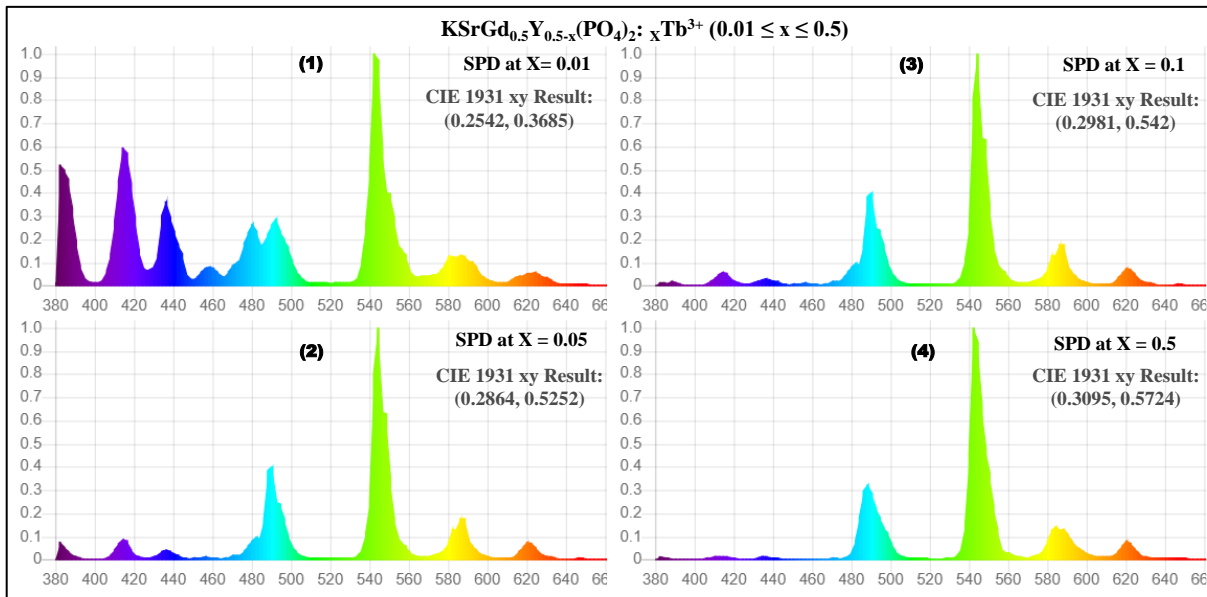


Fig. 5 (a) show the Spectral Power Distribution (SPD)

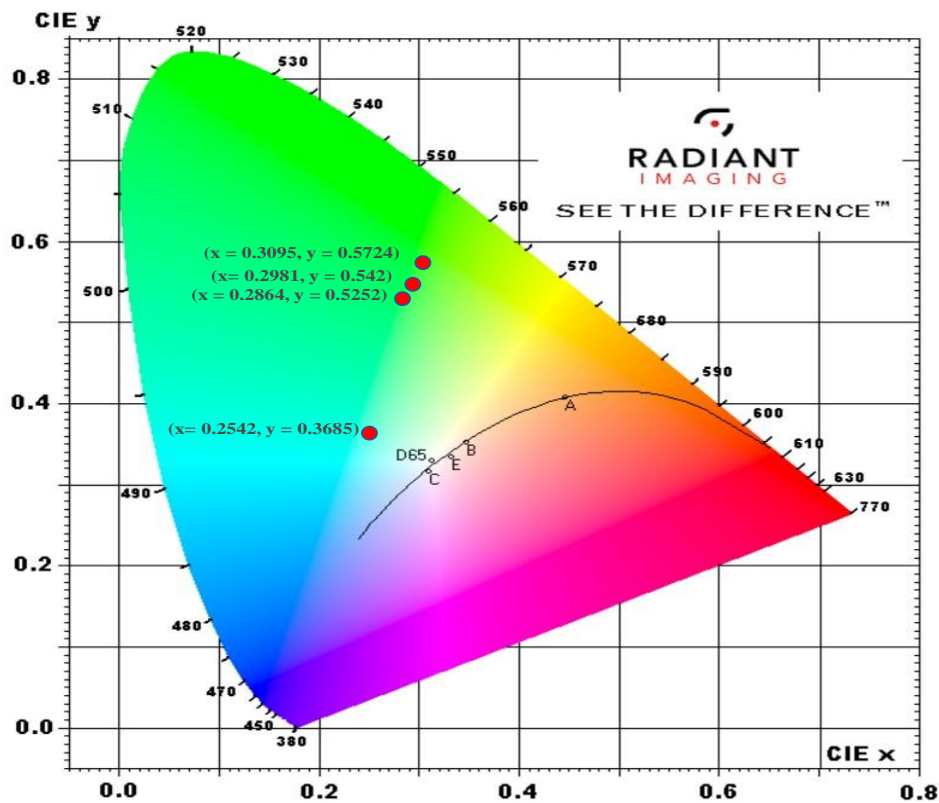


Fig 5 (b): CIE 1931 xy Coordinates of $K Sr Gd_{0.5} Y_{0.5-x} (PO_4)_2: x Tb^{3+}$ ($0.01 \leq x \leq 0.5$)

C. Energy Transfer from Gd^{3+} to Tb^{3+}

To prove ET from Gd^{3+} to Tb^{3+} happens in $K Sr Gd_{0.5} Y_{0.5-x} (PO_4)_2: x Tb^{3+}$ ($0.01 \leq x \leq 0.5$), the emission intensity of Gd^{3+} is measured as a function of Tb^{3+} doping concentration, and the consequences were shown in Fig. 6. Upon direct excitation Gd^{3+} to its 6I_7 level by using a photon with wavelength at 274

nm, emission peak at 312/311 nm that attributed to the ${}^6P_J-{}^8S_{7/2}$ of Gd^{3+} decreases with increasing Tb^{3+} doping concentrations as shown in Figs. 6 (a) and (b), which suggests the occurrence Gd^{3+} to Tb^{3+} ET.

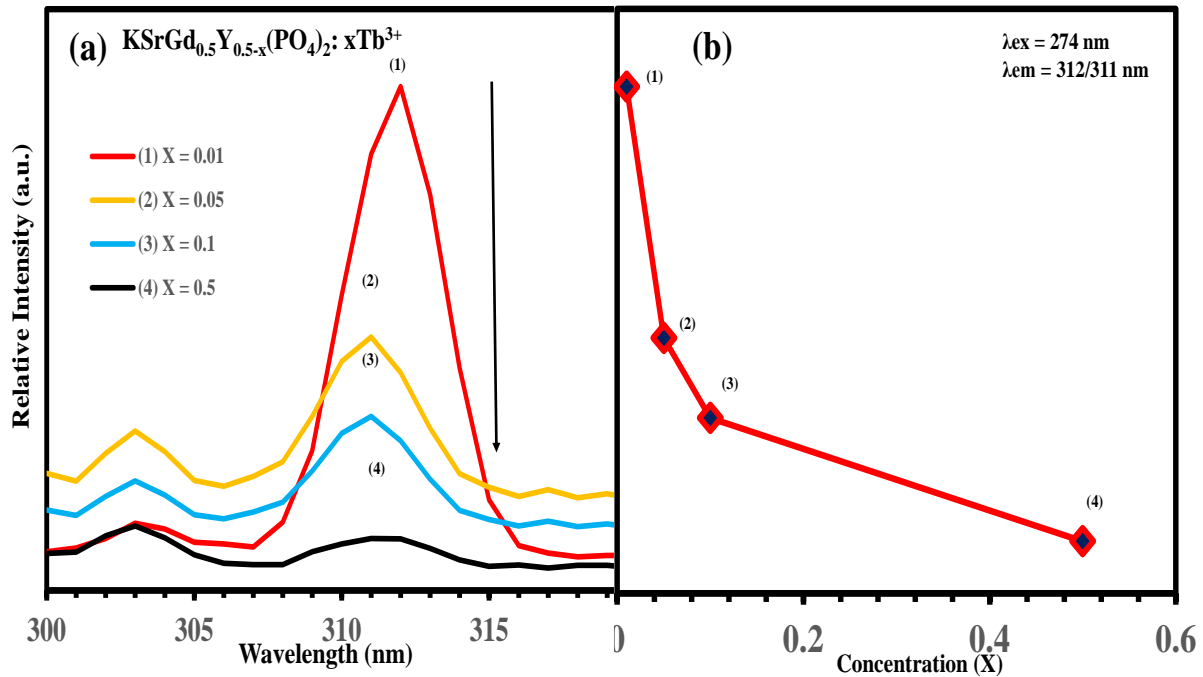


Fig. 6 (a) Emission spectra and (b) emission intensities of Gd^{3+} 6P_J to ${}^8S_{7/2}$ transition under 274 nm excitation as a function of x values in $KSrGd_{0.5}Y_{0.5-x}(PO_4)_2: xTb^{3+}$ ($0.01 \leq x \leq 0.5$) phosphors

D. Quantum Cutting

For Tb^{3+} , there are two different kinds of CRET processes, one is the CRET process between the 5D_3 to 5D_4 and 7F_6 to 7F_0 transitions, which will quench Tb^{3+} 5D_3 emission (blue) and increase Tb^{3+} 5D_4 emission (green) and result in Tb^{3+} emission tuned from blue emission at low Tb^{3+} concentrations to green emission at higher Tb^{3+} doping concentration. The other is the CRET process between the transition from lower $4f5d$ to 5D_3 and 5D_4 to 7F_J , which will result in the QC effect. Figure 7 shows the emission spectra of $KSrGd_{0.5}(PO_4)_2:0.5Tb^{3+}$ and $KSrGd_{0.5}Y_{0.49}(PO_4)_2:0.01Tb^{3+}$ upon ${}^8S_{7/2}-{}^6I_1$ excitation (274 nm) on Gd^{3+} and the excitation (172 and 222 nm) on Tb^{3+} . We have observed that in the sample $KSrGd_{0.5}(PO_4)_2:0.5Tb^{3+}$ the relative intensity of the emission spectra at 172 and 222 nm excitation wavelength is much stronger than emission spectra under excitation 274 nm, indicating that QC occurs in the sample. But in the sample $KSrGd_{0.5}Y_{0.49}(PO_4)_2:0.01Tb^{3+}$ the relative intensity of the emission spectra at 172 and 222 nm excitation wavelength is comparable with emission spectra under excitation 274 nm and hence it is a very small change of QC occurs in the sample.

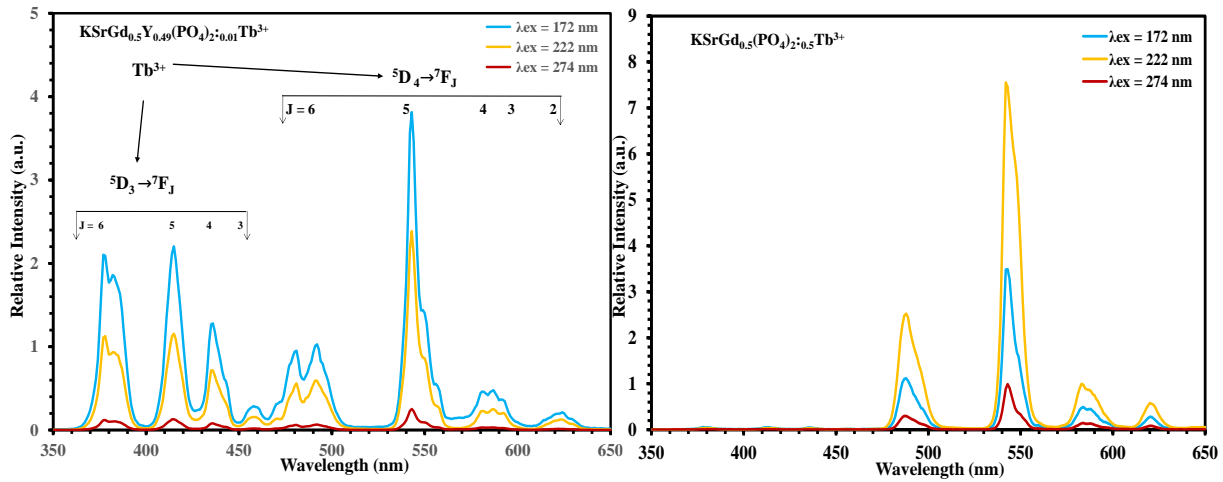


Fig. 7 The emission spectra of $\text{K Sr Gd}_{0.5}(\text{PO}_4)_2:0.5\text{Tb}^{3+}$ and $\text{K Sr Gd}_{0.5}\text{Y}_{0.49}(\text{PO}_4)_2:0.01\text{Tb}^{3+}$ upon $^8\text{S}_{7/2} - ^6\text{I}_J$ excitation (274 nm) on Gd^{3+} and the excitation (172 and 222 nm) on Tb^{3+} .

For more clarification regarding the QE, we calculate the extra QE corresponding to cross-relaxation can be calculated by the emission spectra using the formula [20-24] proposed by Wegh et al. [4] and later modified by Chen et al [7]

$$\eta_{QC} = \eta + \eta_{DT} \tag{1}$$

$$\eta = \frac{P_1}{P_1 + P_2} = \frac{R_2 - R_1}{R_2 + 1} \tag{2}$$

Here P_1 and P_2 are the probabilities of energy transfer from Gd^{3+} to Tb^{3+} through cross-relaxation and direct transfer respectively.

Here $R_2 = \left(^5\text{D}_4 / \text{rest} \right)_{\text{Tb}^{3+}}$ and $R_1 = \left(^5\text{D}_4 / \text{rest} \right)_{\text{Gd}^{3+}}$

$(^5\text{D}_4/\text{rest})$ is the ratio of PL intensity of $^5\text{D}_4$ to that attributed to $^5\text{D}_3$ of Tb^{3+} and $^6\text{P}_{7/2}$ of Gd^{3+} where the subscript designates the excitation is from Tb^{3+} or Gd^{3+} .

The CR efficiency was found to be very small and negligible for the sample $\text{K Sr Gd}_{0.5}\text{Y}_{0.49}(\text{PO}_4)_2:0.01\text{Tb}^{3+}$. This is because of the very low concentration of Tb^{3+} and it increases with increasing Tb^{3+} concentration in the host matrix. The CR efficiency for the sample $\text{K Sr Gd}_{0.5}(\text{PO}_4)_2:0.5\text{Tb}^{3+}$ has to be calculated and the maximum calculated value of CR efficiency from eq.-2 for $\text{K Sr Gd}_{0.5}(\text{PO}_4)_2:0.5\text{Tb}^{3+}$ excited at 222 and 172 nm were found to be 1.55 and 0.015 respectively. Therefore, the resulting value of quantum efficiency was calculated as 255% and 101% at the excitation of 222 and 172 nm respectively.

E. Potential Applications

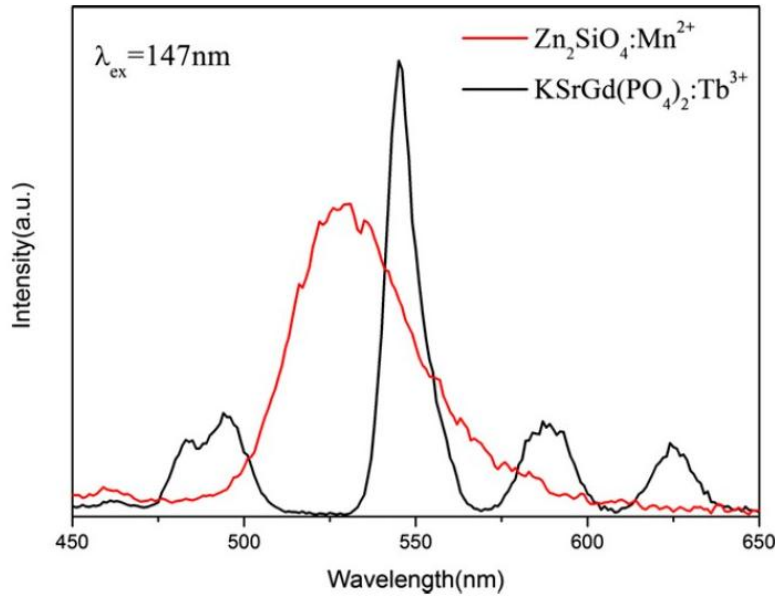


Fig. 8 Shows comparison of the emission spectra of $\text{KSrGd}_{0.5}(\text{PO}_4)_2:0.5\text{Tb}^{3+}$ with commercial green-emitting phosphor $\text{Zn}_2\text{SiO}_4: \text{Mn}^{2+}$ (ZSM) under 147 nm excitation

To further evaluate the application potential of $\text{KSrGd}(\text{PO}_4)_2: \text{Tb}^{3+}$, we have compared the emission spectra of $\text{KSrGd}_{0.5}(\text{PO}_4)_2:0.5\text{Tb}^{3+}$ with that of the commercial green-emitting phosphor $\text{Zn}_2\text{SiO}_4: \text{Mn}^{2+}$ (ZSM) under 147 nm excitation (Fig 8). The integrated emission intensity of $\text{KSrGd}_{0.5}(\text{PO}_4)_2:0.5\text{Tb}^{3+}$ is about 70% of ZSM under 147 nm excitation. $\text{KSrGd}_{0.5}(\text{PO}_4)_2:0.5\text{Tb}^{3+}$ shows a relatively strong emission band under 147 nm excitation, which indicates the phosphor could be a potential application in Hg-free fluorescent lamps, PDPs, and 3D displays.

IV. CONCLUSIONS

The phosphors $\text{KSr}(\text{Gd}, \text{Y})(\text{PO}_4)_2: \text{Tb}^{3+}$ were synthesized using the co-precipitation method. In these phosphors, tunable emission from the blue to yellowish-green was obtained by varying the Tb^{3+} contents cross relaxation under 172 nm excitation. The CR efficiency for the phosphor $\text{KSrGd}_{0.5}(\text{PO}_4)_2:0.5\text{Tb}^{3+}$ excited at 222 and 172 nm was found to be 1.55 and 0.015 respectively. Therefore, the resulting value of quantum efficiency was calculated as 255% and 101% at the excitation of 222 and 172 nm respectively. Under 147 nm excitation, the emission intensity of $\text{KSrGd}_{0.5}(\text{PO}_4)_2:0.5\text{Tb}^{3+}$ is around 70% of that commercial green-emitting phosphor $\text{Zn}_2\text{SiO}_4: \text{Mn}^{2+}$, which could make it a potential application for mercury-free fluorescent lighting, Plasma display panels (PDPs), and Three-dimensional display.

ACKNOWLEDGMENTS

We are grateful to 4B8 VUV spectroscopy beamline scientists of Beijing Synchrotron Radiation Facility (BSRF), China for providing that access to recording VUV on beamline 4B8 under dedicated synchrotron radiation using remote access mode. One of the authors S.R. Jaiswal thankful to the chairman FIST-DST project, Department of Physics Sant Gadge Baba Amravati University, Amravati for providing necessary facilities, and the authors are also thankful to Dr. G.V. Korpe, Principal, Shri Shivaji Science College, Amravati, for moral and official supports.

REFERENCES

- [1] D. Y. Wang, Y. C. Chen, C. H. Huang, B. M. Cheng, and T. M. Chen, *J. Mater. Chem.*, 22 [19] 9957–62 (2012).
- [2] H. A. Höpfe, *Chem. Int. Ed.*, 48 [20] 3572–82 (2009).
- [3] D. Wang, N. Kodama, L. Zhao, and Y. Wang, *J. Electrochem. Soc.*, 157 [6] J233–7 (2010).
- [4] R. T. Wegh, H. Donker, K. D. Oskam, and A. Meijerink, *Science*, 283 [5402] 663–6 (1999).
- [5] P. Ghosh, S. Tang, and A. V. Mudring, *J. Mater. Chem.*, 21 [24] 8640–4 (2011).
- [6] L. Han, Y. Wang, J. Zhang, and Y. Tao, *Mater. Chem. Phys.*, 143 [2] 476–9 (2014).
- [7] T. J. Lee, L. Y. Luo, E. W. G. Diau, T. M. Chen, B. M. Cheng, and C. Y. Appl. Phys. Lett., 89 [13] 131121, 3pp (2006).
- [8] H. Y. Tzeng, B. M. Cheng, and T. M. Chen, *J. Lumin.*, 122, 917–20 (2007).
- [9] D. Wang and N. Kodama, *J. Solid State Chem.*, 182 [8] 2219–24 (2009).
- [10] L. Zhao, Y. Wang, and Y. Tao, *Electrochem. Solid-State Lett.*, 15 [3] B13–6 (2011).
- [11] Z. Tian, H. Liang, W. Chen, Q. Su, G. Zhang, and G. Yang, *Opt. Express*, 17 [2] 956–62 (2009).
- [12] B. Han, H. Liang, Y. Huang, Y. Tao, and Q. Su, *J. Phys. Chem. C*, 114 [14] 6770–7 (2010).
- [13] M. Xie, Y. Tao, Y. Huang, H. Liang, and Q. Su, *Inorg. Chem.*, 49 [24] 11317–24 (2010).
- [14] D. Hou, H. Liang, M. Xie, X. Ding, J. Zhong, Q. Su, and Z. Gao, *Opt. Express*, 19 [12] 11071–83 (2011).
- [15] S. Tie, Q. Su, and Y. Yu, *J. Alloys Compd.*, 227 [1] 1–4 (1995).
- [16] Z. J. Zhang, J. L. Yuan, S. Chen, H. H. Chen, X. X. Yang, J. T. Zhao, and C. S. Shi, *Opt. Mater.*, 30 [12] 1848–53 (2008).
- [17] D. Geng, M. Shang, D. Yang, Y. Zhang, Z. Cheng, and J. Lin, *Dalton Trans.*, 41 [46] 140425 (2012).
- [18] L. L. Han, Y. H. Wang, L. Zhao, J. Zhang, Y. Z. Wang, and Y. Tao, *Mater. Res. Bull.*, 48 [6] 2139–42 (2013).
- [19] G. Pucker, S. Parolin, E. Moser, M. Montagna, M. Ferrari, and L. Del Longo, *Spectrochim. Acta, Part A*, 54 [13] 2133–42 (1998).
- [20] S. R. Jaiswal, N. S. Sawala, P. A. Nagpure, V. B. Bhatkar, and S. K. Omanwar, *J. Mater. Sci. Mater. Electron.* [28] 2407 (2017).
- [21] S. R. Jaiswal, N. S. Sawala, K. A. Koparkar, V. B. Bhatkar, and S. K. Omanwar, *Mater. Discov.* [7] 15 (2017).
- [22] S. R. Jaiswal, N. S. Sawala, P. A. Nagpure, W. S. Barde, and S. K. Omanwar, *Adv. Mater. Res.* [1171] 17–24. <https://doi.org/10.4028/p-wd48sx>.
- [23] S. R. Jaiswal, P. A. Nagpure, and S. K. Omanwar, *J. Sci. Res. Sci. Technol.* 8, 272 (2021).

[24] S. R. Jaiswal, N. S. Sawala, P. A. Nagpure, and S. K. Omanwar, J. Emerg. Technol. Innov. Res. [9] 75 (2022).

¹S. Dubey
²P.K. Sharma
¹A. Mishra
³S.K. Joshi
¹A. Mansuri
⁴S. Vyas

EXAFS studies of some Cu (II) complexes using Synchrotron Radiation Source



Abstract: - Extended X-ray absorption fine structure (EXAFS) analysis of Cu (II) complex (E)-2-(2-(2-hydroxybenzylamino)phenylimino)-1,2-diphenylethanone with other ligands bromide, sulphate, acetate, and nitrate have been studied using EXAFS technique. EXAFS spectra have been recorded at the K-edge of Cu (II) using the energy dispersive EXAFS beam line at 2.5 GeV Indus - 2 synchrotron source at RRCAT, Indore, India. Fourier analysis of experimental EXAFS data of the copper (II) complexes have been also done. Using Fourier transform of the data metal-ligand bond lengths have been obtained. These bond lengths have been compared with the bond lengths obtained from several other known methods viz., Levy's, Lytle's and Lytle, Sayers and Stern's (LSS). The results of bond lengths obtained by different methods compare well. The values of chemical shifts obtained in the present studies for these samples suggest oxidation state +2.

Keywords: EXAFS, Fourier transform, Bond lengths, Chemical Shift.

I. INTRODUCTION

The first transition metal series includes many metals of which Vanadium, Chromium, Manganese, Iron, Cobalt, Nickel, Copper and Zinc complexes have been earlier studied by using X-ray absorption spectroscopy. Even today one of these, Copper occupies very significant position and many research workers are engaged in studying complexes of copper having oxidation states +1, +2 and +3. The beauty of copper is its ability to form coordination compounds or complexes with ligands and it is found in all living organisms as a component of respiratory enzymes, blood pigments, muscles and bones. Copper ores available in nature (only 0.6 %) are chalcocopyrite (CuFeS_2), Bornite (Cu_5FeS_4), Covellite (CuS) and Chalcocite (Cu_2S). Copper has possibilities of various valence states due to 3d incomplete shell. Its electronic configuration is $3d^{10}4s^1$, as such several kinds of samples with oxidation state +1, +2 and +3 may be investigated. In the present paper the X-ray absorption spectra at the K-edge of copper of a series of mixed ligand complexes having (E)-2-(2-(2-hydroxybenzylamino)phenylimino)-1,2-diphenylethanone ligands with bromide, sulphate, acetate and nitrate have been investigated. The X-ray spectra are best recorded using X-ray from synchrotrons. We have recorded the spectra using 2.5 GeV synchrotron facility named Indus-2. This facility is available at Raja Ramanna Centre for Advanced Technology (RRCAT), Indore. The beamline which is suitable for recording X-ray absorption spectra is named as BL-8 dispersive EXAFS beamline.

¹School of Physics, Devi Ahilaya Vishwavidyalaya, Indore, 452001, India

²Govt. Holkar Science College, Indore, 452001, India

³Govt. Arts and Science College, Ratlam, 457001, India

⁴Govt. Madhav Science College, Ujjain, 456010, India

E-mail: *shshankduby@gmail.com

II. EXPERIMENTAL DETAILS

A. Preparation of Complexes :

A solution of o-phenylenediamine (0.005 mol) in alcohol was added to a mixture of 2-hydroxybenzylamino and -1,2-diphenylethanone (0.005 mol) and salicylaldehyde (0.005 mol) in 20 ml alcohol. The mixture was refluxed for about 30 minutes. The mixture was cooled in ice. The resulting precipitate was then filtered, washed with ethanol and dried [1-2]. To an ethanolic solution of the Schiff base ligand with ethanolic solution of the metal copper bromide was added in molar ratio (1:1). The mixture was refluxed for about 30 minutes. The mixture was cooled in ice. The resulting precipitate was then filtered, washed with ethanol and dried. The same procedure was carried out for the other three samples.

I. [Copper(II) (E)-2-(2-(2-hydroxybenzylamino)phenylimino)-1,2-diphenylethanone]bromide

II. [Copper(II) (E)-2-(2-(2-hydroxybenzylamino)phenylimino)-1,2-diphenylethanone]sulphate

III. [Copper(II) (E)-2-(2-(2-hydroxybenzylamino)phenylimino)-1,2-diphenylethanone]acetate

IV. [Copper(II) (E)-2-(2-(2-hydroxybenzylamino)phenylimino)-1,2-diphenylethanone]nitrate

The X-ray absorption spectra at the K-edge of these complexes have been recorded at BL-8 Dispersive EXAFS beamline. On this beamline, the X-ray intensities I_0 and I_t are obtained as the CCD outputs without and with the sample, respectively. Using the relation, $I_t = I_0 e^{-\mu x}$, where μ is the absorption coefficient and x is the thickness of the absorber, the absorption $\mu(E)$ corresponding to the photon energy (E) are obtained [3]. The experimental data have been analyzed using the available computer software packages Origin 6.0 professional and Athena. Firstly, the normalized $\mu(E)$ versus E spectra are obtained, then $\chi(k)$ versus k spectra are obtained, and finally, the Fourier transforms of the latter are obtained [4-7].

III. RESULTS AND DISCUSSION

A. Bond lengths :

The normalized absorption spectrum for complexes studied in this paper are shown in Figs. 1.1 (a), (b), (c) and (d) respectively for complexes I, II, III and IV. Similarly derivative of EXAFS spectrum for these complexes are shown in Figs. 1.2 (a), (b), (c) and (d). Further $\chi(k)$ versus k curves for these complexes are shown in Figs. 1.3 (a), (b), (c), and (d). the bond lengths have been determined for the copper complexes with the help of three methods, i.e., Levy's [8] Lytle's [9] and Lytle, sayers and stern's (L.S.S) [10] methods and the results are given in Table (1.1).

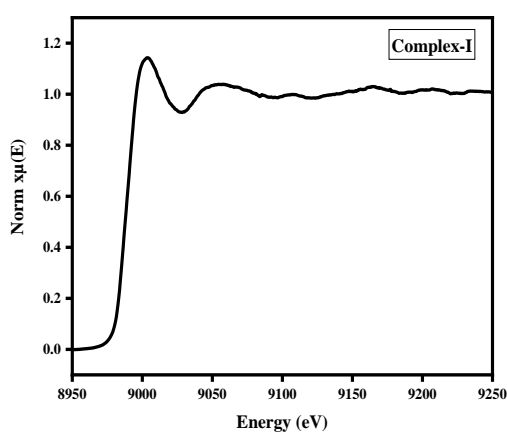


Fig 1.1 (a)

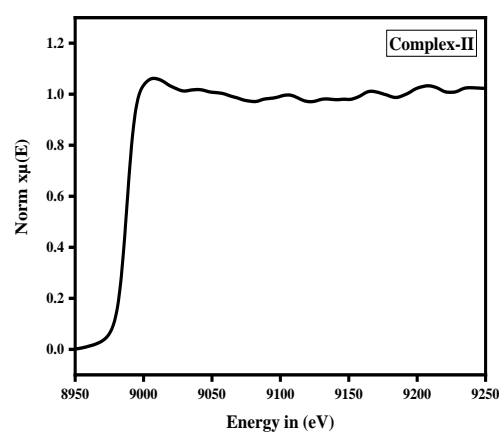


Fig 1.1 (b)

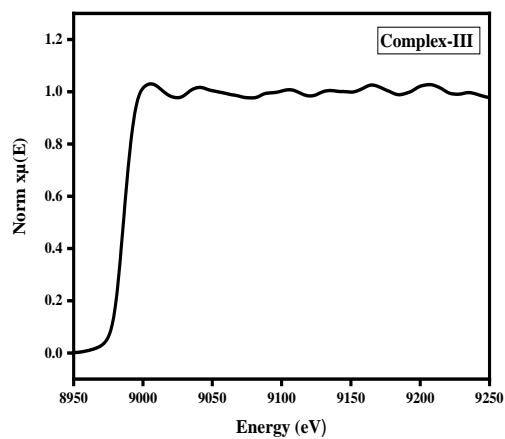


Fig 1.1 (c)

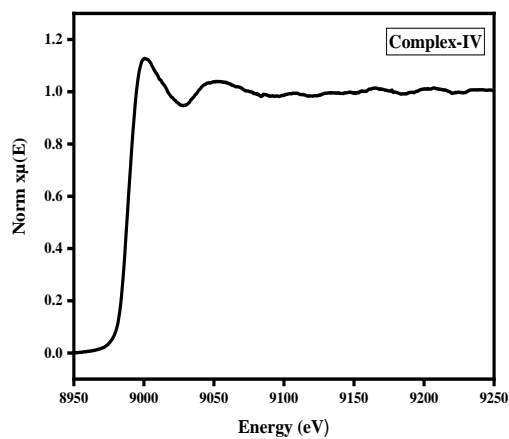


Fig 1.1 (d)

Fig. 1.1 The normalized absorption spectrum for complexes I, II, III and IV.

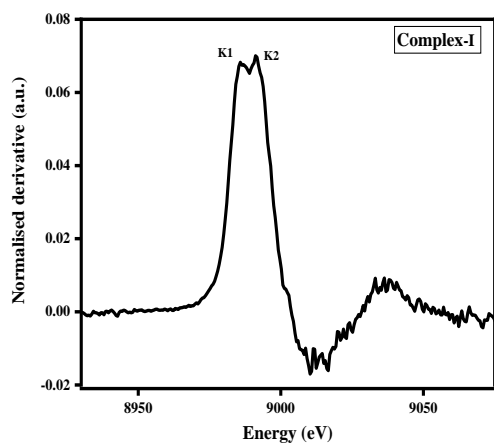


Fig 1.2 (a)

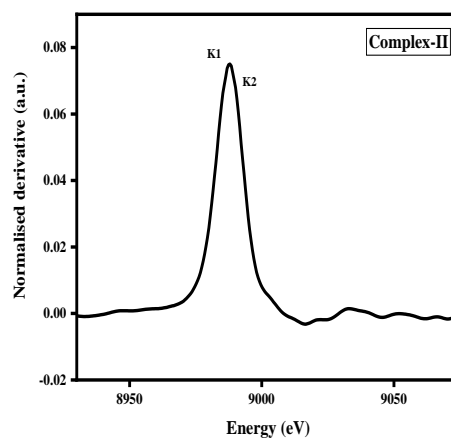


Fig 1.2 (b)

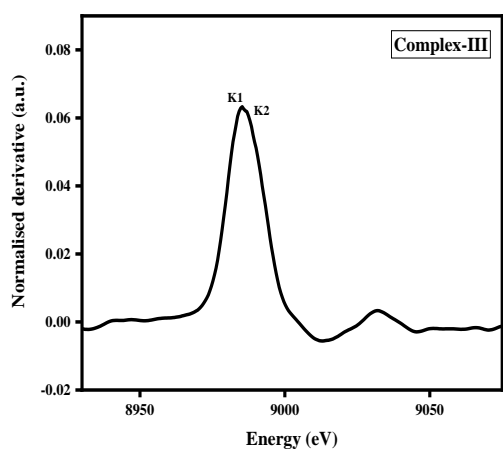


Fig 1.2 (c)

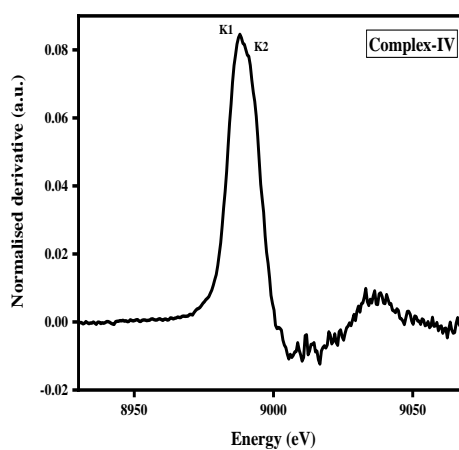


Fig 1.2 (d)

Fig. 1.2 Derivative of XAFS spectrum for complexes I, II, III and IV.

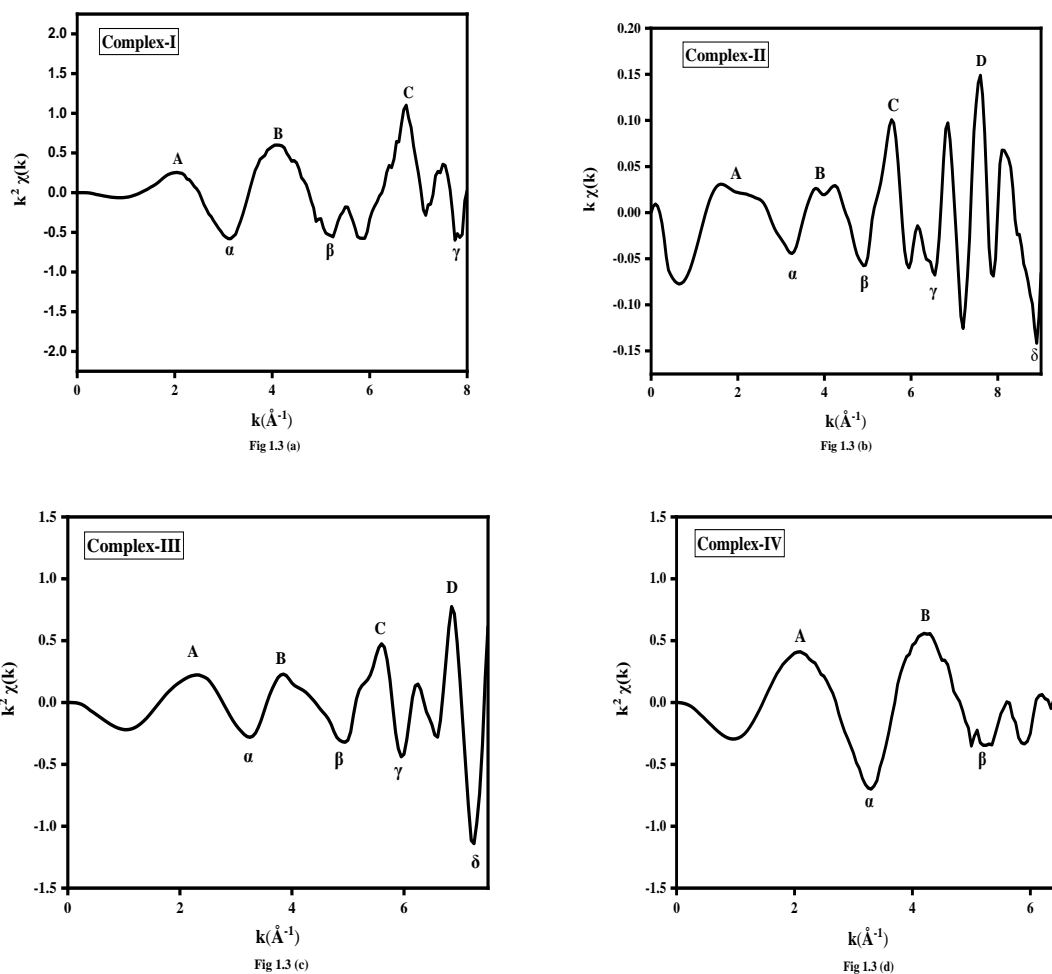


Fig. 1.3 $\chi(K)$ versus k curve for complexes I, II, III and IV.

Table 1.1 Determination of the Bond Lengths Using different Methods

S.No.	Complex	Phase corrected		Phase uncorrected	
		Levy's method R_1	Lytle's method R_s	L.S.S. method $(R_1 - \alpha_1)$	F.T. method R
1	I	1.92	1.53	1.35	1.23
2	II	2.25	1.83	1.67	1.99
3	III	2.03	2.05	2.18	2.06
4	IV	2.00	1.73	1.51	1.29

B. Chemical Shift :

The position of the absorption edge has been found to be sensitive to the metal oxidation state and environment [11,12]. As the electronegativity of the ligands increases, the edge position moves to higher energy. Furthermore, for a given set of ligands, the edge moves to higher energy as the metal oxidation state increases. For complexes involving highly polarisable ligands (e.g. cyanides and sulphur - containing ligands) this shift becomes very small ~ 1 eV or less per oxidation state change. Extensive studies have been reported [13,14] on chemical shifts of X-ray absorption edges. Two main factors contribute to be observed for high energy shifts of X-ray absorption edges, i.e.,

- (I) The tighter binding of the core level because of the change of the effective charge (or screening) of the nucleus caused by the participation of the valence electron in the chemical bond formation.
- (II) Appearance of the energy gap E_g when we go from a metal to a compound or complex.

In general, the chemical shift is towards the high energy side of the metal edge [15] increasing progressively with increase of the valence of the cation. Of course the shift may also be suppressed by the covalent character of the bond or enhanced by the formation of metal – metal bonding. A perusal of Table 1.2 shows that the chemical shift values lie between 4.5 to 7.4 eV.

It is appropriate to compare data of chemical shifts as reported by earlier workers [16-18]. They have reported chemical shifts for various copper complexes and these values have been found to lie in the range 4.5 to 8.5 eV, and all these sample have been suggested to have oxidation state +2. Our chemical shift values also lie in the range 4.5 to 7.4 eV, and on this basis it is obvious that these complexes also possess oxidation state +2. The sequence of variation of chemical shifts follows the trend :

Complex IV > Complex I > Complex II > Complex III
(7.4) (5.3) (5.2) (4.5)

this also indicates the relative ionic character of the bonding in these complexes.

Table 1.2 Data of chemical shifts of Copper (II) complexes.

Complexes	E _{K1} (eV)	E _{K2} (eV)	E _A	Chemical Shift $\Delta E_K = (E_{\text{complex}} - E_{\text{metal}})$
Complex – I	8985.8	8991.1	9003.9	5.3
Complex – II	8985.7	8987.8	9006.0	5.2
Complex – III	8985.0	8987.0	9005.3	4.5
Complex – IV	8987.9	8990.3	9000.9	7.4

Copper Metal K-edge energy 8980.5 eV.

IV. CONCLUSION

It has been observed that the values of the bond lengths as determined from different methods are in good agreement. The values of the chemical shifts suggest that copper is in oxidation state +2 in all of the complexes. Further the sequence of variation of chemical shift values may be taken as representative of the relative ionic character of the bonding in these complexes.

ACKNOWLEDGMENT

One of us (S.D.) is thankful to Dr. B.D.Shrivastava for his valuable support in the completion of data analysis.

REFERENCES

- [1] R.A. Majeed IBN AL-Haitham J.for Pure & Appl. Sci Vol.22(2) 2009.
- [2] Bimal kumar, Rai BK and Nisha Ambastha Synthesis characterization and Antimicrobial screening of cobalt (II), Nickel (II) & copper (II) complexes with Schiff base derived from 2-phenyl Quinoxaline Thiosemicarbazone. Oriental J Chem. 2011;27:1173-1178.
- [3] N Raman, Y Raja Pitchaikani and A Kulandaisamy synthesis and characterization of Cu (II), Ni(II), Mn(II), Zn(II) and Vo(II) Schiff base complexes derived from o-phenylenediamine and acetoacetanilide. Proc Ind Acad Sci.2001;113:183-189.
- [4] D. Bhattacharyya, A.K. Poswal, S.N.Jha, Sangeeta, S.C. Sabharwal, Bull. Mater.,2009 Sci.32103.
- [5] D. Bhattacharyya, A.K. Poswal, S.N.Jha, Sangeeta, S.C. Sabharwal, Nucl. Instrum. Meth.A 2009, 609286.
- [6] N.C.Das, S.N. Jha, D. Bhattacharyya, A.K. Poswal, A.K. Sinha and V.K. Mishra 2004 Sadhna 29545.

- [7] P.L. Lee, M.A. Beno, G. Jennings, M. Ramanathan, G.S. Knapp, K. Huang, J. Bai, P.A. Montano, 1994 Rev. Sci. Instrum 65.
- [8] R.M. Levy, J.Chem.Phys., 1965, 43,1846.
- [9] F.W. Lytle, Advances in X-ray Analysis, 1966,9,398.
- [10] F.W. Lytle, D.E. Sayers and E.A. Stern, 1975 (a), Phys. Rev. B11,4825.
- [11] V.K. Hinge, S.K. Joshi, B.D. Shrivastava, J. Prasad and K. Shrivastava, ICRTP, J. Phys.365 (2012) 012029.
- [12] Shikha Dwivedi, S.K. Joshi, V.K. Hinge, B.D. Shrivastav, J.Prasad . and K. Shrivastava, AIP Conf. Proc. 2100. (2019) 020194.
- [13] C. Bonnelle and C.Mande (Eds), Advances in X-ray Spectroscopy (Pergamon press, New york) (1983).
- [14] S.K. Joshi, B.D. Shrivastava, Bhakta Darshan Shrivastava and A. Mishra, X-ray Spectrom. 33.(2004) 466.
- [15] S.K. Joshi, B.D. Shrivastava & A.P. Deshpande, (Eds) X-ray Spectroscopy and allied areas, (Narosa publishing House, New Delhi), 1998.
- [16] R.K. Katare, S.K. Joshi, B.D. Shrivastava, R.N. Patel, & A. Mishra, Ind. J. of Pure & App. Phys. Vol.40. December 2002, p.p. 908-913.
- [17] S.K. Joshi, R.K. Katare, and B.D. Shrivastava, American Institute of Physics, 2007, 978-0-7354-0384.
- [18] V.K. Hinge, S.K. Joshi, B.D. Shrivastava, J. Prasad & K. Shrivastava, Ind. J. of Pure & App. Phys. Vol.49, March 2011, p.p. 168-172.

¹Shraddha Bansod-
Pande²Seema Ubale

Effect of Sugarcane bagasse ash on the phase transformation and optical properties of Zinc-Borate glass



Abstract: - The aim of this research is fabrication and characterization of zinc-borate glass system derived from ZnO, Borate and sugarcane bagasse ash (BA) as a silica sources. The utilization of sugarcane bagasse ash generated in thermal power plants presents an innovative approach to sustainable glass production. Sugarcane bagasse ash, rich in oxides such as SiO₂, Al₂O₃, Fe₂O₃, and CaO, serves as a valuable raw material for glass formation. The ZnO-Borate glass system was prepared by melt-quench technique. This study investigates the incorporation of sugarcane bagasse ash into Zinc-Borate glass systems, specifically Zinc-Borate sugarcane bagasse ash glass. The impact of progressive addition of sugarcane bagasse ash on phase transformation and optical properties of the resultant glass was examined through various analytical methods, density assessments, X-ray diffraction, FTIR studies and UV-VIS optical absorption technique. X-ray diffraction analysis of the zinc borate glasses shows that the glassy state of the zinc borate glasses increased along with the increment of BA, The vibrational band due to the presence of tridymite was found in the Fourier transform infrared spectroscopy (FTIR) at lowest BA content supporting the XRD result and glass system also shows the formation of zinc borate glasses with the presence of SiO₄ and B-O-B bending vibration of glass. Using UV-VIS spectroscopy optical absorption and transmission characteristics of glass system were discussed.

Keywords: Sugarcane bagasse ash, optical properties, zinc-borate glass

I. INTRODUCTION

Glass is an amorphous material having short range order. It is a transparent and brittle material which has practical; numerous electrical, technical and house hold usages. Glass is also called as super cooled liquid due to its viscosity at room temperature. There are different types of glass depending upon chemical composition, there are different types of glasses with different chemical and physical properties there are various types of glasses which are divided under different categories according to their applications. On the basis of chemical compositions, glasses can be classified as-borate glasses, vanadate glass, alkali borate glasses, silicate glasses, phosphate glasses and zinc-borate glass. Zinc- Borate glass is having low expansion coefficient. This property of zinc borate glass makes it useful in various applications like heat resistant material [1-2]. Addition of silica in zinc borate glass makes it a material having varied properties. In this research an attempt to be made to use sugarcane bagasse ash as a source of silica in glass formation. The making of glass involves three basic types of ingredients. They are a glass former, a flux, and a stabilizer. Silica is the main ingredient of glass, which is a glass former compound. It is found that sugarcane bagasse ash contains large amount of silica. Silica in the form sugarcane bagasse ash serve as one of the glass former [3]. Sugarcane bagasse ash contains other metal oxides along with silica. Study revealed that as compared to other sources sugarcane bagasse contain near about 60% silica [4]. A study explore the possibility of using industrial fly ash waste as a silica source and prepared coloured glass from coal ash which is by product of coal run thermal power plant[5]. Romero M et al has tried to crystallize SiO₂ -CaO-N₂ O glass from sugarcane bagasse and reports the feasibility results of recycling sugar huge amount of surface area, smaller amount of metal impurities and low density [6]. Research reported formation of glass and glass composites from industrial waste and agriculture waste like coal ash, rice husk ash etc. As glass former the roles of B₂O₃ is very important and were explored by previous studies. In addition of B₂O₃ and SiO₂ other metal oxide like ZnO is also important.

II. MATERIAL AND METHODS

The sugarcane bagasse ash (BA) used here was procured from thermal power plant running on biomass fuel, 'Purti Power and Sugar Limited', Bela, District Nagpur (MS) India. The ash was subjected to chemical analysis to confirm the presence of silica form ANACON LAB Nagpur. The percentage of silica, alumina and other fly ash components is as listed in Table1.

Table-1 Chemical analysis of Sugarcane Bagasse Ash

Sr.No.	Parameter	BA
1	Silica	52.64%
2	Alumina	14.05%
3	Iron oxide	7.80%
4	Calcium oxide	3.31%
5	Magnesium oxide	1.72%
6	Potassium oxide	4.74%
7	Titanium dioxide	0.22%
8	Manganese oxide	0.20%
9	Sodium Oxide	0.48%

The glasses were prepared by using BA, Zinc oxide and Boric Oxide (AR grade). The molar composition of the glass sample (with increasing percentage of sugarcane bagasse ash) was taken. The powders were weighed on a monopan K Roy balance digital balance having accuracy 0.0001gm. The powder were mixed for 30 minutes thoroughly by repeated grinding in an agate mortar and pestle. Then mixture was transfer in a fire clay crucible in an electrically heated furnace under ordinary atmospheric conditions at a temperature of about 1000C for 3 h to homogenize the melt. The melted mixture was poured on 2×1 cm² stainless-steel mould to form bulk glass. The glasses were prepared by the melt quench method. The chemical composition of glass sample is given in Table-2.

Table-2 Glass composition

SR.No.	Glass composition	Composition in mole percent (%)
1	BZB-1	60-40-0
2	BZB-2	60-35-5
3	BZB-3	60-30-10
4	BZB-4	60-25-15
5	BZB-5	60-20-20

The quenching rate is 9000C/minute the glasses were immediately transferred to annealing furnace maintained at 3230C for 1 hour. The glass sample polished to form parallel faces to study ultrasonic properties. The density of the glass samples were measured using Archimedes' principle. The amorphous nature of glass sample confirmed by XRD spectra. FTIR of glass samples were studied for confirming the presence of silica and alumina in the glasses [7].

III. RESULTS AND DISCUSSION

1. X-Ray Diffraction

The X-ray diffraction patterns of all glass systems are shown in Fig 1. The X-RD pattern of all glass samples shows no Bragg's peak, but only a broad diffuse humps around low angle region, this is the clear indication of amorphous nature of glass structure [8].

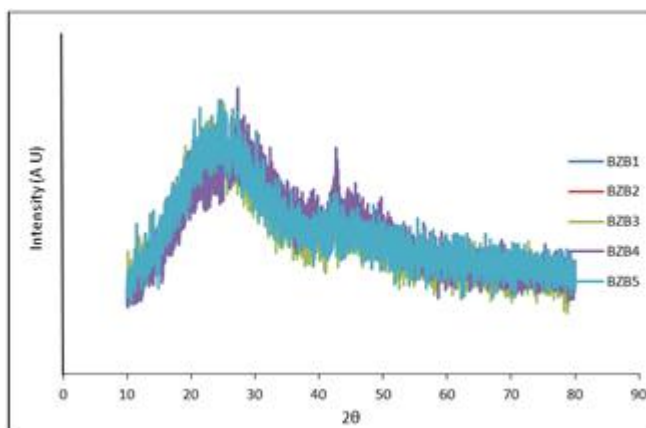


Figure 1 X-ray Diffraction Pattern of bagasse ash glass system

2. Infrared Spectroscopy

The infrared spectra of some selected sample of glass system in the IR region are shown in infrared spectra of glass sample is studied in the range of 400-4000 cm⁻¹ on Perkin Elmer-467 IR spectrometer by using KBr technique shown in Fig 2.

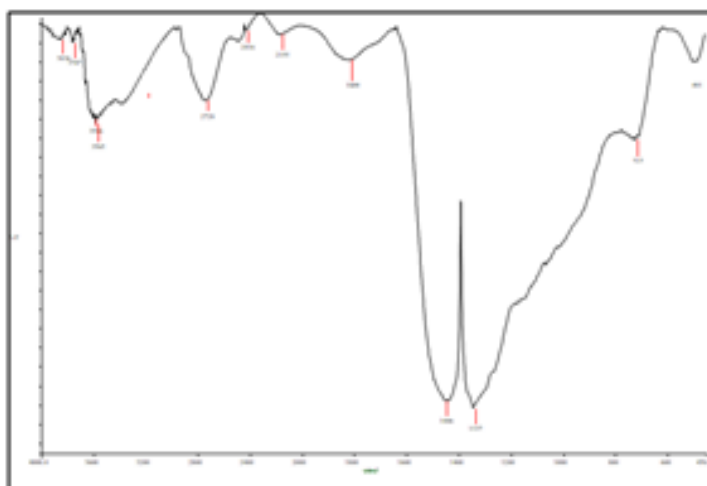


Figure 2: FTIR of Bagasse ash glass sample

The absorption 20 peaks were obtained in glass sample. The peak assignment is consistent with other published work [9]. Absence of peak around 806 cm⁻¹, indicate that borate network does not contain any boroxol ring [10]. The peak near 450cm⁻¹ shows Si-O-Si stretching modes [11]. Presence of peak 440-770cm⁻¹ gives the B-O-B bonding of borate network.1330-1400cm⁻¹ gives the B-O bond stretching of tetrahedral BO₄ units.1446-1826 cm⁻¹ is due to presence of Zn²⁺,peak 2100-2730cm⁻¹ is due to -OH group present in the glass system. Peak at 3565-3747 cm⁻¹suggest the presence of hydroxyl group. The strong bands around at 1200-1600 cm⁻¹ is due to the asymmetric stretching relaxation of B-O bonds of trigonal BO₃ units [12]. Sharp but low intensity peak in the region of 700cm⁻¹ is assigned to the bending vibration of various borate segments. Remarkable changes were observed in the range 800-1800 cm⁻¹upon increasing the content of BA and RHA in the glass network. The vibrations around 806-1442 cm⁻¹ is due to anti-symmetric vibrations of Si-O-Si bonds of [SiO₄] units [13]. In general, it is concluded that sugarcane bagasse ash was become the part of the borate network. Another component in glass network is ZnO which also affects the glass structure.

IV. DENSITY AND MOLAR VOLUME

Density of the sample was measured using Archimedes’ principle using Eq 1

$$\rho = \left(\frac{W_a}{W_a - W_b} \right) \times d \dots\dots\dots(1)$$

Distilled water is used as a buoyant liquid. The molar volume explains the glass structure. Change in molar volume suggests the change in glass network. The density of glass depends upon the number of ions and the way

how they enter in to the glass structure [14]. Inverse relation between density and molar volume is as shown in figure 3. In present glass system BA is in increasing percentage in glass network whereas the B₂O₃ is constant and the ZnO is varied accordingly. Thus the variation in ZnO convert BO₃ triangle in to BO₄ tetrahedral or vice a versa producing non-bridging oxygen. Thus this formation of asymmetric unit is denser than B₂O₃. In addition to the ZnO and silica in the form of BA was also responsible for the formation of asymmetric unit in B₂O₃. These asymmetric units increase density of the glass system. This indicates that the system is in single phase with random glass structure. Fig 3 shows the inverse variation of density and molar volume.

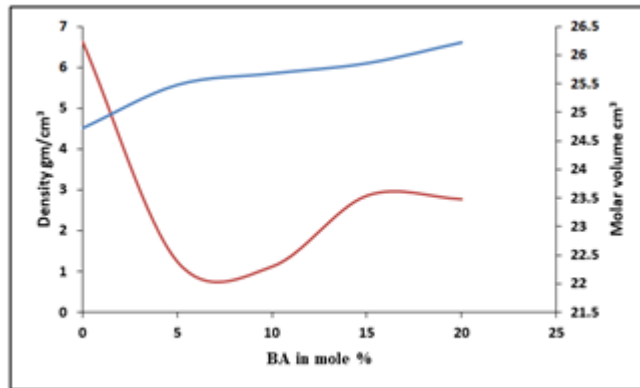


Figure 3: Density and Molar volume of BZB glass system

1. UV-VIS Absorbance

The optical measurement was made in the range of 200 to 800 nm. UV-Visible spectrophotometer (Shimadzu, Japan), was used to measure the optical absorbance in UV region. Absorbance edges were obtained in the ultraviolet region 200-400nm as shown in Fig 4 and transmission spectra of glass system is shown in Fig 5

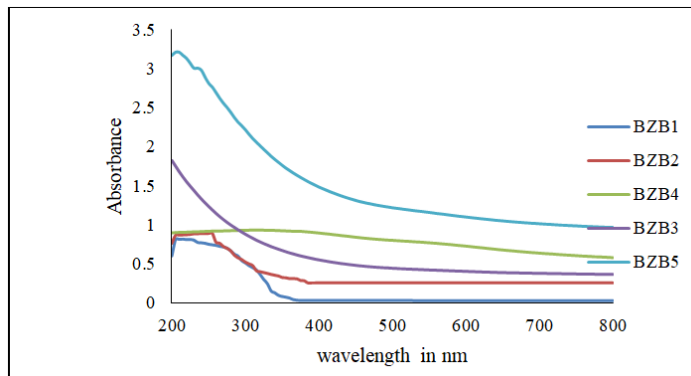
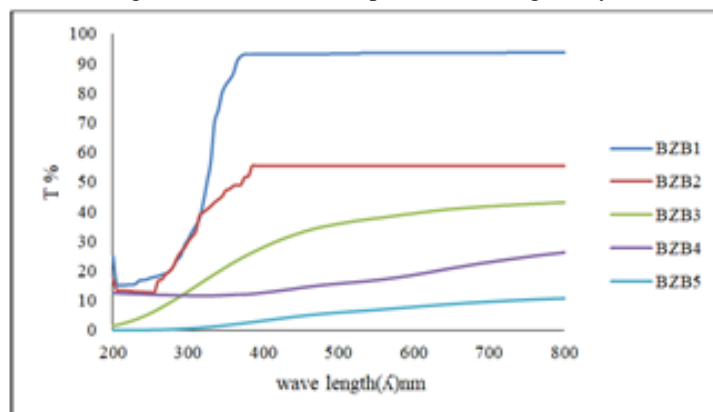


Figure 4: Absorption Spectra of BZB glass system

Figure 5: Transmission spectra of BZB-glass system



Both absorption and transmission spectra shows that absorption edges were not so sharp. Which indicates the glassy or amorphous nature of all samples [15]. It is also observed that with addition of biomass ash the position of the fundamental absorption edge and cut-off wavelength shifted towards higher side. Absorption and transmission spectra are complimentary in nature. The spectra show that the high absorption region for all

glass sample in the ultraviolet range shifts to longer wave length. The prominent increase in the absorption must be shows the formation of hole centres like OHC (oxygen hole centre) or BOHC (Boron –oxygen hole centre). Measurement of optical absorption particularly absorption edge is important in case of electronic structure of amorphous material. The absorption characteristics of this entire glass sample described and discussed with the general qualitative understandings that the absorption edge is determined by the oxygen bond strength in glass forming network. In this present glass system the shift of absorption edge at higher wavelength is justified as, with the addition of silica rich BA and RHA the oxygen environment increases resulting into the formation of bridging oxygen (BO4) is increases [16].The absorption edge of the plot observed in UV region. This plot can be divided in two regions depending on the value of the absorption coefficient α for glassy and amorphous material. This nature of absorption edge suggests the forbidden indirect transition for amorphous material and shows an excellent correlation for the glasses prepared and is consistent with the validity of the relation

$$\alpha = \beta \frac{(h\nu - E_{opt})^{\frac{1}{2}}}{h\nu} \dots\dots\dots(2) \text{ For describing indirect transition [17].}$$

The first region of the graph usually knows as Urbach tail, which is generally characterized with the value of α and depends exponentially upon the photon energy [].Glass samples prepared using sugarcane bagasse ash is shown in Fig 6. [18]



Figure 6: BZB glass samples

V. CONCLUSION

Density of glass sample found to increase with increase in biomass ash content; this is very well associated with the formation of bridging oxygen atoms. Increase in density indicates the formation of network. Molar volume of glass sample varies inversely with the density of glass samples [19].Optical parameters of glasses strongly depend on glass structure.

An attempt has been made to explain the role of bagasse ash as glass former. Bagasse ash used in the present study consist of number of oxides as glass former and glass modifier such as silica. Use of bagasse ash helps in preparation of glass. Addition of bagasse ash as glass former along with borate and zinc oxide leads to change in borate network and resulted in formation of borate and silicate structural units by contributing silica. The results obtained are in agreement with those obtained by other structural properties. Addition of bagasse ash leads to creation of defects, thereby changing the optical band gap [20]. The decrease in optical band gap is also due to decrease of non-bridging oxygen atoms. Bridging oxygen atoms were found to be responsible for the absorption characteristics. Change in value of width of tail emphasizes the degree of disorder in the glass network. From the theoretical fitting of the experimental absorption coefficient for the entire glass sample, it is concluded that the present glass system behaves as an indirect band gap semiconductor and from optical band gap values it is concluded that the present glass system can be used as a UV-ray blocker. Thus the glass composition in present study may be used as new non-linear optical material.

ACKNOWLEDGMENT

Gratitude to all who contributed to this research.

REFERENCES

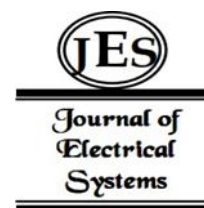
- [1] Ydniane M and Asahara Y, "Glasses for Photonics". Cambridge University Press", 2000.

- [2] Rao K.J. "Structural Chemistry of Glasses" Indian Institute of Science, Bangalore Elsevier: Amsterdam. 2002.
- [3] Ruangtaweepa J, Kaewkhao C, Kedkaewb and P. Limsuwanb "2nd International Science, Social- Science, Engineering and Energy Conference 2010: Engineering Science and Management, Eng Procedia, Investigation of Biomass Fly Ash in Thailand for Recycle to Glass Production" (2010). pp58-61
- [4] Lee CS, Matori KA, Ab Aziz SH, Kamari HM, Ismail I, Zaid MHM. Fabrication and characterization of glass and glass-ceramic from sugarcane bagasse ash as a potent material for opto-electronic applications. *J Mater Sci-Mater Electron* 2017; 28:17611–21.
- [5] Kanjanakul P, Kaewkhao J, Limsuwan P, Kedkaewa C, "Structural and optical properties of alkali borosilicate glass prepared from coal fly ash", *Procedia Engineering*, 32 (2012), 740-744.
- [6] Romero M, Jesus M A, "Crystallization of SiO_2 -CaO-Na₂O Glass Using Sugarcane Bagasse Ash as Silica Source", *J Am Cer. Soc.* (2009), 93(2):450–455 DOI:10.1111/j.1551-2916.2009.03431.K. Elissa, "Title of paper if known," unpublished.
- [7] N. Srisittipokakun, Ruangwaep R, Rachniyom W, Boonin K, CuO, MnO₂ and Fe₂O₃ doped biomass ash as silica source for glass production in Thailand, *Result in physics* vol 7 (2016) 3449-3454
- [8] Bobkova N M and Khot S A, *Glass and Ceramics*, "Zinc Oxide in Borate Glass-Forming Systems," (2005) Vol. 62, No. 5, 167-170. doi:10.1007/s10717-005-0064-7
- [9] Ram S, *Physical Review B* "Infrared Study of the Dynamics of Boroxol Rings in the Crystallization of BaFe₁₂O₁₉ Microcrystal in the Borate Glass," Vol. 51, No. 10, (1995), 6280-6286. doi:10.1103/PhysRevB.51.6280
- [10] Nariyal R.K, Kothari P and Bisht B, *Chemical Science Transactions*, "FTIR Measurements of SiO₂ Glass Prepared by Sol-Gel Technique", (2004), 1064-1066 DOI:10.7598/cst2014.816.3(3)1064-106
- [11] Thirumaran S, Prakash N, "Structural characterisation of some borate glass specimen by ultrasonic method", *Indian J. Pure App. Phys.* (2015), vol 53, pp 82-92
- [12] Shamal N, Raheman A.M, Karmarkar B, "Synthesis and characterisation of chloroborosilicate glass in K₂O-BaO-Al₂O₃-SiO₂-BaCl₂-glass system", *J. Non-Crys. Solid* (2014) pp32-41
- [13] Hassaniena A S, Akhl A A, "Estimation of some physical characteristics of chalcogenide bulk Cd₅₀S₅₀ - xSex glassy systems", *J Non-crys Solids* 428(2015), 112-120
- [14] Kundu V, Dhiman R L, Maan A S, Goyal D R, "Optical and spectroscopic studies of ZnO-Bi₂O₃-B₂O₃ glasses" *Journal of optoelectronics and advanced materials*, (2009) vol. 11, 1595 – 1600
- [15] Sanjay N, Kishore R, Punia R, Dhanlkar S, "Characterization and Optical Properties of Fe₂O₃-PbO-B₂O₃ Glasses", *AIP conference proceedings*, (2016), 1728
- [16] Singh D, Singh K, Singh G, Manupriya, Mohan S, Arora M, Sharma G, "Optical and structural properties of ZnO-PbO-B₂O₃ and ZnO-PbO-B₂O₃-SiO₂ glasses" *J. Phys.: Condens. Matter* 20 (2008) 075228(6pp) doi:10.1088/0953-8984/20/7/075228
- [17] Mott N F, Davis E A, *Electronic Processes in Non-Crystalline Materials* (Clarendon Press Oxford) (1979).
- [18] Samme M A, Awasthi A M, Shripathi T, "Physical and optical properties of mixed alkali borate glasses with three alkali ions", *J Alloys & Compounds*, (2011), 3043-3059
- [19] Halimah M K, Chiew W H, Sidek H A A, Daud W M, Wahab Z A, Khamirul A M & Iskandar S M, *Optical Properties of Lithium Borate Glass (Li₂O)_x (B₂O₃)_{1-x}*, *Sains Malaysiana* 43(6)(2014), 899–902
- [20] Bansod S, Ubale S, "To prepare soda borate glass from biomass fly ash and study its optical properties", *International Journal of Engineering Research & Technology*, Vol. 6 Issue 03, March-2017.

Article in a conference proceedings:

¹P.R. Kandalkar²Y.A. Gadhikar³S.A. Waghuley

ZnO Nanoparticles For Antibacterial Activity Against Clinically Extracted Gram-Positive And Gram-Negative Bacteria



Abstract: - In this research, the antibacterial activity of one pot synthesized zinc oxide (ZnO) nanoparticles (NPs) against clinically extracted Gram-negative and Gram-positive bacteria is determined. *Escherichia coli* (*E. coli*) and *Staphylococcus aureus* (*S. aureus*) were used as test microorganisms. The NPs of ZnO were synthesized by one pot chemical precipitation method using hexamethylenetetramine (HMT). The particle size was found to be 38.78 nm with lattice strain of 0.0095. This was confirmed from SEM analysis. The antibacterial activity of NPs was studied using bacteriological tests of well diffusion agar method. These tests were performed in nutrient broth and nutrient agar following standard method. The minimum inhibitory concentration (MIC) was determined using three different concentrations of ZnO NPs including 0.1, 0.3 and 0.5 mg/ml. The MIC value for both *E. coli* and *S. aureus* was found to be 0.1 mg/ml. The results showed that ZnO NPs have antibacterial inhibition zone of 13 and 15 mm at the concentration of 0.5 mg/ml against *E. coli* and *S. aureus*, respectively. From statistical analysis, it was found the rejection of the null hypothesis. This shows the unequal variances of the two bacteria (*E. coli* and *S. aureus*). ZnO NPs was found to be efficient in killing *E. coli* isolate as compared to *S. aureus* at lower concentration, while, reverse effect was observed at high concentration.

Keywords: Nanoparticles; Zinc oxide; Antibacterial activity; Well diffusion method.

^aDepartment of Zoology, Govt. Vidarbha Institute of Science and Humanities, Amravati 444 604, India

^bDepartment of Physics, Sant Gadge Baba Amravati University, Amravati 444 602, India

1. Introduction

The nanoparticles have different physical and chemical properties in comparison with their bulk size counterparts. Nanoparticles (NPs) are extra known for their account in biological applications including nanomedicine and food safety [1]. As an aliment additive, it is a lot of frequently acclimated zinc antecedent in the barricade of cereal-based foods. Because of its antimicrobial properties, zinc oxide (ZnO) has been congenital into the linings of aliment cans in bales for meat, fish, corn, and peas to bottle colors and to anticipate spoilage [2].

The nanotechnology has potential power of applications in the many aspects of food industry such as disease treatment delivery methods, food safety, new tools for molecular and cellular biology, novel materials for pathogen detection and environment protection. ZnO NPs are not only stable under high temperatures and pressures that are typically needed in food-processing conditions, but also generally regarded as safe for human beings and animals relative to organic materials [3].

Emami-Karvani et al. [4] have carried out the antimicrobial activity of ZnO nanoparticles against Gram-negative (*E. coli*) and Gram-positive (*S. aureus*) bacteria. They have prepared ZnO NPs by multistage chemical method. Mahamuni et al. [5] have reported that facile polyol mediated synthesis and characterization of ZnO NPs and their antimicrobial activities against pathogenic microorganisms. They have prepared ZnO NPs ZnO by by applying different approaches, i) regular synthesis in polyols, ii) in presence of sodium acetate, iii) increasing reaction time. In their study, ZnO synthesized by refluxing zinc acetate precursor in DEG for 3 h in absence of sodium acetate with particle size ~ 15 nm shows maximum activity against *S. aureus* and *Proteus vulgaris*. Siddiqi et al. [6] have written the review article on properties of ZnO NPs and their activity against microbes. They concluded that the ZnO NPs have great potential as a safe antibacterial drug, which may replace antibiotics in future. Alekish et al. [7] have evaluated the antibacterial effects of ZnO NPs and its possible alternative use for the treatment for mastitis in sheep and to determine the minimum inhibitory concentration (MIC) and minimum bactericidal concentration (MBC) of ZnO NPs against multidrug-resistant *S. aureus* and *E. coli* strains isolated from subclinical mastitis cases in sheep. They have synthesized ZnO NPs by multistage chemical method. Also, MIC and MBC values of ZnO NPs are significantly lower for *S. aureus* than that for *E. coli*.

The researchers have studied ZnO NPs as antibacterial agents against *E. coli*, *S. aureus*, *B. subtilis* etc. But they are made ZnO NPs by using very complex route. A single report is not found for antibacterial activity of ZnO NPs synthesized by using one pot method. Also, antibacterial activity of NPs against clinically extracted Gram-negative and Gram-positive bacteria is not observed during literature survey. This is the novelty of the present research work.

This work deals with synthesis of ZnO NPs by one pot chemical precipitation method for the application of antibacterial activity against clinically extracted Gram-negative (*E. coli*) and Gram-positive (*S. aureus*) bacteria through the collection of catheters aseptically in sterile containers..

2. Material and methods

The materials, zinc nitrate $Zn(NO_3)_2$ 98% (Merck), Hexamethylenetetramine (HMT) $C_6H_{12}N_4$ 99% (SD Fine), Nutrient agar, *E. coli* and *S. aureus*, and doubled distilled water were used in this study. In NPs synthesis, metal nitrates of Zn and HMT with a molar ratio of 1:1 were dissolved in doubled distilled water. The solutions were stirred with a magnetic stirrer at 60 °C. Stirring continues till the formation of gel for approximately 2 hours. As the gel was formed, it was allowed to burn at 100 °C. A light fluffy mass was obtained as a result of combustion, which was further annealed at 200 °C for 1 hour to obtain the respective crystalline metal oxide NPs. The metal oxide nanoparticles thus obtained were characterized by X-ray diffraction (XRD)

Antimicrobial activity of the synthesized Zn NPs was tested individually against both Gram-negative (*E. coli*) and Gram-positive (*S. aureus*) bacteria. These microbial were isolated clinically. The isolates; *E-coli* and *S-aureus* were collected from P.D. Medical College and Hospital Laboratory and Microbiology Post Graduate Laboratory, SGB Amravati University, Amravati. They were purified by sub culturing several times to obtain pure cultures. Few biochemical tests were carried out to confirm these isolates before being used for the work. The biochemical tests include; Coagulase test, Mannitol salt agar test, Indole test, Oxidase test, Citrate test and Staining test. The antibacterial activity was evaluated by the agar well-diffusion method.

The method of bacterial extraction was done clinically which follows the collection of catheters aseptically in sterile containers. Small sections 1-2 cm and 3-4 cm from tip of catheter were cut, followed by washing with sterile distilled water and were aseptically suspended in 10 ml Quarter strength Ringers solution. This was subjected to sonication for 5 min at 35 KHz in a transonic water bath and vortexed for two minutes to attain disruption of colonizing bacterium. Bacteria were inoculated on UTI chromogenic media (Himedia make). Predominant bacteria characterized belonged to *E. coli* and *S. aureus*. Fresh bacterial cultures with standardized dilutions were spreaded on Muller Hinton Agar (MHA) plates. Plates were allowed to stand for 10-15 min so that bacteria adhere to the agarized media. The detail is explained in reference [8]. Wells of 6 mm diameter were made in each plate and three dilutions; 0.1, 0.3 and 0.5 mg/ml (fig. 1.) of ZnO NPs were added.

Zone of inhibition (ZOI) was measured in comparison to tetracycline as positive control and distilled water as negative control. Inoculated plates were incubated for 24 h at 37 °C, ZOI was recorded and size of zones was measured. Likewise three dilutions ZnO NPs were tested against each bacterial pathogen. In this way, minimum inhibitory concentration (MIC) was measured against each bacterial pathogen.



Fig. 1. The three dilutions (0.1, 0.3 and 0.5 mg/ml) of ZnO NPs with doubled distilled water.

3. Results and Discussion

In the XRD pattern of ZnO NPs, prominent peaks were observed and they were very well matched with standard data as shown in fig. 2.

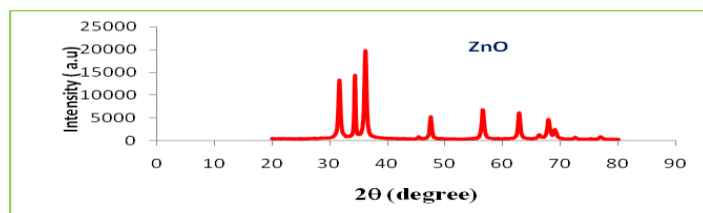


Fig. 2. XRD pattern of one pot synthesized ZnO NPs.

XRD can be utilized to evaluate peak broadening with crystallite size and lattice strain due to dislocation [9]. XRD pattern of ZnO NPs confirms wurtzite crystal structure of the ZnO. The Lattice constants ($a = b = 0.32$ nm and $c = 0.52$ nm) and diffraction peaks corresponding to the planes $\langle 100 \rangle$, $\langle 002 \rangle$ and $\langle 101 \rangle$ obtained from X-ray diffraction data are consistent with the JCPDS data of ZnO. The crystallite size of the ZnO NPs was determined by the X-ray line broadening method using the Scherer equation: $D = k\lambda / \beta \cos\theta$, where D is the crystallite size in nanometers, λ is the

wavelength of the radiation ($\lambda=1.54056 \text{ \AA}$ for $\text{CuK}\alpha$ radiation), k is a constant equal to 0.94, β is the peak width at half maximum intensity, and θ is the peak position. The average crystallite size and lattice strain were found to be 38.78 nm and 0.0095, respectively. The morphology of ZnO NPs was studied by using the SEM, which revealed a flake like shape as shown in fig.3.

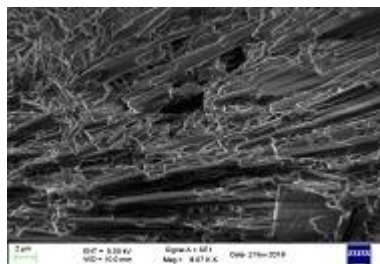


Fig. 3. SEM image of one pot synthesized ZnO NPs.

It clearly shows that the typical SEM image of nano-sized ZnO flakes have large quantity of flake shape with a narrow size distribution. This reveals that the products have uniform flake shape [9]. This may be due to the particle-size broadening from the finite extent and particular morphology of the coherently diffracting domains within the grains. The microstrain broadening may be due to local variations of the d-spacing produced by non uniform crystalline stresses. The flake size observed from morphology exactly matched with XRD.

The antibacterial activity of ZnO NPs was tested by the well diffusion agar methods. The presence of an inhibition zone was clearly indicated the antibacterial effect of ZnO NPs as in photographs of fig. 4. It was seen that by increasing the concentration of ZnO NPs in wells, the growth inhibition has also been increased. The size of inhibition zone was different according to the type of bacteria.

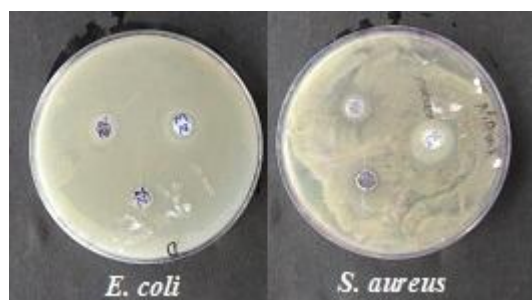


Fig. 4. Antibacterial activities of ZnO NPs against *E. coli* and *S. aureus*.

The antibacterial action of ZnO NPs against *E. coli* and *S. aureus* bacteria is displays as ZOI as shown in table 1. Agar well diffusion method was used to test the antimicrobial sensitivity. The two clinical isolates i.e. *E.coli* and *S. aureus* were selected which are the Gram negative as well as Gram positive species. These clinical isolates were inhibited by ZnO NPs at the minimum concentration of 0.1 mg/ml. The zone of clearance was on an average 11 mm deep for two isolates. Maximum zones of inhibition (ZOI) were observed at 0.5 mg/ml ranging from 13 to 15 mm (table 1 and fig. 4). The minimum inhibitory concentration (MIC) was observed to be equal to both the bacteria.

Table 1. Antibacterial action of ZnO NPs against *E. coli* and *S. aureus* bacteria.

ZnO NPs concentration in wells (mg/ml)	Zone of inhibition (ZOI) (mm)	
	<i>E. coli</i>	<i>S. aureus</i>
0.1	09	08
0.3	11	10
0.5	13	15

The statistical analysis was tested by using F-Test. The F-Test is used to test the null hypothesis that the variances of two bacteria are equal. The F-Test of Two-Bacteria; *E. coli* and *S. aureus* for variances as displayed in table 2.

Table 2. F-Test of *E. coli* and *S. aureus* for variances.

F-Test Two-Bacteria for Variances	<i>E. coli</i>	<i>S. aureus</i>
Mean	11	11
Variance	4	13
Observations	3	3
df	2	2
F	0.307692	
P(F<=f) one-tail	0.235294	
F Critical one-tail	0.052632	

F-Test shows that variance of *E. coli* is lower than the variance of *S. aureus*. The F value was obtained as 0.307692, which is the ratio of *E. coli*/ *S. aureus*. If $F > F$ Critical one-tail then this reject the null hypothesis. In this case, $0.307 > 0.052$. Therefore, the null hypothesis is rejected. The variances of the two bacteria (*E. coli* and *S. aureus*) in this study are unequal.

Existence of efflux mechanism in some bacteria is reported as the cause behind antimicrobial resistance to nanoparticles [8]. ZnO NPs were efficient in killing *E.coli* isolate as compared to *S.aurues* at lower concentration. Whereas, at high concentration, efficient in killing *S.aurues* isolate.

4. Conclusions

One pot synthesis method is the simple and cost effective method to prepare of ZnO NPs. The XRD analysis shows that the average crystallite size and lattice strain found to be 38.78 nm and 0.0095, respectively. SEM image shows the uniform flake shape. There may be a particle-size broadening from the finite extent and particular morphology of the coherently diffracting domains within the grains. The antibacterial activity shows the average 11 mm deep for two isolates from zone of clearance. Maximum zones of inhibition (ZOI) observed at 0.5 mg/ml ranging from 13 to 15 mm for both the isolates. From statistical analysis it is clear that rejection of the null hypothesis, which shows unequal variances of the two bacteria (*E. coli* and *S. aureus*). ZnO NPs found to be efficient in killing *E. coli* isolate as compared to *S. aurues* at lower concentration while at high concentration, shows reverse effect.

Acknowledgements

Authors are very much thankful to the Director, Govt. Vidarbha Institute of Science and Humanities, Amravati, for providing necessary facilities. One of the author (S.A.Waghuley) is very much thankful to Honorable Vice Chancellor, Sant Gadge Baba Amravati University, Amravati for providing the analytical tools..

References

- [1]Min, Y., Caster, J. M., Eblan, M. J. and Wang, A. Z., Clinical translation of nanomedicine, *Chem. Rev.*, 2015, 115, 11147–11190.
- [2]Zhao, C. Y., Tan, S. X., Xiao, X. Y., Qiu, X. S., Pan, J. Q. and Tang, Z. X., Effects of dietary zinc oxide nanoparticles on growth performance and antioxidative status in broilers, *Biol Trace Elem Res.*, 2014, 160, 361-7.
- [3]Espitia, P. J. P., Soares, N. F. F., Coimbra, J. S. R., de Andrade, N. J., Cruz, R. S. and Medeiros, E. A. A., Zinc oxide nanoparticles: synthesis, antimicrobial activity and food packaging applications, *Food Bioprocess Technol.*, 2012, 5, 1447–1464.
- [4]Emami-Karvani, Z. and Chehrazi, P., Antibacterial activity of ZnO nanoparticle on grampositive and gram-negative bacteria, *African Journal of Microbiology Research*, 2011, 5, 1368-1373.

- [5]Mahamuni, P. P., Patil, P. M., Dhanavade, M., Badiger, M. V., Shadij, P. G., Lokhande, A. C. and Bohara, R. A., Synthesis and characterization of zinc oxide nanoparticles by using polyol chemistry for their antimicrobial and antibiofilm activity, *Biochem Biophys Rep*, 2019, 17, 71–80.
- [6]Siddiqi, K. S., Rahman, A., Tajuddin and Husen, A., Properties of zinc oxide nanoparticles and their activity against microbes, *Nanoscale Res. Lett.*, 2018, 13, 141-13.
- [7]Alekish, M., Ismail, Z. B., Albiss, B. and Nawasrah, S., In vitro antibacterial effects of zinc oxide nanoparticles on multiple drug-resistant strains of *Staphylococcus aureus* and *Escherichia coli*: An alternative approach for antibacterial therapy of mastitis in sheep, *Vet. World*, 2018, 11, 1428–1432.
- [8] Kamble, K. D. and Bhagat, S. R., Silver oxide nanoparticle synthesis from *Bacillus* species and its anti-bacterial action against clinical pathogens, *Am. J. Pharm. Health Res.*, 2017, 5, 1-11.
- [9]Sesha Sai Kumar, V. and Venkateswara Rao, K., X-ray peak broadening analysis and optical studies of ZnO nanoparticles derived by surfactant assisted combustion synthesis, *J. Nano Elec. Phy.*, 2013, 5, 02026-6.

Surabhi Jaju Rathi

Research Scholar

E-mail

surabhi.jaju00@gmail.com

ID:

Nanotechnology : A Revolution
in The Era of Renewable
Energy

**Abstract: -**

Nanotechnology, contrary to its name, has massively revolutionized industries around the world. This paper predominantly deals with data regarding the applications of nanotechnology in the modernization of several industries. A comprehensive research strategy is adopted to incorporate the latest data driven from major science platforms. Resultantly, a broad-spectrum overview is presented which comprises the diverse applications of nanotechnology in modern industries. This study reveals that nanotechnology is not limited to research labs or small-scale manufacturing units of nanomedicine, but instead has taken a major share in different industries. Companies around the world are now trying to make their innovations more efficient in terms of structuring, working, and designing outlook and productivity by taking advantage of nanotechnology. From small-scale manufacturing and processing units such as those in agriculture, food, and medicine industries to larger-scale production units such as those operating in industries of automobiles, civil engineering, and environmental management, nanotechnology has manifested the modernization of almost every industrial domain on a global scale. With pronounced cooperation among researchers, industrialists, scientists, technologists, environmentalists, and educationists, the more sustainable development of nano-based industries can be predicted in the future.

Keywords:

Nanotechnology, nano industries, agriculture, foods, medicine, textile, biotechnology, construction, environment, automobiles, cosmetics industry.

VI. INTRODUCTION

Nanotechnology has slowly yet deeply taken over different industries worldwide. This rapid pace of technological revolution can especially be seen in the developed world, where nano-scale markets have taken over rapidly in the past decade. Nanotechnology is not a new concept since it has now become a general-purpose technology. Four generations of nanomaterials have emerged on the surface and are used in interdisciplinary scientific fields; these are active and passive nano assemblies, general nano systems, and small-scale molecular nano systems .

This rapid development of nanoscience is proof that, soon, nano-scale manufacturing will be incorporated into almost every domain of science and technology. This review article will cover the recent advanced applications of nanotechnology in different industries, mainly agriculture, food, cosmetics, medicine, healthcare, automotive, oil and gas industries, chemical, and mechanical industries. Moreover, a brief glimpse of the drawbacks of nanotechnology will be highlighted for each industry to help the scientific community become aware of the ills and benefits of nanotechnology side by side. Nanotechnology is a process that combines the basic attributes of biological, physical, and chemical sciences. These processes occur at the minute scale of nanometers. Physically the size is reduced; chemically, new bonds and chemical properties are governed; and biological actions are produced at the nano scale, such as drug bonding and delivery at particular sites.

Nanotechnology provides a link between classical and quantum mechanics in a grey area called a mesoscopic system. This mesoscopic system is being used to manufacture nano assemblies of nature such as agricultural products, nanomedicine, and nanotools for treatment and diagnostic purposes in the medical industry. Diseases that were previously untreatable are now being curtailed via nano-based medications and diagnostic kits. This technology has greatly affected bulk industrial manufacturing and production as well. Instead of manufacturing materials by cutting down on massive amounts of material, nanotechnology uses the reverse engineering principle, which operates in nature. It allows the manufacturing of products at the nano scale, such as atoms, and then develops products to work at a deeper scale.

Worldwide, millions and billions of dollars and euros are being spent in nanotechnology to utilize the great potential of this new science, especially in the developed world in Europe, China, and America. However, developing nations are still lagging behind as they are not even able to meet the industrial progression of the previous decade. This lag is mainly because these countries are still fighting economically, and they need some

time to walk down the road of nanotechnology. However, it is pertinent to say that both the developed and developing world's scientific communities agree that nanotechnology will be the next step in technological generation. This will make further industrial upgrading and investment in the field of nanotechnology indispensable in the coming years.

With advances in science and technology, the scientific community adopts technologies and products that are relatively cheap, safe, and cleaner than previous technologies. Moreover, they are concerned about the financial standing of technologies, as natural resources in the world are shrinking excessively. Nanotechnology thus provides a gateway to this problem. This technology is clear, cleaner, and more affordable compared to previous mass bulking and heavy machinery.

Moreover, nanotechnology holds the potential to be implemented in every aspect of life. This will mainly include nanomaterial sciences, nanoelectronics, and nanomedicine, being inculcated in all dimensions of chemistry and the physical and biological world. Thus, it is not wrong to predict that nanotechnology will become a compulsory field of study for future generations. This review inculcates the basic applications of nanotechnology in vital industries worldwide and their implications for future industrial progress.

VII. APPLICATIONS OF NANOTECHNOLOGY IN MODERN ERA :

- 2.1 Nanotechnology and Renewable Energy Solar Industries
 - 2.2 Nanotechnology and Computer Industries
 - 2.3 Nanotechnology and Bioprocessing Industries
 - 2.4 Nanotechnology and Agriculture Industries
 - 2.5 Nanotechnology and Food Industries
 - 2.6 Nanotechnology, Poultry and Meat Industries
 - 2.7 Nanotechnology - Fruit and Vegetable Industries
 - 2.8 Nanotechnology and Winemaking Industries
 - 2.9 Nanotechnology and Packing Industries
 - 2.10 Nanotechnology and Construction Industry & Civil Engineering
 - 2.11 Nanotechnology and Textile Industries
 - 2.12 Nanotechnology and Transport & Automobile Industries
 - 2.13 Nanotechnology, Health Care and Medical Industries
 - 2.14 Nano Industry and Dentistry
 - 2.15 Nanotechnology and Cosmetics Industries
 - 2.16 Nanotechnology Industries and Environment
 - 2.17 Nanotechnology - Oil and Gas Industries
 - 2.18 Nanotechnology and Wood Industries
 - 2.19 Nanotechnology and Chemical Industries
- etc.

VIII. NANOTECHNOLOGY AND RENEWABLE ENERGY SOLAR INDUSTRIES :

Renewable energy sources are the solutions to many environmental problems in today's world. This makes the renewable energy industry a major part of the environmental industry. Subsequently, nanotechnology needs to be considered in the energy affairs of the world. Nanotechnologies are increasingly applied in solar, hydrogen, biomass, geothermal, and tidal wave energy production. Although, scientists are convinced that much more needs to be discovered before enhancing the benefits of coupled nanotechnology and renewable energy.

Nanotechnology has procured its application way down the road of renewable energy sources. Solar collectors have been specifically given much importance since their usage is encouraged throughout the world, and with events of intense solar radiation, the production and dependence of solar energy will be helpful for fulfilling future energy needs. Research data are available regarding the theoretical, numerical, and experimental approaches adopted for upgrading solar collectors with the employment of nanotechnologies.

These applications include the nanoengineering of flat solar plates, direct absorption plates, parabolic troughs, and wavy plates and heat pipes. In most of these instruments and solar collection devices, the use of nanofluids is becoming common and plays a crucial role in increasing the working efficiency of these devices.

A gap, however, exists concerning the usage of nanomaterials in the useful manufacturing design of solar panels and their associated possible efficiencies which could be brought to the solar panel industry. Moreover, work needs to be done regarding the cost-effectiveness and efficiency analyses of traditional and nanotechnology-based solar devices so that appropriate measures could be adopted for the future generation of nano solar collectors.

CLOSING REMARK :

Nanotechnology, within a short period, has taken over all disciplinary fields of science, whether it is physics, biology, or chemistry. Now, it is predicted to enormously impact manufacturing technology owing to the evidential and proven benefits of micro scaling. Every field of industry, such as computing, information technology, engineering, medicine, agriculture, and food, among others, is now originating an entire new field in association with nanotechnology. These industries are widely known as nano computer, nanoengineering, nano informatics, nanobiotechnology, nanomedicine, nano agriculture, and nanofood industries. The most brilliant discoveries are being made in nanomedicine, while the most cost-effective and vibrant technologies are being introduced in materials and mechanical sciences.

As every new technology is used in industries, linked social, ethical, environmental, and human safety issues arise to halt the pace of progress. These issues need to be addressed and analyzed along with improving nanotechnology so that this technology easily incorporates into different industries without creating social, moral, and ethical concerns. Wide-scale collaboration is needed among technologists, engineers, biologists, and industrialists for a prospective future associated with the wide-scale application of nanotechnology in diversified fields.

CONCLUSION :

Highly cost-effective and vibrant nanotechnologies are being introduced in materials and mechanical sciences. A comprehensive overview of such technologies has been covered in this study. This review will help researchers and professionals from different fields to delve deeper into the applications of nanotechnology in their particular areas of interest. Indeed, the applications of nanotechnology are immense, yet the risks attached to unlimited applications remain unclear and unpronounced. Thus, more work needs to be linked and carefully ascertained so that further solutions can be determined in the realm of nanotoxicology. Moreover, it is recommended that researchers, technicians, and industrialists should cooperate at the field and educational level to explore options and usefully exploit nanotechnology in field experiments. Additionally, more developments should be made and carefully assessed at the nano scale for a future world, so that we are aware of this massive technology. The magnificent applications of nanotechnology in the industrial world makes one think that soon, the offerings of nanotechnology will be incorporated into every possible industry.

However, there is a need to take precautionary measures to be aware of and educate ourselves about the environmental and pollution concerns alongside health-related harms to living things that may arise due to the deviant use of nanotechnology. This is important because the aspect of sustainability is being increasingly considered throughout the world. So, by coupling the aspect of sustainability with nanotechnology, a prosperous future of nanotechnology can be guaranteed.

REFERENCES

1. Anselmo A.C., Mitragotri S. Nanoparticles in the clinic: An update. *Bioeng. Transl. Med.* 2019;4:e10143. doi: 10.1002/btm2.10143. [[PMC free article](#)] [[PubMed](#)] [[CrossRef](#)] [[Google Scholar](#)]
2. Dubey S.K., Dey A., Singhvi G., Pandey M.M., Singh V., Kesharwani P. Emerging trends of nanotechnology in advanced cosmetics. *Colloids Surf. B Biointerfaces.* 2022;214:112440. doi: 10.1016/j.colsurfb.2022.112440. [[PubMed](#)] [[CrossRef](#)] [[Google Scholar](#)]
3. Hulla J., Sahu S., Hayes A. Nanotechnology: History and future. *Hum. Exp. Toxicol.* 2015;34:1318–1321. doi: 10.1177/0960327115603588. [[PubMed](#)] [[CrossRef](#)] [[Google Scholar](#)]

4. Jaiswal L., Shankar S., Rhim J.-W. Applications of nanotechnology in food microbiology. *Front. Microbiol.* 2019;8:43–60. [[Google Scholar](#)]
5. Khang D., Carpenter J., Chun Y.W., Pareta R., Webster T.J. Nanotechnology for regenerative medicine. *Biomed. Microdevices.* 2008;12:575–587. doi: 10.1007/s10544-008-9264-6. [[PubMed](#)] [[CrossRef](#)] [[Google Scholar](#)]
6. Nanophysics and Nanotechnology: An Introduction to Modern Concepts in Nanoscience. Edward L. Wolf. Copyright © 2004 WILEY-VCH Verlag GmbH.
7. Nanotechnology: principles and practices by Sulabh K Kulkarni.
8. Priyadarsini S., Mukherjee S., Mishra M. Nanotechnology in dentistry-A review. *Int. J. Biol. Med. Res.* 2012;3:1550–1553. [[Google Scholar](#)]
9. Singh A., Dubey S., Dubey H.K. Nanotechnology: The future engineering. *Nanotechnology.* 2019;6:230–233. [[Google Scholar](#)]

----- Thank You -----

© 2024. This work is published under
<https://creativecommons.org/licenses/by/4.0/legalcode>(the“License”).
Notwithstanding the ProQuest Terms and Conditions, you may use this
content in accordance with the terms of the License.

¹Pritesh J.Jadhao
²Kamlesh R Banarse
³S.P. Yawale
⁴S.S. Yawale

**Electrical And Thermal
 Properties of Polyaniline –
 Cadmium Sulphide
 Nanocomposite with Photovoltaic
 Application**



Abstract: - Nanocomposites of conducting polyaniline with CdS nanoparticles have been synthesized by *insitu* polymerization method. A series of nanocomposites have been synthesized by varying the weight percentage of CdS. DC conductivity of the pure PANI polymer and doped with different wt. % of CdS was measured in the temperature range 308 to 328K by using Ohms law. Polyaniline doped with the 5 wt. % CdS shows the maximum value of dc conductivity. Impedance spectroscopy (AC Conductivity) is widely used for investigating the electrical behavior of material over the wide range of frequency and temperature. This helps to separate the real and imaginary components of electrical parameters. The impedance of polyaniline doped with different wt. % of CdS samples was measured at various temperatures over a wide range of frequencies from 0.1-200 KHz. Thermal properties of pure PANI and PANI- CdS nanocomposite were evaluated by TG/DTA in the temperature range 0 °C to 500 °C. The PANI-CdS composite based thin film solar cell device structure consists of glass/ITO/PANI-CdS/Ag. The I-V characteristics is studied to calculate efficiency of the solar cell.

Keywords: Polyaniline, CdS, TG/DTA, DC, Impedance Spectroscopy, Photovoltaic Cell

I. INTRODUCTION

Conducting polymers combine the electronic and optical properties of semiconductors and metals with the attractive mechanical properties and processing advantages of polymers. CPs possesses many advantageous properties in chemical, electrical, physical and optical aspects, compared to normal polymers.

¹ PGT Department of Physics, Gondwana University, Gadchiroli-442605

^{2,3} Department of Physics, Government Vidarbha Institute of Science & Humanities, Amravati, 444604

⁴ Director, Pre IAS-Training Centre, Amravati, 444604

Email: jadhao.pritesh@unigug.ac.in, pritesh.trivendrum@gmail.com, 9403041634

Copyright © JES 2024 on-line: journal.esrgroups.org

These properties cover high conductance, luminescence, electrochromic and high thermal stability. Polyaniline (PANI) is probably the most important industrial CP today. This is due to its facile synthesis and processing, environmental stability and low cost. In addition, PANI has two attractive properties: -intrinsic redox state and reversible doping/de-doping of acid/base. The importance of conducting polymer was celebrated in the form of Nobel Prize in chemistry in 2001 to MacDiarmid, Heeger and Shirakawa [1]. The polymerization mechanism [2], processability [3], and transport mechanism [4] are the main points of academic and scientific attraction. Technological applications include biosensors [5], gas sensors [6], electrochromic [7,8], electromagnetic shielding [9], light emitting devices [10] and photovoltaic applications [11]. Polyaniline is an extensively studied polymer because of its high electrical conductivity, oxidative properties, environmental stability and ease of preparation etc. [12,13]. One of the surprising quotation given by Prof. A.G. MacDiarmid that "there are as many different types of PANI as there are people who synthesize it" [14]. Therefore, the way of synthesis decides the conductivity, band gap, chemical structure, polymerization mechanism and case of attachment and detachment of different functional groups.

Toward the start of nineteenth century, polymer was emerging as the best media for protection. Their wide application as a protective material is the reason they are considered and created in any case. Indeed, these materials are usually utilized for encompassing copper wires and assembling the external structures of electrical machines that keep people from coming in coordinate contact with power. Roughly in 1950 it was polymer can be changed into a conducting structure when electrons are expelled from the spine bringing about cations or added to the spine bringing about anions. Anions and cations go about as charge bearers, bouncing starting with one site then onto the next affected by an electrical field, therefore expanding conductivity.

Among conducting polymers, polyaniline (PANI) is presumably the most generally examined because of its few interesting properties [15,16]. It is simplicity of arrangement, light weight, ease, better electronic, optical properties, exceptionally stable in air and dissolvable in different solvents, and great processability [17-19]. Then again it very well may be utilized in numerous applications, for example, electromagnetic obstruction (EMI) protecting, electro-impetuses, battery-powered battery, light-producing diodes (LEDs), solar cell, chemical sensor, biosensor, erosion gadgets and microwave ingestion [20,21].

Polyaniline-CdS nanocomposite has been as of now utilized in photovoltaic application yet arrangement of ionic side-effects (in the response amid the synthesis that impacts the electrical properties of coming about material), demonstrated a few restrictions in planning of nanocomposites. There are a few reports depicting nanocomposites of polyaniline with semiconducting particles, for example, TiO₂, PbS and CdS [22].

Various metal and metal oxide particles have been epitomized into the conductive polymer to shape nanocomposites (NCs). The NCs show blend of properties like conductivity, electrochemical, reactant and optical properties. The NCs are utilized in applications like electrochromic gadgets, light-

emanating diodes, electromagnetic impedance protecting, optional batteries, electrostatic release frameworks, chemical and biochemical sensors [23]. The photovoltaic marvel has been perceived since 1839, when French physicist Edmond Becquerel could create power by lighting up a metal electrode in a feeble electrolyte arrangement. The photovoltaic impact in solids was first concentrated in 1876 by Adam and Day, who made a sunlight-based cell from selenium that had a proficiency of 1– 2%. The effectiveness of original silicon cells was around 6%, which is extensive lower than that of contemporary sun-based cells (around 14– 20%). Among such polymers, PANI has been examined broadly and is finding expanding utilizes in different fields of innovation, for example, in hostile to consumption coatings, gas sensors, actuators and light emanating shows (LEDs) [24-27]. PANI is known as a semiconducting polymer, with high tunable bandgap, high chemical soundness, processability with a potential application in different fields.

II. Materials and methods

2.1 Materials used

The Aniline hydrochloride (AR grade) and Ammonium Persulphate (AR grade), all received from S.D. Fine Chemicals Mumbai, (India), Acetone, Cadmium Nitrate Tetrahydrate (AR grade) all are obtained from Loba Chem. Mumbai, (India). Ammonium Sulphide (AR grade), Double distilled (DD) water. All the chemicals were used as received.

2.2 Synthesis of pure PANI

Polyaniline (PANI) nanoparticles were prepared by chemical oxidative polymerization method [28]. The synthesis was based on mixing aqueous solutions of aniline hydrochloride 0.2M and ammonium persulfate (APS) 0.25M at room temperature, followed by the separation of PANI hydrochloride precipitate by filtration and drying.

2.3 Synthesis of CdS

CdS nanoparticles were grown by simple chemical precipitation reactions in aqueous medium at room temperature [29]. 100 ml aqueous solution of $\text{Cd}(\text{NO}_3)_2$ (0.085M) was taken in One beaker and 100 ml aqueous solution of $(\text{NH}_4)_2\text{S}$ (0.1M) was in another beaker. Aqueous Solution of $\text{Cd}(\text{NO}_3)_2$ (0.085M) was added drop wise to 100 ml aqueous solution of $(\text{NH}_4)_2\text{S}$ (0.1M) with vigorous stirring. Stirring continued for 5 h. The dark yellow precipitate of CdS nanoparticles was obtained.

2.4 Synthesis of PANI-CdS nanocomposites

Synthesis steps of PANI/CdS nanocomposite are similar to the synthesis method of PANI. Different amount of CdS were dispersed into the APS solution and stirred for 1 h prior to the addition of aniline. Aniline (0.4 mol) stirred with 0.4M H_2SO_4 in 100 ml of distilled water were added drop-wised using burette into the APS-CdS solution and stirred vigorously to form homogeneous dispersion. For convenience, PANI

Composites were prepared with different weight percentages of CdS [30]. The same synthesis conditions were maintained for all composites as that of pure PANI.

III. Characterization

3.1 Thermogravimetric (TG) / Differential Thermal Analysis (DTA):

Thermogravimetric Analysis or thermal gravimetric analysis is a sort of testing performed on tests that decides changes in weight in connection to a temperature program in a controlled atmosphere. Such analysis relies on a high degree of precision in three measurements: weight, temperature, and temperature change. TGA is commonly employed in research to determine characteristics of materials, degradation temperatures, absorbed moisture content of materials, the level of inorganic and organic components in materials, decomposition points of explosives and solvent residues. Thermal Gravimetry Analysis / Differential Scanning Calorimetry is useful for the determination of changes in weight in relation to change in temperature [31]. TGA/DSC study for PANI-CdS Nanocomposites was done at Govt. Vidarbha Institute of Science and Humanities Amravati Thermal properties of pure Polyaniline polymer and PANI doped with Cadmium Sulphide (CdS) were evaluated by TGA/DTA in the temperature range 0 °C to 500 °C at a heating rate of 10 °C /min.

3.2 DC Conductivity:

The DC conductivity of the samples was measured by two probe methods [32], in which resistance of the sample was noted. Samples under investigation were sandwiched in between two silver electrodes for good ohmic contact. Sample was placed in sample holder. A constant dc voltage was applied to the sample and corresponding current was noted. Resistance of the sample is calculated by Ohm's law. DC conductivity is carried out at Department of Physics, Government Vidarbha Institute of Science and Humanities, Amravati.

3.3 Impedance Spectroscopy :

An impedance measurement provides more detailed information on the electrical properties of a system [33]. Impedance measurements are performed by applying a small sinusoidal potential or current to an electrochemical cell and measuring its current or potential response over a wide range of frequencies. The optimized samples were selected for AC conductivity measurement. AC conductivity of the samples was recorded on LCR meter (Wayne Kerr, UK) having range of frequencies from 0.1-200 KHz at different temperature.

IV. Results and discussion

4.1 Thermogravimetric (TG) / Differential Thermal Analysis (DTA):

Thermal properties of pure Polyaniline polymer and PANI doped with Cadmium Sulphide (CdS) were evaluated by TGA/DTA in the temperature range 0 °C to 500°C at a heating rate of 10°C/min (Fig.1).

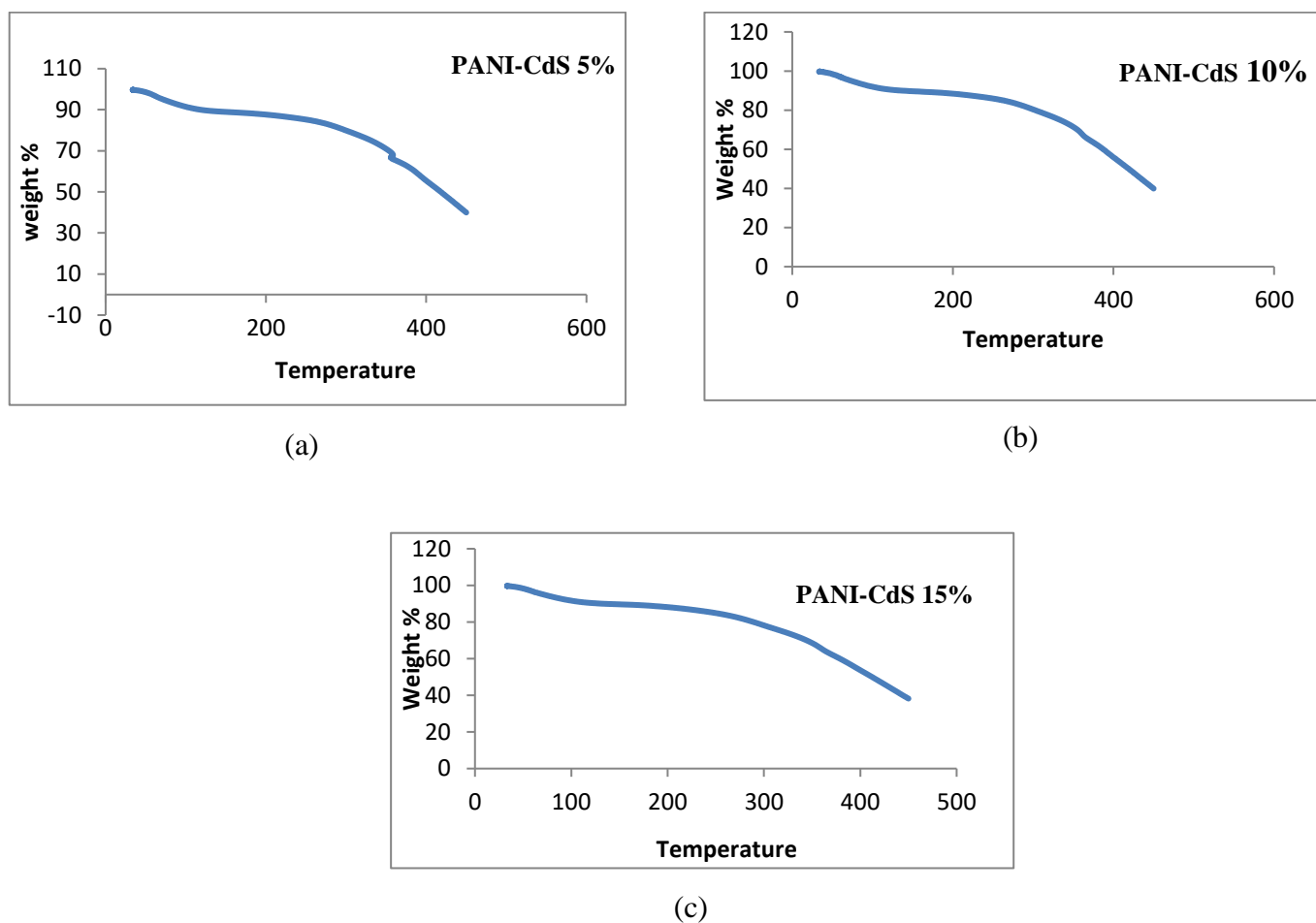


Fig.1 TGA thermographs of PANI doped with wt % of Cadmium Sulphide CdS

TGA thermograph of PANI-CdS nanocomposites shows two step degradation. In the first step the initial weight loss was observed between 35 to 200°C and was attributed to the loss of moisture and low molecular weight compounds in polymer composite. In the second step, a major weight loss was observed from 200 to 450°C and was due to the degradation of polymer composite. Figure 1 shows the two-step degradation of PANI-CdS nanocomposite having 60-65% of its weight loss when it was heated to 500°C. It indicates that 60-65 % of the sample consists of polymers and softeners. The residual about 35-40 % was considered to account for metallic compounds, added as sulphide and dopant.

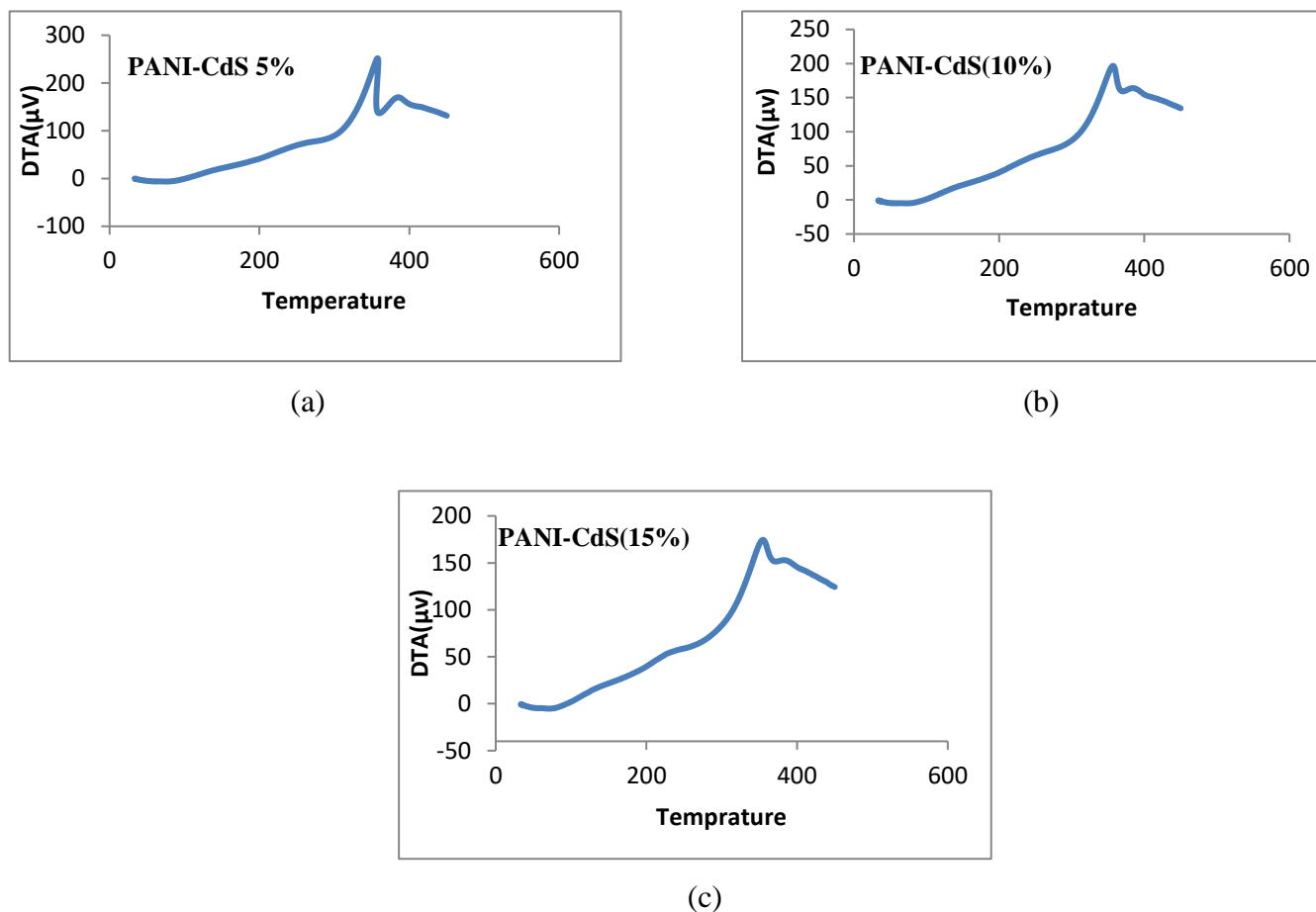


Fig.2 DTA Curve of pure PANI and PANI doped with weight % of Cadmium Sulphide CdS

Figure 2 shows DTA curves of pure Polyaniline and PANI doped with CdS. In DTA curve, the endothermic peak appearing at $\sim 70-80$ °C is probably due to the melting point of PANI that identified as melting of crystalline phase of polymer. The sample PANI-CdS nanocomposite shows the strong and broad exothermic peak in the range 340 to 400 °C accompanied by rapid weight loss can be ascribed to the decomposition of PANI-CdS nanocomposite. This study indicated that polyaniline is thermally stable up to 343 °C.

4.2 DC Conductivity:

DC conductivity of the pure PANI polymer and doped with different wt. % of CdS was measured in the temperature range 308 to 328K by using Ohms law. The resistance of the samples was measured. It is observed that the value of resistance depends on temperature as well as on composition.

The variation of dc conductivity with different wt. % of CdS is shown in fig 3 As compared to pure Polyaniline the conductivity increases with CdS wt. % . Polyaniline doped with the 5 wt. % CdS shows the maximum value of dc conductivity.

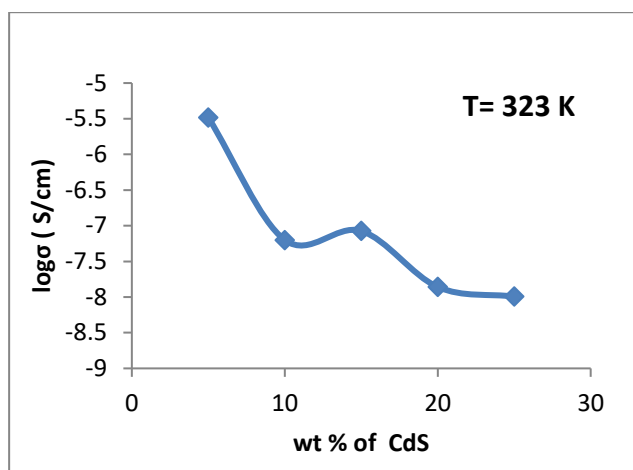


Fig.3 Variation dc conductivity as a function of wt. % of CdS

The variation of dc conductivity as a function of inverse temperature for Polyaniline polymer doped with the different wt. % CdS was estimated. The nature of plots is shown in Figure 4, over the temperature range 308 to 328 K. It can be observed that the dc conductivity for all the compositions of PANI doped with the different wt. % CdS increases with increasing temperature for the entire range.

It tends to be seen that the Arrhenius plots for every one of the examples show a comparative behavior. The dc conductivity esteems increment with the different wt. % CdS at various temperatures.

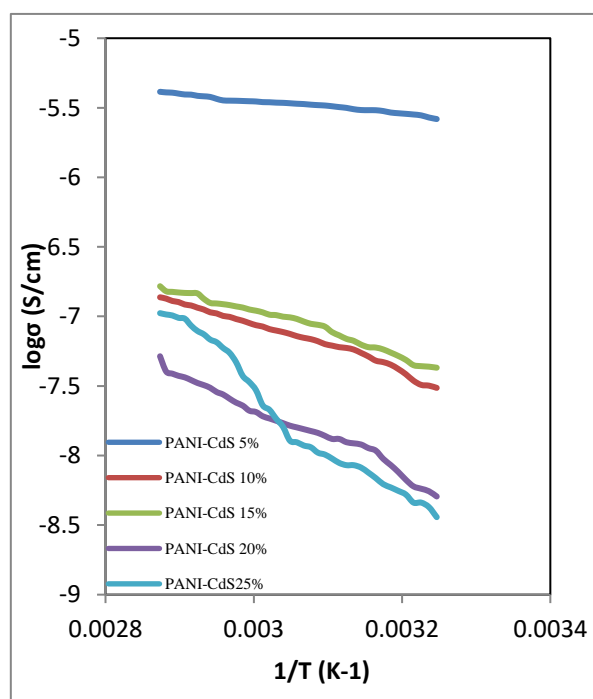


Fig 4: Arrhenius plots of the dc conductivity of PANI-CdS composite for different wt. % of CdS

As the temperature builds, versatility of the ions expands, which results the rise in conductivity. Uppermost curves belong to 5 wt % of CdS for which conductivity is maximum. The conductivity versus temperature curves of all synthesized samples shows the increase in conductivity. The rate of increase of

conductivity is linear for the composite, which may be due to the segmental motion of the ions in the polymer [34].

The natures of the curves are consistent with Arrhenius type charge conduction in polymer composites and the conductivity relationship follows the equation,

$$\sigma = \sigma_0 \exp(-E_a/kT) \quad (1)$$

Where E_a is the activation energy, σ_0 , is the pre-exponential factor and k is the Boltzmann's constant. The slope of each straight line gives the activation energy which lies between 0.039 and 0.36 eV. From figure 5, DC parameters are calculated and noted in table 5.1.

Sr.No.	CdS wt %	Activation Energy E_a (eV)	Conductivity σ (S/cm)
1	5	0.039	3.2833×10^{-6}
2	10	0.146	6.3232×10^{-8}
3	15	0.135	8.4481×10^{-8}
4	20	0.201	1.3852×10^{-8}
5	25	0.364	1.0162×10^{-8}

Table 1: DC parameter for the PANI-CdS Nanocomposite

Plot of activation energy with different wt. % of CdS is illustrated in figure 5.8, which shows that activation energy E_a is found to be maximum for the 25 wt % of CdS. The value of activation energy increases with wt. % CdS.

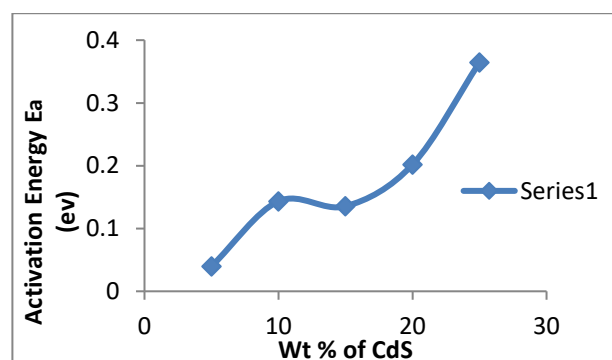


Fig. 5 Variation Activation Energy as a function of wt. % of CdS

4.3 Impedance Spectroscopy:

Impedance spectroscopy (AC Conductivity) is widely used for investigating the electrical behaviour of material over the wide range of frequency and temperature. This helps to separate the real and imaginary component of electrical parameter. Hence provides better understanding of material characteristics.

The variation of imaginary part of impedance with real part of impedance as a function of frequency gives Cole-Cole plots. The impedance of polyaniline doped with different wt. % of CdS samples was measured at various temperatures over a wide range of frequencies from 0.1-200 KHz.

The entire cole-cole plot shows the same trends in the temperature range 308-328K. Many researchers [35-38] reported a similar conductivity isotherm. The impedance spectrum of PANI-CdS nanocomposite with different wt. % of CdS is found to consist of only one arc (fig. 6.) which may be taken to mean that the conduction processes have identical time constants [39]. Also, it may be argued that as the temperature increases the arc of semicircle reduces, indicating the increase in conductivity.

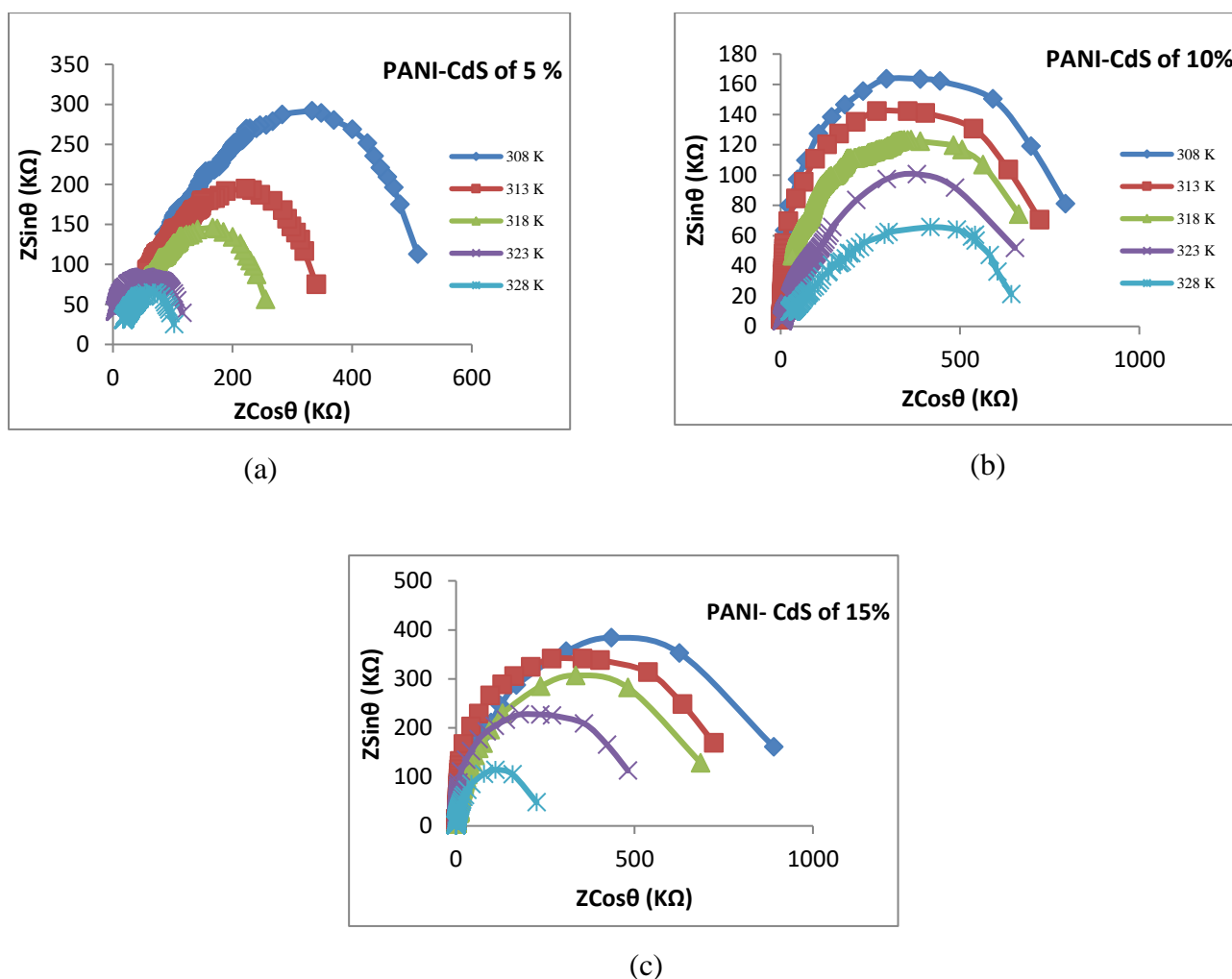


Fig.6 Cole-Cole plots for Polyaniline (PANI) doped with different wt. % of CdS

CdS wt. %	303 K		313 K		318 K		323 K		328 K	
	R_b ($K\Omega$)	C_b (pF)	R_b ($K\Omega$)	C_b (pF)	R_b ($K\Omega$)	C_b (pF)	R_b ($K\Omega$)	C_b (pF)	R_b ($K\Omega$)	C_b (pF)
5	509	121	339	195	254	286	115	693	101	866
10	794	142	722	183	663	236	653	300	642	402

15	890	176	722	271	685	377	481	794	225	-
20	829	121	748	150	618	253	487	402	374	690
25	309	318	276	408	254	521	221	707	154	-

Table 2: Bulk resistance (R_b) and Bulk Capacitance (C_b) of Polyaniline doped with Cadmium Sulphide (CdS) at different temperature

The basic features of the spectra seem to be qualitatively like those obtained by Johnson et al. [40] for polythiophene films and Komura et al. [36] for polypyrrole polystyrene sulfonate composite films in a similar configuration. The arcs are found to be depressing for all films for different temperatures which indicate the distribution of relaxation times [41].

The Bulk resistance (R_b) and bulk capacitance (C_b) can be calculated from the impedance plots and are tabulated in table 1. It is well known from the theory of complex impedance plane analysis that the value of R_b is obtained from the real axis intercept. The capacitance value is obtained from the frequency values corresponding to the maximum of the semicircle in the Impedance plot, using the relation $\omega R_b C_b = 1$ [42].

From table 2 it is observed that the bulk resistance of the sample decreases with the increase in temperature.

The Cole–Cole plots (Fig. 6) show that well-defined semicircles were obtained. The single semicircular plot for a given temperature suggests that the device can be considered as a parallel combination of bulk resistor (R_b)–bulk capacitor (C_b) network only as the plot starts from origin. The impedance plots suggest Debye type behaviour and single relaxation mechanism.

V. Application as a Photovoltaic Cell

The PANI-CdS composite based thin film solar cell device structure consists of glass/ITO/ PANI-CdS/Ag is shown in figure 6. The I-V characteristic is studied to investigate the solar cell parameters.

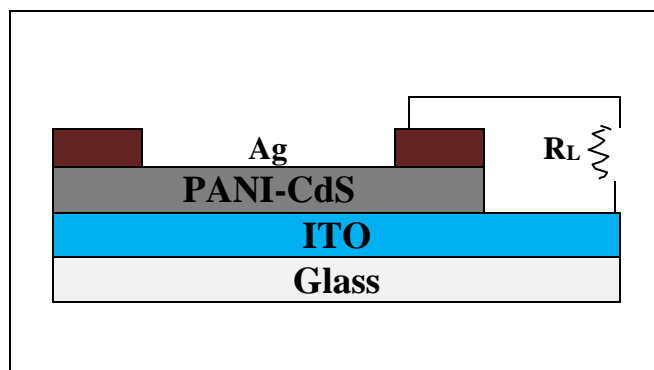


Fig. 7: Schematic diagram of solar cell device with PANI-CdS nanocomposite

The parameters used to calculate the efficiency of the solar cell are the maximum power (P_{max}), energy conversion efficiency (η) and the fill factor (FF). These points are illustrated in Figure 6, which shows a typical forward bias I-V curve of an illuminated PV cell. The maximum power (P_{max}) is the product of the maximum cell current (I_{max}) and the voltage (V_{max}) where the power output of the cell is maximum. This point is situated at the "knee" of the bend. The fill factor (FF) determines how much the I-V characteristics of an actual PV cell differ from those of an ideal cell. I-V response of fabricated PV Cell was done using incandescent light bulb (60W) radiating light power of 3.49 mW/m^2 , measured using Lux meter. The bulb and Photovoltaic cell separation was 30 cm. The fill factor is defined as [43].

$$FF = \frac{I_{max} \times V_{max}}{I_{sc} \times V_{oc}}$$

Where,

I_{max} is the current at the maximum power output (A), V_{max} is the voltage at the maximum power output (V), I_{sc} is the short-circuit current (A) and V_{oc} is the open-circuit voltage (V).

The fill factor is the ratio of the maximum power ($P_{max} = I_{max} \cdot V_{max}$) to the result of the short circuit current (I_{sc}) and the open circuit voltage (V_{oc}). The ideal solar cell has a $FF=1$ but losses from series and shunt resistance decrease the efficiency. Another critical parameter is the transformation efficiency (η), the most extreme power yield to the power contribution to the cell.

$$\eta = \frac{P_{max} \times FF}{P_{in}} \times 100$$

Where

P_{max} is the maximum power output (W) and P_{in} is the power input to the cell defined as the total radiant energy incident on the surface of the cell (W).

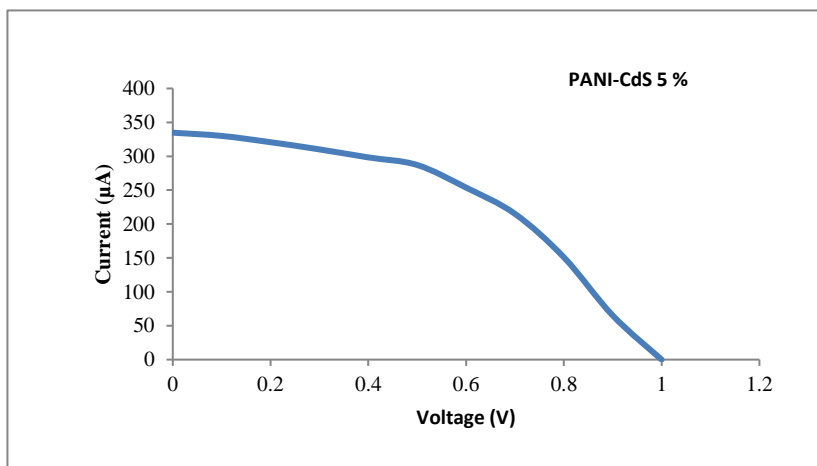


Fig. 8: IV characteristics of PANI-CdS nanocomposite

The maximum value of short circuit current (I_{sc}) was found to be 334.8 μA for optimized PANI-CdS nanocomposite. Similarly, the maximum value of open circuit voltage V_{oc} is 1000 mV. The value of Maximum current and maximum voltage is 287.1 μA and 500 mV respectively. The power conversion efficiency (η) of PANI-CdS composite is 4.1 %. The less efficiency of the PV cell is due to the poor surface morphology of the PANI-CdS composite which absorbs less light limits the electron hopping transport.

VI. CONCLUSION

In this work as compared to pure Polyaniline the conductivity increases with CdS wt. %. Polyaniline doped with the 5 wt. % CdS shows the maximum value of dc conductivity. TGA shows the two-step degradation of PANI-CdS nanocomposite having 60-65% of its weight loss when it was heated to 500^oC. In DTA curve, the endothermic peak appearing at ~ 70-80 ^oC is probably due to the melting point of PANI that identified as melting of crystalline phase of polymer. PV Cell of PANI-CdS nanocomposite has less efficiency and fill factor value. The efficiency of PANI-CdS is found to be 4.1 % under light illumination 3.49 mW/m². The less efficiency caused due to poor absorber morphology which limits the electron hopping transport. The low value of FF is associated with the high value of series and shunt resistances. Such nanocomposite photovoltaic system can be further improved for higher efficiency and more stability of PV cell.

REFERENCES

- [1] A. G. MacDiarmid, Alan J. Heeger, Hideki Shirakawa Rev. Mod. Phys. **73**, No. 3, (2001).
- [2] A. Malinauskas, Polymer **42**, 3957-3972, (2001).
- [3] A. Battacharya, De A. J Macromol Sci. Rev Macromol Chem Phys. **C39**, 17-56, (1999).
- [4] J. Mort, G. Pfister and S. Grammatica., Solid State Commun. **18**, 693, (1976).
- [5] R. Wilson, A.P.F. Turner, Biosensors Bioelectronics, **7**, 16, (1992).
- [6] H. Bai, G. Shi, Sensor **7**, 267, (2007).
- [7] M. H. Ram, N. S. Sunaresan and B. D. Malhotra. J. Mat. Sci. Lett. **13**, 1490, (1994).
- [8] C.K. Chiang, C.R. Fincher, Y.W. Park, A.J. Heeger, H. Shirakawa, E.J. Louis, S.C. Gau and A.G. MacDiarmid, Phys. Rev. Letters **39**, 1098, (1977).
- [9] D.C. Trivedi and S.K. Dhawan., Synth. Met. (1993), **59**, 267.
- [10] N.C. Greeham., S. C. Moratti, D.D.C Bradley, R. H. Friend and A. B. Holmes., Nature (1993) **365**, 628.
- [11] Nalwa, H. S., Ed., Handbook of Organic Conductive Mate. and Poly. (Wiley, New York) (1997).
- [12] A. J. Epstein and A. G. MacDiarmid (1995), **69(1-3)**, 179-182.
- [13] A.F. Diaz, K. K. Kanazava, G. P. Gardini., J. Chem. Soc. chem. Commun. (1979), **24**, 635.
- [14] Irina Sapurina and Jaroslav Stejskal, Polym Int (2008), **57**: 1295–1325.

- [15] L. Li, J. Jiang, F. Xu, *Materials Letters* **61** (2007) 1091–1096.
- [16] R. Mathur, D. R. Sharma, S. R. Vadera, N. Kumar, *Acta mater.* **49** (2001) 181–187.
- [17] L. Li, H. Liu, Y. Wang, J. Jiang, F. Xu, *Colloid and Interface Science* **321** (2008) 265–271.
- [18] A.G. MacDiarmid, A.J. Epstein, *Synthetic Metals* **69** (1995) 86-92.
- [19] J.C. Apesteguy, S.E. Jacobo, *Physica B* **354** (2004) 224–227.
- [20] A. B. Moghaddam, T. Nazari, *Int. J. Electrochem. Sci.*, **3**(2008)768-776.
- [21] A. S. Sarac*, M. Ates and B. Kilic, *Int. J. Electrochem. Sci.*, **3**(2008)777-786.
- [22] D Y Godovsky , A E Varfolomeev , D F Zaretsky , R L N Chandrakanthi, A Kundig, C Weder, W Caseri, *Material Chemistry*, **vol.11, no. 10**, pp. 2465-2469, 2001 .
- [23] S. Hsu, H. Tseng, Y. Lin, *Biomaterials*, **31** (2010), 6796.
- [24] T. Wang and Y.J. Tan, *Corrosion Science* **48**, 2274 (2006).
- [25] Y. Seung-Beom, Y. Eun-Hyea K. Kwang-Bum, *Power Sources* **196 (24)**, 10791 (2011).
- [26] J.E. Albuquerque, L.H.C. Mattoso, D.T. Balogh, R.M. Faria, J. G. Masters, A.G. MacDiarmid, *ynthetic Metals* 113, **19** (2000).
- [27] E.T. Kang, K.G. Neoh, K.L. Tan, *Progress in Polymer Science* **23**, 277 (1998).
- [28] J. Stejskal, R.G. Gilbert, *Pure Appl. Chem.*, **No. 5**, 74 (2002)857.
- [29] Favero, P. P.; Souza-Parise, M. d.; Fernandez, J. L. R.; Miotto, R.; Ferraz, A. C. *Brazilian Journal of Physics* **36**, (2006),1032-1034.
- [30] Shubhangi D. Bompilwara, Subhash B. Kondawarb, Vilas A. Tabhanec, Snehal R. Kargirward, *Pelagia Research Library*, **1 (1)**, (2010),166-173.
- [31] M.A.Golub and R.J. Gargiulo, *Polymeric Lett.*, **10**,(1972), pp.41.
- [32] Yun Ze Long, Jean Luc Duval, *Nanoscale Res Lett.*, **5**, (2010), pp. 237–242.
- [33] J. E. Bauerle, *J. Phys. Chem. Solids*, **30**, (1969), 2657-2670.
- [34] M.H. Cohen, D. Turnbull, *J. Chem. Phys.*, **31** (1959), pp.1164.
- [35] Abdel Salam Hamdy, *Int. J. Electrochem. Sci*, (2006), pp.171-180.
- [36] T. Komura, S. Goisihara, T. Yamaguti, K. Takahashi, *J. Electroanal. Chem.*, **456** (1998). pp.121.
- [37] J. Ross Macdonald, *Annals of Biomedical Engineering*, **20** (1992), pp.289-305.
- [38] R Padma Suvarna, *Bull. Mater. Sci.*, **25(7)**, (2002), pp.647-651.
- [39] J. Hwang, *Solid State Dcs*, **98**(1997), pp.93-104.
- [40] B.W. Johnson, D.C. Read, *J. Electroanal. Chem.*, **364** (1994), pp.103.
- [41] J. Ross Macdonald, *J. Electroanal. Chem*, **223** (1987), pp.25-50.
- [42] A. R. Kulkarni, H S Maiti, *Solid State Ionics*, **14** (1984), pp. 309-317.
- [43] Ramakrishnan Rajaraman, Sudha Janardhanan D & Viswan L R. *RSC Advances*, **2**, (2012), 6228-6236.

¹ S. G. Ibrahim

² D. S. Dhote

A Review Study on Indium Tin Oxide Thin Films: Synthesis and Characterizations



Abstract: - Nanotechnology is one of the reasons in the development of today's world. The things are becoming smaller, thinner and lighter, due to the inventions of new materials and the depositions methods. Researchers are developing new devices which are suitable to work for different applications. One of such material is transparent conducting films which are extensively utilized for numerous applications. The present research reviews, thin films of indium tin oxide deposited by using different deposition methods, deposition substrates and their characterizations.

Keywords: Nanostructured; ITO; Electrical Resistivity; Optical Transparency.

¹ *Nanostructured Thin Film Materials Laboratory, Department of Engineering Physics,
Prof. Ram Meghe College of Engineering & Management, Badnera-444701, Maharashtra, India
² Department of Electronics, Brijlal Biyani Science College, Amravati-444601, Maharashtra, India
Copyright © JES 2024 on-line: journal.esrgroups.org

I. INTRODUCTION

Transparent conductive oxides (TCOs) are unique semiconductors with two fundamental properties: crystal clear materials for light transmission and electricity conducting ones for sensitiveness to light for optical circuits and uses, and for electrical usage respectively. As for TCO, indium tin oxide, namely ITO, is a n-type semiconductor with the big band gap of more than 3.4 eV. ITO has features such as: electrical conductivity and high transparency in visible light, high UV absorption, high infrared reflection, and good surface adhesion to other materials. These qualities depend on the nature of the substrate, the method of deposition, the conditions under which deposition is performed and the heat treatment of the film.

ITO is in wide use in various applications of electronics and optoelectronics like, flat panel display, LED's, heat reflecting mirrors, AR coating, gas sensors, solar cells. In addition, the ITO is also applied as the transparent conductive layer for photocells because the variations in the refractive indices lead to generation of optical losses and ensures that the light transmits through the absorber layer thus enhancing the conversion efficiency.

Various methods were used in the deposition of ITO thin films, these included; Electron Beam evaporation, Sputtering, Pulsed laser deposition, Thermal vacuum evaporation method, Ion beam assisted deposition technique, Sol – gel, Spin-coating, Chemical vapor deposition, and Spray Pyrolysis. However, the techniques that rely on the conditions of vacuum, like RF-DC sputtering are well capable of depositing high quality thin films because of the many benefits these have over the others: the deposition can be carried out at low temperatures, the process is highly reproducible and most importantly, it has relatively high growth rate. The type of thin films and coatings is characterized not only by composition but also by the method of deposition and the conditions of their formation.

This present research reviews, indium tin oxide thin films prepared by various deposition techniques on different deposition substrates, with different deposition temperature and their characterization (Table 1).

Table1: Literature survey for indium tin oxide thin films prepared by various deposition techniques.

Sr. No.	Method for deposition	Temp.	Electrical Resistivity	Optical Transparency	Material used	Substrate	Ref. No.
1	Electron beam evaporation technique	50°C to 350°C	$3 \times 10^{-6} \Omega \text{ m}$	92%	In ₂ O ₃ and SnO ₂	Glass substrates	1
2	Pulsed laser deposition	300°C	$4 \times 10^{-4} \Omega \text{ cm}$	85%	In ₂ O ₃ and SnO ₂	Glass substrates	2
3	Pulsed laser deposition	30°C	$3.3 \times 10^{-4} \Omega \text{ cm}$	Above 90%	ITO pellet containing 5 wt.% SnO ₂	Glass substrates	3
4	Pulsed DC magnetron sputtering	200°C	$2.5 \times 10^{-4} \Omega \text{ cm}$	87%	In ₂ O ₃ and SnO ₂	Glass substrates	4
5	Thermal vacuum evaporation method	350°C	--	88%	In ₂ O ₃ and SnO ₂	Glass substrates	5
6	Ion beam assisted deposition technique	30°C	--	92%	ITO powder pellet	Glass substrates	6
7	Rf magnetron sputtering	150°C	$2.05 \times 10^{-3} \Omega \text{ cm}$	--	In ₂ O ₃ and SnO ₂	Glass substrates	7
8	Sol-gel process	Above 400°C	$1.5 \times 10^{-3} \Omega \text{ cm}$	Above 80%	InCl ₃ and SnCl ₄	Quartz glass substrates	8

9	Spin coating	300°C	4.59×10^{-3} Ω cm	90%	In ₂ O ₃ and SnO ₂	Glass substrates	9
10	Sol-gel spin coating	Post Annealed 500°C	4.14×10^{-3} Ω cm	85.12%	Metal indium and SnCl ₄ ·5H ₂ O	Glass substrates	10
11	Sol-gel spin coating	Post Annealed 450°C - 550°C	--	80%	indium (III) nitrate pentahydrate, tin (IV) chloride	Glass substrates	11
12	Spin-coating	Annealed 550°C	Sheet Resistance 4 k Ω /sq.	91.6%	InCl ₃ and SnCl ₄	Glass substrates	12
13	Spin coating	Post Annealed 120°C - 450°C	8.7×10^{-3} Ω cm	92.66%	ITO Nano powder water dispersion and Sol-gel ITO solution	Glass substrates	13
14	Dip-coating method	Annealed 550°C	Sheet Resistance 17.5k Ω /sq.	90.7%	InCl ₃ , SnCl ₄ and NH ₃ Solutions	Glass substrates	14
15	DC magnetron sputtering	300°C	281×10^{-6} Ω cm	97.1%	In ₂ O ₃ and SnO ₂	Glass substrates	15
16	DC magnetron sputtering	350°C	2×10^{-4} Ω cm	80%	In ₂ O ₃ and SnO ₂	Fused silica and molybdenum substrates	16
17	DC magnetron sputtering	50°C	9×10^{-4} Ω cm	94%	In ₂ O ₃ and SnO ₂	Polyimide and glass substrates	17
18	RF and DC magnetron sputtering	30°C	6.19×10^{-4} Ω cm	91%	In ₂ O ₃ and SnO ₂	Polyethylene terephthalate (PET)	18
19	Rf - magnetron sputtering	250°C	1.51×10^{-3} Ω cm	86%	In ₂ O ₃ and SnO ₂	Fluorophlogopite substrate	19
20	Rf - magnetron sputtering	30°C	1.51×10^{-3} Ω cm (at 156W) and 2.93×10^{-2} Ω cm (at 276W)	87.5% and 92.6%	In ₂ O ₃ and SnO ₂	Flexible fluorophlogopite substrate	20
21	Rf - magnetron sputtering	30°C	2.52×10^{-4} Ω cm	86.6%	In ₂ O ₃ and SnO ₂	Ceramic substrate	21
22	Rf - magnetron sputtering	30°C	--	80%	In ₂ O ₃ and SnO ₂	Glass and Si substrates	22
23	Rf - magnetron sputtering	30°C	2.43×10^{-5} Ω cm	80%	In ₂ O ₃ and SnO ₂	Glass substrates	23
24	Rf -	40°C			In ₂ O ₃ and	Glass substrates	24

	magnetron sputtering		$1.3 \times 10^{-1} \Omega\text{cm}$	60%	SnO ₂		
25	Rf - magnetron sputtering	30°C		85% (glass) 79% (PET)	In ₂ O ₃ and SnO ₂	Glass and PET substrates	25
26	Rf - magnetron sputtering	70°C	$4 \times 10^{-3} \Omega\text{cm}$	--	In ₂ O ₃ and SnO ₂	Epoxy resin and glass substrates	26
27	Rf - magnetron sputtering	300°C	$0.71 \times 10^{-3} \Omega\text{cm}$ $0.94 \times 10^{-3} \Omega\text{cm}$ $0.70 \times 10^{-3} \Omega\text{cm}$	--	In ₂ O ₃ and SnO ₂	PC(polycarbonate), PMMA(polymethyl methacrylate) and glass substrates	27
28	Jet-nebulized spray pyrolysis method	450°C	0.10 Ω m	80%	Indium acetate and tin acetate	Glass substrates	28
29	Jet-nebulized spray pyrolysis method	500°C	$3.9 \times 10^{-4} \Omega\text{cm}$	77%	InCl ₃ and SnCl ₄	Glass substrates	29
30	Spray pyrolysis method	300°C	Sheet Resistance 2786 Ω /sq.	93%	InCl ₃ and SnCl ₄	Glass substrates	30
31	Spray pyrolysis method	500°C	$7.95 \times 10^{-3} \Omega\text{cm}$	88%	InCl ₃ and SnCl ₄	Polyimide substrate	31
32	Chemical vapour deposition	300°C	$6.93 \times 10^{13} \Omega \cdot \text{cm}$	80%	Indium acetate and Tin diacetate	Glass substrates	32
33	Chemical vapour deposition	425°C	$1.4 \times 10^{-4} \Omega\text{cm}$	85%	Indium acetate and Tin acetate	Glass substrates	33
34	Atmospheric pressure chemical vapour deposition	550°C	$3.5 \times 10^{-4} \Omega\text{cm}$	85%	InCl ₃ and SnCl ₄	Boroaluminosilicate glass substrates	34

FUTURE SCOPE

In recent years, the ITO deposition techniques and its applications have been further developed; however, several issues are still arisen such as improving film characteristics and minimizing production costs. The future research work thus should be concentrated on improving the ITO thin film fabrication techniques with higher efficiency and more sustainability, new deposition techniques and finding a solution related to the environmental problems of indium availability.

CONCLUSION

Indium tin oxide (ITO) thin films are unique multifunctional materials useful in electronics and optoelectronics. These two properties make them so valuable for so many technological applications as they are at the same time electrical conductors and optically transparent. Thus, it is possible to consider that the further application of ITO in modern and future devices could still be feasible despite the existing shortcomings and new opportunities could be introduced by means of improved deposition technology. Further studies and investigation on the ITO

thin films are vital to advance the innovation and discoveries in providing better solutions to the current technology industry.

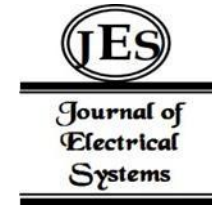
REFERENCES

- [8] George, J., & Menon, C., (2000). Electrical and optical properties of electron beam evaporated ITO thin films. *Surface and Coatings Technology*, 132(1), 45–48. doi:10.1016/s0257-8972(00)00726-x
- [9] Cristian Viespe; Ionut Nicolae; Cornelia Sima; Constantin Grigoriu; Rares Medianu (2007). ITO thin films deposited by advanced pulsed laser deposition. , 515(24), 8771–8775. doi:10.1016/j.tsf.2007.03.167
- [10] Kim, J. H., Jeon, K. A., Kim, G. H., & Lee, S. Y. (2006). Electrical, structural, and optical properties of ITO thin films prepared at room temperature by pulsed laser deposition. *Applied Surface Science*, 252(13), 4834–4837. doi:10.1016/j.apsusc.2005.07.134
- [11] David, C., Tinkham, B. P., Prunici, P., & Panckow, A. (2017). Highly conductive and transparent ITO films deposited at low temperatures by pulsed DC magnetron sputtering from ceramic and metallic rotary targets. *Surface and Coatings Technology*, 314, 113–117. doi:10.1016/j.surfcoat.2016.09.022
- [12] Jain, P., Singh, S., & Pundir, S. K. (2020). Synthesis of Highly Transparent Indium Tin Oxide Thin Films Using Vacuum Evaporation Technique. *Journal of Nanoscience and Nanotechnology*, 20(6), 3845–3853. doi:10.1166/jnn.2020.17505
- [13] Meng, L., Gao, J., Teixeira, V., & dos Santos, M. P. (2008). Indium tin oxide thin films prepared by ion beam assisted deposition technique at different ion beam currents. *Physica Status Solidi (a)*, 205(8), 1961–1966. doi:10.1002/pssa.200778852
- [14] Lee, Chih-Chien; Shih, Chun-Jen; Kumar, Gautham; Biring, Sajal; Sen, Somaditya; Liu, Shun-Wei (2017). Highly efficient exciplex organic light-emitting devices employing a sputtered indium-tin oxide electrode with nano-pinhole morphology. *J. Mater. Chem. C*, (2017)1-3, doi:10.1039.C7TC03500D
- [15] A.B. Chebotareva; G.G. Untila; T.N. Kost; S. Jorgensen; A.G. Ulyashin (2007). ITO deposited by pyrosol for photovoltaic applications. *Thin Solid Films* 515 (2007) 8505–8510, doi:10.1016/j.tsf.2007.03.097
- [16] Sunde, T. O. L., Garskaite, E., Otter, B., Fosshem, H. E., Sæterli, R., Holmestad, R., ... Grande, T. (2012). Transparent and conducting ITO thin films by spin coating of an aqueous precursor solution. *Journal of Materials Chemistry*, 22(31), 15740. doi:10.1039/c2jm32000b
- [17] Dong, L., Zhu, G. S., Xu, H. R., Jiang, X. P., Zhang, X. Y., Zhao, Y. Y., ... Yu, A. B. (2019). Preparation of indium tin oxide (ITO) thin film with (400) preferred orientation by sol–gel spin coating method. *Journal of Materials Science: Materials in Electronics*. doi:10.1007/s10854-019-01126-1
- [18] Aslan, M. H., Oral, A. Y., Demirci, E., & Başaran, E. (2004). Microstructural and Optical Study of ITO Thin Films Prepared by Sol-Gel Method. *Key Engineering Materials*, 264-268, 443–448. doi:10.4028/www.scientific.net/kem.264-268.443
- [19] Kőrösi, L., Papp, S., Beke, S., Pécz, B., Horváth, R., Petrik, P., ... Dékány, I. (2012). Highly transparent ITO thin films on photosensitive glass: sol–gel synthesis, structure, morphology and optical properties. *Applied Physics A*, 107(2), 385–392. doi:10.1007/s00339-012-6765-1
- [20] Xia, N., & Gerhardt, R. A. (2016). Fabrication and characterization of highly transparent and conductive indium tin oxide films made with different solution-based methods. *Materials Research Express*, 3(11), 116408. doi:10.1088/2053-1591/3/11/116408
- [21] Kőrösi, L., Papp, S., & Dékány, I. (2011). Preparation of transparent conductive indium tin oxide thin films from nanocrystalline indium tin hydroxide by dip-coating method. *Thin Solid Films*, 519(10), 3113–3118. doi:10.1016/j.tsf.2010.12.160
- [22] Voisin, L.; Ohtsuka, M.; Petrovska, S.; Sergiienko, R.; Nakamura, T. (2020). Multilayer indium saving ITO thin films produced by sputtering method. *Journal of Alloys and Compounds*, 827(), 154378–. doi:10.1016/j.jallcom.2020.154378
- [23] Al-Kuhaili, M. F. (2020). Electrical conductivity enhancement of indium tin oxide (ITO) thin films reactively sputtered in a hydrogen plasma. *Journal of Materials Science: Materials in Electronics*, 31(4), 2729–2740. doi:10.1007/s10854-019-02813-9
- [24] Klein, E., Huber, K., Paul, O., & Ruther, P. (2019). Low-temperature plasma annealing of sputtered indium tin oxide for transparent and conductive thin-films on glass and polymer substrates. *Thin Solid Films*, 137715. doi:10.1016/j.tsf.2019.137715
- [25] Bazargan, A. M., Sharif, F., Mazinani, S., & Naderi, N. (2016). A high quality ITO/PET electrode for flexible and transparent optoelectronic devices. *Journal of Materials Science: Materials in Electronics*, 28(3), 2962–2969. doi:10.1007/s10854-016-5881-7
- [26] Zhang, H., Zhu, H., Zhang, T., Yu, S., Guo, P., Wang, Y., & Yang, Z. (2021). Effect of sputtering pressure on the optical and electrical properties of ITO film on fluorphlogopite substrate. *Applied Surface Science*, 559, 149968. doi:10.1016/j.apsusc.2021.149968
- [27] Zhu, H., Zhang, H., Zhang, T., Wei, Q., Yu, S., Gao, H., ... Yang, Z. (2021). Effect of Sputtering Power on the Optical and Electrical Properties of ITO Films on a Flexible Fluorphlogopite Substrate. *Crystal Research and Technology*, 2100060. doi:10.1002/crat.202100060
- [28] Kim, S. I., Cho, S. H., Choi, S. R., Yoon, H. H., & Song, P. K. (2009). Properties of ITO films deposited by RF superimposed DC magnetron sputtering. *Current Applied Physics*, 9(3), S262–S265. doi:10.1016/j.cap.2009.01.031

- [29] Hacini, A., Ali, A. H., & Adnan, N. N. (2021). Optimization of ITO thin film properties as a function of deposition time using the swanepoel method. *Optical Materials*, 120, 111411. doi:10.1016/j.optmat.2021.111411
- [30] Z. Ghorannevis; E. Akbarnejad; M. Ghoranneviss (2015). Structural and morphological properties of ITO thin films grown by magnetron sputtering. *Journal of Theoretical and Applied Physics*, 9(4), 285–290. doi:10.1007/s40094-015-0187-3
- [31] Subacius, Andrius; Baloukas, Bill; Bousser, Etienne; Hinder, Steve J.; Baker, Mark A.; Rebholz, Claus; Matthews, Allan (2020). Nanostructural Characterisation and Optical Properties of Sputter-Deposited Thick Indium Tin Oxide (ITO) Coatings. *Coatings*, 10(11), 1127–. doi:10.3390/coatings10111127
- [32] Guillén, C., & Herrero, J. (2005). Comparison study of ITO thin films deposited by sputtering at room temperature onto polymer and glass substrates. *Thin Solid Films*, 480-481, 129–132. doi:10.1016/j.tsf.2004.11.040
- [33] Bragaglia, M., Lamastra, F. R., Tului, M., Di Gaspare, L., Notargiacomo, A., Valentini, M., & Nanni, F. (2019). Low temperature sputtered ITO on glass and epoxy resin substrates: influence of process parameters and substrate roughness on morphological and electrical properties. *Surfaces and Interfaces*, 100365. doi:10.1016/j.surfin.2019.100365
- [34] Liu, J., & Zuo, Y. (2010). Crystallization and conductivity mechanism of ITO films on different substrates deposited with different substrate temperatures. *Journal of Wuhan University of Technology-Mater. Sci. Ed.*, 25(5), 753–759. doi:10.1007/s11595-010-0086-z
- [35] Marikkannu, S., Sanjeeviraja, C., Piraman, S., & Ayeshamariam, A. (2015). Studies on the structural, optical, and electrical properties of jet-nebulized spray pyrolysis ITO thin films. *Journal of Materials Science: Materials in Electronics*, 26(4), 2531–2537. doi:10.1007/s10854-015-2718-8
- [36] Thirumoorthi, M., & Thomas Joseph Prakash, J. (2016). Structure, optical and electrical properties of indium tin oxide ultra thin films prepared by jet nebulizer spray pyrolysis technique. *Journal of Asian Ceramic Societies*, 4(1), 124–132. doi:10.1016/j.jascer.2016.01.001
- [37] Zhou, Y., Wu, G. M., Gao, D. W., Xing, G. J., Zhu, Y. Y., Zhang, Z. Q., & Cao, Y. (2012). Preparation and Physical Properties of ITO Thin Films by Spray Pyrolysis Method. *Advanced Materials Research*, 465, 268–275. doi:10.4028/www.scientific.net/amr.465.268
- [38] Rana, R., Chakraborty, J., Tripathi, S. K., & Nasim, M. (2015). Study of conducting ITO thin film deposition on flexible polyimide substrate using spray pyrolysis. *Journal of Nanostructure in Chemistry*, 6(1), 65–74. doi:10.1007/s40097-015-0177-7
- [39] Maruyama, T., & Tabata, K. (1990). Indium-Tin Oxide Thin Films Prepared by Chemical Vapor Deposition from Metal Acetates. *Japanese Journal of Applied Physics*, 29(Part 2, No. 2), L355–L357. doi:10.1143/jjap.29.l355
- [40] Ikenoue, T., Sakamoto, S., & Inui, Y. (2014). Fabrication and characterization of Cu₂O, ZnO and ITO thin films toward oxide thin film solar cell by mist chemical vapor deposition method. *Physica Status Solidi (c)*, 11(7-8), 1237–1239. doi:10.1002/pssc.201300638
- [41] Gaskell, J. M., & Sheel, D. W. (2012). Deposition of indium tin oxide by atmospheric pressure chemical vapour deposition. *Thin Solid Films*, 520(12), 4110–4113. doi:10.1016/j.tsf.2011.04.191

¹Aniket R.Deshmukh²Nilesh R.Thakare³Sanjay K Devade²GauravS.Chaudhari,

A Literature Review of TiO₂-GO
Composites in Solar Cells: Advances and
Future Prospects



Abstract Over the past two decades, significant progress has been made in developing TiO₂ and graphene oxide (GO) composites for solar cells. This review explores advancements in synthesis, characterization, and application, highlighting their enhanced photovoltaic performance. The integration of GO with TiO₂ has shown improved charge separation and light absorption. The paper also discusses the latest developments in perovskite solar cells using these composites, concluding with suggestions for future research and potential applications in solar energy technologies.

Keywords: TiO₂(TitaniumDioxide),GO(Graphene-Oxide),RGO(ReducedGrapheneOxide),Perovskitesolarcells(PSC),Dye-sensitized solar cells (DSSC), chemical vapor deposition (CVD), Sol-gel method, Hydrothermal, X-ray diffraction (XRD), scanning electron microscopy (SEM), transmission electron microscopy (TEM), and Raman spectroscopy. transparentconductiveoxide(TCO),indiumtinoxide(ITO),fluorine-dopedtinoxide(FTO),HoleTransportLayer (HTL)

I. INTRODUCTION

Research into sustainable and renewable energy sources has led to extensive studies on solar cell technology. Titanium dioxide (TiO₂) stands out for its stability, non-toxicity, and superior charge transport capabilities, making it a prime candidate for dye-sensitized solar cells (DSSCs) and perovskite solar cells (PSCs). However, its broad bandgap and limited visible light absorption necessitate the development of hybrid materials like graphene oxide (GO). GO, produced by oxidizing graphite, is highly soluble in various solvents and interacts strongly with TiO₂, improving charge separation and light absorption.

II. SYNTHESISMETHODSOFTiO₂-GO COMPOSITES

SeveralmethodsareavailableforsynthesizingTiO₂-GO composites:

Sol-gel Process: This involves the hydrolysis and condensation of titanium precursors in the presence of GO, followed by thermal treatment. This method produces uniform composites with high TD uniformity on GO sheets.

HydrothermalSynthesis: This methodofferscontrolled crystallizationand morphology, producing well-defined crystalline structures and enhanced interfacial contact between TiO₂ and GO. Chemical Vapor

Deposition (CVD): This technique allows precise control over TiO₂ deposition on GO substrates, resulting in uniform and well-adhered composite films suitable for large-scale production.

III. CHARACTERIZATIONTECHNIQUES

To understandthephotovoltaicperformanceofTiO₂-GOcomposites,variouscharacterization techniques are employed:

X-rayDiffraction(XRD):Usedtodeterminecrystallinestructureandphasecomposition.

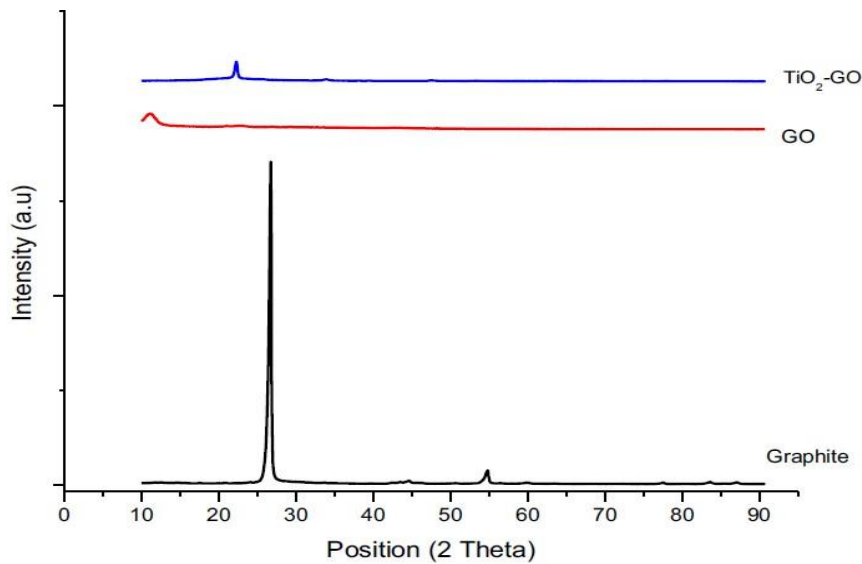


Fig1. XRD patterns of the raw graphite, synthesis GO and TiO₂-GO composite.(Ref-2)

Scanning Electron Microscopy (SEM): Provides detailed images of surface morphology and particle distribution.

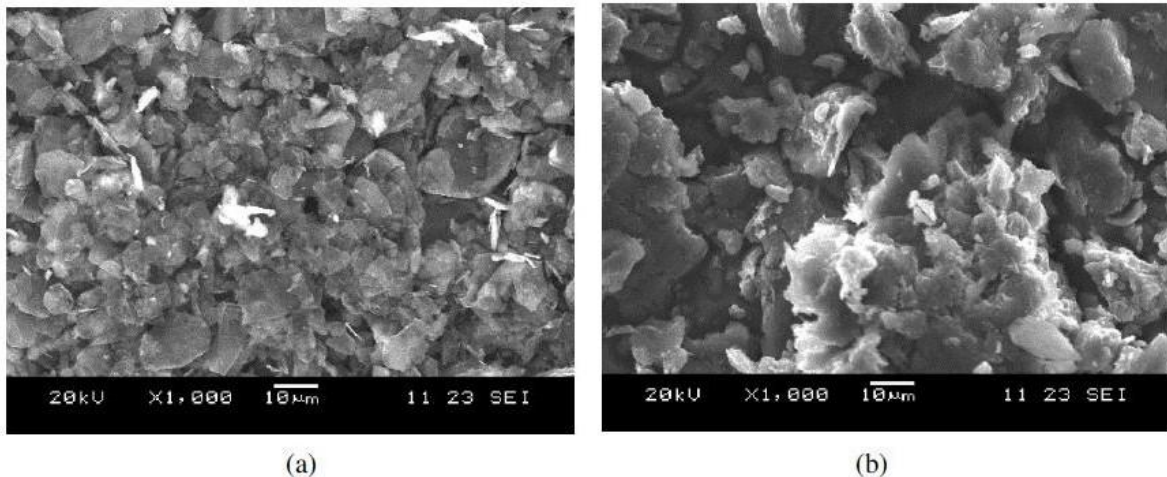


Fig2. SEM for (a) graphite as starting material and (b) GO after synthesis using modified Hummer method (Ref - 2)

Transmission Electron Microscopy(TEM): Offers high-resolution images of the internal structure and interface between TiO₂ and GO.

Raman Spectroscopy: Analyzes vibrational modes and chemical bonding, confirming the successful integration and reduction of GO to RGO.

IV. IMPACT OF DOPANTSON PHOTOVOLTAIC PERFORMANCE

Doping TiO₂-GO composites with metal and non-metal elements can significantly enhance their photovoltaic performance. Metal dopants like silver (Ag) and zinc (Zn) introduce localized surface plasmon resonance effects, enhancing light absorption and electron mobility. Non-metal dopants like nitrogen (N) and carbon (C) modify the bandgap, extending light absorption into the visible range and improving charge separation.

Samples	Calcination temperature (°C)	Surface area (m ² g ⁻¹) ^a	Pore volume (cm ³ g ⁻¹) ^a	Average pore diameter (nm)	Energy gap (eV) ^b	Crystallite size (nm) ^c
TiO ₂	500	45	0.11	12.2	3.0	21
TiO ₂ /5% GO	500	72	0.15	3.6	2.97	19.7
S, N-doped TiO ₂ /5%GO	500	150	0.36	5.4	2.95	15.1
S, N-doped TiO ₂ /5%GO	600	116	0.31	6.1	2.91	15.4
S, N-doped TiO ₂ /5%GO	700	107	0.17	7.3	2.87	25.6

Notes: ^aBET surface area, average pore volume of the as-prepared samples estimated from nitrogen adsorption. ^bCalculated from the UV visible diffuse reflectance spectra study. ^cCalculated from TEM and XRD.(Ref - 3)

1. PerovskiteSolarCellsIncorporatingTiO₂-GOComposites

Perovskite solar cells (PSCs) have revolutionized solar cell technology with their superior light-harvesting capabilities and high efficiency. TiO₂-GO composites further enhance PSC performance by improving charge transport and reducing recombination rates. Various dopants have been explored to enhance the performance of these composites in PSCs, achieving notable efficiency improvements.

2. ConstructionandWorkingofDSSCTiO₂-GOSolarCells

DSSCconstructioninvolvesseverallayers:

SubstratePreparation:UsingTCOglasssubstrateslikeFTOorITO.

Composite Layer: TiO₂ nanoparticles combined with GO, deposited using techniques like doctor bladingor screen printing.

DyeSensitization:AdsorbingaphotosensitivedyeontotheTiO₂-GOcompositelayer.

ElectrolyteLayer:Fillingthespacebetweenthephotoanodeandthecounterelectrodewitharedox electrolyte.

CounterElectrode:Madeofmaterialslikeplatinumorcarbon, facilitatingthereductionoftheredox electrolyte.

3. WorkingPrinciple

The working principle involves light absorptionby dye molecules, excitongenerationand injection, charge separation and transport, and dye regeneration, resulting in continuous electric current generation.

4. EfficacyandPerformanceImprovements

Efficiency improvements in DSSCs using TiO₂-GO composites can be achieved through doping and surface modifications. For instance, sulfur and nitrogen doping enhances photocatalytic activityandphoto- conversion efficiency.

PhotovoltaicparametersofDSSCsemployingdifferenttypes ofCEsandWes

CE/WE	V _{oc} (mV)	J _{sc} (mAcm ⁻²)	FF(%)	η(%)	Reference
WE:TiO ₂ dopedwithtungsten	730	15.10	67	7.42	[7]
WE:TiO ₂ dopedwithscandium	752	19.10	68	9.60	[8]
WE:TiO ₂ dopedwithindium	716	16.97	61	7.48	[9]
WE:TiO ₂ dopedwithboron	660	7.85	66	3.44	[10]
WE:TiO ₂ dopedwithfluorine	754	11	76	6.31	[11]
WE:TiO ₂ dopedwithcarbon	730	20.38	57	8.55	[12]
WE:ONT/FTO	700	10.65	70	5.32	[13]
WE:G-TiO ₂ NPs/TiO ₂ NTs	690	16.59	56	6.29	[14]
WE:TiO ₂ dopedwithCu	591	6.84	56	2.28	[15]
WE:7.5%SnO ₂ dopedTiO ₂	790	14.53	58	6.7	[16]
WE:TiO ₂ :Y _{1.86} Eu _{0.14} WO ₆	757	12.3	43	3.9	[17]
WE:Nb ₂ O ₅	738	6.23	68.3	3.15	[18]
WE:Nanographite-TiO ₂	720	1.69	35	0.44	[19]
CE:PtCo	717	16.96	66	7.64	[20]
CE:Pt+SLGO	670	7.9	65	3.4	[21]
CE:PtMo	697	15.48	62	6.75	[22]

CE:PtCr _{0.05}	739	13.07	71	6.88	[23]
CE:CoNi _{0.25}	706	18.02	66	8.39	[24]
CE:Ni-PANI-G	719	11.56	64	5.32	[25]
CE:PANInanoribbons	720	17.92	56	7.23	[26]
CE:Pd ₁₇ Se ₁₅	700	16.32	65	7.45	[27]
CE:PtCuNi	758	18.30	69	9.66	[28]
CE:g-C ₃ N ₄ /G	723	14.91	66	7.13	[29]
CE:FeN/N-dopedgraphene	740	18.83	78	10.8	[30]
CE:MoS ₂ nanofilm	740	16.96	66	8.28	[31]
CE:Ni _{0.33} Co _{0.67} Semicrosphere	789	17.29	67	9.01	[32]
CE:TubularorthorhombicCoSe ₂	771	17.35	70	9.34	[33]

5. Limitations of DSSC and Perovskite Solar Cell Devices

Despite their potential, DSSCs and PSCs face significant challenges:

DSSC Limitations: Included dye degradation, electrolyte leakage, thermal instability, and complex fabrication processes.

PSCs Limitations: Included moisture sensitivity, thermal instability, UV light degradation, and the use of toxic lead.

6. Future Pathways

To overcome these limitations, several strategies can be pursued:

Material Optimization and Doping: Advanced doping techniques and nanostructuring TiO₂.

Graphene Oxide Functionalization: Chemical functionalization and creating hybrid structures. Interface Engineering:

Introducing buffer and passivation layers to reduce recombination.

Perovskite Layer Enhancements: Composition engineering and defect passivation.

Device Architecture Innovations: Developing tandem and multi-junction cells, and using flexible substrates.

Stability and Durability Enhancements: Advanced encapsulation and thermal management techniques.

Scalability and Manufacturing Improvements: Low-cost fabrication and roll-to-roll manufacturing techniques.

7. Conclusion

Enhancing the performance of TiO₂ and graphene oxide composite solar cells requires a multidimensional approach, including advanced doping, nanostructuring, interface engineering, and innovative device architectures. Ongoing research and interdisciplinary collaboration will unlock the full potential of these materials, paving the way for efficient, stable, and commercially viable solar energy solutions.

8. Acknowledgment

We would like to express our profound gratitude to all of the funding organizations, research centers, and partners whose insightful advice and great assistance made this review possible. We would especially want to thank the laboratory teams for their commitment to the research and data analysis. We also thank peer reviewers for their helpful criticism, which allowed us to improve our work.

REFERENCES

1. D. K. Calvo Ramos, M. Vega González, R. A. Esparza Muñoz, J. Santos Cruz, F. J. De Moure-Flores, S. A. Mayén- Hernández "Obtaining And Characterization Of TiO₂-Go Composites For Photocatalytic Applications," Hindawi, International Journal Of Photoenergy, Volume 2020, Article Id 3489218.
2. N.M.N Azira, D. Murizam, D.S.C. Halin, M.A. Idris And N. F.M. Yunos "Preliminary Study Of Hydrothermal Synthesis Of TiO₂-Go Composites As A High Performance Photocatalyst" Iop Conf. Series: Materials Science And Engineering 957 (2020) 012041.
3. Xiaopengshanga, Minzhanga, Xianbaowangab* Andyingkuiyanga "Sulphur, Nitrogen Doped TiO₂/Graphene oxide composites as a high Performance Photocatalyst" Journal Of Experimental Nanoscience, 2014 Vol.9, No.7, 749-761.
4. Momina Khannam, Shyamalima Sharma, Ranoo Bhargav, Asit Patra And , Swapan Kumar Dolui "Development Of Perovskite Sensitized Thin Film Solar Cells Based On Graphene Oxide/TiO₂ Photoanodes" Sensors & Transducers, Vol. 210, Issue 3, March 2017, Pp. 9-16
5. Ahmad Muslihin Ramli, Mohd Zikri Razali, Norasikin Ahmad Ludin" Performance Enhancement Of Dye Sensitized Solar Cell Using Graphene Oxide Doped Titanium Dioxide Photoelectrode" Malaysian Journal Of Analytical Sciences, Vol 21 No 4(2017):928-940
6. Abdelmajid Timoumi "Reduction Band Gap Energy of TiO₂ Assembled with Graphene Oxide Nanosheets" Scientific Research Publishing, Graphene, 2018, 7, 31-38.
7. Tongz, Pengt, Sunw, Liuw, Guos, Zhaoxz(2014) Introducing an intermediate band into dye-Sensitized solar cells by w₆+Doping Into tio₂ nanocrystalline photoanodes. Jphyschemc 118(30):16892-16895.
8. Latini, Cavallo, Aldibajafk, Gozzidetal(2013) Efficiency improvement of DSSC Photoanode By Scandium Doping Of Mesoporous Titania Beads. Jphyschemc 117(48):25276-25289.
9. Bakhshayesh Am, Farajisafilo N (2015) Efficient Dye-Sensitized Solar Cell based On Uniform In-Doped TiO₂ Spherical Particles.

- Applied Physics A120(1):199–206.
10. Subramaniana, Wanghw (2012) Effects of boron doping in tio2 nanotubes And The Performance Of Dye-Sensitized Solar Cells. *Appl Surf Sci* 258(17):6479–6484.
 11. Song J, Yang Hb, Wang X, Khoo Sy, Wong Cc, Liu Xw, Li Cm (2012) Improved Utilization Of Photogenerated Charge Using Fluorine-Doped Tio(2)Hollowspheresscatteringlayerindy-Sensitizedsolarcells. *AcSapplmaterinterf* 4(7):3712– 3717.
 12. Tabari-Saadi Y, Mohammadi Mr (2015) Efficient Dye-Sensitized Solar Cellsbased On Carbon-Doped Tio2 Hollow Spheres And Nanoparticles. *J Mater Scimater Electron* 26(11):8863–8876.
 13. Lin J, Chen J, Chen X (2011) High-Efficiency Dye-Sensitizedsolar Cells Basedon Robust And Both-End-Open Tio2 Nanotube Membranes. *Nanoscale Reslett* 6:475.
 14. Song Cb, Qiang Yh, Zhao Yl, Gu Xq, Zhu L, Song Cj, Liu X (2014) Dye-Sensitized Solar Cells Based On Graphene-Tio2 Nanoparticles/Tio2nanotubes Composite Films. *Int J Electrochem Sci* 9:8090–8096.
 15. Patlelb, Chaudharia (2016) Performance of dssc with cudoped Tio2 electrode prepared by dipcoating technique. *Int j sci engres* 7(8):1004–1009.
 16. Mao X, Zhou R, Zhangs, Dingl, Wanl, Qins, Chenz, Xuj, Miaos (2016) High Efficiency Dye-Sensitized Solar Cells Constructed With Composites Of tio2 and the hot-Bubbling synthesized ultra Small no2 nanocrystals. *Sci rep* 6:19390.
 17. Llanosj, Britoi, Espinoza d, Sekarr, Maniduraip (2018) A down-Shifting eu3 Doped Y2wo6/Tio2 Photoelectrode For Improved Light Harvesting Indye-Sensitized Solar Cells. *R Soc Open Sci* 5:171054.
 18. Liux, Yuan R, Liu Y, Zhu S, Lin J, Chen X (2016) Niobium Pentoxidenanotube Powder For Efficient Dye-Sensitized Solar Cells. *New J Chem* 40:6276–6280.
 19. Sharma Ss, Sharma K, Sharma V; Nanographite-Tio2 Photoanode For Dyesensitized Solar Cells (2016) *Aip Conference Proceedings* 1728:020515.
 20. Yang Q, Yang P, Duan J, Wang X, Wang L, Wang Z, Tang Q (2016) Ternary platinum Alloy Counter Electrodes For High- Efficiency Dye-Sensitized Solar cells. *Electrochim Acta* 190:85–91.
 21. Ibrayev N, Seliverstova E, Dzhana Bekova R, Serikov T (2018) Photovoltaic properties Of Dssc With Composite Counter Electrodes Based On Pt And slgo. *Mater Sci Eng* 289:012009.
 22. Tangq, Zhangh, Mengy, Heb, Yul (2015) Dis solution engineering of platinum alloy counter electrodes in dye-Sensitized solar cells. *Angewchem Int Ed* 54:11448–11452.
 23. Daovd, Choiy, Yongk, Larinall, Shevaleevskiyo, Choihs (2015) A facile synthesis of bimetallic nanoparticles as a new transparent counter electrode for quantum-Dot-Sensitized Solar Cells. *J power sources* 274:831–838.
 24. Liu J, Tang Q, He B, Yu L (2015) Cost-Effective, Transparent Iron Selenide nanoporous Alloy Counter Electrode For Bifacial Dye-Sensitized Solar Cell. *J power Sources* 282:79–86.
 25. Chen X, Liu J, Qian K, Wang J (2018) Ternary Composites Of Ni–Polyaniline–Graphene As Counter Electrodes For Dye- Sensitized Solar Cells. *Rsc Adv* 8:10948–10953.
 26. Houw, Xiaoy, Hang, Fud, Wur (2016) Serrated, Flexible and ultrathin polyaniline Nanoribbons: An Efficient Counter Electrode For The Dye-Sensitized Solar Cell. *J Power Sources* 322:155–162.
 27. Kukunuri S, Karthicka Sn, Sampath S (2015) Robust, Metallic Pd17se15 And pd7se4 phases from a single source precursor and the iruseas counter electrodes In Dye Sensitized Solar Cells. *J Mater Chem A* 3:17144–17153.
 28. Yangp, Tangq (2016) A branching ni-cu alloy counter electrode for. High-Efficiency dye-Sensitized solar cells. *Appl surf sci* 362:28–34.
 29. Wang G, Zhang J, Kuang S, Zhang W (2016) Enhanced Electrochemical performance Of A Porous G-C3n4/Graphene Composite As A Counter electrode for dye-Sensitized solar cells. *Chem eur j* 22:11763–11769.
 30. Balamurugan J, Thanh Td, Kim Nh, Lee Jh (2016) Nitrogen-Doped graphene nanosheets with fen-core–Shell nanoparticles as high-Performance Counter Electrode materials For Dye-Sensitized Solar cells. *Adv mater interfac* 3:1500348.
 31. Liang J, Li J, Zhu H, Han Y, Wang Y, Wang C, Jin Z, Zhang G, Liu J (2016) One-Step Fabrication Of Large-Area Ultrathin Mos2 Nanofilms With High catalytic activity for photovoltaic devices. *Nanoscale* 8:16017–16025.
 32. Qianx, Lih, Shaol, Jiangx, Hou L (2016) Morphology-Tuned synthesis of Nickel Cobalt Selenides As Highly Efficient Pt-Free Counter Electrode catalysts For Dye-Sensitized Solar Cells. *AcS Appl Mater Interf* 8:29486–29495.
 33. Li H, Qian X, Zhu C, Jiang X, Shao L, Hou L (2017) Template Synthesis Of CoSe2/Co3Se4 nanotubes: Tuning Of Their Crystal Structures For Photovoltaics and Hydrogen Evolution In Alkaline Medium. *J Mater Chem A* 5:4513–4526.

¹M. T. Mundhe²G. K. Biradar³G. B. Todkar⁴R. A. Kunale

Magnetic and electrical properties of nanosized M-type strontium hexaferrite prepared by sol-gel



Abstract: - In present work hexaferrites are synthesized successfully using a sol–gel method. The structural and magnetic properties are investigated. The hexagonal phase is confirmed for all the products. The magnetization is measured with respect to the applied magnetic field. The magnetic parameters including coercivity H_c , and magnetic moment are obtained at room temperatures. It is shown that a substitution decreases the coercivity value. The results on magnetic properties are investigated extensively with respect to the structural and microstructural properties. The obtained H_c values suggest that the synthesized hexagonal ferrites are promising candidates for potential magnetic recording applications..

Keywords: hexagonal ferrite, Magnetic material, electrical properties, coercivity, X-raydiffractin, Hysteresis loop, squareness ratio.

^{1*}Corresponding author : Author ^{1, 4} Physics Department, Kai. Rasika Mahavidyalaya Deoni, India.

²Shr Renukadevi Mahaidyalaya Mahur, Dist. Nanded, India,

³Dayanand Science college Latur, India.

Corresponding Author E-mail:kunalerenuka9@gmail.com

Copyright©JES2024on-line:journal.esrgroups.org

I. INTRODUCTION

The search for new magnetic materials for high performance magnet applications has led to tremendous growth in both the scientific research in this field, and the investment in the development of such materials. This development in materials research was driven by the evolution of new technologies, and the ever increasing demand for the improvement in efficiency, better machine designs, and device miniaturization [1, 2]. The properties of ferrite material depends upon various factor such as synthesis method, sintering temperature, composition of elements, concentration of metal oxide and impurity occur in preparation of ferrite material [3-5].

M-type strontium hexaferrite has been the subject of continuous interest for several years due to its relatively large saturation magnetization, high coercivity and high uniaxial magnetic crystalline anisotropy, chemical stability and corrosion resistivity. It can be therefore used as electronic components, magnetic memories and magnetic substrate for magnetic catalysts.

In addition, the synthesis method has a major influence on the magnetic characteristics. The properties of M type strontium hexaferrite depend on the synthesis method, sintering temperature and type of substituted cations. There are various methods used to prepare SHF, such as hydrothermal flow synthesis [6], pechini method [7], sol-gel method [8] pulsed laser deposition [9] co-precipitation method [10]. The features of sol-gel auto combustion synthesis method are higher temperature achieved with fast heating rates, and shorter reaction times. The sol-gel auto combustion synthesis method is particularly popular method for the manufacture of technologically useful materials at lower costs compared with conventional methods [11, 12]. Thus, in this work, the sol-gel auto combustion approach has been applied.

Strontium hexaferrite's magnetoplumbite structure contains 64 ions per unit cell. The molecular unit of strontium hexaferrite consists of two blocks S (spinel) block and R (hexagonal) block which are cubically as well as hexagonally overlapped giving rise to unit cell formula SRS^*R^* . Where * denotes the rotation of any of the lock through 180° around the c axis [13]. The crystal structure of M-type hexaferrite consists of total 64 ions per unit primitive unit cell occupied on 11 different symmetry sites and crystallizes in a P63/mmc space group.

The unit cell contains 38 oxygen ions, 24 are of Fe^{3+} ion and remaining two of them are cations like Ba, Sr or Pb. The Fe^{3+} ions distributed over five different site namely 2a-octahedral, 2b-trigonal bipyramidal, 12k-octahedral, 4f1- tetrahedral and 4f2- octahedral as shown in Fig 1 [14]. S block contains two oxygen ions (O4–O4) with composition formula $2Fe_3O_4$ and $2 \uparrow$ net spin as shown in table 2. The small cations (Fe) occupy tetrahedral cavities and two types of octahedral ones [15].

R block consists of three large ions (O4–BaO3–O4) with composition formula $BaFe_6O_{11}$ and $2 \uparrow$ net spin as shown in table 2. The outer ones contain exclusively oxygen anions while in the central one there are large cations. Small cations occupy three types of tetrahedral cavities, two types of octahedral cavities and one type of five coordinated bipyramidal cavity, which may also be viewed as two face sharing tetrahedral cavities.

Each Fe^{3+} has magnetic moment $5 \mu_B$, so the net magnetic moment of Fe^{3+} per unit cell is $8 \times 5 \mu_B = 40 \mu_B$. It is known that Fe ions provide the largest positive contribution at the 2b site, a relative weak positive contribution at the 4f1, 4f2, and 2a sites, and a negative contribution at the 12k site [16]. Hence, the intrinsic magnetic properties of Strontium hexaferrite can be increased by substitution Fe ions in different sites with other suitable ions [17].

II. EXPERIMENTAL

Sol gel method is employed to synthesize a strontium hexaferrite with chemical formula $SrNi_{(1-x)}Co_xFe_{12-x}O_{19}$ for $x=0.00, 0.25, 0.50, 0.75$ and 1. High purity (> 99%) (Sigma-aldrich) Strontium nitrate ($Sr(NO_3)_2 \cdot 6H_2O$) and Ferric nitrate ($Fe(NO_3)_3 \cdot 9H_2O$) with citric acid ($C_6H_8O_7 \cdot H_2O$) were taken as starting materials for the synthesis. All the starting materials were mixed in desired stoichiometric amount in sufficient amount of distilled water. The whole mixture is then placed on hot plate with magnetic stirrer. The mixture was continually stirred at constant temperature of $90^\circ C$ and liquid ammonia was added slowly in order to maintain the Ph a constant value 7. After continuously stirring and heating at $90^\circ C$ for 2-3 hours the mixture become viscous and sol was formed and after some time it converts into dried gel, by the process of self-ignition the dried gel was burnt and a fine ash was obtained. The burnt ash is grounded for two hours and then subjected to final sintering at $900^\circ C$ for 6 hours. After final sintering the powders were again grinded for two hours to obtain the fine particles of the final products.

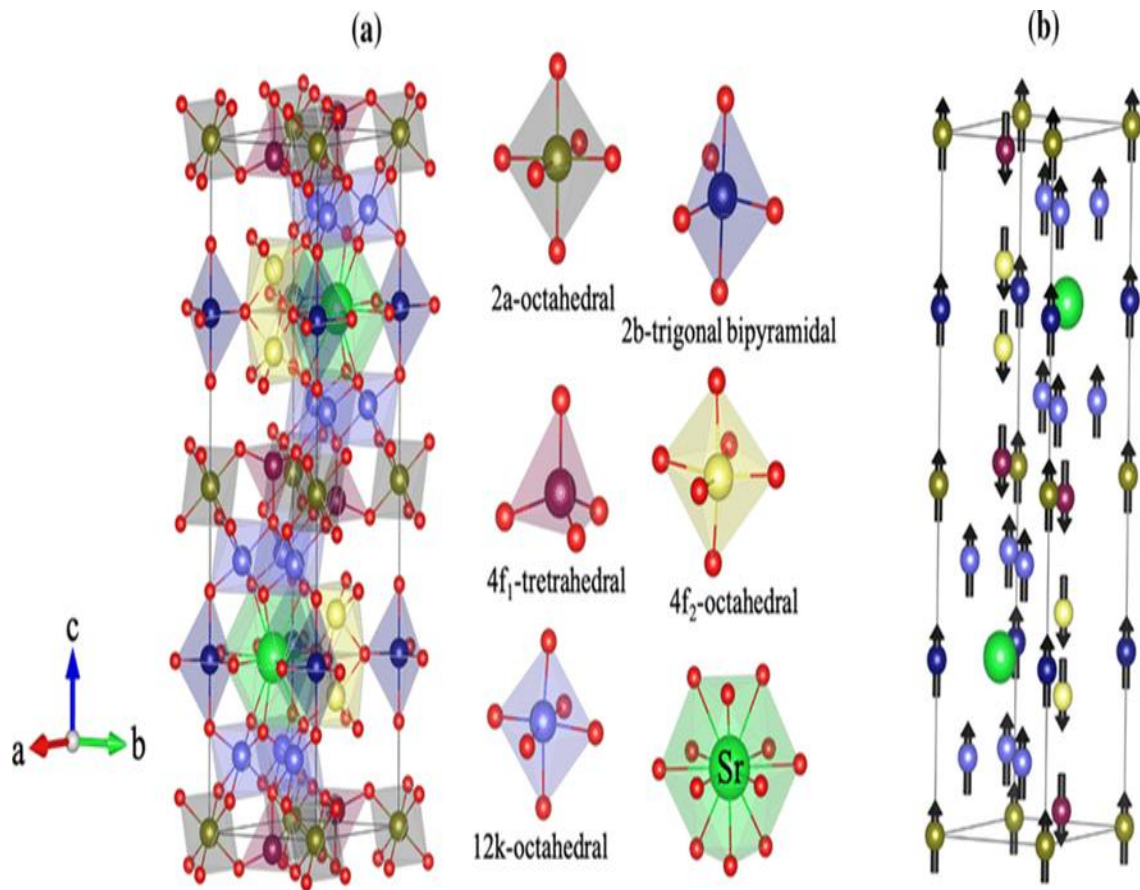


Fig. 1 Unit cell of M-type strontium hexaferrite. (The red spheres are O atoms, and the green spheres are Sr atoms. The Fe ions are at the non-equivalent sites, octahedron (2a), bipyramidal (2b), tetrahedral (4f₁), octahedron (4f₂), and octahedron (12k). b the magnetic moment direction of the Fe ions is shown by arrows; the magnetic moments of Fe ions at 4f₁ and 4f₂ point downward, and at sites 2a, 2b, and 12k sites point upward. For clarity, O atoms are not shown in b.)

III. CHARACTERIZATION

The reaction products were identified by x-ray diffraction (XRD) using Cu-K radiation Scanning electron microscopy (SEM) and transmission electron microscopy (TEM) were used to observe the grain size and morphology of the product. The magnetic properties of the products were observed using a vibrating sample magnetometer (VSM) at room temperature under a maximum field.

IV. EXPERIMENTAL

Sol gel method is employed to synthesize a strontium hexaferrite with chemical formula $\text{SrNi}_{(1-x)}\text{Co}_x\text{Fe}_{12-x}\text{O}_{19}$ for $x=0.00, 0.25, 0.50, 0.75$ and 1 . High purity ($> 99\%$) (Sigma-aldrich) Strontium nitrate ($\text{Sr}(\text{NO}_3)_2 \cdot 6\text{H}_2\text{O}$) and Ferric nitrate ($\text{Fe}(\text{NO}_3)_3 \cdot 9\text{H}_2\text{O}$) with citric acid ($\text{C}_6\text{H}_8\text{O}_7 \cdot \text{H}_2\text{O}$) were taken as starting materials for the synthesis. All the starting materials were mixed in desired stoichiometric amount in sufficient amount of distilled water. The whole mixture is then placed on hot plate with magnetic stirrer. The mixture was continually stirred at constant temperature of 90°C and liquid ammonia was added slowly in order to maintain the Ph a constant value 7. After continuously stirring and heating at 90°C for 2-3 hours the mixture become viscous and sol was formed and after some time it converts into dried gel, by the process of self-ignition the dried gel was burnt and a fine ash was obtained. The burnt ash is grounded for two hours and then subjected to final sintering at 900°C for 6 hours. After final sintering the powders were again grinded for two hours to obtain the fine particles of the final products.

V. CHARACTERIZATION

The reaction products were identified by x-ray diffraction (XRD) using Cu-K radiation Scanning electron microscopy (SEM) and transmission electron microscopy (TEM) were used to observe the grain size and morphology of the product. The magnetic properties of the products were observed using a vibrating sample magnetometer (VSM) at room temperature under a maximum field.

VI. X-RAY CHARACTERIZATION

X-ray diffraction was deployed for determination of crystal structure, crystallite size and bulk density. Physical properties have strong materials depend on the crystal structure which introduced the atomic arrangement so information about crystal chemistry is important to understand and identify the electric and magnetic properties. X-ray diffraction is one of the most significant and non-destructive techniques for structure identify the materials from which we can detect lattice constant, crystallite/particle/grain size and strain. The particle size does not display correlation with the Co dopants concentration. The micro-strain not changes with the Co dopants doping level (x), and it remains nearly constant for all Co dopants. Room temperature X-ray diffraction pattern are taken for all sample in the 2θ range 20-80o for all sample Figure 2 shows the X-ray diffraction pattern of SrNi_(1-x)Co_xFe_{12-x}O₁₉ for x=0.00, 0.25, 0.50, 0.75 and 1.00 samples at room temperature. The X-ray diffraction pattern confirms the formation of M-type crystal structure. The main reflection planes (006), (105), (110), (107), (113), (114), (200), (203), (205), (206), (208), (217), (112), (306), (220) and (317) appear in a x-ray diffraction pattern for all the sample. All these planes are corresponds to hexagonal structure which was confirmed by using standard JCPDS card no. 33-1340. A dominant (114) plane is obtained for all compositions. The intensities of a planes varies with variation of dopant composition may be associated with occupation of Fe³⁺sites by the dopants. The lattice parameter are calculated by using below formula [18],

$$\frac{1}{d^2} = \frac{4}{3} \frac{h^2+hk+k^2}{a^2} + \frac{l^2}{c^2} \tag{1}$$

The calculated values are listed in Table 2. It reveals that as the doping composition increases the lattice parameter decreases it may be due to larger ionic radii of dopant Co²⁺ =0.74 Å[6]as compare to Fe³⁺=0.64 Å [7]. The change in lattice parameter value represents the arrangements of these substituting ions in the structure to occupy vacancy site of Fe³⁺. The c/a parameter can be used to identify the structure type, and the synthesise sample is known to be the M-type magnetoplumbite structure if c/a ratio is lower than 3.98 [8]. As observed from table all samples are founded by measurement those values of c/a ratio are lower than 3.98, which indicate the formation of M-type hexagonal structure. The unit cell volumes of samples were calculated by following equation (2). The average crystallite sizes were calculated from the X-ray diffraction peaks using the following Scherer’s formula (3) [19].

$$V = \frac{\sqrt{3}}{2} a^2 c \tag{2}$$

$$D = \frac{0.9 \lambda}{\beta \cos \theta} \tag{3}$$

Where D is the crystallite size, λ is the X-ray wavelength β is the full width half maxima and θ is the diffraction angle.

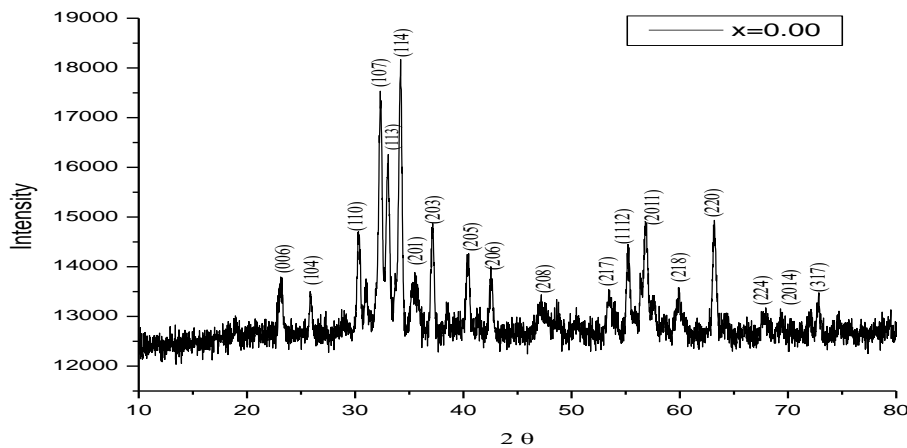


Fig. 2 X-ray diffraction of strontium ferrite

VII. MAGNETIC PROPERTIES

The magnetic properties of the as-synthesized sample of $\text{SrNi}_{(1-x)}\text{Co}_x\text{Fe}_{12-x}\text{O}_{19}$ for $x=0.00, 0.25, 0.75$ and 1 , were measured by VSM at room temperature. Figure 3 and 4 demonstrate the obtained hysteresis loops and the change in magnetic parameters saturation magnetization (M_s), remanence (M_r) and coercive field (H_c). It is known that magnetic properties are influenced by doping of Fe^{3+} with different cations. Theoretically, the coercivity of the M type hexaferrite is influenced by many factors, such as the particle size, morphology, ion substitution, Interface structure, strain and crystal defects [34]. In the present study composition of Ni-Co ions has significant impact on the magnetic properties. The value of coercivity 4.8 KOe obtained for $x=0.00$ ($\text{SrNiFe}_{11}\text{O}_{19}$) sample 6.7 KOe for doped hexaferrite. The obtained H_c values suggest that the synthesized hexagonal ferrites are promising candidates for potential magnetic recording applications [20].

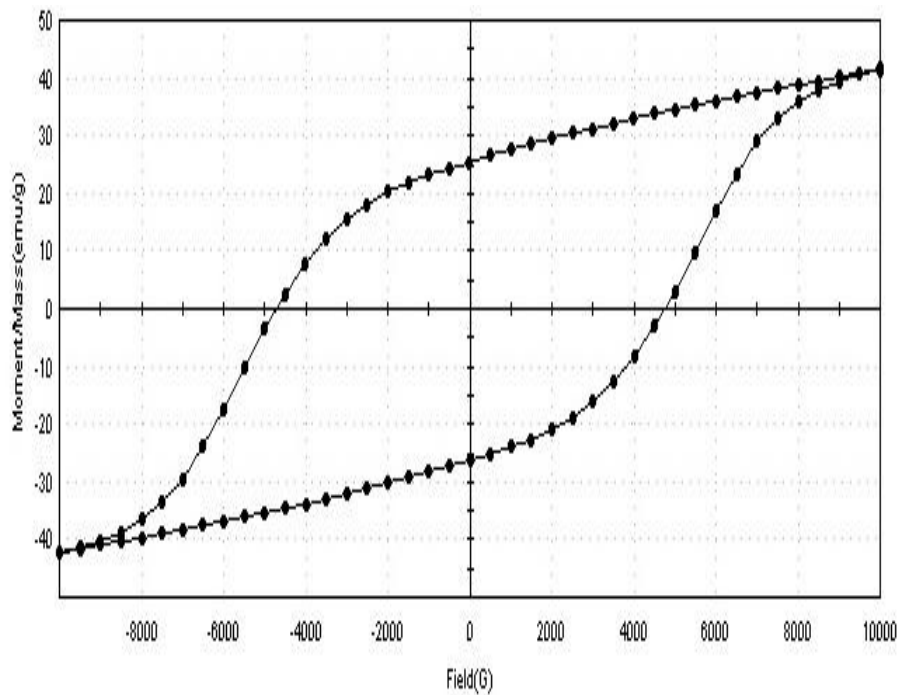


Fig 3 Magnetization of strontium ferrite

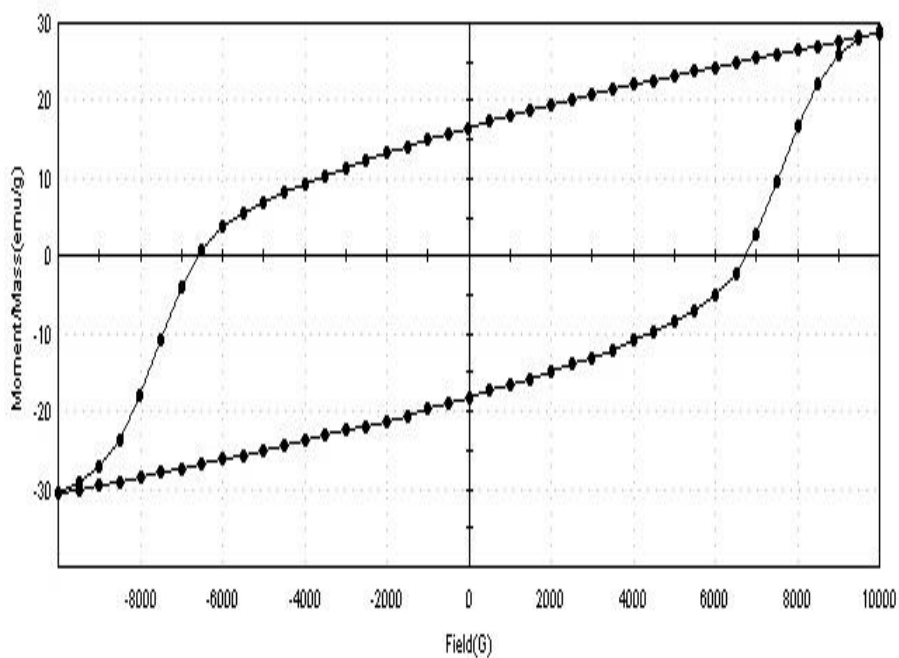


Fig. 4 Magnetization of doped hexaferrite

VIII. ELECTRICAL RESISTIVITY

The DC resistivity of the samples is estimated by two probe methods. Sample made in the form of pellet. A thin layer of silver paste was applied on both the flat surface of the pellets for good electrical contact. The sample holder along with the sample is placed in an electric furnace. The temperature of the furnace was varied using dimmer. A suitable thermocouple was used to measure the temperature of the sample. The resistance of a sample was measured at the regular interval of temperature (5 K). The values of resistivity were calculated using the following equation [21],

$$\rho = \frac{RA}{t} \Omega \cdot \text{cm} \quad (4)$$

Where R: Resistance of the sample; A: Surface area of the sample = πr^2 ; R: Radius of the sample; resistivity was studied as a function of temperature and the plot of $\log \rho$ vs $1000/T$ for all the compositions is shown in Fig.5. It is observed that for all sample resistivity decrease with the increase of temperature. Increase of temperature generally increases the mobility of conduction charge species and, therefore, the resistivity decreases. The ferrite show semiconducting behaviour. The resistivity of a material generally increases with temperature for most metals and decreases for some semiconductors. This behavior is described by the temperature coefficient of resistivity. It is true that increased temperature often increases the mobility of conduction charge species and can decrease resistivity in certain materials, resistivity itself is a more complex property that depends on the balance between carrier mobility, carrier concentration, and scattering mechanisms within the material.

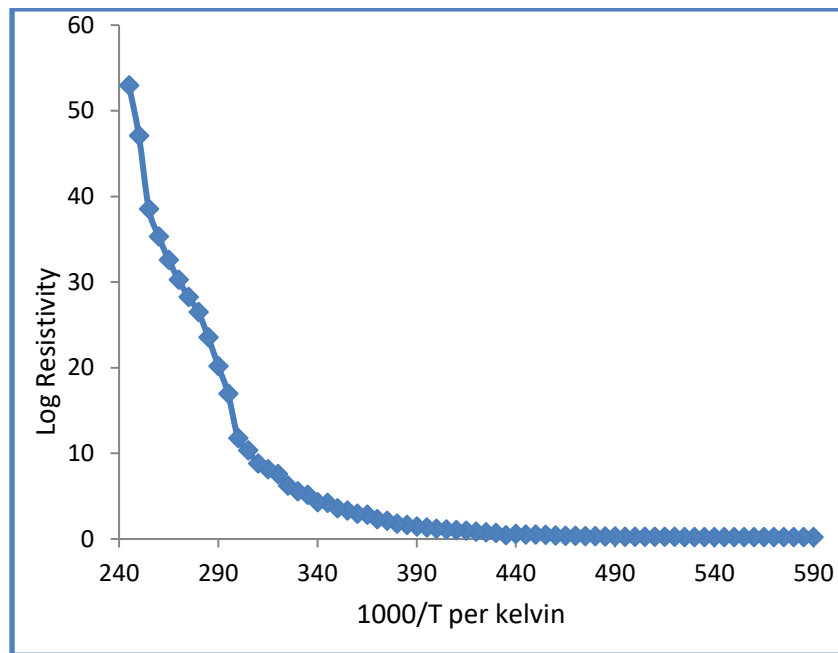


Fig 5. Resistivity graph of strontium hexaferrite

IX. CONCLUSION

We succeeded in the synthesis of a Ni-Co doped strontium hexaferrite nano material by sol-gel method. The sample appears in a hexagonal phase as confirmed by the XRD studies. The lattice parameter found to be decreases as doping increases. The D.C. electrical resistivity increases with decrease in temperature confirming the semiconductor nature. The coercivity of a sample decreases with Ni-Co doping. The value of coercivity 4.8 KOe obtained for $x=0.00$ ($\text{SrNiFe}_{11}\text{O}_{19}$) sample 6.7 KOe for doped hexaferrite. Thus the recent study estimates the potential application of Ni-Co doped strontium for permanent magnet application due to high coercive field.

ACKNOWLEDGMENT

Author Dr. Kunal R. A. is thankful to Swami Ramanand Terth Marathwada University, Nanded , with letter number APDS/Uni.MRP/Sci.& Tech-Physics/2019-20/2836 for financial support to Minor Research Project.

REFERENCES

- [1] Thakur, R.R. Singh, P.B. Barman, *J. Magn. Magn. Mater.* 326 (2012) 35
- [2] Drmota, J. koselj, M. Drogenik, A. Znidarsic, *J. Magn. Magn. Mater.* 324(2012)
- [3] Goldman, *Modern Ferrite Technology*, Marcel Dekker Inc., New York, 1993.
- [4] Chang,S.Kangning,C.Pengfei, *J.Magn.Magn.Mater.*324(2012)802–805.
- [5] M.N. [5]Ashiq,M.J.Iqbal,M.Najam-ul Haq,P.Hernandez Gomez, A.M.Qureshi, *J.Magn.Magn.Mater.* 324(2012)15–19.
- [6] V. G. Harris, A. Geiler, Y. Chen, S. D. Yoon, M. Wu, A. Yang, Z. Chen, P. He, P. V. Parimi, X. Zuo, C. E. Patton, M. Abe, O. Acher, and C. Vittoria, *J. Magn. Magn. Mater.* 321, 2035 (2009).
- [7] S. Nakagawa, N. Matsushita, and M. Naoe, *J. Magn. Magn. Mater.* 235, 337 (2001).
- [8] J. J. Went, G. W. Rathenau, E. W. Gorter, and G. W. van Oosterhout, *Phys. Rev.* 86, 424 (1952).
- [9] A. Xia, C. Zuo, L. Chen, C. Jin, and Y. Lv, *J. Magn. Magn. Mater.* 332, 186 (2013).
- [10] F. N. Tenorio-González, A. M. Bolarín-Miró, F. S.-D. Jesús, P. Vera-Serna, N. Menéndez-González, and J. Sánchez-Marcos, *J. Alloys Compd. C*, 2083 (2017).
- [11] T. Dippong, O. Cadar, I. G. Deac, M. Lazar, G. Borodi, and E. A. Levei, *J. Alloys Compd.* 828, 154409 (2020).
- [12] T. Dippong, E. Andrea Levei, O. Cadar, I. Grigore Deac, M. Lazar, G. Borodi, and I. Petean, *J. Alloys Compd.* 849, 156695 (2020).
- [13] Jorg T., Daniela S.,Jean-Mariele B., Falko L., Vojtech C., Karel K. Helena S.*Journal of Solid State Chemistry*, 226(2015)133–141
- [14] H. Hmok, I. Betancourt, E. Martinez-Aguilar, J. Ribas-Arino, O. R. Herrera, *Theoretical Chemistry Accounts*, (2012)136-140.
- [15] Karl Kouril thesis, Local structure of hexagonal ferrites studied by NMR.
- [16] Y. Xu., G. L. Yang, A.P. Chu, H. R. Zhai, *Phys. Status.solidi B*, 157 (1990)685 18
- [17] B. K. Rai, S.R. Mishra, V. V. Nguyen, J. P. Liu. *Journal of A. and Com.* 550(2013)
- [18] V. K. Chakradhary, M. J. Akhtar*Composites Part B*, 183 (2020) 107667.
- [19] D. Neupane, L. Wang, H. Adhikari, J. Alam, S. R. Mishra, *J. of alloys and comp.* 701(2017)138-146.
- [20] R. Shanker, *J.Mater.Sci.*25 (1990)2465–2570.
- [21] R. A. Kunale, R. H. Kadam, D. R. Mane,*Journal of Advancements in Research & Technology*, 2(2013)37- 40.

¹S. Krishnakumar²Amol V. Pansare³Xavier Gama⁴Guruling. B. Todkar⁵G.K. Brajdar⁶Renuka. A. Kunale

Novel binary polymeric nanocomposite for high performance supercapacitor



Abstract: - We report our research on the production of a novel binary polymeric nanocomposite of $\text{Ni}_{0.7}\text{Mg}_{0.3}\text{Fe}_2\text{O}_4$ ferrite and Polyaniline using in-situ polymerization of monomer aniline for use in high-performance supercapacitors. For structural and morphological analysis, X-ray diffraction (XRD), Field emission scanning electron microscopy (FE-SEM), Field emission gun transmission electron microscopy (FEG-TEM) were used to examine the as-synthesized binary NMF/PANI nanocomposites. Cyclic voltammetry (CV) was used to evaluate the electrochemical performance of pure ferrite and binary NMF/PANI nanocomposite. The binary NMF/PANI nanocomposite at 1 Ag⁻¹ current was found to have a maximum specific capacitance of 193 Fg⁻¹. Binary NMF/PANI nanocomposite is best choice for high performance supercapacitor.

Keywords: Ferrite, Polyaniline, Nanocomposites, Electrochemical, Specific capacity.

^{1*}Corresponding author: Author: ⁶Kai. Rasika Mahavidyalaya Deoni, Dist. Latur, India

^{1,3}Department of Physics, Kittel Science College, Dharwad, Karnataka -580001 India

² Lab Composites Group, Mechanical Systems Engineering, Empa - Swiss Federal Laboratories for Materials Science and Technology, Überlandstrasse 129, 8600 Dübendorf, Switzerland.

³ Dayanand Science College Latur, Maharashtra, 413512, India.

⁵Shr Renukadevi Mahavidyalaya Mahur, Dist. Nanded, India,

Copyright©JES2024on-line:journal.esrgroups.org

I. INTRODUCTION

The harmful effects of greenhouse gas emissions on the environment, coupled with the scarcity of fossil fuels, have created an urgent demand for renewable energy resources, along with their storage and distribution. This situation has been driven by the need to address limited energy sources and the complex issues related to environmental pollution. As a result, there has been intensified development of clean, environmentally friendly, and low-cost alternative energy resources.

Supercapacitors, also known as electrochemical capacitors (ECs), have garnered significant attention in the realm of energy storage due to their exceptional cycling stability and high energy density [1,2]. The performance of supercapacitors is largely influenced by two key factors, electronic conductivity, and the kinetics of ion diffusion. These factors are, in turn, determined by the type of electrode materials and their structural characteristics. The electronic conductivity of the supercapacitor is primarily dictated by the nature of the electrode materials used. Materials with higher conductivity enable more efficient charge transfer, thereby enhancing the overall performance of the supercapacitor. Common materials include carbon-based substances, conducting polymers, and metal oxides, each offering distinct advantages in terms of conductivity and stability. On the other hand, the kinetics of ion diffusion, which refers to the rate at which ions move within the electrode material, is influenced by the structure of the electrode. A well-designed porous structure can facilitate faster ion transport, improving the charge/discharge rates and overall efficiency of the supercapacitor. Advanced fabrication techniques are often employed to create optimized structures that maximize ion accessibility and minimize resistance.

Mixed spinel oxide material of controlled size and shape are of emerging curiosity for both traditional science and technological applications because of their chemical and physical properties [6–8]. In this regard, spinel binary transition metal oxides such as MgCo_2O_4 [3], NiCo_2O_4 [4], MnCo_2O_4 [5], NiFe_2O_4 [6], CuCo_2O_4 [7], MgCo_2O_4 [8], provide a wide range of options for supercapacitor and lithium-ion battery electrodes because of their low cost, eco-friendly properties and excellent electrochemical performances for achieving high-performance energy storage properties [9]. Conducting polymers such as polyaniline and polypyrrole, with their high conductivity, high capacitance, and low cost, have attracted interest in sensors, electrochromical devices, and energy storage devices. Nanocomposites, which blend metal oxide nanoparticles with a conducting polymer and/or carbonaceous material, have been found to dramatically improve the power capacity and rate capacitance of energy devices [10-14]. In this work we report the preparation $\text{Ni}_{0.7}\text{Mg}_{0.3}\text{Fe}_2\text{O}_4$ ferrite and NMF/PANI nanocomposite for supercapacitor electrode. Here, a thorough analysis of binary nanocomposites' electrochemical performance is methodically provided.

II. EXPERIMENTAL DETAILS

The synthesis of NMF ferrite nanoparticles: $\text{Ni}_{0.7}\text{Mg}_{0.3}\text{Fe}_2\text{O}_4$ ferrite powder was synthesized using the sol-gel auto-combustion method. The detailed procedure is as follows. Stoichiometric amounts of $\text{Ni}(\text{NO}_3)_2 \cdot 6\text{H}_2\text{O}$, $\text{Mg}(\text{NO}_3)_2 \cdot 6\text{H}_2\text{O}$, and $\text{Fe}(\text{NO}_3)_3 \cdot 9\text{H}_2\text{O}$ were individually dissolved in deionized water, followed by the addition of a specific amount of lemon juice to the metal nitrate solutions. These cationic solutions were then combined and stirred continuously for one hour to enhance homogeneity. Ammonium hydroxide was added drop wise to adjust the pH to approximately 7.0. The resulting mixed solution was heated at 90°C with constant stirring until it formed a dried gel, which subsequently underwent self-propagating combustion to yield loose precursors [15]. Finally, NMF crystalline powder was obtained by calcining these precursors at 550°C for 4 hours.

Preparation of NMF/ PANI nanocomposite: $\text{Ni}_{0.7}\text{Mg}_{0.3}\text{Fe}_2\text{O}_4$ ferrite/PANI nanocomposite was synthesized via in-situ polymerization in an aqueous medium. Initially, NMF ferrite nanoparticles were dispersed in 70 ml of 1 M hydrochloric acid and stirred for two hours to ensure a homogeneous dispersion. Subsequently, 2 ml of aniline monomer was introduced into the solution, followed by an additional hour of stirring. A solution of ammonium peroxydisulfate (ASP) was prepared by dissolving 4.98 g of ASP in 40 ml of 1 M hydrochloric acid, maintaining a 1:1 molar ratio of ASP to aniline. This solution was then slowly added drop wise to the nanoparticle suspension under constant stirring. The polymerization reaction was carried out over 10 hours at a temperature range of 0°C to 5°C . The resulting suspension was filtered, washed with 1 M hydrochloric acid and deionized water, and then dried in a vacuum oven at 80°C for 48 hours. The final product, a green powder, was characterized using various analytical techniques.

III. CHARACTERIZATION

The ferrite nanoparticles, nanocomposites were made, and their composition, morphology, and structure were investigated. To examine the phase structure and crystalline form of the ferrites and composites, X-ray diffraction (XRD) was used. A field emission scanning electron microscope (FE-SEM) and a high-resolution transmission electron microscope (HR-TEM) were used to analyze the surface morphology. Using an Autolab PGSTAT204 potentiostat for CV, the electrochemical characteristics were investigated.

IV. STRUCTURAL ANALYSIS

Fig. 1 shows the XRD pattern of the as synthesized NMF ferrite nanoparticles and NMF/PANI nanocomposite. In the XRD pattern of NMF nanoparticles, the peaks observed at 18.37, 30.49, 35.92, 37.10, 43.61, 54.00, 57.55, 63.16, 71.58, 74.67, 75.53° correspond to (111), (220), (311), (222), (400), (422), (511), (440), (620), (533) and (622) planes, respectively. The peaks observed in NMF /PANI nanocomposite in the XRD pattern, 18.37, 30.62, 35.92, 37.57, 43.61, 53.00, 57.55, 63.16, 71.58, 74.67, 75.53° correspond to (111), (220), (311), (222), (400), (422), (511), (440), (620), (533) and (622). It was observed that some peaks shift towards higher degree along with two extra peaks formed at 20.68° and 25.6° in nanocomposite. The extra peaks formed at 20.68° and 25.6° are due to polyaniline in the composite [15,16]. The intensity of peaks decreases due to amorphous nature of polyaniline. The average crystallite size of NMF ferrite nanoparticles was calculated using diffraction at (311) plane and was found to be 46nm.

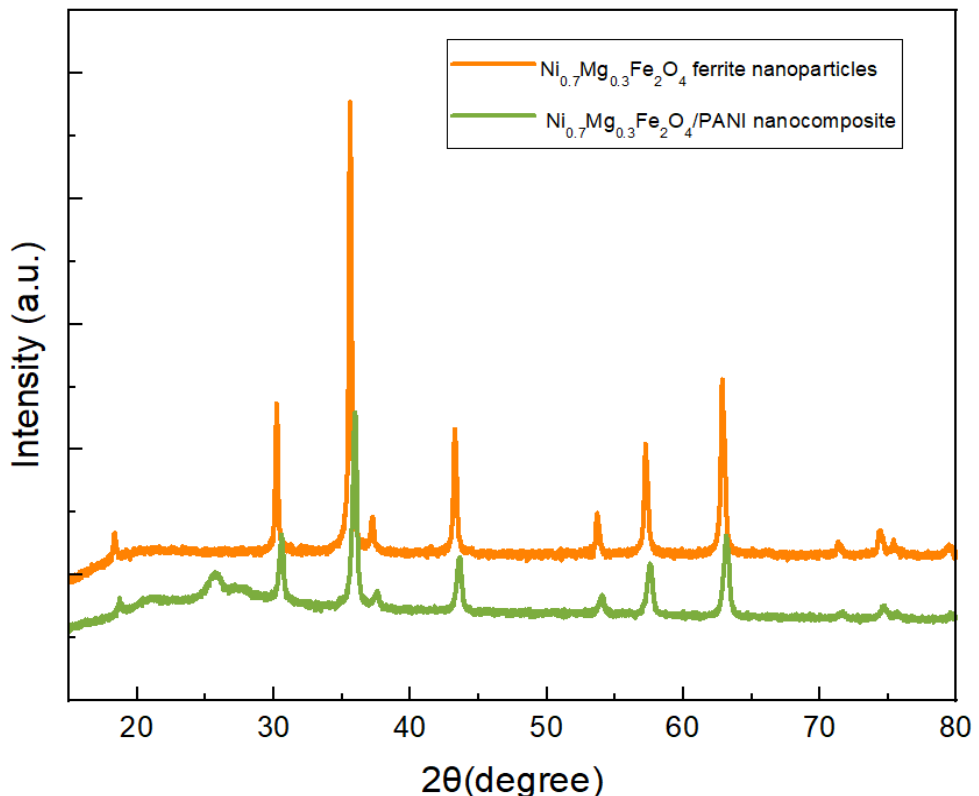


Fig. 1 XRD Patterns of NMF and NMF/ PANI

V. MORPHOLOGICAL CHARACTERIZATION

The FE- SEM images of NMF ferrite nanoparticles and NMF/PANI nanocomposite are shown in Fig.2 (a) and (b). Fig.2 (a) shows NMF ferrite nanoparticles are in a cubic structure and agglomeration of particles due to ferromagnetic properties of material.

The coating of polyaniline on NMF ferrite nanoparticles was observed in Fig.2(b). From FEG-TEM images, the cubic structure of spinel ferrite can be clearly seen and the magnetic dipole interaction gives rise to the agglomeration of ferrite particles as shown in Fig. 3 (a). The average particle size of NMF ferrite nanoparticles was also calculated using FEG-TEM images. The average particle size is found in the range of 46nm, which is calculated using Image-J software. Fig.3 (b) shows the HR- TEM images, particle boundary is clearly observed with light colour coating on the dark coloured spots, which are ferrite nanoparticles and light colour boundary part indicates amorphous polyaniline.

VI. ELECTROCHEMICAL CHARACTERIZATION

NMF ferrite nanoparticles and NMF /PANI nanocomposite are electrochemically investigated using CV in an aqueous electrolyte containing 2 M KOH. At a scan rate of 5 to 80 mV/s, all of the CV curves of NMF ferrite nanoparticles were measured in the voltage range of 0.2 to 0.5 V (vs Ag/AgCl), and that of NMF /PANI nanocomposite in the voltage range of 0.1 to 0.55 V (vs Ag/AgCl). All these curves show strong oxidation and reduction peaks [18-20].

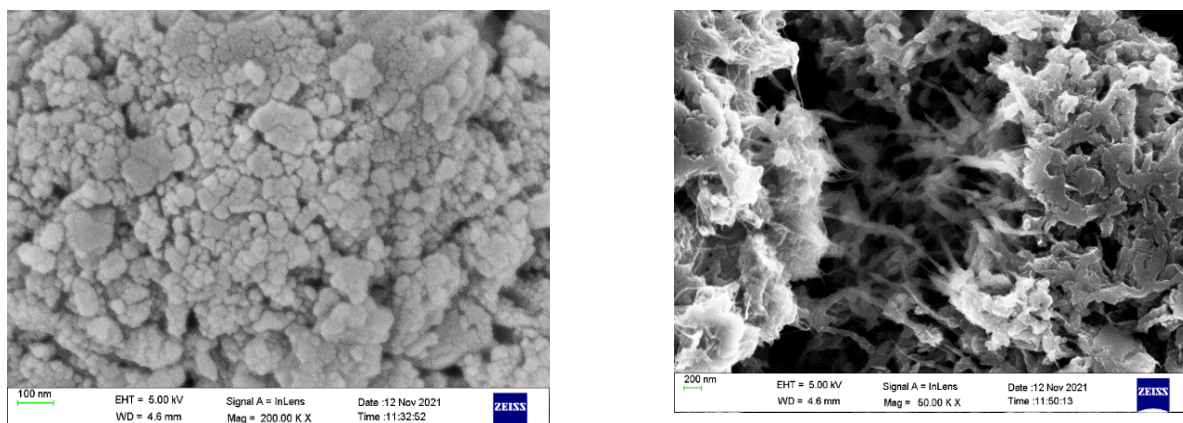


Fig. 2 (a) FE- SEM image of NMF Fig. 2 (b) FE-SEM image of NMF /PANI nanoparticles nanocomposite

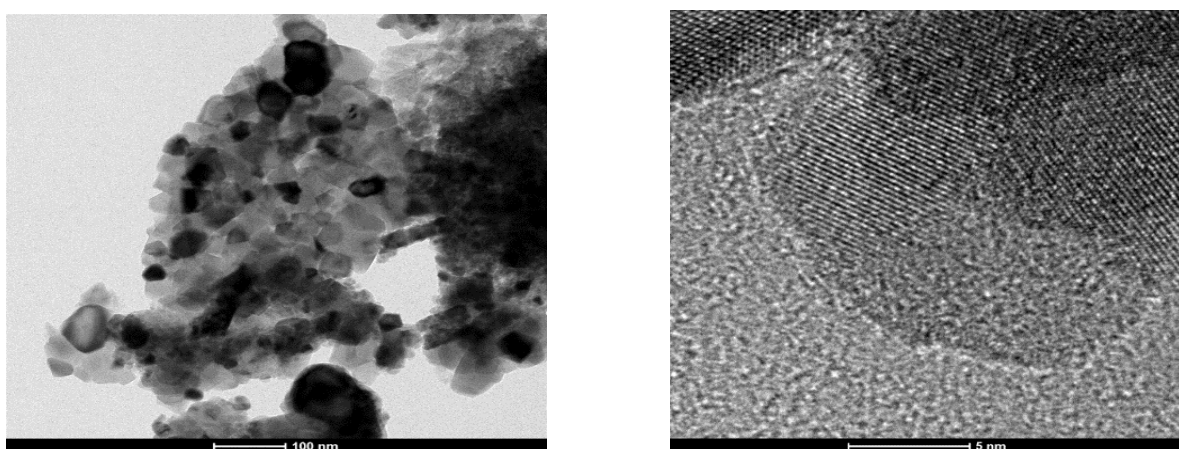


Fig. 3 (a) TEM image of NMF Fig. 3(b) TEM image with HR- TEM of

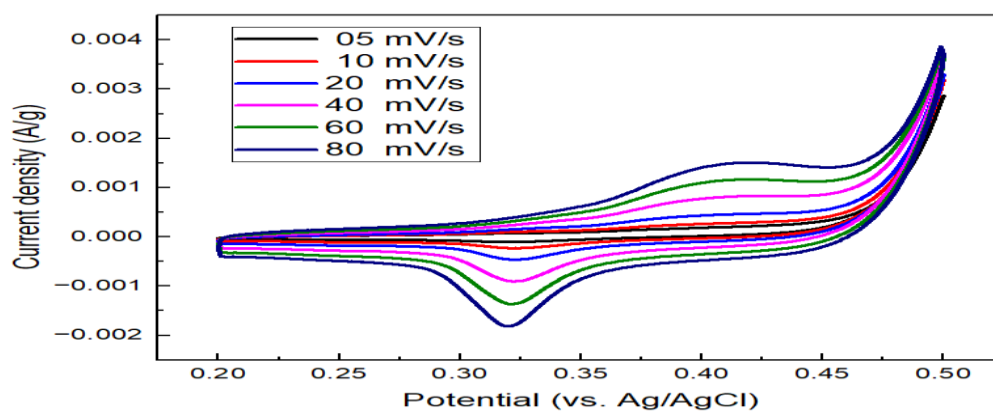


Fig. 4 (a) C V curves of NMF

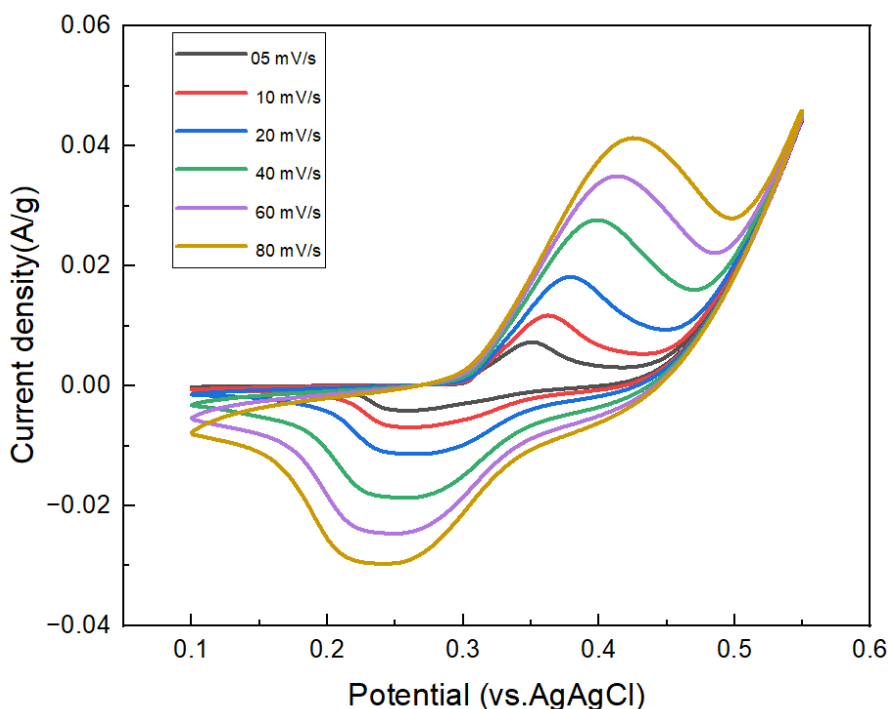


Fig. 4 (b) C V curves of NMF /PANI ferrite nanoparticles.

In a three-electrode configuration system, the CV plots of NMF ferrite nanoparticles and NMF/PANI nanocomposite electrodes at various scan rates (5 mV/s, 10 mV/s, 20 mV/s, 40 mV/s, 60 mV/s, and 80 mV/s) are displayed in Fig. 4 (a) and (b). When PANI is added, the nanocomposite's conducting characteristics improve and grow, improving the specific capacitance and surface area of NMF. Constant conductive network routes created by NMF in the PANI matrix help in ion transport and redox reactions. PANI also improves the electro-chemical performance of the NMF/PANI supercapacitor electrode by minimizing charge transfer resistances and enhancing the interfacial contact between NMF/PANI and electrolyte [21-24]. Using the following formulas, the specific capacitance and energy density were calculated,

$$C_s = \frac{\int I dV}{v \times m \times \Delta V} \dots\dots\dots (1)$$

where, I- Integral area - Scan rate (mVs⁻¹),
 m- Mass of the composites (milligram) and
 ΔV- window potential (volt).

Energy density, E (Wh/kg)

$$E = \frac{0.5 \times C_s \Delta V^2 \times 1000}{3600} \dots\dots\dots (2)$$

The calculated maximum specific capacitance value of NMF nanoparticles and NMF /PANI nanocomposite are 14.85 Fg⁻¹ and 193 Fg⁻¹ at a scan rate of 5 mVsec⁻¹. The energy density value of NMF nanoparticles and NMF/PANI nanocomposite are 0.19 Wh/kg and 9.25 Wh/kg respectively.

VII. CNCLUSION

Magnesium doped nickel ferrite nanoparticles and Magnesium doped nickel ferrite and /Polyaniline nanocomposite were successfully synthesized by sol-gel auto-combustion and In-situ polymerization method. The spinel cubic structure of NMF ferrite and the amorphous nature of polyaniline were verified by the X-ray diffraction pattern. Using XRD and FE-TEM images, the average particle size of the NMF ferrite nanoparticles was determined to be 46 nm. NMF/PANI nanocomposite and NMF ferrite nanoparticles have maximum specific capacitance values of 19.3 Fg⁻¹ and 14.85 Fg⁻¹ at a scan rate of 5 mVsec⁻¹ respectively. NMF ferrite nanoparticles and NMF/PANI nanocomposite have computed energy densities of 0.19 Wh/kg and 9.25 Wh/kg, respectively. The specific capacitance value of NMF/PANI nanocomposite is increased due to conducting polyaniline.

ACKNOWLEDGMENT

The Authors are grateful to Mumbai University Mumbai for providing electrochemical Characterization for our research.

REFERENCES

- [1] Wang Z, Zhang X, Li Y, Liu Z and Hao Z 2013 Synthesis of graphene-NiFe₂O₄ nanocomposites and their electrochemical capacitive behavior *J. Mater. Chem.* 6393–9.
- [2] Zhang G, Xia B Y, Xiao C, Yu L, Wang X, Xie Y and Lou (David) X W, General formation of complex tubular nanostructures of metal oxides for the oxygen reduction reaction and lithium-ion batteries *Angew. Chem.* (2013) 8805–8809.
- [3] Sharma Y, Sharma N, Subba Rao G V and Chowdari B V R Studies on spinel cobaltites, FeCo₂O₄ and MgCo₂O₄ as anodes for Li-ion batteries *Solid State Ion.* (2008) 587–97.
- [4] Jiang H, Ma J and Li C, Hierarchical porous NiCo₂O₄ nanowires for high-rate supercapacitors *Chem. Commun.* (2012) 4465–7.
- [5] Surjit S., Kusha Kumar N., Chandra Sekhar Rout, Electrodeposition of spinel MnCo₂O₄ nanosheets for supercapacitor applications, *Nanotechnology* 26 (2015) 455401.
- [6] Shubhangi B. Bandgar, Madagonda M. Vadiyar, Yong-Chien Ling, Jia-Yaw Chang, Sung-Hwan Han, Anil V. Ghule, and Sanjay S. Kolekar, Metal Precursor Dependent Synthesis of NiFe₂O₄ Thin Films for High-Performance Flexible Symmetric Supercapacitor, *ACS Applied Energy Materials* (2018) 1, 638-648
- [7] S.M. Pawar, B.S. Pawar, P.T. Babar, A.T.A. Ahmed, H.S. Chavan, Y. Jo, S. Cho, J. Kim, B. Hou, A.I. Inamdar, Nanoporous CuCo₂O₄ nanosheets as a highly efficient bifunctional electrode for supercapacitors and water oxidation catalysis, *Appl. Surf. Sci.* 470 (2019) 360–367.
- [8] A.K. Rai, T.V. Thi, J. Gim, J. Kim, Combustion synthesis of MgFe₂O₄/graphene nanocomposite as a high-performance negative electrode for lithium ion batteries, *Mater. Charact.* 95 (2014) 259–265.
- [9] D. Zha, P. Xiong, X. Wang, strongly coupled manganese ferrite/carbon black/ polyaniline hybrid for low-cost supercapacitors with high rate capability, *Electrochim. Acta* 185 (2015) 218–228.
- [10] P. Yu, Z. Zhang, L. Zheng, F. Teng, L. Hu, A novel sustainable flour derived hierarchical nitrogen-doped porous carbon / polyaniline electrode for advanced asymmetric supercapacitors, *Adv. Energy Mater.* 6 (2016) 1601111.
- [11] Yan, B. Jin, D. Li, C. Qian, X. Tan, Temperature dependence of hydrogen bond in the redox process of polyaniline, *J. Electrochem. Soc.* 164 (2017) 521–525.
- [12] W. Wu, Y. Li, L. Yang, Y. Ma, D. Pan, Y. Li, A facile one-pot preparation of dialdehyde starch reduced graphene oxide/polyaniline composite for supercapacitors, *Electrochim. Acta* 139 (2014) 117–126.
- [13] A. Rahy, D.J. Yang, Synthesis of highly conductive polyaniline nanofibers, *Mater. Lett.* 62 (2008) 4311–4314
- [14] Ravindra N. Kambale, Akhilesh Kumar Patel, Sandeep Kumar, K G Suresh, Vaishali Bambole, Green Synthesis, characterization and Microwave absorbing properties of Ni-Cu ferrite nanoparticles, *Research Journey International Multidisciplinary E-Research Journal*, V 168 (B) (2019) 69-72.
- [15] A.K. Rai, T.V. Thi, J. Gim, J. Kim, Combustion synthesis of MgFe₂O₄/graphene nanocomposite as a high-performance negative electrode for lithium ion batteries, *Mater. Charact.* 95 (2014) 259–265.
- [16] Ravindra N Kambale, Sunil M Patange, RA Pawar, Sagar E Shirsath, KG Suresh, Vaishali A Bambole, magnetically recoverable CoFe_{1.9}Gd_{0.1}O₄ ferrite/polyaniline nanocomposite synthesized via green approach for radar band absorption, *Ceramics International* 47, 20 (2021) 28240-28251.
- [17] Ravindra N. Kambale, Krishnakumar M. Sagar, Sunil M. Patange, Sagar E. Shirsath, K. G. Suresh, and Vaishali A. Bambole, Excellent Microwave Absorbing Properties of Nd³⁺Doped Ni–Zn Ferrite/PANI Nanocomposite for Ku Band, *Phys. Status Solidi (a) applications and materials science*, Wiley-VCH GmbH (2022), 2100505-1-2100505- 14.
- [18] Gita Singh, Sudeshna Chandra, Nano-flowered manganese doped ferrite@PANI composite as energy storage electrode material for supercapacitors, *Journal of Electroanalytical Chemistry*, 874, (2020), 114491.
- [19] J. Yan, Y. Huang, C. Chen, X. Liu, H. Liu, The 3D CoNi alloy particles embedded Nd doped porous carbon foam for high-performance microwave absorber, *Carbon* 152 (2019) 545–555.
- [20] Min Fu, Wei Chen, Xixi Zhu, Qingyun Liu, One-step preparation of one dimensional nickel ferrites/graphene composites for supercapacitor electrode with excellent cycling stability, *Journal of Power Sources*, 396, (2018) 41-48.
- [21] P. Chavan, L.R. Naik, P.B. Belavi, G. Chavan, C.K. Ramesha, R.K. Kotnala, Studies on electrical and magnetic properties of Mg-substituted nickel ferrites, *J. Electron. Mater.* 46 (2017) 188–198.
- [22] X. Wang, Y. Fang, B. Shi, F. Huang, F. Rong, R. Que, Three-dimensional NiCo₂O₄@ NiCo₂O₄ core-shell nanocones arrays for high-performance supercapacitors, *Chem. Eng. J.* 344 (2018) 311–319.
- [23] Shaoyun Chen, Huan Cheng, Du Tian, Qi Li, Min Zhong, Jian Chen, Chenglong Hu, and Hongbing Ji, Controllable Synthesis, Core-Shell Nanostructures, and Supercapacitor Performance of Highly Uniform Polypyrrole/Polyaniline Nanospheres, *ACS Applied Energy Materials* (2021) 4, 3701-3711.

¹Vijay R.
Chinchamalature
²Nilesh R. Thakare

**Thermoluminescence Properties of
Fluorophosphate Materials
 $\text{Li}_9\text{Mg}_3[\text{PO}_4]_4\text{F}_3$, $\text{Li}_2\text{Mg}[\text{PO}_4]\text{F}$.**



Abstract: - In this study, the thermoluminescence (TL) properties of fluorophosphate materials $\text{Li}_9\text{Mg}_3[\text{PO}_4]_4\text{F}_3$ and $\text{Li}_2\text{Mg}[\text{PO}_4]\text{F}$ were investigated as potential candidates for dosimetry applications. The results indicate that the irradiated samples display notable thermoluminescence within the temperature range of 100°C to 300°C, with a prominent peak observed at 250°C. The TL spectra exhibit a broad band centered at 400 nm, which is attributed to structural defects in $\text{Li}_9\text{Mg}_3[\text{PO}_4]_4\text{F}_3$ and $\text{Li}_2\text{Mg}[\text{PO}_4]\text{F}$. UV-vis spectroscopy determined that the energy required to excite these defects is 4.4 eV (approximately 280 nm). Further evidence of intrinsic defects was provided by electron paramagnetic resonance (EPR) analysis in $\text{Li}_9\text{Mg}_3[\text{PO}_4]_4\text{F}_3$. This method was used to simulate various intrinsic defects, including single and complex, as well as neutral and charged vacancies. These defects introduce additional electronic states within the band gap, leading to absorption bands in the visible region. Both experimental and theoretical investigations suggest that $\text{Li}_9\text{Mg}_3[\text{PO}_4]_4\text{F}_3$ and $\text{Li}_2\text{Mg}[\text{PO}_4]\text{F}$ are promising optical matrices for dosimetric applications.

Keywords: Thermoluminescence (TL), Fluorophosphate (FP), Microwave-assisted synthesis (MAS)

¹ Associate Professor, Department of Physics, Hutatma Rashtriya Arts and Science College, Ashti, 442202, Distt: Wardha (M.S.), India.
Email: vijay05051970@gmail.com

² Associate Professor, Department of Physics, P. R. Pote Engineering College, Amravati, 444604 (M.S.), India.
Copyright © JES 2024 on-line : journal.esrgroups.org

I. INTRODUCTION

Fluoride-phosphate-based materials have recently garnered significant attention due to their ability to combine the advantages of both anionic species. These fluorophosphate compounds exhibit a range of desirable properties inherited from their phosphate and fluoride components, such as excellent thermal and hydrolytic stability [1]. Cathode materials for Li-ion batteries are known for their high structural diversity and superior properties compared to their phosphate analogs [2,3]. The presence of both fluorine anions and phosphate groups is particularly valuable for optical applications. Phosphates are an appealing choice for crystals used in deep-UV optical materials, as the tetrahedral configuration of PO₄ units aids in achieving a short UV absorption edge [4,5]. Fluorine, owing to its high electronegativity, plays a crucial role in increasing the optical band gap and expanding the transmittance range. Materials belonging to the large family of apatites doped with rare-earth ions, such as NaCa₃Bi(PO₄)₃F:Sm³⁺ [6], Ca₈NaBi(PO₄)₆F₂:Eu [7], Sr₅(PO₄)₃F: Er [8], (Sr,Mn)₅(PO₄)₃(F,Cl) [9], are becoming attractive because of their potential application as efficient phosphors for white light emitting diode devices, as a component of eye-safe devices, optical fiber telecommunication, security systems, and medical imaging. Besides individual compounds that contain both anionic groups, mixed phosphate-fluoride glasses [10] and glass-ceramic compositions [11,12] are also of significant interest. Fluorophosphate phosphors doped with Eu³⁺ and Tb³⁺ are particularly promising candidates for use in fluorescent lamps or white LED devices. Fluoride-containing phosphate-based glass systems are considered a unique class of optical laser glasses with potential applications in color separation optics for high-power laser facilities [13,14]. These glasses are distinguished by their high transparency, ranging from deep ultraviolet to infrared, their capacity to dissolve high concentrations of dopants, low phonon energies, anomalous partial dispersion, and low linear and nonlinear refractive indices [15]. In this study, to evaluate this potential, Li₉Mg₃[PO₄]₄F₃ and Li₂Mg[PO₄]F were synthesized using a microwave-assisted method, and their thermoluminescence properties were thoroughly investigated.

It has been found that X-ray exposed Li₉Mg₃[PO₄]₄F₃ can effectively convert ionizing radiation into detectable light both in real time and after additional thermal stimulation, making it a promising optical matrix for dosimetric applications. The study confirms that all types of luminescence observed are due to intrinsic defects in Li₉Mg₃[PO₄]₄F₃ and Li₂Mg[PO₄]F. Commonly used and well-studied materials for TL dosimetry include Al₂O₃:C single crystals, as well as fluorides, sulfates, borates, and phosphates of alkali and alkaline earth elements. LiF TL phosphor is regarded as one of the most widely used materials for dosimetric applications due to its effective atomic number, $Z_{\text{eff}} = 7.24$, which renders its TL response nearly independent of radiation energy. Similarly, phosphates hold significant importance for radiation dosimetry, primarily because of their chemical and thermal stability and the simplicity of their preparation methods. Among the materials, exhibiting thermally stimulated or optically stimulated luminescence, LiMgPO₄: Tb, B, LiMgPO₄: Er, LiCaPO₄: Eu, NaCaPO₄: Dy were found to be very sensitive radiation dosimetric materials. Incorporating two distinct anionic groups within a crystalline compound offers an extra degree of flexibility in designing new dosimetric materials, making the use of halophosphate phosphors, especially fluorophosphates, a promising strategy.

II. EXPERIMENTAL DETAILS

To prepare Li₉Mg₃[PO₄]₄F₃, Li₂Mg[PO₄]F fluorophosphate, microwave assisted synthesis was used. The appropriate amounts of materials Li₃PO₄ (lithium orthophosphate, 99.9%), LiF (lithium fluoride, 99.9%) and LiMgPO₄ (prepared by the conventional solid-phase method) were mixed and milled in an agate mortar until the average particle size was less than 10 μm. The powder was pressed into a tablet and thermally treated in a microwave muffle furnace at 650 °C.

Then these materials were heated at 800°C for 8 hours, results the compounds of Li₉Mg₃[PO₄]₄F₃, Li₂Mg[PO₄]F in powder forms. The samples were then slowly cooled at room temperature. The resultant polycrystalline mass was crushed to fine particle in a crucible. This powder form was used in further study. The prepared host lattice was analyzed for phase purity and crystallinity using X-ray powder diffraction (XRD). For thermoluminescence (TL) studies, the samples were irradiated with gamma rays from a Co-60 source at room temperature, with a dose rate of 0.994 kGy/h, accumulating a total dose of 5 Gy. After the desired exposure, thermoluminescence (TL) glow curves were obtained for 2 mg of sample at each measurement, with a heating

rate of 2°C/s. The TL glow curves were recorded using a standard setup, which included a small metal plate heated directly by a temperature programmer.

III. CHARACTERIZATION

The experimental X-ray diffraction (XRD) pattern of $\text{Li}_9\text{Mg}_3[\text{PO}_4]_4\text{F}_3$ and $\text{Li}_2\text{Mg}[\text{PO}_4]\text{F}$, prepared via microwave-assisted synthesis, was analyzed. The diffraction peaks were fully indexed to a hexagonal structure with the space group P63. The cell parameters for the fluorophosphate were determined by refining the XRD data, resulting in $a = 12.604(1) \text{ \AA}$ and $c = 5.003(2) \text{ \AA}$. Additionally, traces of Li_3PO_4 , according to JCPDS data, were observed in the XRD pattern. Overall, the XRD pattern is in good agreement with the reported data.

TL glow curves of $\text{Li}_9\text{Mg}_3[\text{PO}_4]_4\text{F}_3$, $\text{Li}_2\text{Mg}[\text{PO}_4]\text{F}$.

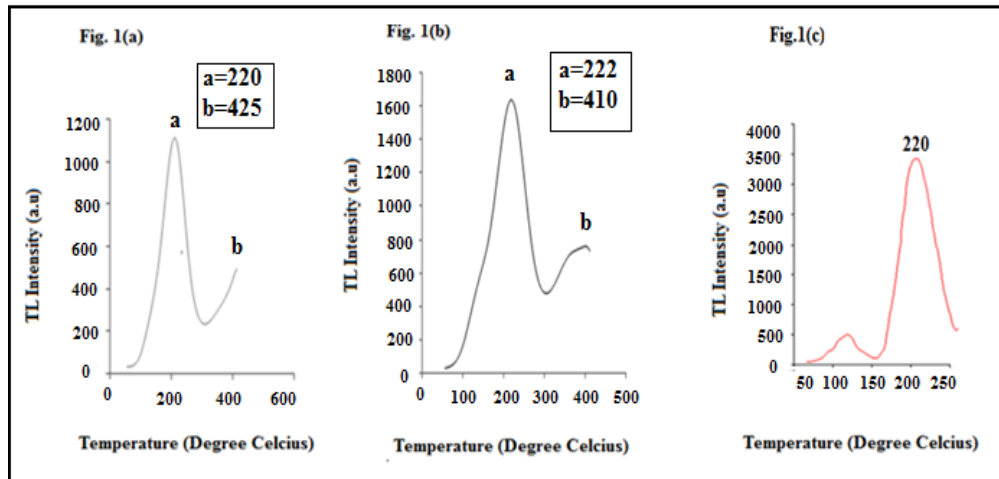


Fig.1: TL glow curves of $\text{Li}_9\text{Mg}_3[\text{PO}_4]_4\text{F}_3$, $\text{Li}_2\text{Mg}[\text{PO}_4]\text{F}$ thermoluminescence materials.

Figure 1(a) shows a typical glow curve for the sample $\text{Li}_9\text{Mg}_3[\text{PO}_4]_4\text{F}_3$, $\text{Li}_2\text{Mg}[\text{PO}_4]\text{F}$ exposed to γ -rays for 5 Gy at a rate of 0.995 kGyh⁻¹. A prominent peak can be seen around 220 °C, 425 °C for 5 mol%, respectively.

Figure 1(b) shows a typical glow curve for the sample $\text{Li}_9\text{Mg}_3[\text{PO}_4]_4\text{F}_3$, $\text{Li}_2\text{Mg}[\text{PO}_4]\text{F}$ exposed to γ -rays for 5 Gy at a rate of 0.995 kGyh⁻¹. A prominent peak can be seen around 222°C and second peak at 410°C for 1 mol%, respectively.

Figure 1(c) shows a typical glow curve for the sample $\text{Li}_9\text{Mg}_3[\text{PO}_4]_4\text{F}_3$, $\text{Li}_2\text{Mg}[\text{PO}_4]\text{F}$ exposed to γ -rays for 5 Gy at a rate of 0.995 kGyh⁻¹. A prominent peak can be seen around 220 °C for 0.1 mol%, respectively. In this phosphor, the appearance of single peak in the glow curve indicates that there is possibly only one kind of trapping sites due to γ -irradiated effect.

Fig 2: TL Characteristics of (a) $\text{Li}_9\text{Mg}_3[\text{PO}_4]_4\text{F}_3$, $\text{Li}_2\text{Mg}[\text{PO}_4]\text{F}$ mol% Mn 0.1 mol%, (b) $\text{Li}_9\text{Mg}_3[\text{PO}_4]_4\text{F}_3$, $\text{Li}_2\text{Mg}[\text{PO}_4]\text{F}$, 1mol%, (c) $\text{Li}_9\text{Mg}_3[\text{PO}_4]_4\text{F}_3$, $\text{Li}_2\text{Mg}[\text{PO}_4]\text{F}$ 5mol% phosphor exposed to γ -rays for 5 Gy at the rate of 0.995 kGyh⁻¹. Fig.2 shows a TL Characteristics curve for the sample $\text{Li}_9\text{Mg}_3[\text{PO}_4]_4\text{F}_3$, $\text{Li}_2\text{Mg}[\text{PO}_4]\text{F}$ 5mol%Mn0.1mol%,Ce 5mol% Dy 0.1mol%, Ce 5mol% phosphor exposed to γ -rays for 5 Gy at the rate of 0.995 kGyh⁻¹.

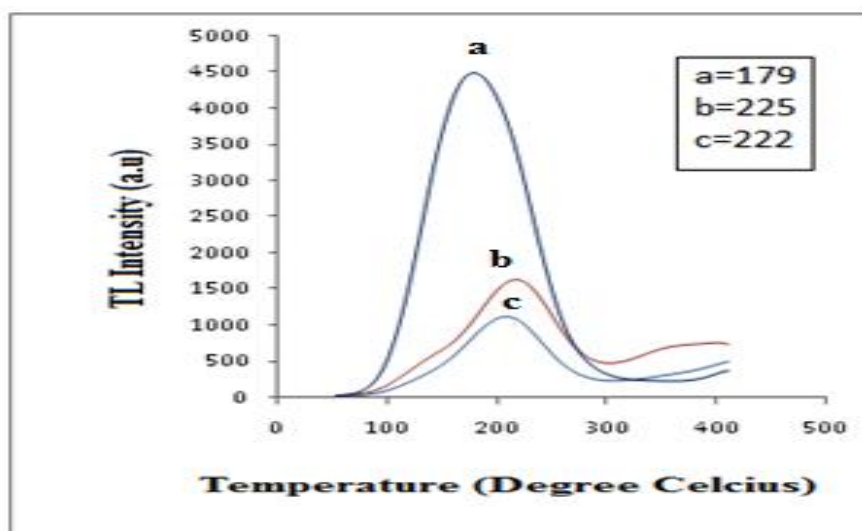


Fig 2: TL Characteristics of (a) $\text{Li}_9\text{Mg}_3[\text{PO}_4]_4\text{F}_3$, $\text{Li}_2\text{Mg}[\text{PO}_4]\text{F}$, mol% Mn 0.1 mol%, (b) $\text{Li}_9\text{Mg}_3[\text{PO}_4]_4\text{F}_3$, $\text{Li}_2\text{Mg}[\text{PO}_4]\text{F}$, 0.1mol% , (c) mol $\text{Li}_9\text{Mg}_3[\text{PO}_4]_4\text{F}_3$, $\text{Li}_2\text{Mg}[\text{PO}_4]\text{F}$, 1 mol%.

A single prominent peak can be seen around (a)179 C, (b) 225 C, and (c) 222 C for Ce 5 mol% Mn 0.1mol%, Ce 5mol% Dy 0.1mol% and Ce 5mol% respectively. It is also observed that there is slightly change in the peak position of Ce 5mol% Mn 0.1mol%, concentration and found to shift toward the lower temperature side. The relative heights of the glow peaks changed for the different concentrations. In this phosphor, it is observed that the intensity is lower for Ce. And it increases after co-doping of Mn and Dy concentrations. The appearance of single peak in the glow curve indicates that there is possibly only one kind of trapping sites due to γ -irradiated effect.

IV. CONCLUSIONS

In this study, $\text{Li}_9\text{Mg}_3[\text{PO}_4]_4\text{F}_3$, $\text{Li}_2\text{Mg}[\text{PO}_4]\text{F}$, was prepared by microwave assisted synthesis method and assigned to the hexagonal structure (P63, Z = 2, a = 12.6054(1) Å, c = 5.0018(2) Å). $\text{Li}_9\text{Mg}_3[\text{PO}_4]_4\text{F}_3$, $\text{Li}_2\text{Mg}[\text{PO}_4]\text{F}$ is shown to melt congruently at 850°C with $\Delta H = -225.1$ J/g. For the first time, comprehensive experimental studies of the TL spectra along with theoretical simulation were carried out for $\text{Li}_9\text{Mg}_3[\text{PO}_4]_4\text{F}_3$. It was found that the irradiated sample exhibits significant thermoluminescence properties in the given sample.

ACKNOWLEDGMENT

I would like to extend my sincere gratitude to all the individuals whose contributions and support have significantly enhanced the quality and rigor of this research.

I also appreciate my friends and colleagues, whose support, and the stimulating academic environment they provided were highly motivating during this research journey. Lastly, I am thankful to my family for their understanding, encouragement, and support.

REFERENCES

- [1] S S Fedotov , N R Khasanova , A Sh , O A Samarin , D Drozhzhin , O M Batuk , J Karakulina, Cathode Material for High-Power Rechargeable Batteries Chem. Mater , vol. 4, pp 411 - 415, 2016.
- [2] H W Yu , J H Young , H P Wu , W G Zhang , J M Rondinelli , structural engineering of pyrophosphates for nonlinear optical applications Chem. Mater , vol. 4 , issue 207, pp 1845 – 1855, 2017.

- [3] Atuchin, Structural and spectroscopic properties of self-activated monoclinic molybdate $\text{BaSm}_2(\text{MoO}_4)_4$, Journal of Alloys Compound., vol.729, pp 843- 849, 2018.
- [4] Ltaief, Structural and optical investigations of new fluorophosphates solid solutions $\text{Li}_x\text{Y}_{1-y}\text{Ln}_y(\text{PO}_4)_{1-x}\text{F}_4$ as phosphors for solid-state lighting, J. Alloys Compd., 29, pp 735-742, 2016.
- [5] Kalinkin, Effect of fluorine on thermoluminescence in LiMgPO_4 , Russ. Journal of Inorganic, Chemistry, vol. 68, pp 216 - 223, 2014.
- [6] Dhabekar, $\text{LiMgPO}_4:\text{Tb}, \text{B}$ - a new sensitive OSL phosphor for dosimetry, Nuclear. Instrumentation Methods Phys. Res., Sect. B, vol. 269, pp 1844-1855, 2015.
- [7] Yahia, Crystal structures of the new fluorophosphates $\text{Li}_9\text{Mg}_3[\text{PO}_4]_4\text{F}_3$ and $\text{Li}_2\text{Mg}[\text{PO}_4]\text{F}$ and ionic conductivities of selected compositions, Journal. Mater. Chem. A, vol. 2, pp 5858-5867, 2019.
- [8] Kellerman, Theoretical and experimental evidences of defects in LiMgPO_4 , J. Alloys Compd., vol.766, pp 626-639, 2019.
- [9] Modak, Exploring the role of vacancy defects in the optical properties of LiMgPO_4 , Phys. Chem. Chem. Phys., vol. 22, pp 1644-1652, 2017.
- [10] Medvedeva, Ab initio simulation of oxygen vacancies in LiMgPO_4 , Mater. Res. Express, vol. 6, pp 1542-1551, 2019.
- [11] Zimoglyad, Nature of defects causing thermostimulated luminescence of calcium halophosphate, Journal of Applied Spectroscopy., vol. 29, pp 1335-1344, 2021.
- [12] Wang, Strongly enhanced photoluminescence and X-ray excited optical luminescence of the hydrothermally crystallized $(\text{Sr},\text{Mn})_5(\text{PO}_4)_3(\text{F},\text{Cl})$ nanorods by composition modulating, J. Alloys Compd., vol.85, pp 241-250, 2016.
- [13] Nieto, Present status and future trends in the development of thermoluminescent materials, Applied Radiation Isotopes., 117, pp 135-144, 2019.
- [14] Gupta, Photoluminescence, thermoluminescence and evaluation of some parameters of Dy^{3+} activated $\text{Sr}_5(\text{PO}_4)_3\text{F}$ phosphor synthesized by sol-gel method, J. Alloys Compd., 688, pp 982-989, 2021.
- [15] Fan, Gamma rays induced defect centres in phosphate glass for radio-photoluminescence dosimeter, Radiation. Meas., vol. 46, pp 45-56, 2022.

^{1*} Sandip M. Parkhi

^{1*} Shaukat A. Shah

² Shruti Dhale

² Ashvini Pusdekar

² N. S. Ugemuge

³ S. V. Moharil

**Combustion Synthesis and
Luminescence in $\text{LiAl}_5\text{O}_8:\text{Ln}^{3+}$
($\text{Ln}^{3+} = \text{Ce, Gd}$) Phosphor for UV
Applications**



Abstract: - $\text{LiAl}_5\text{O}_8:\text{Ln}^{3+}$ ($\text{Ln}^{3+} = \text{Ce, Gd}$) ultraviolet B (UVB) emitting phosphors were synthesized at 500°C within a few minutes through urea assisted combustion synthesis method. A Cubic structure of as synthesized sample was confirmed by using x-ray diffraction method (XRD). The surface morphology and chemical composition confirmed by Scanning Electron Microscopy (SEM) and EDAX. Characteristic luminescence of Ce^{3+} and Gd^{3+} ions were observed in LiAl_5O_8 . The PL spectra of $\text{LiAl}_5\text{O}_8:\text{Ce}^{3+}$ excited at 278 nm consists of a dominant UVB emissions at 362 nm attributed to $5d-4f$ transitions. Also, the PL spectra of $\text{LiAl}_5\text{O}_8:\text{Gd}^{3+}$ excited at 274 nm exhibits an intense emission in the ultraviolet region centered at 313 nm assigned to the ${}^6\text{P}_{7/2} \rightarrow {}^8\text{S}_{7/2}$ transition. The results revealed that Ce^{3+} and Gd^{3+} doped LiAl_5O_8 matrix has potential applications for the UVB emitting phototherapy lamp and other optical devices.

Keywords: Phosphor, Combustion Synthesis, Photoluminescence, Aluminate, UVB applications.

^{1*}Corresponding author: ¹ Department of Chemistry, Anand Niketan College, Anandwan, Warora, 442907, India.

² Department of Physics, Anand Niketan College, Anandwan, Warora, 442907, India.

³ Department of Physics, RTM Nagpur University, Nagpur 440033, India.

I. INTRODUCTION

Inorganic compounds doped with lanthanide ions (Ln^{3+}) have several applications in UV, Visible and NIR region depending upon the dopant ions in selected host matrix. Applications in UV region have technological importance due to its uses in medical and other domains such as phototherapy lamp, scintillators, multimodal imaging probes, induction sterilization, disinfection, insect traps, photochemical reactions, production of vitamin D_3 and the treatment of psoriasis in medical sciences [1]. To attain these applications, Gd^{3+} and Ce^{3+} ions play vital roles as its emission in the range of 200 nm to 400nm on account of f-f transitions [2]. The narrowband UVB radiation (311–315 nm) is identified for the treatment of several disorders and skin diseases [3].

In aluminate host, among all rare earth ions trivalent cerium (Ce^{3+}) ion is one of the most popular dopant ions due to the presence of peculiarity of its $5d \rightarrow 4f$ transition. Ce^{3+} ion has properties to produce an efficient UV emission on account of allowed intra configurational d-f transitions. Ce^{3+} rare earth ion is distinct from all rare earth ions due to presence of $5d-4f$ parity-allowed transitions. Also, Gd^{3+} ion doped phosphor materials have innumerable importance due to their characteristic applications in the UV region as its emission range is 311–315 nm attributed to the ${}^6\text{P}_{7/2} \rightarrow {}^8\text{S}_{7/2}$ transition [4]. Gd^{3+} ion have unpaired 7- electrons in 4f shell and which is extensively used in routine clinical MRI (magnetic resonance imaging) as an optical imaging probe due to their paramagnetic property. As well as it enhances the quality of images to get clear information about abnormalities and diseases which are clearly and noticeable visible on MRI [5]. Gd^{3+} doped up-conversion nanomaterials reported as most important fluorescent imaging agents and T1 -MR material [6]. Gd^{3+} doped phosphors have numerous applications such as microwave applications, compact discs (CD), computer memory, magneto-optical films and imitation of diamonds, green phosphors for color television tubes, etc. Also, in medical science for the treatment of Vitiligo, the UVB phototherapy lamp is most effective [7].

Lithium aluminates-based phosphor compounds have fascinated researchers and industries due to several industrial applications on account of their excellent thermo-chemical and radiation stability, good luminescent materials, artificial illumination, etc. making it a potential candidate for use as a host matrix for active ions, especially rare earth (RE) ones [8]. LiAlO_2 and LiAl_5O_8 are considered as an excellent host phosphor or matrix for several doping impurities. There are three complex oxides in the $\text{Li}_2\text{O}-\text{Al}_2\text{O}_3$ system, Li_5AlO_4 , LiAlO_2 and LiAl_5O_8 , with melting points of 1116, 1785 and 1915°C, respectively [9]. Thus, LiAl_5O_8 has the highest melting point in this system. The phase transitions in LiAl_5O_8 studied by R. K. Datta and Rustum Roy [10]. LiAl_5O_8 with an inverse spinel structure has interesting optical characteristic properties due to acceptance of dopants from rare earth and transition metal ions. Spinel structure is classified into the group of crystals to be used as phosphor, magnetic materials and laser host medium [11]. LiAl_5O_8 possesses two forms: a low temperature primitive cube with ordered, P_432 space group and a high temperature spinel form with disordered, $F4/d \bar{3} 2/m$ space group. LiAl_5O_8 with the space group 213 is commonly used as fluorescent material [12].

There are several reports on the introduction of transition metal ions such as Fe^{3+} , Mn^{2+} , Co^{3+} , Ni^{2+} and Cr^{3+} and rare earth ions such Eu^{3+} , Tb^{3+} , Ce^{3+} and Dy^{3+} for applications in luminescent devices. LiAl_5O_8 doped with Eu^{3+} , Fe^{3+} , or Co^{3+} are also reported. Fe-doped LiAl_5O_8 synthesized by wet chemical route and luminescent properties were studied by Kuttayand Nayak. Recently, Co^{2+} : LiAl_5O_8 nano crystals were synthesized via a citrate sol-gel method [13]. Ce-doped LiAl_5O_8 phosphor also reported. Singh and Rao prepared $\text{LiAl}_5\text{O}_8:\text{Eu}^{3+}$ phosphor using a self-propagating (combustion) synthesis [14]. Shinobu Hashimoto et.al. Applied Self-flux synthesis and studied photoluminescent properties of LiAl_5O_8 [15]. The luminescence properties of Fe^{3+} doped LiAl_5O_8 prepared by a wet chemical processing method have been studied [16]. Fe^{3+} in LiAl_5O_8 a weak luminescence in the green was observed and identified as due to Mn^{2+} impurity [17]. Luminescence of Mn ions ordered and disordered LiAl_5O_8 studied by McNicol and Pott [18]. Luminescence of Cr^{3+} ions in ordered and disordered LiAl_5O_8 studied by Pott and McNicol [19]. Preparation and characterization of Co^{2+} doped LiAl_5O_8 nano-crystal powders by sol-gel technique [20]. LiAl_5O_8 doped with Fe^{3+} or Mn^{2+} is known as a rather efficient phosphor material. Optical properties of Fe^{3+} in LiAl_5O_8 studied. EPR and luminescence properties of combustion synthesized $\text{LiAl}_5\text{O}_8:\text{Mn}^{2+}$ phosphors and Cr^{3+} doped LiAl_5O_8 reported [21].

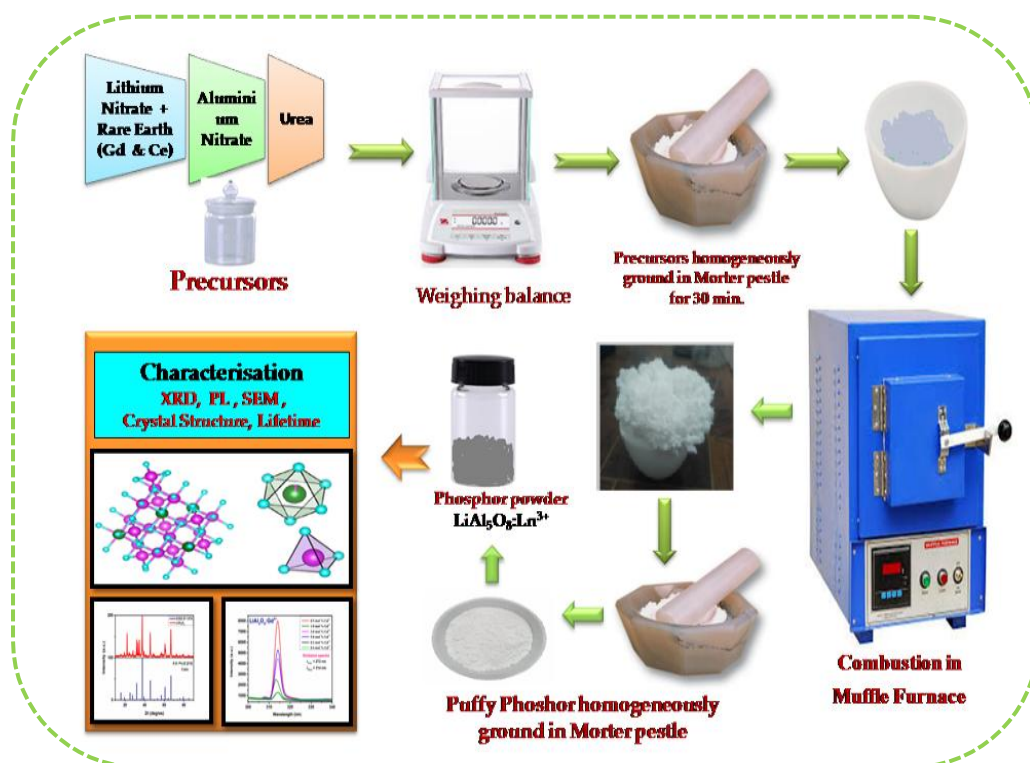
There are several techniques for the synthesis of aluminate-based phosphors including sol-gel method, combustion synthesis, and solid-state reaction method [22] etc. These techniques of preparation of phosphor materials required enormous amount of energy and time. Therefore, to overcome these inadequacies, the combustion synthesis (CS) is most preferred and economic method for the preparation of aluminate-based phosphor on account of its peculiarities such as safe, instantaneous and energy saving. In comparison with these methods, CS has following advantages: (i) control over purity of synthesized product and its composition, (ii)

easy to add dopant ions and (iii) economical, fast and low temperature synthesis. On account of these advantages, we have successfully employed combustion process for the preparation of Gd^{3+} doped LiAl_5O_8 first time and reported in this article along with $\text{LiAl}_5\text{O}_8:\text{Ce}^{3+}$.

From literature, it is observed that there is no report available on Gd^{3+} doped LiAl_5O_8 phosphor therefore in this paper, a facile combustion process was chosen to prepare Ce^{3+} , Gd^{3+} doped LiAl_5O_8 phosphor using combustion process. Besides the synthesis, XRD pattern confirms the crystal structure and phases of compound. Photoluminescence (PL) properties of the synthesized LiAl_5O_8 without dopants were investigated. This phosphor has potential applications in several optoelectronic devices.

II. EXPERIMENTAL

Wherever Times is specified, Times Roman or Times New Roman may be used. If neither is available on your word processor, please use the font closest in appearance to Times. Avoid using bit-mapped fonts if possible. True-Type 1 or Open Type fonts are preferred. Please embed symbol fonts, as well, for math, etc. 2. All the raw materials are procured from the Sigma Aldrich Company, such as LiNO_3 (A.R.99.99%), $\text{Al}(\text{NO}_3)_3 \cdot 9\text{H}_2\text{O}$ (A.R.99.99 %), Urea (A.R.99.99 %), Gadolinium oxide Gd_2O_3 (A.R.99.99 %) and Cerium Oxalate $\text{Ce}_2(\text{C}_2\text{O}_4)_3 \cdot \text{H}_2\text{O}$ (99.99%) A series of $\text{LiAl}_5\text{O}_8:\text{xCe}^{3+}$, $\text{LiAl}_5\text{O}_8:\text{xGd}^{3+}$, $\text{LiAl}_5\text{O}_8:\text{xLn}^{3+}$ ($\text{Ln} = \text{Ce}, \text{Gd}$ and $\text{x} = 0.5, 1, 2, 5$ mol %) precursors are prepared by using the stoichiometric amount of raw materials. The precursors were placed into agate mortar and are ground for half hour to improve the homogeneity. Then the solution was introduced into a china dish and put in muffle furnace and then combust at 500°C for 30 min in muffle furnace. The obtained product was allowed to cool and then grounded for a few minutes with a mortar and pestle. The resulting powder was used for further characterization. Schematic representation of the synthesis procedure of pristine and doped LiAl_5O_8 compound is exhibited in fig.1.



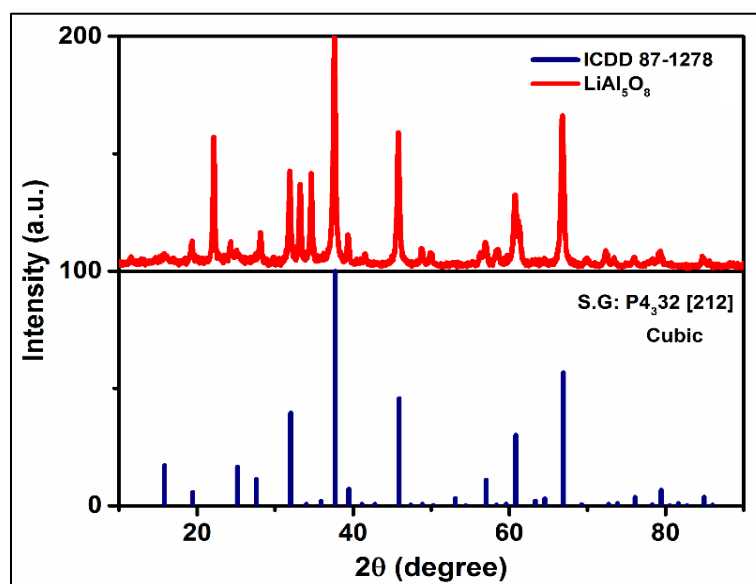
“Fig.1. Schematic diagram of the synthesis procedure of LiAl_5O_8 compound”

III. MATERIAL CHARACTERIZATION

The crystal structure studied by using Powder X-Ray diffraction (Rigaku D-MaxC) using $\text{Cu K}\alpha$ radiation in the range of $2\theta = 10^\circ - 90^\circ$. The particle size, surface morphology and elemental mapping were analyzed through SEM and EDAX techniques. At room temperature PL (photoluminescence) spectra for excitation and emission of sample were taken on instrument Hitachi F-7100 FL spectrophotometer equipped with a 450 W Xe lamp as the excitation source.

IV. RESULTS AND DISCUSSIONS

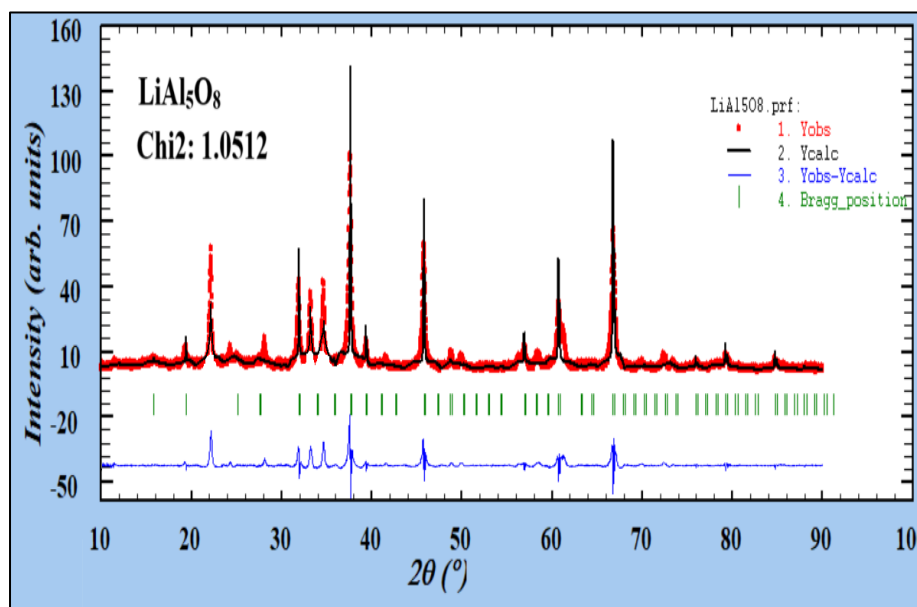
1. X-Ray diffraction Studies



“Fig.2. Powder XRD pattern of LiAl_5O_8 matched with ICDD 87-1278”

The XRD pattern of the as prepared sample is well matched with ICDD 87-1278 is shown in Fig.2. LiAl_5O_8 is described as the cubic crystal system with space group $P4_332$ (212) and the refined lattice parameters are : $a = 7.908 \text{ \AA}$, $b = 7.908 \text{ \AA}$, $c = 7.908$, $\alpha = 90.0000$, $\beta = 90.0000$, $\gamma = 90.0000$ and Unit cell Volume = 494.538356 \AA^3 [23]. Formation of LiAl_5O_8 was ensured by comparing the recorded diffraction patterns with ICDD 87-1278.

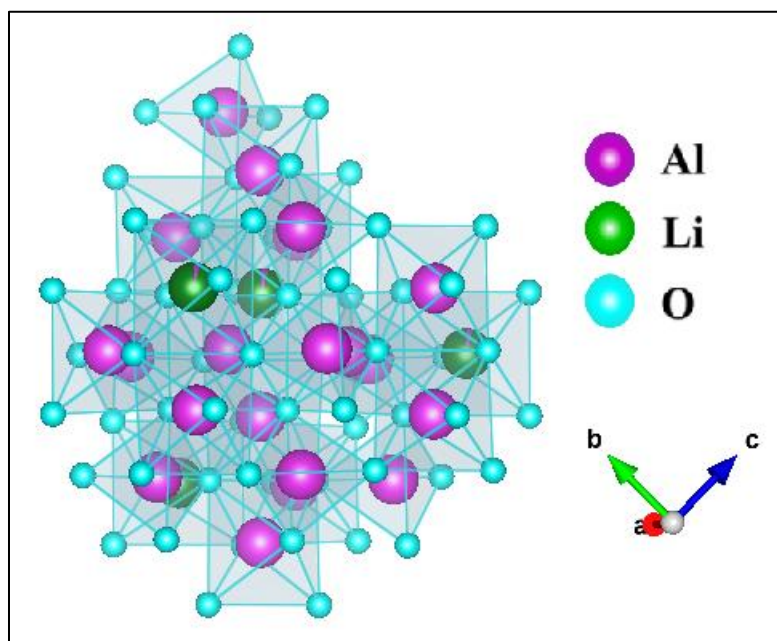
Rietveld refinement is used primarily to refine crystal structure of the as prepared sample. This influential technique of studying X ray diffraction pattern is being increasingly used for obtaining several parameters such as micro structural information, average domain size and crystallite size distribution, texture, strain and stress, and crystalline defect concentration.



“Fig.3. Rietveld refinement of LiAl_5O_8 ”

The FullProf software was used to carry out Rietveld Refinement. Quantitative estimation of the synthesized sample and standard pattern carried out. The results of refinements are shown in fig 3. GOF parameter $\chi^2 = 1.0512$ exhibits an excellent match with standard data.

2. Crystal Structure



“Fig.4. Unit cell of LiAl_5O_8 showing cation coordination and coordination polyhedra”

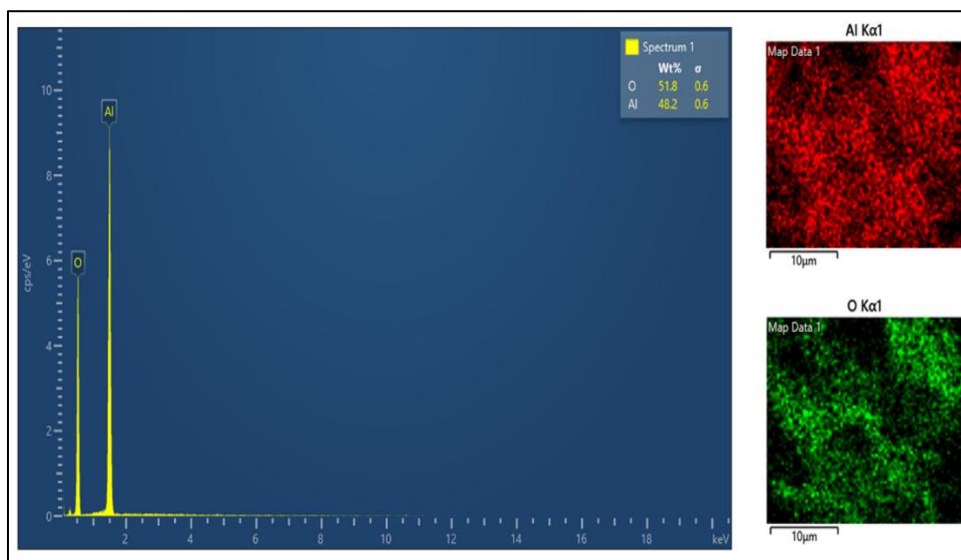
LiAl_5O_8 exists in many forms. The equilibrium high-temperature form (I) has cubic structure. In cubic structure, Al^{3+} ions occupy a tetrahedral and an octahedral (A12 and A13, preferably 12d) sites, while Li^+ occupies only the distorted octahedral (Li1 and Li2, preferably 4b) [24]. Synthesized sample possesses modified spinel structure with cubic symmetry with $P4_332$ space group, shown in Fig. 4. This structure consists of tetrahedral (8c) and two (distorted) octahedral (4b and 12d) sites, in which Al^{3+} ions occupy the tetrahedral (A11) and octahedral (A12 and A13, preferably 12d) sites, while Li^+ occupies only the distorted octahedral (Li1 and Li2, preferably 4b site) [25].

Table 1. Atomic coordinates for LiAl_5O_8

Atom	Label	x/a	y/b	z/c	Occupancy
Li	Li1	0.62500	0.62500	0.62500	0.95700
Li	Li2	0.36860	-0.11860	0.12500	0.01300
Al	A11	-0.00250	-0.00250	-0.00250	1.00000
Al	A12	0.62500	0.62500	0.62500	0.04200
Al	A13	0.36860	-0.11860	0.12500	0.98600
O	O1	0.11460	0.13290	0.38470	1.00000
O	O2	0.38590	0.38590	0.38590	1.00000

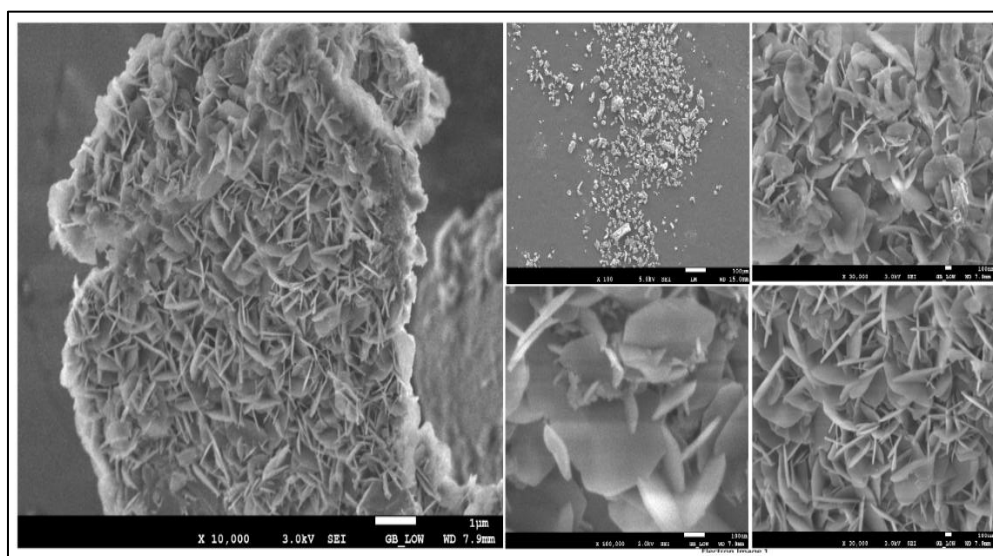
3. SEM, EDS and Elemental mapping

In addition to XRD, formation of pure LiAl_5O_8 matrix is confirmed through EDS spectra and elemental mapping of composition shown in fig.5. The relative atomic percentages of an elements obtained in EDS spectra are close with the molecular formula LiAl_5O_8 . The executed elemental mapping reveals that, all the elements are uniformly and homogeneously distributed. Obtained results show that the phase pure LiAl_5O_8 compound is formed by using simple one step combustion synthesis method.



“Fig.5. EDS spectra and Elemental mapping for pristine LiAl_5O_8 ”

Surface morphology of the as prepared LiAl_5O_8 compound was studied by using FESEM. Fig.6. exhibited typical SEM micrograph of the as prepared compound. Regular rod-shaped particles are observed through SEM. also, the formation of phase of pure LiAl_5O_8 confirmed by SEM.

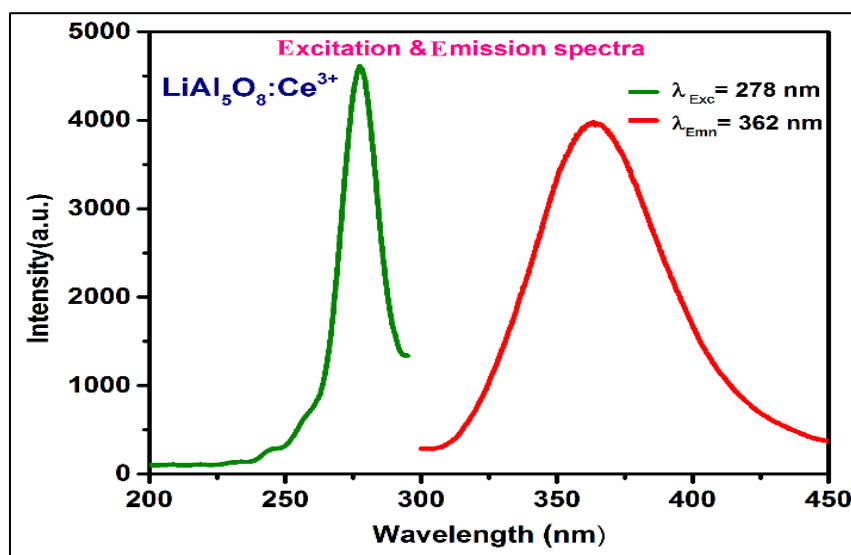


“Fig.6. A typical SEM micrograph for LiAl_5O_8 compound”

4. Photoluminescence Studies (PL)

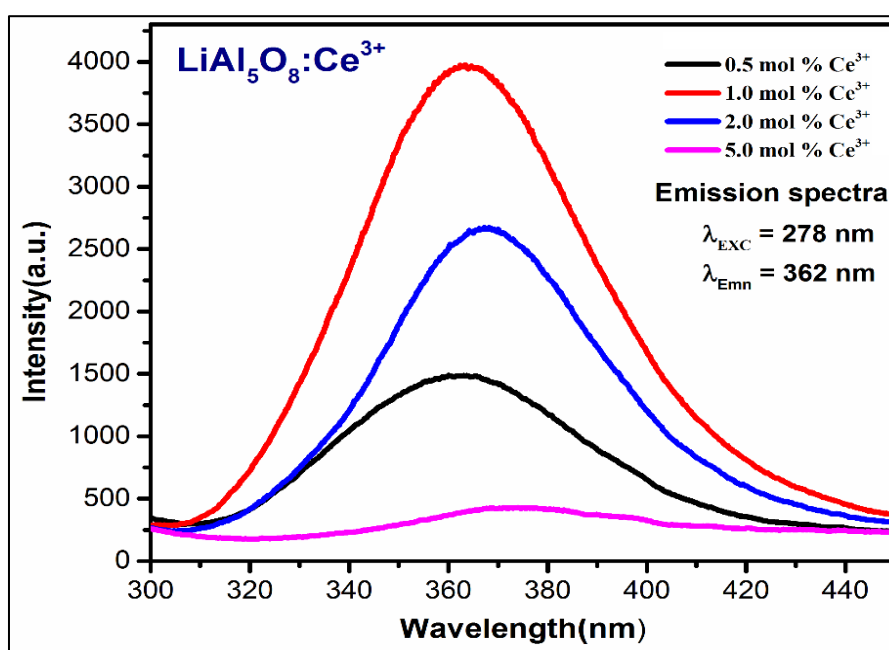
4.1. PL in Ce^{3+} activated LiAl_5O_8 compound

Ce^{3+} is considered as most important activator due to its emission in UV region among all trivalent lanthanide ions. The Ce^{3+} ion possesses $4f^1$ electronic configuration. The excited states for Ce^{3+} ions are attained when electron goes to $5d^1$ shell as it belongs to, the $4f^0,5d^1$ configuration. Thus, in both the ground states and excited states the electronic configuration is the simplest [26]. The ground state in case of Ce^{3+} ion is a doublet because of spin-orbit splitting ($^2F_{5/2}$, $^2F_{7/2}$). The separation of doublet is of the order of 2000 cm^{-1} . In a solid the crystal field is to lower the average energy of the $5d$ electronic configuration and further split $^2D_{3/2}$ and $^2D_{5/2}$ states. In cubic geometry field, the $5d$ states split into two states, t_{2g} and e_g . The relative positions of these states are ruled by the symmetry, and are reversed when symmetry changes from O_h to T . By studying a large number of phosphors hosts the average value for the total splitting is obtained as 10000 cm^{-1} [27]. The outcome of the crystal field on $5d$ bands has been treated by Dorenbos in terms of red shift, centroid shift [28], crystal field splitting. The crystal field splitting, is the separation between top most and the bottom $5d$ orbital band. The centroid shift is difference between the average energy of the Ce^{3+} $5d$ configuration in a solid crystal and the free ion value [29].



“Fig.7. PL and PLE spectra of $\text{LiAl}_5\text{O}_8:\text{Ce}^{3+}$ ”

Fig.7 shows PL emission and excitation spectra for $\text{LiAl}_5\text{O}_8:\text{Ce}^{3+}$. The emission is in form of a typical broad band with peak at 362 nm appeared. This emission corresponds to the transition from the lowest energy bands of $4f^05d^1$ configuration to $(^2F_{5/2}, ^2F_{7/2})$ ground state of $4f^1$ configuration. The corresponding PLE are typical of the splitting of 5d levels observed at 278 nm. Concentration Quenching in Ce^{3+} activated LiAl_5O_8 shown in fig.8. Highest intensity observed at 1.0 mol % after that it decreases.



“Fig.8. Concentration Quenching in Ce^{3+} activated LiAl_5O_8 ”

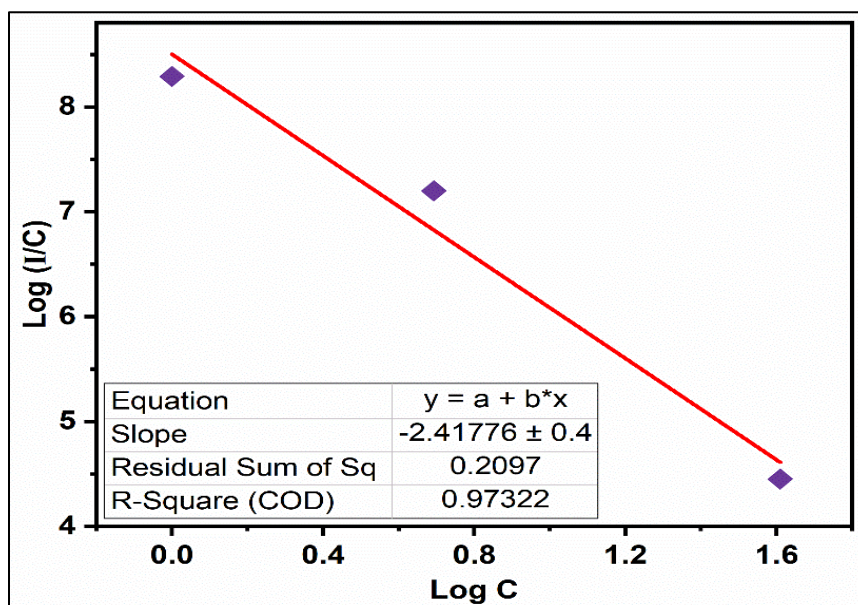
The intensity rises at first till the Ce^{3+} concentration reaches 1.0 % and declines later. These results enable estimation of the minimum separation between Ce^{3+} ions, R_c , that is required to avoid the interaction between them if Blasse [30] equation is used to analyses-

$$R_c = 2 \left(\sqrt[3]{\frac{3V}{4\pi X_c N}} \right)$$

X_c is the amount of Ce^{3+} for which the intensity is maximum (0.01), N is number of sites in a unit cell where Ce^{3+} can be incorporated, V is the volume of the unit cell (512.2372 \AA^3). After substituting the values of the relevant quantities mentioned in the parentheses, R_c value for Ce^{3+} doped LiAl_5O_8 : R_c is 21.4 \AA . Such a high value is not compatible with the exchange mechanism for energy transfer among Ce^{3+} ions. For getting insight

into the mechanism of the concentration quenching, a graph is plotted with $\log I/C$ on the Y axis and $\log C$ on the X (Fig. 10). This graph was analysed in terms of van Uitert equation [31].

$$\frac{I}{C} = k \left[1 + \beta(C)^{\theta/3} \right]^{-1}$$

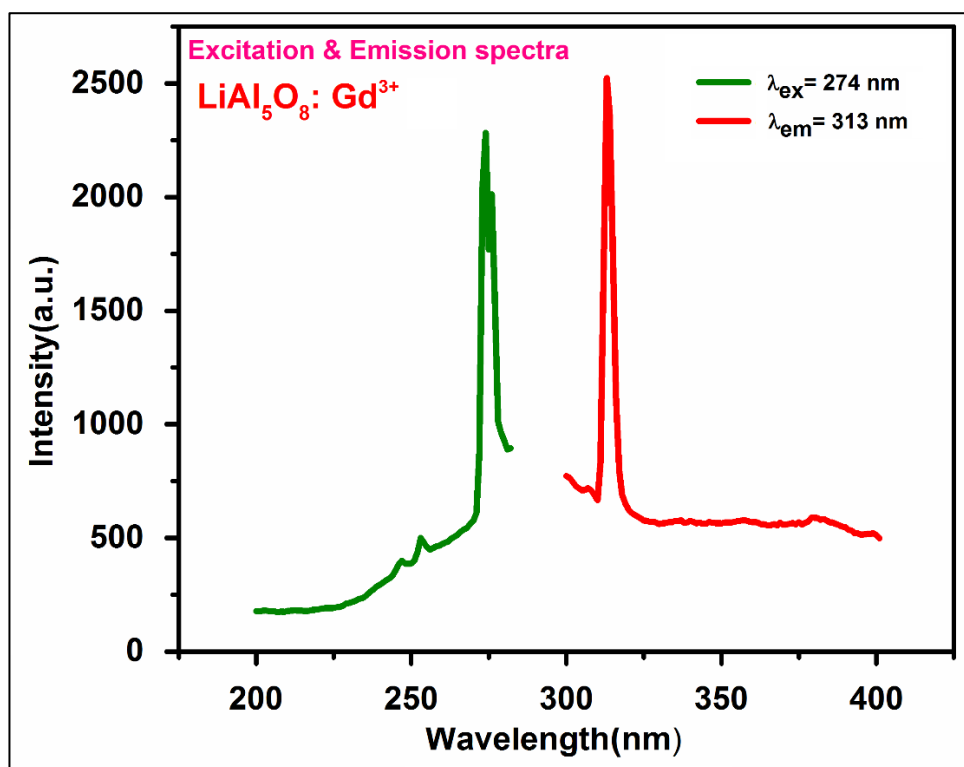


“Fig.9. Van Uitert Plot for Concentration dependence of Ce^{3+} emission”

Slope of the graph throws light on the energy transfer mechanism. It can be seen from the equation that slope equals $-\theta/3$. The multipolar mechanisms can be based on dipole-dipole (d-d), dipole-quadrupole (d-q) and quadrupole-quadrupole (q-q) interactions for which θ values are 6, 8 and 10, respectively. From Fig. 12 we obtain $\theta = 3.3$ which is closer to six and hence energy migration along Ce^{3+} chain in $LiAl_5O_8$ proceeds through d-d interaction.

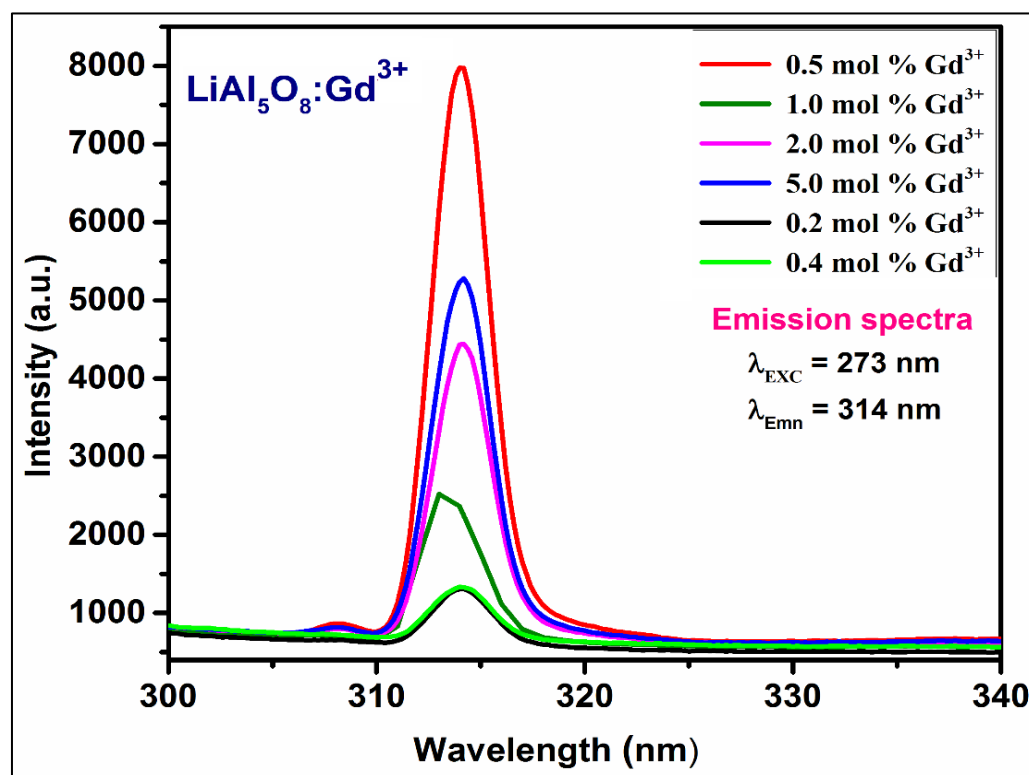
4.2. Photoluminescence in Gd^{3+} activated $LiAl_5O_8$

Gd^{3+} ion is a remarkable lanthanide for a few specific applications related to its magnetic properties arising from 7 unpaired electrons, energy level structure with large gap between the ground state to the first excited state, and large cross section for (n, γ) reaction [32]. Producing cryogenic temperatures (CT) through adiabatic demagnetization [33], Gd^{3+} ion has very abnormal PL properties which do not depend on the host properties. Presence of 7 electrons in 4f gives rise to large number of spectroscopic terms. Only 6 of this viz. 6I_1 , 6P_1 which lie within 50000 cm^{-1} from the ground state $^8S_{7/2}$ are taken in consideration in most of the experiments. Other higher lying levels 6D_1 , 6G_1 become noticeable only for high energy excitations [34]. De-excitation to $^8S_{7/2}$ ground state results in an emission line noticeable at about 314 nm [35]. For luminescence quenching the Critical concentration of Gd^{3+} is very normal. The energy associated with $^6P_{7/2} \rightarrow ^8S_{7/2}$ transition is also very high and cannot be used in the process of phonon formation. Therefore, once Gd^{3+} ion reaches to $^6P_{7/2}$ energy state must emit a UV photon or transfer its energy to nearest luminescence centre. Gd-Gd ion separation is a critical feature in the energy migration along with Gd^{3+} chain.



“Fig.10. PL and PLE spectra of LiAl₅O₈:Gd³⁺”

PL and PLE spectra of LiAl₅O₈:Gd³⁺ is shown in fig.10. Emission of 313 nm is observed for the excitation of 274 nm. The quenching of various mole proportion of Gd³⁺ with LiAl₅O₈ is shown at 314 nm wavelength which is shown in fig. 11.



“Fig.11. Concentration Quenching in Gd³⁺ activated LiAl₅O₈.”

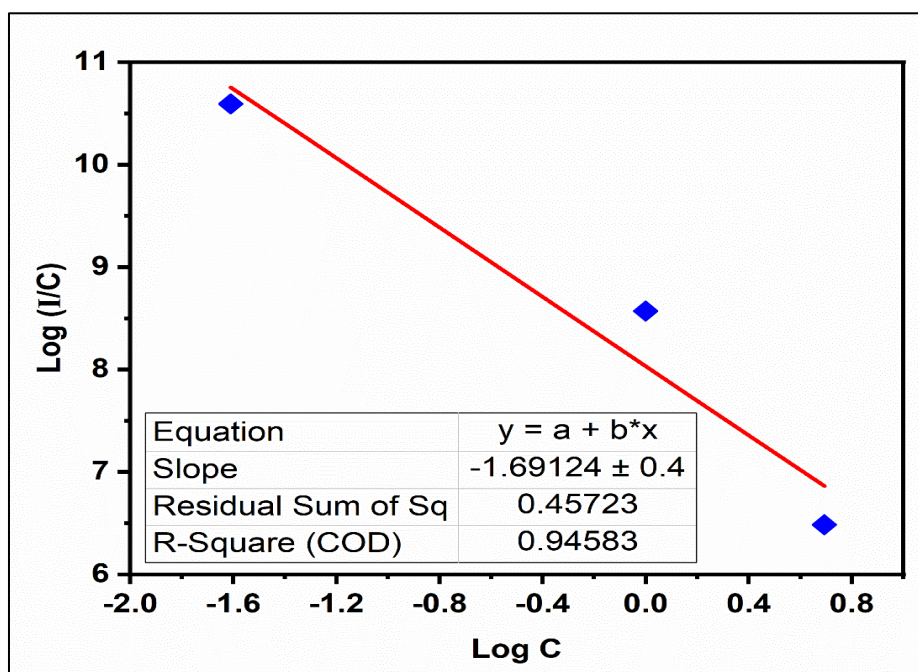
The intensity rises at first till the Gd³⁺ concentration reaches 1.0 % and declines later. These results enable estimation of the minimum separation between Gd³⁺ ions, R_c , that is required to avoid the interaction between them if Blasse [36] equation is used to analyse-

$$R_c = 2 \left(\sqrt[3]{\frac{3V}{4\pi X_c N}} \right)$$

X_c is the amount of Gd^{3+} for which the intensity is maximum (0.01), N is number of sites in a unit cell where Gd^{3+} can be incorporated, V is the volume of the unit cell (512.2372 \AA^3). After substituting the values of the relevant quantities mentioned in the parentheses, R_c value for Gd^{3+} doped $LiAl_5O_8$: R_c is 21.4 \AA . Such a high value is not compatible with the exchange mechanism for energy transfer among Ce^{3+} ions. For getting insight into the mechanism of the concentration quenching, a graph is plotted with $\log I/C$ on the Y axis and $\log C$ on the X (Fig. 10). This graph was analysed in terms of van Uitert equation [37].

$$\frac{I}{C} = k \left[1 + \beta(C)^{\theta/3} \right]^{-1}$$

Slope of the graph throws light on the energy transfer mechanism. It can be seen from the equation that slope equals $-\theta/3$. The multipolar mechanisms can be based on dipole-dipole (d-d), dipole-quadrupole (d-q) and quadrupole-quadrupole (q-q) interactions for which θ values are 6, 8 and 10, respectively. From Fig. 12 we obtain $\theta = 3.3$ which is closer to six and hence energy migration along Gd^{3+} chain in $LiAl_5O_8$ proceeds through d-d interaction.



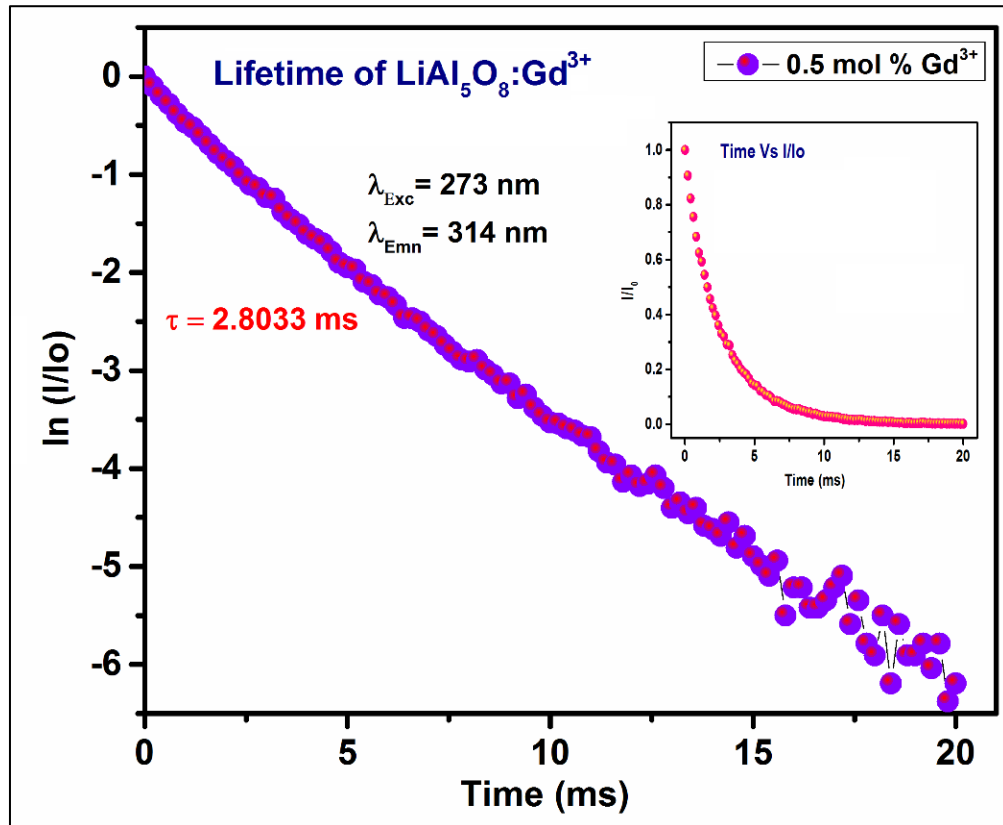
“Fig.12. Van Uitert Plot for Concentration dependence of Gd^{3+} emission.”

Lifetime measurements were also carried out by using emission was sufficiently intense for this purpose. The lifetime was obtained as 2.8033 ms for 0.5 mol.% Gd^{3+} (Fig. 11). At this concentration decay becomes faster due to $Gd^{3+} \rightarrow Gd^{3+}$ energy transfer.

The following equation is used to find the average lifetime,

$$\tau = \frac{\int t \times i(t) dt}{\int i(t) dt}$$

Where, τ represent the average lifetime, t is time and i is the intensity counts.



"Fig.13. Lifetime measurements"

V. CONCLUSION

A series of $\text{LiAl}_5\text{O}_8:\text{Ln}^{3+}$ ($\text{Ln}^{3+} = \text{Ce}, \text{Gd}$) phosphor is prepared by using one step combustion techniques. Phase pure compound formed within few minutes at 500°C temperature. XRD, Rietveld Refinement, EDS and elemental mapping confirm the formation of a phase pure compound and the luminescent studies of $\text{LiAl}_5\text{O}_8:\text{Ln}^{3+}$ ($\text{Ln}^{3+} = \text{Ce}, \text{Gd}$) phosphor samples are carried out and the results discussed in detail. The photoluminescence spectra of $\text{LiAl}_5\text{O}_8:\text{Gd}^{3+}$ phosphor showed prominent emission located at about 313 nm. It is expected that the $\text{LiAl}_5\text{O}_8:\text{Ln}^{3+}$ ($\text{Ln}^{3+} = \text{Ce}, \text{Gd}$) phosphor is potential candidates for ultraviolet LED and other optoelectronic applications.

ACKNOWLEDGMENT

Assistance in obtaining XRD pattern provided by J.Bajaj College of Science, Wardha, (India) is thankfully acknowledged. Also, this work was supported by Anand Niketan College Warora (India) for the assistance in obtaining PL spectra.

VI. REFERENCES

- [1] Liang, B., Pang, D., Jin, C., Li, F., & Wang, Y. (2012). Photo-oxidative degradation of poly (p-dioxanone) under ultraviolet light source. *Polymer degradation and stability*, 97(11), 2162-2169, <https://doi.org/10.1016/j.polymdegradstab.2012.08.011>
- [2] Gai, S., Li, C., Yang, P., & Lin, J. (2014). Recent progress in rare earth micro/nanocrystals: soft chemical synthesis, luminescent properties, and biomedical applications. *Chemical reviews*, 114(4), 2343-2389, <https://doi.org/10.1021/cr4001594>
- [3] Lowe, N. J. (1992). Home ultraviolet phototherapy. In *Seminars in Dermatology*, 11, 284-286, PMID: 1493091
- [4] Singh, V., Sivaramaiah, G., Singh, N., Pathak, M. S., Rao, J. L., Jirimali, H. D., & Natarajan, V. (2018). Investigation of ultraviolet emitting Gd doped $\text{Sr}_2\text{MgSi}_2\text{O}_7$ phosphors. *Optik*, 169, 397-402, <https://doi.org/10.1016/j.ijleo.2018.05.036>
- [5] Yang, D., Kang, X., Shang, M., Li, G., Li, C., & Lin, J. (2011). Size and shape controllable synthesis and luminescent properties of $\text{BaGdF}_5:\text{Ce}^{3+}/\text{Ln}^{3+}$ ($\text{Ln} = \text{Sm}, \text{Dy}, \text{Eu}, \text{Tb}$) nano/submicrocrystals by a facile hydrothermal process. *Nanoscale*, 3(6), 2589-2595, <https://doi.org/10.1039/C1NR10203F>
- [6] Chen, F., Bu, W., Zhang, S., Liu, X., Liu, J., Xing, H., ... & Shi, J. (2011). Positive and negative lattice shielding effects co existing in Gd (III) ion doped bifunctional upconversion nanoprobes. *Advanced Functional Materials*, 21(22), 4285-4294, <https://doi.org/10.1002/adfm.201101663>

- [7] Singh, V., Sivaramaiah, G., Rao, J. L., & Kim, S. H. (2013). Luminescence and electron paramagnetic resonance investigation on ultraviolet emitting Gd doped MgAl₂O₄ phosphors. *Journal of luminescence*, 143, 162-168, <https://doi.org/10.1016/j.jlumin.2013.03.054>
- [8] Silva, A. J., Nascimento, P. A., Andrade, A. B., Sampaio, D. V., Moulton, B. J., Silva, R. S., & Rezende, M. V. D. S. (2018). X-ray excited optical luminescence changes induced by excess/deficiency lithium ions in rare earth doped LiAl₅O₈. *Journal of Luminescence*, 199, 298-301, <https://doi.org/10.1016/j.jlumin.2018.03.066>
- [9] Hashimoto, S., Hattori, K., Inoue, K., Nakahashi, A., Honda, S., & Iwamoto, Y. (2009). Self-flux synthesis and photoluminescent properties of LiAl₅O₈. *Materials Research Bulletin*, 44(1), 70-73, <https://doi.org/10.1016/j.materresbull.2008.04.003>
- [10] Datta, R. K., & Roy, R. (1963). Phase transitions in LiAl₅O₈. *Journal of the American Ceramic Society*, 46(8), 388-390, <https://doi.org/10.1111/j.1151-2916.1963.tb11757.x>
- [11] Duan, X., & Yuan, D. (2005). Synthesis and characterization of Co²⁺ doped lithium aluminum spinel nanocrystals. *Journal of non-crystalline solids*, 351(27-29), 2348-2351, <https://doi.org/10.1016/j.jnoncrysol.2005.05.024>
- [12] De Sousa, O. M. (2018). Study of the structural, electronic, and optical properties of the host matrices of LiAl₅O₈ and LiGa₅O₈ via DFT. *Computational and Theoretical Chemistry*, 1123, 96-101, <https://doi.org/10.1016/j.comptc.2017.11.015>
- [13] Pan, D., Yuan, D., Sun, H., Duan, X., Luan, C., Guo, S., ... & Wang, L. (2006). Preparation and characterization of Co²⁺-doped LiAl₅O₈ nano-crystal powders by sol-gel technique. *Materials chemistry and physics*, 96(2-3), 317-320, <https://doi.org/10.1016/j.matchemphys.2005.07.020>
- [14] Singh, V., & Rao, T. G. (2008). Studies of defects in combustion synthesized europium-doped LiAl₅O₈ red phosphor. *Journal of Solid State Chemistry*, 181(6), 1387-1392, <https://doi.org/10.1016/j.jssc.2008.03.007>
- [15] Hashimoto, S., Hattori, K., Inoue, K., Nakahashi, A., Honda, S., & Iwamoto, Y. (2009). Self-flux synthesis and photoluminescent properties of LiAl₅O₈. *Materials Research Bulletin*, 44(1), 70-73, <https://doi.org/10.1016/j.materresbull.2008.04.003>
- [16] Kutty, T. R. N., & Nayak, M. (1998). Cationic distribution and its influence on the luminescent properties of Fe³⁺-doped LiAl₅O₈ prepared by wet chemical methods. *Journal of alloys and compounds*, 269(1-2), 75-87, [https://doi.org/10.1016/S0925-8388\(98\)00159-5](https://doi.org/10.1016/S0925-8388(98)00159-5)
- [17] Pott, G. T., & McNicol, B. D. (1972). Zeroponon transition and fine structure in the phosphorescence of Fe³⁺ ions in ordered and disordered LiAl₅O₈. *The Journal of Chemical Physics*, 56(11), 5246-5254, <https://doi.org/10.1063/1.1677027>
- [18] McNicol, B. D., & Pott, G. T. (1973). Luminescence of Mn ions in ordered and disordered LiAl₅O₈. *Journal of Luminescence*, 6(4), 320-334, [https://doi.org/10.1016/0022-2313\(73\)90027-6](https://doi.org/10.1016/0022-2313(73)90027-6)
- [19] Pott, G. T., & McNicol, B. D. (1973). Luminescence of Cr³⁺ ions in ordered and disordered LiAl₅O₈. *Journal of Solid State Chemistry*, 7(2), 132-137, [https://doi.org/10.1016/0022-4596\(73\)90145-X](https://doi.org/10.1016/0022-4596(73)90145-X)
- [20] Pan, D., Yuan, D., Sun, H., Duan, X., Luan, C., Guo, S., ... & Wang, L. (2006). Preparation and characterization of Co²⁺-doped LiAl₅O₈ nano-crystal powders by sol-gel technique. *Materials chemistry and physics*, 96(2-3), 317-320, <https://doi.org/10.1016/j.matchemphys.2005.07.020>
- [21] Singh, V., Chakradhar, R. P. S., Rao, J. L., & Kwak, H. Y. (2009). Characterization, EPR and photoluminescence studies of LiAl₅O₈: Cr phosphors. *Solid state sciences*, 11(4), 870-874, <https://doi.org/10.1016/j.solidstatesciences.2009.01.009>
- [22] Shu, W., Qiang, R. F., Xiao, S., Yang, X., & Ding, J. W. (2011). Enhanced red emission in LiAl₅O₈: Fe³⁺ phosphor by B³⁺ doping. *Journal of alloys and compounds*, 509(9), 3886-3888, <https://doi.org/10.1016/j.jallcom.2010.12.144>
- [23] Cao, R., Peng, D., Xu, H., Jiang, S., Luo, Z., Ao, H., & Liu, P. (2016). Synthesis and luminescence properties of NaAl₁₁O₁₇: Mn²⁺ green phosphor for white LEDs. *Journal of Luminescence*, 178, 388-391, <https://doi.org/10.1016/j.jlumin.2016.06.028>
- [24] Silva, A. J., de Freitas, S. M., Nascimento, P. A., Carvalho, I. D. S., Freire, R., Paschoal, C. W. A., & Rezende, M. V. D. S. (2019). Non-stoichiometric Ce-doped LiAl₅O₈ phosphors: Synthesis, structural and optical properties. *Ceramics International*, 45(15), 18994-19001, <https://doi.org/10.1016/j.ceramint.2019.06.140>
- [25] Teixeira, V. C., Rodrigues, L. C., Galante, D., & Rezende, M. V. D. S. (2016). Effect of lithium excess on the LiAl₅O₈: Eu luminescent properties under VUV excitation. *Optical Materials Express*, 6(9), 2871-2878, <https://doi.org/10.1364/OME.6.002871>
- [26] Blasse, G., Schipper, W., & Hamelink, J. J. (1991). On the quenching of the luminescence of the trivalent cerium ion. *Inorganica Chimica Acta*, 189(1), 77-80, [https://doi.org/10.1016/S0020-1693\(00\)80392-8](https://doi.org/10.1016/S0020-1693(00)80392-8)
- [27] Blasse, G., & Brill, A. (1967). Investigation of some Ce³⁺ activated phosphors. *The journal of chemical physics*, 47(12), 5139-5145, <https://doi.org/10.1063/1.1701771>
- [28] Dorenbos, P. (2000). The 5d level positions of the trivalent lanthanides in inorganic compounds. *Journal of Luminescence*, 91(3-4), 155-176, [https://doi.org/10.1016/S0022-2313\(00\)00229-5](https://doi.org/10.1016/S0022-2313(00)00229-5)
- [29] Dorenbos, P. (2000). 5 d-level energies of Ce³⁺ and the crystalline environment. I. Fluoride compounds. *Physical Review B*, 62(23), 15640, <https://doi.org/10.1103/PhysRevB.62.15640>
- [30] Blasse, G. P. R. L. (1968). Energy transfer in oxidic phosphors. *Physics Letters A*, 28(6), 444-445, [https://doi.org/10.1016/0375-9601\(68\)90486-6](https://doi.org/10.1016/0375-9601(68)90486-6)
- [31] Van Uitert, L. G. (1967). Characterization of energy transfer interactions between rare earth ions. *Journal of the electrochemical society*, 114(10), 1048, <https://doi.org/10.1149/1.2424184>
- [32] Fernández, P., & Super-Kamiokande collaboration. (2017, September). Benefits of Gd for high energy neutrinos in superK-Gd. In *Journal of Physics: Conference Series* (Vol. 888, No. 1, p. 012054). IOP Publishing, <https://doi.org/10.1088/1742-6596/888/1/012054>
- [33] Giaque, W. F., & Clark, C. W. (1932). The Conditions for Producing Temperatures below 1 Absolute by Demagnetization of Gd₂(SO₄)₃·8H₂O. *Temperature-Magnetic Field Isentropics*. *Journal of the American Chemical Society*, 54(8), 3135-3142, <https://doi.org/10.1021/ja01347a015>
- [34] Brixner, L. H., & Blasse, G. (1989). X-ray excited 6G and lower term emission from the Gd³⁺ ion. *Chemical physics letters*, 157(4), 283-288, [https://doi.org/10.1016/0009-2614\(89\)87248-3](https://doi.org/10.1016/0009-2614(89)87248-3)
- [35] Blasse, G. (1988). Luminescence of inorganic solids: from isolated centres to concentrated systems. *Progress in Solid State Chemistry*, 18(2), 79-171, [https://doi.org/10.1016/0079-6786\(88\)90004-0](https://doi.org/10.1016/0079-6786(88)90004-0)
- [36] Blasse, G. P. R. L. (1968). Energy transfer in oxidic phosphors. *Physics Letters A*, 28(6), 444-445, [https://doi.org/10.1016/0375-9601\(68\)90486-6](https://doi.org/10.1016/0375-9601(68)90486-6)
- [37] Van Uitert, L. G. (1967). Characterization of energy transfer interactions between rare earth ions. *Journal of the electrochemical society*, 114(10), 1048, <https://doi.org/10.1149/1.2424184>

¹S. P. Pawar*

²P. M. Ardhapurkar

Experimental Investigation and Optimization of Wire Electric Discharge Machining Parameters for Shape Memory Alloy



Abstract: - NiTi Shape Memory alloys are gaining popularity in Aerospace, Medical, Robotics and Automobile sectors for having unique properties- pseudo elasticity and shape memory effect. Most of the Industrial applications demands accurate dimension and tolerances for the use of SMA in product development. Conventional machining of SMA reports difficulty in machining. Therefore, in this paper investigations on machining of SMA were performed using WEDM Non-conventional machining method. The important input parameters - Pulse on Time, Pulse off Time and Gap voltage is considered in the present optimization study. Design of Experiments were done by RSM Box Behkern design. Mathematical models were developed to establish the relation between input and output parameters and validated the developed model through ANOVA analysis and Residual plot. Counter plots are plotted between input and output variable to study the impact. Optimum value of input process parameters was calculated by using RSM composite desirability approach.

Keywords: Shape Memory Alloy, Optimization, Machining, WEDM, RSM

¹ *Research Scholar, Email: satishpawar854@gmail.com

² Professor and Head

Mechanical Engineering Department, MGI's College of Engineering and Technology, Shegaon (MS) – 444203, India

I. INTRODUCTION

Shape Memory alloys possessing certain unique properties which regain their initial shape and size after applying the stress, heat or magnetic field. Unique properties contain Super elasticity, Shape memory effect, Biocompatibility, High wear and Corrosion Resistance. Nickel, titanium, zinc, copper, gold, and iron are used in the various alloys of SMA. On the basis of alloying elements SMAs can be broadly classified as Nickel-Titanium (NiTi) SMAs, Copper (Cu) SMAs, and Iron SMAs. NiTi alloys are very much popular in biomedical applications due to its unique properties [1]. In Biomedical it is mostly used for Vascular, Orthopedic and Orthodontic applications [2]. Machining of shape memory alloys play important role to convert SMA material into any product of biomedical application. It is challenging due to unique properties, presence of nickel and hardness of Shape memory alloys. Past studies [3] on conventional machining of SMA reported tool wear, defects on surface of machined parts, and imprecise dimension. Thus, many researchers find Non-conventional machining is the better option for machining such type of material. Various Non-conventional machining process such as laser machining, Electric discharge machining (EDM), Wire EDM, Electro machining (ECM) and Water jet machining (WJM) can be effectively used to machine SMAs with desired accuracy [4]. Wirecut EDM is widely used to perform machining of difficult to machine materials. In Wire EDM, sparks are generated between the wire and workpiece to remove the material from the work part. Here wire is act as anode and work part act as cathode. It is used to machine complex geometries and difficult to cut material of high hardness. In Wire EDM output of machining process is depends on setting of input parameters which affect the quality of machining, hence controlling these parameters is important to get optimum output. Optimization of input parameters can bring significant improvements in process efficiency [5]. Past studies on optimization of machining process parameters of SMA is discussed below. Saeed Daneshmand et al. [6] chooses the four input parameters for optimization to get desired value of MRR & SR. Optimized values were found out by Taguchi method. Maximum MRR was recorded at higher level of all parameters except pulse off time. Pulse current and Pulse on time found impacting parameters which significantly contribute for higher MRR & lower SR. Gangele et al. [9] also optimized the surface roughness by using Taguchi technique in EDM of SMA. The input parameters considered are same as of Daneshmand [6] except Duty cycle. Pulse off time is the common effective parameter found in both the study. Minimum value of SR was obtained at maximum of Ton and minimum of Toff and discharge current. These researchers [6, 9] shows that minimum SR was obtained at maximum Ton. However, Ton varies from 80 to 150 micro sec. Discharge current is almost same for minimum value of SR. Abibi et al [8] investigate machining of Micro EDM of NiTi alloy with different parameters like Capacitance, Discharge Voltage & Electrode material. Through this optimization, they found that output of the process is majorly affected by the electrode material. Reddy et al. [12], Kulkarni et al. [13], Magbe et al. [14] and Rathi et al. [15] optimized Wire EDM parameters for NiTi SMA by using Taguchi Method. Maximum MRR was recorded almost at the same value of all input process parameters. In all studies, Pulse on Time varies from 110 to 125 micro second. It means Pulse on Time is equally affecting MRR. But Pulse off Time variation is too large. It varies from 9 to 35 micro second in both the studies. Effect of servo voltage is also observed same like Pulse off time. It varies from 40 to 50 V. Lowest surface roughness was obtained at lowest value of Pulse on Time in every case but lot of variation found in values. It may be due to selection of different level of parameters and control of parameter range in different machines. The final optimized values in the above studies are closely matching. Pulse on Time was in the range of 100 to 125 Micro second. 10% variation was observed in Pulse off time and servo voltage. Chaudhari [16] used Taguchi L16 Orthogonal array for DOE in optimization of input parameters and optimization were done by HTS algorithm. In machining operation Nano powder dielectric fluid was used to increase MRR and decrease the SR. It shows the improvement in MRR by 24.01% and 9.35 % in SR.

Sharma et al. [10] and Vinayak N. Kulkarni et al. [13] optimized the input parameters using Response Surface methodology. Results from both papers are closely matching with negligible variations. As discussed in previous papers [6,8,9] of EDM same pattern is found for Wire EDM that is maximum value of MRR was recorded at highest value of Pulse on Time. Therefore, it can be concluded that Maximum MRR can be obtained at Highest Pulse on Time for Wire EDM and EDM of SMA. Pulse off time for Highest MRR is 125 and 130 micro second for [13] & [7] respectively. Servo voltage and Pulse off time values are at middle level for maximum value of MRR. Minimum Surface roughness 1.33 μm and 1.43 μm were found at lowest Pulse on Time. Discharge current and pulse on time found main and effective parameters affecting the MRR & SR. Surface morphology of machined surface of work part was studied by using SEM and EDS analysis in [13]. Chaudhari et al. [17] and [18] has selected the same input parameters for optimization with different grade of Ni Ti material in Wirecut

EDM. The combine approach of RSM and HTS algorithm techniques used for optimization. Same input parameters and their range are used in both [17] and [18]. Input parameters chosen are Ton, Toff Time and current whereas output parameters are MRR, SR and Microhardness for study. Ton and Current significantly affecting the SR and Micro Hardness, whereas Toff and Discharge current shows major effect on MRR. Kulkarni et al [19] optimize the Pulse on Time, Pause time, Wire feed and Servo Voltage by using RSM for optimization. In this servo voltage is the significant parameters for output variables.

Mujumdar et al. [10] and [11] optimized input process parameters to get desired value of SR and microhardness by using GRNN and MOORA (Multi-Objective Optimization by Ratio Analysis). Same results obtained in both the methods. But prediction model developed by GRNN & MOORA Fuzzy logic found different prediction error $\pm 5\%$ and $\pm 10\%$ respectively. H. Soni et al. [20] optimized Ti50 Ni40 Co10 of Wire EDM by using TOPSIS method. Optimum value of input parameters Pulse on time, Pulse off time, Servo voltage, Servo feed and Wire speed were calculated using TOPSIS method. Chaudhari et al. [17] and [21] used combine approach of RSM and HTS algorithm for optimization in machining of SMA. In this they predicted and optimized the output variable at different set of input parameters. HTS algorithm was effectively used to predict the output with +/- 3% to 5% error.

In this paper, WEDM machining operation performed on NiTi SMA. Experiments were designed according to RSM Box Behnken. Experimental runs were conducted on WEDM machine and record the response variables. Mathematical models for each response were developed and check its adequacy using ANOVA analysis. Residual plot analysis conducted to verify ANOVA result. Predicted and actual values of all responses are closely matching.

II. MATERIAL AND METHOD

In this study Shape memory alloy (Ni55.97Ti) is selected for machining on WEDM Machine as a workpart material. Nitinol material of 8 mm dia rod is taken for experimentation. In WDEM process 30 mm length workpiece is cut from Niti rod. Experimental run were performed on CNC Wirecut EDM-Ezeecut-Nxg with dielectric fluid shown in Fig1. Material of wire is Brass with 0.18 mm dia. Wire is act as tool in Wire cut EDM to cut the material. Three input variables Pulse on Time (Ton), Pulse off Time (Toff) and Gap Voltage (V) were selected for the experimentation. In Table 1 input process variables with their range at 3 different level is shown. Input parameters and their range were chosen from the literature and according to machine capability. Experiments are performed according to RSM Box-Behnken Design to reduce number of experiments which will also save the material and machining cost. Three different parameters at three level were considered in Design of Experiments. Total 15 no of experiments were designed and perform in selected range which is presented in Table 2.

Material Removal rate (MRR), Surface roughness (SR) and Hardness were chosen as response variables for study which is useful in various engineering application. MRR is calculated according to below formula. Following Equation shows the MRR calculation

$$MRR = \frac{\Delta W \times 100}{\rho \times t}$$

Where ΔW = difference in weight of workpart before and after machining,

t = time to machine one sample in sec,

ρ (density) = 6.5 g/cm³

Surface Roughness (SR) of machined sample checked by The Mitutoyo Surfatest surface roughness tester. Ra value were checked and recorded to analyze the quality of cut surface. Hardness of the machined sample was measured by Saroj make Brinell Hardness tester Rab 250 at 400 gf at 10 s. Responses for all 15 machined sample were recorded and presented in Table 2.



Fig 1 Wire Electric Discharge Machining Experimental Setup

Table 1 Process Input factors and Levels

Parameters	Level 1	Level 2	Level 3
Pulse on Time (Ton)	35	40	45
Pulse off time (Toff)	5	10	15
Gap Voltage (V)	1	3	5

Table 2 Experiment Results

Sr No	Input Parameter			Output Parameter		
	Ton(μ s)	Toff(μ s)	Gap volt	SR(μ m)	MRR(mm ³ /sec)	Hardness (HV)
1	35	5	3	2.39	1.4935	334.40
2	45	5	3	3.43	1.2769	346.80
3	35	15	3	3.48	1.0544	314.20
4	45	15	3	4.19	1.1324	354.70
5	35	10	1	1.91	1.5080	318.20
6	45	10	1	3.21	1.5266	323.10
7	35	10	5	2.15	1.5025	340.80
8	45	10	5	3.05	1.4413	361.20
9	40	5	1	2.14	1.4343	352.60
10	40	15	1	3.41	1.0069	358.40
11	40	5	5	2.80	1.4267	380.50
12	40	15	5	3.75	1.0293	368.50
13	40	10	3	3.47	1.5914	340.10
14	40	10	3	3.30	1.6573	325.40
15	40	10	3	3.13	1.7303	331.10

RSM is an optimization technique used for investigating how input parameters affect the response variable, optimize and predict the output responses using regression equation. It involves the no of iteration to reach towards optimum value by considering the constraints. Factorial experiments designed by RSM is performed to reach near optimal solution. RSM DOE reduce the number of experiments. It saves experimentation, material cost and time. The factorial experiment design aids in the methodical progression towards the necessary optimum. Experiments in RSM are designed using a variety of techniques, including Box Behnken and CCD. In this study Box Behnken is used to designed experiments. Total 15 experiments were designed at 3 level with 3 input parameters. Minitab 17 is used to analyze RSM in this study.

III. RESULT AND DISCUSSION

Table 2 shows the output of experiments performed on WED machine. All the output variables recorded and presented. SR were obtained in the range of 1.91µm to 4.19 µm. Highest MRR was observed at 1.73 mm3/sec and lowest was found at 1.00 mm3/sec. Hardness was in the range of 318.20 to 380.50 HV. This experimental data of 15 experiments along with input and output response variables were analyzed in the MINITAB 17 statistical software and mathematical models in Equation (1) to (3) were developed. These mathematical models establish the relation between process variables which can be used to predict the output of machining process. Effect of each parameter.

$$SR = -2.061 + 0.0988 \text{ Ton} - 0.1167 \text{ Toff} + 0.847 \text{ Gap Volt} + 0.01092 \text{ Toff*Toff} - 0.1299 \text{ Gap Volt*Gap Volt} \quad (1)$$

$$MRR = -3.00 + 0.2061 \text{ Ton} + 0.1232 \text{ Toff} + 0.1303 \text{ Gap Volt} - 0.00300 \text{ Ton*Ton} - 0.01381 \text{ Toff*Toff} - 0.02251 \text{ Gap Volt*Gap Volt} + 0.00295 \text{ Ton*Toff} \quad (2)$$

$$Hardness = -419 + 40.1 \text{ Ton} - 14.26 \text{ Toff} - 17.16 \text{ Gap Volt} - 0.477 \text{ Ton*Ton} + 0.690 \text{ Toff*Toff} + 3.89 \text{ Gap Volt*Gap Volt} \quad (3)$$

Table 3 ANOVA (SR)

Source	DF	Adj SS	Adj MS	F-Value	P-Value
Model	5	5.52803	1.10561	23.31	0.000
Linear	3	4.16672	1.38891	29.28	0.000
Ton	1	1.95031	1.95031	41.11	0.000
Toff	1	2.07061	2.07061	43.65	0.000
Gap Volt	1	0.14580	0.14580	3.07	0.113
Square	2	1.36130	0.68065	14.35	0.002
Toff*Toff	1	0.27698	0.27698	5.84	0.039
Gap Volt*Gap Volt	1	1.00212	1.00212	21.13	0.001
Error	9	0.42693	0.04744		
Lack-of-Fit	7	0.36913	0.05273	1.82	0.399
Pure Error	2	0.05780	0.02890		
Total	14	5.95496			

R-Sq=92.83% R-sq(adj)=88.85%

Table 4 ANOVA (MRR)

Source	DF	Adj SS	Adj MS	F-Value	P-Value
Model	7	0.736968	0.105281	34.62	0.000
Linear	3	0.252775	0.084258	27.70	0.000
Ton	1	0.004104	0.004104	1.35	0.283
Toff	1	0.247949	0.247949	81.52	0.000
Gap Volt	1	0.000722	0.000722	0.24	0.641
Square	3	0.462496	0.154165	50.69	0.000
Ton*Ton	1	0.020788	0.020788	6.83	0.035
Toff*Toff	1	0.440327	0.440327	144.78	0.000
Gap Volt*Gap Volt	1	0.029930	0.029930	9.84	0.016
2-Way Interaction	1	0.021697	0.021697	7.13	0.032
Ton*Toff	1	0.021697	0.021697	7.13	0.032
Error	7	0.021290	0.003041		
Lack-of-Fit	5	0.011635	0.002327	0.48	0.779
Pure Error	2	0.009655	0.004828		
Total	14	0.758258			

R-Sq=97.19% R-sq (adj)=94.38%

Table 5 ANOVA (Hardness)

Source	DF	Adj SS	Adj MS	F-Value	P-Value
Model	6	4634.98	772.50	10.12	0.002
Linear	3	2024.90	674.97	8.84	0.006
Ton	1	764.40	764.40	10.01	0.013
Toff	1	42.78	42.78	0.56	0.476
Gap Volt	1	1217.71	1217.71	15.95	0.004
Square	3	2610.08	870.03	11.39	0.003
Ton*Ton	1	525.07	525.07	6.88	0.031
Toff*Toff	1	1098.69	1098.69	14.39	0.005
Gap Volt*Gap Volt	1	892.81	892.81	11.69	0.009

Error	8	610.82	76.35		
Lack-of-Fit	6	500.96	83.49	1.52	0.448
Pure Error	2	109.86	54.93		
Total	14	5245.79			

R-Sq=88.36% R-sq (adj)=79.62%

Table 3, 4 and 5 shows the ANOVA analysis for SR, MRR and Hardness respectively. This can be used to check whether the model developed in the analysis is adequate or not. Significance of process parameters can be decided on the basis of P value and F value from ANOVA analysis. If P value of any variables is less than 0.005 at 95% confidence then it is called significant parameters. All the insignificant terms except linear terms are not consider in the analysis. Ton and Toff are significant for SR and Toff is significant for MRR. Toff and Gap volt were significant for Gap volt. P value of lack of Fit for all variables is greater than 0.05 it means the term is insignificant which shows that model is adequate for prediction.

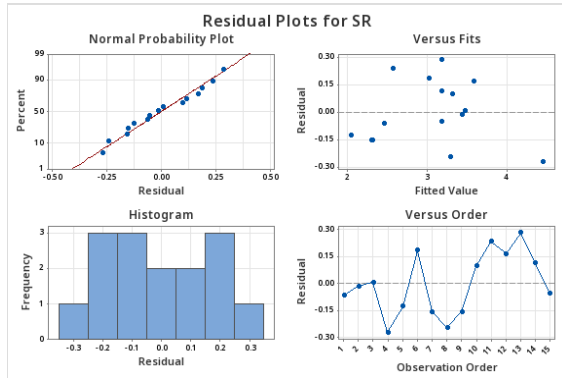


Fig 2 Residual Plot for SR

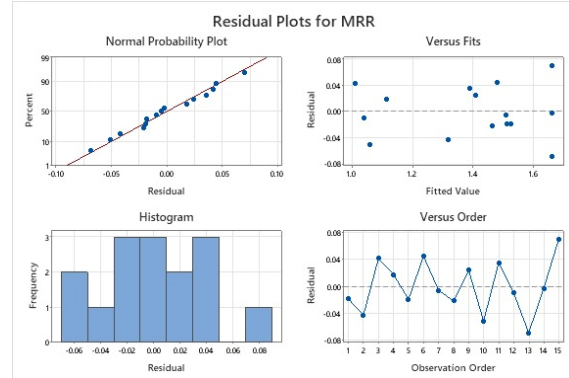


Fig 3 Residual Plot for MRR

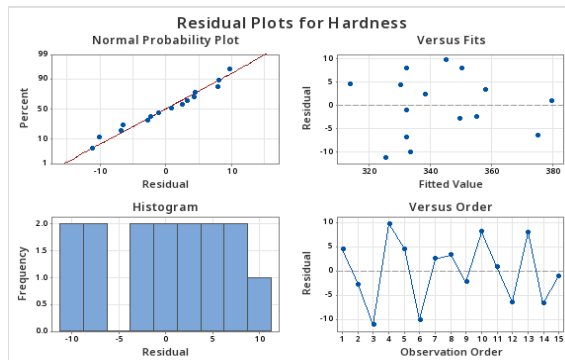


Fig 4 Residual Plot for Hardness

Residual plot for all the responses were shown in Fig 2 to 4. Normal probability plot shows that residuals are arrange in one straight line. It shows that developed model is fit for prediction. In Residual VS fitted plot all the residuals are allocated on both side of the reference line. Histogram shows the normal distribution of the data. No specific pattern was found in observation order plot which shows significance for ANOVA. All the test shows significance of the proposed model.

In contour plot effect of input parameters on response variable can be studied. In one plot two input parameters shows their effect on response variable. Third input parameters are kept constant. Fig 5 shows counter plot of SR in which lowest value of SR was obtained at lowest level of Ton and Gap Volt. As Ton increases the value of SR also increases. In case of Gap volt SR increases till 3v and then again start decreasing. When Gap volt is near to 1 V and Ton is near to 35µs which is at its lowest level SR is recorded at its lowest value (< 2.1µm). Effect of Toff is same like Ton lowest value was observed at 5 µs which is also the lowest level. When Ton and Toff are considered at a time for analysis it shows lowest SR (<2.5 µm) at minimum value of Ton and Toff. Decreasing the Ton and Toff value decreases the SR. Fig 5 shows the counter plot of MRR in this maximum MRR (>1.6 mm³/sec) was observed when Ton varies from 35 to 44 µs and Toff is varied from 6 to 10 µs. Gap volt shows the little variation for Maximum MRR with Ton as compared with Toff. When combines with Ton Maximum MRR was found when gap voltage is in between 2.5 to 3.5 V. and when combines with Toff maximum MRR Gap voltage varies from 1 to 4.5 V. Minimum MRR was observed at the maximum value of input parameters. Fig 6 shows the counter plot of Hardness. Highest value of Hardness was observed when Toff is ranging from 5 to 7 µs

and from 31 to 15 μ s. and Ton is ranging from 37 to 45 μ s. Gap voltage value found from 4.5 to 5 V for maximum Hardness. As observed in ANOVA table Toff is not having any significant effect on Hardness.

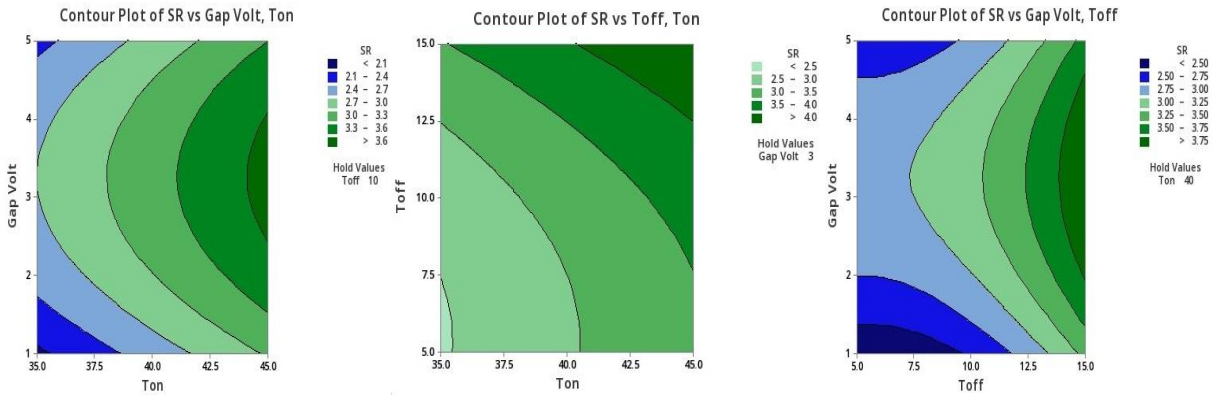


Fig 5 Counter Plot for SR Vs Toff, Ton

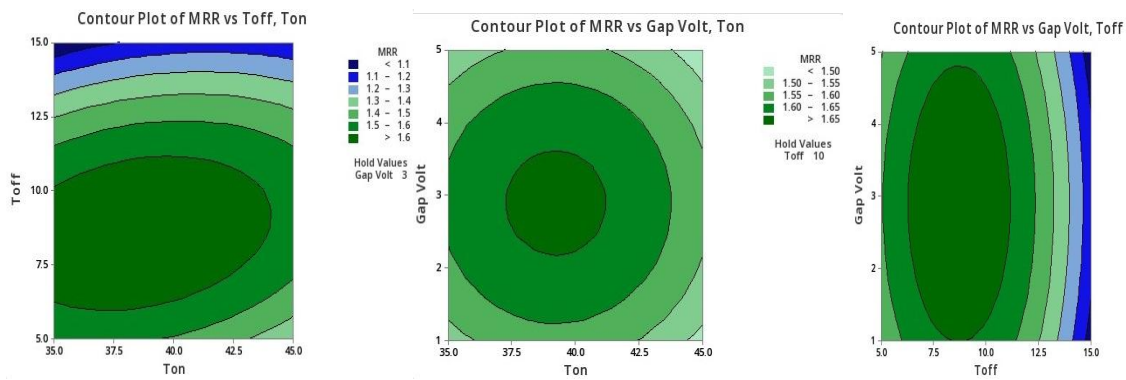


Fig 6 Counter Plot for MRR vs Gap Volt, Toff

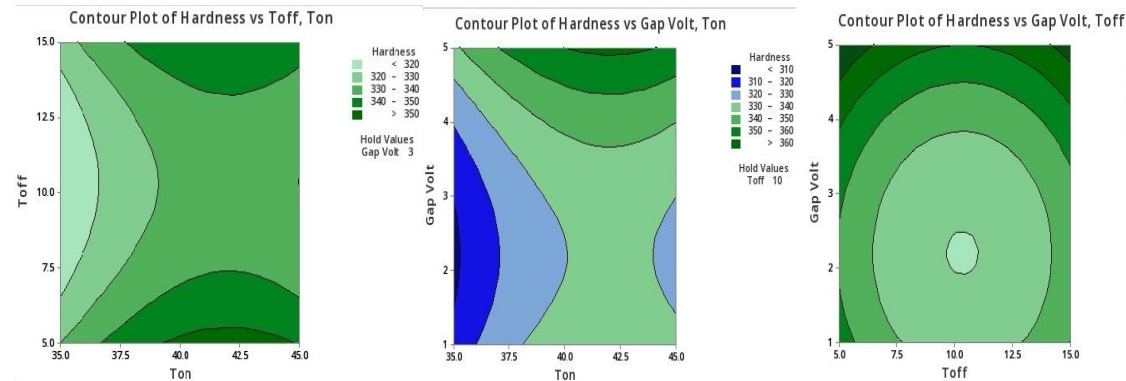


Fig 7 Counter Plot for Hardness vs Gap Volt, Toff

Time series plot for SR, MRR and Hardness shown in fig 8, 9 and 10 respectively. Actual and predicted values are closely matching with each other with slight variation.

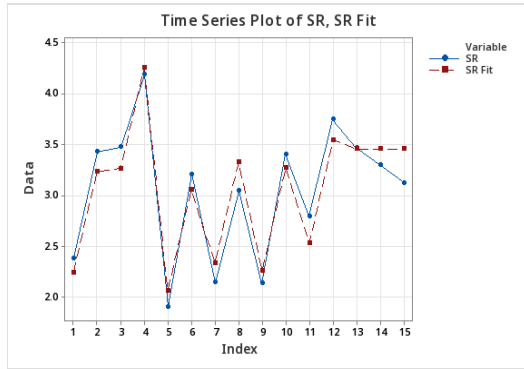


Fig 8 Time Series Plot for SR

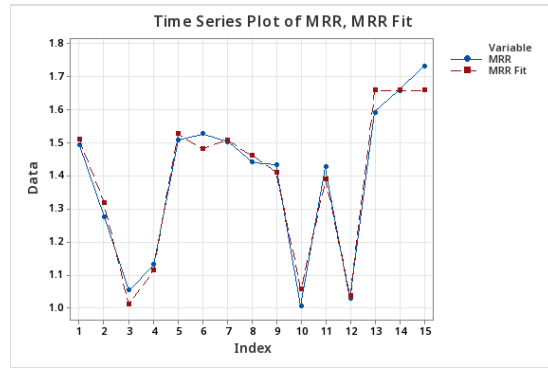


Fig 9 Time Series Plot for MRR



Fig 10 Time Series Plot for Hardness

Table 6 Predicted and Observed value

Response	Fit	SE Fit	95% CI	95% PI
SR	2.288	0.156	(1.936, 2.640)	(1.629, 2.947)
Hardness	368.35	5.67	(355.26, 381.43)	(344.32, 392.37)
MRR	1.4649	0.0379	(1.3754, 1.5544)	(1.3067, 1.6231)

Table 7 Optimum Value of Parameters

Variable	Setting
Ton	37.5253
Toff	5.50505
Gap Volt	5

Table 7 and 8 shows the optimal value of input parameters which is calculated from Multi response optimization using RSM. In this optimization were conducted by aiming all objective simultaneously. In Table 8 optimum value of Ton was found 37.50 μ s which is near to lowest level. Toff was found 5.50 μ s which also the lowest level and Gap volt is 5 v which highest level in range selected for machining.

IV. CONCLUSIONS

- Experiments were conducted as per RSM Box Behnken DOE and recorded the response variable. Experimental data were analyzed and establish the relationship between process variables. Developed mathematical model were found to be robust and confirmed using ANOVA.

- Ton and Toff shows significance for SR whereas Toff is found significant for MRR. Ton and Gap volt are influencing the Gap voltage.

- Value of SR was decreases with decrease in Ton, Toff and Gap volt however decrease in Ton, Toff increases the MRR.

- According to Multi-response desirability approach optimal setting of parameters are found Ton=37.52 μ s, Toff=5.50 μ s and Gap volt 5v.

REFERENCES

- [1] Soni Kumari, Dinbandhu, Kumar Abhishek, "Study of machinability aspects of shape memory alloys: A critical review", *Materials Today: Proceedings* 44 (2021) 1336–1343.
- [2] Rakesh Chaudhari, Jay J. Vora, D.M. Parikh, A Review on application of NiTiNol Shape Memory Alloy, *Recent Advances in Mechanical Infrastructure*, PP123-132
- [3] M. Manjaiah, S. Narendranath, S. Basavarajappa, "Review on non-conventional machining of shape memory alloys", *Transaction of Nonferrous metals Society of China*,2014, pp 12-21
- [4] Barsharani Dash, Manojit Das, Monalisa Das, Trupti R Mahapatra, Debadutta Mishra, "A Concise Review on Machinability of NiTi Shape Memory Alloys" 9th International Conference of Materials Processing and Characterization, ICMPC-2019, *Materials Today: Proceedings* 18 (2019) 5141–5150
- [5] Eren Kaya, Irfan Kaya, "A review on machining of NiTi shape memory alloys: The process and post process perspective", *The International Journal of Advanced Manufacturing Technology* (2019) 100:2045-2087
- [6] Saeed Daneshmand, Ehsan Farahmand Kahrizi, Ali Akbar LotfiNeyestanak, Vahid Monfared, "Optimization Of Electrical Discharge Machining Parameters For Niti Shape Memory Alloy By Using The Taguchi Method" *Journal of Marine Science and Technology*, Vol. 22, No. 4, pp. 506-512 (2014)
- [7] Neeraj Sharma, Tilak Raj, Kamal Kumar Jangra, "Parameter optimization and experimental study on wire electrical discharge machining of porous Ni40Ti60 alloy" *Proc IMechE Part B: J Engineering Manufacture* 2017, Vol. 231(6) 956–970
- [8] Mustafa Haider Abidi, Abdulrahman M. Al-Ahmari, Arshad Noor Siddiquee, Syed Hammad Mian, Muneer Khan Mohammed, Mohammed Sarvar Rasheed, "An Investigation of the Micro-Electrical Discharge Machining of Nickel-Titanium Shape Memory Alloy Using Grey Relations Coupled with Principal Component Analysis" *Metals* 2017, 7, 486; doi:10.3390/met7110486
- [9] Anshul Gangele, Ajay Mishra, "Surface Roughness optimization during machining of NiTi shape memory alloy by EDM through Taguchi technique", *Material Today, Proceedings* 29 (2020) 343-347.
- [10] Himadri Majumder, Kalipada Maity, "Application of GRNN and multivariate hybrid approach to predict and optimize WEDM responses for Ni-Ti shape memory alloy", *Applied Soft Computing* 70 (2018) 665–679.
- [11] H. Majumder, K. Maity, "Prediction and optimization of surface roughness and microhardness using grnn and MOORA-fuzzy-a MCDM approach for nitinol in WEDM", *Measurement* (2018), doi: <https://doi.org/10.1016/j.measurement.2018.01.003>
- [12] Divya Reddy, Hargovind Soni, Narendranath S. "Experimental Investigation and Optimization of WEDM process parameters for Ti50Ni48Co2 Shape Memory Alloy", *Materials Today: Proceedings* 5 (2018) 19063–19072
- [13] Vinayak N Kulkarni, V N Gaitonde, Viranna Hadimanil, Vasant Aiholi "Optimization in Wire Electric Discharge Machining of Nickel -Titanium Shape Memory Alloy", *IOP Conf. Series: Materials Science and Engineering* 577 (2019) 012015 IOP Publishing <https://iopscience.iop.org/article/10.1088/1757-899X/577/1/012015>
- [14] Raymond Magabe, Neeraj Sharma, Kapil Gupta, J Paulo Davim, "Modeling and optimization of Wire-EDM parameters for machining of Ni55.8Ti shape memory alloy using hybrid approach of Taguchi and NSGA-II" *The International Journal of Advanced Manufacturing Technology*, <https://doi.org/10.1007/s00170-019-03287-z>
- [15] Piyush Rathi, Rutvik Ghiya, Hem Shah, Pratyush Srivastava, Shalin Patel, Rakesh Chaudhari and Jay Vora, "Multi-response Optimization of Ni55.8Ti Shape Memory Alloy Using Taguchi Grey Relational Analysis Approach" *Recent Advances in Mechanical Infrastructure* https://doi.org/10.1007/978-981-32-9971-9_2
- [16] Rakesh Chaudhari, Jay Vora, S. S. Mani Prabhu, I. A. Palani, Vivek K Patel, D. M. Parikh, and Luis Norberto Lopez de Lacalle, "Multi-Response Optimization of WEDM Process Parameters for Machining of Superelastic Nitinol Shape-Memory Alloy Using a Heat- Transfer search Algorithm", *Materials* 2019, 12, 1277. <https://doi.org/10.3390/ma12081277>.
- [17] Rakesh Chaudhari, Jay J. Vora, S. S. Mani Prabhu, I. A. Palani, Vivek K. Patel, D. M. Parikh, "Pareto optimization of WEDM process parameters for machining a NiTi shape memory alloy using a combined approach of RSM and heat transfer search algorithm" *Adv. Manuf.* <https://doi.org/10.1007/s40436-019-00267-0>
- [18] Rakesh Chaudhari1 . Jay Vora1 . D. M. Parikh2 . Vishal Wankhede2 . Sakshum Khanna3, "Multi-response Optimization of WEDM Parameters Using an Integrated Approach of RSM–GRA Analysis for Pure Titanium" *J. Inst. Eng. India Ser. D* <https://doi.org/10.1007/s40033-020-00204-7>
- [19] Vinayak N. Kulkarni, V. N. Gaitonde, S. R. Karnik, M. Manjaiah, J. Paulo Davim, "Machinability Analysis and Optimization in Wire EDM of Medical Grade NiTiNOL Memory Alloy", *Materials* 2020, 13, 2184; <https://doi.org/10.3390/ma13092184>
- [20] Hargovind Soni, S. Narendranath, M. R. Ramesh, and P. M. Mashinini, "Enhanced process parameters using TOPSIS method during wire electro discharge machining of TiNiCo shape memory alloy", *AIP Conference Proceedings* 2204, 040005 (2020); <https://doi.org/10.1063/1.5141578> Published Online: 10 January 2020
- [21] Rakesh Chaudhari, Jay Vora, L.N. López de Lacalle, Sakshum Khanna, Vivek K. Patel, Izaro Ayesta, "Parametric Optimization and Effect of Nano-Graphene Mixed Dielectric Fluid on Performance of Wire Electrical Discharge Machining Process of Ni55.8Ti Shape Memory Alloy", *Materials* 2021, 14, 2533. <https://doi.org/10.3390/ma14102>

Dr. S. A. Patil, Asst.Professor,
P. R. Pote Patil College of Engineering
and Management, An Autonomous
Institute, Amravati email id:
sapatil@prpoteatilengg.ac.in

Dr. N. R. Thakare, Asso. Professor,
P. R. Pote Patil College of Engineering
and Management, An Autonomous
Institute, Amravati email id:
nrthakare@prpoteatilengg.ac.in

A review of various Spectroscopic Techniques for cancer diagnosis



Abstract: - India is a developing country with one of the most diverse population and diets in the world. Cancer rates are rapidly increasing in India. Cancer is a fatal disease, as it is very difficult to diagnose in the early stage. The survival of cancer patient mostly depends on early detection and the conventional methods practiced are not that beneficial as they do not produce prominent results to detect cancer at early stage. Many attempts are being made to develop methods to study human cells in situ, non-invasively, not only to provide accurate diagnosis, but also to better understand the genesis of disease at cellular level. Some of the important developing spectroscopic techniques are Laser induced fluorescence, synchronous luminescence spectroscopy, Laser Raman spectroscopy, photoacoustics spectroscopy. In this review article above techniques which are highly sensitive to chemical and morphological changes at the cellular level during cancerous growth are discussed.

Keywords: spectroscopy, cancer, fluorescence, photoacoustic

I. INTRODUCTION (*HEADING 1*)

Since the first report on laser radiation by Maiman (1960), many potential fields for its application have been investigated. Among this medical laser surgery certainly belongs to the most significant advances of our present century. Laser applications and new type of laser devices are used in new branches of medical science such as, Ophthalmology, Dermatology, General, Plastic & Cardiovascular surgery, Neurosurgery, Gynecology, Dentistry, Oncology, Gastroenterology, Orthopedics & others.

In the present article we have concentrated on oncology i.e. We have discussed various laser techniques for cancer diagnosis such as Laser Induced Fluorescence, Synchronous Luminescence Spectroscopy, Laser Raman Spectroscopy, Photoacoustic Spectroscopy.

II. A REVIEW OF LASER INDUCED FLUORESCENCE SPECTROSCOPY FOR CANCER DIAGNOSIS:

In the year 1981 the first laser induced fluorescence was done by Alfano & co-workers. The LIF technique was employed on various tissue regions of teeth (1) for the study of diseases related to oral cavity.

Later on in 1984, Alfano R. et al (2) measured the visible fluorescence spectra from cancerous and normal rat tissues. The spectral profiles from the normal tissues were substantially different and showed characteristic principal and secondary maxima. These peaks were assigned to fluorophores such as flavin and porphyrins in different environment in the 2 types of cell media.

A study was conducted by Mastoid Panjehpour et. al(3) to determine whether laser induced fluorescence could detect high grade dysplasia in Barrettes esophagus. 410 nm lasers light were used to induce auto fluorescence of Barrett's mucosa in 36 patients during routine endoscopy. They concluded that high grade dysplasia in Barrett's esophagus patients can be detected by laser-induced fluorescence spectroscopy.

S.K. Majumdar et.al(4) conducted In-vitro diagnosis of human uterine malignancy. For that they used nitrogen laser-induced auto fluorescence spectroscopy. LIF spectra from concerned and adjoining normal human uterine tissues were recorded. They further concluded that these techniques can provide good discrimination between cancerous and adjoining normal tissues.

In the same year when S. K. Majumdar conducted LIF on cancer & normal tissues i.e. 1996, S. M. Deto(5) et.al conducted Laser-induced auto fluorescence and exogenous fluorescence analysis of normal tissue and

stomach adenocarcinoma. They used helium cadmium laser (8mw, 442 nm) for the analysis. For sensitization of patients, they used five or seven capsules containing hypericin which were administered orally. Strong Yellow-red fluorescence of hypericin in tissue with maximum at 603 nm and auto fluorescence peak at 535 nm gave an intensity ratio of 2-2.5 from cancerous tissue and provided 85% specificity. Further they concluded that preliminary in view results of auto and fluorescence analysis using hypericin photosensitization from one patient with esophageal cancer and eleven patients with stomach cancer proven histological were encouraging and indicated the high reliability of laser induced fluorescence technique with hypericin in detection of early stage malignant lesions.

R. N. Panda et.al(6) in 1989 studied the benign breast tumors fluorescence depolarization and spectral profile analysis. The samples were exposed to the radiation operated at 488nm wave length having 2nm output power and they reported that the typical normalized fluorescence spatial profiles of normal, benign and malignant human breast tissue may be obtained.

Gianary Qu & GianwenHua(7) studied the calibrated fluorescence imaging of tissue in vivo. A laser wavelength at 457nm was used as the excitation source. The fluorescence emitted by the tissue showed distinct features when they were excited by the radiation. The normal and cancerous tissues emitted entirely different spectra.

Table (1) shows a list of biological molecules, which exhibit endogenous fluorescence with their excitation and emission maxima.

Sr. no.	Endogenous fluorophores	Excitation maxima (nm)	Emission Maxima(nm)
1)	Amino acids		
a)	Tryptophan	280	350
b)	Tyrosine	275	300
c)	Phenylalanine	260	280
2)	Structural Proteins		
a)	Collagen	325,360	400,405
b)	Elastin	290,325	340,400
3)	Enzymes & Coenzymes		
a)	FAD, FLAVINS	450	535
b)	NADH	290,351	440,460
c)	NADPH	336	464

NADH -REDUCED NICOTINAMIDE DINUCLEOTIDE

NAD(P)H- REDUCED NICOTINAMIDE DINUCLEOTIDE PHOSPHATE

FAD -FLAVIN ADENINE DINUCLEOTIDE

III. A REVIEW OF SYNCHRONOUS LUMINESCENCE SPECTROSCOPY FOR CANCER DIAGNOSIS:

The synchronous luminous spectra (SLS) of the samples were recorded by simultaneously scanning both emission and excitation wavelength with a fixed interval between them by P. K. Gupta et.al.(8) The offset was kept at 20 nm & the emission was scanned in the range 280-600 nm. The typical spectra full of features and information are obtained.

A.K.Gupta et.al(9) observed that a broad emission band at 401nm is obtained in the fluorescence spectrum. The excitation spectra show a broad band around 320nm, 290nm, in both diseased and normal tissues. The SLS shows an intense characteristics band at 290nm & 365nm for the diseased tissues whereas only as weak band at 290 nm observed for normal tissues.

A study reported by R. S. Jayasree et al (10) on the use of SL spectra in the discrimination of different malignant condition from the normal tissue gives lot of information. The SLS of breast & oral samples were recorded by simultaneously scanning both the emission & the excitation wavelength with a fixed interval between them. Emission was scanned in the 280-600 nm range. The intensity ratio at 360 nm & 320nm was

observed to be larger for both the oral and breast cancerous samples than the corresponding value for the normal tissues.

Alfano R.R. et al(11) studied synchronous luminescence fluorescence spectra of normal, pre malignant & malignant cervical tissues. The SL spectra was measured by scanning both excitation and emission monochromatic simultaneously with a wavelength difference of 20nm. The SL spectra of normal, premalignant and malignant cervical tissues showed the distinct peaks around 300, 350, 525 nm with broad peak around 460 nm. Further they pressured that this may be due to the presence of tryptophan, collagen & flavin respectively. The broad bond around 460 nm may be due to the presence of pyridoxal phosphate, carotenes & lipid pigments.

The SL spectra of normal, benign and malignant breast tissues were also studied by J.Ebenazar, S.Ganesan et al(12) From the study it was observed that the averaged SL spectra of benign having high collagen intensity around 349nm than that of normal & malignant tissues. It was observed that the peak of 514nm for benign and malignant tissues is significantly weaker than that of normal tissues.

In 2007, a synchronous fluorescence imaging system was developed by Quan Liu(13) and group in order to combine the great diagnostic potential of synchronous spectroscopy and the large field of view of imaging for cancer diagnosis. A multispectral imaging system was used to take the fluorescence images of the mouse skin. An optic parametric oscillator (IOPD) pumped by a ND:YAG laser provided excitation light from 420 to 700nm with an average power of 40 mw. The laser pulses were generated at 20Hz. &each pulse lasted for 5ns. Their study revealed that the classification results based on synchronous data analysis can achieve reasonably good accuracy compared to the results based on full spectra analysis when the differential wave Tenth is chosen appropriately. They further concluded that in synchronous fluorescence imaging a much smaller number of data points are required while more than one fluorophores could still be detected.

IV. A DISCUSSION ON RAMAN SPECTROSCOPIC TECHNIQUE FOR CANCER DIAGNOSIS:

Ramaswamy Manoharan(14) & his group demonstrated the ability of Raman spectroscopy to classify accurately normal benign and malignant breast tissues by using a Raman spectroscopic needle probes as a tool for improving the accuracy of needle biopsy.

The study of Raman spectroscopy by A. S. Haka(15) and group reveals that Raman scattering is a spectroscopic technique capable of providing highly detailed chemical information about a tissue sample. In contrast to other optical spectroscopic techniques, there are a large number of Raman active molecules in breast tissues and their spectral signature is sharp & well defined. The ability to probe several different chemicals is of particular importance in studying breast cancer. Further Raman spectroscopy is particularly amendable to in vivo measurements as the powers and excitation wavelengths used are non-destructive to the tissue and have a relatively large penetration depth.

V. PHOTO ACOUSTIC SPECTROSCOPY FOR CANCER DIAGNOSIS:

Photo acoustic imaging is based on the principle of photo acoustic effect. Fundamentally, when laser is incident on a tissue, optical absorption takes place which then results in thermoelastic expansion of tissue. This expansion creates localized pressure waves which are measured in the form of acoustic waves. The detected acoustic waves are plotted in the spectrum against different wavelengths of irradiated light.

Photo acoustic spectroscopy of tissue allows molecules specific detection with high special resolution and penetration depth. (16)

The photo acoustic physio-chemical spectrum of prostate, recorded by Yingna Chen & et.al revealed differences between normal and tumor tissues as the photoacoustic physio-chemical signal of cancer tissues were considerably stronger than that of normal tissues. In the photo acoustic signal intensity, spectra a clear difference in collagen and lipid absorption between normal and cancerous prostate tissue was recorded. It was found that the power spectrum correlation of hemoglobin, collagen and lipid was considerably higher for cancerous than the normal prostate tissue. Yingna Chen & et.al concluded that the complex tumor environment increases the complexity of the photo acoustic spectrum and blurs the distribution characteristics of single substance, thus increases the correlation of photo acoustic spectrum. Thus photo-acoustic physio-chemical spectrum is an

effective tool which records the significant changes in biomacromolecules during tumor development and thus can be useful to diagnose prostate cancer. (17).

VI. CONCLUSION:

The various spectroscopic techniques discussed above are useful in characterizing and diagnosing dreadful disease like cancer. The key characteristics of fluorescence spectroscopy is its high sensitivity. The synchronous luminescence spectra of the samples recorded by simultaneously scanning both the emission and excitation wavelength with a fixed interval between them. The SL spectra recorded shows significant difference in the intensities of different bonds for malignant and normal tissues. The position intensity and shape of peaks in Raman, spectra of cancerous tissue are found to be significantly different compared with those of normal tissues. Certain Biochemical molecules such as nucleic acids, proteins, and lipids have distinctive Raman features that yields structural and environmental information and hence helpful in diagnosing cancer. Photoacoustic spectroscopy is also a promising technique which differentiates between cancerous and normal cell.

REFERENCES

- 1) Preyfus R. W. and Hodgson R. T., Applied Physics Lett., (1972)Vol. 20
- 2) Alfano R.R., Tand G.C., Pradhan A., Lam W. & Chou D.S., IEEE J. of Quantum electronics QE., Vol.20, pp.1507, (1984)
- 3) Masoud Panjehpour, Bergein F. Over Holt, Tran Vo-Dinh, Donnati Edwards, Paul F. Backley III, Joseph F. Decosta, Rodger C. Haggit (April 5, 1996) Advances in Laser and light Spectroscopy to diagnose cancer disease III, optical Biopsy.
- 4) B.K.Majumdar, A. Uppal and P.K.Gupta, (10 May 1996), In-vitro diagnosis of human uterine malignancy using N2 Laser induced auto fluorescence spectroscopy, J current Science, Vol.70.
- 5) Deto G.S.M., Buryi A.N., Melik I.S., Toffe A.V., Rasing T.V. (1996) Proc. SPIE, Optical Biopsies & Microscopic techniques. Vol.2926.
- 6) Panda R.N., Laxmi B.V., Nair N.S., Agrawal A & Pradhan A., (Dec.15- 17, 1999) Proc. of NLS Hyderabad, pp883-384.
- 7) Giananay Qu.& Jianwen Hua.(2000) Appl. Phys.Litt., Vol.76.
- 8) Majumdar S.K. & Gupta P.K. (1997), Laser in surgery & Medicine, Vol.21, pp.117-122.
- 9) Jayasree R.S. & Gupta A.K. & Ragi J.R.(2003). Fluorescence spectra of panels Indians (Indian shrimp) for diagnosis of white spot syndrome. Proc. of NLS-2003.
- 10) Jayasree R.S. & Gupta A.K. Diagnosis of different human mediastival tissues using fluorescence spectroscopy pre-elementary, Proc.NLS-2003.
- 11) Alfano R.R., (2002), Optical Biopsy IV, Vol.4613.
- 12) J.Ebenazar, S.Ganesan, T.Anbupalam, S.Snekalatha & P.Aruna (2002) Proc. of DAE-BRNS National Lases Symposium.
- 13) Quan Liul, Kuichonz, Matthew Martin2, Alan witenberg2, Roberto Lenarduzzi2, Masoud Panjehpour, Bergin F. Overholt & Tuan Vo- Dinth. (October 2007), Optics Express, Vol. 15, No.20.
- 14) Ramasam Manoharan, Karan Shafes, Lev Perelman, Jun Wa, Kun Chen, Geurt Deinum, Maryann Fitzmawice, Janathan Myles, (Jan.2008), Photochemistry and Photobiology Vol.67, issue 1.
- 15) A. S. Haka, Z. Volynskaya, M. S. feld, Research in Biomedical optics.
- 16) Sindhoora Kaniyala Melanthota, Yurg V. Kistenev, Ekaterina Boisova and etal, (2022), Springer, Lasers Med. Sci., Vol. 37(8):3067-3084
- 17) Yingna Chen, Chengdang Xu, Zhoyu Zhang & etal (Sep 2021), Photoacoustics, ELSEVIER, Volume 23, 100280.

¹ Pankaj G. Waghmare,
² Vaibhav Y. Borokar,
² Ashwini S. Ghate,
² Manish G. Patil and
^{2*} Ashok M. Mahajan

Multilayer Deposition of TiO₂: A Versatile Approach for Battery and Biomedical Applications



Abstract: -

Titanium dioxide (TiO₂) stands as a promising material in various technological domains due to its unique properties such as high chemical stability, low toxicity, and excellent biocompatibility. In recent years, the deposition of TiO₂ in multilayer structures has emerged as a versatile strategy to tailor its properties for specific applications, particularly in the fields of battery and biomedical technologies. This paper presents the multilayer deposition techniques using spin coating method. In the context of battery applications, multilayer TiO₂ coatings offer enhanced electrode stability, improved charge/discharge rates, and prolonged cycle life, contributing to the development of high-performance lithium-ion batteries (LIBs), sodium-ion batteries (SIBs), and beyond. In the realm of biomedical applications, multilayer TiO₂ coatings exhibit remarkable potential in diverse areas such as drug delivery systems, biosensors, and implantable medical devices. This paper also discusses the influence of deposition parameters, such as layer thickness, and crystallinity, on the performance of multilayer TiO₂ coatings in battery and biomedical applications and it is characterized by using x-ray diffraction (XRD), Fourier transform infrared spectrometry (FTIR) and UV visible Spectroscopy. Future research directions and challenges associated with scalability, cost-effectiveness, and environmental impact are outlined, aiming to inspire innovative solutions for realizing the full potential of multilayer TiO₂ in diverse technological landscapes.

Keywords: TiO₂, XRD, FTIR, UV etc

¹ BP Arts, SMA Science and KKC College Chalisgaon, Dist Jalgaon (MH)-424101
^{2*} Department Of Electronics, School of Physical Sciences Kavayitri Bahinabai Chaudhari North Maharashtra University, Jalgaon (MH)-425001
Corresponding author Email: ammahajan.ele@gmail.com
Copyright © JES 2024 on-line : journal.esrgroups.org

Introduction

Titanium dioxide (TiO_2) has emerged as a cornerstone material in various technological domains owing to its exceptional properties such as high chemical stability, low toxicity, and excellent biocompatibility [1]. Over the years, significant research efforts have been directed towards harnessing the unique characteristics of TiO_2 for a myriad of applications, particularly in the fields of battery and biomedical technologies. Amongst the various deposition techniques, spin coating deposition stands out as a versatile approach to tailor the properties of TiO_2 for specific application requirements, offering enhanced performance and functionality [2-9]. This paper aims to provide comprehensive characteristics of the multifaceted role of multilayer TiO_2 deposition for both battery and biomedical applications. By systematically exploring the advancements, challenges, and future prospects of this technique, we seek to elucidate its potential to revolutionize these critical technological domains [10].

In the world of energy storage, the need for high performance energy storage devices is increasing with the rapid growth of portable electronics, vehicles, and grid scale energy storage systems. The challenges of electrode stability and charge/discharge rate, as well as cycle life in LIDs, SIBs, and other energy storage solutions, remain challenges that need to be addressed. Multilayer TiO_2 coatings offer a promising way to address these challenges. By controlling the thickness, shape, and composition of the individual layers of TiO_2 , researchers can optimize the electrochemical properties to improve battery performance and usher in a new age of sustainable and energy efficient energy storage solutions [11].

Simultaneously, in the biomedical arena, there is a burgeoning interest in leveraging TiO_2 -based materials for a wide range of applications spanning from drug delivery systems to implantable medical devices. Multilayer TiO_2 coatings offer unique advantages such as controlled drug release kinetics, enhanced cellular adhesion, and minimized biological responses, thereby facilitating advancements in targeted therapy, biosensing, and tissue engineering. The biocompatible nature of TiO_2 further underscores its suitability for biomedical applications, promising safer and more effective solutions for improving human health and well-being [12].

Through a comprehensive examination of the multilayer deposition of TiO₂ by using spin coating techniques, fabrication processes, and performance characteristics of TiO₂ coatings, this paper endeavors to shed light on the transformative potential of this approach in battery and biomedical applications. By elucidating the underlying principles, exploring recent advancements, and identifying future research directions, we aim to inspire continued innovation and collaboration in this dynamic and interdisciplinary area.

Materials and methods

To apply spin coating technology, commercially available TiO₂ nanopowder was used. To prepare the viscous solution, 0.4 g of TiO₂ was dissolved in 5 ml of ethanol and 5 ml of diethylene glycol. The ethanol is used as a solvent, and the diethylene is used as a stabilizer. The mixture is stirred with a magnetic stirrer for 3 days at 60 °C until a homogeneous solution of TiO₂ is obtained. The multi-layer film is prepared using a competitive device. The glass substrate is attached to the spin layer [13]. The speed of the spin layer is set to 3000 rpm. For each model, the turnaround time is 20 seconds. Remove the glass mat after 20 seconds. Dry the multi-layer TiO₂ film on the heater for about 10 minutes. After the first layer of all films is prepared, all three films are placed in an oven at 400 °C. The same process is repeated for the third and fourth layers. A multilayer film is ready for analysis. The characteristics of multi-layered films were determined by transmission x-ray diffraction (XRD). Optical properties were determined by a UV spectrophotometer. The chemical composition of the deposited films was determined by Fourier transform infrared spectroscopy (FTIR)

Results and Discussion

1. X-ray Diffraction Spectroscopy(XRD):

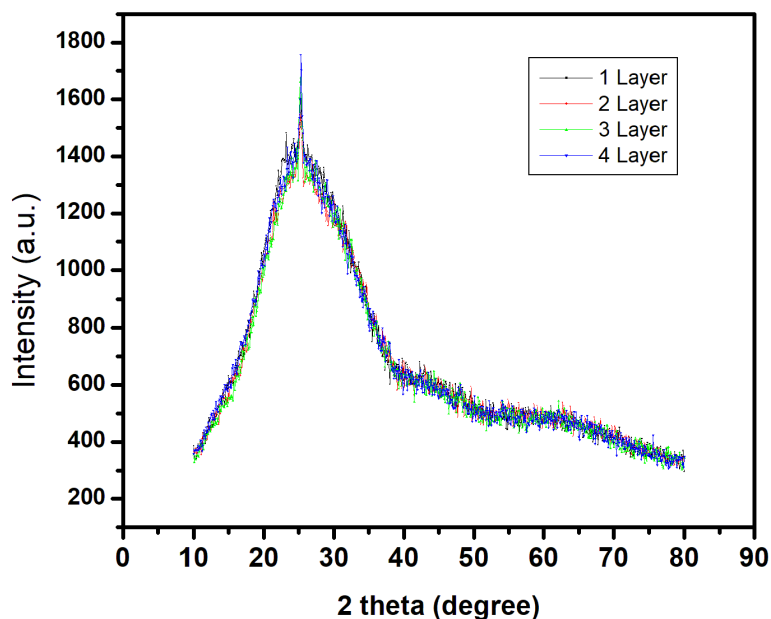


Figure 1. XRD patterns for multilayer TiO₂

Figure 1 displays the XRD patterns of TiO₂ thin films with varying layer numbers, confirming the presence of the anatase phase (tetragonal) of TiO₂. The XRD patterns were obtained using an x-ray diffraction within a 2 theta range of 50 to 900. Notably, all layers exhibited a prominent peak at 25.6810 corresponding to (101) planes of reflection, in accordance with (JCPDS 21-1272) [14, 15]. These findings suggest that increasing the number of deposition layers does not significantly affect the crystallinity of TiO₂. Grain size is calculated by using Debye's Shearer formula

$$\text{i.e. } D = K\lambda / \beta \cos\theta \quad [14,15]$$

The grain size of a single layer of TiO₂ thin film is 1.12 nm at a 2 theta value of 25.6810. This increases to 2.18 nm for two layers, and 3.24 nm for three layers at a 2theta value of 25.2810. When there are four layers, the grain size at the same 2theta value is measured to be 3.10nm. It can be observed that as the number of layers increases, so does the grain size. This phenomenon can be attributed to the increase in number of coating layers, resulting in a reduction of lattice mismatching between them.

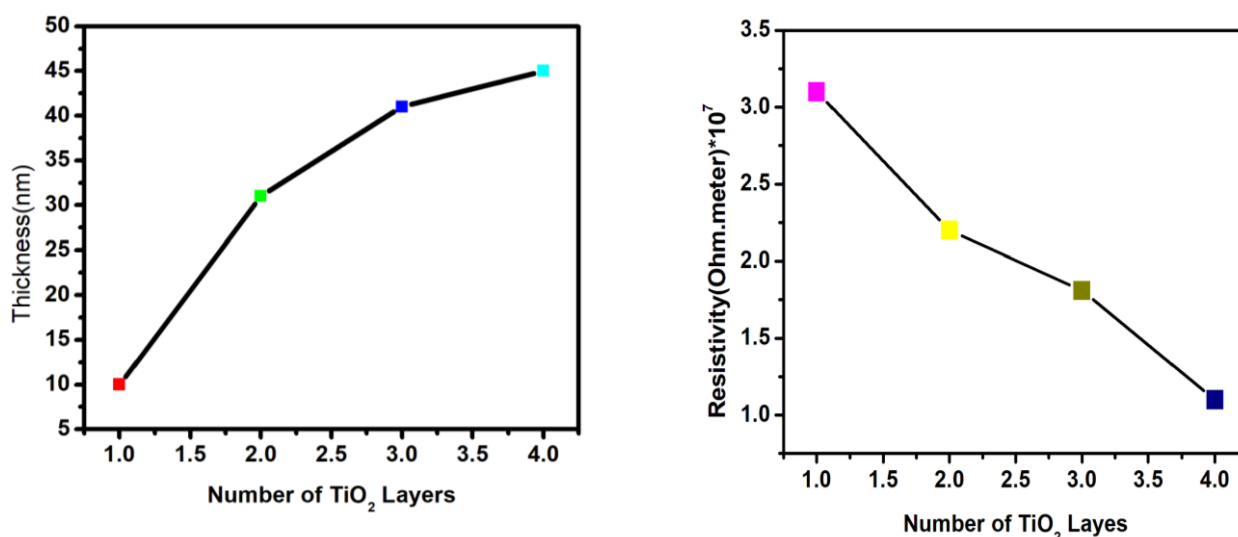


Figure 2. (a) Shows the thickness of TiO₂ deposited films (b) shows the average resistivity of deposited thin films.

The figure 2 illustrates the average resistivity of the deposited material. It is observed that the average resistivity decreases as the number of TiO₂ layers increases. The thickness of the TiO₂ deposited films on the glass substrate is determined using the profilometer Dektak 150. As the number of layers increases, the thickness also increases, as depicted in figure 2. The control of thickness in multilayer deposition is essential for tailoring the material properties to meet the specific requirements of battery and biomedical applications, ensuring optimal performance and longevity. [15].

2. Fourier Transform Infrared Spectroscopy (FTIR).

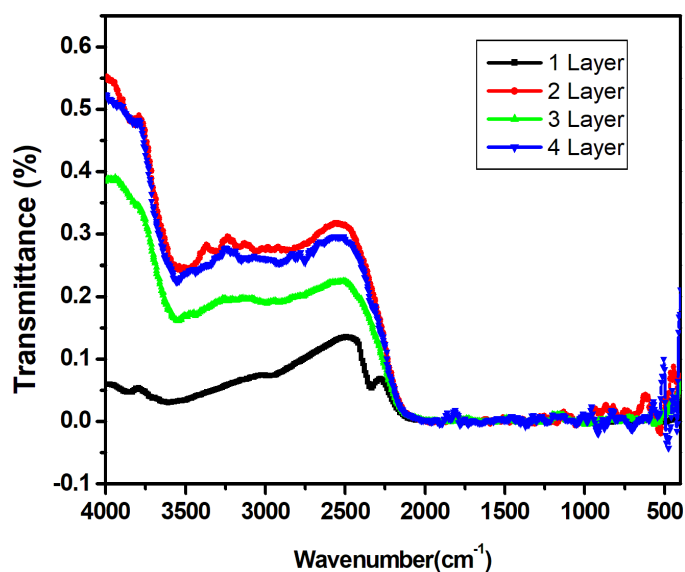


Figure 3. FTIR patterns of multilayer TiO₂

To analyse the chemical composition of the deposited films, Fourier-transform infrared spectroscopy (FTIR) analysis was performed for the vibration bands in the wavenumber range of 400–4000 cm^{-1} . Figure 3 shows the FTIR spectrum of TiO_2 . The peaks at 3390 and 3323 cm^{-1} are related to H-O-H vibrational bonding, and the peaks at 1600 and 1550 cm^{-1} are indexed to OH vibrational bonds, both indicating the presence of absorbed hydroxyl groups in the samples [16, 17]. The groups containing oxygen play an effective role in photocatalytic activity and are thus able to generate more hydroxyl radicals. The increase in hydroxyl group bonds related to the doping process may be related to the fact that this process involves aqueous solutions and aqueous dispersions, even after the oven drying process, as recommended in the literature. The peak at 2280 cm^{-1} signals the Ti-O vibration, which is a very intense bond from the doping process [18]. The peaks shown in the range of 528–458 cm^{-1} are due to the Ti-O group [19]. In the spectrum of undoped TiO_2 (reference), the peaks in the region of 650–1200 cm^{-1} can be attributed to the Ti-O-Ti bond and the TiO stretching vibration.

3. UV visible spectroscopy

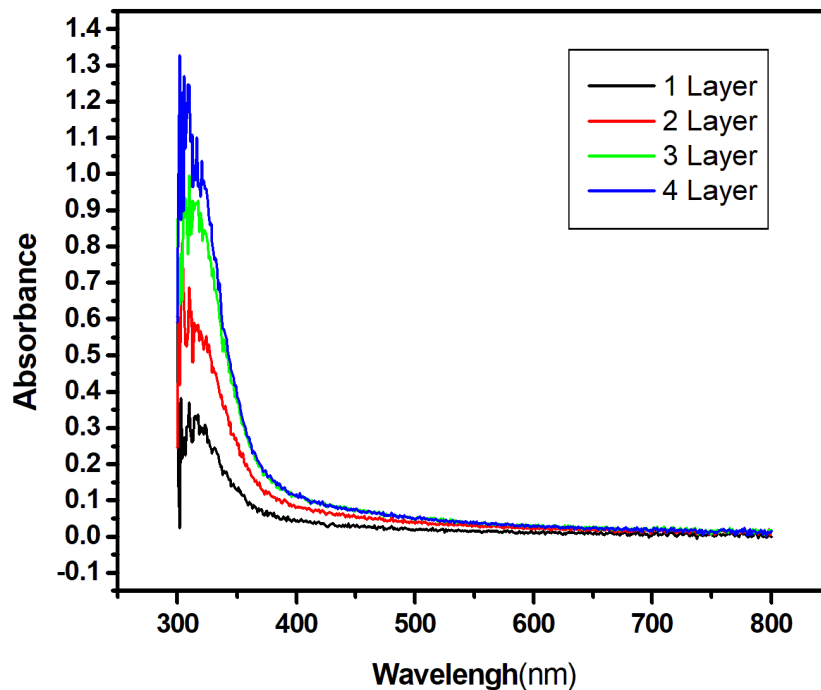


Figure 4. UV Patterns for multilayer TiO_2

The spectra range from 300 to 1000 nm with a peak at the wavelength of 302 nm is presented in figure. 4. It was noted that the absorption of all the multilayer deposited TiO_2 takes place at wavelength of 302 nm

exciton absorption band maximum located at about 300-400 nm range is very distinctive for the band gap of anatase TiO₂, which is well-known and extensively reported [20]. Since TiO₂ is an indirect bandgap semiconductor, the dominant optical absorption arises as the indirect transitions between the valleys [21]. Therefore, we think that the TiO₂ films deposited on glass are anatase phase from the analysis of UV visible spectra. The optical absorption threshold for TiO₂ film has known to increase as the size of layers of TiO₂ films decreases due to the size quantization effect [22-24].

Conclusion

The TiO₂ thin films were successfully deposited on glass substrate by spin coating method. The XRD, FTIR and UV results from this study are indicative to useful for battery and biomedical applications.

References

- [1] Li, Ziliang, et al. "Application of nanostructured TiO₂ in UV photodetectors: A review." *Advanced Materials* 34.28 (2022): 2109083.
- [2] Agrawal, Khushabu S., et al. "Preparation of rare earth CeO₂ thin films using metal organic decomposition method for metal-oxide–semiconductor capacitors." *Journal of Materials Science: Materials in Electronics* 28 (2017): 12503-12508.
- [3] Khairnar, A. G., et al. "Electrical properties of HfO₂ high-k thin-film MOS capacitors for advanced CMOS technology." *Indian Journal of Physics* 89 (2015): 1177-1181.
- [4] Joshi, Bhavana N., and Ashok M. Mahajan. "Deposition characterization of low-k hybrid thin films using methyl methacrylate for ULSI applications." *Materials Science and Engineering: B* 168.1-3 (2010): 182-185.
- [5] Patil, Anil B., and A. M. Mahajan. "Synthesis and characterization of sol-gel derived CeO₂ dielectric thin films for CMOS devices." *Optoelectronics and Advanced Materials, Rapid Communications* 2.12 (2008): 811-813.
- [6] Waghmare, Pankaj G., et al. "CuO/HAp composites: Excellent dielectric materials." *Materials Today: Proceedings* 72 (2023): 2681-2686.

- [7] Borokar, Vaibhav Y., et al. "Growth and characterization of Peald deposited La₂O₃ on SiO₂/Si." *International Journal of Modern Physics B* (2024): 2440017.
- [8] Barhate, Viral Nivrutti, et al. "Post-deposition-annealed lanthanum-doped cerium oxide thin films: structural and electrical properties." *Rare Metals* 40.7 (2021): 1835-1843.
- [9] Agrawal, Khushabu S., Vilas S. Patil, and Ashok M. Mahajan. "Atomic layer deposited HfO₂ ultra-thin films on different crystallographic orientation Ge for CMOS applications." *Thin Solid Films* 654 (2018): 30-37.
- [10] Bhasin, V., et al. "Remarkably high capacity Li ion batteries with rf sputter deposited TiO₂ thin film anodes on SS substrates." *Applied Surface Science* 592 (2022): 153273.
- [11] Shahmohammadi, Mina, Bin Yang, and Christos G. Takoudis. "Applications of titania atomic layer deposition in the biomedical field and recent updates." *Am. J. Biomed. Sci. Res* 8.22 (2020): 465-468.
- [12] Jafari, Sevda, et al. "Biomedical applications of TiO₂ nanostructures: recent advances." *International journal of nanomedicine* (2020): 3447-3470.
- [13] Barhate, Viral, et al. "Spectroscopic study of La₂O₃ thin films deposited by indigenously developed plasma-enhanced atomic layer deposition system." *International Journal of Modern Physics B* 32.19 (2018): 1840074.
- [14] Taha, Sabah, et al. "Development of alcohol sensor using TiO₂-Hydroxyapatite nanocomposites." *Materials Chemistry and Physics* 240 (2020): 122228.
- [15] Khan, M. I., et al. "Structural, electrical and optical properties of multilayer TiO₂ thin films deposited by sol-gel spin coating." *Results in physics* 7 (2017): 1437-1439.
- [16] Toro, Roberta Grazia, et al. "Study of the effect of titanium dioxide hydrosol on the photocatalytic and mechanical properties of paper sheets." *Materials* 13.6 (2020): 1326.
- [17] Jiang, Chi, et al. "Robust fabrication of superhydrophobic and photocatalytic self-cleaning cotton textiles for oil-water separation via thiol-ene click reaction." *Journal of materials science* 54 (2019): 7369-7382.

- [18]Kutte, Vikas, et al. "Gas sensing and dielectric properties of TiO₂/Stilbitenanocomposites." *Materials Today: Proceedings* 92 (2023): 960-966.
- [19] Zhang, Jun-Ying, et al. "Nanocrystalline TiO₂ films studied by optical, XRD and FTIR spectroscopy." *Journal of Non-Crystalline Solids* 303.1 (2002): 134-138.
- [20]Adamczyk, Anna, and Elżbieta Długoń. "The FTIR studies of gels and thin films of Al₂O₃-TiO₂ and Al₂O₃-TiO₂-SiO₂ systems." *SpectrochimicaActa Part A: Molecular and Biomolecular Spectroscopy* 89 (2012): 11-17.
- [21] Ali, Nisreen S., et al. "Performance of a solar photocatalysis reactor as pretreatment for wastewater via UV, UV/TiO₂, and UV/H₂O₂ to control membrane fouling." *Scientific Reports* 12.1 (2022): 16782.
- [22] Li, Saiyao, et al. "Skin bioinspired anti-ultraviolet melanin/TiO₂ nanoparticles without penetration for efficient broad-spectrum sunscreen." *Colloid and polymer science* 299 (2021): 1797-1805.
- [23] Li, Ziliang, et al. "Application of nanostructured TiO₂ in UV photodetectors: A review." *Advanced Materials* 34.28 (2022): 2109083.
- [24] Lee, Song Yeul, et al. "Atomic layer deposition-based synthesis of TiO₂ and Al₂O₃ thin-film coatings on nanoparticle powders for sodium-ion batteries with enhanced cyclic stability." *Journal of Alloys and Compounds* 897 (2022): 163113.

¹Atish Kohale²Sarika A. Khapre

Structure and properties of processible conductive polyaniline-polyethylene oxide composite



Abstract: - The effect of doping of Li_2SO_4 in PANI- Li_2SO_4 -PEO composite films was studied with the help of characterization and thermo gravimetric analysis. PANI- Li_2SO_4 -PEO composite films were prepared by chemical polymerization. The Scanning Electron Microscopy (SEM) has been carried out to characterize the samples. From the IR spectroscopy, it was noticed that, conductive composites were formed and corresponding peak observed, shows the presence of PANI, PEO and Li_2SO_4 . TGA/DTA data shows that, interaction between the polymers. From the TG/DTA, it is observed that PANI-PEO samples with doped Li_2SO_4 gives one step degradation in which weight loss is in the range 95.5 to 97.32 % when heated up to 700K . Thermal analysis is the analysis of a change in a property of a sample, which is related to an imposed change in the temperature. TG measures mass changes in a material as a function of temperature (or time) under a controlled atmosphere and In DTA, the temperature of a sample is compared with that of an inert reference material during a programmed change of temperature.

Keywords: PANI- Li_2SO_4 -PEO composite films, SEM/EDAX, FTIR, TG/DTA.

¹ *Corresponding author: Department of Physics, Shri R. R. Lahoti Science College, Morshi, Dist-Amravati [M.S.], India
Department of Physics, Dr.D.Y. Patil Institute of Technology, Pimpri, Pune -18[M.S.], India.

I. INTRODUCTION

In recent years, synthesis and characterization of conducting polymers fetched attention of researchers because of their electrical, electrochemical, optical properties [1] and their possible applications to sensors, organic batteries, microelectronic devices and electrocatalysis [2]. Polymer composites are advanced materials formed by combining two or more distinct components: a polymer matrix and reinforcing materials. This amalgamation results in a material that exhibits enhanced properties compared to its individual constituents. Polymer composites have gained significant attention and applications across various industries due to their unique combination of strength, light weight, and versatility. However, the major concern in this area is the lack of processibility of these polymers. Nowadays, the rapidly expanding field of nanoconducting polymer composite is generating many exciting new materials with novel properties. Different methods are used for preparation of composites of conducting polymers with conventional polymers. One way of preparing composites is synthesizing the conducting polymer inside the matrices of conventional polymers using chemical [3-5] and electrochemical methods [6-8]. In this work, we have tried to make PANI-Li₂SO₄-PEO blend by chemical polymerization method. These blends have been characterized by elemental analysis, SEM, TG/DTA measurements.

II. EXPERIMENTAL

2.1 Materials

The aniline monomer (AR grade) was obtained from M/S S.D. Fine Chem. (India), Ammonium persulfate [(NH₄)₂S₂O₈] was received from M/S Loba Chemie India and was used as obtained. The concentrated hydrochloric acid was obtained from M/S S.D. Fine Chem. (India), PEO (polyethylene oxide) was received from Merck company. Solvents NMP (1-methyl 2-pyrrolidone), distilled water and methanol were used after purification, Li₂SO₄.H₂O, LiClO₄.3H₂O and LiCl were received from M/S Loba Chemie India and were used as obtained.

2.2 Preparation of Samples

PANI, PEO and Li₂SO₄ were added to NMP (1-methyl 2-pyrrolidone) which was stirred for 30 min [1]. Films containing PANI, PEO and Li₂SO₄.H₂O (Lithium Sulphate) were obtained by drying the mixtures at 750 C for 24 h. Film was deposited on Teflon sheet, so that it is easy for removing the film. Different percentage of composite film have been prepared such as 3,5,7,9,11wt %. In these films the concentration of Li-salt is varied and PANI and PEO is kept constant. The nomenclature and stoichiometry is given in the table.

Table 2.1: Nomenclature and stoichiometry of the films.

wt % of Li-salt in PANI-PEO blend	Polyaniline(PANI) wt (%)	Polyethylene oxide (PEO) wt (%)	Li-salt wt (%)
3	0.1879	1.9	0.064574
5	0.1879	1.9	0.109889
7	0.1879	1.9	0.157154
9	0.1879	1.9	0.206496
11	0.1879	1.9	0.26398

2.3 SEM/EDAX

SEM micrographs of PANI-Li₂SO₄-PEO composite films were taken by scanning electron microscope Model No. JSM-7600F with Resolution: 1.0nm (15 kv), 1.5nm (1 kv), Accelerating Voltage: 0.1 to 30 kv and Magnification: x25 to 1,000,000.

2.4 Thermogravimetric analysis

Thermo gravimetric analysis of PANI- Li₂SO₄-PEO composite films were carried out in a PERKIN ELMER, Diamond TG/DTA thermal analyzer, over a temperature range Ambient to1500°C. Runs were conducted at a heating rate of 0.01°-100° C/min.

2.5 Fourier transforms infrared spectroscopy (FTIR) analysis

The FTIR spectrum of PANI-Li₂SO₄-PEO composite films was recorded on SHIMADZU-FTIR Spectrophotometer at room temperature in the wavelength range 4000 to 400 cm⁻¹

III. RESULTS AND DISCUSSIONS

3.1 Scanning Electron Microscopy images (SEM/EDAX)

The surface morphology of PANI-PEO-Li₂SO₄ blend film was examined by Scanning Electron Microscope (SEM). Fig.1(a-c) illustrate the SEM images of PANI-PEO- Li₂SO₄ blend samples of 5, 7 and 9wt%. It shows that the surface of the film (c) is smooth as compared to (a) and (b), which shows some cracks on the surface, sponge-like appearance observed for the 9 wt% film, indicative of highly inhomogeneous microstructure within the composite [9]. Nature of all film is amorphous.

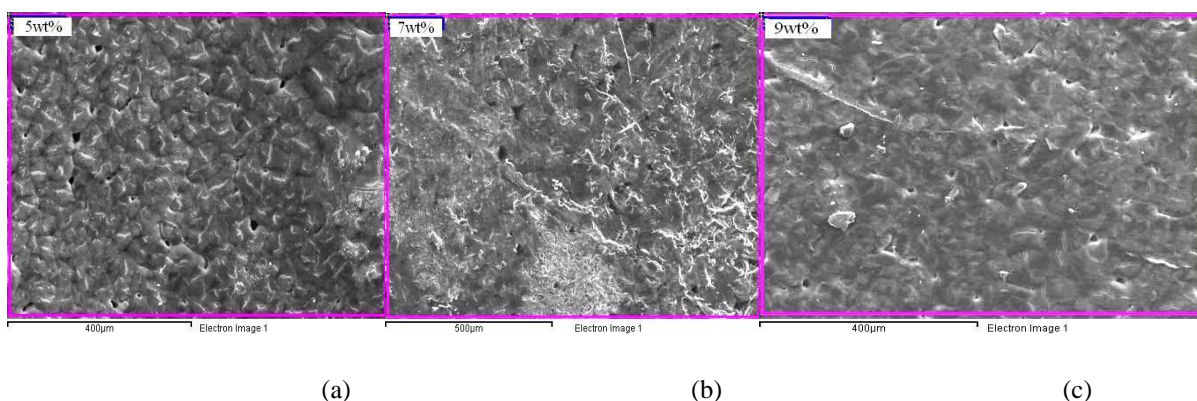
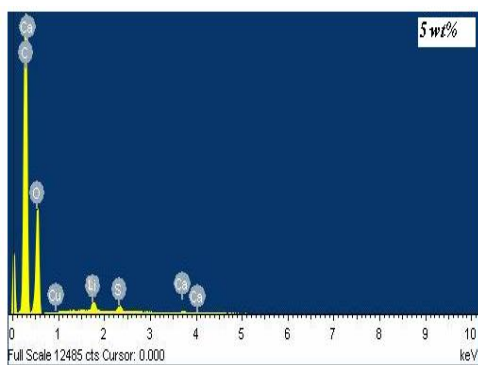


Fig.1 (a-c): Scanning electron micrographs of 5wt%, 7wt% and 9wt% Li₂SO₄ (PANI-PEO- Li₂SO₄) blend.

The elemental composition of PANI-PEO- Li₂SO₄ blend samples is also determined using SEM energy dispersive analytical X-ray (EDAX) spectroscopy. The quantitative analysis for energy dispersive X-ray analysis (EDAX) was performed for Li and S on various samples at different points. The average ratio of atomic percentage of Li:S shows that the samples have S deficiency. The existence of lithium in the composite film is confirmed by EDAX analysis fig 2. A signal corresponding to sulfur also appears on the spectrum. The results of EDAX investigations highlighted are summarized in Table 1(a), (b), (c) for 5,7 and 9wt% Li₂SO₄ (PANI-PEO- Li₂SO₄) respectively. The element (%) and atomic (%) of the Li₂SO₄ (PANI-PEO- Li₂SO₄) blend are shown in table 1(a-c).

Table 1(a)

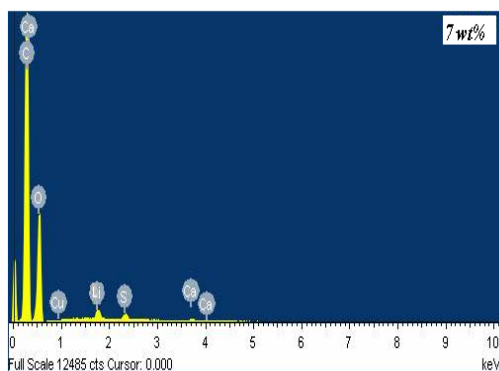
Element	Weight%	Atomic%
C	57.75	64.95
O	40.92	34.55
Li	0.48	0.23
S	0.35	0.15
Ca	0.14	0.05
Cu	0.36	0.08



(a)

Table 1 (b)

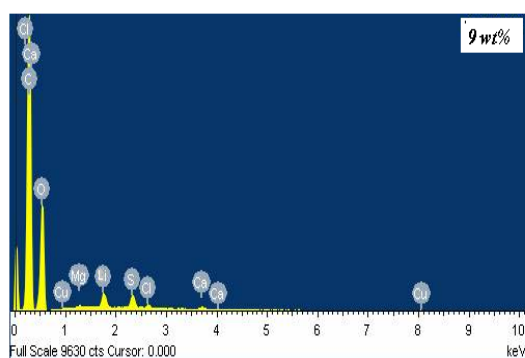
Element	Weight%	Atomic%
C	58.59	65.88
O	39.55	33.38
Li	0.64	0.31
S	0.73	0.31
Ca	0.19	0.06
Cu	0.31	0.07



(b)

Table 1 (c)

Element	Weight%	Atomic%
C	57.6	65.06
O	40.08	33.99
Mg	0.15	0.08
Li	0.72	0.35
S	0.74	0.31
Cl	0.24	0.09
Ca	0.17	0.06
Cu	0.3	0.06



(c)

Fig.2: EDAX spectra of 5, 7 and 9wt% Li_2SO_4 (PAni-PEO- Li_2SO_4) blend.

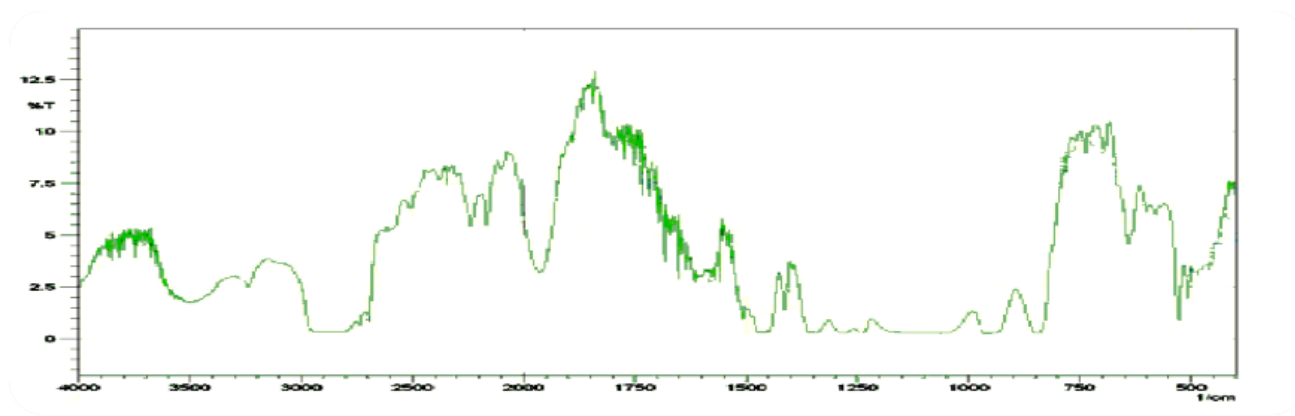
3.2 Fourier transforms infrared spectroscopy (FTIR) analysis :

In order to find the nature of bonding in the film material we studied FTIR spectrum of PANI-PEO - Li₂SO₄ blend. From Fig (3), the strongest lines appear at 1037 cm⁻¹ and 640.37 cm⁻¹ of 5 and 7 wt% respectively which correspond to the (SO₄) and (SO₄) of the sulphate respectively [10]. The peak 486.9 cm⁻¹ of 9 wt% and 1138 cm⁻¹ of 5 wt% indicate vibrations of Li₂SO₄. Several translational modes of Li⁺ ion can be connected due to their presence in the region of 400–450 cm⁻¹ of 7 wt% [11].

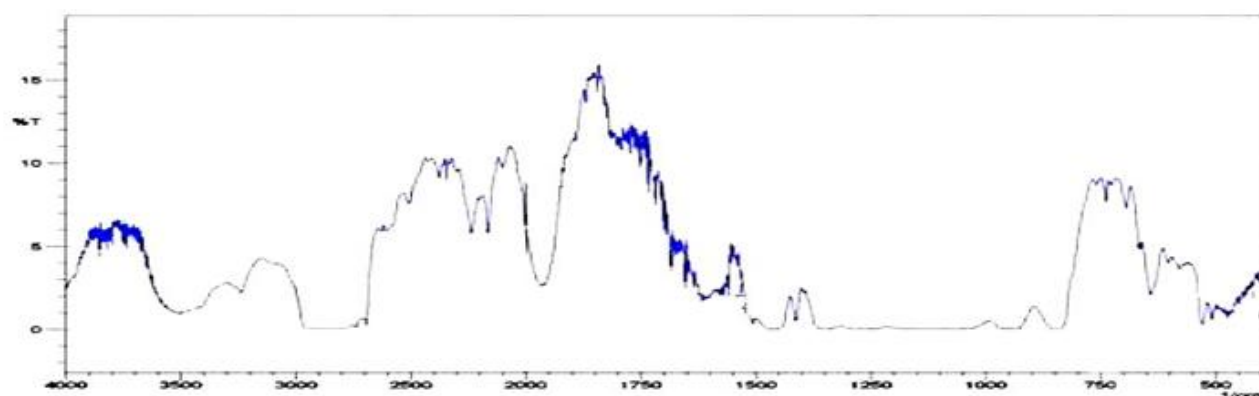
In polyaniline, polarons are responsible for the broad absorption band at wave numbers above 3431.36.8 cm⁻¹ of 7wt% and 2929.87 cm⁻¹ of 9 wt% [12-14]. The absorption band at 1274.95cm⁻¹ of 5wt% is due to C–N stretching of secondary aromatic amine which represents π electron delocalization induced in the polymer by protonation. The band characteristic of the conducting protonated form is observed at about 12334.44 cm⁻¹ of 5wt% which has been interpreted as C-N+• stretching vibration in the polaron structure [15]. The region 900–700 cm⁻¹ corresponds to aromatic ring and out-of-plane C-H deformation vibrations. Their frequencies are mainly determined by the number of adjacent hydrogen atoms in the ring [16]. Also peak 1581.63cm⁻¹, 1355.96 cm⁻¹ of 5 wt% ,these peaks are corresponding to most of the characteristic peaks for PANI as described in literature [17-19], which is same in PANI-PEO blend. PEO exhibit a large broad band of asymmetric CH₂ stretching between 2843.0 cm⁻¹ and narrow band of lower intensity at 2740 cm⁻¹ of 9 wt% [20]. Table 2 shows the Peak position for 5, 7 and 9wt% Li₂SO₄ (PANI-PEO-Li₂SO₄) blend.

Table 2: Peak position for 5, 7 and 9wt% of Li₂SO₄ (PANI-PEO-Li₂SO₄) blend.

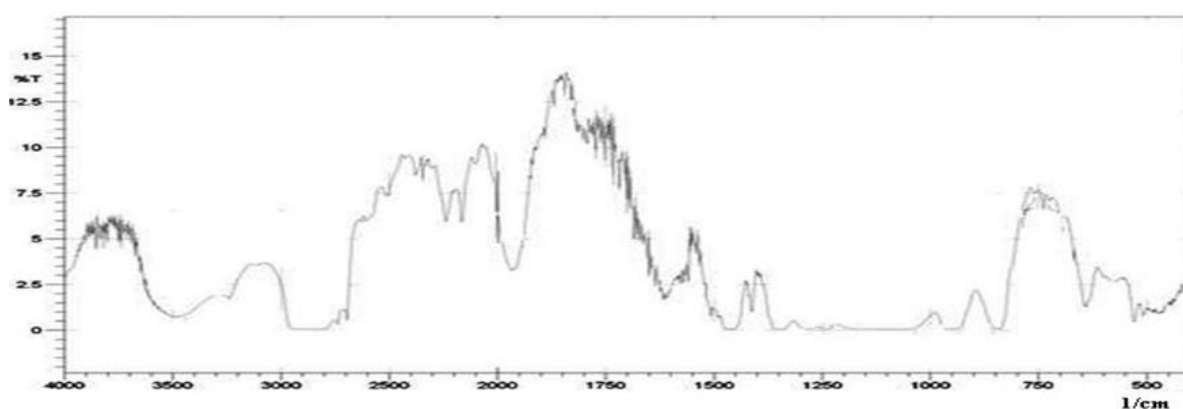
Sr.No.	Peak position cm ⁻¹		
	5%Li ₂ SO ₄ (PANI-PEO-Li ₂ SO ₄)	7%Li ₂ SO ₄ (PANI-PEO-Li ₂ SO ₄)	9%Li ₂ SO ₄ (PANI-PEO-Li ₂ SO ₄)
1	401.19	401.19	-
2	424.34	420.48	-
3	435.91	443.63	-
4	447.49	474.49	486.06
5	694.37	640.37	-
6	727.16	-	727.16
7	738.74	-	738.74
8	759.95	-	759.95
9	839.3	-	837.11
10	933.55	-	856.39
11	941.26	-	939.33
12	952.84	-	-
13	1037.7	-	1037.7
14	1138	1130.29	-
15	1234.44	1230.58	1234.44
16	1274.95	-	-
17	1355.96	1359.82	1359.82
18	1581.63	1533.41	1558.48
19	2740.85	2740.85	2740.85
20	2825.87	-	2843.07
21	2902.87	-	2929.87
22	3415.93	3431.36	3437.15



(a) 5wt%



(b) 7 Wt%



(c) 9wt%

Fig 3: FTIR spectra for a) 5wt% b) 7wt% c) 9wt% of Li_2SO_4 (PANI-PEO- Li_2SO_4) blend.

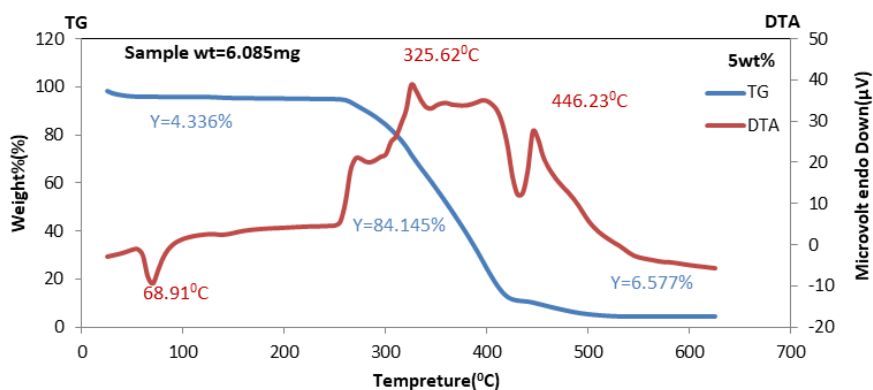
3.3 Thermogravimetry (TG) / Differential thermal analysis (DTA):

Thermo gravimetric analysis was carried out for various polymers to determine the weight loss at different temperatures. Thermal stability of the PANI-PEO- Li_2SO_4 blend was assessed from analysis of the TG and DTA curves Fig. 4 (a-c). The main data is summarized in Table 3.

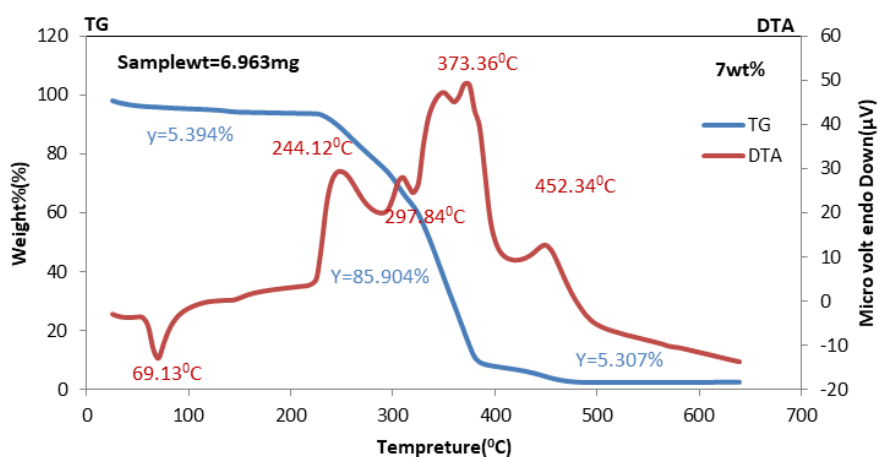
In (Fig. 4.a), film demonstrated one step degradation in the temperature range of 255 to 435°C. One endothermic event and two exothermic events are observed in the PANI-PEO- Li_2SO_4 thermograms (Fig. 4.a). The first event occurs at **68.91°C**

temperature, it is called as glass transition temperature because at this temperature there is transition from a disordered solid to a liquid. The first event is accompanied by a 4.3% weight loss and is related to the removal of the physically adsorbed water. Two exothermic events occur at 325.62°C and 446.23°C. These two events is accompanied 84.145% and 6.577% weight loss.

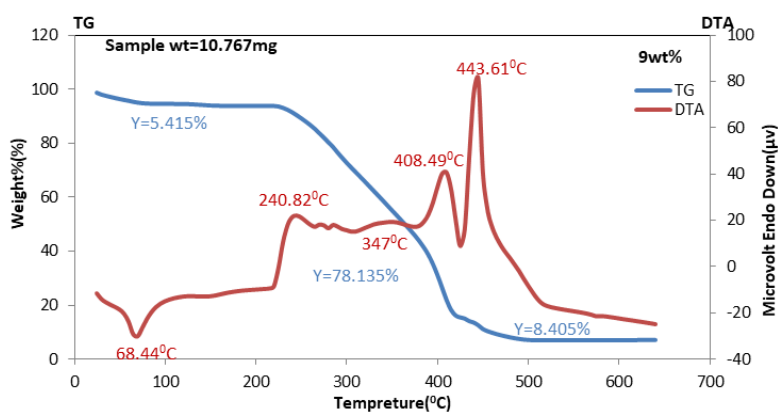
In (Fig. 4. b) the film demonstrated one step degradation. It was in the temperature range of 255 to 425°C. One endothermic event and four exothermic events are observed in the PANI-PEO- Li₂SO₄ thermograms. The first event occurs at 69.13°C temperature, it is called as glass transition temperature. The first event is accompanied by a 5.39% weight loss and is related to the removal of the physically adsorbed water.



(a)



(b)



(c)

Fig 4. TG/DTA curves of a) 5wt% b) 7wt% c) 9wt% of Li₂SO₄ (PANI-PEO-Li₂SO₄) blend.

In (Fig. 4. c) the film demonstrated one step degradation. It was in the temperature range of 250 to 460°C. One endothermic event and four exothermic events are observed in the PANI-PEO- Li₂SO₄ thermograms. The first event occurs at 68.44°C temperature, it is called as glass transition temperature. The first event is accompanied by a 5.415% weight loss and is related to the removal of the physically adsorbed water. Four exothermic events occur at 240.82 °C, 347 °C, 408.49 °C and 443.61 °C. These Four events is accompanied 78.135% and 8.4057% weight loss.

Table 4: TG /DTA data for PANI-PEO- Li₂SO₄ blend samples.

Sample	Peak I (Glass transition) Endothermic events		Peak II Exothermic events		Peak III Exothermic events		Peak IV Exothermic events		Peak V Exothermic events	
	T _{max} (°C)	Peak Height (μV)	T _{max} (°C)	Peak Height (μV)	T _{max} (°C)	Peak Height (μV)	T _{max} (°C)	Peak Height (μV)	T _{max} (°C)	Peak Height (μV)
wt% of Li ₂ SO ₄ (PANI-PEO-Li ₂ SO ₄)										
5	68.98	-9.355	325.62	31.371	446.57	17.702	-	-	-	-
7	69.13	-10.067	244.12	19.988	307.62	6.239	373.36	32.556	452.34	8.028
9	68.44	-13.182	240.82	24.91	347	2.876	408.49	28.846	443.61	79.8

IV. CONCLUSION

The SEM-EDX study in case of PANI-PEO films doped with Li₂SO₄ predicts the presence of dopant Lithium in the films. From the SEM of PANI-PEO- Li₂SO₄ composite, it was observed “sponge-like” appearance and shows a homogeneous surface, with uniformly distributed particles. It shows amorphous nature. FT-IR identifies the presence of certain functional groups of molecule. Also one can use the unique collection of absorption band to confirm the identity of pure compound or to detect the presence of specific impurities. From the IR spectroscopy, it was noticed that, conductive blends were formed and the corresponding peak observed show PANI, PEO and lithium peaks. From the TG/DTA, it is observed that PANI-PEO samples with doped Li₂SO₄ gives one step degradation in which weight loss is in the range 95.5 to 97.32 % when heated up to 700K .

REFERENCES

- [1] T.J. Skotheim (Ed), Handbook of Conducting polymers, Merceel Dekker, New York, 1986.
- [2] G. Inzelt, in: A. J. Bard (ed), Electroanalytical Chemistry, Merceel Dekker, New York 18 (1994) 89.
- [3] H. L. Wang, J.E. Fernandez, *Macromolecules* 25 (1992) 6179.
- [4] T. K. Mandal, B. M. Mandal, *Synth. Met.* 80 (1996) 303.
- [5] S. A. Chen, W. G. Fang, *Macromolecules* 24 (1991) 1242.
- [6] S. E. Lindsey, G. B. Street, *Synth. Met.* 10 (1984) 67.
- [7] H. L. Wang, L. Toppare, J. E. Fernandez, *Macromolecules* 23 (1990) 1053.
- [8] B. Zinger, D. Behar, D. Kijel, *Chem. Mater.* 5 (1993) 778.
- [9] Sanchez, Chantal Ince, *J. Composites Science and Technology* 69 (2009) 1310-1318.
- [10] Xiang-Wu Zhang et al. Center for Electrochemical Systems and Hydrogen Research, Texas Engineering Experiment Station, Texas A & M University, College Station, TX, USA, 31 May(2002) 77843-3402.
- [11] V.DaryaRadziuk and Helmuth Möhwalld ,*Polymers* 3 (2011), 674-692.
- [12] J. Prokes, et.al.,*Polym. Degrad. Stab.*, **78** (2002) 393.
- [13] A .J. Epstein. et. al., *Synth. Met.*, **16**(1986) 305.
- [14] Z.J Ping, *Chem. Soc. Faraday. Trans.*, **92** (1996) 3063.
- [15] S. Quillard, et. al., *Synth. Met.*, **84** (1997) 805.
- [16] G. Socrates, *Infrared Characteristic Group Frequencies*. Wiley, Chichester (1980).
- [17] Z.Shen, P.George, Yi-BingCheng, *Polymer* 43 (2002)4251-4260.
- [18] Mustafa Türk1, Zakir M. O. Rzayev, GülcihanKurucu,*HEALTH* 2 (2010) 51- 61.

¹P. R. Yawale
²N. R. Thakare
²P. P. Chaudhary
³P. S. Parimal
³D. S. Warti
³A. D. Ghatol

Water quality Assessment of Wagholi Lake, Dist. Amravati (MH)



Abstract: - Surface water is the important source of ground water, increasing population, modernization and urbanization are affecting the quality of surface water by disposing sewage and contaminating surface waters like lake water, dam water etc. This study described the assessment of water quality of the Wagholi lake from Amravati district, Maharashtra. For the analysis purpose, 20 water samples were collected from the lake and different physical parameters such as P^H, TDS, Turbidity, Temperature and chemical parameters Total Hardness (TH), Ca²⁺, Mg²⁺, Na⁺, K⁺, HCO₃⁻, CO₃⁻, Cl⁻, NO₃⁻ and SO₄²⁻ were analyzed, followed by the standard analytical procedures. the aim of studying these different physicochemical parameters of the lake water was to find the suitability of water for drinking as well as irrigation purpose. Out of 20 samples (85%) samples shows the value of Fluoride in permissible limit where 15% samples show values higher than the permissible limits of drinking water category. The nitrate values are ranging in between 0.6 ppm to 7.9 ppm.

Keywords: Wagholi Lake, Physicochemical parameters.

¹ *Corresponding author: G.S. Tompe Arts, Commerce and Science College Chandur Bazar, Dist. Amravati. Maharashtra.

² Author Shri Shivaji Science College, Amravati, Amravati, Maharashtra.

³ Author G.S. Tompe Arts, Commerce and Science College Chandur Bazar, Dist. Amravati. Maharashtra.

Copyright © JES 2024 on-line : journal.esrgroups.org

I. INTRODUCTION

Water is the most commonly available solvent which is the most essential part of living things. Water is the crucial thing for the maintenance of ecosystem. Lakes are the best place to store the water on Earth. Human development activities are increasing tremendously and it is one of the reasons affecting the surface or lake water quality dominantly [2]. Wagholi lake is investigated in this study and the main aim to check whether the water quality attributes are in permissible limits or not.

II. STUDY AREA

For the analytical purpose 20 water samples were collected in a screw capped HDPE bottle from Wagholi lake, Dist. Amravati, Maharashtra. Wagholi lake is named from the nearby village Wagholi. The approximate area of lake is 60 acres [1] and geographically it is located at latitude 21°07'47", Longitude 77°08'30". Wagholi lake is near about 21 Km towards North - East from Amravati city. Lake water helps to irrigate approx.500 acres of land and local area people use it for fishing and domestic activities.

III. MATERIALS AND METHODS

In March 2024, 20 water samples were collected from different locations of Wagholi Lake. Temperature, Electrical Conductivity (EC), Total Dissolved Solids (TDS), and P^H readings were taken immediately after sample collection by using portable water analysis kit on field. For calibration of instruments standard solutions, double distilled water, etc used.

Table1: Parameters and methods to analysis of water samples. (APHA standards)

Parameters	Method
p ^H	Digital P ^H meter
Temperature	Mercury Thermometer
Electrical Conductivity	Conductivity meter
Total Dissolved Solids	TDS meter
Alkalinity	Titration method
Chloride	
Calcium	
Magnesium	
Total Hardness	
Carbonate (CO ₃ ²⁻)	
Bicarbonate (HCO ₃ ⁻)	
Fluoride	
Sodium	Flame Photometer
Sulphate	Spectrophotometer
Nitrate	
Potassium	
Iron	

IV RESULT AND DISCUSSION

The turbidity values range from 0.4 to 1.2 NTU with the average value of approximately 0.68 NTU (Nephelometric Turbidity Units). EC values range from 21.5384 to 105.8461 micro-Simmons/Cm indicating varying levels of dissolved ions in the water sample. The variation in the total hardness indicates differences in calcium and magnesium Concentrations.

Carbonate values are relatively consistent, with some variation. Carbonates play an crucial role in buffering water P^H, and their presence indicates the buffering capacity of water. Chloride levels are within acceptable limits for drinking water, though variations exist. Chloride can originate from natural resources such as seawater intrusion, or from anthropogenic sources like road salt and industrial discharge. The variability in iron concentrations suggests differing sources or levels of iron in the samples. Elevated iron levels can cause staining and affect taste of water, but the concentrations observed within acceptable limits. The range of sulphate concentrations is notable in sample no. 19 and 20, with higher levels potentially indicating pollution from industrial or agriculture activities. Sulphate in water can contribute to the taste and may cause scale formation.

V CONCLUSION

The data indicates that the water quality parameters measured are within acceptable limits for the most samples, though some variations exist. Understanding these variations can help identify potential sources of contamination and water management strategies.

REFERENCES

- [1] P.R.Yawale et.al, Study of physicochemical parameters of water samples from Lake near Ratan power Amravati Tahsil, Maharashtra, *Journal of Emerging Technologies and Innovative Research (IJTIR)*, Vol. 10, Feb. 2023.
- [2] Salahuddin and Intzar Hussain, Analysis of Lower Lake water in Bhopal Region of Madhya Pradesh, India, *International Journal of Lakes and Rivers*, Vol. 13, Nov.,2020.
- [3] Srivastava A K and Parimal P S 2012 Assessment of groundwater suitability for irrigation in Purna alluvial basin, Maharashtra; *Gondwana Geol. Mag.*27(1) 79–92.
- [4] APHA 2005 Standard methods for the examination of water and wastewater, 21st edn, American Public Health Association, Washington
- [5] Srivastava A K and Parimal P S 2014 Hydrochemical facies and ionic ratios of groundwater in Purna alluvial basin, Maharashtra; *Gondwana Geol. Mag., Spec. Publ.*14 117–126.
- [6] Srivastava A K and Parimal P S 2015 Hydrogeochemistry of Purna alluvial basin, central India; *J. Geol. Soc. India* 85 673–685.
- [7] Srivastava A K and Kale V M 2018 Purna River, Maharashtra; In: *The Indian Rivers*, Springer Hydrogeology (ed.) Singh D S, Springer Nature Singapore Pte Ltd., pp

Table 2. Physical and chemical parameters

Sr. No	pH	Turbidity in N	EC	TDS (mg/l)	TH (mg/l)	Alkalinity (mg/l)	Carbonate	Bicarbonate	Cl (mg/l)	Fe (mg/l)	F (mg/l)	NO ₃ (mg/l)	SO ₄ (mg/l)	Ca (mg/l)	Mg (mg/l)	Na (mg/l)	K (mg/l)
1	7.3	0.4	41.5384	1067	536	128	24	104	108	0.1	0.88	7.1	162	128	504.896	62	12
2	6.9	0.5	75.3846	1024	548	84	32	52	110	0.1	0.56	7.4	133	129.6	516.5072	52	10
3	7.3	0.6	86.1538	1031	536	100	24	76	106	0.1	0.53	7	121	120	506.84	88	8
4	7.2	0.7	89.2307	1033	552	92	16	76	110	0.1	0.22	7	134	124.8	521.6736	105	11
5	7.3	0.8	81.5384	1028	540	96	16	80	104	0.1	1.03	7.9	131	115.2	512.0064	112	12
6	7.3	0.5	04.6153	1043	528	104	24	80	110	0.1	0.5	7.6	133	112	500.784	109	10
7	7.2	0.5	83.0769	1029	520	96	32	64	106	0.1	0.58	7.4	156	108.8	493.5616	70	7
8	7.2	0.6	86.1538	1031	488	92	24	68	110	0.1	0.44	7.4	122	112	460.784	73	24
9	7.1	0.4	09.2307	1046	528	100	32	68	100	0.1	0.44	7.2	130	116.8	499.6176	70	6
10	7.1	0.5	10.7692	1047	528	92	32	60	100	0.1	0.81	7	124	110.4	501.1728	70	4
13	7.2	0.3	21.5384	1119	528	120	40	80	110	0.1	0.64	1.8	149	128	496.896	90	18
14	6.8	0.4	09.2307	1111	520	80	24	56	104	0.1	0.42	1.4	157	110.4	493.1728	86	14
15	7.3	0.5	12.3076	1113	544	132	24	108	106	0.1	0.76	1.3	166	102.4	519.1168	87	14
16	6.9	0.6	44.6153	1134	540	92	40	52	110	0.1	0.66	0.6	152	110.4	513.1728	84	16
17	6.8	0.5	92.3076	1100	544	72	48	24	108	0.1	0.93	0.9	129	112	516.784	80	13
18	6.9	0.4	73.8461	1088	552	92	40	52	106	0.1	0.86	0.8	156	108.8	525.5616	74	12
19	6.9	0.4	90.7692	1099	572	92	40	52	112	0.1	1.02	1	167	96	548.672	69	10
20	7.2	0.5	72.3076	1087	492	100	24	76	112	0.1	1.08	1.5	164	96	468.672	68	10

¹Bhupesh Nemmaniwar
²Shyam Mokle

**Rheological Study of 2,3-Dichloroaniline and
2-Ethoxyethanol at different Temperatures**



Abstract: -The utilization of rheological analysis emerges as a crucial technique for anticipating the physical attributes of both non-Newtonian (2,3-DCA) and Newtonian (2-EE) fluids, as well as their binary mixtures. While existing literature has explored the rheological behavior of 2,3-DCA+2-EE mixtures, particularly in the realm of thixotropic fluids within binary reactions, comprehensive documentation of their properties remains absent. This study thus endeavors to fill this gap by delving into the rheological characteristics of 2,3-DCA+2-EE binary mixtures across a spectrum of temperatures (293 K to 323 K) and a diverse range of viscosity, torque, and shear strain. With fixed parameters including shear rates (122, 73.4, and 61.2) and RPM (100, 60, and 50), this investigation aims to provide valuable insights into the rheological behavior of these mixtures, shedding light on their behavior under varied conditions and facilitating deeper understanding within the field.

Keywords: brookfield viscometer; 2,3-Dichloroaniline; 2-Ethoxyethanol; Different temperatures; Viscosity; Torque; Shear strain; Shear rates and RPM.

I. INTRODUCTION

Rheology is the science of deformation and flow behavior of fluids [1]. Knowledge properties of fluid and variation with temperature, shear rate and rotation per minute have been globally for industrialization of food technology [2-3], cosmetic [4], Pharmaceuticals [5], Oil and Gas Industry and Polymer Processing [6-7]. Rheology is the study of deformation and flow of fluids in response to stress. To make an incompressible fluid flow, a shear stress must be applied. Fluids include both gases and liquids. Here the focus on the liquids. In fluid, when the increasing shear stress is proportional with increasing shear rate, it is known as Newtonian fluid [8]. The ratio of shear stress and shear rate gives a constant, which is known as viscosity. In a situation where a shear stress is created with a smaller shear rate, the fluid is claimed as having a higher viscosity.

¹Department of Physics, Digambarrao Bindu ACS College Bhokar, Dist. Nanded, MS, India.

e-mail: - bhupesh.nemmaniwar@rediffmail.com

²Department of Chemistry Rajiv Gandhi Mahavidyalaya Mudhkhed, Dist. Nanded, MS, India.

Corresponding author: drmokless@gmail.com

For a fluid to behave as Newtonian, any increase in shear stress should be accompanied with a similar portion increase of shear rate which would result in a constant viscosity. This behaviour indicates the independence of fluid viscosity on the shear rate. However, in reality, fluid does not behave as a Newtonian fluid. 2-Ethoxyethanol commercially known as Cello solves is critical to optimizing their performance in applications such as and widely used as complexes of solvents, coemulsifiers so stabilizers of emulsions, dyes and lacquers.[9]. The aromatic liquid 2,3-DCA is a base substance used in the synthesis of bioactive Schiff's bases, azetidinones, thiazolidinones, pyrazolines, acetohydrazides and in mixture reactions [10-12]. It is an important chemical substance for production of agricultural fungicides, herbicides, insecticides etc. [13-14].

Similarly, in hydraulic fracking applications, the Newtonian viscosity and shear thinning of fracturing fluids determine whether the fluid viscosity is sufficiently large to reduce particle settling rates and sustain fractures of desired geometry against closure stresses imposed by the reservoir [15-16]. Among shear flow and extensional flow, the former is the most common flow behavior. In shear flow, layers of the fluid slide over each other at a speed greater than that of the layer beneath it. The displacement gradient across the fluid layers is called shear strain. When the shear strain continues to increase on the application of shear stress, the velocity gradient is created. The velocity gradient, otherwise called shear rate or strain rate, is the rate of change of strain with time. The behavior of fluid varies with the value of shear rate or shear stress. One such behavior is shear thinning [17]. Shear thinning is a behavior commonly seen in non-Newtonian fluids. It is also called Pseudoplastic flow. Shear thinning results from rearrangements in the microstructure level in fluids. The rearrangements occurring in the plane of applied shear stress change the behavior of fluids. In shear-thinning fluids, as the applied stress increases, the fluid velocity decreases [18].

The present study attempted to characterize the rheological properties of 2,3-DCA+2-EE binary mixtures across a temperature range of 293 K to 323 K, encompassing a wide range of viscosity, torque, and shear strain. Shear rates (122, 73.4, and 61.2) and RPM (100, 60, and 50) were kept constant throughout the experiments.

II. MATERIALS

2,3-Dichloroaniline (GC Grade) is obtained from Sigma-Aldrich and 2-Ethoxyethanol (AR Grade) were obtained from M/S Sd. Fine chemical, Mumbai, India without further purification the two liquids according to their proportions by volume were mixed well and kept 6h in well stoppered bottles to ensure good thermal equilibrium. These liquids used as solute and solvent.

III. MEASUREMENTS

All the measurements are carried out at temperatures 293, 303, 313 and 323 K. by circulating ethylene glycol + water around the liquid cell and temperature is thematically controlled with $\pm 0.50^{\circ}\text{C}$

thermocontrolle using Nevitechpvt. Ltd. Mumbai India. The whole of the equipment is standardized with the help of standard materials like methanol and ethyleneglycol+water (40:60). The viscosities, Torque, Share Stain, Share Rate and RPM of the pure components and their binary mixtures are measured by LVDL V-pro II Brook field viscometer (USA) accuracy range of viscosity is $\pm 1.0\%$, repeatability $\pm 0.2\%$ and temperature accuracy range of viscometer is $\pm 1^\circ\text{C}$ - 100°C to $+149^\circ\text{C}$ [19]

IV. RESULTS AND DISCUSSION

A perusal of Table 1 to 4 provides the experimental values of viscosity (η), Torque (τ), Share Stain (SS), Share Rate [(SR) 122, 73.4 and 61.2] and RPM (100, 60 and 50) of binary liquid mixture of 2,3-DCA+2-EE at 293 to 313K. When the SR decreases from 122, 73.4, and 61.2, and the RPM decreases from 100, 60, and 50, the values of η increase, but τ and SS decrease at all temperatures. In binary mixtures of 2,3-DCA+2-EE, as the mole fraction of 2,3-DCA increases, the values of η , τ , and SS increase.

As the concentration of 2,3-DCA increases in the binary mixtures, the values of η , τ and SS increase but at different temperatures the values of η , τ and SS decrease, the magnitude of variation of mole fraction is in the increasing order. The viscosity values augment with the increasing mole fraction of 2,3-DCA over the whole concentration range, meanwhile, the viscosity, torque and share strain values decrease with the increasing temperature at the same composition and this phenomenon is possibly caused by the weak hydrogen bonding interaction [20].

Table 1 Mole fraction (X) of 2,3-DCA and 2-EE, viscosity (η), Torque (τ), Share Stain (SS), Share Rate (SR) and RPM of binary mixture liquid system of 2,3-DCA+2-EE at 293K

Mole Fraction X	Viscosity (η)	Torque (τ)	Share Stain (SS)	Share Rate (SR)	RPM
0.0000	2.35	42.2	2.41	122	100
	2.75	35.6	2.32	73.4	60
	2.58	30.4	2.11	61.2	50
0.1048	3.12	52.0	3.83	122	100
	3.35	33.5	2.47	73.4	60
	3.40	28.5	2.10	61.2	50
0.2147	3.92	65.5	4.81	122	100
	4.09	40.8	3.00	73.4	60
	4.15	34.7	2.55	61.2	50
0.3298	4.81	70.6	5.94	122	100
	4.96	49.5	3.84	73.4	60
	5.01	41.6	3.05	61.2	50

0.4506	5.67	75.9	6.05	122	100
	5.74	57.6	4.22	73.4	60
	5.77	47.8	3.54	61.2	50
0.5775	6.32	80.2	6.50	122	100
	6.35	53.4	3.90	73.4	60
	6.70	33.6	2.40	61.2	50
0.7110	6.64	84.5	6.70	122	100
	6.68	53.6	3.94	73.4	60
	6.70	32.3	2.40	61.2	50
0.8516	6.70	88.6	6.80	122	100
	6.75	53.8	3.90	73.4	60
	6.80	32.6	2.40	61.2	50
0.0000	6.80	90.8	6.95	122	100
	6.85	58.9	4.29	73.4	60
	7.35	35.0	2.60	61.2	50

Table 2 Mole fraction (X) of 2,3-DCA and 2-EE, viscosity (η), Torque (τ), Share Stain (SS), Share Rate (SR) and RPM of binary mixture liquid system of 2,3-DCA+2-EE at 303K

Mole Fraction X	Viscosity	Torque	Share Stain	Share Rate	RPM
0.0000	2.14	35.5	2.61	122	100
	2.47	24.7	1.82	73.4	60
	2.68	22.4	1.64	61.2	50
0.1048	2.85	28.7	2.13	122	100
	2.89	28.6	2.08	73.4	60
	2.99	25.2	1.83	61.2	50
0.2147	3.31	55.2	4.06	122	100
	3.58	36.6	2.61	73.4	60
	3.70	30.6	2.24	61.2	50
0.3298	3.52	58.6	4.33	122	100
	3.72	37.0	2.70	73.4	60
	3.80	31.4	2.30	61.2	50
0.4506	4.26	71.0	5.22	122	100
	4.32	43.1	3.16	73.4	60
	4.36	36.3	2.67	61.2	50

0.5775	4.73	78.9	5.79	122	100
	4.83	48.4	3.54	73.4	60
	4.86	40.3	2.97	61.2	50
0.7110	5.01	83.4	6.13	122	100
	5.05	50.5	3.70	73.4	60
	5.10	42.3	3.10	61.2	50
0.8516	5.32	89.5	6.57	122	100
	5.33	53.1	3.90	73.4	60
	5.36	44.4	3.26	61.2	50
0.0000	5.35	94.2	6.90	122	100
	5.37	53.6	3.92	73.4	60
	5.58	45.8	3.36	61.2	50

Table 3 Mole fraction (X) of 2,3-DCA and 2-EE, viscosity (η), Torque (τ), Share Stain (SS), Share Rate (SR) and RPM of binary mixture liquid system of 2,3-DCA+2-EE at 313K

Mole Fraction X	Viscosity	Torque	Share Stain	Share Rate	RPM
0.0000	1.70	28.4	2.08	122	100
	2.08	20.8	1.53	73.4	60
	2.32	19.2	1.42	61.2	50
0.1048	1.97	33.0	2.43	122	100
	2.25	22.6	1.64	73.4	60
	2.42	20.0	1.46	61.2	50
0.2147	2.27	37.7	2.77	122	100
	2.47	24.8	1.82	73.4	60
	2.64	22.0	1.62	61.2	50
0.3298	2.62	43.7	3.20	122	100
	2.76	27.5	2.03	73.4	60
	2.92	24.0	1.78	61.2	50
0.4506	2.95	49.1	3.59	122	100
	2.98	30.0	2.19	73.4	60
	3.10	25.8	1.88	61.2	50
0.5775	3.14	52.3	3.84	122	100
	3.24	32.4	2.38	73.4	60
	3.33	27.6	2.02	61.2	50
0.7110	3.41	56.9	4.17	122	100

	3.42	34.2	2.50	73.4	60
	3.45	28.4	2.10	61.2	50
0.8516	3.60	59.9	4.39	122	100
	3.62	36.1	2.66	73.4	60
	3.66	30.5	2.24	61.2	50
0.0000	3.91	65.2	4.78	122	100
	3.92	39.0	2.88	73.4	60
	3.94	32.7	2.41	61.2	50

Table 4 Mole fraction (X) of 2,3-DCA and 2-EE, viscosity (η), Torque (τ), Share Stain (SS), Share Rate (SR) and RPM of binary mixture liquid system of 2,3-DCA+2-EE at 323K

Mole Fraction X	Viscosity	Torque	Share Stain	Share Rate	RPM
0.0000	1.55	25.9	1.89	122	100
	2.01	24.2	1.77	73.4	60
	2.88	20.0	1.48	61.2	50
0.1048	1.68	27.8	2.05	122	100
	1.88	18.8	1.39	73.4	60
	2.02	16.8	1.23	61.2	50
0.2147	1.91	31.8	2.33	122	100
	2.01	21.4	1.57	73.4	60
	3.31	19.1	1.40	61.2	50
0.3298	2.08	34.5	2.53	122	100
	2.24	22.4	1.64	73.4	60
	2.36	19.7	1.45	61.2	50
0.4506	2.27	37.9	2.78	122	100
	2.42	24.2	1.78	73.4	60
	2.51	20.9	1.54	61.2	50
0.5775	2.42	40.3	2.96	122	100
	2.53	25.3	1.86	73.4	60
	2.62	21.7	1.60	61.2	50
0.7110	2.57	42.8	3.14	122	100
	2.66	26.4	1.94	73.4	60
	2.71	22.4	1.66	61.2	50
0.8516	2.76	46.0	3.37	122	100
	2.83	28.3	2.08	73.4	60

	2.89	24.1	1.77	61.2	50
0.0000	3.09	51.4	3.78	122	100
	3.12	31.0	2.28	73.4	60
	3.16	26.2	1.92	61.2	50

IV.CONCLUSION

In summary, the study of a binary liquid mixture of 2,3-DCA+2-EE at temperatures ranging from 293K to 313K reveals intriguing trends. Decreasing shear rate (SR) and RPM coincide with an increase in viscosity (η), while torque (τ) and shear strain (SS) decrease consistently across all temperatures. Additionally, as the mole fraction of 2,3-DCA rises, so do the values of η , τ , and SS, suggesting a correlation between composition and these properties. Notably, variations in temperature lead to contrasting effects: while increasing 2,3-DCA concentration boosts η , τ , and SS, at different temperatures, these values decrease. This inverse relationship hints at the impact of temperature on molecular interactions, potentially driven by weak hydrogen bonding.

ACKNOWLEDGMENT

The authors thanks to the Director, School of Physical Sciences, S.R.T.M. University Nanded for providing necessary laboratory facilities.

REFERENCES

- [1] H.A.Barnes, J.F. Hutton and K. Walters, An Introduction to Rheology, Elsevier, New York, 1989.
- [2] M. Lewis, Chapter 13-Food rheology-Some empirical methods, Food Process Engineering Principles and Data, 2023, pp.107-114.
- [3] J. Ahmed and S. Basu, Food rheology Scientific development and importance to the food industry, Advances in Food Rheology and Its Applications, 2nd ed., 2023.
- [4] D. Grabner and H. Hoffmann, Rheology of Cosmetic Formulations, Cosmetic Science and Technology Theoretical Principles and Applications, 2017, pp.471-488.
- [5] M. Marcos, "General aspects of powder rheology applied to pharmaceutical Formulations," Drug Discovery Today, vol. 29(5), May 2024, pp.1-14, 10.1016/j.drudis.2024.103976.

- [6] D. Shauvik and B.Steffen, “Complex fluids with visco-elastic rheology for applications in oil & gas industry,” *Science Talks*, vol. 3, August. 2022, pp.100036, 1-19, 10.1016/j.sctalk.2022.100036.
- [7] S. Leire, F. Mercedes and S.Antxon, “Polymers and rheology: A tale of give and take,” *Polymer*, vol. 271, April. 2023, pp.125811,1-18,10.1016/j.polymer.2023.125811.
- [8] E.G.Goh, W.B.Wan Nik, M. Fadhli Ahmad and A. Amran, “The Assessment of Rheological Model Reliability in Lubricating Behavior of Vegetable Oils,” *National Tribology Conference*, May 2009, pp.58-65.
- [9] B. Nemmaniwar, “Dielectric Behavior of Binary Mixture of 2-Chloroaniline with 2-Methoxyethanol and 2-Ethoxyethanol, *Orbital Electronic Journal of Chemistry*,” vol.5(1), March 2013, pp.1-6.
- [10] M. Kumar, M.A.Khan, C.P. Yadav, D.Pandey and D. Singh, “Ultrasonic characterization of binary mixture of 2,3-dichloroaniline and polyethylene glycols,” *The Journal of Chemical Thermodynamics*, vol.161, Oct.2021, pp.106557, doi.org/10.1016/j.jct.2021.106557
- [11] K. Zhang, J. Yang, X. Yu, J. Zhang and X. Wei “Densities and Viscosities for Binary Mixtures of Poly (ethylene glycol) 400+Dimethyl Sulfoxide and Poly (ethylene glycol) 600 +Water at Different Temperatures,” *Journal of Chemical Engineering Data*, vol.56 (7), May 2011, pp.3083–3088. doi.org/10.1021/je200148u.
- [12] B. Nemmaniwar, “Dielectric relaxation and dipole moment of binary mixture of 2, 3-dichloroaniline and 2-Ethoxyethanol in 1, 4-dioxane solution using microwave absorption data,” *International Research Journal of Science and Engineering*, vol.5(4), Aug.2017, pp.31-39.
- [13] B.Nemmaniwar and P. Kadam, “Dielectric Relaxation and Dipole Moment Study of Binary Mixture of 2, 3-Dichloroaniline and 2-Propoxyethanol 1, 4-Dioxane Solution Using Microwave Absorption Data,” *International Journal of Sciences: Basic and Applied Research*, vol.17(2), Aug. 2014, pp.143-155.
- [14] B. Nemmaniwar and P. Kadam, “Dielectric Behavior of Binary Mixtures of 2,3-Dichloroaniline with 2-Methoxyethanol Using Microwave X-Band,” *Chemical Science Transactions*, vol. 3(3), 2014, pp.995-1000.
- [15] A.C.Barbati, J. Desroches, A.Robisson, and G.H. McKinley, “Complex fluids and Hydraulic fracturing,” *Annu.Rev. Chem. Biomol.*, vol. 7(1), Jun. 2016, pp.415–453. doi.org/10.1146/annurev-chembioeng-080615-033630.

- [16] J.Adachi, E.Siebrits, A. Peirce and J.Desroches, “ Computer simulation of hydraulic fractures,” *Int.J. Rock Mech. Min.*, vol. 44 (5),Jul.2007,pp.739–757.
doi.org/10.1016/j.ijrmms.2006.11.006
- [17] M. Kevin,R. Noah,and Menard.(2020). *Basic Rheological Concepts. Stress, Strain, and Flow*, book: *DynamicMechanical Analysis*,pp.19-44.
- [18] E.Caroline,A. C.Wagner, J. E.Barbati, S. B.Adam andG.H. McKinley,“Apparent shear thickening at low shear rates in polymer solutionscan bean artifact of non equilibration,”*Applied Rheology*, vol. 26,Sept. 2016,pp. 54091-54096.
<https://doi.org/10.3933/applrheol-26-54091>.
- [19] B. Nemmaniwar,“Dielectric Behaviour of Binary Mixture of 2-Chloroaniline with 2-Methoxyethanol at30⁰CUsing Microwave Frequency,” *Materials Today Proceedings*,vol. 23(2),2020. pp. 324–328.<https://doi.org/10.1016/j.matpr.2020.02.031>.
- [20] B. Nemmaniwar, “Relaxation Time, Excess Relaxation Time and Dipole Moment of Binary Mixture of 2,3-Dichloroaniline and 2-Methoxyethanol using Frequency Domain Reflectometer,” *Orbital Electronic Journal of Chemistry*,vol.12(2),June. 2020. pp. 62–68.
<https://doi.org/10.17807/orbital.v12i2.1368>.

P.L. Harale^{1*},
M.E. Shelke¹,
D.T. Tayade¹,
A.R. Kurhe²

Anticancer Activity of Novel Thiocarbamide Derivatives by MTT Colorimetric Assay

ABSTRACT: - THIOCARBAMIDES WERE PRODUCED FROM AROMATIC AMINES AND THEIR ANTICANCER ACTIVITY WAS EXAMINED THROUGH THE USE OF NOVEL DERIVATIVES THAT REPLACED THIOUREAS. CYTOTOXICITY OF THE THIOCARBAMIDE DERIVATIVES ON THE BREAST CANCER CELL LINE MCF-7 WAS EXAMINED BY THE MTT [3-(4,5-DIMETHYLTHIAZOL-2-YL)-2,5-DIPHENYLTETRAZOLIUM BROMIDE] TEST. BASED ON THE RESULTS OBTAINED FROM THE MTT COLORIMETRIC ASSAY, IT WAS OBSERVED THAT WHEN THE MCF-7 CELL LINE WAS EXPOSED TO DIFFERENT CONCENTRATIONS OF THE SAMPLE OF DERIVATIVES, SUBSTANTIAL CYTOTOXIC ACTIVITY I.E. ACTIVE IN SUPPRESSING MCF-7 CELL GROWTH WAS OBSERVED BY THIOCARBAMIDE DERIVATIVES WITH THE IC₅₀ VALUE 32.35±0.07 µG/ML. AN EFFICIENT MEANS OF PREVENTING CANCER FROM SPREADING MIGHT BE THE DISCOVERY OF NOVEL DRUGS.

Keywords: Thiocarbamide derivatives, Anticancer activity, MTT colorimetric assay, Cytotoxicity

1. INTRODUCTION:

Derivatives of thiocarbamide are practical heterocyclic agents that are synthesized and studied extensively. Because thiocarbamide derivatives hold active thio-amino groups which can form a wide range of therapeutic effects and expose its diverse physiochemical capabilities [1-2]. Cancer has reported for approximately 9.6 to 10 million deaths across the world in 2023 as per the World Health Organization (WHO). Female breast cancer is second ranked occurring (2.3 million cases, 11.6%) in the worldwide and was the leading cause breast cancer deaths (670 000 deaths, 6.9%) reported by International Agency for Research on Cancer (IARC) in 2022. One of the major medical issues that human now face is the rising number of deaths from various types of cancer, and cancer seems to be having an increasingly negative impact on human health globally. Researchers are working to several facets of cancer biology in an attempt to develop medications having anticancer properties. Many effective drugs for the treatment of cancer have been discovered and widely utilized from the pharmaceutical sector [3-7].

1. Department of Chemistry, Govt. Vidarbha Institute of Science and Humanity, Amarawati

2. Research Centre and Department of Chemistry, Padmashri Vikhe Patil College, Pravaranagar.

*Correspondence: prashantharale@gmail.com

Usually in medicinal field use of different substituents is common and most of substituted thiocarbamide derivatives were investigated for their bioactive properties such as antibacterial [8-9], anti-microbial [10-11], anti-inflammatory [12-13], anti-fungal [14-15], anthelmintics [16], antitubercular [17], insecticidal [18], rodenticidal [19] and herbicidal [20].

Thiocarbamide derivatives are one of the active anticancer compounds because of their significant inhibitory effects on protein NADH oxidase, tyrosine kinases (PTKs), Raf kinase, and DNA topoisomerase [21-23]. The present research involved to synthesis of a novel thiocarbamide molecule further characterized by FTIR, NMR, MS, C, H, N, S analysis methods and assuring its cytotoxicity screening against human cancer cell lines by using an MTT colorimetric assay.

2. Result and Discussion:

2.1. Synthesis of thiocarbamide derivatives:

Novel compounds of thiocarbamide derivatives were synthesized from aromatic aniline and different substituted thiourea compounds. 3-chloroaniline (5 mmol) first treated with amino group protecting di-tert-butyl dicarbonate (BOC), further reflux about 4 hrs. with substituted thiourea compounds (5 mmol) in the presence of organic solvent isopropanol then BOC deprotection carried out in presence of acidic condition (4M HCl in methanol) gives 3-thiosubstituted carbamide aniline derivatives were collected by filtration, washed with cold water and dried. Further recrystallized using ethyl alcohol for elucidation of structures of derivatives.

N-(3-aminophenyl)-*N'*-phenyl thiourea

M.F. $C_{13}H_{13}N_3S$; M.P.= 72-74 °C; I.R. (KBr pellets, v/cm^{-1}): (N-H_{stret}) 3282, (Ar-H) 2979, (Ar C=C)1689, (C=S)1282, (C-N) 1153, (p-Ph) 851; 1H NMR (500MHz, $CDCl_3$, δ in ppm): 6.68 (s, 1H, N-H), 6.98 (dt, 1H, Ar-H), 7.15 (dt, 2H, Ar-H), 7.25 (d, 1H, Ar-H), 7.51 (s, 1H, Ar-H)

^{13}C NMR (500MHz, $CDCl_3$, δ in ppm): 77.04 ($CDCl_3$), 116.38, 118.51, 123.03, 129.90, 134.75, 139.57 (Ar-C), 152.40 (C=S); CHNS Analysis: C, H, N, S (%) calc. 64.17, 5.39, 17.27, 13.18, found 58.25, 6.07, 6.26, 0.048; Mass: m/z = 243.5, M.W.= 243.33

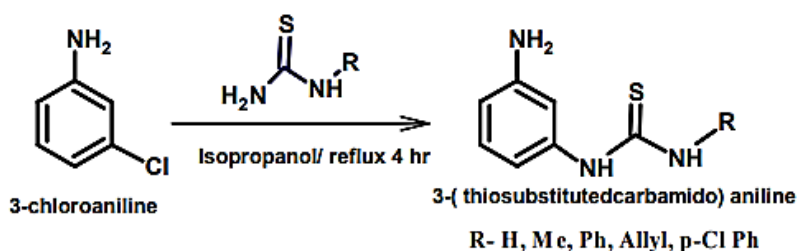


Figure (1): Synthesis route of novel thiocarbamide derivatives

2.2. Pharmacology: (Cancer cell lines)

Human cancer cell lines MCF-7 were procured from the National Centre for Cell Sciences (NCCS), Pune, India. The cells (10000 cells/well) were cultured in 96 well plates for 24 h in DMEM medium supplemented with 10% FBS and 1% antibiotic solution at 37°C in a humidified atmosphere of 5% CO₂ and 95% air. The next day cells were treated from the formulations (different concentrations were prepared in an incomplete medium).

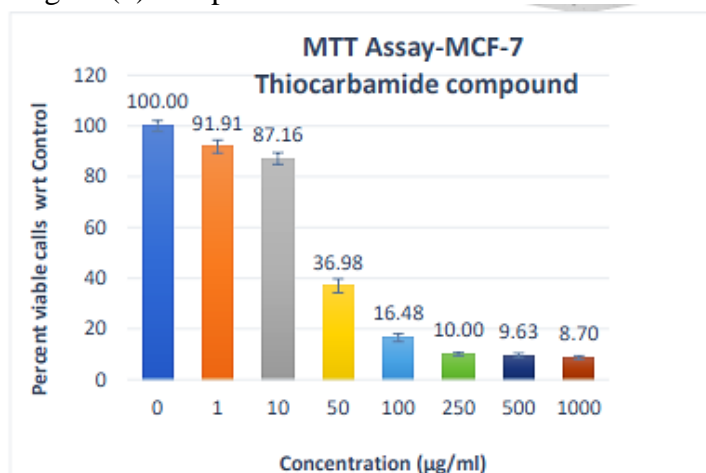
2.3. Cytotoxic activity (MTT colorimetric assay):

Cytotoxicity of the provided samples on the MCF-7 cell line was determined by MTT colorimetric Assay. After incubation for 24 hours, MTT Solution (a final concentration of 250µg/ml) was added to the cell culture and further incubated for 2 h. At the end of the experiment, the culture supernatant was removed and the cell layer matrix was dissolved in 100 µl Dimethyl Sulfoxide (DMSO) and read in an Elisa plate reader (iMark, Biorad, USA) at 540 nm and 660 nm. IC₅₀ was calculated by using the software Graph Pad Prism - 6. Images were captured under an inverted microscope (Olympus ek2) using a Camera (AmScope digital camera 10 MP Aptima CMOS).

Sample Conc. µg/ml	Test	Blank	Corrected value
0	0.478	0.073	0.405
1	0.429	0.057	0.372
10	0.406	0.053	0.353
50	0.201	0.051	0.15
100	0.116	0.049	0.067
250	0.082	0.041	0.041
500	0.077	0.038	0.039
1000	0.0693	0.034	0.035

Table (1). Abs. value w.r.t conc (µg/ml) of test samples and blank

Figure (2): Graph of % viable calls w.r.t control vs conc. (µg/ml)



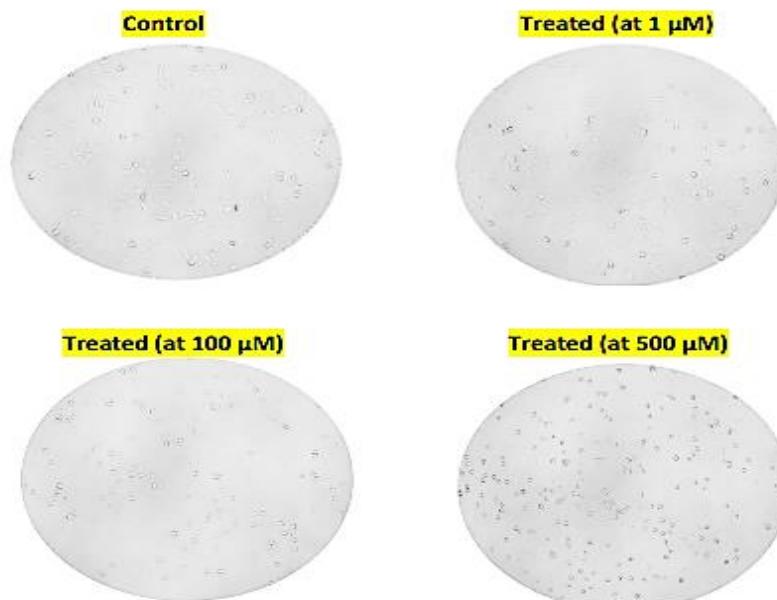


Figure (3): Cytotoxic activity observed for MCF-7 cells at different conc. ($\mu\text{g/ml}$)

3. CONCLUSION:

One area of ongoing research is the discovery of new classes of anticancer agents. Biological screening studies have been given positive anticancer activity for this novel class of thiocarbamide derivatives. These have been reported to be the most potent inhibitor toward MCF-7, breast cancer cell lines, as evidenced by the cytotoxic activity observed at a lower IC_{50} value of $32.35 \pm 0.07 \mu\text{g/ml}$ in the N-(3-aminophenyl)-N'-phenyl thiourea sample at different concentrations when exposed to the MCF-7 breast cell line, as determined by the outcomes of the MTT colorimetric assay.

Acknowledgment:

We thank to Research Center of the Department of Chemistry, Govt. Vidarbha Institute of Science and Humanity, Amaravati and Research Center of the Department of Chemistry, Loknete Dr. Balasaheb Vikhe Patil (Padmabhushan Awardee), Pravara Rural Education Society's, Padmashri Vikhe Patil College Pravaranagar.

Ethical Approval: This has not been published elsewhere and is not currently under consideration for publication elsewhere

Funding: The study did not receive any external funding.

Conflict of interest: The authors declare that they have no conflict of interest.

Informed consent: Written informed consent was obtained from all individual participants included in the study.

Data and materials availability: All data associated with this study are present in the paper.

References:

- [1]. Al-Salim YM, Al-Asadi RH. Synthesis, Anti-breast Cancer Activity, and Molecular Docking Studies of Thiourea Benzamide Derivatives and Their Complexes with Copper Ion. *Tropical Journal of Natural Product Research*. 2023. Jun 1;7(6).
- [2]. Li HQ, Lv PC, Yan T, Zhu HL. Urea derivatives as anticancer agents. *Anti-Cancer Agents in Medicinal Chemistry (Formerly Current Medicinal Chemistry-Anti-Cancer Agents)*. 2009 May 1;9(4):471-80.

- [3]. Gulipalli KC, Ravula P, Bodge S, Endoori S, Cherukumalli PK, Chandra JN, Seelam N. Synthesis and Anticancer Activity of Novel Urea and Thiourea Bearing Thiophene-2-carboxalate Derivatives. *Russian Journal of General Chemistry*. 2020 Jul; 90:1336-44.
- [4]. Yu DD, Wu Y, Shen HY, Lv MM, Chen WX, Zhang XH, Zhong SL, Tang JH, Zhao JH. Exosomes in development, metastasis and drug resistance of breast cancer. *Cancer science*. 2015 Aug;106(8):959-64.
- [5]. Yoshida M, Hayakawa I, Hayashi N, Agatsuma T, Oda Y, Tanzawa F, Iwasaki S, Koyama K, Furukawa H, Kurakata S, Sugano Y. Synthesis and biological evaluation of benzothiazole derivatives as potent antitumor agents. *Bioorganic & medicinal chemistry letters*. 2005 Jul 15;15(14):3328-32.
- [6]. Saeed S, Rashid N, Jones PG, Ali M, Hussain R. Synthesis, characterization and biological evaluation of some thiourea derivatives bearing benzothiazole moiety as potential antimicrobial and anticancer agents. *European journal of medicinal chemistry*. 2010 Apr 1;45(4):1323-31.
- [7]. Lv PC, Li HQ, Sun J, Zhou Y, Zhu HL. Synthesis and biological evaluation of pyrazole derivatives containing thiourea skeleton as anticancer agents. *Bioorganic & medicinal chemistry*. 2010 Jul 1;18(13):4606-14.
- [8]. Khan SA, Singh N, Saleem K. Synthesis, characterization and in vitro antibacterial activity of thiourea and urea derivatives of steroids. *European journal of medicinal chemistry*. 2008 Oct 1;43(10):2272-7.
- [9]. Cui P, Li X, Zhu M, Wang B, Liu J, Chen H. Design, synthesis and antibacterial activities of thiouracil derivatives containing acyl thiourea as SecA inhibitors. *Bioorganic & medicinal chemistry letters*. 2017 May 15;27(10):2234-7.
- [10]. Zhong Z, Xing R, Liu S, Wang L, Cai S, Li P. Synthesis of acyl thiourea derivatives of chitosan and their antimicrobial activities in vitro. *Carbohydrate Research*. 2008 Feb 25;343(3):566-70.
- [11]. Pingaew R, Sinthupoom N, Mandi P, Prachayasittikul V, Cherdtrakulkiat R, Prachayasittikul S, Ruchirawat S, Prachayasittikul V. Synthesis, biological evaluation and in silico study of bis-thiourea derivatives as anticancer, antimalarial and antimicrobial agents. *Medicinal Chemistry Research*. 2017 Dec; 26:3136-48.
- [12]. Nedeljković N, Dobričić V, Bošković J, Vesović M, Brađić J, Anđić M, Kočović A, Jeremić N, Novaković J, Jakovljević V, Vujić Z. Synthesis and investigation of anti-inflammatory activity of new thiourea derivatives of naproxen. *Pharmaceuticals*. 2023 Apr 28;16(5):666.
- [13]. Zhang Y, Zhang X, Qiao L, Ding Z, Hang X, Qin B, Song J, Huang J. Synthesis, structures, drug-likeness, in vitro evaluation and in silico docking on novel N-benzoyl-N'-phenyl thiourea derivatives. *Journal of Molecular Structure*. 2019 Jan 15; 1176:335-45.
- [14]. Thanh ND, Giang NT, Quyen TH, Huong DT, Toan VN. Synthesis and evaluation of in vivo antioxidant, in vitro antibacterial, MRSA and antifungal activity of novel substituted isatin N-(2, 3, 4, 6-tetra-O-acetyl-β-d-glucopyranosyl) thiosemicarbazones. *European Journal of Medicinal Chemistry*. 2016 Nov 10; 123:532-43.
- [15]. Duan LP, Xue J, Xu LL, Zhang HB. Synthesis 1-acyl-3-(2'-aminophenyl) thioureas as anti-intestinal nematode prodrugs. *Molecules*. 2010 Oct 8;15(10):6941-7.
- [16]. Konduri S, Pogaku V, Prashanth J, Siva Krishna V, Sriram D, Basavoju S, Behera JN, Prabhakara Rao K. Sacubitril-based urea and thiourea derivatives as novel inhibitors for anti-tubercular against dormant tuberculosis. *Chemistry Select*. 2021 Apr 28;6(16):3869-74.
- [17]. Kavyasri D, Sundharesan M, Mathew N. Design, synthesis, characterization and insecticidal screening of novel anthranilic diamides comprising acyl thiourea substructure. *Pest Management Science*. 2023 Jan;79(1):257-73.
- [18]. Perry AS, Yamamoto I, Ishaaya I, Perry R, Perry AS, Yamamoto I, Rodenticides. *Insecticides in Agriculture and Environment: Retrospects and Prospects*. 1998:181-6.
- [19]. Li JH, Wang Y, Wu YP, Li RH, Liang S, Zhang J, Zhu YG, Xie BJ. Synthesis, herbicidal activity study and molecular docking of novel pyrimidine thiourea. *Pesticide Biochemistry and Physiology*. 2021 Feb 1; 172:104766.
- [20]. Pingaew R, Prachayasittikul V, Worachartcheewan A, Thongnum A, Prachayasittikul S, Ruchirawat S, Prachayasittikul V. Anticancer activity and QSAR study of sulfur-containing thiourea and sulfonamide derivatives. *Heliyon*. 2022 Aug 1;8(8).
- [21]. Aydemir N, Bilaloğlu R. Genotoxicity of two anticancer drugs, gemcitabine and topotecan, in mouse bone marrow in vivo. *Mutation Research/Genetic Toxicology and Environmental Mutagenesis*. 2003 May 9;537(1):43-51.
- [22]. Yeşilkaynak T, Muslu H, Özpinar C, Emen FM, Demirdöğen RE, Külcü N. Novel thiourea derivative and its complexes: synthesis, characterization, DFT computations, thermal and electrochemical behavior, antioxidant and antitumor activities. *Journal of Molecular Structure*. 2017 Aug 15; 1142:185-93.
- [23]. Abbas SY, Al-Harbi RA, El-Sharief MA. Synthesis and anticancer activity of thiourea derivatives bearing a benzodioxole moiety with EGFR inhibitory activity, apoptosis assay and molecular docking study. *European Journal of Medicinal Chemistry*. 2020 Jul 15; 198:112363.

Anant S. Wadatkar
 Department of Physics,
 Vinayak Vidnyan
 Mahavidyalaya, Nandgaon
 Khandeshwar, Dist.:
 Amravati (M.S.)

**Study of variation of AC Electrical
 Conductivity of 4:1 PS PMMA Polyblend
 thin films doped with Oxalic Acid in
 different weight proportions**



Abstract: - The measurements of the AC conductivity (σ_{ac}) of 4:1 PS PMMA polyblend systems doped with 0%, 5%, 10%, and 15% Oxalic acid (OA) have been carried out in the temperature range 323 K – 373 K and at frequencies in the range 1 kHz – 1 MHz. The experimental results reveal that, The AC conductivity (σ_{ac}) has been found to increase with the increase with weight percentage of Oxalic acid (OA) and frequency.

[Keywords: Polymethyl Methacrylate (PMMA), Polystyrene (PS), Oxalic Acid (OA), AC Electrical Conductivity (σ_{ac})

I INTRODUCTION

Polymers are useful insulators because of their high electrical resistance and can act as dielectric media for capacitors. If electrical conduction could be added to the other useful properties of polymers such as their low densities, flexibility and high resistance to chemical attack, very useful materials would be produced [1]. The dielectric study provides the dispersive behaviour associated with molecular configuration and its ordering which affects the conductivity of the system [2]. The dielectric constant and dielectric loss reveal the information about the physical and chemical properties of polymers which are affected by the presence of a dopant or other polymers [3-7]. These considerations led us to study the AC conduction in the 4:1 PS PMMA polyblend systems doped with Oxalic acid (OA).

II. EXPERIMENTAL

2.1 Sample Preparation:

The Polystyrene (PS) of commercial grade supplied by Poly Chem., Mumbai and Poly Methylmethacrylate (PMMA) obtained from Otto Kemi were used for the present study. The two polymers PS PMMA were taken in the ratio 4:1 were dissolved in the common solvent Tetrahydrofuran (THF). The solution was kept for 3-4 days to allow polymers to dissolve completely to yield uniform solution. The solution mixture was then heated for 1 hour at 60°C to get completely homogeneous solution. A glass plate thoroughly cleaned with water and later with acetone was used as a substrate. To achieve perfect levelling (and uniformity in thickness of the films), a pool of mercury was used in a plastic tray. The solution was poured on the glass plate and was allowed to spread uniformly in all directions on the substrate. The solvent in the solution was thus allowed to evaporate completely and get air-dried. The film on the glass substrate was then removed and cut into small pieces of suitable sizes. In this way the films were prepared by isothermal evaporation technique. Further it was dried for 3 days to remove any traces of solvent. The thickness of the films was measured by digimatic micrometer (Mitutoyo Corporation, Japan).

2.2 Method of preparation of PS PMMA Films using dopant Oxalic Acid:

The 5 %, 10 %, and 15% of Oxalic acid (dopant) means 0.125 gm, 0.25 gm, 0.375 gm were taken and dissolved in the mixture of 4:1 PS PMMA solution. After getting homogenous solution, the same procedure was repeated to prepare the films. The present study has been carried out with the following samples:

- 1) PS PMMA + 0% Oxalic acid [4:1 PSPMMA OA(0)]
- 2) PS PMMA + 5% Oxalic acid [4:1 PSPMMA OA(5)]
- 3) PS PMMA + 10% Oxalic acid [4:1 PSPMMA OA(10)]
- 4) PS PMMA + 15% Oxalic acid [4:1 PSPMMA OA(15)]

2.3 Measurements:

The thickness of the films was measured by digimatic micrometer (Mitutoyo Corporation, Japan). The film was kept between the electrodes of a specially designed sample holder. The AC frequencies were applied (in the range 1 kHz-1 MHz) across the sample by using the 4284 A Precision LCR meter (20 Hz-1MHz) supplied by Agilent Technologies, Singapore and the corresponding Dielectric Constants were measured. From the dielectric data, the values of AC Conductivity of the samples were calculated by using the relation [12],

$$\sigma_{a.c.} = f \epsilon_r \tan \delta / 1.8 \times 10^{10}$$

where, f – frequency applied in Hz
 ϵ_r – Dielectric Constant at frequency f
 $\tan \delta$ - Dielectric loss tangent

III. RESULTS AND DISCUSSIONS

3.1 Results:

Prominent Findings: The prominent results can be summarized as follows,

1. At constant temperature, A C Conductivity ($\sigma_{a.c.}$) increases with the increase of frequency.
2. At constant frequency, A C Conductivity ($\sigma_{a.c.}$) very marginally increases with the increase of temperature.
3. At constant frequency, A C Conductivity ($\sigma_{a.c.}$) increases with the increase in the percentage of dopant.

Graphs:

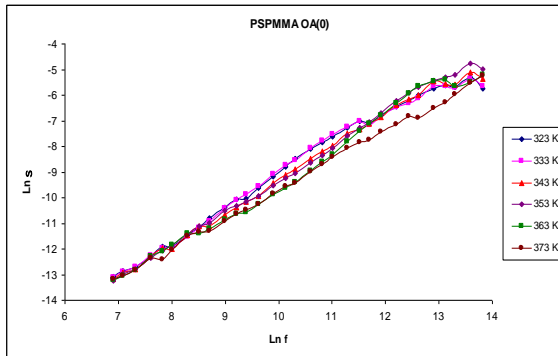


Fig. (a) 0% OA

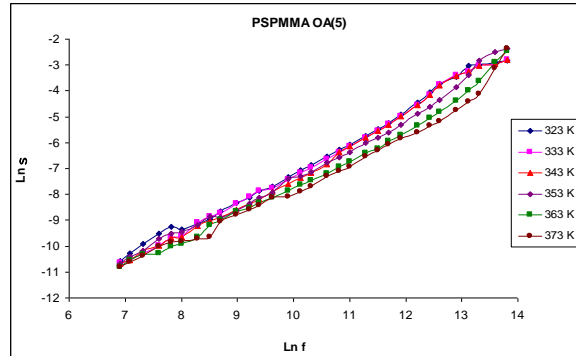


Fig. (b) 5% OA

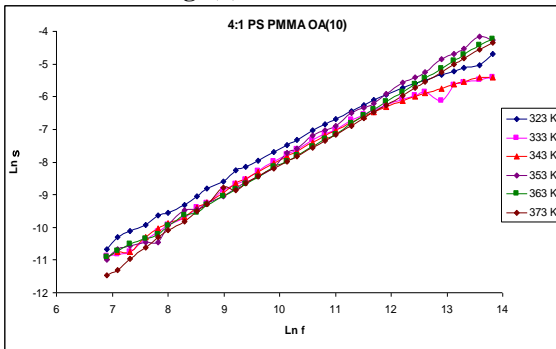


Fig. (c) 10% OA

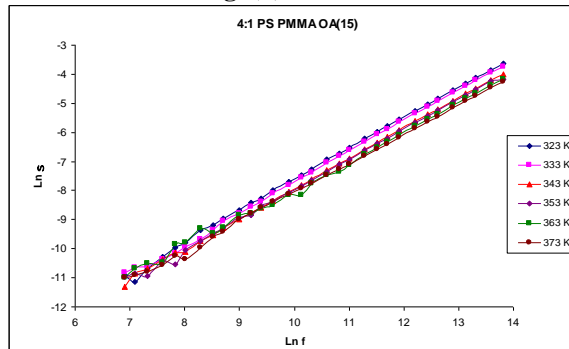
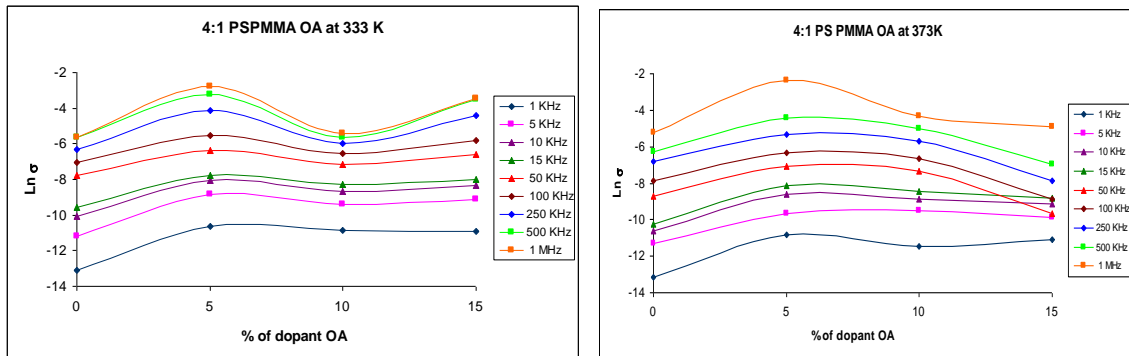


Fig.(d) 15% OA

Variation of Conductivity with frequency (Ln f) at different constant temperatures for 4:1 PS PMMA OA system



Variation of Conductivity with Concentration of dopant at various frequencies for 4:1 PS PMMA OA system

3.2 Discussion of Results:

3.2.1 A.C. conductivity (Effect of frequency):

Our observation that A.C. conductivity of the doped polyblend samples increases with frequency can be explained as under:

When any capacitor consisting of dielectric 4:1 PS PMMA doped with 0%, 5%, 10 %, 15 % oxalic acid is charged under an a.c. voltage or electric field given by, $E = E_0 \cos \omega t$, then there will be a loss current due to ohmic resistance or impedance by heat absorption, Debye relaxation process etc. due to the frictional resistance. Then a.c. conductivity σ_{ac} is given by,

$$\sigma_{ac} = \omega \epsilon'' = \epsilon' \omega \tan \delta \dots\dots\dots(5.9).$$

The above equation shows a linearity of σ_{ac} with angular frequency ω or $f = \omega/2\pi$. But in actual cases frequency dependent σ_{ac} follows a complicated relation of power law in the form,

$$\sigma_{ac} = \epsilon'' \omega^n \dots\dots\dots(5.10)$$

where 'n' may vary from say about 0.5 to 1.5 for crystalline and amorphous film capacitors (Pollock and Geballe,1961; Jonscher,1972; Webb and Brodie 1973). In most cases n lies between 0.5 and 1.

According to Brodie *et al.* ϵ' is proportional to ω^{n-1} hence we have,

$$\sigma_{ac} \propto \omega^{n-1} \tan \delta \omega^n = \tan \delta \omega^{2n-1}$$

In our case, we have a polymer thin films as dielectrics. These films, as shown by XRD spectra and SEM photographs, have small crystalline regions or they are predominantly amorphous in nature.

In such a film capacitor, because of the polycrystalline or amorphous nature of the film and also of the deposition condition, it is expected that there will be some defects, impurities, imperfections in the atomic arrangements of the dielectric field. Frequency dependent conductivity is caused by the hopping of electrons in the localized states near the Fermi level and also due to the excitation of charge carriers to the states in the conduction bands.

If there are some free charge-carriers (due to impact of impurities, defects or imperfections in the polyblend films) then their movements from one band to another band or within the band by hopping process give rise to the conductivity. Frequency dependence of A.C. conductivity can be explained as follows;

Webb and Brodie, in order to understand the frequency dependent conductivity, suggested a multi-component system of conductivity which leads to a relation,

$$\sigma_{Total} = \sigma_{dc} + \sigma_{ac} + \sigma_{relx} \dots\dots\dots(5.11)$$

where, σ_{dc} has significant contribution at room temperature which often masks the contribution of the frequency dependent hopping term.

σ_{ac} is caused by hopping conduction and

σ_{relx} is the contribution from Debye hopping mechanism.

The individual contribution of each component can be expressed in following form,

$$\sigma_{dc} = \sigma_0 \exp(-E_k / 2kT) \quad \dots\dots (5.12)$$

$$\sigma_{ac} = A \omega^n \exp[-E(\omega, T) / kT] \quad \dots\dots(5.13)$$

$$\sigma_{relx} = k \omega^2 \quad \dots\dots(5.14)$$

where, σ_0 , A and k are constants and the other terms have the usual meaning and σ_{ac} and σ_{relx} are frequency dependent terms.

In our case A.C. conductivity almost linearly increases with frequency as indicated by curve (1) in above Fig (5.2). These results are in confirmation with those reported by Khaled *et al.* (2003).

3.2.2 A.C. conductivity (Effect of Temperature):

In the present study we have noticed that the AC Conductivity very marginally increases with temperature which shows almost temperature independence of AC Conductivity. This can be explained on the basis of the model proposed by Mott *et al.* This model is based on the assumption that the energy states in the gap near the fermi level are due to dangling bonds and for exothermic reactions only paired defects are found in the gap (Shukla and Gupta, 1987). Accordingly at low temperatures, a large distribution of relaxation time would be expected contributing towards the dielectric loss. As a result AC Conduction should be almost independent of temperature as observed in the present case.

3.2.3 Effect of dopant on AC Conductivity and Dielectric Constant:

It has been made clear that the addition of dopants Oxalic Acid impart polar character to PS PMMA polyblends. As a result the number of charge carriers and dipoles increases with the increase in the concentration of dopant Oxalic Acid. As a result the AC conductivity increases with the dopant concentration.

III. CONCLUSION

1. At constant temperature, A C Conductivity ($\sigma_{a.c}$) of 4:1 PS PMMA Polyblend thin films doped with Oxalic Acid increases with the increase of frequency.
2. At constant frequency, A C Conductivity ($\sigma_{a.c}$) very marginally increases with the increase of temperature.
3. At constant frequency, A C Conductivity ($\sigma_{a.c}$) increases with the increase in the percentage of dopant.

IV. ACKNOWLEDGEMENT

The author would like to acknowledge Department of Physics, Vidya Bharati Mahavidyalaya, Amravati (India) for providing Research Lab. to carry on this work.

REFERENCES

1. Bower D. I., "An Introduction to Polymer Physics", Cambridge University Press (New York), (2002), 248-251.
2. Saita, Stuhn B., Polymer (UK), 3(35) (1994), 475.
3. Ramu C., Naidu Y. R. V., Sharma A. K., Ferroelectrics, 159 (1994), 275.
4. Mosad M.M., J. Mater. Sci. Lett., 9 (1990), 32.
5. Narayan A. and Singh H. P., Indian J. Pure and Appl Phys, 25 (1987), 30.
6. Bahri and Sood B R, Thin Solid Films, 100 (1983),
7. Belsare N.G. and Deogaonkar V.S., Indian J. Pure and Appl. Phys., 36(1998), 280.
8. Tareev B., "Physics of Dielectric Materials", MIR (Moscow), (1979).
9. Tager A., "Physical Chemistry of Polymers", MIR Publication (Moscow), (1972), 151-155.
10. Seanor D. A., "Electrical Properties of Polymers", Academic Press (New York), (1982).
11. Rao Vijayalakshmi, Ashoakan P.V. and Shridhar M. H., Mater. Sci. and
12. Engg. (Elsevier), A281(2000), 213.
13. Debye P., Physik. Z, 13(1912), 97.
14. Webb J. B., and Brodie D. E., Canad. J. Phy., 51(1973), 1593.

¹Radhika G
Deshmukh
²Amruta
Gaikwad,
³Sanjay J
Dhobale

The Spectroscopic study compound
Na₂BaCa(PO₄)₃:Eu³⁺ red-emitting
phosphor for WLED application



Abstract: - A series of new red phosphors, Na₂BaCa(PO₄)₃:Eu³⁺, was synthesized using the high-temperature solid-phase reaction method. Systematic investigations involving X-ray diffraction (XRD), scanning electron microscopy (SEM), and photoluminescence (PL)spectroscopy were conducted to analyze the microstructure and optical characteristics of the material. The XRD analysis of Na₂BaCa(PO₄)₃:xEu³⁺ shows the sample to be a pure phase. The spectroscopic results show the presence of a red emission peak originated from ⁵D₀ → ⁷F₂ transition, and the quenching mechanism is attributed to interaction between nearest neighboring ions. The CCT of the LED packaged with Na₂BaCa(PO₄)₃:Eu³⁺ was measured to be 4314 K, with the CIE coordinates (0.3658, 0.3600), which is very close to the point of standard white light source. All results indicate that Na₂BaCa(PO₄)₃:0.2Eu³⁺ is suitable for WLED applications.

Keywords Photoluminescence (PL), X-ray diffraction(XRD), Scanning electron microscopy (SEM), Correlated color temperature(CCT), White light emitting diode(WLED)

I INTRODUCTION

In response to the increasing global energy consumption and the resulting energy crisis, effective energy conservation and emission reduction measures are crucial, particularly in the lighting sector, which has significant daily-life implications. White light-emitting diodes (W-LEDs) have emerged as promising green lighting sources due to their low energy consumption, environmental friendliness, fast response times, and long lifespan[1-3]. However, traditional W-LEDs, typically composed of blue InGaN chips combined with yellow phosphors (YAG+), [4-7]suffer from drawbacks such as high correlated color temperature and

poor color rendering index, primarily due to insufficient red-light components.[8-10] In order to address these challenges, a common approach involves using near-ultraviolet (NUV) LED chips to excite blue, green, and red phosphors, thereby achieving composite white light [11-13]. However, existing sulphur oxide and nitrogen oxide-based red phosphors are plagued by issues like poor stability, harsh synthesis conditions, and high costs.[14-16] Hence, there is a critical need for new red phosphors characterized by good stability, ease of synthesis, and excellent light-emitting properties. Recent research has shown that rare earth Eu^{3+} ions, known for their strong red-light emission under near-ultraviolet excitation, are promising candidates for red phosphors. Various Eu^{3+} -doped phosphors,[8] such as $\text{SrAl}_2\text{Si}_2\text{O}_8:\text{Eu}^{3+}$,[8] $\text{LiBaB}_9\text{O}_{15}:\text{Eu}^{3+}$, [17] $\text{CaScO}_4:\text{Eu}^{3+}$,[18] and $\text{Sr}_9\text{LiMg}(\text{PO}_4)_7:\text{Eu}^{3+}$ [19] have demonstrated efficient red light emission properties. The choice of host material significantly influences the final luminescence properties of these phosphors. Eulytite-type orthophosphate-based hosts have gained attention due to their stable physical and chemical properties and relatively low synthesis temperatures. Examples include $\text{Ba}_3\text{Lu}(\text{PO}_4)_3:\text{Eu}^{3+}$ [7] , $\text{Ba}_3\text{Bi}(\text{PO}_4)_3:\text{Eu}^{3+}$ [13] , $\text{Sr}_3\text{La}(\text{PO}_4)_3:\text{Eu}^{3+}$ [20] and $\text{Sr}_3\text{Y}(\text{PO}_4)_3:\text{Eu}^{3+}$ [21-22]. which have shown excellent performance as phosphors.

In this context, $\text{Na}_2\text{BaCa}(\text{PO}_4)_3$, belonging to the eulytite-type structure phosphate, emerges as a novel host material for rare earth doping in phosphors for W-LEDs. Eu^{2+} -doped phosphors are currently gaining significant attention for their applications in solid-state lighting, particularly in white-light-emitting diodes (W-LEDs) that use near-UV chips. The Eu^{2+} ion, with a ground-state electronic configuration of $4f_7$ and an excited-state configuration of $4f_6-5d_1$, exhibits broadband absorption and luminescence attributed to its $4f_7-4f_6-5d_1$ transitions. The emission wavelength of Eu^{2+} varies depending on the host lattice, spanning from ultraviolet to red spectral ranges. Therefore, the choice of host material plays a crucial role in determining the optical properties of Eu^{3+} ions. This study reports on the synthesis of Eu^{3+} -doped $\text{Na}_2\text{BaCa}(\text{PO}_4)_3$ phosphors using a high-temperature solid-phase reaction method, investigating their luminescence properties in detail.

¹Department of physics, Shri Shivaji science college, Amravati - 444603, India

²Department of Physics, R.T.M. Nagpur University, Nagpur – 440033, India

Corresponding author : radhikadeshmukh35@gmail.com

Copyright©JES2024on-line:journal.esrgroups.org

II. Experimental Method

The samples of $\text{Na}_2\text{BaCa}(\text{PO}_4)_3$ ($x = 0.1\%$, 0.3% , 0.5% , 0.7% , 1% molar concentration) were prepared by high-temperature solid-phase reaction method. The raw materials were Na_2O (A.R.), BaO (A.R.), CaO (A.R.), $\text{NH}_4\text{H}_2\text{PO}_4$ (A.R.) and Eu_2O_3 (99.99%, Aladdin), which were weighed in appropriate amounts according to the stoichiometric ratio, and ground in an agate mortar about 30 min. Then the mixed samples were placed into a corundum crucible and heated at 750°C for 12 h to ensure complete decomposition of the reactants, After the samples were naturally cooled to room temperature with the furnace, the obtained phosphors were reground into powder for subsequent testing and characterization. The phase structure of the synthesized samples was characterized by X-ray diffractometer (XRD, the photoluminescence spectra, Sem and all characterization results were measured at room temperature.

III. Results and Discussion

XRD analysis:

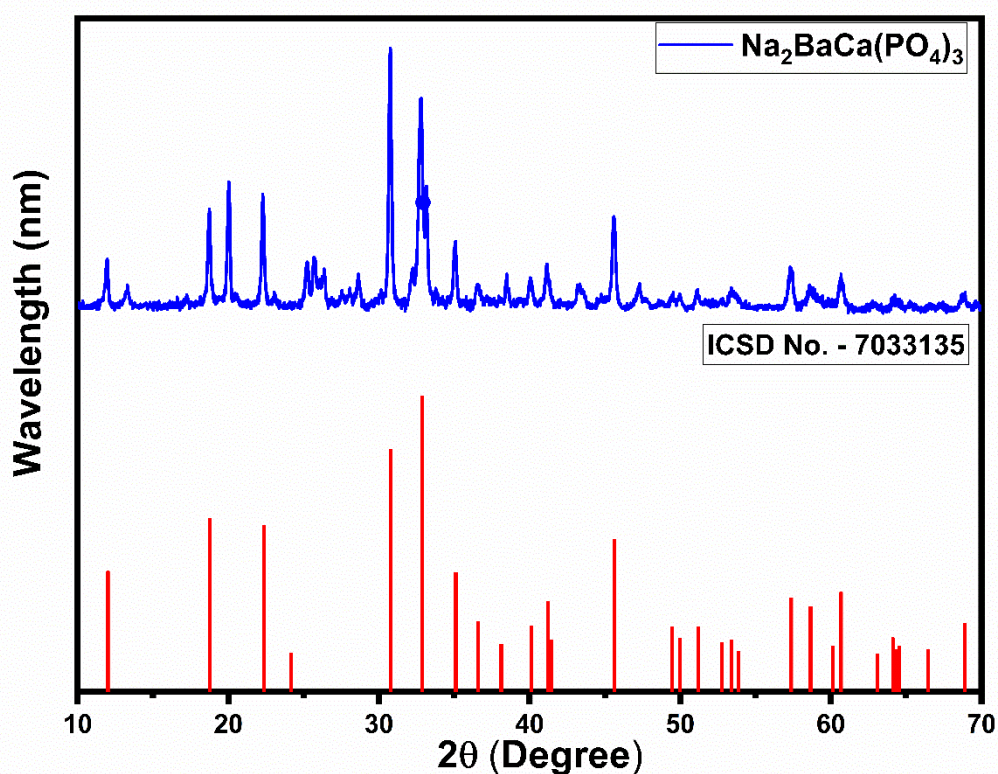


Fig1: Crystalline features observed in the XRD

The sharp crystalline features observed in the XRD profiles indicate micrometer particles with good crystallinity obtained by solid state synthesis method. There is intensity difference between (126) and (206) plane when compared the experimental XRD patterns and CSD standard. Such observation agrees with a preferential crystallization which is strongly dependent on the sintering conditions. As we all know, when the sample is synthesized by the high-temperature solid-phase method, the appropriate synthesis temperature has a greater influence on the phase structure of the sample. Here, in order to determine the optimum synthesis temperature of the sample, In the present study, the structural properties of the prepared material were examined using X-ray powder diffraction (XRD) as shown in Fig. 1. XRD spectra of the $\text{Na}_2\text{BaCa}(\text{PO}_4)_3 : \text{Eu}^{3+}$ samples with different concentrations produced by the conventional solid state diffusion method at 8000 c. We can see clearly that, all XRD spectra of phosphor match the standard inorganic crystal structure database (ICSD) data card no.: 7033135. There are no additional impurity peaks in the XRD spectra of prepared phosphor. Moreover, the proposed sample has a monoclinic crystal structure with lattice parameters is $a = 5.4474$ $b = 5.4474$ $c = 7.3624$ $\alpha = 90.000$ $\beta = 90.000$ $\gamma = 120.000$ with space group I/c (RIR) = 2.94

SEM analysis

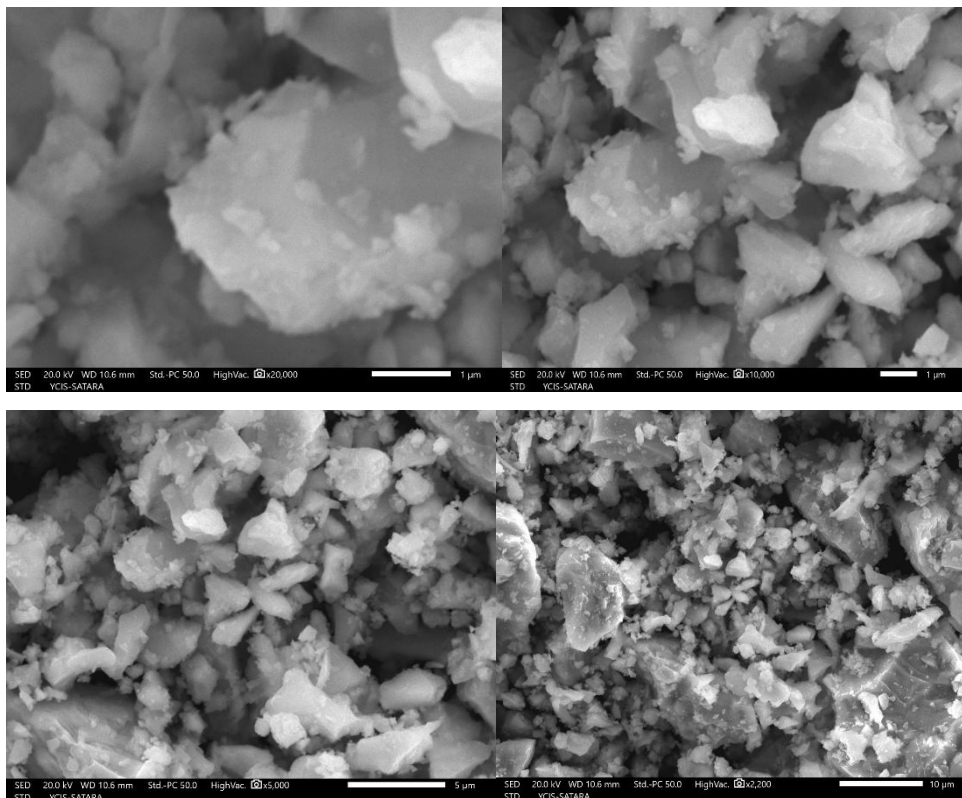


Fig 2: The morphology of the sample was studied using SEM

The morphology of the particles, crystallite size of the sample was studied using SEM. SEM image of $\text{Na}_2\text{BaCa}(\text{PO}_4)_3 : \text{Eu}^{3+}$ doped phosphor with various magnifications of the phosphor under the study of morphology micrographs as shown in Fig. 2. It clearly indicates that the structure of the prepared phosphor

has different sizes and irregular shapes of bunching of flowers with different resolutions. These prepared phosphors can be very easily employed in solid state lighting technology and various coating display illuminating applications.

PL study

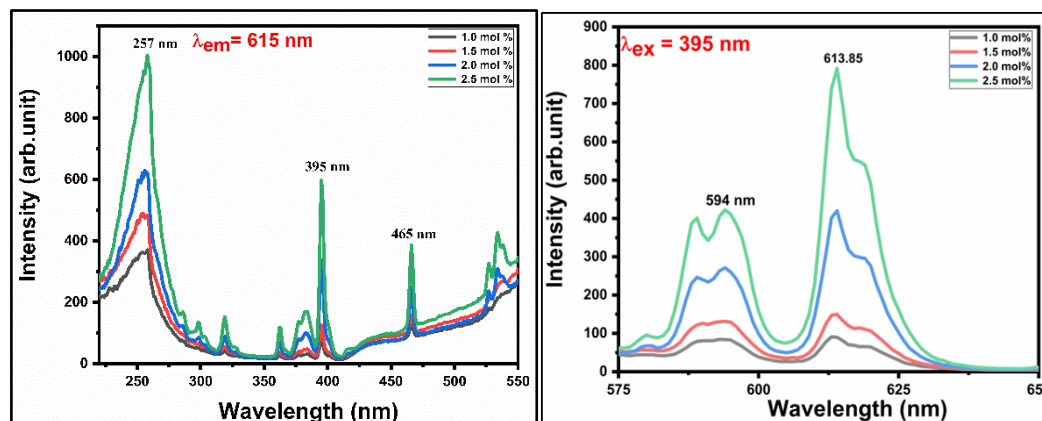


Fig 3: Photoluminescence excitation and emission Peaks

The study photoluminescence excitation and emission of the series $\text{Na}_2\text{BaCa}(\text{PO}_4)_3:\text{Eu}^{3+}$ activated red emitting phosphor are measured as shown in Fig.3. Suggested photoluminescence excitation spectra range from 220 nm to 550 nm. The excitation spectra of $\text{Na}_2\text{BaCa}(\text{PO}_4)_3:\text{Eu}^{3+}$ phosphor exhibits a broadband in the ultraviolet (230–290 nm) region due to the charge transfer transition of $\text{Eu}^{3+}-\text{O}_2^-$. There are five excitation spectrums peak due to intra 4f transitions of Eu^{3+} ions attributed to ${}^7\text{F}_0 \rightarrow {}^5\text{L}_6$, ${}^5\text{D}_2$, ${}^5\text{D}_1$ at wavelengths of 320, 395, 465 nm, respectively. Among these, the band spectrum at 257 nm is higher intensity as compared to the other excitation band spectra. The reason behind highly intense in Charge-transfer transitions is that they are usually both spin- and Laporte allowable; hence, if they occur, the color is often very intense. The excitation band at 395 and 465 nm that the blue LED chip emits at 450 nm and the near-UV LED chip emits at 365 nm. Due to this phosphor being a possible candidate for designing the phosphor-converted WLED that can be effectively excited by both commercial NUV and blue-LED chips. In the emission spectrum, there are two sharp peaks at 595 nm and 618 nm wavelength correspond to ${}^5\text{D}_0 - {}^7\text{F}_j$ ($J = 1, 2$) transitions of Eu^{3+} ions under blue excitation. And here peaks at 575 nm and 615 nm were assigned to magnetic (${}^5\text{D}_0 \rightarrow {}^7\text{F}_1$) and electric (${}^5\text{D}_0 \rightarrow {}^7\text{F}_2$) dipole transitions of Eu^{3+} ions, respectively.

CIE coordinates

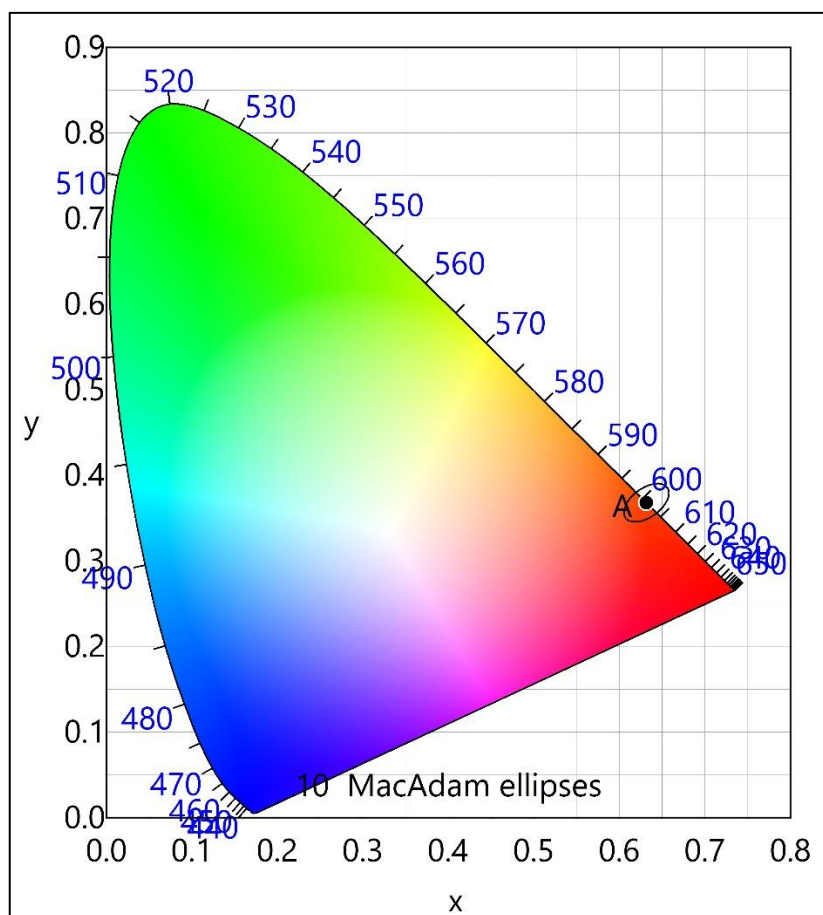


Fig4: (CIE) coordinates

Commission de l'Eclairage chromaticity (CIE) coordinates were analyzed based on the PL emission spectra of the series $\text{Na}_2\text{BaCa}(\text{PO}_4)_3:1 \text{ mol } \% \text{Eu}^{3+}$ activated red emitting phosphor. The color coordinates are predictable from the emission spectra by using the chromaticity coordinate calculation method based on the color calculator software. The values of the CIE coordinates were (0.6314, 0.3682) and emit a bright color in the red region in the CIE chromaticity diagram. These values of CIE of the sample $\text{Na}_2\text{BaCa}(\text{PO}_4)_3:\text{Eu}^{3+}$ the application of solid state lighting. Therefore, the suggested result indicates that $\text{Na}_2\text{BaCa}(\text{PO}_4)_3:\text{Eu}^{3+}$ activated red emitting phosphor has the possible. To check color quality of the achieved white emission color purity can be calculated by following Fred Schubert equation [24],

$$\text{Color Purity} = \frac{\sqrt{(x - x_i)^2} + \sqrt{(y - y_i)^2}}{\sqrt{(x_d - x_i)^2} + \sqrt{(y_d - y_i)^2}} \times 100\%$$

In above equation, values of (x, y) are CIE color coordinate, (x_i, y_i) are coordinates of perfect white light and (x_d, y_d) are coordinates of dominant wavelength in PL emission spectrum [i]. From above equation the color purity was estimated to be 88.60%. Depending on the color temperature, the light sources can be divided into warm and cold colors. Normally, a color temperature around 6500 K is considered a cool color, whereas a color temperature less than 4500 K is considered warm light. A light with low CCT i.e., warm light is more suitable for human eyes. The CCT were calculated by McCamy empirical formula [25].

$$CCT = -449n^3 + 3525n^2 - 6823n + 5520.33$$

Here, $n = (x-x_e)/(y-y_e)$ and (x_e, y_e) are (0.332, 0.186). Therefore, the correlated color temperature (CCT) from above equation was found to be 1175 K which indicate that achieved red light emission is warm light. Thus, this phosphor can be used for the fabrication of WLEDs.

IV. Conclusion

A novel blue-emitting phosphor, $\text{Na}_2\text{BaCa}(\text{PO}_4)_3:\text{Eu}^{3+}$, was synthesized via solid state reaction method. Luminescence properties of this phosphor were examined by steady-state and transient as well as temperature-dependent luminescence spectra. The obtained $\text{Na}_2\text{BaCa}(\text{PO}_4)_3:\text{Eu}^{3+}$ sample shows strong absorption in 220 – 550 nm, and exhibits a tow sharp peaks at 595 nm and 615 nm upon 395 nm excitation. Subsequent SEM analysis revealed that the particle size of the proposed phosphors falls within the sub-micrometer range. The values of the CIE coordinates were (0.6314, 0.3682) and emit a bright color in the red region in the CIE chromaticity diagram and color purity was estimated to be 88.60%. Therefore, the correlated color temperature (CCT) from above equation was found to be 1175 K which indicate that achieved red light emission is warm light. Thus, this phosphor can be used for the fabrication of WLEDs.

V. Ethics declarations

Conflict of Interest

The authors declare that they have no known conflict of financial interests or personal relationships that could have appeared to influence the work reported in this paper.

References:

- [1]. Kadam, A. R., Mishra, G. C., Michalska-Domanska, M., & Dhoble, S. J. (2021). Theoretical analysis of electron vibrational interaction (EVI) parameters in 5d states of Eu^{2+} activated BaSiF_6 downconversion phosphor. *Journal of Molecular Structure*, 1229, 129505.
- [2]. Gupta, S. K., Zuniga, J. P., Abdou, M., Ghosh, P. S., & Mao, Y. (2020). Optical properties of undoped{,} Eu^{3+} doped and Li^+ co-doped $\text{Y}_2\text{Hf}_2\text{O}_7$ nanoparticles and polymer nanocomposite films. *Inorg. Chem. Front.*, 7(2), 505–518.
- [3]. Yan, W., Li, J., Zhang, W., Gao, X., & Zhang, P. (2021). Warm-white luminescence of Dy^{3+} and Sm^{3+} co-doped NaSrPO_4 phosphors through energy transfer between rare earth ions. *Journal of Materials Science: Materials in Electronics*, 32(12), 16648.
- [4]. Kadam, A. R., & Dhoble, S. J. (2021). Energy transfer mechanism of $\text{KAlF}_4:\text{Dy}^{3+}$, Eu^{3+} co-activated down-conversion phosphor as spectral converters: An approach towards improving photovoltaic efficiency by downshifting layer. *Journal of Alloys and Compounds*, 884.
- [5]. Kumar, B. S., Umamahesvari, H., Thyagarajan, K., Ankoji, P., & Vijayakanth, V. (2023). Structural and photoluminescence properties of Dy^{3+} -doped KMgBO_3 phosphors. *Journal of Materials Science: Materials in Electronics*, 34(7), 637.
- [6]. Jamalalah, B. C., & Khan, P. S. (2023). $\text{Sr}_3\text{Gd}(\text{PO}_4)_3:\text{Dy}^{3+}$ phosphors for lighting applications. *Journal of Sol-Gel Science and Technology*, 105(1), 266–277.
- [7]. Krishnapriya, T., Jose, A., Jose, T. A., Saritha, A. C., Joseph, C., & Biju, P. R. (2021). Investigation of the structural and photoluminescence properties of Eu^{3+} doped $\text{Na}_6\text{CaP}_2\text{O}_9$ phosphors for solid state lighting. *Materials Research Bulletin*, 139, 111259
- [8]. Gao, D., Li, Y., Cheng, L., Liu, S., Xu, S., Li, X., Zhang, J., Zhang, X., Cao, Y., Wang, Y., Wang, X., Zhang, Y., Sha, X., Wang, L., & Chen, B. (2022). Concentration effects of fluorescence quenching and optical transition properties of Dy^{3+} doped NaYF_4 phosphor. *Journal of Alloys and Compounds*, 895, 162616.
- [9]. Parauha, Y. R., & Dhoble, S. J. (2021). Photoluminescence and electron-vibrational interaction in 5d state of Eu^{2+} ion in $\text{Ca}_3\text{Al}_2\text{O}_6$ down-conversion phosphor. *Optics & Laser Technology*, 142, 107191.
- [10]. Huo, J., Yu, A., Ni, Q., Guo, D., Zeng, M., Gao, J., Zhang, Y., & Wang, Q. (2020). Efficient Energy Transfer from Trap Levels to Eu^{3+} Leads to Antithermal Quenching Effect in High-Power White Light-Emitting Diodes. *Inorganic Chemistry*, 59(20), 15514–15525.
- [11] Tan, P. M., Ca, N. X., Hien, N. T., Van, H. T., Do, P. V., Thanh, L. D., Yen, V. H., Tuyen, V. P., Peng, Y., & Tho, P. T. (2020). New insights on the energy transfer mechanisms of Eu -doped CdS quantum dots. *Phys. Chem. Chem. Phys.*, 22(11), 6266–6274.

- [12]. Xu, M., Ding, Y., Luo, W., Wang, L., Li, S., & Liu, Y. (2020). Synthesis, luminescence properties and energy transfer behavior of color-tunable KIP2O7: Tb³⁺, Eu³⁺ phosphors. *Optics&LaserTechnology*,121,105829.
- [13].Mofokeng, S. J., Noto, L. L., & Dhlamini, M. S. (2020). Photoluminescence properties of ZnTiO₃:Eu³⁺ phosphor with enhanced red emission by Al³⁺ charge compensation. *Journal of Luminescence*, 228, 117569.
- [14]. Wu, J., Zhuang, W., Liu, R., Liu, Y., Gao, T., Yan, C., Cao, M., Tian, J., & Chen, X. (2021). Broadband near-infrared luminescence and energy transfer of Cr³⁺, Ce³⁺ co-doped Ca₂LuHf₂Al₃O₁₂ phosphors. *Journal of Rare Earths*, 39(3), 269–276.
- [15].Wu, H., Li, H., Jiang, L., Pang, R., Zhang, S., Li, D., Liu, G., Li, C., Feng, J., & Zhang, H. (2021). Synthesis, structure and optical properties of novel thermally robust Dy³⁺-doped Ca₉Sc(PO₄)₇ phosphors for NUV-excited white LEDs. *Journal of Rare Earths*, 39(3),277–283
- [16]. Devi, P., Sehwat, P., Sheoran, M., Dalal, H., Sehwat, N., & Malik, R. K. (2023). Probing the Judd Ofelt parameters and photometric attributes of Eu³⁺- activated Ca₉Y(VO₄)₇ nanomaterials for emerging lighting applications. *Journal of Materials Science: Materials in Electronics*, 34(10), 867
- [17].Patle, Y., Brahme, N., Bisen, D. P., Richhariya, T., Chandrawanshi, E., Choubey, A., & Tiwari, M. (2021). Study of Photoluminescence, Thermoluminescence, and Afterglow properties of Dy³⁺ doped Ba₂ZnSi₂O₇ phosphor. *Optik*, 226, 165896.
- [18]. Zhang, L. H., Zhang, C. Y., Zhou, Y. B., Li, Y. L., & Peng, Q. L. (2024). Energy Transfer and Colorful Emission of Eu³⁺- and Tb³⁺-Co-Doped CaWO₄ Phosphors. *Journal of Applied Spectroscopy*, 90(6), 1346–1351.
- [19].Gupta, I., Singh, D., Singh, S., Kumar, P., Bhagwan, S., & Kumar, V. (2023). Study of structural and spectroscopic characteristics of novel color tunable yellowish-white Dy³⁺ doped Gd₄Al₂O₉ nanophosphors for NUV-based WLEDs. *Journal of Molecular Structure*, 1272, 134199
- [20]
Duan Gao, Yunci Li, Lihong Cheng, Yongze Cao, Yichao Wang, Xin Wang, Yuhang Zhang, Xuezhu Sha, Li Wang, Baojiu Chen (25 February 2022) Concentration effects of fluorescence quenching and optical transition properties of Dy³⁺ doped NaYF₄ phosphor. *Journal of alloys and Compounds*, 162616
- [21]. SonalP. Tatte ^{a,c}, Yatish Parauha ^b, N.S. Dhoble ^c, G.C. Mishra ^a, S.J. Dhoble ^b(2022).Influence of rare earth ions on luminescent properties of self-emitting KCa₂Mg₂(VO₄)₃ phosphors for lighting application. *Optik*, 169976
- [22] Abhijeet R. Kadam, S.J. Dhoble (5 December 2021) Energy transfer mechanism of KAlF₄:Dy³⁺, Eu³⁺ co-activated down-conversion phosphor as spectral converters: An approach towards improving photovoltaic efficiency by downshifting layer. *Journal of alloys and Compounds*,161138. <https://doi.org/10.1016/j.jallcom.2021.161138>
[Get rights and content](#)
- [23]Youfa Tai ^a, Ruirui Cui ^a, Jun Zhang ^b, Chunkai Wang ^a, Tingyu Zhao ^a, Beiqiao Zhang ^a, Chaoyong Deng ^a, (August 2024)Luminescence properties and optical sensing behaviours of Sr₂GdSbO₆:Eu³⁺ phosphors, *Journal of Rare Earths*, Pages 1458-1469. <https://doi.org/10.1016/j.jre.2023.06.009>
[Get rights and content](#)